CODEN: JASMAN 4966

THE JOURNAL of the Acoustical Society of America

Vol. 107, No. 3 March 2000

SOUNDINGS SECTION

GENERAL LINEAR ACOUSTICS [20]

NONLINEAR ACOUSTICS [25]

(Continued)

CONTENTS—*Continued from preceding page*

UNDERWATER SOUND [30]

ULTRASONICS, QUANTUM ACOUSTICS, AND PHYSICAL EFFECTS OF SOUND [35]

TRANSDUCTION [38]

STRUCTURAL ACOUSTICS AND VIBRATION [40]

NOISE: ITS EFFECTS AND CONTROL [50]

ARCHITECTURAL ACOUSTICS [55]

ACOUSTIC SIGNAL PROCESSING [60]

(Continued)

CONTENTS—*Continued from preceding page*

PHYSIOLOGICAL ACOUSTICS [64]

PSYCHOLOGICAL ACOUSTICS [66]

SPEECH PRODUCTION [70]

(Continued)

CONTENTS—*Continued from preceding page*

SPEECH PERCEPTION [71]

SPEECH PROCESSING AND COMMUNICATION SYSTEMS [72]

BIOACOUSTICS [80]

LETTERS TO THE EDITOR

ACOUSTICS RESEARCH LETTERS ONLINE

CUMULATIVE AUTHOR INDEX

Shape and extinction thresholds in sonoluminescence parameter space

Jeffrey A. Ketterling* **and Robert E. Apfel**

Department of Mechanical Engineering, Yale University, New Haven, Connecticut 06520
ketterling@rrinyc.org, robert.apfel@yale.edu

Abstract: Experimental single bubble sonoluminescence (SBSL) ambient radius, acoustic drive pressure (R_o-P_a) phase diagrams are compared with predictions of the Dissociation Hypothesis (DH) and calculations of the $n = 2, 3, 4$ shape thresholds, focusing on the location of unstable SBSL and the extinction threshold. A phase diagram for experimental runs with a 20% air saturation is shown to indicate the location of the SBSL extinction threshold. Mixtures with appropriate concentrations of argon and nitrogen are presented to show the location of unstable SBSL. The results are consistent with the DH and show that unstable SBSL and the extinction threshold appear to coincide more closely with the $n = 4$ shape threshold.

PACS numbers: 43.35.Ei, 78.60.Mq

1. Introduction

A single, gas-filled bubble in the presence of an acoustic standing wave can emit a pulse of light as the bubble violently collapses each acoustic cycle. This process has been labeled single bubble sonoluminescence (SBSL).[1] Some of the interesting early observations concerning SBSL were the need for a noble gas to obtain light emission,[2] the apparent violation of mass diffusion for a single stable bubble,[3] and a "dissolution island" in parameter space where stable bubbles were observed when they would normally be expected to dissolve.[4] These observations helped to support what is commonly referred to as the Dissociation Hypothesis (DH) of SBSL.[5–8]

DH permits predictions of bubble behavior in the ambient radius, acoustic drive pressure (R_o-P_a) parameter space under the assumption that the diatomic gases in the bubble begin to dissociate as P_a increases and the bubble collapse becomes more violent. Stable non-SL occurs at lower P_a, as the bubble enters a stable dissociation equilibrium where the amount of diatomic gas dissociated each acoustic cycle equals the amount diffusing back into the bubble. In parameter space, the calculated dissociation equilibrium has a negative slope. Stable SL occurs at higher P_a, once all of the diatomic gases have "burned" off, and the bubble enters a stable diffusive equilibrium based on the noble gas content remaining in the bubble. In parameter space, the calculated stable diffusive equilibrium has a positive slope.

The predictions of DH for stable bubble behavior agree very well with experimental results.[9–11] For sufficiently high noble gas concentrations, DH also predicts that unstable SL will occur as the bubble intersects a shape stability threshold as it grows by rectified diffusion,[12] just as bubbles do under low P_a, non-SL conditions.[4,9] In this letter, we show experimental results for air and argon-nitrogen mixtures and compare them with calculations of the shape stability threshold. A brief background of DH as it relates to shape instabilities is given, and the experimental apparatus is summarized. The experimental results are then presented.

*Present address: Riverside Research Institute, 330 West 42nd Street, New York, NY, 10036

2. Background

There exist regions of R_o-P_a parameter space where shape instabilities are likely.[4,5,13–15] In DH, the shape stability threshold (SST) acts as the upper bound for unstable SL and non-SL bubbles. However, the first mode to set in ($n = 2$) may not be sufficient to cause the bubble to "dance" or break up. Therefore, we also consider higher order modes. When the bubble reaches a SST, several things may happen. First, it may become unstable and pinch off a microbubble causing it to drop to a lower R_o and then grow back in size until it intersects the SST again. This behavior is sometimes referred to as "dancing."[1,4,16] Second, the bubble may remain oscillating in a "stable" fashion for a long time period with the resonant mode present.[4,17,18] This behavior becomes less likely with increasing mode number, because higher order modes have increased damping. Finally, a fast time scale instability may step in and cause the bubble to suddenly break up with a small change in P_a.[19] The sudden break up of the bubble is often referred to as the SL extinction threshold. What initiates the sudden extinction is not well understood but may relate to the Rayleigh-Taylor instability,[13] Richtmyer-Meshkov instability,[20] or the translation experienced by the bubble from the instantaneous Bjerknes force.[19,21]

We will consider the SST to also act as the extinction threshold even though this may not be strictly true. The boundary in parameter space between where the SST causes unstable behavior and extinction is not clearly defined. Experimentally, extinction is more likely to occur at higher P_a.

A SST is defined as the location in parameter space where the amplitude of a shape mode of order n ($a_n(t)$) begins to maintain a steady, nonzero value.[5,14,15] The location of the SSTs for $n = 2$ (solid with $+$), $n = 3$ (solid with $\times$), and $n = 4$ (solid with $*$) are shown in Fig. 1. These curves were calculated by Wu[20] at 33 kHz using the method described in Ref. 14. Recent calculations by Hao[22] and Hilgenfeldt[23] agree with the $n = 2$ SST calculated by Wu.

3. Apparatus

The apparatus has been described in more detail elsewhere.[10,11] It consisted of a cylindrical levitation cell acoustically excited at 32.8 kHz. Before running an experiment, fluid was prepared with a gas-handling system, which allowed accurate control of the gas content of the fluid. Once a bubble was levitated, its oscillation was captured with a stroboscopic imaging system (SIS).[18] From the digital images acquired with the SIS, we were able to construct a time averaged radius-time $R(t)$ history of the bubble oscillation. From this curve we extracted a value for the maximum radius R_{max} (± 1.1 μm) and R_o (± 0.9 μm). These values were used to determine P_a (± 0.07 atm) via a numerical fit to the Rayleigh-Plesset equation.[10] Assembling the collection of $R(t)$ curves for a single gas saturation permitted the construction of a R_o-P_a phase diagram.

4. Results and discussion

4.1 Air saturated to 20%

Figure 1 shows a phase diagram for five experimental runs with a 20% air saturation. The final argon concentration in the fluid for this case is $C = 0.2\%$, where $C = 100\%$ would be complete saturation of the fluid. The data sets were taken over a period of several months which indicates the repeatability of the experiments. Each data point represents data from a single $R(t)$ curve. The data have one of four types of behavior: stable non-SL (square) (Mm. 1), unstable non-SL (circle) (Mm. 2), stable SL (upward pointing triangle) (Mm. 3), and unstable SL (downward pointing triangle) (Mm. 4).

Mm. 1. One cycle of typical stable non-SL captured with the SIS with $P_a \approx 1.25$ atm. Note the small R_{max} and the relatively strong afterbounces just after collapse. The horizontal width (true vertical) of the image is equivalent to 160 μm. The duration of the acoustic cycle is 30.5 μs, and the 75 frames of the animation are each separated by ≈400 ns. Light passing directly through the bubble causes the bright spot at the center the bubble (173 kb).

Mm. 2. One cycle of typical unstable non-SL captured with the SIS with $P_a \approx 1.1$ atm. Note that the bubble reaches a slightly larger R_{max} with the lower P_a, and the bubble tends to return to the same location. Afterbounces are also still visible (284 kb).

Mm. 3. One cycle of typical stable SL captured with the SIS with $P_a \approx 1.5$ atm. Note that R_{max} is now much larger, and afterbounces are weak because energy is lost to light emission (362 kb).

Mm. 4. One cycle of typical unstable SL captured with the SIS with $P_a \approx 1.6$ atm. Note the large R_{max}, the lack of strong afterbounces, and that the bubble tends to move along the same path. The unstable behavior is more "orderly" than that which was seen in Mm. 1 (324 kb).

Shown in the figure are the curves for the $C = 0.2\%$ diffusive equilibrium[24,25] (solid), the stable dissociation equilibrium for 20% air (dash dotted) computed by Arlman,[26,27] and the $n = 2, 3, 4$ SSTs (solid with $+$, $\times$, and $*$) calculated by Wu.[20] The behavior of the bubble with increasing P_a is described elsewhere[10] and is similar to what has been reported by others.[1,4,16] As DH predicts, the stable SL points agree with the $C = 0.2\%$ curve, and the stable non-SL points agree with the dissociation equilibrium.

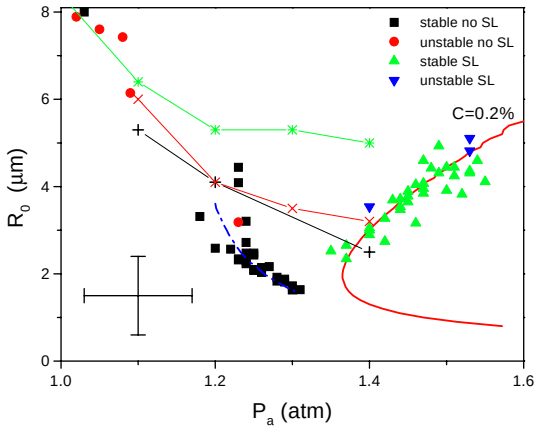

Fig. 1. Phase diagram for five experimental runs with air saturated to 20%. The curves represent theoretical calculations of the stable diffusive equilibrium $C = 0.2\%$ (solid), the stable dissociation equilibrium for a 20% air saturation computed by Arlman (dash dotted), and the $n = 2, 3, 4$ shape thresholds computed by Wu (solid with $+$, $\times$, and $*$). The bubble behavior is represented by a symbol shape (square, circle, upward pointing triangle, and downward pointing triangle). The cross hairs represent the experimental error.

In some of the runs, unstable SL was visible near the extinction threshold for SL. In these cases, the bubble was unstable, but the instability was not severe enough to destroy the bubble. Interestingly, SL bubbles appear stable well above the $n = 2, 3$ SSTs, and the extinction threshold appears to coincide with the $n = 4$ SST.

4.2 Argon-nitrogen mixture with $C = 1.2\%$ final argon concentration

To see unstable SL behavior over a wider pressure range, the argon concentration needs to be increased above $C \approx 0.7\%$.[5] According to DH, as noble gas concentration increases, the diffusive stability curve takes on a more and more positive slope causing it to intersect the SST at lower and lower P_a. Because extinction does not usually occur at lower values of P_a (< 1.45 atm), the bubble instead follows the SST as P_a increases, undergoing repeated pinch off and growth until at some point it reaches the extinction threshold.

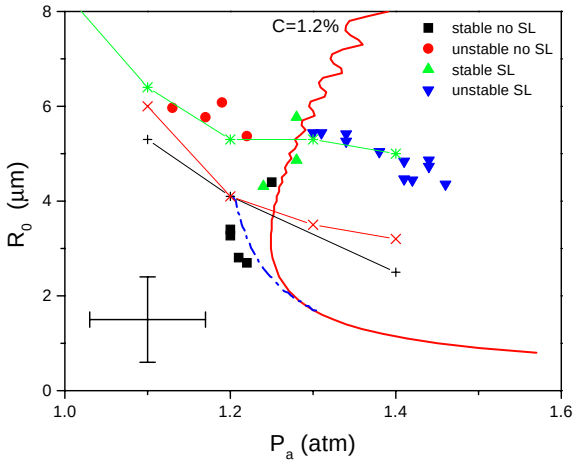

Fig. 2. Phase diagram for two experimental runs with a 12% argon and 88% nitrogen mixture saturated to 10%. The curves represent theoretical calculations of the stable diffusive equilibrium $C = 1.2\%$ (solid), the stable dissociation equilibrium for 10% air (dash dotted), and the $n = 2, 3, 4$ shape thresholds (solid with $+$, $\times$, and $*$).

Figure 2 shows the phase diagram for two 12% argon and 88% nitrogen mixtures saturated to 10%, which gives a final argon concentration in the fluid of $C = 1.2\%$. Also shown are the $n = 2, 3, 4$ SSTs (solid with $+$, $\times$, and $*$). As DH predicts, the stable SL points (upward pointing triangles) show agreement with the $C = 1.2\%$ curve (solid) until they intersect the $n = 4$ SST at $P_a \approx 1.3$ atm. Between $P_a = 1.3 - 1.45$ atm there is a region of unstable SL (downward pointing triangles) as also predicted by DH. For $P_a > 1.45$ atm, the bubble reaches the extinction threshold and rapidly breaks up.

For lower P_a where no SL is observed, it has been shown that the calculated $n = 2$ mode[14,15] is in fairly good agreement with experimental data.[4] The agreement is also seen for the $n = 3, 4$ modes, since all the modes lie fairly close together at low P_a. However, as seen in Fig. 2, the agreement between the data and the $n = 2$ mode does not appear to occur at higher P_a where SL was observed. This may imply that the higher order modes are more destructive to the bubble and contribute to unstable SL and SL extinction. It may also simply mean that the criterion used to define the SST[5,14,15] is not sufficient to describe unstable behavior and extinction.

4.3 Argon-nitrogen mixture with $C > 2\%$ final argon concentration

With an amount of final argon concentration $C > 2\%$, DH predicts that neither stable SL nor stable non-SL should be observed. Figure 3 shows a phase diagram for two mixtures of $> 10\%$ argon in nitrogen saturated to 20%. The exact ratio of gases in the mixture was unknown due to an error in preparation. If we assume the initial gas mixture was 15% argon and 85% nitrogen, then the final argon concentration in the fluid would be

$C = 3\%$ (solid curve). This curve has no stable SL equilibria, and because it also nearly overlaps the dissociation equilibrium for 20% air (dash dotted), there is also no stable non-SL. Therefore, only unstable behavior is possible as was observed experimentally. Below $P_a \approx 1.3$ atm there were only "dancing", nonluminescing bubbles (circles), and above $P_a \approx 1.3$ atm there were only unstable, luminescing bubbles. As in the previous case, the unstable SL behavior shows close agreement to the $n = 4$ SST (solid with $*$).

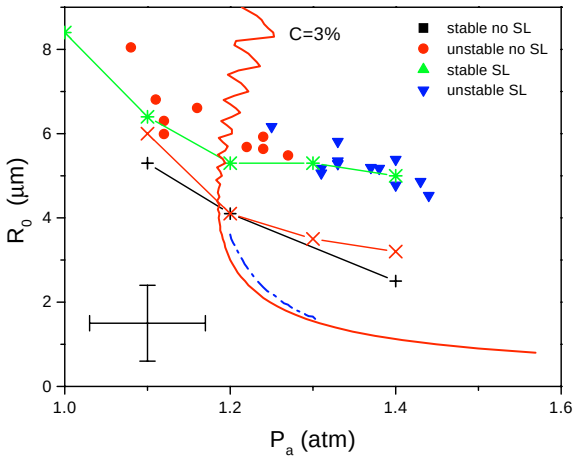

Fig. 3. Phase diagram for two experimental runs with an argon-nitrogen mixture having $> 10\%$ argon saturated to 20%. The curves represent theoretical calculations of the unstable diffusive equilibrium $C = 3\%$ (solid), the stable dissociation equilibrium for 20% air (dash dotted), and the $n = 2, 3, 4$ shape thresholds (solid with $+$, $\times$, and $*$).

5. Conclusions

The experimental results presented here confirm that the predictions of DH for unstable SL are valid. For sufficiently high noble gas concentrations, the SST limits the growth of bubbles, resulting in "dancing" behavior. The SST also appears to coincide with the extinction threshold. The results raise new questions about what actually causes unstable bubble behavior and SL extinction. Previously, the $n = 2$ (quadrupole) mode was believed to be the cause;[5] however, the work presented here suggests higher order modes may actually be more destructive to the bubble. In fact, we occasionally observed a luminescing bubble that appeared to have a shape instability, yet it showed no signs of "dancing". Holt and Gaitan[4] and Tian *et al.*[18] have observed similar behavior, but for non-SL bubbles at lower P_a. These observations suggest that surfactants that suppress higher order shape modes[28] could be very useful for extending the region of stable SL in parameter space. Performing SBSL experiments in microgravity[29–31] may also help stabilize the bubble by eliminating the translation induced by the Bjerknes force.[21]

Acknowledgements

We wish to acknowledge many valuable discussions with G. Holt, T. Matula, S. Hilgenfeldt, and R. Roy. We also wish to thank C. Wu, T. Arlman, and Y. Hao for sharing the results of their numerical calculations.

References and links

[1]D. F. Gaitan, L. A. Crum, C. C. Church, and R. A. Roy, "Sonoluminescence and bubble dynamics for a single, stable, cavitation bubble," J. Acoust. Soc. Am. **91,** 3166–3183 (1992).

[2]R. Hiller, K. Weninger, S. J. Putterman, and B. P. Barber, "Effect of noble-gas doping in single-bubble sonoluminescence," Science **266,** 248–250 (1994).
[3]R. Löfstedt, K. Weninger, S. Putterman, and B. P. Barber, "Sonoluminescing bubbles and mass diffusion," Phys. Rev. E **51,** 4400–4410 (1995).
[4]R. G. Holt and D. F. Gaitan, "Observation of stability boundaries in the parameter space of single bubble sonoluminescence," Phys. Rev. Lett. **77,** 3791–3794 (1996).
[5]S. Hilgenfeldt, D. Lohse, and M. P. Brenner, "Phase diagrams for sonoluminescing bubbles," Phys. Fluids **8,** 2808–2826 (1996).
[6]D. Lohse, M. P. Brenner, T. F. Dupont, S. Hilgenfeldt, and B. Johnston, "Sonoluminescing air bubbles rectify argon," Phys. Rev. Lett. **78,** 1359–1362 (1997).
[7]D. Lohse and S. Hilgenfeldt, "Inert gas accumulation in sonoluminescing bubbles," J. Chem. Phys. **107,** 6986–6997 (1997).
[8]S. Hilgenfeldt, S. Grossmann, and D. Lohse, "A simple explanation of light emission in sonoluminescence," Nature **398,** 402–404 (1999).
[9]D. F. Gaitan and R. G. Holt, "Experimental observations of bubble response and light intensity near the threshold for single bubble sonoluminescence in an air-water system," Phys. Rev. E **59,** 5495–5502 (1999).
[10]J. A. Ketterling and R. E. Apfel, "Experimental validation of the dissociation hypothesis for single bubble sonoluminescence," Phys. Rev. Lett. **81,** 4991–4994 (1998).
[11]J. A. Ketterling, "An experimental validation of the dissociation hypothesis for sonoluminescence and an extension to the analysis of multiple frequency drives," Ph.D. dissertation, Yale University (1999).
[12]L. A. Crum, "Acoustic cavitation series part five - Rectified diffusion," Ultrasonics **22,** 215–223 (1984).
[13]M. P. Brenner, D. Lohse, and T. F. Dupont, "Bubble shape oscillations and the onset of sonoluminescence," Phys. Rev. Lett. **75,** 954–957 (1995).
[14]C. C. Wu and P. H. Roberts, "Bubble shape instability and sonoluminescence," Phys. Lett. A **250,** 131–136 (1998).
[15]A. Prosperetti and Y. Hao, "Modelling of spherical gas bubble oscillations and sonoluminescence," Phil. Trans. R. Soc. Lond. A **357,** 203–224 (1999).
[16]B. P. Barber, C. C. Wu, R. Löfstedt, P. H. Roberts, and S. J. Putterman, "Sensitivity of sonoluminescence to experimental parameters," Phys. Rev. Lett. **72,** 1380–1383 (1994).
[17]R. G. Holt, J. Holzfuss, A. Judt, A. Phillip, and S. Horsburgh, "Forced nonlinear oscillations of single air bubbles in water: Experimental results," In *Proc. of the 12th Int. Symp. on Nonlinear Acoustics, Austin, Texas*, M. Hamilton and D. Blackstock, eds., p. 497 (Elsevier, New York, 1990).
[18]Y. Tian, J. A. Ketterling, and R. E. Apfel, "Direct observation of microbubble oscillations," J. Acoust. Soc. Am. **100,** 3976–3978 (1996).
[19]S. M. Cordry, "Bjerknes forces and temperature effects in single-bubble sonoluminescence," Ph.D. dissertation, University of Mississippi (1995).
[20]C. C. Wu, (private communication).
[21]T. J. Matula, S. M. Cordry, R. A. Roy, and L. A. Crum, "Bjerknes force and bubble levitation under single-bubble sonoluminescence conditions," J. Acoust. Soc. Am. **102,** 1522–1527 (1997).
[22]Y. Hao, (unpublished data).
[23]S. Hilgenfeldt, (unpublished data).
[24]A. Eller and H. G. Flynn, "Rectified diffusion during nonlinear pulsations of cavitation bubbles," J. Acoust. Soc. Am. **37,** 493–503 (1965).
[25]M. M. Fyrillas and A. J. Szeri, "Dissolution or growth of soluble spherical oscillating bubbles," J. Fluid Mech. **277,** 381–407 (1994).
[26]T. Arlman, S. Hilgenfeldt, and D. Lohse, (preprint).
[27]The curve is actually calculated for a mixture of 1% Xe and 99% nitrogen. However, since the nitrogen mainly influences the location of the curve, the curve for air would show little difference. The calculation includes the effect of water vapor on the internal temperature of the bubble.
[28]T. R. Stottlemyer and R. E. Apfel, "The effects of surfactant additives on the acoustic and light emissions from a single stable sonoluminescing bubble," J. Acoust. Soc. Am. **102,** 1418–1423 (1997).
[29]R. G. Holt and R. A. Roy, "Sonoluminescence: The critical role of buoyancy in the stability and emission mechanisms," In *Proc. of the 4th Microgravity Fluid Phys. Conf.*, pp. 347–352 (NASA, 1998).
[30]D. B. Thiessen, J. E. Young, M. J. Marr-Lyon, S. L. Richardson, C. D. Breckon, S. G. Douthit, P. S. Jian, W. E. Torruellas, and P. L. Marston, "Single bubble sonoluminescence in low gravity and optical radiation pressure positioning of the bubble," In *Proc. of the 4th Microgravity Fluid Phys. Conf.*, pp. 379–383 (NASA, 1998).
[31]T. J. Matula, (private communication).

SOUNDINGS

Section Editor: Richard Stern

This front section of the *Journal* includes acoustical news, views, reviews, and general tutorial or selected research articles chosen for wide acoustical interest and written for broad acoustical readership.

ACOUSTICAL NEWS—USA

Elaine Moran
Acoustical Society of America, Suite 1NO1, 2 Huntington Quadrangle, Melville, NY 11747-4502

Editor's Note: *Readers of this Journal are asked to submit news items on awards, appointments, and other activities about themselves or their colleagues. Deadline dates for news items and notices are 2 months prior to publication.*

139th Meeting of the Acoustical Society of America Meeting Announcement

The 139th meeting of the Acoustical Society of America (ASA) will be held Tuesday through Saturday, 30 May–3 June 2000, at the Westin Peachtree Plaza in Atlanta, Georgia, USA.

Technical Program and Special Sessions

The technical program will consist of lecture and poster sessions. Technical sessions will be scheduled Tuesday through Saturday, 30 May–3 June.

The special sessions described below will be organized by the ASA Technical Committees/Groups.

Acoustical Oceanography (AO)

Acoustical surveys of ocean bottom geology (Joint with Underwater Acoustics)
Comparisons of acoustical and conventional measurements of ocean thermohaline structure

Animal Bioacoustics (AB)

Animal hearing sensitivity and characteristics
Auditory temporal processing in animals (Joint with Signal Processing in Acoustics)
Cognition of complex sounds by animals (Joint with Psychological and Physiological Acoustics and Speech Communication)

Architectural Acoustics (AA)

Acoustical design of learning spaces
Classroom acoustics poster session
Electronic enhancement and the traditionally unamplified art form: Philosophy and techniques
Stadium and arena acoustics

Biomedical Ultrasound/Bioresponse to Vibration (BB)

Cavitation detection and monitoring (Joint with Physical Acoustics)
New techniques in biomedical imaging (Joint with Physical Acoustics)
Ultrasound for disease treatment and diagnosis

Education in Acoustics (ED)

Take fives
Publishing excellence in JASA

Engineering Acoustics (EA)

Combustion acoustics (Joint with Physical Acoustics)

Musical Acoustics (MU)

Audio signal data compression for musical applications (Joint with Signal Processing in Acoustics)
Choral and solo vocal performance
Modeling and perception of musical sound sources
Visualization methods for musical instrument acoustics

Noise (NS)

Educating the public on the perils of overexposure to noise (Joint with Education in Acoustics)
Noise and vibration exposure
Student papers in noise control and noise effects

Physical Acoustics (PA)

Signal processing for low diffraction beams (Joint with Signal Processing in Acoustics)
Acoustics of multiphase flow
Acoustics of sand, paper and foam

Psychological and Physiological Acoustics (PP)

Characterization and possible neural bases of age-related hearing loss (Joint with Speech Communication)

Signal Processing in Acoustics (SP)

Acoustical imaging and tomography (Joint with Biomedical Ultrasound/Bioresponse to Vibration, Underwater Acoustics and Acoustical Oceanography)
Time frequency (TF) and wavelet processing (WP) in acoustics (Joint with Noise)

Speech Communication (SC)

Franklin Cooper: A legacy in speech acoustics

Structural Acoustics and Vibration (SA)

Aeroelasticity and flow-induced noise and vibration
Combining active and passive control of vibration and noise
Tire vibration

Underwater Acoustics (UW)

Model-based processing of sources in motion (Joint with Signal Processing in Acoustics and Acoustical Oceanography)

Other Technical Events

A ''Hot Topics'' session sponsored by the Tutorials Committee is scheduled. The Committee on Archives and History will jointly sponsor the next in a series of lectures on the history of acoustics with the Technical Committees on Architectural Acoustics and Engineering Acoustics.

Meeting Program

An advance meeting program summary will be published in the April issue of JASA and a complete meeting program will be mailed as Part 2 of the May issue. Abstracts will be available on the ASA Home Page in April.

Student Transportation Subsidies

A student transportation subsidies fund has been established to provide limited funds to students to partially defray transportation expenses to meetings. Students presenting papers who propose to travel in groups using economical ground transportation will be given first priority to receive subsidies, although these conditions are not mandatory. No reimbursement is intended for the cost of food or housing. The amount granted each student depends on the number of requests received. To apply for a subsidy, submit a proposal (e-mail preferred) to be received by 10 April: Elaine Moran, E-mail: asa@aip.org ASA, Suite 1NO1, 2 Huntington Quadrangle, Melville, NY 11747-4502, 516-576-2360, Fax: 516-576-2377. The proposal should indicate your status as a student, whether you have submitted an abstract,

 0001-4966/2000/107(3)/1077/3/$17.00

whether you are a member of ASA, method of travel, whether you will travel alone or with other students, names of those traveling with you, and approximate cost of transportation.

Young Investigator Travel Grants

The Committee on Women in Acoustics is sponsoring a Young Investigator Travel Grant to help with travel costs associated with presenting a paper at the Atlanta ASA meeting. This award is designed for young professionals who have completed the doctorate in the past five years (not currently enrolled as a student), who plan to present a paper at the Atlanta meeting. Up to $500 in support for travel and lodging costs is available. Applicants should submit a request for support, a copy of the abstract they have submitted for the meeting and a current resume/vita to Jan Weisenberger, Speech and Hearing Science, Ohio State University, 1070 Carmack Road, Columbus, OH 43210 (614-292-1281, jan+@osu.edu). Deadline for receipt of applications is 10 April 2000.

Students Meet Members for Lunch

The Education Committee has established a program for students to meet with members of the ASA over lunch. Students are strongly encouraged to contact Scott Sommerfeldt, N241 ESC, P.O. Box 24673, Brigham Young University, Provo, UT 84602-4673, USA; Tel: 801-378-2205; E-mail: s_sommerfeldt@byu.edu prior to the meeting. There will also be a sign up sheet available at the registration desk for those students who have not responded prior to the meeting.

Members who wish to participate are also encouraged to contact Scott Sommerfeldt. Participants are responsible for the cost of their own meal.

Plenary Session, Awards Ceremony, Fellows' Luncheon and Social Events

Complimentary buffet socials with cash bar will be held early on Wednesday and Friday evenings at the Westin Peachtree Plaza. The Plenary session will be held on Thursday afternoon where Society awards will be presented and recognition of Fellows will be announced. A Fellows' Luncheon will be held on Friday. The speaker will be Professor Steven Garrett of the Pennsylvania State University who will discuss Thermoacoustics. Each ASA Fellow may bring one guest to the luncheon; tickets may be purchased using the registration form that can be found in the meeting Call for Papers which was sent to all members or online at ⟨http://asa.aip.org/atlanta/atlanta.html⟩

Paper Copying Service

Authors are requested to provide one paper copy of their projection material and/or paper(s) to the Paper Copies Desk upon arrival. The copy should contain material on one side only on 8-1/2×11 inch or A4 paper suitable for photocopy reproduction. Copies of available papers will be made for a nominal charge.

Technical Tours

Technical tours have been arranged to visit the Fox theater. There will also be an open house at the Acoustical Laboratories of the Woodruff School of Mechanical Engineering at Georgia Tech and the Aeroacoustics Laboratories (formerly Lockheed facilities) of the Georgia Tech Research Institute. Bus transportation will be provided at cost. A schedule of tours and sign-up sheets will be available at the meeting.

Assistive Listening Devices

Anyone planning to attend the meeting who will require the use of an assistive listening device is requested to advise the Society in advance of the meeting by writing to: Acoustical Society of America, Suite 1NO1, 2 Huntington Quadrangle, Melville, NY 11747-4502, asa@aip.org.

Accompanying Persons Program

We hope that spouses and other visitors will come to Atlanta because we have an exciting program planned for you. A hospitality room, specifically designated for accompanying persons, will be open from 8:00 to 11:00 a.m. daily, Tuesday through Friday, at the Westin Peachtree Plaza. Information will be available about activities in Atlanta and its environs, such as restaurants, shopping, sports, museums, parks, nightlife, cultural events, historical attractions and other sights not on the planned tours. Some special activities, such as speakers, are being planned for your early morning enjoyment in the hospitality room. Also, Atlanta Arrangements has helped us devise an ambitious tour program for your enjoyment of our city. One tour is scheduled for each day, Tuesday through Friday. These are: City Highlights; Atlanta's Legacy of Leaders Tour, which includes a visit to the Carter Center and the Martin Luther King, Jr. Historic District; Mansions and Magnolias Tour, where you will spend a day in the old South; and Atlanta Past and Present, which includes the beautiful Swan House. Details about these tours and sign-up information may be found on the Visitors' Program Page in the Call for Papers or online at ⟨http://asa.aip.org/atlanta/atlanta.html⟩. We encourage you to sign up and pay for the tours in advance, as they might be cancelled if we don't have enough preregistrations.

In addition to tours, you might shop at Lenox Square, visit the pandas in the Atlanta Zoo, see the Civil War at the Cyclorama, attend an Atlanta Braves baseball game in Turner Stadium, visit Stone Mountain Park, go to the High Museum, attend the symphony or theater at the Woodruff Arts Center, or visit Georgia Tech and Emory, our highly-ranked universities. These are only some of the things to do in Atlanta. We hope to see you in Atlanta and look forward to welcoming you.

Air Transportation

Hartsfield International Airport in Atlanta is served by all major airlines and is a hub for Delta Airlines. The airport designation is ATL.

Ground Transportation

The Westin Peachtree Plaza is located 12 miles from Hartsfield International Airport. Transportation from the airport to the hotel may be by car, taxi, shuttle service, or public transportation. Public metro system (MARTA) is the recommended mode of transportation. From the airport baggage claim area, follow the signs for MARTA. The fare is $1.50. Exit at the Peachtree Center station. The Westin Peachtree Plaza is half a block from the exit. The one-way taxi fare is approximately $18. The Airport Shuttle costs $10 one-way and $17 round trip. It leaves every 30 minutes. Reservations are only needed after 7:10 p.m. Call (404) 524-3400.

Room Sharing

ASA will compile a list of those who wish to share a hotel room and its cost. To be listed, send your name, telephone number, email address, gender, smoker or nonsmoker, by 17 April to the Acoustical Society of America, by email: asa@aip.org or by postal mail to Attn.: Room Sharing, Suite 1NO1, 2 Huntington Quadrangle, Melville, NY 11747-4502. The responsibility for completing any arrangements for room sharing rests solely with the participating individuals.

Weather

Atlanta has a moderate climate and four distinct colorful seasons. Early June temperatures will range from daytime highs of 75 to 85 degrees F, to nighttime lows of 60 to 70 degrees F.

Hotel Reservation Information

Guest rooms at discounted rates have been reserved for conference participants at the Westin Peachtree Plaza. To reserve a room, please contact the hotel directly. Early reservations are strongly recommended. Note that the conference rates are not guaranteed after 27 April. Please reference the Acoustical Society of America when making your reservation.

The Westin Peachtree Plaza, America's Tallest Hotel, is an Atlanta landmark. Located in the very heart of the city, and only 20 minutes from Hartsfield International Airport, it is connected to the Peachtree Center Mall, with dozens of offices, shops, restaurants and attractions.

Guests can enjoy the health club, year-round indoor-outdoor pool, business center, and three specialty restaurants. Amenities include wall safes, irons, ironing boards, coffee makers and coffee, hair dryers, and video account review. Outside the floor-to-ceiling windows, is a breathtaking 180-degree panoramic view of the Atlanta skyline.

All reservations at The Westin Peachtree Plaza require a one night's room and tax deposit made by check, money order or a major credit card. In

order to receive a refund of your deposit, you must cancel your reservation at least 72 hours before your arrival date. Any changes to departure after check-in will result in a $25.00 administration fee.

A limited number of rooms will be available at the government rate. To obtain this rate, a government ID must be presented at check-in and the room must be charged to a government credit card.

Please make your reservations directly with the hotel: The Westin Peachtree Plaza, 210 Peachtree Street, NW, Atlanta, GA 30303; Tel.: 404-659-1400; Central Reservations: 1-800-WESTIN1; Fax: 404-589-7424.

Room rates: $115, plus 14% tax. Single; $126, plus 14% tax. Double; $146, plus 14% tax. Triple (3 persons); $166, plus 14% tax. Quad (4 persons). Daily parking is available for $18.

Reservation cut-off date: 27 April 2000.

Preregistration and Registration

The registration desk at the meeting will open on Tuesday morning, 30 May, at 7:30 a.m. on the 7th Level Terrace at the Westin Peachtree Plaza. To preregister, use the form in the meeting Call for Papers or online at ⟨http://asa.aip.org/atlanta/atlanta.html⟩. Preregistration and registration fees are as follows:

Category	Preregistration by 27 April	Registration after 27 April
Acoustical Society Members	$200	$250
Acoustical Society Members One-Day	$100	$125
Nonmembers	$245	$295
Nonmembers One-Day	$125	$150
Nonmember Invited Speakers	$200	$250
(Note: The fee is waived for these speakers if they attend the meeting on the day of their presentation only)		
Students (with current ID cards)	Fee waived	Fee waived
Emeritus members of ASA	$35	$45
(Emeritus status pre-approved by ASA)		
Accompanying Persons	$35	$45
(For registrants who will not participate in the technical sessions)		

Nonmembers who simultaneously apply for Associate Membership in the Acoustical Society of America will be given a $50 discount off their dues payment for the first year of membership. (Full price for dues: $100.)

Invited speakers who are members of the Acoustical Society of America are expected to pay the registration fee, but nonmember invited speakers who participate in the meeting for one day only may register without charge. Nonmember invited speakers who wish to participate in the meeting for more than one day will be charged the member registration fee, which will include a one-year membership in the ASA upon completion of an application form at the meeting.

NOTE: A $25 PROCESSING FEE WILL BE CHARGED TO THOSE WHO WISH TO CANCEL THEIR REGISTRATION AFTER 1 MAY.

Regional Chapter New Washington, DC

Help us organize a meeting of the Washington DC Chapter. Charles F. Gaumond thinks that a meeting should be held in the springer of 2000 in order to nominate new officers and reorganize and revitalize the Washington, DC Chapter. If you would like to help, call him at (202) 404-4811 (work), (301) 567-0755 (home) or e-mail him at gaumond@nrl.navy.mil. The greater Washington DC area has many acousticians with widely varied interests. Meetings in the past have been interesting, professionally broadening, and enjoyable.

USA Meetings Calendar

Listed below is a summary of meetings related to acoustics to be held in the U.S. in the near future. The month/year notation refers to the issue in which a complete meeting announcement appeared.

2000

6–9 Mar	Society of Automotive Engineers Congress, Detroit, MI [SAE Headquarters, 400 Commonwealth Dr., Warrendale, PA 15096-0001; Fax: 724-776-1830; E-mail: congress2000@sae.org].
17–19 May	ASNE Day 2000, Arlington, VA [Andrea Zari, Meetings Department, American Society of Naval Engineers, 1452 Duke St., Alexandria, VA 22314-3458; Tel.: 703-836-6727; Fax: 703-836-7491; E-mail: azari@navalengineers.org].
30 May–3 June	139th meeting of the Acoustical Society of America, Atlanta, GA [Acoustical Society of America, Suite 1NO1, 2 Huntington Quadrangle, Melville, NY 11747-4502; Tel.: 516-576-2360; Fax: 516-576-2377; E-mail: asa@aip.org; WWW: asa.aip.org].
8–10 June	Synaptic Function in Hearing and Balance Symposium, Baltimore, MD [Paul Fuchs, Tel.: 410-955-6311; E-mail: sfhb@bme.jhu.edu].
22–24 June	Binaural Hearing, Hearing Loss & Hearing Aids, Iowa City, IA [Rich Tyler, Tel.: 319-356-2471; E-mail: tyler@uiowa.edu; WWW: www.medicine.uiowa.edu/otolaryngology/news/news].
25–26 June	NIH Bioengineering Symposium—2000, Nanoscience and Nanotechnology: Shaping Biomedical Research, Bethesda, MD [Mark Brown, MasiMaxi Resources Inc., Tel.: 240-632-5618; E-mail: mbrown@masimax.com].
13–16 July	ClarinetFest 2000, Norman, OK [Dr. Keith Koons, Music Dept., Univ. of Central Florida, P.O. Box 161354, Orlando, FL 32816-1354; Tel.: 407-823-5116; E-mail: kkoons@pegasus.cc.ucf.edu].
4–8 December	Joint Meeting: 140th meeting of the Acoustical Society of America/NoiseCon 2000, Newport Beach, CA [Acoustical Society of America, Suite 1NO1, 2 Huntington Quadrangle, Melville, NY 11747-4502; Tel.: 516-576-2360; Fax: 516-576-2377; E-mail: asa@aip.org; WWW: asa.aip.org].

2001

30 April–3 May	2001 SAE Noise & Vibration Conference & Exposition, Traverse City, MI [Patti Kreh, SAE Int'l., 755 W. Big Beaver Rd., Suite 1600, Troy, MI 48084; Tel.: 248-273-2474; Fax: 248-273-2494; E-mail: pkreh@sae.org]. Deadline for submitting abstracts: 14 July 2000

REVIEWS OF ACOUSTICAL PATENTS

Lloyd Rice
11222 Flatiron Drive, Lafayette, Colorado 80026

The purpose of these acoustical patent reviews is to provide enough information for a Journal reader to decide whether to seek more information from the patent itself. Any opinions expressed here are those of reviewers as individuals and are not legal opinions. Printed copies of United States Patents may be ordered at $3.00 each from the Commissioner of Patents and Trademarks, Washington, DC 20231.

Reviewers for this issue:

GEORGE L. AUGSPURGER, *Perception, Incorporated, Box 39536, Los Angeles, California 90039*
CARL J. ROSENBERG, *Acentech Incorporated, 33 Moulton Street, Cambridge, Massachusetts 02138*

5,802,195

43.38.Fx HIGH DISPLACEMENT SOLID STATE FERROELECTRIC LOUDSPEAKER

Curtis R. Regan *et al.*, assignors to the United States of America—National Aeronautics and Space Administration
1 September 1998 (Class 381/190); filed 11 October 1994

A dome-shaped piezoelectric diaphragm is described which can generate excursions of more than one millimeter at its apex. This is directly coupled to a conventional loudspeaker cone assembly or planar diaphragm.—GLA

5,802,196

43.38.Fx SPEAKER FOR RADIATING SOUND WAVES IN ALL DIRECTIONS RELATIVE TO A SPEAKER SUPPORTING SURFACE

Takeshi Nakamura, assignor to Murata Manufacturing Company, Limited
1 September 1998 (Class 381/202); filed in Japan 14 December 1995

Hemispherical piezoelectric assembly 14 directly radiates sound upward and outward. Sound energy produced at its rear surface travels through horn throat 28 and emerges from the radial horn formed between surface 26 and a flat table or other mounting panel (not shown). ''Therefore, the sound waves generated by this speaker are transmitted in a omni-directional manner relative to an installation surface, in directions both toward and away from the installation surface.'' Assuming that directional response is averaged over a sufficiently wide bandwidth, the assertion is probably justified.—GLA

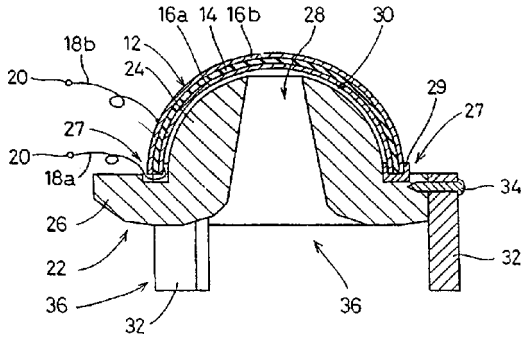

5,802,190

43.38.Hz LINEAR SPEAKER ARRAY

Bran Ferren, assignor to The Walt Disney Company
1 September 1998 (Class 381/182); filed 4 November 1994

A vertical linear array of small loudspeakers is electrically separated into upper and lower groups driven by two signals. Speech reinforcement is concentrated in the upper group. The lower group is driven by a signal in which speech is substantially attenuated. This arrangement is intended to provide more uniform sound coverage to a large group of people, many of whom will be in the near field of the array. It is also intended to minimize feedback when a roving microphone is brought close to the array.—GLA

5,809,153

43.38.Hz ELECTROACOUSTICAL TRANSDUCING

J. Richard Aylward *et al.*, assignors to Bose Corporation
15 September 1998 (Class 381/155); filed 4 December 1996

Small arrays of two or more loudspeakers can be driven through simple phase-shift networks to achieve substantial directivity at low frequencies. At high frequencies, the directivity of the speakers themselves is brought into play. The patent describes every conceivable variant of this idea in 40 illustrations, six pages of text, and 44 claims.—GLA

5,812,685

43.38.Ja NON-DIRECTIONAL SPEAKER SYSTEM WITH POINT SOUND SOURCE

Takeshi Fujita, Yokohama, and Kenji Murata, Tokyo, both of Japan
22 September 1998 (Class 381/90); filed 7 March 1996

Every ten years or so someone decides to simulate a point source by mounting twenty or thirty loudspeakers on a spherical enclosure. The resulting high frequency comb filter is ignored in this patent. Instead, the invention is concerned with correcting low frequency response through the use of digital FIR equalization, thereby correcting both amplitude and phase irregularities.—GLA

 0001-4966/2000/107(3)/1085/6/$17.00

5,812,686

43.38.Ja DEVICE FOR ACTIVE SIMULATION OF AN ACOUSTICAL IMPEDANCE

Maxmillian Hans Hobelsberger, Wurenlingen, Switzerland
22 September 1998 (Class 381/96); filed in Switzerland 24 March 1992

Although the invention can be used as a stand-alone active absorber, this patent and the inventor's two earlier patents are mainly concerned with making a small sealed box behave like a much larger, or even an infinite, air volume behind a loudspeaker. In this variant, signals from pressure transducer 4 and velocity sensor 5 are electronically combined to provide the desired acoustic function. Partition openings 11a are stuffed with fibrous material 11b to form a lowpass filter. The resulting pressure difference between chambers 14 and 15 is not mentioned.—GLA

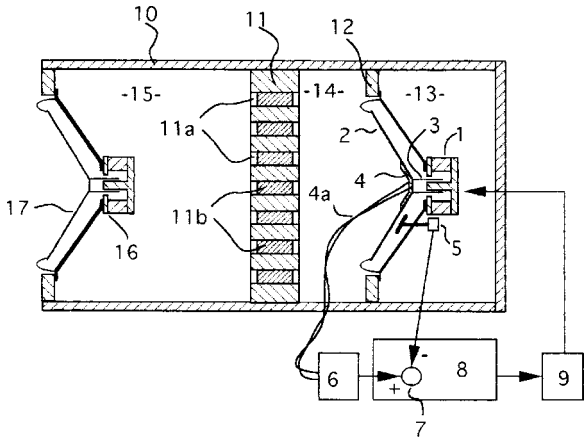

5,818,942

43.38.Ja MULTIMEDIA STEREO SOUND SOURCE

Tommyca Freadman, Goshen, NY
6 October 1998 (Class 381/24); filed 2 November 1994

Back chambers for computer stereo speakers 10 are vented through pipes 32 to a common chamber 30 and from there to the outside world. The arrangement shown appears to waste almost half of the available volume.—GLA

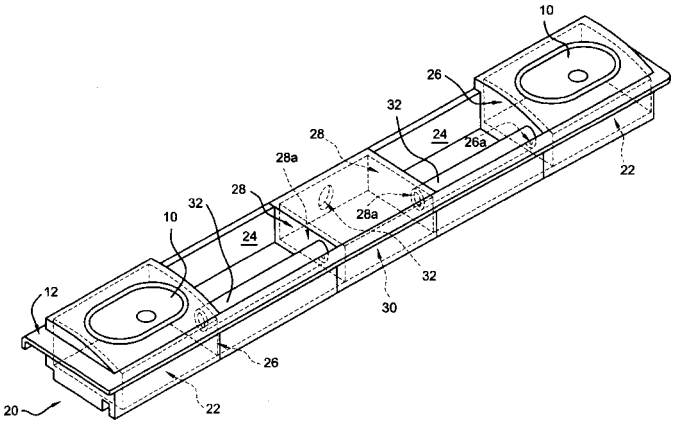

5,821,470

43.38.Ja BROADBAND ACOUSTICAL TRANSMITTING SYSTEM

John D. Meyer and Paul J. Kohut, assignors to Meyer Sound Laboratories, Incorporated
13 October 1998 (Class 181/155); filed 8 April 1997

Parabolic reflector 15 concentrates sound from high frequency horn 38 into a highly directional beam. Low frequency loudspeaker 57 extends the usable bandwidth of the system down into the 125 Hz region. Fairly elaborate signal processing is included to maintain smooth response and uniform beamwidth through the crossover region.—GLA

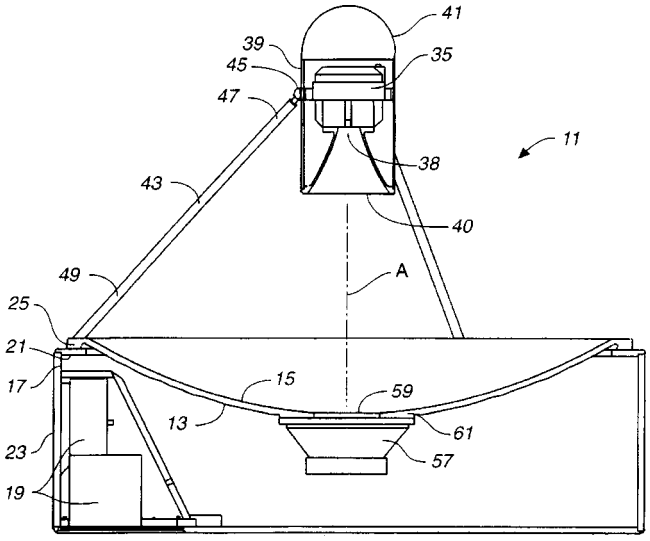

5,821,471

43.38.Ja ACOUSTIC SYSTEM

Mark A. McCuller, Fremont, CA
13 October 1998 (Class 181/156); filed 30 November 1995

A loudspeaker is mounted on one end of a folded, undamped pipe. The patent includes more than 100 illustrations of various ways in which a pipe can be folded. In all cases, the result is '' . . . a plurality of inner openings, for causing a selective cancellation of sounds at predetermined frequencies, while preserving sounds at other frequencies.'' Since some of the illustrations appear to show known prior art, it is a little difficult to understand exactly what has been patented.—GLA

5,822,441

43.38.Lc POWER AMPLIFIER/LOUDSPEAKER INTERFACE

Jean-Marie DeHaeze, Chaville, France
13 October 1998 (Class 381/94.6); filed in France 1 December 1993

In a conventional two-way loudspeaker system, the resistance of the connecting cable generates a certain amount of crosstalk between high- and low-frequency filters. For this reason, high-quality loudspeakers often provide two sets of terminals to allow for bi-wiring, using separate cables for the two sets of components. The invention takes the process one step further by using separate return conductors for each loudspeaker and each filter section. The patent text asserts that, although this is contrary to the techniques of the art,'' the dynamic is substantially improved, the sound is more natural and rich, the timbre of the instruments is quite realistic.''—GLA

5,812,971

43.38.Vk ENHANCED JOINT STEREO CODING METHOD USING TEMPORAL ENVELOPE SHAPING

Juergen Heinrich Herre, assignor to Lucent Technologies Incorporated
22 September 1998 (Class 704/230); filed 22 March 1996

In joint stereo coding, one or more of the processing steps share information across channels to improve the coding efficiency. In this method for encoding stereo audio data, channel-independent high-resolution filter bank analysis, perceptual adaptation and linear prediction of the band outputs are followed by steps in which the cross-channel LP band coefficients are compared to reduce redundancies. A single set of band coefficients is transmitted along with channel-specific band intensity scaling information.—DLR

5,846,629

43.40.Tm CUSHIONING HANDLE WRAP FOR ISOLATING VIBRATION

James T. Gwinn, assignor to Lord Corporation
8 December 1998 (Class 428/68); filed 31 May 1996

This patent describes a continuous strip of a rectangular elastomeric body filled with foam. The strip is to be wrapped around the controls of a vibrating source, like the steering wheel of a motorcycle or the handle of a chain saw, in order to isolate the transmission of high frequency vibrations from the user's hands. This should reduce the incidence of occupational disabilities associated with the use of these vibrating sources.—CJR

5,889,869

43.50.Ki INVISIBLE ACOUSTIC SCREEN FOR OPEN-PLAN OFFICES AND THE LIKE

Radamis Botros and Rafik A. Goubran, assignors to Botrus Teleconferencing & Acoustics Consulting, Limited
30 March 1999 (Class 381/71.11); filed in Canada 24 June 1996

The invisible screen is an active noise cancellation setup, to deal with the signal generated by handsfree telephones, loudspeaking computer terminals and such where the source location is clearly defined and localized. The intent is to reduce sound leakage and improve acoustical privacy for neighbors of offices where there are such loudspeakers.—CJR

5,817,992

43.55.Br PLANAR BINARY AMPLITUDE DIFFUSOR

Peter D'Antonio, assignor to RPG Diffusor Systems, Incorporated
6 October 1998 (Class 181/295); filed 5 March 1997

This latest development from this prolific inventor is a basically flat-faced panel with a series of alternating reflective and absorptive regions defined by a binary sequence. The combination of regions or patches results in a combination of absorption and diffusion.—CJR

5,816,016

43.55.Dt METHOD OF INSTALLING ACOUSTICAL PANELS IN AN ARENA

Bernard F. Zarnick, Rocky River, OH
6 October 1998 (Class 52/747.1); filed 11 December 1995

The installation method described in the patent relates to hanging large acoustical panels (as big as 10 feet by 40 feet) from I-beams high up in the ceiling of a large space. The method involves a harness and tightrope for a worker to stand on as he works his way across the space.—CJR

5,874,161

43.55.Ev PLAIN SURFACE ACOUSTICAL PRODUCT AND COATING THEREFOR

James D. Pape and Darryl L. Sensenig, assignors to Armstrong World Industries, Incorporated
23 February 1999 (Class 428/206); filed 9 November 1995

The patent describes two configurations of decorative wall board, with or without a laminated porous nonwoven scrim. In both cases, the basic board underneath is a fiberboard substrate that is either perforated to make it porous and sound absorptive, or nonperforated, in which case it is not absorptive.—CJR

5,884,436

43.55.Nd REVERBERATION ROOM FOR ACOUSTICAL TESTING

Gordon L. Ebbitt, assignor to Lear Corporation
23 March 1999 (Class 52/79.4); filed 9 May 1995

This reverberation room is an improvement over typical designs because of the shape of the room, the placement of the loudspeakers, and the location of the windows for transmission loss measurements.—CJR

5,907,932

43.55.Ti WALL STRUCTURE HAVING ENHANCED SOUND TRANSMISSION LOSS

Alain LeConte and Ronald Moulder, assignors to CertainTeed Corporation
1 June 1999 (Class 52/144); filed 1 August 1997

A fastening device between two metal studs provides sound isolation

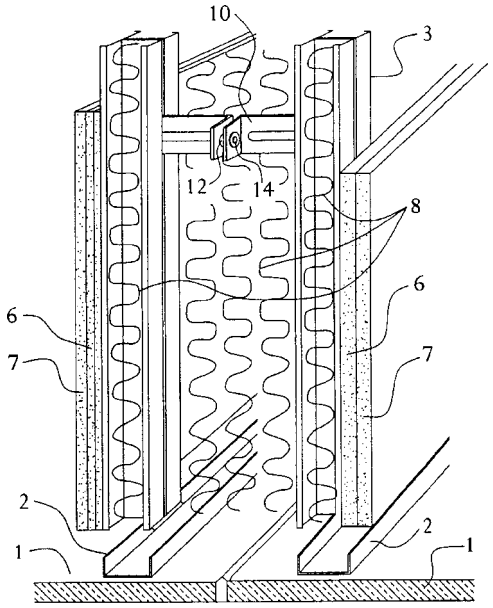

due to the high vibration loss across the device.—CJR

5,815,987

43.55.Ti TURNTABLE WITH ACOUSTIC DOOR AND WALL PANEL

Rex W. Beasley, Venice, CA
6 October 1998 (Class 52/65); filed 13 August 1996

Here is a turntable on which sits a small office. On the turntable is a door and at least one wall panel that engages adjacent permanent building structure elements, and the patent includes acoustical seals for different configurations of the turntable.—CJR

5,812,969

43.60.Cg PROCESS FOR BALANCING THE LOUDNESS OF DIGITALLY SAMPLED AUDIO WAVEFORMS

Alfred D. Barber, Jr. *et al.*, assignors to Adaptec, Incorporated
22 September 1998 (Class 704/224); filed 6 April 1995

When combining audio signals from multiple sources, it is often necessary to adjust the loudness levels to an acceptable uniform loudness. According to the patent, each signal is tested to determine the maximum gain which will avoid distortion. All signals are then adjusted such that each has its maximal loudness set equal to the minimum of the non-distorting loudness maxima.—DLR

5,820,588

43.64.Me METHOD FOR PASSING INFORMATION BETWEEN A PATIENT'S AUDITORY CORTEX AND A SPEECH PROCESSOR

Matthew A. Howard III, assignor to The University of Iowa Research Foundation
13 October 1998 (Class 604/93); filed 9 February 1994

This is a wireless, implantable, multi-electrode prosthesis designed for direct insertion into the primary auditory cortex of a hearing-impaired patient. As many as a few hundred contacts are spaced along a support of a few millimeters in length. Using MRI scans as a reference, the electrode is placed longitudinally within the tonotopical region of the auditory cortex. An external audio processor transmits signals to the implant.—DLR

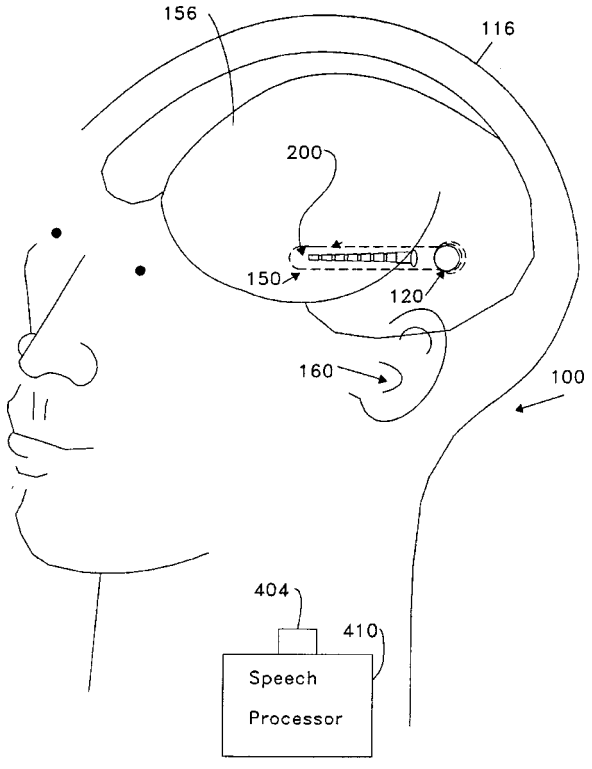

5,819,217

43.72.Ar METHOD AND SYSTEM FOR DIFFERENTIATING BETWEEN SPEECH AND NOISE

Vijay Rangan Raman, assignor to NYNEX Science & Technology, Incorporated
6 October 1998 (Class 704/233); filed 21 December 1995

The patent describes a speech/noise/silence detector which uses a decision tree frame classifier operating on measurements taken within each speech frame. Various frame-to-frame operations include the monotone test (energy level similarities), the pulse test (many samples near the maximum), the transition deviation test (energy level change) and the speech level test (energy above a threshold).—DLR

5,812,970

43.72.Dv METHOD BASED ON PITCH-STRENGTH FOR REDUCING NOISE IN PREDETERMINED SUBBANDS OF A SPEECH SIGNAL

Joseph Chan and Masayuki Nishiguchi, assignors to Sony Corporation
22 September 1998 (Class 704/226); filed in Japan 30 June 1995

This device reduces noise in a speech signal by taking a variety of energy and other measures on spectral bands from two separate FFT analyses. Speech detection and a pitch estimate are based on a type of autocorrelation done on the spectral data. A comparison of frame-to-frame filtered amplitudes and *n*-frame minima provides a phonetic measure described as a consonant indicator.—DLR

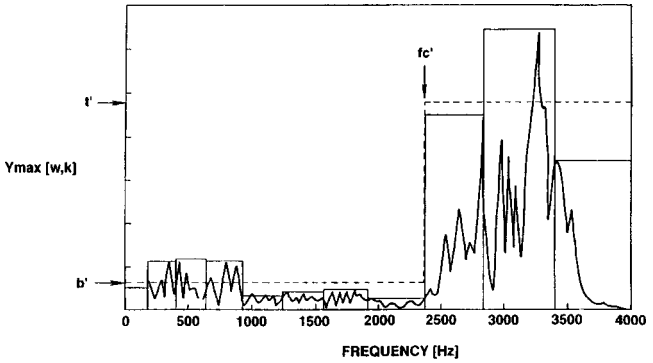

5,819,212

43.72.Gy VOICE ENCODING METHOD AND APPARATUS USING MODIFIED DISCRETE COSINE TRANSFORM

Jun Matsumoto *et al.*, assignors to Sony Corporation
6 October 1998 (Class 704/219); filed in Japan 26 October 1995

This variable bitrate vocoder performs a filter bank analysis, followed by linear prediction of each spectral band. Long-term pitch prediction on low frequency bands leaves a pitch residual, which is then transformed using a type of discrete cosine transform. The bitrate setting adjusts various constants such as sample rates, predictor orders and mappings of certain bands to baseband throughout the system.—DLR

5,812,972

43.72.Ne ADAPTIVE DECISION DIRECTED SPEECH RECOGNITION BIAS EQUALIZATION METHOD AND APPARATUS

Biing-Hwang Juang *et al.*, assignors to Lucent Technologies Incorporated
22 September 1998 (Class 704/234); filed 30 December 1994

This speech recognition system includes a method for adaptively equalizing the signal spectrum at the point of phonetic feature analysis. The adaptation is done by comparing the values of spectral-based phonetic features following a segmentation step. The adapted features may also be recycled through the segmentation step, again adjusting the equalization vector.—DLR

5,812,974

43.72.Ne SPEECH RECOGNITION USING MIDDLE-TO-MIDDLE CONTEXT HIDDEN MARKOV MODELS

Charles T. Hemphill *et al.*, assignors to Texas Instruments Incorporated
22 September 1998 (Class 704/256); filed 26 March 1993

This hidden Markov model (HMM)-based speech recognition system improves the detection of coarticulated words by training unique HMM state sequences for each word boundary. Designed for a limited word vocabulary,

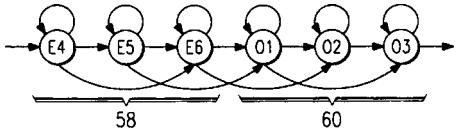

word transitions are defined from near the end of one word into the beginning of the next.—DLR

5,819,220

43.72.Ne WEB TRIGGERED WORD SET BOOSTING FOR SPEECH INTERFACES TO THE WORLD WIDE WEB

Ramesh Sarukkai and Sekhar Sarukkai, assignors to Hewlett-Packard Company
6 October 1998 (Class 704/243); filed 30 September 1996

This speech recognizer is designed for enhanced recognition of the words which occur in a World Wide Web document. A document scan produces a list of the words considered most likely to be spoken in the current context. Language and acoustic models are then adjusted dynamically to reflect the new word set.—DLR

5,819,221

43.72.Ne SPEECH RECOGNITION USING CLUSTERED BETWEEN WORD AND/OR PHRASE COARTICULATION

Kazuhiro Kondo *et al.*, assignors to Texas Instruments Incorporated
6 October 1998 (Class 704/255); filed 31 August 1994

This speech recognition system uses additional phonetic models added after the standard training to model the between-word and between-phrase coarticulated phonetic sequences. Clustering techniques are used to limit the proliferation of phonetic models. The patent is not specific as to the type of model to be used, although hidden Markov models are employed in the examples given.—DLR

5,819,222

43.72.Ne TASK-CONSTRAINED CONNECTED SPEECH RECOGNITION OF PROPAGATION OF TOKENS ONLY IF VALID PROPAGATION PATH IS PRESENT

Samuel Gavin Smyth and Simon Patrick Alexander Ringland, assignors to British Telecommunications public limited company
6 October 1998 (Class 704/256); filed in European Patent Office 31 March 1993

The patent describes a method of backtracking control to allow optimizing the search path during the operation of a speech recognition system. As each node in a grammar network is matched against a speech feature

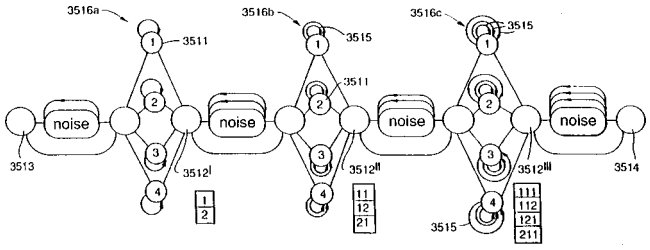

vector, a signature is saved which represents the quality of the match and the progress through the network. When a phrase-final mode is matched, the entire matching sequence is available in the signatures.—DLR

5,819,223

43.72.Ne SPEECH ADAPTATION DEVICE SUITABLE FOR SPEECH RECOGNITION DEVICE AND WORD SPOTTING DEVICE

Keizaburo Takagi, assignor to NEC Corporation
6 October 1998 (Class 704/256); filed in Japan 26 January 1995

The patent describes a speech recognition system supposedly able to recognize speech using an arbitrary vocabulary. Vocabulary-independent reference patterns, such as Japanese mora, are stored for a preliminary matching pass. After the first matching pass, both the speech features and all matched reference patterns are adapted in an attempt to improve the match.—DLR

5,822,727

43.72.Ne METHOD FOR AUTOMATIC SPEECH RECOGNITION IN TELEPHONY

Roger Borgan Garberg and M. Yudkowski, assignors to AT&T Corporation
13 October 1998 (Class 701/243); filed 30 March 1995

The patent discloses a method of obtaining training speech data for a template recognition system using available data such as a telephone subscriber database. For example, names from a phone user's calling list would be synthesized using a standard text-to-speech device. The synthesized speech would be used in a preliminary training pass for the recognizer.—DLR

5,822,728

43.72.Ne MULTISTAGE WORD RECOGNIZER BASED ON RELIABLY DETECTED PHONEME SIMILARITY REGIONS

Ted H. Applebaum and Philippe R. Morin, assignors to Matsushita Electric Industrial Company, Limited
13 October 1998 (Class 704/254); filed 8 September 1995

This speech recognition system processes the acoustic feature vectors through a sequence of matching steps. The first reference contains targets describing the location and shape of stable peaks of phonetic similarity for each stored word. The second stage represents each word by a prototype consisting of phoneme targets, word duration and average training match scores.—DLR

5,822,729

43.72.Ne FEATURE-BASED SPEECH RECOGNIZER HAVING PROBABILISTIC LINGUISTIC PROCESSOR PROVIDING WORD MATCHING BASED ON THE ENTIRE SPACE OF FEATURE VECTORS

James Robert Glass, assignor to Massachusetts Institute of Technology
13 October 1998 (Class 704/255); filed 5 June 1996

Early speech recognizers typically matched each input acoustic feature set against all stored reference features, often using clustering or other means of reducing the reference database. Later models added a stage of feature processing, such as segmentation or landmark analysis, reducing the computational load by limiting the set of feature vectors at each match. This invention restores the full set of feature vectors at each match, but may include segmentation, landmark or other levels, retaining the advantage of features specific to the additional levels.—DLR

5,822,730

43.72.Ne LEXICAL TREE PRE-FILTERING IN SPEECH RECOGNITION

Robert Roth *et al.*, assignors to Dragon Systems, Incorporated
13 October 1998 (Class 704/255); filed 22 August 1996

This speech recognition system has a lexical store in the form of trees, grouping words having common initial phonetic sequences. As each feature vector is matched, a tree search begins at the corresponding phonetic unit.

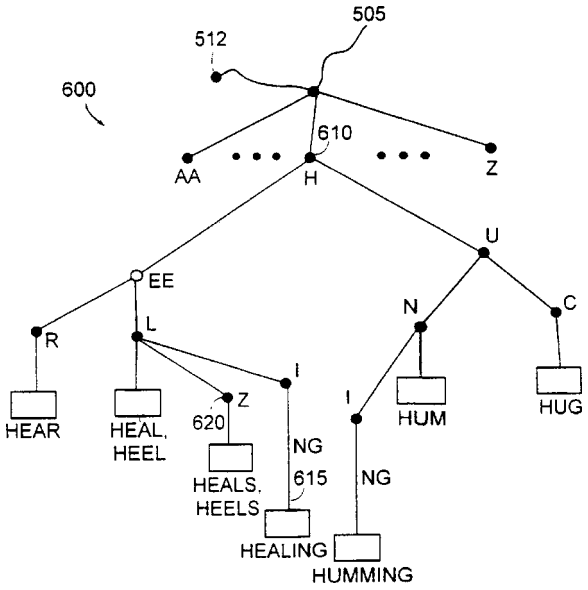

At other time points in the input stream, competing word trees may also be started. Terminal nodes in each word group represent complete words and signal that a word has been matched.—DLR

Optimum and standard beam widths for numerical modeling of interface scattering problems

Ralph A. Stephen[a)]
Woods Hole Oceanographic Institution, Woods Hole, Massachusetts 02543

(Received 19 October 1998; revised 26 October 1999; accepted 16 November 1999)

Gaussian beams provide a useful insonifying field for surface or interface scattering problems such as encountered in electromagnetics, acoustics and seismology. Gaussian beams have these advantages: (i) They give a finite size for the scattering region on the interface. (ii) The incident energy is restricted to a small range of grazing angles. (iii) They do not have side lobes. (iv) They have a convenient mathematical expression. The major disadvantages are: (i) Insonification of an interface is nonuniform. The scattered field will depend on the location of the scatterers within the beam. (ii) The beams spread, so that propagation becomes an integral component of the scattering problem. A standard beam parameterization is proposed which keeps propagation effects uniform among various models so that the effects of scattering only can be compared. In continuous wave problems, for a given angle of incidence and incident amplitude threshold, there will be an optimum Gaussian beam which keeps the insonified area as small as possible. For numerical solutions of pulse beams, these standard parameters provide an estimate of the smallest truncated domain necessary for a physically meaningful result. [S0001-4966(00)05202-4]

PACS numbers: 43.20.Bi, 43.20.Fn, 43.30.Gv, 43.30.Hw [ANN]

INSONIFYING FIELDS FOR SCATTERING PROBLEMS

Many representations of scattering functions are based on the notion of an incident plane wave (Bass and Fuks, 1979; Beckman and Spizzichino, 1963; Felsen and Marcuvitz, 1973; Ishimaru, 1978; Ogilvy, 1991). To avoid edge effects at non-normal angles of incidence and to localize the scattering area on the interface, however, some form of tapering at the edges of the plane wave is often employed in theoretical approaches (Pott and Harris, 1984; Thorsos, 1988; Zeroug and Felsen, 1994, for example), numerical approaches (Hastings *et al.*, 1995; Jensen and Schmidt, 1987; Stephen and Swift, 1994; for example) and in laboratory experiments (Breazeale *et al.*, 1977; Chimenti *et al.*, 1994; Muir *et al.*, 1979, for example). In numerical scattering formulations, particularly, it is important to minimize the insonified area to keep computer memory and computation times as small as possible. In this paper we use the Gaussian beam description given by Červený *et al.* (1982) to predict the minimum width of a two-dimensional continuous wave (cw) beam for a given grazing angle and incident amplitude threshold. Since in numerical solutions to wave scattering and propagation problems it is advantageous to keep the computational domain as small as possible, the ''minimum'' width beams are considered ''optimum.'' An extension of this parameterization to pulse beams leads to a definition of standard beams for validity testing and benchmark models.

The concept of an infinite plane wave as the incident field originates from Fresnel reflection coefficient theory (Jackson, 1975, Sec. 7.3) in electromagnetics, and similar treatments for plane wave reflection coefficients in acoustics (Pierce, 1989, Sec. 3.6) and seismology (Aki and Richards, 1980, Sec. 5.2). In these cases, semi-infinite plane waves are incident on infinite planar surfaces separating semi-infinite half-spaces. When coupled with the plane or cylindrical wave decomposition of a point source (Aki and Richards, 1980, Chap. 6; Sommerfeld, 1909; Von Weyl, 1919), the reflection coefficients can be used to solve the problem of a point source over a planar interface separating two semi-infinite media. In seismology these are referred to as Lamb's problems (Lamb, 1904). All of these problems are well posed notions completely consistent with the wave equations. The propagation and scattering (reflection and transmission) are both correct simultaneously. The solutions are exact and they lead to a number of convenient and powerful concepts in wave theory such as wave number vector decompositions.

However, problems arise when truncating the time and space domains. The integral transforms can no longer be evaluated to infinity and the convenient concepts only apply approximately over certain bandwidths or in given spatial domains. Scattering problems from surface roughness and volume heterogeneities introduce ''length scales'' to the problem which are not present in the problems of Fresnel, Lamb, Weyl, and Sommerfeld. In stratified media or in the geometrical optics (high frequency) limit, the introduction of a length scale is not a problem if one is careful in defining the bandwidth and the smoothness (wave number content) of the medium. In scattering theory for infinite surfaces with small stochastic roughness or for infinite surfaces with periodic discrete scatterers, it is still valid to consider incident and scattered semi-infinite plane waves. If the domain is truncated, however, either explicitly by tapering the incident field (Thorsos, 1988, for example) or implicitly by adding a single discrete scattering element on the interface, semi-infinite plane waves are no longer well posed. It is at this point that the trade-off between angle resolution and spatial resolution is introduced if one wants to do both the propaga-

a)Electronic mail: rstephen@whoi.edu

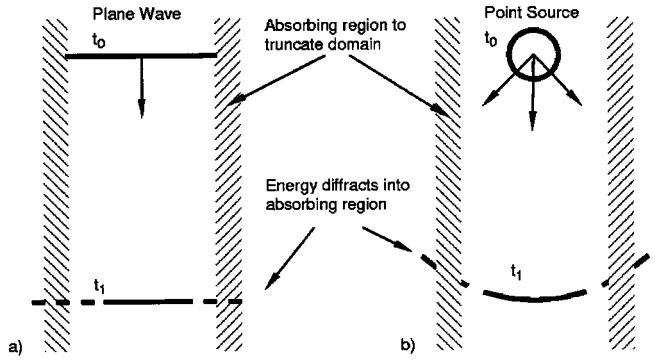

FIG. 1. In some numerical solutions to wave equations, such as time-domain finite-differences, it is necessary to make the computational domain in space as small as possible. This is accomplished by adding absorbing regions (hashed) around the spatial domain of interest. The examples in (a) and (b) show a truncated plane wave and a point source, respectively, propagating in a homogeneous medium. Because of diffraction of energy into the absorbing region, neither of these examples correctly portrays propagation in infinite, homogeneous media. Similar but less obvious effects occur in many applications where the medium is more complex. As an alternative to plane waves and point sources, Gaussian beams provide a convenient and useful incident field in these cases of dramatically truncated domains.

tion and scattering problems simultaneously. Large domains permit small angle spread and small domains require larger angle spread. Gaussian beams provide a mechanism to address this trade-off quantitatively.

This study has been motivated by the computational necessity, in time-domain numerical solutions to wave equations, to keep the spatial and temporal domains as small as possible. Spatial domains of only a few hundred wavelengths on a side in two-dimensional problems or only a few tens of wavelengths on a side for three-dimensional problems challenge even the fastest and largest computers. It is tempting to use spatial domains that are so small or have such a narrow aspect ratio that even results for homogeneous media will not be valid.

As an example, consider propagation in a homogeneous, two-dimensional medium (Fig. 1). Figure 1(a) is an example similar to acoustic well logging problems. The incident field is a vertically propagating plane wave, but in an effort to minimize the computational domain absorbing boundaries are placed close together and parallel to the propagation direction. In this case energy diffracts from the edges of the plane wave into the absorbing regions on either side. After propagating a short distance, the planar wave front inside the domain no longer agrees with the intended solution of an infinite plane wave. This problem is closely related to the radiated field from a vibrating piston (Pierce, 1989, Chap. 5). Figure 1(b) is an example similar to many problems in controlled source or earthquake modeling. It shows a point source in homogeneous media where the domain has been truncated by absorbing boundaries parallel to the propagation direction of interest. This is often done in an effort to minimize the computational domain. In this problem, energy also diffracts into the absorbing boundaries, and the solutions for even homogeneous media will be incorrect. Although these examples are trivial, similar but less obvious effects occur in many applications where the medium is more complex.

I. GAUSSIAN BEAMS

Gaussian beams are a useful way to restrict the angular (or horizontal wave number) content of the incident field while keeping the interaction localized on the surface (Červený *et al.*, 1982; Chimenti *et al.*, 1994; Felsen, 1976). However, by truncating a plane wave the additional complexity of beam spreading (Huygen's principle) must be considered. This introduces propagation issues into scattering problems.

In this paper we are interested in actual Gaussian beams in homogeneous media which can be used as insonifying fields for scattering problems (Bertoni and Tamir, 1973; Choi and Harris, 1989; Felsen, 1976; Jensen and Schmidt, 1987; Zeroug and Felsen, 1994, for example). There is extensive literature on the Gaussian beam summation method for computing wave fields from point and line sources in inhomogeneous media (Červený *et al.*, 1982; George *et al.*, 1987; Klimeš, 1989; Nowack and Aki, 1984; Weber, 1988; White *et al.*, 1987, for example). The Gaussian beam summation method is not being addressed here. Rather we consider Gaussian beams as a physical reality.

Assume that the medium is homogeneous and that we are in a two-dimensional Cartesian coordinate system. For a beam waist centered at (x_p, z_p) with a half-width at the waist of L_M, and an angle of incidence α, the pressure at (x,z) is given by (Červený *et al.*, 1982),

$$\Phi(x,z) = \sqrt{\frac{\sqrt{2\pi}L_M}{s+\epsilon}} \exp\{2\pi i[s+n^2/(2(s+\epsilon))]\},$$

where

$$\epsilon = -i\pi L_M^2,$$

$$s = (x-x_p)\sin(\alpha) + (z-z_p)\cos(\alpha),$$

$$n = (x-x_p)\cos(\alpha) - (z-z_p)\sin(\alpha). \tag{1}$$

This is an asymptotic solution to the time harmonic, two-dimensional parabolic wave equation, obtained using a parabolic approximation to the wave equation about the beam axis. The beam coordinates are (s, n), where s is the propagation distance from the beam waist and n is the direction normal to the beam axis (Fig. 2). All distances are in terms of wavelengths. The normalized power, the area under $|\Phi|^2$ as a function of wavelength across the beam, is unity. If Φ is pressure (in Pascals), ρ is density (in kg/m^3) and f is frequency (in Hertz), then the power in the beam (in Watts) is

$$P = \frac{1}{\rho f}\int |\Phi|^2 dn = \frac{1}{\rho f}. \tag{2}$$

An equation similar to Eq. (1), with differences in the phase and amplitude normalization, can also be derived using the complex source point method (Zeroug and Felsen, 1994).

In ray coordinates, Eq. (1) can be rewritten as

$$\Phi(s,n) = \sqrt{\frac{\sqrt{2\pi}L_M}{s-i\pi L_M^2}} \exp\left\{2\pi i[s+n^2K(s)] - \frac{n^2}{L^2(s)}\right\},$$

where

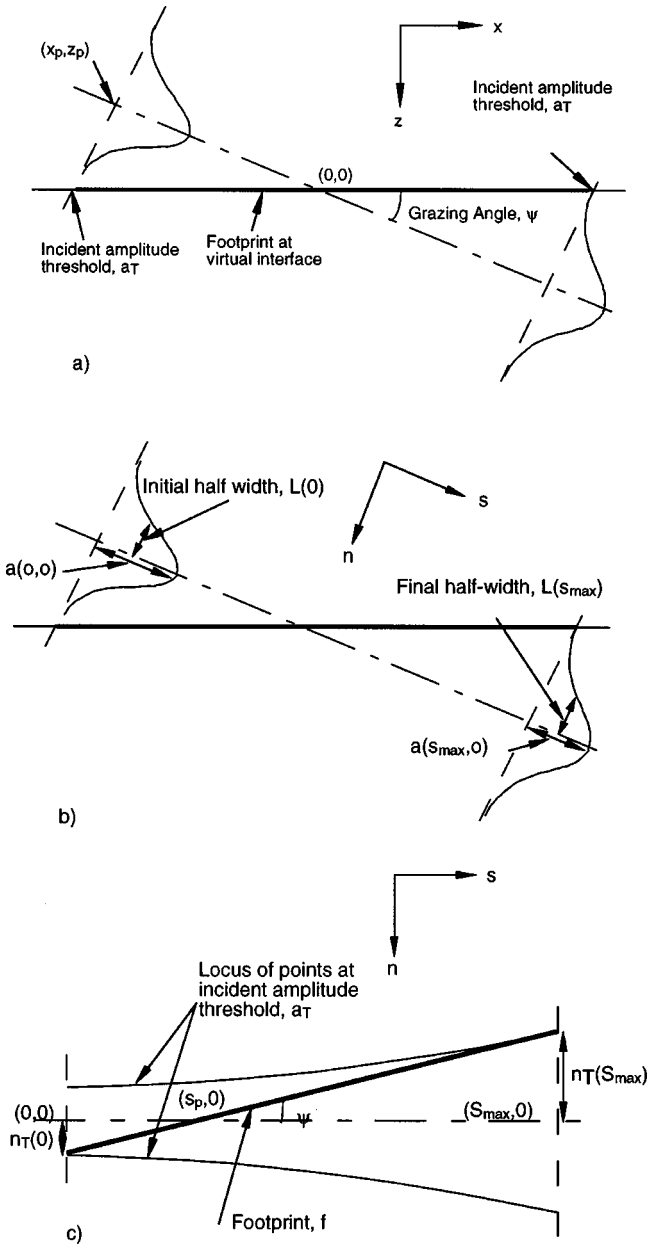

FIG. 2. (a) The optimum Gaussian beam for surface scattering problems is defined on the notion that the beam will spread as it propagates across a flat virtual interface at the mean level of the surface. Optimum beam parameters are constrained by the grazing angle and the incident amplitude threshold. The incident amplitude threshold is the maximum acceptable incident amplitude at the edges of the scattering region and is chosen based on an acceptable level of artifacts from edge effects. The minimum half-width occurs at the beam waist. The origin is defined as the intersection of the beam axis and the virtual interface. The center of the beam waist is located at (x_p, z_p). The footprint size is the distance along the virtual interface between the lower and upper incident amplitude threshold points. (b) To compute parameters for the optimum beam it is convenient to work in beam coordinates (s,n). Two parameters that define the shape of the beam are the incident amplitude threshold, a_T, and the propagation distance, $S_{\max}$. From these one can compute the half-width at the beam waist, $L(0)$, the size of the footprint on the virtual interface, f, and the ''nominal'' angle of incidence, ψ. By the inverse coordinate transform in Eq. (1) one can also locate the beam waist in (x,z) coordinates, (x_p, z_p). (c) The locus of points which have an amplitude a_T is shown in beam coordinates.

$$K(s)=\frac{s}{2[s^2+(\pi L_M^2)^2]},$$

$$L(s)=\sqrt{L_M^2+\left(\frac{1}{\pi L_M}\right)^2 s^2}. \tag{3}$$

$K(s)$ controls the divergence of the beam energy or curvature of the surfaces of constant phase. The profile of the beam is Gaussian with an ''effective half-width,'' $L(s)$. This is the half-width to the point where the amplitude decreases to e^{-1} of the value which occurs at the beam axis. The function $L(s)$ defines the beam envelope as a half-width and is hyperbolic. If the beam envelope is defined by an absolute amplitude, however, there is a small additional factor to account for the change in amplitude along the beam axis. The amplitude of the beam is

$$a(s,n)=\sqrt{\frac{\sqrt{2\pi}L_M}{\sqrt{s^2+(\pi L_m^2)^2}}}\exp\left\{-\frac{n^2}{L^2(s)}\right\}. \tag{4}$$

The power on lines normal to the beam is constant and the amplitude on the beam axis, $a(s,0)$, is related to the half-width, $L(s)$, by

$$a^2(s,0)L(s)=\sqrt{\frac{2}{\pi}}. \tag{5}$$

For a given path length, $S_{\max}$, in homogeneous media there is an initial beam half-width, L_M^{opt}, which will yield the narrowest beam, as defined by half-width

$$L_M^{\text{opt}}=\sqrt{S_{\max}/\pi}. \tag{6a}$$

The corresponding half-width at $S_{\max}$ is

$$L(S_{\max})=\sqrt{2S_{\max}/\pi}. \tag{6b}$$

Gaussian beams are a convenient incident field for interface scattering problems because they have such a simple analytic expression for the beam divergence and they have a predictable minimum width for a given propagation distance. For initial beam half-widths less than L_M^{opt}, the beam spreads more, so that the half-width at $S_{\max}$ is greater than $\sqrt{2S_{\max}/\pi}$. For initial beam half-widths greater than L_M^{opt}, the beam spreads less but the resultant half-width at $S_{\max}$ is still greater than $\sqrt{2S_{\max}/\pi}$.

Bessel beams have many of the same advantages as Gaussian beams and, in addition, they are diffraction-free and do not spread (Durnin and Miceli, 1988). The major disadvantage of Bessel beams for interface scattering problems is that they have multiple lobes and zeros within the beam. Insonification across the beam footprint is dramatically nonuniform.

Felsen and coauthors (Chimenti *et al.*, 1994; Felsen, 1984; Zeroug and Felsen, 1992) use the complex source point (CSP) method to generate beams which are close approximations to plane waves with a Gaussian profile when the Fresnel length [πL_M^2 in Eq. (1)] is greater than a wavelength. The beam is constructed by interference of evanescent (inhomogeneous) plane waves. Their approach has been applied to the study of reflection of Gaussian beams from fluid loaded elastic structures (Chimenti *et al.*, 1994) and the coupling of beams to leaky modes (Zeroug and Felsen, 1994). Good agreement between the CSP method and laboratory observations was obtained (Chimenti *et al.*, 1994).

A number of investigators have used bounded beams to study reflection and refraction at planar fluid-solid interfaces (Bertoni and Tamir, 1973; Breazeale *et al.*, 1977; Pott and

Harris, 1984, for example). Deterministic scattering of bounded beams from rough seafloors has been discussed by Stephen and Swift (1994), from volume heterogeneities below a fluid-solid boundary by Swift and Stephen (1994), and from a rough sea surface by Thorsos (1996), Stephen (1996) and Hastings *et al.* (1997). In this paper we propose a standard beam configuration for all types of interface and surface scattering problems including flat interfaces between homogeneous media, interfaces with volume heterogeneity in the lower medium, interfaces with fine scale roughness and interfaces with discrete scatterers.

II. THE ''OPTIMUM'' GAUSSIAN BEAM

When applying Gaussian beams to interface scattering problems it is desirable to minimize the footprint on the interface while keeping the half-width of the beam, the amplitude of the incident field, and the angle of incidence as constant as possible across the footprint. The ''optimum'' Gaussian beam is defined by considering propagation in a homogeneous medium with the beam incident on a virtual interface normal to the z axis in a Cartesian coordinate system [Fig. 2(a)]. The virtual interface is transparent to the optimum beam. The virtual interface, however, specifies the location of the mean surface for actual scattering problems and is the reference for defining the beam parameters.

We choose the origin in (x,z) coordinates to be at the intersection of the axis of the beam and the virtual interface. The beam axis intersects the virtual interface with the nominal grazing angle, ψ. Since the beam diverges as it propagates across the virtual interface [because of the curvature factor $K(s)$ in Eq. (3)], the actual grazing angle [defined in this context as the inverse cosine of the slope of the phase curve in cycles per wavelength (Stephen, 1996)] varies with range along the interface.

For a given angle of incidence and a given incident amplitude threshold, the optimum Gaussian beam will minimize the insonified area, or footprint, on the virtual surface. The incident amplitude threshold, a_T, is the largest incident amplitude that is acceptable at the end of the tapers on the left and right edges of the scattering region [Fig. 2(a)]. It can be expressed in decibels down from a reference amplitude,

$$\hat{A}_T = 20\log_{10}(\hat{a}_T) = 20\log_{10}\left(\frac{a_T}{a(0,0)}\right). \tag{7}$$

For a reference amplitude we choose the peak amplitude at the beam waist, $a(0,0)$, which in homogeneous media is the largest amplitude in the problem. (In this paper we use $\log_{10}$ to indicate logarithms to the base 10 and log to indicate natural logarithms.) As the beam propagates along its axis from the waist, its half-width, $L(s)$, increases and its on-axis amplitude, $a(s,0)$, decreases according to Eqs. (3) and (5). The normalized amplitude, $\hat{a}$, can be expressed in terms of the waist half-width only,

$$\hat{a}(s,n) = \sqrt{\frac{\pi L_M^2}{\sqrt{s^2+(\pi L_M^2)^2}}}\exp\left\{\frac{-n^2}{L^2(s)}\right\},$$

$$L^2(s) = L_M^2 + \left(\frac{1}{\pi L_M}\right)^2 s^2. \tag{8}$$

The beam half-width from the axis to the normalized amplitude $\hat{a}$ is

$$n(s) = \pm\left(L_M^2 + \left(\frac{s}{\pi L_M}\right)^2\right)^{1/2}\left[-\log(\hat{a}) - \log\left(\sqrt{\frac{\sqrt{s^2+(\pi L_M^2)^2}}{\pi L_M^2}}\right)\right]^{1/2}. \tag{9}$$

The first expression on the right side represents the hyperbolic spreading of the beam half-width corresponding to an amplitude of $1/e$. The first term in the square brackets modifies the $1/e$ half-width to the half-width at the normalized amplitude. The second term in square brackets allows for the decay in amplitude along the beam axis. For a fixed distance, s, the term in square brackets varies much more slowly with respect to the waist half-width, than the preceding hyperbolic spreading term. The waist half-width which gives the narrowest beam in terms of half-width [Eq. (6)] also gives the narrowest beam in terms of constant amplitude. The beam half-width to the normalized amplitude can then be expressed as a function of the propagation distance, $S_{\max}$,

$$n(s) = \pm\left(\frac{S_{\max}^2+s^2}{\pi S_{\max}}\right)^{1/2}\left[-\log\left(\hat{a}\sqrt{\frac{\sqrt{S_{\max}^2+s^2}}{S_{\max}}}\right)\right]^{1/2}. \tag{10}$$

To compute parameters for the optimum beam it is convenient to work in beam coordinates, (s,n) [Fig. 2(b)]. The beam shape is defined by the locus of points at the amplitude threshold, $\hat{a}_T$. The beam half-width, from the axis to the amplitude threshold, is $n_T(s)$. The angle that the beam axis makes with the virtual interface is the grazing angle, ψ. The initial and final beam half-widths, $n_T(0)$ and $n_T(S_{\max})$, are

$$n_T(0) = \pm\sqrt{\frac{S_{\max}}{\pi}(-\log\hat{a}_T)},$$
$$n_T(S_{\max}) = \pm\sqrt{\frac{2S_{\max}}{\pi}(-\log\hat{a}_T - \log\sqrt[4]{2})}. \tag{11}$$

Now $\tan\psi$ is the sum of these initial and final beam half-widths divided by the propagation distance, $S_{\max}$ [Fig. 2(c)]. So for a given grazing angle and a given incident amplitude threshold, the propagation distance for the optimum Gaussian beam can be obtained,

$$S_{\max} = \frac{\left[\sqrt{-\log\hat{a}_T} + \sqrt{2(-\log\hat{a}_T - \log\sqrt[4]{2})}\right]^2}{\pi\tan^2\psi}. \tag{12}$$

Once $S_{\max}$ is determined, the waist half-width is obtained by (6) and the beam shape is defined by (3). The footprint on the virtual interface, f, is

$$f = \frac{S_{\max}}{\cos\psi}. \tag{13}$$

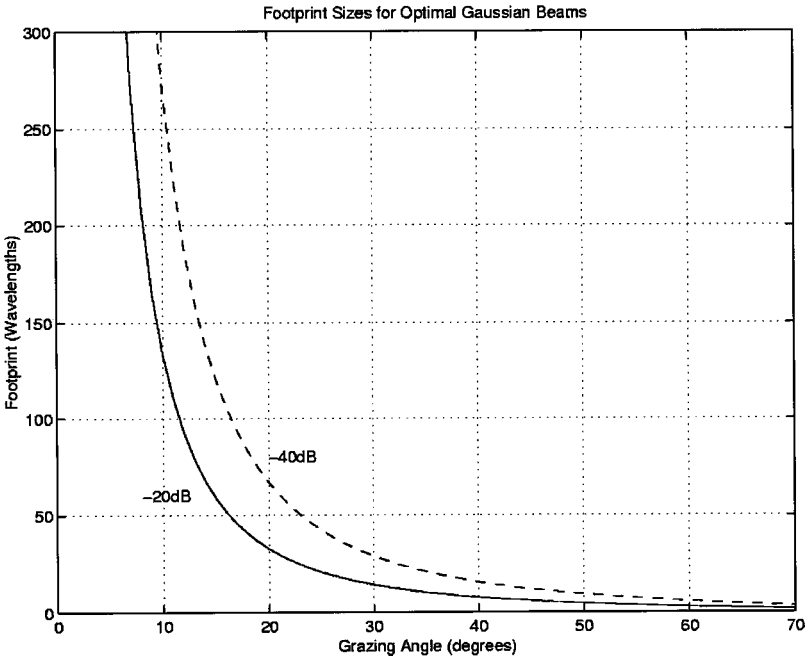

FIG. 3. Footprint sizes are shown as a function of grazing angle for amplitude threshold values of −20 and −40 dB. Using minimum footprints is particularly important at low grazing angles where the footprint size exceeds 100 wavelengths. At higher grazing angles, where the optimum footprint size goes to zero, other issues may constrain the footprint size. For example, it may be necessary to have a sufficiently large number of scattering elements on the interface to adequately represent the statistical distribution of scatterers. Since angle spread increases with decreasing beam waist widths, defining the beam in terms of grazing angle and acceptable angle spread may be more useful.

The center of the beam waist in (x,z) coordinates, (x_p, z_p) is

$$x_p = -n_T(0)\frac{\cos\psi}{\tan\psi}, \quad z_p = -n_T(0)\cos\psi, \tag{14}$$

Footprint sizes as functions of grazing angle for the optimum Gaussian beams are shown in Fig. 3 for incident amplitude thresholds of −20 and −40 dB. For thresholds less than −20 dB, footprints greater than 130 wavelengths are necessary for grazing angles less than about 10°. For thresholds greater than −40 dB, at grazing angles near 50° the footprints drop below about 10 wavelengths. At grazing angles greater than 50° there will be criteria other than beam spreading which control the footprint size. For example, one needs a footprint sufficiently large that there will be enough scattering elements to adequately represent a particular phenomenon. Since angle spread increases with decreasing beam waist widths, defining beams in terms of grazing angle and acceptable angle spread may be more useful.

III. EXAMPLES AND DISCUSSION

As an example of an optimum Gaussian beam, consider a 400 Hz beam insonifying a surface at 10° grazing angle in water (velocity of 1500 m/s, density of 1000 kg/m^3) (Fig. 4). This is similar to the incident field used in Test Case 1 of Thorsos (1996) which was generated by a vertical array. Gaussian beams for Test Case 1 are also discussed in Stephen (1996). Figure 5 shows the projection of the incident optimum Gaussian beam on the surface for an incident amplitude threshold of −40 dB. The footprint size is 1023 m (273 wavelengths) compared to the 750 m (200 wavelengths) footprint used in Test Case 1. Figure 6 shows the corresponding grazing angle across the surface. Even though the nominal grazing angle was 10°, the actual grazing angle varies from about 7 to 10.5°. The angle spread for the optimum Gaussian beam of 3.5° is narrower by about 1° than the angle spread for the beam used in Test Case 1. The waist half-width of the optimum beam is 34.68 m and is considerably wider than the half-width of the vertical taper used in Test Case 1, 27.55 m. The depth of the midpoint of the waist is also deeper, 73.30 compared to 66.12 m. [The ''optimum Gaussian beam'' discussed in Stephen (1996) was based on slant range, rather than the amplitude threshold criteria defined in Eq. (12). This gave a more meaningful comparison with the other beams discussed in that paper but was not as rigorous in terms of incident amplitude constraints.]

In some formulations of the scattering problem (Hastings *et al.*, 1995; Thorsos, 1988, for example), the incident field is ''layed-down'' on the scattering surface, rather than propagating the incident field up to the scattering surface. The scattered fields are compared with theoretical results for incident plane waves. Gaussian tapers, however, are used on the mean scattering surface to truncate the domain, and the incident field in the medium adjacent to the scattering surface is undefined and could be quite complicated. Comparison with results from other methods, where it is impractical to ''lay-down'' the incident field, would be difficult. In these formulations, the optimum Gaussian beams defined here would provide useful incident fields with simple and well-

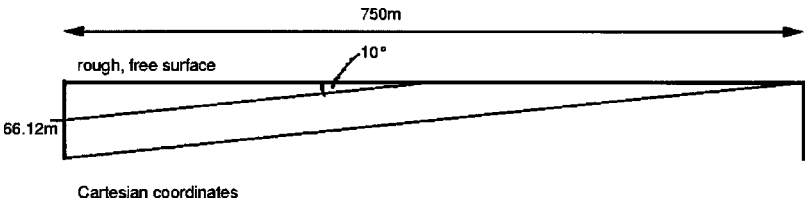

FIG. 4. As an example of an optimum beam calculation, consider a 400 Hz beam insonifying a free surface at 10° grazing angle in water (velocity of 1500 m/s, density of 1000 kg/m^3).

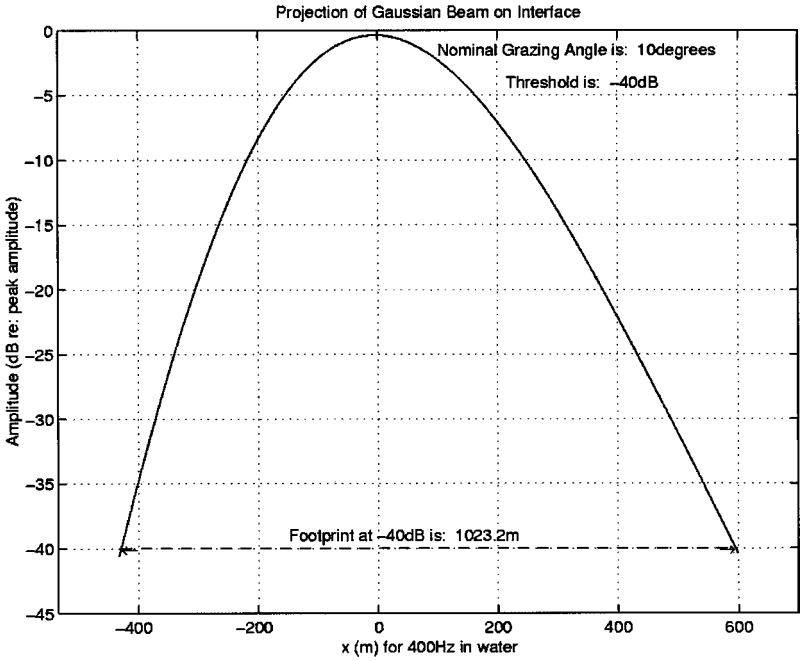

FIG. 5. The optimum beam projection on the interface for the example shown in Fig. 4 has a footprint of over 1000 m for an incident threshold value of −40 dB. If beam spreading were ignored and geometrical optics was used to project the beam, the footprint size would be only 750 m. The projection of the Gaussian beam on the horizontal surface is asymmetrical because of beam spreading.

defined propagation characteristics. In one example, Hastings *et al.* (1995) for a rough sea surface with a grazing angle of 10° used a footprint of 180 wavelengths and a half-width for the Gaussian taper of 40 wavelengths. The optimum Gaussian beam with an incident amplitude threshold of −36 dB has a footprint of 245 wavelengths and the profile on the footprint has a half-width of about 54 wavelengths. It is beyond the scope of this paper to investigate the numerical implications of using optimum Gaussian beams in these methods, but it would be worth considering them. The optimum beam profile could be used in these calculations with very little additional computational effort. In addition to having the propagation of the incident field well defined, the angle spread over the footprint would also be well defined. In this case it is less than 3.5°.

In a third example, Stephen and Swift (1994) use a Gaussian pulse-beam as the insonifying field for seafloor scattering problems in a Numerical Scattering Chamber using time-domain finite-differences. Their footprint calculations assume a uniform ''channel width,'' rather than a minimum incident amplitude threshold. The optimum Gaussian beam, based on the peak frequency in pressure, for a grazing angle of 15° and an incident amplitude threshold of −20 dB, would have a waist half-width of 4.25 wavelengths located at (−23.27, −6.24). The footprint would be only 58.9 wavelengths compared to the 72 wavelengths used in the earlier study. The depth of the computational domain would not change appreciably, but there would be a reduction in the length by 20% and computational time would be reduced by 35% for the same problem. The divergence, caused by the

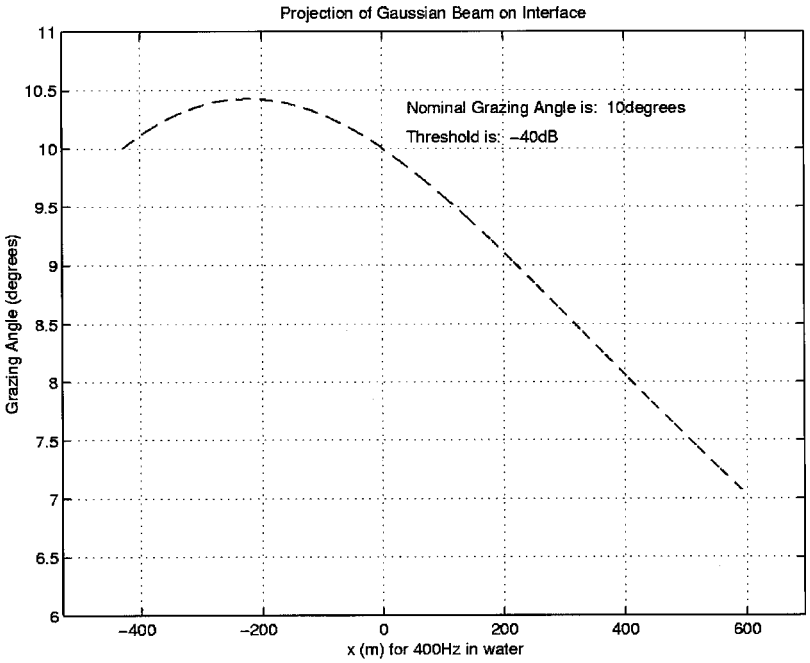

FIG. 6. Grazing angles for the optimum Gaussian beam in Fig. 4, with a nominal grazing angle of 10°, actually vary from about 7.0 to 10.5°. Narrower angle ranges (less diffraction) can be obtained by using wider footprints.

TABLE I. Frequency effects on beam parameters.

At $s=0$:	$L(0)$-meters	$\hat{a}(0,n_T(0))$
Peak frequency (10 Hz)	638.1	0.1000
Upper half-power frequency (13.6 Hz)	638.1	0.0707
Lower half-power frequency (6.8 Hz)	638.1	0.0707
At $s=S_{\max}$:	$L(S_{\max})$-meters	$\hat{a}(S_{\max},n_T(S_{\max}))$
Peak frequency (10 Hz)	902.4	0.1000
Upper half-power frequency (13.6 Hz)	792.8	0.0402
Lower half-power frequency (6.8 Hz)	1132	0.1373

curvature of the phase fronts, of the optimum Gaussian beam would be about 5°.

In a Gaussian pulse-beam the various frequency components of the beam will spread at different rates. For the same initial half-width and propagation distance (in meters, not wavelengths), lower frequency beams will spread more. Table I shows half-widths and normalized amplitude thresholds at the peak frequency and upper and lower half-power frequencies for the time wavelet used in Stephen and Swift (1994). The table assumes a peak frequency of 10 Hz and a propagation velocity of 1500 m/s. At the lower half-power frequency the beam has spread 25% more, and the threshold amplitude at $[S_{\max},n_T(S_{\max})]$ is 37% greater than at the peak frequency. If these discrepancies are judged to be significant, a more conservative value of the incident amplitude threshold should be used in the beam design.

By considering Gaussian beams as the incident field, we gain some insight into the problem of backscatter in the limit as grazing angle goes to zero. It is challenging to imagine a plane wave incident on an interface at 0° grazing angle. It is quite natural, however, to consider a Gaussian beam, such as in Fig. 2(c), propagating at 0° just above an interface with a particular incident amplitude threshold. The optimum beam notion, discussed above, would not apply, but the incident field into the interface would consist solely of diffracted energy from beam spreading. The insonified length between incident amplitude thresholds would still be bounded because of decay in amplitude along the beam axis. Scattering elements, either roughness on the interface or sub-bottom heterogeneity, would scatter a finite amount of energy back into the upper medium in all directions.

Although in this paper we considered Gaussian beams in two-dimensional media, a similar approach can be taken to obtain optimum beams for interface scattering problems in three dimensions using the formulas for three-dimensional Gaussian beams (Červený, 1985, Sec. 9; Pott and Harris, 1984; Wang and Waltham, 1995; Zeroug and Felsen, 1994, for example).

IV. CONCLUSIONS

In applying cw Gaussian beams to seafloor scattering problems there are optimum beam parameters which minimize the size of the scattering region on the interface. For a given footprint size, these optimum Gaussian beams have the most uniform half-width and the least angle spread across the footprint. The optimum beam parameters are constrained by the angle of incidence and the incident amplitude threshold. In finite bandwidth, pulse-beam problems, standard beams can be defined by applying the optimum beam parameters at the peak or center frequencies. By using optimum Gaussian beams investigators can minimize and standardize the propagation effects in beam scattering problems.

ACKNOWLEDGMENTS

I would like to thank Eric Thorsos for helpful discussions and two anonymous reviewers for constructive comments. This work was carried out under Office of Naval Research Grant Nos. N00014-90-I-1493, N00014-96-1-0460, and N00014-95-1-0506 and under a Mellon Independent Study Award from Woods Hole Oceanographic Institution. Woods Hole Oceanographic Institution Contribution Number 10094.

Aki, K., and Richards, P. G. (**1980**). *Quantitative Seismology: Theory and Methods* (Freeman, San Francisco), Vol. 1.

Bass, F. G., and Fuks, I. M. (**1979**). *Wave Scattering from Statistically Rough Surfaces* (Pergamon, Oxford).

Beckman, P., and Spizzichino, A. (**1963**). *The Scattering of Electromagnetic Waves from Rough Surfaces* (Pergamon, Oxford).

Bertoni, H. L., and Tamir, T. (**1973**). ''Unified theory of Rayleigh-Angle phenomena for acoustic beams at liquid-solid interfaces,'' Appl. Phys. **2**, 157–172.

Breazeale, M. A., Alder, L., and Scott, G. W. (**1977**). ''Interaction of ultrasonic waves incident at the Rayleigh angle onto a liquid-solid interface,'' J. Appl. Phys. **48**, 530–537.

Červený, V. (**1985**). ''The application of ray tracing to the numerical modeling of seismic wavefields in complex structures,'' in *Seismic Shear Waves, Part A: Theory, Handbook of Geophysical Exploration*, edited by G. Dohr (Geophysical, London), Vol. 15A, pp. 1–124.

Červený, V., Popov, M. M., and Pšenčík, I. (**1982**). ''Computation of wave fields in inhomogeneous media—Gaussian beam approach,'' Geophys. J. R. Astron. Soc. **70**, 109–128.

Chimenti, D. E., Zhang, J.-G., Zeroug, S., and Felsen, L. B. (**1994**). ''Interaction of acoustic beams with fluid-loaded elastic structures,'' J. Acoust. Soc. Am. **95**, 45–59.

Choi, H.-C., and Harris, J. G. (**1989**). ''Scattering of an ultrasonic beam from a curved interface,'' in *Wave Motion II*, edited by N. Holland (Elsevier Science, New York), pp. 383–406.

Durnin, J., and Miceli, Jr., J. (**1988**). ''Comparison of Bessel and Gaussian beams,'' Opt. Lett. **13**, 79–80.

Felsen, L. B. (**1976**). ''Complex-point-source solutions of the field equations and their relation to the propagation and scattering of Gaussian beams,'' in *Symposia Matematica*, edited by Istituto Nazionale di Alta Matematica (Italy) (Academic, New York), Vol. 18, pp. 39–56.

Felsen, L. B. (**1984**). ''Geometrical theory of diffraction, evanescent waves, complex rays and Gaussian beams,'' Geophys. J. R. Astron. Soc. **79**, 77–88.

Felsen, L. B., and Marcuvitz, N. (**1973**). *Radiation and Scattering of Waves* (Prentice-Hall, Englewood Cliffs).

George, T., Virieux, J., and Madariaga, R. (**1987**). ''Seismic wave synthesis by Gaussian beam summation: A comparison with finite differences,'' Geophysics **52**, 1065–1073.

Hastings, F. D., Schneider, J. B., and Broschat, S. L. (**1995**). ''A Monte Carlo FDTD technique for rough surface scattering,'' IEEE Trans. Antennas Propag. **43**, 1183–1189.

Hastings, F. D., Schneider, J. B., and Broschat, S. L. (**1997**). ''A finite-difference time-domain solution to scattering from a rough pressure-release surface,'' J. Acoust. Soc. Am. **102**, 3394–3400.

Ishimaru, A. (**1978**). *Wave Propagation and Scattering in Random Media* (Academic, New York).

Jackson, J. D. (**1975**). *Classical Electrodynamics* (Wiley, New York).

Jensen, F. B., and Schmidt, H. (**1987**). ''Subcritical penetration of narrow Gaussian beams into sediments,'' J. Acoust. Soc. Am. **82**, 574–579.

Klimeš, L. (**1989**). ''Optimization of the shape of Gaussian beams of a fixed length,'' Stud. Geophys. Geod. **33**, 146–163.
Lamb, H. (**1904**). ''On the propagation of tremors over the surface of an elastic solid,'' Philos. Trans. R. Soc. London, Ser. A **203**, 1–42.
Muir, T. G., Horton, Sr., C. W., and Thompson, L. A. (**1979**). ''The penetration of highly directional acoustic beams into sediments,'' J. Sound Vib. **64**, 539–551.
Nowack, R., and Aki, K. (**1984**). ''The 2-D Gaussian beam synthetic method testing and application,'' J. Geophys. Res. **89**, 7797–7819.
Ogilvy, J. A. (**1991**). *Theory of Wave Scattering from Random Rough Surfaces* (Adam Hilger, Bristol).
Pierce, A. D. (**1989**). *Acoustics: An Introduction to its Physical Principles and Applications* (Acoustical Society of America, Woodbury).
Pott, J., and Harris, J. G. (**1984**). ''Scattering of an acoustic Gaussian beam from a fluid-solid interface,'' J. Acoust. Soc. Am. **76**, 1829–1838.
Sommerfeld, A. (**1909**). ''Uber die ausbreitung der wellen in der drahtlosen telegraphie,'' Ann. Phys. (Leipzig) **28**, 665–736.
Stephen, R. A. (**1996**). ''Modeling sea surface scattering by the time-domain finite difference method,'' J. Acoust. Soc. Am. **100**, 2070–2078.
Stephen, R. A., and Swift, S. A. (**1994**). ''Modeling seafloor geoacoustic interaction with a numerical scattering chamber,'' J. Acoust. Soc. Am. **96**, 973–990.
Swift, S. A., and Stephen, R. A. (**1994**). ''The scattering of a low-angle pulse beam by seafloor volume heterogeneities,'' J. Acoust. Soc. Am. **96**, 991–1001.
Thorsos, E. I. (**1988**). ''The validity of the Kirchhoff approximation for rough surface scattering using a Gaussian roughness spectrum,'' J. Acoust. Soc. Am. **83**, 78–92.
Thorsos, E. I. (**1996**). ''Test Case 1: Sea surface forward scattering,'' in *Benchmark Solutions in Reverberation and Scattering: Proceedings of the Reverberation and Scattering Workshop, May 2–5, 1994*, edited by D. B. King, S. A. Chin-Bing, J. A. Davis, and R. B. Evans, Naval Research Laboratory Book Contribution NRL/BE/7181-96-001 (U.S. Government Printing Office), pp. 3.2–3.20.
Von Weyl, H. (**1919**). ''Ausbretung elektromagnetischer wellen uber einen ebenen leiter,'' Ann. Phys. (Leipzig) **60**, 481–500.
Wang, T. K., and Waltham, D. A. (**1995**). ''Seismic modelling over 3-D homogeneous layered structures-summation of Gaussian beams,'' Geophys. J. Int. **122**, 161–174.
Weber, M. (**1988**). ''Computation of body-wave seismograms in absorbing 2-D media using the Gaussian beam method: Comparison with exact methods,'' Geophys. J. **92**, 9–24.
White, B. S., Norris, A., Bayliss, A., and Burridge, R. (**1987**). ''Some remarks on the Gaussian beam summation method,'' Geophys. J. R. Astron. Soc. **89**, 579–636.
Zeroug, S., and Felsen, L. B. (**1992**). ''Multiple reflected beam synthesis of fields excited by a high-frequency oblique beam input in an elastic plate,'' J. Acoust. Soc. Am. **91**, 2016–2024.
Zeroug, S., and Felsen, L. B. (**1994**). ''Nonspecular reflection of two- and three-dimensional acoustic beams from fluid-immersed plane-layered elastic structures,'' J. Acoust. Soc. Am. **95**, 3075–3089.

A boundary that sustains a negligible specular reflection coefficient over a wide frequency band

G. Maidanik and J. Dickey[a)]
CDNSWC (DTMB), 9500 MacArthur Boulevard, W. Bethesda, Maryland 20817

(Received 8 July 1999; accepted for publication 14 December 1999)

In a previous paper the authors analyzed and discussed the specular reflection coefficient of a plane boundary comprised of a plate, a compliant layer, and a fluid. The analysis showed that a negligible specular reflection coefficient may be derived provided specific resonance conditions are met. The resonance of concern is that between the surface mass of the plate and the surface stiffness of the compliant layer. The conditions of resonance included the value that must be assigned to the loss factor in the compliant layer. In the present paper, an attempt is made to determine the conditions that must be placed on the surface stiffness of the compliant layer in order to increase the frequency range over which a negligible specular reflection coefficient may be maintained. The tolerances in these conditions are also estimated. © *2000 Acoustical Society of America.*
[S0001-4966(00)05203-6]

PACS numbers: 43.20.El, 43.40.Fz [DEC]

LIST OF SYMBOLS

$A=\lvert(1+\eta_2^2)-(\overline{fZ_g})\rvert^2$	a positive definite and dimensionless quantity
$B_c(\omega,\theta)=(\omega/\omega_c)\times[\cos(\theta)/\mathcal{E}_c]$	a dimensionless quantity dependent on the normalized frequency (ω/ω_c) and on the angle of incidence (θ)
c	the speed of sound in the fluid
$(f)^{-1}=(K/K_{12})$	the surface stiffness modification parameter of the compliant layer
$(\overline{f})^{-1}=(\omega_0/\omega)^2(f)^{-1}$	the surface stiffness modification factor of the compliant layer
$g=(1+\eta_2^2)(\lvert\mathbf{k}\rvert/k_p)^n$	the normalized surface stiffness impedance of the panel
K	the surface stiffness of the compliant layer
K_{12}	a constant (independent of $\{\mathbf{k},\omega\}$) surface stiffness
k_p	the free wave number in the panel; $k_p^2=(\omega\omega_c/c^2)$
$\mathbf{k}=\{k,k_y\}$	the wave vector variable
$\{\mathbf{k},\omega\}$	the spectral vector variable
$(k_3^2+\lvert\mathbf{k}\rvert^2)=(\omega/c)^2$	is a statement of the wave equation in the fluid; $\overline{k}_3=(k_3c/\omega)$
$M_2=M(1+\eta_2^2)$	the surface mass of the panel; $\overline{M}_2=[M_2/(\rho c)]$
$(i\omega)M$	the surface mass impedance of the panel
n	the flexural index; $n=2$ a membrane, $n=4$ a plate
$R(\mathbf{k},\omega)$	the specular reflection coefficient of the boundary
$Z(\mathbf{k},\omega)$	the mechanical surface impedance of the boundary; $\overline{Z}(\mathbf{k}\omega)=[\underline{Z}(\mathbf{k}\omega)/(\rho c)]=Z_R(\mathbf{k}\omega)+iZ_I(\mathbf{k}\omega)$
$Z_1(\mathbf{k},\omega)=(\rho c)(\overline{k}_3)^{-1}$	the surface impedance of the fluid in the plane of the boundary; $\overline{Z}_1=(\overline{k}_3)^{-1}=[Z(\mathbf{k},\omega)/(\rho c)]$
$\overline{Z}_2(\mathbf{k},\omega)=(i\omega)\times M\overline{Z}_g(\mathbf{k},\omega)$	the surface impedance of the panel; $\overline{Z}_2(\mathbf{k},\omega)=[Z_1(\mathbf{k},\omega)/(\rho c)]$ $[(1-g)-i\eta]$
$\overline{Z}_g(\mathbf{k},\omega)=[Z_2(\mathbf{k},\omega)/(i\omega M)]$	
$Z_{12}(\mathbf{k},\omega)=(K/i\omega)(1+i\eta_{12})$	surface impedance of the compliant layer; $\overline{Z}_{12}(\mathbf{k},\omega)=[Z_{12}(\mathbf{k},\omega)/(\rho c)]$
$\gamma=(\lvert\mathbf{k}\rvert c/\omega)$	the normalized wave number variable; $\gamma<1$ defines the supersonic spectral range; and $\gamma>1$ defines the subsonic spectral range
Δ	designates an elemental variation in the quantity on which it operates
$\mathcal{E}$	degree of smallness; $\lvert\mathcal{E}\rvert\ll1$
$\mathcal{E}_2$	$(1+\eta_2^2)^{-1}\mathcal{E}_c$=the fluid loading parameter; $\mathcal{E}_2=(\omega_c\overline{M}_2)^{-1}$ and $\mathcal{E}_c=(\omega_cM)^{-1}$
$\eta=\eta_2+g\eta_p$	the loss factor in the isotropic panel; η_2 is the mass attributed loss factor and $(g\eta_p)$ is the stiffness attributed loss factor
η_{12}	the loss factor in the compliant layer
$\{\theta,\phi\}$	the angular vector of incidence
ρ	the density of the fluid
(ρc)	the characteristic impedance of the fluid
$\omega_0=(K_{12}/M)^{1/2}$	the resonance frequency; $\omega_0^2=\omega_1^2(1+\eta_2^2)$
ω_c	the critical frequency in the isotropic panel
$[\cdots]_0$	encloses a quantity that is evaluated for a negligible specular reflection coefficient

[a)]Present address: Center for Nondestructive Evaluations, Maryland Hall, 3400 N. Charles St., The Johns Hopkins University, Baltimore, MD 21218.

INTRODUCTION

The achievement of several noise control goals relies on the presence of a resonance. For example, a negligible specular reflection coefficient of a plane boundary may be achieved if the incident pressure wave perceives a matching surface impedance in the mechanical boundary.[1] Another example is the achievement of vibration reduction by a resonant sprung mass (a dynamic absorber) placed on a machinery piece that excessively vibrates at the sprung-mass resonance frequency.[2–4] In these examples and others, the operation of the noise control devices are largely effective at and in the immediate vicinity of the resonance frequency. This paper deals largely with a noise control device that renders negligible the specular reflection coefficient of a boundary. Since the surface impedance of the fluid is real, to match this fluid surface impedance the mechanical surface impedance of the boundary also needs to be real. The fluid surface impedance is that pertaining to an incident propagating pressure wave. To render the mechanical surface impedance of the boundary real, a resonance may be employed; at resonance, the surface impedance of the boundary is real. Moreover, the magnitude of that real surface impedance is inversely proportional to the loss factor associated with the boundary. To achieve a matching surface impedance with that pertaining to the incident pressure wave, the loss factor needs to assume a specific value. However, when the incident pressure wave enters the boundary, its initial vision of an endless propagation, into an apparent infinite fluid medium is shattered. It transpires that the specific value of the loss factor in the resonant boundary is just right for efficiently dissipating the incident pressure wave before it can re-emerge into the fluid. In this manner, a resonating boundary, with the right loss factor, may possess a negligible specular reflection coefficient. The conditions that bestow a resonant boundary with a surface impedance matching the fluid surface impedance, are enumerated and discussed in Ref. 1. Also discussed, in that reference, are the sensitivities of these conditions when the demand for achieving a strictly negligible specular reflection coefficient is relaxed. A brief account of the conditions and their sensitivities under these circumstances is included herein, which may help to introduce the wider scope of the present paper.

Noise control devices, that rely on a resonance for achieving a desired goal, are largely effective only in the immediate vicinity of the resonance frequency. Means to extend the operational frequency band of these resonant devices are constantly sought.[3–14] An obvious extension is one in which a series of adjacent and appropriately tailored resonances are designed into the device with associated loss factors that obey the ''modal overlap'' condition.[5–13] Although such an extension is obvious, implementation is not always that straightforward. Indeed, in certain situations implementation may not even be physically realizable.[10–13,15] It may be useful, nonetheless, to suspend the question of realization and examine the analytical implications involved in such an extension, employing a simple generic device. With the notable exception of Ref. 15, most of the references just quoted relate to the analysis of structural fuzzies and, as such, they are only obliquely relevant to the present paper.[6] As already mentioned, the subject of interest herein is the analysis of a noise control device that renders negligible the specular reflection coefficient of a boundary. Of particular interest is the sustenance of this quality of the boundary over a wider frequency band as well as a wider angular incidence.[15,16] The conditions that sustain a negligible specular reflection coefficient over a wide frequency band and the sensitivities of these conditions to variations in the material properties of a generic boundary are detailed in this paper. The generic boundary is to be composed merely of a compliant layer facing a compressible fluid and backed by a thin plate[1] [cf. Figs. 1 and 2(a)]. The compliant layer is backed by the thin plate only. In this case the mechanism for achieving a wide frequency band is associated with designing the surface stiffness of the compliant layer to be frequency dependent. The analysis of this frequency dependence allows one to demonstrate, in a straightforward manner, the conditions, and the tolerances on these conditions, that need to be satisfied in order to achieve the desired boundary. Although this approach is of limited scope, it addresses questions that are relevant to any other attempt to achieve a boundary of negligible specular reflection coefficient over a wide frequency band.

I. A NEGLIGIBLE SPECULAR REFLECTION COEFFICIENT FOR A BOUNDARY FACING A SEMI-INFINITE FLUID ATOP

The specular reflection coefficient $R(\mathbf{k},\omega)$ of a plane surface that interfaces with a semi-infinite fluid atop and that possesses a uniform mechanical surface impedance $Z(\mathbf{k},\omega)$, is familiarly given by

$$R(\mathbf{k},\omega)=[Z(\mathbf{k},\omega)-Z_1(\mathbf{k},\omega)][Z(\mathbf{k},\omega)+Z_1(\mathbf{k},\omega)]^{-1},\quad \mathbf{k}=\{k,k_y\}, \tag{1}$$

where $Z_1(\mathbf{k},\omega)$ is the surface impedance of the fluid on the plane, $(\mathbf{k})$ is the wave-vector variable in the plane, and (ω) is the frequency variable; see Fig. 1.[1,17] The surface impedance of the fluid on that plane is expressed in the form

$$Z_1(\mathbf{k},\omega)=(\rho c/\overline{k_3}), \tag{2a}$$

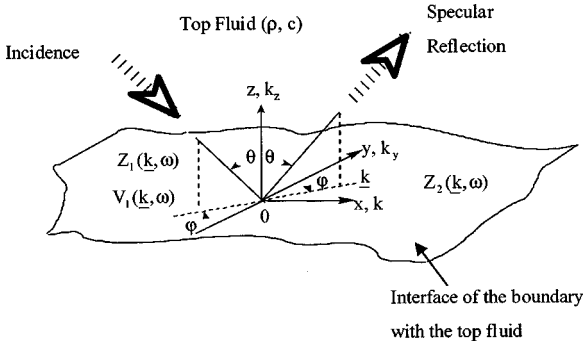

FIG. 1. Incidence and specular reflection as defined by the angular vector $\{\theta,\phi\}$. The velocity $V_1(\mathbf{k},\omega)$ is on the interface of the boundary and the top fluid. The surface impedance $Z_1(\mathbf{k},\omega)$ is that of the top fluid and $Z_2(\mathbf{k},\omega)$ is the surface impedance of the basic boundary; e.g., a backing plate.

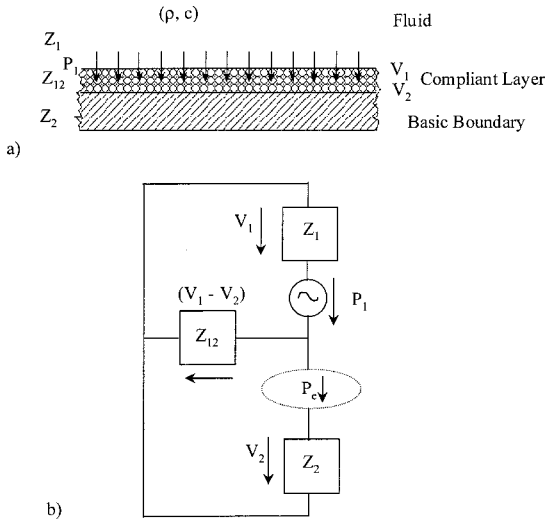

FIG. 2. (a) A boundary composed of a basic boundary and a compliant layer. The top surface of the compliant layer is facing a semi-infinite space filled with fluid. The surface impedances Z_1, Z_{12}, and Z_2 of the fluid, the compliant layer and the basic boundary, respectively, are indicated. Also indicated, are the velocities V_1 and V_2 on top and bottom surfaces of the compliant layer, respectively. An external drive, P_1, is shown applied at the interface of the compliant layer and the fluid. (b) Equivalent circuit diagram of the model depicted in Fig. 2a showing also the possibility than an external drive, P_e, may be applied directly to the basic boundary. When $P_1=0$, the radiated pressure is $P_{\text{rad}}=Z_1V_1$.

$$\overline{k}_3(\mathbf{k},\omega)=(1-\gamma^2)^{1/2}U(1-\gamma^2)-i(\gamma^2-1)^{1/2}U(\gamma^2-1),$$
$$\gamma=(|\mathbf{k}|c/\omega), \tag{2b}$$

where (ρ) and (c) are the density and speed of sound in the fluid, respectively, U is the step function, and $\{\mathbf{k},\omega\}$ defines the incidence on and the specular reflection from the plane boundary; again, see Fig. 1.[1,17] From Eqs. (1) and (2a) one obtains

$$R(\mathbf{k},\omega)=[\overline{Z}(\mathbf{k},\omega)\overline{k}_3-1][\overline{Z}(\mathbf{k},\omega)\overline{k}_3+1]^{-1},$$
$$\overline{Z}(\mathbf{k},\omega)=[Z(\mathbf{k},\omega)/(\rho c)]. \tag{3}$$

The normalized surface impedance $\overline{Z}(\mathbf{k},\omega)$ is a complex quantity that can be expressed in the form

$$\overline{Z}(\mathbf{k},\omega)=\overline{Z}_R(\mathbf{k},\omega)+i\overline{Z}_I(\mathbf{k},\omega), \tag{4}$$

where $\overline{Z}_R$ and $\overline{Z}_I$ are real quantities and for the structural system to be stable it requires that

$$\overline{Z}_R(\mathbf{k},\omega)+\mathrm{Re}\{(\overline{k}_3)^{-1}\}>0. \tag{5}$$

In this connection it is observed, from Eq. (2b), that the normalized surface impedance $(\overline{k}_3)^{-1}$ of the fluid on the plane is either wholly real or wholly imaginary.[17] A real $(\overline{k}_3)^{-1}$ defines the supersonic spectral range; i.e., the range $\gamma<1$, and an imaginary $(\overline{k}_3)^{-1}$ defines the subsonic spectral range, i.e., the range $\gamma>1$. In the vicinity of $\gamma=1$, $|(\overline{k}_3)^{-1}|$ is large, at $\gamma=1$, $|(\overline{k}_3)^{-1}|$ is singularly large. A propagating incidence is commensurate with a normalized surface fluid impedance that is wholly real and, therefore, may be cast in the form

$$[\overline{Z}_1(\mathbf{k},\omega)]^{-1}=\overline{k}_3(\mathbf{k},\omega)=\cos\theta,$$
$$\gamma<1, \quad 0\leqslant\theta<(\pi/2), \tag{6a}$$
$$(\mathbf{k}c/\omega)=\{\sin(\theta)\cos(\phi),\ \sin(\theta)\sin(\phi)\}, \tag{6b}$$

where $\{\theta,\ \phi\}$ is the angular vector of incidence; see Fig. 1.[17] To obtain a substantially negligible specular reflection coefficient; namely,

$$R(\mathbf{k},\omega)=(\mathcal{E}/\sqrt{2})[1+\mathcal{E}+(\mathcal{E}^2/2)]^{-(1/2)}, \quad |\mathcal{E}|\ll 1, \tag{7}$$

the following conditions need to be satisfied simultaneously:

$$\overline{Z}_R(\mathbf{k},\omega)\cos(\theta)=(1+\mathcal{E}), \quad \overline{Z}_I(\mathbf{k},\omega)\cos(\theta)=\mathcal{E}, \quad \gamma<1, \tag{8}$$

where the smallness of $|\mathcal{E}|$, as compared with unity, is yet to be specified. The conditions just stated in Eq. (8) may be satisfied were the mechanical boundary to resonate; the normalized mechanical surface impedance $\overline{Z}(\mathbf{k},\omega)$ in the immediate vicinity of the resonance frequency is largely real. Thus, at resonance the specular reflection coefficient may be necessarily, but not sufficiently, small enough to be considered negligible. A generic mechanical boundary that appropriately admits to a resonance may comprise a panel and a compliant layer with the compliant layer facing the fluid. If the advantages, that the resonance bestows upon this generic boundary, are to be sustained over a wider and wider frequency band, means to maintain the resonance conditions in the boundary, over such a frequency bandwidth, must be devised.

II. NORMALIZED SURFACE IMPEDANCE OF A BOUNDARY COMPRISING A PANEL AND A COMPLIANT LAYER

The elements of a fluid-loaded boundary of this kind are depicted in Fig. 2(a) and the equivalent circuit diagram is shown in Fig. 2(b).[1] An isotropic panel is characterized by the normalized surface impedance

$$\overline{Z}_2(\mathbf{k},\omega)=i\omega\overline{M}\overline{Z}_g(\mathbf{k},\omega)=i(\omega/\omega_c\mathcal{E}_c)\overline{Z}_g(\mathbf{k},\omega),$$
$$\overline{M}=[M/(\rho c)], \tag{9a}$$
$$\overline{Z}_g(\mathbf{k},\omega)=[(1-g)-i\eta],$$
$$\eta=[\eta_2+(g\eta_p)], \tag{9b}$$
$$g=(1+\eta_2^2)(|\mathbf{k}|/k_p)^n$$

and if $n=4$, $k_p^2=(\omega\omega_c/c^2)$,

$$\overline{M}=(1+\eta_2^2)^{-1}\overline{M}_2, \quad \overline{M}_2=[M_2/(\rho c)],$$
$$\mathcal{E}_c=(\omega_c\overline{M})^{-1}, \tag{9c}$$
$$\mathcal{E}_2=(\omega_c\overline{M}_2)^{-1}=(1+\eta_2^2)^{-1}\mathcal{E}_c, \quad \eta=(\eta_2+g\eta_p),$$

where (M_2) is the surface mass, (k_p) is the free wave number, (ω_c) is the critical frequency with respect to the speed of sound (c) in the fluid, $(\mathcal{E}_2)$ is the fluid loading parameter, (n) is the flexural index [(n) is equal either to (2) or (4)], $(g\eta_p)$ and (η_2) are the loss factors associated with the surface stiffness and the surface mass of the panel, respectively, and it is to be understood that the explicit dependence of quantities

and parameters on the vector variable $\{\mathbf{k},\omega\}$ may, at times, be omitted as obvious; e.g., $g=g(\mathbf{k},\omega)$ and $\eta_p=\eta_p(\mathbf{k},\omega)$ in the above equations.[18] For the sake of simplicity the panel is considered to be an isotropic plate so that $(k_pc/\omega)=(\omega_c/\omega)^{1/2}$ and $n=4$ reign. The extension to include orthotropic panels, that are or are not plates, may be readily prescribed when the need arises.[19]

The compliant layer is characterized by the normalized surface impedance

$$\overline{Z}_{12}(\mathbf{k},\omega)=(\overline{K}/i\omega)(1+i\eta_{12}),\quad f=(\overline{K}_{12}/\overline{K}),\quad \omega_1^2=(\overline{K}_{12}/(\overline{M}_{12}), \tag{10a}$$

$$\overline{f}=(\omega/\omega_0)^2 f,\quad \omega_0^2=(\overline{K}_{12}/\overline{M})=\omega_1^2(1+\eta_2^2),\quad \overline{K}_{12}=[K_{12}/(\rho c)], \tag{10b}$$

where, again, the surface impedance of the compliant layer is considered to be isotropic, (K_{12}) is a constant (independent of $\{\mathbf{k},\omega\}$) surface stiffness, (η_{12}) is the loss factor associated with the compliant layer, and (f) is a dimensionless and a real function of the normalized frequency (ω/ω_0); namely, $f=f(\omega/\omega_0)$. The normalizing frequency (ω_0) is defined in Eq. (10). The factor $(f)^{-1}$ is a surface stiffness modification parameter (or simply a modification parameter) that defines the actual surface stiffness (K) of the compliant layer in terms of the constant surface stiffness (K_{12}), again, as defined in Eq. (10). In this context, $(\overline{f})^{-1}$ is termed the modification factor and (f) is, then, the inverse modification factor.

The normalized surface impedance $\overline{Z}\{\mathbf{k},\omega\}$, of the boundary, that is sketched in Fig. 2(a), is

$$\overline{Z}(\mathbf{k},\omega)=\overline{Z}_{12}(\mathbf{k},\omega)\overline{Z}_2(\mathbf{k},\omega)[\overline{Z}_{12}(\mathbf{k},\omega)+\overline{Z}_2(\mathbf{k},\omega)]^{-1}, \tag{11}$$

as can be verified with the help of Fig. 2(b). Substituting Eqs. (4) and (9)–(11) one obtains

$$\overline{Z}(\mathbf{k},\omega)=(i\omega\overline{M})(\overline{Z}_g)(1+i\eta_{12})[(1+i\eta_{12})-\overline{f}\overline{Z}_g]^{-1}, \tag{12a}$$

or equivalently

$$[\overline{Z}_R\cos(\theta)]=B_c(\omega,\theta)[\eta_{12}\overline{f}|\overline{Z}_g|^2+\eta(1+\eta_{12}^2)]/A, \tag{12b}$$

$$[\overline{Z}_I\cos(\theta)]=B_c(\omega,\theta)[(1+\eta_{12}^2)(1-g)-\overline{f}|\overline{Z}_g|^2]/A, \tag{12c}$$

where

$$B_c(\omega,\theta)=(\omega/\omega_c)[\cos(\theta)/\mathcal{E}_c], \tag{13a}$$

$$A=|(1+i\eta_{12})-\overline{f}\overline{Z}_g|^2, \tag{13b1}$$

which, in turn, may be cast either in the form

$$A=[\{1-\overline{f}(1-g)\}^2+\{\eta_{12}\overline{f}\eta\}^2], \tag{13b2}$$

or, equivalently, in the form

$$A=[(1+\eta_{12}^2)+\overline{f}^2|\overline{Z}_g|^2-2\overline{f}\{(1-g)-\eta_{12}\eta\}], \tag{13b3}$$

$$\overline{Z}(\mathbf{k},\omega)=\overline{Z}_R(\mathbf{k},\omega)+i\overline{Z}_I(\mathbf{k},\omega),\quad \overline{Z}_g^*=[(1-g)+i\eta],$$

$$|\overline{Z}_g|^2=[(1-g)^2+\eta^2]. \tag{13c}$$

As already indicated in Eqs. (12b) and (12c) and hereafter, quantities that are dependent on $\{\mathbf{k},\omega\}$, but are to be evaluated in the supersonic range only, are to be stated free of this explicit dependence. Thus, for example,[17]

$$R(\mathbf{k},\omega)\equiv R\{(\omega/c)\sin(\theta)\cos(\phi),(\omega/c)\sin(\theta)\sin(\phi),\omega\}\rightarrow R. \tag{6c}$$

Subjecting Eq. (12) to the conditions stated in Eq. (8) and imposing, in addition, that $\mathcal{E}=0$, one obtains

$$[Z_R\cos(\theta)]_0\rightarrow[B(\omega,\theta)|\overline{Z}_g|^2\{\eta_{12}(1-g)+\eta\}^{-1}]_0=1, \tag{14a}$$

$$[Z_I\cos(\theta)]_0\rightarrow 0,\quad [(1+\eta_{12}^2)(1-g)=\overline{f}|\overline{Z}_g|^2]_0, \tag{14b}$$

$$[A]_0\rightarrow[\overline{f}(1-g)^{-1}\{\eta_{12}(1-g)+\eta\}^2]_0. \tag{14c}$$

The brackets $[\cdots]_0$ evaluate the enclosed quantity with $\mathcal{E}=0$ [cf. Eq. (8)]. Were Eq. (14) satisfied, the specular reflection coefficient R, stated in Eq. (3) with Eq. (6) imposed, would be equal to zero. Thus, Eq. (14) constitutes the design criteria for achieving a boundary of negligible specular reflection coefficient. The boundary of concern is depicted in Fig. 2(a) and its mechanical surface impedance is stated in Eqs. (12) and (13). If Eq. (14) is only nearly satisfied, the specular reflection coefficient R, stated in Eq. (3) with Eq. (6) imposed, would deviate from its value of zero. One may then request that the deviation in $|R|$ does not exceed a predetermined value and request the limits on the parametric variations that would ensure that this predetermined value for $|R|$ would not be exceeded. These parametric variations constitute the design criteria tolerances for the construction of a surface for which the absolute values for the specular reflection coefficient remain tightly bounded within these preset values.

III. DESIGNING A NEGLIGIBLE SPECULAR REFLECTION COEFFICIENT FOR THE BOUNDARY SPECIFIED IN SEC. II

To establish an appropriate connection with Ref. 1 and to duplicate the results thereof, one needs merely conform some of the quantities and parameters to those used in Ref. 1; namely

$$g\rightarrow 0,\quad (g\eta_p)\rightarrow 0,\quad \eta\rightarrow\eta_2,\quad f=1. \tag{15}$$

Substituting Eq. (15) in Eq. (14) one immediately recovers Eq. (30) of Ref. 1. [Erratum: (m) in Eq. (30c) of Ref. 1 should be corrected to read (M_2).] In Ref. 1 it was found that a negligible specular reflections coefficient, under the conditions stated in Eqs. (7) and (15), is achieved for a frequency (ω) that is very nearly equal to (ω_1) and for an angle (θ) defined by the relationship

$$(\omega/\omega_1)^2=(1+\eta_{12}^2),\quad (\overline{K}_{12}/\omega)\cos(\theta)\simeq(\eta_{12}+\eta_2)(1+\eta_{12}^2)^{-1},\quad (\omega\overline{M}_2)\cos(\theta)\simeq(\eta_{12}+\eta_2) \tag{16}$$

[cf. Eq. (30) of Ref. 1].

The purpose of this paper is to examine the parametric values of the boundary that are needed to achieve a negligible specular reflection coefficient over a wider frequency bandwidth and/or a wider angle of incidence than that achieved in Ref. 1. To set the stage it may be useful to assume, again, that the surface impedance of the panel is largely surface mass controlled; namely

$$\overline{Z}_2(\mathbf{k},\omega)\rightarrow i\omega\overline{M}(1-i\eta_2), \quad g\rightarrow 0, \quad g\eta_p\rightarrow 0, \quad \eta\rightarrow\eta_2. \tag{17}$$

Substituting Eq. (17) in Eqs. (12)–(14) yields

$$[Z_R\cos(\theta)]=B_c(\omega,\theta)[\eta_{12}\overline{f}(1+\eta_{12}^2)+\eta_2(1+\eta_{12}^2)]/A, \tag{18a}$$

$$[Z_I\cos(\theta)]=B_c(\omega,\theta)[(1+\eta_{12}^2)-\overline{f}(1+\eta_2^2)]/A, \tag{18b}$$

$$A=[(1+\eta_{12}^2)+(\overline{f})^2(1+\eta_2^2)-2\overline{f}\{1-\eta_{12}\eta_2\}], \tag{18c}$$

$$[Z_R\cos(\theta)]_0=[B_c(\omega,\theta)(1+\eta_2^2)(\eta_{12}+\eta_2)^{-1}]_0=1, \tag{19a}$$

$$[Z_I\cos(\theta)]_0\rightarrow 0, \quad [(1+\eta_{12}^2)=\overline{f}(1+\eta_2^2)]_0, \tag{19b}$$

$$[A]_0\rightarrow[\overline{f}\{(\eta_{12}+\eta_2)\}^2]_0, \quad \overline{Z}_g^*=(1+i\eta_2), \quad |\overline{Z}_g|^2=(1+\eta_2^2). \tag{19c}$$

From Eqs. (9c) and (10b), Eqs. (19a) and (19b) may be cast in the form

$$[(\eta_{12})]_0=[\{B_c(\omega,\theta)(1+\eta_2^2)-\eta_2\}]_0, \tag{20a}$$

$$[(\overline{f})]_0=(1+\eta_2^2)^{-1}\{1+[(\eta_{12})]_0^2\}, \tag{20b}$$

where $B_c(\omega,\theta)$ and (η_2) are stated in Eqs. (13a) and (9), respectively, and, again, $[\cdots]_0$ encloses parameters that are evaluated for negligible specular reflection coefficients. For a given boundary (ω_0/ω_c), $(\mathcal{E}_c)$, and (η_2) are assumed to be specified parameters; the variables in Eq. (20) are then (ω/ω_0) and $[\cos(\theta)]$. The loss factor $[(\eta_{12})]_0$ and the inverse modification factor $[(\overline{f})]_0$ are depicted, as functions of (ω/ω_0) and $[\cos(\theta)]$, for several values of (ω_0/ω_c), $(\mathcal{E}_c)$ and (η_2), in Figs. 3 and 4, respectively. For checking purposes, the corresponding absolute values of the specular reflection coefficients $[|R\{(\omega/\omega_0),\ \cos(\theta)\}|]_0$, as functions of (ω/ω_0) and $[\cos(\theta)]$, are depicted in Fig. 5. Figures 3–5 clearly demonstrate that extended regions in which values of $[(\eta_{12})]_0$ and $[(\overline{f})]_0$ can be found and that these values indeed yield, in these extended regions, negligible specular reflection coefficients; $[R]_0\rightarrow 0$. Moreover, Eq. (20b) shows that a constraint exists between the inverse modification factor $[(\overline{f})]_0$ and the loss factor $[(\eta_{12})]_0$. This constraint, which is fundamental to achieving a boundary of negligible specular reflection coefficient, is depicted in Fig. 6 for two values of (η_2); $\eta_2=10^{-2}$ and 10^{-1}. In addition, Eq. (20) states that a boundary of negligible reflection coefficient requires the loss factor $[(\eta_{12})]_0$ to be linearly dependent on the normalized frequency (ω/ω_0) and on the angular function $[\cos(\theta)]$. In this connection one realizes that the damping of the boundary is contributed by both, the damping in the panel, as measured by (η_2), and in the compliant layer, as measured by (η_{12}). The combined loss factor $(\eta_{12}+\eta_2)$ may exceed the loss factor necessary to achieve a negligible reflection coefficient. In such a case one may be required to introduce a component in the loss factor that is negative. This requirement cannot be achieved passively. Then, to achieve a negligible specular reflections coefficient, a call for an active control surface impedance may become mandatory.

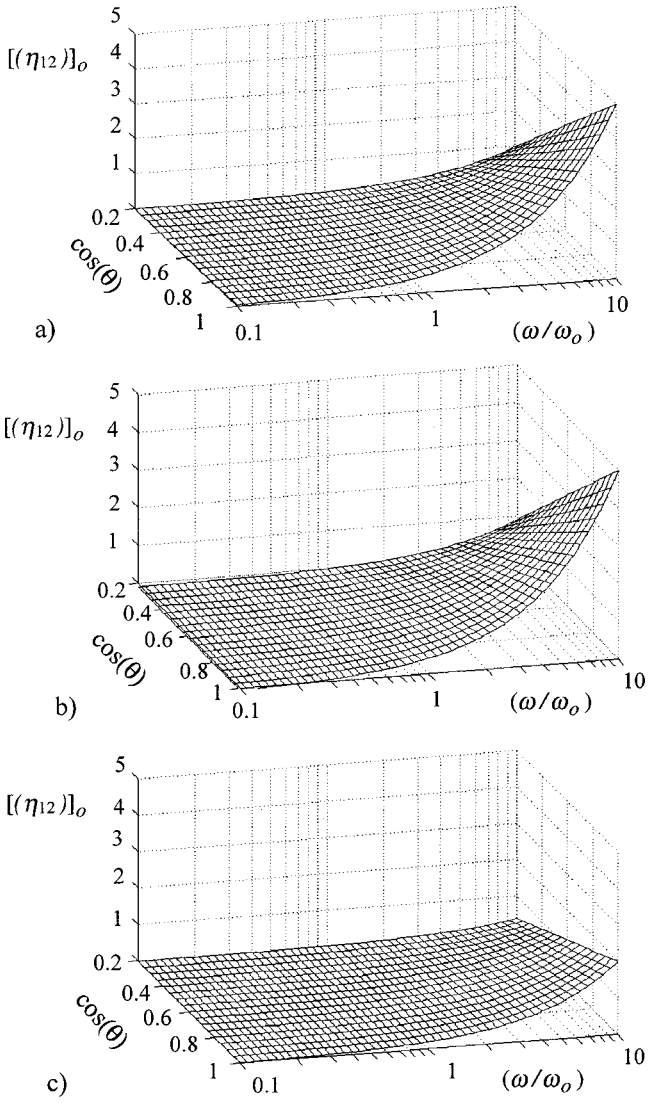

FIG. 3. The loss factor $[(\eta_{12})]_0$ as a function of (ω/ω_0) and $\cos(\theta)$: (a) $(\omega_0/\omega_c)=(1/20)$, $\eta_2=10^{-2}$; (b) $(\omega_0/\omega_c)=(1/20)$, $\eta_2=10^{-1}$; (c) $(\omega_0/\omega_c)=(1/50)$, $\eta_2=10^{-2}$.

Although the surface stiffness modification factor $[(\overline{f})^{-1}]_0$ is a natural quantity in the analysis, data relating to the surface stiffness of the compliant layer is often cast in terms of (K) or equivalently $(K_{12})^{-1}(K)$. It may, therefore, be of interest to exhibit, at least once, the surface stiffness in terms of the modification parameter $[(f)^{-1}]_0$. For this purpose a portion of Eq. (10) is recalled in the form

$$\{f(\omega/\omega_0)\}^{-1}=(K_{12})^{-1}K(\omega/\omega_0), \tag{21a}$$

$$[\{f(\omega/\omega_0)\}^{-1}]_0=(K_{12})^{-1}[K(\omega/\omega_0)]_0, \tag{21b}$$

where K_{12} is a constant independent of frequency. Again, using Eq. (20), the dependence of the modification parameter $[(f)^{-1}]_0$, and hence the dependence of the surface stiffness $[(K)]_0$, on (ω/ω_0) and $[\cos(\theta)]$ is depicted in Fig. 7 [cf. Fig. 4]. Figure 7 shows that in the lower range of the loss factor

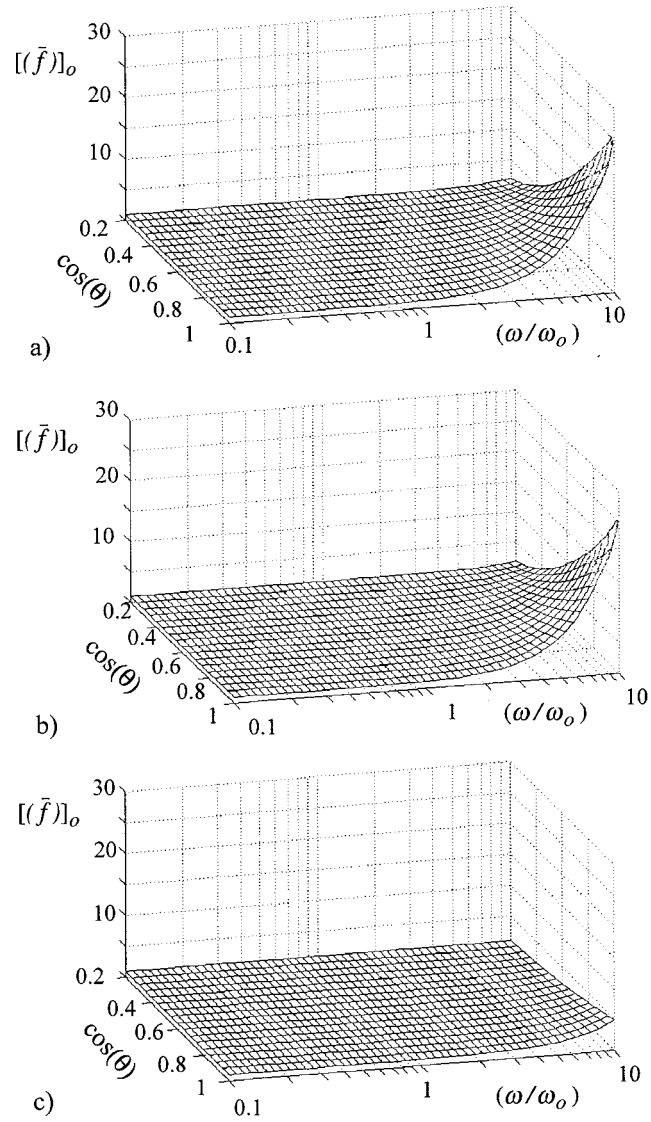

FIG. 4. The inverse modification factor $[(\bar{f})]_0$ as a function of (ω/ω_0) and $\cos(\theta)$: (a) $(\omega_0/\omega_c)=(1/20)$, $\eta_2=10^{-2}$; (b) $(\omega_0/\omega_c)=(1/20)$, $\eta_2=10^{-1}$; (c) $(\omega_0/\omega_c)=(1/50)$, $\eta_2=10^{-2}$.

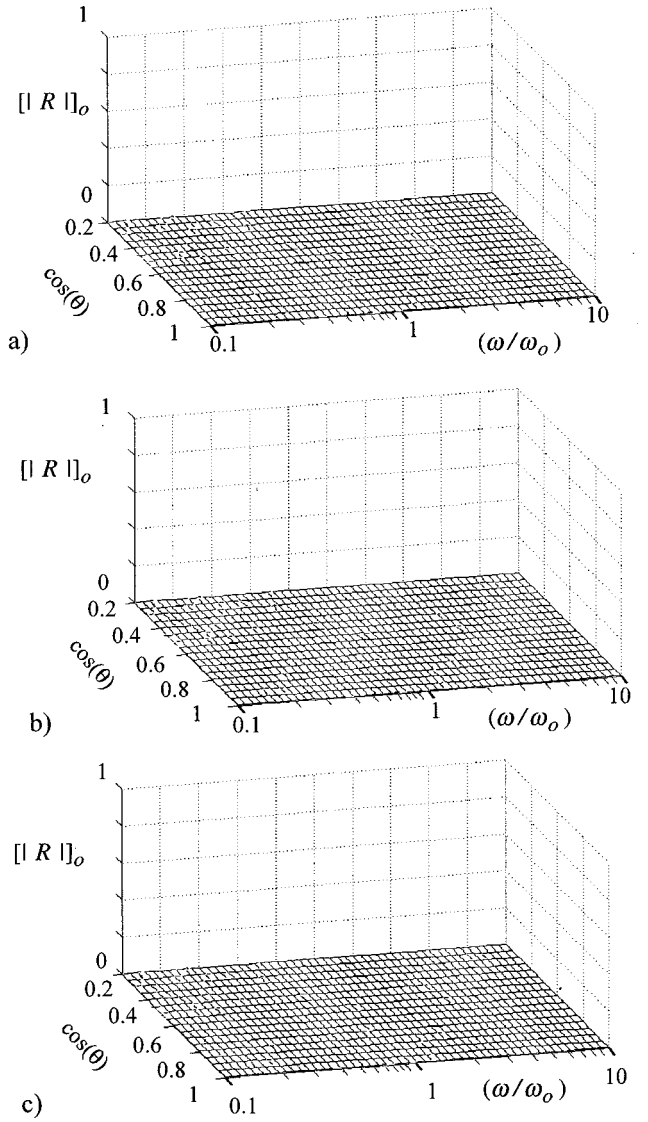

FIG. 5. The specular reflection coefficient $[|R|]_0$ as a function of (ω/ω_0) and $\cos(\theta)$: (a) $(\omega_0/\omega_c)=(1/20)$, $\eta_2=10^{-2}$; (b) $(\omega_0/\omega_c)=(1/20)$, $\eta_2=10^{-1}$; (c) $(\omega_0/\omega_c)=(1/50)$, $\eta_2=10^{-2}$.

in the compliant layer; i.e., when $[(\eta_{12})]_0 \leqslant (1/2)$, $[(f)^{-1}]_0$ is quadradically dependent on the normalized frequency (ω/ω_0) and is largely independent of the angular function $[\cos(\theta)]$ (cf. Fig. 3). As the loss factor $[(\eta_{12})]_0$ increases into the higher range; i.e., when $[(\eta_{12})]_0 \geqslant (3/2)$, the modification parameter $[(f)^{-1}]_0$ becomes asymptotically independent of the normalized frequency (ω/ω_0), but becomes inversely proportional to $[\cos^2(\theta)]$. Whether, the data exhibited in Fig. 6 and/or Fig. 7 may constitute a practical proposition, lies, however, beyond the scope of the present paper. Here it is assumed that all data are analytically acceptable.

IV. VARIATIONS OF $[(\eta_{12})]_0$ AND OF $[(\bar{f})]_0$

Although a negligible specular reflection coefficient may be a design goal, often achieving an absolute value for the specular reflection coefficient that is small compared with unity may suffice. Indeed, for many practical purposes a $|R|(=|R(\mathbf{k},\omega)|$ that lies in the supersonic range, where $\gamma=(|\mathbf{k}|c/\omega)<1)$ that is less than one third is satisfactory enough. The extreme of this value indicates and absorption of 90% of the incident spectral density. Of course, the limits on the variation in $|R|$ may be practically induced by the inability to meet the prescribed values of the loss factor $[(\eta_{12})]_0$ and the inverse modification factor $[(\bar{f})]_0$. Using Eqs. (18) and (19) one may derive relationships between the values of $|R|$ and the proportional variations of $[(\eta_{12})]_0$ and of $[(\bar{f})]_0$. These variations and relationships are readily derived to be

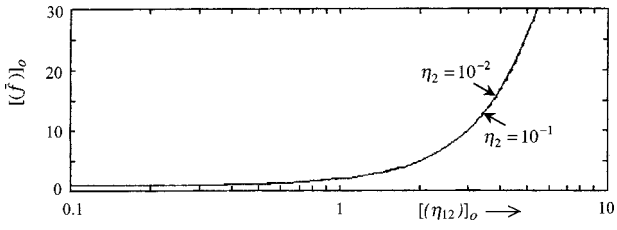

FIG. 6. The relationship between $[(\eta_{12})]_0$ and $[(\bar{f})]_0$ curves for $\eta_2=10^{-2}$ and 10^{-1} are largely indistinguishable.

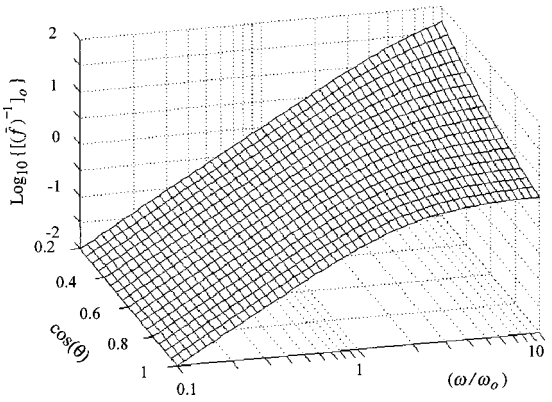

FIG. 7. The modification parameter $[(f)^{-1}]_0$ as a function of (ω/ω_0) and $\cos(\theta)$.

$$[(\eta_{12})^{-1}]_0\Delta(\eta_{12}) = \pm 2|R|[1+(\eta_2/\eta_{12})]_0 \times\{[1+2\eta_{12}\eta_2)^{-1}]_0^2 + [2\eta_{12}(1+\eta_{12}^2)^{-1}]_0^2\}^{-(1/2)}, \quad (22a)$$

$$[(\bar{f})^{-1}]_0\Delta(\bar{f}) \equiv [(\bar{f})]_0\Delta(\bar{f})^{-1} = \pm 2|R|[1+(\eta_2/\eta_{12})]_0 \times\{[\eta_{12}^2(1+\eta_{12}^2)^{-1}]_0\}^{1/2}, \quad (22b)$$

where (Δ) designates a variation in the quantity on which it operates. In Figs. 8 and 9 the ratios $\{|R|[\eta_{12}]_0\}^{-1}\Delta(\eta_{12})$ and $\{|R|[(f)]_0\}^{-1}\Delta(f)$ are depicted as functions of $[(\eta_{12})]_0$ and of $[(f)]_0$, respectively, for values of (η_2) equal to 10^{-2} and to 10^{-1}. It is immediately clear from Figs. 8 and 9 that when $[(\eta_{12})]_0 \leqslant 1$ or equivalently when $[(\bar{f})]_0 = [(1+\eta_{12}^2)]_0(1+\eta_2^2)^{-1} \leqslant 2$, the permissible variations of $[(\eta_{12})]_0$ are much less stringent than those of $[f]_0$, if reasonable low values are to be achieved in the designed $|R|$; $|R|$, again, is the specular reflection coefficient of the generic boundary in the supersonic range of spectral space [cf. Eqs. (3)–(6)]. On the other hand, when $[(\eta_{12})]_0 \geqslant 1$ or equivalently when $[(\bar{f})]_0 = [(1+\eta_{12}^2)]_0(1+\eta_2^2)^{-1} \geqslant 2$, the permissible variations of $[(\eta_{12})]_0$ are comparable to those of $[(\bar{f})]_0$. Moreover, in this range of values the variations of $[(\eta_{12})]_0$ and of $[(\bar{f})]_0$ are comparable to those regarding $|R|$; i.e., if in the supersonic range of spectral space $|R|$ is allowed to reach (1/3), the proportional variations of $[(\eta_{12})]_0$ and of $[(\bar{f})]_0$ are allowed approximately the same reach. The situations just discussed are illustrated in Figs. 10

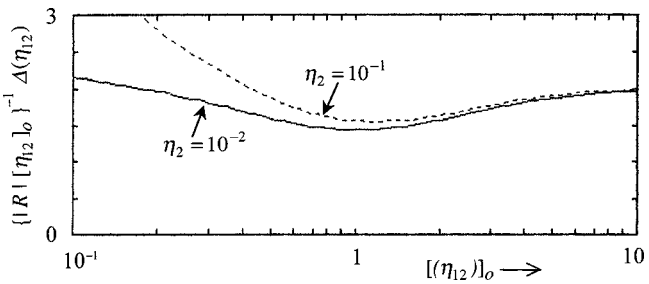

FIG. 8. The allowed normalized variations in (η_{12}) as a function of $[(\eta_{12})]_0$.

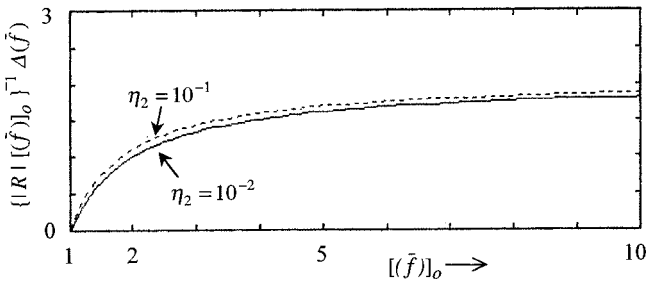

FIG. 9. The allowed normalized variations in $(\bar{f})$ as a function of $[(\bar{f})]_0$.

and 11. In these figures $|R|$ is determined with $(\eta_{12}) = 1.2[(\eta_{12})]_0$ and with $(f) = 1.1[(f)]_0$, respectively. The range in which $|R| < 0.3$ and the range in which $|R| > 0.3$ are separated by a solid line. The variational limits depicted in Figs. 8 and 9 are properly reflective in Figs. 10 and 11, respectively. Whether the maintenance of the parameters $[(\eta_{12})]_0$ and $[(f)]_0$ can be kept within the required limits, in any practical situation designed to sustain $|R| \leqslant 0.3$, is yet to be tested. The elements of the design and the form of the testing are, however, in hand, in part, due to this paper.

V. CONCLUDING REMARKS

In Ref. 1, the sensitivity of $|R|$ to variations in the values of (K_{12}/ω_c) and of (η_{12}) are investigated. In this investigation, $|R|$ is restricted not to exceed (10^{-1}) and $[\mathcal{E}_c/\cos^2(\theta)]$ is maintained at (10^{-1}). The sensitivity of $|R|$ to these variations seems to be supported by the analysis presented in the preceding section. Indeed, both Figs. 5 and 6 of Ref. 1 are so supported by Figs. 10 and 11.

In the same vein, the greater laxity in the sensitivity of the specular reflection coefficient $|R|$ to variations in the values of (η_{12}) as compared to those in the values of (f) is significant to the design process. If one focuses on the limited range in which $[(\eta_{12})]_0 \leqslant 1$ and, therefore, $[(f)]_0 \leqslant 2$, the specification of these parameters becomes strict, especially with respect to the specification of $[(f)]_0$. The tolerances that are imposed, in the design processes, on the value of $[(\eta_{12})]_0$ and, especially, on the value of $[(f)]_0$ that lie within the range of these inequalities may thus become too demanding. Without mentioning specific cases, failure to

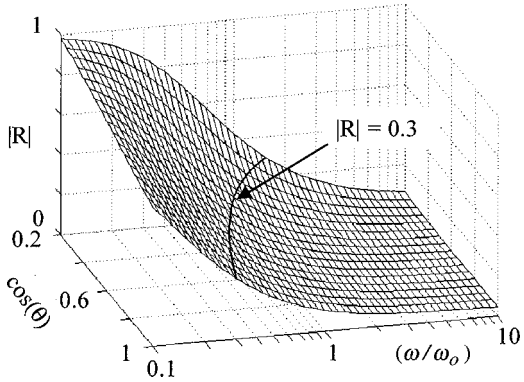

FIG. 10. The specular reflection coefficient $|R|$ as a function of (ω/ω_0) and $\cos(\theta)$ where the inverse modification factor $[(\bar{f})]_0$ is deviated by a 10%; i.e., $[(\bar{f})^{-1}]_0\ \Delta\bar{f} = \pm 0.1$.

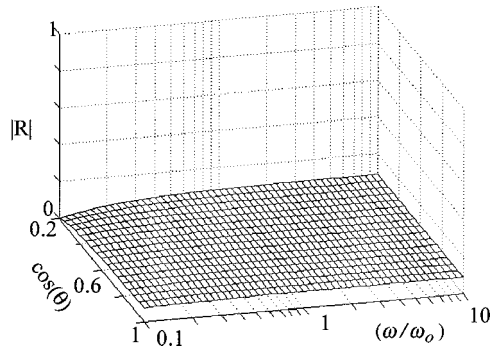

FIG. 11. The specular coefficient $|R|$ as a function of (ω/ω_0) and $\cos(\theta)$ where the loss factor $[(\eta_{12})]_0$ is deviated by 20%; i.e., $[(\eta_{12})^{-1}]_0$, $\Delta\eta_{12} = \pm 0.2$.

meet these kind of values and tolerances have already been encountered.[16] Failure of this type and in this range is caused not only as a result of the overly strict tolerances, but also because the dependence of the modification parameter $[(f)^{-1}]_0$ on the normalized frequency (ω/ω_0) is steep; essentially quadratic. The former is illustrated in Figs. 8 and 9 and the latter in Fig. 7. It appears, therefore, that in trying to design a viable compliant layer, the range defined by the inequality $[(\eta_{12})]_0 \gtrsim 1$ and, therefore, also the inequality $[(f)]_0 \gtrsim 2$, needs to be imposed. In this range, not only are the tolerances more reasonable, but the frequency dependence of the modification parameter is less demanding, notwithstanding that the dependence on $[\cos(\theta)]$ is more severe in this range than in the previous lower range, where $[(\eta_{12})]_0 \lesssim 1$ and $[(f)]_0 \lesssim 2$ [cf. Figs. 7–9 and remarks post Eq. (21)]. Clearly, criteria and tolerances on these criteria, that are involved in the design of a compounded structure for the boundary may follow similar treatments with largely similar conclusions, notwithstanding that more compounded and more complex, but properly designed, boundaries are expected to exhibit more robust sensitivities to variations in the material properties of the elements that compose these boundaries. Nonetheless, it emerges that not only the practical design criteria of the material properties of the elements composing the boundary need to be specified, but an examination of the tolerances on the design criteria must become an integral part of the design process if the desired boundaries are to be achieved in practice.

[1] G. Maidanik and J. Dickey, ''Designing a negligible specular reflection coefficient for a panel with a compliant layer,'' J. Acoust. Soc. Am. **90**, 2139–2145 (1991).

[2] G. Maidanik, ''Power dissipation in a sprung mass attached to a master structure,'' J. Acoust. Soc. Am. **98**, 3527–3533 (1995).

[3] M. Strasberg and D. Feit, ''Vibration damping of large structures induced by attached small resonant substructures,'' J. Acoust. Soc. Am. **99**, 335–344 (1996).

[4] M. J. Brennan, ''Wideband vibration neutralizer,'' Noise Control Eng. J. **45**, 201–207 (1997).

[5] R. Ohayon and C. Soize, *Structural Acoustics and Vibrations* (Academic, San Diego, 1998).

[6] C. Soize, ''Probabilistic structural modeling in linear dynamic analysis of complex mechanical systems,'' Rech. Aerosp. **1986-3**, 23–48 (1986).

[7] G. Maidanik and K. J. Becker, ''Noise control of a master harmonic oscillator that is coupled to a set of satellite harmonic oscillators,'' J. Acoust. Soc. Am. **104**, 2628–2637 (1998).

[8] M. Strasberg, ''Continuous structures as 'fuzzy' substructures,'' J. Acoust. Soc. Am. **100**, 3456–3459 (1996).

[9] M. Strasberg, ''Is the dissipation induced by 'fuzzy' substructures real or apparent,'' J. Acoust. Soc. Am. **102**, 3130 (1997).

[10] T. L. Smith, K. Rao, and I. Dyer, ''Attenuation of plate flexural waves by a layer of dynamic absorbers,'' Noise Control Eng. J. **26**, 56–60 (1986).

[11] G. Maidanik and J. Dickey, ''Singly and regularly ribbed panels,'' J. Sound Vib. **123**, 309–314 (1988).

[12] G. Maidanik and K. J. Becker, ''Characterization of multiple-sprung masses for wideband noise control,'' J. Acoust. Soc. Am. (in press).

[13] R. J. Nagem, I. Velikovic, and G. Sandri, ''Vibration damping by a continuous distribution of undamped oscillators,'' J. Sound Vib. **207**, 429–434 (1997).

[14] Indeed, establishing techniques and mechanisms for implementing a wide frequency band device has been actively pursued; e.g., an implementation of a mechanical boundary that sustains a negligible specular reflection coefficient over a wide frequency band had been proposed and analyzed by Sheiba and Colleagues at EG&G during the late 1980s and early 1990s (Ref. 15). Usually these techniques and mechanisms call upon an elaborate compliant layer that is placed on a basic boundary, a compounded combination of surface stiffnesses and surface masses, and/or, in addition, an inclusion of even nonmechanical elements. On the other hand, a corresponding attempt has been undertaken with respect to dynamic absorbers. In this attempt a number of sprung masses, with a wide distribution of resonance frequencies, replaces the single sprung mass (Refs. 3–13). In an analogous manner, one may then analyze and discuss the implications involved in rendering a noise control device that passively maintains these wider frequency bandwidths. Moreover, one may even address, in this context, as to whether an actively controlled boundary may be devised with the appropriate properties to maintain these wider frequency bandwidths. However, such an esoteric analysis lies outside the scope of the present paper.

[15] L. S. Sheiba and P. A. Wlodkowski, ''Underwater sound coatings design on the basis of non-uniform materials,'' EG&G TR-F028-28 RATLAB, 1995.

[16] J. J. Dlubac (private communication).

[17] A. P. Dowling and J. E. Fowcs Williams, *Sound and Sources of Sound* (Ellis Horwood Limited, Chichester, 1983).

[18] L. Cremer, M. Heckl, and E. Ungar, *Structure-Borne Sound, Structural Vibrations and Sound Radiation at Audio Frequencies*, 2nd ed. (Springer-Verlag, Berlin, 1988).

[19] M. Heckl, ''Untersuchungen an orthotropen platten,'' Acustica **10**, 109–115 (1960) and also G. Maidanik, ''Influence of fluid loading on the radiation from orthotropic plates,'' J. Sound Vib. **3**, 288–299 (1966).

Inversion of penetrable obstacles from far-field data on narrow angular apertures

J. A. Warner
Naval Research Laboratory, Code 7130, 4555 Overlook Avenue, Washington, D.C. 20375-5350

D. N. Ghosh Roy
SFA, Inc., 1401 McCormick Drive, Landover, Maryland 20785

J. Bucaro and L. Couchman
Naval Research Laboratory, Code 7130, 4555 Overlook Avenue, Washington, D.C. 20375-5350

(Received 13 May 1999; revised 12 November 1999; accepted 17 November 1999)

Reported in this paper are reconstructions of shape and material parameters of two-dimensional, homogeneous, acoustic, penetrable obstacles of arbitrary cross-sections which are immersed in an infinite, homogeneous ambience. Reconstructions are based on the far-field scattering patterns of multiple incident plane acoustic waves. For remotely acquired data, practical necessities require not only that the entire data collection region be less than 2π, but also that each received ''sees'' the object over as narrow an angular aperture as possible. The inversions presented here were obtained under such conditions. Two types of data were used for each incidence namely, ''near-monostatic'' fields of narrow angular apertures (the narrowest aperture reported is 2°), and a ''duostatic'' geometry consisting of backscatter plus one other receiver angle. These data sets were acquired for a series of incident angles. The theoretical formalism for inversion is algebraic in nature, requires no integral equation, and possesses a number of advantages for the implementation of a Gauss–Newton type of inversion that was used in this study. Moreover, the algorithm is shown to be inheritently parallelizable. © *2000 Acoustical Society of America.* [S0001-4966(00)00303-9]

PACS numbers: 43.20.Fn, 43.60.Pt, 43.30.Pc, 43.40.Le [DLB]

INTRODUCTION

The inverse problem of recovering a scattering obstacle from the knowledge of the scattered fields is an important problem that occurs frequently in numerous applications in engineering, physics, and mathematics. Both in direct and inverse scattering, two cases must be distinguished, namely, whether the scatterer is an obstacle (i.e., there is a discontinuity in the material parameters) or an inhomogeneity (no discontinuity between the scattering region and the surrounding). The latter case is described by the Lippmann–Schwinger integral equation (Colton and Kress, 1992). On the other hand, scattering, scattering from obstacles is governed by Helmholtz's equation subject to the appropriate boundary data and Sommerfeld's radiation condition at infinity. The boundary data are of two types depending upon whether the wave is totally reflected or undergoes refraction at the boundary. These correspond to the impedance and transmission condition, respectively. There thus arise two types of inverse problems in obstacle scattering. For obstacles with impedance boundary conditions, such as Dirichlet, Neumann, or Robin scatterers, the inverse problem consists of recovering only the boundary of the obstacle (Colton and Kress, 1992; Jones and Mao, 1989; Crostar, 1997). For transmission objects, on the other hand, the inversion is not only for the boundary (Colton and Monk, 1987), but for the material parameters of the scatterer as well. From both practical and realistic viewpoints, the transmission inverse problem is of particular importance. It is this inverse transmission obstacle problem that is addressed in this paper.

In several recent publications (Ghosh Roy *et al.*, 1997, Couchman *et al.*, 1998 and Ghosh Roy *et al.*, 1998), a non-integral equation approach to the solution of the obstacle scattering problem was developed and applied to inversions of penetrable and impenetrable two-dimensional obstacles of various shapes, orientations, and material compositions. The method is a combination of the shape deformation technique and the Padé extrapolation (Kirsch, 1998; Hettlich, 1995; Bruno and Reitich, 1995). The reconstructions reported in these papers were based on data (both near- and far-field) collected over a range of receiver angles with a fixed source (a bistatic measurement). In many applications it is more practical to use a co-located source and receiver to measure backscatter as a function of incident angle (the monostatic case). This paper presents reconstructions based on data collected in backscattering over small angular apertures (a monostatic array). Also considered is a special geometry where, for a given incident wave, the data are collected monostatically and also bistatically by a single second receiver which can be widely separated in angle from the direction of incidence. This is referred to as ''duostatic'' data here.

The analysis presented in this paper applies only to homogeneous obstacles. Its straightforward extension to arbitrarily inhomogeneous scatterers would be difficult. However, the method can be useful for a class of problems which frequently occur in practice. This is comprised of obstacles which possess uniform backgrounds of strong contrast to the ambient (far beyond the range of linearized techniques of

Born or Rytov approximation) with inhomogeneous perturbations superimposed on them. At present, such problems are handled via the distorted-wave Born (DWBA) or Rytov (DWRA) which recover only the perturbations and must perforce assume that the uniform background must be known (Bates *et al.*, 1991). Recall that the linearized techniques depend critically on the assumption that the incident field is not affected by scattering from the perturbations. Assuming the validity of this assumption, the application of the technique presented here would lead to the recovery of the strongly contrasting background. As a result, a DWBA or DWRA can still be applied, but without the need to know the background *a priori*. Finally, it should be pointed out that the method presented here can also be applied to obstacles with homogeneous internal structures. The computations will naturally be more intensive. The degree of the added complexities will depend on the specific problem at hand.

The plan of the article is as follows. Section I describes the basic formalisms which is a modified version of the algorithm presented in Ghosh Roy *et al.* (1998) and leads to faster reconstructions. Also discussed in this section is the parallelizability of the algorithm which can further enhance the speed of inversions. The results of numerical reconstructions are discussed in Sec. II. It is demonstrated that both monostatic array and duostatic data result in excellent reconstructions. (However, the reconstructions are approximately an order of magnitude more computationally intensive than in the bistatic case.) Further details appear later in the text.

I. THE METHOD

Since the details of the method were described in Ghosh Roy *et al.* (1998) it is reviewed here only briefly. The starting point is the decomposition of the scatterer boundary, Γ_{sc}, into an underlying canonical geometry, Γ_c (a circle in two-dimensions), with a deformation $\delta\Gamma$ superimposed on it. This deformation need not be an infinitesimally small perturbation, but can have a magnitude of finite amount. Then

$$\Gamma_{sc}=\Gamma_c+\delta\Gamma=\Gamma_c+\lambda f(\theta), \quad \lambda\in[0,\lambda_0)\subset\mathbf{R}^1.$$

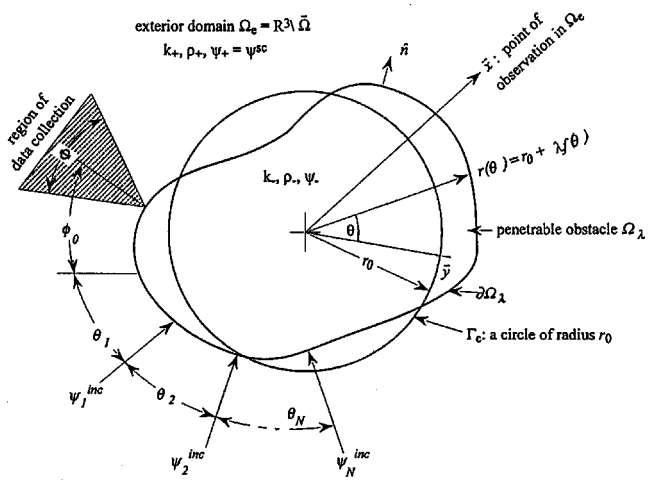

FIG. 1. The geometry of scattering. The scatterer shape is given by $r(\theta)=r_0+\lambda f(\theta)$, $0\leq\theta\leq 2\pi$. $\Phi_0\leq\Phi\leq 2\pi$, $\Phi_0>0$.

$f(\theta)$ is a smooth function of θ, and λ the magnitude of the deformation $\delta\Gamma$. The following Fourier expansions are used:

$$f(\theta)=\sum_{l=-L}^{L} c_{1,l}e^{il\theta} \tag{1}$$

and

$$(f(\theta))^p=\sum_{l=-pL}^{pL} c_{p,l}e^{il\theta}, \quad p\in\mathbf{Z}^+, \tag{2}$$

where the restriction $c_{p,l}=-c_{p,l}^*$, * denoting the complex conjugate, is enforced. For small λ, the scattered field is expanded in a Taylor series around $\lambda=0$, namely

$$\psi_\lambda^{sc}(x;\lambda,\xi)=\sum_{m=0}^{\infty}\tilde{\psi}^{(m)}(x;\xi)\lambda^m, \tag{3}$$

where

$$\tilde{\psi}^{(m)}=\frac{1}{m!}\left(\frac{\partial^m\psi_\lambda^{sc}}{\partial\lambda^m}\right)_{\lambda=0},$$

and $\xi=[\{c_{1,l}\}_{l=-L}^{L},k_-,\rho_-]\in\mathbf{R}^{2L+3}$. Next $\tilde{\psi}^{(m)}$ is expanded as

$$\tilde{\psi}^{(m)}(x;\xi)=\sum_{n=-\infty}^{\infty}\alpha_n^{(m)}(\xi)(-i)^nH_n(k|x|)e^{in\theta}. \tag{4}$$

The actual solution corresponding to λ beyond the radius of convergence of the Taylor series is obtained by extrapolating $\tilde{\psi}^{(m)}$, or what is the same thing, the Taylor series

$$\sum_{m=0}^{\infty}\alpha_n^{(m)}\lambda^m$$

via the Padé approximation (Baker and Graves-Morris, 1984; Ghosh Roy *et al.*, 1997).

Essentially then, the forward problem is to determine $\alpha_n^{(m)}$, $\forall\, m,n$, which are functions of the elements of ξ, that is, the Fourier coefficients of $f(\theta)$ and the material parameters k_- and ρ_- of the obstacle. The inverse problem is to recover the unknown vector ξ itself from the knowledge of the scattered fields. The formalism is next applied to the transmission obstacle problem and is described below.

A. The forward problem

Let us consider scattering from a domain in $\mathbf{R}^2$, that is, a bounded and simply connected region Ω_λ having a boundary $\partial\Omega_\lambda=\partial\Omega_c+\lambda f(\theta)$. The decomposition of the boundary and the geometry of scattering are shown in Fig. 1. The subscripts $+$, $-$ refer to the exterior domain Ω_e and the obstacle Ω_λ, respectively. The mass density ρ_- and the wave number k_- are assumed to remain constant within the obstacle. The BVP for the penetrable obstacle scattering is given by

$$\begin{aligned}&(\Delta+k_+^2)\psi_\lambda^+=0 \quad \text{in } \Omega_{e\lambda},\\ &(\Delta+k_-^2)\psi_\lambda^-=0 \quad \text{in } \Omega_\lambda,\\ &\psi_\lambda^+=\psi_\lambda^- \quad \text{on } \partial\Omega_\lambda,\end{aligned} \tag{5}$$

and

$$\frac{\partial \psi_\lambda^+}{\partial n_\lambda} = C_0 \frac{\partial \psi_\lambda^-}{\partial n_\lambda} \quad \text{on} \quad \partial\Omega_\lambda .$$

In Eq. (5), $C_0 = \rho_+ / \rho_-$ and $\psi_\lambda^+ = \psi_\lambda^{sc} + \psi^{\text{inc}}$ is the total field, $\psi^{\text{inc}} = \exp(ik_+ \hat{k}_+ \cdot x)$ propagating along $\hat{k}_+$.

$\psi_\lambda^\pm$ are expanded as in Eq. (4), the coefficients of expansion being $(\alpha_\pm)_n^{(m)}$. Following the procedures outlined in Ghosh Roy *et al.* (1998) and using Eqs. (1)–(4) in the boundary conditions of the Helmholtz problem Eq. (5), two recursion relations are obtained for two sets of unknowns α_+ and α_-. These are found to be

$$\begin{aligned}
&(\alpha_+)_n^{(m)} H_n(\xi_+) - (\alpha_-)_n^{(m)} J_n(\xi_-) \\
&\quad = -\frac{k_+^m}{m!} \sum_{q=n-mL}^{n+mL} e^{i(n-q)\theta_0} (-i)^{q-n} c_{m,n-q} J_q^{(m)}(\xi_+) \\
&\qquad - \sum_{j=0}^{m-1} \sum_{q=n-(m-j)L}^{n+(m-j)L} (-i)^{q-n} \frac{1}{(m-j)!} c_{m-j,n-q} \\
&\qquad \cdot [(\alpha_+)_q^{(j)} k_+^{m-j} H_q^{(m-j)}(\xi_+) \\
&\qquad - (\alpha_-)_q^{(j)} k_-^{m-j} J_q^{(m-j)}(\xi_-)], \qquad (6)
\end{aligned}$$

and

$$\begin{aligned}
&(\alpha_+)_n^{(m)} k_+ H_n^{(1)}(\xi_+) - (\alpha_-)_n^{(m)} C_0 k_- J_n^{(1)}(\xi_-) \\
&\quad = -\frac{k_+^{m+1}}{m!} \sum_{l=-Lm}^{Lm} e^{i(n-q)\theta_0} (-i)^{-l} c_{m,l} \left\{ J_{n-l}^{(m+1)}(\xi_+) + l(n-l) \frac{d^{(m-1)}}{dr^{m-1}} \frac{J_{n-l}(\xi_+)}{r^2} \right\} \\
&\qquad - \sum_{j=0}^{m-1} \sum_{l=-(m-j)L}^{(m-j)L} (-i)^{-l} c_{m,l} \cdot \left\{ k_+^{m-j+1} (\alpha_+)_{n-l}^{(j)} \left(H_{n-l}^{(m-j+1)}(\xi_+) + l(n-l) \frac{d^{(m-j-1)}}{dr^{m-j-1}} \frac{H_{n-l}}{r^2} \right) \right. \\
&\qquad \left. - C_0 k_-^{m-j+1} (\alpha_-)_{n-l}^{(j)} \left(J_{n-l}^{(m-j+1)}(\xi_-) - l(n-l) \frac{d^{(m-j-1)}}{dr^{m-j-1}} \frac{J_{n-l}(\xi_-)}{r^2} \right) \right\}. \qquad (7)
\end{aligned}$$

J_ν and H_ν in Eqs. (6) and (7) are integer order ordinary Bessel function and Hankel function of the first kind, respectively. Identifies (6) and (7) are the simplified versions of the corresponding expressions [Eqs. (22)–(23)] in Ghosh Roy *et al.* (1998). As pointed out earlier, expansions (3) and (6) give rise to the Taylor series for $\alpha_\pm$, namely

$$A_n^\pm = \sum_{m=0}^{\infty} (\alpha_\pm^{(m)})_n \lambda^m .$$

$A_n^\pm$ is then Padé extrapolated for an arbitrary $\lambda \in [0, \lambda_0)$. If B_n^+ is the Padé extrapolated A_n^+, then the solution to the exterior Helmholtz problem corresponding to Eq. (5) is

$$\psi_+(x) = \sum_{n=-\infty}^{\infty} B_n^+ (-i)^n H_n(k_+ |x|) e^{in\theta}. \qquad (8)$$

B. The inverse problem

The far-field data were inverted for the $(2L+3)$ unknown components of the vector ξ in Eq. (3), namely, the $(2L+1)$ Fourier coefficients $c_{1,l}$, and the material parameters k_- and ρ_-. However, in actual numerics the quantities $k_{\text{ratio}} = k_+ / k_-$ and $\rho_{\text{ratio}} = \rho_+ / \rho_-$ were considered in place of k_- and ρ_-, respectively. Inversions were achieved through a Gauss–Newton iteration scheme using the Levenberg–Marquardt procedures for nonlinear parameter estimation. The objective function minimized was

$$Q = \sum_{i=1}^{I} |\rho_i|^2 . \qquad (9)$$

I is the number of observation points, and ρ_i is the residual at the ith position x_i, namely

$$\rho_i = \psi_p^{sc}(x_i; \xi) - \psi_m^{sc}(x_i; \xi_0).$$

Subscripts p, m indicate predicted and ''measured'' field, respectively. ξ and ξ_0 are the iteratively updated and the true parameter vector, respectively, which are elements in a $(2L+3)$-dimensional Euclidean space as mentioned earlier. ''Measured'' data were obtained from an independent finite element solution. Random noise was added to the data, and no regularization was used.

The Levenberg–Marquardt procedure requires the calculation of the Jacobian J_{sc} of the scattered field. J_{sc} consists of the derivatives of ψ^{sc} with respect to ξ. This is the most computationally intensive part of the calculation, and so the manner in which J_{sc} is calculated is of critical importance. The simplifications introduced by the present method in the determination of the Jacobian matrix was discussed in detail in Couchman *et al.* (1998). The other advantages of the formalism were discussed in Ghosh Roy *et al.* (1998).

C. Parallelization of the algorithm

As can be seen from Eqs. (6) and (7), not only is it true that each incident frequency is completely independent of all the others, but so is each incident angle. This leads directly to a very simple but powerful parallelization of the algorithm whereby a separate processor can be given the task of computing the forward problem (or the Jacobian) for each individual incident wave, be the difference simply the angle of

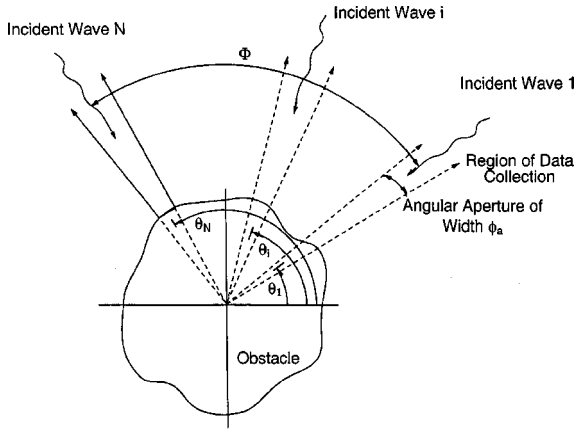

FIG. 2. The geometry of limited-angle, near-monostatic data collection for N number of incident waves. Φ denotes the angular region on which the entire data set corresponding to all N waves is acquired. ϕ_a is the angular aperture of the near-monostatic data for one incidence. At the ith position, $\theta_i = \theta_1 + (i-1)*\theta_0$, θ_0 being the angular interval of scanning. When $N=1$, $\Phi = \phi_a$. For full-circle data, $\Phi = 360°$.

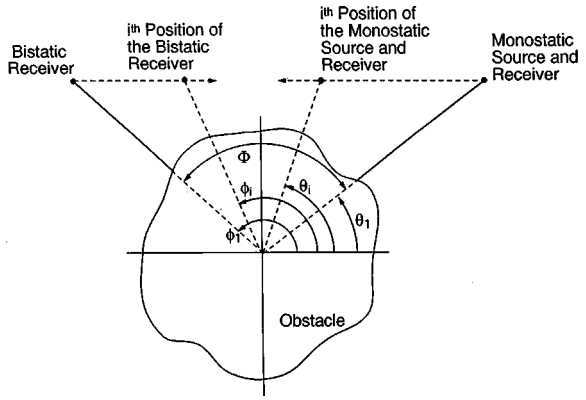

FIG. 3. A schematic of data collection in duostatic configuration. For each incidence, data are acquired simultaneously monostatically and bistatically at a receiver which is angularly separated from the source. The complete data set is acquired by moving the source and the bistatic detector simultaneously. In the ith positions of the source and the bistatic receiver, $\theta_i = \theta_1 + (i-1)*\theta_0$ and $\phi_i = \phi_1 - (i-1)*\theta_0$, θ_0 being the interval at which the detecrots are moved. For full-circle data, $\Phi = 360°$.

incidence and/or the frequency. This simple process has the potential to yield significant wall-clock savings.

In any discussion of parallelization, the question of the volume of interprocess communications (IPC) becomes salient. The IPC comes in two forms: first the communication down to the secondary processes (which do the computations for each incident wave separately), and then the communication back to the primary process. Communication down to the secondary process consists of the problem definition, and includes the components of ξ, along with the incident angle, r_0, and k_+. For a problem with $L=8$, for example, this amounts to 20 real numbers or 160 bytes being sent to each secondary process, a trivial volume of data flow. The calculation of the amount of secondary to primary IPC is slightly more complicated. What each secondary process must calculate are the coefficients necessary to calculate ψ_+. In Eq. (8), the summation for $\psi_+(\mathbf{x})$ is over infinite limits. In practice, however, only definite limits can be imposed on the sum. Given limits of $\pm N$ on the sum, the total amount of data that needs to be transmitted between processes for a forward problem calculation are the $(2N+1)$ complex numbers comprising the full set of the coefficients B_n^+. The largest typical N used in the computations presented here was 15, giving a total of 31 complex numbers or 496 bytes of IPC for each secondary process, a very manageable number.

II. RESULTS AND DISCUSSIONS

The method described above was applied to the reconstructions of a number of penetrable obstacles. Both the boundary as well as the material parameters (ρ_-, k_-) were recovered. The scatterers were assumed to be homogeneous. The reconstructions presented here used multiple incident angles, full-circle, or limited-angle data (see the Introduction) in either monostatic array or duostatic geometry. All reconstructions used far-field data and a total of nine frequencies for each incident angle, ranging from $k_+ = 1.0$ to $k_+ = 5.0$ at even intervals. Figure 2 shows the geometry for acquiring limited-angle monostatic array data, while the corresponding duostatic data collection is schematized in Fig. 3.

In Fig. 2, the angle Φ defines the range of incident angles θ_i, whereas the angle ϕ_a denotes the angle spanned by the receivers of the monostatic array. For the duostatic geometry shown in Fig. 3, two individual receivers are used, one for the monostatic and the other for a single bistatic measurement. These two detectors are moved simultaneously, thereby scanning the entire angle of data collection which can vary between 0° and 360°.

It is interesting to compare the duostatic configuration with that of multiple incidence, bistatic measurement. If M is the number of incident waves, then in the duostatic case, the total number of measurements is simply $2M$. In the bistatic situation, on the other hand, with M incident waves, the total number of data points is MN, N being the number of detectors within the angle of data collection which is assumed to remain constant for each incidence. Thus in order for the duostatic data to possess the same information content as that of the limited-angle, multiple incidence, bistatic data having MN data points, the number of incidence angles M in the duostatic configuration must be $MN/2$. This may involve a large number of incident waves, and consequently, may result in longer inversion times. However, this may be well compensated by the fact that in practice data collection using the duostatic geometry may prove to be much simpler compared to that in the bistatic configuration. Moreover, the parallel nature of the algorithm (discussed in Sec. I C) may be gainfully exploited to enhance the speed of computation.

The ''measured'' data were generated by solving the transmission problem Eq. (5) numerically by the finite-element method (FEM). The FEM solution was then used in the objective function Eq. (9), the minimization of which led to the inverse solution. Calculations were performed on an SGI Indy machine with a 174-MHz R440 CPU.

The inversions were performed for a cloverleaf, a wing shape, and for an asymmetric obstacle. The boundary parameterizations for the cloverleaf and the wing appear in the

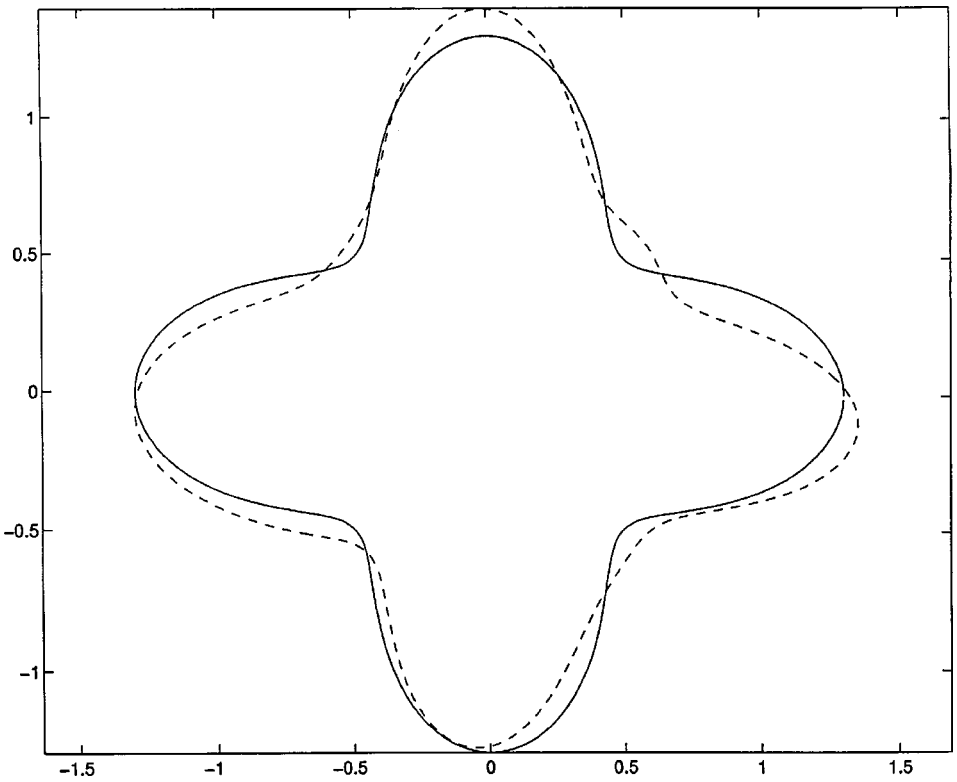

FIG. 4. Reconstruction of a cloverleaf from near-monostatic data (2° aperture). True $k_{\text{ratio}}=2.0$ and true $\rho_{\text{ratio}}=0.5$. Recovered $k_{\text{ratio}}=1.985$ and recovered $\rho_{\text{ratio}}=0.522$. The highest order Padé Approximant used was [6/6]. The cloverleaf shape is given by $r(\theta)=1.0+0.3\cos(4\theta)$. Frequencies used were $k_{+}=1.0$ through 5.0.

figure captions, whereas the structure of the third scatterer is shown separately in the inset in Fig. 6. The results are shown in Figs. 4–10, in which the true and reconstructed shapes and values of k_{ratio} and ρ_{ratio} are compared. (Unless otherwise specified, the true shape is given by the solid line, and the reconstructed shape is given by the dashed line.) Also shown in the figures are the highest orders of the Padé approximants used. The underlying canonical geometry Γ_c was assumed to be a circle of radius $r_0=1$, and the starting guesses for k_{ratio} and ρ_{ratio} were set to be unity (i.e., the material parameters of the scatterer were equal to those of the ambient medium). All the obstacles considered here were parameterized by 17 Fou-

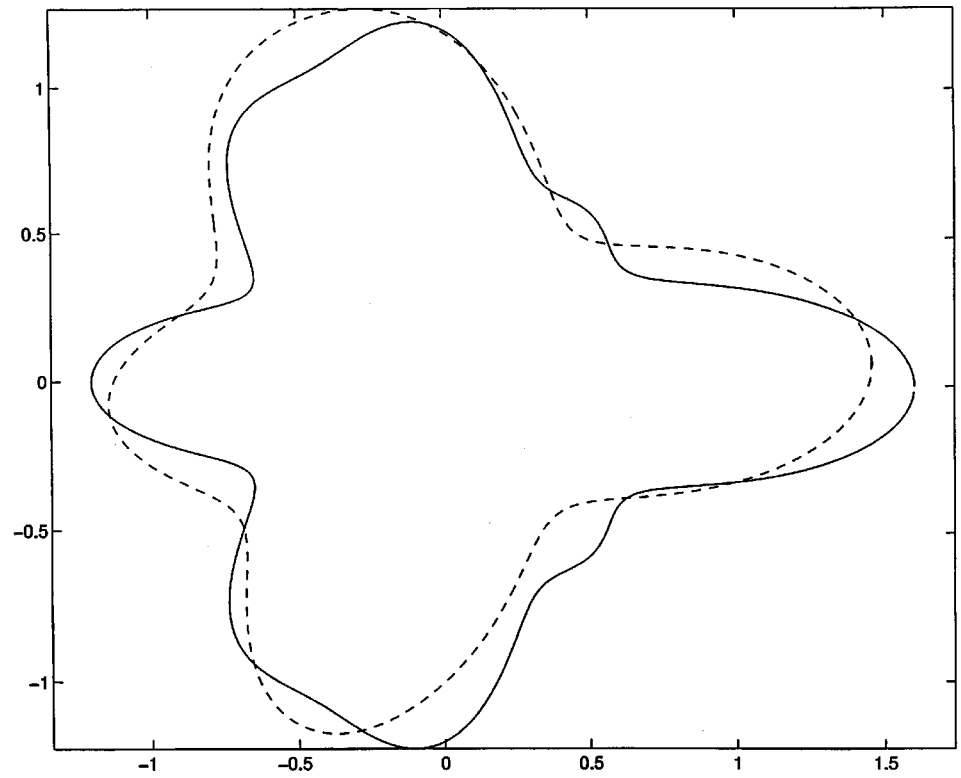

FIG. 5. Reconstruction of a wing from near-monostatic data (4° aperture). True $k_{\text{ratio}}=2.0$ and true $\rho_{\text{ratio}}=0.5$. Recovered $k_{\text{ratio}}=1.999$ and recovered $\rho_{\text{ratio}}=0.518$. The highest order Padé Approximant used was [6/6]. The wing shape is given by $r(\theta)=1.0+0.2\cos(3\theta)+0.2\cos(4\theta)+0.1\times\cos(6\theta)+0.1\cos(8\theta)$. Frequencies used were $k_{+}=1.0$ through 5.0.

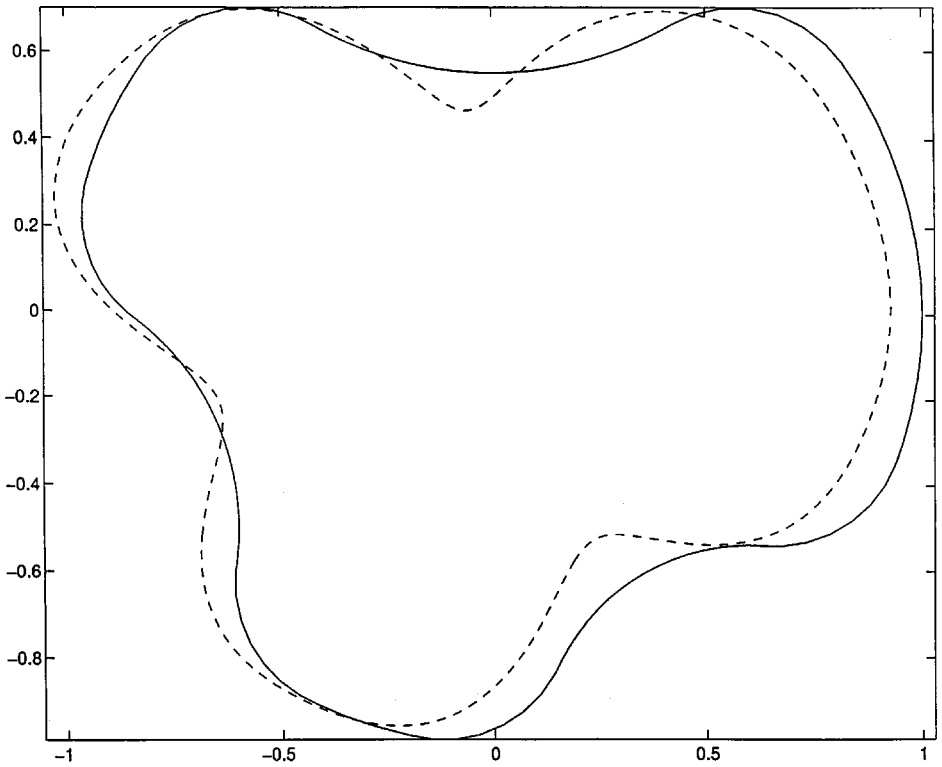

FIG. 6. Reconstruction of an asymmetric figure from near-monostatic data (2° aperture). True $k_{\text{ratio}}=2.0$ and true $\rho_{\text{ratio}}=0.5$. Recovered $k_{\text{ratio}}=2.102$ and recovered $\rho_{\text{ratio}}=0.526$. The highest order Padé Approximant used was [6/6]. Frequencies used were $k_+=1.0$ through 5.0.

rier coefficients, so that a total of 19 unknown parameters were recovered.

Figures 4–8 depict reconstructions from near-monostatic data. Figure 4 shows the reconstruction of the cloverleaf using a 2° angular aperture (the data collection configuration as in Fig. 2), where there insonification occurred only along the upper edge of the figure. A total of 25 incident angles were used between 20° and 140° (with respect to the positive x-axis) at equal intervals of 5°. That is, in reference to Fig. 2, $\theta_1=20°$, $\theta_N=140°$, $\theta_0=5°$, and $\phi_a=2°$. The reconstruction of the wing using 4° wedges of data (i.e., $\phi_a=4°$) taken at 10° intervals ($\theta_0=10°$) around the full circle (i.e., 36 incident waves and $\theta_N=360°$) is shown in Fig. 5. Figure 6 shows the reconstruction of the asymmetric body also using a full-circle, 36 incident angles, but with an aperture of 2°. These apertures appear to be the

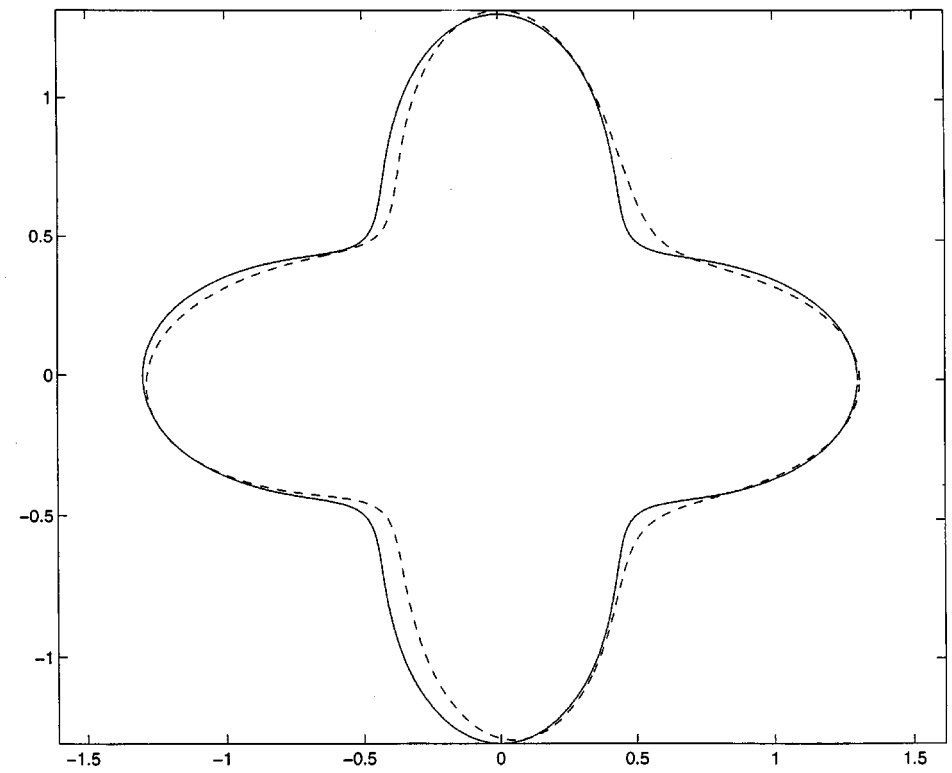

FIG. 7. Reconstruction of a cloverleaf from near-monostatic data (10° aperture). True $k_{\text{ratio}}=2.0$ and true $\rho_{\text{ratio}}=0.5$. Recovered $k_{\text{ratio}}=1.954$ and recovered $\rho_{\text{ratio}}=0.506$. The highest order Padé Approximant used was [6/6]. The cloverleaf shape is given by $r(\theta)=1.0+0.3\cos(4\theta)$. Frequencies used were $k_+=1.0$ through 5.0.

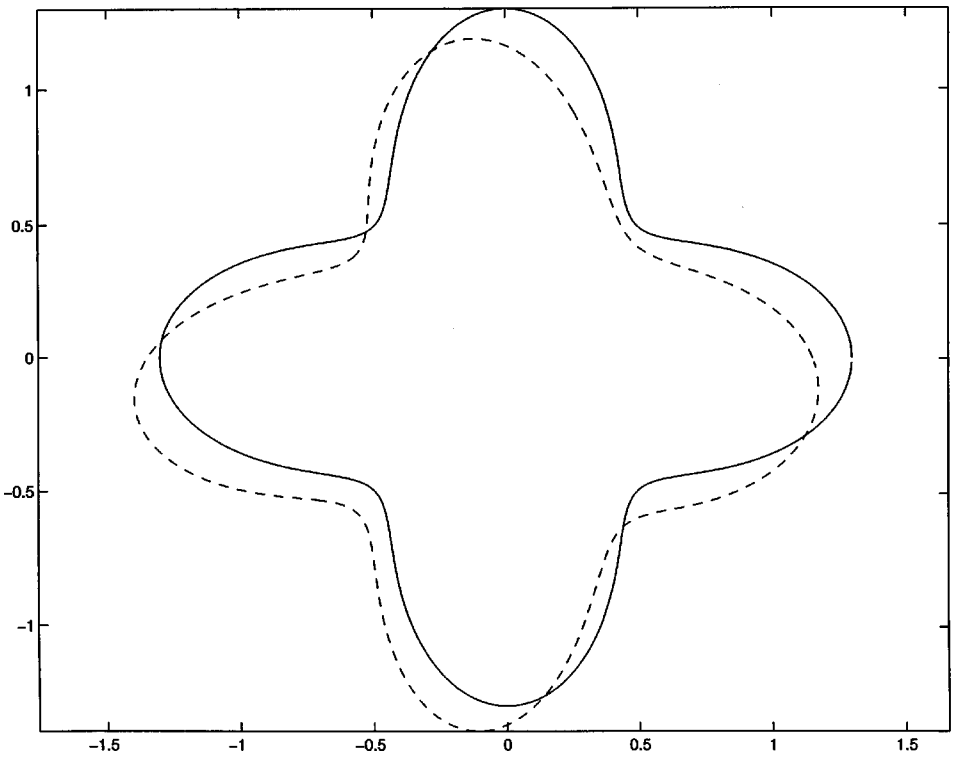

FIG. 8. Reconstruction of a cloverleaf from near-monostatic data (2° aperture). True $k_{\text{ratio}}=2.5$ and true $\rho_{\text{ratio}}=0.250$. Recovered $k_{\text{ratio}}=2.411$ and recovered $\rho_{\text{ratio}}=0.298$. The highest order Padé Approximant used was [6/6]. The cloverleaf shape is given by $r(\theta)=1.0+0.3\cos(4\theta)$. Frequencies used were $k_+=1.0$ through 5.0.

minimum possible for which satisfactory resolutions could still be obtained. Increasing the aperture, of course, improved the accuracy of the reconstructions. For the sake of illustration, the reconstruction of the cloverleaf using 10° aperture data (with all other parameters remaining the same) is shown in Fig. 7. Additional incident waves were also beneficial, but the improvements were not as dramatic. To further illustrate the robustness of our algorithm, we reconstructed the cloverleaf shape using 2° data wedges taken at 15° intervals around the full circle (i.e., $\phi_a=2°$, with 24 incident waves and $\theta_N=360°$), but this time with different material parameters than we used before. The results is shown in Fig. 8. A comparison of Figs. 4 and 8 shows that they give substantially the same result, notwithstanding markedly different values of the material constants.

Figures 9–12 show reconstructions of the same shapes

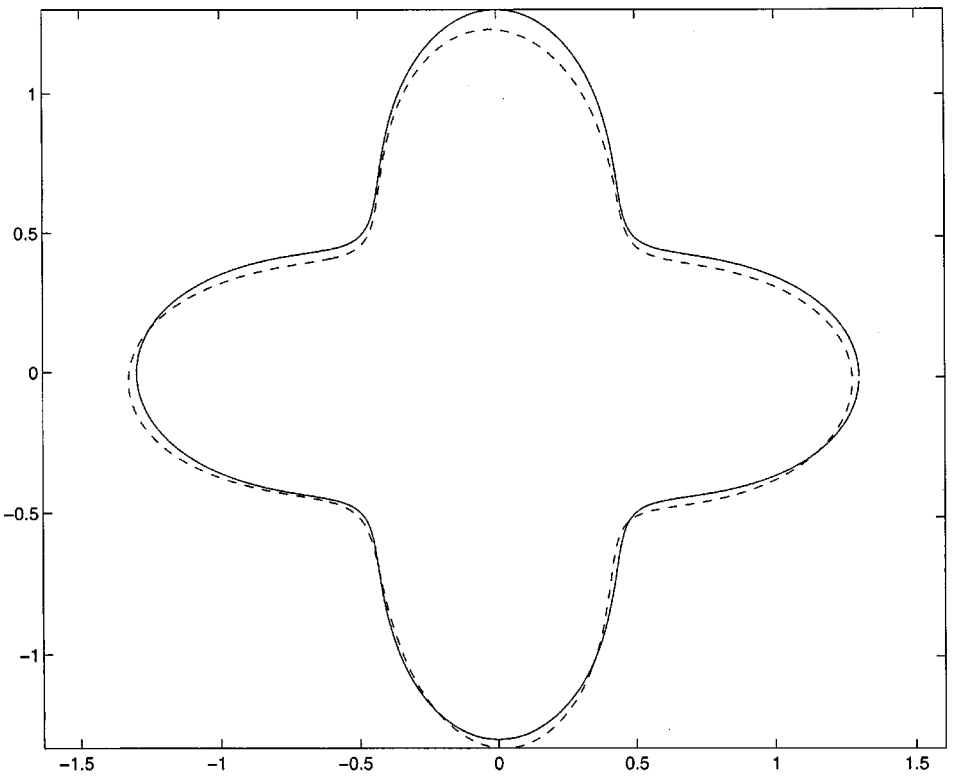

FIG. 9. Reconstruction of a cloverleaf from duostatic data. True $k_{\text{ratio}}=2.0$ and true $\rho_{\text{ratio}}=0.5$. Recovered $k_{\text{ratio}}=2.003$ and recovered $\rho_{\text{ratio}}=0.491$. The highest order Padé Approximant used was [6/6]. The cloverleaf shape is given by $r(\theta)=1.0+0.3\cos(4\theta)$. Frequencies used were $k_+=1.0$ through 5.0.

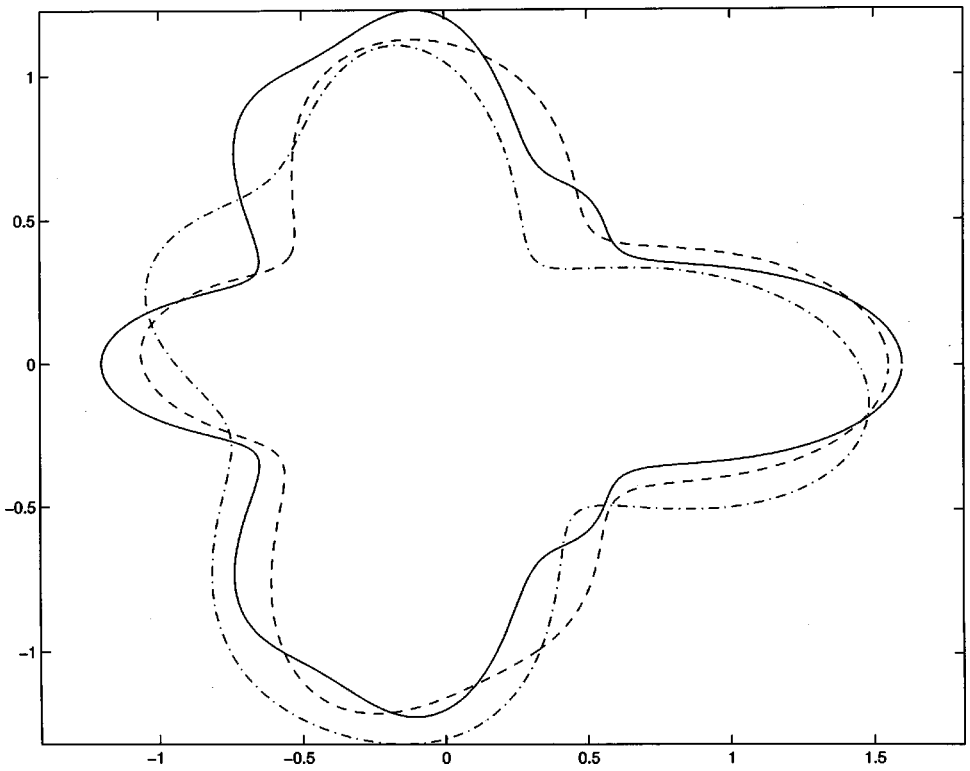

FIG. 10. Reconstruction of a wing from duostatic data. True $k_{\text{ratio}}=2.0$ and true $\rho_{\text{ratio}}=0.5$. Recovered $k_{\text{ratio}}=1.976$ and recovered $\rho_{\text{ratio}}=0.527$ (dashed line). Recovered $k_{\text{ratio}}=2.074$ and recovered $\rho_{\text{ratio}}=0.503$ (dash-dot line). The highest order Padé Approximant used was [6/6]. The wing shape is given by $r(\theta)=1.0+0.2\cos(3\theta)+0.2\cos(4\theta)+0.1\times\cos(6\theta)+0.1\cos(8\theta)$. Frequencies used were $k_+=1.0$ through 5.0.

from the duostatic data. Figure 9 shows the reconstruction of the cloverleaf where, as in the near-monostatic case, the insonification occurred only across the upper portion of the figure, again using incident angles (θ_i in Fig. 3) between 20° and 140° from the positive x-axis. Duostatic data were collected every 5° (i.e., $\theta_0=5°$) within this range. Thus comparing to Fig. 3, for the 140° incident wave (θ_1 in Fig. 3 is 140°), data were collected monostatically at 140° and bistatically at 20° (ϕ_1); for the 135° incident wave (θ_2), data were collected monostatically at 135° and bistatically at 25° (ϕ_2), and so on. The reconstruction of the wing (Fig. 10) was done in two ways. First (dashed line), we used 24 incident angles taken every 15° ($\theta_0=15°$) around the body, with the second data point collected at similar intervals, but in the opposite direction. That is, for the 0° incident wave ($\theta_1=0°$), data were collected at 0° and 345° (i.e., $\phi_1=345°$), for the 15° incidence, the corresponding data collection angles were 15° and 330°, and so on. Second (dash-dot line), for purposes of

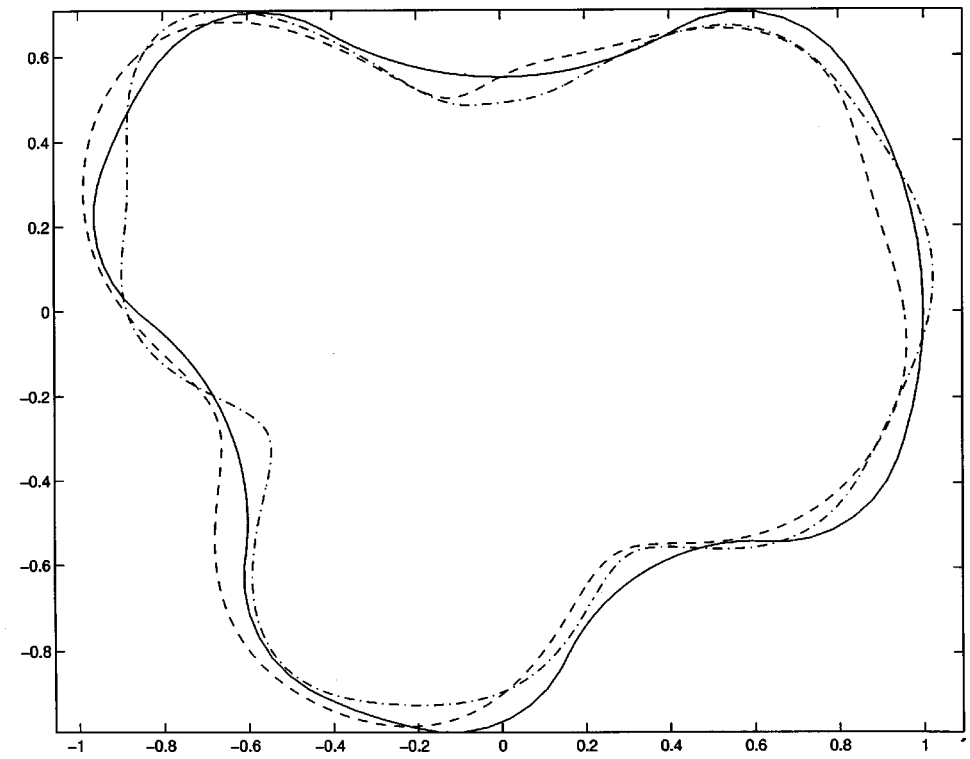

FIG. 11. Reconstruction of an asymmetric figure from duostatic data. True $k_{\text{ratio}}=2.0$ and true $\rho_{\text{ratio}}=0.5$. Recovered $k_{\text{ratio}}=2.062$ and recovered $\rho_{\text{ratio}}=0.542$ (dashed line). Recovered $k_{\text{ratio}}=2.131$ and recovered $\rho_{\text{ratio}}=0.545$ (dash-dot line). The highest order Padé Approximant used was [6/6]. Frequencies used were $k_+=1.0$ through 5.0.

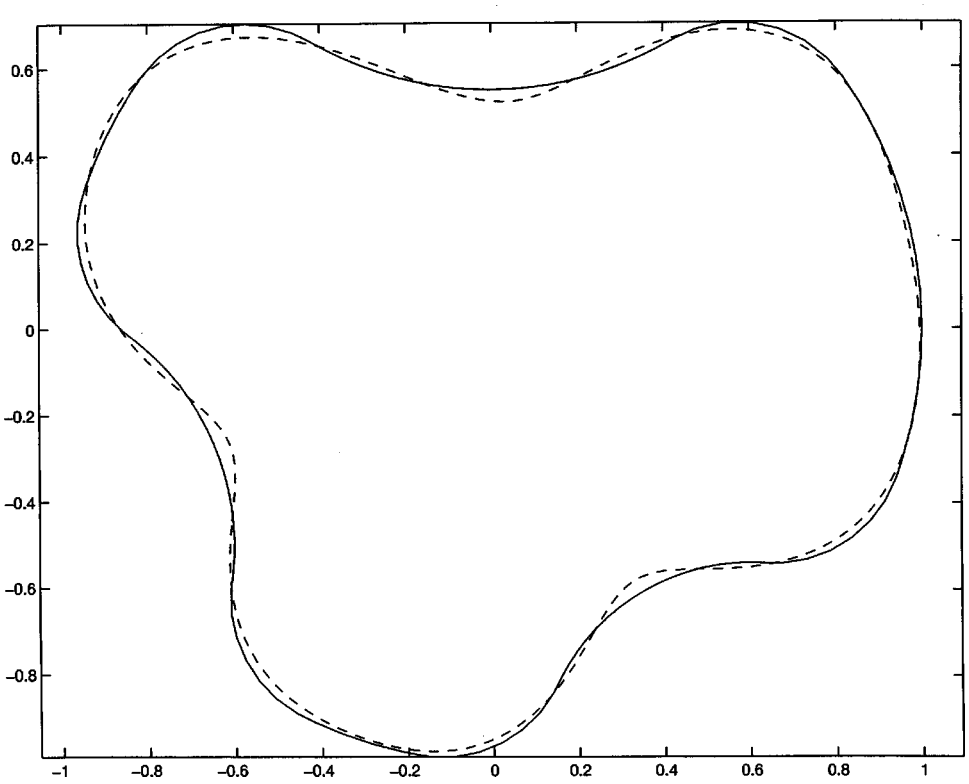

FIG. 12. Reconstruction of an asymmetric figure from duostatic data. True $k_{\text{ratio}}=2.5$ and true $\rho_{\text{ratio}}=0.333$. Recovered $k_{\text{ratio}}=2.634$ and recovered $\rho_{\text{ratio}}=0.338$. The highest order Padé Approximant used was [6/6]. Frequencies used were $k_+=1.0$ through 5.0.

comparison, we used the same data configuration as was used for the cloverleaf reconstruction in Fig. 9. In comparing the two reconstructions, we note the marked decrease in accuracy when using the limited aperture data in this case. The asymmetric shape was also reconstructed using two different data configurations (Fig. 11). First (dashed line), we used 36 incident waves taken every 10° around the body, again with the second data point collected at similar intervals but in the opposite direction, as just described. Second (dash-dot line), for purposes of comparison, we again used the same data configuration as was used for the cloverleaf reconstruction in Fig. 9. In comparing the two reconstructions, we see that in this case the accuracy when using the limited aperture data is comparable to that of the full circle data. As an added example of the method's capabilities, Fig. 12 shows the reconstruction of the asymmetric shape, using the same data configuration as outlined for Fig. 11, but this time the obstacle had different material parameters, more dissimilar to those of the ambient medium than in the previous case. A comparison of the two figures shows that this reconstructed shape is even closer to the true value than the other, with reporting of the material properties of the scatterer extremely accurate. As can be appreciated from the reconstructions reported, the near-monostatic as well as the duostatic data yield more than satisfactory recovery of penetrable acoustic targets from the far-field patterns.

III. SUMMARY

In summary, reconstructions of homogeneous, acoustic, penetrable obstacles in an infinite, homogeneous ambience from the far-field patterns of incident plane acoustic waves in two space dimensions are reported. Both the shape and the material parameters of the scatterers were recovered. Data were collected both full-circle and limited-angle configuration. Two types of data were used for inversion, namely, ''near-monostatic'' data of very narrow angular aperture (the narrowest aperture was 2°), and a ''duostatic'' geometry consisting of monostatic and a single bistatic measurement. The reconstructions were found to be more than satisfactory. Finally, it is shown that the algorithm presented here is parallelizable, and hence has the capability of enhancing the speed with which the inversions can be performed.

ACKNOWLEDGMENTS

This work was supported by the Naval Research Laboratory and the Office of Naval Research.

Baker, G. A., and Graves-Morris, P. (**1981**). *Padé Approximants. Part I: Basic Theory* (Addison-Wesley, Reading).

Bates, R. H. T., Smith, V. A., and Murch, R. D. (**1991**). ''Manageable multidimensional inverse scattering theory,'' Phys. Rep. **201**, 185–277.

Bruno, O. P., and Reitich, F. (**1995**). ''A new approach to the solution of problems of scattering by bounded obstacles,'' Int. Soc. Opt. Eng. **2192**, 20–28.

Crosta, G. (**1997**). ''The obstacle reconstruction problem in acoustics: Error analysis of an inversion algorithm set in the subspace of outgoing spherical wave functions,'' Nonlinear Analysis, Theory, Methods, & Applications **30**, 3481–3492.

Colton, D., and Kress, R. (**1992**). *Inverse Acoustic and Electromagnetic Scattering Theory* (Springer, New York).

Colton, D., and Monk, P. (**1987**). ''The inverse scattering problem for time-harmonic acoustic waves in a penetrable medium,'' Quart. J. Mech. Appl. Math. **40**, 189–212.

Couchman, L. S., Ghosh Roy, D. N., and Warner, J. (**1998**). ''Inverse Neumann obstacle problem,'' J. Acoust. Soc. Am. **104**, 2615–2621.

Ghosh Roy, D. N., Couchman, Louise, and Warner, J. (**1997**). ''Scattering and inverse scattering of sound-hard obstacles via shape deformation,'' Inverse Probl. **13**, 585–606.
Ghosh Roy, D. N., Warner, J., Couchman, L. S., and Shirron, J. (**1998**). ''Inverse obstacle transmission problem in acoustics,'' Inverse Probl. **14**, 903–929.
Hettlich, F. (**1995**). ''Frechet derivatives in inverse obstacle scattering,'' Inverse Probl. **11**, 371–382.
Jones, D. S., and Mao, X. Q. (**1989**). ''The inverse problem in hard acoustic scattering,'' Inverse Probl. **5**, 731–748.
Kirsch, A. (**1993**). ''The domain derivative and two applications in inverse scattering theory,'' Inverse Probl. **9**, 81–96.

Acoustic scattering by baffled flexible surfaces: The discrete optical theorem

G. A. Kriegsmann
Department of Mathematical Sciences, Center for Applied Mathematics and Statistics, New Jersey Institute of Technology, Newark, New Jersey 07102

(Received 13 September 1999; revised 13 December 1999; accepted 15 December 1999)

The optical theorem for acoustic scattering by baffled membranes and plates relates the total cross section of the scattered field, the directivity factor in the specular direction, and the energy dissipated by the structure. It is basically a statement of conservation of power. In this paper it is demonstrated that the discrete formulation of these problems, obtained by a Galerkin approximation, exactly satisfies the optical theorem. This discrete relationship holds regardless of the choice of basis functions and the size of the truncated system N. Thus, the adherence of the approximate numerical results to the power conservation law does not necessarily imply its accuracy. © *2000 Acoustical Society of America.* [S0001-4966(00)05103-1]

PACS numbers: 43.20.Fn, 43.40.Fz, 43.40.Rj, 45.10.−b [ANN]

INTRODUCTION

The scattering of a plane, time harmonic acoustic wave by a baffled compact flexible surface, such as a membrane or plate, is a prototypical problem in structural acoustics. It possesses many of the salient physical and mathematical features of scattering by more complex structures, but is more amenable to asymptotic and numerical approximations. In the former camp there are light[1,2] and heavy loading[3] approximations, short wavelength approximations,[4] and impedance approximations,[5,6] all of which decouple the motion of the acoustic fluid from the dynamics of the flexible structure. When the physical parameters of the acoustic fluid and structure do not warrant any of these approximations, then the scattering problem must be resolved numerically by Galerkin methods, finite difference techniques, or finite element methods.

The scattering problem considered here involves the interaction of the incident plane wave with either a membrane or plate. This physical problem has a conservation law which can be recast as an optical theorem[7,8] which relates the total cross section of the scattered field, the directivity factor in the specular direction, and the energy dissipated by losses in the flexible surface. It would be a very desirable feature of the approximate and numerical methods listed above to reproduce this optical theorem. A failure to do so would clearly indicate a deficiency in the method. However, as has been shown in other scattering problems, the adherence of a method to this conservation law does not imply accuracy.[9,10]

In this note it will be shown that any Galerkin approximation to the scattering problem, not necessarily using normal modes, will exactly satisfy the optical theorem. This adherence is completely independent of the choice of basis functions and of the order of approximation. Thus, for this problem too, satisfying the optical theorem is no indication of the accuracy of the approximation.

The remainder of this paper will now be outlined. The scattering problem will be outlined in Sec. I for both the membrane and plate. A new derivation of the optical theorem will be presented in Sec. II. Unlike previous derivations given for two-dimensional[8] and three-dimensional[7] cases, no stationary phase methods are employed. The present derivation sets the stage for Sec. III in which the optical theorem is proved for any Galerkin approximation.

I. FORMULATION

A plane time harmonic acoustic wave impinges upon a compact flexible surface, such as a membrane or plate, which is set into an infinite, rigid baffle that coincides with the plane $z=0$. The resulting total pressure $P(\mathbf{x})$ in the region $z>0$ satisfies the Helmholtz equation

$$\nabla^2 P + k^2 P = 0, \tag{1a}$$

where $k=\omega L/c_0$, ω is the frequency of the excitation, c_0 is the sound speed in $z>0$, and L is a nominal measure of the size of the flexible structure, such as its maximal diameter. The region below the baffle and structure, $z<0$, is taken to be a vacuum.

The total pressure is given by

$$P = P^I(x,y,z,\phi_I) + P^I(x,y,-z,\phi_I) + P^S(x,y,z), \tag{1b}$$

$$P^I(x,y,z,\phi^I) = e^{ik(y\sin\phi^I - z\cos\phi^I)}, \tag{1c}$$

where the first term in (1b) is the incident plane wave, the second is the specularly reflected wave from the plane $z=0$, and the third is the scattered field caused by the presence of the flexible surface. These pressures and the independent variables are dimensionless, having been normalized by the amplitude of the incident wave and L, respectively. In addition, the unit vector in the propagation direction of the incident wave is defined by $\mathbf{e}_I=(0,\sin\phi^I,-\cos\phi^I)$, where, without loss of generality, $\mathbf{e}_I$ is orientated to be orthogonal to the x axis. The total field satisfies the boundary condition

$$\frac{\partial}{\partial z}P(x,y,0)=0, \quad (x,y)\notin\Omega, \tag{2a}$$

where Ω is the region occupied by the flexible surface and B is its boundary.

Since the sum of the incident and specularly reflected waves satisfies (2a) on the entire plane $z=0$, it follows from (1b) that

$$\frac{\partial}{\partial z}P^S(x,y,0)=0, \quad (x,y)\notin\Omega, \tag{2b}$$

and

$$\frac{\partial}{\partial z}P(x,y,0)=\frac{\partial}{\partial z}P^S(x,y,0), \quad (x,y)\in\Omega. \tag{2c}$$

In addition, the scattered field satisfies the far field condition

$$P^S(\mathbf{x})=A(\mathbf{e}_I,\hat{\mathbf{r}})\frac{e^{ikr}}{r}+O(1/r^2), \quad r\gg 1, \tag{3}$$

where the directivity factor A depends upon the propagation direction $\mathbf{e}_I$ and the observation direction $\hat{\mathbf{r}}\equiv\mathbf{x}/r$. A time factor of $e^{-i\omega t}$ has been assumed so that P^S is an outgoing wave at infinity.

The flexible surfaces to be considered here are membranes and plates. The displacement of the former satisfies

$$L_m w\equiv\nabla_0^2 w+k^2c^2w=\frac{L^2}{T}P(x,y,0),$$
$$(x,y)\in\Omega; \quad w=0, \quad (x,y)\in B, \tag{4a}$$

where ∇_0^2 is the Laplace operator in the $x-y$ plane, while the displacement of the latter satisfies

$$L_p w\equiv\nabla_0^4 w-k^2b^2w$$
$$=-\frac{L^4}{D}P(x,y,0),$$
$$(x,y)\in\Omega; \quad w=\mathbf{n}\cdot\nabla w=0, \quad (x,y)\in B, \tag{4b}$$

where $\mathbf{n}$ is the outward pointing unit normal to B. The parameters in (4a) are defined by $c=c_0/c_m$, $c_m=(T/\rho_m)^{1/2}$, ρ_m is the density per unit area of the membrane and T is the tension applied to the membrane. Similarly, the parameters in (4b) are defined by $b=c_0/c_p$, $c_p=(D/\rho_p hL^2)^{1/2}$, $D=Eh^3/12(1-\nu^2)$, h is the thickness of the plate, ν is Poisson's ratio, E is Young's modulus, and ρ_p is the density of the plate. The boundary condition in (4b) implies the plate is clamped; pinned plates can also be considered.

In addition to satisfying Eqs. (1)–(4), the pressure in the acoustic fluid and the displacement of the flexible surface are connected by the boundary condition

$$\frac{\partial}{\partial z}P(x,y,0)=L\omega^2\rho_0 w(x,y), \quad (x,y)\in\Omega, \tag{5a}$$

where ρ_0 is the density of the acoustic fluid in the region $z>0$. This is just the statement that the vertical velocities of the fluid and flexible surface are continuous. Equation (2c) can be used to simplify (5a) to

$$\frac{\partial}{\partial z}P^S(x,y,0)=L\omega^2\rho_0 w(x,y), \quad (x,y)\in\Omega. \tag{5b}$$

This boundary condition along with a standard Green's function argument gives the scattered pressure in the acoustic fluid as

$$P^S(x,y,z)=\frac{L\omega^2\rho_0}{2\pi}\int\int_\Omega w(x',y')\frac{e^{ik\rho}}{\rho}dx'\,dy', \tag{6a}$$

$$\rho=\sqrt{(x-x')^2+(y-y')^2+z^2}. \tag{6b}$$

Finally, the boundary value problem (1)–(5) can be recast as an integral-differential equation for the displacement w alone. This follows by inserting (1b) into (4) and using (6a), all evaluated at $z=0$; the result is

$$L_l w=F_l\left[2P^I(x,y,0)+\frac{L\omega^2\rho_0}{2\pi}\right.$$
$$\left.\times\int\int_\Omega w(x',y')\frac{e^{ik\tau}}{\tau}dx'\,dy'\right], \tag{7a}$$

$$\tau=\sqrt{(x-x')^2+(y-y')^2}, \tag{7b}$$

where $l=m$ and $F_m=L^2/T$ correspond to the membrane, and $l=p$ and $F_p=-L^4/D$ to the plate. The displacement still satisfies the corresponding boundary conditions in (4a) and (4b), respectively.

II. THE OPTICAL THEOREM

In this section the optical theorem is derived in a slightly different manner than presented in Ref. 7. The present derivation does not use the method of stationary phase, as will now be shown.

The first step begins by observing that both P^S and its complex conjugate P^{S*} satisfy (1a). It then follows in the usual manner that $\nabla\cdot(P^{S*}\nabla P^S-P^S\nabla P^{S*})=0$. Integrating this relationship in the hemispherical region $\{z>0,r\leqslant R\}$, where $R\gg 1$, using the divergence theorem, (2b), and (3), it is readily deduced that

$$k\sigma^T=\mathrm{Im}\left\{\int\int_\Omega P^{S*}(x',y',0)\frac{\partial}{\partial z}P^S(x',y',0)\,dx'\,dy'\right\}, \tag{8a}$$

$$\sigma^T\equiv\int_0^{2\pi}\int_0^{\pi/2}|A|^2\sin\theta\,d\theta\,d\phi, \tag{8b}$$

where Im denotes the imaginary part of a complex number and $|\ |$ its modulus. The parameter σ^T is the total cross section of the scattered pressure P^S.

The second step commences by approximating (6a) in the far field, $r\gg 1$, using the law of cosines, and recalling the definition of A in (3). The result is

$$A(\mathbf{e}_I,\hat{\mathbf{r}})=\frac{L\omega^2\rho_0}{2\pi}\int\int_\Omega w(x',y')e^{-ik\mathbf{x}'\cdot\hat{\mathbf{r}}}dx'\,dy', \tag{9a}$$

where $\mathbf{x}'=(x',y',0)$. Evaluating this expression for $\hat{\mathbf{r}}=\mathbf{e}_R=(0,\sin\phi^I,\cos\phi^I)$, namely in the specularly reflected direction, and recalling the definition of the incident pressure (1c), it follows that

$$A(\mathbf{e}_I,\mathbf{e}_R)=\frac{L\omega^2\rho_0}{2\pi}\times\int\int_\Omega w(x',y')P^{*I}(x',y',0)\,dx'\,dy'. \tag{9b}$$

The third step begins by inserting (5b) into (8a) to yield the total cross section in terms of P^{S*} and w. Then, the imaginary part of (9b) is combined with this expression and (1b) to give

$$k\sigma^T+4\pi\,\mathrm{Im}\{A(\mathbf{e}_I,\mathbf{e}_R)\}=L\omega^2\rho_0\,\mathrm{Im}\left\{\int\int_\Omega w(x',y')P^*(x',y',0)\,dx'\,dy'\right\}, \tag{10}$$

where $P(x',y',0)$ is the total pressure on the flexible surface.

The final step begins, in the case of the membrane, by taking the complex conjugate of (4a), multiplying it by w, and integrating the resulting expression over Ω. Applying Green's theorem and the boundary condition on B yields the result

$$\int\int_\Omega[k^2c^{*2}|w|^2-|\nabla_0 w|^2\,dx\,dy=F_m\int\int_\Omega wP^*\,dx\,dy, \tag{11a}$$

from which it follows by taking the imaginary part of this equation,

$$\mathrm{Im}\left\{\int\int_\Omega wP^*\,dx\,dy\right\}=\frac{k^2\,\mathrm{Im}(c^{*2})}{F_m}\int\int_\Omega|w|^2\,dx\,dy. \tag{11b}$$

Here $\mathrm{Im}(c^{*2})\geqslant 0$, which allows for loss in the structure and the right-hand side of (11b) is just that loss. A similar analysis shows that (11b) also holds for the plate with F_m replaced by F_p and $\mathrm{Im}(c^{*2})$ by $-\mathrm{Im}(b^{*2})$. Then, for either flexible surface the optical theorem is obtained by inserting this result into (10) to obtain

$$k\sigma^T+4\pi\,\mathrm{Im}\{A(\mathbf{e}_I,\mathbf{e}_R)\}=\frac{k^2L\omega^2\rho_0\,\mathrm{Im}(\nu^2)}{F_l}\times\int\int_\Omega|w|^2\,dx\,dy, \tag{12}$$

where $\nu^2=c^{*2}$ for the membrane and $-b^{*2}$ for the plate.

In closing this section there are two things to note. The first is the lack of stationary phase arguments required to derive (12). The replacement step was the application to the law of cosines on (6) to obtain (9a) from which (9b) followed. Second, and perhaps more importantly, it follows from Eq. (10) that a necessary and sufficient condition for the optical theorem to hold is just (11b). This observation will be used in the next section.

III. THE GALERKIN APPROXIMATION: THE DISCRETE OPTICAL THEOREM

The Galerkin method is a standard procedure for obtaining approximate solutions to the integral differential equation (7) for either membranes or plates.[11,12] This technique yields an approximation of the surface displacement from which an approximation to the scattered field is obtained from (6). It will be demonstrated that the directivity factor of this approximate scattered field exactly satisfies the optical theorem (12).

The first step is to introduce a set of basis functions $\{\psi_n\}$ that are sufficiently smooth, independent, and each satisfying the boundary condition $\psi_n=0$ on B for the membrane and $\psi_n=\mathbf{n}\cdot\nabla\psi_n=0$ on B for the plate. These functions need not be the eigenfunctions for the structure in a vacuum. The approximate displacement is taken to be

$$w_N=\sum_{n=1}^{N}\alpha_n\psi_n, \tag{13}$$

where $N>1$ is a fixed integer and the amplitudes α_n are to be determined. This expression is then substituted into (7) to yield

$$L_l w_N=F_l\left\{2P^I(x,y,0)+\frac{L\omega^2\rho_0}{2\pi}\times\int\int_\Omega w_N(x',y')\frac{e^{ik\tau}}{\tau}dx'\,dy'\right\}+R_l^N(x,y), \tag{14}$$

where R_l^N denotes the residual error made by the approximation (13) and again $l=m$ corresponds to the membrane and $l=p$ to the plate. By requiring that this residual error is orthogonal to each of the ψ_j, i.e.,

$$\int\int_\Omega R_l^N(x,y)\psi_j^*\,dx\,dy=0,\quad j=1,2,\ldots,N, \tag{15}$$

a set of N linear equations is obtained for the α_n. These can be solved and along with (13) give the desired approximation to the displacement.

In the next step the approximate displacement w_N is inserted into (6) to give the approximate scattered field P_N^S. This field satisfies (1a) and the boundary conditions (2b) and (5b), with w replaced by w_N, by virtue of the properties of the kernel function in (6a). Denoting by A_N the directivity factor of P_N^S and σ_N^T the corresponding total cross section, it follows by arguments, identical to those of the previous section, that

$$k\sigma_N^T+4\pi\,\mathrm{Im}\{A_N(\mathbf{e}_I,\mathbf{e}_R)\}=L\omega^2\rho_0\,\mathrm{Im}\left\{\int\int_\Omega w_N(x,y)P_N^*(x,y,0)\,dx\,dy\right\}, \tag{16a}$$

$$\sigma_N^T\equiv\int_0^{2\pi}\int_0^{\pi/2}|A_N|^2\sin\theta\,d\theta\,d\phi, \tag{16b}$$

where $P_N^*=2P^{*I}(x,y,0)+P_N^{S*}$.

The final step is now to show that the right-hand side of (16a) is the corresponding approximate energy loss of the

flexible surface. This is readily deduced from (14) and (15) as follows. Rewriting the complex conjugate of (14), for the membrane, as

$$\nabla_0^2 w_N^* + k^2 c^{*2} w_N^* = F_m P_N^* + R_l^{*N}, \tag{17a}$$

multiplying it by w_N, integrating the result over Ω, and applying Green's theorem gives the analog of (11a),

$$\int \int_\Omega [k^2 c^{*2} |w_N|^2 - |\nabla_0 w_N|^2 \, dx \, dy$$

$$= F_m \int \int_\Omega w_N P_N^* \, dx \, dy + \int \int_\Omega R_l^{*N} w_N \, dx \, dy. \tag{17b}$$

Then, taking the imaginary part of this equation and applying (13) gives

$$F_m \operatorname{Im}\left\{ \int \int_\Omega w_N P_N^* \, dx \, dy \right\} - k^2 \operatorname{Im}(c^{*2}) \int \int_\Omega |w_N|^2 \, dx \, dy$$

$$= -\sum_{n=0}^{N} \alpha_n \left\{ \int \int_\Omega R_l^{*N} \psi_n \, dx \, dy \right\}. \tag{18a}$$

Taking the complex conjugate of (15) implies the right-hand side of (18) vanishes and thus,

$$\operatorname{Im}\left\{ \int \int_\Omega w_N P_N^* \, dx \, dy \right\} = \frac{k^2 \operatorname{Im}(c^{*2})}{F_m} \int \int_\Omega |w_N|^2 \, dx \, dy. \tag{18b}$$

The same result holds for the plate with F_m replaced by F_p and c^{*2}, by $-b^{*2}$.

Finally, inserting (18b) into (16a) yields the relationship

$$k \sigma_N^T + 4\pi \operatorname{Im}\{A_N(\mathbf{e}_I, \mathbf{e}_R)\} = \frac{k^2 L \omega^2 \rho_0 \operatorname{Im}(\nu^2)}{F_l} \times \int \int_\Omega |w_N|^2 \, dx \, dy, \tag{19}$$

which is the desired result. This relationship is identical in form and content to the optical theorem given by Eq. (12). It holds for any choice of basis functions $\{\psi_n\}$, as long as they are sufficiently smooth and satisfy the appropriate boundary conditions on B, and any order of approximation N. Thus, the fact that the Galerkin approximation satisfies the discrete optical theorem (19) is no indication of its accuracy. Rather, Eq. (19) should be interpreted as a condition which should be met by any viable candidate for an approximation.

IV. EXTENSIONS

The results of the preceding sections hold when a rigid cup is placed beneath the flexible surface with its edge in perfect contact with the baffle. This forms a resonator whose only access to the acoustic fluid in the region $z>0$ is through the flexible surface Ω. The cavity can be filled with a different lossless acoustic fluid having density ρ_c and sound speed c_c. The only difference in the preceding formulation is the addition of an extra term, due to the additional acoustic fluid in the cavity, in the total pressure on the flexible structure. The arguments follow along almost identical paths. The results are identical with A, now the directivity factor of the flexible surface-cavity-baffle system.

Similarly, the results of the preceding sections hold when the region $z<0$ under the baffled structure is filled with a different lossless acoustic fluid of density ρ_1 and sound speed c_1. The only slight modification is that the total cross section defined in (8b) is replaced by

$$\hat{\sigma}^T = \int_0^{2\pi} \int_0^{\pi} \eta(\theta) |A|^2 \sin\theta \, d\theta \, d\phi, \tag{20a}$$

$$\eta(\theta) = \begin{cases} 1, & 0 < \theta < \pi/2, \\ c_0 \rho_1 / c_1 \rho_0, & \pi/2 < \theta < \pi, \end{cases} \tag{20b}$$

and a similar expression for the approximation $\hat{\sigma}_N^T$.

Finally, it should be noted that optical theorems have been proved for several interesting and important related problems. Several authors have considered acoustic scattering by an infinite flexible plate or planar shell with a compact inclusion, such as a rib support or variable density,[8,13–16] and have derived expressions analogous to (8b). When fluid loading is neglected,[14] the scattering is initiated by a flexural wave and the compact obstacle produces an outgoing cylindrical wave on the surface of the plate. The cross section of this wave also satisfies an analogous optical theorem. In addition, the acoustic scattering by a rigid obstacle above an infinite plate has also been recently studied;[8,15] there a result similar to (8b) is proved.

Although Galerkin methods were not used in these problems, it seems plausible that they will preserve the optical theorems derived therein. Indeed this would be an interesting sequence of calculations to perform and is the topic of ongoing research.

ACKNOWLEDGMENTS

This work was supported by the Air Force Office of Scientific Research under Grant No. AFOSR F49620-94-1-0338.

[1] F. G. Leppington, ''Scattering of sound waves by finite membranes and plates near resonance,'' Q. J. Mech. Appl. Math. **29**, 527–546 (1976).

[2] G. A. Kriegsmann, A. N. Norris, and E. L. Reiss, ''Acoustic scattering by baffled membranes,'' J. Acoust. Soc. Am. **75**, 685–691 (1984).

[3] I. D. Abrahams, ''Scattering of sound by a heavily loaded finite plate,'' Proc. R. Soc. London, Ser. A **378**, 89–117 (1981).

[4] B. P. Belinskiy, ''The integral equations of stationary problems on the diffraction of short waves at obstacles of the segment type,'' J. Comput. Math. Math. Phys. **13**, 125–140 (1973).

[5] G. A. Kriegsmann and C. L. Scandrett, ''Assessment of a new radiation damping model for structural acoustic interactions,'' J. Acoust. Soc. Am. **86**, 788–794 (1989).

[6] T. L. Geers, ''Doubly asymptotic approximations for transient motion of submerged plates,'' J. Acoust. Soc. Am. **64**, 1500–1508 (1978).

[7] G. A. Kriegsmann, A. N. Norris, and E. L. Reiss, ''An optical theorem for acoustic scattering by baffled flexible surfaces,'' J. Sound Vib. **99**, 301–307 (1985).

[8] B. P. Belinskiy and D. P. Kouzov, ''The optical theorem for the plate-liquid system,'' Sov. Phys. Acoust. **26**, 8–11 (1980).

[9] N. Amitay and V. Galindo, ''On energy conservation and the method of moments in scattering problems,'' IEEE Trans. Antennas Propag. **17**, 747–751 (1969).

[10] G. A. Kriegsmann, ''The flanged waveguide antenna: Discrete reciprocity and conservation,'' Wave Motion **29**, 81–95 (1997).
[11] B. E. Sandman and J. Vieira, Jr., ''The experimental and theoretical dynamics of fluid-loaded plates,'' *Proceedings of the 14th MidwesternMechanics Conference*, Vol. 8, pp. 295–311, 1977.
[12] P. M. Morse and K. U. Ingard, *Theoretical Acoustics* (McGraw-Hill, New York, 1968).
[13] B. P. Belinskiy, ''Comments on an optical theorem for acoustic scattering by baffled flexible surfaces,'' J. Sound Vib. **139**, 522–532 (1990).
[14] A. N. Norris and C. Vemula, ''Scattering of flexural waves on thinplates,'' J. Sound Vib. **181**, 115–125 (1995).
[15] Y. P. Guo, ''On sound energy scattered by a rigid body near a compliant surface,'' Proc. R. Soc. London, Ser. A **451**, 543–553 (1995).
[16] I. V. Andromov and B. P. Belinskiy, ''Acoustic scattering on an elastic plate described by the Timoshenko model: Contact conditions and uniqueness of the solution,'' J. Acoust. Soc. Am. **103**, 673–682 (1998).

Effects of thermal diffusion on sound attenuation in evaporating and condensing gas-vapor mixtures in tubes

Craig J. Hickey, Richard Raspet, and William V. Slaton
National Center for Physical Acoustics, University of Mississippi, University, Mississippi 38677

(Received 26 March 1999; accepted for publication 21 October 1999)

An investigation of sound propagation in an air–water vapor mixture contained in a cylindrical tube with wet walls was recently presented [Raspet *et al.*, J. Acoust. Soc. Am. **105**, 65–73 (1999)]. The formulation of the problem paralleled the ''low reduced frequency method'' of Tijdeman [J. Sound Vib. **39**, 1–33 (1975)]. It was pointed out that a term of reduced frequency order had been neglected in the radial component of the diffusion equation [G. Swift, personal communication (1999)]. This term represents the additional mass diffusion driven by the temperature gradient, or Soret effect, and is proportional to the thermal diffusion ratio. The solution for the complex wave number of the acoustic mode with this additional term is presented here. Numerically calculated predictions for the air–water vapor mixture show little change in acoustic attenuation due to the coupling. Therefore, a description of the acoustic attenuation where the viscous, thermal, and diffusion processes are decoupled is adequate for the specific case previously discussed by Raspet *et al.* [J. Acoust. Soc. Am. **105**, 65–73 (1999)]. [S0001-4966(00)01402-8]

PACS numbers: 43.20.Hq, 43.20.Mv [DEC]

INTRODUCTION

In this paper we extend the results of a recent paper[1] which modeled the attenuation of sound in a wet tube filled with an air–water vapor mixture. The model included dissipation of acoustic energy due to diffusion, thermal relaxation, and viscous relaxation. The tube wall was assumed wet so as to allow mass transfer of vapor to and from the wall. Further, it is assumed that the temperature of the tube wall and the layer of liquid do not fluctuate, the air component cannot penetrate the tube wall or the liquid layer, and that the air–vapor mixture does not slip with respect to the liquid layer.

The formulation of the problem paralleled the ''low reduced frequency method'' of Tijdeman.[2] In using this approach, the basic equations governing sound propagation in an ideal air–vapor mixture are recast into cylindrical coordinates. It is assumed that the tubes are sufficiently small that any polar dependence may be ignored. Nondimensional variables in the axial and radial directions are then defined. The reduced frequency is also defined as

$$\Omega = \frac{\omega R}{c}, \tag{1}$$

where ω is the angular frequency, R is the tube radius, and c is the speed of sound in the mixture.

The principal approximation of the ''low reduced frequency method'' is to require that the reduced frequency, Ω, be small. A second criterion requiring that the radial velocity terms be treated as first order in the reduced frequency, Ω, is also imposed to retain terms that would otherwise be neglected. In the previous paper,[1] the resulting equations, Eqs. (22)–(28), were decoupled. The wave number of the acoustic mode was then determined by directly integrating the equations.

Swift pointed out that a term of order Ω in the radial component of the diffusion equation, i.e., Eq. (28), had been neglected.[3] This term represents the thermally assisted mass diffusion, i.e., the Soret effect, and is proportional to the thermal diffusion ratio, k_T. A second term containing k_T expressing diffusion assisted heat flow was retained. Therefore, the effect of diffusion on heat transport was accounted for but the effect of temperature gradients on mass transport was neglected. The thermal diffusion ratio, k_T, is defined by Hirschfelder *et al.*,[4] as a measure of the relative importance of the thermal and ordinary diffusion. The value of the thermal diffusion ratio, k_T, for an air–water vapor mixture is of the O (10^{-4}) at 0 °C and O (10^{-2}) at 100 °C when the ambient air pressure is one atmosphere. It was concluded in the previous paper that the heat flux associated with the diffusion was not a significant contribution to the overall attenuation.

The solution for the acoustic wave number including the Soret effect is presented here. The equations can no longer be integrated directly to obtain an expression for the acoustic wave number because the entropy and diffusion equations are now coupled. The expressions for the dimensionless thermal wave number, λ_T, and the dimensionless diffusion wave number, λ_D, are altered on account of this coupling.

NEW SOLUTION

The principal approximation in the ''low reduced frequency method'' is to require that the reduced frequency be small:

$$\Omega = \frac{\omega R}{c} = \frac{2\pi R}{\lambda} \ll 1. \tag{2}$$

This spans a wide range of frequencies for small tubes and in fact includes regions where the Kirchoff wide tube approxi-

mation holds, as well as the Rayleigh narrow tube/low frequency region. In the analysis of sound propagation in an air–water vapor mixture contained in a cylindrical tube with wet walls a second set of criteria are also used to retain some terms that would otherwise be neglected:

$$u \gg v \tag{3}$$

and

$$v \approx V. \tag{4}$$

The first condition is met since the radial velocity must be zero at the center and the displacement per cycle is at most on the order of one radius. The second condition arises since v and V are the same order of magnitude at the wall and both are zero at the center.

We rewrite the equations retaining the lowest order terms in Ω. We treat terms in v and V as first order terms in Ω. With the definitions in the previous paper[1] and the application of the low reduced frequency approximation, the complete system of equations are presented below to facilitate the presentation of the solution. The axial component of the Navier–Stokes equation is

$$iu = \frac{1}{\gamma}\frac{\partial p^*}{\partial \xi} - \frac{1}{\lambda_\mu^2}\left[\frac{\partial^2 u}{\partial \eta^2} + \frac{1}{\eta}\frac{\partial u}{\partial \eta}\right], \tag{5}$$

and the radial component becomes

$$\frac{1}{\gamma}\frac{\partial p^*}{\partial \eta} = 0. \tag{6}$$

The continuity equation for the mixture gives

$$i\Omega \rho^* = \Omega \frac{\partial u}{\partial \xi} + \frac{\partial v}{\partial \eta} + \frac{v}{\eta}, \tag{7}$$

and the equation of state becomes

$$\Omega[p^* - \rho^* - T^*] = i\frac{n_1 n_2}{n\rho_0}(m_1 - m_2)\left[\Omega \frac{\partial U}{\partial \xi} + \frac{1}{\eta}\frac{\partial \eta V}{\partial \eta}\right]. \tag{8}$$

The entropy equation for the mixture becomes

$$T^* - \frac{\gamma - 1}{\gamma}p^* - \frac{i}{\lambda_T^2}\left[\frac{\partial^2 T^*}{\partial \eta^2} + \frac{1}{\eta}\frac{\partial T^*}{\partial \eta}\right] + i\frac{k_T}{\Omega}\frac{\gamma - 1}{\gamma}\left(\frac{1}{\eta}\frac{\partial \eta V}{\partial \eta} + \Omega \frac{\partial U}{\partial \xi}\right) = 0. \tag{9}$$

The second term represents the temperature change due to adiabatic heating, the third term is the temperature change due to heat conduction, and the fourth term is the temperature change associated with diffusion assisted heat flux. The axial component of the diffusion equation is

$$iU = 0, \tag{10}$$

implying there is no mass flux in the direction of propagation of the acoustic wave. Equations (5)–(10) are unchanged from the previous paper.[1] The corrected radial component of the diffusion equation is

$$iV = \frac{-1}{\lambda_D^2}\frac{\partial}{\partial \eta}\left[\frac{1}{\eta}\frac{\partial \eta V}{\partial \eta} + \Omega \frac{\partial U}{\partial \xi}\right] - i\Omega \frac{(m_2 - m_1)}{\lambda_D^2}\frac{n}{\rho_0}\frac{\partial p^*}{\partial \eta} - i\Omega \frac{k_T}{\lambda_D^2}\frac{n^2}{n_1 n_2}\frac{\partial T^*}{\partial \eta}. \tag{11}$$

Since V is $O(\Omega)$, all terms in this equation are the same order and all terms should be retained in the low reduced frequency approximation. The first term on the right hand side is the ordinary diffusion which is attributed to concentration gradients of the components present in the mixture. The second term on the right hand side represents the pressure diffusion and does not contribute as a consequence of Eq. (6). This equation differs from the previous paper[1] by the addition of the third term on the right hand side that is proportional to the thermal diffusion ratio, k_T. This term represents the thermal diffusion. Furthermore, Eq. (10) will be used to eliminate the $\partial U/\partial \xi$ term in Eq. (8), Eq. (9), and Eq. (11).

In the previous paper the use of the low reduced frequency approximation decoupled the equations so that the wave number of the acoustic mode could be determined by directly integrating the equations. However, now that the equation for V, Eq. (11), is coupled to the entropy equation, Eq. (9), they must be solved simultaneously. From inspection of Eq. (9) and Eq. (11) we assume solutions of the following forms:

$$T^* = AJ_0(\sqrt{i}\lambda_x \eta) + BJ_0(\sqrt{i}\lambda_y \eta) + \frac{\gamma - 1}{\gamma}p^* \tag{12}$$

and

$$V = CJ_1(\sqrt{i}\lambda_x \eta) + DJ_1(\sqrt{i}\lambda_y \eta), \tag{13}$$

where J_0 is the Bessel function of the first kind of order zero and J_1 is the Bessel function of the first kind of order one. A, B, C, and D are complex valued coefficients which will be determined using boundary conditions.

Substitution of Eq. (12) and Eq. (13) into Eqs. (9) and (11) yields the same eigenvector equation for λ_x and λ_y:

$$\left(1 - \frac{\lambda_{x,y}^2}{\lambda_T^2}\right)\left(1 - \frac{\lambda_{x,y}^2}{\lambda_D^2}\right) = \frac{n^2}{n_1 n_2}k_T^2 \frac{\gamma - 1}{\gamma}\frac{\lambda_{x,y}^2}{\lambda_D^2}. \tag{14}$$

The two solutions to this equation are λ_x and λ_y. Inspection of these solutions shows that one solution approaches λ_T and one approaches λ_D for small k_T so we denote these as ${}^*\lambda_T$ and ${}^*\lambda_D$:

$${}^*\lambda_T^2 = \frac{\lambda_T^2(1+\Phi)}{2}\left[1 + \sqrt{1 + \frac{4\lambda_T^2\lambda_D^2\Phi}{[\lambda_T^2(1+\Phi) - \lambda_D^2]^2}}\right] + \frac{\lambda_D^2}{2}\left[1 - \sqrt{1 + \frac{4\lambda_T^2\lambda_D^2\Phi}{[\lambda_T^2(1+\Phi) - \lambda_D^2]^2}}\right], \tag{15}$$

$$*\lambda_D^2=\frac{\lambda_D^2}{2}\left[1+\sqrt{1+\frac{4\lambda_T^2\lambda_D^2\Phi}{[\lambda_T^2(1+\Phi)-\lambda_D^2]^2}}\right]+\frac{\lambda_T^2(1+\Phi)}{2}\times\left[1-\sqrt{1+\frac{4\lambda_T^2\lambda_D^2\Phi}{[\lambda_T^2(1+\Phi)-\lambda_D^2]^2}}\right], \tag{16}$$

where

$$\Phi=\frac{n^2}{n_1n_2}k_T^2\frac{\gamma-1}{\gamma}. \tag{17}$$

Four equations are required to determine coefficients *A, B, C,* and *D*. The first two equations are obtained by substituting Eq. (12) and Eq. (13), with the above values for $*\lambda_T$ and $*\lambda_D$, into Eqs. (9) and (11), respectively. The other two equations are obtained from the boundary conditions. The boundary condition on temperature fluctuations, $T^*=0$, at the tube wall, $\eta=1$, yields

$$AJ_0(\sqrt{i}*\lambda_T)+BJ_0(\sqrt{i}*\lambda_D)+\frac{\gamma-1}{\gamma}p^*=0. \tag{18}$$

The boundary condition on the vapor pressure, $p_2=0$, at the tube wall, $\eta=1$, yields

$$i\Omega p^*=\frac{n_1}{n}[\sqrt{i}*\lambda_TJ_0(\sqrt{i}*\lambda_T)C+\sqrt{i}*\lambda_DJ_0(\sqrt{i}*\lambda_D)D]. \tag{19}$$

The solutions for *A, B, C,* and *D* are substituted into Eq. (12) to obtain an equation for the temperature as a function of pressure as

$$T^*=\frac{\gamma-1}{\gamma}p^*\left[1-\left(\frac{\lambda_T^2-*\lambda_D^2}{*\lambda_T^2-*\lambda_D^2}\right)\frac{J_0(\sqrt{i}*\lambda_T\eta)}{J_0(\sqrt{i}*\lambda_T)}+\left(\frac{\lambda_T^2-*\lambda_T^2}{*\lambda_T^2-*\lambda_D^2}\right)\frac{J_0(\sqrt{i}*\lambda_D\eta)}{J_0(\sqrt{i}*\lambda_D)}+\frac{\lambda_T^2}{*\lambda_T^2-*\lambda_D^2}k_T\times\frac{n}{n_1}\left(\frac{J_0(\sqrt{i}*\lambda_D\eta)}{J_0(\sqrt{i}*\lambda_D)}-\frac{J_0(\sqrt{i}*\lambda_T\eta)}{J_0(\sqrt{i}*\lambda_T)}\right)\right]. \tag{20}$$

Substitution into Eq. (13) gives the radial component of the diffusion velocity as

$$V=\frac{i\Omega}{k_T}p^*\left(\frac{\lambda_T^2}{*\lambda_T^2-*\lambda_D^2}\right)\left[\left(1-\frac{*\lambda_T^2}{\lambda_T^2}\right)\left(1-\frac{*\lambda_D^2}{\lambda_T^2}\right)\times\left(\frac{J_1(\sqrt{i}*\lambda_D\eta)}{\sqrt{i}*\lambda_DJ_0(\sqrt{i}*\lambda_D)}-\frac{J_1(\sqrt{i}*\lambda_T\eta)}{\sqrt{i}*\lambda_TJ_0(\sqrt{i}*\lambda_T)}\right)+\frac{n}{n_1}k_T\left(\frac{\lambda_T^2-*\lambda_D^2}{*\lambda_T^2}\frac{J_1(\sqrt{i}*\lambda_D\eta)}{\sqrt{i}*\lambda_DJ_0(\sqrt{i}*\lambda_D)}-\frac{\lambda_T^2-*\lambda_T^2}{*\lambda_T^2}\frac{J_1(\sqrt{i}*\lambda_T\eta)}{\sqrt{i}*\lambda_TJ_0(\sqrt{i}*\lambda_T)}\right)\right]. \tag{21}$$

From this point on the approach to obtaining a solution for the acoustic mode parallels the procedure of the previous paper.[1] The new solution for the wave number squared of the acoustic mode is

$$k^2=\frac{\gamma}{F(\lambda_\mu)}\frac{\omega^2}{c^2}\left[1+\frac{n_2}{n_1}-\frac{\gamma-1}{\gamma}\left[1-\frac{\lambda_T^2-*\lambda_D^2}{*\lambda_T^2-*\lambda_D^2}(1-F(*\lambda_T))+\frac{\lambda_T^2-*\lambda_T^2}{*\lambda_T^2-*\lambda_D^2}(1-F(*\lambda_D))\right]+\frac{n_2}{n_1}\frac{\lambda_T^2-*\lambda_D^2}{*\lambda_T^2-*\lambda_D^2}\left[\frac{\lambda_T^2-*\lambda_T^2}{\lambda_T^2-*\lambda_D^2}F(*\lambda_T)-F(*\lambda_D)\right]+\frac{n_2}{nk_T}\frac{\lambda_T^2-*\lambda_T^2}{\lambda_T^2}\left(\frac{\lambda_T^2-*\lambda_D^2}{*\lambda_T^2-*\lambda_D^2}\right)[F(*\lambda_T)-F(*\lambda_D)]-\frac{\gamma-1}{\gamma}\frac{\lambda_T^2}{*\lambda_T^2-*\lambda_D^2}k_T\frac{n}{n_1}[F(*\lambda_T)-F(*\lambda_D)]\right], \tag{22}$$

where

$$F(\lambda_j)=1-\frac{2J_1(\sqrt{i}\lambda_j)}{\sqrt{i}\lambda_jJ_0(\sqrt{i}\lambda_j)}, \tag{23}$$

with λ_j representing the viscous wave number, modified thermal wave number, and the modified diffusion wave number. Equation (22) above reduces to the acoustic wave number obtained in the previous paper in the limit of $*\lambda_T\to\lambda_T$ and $*\lambda_D\to\lambda_D$. Making use of the fact that the sum of Eq. (15) and Eq. (16) is

$$*\lambda_D^2+*\lambda_T^2=\lambda_D^2+(1+\Phi)\lambda_T^2, \tag{24}$$

and the product is

$$*\lambda_D^2*\lambda_T^2=\lambda_D^2\lambda_T^2, \tag{25}$$

allows Eq. (22) to be somewhat simplified to

$$k^2=\frac{\gamma}{F(\lambda_\mu)}\frac{\omega^2}{c^2}\left[1+\frac{n_2}{n_1}+\left[-\frac{\gamma-1}{\gamma}\left(\frac{\lambda_T^2-*\lambda_D^2}{*\lambda_T^2-*\lambda_D^2}\right)+\frac{n_2}{n_1}\left(\frac{\lambda_T^2-*\lambda_T^2}{*\lambda_T^2-*\lambda_D^2}\right)\right]F(*\lambda_T)+\left[\frac{\gamma-1}{\gamma}\left(\frac{\lambda_T^2-*\lambda_T^2}{*\lambda_T^2-*\lambda_D^2}\right)-\frac{n_2}{n_1}\left(\frac{\lambda_T^2-*\lambda_D^2}{*\lambda_T^2-*\lambda_D^2}\right)\right]F(*\lambda_D)-2\left[k_T\frac{n}{n_1}\frac{\gamma-1}{\gamma}\frac{\lambda_T^2}{*\lambda_T^2-*\lambda_D^2}\right][F(*\lambda_T)-F(*\lambda_D)]\right], \tag{26}$$

but obtaining the expression of the previous paper is not as

obvious. If we choose to ignore the coupling between thermal and diffusion processes, substituting $k_T=0$ into Eq. (26) gives

$$k^2=\frac{\gamma}{F(\lambda_\mu)}\frac{\omega^2}{c^2}\left[1-\frac{\gamma-1}{\gamma}F(\lambda_T)+\frac{n_2}{n_1}(1-F(\lambda_D))\right]. \qquad (27)$$

The real and imaginary parts of the wave number can be evaluated numerically from the expressions above. The imaginary part of k yields the attenuation and the real part is ω/v_{ph}, where v_{ph} is the phase velocity.

COMPARISON OF NUMERICAL PREDICTIONS FOR AN AIR-WATER VAPOR MIXTURE

Calculating the attenuation of sound from the above expressions requires values for the properties of the components as well as values for the effective properties of the mixture. These properties are calculated using the same approach as in the previous paper.[1] The ratio of specific heats and the specific heat at constant pressure for the components are independent of temperature and are calculated from basic kinetic theory, whereas the temperature dependence of the ambient sound speed of the components is taken into account. The ratio of specific heats, the specific heat at constant pressure, and the temperature dependence of ambient sound speed of the mixture are derived based upon an average energy of the mixture. The temperature dependence of the viscosity and thermal conductivity of the components and of the binary mixture are accounted for. The temperature and pressure dependence of mass diffusion and the thermal diffusion ratio of the binary mixture are also accounted for.

Varying the temperature changes the properties of the components and mixture as well as changing the mole fractions of the components. The variation in properties of air, water vapor, and the mixture as a function of temperature are shown in Fig. 2 of the previous paper.[1] For an air–water vapor mixture, the diffusion coefficient is of O(10^{-5}) m^2/s and exhibits a maximum at about 50 °C. The thermal diffusion ratio, k_T, tends to zero as the mole fraction of either component goes to zero. For an air–water vapor mixture the thermal diffusion ratio increases with increasing temperature to about 0.01 at a temperature of 100 °C.

It is quite common to calculate dimensionless numbers to estimate the relative importance of various process. Figure 1 shows the values of Prandtl number, Schmidt number, or Prandtl mass transfer number, and the Lewis number for the air–water vapor mixture. The Prandtl number is the ratio of momentum (viscous) to thermal effects. The Prandtl number increases slightly with increasing temperature and is always larger than the near $\frac{2}{3}$ value for pure monatomic ideal gases. The Schmidt number is the ratio of momentum (viscous) to mass diffusion effects. It remains fairly constant over the range of temperature considered here. It is smaller than the Prandtl number. The Lewis number is the ratio of mass diffusion to thermal effects. It can be calculated as the ratio of Prandtl to Schmidt number. It varies slightly with temperature and is greater than one. This implies that the mass diffusion effects are larger than the thermal effects.

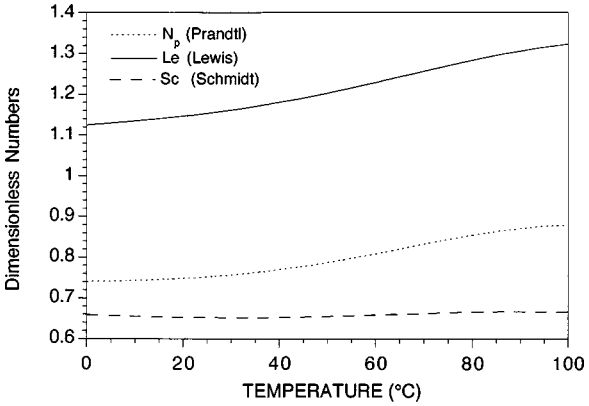

FIG. 1. Calculated Prandtl number, Schmidt number, and Lewis number of the air–water vapor mixture as a function of temperature.

When coupling between mass diffusion and thermal processes are accounted for the expressions for the dimensionless thermal wave number, $*\lambda_T$, and the dimensionless diffusion wave number, $*\lambda_D$, are given by Eq. (15) and Eq. (16), respectively. Figure 2 shows the differences in thermal and diffusion wave numbers with and without the coupling. The thermal wave number is increased, i.e., the thermal penetration depth is decreased, due to the effect of diffusion. The diffusion wave number is decreased, i.e., the diffusion penetration depth is increased, due to the temperature gradient. The value of k_T and the differences between λ_j's and $*\lambda_j$'s go to small nonzero values as the temperature approaches zero. The largest differences between λ_j's and $*\lambda_j$'s are quite small for this case. The differences between λ_j's and $*\lambda_j$'s plotted in Fig. 2 are independent of tube size and frequency and depend solely on the properties of the gas mixture.

Predictions of attenuation of 10-kHz sound in a wet tube of radius 0.5 mm filled with an air–water vapor mixture is shown in Fig. 3. For reference, the magnitude of λ_j's in this case are O(30). Calculations for the mixture-filled tube show a decrease in attenuation if the mixture is treated as an effective fluid, i.e., without mass transfer. This is due to the decrease in the kinematic viscosity of the mixture. An increase in attenuation is predicted if mass transfer is included.

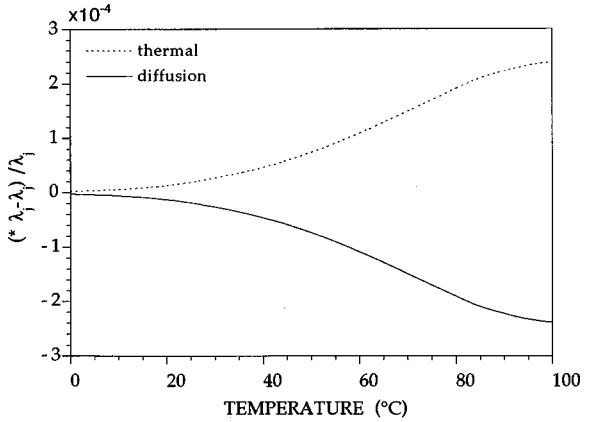

FIG. 2. Differences in thermal wave number, λ_T, and diffusion wave number, λ_D of the mixture with $k_T=0$ and with coupling of diffusion and thermal processes.

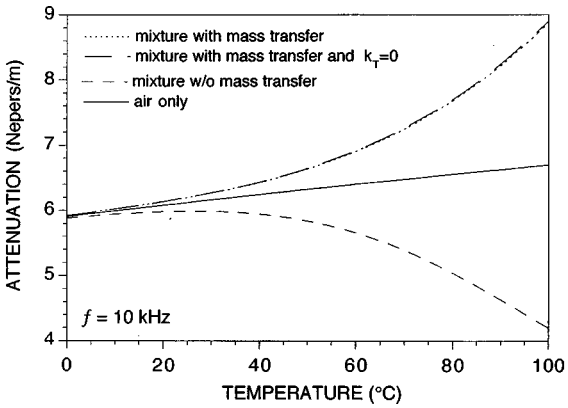

FIG. 3. Predicted attenuation of sound in a tube filled with an air–water vapor mixture with mass transfer, an air–water vapor mixture with mass transfer but neglecting coupling between diffusion and thermal, an air–water vapor mixture treated as an effective fluid and only air as a function of temperature. The frequency is 10 kHz and the air pressure is 1 atm.

The increase in attenuation due to mass transfer is associated with the phasing of the pressure perturbation of the acoustic wave and the evaporation-condensation of water vapor from the wall. The predicted attenuation with and without coupling between thermal and diffusion process are almost the same. This implies that the coupling does not significant alter the attenuation. The thermal diffusion ratio, k_T, representing the coupling between diffusion and heat flux is of the O (10^{-2}) for this case. The thermal diffusion ratio of other binary mixtures of various gases can be an order of magnitude larger than for case considered here.[5] Therefore, the coupling between mass diffusion and heat flux might be important for other mixtures.

CONCLUSIONS

The low reduced frequency method of Tijdeman[2] can be used to produce predictions of the effect of wet walls on sound propagation in air-filled tubes. The solution for the acoustic wave number including the coupling between mass diffusion and thermal effects has been derived. The expressions for the dimensionless thermal wave number, λ_T, and the dimensionless diffusion wave number, λ_D, are altered due to the coupling. However, these changes are quite small for the case of an air–water vapor mixture. The attenuation of a 10-kHz acoustic wave propagating in the tube also shows little change due to the coupling. The contribution can be shown to be small for a wide range of λ_j's. Therefore, a description of attenuation where the viscous, thermal, and diffusion processes are decoupled, i.e., $k_T=0$, is adequate for the air–water vapor mixture discussed in the previous paper.[1]

ACKNOWLEDGMENTS

We wish to thank Greg Swift for pointing out our neglect of thermal diffusion from Eq. (28) of Ref. 1. This work is supported jointly by the Office of Naval Research and the USDA-ARS National Sedimentation Laboratory. We thank the referees for their comprehensive reviews of this article.

[1] R. Raspet, C. J. Hickey, and J. M. Sabatier, ''The effect of evaporation-condensation on sound propagation in cylindrical tubes using the low reduced frequency approximation,'' J. Acoust. Soc. Am. **105**, 65–73 (1999).

[2] H. Tijdeman, ''On the propagation of sound waves in cylindrical tubes,'' J. Sound Vib. **39**, 1–33 (1975).

[3] G. Swift, personal communication (1999).

[4] The definition of the thermal diffusion ratio, k_T, is given by Eq. 8.1–10 with further discussion on pages 518–520 of J. V. Hirschfelder, C. Curtiss, and R. B. Bird, *Molecular Theory of Gases and Liquids* (Wiley, New York, 1954).

[5] Values for the thermal diffusion ratio, k_T, of various binary gas mixtures are given in Table 8.4–14 on pages 584–585 of J. V. Hirschfelder, C. Curtiss, and R. B. Bird, *Molecular Theory of Gases and Liquids* (Wiley, New York, 1954).

A transfer-matrix approach for estimating the characteristic impedance and wave numbers of limp and rigid porous materials

Bryan H. Song and J. Stuart Bolton[a)]
1077 Ray W. Herrick Laboratories, School of Mechanical Engineering, Purdue University, West Lafayette, Indiana 47907-1077

(Received 10 February 1999; accepted for publication 10 November 1999)

A method for evaluating the acoustical properties of homogeneous and isotropic porous materials that may be modeled as fluids having complex properties is described here. To implement the procedure, a conventional, two-microphone standing wave tube was modified to include: a new sample holder; a section downstream of the sample holder that accommodated a second pair of microphone holders and an approximately anechoic termination. Sound-pressure measurements at two upstream and two downstream locations were then used to estimate the two-by-two transfer matrix of porous material samples. The experimental transfer matrix method has been most widely used in the past to measure the acoustical properties of silencer system components. That procedure was made more efficient here by taking advantage of the reciprocal nature of sound transmission through homogeneous and isotropic porous layers. The transfer matrix of a homogeneous and isotropic, rigid or limp porous layer can easily be used to identify the material's characteristic impedance and wave number, from which other acoustical quantities of interest can be calculated. The procedure has been used to estimate the acoustical properties of a glass fiber material: good agreement was found between the estimated acoustical properties and those predicted by using the formulas of Delany and Bazley. © *2000 Acoustical Society of America.* [S0001-4966(00)04302-2]

PACS numbers: 43.20.Jr, 43.20.Mv, 43.55.Ev, 43.58.Bh [DEC]

INTRODUCTION

Many types of sound-absorbing materials are used in noise-control applications. These materials include, for example: glass fiber, polymeric fibrous materials, and various types of foams. It is of interest to be able to predict the noise-control impact of these materials, whether in sound absorption or barrier applications, at the design stage: finite element, boundary element, and statistical energy analysis programs make that possible in principle. However, to take full advantage of these software capabilities, it is necessary to have detailed knowledge of the acoustical properties of the noise-control materials. In particular, it is usually necessary to know their characteristic impedance and wave number. A procedure addressing that need is presented here.

We will consider, in particular, porous materials that are homogeneous (i.e., materials whose properties are spatially uniform) and isotropic (i.e., materials whose properties are independent of direction), and whose expanded solid phase may be assumed to be either perfectly rigid or perfectly limp. In general, most noise-control materials are poroelastic: i.e., they can support two compressional waves and a transverse wave. However, in certain frequency or material property regimes, certain porous materials behave as though they were rigid, i.e., their solid phase motion is negligible compared to that of the fluid phase owing to weak coupling or the relatively high density or stiffness of the solid phase. In other regimes, certain materials such as low density, high flow resistivity, unreinforced glass fibers may be approximated as limp: i.e., the *in vacuo* stiffness of their bulk solid phase is negligible compared to that of the saturating fluid. For practical purposes, many fibrous materials and foams fall into these two categories in specific frequency ranges of interest. Air-saturated, homogeneous, and isotropic porous materials that can be approximated as either rigid or limp may be considered to support only a single dilational wave type and may thus be modeled as dissipative fluids having complex physical properties: e.g., characteristic impedance and wave number.[1] The acoustical properties of such a medium are completely specified when the latter two quantities, or two independent properties derived from them (e.g., complex density and complex sound speed) are known. Thus, it is of interest to be able to determine experimentally the wave number and the characteristic impedance of a homogeneous and isotropic porous material.

The current effort is an extension of work reported earlier by Bolton *et al.*[2] In that work, a four-microphone, standing wave tube measurement of the normal incidence reflection and transmission coefficients of automotive sealant materials was described. The success of that procedure depended on the provision of an anechoic termination for the standing wave tube. Here, it is shown that the same measured data may be used to determine the transfer matrix of the material under test even though no conditions are imposed on the tube termination properties. The transfer matrix elements may then be related in closed form to the porous material's characteristic impedance and wave number. Note that the latter property, in particular, yields both the phase speed and the spatial rate of energy dissipation within the material. Note also that when the transfer matrix of a layer of acoustical material is known, it may be combined with transfer matrices of other acoustical elements (e.g., barrier or resistive layers) to form the complete transfer matrix of a multilayer noise control treatment.[3] The latter matrix may

[a)]Author to whom correspondence should be addressed. Electronic mail: bolton@ecn.purdue.edu

then be used to predict and optimize the absorption and barrier properties of the treatment.

The transfer matrix method has been widely used in the past to analyze and to measure the acoustical properties of flow system elements (e.g., automotive mufflers). The particular implementation of the transfer matrix method described here was made possible by taking advantage of the reciprocal nature of sound transmission through typical acoustical materials: that reciprocity places conditions on the structure of the transfer matrices of these materials. The resulting mathematical constraints make it possible to determine the acoustical properties of homogeneous and isotropic porous materials by using fewer measurements than are typically necessary when using a transfer matrix approach.

The procedure is demonstrated here through measurements of the acoustical properties of aviation-grade glass fibers. Good agreement was found between the measured acoustical properties of these materials and predictions made using well-established semiempirical formulas. Note, however, that the procedure applied here cannot be applied directly in its present form to materials that must be modeled as poroelastic: i.e., those materials in which two compressional waves and a transverse wave contribute significantly to the materials' acoustical properties.

I. BACKGROUND

In 1946, Scott described a technique for directly measuring the propagation constant and for inferring the characteristic impedance of a porous material.[4] The propagation constant, or wave number, as defined by Scott comprised a real component, the propagation factor, governing the phase change per unit length and an imaginary component, the attenuation factor, governing the exponential decay of sound pressure within the porous material. The attenuation factor at a single frequency was determined by passing a microphone probe through a deep sample and measuring the decay of mean-square sound pressure with position. The propagation factor was determined at the same time by measuring the sound field's phase change with distance. The characteristic impedance was inferred by measuring the normal specific acoustic impedance of a sample sufficiently deep that reflection from the tube termination was negligible. The same approach was also described by Beranek.[5] The disturbance of the acoustical material caused by the microphone probe has proven to be a problem with Scott's technique in application to some types of materials. More recently, a nonintrusive version of Scott's wave number measurement was described by Lambert and Tesar.[6] In their procedure, a long sample of porous material was placed in a standing wave tube as in Scott's approach. However, the single-frequency sound field within the porous material was sampled at 1-cm intervals along its length by means of a probe microphone inserted through the tube wall. The real and imaginary parts of the wave number can easily be calculated from the latter data.

Following Scott's work, Beranek[7] used an elastic porous material theory similar to that of Zwikker and Kosten[8] to relate the wave number and characteristic impedance of a porous material to its macroscopic physical properties: i.e., flow resistance, structure factor (as then defined), porosity, density, and the volume stiffness coefficients for the air and structure. He suggested that the theory could be used as an alternative to direct measurement of the wave numbers and characteristic impedances of either limp or rigid porous material.

Ferrero and Sacerdote subsequently proposed a second style of material property measurement based on two measurements of surface-normal impedance.[9] In particular, they showed that it was possible to determine the characteristic impedance and wave number of a porous material graphically and analytically by measuring at a single frequency the surface-normal specific acoustic impedance of two different thicknesses of the same porous material, one thickness being double the other. Their particular procedure has since become known as the two-thickness method. When using this technique, however, it is sometimes difficult to mount a second sample without disturbing the first, and the procedure becomes inaccurate when the product of the attenuation factor and the sample depth is sufficiently large that the difference between the surface impedances of the two thicknesses of material is relatively small. The latter problem is particularly significant for fibrous materials having high flow resistivities.

Yaniv eliminated problems associated with the use of two thicknesses of material by introducing the two-cavity, single-frequency method: during the first surface impedance measurement the sample was backed by a rigid wall, while in the second measurement the sample was backed by a one-quarter-wavelength deep cavity terminated by a rigid wall.[10] The wave numbers and characteristic impedances of a number of materials obtained by using this procedure were compared both with predictions made using the Beranek theory and with results obtained by using Scott's method. The two-cavity method was shown to give results in good agreement with Beranek's theory over the frequency range considered: Scott's method was found to be less accurate for the materials that Yaniv considered. Like the two-thickness method, however, the two-cavity method can become inaccurate when the sample material is highly dissipative: i.e., when the surface-normal impedance is relatively insensitive to backing conditions.

Smith and Parott have also evaluated the two-thickness method, the two-cavity method, and Scott's method.[11] They found that the significant advantage of the two-cavity method compared with the two-thickness method lies in the reduction of both measurement times and the variation associated with mounting test materials that is made possible by using the former method.

Utsuno *et al.* subsequently described a cross-spectral implementation of the two-cavity method based on the two-microphone method for measuring surface-normal impedance.[12,13] In their procedure, the wave number and characteristic impedance were estimated on the basis of two measurements of the surface impedance of a sample insonified by broadband noise: first when backed by a hard termination and then by an arbitrarily deep air space. Their approach allows results to be obtained over a broad range of frequencies simultaneously and eliminates the need for a different backing depth at each frequency. However, in com-

mon with other techniques based on surface-normal impedance measurement, this approach can be inaccurate when applied to highly dissipative materials.

To address the latter concern, a third general type of estimation procedure combining surface impedance information with measurements of transfer properties across the sample has been developed by a number of investigators. Such a procedure was implemented by Bordone-Sacerdote and Sacerdote.[14] In their procedure, transfer functions were measured in two directions across a porous sample that divided a short tube terminated at both ends by acoustic drivers. By taking advantage of the reciprocal nature of sound transmission through the sample, they were able to determine parameters related directly to the wave number and characteristic impedance of the material under test. Although the authors' intention was to develop a procedure specifically useful at very low frequencies, and which could also be used to measure the material's dynamic flow resistivity, there appears to be no reason that this procedure could not work at any frequency in the plane wave range. Note, however, that the acoustic drivers which terminate the tube are required to present a zero-velocity boundary condition when not in use: this requirement may be difficult to satisfy when using conventional loudspeakers.

Some time later, Ingard and Dear described a simplified two-microphone procedure for measuring the dynamic flow impedance of a sample thin enough so that the acoustic particle velocities on its two surfaces are negligibly different.[15,16] The latter requirement restricts the use of their procedure to low frequencies. In this procedure a sample is placed in a standing wave tube at a distance L from a rigid termination, and the sound pressure is measured both at the termination and at the front surface of the sample. At frequencies such that L is an odd number of quarter wavelengths, the normalized flow impedance of the sample is directly related to a ratio of the two sound pressures. This procedure is of interest since the flow impedance as defined by the authors may be related to the material's characteristic impedance. However, owing to the requirement that the sample depth be very small compared to a wavelength, this procedure cannot be used to estimate a material's wave number, and as noted, it may only be applied at a discrete set of frequencies determined by the length of the terminating air space.

McIntosh *et al.* subsequently described a more general apparatus and procedure for measuring the low frequency, dynamic flow impedance of a sample.[17] Their apparatus was similar to that of Ingard and Dear except that a linear array of microphones positioned in front of the incident surface of the sample was used to estimate the complex pressure and particle velocity on the incident face of the sample at each frequency of interest. The sound pressure measured at a microphone mounted flush with the rigid termination was used to estimate the same information at the transmission face of the sample without restriction on frequency. The pressure and particle velocity information could then be used to estimate the dynamic flow resistivity at low frequencies: i.e., when the sample thickness was small compared to a wavelength. However, McIntosh *et al.* noted that the same information could be combined with a single-wave model for sound propagation within the porous layer to determine the latter's characteristic impedance and wave number at any frequency in the plane wave region by means of an iterative, numerical solution. Measured results for an open cell foam were in generally good agreement with appropriate theoretical predictions.

Champoux and Stinson have described a procedure similar in some respects to that of McIntosh *et al.* that entails measurement of both the surface impedance of a sample backed by a fixed-depth air space and the pressure transfer function across the sample.[18] The latter quantity was estimated by using a reference microphone at the front surface of the sample and a cavity microphone behind the sample. The shallow cavity behind the sample was terminated by a rigid backing. The procedure implemented by Champoux and Stinson was based on the use of a traversing probe tube to estimate the surface-normal impedance of the sample, and so measurements were made one frequency at a time. The surface impedance and the transfer function across the sample together provide the information necessary to calculate the characteristic impedance and the wave number of the material in closed form. The direct measurement of the transfer function across the sample makes it possible for this method to yield accurate estimates of the characteristics of dissipative materials having high flow resistivities. The latter property is shared with all the other procedures described here that involve measurements on both sides of the sample.[14–17] Note that a procedure essentially identical to that of Champoux and Stinson, save for the elimination of the air space behind the sample, has recently been described by Iwase *et al.*[19] Note finally that the Ingard and Dear, McIntosh *et al.*, and Champoux and Stinson procedures are similar in some respects to one- and two-microphone techniques that were developed for measuring the impedance of duct lining materials: see, for example, Ref. 20.

All of the procedures described above entail the use of a sample placed in sealed standing wave tube. More recently, Amedin *et al.* developed a measurement procedure based on sound transmission from a standing wave tube to a free field.[21] Their method involved a two-microphone measurement inside an impedance tube, and one sound-pressure measurement immediately above a plug of porous material at the tube termination: the tube termination was itself mounted flush with a large baffle. The authors claimed that the direct measurement of the sound pressure above the sample material resulted in high sensitivity and accurate results.

The procedure to be described here is of the same family as those described in Refs. 14–21 in the sense that measurements are made on both sides of a cylindrical plug of material placed in a standing wave tube. However, the present procedure differs from earlier approaches since knowledge of the tube termination condition is not required and because it is based more closely on techniques previously used to measure the acoustical performance of flow system components: i.e., transfer matrix methods.

Transfer matrix approaches have found frequent application in acoustics, and they have also been used in hydraulics applications where this approach is sometimes known as

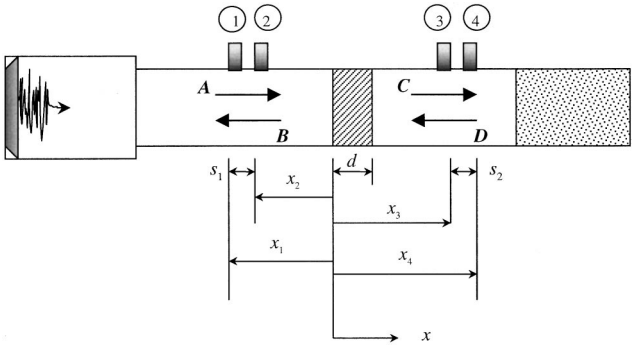

FIG. 1. Schematic diagram of the standing wave tube.

the two-port or four-pole method.[22] As a result, there is a large body of literature related to the measurement of the properties of acoustical elements based on transfer matrix, or two-port, representations.[14,23–28] The transfer matrix method has most often been applied to the characterization of air duct system components, exhaust silencers, etc. The transfer matrix method can also be applied as an adjunct to the boundary element method or the finite element method in noise-control design procedures.[29,30]

An important observation related to the application of the transfer matrix method to acoustical elements was made by Pierce, who noted the constraints placed on the transfer matrix elements by the requirements of symmetry when the acoustical element was reciprocal.[31] Those constraints had been used earlier, without comment, by Bordone-Sacerdote and Sacerdote.[14]

In the present study, an experimental transfer matrix approach of the type previously used to measure the performance of flow system elements was combined with the constraints imposed by sample symmetry and reciprocity to make possible the efficient measurement of porous material properties by using a suitably modified standing wave tube.

II. THEORY OF THE TRANSFER MATRIX METHOD

A. Sound-field representation

In the approach considered here, a loudspeaker was used to generate a plane wave field in a standing wave tube, and a single microphone was used to measure the transfer functions between the signal provided to the loudspeaker and the sound pressure at the four locations shown in Fig. 1. Those transfer functions are denoted P_1 to P_4. In subsequent calculations, the quantities P_1 to P_4 always appear in ratios, with the result that the spectral characteristic of the input signal is canceled. Thus, for present purposes P_1 to P_4 may be considered to represent the complex sound pressure at the four measurement locations x_1 to x_4, i.e.,

$$P_1=(Ae^{-jkx_1}+Be^{jkx_1})e^{j\omega t}, \tag{1a}$$

$$P_2=(Ae^{-jkx_2}+Be^{jkx_2})e^{j\omega t}, \tag{1b}$$

$$P_3=(Ce^{-jkx_3}+De^{jkx_3})e^{j\omega t}, \tag{1c}$$

$$P_4=(Ce^{-jkx_4}+De^{jkx_4})e^{j\omega t}. \tag{1d}$$

Here, k represents the wave number in the ambient fluid and an $e^{+j\omega t}$ sign convention has been adopted. The four complex pressures, P_1 to P_4, comprise various superpositions of positive- and negative-going plane waves in the up- and downstream segments of the standing wave tube; the complex amplitudes of those waves are represented by the coefficients A to D. Equations (1a)–(1d) yield four equations for the coefficients A to D in terms of the four measured sound pressures, i.e.,

$$A=\frac{j(P_1e^{jkx_2}-P_2e^{jkx_1})}{2\sin k(x_1-x_2)}, \tag{2a}$$

$$B=\frac{j(P_2e^{-jkx_1}-P_1e^{-jkx_2})}{2\sin k(x_1-x_2)}, \tag{2b}$$

$$C=\frac{j(P_3e^{jkx_4}-P_4e^{jkx_3})}{2\sin k(x_3-x_4)}, \tag{2c}$$

$$D=\frac{j(P_4e^{-jkx_3}-P_3e^{-jkx_4})}{2\sin k(x_3-x_4)}. \tag{2d}$$

The latter coefficients provide the input data for subsequent transfer matrix calculations. Note that the wave number, k, should be made complex to account for the effects of viscous and thermal dissipation in the oscillatory, thermoviscous boundary layer that forms on the inner surface of the duct. In the present work, formulas appropriate for wide ducts given by Pierce were used to calculate the real and imaginary parts of the wave number.[31]

B. Transfer matrix formulation

Here, the transfer matrix is used to relate the sound pressures and normal acoustic particle velocities on the two faces of a porous layer extending from $x=0$ to $x=d$ as in Fig. 1, i.e.,

$$\begin{bmatrix} P \\ V \end{bmatrix}_{x=0}=\begin{bmatrix} T_{11} & T_{12} \\ T_{21} & T_{22} \end{bmatrix}\begin{bmatrix} P \\ V \end{bmatrix}_{x=d}. \tag{3}$$

In Eq. (3), P is the exterior sound pressure and V is the exterior normal acoustic particle velocity. The pressures and particle velocities on the two surfaces of the porous layer may easily be expressed in terms of the positive- and negative-going plane wave component amplitudes, i.e.,

$$P|_{x=0}=A+B, \tag{4a}$$

$$V|_{x=0}=\frac{A-B}{\rho_0 c}, \tag{4b}$$

$$P|_{x=d}=Ce^{-jkd}+De^{jkd}, \tag{4c}$$

$$V|_{x=d}=\frac{Ce^{-jkd}-De^{jkd}}{\rho_0 c}, \tag{4d}$$

where ρ_0 is the ambient fluid density and c is the ambient sound speed. Thus, when the plane wave components are known based on measurements of the complex pressures at four locations, the pressures and the normal particle velocities at the two surfaces of the porous layer can be determined.

It is then of interest to determine the elements of the transfer matrix since, as will be shown below, the elements

of that matrix may be directly related to the properties of the porous layer. However, first note that Eq. (3) represents two equations in four unknowns: T_{11}, T_{12}, T_{21}, and T_{22}. Thus, two additional equations are required in order to be able to solve for the transfer matrix elements. Those equations may be generated, for example, by making a second measurement at the four microphone positions after changing the impedance terminating the downstream section of the standing wave tube; that approach is the basis of the so-called two-load method.[25]

However, instead of making a second set of measurements it is possible to take advantage of the reciprocal nature of a layer of homogeneous and isotropic porous material to generate two additional equations. Pierce noted that reciprocity requires that the determinant of the transfer matrix be unity.[31] Ingard has noted that the latter constraint is a general property of passive, linear four-pole networks.[16] Allard has also shown that this condition follows directly from the requirement that the transmission coefficient of a planar, arbitrarily layered acoustical system be the same in both directions.[32] Further, Pierce notes that for symmetrical systems, $T_{11}=T_{22}$. It may easily be shown that the latter condition follows when the plane wave reflection coefficients from the two surfaces of a planar, layered system are the same (see the Appendix). Thus, given reciprocity and symmetry, it follows that

$$T_{11}=T_{22}, \tag{5a}$$

$$T_{11}T_{22}-T_{12}T_{21}=1. \tag{5b}$$

The latter two constraint conditions complete the set of four equations necessary to solve for the transfer matrix elements.

By combining Eqs. (3) and (5), the transfer matrix elements can be expressed directly in terms of the pressures and velocities on the two surfaces of the porous layer, i.e.,

$$T_{11}=\frac{P|_{x=d}V|_{x=d}+P|_{x=0}V|_{x=0}}{P|_{x=0}V|_{x=d}+P|_{x=d}V|_{x=0}}, \tag{6a}$$

$$T_{12}=\frac{P|_{x=0}^2-P|_{x=d}^2}{P|_{x=0}V|_{x=d}+P|_{x=d}V|_{x=0}}, \tag{6b}$$

$$T_{21}=\frac{V|_{x=0}^2-V|_{x=d}^2}{P|_{x=0}V|_{x=d}+P|_{x=d}V|_{x=0}}, \tag{6c}$$

$$T_{22}=\frac{P|_{x=d}V|_{x=d}+P|_{x=0}V|_{x=0}}{P|_{x=0}V|_{x=d}+P|_{x=d}V|_{x=0}}. \tag{6d}$$

Once the transfer matrix elements are known, all of the other acoustical properties of a porous layer, e.g., the reflection and transmission coefficients, can be calculated, as will be demonstrated next.

C. Calculation of reflection and transmission coefficients

For example, consider a porous layer of depth d backed by an anechoic termination, so that it can be assumed that D is negligible compared to C in the downstream tube section. When the incident plane wave is assumed to have unit amplitude, the sound pressures and particle velocities on the two surfaces of the porous layer become

$$P|_{x=0}=1+R, \tag{7a}$$

$$V|_{x=0}=\frac{1-R}{\rho_0 c}, \tag{7b}$$

$$P|_{x=d}=Te^{-jkd}, \tag{7c}$$

$$V|_{x=d}=\frac{Te^{-jkd}}{\rho_0 c}, \tag{7d}$$

where $R=B/A$ and $T=C/A$ are the plane wave reflection and transmission coefficients, respectively. When Eqs. (7) are substituted into Eq. (3), the normal incidence pressure transmission and reflection coefficients for the case of an anechoic termination, T_a and R_a, respectively, can be expressed as

$$T_a=\frac{2e^{jkd}}{T_{11}+(T_{12}/\rho_0 c)+\rho_0 c T_{21}+T_{22}}, \tag{8}$$

$$R_a=\frac{T_{11}+(T_{12}/\rho_0 c)-\rho_0 c T_{21}-T_{22}}{T_{11}+(T_{12}/\rho_0 c)+\rho_0 c T_{21}+T_{22}}. \tag{9}$$

In contrast, when the porous layer of depth d is positioned against a rigid backing, $V|_{x=d}=0$. Then, when the latter condition and Eqs. (7a) and (7b) are substituted into Eq. (3), the normal incidence reflection coefficient for the hard-backing case, R_h, is obtained as

$$R_h=\frac{T_{11}-\rho_0 c T_{21}}{T_{11}+\rho_0 c T_{21}}. \tag{10}$$

Similar expressions may easily be derived for the case of a porous layer backed by an arbitrary impedance.

D. Calculation of wave number and characteristic impedance

Next, note that the normal incidence transfer matrix for a finite depth layer of a homogeneous, isotropic porous material that can be considered to be either limp or rigid is[16,32]

$$\begin{bmatrix} T_{11} & T_{12} \\ T_{21} & T_{22} \end{bmatrix}=\begin{bmatrix} \cos k_p d & j\rho_p c_p \sin k_p d \\ j \sin k_p d/\rho_p c_p & \cos k_p d \end{bmatrix}. \tag{11}$$

In Eq. (11), k_p is the wave number in the acoustical material, d is the layer thickness, and $\rho_p c_p$ is the characteristic impedance of the material. Thus, the four transfer matrix elements may be directly associated with the acoustical properties of the porous material. In particular, the wave number can be evaluated either as

$$k_p=\frac{1}{d}\cos^{-1} T_{11}, \tag{12a}$$

or

$$k_p=\frac{1}{d}\sin^{-1}\sqrt{-T_{12}T_{21}}, \tag{12b}$$

and the characteristic impedance of the acoustical material can be calculated most directly as

$$\rho_p c_p = \sqrt{\frac{T_{12}}{T_{21}}}. \tag{13}$$

Quantities such as the complex sound speed, $c_p = \omega/k_p$, and complex density, $\rho_p = \rho_p c_p / c_p$, can easily be determined when k_p and $\rho_p c_p$ are known.

III. EXPERIMENTAL PROCEDURE

The experimental procedure used in the present work was based very closely on the earlier work by Bolton *et al.*,[2] and will be summarized only briefly here. The measurements were made using a modified standing wave tube (the Brüel & Kjær two-microphone impedance measurement tube type 4206). A loudspeaker at one end of the tube was used to generate a broadband random signal over the frequency range 100 to 6400 Hz and the transfer function between the input signal to the loudspeaker and the microphone output at each of the four measurement positions was measured over that band by using a Brüel and Kjær 2032 frequency analyzer. Note that the Brüel and Kjær two-microphone impedance measurement tube type 4206 is suitable for both low-frequency (100 to 1600 Hz) and high frequency (500 to 6400 Hz) measurements. In the work presented here, only the 2.9-cm inner diameter, high-frequency tube was used, so that the results presented, with one exception, are confined to the high-frequency range. Note also that a single-microphone approach was adopted here as a matter of convenience: i.e., a two-channel analyzer could be used to make the measurements and there was no need to phase-calibrate the microphone. Given access to four phase-matched microphones and a multichannel data acquisition procedure, it would not be difficult to implement a multimicrophone version of the present procedure. Note that when using the single-microphone approach, a greater number of averages should be used when estimating the transfer functions than might normally be the case in a four-microphone measurement.[2,33] In addition, it is necessary to compensate for the propagation delay between the loudspeaker and the various microphones to avoid the introduction of a time-delay bias error.[34] Note finally that it may be desirable in future implementations to base the single-microphone procedure on the measurement of transfer functions between a fixed microphone placed near the sample and the roving microphone placed at each of the four measurement positions in turn.[34] The latter approach ensures that loudspeaker nonlinearities do not affect the results.

In the present application, the standing wave tube was modified by the addition of a second high-frequency microphone holder and the first section of a high-frequency sample holder to create a new downstream section: see Fig. 2. The downstream section was separated from the upstream section by a sample holder of the same internal diameter as the up- and downstream sections. The two measurement positions in the up- and downstream tube sections were separated by a distance of 2 cm; measurement position 2 was in all cases 21.2 cm from the front surface of the sample, and measurement position 3 was 13.6 cm downstream of the rear surface of the sample when 7.5-cm-deep samples were used; this distance increased to 16.1 and 18.6 cm, respectively, when

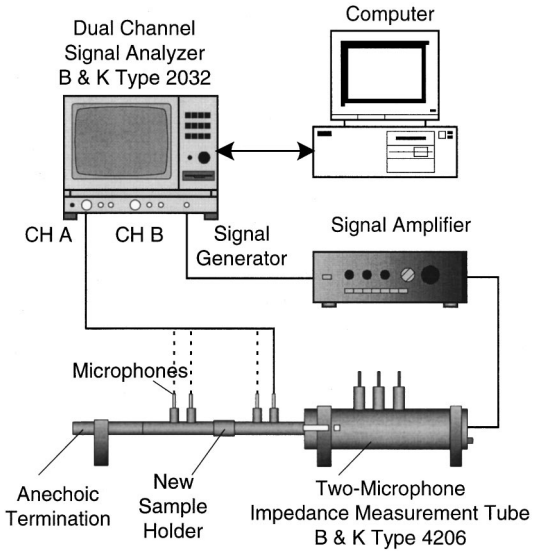

FIG. 2. Schematic of the measurement setup.

5.0-cm and 2.5-cm-thick samples were used. Note that recent work suggests that there is a frequency-dependent, optimum microphone separation for multimicrophone measurements of the type reported here.[35] The latter effect should be investigated in the future to ensure the selection of an appropriate microphone separation given the frequency range of interest.

A subsequent structural modal analysis of the sample holder used in the present work revealed that its first two natural frequencies fell within the frequency range of interest: at approximately 4.6 and 4.9 kHz. The first mode involved a longitudinally uniform ovalling of the sample holder; in the second mode the ovalling was out of phase at the two ends of the sample holder. Both of these motions can presumably couple well with the first, higher-order acoustical circumferential mode within the sample contained within the holder. It is believed that this effect accounted for some of the anomalies in the measured results that are visible between 4 and 5 kHz; see Sec. IV. In future work the sample holder will be stiffened to raise its first natural frequencies above the frequency range of interest.

The downstream section was terminated by an approximately anechoic termination that was created by loosely packing the standard sample holder with 66 cm of 3M Thinsulate sound-absorbing material. The absorption coefficient of this termination was greater than 0.97 in the frequency range of interest (500 to 6400 Hz).[2] Note that an anechoic termination is not required by the measurement procedure used here; in principle, the termination impedance can be arbitrary, and its value need not be known: see Sec. V B. However, the presence of the anechoic termination causes the sound field in the downstream section to be almost purely propagational, thus minimizing the possibility of error in the downstream transfer function estimates. Note also that when the downstream termination impedance is known either *a priori* (e.g., if there is a rigid termination) or by independent measurement, the relation between the coefficients C and D in Eqs. (1) can be determined. In that case only a single downstream sound-pressure measurement would be required, and the current procedure would become, in effect, a broad-

TABLE I. The physical properties of the glass fiber materials.

Sample	Bulk density [kg/m^3]	Flow resistivity [MKS Rayls/m]	Std. dev. of flow resistivity [MKS Rayls/m]
A	6.7	1.5×10^4	1.4×10^3
B	9.6	2.4×10^4	2.5×10^3

band implementation of the Champoux and Stinson technique described above.[18]

The material tested in the present work was aviation-grade glass fiber; the properties of the materials used are listed in Table I. The sheets of glass fiber from which the samples were cut were nominally 2.5 cm thick, and cylindrical samples of the lining material were carefully cut to fit snugly inside the sample holder. The measurements reported here were made using either three, two, or one layer(s) of lining material to give total sample thicknesses of 7.5, 5.0, or 2.5 cm, respectively. Lining materials were carefully inserted into the sample holder so that the depth of the individual layers comprising the complete sample was preserved. To reduce the effect of mounting sample errors and material variability, in each case ten different measurements were performed using a total of 30, 2.5-cm-deep samples in the case of 7.5-cm total depth, and correspondingly fewer pieces for the smaller total sample depths; the results of the ten individual tests were then averaged to give the results presented here.

IV. RESULTS AND DISCUSSION

A. Transmission loss

Consider first the normal incidence transmission loss of 7.5-cm depths of the two materials; see Fig. 3. This quantity was calculated as $\mathrm{TL}=20\log|C|/|A|$ and represents an approximation to the transmission loss since the magnitude of the plane wave component reflected from the termination, D, although small, is still finite.[2] Note also that the results are plotted here from 100 to 6400 Hz. Although the results are not certain to be accurate below 500 Hz owing to the 2-cm intermicrophone spacing, they are believed to be accurate in character owing to the low reactivity of the sound field in both the up- and downstream segments of the standing wave tube.

While the transmission loss of both materials increases with increasing frequency above 1 kHz as would be expected, note that the transmission loss also increases with decreasing frequency below a minimum near 400 Hz (sample A) and 500 Hz (sample B). This behavior is typical of the effect of sample-edge constraint on the normal incidence transmission loss of an elastic porous material,[2,36,37] an effect first noted by Beranek in the context of normal incidence absorption measurements.[5] This effect is primarily significant at low frequencies owing to the strong viscous coupling between the solid and fluid phases of the porous material in that region. In the present case, it was concluded that the sample-edge constraint caused the measured results to differ from those of a laterally infinite plane sheet at frequencies below 1 kHz. It is expected that the edge-constraint effect would be mitigated by the use of larger diameter samples; this suggestion will be investigated in future work.

B. Transfer matrix

The magnitudes and phases of the averaged transfer matrix elements for the two materials considered here, calculated using Eqs. (6), are plotted in Fig. 4. Each of the elements is significant in this case, and each has a particular physical meaning. Note first that the elements T_{11} and T_{22} are identical owing to the constraint, Eq. (5a), imposed by

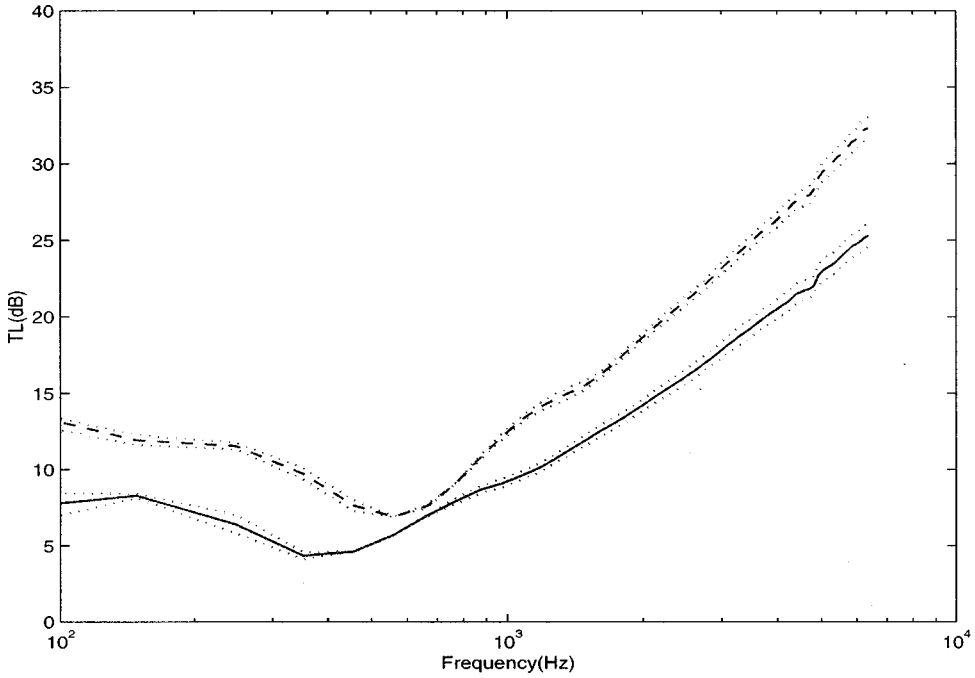

FIG. 3. Normal incidence transmission loss of lining materials A and B. Solid line: sample A; dashed line: sample B. Dotted lines indicate ± one standard deviation.

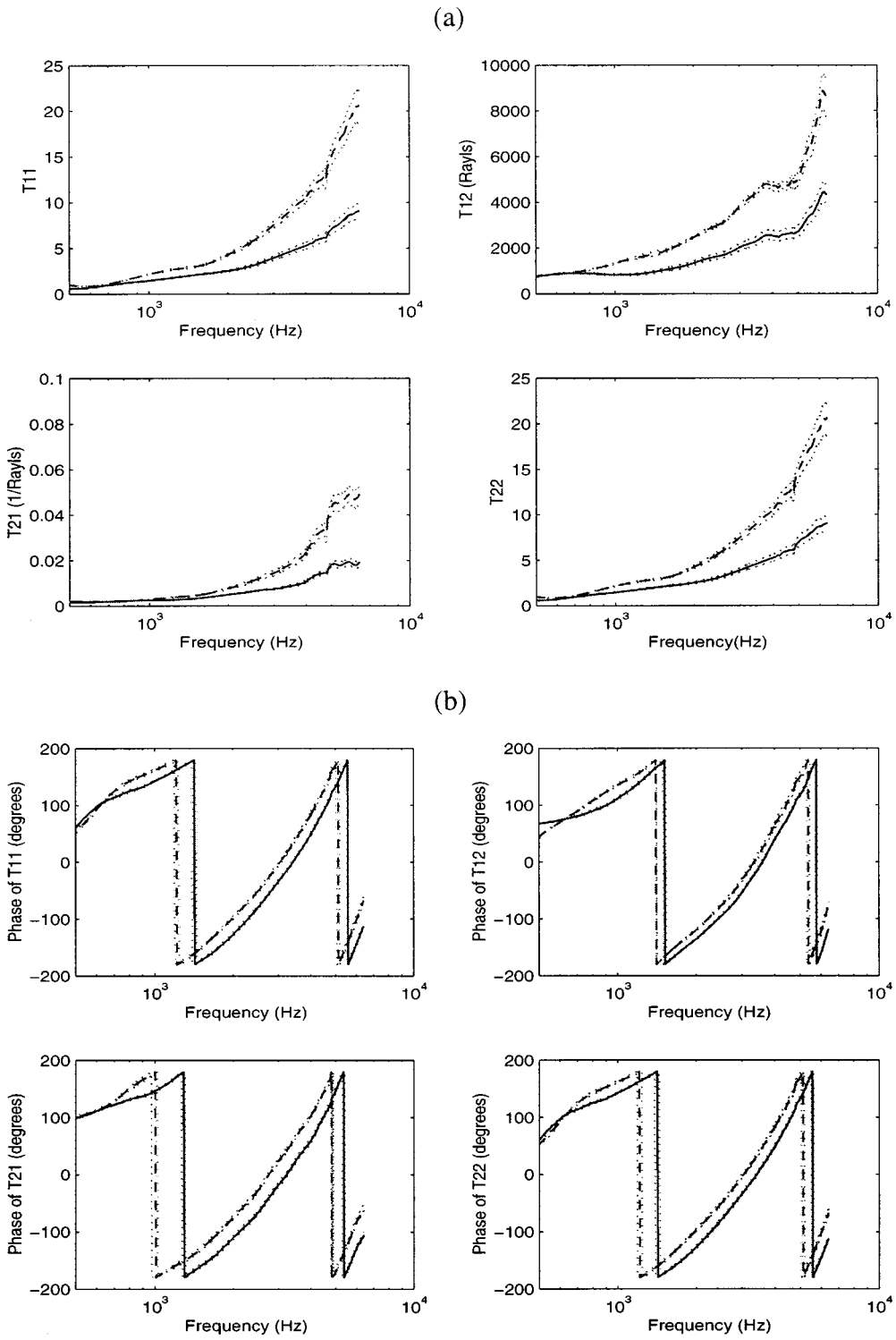

FIG. 4. Transfer matrix elements for samples A and B. Dotted lines indicate ± one standard deviation. (a) Magnitude, and (b) phase. Solid line: sample A; dashed line: sample B.

symmetry. Further, the element T_{11} is the ratio of the upstream and downstream pressures in the case of a zero velocity state at the downstream layer surface, and it is thus dimensionless. The element T_{12} is the ratio of the upstream pressure and downstream velocity when a zero-pressure state exists at the downstream surface of the sample, and thus it has the units of impedance. Conversely, T_{21} represents the ratio of the upstream velocity and the downstream pressure when the downstream surface velocity state is zero; i.e., for the case of a hard-backing boundary condition at the downstream surface of the sample. The element T_{21} thus has the units of admittance.

C. Wave number and characteristic impedance

The wave numbers and normalized characteristic impedances of the materials considered here are plotted in Figs. 5

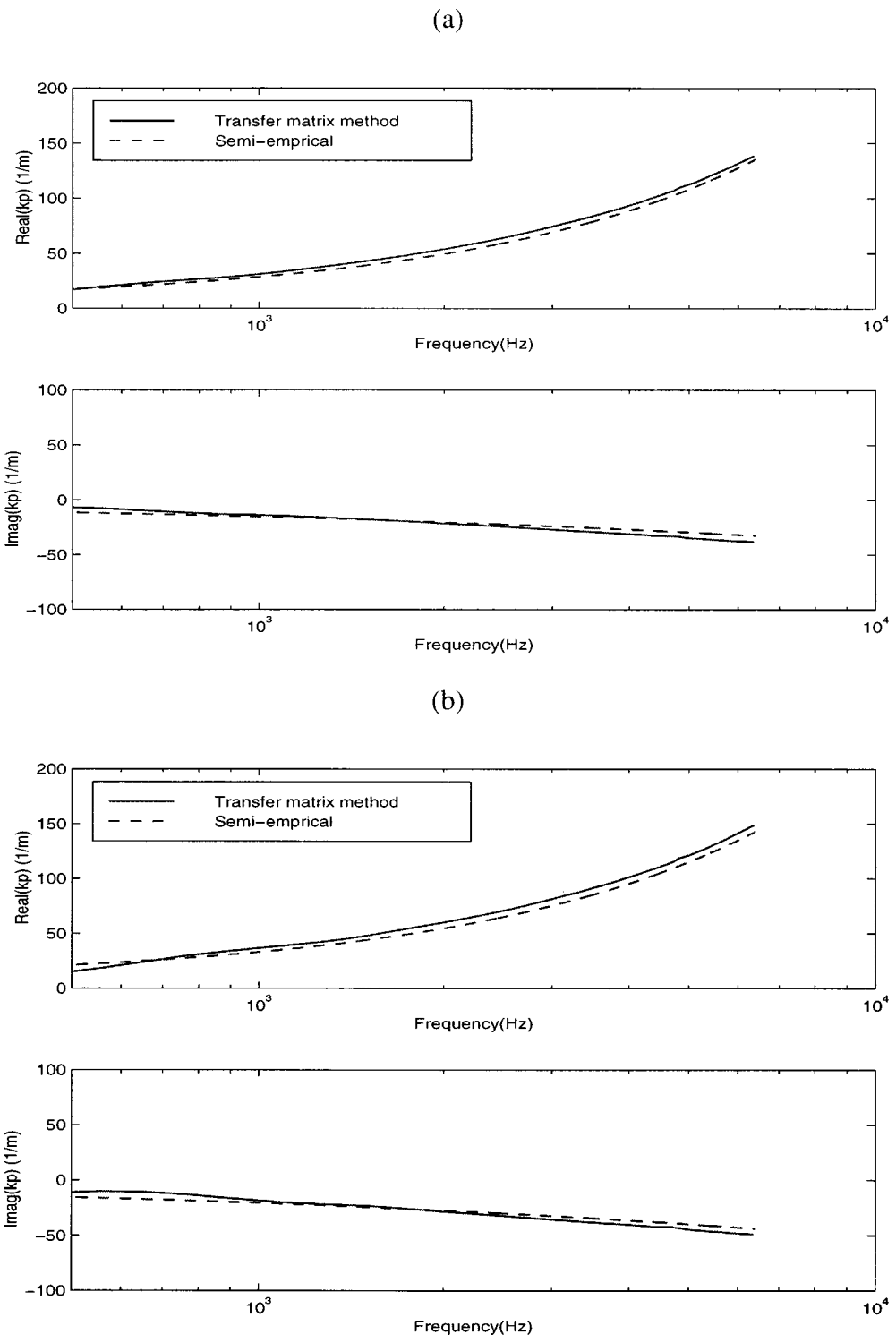

FIG. 5. Wave number within lining material determined by using transfer matrix method and predicted using semiempirical formulas: (a) sample A; (b) sample B.

and 6, respectively. Predictions made using the Delany and Bazley semiempirical formulas[38] for fibrous materials are also plotted. It can be seen that the measured and predicted wave numbers are in good agreement over the entire frequency range. The measured characteristic impedances agree reasonably well with the predictions except at low frequencies; it is believed that the low-frequency discrepancy results from the constraint of the sample around its edges, as discussed above.

It is also of interest to plot the wave number components in a more immediately meaningful form. For example, the phase speed in the porous material, c_{ph}, can be expressed in normalized form as

$$\frac{c_{\mathrm{ph}}}{c} = \frac{\omega}{c\beta_p}, \tag{14}$$

where β_p is the real part of k_p. The normalized phase speeds

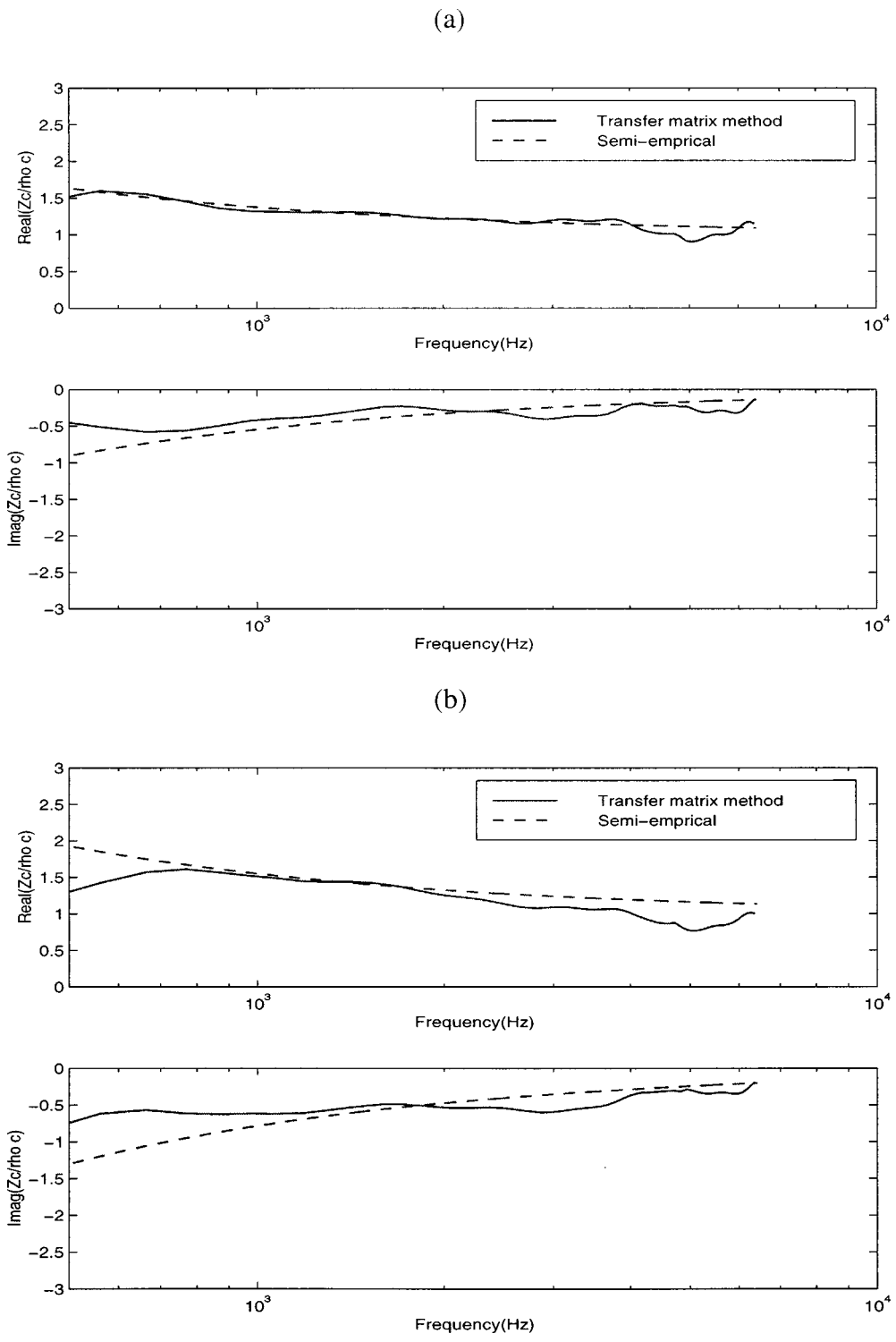

FIG. 6. Normalized characteristic impedance of lining material determined by using transfer matrix method and predicted using semiempirical formulas: (a) sample A; (b) sample B.

are plotted in Fig. 7, where it can be seen that there is reasonable agreement between the measurements and the Delany and Bazley prediction (except at the lowest frequencies, for the reasons discussed above).

Note that, as expected, the phase speed is reduced in the porous medium compared to that in air. As a result, higher-order duct modes may ''cut on'' within the porous material at frequencies lower than they would in air, approximately by the ratio of the sound speeds (although in a dissipative medium there is, of course, no longer a strict distinction between propagating and nonpropagating modes). In the present instance, these modes may be closely coupled, in the frequency range about 4 kHz, with the sample holder modes that were noted in Sec. III. This effect may be responsible for the feature visible in T_{12} (see Fig. 3) above 4 kHz for both materials, as well as for the features in the real part of the

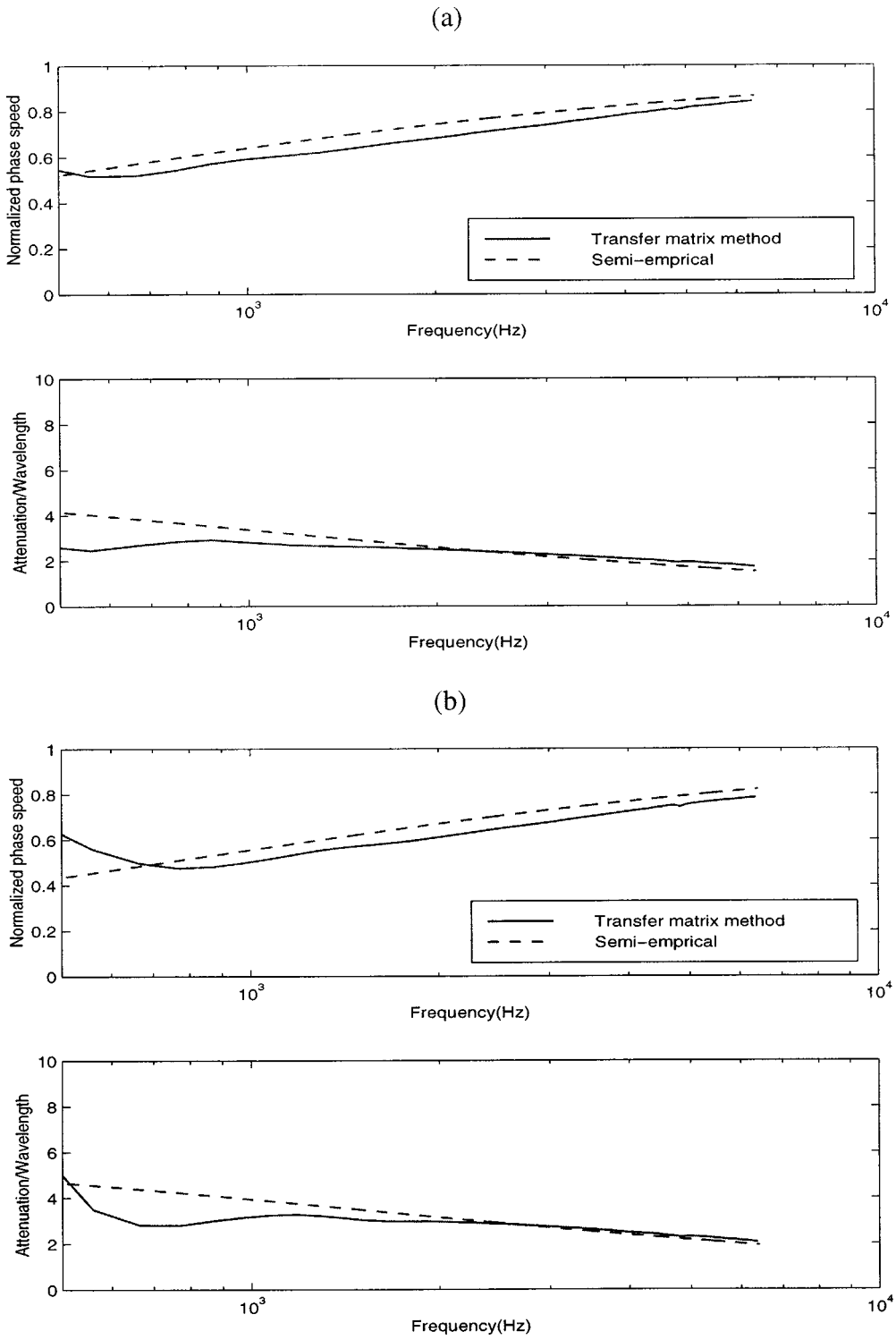

FIG. 7. Normalized phase speed and attenuation per wavelength determined by using transfer matrix method and predicted using semiempirical formulas: (a) sample A; (b) sample B.

characteristic impedance in the same frequency range; see Fig. 6.

The acoustical dissipation within a porous material may be expressed in terms of the attenuation per wavelength, which is also plotted in Fig. 7. This quantity is calculated as $\alpha_p \lambda_p$ where α_p is the imaginary part of the wave number in the porous material, and $\lambda_p = f/c_{\mathrm{ph}}$ (where f is the frequency) is the wavelength within the material. The attenuation per wavelength may thus be calculated as

$$\alpha_p \lambda_p = 2\pi \alpha_p / \beta_p . \tag{15}$$

It may be seen that there is good agreement between the measurements and predictions at frequencies above 1 kHz.

D. Complex density and sound speed

As mentioned in the Introduction, homogeneous and isotropic limp or rigid porous materials may be modeled as

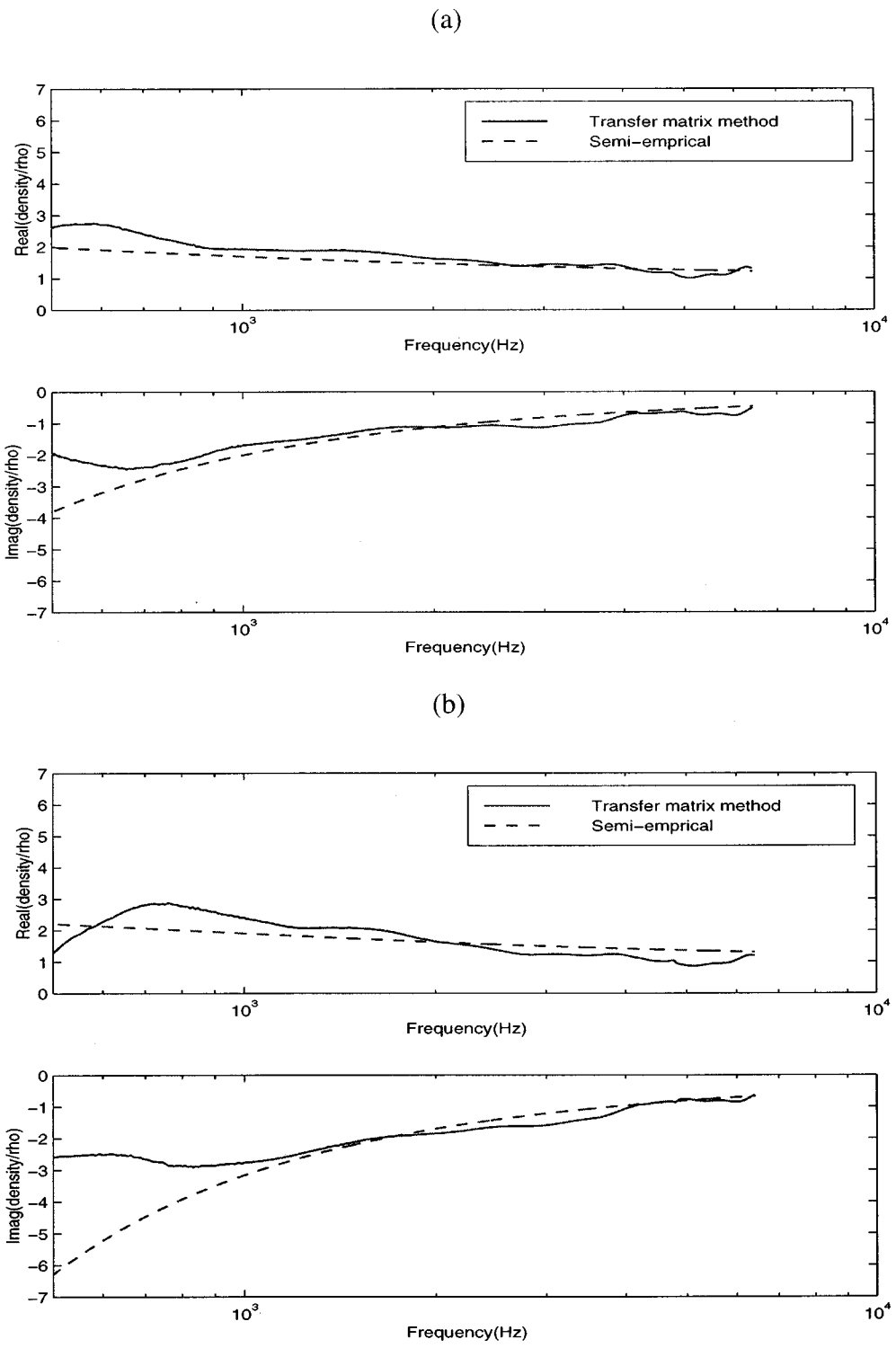

FIG. 8. Normalized complex density determined by using transfer matrix method and predicted using semiempirical formulas: (a) sample A; (b) sample B.

fluids having complex properties. Thus, arbitrarily shaped porous material domains may be modeled by using existing finite and boundary element codes so long as provision has been made for complex material properties; see Ref. 39 for a recent example of this approach. The input data most often required by these programs are complex density and the complex sound speed within the porous material. The complex density can be calculated in normalized form as

$$\frac{\rho_p}{\rho_0} = \frac{(\rho_p c_p) k_p}{\rho_0 \omega}, \tag{16}$$

and the normalized complex sound speed as

$$\frac{c_p}{c} = \frac{\omega}{k_p c}. \tag{17}$$

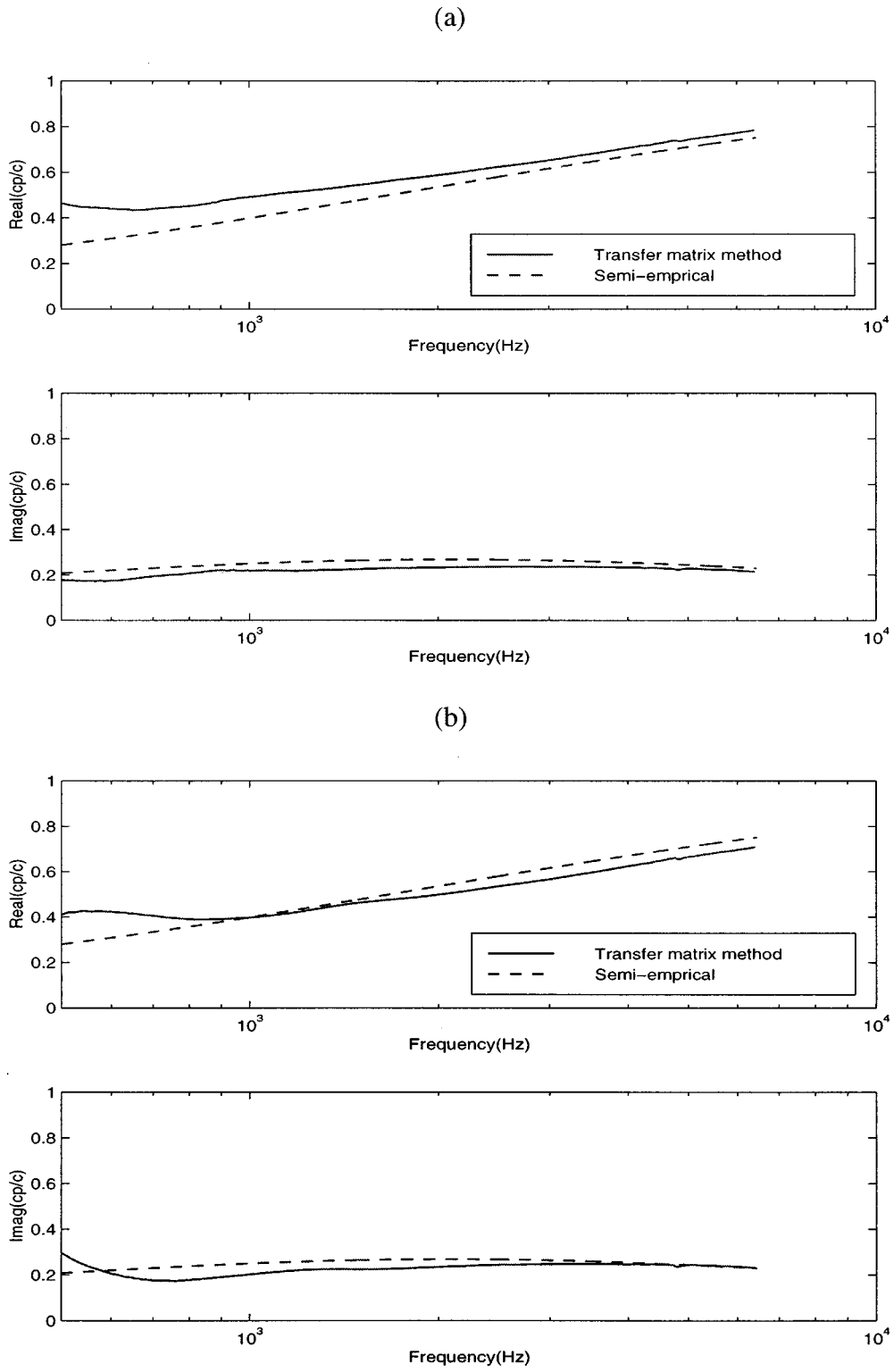

FIG. 9. Normalized complex sound speed determined by using transfer matrix method and predicted using semiempirical formulas: (a) sample A; (b) sample B.

The normalized complex densities of the present materials are shown in Fig. 8, where it can be seen that there is good agreement with the theoretical prediction at frequencies above 1 kHz. Note that the complex density used here is a bulk density in contrast to the pore-based complex density referred to in Ref. 32: the two quantities differ by a factor of porosity. The normalized complex sound speeds are shown in Fig. 9, where again it can be seen that there is good general agreement with the theoretical predictions.

E. Prediction of reflection coefficient for the hard-termination case

Once the transfer matrix of a porous layer is known, the performance of the latter may be predicted in a variety of

(a)

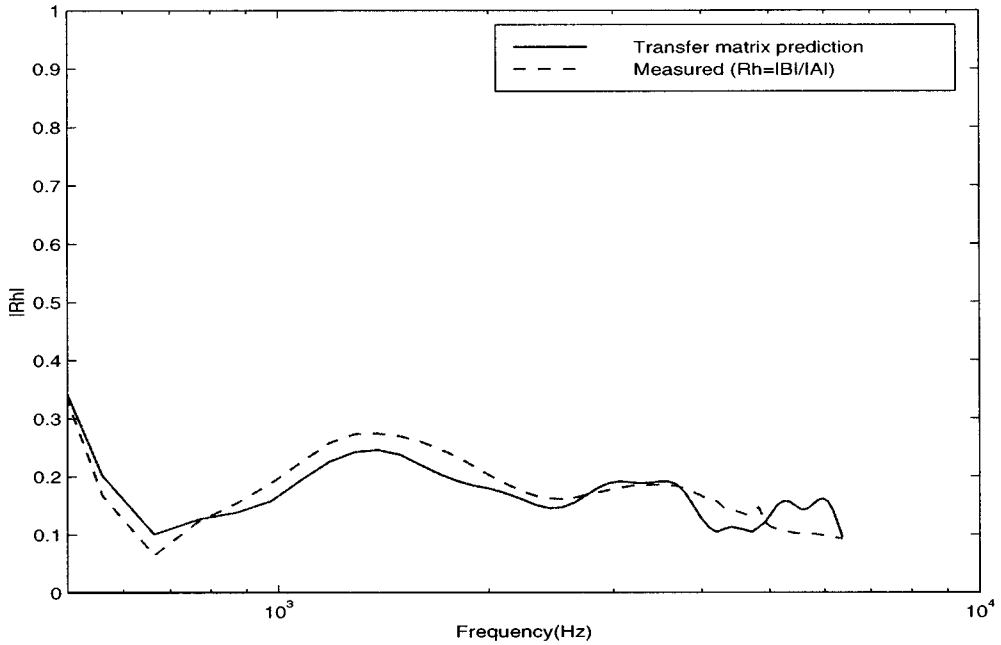

(b)

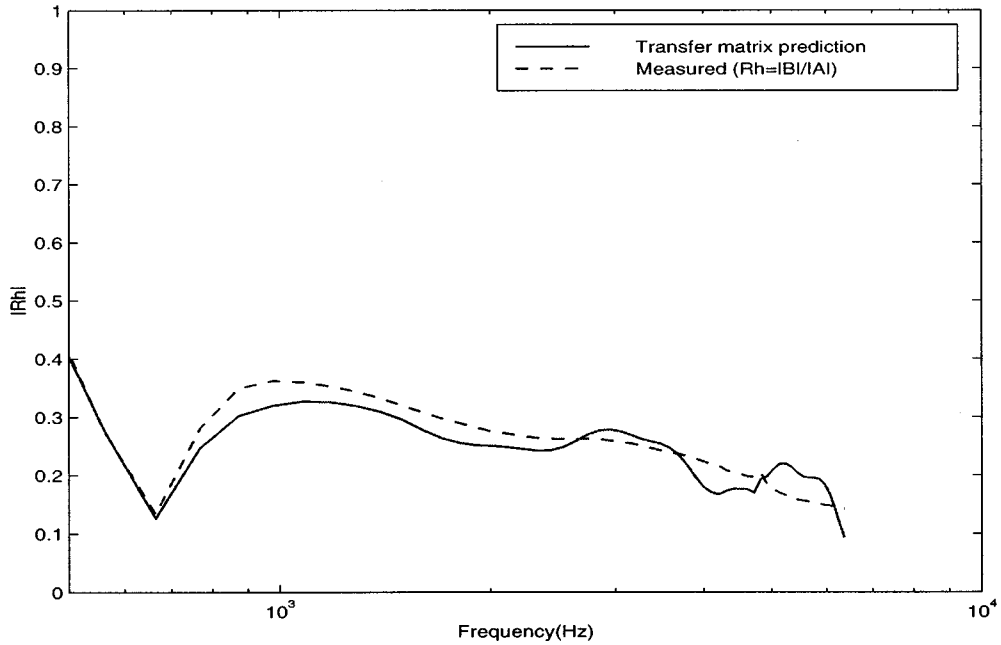

FIG. 10. Reflection coefficients in the hard-termination case: (a) sample A; (b) sample B.

applications. For example, the reflection coefficient of a porous layer positioned in front of either an anechoic or rigid termination can be calculated based on a knowledge of the transfer matrix elements by using Eqs. (9) and (10), respectively. In Fig. 10, the magnitudes of the directly measured reflection coefficients for the two materials in the hard-termination configuration (evaluated as $R_h=|B|/|A|$) are compared with the predicted ones based on the measured transfer matrix elements.

The measured results shown are the average of ten individual measurements of 7.5-cm-deep layers assembled from the same 30, 2.5-cm-deep samples used in the transfer matrix measurements. The results were not expected to be particularly accurate below 1000 Hz owing to the sample edge-constraint effect described above, nor above 4 kHz owing to the effect of sample holder modes. Nonetheless, the predictions based on the measured transfer matrix elements faithfully capture the character of the directly measured results.

Note that once the wave number and characteristic impedance of a particular porous material are known, predic-

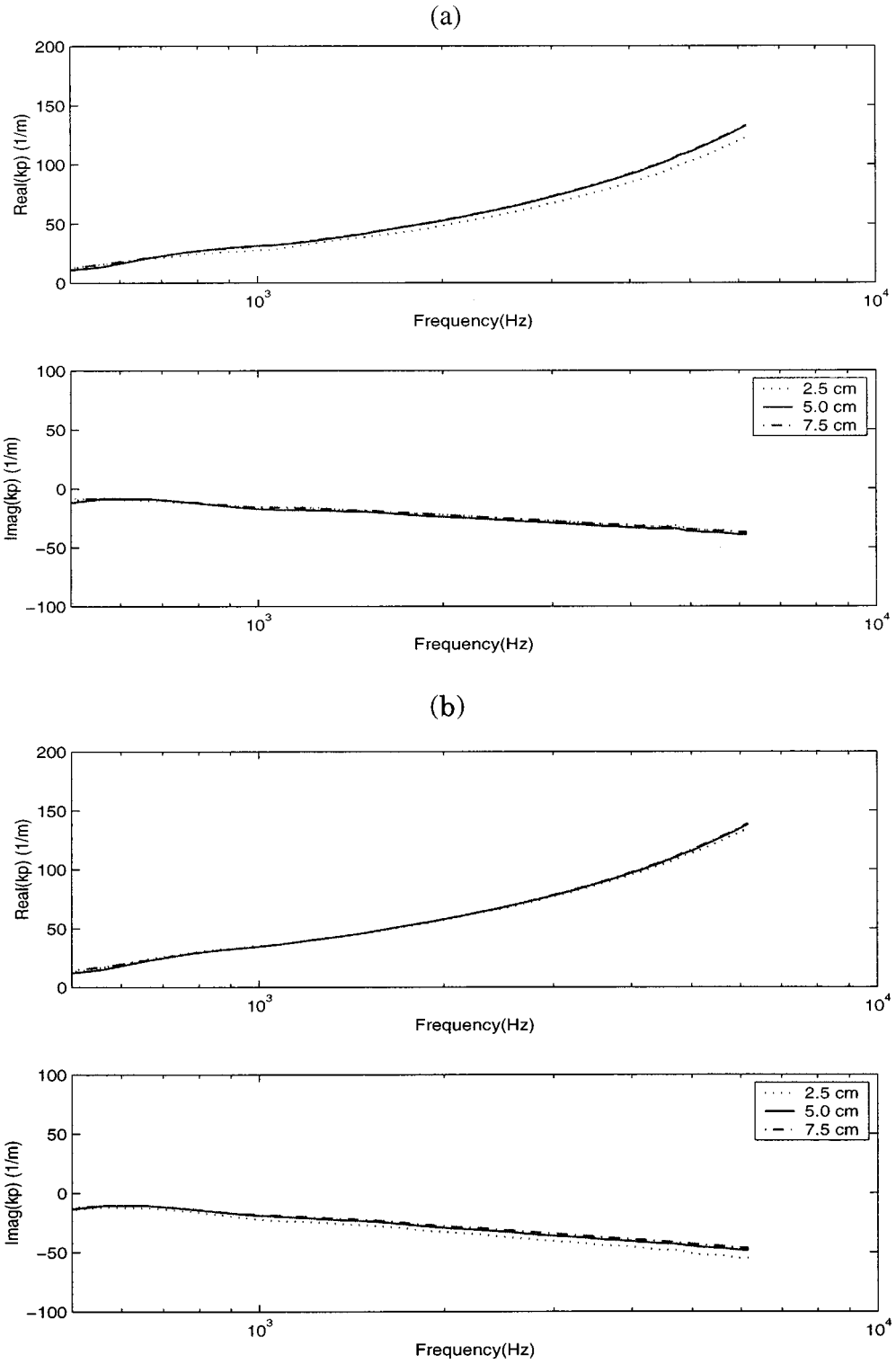

FIG. 11. Wave number within lining material determined by using transfer matrix method in combination with different sample thicknesses, as noted: (a) sample A; (b) sample B.

tions of the reflection or transmission coefficients of an arbitrary thickness of that material may be made by using the transfer matrix approach. In addition, the transfer matrix approach may be extended to non-normal incidence cases to predict the oblique incidence behavior of sheets of porous materials, either alone or in combination with other acoustical elements.[3,16,32]

V. VERIFICATION STUDIES

A. Effect of sample depth

Finally, it was of interest to perform a sequence of experiments to verify the capabilities of the transfer matrix procedure described here. First, the effect of sample depth will

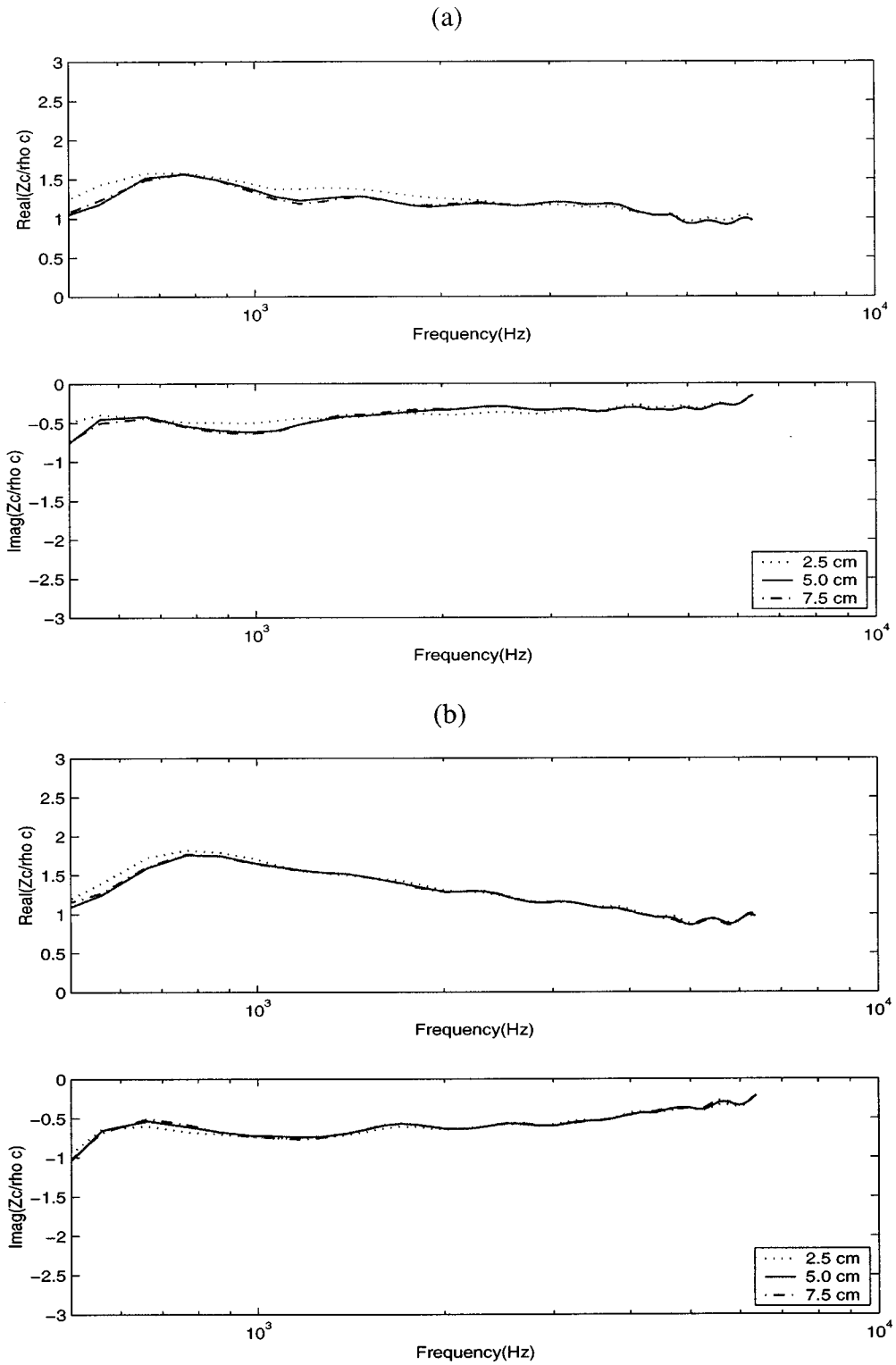

FIG. 12. Normalized characteristic impedance of lining material determined by using transfer matrix method in combination with different sample thickness: (a) sample A; (b) sample B.

be demonstrated. The wave number and characteristic impedance are both inherent properties of a homogeneous fibrous material, and thus, if the proposed procedure works properly, the estimated values of these quantities should not depend on the depth of the sample under test. Here, measurements were made using ten 5-cm-deep samples and ten 2.5-cm-deep samples of both materials A and B: those results were compared with the estimates made using the 7.5-cm-deep samples that were presented earlier. Shown in Fig. 11 are the averaged wave numbers estimated using the three sample depths. It may be seen that the propagation constants are essentially identical in the 5.0- and 7.5-cm cases, but that there is a slight discrepancy in the 2.5-cm case. It is possible that the latter discrepancy resulted from leakage around the edge of the sample; it was difficult to mount the relatively thin and light 2.5-cm samples in the sample holder without

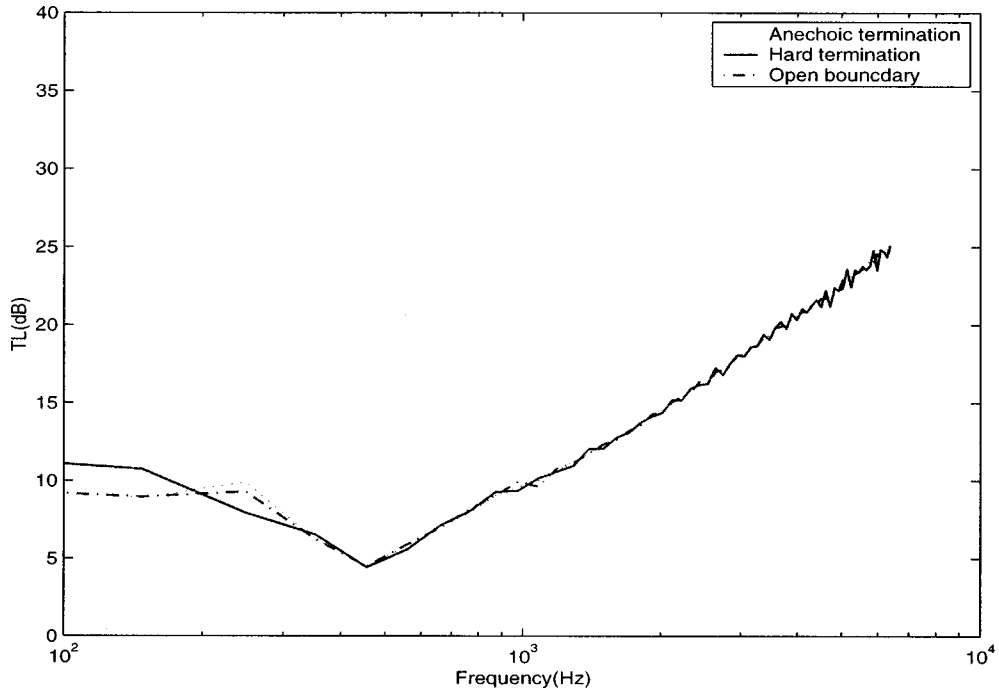

FIG. 13. Normal incidence transmission losses of lining material A estimated by using the transfer matrix method in combination with three different termination conditions.

creating small gaps around the edge of the samples. Leakage appeared not to be a problem with the deeper samples. Effects of sample inhomogeneity are also likely to be exaggerated when using thin samples (since a smaller total amount of material is involved in ten 2.5-cm-deep samples than in ten 5.0-cm-deep samples, etc.). The characteristic impedance results are shown in Fig. 12. It may be seen that there was good agreement between the estimated values in all three cases although, once again, the estimates based on the 2.5-cm samples deviate slightly from the other results. However, taken together, the wave number and characteristic impedance results do indicate that estimates of the fundamental properties of the sample materials were independent of sample depth, as expected, except, that is, when relatively thin samples were used, in which case edge leakage and intersample inhomogeneities may have affected the results.

B. Effect of tube-termination conditions

It was pointed out earlier that a knowledge of the tube-termination impedance is not required when using the present approach: it was of interest to confirm this feature of the transfer matrix method. Second, it was of interest to illustrate the errors introduced in transmission loss estimates when no account was made of reflections from the termination. Measurements of the transmission loss of the 7.5-cm depths of sample A made using the transfer matrix procedure in combination with three termination conditions (nearly anechoic as described in Sec. III, rigid and open) are shown in Fig. 13. It may be seen that the differences between the three estimates are small even when the termination conditions are dramatically different. Noticeable discrepancies occur below 500 Hz, which, however, is the lower limit of the frequency range over which results are known to be accurate when using the present microphone spacing. In addition, in the case of the hard termination, there is a small oscillatory error in the transmission loss results at high frequencies, presumably resulting from the highly reactive standing wave field in the downstream tube section in this case. The results shown in Fig. 14 indicate that neither the estimates of the wave number or characteristic impedance are significantly affected by the tube termination conditions. Together, these results support the claim that the transfer matrix procedure results are essentially independent of termination conditions, at least in application to fibrous material properties, of the type considered here.

Shown in Fig. 15 are estimates of the transmission loss of a 7.5-cm depth of sample A based simply on the use of $T=|C|/|A|$: i.e., no accounting was made of the reflection from the tube termination. The results shown are the average of ten individual measurements. It can be seen that the estimated transmission losses can be significantly in error in these cases: only the anechoic termination case approaches the results obtained using the transfer matrix method.

C. Comparison with two-load method

Finally, it was of interest to compare results obtained using the proposed transfer matrix method and the two-load method.[25] The two-load method was implemented using the same approach as for the transfer matrix method, except that measurements at the four microphone locations were made in sequence for two termination conditions: nearly anechoic and rigid. Those data were then used in conjunction with Eq. (3), written twice, to solve for the transfer matrix elements. In the two-load measurements, the 7.5-cm-deep samples of material A were used. The results of ten individual measure-

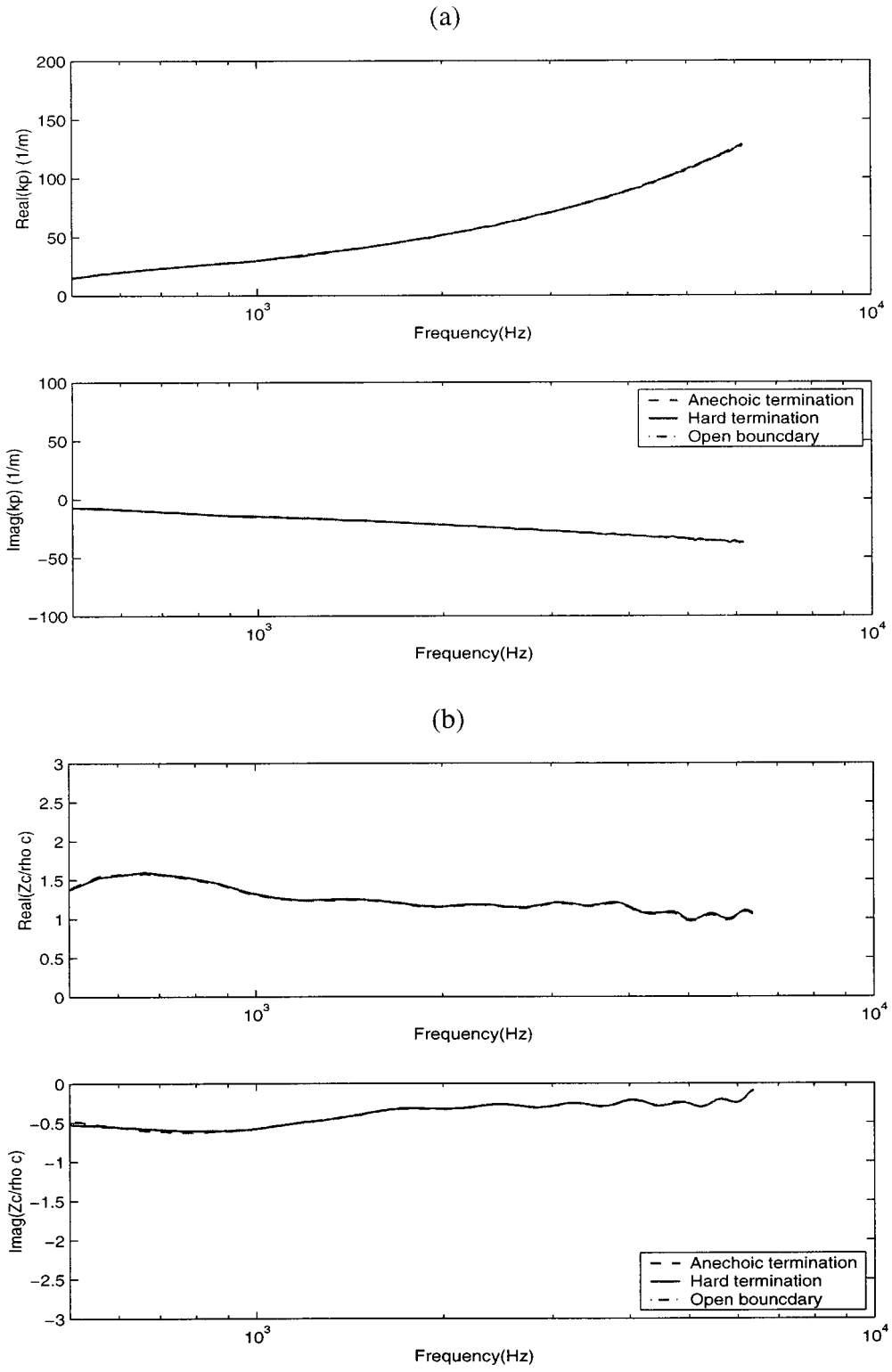

FIG. 14. (a) Wave number and (b) normalized characteristic impedance estimated for material A by using the transfer matrix method in combination with three different termination conditions.

ments were averaged as before. It may be seen from Fig. 16 that the two procedures yield essentially identical estimates of the transmission loss except at frequencies below which the present intermicrophone spacing is not guaranteed to yield accurate results. Close agreement was also found when estimating the wave number and characteristic impedances, as may be seen from Fig. 17. Note, however, that the two-load results are distorted by a small oscillatory error at high frequencies that presumably results from the highly reactive downstream sound field in the rigid termination case. Thus, it may be concluded that the transfer matrix method presented here yields results that are of the same or better quality than

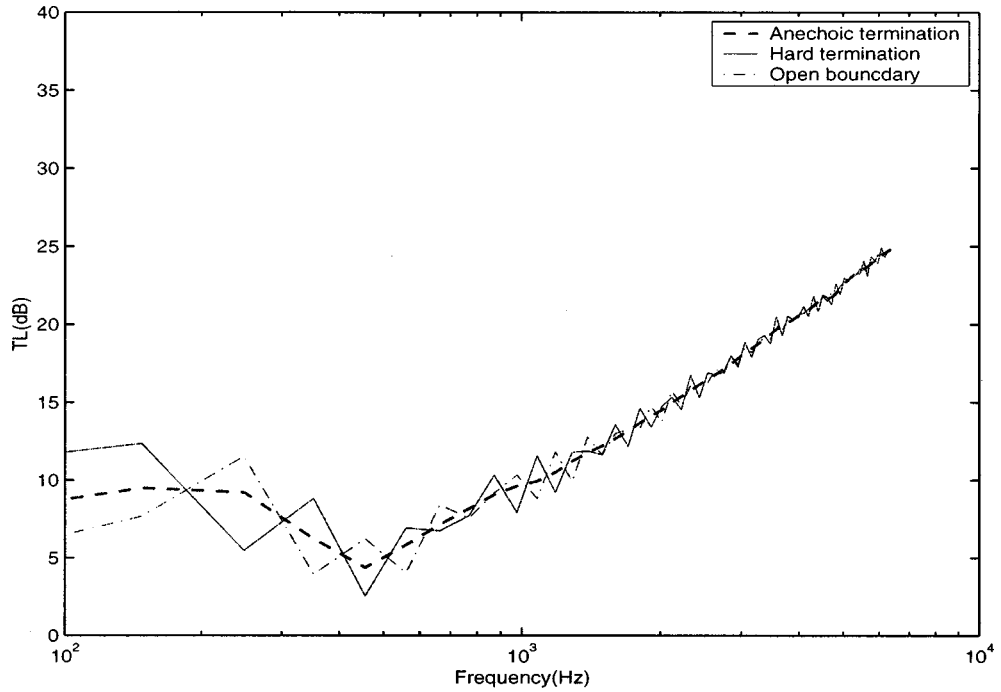

FIG. 15. Normal incidence transmission losses of lining material A estimated using the ratio $|C|/|A|$ for three different termination conditions.

those of the two-load method, even though only half the number of measurements are required when using the former procedure.

VI. CONCLUSIONS

The intention of the present work was to develop a quick and convenient method for determining the fundamental acoustical properties (i.e., the wave number and characteristic impedance) of commonly used porous materials. The procedure described here was based on well-known transfer matrix methods, but the number of measurements required was reduced compared to earlier methods by taking advantage of the reciprocal nature of sound transmission through homogeneous and isotropic porous layers. The kind of information that can be derived from the present method, e.g., complex density and sound speed, is the information required to model limp or rigid porous materials in finite or boundary element procedures, and so the present procedure may prove a useful adjunct to modern noise-control design procedures.

Note, finally, that elastic porous materials such as foams can support two longitudinal waves and a single transverse

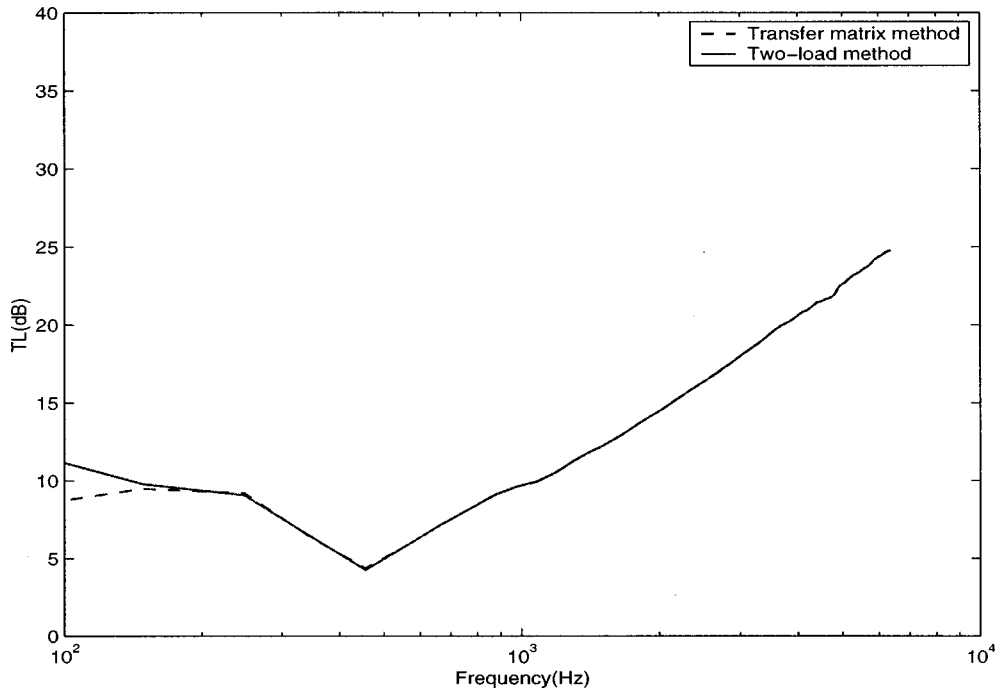

FIG. 16. Comparisons of the normal incidence transmission loss of sample A estimated by using the transfer matrix method and two-load method.

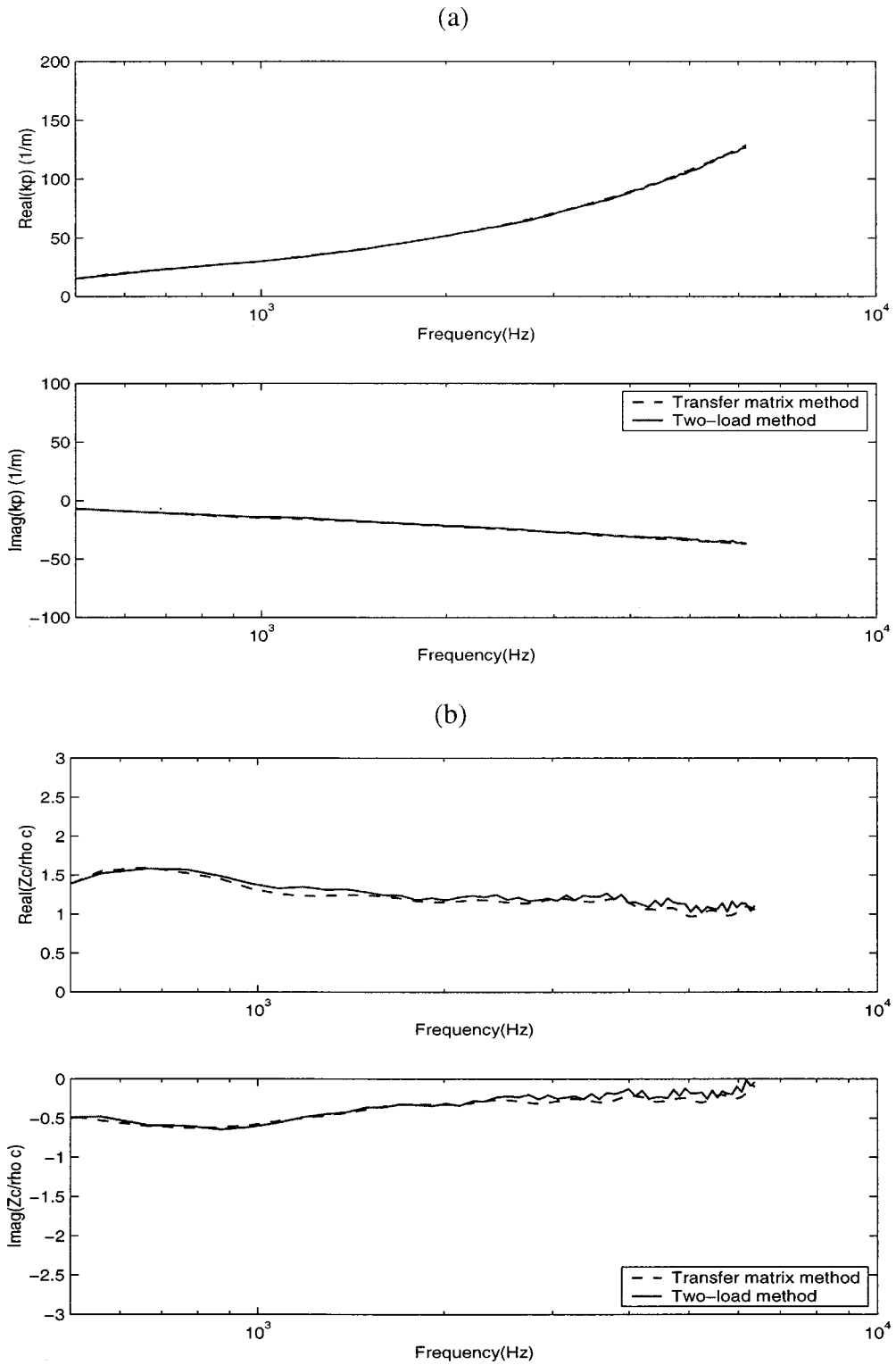

FIG. 17. (a) Wave number, and (b) normalized characteristic impedance for material A estimated by using the transfer matrix method and two-load method.

wave.[40] Although a single airborne wave is often dominant in unfaced noise-control foams, in which case they can be modeled as effective fluids (see Ref. 39, for example), the other two wave types may sometimes contribute very significantly, depending on the details of the foams' surface boundary conditions.[41] Thus, in principle, a transfer matrix representation of a foam layer is much more complicated than that presented here as Eq. (10).[16,32] The reader should therefore be cautious when applying the present method to foams.

ACKNOWLEDGMENTS

This paper was written while the authors were visiting the Center for Noise and Vibration Control (NOVIC) in the Department of Mechanical Engineering of the Korea Advanced Institute of Science and Technology. We are grateful for the hospitality extended by the NOVIC faculty, students and staff. The second author extends his thanks, in particular, to Professor Yang-Hann Kim and Professor Jeong-Guon Ih

for arranging his visit and helping to make it productive, and to the Korea Research Foundation for providing financial support. We are also grateful to Joseph Pope, who suggested the use of a four-microphone method to measure the transmission loss of porous materials and to David Apfel of L & L Products of Romeo, Michigan, whose initial financial support helped to make this work possible. Finally, our thanks go to Robert Schlinker of the United Technologies Research Center, who arranged the financial support that made it possible to complete the present work.

APPENDIX A: IMPLICATIONS OF RECIPROCAL SOUND TRANSMISSION AND REFLECTION

In this Appendix, normal incidence sound transmission through, and sound reflection from, an arbitrarily layered medium represented by a two-by-two transfer matrix are considered. The approach followed is similar to that of Allard, who previously considered the implications of reciprocal sound transmission.[32] The configurations considered are shown in Fig. A1, where the two surfaces of the layered system are labeled A and B. Note that the only difference between the two configurations is the location of the x-coordinate origin which is shifted in case (b) with respect to case (a) as a matter of convenience. In case (a), a unit amplitude plane wave is assumed to be incident on surface A, and the reflection and transmission coefficients are denoted R_1 and T_1, respectively. In case (b), a plane wave is incident on surface B, and the reflection and transmission coefficients are similarly denoted R_2 and T_2.

In case (a), the sound pressures and normal particle velocities at surfaces A and B are related by

$$\begin{bmatrix} P(A) \\ V(A) \end{bmatrix} = \begin{bmatrix} T_{11} & T_{12} \\ T_{21} & T_{22} \end{bmatrix} \begin{bmatrix} P(B) \\ V(B) \end{bmatrix}, \tag{A1}$$

where

$$P(A) = 1 + R_1, \tag{A2}$$

$$V(A) = \frac{1 - R_1}{\rho_0 c}, \tag{A3}$$

$$P(B) = T_1 e^{-jkd}, \tag{A4}$$

$$V(B) = \frac{T_1 e^{-jkd}}{\rho_0 c}. \tag{A5}$$

In case (b), the sound pressures and normal particle velocities at surfaces A and B are related by

$$\begin{bmatrix} P'(A) \\ V'(A) \end{bmatrix} = \begin{bmatrix} T_{11} & T_{12} \\ T_{21} & T_{22} \end{bmatrix} \begin{bmatrix} P'(B) \\ V'(B) \end{bmatrix}, \tag{A6}$$

where, in this case

$$P'(A) = T_2 e^{-jkd}, \tag{A7}$$

$$V'(A) = -\frac{T_2 e^{-jkd}}{\rho_0 c}, \tag{A8}$$

$$P'(B) = 1 + R_2, \tag{A9}$$

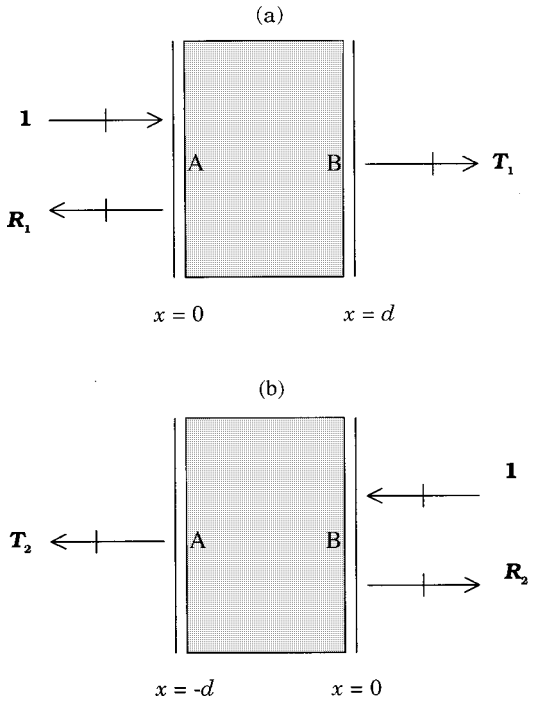

FIG. A1. Sound transmission and reflection cases (a) and (b).

$$V'(B) = \frac{R_2 - 1}{\rho_0 c}. \tag{A10}$$

When Eqs. (A2)–(A5) and (A7)–(A10) are substituted into Eqs. (A1) and (A6), respectively, it is possible to solve for R_1, T_1, R_2, T_2 in terms of the transfer function elements, i.e.,

$$R_1 = \frac{T_{11} + (T_{12}/\rho_0 c) - T_{21}\rho_0 c - T_{22}}{T_{11} + (T_{12}/\rho_0 c) + T_{21}\rho_0 c + T_{22}}, \tag{A11}$$

$$T_1 = \frac{2e^{jkd}}{T_{11} + (T_{12}/\rho_0 c) + T_{21}\rho_0 c + T_{22}}, \tag{A12}$$

$$R_2 = \frac{-T_{11} + (T_{12}/\rho_0 c) - T_{21}\rho_0 c + T_{22}}{T_{11} + (T_{12}/\rho_0 c) + T_{21}\rho_0 c + T_{22}}, \tag{A13}$$

$$T_2 = \frac{2e^{jkd}(T_{11}T_{22} - T_{12}T_{21})}{T_{11} + (T_{12}/\rho_0 c) + T_{21}\rho_0 c + T_{22}}. \tag{A14}$$

It can be seen by comparing Eqs. (A11) and (A13) that when $R_1 = R_2$, i.e., when the layer is symmetrical in the x direction, it follows that

$$T_{11} = T_{22}. \tag{A15}$$

Similarly, by comparing Eqs. (A12) and (A14) it is clear that when $T_1 = T_2$, i.e., when the sound transmission through the layer is reciprocal, it follows that

$$T_{11}T_{22} - T_{12}T_{21} = 1. \tag{A16}$$

[1] K. Attenborough, ''Acoustical characteristics of porous materials,'' Phys. Rep. **82**, 179–227 (1982).
[2] J. S. Bolton, R. J. Yun, J. Pope, and D. Apfel, ''Development of a new sound transmission test for automotive sealant materials,'' SAE Trans., J. Pass. Cars **106**, 2651–2658 (1997).
[3] H.-Y. Lai, S. Katragadda, J. S. Bolton, and J. H. Alexander, ''Layered

fibrous treatments for sound absorption and transmission,'' SAE Trans., J. Pass. Cars **106**, 3311–3318 (1997).
[4] R. A. Scott, ''The absorption of sound in a homogeneous porous medium,'' Proc. Phys. Soc. London **58**, 358–368 (1946).
[5] L. L. Beranek, ''Some notes on the measurement of acoustic impedance,'' J. Acoust. Soc. Am. **19**, 420–427 (1947).
[6] R. F. Lambert and J. S. Tesar, ''Acoustic structure and propagation in highly porous, layered, fibrous materials,'' J. Acoust. Soc. Am. **73**, 1231–1237 (1984).
[7] L. L. Beranek, ''Acoustical properties of homogeneous, isotropic rigid tiles and flexible blankets,'' J. Acoust. Soc. Am. **19**, 556–568 (1947).
[8] C. Zwikker and C. W. Kosten, *Sound Absorbing Materials* (Elsevier, Amsterdam, 1949).
[9] M. A. Ferrero and G. G. Sacerdote, ''Parameters of sound propagation in granular absorption materials,'' Acustica **1**, 135–142 (1951).
[10] S. L. Yaniv, ''Impedance tube measurement of propagation constant and characteristic impedance of porous acoustical material,'' J. Acoust. Soc. Am. **54**, 1138–1142 (1973).
[11] C. D. Smith and T. L. Parott, ''Comparison of three methods for measuring acoustic properties of bulk materials,'' J. Acoust. Soc. Am. **74**, 1577–1582 (1983).
[12] Anonymous, ''Standard test method for impedance and absorption of acoustical materials using a tube, two microphones, and a digital frequency analysis system,'' ASTM Standard E 1050-90 (1990).
[13] H. Utsuno, T. Tanaka, T. Fujikawa, and A. F. Seybert, ''Transfer function method for measuring characteristic impedance and propagation constant of porous materials,'' J. Acoust. Soc. Am. **86**, 637–643 (1989).
[14] C. Bordone-Sacerdote and G. G. Sacerdote, ''A method for measuring the acoustic impedance of porous materials,'' Acustica **34**, 77–80 (1975).
[15] K. U. Ingard and T. A. Dear, ''Measurement of acoustic flow resistance,'' J. Sound Vib. **103**, 567–572 (1985).
[16] K. U. Ingard, *Notes on Sound Absorption Technology* (Noise Control Foundation, Poughkeepsie, NY, 1994).
[17] J. D. McIntosh, M. T. Zuroski, and R. F. Lambert, ''Standing wave apparatus for measuring fundamental properties of acoustic materials in air,'' J. Acoust. Soc. Am. **88**, 1929–1938 (1990).
[18] Y. Champoux and M. Stinson, ''Measurement of the characteristic impedance and propagation constant of materials having high flow resistivity,'' J. Acoust. Soc. Am. **90**, 2182–2191 (1991).
[19] T. Iwase, Y. Izumi, and R. Kawabata, ''A new measuring method for sound propagation constant by using sound tube without any air spaces back of a test material,'' in *Proceedings INTER-NOISE 98* (CD-ROM edition, Causal Productions, Australia, 1998).
[20] P. Dean, ''An *in situ* method of wall acoustic impedance measurement in flow ducts,'' J. Sound Vib. **34**, 97–130 (1974).
[21] C. K. Amedin, Y. Champoux, and A. Berry, ''Acoustical characterization of absorbing porous materials through transmission measurements in a free field,'' J. Acoust. Soc. Am. **102**, 1982–1994 (1997).
[22] D. N. Johnston, D. K. Longmore, and J. E. Drew, ''A technique for the measurement of the transfer matrix characteristics of two-port hydraulic components,'' Fluid Power Sys. Tech. **1**, 25–33 (1994).
[23] M. Fukuda, ''A study on the exhaust muffler of internal combustion engine,'' Bull. JSME **6**, 255–269 (1963).
[24] T. Y. Lung and A. G. Doige, ''A time-averaging transient testing method for acoustic properties of piping systems and mufflers with flow,'' J. Acoust. Soc. Am. **73**, 867–876 (1983).
[25] M. L. Munjal, *Acoustics of Ducts and Mufflers* (Wiley-Interscience, New York, 1987).
[26] A. G. Doige, M. L. Munjal, and H. S. Alves, ''An improved experimental method for determining transfer matrices of pipeline elements with flow,'' in *Proceedings of NOISE-CON 88*, pp. 481–486 (Noise Control Foundation, Poughkeepsie, NY, 1988).
[27] M. L. Munjal and A. G. Doige, ''Theory of two source-location method for direct experimental evaluation of the four-pole parameters of an aeroacoustic element,'' J. Sound Vib. **141**, 323–333 (1990).
[28] K. S. Peat, ''A transfer matrix for an absorption silencer element,'' J. Sound Vib. **146**, 353–360 (1991).
[29] T. Tanaka, T. Fujikawa, T. Abe, and H. Utsuno, ''A method for the analytical prediction of insertion loss of a two-dimensional muffler model based on the transfer matrix derived from the boundary element method,'' Trans. ASME **107**, 86–92 (1985).
[30] U. R. Kristiansen and T. E. Vigran, ''On the design of resonant absorbers using a slotted plate,'' Appl. Acoust. **43**, 39–48 (1994).
[31] A. D. Pierce, *Acoustics: An Introduction to its Physical Principles and Applications* (McGraw-Hill, New York, 1981).
[32] J. F. Allard, *Propagation of Sound in Porous Media* (Elsevier Applied Science, London and New York, 1993).
[33] M. Kompella, P. Davies, D. J. Ufford, and R. J. Bernhard, ''A technique to identify the number of incoherent sources contributing to the response of a system,'' Mech. Sys. Sig. Proc. **8**, 363–380 (1994).
[34] J. Kruger and M. Quickent, ''Determination of acoustic absorber parameters in impedance tube,'' Appl. Acoust. **50**, 79–89 (1997).
[35] S.-H. Jang and J.-G. Ih, ''On the multiple microphone method for measuring induct acoustic properties in the presence of mean flow,'' J. Acoust. Soc. Am. **103**, 1520–1526 (1998).
[36] Y. J. Kang and J. S. Bolton, ''A finite element model for sound transmission through foam-lined double panel structures,'' J. Acoust. Soc. Am. **99**, 2755–2765 (1996).
[37] Y. J. Kang and J. S. Bolton, ''Sound transmission through elastic porous wedges and foam layers having spatially graded properties,'' J. Acoust. Soc. Am. **102**, 3319–3332 (1997).
[38] M. E. Delany and E. N. Bazley, ''Acoustic properties of fibrous absorbent materials,'' Appl. Acoust. **3**, 105–116 (1971).
[39] A. F. Seybert, R. A. Seman, and M. D. Lattuca, ''Boundary element prediction of sound propagation in ducts containing bulk absorbing materials,'' Trans. ASME, J. Vib. Acoust. **120**, 976–981 (1998).
[40] J. S. Bolton and Y. J. Kang, ''Elastic porous materials for sound absorption and transmission control,'' SAE Trans., J. Pass. Car **106**, 2576–2591 (1997).
[41] J. S. Bolton, N.-M. Shiau, and Y. J. Kang, ''Sound transmission through multi-panel structures lined with elastic porous materials,'' J. Sound Vib. **191**, 317–347 (1996).

Eigenmode analysis of arbitrarily shaped two-dimensional cavities by the method of point-matching

Sang Wook Kang and Jang Moo Lee[a)]
Seoul National University, Department of Mechanical Design and Production Engineering, San 56-1, Shinlim-Dong, Kwanak-Gu, Seoul, 151-742, Korea

(Received 9 December 1998; revised 4 October 1999; accepted 8 October 1999)

In the proposed method, as in the boundary element method (BEM), a field problem is solved on its boundary along which nodes are distributed. The distinct feature of the proposed method is related to the fact that no interpolation functions between the nodes are required, so that the basic collocation method is employed to satisfy a given boundary condition. This approach reduces a large amount of numerical calculation induced due to the interpolation functions. Unlike the method of auxiliary sources (MAS), in the proposed method only the *regular* functions that have finite functional values everywhere including the origins are employed as basis functions. As a result, the proposed method does not need the auxiliary surface, the construction of which is a troublesome work because its form, dimension, shifting, etc. strongly influence the accuracy of the MAS. The eigenvalues calculated by the proposed method rapidly converge to the exact values thanks to the simplicity of the method. Moreover, the method gives mode shapes successfully without using the interpolation functions between the nodes. The efficiency and accuracy of the method are verified through several applications. © *2000 Acoustical Society of America.* [S0001-4966(00)06101-4]

PACS numbers: 43.20.Ks, 43.20.Rz [ANN]

INTRODUCTION

The boundary element method[1,2] and finite element[3] method have been used as common techniques to solve the eigenvalue problem of an arbitrarily shaped cavity. Furthermore, a variety of approximate methods, for example, the finite difference method,[4,5] collocation,[6–8] Rayleigh–Ritz,[9] and Galerkin[10] methods have been applied to find out cutoff frequencies of a waveguide problem, which is analogous to two-dimensional cavity problems considered in this paper. Most of these methods are based on the superposition procedure of independent approximate solutions that are two-dimensional functions of two independent variables. If a polar system of coordinates is selected, the radial and angular coordinates are involved in the two-dimensional functions. Thus, a large amount of numerical calculation is required and its accuracy and convergence are limited as the number of independent solutions is increased for higher order modes.

In this paper, a simple method of solving an arbitrarily shaped two-dimensional cavity by employing a so-called *nondimensional* Green's function is introduced. The function is a solution of the homogeneous Helmholtz equation that governs eigenfields, and is a wave-type, simple function that propagates omnidirectionally from its origin to infinite extent. Physically the function represents a circularly symmetric waveform of which the center has a unit pressure in amplitude and coincides with the origin. Thus, in the case of using polar coordinates, the Bessel function of only the first kind of zero order, which is *bounded* everywhere including the origin, is selected (note that the Bessel function of the second kind of order zero is discarded because it has an infinite functional value at its origin). Strictly speaking, the selected function is the sum of an incoming and outgoing Hankel function.

The method presented in this paper may appear to be similar to the method of auxiliary sources (MAS)[11] that has been used mainly for scattered-field problems, in a sense that the two methods commonly use the collocation method when they apply the given boundary condition to a previously determined approximate solution. However, the proposed method uses a simpler approximate solution than that in the MAS, i.e., while the MAS employs Bessel functions of the first and second kinds of zero order as the basis functions, the proposed method employs only the Bessel function of the first kind of zero order, which has finite values everywhere including the origin. Thus, the numerical calculation is simpler than that in the MAS. Besides, the proposed method can calculate the eigenvalues of arbitrarily shaped cavities without the subsidiary surface, the construction of which is a troublesome work because its form, dimension, shifting, etc. strongly influence the accuracy of the MAS.

Unlike the boundary element method, the proposed method uses the discretization scheme that the boundary of a cavity is discretized by a finite number of nodes between which no interpolation functions are used, and employs the collocation technique to apply the given boundary conditions. As a result, no numerical integration procedures are involved in the development of the theoretical formulations. Although a couple of approximations are made, the eigenvalues obtained from the present method are found to be accurate, and the eigenmodes are also successfully extracted by the simple numerical calculations. Besides, the eigenvalues converge to the exact solutions even when a small number of

[a)]Author to whom correspondence should be addressed. Electronic mail: leejm@gong.snu.ac.kr

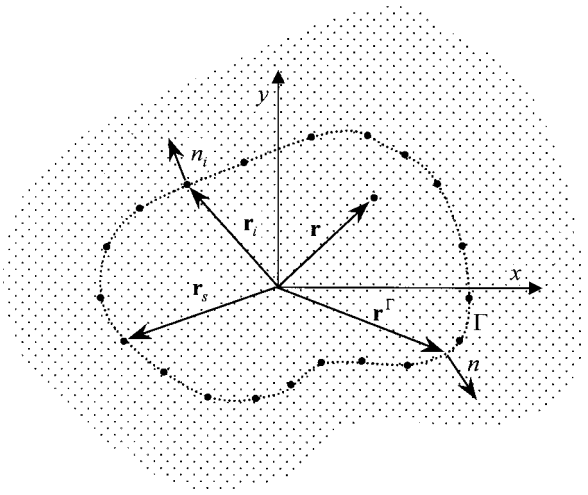

FIG. 1. Two-dimensional infinite acoustic field with the nodes located on the fictitious boundary Γ.

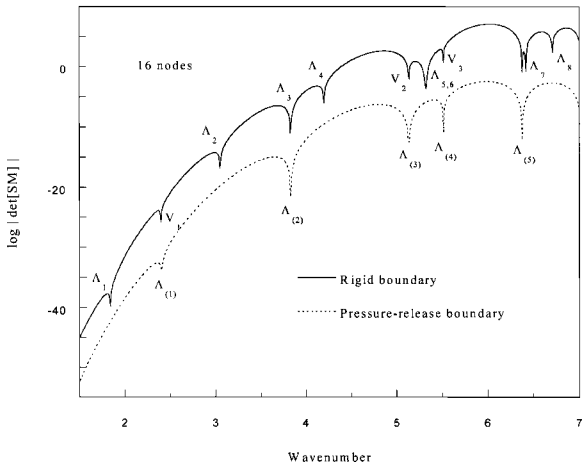

FIG. 2. Determinant of the system matrix vs wave number for a circular cavity.

boundary nodes are used. The basic idea underlying this study can be extended to cavities with a multiply connected region; related works are presently being carried out.

I. THEORETICAL FORMULATION

A. Nondimensional Green's function

In an infinite acoustic field, imagine a waveform that spreads circularly outward from the center. Since the field is infinite in extent, the waveform will depend on the scalar distance from the center point $\mathbf{r}_0$ to the field point $\mathbf{r}$, $r=|\mathbf{r}-\mathbf{r}_0|$. The wave equation in this case reduces to

$$\frac{1}{r}\frac{\partial}{\partial r}\left(r\frac{\partial p}{\partial r}\right)=\frac{1}{c^2}\frac{\partial^2 p}{\partial t^2}. \tag{1}$$

In the case of harmonic problems with a time-dependent term $e^{j\omega t}$, the relation $p=P(r)\,e^{j\omega t}$ leads Eq. (1) to

$$\frac{1}{r}\frac{\partial}{\partial r}\left(r\frac{\partial P}{\partial r}\right)+k^2P=0, \tag{2}$$

where $k=\omega/c$ (ω and c are the angular frequency and the speed of sound, respectively).

If the physical consideration that pressure is *bounded* at the center point $\mathbf{r}_0$ ($r=0$) is given, a unique solution of Eq. (2) is the Bessel function of the first kind of zero order, $J_0(kr)$, which is finite everywhere including the center point. Note that the Bessel function of the second kind of zero order $Y_0(kr)$ is discarded since it is infinite at the center point ($r=0$). Now, $J_0(kr)$ is termed a *nondimensional* Green's function in a two-dimensional infinite acoustic field. This function physically represents the *pressure* at a field point due to *unit pressure* at the center point of a wave that spreads circularly in the infinite region. Note also that the argument of $J_0(kr)$ used in this study is dimensionless, and that the nondimensional Green's function satisfies the homogeneous Helmholtz equation

$$\nabla^2P+k^2P=0, \tag{3}$$

TABLE I. Comparison of the eigenvalues of the circular cavity with a rigid or pressure-release boundary, obtained by the proposed method.

Rigid boundary condition					Pressure-release boundary condition				
$N=12$	$N=16$	$N=20$	Singular values	Exact solution	$N=12$	$N=16$	$N=20$	Singular values	Exact solution
1.8412	1.8412	1.8412	Λ_1	1.8412					
2.4048	2.4048	2.4048	V_1		2.4048	2.4048	2.4048	$\Lambda_{(1)}$	2.4048
3.0563	3.0542	3.0542	Λ_2	3.0542					
3.8317	3.8317	3.8317	Λ_3	3.8317	3.8317	3.8317	3.8317	$\Lambda_{(2)}$	3.8317
4.2012	4.2012	4.2012	Λ_4	4.2012					
5.1356	5.1356	5.1356	V_2		5.1356	5.1356	5.1356	$\Lambda_{(3)}$	5.1356
5.3306	5.3176	5.3176	Λ_5	5.3176					
5.3314	5.3314	5.3314	Λ_6	5.3314					
5.5201	5.5201	5.5201	V_3		5.5201	5.5201	5.5201	$\Lambda_{(4)}$	5.5201
6.3681	6.3802	6.3802	V_4		6.3790	6.3802	6.3802	$\Lambda_{(5)}$	6.3802
6.7099	6.4160	6.4156	Λ_7	6.4156					
6.8318	6.7061	6.7061	Λ_8	6.7061					

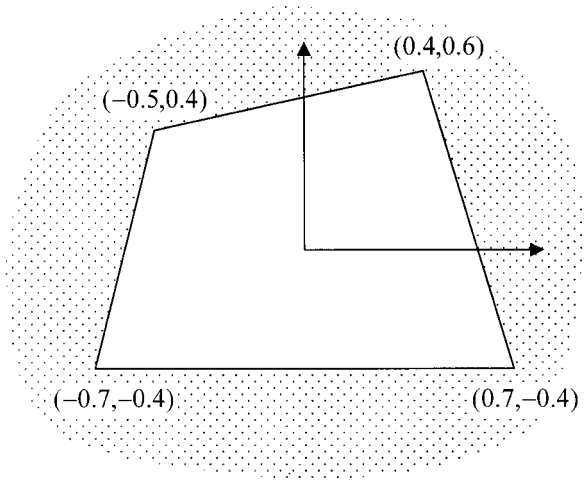

FIG. 3. Dimensions of a quadrilateral cavity with unequal length of edges (unit: meter).

which is a governing differential equation of eigenvalue problems.

B. Linear superposition of the nondimensional Green's functions

In an infinite acoustic field, N nodes are distributed along the fictitious contour, the shape of which is exactly the same as the boundary of the cavity of interest, which is depicted by the dotted line in Fig. 1. Next, we consider that N waves, of which the forms are given by the nondimensional Green's functions, spread circularly from each of the nodes. Then, the pressure at field point $\mathbf{r}$ can be obtained by linearly superposing the nondimensional Green's functions

$$P(\mathbf{r})=\sum_{s=1}^{N} A_s J_0(k|\mathbf{r}-\mathbf{r}_s|), \tag{4}$$

which also satisfies the Helmholtz equation Eq. (3) because each of the nondimensional Green's functions does. Thus, Eq. (4) can be employed as a trial solution for solving the eigenfield of the finite-sized cavity represented by the dotted line in Fig. 1.

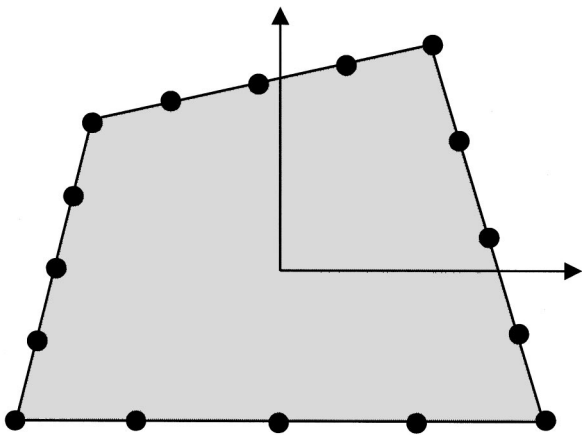

FIG. 4. Location of the nodes distributed along the boundary of the quadrilateral cavity for $N=16$.

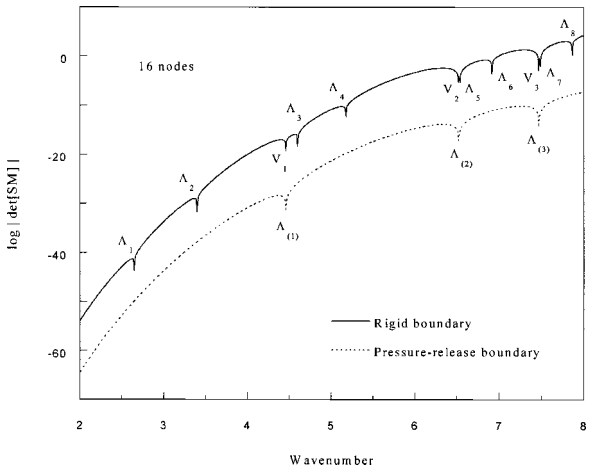

FIG. 5. Determinant of the system matrices $\mathbf{SM}_{\partial P/\partial n=0}$ and $\mathbf{SM}_{P=0}$ vs wave number for the quadrilateral cavity.

The unknown coefficients $A_1 \sim A_N$ involved in the trial function are determined by applying a given boundary condition to the function. As in the collocation technique, the Dirichlet boundary condition defined continuously along the boundary is discretized so as to be satisfied only at previously located nodes to obtain the trial function, i.e.,

$$P(\mathbf{r}_i)=\overline{P}(\mathbf{r}_i), \quad i=1,2,...,N. \tag{5}$$

Note that the discrete boundary condition converges to the continuous boundary condition as $N\to\infty$. To determine the coefficients, applying the discrete boundary condition to the trial function Eq. (4) gives

$$\sum_{s=1}^{N} A_s J_0(k|\mathbf{r}_i-\mathbf{r}_s|)=\overline{P}(\mathbf{r}_i), \quad i=1,2,...,N. \tag{6}$$

In the case where the Neumann boundary condition is given in the form

$$\frac{\partial P(\mathbf{r}_i)}{\partial n_i}=\overline{V}_n(\mathbf{r}_i), \quad i=1,2,\ldots,N, \tag{7}$$

the same procedure as above is conducted. In Eq. (7), n_i denotes the normal direction from the boundary at $\mathbf{r}=\mathbf{r}_i$, as shown in Fig. 1. If the contour has a nonsmooth geometry, such as when two normal vectors are given at a corner, the unique normal direction is approximately determined by the vector sum of the two. Substituting the eigensolution Eq. (4) into the discrete boundary condition Eq. (7) gives

$$\sum_{s=1}^{N} A_s \frac{\partial}{\partial n_i} J_0(k|\mathbf{r}_i-\mathbf{r}_s|)=\overline{V}_n(\mathbf{r}_i), \quad i=1,2,...,N. \tag{8}$$

Both Eq. (6) and Eq. (8) can be written into the single common matrix form

$$\mathbf{SM}(k)\mathbf{A}=\mathbf{B}, \tag{9}$$

where the system matrix $\mathbf{SM}(k)$ of order $N\times N$ is given by $\mathrm{SM}_{i\,s}=J_0(k|\mathbf{r}_i-\mathbf{r}_s|)$ for Eq. (6) and $\mathrm{SM}_{i\,s}=(\partial/\partial n_i)J_0(k|\mathbf{r}_i$

TABLE II. Comparison of the eigenvalues of the quadrilateral cavity with a rigid or pressure-release boundary, obtained by the proposed method.

Rigid boundary condition					Pressure-release boundary condition				
$N=12$	$N=16$	$N=20$	Singular values	FEM: 961 nodes	$N=12$	$N=16$	$N=20$	Singular values	FEM: 961 nodes
2.6594	2.6500	2.6622	Λ_1	2.6620					
3.4106	3.3977	3.4062	Λ_2	3.3980					
4.4596	4.4601	4.4628	V_1		4.4597	4.4601	4.4628	$\Lambda_{(1)}$	4.4651
4.6137	4.6055	4.6071	Λ_3	4.6089					
5.1947	5.1785	5.1910	Λ_4	5.1909					
6.4595	6.5257	6.5292	V_2		6.4521	6.5244	6.5292	$\Lambda_{(2)}$	6.5375
6.5661	6.5354	6.5286	Λ_5	6.5448					
6.8622	6.9161	6.8975	Λ_6	6.9191					
7.4584	7.4702	7.4714	V_3		7.4435	7.4739	7.4714	$\Lambda_{(3)}$	7.4847
7.5233	7.4911	7.4905	Λ_7	7.5207					
7.8994	7.8656	7.8662	Λ_8	7.8865					

$-\mathbf{r}_s|$) for Eq. (8); the column vector $\mathbf{B}$ of order $N\times 1$ is also given by $B_i=\overline{P}(\mathbf{r}_i)$ for Eq. (6) and $B_i=\overline{V}_n(\mathbf{r}_i)$ for Eq. (8); the elements of the column vector $\mathbf{A}$ of order $N\times 1$ represent the unknown coefficients. From Eq. (9), the unknown coefficients can be found as follows:

$$\mathbf{A}=\mathbf{SM}(k)^{-1}\mathbf{B}. \tag{10}$$

C. Eigenvalues and eigenmodes

The above formulas are applied for eigenmode analysis of arbitrarily shaped cavities with a pressure-release boundary ($P=0$) or a rigid boundary ($\partial P/\partial n=0$). In these cases, all elements of the vector $\mathbf{B}$, which is evaluated from the given boundary condition, become zeros, i.e., $\mathbf{B}=\mathbf{0}$. Then, Eq. (9) reduces to the system equation

$$\mathbf{SM}(k)\mathbf{A}=\mathbf{0}. \tag{11}$$

For a nontrivial solution, the determinant of the system matrix $\mathbf{SM}(k)$, which is a function of the wave number, must become zero, i.e.,

$$\det[\mathbf{SM}(k)]=0. \tag{12}$$

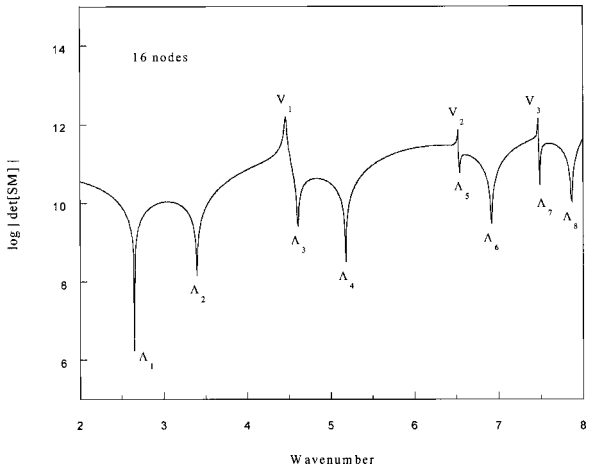

FIG. 6. Determinant of the system matrix $\mathbf{SM}^{(\mathrm{net})}_{\partial P/\partial n=0}$ vs wave number for the quadrilateral cavity with the rigid boundary.

Eigenvalues and eigenvectors may be calculated from Eq. (12) and Eq. (11), respectively. Mode shapes for the calculated eigenvalues can be plotted from Eq. (4), into which the corresponding eigenvectors are substituted.

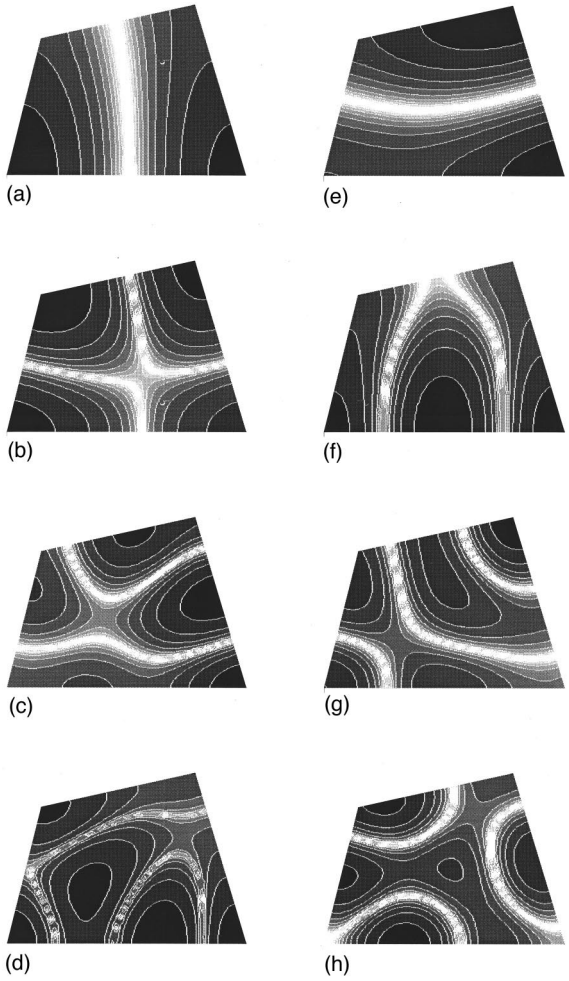

FIG. 7. Mode shapes of the quadrilateral cavity with a rigid boundary, obtained by the proposed method in the case of 16 nodes; (a)–(h): first–eighth mode.

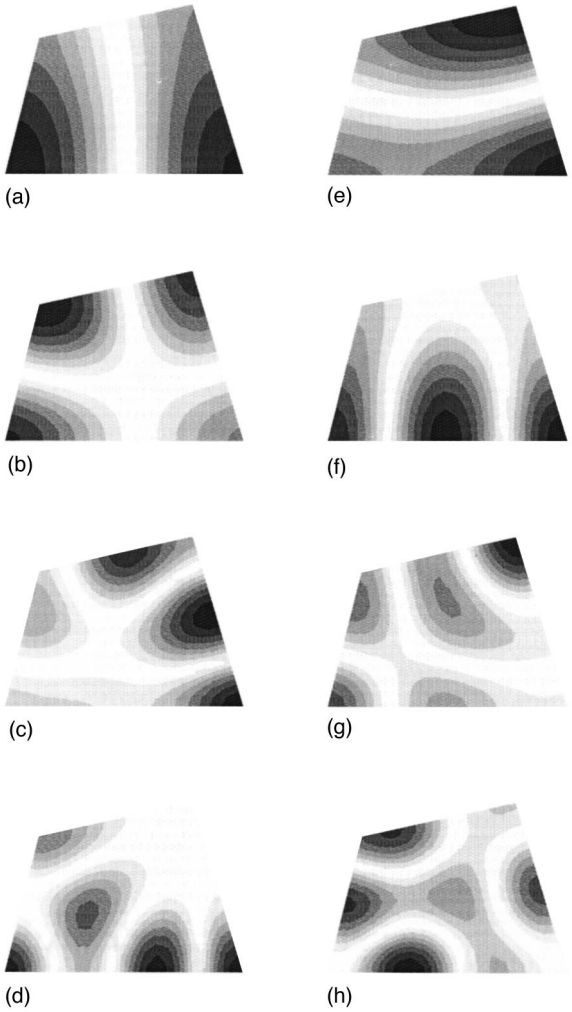

FIG. 8. Mode shapes of the quadrilateral cavity with the rigid boundary, obtained by the FEM (SYSNOISE) in the case of 441 nodes; (a)–(h): first–eighth mode.

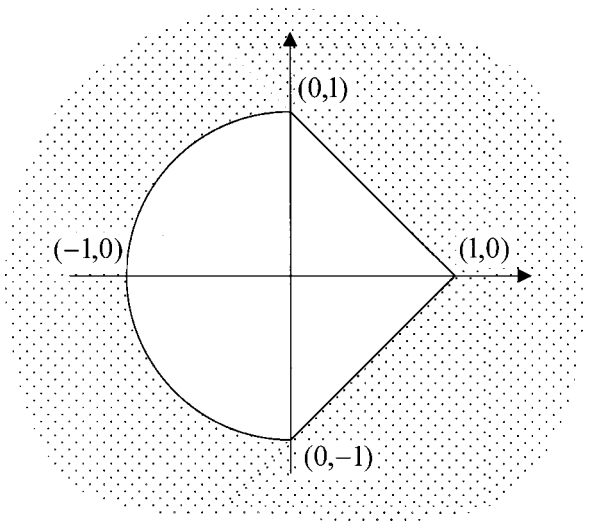

FIG. 9. Dimensions of an arbitrarily shaped cavity with one semicircle and two edges (unit: meter).

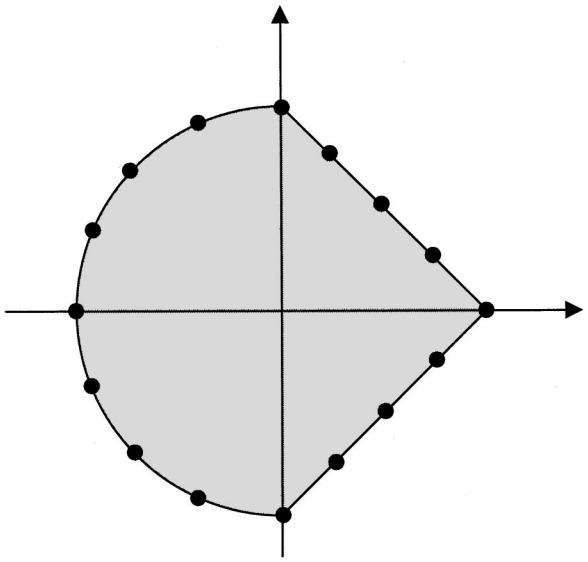

FIG. 10. Location of the nodes distributed along the boundary of the arbitrarily shaped cavity for $N=16$.

II. FUNCTIONAL DEPENDENCE OF THE TRIAL FUNCTION

In this section, it is investigated through a numerical application whether or not the nondimensional Green's functions used as basis functions of the trial function are functionally independent of each other. The proposed method is applied to a circular cavity of unit radius with a rigid boundary. In order to illustrate the functional dependence of the trial function, the method is applied to another cavity of the same radius with a pressure-release boundary. First, N equally spaced nodes are distributed along the boundary of the cavity.

The determinant curves for $N=16$ are shown in Fig. 2, where the wave numbers corresponding to the troughs represent singular values of the system matrix $\mathbf{SM}(k)$. Although the determinant curves for $N=12$ and $N=20$ are omitted, the singular values for $N=12$, $N=16$, and $N=20$ are summarized in Table I. It may be said from the comparison of the present results and the exact results that the proposed method gives very accurate eigenvalues close to the exact ones.

It is also confirmed from Table I that some of the singular values in the case of the *rigid boundary condition*, V_1-V_4, coincide with the exact eigenvalues for the *pressure-release boundary*, and that, in the case of the *pressure-release boundary condition*, all the singular values, $\Lambda_{(1)}-\Lambda_{(5)}$, correspond to the exact eigenvalues. Thus, additional work may be required to discriminate V_1-V_4 from $\Lambda_1-\Lambda_8$ in the case of the rigid boundary.

III. EVALUATION OF THE NET SINGULAR VALUES

In the present approach, eigenvalues are found from the troughs that appear in the determinant curve. However, not all the troughs correspond to the eigenvalues of the cavity with a rigid boundary. A part of the troughs, which are created owing to the functional dependence of the trial function, corresponds to the eigenvalue of the same cavity with a pressure-release boundary, as has been confirmed from the

TABLE III. Comparison of the eigenvalues of the arbitrarily shaped cavity with a rigid or pressure-release boundary, obtained by the proposed method.

Rigid boundary condition					Pressure-release boundary condition				
$N=12$	$N=16$	$N=20$	Singular values	FEM: 1321 nodes	$N=12$	$N=16$	$N=20$	Singular values	FEM: 1321 nodes
1.9555	1.9582	1.9590	Λ_1	1.9587					
2.0217	2.0250	2.0244	Λ_2	2.0263					
2.7039	2.7076	2.7089	V_1		2.7038	2.7076	2.7089	$\Lambda_{(1)}$	2.7098
3.0731	3.0824	3.0839	Λ_3	3.0869					
3.6268	3.6326	3.6357	Λ_4	3.6403					
3.9895	3.9957	3.9998	Λ_5	4.0096					
4.2033	4.2190	4.2253	V_2		4.2027	4.2190	4.2253	$\Lambda_{(2)}$	4.2340
4.3584	4.3579	4.3579	V_3		4.3585	4.3579	4.3579	$\Lambda_{(3)}$	4.3605
4.5514	4.5780	4.5818	Λ_6	4.5957					
4.7219	4.7357	4.7410	Λ_7	4.7518					
5.3872	5.3787	5.3761	Λ_8	5.3976					

numerical test. In this section, a way for eliminating the unwanted troughs due to the functional dependence is devised. Moreover, the devised way is verified through two shapes of arbitrarily shaped cavities with rigid boundaries.

A. Manipulation of system matrices

First, we define four system matrices $\mathbf{SM}_{P=0}$, $\mathbf{SM}_{\partial P/\partial n=0}$, $\mathbf{SM}^{(\mathrm{net})}_{P=0}$, and $\mathbf{SM}^{(\mathrm{net})}_{\partial P/\partial n=0}$ in order to simply illustrate a way for eliminating the unwanted troughs. $\mathbf{SM}_{P=0}$ and $\mathbf{SM}_{\partial P/\partial n=0}$ represent the system matrices created when the boundary conditions $P=0$ and $\partial P/\partial n=0$ are, respectively, applied to the trial function of the proposed method. $\mathbf{SM}^{(\mathrm{net})}_{P=0}$ and $\mathbf{SM}^{(\mathrm{net})}_{\partial P/\partial n=0}$ represent the net system matrices of which the singular values correspond to only the eigenvalues of the cavity with the pressure-release boundary and the rigid boundary, respectively. Since the singular values of $\mathbf{SM}^{(\mathrm{net})}_{\partial P/\partial n=0}$ including those of $\mathbf{SM}^{(\mathrm{net})}_{P=0}$ are obtained from $\det[\mathbf{SM}_{\partial P/\partial n=0}]$, as has been confirmed in Table I, $\det[\mathbf{SM}_{\partial P/\partial n=0}]$ may be subdivided into

$$\det[\mathbf{SM}_{\partial P/\partial n=0}]=\det[\mathbf{SM}^{(\mathrm{net})}_{\partial P/\partial n=0}]\times\det[\mathbf{SM}^{(\mathrm{net})}_{P=0}], \quad (13)$$

which is valid under the precondition that the singular values of $\mathbf{SM}^{(\mathrm{net})}_{\partial P/\partial n=0}$ do not coincide with any value of those of $\mathbf{SM}^{(\mathrm{net})}_{P=0}$. In the case of arbitrarily shaped cavities, except circular or rectangular cavities, the precondition is satisfied.

In Eq. (13), $\det[\mathbf{SM}^{(\mathrm{net})}_{P=0}]$ can be replaced by $\det[\mathbf{SM}_{P=0}]$, because both the determinants give the same singular values ($\det[\mathbf{SM}_{P=0}]$ was confirmed to offer the singular values corresponding to the eigenvalues of the cavity with the pressure-release boundary). From Eq. (13), $\det[\mathbf{SM}^{(\mathrm{net})}_{\partial P/\partial n=0}]$ can be evaluated as follows:

$$\det[\mathbf{SM}^{(\mathrm{net})}_{\partial P/\partial n=0}]=\det[\mathbf{SM}_{\partial P/\partial n=0}]\div\det[\mathbf{SM}^{(\mathrm{net})}_{P=0}]. \quad (14)$$

The net singular values corresponding to the eigenvalues of the cavity with the rigid boundary are found by equalizing Eq. (14) to zero

$$\det[\mathbf{SM}^{(\mathrm{net})}_{\partial P/\partial n=0}]=0. \quad (15)$$

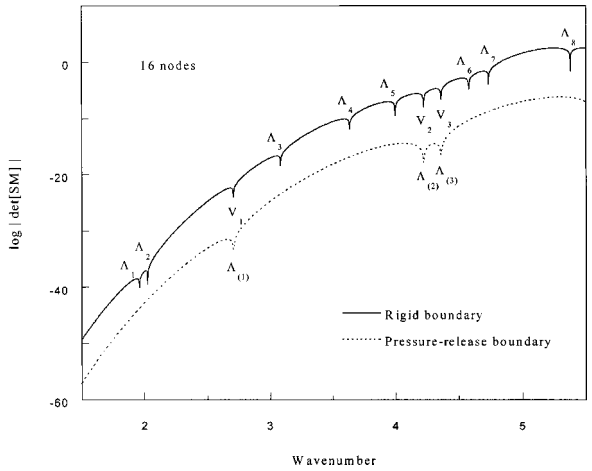

FIG. 11. Determinant of the system matrices $\mathbf{SM}_{\partial P/\partial n=0}$ and $\mathbf{SM}_{P=0}$ vs wave number for the arbitrarily shaped cavity.

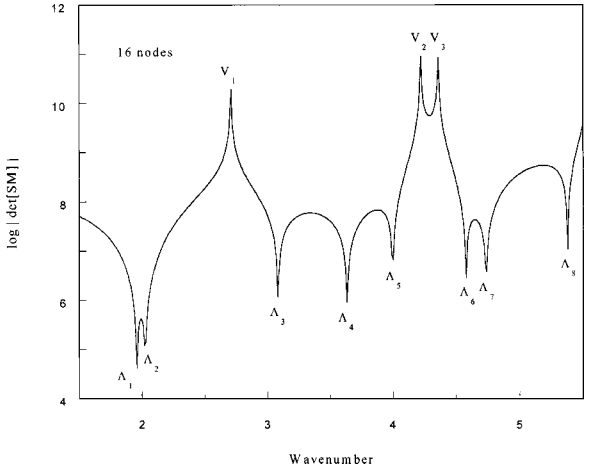

FIG. 12. Determinant of the system matrix $\mathbf{SM}^{(\mathrm{net})}_{\partial P/\partial n=0}$ vs wave number for the arbitrarily shaped cavity with a rigid boundary.

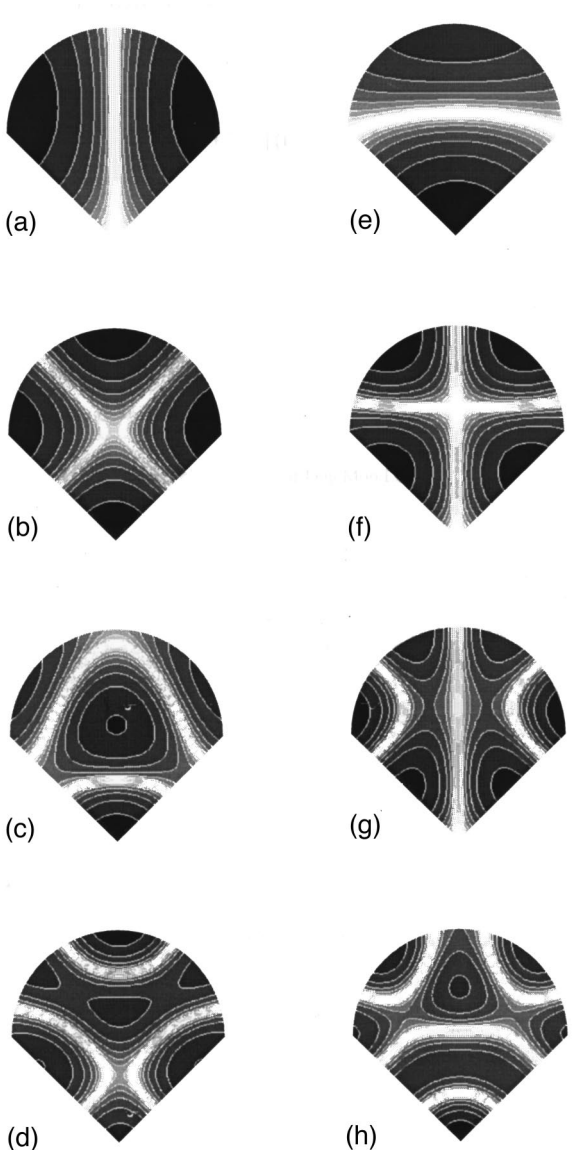

FIG. 13. Mode shapes of the arbitrarily shaped cavity with a rigid boundary, obtained by the present method in the case of 16 nodes; (a)–(h): first–eighth mode.

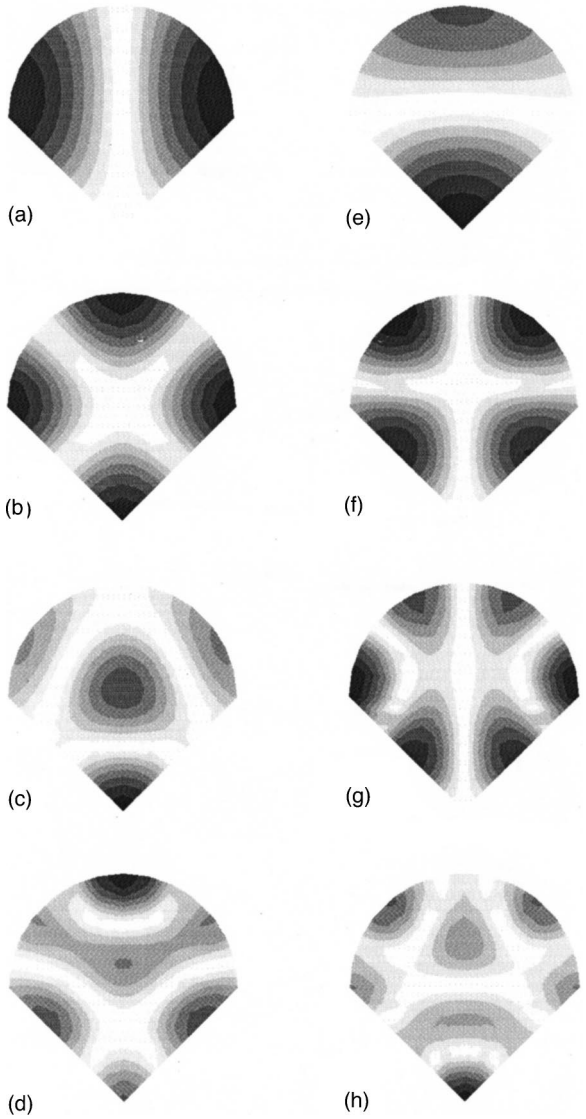

FIG. 14. Mode shapes of the arbitrarily shaped cavity with a rigid boundary, obtained by the FEM (SYSNOISE) in the case of 841 nodes; (a)–(h): first–eighth mode.

B. Numerical applications

Sample computations are presented to verify the usefulness and validity of the developed formulas when the proposed method is applied to general shapes of cavities with the rigid boundary.

1. Quadrilateral cavity

Figure 3 shows the dimensions of a quadrilateral cavity that is solved by the proposed method. The location of the boundary nodes for $N=16$ is illustrated by Fig. 4, where the nodes are equally spaced. For $N=16$, logarithm curves for $\det[\mathbf{SM}_{\partial P/\partial n=0}]$ and $\det[\mathbf{SM}_{P=0}]$ are plotted in Fig. 5, where the values of the wave number corresponding to the troughs represent the singular values of the system matrices $\mathbf{SM}_{\partial P/\partial n=0}$ and $\mathbf{SM}_{P=0}$. A comparison of the two curves reinforces that in the case of the rigid boundary the proposed method gives singular values corresponding to the eigenvalues of the cavity with the rigid boundary including those with the pressure-release boundary. In Table II the singular values obtained from the determinant curves for $N=12$, $N=16$, and $N=20$ are summarized. Although the unwanted singular values V_is are not eliminated in the case of the rigid boundary, the present results converge nearly to the eigenvalues computed by SYSNOISE, which is a commercial FEM solver.

The elimination of the unwanted singular values is conducted in the way that was proposed in Sec. III A. For $N=16$, a logarithm curve for $\mathbf{SM}^{(\mathrm{net})}_{\partial P/\partial n=0}$ is plotted in Fig. 6 where the troughs and the crests represent the eigenvalues and the unwanted singular values, respectively. Moreover, it may be said from the comparison of Figs. 7 and 8 that the mode shapes obtained by the proposed method agree well with those obtained by the SYSNOISE. In the mode shapes for both analyses, the regions with high brightness represent the nodal lines.

2. Arbitrarily shaped cavity

Figure 9 shows the dimensions of an arbitrarily shaped cavity that is considered in the present work. In the same

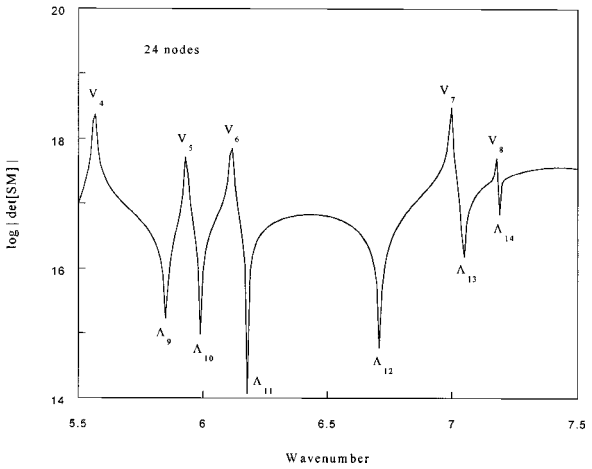

FIG. 15. Determinant of the system matrix $\mathbf{SM}^{(\mathrm{net})}_{\partial P/\partial n=0}$ vs wave number for the arbitrarily shaped cavity with a rigid boundary in the high wave-number range.

manner as in the previous example, 12, 16, and 20 nodes are distributed along the boundary of the cavity for the construction of discretized models. As an example, the discretized model for $N=16$ is illustrated in Fig. 10. Table III presents the singular values of the system matrices, $\det[\mathbf{SM}_{\partial P/\partial n=0}]$ and $\det[\mathbf{SM}_{P=0}]$ in the two cases of the rigid boundary and the pressure-release boundary. It may be said that for $N=20$, the eigenvalues are nearly equal to the SYSNOISE results. For $N=16$, the determinant curves for the system matrices are plotted in Fig. 11, where it may be seen that the unwanted troughs for $\det[\mathbf{SM}_{\partial P/\partial n=0}]$ coincide with those for $\det[\mathbf{SM}_{P=0}]$. However, the determinant curve for $\mathbf{SM}^{(\mathrm{net})}_{\partial P/\partial n=0}$ gives the troughs corresponding only to the eigenvalues of the cavity with the rigid boundary, as shown in Fig. 12 where the crests represent the unwanted singular values.

Figures 13 and 14 show the mode shapes of the cavity obtained by the proposed method and SYSNOISE, respectively. It is confirmed from these results that the mode shapes obtained by the present method agree well with those obtained by the numerical method.

IV. HIGH WAVE-NUMBER RANGE

In order to show the accuracy and validity of the proposed method in the high wave-number range, the method is applied to the arbitrarily shaped cavity that was dealt with in the previous section. In the following numerical test, the 9th–14th eigenvalues of the cavity with the rigid boundary are found from the determinant curve for $\mathbf{SM}^{(\mathrm{net})}_{\partial P/\partial n=0}$. For more accurate evaluation of higher modes, 24 nodes are distributed along the boundary. Figure 15 shows the determinant curve where the troughs and the crests represent the eigenvalues for the rigid boundary and those for the pressure-release boundary, respectively. The eigenvalues $\Lambda_9-\Lambda_{14}$ and the FEM results are summarized in Table IV, from which the accuracy of the proposed method is confirmed in the high wave-number range.

TABLE IV. Comparison of the higher eigenvalues of the arbitrarily shaped cavity with a rigid boundary, obtained by the proposed method and the FEM (SYSNOISE).

Sequence	9th	10th	11th	12th	13th	14th
Present ($N=24$)	5.852	5.991	6.180	6.711	7.046	7.189
FEM (1321 nodes)	5.872	6.020	6.209	6.748	7.097	7.238

V. CONCLUSIONS

This paper is concerned with a method using the superposition of circularly spreading waves, the forms of which are represented by nondimensional Green's functions. The functions are employed as basis functions of the trial function for the eigensolution. Since the basis functions are bounded at the origins of the function, unlike in the method of auxiliary sources, the proposed method does not require the auxiliary surface, the construction of which is a troublesome work.

The calculation scheme utilized in this study is very simple because the basis functions depend only on the scalar distance between the two boundary nodes and no subsidiary surface is required. Therefore, the numerical calculations are also very simple and the rapid convergence to the exact solutions may be guaranteed in spite of small numbers of nodes.

[1] C. A. Brebbia, J. C. F. Telles, and L. C. Wrobel, *Boundary Element Techniques* (Springer, New York, 1984).
[2] C. A. Brebbia, *The Boundary Element Method for Engineers* (Wiley, New York, 1978).
[3] J. R. Hughes, *The Finite Element Method* (Prentice-Hall, Englewood Cliffs, NJ, 1987).
[4] J. B. Davies and C. A. Muilwyk, ''Numerical solutions of uniform hollow waveguides with boundaries of arbitrary shape,'' Proc. Inst. Electr. Eng. **113**, 277–284 (1966).
[5] C. W. Steele, ''Numerical computation of electric and magnetic fields in a uniform waveguide of arbitrary cross section,'' J. Comput. Phys. **3**, 148–153 (1968).
[6] H. Y. Yee, ''On determination of cutoff frequencies of waveguides with arbitrary cross-section,'' Proc. Inst. Electr. Eng. **54**, 64 (1966).
[7] H. Y. Yee and N. F. Audeh, ''Cutoff frequencies of eccentric waveguides,'' IEEE Trans. Microwave Theory Tech. **MTT-14**, 487–493 (1966).
[8] R. H. T. Bates, ''The theory of the point-matching method for perfectly conducting waveguides and transmission lines,'' IEEE Trans. Microwave Theory Tech. **MTT-17**, 294–301 (1969).
[9] R. M. Bulley and J. B. Davies, ''Computation of approximate polynomial solutions to TE modes in an arbitrary shaped waveguide,'' IEEE Trans. Microwave Theory Tech. **MTT-17**, 440–446 (1969).
[10] P. A. Laura, ''A simple method for determination of cutoff frequencies of waveguides with arbitrary cross sections,'' Proc. Inst. Electr. Eng. **54**, 1495–1497 (1966).
[11] R. Zaridze, G. Bit-Babik, D. Karkasshadze, R. Jobava, D. Economou, and N. Uzunoglu, ''The Method of Auxiliary Sources (MAS): Solution of Propagation, Diffraction and Inverse Problems using MAS,'' Irans Black Sea Region Union of Applied Electrodynamics, 24–29 (1998).

Time-harmonic torsional waves in a composite cylinder with an imperfect interface

J. R. Berger[a)]
Division of Engineering, Colorado School of Mines, Golden, Colorado 80401

P. A. Martin[b)]
Department of Mathematics, University of Manchester, Manchester M13 9PL, United Kingdom

S. J. McCaffery[c)]
Division of Engineering, Colorado School of Mines, Golden, Colorado 80401

(Received 24 June 1999; accepted for publication 12 November 1999)

In this paper, the propagation of time-harmonic torsional waves in composite elastic cylinders is investigated. An imperfect interface is considered where tractions are continuous across the interface and the displacement jump is proportional to the stress acting on the interface. A frequency equation is derived for the rod and dispersion curves of normalized frequency as a function of normalized wave number for elastic bimaterials with varying values for the interface constant F are presented. The analysis is shown to recover the dispersion curves for a bimaterial rod with a perfect (welded) interface ($F=0$), and has the correct limiting behavior for large F. It is shown that the modes, at any given frequency, are orthogonal, and it is outlined how the problem of reflection of a torsional mode by a planar defect (such as a circumferential crack) can be treated. © *2000 Acoustical Society of America.* [S0001-4966(00)04402-7]

PACS numbers: 43.20.Mv, 43.20.Gp, 43.35.Cg, 43.38.Dv [ANN]

INTRODUCTION

The motivation for this study comes from the application of electromagnetic–acoustic transducers (EMATs) to the nondestructive testing of reinforced cables. We model the cable as an infinitely long bimaterial cylinder, with a core of circular cross section surrounded by a coaxial cladding; the core and the cladding are different homogeneous isotropic elastic solids.

Applications of EMATs are reviewed by Frost (1979) and by Hirao and Ogi (1997). We are interested in the use of time-harmonic torsional waves in the composite cylinder. Johnson *et al.* (1994) have used EMATs to study standing torsional modes in a single-material circular cylinder. This is a classical problem originally studied by Pochhammer (see, for example, Achenbach, 1973, sec. 6.10, or Miklowitz, 1978, sec. 4.4).

Propagation of time-harmonic torsional waves in a rod composed of two or more elastic layers has also been studied; see Thurston's paper (1978) for a comprehensive review. Perhaps the earliest work is by Armenàkas (1965, 1967, 1971). He studied the dispersion of harmonic waves and established the displacements and stresses at the interface of each layer analytically. A frequency equation was obtained by enforcing continuity conditions at the interface and a stress-free boundary condition on the lateral surfaces of the cylindrical rod.

Charalambopoulos *et al.* (1998) have considered the free vibration of a bimaterial elastic rod of finite length. The problem was solved for time-harmonic waves using the Helmholtz decomposition of the three-dimensional elasticity equations. The interface between the layers was considered as perfect, providing continuity of displacement and traction. The frequency equation for the full three-dimensional rod was found in terms of a 9×9 determinantal equation whose roots yield the dispersion relations for the rod.

Rattanawangcharoen and Shah (1992) have also considered the layered cylindrical rod, but they studied the problem from a more general perspective in that their formulation allowed many layers. A propagator matrix approach was used which related the stresses and displacements of one layer to the next. The propagator matrix was found to implicitly generate the frequency equation for the rod. The main motivation for the paper was to arrive at an efficient computational scheme for the many-layer problem which did not rely on a homogenization method such as integrating through the layers.

In this paper, we consider the bimaterial elastic cylinder with an imperfect interface between the core and the cladding. We do this because it is unrealistic to assume a perfectly bonded (welded) interface for our intended application to reinforced cables. We model the imperfect interface using a (linear) modification to the standard perfect-interface conditions, allowing some slippage. The interface conditions involve a single dimensionless parameter F. We study the effect of varying F on the dispersion relations. Note that the results for a perfectly bonded interface can be recovered by setting $F=0$.

EMATs can be used to excite propagating modes with a specified axial wavelength λ, where λ is determined by the physical spacing between the magnets of alternating polarity.

[a)]Electronic mail: jberger@mines.edu
[b)]Present address: Department of Mathematical and Computer Sciences, Colorado School of Mines, Golden, CO 80401; electronic mail: pamartin@mines.edu
[c)]Present address: CIRES, University of Colorado, Boulder, CO 80309.

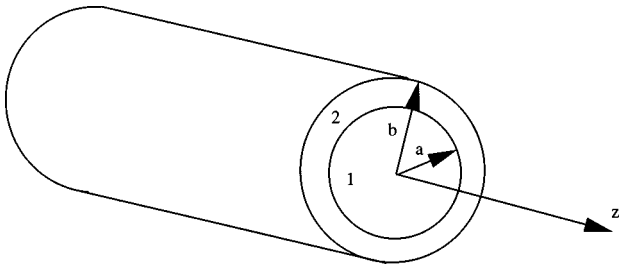

FIG. 1. Geometry of the bimaterial cylinder.

One then adjusts the frequency ω until one of the propagating torsional modes is excited. When such a mode interacts with a defect in the composite cylinder, other allowable modes at the frequency ω, but with various wavelengths, will be stimulated; evanescent modes (decaying exponentially with distance from the defect) will also be present, in general. We show that the torsional modes at a given frequency are orthogonal, extending a proof due to Gregory (1983). We also discuss the evanescent modes and their computation.

Finally, we outline how our knowledge of the modal structure for the composite cylinder can be used to model the problem of reflection of a torsional mode by a thin defect in a cross-sectional plane. The EMAT system can only receive waves with the same wavelength as the incident mode, so that some information at the excitation frequency ω is lost; but the experiment can be repeated at other modal frequencies.

I. FORMULATION

Let (r,θ,z) be cylindrical polar coordinates. We consider the infinite isotropic elastic bimaterial cylinder shown in Fig. 1. The cylinder consists of a solid core, $r<a$, surrounded by an annular cladding, $a<r<b$; the core and cladding are made of materials 1 and 2, respectively. Material m has Lamé moduli λ_m and μ_m, $m=1,2$. The analysis presented here generally follows Armenàkas (1965).

In general, the displacement field $\mathbf{u}=(u,v,w)$ in each portion of the bimaterial can be written using the Lamé scalar potential ϕ and vector potential $(\psi_r,\psi_\theta,\psi_z)$; see, for example, Achenbach, 1973, sec. 2.13. We are interested in torsional waves, for which the only non zero displacement component is the tangential displacement v, and v itself is required to be independent of θ. Hence, the only potential needed is the z-component of the vector potential, $\psi_z\equiv\psi$, say. In terms of ψ, we have

$$v=-\frac{\partial\psi}{\partial r}. \tag{1}$$

The only nontrivial stress components are

$$\sigma_{r\theta}=\mu\left(\frac{\partial v}{\partial r}-\frac{v}{r}\right) \tag{2}$$

and

$$\sigma_{\theta z}=\mu\frac{\partial v}{\partial z}. \tag{3}$$

The potential ψ satisfies

$$\Delta\psi=\frac{1}{c^2}\frac{\partial^2\psi}{\partial t^2}, \tag{4}$$

where Δ is the Laplace operator and c is the shear wave speed. For waves propagating in the positive z-direction, the appropriate solution of (4) can be written as

$$\psi(r,z,t)=\Psi(r)e^{i(kz-\omega t)}, \tag{5}$$

where i is $\sqrt{-1}$, k and ω are real, and Ψ solves

$$\frac{1}{r}\frac{d}{dr}(r\Psi')+((\omega/c)^2-k^2)\Psi=0. \tag{6}$$

This is Bessel's equation of order zero. Its solutions depend on the sign of $\omega^2-k^2c^2$. Thus, define

$$Z_n=J_n,\quad W_n=Y_n,\quad \text{and } q=\sqrt{(\omega/c)^2-k^2}\quad \text{if } \omega^2>k^2c^2, \tag{7}$$

and

$$Z_n=(-1)^nI_n,\quad W_n=K_n,\quad \text{and } q=\sqrt{k^2-(\omega/c)^2}\quad \text{if } \omega^2<k^2c^2, \tag{8}$$

where J_n and Y_n are Bessel functions and I_n and K_n are modified Bessel functions. The factor $(-1)^n$ will allow a unified treatment for all frequencies. The behavior of the solution as $q\to0$ will be examined in some detail later; for now we assume that $q>0$ $(\omega^2\neq k^2c^2)$.

So, the appropriate solution of (6) is

$$\Psi(r)=q^{-2}AZ_0(qr)+b^2BW_0(qr), \tag{9}$$

where A and B are arbitrary constants, and the factors q^{-2} and b^2 have been introduced for later convenience, implying that A and B are dimensionless; recall that b is the outer radius.

The displacement field obtained by substituting (5) and (9) in (1) is

$$v=\{q^{-1}AZ_1(qr)+qb^2BW_1(qr)\}e^{i(kz-\omega t)}, \tag{10}$$

as $Z_0'(x)=-Z_1(x)$ and $W_0'(x)=-W_1(x)$. (Note that $I_0'=I_1$.) From (2), we obtain for the stress,

$$\sigma_{r\theta}=-\mu\{AZ_2(qr)+(qb)^2BW_2(qr)\}e^{i(kz-\omega t)}, \tag{11}$$

as $Z_1'(x)-x^{-1}Z_1(x)=-Z_2(x)$ and $W_1'(x)-x^{-1}W_1(x)=-W_2(x)$.

Let us now use the expressions above, using subscripts 1 and 2 to indicate quantities in the core and cladding, respectively. Thus, from (10), the displacement in the cladding is

$$v_2=\{q_2^{-1}A_2Z_1(q_2r)+q_2b^2B_2W_1(q_2r)\}e^{i(kz-\omega t)}. \tag{12}$$

For the core, the solution for v_1 must be bounded at the origin so we have

$$v_1=q_1^{-1}A_1Z_1(q_1r)e^{i(kz-\omega t)}. \tag{13}$$

In these expressions, q_j is defined by

$$q_j=\begin{cases}\sqrt{k_j^2-k^2} & \text{if } k_j^2>k^2,\\ \sqrt{k^2-k_j^2} & \text{if } k_j^2<k^2,\end{cases}\quad j=1,2, \tag{14}$$

where $k_j=\omega/c_j$. Note that the wave number, k, is the same in the expressions for q_1 and q_2; this observation gives a

relation between q_1 and q_2, which we will discuss later.

With reference to Fig. 1, we now consider boundary and interface conditions on the displacement field given by (12) and (13). At the outer surface, we have the traction-free boundary condition

$$\sigma_{r\theta}=0 \quad \text{at } r=b. \tag{15}$$

We consider the interface conditions in the following section.

A. Interface conditions

A variety of conditions may be taken on the interface $r=a$ in order to represent imperfect interface conditions. A review of interface conditions for elastic wave problems has been presented by Martin (1992). For most models, the displacement $\mathbf{u}^+$ and traction $\mathbf{t}^+$ on one side of the interface are assumed to be linearly related to the displacement $\mathbf{u}^-$ and traction $\mathbf{t}^-$ on the other side of the interface. For example, the model of Rokhlin and Wang (1991), originally derived for plane interfaces, takes interface conditions of the form

$$[\mathbf{t}]=\mathbf{G}\mathbf{u}^-+\mathbf{B}\mathbf{t}^-, \quad [\mathbf{u}]=\mathbf{F}\mathbf{t}^-+\mathbf{A}\mathbf{u}^-,$$

where **A**, **B**, **F**, and **G** are 3×3 matrices, and the square brackets indicate a jump in the quantity across the interface; for example, if the interface is at $r=a$, we have

$$[\mathbf{u}]=\mathbf{u}^+-\mathbf{u}^-=\mathbf{u}(a^+,\theta)-\mathbf{u}(a^-,\theta), \tag{16}$$

suppressing the dependence on z and t. If the coupling term **G** can be neglected, and furthermore if **A** and **B** are set equal to zero, we recover the model of Jones and Whittier (1967) for a flexibly bonded interface,

$$[\mathbf{t}]=0, \tag{17}$$

$$[\mathbf{u}]=\mathbf{F}\mathbf{t}^-, \tag{18}$$

where **F** is a constant diagonal matrix. For simplicity, we will use the Jones–Whittier model for the analysis presented here. For thin, elastic interfacial layers, the elements of **F** have been related to the thickness and elastic constants of the layer by, for example, Jones and Whittier (1967), Mal and Xu (1989), and Pilarski and Rose (1988).

For torsional waves, **u** reduces to a scalar for the tangential displacement v and **t** reduces to a scalar for the tangential shear stress $\sigma_{r\theta}$. The interface conditions are then

$$\sigma_{r\theta}(a^-)=\sigma_{r\theta}(a^+) \tag{19}$$

and

$$[v]=(a/\mu_1)F\sigma_{r\theta}(a), \tag{20}$$

where $[v]=v_2(a^+)-v_1(a^-)$ and F is a dimensionless scalar. Our goal is to investigate solutions which satisfy (15), (19), and (20) as the interface parameter F is varied. We note that if $F=0$, the perfect interface conditions of continuity of traction and displacement are recovered.

II. FREQUENCY EQUATION FOR THE ROD

We now present the details for the set of equations which will determine the dispersion relations in the bimaterial rod. Substituting the displacement field of (12) in the boundary condition, (15), yields

$$A_2Z_2(q_2b)+(q_2b)^2B_2W_2(q_2b)=0. \tag{21}$$

Following the Jones-Whittier model, we have for continuity of traction across the interface, from (12), (13), and (19),

$$(\mu_1/\mu_2)A_1Z_2(q_1a)-A_2Z_2(q_2a)-(q_2b)^2B_2W_2(q_2a)=0. \tag{22}$$

Note that neither of these equations changes in the case of the perfectly bonded interface. The displacement jump across the interface is given by (20). We then have

$$(q_1b)^{-1}A_1\{Z_1(q_1a)-Fq_1aZ_2(q_1a)\}-(q_2b)^{-1}A_2Z_1(q_2a) - q_2bB_2W_1(q_2a)=0. \tag{23}$$

Equations (21)–(23) provide three equations in the three unknown constants A_1, A_2, and B_2. In matrix form, the system of equations is

$$\mathbf{D}\mathbf{b}=\mathbf{0}, \tag{24}$$

where the elements of the nonsymmetric matrix **D** are obtained directly from (21)–(23) and $\mathbf{b}=(A_1,A_2,B_2)^T$.

For a nontrivial solution we then require

$$\det \mathbf{D}=0. \tag{25}$$

This is the frequency equation for the rod.

The quantity $\det \mathbf{D}$ seems to depend on only five dimensionless parameters, namely

$$q_1b, \quad q_2b, \quad a/b, \quad \mu_1/\mu_2, \quad \text{and } F; \tag{26}$$

in particular, the density ratio (or, equivalently, c_1/c_2) does not appear explicitly. However, this is illusory: we have to know how to choose Z_n (J_n or $(-1)^nI_n$?) and W_n (Y_n or K_n?) in each material, and these choices depend on the relative sizes of k^2, k_1^2, and k_2^2, information that we cannot extract from a knowledge of (26) alone.

Thus we proceed as follows. Assume that we are given values for a/b, μ_1/μ_2, F, and

$$c_2/c_1=k_1/k_2=\alpha, \tag{27}$$

say. Choose a value for the axial wave number kb. We now seek values of k_2b, say, so that (25) is satisfied. Note that $k_1b=\alpha k_2b$, and then q_1b and q_2b are defined by (14), with the associated selections of Z_n and W_n dictated by (7) and (8). In fact, the relations between q_1, q_2, k_1, k_2, k, and α are complicated, because they depend on the relative magnitudes of k^2, k_1^2, and k_2^2; there are four cases, as summarized in Table I. In this table, the second column specifies the four cases in terms of the shear wave speeds of the two materials (these are material constants) and the axial wave speed $c_a=\omega/k$. A similar table was given by Kleczewski and Parnes (1987) in their study of torsional modes when the cladding is unbounded ($b\to\infty$ in our notation).

In order to compare with Armenàkas (1965) (for $F=0$), we have determined the dispersion curves of normalized frequency,

TABLE I. Relations between q_1 and q_2, in which $\alpha = c_2/c_1 = k_1/k_2$ and $c_a = \omega/k$.

Wave numbers	Wave speeds	q_1^2	q_2^2	Relation between q_1 and q_2
$k^2 < k_1^2 \leqslant k_2^2$ $k^2 < k_2^2 \leqslant k_1^2$	$c_1 \leqslant c_2 < c_a$ $c_2 \leqslant c_1 < c_a$	$k_1^2 - k^2$	$k_2^2 - k^2$	$q_1^2 = \alpha^2 q_2^2 - k^2(1-\alpha^2)$
$k_2^2 < k^2 < k_1^2$	$c_1 < c_a < c_2$	$k_1^2 - k^2$	$k^2 - k_2^2$	$q_1^2 = -\alpha^2 q_2^2 - k^2(1-\alpha^2)$
$k_1^2 < k^2 < k_2^2$	$c_2 < c_a < c_1$	$k^2 - k_1^2$	$k_2^2 - k^2$	$q_1^2 = -\alpha^2 q_2^2 + k^2(1-\alpha^2)$
$k_1^2 \leqslant k_2^2 < k^2$ $k_2^2 \leqslant k_1^2 < k^2$	$c_a < c_1 \leqslant c_2$ $c_a < c_2 \leqslant c_1$	$k^2 - k_1^2$	$k^2 - k_2^2$	$q_1^2 = \alpha^2 q_2^2 + k^2(1-\alpha^2)$

$$\Omega_2 = k_2(b-a)/\pi = \omega(b-a)/(\pi c_2),$$

as a function of normalized axial wave number,

$$\xi = k(b-a)/\pi,$$

for a given value of the interface parameter F. We note that the frequency equation determined here cannot be written in terms of a single argument such as qa, which can be done in the case of a rod made from a single material. As such, we study numerical solutions to (25) in the next section for values of a/b, F, and the elastic constants.

III. DISPERSION CURVES WITH VARYING INTERFACE CONDITIONS

To benchmark the analysis presented here, we first present results which can be directly compared with Armenàkas (1965) in the case of a perfect interface, $F=0$. We take $a/b=0.25$, $\mu_1/\mu_2=10$, and $c_1/c_2=1.83$ (so that the density ratio, $\rho_1/\rho_2=3$). We show the dispersion curves of frequency, Ω_2, versus wave number, ξ, for $F=0$, $F=1$, $F=10$, and $F=100$ for the second mode in Fig. 2 and the third mode in Fig. 3. The first mode will be analyzed in a subsequent section. The dispersion curve for $F=0$ agrees exactly with the analysis of Armenàkas (1965). As the interface parameter is increased, note the decrease in Ω_2, especially at the smaller values of ξ. At higher values of ξ, the loss of perfect continuity at the interface has a reduced effect.

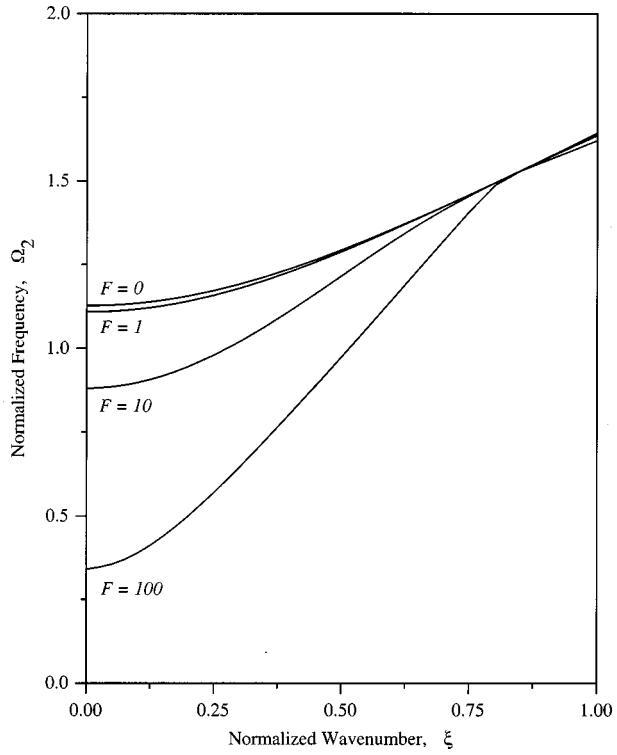

FIG. 2. Dispersion curves for the second mode in the bimaterial cylinder.

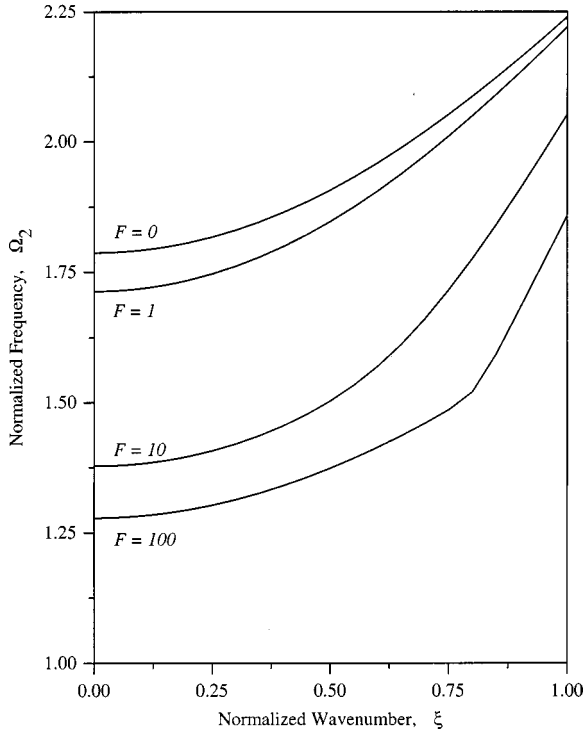

FIG. 3. Dispersion curves for the third mode in the bimaterial cylinder.

One feature of note in Fig. 3 is the curve for $F=100$, which exhibits a corner at $\xi \simeq 0.8$. This is not a numerical artifact: the figure was produced using very small increments in ξ. Similar behavior was found for other (large) values of F.

A second way of visualizing the behavior of the dispersion curves as the interface parameter is varied is illustrated in Fig. 4. In the figure, we show results for the second mode and plot frequency, Ω_2, versus the interface parameter, F, as the wave number ξ is varied. As expected, we see a much greater effect on Ω_2 by F at the smaller wave numbers. This suggests a possible measurement approach for determining F where ξ is fixed, Ω_2 is measured, and then F is determined from the figure.

The curves shown in Fig. 4 appear to be approaching asymptotic values for large F. With reference to the interface conditions given by (20), we see that in the limit as $F \to \infty$ we recover the boundary condition

$$\sigma_{r\theta}(a) = 0.$$

This is the appropriate boundary condition for the outer boundary of a solid rod of radius a and for the inner boundary condition for a hollow tube with inner radius a. In the case of $F \to \infty$, the frequency equation given by (25) reflects this change in boundary condition,

$$Z_2(q_1 a)\, g(q_2 a, q_2 b) = 0, \tag{28}$$

where

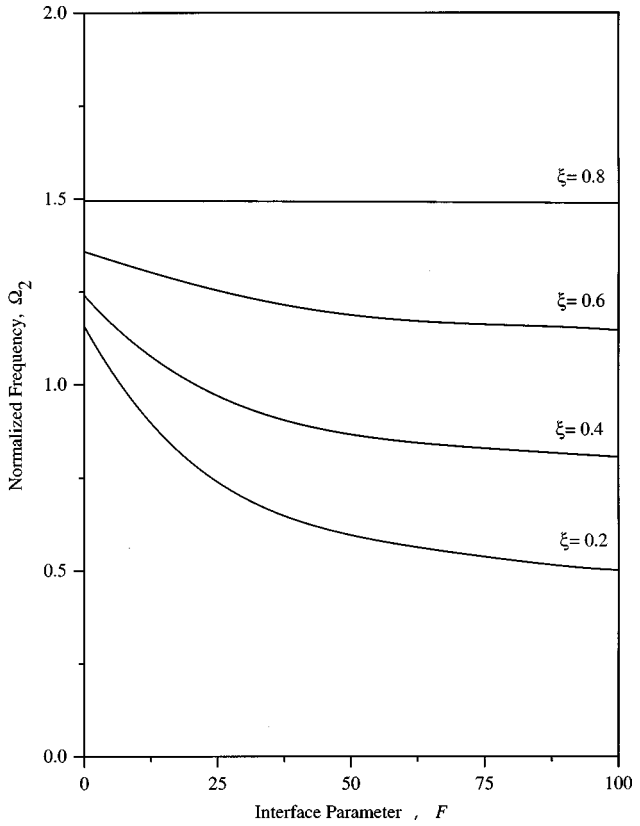

FIG. 4. Normalized frequency vs interface parameter at fixed wave number in the bimaterial cylinder for the second mode.

$$g(q_2a,q_2b)=Z_2(q_2a)W_2(q_2b)-Z_2(q_2b)W_2(q_2a).$$

The frequency equation (28) has two sets of solutions, one given by $Z_2(q_1a)=0$ and the other given by $g(q_2a,q_2b)=0$. The first of these is the frequency equation for a solid rod of radius a, whereas the second is the frequency equation for a hollow tube of inner radius a and outer radius b. So, the imperfect interface formulation has the expected behavior for large values of F.

Numerically, one must be somewhat careful in handling the limit as $F\to\infty$ and check if the relations between q_1 and q_2 given in Table I still hold. We present some typical results in Table II where we have used $F=1\times10^{10}$. Note in the table that we report values of normalized frequency Ω_2 as we have throughout this paper, even for the solid rod modes in material 1 reported in the table. From the table, we see that the asymptotic values of frequency, Ω_2, for the second mode in the composite rod, are the nondispersive first modes $(q_1a=0)$ in the solid rod. Also, the asymptotic values of frequency, Ω_2, for the third mode in the composite rod correspond to the second mode frequencies in the hollow tube.

TABLE II. Frequencies for the second and third modes in the composite rod with $F=1\times10^{10}$, and corresponding frequencies for the first mode in a solid rod and the second mode in a hollow tube.

ξ	Ω_2 second mode	Ω_2 third mode	Ω_2, hollow tube second mode	Ω_2, solid rod first mode
0.2	0.365	1.286	1.286	0.365
0.4	0.730	1.332	1.332	0.730
0.6	1.095	1.405	1.405	1.095

Some discussion on the interface parameter F is perhaps in order. As mentioned in the Introduction, the application motivating the analysis presented here is the nondestructive evaluation of reinforced cables. Typically these cables are fabricated with a steel core surrounded by an aluminum cladding. Because of the underlying wire-rope structure of the core and the cladding, the interface conditions are imperfect. Our approach here is to treat the interface parameter in a phenomenological manner to account for the imperfect interface. As such, we do not stipulate a strict physical interpretation to the numerical value of F, nor do we attempt to relate the value of F to elastic constants.

IV. FIRST TORSIONAL MODE

Armenàkas (1965) noted that the first torsional mode is not properly described by the solution of the Bessel equation, unlike the higher torsional modes analyzed above. Therefore, special consideration of the first torsional mode is necessary, and this is carried out next. For example, when $q_2=0$, there can be a nondispersive mode propagating in the cladding of the rod with dispersive modes in the core.

Suppose that $\omega^2=k^2c^2$, so that $q=0$ and (6) reduces to

$$\frac{d}{dr}(r\Psi')=0,$$

with general solution

$$\Psi(r)=A+B\log r.$$

This gives a solution for v proportional to B/r, which cannot be the general solution as it involves only one arbitrary constant, B. As we are interested in Ψ' rather than Ψ, we return to (6); differentiation with respect to r gives

$$\frac{d}{dr}\left(\frac{1}{r}\frac{d}{dr}(r\Psi')\right)+((\omega/c)^2-k^2)\Psi'=0,$$

a second-order ordinary differential equation for Ψ'. When $\omega^2=k^2c^2$, the general solution of this equation is

$$\Psi'(r)=Ar+B/r.$$

Hence, in dimensionless form, we have

$$v(r,z,t)=(Ar+Bb^2/r)e^{i(kz-\omega t)} \tag{29}$$

and

$$\sigma_{r\theta}(r,z,t)=-2\mu B(b/r)^2e^{i(kz-\omega t)}. \tag{30}$$

Note that the expressions (29) and (30) can also be obtained by taking the limit $q\to0$ in (10) and (11) (apart from some numerical factors which can be absorbed into A and B). This accounts for the various q-factors in (10): they lead to meaningful (bounded) expressions for small q.

Let us assume that $q_2=0$. The outer boundary condition (15) implies that $B_2=0$, whence $\sigma_{r\theta}\equiv0$ in the cladding and

$$v_2=A_2re^{i(kz-\omega t)}. \tag{31}$$

Within the core, v_1 is given by (13). For continuity of tractions across $r=a$, (19) gives

$$A_1 Z_2(q_1 a) = 0, \tag{32}$$

whereas the imperfect-interface condition (20) gives

$$A_1 Z_1(q_1 a) - q_1 a A_2 = 0. \tag{33}$$

Now, for nontrivial solutions, we require $k^2 > k_1^2$, so that (32) gives $q_1 a = j_{2,s}$, the s-th zero of $J_2(x)$. Then A_1 is arbitrary with A_2 given by (33) (with $Z_1 = J_1$). It is interesting to note that the interface parameter F does not enter into any of the equations, so that the dispersion curves for the first torsional mode when $q_2 = 0$ are identical, regardless of whether the interface is perfect or imperfect. This is consistent with the fact that since $q_2 = 0$, a nondispersive mode is propagating in the cladding and (32) is simply the frequency equation for the dispersive modes in the core.

Alternatively, let us assume that $q_1 = 0$; for bounded displacements in the core, we obtain

$$v_1(r,z,t) = A_1 r e^{i(kz - \omega t)}.$$

Within the cladding, v_2 is given by (12), so that the outer boundary condition gives (21). The interface condition (19) gives

$$A_2 Z_2(q_2 a) + (q_2 b)^2 B_2 W_2(q_2 a) = 0;$$

the frequency equation is then obtained by combining this equation with (21): it is the same equation as for a hollow cylindrical tube. The other interface condition, (20), then determines A_1 as

$$A_1 = (q_2 a)^{-1} A_2 Z_1(q_2 a) + (q_2 b^2/a) B_2 W_1(q_2 a).$$

Again, these equations do not involve F.

V. EVANESCENT MODES

So far, we have only considered propagating torsional modes. However, cylinders can also support evanescent modes, which decay exponentially with z. Such modes can be constructed by writing

$$\psi(r,z,t) = \Psi(r) e^{-kz - i\omega t},$$

where Ψ solves

$$\frac{1}{r}\frac{d}{dr}(r\Psi') + ((\omega/c)^2 + k^2)\Psi = 0,$$

whence

$$\Psi(r) = q^{-2} A J_0(qr) + b^2 B Y_0(qr)$$

with $q = \sqrt{(\omega/c)^2 + k^2}$. Then, proceeding exactly as before, we arrive at the frequency equation (25) in which Z_n and W_n are to be replaced by J_n and Y_n, respectively.

VI. DISCUSSION ON MODE ORTHOGONALITY

We have constructed various torsional modes for the composite cylinder in the general form

$$\mathbf{u}(r,\theta,z,t) = \mathrm{Re}\{\mathbf{U}(r,\theta) e^{i(kz - \omega t)}\}.$$

In our computations, we have fixed the axial wave number k and then calculated the frequencies ω of the allowable modes. This is convenient for comparisons with Armenàkas (1965) and it is appropriate for the application to EMATs; these can be used to excite propagating modes of a specified axial wavelength. However, once such a mode has been excited, we are interested in studying its reflection by defects in the cylinder. This is most conveniently done by specifying the frequency and then determining all the allowable modes at that frequency. With this in mind, we write a typical mode as

$$\mathbf{u}^{(n)}(r,\theta,z,t) = \mathrm{Re}\{\mathbf{U}^{(n)}(r,\theta) e^{i(k^{(n)} z - \omega t)}\},$$

where the wave number $k^{(n)}$ need not be real.

These modes are biorthogonal. To be more explicit, denote the stresses corresponding to $\mathbf{u}^{(n)}$ by

$$\boldsymbol{\sigma}^{(n)}(r,\theta,z,t) = \mathrm{Re}\{\mathbf{S}^{(n)}(r,\theta) e^{i(k^{(n)} z - \omega t)}\}.$$

Then, if $k^{(n)} \neq \pm k^{(m)}$, we have

$$\int_{\mathcal{A}} \{U_z^{(m)} S_{zz}^{(n)} - S_{rz}^{(m)} U_r^{(n)} - S_{\theta z}^{(m)} U_\theta^{(n)}\} r\, dr\, d\theta = 0, \tag{34}$$

where $\mathcal{A}$ is the cross section of the composite cylinder. This relation can be proved by a simple extension of the proof given by Gregory (1983). (One applies the elastic reciprocal theorem twice, once in the core and once in the cladding, and then adds the results; the interface conditions imply that the contributions from integrating over the two sides of the interface cancel.) In fact, (34) holds for all modes in composite cylinders of any cross section, and with any number of imperfect (cylindrical) interfaces. For our problem, with torsional modes given by

$$v^{(n)}(r,z,t) = \mathrm{Re}\{V^{(n)}(r) e^{i(k^{(n)} z - \omega t)}\},$$

Eq. (34) reduces to

$$\int_0^b V^{(m)}(r) V^{(n)}(r) r\, dr = 0, \quad m \neq n, \tag{35}$$

so that torsional modes are actually orthogonal. This orthogonality relation is useful when the reflection of a torsional mode by certain defects is examined. For example, we may consider a bimaterial cylinder with a planar break (crack) perpendicular to the cylinder's axis, giving an idealized model of a damaged cable. Specifically, we partition the cross-section $\mathcal{A}$ into a broken part $\mathcal{A}_b$ and an unbroken part $\mathcal{A}_u$, so that $\mathcal{A} = \mathcal{A}_b \cup \mathcal{A}_u$. The boundaries of $\mathcal{A}_b$ and $\mathcal{A}_u$ are concentric circles; for example, we might take $\mathcal{A}_u$ to be the circle $0 \leqslant r < c$, with $\mathcal{A}_b$ as the annulus $c < r < b$, so that the cable is circumferentially cracked. Then, if a torsional mode is incident on the defect, the reflected and transmitted fields can be written as modal sums. This is a standard approach for planar obstacles in waveguides. In the context of torsional waves, it has been used recently by Engan (1998) to analyze the effect of a step-change in radius of homogeneous circular cylinders. For the present problem, application of the boundary conditions at the defect plane leads to a system of equations for the reflection and transmission coefficients; of particular interest are the reflected and transmitted modes with the same wavelength as the incident mode, because these are the only modes that can be detected by the EMAT. Again, in a standard way, one can derive integral equations and/or variational expressions for the reflection and transmis-

sion coefficients; see, for example, Schwinger and Saxon (1968) for a detailed discussion on related scattering problems.

VII. CONCLUSIONS

We have presented an analysis for torsional waves propagating in a bimaterial rod with imperfect interface conditions. To the authors' knowledge, the effect of imperfect interface conditions on dispersive wave motion has not been studied for rods. We find the expected behavior for waves in the rod when we take the interface parameter $F=0$ and $F \rightarrow \infty$. When $F \neq 0$ we find that the frequency decreases with increasing F at a given wave number in the dispersion relations. This effect was shown to be more pronounced at small wave numbers. The propagation of nondispersive modes in the cladding was also investigated, and the frequency equation for dispersive modes in the core was recovered. We also showed that, at any given frequency, the modes are orthogonal. This fact can be exploited in the solution of a scattering problem, where an incident torsional mode interacts with an annular defect in the bimaterial rod. The model developed here should be useful in analyzing nondestructive evaluation measurements in reinforced cables where perfect interface conditions may not exist.

ACKNOWLEDGMENTS

Two of us (J.R.B. and S.J.M.) gratefully acknowledge the support received from the Center for Advanced Control of Energy and Power Systems, a National Science Foundation Industry/University Cooperative Research Center, at the Colorado School of Mines. J.R.B. also acknowledges the additional support provided by the Engineering and Physical Sciences Research Council as a visiting fellow in the Department of Mathematics at the University of Manchester.

Achenbach, J. D. (**1973**). *Wave Propagation in Elastic Solids* (North-Holland, New York).

Armenàkas, A. E. (**1965**). ''Torsional waves in composite rods,'' J. Acoust. Soc. Am. **38**, 439–446.

Armenàkas, A. E. (**1967**). ''Propagation of harmonic waves in composite circular cylindrical shells. I: Theoretical investigation,'' AIAA J. **5**, 740–744.

Armenàkas, A. E. (**1971**). ''Propagation of harmonic waves in composite circular cylindrical shells. Part II: Numerical analysis,'' AIAA J. **9**, 599–605.

Charalambopoulos, A., Fotiadis, D. I., and Massalas, C. V. (**1998**). ''Free vibrations of a double layered elastic isotropic cylindrical rod,'' Int. J. Eng. Sci. **36**, 711–731.

Engan, H. E. (**1998**). ''Torsional wave scattering from a diameter step in a rod,'' J. Acoust. Soc. Am. **104**, 2015–2024.

Frost, H. M. (**1979**). ''Electromagnetic-ultrasound transducers: Principles, practice, and applications,'' in *Physical Acoustics*, edited by W. P. Mason and R. N. Thurston (Academic, New York), Vol. 14, pp. 179–275.

Gregory, R. D. (**1983**). ''A note on bi-orthogonality relations for elastic cylinders of general cross section,'' J. Elast. **13**, 351–355.

Hirao, M., and Ogi, H. (**1997**). ''Electromagnetic acoustic resonance and materials characterization,'' Ultrasonics **35**, 413–421.

Johnson, W., Auld, B. A., and Alers, G. A. (**1994**). ''Spectroscopy of resonant torsional modes in cylindrical rods using electromagnetic-acoustic transduction,'' J. Acoust. Soc. Am. **95**, 1413–1418.

Jones, J. P., and Whittier, J. S. (**1967**). ''Waves at a flexibly bonded interface,'' J. Appl. Mech. **34**, 905–909.

Kleczewski, D., and Parnes, R. (**1987**). ''Torsional dispersion relations in a radially dual elastic medium,'' J. Acoust. Soc. Am. **81**, 30–36.

Mal, A. K., and Xu, P. C. (**1989**). ''Elastic waves in layered media with interface features,'' in *Elastic Wave Propagation*, edited by M. F. McCarthy and M. A. Hayes (North-Holland, Amsterdam), pp. 67–73.

Martin, P. A. (**1992**). ''Boundary integral equations for the scattering of elastic waves by elastic inclusions with thin interface layers,'' J. Nondestruct. Eval. **11**, 167–174.

Miklowitz, J. (**1978**). *The Theory of Elastic Waves and Waveguides* (North-Holland, Amsterdam).

Pilarski, A., and Rose, J. L. (**1988**). ''A transverse-wave ultrasonic oblique-incidence technique for interfacial weakness detection in adhesive bonds,'' J. Appl. Phys. **63**, 300–307.

Rattanawangcharoen, N., and Shah, A. H. (**1992**). ''Guided waves in laminated isotropic circular cylinder,'' Comput. Mech. **10**, 97–105.

Rokhlin, S. I., and Wang, Y. J. (**1991**). ''Analysis of boundary conditions for elastic wave interaction with an interface between two solids,'' J. Acoust. Soc. Am. **89**, 503–515.

Schwinger, J., and Saxon, D. S. (**1968**). *Discontinuities in Waveguides* (Gordon & Breach, New York).

Thurston, R. N. (**1978**). ''Elastic waves in rods and clad rods,'' J. Acoust. Soc. Am. **64**, 1–37.

Fast analysis of transient acoustic wave scattering from rigid bodies using the multilevel plane wave time domain algorithm

A. A. Ergin,[a] B. Shanker, and E. Michielssen
Center for Computational Electromagnetics, Department of Electrical and Computer Engineering, University of Illinois at Urbana-Champaign, 1406 West Green Street, Urbana, Illinois 61801

(Received 19 July 1999; accepted for publication 12 November 1999)

The analysis of transient wave scattering from rigid bodies using integral equation-based techniques is computationally intensive: if carried out using classical schemes, the evaluation of the velocity potential on the surface of a three-dimensional scatterer, represented in terms of N_s spatial basis functions for N_t time steps, requires $O(N_t N_s^2)$ operations. The recently developed plane wave time domain (PWTD) algorithm permits the rapid evaluation of transient fields that are generated by bandlimited source distributions. It has been shown that incorporation of the PWTD algorithm into integral equation-based solvers in a two-level setting reduces the computational complexity of a transient analysis to $O(N_t N_s^{1.5} \log N_s)$. In this paper, it is shown that casting the PWTD scheme into a multilevel framework permits the analysis of transient acoustic surface scattering phenomena in $O(N_t N_s \log^2 N_s)$ operations using $O(N_t N_s)$ memory. Numerical examples that demonstrate the efficacy of the multilevel implementation are also presented. © *2000 Acoustical Society of America.* [S0001-4966(00)04802-5]

PACS numbers: 43.20.Px, 43.20.Fn, 02.70.Pt [ANN]

INTRODUCTION

Transient acoustic wave scattering phenomena can be analyzed using either differential equation (DE)-based or integral equation (IE)-based techniques. When the scatterer is impenetrable/homogeneous and immersed in an unbounded homogeneous medium, IE-based methods enjoy two important advantages over DE-based techniques. First, IE-based solvers implicitly impose the radiation condition. DE-based techniques, in contrast, have to be supplemented with boundary conditions that emulate a free-space environment. Second, IE techniques only require that the unknown fields be discretized on the scatterers surface, whereas DE-based methods call for a discretization of these fields throughout a volume enclosing the scatterer. Despite these advantages, IE-based methods for analyzing transient scattering phenomena historically have not enjoyed widespread popularity as they were long thought to be intrinsically unstable and computationally expensive. Recent research, however, has resulted in techniques to suppress instabilities[1–4] in IE-based solvers, and schemes have surfaced for reducing their exorbitant computational requirements.

A typical IE-based solver for analyzing acoustic surface scattering phenomena operates as follows. Given a scatterer that resides in an infinite homogeneous medium, the extinction theorem states that the fields can be evaluated anywhere in space upon specification of the incident field and the total field (and its normal derivative) on the scatterers surface. The total surface field can be related to the incident field through a time-domain boundary integral equation (BIE), which can be solved using so-called marching-on-in-time (MOT) schemes.[1,5–7] To this end, the surface field is represented in terms of a set of spatial and temporal basis functions. Then, the instantaneous total field is expressed as a superposition of the incident and scattered fields. Evaluation of the latter requires the computation of a retarded time boundary integral over the basis functions representing the field. This procedure leads to a system of equations that can be solved for the coefficients of the basis functions representing the surface field at a given time step. Depending on the choice of the time step size, the basis functions, and the testing procedure, the matrix to be inverted is diagonal or sparse, yielding explicit or implicit time stepping schemes, respectively. It has been empirically shown that implicitness and accurate evaluation of retarded time boundary integrals contribute to the stability of a MOT scheme.[1–3,7,8]

Forming the right-hand side of the aforementioned matrix equation at each time step is computationally expensive because it calls for the evaluation of the scattered fields on the surface in terms of the past values of the total surface fields. If N_s spatial and N_t temporal basis functions are used to represent the surface fields, then the computational cost of forming the excitation vector for all N_t time steps scales as $O(N_t N_s^2)$. A technique for reducing this cost, albeit at the expense of accuracy, was suggested by Dodson *et al.*[9] In this approach, ''integration over regions of low retarded field'' is omitted and field values are computed only in regions where the field is anticipated to be significant. However, cost savings only seem attainable when the scatterer is long compared to the width of the incident pulse along its direction of propagation. The plane wave time domain (PWTD) algorithm,[10,11] which can be considered the time-domain counterpart of the frequency domain fast multipole method,[12–14] provides an alternative approach to reducing the cost of MOT schemes. This algorithm relies on a decomposition of transient wave fields in terms of propagating

[a]Electronic mail: aergin@decwa.ece.uiuc.edu

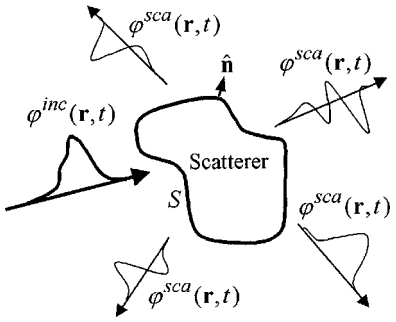

FIG. 1. The surface scattering problem. The incident field $\varphi^{\mathrm{inc}}(\mathbf{r},t)$ interacts with the scatterer bounded by the surface S and produces the scattered field $\varphi^{\mathrm{sca}}(\mathbf{r},t)$.

plane waves and permits the accurate and fast computation of fields that are radiated by known and bandlimited sources. Two-level PWTD enhanced MOT solvers have been used successfully in analyzing both acoustic and electromagnetic transient scattering phenomena.[15,16] It has been shown that the cost of analyzing surface scattering phenomena using these solvers scales as $O(N_t N_s^{1.5} \log N_s)$, resulting in considerable cost savings when compared to a classical MOT solver. It also has been conjectured that more efficient schemes can be constructed by embedding the PWTD algorithm in a hierarchical framework.[10,11]

This paper describes a multilevel PWTD enhanced MOT solver for analyzing acoustic surface scattering from rigid bodies. In Sec. I, the BIE used for the transient scattering analysis is introduced, and the formulation of the MOT scheme for solving it is presented. The PWTD algorithm is reviewed in Sec. II. In Sec. III the incorporation of the multilevel PWTD algorithm into the MOT solver is elucidated. Specifically, a detailed description of the operations unique to the multilevel scheme is presented, and the $O(N_t N_s \log^2 N_s)$ computational complexity and $O(N_t N_s)$ memory requirements of the algorithm are derived in this section. In Sec. IV numerical examples that demonstrate the effectiveness of the proposed multilevel scheme in solving large-scale scattering problems are presented, and our conclusions are stated in Sec. V.

I. MARCHING-ON-IN-TIME FORMULATION FOR ACOUSTIC WAVE SCATTERING ANALYSIS

Let $\varphi^{\mathrm{inc}}(\mathbf{r},t)$ denote the velocity potential of a field that propagates in a medium with wave speed c and ambient fluid density ρ_0, and that impinges on a rigid body with surface S (Fig. 1). The interaction between the incident field and the rigid body produces a scattered field with velocity potential $\varphi^{\mathrm{sca}}(\mathbf{r},t)$. This field is completely specified, everywhere in space, by the total velocity potential $\varphi(\mathbf{r},t)=\varphi^{\mathrm{inc}}(\mathbf{r},t)+\varphi^{\mathrm{sca}}(\mathbf{r},t)$ on the surface S via a retarded time boundary integral. It is assumed that the temporal spectrum of $\varphi^{\mathrm{inc}}(\mathbf{r},t)$ vanishes for $\omega>\omega_{\max}$ [the same therefore holds true for $\varphi(\mathbf{r},t)$ and $\varphi^{\mathrm{sca}}(\mathbf{r},t)$], that $\varphi^{\mathrm{inc}}(\mathbf{r},t)$ does not interact with S for $t<0$ [i.e., that $\varphi^{\mathrm{sca}}(\mathbf{r},t)=0$ for $t<0$], that S is a volume enclosing (closed) surface, and that $\varphi(\mathbf{r},t)$ for $0<t<T$ is to be calculated on S.

Imposing the condition that the total pressure field $p(\mathbf{r},t)=-\rho_0\partial_t\varphi(\mathbf{r},t)$ vanishes inside S yields the Kirchhoff integral equation.[17] However, this integral equation is prone to the ''thin-body difficulty'' when the scatterer is slender (or, in the limit, when S is open).[18,19] Alternatively, imposing the condition that the normal component of the velocity field $\hat{\mathbf{n}}\cdot\mathbf{v}(\mathbf{r},t)=\hat{\mathbf{n}}\cdot\nabla\varphi(\mathbf{r},t)$ vanishes on S—here $\hat{\mathbf{n}}$ is the position-dependent outward pointing unit normal to S—yields the normal derivative of the Kirchhoff integral equation,[20] which is devoid of the thin-body difficulty. It was shown in Ref. 4 that the numerical solutions to both these time-domain integral equations are susceptible to corruption by resonance modes of the corresponding interior problem. In that same paper it was also suggested that corruption by resonance modes can be avoided by using a linear combination of these integral equations given by

$$(1-\alpha)\partial_t\varphi^{\mathrm{inc}}(\mathbf{r},t)+\alpha c\hat{\mathbf{n}}\cdot\nabla\varphi^{\mathrm{inc}}(\mathbf{r},t)=\mathcal{L}_c\{\varphi(\mathbf{r},t)\},\quad \mathbf{r}\in S, \tag{1}$$

where

$$\mathcal{L}_c\{\varphi(\mathbf{r},t)\}=-(1-\alpha)\mathcal{L}_p\{\varphi(\mathbf{r},t)\}+\alpha c\mathcal{L}_v\{\varphi(\mathbf{r},t)\}, \tag{2}$$

$$\mathcal{L}_p\{\varphi(\mathbf{r},t)\}=-\tfrac{1}{2}\partial_t\varphi(\mathbf{r},t)+\partial_t\int\!\!\!\!\!\!-_S d\mathbf{r}'\,\varphi(\mathbf{r}',t)*\hat{\mathbf{n}}'\cdot\nabla'\frac{\delta(t-R/c)}{4\pi R}, \tag{3}$$

$$\mathcal{L}_v\{\varphi(\mathbf{r},t)\}=-\int\!\!\!\!\!\!=_S d\mathbf{r}'\,\varphi(\mathbf{r}',t)*\hat{\mathbf{n}}\cdot\nabla\hat{\mathbf{n}}'\cdot\nabla'\frac{\delta(t-R/c)}{4\pi R}. \tag{4}$$

In the above equations, $*$ denotes a temporal convolution, $R=|\mathbf{r}-\mathbf{r}'|$, $\delta(\cdot)$ is the Dirac pulse, $0\leq\alpha\leq1$ is a real constant, and single and double dashes on the integral signs denote that the principal value and the finite part of the integrals are to be evaluated, respectively. Note that Eq. (1) reduces to (the time derivative of) the Kirchhoff integral equation for $\alpha=0$ and to the normal derivative of the Kirchhoff integral equation for $\alpha=1$. As was experimentally shown in Ref. 4, for $0<\alpha<1$ the numerical solutions to Eq. (1) are accurate and devoid of interior resonance modes.

The first step towards obtaining a numerical solution to Eq. (1) using the MOT is to represent the unknown potential $\varphi(\mathbf{r},t)$ on S for $0\leq t\leq T$ in terms of N_s spatial basis functions $f_n(\mathbf{r})$ and N_t temporal basis functions $T_i(t)=T(t-i\Delta_t)$ (Δ_t is the MOT time step, see Sec. II) as

$$\varphi(\mathbf{r},t)=\sum_{n=1}^{N_s}\sum_{i=1}^{N_t}\varphi_{i,n}f_n(\mathbf{r})T_i(t), \tag{5}$$

where $\varphi_{i,n}$ are unknown expansion coefficients to be determined. Substituting Eq. (5) in Eq. (1) and testing the resulting equation at $t=t_j=j\Delta_t$ with $\tilde{f}_m(\mathbf{r})$, $m=1,...,N_s$, yields a system of equations that can be expressed as

$$\overline{\mathbf{Z}}_0\mathbf{\Phi}_j=\mathbf{F}_j^{\mathrm{inc}}-\sum_{k=1}^{j-1}\overline{\mathbf{Z}}_k\mathbf{\Phi}_{j-k}, \tag{6}$$

where $\mathbf{\Phi}_j$ and $\mathbf{F}_j^{\mathrm{inc}}$ are vectors with elements

$$\mathbf{\Phi}_{j,n}=\varphi_{j,n}, \tag{7}$$

$$\mathbf{F}^{\mathrm{inc}}_{j,m} = \int_S d\mathbf{r} \tilde{f}_m(\mathbf{r}) [(1-\alpha)\partial_t \varphi^{\mathrm{inc}}(\mathbf{r},t) + \alpha c \hat{\mathbf{n}} \cdot \nabla \varphi^{\mathrm{inc}}(\mathbf{r},t)]|_{t=t_j}, \quad (8)$$

and an element of the $\overline{\mathbf{Z}}_k$ matrix is given by

$$\overline{\mathbf{Z}}_{k,mn} = \int_S d\mathbf{r} \tilde{f}_m(\mathbf{r}) \mathcal{L}_c\{f_n(\mathbf{r}) T_{j-k}(t)\}|_{t=t_j}. \quad (9)$$

Equation (6) forms the basis of the MOT method. It relates $\varphi(\mathbf{r},t)$ at time $t=t_j$ to the incident field at that time and to $\varphi(\mathbf{r},t)$ on S at earlier times. At the jth time step of the MOT scheme, the right-hand side of Eq. (6) is formed from the incident field and $\mathbf{\Phi}_i$, $i=1,...,j-1$, and the vector $\mathbf{\Phi}_j$, representing the potential on S at the current time step, is solved for. The stability and accuracy of this scheme depend on the choice of the temporal and spatial basis functions as well as on the time step size Δ_t. In this study, S is modeled as a collection of N_s flat triangular facets and the spatial bases $f_n(\mathbf{r})$ are chosen to be unit pulse functions over these facets. The testing functions are chosen as $\tilde{f}_m(\mathbf{r}) = \delta(\mathbf{r} - \mathbf{r}^c_m)$, where $\mathbf{r}^c_m$ is the centroid of the mth triangular facet, rendering the testing procedure conventional collocation. Cubic interpolants are used as the temporal basis functions. Detailed descriptions of these bases as well as the numerical evaluation of the integrals in Eqs. (8) and (9) can be found in Ref. 4. The time step size is chosen—independent of the spatial mesh size—as $\Delta_t = 2\pi/(\beta\omega_{\max})$. How to specify the parameter β is a topic of ongoing research.[8] Within the present study, $\beta=10$ has yielded stable and accurate results. Finally, it should be noted that the above MOT formulations, as well as all PWTD derivations in the remainder of this paper, are independent of the choice of basis functions and also apply to more sophisticated ones than used here, e.g., those of Bluck and Walker.[1]

Solution of the matrix equation (6) at each time step with a nonstationary iterative solver proves to be an inexpensive procedure. Since the interaction matrix $\overline{\mathbf{Z}}_0$ is sparse, the solution is obtained in $O(\kappa N_s)$ operations, where κ denotes the number of iterations. Setting the initial guess of the iterative solver at a time step equal to the solution obtained in the previous step reduces κ significantly. By far the most expensive part of the MOT scheme is the evaluation of the summation on the right-hand side of Eq. (6). This operation is equivalent to evaluating $\mathcal{L}_c\{\varphi(\mathbf{r},t)\}$ at $O(N_s)$ observation points due to $O(N_s)$ sources and requires $O(N_s^2)$ operations. Hence, the complexity of a MOT analysis with N_t time steps scales as $O(N_t N_s^2)$. This scaling law renders the application of classical MOT methods to the analysis of large-scale scattering phenomena prohibitively expensive.

II. THE PLANE WAVE TIME DOMAIN ALGORITHM

The computational bottleneck posed by the evaluation of $\mathcal{L}_c\{\varphi(\mathbf{r},t)\}$ can be relieved by expanding the latter in a basis of propagating plane waves. In this section, a plane wave expansion of $\mathcal{L}_c\{\varphi(\mathbf{r},t)\}$ will be presented without proof (a detailed derivation of this expansion can be found in Ref. 15 and references therein). Such a representation facilitates the efficient evaluation of $\mathcal{L}_c\{\varphi(\mathbf{r},t)\}$ using the three-stage PWTD algorithm,[10,11] which is also briefly reviewed below.

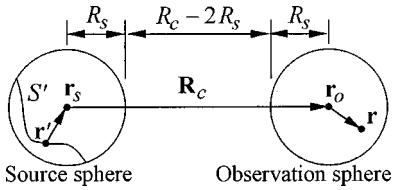

FIG. 2. Definitions of vectors used in the PWTD algorithm.

Consider two fictitious spheres of equal radius R_s that are centered at $\mathbf{r}_s$ and $\mathbf{r}_o$ as depicted in Fig. 2, and let $\mathbf{R}_c$ denote the vector $\mathbf{r}_o - \mathbf{r}_s$. It is assumed that the spheres do not overlap, i.e., $R_c = |\mathbf{R}_c| > 2R_s$. Assume that a source distribution $\varphi(\mathbf{r},t)$ resides on a surface S' enclosed by the sphere centered at $\mathbf{r}_s$ and that the field $\mathcal{L}_c\{\varphi(\mathbf{r},t)\}$ due to this source distribution is observed inside the other sphere.

As shown in Ref. 15, if the duration of the source distribution $\varphi(\mathbf{r},t)$ is bounded by $T_s < T_{s,\max} = (R_c - 2R_s)/c$, then $\mathcal{L}_c\{\varphi(\mathbf{r},t)\}$ can be recovered directly from the plane wave expansion introduced below. However, if the duration of $\varphi(\mathbf{r},t)$ exceeds $T_{s,\max}$, then the PWTD scheme requires that $\varphi(\mathbf{r},t)$ be broken up into L subsignals $\varphi_l(\mathbf{r},t)$, $l=0,...,L-1$, each of duration less than $T_{s,\max}$. Such decomposition can be achieved in many ways, e.g., by interpolating $\varphi(\mathbf{r},t)$ using basis functions $\psi(t)$ as

$$\varphi_l(\mathbf{r},t) = \sum_{i=lM_t}^{(l+1)M_t-1} \varphi(\mathbf{r}, i\Delta_t)\psi(t - i\Delta_t). \quad (10)$$

Here, $\psi(t)$ is the bandlimited and quasi time-limited (local) interpolant

$$\psi(t) = \frac{\omega_+}{\omega_s} \frac{\sin(\omega_+ t)}{\omega_+ t} \frac{\sinh(p_t \Delta_t \omega_- \sqrt{1 - t^2/(p_t\Delta_t)^2})}{\sinh(p_t\Delta_t\omega_-)\sqrt{1 - t^2/(p_t\Delta_t)^2}}, \quad (11)$$

where $\omega_s = \pi/\Delta_t = \chi_1 \omega_{\max}$ ($\chi_1 > 1$ is the spectral oversampling factor), and $\omega_\pm = 0.5(\omega_s \pm \omega_{\max})$. The function $\psi(t)$ is bandlimited to ω_s and essentially spans a total duration of $2p_t + 1$ time steps. That is, with the proper choice of parameters χ_1 and p_t, $\psi(t)$ becomes vanishingly small outside of the interval $[-p_t\Delta_t, p_t\Delta_t]$, and the error that is incurred upon truncating $\psi(t)$ outside this interval decreases exponentially fast with increasing χ_1 and p_t.[10,21] In Eq. (10), M_t denotes the number of samples of the original signal used in the construction of the subsignal $\varphi_l(\mathbf{r},t)$, which is of duration $T_s = (M_t + 2p_t)\Delta_t$. The restriction $T_s < T_{s,\max}$ dictates that M_t should be chosen as

$$M_t \leq \lfloor (R_c - 2R_s)/(c\Delta_t) \rfloor - 2p_t. \quad (12)$$

Given the above partitioning of the source signal into subsignals, the linearity of the operator $\mathcal{L}_c$ ensures that $\mathcal{L}_c\{\varphi(\mathbf{r},t)\}$ can be expressed as

$$\mathcal{L}_c\{\varphi(\mathbf{r},t)\} = \sum_{l=0}^{L-1} \mathcal{L}_c\{\varphi_l(\mathbf{r},t)\}. \quad (13)$$

Next, each $\mathcal{L}_c\{\varphi_l(\mathbf{r},t)\}$ is expressed as a time gated superposition of a finite number of propagating plane waves as[15]

$$\mathcal{L}_c\{\varphi_l(\mathbf{r},t)\}=\begin{cases}0; & t<t_l^{\max},\\ \tilde{\mathcal{L}}_c\{\varphi_l(\mathbf{r},t)\}; & t\geqslant t_l^{\max},\end{cases} \tag{14}$$

where

$$\begin{aligned}\tilde{\mathcal{L}}_c\{\varphi_l(\mathbf{r},t)\}=\sum_{p=0}^{K}\sum_{q=-K}^{K} w_{pq}\Big\{&((1-\alpha)-\alpha\hat{\mathbf{n}}\cdot\hat{\mathbf{k}}_{pq})\\ &\times\delta[t-\hat{\mathbf{k}}_{pq}\cdot(\mathbf{r}-\mathbf{r}_o)/c]\\ &*\mathcal{T}(\hat{\mathbf{k}}_{pq},\mathbf{R}_c,t)*\int_{S'}d\mathbf{r}'\,\hat{\mathbf{n}}'\\ &\cdot\hat{\mathbf{k}}_{pq}\delta[t+\hat{\mathbf{k}}_{pq}\cdot(\mathbf{r}'-\mathbf{r}_s)/c]*\varphi_l(\mathbf{r}',t)\Big\}.\end{aligned} \tag{15}$$

Here, the translation function $\mathcal{T}(\hat{\mathbf{k}}_{pq},\mathbf{R}_c,t)$ is given by

$$\mathcal{T}(\hat{\mathbf{k}}_{pq},\mathbf{R}_c,t)=\begin{cases}0; & |t|>R_c/c,\\ \dfrac{\partial_t^3}{16\pi^2 cR_c}\displaystyle\sum_{k=0}^{K}(2k+1) & \\ \quad\times P_k(ct/R_c)P_k(\hat{\mathbf{k}}_{pq}\cdot\mathbf{R}_c/R_c); & |t|\leqslant R_c/c.\end{cases} \tag{16}$$

In the above equations, $t_l^{\max}=[(l+1)M_t-1+p_t]\Delta_t$ (such that $\varphi_l(\mathbf{r},t)=0$ for $t\geqslant t_l^{\max}$), $K=\lceil 2\chi_2 R_s\omega_s/c\rceil$ ($\chi_2>1$ is the excess bandwidth factor[22]), $\hat{\mathbf{k}}_{pq}=\hat{\mathbf{x}}\sin\theta_p\cos\phi_q+\hat{\mathbf{y}}\sin\theta_p\times\sin\phi_q+\hat{\mathbf{z}}\cos\theta_p$, $\phi_q=q2\pi/(2K+1)$, θ_p is the $(p+1)^{th}$ zero of $P_{K+1}(\cos\theta)$, $P_k(\cdot)$ is the Legendre polynomial of degree k, and the weights w_{pq} are given by

$$w_{pq}=\frac{4\pi(1-\cos^2\theta_p)}{(2K+1)[(K+1)P_K(\cos\theta_p)]^2}. \tag{17}$$

Note that by defining $\chi=\chi_1\chi_2$, K can also be written as $K=\lceil 2\chi R_s\omega_{\max}/c\rceil$. It can be shown that, given $\omega_{\max}$, Δ_t, and R_s, the free parameters χ and p_t can be chosen *a priori* to achieve the desired level of accuracy in evaluating $\mathcal{L}_c\{\varphi(\mathbf{r},t)\}$.[10,11]

Equations (13)–(16) constitute the crux of the three-stage PWTD algorithm. In the first stage, the integral over the source domain S' maps the source distribution $\varphi_l(\mathbf{r},t)$ onto a set of plane waves that emanate from the source sphere and propagate in the $\hat{\mathbf{k}}_{pq}$ directions. This mapping is termed the slant stack transform (SST) and the plane waves generated by it are termed *outgoing rays*. In practice, the integration over S' is evaluated by a quadrature rule chosen in accordance with the spatial basis functions used in expanding $\varphi(\mathbf{r},t)$. In our implementations, a seven-point Gaussian quadrature rule is used over each triangular facet that approximates S'. The entire set of outgoing rays associated with the lth subsignal can be generated by performing the SST at $t=t_l^{\max}$. These outgoing rays—each lasting a maximum duration of T_s+2R_s/c—describe the time-dependent radiation pattern of the source distribution.[23] In the second stage, the outgoing rays that emanate from the source sphere are mapped onto *incoming rays* that impinge upon the observation sphere by convolving each ray with the translation function $\mathcal{T}(\hat{\mathbf{k}}_{pq},\mathbf{R}_c,t)$ at $t=t_l^{\max}$. Note that performing the translation operation at $t=t_l^{\max}$ implicitly implements the time gating suggested in Eq. (14) because the contribution of $\varphi_l(\mathbf{r},t)$ to the incoming rays is taken into account only after this time. In the third stage of the PWTD algorithm, the incoming rays are aggregated with appropriate delays, yielding the field $\mathcal{L}_c\{\varphi_l(\mathbf{r},t)\}$.

The PWTD algorithm described by Eqs. (13)–(16) can be used to accelerate the evaluation of the sum appearing on the right-hand side of Eq. (6). The two-level PWTD enhanced MOT solver described in Ref. 15 is the simplest scheme that accomplishes such acceleration, and it operates as follows. First, the scatterer is partitioned into subscatterers, each of which is contained in a sphere of radius R_s. Then, contributions to the above sum due to combinations of basis/testing functions residing in each other's immediate vicinity, i.e., involving a pair of identical or adjacent subscatterers, are evaluated classically. The rest of the contributions are accounted for by invoking the PWTD algorithm for all remaining pairs of subscatterers. The computational complexity of this scheme is of $O(N_t N_s^{1.5}\log N_s)$ provided that the dimensions of the subscatterers are chosen judiciously.

III. THE MULTILEVEL FAST ALGORITHM

Computational and memory savings beyond those achieved by the two-level PWTD schemes can be attained by casting the PWTD algorithm into a multilevel framework. Just like in the two-level scheme, multilevel PWTD schemes assume that the scatterer is partitioned into a large set of subscatterers, and interactions between nearby subscatterers are accounted for classically. Contrary to the two-level algorithm, however, subscatterers are hierarchically aggregated into composite entities and the PWTD scheme is only invoked to account for interactions between composite subscatterers when continued aggregation would render the PWTD scheme inapplicable. The efficiency of the proposed multilevel scheme hinges on that of the operations that establish communication between the different levels in the hierarchical structure. In this section, first the notation related to the multilevel framework will be introduced. Then, four operations—namely interpolation, splicing, resection, and anterpolation operations—that permit the transfer of information across levels will be described in detail. Finally, the multilevel fast algorithm will be outlined and its computational complexity and memory requirements estimated.

A. Notation

A multilevel subdivision of the scatterer S is accomplished by recursively subdividing a fictitious cubical box that encloses S. Initially, this box is divided into eight boxes of equal size. Each resulting ''child'' box is recursively subdivided into eight smaller boxes until the linear dimensions of the smallest boxes so obtained measure approximately one wavelength at $\omega_{\max}$ (or a fixed fraction thereof). These finest

boxes are termed ''level 1 boxes,'' and the collection of spatial basis functions that fall into a level 1 box is said to form a ''level 1 group'' (or a ''level 1 subscatterer''). Higher level boxes and groups are similarly defined. For levels $i=1,...,N_l$, let $N_g(i)$ denote the number of groups (nonempty boxes), $M_s(i)=N_s/N_g(i)$ denote the average number of spatial basis functions per group, $R_s(i)$ denote the radius of the sphere that encloses a level i box, and $K(i)=\lceil 2\chi R_s(i)\omega_{\max}/c\rceil$ denote the number of spherical harmonics to be used in Eqs. (15) and (16) whenever a level i box participates in a PWTD translation. From Eq. (15) it is evident that $D(i)=(K(i)+1)(2K(i)+1)$ directions are required to properly represent fields at level i. It should be noted that, for a surface scatterer, $M_s(i)$ and $K(i)$ scale proportional to $(R_s(i))^2$ and $R_s(i)$, respectively, and therefore $D(i)$ is of $O(M_s(i))$. Also, as the linear dimensions of the level 1 boxes are chosen proportional to the wavelength at $\omega_{\max}$, it follows that $(R_s(1)\omega_{\max}/c)$ and $M_s(1)$ are of $O(1)$, that $N_g(1)\propto N_s$, and that $N_l\propto\log N_s$. Finally, note that, for a surface scatterer, $N_g(i+1)\approx N_g(i)/4$ and $M_s(i+1)\approx 4M_s(i)$.

In the aforementioned two-level algorithm, all sufficiently remote group pairs interact, i.e., exchange information through a PWTD translation, at the lowest level. This is not so in the multilevel algorithm, where lowest level groups are recursively aggregated into larger entities. Indeed, as long as the spheres circumscribing these composite groups are sufficiently remote, it turns out to be more efficient to have composite structures interact rather than to have their constituents exchange information individually. Therefore, it is important to identify all group pairs that interact at a given level (this is a subset of all group pairs that exist at that level). To this end, the fundamental subsignal duration at level i is defined as $T_s(i)=(M_t(i)+2p_t)\Delta_t$ with $M_t(i)=2^{(i-1)}M_t(1)$ and $M_t(1)\propto R_s(1)/(c\Delta_t)$. The constraint that $T_s\leqslant(R_c-2R_s)/c$, stated in Sec. II for a two-sphere setting, dictates that the PWTD algorithm can be applied to sphere pairs at level i whose centers are separated by at least $2R_s(i)+cT_s(i)$. Hence, starting at level N_l, all box pairs whose centers are separated by more than $2R_s(N_l)+cT_s(N_l)$ are identified as ''level N_l far-field pairs.'' Then, all level N_l-1 group pairs with group centers separated by more than $2R_s(N_l-1)+cT_s(N_l-1)$ and describing interactions that have not yet been accounted for by any of the level N_l pairs are identified as ''level N_l-1 far-field pairs.'' This process is continued and far-field pairs are identified at each level (including level 1) as those pairs that are considered well separated at a given level and that have not yet been accounted for at a higher level. The level 1 pairs with group centers separated by less than $2R_s(1)+cT_s(1)$ are classified as near-field pairs. In this way, each and every source/observer (basis/testing function) combination belongs to one and only one pair that is classified as either a far-field or a near-field pair. Also, distant source/observer combinations tend to belong to higher level far-field pairs than those that reside close to one another. This classification of group pairs is illustrated in Fig. 3.

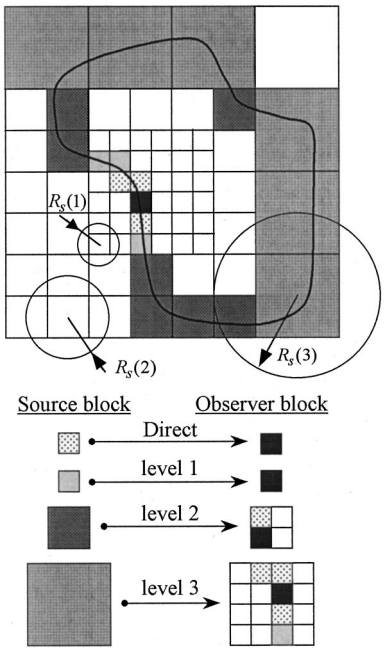

FIG. 3. Cross-sectional view of the multilevel partitioning of S.

B. Multilevel operations

For a given level i far-field group pair (γ, γ'), the field at group γ due to $\varphi(\mathbf{r},t)$ in group γ' (and vice versa) will be calculated using the three-stage PWTD algorithm. The first stage of this algorithm calls for the evaluation of the SSTs to form the outgoing rays associated with group γ' along $D(i)$ directions. For $i=1$, the outgoing rays can be obtained by directly integrating over S' in Eq. (15). However, for higher levels, direct evaluation of the SSTs is computationally expensive. The fact that the same source information is to be used to construct outgoing rays at each level suggests that rays at level $i>1$ can be constructed economically by reusing information already stored in level $i-1$ rays. This is achieved by two operations that are termed *interpolation* and *splicing*. Interpolation is needed as more rays are to be associated with a parent group than with one of its children and splicing is used in assembling a single parent group ray from interpolated child rays. Similarly, the last stage of the PWTD algorithm calls for a projection of incoming rays onto observers. Directly projecting the incoming rays at level $i>1$ onto the observers is more expensive than disaggregating these rays into level $i-1$ rays and propagating the information contained in these rays through the multilevel structure until level 1 rays are projected onto the observer locations. Two operations, termed *resection* and *anterpolation* (these are complementary to the splicing and interpolation operators), construct level $i-1$ incoming rays for a group from those of its parent. Implementation of these four operations is discussed next.

First, consider the interpolation and anterpolation operations. As mentioned in Sec. II, the outgoing rays associated with a group describe the time-dependent radiation pattern of the source distribution associated with that group. Because the radiation pattern of a source distribution that is spatially bounded by a sphere of radius $R_s(i)$ and spectrally bandlim-

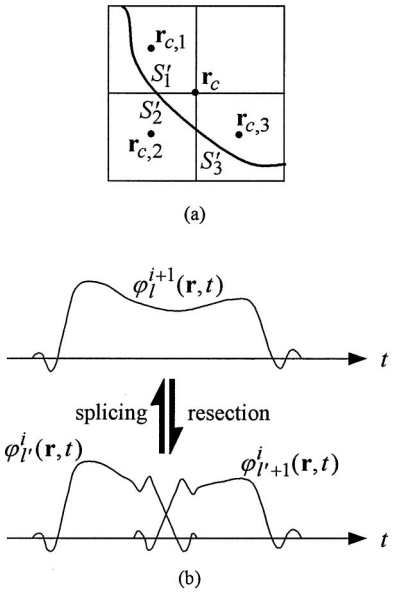

FIG. 4. Schematic description of the splicing and resection operations.

ited to ω_s can be expressed in terms of $K(i)$ spherical harmonics,[24] the interpolation operator increases the sampling rate and zero-pads the excess spherical spectrum introduced. Similarly, anterpolation operations call for the application of a spherical filter with uniform resolution to a set of outgoing or incoming rays. In other words, anterpolation is equivalent to truncating the spherical harmonic content and lowering the sampling rate over the sphere. If implemented as described by Jakob-Chien and Alpert,[25] the application of interpolation and anterpolation operators between levels i and $i+1$ can be completed in $O(K^2(i)\log K(i))$ operations per time step and per child–parent group pair. This yields approximately $O(N_s \log K(i))$ operations per time step at level i, and an overall computational cost of order less than $O(N_t N_s \log^2 N_s)$.

The nature of the splicing and resection operations can be understood by inspecting Eq. (15). With reference to Fig. 4(a), assume that an outgoing ray of a level $i+1$ box, whose center is denoted by $\mathbf{r}_c$, is to be formed. Denoting the centers of the N_c child boxes associated with this level $i+1$ box as $\mathbf{r}_{c,\xi}$, $\xi=1,...,N_c$, and the part of the surface S' that lies inside each of these level i boxes as S'_ξ, the expression for an outgoing ray of the parent box takes the form

$$\int_{S'} d\mathbf{r}'\hat{\mathbf{n}}'\cdot\hat{\mathbf{k}}_{pq}\,\delta[t+\hat{\mathbf{k}}_{pq}\cdot(\mathbf{r}'-\mathbf{r}_c)/c]*\varphi_l^{i+1}(\mathbf{r}',t)$$
$$=\sum_{\xi=1}^{N_c}\delta[t+\hat{\mathbf{k}}_{pq}\cdot(\mathbf{r}_{c,\xi}-\mathbf{r}_c)/c]*\int_{S'_\xi} d\mathbf{r}'\hat{\mathbf{n}}'$$
$$\cdot\hat{\mathbf{k}}_{pq}\,\delta[t+\hat{\mathbf{k}}_{pq}\cdot(\mathbf{r}'-\mathbf{r}_{c,\xi})/c]*\varphi_l^{i+1}(\mathbf{r}',t). \tag{18}$$

In Eq. (18), the superscript $i+1$ on $\varphi_l(\mathbf{r}',t)$ signifies the fact that the source subsignal is of duration $T_s(i+1)$, and $\hat{\mathbf{k}}_{pq}$ denotes a ray direction at level $i+1$. Since each $\varphi_l^{i+1}(\mathbf{r},t)$ can be obtained by splicing two level i subsignals $\varphi_{l'}^{i}(\mathbf{r},t)$ and $\varphi_{l'+1}^{i}(\mathbf{r},t)$ for some l' as shown in Fig. 4(b), the outgoing ray of the parent box can be expressed as

$$\sum_{\zeta=l'}^{l'+1}\sum_{\xi=1}^{N_c}\delta[t+\hat{\mathbf{k}}_{pq}\cdot(\mathbf{r}_{c,\xi}-\mathbf{r}_c)/c]*\int_{S'_\xi} d\mathbf{r}'\hat{\mathbf{n}}'$$
$$\cdot\hat{\mathbf{k}}_{pq}\,\delta[t+\hat{\mathbf{k}}_{pq}\cdot(\mathbf{r}'-\mathbf{r}_{c,\xi})/c]*\varphi_\zeta^{i}(\mathbf{r}',t). \tag{19}$$

Note that the integral over each S'_ξ is nothing but an outgoing ray of a child box propagating along direction $\hat{\mathbf{k}}_{pq}$. Hence, Eq. (19) clearly indicates that once the outgoing rays of the child boxes are interpolated to level $i+1$ directions $\hat{\mathbf{k}}_{pq}$, they can be time advanced by an amount $s_\xi(\hat{\mathbf{k}}_{pq})=\hat{\mathbf{k}}_{pq}\cdot(\mathbf{r}_{c,\xi}-\mathbf{r}_c)/c$ and spliced together to form the outgoing rays of the parent box. In a completely complementary manner, it can be shown that the incoming rays of a level i group can be obtained by resecting the incoming rays of its parent box as depicted in Fig. 4(b), delaying these rays by an amount $s_\xi(\hat{\mathbf{k}}_{pq})$, and anterpolating the resulting rays to level i directions.

C. The algorithm and its computational complexity

Now that requisite notation has been introduced and multilevel operations described, an algorithm for efficiently evaluating the summation in Eq. (6) can be outlined. Note, once again, that the evaluation of this summation is equivalent to testing by N_s spatial testing functions the field $\mathcal{L}_c\{\varphi(\mathbf{r},t)\}$ generated by N_s spatial basis functions at time $t=t_j$.

(1) *Evaluation of the near-field interactions*: For each near-field group pair (γ,γ'), the tested fields in group γ are calculated classically, i.e., without invoking the PWTD scheme, as

$$\sum_{k=1}^{j-1}\overline{\mathbf{Z}}_k^{\gamma\gamma'}\mathbf{\Phi}_{j-k}^{\gamma'}, \tag{20}$$

where $\overline{\mathbf{Z}}_k^{\gamma\gamma'}$ is the matrix made up of those elements of the matrix $\overline{\mathbf{Z}}_k$ that relate the fields over group γ to the sources residing in group γ', and $\mathbf{\Phi}_{j-k}^{\gamma'}$ is a vector comprised of the coefficients $\varphi_{j-k,n}$ for all n in group γ'. The multilevel partitioning of the scatterer constructed earlier guarantees that all the near-field pairs reside at level 1 and that each level 1 group participates in only a small number of near-field interactions. Hence, at each time step, the evaluation of the sum (20) requires $O(N_s)$ operations since there are $O(N_s)$ near-field pairs with $O(1)$ interactions per pair.

(2) *Evaluation of the far-field interactions*: All interactions between a pair of far-field groups (γ,γ') are calculated via the three-stage PWTD algorithm:

(a) When the time step is a multiple of $M_t(i)$, the outgoing rays emanating from groups at level i are generated. For level 1 groups, this is accomplished by numerical evaluation of the integral over S' in Eq. (15). Since this operation maps the signal over each of N_s sources to $D(1)\propto O(1)$ directions, outgoing rays at level 1 can be constructed in $O(N_s)$ operations per time step. At higher levels, the outgoing rays of a group are calcu-

lated from those of its children using the interpolation and splicing operations at a cost that scales as $O(N_s \log^2 N_s)$ per time step.

(b) Once the outgoing rays at level i have been generated, translation between each level i far-field pair (γ, γ') can be performed. This is accomplished by convolving the outgoing rays of the source group γ' with the appropriate translation function and superimposing the resulting rays onto the incoming rays of the observer group γ. The duration of both the outgoing rays and the translation functions are proportional to the box size at the level with which they are associated and hence are described by $O(M_t(i))$ samples. Therefore, it is possible to evaluate the convolution of these two signals in $O(M_t(i)\log M_t(i))$ operations using fast Fourier transforms. However, as the translation function $\mathcal{T}(\hat{\mathbf{k}},\mathbf{R}_{c,\gamma\gamma'},t)$ is not bandlimited in time, its Fourier transform needs to be evaluated analytically at $O(M_t(i))$ frequencies. To this end, note that the Fourier transform of $\mathcal{T}(\hat{\mathbf{k}},\mathbf{R}_{c,\gamma\gamma'},t)$ is given by

$$\begin{aligned}\mathcal{F}\{\mathcal{T}(\hat{\mathbf{k}},\mathbf{R}_{c,\gamma\gamma'},t)\} &= \int_{-\infty}^{+\infty} \mathcal{T}(\hat{\mathbf{k}},\mathbf{R}_{c,\gamma\gamma'},t)e^{-j\omega t}dt \\ &= \frac{(j\omega)^3}{8\pi^2 c^2}\sum_{k=0}^{K}(2k+1) \\ &\quad \times (-j)^k j_k(\omega R_{c,\gamma\gamma'}/c)P_k(\cos\theta) \\ &= \frac{c}{R_{c,\gamma\gamma'}^3}\tilde{\mathcal{T}}(\theta,\Omega), \qquad (21)\end{aligned}$$

where $\Omega = \omega R_{c,\gamma\gamma'}/c$ is the normalized frequency, $\cos\theta = \hat{\mathbf{k}}\cdot\mathbf{R}_{c,\gamma\gamma'}/R_{c,\gamma\gamma'}$, and $j_k(\cdot)$ denotes the spherical Bessel function of order k. Since $\tilde{\mathcal{T}}(\theta,\Omega)$ is bandlimited both in θ and Ω, the Fourier transform of $\mathcal{T}(\hat{\mathbf{k}},\mathbf{R}_{c,\gamma\gamma'},t)$ for any group pair can be evaluated from the samples of $\tilde{\mathcal{T}}(\theta,\Omega)$ in $O(M_t(i))$ operations for a given direction. As the translation operation is repeated for $N_t/M_t(i)$ time intervals, for $D(i)\propto M_s(i)$ directions per far-field pair, for $O(N_g(i))$ pairs per level, and for all $\log N_s$ levels, the overall cost of this step scales no worse than $O(N_t N_s \log^2 N_s)$.

(c) When the time step is a multiple of $M_t(i)$ for a level i, the incoming rays at that level are obtained by resecting and anterpolating the incoming rays at a higher level. This process has to be carried out starting from the highest level, as the incoming rays at a level have to be formed completely before they are resected to form the rays at lower levels. Finally, the tested fields are evaluated by convolving the incoming rays at level 1 with

$$-\int_S d\mathbf{r}\tilde{f}_m(\mathbf{r})[(1-\alpha)\partial_t + \alpha\hat{\mathbf{n}}\cdot\hat{\mathbf{k}}_{pq}]\delta(t-\hat{\mathbf{k}}_{pq}\cdot(\mathbf{r}-\mathbf{r}_c)/c), \qquad (22)$$

where $\mathbf{r}_c$ is the center of the box that contains $f_m(\mathbf{r})$, and summing over all level 1 ray directions $\hat{\mathbf{k}}_{pq}$ as in Eq. (15). This step, which is conceptually the transpose of forming the outgoing rays, can also be accomplished in $O(N_t N_s \log^2 N_s)$ operations.

Summing up the cost of each step, it is seen that the computational cost of this algorithm, which evaluates the summation in Eq. (6) N_t times, scales as $O(N_t N_s \log^2 N_s)$. This computational complexity is significantly lower than the $O(N_t N_s^2)$ complexity of the classical MOT algorithms.

It is important to point out that the reduction in the computational complexity in the multilevel algorithm is *not* achieved at the expense of increased memory requirements. As the surface field values throughout the analysis have to be stored in any MOT scheme, the essential storage requirements associated with all MOT schemes scale as $O(N_t N_s)$. In a classical MOT implementation, one can either only require $O(N_t N_s)$ storage by calculating the $O(N_s^2)$ nonzero elements of the $\overline{\mathbf{Z}}_k$ matrices every time step, or compute these matrix elements once and for all and store them. The first approach, although highly memory efficient, consumes an exorbitant amount of computation time, even for very small problems. On the other hand, the second approach reduces computation time at the cost of $O(N_s^2)$ memory requirements. As the focus of this paper is to minimize the computation time, the second approach is adopted in the section on numerical results for comparison purposes. As for the memory requirements of the multilevel algorithm, it can be shown that the storage of the incoming and outgoing rays dominates the memory complexity. The memory required for storing the rays at level i is proportional to the number of groups at that level, $N_g(i) = N_s/M_s(i)$, the number of ray directions per group, $D(i)\propto M_s(i)$, and the total duration of the rays stored per direction, $O(M_t(i))$. Hence the amount of storage per level is $O(M_t(i)N_s)$. Noting that $M_t(N_l) \propto N_t$ and making use of the fact that $M_t(i-1) = 0.5M_t(i)$ yields an overall memory complexity of $O(N_t N_s)$, which scales as the essential amount of required storage. Note that for a typical surface scatterer, N_t typically scales as $O(N_s^{0.5})$, and in such cases the derived memory complexity is of $O(N_s^{1.5})$ as opposed to $O(N_s^2)$ for the classical scheme (when all interactions are stored).

IV. NUMERICAL RESULTS

In this section, the accuracy and efficiency of the proposed multilevel PWTD enhanced MOT (ML-PWTD) scheme are demonstrated by applying it to analysis of plane wave scattering from several rigid bodies. The ML-PWTD scheme is validated by comparing the results obtained using this method either directly to those obtained using a MOT scheme, or indirectly, upon Fourier transformation, to those obtained using a frequency domain boundary element method (FD-BEM). The FD-BEM code uses the same spatial basis functions as the ML-PWTD scheme, circumvents the nonuniqueness difficulty by using the Burton–Miller approach, and has been validated independently. Since all the scatterers analyzed in this section are closed bodies, α in Eq. (1) is set to 0.5. In all time domain simulations, the excitation is a modulated Gaussian plane wave defined as

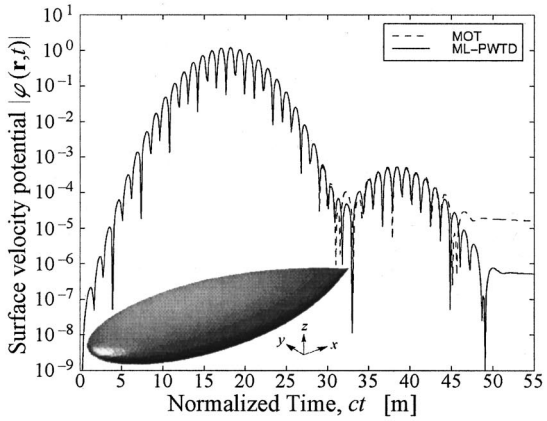

(a)

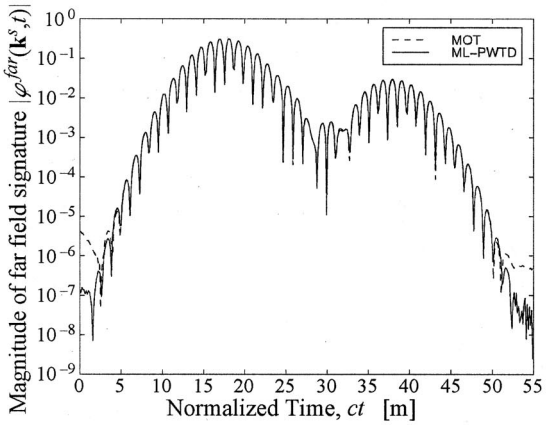

(b)

FIG. 5. Scattering from an almond. (a) Surface velocity potential $\varphi(\mathbf{r},t)$ near the round end of the almond. (b) Back-scattered far field signature.

$$\varphi^{\text{inc}}(\mathbf{r},t)=\cos[(ct-\mathbf{r}\cdot\hat{\mathbf{k}}^{\text{inc}})2\pi f_o/c]\times\exp[-(ct-\mathbf{r}\cdot\hat{\mathbf{k}}^{\text{inc}}-6\sigma)^2/2\sigma^2], \quad (23)$$

where f_o is the center frequency of the pulse, σ is a measure of the pulse's temporal width, and $\hat{\mathbf{k}}^{\text{inc}}$ is its propagation direction. This pulse safely can be assumed to be bandlimited to $\omega_{\max}=2\pi f_o+6c/\sigma$ since at that frequency the spectral content of the pulse is down by more than 150 dB from its peak value at f_o. Finally, the system of equations in Eq. (6) is solved using a transpose-free quasi-minimal residual algorithm[26] with diagonal preconditioning. Using the result from the previous time step as the initial guess vector, a relative residual error of 10^{-6} was obtained in $\kappa<20$ iterations even for the example with the largest number of spatial basis functions.

As a first example, plane wave scattering from an almond [depicted in the inset of Fig. 5(a)] is analyzed. The almond, which is modeled by 8044 triangular facets, is a scaled version of that described by Woo *et al.*[27] with a total length of 10 m. The parameters of the incident wave are chosen as $f_o/c=0.4373\,\text{m}^{-1}$, $\sigma=2.9776\,\text{m/rad}$, and $\hat{\mathbf{k}}^{\text{inc}}=\hat{\mathbf{x}}$. The surface velocity potential is calculated using both the classical MOT method and the ML-PWTD scheme. In the multilevel scheme, approximately 76% of the interactions were calculated by the PWTD algorithm with three levels, and the parameters that control the accuracy were set to $p_t=4$ and $\chi=5.0$. The absolute value of the surface velocity potential near the round end calculated by both methods is plotted on a logarithmic scale with respect to normalized time ct in Fig. 5(a) and excellent agreement is observed. The L_2 norm of the difference of the two results divided by the L_2 norm of the one calculated by the classical method is found to be 3.99×10^{-4}. This difference can be made smaller by increasing p_t and χ. This test demonstrated the accuracy of the near field computed using the ML-PWTD scheme at a given point on the scatterer. To check the accuracy of the calculated fields all over the scatterer surface, the far-field signature associated with the surface velocity potential $\varphi(\mathbf{r},t)$ along a direction $\hat{\mathbf{k}}^s$ given by

$$\varphi^{\text{far}}(\hat{\mathbf{k}}^s,t)=\lim_{r\to\infty}2\sqrt{\pi}r\varphi^{\text{sca}}(r\hat{\mathbf{k}}^s,t+r/c)\cong\frac{\partial_t}{2c\sqrt{\pi}}\int_S d\mathbf{r}'(\hat{\mathbf{n}}'\cdot\hat{\mathbf{k}}^s)\varphi(\mathbf{r}',t+\hat{\mathbf{k}}^s\cdot\mathbf{r}'/c) \quad (24)$$

is calculated in the backscatter direction $\hat{\mathbf{k}}^s=-\hat{\mathbf{x}}$ [Fig. 5(b)]. Again, the agreement between the far-field signatures calculated via the classical and PWTD enhanced codes is excellent.

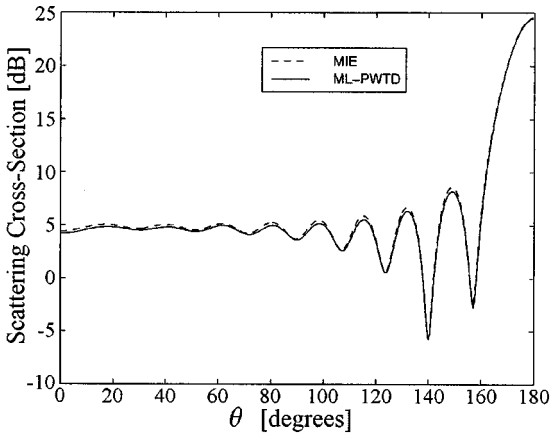

(a)

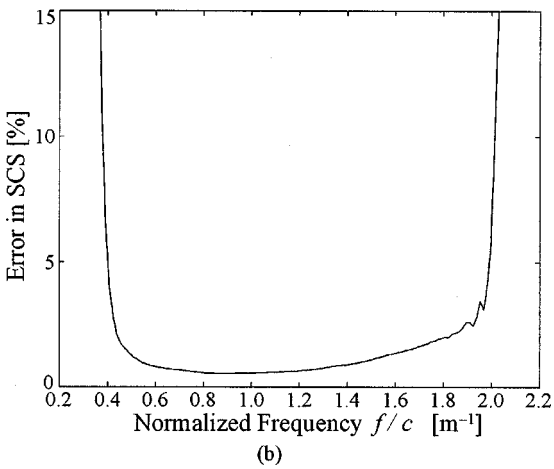

(b)

FIG. 6. (a) SCS pattern of a unit radius sphere for $f/c=1.822\,\text{m}^{-1}$. (b) Percent error in SCS over a range of frequencies.

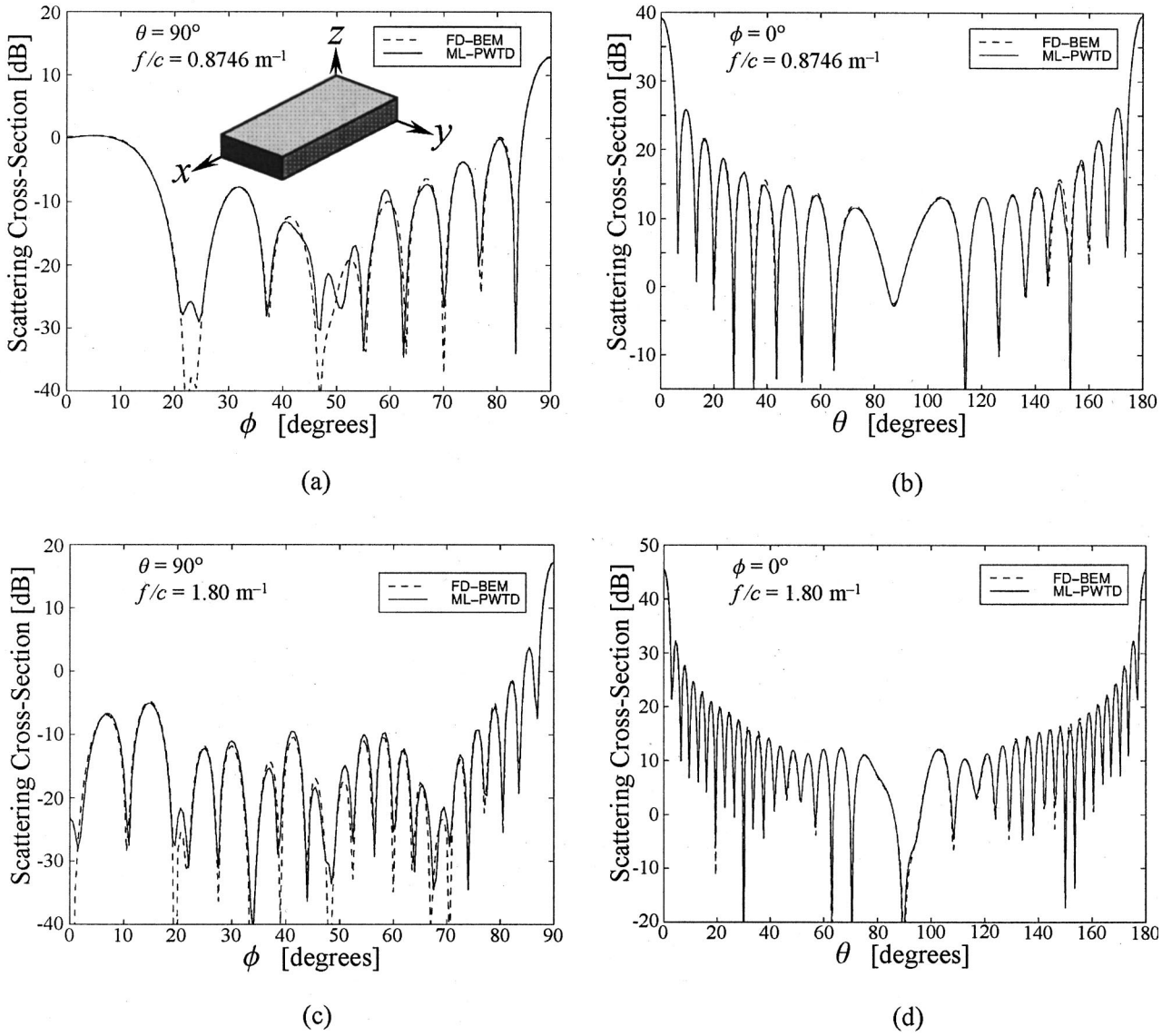

FIG. 7. SCS patterns of a $10\times3\times1$-m^3 box modeled with 107 500 triangular facets in (a) *xy*-plane at $f/c=0.8746\ \mathrm{m}^{-1}$, (b) *xz*-plane at $f/c=0.8746\ \mathrm{m}^{-1}$, (c) *xy*-plane at $f/c=1.80\ \mathrm{m}^{-1}$, and (d) *xz*-plane at $f/c=1.80\ \mathrm{m}^{-1}$.

Next, the efficacy of the fast method in generating scattering cross-section (SCS) data over a broad range of frequencies is inspected. To this end, a sphere of radius 1 m is modeled with 25 246 triangular patches and is excited by a wave with $f_o/c=1.166\ \mathrm{m}^{-1}$, $\sigma=0.9358$ m/rad, and $\hat{\mathbf{k}}^{\mathrm{inc}}=-\hat{\mathbf{z}}$. The evolution of the velocity potential at the surface of the sphere is computed by the ML-PWTD scheme, and the far-field signatures are evaluated using Eq. (24) for a number of elevation angles. Then, the SCSs of the scatterer along these directions are extracted at particular frequencies from the far-field signatures via a discrete time Fourier transform and compared to analytical values obtained using a Mie series. One such comparison, at $f/c=1.822\ \mathrm{m}^{-1}$, is shown in Fig. 6(a). It is seen that the agreement between the MOT result and the analytical one is good, even though the incident signal power at this frequency is 64.6 dB lower than the power at the center frequency. The L_2 norm of the error in the SCS at different frequencies normalized to the L_2 norm of the SCS at each frequency is plotted in Fig. 6(b). It is seen that the time domain simulation provides accurate far-field information over a broad range of frequencies.

In the next example, the PWTD enhanced MOT scheme is pushed to its limits insofar as the computational resources are concerned. The scatterer [depicted in the inset of Fig. 7(a)] is a $10\times3\times1$-m^3, rectangular box modeled using 107 500 triangular facets, and the parameters of the incident field are chosen as $f_o/c=1.365\ \mathrm{m}^{-1}$, $\sigma=1.048$ m/rad, and $\hat{\mathbf{k}}^{\mathrm{inc}}=-\hat{\mathbf{z}}$. Approximately 98% of the interactions were handled by the multilevel PWTD algorithm, which utilized five levels for this case. The results obtained by this simulation are validated by comparing the SCS patterns extracted at different frequencies to those obtained using the FD-BEM code. Figure 7 shows how the SCS data in the *xy*- and *xz*-planes generated by the two methods compare at $f/c=0.8746\ \mathrm{m}^{-1}$ and $f/c=1.80\ \mathrm{m}^{-1}$. Note that these frequencies are near the edges of the frequency band occupied by the incident pulse as the incident power levels at these frequencies are 45.28 and 35.63 dB below the power at the center

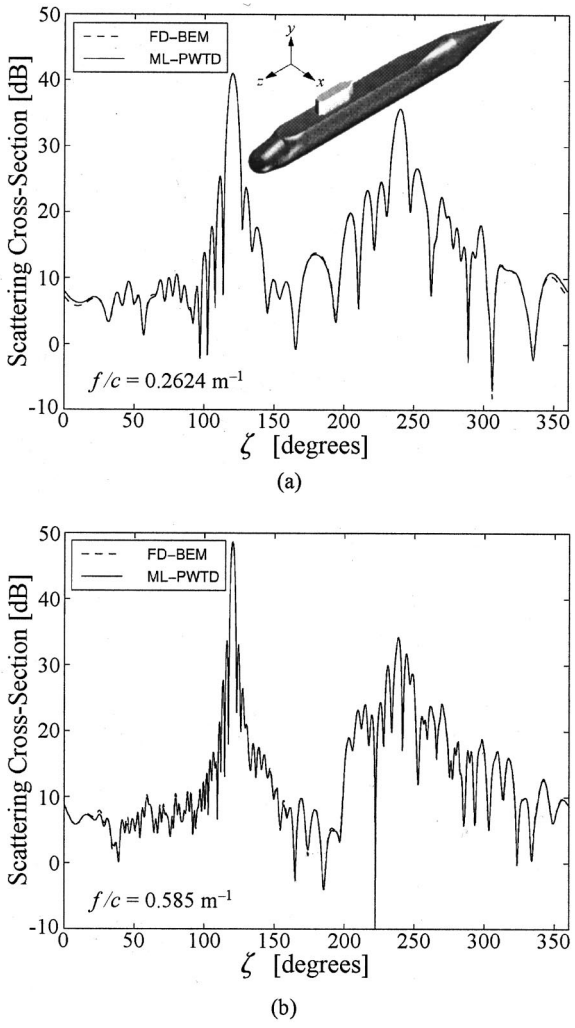

FIG. 8. SCS patterns of an obliquely insonified submarine modeled with 91 366 triangular facets at (a) $f/c=0.2624\,\mathrm{m}^{-1}$ and (b) $f/c=0.585\,\mathrm{m}^{-1}$.

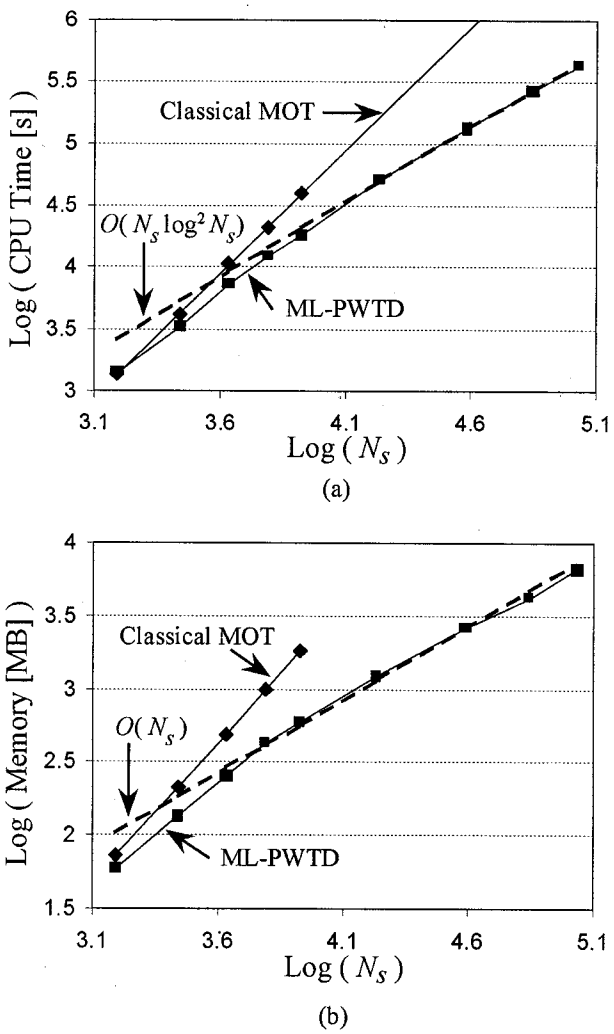

FIG. 9. (a) Computational and (b) memory requirements of the classical MOT and ML-PWTD schemes.

frequency. At both frequencies, the agreement is very good in spite of the low power levels. Similar tests were carried out at several other frequencies with higher incident field powers, and, as expected, even better agreement between the ML-PWTD and FD-BEM results were observed.

As a more realistic example, the SCS of a submarine was calculated for an incident wave characterized by $f_o/c=0.4373\,\mathrm{m}^{-1}$, $\sigma=3.275$ m/rad, and $\hat{\mathbf{k}}^{\mathrm{inc}}=-0.224\hat{\mathbf{x}}-0.8365\hat{\mathbf{y}}-0.5\hat{\mathbf{z}}$. The scatterer, which is 4.432 m wide, 7.585 m tall, and 46 m long, is modeled with 91 366 triangular facets and oriented as depicted in the inset of Fig. 8(a). The model is designed to include a variety of generic surface shapes like a spheroidal cap at the front end and a conical tip at the tail as well as smooth surfaces and wedgelike structures at the top. The SCS patterns in the plane that includes the $\hat{\mathbf{k}}^{\mathrm{inc}}$ and $\hat{\mathbf{z}}$ vectors are plotted in Fig. 8 for $f/c=0.2624\,\mathrm{m}^{-1}$ and $f/c=0.585\,\mathrm{m}^{-1}$. In these plots, the angle ζ is measured from the $+z$ axis, and the angle $\zeta=120°$ indicates the forward scattering direction. Again, agreement between the results obtained by the two methods is excellent.

Finally, the computational and memory complexities of the proposed ML-PWTD scheme are verified. To this end, the $10\times3\times1$-m^3 rectangular box was first modeled with 1548 triangular facets (N_s), and this number was increased progressively to as large as $N_s=107\,500$. In addition, the center frequency and width of the incident pulse were scaled such that the average edge length of the triangular facets was $\frac{1}{10}$ of the wavelength at the highest frequency. The surface velocity potential was calculated in each case for $N_t=500$ time steps. The CPU times and the amount of memory required to complete the analysis using the classical and the proposed schemes are shown in Fig. 9(a) and (b), respectively. Also, to serve as a reference, the curve $C_cN_s\log^2 N_s$ is plotted in Fig. 9(a), as is the curve C_mN_s in Fig. 9(b). The constants C_c and C_m are chosen so that the reference curves match the values for the PWTD enhanced method at $N_s=38\,700$. Evidently, the multilevel PWTD enhanced MOT scheme performs with the predicted complexities and becomes more advantageous to employ when N_s exceeds approximately 1600.

V. CONCLUSIONS

This paper elucidated the implementation of multilevel PWTD enhanced MOT solvers for analyzing transient scattering from rigid bodies. It should be noted that the presented scheme is not contingent on the actual integral equation pre-

sented herein nor on the discretization scheme used to solve it, and that the scheme can be adapted to any retarded time integral equation describing linear wave scattering from a homogenous scatterer. It was also shown that the memory requirements and computational complexity of the multilevel PWTD scheme scale as $O(N_t N_s)$ and $O(N_t N_s \log^2 N_s)$, respectively. Numerical experiments indicate that the multilevel PWTD enhanced MOT scheme becomes more efficient than the classical MOT method when $N_s \geqslant 1600$.

ACKNOWLEDGMENTS

This work was supported in part by a grant from AFOSR via the MURI program under Contract No. F49620-96-1-0025, and the Gebze Institute of Technology, Turkey. The authors would also like to acknowledge the National Center for Supercomputing Applications for granting access to its computational facilities.

[1] M. J. Bluck and S. P. Walker, ''Analysis of three-dimensional transient acoustic wave propagation using the boundary integral equation method,'' Int. J. Numer. Methods Eng. **39**, 1419 (1996).
[2] M. Bluck and S. Walker, ''Time-domain BIE analysis of large three-dimensional electromagnetic scattering problems,'' IEEE Trans. Antennas Propag. **45**, 894 (1997).
[3] J. Garrett, A. Ruehli, and C. Paul, ''Accuracy and stability improvements of integral equation models using the partial element equivalent circuit (PEEC) approach,'' IEEE Trans. Antennas Propag. **46**, 1824 (1998).
[4] A. A. Ergin, B. Shanker, and E. Michielssen, ''Analysis of transient wave scattering from rigid bodies using a Burton-Miller approach,'' J. Acoust. Soc. Am. **106**, 2396–2404 (1999).
[5] M. Friedman and R. Shaw, ''Diffraction of pulses by cylindrical obstacles of arbitrary cross section,'' J. Appl. Mech. **29**, 40 (1962).
[6] A. Tijhuis, *Electromagnetic Inverse Profiling: Theory and Numerical Implementation* (VNU Science, Utrecht, The Netherlands, 1987).
[7] Y. Ding, A. Forestier, and T. H. Duong, ''A Galerkin scheme for the time domain integral equation of acoustic scattering from a hard surface,'' J. Acoust. Soc. Am. **86**, 1566 (1989).
[8] S. Dodson, S. Walker, and M. Bluck, ''Implicitness and stability of time domain integral equation scattering analysis,'' Appl. Comput. Electromagn. Soc. J. **13**, 291 (1998).
[9] S. Dodson, S. Walker, and M. Bluck, ''Costs and cost scaling in time-domain integral-equation analysis of electromagnetic scattering,'' IEEE Antennas Propag. Mag. **40**, 12 (1998).
[10] A. A. Ergin, B. Shanker, and E. Michielssen, ''Fast evaluation of three-dimensional transient wave fields using diagonal translation operators,'' J. Comput. Phys. **146**, 157 (1998).
[11] A. A. Ergin, B. Shanker, and E. Michielssen, ''The plane wave time domain algorithm for the fast analysis of transient wave phenomena,'' IEEE Antennas Propag. Mag. **41**, 39 (1999).
[12] M. F. Gyure and M. A. Stalzer, ''A prescription for the multilevel Helmhotz FMM,'' IEEE Comput. Sci. Eng. **5** (3), 39 (1998).
[13] V. Rokhlin, ''Diagonal forms of translation operators for the Helmholtz equation in three dimensions,'' Appl. Comput. Harmon. Anal. **1**, 82 (1993).
[14] J. Song and W. Chew, ''Multilevel fast-multipole algorithm for solving combined field integral equations of electromagnetic scattering,'' Microwave Opt. Technol. Lett. **10**, 14 (1995).
[15] A. Ergin, B. Shanker, and E. Michielssen, ''Fast transient analysis of acoustic wave scattering from rigid bodies using two-level plane wave time domain algorithm,'' J. Acoust. Soc. Am. **106**, 2405–2416 (1999).
[16] B. Shanker, A. Ergin, K. Aygun, and E. Michielssen, ''Analysis of transient electromagnetic scattering phenomena using a two-level plane wave time domain algorithm,'' IEEE Trans. Antennas Propag. (2000), accepted for publication.
[17] P. H. L. Groenenboom, ''Wave propagation phenomena,'' in *Progress in Boundary Element Methods*, edited by C. A. Brebbia (Pentech, London, 1983), Vol. 2, pp. 24–52.
[18] R. Martinez, ''The thin-shape breakdown (TSB) of the Helmholtz integral equation,'' J. Acoust. Soc. Am. **90**, 2728 (1991).
[19] T. Wu, ''A direct boundary element method for acoustic radiation and scattering from mixed regular and thin bodies,'' J. Acoust. Soc. Am. **97**, 84 (1995).
[20] S. Hirose and J. Achenbach, ''BEM method to analyze the interaction of an acoustic pulse with a rigid circular disk,'' Wave Motion **10**, 267 (1988).
[21] J. J. Knab, ''Interpolation of band-limited functions using the approximate prolate series,'' IEEE Trans. Inf. Theory **25**, 717 (1979).
[22] O. M. Bucci, C. Gennarelli, and C. Savarese, ''Optimal interpolation of radiated fields over a sphere,'' IEEE Trans. Antennas Propag. **39**, 1633 (1991).
[23] A. Shlivinski, E. Heyman, and R. Kastner, ''Antenna characterization in the time domain,'' IEEE Trans. Antennas Propag. **45**, 1140 (1997).
[24] O. M. Bucci and G. Franceschetti, ''On the spatial bandwidth of scattered fields,'' IEEE Trans. Antennas Propag. **35**, 1445 (1987).
[25] R. Jakob-Chien and B. K. Alpert, ''A fast spherical filter with uniform resolution,'' J. Comput. Phys. **136**, 580 (1997).
[26] R. W. Freund, ''A transpose-free quasi-minimal residual algorithm for non-hermitian linear systems,'' SIAM J. Sci. Comput. (USA) **14**, 470 (1993).
[27] A. C. Woo, H. T. Wang, M. J. Schuh, and M. L. Sanders, ''Benchmark radar targets for the validation of computational electromagnetics programs,'' IEEE Antennas Propag. Mag. **35**, 84 (1993).

Transient acoustic radiation from impulsively accelerated bodies by the finite element method

K. G. Manoj and S. K. Bhattacharyya
Ocean Engineering Centre, IIT Madras-600 036, India

(Received 16 June 1997; revised 8 November 1999; accepted 15 December 1999)

Bodies under impulsive motion, immersed in an infinite acoustic fluid, severely put to test any numerical method for the transient exterior acoustic problem. Such problems, in the context of the finite element method (FEM), are not well studied. FE modeling of such problems requires truncation of the infinite fluid domain at a certain distance from the structure. The volume of computation depends upon the extent of this domain as well as the mesh density. The modeling of the fluid truncation boundary is crucial to the economy and accuracy of solution and various boundary dampers have been proposed in the literature for this purpose. The second order damper leads to unsymmetric boundary matrices and this necessitates the use of an unsymmetric equation solver for large problems. The present paper demonstrates the use of FEM with zeroth, first and second order boundary dampers in conjunction with an unsymmetric, out of core, banded equation solver for impulsive motion problems of rigid bodies in an acoustic fluid. The results compare well with those obtained from analytical methods.
[S0001-4966(00)05003-7]

PACS numbers: 43.20.Px, 43.20.Tb, 43.40.Rj [ANN]

INTRODUCTION

For calculating the transient acoustic field generated by a body of an arbitrary shape in a free space, the Kirchhoff integral formulation (KIF) can be used.[1] The integrals in the Kirchhoff integral equation must be discretized in both temporal and spatial domains. Mitzner[2] first introduced direct numerical solution of the classical KIF for the transient scattering from a hard surface of arbitrary shape. Farn and Huang[3] developed a similar integral formulation based on a simple source method for transient acoustic radiation from an arbitrary body subjected to time-dependent excitation. Since the surface integrals were discretized in both space and time simultaneously, the numerical implementation was quite complicated even for a spherical surface, and was extremely sensitive to the time step used in integration.

For finding the transient acoustic field, Ebenezer and Stepanishen[4] developed both wave-vector-time domain and Kirchhoff integral methods. In the latter approach, the integral formulation was discretized in both spatial and temporal domains and the acoustic pressure on each element was expressed in terms of Taylor's series and determined by marching forward in time. For predicting the sound radiation from vibrating objects, Kirchhoff integral theory has been used.[5–9]

Direct solution of KIF is difficult because the acoustic quantities are both time and space dependent. Therefore, the surface integrals in this formulation must be discretized into both temporal and spatial domains, which complicates the numerical implementation. An explicit solution to this integral equation cannot be found when the surface is of arbitrary shape. Hence, in this approach one cannot use the fast Fourier transform (FFT) technique to solve for the surface acoustic pressure in the frequency domain first and then convert it into time domain by taking an inverse Fourier transform.

Morgans[10] and Farassat and Myers[11] had derived extended KIF for predicting the sound radiation from a vibrating object in motion. When the object vibrates at a constant frequency, all these formulations can be easily implemented for numerical computation. Numerical implementation becomes quite complicated, when the object is subjected to arbitrary time-dependent or impulsive excitation, because the acoustic quantities are time dependent and each element on the surface has a different emission time for an observer in a fixed coordinate system. Hence, it is clear that the surface integrals in all the aforementioned formulations must be discretized in both temporal and spatial domains simultaneously.

Wu and Akay[12] presented an integral formulation for predicting the sound radiation from a vibrating body in motion. This formulation involves both surface and volume integrals, in which the latter represents the effect of a turbulent field induced by the motion of the vibrating body, whereas the surface integrals represent the combined effects of the gradient of the turbulent stress field and unsteady force exerted on the fluid by the surface as well as the surface displacement effect. Numerical examples of sound radiation from the dilating and transversely oscillating spheres moving rectilinearly in space at constant subsonic speeds were presented.

Wu[13] demonstrated that for an impulsively accelerated body, an explicit form of solution for the radiated acoustic pressure could be derived from the classical Kirchhoff's integral theorem by using FFT. The basic principle is that the surface velocity distribution is expressible as generalized functions, when the body is impulsively accelerated. This approach is also applicable when the body is subjected to an arbitrary time-dependent excitation. Also, the solutions for the radiated acoustic pressure for the exterior region are unique at all frequencies. Wu and Wang[14] developed an FFT based numerical technique for KIF using the numerical

model.[13] The advantages of this technique are: (i) it enables one to decouple the temporal domain from the spatial one during the discretization process, (ii) it enables one to use the commercially available FFT software packages and (iii) the algorithm is free of the nonuniqueness difficulties inherent in the classical Kirchhoff integral theory.

KIF is a natural approach to problems of transient acoustic radiation and scattering from a body of arbitrary shape in free space. The finite element method (FEM), due to its simplicity and versatility, can be used to model such acoustic problems involving complicated geometries and loading conditions. In this domain decomposition approach, the problem can be modeled as an exterior acoustic problem in an infinite medium and it requires the solution of the wave equation subjected to Sommerfeld radiation condition at the far field.

There is a continued interest in the development of more accurate radiation boundary conditions to model the far field at a finite distance away from a radiating source. Various formulations and performance assessment of such nonreflecting boundary conditions are being pursued actively.[15] Of these, very few are applicable to both time-harmonic and direct-transient analysis. Similarly, many are restricted to special geometries and many have other mathematical restrictions. The simplest approximate radiation boundary conditions are the plane wave and curved wave dampers. Bayliss and Turkel[16] and Bayliss *et al.*[17] have introduced a sequence of boundary operators which are based on an asymptotic expansion in powers of $1/r$ (r: radial coordinate) of the exact time-dependent solution. The operators in this sequence are of progressively higher order (and are progressively more difficult to implement) but provide increasing accuracy.

The interest in modeling the propagation of sound from impulsively accelerated bodies stems not only from the intrinsic challenge of the problem but also from its wide application in many engineering areas. Notably, solution of such problems throws light on the generation and propagation of shock waves, which is required to predict the survival of engineering structures subject to shock. In addition, the impulsive motion of baffled/unbaffled circular disks has many practical applications. The theoretical and numerical modeling of this class of problem has been a major area of interest in the acoustic community. The present paper demonstrates the use of a general finite element method to tackle the sound radiation from impulsively accelerated bodies, which can be used for arbitrary body geometries. In the finite element context, the problem becomes unsymmetric when a second order nonreflecting boundary damper is used. The finite element method, when used for practical problems, leads to a large system of equations, which cannot be solved ''in core'' of the computer memory. For this purpose, an ''out of core'' solver for banded unsymmetric matrices has been developed by Manoj and Bhattacharyya[18] and has been used in the work reported here.

I. GOVERNING EQUATIONS AND BOUNDARY CONDITIONS

Exterior transient acoustic problems can be modeled as a boundary value problem governed by the wave equation in time domain exterior to the body with the Neumann/Dirichlet boundary condition at the body boundary and suitable radiation boundary condition at the truncation boundary. Here the body is treated as rigid and is embedded in an unbounded linear acoustic medium (Fig. 1). FEM is used for computing the pressure field in the fluid domain (Ω_F). Radiation boundary dampers are used on the finite truncation boundary (S_R) and the pressure field is computed by employing either the Neumann or Dirichlet boundary condition on the body boundary (S_B).

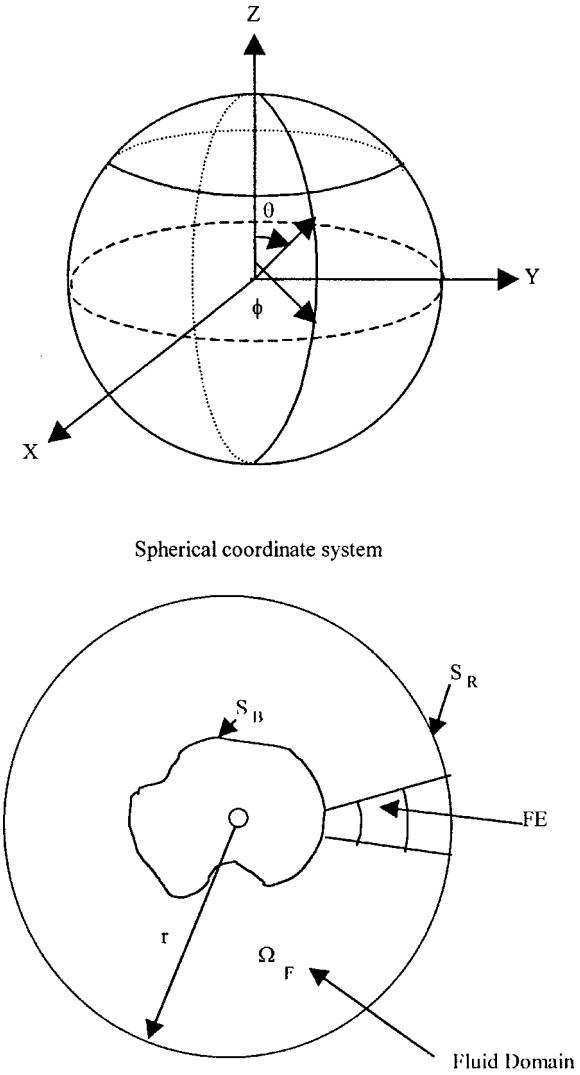

FIG. 1. Geometry of a typical infinite domain problem.

The acoustic pressure field generated by a rigid oscillating body in an infinite domain can be described by classical linear acoustic wave equation

$$\nabla^2 p = \frac{\ddot{p}}{c^2} \quad \text{in} \quad \Omega_F, \tag{1}$$

where ∇^2 is the Laplace operator, p (t) denotes the acoustic pressure at time t, $\ddot{p} = \partial^2 p / \partial t^2$ and c the speed of sound in the acoustic medium.

The boundary conditions on S_B can be a combination of

$$p_{,n} = -\rho \ddot{\bar{u}}_n \quad \text{and} \quad p = \bar{p}, \tag{2}$$

where $p_{,n}=\partial p/\partial n$, $\overline{\ddot{u}}_n$ ($\ddot{u}_n=\partial^2 u/\partial t^2$) is the prescribed acceleration normal to S_B (an overbar denotes a prescribed value), ρ is the density of the acoustic fluid and $\overline{p}$ is the prescribed pressure at time t and n is the outward normal on S_B. The boundary condition on S_R is

$$\lim_{r\to\infty} r^{\frac{h-1}{2}}\left[p_{,r}+\frac{\dot{p}}{c}\right]=O\left(\frac{1}{r}\right), \tag{3}$$

where $p_{,r}=\partial p/\partial r$, $\dot{p}=\partial p/\partial t$, $h=2$ or 3 for two-dimensional (2D) or three-dimensional (3D) problems respectively, and r is the outward radial distance from the reference point *w.r.t.* which the waves are assumed to be cylindrically (2D) or spherically (3D) symmetric. This radiation condition ensures that all waves are outgoing at S_R. The hierarchy of boundary dampers[16] is an alternative to the limiting condition [Eq. (3)] which cannot be readily accommodated in a FE model. This radiation condition has to be properly modeled as a Neumann condition for FE implementation. The boundary conditions[19,20] on S_R can be stated to any desired accuracy in $(1/r)$ as

$$B_m p=0, \tag{4a}$$

$$B_m=\prod_{J=1}^{m}\left(\frac{\partial}{\partial r}+\frac{1}{c}\frac{\partial}{\partial t}\right) \quad \text{for } m=0; \tag{4b}$$

$$B_m=\prod_{J=1}^{m}\left(\frac{\partial}{\partial r}+\frac{1}{c}\frac{\partial}{\partial t}+\frac{2J-1}{r}\right) \quad \text{for } m\geqslant 1.$$

In the above, B_m is the damper operator and m the order of the damper.

II. FINITE ELEMENT FORMULATION

Consider the functional $I(p)$ defined as follows:[21]

$$I(p)=\int_{t_1}^{t_2}\left\{\frac{1}{2}\left[\int_{\Omega_F}\nabla p.\nabla p\,d\Omega+\frac{1}{c^2}\int_{\Omega_F}\dot{p}^2\,d\Omega\right]+\rho\int_{S_B}\overline{\ddot{u}}_n p\,ds-\int_{S_B}\overline{p}\,p\,ds-\int_{S_R}S_m p\,ds\right\}dt. \tag{5}$$

In the above, S_m is the FE operator which corresponds to B_m. Taking the variation, $\delta I=0$, Eq. (5) becomes

$$\int_{\Omega_F}\nabla p.\delta(\nabla p)\,d\Omega+\frac{1}{c^2}\int\dot{p}\,\delta\dot{p}\,d\Omega+\rho\int_{S_B}\overline{\ddot{u}}_n\,\delta p\,ds-\int_{S_B}\overline{p}\,\delta p\,ds-\int_{S_R}S_m\,\delta p\,ds=0. \tag{6}$$

Now assume

$$p=\sum_e N_F^e\{p_e\}, \tag{7}$$

where $\{p_e\}$ denotes the field variable corresponding to an element, N_F^e is the fluid shape function vector at element level, and Σ_e denotes summation over all elements. Using the approximation of Eq. (7) into Eq. (6), and since δp_e is arbitrary, the various terms can be written as follows:

$$\int_{\Omega_F}\nabla p\cdot\delta(\nabla p)\,d\Omega=\sum_e\int_{\Omega_F^e}\nabla N_F^{eT}\nabla N_F^e\,d\Omega\{p_e\}, \tag{8}$$

$$\int_{\Omega_F}\dot{p}\,\delta\dot{p}\,d\Omega=\sum_e\frac{1}{c^2}\int_{\Omega_F^e}N_F^{eT}N_F^e\,d\Omega\{\ddot{p}_e\}, \tag{9}$$

$$\rho_F\int_{S_B}\overline{\ddot{u}}_n\delta p\,ds=\sum_e\rho_F\int_{S_F^e}N_F^{eT}\overline{\ddot{u}}_n\,ds, \tag{10}$$

$$\int_{S_B}\overline{p}\,\delta p\,ds=\sum_e\int_{S_B}N_F^{eT}\overline{p}\,ds. \tag{11}$$

The last term in Eq. (6) has to be expanded according to the type of radiation damper adopted. The details regarding the FE implementation of various dampers are given in the subsequent sections.

A. Plane wave damper $B_0 p$

For $m=0$, the operator B_m in Eq. (4b) is

$$B_0 p=p_{,r}+\frac{\dot{p}}{c}=O\left(\frac{1}{r}\right), \tag{12}$$

and the corresponding FE operator can be written as

$$S_0 p=-\frac{\dot{p}}{c}. \tag{13}$$

By using Eqs. (7) to (11) and (13), semi-discrete finite element equations can be written as

$$\sum_e\int_{\Omega_F^e}\nabla N_F^{eT}\nabla N_F^e\,d\Omega\{p_e\}+\frac{1}{c}\int_{S_R^e}N_F^{eT}N_F^e\,ds\{\dot{p}_e\}+\frac{1}{c^2}\int_{\Omega_F^e}N_F^{eT}N_F^e\,d\Omega\{\ddot{p}_e\}=F_1(t)+F_2(t), \tag{14}$$

or

$$[K]\{p\}+[C]\{\dot{p}\}+[M]\{\ddot{p}\}=\{F(t)\}, \tag{15}$$

where

$$[K]=[K_F], \tag{16}$$

$$[C]=[C_{R1}], \tag{17}$$

$$[M]=[M_F], \tag{18}$$

$$[K_F]=\sum_e\int_{\Omega_F^e}\nabla N_F^{eT}\nabla N_F^e\,d\Omega, \tag{19}$$

$$[M_F]=\sum_e\frac{1}{c^2}\int_{\Omega_F^e}N_F^{eT}N_F^e\,d\Omega, \tag{20}$$

$$[C_{R1}]=\sum_e\frac{1}{c}\int_{S_R^e}N_F^{eT}N_F^e\,ds, \tag{21}$$

$$\{F_1(t)\}=-\rho_F\int_{S_B^e}N_F^{eT}\overline{\ddot{u}}_n\,ds, \tag{22}$$

$$\{F_2(t)\}=\int_{S_B^e} N_F^{e^T}\,\overline{p}\,ds, \tag{23}$$

where $[K_F]$ is the fluid stiffness matrix, $[C_{R1}]$ is the radiation damping matrix, $[M_F]$ is the fluid mass matrix, $\{F_1(t)\}$ is the force vector corresponding to the prescribed normal acceleration $(\overline{\ddot{u}}_n)$, $\{F_2(t)\}$ is the force vector corresponding to prescribed pressure $(\overline{p})$, $[K]$, $[M]$ and $[C]$ are the total stiffness, damping and mass matrices and $\{F(t)\}$ is the global load vector. This is the simplest form of the damper, which applies the Sommerfeld radiation condition as a natural boundary condition on the truncated fluid boundary (S_R). It may be noted that the performance of any damper, though exact at infinite distance from the radiating body, deteriorates as S_R approaches the source of perturbation. In practice this means that if the S_R boundary is several wavelengths away from the body, the damper performs well. On the other hand, if this distance is comparable to the wavelength, the effectiveness of the damper will be downgraded significantly.

B. Spherical damper B_1p

For $m=1$, the operator B_m in Eq. (4b) reduces to

$$B_1p=p_{,r}+\frac{\dot{p}}{c}+\frac{p}{r}=O\left(\frac{1}{r^3}\right), \tag{24}$$

and the corresponding FE operator can be written as

$$S_1p=-\frac{p}{r}-\frac{\dot{p}}{c}. \tag{25}$$

By using Eqs. (5)–(11), (24) and (25), the semidiscrete finite element equations can be written as

$$\sum_e \left\{\int_{\Omega_F^e}\nabla N_F^{e^T}\nabla N_F^e\,d\Omega+\frac{1}{r}\int_{S_R^e}N_F^{e^T}N_F^e\,ds\right\}\{p_e\}+\frac{1}{c}\int_{S_R^e}N_F^{e^T}N_F^e\,ds\{\dot{p}_e\}+\frac{1}{c^2}\int_{\Omega_F^e}N_F^{e^T}N_F^e\,d\Omega\{\ddot{p}_e\}=\{F(t)\}. \tag{26}$$

From the correspondence with Eq. (15), one obtains

$$[K]=[K_F]+[K_{R1}], \tag{27}$$

$$[C]=[C_{R1}], \tag{28}$$

$$[M]=[M_F], \tag{29}$$

$$[K_{R1}]=\sum_e\frac{1}{r}\int_{S_R^e}N_F^{e^T}N_F^e\,ds, \tag{30}$$

$$[C_{R1}]=\sum_e\frac{1}{c}\int_{S_R^e}N_F^{e^T}N_F^e\,ds, \tag{31}$$

where $[K_{R1}]$ and $[C_{R1}]$ are the radiation stiffness and radiation damping matrices arising from the truncated fluid boundary. This radiation condition is referred to as a spherical damper since the operator absorbs radially symmetric spherical waves.

C. Second order damper B_2p

For $m=2$, by Eq. (4b) the operator B_2 can be written as

$$B_2p=p_{,rr}+\frac{2}{c}\dot{p}_{,r}+\frac{2}{r^2}p+\frac{4}{r}p_{,r}+\frac{4}{rc}\dot{p}+\frac{\ddot{p}}{c^2}. \tag{32}$$

The corresponding S_2 operator can be written as

$$S_2p=-\frac{r}{c}p_{,r}-\frac{(2-D)}{2r}p-\frac{2}{c}\dot{p}-\frac{r}{c^2}\ddot{p}, \tag{33}$$

where

$$D=\frac{1}{\sin\theta}\frac{\partial}{\partial\theta}\left(\sin\theta\frac{\partial}{\partial\theta}\right)+\frac{1}{\sin^2\theta}\frac{\partial^2}{\partial\phi^2}.$$

By using Eqs. (5)–(11), (32) and (33), the semidiscrete finite element equations can be written as

$$\sum_e\left\{\int_{\Omega_F^e}\nabla N_F^{e^T}\nabla N_F^e\,d\Omega+\frac{1}{r}\int_{S_R^e}N_F^{e^T}N_F^e\,ds+\frac{1}{2r}\int_{S_R^e}\left[N_{F,\theta}^{e^T}N_{F,\theta}^e+\frac{1}{\sin^2\theta}N_{F,\phi}^{e^T}N_{F,\phi}^e\right]ds\right\}\{p_e\}+\left\{\frac{2}{c}\int_{S_R^e}N_F^{e^T}N_F^e\,ds+\frac{r}{c}\int_{S_R^e}N_{F,r}^{e^T}N_F^e\,ds\right\}\{\dot{p}_e\}+\left\{\frac{1}{c^2}\int_{\Omega_F^e}N_F^{e^T}N_F^e\,d\Omega+\frac{r}{c^2}\int_{S_R^e}N_F^{e^T}N_F^e\,ds\right\}\{\ddot{p}_e\}=F(t). \tag{34}$$

From the correspondence with Eq. (15), one obtains

$$[K]=[K_F]+[K_{R1}]+[K_{R2}], \tag{35}$$

$$[C]=[C_{R1}]+[C_{R2}], \tag{36}$$

$$[M]=[M_F]+[M_{R1}], \tag{37}$$

$$[K_{R1}]=\sum_e\frac{1}{r}\int_{S_R^e}N_F^{e^T}N_F^e\,ds, \tag{38}$$

$$[K_{R2}]=\sum_e\frac{1}{2r}\int_{S_R^e}\left[N_{F,\theta}^{e^T}N_{F,\theta}^e+\frac{1}{\sin^2\theta}N_{F,\phi}^{e^T}N_{F,\phi}^e\right]ds, \tag{39}$$

$$[C_{R1}]=\sum_e\frac{2}{c}\int_{S_R^e}N_F^{e^T}N_F^e\,ds, \tag{40}$$

$$[C_{R2}]=\sum_e\frac{r}{c}\int_{S_R^e}N_{F,r}^{e^T}N_F^e\,ds, \tag{41}$$

$$[M_{R1}]=\sum_e\frac{r}{c^2}\int_{S_R^e}N_F^{e^T}N_F^e\,ds, \tag{42}$$

where $[K_{R1}]$ and $[K_{R2}]$ are the radiation stiffness matrices, $[C_{R1}]$ and $[C_{R2}]$ are the radiation damping matrices and $[M_{R1}]$ is the radiation mass matrix arising from the truncated fluid boundary.

D. Second order damper $B_2\dot{p}$

Another type of second order damper based on the $\dot{p}$ condition (instead of p, which is usually adopted) will be discussed next.

The B_2 operator, after elimination of higher order radial derivatives (p_{rr}), can be written as

$$B_2\dot{p}=\frac{2}{r}p_{,r}+\frac{2}{c}\dot{p}_{,r}-\frac{(D-2)}{r^2}p+\frac{4}{rc}\dot{p}+\frac{2}{c^2}\ddot{p}. \tag{43}$$

The damper operator $S_2\dot{p}$ in FE formulation can be written as

$$S_2\dot{p}=-\frac{c}{r}p_{,r}-\frac{c\,(2-D)}{2\,r^2}p-\frac{2}{r}\dot{p}-\frac{\ddot{p}}{c}. \tag{44}$$

By using Eqs. (5)–(11), (43) and (44), the semidiscrete finite element equations can be written as

$$\sum_e \left\{ \int_{\Omega_F^e} \nabla N_F^{eT}\,\nabla N_F^e\,d\Omega + \frac{c}{r}\int_{S_R^e} N_{F,r}^{eT} N_F^e\,ds + \frac{1}{2r^2}\int_{S_R^e}\left(N_{F,\theta}^{eT}N_{F,\theta}^e + \frac{1}{\sin^2\theta}N_{F,\phi}^{eT}N_{F,\phi}^e\right) ds + \frac{c}{r^2}\int_{S_R^e} N_F^{eT}N_F^e\,ds\right\}\{p_e\} + \frac{2}{r}\int_{S_R^e} N_F^{eT}N_F^e\,ds\,\{\dot{p}_e\} + \left\{\frac{1}{c^2}\int_{\Omega_F^e} N_F^{eT}N_F^e\,d\Omega + \frac{1}{c}\int_{S_R^e} N_F^{eT}N_F^e\,ds\right\}\{\ddot{p}_e\}=\{F(t)\}. \tag{45}$$

From the correspondence with Eq. (15), one obtains

$$[K]=[K_F]+[K_{R1}]+[K_{R2}]+[K_{R3}], \tag{46}$$

$$[C]=[C_{R1}], \tag{47}$$

$$[M]=[M_F]+[M_{R1}], \tag{48}$$

$$[K_{R1}]=\sum_e \frac{c}{r}\int_{S_R^e} N_{F,r}^{eT}N_F^e\,ds, \tag{49}$$

$$[K_{R2}]=\sum_e \frac{1}{2r^2}\int_{S_R^e}\left(N_{F,\theta}^{eT}N_{F,\theta}^e + \frac{1}{\sin^2\theta}N_{F,\phi}^{eT}N_{F,\phi}^e\right) ds, \tag{50}$$

$$[K_{R3}]=\sum_e \frac{c}{r^2}\int_{S_R^e} N_F^{eT}N_F^e\,ds, \tag{51}$$

$$[C_{R1}]=\sum_e \frac{2}{r}\int_{S_R^e} N_F^{eT}N_F^e\,ds, \tag{52}$$

$$[M_{R1}]=\sum_e \frac{1}{c}\int_{S_R^e} N_F^{eT}N_F^e\,ds, \tag{53}$$

where $[K_{R1}]$, $[K_{R2}]$, and $[K_{R3}]$ are the radiation stiffness matrices, $[C_{R1}]$ is the radiation damping matrix and $[M_{R1}]$ is the radiation mass matrix arising from the truncated fluid boundary.

III. COMPUTATIONAL ASPECTS

A FORTRAN program has been developed using 20 (quadratic) and 8 (linear) noded hexahedron (or brick) isoparametric C^0 type acoustic fluid elements which are used for volume modeling and the matching 8 and 9 noded quadrilateral elements for surface modeling. The details of isoparametric formulation[21] are well known and hence are not reproduced here. All the boundary dampers discussed earlier have been implemented in the present code. It seems that the $B_2\dot{p}$ has not been implemented elsewhere in the literature. The system of equations will be unsymmetric when higher order dampers ($m=2$) are employed. For this purpose, an unsymmetric block solver capable of handling a sparse, banded, and large unsymmetric system of equations has been developed[19] which is ''out of core'' type and uses the Crouts L-U decomposition procedure.[22]

The simplest and most popular direct integration scheme, known as generalized Newmark's method,[23–25] with $\beta=0.25$ and $\gamma=0.5$, is adopted in the present work. The development of the so-called α-method[26] is noteworthy and has been shown to filter the higher modes. The use of $\beta=0.3025$ and $\gamma=0.6$ in the Newmark method renders a strong filtering characteristic to it for higher modes.

IV. NUMERICAL EXAMPLES, RESULTS AND DISCUSSION

A. Explosively expanding sphere

This example concerns the transient acoustic radiation from an explosively expanding sphere of radius a. The term ''explosively expanding'' means that at $t=0$, the velocity on the surface of the sphere rises instantaneously from zero to a finite value v_s. Therefore at $t=0$, one can write the finite element boundary condition on the surface of the sphere ($r=a$) as

$$p=\rho\,c\,v_s \quad \text{at } r=a. \tag{54}$$

The analytical solution of this problem[13] can be written as

$$p(r,t)=(\rho\,c\,v_s\,a/r)\,e^{-(ct-r)}\,H(t-r/c), \tag{55}$$

where $H(t-r/c)$ is the Heaviside step function, which is unity for $t\geqslant r/c$ and zero for $t<r/c$. Equation (55) is based on the assumption that the wave radiates from the center of the sphere, which has to be modified to suit the time origin at $r=a$, so that it can be compared with FEM results. The shift of origin gives

$$p(r,t)=(\rho\,c\,v_s\,a/r)\,e^{-(ct-(r-a))}\,H(t-(r-a)/c). \tag{56}$$

Since Eq. (54) is a condition on p, it is a Dirichlet problem. A transient FE solution of the above problem with $a=1$ m was obtained using mesh which consists of a single stack of 20 noded brick elements in the radial direction from $r=1$ to $r=15$ m. The radial length of each element is about 0.03 m and it extends 10° in both θ and ϕ directions. This gives 450 elements in the stack. The system starts from rest at $t=0$ and the Newmark integration scheme is adopted with a time step of 10 μs. The damping boundary is kept at $r=15$ m and $c=340$ m/s and $\rho=1.2$ kg/m^3 are adopted.

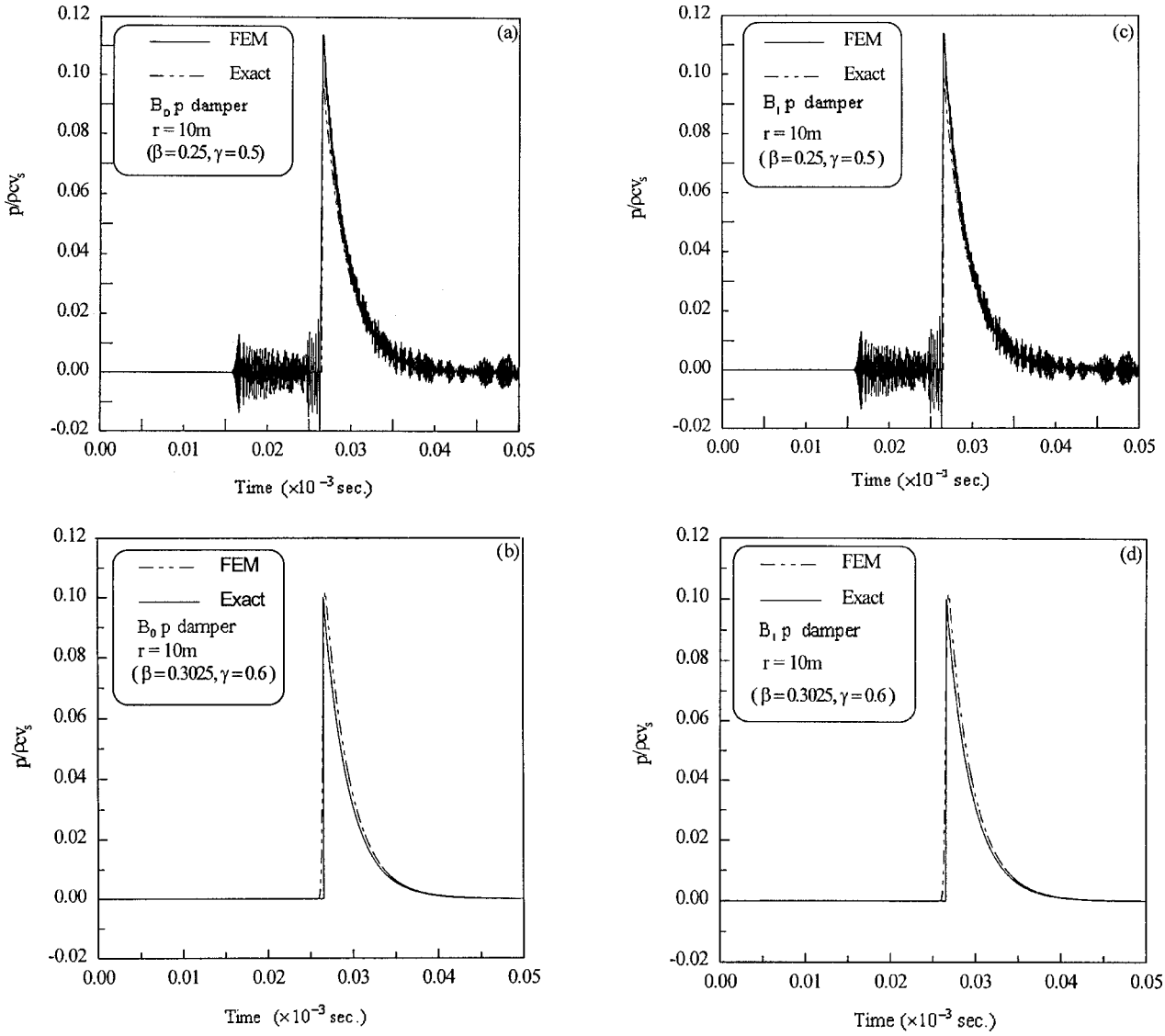

FIG. 2. Dimensionless acoustic pressure for the explosively expanding sphere.

The finite element results are obtained with B_0p, B_1p, B_2p, and $B_2\dot{p}$ dampers using Newmark integration method with both undamped ($\beta=0.25$, $\gamma=0.5$) and damped ($\beta=0.3065$, $\gamma=0.6$) formulations. The comparison with exact results at $r=10$ m is given in Fig. 2. From a study of these results the following observations can be made:

(a) The undamped Newmark method introduces spurious oscillations for all dampers [Fig. 2(a), (c), (e), and (g)], whereas the damped Newmark method has excellent filtering properties [Fig. 2(b), (d), (f), and (h)] so that it entirely eliminates all spurious oscillations for all dampers.

(b) The spurious oscillations associated with the undamped Newmark method are more pronounced in the case of B_2p than $B_2\dot{p}$. Both B_0p and B_1p fare somewhat better in this regard.

(c) The comparison with theoretical result is excellent and of identical accuracy for all dampers [Fig. 2(b), (d), (f), and (h)] when the damped Newmark method is used.

An efficient computational method for step-by-step integration of linear dynamic equations should be endowed with the attributes of (i) unconditional stability, (ii) second order accuracy, (iii) controllable algorithmic dissipation in the higher modes and (iv) self-starting. The Newmark family of algorithms enjoys widespread use, especially in structural dynamics, but it cannot possess the attributes of second order accuracy and dissipation characteristics simultaneously. It possesses the other attributes, however. Since the higher modes of semidiscrete equations are artefacts of the discretization process, they are not a true representation of the governing partial differential equation. It is desirable to filter out these modes by some form of artificial damping without affecting the order of accuracy. The development of the so-called α-method,[26,27] when used in conjunction with the Newmark family, significantly improves the algorithmic dissipation which is controllable and at the same time preserves the order of accuracy. A Newmark algorithm embeds two constants, β and γ. When $\beta=0.25$ and $\gamma=0.5$, it is unconditionally stable and second-order accurate but possesses no

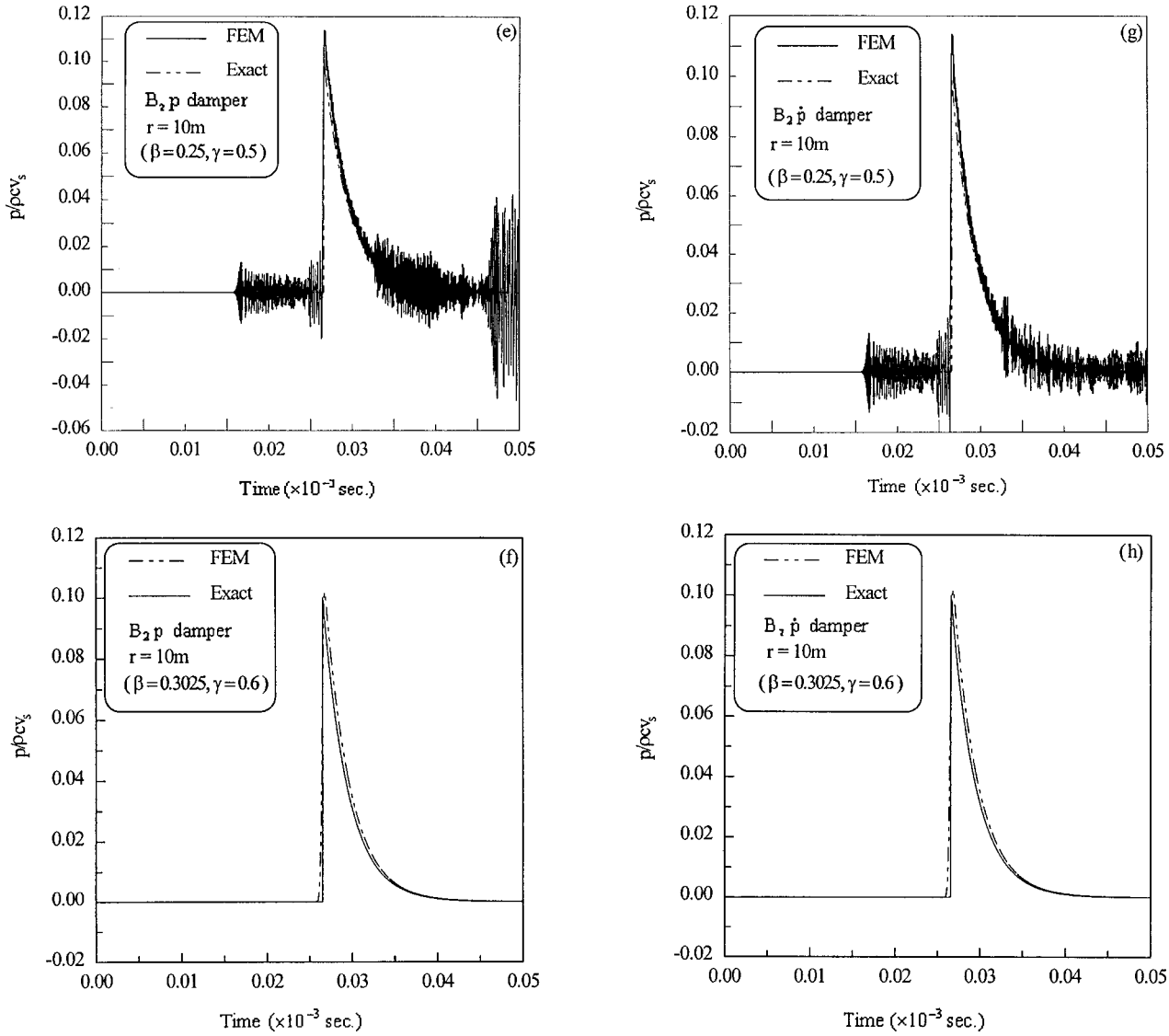

FIG. 2. (*Continued.*)

dissipation. This is referred to as the undamped Newmark method. Therefore, spurious oscillations, which can be due to the numerical instability of the domain decomposition technique, will appear in the results as the time integration scheme is unable to filter it. In the α-method, one adopts $\beta=(1-\alpha)^2/4$ and $\gamma=0.5-\alpha$ with $\alpha\in[-1/3,0]$. Since $\alpha\leqslant 0$, $\gamma\geqslant 0.5$ and for nonzero α, numerical dissipation is imparted to the integration scheme. This is the damped Newmark method, which damps out the spurious oscillations. A value $\alpha=-0.1$ (hence $\beta=0.3025$ and $\gamma=0.6$) has been used with excellent results in the present calculations.

B. Impulsively accelerated rigid sphere

This example concerns the transient sound radiation from a rigid sphere of radius a accelerated impulsively in the positive z direction. Examination of symmetry shows that the acoustic quantities on the surface and in the field are axisymmetric about the z axis and depend on the angle θ with respect to the z-axis.

The finite element boundary condition is

$$p=\rho\, c\, v_s \cos\theta. \tag{57}$$

The analytical solution of the problem[13] can be written as

$$p(r,t)=\frac{\rho c v_s \cos\theta}{r} e^{-(ct-r)/a} H\left(t-\frac{r}{c}\right) \times\left[\cos\left(\frac{ct-r}{a}\right)-\left(1-\frac{a}{r}\right)\sin\left(\frac{ct-r}{a}\right)\right]. \tag{58}$$

Shifting the origin as in the earlier problem, Eq. (58) can be written as

$$p(r,t)=\frac{\rho\, c\, v_s \cos\theta}{r} e^{(ct-(r-a))/a} H\left(t-\frac{(r-a)}{c}\right) \times\left[\cos\left(\frac{ct-(r-a)}{a}\right)\left(1-\frac{a}{r}\right)\sin\left(\frac{ct-(r-a)}{a}\right)\right]. \tag{59}$$

A transient FE solution of this problem was obtained using the same mesh as in the earlier problem. The other data

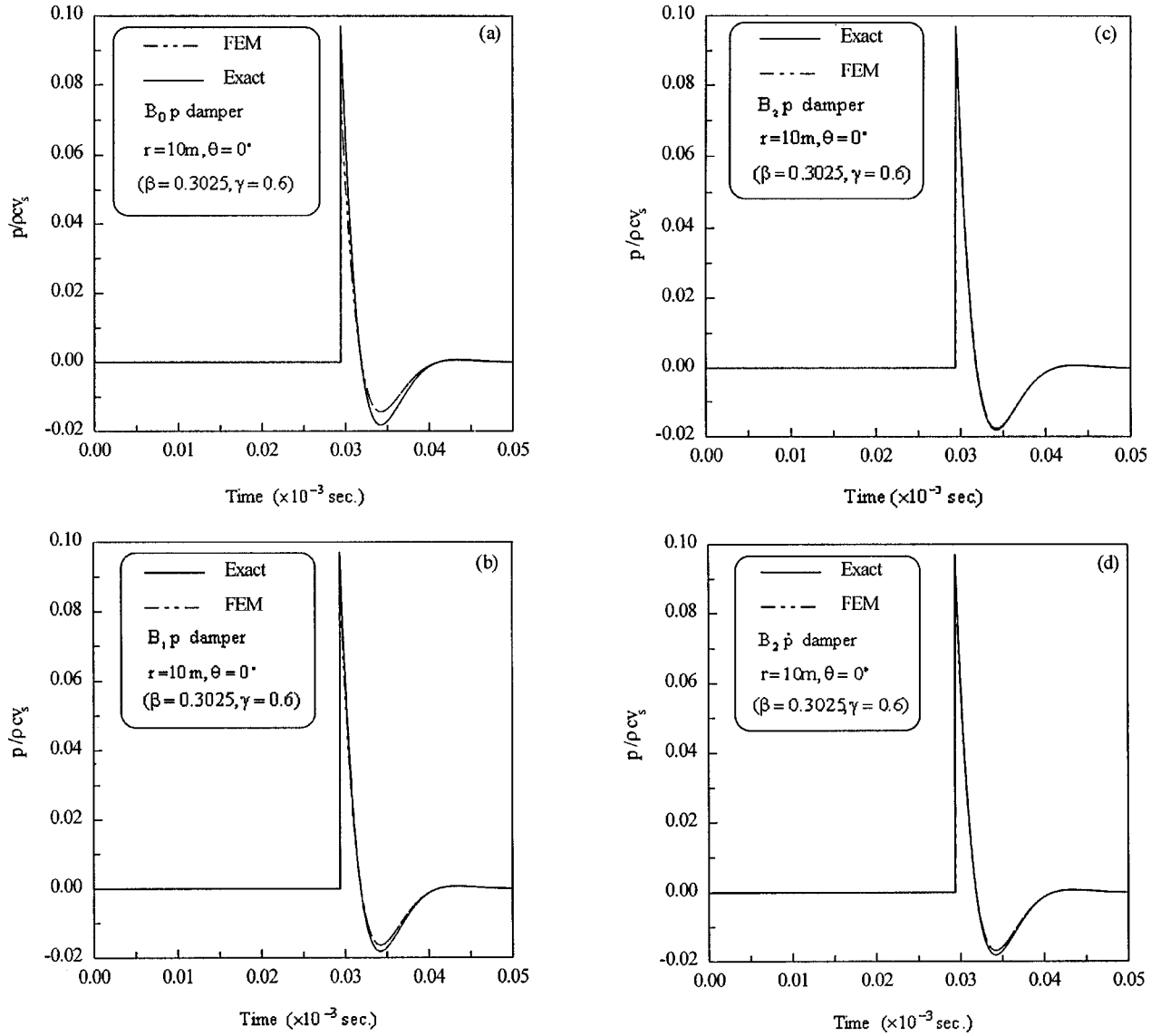

FIG. 3. Dimensionless acoustic pressure for the impulsively accelerated sphere.

are also the same. The finite element results are obtained for all four dampers using both damped and undamped Newmark methods. Spurious oscillations are observed in the undamped Newmark case like in the previous example, whereas excellent comparisons have been obtained with the damped Newmark case. Hence, the results for the latter case at $r=10$ m only are given for $\theta=0^0$ (Fig. 3). The quality of comparison for $\theta\neq 0^0$ has been found to be similar. As can be seen, all the dampers give excellent comparison, though $B_0 p$ damper fares marginally worse.

C. Explosively expanding ellipsoid

At this stage, it should be recognized that though the two problems solved above pertain to spherical geometry, the finite element method developed is by no means restricted to any specific geometry. This fact is demonstrated by an example.

This example concerns the transient acoustic radiation from an explosively expanding ellipsoid of major to minor axis ratio 2:1. At $t=0$, the velocity on the surface of the ellipsoid rises instantaneously from zero to a finite value v_s. Therefore at $t=0$, one can write the finite element boundary condition on the entire surface of the ellipsoid as

$$p=\rho c v_s, \tag{60}$$

There is no published result for the analytical solution of this problem. Hence, the FE solution of this problem cannot be compared. This, then, demonstrates the applicability of the FEM to general 3D bodies under impulsively accelerated motion.

A transient FE solution of the above problem with the radiation boundary at $r=3$ m was obtained using 8-noded brick elements. The radial length of each element is about 0.03 m and it extends 10^0 in both θ and ϕ directions (see Fig. 1). The number of elements in this problem is 8000. The system starts from rest at $t=0$ and Newmark integration scheme is adopted with a time step of 10 μs. The other data of the problem are the same as in the last two problems.

The finite element results are obtained with $B_0 p$, $B_1 p$, $B_2 p$, and $B_2 \dot{p}$ dampers using the Newmark integration

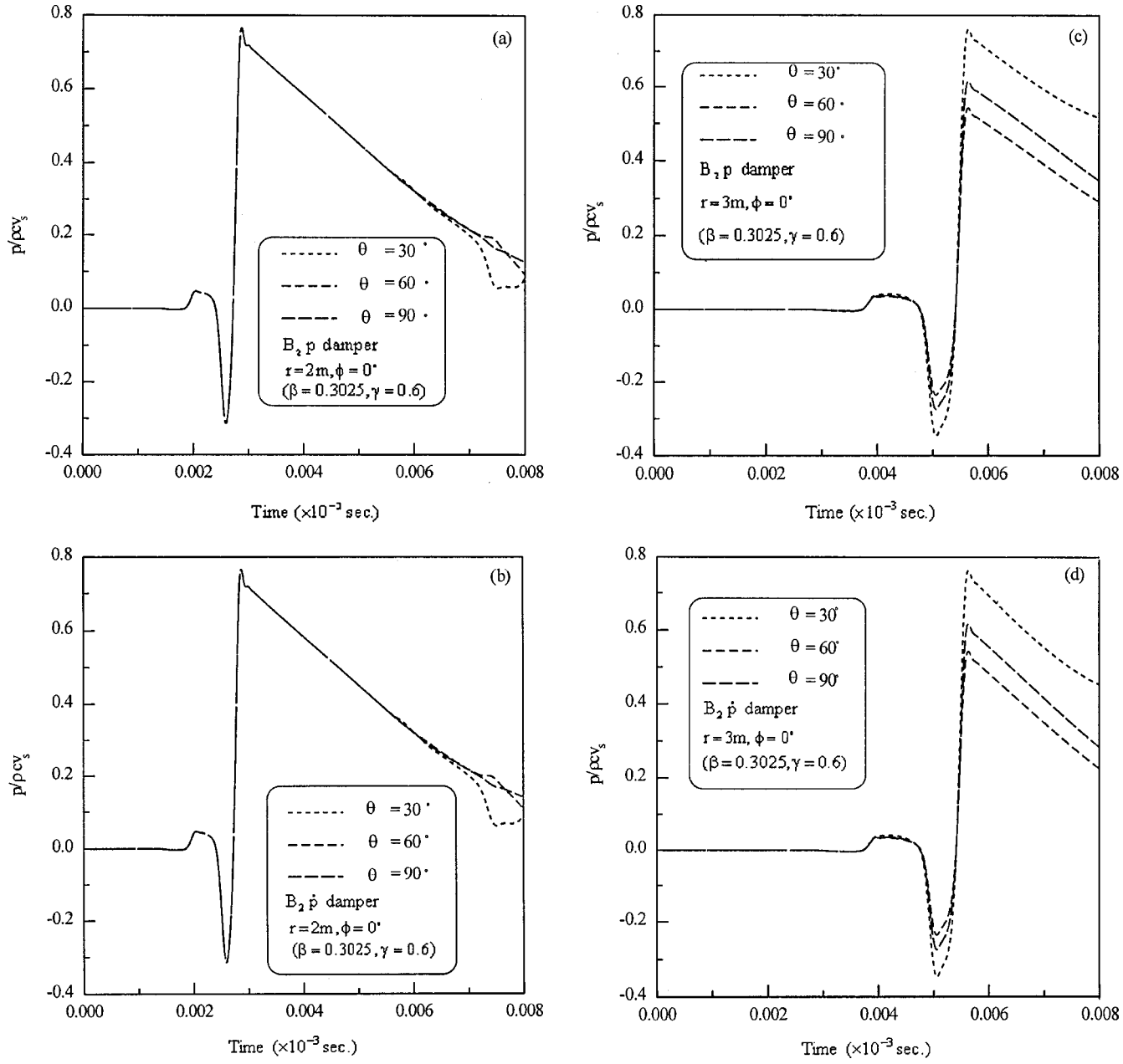

FIG. 4. Dimensionless acoustic pressure for the explosively expanding ellipsoid.

method with both undamped (β=0.25, γ=0.5) and damped (β=0.3025, γ=0.6) formulations. Spurious oscillations are observed in the undamped Newmark case. The dimensionless acoustic pressure at various locations within the computational fluid domain using B_2p and $B_2\dot{p}$ are given in Fig. 4 for the damped Newmark case only. It can be seen that the shock wave front is well captured at various locations. The results show no difference between B_2p and $B_2\dot{p}$ dampers.

The correct and optimum choice of mesh density and the distance of the radiation boundary from the body are two aspects for which some preliminary guidelines are required to obtain a reliable FE solution with reasonable computer time. In general, there should be ten linear elements per acoustic wavelength in a given problem. However, for impulsive problems, a FFT analysis of the excitation will show the frequency content and this can be used as a guidance to choose the mesh density. In a time domain problem of this type, the radiation boundary can be located a little away from the point where the pressure time history is sought. It has been found that with radiation boundary at r=15 m in the first two problems, the results of pressure match quite well with the analytical solution up to r=14 m. The comparison is particularly unrealistic exactly at r=15 m.

V. CONCLUSION

A comprehensive finite element method has been developed and implemented for transient sound radiation from impulsively accelerated bodies of arbitrary shape. A variety of transient nonreflecting boundary conditions have been implemented. Of these, the second-order damper with time derivative of pressure as the variable is implemented for the

first time. The FEM results have been validated with theoretical results and the comparisons were found to be excellent. The importance of adopting the damped Newmark method for such impulsively loaded systems is clearly brought out. An ''out of core'' (or block) solver is used in the FE code so that it can be used for large problems which arise in practice.

ACKNOWLEDGMENT

The authors express their thanks to Professor C. P. Vendhan for his helpful suggestions during the course of this work.

[1] A. D. Pierce, *Acoustics: An Introduction to its Physical Principles and Applications* (McGraw-Hill, New York, 1981).
[2] K. M. Mitzner, J. Acoust. Soc. Am. **42**, 391–397 (1967).
[3] C. L. S. Farn and H. Huang, J. Acoust. Soc. Am. **43**, 252–257 (1968).
[4] D. D. Ebenezer and P. R. Stepanishen, J. Acoust. Soc. Am. **94**, 542–553 (1991).
[5] F. H. Fenlon, Proc. IEEE **57**, 291–306 (1969).
[6] P. H. Rogers, J. Acoust. Soc. Am. **54**, 1662–1666 (1973).
[7] A. F. Seybert, B. Soenarko, F. J. Rizzo, and D. J. Shippy, ASME J. Vib., Acoust. Stress Reliab. Des. **106**, 414–420 (1984).
[8] X. F. Wu, A. D. Pierce, and J. H. Ginsberg, IEEE J. Ocean Eng. **12**, 412–418 (1987).
[9] J. H. Ginsberg, P. T. Chen, and A. D. Pierce, J. Acoust. Soc. Am. **44**, 41–58 (1990).
[10] W. R. Morgans, Philos. Mag. **9**, 141–161 (1980).
[11] F. Farassat and M. K. Myers, J. Sound Vib. **123**, 451–460 (1988).
[12] X. F. Wu and A. Akay, J. Acoust. Soc. Am. **91**, 2544–2555 (1992).
[13] S. F. Wu, J. Acoust. Soc. Am. **94**, 542–553 (1993).
[14] S. F. Wu and Z. Wang, *FFT-KIT: An Effective Means for Predicting Sound Radiation* (Third International Congress on Air and Structure-Borne Sound and Vibration, Montreal, Canada, 1994).
[15] M. J. Grote and J. B. Keller, J. Comput. Phys. **127**, 52–65 (1996).
[16] A. Bayliss and E. Turkel, Commun. Pure Appl. Math. **33**, 707–725 (1980).
[17] A. Bayliss, M. Gunzburger, and E. Turkel, SIAM (Soc. Ind. Appl. Math.) J. Appl. Math. **42**, 430–451 (1982).
[18] K. G. Manoj and S. K. Bhattacharyya, Int. J. Numer. Methods Eng. **40**, 3279–3295 (1997).
[19] P. M. Pinsky and N. N. Abboud, Comput. Methods Appl. Mech. Eng. **85**, 311–348 (1991).
[20] P. M. Pinsky, L. L. Thompson, and N. N. Abboud, J. Acoust. Soc. Am. **91**, 1320–1335 (1992).
[21] O. C. Zienkiewicz and R. L. Taylor, *The Finite Element Method: Basic Formulation and Linear Problems*, 4th ed. (McGraw-Hill, London, 1989), Vol. 1.
[22] S. C. Chapra and R. P. Canale, *Numerical Methods for Engineers* (McGraw-Hill, New York, 1989).
[23] K. J. Bathe and E. L. Wilson, *Finite Element Procedures in Engineering Analysis* (Prentice-Hall, New Jersey, 1982).
[24] T. J. R. Hughes and T. Belytschko, ASME Trans. J. Appl. Mech. **50**, 1033–1041 (1983).
[25] T. J. R. Hughes, *The Finite Element Method* (Prentice-Hall, New Jersey, 1987).
[26] H. M. Hilber and T. J. R. Hughes, Earthq. Eng. Struct. Dyn. **6**, 99–118 (1978).
[27] H. M. Hilber, T. J. R. Hughes, and R. L. Taylor, Earthq. Eng. Struct. Dyn. **5**, 283–292 (1977).

Sound cancellation by the use of secondary multipoles: Experiments

Thierry A. Beauvilain[a] and J. Stuart Bolton
1077 Ray W. Herrick Laboratories, School of Mechanical Engineering, Purdue University, West Lafayette, Indiana 47907-1077

Bryce K. Gardner[b]
Automated Analysis Corporation, 2805 S. Industrial, Suite 100, Ann Arbor, Michigan 48104

(Received 10 February 1999; accepted for publication 2 December 1999)

Theory related to global, free-field cancellation of a primary monopole field by the use of a displaced, secondary multipole was presented previously: a corresponding experimental investigation is presented here. The construction of multipole source components to octopole order is described, as are procedures for determining their source strengths. Dipoles, longitudinal quadrupoles, and longitudinal octopoles that conformed closely to their theoretical models were constructed using arrays of unbaffled loudspeakers. Two methods of calculating the multipole strengths required to cancel a primary monopole field were implemented in an open-loop manner: a ''direct'' approach based on a multipole expansion of the primary field, and a least-squares procedure based on fitting the secondary field to the primary field either along a circle enclosing a secondary source, or along a segment of that circle. Cancellation measurements were made on a 1-m-radius circle centered on the secondary source: the primary-to-secondary source separation was approximately 0.2 wavelengths. It was found both that a secondary multipole could provide far greater cancellation than a monopole placed at the same distance from the primary source and that the least-squares approach resulted in greater far-field cancellation than did the direct approach.
 [S0001-4966(00)01803-8]

PACS numbers: 43.20.Rz, 43.38.Ja, 43.50.Ki [DEC]

INTRODUCTION

The present article is a companion to an earlier one in which theory related to global, free-field cancellation of a primary monopole field by the use of a secondary multipole was presented.[1] Here, a corresponding experimental investigation is described. Both pieces of work were motivated by the observation that little work has been devoted to the use of secondary sources of higher than monopole order in the context of free-field sound cancellation. In some cases, the action of arrays of secondary monopoles has been interpreted in multipole terms, however: see, for example, Refs. 2–4.

Kempton appears to have been the first to suggest the use of a single multipole secondary source for active control of sound radiated into a free field.[5] Kempton showed that within a specified region of convergence, the field of a monopole could be exactly represented as originating at an infinite-order multipole placed at finite distance from the monopole. By inverting the phase of the multipole with respect to the monopole, it is then possible in principle to cancel completely the monopole's sound field in a region exterior to a sphere centered on the secondary source and enclosing the primary source. In our earlier article, it was shown analytically that the sound field of a primary monopole could be canceled effectively by using a finite-order secondary multipole whose various multipole component source strengths were identified from a direct Taylor series expansion of the primary field about the secondary source location.[1] It was shown, in particular, that the attenuation provided by a displaced multipole can be much larger than that afforded by an out-of-phase monopole placed at the same location. Equivalently, a secondary multipole can be placed much further from the primary source than a secondary monopole while delivering the same level of cancellation.

However, in the same article it was also shown that the direct approach suggested by Kempton is not optimal. That is, it was found that significantly greater levels of far-field attenuation could be obtained when the multipole component source strengths were chosen to minimize the sound power radiated by the combination of the primary monopole and the secondary multipole. A similar sound-power minimization procedure was followed earlier by Nelson *et al.* to identify optimal arrays of secondary monopoles.[3,4]

In Ref. 1, formulas for the optimal component strengths of secondary sources truncated at monopole, dipole, quadrupole, and octopole order were given. Those results may seem limited in their application, since few practical noise sources behave like true monopoles. However, it has been shown that sound radiation from complex sources may be modeled as being created by an array of monopole sources notionally located within the actual source.[6] Thus, by linearly superposing the multipole components required to cancel each of the component monopoles, it may be possible to cancel sound radiation from a complex source by using a single, higher-order secondary source.

The objective of the work described in the present article

[a]Present address: Creos Creica, Ingenieurie de la Division des Vehicules Utilitaires RENAULT, Service 5080: Acoustique et Vibrations, 42 route de Beynes, 78640 Villiers St Frederic, France.
[b]Present address: M/S 157-410, Jet Propulsion Laboratory, California Institute of Technology, 4800 Oak Grove Drive, Pasadena, CA 91109-8099.

was to complement the earlier theoretical work by demonstrating experimentally that the field generated by a primary monopole could indeed be canceled either globally or in particular target regions by using a displaced multipole secondary source. The secondary source considered here comprised monopole, dipole, linear quadrupole, and linear octopole elements.

The practical noise sources that have perhaps received the most attention in the context of free-field active control are electrical transformers; their radiated sound fields usually result from core vibration caused by magnetostriction. The latter process generates sound at the line frequency and its harmonics. Conover,[7] Kido,[8] Hesselman,[9] Ross,[10] Jessel and Angevine,[11] Angevine,[12] and Craig and Angevine[13] have all investigated active control of transformer noise. Transformer noise is potentially very susceptible to active control since transformer hum occurs at low frequencies, and because it is tonal and stable. Almost without exception, the secondary sources used to control transformer noise have been monopole-like, and were created by using baffled loudspeakers or equivalent structures. It does not appear that there have been attempts to use multipole sources in this role, although structural actuators have been used to supplement secondary acoustical sources.[14] A number of studies with application to cancellation of free-field radiation from automotive exhaust systems have also been reported: for example, by Davis,[15] Kanai *et al.*,[16] and Hall *et al.*[17] In all those cases, the secondary source comprised one or more secondary monopoles. Thus, it appears that very little effort has been directed towards the direct use of secondary sources of higher than monopole order.

The contents of this article are as follows. The construction, testing, and acoustical characteristics of the secondary multipole elements are described in the first three sections below. Next, the experimental procedures used to conduct the cancellation measurements are described. Then, in the next two sections, the cancellation that can be obtained along a complete circle, or along angular sectors of the plane containing the primary and secondary source, is demonstrated. In the former case the degree of cancellation obtained when the secondary multipole components strengths were determined using a direct Taylor series expansion of the monopole field are compared with the cancellation obtained when the secondary component strengths were calculated using a least-squares approach.

Note that the experiments reported here are intended simply to demonstrate the feasibility of the use of multipole secondary sources in active noise-control applications. The multipole secondary source used in the present experiments was constructed using an array of loudspeakers and was operated in an open-loop manner. In a practical application it would be necessary to devise a more compact secondary source and to operate it adaptively to account for time-varying source, environmental and transducer characteristics.

I. CONSTRUCTION OF MULTIPOLE ELEMENTS

To perform the experiments described here, it was necessary to construct secondary source elements extending to octopole order that conformed to theoretical models of multipole behavior. The construction of those various sources is described in this section. Note that all of the experiments described here were for the case of a pure-tone primary signal at 250 Hz.

The primary and secondary monopoles were identical in their construction. They both comprised a University Sound model 1829 compression driver mounted to a half-wavelength source tube whose exterior diameter was 5 cm and whose inner diameter was 4 cm. These compression drivers were designed to operate at frequencies above 1000 Hz. The half-wavelength tube was thus designed to enhance the output of the driver at 250 Hz; in this way it was not necessary to overload the driver in order to generate acceptably high output levels. It was also anticipated that the tube exit would act more like a monopole than would the driver without a tube attached.

The creation of a dipole was straightforward since unbaffled loudspeakers are known to behave as dipoles when the wavelength of the signal is much longer than the physical dimensions of the loudspeaker. The loudspeaker used to represent the dipole in the present instance was an Infinity RS 2000 having a diaphragm diameter of approximately 15 cm (i.e., approximately 0.1 wavelengths).

The construction of a longitudinal quadrupole entails the use of two unbaffled loudspeakers driven in phase but placed face-to-face. A longitudinal octopole source can then be created from two opposing longitudinal quadrupoles: i.e., four unbaffled loudspeakers are required to create the longitudinal octopole. In order to create sources that conformed as closely as possible to their theoretical models, it was necessary that the four loudspeakers be closely matched in their phase and amplitude responses. The Infinity RS 2000 loudspeakers used in the present work were found to be sufficiently well matched that they could be used without the need for additional amplitude and phase correction.

For the sake of compactness it was decided to create the quadrupole and octopole sources by using a single array of four loudspeakers. That is, the two central loudspeakers of the octopole array were used to represent the quadrupole. The arrangement of the loudspeakers, and the signals that were sent to them, is shown in Fig. 1. The two central loudspeakers, LS 2 and LS 3, were separated by 10 cm while the distance between LS 1 and LS 2, and between LS 3 and LS 4, was 12.5 cm. The latter distance was of necessity different from the distance separating the two central loudspeakers owing to the back-to-back arrangement of the outer loudspeakers.

Summation amplifiers were connected to loudspeakers LS 2 and LS 3. When signal 2 was turned off, signal 1 was fed to loudspeakers LS 2 and LS 3, thus creating the longitudinal quadrupole source. Conversely, when signal 1 was turned off, signal 2 was fed to loudspeakers LS 1 and LS 2 with the same phase while at the same time it was phase-shifted by 180 deg before being delivered to loudspeakers LS 3 and LS 4. Thus, the pair of loudspeakers LS 1 and LS 2 represented one longitudinal quadrupole while the pair of loudspeakers LS 3 and LS 4 represented a second longitudinal quadrupole 180 deg out of phase with the first. When operated together, the two quadrupoles formed a longitudinal

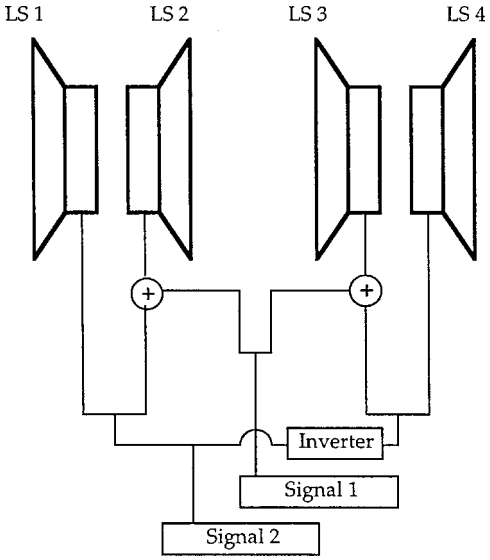

FIG. 1. Arrangement of loudspeakers and signals used for simultaneous operation of longitudinal quadrupole and longitudinal octopole sources.

octopole. Then, by delivering the appropriate signals 1 and 2 it was possible to generate independent quadrupole and octopole sound-pressure fields simultaneously. The procedure used to confirm that the sources described here did indeed conform to their theoretical models is described in the next section.

II. SOURCE CHARACTERIZATION

A. Experimental arrangements

The source characterization setup is shown in Fig. 2. It comprised a Wavetek model 75 signal generator, a Crown 5507 power amplifier, a 12-mm Bruel & Kjaer microphone model 4130, a Bruel & Kjaer microphone preamplifier model 2810, a Krohn–Hite model 6400 phase meter, and a Bruel & Kjaer model 2107 voltmeter. Since all the experiments were performed using a 250-Hz tone, and since there was no evidence of significant nonlinear distortion (even though the responses of the various loudspeakers were found to be slightly nonlinear with respect to input level: see below), no filtering was applied during the tests, thus avoiding the introduction of spurious phase shifts. The phases of all the signals provided to the multipole components were referenced to the output of the signal generator.

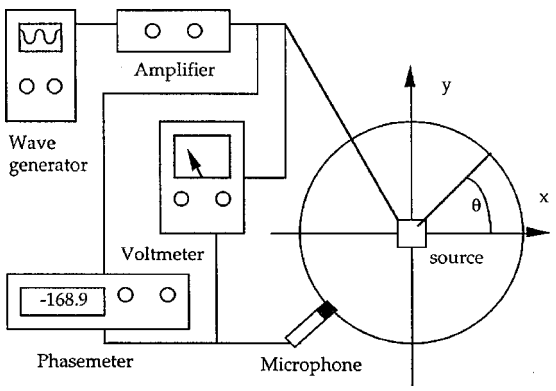

FIG. 2. Experimental arrangement for source characterization measurements.

The source to be characterized in any particular instance was fixed in place at the center of the Ray W. Herrick Laboratories' anechoic chamber: that position represented the coordinate origin. The microphone was mounted facing the source at a radial distance of 1 m from the coordinate origin on a rotating boom that could be moved around the source in a circle on the *x*-*y* plane. Measurements made at one circumferential position were used to determine the source strength of each multipole component; to determine the directivity of the sources, the microphone output voltage was measured at increments of 30 deg around the 1-m-radius circle centered on the source while a constant amplitude input voltage was provided to the latter. Note that the microphone output voltage, v_m, was converted to a sound pressure by the use of an appropriate calibration factor: i.e., $P=20\times10^{-6}$ (v_m/Cal) (Pa) where v_m was the rms microphone output value and Cal was 0.77 volts/Pa for the microphone and signal-conditioning equipment used in the experiments reported here.

When determining the primary and secondary monopole source strengths, the source tube exits were placed at the origin of the *x*-*y* coordinate system, the length of the tube being placed in the *z* direction: i.e., perpendicular to the *x*-*y* plane. The center of the diaphragm of the loudspeaker used to represent the dipole was placed at the origin of the *x*-*y* coordinate system, and the diaphragm was placed perpendicular to the *x* axis so that its front surface faced in the positive *x* direction. When the quadrupole/octopole array was tested, it was positioned so that its longitudinal axis coincided with the *x* axis and so that the coordinate origin lay on the array's longitudinal axis at a point midway between the central pair of loudspeakers.

B. Source models

Theoretical expressions for the sound fields radiated by the primary and secondary monopole sources are given here as Eqs. (1) and (2): the corresponding expressions for the secondary dipole, quadrupole, and octopole fields are given in Eqs. (3) to (5), respectively

$$P_{\mathrm{pm}}=j\omega\rho\frac{Q_{\mathrm{pm}}}{4\pi}\frac{e^{-jkr_h}}{r_h}, \tag{1}$$

$$P_{\mathrm{sm}}=j\omega\rho\frac{Q_{\mathrm{sm}}}{4\pi}\frac{e^{-jkr}}{r}, \tag{2}$$

$$P_{\mathrm{sd}}=\omega\rho k\frac{Q_{\mathrm{sd}}}{4\pi}\cos\theta\left(1+\frac{1}{jkr}\right)\frac{e^{-jkr}}{r}, \tag{3}$$

$$P_{\mathrm{sq}}=-\omega\rho k^2\frac{Q_{\mathrm{sq}}}{4\pi}\left[\left(1+\frac{3}{jkr}+\frac{3}{(jkr)^2}\right)\cos^2\theta-\left(\frac{1}{jkr}+\frac{1}{(jkr)^2}\right)\right]\frac{e^{-jkr}}{r}, \tag{4}$$

TABLE I. Experimentally determined polynomial coefficients characterizing primary and secondary source strengths in Eq. (6).

Source	a_1	a_2	b_0	b_1	b_2
Q_{pm}	4.25×10^{-4}	-2.75×10^{-5}	1.69π	1.77×10^{-1}	-1.61×10^{-2}
Q_{sm}	4.88×10^{-4}	-3.56×10^{-5}	1.69π	1.54×10^{-1}	-1.34×10^{-2}
Q_{sd}	4.38×10^{-5}	-1.02×10^{-6}	2.40π	⋯	⋯
Q_{sq}	4.28×10^{-6}	-1.17×10^{-7}	-0.47π	⋯	⋯
Q_{so}	1.60×10^{-6}	-3.64×10^{-8}	0.45π	⋯	⋯

$$P_{so}=-\omega\rho k^3\frac{Q_{so}}{4\pi}\left[\left(1+\frac{6}{jkr}+\frac{15}{(jkr)^2}+\frac{15}{(jkr)^3}\right)\cos^3\theta-\left(\frac{3}{jkr}+\frac{9}{(jkr)^2}+\frac{9}{(jkr)^3}\right)\cos\theta\right]\frac{e^{-jkr}}{r}. \quad (5)$$

Note that near-field forms of the multipole component sound fields were used, since as a matter of practical necessity the experimental measurements were not made sufficiently far from the various sources to be considered in the far field: i.e., the measurement circle had a radius of approximately three-quarters of a wavelength. In Eqs. (1) to (5), Q_{pm}, Q_{sm}, Q_{sd}, Q_{sq}, and Q_{so} are the source strengths of the primary monopole, the secondary monopole, the secondary dipole, the secondary quadrupole, and the secondary octopole, respectively. The quantity r_h is the distance from the primary monopole to the observation point, and $r_h=[(h+r\cos\theta)^2+(r\sin\theta)^2]^{1/2}$ where h is the displacement of the primary source from the coordinate origin in the negative x direction, θ is the angle from the positive x axis as shown in Fig. 2, and $r=[x^2+y^2]^{1/2}$ is the distance from the coordinate origin to the observation point in the x-y plane. Note that during the source characterization measurements, h was set to zero: i.e., the primary monopole was placed at the coordinate origin. Finally, ρ is the ambient fluid density (here air), k is the wave number in the ambient fluid (equal to ω/c where ω is the circular frequency and c is the ambient sound speed) and $j=-1^{1/2}$.

C. Determination of component source strengths

To perform an open-loop cancellation of the sound field radiated by a primary monopole whose source strength, Q_{pm}, is known, it is necessary to be able to specify the source strengths of the primary and the various secondary sources, i.e., the Qs in Eqs. (2) to (5), in terms of their input voltages. For that purpose, the microphone was positioned at $r=1$ m, $\theta=0$ deg, and the microphone output level and phase were measured when ten different input voltage levels were applied to each of the sources in turn. At each input level, the microphone output voltage was converted to a sound pressure. Then, the appropriate one of Eqs. (1) to (5) was used to determine the source strength at each input level. Since all of the sources were found to be slightly nonlinear in their response, it was convenient to express their source strengths in the form

$$Q=(a_1v+a_2v^2)e^{j(b_0+b_1v+b_2v^2)}, \quad (6)$$

where v is the applied voltage. The values of the a's and b's in the latter equation were determined by performing a least-squares fit to the source strength vs input voltage data: the results for the various sources are given in Table I.

Note that the phase responses of both the primary and secondary monopoles were nonlinear: i.e., b_1 and b_2 in Eq. (6) were observed to be nonzero. The latter effect may have resulted from nonlinearities either of the compression driver itself (which was operated at a frequency well below its nominal range), or may have resulted from the relatively high velocity fluid motion in the vicinity of the source tube exit. In contrast, the phase responses of the dipole, quadrupole, and octopole secondary sources were not found to depend on input level: i.e., in each case b_1 and b_2 were found to be negligibly small.

In the next section, the measured and predicted sound fields radiated by the primary and secondary sources are compared. It will be seen that, with a few exceptions, there was excellent agreement between the theoretical multipole component models and the experimental realizations of those sources.

III. COMPARISON OF MEASURED AND PREDICTED SOURCE LEVELS AND DIRECTIVITIES

Equations (1) to (5) can be used in conjunction with Eq. (6) and the data of Table I to predict the sound-pressure levels and phases of the fields radiated by the various sources as a function of observation position and input voltage. By comparing the measured and predicted sound levels and phases on a 1-m-radius circle around the sources, it was found that the various sources were consistent with the appropriate theoretical models: see Fig. 3. In Fig. 3 the measured data are shown as dots, while the theoretical predictions are plotted as solid lines.

The results for the primary monopole at an input voltage of 2 V rms are shown in Fig. 3(a). It can be seen that there is good agreement between predictions and measurements. The slight deviation of the measured phase from its ideal value may have resulted from the source not being perfectly centered with respect to the measurement circle. In addition, there was perhaps a ±12-mm uncertainty in the radius at each angle, which would result in a phase uncertainty of ±3.3 deg at 250 Hz. It can be seen that the phase discrepancy lies within that bound. The agreement between the predicted and measured phase- and sound-pressure levels for the secondary monopole was similar to that for the primary monopole, and those results are not presented here.

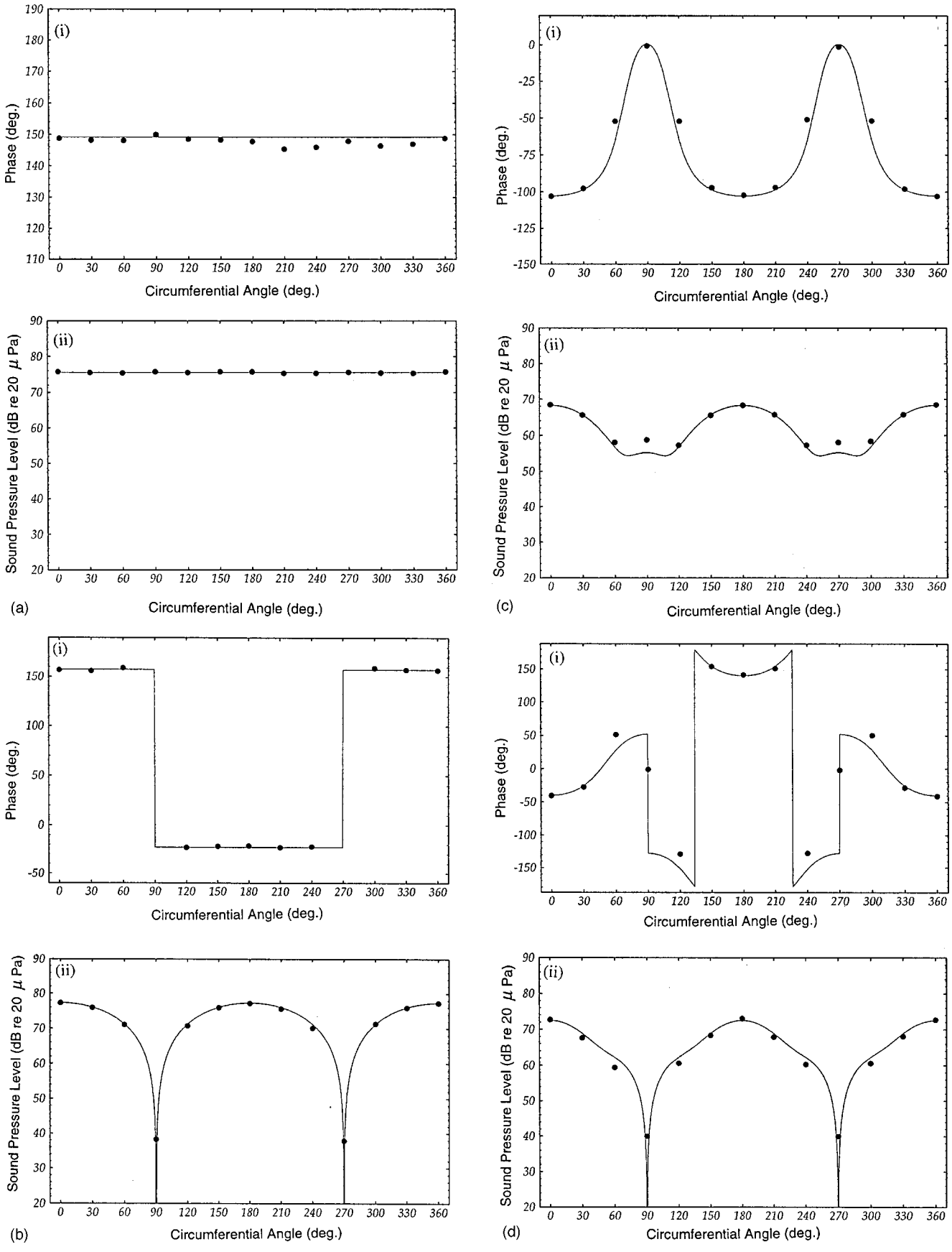

FIG. 3. (i) Phase and (ii) sound-pressure level at 250 Hz vs circumferential angle on a 1-m-radius circle centered on the origin. Dots: measurements; solid line: predictions. (a) Primary monopole; (b) secondary dipole; (c) secondary quadrupole; and (d) secondary octopole.

The results for the secondary dipole operated at an input voltage of 5 V rms are shown in Fig. 3(b). Note that in this case the phase of the microphone signal could not be measured accurately at the angle 90 and 270 deg since the microphone voltage at those positions was very small. At those angles, the dipole seemed to manifest a small monopole component since the sound pressure did not go exactly to zero. It was not clear in the first instance whether the loudspeaker was truly displaying a monopole component, or whether the result was nonzero because the pressure gradient (as a function of θ) was so large near those angles: i.e., the minimum region is very narrow. Even at 1 m from the source, a 12-mm-diameter microphone may be too large to distinguish the zero-pressure plane of a dipole-like source. The depth of the minima at 90 and 270 deg may also have been limited by electronic and ambient noise levels; see Secs. V and VI below. Nonetheless, for practical purposes the source was judged to behave like a ''true'' dipole with respect to both sound pressure and phase.

The quadrupole results for a 4 V rms input are shown in Fig. 3(c). Once again, good agreement was found between measurements and predictions except for slight discrepancies in levels near the minima at 90 and 270 deg. It was therefore judged that for practical purposes the source behaved like a true longitudinal quadrupole.

Finally, the secondary octopole results for a 4 V rms input are shown in Fig. 3(d). There was generally good agreement between measured and predicted levels, but it can be seen that at the angles of 60, 120, 240, and 300 deg the measured phases do not correspond precisely to their predicted values. This effect may have resulted from diffraction from the edges of the two central loudspeakers. If one draws cones having their vertices at the axial center of the loudspeaker array and having their surfaces tangent to the edges of the central loudspeakers, the half angle of that cone is approximately 60 deg. Hence, it seems possible that the phase distortion at those angles originated in diffraction from the loudspeaker edges.

Note that if it had been assumed that the four loudspeakers used to build the quadrupole and the octopole were identical with one another, and to the one used to represent the dipole, it would have been possible to estimate the source strengths of the quadrupole and octopole without performing any measurements. That is, it would be enough to know the dipole strength of any single loudspeaker and the distance between the various loudspeakers in the array. For example, since the two central loudspeakers were separated by 0.10 m, the source strength of the quadrupole they simulate could have been approximated as the product of their separation distance and the dipole source strength of the individual loudspeakers. In fact, when Q_{sd} is multiplied by 0.10 m, the result is close to the experimentally determined value of Q_{sq}. The octopole comprises two quadrupoles that are separated by a center-to-center distance of 0.225 m. Each of the quadrupoles in turn is composed of two dipoles separated by 0.125 m. Therefore, the source strengths of each quadrupole could be approximated as $0.125Q_{\mathrm{sd}}$, and the source strength of the octopole could in turn be approximated as $(0.225 \times 0.125)Q_{\mathrm{sd}}$. Those approximations match well with the source strengths that were estimated directly from the measurements. The latter observation thus helps to confirm that the various sources conformed closely to their theoretical models.

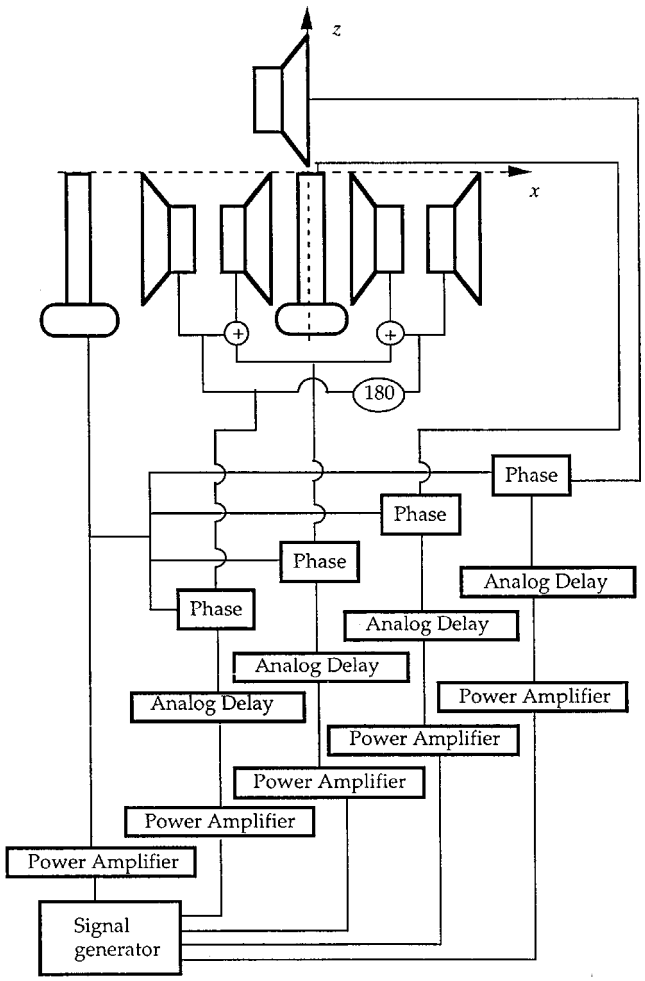

FIG. 4. Schematic of primary and secondary source arrangements and of signal paths used to conduct cancellation measurements.

IV. EXPERIMENTAL PROCEDURES FOR CANCELLATION MEASUREMENTS

Next, it was of interest to establish the degree of cancellation that could be achieved in practice by using a multipole secondary source. Recall that here we are concerned only with the open-loop cancellation of a monopole sound field by the use of a displaced multipole source. The experimental apparatus used to perform the cancellation measurements is described in this section.

A schematic representation of the experimental apparatus is shown in Fig. 4. The figure also illustrates the loudspeaker arrangement that was adopted so that the secondary source was as compact as possible. It can be seen that the secondary monopole source tube was run through the middle of the quadrupole/octopole loudspeaker array, and that the source tube exit was placed at the origin of the coordinate system. The quadrupole/octopole array was itself positioned below the *x-y* plane so that the top of the loudspeakers were tangent with the *x-y* plane. In this arrangement, the longitu-

TABLE II. Global cancellation: direct approach. Secondary source parameters and cancellation performance.

Secondary source component	Component source strength	Component source strength magnitude	Applied voltage (rms V)	Phase shift (radians)	Average attenuation measured on 1-m-radius circle (dB)	Estimated sound-power-level reduction (dB)
Q_{sm}	$-Q_{pm}$	3.975×10^{-4}	0.86	1.014π	4.9	3.3
Q_{sd}	$-hQ_{pm}$	1.073×10^{-4}	2.61	0.345π	10.5	9.6
Q_{sq}	$-(h^2/2)Q_{pm}$	1.448×10^{-5}	3.77	1.215π	19.4	18.7
Q_{so}	$-(h^3/3!)Q_{pm}$	1.304×10^{-6}	0.83	0.295π	25.4	29.9

dinal axis of the loudspeaker array was 7.5 cm below and parallel with the x axis. The single unbaffled loudspeaker representing the secondary dipole was placed immediately above the secondary monopole, its lower edge being 2 cm above the secondary monopole source tube exit. The center of the loudspeaker diaphragm was therefore 9.5 cm above the x-y plane. The loudspeaker's diaphragm was positioned in the y-z plane, facing in the positive x direction. The exit of the primary monopole source tube was positioned at $x=-0.27$ m, $y=0$, $z=0$ for the global cancellation experiments described in Sec. V, and at $x=-0.20$ m, $y=0$, $z=0$ for the sector cancellation experiments described in Sec. VI.

A 250-Hz sinusoidal signal was used in all the experiments reported here. Thus, the primary and secondary sources were separated by a distance of approximately 0.2 wavelengths in the case of the global cancellation experiments. A single signal source was used to drive all of the acoustical sources so as to avoid spurious phase differences between the signals sent to the various sources. The amplitude of the sine wave fed to the primary source was 1 V rms during the global cancellation experiments and 2 V rms during the sector cancellation experiments. Knowledge of that input voltage makes it possible to calculate the primary source strength by the use of Eq. (6). The secondary source strengths were then calculated using procedures described in the next section. Finally, the corresponding input voltages and phase angles were found by using Eq. (6) in combination with the source strength data of Table I. The signals delivered to the secondary sources were amplified or attenuated as appropriate and phase-shifted with respect to the signal sent to the primary monopole, the latter signal serving as the phase reference in all cases.

V. GLOBAL CANCELLATION EXPERIMENTS

A. Cancellation procedures

When the primary monopole source strength is known, it is possible to use several approaches to calculate the secondary source strengths required to achieve cancellation. In a previous article,[1] the relative efficacy of two approaches were compared: the ''direct'' approach and an approach in which the sound power radiated by the combination of the primary and secondary sources was minimized.

In the direct approach, the secondary source strengths are identified from a Taylor series expansion of the primary monopole sound field about the location of the secondary multipole. Each term in that series expansion represents the contribution of a multipole component. When the primary source displacement is in the direction of one of the coordinate axes, the nonzero terms comprise a monopole, a dipole, a longitudinal quadrupole, a longitudinal octopole, etc., the higher-order terms having their axes aligned with the coordinate axis. Thus, by positioning an appropriately weighted multipole source at the expansion point, and inverting its phase with respect to the primary monopole, cancellation of the latter's field may be achieved.

However, it was shown in the earlier paper that an approach in which the strengths of the secondary multipole components were chosen to minimize the total sound power radiated by the primary and secondary sources resulted in greater far-field attenuation than did the direct approach. It was also noted that in the optimal case all of the secondary source components were 180 deg out of phase with respect to the primary source.[1]

Here, an approach that differed slightly from the latter one was adopted owing to the nature of the present experimental arrangements. In particular, secondary source strengths were chosen to match the primary sound field as closely as possible in a least-squares sense at a number of discrete points distributed along a 1-m-radius circle centered on the secondary source array. The phases of the various secondary source components were then inverted to cancel the primary field. Note that owing to the cylindrical symmetry of the arrangement considered here, the latter approach also ensures global (although not quite optimal) reduction of the radiated sound power.

B. Cancellation by the direct approach

When a Taylor series expansion of the primary monopole sound-pressure field (the primary monopole having a source strength Q_{pm} and being placed at $-h$ on the x axis) is performed, it is found that the secondary monopole source strength should be equal to the primary's in magnitude and opposite in phase to achieve control: i.e., $Q_{sm}=-Q_{pm}$. Recall that the secondary source is placed at the coordinate origin, so that h is also the separation between the primary and secondary sources. From the Taylor series expansion, it is also found that the secondary dipole source strength should be $Q_{sd}=-hQ_{pm}$, that the secondary quadrupole source strength should be $Q_{sq}=-(h^2/2)Q_{pm}$, and that the secondary octopole source strength should be $Q_{so}=-(h^3/3!)Q_{pm}$: these results are summarized in Table II.

When a 250-Hz sinusoid of 1 V rms was delivered to the primary source, the resulting primary monopole source

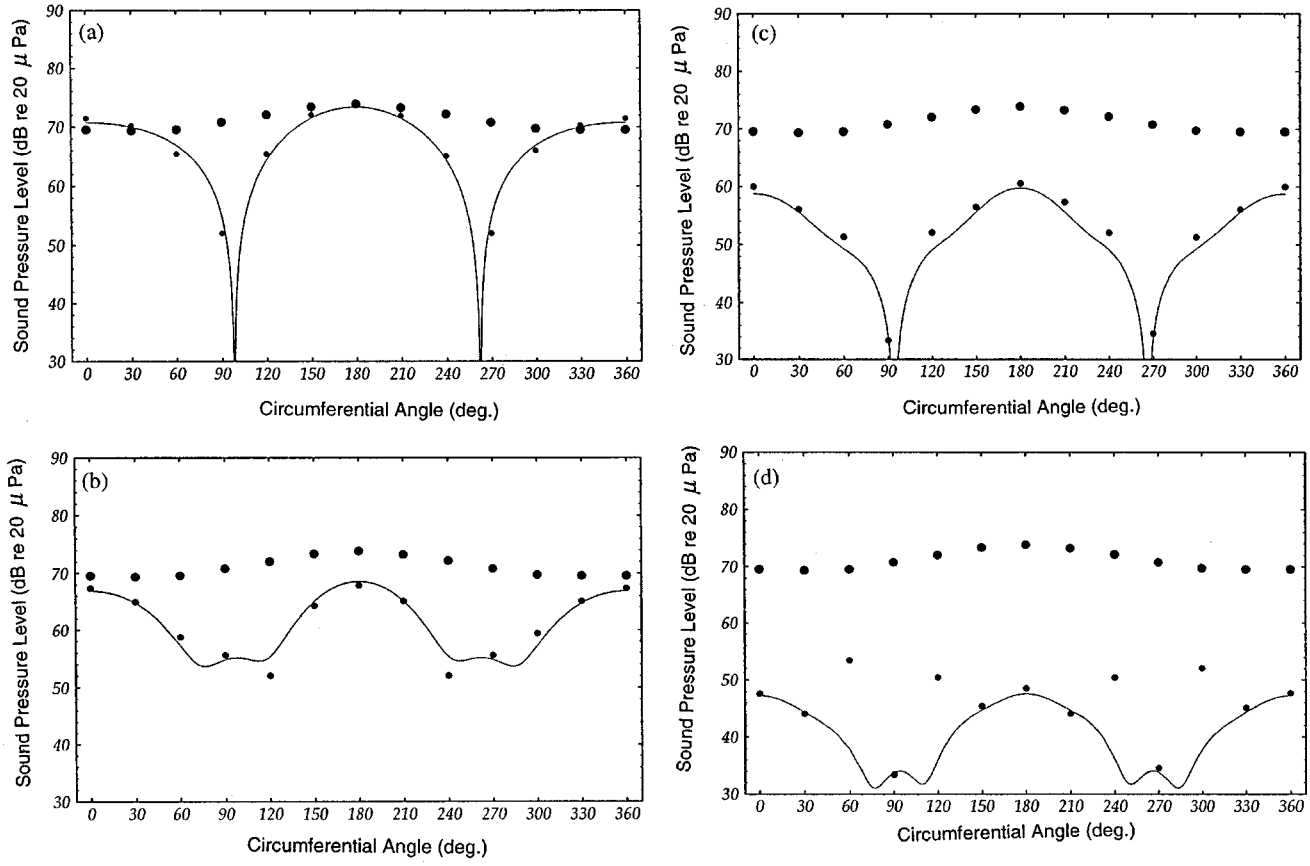

FIG. 5. Cancellation by the direct approach: $f=250$ Hz, $h=0.27$ m. Sound-pressure level vs circumferential angle on a 1-m-radius circle centered on the origin. Large dots: measured primary sound field; small dots: measured primary plus secondary sound field; solid line: prediction. Secondary source: (a) monopole; (b) monopole and dipole; (c) monopole, dipole, and quadrupole; (d) monopole, dipole, quadrupole, and octopole.

strength was $Q_{\mathrm{pm}}=3.975\times10^{-4}e^{j1.745\pi}$ m^3/s. The corresponding secondary multipole component source strengths are listed in Table II along with the matching source voltages and phase shifts required to achieve the specified component source strength and to ensure that each secondary source was operated 180 deg out of phase with respect to the primary source.

The calculated parameters were implanted using the experimental apparatus shown in Fig. 4, and the attenuations that were achieved by using progressively higher-order secondary sources are illustrated in Fig. 5. In Fig. 5 the larger dots represent the measured sound-pressure levels before control, the smaller dots the measured sound-pressure levels after control, and the solid line the predictions that were made based on the direct approach. The measured, space-averaged attenuation of the primary field sound-pressure level achieved in each case is also listed in Table II, along with estimates of the corresponding sound-power-level reductions (see below).

In Fig. 5(a) it can be seen that there was good agreement between the predicted and measured cancellation when the secondary monopole was operated. Note that the action of the secondary monopole was to cause the residual sound field to resemble that of a dipole: compare Figs. 3(b) and 5(a). The attenuation averaged along the measurement circle was found to be 4.9 dB. Note also that there was a slight reinforcement of the level in the region from 330 to 30 deg, i.e., on the opposite side of the secondary source from the primary source.

The results obtained when the secondary dipole was added are shown in Fig. 5(b). Again, there was good agreement between the predictions and measurements. In this case

TABLE III. Global cancellation: least-mean-square fitting procedure, monopole and dipole cases. Secondary source parameters and cancellation performance.

Secondary source component	Component source strength magnitude	Applied voltage (rms V)	Phase shift (radians)	Average attenuation measured on 1-m-radius circle (dB)	Estimated sound-power-level reduction (dB)	Maximum possible sound-power-level reduction (dB)
Q_{sm}	2.653×10^{-4}	0.57	1.027π	3.9	3.7	3.8
Q_{sd}	0.898×10^{-4}	2.15	0.395π	13.6	12.7	13.6

TABLE IV. Global cancellation: least-mean-square fitting procedure, quadrupole case. Secondary source parameters and cancellation performance.

Secondary source component	Component source strength magnitude	Applied voltage (rms V)	Phase shift (radians)	Average attenuation measured on 1-m-radius circle (dB)	Estimated sound-power-level reduction (dB)	Maximum possible sound-power-level reduction (dB)
Q_{sm}	3.941×10^{-4}	0.86	1.210π	⋯	⋯	⋯
Q_{sd}	0.898×10^{-4}	2.15	0.395π	⋯	⋯	⋯
Q_{sq}	1.298×10^{-5}	3.29	1.255π	28.3	26.7	27.1

the residual field approximates that of a longitudinal quadrupole: compare Figs. 3(c) and 5(b). The attenuation averaged along the measurement circle was found to be 10.5 dB in this case: i.e., 5.6 dB more than was obtained when using a single secondary monopole.

When the quadrupole secondary source was added, the cancellation shown in Fig. 5(c) was obtained. The measurements agree well with the predictions, and the residual field resembled that of a longitudinal octopole: compare Figs. 3(d) and 5(c). The spatially averaged attenuation was found to be 19.4 dB, i.e., 8.9 dB more than that obtained when using a secondary source comprising a monopole and a dipole.

Finally, the secondary octopole was added: the resulting cancellation is shown in Fig. 5(d). In this case there was generally good agreement between measurement and prediction except at 60, 120, 240, and 300 deg where problems possibly arising from diffraction around the edges of the loudspeakers may have interfered with the cancellation process. At those angles the cancellation was not as great as predicted but was nonetheless quite large. The measured spatially averaged attenuation was 25.4 dB in this case, i.e., 6.0 dB more than that obtained using a quadrupole order secondary source. In theory the spatially averaged attenuation would have been 29.5 dB had problems not occurred at 60, 120, 240, and 300 deg.

Listed in the last column of Table II are the sound-power-level reductions expected when using the direct approach. The sound-power-level reduction in this case is a function of the nondimensional primary–secondary source separation distance, kh, and the secondary multipole truncation order only. The sound-power-level reductions were calculated using Eq. (44) of Sec. IV A of Ref. 1. It may be seen that even though the 1-m-radius measurement circle was not strictly in the far field of the source, the value of the sound-pressure-level reduction when averaged around the circle was within approximately 1 decibel of the predicted sound-power-level reduction (except in the octopole case, for the reasons discussed above), presumably because of the cylindrical symmetry of the experimental geometry.

In summary, the results presented in this subsection show that the degree of cancellation predicted by using the direct approach can, within reason, be achieved in practice. Note also that the action of adding each progressively higher multipole component causes the residual sound-pressure field to approximate that of the next higher multipole order as noted by Kempton.[5] Finally, as a consequence of the latter effect, note that there are rather large variations in the degree of cancellation as a function of circumferential angle, i.e., the cancellation is much larger in some directions than in others. The latter behavior, which was also demonstrated using theoretical calculations in Ref. 1, contrasts in some instances with the spatial character of the attenuation that can be achieved when using the least-mean-square fitting procedure, to be considered next.

C. Cancellation by a least-mean-square fitting procedure

In this subsection a least-mean-squares fitting procedure for identifying component multipole secondary source strengths up to octopole order is presented. Here, the objective was to cancel along a 1-m-radius circle centered on the coordinate origin the sound field that was created by a primary monopole placed at $-h$ on the x axis. As before, the primary monopole was operated at 1 V rms, and the primary source was placed at $x=-0.27$ m. The approach followed

TABLE V. Global cancellation: least-mean-square fitting procedure, octopole case. Secondary source parameters and cancellation performance.

Secondary source component	Component source strength magnitude	Applied voltage (rms V)	Phase shift (radians)	Average attenuation measured on 1-m-radius circle (dB)	Estimated sound-power-level reduction (dB)	Maximum possible sound-power-level reduction (dB)
Q_{sm}	3.941×10^{-4}	0.86	1.210π	⋯	⋯	⋯
Q_{sd}	1.070×10^{-4}	2.60	0.378π	⋯	⋯	⋯
Q_{sq}	1.298×10^{-5}	3.29	1.255π	⋯	⋯	⋯
Q_{so}	1.210×10^{-6}	0.77	0.327π	42.5[a]	43.0	43.1

[a]Theoretical prediction (see the text).

here was to identify the multipole component strengths required to most nearly replicate (in a least-squares sense) the primary sound field on the 1-m-radius circle. After having identified the complex source strengths in this way, their phases were inverted to achieve cancellation.

The least-mean-squares approach can be expressed most compactly in terms of the following vectors and matrices. Let Y be the vector of complex sound pressures at $r=1$ m and at a number of different angles encircling the source (here denoted θ_i). Note that, when the primary monopole source strength is known, it is possible to calculate each component of the Y vector by using Eq. (1). The columns of the matrix A comprise the field components contributed by the unit amplitude elements of the multipole source, i.e., the monopole, dipole, quadrupole, or octopole sound pressures: these terms were calculated using normalized versions of Eqs. (2) to (5). Finally, X is the vector comprising the secondary source strengths, i.e., Q_{sm}, Q_{sd}, Q_{sq}, Q_{so}, respectively. In explicit form

$$Y^T=[P_{\mathrm{pm}}(\theta_1),P_{\mathrm{pm}}(\theta_2),\ldots,P_{\mathrm{pm}}(\theta_n)], \tag{7}$$

$$A=\begin{bmatrix} \frac{P_{\mathrm{sm}}(\theta_1)}{Q_{\mathrm{sm}}}, \frac{P_{\mathrm{sd}}(\theta_1)}{Q_{\mathrm{sd}}}, \frac{P_{\mathrm{sq}}(\theta_1)}{Q_{\mathrm{sq}}}, \frac{P_{\mathrm{so}}(\theta_1)}{Q_{\mathrm{so}}} \\ \frac{P_{\mathrm{sm}}(\theta_2)}{Q_{\mathrm{sm}}}, \frac{P_{\mathrm{sd}}(\theta_2)}{Q_{\mathrm{sd}}}, \frac{P_{\mathrm{sq}}(\theta_2)}{Q_{\mathrm{sq}}}, \frac{P_{\mathrm{so}}(\theta_2)}{Q_{\mathrm{so}}} \\ \cdots \\ \frac{P_{\mathrm{sm}}(\theta_n)}{Q_{\mathrm{sm}}}, \frac{P_{\mathrm{sd}}(\theta_n)}{Q_{\mathrm{sd}}}, \frac{P_{\mathrm{sq}}(\theta_n)}{Q_{\mathrm{sq}}}, \frac{P_{\mathrm{so}}(\theta_n)}{Q_{\mathrm{so}}} \end{bmatrix}, \tag{8}$$

$$X^T=[Q_{\mathrm{sm}},Q_{\mathrm{sd}},Q_{\mathrm{sq}},Q_{\mathrm{so}}]. \tag{9}$$

The secondary multipole component strengths that result in the sound field that most nearly replicates the primary sound field is then

$$X=(A^{\mathrm{HT}}A)^{-1}A^{\mathrm{HT}}Y, \tag{10}$$

where A^{HT} denotes the Hermitian transpose of A. Cancellation is then obtained by inverting the phase of the multipole components.

Here, the least-mean-square fitting procedure was based on the complex sound pressure evaluated at 24 equally spaced points around the 1-m-radius circle, i.e., at 15-deg intervals. The secondary source parameters required to implement this procedure for various secondary source orders are given in Tables III–V, and the resulting measured and predicted cancellations are shown in Fig. 6. Also listed in Tables III–V are the sound-pressure-level attenuations averaged along the 1-m-radius circle, the estimated sound-power-level reductions based on the secondary component source strengths determined in the various cases [calculated using Eqs. (18), (23), (26), and (30) of Ref. 1], and the maximum possible sound-power-level reduction [calculated using Eqs. (48), (50), (52), and (53) of Ref. 1]. [Note that there is a misprint in Eq. (30) of Ref. 1: the last term within the square brackets should be proportional to k^4, not k^3.] Note also that the phase delays listed in Tables III–V are as implemented during the experiments. It was necessary to adjust the phase delays slightly from their nominal values to achieve maximum attenuation (as measured at 0 deg). It was necessary to increase the phase shift by approximately 10 deg to achieve maximum attenuation. This effect may have resulted from temperature variations during the experiments (hence changing the sound speed) or from a slight change of the primary source characteristics between the time that the source characterization and least-squares cancellation measurements were performed.

When a single secondary monopole was used, the secondary monopole source parameters were as given in the first row of Table I. Note that the secondary monopole source strength was approximately two-thirds of that determined by using the direct approach. The resulting cancellation is shown in Fig. 6(a), where it can be seen that there is good agreement between measured and predicted results. In contrast with the result of the direct approach in the monopole case, the residual sound-pressure field is not similar to that of a dipole: instead, the residual sound field exhibits a smaller angular variation than before; compare with Fig. 5(a). The latter effect has been noted previously.[1] The attenuation averaged over the measurement circle in this case was 3.9 dB. That attenuation was less than that resulting from an application of the direct approach. However, at no point was the sound field reinforced by the secondary source: that is the major improvement resulting from the application of the least-mean-square approach in the monopole case.

When a secondary source comprising a monopole and a dipole was considered, the source parameters were those given in the complete Table III. Note that the monopole source strength is unchanged from the previous case since there is no interaction between the monopole and the dipole: that point has been discussed previously.[1] The cancellation results in this case are shown in Fig. 6(b), where it can be seen that the measured results are in good agreement with the predictions and that there is a net improvement in performance compared with the direct approach [compare to Fig. 5(b)]. The spatially averaged attenuation in this case was 13.6 dB, i.e., 3.1 dB more than the attenuation achieved by using the direct approach.

Next, the quadrupole component was added to the secondary source. Since the monopole and quadrupole components can interact,[1] the optimal value of the former component is different than in the previous two cases. However, the dipole and quadrupole components are independent, so the dipole strength is unchanged. The secondary source parameters in this case are given in Table IV and the resulting cancellation is shown in Fig. 6(c). The spatially averaged attenuation in this case was 28.3 dB, which is 8.9 dB more than that obtained using the direct approach; compare with Fig. 5(c). There was again good agreement between predictions and measurements, and the spatial variance of the sound-pressure level is arguably smaller in this case than in the direct case [compare with Fig. 5(c)].

When the octopole component is added, the monopole and quadrupole source strengths do not change compared with the last case, but the dipole component does since the dipole can interact with the octopole.[1] The secondary source parameters in this case are given in Table V and the predicted cancellation is shown in Fig. 6(d). Unfortunately, it

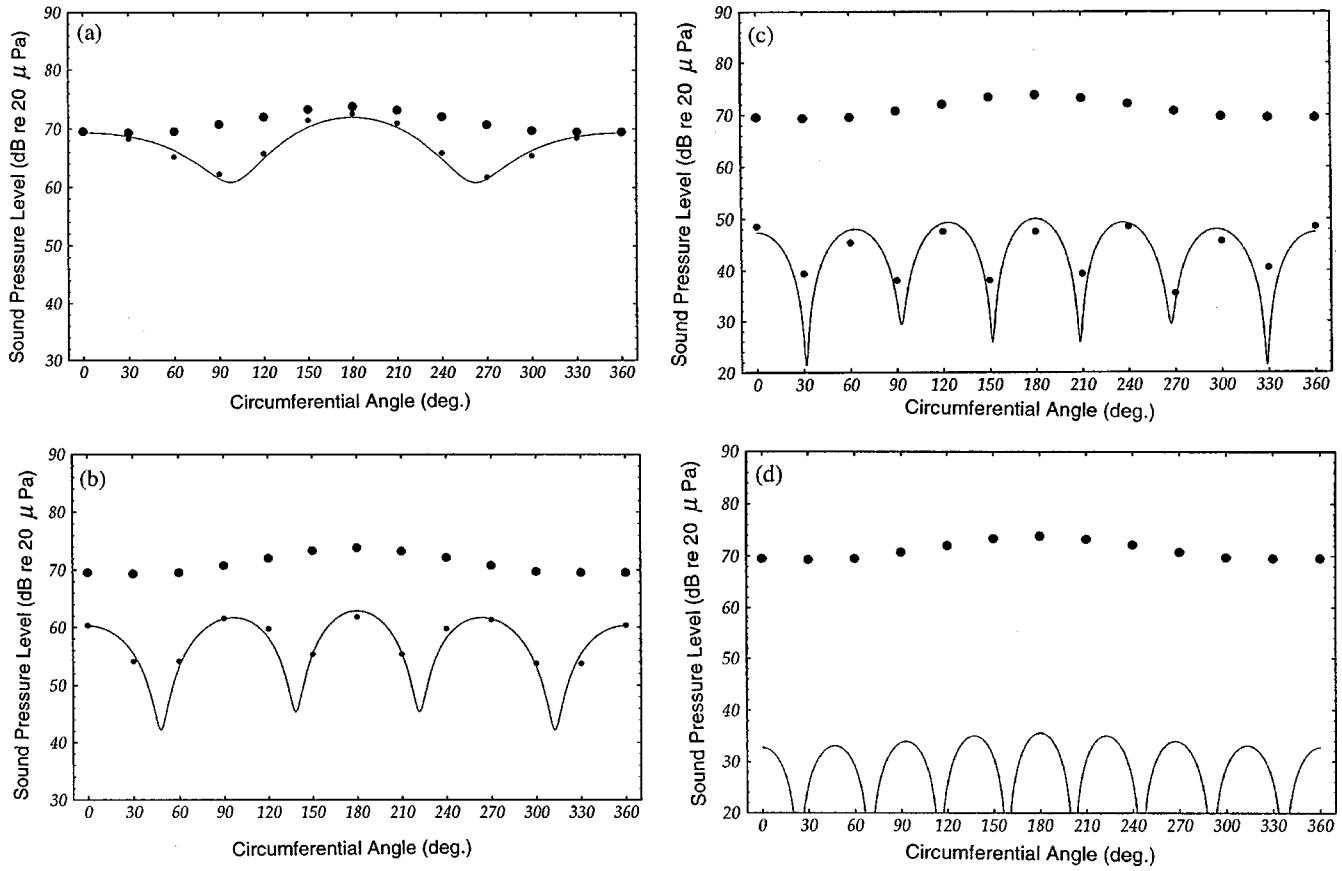

FIG. 6. Cancellation by the least-mean-square fitting procedure: $f=250$ Hz, $h=0.27$ m. Sound-pressure level vs circumferential angle on a 1-m-radius circle centered on the origin. Large dots: measured primary sound field; small dots: measured primary plus secondary sound field; solid line: prediction. Secondary source: (a) monopole; (b) monopole and dipole; (c) monopole, dipole, and quadrupole; (d) monopole, dipole, quadrupole, and octopole.

was not possible to make accurate measurements of the cancellation in this case since the sound-pressure levels after cancellation were comparable with the ambient background and the electronic noise levels. Nonetheless, the cancellation was judged to be effective from a subjective point of view, since the 250-Hz tone became inaudible when the secondary source to octopole order was operated using the parameters of Table V. The spatially averaged attenuation was predicted to be 42.5 dB for this case; that is, 13.0 dB more than the attenuation predicted in the corresponding direct case; compare with Fig. 5(d).

In all the cases considered here, control was strictly achieved only on the circle of 1-m radius centered on the secondary source. However, owing to the cylindrical symmetry of the experimental arrangement, it is to be expected that similar levels of control were achieved over the whole sphere surrounding the source. Note that the minimization of sound pressure at equally spaced discrete points along a circle, as here, does not necessarily result in minimization of total radiated sound power owing both to the fact that the sound pressures on which the fitting procedure were based were not in the far field of the secondary source, and to the fact that a spherical area weighting was not applied to the sound pressures on the 1-m circle as would have been the case in a sound-power minimization. However, the measured, space-averaged sound-pressure-level reductions were in fact very close both to the estimated sound-power-level reductions in each case (based on the secondary source component strengths required to optimally match the sound pressure on the 1-m-radius circle), and to the maximum possible sound-power-level reduction given the nondimensional primary-to-secondary source separation and the secondary source truncation order; see the final three columns in Tables III–V.

The results presented in this subsection suggest that it is thus possible to achieve higher levels of both sound-pressure and sound-power reduction by using a least-mean-squares procedure than by using the direct approach. The results also suggest that the spatial variation of the residual sound field is less marked in the former case than in the latter.

Note that it is also possible to use the approach described in this subsection to achieve control in specific regions of space: for example, to reduce sound radiation into particularly sensitive angular sectors. The next section is devoted to a discussion of sector cancellation by the use of the least-mean-squares method.

VI. SECTOR CANCELLATION BY THE LEAST-MEAN-SQUARE FITTING PROCEDURE

In this section, cancellation results obtained for the two regions shown in Fig. 7 are presented. The two angular sectors of interest were sector 1 extending from −60 to 60 deg, and sector 2, extending from 120 to 240 deg, both sectors lying on a 1-m-radius circle centered on the coordinate ori-

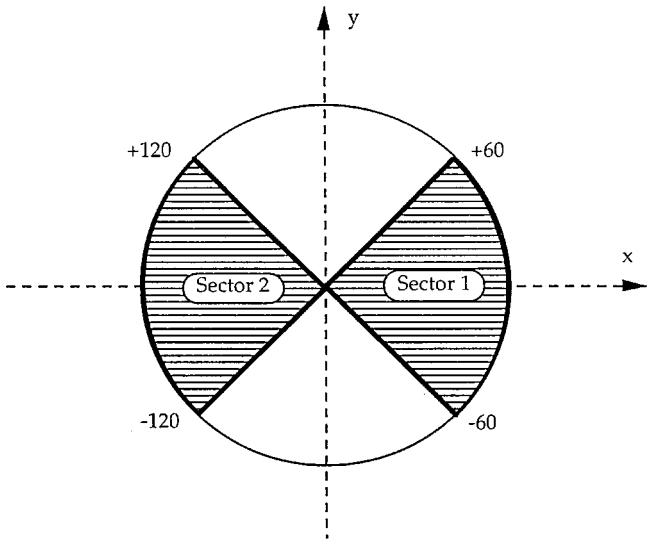

FIG. 7. Definition of cancellation sectors 1 and 2.

gin. Note that in the case of sector 1, the secondary source lies between the primary source and the region of control, while in the sector 2 case the secondary source and the region of control lie on opposite sides of the primary source. The cancellation was performed by using a secondary source comprising a monopole, a dipole, and a quadrupole, and the least-mean-square fitting procedure described in Sec. V C was used to calculate the required secondary source strengths.

Once again, a 250-Hz signal was used in the experiments; however, the primary-to-secondary source separation in this case was chosen to be $h=0.20$ m. The least-mean-square fitting procedure was applied using sound pressures at nine points separated by 15 deg, spanning the sector of interest. Note also that the secondary quadrupole used in these experiments differed slightly from the one described in Sec. II. By repeating the source characterization measurement procedures described in Sec. II, the quadrupole source parameters at 250 Hz were found to be: $a_1=3.64\times10^{-6}$, $a_2=-4.08\times10^{-8}$, and $b_0=2.38\pi$. A 250-Hz sinusoidal signal of 2 V rms was delivered to the primary source which resulted in a primary source strength of $Q_{\mathrm{pm}}=7.40\times10^{-4}e^{j1.75\pi}$ m^3/s. The component source strengths required to achieve control in sectors 1 and 2 are given in Tables VI and VII, respectively, and the cancellation results are presented in Fig. 8.

The sector 1 cancellation results are shown in Fig. 8(a),

TABLE VI. Sector cancellation, −60 to 60 deg: least-mean-square fitting procedure. Secondary source parameters and measured cancellation performance.

Secondary source component	Component source strength magnitude	Applied voltage (rms V)	Phase shift (radians)	Average measured sector attenuation (dB)
Q_{sm}	7.810×10^{-4}	1.77	1.000π	⋯
Q_{sd}	1.483×10^{-4}	3.70	0.309π	⋯
Q_{sq}	0.935×10^{-5}	2.65	0.189π	38.7

TABLE VII. Sector cancellation, 120 to 240 deg: least-mean-square fitting procedure. Secondary source parameters and measured cancellation performance.

Secondary source component	Component source strength magnitude	Applied voltage (rms V)	Phase shift (radians)	Average measured sector attenuation (dB)
Q_{sm}	6.28×10^{-4}	1.40	1.022π	⋯
Q_{sd}	1.90×10^{-4}	4.90	0.294π	⋯
Q_{sq}	2.39×10^{-5}	7.15	0.577π	36.0

where the larger dots represent the measured sound-pressure levels before control, the smaller dots the measured sound-pressure levels after control, and the solid lines shows the predicted results. It can be seen that there was excellent agreement between the predictions and the measurements in the range 90 to 270 deg, and that in the sector of interest (i.e., from 60 to −60 deg) substantial attenuation was achieved, although it was not as large as that predicted. In theory, the sound levels in sector 1 should have been less than 10 dB after control, but as previously noted it was not possible to measure levels that were below 30 dB owing to the noise floor of the electronics and the ambient background noise in the anechoic chamber. Nonetheless, the measured average

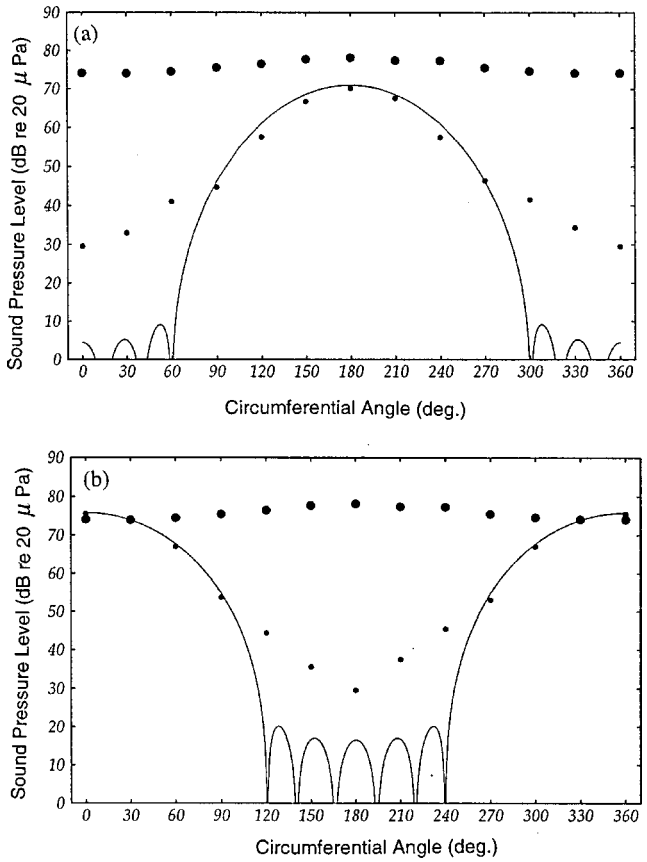

FIG. 8. (a) Sector 1 and (b) sector 2 cancellation by the least-mean-square fitting procedure: $f=250$ Hz, $h=0.20$ m. Sound-pressure level vs circumferential angle on a 1-m-radius circle centered on the origin. Secondary source: monopole, dipole, and quadrupole. Large dots: measured primary sound field; small dots: measured primary plus secondary sound field; solid line: prediction.

attenuation across sector 1 was 38.7 dB. The latter compares with 28.3 dB of attenuation obtained when the sound field was canceled around the whole 1-m-radius circle by using the least-mean-square approach. Note also that the sound level was not reinforced anywhere in the space outside the region of control. Thus, it was possible to suppress sound radiation into a particular angular sector without reinforcing it elsewhere.

The same procedure was repeated for sector 2; the cancellation results in this case are shown in Fig. 8(b). It can be seen that there was good agreement between the predictions and the measurements for all the sound levels that were above 40 dB (again, it was not possible to make accurate measurements of sound levels below 30 dB). Note that the dipole and quadrupole source strengths are significantly higher than in the sector 1 case. The latter effect apparently results from the change of relative position of the primary and secondary sources with respect to the region of control when compared to the sector 1 case. It may also be seen that neither the predicted nor measured attenuation were as large as in the sector 1 case. The measured, space-averaged attenuation over sector 2 was 36.0 dB compared to 38.7 dB over sector 1. In addition, note that the sound level was reinforced slightly near 0 deg. The results of these experiments suggest that it is easier to cancel sound in a particular region when the secondary source lies between the primary source and the region in which one wishes to achieve cancellation (sector 1 case) rather than when the secondary source and the region of interest lie on opposite sides of the primary source (sector 2 case).

VII. CONCLUSIONS

Sound-field cancellation by the use of secondary sources of higher than monopole order has been demonstrated in the present work. It has been shown that dipole, longitudinal quadrupole, and octopole sources that conform to their theoretical models at low frequencies can be constructed by using unbaffled loudspeakers. Their source strengths can be determined by simple measurements and can be used in combination with the mathematical model to predict the sound-pressure field radiated by each type of source.

Two methods for calculating the secondary source strengths required to globally cancel the sound field generated by a primary monopole were investigated. Both a direct approach derived from a multipole expansion of the primary monopole sound field and a least-squares fitting procedure were implemented. The latter approach was shown to yield greater cancellation under most circumstances than the direct approach and to result in near-optimal global sound-power-level reductions. The least-squares procedure was also successfully employed to cancel the sound field of a primary monopole in specific angular sectors of interest.

Although cancellation was demonstrated only on a 1-m-radius circle around the secondary source, the cylindrical symmetry of the experimental arrangement makes it reasonable to suggest that global cancellation can be achieved by using the approaches described here. That conclusion was reinforced by the calculations of sound-power-level reductions based on theory presented earlier.[1]

In the present work, only control of pure tones has been demonstrated. Clearly, it would be of interest in the future to study multipole control of broadband noise, particularly with respect to limitations imposed by the frequency response and dynamic range characteristics of the secondary sources. In addition, the cancellation experiments reported here were performed by using a nonadaptive, open-loop approach. If the use of multipole secondary sources is to be practical in the future, it will be necessary to control the secondary source components adaptively to account for time-varying source, environmental and transducer characteristics. That point is emphasized by the fact that in some instances it was necessary to fine-tune the phase of the secondary source components to achieve the predicted cancellation performance. Clearly, only a small number of practical sources have the character of pure monopoles. Thus, it would also be of interest to demonstrate the application of secondary multipoles to the cancellation of arbitrarily complicated primary fields. In the latter case, it would be useful, as suggested by Koopmann *et al.*,[6] to model the primary sound field as being radiated by a collection of monopoles contained within the actual source. The secondary multipole component strengths required to cancel each of the monopoles may then in principle be superposed to cancel the sound field of the complete primary source. It would be useful to demonstrate the latter concept experimentally.

In the first instance it may prove profitable to apply the present technique to the cancellation of external, low-frequency sound fields radiated from exhaust pipes or duct terminations. Those sources may often be successfully modeled as monopoles. It may also be useful to apply the present procedures to the cancellation of electrical transformer noise owing to the harmonic nature of those noise sources. In that instance, it may be particularly appropriate to employ sector cancellation techniques to suppress sound radiation in particularly sensitive directions.

ACKNOWLEDGMENTS

The authors are grateful to the U.S. Army Construction Engineering Research Laboratory, which provided partial financial support for this work. The authors are also grateful to Rick Weisman, formerly of Harmon International, for providing the loudspeakers used to construct the dipole, quadrupole, and octopole sources used in the present experiments. This article was completed while the second author was on sabbatical leave at the Center for Noise and Vibration Control (NOVIC), Department of Mechanical Engineering, Korea Advanced Institute of Science and Technology (KAIST), Taejon, Korea: his thanks go in particular to Professor Yang-Hann Kim and Professor Jeong-Guon Ih for making his visit possible and productive, and to the Korea Research Foundation for providing financial support.

[1] J. S. Bolton, B. K. Gardner, and T. A. Beauvilain, ''Sound cancellation by the use of secondary multipoles,'' J. Acoust. Soc. Am. **98**, 2343–2362 (1995).
[2] I. Brown, ''The application of simple source theory to active noise control,'' Proc. Inst. Acoust. **7**, 73–78 (1982).
[3] P. A. Nelson, A. R. D. Curtis, and S. J. Elliot, ''Optimal multipole source

distributions for the active suppression and absorption of acoustic radiation,'' Proc. Euromech Colloq. **213** (1986).
[4] P. A. Nelson, A. R. D. Curtis, S. J. Elliot, and A. J. Bullmore, ''The minimum power output of free field point source and the active control of sound,'' J. Sound Vib. **116**, 397–414 (1987).
[5] A. J. Kempton, ''The ambiguity of acoustic sources: a possibility for active noise control?'' J. Sound Vib. **48**, 475–483 (1976).
[6] G. H. Koopmann, L. Song, and J. B. Fahnline, ''A method for computing acoustic fields based on the principle of wave superposition,'' J. Acoust. Soc. Am. **86**, 2433–2438 (1989).
[7] W. B. Conover, ''Fighting noise with noise,'' Noise Control **92**, 78–82 (1956).
[8] K. Kido, ''Reduction of noise by the use of additional sound sources,'' Proc. INTER-NOISE **75**, 647–650 (1975).
[9] N. Hesselman, ''Investigation of noise reduction in a 100 KVA transformer tank by means of active methods,'' Appl. Acoust. **11**, 27–34 (1978).
[10] C. F. Ross, ''Experiments on the active control of transformer noise,'' J. Sound Vib. **61**, 473–480 (1978).
[11] M. Jessel and O. L. Angevine, ''Active acoustic attenuation of a complex noise source,'' Proc. INTER-NOISE **80**, 689–694 (1980).
[12] O. L. Angevine, ''Active acoustic attenuation of transformer noise,'' Proc. INTER-NOISE **81**, 303–306 (1981).
[13] S. E. Craig and O. L. Angevine, ''Active control of hum from large power transformers—The real world,'' Proceedings of the Second Conference on Recent Advances in Active Control of Sound and Vibration, 279–290 (1993).
[14] M. McLoughlin, S. Hildebrand, and Z. Hu, ''A novel active transformer quieting system,'' Proc. INTER-NOISE **94**, 1323–1326 (1994).
[15] M. R. Davis, ''Reduction of noise from open pipe terminations,'' J. Sound Vib. **132**, 213–225 (1989).
[16] H. Kanai, M. Abe, and K. Kido, ''A new method to arrange an additional sound source used in active noise control,'' Acustica **70**, 258–264 (1990).
[17] H. R. Hall, W. B. Ferren, and R. J. Bernhard, ''Active control of radiated sound from ducts,'' Trans. ASME, J. Vib. Acoust. **114**, 338–346 (1992).

Experimental investigation of transient pressure waves produced in dielectric liquids

F. Jomni,[a] F. Aitken, and A. Denat
Laboratoire d'Electrostatique et de Matériaux Diélectriques, CNRS-Joseph Fourier University 25, av. des Martyrs, 38042 Grenoble, France

(Received 27 August 1998; accepted for publication 12 August 1999)

The experimental results reported in this paper mainly concern the two first transient pressure waves emitted after a fast (~ns) and localized (~μm) injection of electrical energy W_i in insulating liquids. The influence of various parameters (hydrostatic pressure P_∞, injected energy W_i, etc.) on the relative amplitude of these two transient pressure waves are presented and discussed. The analysis shows clearly a difference of behavior, in particular their dependence as a function of hydrostatic pressure, between these two waves. Basically, the physical processes leading to their emission are quite different. The first pressure transient is a consequence of the plasma relaxation, whereas the second one is due to the bubble collapse. According to these results, the chronology of the events is more improved, as well as the theoretical analysis. © *2000 Acoustical Society of America.* [S0001-4966(99)01512-X]

PACS numbers: 43.25.Cb, 43.25.Vt, 43.25.Yw [MFH]

INTRODUCTION

Dielectric liquids such as mineral oil, silicon oil, cryogenic liquids, etc., are used in high-voltage devices as an electrical insulator and/or as coolant. They represent a weakness of these devices in that their failure to maintain a high applied voltage between component electrodes generally means the breakdown and the partial or complete damage of the device. The understanding of breakdown processes is consequently very important from a fundamental and economical point of view. Well-known, but not necessarily well understood, breakdown is the final step of a series of prebreakdown events such as a local deposition of electrical energy, the generation and propagation of streamers, etc.[1,2] Effort is now focused on the initial step (i.e., the local deposition of electrical energy) of prebreakdown phenomena which corresponds to very low injected energy in a large hydrostatic pressure range (this can be larger than the critical pressure of the fluid).

Previous studies of electrical conduction in highly purified nonpolar liquids, in point–plane geometry and for point cathode have shown the existence of a current pulse regime when the applied dc voltage is raised above a given threshold V_T.[3] Each current pulse (i.e., electron avalanches of some ns) corresponds to a localized injection of energy (~nJ) in the liquid close to the point, on a distance of the order of a point radius (~μm) which is much smaller than the needle–plane distance (~mm). The discharge volume (~μm^3) evolves to bring about the emission of a transient pressure wave, the formation of a microscopic bubble, and then, the emission of pressure waves due to the successive collapses of the bubble.[4] All the processes occur under a constant dc voltage and are entirely reproducible. Furthermore, the presence of these phenomena has appeared to be, in some conditions, the precursor of streamer generation leading to liquid breakdown (=spark discharge). The transition from a single microscopic bubble to a propagating gaseous canal (i.e., a streamer) requires a fast and repetitive energy injection into this initial bubble.[5] Hence, the study of these hydrodynamic processes appears to be of great interest in understanding prebreakdown mechanism in dielectric liquids. Moreover, these experimental conditions have been found to be a good tool for the study of the initial step of prebreakdown phenomena. Events were very reproducible and well localized close to the point. This experimental method leads to a series of events which is qualitatively comparable to those obtained in the field of optical breakdown.[6] An energy model has been developed to model the series of processes following the occurrence of an electron avalanche in a liquid.[7] Comparison between experimental and theoretical results (in the range of ~nJ to ~mJ and for an injection time duration of ~ns) was particularly good. For instance, the values of the experimental maximum bubble size as a function of energy injection and hydrostatic pressure (0.1–10 MPa) are well predicted by the model.[4,7]

Another way to produce similar phenomena (pressure waves and bubble formation) is to use spark discharge in liquid.[8–10] However, in this case, bubble formation takes place after a series of very complex events occurring into a propagating canal discharge created between the electrodes (electron avalanches, phase change, streamer, and leader formation, etc.) leading to the total collapse of the voltage, a large energy injection (mJ to kJ) and, therefore, a large bubble size (mm to m). Moreover, here the injected energy is deposited in some μs in medium of evoluting characteristics in time from the liquid phase to a gaseous canal at low temperature (streamer) and then to a canal at high temperature (arc). Here, we do not attempt to treat such complex phenomena as we are mainly interested in understanding and modeling prebreakdown mechanisms.

The object of the present study is to investigate the spa-

[a]Present address: Physics Department, Faculty of Sciences of Tunis, 1060, Tunisia.

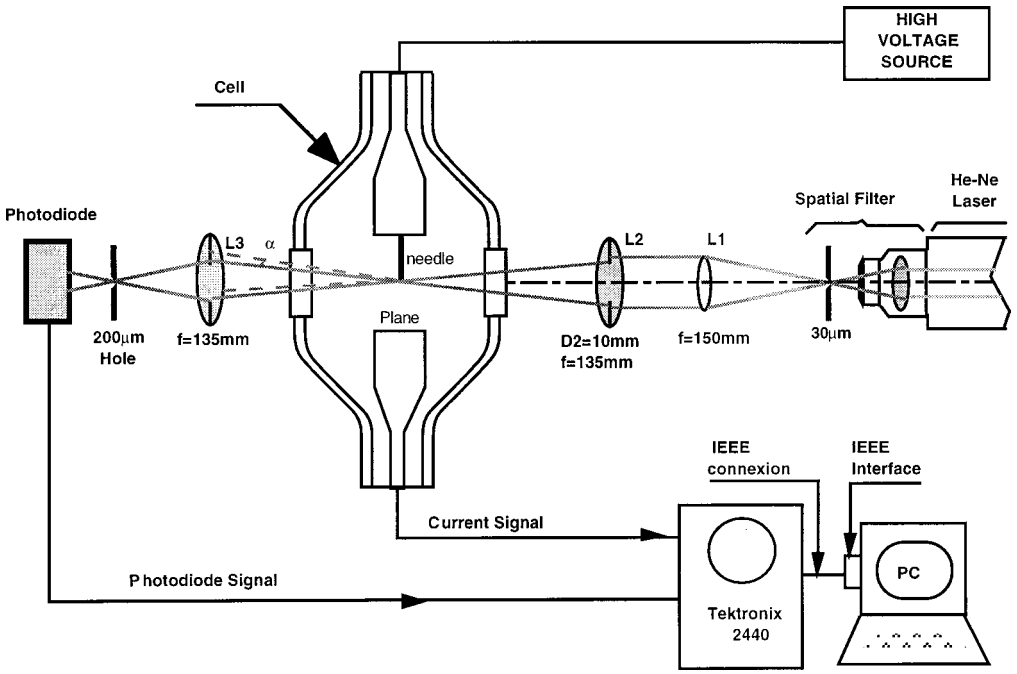

FIG. 1. Experimental arrangement using a probe-beam deflection technique.

tiotemporal evolution of the first two transient pressure waves induced by one current pulse of ns duration. It is clearly shown for the first time that the first and second pressure pulses are generated by two different mechanisms. Moreover, the formation of a transient pressure wave and a bubble has been analyzed as a function of various parameters: injected energy W_i ($0.1<W_i<100$ nJ) and applied hydrostatic pressure P_∞ ($0.1<P_\infty<10$ MPa). This will allow us to clarify the chronology of the events and to better improve the theoretical analysis.

I. EXPERIMENTAL PROCEDURE

Liquids were degassed, purified by passage through columns of activated molecular sieves, columns of silicagel, and then filtered in order to remove all traces of oxygen, water, solid particles, etc. The liquid was transferred into experimental cells by vacuum distillation. In order to measure current pulse in the nanosecond range without reflections or oscillations, coaxial test cells with a well-defined wave impedance of 50 Ω were constructed. The electrode geometry being point–plane geometry, the point radius r_p and the electrode gap d were varied independently from 0.3 to 10 μm and from 0.5 to 3 mm, respectively. The cells could be pressurized up to 12 MPa via a nitrogen-operated piston. Each cell was mounted on an $X-Z$ translation stage with a spatial resolution of 10 μm along the X-axis and 5 μm along the Z-one. The temporal study of pressure waves was achieved by a laser–Schlieren technique (Fig. 1), which appears to offer the best combination of resolution and sensitivity for fast events.[6] The probe beam from a 5-mW He–Ne laser is spatially filtered, expanded to a 10-mm-diameter collimated beam and focused into the cell on the tip needle (or at some known distance of it). The focusing lens has a focal length of 135 mm. The theoretical diffraction-limited diameter of the focal spot is 15 μm; however, experimentally we measured a spot size of about 25 μm. This yields to a temporal resolution of 20 ns, which corresponds to the time necessary for acoustic transients to travel through the probe-beam focus. The probe beam continues its travel outside the cell by passing through a second focusing lens ($f=135$ mm) with a circular aperture $D2$ of a diameter equal to the laser beam and is imaged onto the sensitive area of a fast photodiode. The active area of this photodiode is 1 mm^2 and its rise time <1 ns. Both the current and photodiode signals were recorded simultaneously on an oscilloscope (Tektronix 2440, 300-MHz bandwidth) and then transferred to a computer for processing.

When a transient pressure wave passes through the probe-beam focus (spot size 25 μm), a refractive index change occurs which produces a transient angular deflection ϕ of the probe. As a result, the probe beam is partially blocked out by the aperture $D2$ and the intensity of the light transmitted to the photodiode is modulated. The photodiode signal is proportional to the modulus of the time derivative of the pressure pulse, at the probe-beam position in the liquid, and is given by[11]

$$U_0-U(t)\propto\left|\frac{\partial P(r,t)}{\partial t}\right|, \tag{1}$$

where U_0 is the photodiode voltage for $\phi=0$ and $\partial P(r,t)/\partial t$ is the temporal pressure change.

The light beam was checked periodically to assure alignment of the laser beam with the test section by maximizing signal intensity. The photodiode signal and then the pressure pulse can be measured along the X and Z axes (see Fig. 2) in order to verify the wave's sphericity.

Unfortunately, the calibration of the photodiode signal, as it has been done in the case of optical breakdown (e.g., by using piezoelectric transducers), turned out to be impossible in our case. The very low amplitude of the emitted pressure

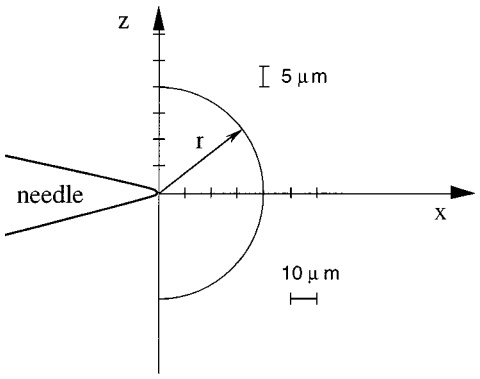

FIG. 2. Displacement r of the needle in two directions from the laser spot focus. The cell is mounted on $X-Z$ translators.

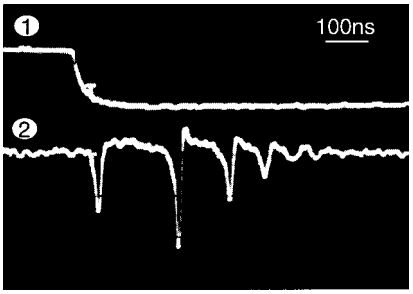

FIG. 4. Temporal profile (curve 2) of the acoustic transients in *n*-pentane at $r=40\ \mu$m from the emission center, $P_\infty=0.8$ MPa, and $W_i=14.2$ nJ. The initial peak is followed by pressure transients corresponding to the successive bubble collapses. Curve 1: the integrated current pulse.

waves requires putting the probe very close to the point electrode where a constant high dc voltage is constantly operative. The existence of such a high electric field close to the emission center strongly influences the transducer signal and makes its use impossible. Hence, our experimental results are qualitative, since we only observed the variation of the amplitude of the photodiode signal which is proportional to the time derivative of $P(t)$ [relation (1)].

An optical scattering setup, similar to the above, was used to measure the bubble radius vs time.[12] The focal spot was adjusted so that the diameter of the focal spot was always greater than the maximum bubble size to be measured. The calibration of this detection was made using the high-speed visualization device previously described.[5,12]

II. EXPERIMENTAL RESULTS AND DISCUSSION

A. Chronology of events

After each current impulse, the sequence of events is as follow: a cold plasma appears as the immediate result of electron avalanches. In hydrocarbons, the plasma size is of the order of the point radius r_p.[13] When the probe beam is focused on the needle tip, we observed the typical signals shown in Fig. 3, the integrated current pulse and the photodiode signal being taken simultaneously. As the plasma is produced very close to the point tip, when the probe beam is focused on the point, we can define this as the position of the emission center. The uncertainty about the position of the emission center is of the order of the radius of the focus spot

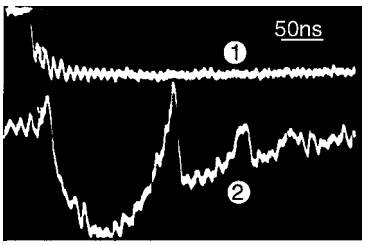

FIG. 3. Illustration of events: Oscillogram of (1) the integrated current pulse ($Q_i=2.85$ pC) (2) the photodiode signal close to the emission center. It records the disturbances of the medium induced by the initial acoustic transient, the bubble, and the pressure waves emitted upon bubble collapses. (cyclohexane, $P_\infty=2$ MPa, $W_i=18.50$ nJ). The laser beam is focused on the point tip. The spot size at focus is $\sim 25\ \mu$m. Every perturbation occurring in this region leads to change of the refractive index of the medium.

(i.e., about 10 μm). The very localized injection of energy ($\sim$ns time duration) gives rise to the emission of a spherical pressure/shock wave (first peak on the photodiode signal shown in Fig. 3), followed some ns later by the formation of a bubble which rebounds several times before disappearing (see Fig. 3). At the end of each expansion–collapse cycle, we can also observe the emission of a pressure/shock wave.

Figure 4 shows the integrated current and photodiode signals taken at a distance r of 40 μm from the emission center. This r is large compared to the plasma size (2–3 μm) and also to the maximum bubble radius $R_{\max}=6\ \mu$m. These results, which are independent of the direction of observation (X or Z axis), indicate the pressure wave sphericity. In these conditions, we detect only transient pressure waves: the first one which appears at a perfectly determined delay time with respect to the starting time of the current pulse (and independently of the external conditions) corresponds to a pressure/shock wave generated by the relaxation of the plasma. The following ones have delay times with respect to the starting time of the current pulse depending on the external conditions (mainly P_∞) and therefore correlated to the successive rebounds of the bubble. The pressure waves have a time duration of about 25 ns at half-width and a similar shape. In addition, we note in Fig. 4 that the amplitude of the second pressure pulse (i.e., that emitted after the first collapse of the bubble) is higher than the initial one. This behavior has always been observed in our experiments. In optical breakdown, the converse case can also be observed.[14]

Figures 3 and 4 show typical signals of the formation and collapse of a bubble which are qualitatively comparable to those already observed in the field of cavitation bubbles produced by laser light pulses, shock tubes, electrical sparks, etc. In previous works,[5,12] we have shown that the time Δt between the first and second pressure pulses corresponded exactly to the first growth and collapse phase of the bubble and, in low-viscosity liquids such as cyclohexane, followed Rayleigh's equation (i.e., $\Delta t=1.83R_{\max}\sqrt{\rho_\infty/P_\infty}$; here, ρ_∞ denotes the density of the liquid at P_∞) in the entire studied hydrostatic pressure range 0.1–10 MPa.

Due to the different origins of the initial and second transient pressure/shock waves, we are going to analyze them separately. Pressure waves mean that liquid compressibility is a factor which must be taken into account and this requires the knowledge of an equation of state for the liquid.

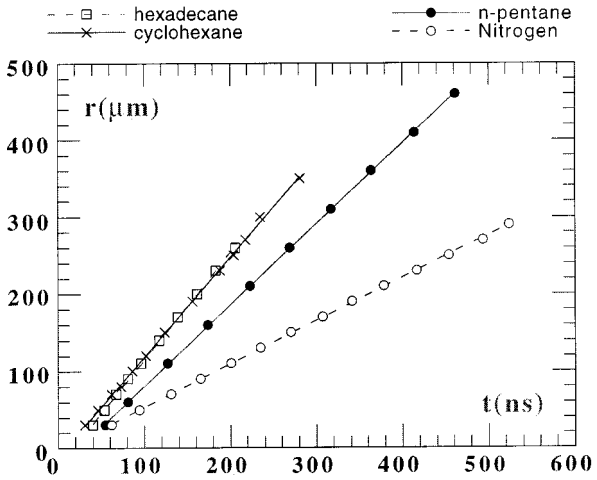

FIG. 5. The propagation distance of the initial acoustic transient from the emission center as a function of the delay time for different liquids at $P_\infty = 2.6$ MPa. The slope of each curve represents the velocity of sound in the liquid which is roughly constant far from the emission center ($r \geqslant 50\ \mu$m).

B. Equation of state

The choice of an equation of state depends on the range of pressure generated by these phenomena. We cannot measure the absolute value of the amplitude of the pressure waves, only their propagation velocity. However, with the pressure being related to the values of the propagation velocity, it is possible to get back to the equation of state this way.

The initial pressure/shock wave being well-defined in time, the distance r traveled by this wave from the emission center can be accurately plotted as a function of time t for different hydrostatic pressures and liquids. Its velocity is then determined from the slopes of the curve $r(t)$. At a distance over approximately 50 μm from the point tip (the emission center), we observed that the propagation velocity stays constant with the distance r and is very close to the sound velocity in the liquid for a given P_∞ (Fig. 5). The observed processes can be considered as adiabatic. Consequently, the pressure in the initial wave which can be evaluated in the first approximation by $(1/2)\rho_\infty c_\infty^2$ is of the order of a few hundred MPa. Here, c_∞ denotes the speed of sound in the liquid at P_∞.

When studying underwater explosions, especially shock waves, Kirkwood proposed an equation of state (EOS) for liquids which is accurate enough to describe high-pressure phenomena in a pressure range of a few hundred MPa.[15] This EOS consists of a rectangular branch of hyperbola for representing the adiabatic compressibility coefficient as a function of pressure P; this idea was first introduced by Tait in 1888 but in a slightly different way.[16] The modified Tait equation (MTE), the name already given by Richardson *et al.*,[17] is given by the following expression:

$$[P+B(S)]V^n = F(S) \quad \text{with} \quad F(S) = [P_0 + B(S)]V_0^n, \tag{2}$$

where V is the specific volume and $V_0 = V(P_0, S)$ is the specific volume at the pressure reference P_0. The MTE is a complete EOS in which the coefficient n is assumed constant and $B(S)$ is a function of entropy alone. Now, if we suppose that the internal energy $e(S,V)$ of the studied liquids verifies the standard inequalities of the thermodynamic such that $(\partial P/\partial V)_S < 0$ and $(\partial P/\partial S)_V > 0$,[18] we obtain that $n > 0$ and $B'(S) > 0$, where the prime index denotes the first derivative of the function with respect to S.

Generally, the function $B(S)$ is taken as a constant B_0, which means that the MTE becomes a relation of barotropy with a polytropic evolution; we then deduce from this that the internal energy is the sum of two independent functions such that $e(S,V) = e_0(S) + e_1(V)$, and that the Grüneisen coefficient is equal to zero.[19] This assumption leads to the following conclusions:

(i) the isobar and isochor specific heats are equal;
(ii) the adiabatic and isotherm compressibilities are equal;
(iii) the coefficient of thermal expansion at constant pressure is equal to zero and the temperature is determined by $T = e_0'(S)$.

We can see also that this hypothesis is very strong and can only be made if temperature changes occurring in the problem are small. This is generally the case for the weak shock waves emitted after localized electrical breakdown.

However, it is possible to determine from the MTE the adiabatic sound velocity as

$$c^2 = \left.\frac{\partial P}{\partial \rho}\right|_S = n\,\frac{P+B(S)}{\rho} \quad \text{with} \quad \rho = 1/V. \tag{3}$$

By plotting the variation of the square sound velocity as a function of hydrostatic pressure P_∞, we can deduce the parameters n and B. We have calculated these parameters for various studied liquids (Table I). These values are in good agreement with those obtained by Macdonald.[20] Then, we are able to deduce from our experimental measurement the parameters of the state equation for each of the liquids; this is very important for the remainder of this study.

If the propagation of this transient pressure wave is really acoustic, the theory predicts, for a spherical wave, a decrease of the amplitude with the distance r traveled from the source in $1/r$.[21] This is a behavior which can be observed in Fig. 6. This result, associated with the velocity of propagation, shows that this wave has the characteristics of a spherical acoustic wave for distances over 50 μm from the emission center.

If we analyze more accurately the $r(t)$ curves for distances lower than 50 μm from the emission center, this curves show a marked bending. This phenomenon is mainly observed for the high values of the injected energy (e.g., in

TABLE I. Parameters n, B of the MTE, and the sound velocity c_∞ calculated at $P_\infty = 2.6$ MPa.

Liquids	n	B (MPa)	c_∞ (m/s) ($P_\infty = 2.6$ MPa)
Cyclohexane (293 K)	10.7	121.8	1292
n-pentane (293 K)	11.3	58.3	1055
n-decane (293 K)	10	115	1269
Hexadecane (295 K)	13.62	105.5	1382
Nitrogen (115 K)	17.9	3.7	558
Argon (91.7 K)	9.7	89.2	807

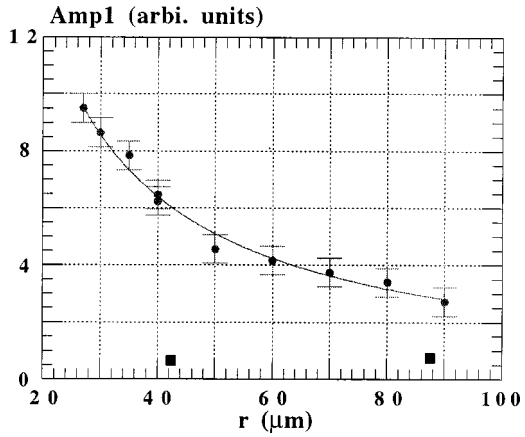

FIG. 6. Variation of the initial shock/pressure wave amplitude as a function of its traveled distance (cyclohexane, $W_i = 13.3$ nJ, $P_\infty = 1.1$ MPa). The term Amp represents the maximum relative amplitude of the temporal profile recorded by the photodiode (no calibration). Ampl corresponds to the initial shock/pressure wave due to the plasma relaxation.

cyclohexane for $W_i > 20$ nJ). However, measurements are only possible at a distance greater than 20 μm, because there are considerable fluctuations of the photodiode signal due to the disturbed medium near the emission center. From the example given in Fig. 7, we determined a propagation velocity of up to 2150 m/s close to the emission center (for the three first points in Fig. 7), which lasts only a few tens of ns, and rapidly slows to a velocity of about 1280 m/s, corresponding to the sonic velocity in cyclohexane. This decrease in slope when moving away from the emission center is more easily detectable in the case of optical breakdown,[22,23] since the characteristic time of the phenomena is very large compared to our case; thus, the transition from the supersonic stage to the acoustic one of the transient pressure is determined more accurately. From this analysis we can assume that the first pressure pulse has the characteristics of a shock wave in its first stage of propagation. So, we will further treat it theoretically as a weak shock wave.

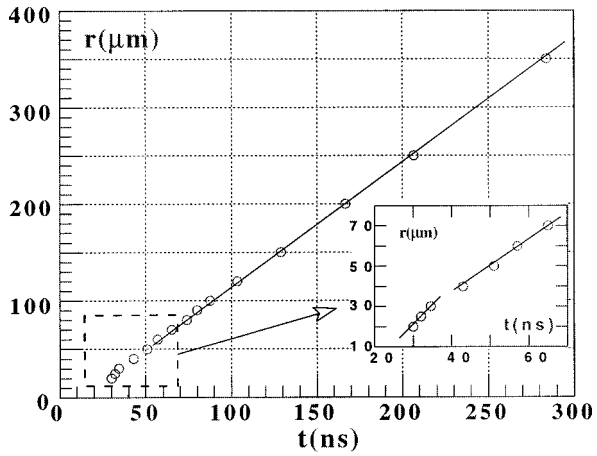

FIG. 7. The propagation distance of the initial acoustic transient as a function of the delay time in cyclohexane at $P_\infty = 1.6$ MPa. In the zoom, we can observe a slight increase in the slope ($\approx$40%) near the emission center which characterize the initial supersonic propagation of the shock (spatial resolution = 5 μm).

C. Initial transient pressure/shock wave characteristics

In this section, we present a theoretical analysis about the initial transient pressure assumed as a weak shock wave in order to understand our experimental results.

Experimentally in optical breakdown, between 10% to 20% of the injected energy W_i is typically lost to an initial pressure transient (or shock wave), less than 5% to the bubble, and the remaining 80% or so is transformed into heat.[6] According to these experimental evidences, the injected energy is broken up into thermal components (E_T) and mechanical components (E_P) such that

$$W_i = E_T + E_P . \tag{4}$$

This relation has also been demonstrated theoretically by Aitken *et al.*[24]

According to Teslenko,[25] the mechanical energy is further divided into that taken by the shock wave E_{sw} and that of the bubble itself, E_b

$$E_P = E_{\mathrm{sw}} + E_b = k_0 W_i , \tag{5}$$

where k_0 is a coefficient corresponding to the part of energy converted to mechanical energy which denoted hydraulic efficiency of the discharge.

Our experimental observations indicate that the behavior of the shock wave is similar to that of an acoustic wave in the case of spherical symmetry; consequently we can use the theoretical approach of Arons *et al.*:[26] they associated the Hugoniot–Rankine equations with the work done by a divergent sonic wave in displacement of spherical surface having a radius r_c, that is to say: $4\pi r_c^2 \int_0^t \Delta P u \, dt$; this implies the following relation:

$$E_{\mathrm{sw}} = \frac{4\pi r_c^2}{\rho_\infty} \left\{ \int_0^{t_1} \frac{(\Delta P)^2}{U_c - (\Delta P/\rho_\infty U_c)} dt + \frac{1}{r_c} \int_0^{t_1} \left[\Delta P \int_0^{t_1} \Delta P dt \right] dt \right\}, \tag{6}$$

where $\Delta P = P - P_\infty$, U_c is the shock wave velocity, and t_1 is an arbitrary limit of integration. The first term in bracket represents the acoustic radiated energy in an irreversible way, while the second, denoted ''afterflow'' by Cole,[15] represents the energy stored reversibly behind the shock wave. However, this last term becomes rapidly negligible with regard to the first one and hence: ''The energy flux density is estimated by the first term only in Eq. (6). This term in itself is not exact, because it is obtained in the acoustic approximation.'' [15]

Now, if we express the shock wave velocity U_c by the well-known relation[15] $U_c = c_\infty [1 + ((n+1)/4c_\infty) u_1]$, such that $u_1 = \Delta P/\rho_\infty c_\infty$, we obtain, if we consider only the first-order terms, the following expressions:

$$E_{\mathrm{sw}} = \frac{4\pi r_c^2}{\rho_\infty c_\infty} \int_0^{t_1} (\Delta P)^2 \left[1 - \left(\frac{n+1}{4} - 1 \right) \frac{\Delta P}{\rho_\infty c_\infty^2} \right] dt. \tag{7}$$

However, this approximation is only valid for weak shocks; the correction term in $(\Delta P)^3$ contributes only for a few percent in the range of pressure concerned; hence, the neglect-

ing of this term is well justified. The pressure transient/shock wave energy is then given by the impulse expression:[26]

$$E_{sw}=\frac{4\pi r_c^2}{\rho_\infty c_\infty}\int_0^\infty (P(t)-P_\infty)^2 dt, \tag{8}$$

where c_∞ is the speed of sound in the liquid at (P_∞, T_∞), where P_∞ and T_∞ are the undisturbed liquid pressure and temperature, respectively, and ρ_∞ is the liquid density under the same conditions. To express this integral, we have to find a representation of the pressure variation as a function of the maximum pressure $(P_{mo}-P_\infty)$ in the shock wave. We simply use the exponential decay in time observed experimentally by Cole *et al.*[27]

The MTE is assumed to be verified and, if the initial pressure distribution in the plasma is chosen to be Gaussian, we obtain a relation between the maximum pressure amplitude $(P_{mo}-P_\infty)$ of the shock wave and the initial bubble energy[7]

$$P_{mo}-P_\infty=\frac{b+\sqrt{\Delta}}{2}, \tag{9}$$

where $\Delta=b^2-4C$ and

$$b=\frac{\rho_\infty c_\infty^2}{6}\frac{3\sqrt{\frac{\pi}{2}}\left(\frac{\sigma}{r_0}\right)^3\Psi\left(\frac{3}{2},\frac{r_0^2}{2\sigma^2}\right)-\exp\left(-\frac{r_0^2}{2\sigma^2}\right)}{1-\exp\left(-\frac{r_0^2}{2\sigma^2}\right)},$$

$$C=\frac{\rho_\infty c_\infty^2}{8\pi r_0^3}E_b.$$

Here, σ is the Gaussian standard deviation, r_0 is plasma radius (typically the plasma zone has the same dimension as r_p), and Ψ is the incomplete gamma function.

It is known that the bubble energy E_b is proportional to the injected energy W_i,[28,4] giving a direct relationship between $(P_{mo}-P_\infty)$ and $W_i^{1/2}$. This variation seems in good accordance with experimental results: $(P_{mo}-P_\infty)=a_1+a_2W_i^\beta$, ($a_1$ and a_2 are two constants); $\beta=0.52$ in *n*-pentane (Fig. 8). The same experimental value for β was obtained by laser-induced breakdown in water.[29,30]

When looking at (9), it can be seen that the terms which depend on P_∞ are the sound velocity c_∞ and the density ρ_∞, but these terms can be taken as constants as long as P_∞ is much smaller than the Tait coefficient *B*. Moreover, the bubble energy does not depend on P_∞,[28] we intend to find that the amplitude $(P_{mo}-P_\infty)$ does not vary with P_∞. This behavior is experimentally observed in Fig. 9 for one liquid and three different injected energies. This implies that the relative amplitude of the shock wave is directly proportional to the square root of energy. This indicates too that the value of the constant ''a_1'' is small. Thus, the theoretical predictions are in good accordance with our experimental results.

D. Second transient pressure wave characteristics

We have also measured the velocity of the pressure wave emitted by the first collapse of the bubble. For $r>50\ \mu$m, we obtain practically the same values of the propagation velocity as those of the initial transient pressure wave in its sonic stage for different studied liquids (see Fig. 10) (e.g., from Fig. 10 we determined a velocity of 1059 m/s in *n*-pentane and 1314 m/s in hexadecane at $P_\infty=2.6$ MPa). For distances lower than 50 μm, no conclusive results have been obtained concerning the propagation velocity. This can be explained by the following reason: the distance traveled by this pressure wave depends not only on the distance between the laser spot and the emission center but also on the lifetime of the first expansion–implosion cycle of the bubble. This lifetime fluctuates with the statistical variation of the injected energy, which leads to a large spatial error. In the case of optical breakdown, the supersonic propagation of this second transient pressure wave has also been observed.[31] In this way, some theories on the influence of the amount of vapor or gas inside the bubble and the physical behavior of the gas on the collapse process have been investigated.[32] It has been

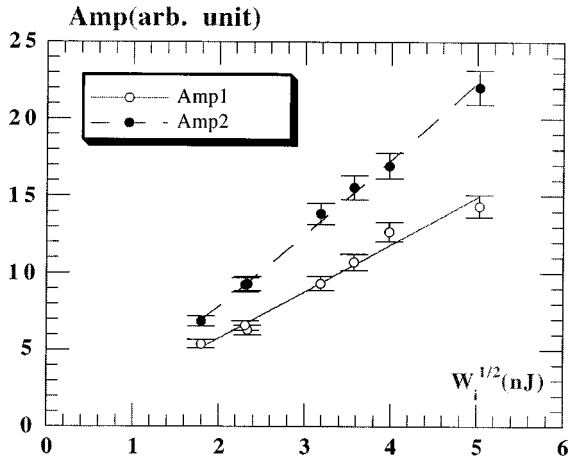

FIG. 8. The initial and the second shock/pressure wave amplitudes as a function of the square root of the injected energy (*n*-pentane, $P_\infty=1.6$ MPa). The measurements were done at the distance $r=160\ \mu$m from the emission center. Amp2 corresponds to the relative amplitude of the acoustic transient emitted by the first bubble collapse.

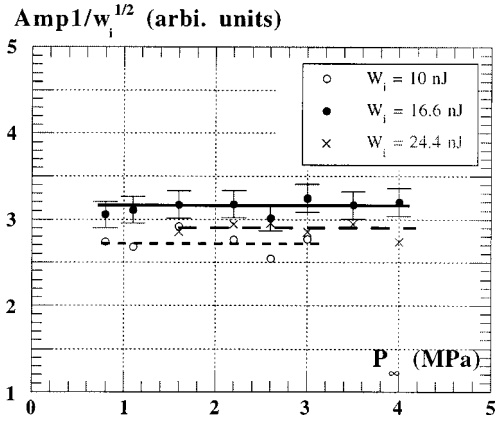

FIG. 9. Relative amplitude of the initial shock/pressure wave normalized to $W_i^{1/2}$ as a function of the applied hydrostatic pressure in *n*-pentane for three injected energies. As we can see, the ratio of the amplitude to the square root of energy has practically the same value when we take into account the error induced by the experimental setup (for figure clarity, error bars are shown only in one experiment). This implies that the relative amplitude of the initial shock/pressure wave is roughly proportional to the square root of energy.

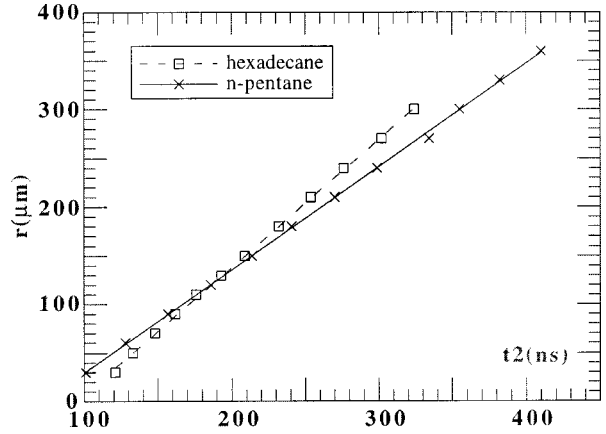

FIG. 10. The propagation distance of the second acoustic transient emitted by the first bubble collapse as a function of the delay time for two different liquids (at $P_\infty = 2.6$ MPa).

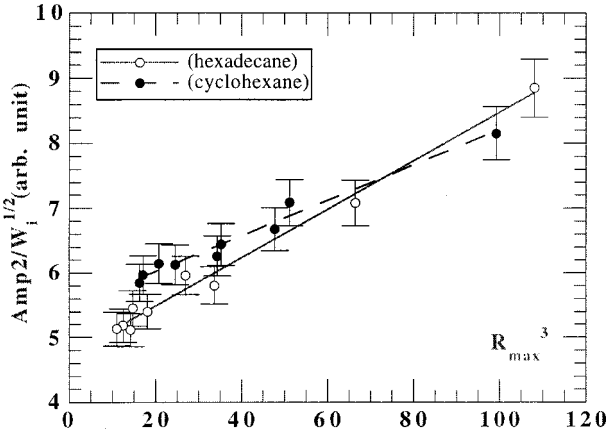

FIG. 12. Variation of the relative amplitude of the second acoustic transient normalized to the square root of the injected energy as a function of $R_{\max}^3$ for two different liquids (same conditions as Fig. 11).

shown that the velocity of propagation is as important as the initial pressure inside the bubble is weak. It implies that the two propagation stages can be observed. But, the fact that in our experiments the measured values correspond only to sonic velocities for distances of about five to ten times greater than the maximum bubble radius suggests that the gas pressure inside the bubble during the collapse process becomes important compared to the hydrostatic pressure of the liquid.

In the same manner as for the initial transient pressure wave, we have studied the amplitude of the transient wave emitted by the first bubble collapse as a function of the injected energy and of the applied hydrostatic pressure.

In Fig. 8, we observe that the maximum amplitude of the pressure wave $(P_{\max}-P_\infty)$ emitted by the first collapse of the bubble is almost proportional to W_i^β with $\beta=0.57$ in the *n*-pentane. This value can be explained if we assume that in the first approximation the liquid is incompressible and we neglect liquid viscosity and surface tension; in this case, Shima *et al.*[33] have obtained the following expression:

$$P_{\max}=P_{g0}\left[1+(\gamma_0-1)\frac{1-g}{m}\right]^{\gamma_0/\gamma_0-1}. \tag{10}$$

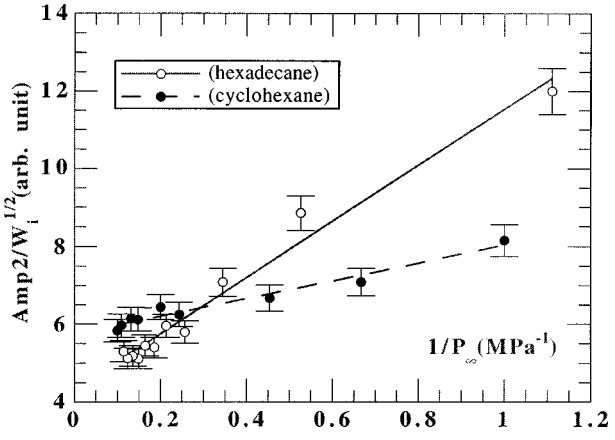

FIG. 11. Variation of the relative amplitude of the second acoustic transient normalized to the square root of the injected energy as a function of $1/P_\infty$ for two different liquids: (1) cyclohexane: $W_i=18$ nJ at $r=40$ μm from the emission center; (2) hexadecane: $W_i=18.6$ nJ at $r=45$ μm.

Here, γ_0 is the ratio of specific heats, $m=P_{g0}/P_\infty$, and $g=P_v(T_\infty)/P_\infty$ where $P_v(T)$ is the vapor pressure. The relation (10) shows that the maximum amplitude $P_{\max}$ is, in the first approximation, proportional to the initial gas pressure P_{g0} at the bubble wall; Aitken *et al.*[7] have shown that $(P_{g0}-P_\infty)$ is almost proportional to $W_i^{1/2}$. Then, we deduce that the theoretical variation of $(P_{\max}-P_\infty)$ is such that: $P_{\max}-P_\infty \approx kW_i^{1/2}$ where k is a constant.

So, the effect of hydrostatic pressure on the maximum wave amplitude is investigated by using the normalized variable $P_{\max}-P_\infty/\sqrt{W_i}$. Indeed, this also takes into account the statistical fluctuations of W_i as well as the increase of W_i with time (due to the erosion of the needle tip by the corona discharges as $W_i \approx r_p^\alpha, \alpha \sim 3$) observed experimentally. In Fig. 11, we observed a power decrease of the maximum amplitude $(P_{\max}-P_\infty)$ such that $P_{\max}-P_\infty/\sqrt{W_i} \propto 1/P_\infty$. This means that, contrary to the initial transient pressure wave, this one depends on P_∞. We know too that the maximum radius $R_{\max}$ of the bubble varies as $(W_i/P_\infty)^{1/3}$,[12] so we intend to find that $P_{\max}-P_\infty/\sqrt{W_i}$ is also proportional to $R_{\max}^3$ for the W_i constant. This is experimentally observed in Fig. 12 for different liquids. This variation allows us to deduce some results which are, at the present time, very difficult to obtain experimentally. Now, if we consider the Rayleigh–

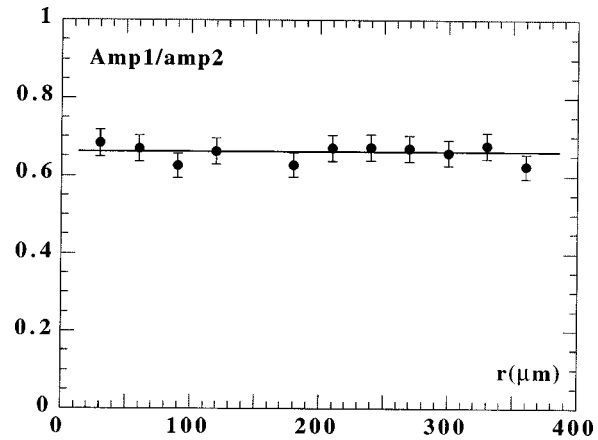

FIG. 13. Variation of the ratio Amp1/Amp2 as a function of the propagation distance in *n*-pentane for $r \geqslant 40$ μm.

TABLE II. Characteristic dimensions of phenomena in the case of electrical prebreakdown (Refs. 5 and 12) and optical breakdown (Refs. 6, 22, and 28) for similar energy injection time duration.

Electrical prebreakdown	Optical breakdown
Time duration of the current pulse: ~ns	Time duration of the laser pulse: ~ns
Energy: $1 < W_i < 100$ nJ	Energy: from few hundred μJ up to mJ
Plasma size: of the order of point radius, i.e., 0.5 to 5 μm	Plasma size: 30–100 μm
Minimum distance from the emission center: ~20 μm	Minimum distance from the emission center: ~80 μm
Supersonic stage for $r < 50$ μm	Supersonic stage for $r < 200$ μm
Maximum bubble radius: 1–10 μm	Maximum bubble radius: 100 μm to few mm

Plesset equation treating the bubble dynamics in isothermal evolution,[34] this equation shows that $P_{\max} - P_\infty \propto (R_{\max}/R_{\min})^3$. As we also know that $R_{\max}$ is proportional to $(W_i/P_\infty)^{1/3}$, $P_{\max} - P_\infty$ therefore has to vary as $W_i/P_\infty R_{\min}^3$. Then, from Fig. 12 we can deduce as a consequence that $R_{\min}^3$ must vary as $\sqrt{W_i}$ and be independent of P_∞. We have already obtained this result experimentally when studying bubble dynamics.[35] Although, the Rayleigh–Plesset model cannot describe the pressure waves propagation, it can be used to evaluate the maximum amplitude of the pressure waves. Finally, the Rayleigh–Plesset equation, when considering isothermal evolution of the gas, is certainly a good qualitative representation of the evolution of the maximum amplitude of the pressure wave due to bubble collapse. This would indicate that the thermal exchanges of the bubble with the surrounding liquid occur mainly during the collapse phase, the expansion phase being nearly adiabatic.

III. CONCLUSIONS

In this paper, we have clarified the relation between the energy injection, due to electron avalanches of ns duration, into the liquid and the formation of pressure transients and the bubble.

Our analysis of the transient pressure waves shows clearly the difference between the first two. Basically, the physical processes leading to their emission are quite different. The first pressure transient is a consequence of the plasma relaxation, whereas the second one is due to the bubble collapse. First, the main difference of behavior between the two waves is their behavior as a function of hydrostatic pressure. In fact, the first one, whose amplitude depends on the plasma size, and so on the deposited energy (and eventually on the nature of the liquid), is independent of P_∞. On the other hand, the amplitude of the second one, which is correlated to the bubble size and its dynamics, depends on P_∞. This latter fact makes it quite obvious, as we have already shown in previous studies,[35] that the hydrostatic pressure strongly affected the bubble (i.e., lifetime and size) and its dynamics.

We have also suggested that the velocity of the first pressure transient is supersonic for distances close to the emission center (i.e., for $r \leqslant 50$ μm). This supersonic stage is only detected for the high values of the injected energy. For the second one, we are unable to confirm the existence of a supersonic regime.

However, far from the emission center ($r \geqslant 50$ μm), for a given P_∞ the two pressure waves present a similar behavior which can be interpreted as those characterizing an acoustical spherical wave. This propriety is shown in Fig. 13, which depicts the variation of the ratio Amp1/Amp2 as a function of the propagation distance. We note that this ratio remains constant, whatever the distance. This implies that they verify the same law of attenuation.

Moreover, we have also studied these phenomena in more viscous liquids ($\mu \geqslant 3\,10^{-3}$ Pa s). Our experiments show only the appearance of the pressure transient due to the current pulse, and no pressure wave emitted by the bubble was detected, since its dynamics is described only by one dissymmetrical cycle and no rebounds.[4] This dissymmetry is due to the effect of viscosity which particularly affects the time of the bubble collapse; this collapse time becomes more and more important the higher the liquid viscosity.

Our experimental results are qualitatively similar to those obtained by nanoseconds laser-induced breakdown, and therefore, present an extrapolation to smaller characteristic scales of the results obtained by optical cavitation (see Table II).

ACKNOWLEDGMENT

The authors thank Dr. N. Bonifaci for continuing help and technical assistance on the study of cryogenic fluids.

[1] A. H. Sharbaugh, J. C. Devins, and S. J. Rzad, ''Progress in the field of electric breakdown in dielectric liquids,'' IEEE Trans. Electr. Insul. **13**, 249–276 (1978).
[2] O. Lesaint and R. Tobazéon, ''Streamer generation and propagation in transformer oil under ac divergent field conditions,'' IEEE Trans. Electr. Insul. **23**, 941–954 (1988).
[3] A. Denat, J. P. Gosse, and B. Gosse, ''Electrical conduction of purified cyclohexane in a divergent electric field,'' IEEE Trans. Electr. Insul. **23**, 545–554 (1988).
[4] F. Jomni, ''Etude des phénomènes hydrodynamiques engendrés dans les liquides diélectriques par un champ électrique très intense,'' Thesis, Joseph Fourier University, Grenoble I, 1997.
[5] R. Kattan, A. Denat, and N. Bonifaci, ''Formation of vapor bubbles in non-polar liquids initiated by current pulses,'' IEEE Trans. Electr. Insul. **26**, 656–662 (1991).
[6] A. Vogel and W. Lauterborn, ''Acoustic transient generation by laser-produced cavitation bubbles near solid boundaries,'' J. Acoust. Soc. Am. **84**, 719–731 (1988).
[7] F. Aitken, F. M. J. McCluskey, and A. Denat, ''An energy model for artificially generated bubbles in liquids,'' J. Fluid Mech. **327**, 373–392 (1996).

[8] M. Harrison, ''An experimental study of single bubble cavitation noise,'' J. Acoust. Soc. Am. **24**, 776–782 (1952).
[9] P. K. Watson, W. G. Chadband, and W. Y. Mak, ''Bubble growth following a localized electrical discharge and its relationship to the breakdown of triggered spark gaps in liquids,'' IEEE Trans. Electr. Insul. **EI-20**, 275–280 (1985).
[10] J. A. Cook, A. M. Gleeson, R. M. Roberts, and R. L. Rogers, ''A spark-generated bubble model with semi-empirical mass transport,'' J. Acoust. Soc. Am. **101**, 1908–1920 (1997), and references therein.
[11] B. Sullivan and A. C. Tam, ''Profile of laser-produced acoustic pulse in a liquid,'' J. Acoust. Soc. Am. **75**, 437–441 (1984).
[12] R. Kattan, A. Denat, and O. Lesaint, ''Generation, growth, and collapse of vapor bubbles in hydrocarbon liquids under a high divergent electric field,'' J. Appl. Phys. **66**, 4062–4066 (1989).
[13] N. Bonifaci, A. Denat, and V. M. Atrazhev, ''Work functions for a HV cathode in nonpolar liquids,'' IEEE Trans. Dielectr. Electr. Insul. **1**, 657–662 (1994).
[14] P. Alloncle, private communication (Grenoble, 1996).
[15] R. H. Cole, *Underwater Explosions* (Dover, New York, 1965).
[16] J. H. Dymond and R. Malhotra, ''The Tait Equation: 100 years on,'' Int. J. Thermophys. **9**, 941–951 (1988).
[17] J. M. Richardson, A. B. Arons, and R. R. Halverson, ''Hydrodynamic properties of sea water at the front of a shock wave,'' J. Chem. Phys. **15**, 785–794 (1947).
[18] H. Weyl, ''Shock waves in arbitrary fluids,'' Commun. Pure Appl. Math. **2**, 103–122 (1949).
[19] R. Menikoff and B. J. Plohr, ''The Riemann problem for fluid flow of real materials,'' Rev. Mod. Phys. **61**, 75–130 (1989).
[20] J. R. Macdonald, ''Some simple isothermal equations of states,'' Rev. Mod. Phys. **38**, 669–679 (1966).
[21] L. Landau and E. Lifchitz, *Physique Théorique, Tome 6. Mécanique des Fluides* (Ed. Librairie du globe, Editions MIR, Moscow, 1989), Chap. 8.
[22] A. P. Alloncle, D. Dufresne, and M. Autric, ''Characterisation of pressure waves in liquids using an interferometric method,'' IUTAM Symposium on Bubble Dynamics and Interface Phenomena, Birmingham, UK, 1993.
[23] A. Vogel, S. Busch, and U. Parlitz, ''Shock wave emission and cavitation bubble generation by picosecond and nanosecond optical breakdown in water,'' J. Acoust. Soc. Am. **100**, 148–165 (1996).
[24] F. Aitken, F. Jomni, and A. Denat, ''Bubble formation by a corona discharge in dielectric liquids,'' Third International Symposium on Cavitation, April 1998, Grenoble, France.
[25] V. S. Teslenko, ''Investigation of photoacoustic and photohydrodynamic parameters of laser breakdown in liquids,'' Sov. J. Quantum Electron. **7**, 981–984 (1977).
[26] A. B. Arons and D. R. Yennie, ''Energy partition in underwater explosion phenomena,'' Rev. Mod. Phys. **20**, 519–536 (1948).
[27] R. H. Cole and J. S. Coles, ''Propagation of spherical shock waves in water,'' Phys. Rev. **71**, 128–129 (1947).
[28] P. Giovanneschi-Testud, ''Contribution à l'étude de la cavitation à bulles isolées initiées par un rayonnement laser de grande intensité,'' Doctoral thesis, University of Aix-Marseille II, 1987.
[29] H. Shoeffmann, H. Schmidth-Kloiber, and E. Reichel, ''Time-resolved investigations of laser-induced shock waves in water by use of polyvinylidenefluoride hydrophones,'' J. Appl. Phys. **63**, 46–51 (1987).
[30] J. Noak and A. Vogel, ''Streak-photographic investigation of shock wave emission after laser-induced plasma formation in water,'' Proc. SPIE **2391A**, 284–293 (1995).
[31] G. V. Dreiden, A. P. Dmitriev, Yu. I. Ostrovskii, and M. Etinberg, ''Experimental investigation of shock waves produced in water when a cavitation bubble collapses,'' Sov. Phys. Tech. Phys. **28**, 191–193 (1983).
[32] R. Hickling and M. S. Plesset, ''Collapse of a spherical bubble in water,'' Phys. Fluids **7**, 7–14 (1964).
[33] A. Shima and Y. Tomita, ''On the impulse pressure accompanying spherical bubble collapse in liquids,'' Rep. Inst. High Speed Mech., Tohoku Univerity, **31**, 97–135 (1975).
[34] J. P. Franc, F. Avellan, B. Belahadj, Y. V. Billard, L. Brianson-Marjollet, D. Fréchov, D. H. Froman, A. Karimi, J. L. Kveny, and J. M. Michel, *La Cavitation*, Mécanismes Physiques (Presses Universitaires de Grenoble, 1995), p. 64.
[35] F. Jomni, F. Aitken, and A. Denat, ''Dynamics of microscopic bubbles generated by a corona discharge in insulating liquids: influence of pressure,'' J. Electrost. (in press).

Higher-order harmonics of limited diffraction Bessel beams

Desheng Ding
Department of Electronic Engineering, Southeast University, Nanjing 210096, People's Republic of China

Jian-yu Lu
Ultrasound Laboratory, Department of Bioengineering, The University of Toledo, Toledo, Ohio 43606-3390

(Received 18 February 1999; accepted for publication 16 November 1999)

We investigate theoretically the nonlinear propagation of the limited diffraction Bessel beam in nonlinear media, under the successive approximation of the KZK equation. The result shows that the nth-order harmonic of the Bessel beam, like its fundamental component, is radially limited diffracting, and that the main beamwidth of the nth-order harmonic is exactly $1/n$ times that of the fundamental. © *2000 Acoustical Society of America.* [S0001-4966(00)00503-8]

PACS numbers: 43.25.Jh [MFH]

INTRODUCTION

Bessel beams were first developed in 1941 by Stratton and were named undistorted progressive waves.[1] In the past decade, both Bessel beams and a more general type of beam called *X* wave have been widely investigated in the fields of acoustics and optics.[2,3] Theoretically, a J_0 Bessel beam (the lowest-order Bessel beam) with an infinite aperture has a beam profile of the *zero*th-order Bessel function of the first kind in the transverse plane and can travel to an infinite distance without changing its beam profile and amplitude. Numerical simulations and experiments show that even when produced with a finite aperture, this beam has a very large depth of field where the beam profile approximately maintains a J_0 Bessel function distribution. Because of these properties, the Bessel beam may have many potential applications,[2–6] such as ultrasonic imaging. It may also be applied to harmonic imaging developed recently.[3,5,7–9] In addition, the dispersion feature of the J_0 beam has been demonstrated to be applicable in nonlinear optics, where this beam can be viewed as a light beam with a tunable wavelength.[10]

In previous work, we studied theoretically the second harmonic generation of the Bessel beam.[7] Analysis indicates that the second harmonic of this beam is limited diffracting in the radial direction and the main beamwidth of the second harmonic is equal to one-half of that of the fundamental component in the Bessel field. In this paper, we investigate a more general case. It will be shown that for a J_0 Bessel beam, the harmonic of an order n is also radially limited diffracting and its main beamwidth is exactly $1/n$ times that of the fundamental component.

I. THEORY AND RESULTS

Assuming that an axial-symmetric source, with an angular frequency ω and a characteristic radius a, oscillates harmonically in time and that the sound absorption of the medium can be neglected (in attenuating medium, an exponential decay of the fundamental may occur), from the KZK (Khokhlov–Zabolotskaya–Kuznetsov) equation[7,11] and the perturbation method, we obtain the solution for the fundamental component of waves in terms of dimensionless variables[11]

$$\overline{q_l}(\xi,\eta)=\frac{2}{i\eta}\int_0^\infty \exp\left(i\frac{\xi^2+\xi'^2}{\eta}\right)J_0\left(\frac{2\xi\xi'}{\eta}\right)\overline{q_l}(\xi')\xi'\,d\xi', \tag{1}$$

and the solution for the nth-order harmonic component

$$\overline{q_n}(\xi,\eta)=\sum_{l=1}^{n-1}\overline{q}_{nlm}(\xi,\eta), \tag{2a}$$

where

$$\overline{q}_{nlm}(\xi,\eta)=\frac{n^2}{8}\int_{\eta'=0}^{\eta}\int_{\xi'=0}^{\infty}\frac{\xi'}{\eta-\eta'}\times\exp\left(\frac{in(\xi^2+\xi'^2)}{\eta-\eta'}\right)J_0\left(\frac{2n\xi\xi'}{\eta-\eta'}\right)\times\overline{q_l}(\xi',\eta')\overline{q_m}(\xi',\eta')d\xi'\,d\eta', \tag{2b}$$

and $n=l+m$. [Notice that in Eq. (2a) we have ignored the production of lower harmonics from higher harmonics because the pressure amplitude of the $(m+1)$th-order harmonic is assumed to be much smaller than that of the mth-order harmonic.] In these equations, $\xi=r/a$ and $\eta=2z/ka^2$ are the radial and axial dimensionless coordinates, $k=\omega/c$, and c is the speed of sound of medium. Correspondingly, the notations r and z denote the radial and axial coordinates. $\overline{q_l}(\xi')$ is the distribution function of the sound beam on the plane $\eta=0$. Equations (1) and (2) can be viewed as the complex-valued pressure amplitudes in a dimensionless form for the fundamental and nth-order harmonic components, respectively. These solutions are derived under the conditions that the Mach number $\varepsilon\ll 1$ and $(ka)^2\gg 1$.

Assume that the J_0 beam with a scaling parameter α has the form

$$\overline{q_l}(\xi')=J_0(\alpha\xi') \tag{3}$$

at the source. In previous work[7] it has been shown that the fundamental component of this beam is given by

$$\overline{q_l}(\xi,\eta)=J_0(\alpha\xi)\exp\left(-\frac{i}{4}\alpha^2\eta\right), \tag{4}$$

and the second harmonic under an asymptotic condition ($\alpha^2\eta$ is sufficiently large) can be expressed as

$$\overline{q_2}(\xi,\eta)=\sqrt{2}\left(\frac{e^{i3\pi/4}}{4\alpha\sqrt{\pi}}\right)J_0(2\alpha\xi)\,\eta^{1/2}\exp\left(-\frac{i\alpha^2}{2}\eta\right). \quad (5)$$

In the following, we will derive a more general case that the nth-order harmonic component of the Bessel beam has the $J_0(n\alpha\xi)$ function distribution in the radial distance. From Eqs. (4) and (5), we can assume in general that under the asymptotic condition ($\alpha^2\eta$ is sufficiently large) the lth- and mth-order harmonics of the Bessel beam are given by

$$\overline{q_l}(\xi,\eta)=A_lJ_0(l\alpha\xi)\,\eta^{(l-1)/2}\exp\left(-\frac{il}{4}\alpha^2\eta\right) \quad (6)$$

and

$$\overline{q_m}(\xi,\eta)=A_mJ_0(m\alpha\xi)\,\eta^{(m-1)/2}\exp\left(-\frac{im}{4}\alpha^2\eta\right), \quad (7)$$

respectively. From Eq. (2b), it follows that (notice that $\hat{q}_{mln}$ is different from $\overline{q}_{mln}$ by a constant)

$$\begin{aligned}\hat{q}_{nlm}(\xi,\eta)=&\int_{\eta'=0}^{\eta}\int_{\xi'=0}^{\infty}\frac{\xi'}{\eta-\eta'}\\&\times\exp\left(\frac{in(\xi^2+\xi'^2)}{\eta-\eta'}\right)J_0\left(\frac{2n\xi\xi'}{\eta-\eta'}\right)\\&\times J_0(l\alpha\xi')J_0(m\alpha\xi')\\&\times\exp\left(-\frac{in}{4}\alpha^2\eta'\right)\eta'^{(n/2)-1}\,d\xi'\,d\eta'. \quad (8)\end{aligned}$$

To simplify, we change Eq. (8) first to a triple integral

$$\begin{aligned}\hat{q}_{nlm}(\xi,\eta)=&\frac{1}{\pi}\int_{\eta'=0}^{\eta}\int_{\xi'=0}^{\infty}\int_{t'=0}^{\pi}\frac{\xi'}{\eta-\eta'}\\&\times\exp\left(\frac{in(\xi^2+\xi'^2)}{\eta-\eta'}\right)J_0\left(\frac{2n\xi\xi'}{\eta-\eta'}\right)\\&\times J_0(\lambda\alpha\xi')\exp\left(-\frac{in}{4}\alpha^2\eta'\right)\\&\times\eta'^{(n/2)-1}\,d\xi'\,d\eta'\,dt', \quad (9)\end{aligned}$$

where $\lambda=(l^2+m^2-2lm\cos t')^{1/2}$ and the formula

$$\pi J_0(X)J_0(x)=\int_0^{\pi}J_0[(X^2+x^2-2Xx\cos t)^{1/2}]dt \quad (10)$$

has been used. Applying the following

$$\begin{aligned}&\int_0^{\infty}J_0(\alpha t)J_0(\beta t)e^{\pm i\gamma^2t^2}t\,dt\\&=\pm\frac{i}{2}\gamma^{-2}\exp\left[\mp\frac{i}{4}\gamma^{-2}(\alpha^2+\beta^2)\right]J_0\left(\frac{1}{2}\alpha\beta\gamma^{-2}\right), \quad (11)\end{aligned}$$

we have

$$\begin{aligned}\hat{q}_{nlm}(\xi,\eta)=&\frac{i}{2\pi n}\int_{\eta'=0}^{\eta}\int_{t'=0}^{\pi}J_0(\lambda\alpha\xi)\exp\left(-\frac{i\alpha^2\lambda^2\eta}{4n}\right)\\&\times\exp\left[-\frac{i\alpha^2}{4}\eta'\left(\frac{\lambda^2}{n}-n\right)\right]\eta'^{(n/2)-1}\,d\eta'\,dt'. \quad (12)\end{aligned}$$

Formally, the integral about η' in the equation above can be expressed in terms of the incomplete Gamma function $P(a,z)$, which is defined by formula 6.5.1 from Ref. 12. We then obtain

$$\begin{aligned}\hat{q}_{nlm}(\xi,\eta)=&\frac{2i}{\pi n}\exp\left(-\frac{in\alpha^2}{4}\eta\right)\int_{t=0}^{\pi/2}J_0(\lambda\alpha\xi)b^{-n/2}\\&\times\exp(b\eta)\Gamma\left(\frac{n}{2}\right)P\left(\frac{n}{2},b\eta\right)dt, \quad (13)\end{aligned}$$

with $b=i\alpha^2(lm/n)\cos^2t$ and the transformed variable $t=t'/2$. In order to analyze Eq. (13), we concentrate on the function

$$f_n(t)=b^{-n/2}\exp(b\eta)\Gamma\left(\frac{n}{2}\right)P\left(\frac{n}{2},b\eta\right). \quad (14)$$

Note that this function resembles function (11) of Ref. 7, and its real and imaginary parts are extremely similar to the delta function under the asymptotic condition mentioned above. Therefore, Eq. (13) can be approximated well under this condition with

$$\begin{aligned}\hat{q}_{nlm}(\xi,\eta)=&\frac{2e^{i3\pi/4}}{\sqrt{\pi}n^2\alpha}\exp\left(-\frac{in\alpha^2}{4}\eta\right)\\&\times J_0(n\alpha\xi)\,\eta^{(n-1)/2}\sqrt{\frac{n}{lm}}. \quad (15)\end{aligned}$$

From Eqs. (2) and (15), one obtains the nth-order harmonic component of the Bessel beam

$$\overline{q_n}(\xi,\eta)=A_nJ_0(n\alpha\xi)\,\eta^{(n-1)/2}\exp\left(-\frac{in}{4}\alpha^2\eta\right). \quad (16)$$

The coefficient A_n is given by the following recursive relationship [obtained by inserting both Eqs. (16) and (15) into Eq. (2a)]

$$A_n=\frac{\sqrt{n}e^{i3\pi/4}}{4\sqrt{\pi}\alpha}\sum_{l=1}^{n-1}A_lA_m\sqrt{\frac{1}{lm}}. \quad (17)$$

Let

$$A_n=\sqrt{n}\left(\frac{e^{i3\pi/4}}{4\sqrt{\pi}\alpha}\right)^{n-1}C_n, \quad (18)$$

from Eq. (17), we have

$$C_n=\sum_{l=1}^{n-1}C_lC_m \quad \text{or} \quad C_n=\sum_{l=1}^{n-1}C_lC_{n-l}, \quad (19)$$

where C_n is the Catalan number. The first two terms of C_n are given by $C_1=1$ and $C_2=1$, and generally

$$C_n=\frac{1}{n}\binom{2n-2}{n-1}. \quad (20)$$

Finally, the nth-order harmonic component of the Bessel beam can be expressed by

$$\overline{q_n}(\xi,\eta)=\sqrt{n}C_n\left(\frac{e^{i3\pi/4}}{4\sqrt{\pi}\alpha}\right)^{n-1}\exp\left(-\frac{in\alpha^2}{4}\eta\right)$$
$$\times J_0(n\alpha\xi)\,\eta^{(n-1)/2}. \tag{21}$$

Notice that Eq. (21) is obtained by assuming the interaction of nonlinear components in the nearfiled is negligible so that the asymptotic results in Eqs. (6) and (7) can be inserted into Eq. (2) to get Eq. (8).

II. DISCUSSION

From Eq. (21), we see that under the asymptotic condition ($\alpha^2\eta$ is sufficiently large) the nth-order harmonic of the Bessel beam is radially limited diffracting and its beamwidth is exactly $1/n$ times that of the fundamental. Many advantages of the Bessel fundamental beam have been demonstrated in the fields of ultrasonic imaging and tissue characterization.[5,3] Here we point out an additional advantage of this beam when it is applied to harmonic imaging due to the nonlinearity of media.[7–9] It is known theoretically and experimentally that for conventional ultrasonic beams (focused or not), the beamwidth of the nonlinearly generated nth-order harmonic is generally $1/\sqrt{n}$ times that of the fundamental.[13,14] The present analysis indicates that in ultrasonic imaging due to the signal of the nth-order harmonic component, higher resolution can be obtained by using the Bessel beam rather than conventional beams that have the same resolution at the fundamental frequency. It should be noticed that in frequency-dependent attenuating media such as biological soft tissues, harmonics of very high orders are very weak and thus cannot be measured in practice. However, this is true for both limited diffraction Bessel beams and conventional beams.

We must emphasize the validity of Eq. (21) that is derived based on the so-called quasilinear (or successive) approximation method. This equation is not a uniformly accurate expression for the nth-order harmonic component of the Bessel beam. From the perturbation theory, the analysis in this paper is valid when the following inequality is satisfied:

$$\left(\frac{2}{\pi}\right)^{1/2}\frac{\beta(ka)^2}{\alpha}\left(\frac{u_0}{c}\right)\eta^{1/2}<\frac{1}{\sqrt{2}}, \tag{22}$$

where β is the acoustic nonlinearity coefficient of the medium and u_0 is the vibration velocity at the source center. This condition coincides with that obtained in the second harmonic case.[7] This indicates that the nth-order harmonic Bessel beam has a finite depth of field. In fact, the depth of field of the harmonics may be similar to that of the fundamental.

The current analysis is based on the ''ideal'' case under which the aperture of the sound source, i.e., the Bessel beam function, is infinite. In this case, the depth of field of the Bessel fundamental beam is extended into infinity. Accordingly, the depth of field of an nth-order harmonic, as predicted by Eq. (21), is also infinite. In practical applications, however, the aperture sizes of beams are always finite. With a finite aperture, the depth of field[2,4] of a Bessel beam is finite, and is a function of the scaling parameter, the aperture radius, and the wavelength of the beam. Within the depth of field, the property of the fundamental Bessel beam can still be characterized by Eq. (4) and the same may also be true for the nth-order harmonic [Eq. (21)] of the Bessel beam but with a beamwidth that is n times smaller than that of the fundamental. This has been verified numerically in the case of the second harmonic.[8]

Finally, our analysis has ignored the attenuation of sound in media. Although this has little influence on the radial distribution of sound beams, it leads to an exponential decay of the amplitudes in axial direction. In medical applications, higher harmonics have a higher attenuation that may limit the depth of penetration. A further theoretical and experimental study will be conducted for the higher harmonics in attenuating media.

III. CONCLUSION

We have obtained a theoretical expression of an nth-order harmonic component of the Bessel beam. The result shows that an nth-order harmonic of the Bessel beam is also limited diffracting in the radial direction and the main beamwidth is exactly $1/n$ times that of the fundamental component.

ACKNOWLEDGMENTS

This work was supported in part by the National Natural Science Foundation of China via Research Grant No. C-AD40502-19904003, and by Grant No. HL60301 from the National Institute of Health, USA.

[1] J. A. Stratton, *Electromagnetic Theory* (McGraw-Hill, New York, 1941), p. 356.
[2] J. Durnin, J. Opt. Soc. Am. A **4**, 651 (1987).
[3] J.-y. Lu, IEEE Trans. Ultrason. Ferroelectr. Freq. Control **44**, 839 (1997), and references therein.
[4] J. Durnin, J. J. Miceli, and J. H. Eberly, Phys. Rev. Lett. **58**, 1499 (1987).
[5] J.-y. Lu and J. F. Greenleaf, IEEE Trans. Ultrason. Ferroelectr. Freq. Control **37**, 438 (1990).
[6] J.-y. Lu and J. F. Greenleaf, IEEE Trans. Ultrason. Ferroelectr. Freq. Control **39**, 19 (1992).
[7] D. Ding and Z. Lu, Appl. Phys. Lett. **68**, 608 (1996); *ibid.*, **71**, 723 (1997).
[8] J. Synnevag and S. Holm, IEEE Ultrason. Symp., Sendai, Oct. 1998.
[9] M. A. Averkiou, D. N. Roundhill, and J. E. Powers, IEEE Ultrason. Symp., Toronto, Oct. 1997.
[10] T. Wulle and S. Herminghaus, Phys. Rev. Lett. **70**, 1401 (1993).
[11] S. Aanonsen, T. Barkve, J. N. Tjøtta, and S. Tjøtta, J. Acoust. Soc. Am. **75**, 749 (1984).
[12] M. Abramowitz and I. A. Stegun, *Handbook of Mathematical Functions with Formulas, Graphs and Mathematical Tables* (Dover, New York, 1964).
[13] L. Germain and J. D. N. Cheeke, J. Acoust. Soc. Am. **83**, 942 (1988).
[14] D. Rugar, J. Appl. Phys. **56**, 1338 (1984).

Mechanisms for subcritical penetration into a sandy bottom: Experimental and modeling results

Alain Maguer, Warren L. J. Fox,[a] Henrik Schmidt,[b] Eric Pouliquen, and Edoardo Bovio
NATO SACLANT Undersea Research Centre, Viale San Bartolomeo 400, 19138 La Spezia, Italy

(Received 11 May 1998; revised 3 August 1999; accepted 18 August 1999)

This paper presents preliminary results of a recent study whose overall objectives are to determine the mechanisms contributing significantly to subcritical acoustic penetration into ocean sediments, and to quantify the results for use in sonar performance prediction for the detection of buried objects. *In situ* acoustic measurements were performed on a sandy bottom whose geoacoustical and geomorphological properties were also measured. A parametric array mounted on a tower moving on a rail was used to insonify hydrophones located above and below the sediment interface. Data covering grazing angles both above and below the nominal critical angle and in the frequency range 2–15 kHz were acquired and processed. The results are compared to two models that account for scattering of sound at the rough water–sediment interface into the sediment. Although all possible mechanisms for subcritical penetration are not modeled, the levels predicted by both models are consistent with the levels observed in the experimental data. For the specific seafloor and experimental conditions examined, the analysis suggests that for frequencies below 5–7 kHz sound penetration into the sediment at subcritical insonification is dominated by the evanescent field, while scattering due to surface roughness is the dominant mechanism at higher frequencies. [S0001-4966(00)02401-2]

PACS numbers: 43.30.Bp, 43.30.Gv [DLB]

INTRODUCTION

Sonars are important tools for the detection of buried objects such as pipelines or sea mines. The detection of such objects by conventional high frequency sonars (on the order of 100 kHz), which are typically used for imaging objects lying proud on the seabed, is limited by the physics of sound penetration into the sediment.

Various research institutions have proposed buried object detection and classification systems using lower frequencies (on the order of 10 kHz), and normal incidence or swath approaches designed to work above the critical grazing angle. The NATO SACLANT Undersea Research Center (SACLANTCEN) has investigated an alternative approach to buried object detection using a parametric source (with secondary frequencies in the range 2–15 kHz) at low, including subcritical, grazing angles. This approach would provide higher coverage rates compared to normal incidence or swath approaches assuming equivalent detection performance.

In order to pursue this approach, it is very important to understand the basic physics underlying the penetration of acoustic energy into ocean sediments. Snell–Descartes analysis[1] predicts evanescent energy propagating in the sediment for subcritical grazing angles. Recent investigations[2,3] have shown experimental evidence of ''anomalous'' acoustic penetration below the critical grazing angle, where anomalous refers to levels above those predicted for the evanescent field. Several theoretical explanations have been promulgated for this phenomenon, including: scattering due to roughness of the water–sediment interface,[4] the effect of using a narrow beamwidth,[5] the porous nature of the sediment that leads to a second ''slow'' compressional wave with a wave speed less than the speed of sound in water,[6] and volume inhomogeneities within the sediment that have shown a role in backscattering and may also scatter the evanescent wave.[7–10]

The overall goal of this work is to determine the main physical mechanisms for anomalous acoustic penetration into sandy sediments, and to quantify the effect to aid in buried object detection sonar design and performance prediction. Preliminary acoustic measurements addressing this penetration issue were performed using a parametric sonar. This paper describes the analysis of data obtained for hydrophones deployed at two different depths into the sediment (30 and 60 cm) for a wide range of grazing angles and frequencies of the incident beam. Section I describes the experimental setup, including the acoustic equipment used and the rail facility specially designed for this kind of experiment. The results and interpretation of environmental characterization measurements are also given. Section II describes the results obtained after processing the collected data. First, the time domain signals measured on the buried hydrophones are described. Then the variation of the received levels in the sediment is given as a function of the grazing angle, the frequency, and the hydrophone burial depth. Section III succinctly presents the different theoretical approaches and the associated numerical models used for comparison with the data. The first model uses a combination of the standard OASES code[11] and a perturbation approach to compute the 3-D scattered field[12] in the sediment. The second model corresponds to a 3-D simulation of the scattered field in the sediment using Helmholtz–Kirchhoff theory on a rough surface.[13] The two models operated on the same realization of a rough surface with characteristics similar to that mea-

[a]Currently with: Applied Physics Laboratory, University of Washington, Seattle, WA 98105.
[b]Currently with: Ocean Engineering Department, MIT, Cambridge, MA 02139.

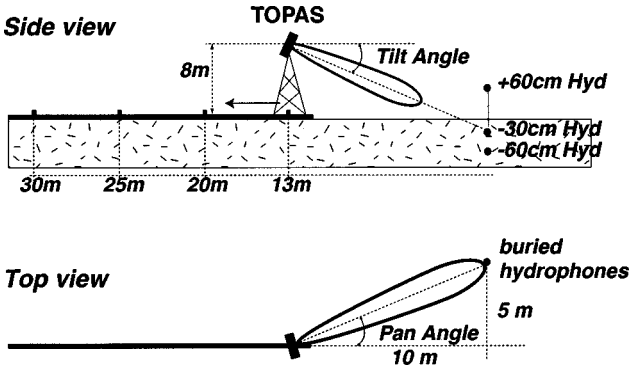

FIG. 1. Side and top views of the experimental geometry.

sured by divers during the at-sea experiment. Section IV presents the comparison of the data to the models. The analysis suggests that, for the specific seafloor and experimental conditions examined, subcritical penetration is dominated by the evanescent field below 5–7 kHz, while scattering due to surface roughness is the dominant mechanism for higher frequencies. Section V summarizes the effort and gives directions for future work.

I. EXPERIMENTAL SETUP

A. Equipment and geometry

The sonar used for this experiment was the commercial TOPAS PS 040 (TOpographic PArametric Sonar).[14] This transducer transmits a weighted high frequency, or ''primary'' frequency, burst centered around 40 kHz. The nonlinear properties of the water produce a low frequency, or ''secondary'' frequency, superdirective radiation in the frequency range 2–15 kHz. The source level is approximately 238 dB *re*: 1 μPa @ 1 m for the primary frequency. The secondary frequency source levels vary from about 190 to 203 dB *re*: 1 μPa @ 1 m in the 2–15 kHz frequency band. The broadband beamwidth in the secondary frequency band is roughly 3.5 by 7.0 degrees. A complete calibration of the TOPAS transmitter may be found in Ref. 14.

Figure 1 shows side and top views of the experimental geometry for the penetration measurements. The transmitter was mounted on a tower fixed 8 m from the seafloor. The tower, with a stabilizing structure underneath as seen in Fig. 2, was then mounted on a 24-m-long linear rail along which it could be precisely positioned using a pneumatic motor. A small video camera was mounted on the structure, trained on markings on the rail, in order to provide an accurate measure of the lateral position of the tower.

The TOPAS transmitter was mounted in a pan-and-tilt assembly with a motion reference unit (MRU) so that the pointing direction of the sonar could be accurately controlled and measured. Figure 3 shows the structure used to support the transmitter, and the pan-and-tilt motors. The 16-element

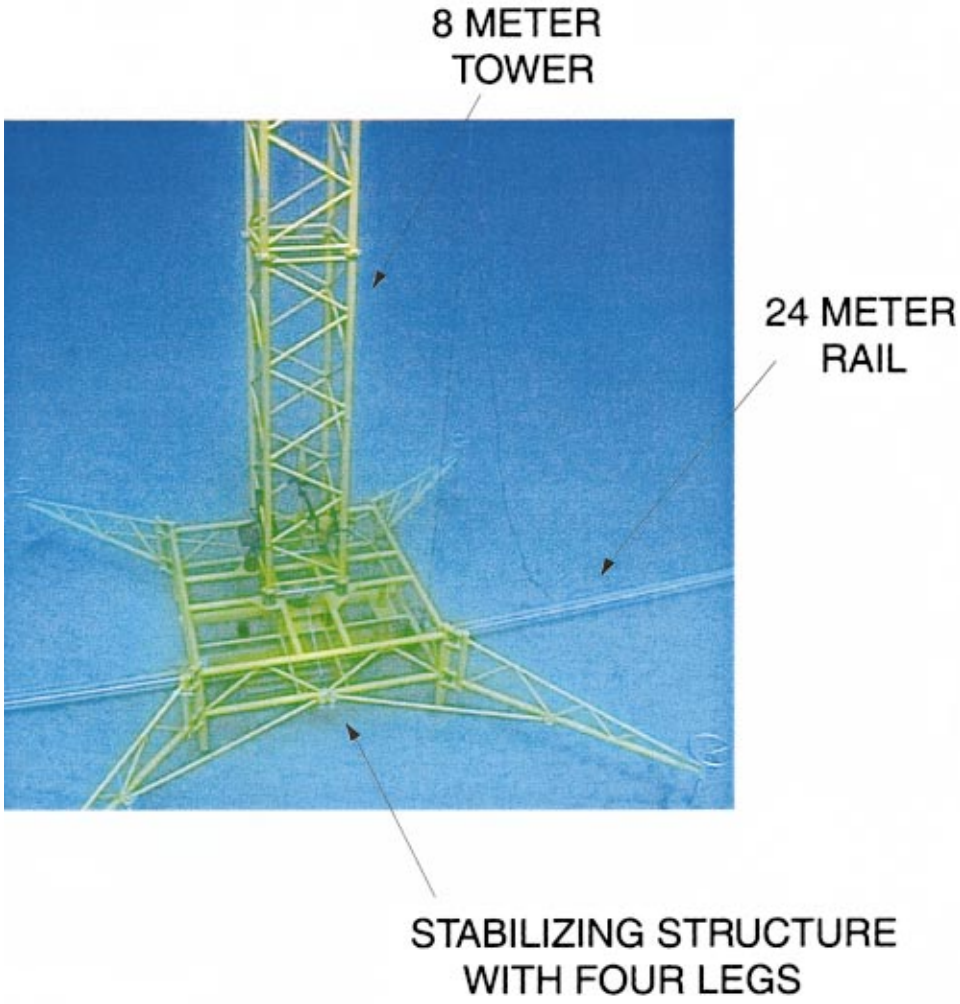

FIG. 2. Tower, stabilizing structure, and rail.

FIG. 3. TOPAS parametric sonar with pan-and-tilt motors.

array shown in the figure was used as a receiver for a different portion of the trial.

As seen in the side view of Fig. 1, three receiving hydrophones were used (Reson type TC4034), mounted on a rigid vertical stick. One was suspended 60 cm above the sea floor. The two other hydrophones were buried into the sediment at -30 cm and -60 cm, respectively. The hydrophone pre-amplifiers were specifically designed to reject the primary frequency band of the parametric sonar, thereby providing better dynamic range for the secondary frequency signals. The grazing angle was varied by moving the tower along the rail. For a given lateral position on the rail, the transmitter was mechanically steered via the pan-and-tilt unit so that the main response axis of the transmit beam was pointing to the patch of seafloor above the buried hydrophones. Subsequently, a series of pulses was transmitted and the signals received on the three hydrophones were recorded.

Of some concern in an experiment like this is the use of a parametric source, since it has been previously shown that they can produce sediment penetration effects significantly different from conventional linear sources when the primary near field is truncated by the water–sediment interface.[15] For the TOPAS, the primary near-field distance is calculated to be 10.67 m.[14] Since this is less than the ranges considered in the experiment, this truncation effect is not considered as a contributor to any penetration effects.

B. Bottom properties

The experiment was performed in 10-m water depth on a sandy bottom in the Biodola Gulf on the north side of Elba Island, Italy. A sub-bottom profiling (''boomer'') survey was performed in the area before burying the hydrophones. The first layer of sand was found to be approximately 1.8 m thick. Cores (30 cm deep) were collected in order to measure the average sound speed (1720 m/s), porosity (44.6%), grain size (0.2-mm mean diameter), and density (1.92 g/cm^3) of the sediment. CTD measurements in the water column indicated a sound speed of 1530 m/s, resulting in a nominal critical angle of arccos (1530/1720)$\cong$27.2 degrees. It is important to note that the sediment sound speed was measured with laboratory equipment operating at 200 kHz. The relevance of this measurement to the low frequency penetration is an important issue which will be addressed in Sec. IV and in the Appendix.

Measurement of the bottom roughness was performed by divers who estimated the sand ripple height and wavelength. It was found that the rms roughness was on the order of 2.5 cm, and the mean sand ripple wavelength was estimated to be 20 cm. The mean sand ripple orientation relative to the rail was estimated to be roughly 30 degrees.

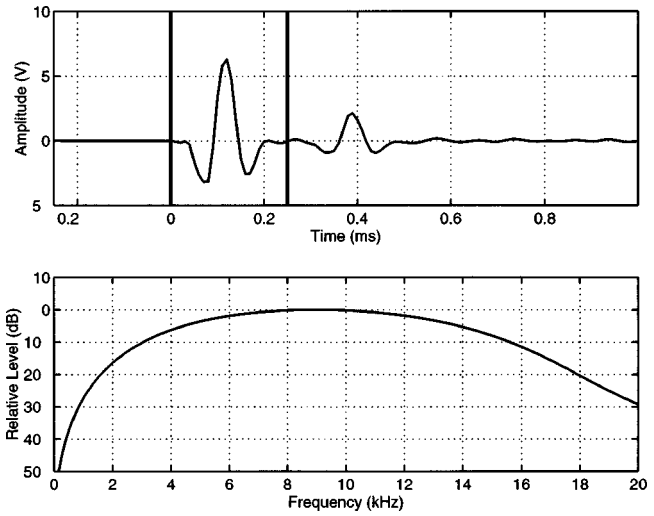

FIG. 4. Example of a signal recorded on the hydrophone in the water (top). The direct path signal (between 0 and 0.25 ms) is considered as a reference transmit signal for further processing, and is shown in the frequency domain in the bottom plot. The other signal centered at 0.4 ms is due to the bottom bounce path.

II. EXPERIMENTAL RESULTS

As mentioned in the previous section, the penetration data were collected by mechanically steering the transmitter to the buried hydrophones and transmitting a series of pings. By steering to the hydrophone in the water, reference signals were also recorded. An example can be seen in Fig. 4. The top plot shows the reference signal in the time domain. The portion of the signal between 0 and 0.25 ms (between the two dark vertical bars) is the direct path transmitted signal. This gated portion of the signal is then the reference transmitted signal used for further processing. The other arrival centered near 0.4 ms is due to the bottom bounce path. This roughly 0.25-ms pulse (often called a ''Ricker'' pulse) is a common seondary frequency transmit signal for parametric sources like the TOPAS.[14] Reference signals were collected for each rail position (and, hence, range and grazing angle). The bottom plot of Fig. 4 shows the gated reference signal in the frequency domain.

Figure 5 shows the received signals on the −30-cm buried hydrophone for four grazing angles: 30, 22, 18, and 15 degrees. The grazing angle (GA) is marked at the top of each plot. These signals are the result of coherently averaging the received time series over a set of consecutive transmissions in order to maximize signal to noise ratio. Between 30 and 50 pings were used for the various averages. Note that the vertical scales are not the same from plot to plot. The time scales are relative, with the 0-ms reference chosen to be the estimated received signal starting time for each signal. For all grazing angles, the signals are characterized by an initial pulse that looks much like the reference signal of Fig. 4, followed in time by lower level signals that grow in relative amplitude (with respect to the initial pulse) at lower grazing angles. Figure 6 shows the corresponding received signals on the −60-cm buried hydrophone. The 30 degree grazing angle signal is much like those seen on the −30-cm hydrophone. The other three signals, however, tend to be dominated by the signals following the initial pulse. Further interpretation

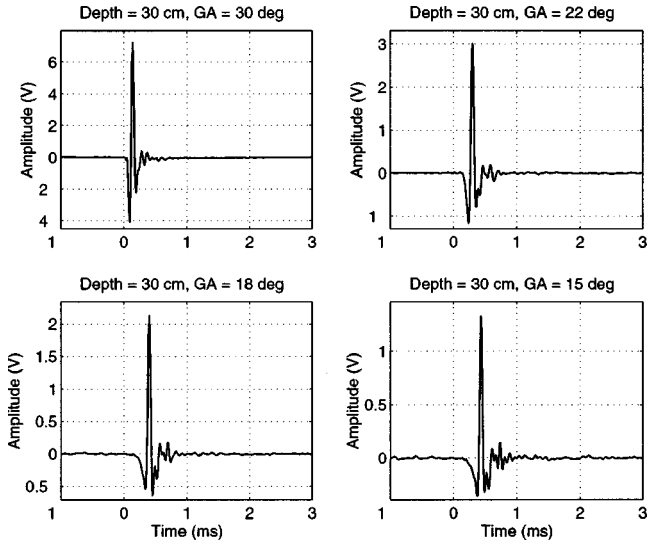

FIG. 5. Received signals at different grazing angles (30, 22, 18, and 15 degrees) for the hydrophone buried −30 cm in the sediment.

of these signals will appear in the section dealing with comparison to models (Sec. IV).

In order to quantify the acoustic penetration into the sediment for comparison to the models used in this study, a measure called the ''penetration ratio'' was devised. For a given frequency, the penetration ratio is defined as the magnitude squared of the ratio of the pressure at a point in the sediment to a reference pressure,

$$PR(f)=\left|\frac{P_{\mathrm{sed}}(f)}{P_{\mathrm{ref}}(f)}\right|^2=\frac{|P_{\mathrm{sed}}(f)|^2}{|P_{\mathrm{ref}}(f)|^2}. \tag{1}$$

The reference pressure is an idealized pressure that would exist at the location in space directly above the buried hydrophone at the water–sediment interface in the absence of the sediment. In the case of a plane wave, the reference pressure would simply be the incident field. In our case, the reference pressure is taken from the frequency domain description of the gated reference signal as described earlier.

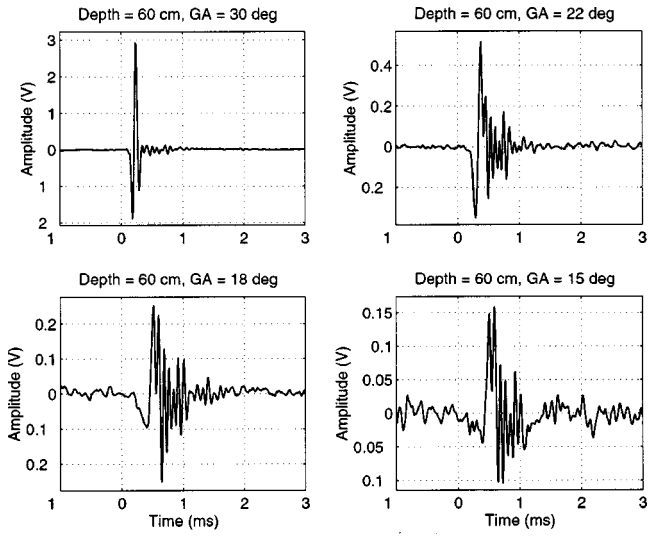

FIG. 6. Received signals at different grazing angles (30, 22, 18, and 15 degrees) for the hydrophone buried −60 cm in the sediment.

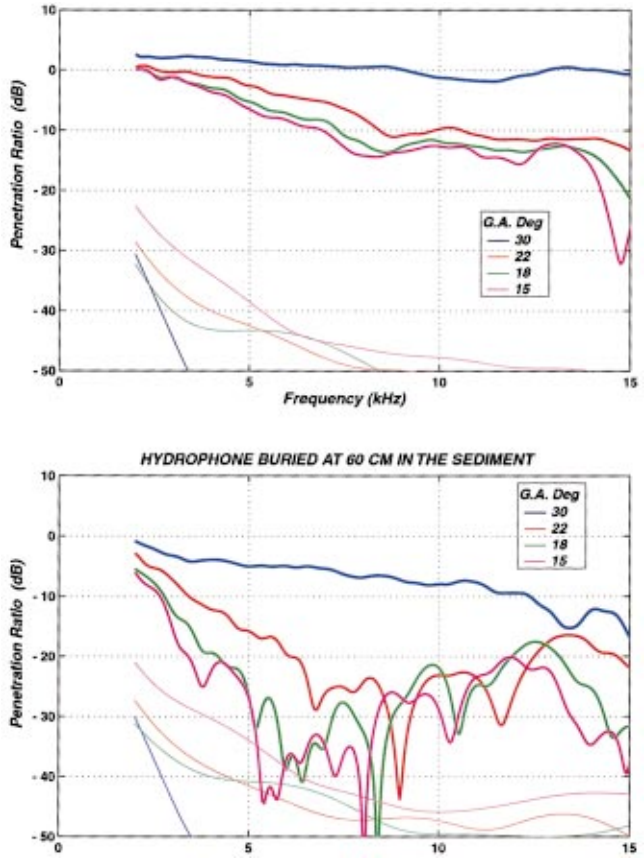

FIG. 7. Penetration ratio in dB (thick lines) versus frequency and grazing angle for the −30-cm (top plot) and −60-cm (bottom plot) buried hydrophones. The thin lines correspond to estimated background noise levels.

Figure 7 displays the computed penetration ratios in dB (thick lines) for the data on the −30-cm (top plot) and −60-cm (bottom plot) buried hydrophones at the four grazing angles. The $P_{\mathrm{sed}}(f)$ values were computed by gating the signals from Figs. 5 and 6 between 0 and 2.0 ms, zero padding, and Fourier transforming. The $P_{\mathrm{ref}}(f)$ values were computed from the appropriate reference signals. The thin lines in Fig. 7 are estimates of the background noise levels in terms of the penetration ratio. The raw noise level estimates were computed by taking a 2-ms window of data before the gated signals used to compute $P_{\mathrm{sed}}(f)$, and applying standard techniques for spectral analysis of stationary random signals with a Hamming data taper and Parzen lag window (see Ref. 16 for details). These raw noise level estimates were then ''normalized'' with the reference signal [similar to the way in which the $|P_{\mathrm{sed}}(f)|^2$ values are ''normalized'' via Eq. (1)] in order to give an indication of the background noise levels for the penetration ratios.

For the −30-cm case (top plot of Fig. 7), the estimated signal-to-noise ratios (SNRs) are in general quite high, with values greater than 20 dB. The penetration ratios for the lowest three grazing angles are characterized by a nearly linear falloff versus frequency until 7 or 8 kHz, and a levelling out at higher frequencies. For any given frequency, the penetration ratio also tends to decrease with grazing angle. The penetration ratio for the highest grazing angle (30 degrees) is at an overall higher level than the other three, and the higher frequency phenomenon noted above is not as obvious.

For the −60-cm case (bottom plot of Fig. 7), the SNRs are generally lower, especially for the lowest grazing angle (15 degrees) below roughly 8 kHz. As for the −30-cm case, the highest grazing angle exhibits an overall higher penetration ratio than the other grazing angles, and shows a nearly linear falloff versus frequency across the band. The other grazing angles show a tendency toward a linear falloff versus frequency in the lower part of the band (as for the −30-cm case), with increasing (although erratic) levels between roughly 8 and 15 kHz. Note that the SNRs for the three lowest grazing angles are quite high (roughly 20–30 dB) in the higher frequency regime.

The following section (Sec. III) will describe the models used to compare with the data. Some of the features seen in the data will be addressed more fully in the data-models comparison section (Sec. IV).

III. MODEL DESCRIPTIONS

The experimental penetration data have been compared to two models based on different approximations to the handling of the bottom penetration problem, although both consider roughness scattering. Both models include the evanescent component as well as the roughness scattering contribution, but one uses a low frequency approximation for modeling the scattering contribution, while the other uses a high frequency approximation. The frequencies involved in the experiments are in the transition region between the two approximations, so the performance of both modeling approaches was *a priori* uncertain. In addition, neither of the models had earlier been compared against other models or experimental data for the penetration problem. Therefore, the present study also served an important model validation purpose. The models considered here were mainly used to validate the obtained experimental results and to qualitatively (and not quantitatively) identify the main mechanisms responsible for the sub-critical penetration.

The first model is based on OASES-3D[12] which uses wave number integration in combination with a perturbation approach to compute the three-dimensional coherent and scattered fields in stratified ocean waveguides with rough interface patches (a low frequency approximation). The second model uses Helmholtz–Kirchhoff theory for penetration through a rough surface[13] (a high frequency approximation).

A. OASES-3D bottom penetration modeling

The three-dimensional version of the OASES propagation model has recently been combined with a perturbation approach in order to model scattering from rough seabeds. This technique allows full wave theory modeling of the 3-D field associated with bottom interaction of narrow-beam sonars such as the TOPAS parametric source used in this investigation.[12] The new OASES-3D model consistently handles both the coherent component of the full waveguide field including the evanescent bottom penetration, and the scattering produced by seabed roughness.

As a first step, the standard OASES code is applied to compute the field in a waveguide with smooth interfaces.

Subsequently, the interface scattering is computed using the perturbation approach to rough elastic interface scattering developed by Kuperman and Schmidt.[17,18] The original perturbation theory is based on a 2-D Fourier transform formulation for interfaces of infinite extent. For computational reasons this approach is only feasible for evaluation of the scattered field in a plane geometry with one-dimensional roughness.[18] However, many sonar problems are characterized by a sonar ''footprint'' or ''patch'' of limited spatial extent, as is the case for the TOPAS. An alternative implementation of the perturbation theory has therefore been devised, which in effect represents the insonified roughness patch as a virtual source distribution. The field produced by this source distribution can then be very efficiently evaluated by wave number integration models such as OASES using azimuthal Fourier synthesis.[19]

The approach used in OASES-3D uses a spatial realization of the roughness statistics, or a directly measured roughness patch, to generate a single field realization. The coherent component of the field, including the evanescent bottom field, is computed by the OASES code[11] using standard wave number integration for stratified waveguides.[20] This approach expresses the field produced by a point source of time dependence $\exp(-i\omega t)$ in each layer l in the stratification in terms of an integral representation,

$$\chi_l(r)=\int_0^\infty [\tilde{\chi}_l^+(k_r)e^{ik_z z}+\tilde{\chi}_l^-(k_r)e^{-ik_z z}]k_r J_0(k_r r)dk_r . \tag{2}$$

Here z and r are the depth and range coordinates, and k_r is the horizontal wave number. The depth dependence of the field is represented by the exponentials, with k_z being the vertical wave number, defined as

$$k_z=\begin{cases} \sqrt{k_l^2-k_r^2}, & k_r \leqslant k_l , \\ i\sqrt{k_r^2-k_l^2}, & k_r > k_l , \end{cases} \tag{3}$$

where $k_l=\omega/c_l$ is the medium wave number for layer l. In this form, the integral representation clearly separates the field into waves propagating vertically in the layer ($k_r \leqslant k_l$), and waves which are exponentially growing or decaying, the evanescent waves ($k_l \leqslant k_r$), separated by the critical wave number $k_r=k_l$. The amplitudes $\tilde{\chi}_l^{\pm}(k_r)$ are found by matching the boundary conditions of continuous particle motion and stresses (pressure) at all interfaces in the stratification.

Following the computation of the coherent field by wave number integration, the scattering by rough interfaces can be consistently handled using the method of small perturbations developed by Kuperman and Schmidt.[17] Here, the term ''small'' is intended with respect to the acoustic wavelength. For arbitrary fluid-elastic stratifications, this theory decomposes the wave field into coherent and scattered components of the field potential χ_l in layer number l,

$$\chi_l=\langle\chi_l\rangle+s_l . \tag{4}$$

Away from physical sources and the rough interfaces, the scattered potential satisfies the same homogeneous Helmholtz equations as the coherent field with the same boundary conditions. However, the physical sources are replaced by a virtual source distribution resulting from perturbation theory as a convolution of roughness and the coherent field.[17,21,22]

For a finite size roughness patch or sonar footprint, the scattered field can then be represented by a spatial integral over the patch P,

$$s(\mathbf{x})=\int_P G_v(\mathbf{x},\mathbf{x}_v)d^2\mathbf{x}_v , \tag{5}$$

where $G_v(\mathbf{x},\mathbf{x}_v)$ is a generalized Green's function satisfying the standard Helmholtz equation and the virtual source distribution. The result is a representation of the scattered field as an azimuthal Fourier series of wave number integrals given by

$$s(r,\theta)=\sum_{m=-\infty}^{\infty}\exp(im\theta)\int dqqJ_m(rq) \times\left[\int_P \tilde{G}_v^m(q,r_v,\theta_v)r_v\,dr_v\,d\theta_v\right]. \tag{6}$$

B. Helmholtz–Kirchhoff bottom penetration modeling

This approach is based on the Helmholtz–Kirchhoff integral and the Kirchhoff approximation.

In the case of water–seafloor–water scattering, according to Brekhovskikh,[23] for a deterministic surface, the following local criterion (Rayleigh criterion) has to be satisfied in order that the Helmholtz–Kirchhoff approximation may be used:

$$P=2kr_c\sin\theta_g \gg 1. \tag{7}$$

k is the wave number, r_c is the local radius of curvature, and θ_g is the local grazing angle of the incident sound wave.

In Ref. 13, it was found, considering the variation of the Rayleigh parameter for a random rough surface, that any model based on the Kirchhoff approximation intending to quantify the sub-critical penetration into sandy seafloors should not be used at grazing angles lower than 10° to 15° if the frequency is as low as 2–3 kHz. The Kirchhoff approximation is only valid for gently undulating surfaces, i.e., for surfaces whose ratio σ_s/l is small, where σ_s is the seafloor rms roughness and l the average correlation length. For example, at 5 kHz, in the 10°–30° range, the condition [Eq. (7)] is not satisfied for seafloors having a ratio σ_s/l larger than 0.15.

A full description of this model and discussion of its validity regions is beyond the scope of this paper, and may be found in Ref. 13. An overview of the modeling method is presented here.

Figure 8 shows a schematic of the geometry considered for the calculation. The model first analyticaly expresses the elementary pressure contribution $dp(\mathbf{R}')$ received at a fixed point $\mathbf{R}'$ within the sediment from a point $\mathbf{R}$ located on the water–sediment surface.

Considering a directional source at $\mathbf{P}$ transmitting a pulse $p_0e(t)$ with a beam directivity gain $D_i(\mathbf{P}-\mathbf{R},f)$, $dp(\mathbf{R}')$ takes the form (in the time domain)

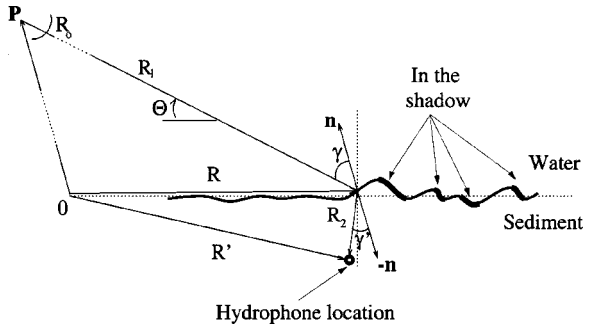

FIG. 8. Geometry of the Helmholtz–Kirchhoff formulation. The source is located at **P** and is transmitting an acoustic signal towards the seafloor. A hydrophone is located at $\mathbf{R}'$ in the sediment. The element of surface $d\mathbf{S_r}$ is located at **R**. **n** is the local normal to the surface. γ is the angle between the normal vector **n** and the incident direction. γ' is the angle between the normal vector **n** and the vector $\mathbf{R_2}$. θ is the grazing angle.

$$dp(\mathbf{R}',t)=\frac{p_0R_0}{4\pi c_1R_1R_2}[1+\Re_{12}(\mathbf{R})]e'\left(t-\frac{R_1+\overline{n_2'}R_2}{c_1}\right)\times[\cos(\gamma(\mathbf{R}))+\overline{n_2}\cos(\gamma'(\mathbf{R}))]*\mathcal{F}^{-1}\{e^{-(\alpha f R_2)/2}\}*\mathcal{F}^{-1}\{D_i(\mathbf{P}-\mathbf{R},f)\}d\mathbf{S_R}, \quad (8)$$

where $1+\Re_{12}(\mathbf{R})$ is the local water–sediment plane wave transmission coefficient, $\gamma(\mathbf{R})$ is the angle made between the incident direction and the normal vector **n** to the surface at **R**, $\gamma'(\mathbf{R})$ is the angle made between the refracted direction and the normal vector $-\mathbf{n}$ to the surface at **R**, $\overline{n_2'}$ is the real part of the mean water–sediment index of refraction $\overline{n_2}$, and c_1 is the average sound speed in water. The term $d\mathbf{S_R}$ corresponds to a surface element of the seafloor at **R**. $\mathcal{F}^{-1}$ denotes an inverse Fourier transform and $*$ denotes convolution. The term α is the attenuation term assuming a linear dependence with frequency.

The surface ensemble is defined as all the seafloor elementary surfaces (S_t) which are seen from the source at **P**, i.e., those which are not in the ''shadow zones,'' therefore assuming geometric scattering from the interface. It must be mentioned that the implementation of the shadowing by abruptually truncating the surface field at the shadow edges may cause unphysical diffraction from these edges.

The second step of the model consists of computing the total pressure field received at the hydrophone $p(\mathbf{R}',t)$ by summing all the elementary pressures $dp_{(S)}(\mathbf{P}',t)$ over the surface (S_t),

$$p(\mathbf{R}',t)=\int_{(S_t)}dp(\mathbf{R}',t). \quad (9)$$

C. Rough water–sediment interface modeling

Both modeling approaches differ from some traditional scattering computations in that they do not use formal averaging to achieve field statistics. Instead the scattered fields are computed deterministically using modeled realizations of a seabed with given roughness statistics. In the studies performed here, both models use the same synthetic rough surface with spatial characteristics similar to those observed during the experiment.

A filtered Gaussian spectrum (following the method of Pouliquen *et al.*[13]) that accounts for both isotropic and anisotropic features was chosen to describe the seafloor interface. It is expressed in the general form

$$W_s(\mathbf{K})=Q_s(\mathbf{K},\mathbf{K_c})+Q_s(\mathbf{K},-\mathbf{K_c}), \quad (10)$$

where $\mathbf{K}=(K_x,K_y)$ is the spatial frequency, $\mathbf{K_c}=(K_{xc},K_{yc})$ describes the average ripple wavelength, and

$$Q_s(\mathbf{K},\mathbf{K_c})=\begin{cases} C\exp\left(\dfrac{2\rho l_x l_y(K_x-K_{xc})(K_y-K_{yc})-l_x^2(K_x-K_{xc})^2-l_y^2(K_y-K_{yc})^2}{2(1-\rho^2)}\right), & |K|>K_{hp}, \\ 0, & |K|\leqslant K_{hp}. \end{cases} \quad (11)$$

Here, l_x and l_y are the components of the correlation length, and ρ is the correlation coefficient between the x and the y direction (ρ will be set to 0 in this study for simplicity). The spatial frequency K_{hp} sets the limit of a high-pass filter which is necessary for typical seafloors for which low frequency content is absent (the first moment of the sea floor height field is expected to be zero). This filter removes very large-scale features. C is a normalizing factor such that

$$\int_s W_s(\mathbf{K})d\mathbf{K}=\sigma_s^2, \quad (12)$$

where σ_s is the rms roughness.

The spectrum defined above is used for generating realizations of the water–sediment interface based on the Fourier synthesis method.[24] To generate a seafloor realization, a surface height power spectrum is first generated by randomizing part of the phase and amplitude of $W_s(\mathbf{K})$. It is then converted to an amplitude field in the spatial domain using an inverse Fourier transform. Figure 9 shows an example of a generated seafloor interface height field used for the simulations to follow. Using the information about the seafloor gathered during the experiment, the rms roughness σ_s is set to 2.5 cm, $|\mathbf{K_c}|$ is 31.5 rad/m (giving a ripple wavelength of 20 cm), K_{hp} is 10 rad/m, and the ripple direction (skewness) is 30 degrees.

IV. DATA-MODELS COMPARISON

As mentioned in the previous section, both models account for the coherent component of the sound field in the

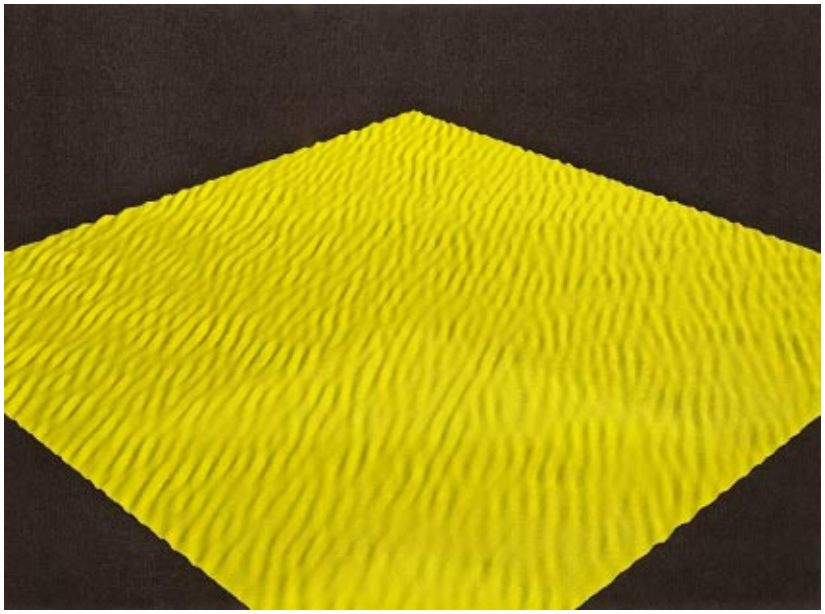

FIG. 9. 3-D display of a 10 m by 10 m seafloor realization. The rms roughness $\sigma_s = 2.5$ cm, $|\mathbf{K}_c| = 31.5$ rad/m (giving a ripple wavelength of 20 cm), and spatial frequency for the high-pass filter $K_{hp} = 10$ rad/m.

sediment, as well as a component due to scattering from the rough water–sediment interface. While the first component can be thought of in a deterministic sense, the second should be considered in a stochastic sense, i.e., the particular seafloor above the buried hydrophones is a realization of a two-dimensional random process. It must be kept in mind, therefore, that since the given realization present during the experiment could not be reproduced exactly for the simulations, more qualitative interpretations of the levels for the scattering phenomenon are necessary.

The models were run assuming the experimental geometry presented in Sec. I, the measured density of the sediment (1.92 g/cm^3), and the realization of the seafloor roughness shown in Fig. 9. A compressional wave attenuation of 0.5 dB/λ (where λ is the wavelength in m) was assumed, which is a nominal value for this type of sediment.[20] During the data-models comparison, however, it was found that a sediment sound speed of 1685 m/s was necessary in order to bring the model results into agreement with the data. Although this sound speed is within the estimated error (1720 m/s $\pm 3\%$) of the sound speed measurement system used on the cores (travel time measurements using short acoustic pulses centered at 200 kHz), a possible theoretical explanation for lower sound speed at lower frequencies is presented in the Appendix. Also note that the use of this sound speed implies a change of the nominal critical angle to $\arccos(1530/1685) \cong 24.8$ degrees.

Figure 10 shows the comparison of the penetration ratio data from the -30-cm hydrophone at 30 degree grazing angle (solid green line) to the various model results. Assuming plane wave isonification, OASES predicts the solid red line, which is somewhat above the data. The dashed blue line shows the results from OASES when the finite width of the TOPAS beam is approximated by using a focused vertical array.[5] It must be mentioned that the achieved beamwidth with this technique is not meant to exactly reproduce the TOPAS beampattern. The main objective of this simulation is to show qualitatively the influence of a relatively narrow beamwidth on the penetration. Note that the finite beamwidth lowers the penetration ratio at this supercritical angle. The reason is that the finite beamwidth generates paths that, in the vicinity of the critical angle, are below the critical angle, and therefore contribute less than the above critical angle paths to the penetration.

The dash-dot black line in Fig. 10 shows the results of the Helmholtz–Kirchhoff model. The levels predicted are fairly consistent with the data, although they tend to fall off slightly at the lower frequencies. The black crosses show the results of the penetration ratio due to surface scattering calculated by OASES-3D. They are well below the coherent field predicted by OASES. In order to mitigate somewhat the realization specific fluctuations of the model output, the

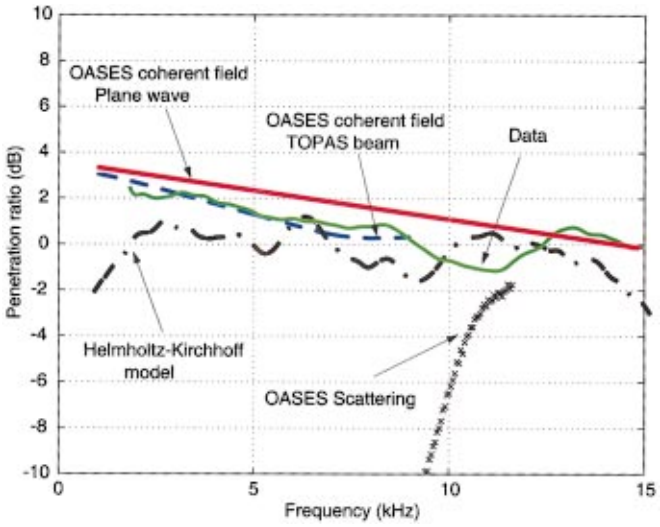

FIG. 10. Measured and modeled penetration ratio for hydrophone at -30 cm. The grazing angle is 30 degrees. The data are shown in green. The OASES coherent field is shown in solid red line (plane wave) and dashed blue line (TOPAS beam). The OASES scattered field is shown by black crosses. The Helmholtz–Kirchhoff model results are shown in dash-dot black line.

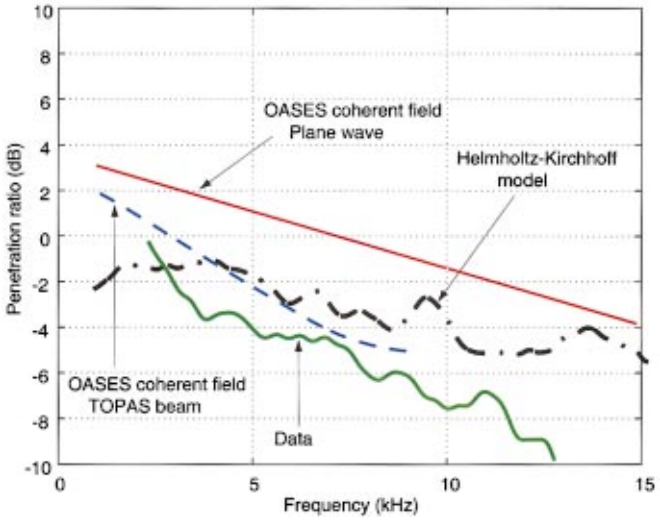

FIG. 11. Measured and modeled penetration ratio for hydrophone at −60 cm. The grazing angle is 30 degrees. The data are shown in green. The OASES coherent field is shown in solid red line (plane wave) and dashed blue line (TOPAS beam). The contribution of the OASES scattered field was not high enough to be shown on the figure. The Helmholtz–Kirchhoff model results are shown in dash-dot black line.

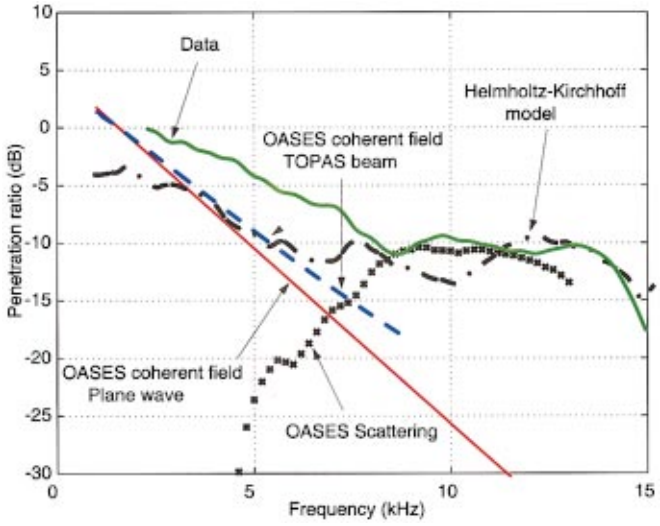

FIG. 12. Measured and modeled penetration ratio for hydrophone at −30 cm. The grazing angle is 18 degrees. The data are shown in green. The OASES coherent field is shown in solid red line (plane wave) and dashed blue line (TOPAS beam). The OASES scattered field is shown by black crosses. The Helmholtz–Kirchhoff model results are shown in dash-dot black line.

OASES-3D scattering result was obtained by averaging the penetration ratio over five spatially separated hydrophone locations at the same depth (−30-cm depth in this case, with one simulated hydrophone at the center of the illuminated patch, and four others 0.5 m to the left, right, front, and back). This procedure is also followed for the other OASES-3D results to be be shown. In sum, these results imply that the energy in the sediment for this geometry across the frequency band of interest is dominated by the coherent field.

Figure 11 shows the comparison of the penetration ratio on the −60-cm hydrophone at 30 degree grazing angle (solid green line) to model results. As in the −30-cm case for this grazing angle, the TOPAS beam simulation (dashed blue line) shows a lower penetration ratio than the plane wave results (solid red line), and is relatively consistent with the data values. The Helmholtz–Kirchhoff model output (dash-dot black line) also shows a level and trend similar to that of the data. The results of the OASES-3D scattering model are too low to appear on the plot. Again, in an overall sense, these results imply that the energy measured in the sediment for this case is dominated by the coherent field across the frequency band examined.

Figure 12 shows the data-models comparison for the −30-cm hydrophone at 18 degree grazing angle, well below the nominal critical angle. Note that the penetration ratio axis of this plot extends to −30 dB, as opposed to the two previous comparisons that only extend to −10 dB. For subcritical cases, the TOPAS beam simulation (dashed blue line) gives a higher penetration ratio than the plane wave results (solid red line). This is due to the finite spatial spectrum of the source, i.e., some of the energy is arriving at the water–sediment interface above the ''geometrical'' critical angle assumed for a plane wave.[5] The level of the OASES-3D scattering result (black crosses) is consistent with the data above roughly 8 kHz, where this component is dominating the coherent prediction of OASES. The Helmholtz–Kirchhoff results are also consistent with the data in this frequency regime. Unfortunately, there does appear to be a roughly 5-dB upward bias of the data compared to the models below 8 kHz in this case. This may be attributable to beampattern effects that are not completely taken into account by the models, but it remains a result that is not entirely consistent with the other data-model comparisons. It is important to mention that the Helmholtz–Kirchhoff approximation, as already mentioned previously, tends to be less and less valid as long as the frequency decreases, which could also explain the mismatch between the data and the

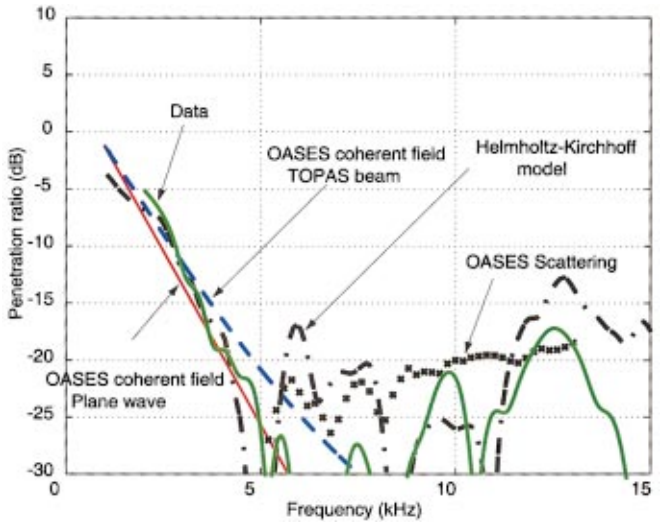

FIG. 13. Measured and modeled penetration ratio for hydrophone at −60 cm. The grazing angle is 18 degrees. The data are shown in green. The OASES coherent field is shown in solid red line (plane wave) and dashed blue line (TOPAS beam). The OASES scattered field is shown by black crosses. The Helmholtz–Kirchhoff model results are shown in dash-dot black line.

Helmholtz–Kirchhoff model results at the lower frequencies of our band of interest.

Finally, Fig. 13 shows the data-models comparison for the −60-cm hydrophone at 18 degree grazing angle. The data (solid green line), OASES coherent field results (plane wave is solid red, TOPAS beam is dashed blue), and Helmholtz–Kirchoff result (dash-dot black) show good consistency below 5 kHz, where it appears that the evanescent field is the dominant component of the field. Above this frequency, the models show moderate agreement (in terms of mean level) with the data. The OASES scattering result (black crosses) shows a smoother variation with frequency due to the spatial averaging performed.

Referring back to Figs. 5 and 6, we can now attempt to interpret some of the features seen in the time domain signals. For the signals on the −30-cm hydrophone (Fig. 5), the initial pulse can be seen to widen in time, which can be associated with the effective ''filtering'' the sediment has performed on the signal via the exponential decay versus frequency of the evanescent wave. Also, the signals arriving after the main pulse both at −30 and −60 cm are consistent with the interface scattering mechanism as described by Thorsos *et al.*[4]

Although not presented in detail here, two other separate modeling efforts were made which are worthy of note. Using OASES, shear speeds of 400 m/s and less (typical values for this type of sediment) were assigned to the sediment layer, but the model output did not show any significant penetration effect with this addition (the model results presented previously assumed no support for shear waves in the sediment). Also using OASES, the sediment was treated as a poroelastic medium via Biot theory. Since many of the Biot parameters were not available, nominal values were used and varied within reasonable ranges (see also the Appendix). The levels of the generated slow wave observed in these simulations was far below any of the levels observed in the data.

Several shortcomings of these data have prevented meaningful time domain, ''arrival separation'' type processing: the sparsity of the measurements in receiver position and grazing angle, and the low SNR in parts of the frequency band on the −60-cm hydrophone. This type of processing could help to separate and define the mechanisms contributing to the penetration. Lacking this, we can only say that the mechanisms modeled (finite beamwidth and interface scattering) provide a reasonable explanation for the levels of energy observed in the sediment, although other mechanisms cannot be definitively ruled out at this time.

V. CONCLUSION

This paper has described an initial attempt to determine the cause of sound penetration into sediments in the frequency band 2–15 kHz and to quantify the amount of energy received on buried hydrophones for insonification below the critical angle. The comparison between the data and the models dealing with the evanescent wave and the roughness scattering suggests, for this bottom type, the presence of two main mechanisms, the relative significance of which depends on the frequency range. For low frequency (up to 5–7 kHz for the seabed examined), the main contribution to the penetration is the evanescent coupling in combination with the finite beamwidth effect, while roughness scattering provides a reasonable explanation for the anomalous levels observed at higher frequencies.

It was also observed that significant amounts of energy are penetrating in the bandwidth 2–3 kHz, even for low grazing angles. This suggests a potential benefit from using sonars in this frequency range for the detection of buried objects.

It must be mentioned that, to our knowledge, this is the first time that a quantification of the contributions of the evanescent field and, potentially, roughness scattering to the penetration into the sediment has been obtained from an at-sea experiment. Moreover, the obtained results were consistent with levels predicted by two different models. Even though more experimental validation is needed, this study has already provided an important initial verification of these two models.

Future work will be dedicated to the validation and extension of these results through further at-sea experiments and model development. Some of the shortcomings of the current experiment, such as measurement sparsity and low SNR, will be addressed in further work so that more definitive statements can be made about the mechanisms at work.

ACKNOWLEDGMENTS

The authors would like to thank the crew of the R/V Manning, the Center's Engineering Technology Division (especially E. Michelozzi, P. A. Sletner, R. Chiarabini, and A. Figoli) the Mine Countermeasures Group technicians (M. Mazzi and M. De Grandi), and the team of divers for their help and constant availability during the experiment. All contributed greatly to the success of the experiment and the quality of the data collected. Many thanks also go to N. G. Pace and A. P. Lyons for their many useful discussions and suggestions during preparation of the paper, and to the anonymous reviewers whose comments led to significant improvements to the original manuscript.

APPENDIX: SEDIMENT SOUND SPEED VARIATION

As mentioned in the main text, it was found that using a sound speed of 1685 m/s in the sediment as input to the acoustic models instead of the the 1720 m/s measured from the sample cores provided better data-model fits. An example of the sensitivity of the penetration ratio to sediment sound speed can be seen in Fig. A1, where above (32 degree) and below (18 degree) critical angle geometries are modeled for sediment sound speeds of 1650, 1685, and 1720 m/s (with associated critical angles of 22.0, 24.8, and 27.2 degrees, respectively). For the above critical case, the variation with sound speed is insignificant. Below critical angle, the differences in penetration ratio grow with increasing frequency. For our case (1685 vs 1720 m/s), there is a roughly 4-dB difference in the levels at 5 kHz, and 7-dB difference at 10 kHz.

The value of 1720 m/s was calculated based on travel time measurements through the cores of short pulses cen-

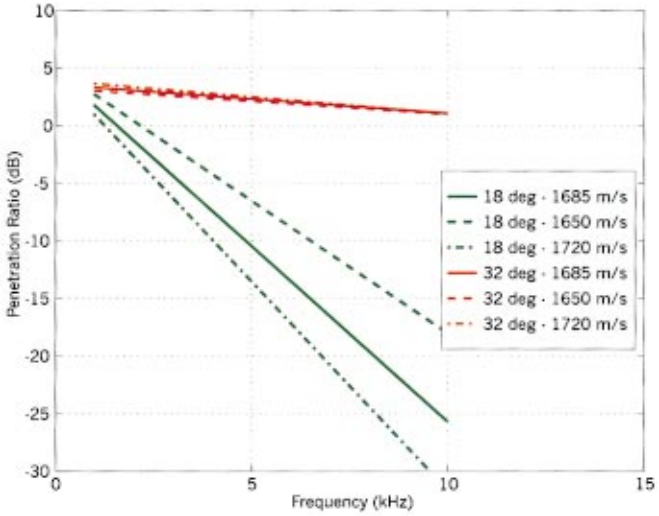

FIG. A1. Penetration ratio in dB for 30-cm deep hydrophone, for plane wave incident at 18 degrees (green) and 32 degrees (red) grazing angles. The water sound speed is 1530 m/s, while the bottom sound speed is varied: 1685 m/s (solid), 1650 m/s (dashed), and 1720 m/s (dash-dot).

tered at 200 kHz. The penetration measurements themselves, however, took place at much lower frequencies (2–15 kHz). A possible explanation for this apparent frequency dependence of the sediment sound speed can be provided by the Biot theory for poroelastic sediments, which can be modeled within OASES. An important parameter for this model is the sediment permeability, which was unfortunately not measured on the sample cores. Therefore, Fig. A2 shows model results for sediment compressional wave speed versus frequency for two different values of permeability that are representative of historically observed values for this type of sand: $k=1\times10^{-10}\,\mathrm{m}^2$ and $k=4\times10^{-11}\,\mathrm{m}^2$. The other parameters measured from the cores (density and porosity) were used, and the other free Biot parameters were adjusted to yield 1720 m/s at 200 kHz. The model predicts a decrease

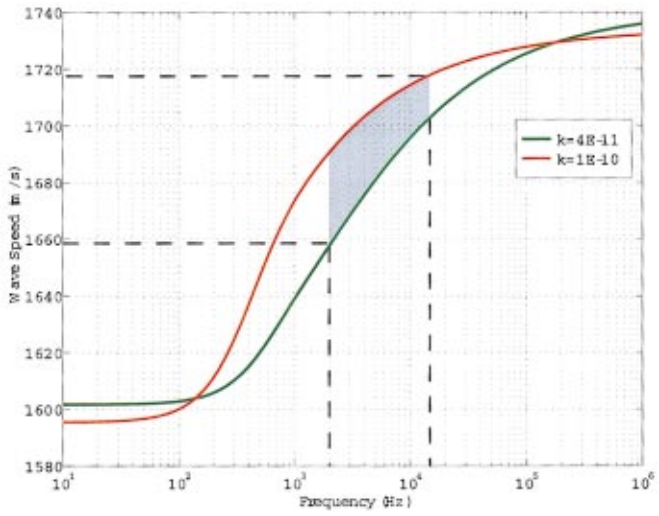

FIG. A2. Frequency dependence of the sound speed in sand. The two curves show the results for two different permeabilities within the range typical for this type of sand.

in sound speed for decreasing frequency such that an average value of 1685 m/s in the 2–10 kHz regime is not unrealistic.

[1] L. M. Brekhovskikh, *Waves in Layered Media*, 2nd ed. (Academic, New York, 1980).
[2] J. L. Lopes, ''Observations of anomalous acoustic penetration into sediment at shallow grazing angles,'' J. Acoust. Soc. Am. **99**, 2473–2474 (1996).
[3] N. P. Chotiros, A. M. Mautner, A. Løvik, Å. Kristensen, and O. Bergem, ''Acoustic penetration of a silty sand sediment in the 1–10 kHz band,'' IEEE J. Ocean Eng. **22**, 604–615 (1997).
[4] E. I. Thorsos, D. R. Jackson, J. E. Moe, and K. L. Williams, ''Modeling of subcritical penetration into sediments due to interface roughness,'' in *High Frequency Acoustics in Shallow Water*, edited by N. G. Pace, E. Pouliquen, O. Bergem, and A. P. Lyons, no. CP-45 in SACLANTCEN Conference Proceedings Series (La Spezia, Italy), pp. 563–569, NATO SACLANT Undersea Research Centre, June 1997.
[5] F. B. Jensen and H. Schmidt, ''Subcritical penetration of narrow Gaussian beams into sediment,'' J. Acoust. Soc. Am. **82**, 574–579 (1987).
[6] N. P. Chotiros, ''Biot model of sound penetration in water saturated sand,'' J. Acoust. Soc. Am. **97**, 199–214 (1995).
[7] D. R. Jackson, K. B. Briggs, K. L. Williams, and M. D. Richardson, ''Tests of models for high-frequency seafloor backscatter,'' IEEE J. Ocean Eng. **21**, 458–70 (1996).
[8] A. N. Ivakin and Y. P. Lysanov, ''Theory of underwater sound scattering by random inhomogeneities of the bottom,'' Sov. Phys. Acoust. **27**, 61–64 (1981).
[9] P. C. Hines, ''Theoretical model of acoustic backscatter from a smooth seabed,'' J. Acoust. Soc. Am. **88**, 324–334 (1990).
[10] A. P. Lyons, A. L. Anderson, and F. S. Dwan, ''Acoustic scattering from the sea floor: Modeling and data comparison,'' J. Acoust. Soc. Am. **95**, 2441–2451 (1994).
[11] H. Schmidt, OASES: Version 2.1. User Guide and Reference Manual, Massachusetts Institute of Technology, 1997.
[12] H. Schmidt, J. Lee, H. Fan, and K. LePage, ''Multistatic bottom reverberation in shallow water,'' in *High Frequency Acoustics in Shallow Water*, edited by N. G. Pace, E. Pouliquen, O. Bergem, and A. P. Lyons, no. CP-45 in SACLANTCEN Conference Proceedings Series (La Spezia, Italy), pp. 475–481, NATO SACLANT Undersea Research Centre, June 1997.
[13] E. Pouliquen, A. P. Lyons, and N. G. Pace, ''Penetration of acoustic waves into sandy seafloors at low grazing angles: The Helmholtz–Kirchhoff approach,'' SR-290, NATO SACLANT Undersea Research Centre, La Spezia, Italy, Aug. 1998.
[14] O. Bergem and N. G. Pace, ''Calibration of the TOPAS PS040. Part I: Measurements recorded with TOPAS acquisition system,'' M-119, NATO SACLANT Undersea Research Centre, La Spezia, Italy, Jan. 1996.
[15] D. J. Wingham, N. G. Pace, and R. V. Ceen, ''An experimental study of the penetration of a water-sediment interface by a parametric beam,'' J. Acoust. Soc. Am. **79**, 363–374 (1986).
[16] D. B. Percival and A. T. Walden, *Spectral Analysis for Physical Applications* (Cambridge University Press, Cambridge, 1993).
[17] W. A. Kuperman and H. Schmidt, ''Self-consistent perturbation approach to rough surface scattering in stratified elastic media,'' J. Acoust. Soc. Am. **86**, 1511–1522 (1989).
[18] H. Schmidt and W. A. Kuperman, ''Spectral representations of rough interface reverberation in stratified ocean waveguides,'' J. Acoust. Soc. Am. **97**, 2199–2209 (1995).
[19] H. Schmidt and J. Glattetre, ''A fast field model for three-dimensional wave propagation in stratified environment based on the global matrix method,'' J. Acoust. Soc. Am. **78**, 2105–2114 (1985).
[20] F. B. Jensen, W. A. Kuperman, M. B. Porter, and H. Schmidt, *Computational Ocean Acoustics* (AIP Press, New York, 1994).
[21] K. LePage, ''Elastic scattering in oceanic waveguides,'' Ph.D. thesis, Massachusetts Institute of Technology, June 1992.
[22] B. H. Tracey and H. Schmidt, ''Seismo-acoustic field statistics in shallow water,'' IEEE J. Ocean Eng. **22**, 317–331 (1997).
[23] L. M. Brekhovskikh and Y. Lysanov, *Fundamentals of Ocean Acoustics* (Springer-Verlag, New York, 1982).
[24] M. F. Barnsley, R. L. Devaney, B. B. Mandelbrot, H. O. Peitgen, D. Saupe, and R. F. Voss, *The Science of Fractal Images* (Springer-Verlag, New York, 1988).

Impedance-matched absorbers for finite-difference parabolic equation algorithms

David Yevick
Department of Physics, University of Waterloo, 200 University Avenue West, Waterloo, Ontario N2L 3G1, Canada

David J. Thomson
Defence Research Establishment Atlantic, P.O. Box 1012, Dartmouth, Nova Scotia B2Y 3Z7, Canada

(Received 25 November 1998; revised 22 November 1999; accepted 11 December 1999)

In this paper, a perfectly matched layer (PML) absorber, recently introduced into the electromagnetic propagation literature by Bérenger [J. Comput. Phys. **114**, 185–200 (1994)], is adapted for use with both paraxial and wide-angle acoustic parabolic equations (PEs). Our procedure incorporates an imaginary component into the transverse coordinate that mimics the introduction of a fictitious absorber on the edge of the computational grid. Use of such an impedance-matched layer can significantly reduce spurious reflections compared to physical absorbing layer methods and thus allows a smaller number of boundary points to be employed in PE calculations. Numerical results obtained with several higher-order propagator approximations confirm that such impedance-matched absorbers efficiently eliminate reflections.
[S0001-4966(00)04703-2]

PACS numbers: 43.30.Bp [SAC-B]

INTRODUCTION

Several one-way propagation procedures currently exist for solving various parabolic equations relevant to underwater acoustics (see Ref. 1, pp. 343–412 and the references therein). In particular, numerical methods have been developed to treat both range-independent and range-dependent inelastic and elastic media that accurately account for discontinuous changes in material properties, highly divergent fields and bidirectional field propagation.[2] Each parabolic equation must be supplemented with relevant boundary conditions along the cross-range edges of the computational grid. For underwater sound propagation, the ocean surface is usually modeled simply as a pressure-release boundary. A more complicated procedure is required, however, to treat the interaction of the field beneath a penetrable sea-bottom where a downgoing radiation condition usually applies.

In treating radiation conditions, two cases can be distinguished. The first of these results if the field physically undergoes further reflection at the position of the computational window boundary or at some distance beyond this location. Sometimes, the boundary interaction can be described in terms of a local impedance condition as in radar[3] and atmospheric sound[4] propagation near the Earth's surface. In underwater acoustics, however, such locally reacting conditions are generally not applicable, and nonlocal boundary conditions that incorporate the full spectral behavior of the reflection coefficient describing the interaction with the subbottom must be used instead.[5]

A second case results if the subbottom is assumed to be homogeneous and semi-infinite so that all power leaving the computational domain should physically radiate downward to infinity. Numerous local and nonlocal boundary conditions of varying degrees of accuracy may then be applied to remove this component of the acoustic field. The most direct procedure is to introduce a physical absorbing layer which, if the absorber strength increases sufficiently gradually, removes a large fraction of the incident field by an attenuation mechanism without introducing spurious reflections.[6–12] Generally, the absorber is terminated by imposing a pressure-release condition at the base of the layer. For some problems, the use of physical absorbers necessitates a large number of grid points, and can be computationally inefficient. Consequently, several alternate approaches for handling the downgoing radiation field have been proposed. The most accurate of these involve nonlocal procedures that employ the previous history of the acoustic field along the computational window edges to determine the downgoing boundary condition at the successive propagation step.[5,13–19] While such nonlocal methods can be made arbitrarily precise,[20] their implementation requires more effort compared to local methods. Moreover, they cannot easily be adapted to three-dimensional problems or extended to accommodate multiterm Padé[21] or split-step Padé PEs.[22]

Recently, several researchers have examined an alternative absorbing mechanism that is equivalent to introducing a fictitious imaginary component into the transverse coordinates. Such a procedure greatly reduces any unphysical (and unwanted) reflections from the boundary layer.[23–33] Although this observation had its roots in early analytic work on electromagnetic modes,[23] its first major application was in the area of finite-difference time-domain analysis of electromagnetic fields.[24] A considerable amount of work has since been expended on developing a theoretical basis for the method and on applying this knowledge to the generation of increasingly accurate radiation boundary conditions. The formalism has since been adapted to one-way wave propagation by several authors,[34,35] as well as to elastic fields.[36] Careful analyses of the errors arising from grid-point discretization

have been performed and compared to numerical results.[32,37,38]

In this paper, we address a key element that extends previous work[38] on this so-called perfectly matched layer (PML) method, especially as it relates to frequency-domain propagation in underwater acoustics. Namely, we perform a detailed numerical study of the manner in which the reflectivity of such layers depends on the wide-angle capability of the underlying propagation technique. Our results indicate that in fact the reflection coefficient is almost unchanged with the wide-angle order of the propagation method, from which we conclude that the detailed theory that has been derived for paraxial methods should apply as well to higher-order wide-angle techniques.

I. PE PROPAGATORS

As a first step, we construct several one-way propagation equations for a medium with a varying density $\rho(z)$ located between the surface ($z=0$) and bottom ($z=z_b$) of a stratified ocean. The sound speed and absorption are designated by $c(z)$ and $\alpha(z)$, respectively. Defining a reference wave number $k_0=\omega/c_0$, we relate the field ψ to the complex pressure p according to

$$p(r,z)=\frac{\psi(r,z)\exp(ik_0r)}{\sqrt{k_0r}}. \tag{1}$$

In terms of the square-root operator $\sqrt{1+X}$, which is composed of the dimensionless expression

$$X=N^2-1+k_0^{-2}\rho\frac{\partial}{\partial z}\left(\rho^{-1}\frac{\partial}{\partial z}\right), \tag{2}$$

with $N(z)=n(z)[1+i\alpha(z)]$ and $n(z)=c_0/c(z)$, outgoing propagating waves in the far-field ($k_0r\gg1$) can be described formally by the exact ''one-way'' evolution equation[7–9]

$$\frac{\partial\psi}{\partial r}=ik_0\{-1+\sqrt{1+X}\}\psi. \tag{3}$$

The propagation operator associated with this equation is

$$\psi(r+\Delta r,z)=\exp\{-\delta+\delta\sqrt{1+X}\}\psi(r,z), \tag{4}$$

where we have set $\delta=ik_0\Delta r$. Combined with appropriate boundary conditions, Eq. (4) yields the exact solution of the discretized one-way propagation problem.

The standard, paraxial PE results if the square-root operator in Eq. (3) is approximated by

$$-1+\sqrt{1+X}\approx\tfrac{1}{2}X. \tag{5}$$

Substituting Eq. (5) into Eq. (3) yields

$$\frac{\partial\psi}{\partial r}=\tfrac{1}{2}ik_0X\psi, \tag{6}$$

with the associated one-way propagator

$$\psi(r+\Delta r,z)=\exp\{\tfrac{1}{2}\delta X\}\psi(r,z). \tag{7}$$

The accuracy of the paraxial equation is limited to acoustic waves whose dominant horizontal wave numbers lie close to the value chosen for k_0. Sound energy emitted from more highly divergent radiation sources is more accurately described by wide-angle equations. Two procedures are commonly employed to construct energy-conserving wide-angle equations and propagators from Eq. (3) and Eq. (7).

In the first procedure, a $[M,M]$-Padé approximation is applied to $\sqrt{1+X}$ followed by M [1,1]-Padé approximants with respect to δ. That is, first write[21]

$$\psi(r+\Delta r,z)=\exp\left\{\sum_{m=1}^{M}\frac{\delta a_{m,M}X}{1+b_{m,M}X}\right\}\psi(r,z), \tag{8}$$

where the real coefficients $a_{m,M}$ and $b_{m,M}$ are given by

$$a_{m,M}=\frac{2}{2M+1}\sin^2\frac{m\pi}{2M+1}, \tag{9}$$

$$b_{m,M}=\cos^2\frac{m\pi}{2M+1}, \tag{10}$$

followed by the unitary single-term approximations

$$\exp\frac{\delta a_{m,M}X}{1+b_{m,M}X}\approx\frac{1+c^{+}_{m,M}X}{1+c^{-}_{m,M}X}, \tag{11}$$

with $c^{\pm}_{m,M}=b_{m,M}\pm\frac{1}{2}\delta a_{m,M}$.

The lowest-order ($M=1$) equation of this series gives $a_{1,1}=1/2$ and $b_{1,1}=1/4$ and leads to the rational-linear approximation

$$-1+\sqrt{1+X}\approx\frac{\frac{1}{2}X}{1+\frac{1}{4}X}. \tag{12}$$

The resulting third-order PE,

$$\left(1+\frac{1}{4}X\right)\frac{\partial\psi}{\partial r}=\frac{1}{2}ik_0X\psi, \tag{13}$$

is due to Claerbout[39] and can be put in the implicit finite-difference form

$$\{1+\tfrac{1}{4}(1-\delta X)\}\psi(r+\Delta r,z)=\{1+\tfrac{1}{4}(1+\delta X)\}\psi(r,z). \tag{14}$$

It should be noted that although a higher-order Padé approximant to the propagator will generally allow larger range steps to be taken, the accuracy of the overall approximation with respect to X will not be improved.

Once Eq. (8) has been evaluated to the desired (transverse) Padé order in X, the exponential of the sum of commuting terms may be written as the product of exponentials of the individual terms and a [1,1]-Padé approximant can then be applied to each of these partial propagators. Alternatively, a $[M,M]$-Padé approximation may be applied to the exponential of the full sum and the numerator and denominator of the resulting expression factored into the products of first-order polynomial expressions in X. In either case, once δ is specified, the algebraic expressions for the propagator can be recast numerically into the partial fraction form

$$\exp\{-\delta+\delta\sqrt{1+X}\}=1+\sum_{m=1}^{M}\frac{\tilde{a}_{m,M}X}{1+\tilde{b}_{m,M}X}. \tag{15}$$

Consequently, in a multiprocessing system, each processor can be assigned one of the terms, $m=1,\ldots,M$ on the right-hand side of the expression

$$\psi(r+\Delta r,z)=\psi(r,z)+\sum_{m=1}^{M}\frac{\tilde{a}_{m,M}X}{1+\tilde{b}_{m,M}X}\psi(r,z), \tag{16}$$

so that all M terms may be evaluated in parallel and then summed. In two dimensions, all of the above procedures involve numerically efficient routines for multiplying and inverting tridiagonal matrices and have therefore been widely applied.

Due to the use of $[1,1]$-Padé approximants with respect to δ, however, the above procedure requires sufficiently small values of δ in order to maintain accuracy. We therefore consider a second procedure which permits larger values of δ for a desired level of accuracy.[22] In particular, we apply a $[M,M]$-Padé approximation with respect to X directly to the exact exponential propagation operator to generate an expression of the form

$$\exp\{-\delta+\delta\sqrt{1+X}\}=\frac{1+G_M(\delta,X)}{1+G_M^*(\delta,X)}, \tag{17}$$

where * denotes complex conjugate. In the $M=2$ case, for example, we find G_2 given by

$$G_2(\delta,X)=\frac{g_{2,1}(\delta)X+g_{2,2}(\delta)X^2}{g_2(\delta)}, \tag{18}$$

with

$$g_2(\delta)=\delta^2-3, \tag{19}$$

$$g_{2,1}(\delta)=\tfrac{1}{4}\delta^3+\tfrac{1}{2}\delta^2-\tfrac{3}{4}\delta-\tfrac{9}{4}, \tag{20}$$

$$g_{2,2}(\delta)=\tfrac{1}{48}\delta^4+\tfrac{1}{16}\delta^3-\tfrac{1}{16}\delta^2-\tfrac{27}{16}\delta-\tfrac{27}{16}. \tag{21}$$

The corresponding $M=3$ propagator is derived from

$$G_3(\delta,X)=\frac{g_{3,1}(\delta)X+g_{3,2}(\delta)X^2+g_{3,3}(\delta)X^3}{g_3(\delta)}, \tag{22}$$

in which

$$g_3(\delta)=\delta^6-18\delta^4+135\delta^2-135, \tag{23}$$

$$g_{3,1}(\delta)=\tfrac{1}{4}\delta^7+\tfrac{3}{4}\delta^6-\tfrac{9}{2}\delta^5-\tfrac{33}{2}\delta^4+\tfrac{135}{4}\delta^3+\tfrac{585}{4}\delta^2-\tfrac{135}{4}\delta-\tfrac{675}{4}, \tag{24}$$

$$g_{3,2}(\delta)=\tfrac{1}{40}\delta^8+\tfrac{1}{8}\delta^7-\tfrac{3}{8}\delta^6-3\delta^5+\tfrac{3}{4}\delta^4+\tfrac{225}{8}\delta^3+\tfrac{225}{8}\delta^2-\tfrac{135}{4}\delta-\tfrac{405}{8}, \tag{25}$$

$$g_{3,3}(\delta)=\tfrac{1}{960}\delta^9+\tfrac{1}{160}\delta^8-\tfrac{1}{64}\delta^7-\tfrac{11}{64}\delta^6-\tfrac{3}{64}\delta^5+\tfrac{57}{32}\delta^4+\tfrac{45}{16}\delta^3-\tfrac{135}{64}\delta^2-\tfrac{405}{64}\delta-\tfrac{135}{64}. \tag{26}$$

For $M=2$ and $M=3$, respectively, these results are equivalent to applying a $[M,M]$-Padé approximation to the square-root operator followed by a $[M,M]$-Padé approximation to the resulting exponential function. This equivalence holds for any M. Since propagator approximations for $M>3$ are tedious to express analytically, however, it is expedient to compute them numerically once δ is specified.

II. ABSORBING LAYERS

A central problem encountered when underwater acoustic fields are propagated numerically is that of removing downward radiating field components at the computational boundary. In this section, we analyze two procedures for attenuating radiated energy that are based on using a physical absorbing layer and a perfectly matched layer, respectively. We first consider the standard parabolic equation and apply the half-range Fourier transform

$$\Psi(s,z)=\int_0^\infty \psi(r,z)\exp(-isr)\,dr \tag{27}$$

to Eq. (6) to obtain

$$\frac{\partial^2\Psi}{\partial z^2}+\gamma^2(s)\Psi=0, \tag{28}$$

where $\gamma^2(s)=k_0^2(N^2-1-2s/k_0)$ is the squared vertical wave number and we have chosen the branch $\Im\gamma>0$. The horizontal wave number s of the standard PE is related to the horizontal wave number k of the scalar wave equation by the mapping $k=k_0\sqrt{1+2s/k_0}$ (see, e.g., Ref. 15).

Consider a uniform layer of thickness h appended to the base $z=z_b$ of the PE computational domain. Within a thin homogeneous layer just above $z=z_b$, the solution to Eq. (28) can be written as

$$\Psi_-=\exp[i\gamma_-|z-z_b|]+R\exp[-i\gamma_-|z-z_b|]. \tag{29}$$

Here, the subscripts ''$\pm$'' are used to denote quantities at $z=z_b\pm 0$, R is the plane wave reflection coefficient, and the dependence on s has been suppressed. In $z_b<z<z_b+h$, we set $\rho_+=\rho_-$, $n_+=n_-$ and impose a Dirichlet boundary condition on the field at $z=z_b+h$.

In the case of a physical absorber, we set $N_+=n_+(1+i\alpha_+)$ and obtain for the field in the layer

$$\Psi_+=T\exp[i\gamma_+(z-z_b)]-T\exp[-i\gamma_+(z-z_b-2h)]. \tag{30}$$

Imposing the continuity of Ψ and $\rho^{-1}\Psi_z$ across $z=z_b$ then yields the reflection coefficient of the physical absorbing layer in the form

$$R=\frac{R_0-\exp(2i\gamma_-h)}{1-R_0\exp(2i\gamma_-h)}=R_0+(R_0^2-1)\exp(2i\gamma_-h)+\ldots, \tag{31}$$

where $R_0=(\gamma_--\gamma_+)/(\gamma_-+\gamma_+)$ is the reflection coefficient associated with the top of the layer. The second term in Eq. (31) corresponds to the amplitude reduction due to a round-trip passage of the wave in the lossy layer. The apparent reflection loss of this wave component is given by

$$R\approx\exp(2i\gamma_-h)\Rightarrow|R|\approx\exp(-2\Im\gamma_-h). \tag{32}$$

Clearly, the jump in absorption across $z=z_b$ must be small to keep $|R_0|$ small. However, in order to significantly attenuate the round-trip component of the reflected field, smaller values of α_+ must be compensated by larger values of h. An acceptable trade-off between these requirements can be realized by smoothly tapering the absorber strength $\alpha(z)$ within

the layer. This can render $R_0 \approx 0$ for a given maximum value of α without changing h.[6–12]

In a perfectly matched layer, we instead set the refractive index $N_+ = N_-$ (so that $\gamma_+ = \gamma_-$) and stretch the z-coordinate for $z_b < z < z_b + h$ according to $z^* = z(1+ia)$. Accordingly, inserting

$$\frac{\partial}{\partial z} \rightarrow \frac{\partial}{\partial z^*} = (1+ia)^{-1} \frac{\partial}{\partial z} \tag{33}$$

in Eq. (28), transforms the standard PE for $\Psi^*(z) = \Psi(z^*)$ in the layer into

$$(1+ia)^{-2} \frac{\partial^2 \Psi^*}{\partial z^2} + \gamma_+^2(s) \Psi^* = 0. \tag{34}$$

Proceeding as in the case of the physical absorber, we find that the field just above $z = z_b$ still has the form of Eq. (29), while inside the layer the solution that satisfies a pressure-release condition at the stretched depth $z^* = z_b + h^*$ can be written as

$$\Psi_+^* = T \exp[i\gamma_+(z^* - z_b)] - T \exp[-i\gamma_+(z^* - z_b - 2h^*)]. \tag{35}$$

For constant a, the continuity conditions across $z = z_b$ become $\Psi_- = \Psi_+^*$ and $\partial_z \Psi_- = (1+ia)^{-1} \partial_z \Psi_+^*$. Applying these conditions to Eq. (29) and Eq. (35) yields the result

$$R = -\exp[2i\gamma_+ h^*] \Rightarrow |R| = \exp[-2(a\Re\gamma_+ + \Im\gamma_+)h]. \tag{36}$$

Note that $\Im\gamma_+ > 0 \Rightarrow \Re\gamma_+ > 0$. The formula for R in Eq. (36) corresponds to the expression obtained by Bérenger in an electromagnetic context.[24] It exhibits the remarkable feature that a reflected wave from the top of the PML layer is absent.

While increasing the value of α_+ in Eq. (32) yields unacceptably large values of $|R_0|$, this restriction does not appear to apply to a in Eq. (36). This attractive PML property for continuous media does not hold true, however, when the continuous problem is discretized on a computational grid.[37,38] In this case, the use of a suitably tapered profile $a(z)$ can significantly reduce the discretization-induced reflections. For this purpose, we choose for $0 < z - z_b < h$ an $a(z)$-profile of the form[37]

$$a(z) = \tfrac{1}{2} p \{1 - \cos[(z - z_b)\pi/h]\}^q \equiv H(p,q) \tag{37}$$

in our subsequent finite-difference calculations incorporating perfectly matched layer absorbers.

Within the absorbing layer, the numerical implementation of the loss mechanisms differ for the two procedures. This is seen by inspection of the standard PE of Eq. (6), which we write as

$$\frac{\partial \psi}{\partial r} = \underbrace{\frac{1}{2} i k_0 (N^2 - 1)\psi}_{\text{lens}} + \underbrace{\frac{1}{2}(i/k_0)\frac{\partial^2 \psi}{\partial z^2}}_{\text{diffraction}}. \tag{38}$$

For the physical absorber, the introduction of loss into the refractive index affects the coefficient of ψ in the lens term. In contrast, for the perfectly matched layer, the introduction of a stretched depth coordinate z^* affects the computation of the Laplacian in the diffraction term.

The above analysis for the standard PE also applies to the higher-order PEs of Eq. (15). These equations only differ from the paraxial equation in the form of the expression for the vertical wave number associated with a given PE approximation, which only affects the PE dispersion relation. That is, the squared vertical wave number for the Mth-order Padé approximation given in Eq. (15) is given by[40]

$$\gamma_M^2 = k_0^2 \{N^2 - 1 - 2s/k_0 - s^2/k_0^2\} + O(s^{2M+1}). \tag{39}$$

Replacing γ in the above analysis with γ_M in Eq. (39) yields the same expression for R in both Eq. (32) and Eq. (36).

Comprehensive analytical and graphical results for the reflection coefficient as a function of angle for both absorbing and impedance-matched boundary layers are presented elsewhere.[37] A key finding of this reference is that for a physical absorber the discretization-induced reflection loss from an inhomogeneous layer defined by $\alpha(z_l) \equiv \Im N(z_l)/n(z_l)$ at grid positions $z_l = z_b + l\Delta z$, $\Delta z = h/L$ for $l = 0, \ldots, L$, is given to the first nontrivial order in the grid point spacing by

$$|R| \approx \exp\left[-2\Delta z \sum_{l=0}^{L} \Im\gamma(z_l)\right]. \tag{40}$$

In comparison, for an impedance-matched layer, a z-dependent imaginary stretching of the grid point spacing is obtained by setting the complex distance between grid points z_l and z_{l+1} to

$$\Delta z_l^* = [1 + ia(z_l)]\Delta z, \tag{41}$$

which generates the continuous reflection loss

$$|R| = \exp\left\{-2\Delta z \sum_{l=0}^{L} [a(z_l)\Re\gamma(z_l) + \Im\gamma(z_l)]\right\}. \tag{42}$$

As noted earlier, the discrete nature of the grid points results in additional contributions to the reflection coefficient of Eq. (40) and Eq. (42). For a perfectly matched layer, the discrete reflection coefficient can be shown to be[37]

$$R(z_l) = \tfrac{1}{16}(2i + a_{l-1} + a_{l+1})(a_{l-1} - a_{l+1})\Gamma^2 + O(\Gamma^4), \tag{43}$$

where $\Gamma^2 = 2 - 2\cos(\gamma\Delta z)$ and we have set $a_l = a(z_l)$. Defining a ''mathematically equivalent'' lossy absorber defined by the requirement that the transverse decay of a plane wave in an isotropic PML medium equals that of an impedance-matched layer with a specified $a(z_l) \equiv H_l(p,q)$, we find that the extra reflection to Eq. (40) attributed to the discrete grid point spacing is

$$R(z_l) = \frac{a_l - a_{l+1}}{2i + a_l + a_{l+1}} + O(\Gamma). \tag{44}$$

Since Eq. (43) is second-order rather than zero-order in Γ, the discretization-induced reflection for the perfectly matched layer is typically several orders of magnitude smaller than that associated with a physical absorber.

Finally, we remark that to implement the above z-dependent stretching of the imaginary part of the z-coordinate, the finite-difference approximation to the La-

placian operator is constructed from the standard three-point expression for non-equidistant grid points z_{l-1}^*, z_l^*, and z_{l+1}^*, namely,

$$\left.\frac{\partial^2\psi}{\partial z^{*2}}\right|_{z=z_l} \approx \frac{2/\Delta z^2}{2+ia_l+ia_{l+1}}\left\{\frac{\psi_{l+1}-\psi_l}{1+ia_{l+1}}-\frac{\psi_l-\psi_{l-1}}{1+ia_l}\right\}. \tag{45}$$

Pressure-release boundary conditions can be applied at the computational window boundary since, for sufficiently large a_l, the overall reflection from an impedance-matched layer is nearly independent of the boundary condition at the layer endpoint except at nearly grazing incidence.[41]

III. NUMERICAL RESULTS

Three test cases were chosen to examine the degree to which a numerical implementation of the impedance-matched absorbing boundary condition eliminates reflections from the edges of the computational domain. The first case involves the reflection of a Gaussian acoustic beam that is steered obliquely toward an impedance-matched layer. This case is intended to establish the degree to which the reflection coefficient depends on the type of propagator employed. The second case involves a modified Lloyd mirror configuration adapted from PE Workshop II Test Case 1[2] and is designed to study the ability of the impedance-matched layer (IML) to absorb highly divergent radiation from a point source. Finally, in the third case, a leaky waveguide configuration (Ref. 1, pp. 249–251) due to Bucker is used to compare the effectiveness of the impedance-matched layer with that of previous methods based on the use of absorbing layers and nonlocal boundary conditions.[15,19]

A. Example 1: Gaussian beam

The field of a single-frequency acoustic Gaussian beam has a z-dependent profile at $r=0$ in the form ($w=30$ m)

$$\psi(z)=\exp[-(z-z_0)^2/w^2+ik_0\sin\theta z)]. \tag{46}$$

Specifically, we consider a 40-Hz beam steered downwards at an angle of $\theta=45°$ with respect to the pressure-release ocean surface along $z=0$. The medium in $z>0$ is taken to be lossless with a uniform sound speed and density of 1500 m s^{-1} and 1 g cm^{-3}, respectively. The beam is propagated downrange on a computational mesh of range step $\Delta r=10$ m and depth step $\Delta z=4$ m and is allowed to interact with an impedance-matched boundary layer that occupies the region $840<z<1000$ m. For the purpose of this test case, the 40-point PML is parameterized by $H_l(4,1)$ in Eq. (37). Numerical experience indicates that a considerably thinner absorbing region could be employed subject to a careful optimization of the layer properties.

For each calculation, the operator X is first constructed by discretizing the appropriate approximations to Eq. (3), together with the impedance-matched or absorbing boundary conditions on the 250-point transverse spatial grid. Subsequently, each relevant propagator, Eqs. (4), (7), (8) or (17), is evaluated numerically by performing the indicated matrix inversions, multiplications, square-root operations and/or exponentiations exactly as specified in the relevant expression. The resulting matrix representation of the propagator is then applied to advance the initial acoustic field in Eq. (46) through repeated matrix-vector multiplications. For example, the acoustic field amplitude profile at $r=500$ m, calculated with a [4,4]-Padé approximation to the square-root function using this technique, is displayed in Fig. 1. The propagated field (solid line) at the lower computational window boundary is observed to be negligible in accordance with Eq. (42). Therefore, the reflection from the boundary layer is dominated by the reflectivity induced by the discrete grid, except for very small transverse wave vector components. In contrast, the non-negligible incident field (dashed line) at the upper window boundary persists downrange due to the interaction with the pressure-release surface.

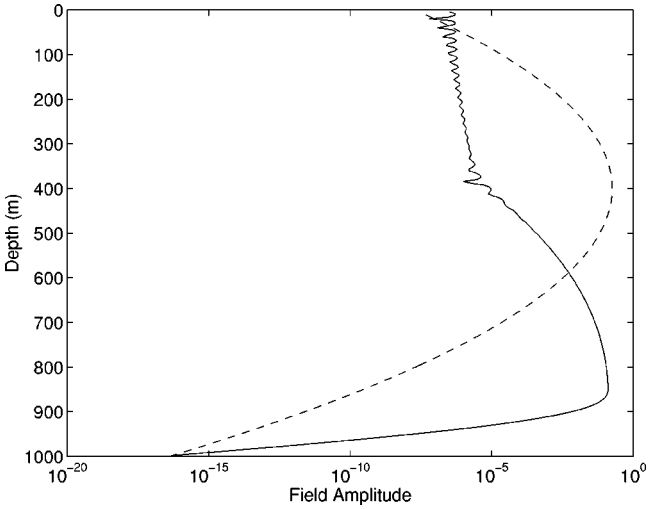

FIG. 1. Amplitude of the acoustic field at a range $r=500$ m (solid line) from the Gaussian source field incident at $r=0$ m (dashed line).

In Fig. 2, we display for the exact propagator the power loss $P(r)$ of the propagating field as a function of range, defined as

$$P(r)=-10\log_{10}\frac{\int|\psi(r,z)|^2dz}{\int|\psi(0,z)|^2dz}. \tag{47}$$

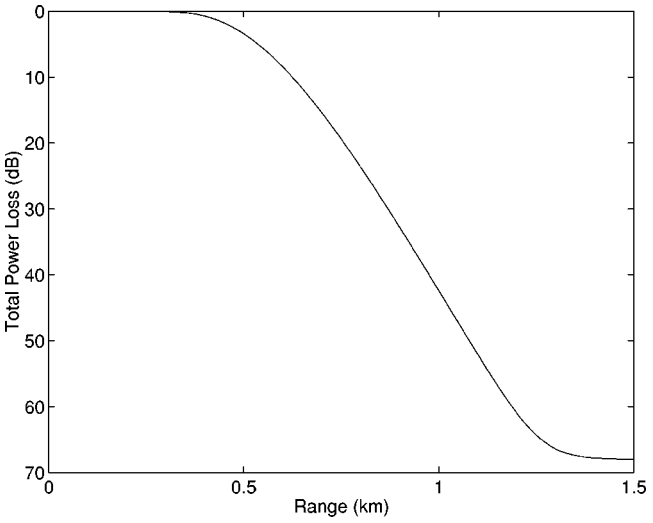

FIG. 2. Total field amplitude as a function of range for the Gaussian beam.

TABLE I. Relative field amplitude of a Gaussian beam after a single reflection from an impedance-matched layer.

Propagator	Total field amplitude
Paraxial	$3.977\,34\times10^{-4}$
Eq. (17), $M=2$	$3.981\,19\times10^{-4}$
Eq. (17), $M=3$	$3.960\,38\times10^{-4}$
Eq. (8), $M=2$	$3.967\,05\times10^{-4}$
Eq. (8), $M=4$	$3.959\,55\times10^{-4}$
Eq. (8), $M=8$	$3.959\,46\times10^{-4}$
Exact propagator	$3.959\,46\times10^{-4}$

Accounting for the effects of the Gaussian field shape, this curve clearly demonstrates that the field amplitude falls exponentially once the beam is in contact with the impedance-matched boundary layer and then stabilizes after it has fully reflected away from the boundary. The value of the field amplitude after a full reflection from the boundary, which occurs near $r=1500$ m for the exact propagator, provides a convenient measure of the effectiveness of the impedance-matched layer for a given acoustic propagator. This full reflection distance increases to $r\approx1700$ m for the paraxial and low-order Padé propagator approximations since the effective propagation angle that results when these propagators are applied is less than the true 45° beam angle.

In Table I, the relative amplitude calculated after a full reflection (at $r=r'$), namely

$$\exp\{-P(r')/20\}\equiv\left(\frac{\int|\psi(r',z)|^2dz}{\int|\psi(0,z)|^2dz}\right)^{1/2}, \tag{48}$$

is listed for various acoustic propagators. These values are within 1% of each other, and indicate that the magnitude of the reflectivity from the impedance-matched layer, Eq. (42), is comparable for both paraxial and wide-angle methods. Moreover, varying the total propagation distance by ±100 m also changes the predicted loss by less than 1%. We are therefore justified in applying the impedance-matched procedure to realistic wide-angle acoustic calculations in the following section.

B. Example 2: Lloyd mirror

In this example, we consider a fluid medium with the same properties as in the previous example, but with the Gaussian beam source replaced by a 40-Hz point acoustic source located at a depth $z_0=150$ m. The exact solution to this Lloyd mirror problem is given analytically by

$$\psi(r,z)=\sqrt{r}\exp(-ik_0r)\left\{\frac{\exp(ik_0R_-)}{R_-}-\frac{\exp(ik_0R_+)}{R_+}\right\}, \tag{49}$$

where the slant ranges to a receiver from the source and its geometric image about the plane $z=0$ are defined by $R_\pm^2=r^2+(z\pm z_0)^2$. All computations were performed using a 10-m range step, a 0.5-m transverse depth step and a 500-m thick transverse computational domain. To reduce sampling issues associated with the field divergence at the source position, the analytic field in Eq. (49) at a range of 25 m from the source was used to initialize the input acoustic field. The calculation further incorporates a 20-point impedance-matched boundary layer parameterized by $H_l(10,1)$ in Eq. (37).

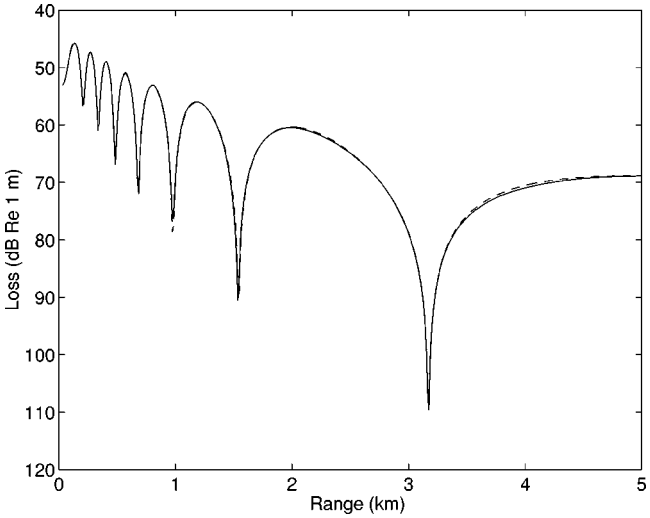

FIG. 3. Finite-difference PE transmission loss versus range curves for the Lloyd mirror test case and the exact PE propagator. Solid line—analytic calculation. Dashed line—calculation with the exact propagator and the impedance-matched layer.

In Figs. 3–6, the computed transmission losses $[-10\log_{10}|p(r,z)|^2]$ versus range to a receiver at a depth of $z=400$ m are shown for several propagators together with the known analytic solution given by Eq. (49) (solid line). The dashed line in each figure corresponds to the result obtained using a selected propagator. In particular, the dashed line in Fig. 3 shows the result obtained using the exact propagation formula Eq. (4). Similarly, the dashed lines in Fig. 4 and Fig. 5 correspond, respectively, to the $M=1$ and $M=3$ propagators defined by Eq. (8). In the limit of small δ, the $M=1$ propagator approaches the result of the Crank-Nicolson form of the third-order Claerbout equation, Eq. (14). Finally, in Fig. 6, the dashed line corresponds to the [15,15]-Padé approximant with respect to X to the full

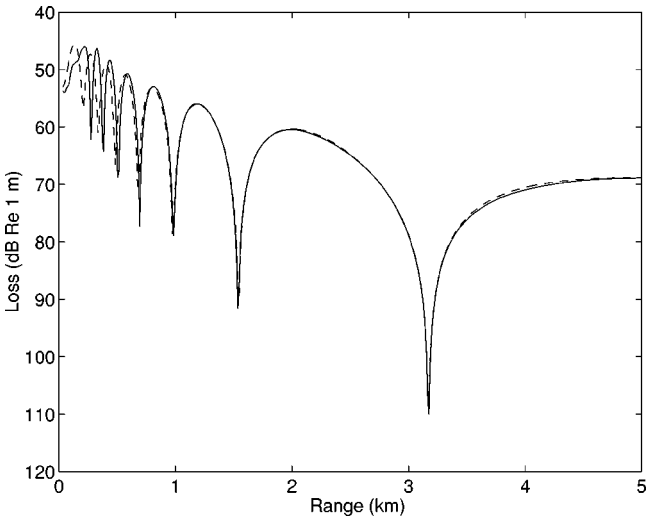

FIG. 4. Finite-difference PE transmission loss versus range curves for the Lloyd mirror test case and a propagator based on a [1,1] Padé square-root approximation. Solid line—analytic calculation. Dashed line—calculation with the approximate propagator and the impedance-matched layer.

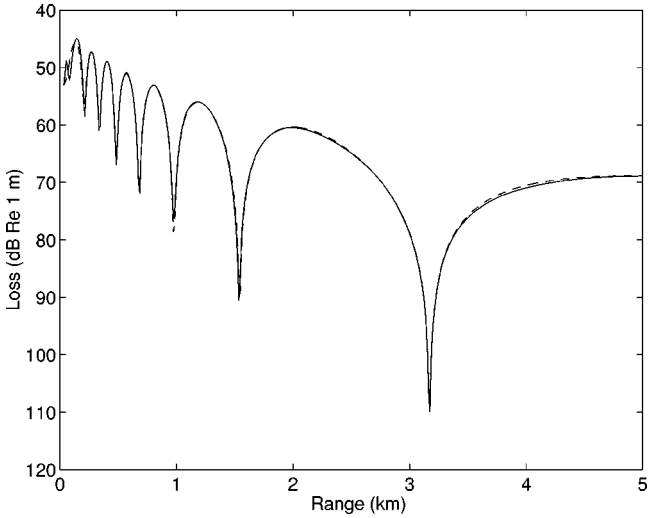

FIG. 5. Finite-difference PE transmission loss versus range curves for the Lloyd mirror test case and a propagator based on a [3,3]-Padé approximant to the full propagator. Solid line—analytic calculation. Dashed line—calculation with the approximate propagator and the impedance-matched layer.

propagation operator given by Eq. (15). For all propagators, the results shown are highly insensitive to the strength or width of the impedance-matched layer.

Beginning with Fig. 3, we observe that a slight difference exists in the calculated loss (<0.5 dB) at large ranges between the analytical result and the result obtained using the numerical implementation of the exact propagator. This effect is a result of the finite transverse grid point spacing used in the numerical work, and is therefore common to all of the calculations for the Lloyd mirror example. Next, Fig. 4 clearly demonstrates the wide-angle nature of our calculation, as the exact and Claerbout curves do not agree until the lower-angle energy is dominant beyond a distance of ≈ 1 km. The reduction of the error associated with the wide-angle components of the field afforded by the [3,3]-Padé approximant to the full exponential operator is evident from

TABLE II. Geoacoustic profile for the Bucker example.

Depth (m)	Sound speed ($m\,s^{-1}$)	Density ($g\,cm^{-3}$)	Attenuation dB λ^{-1}
0	1500	1.0	0.0
120	1498	1.0	0.0
240	1500	1.0	0.0
>240	1505	2.1	0.0

the calculated loss curve of Fig. 5, which agrees with the analytic result except for a small region within 100 m of the initial field position. Finally, even this residual error is eliminated by use of the $M=15$ Padé approximation to the square-root operator, which almost precisely coincides with the exact result as shown in Fig. 6. From the excellent agreement between the analytic and numerical curves, we conclude that impedance-matched layers can be employed to absorb the radiation field in wide-angle calculations without degrading the calculational accuracy of the underlying computational algorithm.

C. Example 3: Bucker profile

Finally, we examine the leaky waveguide example given in Table II which is a shallow water problem originally studied by H. Bucker (Ref. 1, pp. 249–251). In the water column, the geoacoustic parameters vary linearly between points. Both sound speed and density undergo jump discontinuities along the ocean bottom. The lossless region $z>240$ m has a uniform sound speed and density of 1505 $m\,s^{-1}$ and 2.1 $g\,cm^{-3}$, respectively. This example has been used previously to examine the effectiveness of absorbing boundary conditions.[15,19]

The transmission loss versus range curves are shown in Fig. 7 for a 100-Hz acoustic source located at $z=30$ m and a receiver depth of $z=90$ m. The solid line in this figure was obtained using the spectral integration model SAFARI.[42] The two other curves were computed using the Claerbout PE in

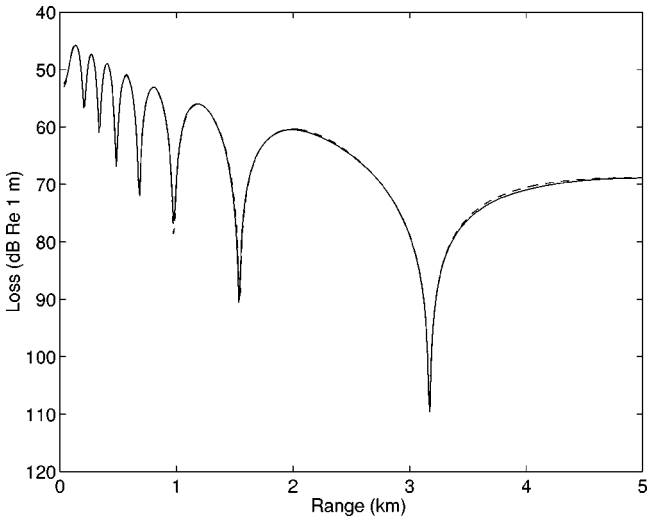

FIG. 6. Finite-difference PE transmission loss versus range curves for the Lloyd mirror test case and a propagator based on a [15,15]-Padé square-root approximation. Solid line—analytic calculation. Dashed line—calculation with the approximate propagator and the impedance-matched layer.

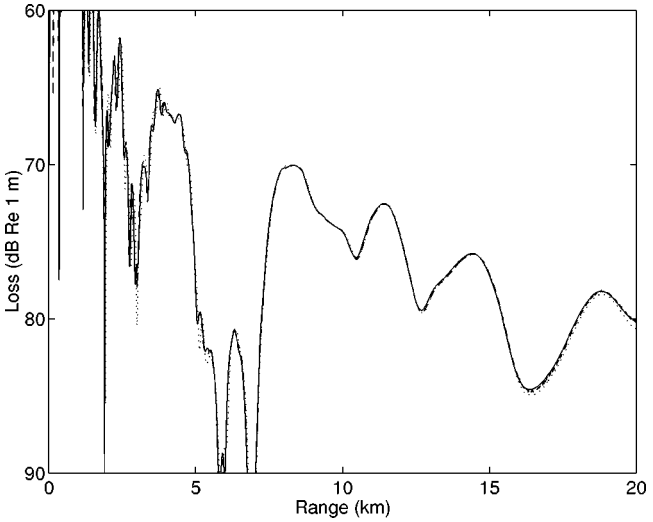

FIG. 7. Finite-difference PE transmission loss versus range curves for the Bucker profile. Solid line—Claerbout PE calculation with the nonlocal boundary condition. Dashed line—SAFARI. Dotted line—Claerbout PE with the impedance-matched layer.

conjunction with an impedance-matched boundary layer (dotted line) as well as the exact, nonlocal boundary condition (NLBC, dashed line) presented in Ref. 19. The 20-point impedance-matched layer in the region $260<z<300$ m is given by $a_l=H_l(10,2)$ in Eq. (37) while the NLBC was applied at a depth of $z=250$ m (10 m below the sea-bottom interface). Both PE calculations used a range step size of $\Delta r=10$ m, a depth step size of $\Delta z=2$ m, and a value of $c_0=1500\ \mathrm{m\,s^{-1}}$ for the reference sound speed.

The excellent agreement between the computed impedance-matched layer transmission losses and the SAFARI and PE+NLBC results demonstrates the practical efficiency of this method. The small discrepancies at long range are attributable to discretization-induced reflection, as explained above, as well as to numerical errors in the excitation field arising from the finite number of grid points, as we have verified by repeating our impedance-matched calculation with different window widths. (In fact, the latter effects were previously observed in calculations using the Papadakis nonlocal boundary conditions.) Although as before, the layer strength and width have not been optimized, our results compare favorably with those obtained using a traditional linearly increasing absorber, which requires a typical thickness of 500–1000 m to achieve equivalent accuracy.

IV. CONCLUSIONS

In this paper, we have demonstrated that an impedance-matched layer can be constructed for both paraxial and wide-angle acoustic wave propagation that yields a highly efficient procedure for absorbing radiating fields at the computational boundary. In particular, we first considered the reflection of a Gaussian beam from an impedance-matched boundary and found that the computed reflection coefficient is nearly independent of the angular accuracy of the underlying propagator. We further examined two standard acoustic test problems using different paraxial and wide-angle propagators. In all cases the results agreed very well with exact results even for very thin impedance-matched layer regions. Use of a traditional absorbing layer typically requires far more grid points in these cases to achieve a similar level of accuracy. Accordingly, we conclude that while transparent boundary conditions such as those of Refs. 14, 15, and 19 are optimal for two-dimensional near-paraxial propagation problems that can be modeled with either the Fresnel or Claerbout equations, the impedance-matched condition investigated above can be applied to two-dimensional wide-angle as well as paraxial and wide-angle three-dimensional problems for which accurate and convenient nonlocal boundary conditions remain to be formulated.

[1] F. B. Jensen, W. A. Kuperman, M. B. Porter, and H. Schmidt, *Computational Ocean Acoustics* (AIP, New York, 1994).

[2] M. D. Collins, ''Higher-order, energy-conserving, two-way, and elastic parabolic equations,'' in *PE Workshop II: Proceedings of the Second Parabolic Equation Workshop*, edited by S. A. Chin-Bing, D. B. King, J. A. Davis, and R. B. Evans (Naval Research Laboratory, U.S. Government Printing Office, 1993), pp. 145–168.

[3] J. R. Kuttler and G. D. Dockery, ''Theoretical description of the parabolic approximation/Fourier split-step method of representing electromagnetic propagation in the troposphere,'' Radio Sci. **26**, 381–393 (1991).

[4] K. E. Gilbert and X. Di, ''A fast Green's function method for one-way sound propagation in the atmosphere,'' J. Acoust. Soc. Am. **94**, 2343–2352 (1993).

[5] J. S. Papadakis, M. I. Taroudakis, P. J. Papadakis, and B. Mayfield, ''A new method for a realistic treatment of the sea bottom in the parabolic approximation,'' J. Acoust. Soc. Am. **92**, 2030–2038 (1992).

[6] S. M. Flatte and F. D. Tappert, ''Calculation of the effect of internal waves on oceanic sound transmission,'' J. Acoust. Soc. Am. **58**, 1151–1159 (1976).

[7] F. D. Tappert, ''The parabolic approximation method,'' in *Wave Propagation and Underwater Acoustics*, edited by J. B. Keller and J. S. Papadakis (Springer, New York, 1977), Chap. 5, pp. 224–287.

[8] J. A. Davis, D. White, and R. C. Cavanagh, ''NORDA Parabolic Equation Workshop, 31 March–3 April 1981,'' Naval Ocean Research and Development Activity, NSTL Station, MS, Tech. Note 143, 1982.

[9] D. J. Thomson, ''Wide-angle parabolic equation solutions to two range-dependent benchmark problems,'' J. Acoust. Soc. Am. **87**, 1514–1520 (1990).

[10] D. Yevick, J. Yu, and Y. Yayon, ''Optimal absorbing boundary conditions,'' J. Opt. Soc. Am. A **12**, 107–110 (1995).

[11] C. Vassallo and F. Collino, ''Highly efficient absorbing boundary conditions for the beam propagation method,'' J. Lightwave Technol. **14**, 1570–1577 (1996).

[12] D. T. Prescott and N. V. Shuley, ''Reflection analysis of FDTD boundary conditions—Part I: Time-space absorbing boundaries,'' IEEE Trans. Microwave Theory Tech. **45**, 1162–1170 (1997).

[13] S. W. Marcus, ''A hybrid (finite-difference–surface Green's function) method for computing transmission losses in an inhomogeneous atmosphere over irregular terrain,'' IEEE Trans. Antennas Propag. **40**, 1451–1458 (1992).

[14] J. S. Papadakis, ''Exact, nonreflecting boundary conditions for parabolic-type approximations in underwater acoustics,'' J. Comput. Acoust. **2**, 83–98 (1994).

[15] D. J. Thomson and M. E. Mayfield, ''An exact radiation condition for use with the *a posteriori* PE method,'' J. Comput. Acoust. **2**, 113–132 (1994).

[16] F. Schmidt and P. Deuflhard, ''Discrete transparent boundary condition for the numerical solution of Fresnel's equation,'' Comput. Math. Appl. **29**, 53–76 (1995).

[17] A. V. Popov, ''Accurate modeling of transparent boundaries in quasi-optics,'' Radio Sci. **31**, 1781–1790 (1996).

[18] M. F. Levy, ''Transparent boundary conditions for parabolic equation solutions of radiowave propagation problems,'' IEEE Trans. Antennas Propag. **45**, 66–72 (1997).

[19] D. Yevick and D. J. Thomson, ''Nonlocal boundary conditions for finite-difference parabolic equation solvers,'' J. Acoust. Soc. Am. **106**, 143–150 (1999).

[20] F. Schmidt and D. Yevick, ''Analysis of boundary conditions for the Fresnel equation,'' J. Comput. Phys. **134**, 96–107 (1997).

[21] M. D. Collins, ''Benchmark calculations for higher-order parabolic equations,'' J. Acoust. Soc. Am. **87**, 1535–1538 (1990).

[22] M. D. Collins, ''A split-step Padé solution for the parabolic equation method,'' J. Acoust. Soc. Am. **93**, 1736–1742 (1993).

[23] V. Shevshenko, ''The expansion of the fields of open waveguides in proper and improper modes,'' Radiophys. Quantum Electron. **14**, 972–977 (1974).

[24] J.-P. Bérenger, ''A perfectly matched layer for the absorption of electromagnetic waves,'' J. Comput. Phys. **114**, 185–200 (1994).

[25] D. Katz, E. Thiele, and A. Taflove, ''Validation and extension to three dimensions of the Berénger PML absorbing boundary condition for FD-TD meshes,'' IEEE Microwave Guid. Wave Lett. **4**, 268–270 (1994).

[26] W. C. Chew and W. H. Weedon, ''A 3D perfectly matched medium from modified Maxwell's equations with stretched coordinates,'' Microwave Opt. Technol. Lett. **7**, 599–604 (1994).

[27] R. Mittra and Ü. Pekel, ''A new look at the perfectly matched layer (PML) concept for the reflectionless absorption of electromagnetic waves,'' IEEE Microwave Guid. Wave Lett. **5**, 84–86 (1995).

[28] C. Rappaport, ''Perfectly matched absorbing boundary conditions based on anisotropic lossy maping of space,'' IEEE Microwave Guid. Wave Lett. **5**, 90–92 (1995).

[29] B. Chen and D. G. Fang, ''Modified Berénger's PML absorbing boundary conditions for FD-TD meshes,'' IEEE Microwave Guid. Wave Lett. **5**, 399–401 (1995).

[30] J. Fang and Z. Wu, ''Generalized perfectly matched layer–An extension of Berénger's perfectly matched layer boundary condition,'' IEEE Microwave Guid. Wave Lett. **5**, 451–453 (1995).

[31] Q. H. Liu and J. Tao, ''The perfectly matched layer for acoustic waves in absorbtive media,'' J. Acoust. Soc. Am. **102**, 2072–2081 (1997).
[32] D. M. Sullivan, ''An unsplit step 3-D PML for use with the FDTD method,'' IEEE Microwave Guid. Wave Lett. **7**, 184–186 (1997).
[33] J.-P. Bérenger, ''An effective PML for the absorption of evanescent waves in waveguides,'' IEEE Microwave Guid. Wave Lett. **8**, 188–190 (1998).
[34] W.-P. Huang, C. L. Xu, W. Lui, and K. Yokoyama, ''The perfectly matched layer boundary condition for modal analysis of optical waveguides: Leaky mode calculations,'' IEEE Photonics Technol. Lett. **8**, 652–654 (1996).
[35] W. W. Lui, K. Magari, N. Yoshimoto, S. Oku, T. Hirono, K. Yokoyama, and W.-P. Huang, ''Modeling and design of bending waveguide based semiconductor polarization rotators,'' IEEE Photonics Technol. Lett. **9**, 1379–1381 (1997).
[36] W. C. Chew and Q. H. Liu, ''Perfectly matched layers for elastodynamics: A new absorbing boundary condition,'' J. Comput. Acoust. **4**, 72–79 (1996).
[37] D. Yevick, J. Yu, and F. Schmidt, ''Analytic studies of absorbing and impedance-matched boundary layers,'' IEEE Photonics Technol. Lett. **9**, 73–75 (1997).
[38] F. Collino, ''Perfectly matched absorbing layers for the paraxial equations,'' J. Comput. Phys. **131**, 164–180 (1997).
[39] J. F. Claerbout, ''Coarse grid calculations of waves in inhomogeneous media with application to delineation of complicated seismic structure,'' Geophysics **35**, 407–418 (1970).
[40] G. H. Brooke and D. J. Thomson, ''Non-local boundary conditions for high-order PE models with application to scattering from a rough surface,'' Defence Research Establishment Atlantic, Dartmouth, N.S., Tech. Memo. DREA TM 1999–121, August 1999.
[41] D. T. Prescott and N. V. Shuley, ''Reflection analysis of FDTD boundary conditions—Part II: Bérenger's PML absorbing layers,'' IEEE Trans. Microwave Theory Tech. **45**, 1171–1178 (1997).
[42] H. Schmidt, ''SAFARI Seismo-acoustic fast field algorithm for range-independent environments,'' SACLANT Undersea Research Centre, San Bartolomeo, Italy, Rep. SR-113, 1988.

Traction-free vibration of layered elastic and piezoelectric rectangular parallelepipeds

Paul Heyliger
Department of Civil Engineering, Colorado State University, Fort Collins, Colorado 80523

(Received 12 January 1998; accepted for publication 24 November 1998)

A variational method is developed to study the traction-free vibration of layered rectangular elastic and piezoelectric parallelepipeds. The weak form of the equations of motion and the charge equation are formulated in rectangular Cartesian coordinates. Approximate solutions to these equations are sought in a form that combines piecewise linear or quadratic Lagrange basis functions through the layered dimension of the solid with continuous global polynomial or trigonometric functions in the plane. This allows for the necessary discontinuity in the shear strain and normal potential gradient across the interface between layers caused by the mismatch in material properties. Numerical results compare very well with those computed by other techniques for layered elastic and piezoelectric plates with simple support and homogeneous parallelepipeds under stress-free conditions. New results are presented for layered systems. © *2000 Acoustical Society of America.*
[S0001-4966(00)03702-4]

PACS numbers: 43.30.Dx [PJR]

INTRODUCTION

The unrestrained, traction-free vibration of solid spheres, cylinders, and parallelepipeds has formed the foundation for the computation of elastic properties, internal friction, and the presence of internal voids or flaws in a wide variety of materials. By comparing the measured frequencies with those predicted by approximate solutions to the equations of motion for linear elasticity, estimates to elastic constants and other parameters can be obtained by minimizing the differences between theory and experiment. For parallelepipeds, most computational schemes for the solution of the equations of motion have been based on algorithms based on the studies of Demarest[1] and Eer Nisse.[2] Using Hamilton's principle, the weak form of the equations of motion was solved in approximate fashion by expanding the displacements in terms of Legendre polynomials. This provided an accurate and relatively simple solution to a practical problem with no existing closed-form solution. This methodology was extended to orthorhombic materials by Ohno[3] and later used in a vast number of studies on material properties and vibration mechanics.[4] An important and powerful extension of the general method of analysis was developed by Visscher and co-workers[5] using power series as a basis for the displacement components. Using appropriate transformations, this allowed for the analysis of a wide variety of different shapes including spheres, cylinders, parallelepipeds, and cones.

One disadvantage of the general strategy employed in previous studies is that the approximation functions used, including power series or Legendre polynomials, yield continuous derivatives in the displacements at all points within the solid. While this is a valid and useful trait for homogeneous media, such an approach is flawed when considering dissimilar media. At an interface between two materials that differ in elastic, piezoelectric, and dielectric properties, two of the shear stresses and the normal electric displacement are continuous. However, the material properties are discontinuous. This results in a discontinuity in the gradient of displacement components and the electrostatic potential.

The objective of this study is to develop a solution technique for layered elastic and piezoelectric parallelepipeds that can account for the discontinuity in slope across a dissimilar interface for the problem of unrestrained free vibration. Using one-dimensional basis functions through the thickness combined with global or continuous approximation functions in the plane parallel to the interface, a more accurate estimate of the theoretical frequencies can be generated while maintaining much of the efficiency of earlier models. Similar approaches have been used in related problems by Pauley and Dong[6] for wave propagation in laminated piezoelectric media, and a generalized discrete-layer approach for elastic laminates by Reddy.[7] The solution strategy is formulated for elastic and piezoelectric media and examples are given for both materials. Although the focus of the study is on geometries that are most accurately described as blocks, the wealth of comparisons available in the literature requires that some attention be focused on the geometrically extreme case of the layered plate. Both are considered in this study.

I. GOVERNING EQUATIONS

A. Linear piezoelectricity

We consider a rectangular parallelepiped composed of an arbitrary number elastic or piezoelectric layers. The parallelepiped has dimensions L_x, L_y, and L_z, and the z direction is perpendicular to each dissimilar material interface and is also the poling direction if the layer is piezoelectric. Each layer has the constitutive equations that can be expressed as given as[8]

$$\begin{aligned} \sigma_{ij} &= C_{ijkl} S_{kl} - e_{nij} E_n , \\ D_m &= e_{mkl} S_{kl} + \epsilon_{mn} E_n . \end{aligned} \tag{1}$$

Here, σ_{ij} are the components of the stress tensor, C_{ijkl} are the elastic stiffness components, S_{ij} are the components of

infinitesimal strain, e_{nij} are the piezoelectric coefficients, E_n are the components of the electric field, D_n are the components of the electric displacement, and ϵ_{mn} are the dielectric constants. The indices i and j range over 1,...,6 and m and n range over 1,...,3.

The strain-displacement relations are given by

$$S_{ij}=\frac{1}{2}\left(\frac{\partial u_i}{\partial x_j}+\frac{\partial u_j}{\partial x_i}\right). \tag{2}$$

Here, S_{ij} are the components of the infinitesimal stain tensor and u_i represents the displacement components. The electric field components E_m are related to the electrostatic potential ϕ using the relation

$$E_m=-\frac{\partial \phi}{\partial x_m}. \tag{3}$$

The materials used here allow for nonzero values for e_{ij} as e_{31}, e_{32}, e_{33}, e_{24}, e_{15}, e_{25}, e_{14}, e_{36}, e_{16}, e_{21}, and e_{22}. The nonzero elastic stiffnesses C_{ij} are C_{11}, C_{12}, C_{13}, C_{14}, C_{16}, C_{22}, C_{23}, C_{24}, C_{26}, C_{33}, C_{36}, C_{44}, C_{45}, C_{55}, C_{56}, and C_{66}. The dielectric constants are given by ϵ_{11}, ϵ_{12}, ϵ_{22}, and ϵ_{33}.

Hamilton's principle forms the basis for the weak form of the equations of motion and the charge equation. This can be expressed for a piezoelectric medium[8] as

$$\delta\int_{t_0}^{t}dt\int_V\left[\frac{1}{2}\rho\dot{u}_j\dot{u}_j-H(S_{kl},E_k)\right]dV + \int_{t_0}^{t}dt\int_S(\overline{T}_k\delta u_k-\overline{\sigma}\delta\phi)dS=0. \tag{4}$$

Here, t is time, V and S are the volume and surface occupied by and bounding the solid, respectively, $\overline{T}$ and $\overline{\sigma}$ are the specified surface tractions and surface charge, respectively, δ is the variational operator, the $\cdot$ superscript represents differentiation with respect to time, and H represents the electric enthalpy. The electric enthalpy is given by

$$H=\tfrac{1}{2}C_{ijkl}S_{ij}S_{kl}-e_{ijk}E_iS_{jk}-\tfrac{1}{2}\epsilon_{ij}E_iE_j. \tag{5}$$

B. Variational statement

The weak form of the governing equations, as well as the governing differential equations themselves, can be found by substituting the above relations into Hamilton's principle. It is common to use the contracted notation for the elastic and piezoelectric stiffnesses C_{ijkl} and e_{mij} by compressing the ij and kl indices into a single index ranging from 1 to 6, and maintaining the range of m from 1 to 3. For example, C_{1122} is reduced to C_{12} and e_{312} to e_{36}. In rectangular Cartesian coordinates, we set $x_1=x$, $x_2=y$, and $x_3=z$, with the displacements as $u_1=u(x,y,z)$, $u_2=v(x,y,z)$, and $u_3=w(x,y,z)$. Using this nomenclature, the weak form can be expressed as

$$\begin{aligned}
0=\delta\int_{t_0}^{t}dt\int_V\Big[&\rho(\dot{u}\,\delta\dot{u}+\dot{v}\,\delta\dot{v}+\dot{w}\,\delta\dot{w})-\Big[C_{11}\frac{\partial u}{\partial x}\frac{\partial\delta u}{\partial x}+C_{12}\frac{\partial u}{\partial x}\frac{\partial\delta v}{\partial y}+C_{13}\frac{\partial u}{\partial x}\frac{\partial\delta w}{\partial z}+C_{14}\frac{\partial u}{\partial x}\left(\frac{\partial\delta v}{\partial z}+\frac{\partial\delta w}{\partial y}\right)\\
&+C_{16}\frac{\partial u}{\partial x}\left(\frac{\partial\delta u}{\partial y}+\frac{\partial\delta v}{\partial x}\right)+C_{12}\frac{\partial v}{\partial y}\frac{\partial\delta u}{\partial x}+C_{22}\frac{\partial v}{\partial y}\frac{\partial\delta v}{\partial y}+C_{23}\frac{\partial v}{\partial y}\frac{\partial\delta w}{\partial z}+C_{24}\frac{\partial v}{\partial y}\left(\frac{\partial\delta v}{\partial z}+\frac{\partial\delta w}{\partial y}\right)\\
&+C_{26}\frac{\partial v}{\partial y}\left(\frac{\partial\delta u}{\partial y}+\frac{\partial\delta v}{\partial x}\right)+C_{13}\frac{\partial w}{\partial z}\frac{\partial\delta u}{\partial x}+C_{23}\frac{\partial w}{\partial z}\frac{\partial\delta v}{\partial y}+C_{33}\frac{\partial w}{\partial z}\frac{\partial\delta w}{\partial z}+C_{36}\frac{\partial w}{\partial z}\left(\frac{\partial\delta u}{\partial y}+\frac{\partial\delta v}{\partial x}\right)\\
&+C_{44}\left(\frac{\partial v}{\partial z}+\frac{\partial w}{\partial y}\right)\left(\frac{\partial\delta v}{\partial z}+\frac{\partial\delta w}{\partial y}\right)+C_{45}\left(\frac{\partial v}{\partial z}+\frac{\partial w}{\partial y}\right)\left(\frac{\partial\delta u}{\partial z}+\frac{\partial\delta w}{\partial x}\right)+C_{45}\left(\frac{\partial u}{\partial z}+\frac{\partial w}{\partial x}\right)\left(\frac{\partial\delta v}{\partial z}+\frac{\partial\delta w}{\partial y}\right)\\
&+C_{55}\left(\frac{\partial u}{\partial z}+\frac{\partial w}{\partial x}\right)\left(\frac{\partial\delta u}{\partial z}+\frac{\partial\delta w}{\partial x}\right)+C_{56}\left(\frac{\partial u}{\partial z}+\frac{\partial w}{\partial x}\right)\left(\frac{\partial\delta u}{\partial y}+\frac{\partial\delta v}{\partial x}\right)+C_{16}\left(\frac{\partial u}{\partial y}+\frac{\partial v}{\partial x}\right)\frac{\partial\delta u}{\partial x}+C_{26}\left(\frac{\partial u}{\partial y}+\frac{\partial v}{\partial x}\right)\frac{\partial\delta v}{\partial y}\\
&+C_{36}\left(\frac{\partial u}{\partial y}+\frac{\partial v}{\partial x}\right)\frac{\partial\delta w}{\partial z}+C_{66}\left(\frac{\partial u}{\partial y}+\frac{\partial v}{\partial x}\right)\left(\frac{\partial\delta u}{\partial y}+\frac{\partial\delta v}{\partial x}\right)+C_{14}\frac{\partial\delta u}{\partial x}\left(\frac{\partial v}{\partial z}+\frac{\partial w}{\partial y}\right)+C_{24}\frac{\partial\delta v}{\partial y}\left(\frac{\partial v}{\partial z}+\frac{\partial w}{\partial y}\right)+C_{56}\left(\frac{\partial\delta u}{\partial z}+\frac{\partial\delta w}{\partial x}\right)\\
&\times\left(\frac{\partial u}{\partial y}+\frac{\partial v}{\partial x}\right)-e_{14}\delta E_1\left(\frac{\partial v}{\partial z}+\frac{\partial w}{\partial y}\right)-e_{15}\delta E_1\left(\frac{\partial u}{\partial z}+\frac{\partial w}{\partial x}\right)-e_{24}\delta E_2\left(\frac{\partial v}{\partial z}+\frac{\partial w}{\partial y}\right)-e_{25}\delta E_2\left(\frac{\partial u}{\partial z}+\frac{\partial w}{\partial x}\right)-e_{16}\delta E_1\left(\frac{\partial u}{\partial y}+\frac{\partial v}{\partial x}\right)\\
&-e_{16}E_1\left(\frac{\partial\delta u}{\partial y}+\frac{\partial\delta v}{\partial x}\right)-e_{31}\delta E_3\frac{\partial u}{\partial x}-e_{32}\delta E_3\frac{\partial v}{\partial y}-e_{33}\delta E_3\frac{\partial w}{\partial z}-e_{36}\delta E_3\left(\frac{\partial u}{\partial y}+\frac{\partial v}{\partial x}\right)-e_{21}\delta E_2\frac{\partial u}{\partial x}-e_{21}E_2\frac{\partial\delta u}{\partial x}-e_{22}\delta E_2\frac{\partial v}{\partial y}\\
&-e_{22}E_2\frac{\partial\delta v}{\partial y}-\epsilon_{11}E_1\delta E_1-\epsilon_{22}E_2\delta E_2-\epsilon_{33}E_3\delta E_3-\epsilon_{12}E_1\delta E_2-\epsilon_{12}E_2\delta E_1-e_{14}E_1\left(\frac{\partial\delta v}{\partial z}+\frac{\partial\delta w}{\partial y}\right)-e_{15}E_1\left(\frac{\partial\delta u}{\partial z}+\frac{\partial\delta w}{\partial x}\right)\\
&-e_{24}E_2\left(\frac{\partial\delta v}{\partial z}+\frac{\partial\delta w}{\partial y}\right)-e_{25}E_2\left(\frac{\partial\delta u}{\partial z}+\frac{\partial\delta w}{\partial x}\right)-e_{31}E_3\frac{\partial\delta u}{\partial x}-e_{32}E_3\frac{\partial\delta v}{\partial y}-e_{33}E_3\frac{\partial\delta w}{\partial z}-e_{36}E_3\left(\frac{\partial\delta u}{\partial y}+\frac{\partial\delta v}{\partial x}\right)\Big]\Big]dV\\
&+\int_{t_0}^{t}dt\int_S(\overline{T}_k\delta u_k-\overline{\sigma}\delta\phi)dS=0.
\end{aligned} \tag{6}$$

It is possible to perform the integration by parts and collect the coefficients of the first variations of u, v, w, and ϕ to yield the equations of motion and charge, but that is not necessary here as it is the weak form that is used to develop the approximate solution by a variational method.

C. Discrete-layer approximation

In past studies, approximations to the three displacements (for elastic media) and the three displacements and electrostatic potential (for piezoelectric media) were generated in terms of the global (x,y,z) coordinates. In this study, the dependence of the displacements on the z coordinate is separated from the functions in x and y. This allows for global functions in x and y that result in a subsequent reduction of the size of the computational problem. Hence, approximations for the four unknown field quantities are sought in the form (see Ref. 7)

$$\begin{aligned}
u(x,y,z,t) &= \sum_{j=1}^{n} U_j(x,y,t)\overline{\Psi}_j^u(z) \\
&= \sum_{i=1}^{m}\sum_{j=1}^{n} U_{ji}(t)\Psi_i^u(x,y)\overline{\Psi}_j^u(z), \\
v(x,y,z,t) &= \sum_{j=1}^{n} V_j(x,y,t)\overline{\Psi}_j^v(z) \\
&= \sum_{i=1}^{m}\sum_{j=1}^{n} V_{ji}(t)\Psi_i^v(x,y)\overline{\Psi}_j^v(z), \\
w(x,y,z,t) &= \sum_{j=1}^{n} W_j(x,y,t)\overline{\Psi}_j^w(z) \\
&= \sum_{i=1}^{m}\sum_{j=1}^{n} W_{ji}(t)\Psi_i^w(x,y)\overline{\Psi}_j^w(z), \\
\phi(x,y,z,t) &= \sum_{j=1}^{n} \Phi_j(x,y,t)\overline{\Psi}_j^\phi(z) \\
&= \sum_{i=1}^{m}\sum_{j=1}^{n} \Phi_{ji}(t)\Psi_i^\phi(x,y)\overline{\Psi}_j^\phi(z).
\end{aligned} \tag{7}$$

The approximations for each of the four field quantities are constructed in such a way as to separate the dependence in the plane with that in the direction perpendicular to the interface. The reason for this is that the change in the material properties forces a break in the gradients of the displacements across an interface. This can be easily seen by considering the specialized case of elastostatic and electrostatics. In the former case, the shear stress must be continuous across an interface, but the shear modulus is different for two layers. Hence, the shear strain must be different, implying changes in the slope of the displacement variables across the interface. Similar behavior is true in electrostatics since the electric displacement must be continuous and the dielectric constants are different.

In the thickness direction, one-dimensional Lagrangian interpolation polynomials are used for $\overline{\Psi}_j(z)$. For the in-plane approximations, different types of approximations can be used for the two-dimensional functions $\Psi_j(x,y)$, but power and Fourier series are those most commonly selected. For a parallelepiped with n layers, $(n-1)$ is the number of subdivisions through the parallelepiped thickness (typically taken equal to or greater than the number of layers in the parallelepiped), and Γ_{ji} is the value of component γ at height j corresponding to the ith in-plane approximation function.[7]

Substituting these approximations into the weak form in Eq. (6), introducing the assumption of periodic motion, collecting the coefficients of the variations of the displacements, and placing the results in matrix form yields the result

$$\begin{bmatrix} [M^{11}] & [0] & [0] & [0] \\ [0] & [M^{22}] & [0] & [0] \\ [0] & [0] & [M^{33}] & [0] \\ [0] & [0] & [0] & [0] \end{bmatrix} \begin{Bmatrix} \{\ddot{u}\} \\ \{\ddot{v}\} \\ \{\ddot{w}\} \\ \{\ddot{\phi}\} \end{Bmatrix} + \begin{bmatrix} [K^{11}] & [K^{12}] & [K^{13}] & [K^{14}] \\ [K^{21}] & [K^{22}] & [K^{23}] & [K^{24}] \\ [K^{31}] & [K^{32}] & [K^{33}] & [K^{34}] \\ [K^{41}] & [K^{42}] & [K^{43}] & [K^{44}] \end{bmatrix} \times \begin{Bmatrix} \{u\} \\ \{v\} \\ \{w\} \\ \{\phi\} \end{Bmatrix} = \begin{Bmatrix} \{F^1\} \\ \{F^2\} \\ \{F^3\} \\ \{Q\} \end{Bmatrix}. \tag{8}$$

The elements of these submatrices are themselves submatrices whose elements are determined by evaluating the preintegrated elastic stiffnesses, piezoelectric coefficients, or dielectric constants through the thickness multiplied by the various shape functions or their derivatives as determined by the variational statement. If these submatrices, each of order $(n+1)$, are defined by the subscripts α and β, the corresponding elements can be expressed in fairly compact form. These are given in the Appendix.

Formulating the problem in this fashion has a number of advantages. Primarily, the matrix equations are generic and can accommodate approximating functions in (x,y) that are either global and analytic (such as Fourier or power series) or local and exactly evaluated (such as finite element polynomials). Also, the dependence on the z coordinate has been eliminated by preintegrating, which manifests itself in the matrix equations above. Because of the nature of the approximating functions themselves, the derivative of the displacement and potential is continuous only over a specific sublayer. If the material is homogeneous, this is still an acceptable approximation even for a subdivided layer because the behavior trends toward a continuous derivative as the number of layers increases. For the case of dissimilar media, the functions allow a break in the slope, which matches physical reality much more accurately than a global approximation.

II. NUMERICAL EXAMPLES

The focus of this study is the natural vibrations of unrestrained, traction-free, layered parallelepipeds. However, these solids have relatively few results in the literature with which to compare. To assess the accuracy of the discrete-layer model used here, specific geometries were considered

TABLE I. Dimensionless frequencies of laminated isotropic plate.

ν_1	ρ_1/ρ_2	G_1/G_2	# Layers	Present	Exact	CLT
0.3	1	1	1	0.102 907	0.093 15	0.096 318
0.3	1	1	2	0.095 915	0.093 15	0.096 318
0.3	1	1	4	0.093 864	0.093 15	0.096 318
0.3	1	1	16	0.093 195	0.093 15	0.096 318
0.3	1	1	40	0.093 157	0.093 15	0.096 318
0.3	1	2	40	0.112 491	0.112 483	0.117 493
0.3	1	5	40	0.153 849	0.153 84	0.165 49
0.3	1	15	40	0.229 591	0.229 58	0.269 553
0.3	2	15	40	0.209 477	0.209 468	0.246 065
0.3	3	15	40	0.193 863	0.193 853	0.227 81
0.2	1	1	40	0.090 379	0.090 373	0.093 333

which were not unrestrained but can still be studied using the present approach and also provide a means of comparison. These are the somewhat geometrically extreme parallelepiped: the layered plate. Because of the large number of studies for these types of solids using both individual layer and equivalent single-layer theories, they are useful in this context to assess the accuracy for the thickness approximation. Several exact and approximate solutions exist for simply supported laminated rectangular plates, and these results were used to compare with those of the present approach. The in-plane functions in (x,y) are easily described as the harmonics of the plane in terms of sine and cosine functions. Hence, the main focus of accuracy is the one-dimensional behavior through the thickness.

A. Free vibrations of simply supported laminated isotropic plates

The natural frequencies of a simply supported laminated plate composed of dissimilar isotropic materials have been computed by Srinivas[9] using an exact method. This problem was treated here using the discrete-layer model for the fundamental in-plane mode. The exact in-plane harmonics are used as the approximation functions in (x,y), which effectively makes the problem one-dimensional. A three-ply plate was considered with the material properties as follows: $\rho_1=\rho_3$, $G_1=G_3$, $\nu_1=\nu_3$, $\nu_2=0.3$, $h_1/h=0.1$, $h_1=h_3$, $h_2/h=0.8$, $a/h=10.0$. Here, h is the total thickness of the plate and a is the length of a side of the plate. A convergence study was completed first for the case of a completely isotropic plate. The material parameters were then varied and the remaining results were calculated using a 40-layer discretization through the thickness. For all discretizations, layers of equal thickness were used, and linear approximations were used in the thickness direction.

The results are presented using the dimensionless frequency parameter $\lambda=\Omega(\rho_2 h^2/G_2)^{1/2}$, and are shown in Table I. Even for a fairly small number of layers, the present results are in excellent agreement with the exact values. Changing the material properties to correspond to different materials does not lessen the accuracy.

B. Free vibrations of simply supported cross-ply laminates

A problem that is similar to the laminated isotropic plate is the analysis of the free vibrations of simply supported cross-ply laminates composed of orthotropic materials. The material properties in this case were taken to be $E_1/E_2=40$, $G_{12}/E_2=G_{13}/E_2=0.6$, $G_{23}/E_2=0.5$, $\nu_{12}=\nu_{13}=\nu_{23}=0.25$. A square plate was used with length a, thickness h, and $a/h=5$ unless noted. Results were calculated using the dimensionless fundamental frequency given by $\bar{\omega}=\omega(\rho h^2/E_2)^{1/2}$. Results are presented in Tables II(a)–(d). The results are compared with those of Noor,[10] Putcha and Reddy,[11] Khdier,[12] and classical lamination theory. The parameter N is used to denote the total number of sublayers modeled using linear polynomials by the present methodology. For example, for the three-ply plate whose results are given in Table II(a), one linear discrete layer is used for each ply $(N=3)$, then this discretization is refined to provide 10 linear layers per ply $(N=30)$. Very good agreement is found for all cases considered.

TABLE II. (a) Fundamental frequency of [0/90/0] laminate. (b) Fundamental frequency of [0/90/90/0] laminate. (c) Frequencies of [0/90/0] laminate for first three modes. One lamina per layer used $(N=3)$, $E_1/E_2=40$, $a/h=10$. (d) Fundamental frequency of unsymmetric cross-ply: $[0/90/\cdots]$ $(\nu_{23}=0.49$, $a/h=5)$.

(a)

	E_1/E_2			
Theory	10	20	30	40
Present $(N=3)$	0.333 06	0.380 26	0.409 17	0.426 73
Present $(N=30)$	0.327 73	0.373 72	0.398 85	0.415 06
Noor	0.328 41	0.382 41	0.410 89	0.430 06
Pitcha	0.330 95	0.381 12	0.410 94	0.431 55
Khdier	0.326 04	0.369 39	0.393 90	0.410 53
CLT	0.425 99	0.557 93	0.664 19	0.755 65

(b)

	E_1/E_2			
Theory	10	20	30	40
Present $(N=4)$	8.3371	9.6528	10.4000	10.8887
Present $(N=40)$	8.2488	9.5018	10.2024	10.6567
Noor	8.2103	9.5603	10.272	10.752
Khdier	8.2718	9.5263	10.272	10.787
CLT	10.65	13.948	16.605	18.891

(c)

	Mode number		
Theory	1	2	3
Present	14.9068	20.8413	31.4874
Khdier	14.702	21.904	35.982
CLT	18.891	26.938	46.208

(d)

	E_1/E_2		
Theory	3	20	40
Present $(N=2)$	0.256 56	0.310 74	0.346 30
Noor	0.250 81	0.306 98	0.342 50
Khdier	0.249 12	0.311 15	0.358 91
Present $(N=4)$	0.262 78	0.381 23	0.435 95
Noor	0.261 82	0.376 22	0.427 19
Khdier	0.260 67	0.386 62	0.448 51
Present $(N=10)$	0.264 61	0.402 34	0.464 66
Noor	0.265 83	0.403 37	0.464 98
Khdier	0.263 93	0.403 37	0.465 69

C. Free vibrations of simply supported piezoelectric laminates

Several different studies have appeared for piezoelectric laminates. Ricketts[13] used an approximate single-layer

TABLE III. Convergence of fundamental frequency for single layer of PZT-4.

a/h	4		10		50	
N	Open	Closed	Open	Closed	Open	Closed
1	110 189	104 105	20 485.7	20 217.4	848.586	848.094
2	102 599	100 294	18 761.5	18 656.2	773.651	773.458
4	99 454	97 915	18 255.4	18 180.8	753.622	753.525
8	98 456	97 186	18 122.4	18 055.7	748.576	748.452
16	98 311	96 994	18 088.9	18 024.0	747.299	747.177
32	98 251	96 946	18 080.6	18 016.0	746.979	746.859
64	98 236	96 934	18 078.4	18 014.0	746.898	746.779
Exact	98 232	96 930	18 077.8	18 013.4	746.873	746.752

theory to study piezoelectric plate vibrations. Exact frequencies for piezoelectric laminates under simple support have been given by Heyliger and Saravanos.[14] We use the results of the latter study to examine the convergence of the discrete-layer model for piezoelectric media.

A square plate composed of a single layer of the piezoceramic PZT-4 is considered first. The length of each side is taken as $L_x = L_y = a$. The height is taken as h, and three a/h ratios are studied: 4, 10, and 50. The fundamental through-thickness frequency is of most interest, and is given as a function of the number of layers used to describe the piezoelectric layer. The results are shown in Table III. The frequencies are represented in the tables in terms of the parameter $\omega h/\rho$.

A second plate is composed of two dissimilar piezoelectric materials modeled after PZT-4[15] and PVDF.[16] The densities of the two materials are taken to be the same. A three-ply laminate is constructed with the configuration [PZT/PVDF/PZT], with the PVDF layer oriented at 0 deg. The thickness of each PZT layer is $0.25h$. Both open ($D_z = 0$) and closed-circuit ($\phi = 0$) conditions are considered on the upper and lower laminate faces, with the length/thickness ratios of 4 and 50 studied. The convergence of the first six modes as a function of a number of sublayers is shown and compared with the exact frequencies in Table IV. For both of these examples, it is clear that even a small number of layers yields frequencies accurate well within several percent.

All remaining examples consider the case of fully unrestrained free vibration, for which there are no exact or single-term solutions. This type of behavior is much more complex and computationally intensive than those with simple support. Also, the shapes of interest tend to be blocks, not plates.

D. Homogeneous orthotropic and trigonal parallelepipeds

The homogeneous orthotropic parallelepiped under traction-free vibration can be studied using the original Ritz method of Demarest[1] as reported by Ohno.[3] The specimen

TABLE IV. Convergence of frequencies for 3-ply piezoelectric laminate.

	Mode					
$a/h = 4$: C	1	2	3	4	5	6
$N = 4$	74.7732	197.353	329.301	342.387	447.653	549.479
$N = 8$	72.8253	195.402	311.843	338.628	432.976	534.030
$N = 16$	72.3376	194.920	307.606	337.504	426.810	530.343
$N = 32$	72.2152	194.800	306.558	337.207	425.160	529.432
$N = 64$	72.1846	194.770	306.296	337.132	424.742	529.205
Exact	72.1744	194.760	306.209	337.107	424.602	529.129
$a/h = 44$: O	1	2	3	4	5	6
$N = 4$	74.8023	197.483	329.691	342.481	447.733	550.079
$N = 8$	72.8451	195.525	312.190	338.718	433.049	534.493
$N = 16$	72.3554	195.042	307.940	337.593	426.875	530.769
$N = 32$	72.2325	194.921	306.888	337.296	425.223	529.849
$N = 64$	72.2017	194.891	306.626	337.221	424.804	529.620
Exact	72.1915	194.881	306.539	337.196	424.664	529.543
$a/h = 50$: C	1	2	3	4	5	6
$N = 4$	0.637 707	16.4328	28.5365	292.035	379.322	400.300
$N = 8$	0.634 494	16.4315	28.5356	273.945	359.391	379.362
$N = 16$	0.633 687	16.4312	28.5353	269.563	354.642	371.982
$N = 32$	0.633 485	16.4311	28.5353	268.479	353.469	370.048
$N = 64$	0.633 434	16.4311	28.5353	268.208	353.177	369.559
Exact	0.633 417	16.4311	28.5352	268.118	353.079	369.396
$a/h = 50$: O	1	2	3	4	5	6
$N = 4$	0.637 786	16.4426	28.5566	295.866	390.811	400.301
$N = 8$	0.634 566	16.4413	28.5556	277.248	369.149	379.363
$N = 16$	0.633 757	16.4410	28.5554	272.717	363.958	371.982
$N = 32$	0.633 555	16.4409	28.5554	271.595	362.674	370.048
$N = 64$	0.633 506	16.4409	28.5553	271.315	362.354	369.560
Exact	0.633 487	16.4409	28.5553	271.222	362.248	369.396

TABLE V. Groupings of approximation functions.

Group	Displacement	x	y	z	Group	Displacement	x	y	z
	u	O	E	E		u	O	O	O
OD	v	E	O	E	OX	v	E	E	O
	w	E	E	O		w	E	O	E
	u	O	O	E		u	O	E	O
EY	v	E	E	E	EZ	v	E	O	O
	w	E	O	O		w	E	E	E
	u	E	E	E		u	E	O	O
EX	v	O	O	E	EV	v	O	E	O
	w	O	E	O		w	O	O	E
	u	E	E	O		u	E	O	E
OY	v	O	O	O	OZ	v	O	E	E
	w	O	E	E		w	O	O	O

studied is olivine, with the dimensions given as $2.745 \times 2.832 \times 2.015$ (all mm), the density by 3.316 (g/cm^3), and the elastic stiffnesses $C_{11}=324$ (all C_{ij} in GPa), $C_{22}=196$, $C_{33}=232$, $C_{44}=63.9$, $C_{55}=77.9$, $C_{66}=78.8$, $C_{12}=71.5$, $C_{13}=71.5$, and $C_{23}=68.8$. These results are very useful for comparing the resulting frequencies of the present model. The frequencies were computed using 16 layers and linear approximations in the thickness direction of the the parallelepiped. In the $x-y$ plane, Legendre polynomials of up to seventh order were used to describe the displacements.

The methodology used by Ohno has one distinct advantage over the present technique in that symmetry of the specimen can be used to greatly reduce the computational size of the eigenvalue problem that approximates the weak form of the equations of periodic motion. For example, if polynomials up to order 5 are used to describe each of the three displacements, the size of the global $[K]$ or $[M]$ matrix is $3 \times 6^3 = 648$ terms, where the first three represent the three displacements, 6 is the number of functions for polynomials up to order 5, raised to the third power in three-space. As shown by Ohno,[3] this problem can be broken down into eight smaller problems of dimension 81 using group theory for orthotropic, hexagonal, cubic, or isotropic materials. The nature of these groupings is shown in Table V, where the eight groups are defined by labels as characterized by Ohno and others as *OD* (breathing and longitudinal modes), *EX*, *EY*, and *EZ* (symmetric flexure modes), *OX*, *OY*, and *OZ* (torsional modes), and *EV* (asymmetric flexure). These are grouped according to the pairings of the odd or even (O or E) nature of the displacement functions in the three spatial coordinates.

For the present method, there is no inherent symmetry of the one-dimensional Lagrangian basis functions in the z direction that is used to approximate the displacements. Hence, for orthorhombic symmetry, only four smaller groups can be constructed, with either odd or even functions used for the three displacement components. These groups are formed by combining (*EX*,*OY*), (*OZ*,*EV*), (*EY*,*OX*), and (*OD*,*EZ*). As can be seen from Table V, each of these pairings has identical properties in x and y, but they cannot be split into two smaller groups because of the layerwise approximation in z as opposed to a global approximation. For the present example, the total size of the problem for 16 layers and terms up to order 7 is $3 \times 8^2 \times 17 = 3264$, where the three displacements are represented by 64 total terms in the $x-y$ dimension and 17 total bounding surfaces of the 16 layers. However, since the 64 in-plane terms can be split, the problem reduces to four separate problems of dimension 816. Clearly, this method is not competitive with algorithms that use global basis functions for homogeneous solids, as it is computationally easier to solve problems that can be split into eight smaller problems rather than the four. It is only when the through-thickness symmetry is destroyed (i.e., layered materials) that this approach yields significant benefits.

The first six frequencies for an unrestrained solid are zero, corresponding to the rigid-body modes. The values for the first 19 nonzero frequencies as computed by the present model are shown in Table VI and are compared with the results of Ohno.[3] Excellent agreement is obtained, with even the higher frequencies within a fraction of a percent. The results of Ohno are based on continuous Legendre polynomials as basis functions in each direction of the solid, which is in general a more accurate approach for a homogeneous solid. The higher accuracy of the present approach, demonstrated here through the lower frequencies, is primarily

TABLE VI. Frequencies for orthotropic cube (MHz).

Mode	Present	Ohno
1	0.6931	0.6937
2	0.9300	0.9307
3	1.0294	1.0302
4	1.0391	1.0401
5	1.0895	1.0904
6	1.1589	1.1606
7	1.2096	1.2100
8	1.2251	1.2264
9	1.2314	1.2324
10	1.3113	1.3129
11	1.3172	1.3181
12	1.4119	1.4124
13	1.4133	1.4152
14	1.5407	1.5434
15	1.6363	1.6370
16	1.6496	1.6511
17	1.6553	1.6573
18	1.6809	1.6844
19	1.6826	1.6849

TABLE VII. Frequencies for (trigonal) alpha-quartz (MHz).

Mode	Present	Ohno	Group
1	0.5216	0.5213	*AU-BG*
2	0.5944	0.5941	*AU-BG*
3	0.6435	0.6429	*BU-AG*
4	0.6678	0.6676	*AU-BG*
5	0.7002	0.6994	*AU-BG*
6	0.7010	0.7004	*BU-AG*
7	0.7219	0.7215	*BU-AG*
8	0.7452	0.7449	*BU-AG*
9	0.7951	0.7946	*AU-BG*
10	0.8002	0.7993	*AU-BG*
11	0.8026	0.8022	*BU-AG*
12	0.8144	0.8140	*BU-AG*
13	0.8339	0.8332	*BU-AG*
14	0.8540	0.8535	*BU-AG*
15	0.8663	0.8657	*AU-BG*
16	0.9130	0.9123	*BU-AG*
17	0.9186	0.9182	*BU-AG*
18	0.9490	0.9485	*AU-BG*
19	0.9745	0.9741	*BU-AG*

caused by the relatively large number of layers and terms used to approximate the displacement components.

A parallelepiped of alpha-quartz was also studied and compared with the global approximation results of Ohno.[17] This material has trigonal elastic and piezoelectric symmetry, but only the elastic frequencies are studied here for a comparison for materials with trigonal symmetry. For global basis functions as described in the earlier section, the appearance of the C_{14}, C_{24}, and C_{56} terms indicates that not eight but rather four smaller groups can be used to decompose the total eigenvalue problem. These are referred to as groups A_u (*EX* and *EV*), A_g (*OD* and *OX*), B_u (*EY* and *EZ*), and B_g (*OY* and *OZ*) in Ohno's paper. Once again, the use of Lagrange piecewise-linear basis functions in the z direction destroys the symmetry about the $x-y$ plane, and only two smaller subgroups are possible: the combined groups A_u-B_g and B_u-A_g. The nature of the displacement field characteristics are discussed further in Ohno's paper and are not replicated here. The specimen has density of 2648 kg/m^3, edge lengths $3.219\times2.913\times3.690$ mm^3, and independent elastic constants as reported by Bechmann[18] as $C_{11}=86.80$, $C_{33}=105.75$, $C_{44}=58.20$, $C_{12}=7.04$, and $C_{13}=11.91$ in GPa.

A total of 32 layers and power series up to order 5 are used to represent the displacement components. The study of Ohno used Legendre polynomials up to order 10 in all directions. Hence, the thickness (or z) direction is more finely modeled using the present approach, with a less accurate approximation used in $x-y$. The results are given in Table VII. Excellent agreement is found, with the present method yielding expected higher results in frequency.

E. Homogeneous piezoelectric parallelepiped

We also consider the homogeneous parallelepiped of $LiNbO_3$ monocrystal considered by Dunn and co-workers.[19] This specimen has trigonal structure of class $3m$. The specimen has dimensions $0.504\times0.507\times0.497$ cm, with density 4.636 g/cm^3. The independent constants are $C_{11}=203.0$ (all C_{ij} in GPa), $C_{12}=53.0$, $C_{13}=75.0$ $C_{14}=9.0$, $C_{33}=245.0$, $C_{44}=60.0$, $e_{31}=0.2$ (all e_{mi} in C/m^2), $e_{33}=1.3$, $e_{15}=3.7$, $e_{22}=2.5$, and the relative dielectric constants are $\epsilon_{11}=44.0$, $\epsilon_{33}=29.0$.

TABLE VIII. Frequencies for $LiNbO_3$(kHz).

	Elastic		Piezoelectric	
Mode	Power series	Present	Power series	Present
1	326.31	326.74	326.70	327.13
2	341.87	342.40	399.98	400.64
3	437.71	438.44	490.21	491.00
4	440.27	441.09	493.26	494.09
5	458.85	459.46	497.24	498.09
6	477.27	477.92	510.29	510.89
7	485.72	486.35	520.78	521.80
8	498.89	499.25	542.52	543.23
9	511.56	512.34	561.14	561.90
10	550.26	550.70	569.24	570.21
11	550.29	552.22	578.69	579.13
12	555.24	557.23	585.25	586.81
13	557.15	557.92	592.66	593.05
14	560.37	560.82	594.03	595.60
15	561.49	562.33	615.19	616.10
16	575.41	575.76	616.91	617.42
17	617.79	618.98	646.19	649.39
18	640.08	642.79	661.10	661.97
19	653.59	654.54	662.06	663.73
20	656.50	657.85	683.78	684.96

The frequencies are computed two ways. The first is using the global Ritz method with power series used as the approximation functions, similar to that used by Ohno[17] with terms up to and including 11th order in the approximation. Next, the present approach is used with 16 layers and terms up to order 7. The outer faces of the block have zero traction and zero charge. The results are given in Table VIII for both piezoelectric and elastic frequencies, the latter of which are obtained by completing an analysis with all piezoelectric constants set equal to zero. The agreement is very good, with the present method yielding slightly higher values because of the lower order of approximation. The results are also in good agreement with measurements reported by Dunn and co-workers.[19] The difference between piezoelectric and elastic frequencies is quite high because of the relative strength of the piezoelectric coefficients. Alpha-quartz, for example, has much smaller differences between elastic and electric frequencies.[17]

F. Layered elastic parallelepiped

Visscher and co-workers have presented a relatively simple yet highly effective and very accurate method of computing free-vibration frequencies for a wide variety of shapes using power series as basis functions to describe each of the three displacement components.[5] One of the examples studied in their work was a problem termed the ''layered sandwich,'' which is one of the problems of interest in the present study. The layered sandwich is rectangular parallelepiped made of two smaller parallelepipeds of dissimilar materials. One of the configurations considered by Visscher and co-workers has lengths in the x, y, and z directions of dimension 0.4, 0.6, and 0.8. The two smaller parallelepipeds are identical in size but have different material properties. The

TABLE IX. Group structure for layered isotropic bimaterial.

Group	Displacement	x	y
1	u	e	e
	v	o	o
	w	o	e
2	u	e	o
	v	o	e
	w	o	o
3	u	o	o
	v	e	e
	w	e	o
4	u	o	e
	v	e	o
	w	e	e

top layer is denoted as layer 1 and has $\rho=2.0$, $C_{11}=1.2$, and $C_{12}=0.4$. The bottom layer is layer 2, with $\rho=10.0$, $C_{11}=6.0$, and $C_{12}=2.0$.

One of the limitations of using global basis functions to describe the displacement of components of this type is that the derivatives of the displacements are by assumption continuous across a dissimilar material interface. The physical conditions are such that, though the tractions and the displacements are continuous, the shear strain is discontinuous across such an interface because of the mismatch in the shear modulus. Hence, there is a break or kink in the displacement field across the interface that simple power series cannot represent. The present approach can model this effect and therefore does not have this limitation.

As discussed earlier, the general eigenvalue problem that results following numerical approximation can be split into smaller groups depending on the symmetry of the material and the nature of the approximations being used. For isotropic materials and global basis functions, such a splitting results in solution of eight smaller problems. In this case, the symmetry about the $x-y$ plane is destroyed by the layered material, and no grouping is possible in z. Hence, the eight groups must be grouped into the four groups mentioned in the section on homogeneous orthorhombic materials. The explicit form of these four groups is shown in Table IX.

The results for the layered parallelepiped are listed in Table X. The present results are compared with those of Visscher, who included results for only one symmetry group for a large variety of layer-thickness ratios. Here, we focus only on the thickness ratio of 1:1, but include all frequencies as computed by the present algorithm using 16 layers (eight per material) and eight terms in the in-plane approximation. The frequencies from Visscher are taken from a table, and the accuracy of the third digit may be limited. It is clear from these results that using a global approximation function with C^1 continuity across an interface can introduce significant errors in frequency. The results of Visscher are significantly higher than those computed using the present approach, especially for the lower modes. Specifically, the lower two modes are slightly over five percent larger than the discrete-layer results. The present methodology converges from above; hence, enforcing continuity of slope displacement that does not physically exist stiffens the system and results in higher frequencies. As the mode number increases, the difference between the two approaches is lessened, but the present method yields consistently lower values.

TABLE X. Frequencies for layered elastic bimaterial.

Mode	Present	Visscher	Group	Mode	Present	Visscher	Group
1	0.236		2	26	0.771		4
2	0.251		1	27	0.775		2
3	0.278	0.295	3	28	0.780	0.787	3
4	0.399		2	29	0.794		4
5	0.431		4	30	0.797		4
6	0.436		1	31	0.799	0.802	3
7	0.452	0.476	3	32	0.821	0.821	3
8	0.477		4	33	0.832		4
9	0.481		1	34	0.836		2
10	0.514		2	35	0.859		4
11	0.526		1	36	0.859	0.861	3
12	0.540		4	37	0.864		2
13	0.575		2	38	0.876	0.882	3
14	0.585		4	39	0.879		1
15	0.591		2	40	0.883		1
16	0.608	0.613	3	41	0.888		4
17	0.652		4	42	0.889	0.892	3
18	0.664		1	43	0.906		1
19	0.671		2	44	0.911		4
20	0.703	0.703	3	45	0.920		2
21	0.710		1	46	0.926	0.929	3
22	0.716		1	47	0.939		1
23	0.737		1	48	0.942	0.950	3
24	0.751		4	49	0.945		2
25	0.759		1	50	0.946		4

Part of the reason for this difference can been seen by examination of the through-thickness plots of the displacement component modal distributions. Figures 1 and 2 show the plots for the normalized v and w displacement components through the thickness of the block at the outermost corner ($x=0.2$,$y=0.3$) for the first five modes of group 3 (i.e., modes 3, 7, 16, 20, and 28). The displacement vector is normalized for each mode: hence, the maximum value of either u, v, or w is set equal to 1, with the remaining values given relative to this scaling. The plot of u is not shown primarily because the magnitude of this component for the modes considered is small.

The modal distributions for mode 3 (solid line), 7 (dotted line), 16 (dashed line), 20 (long-dashed line), and 28

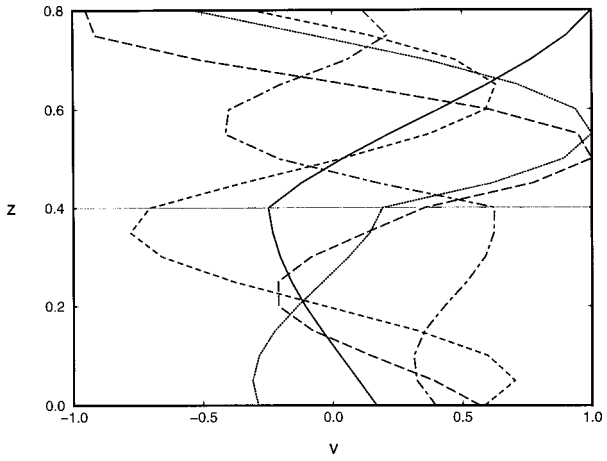

FIG. 1. Through-thickness modal distribution of v at corner of bimaterial.

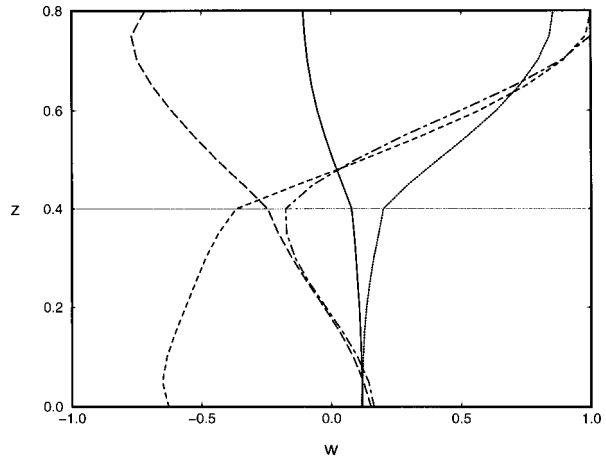

FIG. 2. Through-thickness modal distribution of w at corner of bimaterial.

(dot–dashed line) are shown as a function of thickness coordinate z, with the displacement shown at each sublayer interface. Many of the kinks in the curves are a result of the linear thickness approximation, but even so it is clear that breaks in the slope occur which would be difficult to represent using functions with continuous derivatives. As a general rule, the higher modes are much smoother, with several of the modes having very small breaks in slope. The better agreement of frequencies at higher modes also reflects this condition.

G. Layered piezoelectric parallelepiped

As a final example, we consider the traction-free case of the layered piezoelectric block. A two-layer bimaterial composed of $LiNbO_3$ bonded to PZT-5 is considered. The dimensions of the block are the same as those used for the homogeneous $LiNbO_3$ example considered in an earlier section. In the thickness direction, the block is divided into two equal halves, with the lower composed of $LiNbO_3$ and the upper of PZT-5. The PZT-5 has hexagonal symmetry, with the properties $\rho=7500\,\mathrm{kg/m^3}$, $C_{11}=139.0$, $C_{33}=115.0$, $C_{44}=25.6$, $C_{12}=77.8$, and $C_{13}=74.3$ in GPa, $e_{31}=-5.2$, $e_{33}=15.08$, $e_{15}=12.72$ in $\mathrm{C/m^2}$, and relative dielectric constants of $\epsilon_{11}/\epsilon_0=1475$ and $\epsilon_{33}/\epsilon_0=1300$.

Three different cases are explored. The elastic frequencies are computed first, which requires all $e_{ij}=0$. For the remaining two cases, the piezoelectric coefficients are nonzero and two surface boundary conditions are explored: zero normal electric displacement ($D_n=0$) and zero electrostatic potential ($\phi=0$). The first condition is satisfied in a weak sense on the surfaces regardless of the type of approximation function being used. The second condition must be enforced by the appropriate selection of the approximation functions in (x,y). Using polynomials as before, the following functions are used for ϕ:

$$\Psi_{ij}^{\phi}(x,y)=\left(x^{i+1}-\frac{x^{i-1}L_x^2}{4}\right)\left(y^{j+1}-\frac{y^{j-1}L_y^2}{4}\right). \tag{9}$$

These functions satisfy the essential boundary condition of zero potential at the outer surfaces. The upper and lower faces are fixed at zero potential by forcing the coefficients of the appropriate functions to be equal to zero at these locations. The results are shown in Table XI for the three cases.

TABLE XI. Frequencies (kHz) for layered piezoelectric block.

Mode	Elastic	Piezoelectric: $D_n=0$	Piezoelectric: $\phi=0$
1	215.29	219.19	215.42
2	219.09	223.95	219.10
3	271.90	275.87	275.38
4	281.31	293.84	283.30
5	282.31	295.66	284.15
6	291.02	334.38	294.87
7	291.20	336.98	296.20
8	318.45	337.75	325.60
9	324.83	347.34	328.35
10	326.09	355.88	336.44
11	339.30	356.72	347.25
12	345.38	363.28	348.21
13	345.93	372.10	352.67
14	350.97	372.35	354.24
15	351.79	372.84	357.95
16	369.71	377.40	374.09
17	390.24	428.80	390.69
18	423.98	434.64	424.02
19	441.06	450.10	442.83
20	448.80	451.39	444.44
21	462.20	492.88	466.12
22	462.78	494.98	466.35
23	464.56	496.59	474.49
24	466.74	497.17	475.65
25	475.84	502.28	479.08

As one might expect, the elastic frequencies are the lowest, with the homogeneous electric displacement yielding the highest frequencies. As in the case of the layered elastic block, it is theoretically possible to back calculate the properties of both materials as in conventional resonant ultrasound using an inverse approach, but such an attempt was not made here.

III. CONCLUSION

Using global basis functions to approximate displacement components for rectangular parallelepipeds using the Ritz method is unquestionably a more efficient approach for the traction-free vibration problem of homogeneous materials than splitting the nature of the approximations as done here. This is especially true when symmetry of the material properties can be exploited to reduce the size of the problem. When the parallelepiped is layered, however, the discontinuity in material properties across the material interface can result in a break in the slope of the displacement components and also the potential if the material is piezoelectric. We have shown that use of approximation functions with C^0 continuity in the thickness direction can model this behavior more accurately. Although the efficiency is reduced because of the loss of forced symmetry in the basis functions, it is still possible to maintain some of these reductions in the plane. The present approach is ideally suited for traditional applications of resonant ultrasound spectroscopy, including materials characterization and flaw detection.

ACKNOWLEDGMENT

This study was funded in part by Grant No. 9702548 from the United States Department of Agriculture. This support is gratefully acknowledged.

APPENDIX

The entries in the element coefficients can be expressed as

$$[K^{11}]_{\alpha\beta}=\int_A\Bigg[[A^{11}]\frac{\partial\Psi^u_\alpha}{\partial x}\frac{\partial\Psi^u_\beta}{\partial x}+[A^{16}]\Bigg(\frac{\partial\Psi^u_\alpha}{\partial y}\frac{\partial\Psi^u_\beta}{\partial x}+\frac{\partial\Psi^u_\alpha}{\partial x}\frac{\partial\Psi^u_\beta}{\partial y}\Bigg)+[D^{55}]\Psi^u_\alpha\Psi^u_\beta+[B^{56}]\frac{\partial\Psi^u_\alpha}{\partial y}\psi^u_\beta+[B^{56}]^T\psi^u_\alpha\frac{\partial\Psi^u_\beta}{\partial y}+[A^{66}]\frac{\partial\Psi^u_\alpha}{\partial y}\frac{\partial\Psi^u_\beta}{\partial y}\Bigg]dxdy, \quad \text{(A1)}$$

$$[K^{12}]_{\alpha\beta}=\int_A\Bigg[[A^{12}]\frac{\partial\Psi^u_\alpha}{\partial x}\frac{\partial\Psi^v_\beta}{\partial y}+[A^{26}]\frac{\partial\Psi^u_\alpha}{\partial y}\frac{\partial\Psi^v_\beta}{\partial y}+[D^{45}]\Psi^u_\alpha\Psi^v_\beta+[A^{16}]\frac{\partial\Psi^u_\alpha}{\partial x}\frac{\partial\Psi^v_\beta}{\partial x}+[B^{14}]\frac{\partial\Psi^u_\alpha}{\partial x}\psi^v_\beta+[B^{56}]^T\psi^u_\alpha\frac{\partial\Psi^v_\beta}{\partial x}+[A^{66}]\frac{\partial\Psi^u_\alpha}{\partial y}\frac{\partial\Psi^v_\beta}{\partial x}\Bigg]dxdy, \quad \text{(A2)}$$

$$[K^{13}]_{\alpha\beta}=\int_A\Bigg[[B^{13}]\frac{\partial\Psi^u_\alpha}{\partial x}\Psi^w_\beta+[B^{36}]\frac{\partial\Psi^u_\alpha}{\partial y}\Psi^w_\beta+[\bar{B}^{45}]\Psi^u_\alpha\frac{\partial\Psi^w_\alpha}{\partial y}+[A^{56}]\frac{\partial\Psi^u_\alpha}{\partial y}\frac{\partial\Psi^w_\beta}{\partial x}+[A^{14}]\frac{\partial\Psi^u_\alpha}{\partial x}\frac{\partial\Psi^w_\beta}{\partial y}+[\bar{B}^{55}]\Psi^u_\alpha\frac{\partial\Psi^w_\alpha}{\partial x}\Bigg]dxdy, \quad \text{(A3)}$$

$$[K^{14}]_{\alpha\beta}=\int_A\Bigg[[E^{31}]\frac{\partial\Psi^u_\alpha}{\partial x}\Psi^\phi_\beta+[E^{36}]\frac{\partial\Psi^u_\alpha}{\partial y}\Psi^\phi_\beta+[\bar{E}^{15}]\Psi^u_\alpha\frac{\partial\Psi^\phi_\beta}{\partial x}+[\bar{E}^{16}]\frac{\partial\Psi^u_\alpha}{\partial y}\frac{\partial\Psi^\phi_\beta}{\partial x}+[\bar{E}^{21}]\frac{\partial\Psi^u_\alpha}{\partial x}\frac{\partial\Psi^\phi_\beta}{\partial y}+[\bar{E}^{25}]\Psi^u_\alpha\frac{\partial\Psi^\phi_\alpha}{\partial y}\Bigg]dxdy, \quad \text{(A4)}$$

$$[K^{22}]_{\alpha\beta}=\int_A\Bigg[[A^{22}]\frac{\partial\Psi^v_\alpha}{\partial y}\frac{\partial\Psi^v_\beta}{\partial y}+[A^{26}]\Bigg(\frac{\partial\Psi^v_\alpha}{\partial x}\frac{\partial\Psi^v_\beta}{\partial y}+\frac{\partial\Psi^v_\alpha}{\partial y}\frac{\partial\Psi^v_\beta}{\partial x}\Bigg)+[D^{44}]\Psi^v_\alpha\Psi^v_\beta+[B^{24}]^T\Psi^v_\alpha\frac{\partial\Psi^v_\beta}{\partial y}+[B^{24}]\frac{\partial\Psi^v_\alpha}{\partial y}\Psi^v_{beta}+[A^{66}]\frac{\partial\Psi^v_\alpha}{\partial x}\frac{\partial\Psi^v_\beta}{\partial x}\Bigg]dxdy, \quad \text{(A5)}$$

$$[K^{23}]_{\alpha\beta}=\int_A\Bigg[[B^{23}]\frac{\partial\Psi^v_\alpha}{\partial y}\Psi^w_\beta+[B^{36}]\frac{\partial\Psi^v_\alpha}{\partial x}\Psi^w_\beta+[\bar{B}^{44}]\Psi^v_\alpha\frac{\partial\Psi^w_\alpha}{\partial y}+[A^{56}]\frac{\partial\Psi^v_\alpha}{\partial x}\frac{\partial\Psi^w_\beta}{\partial x}+[A^{24}]\frac{\partial\Psi^v_\alpha}{\partial y}\frac{\partial\Psi^w_\beta}{\partial y}+[\bar{B}^{45}]\Psi^v_\alpha\frac{\partial\Psi^w_\alpha}{\partial x}\Bigg]dxdy, \quad \text{(A6)}$$

$$[K^{24}]_{\alpha\beta}=\int_A\Bigg[[E^{32}]\frac{\partial\Psi^v_\alpha}{\partial y}\Psi^\phi_\beta+[E^{36}]\frac{\partial\Psi^v_\alpha}{\partial x}\Psi^\phi_\beta+[\bar{E}^{14}]\Psi^v_\alpha\frac{\partial\Psi^\phi_\alpha}{\partial x}+[\bar{E}^{24}]\Psi^v_\alpha\frac{\partial\Psi^\phi_\alpha}{\partial y}+[\bar{E}^{16}]\frac{\partial\Psi^v_\alpha}{\partial x}\frac{\partial\Psi^\phi_\beta}{\partial x}+[\bar{E}^{22}]\frac{\partial\Psi^v_\alpha}{\partial y}\frac{\partial\Psi^\phi_\beta}{\partial y}\Bigg]dxdy \quad \text{(A7)}$$

$$[K^{33}]_{\alpha\beta}=\int_A\Bigg[[A^{44}]\frac{\partial\Psi^w_\alpha}{\partial y}\frac{\partial\Psi^w_\beta}{\partial y}+[A^{45}]\Bigg(\frac{\partial\Psi^w_\alpha}{\partial x}\frac{\partial\Psi^w_\beta}{\partial y}+\frac{\partial\Psi^w_\alpha}{\partial y}\frac{\partial\Psi^w_\beta}{\partial x}\Bigg)+[D^{33}]\Psi^w_\alpha\Psi^w_\beta+[A^{55}]\frac{\partial\Psi^w_\alpha}{\partial x}\frac{\partial\Psi^w_\beta}{\partial x}\Bigg]dxdy, \quad \text{(A8)}$$

$$[K^{34}]_{\alpha\beta}=\int_A\Bigg[[\hat{E}^{14}]\frac{\partial\Psi^w_\alpha}{\partial y}\frac{\partial\Psi^\phi_\beta}{\partial x}+[\hat{E}^{15}]\frac{\partial\Psi^w_\alpha}{\partial x}\frac{\partial\Psi^\phi_\beta}{\partial x}+[\hat{E}^{24}]\frac{\partial\Psi^w_\alpha}{\partial y}\frac{\partial\Psi^\phi_\beta}{\partial y}+[\hat{E}^{25}]\frac{\partial\Psi^w_\alpha}{\partial x}\frac{\partial\Psi^\phi_\beta}{\partial y}+[\check{E}^{33}]\Psi^w_\alpha\Psi^\phi_\beta\Bigg]dxdy, \quad \text{(A9)}$$

$$[K^{44}]_{\alpha\beta}=-\int_A\Bigg[[G^{11}]\frac{\partial\Psi^\phi_\alpha}{\partial x}\frac{\partial\Psi^\phi_\beta}{\partial x}+[G^{22}]\frac{\partial\Psi^\phi_\alpha}{\partial y}\frac{\partial\Psi^\phi_\beta}{\partial y}+[\hat{G}^{33}]\Psi^\phi_\alpha\Psi^\phi_\beta\Bigg]dxdy. \quad \text{(A10)}$$

The submatrices listed above are computed by preintegrating the functions in z. For any general approximation through thickness, these can be expressed as

$$A^{km}_{ij}=\sum_{l=1}^{N}\int_{z_l}^{z_{l+1}}C_{km}\bar{\Psi}_i(z)\bar{\Psi}_j(z)dz, \quad \text{(A11)}$$

$$B^{km}_{ij}=\sum_{l=1}^{N}\int_{z_l}^{z_{l+1}}C_{km}\bar{\Psi}_i(z)\frac{d\bar{\Psi}_j(z)}{dz}dz, \quad \text{(A12)}$$

$$\bar{B}^{km}_{ij}=\sum_{l=1}^{N}\int_{z_l}^{z_{l+1}}C_{km}\bar{\Psi}_i(z)\bar{\Psi}_j(z)dz, \quad \text{(A13)}$$

$$D^{km}_{ij}=\sum_{l=1}^{N}\int_{z_l}^{z_{l+1}}C_{km}\frac{d\bar{\Psi}_i(z)}{dz}\frac{d\bar{\Psi}_j(z)}{dz}dz, \quad \text{(A14)}$$

$$E^{km}_{ij}=\sum_{l=1}^{N}\int_{z_l}^{z_{l+1}}e_{km}\bar{\Psi}_i(z)\frac{d\bar{\Psi}_j(z)}{dz}dz, \quad \text{(A15)}$$

$$\bar{E}^{km}_{ij}=\sum_{l=1}^{N}\int_{z_l}^{z_{l+1}}e_{km}\bar{\Psi}_i(z)\bar{\Psi}_j(z)dz, \quad \text{(A16)}$$

$$\hat{E}^{km}_{ij}=\sum_{l=1}^{N}\int_{z_l}^{z_{l+1}}e_{km}\bar{\Psi}_i(z)\bar{\Psi}_j(z)dz, \quad \text{(A17)}$$

$$\check{E}_{ij}^{km}=\sum_{l=1}^{N}\int_{z_l}^{z_{l+1}} e_{km}\frac{d\overline{\Psi}_i(z)}{dz}\frac{d\overline{\Psi}_j(z)}{dz}dz, \tag{A18}$$

$$G_{ij}^{km}=\sum_{l=1}^{N}\int_{z_l}^{z_{l+1}} \epsilon_{km}\overline{\Psi}_i(z)\overline{\Psi}_j(z)dz, \tag{A19}$$

$$\hat{G}_{ij}^{km}=\sum_{l=1}^{N}\int_{z_l}^{z_{l+1}} \epsilon_{km}\frac{d\overline{\Psi}_i(z)}{dz}\frac{d\overline{\Psi}_j(z)}{dz}dz. \tag{A20}$$

[1] H. H. Demarest, Jr., ''Cube Resonance Method to Determine the Elastic Constants of Solids,'' J. Acoust. Soc. Am. **49**, 768–775 (1971).
[2] E. P. Eer Nisse, ''Variational Method for Electroelastic Vibration Analysis,'' IEEE Trans. Sonics Ultrason. **SU-14**, 153–160 (1967).
[3] I. Ohno, ''Free Vibration of a Rectangular Parallelepiped Crystal and its Application to Determination of Elastic Constants of Orthorhombic Crystals,'' J. Phys. Earth **24**, 355–379 (1976).
[4] A. Migliori and J. L. Sarrao, *Resonant Ultrasound Spectroscopy: Applications to Physics, Materials Measurements and Non-Destructive Evaluation* (Wiley, New York, 1997).
[5] W. M. Visscher, A. Migliori, T. M. Bell, and R. A. Reinert, ''On the Normal Modes of Free Vibration of Inhomogeneous and Anisotropic Elastic Objects,'' J. Acoust. Soc. Am. **90**, 2154–2162 (1991).
[6] K. E. Pauley and S. B. Dong, ''Analysis of Plane Waves in Laminated Piezoelectric Plates,'' Wave Electron. **1**, 265–285 (1976).
[7] J. N. Reddy, ''A Generalization of Displacement-Based Laminate Theories,'' Commun. App. Numer. Meth. **3**, 173–181 (1987).
[8] H. F. Tiersten, *Linear Piezoelectric Plate Vibrations* (Plenum, New York, 1969).
[9] S. Srinivas, C. V. Joga Rao, and A. K. Rao, ''Some Results From an Exact Analysis of Thick Laminates in Vibration and Buckling,'' J. Appl. Mech. **37**, 868–870 (1970).
[10] A. K. Noor, ''Free Vibrations of Multilayered Composite Plates,'' AIAA J. **11**, 1038–1039 (1973).
[11] N. S. Putcha and J. N. Reddy, ''Stability and Natural Vibration Analysis of Laminated Plates,'' J. Sound Vib. **104**, 285–300 (1986).
[12] A. Khdeir, ''Free Vibration and Buckling of Unsymmetric Cross-Ply Laminated Plates Using a Refined Theory,'' J. Sound Vib. **128**, 377–395 (1989).
[13] D. Ricketts, ''The Frequency of Flexural Vibrations of Completely Free Piezopolymer Plates,'' J. Acoust. Soc. Am. **80**, 723–726 (1986).
[14] P. Heyliger and D. A. Saravanos, ''Exact Free-Vibration Analysis of Laminated Plates with Embedded Piezoelectric Layers,'' J. Acoust. Soc. Am. **98**, 1547–1557 (1995).
[15] D. A. Berlincourt, D. R. Curran, and H. Jaffe, ''Piezoelectric and Piezomagnetic Materials and Their Function in Transducers,'' in *Physical Acoustics*, edited by W. P. Mason (Academic, New York, 1964), Vol. 1, pp. 169–270.
[16] K. Tashiro, H. Tadokoro, and M. Kobayashi, ''Structure and Piezoelectricity of Poly(Vinylidene Flouride),'' Ferroelectrics **32**, 167–175 (1981).
[17] I. Ohno, ''Rectangular Parallelepiped Resonance Method for Piezoelectric Crystals and Elastic Constants of Alpha-Quartz,'' Phys. Chem. Miner. **17**, 371–378 (1990).
[18] R. Bechmann, ''Elastic and Piezoelectric Constants of Alpha-Quartz,'' Phys. Rev. **110**, 1060–1061 (1958).
[19] M. Dunn, H. Ledbetter, and P. Heyliger, ''Free Vibration of Piezoelectric Solids: Application to Determination of Elastic and Piezoelectric Constants,'' in *Engineering Mechanics: Proceedings of the 10th Conference*, edited by S. Sture (American Society of Civil Engineers, Washington, D. C., 1995), pp. 204–210.

Acoustic scattering by a three-dimensional elastic object near a rough surface

Raymond Lim
Coastal Systems Station/Dahlgren Division, Naval Surface Warfare Center, Code R22, 6703 West Highway 98, Panama City, Florida 32407-7001

Kevin L. Williams and Eric I. Thorsos
Applied Physics Laboratory, University of Washington, 1013 N.E. 40th Street, Seattle, Washington 98105

(Received 8 April 1999; revised 22 October 1999; accepted 29 October 1999)

The ensemble-averaged field scattered by a smooth, bounded, elastic object near a penetrable surface with small-scale random roughness is formulated. The formulation consists of combining a perturbative solution for modeling propagation through the rough surface with a transition (*T*-) matrix solution for scattering by the object near a planar surface. All media bounding the rough surface are assumed to be fluids. By applying the results to a spherical steel shell buried within a rough sediment bottom, it is demonstrated that the ensemble-averaged ''incoherent'' intensity backscattered by buried objects illuminated with shallow-grazing-angle acoustic sources can be well enhanced at high frequencies over field predictions based on scattering models where all environmental surfaces are planar. However, this intensity must compete with the incoherent intensity scattered back from the interface itself, which can defeat detection attempts. The averaged ''coherent'' component of the field maintains the strong evanescent spectral decay exhibited by flat interface predictions of shallow-angle measurements but with small deviations. Nevertheless, bistatic calculations of the coherent field suggest useful strategies for improving long-range detection and identification of buried objects.
[S0001-4966(00)02002-6]

PACS numbers: 43.30.Gv, 43.30.Ma [DLB]

INTRODUCTION

Sound transmission into sandy sediments has been found to be anomalously high when the incident sound field enters the ocean bottom at a shallow grazing angle; especially at angles shallower than the critical angle for total reflection at an analogous nonlossy flat bottom.[1–3] To explain this effect, standard assumptions in underwater bottom propagation models are being questioned. For example, the assumption that low-shear ocean sediments can be modeled as attenuating fluids has been challenged by formulating more general models based on a poroelastic description of sandy sediments. These models have suggested the possibility of higher sound penetration at shallow grazing angles by mode conversion into a slowly propagating wave that is unique to poroelastic media.[4] In addition, scattering models that allow for targets to be embedded in poroelastic environments can predict enhanced backscatter at long ranges from the targets.[5,6] However, the sensitivity of these effects to input parameters that are not easily measured has made penetration mechanisms based on poroelasticity difficult to verify.

Recently, it has been suggested that the penetration effects might also be explained by sound diffusely scattered by small-scale roughness of the water/sediment interface or sediment inhomogeneities near the interface.[7] Surface roughness and inhomogeneities within the bottom are usually expected to act as noise sources and, their effect, to reduce the strength of any coherent signal transmitted into the bottom. Since the evidence of anomalous transmission most often cited is based on data analyzed with incoherent processing techniques, it is possible that the effects observed are merely a manifestation of the diffusely scattered field from the rough sediment surface; i.e., the ''incoherent'' part of the transmitted field. Calculations[7,8] of the incoherent intensity transmitted through an interface by small-scale random roughness modeled with a filtered power-law roughness spectrum have been found to compare favorably with the intensity measurements described in Refs. 1 and 2. However, the measurements performed by Lopes *et al.*[3] in Duck, NC exhibited not only anomalous transmission levels at shallow grazing angles but also good signal compression when coherently correlated with the transmitted pulse; thus, indicating little signal distortion. This is somewhat unexpected since an elongated, distorted signal might have been expected to result after a pulse is diffracted by random roughness. In any case, these observations do not invalidate the roughness mechanism but they do accentuate the need for more study into the effects of roughness.

In this paper, the effect that random surface roughness has on the acoustic scattering by a completely buried, simple, smooth, elastic object will be investigated. Effects due to the roughness are isolated from possible effects due to (poro)elasticity of the sediment by modeling the bottom as a fluid. The method used is to incorporate generalized reflection and transmission coefficients based on a perturbative treatment of plane-wave transmission through the rough interface into a deterministic *T*-matrix solution for a buried object. This results in a formulation of the field scattered by

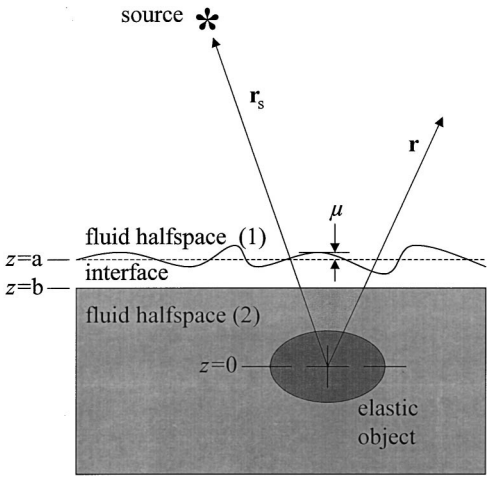

FIG. 1. The scattering geometry to be modeled.

the object that can then be analytically averaged over an ensemble of randomly rough interfaces above the object using a realistic statistical description of the roughness. The ability to formulate such an averaged solution is particularly significant when a completely deterministic scattering solution for an object under a given surface roughness configuration is of limited value; e.g., when quantitative comparisons with field measurements are desired but the roughness configuration cannot be known and is likely to be dynamic.

An interesting finding is that, for shallow-grazing-angle incident fields in the water column, the diffuse field scattered down by small-scale surface roughness can significantly enhance the average intensity backscattered by a buried object. By comparing this backscatter level with existing model predictions for the average surface reverb level, signal-to-noise predictions can be made that suggest conditions under which surface roughness effects might enhance the shallow-angle observability of a buried object. In addition, it is noted that the enhancements of the object's intensity due to surface roughness can be comparable to that predicted by models that embed an object in a poroelastic half-space under a flat interface when bottom parameters proposed by Chotiros[4] are used. By contrasting the predictions of such scattering models, it is hoped that clues to aid in distinguishing the actual transmission mechanism in field measurements will result.

I. DETERMINISTIC SOLUTION

A. Background

A solution is desired for the field scattered by an object in a layered fluid environment. Figure 1 depicts the scattering configuration to be considered. A source in the upper fluid half-space insonifies the bottom which consists of a fluid transition layer over another fluid half-space. The transition layer has a randomly rough top interface with an average vertical coordinate at $z=\mathrm{a}$ and a planar lower interface at $z=\mathrm{b}$. A smooth elastic three-dimensional bounded object is centered on the coordinate origin located below the transition layer.

When the transition layer has no rough boundaries, a time-harmonic scattering solution can be formulated in terms of a T matrix as discussed in Ref. 9. The total pressure field $\Phi(\mathbf{r})$ is decomposed as a sum of fields incident upon and scattered by the object which are expanded in regular and outgoing basis functions appropriate for the layered environment; i.e.,

$$\Phi(\mathbf{r})=\Phi^{\mathrm{inc}}(\mathbf{r})+\Phi^{\mathrm{scatt}}(\mathbf{r}), \tag{1a}$$

$$\Phi^{\mathrm{inc}}(\mathbf{r})=\sum_n \hat{\psi}_n(\mathbf{r})a_n(\mathbf{r}_s), \tag{1b}$$

$$\Phi^{\mathrm{scatt}}(\mathbf{r})=\sum_n \psi_n(\mathbf{r})f_n. \tag{1c}$$

Here, following the standard spectral approach, a monochromatic time factor, $e^{-i\omega t}$, is suppressed. The summation index, n, represents a set of indices that range over all values required to specify a complete set of basis functions and a hat denotes the set that is regular at the origin. For a region layered in the vertical direction, it is sufficient to use an incident field expansion that is convergent for points $\mathbf{r}$ within the largest origin-centered spherical surface that does not overlap any layer boundaries and source points $\mathbf{r}_s$ outside this sphere. Under these conditions the regular spherical functions are assumed to form a viable basis set for the expansion. Given an origin centered on a scatterer in the bottom half-space, these functions are given by

$$\hat{\psi}_{\sigma ml}(\mathbf{r})=\mathrm{j}_l(k_2 r)Y_{\sigma ml}(\theta,\phi), \tag{2}$$

where k_2 is the wave number of the bottom (which is allowed to be complex for an attenuating bottom), j_l is a regular spherical Bessel function and the normalized real spherical harmonics are

$$Y_{\sigma ml}(\theta,\phi)=\left(\epsilon_m\frac{2l+1}{4\pi}\frac{(l-m)!}{(l+m)!}\right)^{1/2}P_l^m(\cos\theta)\times\begin{Bmatrix}\cos m\phi, & \sigma=e\\ \sin m\phi, & \sigma=o\end{Bmatrix}. \tag{3}$$

P_l^m is the associated Legendre function of order l and rank m. The parameter $\epsilon_m=2$ for $m>0$ and $\epsilon_m=1$ for $m=0$. For the $\hat{\psi}$'s to form a complete basis, it is sufficient to specify their indices in the following way: the parity index, σ, is either even or odd, the rank index, m, takes integer values, $0\leqslant m\leqslant l$, and the order index, l, takes integer values, $0\leqslant l<\infty$. Corresponding to this basis, the expansion coefficients of the incident field for a point source at $\mathbf{r}_s$ in the top half-space may be expressed as the following plane-wave superposition:

$$a_{\sigma ml}(\mathbf{r}_s)=\frac{Ci^{m+1}}{2\pi}\left(\frac{\epsilon_m}{2\pi}\right)^{1/2}\int_0^{2\pi}d\xi\int_0^{\infty}\frac{q\,dq}{h_1(q)}\times e^{-iq\zeta_s\cos(\xi-\phi_s)}B_{ml}\left(-\frac{h_2(q)}{k_2}\right)e^{-ih_1(q)(\mathrm{a}-z_s)}\times W_{1\to 2}(q)e^{ih_2(q)\mathrm{b}}\begin{pmatrix}\cos m\xi, & \sigma=e\\ \sin m\xi, & \sigma=o\end{pmatrix}, \tag{4}$$

where C is a factor included for specifying amplitude units, and

$$B_{ml}\left(\frac{h_p(q)}{k_p}\right)=i^{l-m}\left(\frac{2l+1}{2}\frac{(l-m)!}{(l+m)!}\right)^{1/2}P_l^m\left(\frac{h_p(q)}{k_p}\right). \quad (5)$$

In the integrand, $\mathbf{r}_s$, is expressed in the cylindrical coordinates (ζ_s,ϕ_s,z_s), $h_p(q)=\sqrt{k_p^2-q^2}$ is the vertical component of the wave vector in region p, q is the magnitude of the transverse component of the wave vector, and k_p is the total magnitude of the wave vector (i.e., the wave number) in region p. Here, p equals 1, 2, or i in reference to the upper, lower, or interfacial regions. To ensure convergence, $h_p(q)$ is evaluated on its ''physical sheet'' defined by $\mathrm{Im}(h_p(q))>0$ in the complex q plane. $W_{1\to 2}$ is a plane-wave transmission coefficient for propagation of the pressure field from the top half-space to the bottom half-space. Although the construction of the interfacial region can be quite general, we will merely assume that it is a single homogeneous layer. Therefore, $W_{1\to 2}$ may be expressed as given by Brekhovskikh;[10] i.e.,

$$W_{1\to 2}(q)=\frac{1+V_1(q)}{\cos(|\mathrm{a}-\mathrm{b}|h_\mathrm{i}(q))-i(Z_\mathrm{i}(q)/Z_2(q))\sin(|\mathrm{a}-\mathrm{b}|h_\mathrm{i}(q))}, \quad (6)$$

where V_1 is the reflection coefficient for plane waves incident on the interface from above given by

$$V_1(q)=\frac{Z_\mathrm{i}(q)[Z_2(q)-Z_1(q)]+i[Z_1(q)Z_2(q)-Z_\mathrm{i}^2(q)]\tan(|\mathrm{a}-\mathrm{b}|h_\mathrm{i}(q))}{Z_\mathrm{i}(q)[Z_1(q)+Z_2(q)]-i[Z_1(q)Z_2(q)+Z_\mathrm{i}^2(q)]\tan(|\mathrm{a}-\mathrm{b}|h_\mathrm{i}(q))}, \quad (7)$$

$Z_p(q)=\rho_p/h_p(q)$, and ρ_p is the density of region p.

The outgoing basis functions for expanding the scattered field in the layered host may be specified for $\mathbf{r}$ in any layer as long as $\mathbf{r}$ is outside a spherical surface circumscribing the object at the origin. For $\mathbf{r}$ in the top or bottom half-space, these functions may be expressed as

$$\begin{aligned}\psi_{\sigma ml}(\mathbf{r})&=\frac{1}{2\pi i^m}\left(\frac{\epsilon_m}{2\pi}\right)^{1/2}\int_0^{2\pi}d\xi\int_0^\infty\frac{q\,dq}{k_2h_2(q)}\\&\quad\times B_{ml}\left(-\frac{h_2(q)}{k_2}\right)e^{ih_2(q)\mathrm{b}}W_{2\to 1}(q)\\&\quad\times e^{ih_1(q)(z-\mathrm{a})+iq\zeta\cos(\xi-\phi)}\begin{pmatrix}\cos m\xi, & \sigma=e\\ \sin m\xi, & \sigma=o\end{pmatrix},\\&\quad z>\mathrm{a}, \quad (8)\\&=\mathrm{h}_l^{(1)}(k_2r)Y_{\sigma ml}(\theta,\phi)\\&\quad+\frac{1}{2\pi i^m}\left(\frac{\epsilon_m}{2\pi}\right)^{1/2}\int_0^{2\pi}d\xi\int_0^\infty\frac{q\,dq}{k_2h_2(q)}\\&\quad\times B_{ml}\left(-\frac{h_2(q)}{k_2}\right)e^{ih_2(q)\mathrm{b}}\\&\quad\times U_2(q)e^{-ih_2(q)(z-\mathrm{b})+iq\zeta\cos(\xi-\phi)}\\&\quad\times\begin{pmatrix}\cos m\xi, & \sigma=e\\ \sin m\xi, & \sigma=o\end{pmatrix},\quad z<\mathrm{b}, \quad (9)\end{aligned}$$

where $\mathrm{h}_l^{(1)}$ is a spherical Hankel function of the first kind, U_2 is the reflection coefficient for plane waves incident on the interface from below, and $W_{2\to 1}$ is a plane-wave transmission coefficient for propagation from the bottom half-space to the top half-space. Both $W_{2\to 1}$ and U_2 may be determined using Eqs. (6) and (7) by exchanging material properties. To maintain a complete set of outgoing functions, the same restrictions on the indices are maintained as for the regular functions in Eq. (2).

The expansion coefficients of the scattered field, $f_{\sigma ml}$, are obtained by invoking the T matrix for the system via the relation

$$f_{\sigma ml}=\sum_{\sigma' m' l'}\mathcal{T}_{\sigma ml;\sigma' m' l'}a_{\sigma' m' l'}(\mathbf{r}_s), \quad (10)$$

where the T matrix in a plane-stratified fluid, $\mathcal{T}$, takes the form

$$\mathcal{T}=[\mathbf{T}^{-1}-\mathbf{R}]^{-1}. \quad (11)$$

Here, $\mathbf{T}$ is the free-field T matrix of the object defined with the material parameters of the embedding medium and $\mathbf{R}$ is a symmetric rescattering matrix with elements that, for the present system, reduce to

$$\begin{aligned}R_{\sigma ml;\sigma' m' l'}&=2\delta_{\sigma\sigma'}\delta_{mm'}\int_0^\infty\frac{q\,dq}{k_2h_2(q)}B_{ml}\left(-\frac{h_2(q)}{k_2}\right)\\&\quad\times B_{ml'}\left(-\frac{h_2(q)}{k_2}\right)U_2(q)e^{2ih_2(q)\mathrm{b}}. \quad (12)\end{aligned}$$

B. Rough interface

The scattering formulation presented so far constitutes an exact solution of the Helmholtz equation for an environment with planar interfaces. An advantage of it is that its structure is such that one can isolate all effects associated with propagation of the source field to the object in the coefficients of Eq. (4), all effects associated with propagation of the scattered field to $\mathbf{r}$ in the outgoing basis functions of Eqs. (8) and (9), and all scattering and environmental interaction effects due to the presence of the object in the T matrix. Since the details of these effects are given in terms of a superposition of plane waves, it becomes straightfor-

ward to account for roughness at interfaces of the environment by replacing the plane-wave reflection and transmission coefficients for planar boundaries with generalizations appropriate for rough boundaries.

In this paper, generalizations formulated by Moe[8] and Moe and Jackson[11] for an interface with small-scale random roughness will be used. In this formulation, roughness on the interface at $z=\mathrm{a}$ is defined by

$$z-\mathrm{a}=\mu \mathrm{F}(\tilde{\mathbf{r}}), \tag{13}$$

where μ is the root-mean-square (rms) height and $\mathrm{F}(\tilde{\mathbf{r}})$ specifies height variations as a function of the two-dimensional projection $\tilde{\mathbf{r}}$ of the position vector $\mathbf{r}$ onto the plane at $z=\mathrm{a}$. Roughness causes a plane-wave propagating with transverse wave vector $\mathbf{q}'$ in the top half-space to be transformed upon reflection or transmission into a continuous spectrum of wave vector components. Therefore, the total contribution to the complex amplitude of the reflected or transmitted plane wave with transverse wave vector $\mathbf{q}$ involves an integration over all wave vectors $\mathbf{q}'$ incident on the roughness. Only transverse wave vectors need to be integrated because the vertical components are constrained by the value of the wave number in each medium. Denoting the plane-wave amplitudes with a script A, the reflected, and transmitted amplitudes are related to the incident amplitude by

$$\mathcal{A}^{\mathrm{re}}(\mathbf{q})=\int_0^{2\pi} d\xi' \int_0^{\infty} q'\, dq'\, \mathbf{V}_1(\mathbf{q},\mathbf{q}')\mathcal{A}^{\mathrm{inc}}(\mathbf{q}') \tag{14}$$

and

$$\mathcal{A}^{\mathrm{tr}}(\mathbf{q})=\int_0^{2\pi} d\xi' \int_0^{\infty} q'\, dq'\, \mathbf{W}_{1\to 2}(\mathbf{q},\mathbf{q}')\mathcal{A}^{\mathrm{inc}}(\mathbf{q}'), \tag{15}$$

where q' and ξ' are the two-dimensional polar coordinates of $\mathbf{q}'$. The corresponding field at a given space point is obtained by multiplying these amplitudes by the appropriate plane wave and integrating over the transverse wave vector; i.e.,

$$\Phi^{\mathrm{re}}(\mathbf{r})=\int_0^{2\pi} d\xi \int_0^{\infty} q\, dq \mathcal{A}^{\mathrm{re}}(\mathbf{q}) e^{ih_1(q)(z-\mathrm{a})+i\mathbf{q}\cdot\mathbf{r}}, \tag{16a}$$

$$\Phi^{\mathrm{tr}}(\mathbf{r})=\int_0^{2\pi} d\xi \int_0^{\infty} q\, dq \mathcal{A}^{\mathrm{tr}}(\mathbf{q}) e^{-ih_1(q)(z-\mathrm{b})+i\mathbf{q}\cdot\mathbf{r}}. \tag{16b}$$

By satisfying boundary conditions through second order in $k_1\mu$, the functions specifying the transformation of waves with transverse wave vector $\mathbf{q}'$ into wave vector $\mathbf{q}$ in Eqs. (14) and (15) may be expressed in the form

$$\begin{aligned}\mathbf{V}_1(\mathbf{q},\mathbf{q}')=&V_1\delta(\mathbf{q}-\mathbf{q}')+k_1\mu H_{11}(\mathbf{q},\mathbf{q}')F(\mathbf{q}-\mathbf{q}')\\&+\frac{(k_1\mu)^2}{2}\Bigg[G_{11a}(\mathbf{q},\mathbf{q}')\int d\mathbf{q}''F(\mathbf{q}-\mathbf{q}'')\\&\times F(\mathbf{q}''-\mathbf{q}')+\int d\mathbf{q}''F(\mathbf{q}-\mathbf{q}'')F(\mathbf{q}''-\mathbf{q}')\\&\times G_{11b}(\mathbf{q},\mathbf{q}'',\mathbf{q}')\Bigg]+O((k_1\mu)^3)\end{aligned} \tag{17}$$

and

$$\begin{aligned}\mathbf{W}_{1\to 2}(\mathbf{q},\mathbf{q}')=&W_{1\to 2}\delta(\mathbf{q}-\mathbf{q}')+k_1\mu H_{12}(\mathbf{q},\mathbf{q}')\\&\times F(\mathbf{q}-\mathbf{q}')+\frac{(k_1\mu)^2}{2}\Bigg[G_{12a}(\mathbf{q},\mathbf{q}')\int d\mathbf{q}''\\&\times F(\mathbf{q}-\mathbf{q}'')F(\mathbf{q}''-\mathbf{q}')\\&+\int d\mathbf{q}''F(\mathbf{q}-\mathbf{q}'')F(\mathbf{q}''-\mathbf{q}')\\&\times G_{12b}(\mathbf{q},\mathbf{q}'',\mathbf{q}')\Bigg]+O((k_1\mu)^3).\end{aligned} \tag{18}$$

Here, $F(\mathbf{q})$ is the 2D Fourier transform of $\mathrm{F}(\tilde{\mathbf{r}})$, and the explicit forms of H_{11}, H_{12}, G_{11a}, G_{11b}, G_{12a}, and G_{12b} are given in Appendix A.

To account for the effects of the rough interface on propagation to and from the buried object in the present scattering model, the integrands of Eqs. (4), (8), and (9) are modified with Eqs. (14) and (15). Hence, the coefficients, $a_{\sigma ml}$, become

$$\begin{aligned}a_{\sigma ml}(\mathbf{r}_s)=&\frac{Ci^{m+1}}{2\pi}\left(\frac{\epsilon_m}{2\pi}\right)^{1/2}\int_0^{2\pi} d\xi \int_0^{\infty} q\, dq B_{ml}\left(-\frac{h_2(q)}{k_2}\right)\\&\times e^{ih_2(q)\mathrm{b}}\begin{pmatrix}\cos m\xi, & \sigma=e\\ \sin m\xi, & \sigma=o\end{pmatrix}\\&\times\int_0^{2\pi} d\xi' \int_0^{\infty}\frac{q'\, dq'}{h_1(q')}\mathbf{W}_{1\to 2}(\mathbf{q},\mathbf{q}')\\&\times e^{-iq'\xi_s\cos(\xi'-\phi_s)-ih_1(q')(\mathrm{a}-z_s)},\end{aligned} \tag{19}$$

where factors associated with the field incident upon and transmitted through the interface are now separated by $\mathbf{W}_{1\to 2}(\mathbf{q},\mathbf{q}')$ and two sets of integrations over transverse wave vector. Likewise, by grouping factors associated with plane waves propagating to and away from the interface, expressions for the basis functions, $\Psi_{\sigma ml}$, become

$$\begin{aligned}\psi_{\sigma ml}(\mathbf{r})=&\frac{1}{2\pi i^m}\left(\frac{\epsilon_m}{2\pi}\right)^{1/2}\\&\times\int_0^{2\pi} d\xi \int_0^{\infty} q\, dq e^{iq\zeta\cos(\xi-\phi)+ih_1(q)(z-\mathrm{a})}\\&\times\int_0^{2\pi} d\xi' \int_0^{\infty}\frac{q'\, dq'}{k_2h_2(q')}\mathbf{W}_{2\to 1}(\mathbf{q},\mathbf{q}')\\&\times B_{ml}\left(-\frac{h_2(q')}{k_2}\right)e^{ih_2(q')\mathrm{b}}\begin{pmatrix}\cos m\xi', & \sigma=e\\ \sin m\xi', & \sigma=o\end{pmatrix},\\&z>\mathrm{a},\end{aligned} \tag{20}$$

$$= h_l^{(1)}(k_2 r) Y_{\sigma ml}(\theta,\phi) + \frac{1}{2\pi i^m}\left(\frac{\epsilon_m}{2\pi}\right)^{1/2} \times \int_0^{2\pi} d\xi \int_0^{\infty} q\, dq e^{iq\zeta\cos(\xi-\phi) - ih_2(q)(z-\mathrm{b})} \times \int_0^{2\pi} d\xi' \int_0^{\infty} \frac{q'\, dq'}{k_2 h_2(q')} \mathbf{U}_2(\mathbf{q},\mathbf{q}') B_{ml}\left(-\frac{h_2(q')}{k_2}\right) \times e^{ih_2(q')\mathrm{b}} \begin{pmatrix} \cos m\xi', & \sigma = e \\ \sin m\xi', & \sigma = o \end{pmatrix}, \quad z < \mathrm{b}. \tag{21}$$

In Eqs. (20) and (21), the quantities $\mathbf{U}_2(\mathbf{q}',\mathbf{q})$ and $\mathbf{W}_{2\to1}(\mathbf{q}',\mathbf{q})$ are analogous to Eqs. (17) and (18), respectively, but for propagation from medium 2 to medium 1. They may be determined using the perturbation theory of Refs. 8 and 11 but, since the present work will not require the reflection coefficient, determining $\mathbf{U}_2(\mathbf{q}',\mathbf{q})$ will be left to later investigations. However, $\mathbf{W}_{2\to1}(\mathbf{q}',\mathbf{q})$ will be determined via the relation

$$\mathbf{W}_{2\to1}(\mathbf{q}',\mathbf{q}) = \frac{\rho_1 h_2(q)}{\rho_2 h_1(q')} \mathbf{W}_{1\to2}(-\mathbf{q},-\mathbf{q}'), \tag{22}$$

which is required in order for the Green's function to remain reciprocal for propagation between the two half-spaces. This consequence of reciprocity is shown in Appendix B.

With Eqs. (19)–(21), a new rescattering matrix can also be formulated to update Eq. (12). This task is done in Appendix C. By then updating the planar-surface scattering solution using Eqs. (19)–(21) and the rescattering elements exhibited in Eq. (C5), a perturbative, but deterministic, scattering solution for an object under a surface with small-scale roughness is obtained. However, given the complexity of this solution, it will be convenient to adopt some simplifying assumptions to avoid some numerical labor later. In the subsequent development, the source of the incident field will be assumed far enough away to approximate the field in the vicinity of the scatterer as that due to transmitting a plane wave through the roughness above the scatterer and the scattered field will be predicted in the far field. Therefore, the number of required integrations can be reduced by applying a stationary phase approximation for large r and r_s.[12] This results in the following simpler expressions for the field coefficients and basis functions:

$$a_{\sigma ml}(\theta_s,\phi_s) = 2i^m\sqrt{2\pi\epsilon_m} e^{-ik_1 \mathrm{a}\cos\theta_s} \times \int_0^{2\pi} d\xi \int_0^{\infty} q\, dq B_{ml}\left(-\frac{h_2(q)}{k_2}\right) e^{ih_2(q)\mathrm{b}} \times \begin{pmatrix} \cos m\xi, & \sigma = e \\ \sin m\xi, & \sigma = o \end{pmatrix} \times \mathbf{W}_{1\to2}(\mathbf{q},\mathbf{q}')\Big|_{q'=k_1\sin\theta_s,\,\xi'=\phi_s+\pi}, \tag{23}$$

$$\psi_{\sigma ml}(\mathbf{r}) = \frac{k_1\cos\theta}{i^{m+1}}\left(\frac{\epsilon_m}{2\pi}\right)^{1/2} \frac{e^{ik_1(r-\mathrm{a}\cos\theta)}}{r} \times \int_0^{2\pi} d\xi \int_0^{\infty} \frac{q\, dq}{k_2 h_2(q)} B_{ml}\left(-\frac{h_2(q)}{k_2}\right) e^{ih_2(q)\mathrm{b}} \times \begin{pmatrix} \cos m\xi, & \sigma = e \\ \sin m\xi, & \sigma = o \end{pmatrix} \mathbf{W}_{2\to1}(\mathbf{q}',\mathbf{q})\Big|_{q'=k_1\sin\theta,\,\xi'=\phi}, \quad k_1 r, k_1 z \gg 0, \tag{24}$$

$$\psi_{\sigma ml}(\mathbf{r}) = \frac{e^{ik_2 r}}{i^{m+1}k_2 r}\left(\frac{\epsilon_m}{2\pi}\right)^{1/2} \begin{pmatrix} \cos m\phi, & \sigma = e \\ \sin m\phi, & \sigma = o \end{pmatrix} \times B_{ml}\left(\frac{h_2(k_2\sin\theta)}{k_2}\right) + \frac{k_2\cos\theta}{i^{m+1}}\left(\frac{\epsilon_m}{2\pi}\right)^{1/2} \frac{e^{ik_2(r+\mathrm{b}\cos\theta)}}{r} \times \int_0^{2\pi} d\xi \int_0^{\infty} \frac{q\, dq}{k_2 h_2(q)} B_{ml}\left(-\frac{h_2(q)}{k_2}\right) e^{ih_2(q)\mathrm{b}} \times \begin{pmatrix} \cos m\xi, & \sigma = e \\ \sin m\xi, & \sigma = o \end{pmatrix} \mathbf{U}_2(\mathbf{q}',\mathbf{q})\Big|_{q'=k_2\sin\theta,\,\xi'=\phi}, \quad k_1 r, -k_1 z \gg 0. \tag{25}$$

In Eq. (23), the scale factor C was set so that the plane wave would have a unit amplitude in medium 1.

A further simplification can be made by noting that effects due to multiple scattering between the object and the rough surface embodied in Eq. (C5) can be small for burial much deeper than 1.5 radii of the sphere circumscribing the object. At depths greater than about 1.25 radii, backscatter calculations with a sphere buried under a flat interface exhibit little rescattering effects even when the source is placed directly above the sphere. Therefore, in the present work, it will be assumed that these effects can be ignored; i.e., $\mathbf{R} = 0$. Finally, a spherical object will be studied since the free-field T matrix is simplest for this case.

II. AVERAGED FIELDS

A. Bistatic coherent solution

Rather than apply the scattering formulation given in the previous section directly on a specific surface configuration, the goal here is to use the formulation to establish the average properties. For example, the steady-state coherent field scattered by a buried sphere is calculated with an ensemble average over interface roughness as

$$\langle \Phi^{\mathrm{scatt}}(\mathbf{r})\rangle = \sum_{ml} T_{ml} \sum_{\sigma} \langle \psi_{\sigma ml}(\mathbf{r}) a_{\sigma ml}(\theta_s,\phi_s)\rangle, \tag{26}$$

where the second set of spherical indices on the T matrix have been suppressed because the free-field T matrix for a sphere is diagonal; therefore, averages of off-diagonal products of basis functions and source field coefficients are not needed in the summations. The parity index dependence has also been removed from the T matrix because it is unneces-

sary for an axisymmetric object suspended in a fluid.[13]

Of primary interest is the field scattered back into the upper half-space given a plane-wave incident on the bottom from above. For $\mathbf{r}$ and $\mathbf{r}_s$ sufficiently far away from the sphere, this field can be computed using Eqs. (23) and (24) to form the quantity

$$\sum_{\sigma} \langle \psi_{\sigma ml}(\mathbf{r}) a_{\sigma ml}(\theta_s, \phi_s) \rangle$$
$$= \frac{2\epsilon_m k_1 \cos\theta}{ir} e^{ik_1[r - a(\cos\theta + \cos\theta_s)]}$$
$$\times \int_0^{2\pi} d\xi \int_0^{\infty} \frac{q\, dq}{k_2 h_2(q)} \int_0^{2\pi} d\xi' \int_0^{\infty} q'\, dq' \cos m(\xi - \xi')$$
$$\times B_{ml}\left(-\frac{h_2(q)}{k_2}\right) B_{ml}\left(-\frac{h_2(q')}{k_2}\right)$$
$$\times e^{i[h_2(q) + h_2(q')]b} \langle \mathbf{W}_{2\to 1}(\mathbf{q}_1, \mathbf{q})|_{q_1 = k_1 \sin\theta, \xi_1 = \phi}$$
$$\times \mathbf{W}_{1\to 2}(\mathbf{q}', \mathbf{q}_1')|_{q_1' = k_1 \sin\theta_s, \xi_1' = \phi_s + \pi} \rangle. \quad (27)$$

In the following, it will be convenient to reexpress the correlation of rough surface transmission coefficients as

$$\langle \mathbf{W}_{2\to 1}(\mathbf{q}_1, \mathbf{q}) \mathbf{W}_{1\to 2}(\mathbf{q}', \mathbf{q}_1') \rangle$$
$$= \frac{\rho_1 h_2(q)}{\rho_2 h_1(q_1)} [\langle \mathbf{W}_{1\to 2}(-\mathbf{q}, -\mathbf{q}_1) \rangle \langle \mathbf{W}_{1\to 2}(\mathbf{q}', \mathbf{q}_1') \rangle$$
$$- \langle \delta\mathbf{W}_{1\to 2}(-\mathbf{q}, -\mathbf{q}_1)\, \delta\mathbf{W}_{1\to 2}(\mathbf{q}', \mathbf{q}_1') \rangle], \quad (28)$$

where the reciprocity relation in Eq. (22) and the difference $\delta\mathbf{W}_{1\to 2} = \mathbf{W}_{1\to 2} - \langle \mathbf{W}_{1\to 2} \rangle$ have been introduced.

By assigning statistical properties to the height function $F(\tilde{\mathbf{r}})$, the ensemble average of the transmission coefficient in Eq. (18) can be determined to second order in $k_1\mu$. In the present work, it will be assumed that $F(\tilde{\mathbf{r}})$ is a Gaussian, wide-sense stationary process with zero mean and unit variance. The identities[8]

$$\langle \int d\mathbf{q}'' F(\mathbf{q} - \mathbf{q}'') F(\mathbf{q}'' - \mathbf{q}') \rangle = \delta(\mathbf{q} - \mathbf{q}') \quad (29)$$

and

$$\langle \int d\mathbf{q}'' F(\mathbf{q} - \mathbf{q}'') F(\mathbf{q}'' - \mathbf{q}') G_{12b}(\mathbf{q}, \mathbf{q}'', \mathbf{q}') \rangle$$
$$= \delta(\mathbf{q} - \mathbf{q}') \int d\mathbf{q}'' G_{12b}(\mathbf{q}, \mathbf{q}'', \mathbf{q}) D(\mathbf{q}'' - \mathbf{q}) \quad (30)$$

may then be invoked. In Eq. (30) the factor $D(\mathbf{q}'' - \mathbf{q})$ is the spectrum of the surface autocorrelation function which is defined in terms of the identity

$$\langle F^*(\mathbf{q} - \mathbf{q}_1) F(\mathbf{q}' - \mathbf{q}_1') \rangle = D(\mathbf{q} - \mathbf{q}_1)\, \delta(\mathbf{q} - \mathbf{q}_1 - \mathbf{q}' + \mathbf{q}_1'). \quad (31)$$

The functional form chosen for D is

$$D(\mathbf{q} - \mathbf{q}_1) = \frac{\beta}{\mu^2 |\mathbf{q} - \mathbf{q}_1|^{\gamma}} [1 - e^{-(|\mathbf{q} - \mathbf{q}_1|\alpha)^2/2}]^2. \quad (32)$$

Equation (32) corresponds to assuming the interface is isotropically rough with a filtered power-law spatial roughness spectrum of strength β and exponent γ, where low spatial frequencies (i.e., large-scale spatial components) are removed according to the filter parameter α. By filtering the power-law spectrum, the rms roughness height μ becomes finite and is related to α, β, and γ by

$$\mu = \sqrt{\frac{2\pi\beta\alpha^{\gamma - 2}}{\gamma - 2} \Gamma\left(2 - \frac{\gamma}{2}\right) (2^{2 - (\gamma/2)} - 1)}. \quad (33)$$

Power-law spectral assumptions have been found to provide a good description of roughness on the seafloor.[14–16]

Using the statistical relations above and the zero-mean property of $F(\tilde{\mathbf{r}})$ in Eq. (18) to eliminate the first order terms, the average transmission coefficient to second order in $k_1\mu$ becomes

$$\langle \mathbf{W}_{1\to 2}(\mathbf{q}, \mathbf{q}') \rangle = \left\{ W_{1\to 2}(q) + \frac{(k_1\mu)^2}{2} \left[G_{12a}(\mathbf{q}, \mathbf{q}) + \int d\mathbf{q}'' G_{12b}(\mathbf{q}, \mathbf{q}'', \mathbf{q}) D(\mathbf{q} - \mathbf{q}'') \right] \right\} \times \delta(\mathbf{q} - \mathbf{q}'). \quad (34)$$

Subtracting this quantity from the transmission coefficient in Eq. (18), the leading term in the correlation of the difference in Eq. (28) then becomes

$$\langle \delta\mathbf{W}_{1\to 2}(-\mathbf{q}, -\mathbf{q}_1)\, \delta\mathbf{W}_{1\to 2}(\mathbf{q}', \mathbf{q}_1') \rangle$$
$$= (k_1\mu)^2 H_{12}(\mathbf{q}, \mathbf{q}_1) H_{12}(\mathbf{q}', \mathbf{q}_1') D(\mathbf{q} - \mathbf{q}_1)$$
$$\times \delta(\mathbf{q} - \mathbf{q}_1 - \mathbf{q}' + \mathbf{q}_1'). \quad (35)$$

Inserting these results in Eqs. (26) and (27), the following far-field expression for the scattered coherent field in the upper half-space is obtained to second order in $k_1\mu$, ignoring multiple scattering effects and assuming a unit-amplitude plane wave is incident on the bottom half-space:

$$\langle \Phi^{\mathrm{scatt}}(\mathbf{r})\rangle = \frac{2k_1\cos\theta}{ir} e^{ik_1[r-\mathrm{a}(\cos\theta+\cos\theta_s)]} \sum_{ml} T_{ml}\epsilon_m \Bigg\{ \frac{\rho_1(-1)^m}{k_1k_2\cos\theta\rho_2}\cos m(\phi-\phi_s) B_{ml}\Bigg(-\frac{h_2(k_1\sin\theta)}{k_2}\Bigg)$$
$$\times B_{ml}\Bigg(-\frac{h_2(k_1\sin\theta_s)}{k_2}\Bigg) e^{i[h_2(k_1\sin\theta)+h_2(k_1\sin\theta_s)]\mathrm{b}} \Bigg[W_{12}(k_1\sin\theta) W_{12}(k_1\sin\theta_s)[1+\mu^2(k_{\mathrm{i}}^2-k_1^2)]$$
$$+\frac{(k_1\mu)^2}{2} W_{12}(k_1\sin\theta)\int d\mathbf{q} G_{12b}(\mathbf{q}_1',\mathbf{q},\mathbf{q}_1') D(\mathbf{q}-\mathbf{q}_1') + \frac{(k_1\mu)^2}{2} W_{12}(k_1\sin\theta_s)$$
$$\times \int d\mathbf{q} G_{12b}(\mathbf{q}_1,\mathbf{q},\mathbf{q}_1) D(\mathbf{q}-\mathbf{q}_1)\Bigg] + (k_1\mu)^2 \int_0^{2\pi} d\xi \int_0^{\infty} \frac{q\,dq}{k_2 h_2(q)} \cos m(\xi-\xi')$$
$$\times B_{ml}\Bigg(-\frac{h_2(q)}{k_2}\Bigg) B_{ml}\Bigg(-\frac{h_2(q')}{k_2}\Bigg) e^{i[h_2(q)+h_2(q')]\mathrm{b}} H_{12}(\mathbf{q},\mathbf{q}_1) H_{12}(\mathbf{q}',\mathbf{q}_1') D(\mathbf{q}-\mathbf{q}_1)\Bigg\}, \quad z>\mathrm{a}, \tag{36}$$

where the vectors $\mathbf{q}_1$ and $\mathbf{q}_1'$ are specified in terms of the polar magnitude and angle coordinates $(k_1\sin\theta,\phi)$ and $(k_1\sin\theta_s,\phi_s+\pi)$, respectively, and $\mathbf{q}'=\mathbf{q}+\mathbf{q}_1'-\mathbf{q}_1$. Given that transverse wave vectors lie in the *x*-*y* plane, the magnitude q' and polar angle ξ' are specified by solving the two simultaneous equations

$$q'\cos\xi' = q\cos\xi - k_1\sin\theta_s\cos\phi_s - k_1\sin\theta\cos\phi, \tag{37a}$$

$$q'\sin\xi' = q\sin\xi - k_1\sin\theta_s\sin\phi_s - k_1\sin\theta\sin\phi. \tag{37b}$$

At this point, it is worth noting that the last term in Eq. (36) arises in addition to the terms that would result from replacing the transmission coefficients in the scattering solution for a flat interface with averaged transmission coefficients. Since this last term does not exhibit the explicit exponential (evanescent wave) decay with frequency expected when $k_1>k_2$ and θ or θ_s are near 90° (note the $e^{i[h_2(k_1\sin\theta)+h_2(k_1\sin\theta_s)]\mathrm{b}}$ factor multiplying the other terms), it is possible for this term to be important compared to the terms resulting from the averaged coefficients. This is mentioned because it has been suggested[17] that reflection and transmission of the coherent field at a rough surface can be treated effectively using a flat interface with effective reflection and transmission coefficients. As indicated by Eq. (28), the last term in Eq. (36) measures the correlation of the roughness-modified component of the field transmitted from the top half-space to the bottom with that scattered back up in the opposite sense. To the extent that these correlations are an important contribution to the roughness correction of the scattered field, the use of effective flat-interface models need to be considered carefully.

B. Backscattered intensity

The total steady-state intensity scattered by a buried sphere is composed of a coherent and an incoherent component when the sphere is under a randomly rough surface. The coherent component is given by the square of the magnitude of the coherent field evaluated above. Therefore, the incoherent component is simply the difference $\langle|\Phi^{\mathrm{scat}}(\mathbf{r})|^2\rangle - |\langle\Phi^{\mathrm{scat}}(\mathbf{r})\rangle|^2$. However, before proceeding with an evaluation of the intensity, it will be helpful to discuss the relevant order of approximation a bit further. Since the coherent field is given to second order in $k_1\mu$, the corresponding intensity can, in principle, be completely determined to second order. This choice of truncation presumes that $k_1\mu$, being the perturbation parameter, is the only relevant small parameter. As mentioned previously, this is not true for all source/receiver geometries of interest since the last term in Eq. (36) can be expected to dominate the others under certain circumstances such as when the plane wave incident on the bottom approaches at a shallow grazing angle. A calculation of the leading terms in the coherent intensity should also include terms that are low order in the exponential decay factors responsible for removing ordinarily dominant terms from the perturbation series. Therefore, a term fourth order in $k_1\mu$ is kept in determining the coherent intensity.

To completely determine the total intensity up to fourth order would be cumbersome due to the complexity and number of terms required. Therefore, the present effort will focus on circumstances relevant to understanding the transmission anomalies observed with shallow-grazing-angle sonar. Of particular interest is the possibility of enhanced shallow-grazing-angle backscatter by objects buried in fast ocean bottoms. To study this problem only a few additional terms in the intensity beyond those worked out for the coherent part are needed. For low frequencies it is expected that the low-order terms in the coherent part will dominate the intensity but at higher frequencies (but not so high that $k_1\mu\gg 1$) terms that are low order in the exponentially decaying factors may dominate. Because these exponential factors decay so quickly as a function of frequency, it should be sufficient to retain terms that are zeroth order in these factors.

By using Eqs. (18), (23), and (24) to form the product $\psi_{\sigma ml}(\mathbf{r})\psi^*_{\sigma' m' l'}(\mathbf{r}) a_{\sigma ml}(\theta,\phi) a^*_{\sigma' m' l'}(\theta,\phi)$, it is easy to see that exponential decay factors show up in those terms that include zero-order factors from any of the basis functions $\psi_{\sigma ml}$ or source field coefficients $a_{\sigma ml}$. [Here the generalized transmission coefficient in Eq. (18) is assumed known out to fourth order in $k_1\mu$ and a backscatter configuration is imposed by setting $\theta_s=\theta$ and $\phi_s=\phi$.] The leading terms from the product that do not contain a decaying exponential are formed by taking a term first order in $k_1\mu$ from each basis

function and source field coefficient. Therefore, the high frequency behavior for shallow-angle backscatter will be described by an expression of the form

$$\left\langle \left| \sum_{\sigma ml} T_{ml} \psi_{\sigma ml}(\mathbf{r}) a_{\sigma ml}(\theta,\phi) \right|^2 \right\rangle \sim (k_1\mu)^4 \frac{4|k_1|^2 \cos^2\theta}{r^2} \int_0^{2\pi} d\xi \int_0^{\infty} \frac{q\, dq}{k_2 h_2(q)} \int_0^{2\pi} d\xi' \int_0^{\infty} q'\, dq' \int_0^{2\pi} d\xi'' \int_0^{\infty} \frac{q''\, dq''}{k_2^* h_2^*(q'')}$$
$$\times \int_0^{2\pi} d\xi^{(3)} \int_0^{\infty} q^{(3)}\, dq^{(3)} \sum_{\sigma ml} \sum_{\sigma' m' l'} \epsilon_m \epsilon_{m'} T_{ml} T^*_{m'l'}$$
$$\times \begin{pmatrix} \cos m\xi \cos m\xi', & \sigma = e \\ \sin m\xi \sin m\xi', & \sigma = o \end{pmatrix} \begin{pmatrix} \cos m'\xi'' \cos m'\xi^{(3)}, & \sigma' = e \\ \sin m'\xi'' \sin m'\xi^{(3)}, & \sigma' = o \end{pmatrix} B_{ml}\left(-\frac{h_2(q)}{k_2} \right)$$
$$\times B_{ml}\left(-\frac{h_2(q')}{k_2} \right) B^*_{m'l'}\left(-\frac{h_2(q'')}{k_2} \right) B^*_{m'l'}\left(-\frac{h_2(q^{(3)})}{k_2} \right) e^{i(h_2(q)+h_2(q')-h_2^*(q'')-h_2^*(q^{(3)}))^{\mathrm{b}}}$$
$$\times H_{12}(\mathbf{q},\mathbf{q}_1) H_{12}(\mathbf{q}',-\mathbf{q}_1) H^*_{12}(\mathbf{q}'',\mathbf{q}_1) H^*_{12}(\mathbf{q}^{(3)},-\mathbf{q}_1)$$
$$\times \langle F^*(\mathbf{q}-\mathbf{q}_1) F(\mathbf{q}'+\mathbf{q}_1) F(\mathbf{q}''-\mathbf{q}_1) F^*(\mathbf{q}^{(3)}+\mathbf{q}_1) \rangle. \tag{38}$$

As before, the transverse vector $\mathbf{q}_1$ designates the polar magnitude and angle coordinates $(k_1 \sin\theta, \phi)$. The correlation of transformed height functions is evaluated by performing the Gaussian factorization

$$\begin{aligned} &\langle F^*(\mathbf{q}-\mathbf{q}_1) F(\mathbf{q}'+\mathbf{q}_1) F(\mathbf{q}''-\mathbf{q}_1) F^*(\mathbf{q}^{(3)}+\mathbf{q}_1) \rangle \\ &\quad = \delta(\mathbf{q}'+\mathbf{q}'')\, \delta(\mathbf{q}+\mathbf{q}^{(3)}) D(\mathbf{q}'+\mathbf{q}_1) D(\mathbf{q}^{(3)}+\mathbf{q}_1) \\ &\qquad + \delta(\mathbf{q}'-\mathbf{q}^{(3)})\, \delta(\mathbf{q}''-\mathbf{q}) D(\mathbf{q}'+\mathbf{q}_1) D(\mathbf{q}''-\mathbf{q}_1) \\ &\qquad + \delta(\mathbf{q}'-\mathbf{q}+2\mathbf{q}_1)\, \delta(\mathbf{q}''-\mathbf{q}^{(3)}-2\mathbf{q}_1) D(\mathbf{q}'+\mathbf{q}_1) \\ &\qquad \times D(\mathbf{q}''-\mathbf{q}_1). \end{aligned} \tag{39}$$

When inserted into Eq. (38) the last term in Eq. (39) reproduces the square magnitude of the last term in Eq. (36) in the case that backscatter ($\mathbf{q}_1 = -\mathbf{q}_1'$) is considered. After some simplification, the remaining terms lead to the following form for the total intensity:

$$\begin{aligned} &\left\langle \left| \sum_{\sigma ml} T_{ml} \psi_{\sigma ml}(\mathbf{r}) a_{\sigma ml}(\theta,\phi) \right|^2 \right\rangle \\ &\quad = (k_1\mu)^4 \frac{4|k_1|^2 \cos^2\theta}{r^2} \\ &\qquad \times \sum_{\sigma ml} \sum_{\sigma' m' l'} \epsilon_m \epsilon_{m'} (-1)^{m+m'} T_{ml} T^*_{m'l'} \\ &\qquad \times [I_{\sigma ml;\sigma' m' l'}(0,0,\mathbf{q}_1) I_{\sigma ml;\sigma' m' l'}(1,1,\mathbf{q}_1) \\ &\qquad + I_{\sigma ml;\sigma' m' l'}(0,1,\mathbf{q}_1) I_{\sigma ml;\sigma' m' l'}(1,0,\mathbf{q}_1)] \\ &\qquad + \textit{terms from coherent intensity}, \end{aligned} \tag{40}$$

where $I_{\sigma ml;\sigma' m' l'}$ represents the integral

$$\begin{aligned} &I_{\sigma ml;\sigma' m' l'}(n,n',\mathbf{q}_1) \\ &\quad = \int_0^{2\pi} d\xi \int_0^{\infty} \frac{q\, dq}{[k_2 h_2(q')]^n [k_2^* h_2^*(q')]^{n'}} \\ &\qquad \times A_{\sigma m;\sigma' m'}(\xi) e^{-2\,\mathrm{Im}(h_2(q))^{\mathrm{b}}} B_{ml}\left(-\frac{h_2(q)}{k_2} \right) \\ &\qquad \times B^*_{m'l'}\left(-\frac{h_2(q)}{k_2} \right) |H_{12}(\mathbf{q},\mathbf{q}_1)|^2 D(\mathbf{q}-\mathbf{q}_1). \end{aligned} \tag{41}$$

Finally, the elements $A_{\sigma m;\sigma' m'}(\xi)$ in Eq. (41) are specified as follows:

$$A_{em;em'}(\xi) = \cos m\xi \cos m'\xi, \tag{42a}$$
$$A_{em;om'}(\xi) = \cos m\xi \sin m'\xi, \tag{42b}$$
$$A_{om;em'}(\xi) = \sin m\xi \cos m'\xi, \tag{42c}$$
$$A_{om;om'}(\xi) = \sin m\xi \sin m'\xi. \tag{42d}$$

III. NUMERICAL RESULTS

The ensemble-averaged results above will now be used to investigate the consequences of bottom roughness on sonar detection of buried underwater objects. This requires evaluation of the integrations in Eqs. (36) and (40), which are performed by segmenting the integration region and using standard Gauss–Legendre quadrature over enough segments to ensure convergence. Consistent with the assumptions used to obtain Eqs. (36) and (40), the target is an evacuated spherical steel shell with a thickness of 11% of the outer radius a, which will be assumed to be 0.25 m. The explicit form of the free-field T matrix needed for this type of scatterer has been presented elsewhere[18,19] and need not be discussed further here. External to the shell, the environment consists of a water half-space above a sediment transition layer of average thickness $0.1a$. This, in turn, is above a sediment half-space which contains the steel shell. The material parameters assumed for the shell and the environment are presented in Table I. Of these, the sound speeds in the bottom have been assigned complex values to allow for propagation loss. The loss chosen for the sediment half-space is typical of attenuation levels observed in sand sediments and corresponds to 0.453 dB/m/kHz. A lower attenuation level of 0.30 dB/m/kHz was chosen for the transition layer.

Also presented in Table I are parameters specifying the spatial roughness spectrum [Eq. (32)] of the upper transition layer interface. Values for two rms roughness levels are

TABLE I. Parameters of the shell and its environment.

Parameter	Value
steel density	7900 kg/m^3
steel compressional speed	5.79×10^3 m/s
steel shear speed	3.10×10^3 m/s
water density	1000 kg/m^3
water sound speed	1.50×10^3 m/s
interfacial layer density	1780 kg/m^3
interfacial layer sound speed	$(1.657\times10^3, -15.0)$ m/s
sediment density	2000 kg/m^3
sediment sound speed	$(1.70\times10^3, -24.0)$ m/s
α ($\mu=1$ mm)	0.01 m
β ($\mu=1$ mm)	2.17×10^{-5} m
γ ($\mu=1$ mm)	3.0
α ($\mu=1.2$ cm)	0.5 m
β ($\mu=1.2$ cm)	6.2×10^{-5} m
γ ($\mu=1.2$ cm)	3.0

given: $\mu=1$ mm and $\mu=1.2$ cm. The values given for the low roughness case correspond to those chosen by Moe[8] to represent the sediment surface roughness in the tank experiment described by Boyle and Chotiros.[2] The higher roughness case uses values chosen to represent the surface roughness at a sandy site off Panama City, FL where transmission experiments were recently performed by Chotiros.[4]

In the present investigation, a source is assumed to produce a unit-amplitude plane wave that strikes the bottom at an incident angle of 70° from vertical in the vicinity of the shell. For the bottom parameters used, this angle is past the ''critical'' angle beyond which high reflection is expected from a flat bottom. This choice is motivated by the desire to detect objects at long ranges to optimize the rate of search; thus, requiring illumination of the bottom at a shallow grazing angle. The field scattered by the shell is initially detected in the backscatter direction, 25 m from the center of the shell.

In Fig. 2 backscattered intensity predictions are presented for the steel shell buried by 1.5a below a rough interface. The depth is measured from the mean level of the interface to the center of the sphere. Predicted coherent and total intensities and the corresponding flat interface result [given by the zeroth order term in Eq. (36)] are compared as a function of the scaled wave number of water, k_1a, for each roughness level provided for in Table I. For the 0.5-m-diam shell, the plotted interval $0<k_1a<25$ corresponds to frequencies up to 23.9 kHz. The upper end of this interval is also close to the expected limit of validity of perturbation theory when applied to 1.2-cm rms roughness. In that case, $k_1\mu=1.2$ although Thorsos[20] has shown that perturbation theory gives good results for transmission due to rough surface scattering at $k_1\mu$ as high as 2.0. The T-matrix summation was truncated after 30 l and m values for these calculations and a resolution of 200 line-connected wave number points is maintained in each curve.

It is seen that roughness causes the total intensity to diverge from the flat interface calculation increasely with frequency. The enhancements are greater and start at lower frequencies for the case with higher roughness. Nevertheless, the coherent part of the backscattered intensity is indistinguishable from the flat interface result when the roughness is low and only slightly enhanced at the higher frequencies for the higher roughness case. Although not large, it is recognized in passing that the observed enhancement of the coherent intensity in the last case is predominantly due to the last term in Eq. (36). Aside from this, the bulk of the enhancement of the total intensity is clearly due to incoherent scattering. Also of note, spectral features are preserved in the flat interface and coherent calculations but washed out of the total intensity. While this is not unexpected, it means that the incoherent part of the backscatter may be useful for detecting a buried object but not so useful for probing its dynamics; for example, as a means to determine its identity.

Despite the greater magnitude of the total intensity due to incoherent scattering, using this to detect the shell depends on this intensity being greater than the reverberant noise level from the rough surface itself. The noise level at $\mathbf{r}$ due to reverberation from a surface patch of area ΔA centered at $\mathbf{r}'$ may be estimated using the formula [8,11,21]

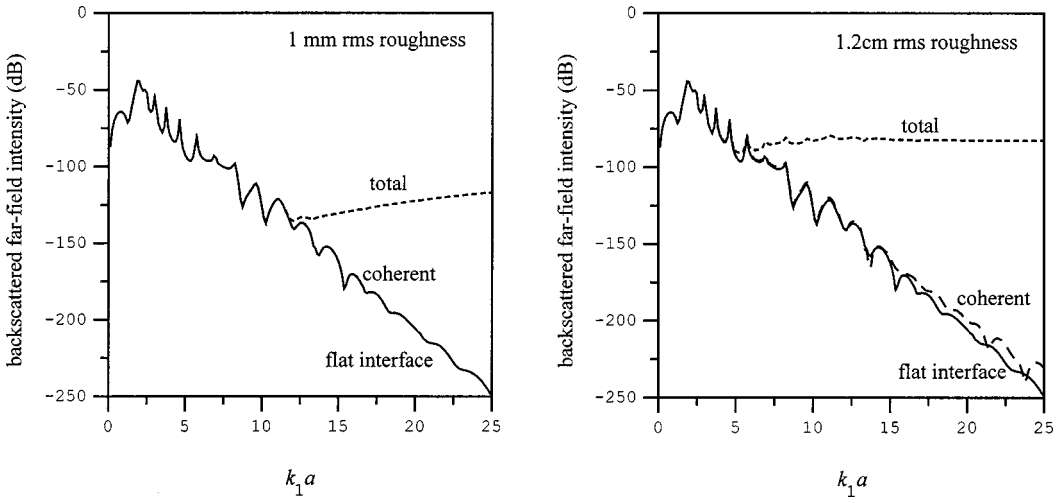

FIG. 2. Total, coherent, and flat-interface itensities as a result of scattering a unit-amplitude plane wave in the water half-space from an 11% steel shell buried by 1.5a in the sediment halfspace. The plane wave is incident at a 20° grazing angle from the mean plane of the rough water/sediment interface.

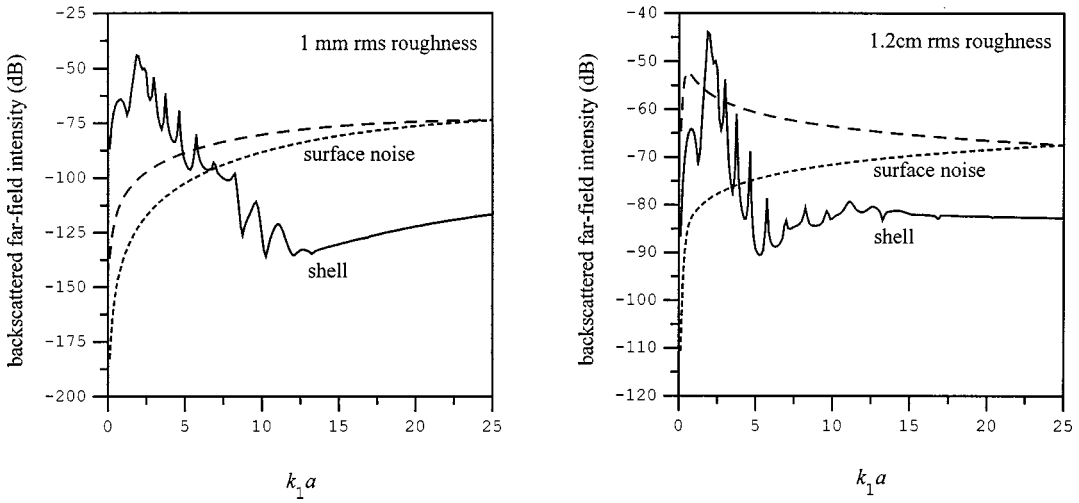

FIG. 3. A comparison of the total intensity scattered by the shell in Fig. 2 with surface noise levels. The dashed line corresponds to holding the source beam resolution constant and the long-dashed line corresponds to holding the source aperture and bandwidth constant.

$$\langle|\Phi^{\mathrm{rev}}(\mathbf{r})|^2\rangle = \frac{\Delta A|\Phi^{\mathrm{inc}}(\mathbf{r}')|^2}{|\mathbf{r}-\mathbf{r}'|^2} k_1^4\mu^2 \times \cos^2(\theta)|H_{11}(\mathbf{q},\mathbf{q}')|^2 D(\mathbf{q}-\mathbf{q}'), \quad (43)$$

which follows from a sonar equation calculation based on a bistatic cross section. Here, $\mathbf{q}'$ and $\mathbf{q}$ are the transverse wave vectors incident on and scattered from the surface patch. For the purposes of comparison, $|\Phi^{\mathrm{inc}}(\mathbf{r}')|^2$ can be set to unity since a unit-amplitude plane wave is assumed incident on the surface in the vicinity of the shell. The factor $\Delta A/(|\mathbf{r}-\mathbf{r}|^2)$ will be assigned a value of 9.6×10^{-5} at $k_1a=25$, which corresponds to using an acoustic source with sufficient aperture and bandwidth to illuminate a 0.40 m×0.15 m patch (0.4 m in the down range direction and 0.15 m transverse to that direction) of the bottom above the shell. The patch size is chosen to illustrate the case with the highest realistic signal-to-noise, using Eq. (43) to calculate the noise level and Eq. (40) to calculate the signal level. (The signal level calculation does not restrict the surface area being illuminated by the incident wave.) This is an important point that warrants further discussion.

Reference 21 treats the penetration problem in terms of a sonar equation calculation and shows that, at shallow angles (below critical), the region of the water/sediment interface contributing to a buried receiver is highly localized and nearly overhead. A calculation was carried out for a 20-kHz source 7.3 m above the sediment interface and displaced 20 m horizontally from a receiver buried 0.12 m into the sediment. (This geometry gives a 70° incident angle at the point above the receiver.) The result shows that illumination of a 0.4 m×0.15 m area of the bottom above the receiver (and displaced 0.15 m toward the source) yields a signal at the receiver within 1.5 dB of the result for illumination of the entire bottom. This is equivalent to saying that for the present discussion the penetration scattering cross section can be approximated as constant over the 0.4 m×0.15 m area and zero outside this area.

With this test geometry and sonar equation approximation it is clear that as the illuminated area is made larger than 0.4 m×0.15 m the signal-to-noise would diminish since the signal would stay constant and the noise [Eq. (43)] is proportional to ΔA. If the area is smaller than 0.4 m×0.15 m, both the signal and the noise will diminish at least as fast as ΔA so that the signal-to-noise ratio will not improve with further reduction of area. This line of reasoning implies that a calculation using 0.4 m×0.15 m should be indicative of the highest signal-to-noise obtainable for the surface conditions, material parameters, and geometry examined here.

A second consideration in plotting noise curves is that the resolution is not commonly kept constant as frequency is altered. If the aperture and fractional bandwidth are constant, the illuminated area will be proportional to $1/\nu^2$, where ν is the center frequency of the source. A $1/\nu^2$ dependence of resolution and a constant resolution should yield reasonable noise bounds for actual sonar systems. In the following, both choices will be compared to the backscatter level of the buried shell using a resolution of 0.4 m×0.15 m at $k_1a=25$ as a reference point.

In Fig. 3, the total intensity backscattered from the shell is compared with the two estimated noise levels of the surface for the two roughness levels considered. For low roughness levels, the shell dominates the low frequency part of the spectrum but the surface noise dominates the high frequency part. The same is true for the higher roughness case but only when the source beam resolution can be held constant, which may not be the most realistic case. When a $1/\nu^2$ resolution dependence is assumed, the noise level still dominates the signal level at higher frequencies but continues to remain a problem even at the low end. While the difference between the intensity of the shell and both noise curves at the upper frequency range is smaller for 1.2-cm rms roughness, increasing the rms roughness amplitude further by increasing the filter parameter α did not help close this gap. This is because the original value of α already accounts for most spatial frequency components of the interface responsible for enhancing the shell's intensity. The larger scale spatial components included by increasing α diffract energy down to the shell less efficiently at the higher frequencies. In any case,

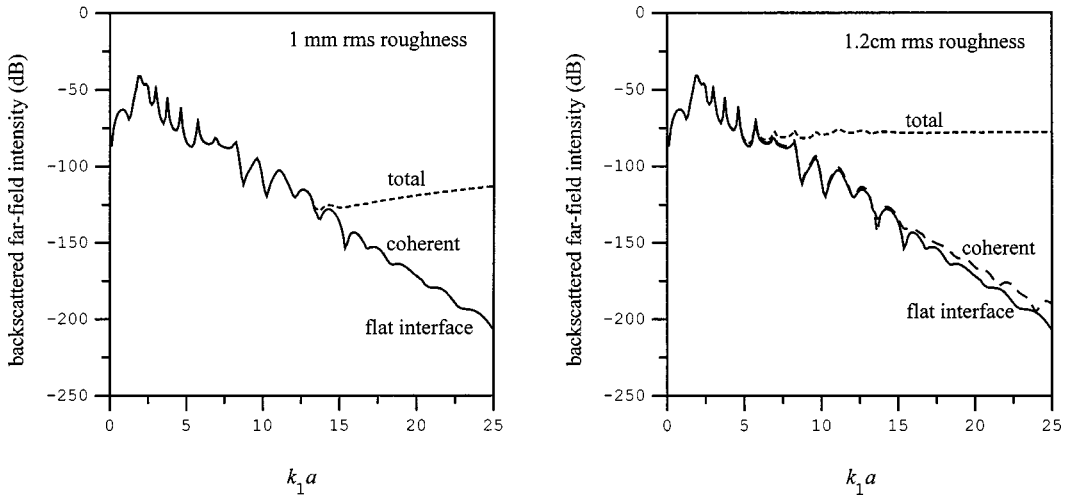

FIG. 4. Total, coherent, and flat-interface itensities as a result of scattering a unit-amplitude plane wave in the water halfspace from an 11% steel shell buried by $1.2a$ in the sediment halfspace. The plane wave is incident at a 20° grazing angle from the mean plane of the rough water/sediment interface.

when the bottom roughness is described by typical power law spectra, the present calculations indicate that low frequencies are best for finding the buried shell using shallow-grazing-angle sonar.

The dependence of the roughness induced enhancements seen in Fig. 2 and their comparison with the noise level may also be examined as a function of the depth of the shell. In Figs. 4 and 5, results analogous to Figs. 2 and 3 are presented except that now the shell is buried by only $1.2a$. Compared to the results at $1.5a$ burial, Fig. 4 shows that the enhanced region of the backscattered intensity has increased much less than the intensity for a flat interface. This is consistent with the fact that the intensity for the shell under a flat interface is due to scattering evanescent waves, which decay exponentially in amplitude as depth increases. The roughness induced enhancements are due to scattering waves diffracted down to the shell, which suffer only the usual propagation losses in sediment over the short distance between the shell and the interface above. It is notable, however, that the noise level associated with 1.2-cm rms roughness (Fig. 5) is becoming less dominant over the shell's total intensity in the upper frequency range. This suggests that shallowly buried objects of high target strength may be observable above the surface noise level at high frequencies, which is consistent with field observations of buried corner reflectors (0-dB target strength) by Lopes.[3]

As a final examination of roughness effects on the scattering by a buried shell, calculations of the coherent bistatic spectral response of the sphere is given in Figs. 6 and 7. In both cases, the geometry of the incident plane wave and shell is as described previously for Fig. 2. However, in Fig. 6, the position of the receiver is moved in angle along an origin-centered circular arc that is contained in the vertical plane containing both the wave vector of the incident plane wave and the origin. Low angles correspond to the receiver near the interface on the same side of the origin as the source. In Fig. 7, the angle of the receiver position vector to the interface is held constant at 20°, but its azimuthal angle (ϕ) around the vertical axis at the origin is scanned from 0° (backscatter) to 180°. An interfacial roughness of 1.2-cm rms is assumed. Results are presented as gray-scaled intensity levels plotted against k_1a and the corresponding angle to the

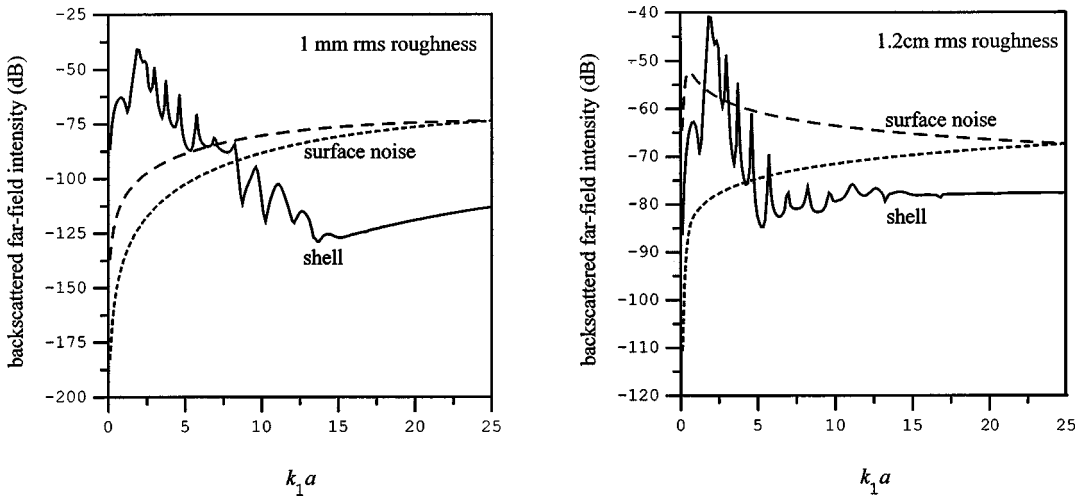

FIG. 5. A comparison of the total intensity scattered by the shell in Fig. 4 with surface noise levels. The dashed line corresponds to holding the source beam resolution constant and the long-dashed line corresponds to holding the source aperture and bandwidth constant.

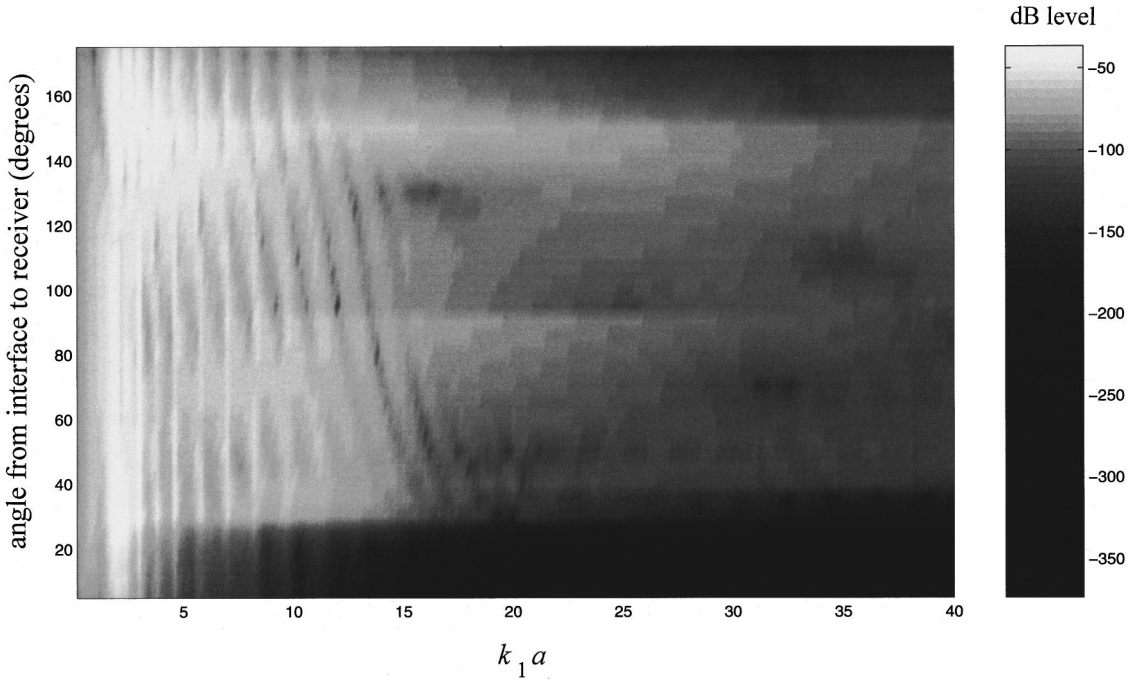

FIG. 6. Bistatic coherent intensity scattered by an 11% steel shell buried 1.5*a* under a water/sediment interface with 1.2-cm rms roughness. A plane wave is incident on the interface above the shell at a 20° grazing angle.

receiver. The truncation of the *T*-matrix summation was increased to 60 *l* and *m* values so that results out to $k_1 a = 40$ could be obtained. A resolution of 200 wave number points by 35 (Fig. 6) or 37 (Fig. 7) angle points is displayed. Intensity variations are smoothed with interpolated shading.

A few details are worth mentioning. First, note that spectral features are visible in both plots as ripples in the intensity. However, the shading in Fig. 6 suggests a compression of these features toward lower $k_1 a$ as the angle increases toward 180°. Such a compression cannot reflect a shifting of the elastic resonances that give rise to these features because resonances cannot shift to lower frequencies with a change in observation angle. The apparent shift is likely an illusion caused by variations in the shape of the spectral features with angle. Such variations might arise as a consequence of how the radiating resonant field interferes with the specular field in the observation direction. This agrees with the general ''straightness'' of the high intensity

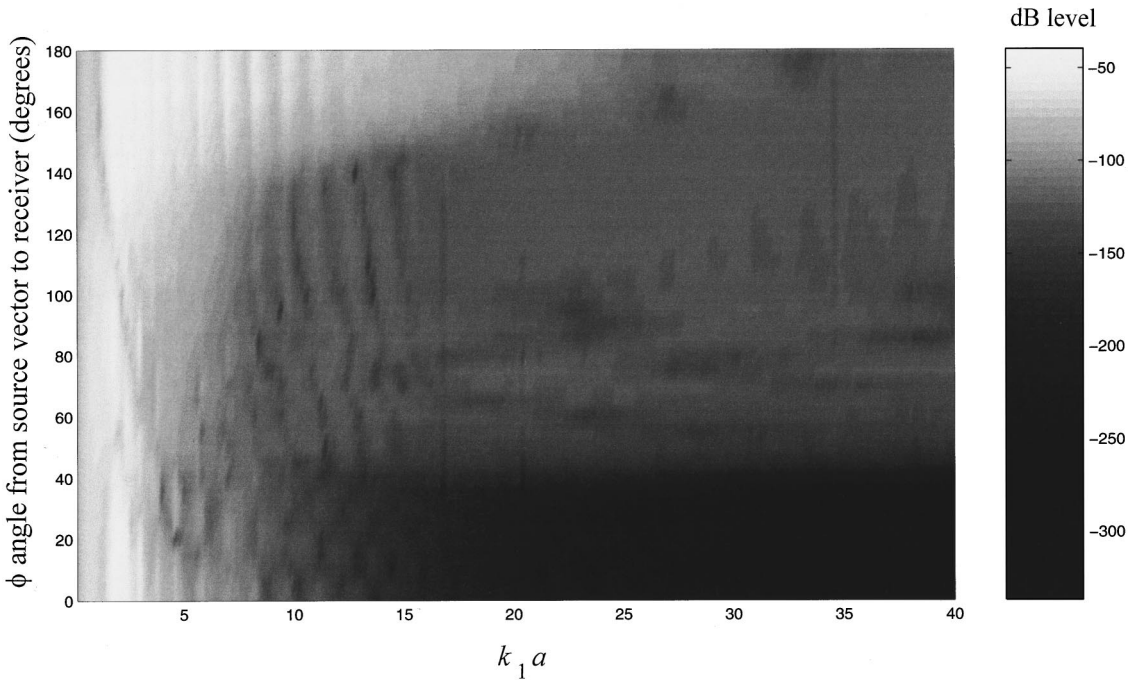

FIG. 7. Bistatic coherent intensity scattered by an 11% steel shell buried 1.5*a* under a water/sediment interface with 1.2-cm rms roughness. A plane wave is incident on the interface above the shell at a 20° grazing angle.

ridges at the low $k_1 a$ end, where the resonant contribution to the intensity is strongest and least modified by the specular contribution.

Aside from this, there is also an expected general decline in intensity with increasing frequency. This is a manifestation of the decay of at least one of the two phase factors in the lowest order term of Eq. (36) resulting from transmission through the interface at shallow grazing angles. When the angle from the interface to the receiver is not shallow as in the region between 30° and 150° in Fig. 6, the decay is less severe because propagation to the receiver is not associated with an evanescent phase factor. One might take advantage of this extra amplitude with a sonar system configured for backscatter over extended ranges by inspecting reflections off other layer interfaces (e.g., an air–water interface).

However, it is notable that, at shallow angles near backscatter (i.e., angles less than 30° in Fig. 6), the coherent intensity declines with frequency much faster than at shallow angles near the specular direction (angles greater 150° in Fig. 6). This asymmetry is not a consequence of the roughness since it is also manifested for a flat interface. It occurs because the scattering modes describing energy distribution in the ϕ direction add up destructively in the back direction but constructively in the specular direction. This is analogous to what happens in high frequency free-field scattering, where enhanced forward scattering lobes develop that interfere with the incident field to create a shadow zone. In the present configuration, the evanescent wave vectors produced when the scattered grazing angle is shallow lead to large factors in the scattering coefficients that further magnify the asymmetry between back and specular scattering. For the 20° scattered grazing angle, Fig. 7 shows significantly slower decay of the intensity with frequency beyond $\phi = 40°$. This indicates that bistatic sonar configurations could have an advantage in detecting more of the object's low frequency spectrum, which might be used to identify the object.

Unlike the total intensity, the averaged coherent response of the shell does not exhibit large departures from the standard flat-interface prediction, but an assessment of less dramatic effects due to roughness is also of interest. Such an assessment is presented in Fig. 8 which compares the temporal response of the shell buried by $1.5a$ under a flat interface and the interface with 1.2-cm rms roughness. A bistatic but shallow angle scattering geometry is considered, corresponding to detection at a point 25 m from the shell at the 180° receive ϕ angle in Fig. 7. An incident pulse, depicted in Fig. 8(a), with a flat frequency response in the $10 < k_1 a < 25$ band but zero amplitude outside this band is assumed. By inverse transforming this band in the steady-state spectra, the corresponding echos for the flat interface and roughness averaged cases are presented in Fig. 8(b) and (c), respectively. The time delay of each echo is set such that the maximum of the pulse resembling the specular is lined up with the transmit pulse maximum in Fig. 8(a).

Both echos appear very similar. The initial specular reflection appears quite dispersed compared to the incident pulse. This is clearly a result of the spectral attenuation associated with scattering evanescent waves. The dispersive secondary pulse following the specular is likely due to reradiation by a flexural wave excited on the shell. Aside from these common features, it is noted that the echo resulting from the rough interface exhibits a higher amplitude than the flat-interface prediction. This may be a result of the additional energy diffracted down by the roughness on the interface.

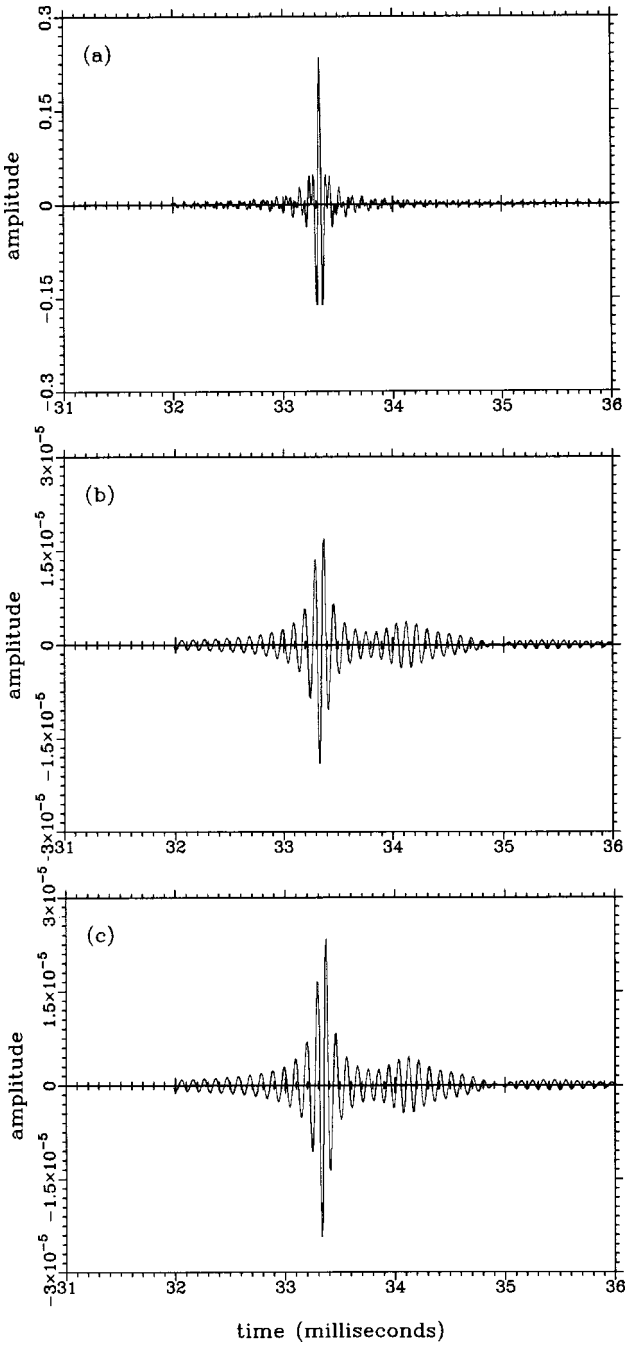

FIG. 8. Time waveforms of (a) the pulse incident on the interface above a spherical shell, (b) the pulse scattered by the shell when the interface is flat, and (c) the ensemble-averaged coherent pulse scattered by the shell when the interface is rough.

IV. SUMMARY AND DISCUSSION

Effects of ocean bottom roughness on underwater acoustic scattering by a completely buried, simple, smooth, elastic object have been studied here. The approach taken combines

a perturbative statistical treatment of a randomly rough water/sediment interface with a deterministic scattering solution for a buried object. Due to the complexity of the resulting formulation, a number of simplifications are imposed before ensemble-averaged predictions are made: steady-state field quantities are considered, the buried object is spherical, it is assumed to be buried deep enough to neglect rescattering events between the sphere and the rough surface, the source field is a unit-amplitude plane wave, the scattered field is detected in the far field, the rough surface obeys Gaussian statistics with a filtered power law roughness spectrum, the coherent field is formulated to second order in the rms roughness μ, the total intensity is formulated only for shallow-grazing-angle backscatter including the coherent part and an incoherent part that is zeroth order in evanescent decay factors, and the perturbation theory is assumed to remain valid up to about $k_1\mu=2$. For developing an understanding of roughness-induced scattering effects observed with underwater sonar operated at shallow grazing angles, these simplifications are expected to be reasonable.

Based on the calculations presented, a few points can be made regarding the effect of ocean bottom surface roughness on using sonar to detect a buried object at long ranges. When the bottom is illuminated at shallow grazing angles with frequencies typically used to image an object ($k_1a\gg1$), the ensemble-averaged total backscattered intensity is well-enhanced relative to the flat-interface prediction. However, it must compete to be observed with the reverberant noise scattered back by the roughness itself. Observation becomes increasingly problematic as the frequency increases. It is anticipated that, for the power law spectrum surfaces examined here, the intensity of the object can be higher than that of the noise if the illuminated area of the bottom is kept small and the object is shallowly buried, or it has a high target strength. But detection strategies based on low frequencies ($k_1a\sim1$), where evanescent transmission remains strong, will lead to the best signal-to-noise.

Furthermore, the bistatic scattering predictions of the coherent field suggest that schemes focusing on coherent field detection of buried objects at extended ranges (i.e., with shallow angle illumination and reception) may be enhanced by adopting bistatic configurations. This is because, even when the angle to the receiver remains shallow, the coherent field can decay at a rate low enough compared to backscatter that it may be possible to detect scattered evanescent waves over a broader frequency band than suggested by the backscatter intensity calculations. In addition, spectral features that might be useful for object identification do not appear strongly modified by roughness effects. Of course, the prospects for moderate to high frequency coherent detection of a buried target would still require high receive sensitivity, being able to sample enough different realizations of the rough interface to filter out incoherent contributions to the higher frequency components, and being able to separate the coherent part of the surface reverberation. Also, detection of either the coherent intensity or the total intensity of the shell could be further defeated by noise due to volume inhomogenieties although this effect cannot be quantified here. Nevertheless, the use of bistatic detection represents a possible alternative strategy for searching for buried objects.

Scattering predictions made with models allowing for periodically rough ocean bottoms[22–24] or flat bottoms with poroelastic properties[5,6] also exhibit enhanced backscatter, and it is interesting to contrast the present results with those. Using a two-dimensional plane-wave decomposition formulation, Fawcett[24] demonstrated that a cylinder buried by 2 radii below a periodic sinusoidal water/sediment interface can exhibit backscatter enhancement for a sonar beam incident at a (subcritical) 20° grazing angle on the bottom above the cylinder. When the spatial frequency of the roughness falls within an optimal acoustic band, the sinusoidal interface produces a much greater enhancement compared to the results given here for the average intensity of a sphere under a random interface. Furthermore, the reverberant noise from the sinusoidal interface is shown to decay at high frequencies so that the corresponding enhancement becomes noise free. Of course, these comparisons are merely suggestive; different object dimensionalities are involved and the sinusoidal interface results are not averaged in any way. Nevertheless, what is inferred from this is that the level of backscatter enhancement as well as the noise level can depend strongly on how the rough interface is represented. Bottom features such as sand ripples might appear to be a periodic roughness, but reality is likely to be complicated enough to preclude quantitative agreement with a rough interface model consisting of a single spatial frequency. While such approaches are informative, it is hoped that the present scattering formulation will be of more predictive value if the roughness is random and not easily mapped; i.e., where effects become difficult to quantify except in an average sense.

Scattering models based on plane-stratified bottoms with poroelastic properties can also exhibit enhanced backscatter by buried objects, although this mechanism does not lead to any unusual enhancement[5,6] unless the sediment has poroelastic properties within a special range. Nonetheless, if shallow-grazing-angle backscatter enhancements are observed in measurements, it might be possible to determine the mechanism driving the enhancement by comparing the spectral response to the corresponding predicted response. Therefore, a few differences between predictions based on the poroelastic mechanism and the roughness mechanism are worth noting. First, it was shown previously[5,6] that scattering models incorporating flat poroelastic bottoms exhibit a marked dependence on properties such as permeability. Variations in such properties have no effect in fluid-sediment models based on interface roughness. Second, when the poroelastic mechanism is most effective, it modifies the low frequency ($k_1a<3$) spectral features in the intensity of a buried spherical object (for shallow-angle illumination) from the case of the sphere buried in a medium with just fluid properties. In the present calculations, bottom roughness does not have an analogous effect; the low frequency backscatter spectrum is indistinguishable whether a rough or flat interface is used. Third, the poroelastic bottom retains a general exponential decay in the shallow-grazing-angle backscatter intensity as the frequency increases, albeit with a shallower slope than expected with a fluid bottom when the

intensity is enhanced. On the other hand, interface roughness appears to change the exponential decay expected with a flat bottom to a level frequency dependence on average as frequency is increased. Finally, since the poroelastic models assume flat interfaces for the bottom, they predict an enhancement in the coherent backscatter field. The roughness mechanism produces an enhancement primarily in the average incoherent part of the backscattered field. Differences such as these may help resolve the actual mechanism for anomalous shallow-grazing-angle bottom transmission and scattering effects observed with underwater sonar.

ACKNOWLEDGMENTS

This work was supported by the Office of Naval Research's Ocean Acoustics Program and the Coastal Systems Station's Independent Research Program.

APPENDIX A

Explicit forms for H_{11}, H_{12}, G_{11a}, G_{11b}, G_{12a}, and G_{12b} [see Eqs. (16) and (17)] are given below using the notation adopted in this work. Moe[8] and Moe and Jackson[11] originally derived these expressions for propagation into a region bounded from above by a rough surface and below by a plane-stratified region. For the purpose of the present work, it is a simple matter to reinterpret them so that they account for propagation through the interfacial region, into the bottom half-space. This is accomplished by rearranging the existing expressions so that the dependence on the flat surface transmission coefficient is explicitly displayed and then using Eq. (6) in place of the transmission coefficient specified by Moe and Jackson. The results are as follows:

$$H_{11}(\mathbf{q},\mathbf{q}')=\frac{k_1}{2ih_1(q)}[\beta(1-V_1(q))(1-V_1(q')) + \alpha(1+V_1(q))(1+V_1(q'))], \tag{A1}$$

where

$$\alpha=1-\frac{k_i^2\rho_1}{k_1^2\rho_i}+\left(\frac{\rho_1}{\rho_i}-1\right)\frac{\mathbf{q}\cdot\mathbf{q}'}{k_1^2}, \tag{A2}$$

and

$$\beta=\frac{h_1(q)h_1(q')}{k_1^2}\left(\frac{\rho_i}{\rho_1}-1\right); \tag{A3}$$

$$H_{12}(\mathbf{q},\mathbf{q}')=\frac{W_{1\to2}(q)k_1}{2ih_1(q)}[\alpha(1+V_1(q'))-\beta(1-V_1(q'))]; \tag{A4}$$

$$G_{11a}(\mathbf{q},\mathbf{q}')=\frac{1}{2}\left(\frac{k_i^2}{k_1^2}-1\right)\left[(1+V_1(q))(1-V_1(q'))\frac{h_1(q')}{h_1(q)} - (1-V_1(q))(1+V_1(q'))\right]; \tag{A5}$$

$$G_{11b}(\mathbf{q},\mathbf{q}',\mathbf{q}'')=\frac{iH_{11}(\mathbf{q}',\mathbf{q}'')}{k_1h_1(q)}[(\mathbf{q}\cdot\mathbf{q}'-k_1^2)(1+V_1(q)) - h_1(q)h_1(q')(1-V_1(q))] - \frac{iH_{12}(\mathbf{q}',\mathbf{q}'')}{k_1h_1(q)W_{1\to2}(q')}\left[\frac{\rho_1}{\rho_i}(\mathbf{q}\cdot\mathbf{q}'-k_i^2) \times(1+V_1(q))(1+V_1(q')) + \frac{\rho_i}{\rho_1}h_1(q)h_1(q') \times(1-V_1(q))(1-V_1(q'))\right]; \tag{A6}$$

$$G_{12a}(\mathbf{q},\mathbf{q}')=\frac{W_{1\to2}(q)}{1+V_1(q)}\left[(1+V_1(q'))\left(\frac{k_i^2}{k_1^2}-1\right) + G_{11a}(\mathbf{q},\mathbf{q}')\right]; \tag{A7}$$

$$G_{12b}(\mathbf{q},\mathbf{q}',\mathbf{q}'')=\frac{W_{1\to2}(q)}{1+V_1(q)}\left[\frac{2ih_1(q')}{k_1}H_{11}(\mathbf{q}',\mathbf{q}'') + \frac{2i\rho_ih_1(q')(1-V_1(q'))}{\rho_1k_1W_{1\to2}(q')}H_{12}(\mathbf{q}',\mathbf{q}'') + G_{11b}(\mathbf{q},\mathbf{q}',\mathbf{q}'')\right]. \tag{A8}$$

APPENDIX B

In the following, reciprocity will be used to establish Eq. (22). The Green's function for propagation of the pressure field through an intermediate region containing roughness is obtained by combining Eqs. (15) and (16) with the incident field specified by[8]

$$\mathcal{A}^{\mathrm{inc}}(\mathbf{q})=\frac{ir_0u}{2\pi h_1(q)}e^{-ih_1(q)(a-z_s)-i\mathbf{q}\cdot\mathbf{r}_s}, \tag{B1}$$

where the parameters $r_0=1$ m and u has unit magnitude and dimensions of pressure×time so that the source corresponds to a point in medium 1 at $\mathbf{r}_s$ with unit pressure magnitude at 1-m distance. Therefore, the field propagated to $\mathbf{r}$ in medium 2 takes the form

$$G(\mathbf{r}_s,\mathbf{r})=\frac{ir_0u}{2\pi}\int_0^{2\pi}d\xi\int_0^{\infty}q\,dq\int_0^{2\pi}d\xi'\int_0^{\infty}\frac{q'\,dq'}{h_1(q')} \times e^{-ih_2(q)(z-b)+i\mathbf{q}\cdot\mathbf{r}}\mathbf{W}_{1\to2}(\mathbf{q},\mathbf{q}') \times e^{-ih_1(q')(a-z_s)-i\mathbf{q}'\cdot\mathbf{r}_s}. \tag{B2}$$

For the opposite case of $\mathbf{r}_s$ in medium 2 and $\mathbf{r}$ in medium 1, a similar expression results; i.e.,

$$G(\mathbf{r}_s,\mathbf{r}) = \frac{ir_0u}{2\pi}\int_0^{2\pi} d\xi \int_0^{\infty} q\,dq \int_0^{2\pi} d\xi' \int_0^{\infty} \frac{q'\,dq'}{h_2(q')} \times e^{ih_1(q)(z-\mathrm{a})+i\mathbf{q}\cdot\mathbf{r}}\mathbf{W}_{2\to1}(\mathbf{q},\mathbf{q}') \times e^{ih_2(q')(\mathrm{b}-z_s)-i\mathbf{q}'\cdot\mathbf{r}_s}. \tag{B3}$$

Reciprocity requires the pressure field Green's function to satisfy the relation[25]

$$\rho_1 G(\mathbf{r}_s,\mathbf{r}) = \rho_2 G(\mathbf{r},\mathbf{r}_s) \tag{B4}$$

when the positions of the source and receiver are interchanged. Using Eq. (B3) to represent the right hand side, this means

$$\begin{aligned} G(\mathbf{r}_s,\mathbf{r}) &= \frac{\rho_2}{\rho_1}\frac{ir_0u}{2\pi}\int_0^{2\pi} d\xi \int_0^{\infty} q\,dq \int_0^{2\pi} d\xi' \int_0^{\infty} \frac{q'\,dq'}{h_2(q')} \times e^{ih_1(q)(z_s-\mathrm{a})+i\mathbf{q}\cdot\mathbf{r}_s}\mathbf{W}_{2\to1}(\mathbf{q},\mathbf{q}') \times e^{ih_2(q')(\mathrm{b}-z)-i\mathbf{q}'\cdot\mathbf{r}} \\ &= \frac{\rho_2}{\rho_1}\frac{ir_0u}{2\pi}\int_0^{2\pi} d\xi' \int_0^{\infty} q'\,dq' \int_0^{2\pi} d\xi \int_0^{\infty} \frac{q\,dq}{h_2(q)} \times e^{-ih_1(q')(\mathrm{a}-z_s)-i\mathbf{q}'\cdot\mathbf{r}_s}\mathbf{W}_{2\to1}(-\mathbf{q}',-\mathbf{q}) \times e^{-ih_2(q)(z-\mathrm{b})+i\mathbf{q}\cdot\mathbf{r}} \\ &= \frac{ir_0u}{2\pi}\int_0^{2\pi} d\xi \int_0^{\infty} q\,dq \int_0^{2\pi} d\xi' \int_0^{\infty} \frac{q'dq'}{h_1(q')} \times e^{-ih_2(q)(z-\mathrm{b})+i\mathbf{q}\cdot\mathbf{r}}\left[\frac{\rho_2 h_1(q')}{\rho_1 h_2(q)}\mathbf{W}_{2\to1}(-\mathbf{q}',-\mathbf{q})\right] \times e^{-ih_1(q')(\mathrm{a}-z_s)-i\mathbf{q}'\cdot\mathbf{r}_s}. \end{aligned} \tag{B5}$$

A change of dummy integration variables corresponding to $\mathbf{q}\to-\mathbf{q}'$ and $\mathbf{q}'\to-\mathbf{q}$ was made in the second equality. By comparing the last equality with Eq. (B2), the desired relationship between the generalized transmission coefficients is deduced.

APPENDIX C

In this Appendix, the form of the rescattering matrix, **R**, is reformulated to account for multiple-scattering effects between the rough interface and a buried object. The method is similar to the derivation of **R** for a flat interface as presented by Hackman and Sammelmann,[26] where **R** is identified as an operator needed to modify the field created by the source in the absence of the buried object so that the field effectively incident on the object results. This ''effective'' field is defined in the following way:

$$\Phi^{\mathrm{eff}}(\mathbf{r}) = \Phi^{\mathrm{inc}}(\mathbf{r}) + [\Phi^{\mathrm{scatt}}(\mathbf{r}) - \Phi^{\mathrm{dir}}(\mathbf{r})], \tag{C1}$$

where $\Phi^{\mathrm{dir}}(\mathbf{r})$ is the part of the scattered field that is scattered by the object directly to **r** without interacting with any interfaces. Therefore, the quantity in brackets represents the part of the scattered field returned to **r** directly as a result of the presence of the interface. For **r** in the bottom half-space near the origin, the effective incident field is assumed to be expandable in regular spherical basis functions as

$$\Phi^{\mathrm{eff}}(\mathbf{r}) = \sum_{\sigma m l} e_{\sigma m l}\hat{\psi}_{\sigma m l}(\mathbf{r}). \tag{C2}$$

In terms of the free-field T matrix for scattering in the bottom half-space medium, the expansion coefficients of the scattered field must be given by

$$f_{\sigma m l} = \sum_{\sigma' m' l'} T_{\sigma m l;\sigma' m' l'} e_{\sigma' m' l'}. \tag{C3}$$

Also, since the direct field to **r** includes no interactions with the interface, it can be expanded in a standard outgoing spherical basis as

$$\Phi^{\mathrm{dir}}(\mathbf{r}) = \sum_{\sigma m l} f_{\sigma m l}\mathrm{h}_l^{(1)}(k_2 r)Y_{\sigma m l}(\theta,\phi). \tag{C4}$$

Using this with Eqs. (1) and (21), the bracketed term in Eq. (C1) takes the form

$$\begin{aligned} &\Phi^{\mathrm{scatt}}(\mathbf{r}) - \Phi^{\mathrm{dir}}(\mathbf{r}) \\ &= \sum_{\sigma m l}\frac{1}{2\pi i^m}\left(\frac{\epsilon_m}{2\pi}\right)^{1/2}\int_0^{2\pi} d\xi \int_0^{\infty} q\,dq \times e^{iq\zeta\cos(\xi-\phi)-ih_2(q)(z-\mathrm{b})}\int_0^{2\pi} d\xi' \int_0^{\infty}\frac{q'\,dq'}{k_2 h_2(q')} \times \mathbf{U}_2(\mathbf{q},\mathbf{q}')B_{ml}\left(-\frac{h_2(q')}{k_2}\right)e^{ih_2(q')\mathrm{b}} \times \begin{pmatrix}\cos m\xi', & \sigma=e\\ \sin m\xi', & \sigma=o\end{pmatrix}\sum_{\sigma' m' l'} T_{\sigma m l;\sigma' m' l'}e_{\sigma' m' l'} \\ &= \sum_{\sigma'' m'' l''}\hat{\psi}_{\sigma'' m'' l''}(\mathbf{r})\sum_{\sigma m l}\frac{\sqrt{\epsilon_m\epsilon_{m''}}}{\pi i^{m-m''}}\int_0^{2\pi} d\xi \int_0^{\infty} q\,dq \times B_{m'' l''}\left(-\frac{h_2(q)}{k_2}\right)e^{ih_2(q)\mathrm{b}}\begin{pmatrix}\cos m''\xi, & \sigma''=e\\ \sin m''\xi, & \sigma''=o\end{pmatrix} \times \int_0^{2\pi} d\xi' \int_0^{\infty}\frac{q'\,dq'}{k_2 h_2(q')}\mathbf{U}_2(\mathbf{q},\mathbf{q}')B_{ml}\left(-\frac{h_2(q')}{k_2}\right) \times e^{ih_2(q')\mathrm{b}}\begin{pmatrix}\cos m\xi', & \sigma=e\\ \sin m\xi', & \sigma=o\end{pmatrix} \times \sum_{\sigma' m' l'} T_{\sigma m l;\sigma' m' l'}e_{\sigma' m' l'} \\ &\equiv \sum_{\sigma'' m'' l''}\hat{\psi}_{\sigma'' m'' l''}(\mathbf{r})\sum_{\sigma m l} R_{\sigma'' m'' l'';\sigma m l} \times \sum_{\sigma' m' l'} T_{\sigma m l;\sigma' m' l'}e_{\sigma' m' l'}. \end{aligned} \tag{C5}$$

In the second equality, the following spherical expansion of a plane wave[27] was substituted:

$$e^{iq\zeta\cos(\xi-\phi)-ih_2(q)z}=\sum_{\sigma ml} i^m\sqrt{8\pi\epsilon_m}B_{ml}\left(-\frac{h_2(q)}{k_2}\right)\times\begin{pmatrix}\cos m\xi, & \sigma=e\\ \sin m\xi, & \sigma=o\end{pmatrix}\hat{\psi}_{\sigma ml}(\mathbf{r}). \tag{C6}$$

Finally, by using Eqs. (C2) and (C5) and the incident field expansion from Eq. (1) in Eq. (C1), it is simple to show that, in analogy to the case of a plane-stratified environment, the vector of ''effective'' field coefficients **e** is related to the vector of incident field coefficients **a** according to the matrix relation

$$\mathbf{e}=(1-\mathbf{RT})^{-1}\mathbf{a}. \tag{C7}$$

Here, matrix/vector products imply a contraction over the range of a complete set of spherical mode indices and the new rescattering matrix **R** consists of the $R_{\sigma''m''l'';\sigma ml}$ elements defined through Eq. (C5).

[1] N. P. Chotiros, ''High frequency acoustic bottom penetration: Theory and experiment,'' in *Proceedings of Oceans '89* (IEEE Publication No. 89CH2780-5) (IEEE, New York, 1989), Vol. 3.

[2] F. A. Boyle and N. P. Chotiros, ''Experimental detection of a slow acoustic wave in sediment at shallow grazing angles,'' J. Acoust. Soc. Am. **91**, 2615–2619 (1992).

[3] J. L. Lopes, ''Observations of anomalous acoustic penetration into sediment at shallow grazing angles,'' J. Acoust. Soc. Am. **99**, 2473–2474 (1996) (A).

[4] N. P. Chotiros, ''Biot model of sound propagation in water-saturated sand,'' J. Acoust. Soc. Am. **97**, 199–214 (1995).

[5] R. Lim, ''Scattering by an obstacle in a plane-stratified poroelastic medium: Application to an obstacle in ocean sediments,'' J. Acoust. Soc. Am. **95**, 1223–1244 (1994).

[6] R. Lim, ''Acoustics of layered poroelastic obstacles in poroelastic hosts,'' in *Proceedings Design Technical Conference: Acoustics Vibrations and Rotating Machines* (ASME, New York, 1995), Vol. 2, Pt. 3B.

[7] E. I. Thorsos, D. R. Jackson, and K. L. Williams, ''Modeling of subcritical penetration into sediments due to interface roughness,'' J. Acoust. Soc. Am. **107**, 263–277 (2000).

[8] J. E. Moe, ''Near- and far-field acoustic scattering through and from two-dimensional fluid–fluid rough interfaces,'' Applied Physics Laboratory, Seattle, WA, Tech. Rep. APL-UW TR 9606, October 1996.

[9] R. Lim, J. L. Lopes, R. H. Hackman, and D. G. Todoroff, ''Scattering by objects buried in underwater sediments: Theory and experiment,'' J. Acoust. Soc. Am. **93**, 1762–1783 (1993).

[10] L. M. Brekhovskikh, *Waves in Layered Media*, 2nd ed. (Academic, New York, 1980).

[11] J. E. Moe and D. R. Jackson, ''Near-field scattering through and from a two-dimensional fluid–fluid rough interface,'' J. Acoust. Soc. Am. **103**, 275–287 (1998).

[12] N. Bleistein and R. A. Handelsman, *Asymptotic Expansion of Integrals* (Dover, New York, 1986), Sec. 8.4.

[13] P. C. Waterman, ''New formulation of acoustic scattering,'' J. Acoust. Soc. Am. **45**, 1417–1429 (1969).

[14] C. G. Fox and D. E. Hayes, ''Quantitative methods for analyzing the roughness of the seafloor,'' Rev. Geophys. **23**, 1–48 (1985).

[15] J. A. Goff and T. H. Jordan, ''Stochastic modeling of seafloor morphology: Resolution of topographic parameters by sea beam data,'' IEEE J. Ocean Eng. **14**, 326–337 (1989).

[16] K. B. Briggs, ''Microtopographical roughness of shallow-water continental shelves,'' IEEE J. Ocean Eng. **14**, 360–367 (1989).

[17] See, for example, J. D. Sheard and M. Spivak, ''Wave scattering in a rough elastic layer adjoining a fluid half-space,'' J. Acoust. Soc. Am. **97**, 72–83 (1995).

[18] R. R. Goodman and R. Stern, ''Reflection and transmission of sound by elastic spherical shells,'' J. Acoust. Soc. Am. **34**, 338–344 (1962).

[19] B. Peterson and S. Ström, ''Matrix formulation of acoustic scattering from multilayered scatterers,'' J. Acoust. Soc. Am. **57**, 2–13 (1975).

[20] E. I. Thorsos, ''The accuracy of perturbation theory for acoustic penetration of sediment due to interface,'' J. Acoust. Soc. Am. **99**, 2475 (1996).

[21] K. L. Williams and D. R. Jackson, ''A model for bistatic scattering into ocean sediments for frequencies from 10–100 kHz,'' Technical Report No. 9505, Applied Physics Laboratory, University of Washington, June, 1996.

[22] G. Bishop and J. Smith, ''Scattering from an elastic shell and a rough fluid-elastic interface,'' J. Acoust. Soc. Am. **101**, 767–788 (1997).

[23] G. Bishop and J. Smith, ''Scattering from fluid-loaded elastic targets near penetrable sediments,'' J. Acoust. Soc. Am. **103**, 2813(A) (1998).

[24] J. A. Fawcett, ''Scattering from an elastic cylinder buried beneath a rough water/sediment interface,'' in *High Frequency Acoustics in Shallow Water* (NATO SACLANT, La Spezia, Italy, 1997).

[25] A. D. Pierce, *ACOUSTICS An Introduction to its Physical Principles and Applications* (Acoustical Society of America, New York, 1989), Sec. 4-9.

[26] R. H. Hackman and G. S. Sammelmann, ''Multiple-scattering analysis for a target in an oceanic waveguide,'' J. Acoust. Soc. Am. **84**, 1813–1825 (1988).

[27] See, for example, J. A. Stratton, *Electromagnetic Theory* (McGraw-Hill, New York, 1941), Sec. 7.6.

High-resolution geoacoustic inversion in shallow water: A joint time- and frequency-domain technique

Charles W. Holland[a] and John Osler
SACLANT Undersea Research Centre, Viale S. Bartolomeo, 400, 19138-La Spezia, Italy

(Received 14 December 1998; revised 22 October 1999; accepted 29 October 1999)

High-resolution geoacoustic data are required for accurate predictions of acoustic propagation and scattering in shallow water. Since direct measurement of geoacoustic data is difficult, time-consuming, and expensive, inversion of acoustic data is a promising alternative. However, the main problem encountered in geoacoustic inversion is the problem of uniqueness, i.e., many diverse geoacoustic models can be made to fit the same data set. A key, and perhaps unique, aspect of this approach is the combination of data analysis in both the space–time and the space–frequency domains. This combination attempts to ameliorate the uniqueness problem by exploiting as much independent data as possible. In order to meet the stringent requirements of high spatial resolution and uniqueness, an entire method has been developed including a new measurement technique, processing/analysis technique, and inversion strategy. These techniques are described and then illustrated with a shallow-water data set. Sound-speed gradients in the upper few meters of the sub-bottom appear to be much higher (one order of magnitude) than generally assumed. And, although often ignored, a large density gradient was observed in the top layer that played an acoustically significant role. © *2000 Acoustical Society of America.* [S0001-4966(00)03402-0]

PACS numbers: 43.30.Pc, 43.30.Ma [DLB]

INTRODUCTION

Shallow-water[1] acoustic propagation is often constrained by interaction with the seafloor. Prediction accuracy is generally limited by knowledge of the seafloor properties rather than model physics. Therefore, there is a need for methods by which the seafloor properties can be estimated. A simplified description of the seafloor properties that controls seafloor interaction over a particular frequency band of interest is called a geoacoustic model. The model includes compressional[2] speed, density, and attenuation as a function of depth and the latter as a function of frequency.

Our application for the geoacoustic model requires high spatial resolution, since we require the geoacoustics for both propagation and scattering[3] or reverberation. This concept of a self-consistent geoacoustic model, i.e., a model capable of treating both the propagation and the scattering with the same physical descriptors, is different from the common approach of treating the propagation with a geoacoustic model and the scattering with an empirical scattering kernel. The concept of a self-consistent geoacoustic model was explored in a deep-water environment in Holland and Neumann (1998). In this paper, the problem of high-resolution geoacoustic inversion is addressed. In a later study, the application of these data to propagation and scattering will be examined.

Since direct measurement of geoacoustic properties is difficult, time-consuming, and expensive, inversion of acoustic data is a promising alternative. However, the main problem encountered in geoacoustic inversion is the problem of uniqueness, i.e., many diverse geoacoustic models can be made to fit the same data set. For some applications this does not pose a serious problem since only a parametrization that fits the data is required without a requirement that the parameters represent actual physical properties. However, for our application the sediment physical properties, not just parameters, are required. One way to reduce uniqueness problems, i.e., improve the likelihood of obtaining properties and not geo-parameters, is to employ more (independent) data. For example, one approach that has been widely used is to employ data over a broad frequency band [e.g., Hermand and Gerstoft (1996)]. In our method, we attempt to use as much independent data as possible over three domains: time, frequency, and space.

Our inversion technique is based on a novel combination of a time-domain inversion and frequency-domain extraction. The time-domain inversion uses the wide-angle reflection data to obtain layer thicknesses and interval velocities; this step solves a second problem in geoacoustic inversion which is to adequately define the initial parametrization (e.g., how many layers should be considered in the solution space). The reflectivity (or bottom loss) analysis in the frequency domain provides attenuation as a function of depth and frequency and density as a function of depth. A new analysis technique exploits cumulative time windowing of the bottom loss to improve resolution in depth for the density and attenuation estimates.

In order to meet the stringent requirements of high spatial resolution and uniqueness, an entire method has been developed including a new measurement technique, processing/analysis technique, and inversion strategy. In this paper we describe each of these techniques and then show how they were applied. Details of the experiment design and processing are provided in Secs. I and II. Section III describes the inversion and modeling procedures and Sec. IV provides discussion of the results at a shallow-water site in the Mediterranean Sea.

[a]Electronic mail: holland@saclantc.nato.int

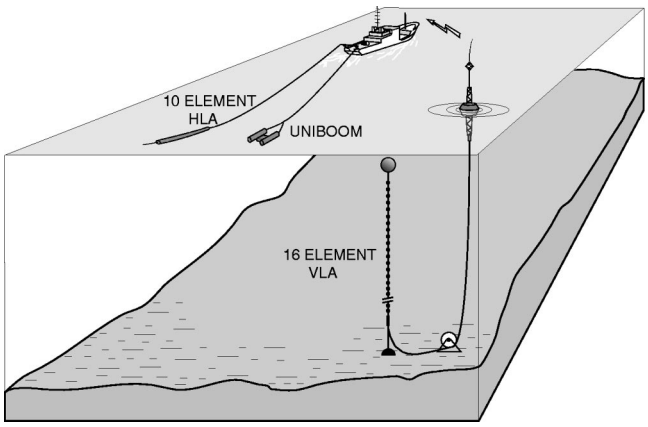

FIG. 1. Experiment geometry.

I. EXPERIMENT DESIGN

A common method of geoacoustic inversion in shallow water is to employ propagation data over spatial scales of kilometers or tens of kilometers; the resulting data therefore represent a spatial average over a large measurement aperture. The requirement for high regional range resolution in our approach was met by using the strategy of making multiple, very short aperture (termed ''local'') measurements, with spatial averaging over scales of a few hundred meters. In addition to the advantage of a smaller spatial averaging footprint, the local measurements have the additional advantage of being less sensitive to oceanographic variability that sometimes plagues shallow-water geoacoustic inversion. Interpolation between local measurements using seismic reflection data has the potential for a regional range-dependent model with high resolution. In this paper we address the local measurement and inversion problem.

The requirement for high resolution in depth suggests that the source pulse length should be short (which also fits the requirement of obtaining data over a broad bandwidth) with dense along-track sampling. A Uniboom source was selected because it transmits a short repeatable pulse at high repetition rates. A sparker source was also examined but later discarded because the pulse was neither repeatable nor sufficiently short.

The experiment geometry as shown in Fig. 1 consists of the towed Uniboom source and a bottom moored receiver. This measurement technique has been conducted at several sites in the northern Tyrrhenian Sea as shown in Fig. 2. In this case, a 16-element vertical line array (VLA) was employed, although the analysis here uses data from the deepest hydrophone[4] which was 12 m above the seafloor. After deployment, the VLA geographic position was fixed within an estimated rms error of less than 8.5 m using transponders on the hull and bottom of the VLA. The array localization was required for positioning the experimental track.

The acoustic data were collected along orthogonal tracks with the center intended to be directly over the array position. This pattern allows data to be acquired over a wide range of grazing angles in four azimuths around the array. The length of each leg is determined based upon the local sound-speed profile, water depth, and array depth, but a typical spatial aperture of the measurement is of order 1 km. The close proximity of the ship to the array required gas turbines to be used in order to minimize contamination from ownship noise. Differential Global Positioning System (DGPS) was employed for navigation and timing. Supporting environmental data included seismic reflection profiling, conductivity temperature-depth (CTD)/expendable bathythermograph (XBT) bathymetry, gravity and piston cores, and sidescan data.

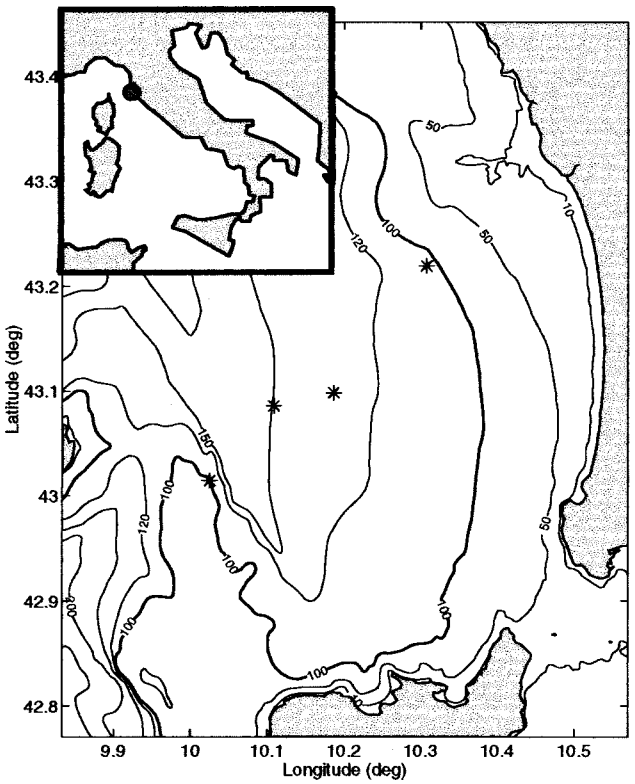

FIG. 2. Capraia Basin area showing test sites (*). The analysis reported in this paper pertains to site 2, which is on the 150-m depth contour. Elba Island is on the southern edge of the map. Insert shows the experiment location on the northwest coast of Italy.

A. Source

The source was an EG&G model 265 Uniboom which had desirable qualities of a repeatable short pulse length and broad bandwidth (600–6000 Hz). Its electromechanical assembly consists of an insulated round metal plate of radius 0.2 m and rubber diaphragm adjacent to a flat-wound electrical coil. A short-duration, high-energy (300 J) electrical pulse discharges into the coil and the resultant magnetic field explosively repels the metal plate. The plate motion in the water generates a single broadband acoustic pressure pulse less than 1 ms in duration (see Fig. 3) with a broadband source level of 207 dB *re* 1 μPa. The source was mounted on a catamaran with a source depth of about 0.2 m and tow speed of 4 kn. The pulse repetition rate was 15 pulses per min or 1 pulse approximately every 8 m. This repetition rate yielded a high data density for the measured wide-angle reflection seismogram and an excellent resolution in grazing angle for the bottom loss data. Uniboom pulses are initiated by a trigger controlled from a GPS clock. The data acquisition was also keyed to GPS, avoiding the tedious and error-prone task of clock synchronization.

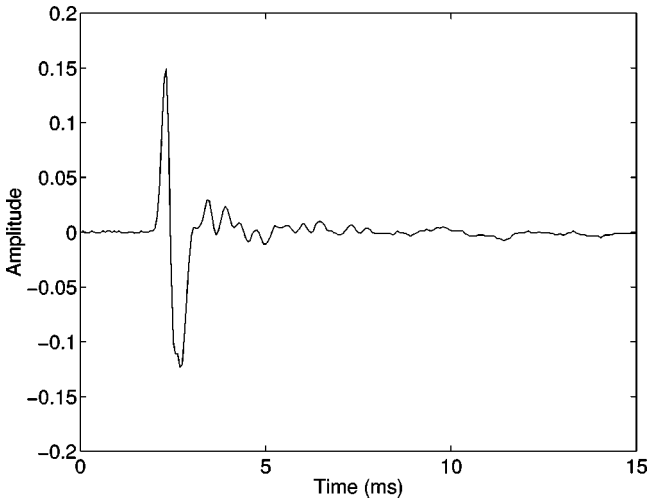

FIG. 3. Uniboom source pulse at 19-cm depth received at a depth and offset of about 138 and 15 m, respectively.

The difficulty in using the Uniboom as opposed to more conventional sources is that the source characteristics were not known. Also, the catamaran has a slight, but unknown, tilt when towed. The source characteristics were estimated by using the direct path arrival on the vertical array. Figure 4 shows a ray diagram of the experiment including the direct and bottom reflected paths. The source beam pattern and presence of the image path eliminates the possibility of performing a self-calibrating technique. Instead, we use the direct path to extract source level as follows:

$$\mathrm{SL}(f,r:\phi)=\mathrm{RL}_{\mathrm{dir}}(f,r)+\mathrm{TL}_{\mathrm{dir}}(f,r), \tag{1}$$

where $\mathrm{TL}_{\mathrm{dir}}$ and $\mathrm{RL}_{\mathrm{dir}}$ are the theoretical transmission loss and measured received level for the direct path (including the surface image) over a 1/3-octave bandwidth. $\mathrm{TL}_{\mathrm{dir}}$ is computed using two rays coherently summed then frequency averaged.

Figure 5 shows a comparison of the measured source level for an integration time[5] of 15 ms with a model based on the classical radiation from a plane, circular, baffled, piston. While this model predicts the general frequency and angular dependence of the data, a better fit to the data was desirable. The source level used in the analysis, given in the solid curve, is a sixth-order polynomial fit to the measured data. This fit is done for each leg since the sled tilt is different depending on whether the leg is approaching or receding from the array.

The low-frequency ringing of the transducer following the electrical discharge is small (see Fig. 3) but not negligible. The source ringing has two undesirable effects. First, it places a lower limit on the receiver height above the seafloor (a receiver close to the seafloor may be contaminated by the extended source pulse, depending on the magnitude of the bottom reflectivity). Second, the source level is a function of integration time which places limits on the bottom loss integration times. Figure 6 shows the dependence of the source level (direct path) received level on integration time. The data have been normalized to the longest integration time of 48 ms. For data above 1000 Hz, the source level appears to be independent of integration time for times greater than 6 ms. For longer integration times, lower frequencies can be used. For the data shown in this paper, 630 Hz was the lowest frequency analyzed.

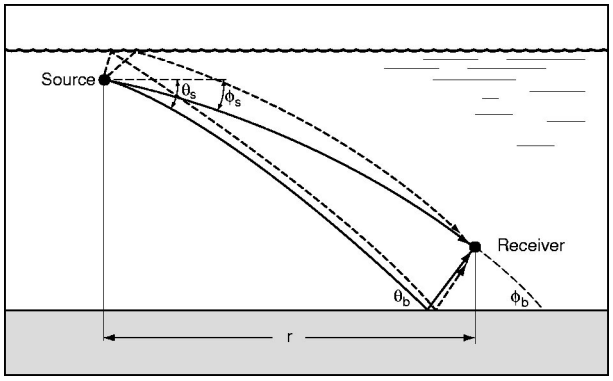

FIG. 4. Ray diagram of direct and bottom bounce paths with the associated surface reflections.

B. Receiver

The receiver consisted of 16 Benthos AQ-4 hydrophones spaced irregularly over a 62-m aperture. The data were sampled at 24 kHz and low-pass filtered at 8 kHz with a seven-pole six–zero elliptic (70 dB per octave roll off) antialias filter. The variable RC high-pass filter (6 dB per octave roll off) was set at 150 Hz. A high-speed digital link within the array provided programmable signal conditioning, digitization, and serialization of the signals. Nonacoustic data (gains, filter settings, etc.) were interleaved in the serial stream and telemetered to the NATO research vessel (NRV) ALLIANCE. The system filter and gain settings (0–84 dB in 6-dB steps) are user-programmable via telemetry.

The limited dynamic range of the VLA (about 60 dB) meant that gains had to be manually changed frequently near the VLA. Also, the close approach to the VLA meant that the rf antennae had to be manually steered, resulting in some data dropouts. Nevertheless, the overall quality of the data was very high.

II. DATA PROCESSING

In this section, the processing of the data in the time and frequency domains is discussed. One of the assumptions in the processing and analysis is that the environment can be approximated as range independent. The short spatial aperture over which the measurements are conducted makes this assumption valid for environments that we have investigated. For example, at site 2 where the maximum offset (horizontal source–receiver separation) was 800 m, acoustic interaction with the seafloor interface occurs within 100 m of the array for the bottom phone. Interaction with sub-bottom layers spans a somewhat larger offset of approximately 300 m (depending on the sub-bottom sound-speed structure). Seismic reflection data indicate that the range-independent assumption is justified over these range scales.

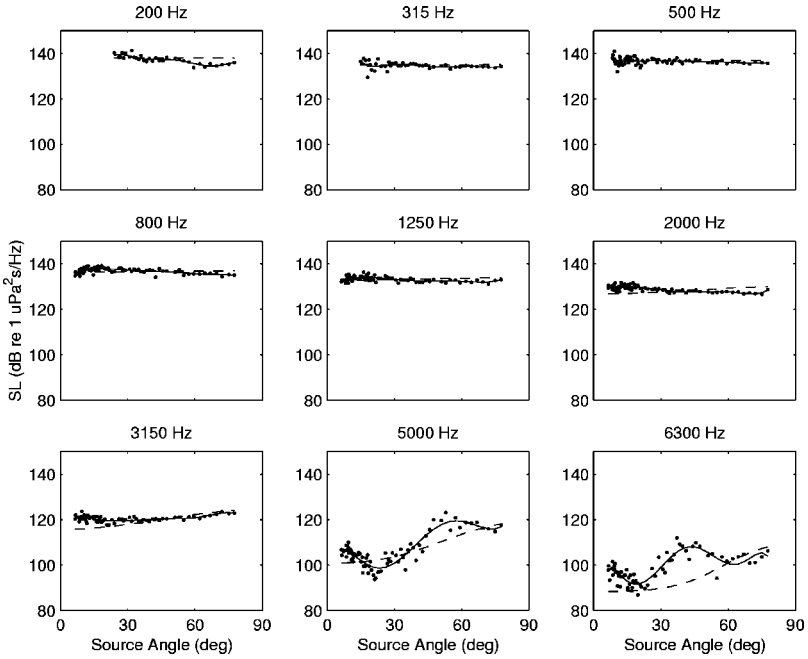

FIG. 5. Comparison of measured source level (·) with extracted beam pattern (solid line) and a piston model (dashed line).

A. Time domain

Quality control checks are applied to the time-domain data, including the removal of seismograms which are contaminated by rf or other spurious noise and ensuring that array gain changes have been properly logged and applied to the data. Seismograms which are clipped, usually on the direct arrival, are removed from the bottom loss analysis. However, they are not removed from the time-domain analysis as the clipping has little effect, with the possible exception of comparison of synthetic and data.

Initial attempts to construct $t-x$ sections using horizontal source–receiver offsets based on the DGPS position of the NRV ALLIANCE and the array position failed due to insufficient accuracy. Instead, horizontal source–receiver offsets are calculated using time of flight of the direct arrival, the experimental geometry (source, receiver, and water-depths), and an eigenray model (Westwood and Vidmar, 1987) using the measured sound-velocity profile.[6]

B. Frequency domain—bottom loss

Bottom loss has historically been a deep-water measurement. In shallow water, the short intervals between multipaths make separation of the bottom arrivals difficult. In our experiment geometry, the separation of multipaths is possible because of the very shallow tow depth (the surface and nonsurface reflected path have nearly the same characteristics), the short duration of the transmit pulse, and the relatively short measurement aperture.

Bottom loss as a function of frequency, f, and specular angle, θ_b, at the water–sediment interface and integration

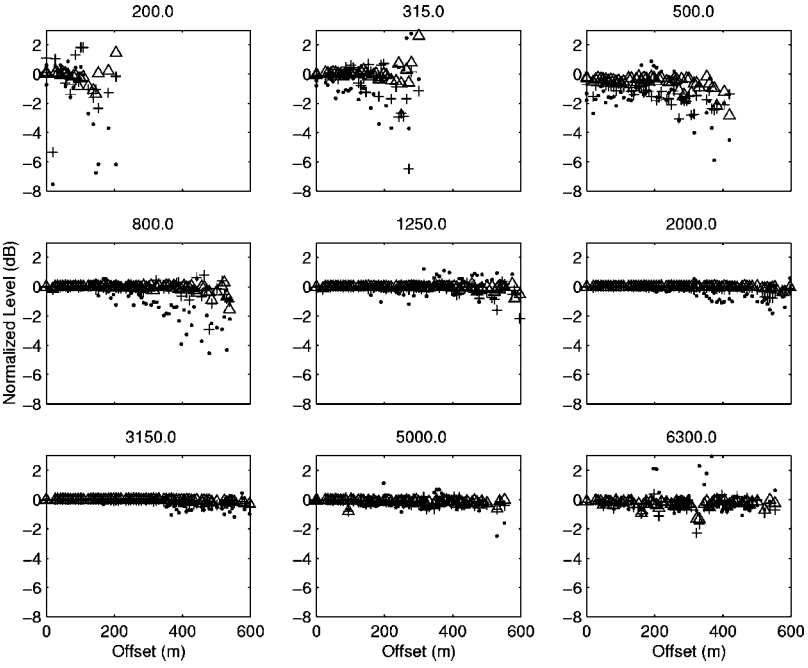

FIG. 6. Dependence of source characteristics (direct path received level) on integration time for integration times of 24 ms (triangle), 12 ms (+), and 6 ms (dot). Data are plotted relative to an integration time of 48 ms.

time τ_i can be calculated from a simple sonar equation as

$$\mathrm{BL}(f,\theta_b,\tau_i)=\mathrm{SLF}(f,\theta_s)-\int_0^{\tau_i}\mathrm{RL}_{bb}(f,r)dt - \mathrm{TLP}_{bb}(f,r{:}\,\vartheta_b), \tag{2}$$

where TLP_{bb} is the theoretical transmission loss from a perfectly reflecting bottom, RL_{bb} is the measured received level in one-third-octave bands associated with the bottom interacting arrival, and SLF is the fitted source level from Eq. (1) at angles corresponding to the bottom bounce path. A signal-to-noise criterion of 6 dB was used both for the individual data points and a fitted curve.

Traditionally, bottom loss has been processed as a total energy quantity, i.e., integrated over all bottom arrivals. However, this method generally leads to severe uniqueness problems inasmuch as there can be many diverse parameter sets that explain the data equally well. In order to hone in on the ''true'' solution, the bottom loss data are processed for selected cumulative time (or equivalently, sub-bottom depth) intervals τ_i: first across just the water–sediment interface, then across the water–sediment interface plus the next layer, and continuing until all layers are included in the integration. This layering stripping approach has been used in the time domain, for example by Yagle and Levy (1984).

In our analysis, the geoacoustics are first extracted starting from the BL data at the water–sediment interface. Then, those properties are fixed and the next BL data set including the next horizon is analyzed, and so forth until the last data set, which is integrated over all arrivals. In this way the gradients in velocity, density, and attenuation can be better constrained. The cumulative approach also has the advantage of indicating sensitivity of the BL to deeper layers. Data windowing is limited, of course, by the pulse length and the relative interval velocity between adjacent layers. In practice, the time windows are placed between layers or layer groups in such a way that there is no danger of cutting across layer boundaries.

Frequently, bottom loss data are smoothed over some range of angles as an attempt to reduce ''random'' scatter arising from imprecise knowledge of the geometry and environment. However, in order to maximize resolution in angle space, no smoothing was applied in our processing. This approach preserves information in the angular dependence that can be useful for geoacoustic inversion.

Standard bottom loss processing [e.g., Eq. (2)] makes the implicit assumption that the bottom is a half-space since the correction for the transmission loss in the water is applied only to the sediment reflected path at θ_b. When sub-bottom paths contribute, as in Fig. 7, the measurement represents a non-plane-wave bottom loss [e.g., Stickler (1977), Spofford (1980), Chapman *et al.* (1990)]. That is, the measurement includes energy from multiple angles. The presence of sub-bottom paths leads to artifacts in the data including the infamous ''negative bottom loss'' anomaly. Thus, it is possible in processing such as Eq. (2) to arrive at the wholly undesirable result of different bottom loss values depending upon source–receiver geometry. Using a source with a beam pattern further complicates matters. In the case of the Uniboom, it means that at moderate[7] frequencies, the beam pattern is corrected only at the angle of the sediment-reflected path, and not for any other sub-bottom paths (even though the loss may be dominated by the sub-bottom paths).

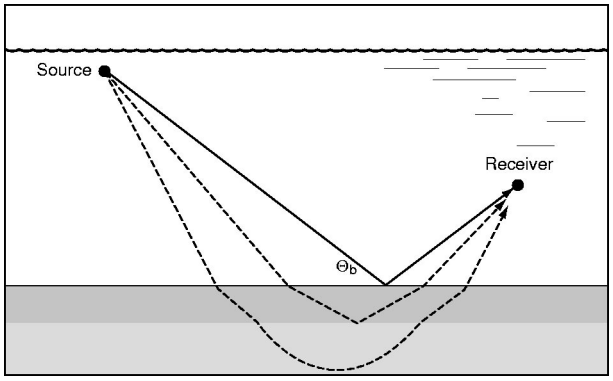

FIG. 7. Ray diagram of the experiment geomtry showing the non-plane wave nature of the measurement technique. That is, sub-bottom paths arrive at different angles than the specular.

These problems (relating to the incorrect half-space assumption) can be addressed either in the data processing stage or in the modeling stage. For purposes here, it is more convenient to treat these problems in the modeling and retain simplicity in the data processing.

III. MODELING, EXTRACTION, AND INVERSION

The objective of the inversion and extraction techniques is to recover the deterministic sediment geoacoustic properties. A unique aspect is the coordinated analysis of data in both the time–space and frequency–space domains. The analyses performed in each domain are not necessarily new, but their combination is new (according to the authors' knowledge). Our technique attempts to use as much independent data as possible (across time, frequency, and space) and to extract information from each data type that is most suitable. For example, sound-speed information is best extracted from the time domain, whereas attenuation is best extracted from the frequency domain.

The first step in the technique is to use the time-domain data to invert for the interval velocity and thickness of each layer. This provides the crucial initial parametrization, in terms of identifying the number of layers and provides an important advantage over many geoacoustic inversion techniques that have no basis for selecting the number of layers on which to perform the inversion. The second major step is to use the frequency-domain data (bottom loss) to extract density and attenuation, as well as to refine the velocity structure. Finally, the geoacoustic properties are refined by alternating between the synthetic seismogram analysis and the bottom loss analysis.

A. Time domain—inversion method

Assuming that the velocity structure above a given layer is a function of depth only, Dix (1955) showed that it is possible to determine the velocity and thickness of a homogeneous layer embedded in an arbitrary sequence of layers, without prior knowledge of the overlying structure. The in-

terval velocity, v_n, of a layer is determined from the root-mean-square (rms) velocities of the wide-angle reflections from the top, $v_{\mathrm{rms}_{n-1}}$, and bottom, v_{rms_n}, interfaces of the layer,

$$v_n^2 = \frac{v_{\mathrm{rms}_n}^2 \Sigma_1^n \Delta t_i - v_{\mathrm{rms}_{n-1}}^2 \Sigma_1^{n-1} \Delta t_i}{\Delta t_n}, \tag{3}$$

where the root-mean-square velocity is defined as $v_{\mathrm{rms}} = \sqrt{\Sigma v_i^2 \Delta t_i / \Sigma \Delta t_i}$, with t_i being the zero-offset travel time within a layer. Le Pichon *et al.* (1968) incorporated the Dix method to calculate an initial velocity structure of deep-sea sediments in their technique that used conventional sonobuoys deployed while the vessel was underway conducting seismic reflection profiling. This velocity structure was then revised by iterative forward modeling to improve the fit between measured and modeled travel times, progressing from shallower to deeper layers. Implicit in this technique is the assumption that the velocity structure may be treated as a sequence of isovelocity layers, including the water layer, thus assuming straight-line ray paths segments in each layer.

As documented by Bryan (1974, 1980), the application of straight-line paths to layers which are not homogeneous leads to errors which may be significant in certain cases. In particular, errors in the water column which are negligible in comparison with the times and offsets involved in the water column can be appreciable as the error is magnified as a subseabed layer gets thinner. In the absence of a detailed water velocity structure to overcome the assumption of straight-line ray paths, the method of Le Pichon *et al.* is limited to water depth/layer thickness ratios of up to about 15 (Bryan, 1974).

Bryan (1974, 1980) presented an alternative approach, the ray-parameter method (see the Appendix), which he used for characterizing relatively thin layers near the seafloor in deep water. His experimental data involved both the source and receiver located on the seabed, an optimal configuration from the standpoint of avoiding lateral variations in the water column. However, the theory is more general and allows for diverse experimental geometries such as the surface towed source and bottom-moored receiver as used in our experiments. Since this method allows the resolution of thinner layers and is valid over a wider range of incident angles, it is a suitable choice for the inversion of wide-angle reflection data in shallow water.

The implementation of the Bryan inversion method involves fitting a hyperbola to each of the wide-angle reflections which determines the zero-offset travel time and stacking velocity, t_0^2 and v_{ST}^2 (see the Appendix for details on the theory). The hyperbola fitting is done interactively with a visual display of data, presented as a reduced travel time ($t^2 - x^2/v_W^2$, where v_W is the reducing velocity generally chosen to be the depth-averaged sound speed in the water column) versus offset plot. Hyperbolas were fitted qualitatively, i.e., ''by eye.'' Once the hyperbolas have been defined, the layer thicknesses and interval velocities are immediately computed from Eq. (A3).

Interval velocities recovered from the Bryan method are averaged both on a micro and macro scale. That is, there are fine-scale fluctuations in the velocity structure within a layer as well as larger scale variability, e.g., velocity gradients. The small-scale velocity fluctuations are not addressed in this paper. Velocity gradients are extracted at a later point in the analysis.

B. Time domain—synthetic seismograms

The objective for the synthetic seismograms was to (1) aid in interpreting the measured data, (2) guide the time-domain pick criteria, and (3) refine the geoacoustic model. The generation of the synthetic seismograms follows Westwood and Vidmar (1987). It uses the same ray-based approach as in the bottom loss modeling (see the next section), except that no attempt is made to correct for the source beam pattern. The receiver response for individual eigenrays [see the first term in Eq. (4)] are calculated then summed with the proper delay based on the travel times. An approximate source function was employed using the source data of Fig. 3 with the surface reflection removed. The sampling frequency in the synthetics is 16 384 Hz, with a bandpass filter of 800–7000 Hz and Hamming window roll offs of 400 Hz below and above the band.

The synthetics provided a solution to a puzzling phenomenon where the water–sediment interface arrival was only visible for offsets shorter than 200 m. From the synthetics, it was found that for a low velocity layer at the water–sediment interface that the arrival structure would be masked beyond an offset of about 200 m due to the classical angle of intromission. Since the water–sediment interface arrival is obscured at large offsets, the model results are used to guide the picking process for the time-domain inversion.

C. Frequency domain

1. Modeling

The bottom loss modeling attempts to account for all of the artifacts noted in Sec. II B. The idea is to model the environmental effects (e.g., sub-bottom paths and source–receiver geometry) as faithfully as possible and then process the results using the same assumption used in the data processing [i.e., Eq. (2)]. Thus, the model and data should be directly comparable (artifacts included). The processed bottom loss is modeled as follows:

$$\mathrm{BL}(f,\theta_b,N) = 10\log_{10}\left[\int \left|\sum_i^N \kappa(f,\theta_i)\,\gamma(r{:}\,\theta_i) g(r{:}\,\theta_i) \times e^{-j2\pi f\tau - \alpha_i f}\right|^2 df\right] + \mathrm{BP}(f,\phi_s) - \mathrm{TLP}_{bb}(f,r{:}\,\theta_b), \tag{4}$$

where θ_b is the specular angle at the water–sediment interface. The first term is the received level; that is a coherent sum of eigenrays rays at offset r including the effect of the normalized beam pattern $\kappa = 10^{\mathrm{SL\text{-}SL}_{\max}}$. The number of eigenrays, N, will be proportional to the integration time, τ_i.

The 1/3-octave frequency average is performed incoherently. Ray quantities γ, g, τ, and α, respectively, are the combined pressure reflection/transmission coefficient, the

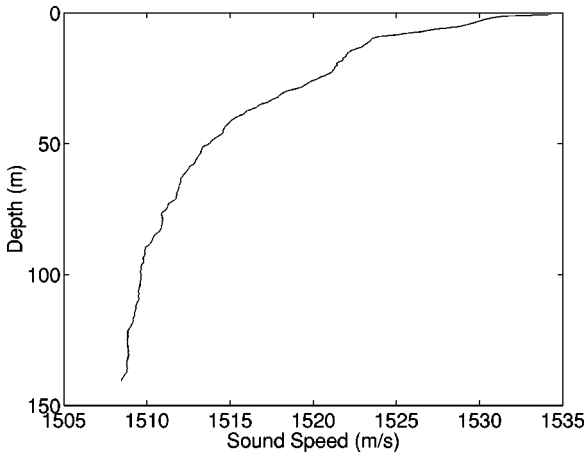

FIG. 8. Sound-speed profile at site 2.

geometrical spreading, travel time, and attenuation for each ray i as computed following Westwood and Vidmar (1987). The model is capable of predicting effects of shear waves. However, for the environment examined in this paper, shear waves contributed negligibly and thus are not included in the analysis. The second and third terms mirror the assumptions in the data processing [Eq. (2)] by introducing a normalized beam-pattern correction BP at the nominal source angle ϕ_s and a correction for the transmission loss TLP_{bb} at the nominal bottom angle θ_b.

2. Geoacoustic extraction

The frequency-domain solution contains clues about the velocity structure of the sub-bottom that can refine the time-domain picks. The frequency-domain solution also contains important clues about the attenuation and density, the former being the most notoriously difficult parameter in a geoacoustic model to estimate.

As an initial geoacoustic model, density and attenuation are computed from empirical relationships following Bachman (1985) and Hamilton (1980),[8] respectively, using the velocity data as the known parameter. Forward modeling is then employed to refine these estimates by comparing the model output with the measured data over frequency and angular regions that are sensitive to each parameter. For example, the slope (in angle) of low-angle bottom loss is often highly sensitive to the attenuation. This is due to the fact that at low frequencies, the dominant path for the energy is often refraction through the sediment. A linearly frequency-dependent attenuation is assumed. There was no indication in the measured data that a nonlinear frequency dependence was justified. Density effects are generally best observed near normal incidence where reflection rather than refraction dominates.

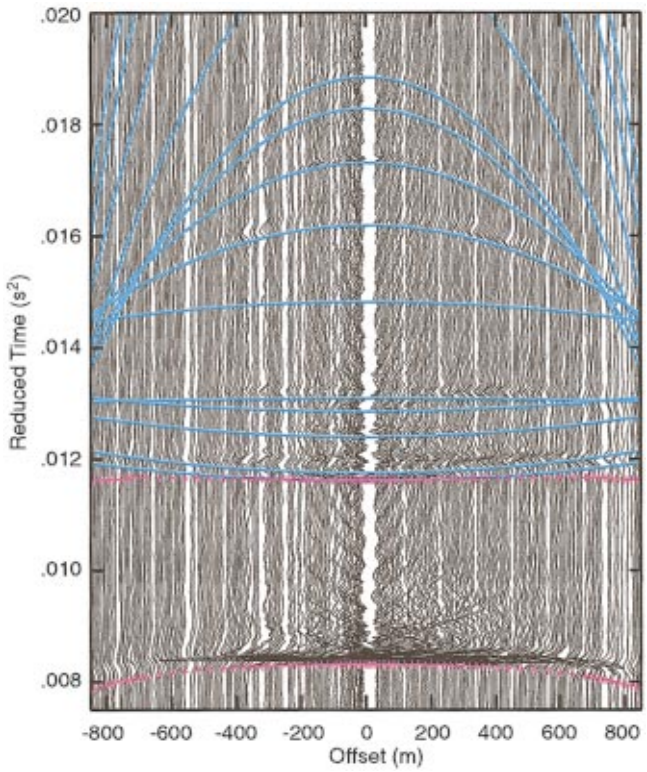

FIG. 9. Wide-angle reflection data at site 2 from a phone 11.5 m above the seafloor. The reducing velocity is 1513.4 m/s. The hyperbolic picks are also shown.

IV. DISCUSSION OF RESULTS

Our method has been employed at various locations in a shallow-water region known as Capraia Basin in the northern Tyrrhenian Sea (see Fig. 2) as well as on the Malta Plateau. Data from the north–south track at Capraia site 2 on a hydrophone 12 m above the seafloor will be presented in this section. Bathymetry was essentially flat (150-m water depth) across the measurement area and the limiting angle at the seafloor based on the sound-speed profile (see Fig. 8) is approximately 11°.

A. Time domain—Bryan method

In Fig. 9, the wide-angle reflection data on the bottom hydrophone of the VLA are presented versus reduced time. This mapping has the desirable property that reflectors with the same stacking velocity (see the Appendix) have the same curvature regardless of their zero-offset intercept time. It also allows a visual indication of where layers of lower sound speed relative to surrounding layers are located. The ''picked'' wide-angle reflections used to obtain the thickness and interval velocity of the layers are also shown in this figure.

The velocity versus depth solution from the picks (converted to travel time) is superimposed on the reflection seismogram in Fig. 10. Note that in the reflection seismogram that the subseabed reflectors are laterally continuous and exhibit little range dependence. The interval velocity and thickness of the layers are provided in Table I along with the initial density and attenuation values.

B. Frequency domain

In this section, results of the bottom loss (frequency-domain) analysis are provided. In order to obtain the best possible depth resolution in the extracted geoacoustics, the bottom loss data were processed in cumulative time intervals. At this site, three cumulative windows were chosen, the

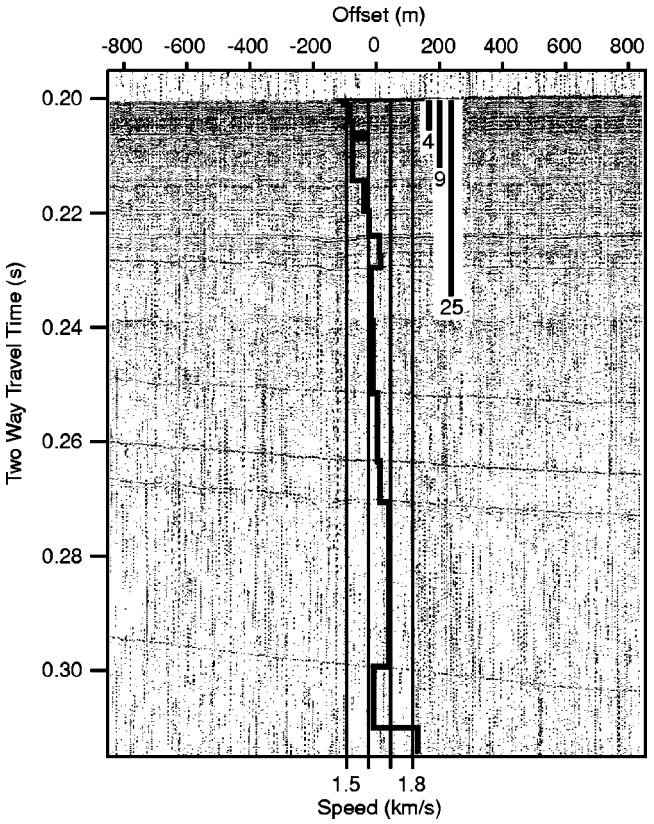

FIG. 10. Reflection seismogram along the track. Also shown is the velocity and thickness solution from the time picks of Fig. 9.

first from 0–4-m sub-bottom, the second from approximately 0–9-m sub-bottom depth, and the third from 0–25-m sub-bottom. In the following discussion, we refer to the depth of these windows not in terms of the actual window length but rather in terms of the depth of the last layer horizon in the window. These windows were at 3, 6, and 24 m, respectively, sub-bottom.

TABLE I. Initial geoacoustic model.

Thickness (m)	Depth (m)	Velocity (m/s)	Density (g/cc)	Attenuation (dB/m/kHz)
0.5	0.5	1486	1.38	0.07
2.2	2.7	1516	1.48	0.09
1.5	4.2	1527	1.51	0.1
0.8	5	1591	1.68	0.4
5.6	10.6	1525	1.5	0.1
4.3	14.9	1582	1.66	0.33
3.5	18.4	1604	1.71	0.5
3	21.4	1648	1.81	0.78
1.7	23.1	1656	1.83	0.74
7.5	30.6	1612	1.73	0.55
10.4	41	1620	1.75	0.61
9.9	50.9	1641	1.8	0.74
6	56.9	1651	1.82	0.76
24.7	81.6	1693	1.9	0.55
8.8	90.4	1623	1.76	0.63
59.2	149.6	1823	2.06	0.48

Bottom loss data on the incoming leg (south of the array) were essentially identical to the data on the outgoing leg (north of the array), indicating that the measurement area is laterally homogeneous. Data are presented from the incoming leg.

Figure 11 shows bottom loss data integrated to 3-m depth in sub-bottom. First note the characteristics of the measured data. The unusually high data density and lack of ''random'' scatter[9] in the data provides features which can be exploited for extracting geoacoustic data. Now, consider the model predictions shown in the solid line. Predictions from the baseline geoacoustic model (Table I, first three layers only) are quite poor, especially at shallow grazing angles. A more careful examination of the time-domain data indicated the presence of another layer between the first and second. These layer properties were estimated by a combination of the time- and frequency-domain data and are given in

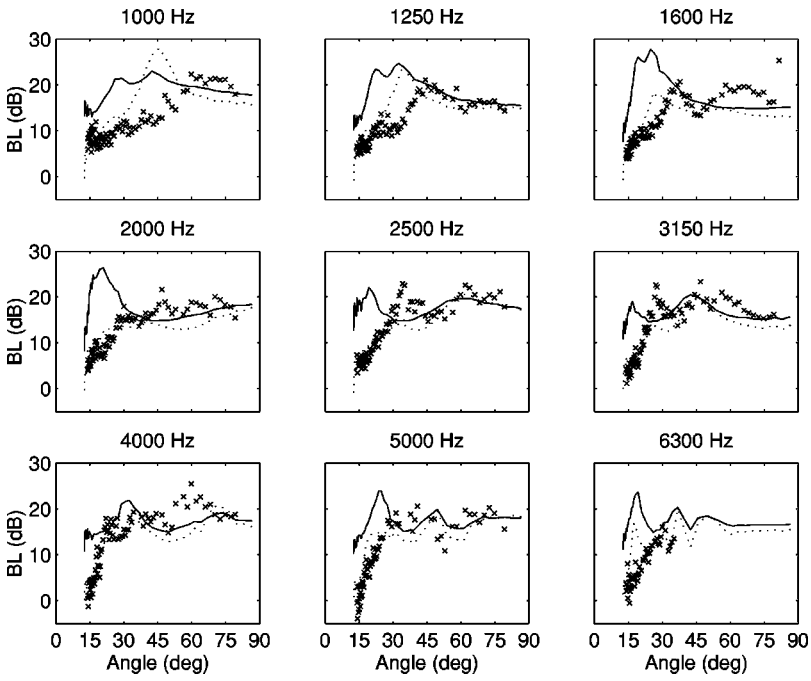

FIG. 11. Bottom loss data (×) with model predictions for upper 3 m: solid line is original geoacoustic model (Table I) and dashed line is with additional layer (Table II).

TABLE II. Updated geoacoustic model for upper 3 m.

Thickness (m)	Depth (m)	Velocity (m/s)	Density (g/cc)	Attenuation (dB/m/kHz)
0.5	0.5	1486	1.38	0.07
0.6	1.1	1551	1.58	0.1
2.2	3.3	1516	1.48	0.09
⋯		1527	1.51	0.1

TABLE III. Geoacoustic model for upper 6 m.

Thickness (m)	Depth (m)	Velocity (m/s)	Density (g/cc)	Attenuation (dB/m/kHz)
0.5	0.5	1470–1502	1.15–1.30	0.07
0.6	1.1	1551	1.58	0.1
2.2	3.3	1516	1.48	0.09
1.5	4.8	1527	1.51	0.1
0.8	5.6	1591	1.68	0.4
⋯		1525	1.50	0.1

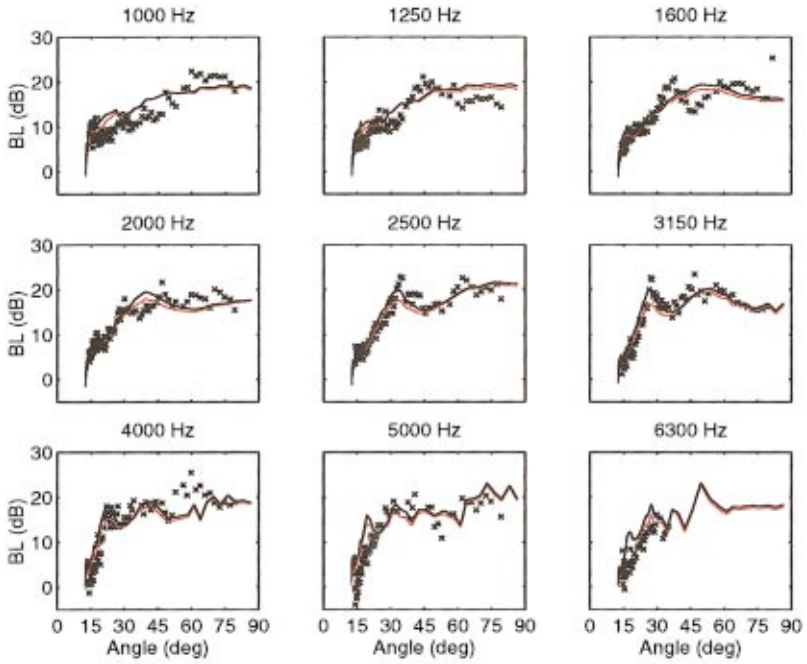

FIG. 12. Bottom loss data (×) with model predictions for upper 3 m: including a linear density profile from 1.15–1.30 g/cc in the first sedimentary layer (red line) and including both the density gradient and a velocity gradient of 1470–1502 m/s (black line).

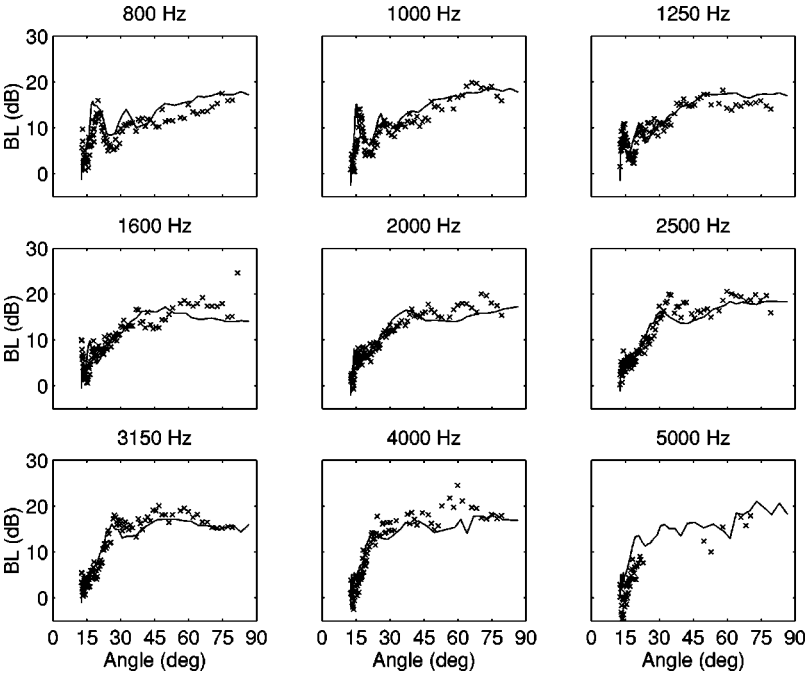

FIG. 13. Bottom loss data (×) and model predictions (solid line) for upper 6 m.

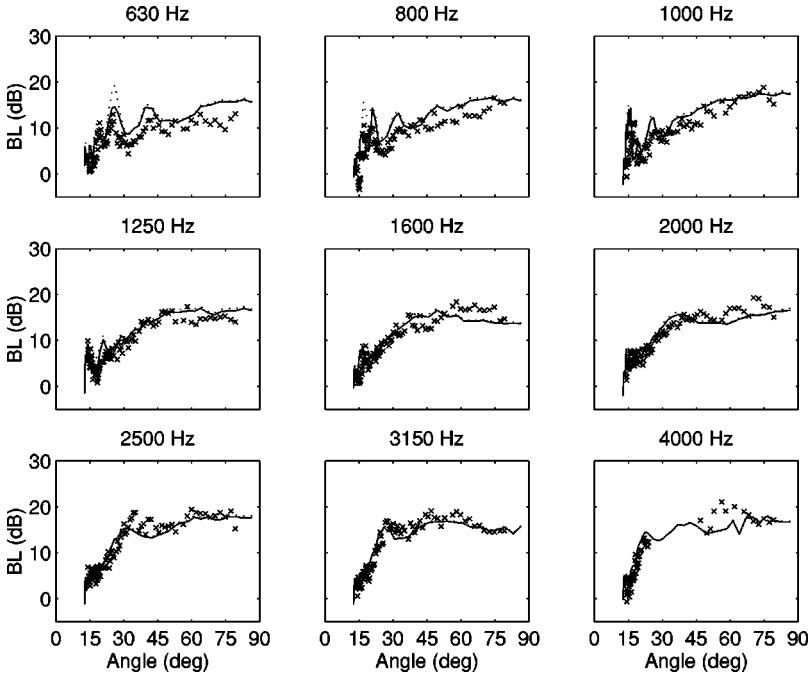

FIG. 14. Bottom loss data (×) and model predictions for upper 24 m: dashed line uses initial attenuation estimate (see Table I); solid line is modified attenuation (see Table IV).

Table II (second layer). The resulting prediction (dotted line) in Fig. 11 is considerably better, especially at higher frequencies.

An even higher quality geoacoustic model was desired which led to a sensitivity study. The sensitivity analysis showed that the bottom loss was very sensitive to density gradients in the first layer. Since the first layer has such a low velocity indicative of a very soft silty clay, a large gradient could be suggestive of the transition from a suspension to a sediment. Figure 12 shows the predictions using a linear density profile from 1.15–1.30 g/cc in the first layer (red line); note that the fit is now quite good across angle and frequency. Some of the details in angular dependence are exceptionally well-modeled. That the bottom loss was sensitive to the density gradient was a somewhat surprising result inasmuch as density gradients are often assumed to be unimportant in geoacoustic modeling [e.g., Rutherford and Hawker (1978)]. Corresponding to the density gradient, there is almost certainly a velocity gradient. The predictions, however, are not sensitive to typical velocity gradients (less than 10 s^{-1}) in the upper layer. The predictions are sensitive to very large velocity gradients of order 50 s^{-1}. For such large gradients, the model predicts higher peaks in the bottom loss near 30° at 2500 and 3150 Hz in even greater accord with the measurements (see black line of Fig. 12). An analysis of sensitivity to attenuation for this three layer model indicated that Hamilton values were an upper bound. In other words, higher attenuation values gave poorer fits (especially at low angles and high frequencies), but lower values did not change the prediction at all. In general, for such short path lengths (3 m to last reflecting horizon in the window) the model is not very sensitive to attenuation.

With the geoacoustic model thus obtained for the upper 3 m, the next two layers from Table I are now added as shown in Table III. Figure 13 shows bottom loss data integrated to 6-m depth in sub-bottom with the corresponding predictions. The predictions are quite good across angle and frequency, indicating that the geoacoustic model is reasonable. Note for example the capability of the model to predict the low angle interference pattern caused by interference between reflections from the two higher-speed layers. Also, note the excellent predictions from 2000 and 3150 Hz. A sensitivity analysis for attenuation in the upper 6 m indicated again that the Hamilton values were an upper bound.

Next, the bottom loss data over the upper 24 m are analyzed. The initial geoacoustic model is obtained by adding the next five lower layers from Table I onto Table III. Model predictions (dotted line) are shown in Fig. 14. Overall, the predictions are reasonable. A sensitivity study of the attenuation, however, indicated that the attenuation in the lower layers was too high. The data were fit better by lower attenuation values (solid line) as given in Table IV, although there is not enough information to extract the structure of the attenuation profile over the lower 20 m. The attenuation values given in Table IV should be viewed as an averaged value over this part of the sediment column.

In order to demonstrate the sensitivity of the data to the fine-scale layering structure, Fig. 15 shows the model predic-

TABLE IV. Geoacoustic model for upper 24 m based on bottom loss analysis.

Thickness (m)	Depth (m)	Velocity (m/s)	Density (g/cc)	Attenuation (dB/m/kHz)
0.5	0.5	1470–1502	1.15–1.30	0.07
0.6	1.1	1551	1.58	0.1
2.2	3.3	1516	1.48	0.09
1.5	4.8	1527	1.51	0.1
0.8	5.6	1591	1.68	0.4
5.6	11.2	1525	1.50	0.1
4.3	15.5	1582	1.66	0.015
3.5	19	1604	1.71	0.015
3.0	22	1648	1.81	0.015
1.7	23.7	1656	1.83	0.015
…		1612	1.73	0.015

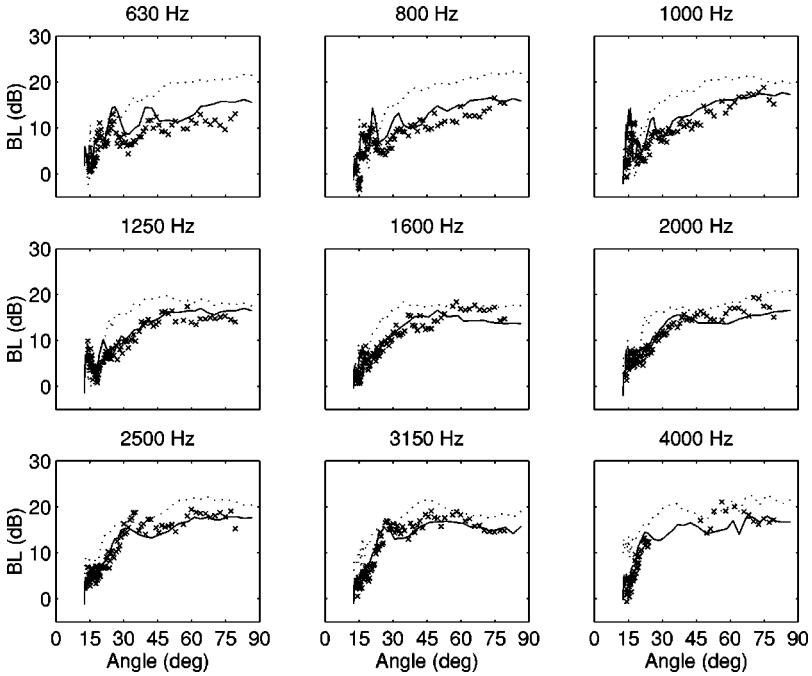

FIG. 15. Bottom loss data (×) and model predictions for upper 24 m: solid line is with all layers (see Table IV); dotted line is with the intercalating layers (layers 2 and 5) removed.

tions with (solid line) and without (dotted line) the two near-surface thin intercalating layers (layers 2 and 5). The point is that the bottom reflectivity is very sensitive to these layers. If the fine-scale layers were not included in the analysis, the resulting geoacoustic inversion would yield ''effective parameters'' rather than ''geoacoustic properties.''

C. Time-domain synthetics

The resulting geoacoustic model can now be tested and refined by returning to analyses in the time domain. Figure 16 shows the synthetic seismogram (using the geoacoustics from Table I) for the upper 24 m of sediment which can be compared with the measured data of Fig. 17. Concentrating on the data at positive offsets, it can be seen that the synthetics give a reasonable match. The data on the negative offsets have a lower level due to the source asymmetry (source sled tilt). The ''arrivals'' with a hyperbolic shape between the direct path (0.008 s^2) and the bottom bounce (0.012 s^2) are due to the low frequency source ringing. The apparent ring-

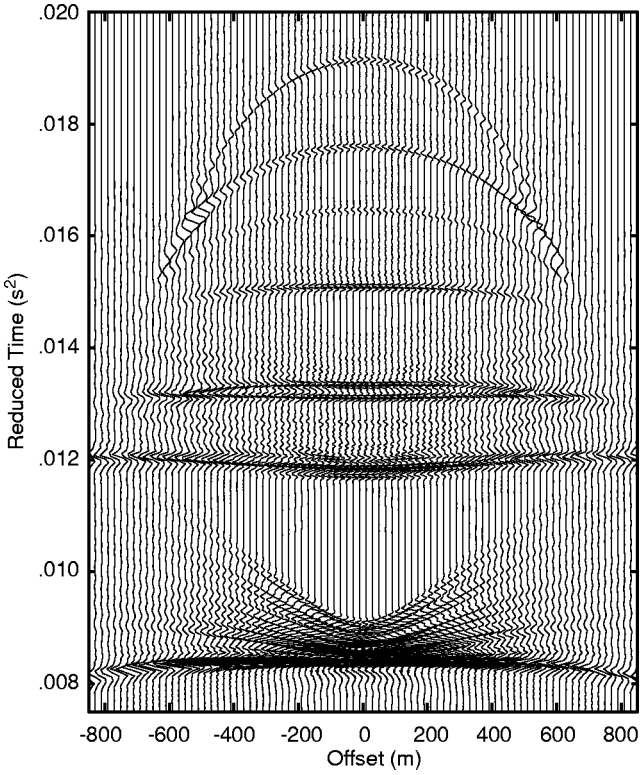

FIG. 16. Synthetic seismogram for upper 24 m of sediment using inputs from Table IV.

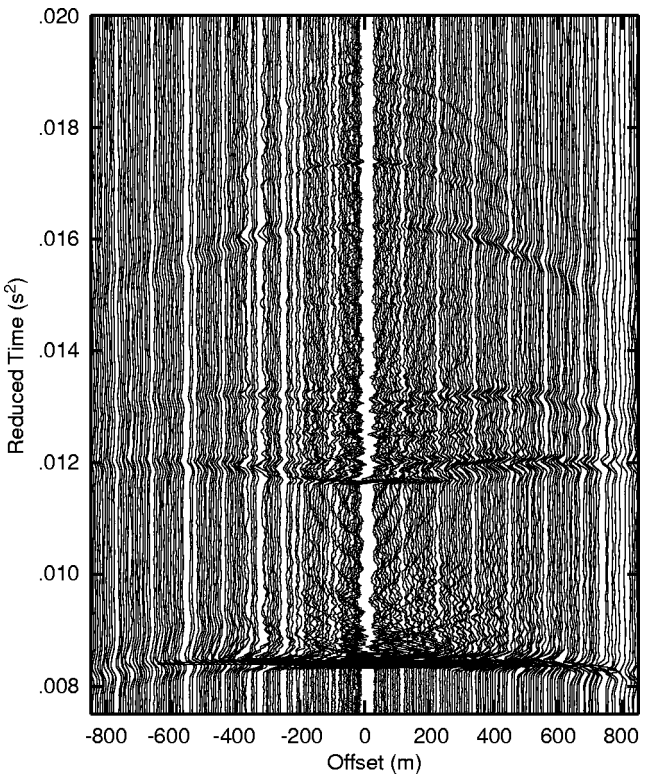

FIG. 17. Wide-angle seismogram for upper 24 m of sediment.

TABLE V. Geoacoustic model for upper 24 m based on time domain and bottom loss analysis.

Thickness (m)	Depth (m)	Velocity (m/s)	Density (g/cc)	Attenuation (dB/m/kHz)
0.5	0.5	1470–1502	1.15–1.30	0.07
0.6	1.1	1551	1.58	0.1
2.2	3.3	1516	1.48	0.09
1.5	4.8	1527	1.51	0.1
0.8	5.6	1591	1.68	0.4
9.5	15.1	1555	1.60–1.70	0.015
0.2	15.3	1674	1.91	0.1
3.5	18.8	1604	1.71	0.015
3.0	21.8	1648	1.81	0.015
1.7	23.5	1656	1.83	0.015
0.2	23.7	1720	1.94	0.1
⋯		1612	1.73	0.015

ing in the synthetics is of a shorter duration than for the data simply because the source waveform was truncated to about 5 ms.

While the synthetics capture the general characteristics, there are several details which can be improved. Note in the synthetics that the layer reflectivity at 0.015 s^2 is too strong and that of the following layer (at 0.016 s^2) is too weak. For this latter layer, there was no reasonable combination of density, attenuation, and sound-speed gradient that would adequately match the measured data. Our interpretation is that there is a thin (smaller than the pulse resolution) high-impedance layer at this horizon separating an otherwise homogeneous sediment. The existence of such a layer is consistent with the depositional history observed in the upper sedimentary layers, where alternating layers of mud and shelly sand were observed probably related to eustatic variations. The properties of the layer were obtained by trial and error. The modification to the geoacoustic model of Table V yields a more satisfactory seismogram as shown in Fig. 18.

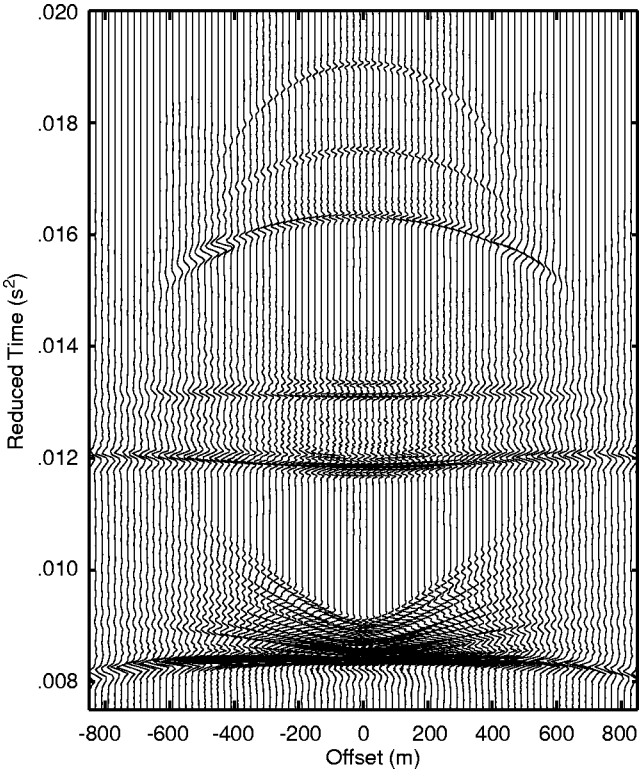

FIG. 18. Synthetic seismogram for upper 24 m of sediment using inputs from Table V.

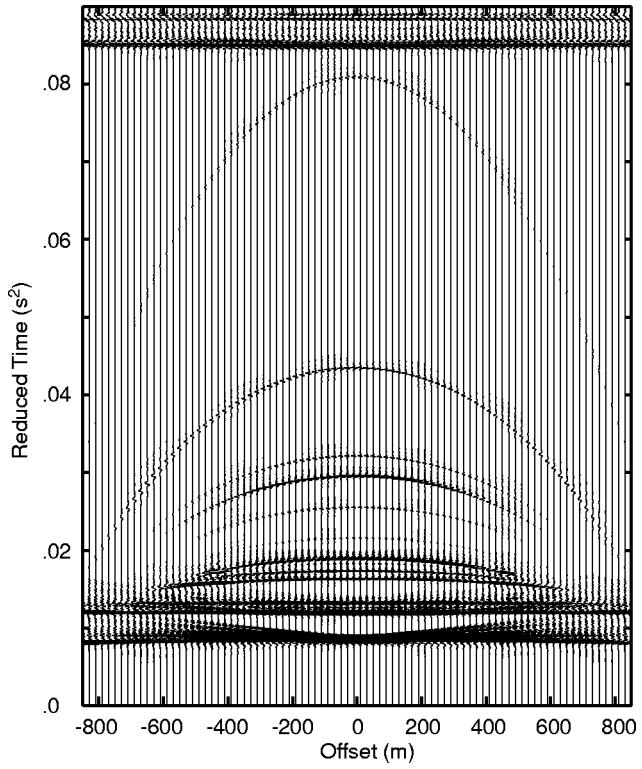

FIG. 19. Synthetic seismogram for upper 150 m of sediment using inputs from Table VI.

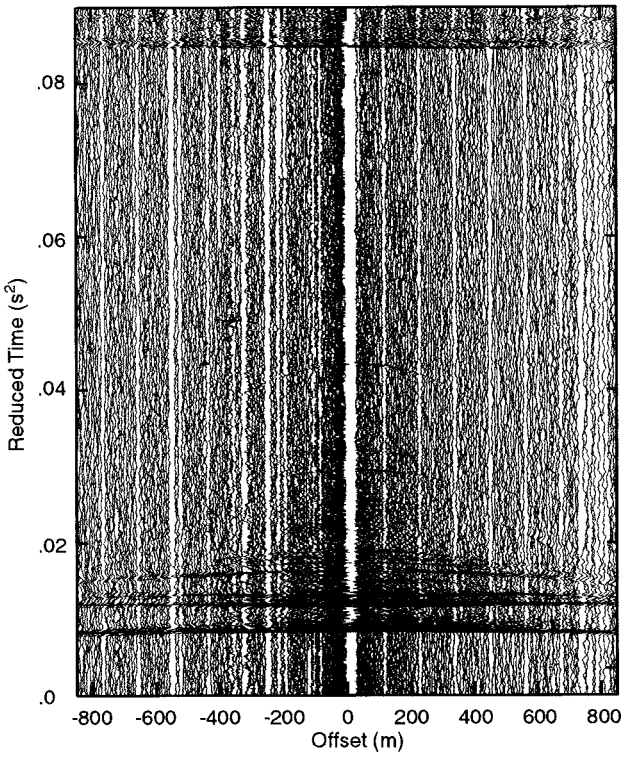

FIG. 20. Wide-angle seismogram for upper 150 m of sediment.

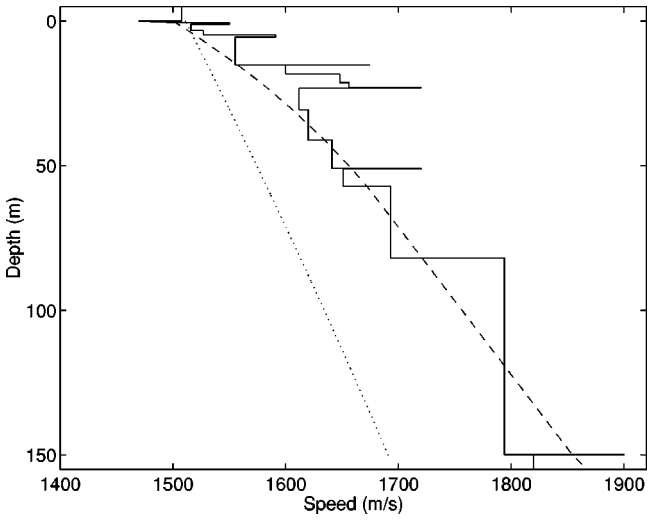

FIG. 21. Interval velocity structure from the inversion (solid stair-step line) compared with Hamilton's empirical equation (dotted line) and a fit through the center of the layers (solid curved line) that appear to be the same sediment type.

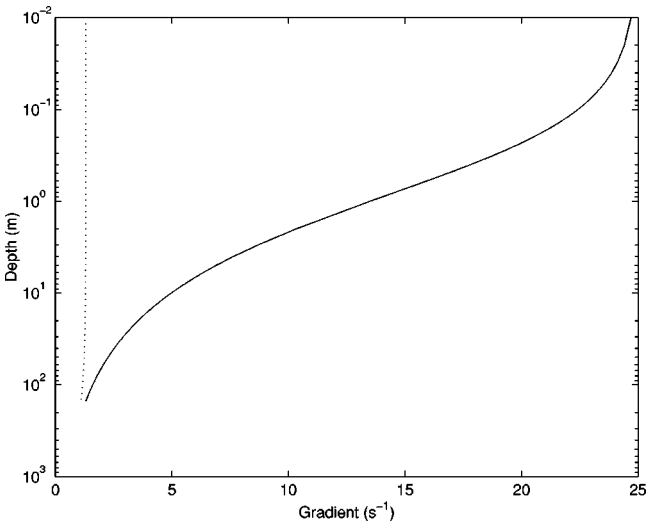

FIG. 22. Sound-speed gradient from Hamilton's deep-water empirical equation (dotted line) compared with the smoothed inversion from this study (solid line).

This modified geoacoustic model also fits the bottom loss data.

Below 24-m sub-bottom, the cumulative bottom loss (greater than 630 Hz) is no longer sensitive to sediment parameters. However, a comparison of the measured and synthetic seismograms can be used to refine the geoacoustic model. The strength of the reflectors observed in the data at several horizons suggests (just as in the analysis in the upper 24-m sub-bottom) the presence of thin sandy intercalating layers. Thus, the picture emerges of a relatively homogeneous silty clay (with gradients induced by overburden pressure) and interspersed sandy layers that provide sufficient velocity contrast for a reflecting horizon to be visible in the seismic data.

Figures 19 and 20 show the synthetic and measured seismograms, respectively, for the entire observable arrival structure (to 150-m sub-bottom). The surface multiple is seen at about 0.08 (s^2).[10] Note that the curvature of each layer is well-modeled, meaning that the velocity structure is correct. Thin intercalating layers have been inserted at the appropriate points. Their existence is strongly evident in the data; however, their geoacoustic characteristics (thickness, sound speed, density, and attenuation) are not particularly well constrained. The final geoacoustic model is shown in Table VI.

Figure 21 shows the inverted interval velocity along with the empirical depth function suggested by Hamilton (1980) for deep-water terrigenous sediments (silt clays, turbidites, mudstone shale). Note that in this shallow-water environment the sound-speed gradients, are considerably higher than the Hamilton model allow, especially near the water–sediment interface. An alternative fit to the interval velocity is also shown which was based on a form for the sediment sound speed $c(z)$ as proposed by Spofford *et al.* (1983)

$$c(z)=c_0[(1+\beta)(1+2g_0z/(c_0(1+\beta)))^{1/2}-\beta], \qquad (5)$$

where z is depth in meters, c_0 is the speed at the top of the sediment, g_0 is the initial gradient, and β is a parameter that controls the curvature. For the fit in Fig. 21 we have used $c_0=1470$ m/s (from the inversion results), $g_0=25\,\mathrm{s}^{-1}$, and $\beta=0.986$. Figure 22 shows a quantitative comparison of the depth dependence of the sound-speed gradient from the fitted model and the Hamilton empirical equation.

D. Ground truthing

It would be desirable to compare the geoacoustic model of Table VI with independent ground truth. However, there does not exist any reliable ground-truthing method for the complete model, to 150 m in sub-bottom depth. One potential means is by coring; however, coring has limitations because the sediment fabric is often disturbed by the coring operation as well as by postcore handling. Also, core velocity measurements are prone to error because they are taken at

TABLE VI. Geoacoustic model for upper 150 m based on time domain and bottom loss analysis.

Thickness (m)	Depth (m)	Velocity (m/s)	Density (g/cc)	Attenuation (dB/m/kHz)
0.5	0.5	1470–1502	1.15–1.30	0.07
0.6	1.1	1551	1.58	0.1
2.2	3.3	1516	1.48	0.09
1.5	4.8	1527	1.51	0.1
0.8	5.6	1591	1.68	0.4
9.5	15.1	1555	1.60–1.70	0.015
0.2	15.3	1674	1.91	0.1
3	18.3	1604	1.71	0.015
3	21.3	1648	1.81	0.015
1.7	23	1656	1.83	0.015
0.2	23.2	1720	1.94	0.1
7.5	30.7	1612	1.73	0.015
10.4	41.1	1620	1.75	0.015
9.9	51	1641	1.8	0.015
0.2	51.2	1720	1.94	0.1
6	57.2	1651	1.82	0.015
24.7	81.9	1693	1.9	0.015
68	149.9	1794	2.04	0.015
0.2	150.1	1900	2.2	0.1
…		1820	2.06	0.015

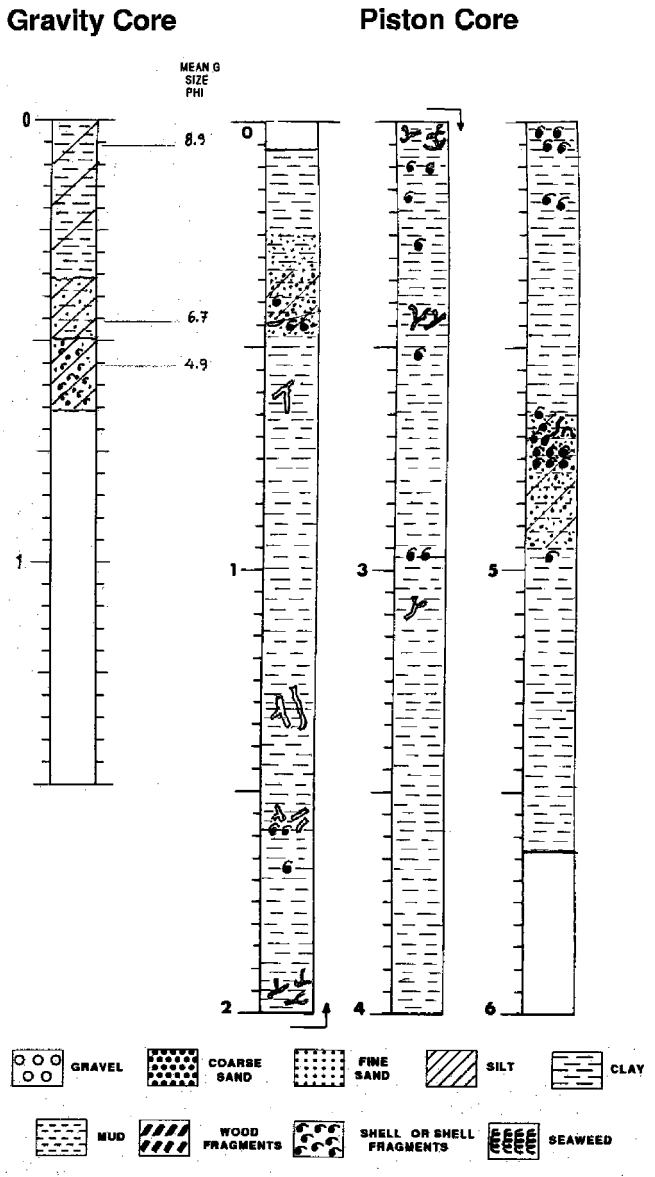

FIG. 23. Core lithologies at site 2. Core 3637 is a short gravity core; core 3638 is a piston core. Note that the top layer is compressed in the piston core relative to the gravity core. That is, the shell layer appears shallower in depth in the piston core.

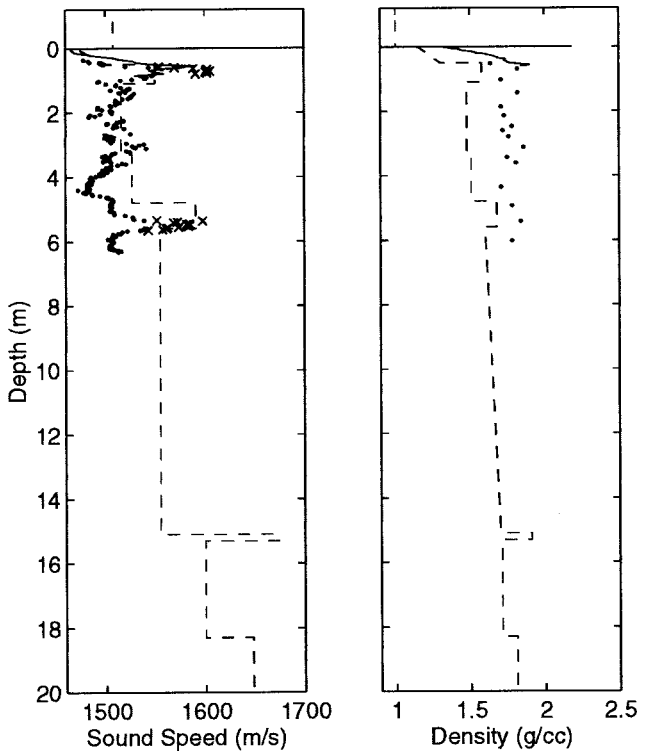

FIG. 24. Comparison of inversion results (dashed line) with piston core (dots) and wide-barrel gravity core (solid line) measurements. The sound measurements were conducted at 200 kHz and in the shelly sand layers at 50 kHz (×). The water column values of density and sound speed are shown above the water–sediment interface (0 m).

much higher frequencies (200 kHz and in some cases 50 kHz) and suffer from scattering from small pebbles and shell fragments. Thus, core data can be considered as valuable additional information, but not necessarily ground truth.

Two cores were taken at this site (within 100 m of the array location), a wide diameter, thin-walled 1-m gravity core specially designed to minimize disturbance of the sediment and an 8-m piston core intended for deeper penetration with greater likelihood of sediment disturbance. Sound-speed and magnetic susceptibility measurements were conducted shortly after the cores were collected. The gravity core measurements were conducted with the core vertical; the length of the piston core necessitated a horizontal measurement geometry. The lithology of the cores is shown in Fig. 23, which shows a predominantly mud bottom with intercalating layers of shelly sand with some coral fragments.[11] Comparison of the depth of the sandy layer (at 35 cm in the gravity core versus 25 cm in the piston core) indicates that about 10 cm of sediment at the top of the piston core were lost. The magnetic susceptibility measurements were employed to correct the piston core depths for core compression and loss of material in the upper part of the core [for details, see Osler *et al.* (1999)]. The corrected depths were applied to sound speed and density data, but not to the lithology.

Several months after collection, the cores were split, logged, and measured for mass properties (including density). Some of the cores showed evidence of settling from 2–4 cm over this time period. Therefore, the velocity measurements are the most reliable in terms of minimal core disturbance caused by handling. In the shelly layers, the shells were quite large, having length scales on the order of 2–4 cm; the largest had an area of about 6 by 6 cm. Since these densely packed inclusions are larger than a wavelength (even for the 50-kHz data), the velocity measurements in the shelly layers are probably not reliable.

Figure 24(a) compares the sound-speed inversion results with the core measurements. There are a number of promising similarities between the inversion results and the core data. First, both show the 50-cm low-speed layer at the water–sediment interface. Both also show large gradients in this layer, although the measured gradients are even larger than the inversion results. Second, note the manifestation of the high-speed shelly layers in both the inversion and the core data. Since the core velocity measurements are probably contaminated in this layer, a quantitative comparison cannot be made, except to say that the sub-bottom depths are in good agreement. Between the two shelly layers the inversion

and core sound speeds compare quite favorably. Below the shelly layer at 6 m the core measurements are lower than the inversion results. However, the inversion results represent an interval velocity over the entire 9.5-m layer, and the core data do not extend deep enough into the sediment to make a just comparison.

The density inversion and core measurements are shown in Fig. 24(b). Note that the density gradient (crucial for the good model-to-data agreement in Fig. 12) also appears in the core data. Two main differences between the inversion and core results should be noted. First, there is an overall bias between the inversion and core densities. The reason for this bias is not fully understood; however, it is possible that the core densities may be higher due to compression during the coring process and/or core disturbance during transportation and storage. Second, note that the piston core-density measurements show less contrast between the shelly sand and the silty clay layers than the inversion. This is probably due to the fact that the core-density measurements are conducted from a sample size smaller than the shell and coral fragments (i.e., do not include shell and coral fragments) and thus do not give an accurate measurement of the bulk sediment properties.

V. SUMMARY

A method has been presented for obtaining high-resolution geoacoustic properties from the seafloor. The high resolution in depth stems from using a short pulse, with a dense spatial sampling over a fairly short aperture (of order several hundred meters). Layers of order 50 cm were identified and geoacoustic data were recovered to depths greater than 100 m. The best quality data were extracted from the upper 24 m. In general, depth of penetration will be depend on the sub-bottom structure with a maximum penetration of the difference between source and receiver depths.

The short measurement aperture means that the measurements are ''local,'' i.e., they are applicable over a confined area. A later paper will explore the potential for extrapolating these local measurements to regional scales using seismic data to connect various sites. However, the short aperture will actually be advantageous for some applications, e.g., geoacoustic properties extraction in support of direct path scattering measurements where the spatial averaging typical of long-range geoacoustic inversion approaches should be avoided.

The strength of the method lies in the wide range of data employed: including the time, frequency, and spatial domains. Using as much independent data as possible provides the basis for inversion of geoacoustic properties rather than effective parameters. Core velocity and density data in the upper 6 m compared favorably with the inverted data.

The geoacoustic properties of this shallow-water site offered several important insights. First, a large density gradient in the upper layer had a measurable influence upon reflection. This is significant because often density gradients are ignored in geoacoustic modeling. Second, sound-speed gradients appear to be much larger in this shallow-water environment than the Hamilton empirical equations would suggest, especially in the upper part of the sediment column. Near-surface (within the first meter) velocity and density gradients were extremely large, approximately 150 s^{-1} and 1.2 g/cc/m, respectively.

ACKNOWLEDGMENTS

We gratefully acknowledge the North Atlantic Treaty Organization as sponsoring agency of this work. We also wish to acknowledge the captain, officers, crew, and the entire scientific crew aboard the NRV ALLIANCE who managed the ship maneuvers and data collection effort with adeptness and aplomb. We express particular appreciation Mr. Luigi Troiano and Mr. Piero Boni, whose engineering and data acquisition skills and initiative were crucial to the success of the experiment. Special thanks to Mr. Reg Hollett for help in the bottom loss data processing.

APPENDIX

A. Theory

Following Bryan (1974, 1980) and Claerbout (1978), consider a homogeneous layer of velocity, v_i, bounded by reflectors at depths, h, and $h+h_i$. As with Dix (1955) and Le Pichon *et al.* (1968), it is assumed that velocity is a function of depth only. A given ray parameter, p, defines a path to each reflector (Fig. A1). In the ray-parameter approach, these two paths are not associated with the same value of x (as would be the case in the Dix method), but rather with the same value of p, and above h, they are everywhere parallel. Thus, the contribution from the structure above h has canceled out because of the choice of paths. The difference in travel time and offset for these two paths is

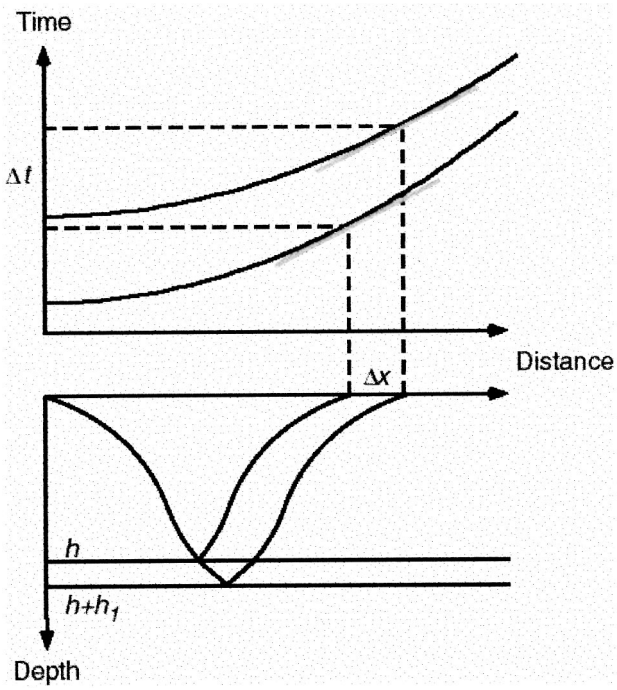

FIG. A1. Schematic diagram of the ray-parameter method (after Bryan, 1974). Note that the two ray paths are everywhere parallel above the first reflector at depth h.

$$\Delta x(p) = 2\int_{h}^{h+h_i} pv/\sqrt{1-p^2v^2}\,dh$$

and (A1)

$$\Delta t(p) = 2\int_{h}^{h+h_l} 1/(v\sqrt{1-p^2v^2})\,dh.$$

For a uniform velocity in the layer, v_i, Eqs. (A1) can be integrated to give

$$\Delta x = 2pv_i h_i/\sqrt{1-p^2v_i^2} \quad \text{and} \quad \Delta t = 2h_i/v_i\sqrt{1-p^2v_i^2}, \tag{A2}$$

which can be solved for the velocity and thickness of the layer,

$$v_i = \sqrt{\frac{\Delta x}{p\Delta t}} \quad \text{and} \quad h_i = \frac{v_i \Delta t\sqrt{1-p^2v_i^2}}{2}. \tag{A3}$$

B. Implementation

For a horizontally layered medium, it is common practice to express the squared travel time, t^2, for a reflected signal as an infinite series of the squared source–receiver offset, x^2,

$$t^2 = a_1 + a_2x^2 + a_3x^4 + a_4x^6 + \cdots, \tag{A4}$$

where the coefficients $a_1, a_2, a_3, a_4, \ldots$, are functions of h_i and v_i, $i = 1,2,3,4,\ldots,n$, the layer thicknesses and interval velocities. Following Taner and Koehler (1969), Eq. (A4) can be written as

$$t^2 = t_0^2 + x^2/v_{\text{rms}}^2 + O(x^4), \tag{A5}$$

where $t_0 = \Sigma\Delta t_i$ is the zero-offset travel time (the sum of the zero-offset travel times of the individual layers comprising the velocity structure) and v_{rms} is defined above. Within a limited horizontal source–receiver offset, the $t-x$ relation can be approximated by the simple hyperbolic formula

$$t^2 = t_0^2 + x^2/v_{\text{ST}}^2, \tag{A6}$$

where v_{ST} is the stacking velocity. For a given wide-angle reflection, v_{ST}^2 corresponds to the slope of a least-squares fit through the travel times in a plot of t^2 versus x^2. The bias between v_{ST} and v_{rms} is a complicated non-negative function of the velocity and thickness of the component layers. It increases in magnitude with increasing heterogeneity in the velocity structure and with increasing ray parameter. The bias may be reduced by including a fourth-order term in the $t-x$ polynomial [Eq. (A4)]; however, this increases the variance in the estimate of v_{rms}. This is of particular concern in the Dix method, which requires that values of v_{rms} be provided for the wide-angle reflections which bound the layer under consideration.

The Bryan method does not presuppose any functional relationship for the $t-x$ curves, requiring instead that values of Δx and Δt be determined for a given bounding pair of wide-angle reflections at a specified value of p. However, the use of the hyperbolic formula [Eq. (A6)] to define the functional relationship for wide-angle reflections in the Bryan method leads to a straightforward analytical implementation. At the tangent point, the travel time for a hyperbola and an intersecting line with slope p are equal. In addition, p is equal to the derivative of the hyperbola. This set of equations may be solved for the horizontal offset at the tangent point, x_T, and a zero-offset travel time. For a given pair of wide-angle reflections, the interval velocity, v_i, and layer thickness, h_i, may be determined using $\Delta x = x_{T_{i+1}} - x_{T_i}$ and $\Delta t = b_{i+1} - b_i$. Solutions can, and are, repeated for several values of p. With this approach, errors tend to be larger as p approaches its minimal and maximal value. In the former case, this is because the values of Δx are very small and in the latter case, because it is increasingly rapidly.

As wide-angle reflections are represented by hyperbolas [Eq. (A6)] the maximum horizontal offset that is used must be selected with care. In order to work at larger horizontal source–receiver offsets, the use of a fourth-order polynomial to represent the $t-x$ curves was pursued. However, there are no straightforward analytical solutions to the system of equations described above and numerical solutions using Newton's method were prone to finding local minima. An alternate approach, therefore, was also to consider the maximum horizontal source–receiver offset which could be employed when testing the layer thickness and velocity resolution capabilities of the Bryan method with synthetic data.

C. Testing

A number of test geoacoustic models were constructed and are described in detail in Osler *et al.* (in press). They all included a water depth of 150 m (characteristic of the depths in which SACLANTCEN shallow-water experiments have been conducted) underlain by a seabed comprised of multiple isovelocity layers, including cases with low velocity zones. The thickness of the three seabed layers was varied in unison from 50 to 1 m, yielding water-depth-to-layer-thickness ratios ranging from 3 to 150. For each geoacoustic model, theoretical travel times are calculated and then subjected to the analysis procedure outlined above.

Test results in Bryan (1974) using synthetic data indicate that solutions using the exact ray-parameter method deteriorate for thickness ratios of 100 or greater due to increasing relative error in Δx [Eq. (3)] as Δx itself decreases with layer thickness. Further, his experience with real data suggest the method was useful up to thickness ratios of 25 and that another method, the thin layer approximation, should be used for thickness ratios greater than 50. When an appropriate horizontal source–receiver offset is selected, our test results suggest that the exact ray-parameter method is well behaved over a wider range of thickness ratios. The discrepancy between test results likely stems from different implementations of the method. Unfortunately, Bryan provides few details, but a potential explanation is that our analytical implementation serves to minimize errors in Δx.

[1]By shallow water we generally mean continental shelf regions; however, it can mean by extension any bottom-limited region.

[2]The inversion technique is capable of including shear waves. However, for the environment examined in this paper, shear waves contributed negligibly and thus are not included in the geoacoustic model.

[3]The scattering from sub-bottom sediment volume inhomogeneities requires

substantially higher resolution in the geoacoustics than does the propagation.

[4]The data quality on all of the hydrophones was very good. The deepest hydrophone was selected because it provides the longest time window (i.e., greatest sub-bottom penetration) for analysis, i.e., the longest time before the second bottom bounce arrives. The amount of sub-bottom penetration is limited by the difference between source and receiver depths.

[5]Integration times vary depending upon source–receiver offset. All integration times are given referenced to the value at normal incidence.

[6]Thus, the 8.5 rms error for the array position does not affect our analysis results.

[7]At low frequencies (roughly below 1 kHz) the Uniboom is omnidirectional, and at high frequencies (very roughly above 5 kHz but strongly dependent upon sediment properties) the sub-bottom paths contribute negligibly because of attenuation.

[8]The attenuation is derived from the porosity which is estimated using the Bachman (1985) relation between velocity and porosity.

[9]The usual angle averaging was not done.

[10]That is, the pair of paths that have interacted with the bottom once and then the sea surface.

[11]The shells and shell fragments were bivalves (from the *Tellinid* and *Pettinid* families) and prosobranches (*Turritellid* and *Vermetid* families). The coral fragments were *Arborascente*.

Bachman, R. T. (**1985**). ''Acoustic and physical property relationships in marine sediments,'' J. Acoust. Soc. Am. **78**, 616–621.

Bryan, G. M. (**1980**). ''The hydrophone-pinger experiment,'' J. Acoust. Soc. Am. **68**, 1403–1408.

Bryan, G. M. (**1974**). ''Sonobuoy measurements in thin layers,'' in *Physics of Sound in Marine Sediments*, edited by Lloyd Hampton (Plenum, New York), pp. 119–130.

Chapman, N. R., Bannister, R. W., and Falconer, R. K. H. (**1990**). ''The effect of an elastic basement in the interpretation of bottom loss data,'' J. Acoust. Soc. Am. **87**, 2044–2050.

Claerbout, J. F. (**1978**). ''How to derive interval velocities using a pencil and a straight edge,'' Stanford Exploration Project Report No. 14.

Dix, C. H. (**1955**). ''Seismic velocities from surface measurements,'' Geophysics **20**, 68–86.

Hamilton, E. L. (**1980**). ''Geoacoustic modeling of the seafloor,'' J. Acoust. Soc. Am. **68**, 1313–1339.

Hermand, J. P., and Gerstoft, P. (**1996**). ''Inversion of broadband multi-tone acoustic data from the YELLOW SHARK Summer Experiments,'' IEEE J. Ocean Eng. 324–346.

Holland, C. W., and Neumann, P. (**1998**). ''Sub-bottom scattering: A modeling approach,'' J. Acoust. Soc. Am. **104**, 1363–1373.

Le Pichon, X., Ewing, J., and Houtz, R. E. (**1968**). ''Deep-sea sediment velocity determination made while reflection profiling,'' J. Geophys. Res. **73**, 2597–2614.

Osler, J. C., Holland, C. W., and Fracassi, U. (**2000**). ''High-resolution velocity inversion from shallow water wide angle seismic reflection measurements,'' SACLANTCEN Memorandum SM-353 (in press).

Osler, J. C., Gualdesi, L., Michelozzi, E., and Tonarelli, B. **(1999)**. ''Piston coring capabilities at SACLANTCEN: minimizing and assessing core disturbance,'' SACLANTCEN Report SR-321.

Rutherford, S. R., and Hawker, K. E. (**1978**). ''Effects of density gradients on bottom reflection loss for a class of marine-sediments,'' J. Acoust. Soc. Am. **63**, 750–757.

Spofford, C. W., Greene, R. R., and Hersey, J. B. **(1983)**. ''The estimation of geoacoustic ocean sediment parameters from measured bottom-loss data,'' SAIC Technical Report 83-879-WA, McLean, VA.

Spofford, C. W. (**1980**). ''Inference of geo-acoustic parameters from bottom loss data,'' in *Bottom-Interacting Ocean Acoustics*, edited by W. A. Kuperman and F. B. Jensen (Plenum, New York).

Stickler, D. C. (**1977**). ''Negative bottom loss, critical angle shift, and the interpretation of the bottom reflection coefficient,'' J. Acoust. Soc. Am. **61**, 707–710.

Taner, M. T., and Koehler, F. (**1969**). ''Velocity spectra-digital computer derivation of velocity functions,'' Geophysics **34**, 859–881.

Westwood, E. K., and Vidmar, P. J. (**1987**). ''Eigenray finding and time series simulation in layered bottom ocean,'' J. Acoust. Soc. Am. **81**, 912–924.

Yagle, A. E., and Levy, B. C. (**1984**). ''Application of the Schur algorithm to the inverse problem for a layered acoustic medium,'' J. Acoust. Soc. Am. **76**, 301–308.

Target strength of an oily deep-water fish, orange roughy (*Hoplostethus atlanticus*) II. Modeling

Sam McClatchie[a]
National Institute of Water and Atmospheric Research Ltd., P.O. Box 14901. Kilbirnie, Wellington, New Zealand

Zhen Ye
Department of Physics and Center for Complex System Studies, National Central University, Taiwan, Republic of China

(Received 23 February 1998; revised 17 August 1999; accepted 16 November 1999)

Orange roughy consist of ~18% lipids by weight, mostly as wax esters, and the lipids must be taken into account when modeling target strength. A deformed cylinder model incorporating the effect of temperature and pressure on sound speed through wax ester was used to scale experimental measurements of target strength to the temperatures and pressures where orange roughy live (~6 °C, depths ~800–1300 m). The effect of decreasing temperature and increasing pressure is to increase the sound speed in orange roughy lipids. Modeling shows that the net effect of this is to reduce tilt-averaged target strength, $\langle TS \rangle$, by ~2 dB. Adjusting experimental results to compensate for temperature and pressure effects gives a predicted $\langle TS \rangle$ for a 35-cm orange roughy of −48.3 dB. Adjusting *in situ* estimates of orange roughy $\langle TS \rangle$ for avoidance behavior [McClatchie *et al.*, J. Acoust. Soc. Am. **106**, 131–142 (1999)] suggests the correct $\langle TS \rangle$ is ~−47.5 dB, rather than −50 dB as previously reported [Kloser *et al.*, ICES J. Mar. Sci. **54**, 60–71 (1997)]. We conclude that experimental and *in situ* estimates now converge at a $\langle TS \rangle$ of ~−48 dB for a 35-cm fish. © *2000 Acoustical Society of America.* [S0001-4966(00)05302-9]

PACS numbers: 43.30.Sf, 43.30.Ft [SAC-B]

INTRODUCTION

Orange roughy (*Hoplostethus atlanticus*) are the subject of a valuable deep-water fishery in New Zealand waters. Echo integration survey techniques are now being applied to estimate the biomass of orange roughy. The accuracy of the relationship predicting tilt-averaged target strength, $\langle TS \rangle$, from fish length has an important effect on the accuracy of the biomass estimate. At present, there is some debate as to what the most accurate estimates of target strength are. Our method for obtaining reliable $\langle TS \rangle$ estimates of fish is to use three independent techniques: (1) experimental measurements on live fish,[1] (2) *in situ* estimates using a deep towed split beam echosounder, and (3) modeling that incorporates morphology and flesh characteristics. The modeling results for orange roughy $\langle TS \rangle$ are the subject of this paper. In this paper we refer to tilt-averaged target strength, or $\langle TS \rangle$, as the target strength averaged with respect to fish orientation for a given size of fish.

The target strength of orange roughy has been measured using a variety of methods and a wide range of results have been obtained (reviewed by Refs. 1 and 2). The principal reasons behind the discrepancies appear to be related to three factors. First, measurements made on dead fish are affected by changes in the fish body composition over time,[3] and the magnitude of these changes is compounded by using specimens that were previously frozen.[1] Consequently, measurements on dead orange roughy can be regarded as erroneous unless the measurements are taken after the fish tissue composition has stabilized.[1] Second, at least some of the differences between *in situ* and experimental measurements of target strength made on live orange roughy are due to differences in the orientation of the fish. These differences are exaggerated by the avoidance behavior of orange roughy to a transducer lowered close enough to the fish (i.e., within 150 to 100-m range) to estimate target strength directly.[4] The effect of avoidance must be incorporated into measurements of *in situ* $\langle TS \rangle$. Avoidance is not a problem during surveys because the transducer is farther from the fish than is the case during $\langle TS \rangle$ measurements. Third, both temperature and pressure affect the sound-speed ratio, which affects the target strength of orange roughy. These effects need to be considered when extrapolating experimental measurements made at the surface to the depths at which the fish are found in nature (800–1300 m).

The tissues of orange roughy have very high lipid content.[5–7] Unlike other swimbladder fish, for which the gas-filled swimbladder dominates the backscattering of sound, orange roughy store a large amount of semi-solid lipid in their swimbladders. From 66% to 90% of the tissue in the swimbladder is lipid.[8,9] The composition of the swimbladder lipid is 94%–99% wax esters.[7,10] These wax esters have low acoustic contrast to the water and as a result the target strength of orange roughy is low. Several other tissues also contain large quantities of lipid. The lipid content of whole orange roughy is ~18% by weight.[7,8,11]

We first describe the model used to estimate $\langle TS \rangle$ and then present new experimental measurements on the temperature and pressure dependence of sound speed through orange roughy lipids. We then compare the model $\langle TS \rangle$ with our previous experimental measurements of $\langle TS \rangle$ of live orange roughy. Next, we use the sound-speed measurements

[a]Electronic mail: s.mcclatchie@niwa.cri.nz

and the model to compensate for differences of pressure and temperature between the experimental conditions and orange roughy habitat. This allows us to extrapolate our experimental measurements of $\langle TS \rangle$ to the depths at which the fish are found in nature.

METHODS

The model

The Kirchhoff approximation has been used to model target strength of orange roughy.[2] Although it is relatively simple, we found it to be inaccurate, and consequently we use the deformed cylinder approximation. The sound scattering by an elongated target can be calculated using the approximation that regards the target as a slender body of revolution (the deformed cylinder, which in this case is a prolate spheroid). It assumes that a differential element of the target along the longitudinal axis is a small piece of cylinder, and it scatters sound as though it were a part of an infinite cylinder of the same radius. The total scattering function is then the sum of the scattering functions of each differential element. It can be written, following Ye *et al.*,[12] as

$$f(\mathbf{k}_i,\mathbf{k}_s)=\int dz \frac{-i}{\pi}\sum_{n=0}^{\infty} B_n(z)F_n(z)(-i)^n \times \cos(n\phi(z))e^{i\mathbf{k}_i\cdot\mathbf{r}(z)-i\mathbf{k}_s\cdot\mathbf{r}(z)}, \quad (1)$$

where the integration is done along the deformed cylinder axis, dz is a segment of the integration which can be a length element along the axis, $\mathbf{k}_i$ and $\mathbf{k}_s$ are incident and scattered wave vector, respectively, $i=\sqrt{-1}$, $B_n(z)$, and $F_n(z)$ are n-th order expansion coefficients including element radii which generally change along the axis. The expressions for $B_n(z)$ and $F_n(z)$ are given in Ye *et al.*[12] Both coefficients depend on the acoustic properties through the boundary conditions that are expressed in the values of the density and sound-speed ratios (g and h). The sound speed of the water surrounding the fish was calculated using Mackenzie's equation,[13] which incorporates the effects of temperature, pressure, and salinity on sound speed. $\phi(z)$ is the azimuthal angle between the incident and scattering directions, and $r(z)$ is the range from an arbitrary reference point.

The differential scattering cross section is defined as

$$\sigma(\mathbf{k}_i,\mathbf{k}_s)=|f(\mathbf{k}_i,\mathbf{k}_s)|^2, \quad (2)$$

and the backscattering cross section is given by

$$\sigma_{bs}=|f(\mathbf{k}_i,-\mathbf{k}_s)|. \quad (3)$$

The backscattering target strength is given by $TS=10\log_{10}\sigma_{bs}$.

The averaged target strength is related to the averaged backscattering cross section as

$$\langle TS\rangle = 10\log_{10}\langle\sigma_{bs}\rangle, \quad (4)$$

where $\langle\sigma_{bs}\rangle$ is averaged for the orientation distribution and is expressed by

$$\langle\sigma_{bs}\rangle=\int P(\theta)\sigma_{bs}(\theta)d\theta, \quad (5)$$

where $P(\theta)$ is the probability function for fish tilt orientation and θ is the incident angle (tilt angle), implicit in Eq. (1), with respect to the longitudinal axis of the target. TS_θ is the target strength at a particular angle, where $\theta=0$ corresponds to the dorsal aspect. The tilt angle distribution is approximated by a normal distribution with a standard deviation of 18.7°.[1] $TS_{\max}$ is the maximal target strength measured from a fish that is generally in near dorsal aspect (i.e., fish normal to the axis of the acoustic beam) but is often measured at an orientation angle that is offset from true dorsal aspect in both swimbladder and non-swimbladder fish.

The practical implementation of the deformed cylinder requires the following steps. First, the physical dimensions of the scatterer are recorded in a geometrical reference frame (see Morphological measurements section). The physical structure is dissected into a series of short cylindrical or approximately cylindrical segments, for which the cross section is approximated as circular, and the radius is the averaged value of the widths in two perpendicular directions. Third, the length of the segment replaces dz in Eq. (1), and for each i-th segment (denoted by dz_i), we compute the scattering and incident angles with respect to its axis and compute the coefficients $B_n(z_i)$ and $F_n(z_i)$. The scattering function for each segment is then calculated. The total scattering function is the summation of the scattering functions from individual segments. In this way, integration in Eq. (1) is approximated by the summation of a finite series.

We tested for the importance of scattering by wax ester by calculating the $\langle TS\rangle$ from the model of the fish body without wax ester and comparing it to experimentally measured $\langle TS\rangle$. We were unable to match the model and experimental $\langle TS\rangle$ values unless we used values for density and sound-speed contrast (g and h) in the model that were appropriate for wax ester. This led us to consider that the wax ester component must have a significant effect on the scattering.

We modeled the fish body as a fluid-filled prolate spheroid with length 35 cm, aspect ratio, $e=0.15$, insonified by a plane-wave of frequency 38 kHz which is the same as used in the experimental measurements. Aspect ratio, e, is defined as the ratio between the short and long semiaxes of the prolate spheroid. Sound speed in fish flesh was taken from Gytre.[3] We modeled the wax ester as a prolate spheroid shape located in the anterior one-third of the fish body, with the same aspect ratio as the fish body. We aligned the axis of the wax ester with that of the fish body.

Morphological measurements

A video camera was used to capture separate lateral and dorsal views of individual orange roughy (Fig. 1). To capture the dorsal images the thawed fish was placed on a clear perspex stand with the background scale raised 15 cm off the ground and level with the midline of the fish. The camera was then raised 15 cm to maintain the same magnification as in the lateral view. Images were sharpened and adjusted for contrast. Measurements were made along the longitudinal axis from the snout to the fleshy tip of the tail, excluding fin rays. These were done at 5-mm intervals for the head anterior to the gill covers and the tail posterior to the anus, and at 10-mm intervals for the rest of the trunk; these intervals de-

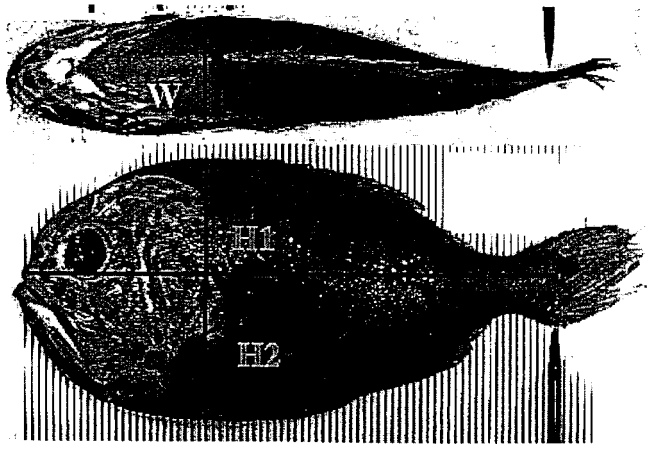

FIG. 1. An example of the video image of an orange roughy used to obtain measurements for modeling $\langle TS \rangle$. Measurements recorded were the maximum distance from the midline (drawn from the snout to the middle of the fleshy tip of the tail) to the dorsal surface ($H1$), and the maximum distance from the midline to the ventral surface ($H2$). The body width (W) was measured in dorsal view.

fine the length of the segments. For each position along the longitudinal axis three measurements were recorded (Fig. 1). These were from the lateral view, the height ($H1$) above a line (referred to as the midline) drawn from the snout to middle of the tail, the height ($H2$) below the midline, and the width of the body in dorsal view (W). The averaged radius for the segment is approximated as $(H1+H2)/2 + W/2$.

Sound-speed measurements

Sound speed was measured as a function of temperature and pressure in lipid extracted from two orange roughy. Fish were captured live (see McClatchie *et al.*[1]) and kept alive until just before they were used for lipid extraction. Their lipid was extracted using the method of Folch *et al.*[14] Lipid was extracted from the entire fish. Sound speed was measured over a range of temperatures and pressures.[15] For each pressure level, sound-speed measurements were made at a range of temperatures starting at ~20 or ~25 °C and decreasing the temperature in ~2 °C steps. The temperature range covered 20.0 down to 3.9°C for the first lipid sample and 25.8 down to 1.3 °C for a second lipid sample. The temperature was then increased again to 20 °C and several spot measurements were made at selected temperatures as the apparatus was cooled. Cycling the temperature in this manner served to test the heat stability of the lipid (which was found to be stable). The pressure range was 0 to 105 atm for the first sample and 0 to 120 atm for the second sample.

RESULTS

Comparison of experimental and modeling results

In Fig. 2, TS_θ for the fish body is plotted against the tilt angles for various density and sound-speed ratios, g and h. This shows that the overall target strength increases as g and h increase, but that the oscillatory structure in the scattering function does not vary with changes in g and h. We conclude that this oscillatory structure is purely a manifestation of the

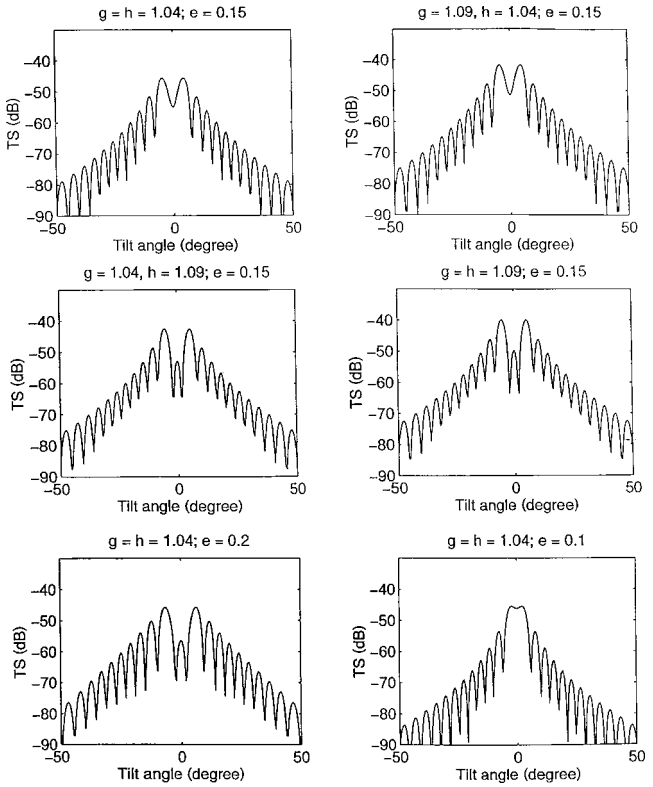

FIG. 2. Target strength (TS_θ) of the fish body (excluding the wax ester) for a 35-cm orange roughy as a function of angle of orientation (θ) estimated using the deformed cylinder model for different theoretical values of the density ratio (g), sound-speed ratio (h), *and* aspect ratio (e) of a prolate spheroid (see Table I).

scattering geometry. However, in order to make the model tilt-averaged target strength, $\langle TS \rangle$, match the experimentally measured $\langle TS \rangle$ for a 35-cm fish (≈ -46 dB[1]), we have to use 1.09 for the values of g and h, assuming that the fish body dominates the scattering (Table I). These values for g and h are unrealistic, given that measurements of g for fish flesh: seawater[16] and h for orange roughy lipid: seawater (from this study) mostly fall below 1.04. This result implies that the scattering by wax ester must be incorporated into the model. Consequently, we included both the fish body and the wax ester in subsequent model estimates of $\langle TS \rangle$.

The model was run on 19 fish. Seven of the 16 fish used in the live fish $\langle TS \rangle$ experiments were also used for modeling, so we were able to directly compare the model with experimental results for these fish (Fig. 3 and Table II). We made five comparisons between model and experimental results: (1) the magnitude of $\langle TS \rangle$, (2) the magnitude of $TS_{\max}$,

TABLE I. Estimates of $\langle TS \rangle$ (dB) calculated from a prolate spheroid model of a 35-cm-length orange roughy body without the wax ester (see Model section in Methods). $\langle TS \rangle$ was estimated for two different values of density and sound-speed ratios (g and h), as well as for three different values for the aspect ratio of the prolate spheroid *(e)* (see Fig. 2).

	$g=1.04$	$g=1.09$
$h=1.04$	-55 $(e=0.1)$	⋯
$h=1.04$	-52 $(e=0.15)$	-48 $(e=0.15)$
$h=1.04$	-54 $(e=0.2)$	⋯
$h=1.09$	-49 $(e=0.15)$	-46 $(e=0.15)$

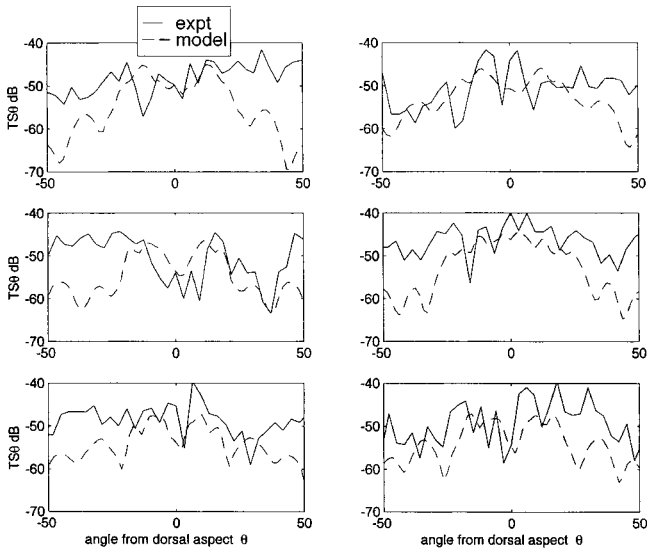

FIG. 3. Target strength as a function of fish tilt angle (TS_θ) calculated using the deformed cylinder model, including the wax ester, compared with experimental measurements made on the same live orange roughy (only six of the seven fish in Table II are shown). Positive angles represent head-up orientation in the pitch plane.

(3) the location of $TS_{\max}$ with respect to θ, (4) the correspondence of peaks and nulls in TS_θ, and (5) the $\langle TS\rangle$-length regression.

Model $\langle TS\rangle$ and experimentally measured $\langle TS\rangle$ were within 3 dB in six out of seven cases where we had model and experimental measurements on the same fish (Table II). In one case the model estimate was ~4 dB lower than the experimentally measured $\langle TS\rangle$. $TS_{\max}$ values did not correspond as closely between the model and the experimental results because the experimental data generally had sharper peaks and nulls than predicted by the model (Fig. 3). The pattern of peaks and nulls is not consistent between the model and the experimental results, although some coherence is evident (Fig. 3). Both the model and the experimental results show that $TS_{\max}$ does not necessarily occur at dorsal aspect orientation.

TABLE II. Tilt-averaged target strength, $\langle TS\rangle$, calculated from the deformed cylinder model on 19 fish, including 7 of the 16 live fish for which both model estimates and experimental estimates of $\langle TS\rangle$ are available. Note that the length of the fish changed slightly after frozen storage between when experiments were done and the measurements for the modeling were obtained. This is due to distortion of the tissues during thawing.

Thawed length cm	Fresh length cm	Model $\langle TS\rangle$ dB	Experimentally measured $\langle TS\rangle$ dB	$\lvert\Delta TS\rvert$
29	30	−48.25	⋯	
30	30	−49.03	⋯	
32.5	32.3	−48.06	−48.68	0.62
30	30.8	−49.29	−47.37	1.92
30	30.2	−49.44	−46.49	2.95
31	30	−50.39	−48.37	2.02
36	36.3	−47.59	−45.39	2.22
31.5	32.7	−48.58	⋯	3.98
31	32.4	−51.13	−47.15	2.99
32.5	32.7	−50.48	−47.49	
31	31	−51.58	⋯	
36	39	−50.91	⋯	
38	40	−48.97	⋯	
31	31	−47.76	⋯	
29	28.5	−49.12	⋯	
16	16	−57.16	⋯	
27.5	27	−54.26	⋯	
34.5	34	−46.99	⋯	
30	30	−49.81	⋯	

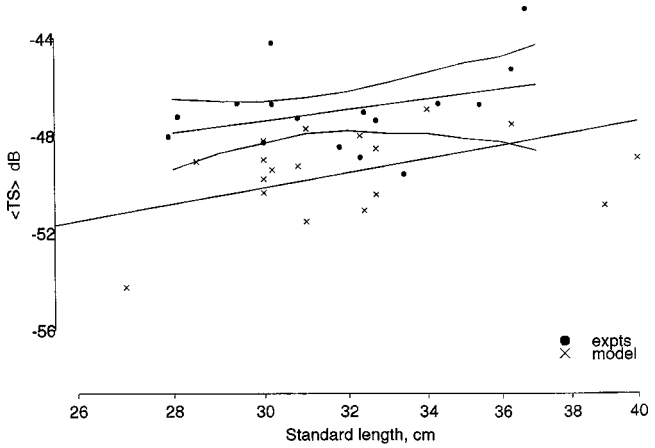

FIG. 4. Comparison of the target strength–length regression for live orange roughy ($n=16$) with a subset of the deformed cylinder model results ($n=18$) at the same temperature and pressure. Note that the 16-cm fish in Table II is excluded from this plot because there were no experimental measurements on such small fish. The regression equation for the live fish data is: $\langle TS\rangle = 16.374 \log_{10}$ standard length—71.621, where $\langle TS\rangle$ is in dB and standard length is in cm. Ninety-five percentile confidence limits for live fish data were estimated by bootstrapping. A regression line fitted to the model data is used to estimate the offset between model and experimental results. Length is plotted on a log scale, and length for the model data are fresh lengths rather than thawed lengths (see Table II).

When the $\langle TS\rangle$-length relationships are compared for the model and the experimental data it is apparent that the model predicts lower $\langle TS\rangle$ for a given size of fish. The difference between model and experimental regression lines is 2.2 to 2.9 dB (Fig. 4).

Effect of pressure and temperature

The effect of increasing pressure and decreasing temperature is to increase the speed of sound through orange roughy lipid (Fig. 5). Speed is increased by ~35 m s^{-1} as temperature falls from 13.5 to 6 °C (i.e., from the temperature at which the experimental measurements were made to the temperature at which the fish live). The effect of increasing pressure from the surface to that at 1050-m depth and decreasing temperature from 13.5 to 6 °C is to increase the sound speed through orange roughy lipid by ~57 m s^{-1} (Fig. 5). We used 1050 m as a representative depth for roughy in nature. We used these results to adjust h in the model in order to scale the experimental results to compensate for temperature and pressure. This is reasonable because we can reliably calculate the effect of temperature and pressure on the sound-speed ratio, h, even though the model $\langle TS\rangle$ is generally lower than the experimentally measured $\langle TS\rangle$. We assume that the experimental results are correct for surface pressures and temperatures and simply use the model to scale the experimental $\langle TS\rangle$ to the depth at which the fish live. The net result of the sound-speed increase is to decrease $\langle TS\rangle$ by ~2 dB.

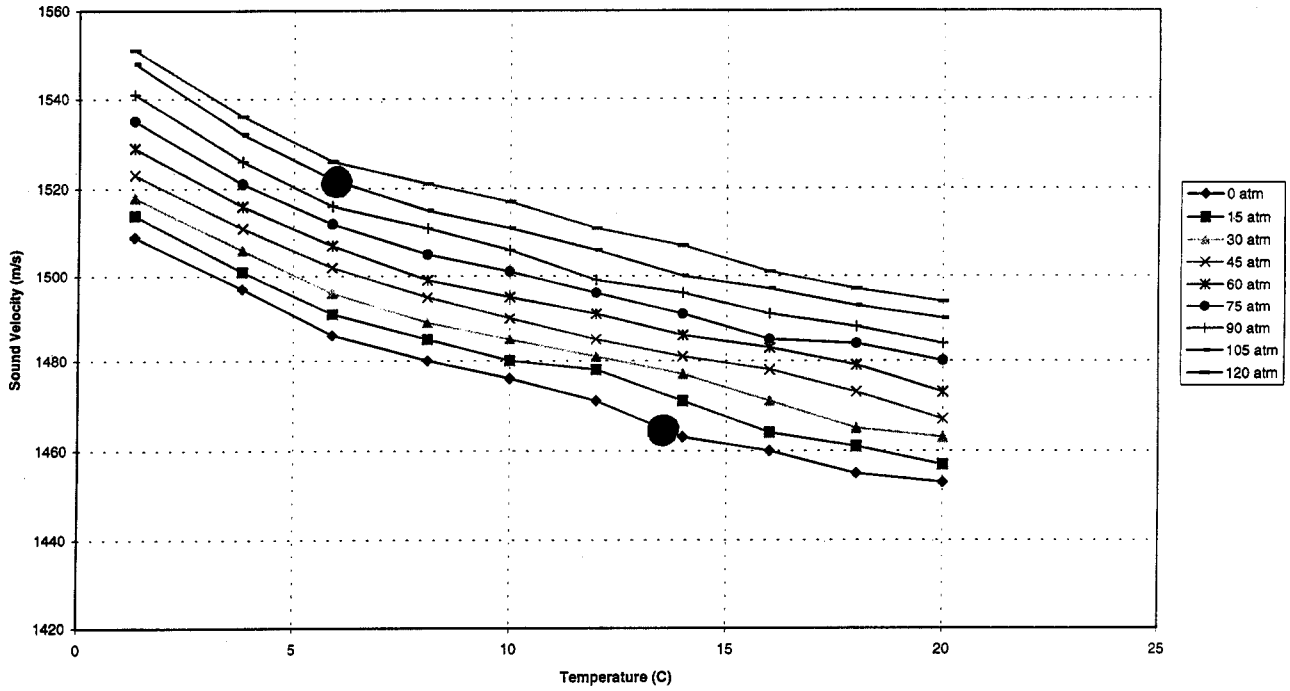

FIG. 5. Effect of temperature and pressure on the sound speed in orange roughy lipid. Sound speed decreased approximately linearly with temperature and pressure over the range of temperatures (13.5 to 6 °C) and pressures (0 to 105 atm) of interest in this study. The lower large filled circle is the sound speed at the temperature and pressure for experimentally measured $\langle TS \rangle$ data (13.5 °C and 0 atm). The upper large filled circle is the sound speed at a representative temperature and pressure for the depths where orange roughy live (6 °C and 105 atm).

DISCUSSION

The model is not expected to exactly replicate the experimental measurements, but rather to provide a theoretical trend with regard to frequency response and overall variations of the averaged target strength as a function of temperature, pressure, and fish length. It is generally necessary to adjust models of target strength with a ''local calibration'' because fish structures are more complicated scatterers than the comparatively simple models.[17]

The exact position of $TS_{\max}$ with respect to fish orientation does not match, because in the model the wax ester in the anterior one-third of the body is aligned with the body axis, but in real fish the lipid is distributed in various body locations, primarily the head region (including the swimbladder and neurocranial cavity), as well as in muscle, skin, and gut. Consequently, scattering from the model is symmetric, but is not necessarily so in the real fish.

In the discussion that follows, we refer to a single size of orange roughy because 35 cm is a common modal size for length frequency distributions of commercially exploited populations, and as such, it provides a useful reference point for comparing target strength values between studies. On first inspection it appears that the *in situ* estimate of $\langle TS \rangle$ for a 35-cm orange roughy of ~ -50 dB[2] is considerably lower than the experimentally measured estimate of ~ -46.3 dB.[1] The question then arises as to which of these estimates is correct and which estimate should be used in the biomass assessment for orange roughy. This issue is far from trivial given that acoustic survey is used to assess the biomass of this high value New Zealand fishery (NZ$ 123 million in 1995[18]). Our research in this and a previous paper[1] shows that neither the *in situ* nor the experimental estimates should be used without adjustment. The *in situ* results need to be corrected for the avoidance behavior of the fish.[1] The effect of this correction is to raise the $\langle TS \rangle$ value by ~ 2.5 dB.[1] The experimentally measured $\langle TS \rangle$ result needs to be adjusted for the effects of pressure and temperature on the sound-speed ratio between lipid and seawater. This adjustment lowers the $\langle TS \rangle$ value by ~ 2 dB. The net result is that the adjusted *in situ* $\langle TS \rangle$ and the adjusted experimentally measured $\langle TS \rangle$ converge on a value of ~ -48 dB for a 35-cm fish.[1] The apparent conflict between the *in situ* and the experimental estimates of $\langle TS \rangle$ now appears to be resolved.

ACKNOWLEDGMENTS

Sound-speed measurements in orange roughy lipid were made by J. C. Goold, School of Ocean Sciences, University of Wales, Bangor, under contract to the National Institute of Water and Atmospheric Research Ltd. We are grateful to Alan Hart for extracting the orange roughy lipid and to Paul Grimes for making the morphological measurements. Gavin Macaulay provided a helpful review of the manuscript. Funding for this research was provided by the New Zealand Ministry of Fisheries (Project No. DEOR02) and by a NIWA Visiting Scientist award to Z. Ye. Painstaking comments by an anonymous reviewer were appreciated and led to a greatly improved manuscript.

[1] S. McClatchie, G. Macaulay, R. F. Coombs, P. Grimes, and A. Hart, ''Target strength of the oily deep-water fish, orange roughy (*Hoplostethus atlanticus*). Part I: Experiments,'' J. Acoust. Soc. Am. **106**, 131–142 (1999).

[2] R. J. Kloser, A. Williams, and J. A. Koslow, ''Problems with acoustic target strength measurements of a deepwater fish, orange roughy (*Hoplostethus atlanticus*, Collett),'' ICES J. Mar. Sci. **54**, 60–71 (1997).

[3] T. Gytre, ''Ultrasonic methods for fish tissue characteristics,'' International Council for the Exploration of the Sea, ICES CM. 1987/G:14.
[4] A. J. Koslow, R. Kloser, and C. A. Stanley, ''Avoidance of a camera system by a deepwater fish, the orange roughy (*Hoplostethus atlanticus*),'' Deep-Sea Res., Part I **42**, 233–244 (1995).
[5] K. Hayashi and T. Takagi, ''Occurrence of unusually high levels of wax esters in deep-sea teleost fish muscle, *Hoplostethus atlanticus*,'' Bull. Jpn. Soc. Sci. Fish. **46**, 459–463 (1980).
[6] J. R. Sargent, R. R. Gatten, and N. R. Merrett, ''Lipids of *Hoplostethus atlanticus* and *H. mediterraneus* (Beryciformes: Trachichthyidae) from deep water to the west of Britain,'' Mar. Biol. (Berlin) **74**, 281–286 (1983).
[7] P. Vlieg, ''Proximate composition of New Zealand marine fish and shellfish,'' DSIR Biotechnology Division, Department of Scientific and Industrial Research Internal Report.
[8] P. Vlieg, ''Transmission oil from fish,'' Catch '83 **10**, 21–22 (1983).
[9] M. R. Grigor, W. H. Sutherland, and C. F. Phleger, ''Wax-ester metabolism in the orange roughy *Hoplostethus atlanticus* (Beryciformes: Trachichthyidae),'' Mar. Biol. (Berlin) **105**, 223–227 (1990).
[10] C. F. Phleger and M. R. Grigor, ''Role of wax esters in determining buoyancy in *Hoplostethus atlanticus* (Beryciformes: Trachichthyidae),'' Mar. Biol. (Berlin) **105**, 229–233 (1990).
[11] D. H. Buisson, D. R. Body, G. J. Dougherty, L. Eyres, and P. Vlieg, ''Oil from deep water fish species as a substitute for sperm whale and jojoba oil,'' J. Am. Oil Chem. Soc. **59**, 390–395 (1982).
[12] Z. Ye, ''A novel approach to sound scattering by cylinders of finite length,'' J. Acoust. Soc. Am. **102**, 877–884 (1997).
[13] K. V. Mackenzie, ''Nine-term equation for sound speed in the oceans,'' J. Acoust. Soc. Am. **70**, 807–812 (1981)
[14] J. Folch, M. Lees, and G. H. Sloane-Stanley, ''A simple method for the isolation and purification of total lipids from animal tissues,'' J. Biol. Chem. **226**, 497–509 (1957).
[15] J. C. Goold, J. D. Bennell, and S. E. Jones, ''Sound velocity measurements in sperm whale oil under the combined influences of temperature and pressure,'' Deep-Sea Res., Part I **43**, 961–969 (1996).
[16] K. Shibata, ''Study on details of ultrasonic reflection from individual fish,'' Bull. Faculty Fish. Nagasaki Univ. **29**, 1–82 (1970).
[17] C. S. Clay and H. Medwin, ''Marine bioacoustics: A physical basis for biological measurements using sonar systems,'' (in preparation).
[18] Anonymous, ''The New Zealand seafood industry economic review 1994–96,'' New Zealand Fishing Industry Board, 1996.

Matched-field processing, geoacoustic inversion, and source signature recovery of blue whale vocalizations

Aaron M. Thode, G. L. D'Spain, and W. A. Kuperman
Marine Physical Laboratory, Scripps Institution of Oceanography, San Diego, California 92093-0205

(Received 28 December 1998; revised 25 October 1999; accepted 27 October 1999)

Matched-field processing (MFP) and global inversion techniques have been applied to vocalizations from four whales recorded on a 48-element tilted vertical array off the Channel Islands in 1996. Global inversions from selected whale calls using as few as eight elements extracted information about the surrounding ocean bottom composition, array shape, and the animal's position. These inversion results were then used to conduct straightforward MFP on other calls. The sediment sound-speed inversion estimates are consistent with those derived from sediment samples collected in the area. In general, most animals swam from the east to west, but one animal remained within ~500 m of its original position over 45 min. All whales vocalized between 10 and 40 m depth. Three acoustic sequences are discussed in detail: the first illustrating a match between an acoustic track and visual sighting, the second tracking two whales to ranges out to 8 km, and the final sequence demonstrating high-resolution dive profiles from an animal that changed its course to avoid the research platform FLIP (floating instrument platform). This last whale displayed an unusual diversity of signals that include three strong frequency-modulated (FM) downsweeps which contain possible signs of an internal resonance. The arrival of this same whale coincided with a sudden change in oceanographic conditions.
[S0001-4966(00)02802-2]

PACS numbers: 43.30.Pc, 43.30.Sf [WA]

INTRODUCTION AND REVIEW OF PREVIOUS WORK

In this paper, matched-field processing[1–3] (MFP) methods have been applied to blue whale (*Balaenoptera musculus*) vocalizations, recorded off the California coast in 1996. The research upon which this work is based is an outgrowth of initial work by the Marine Physical Laboratory to conduct MFP on whales during an unrelated experiment in 1994,[4,5] and to use whale vocalizations for geophysical inversions.[6] The results presented in this paper show how these techniques can obtain high-resolution ranges and depths of blue whale positions out to ranges of 8 km under complex propagation conditions, using as few as eight hydrophones. No previous knowledge of the surrounding ocean bottom was required, because the needed information was extracted from the vocalizations themselves, using global inversion techniques. When combined with the acoustic vector intensity measured from a DIFAR[7] sonobuoy, a three-dimensional localization was achieved. Propagation effects could then be removed from the calls, using the derived locations and inferred ocean bottom properties. This procedure obtained estimates of both the source time signatures and source levels of different vocalization types.

Most localization work on baleen whales has focused on obtaining azimuth and range, usually by employing widely spaced hydrophone assemblies. Recent examples of these approaches are given in Refs. 8–11. Previous depth estimates from cetacean vocalizations have been obtained only under restricted conditions, where the acoustic signal has been assumed to travel directly from the animal to each receiver, allowing standard time-of-arrival methods[12] to be employed. Some examples of this approach have included captive dolphins in a concrete tank,[13] and sperm whales in deep water.[14] However, acoustic signals generated by baleen whales along the coast generally propagate over ranges greater than the local water depth, and they become substantially altered through interaction with the surface and ocean bottom, making the application of standard time-of-arrival methods difficult.[12] The MFP techniques used in this paper have no such limitations; indeed, some signals discussed here have been localized in depth and range to distances greater than 60 times the local water depth, and thus experienced multiple surface reflections and bottom refractions before being recorded. In this case no direct acoustic path between the whale and the receiving array existed.

After a review of the experimental location, geometry, and data analysis procedures in Sec. I, the MFP results are presented in Sec. II A, using data from three distinct acoustic sequences, recorded over a 40-hour time period in 1996 off the northern Channel Islands in the Southern California Bight region. The first sequence (case 1) demonstrates a match between an acoustic track and a visual observation of two blue whales. The next sequence (case 2) demonstrates the maximum ranges obtained from the experiment, covering a 90-min period wherein two different whales are tracked to ranges of several kilometers. The final sequence (case 3) illustrates a high-resolution track of a single whale that swam toward the research platform FLIP, then altered its course to avoid the experiment. This sequence contains three unusual FM signals and three detailed dive profiles.

Section II B compares the sediment properties extracted from the whale vocalizations with those derived from sediment cores taken from the same region. Section II C uses the MFP positions to compute source levels for the animals in cases 2 and 3, and Sec. III D uses multichannel deconvolution techniques[15,16] to strip away propagation effects from three FM sweeps in case 3, demonstrating that the unusual

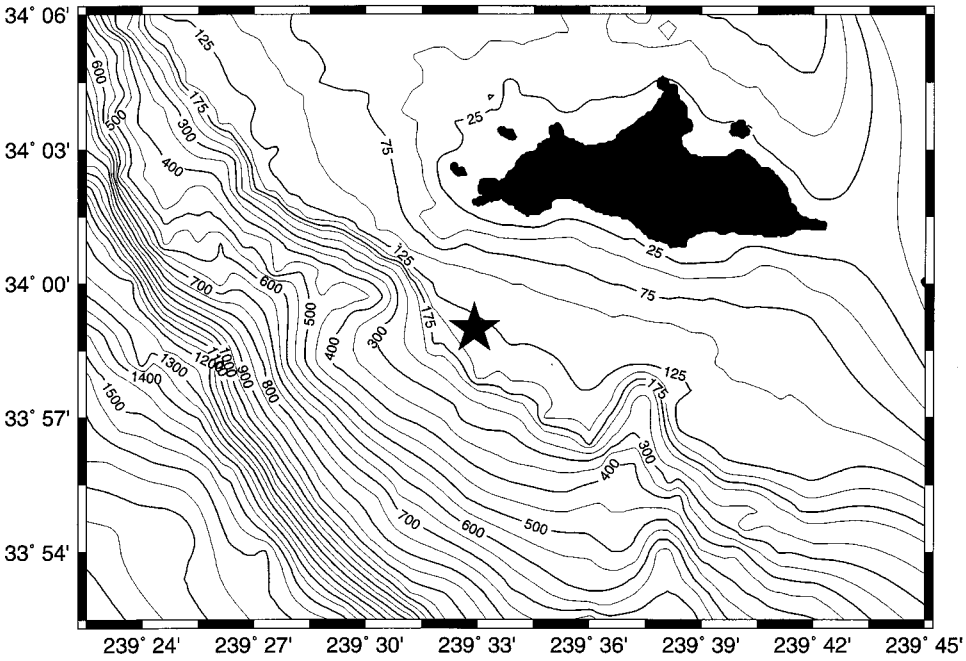

FIG. 1. Bathymetry around the 1996 experiment site. The contour interval is 25 m until 300-m depth, and then increases to 50 m for deeper depths. FLIP location is given by star. Note how the bathymetry to the east and northwest is only mildly range-dependent.

features present in the call are produced within the whale itself, and are not waveguide effects. The discussion in Sec. III discusses whether the unusual FM sweeps in the latter case might indicate an internal resonance, and notes how the presence of this whale coincides with a sudden change in ocean conditions in the area.

The ''type A'' and ''type B'' eastern Pacific blue whale vocalizations discussed here are described in greater detail elsewhere.[8–10,17,18] References on blue whale sounds in other regions of the world,[19–25] MFP,[1,2,26,27] and geoacoustic inversion methods,[26,28–34] have also been provided.

I. METHODS

A. Experiment location and geometry

The 1996 experiment was conducted using the research platform FLIP (floating instrument platform)[35] from July 18 through July 22 off the south coast of San Miguel Island, at 33°59′ N, 120°27.221′ W. This location lies within the boundaries of the Channel Islands National Marine Sanctuary,[36] administered by the National Oceanic and Atmospheric Administration. Surveys over the past ten years have observed concentrations of blue, fin, and humpback whales in the region during the summer months. ''Whale Habitat and Prey Study (WHAPS)'' surveys[37] conducted by the National Marine Fisheries Service, Southwest Fisheries Science Center (SWFSC) have concluded that around 100 blue whales frequent the area each summer. The animals are believed to be feeding off krill, which in turn feed off the plankton blooms growing in the nutrient-rich water upwelling around the islands.[38]

Figure 1 illustrates the bathymetry around the experimental site. The contour maps were constructed using fathometer-corrected data downloaded from the National Oceanographic Service and National Geological Data Center databases. Depending on the tide level, the water depth at the experiment site varied between 129 and 133 m. The vocalizations presented here will be from animals swimming from the E to SE of FLIP, a region where the water depth changes by only 30 m over 10 km.

The experimental deployment is illustrated in Fig. 2, and consisted of a 48-element[39] vertical array with a hydrophone spacing of 1.875 m, sampled at a rate of 1500 Hz. A General Oceanics inclinometer was attached 1.7 m above the shallowest hydrophone element, and recorded the array tilt magnitude and direction, inclinometer depth, and water temperature every 90 sec. Data from the vertical array were used to conduct the MFP, while information from both the vertical array tilt and an occasional DIFAR sonobuoy[7] estimated

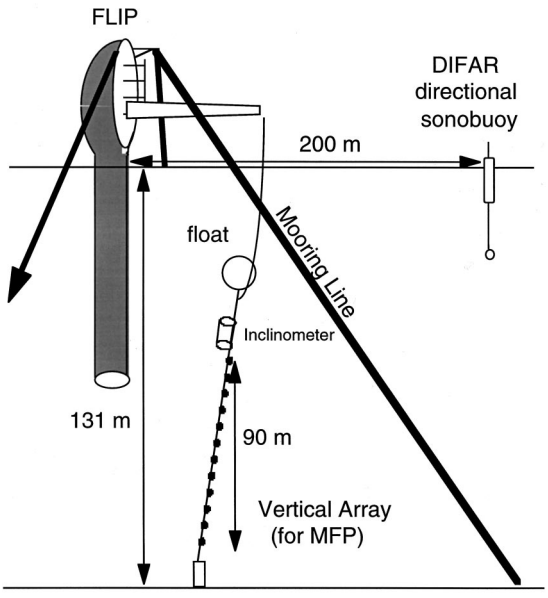

FIG. 2. Experimental setup of the MFP experiment. The vertical array is used to compute range and depth of calling animals. Source azimuth could occasionally be estimated by using either a DIFAR directional sonobuoy (as in case 2), or by taking advantage of the vertical array tilt caused by strong currents in the area (Sec. I C). The thick dark lines represent mooring lines.

source azimuth,[40,41] thus yielding a three-dimensional location. Subsequent work showed that localization could be accomplished using as few as eight hydrophones as long as they spanned 90 m of vertical aperture.

B. Data analysis and inversion procedures

Traditional MFP requires information about the ocean depth, bottom composition, sound-speed profile, and tilt of the vertical array, in order to construct an accurate model of the acoustic field received at the area. Bathymetry information was independently available, but the other environmental information was sparse or unknown. The analysis for each case presented in Sec. II began by selecting several large signal-to-noise ratio (SNR) calls throughout the sequence for ''focalization'' or inversion. By applying a genetic algorithm[42,43] inversion software package[34] to a normal-mode numerical model,[44] the required environmental parameters were extracted from the vocalizations themselves, while simultaneously recovering the best-fit range and depth of the whale. The fitness criteria used were the normalized output of the Bartlett processor, incoherently averaged over 3–10 frequencies between 16 and 130 Hz. Identical global optimization procedures were used for each inversion, which adjusted 18 parameters in an attempt to maximize the peak correlation of the incoherently frequency-averaged ambiguity surfaces. Each inversion was repeated 40 times for each vocalization sample, using a different initial population of trial solutions, and the inversion run that yielded the largest correlation was retained.

Nine of the 18 inverted parameters defined a geoacoustic model of the ocean bottom that assumed a sediment layer overlaying an infinite basement layer. The sediment thickness was set to 70 m, deeper than the expected bottom penetration for all frequencies except possibly 17 Hz. A sediment sound-speed profile was constructed by allowing the inversion to adjust the sediment sound-speed at depths of 23, 46, and 70 m beneath the water/sediment interface, as well as the bottom half-space sound-speed. The sediment sound-speed at the water/sediment interface was allowed to vary between realistic values of 1450 and 4000 m/s, and the sound-speed was allowed to increase between 0 and 1000 m/s every 23 m, ensuring the physically realistic result that the bottom velocity would increase with depth. The inversions did not solve for possible large shear speeds in either the sediment layer or half-space, as the normal-mode models used for the inversion incorporated a perturbation approach to compute shear, which is valid only for small shear values.[2]

Baseline water-borne sound-speed profiles were constructed using temperature data from five XBT casts. The technique of empirical orthogonal functions (EOFs) was applied to enable inversion of the water column sound-speed profile using only a few parameters.[45] The MFP results were insensitive to the exact shape of the sound-speed profile used. The inversion techniques were benchmarked by performing inversions on the Swellex-3[27] data set, where the geoacoustic parameters were already known.

Once acquired, the inversion parameters were used to perform MFP on the rest of the calls in the sequence, while ensuring that updated ''snapshots'' of the vertical array geometry were used. Once a time series was selected, a single global inversion typically took 10–20 min using a Sun Ultra workstation. A MFP computation using the inversion results took 30–60 sec per call, using routines developed in MATLAB.

C. Interpreting inverted array tilt

Imagine a tilted vertical array with a total offset H between the top and bottom hydrophones. Because MFP models the two-dimensional acoustic field between the source and receiver, it is only the projection (H') of the total offset onto the MFP plane that influences the received acoustic field. If the source bearing is the same as the tilt direction, then $H'=H$; if the source bearing is perpendicular to the tilt bearing, then $H'=0$—the projected offset is zero. Because the maximum array tilt and tilt direction were independently measured by an inclinometer, the projected offset can be converted into a rough source bearing estimate. The convention used in this paper is that a negative value of H' indicates the array is tilting away from the source. One important consequence of this behavior is that if the projected array tilt remains constant over time while the range decreases, then the source must be moving toward the array.

II. RESULTS

In this paper all dB units have been expressed in terms of pressure spectral density (*re* 1 μPa^2/Hz), and source levels in terms of source pressure level spectral density (*re* 1 μPa^2/Hz @ 1 m).

A. MFP tracks

1. Case 1—demonstration of an acoustic/visual match

The ocean conditions were calm over the 15-min period shown in Fig. 3, beginning at 14:01 GMT, Julian Day 204, 1996, and are among the last calls recorded during the experiment. The myriad 20–30-Hz pulses that are prominent around 750 sec may be fin whale calls.[46–48] In addition, at least three blue whales are vocalizing during this time, generating two types of signals known to be produced by blue whales.[9,17,18,20,49,50] The broadband pulsed call is conventionally called ''type A,'' and the harmonic FM sweep is labeled ''type B.'' One animal is producing very faint B calls ($\sim$100 dB *re* 1 μPa^2/Hz), with only the 50-Hz tone visible, suggesting that it is greater than 5 km away. Another animal generated the two A-B sequences that begin at roughly 100 and 310 sec along the time axis in Fig. 3. A third animal has produced the intense broadband type A calls recorded at 293, 505, and 718 sec (labeled ''a,'' ''b,'' and ''c'' in the figure), and these calls are the focus of this case. Of the three calls, the 505-sec call has the best signal-to-noise ratio. The 293-sec call is also of good quality, but the 718-sec signal suffers from contamination from pulsing broadband noise and possible fin whale pulses.

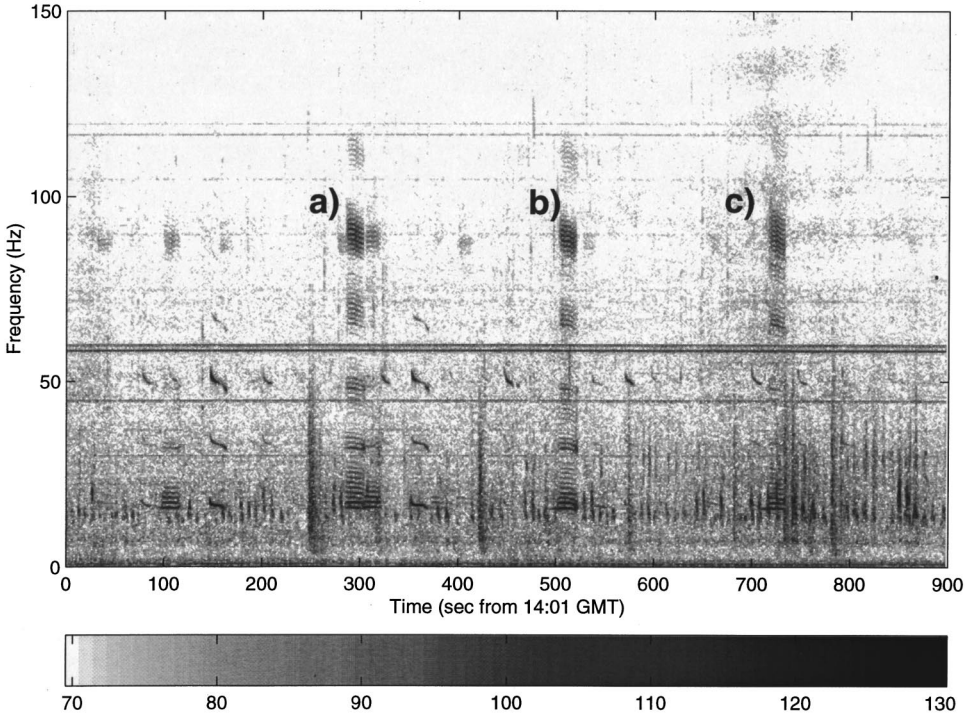

FIG. 3. Spectrogram of case 1, Julian Day 204 time sequence, starting at 14:01 GMT. Power spectral density levels are in units of dB *re* 1 μPa^2/Hz. Note the three strong type A calls at 290 (''a''), 505 (''b''), and 720 (''c'') seconds. The multiple vertical energy bands between 20 and 30 Hz may be fin whale vocalizations.

The inversion procedure was performed on each of the three high-level type A calls, using an incoherent average of 8–10 frequencies between 16 and 112 Hz. The inversion results are graphically displayed in Fig. 4. The inverted sediment sound-speed profiles from the three calls are generally consistent to within ± 50 m/s down to depths of 46 m beneath the surface, with a mean speed around 1621 m/s at the water sediment interface. The accuracy of these geophysical estimates is explored further in Sec. II B.

The multiple arrival paths from a propagating acoustic signal generate an interference pattern in the received pressure field along the array, as a function of depth. To compare the received data from the ''b'' call with that of the best-fit model, the measured vs modeled pressure magnitude across the vertical aperture of the array is plotted in Fig. 5, for six different frequency components. The fit is excellent across a wide range of frequencies, particularly in the high signal-to-noise (SNR) ratio band between 85 and 95 Hz.

The frequency-averaged ambiguity surfaces for each call are displayed in Fig. 6, using the adaptive white-noise constraint (WNC) MFP processor,[51,52] where the constraint has been set to 3 dB below the maximum white-noise gain. The WNC correlation output is generally less than that of the Bartlett processor.

Clues about the whale's azimuthal position are provided by the projected array geometry obtained from the inver-

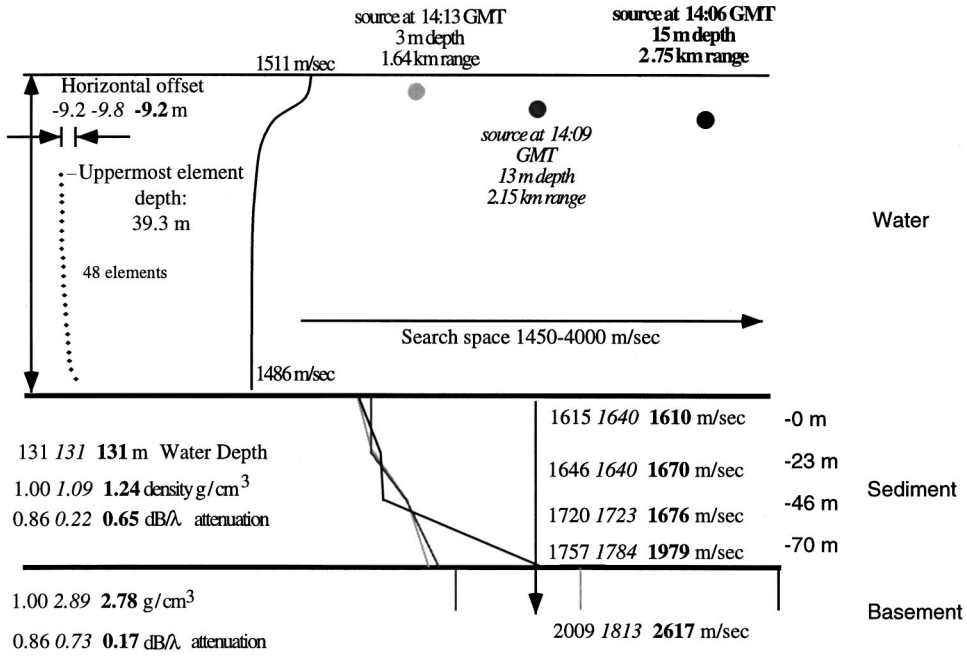

FIG. 4. Illustration of best-fit inversion model for the three type A calls from case 1. Parameters obtained from the same call share the same shading and text style.

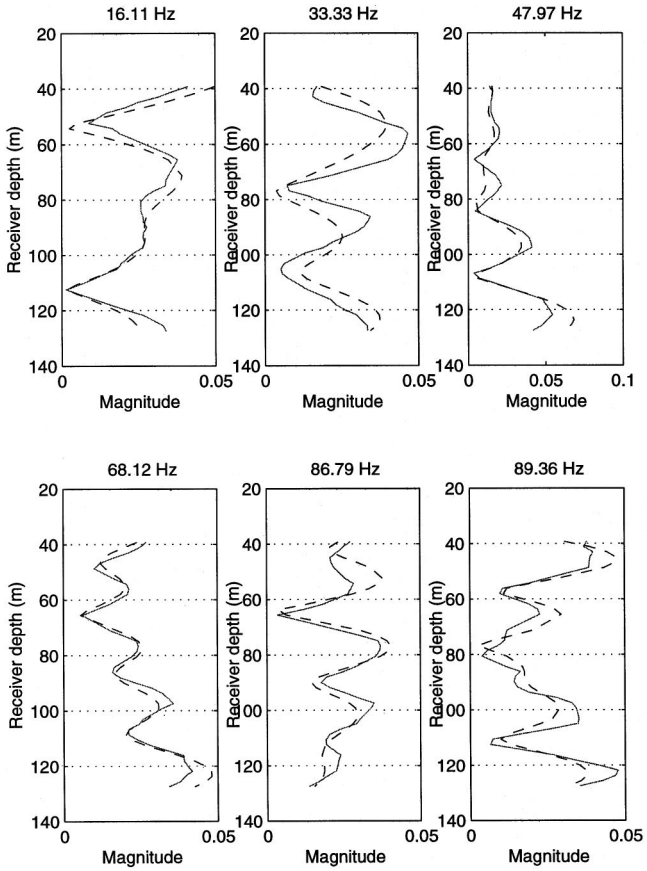

FIG. 5. Comparison between the normalized sound pressure magnitude from the middle type A call (dotted line), and that predicted by the best-fit inversion, as a function of depth for six different frequency components.

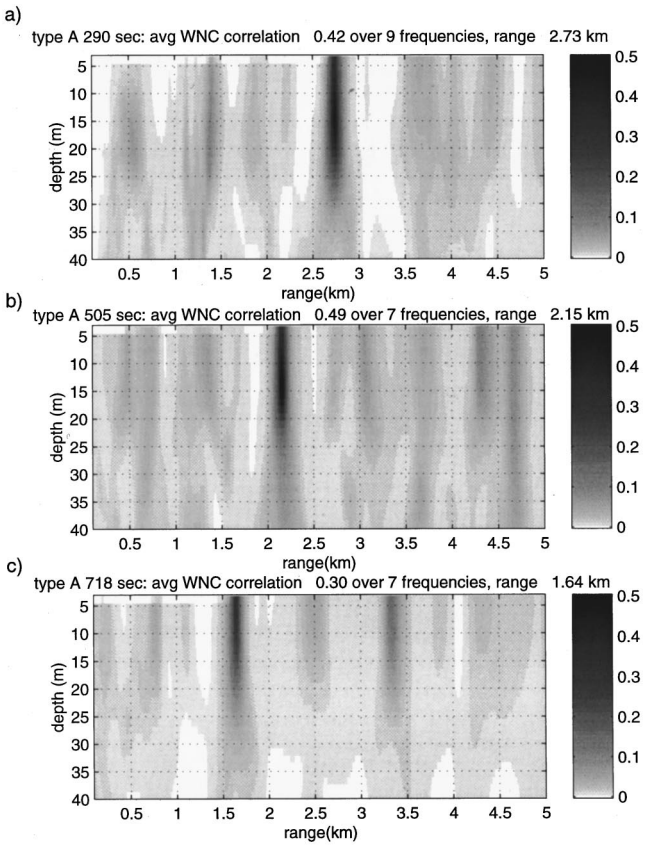

FIG. 6. Ambiguity surfaces from case 1 calls shown in Fig. 3, using the white-noise constraint (WNC) processor. The constraint has been set to 3 dB below the maximum white-noise gain. Frequencies have been selected from the 32-, 48-, 65-, 90-, and 112-Hz bands. Generally correlation values of the WNC are lower than Bartlett values. (a) 290-sec call, average of nine frequencies between 17 and 112 Hz; (b) 505-sec call, average of seven frequencies between 17 and 112 Hz; (c) 720-sec call, average of seven frequencies between 17 and 112 Hz.

sions. For example, the projected horizontal offset H' between the top and bottom hydrophone remained constant at about -9.5 m, so the whale must have been swimming along a radial directly toward FLIP. Had the bearing of the animal relative to FLIP changed significantly during the calling sequence, the inverted array tilt would have changed with time. The negative tilt values indicate the array was tilting away from the whale, and since the array was tilting toward the NW, the bearing of the animal must be to the E or SE. The whale moved 1.1 km over about 430 sec. Its average speed over this time was therefore 2.6 m/s (9.2 km/hr), consistent with estimated swimming speeds between 5 to 33 km/hr for blue whales.[53]

Given the long duration of these calls (around 15 sec), it is possible to perform MFP on sequential time segments within a call, obtaining the animal's dive profile while vocalizing. The ranges and depths from the resulting ambiguity surface mainlobes are plotted in Fig. 7, at 1-sec intervals, for the 505-sec (''b'') call. While calling, the animal's range decreases by 2.5 to 3 m/s, consistent with the long-term swimming speed derived from Fig. 6.

The animal seems to remain at a constant depth over the duration of the 505-sec call, to within the resolution of the MFP processor. This theoretical resolution limit, based on the Cramer–Rao lower bound,[3] is expected to be around ± 2 m in depth and ± 10 m in range, for a 89-Hz signal with a 20-dB signal-to-noise ratio (SNR). Bathymetry mismatch also introduces a depth uncertainty, as the true ocean bottom is not flat. At 2.1-km range, the water depth lies between 110 and 150 m, depending on the azimuth used, which translates into an absolute source depth uncertainty of about ± 3 m[54] and a range uncertainty of about 15%. Thus the relative ranges and depths in Figs. 6 and 7 are probably accurate, but the absolute ranges and depths have uncertainties of ± 3 m in depth and ± 300 m in range.

Both Figs. 6 and 7 suggest a swimming speed of 2.6 m/s toward FLIP. Therefore this whale would have taken about 10.5 min to cover the remaining 1.6 km to the vertical array, suggesting that a visual sighting of an animal from FLIP should have been noted between 14:23 and 14:24 GMT on Julian Day 204. Indeed, this was the case.

Beginning at 14:23 GMT, a videotape of two whales approaching FLIP was recorded using a Cannon Hi 8-mm ES5000 camcorder. During this period, the animals approached from the E/SE, performed a shallow dive (about 30 m away from FLIP), then altered course slightly to swim away to the NW. Scientists at Southwest Fisheries Science Center identified both animals on the videotape as blue whales.[55] If these whales were indeed responsible for the recorded calls, then it seems likely that only one of them vocalized, due to the consistency in style and timing of the

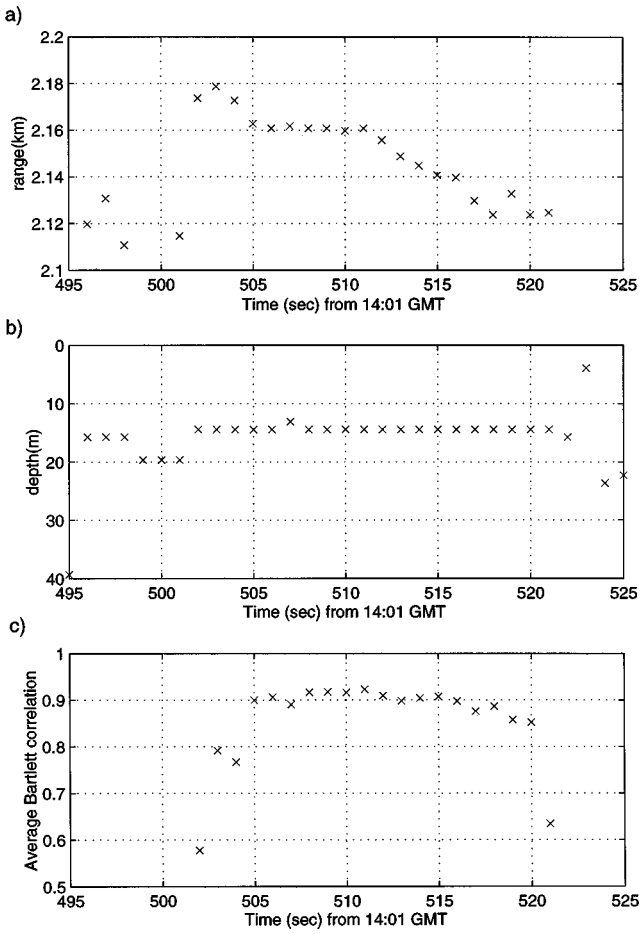

FIG. 7. Estimated changes in (a) range and (b) depth during ''b'' type A vocalization. Seven frequencies between 30 and 120 Hz were used in the MFP processing. Plot (c) shows the average correlation of the MFP peak over time. Estimated Cramer–Rao bound resolution is ± 3 m in absolute depth, ± 10 m in absolute range.

type A calls. One animal was somewhat smaller than the other, so perhaps the pair was a mother and her calf—but this will remain a speculation.

2. Case 2—maximum ranges obtained from MFP

The 90-min sequence analyzed here, beginning at 19:52 GMT on Julian Day 203, demonstrates for the first time how MFP can track calling whales to ranges in excess of 60 water depths, a situation where no direct path between the source and receiver exists. While case 1 analyzed three type A calls over a 15-min period, case 2 contains data from 67 type B and 39 type A calls from two different animals, one out to a range of over 8 km. Azimuthal information provided by a DIFAR sonobuoy was also available during part of the sequence, enabling high-resolution three-dimensional position estimates.

At first, only a single whale called, making type A-B doublet patterns. At approximately 20:36 GMT (44 min into the sequence), a second whale began calling. This animal had a different vocalization pattern, making three to five B calls for every pulsed A call. Both whales called at predictable intervals, and both also had their own characteristic FM downsweeps, making it easy to separate individuals from the spectrograms. For 30 min both animals called simultaneously, before the first whale fell silent at around 21:07 GMT (75 min into the sequence). Fortunately, a DIFAR sonobuoy had begun recording data 5 min earlier, and so precise azimuthal estimates were obtained for both animals. The second animal continued calling for another 15 min before suddenly lapsing into silence shortly past 21:22 GMT. Signal harmonics as high as 135 Hz were detected during this whale's final vocalizations.

Several strong type B calls produced by the second whale around 21:20 GMT (88 min into the sequence) provided excellent inversion sources, due to their high SNR and the presence of many harmonics. The resultant range and depth tracks from both animals, assuming a range-independent bathymetry, are plotted in Fig. 8(a) and (b). Only the 32-, 50-, and 65-Hz frequency bands have been averaged to generate these plots, because they were the only components present in all calls. Incorporating the higher-frequency components, whenever they were present, did not significantly alter these results. Each data point represents a covariance matrix constructed from 4096 pts (2.4 sec) of data. Adjacent data points were spaced 1 sec apart, so a single call yielded 10 to 15 range/depth estimates. Only points whose frequency-averaged peak correlation was greater than 0.7 have been plotted. Because of the higher SNR of the type B tones, the correlations of the type B calls are generally better than the type A estimates.

The first whale was detected at nearly 9-km range, which steadily decreased at a rate of about 8.2 km/hr, again consistent with known swimming speeds. The depth estimates show high scatter until the range became less than 5 km, and then they settle to values between 20 and 30 m. This animal swam within 1.4 km of FLIP at its closet point of approach.

The second whale's behavior provides an interesting contrast, in that its range remained relatively constant over 45 min. Gaps in vocalization are visible, which probably occurred when the animal surfaced. When first detected, the whale's apparent depth was shallow, at around 10 m. Over the next 10 min the source depths increased to a final average value of 20 m, where it remained for the rest of the sequence.

Figure 8(c) shows the best-fit projected array offsets (H') from 17 global inversions, computed at various times from both animals. As discussed in Sec. II C, projected array tilts can be converted to azimuthal estimates if assumptions about the array geometry are made. Because the array was tilting toward the west, the initial negative array offsets indicate that both animals were first detected roughly east of FLIP. The second whale's projected tilt remains fixed between -24 to -26 m, suggesting that its bearing did not change much over this time. By contrast, the azimuth of the first whale changes considerably, as the projected offset shifts from -25 to $+25$ m over 90 min. If the total array offset is assumed to lie between 25 and 30 m, then both whales were first detected at a bearing of around 95°, almost due east of FLIP. The first (transiting) whale reached its closest approach to FLIP at roughly 330° bearing, and stopped calling at approximately 315° bearing. The second whale, whose apparent bearing never changed, had a final estimated bearing of $105 \pm 40°$. The DIFAR results from this

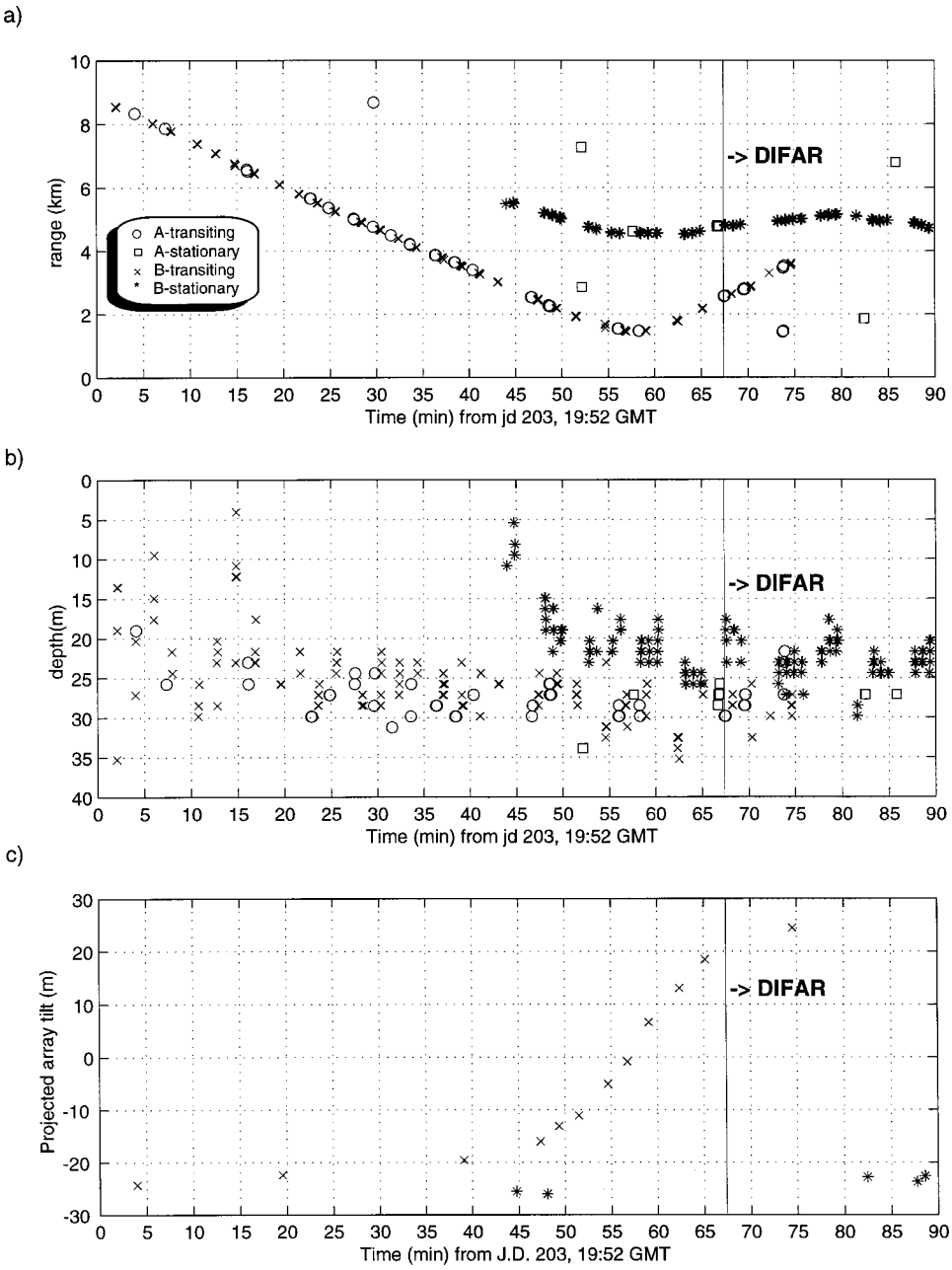

FIG. 8. Computed ranges and depths from case 2, for two animals over 90 min, starting from 19:52 GMT on J.D. 203. The 32-, 50-, and 65-Hz frequency bands were used in the MPF processing, assuming a range-independent bathymetry. A DIFAR sonobuoy begins recording data at 21:01 GMT. Each data point represents 2.5 sec of data, spaced 1 sec apart within a call. (a) range versus time; (b) depth versus time; (c) inverted horizontal array offset versus time. Whale bearing can be estimated from array offset.

time confirmed the second whale was calling from a bearing of 105°, and that the final bearing of the transiting whale was 340°. Both measurements thus agree with the rough inverted-array tilt predictions.

Because the azimuths of these calls were available, the effects of incorporating a more accurate bathymetric profile could be evaluated. For example, the true bathymetry along a 105° bearing from FLIP changes from 133 to 118 m over 5 km. When range-dependent replicas were recomputed using a parabolic-equation model,[56] the second whale's range estimate became 4.6 km, instead of the 5-km range obtained from assuming a flat bottom. The estimated depth also became about 2 m shallower, in agreement with theoretical expectations.[54] The effects of range-dependent bathymetry were therefore concluded to be mild for animals approaching from the east, or for animals less than 3 km away from FLIP.

3. Case 3—close approach with unusual vocal behavior

Case 3, the hour-long sequence analyzed here, began with a single type A-B doublet recorded on Julian Day 204, 1996, at 8:30 GMT. After a 10-min gap, two strong bouts of unusual calls appeared, lasting about 14 min. These vocalization bouts were striking in their variety. Each FM sweep had a different modulation, from straightforward downsweeps to U-shaped contours. The animal switched between type A-B doublets and type A calls followed by multiple Bs.

Between 29 and 30 min, the whale generated several heavily modulated type B calls and two unusual FM (''type D^{10}'') sweeps, which are plotted in Fig. 9(a). The whale made a third type D call around 100 sec later, then continued calling before lapsing into another 6-min period of silence beginning around 34 min. At 40 min, the animal generated

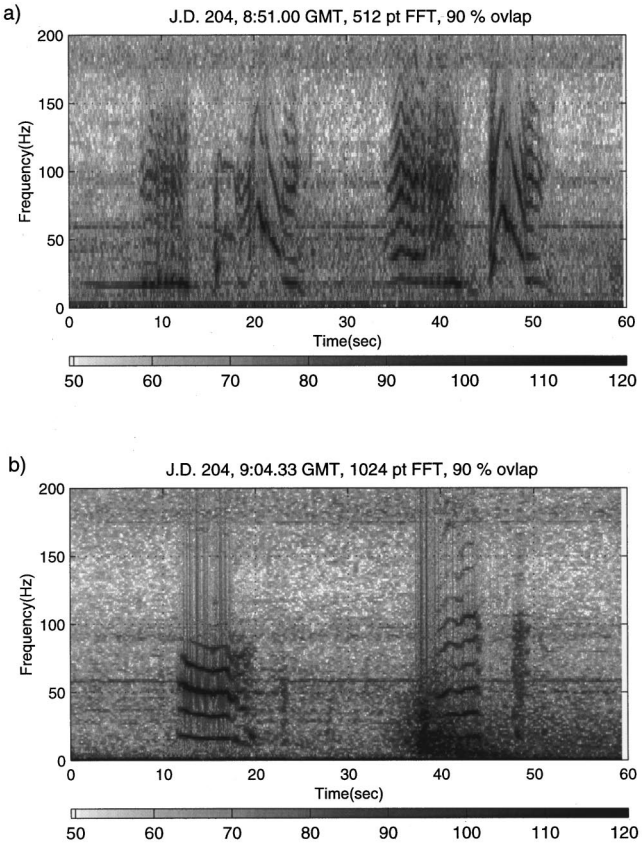

FIG. 9. Spectrograms of 60-sec segments of unusual calls recorded during case 3, expressed in units of pressure spectral density (dB *re* 1 μPa^2/Hz @ 1 m). Both sets of calls were produced when the animal was near the bottom of its dive profile: (a) Strongly modulated type B and D downsweeps, beginning at 8:51 GMT; (b) other examples of highly modulated calls, beginning at 9:04:30 GMT.

two more bouts of vocalizations, separated by an apparent breathing gap at 45.5 min. Some examples of calls generated over a 1-min period during the last bout are shown in Fig. 9(b). The whale finally fell silent at 55 min, or 9:17 GMT.

Figure 10 shows the final MFP results for this track, assuming a flat bathymetry. As with Fig. 8, the results displayed here use frequency components picked from the 32-, 50-, and 60-Hz bands, each point represents an analysis of 2.4 sec of data, and adjacent points are spaced 1 sec apart. By using only these three frequency components, all calls could be included. Using higher-frequency components, when available, did not change the localization estimates.

Figure 10(a) shows the isolated type A-B doublet was generated at around 3 km range, at around 30-m depth. The first strong vocalization bout started at 1.67-km range, which steadily decreased at an average rate of 1.5 m/s to a minimum range of 386 m, after which the whale ceased calling. After the 6 min gap, the animal produced two more calling bouts, both showing the animal's range now increasing. The animal's radial velocity seemed to increase from 0.58 to 1.23 m/s between the two bouts. The last fix on the animal yielded a range of 1.24 km, after which it fell silent.

The depth estimates in Fig. 10(b) show four complete dive profiles. The scatter of adjacent data points (± 4 m) is consistent with theoretical predictions at these frequencies and ranges. Generally, the animal began calling at 20-m depth, and over 2–3 min descended to a depth of 30 to 35 m. After holding this depth for another 2–3 min, the animal began ascending while continuing to vocalize. The final calls were made between 15- to 20-m depth, with an estimated depth resolution of ± 5 m. The animal took about 2 min to surface and breathe, before descending for the next calling bout.

Figure 10(c) shows the inverted projected array offsets of the vertical array. The projected array tilt remained constant at -10 m as the animal approached FLIP, except for a small excursion at 20 min. At this time the array was leaning WNW, so the animal must have arrived from an easterly bearing, similar to those obtained in the previous sections. The constant projected tilt indicated the animal was swimming directly toward FLIP, just like the two whales in case 1. After the 6-min calling gap, the third calling bout produced a projected array tilt of 0, indicating that the animal had veered off to the side of FLIP, increasing its range to 490 m. The increasing positive tilt values following this time suggest that the animal had swum past FLIP, steadily changing its bearing with respect to FLIP, and thus swimming along a different route than its earlier approach.

Separate estimates of the whale's bearing were obtained by converting the projected array tilt into a bearing estimate (Sec. I C), and by using range-dependent MFP runs to obtain the best-fit bathymetry profile between FLIP and the whale, which can be converted into a bearing estimate.[57] The combined analyses suggest the whale arrived from a bearing between 80 and 120°, while swimming directly toward FLIP to within a range of 390 m. The animal then veered to the north, and may have swum a partial circle around FLIP, before finally swimming toward 340–350°. Thus the initial and final bearings of this whale are similar to those obtained from the transiting whale in case 2. However, this whale clearly made a course correction to avoid FLIP.

B. Evaluation of geoacoustic inversion results

This section summarizes the results from the 48 geophysical inversions extracted from the whale vocalizations discussed in cases 1–3, and compares the estimated sediment speeds with those expected from core samples collected from the region. Most inversions used type B calls, due to their high SNR ratio. Each inversion also optimized the waterborne sound-speed profile, but the results were relatively insensitive to the details of the profile shape. The low frequencies used in the inversion were probably the reason for this insensitivity; for frequencies greater than 150 Hz, the sound-speed profile structure should have more influence on the vertical field structure.

The most important geoacoustic inversion parameters were the sediment sound-speeds at the water/sediment interface, and at depths of 23, 46, and 70 m beneath this interface. The inversion also solved for the best-fit sediment density and attenuation, and for the speed, density, and attenuation of the acoustic half-space that was assumed to lie beneath the sediment. The half-space properties will be ignored here, because the acoustic field energy was not expected to penetrate deeper than 70 m. The inversion results confirmed this ex-

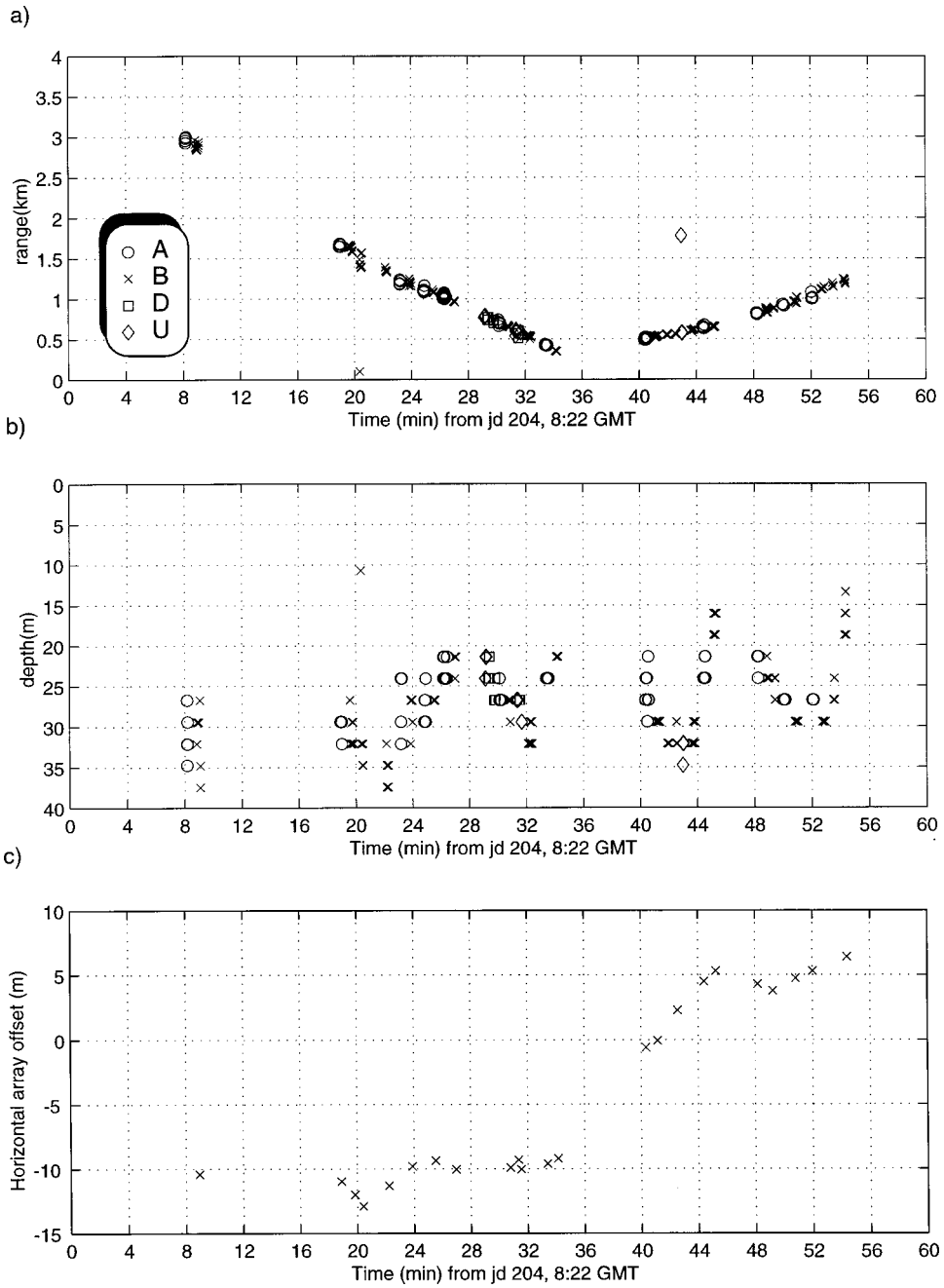

FIG. 10. MFP track of case 3. The track was generated using the 34-, 50-, and 67-Hz signal components, assuming a range-independent bathymetry. Each data point represents 2.5 sec of data, spaced 1 sec apart. The ''U'' label represents highly modulated type B calls. (a) Blue whale range; (b) blue whale depth; (c) projected horizontal array offset estimated from global inversions.

pectation: the inverted half-space parameters were essentially randomly distributed.

The inversions assumed sediment properties were not a function of source location. In reality the bottom was heterogeneous, so the results presented here represented a range-averaged estimate of the bottom properties between each source and FLIP.

Figure 11 displays the inverted interface sediment sound-speeds as both a function of range from FLIP and the whale used as the inversion source. As discussed previously, the precise azimuths of the calling whales were difficult to determine, except when DIFAR sonobuoy data were available. However, each inversion indicated whether a particular call arrived from the east or west, by combining the projected array tilt with knowledge of the array tilt direction. Figure 11 incorporates this information by plotting easterly data as negative ranges, and westerly data as positive ranges.

This sound-speed parameter was allowed to vary between 1450 m/s (representative of water-saturated mud) and 4000 m/s (typical basalt values) during the inversions. Despite this wide range, all inversion results lie between 1550 and 1800 m/s, with 75% lying between 1600 and 1700 m/s, or 4% of the allowed search space. These values are associated with silty/sandy bottoms.[58] Inversions obtained from the same animal over a small range interval also yielded consistent results; the scatter of these adjacent inversion points is about ± 25 m/s. The scatter is much larger between different cases at similar ranges, because the animals are probably calling from different bearings, and the acoustic energy is sampling different sediment profiles. There was no obvious correlation between the spread of the results and the number of frequencies used in the inversion. One might have ex-

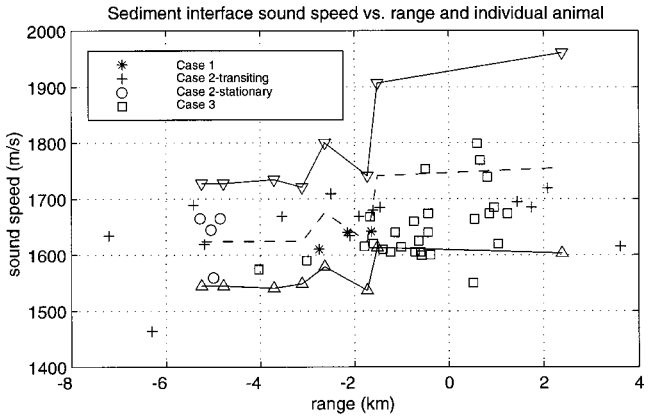

FIG. 11. Inversion results for sediment interface speed, as a function of inversion range and whales used as the acoustic source. The dashed line shows the sound-speeds derived from sediment core mean grain sizes. The solid lines show the sound-speeds computed from grain sizes one standard deviation from the mean. Triangles indicate the ranges of the core samples from FLIP. Negative ranges represent locations east of FLIP, and positive ranges are to the west. The ''stationary'' whale mentioned in the legend refers to the animal in case 2 that held its bearing fixed at a steady range of about 5 km.

pected the precision to increase as higher-frequency components are included; however, higher frequencies also penetrate less deeply into the sediment, and thus involve a different spatial average.

The recovered surface sediment speed is the only geoacoustic parameter for which independent information exists, in the form of sediment cores collected in the region by various institutions, particularly the United States Geological Survey (USGS) and the University of Southern California (USC)[59] over the past several decades. The penetration depth of these cores is generally less than a meter.

The sediment core data report the grain size distribution using a logarithmic measure $\varphi = \log_2$ (grain size in mm). Considerable variation exists in the particle sizes within a particular sample, so both the mean and standard deviation of φ are recorded. Sediment grain sizes can be converted to bottom sound-speed estimates via an empirical fit,[60] using a measured water sound-speed of 1485 m/s. Three sediment sample speeds are plotted in Fig. 11. The dashed line uses the mean φ, and the two solid lines use φ values lying one standard deviation on either side of the mean. The triangles indicate the ranges of the individual cores from the FLIP position. The plotted core data are restricted to those obtained within 8 km of FLIP, in water depths between 100 and 200 m. The reason for restricting the water depth is that there is a correlation between water depth and sediment sound-speed. For example, as the water shallows while approaching San Miguel shore, both the particle size and sediment sound-speed increase. Even with this depth restriction, the sediment sound-speed apparently changes west of FLIP. Part of this change may reflect the fact that only one core is available west of FLIP (for some reason a gap in sampling occurs to the west in an otherwise well-covered area).

East of FLIP, the whale inversion data lie within ± 50 m/s of the average sediment core sound-speed. The inversions underestimate the mean sound-speed between -1 and $+4$ km range, but this comparison is based on only two sediment cores. In general, the inversion results show a good match with the limited ground truth information available, particularly considering that the animals' bearings are imperfectly known.

Table I summarizes the properties and locations of the sediment cores used in this section. The ''AHF#'' column refers to the indexing system used by USC to record their samples.

C. Source level estimates

Using the range and depth information in Figs. 8 and 10, multichannel deconvolution techniques[15,16,61] were applied to estimate the source levels of the harmonic frequencies for the three whales in cases 2 and 3. Because the whales' acoustic power output varied considerably during a single vocalization, it is necessary to perform multiple estimates per call to estimate the maximum source levels.

Figure 12 displays the source spectral density levels (dB *re* 1 μPa^2/Hz @ 1 m) for the five lowest-frequency harmonics of the whales in case 2. To convert spectral densities into tonal spectral level, 4 dB should be subtracted from these values (to account for the 0.4-Hz frequency bin width). The uncertainty in these estimates are about ± 5 dB.

Some interesting results are that the 50-Hz tone source level is within 5 dB of the 17-Hz tone level, and that both animals consistently maintain a maximum source spectral density level of about 185 dB *re* 1 μPa^2/Hz @ 1 m (thus total power between 10–100 Hz is about 180 dB *re* 1 μPa @ 1

TABLE I. Sediment core interface sound-speed estimates, based on a water sound-speed of 1485 m/s.

AHF#	Latitude	Longitude	Range (km) from FLIP	Water depth (m)	φ	Skewness	Expected sound-speed (m/sec) over ± 1 standard deviation: Min.	Mean	Max.
24237	33.97	120.45	1.51	169	2.3 ± 2.1	1.3	1613	1741	1907
24238	33.967	120.433	2.63	135	3.3 ± 1.8	2	1579	1676	1741
24239	33.968	120.418	3.71	128	4.2 ± 1.8		1540	1624	1735
23159	33.983	120.435	1.73	115	4.2 ± 1.9	2	1537	1624	1742
23163	33.983	120.42	3.11	107	4.2 ± 1.6	6.5	1548	1624	1721
23164	33.985	120.402	4.78	100	4.2 ± 1.6		1548	1624	1727
23184	33.968	120.400	5.24	115	4.2 ± 1.7	2.5	1544	1624	1728
25192	34.00	120.47	2.39	110	2.1 ± 2.5	0.5	1608	1761	1968
FLIP	33.98	120.454		130					

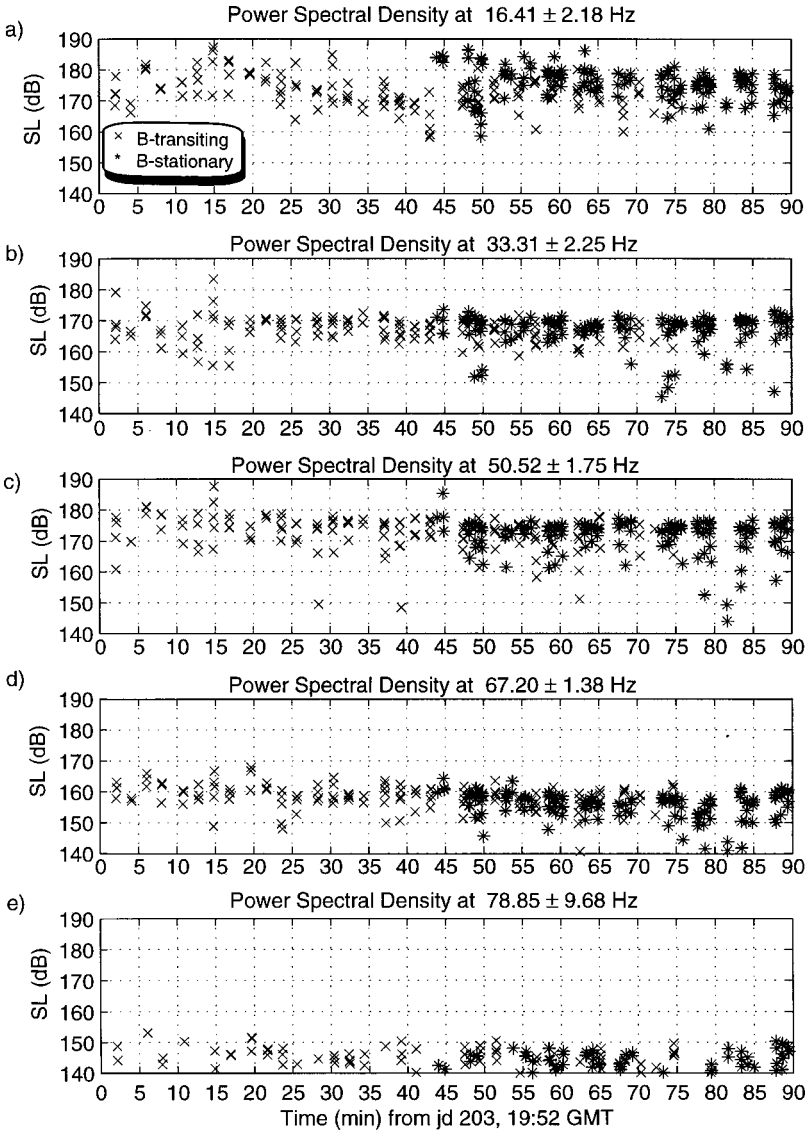

FIG. 12. Blue whale type B call source levels for case 2, estimated using locations given in Fig. 8. Levels are given in terms of pressure spectral density (dB *re* 1 μPa^2/Hz @ 1 m). (a) 16-Hz band; (b) 32-Hz band; (c) 51-Hz band; (d) 67-Hz band; (e) 79-Hz band.

m). In addition, 43 min into the sequence both animals were calling within 2 km of each other, yet neither animal appeared to alter its movements or vocalization patterns in response to the other's presence.

The source levels estimated from case 3 are plotted in Fig. 13. The 17-Hz tones are surprisingly weak, reaching a typical spectral density level of only 160–170 dB *re* μPa^2/Hz @ 1 m, around 10 dB weaker than the levels plotted in Fig. 12. However, the source levels of the harmonics are similar for both cases.

D. Source signature recovery for case 3

Precise knowledge of a blue whale's acoustic location allows not only the source levels to be recovered, but also the relative phase between frequency components of a call. Thus the original time series produced by the whale can be estimated, using multichannel deconvolution methods.[15,16,61]

During its final dive before passing FLIP, this whale generated three strong ''type D'' FM downsweeps,[10] plotted in Fig. 9(a). Single-element spectrograms of these signals revealed interesting narrow-band regions of high intensity levels between 60 and 120 Hz. To verify that these regions were not products of waveguide propagation effects, as might be reasonably expected,[62] the source time signatures were estimated for the three calls using a Gauss–Markov estimate [Eq. (4) in Ref. 15]. Calibrated spectrograms of these reconstructed signal estimates are shown in Fig. 14, where the gray scale is in units of source pressure spectral density (dB *re* μPa^2/Hz @ 1 m). The theoretical depth resolution of the MFP results presented here is expected to be within ± 2 m, because frequencies greater than 110 Hz were used in the inversions.

These narrow-band high-intensity regions (indicated by white arrows) are not propagation effects, but seem to be generated within the animal itself. Whenever a harmonic of the FM fundamental passes through this region, the signal level increases by around 5–10 dB.

III. DISCUSSION AND SPECULATIONS

A. General comments

The four whales tracked in this paper provide interesting insights into their acoustic behavior. While blue whales are capable of descending to 100-m depth to feed,[38] all the

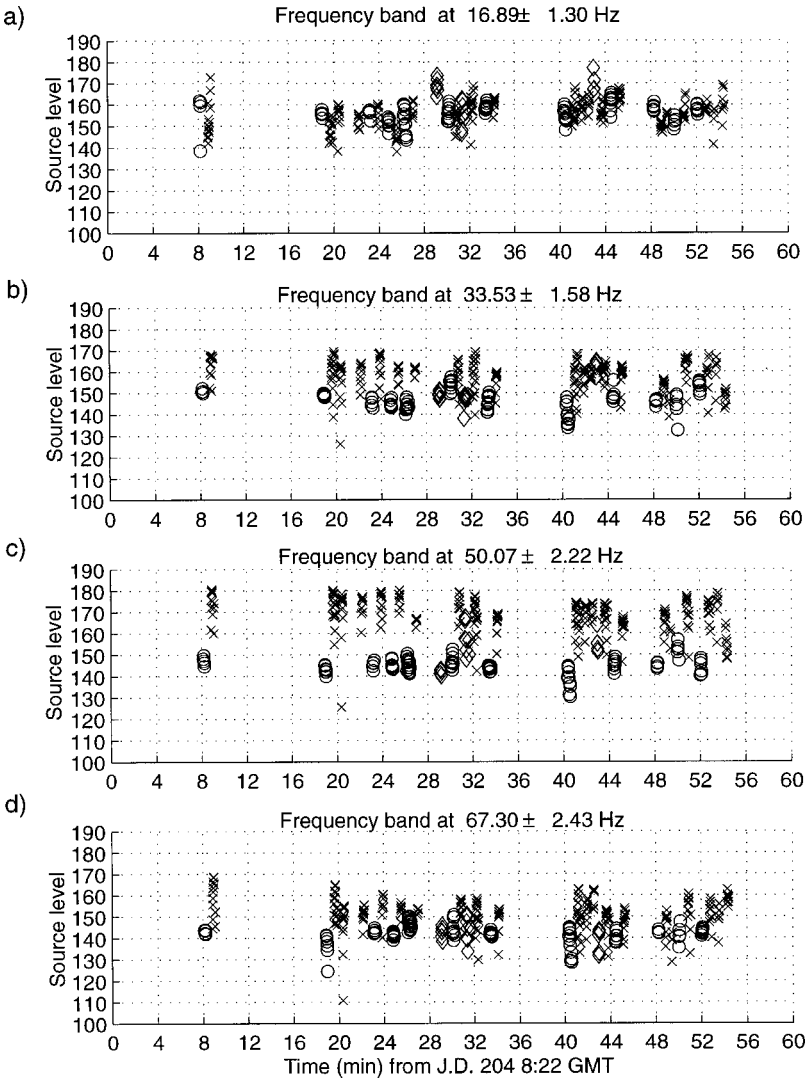

FIG. 13. Estimated source pressure spectral densities in different frequency bands of type A and B calls (dB *re* 1 μPa^2/Hz @ 1 m) for case 3. Call locations were estimated using 30-, 50-, and 65-Hz band information. Circles represent type A calls, ''×'' represents type B, and diamonds represent strongly modulated B and D calls. (a) 17-Hz band; (b) 33-Hz band; (c) 50-Hz band; (d) 67-Hz band.

whales tracked here vocalized between 10- and 40-m depth, whether stationary or transiting. The animal in case 3 yielded four complete dive profiles that show the animal's depth changes only gradually while calling. Most animals swam from east to west at rates of around 2–3 m/s, but one animal remained within 500 m of its original position for 45 min. The case 2 sequence tracked two vocalizing whales simultaneously, including a period when the animals passed within 2 km of each other. However, neither animal appeared to alter its course in response to the other's presence.

Having constructed an environmental propagation model, it is a simple matter to compute both the optimal frequency of propagation, and the depth at which an acoustic source should be placed to minimize transmission losses.[63] The optimum depth for transmitting frequencies between 10–150 Hz in a 130-m deep environment is about 80 m. Over a 10-km propagation range, a 17-Hz source shallower than 40 m would suffer a large transmission loss due to destructive interference between the source and surface reflection. Given the fact that most of the energy in blue whale vocalizations lie under 20 Hz, it seems clear that the vocalization depths of the animals were not acoustically optimized for propagation under the shallow-water conditions present around FLIP.

B. Do blue whales display an internal resonance?

The results of Sec. II D suggest the presence of a possible internal resonance within the animal. A mechanical resonance might be present in the oscillating source (generally assumed to be or near the arytenoid cartilages, see references in Ref. 64), or an air-filled space may act as a resonator that couples with the oscillator, similar in manner to the way the vibration of the double reed within an oboe is influenced by the resonant characteristics of the tube.[65]

The limited samples present here suggest an air-filled resonator may be more likely, because the frequency of this hypothetical resonance seems to increase with the animal's depth, which is what would be expected if an air-filled cavity were being compressed. Unfortunately, the depth-frequency relationship visible does not fit any simple resonator model. For example, the resonant frequency of a bubble of fixed size is proportional to the square root of the external pressure.[66] The first and last call depths are 20 and 30 m, so the resulting external water pressure increase is about 33%, and the expected frequency shift for a resonating bubble is 15%. The regions indicated by the arrows show a much greater frequency shift. In fact, the hypothetical resonance frequency seems to be proportional to the external pressure squared,

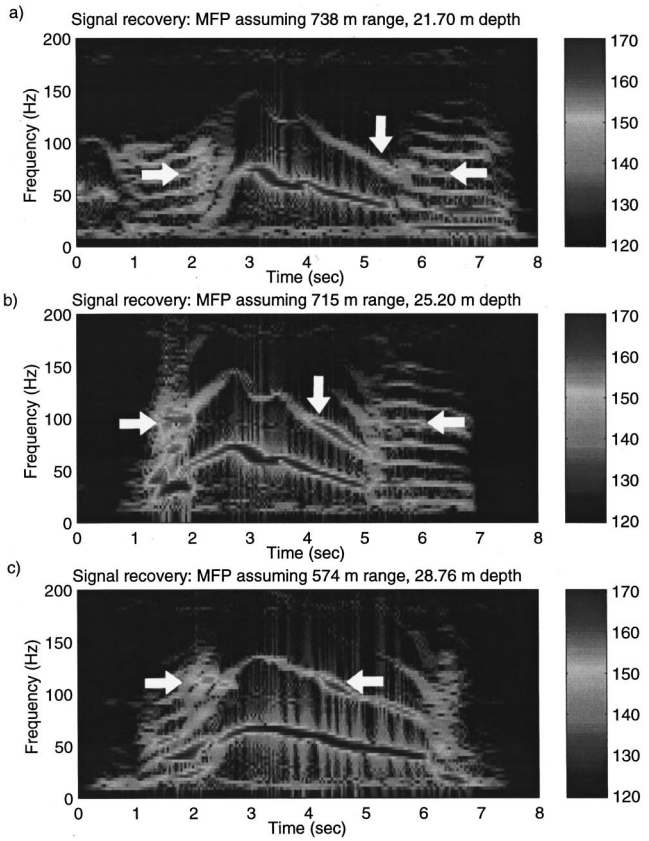

FIG. 14. Source pressure spectral density spectrograms (*re* dB *re* 1 μPa^2/Hz @ 1 m) of estimated source signatures for three ''type D'' FM downsweeps, obtained using multichannel deconvolution and an optimized inverted environment. White arrows indicate speculated resonances of sound-production mechanism: (a) Starting at J.D. 204, 8:51:18 GMT, 738±10 m range, 22 ±2 m depth. (b) Starting at J.D. 204, 8:51:45 GMT, 715±10 m range, 25 ±2 m depth. (c) Starting at J.D. 204, 8:53:28 GMT, 574±10 m range, 29 ±2 m depth.

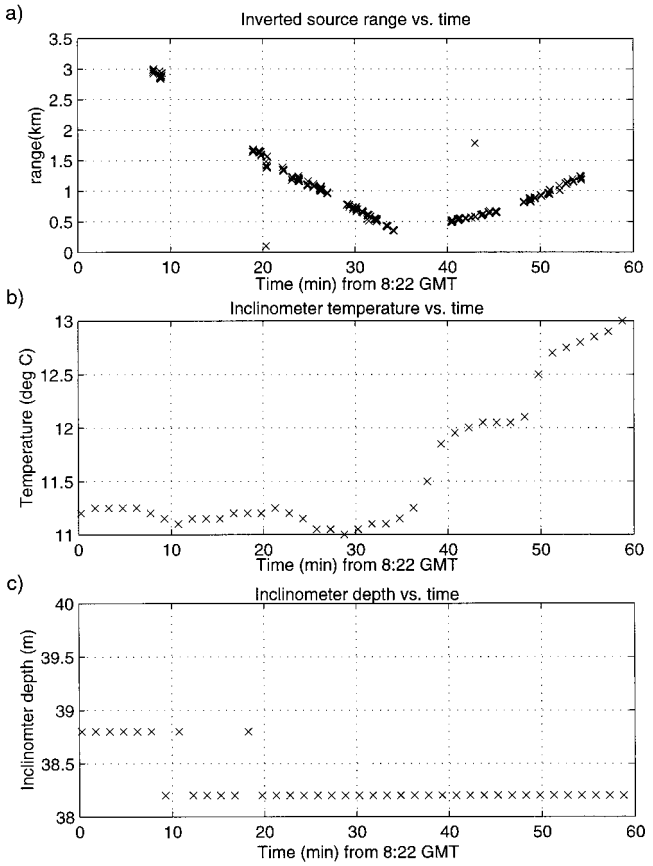

FIG. 15. Comparison between case 3 whale location and local environmental conditions. (a) Range track of blue whale versus time; (b) water temperature (°C) measured at inclinometer versus time; (c) measured inclinometer depth versus time.

instead of the square root. A Helmholtz resonator[66] would also show the same square root dependence on ambient pressure, and a bubble resonator allowed to collapse in volume with depth would still only show a linear dependence on external pressure. It is clear that more samples of these FM downsweeps would be required to answer these questions.

C. Do whales associate with tidal bores?

Another interesting feature associated with case 3 is that the animal's arrival corresponds with a sudden change in oceanic conditions. Figure 15 demonstrates this association by replotting the whale's range versus time in (a), the water temperature at the array inclinometer vs time in (b), and the inclinometer depth in (c). This last plot shows that the temperature change is not caused by a sudden change in the temperature sensor depth (note that the inclinometer depth measurements are quantized in increments of about 0.5 m).

To within the timing resolution of the inclinometer (90 s), the point at which the whale reached its closest approach to FLIP was associated with a 1.0 °C jump in water temperature, followed 10 min later by another 1.0 °C jump. The eventual total temperature increase is 2.5 °C over 30 min. During the previous 11 hours the temperature had remained within 0.5 of 11 °C. This temperature jump was the largest short-term temperature change recorded over the 42 hours of the experiment, and was accompanied by a rapid rotation in the array tilt direction from 300° bearing to about 200°. Unfortunately, heavy cloud cover in the area blocked any useful SST satellite measurements recorded at this time.

An examination of the complete temperature/array tilt record showed that three strong disturbances occur approximately every 12 hours, during which the water temperature rises quickly, and the array tilts to the south. The closest approach of the transiting whale in case 2 also took place in the middle of the previous strong disturbance. These disturbances last less than 2 hours, and then the ocean returns to baseline conditions. The 12-hour spacing of these events suggests a tidal mechanism, during times when the tide level is changing most rapidly. Such behavior might be associated with tidal bores generated along the shelf of San Miguel.[66]

There is anecdotal evidence[67] relating the sightings of whales and other sea life with the presence of strong ocean fronts. Recent work has shown that shorward-propagating internal bores concentrate zooplankton,[68] a propperty that might be exploited by a whale. However, more observations will be required to establish whether whales feed along tidal bores.

IV. CONCLUSION

Matched-field processing (MFP) and global inversion methods have been used to plot the three-dimensional trajec-

tories of four blue whales over periods of up to 90 min and ranges to 8 km. The information needed for the computational models was extracted from the whale calls themselves, using as few as eight hydrophones, spread over a 90-m depth. The extracted values for surface sediment sound-speed estimates lie within ± 50 m/s of those derived from sediment samples collected in the area. These results are believed to be the first successful three-dimensional localizations of a vocalizing baleen whale over long periods of time, and the first successful three-dimensional localizations of marine mammal vocalizations recorded at ranges greater than several water depths from the hydrophone.

The MFP localization and source signature recoveries have raised several interesting questions about the purpose and production mechanism for these calls. The whale in case 3 produced heavily modulated signals that were not stereotyped, atypical behavior for blue whales in this region. In addition, the source level of its fundamental frequency was nearly 20 dB lower than the whales in case 2. These two feature suggest the possibility that this animal might have been a juvenile. This whale's arrival also closely coincided with the arrival of a prominent but short-lived ocean disturbance that changed the ocean temperature by over 2.0 °C over 20 min. Finally, certain FM downsweeps made by this animal display signs of an internal resonance that may be depth-dependent.

Clearly much remains to be learned about the natural acoustic lives of baleen whales, as well as their responses to short- and long-term anthropogenic activities. We hope the potential of some powerful new tools to address these questions has been demonstrated.

ACKNOWLEDGMENTS

The authors would like to thank MPL technical staff and the crew of the R/P FLIP for making the collection of the data used in this paper possible. In particular, the assistance of James Murray and Dave Ensberg is particularly appreciated. They would also like to thank myriad individuals within the Southwest Fisheries Science Center, including Paul Fielder, Alexandra von Saunder, Wayne Perryman, and Jay Barlow. Stu Smith of the Geological Data Center at Scripps provided us with bathymetric information, and useful sediment data was provided by Donn Gorsline of the Department of Marine Geology of the University of Southern California. Peter Gerstoft wrote the extremely useful genetic algorithm inversion package SAGA, and provided a great deal of advice on how to use it. Lisa Schlender of Cascadia Research tried to identify the individual whales videotaped on Julian Day 203. Mike Porter, Mark McDonald, and Dave Mellinger contributed helpful suggestions and insights to the paper. Demultiplexing of the DIFAR sonobuoy data was conducted using software acquired from Greeneridge Sciences, Inc., in Santa Barbara, California. This research was funded by the Office of Naval Research Grant Nos. N00014-97-0593 and N00014-96-1-0603.

[1] A. B. Baggeroer, W. A. Kuperman, and P. N. Mikhalevsky, ''An overview of matched field methods in ocean acoustics,'' IEEE J. Ocean Eng. **18**, 401–424 (1993).

[2] F. B. Jensen, W. A. Kuperman, M. B. Porter, and H. Schmidt, *Computational Ocean Acoustics* (AIP, New York, 1994).

[3] A. B. Baggeroer, W. A. Kuperman, and H. Schmidt, ''Matched field processing: Source localization in correlated noise as an optimum parameter estimation problem,'' J. Acoust. Soc. Am. **83**, 571–587 (1988).

[4] G. D'Spain, W. A. Kuperman, W. S. Hodgkiss, and L. P. Berger, ''3-D localization of a blue whale,'' Scripps Institution of Oceanography, Technical Memorandum MPL TM 447 (1995).

[5] G. L. D'Spain, W. A. Kuperman, W. S. Hodgkiss, and L. P. Berger, ''Three-dimensional localization of a blue whale using broadband matched-field processing for range and depth, and plane-wave adaptive beamforming for azimuth,'' J. Acoust. Soc. Am. **97**, 3353 (A) (1995).

[6] G. L. D'Spain, W. A. Kuperman, C. W. Clark, and D. K. Mellinger, ''Simultaneous source ranging and bottom geoacoustic inversion using shallow water, broadband dispersion of fin whale calls,'' J. Acoust. Soc. Am. **97**, 3353 (A) (1995).

[7] ''Sonobuoy Instruction Manual,'' Naval Weapons Support Center NAVAIR 28-SSQ-500-1 (1983).

[8] K. M. Stafford, C. G. Fox, and D. S. Clark, ''Long-range acoustic detection and localization of blue whale calls in the northeast Pacific Ocean,'' J. Acoust. Soc. Am. **104**, 3616–3625 (1998).

[9] M. A. McDonald, J. A. Hildebrand, and S. C. Webb, ''Blue and fin whales observed on a seafloor array in the Northeast Pacific,'' J. Acoust. Soc. Am. **98**, 712–21 (1995).

[10] A. M. Teranishi, J. A. Hildebrand, M. A. McDonald, S. E. Moore, and K. M. Stafford, ''Acoustic and visual studies of blue whales near the California Channel Islands,'' J. Acoust. Soc. Am. **102**, 3121 (1997).

[11] M. A. McDonald and C. G. Fox, ''Passive acoustic methods applied to fin whale population density estimation,'' J. Acoust. Soc. Am. **1015**, 2643–2651 (1999).

[12] W. A. Watkins and W. E. Schevill, ''Sound source location by arrival times on a non-rigid three-dimensional hydrophone array,'' Deep-Sea Res. **19**, 691–706 (1972).

[13] L. E. Freitag and P. L. Tyack, ''Passive acoustic localization of the Atlantic bottlenose dolphin using whistles and echolocation clicks,'' J. Acoust. Soc. Am. **93**, 2197–2205 (1993).

[14] D. E. McGehee, ''1997 Sperm Whale Abundance and Population Structure Cruise Leg II Sonobuoy Project, Final Report,'' Tracor Applied Sciences T-97-56-0002-U (1997).

[15] S. Finette, P. C. Mignerey, and J. F. Smith, ''Broadband source signature extraction using a vertical array,'' J. Acoust. Soc. Am. **94**, 309–318 (1993).

[16] P. C. Mignerey and S. Finette, ''Multichannel deconvolution of an acoustic transient in an oceanic waveguide,'' J. Acoust. Soc. Am. **92**, 351–364 (1992).

[17] J. A. Rivers, ''Blue whale, *Balaenoptera musculus*, vocalizations from the waters off central California,'' Marine Mammal Science **13**, 186–195 (1997).

[18] P. O. Thompson, L. T. Findley, O. Vidal, and W. C. Cummings, ''Underwater sounds of blue whales, *Balaenoptera musculus*, in the Gulf of California, Mexico,'' Marine Mammal Science **12**, 228–293 (1996).

[19] A. Alling, E. M. Dorsey, and J. C. D. Gordon, ''Blue whales (*Balaenoptera musculus*) off the Northeast Coast of Sri Lanka: Distribution, feeding and individual identification,'' in *Cetaceans and Cetacean Research in the Indian Ocean Sanctuary*, United Nations Mar. Mammal. Tech. Rep. 3, edited by S. Leatherwood and G. P. Donovan (Nairobi, Kenya, 1991), pp. 248–258.

[20] W. C. Cummings and P. O. Thompson, ''Underwater sounds from the blue whale, *Balaenoptera musculus*,'' J. Acoust. Soc. Am. **50**, 1193–1198 (1971).

[21] P. L. Edds, ''Vocalizations of the blue whale, *Balaenoptera musculus*, in the St. Lawrence River,'' J. Mammal. **63**, 345–347 (1982).

[22] A. C. Kibblewhite, R. N. Denham, and D. J. Barnes, ''Unusual low-frequency signals observed in New Zealand waters,'' J. Acoust. Soc. Am. **41**, 644–655 (1967).

[23] D. K. Mellinger and C. W. Clark, ''Characteristics of fin and blue whale vocalizations recorded from IUSS in the north and west Atlantic,'' 11th Biennial Conference on the Biology of Marine Mammals, Orlando, FL, 1995.

[24] J. W. Northrup and W. C. Cummings, ''Underwater 20-Hz signals recorded near Midway Island,'' J. Acoust. Soc. Am. **49**, 1909–1910 (1971).

[25] P. O. Thompson and W. A. Friedl, ''A long term study of low frequency sounds from several species of whales off Oahu, Hawaii,'' Cetology **19**, 1–19 (1982).

[26] J. S. Perkins and W. A. Kuperman, ''Environmental signal processing: Three-dimensional matched-field processing with a vertical array,'' J. Acoust. Soc. Am. **87**, 1553–1556 (1990).
[27] N. O. Booth, P. A. Baxley, J. A. Rice, P. W. Schey, W. S. Hodgkiss, G. L. D'Spain, and J. J. Murray, ''Source localization with broad-band matched-field processing in shallow water,'' IEEE J. Ocean Eng. **21**, 402–412 (1996).
[28] M. D. Collins and W. A. Kuperman, ''Focalization: Environmental focusing and source localization,'' J. Acoust. Soc. Am. **90**, 1410–1422 (1991).
[29] D. F. Gingras and P. Gerstoft, ''Inversion for geometric and geoacoustic parameters in shallow water: Experimental results,'' J. Acoust. Soc. Am. **97**, 3589–3598 (1995).
[30] S. E. Dosso, M. L. Yeremy, J. M. Ozard, and N. R. Chapman, ''Estimation of ocean bottom properties by matched-field inversion of acoustic field data,'' IEEE J. Ocean Eng. **18**, 232–239 (1993).
[31] P. Gerstoft, ''Inversion of seismoacoustic data using genetic algorithms and a posteriori probability distributions,'' J. Acoust. Soc. Am. **95**, 770–782 (1994).
[32] P. Gerstoft, ''Inversion of acoustic data using a combination of genetic algorithms and the Gauss-Newton approach,'' J. Acoust. Soc. Am. **97**, 2181–2190 (1995).
[33] P. Gerstoft and D. F. Gingras, ''Parameter estimation using multifrequency range-dependent acoustic data in shallow water,'' J. Acoust. Soc. Am. **99**, 2839–2851 (1996).
[34] P. Gerstoft, ''SAGA Users Guide 2.0, an inversion software package,'' SACLANT Undersea Research Centre SM-333 (1997).
[35] E. D. Bronson and L. R. Glosten, ''FLIP; Floating Instrument Platform,'' Marine Physical Laboratory, SIO, MPL Tech. Memo MPL-U-27/85 (1985).
[36] ''http://www.nos.noaa.gov/ocrm/nmsp/nmschannelislands.html,'' Vol. 1996, NOAA, 1999.
[37] K. F. Mangels and P. Fiedler, ''Cruise announcement: Whale habitat and prey study (WHAPS95), a marine mammal habitat survey off southern California,'' U. S. Dept. of Commerce, Nat'l Oceanic and Atmos. Admin., Nat'l Marine Fish. Service, Southwest Fish. Sci. Center, Feb (1995).
[38] P. C. Fiedler, S. Reilly, R. P. Hewitt, D. Demer, V. A. Philbrick, S. Smith, W. Armstrong, D. A. Croll, B. R. Tershey, and B. R. Mate, ''Blue whale habitat and prey in the Channel Islands,'' Deep-Sea Res. II **45**, 1781–1801 (1998).
[39] W. S. Hodgkiss, J. C. Nickles, G. L. Edmonds, R. A. Harriss, and G. L. D'Spain, ''A large dynamic range vertical array of acoustic sensors,'' *Full Field Inversion Methods in Ocean and Seismic Acoustics*, edited by O. Diachok (Kluwer, Dordrecht, The Netherlands, 1995).
[40] G. L. D'Spain and W. S. Hodgkiss, ''Array processing with acoustic measurements at a single point in the ocean,'' J. Acoust. Soc. Am. **91**, 2364 (A) (1992).
[41] G. L. D'Spain, W. S. Hodgkiss, and G. L. Edmonds, ''Energetics of the deep ocean's infrasonic sound field,'' J. Acoust. Soc. Am. **89**, 1134–1158 (1991).
[42] L. Davis, *Genetic Algorithms and Simulated Annealing* (Pitman, London, 1987).
[43] D. E. Goldberg, *Genetic Algorithms in Search, Optimization, and Machine Learning* (Addison-Wesley, Reading, MA, 1989).
[44] M. B. Porter, ''The KRAKEN normal mode program,'' SACLANTCEN, Memorandum SM-245, 1991.
[45] J.-M. Q. D. Tran and W. S. Hodgkiss, ''Sound-speed profile inversion using a large aperture vertical line array,'' J. Acoust. Soc. Am. **93**, 803–812 (1993).
[46] P. O. Thompson, ''20-Hz pulses and other vocalizations of fin whales, *Balaenoptera physalus*, in the Gulf of California, Mexico,'' J. Acoust. Soc. Am. **92**, 3051–3057 (1992).
[47] W. A. Watkins, ''Activities and underwater sounds of fin whales,'' Sci. Rep. Whal. Res. Inst. **33**, 83–117 (1981).
[48] W. A. Watkins, P. Tyack, K. E. Moore, and J. E. Bird, ''The 20-Hz signals of finback whales (*Balaenoptera physalus*),'' J. Acoust. Soc. Am. **82**, 1901–1912 (1987).
[49] W. J. Richardson, C. R. Greene, C. I. Malme, and D. H. Thomson, *Marine Mammals and Noise* (Academic, San Diego, 1995).
[50] J. Northrop, W. Cummings, and P. Thompson, ''20-Hz signals observed in the central Pacific,'' J. Acoust. Soc. Am. **43**, 383–384 (1968).
[51] H. Cox, R. M. Zeskind, and M. M. Owen, ''Robust adaptive beamforming,'' IEEE Trans. Acoust., Speech, Signal Process. **35**, 1365–1375 (1987).
[52] R. A. Gramann, ''ABF algorithms implemented at ARL:UT,'' Applied Research Laboratories, University of Texas, ARL-TL-EV-92-31 (1992).
[53] P. K. Yochem and S. Leatherwood, ''Blue Whale,'' in *Handbook of Marine Mammals*, edited by S. H. Ridgway and S. R. Harrison (Harcourt Brace Jovanovich, San Diego, 1985), Vol. 3, p. 223.
[54] G. L. D'Spain, J. J. Murray, W. S. Hodgkiss, N. O. Booth, and P. W. Schey, ''Mirages in shallow water matched field processing,'' J. Acoust. Soc. Am. **105**, 3245–3265 (1999).
[55] W. Perryman, personal communication, 1996.
[56] M. D. Collins, R. J. Cederberg, D. B. King, and S. A. Chin-Bing, ''Comparison of algorithms for solving parabolic wave equations,'' J. Acoust. Soc. Am. **100**, 178–82 (1996).
[57] W. A. Kuperman, M. B. Porter, and J. S. Perkins, ''Rapid computation of acoustic fields in three-dimensional ocean environments,'' J. Acoust. Soc. Am. **89**, 125–33 (1991).
[58] E. L. Hamilton, ''Geoacoustic modeling of the sea floor,'' J. Acoust. Soc. Am. **68**, 1313–1339 (1980).
[59] D. Gorsline, unpublished station data, 1997.
[60] R. T. Bachman, ''Estimating velocity ratio in marine sediment,'' J. Acoust. Soc. Am. **86**, 2029–2031 (1989).
[61] T. C. Yang, ''Broadband source localization and signature estimation,'' J. Acoust. Soc. Am. **93**, 1797–1806 (1993).
[62] S. D. Chuprov, ''Interference structure of a sound field in a layered ocean,'' in *Akustika Okeana. Sovremennoe sostoyanie* (*Ocean Acoustics, Current State*), edited by L. M. Brekhovskikh and I. B. Andreevoi (Nauka, Moscow, 1982), pp. 71–91.
[63] F. B. Jensen and W. A. Kuperman, ''Optimum frequency of propagation in shallow water environments,'' J. Acoust. Soc. Am. **73**, 813–819 (1983).
[64] M. A. McDonald, J. A. Hildebrand, and S. C. Webb, ''On the sound production mechanism of blue whales'' (unpublished).
[65] N. H. Fletcher, *The Physical of Musical Instruments* (Springer-Verlag, New York, 1991).
[66] M. Hendershott, personal communication, 1999.
[67] J. Barlow, personal communication, 1999.
[68] J. Pineada, ''Circulation and larval distribution in internal tidal bore warm fronts,'' Limnology and Oceanography **44**, 1400–1414 (1999).

Matched-field replica model optimization and bottom property inversion in shallow water

Paul A. Baxley and Newell O. Booth
Space and Naval Warfare Systems Center, San Diego, Electromagnetics and Advanced Technology Division, Acoustic Branch, Code D857, San Diego, California 92152-5001

William S. Hodgkiss
Marine Physical Laboratory, Scripps Institution of Oceanography, University of California San Diego, San Diego, California 92152-6400

(Received 3 November 1998; revised 2 November 1999; accepted 16 November 1999)

Matched-field replica models based on an inaccurate knowledge of geoacoustic parameters such as bottom attenuation, shear, and interfacial sound-speed discontinuities, can predict an incorrect number of propagating modes for a shallow-water channel. The resulting degradation in the matched-field ambiguity surface can be substantially reduced by obtaining optimal replica models via modal-sum-limit optimization or bottom-property inversion. The use of these techniques for multi-tone (70, 95, 145, and 195 Hz) source-tow data recorded near San Diego during the first Shallow-Water Evaluation Cell Experiment (SWellEX-1) significantly increased matched-field correlation levels and improved source localization relative to results obtained with a previous nonoptimized model. The predicted number of propagating modes was also reduced substantially. The inversion for bottom properties (attenuation, interfacial sound-speed discontinuities, no shear) provided sediment attenuation estimates which agree well with Hamilton's models and were an order-of-magnitude greater than that used in the nonoptimized model, which accounts for the reduction in the number of modes. A simulated modal decomposition using the inverted optimal replica model verifies the number of modes predicted by the modal-sum-limit optimization. [S0001-4966(00)00103-X]

PACS numbers: 43.30.Pc, 43.30.Wi, 43.30.Bp [DLB]

INTRODUCTION

The ability of a matched-field processor[1–4] (MFP) to successfully localize an underwater sound source is highly dependent upon the accuracy of the replica model to which data are matched. Hence, a large body of work has been devoted to studying the sensitivity of MFP localization to mismatch errors since the mid-1980's. These have included examinations of mismatch in sound-speed profile,[1,5–13] water depth,[9,13–15] bottom properties,[5–6,9,10,13,15,16] array parameters (array tilt or placement, or element locations),[8,11,15,16] and errors introduced by sea surface roughness[17–19] and internal waves.[18,20,21]

A high sensitivity to mismatch, however, does not render the source localization problem hopeless, for this sensitivity enables one to invert for mismatched parameters by performing searches over these parameters until an optimal response is obtained. In essence the search space for the inverse problem is widened from simply source location to the number of parameters believed to be controlling the acoustic propagation. While the techniques vary from simple recalculations for each combination of parameters to complex nonlinear search techniques such as simulated annealing or genetic algorithms, successful inversions have been performed for parameters such as under-ice reflection amplitudes and phases,[22] ocean sound-speed structure,[23–26] bottom properties,[5,27–30] array tilt,[15] and array element locations.[31]

The purpose of this study is to obtain an optimal replica model for a shallow-water testbed off the coast of San Diego, California, thus providing a ''ground truth'' baseline for ongoing MFP studies[32–36] in this area. This is accomplished via an analysis of nearly constant-water-depth multi-tone source-tow data recorded on a vertical line array (VLA) during the first Shallow-Water Evaluation Cell Experiment (SWellEX-1), which took place in August 1993. Since an extensive CTD survey performed during the experiment revealed a stable sound-speed structure in both space and time, a constant sound-speed profile was assumed. Therefore, the replica model optimization will only address the issues of bottom-induced mismatch, neglecting the effects water mass fluctuations (e.g., internal waves).

Optimizations presented here focus on the reduction of mismatch effects which result in an incorrect prediction of the number of propagating modes. This may be caused by inaccurate knowledge of geoacoustic parameters such as bottom (intrinsic) attenuation, interfacial sound-speed discontinuities, or from conversion to shear waves, multiple reflections in layers, reflector roughness, and scattering by inhomogeneities. Since these causes manifest themselves in one major parameter, namely, the modal-sum-limit, an optimal replica model can be determined by varying this parameter until the correlation is optimized. This approach uses the total ''effective'' attenuation as its basis for optimization, without regard for the determination of specific bottom parameters which may contribute to this total effect. A second approach is to invert directly for specific bottom parameters thought to be prime contributors to the modal-sum-limit er-

ror, via repeated solutions of the forward problem for combinations of these parameters.

A description of the SWellEX-1 data set used in this analysis is presented in Sec. I along with a discussion of the acoustic environment and the original replica model used to characterize it. The performance for this nonoptimized model provides the baseline to which that for the optimized models will be compared. Evidence that the original replica model overestimates the number of propagating modes is provided. Section II presents the Bartlett estimator, used for all matched-field calculations. Section III discusses the two approaches used to obtain optimal replica models, namely, modal-sum-limit optimization (MSLO) and explicit bottom property inversion. Section IV presents the optimization results at selected times for these two approaches along with an optimization to determine the position of the array in the water column. The MFP performance using the optimized models over the entire period of the source-tow is compared to the original baseline model in Sec. V. Conclusions and recommendations are discussed in Sec. VI.

I. SWELLEX-1 DATA SET

A. SWellEX-1 experiment description

The first Shallow-Water Evaluation Cell Experiment (SWellEX-1)[37] (as well as SWellEX-3[38] and SWellEX-96[39]) was conducted in 50–200-m water southwest of Point Loma (the entrance to San Diego Harbor). A 48-element, 88.125-m aperture vertical line array (VLA) was mounted beneath the research platform FLIP in 198 m of water (32°, 36 42′ N, 117° 21.48′ W). This study only considers data recorded by the VLA during a range-independent constant-wavelength-comb (CW-comb) source-tow on August 17, 1993. The source-tow track (G-to-I track, 1615 to 1735 Zulu), shown in Fig. 1 with the location of FLIP and the bathymetric contours, is directed northward from FLIP, following roughly the 200-m isobath (except near the end of the northward excursion). The entire northward track represents approximately 80 min of data (from 1615 to 1735 Zulu). The CW-comb source transmitted tonals at 70, 95, 145, 195, 275, 370, 550, and 745 Hz, but only the first four were analyzed because of the poor data quality at the higher frequencies. The average source depth and speed for the track were 83.3 m and 1.58 m/s (3.07 knots), respectively. Figure 2 shows the source depth, bathymetry, and bottom layer profile along the track and the position of the VLA in the water column. Although there is lateral variability, particularly near the end of the track, it appears to be mild enough to warrant a range-independent assumption.

The VLA was deployed such that the 88.125-m aperture occupied the lower portions of the 198-m water column. The element spacing was 1.875 m and the bottom phone was originally assumed to be 4.5 m above the seafloor. Optimization results presented in Sec. IV suggest that a bottom-phone-depth of 8.5 m is more accurate. Since the VLA was suspended below FLIP and the motion of the lower end of the array was unconstrained, it was subject to deviations from the vertical orientation resulting from the surface-wave-induced motion of FLIP. Tilt angles oscillating in a translating pendulum fashion between ±1° with a period of roughly 50 s were observed, corresponding to the 53-s period of FLIP's rocking motion. The effect of this tilt on MFP performance appears to be negligible at the frequencies considered.

The entire 80-min data set was processed using 8192-point FFTs with 50% overlap, resulting in a total of 1775 FFT samples. With a sampling rate of 1500 samples/s, the binwidth was 0.1831 Hz, the FFT length was 5.46 s, and the time between consecutive samples was 2.73 s. For this analysis, only the tonal bins were saved for processing. The center frequencies of the bins containing the four tonals considered were 69.95 Hz, 95.03 Hz, 145.02 Hz, and 195.01 Hz.

B. Original replica model

The environmental properties used in previous analyses[40] for the original replica model for this area are summarized graphically in Fig. 3. Figure 3(a) shows both the water column and the bottom, while Fig. 3(b) shows a close-up for the water column. These are based on CTD measurements at the array site and a geoacoustic model developed by Bachman.[41,42] The bottom depth was assumed to be 198 m and range independent. The bottom was modeled as a 30-m silty-sand sediment layer overlying an 800-m mudstone (Tertiary) basement above a Cretaceous sandstone subbottom (modeled as a semi-infinite half-space). The bottom properties for each layer are summarized in tabular form in Table I. A linear upward refracting compressional sound-speed profile is assumed for the sediment and mudstone, while the subbottom is assumed to be isovelocity. The density and compressional wave attenuation is assumed constant in each layer with the exception of the compressional wave attenuation in the sediment, which increases slightly with depth. All media are assumed to be fluid (no shear).

The performance using this original replica model provides the baseline to which that obtained for optimized models will be compared. In performing MFP for this baseline case, replicas were calculated via the inclusion of modes with phase velocities up to 2100 m/s (corresponding to 21 modes at 70 Hz, 28 modes at 95 Hz, 43 modes are 145 Hz, and 58 modes at 195 Hz). Modes with higher phase velocities have been found to contribute little to the field.

C. Data model comparison

The general quality of a replica model can be easily tested by comparing its predicted power across the array as a function of source range with the measured value. Figure 4 shows such a comparison for the 70-Hz tonal. Figure 4(a) presents the uncalibrated data power across the array as a function of time, while Fig. 4(b) presents the simulated power calculated by the KRAKEN[43] normal mode code for the environmental model of Fig. 3. The ranges in the range axis of the simulation correspond approximately to those traversed by the nearly constant-speed source over the 80-min period. The source depth in these simulations was assumed to be 83 m, which is the average depth over the track. To facilitate comparison the dynamic range for both the data and simulation was set at 50 dB, with the data scale being trans-

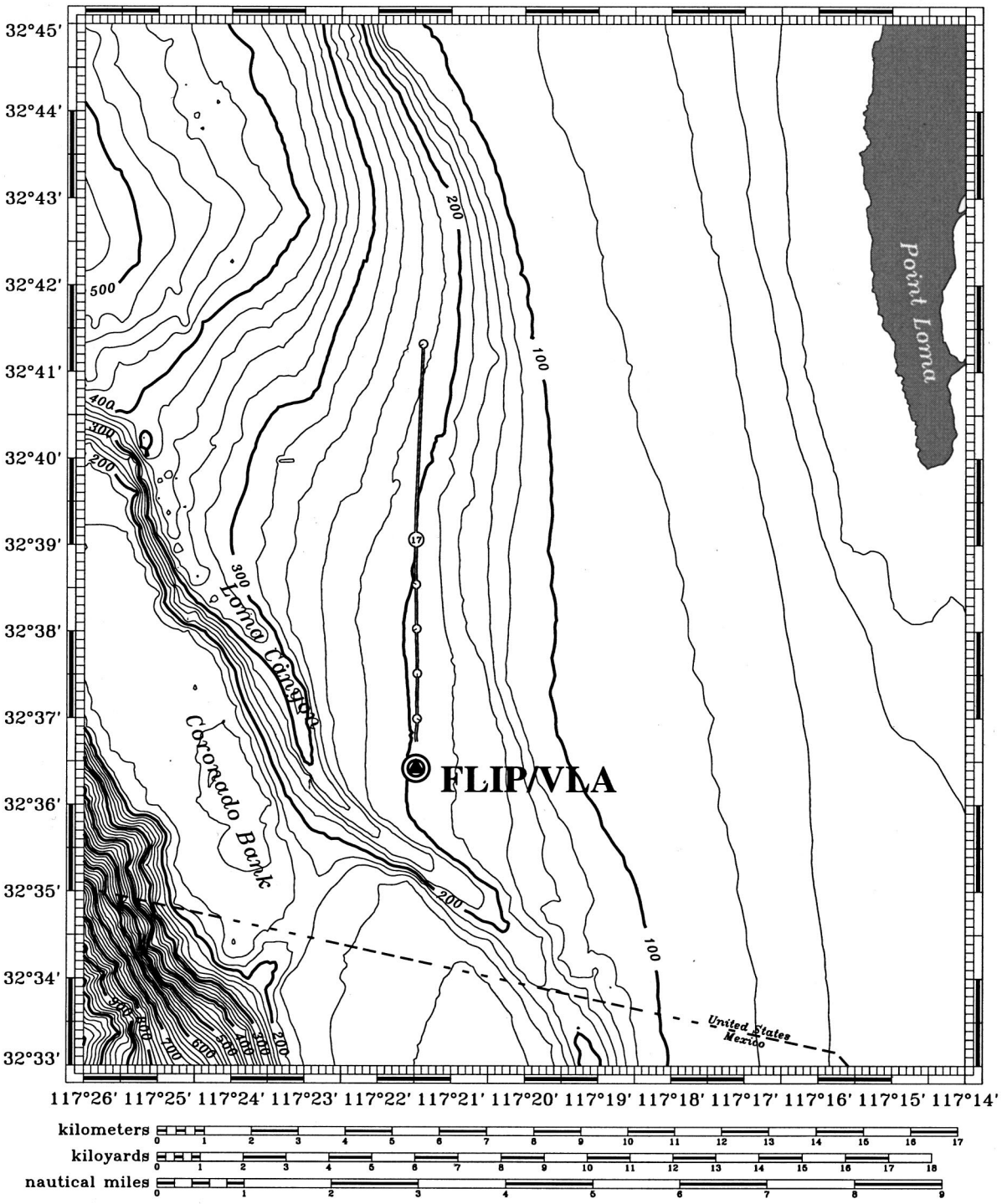

FIG. 1. SWellEX-1 test site and source-tow track analyzed in this study. Isobath intervals are 20 m. Source-tow direction is northward from FLIP. (Courtesy of Joe Rice, SSC San Diego, Code D857.)

lated until comparison was optimized. Clearly, the simulated field exhibits a much finer structure than that observed in the data. The obvious conclusion is that more modes are surviving in the replica model than observed in the data. Similar comparisons for the other tonals yield the same conclusion.

Optimizations to remedy this incorrect prediction of the number of propagating modes are clearly required. Replica model mismatch of several bottom properties can account for this error. Of major significance are intrinsic attenuation, which directly determines which modes are stripped out of the field, and interfacial sound-speed discontinuities, which determine the partitioning of reflected and transmitted energy via the critical angle. Conversion of compressional energy to shear waves can also be a factor. The effects of variations in the first two of these properties are the focus of this study.

II. BARTLETT MFP

The measure of the match or correlation between the observed pressure p_n^o at each phone of an N-phone array and

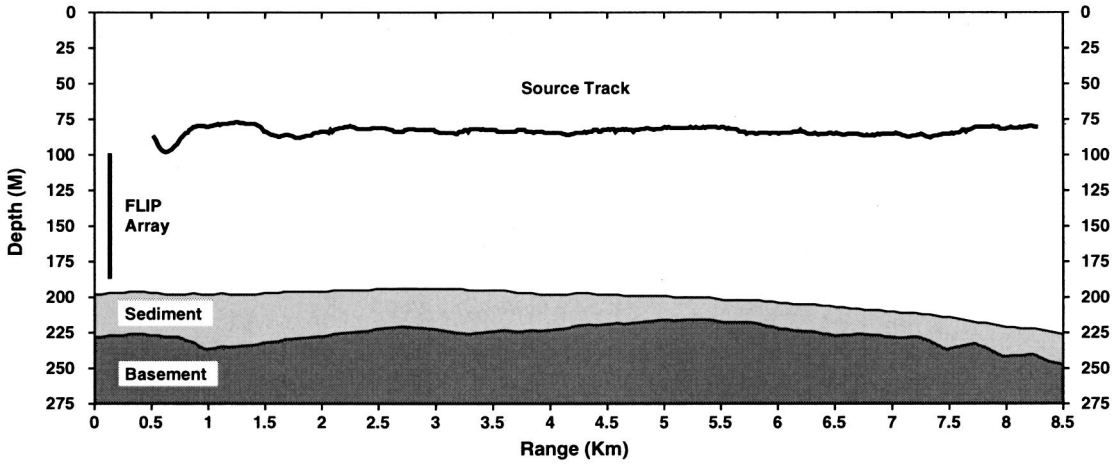

FIG. 2. Bathymetry and bottom layer profile along source-tow track. (Courtesy of Phil Schey, SSC San Diego, Code D857.)

the predicted pressure $p_n(\mathbf{x})$ at the same phones for an assumed target location $\mathbf{x}$ may be given by the normalized Bartlett estimator:[4]

$$\hat{B}_{\mathrm{BART}}(\mathbf{x}) = \frac{\Sigma_{n=1}^{N}\Sigma_{m=1}^{N} p_m^*(\mathbf{x})\hat{R}_{mn}p_n(\mathbf{x})}{\Sigma_{n=1}^{N}|p_n(\mathbf{x})|^2}, \tag{1}$$

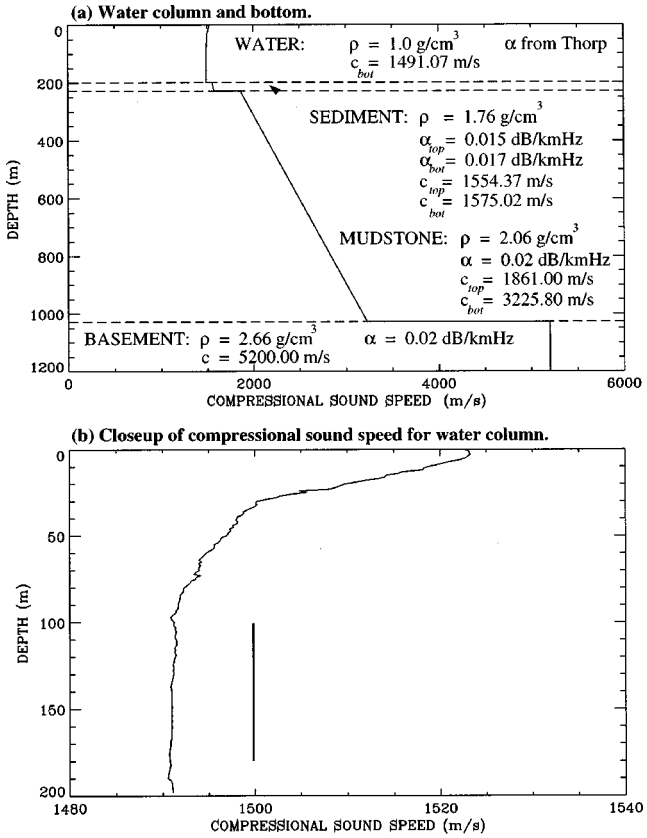

FIG. 3. Original replica model used in previous analyses (Ref. 40). (a) Water column and bottom. (b) Close-up of compressional sound-speed profile in water column and position of VLA. In the computation of replica pressures, this model is assumed to valid over the entire source-tow track and only modes with phase velocities less than 2100 m/s are included in the modal sum. In each layer, c is the compressional sound speed, ρ is the density, and α is the intrinsic volume attenuation. The subscripts *top* and *bot* indicate values at the top and bottom of a layer, respectively. The absence of a subscript implies the parameter is constant throughout the layer.

where $\hat{R}_{mn}$ is the normalized time-averaged cross-spectral matrix. In this study, $R_{mn}=\overline{p_m^o p_n^{o*}}$ is normalized by its trace as follows:

$$\hat{R}_{mn} = \frac{R_{mn}}{\Sigma_{l=1}^{N}|p_l^o|^2}. \tag{2}$$

For the case of a VLA in an azimuthally symmetric (range-independent) environment, $\mathbf{x}$ is a two-dimensional vector with components r, source range, and d, source depth. Therefore Eq. (1) applied to a VLA is a surface, commonly referred to as an ambiguity surface, which plots correlation as a function of candidate source ranges and depths. The highest correlation should provide an estimate of the true source location. However, because of the repetitive nature of the modal-interference pattern in shallow water, high correlations will also occur at source locations that produce an acoustic field at the VLA resembling the field produced by the actual source at the true location. These false peaks, or sidelobes, can be quite large in shallow-water waveguides, but will be lower than the true peak if the replica model is known exactly. Inaccurate knowledge of some parameters in the replica model can, depending on the degree of the inaccuracy, degrade the main peak to the extent that it is no longer the maximum. The result is an incorrect estimate of the source location, reporting either a sidelobe as the main peak, or a peak caused by noise in the data.

With the exception of the modal-sum-limit optimizations presented in Sec. IV, 500 candidate source ranges from 20 m to 10 km at 20-m increments and 100 candidate source

TABLE I. Bottom properties of the original replica model.

Depth (m)	Compressional wave speed (m/s)	Compressional wave attenuation [dB/km Hz]	Density (g/cm^3)	Bottom type
198.0	1554.37	0.015	1.76	sediment
228.0	1575.02	0.017	1.76	
228.0	1861.0	0.020	2.06	mudstone
1028.0	3225.80	0.020	2.06	
1028.0	5200.00	0.020	2.66	basement

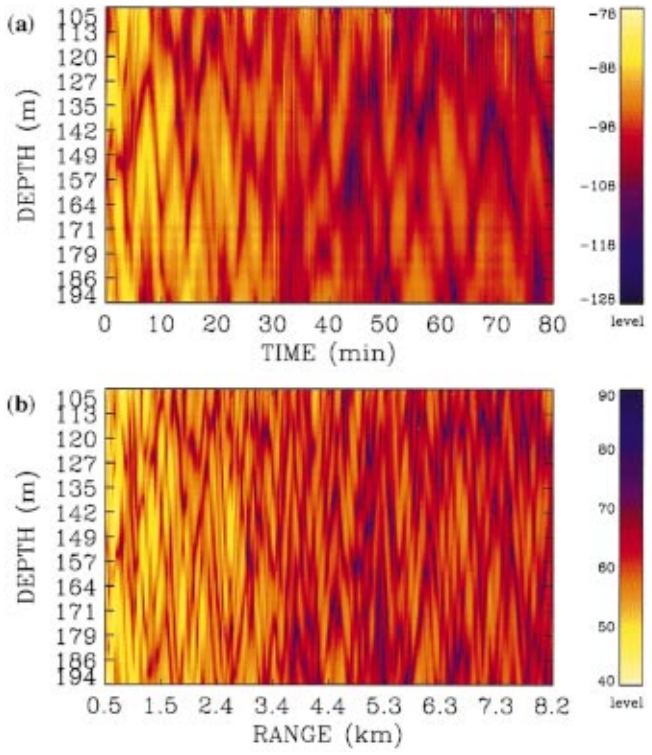

FIG. 4. 70-Hz data-model power comparison across VLA. (a) Uncalibrated data power across VLA versus time. (b) Simulated transmission loss (KRAKEN normal-mode solution) across VLA using original replica model in Fig. 3 versus source range traversed during source-tow. Vertical axes span the aperture of the VLA.

depths from 2 m to 200 m at 2-m increments were used in the generation of the ambiguity surfaces. The modal-sum-limit optimizations differed only in that 40 source depths from 5 to 200 m at 5-m increments were used.

III. OPTIMIZATION APPROACHES

In the discussion of the optimization approaches, it is useful to use the mode characterization of the acoustic field. According to normal mode theory,[43,44] the single-frequency complex pressure at a depth z and range r produced by a source at depth z_s in a constant-water-depth waveguide with arbitrary sound speed profile $c(z)$ is given by

$$p(r,z)=Cr^{-1/2}\sum_{m=1}^{\infty}\phi_m(z_s)\phi_m(z)k_m^{-1/2}e^{ik_m r}, \tag{3}$$

where ϕ_m are the depth-dependent mode functions, k_m are the horizontal propagation constants for each mode, and $C=ie^{-i\pi/4}/\rho(z_s)\sqrt{8\pi}$ characterizes the source strength, ρ being the depth-dependent density of the medium. The quantity $\nu_{p_m}=\omega/re(k_m)$ is known as the phase velocity of the mth mode. The modal grazing angle of mode m is defined as $\theta_{m_g}=\cos^{-1}(c_w/\nu_{p_m})$, where c_w is the sound speed of the water at the seafloor. An incorrect prediction of the number of propagating modes results primarily from an inaccurate estimate of the imaginary part of the horizontal propagation constant k_{m_i}.

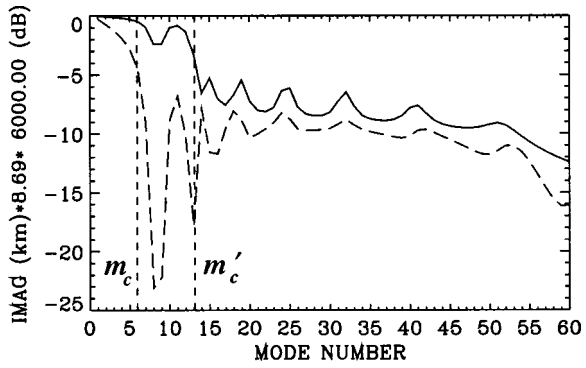

FIG. 5. Effect of sediment attenuation variation on the 70-Hz, 6-km modal attenuation, Imag(k_m)*8.69*6000, versus mode number. Solid line: original replica model ($\alpha=0.015$ to 0.017 dB/km Hz). Dashed line: original replica model with sediment attenuation increased by a factor of 10 ($\alpha=0.15$ to 0.17 dB/km Hz). Vertical dashed lines indicate the modes m_c and m_c' for which the modal grazing angle at the water-sediment interface first exceeds (1) the critical angle at water-sediment interface θ_c, and (2) the grazing angle θ_c' at water-sediment interface giving rise to a critical angle at the sediment-mudstone interface.

A. Effect of bottom properties on modal attenuation k_{m_i}

Figures 5 and 6 demonstrate how variations in sediment attenuation and water/sediment sound-speed discontinuity, respectively, can affect the value of k_{m_i}. The solid line in these figures represents the 70-Hz KRAKEN solution for k_{m_i} using the original replica model of Fig. 3. The value of k_{m_i} has been rescaled to provide the modal attenuation in decibels at a range of 6.0 km ($10\log[8.69\cdot k_{m_i}\cdot 6000]$, where k_{m_i} is in units of nepers/m).[43] The vertical dashed lines indicate the modes m_c and m_c' for which the modal grazing angle at the water-sediment interface θ_{m_g} first exceeds (1) the critical angle at the water-sediment interface θ_c and (2) the grazing angle at the water-sediment interface θ_c' which gives rise to a critical angle at the sediment-mudstone interface. Figure 5 shows the effect of increasing the sediment attenuation by a factor of 10 (from $\alpha=0.015$ dB/km Hz to $\alpha=0.15$ dB/km Hz at the water/sediment interface; dashed curve).

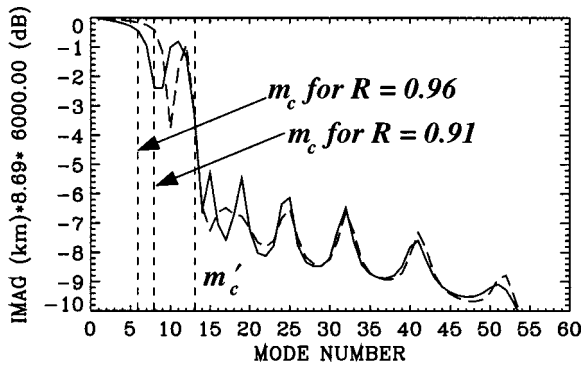

FIG. 6. Effect of water/sediment sound-speed discontinuity variation on the 70-Hz, 6-km modal attenuation, Imag(k_m)*8.69*6000, versus mode number. Solid line: original replica model (R = water-to-sediment sound speed ratio at seafloor = 0.96). Dashed line: original replica model with sound speed in sediment increased by 5% ($R=0.91$). Vertical dashed lines indicate the modes m_c and m_c' as in Fig. 5. Note that m_c is increased from 6 to 8 as the sound speed in the sediment is increased by 5%.

Figure 6 shows the effect of decreasing the ratio of water sound speed to sediment sound speed at the water-sediment interface R by 5% (from $R=1491.07/1554.37=0.96$ to $R=1491.07/1632.09=0.91$; dashed curve). In both figures, the first major increase in modal attenuation is seen to coincide with the transition to supercritical modes ($\theta_{m_g}>\theta_c$) at $m_c=6$, while the second increase occurs when $\theta_{m_g}>\theta_c'$ at $m_c'=13$. The effect of increasing the intrinsic attenuation in Fig. 5 is an increase in modal attenuation, primarily for modes between m_c and m_c'. The basic shape of the distribution, however, remains unchanged. The main effect of decreasing R in Fig. 6 is seen to be a change in the shape of the modal distribution; the curve is shifted in the direction of higher modes and compressed against the m_c' boundary. This is a result of the increase of θ_c caused by the increase in the sound speed in the sediment. The resulting increase in m_c to higher modes causes modes which were highly attenuated in the original model to be propagated. These effects on k_{m_i} obviously effect the number of propagating modes; errors in intrinsic attenuation inaccurately describe the attenuation of each mode, while errors in R inaccurately describe the partitioning of reflected and transmitted energy, and hence how the modes are filtered.

It should be noted here that changes in sediment attenuation and interfacial sound-speed discontinuities were observed to have very little effect on the real part of the horizontal propagation constant k_{m_r} or the mode functions ϕ_m. This suggests that the major impact of variations in these parameters will be a change in the number of propagation modes, and not the shape of the mode functions themselves.

The number of propagating modes may also depend on the conversion of compressional wave energy in the water column to shear wave energy, if the seafloor is elastic. At frequencies above 10 Hz, however, shear waves normally experience greater absorption than compressional waves as they propagate through the bottom layers. In addition, the shear speed in the seabed is often much less than the compressional sound speed in the water, so that energy is propagated downward at steep angles and seldom returns to the water column.[45] This extraction of energy from the problem is manifested as an increased attenuation in the bottom. An application of Tindle and Zhang's[46] equivalent-fluid approximation at the water-sediment interface of the original replica model, with shear added to the sediment ($c_s=112.6$ m/s, $\alpha_s=17.0$ db/km Hz), verifies this by predicting an effective increase in the sediment compressional attenuation of 0.005 dB/km Hz. Shear wave effects on the number of propagating modes may therefore simply be incorporated into the attenuation parameter.

B. Modal-sum-limit optimization

The mode-filtering character of the k_{m_i} distribution implies that the modal sum of Eq. (3) need not be extended to infinity in practice. Instead, the sum may be taken up to a practical modal-sum-limit M, beyond which the influence of the higher modes is negligible. Therefore, assuming that the mode functions ϕ_m accurately describe the measured field, a replica model based on Eq. (3) with a modal-sum-limit of M should yield a correlation close to unity at the correct source location. If, however, the replica model predicts significantly different values for k_{m_i}, it will predict $L\neq M$ propagating modes. Since the correlation in Eq. (1) is now attempting to match a sum of M significant terms (in p_n^o) to a sum of $L\neq M$ significant terms (in p_n), the result at the true source location will be a value less than unity. This, in turn, decreases the chances of this value remaining the maximum throughout the surface, destroying localization.

Modal-sum-limit optimization disregards the specific geoacoustic parameters responsible for the mismatch in the number of propagating modes, and simply attempts to determine the optimal number of propagating modes directly. This is accomplished via repeated evaluations of the Bartlett estimator in Eq. (1) with the predicted pressures $p_n(\mathbf{x})$ calculated by Eq. (3) for varying values of the modal-sum-limit M. The mode functions ϕ_m are computed using KRAKENC, a version of KRAKEN[43] which finds eigenvalues in the complex plane. A maximum value of the Bartlett estimator at the true source location then occurs for the optimal modal-sum-limit. The technique has been used previously by Livingston and Diachok[22] to determine the number of waterborne propagating modes in a deep-water Arctic environment. This approach represents at attempt to optimize over the total ''effective'' modal attenuation, without regard to the causes contributing to that total. Implied in this approach is the assumption that the shape of the mode functions is little effected by the mismatched parameters causing the errors in the predicted number of propagating modes; a reasonable assumption based on the simulations that produced Figs. 5 and 6.

Since the VLA does not span the full water column, a determination of the exact number of propagating modes requires that the true number of propagating modes in the data is less than or equal to the number of modes that can be resolved by the VLA. However, even if this condition does not hold, the technique can be used to estimate the modal-sum-limit, since the VLA can discriminate between groups of modes. Hence, the modal-sum-limit is estimated by selecting the mode number with the highest correlation among a set of modes with similar correlation levels. A modal decomposition can also be used to determine the upper limit of the propagating modes; however, the reduced modal resolution for the limited-aperture VLA makes accurate determination of the limit difficult.

C. Bottom-property inversion

If geoacoustic parameter determination, as well as replica model optimization, is an objective, then geoacoustic-parameter inversion must be performed. This process focuses on the determination of the specific physical causes of the mismatch errors. This technique is implemented by repeated evaluations of the Bartlett estimator in Eq. (1) with the predicted pressures $p_n(\mathbf{x})$ calculated by Eq. (3) for varying values of the bottom parameters which significantly impact the solution. The mode functions ϕ_m are computed using KRAKENC. A maximum value for the Bartlett estimator at the true source location then occurs for the optimal set of bottom

parameters, thus providing the optimal inverted replica model. While the modal-sum-limit approach is specialized to situations in which the main mismatch effect is an incorrect prediction of the number of modes, the bottom-property inversion approach has general applicability to any type of mismatch effect.

This approach can be much more time consuming and computationally intensive than the modal-sum-limit optimization approach, since the number of search parameters can be large. However, if the primary mismatch effect is an incorrect prediction of the number of modes, as is postulated to be the case for the SWellEX-1 data, then the search space can be reduced to those parameters known to produce such an effect. It will be assumed that the major properties impacting the modal-sum-limit M are intrinsic bottom attenuation in the bottom layers and interfacial sound-speed discontinuities between the layers. As already noted, the effects of shear wave conversion are believed to be small, and will be incorporated into the attenuation parameters.

In setting up the search space, it is noted from Fig. 3 that the large thickness of the mudstone layer (800 m) effectively prevents energy from interacting with the basement, at least at any significant range from the source. Therefore, basement properties and the mudstone-basement interface need not be considered in the inversion. This means then that the minimum search space is composed of four parameters: (1) the intrinsic attenuation in the sediment; (2) the intrinsic attenuation in the mudstone; (3) the sound-speed discontinuity at the water-sediment interface; and (4) the sound-speed discontinuity at the sediment-mudstone interface. This does not necessarily imply, however, that all four parameters need to be searched simultaneously. Figures 5 and 6 suggest that effects caused by changes in bottom layer attenuation may be independent of effects caused by changes in interfacial sound-speed discontinuities. If this is assumed to be true, then a two-parameter search for the intrinsic attenuation in the sediment and mudstone layers can first be performed, followed by a second two-parameter search for the interfacial sound-speed discontinuity at the water-sediment and sediment-mudstone interfaces. The second search uses the optimal values for the attenuations determined in the first search. Variations of the sound-speed parameters were accomplished via a translation of the sound-speed profile in the sediment and mudstone layers; hence the search parameters were actually the sound speed at the top of each layer. Finally, the assumption of independent effects can be tested by repeating the attenuation search using the optimal values obtained by the sound-speed discontinuity search; if the final estimates of the attenuations differ little from those obtained by the first search, then the assumption is validated.

D. Array position optimization (APO)

Since array element localization (AEL) measurements were not performed during the time period for the data analyzed, the exact vertical placement of the VLA in the water column was not known *a priori*. An optimization was therefore performed for this parameter in order to maximize the MFP correlations. This was accomplished via the repeated evaluation of the Bartlett estimator in Eq. (1) with the predicted pressures $p_n(\mathbf{x})$ calculated by Eq. (3) for varying phone depths resulting from vertical translations of the VLA. Since the phone separations remain constant, the translation of the VLA was characterized by the variation of a single parameter; namely, the bottom-phone height above the seafloor. A maximum value of the Bartlett estimator at the true source location then occurs for the optimal bottom-phone height. The optimization was only performed for the 195-Hz tonal, since performance is most sensitive to these errors at the higher frequencies. The modal-sum-limit optimization was performed with and without array position optimization, so that the magnitude of errors in array position could be identified. All bottom-property inversions used the optimal array position.

IV. OPTIMIZATION RESULTS

A. Modal-sum-limit optimization

The modal-sum-limit optimization was performed at a time 54.6 min (FFT number 1201) from the start of the track, when the source was at a range of 5.76 km and a depth of 85 m. FFT averaging was not performed so that only 5.46 s (the FFT length) was involved. Matched-field ambiguity surfaces were calculated via the Bartlett estimator in Eq. (1) with the modal-sum-limit M in the predicted pressures $p_n(\mathbf{x})$ [Eq. (3)] taking on values from 1 to 40.

Figure 7 plots the maximum correlation in the full ambiguity surface (solid line) and the maximum correlation in a small window containing the true source location (extending from 5.4 to 6.2 km in range and 60 to 100 m in depth; dashed line) as a function of the number of modes M included in the sum of Eq. (3). Figure 7(a) is for the 70-Hz tonal, 7(b) for the 95-Hz tonal, 7(c) for the 145-Hz tonal, and 7(d) for the 195-Hz tonal. The observed trend with increasing M is an initial increase in the maximum level up to a peak at some number of modes M_0, followed by a decrease which levels off to a nearly constant level for further increases of M. M_0 is the optimal number of modes. The lower correlations for $M<M_0$ indicate that too few modes have been included in the replica sum, while the those for $M>M_0$ indicate that too many modes have been included. The constant value at the higher modes indicates that these modes are insignificant in both the data and the replica model.

For the 70-Hz and 95-Hz tonals, the peak at M_0 in the window coincides with that over the entire surface; however, the maximum correlations drop to lower levels at higher M for the windowed case. The divergence of the two curves for the 145-Hz and 195-Hz tonals will be shown in the next section to be the result of an inaccurate assumption regarding the vertical placement of the array in the water column, which affects performance primarily at the higher frequencies. But even with these discrepancies, the curves for the windowed case exhibit a peak near the same mode numbers for which a peak is observed in the full surface. Considering only the full-surface curves, the optimal number of modes M_0 is presented in Table II.

Also shown in Table II is the critical mode number M_c, which indicates the first mode whose modal grazing angle θ_{m_g} at the water-sediment interface exceeds the critical angle

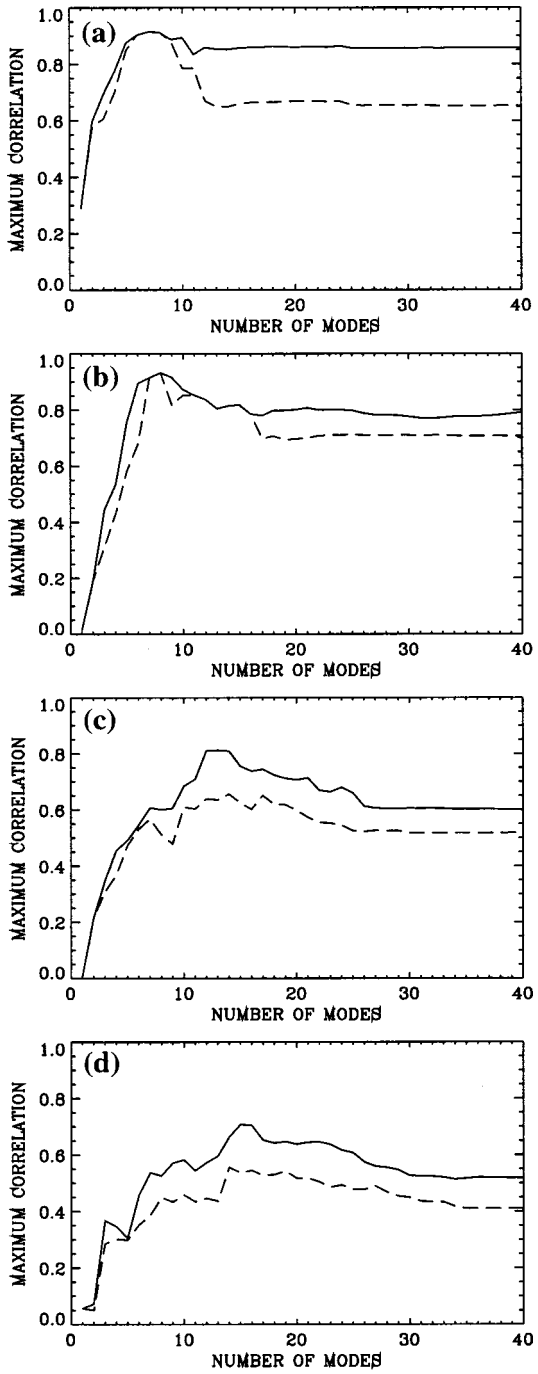

FIG. 7. Modal-sum-limit optimization via MFP ambiguity surface optimization without array position optimization. Maximum correlation in entire ambiguity surface (solid line) and in windowed ambiguity surface containing true source location (dashed line) versus modal-sum-limit for (a) 70-Hz tonal, (b) 95-Hz tonal, (c) 145-Hz tonal, (d) 195-Hz tonal. Optimization performed 54.6 min from start of track. Source range=5.76 km. Source depth=85 m. Windowed surface is from 5.4 to 6.2 km in range and from 60 to 100 m in depth.

θ_c (for the original replica model, $\theta_c = 16.4°$) at that interface. Clearly, the fact that M_0 is close to M_c suggests that only subcritical modes survive out to a range of 5.76 km, as expected. In addition, the decrease in correlation for $M > M_0$ strongly suggests that either (1) the intrinsic attenuation in the sediment of the replica model is too low, allowing the survival of supercritical modes; or (2) the sound-speed discontinuity at the water-sediment interface of the replica model is too large, producing a larger critical angle than in the data. If there were no mismatch in either the sediment attenuation or the water-sediment sound-speed discontinuity, the curves in Fig. 7 would not decrease beyond $M = M_0$, but would remain at a constant level.

TABLE II. Optimal number of modes M_0 from ambiguity surface optimization.

Frequency (Hz)	Optimal mode number M_0	Critical mode number M_c
70	7	6
95	8	8
145	13	11
195	15	15

The decrease in correlation beyond $M = M_0$ appears to be associated with the descent of the deepest antinode of a mode into the sediment layer. This is demonstrated in Fig. 8, which plots the mode functions for modes 6 through 9 for the 70-Hz tonal. This suggests that a probable cause for the degradation is an underestimate of the intrinsic attenuation in the sediment. While an overestimate of the sound-speed discontinuity at the water-sediment interface could also cause a degradation, this would require a change in the mode functions such that the critical mode number increases. For example, an increase of the sediment sound speed by 5% (from 1554.37 to 1632.09 m/s, or a change in θ_c from 16.4° to 20°) delays the entrance of the deepest antinode into the sediment to mode 8, and increases the critical mode number M_c from 6 to 9. Hence, an overestimate of the sound speed discontinuity by 5% will predict the survival of the two or three more modes than actually present in the data. However, this large change in sound-speed discontinuity is much larger than the expected error of this parameter in the replica model. In addition, note from Fig. 7(a) that at least five modes beyond M_0 are affected by the error, which would imply a discontinuity error in excess of 5%. For this reason, an error in the intrinsic attenuation in the sediment is therefore thought to be the primary source of the degradation on correlation beyond M_0. The leveling off of the maximum

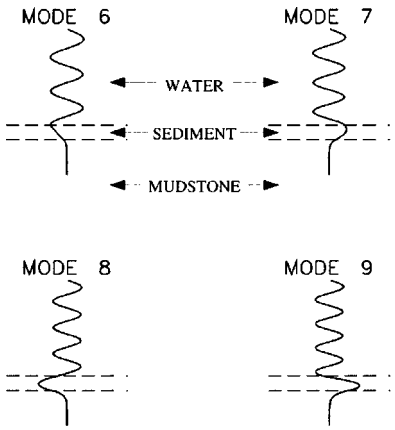

FIG. 8. 70-Hz mode functions for mode 6 through 9 for original replica model. Depth extent is from 0 to 300 m. Dashed horizontal lines indicate water-sediment interface (depth=198.0 m) and sediment-mudstone interface (depth=228.0 m).

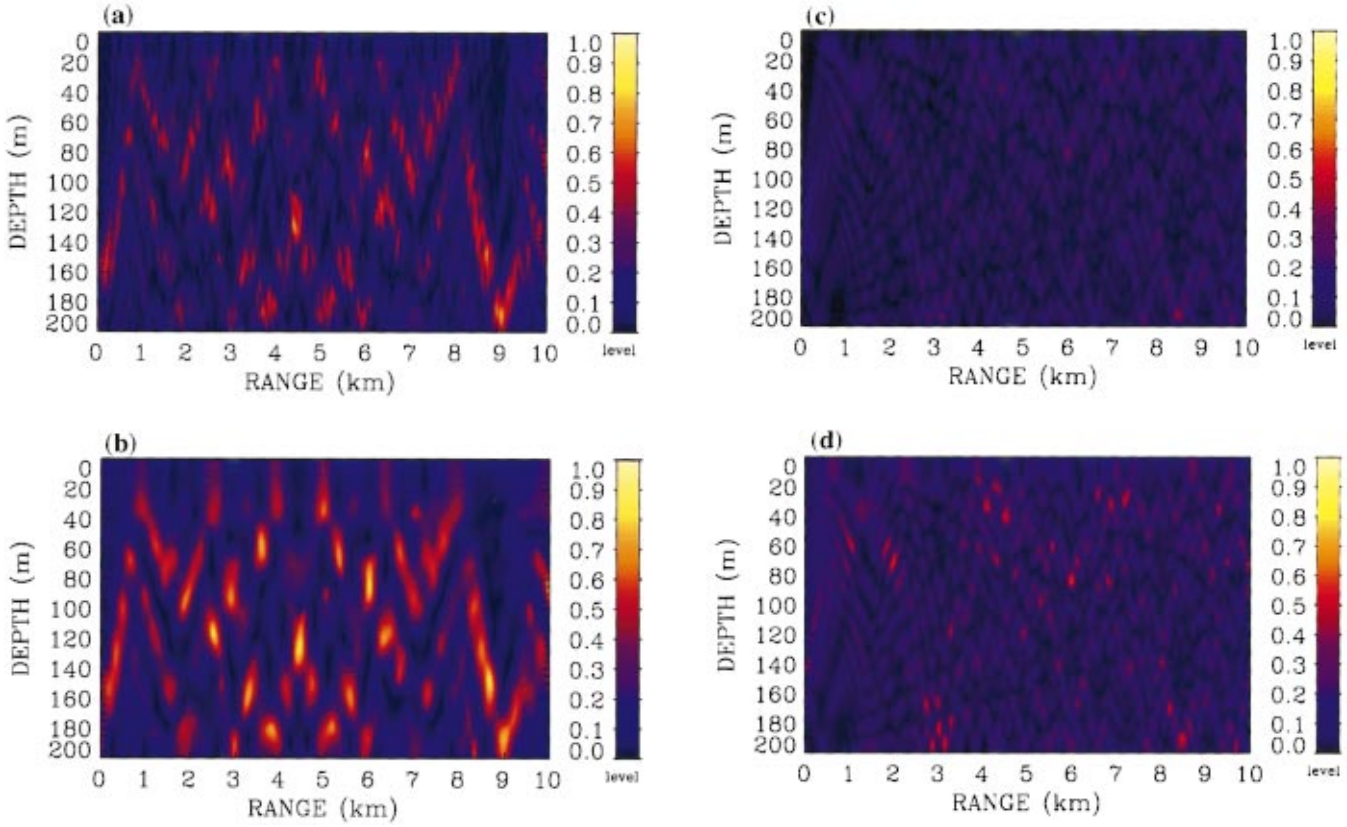

FIG. 9. Optimal modal-sum-limit enhancement of 70-Hz and 195-Hz MFP ambiguity surfaces. (a) 70-Hz original replica model with modal-sum-limit of 21 modes (modal phase velocities less than 2100 m/s). (b) 70-Hz optimal replica model with modal-sum-limit of 7 modes [as determined in MFP ambiguity surface optimization in Fig. 7(a)]. (c) 195-Hz original replica model with modal-sum-limit of 58 modes (modal phase velocities less than 2100 m/s). (d) 195-Hz optimal replica model with modal-sum-limit of 15 modes [as determined in MFP ambiguity surface optimization in Fig. 7(d)]. Time = 54.6 min from start of track. Source range = 5.76 km. Source depth = 85 m.

correlation to a nearly constant level for modes beyond mode 12 in Fig. 7(a) is associated with an increased interaction of the deepest antinode of a mode with the mudstone layer, resulting in a high attenuation of these modes at this range.

The enhancement of range-depth ambiguity surfaces using the optimal replica model is illustrated in Fig. 9 for the 70-Hz and 195-Hz tonals. Figure 9(a) is the 70-Hz surface obtained for the original replica model in which 21 modes (phase velocities less than 2100 m/s) were included in the modal sum, while Fig. 9(b) is the surface resulting from the restriction that $M = M_0$. Figure 9(c) and (d) is the corresponding surfaces for the 195-Hz tonal. Clearly, for both frequencies, the target peak near the true target location of 5.76 km and 85 m is greatly enhanced when using the optimal replica model. In addition, since the main peak cannot be enhanced without enhancing its ambiguities (since a source at an ambiguous location produces a field at the array similar to that produced by the true source), correlations over the entire ambiguity surface are also increased. It is also observed that the surface is smoother, and peaks are wider, because of the rejection of the higher modes. The range-depth resolution is higher for the 195-Hz tonal, because of the greater number of propagating modes. However, correlations levels are lower because of the increased effect of unknown mismatch at higher frequencies.

B. Array position optimization

The modal-sum-limit optimization results presented in the previous section were obtained with the assumption of a vertically straight VLA and a bottom-phone height above the seafloor of 4.5 m, which is based on estimates reconstructed from deployment logs and array design. The discrepancies between the full-surface and windowed curves at the higher frequencies in Fig. 7 suggest that this estimate for the bottom-phone height is in error. In essence, the finer field structure caused by the presence of more higher-order modes increases the sensitivity to mismatch in this parameter at the higher frequencies. The degradation in correlation in Fig. 7(c) and (d) is such that the actual target peak, which should reside in the 800-m (range) by 40-m (depth) window, is no longer the maximum for the full ambiguity surface; the maximum has moved to a point outside the window.

A better estimate of the bottom-phone height was therefore sought via an optimization for this parameter. Implied in this approach is the assumption that the VLA remained perfectly straight and vertical (ignoring the known tilt of the VLA) so that the phone separations remained constant at 1.875 m. Since a determination of the vertical placement of the VLA should be enhanced at close range, where the direct path fully ensonifies the VLA, the optimization was performed at a time 15.0 min (FFT number 330) from the start of the track, where the source was at a range of 2.0 km and

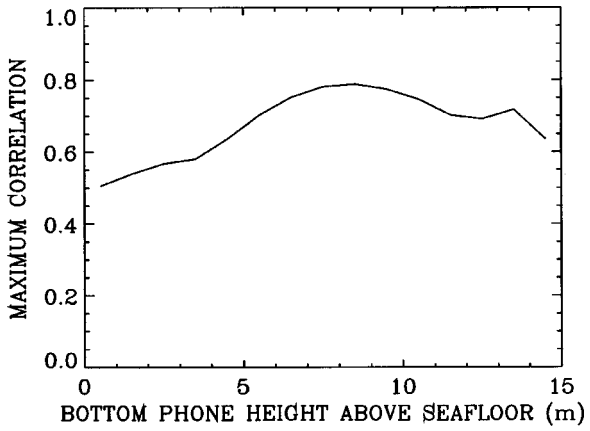

FIG. 10. Array position optimization for 195-Hz tonal. Maximum correlation in a windowed ambiguity surface containing the true source location versus bottom-phone height above the seafloor. Optimization performed 15.0 min from start of track. Source range=2.0 km. Source depth=84 m. Windowed surface is from 1.5 to 2.5 km in range and 80 to 90 m in depth.

a depth of 84 m. The search was only performed for the 195-Hz tonal and no FFT averaging was performed. Matched-field ambiguity surfaces were calculated via the Bartlett estimator in Eq. (1) with the bottom-phone height taking on values from 0.5 m to 14.5 m at 1.0-m increments. The modal-sum-limit in the predicted pressures $p_n(\mathbf{x})$ [Eq. (3)] was set at 15, the value of the optimal mode number M_0 at 195 Hz. Figure 10 plots the maximum correlation in a small window of the ambiguity surface containing the true source location (extending from 1.5 to 2.5 km in range and from 80 to 90 m in depth) as function of bottom-phone height above the seafloor. The correlation is seen to be optimized for a bottom-phone height of 8.5 m.

As a check on the accuracy of this new estimate for the bottom-phone height, the modal-sum-limit optimizations of the previous section were recomputed with this new value. Figure 11 presents results similar to Fig. 7 but with the bottom-phone height increased to 8.5 m. It is first noted that the 70-Hz and 95-Hz curves in Fig. 11(a) and (b) differ little from those in Fig. 7(a) and (b), which is expected since exact vertical placement of the VLA is less important at the lower frequencies. For the 145-Hz and 195-Hz tonals, however, the discrepancies between the full-surface curves and the windowed curves observed in Fig. 7(c) and (d) are eliminated in Fig. 11(c) and (d); This is strong evidence that the bottom-phone height of 8.5 m is a good estimate. While the values of M_0 in Fig. 11(c) and (d) differ somewhat from those in Fig. 7(c) and (d) and Table II, the broad plateaulike peaks in the curves imply that the modes in a band of modes will produce similar optimal performance. For this reason the values of M_0 in Table II will be retained as the final modal-sum-limit estimates.

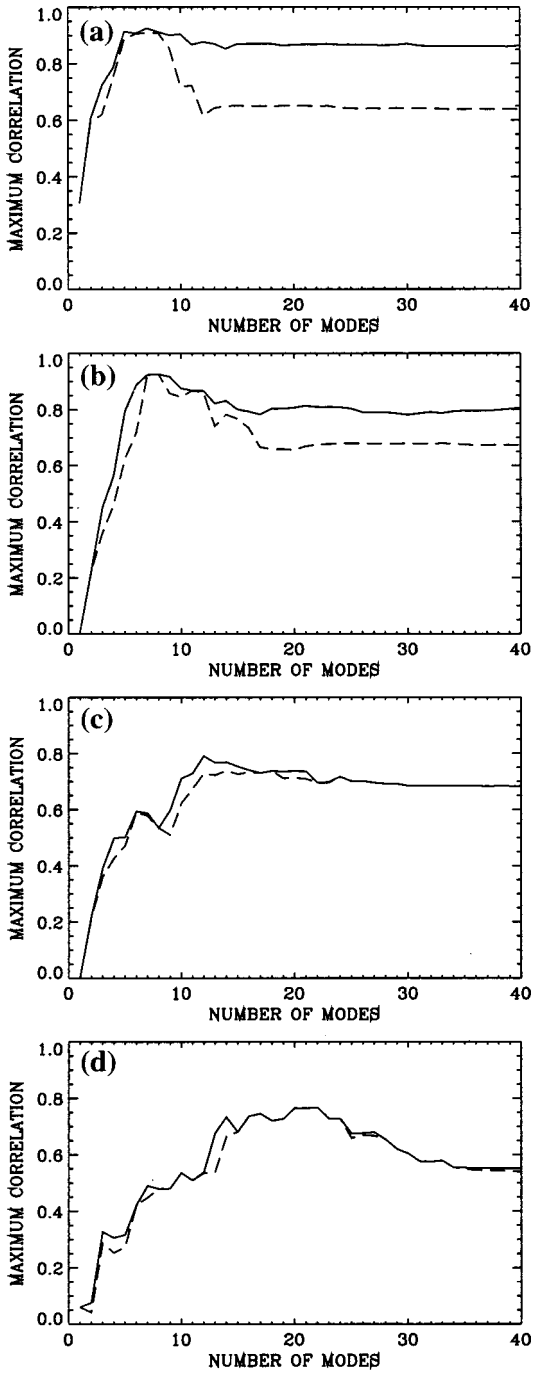

FIG. 11. Modal-sum-limit optimization via MFP ambiguity surface optimization with array position optimization. Optimal bottom-phone height=8.5 m as obtained in array position optimization of Fig. 10. Maximum correlation in entire ambiguity surface (solid line) and in windowed ambiguity surface containing true source location (dashed line) versus modal-sum-limit for (a) 70-Hz tonal, (b) 95-Hz tonal, (c) 145-Hz tonal, (d) 195-Hz tonal. Optimization performed 54.6 min from start of track. Source range=5.76 km. Source depth=85 m. Windowed surface is from 5.4 to 6.2 km in range and from 60 to 100 m in depth.

C. Bottom-property inversion

All bottom-property inversions were performed for the 70-Hz tonal. Assuming that sound speed is constant with frequency and that intrinsic attenuation is scales linearly with frequency (as implied by the units of dB/km Hz), estimates obtained at one frequency can be assumed to be valid at other frequencies. The validity of the assumption of the linear dependence of attenuation with frequency is currently under debate.[47] Nevertheless, results to be presented in Sec. V suggest that the use of parameter obtained at 70 Hz work well at the other frequencies.

Inversions were performed at the three times or stations indicated in Fig. 12, which also displays the sound-speed

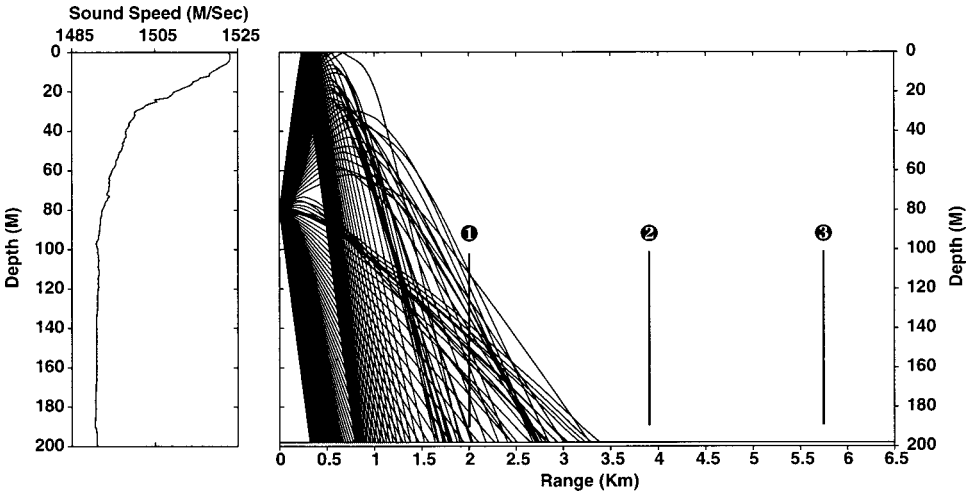

FIG. 12. Bottom-property inversion stations along source-tow track. Placement of VLA relative to sound speed profile and nonbottom-reflected energy at each station is indicated approximately. Station 1: time=15.0 min, source range=2.0 km, source depth=84 m. Station 2: time=35 min, source range=3.9 km, source depth=84 m. Station 3: time=54.6 min, source range=5.76 km, source depth=85 m. All times are from start of track.

profile, a ray-trace of nonbottom-reflected energy, and the placement of the VLA array in the water column. The range of the source from the VLA was 2.00 km at Station 1, 3.90 km at Station 2, and 5.76 km at Station 3. The source depth was 84 m at Stations 1 and 2 and 85 m at Station 3. The quality of the inverted bottom-property estimates, however, varied between each station because of the nature of the acoustic field at each site. Station 1 was generally unsuitable for attenuation inversions because the array is immersed in direct-path and subcritical bottom-interacting energy, which overpowers the attenuation-sensitive supercritical energy. On the other hand, inversions for interfacial sound-speed discontinuities could be performed at Station 1 since changes in this parameter affect how the energy is partitioned between the subcritical and supercritical energy. Because of its location outside of the influence of direct-path energy, Station 2 was considered a good site for inversion of both parameters; however, a strong interferer present during this period significantly degraded the matched-field correlation, rendering inversions difficult. Consequently, the results at Station 2 will not be reported here. Station 3 proved to be useful for the inversion of sediment parameters because of high signal-to-noise conditions present at this time. However, because mudstone-interacting energy is highly attenuated, inversion for mudstone properties is difficult at this range.

For all bottom-property inversions, the maximum correlation in a small window of the ambiguity surface containing the true source location was selected to be the optimization metric. The windows used in determining the maximum extended in range from 1.5 to 2.5 km for Station 1 and from 5.3 to 6.3 km for Station 3; the depth extent of the windows was from 60 to 100 m for all stations. In all cases, the optimal bottom-phone height of 8.5 m, obtained previously, was used.

1. First-iteration sediment and mudstone attenuation inversion

To gain an initial understanding of the sensitivity of matched-field performance to variations in bottom attenuation, a coarse-grid search was first performed at Station 3. Matched-field ambiguity surfaces were calculated using the Bartlett estimator in Eq. (1) for all combinations of candidate sediment and mudstone attenuations. Attenuations considered consisted of values in the original replica model ($\alpha = 0.015$ dB/km Hz at top of sediment layer, $\alpha = 0.02$ dB/km Hz in mudstone layer) and repeated doublings of those values. No FFT averaging was performed for this analysis. Figure 13 plots the maximum correlation in the small window of the ambiguity surface containing the true source location as function of the sediment and mudstone attenuation. Note that the attenuation axes are on a $\log_2$ scale. The black dot in part (a) marks the data point of the original replica model, while the gray dot marks the point of maximum correlation. At low values of the mudstone attenuation, the correlation is seen to be optimized along the sediment attenuation direction at 0.24 dB/km Hz, a value greater that ten times that in the original replica model. In the mudstone attenuation direction, however, the correlation does not peak, but continues to rise with increasing mudstone attenuation. The large mudstone attenuations (>0.2 dB/km Hz) toward which the optimization appears to be approaching are known to be nonphysical for this environment, thus illustrating the caution which must be exercised in interpreting inversion results. Incorrect estimates of parameters may effectively maximize correlation if the effects of variations in those parameters are of the same nature as other parameters,

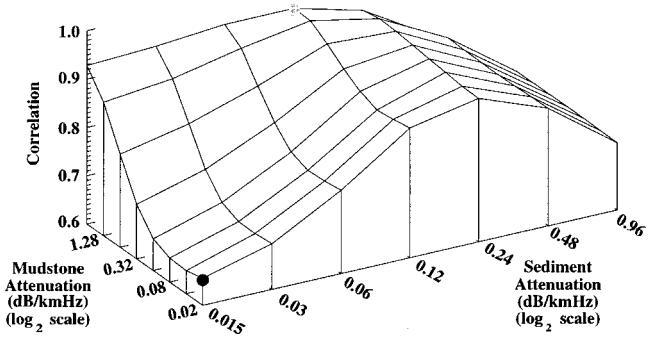

FIG. 13. Station 3 coarse-grid sediment and mudstone attenuation inversion results. Attenuation axes are $\log_2$ scales. Time=54.6 min from start of track. Source range=5.76 km. Source depth=85 m. Black dot marks the result for the original replica model while gray-shaded dot marks the point of maximum correlation. Correlation values range from 0.65 (sediment attenuation =0.015 dB/km Hz, mudstone attenuation=0.04 dB/km Hz) to 0.95 (sediment attenuation=0.12 dB/km Hz, mudstone attenuation=2.56 dB/km Hz) over the entire surface.

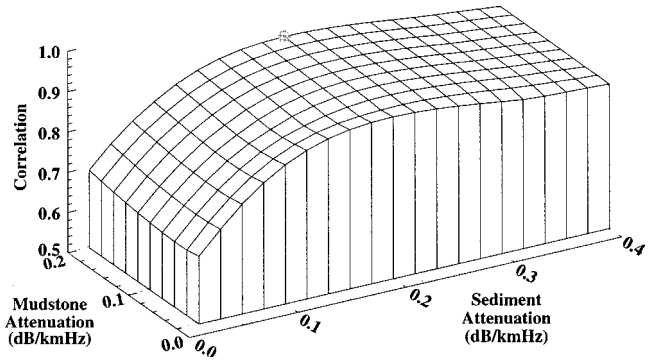

FIG. 14. First-iteration Station 3 sediment and mudstone attenuation inversion results. Time=54.6 min from start of track. Source range=5.76 km. Source depth=85 m. Gray-shaded dot marks the point of maximum correlation. Correlation values range from 0.66 (sediment attenuation=0.02 dB/km Hz, mudstone attenuation=0.06 dB/km Hz) to 0.91 (sediment attenuation=0.20 dB/km Hz, mudstone attenuation=0.20 dB/km Hz) over the entire surface.

or if other important parameters have been neglected from the model. Based on this coarse-grid study, it was concluded that sediment attenuations below about 0.4 dB/km Hz and mudstone attenuations below about 0.2 dB/km Hz (based on known physical limits) need only be considered in the attenuation inversions. The latter value is a rough estimate based on available geoacoustic data for this environment.

Having established the limits of the attenuation search, a finer-grid search was then performed for the three stations in Fig. 12. For these optimizations, sediment attenuations were allowed to vary from 0.02 to 0.40 dB/km Hz at 0.02-dB/km Hz increments, while mudstone attenuations were allowed to vary from 0.02 to 0.20 dB/km Hz at 0.02-dB/km Hz increments. The maximum correlation in the small window of the ambiguity surface containing the true source location is plotted as function of the sediment and mudstone attenuation for Station 3 in Fig. 14. A maximum correlation of 0.91 occurs for a sediment attenuation of 0.20 dB/km Hz and a mudstone attenuation of 0.20 dB/km Hz (indicated by the gray dot). Clearly, the correlations are highly sensitive to changes in sediment attenuation, but nearly constant with changes in mudstone attenuation. This suggests that the VLA is primarily sensing strong sediment-interacting energy, with the mudstone-interacting energy being nearly eliminated at this range. Since correlations only vary between 0.90 and 0.91 with changes in mudstone variation for a sediment attenuation fixed at 0.2 dB/km Hz, a determination of an optimal value for the mudstone attenuation is not possible. Ignoring the slight changes with mudstone-attenuation variation, the optimal sediment attenuation occurs at around 0.2 or 0.22 dB/km Hz. Since the correlations vary little between these two values, the lower value was selected as the inversion estimate at this station.

The value of 0.2 dB/km Hz for the sediment attenuation agrees well with predictions based on Hamilton's[48,49] semi-empirical models. These predictions are obtained from curves fit to intrinsic attenuation (in units of dB/km Hz) at the top of the sediment layer, $\alpha(0)$, versus mean grain size data measured off the coast of San Diego. The mean grain size is in ϕ units, defined as $\phi = -10\log_2$ (grain diameter in mm). Bachman[41,42,50] has provided estimates of the mean grain size along the range-independent source-tow track, with values varying from about 5.00 up to nearly 5.25. By taking a linear fit to Hamilton's compilation of data over a regime containing these grain sizes, the appropriate equation for Hamilton's sediment attenuation prediction is $\alpha(0) = 1.206\,85 - 0.197\,851\,7\,\phi$. The range-averaged value of ϕ between the array and the station range was 5.14, which yields a value for $\alpha(0)$ of 0.19 dB/km Hz when substituted in the above equation fit to Hamilton's data.

It should be noted that an inversion performed at Station 2 yielded a sediment attenuation estimate of 0.18 dB/km Hz, in close agreement with that obtained for Station 3, with a mudstone attenuation estimate of 0.06 dB/km Hz. However, the correlations were much lower overall (maximum level was 0.64), because of the presence of the interferer, and the correlation difference between a mudstone attenuation of 0.06 and 0.02 dB/km Hz was insignificant. For this reason, the mudstone attenuation of the original replica model, namely, 0.02 dB/km Hz, was retained for the sound-speed inversions to follow.

2. Sediment and mudstone sound-speed inversion

Inversions for the sediment and mudstone sound speeds were next performed with sediment and mudstone attenuations fixed at the best estimates obtained in the previous section. The sediment sound-speed search was restricted to values producing critical angles θ_c at the water-sediment interface roughly between 10° and 25°. This decision was based on an observation in the data that the vertical beam response drops sharply as vertical arrival angle is increased past approximately 25°, which approximates the critical angle. The sound speed at the top of the sediment layer was hence allowed to vary from 1514.37 m/s ($\theta_c = 10.06°$) up to 1654.37 m/s ($\theta_c = 25.67°$) at 10-m/s increments. The limits for the mudstone sound-speed search are less obvious, since a distinct change associated with the critical angle at the sediment-mudstone interface is not observable because of the low levels of mudstone-interacting energy. The sound speed at the top of the mudstone layer was therefore arbitrarily allowed to vary from 1781.0 m/s up to 1941.0 m/s at 10-m/s increments, with the higher values being more representative of those based on the geoacoustic models of Bachman.[41,42] The 10-m/s grid spacing for both searches proved to be adequate to produce smooth surfaces.

The maximum correlation in a small window of the ambiguity surface containing the true source location is plotted as function of the sediment and mudstone sound speed at the top of their respective layers for the Station 1 in Fig. 15. Matched-field correlations are observed to be significantly sensitive to variations in bottom layer sound speeds, for reasons already noted. The structure of the surface, however, is not as smooth as may be desired for accurate parameter estimation. Several ambiguous peaks possess nearly the same correlation ($\sim$0.92) in a region between mudstone sound speeds of 1671 and 1721 m/s. The multiple peaks in this region implies that the critical angle on one interface may be compensating for an inaccurate critical angle at the other interface.

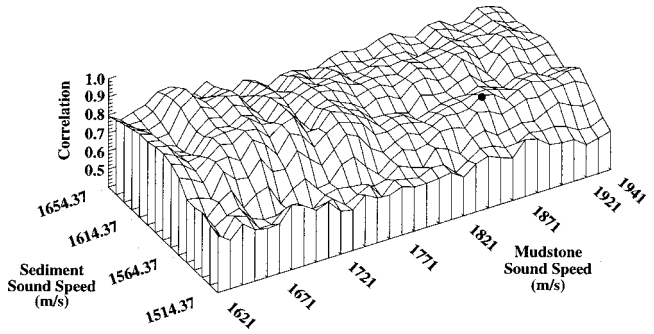

FIG. 15. Station 1 sediment and mudstone sound-speed inversion results. Time=15.0 min from start of track. Source range=2.00 km. Source depth=84 m. Black dot marks the results for the original replica model. Correlation values range from 0.58 (sediment sound speed=1514.37 m/s, mudstone sound speed=1921.0 m/s) to 0.92 (sediment sound speed =1624.37 m/s, mudstone sound speed=1671.0 m/s) over the entire surface.

The sound-speed inversion results for Station 3 in Fig. 16 reveal a distinct ridge of maxima along the 1574.37-m/s sediment-sound-speed line at the higher mudstone sound speeds. As mudstone sound speed in decreased, however, the ridge breaks up and maxima tend toward higher sediment sound speeds, in a fashion similar to that observed at Station 1. The highest peaks, which occur in both the high and low mudstone regions, possess a correlation of approximately 0.96, significantly higher than the value of 0.92 obtained after the previous attenuation inversion.

The complicated structure of the surfaces in Figs. 15 and 16 precludes exact determination of the bottom sound speeds. The similar correlation levels of the peaks suggest that performance will not vary much for estimates based on those peaks; this will be verified in Sec. V. However, Figs. 15 and 16 suggest a natural division of the problem into a low (<1771 m/s) and high (>1771 m/s) mudstone-sound-speed regime. At short range (Station 1), the low mudstone sound speeds appear optimal, and any of the peaks in this regime will enhance performance. At long range (Station 3), the high mudstone sound speeds appear optimal, since the relative sensitivity with mudstone sound speed in this regime is consistent with the previous observation that mudstone energy has been greatly attenuated at this range. For the

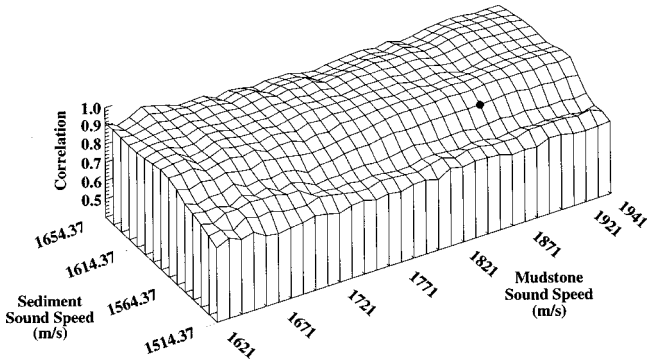

FIG. 16. Station 3 sediment and mudstone sound-speed inversion results. Time=54.6 min from start of track. Source range=5.76 km. Source depth=85 m. Black dot marks the results for the original replica model. Correlation values range from 0.78 (sediment sound speed=1514.37 m/s, mudstone sound speed=1671.0 m/s) to 0.96 (sediment sound speed =1584.37 m/s, mudstone sound speed=1641.0 m/s) over the entire surface.

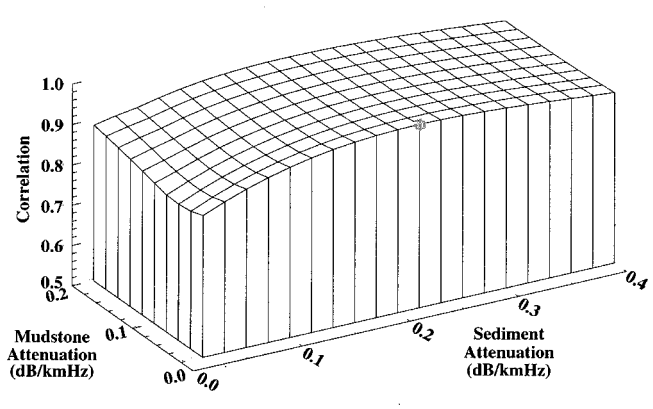

FIG. 17. Second-iteration Station 3 sediment and mudstone attenuation inversion results. Time=54.6 min from start of track. Source range=5.76 km. Source depth=85 m. Gray-shaded dot marks the point of maximum correlation. Correlation values range from 0.84 (sediment attenuation=0.02 dB/km Hz, mudstone attenuation=0.06 dB/km Hz) to 0.96 (sediment attenuation=0.22 dB/km Hz, mudstone attenuation=0.02 dB/km Hz) over the entire surface.

high-mudstone-sound-speed regime, the optimal sediment sound speed is 1574.37 m/s, the value along the high-correlation ridge. Since a cluster of maxima occur near this value for the low-mudstone-sound-speed regime, 1574.37 m/s was selected as the inverted sediment sound speed for both regimes. This value is also agrees best with the prediction of 1550.0 m/s by Richardson and Briggs.[51] This prediction is based on an expression for the ratio of sediment sound speed c_{b_1} to bottom water sound speed c_w given by $c_{b_1}/c_w = 1.180 - 0.034\phi + 0.0013\phi^2$, where ϕ is the grain size in ϕ units. Since performance is insensitive to variation in mudstone sound speed in the high-mudstone-sound-speed regime, the mudstone sound speed was set at 1861 m/s, a value based on borehole measurements in 90-m water west of San Diego.[52] For the low-mudstone-sound-speed regime, however, the mudstone sound speed was set at 1691 m/s, which is the value for the largest peak among the cluster of maxima near the lower sediment sound speeds. This mudstone estimate is observed to be 170 m/s lower than that predicted by the borehole measurement. However, it should be noted that the borehole measurement was made in much shallower water, and the actual sound speed at the sediment-mudstone interface was extrapolated using trends measured at a greater depth (measurements were not recorded in the upper 250 m of the mudstone layer).

Since the correlation levels are similar for either choice of mudstone sound speed, the value of 1691 m/s will be used in the remaining inversion to follow. The difference between using 1691 m/s and 1861 m/s will be investigated further in the performance evaluations of Sec. V.

3. Second-iteration sediment and mudstone attenuation inversion

To complete the inversion cycle, sediment and mudstone attenuation inversions were repeated with the sediment and mudstone sound speed fixed at 1574.37 m/s and 1691 m/s, respectively, as determined in the previous section. The results for Station 3 are presented in Fig. 17. The correlation

levels are higher overall than those observed for the first-iteration attenuation inversions in Fig. 14, since optimal sound speeds are now used in the bottom layers. The sensitivity to changes in sediment attenuation, and the near insensitivity to changes in mudstone attenuation, observed in the initial inversion results at Station 3 are seen to be preserved in Fig. 17. The general shape of the correlation surface has remained the same, although the drop in correlation at the low sediment attenuations has become less drastic. A maximum peak of 0.96 occurs for a sediment attenuation of 0.22 dB/km Hz and a mudstone attenuation of 0.02 dB/km Hz; however, the performance is nearly the same for all mudstone attenuations. Closer examination of Fig. 17 reveals that the maximum in the sediment attenuation direction shifts to 0.20-dB/km Hz sediment attenuation at the higher mudstone attenuations, an effect also observed in Fig. 14. The sediment attenuation estimate at this range is therefore concluded to be 0.20–0.22 dB/km Hz, while the mudstone attenuation is indeterminate, which is in agreement with the initial inversion results.

Since the performance at all stations was little affected by changes in mudstone attenuation, the original value of 0.02 dB/km Hz was selected for the mudstone attenuation. Since sediment attenuation tended toward 0.22 at the low mudstone attenuations, this value was selected as the optimal value for this parameter in the optimal replica model. In summary, the final estimates for the sediment and mudstone attenuation are 0.22 dB/km Hz and 0.02 dB/km Hz, respectively.

As already noted, the sediment attenuation estimate above is in good agreement with predicted values of Hamilton.[48,49] However, several of the more recent studies[53–56] record attenuations an order of magnitude lower than the inverted estimate. Anderson and Blackman,[54] for instance, report values of 0.015 dB/km Hz in terrigenous turbidite sediments and 0.030 dB/km Hz in calcareous sediments. Measurements like these provided the basis for the use of 0.02 dB/km Hz in the original replica model (Table I and Fig. 4). The inversion analysis presented here, however, concludes that the low end of Hamilton's data (see Fig. 3 of Ref. 48) more accurately represents this environment.

The fact that the first and second attenuation inversions are in general agreement suggests that the inverted sound speed and attenuation values are reasonable. A combined simultaneous four-parameter (sound speed and attenuation in each layer) search is required to determine if they indeed correspond to the global optimum. Nevertheless, results in Sec. V indicate that the inverted values significantly enhance localization performance.

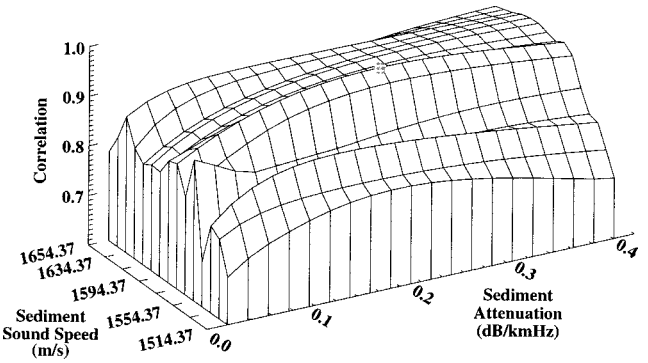

FIG. 18. Station 3 sediment attenuation and sound-speed inversion results. Time=54.6 min from start of track. Source range=5.76 km. Source depth=85 m. Gray-shaded dot marks the point of maximum correlation. Correlation values range from 0.69 (sediment attenuation=0.02 block/dB/km Hz, sediment sound speed=1544.37 m/s) to 0.96 (sediment attenuation =0.22 dB/km Hz, sediment sound speed=1574.37 m/s) over the entire surface.

4. Sediment attenuation and sound-speed inversion

It is clear from the preceding discussions of inversion results that the bottom parameters having the greatest impact on matched-field performance are those in the sediment layer. This is because energy reaching the mudstone is higher-angle (or higher-mode) supercritical energy which has already been greatly attenuated by its passage through the sediment. It is therefore instructive to examine an inversion result for a search over attenuation and sound speed in the sediment layer alone. Figure 18 presents such a result of a two-parameter search for sediment attenuation and sound speed at Station 3, which provided the best overall estimates in the preceding inversion. For this case the mudstone attenuation and sound speed were set equal to those obtained in the previous sections (namely, a 0.02-dB/km Hz attenuation and a 1691.0-m/s upper sound speed). A distinctive peak of 0.96 occurs at a sediment attenuation of 0.22 dB/km Hz and a upper sediment sound speed of 1574.37 m/s, in agreement with the values obtained in previous sections.

5. Optimal replica model using inversion estimates

The optimal parameters obtained via the preceding inversions were used to define the optimal inverted replica modal in Table III. Layer densities and profile gradients are

TABLE III. Bottom properties for the inverted optimal replica model.

Depth (m)	Compressional wave speed (m/s)	Shear wave speed (m/s)	Density (g/cm^3)	Compressional wave attenuation [dB/km Hz]	Shear wave attenuation [dB/km Hz]	Bottom type
198.0	1574.37	0.0	1.76	0.22	0.0	sediment
228.0	1595.02	0.0	1.76	0.24	0.0	
228.0	1691.0	0.0	2.06	0.020	0.0	mudstone
1028.0	3055.80	0.0	2.06	0.020	0.0	
1028.0	5200.00	0.0	2.66	0.020	0.0	basement

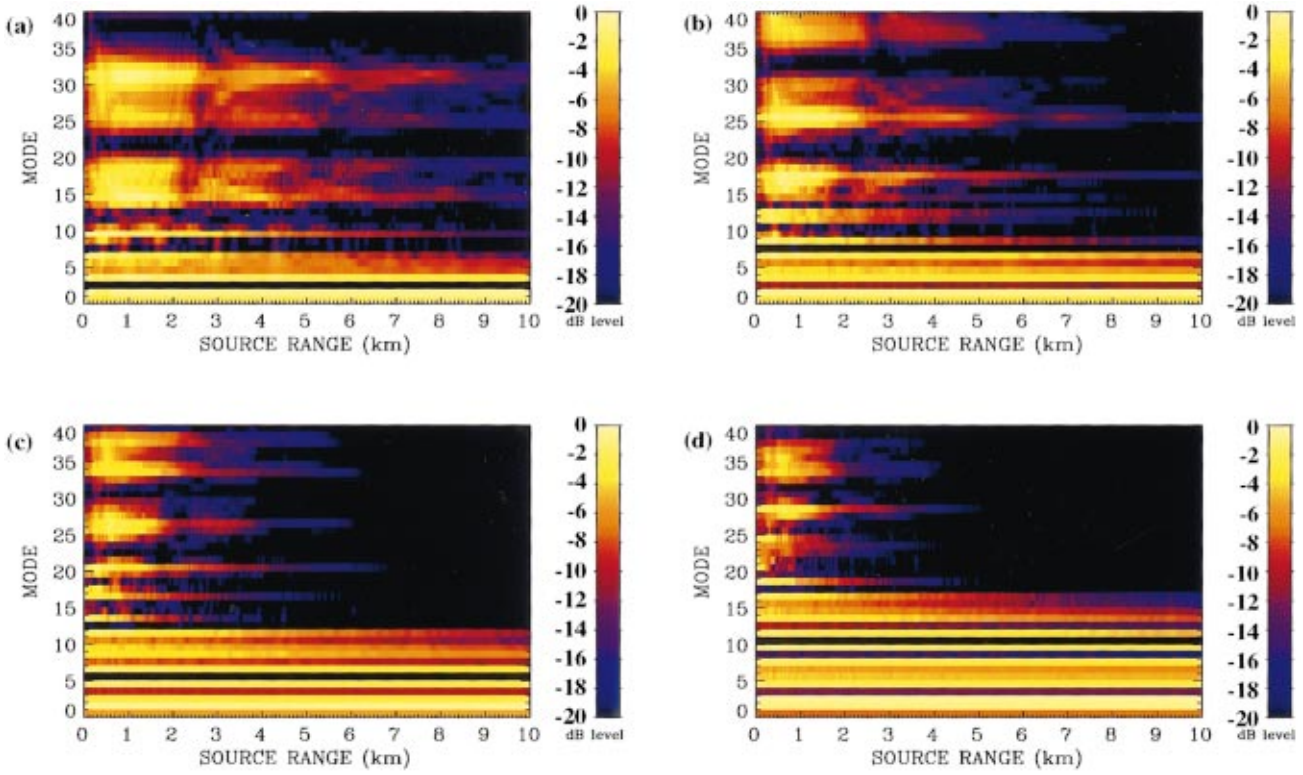

FIG. 19. Synthetic modal decompositions using inverted optimal replica model in Table III. Modal distributions versus range for (a) 70-Hz tonal, (b) 95-Hz tonal, (c) 145-Hz tonal, (d) 195-Hz tonal. Obtained for a fictitious VLA spanning the water column and bottom layers. Distributions are normalized at each time so that the maximum power=0.0 dB.

the same as those used in the original replica model of Table I. The mudstone attenuation is also the same as that in the original replica model, since inversion for this parameter was unsuccessful, and 0.02 dB/km Hz is the value predicted by Mitchell and Focke.[53]

D. Synthesized modal decomposition using inversion estimates

If the primary bottom parameters impacting the number of propagating modes have been included in the inversion process, the inverted optimal replica model should predict a number of propagating modes in agreement with those predicted by the modal-sum-limit optimization approach. This can be checked via an examination of the modal content of the inverted-parameter replica model via a synthesized modal decomposition for a fictitious VLA which spans the full water column and extends into the bottom (to ensure orthogonality). For a VLA, the energy $E_m(r)$ in mode m (or modal coefficients) at range r may be obtained using

$$E_m(r)=\sum_{i=1}^{N}\frac{p(r,z_i)\phi_m(z_i)}{\rho(z)}\Delta z,$$

where $p(r,z_i)$ is the pressure at the ith phone at depth z_i, ϕ_m is the mode m mode function, Δz is the phone spacing, $\rho(z)$ is the density, and N is the number of phones. Synthesized modal power $(10\log_{10}E_m^2)$ using the inverted-parameter optimal replica model of Table III for the four tonals is presented in Fig. 19 as a function of source range. The fictitious array used for the simulation contained 1025 elements, extending from a depth of 1 m down to 1025 m (1-m spacing), which is 3 m above the subbottom. The source depth was fixed at 84 m, the average depth of the source during the source-tow, in all cases. The power scales in Fig. 19 are from 20 dB below the maximum level up to the maximum level, which is normalized to be 0 dB at each range. While higher-order modes are observed to be present at short range, a distinctive feature of the modal distributions for all four tonals is the presence of bands of low-order modes that predominate over all ranges. These bands identify the propagating modes. The high-end cutoff of these bands represent a modal-sum-limit which can be compared to the results of the modal-sum-limit optimization technique. From Fig. 19, modal-sum-limits of 7 for the 70-Hz tonal, 7 for the 95-Hz tonal, 12 for the 145-Hz tonal, and 17 for the 195-Hz tonal, are observed. These are in good agreement with the predictions obtained by modal-sum-limit optimization in Table II. A similar analysis performed for the original replica model of Table I results in modal-sum-limits of approximately 13 for the 70-Hz tonal, 19 for the 95-Hz tonal, 27 for the 145-Hz tonal, and 35 for the 195-Hz tonal.

V. PERFORMANCE COMPARISONS

In this section, the performance of each optimization technique is evaluated and compared to the performance of the original replica model as a function of time for the entire source-tow track. The quality of the performance is measured by the maximum correlation of the ambiguity surface, and the accuracy of the source location (range and depth) estimate corresponding to that maximum correlation, at each time. The accuracy of the source location estimate is judged

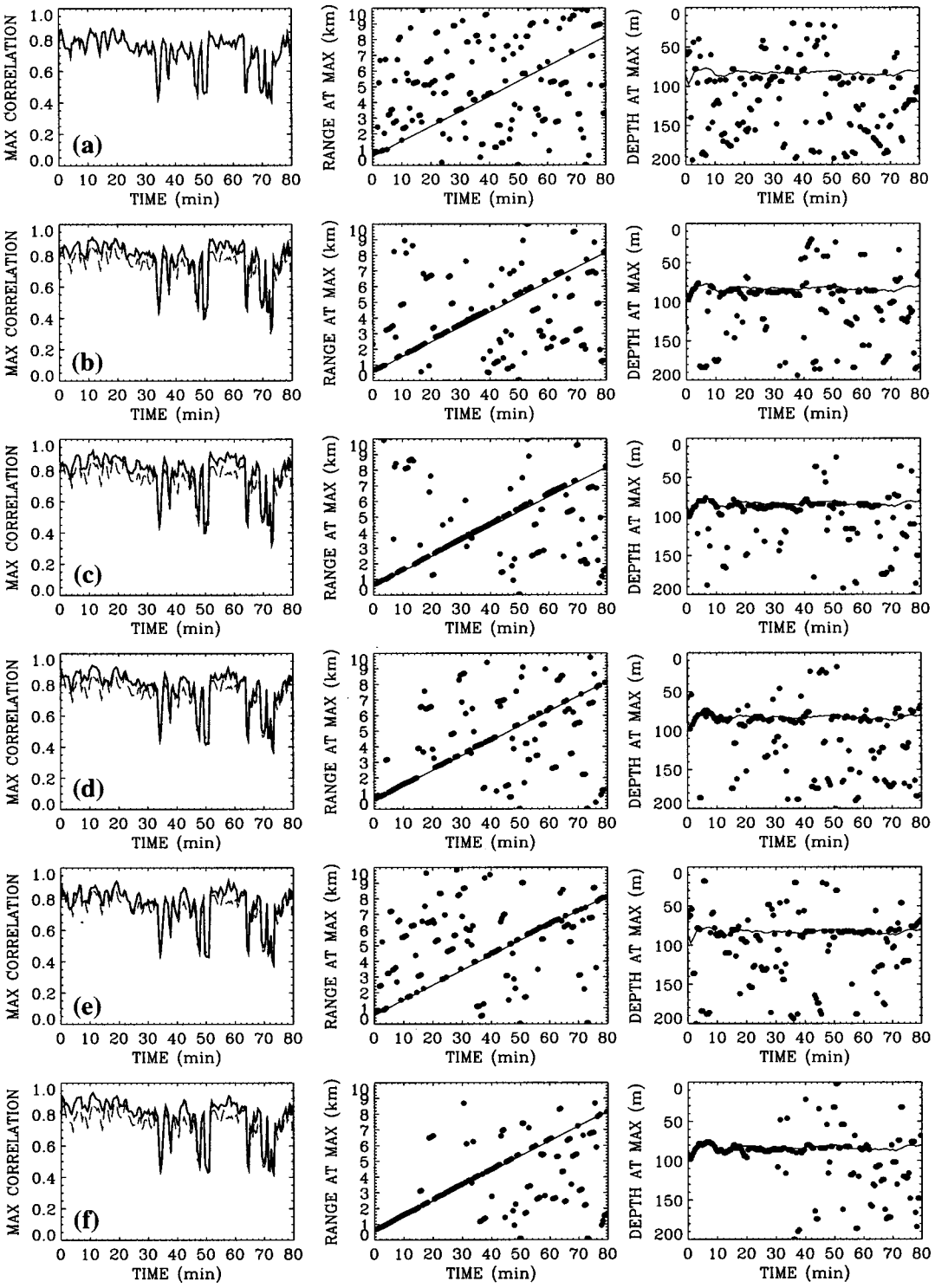

FIG. 20. Comparison of 70-Hz MFP ambiguity surface maxima, range at maxima, and depth at maxima versus time during source-tow track using various replica models. Replica models used in Bartlett processor are (a) original replica model, and optimal replica models obtained by (b) modal-sum-limit optimization, (c) modal-sum-limit optimization with array position optimization, (d) bottom-property inversion, (e) replica model in part (d) with upper mudstone sound speed increased to 1861 m/s, and (f) replica model in part (d) with mudstone attenuation increased to 1.28 dB/km Hz.

via a comparison to the known source-tow location. For all analyses, 21 FFT samples were averaged (for a total averaging time of 54.6 s) with 50% overlap, resulting in 176 averaged samples separated by 27.3 s. Matched-field ambiguity surface samples were generated for each sample using the Bartlett estimator in Eq. (1).

While performance analyses were performed for each of the four tonals, only the results for the 70-Hz and 195-Hz tonals will be presented as representative of high- and low-frequency regimes. Results for the 95-Hz and 145-Hz tonals essentially demonstrate a smooth transition of performance between these regimes. Figures 20 and 21 plot the maximum correlation in the ambiguity surface samples, and the range and depth at which this maximum occurs, as a function of

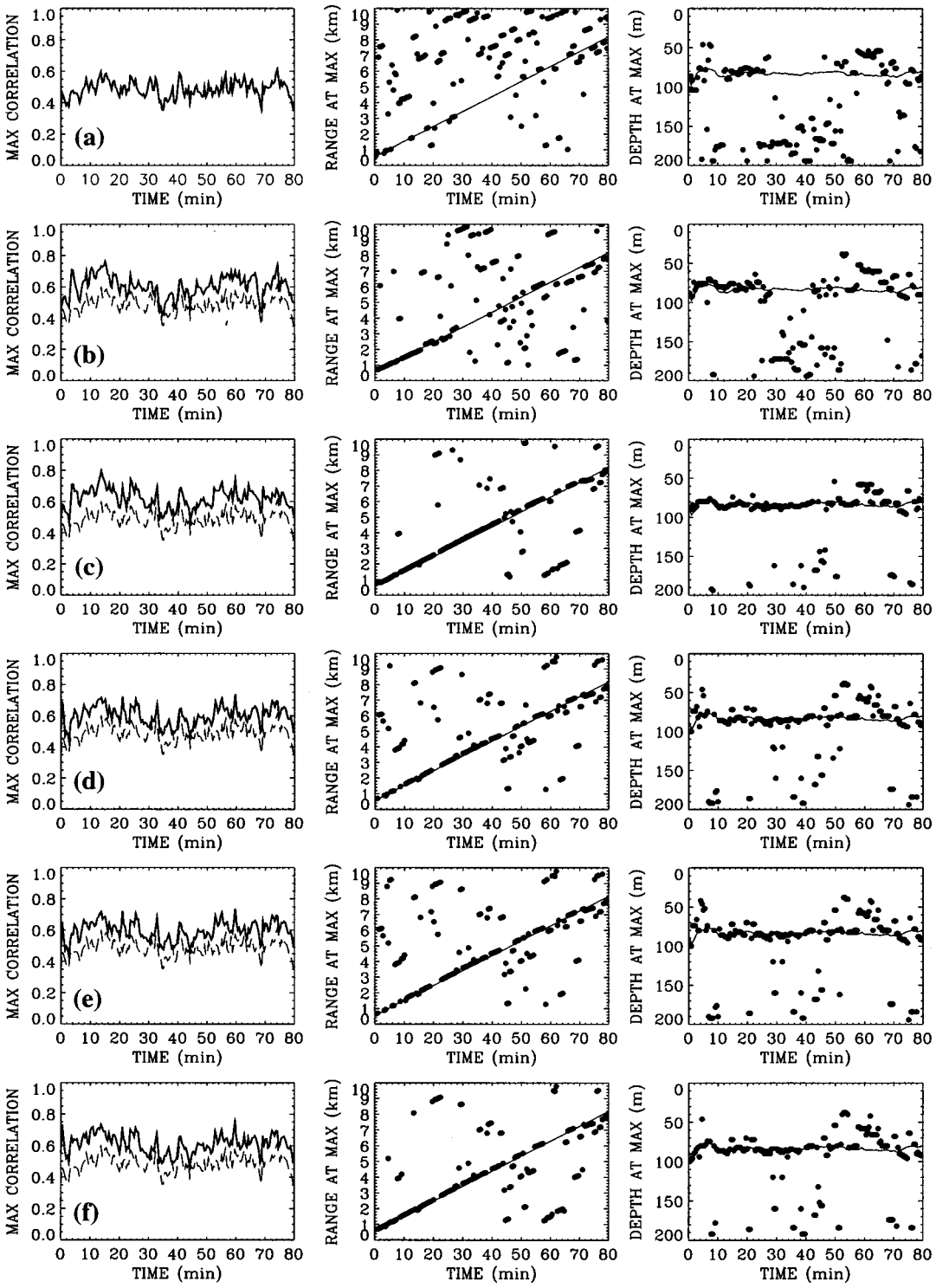

FIG. 21. Comparison of 195-Hz MFP ambiguity surface maxima, range at maxima, and depth at maxima versus time during source-tow track using various replica models. Replica models used in Bartlett processor are (a) original replica model, and optimal replica models obtained by (b) modal-sum-limit optimization, (c) modal-sum-limit optimization with array position optimization, (d) bottom-property inversion, (e) replica model in part (d) with upper mudstone sound speed increased to 1861 m/s, and (f) replica model in part (d) with mudstone attenuation increased to 1.28 dB/km Hz.

time. Figure 20 is for the 70-Hz tonal while Fig. 21 is for the 195-Hz tonal. In both of these figures, part (a) corresponds to the original replica model, part (b) to the optimal replica model obtained by the modal-sum-limit optimization without APO, part (c) to the optimal replica model obtained by modal-sum-limit optimization with APO, and part (d) to the optimal replica model obtained by bottom-property inversion with APO in Table III. Part (e) corresponds to the inverted optimal replica model of part (d) with the mudstone profile shifted so that the upper mudstone sound speed is 1861 m/s, instead of 1691 m/s. This part has been added to investigate the difference in performance between the high and low mudstone sound-speed regimes discussed in Sec. IV. Part (f) corresponds to the inverted optimal replica model of part (d)

with the mudstone attenuation increased from 0.02 dB/km Hz to 1.28 dB/km Hz. This part has been added to observe the effective performance optimization which may be obtained by a higher, but nonphysical, value for this parameter. In all figures, the solid line in the range versus time and depth versus time plots represents values for the known true source track, and the maximum correlation versus time in part (a) is redrawn in parts (b)–(f) as a dashed line to indicate correlation enhancement.

It is first observed in Figs. 20(a) and 21(a) that the maximum peak seldom occurs at the known source location using the original replica model. While peaks do occur at the proper location (see Fig. 9), mismatch has caused them to drop below sidelobe levels. For all tonals, the use of the optimal replica model obtained by modal-sum-limit optimization without APO increases the maximum correlation [part (b)] at all times, thereby increasing the frequency at which the maximum peak occurs at the known source location. The localization improvement for the higher frequencies (195 Hz), however, is largely restricted to shorter ranges (or times). Inclusion of APO in Fig. 21(c) greatly improved localization in both range and depth at the higher frequencies over the majority of the source-tow. Improved localization was also observed for the lower frequencies (70 Hz), although to a lesser extent because of the lower impact of array geometry mismatch at the lower frequencies. The maximum peaks are seen to closely follow the true source track in Figs. 20(c) and 21(c). In particular, note how the maximum peaks follow the depth excursions at the beginning of the track, caused by changes in the speed of the tow-ship as it began its course. It is also remarkable that the small increases in maximum level observed in going from part (b) to part (c) are enough to cause the peaks at the true source locations to become the maxima over the entire surface.

A comparison of part (d) with part (c) in Figs. 20–21 reveals that the localization performance for the bottom-property-inverted optimal replica model with APO is of comparable quality to that for the modal-sum-limit optimization with APO, although the latter is generally superior. In particular, the depth of the maximum peak disagrees with the true depth more often when using the inverted optimal replica model. The superior performance of the modal-sum-limit optimization is expected since this technique is based on an optimization of the total attenuating effect of the geoacoustic properties. The inability to include all possible mechanisms in the inversion technique renders the accurate determination of geoacoustic parameters which yield that total effect difficult, resulting in slightly poorer performance.

The performance obtained using a mudstone sound speed of 1861 m/s is observed to differ little from that obtained with the lower value of 1691 m/s at 195 Hz [compare Fig. 21(e) with Fig. 21(d)]. This was also observed to be the case for the 95- and 145-Hz tonals. From this it is concluded that the precise value of the mudstone sound speed is of little consequence at the higher frequencies. For the 70-Hz tonal, however, localization performance is significantly affected by the value of this parameter. While the low-mudstone-sound-speed model [Fig. 20(d)] has generally good localization performance over the full track, performance is slightly better at the shorter ranges (at times less than 40 min from the start of the track). The performance for the high-mudstone-sound-speed model [Fig. 20(e)], on the other hand, appears better at the long ranges. This is in agreement with the observation of a high and low mudstone-sound-speed regime in Sec. IV. The reason for this difference may be the deviation from the range-independent assumption as the source moves away from the VLA. Figure 3 indicates that sediment thickness varies along the source-tow track. In addition, the composition of the bottom layers may vary laterally. Figure 20(d) and (e) suggests that the environment at ranges less than 5 km is best modeled by the low-mudstone-sound-speed model, while that at ranges greater than 5 km is best modeled by the high-mudstone-velocity model. It is possible that the mudstone ridge near a range of 5 km from the VLA, as seen in Fig. 3, may be stripping out modes present at closer ranges, or that bottom properties on either side of this ridge differ substantially. The small differences in correlation between Fig. 20(d) and (e) renders determination of the exact cause for the difference in performance extremely difficult.

It will be recalled from the coarse-grid attenuation inversion of Fig. 13 that large matched-field correlations could be realized if the mudstone attenuation was increased to values greater than those thought to be realistic for this region (>1 dB/km Hz). Such values therefore do not represent valid inversion estimates for the mudstone attenuation, but rather are values of this parameter which ''effectively'' optimize performance. To study this effect, parts (f) of Figs. 20 and 21 present the performance results using the inverted optimal replica model with the mudstone attenuation increased from 0.02 dB/km Hz to 1.280 dB/km Hz. A comparison of Fig. 21(f) with Fig. 21(c) and Fig. 21(d) reveals that for the higher frequencies (195 Hz), the localization performance for the model with a 1.28 dB/km Hz mudstone sound speed resembles that of the modal-sum-limit optimization with APO [Fig. 21(c)] more closely than that for the inverted optimal replica model with APO [Fig. 21(d)]. In essence, any energy penetrating the mudstone is highly attenuated, effectively producing the same result as a truncation of all modes which extend below the sediment-mudstone interface. At the lower frequencies (70 Hz), the source-localization performance in Fig. 20(f) appears to exceed that in Fig. 20(c), particularly at the shorter ranges.

Previous studies[3,4,32–34,36] have demonstrated that matched-field localization can be significantly improved by taking the incoherent average of the ambiguity surfaces obtained for individual frequencies. Figure 22 presents performance results for ambiguity surfaces incoherently averaged over the four tonals. Figure 22(a) corresponds to the original replica model, Fig. 22(b) to the optimal replica model obtained by modal-sum-limit optimization with APO, and Fig. 22(c) to the optimal replica model obtained by bottom-property inversion with APO in Table III. It is observed that the source is tracked extremely well in both range and depth, even with the significant mismatch inherent in the original replica model [Fig. 22(a)]. This is a result of the fact that sidelobes in the matched-field signal function occur at different locations for different frequencies, which results in sig-

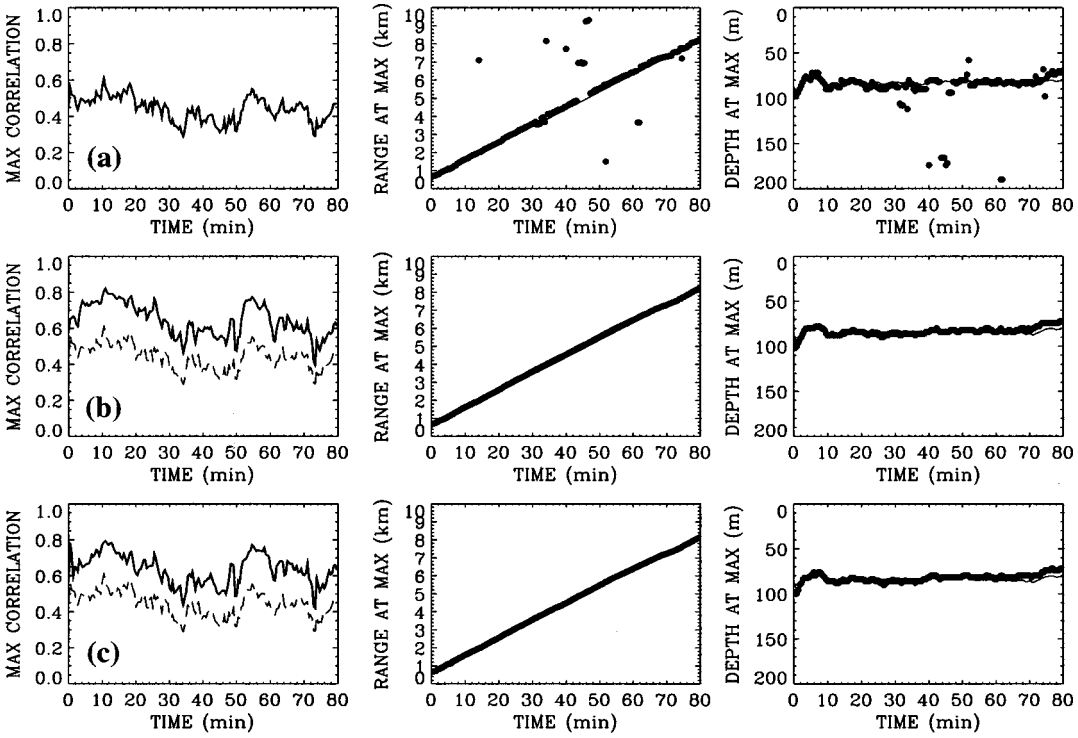

FIG. 22. Comparison of four-tone frequency-averaged MFP ambiguity surface maxima, range at maxima, and depth at maxima versus time during source-tow track using various replica models. Replica models used in Bartlett processor are (a) original replica model, and optimal replica models obtained by (b) modal-sum-limit optimization with array position (c) bottom-property inversion.

nificant sidelobe reduction when the ambiguity surfaces are summed. Consequently the competition between the sidelobes and the main peak for the maximum value is removed. Most of the deviations from the true source track are eliminated, and the maximum correlation in the surface enhanced, when either the modal-sum-limit-optimized replica model with APO [Fig. 22(b)] or the inverted optimal replica model with APO [Fig. 22(c)] is used. The main deviation from the known source track occurs at times beyond 70 min, in which the maximum averaged peak occurs at slightly shallower depths and slightly shorter ranges than those for the known source-tow track. This deviation is caused by the break down of the range-independence assumption for the bathymetry; Figs. 1 and 3 indicate that the depth of the seafloor increases substantially near the end of the source-tow track. The magnitude of these errors is consistent with that predicted by D'Spain *et al.*[32–34] using adiabatic normal mode theory. The performance for the other replica models considered in Figs. 20–21 is essentially identical. While it is remarkable that exceptional source localization performance can be realized using frequency averaging without any replica model optimization, it should be noted that the enhanced correlations provided by such optimizations provide significant advantages for the detection problem. In addition, the agreement between the source location estimates and the true track suggests that the neglect of water mass fluctuations is reasonable.

While not presented here, localization data like that presented in Fig. 22(c) were obtained for the case in which a single bottom parameter (such as water depth or sediment thickness, density, sound speed, or attenuation) was varied from the value in the inverted replica model in Table III. In all cases, the best performance (highest correlation and best tracking) occurred at all ranges when the parameter coincided with the value of the inverted replica model. This is strong evidence that the inverted parameters (sediment sound speed and attenuation) are near-optimal, and that the noninverted parameters (water depth, sediment thickness, and density) were originally good estimates and could validly be treated as known.

Since the difference in the maximum correlation level for the various optimization schemes is difficult to observe visually in Figs. 20–22, Fig. 23 compares the range-averaged (over the entire source-tow track) maximum correlation level for each scheme with that for the original replica model in bar-chart form. These results are also tabulated in Table IV. It is clear from these summaries that the all optimal replica models [including the modified forms for (e) and (f)], on average, substantially increase the maximum correlation above that for the original replica model for all tonals and their average. The improvement is seen to increase with increasing frequency; correlation enhancements between 6.5% and 8.2% at 70 Hz increase to between 23.1% and 27.8% at 195 Hz. This behavior is reasonable since impact of mismatch is greatest at the higher frequencies. For the modal-sum-limit techniques [(b) and (c)], the inclusion of APO (c) has the greatest influence at the higher frequencies, as expected, but its contribution to the overall correlation increase is still relatively small compared to that caused by the modal-sum-limit optimization alone (b).

It is interesting to note that the range-averaged maximum correlation for the four-tone average is in all cases less than the average of the maximum correlations shown for the individual tones. In fact, the four-tone average values for the

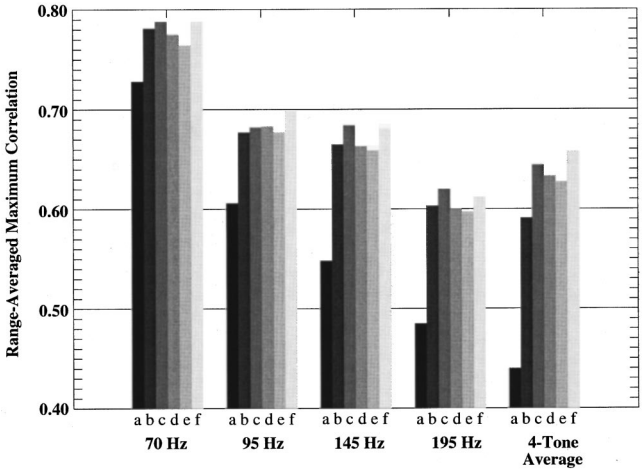

FIG. 23. Summary of range-averaged MFP maximum correlation using various replica models. Replica models used in Bartlett processor are (a) original replica model, and optimal replica models obtained by (b) modal-sum-limit optimization, (c) modal-sum-limit optimization and array position optimization, (d) bottom-property inversion, (e) replica model in part (d) with upper mudstone sound speed increased to 1861 m/s, and (f) replica model in part (d) with mudstone attenuation increased to 1.28 dB/km Hz. Categories (a) through (f) correspond to parts (a) through (f) of Figs. 20–21.

original replica model (a), and the modal-sum-limit optimized model without APO (b), are below those for the highest-frequency tonal. The only possible explanation for this behavior is that, at a given time, the location of the main peak varies with frequency, causing a degradation in the average. That this is indeed the case is demonstrated in Fig. 24, which plots the range and depth error (relative to the known true location) of the main peak versus time and frequency for the original replica model [part (a)], the modal-sum-limit-optimized model [part (b)], and the modal-sum-limit-optimized and array-position-optimized model [part (c)]. In these plots, the closed circles are for the 70-Hz tonal, the open circles for the 95-Hz tonal, the plus signs for the 145-Hz tonal, and the open triangles for the 195-Hz tonal. It is observed that the location of the main peak for the original replica model exhibits substantial scatter. However, because each peak possesses a thickness in both the range and depth directions, the peaks overlap. The average of these peaks will therefore be significantly lower than the average obtained if the peaks were coincident, but not totally destroyed because of the overlap. The scatter of the main peak location is seen to be reduced for the modal-sum-limit-optimized model, causing the four-tone average in Fig. 23 to increase to a value closer to the theoretical average which would be obtained for coincident peaks. The addition of the APO causes the main peaks for each tonal to move closer together, further enhancing the four-tone average. This accounts for the larger increase in going from (b) to (c) for the four-tone average, than for the individual tonals, in Fig. 23. In theory, the value of the four-tone average should approach the value obtained if the peaks were coincident as mismatch and noise are eliminated. Even while localization performance using the original replica with frequency averaging was seen to be nearly as good as that for the optimal models (Fig. 22), Fig. 24 clearly demonstrates that the use of optimal replica models greatly increases correlation and hence detection performance.

The range-averaged maximum correlation for the optimal replica model obtained via bottom-property inversion with APO (d) is generally, with the exception of the 95-Hz tonal, less than that obtained via modal-sum-limit optimization with APO (c). As indicated previously, this is because of the inability to account for all parameters in the inversion process. The modal-sum-limit optimization, on the other hand, implicitly includes effects of these parameters by effectively optimizing over the total effective attenuation. The effect of increasing the upper mudstone sound speed to 1861 m/s (e) is seen to have little overall effect on the maximum correlation, the greatest effect (a degradation) is observed for the 70-Hz tonal, consistent with the previous discussions on this matter. And finally, it is interesting to note that the inverted optimal model with the mudstone attenuation increased to 1.28 dB/km Hz (f) produces a maximum correla-

TABLE IV. Range-averaged maximum correlation for various replica models. Replica models: (a) original; (b) obtained by modal-sum-limit optimization without APO; (c) obtained by modal-sum-limit optimization with APO; (d) obtained by bottom-property inversion with APO; (e) same as (d) but with upper mudstone sound speed increased to 1861 m/s; (e) same as (d) but with mudstone attenuation increased to 1.28 dB/km Hz. The above labels correspond to the parts in Figs. 20–21. Parenthetical values represent the percent increase above the value for the original replica model.

Replica model	Range-averaged maximum correlation				
	70 Hz	95 Hz	145 Hz	195 Hz	Frequency average
(a)	0.728	0.606	0.548	0.485	0.440
(b)	0.781 (+7.3%)	0.677 (+11.7%)	0.665 (+21.4%)	0.603 (+24.3%)	0.591 (+34.3%)
(c)	0.788 (+8.2%)	0.682 (+12.5%)	0.684 (+24.5%)	0.620 (+27.8%)	0.644 (+46.4%)
(d)	0.775 (+6.5%)	0.683 (+12.7%)	0.663 (+21.0%)	0.600 (+23.7%)	0.633 (+43.9%)
(e)	0.764 (+4.9%)	0.677 (+11.7%)	0.659 (+20.3%)	0.597 (+23.1%)	0.627 (+42.5%)
(f)	0.788 (+8.2%)	0.698 (+15.2%)	0.681 (+24.3%)	0.612 (+26.2%)	0.658 (+49.5%)

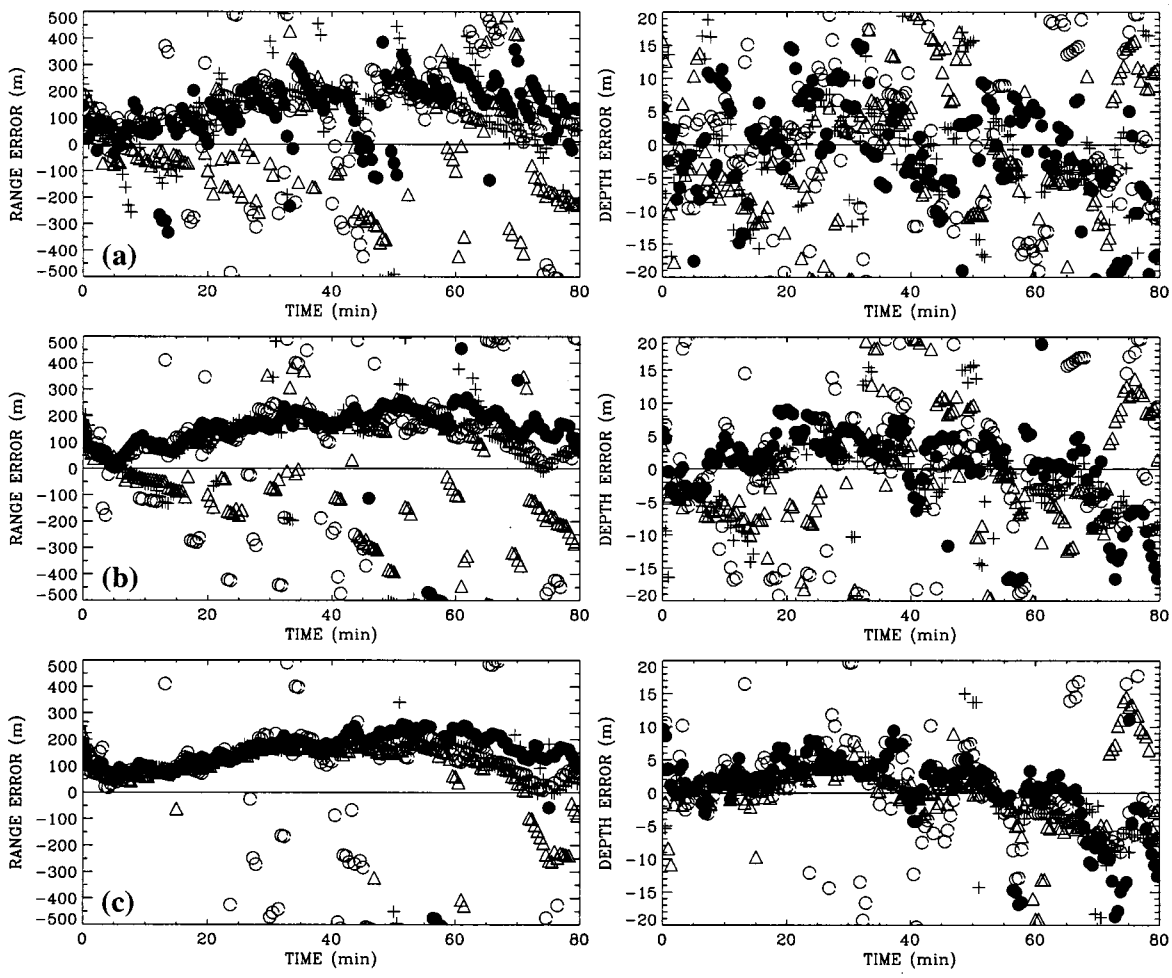

FIG. 24. Ambiguity surface main peak range and depth error (relative to known true location) versus time during source-tow track and tonal frequency. Replica models used in Bartlett processor are (a) original replica model, and optimal replica models obtained by (b) modal-sum-limit optimization, and (c) modal-sum-limit optimization with array position optimization. Closed circles: 70-Hz tonal. Open circles: 95-Hz tonal. Plus signs: 145-Hz tonal. Open triangles: 195-Hz tonal. Main peak location determined by finding the maximum correlation in a window (1-km wide in range, 40-m wide in depth) centered on the true source location at each time.

tion closer to, and sometimes above (at 95 Hz and the four-tone average) that for the modal-sum-limit optimization with array position optimization. This implies that this high mud-stone attenuation model is effectively accomplishing the same effect as the modal-sum-limit optimization; namely the elimination of modes not present in the data.

VI. CONCLUSIONS AND RECOMMENDATIONS

The overall objective of this study has been to optimize MFP performance in the shallow-water SWellEX-1 environment via the determination of an optimal replica model. Having determined that an initial estimate for a replica model used in previous studies predicted a number of propagating modes in excess of that actually present in the data, two optimization approaches were implemented to correct for this mismatch. Since the number of propagating modes depends on the nature of the bottom interactions of the acoustic energy, these techniques involve attempts to determine replica models that best model these interactions. The first technique, termed modal-sum-limit optimization, seeks the model which best models the total ''effective'' modal attenuation by explicitly determining the number of modes present in the data. The second technique for replica model optimization is to invert for the major bottom parameters thought to be responsible for the modal-sum-limit error, via repeated solutions of the forward problem for combinations of these parameters.

Both techniques for replica model optimization greatly improved correlation levels and localization performance at all frequencies. For the 70-Hz tonal, maximum correlations of 0.96 were achieved during very high signal-to-noise ratio periods. The degree of correlation enhancement increased with increasing frequency, since mismatch effects are greater at higher frequencies, increasing from around 7% to 8% (relative to the original replica model) at 70 Hz up to 24%–28% at 195 Hz. In most cases, the performance for the modal-sum-limit optimized model was superior to that for the inverted model, suggesting that the inverted bottom properties account for most, but not all, of the mismatch contained in the original replica model. This superior performance, coupled with an inherent computational simplicity, renders the modal-sum-limit approach an attractive choice for practical problems, and may be conducive to optimization automation. The performance enhancement obtained via

array position optimization is greatest at the higher frequencies, as expected.

In performing the bottom-property inversion, it was noted that inversion for sediment properties was more easily accomplished than for mudstone properties, because of the small effects with variation in mudstone attenuation. Apparently, mudstone-interacting energy has simply been too highly attenuated at the inversion stations considered to yield reliable results for mudstone attenuation. While the effects of mudstone sound-speed variation were more dramatic, estimates for this parameters were highly ambiguous. At the higher frequencies (95, 145, and 195 Hz) MFP performance was essentially identical using either the low (1691 m/s) or the high (1871 m/s) mudstone sound-speed estimate. At 70 Hz, the value of 1691 m/s produced better localization performance at the shorter ranges (<5 km), while the value of 1861 m/s produced better performance at the larger ranges (>5 km). It is surmised that a significant deviation from the range-independence assumption for the sediment-mudstone interface may be responsible for this behavior; further study into the reason for this effect is warranted. As for the sediment property inversions, best results were generally obtained at the inversion station at a range of 5.76 km from the source, beyond the influence of the direct path energy and the unknown interferer.

The quality of the inverted replica model was validated is several ways. First, extremely high correlations (0.96) were obtained during periods of high signal-to-noise ratio. Second, a synthetic modal decomposition as a function of source range using the inverted replica model and a fictitious array spanning the water column and bottom layers indicates that modal power drops significantly at mode numbers close to those predicted by the modal-sum-limit optimization. Third, estimates for the sediment attenuation are observed to be in agreement with those predicted by Hamilton.[48] The general enhancement at all frequencies, obtained using an attenuation estimate (in dB/km Hz) at one frequency (70 Hz), also supports Hamilton's assumption that attenuation varies as the first power of frequency. Last, while not presented here, recent work by Hodgkiss *et al.*[35] has shown that the use of a replica model close to the inverted model obtained in this study, results in good high-resolution localization performance of the MFP minimum-variance distortionless response (MVDR) estimator, which is much more sensitive to mismatch errors than the Barlett estimator in Eq. (1).

It has also been demonstrated that MFP performance optimization may be accomplished using replica models known to be nonphysical. MFP localization performance and correlation enhancement was observed to be excellent, agreeing more consistently with the results of the modal-sum-limit optimization, when an unrealistic value of 1.28 dB/km Hz was used for the mudstone attenuation. This implies that it may be possible to find a replica model with a simple bottom structure (such as a single continuous half-space) with parameters which provide very good MFP performance. It is believed that a study of such an approach might prove beneficial for practical applications of MFP.

Incoherently averaging the ambiguity surfaces for the four tonals greatly enhanced localization performance via the reduction of signal sidelobes. This was even the case for the nonoptimized original replica model. However, optimized models greatly enhanced the correlation levels of the main peak, thus increasing the detection of the signal. Compared to the frequency-averaged results for the original replica model, maximum correlations were on average 46.4% greater for the modal-sum-limit approach and 43.9% greater for the bottom-property inversion.

ACKNOWLEDGMENTS

This work was supported by the Office of Naval Research, ONR-321US. The authors thank Phil Schey of the Space and Naval Warfare Systems Center, San Diego (SSCSD) for the initial reduction of SWellEX-1 data and his valuable insights into the problem. Appreciation is also expressed to Richard Bachman of SSCSD for providing initial geoacoustic models and insights into geoacoustic character of the seafloor.

[1] H. P. Bucker, ''Use of calculated sound fields and matched field detection to locate sound sources in shallow water,'' J. Acoust. Soc. Am. **59**, 368–373 (1976).
[2] R. G. Fizell, ''Application of high-resolution processing to range and depth estimation using ambiguity function methods,'' J. Acoust. Soc. Am. **82**, 606–613 (1987).
[3] A. B. Baggeroer, W. A. Kuperman, and H. Schmidt, ''Matched field processing: Source localization in correlated noise as an optimum parameter estimation problem,'' J. Acoust. Soc. Am. **83**, 571–587 (1988).
[4] A. Tolstoy, *Matched Field Processing for Underwater Acoustics* (World Scientific, Singapore, 1993).
[5] M. B. Porter, R. Dicus, and R. G. Fizell, ''Simulation of matched-field processing in a deep-water Pacific environment,'' IEEE J. Ocean Eng. **12**, 173–181 (1987).
[6] C. Feuillade, D. R. Del Balzo, and M. M. Rowe, ''Environmental mismatch in shallow-water matched-field processing: Geoacoustic parameter variability,'' J. Acoust. Soc. Am. **85**, 2354–2364 (1989).
[7] A. Tolstoy, ''Sensitivity of matched field processing to sound-speed profile mismatch for vertical arrays in a deep water Pacific environment,'' J. Acoust. Soc. Am. **85**, 2394–2404 (1989).
[8] D. F. Gingras, ''Methods for predicting the sensitivity of matched-field processors to mismatch,'' J. Acoust. Soc. Am. **86**, 1940–1949 (1989).
[9] R. M. Hamson and R. M. Heitmeyer, ''Environmental and system effects on source localization in shallow water by the matched-field processing of a vertical array,'' J. Acoust. Soc. Am. **86**, 1950–1959 (1989).
[10] T. C. Yang, ''Effectiveness of mode filtering: A comparison of matched-field and matched-mode processing,'' J. Acoust. Soc. Am. **87**, 2072–2084 (1990).
[11] H. Schmidt, A. B. Baggeroer, W. A. Kuperman, and E. K. Scheer, ''Environmentally tolerant beamforming for high-resolution matched-field processing: Deterministic mismatch,'' J. Acoust. Soc. Am. **88**, 1851–1862 (1990).
[12] G. B. Smith, H. A. Chandler, and C. Feuillade, ''Performance stability of high-resolution matched-field processors to sound-speed mismatch in a shallow-water environment,'' J. Acoust. Soc. Am. **93**, 2617–2626 (1993).
[13] E. C. Shang and Y. Y. Wang, ''Environmental mismatching effects on source localization processing in mode space,'' J. Acoust. Soc. Am. **89**, 2285–2290 (1991).
[14] D. R. Del Balzo, ''Effects of water-depth mismatch on matched-field localization in shallow water,'' J. Acoust. Soc. Am. **83**, 2180–2185 (1988).
[15] C. Feuillade, W. A. Kinney, and D. R. DelBalzo, ''Shallow-water matched-field processing off Panama City, Florida,'' J. Acoust. Soc. Am. **88**, 423–433 (1990).
[16] S. M. Jesus, ''Normal-mode matching localization in shallow water: Environmental and system effects,'' J. Acoust. Soc. Am. **90**, 2034–2041 (1991).
[17] R. Klemm, ''Range and depth estimation by line arrays in shallow water,'' Signal Process. **3**, 333–334 (1981).
[18] J. R. Daugherty, and J. F. Lynch, ''Surface wave, internal wave, and source motion effects on matched-field processing in a shallow water

waveguide,'' J. Acoust. Soc. Am. **87**, 2503–2526 (1990).
[19] C. L. Byrne, ''Effects of modal phase errors on eigenvector and nonlinear methods for source localization in matched-field processing,'' J. Acoust. Soc. Am. **92**, 2159–2164 (1992).
[20] J. M. Q. D. Tran and W. S. Hodgkiss, ''Experimental observation of temporal fluctuations at the output of the conventional matched-field processor,'' J. Acoust. Soc. Am. **89**, 2291–2302 (1991).
[21] D. R. Jackson and T. E. Ewart, ''The effect of internal waves on matched-field processing,'' J. Acoust. Soc. Am. **96**, 2945–2955 (1994).
[22] E. Livingston and O. Diachok, ''Estimation of average under-ice reflection amplitudes and phases using matched-field processing,'' J. Acoust. Soc. Am. **86**, 1909–1919 (1989).
[23] A. Tolstoy, O. Diachok, and L. N. Frazer, ''Acoustic tomography via matched-field processing,'' J. Acoust. Soc. Am. **89**, 1119–1127 (1991).
[24] A. Tolstoy, ''Linearization of the matched field processing approach to acoustic tomography,'' J. Acoust. Soc. Am. **91**, 781–787 (1992).
[25] J. M. Q. D. Tran and W. S. Hodgkiss, ''Sound-speed profile inversion using a large aperture vertical line array,'' J. Acoust. Soc. Am. **93**, 803–812 (1993).
[26] C. C. Karangelen and O. Diachok, ''Experimental demonstration of sound-speed inversion with matched-field processing,'' J. Acoust. Soc. Am. **93**, 2649–2655 (1993).
[27] S. E. Dosso, J. M. Ozard, and J. A. Fawcett, ''Inversion of acoustic field data for bathymetry and bottom sound speed via simulated annealing,'' in *Acoustic Signal Processing for Ocean Exploration*, edited by J. M. F. Moura and I. M. G. Lourtie (Kluwer, Dordrecht, 1993).
[28] M. D. Collins, W. A. Kuperman, and H. Schmidt, ''Nonlinear inversion for ocean-bottom properties,'' J. Acoust. Soc. Am. **92**, 2770–2783 (1992).
[29] P. Gerstoft, ''Inversion of seismoacoustic data using genetic algorithms and *a posteriori* probability distributions,'' J. Acoust. Soc. Am. **95**, 770–782 (1994).
[30] D. F. Gingras and P. Gerstoft, ''Inversion for geometric and geoacoustic parameters in shallow water: Experimental results,'' J. Acoust. Soc. Am. **97**, 3589–3598 (1995).
[31] J. M. Q. D. Tran and W. S. Hodgkiss, ''Array surveying using matched-field processing,'' J. Acoust. Soc. Am. **94**, 2851–2858 (1993).
[32] G. L. D'Spain, J. J. Murray, W. S. Hodgkiss, N. O. Booth, and P. W. Schey, ''Mirages in shallow water matched-field processing,'' J. Acoust. Soc. Am. **105**, 3245–3265.
[33] G. L. D'Spain, J. J. Murray, W. S. Hodgkiss, and N. O. Booth, ''Predicting the broadband matched field processing results for the arc event during SWellEx-3,'' Marine Physical Laboratory, Scripps Institution of Oceanography: San Diego, CA, MPL TM-442 (1994).
[34] G. L. D'Spain, W. S. Hodgkiss, and W. A. Kuperman, ''Broadband matched field processing in shallow water,'' Proc. 15th Int'l Conf. on Acoustics, Trondheim, Norway, 1995 (Acoustical Society of Norway under the aegis of the International Union of Pure and Applied Physics, 1995), Vol. I, pp. 231–234.
[35] W. S. Hodgkiss, K. H. Kim, J. J. Murray, and J. L. Krolik, ''Robust MFP processor performance with SWellEx data,'' presented at the Eighth International Workshop on Matched-Field Processing and Model-Based Signal Processing, Victoria, British Columbia, Canada, 12–14 June 1996.
[36] N. O. Booth, P. A. Baxley, J. A. Rice, P. W. Schey, W. S. Hodgkiss, G. L. D'Spain, and J. J. Murray, ''Source localization with broad-band matched-field processing in shallow water,'' IEEE J. Ocean Eng. **21**, 402–412 (1996).
[37] SWellEX-1 Test Plan, unpublished Space and Naval Warfare Systems Center, San Diego document, August 1993.
[38] SWellEX-3 Data Report, unpublished Space and Naval Warfare Systems Center, San Diego document, June 1993.
[39] SWellEX-96 Preliminary Data Report, unpublished Space and Naval Warfare Systems Center, San Diego document, May 1996.
[40] P. Schey and F. Ryan, ''Matched-field processing and source depth localization in a shallow-water environment (SWellEX-3),'' J. Acoust. Soc. Am. **95**, 2981 (1994).
[41] R. T. Bachman, unpublished Space and Naval Warfare Systems Center, San Diego document, September 1994.
[42] R. T. Bachman, P. W. Schey, N. O. Booth, and F. J. Ryan, ''Geoacoustic databases for matched-field processing: Preliminary results in shallow water of San Diego, California,'' J. Acoust. Soc. Am. **99**, 2077 (1996).
[43] M. B. Porter, ''The KRAKEN normal mode code,'' SACLANT Undersea Research Centre memorandum SM-245, September 1991.
[44] L. Brekhovskikh and Y. Lysanov, *Fundamentals of Ocean Acoustics* (Springer-Verlag, Berlin, 1982).
[45] F. D. Tappert, ''Parabolic equation modeling of shear waves,'' J. Acoust. Soc. Am. **78**, 1905 (1985).
[46] C. T. Tindle and Z. Y. Zhang, ''An equivalent fluid approximation for a low shear speed ocean bottom,'' J. Acoust. Soc. Am. **91**, 3248 (1992).
[47] M. J. Buckingham, ''Theory of acoustic attenuation, dispersion, and pulse propagation in unconsolidated granular materials including marine sediments,'' J. Acoust. Soc. Am. **102**, 2579 (1997).
[48] E. L. Hamilton, ''Compressional wave attenuation in marine sediments,'' Geophysics **37**, 620–646 (1972).
[49] E. L. Hamilton, ''Geoacoustic modeling of the sea floor,'' J. Acoust. Soc. Am. **68**, 1313–1340 (1980).
[50] R. T. Bachman, personal communication.
[51] M. D. Richardson and K. B. Briggs, ''On the use of acoustic impedance values to determine sediment properties,'' in Proceedings of the Institute of Acoustics, Vol. 15, Part 2, Bath, U.K., 1993 (Institute of Acoustics, 1993), pp. 15–24.
[52] R. T. Bachman, personal communication.
[53] S. K. Mitchell and K. C. Focke, ''New measurements of compressional wave attenuation in deep ocean sediments,'' J. Acoust. Soc. Am. **67**, 1582 (1980).
[54] R. S. Anderson and A. Blackman, ''Attenuation of low frequency sound waves in sediments,'' J. Acoust. Soc. Am. **44**, 786 (1971).
[55] R. D. Stoll, ''Acoustic waves in marine sediments,'' in *OceanSeismoAcoustics*, edited by T. Akal and J. M. Berkson (Plenum, New York, 1986).
[56] G. V. Frisk, J. A. Doutt, and E. E. Hays, ''Bottom interaction of low frequency acoustic signals at small grazing angles in the deep ocean,'' J. Acoust. Soc. Am. **69**, 84 (1981).

A matched-peak inversion approach for ocean acoustic travel-time tomography

E. K. Skarsoulis
Institute of Applied and Computational Mathematics, Foundation for Research and Technology Hellas, P.O. Box 1527, 711 10 Heraklion, Crete, Greece

(Received 11 May 1999; revised 5 November 1999; accepted 18 November 1999)

A new approach for the inversion of travel-time data is proposed, based on the matching between model arrivals and observed peaks. Using the linearized model relations between sound-speed and arrival-time perturbations about a set of background states, arrival times and associated errors are calculated on a fine grid of model states discretizing the sound-speed parameter space. Each model state can explain (identify) a number of observed peaks in a particular reception lying within the uncertainty intervals of the corresponding predicted arrival times. The model states that explain the maximum number of observed peaks are considered as the more likely parametric descriptions of the reception; these model states can be described in terms of mean values and variances providing a statistical answer (matched-peak solution) to the inversion problem. A basic feature of the matched-peak inversion approach is that each reception can be treated independently, i.e., no constraints are posed from previous-reception identification or inversion results. Accordingly, there is no need for initialization of the inversion procedure and, furthermore, discontinuous travel-time data can be treated. The matched-peak inversion method is demonstrated by application to 9-month-long travel-time data from the Thetis-2 tomography experiment in the western Mediterranean sea. [S0001-4966(00)00203-4]

PACS numbers: 43.30.Pc, 43.30.Bp, 43.60.Lq [DLB]

INTRODUCTION

Ocean acoustic travel-time tomography was introduced by Munk and Wunsch[1,2] as a remote-sensing technique for monitoring the ocean interior over large sea areas using low-frequency sound waves. Measuring the travel times of pulsed acoustic signals propagating through the water mass over a multitude of different paths, and exploiting the knowledge about how travel times are affected by the sound-speed (temperature) distribution in the water, the latter can be obtained by inversion.

Various modeling approaches have been used for establishing functional relations (model relations) between sound-speed and travel-time variations, based on the notion of ray arrivals,[3,4] modal arrivals,[3,5] or peak arrivals.[6,7] Assuming small perturbations of the ocean, the model relations are usually linearized about a single background state permitting the rapid computation of arrival times directly for any given sound-speed profile. By replacing the single background state through a discrete set of background states, the linearization approach can be extended to cover cases where the initial model relations exhibit significant nonlinearity, either due to the extent of ocean variability (e.g., large variations) or due to the particular propagation conditions.[8,9]

Before addressing the inversion problem in travel-time tomography, the peak identification problem has to be solved, i.e., the model peaks must be associated with the observed ones.[10,11] Traditionally this problem is solved by first obtaining observed peak tracks (tracking problem) which are then associated with model peaks (identification problem). Various automatic tracking and identification approaches have been developed based on adaptive filtering,[12,13] statistical decision theory,[14,15] or using additional arrival-angle information.[16,17] More recently, unified model-based approaches were proposed treating the peak tracking and identification problem in close relation to the inversion problem.[7,18,19]

A common feature of the automatic tracking and identification algorithms is that identification/inversion results from previous receptions are used to constrain the set of trial identifications in the current reception. Although this approach in general works well in the case of low-noise receptions with stable and well-separated peaks, in cases of noisy data with peaks fading in and out or in case of nonsmooth evolution of arrival times, from reception to reception, tracking may become ambiguous and misidentifications are probable. In such cases, a misidentification in a particular reception may become fatal for the inversions in the subsequent receptions, which may lose track of the correct peaks.[19]

A matched-peak inversion approach is proposed here which bypasses the explicit solution of the identification problem and the above inherent difficulties. Using the linearized model relations between sound-speed and arrival-time perturbations, about a set of background states, arrival times and associated model errors are calculated on a fine grid of model states discretizing the parameter space. Each model state can explain (identify) a number of observed peaks in a particular reception lying within the error intervals of the corresponding predicted arrival times. The model states that explain the maximum number of observed peaks are considered as the more likely parametric descriptions of the reception; these model states can be described in terms of mean values and variances providing a statistical answer (matched-peak solution) to the inversion problem. This approach can

be considered as an extension of the matched-field/waveform approach[20–22] to the case of travel-time data. An advantage of the proposed method is that each reception can be analyzed independently of the previous receptions, i.e., no constraints are posed using results from the previous reception(s). This has an important consequence that there is no need for initialization of the inversions, i.e., no need for additional initialization data, whereas it enables the treatment of discontinuous (gapped) data.

The contents of the work are organized as follows: Sec. I deals with the parametrization of the sound-speed profile, the model relations between the sound-speed parameters and the peak arrival times, as well as with the linearization of the model relations. Section II describes the matched-peak approach starting with the discretization of the parameter space. An association between observed and model peaks is proposed, taking into account the discretization error as well as the observation/model error. In Sec. III the proposed method is applied to 9-month-long tomography data from the Thetis-2 experiment conducted from January to October 1994 in the western Mediterranean sea. Finally, in Sec. IV the main features of the method are discussed and conclusions are drawn.

I. MODEL RELATIONS

A tomographic setting is considered with a broadband source and a receiver at fixed locations in a range-independent ocean. The variability of the sound-speed profile $c(z)$ within the water column can be represented parametrically through a modal expansion of the form

$$c(z)=c_0(z)+\sum_{l=1}^{L}\vartheta_l\phi_l(z), \tag{1}$$

where $c_0(z)$ is a basic reference profile and $\{\phi_l(z)\}$ is a set of sound-speed modes, e.g., planetary modes or empirical orthogonal functions (EOFs) for the area of interest. The parameter vector $\boldsymbol{\vartheta}=\{\vartheta_l\}$ takes values from the domain Θ spanning the anticipated sound-speed variability.

The solution of the direct problem in ocean acoustic travel-time tomography leads to a set of model relations

$$\tau_i=g_i(\boldsymbol{\vartheta}),\quad i=1,2,...,I,\quad \boldsymbol{\vartheta}\in\Theta, \tag{2}$$

nonlinear in general, between the parameter vector $\boldsymbol{\vartheta}$ and the arrival times τ_i, $i=1,2,...,I$. Arrival times may be defined in various ways, using ray theory (ray arrival times),[1,4] normal-mode theory (modal arrival times),[3,5] or a unified peak-arrival approach[6,7] able to cope with either ray- or wave-theoretic modeling approaches. The precise form of Eq. (2) depends on the definition of arrival times and the propagation modeling used. The selection of one or the other definition and approach relies on the ability to resolve the particular model observables in the measured arrival patterns.

For small sound-speed variations, the relations (2) are usually linearized about a mean background state $\boldsymbol{\vartheta}=\boldsymbol{\vartheta}^{(b)}$, $\tau_i^{(b)}=g_i(\boldsymbol{\vartheta}^{(b)})$

$$\tau_i(\boldsymbol{\vartheta})=\tau_i^{(b)}+\sum_{l=1}^{L}\frac{\partial g_i(\boldsymbol{\vartheta}^{(b)})}{\partial\vartheta_l}[\vartheta_l-\vartheta_l^{(b)}]. \tag{3}$$

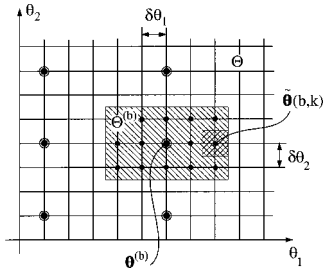

FIG. 1. A schematic diagram of the discretization of the parameter domain for the two-dimensional case.

The derivatives $\partial g_i/\partial\vartheta_l$, called influence coefficients, can be expressed and calculated in terms of background quantities and sound-speed modes.[4–6] Equation (3) can be used as a basis for linear inversions of travel-time data.

Replacing the single background state with a set of background states, the above linearization approach can also be extended to cover cases where the initial model relations exhibit significant nonlinearity, either due to the extent of ocean variability (e.g., large variations) or due to the particular propagation conditions. The superscript b is considered as a variable index in this case, $b\in\mathcal{B}$, from the background set $\mathcal{B}$. The set of background states $\boldsymbol{\vartheta}^{(b)}$, $b\in\mathcal{B}$, divides the initial parameter domain Θ into a number of local subdomains $\Theta^{(b)}$, as shown in Fig. 1 (for the two-dimensional case), over which the linearized model relations (3) can be used. In this way, the initial nonlinear model relations (2) are replaced by a set of linear ones.

Ocean acoustic tomography aims at obtaining the range-averaged ocean properties from a single source–receiver pair. In this connection, the model relations (2) and (3) describe the functional dependence of arrival times on variations of the sound-speed profile $c(z)$ for the range-independent case. Nevertheless, the effects of range dependence, which is present either in the medium (e.g., mesoscale eddies) or at the boundaries (e.g., sea-surface roughness), are contained in the received signals and their description/modeling is necessary in order either to correct or to invert for them. Previous studies have shown that the effects of range dependence on the arrival times are primarily of second order.[23–25] In the following, it is assumed that the main range-dependence effects have been either corrected for (cf. Sec. III A and Ref. 19) or taken into account as part of the observation error.

II. MATCHED-PEAK INVERSION

The matched-peak solution to the inversion problem consists of finding the population of model states that interpret (identify) the maximum number of peaks in each reception. For this purpose the parameter domain is discretized into a finite set of model states. Using the linearized model relations, arrival times are predicted for each model state and compared with the observed ones seeking to maximize the number of matched peaks.

A. Parameter-domain discretization

Besides the grid of background states, a finer grid of model states is introduced with resolution defined by $\delta\theta_l$,

$l=1,...,L$, as shown in Fig. 1. The discrete model states within each local parameter domain $\Theta^{(b)}$ are denoted by $\tilde{\boldsymbol{\vartheta}}(b,k)$, where $b\in\mathcal{B}$ is the background index and $k\in\mathcal{K}$ is a local grid index. The linearized model relations can be used within each local parameter grid to calculate the corresponding arrival times

$$\tilde{\tau}_i(b,k)=\tau_i^{(b)}+\sum_{l=1}^{L}\frac{\partial g_i(\boldsymbol{\vartheta}^{(b)})}{\partial\vartheta_l}[\tilde{\vartheta}_l(b,k)-\vartheta_l^{(b)}]. \tag{4}$$

Due to the finite resolution of the model grid, certain tolerances (discretization errors) have to be accounted for when associating model arrivals and observed peaks. Considering the influence area of each discrete model state to extend half the way to the neighboring model states—cf. Fig. 1, i.e., over the domain described by the Cartesian product $\Pi_{l=1}^{L}[\tilde{\vartheta}_l(b,k)-\delta\vartheta_l/2,\tilde{\vartheta}_l(b,k)+\delta\vartheta_l/2]$, and exploiting the linearized model relations about the corresponding background state, an estimate for the upper bound of the discretization error can be obtained

$$d_i(b,\delta\boldsymbol{\vartheta})=\frac{1}{2}\sum_{l=1}^{L}\left|\frac{\partial g_i(\boldsymbol{\vartheta}^{(b)})}{\partial\vartheta_l}\delta\vartheta_l\right|. \tag{5}$$

The discretization error depends on the particular model peak, the background state, and the discretization step. If a larger step size, i.e., a coarser model grid, is used, the discretization error increases. With decreasing step size (finer model grid), the discretization error decreases accordingly.

Apart from the discretization error, the predicted arrival times are also subject to a modeling error (e.g., due to linearization or range-dependence effects), whereas the arrival-time observation is subject to an error as well. Denoting by n_i the cumulative observation and modeling error, the total tolerance that has to be allowed for when matching predicted arrival times, corresponding to the discrete model states, with observed travel-time data is given by the sum

$$\varepsilon_i(b,\delta\boldsymbol{\vartheta})=d_i(b,\delta\boldsymbol{\vartheta})+n_i. \tag{6}$$

B. Peak matching

The observed arrival times τ_j^{obs}, $j=1,...,J$ are allowed to associate with the model arrival times $\tilde{\tau}_i(b,k)$, $i=1,...,I$ corresponding to the discrete model state $\tilde{\boldsymbol{\vartheta}}(b,k)$, where $b\in\mathcal{B}$, $k\in\mathcal{K}$, if their time difference is smaller than the tolerance ε_i. Accordingly, an association set can be built for each model peak and each discrete model state

$$\mathcal{J}(i;b,k)=\{j\in\{1,...,J\}:|\tilde{\tau}_i(b,k)-\tau_j^{\mathrm{obs}}|<\varepsilon_i(b,k)\}, \tag{7}$$

describing the identifiable observed peaks by the particular model peak and model state. Since the search windows may overlap each other, the sets $\mathcal{J}(i;b,k)$ may also partially or totally overlap each other. The number of peaks that a particular model state (b,k) can explain (identify) can be obtained through successive inspection of all association sets by assigning the first available (i.e., not already assigned) observed peak in each association set to the corresponding model peak. This recursive process can be formulated as follows: Assign the first observed peak from $\mathcal{J}(1;b,k)$ to the first model peak. A zero denotes empty window, i.e., no assignment

$$j_a(1;b,k)=\min(\mathcal{J}(1;b,k)\cup\{0\}). \tag{8}$$

For each subsequent set $\mathcal{J}(i;b,k)$, $i=2,...,I$ assign the first available (not already assigned) peak to the corresponding model peak. A zero denotes no assignment, either due to an empty window or due to the assignment of all peaks within the particular window to previous model peaks.

$$j_a(i;b,k)=\min(\{j\in\mathcal{J}(i;b,k):j>j_a(i-1;b,k)\}\cup\{0\}),\quad i=2,...,I. \tag{9}$$

The number of identified (assigned) peaks can be calculated by introducing a binary counter $m(i;b,k)$ for each model peak, which is 0 if the peak is not identified in the data and 1 if the peak is identified

$$m(i;b,k)=\begin{cases}1, & \text{for } j_a(i;b,k)\neq 0,\\ 0, & \text{for } j_a(i;b,k)=0.\end{cases} \tag{10}$$

The number of peaks identified by the particular model state, called matching index, is given by the sum $M(b,k)=\Sigma_i m(i;b,k)$. M is an integer number corresponding to each discrete model state and offers a measure of how well the particular observation can be interpreted in terms of identified peaks. The matching index can be calculated very simply and rapidly using the above algorithm. In contrast, automatic identification algorithms have to build up the set of all possible associations between model and observed peaks, which is a computationally intensive procedure since the number of possible combinations may be very large.

In the matched-peak approach, the model states with the largest matching indices, i.e., interpreting the maximum number of observed peaks, are considered the more likely parametric descriptions of the reception

$$Q=\{(\hat{b},\hat{k})\in\mathcal{B}\times\mathcal{K}:M(\hat{b},\hat{k})=\max_{b,k}M(b,k)\}. \tag{11}$$

C. *A posteriori* statistics

The population Q of the more likely model states can be statistically described in terms of the mean value of the sound-speed parameters

$$\overline{\vartheta}_l=\frac{1}{N}\sum_{(b,k)\in Q}\tilde{\vartheta}_l(b,k), \tag{12}$$

and the corresponding covariance matrix

$$D_{\vartheta\vartheta,l\lambda}=\frac{1}{N}\sum_{(b,k)\in Q}(\tilde{\vartheta}_l(b,k)-\overline{\vartheta}_l)(\tilde{\vartheta}_\lambda(b,k)-\overline{\vartheta}_\lambda), \tag{13}$$

where N is the cardinality of the set Q, i.e., the number of selected model states. Using the parametric expression (1) for the sound speed, the mean sound-speed profile $\overline{c}(z)$ can be calculated from the mean parameter vector $\overline{\boldsymbol{\vartheta}}$. Further, the sound-speed variance $\langle\delta c^2(z)\rangle=\langle[c(z)-\overline{c}(z)]^2\rangle$ can be expressed as

$$\langle\delta c^2(z)\rangle=\mathrm{diag}[\boldsymbol{\phi}'(z)\mathbf{D}_{\vartheta\vartheta}\boldsymbol{\phi}(z)], \tag{14}$$

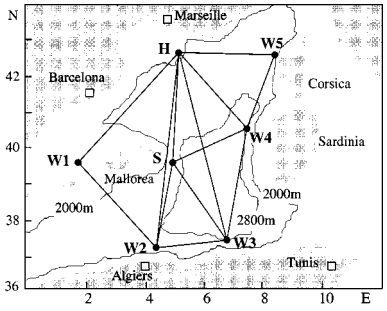

FIG. 2. The geometry of the Thetis-2 experiment in the western Mediterranean.

where $\boldsymbol{\phi}(z)=\{\phi_l(z)\}$ is the vector (column matrix) containing the values of the sound-speed modes at depth z, and $\mathbf{D}_{\vartheta\vartheta}$ is the covariance matrix calculated in (13). The variance for the depth-averaged sound speed (over a particular depth layer) is given by $\langle \overline{\delta c}^2 \rangle = \overline{\boldsymbol{\phi}}' \mathbf{D}_{\vartheta\vartheta} \overline{\boldsymbol{\phi}}$, where the overbars denote depth-averaged quantities.

III. APPLICATION TO THETIS-2 DATA

The matched-peak inversion method is applied in the following to the Thetis-2 experiment conducted from January to October 1994 in the western Mediterranean sea.[26,27] Figure 2 shows the experimental site and geometry. The tomographic array contained seven moored transceivers all deployed at a nominal depth of 150 m. A low-frequency (HLF-5) acoustic source, marked by H in Fig. 2, of central frequency 250 Hz and effective bandwidth 62.5 Hz, insonified the basin at 8-h intervals. The remaining six sources ($W1-W5$ and S), transmitting six times per day, were of Webb type with central frequency 400 Hz and effective bandwidth 100 Hz. The receiver parts of $W1-W5$ were modified to listen to both the 400-Hz and 250-Hz signals. Along the section $W3-H$ an expenddable bathythermograph (XBT) verification line was occupied every 2 weeks using a commercial vessel connecting Marseilles (France) to Skikda (Algeria). In particular, the positions of H and $W3$ were aligned with the ship's route to allow detailed comparisons between tomographic inversions and XBT data. Tomography data from this particular transect (receptions at $W3$ from H) spanning the period from 24 January to 16 October 1994 (yeardays 24.4–289.4) are analyzed in the following.

A. The data

Figure 3(a) shows the sequence of acoustic receptions at $W3$ from H over the 9-month duration of the experiment, after correlation (matched-filter) processing, clock-drift correction, mooring-motion correction, and offset calibration.[19,26] A 3-day sliding average has been applied, i.e., for each calendar day the arrival patterns measured from the preceding to the following day have been incoherently averaged. Finally, the arrival patterns in Fig. 3(a) are normalized with respect to the noise rms level. The parts of each reception lying higher than 2.5 times the rms noise level are considered as containing useful signal and they are used for the calculation of the signal-to-noise ratio (SNR) shown in Fig. 3(b). It is seen from both Fig. 3(a) and (b) that there are

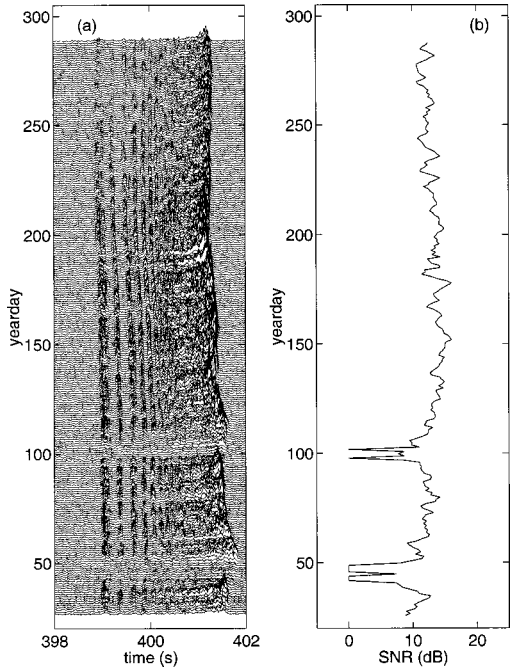

FIG. 3. The acoustic receptions at $W3$ from H. (a) The arrival patterns (3-day incoherent averages) after clock-drift, mooring-motion correction, and offset calibration. (b) The signal-to-noise ratio of the receptions.

two periods, from yearday 37 to 51 and from 96 to 105, characterized by particularly low SNR; over these two periods the transmissions are practically interrupted. A threshold to separate meaningful and poor receptions is 10 dB.

In the first half of most receptions five to six arrival groups can be distinguished which can be associated with particular ray groups corresponding to steep propagation angles. The remaining intermediate and late arrivals are difficult to interpret in terms of ray arrivals because ray groups overlap each other in this interval. To exploit the maximum of information contained in the intermediate and late part of the arrival patterns, the peak-arrival approach[6,7] is used for describing the observables, combined with normal-mode propagation modeling.

Figure 4 shows the observed peak arrival times corresponding to the receptions of Fig. 3(a). The horizontal axis of this figure represents yeardays of 1994 and spans the pe-

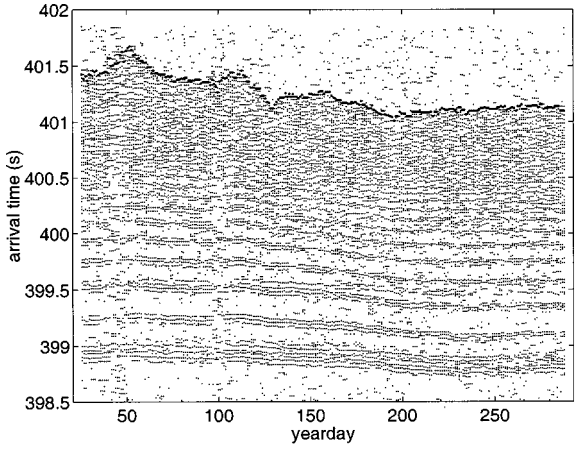

FIG. 4. Measured acoustic arrival times at $W3$ from H. The cutoff peaks are denoted by heavier dots.

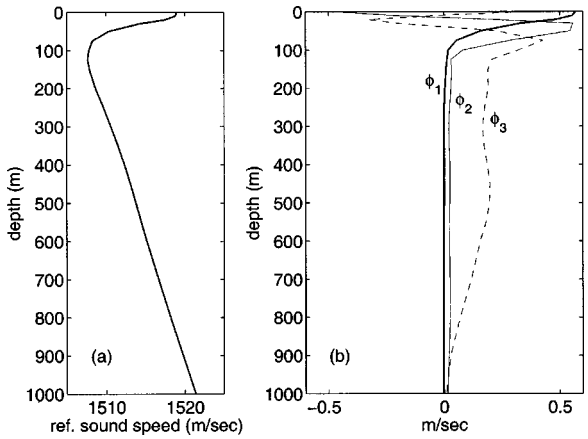

FIG. 5. (a) The basic reference sound-speed profile, and (b) the three most significant empirical orthogonal functions (EOFs) for the western Mediterranean basin.

riod of the experiment, whereas the vertical axis measures arrival time. The 55–60 more-significant peaks in each reception are shown through dots. The location of the cutoff peaks, defined as the last of the five highest peaks in each reception, is shown through heavier dots.

In Fig. 5 the first three empirical orthogonal functions (EOFs) for the western Mediterranean basin are shown along with the basic reference profile. The rms values of the EOF amplitudes are $\vartheta_{1,\mathrm{rms}}=18.48$, $\vartheta_{2,\mathrm{rms}}=2.88$, and $\vartheta_{3,\mathrm{rms}}=0.96$. EOF-1 accounts for the bulk of the seasonal variability taking place close to the surface, and this explains the large rms value of the corresponding amplitude, whereas higher-order EOFs extend to increasingly deep layers. The first three EOFs explain 99.6% of the total variance.

Figure 6(a) shows variations of the reference profile (upper 300 m) in the direction of the first EOF over the ϑ_1 interval $[-50,50]$, covering 2.5 standard deviations of the corresponding amplitude and spanning the gross seasonal variability expected. Large negative values for ϑ_1 correspond to winter conditions (upward-refracting profile) and large positive values to summer conditions (channeled profiles).

Figure 6(b) shows the predicted peak-arrival times corresponding to the different ϑ_1 values for 33 model peaks, from the early arrivals to the final cutoff peak, which could be traced throughout the range of variability. A clear nonlinear behavior can be seen, caused by the passage from surface-reflected propagation in winter to refracted propagation in summer. This passage takes place at different ϑ_1 values for the different peaks, corresponding to sound-speed values at the surface equal to the values at the different turning depths. For an efficient description of the nonlinearity, a fine discretization of the ϑ_1 axis is required.

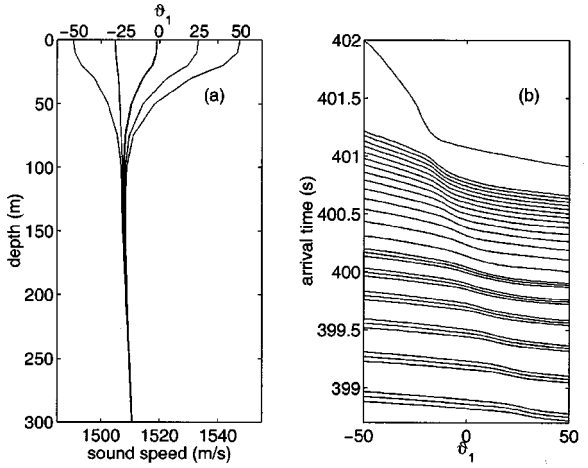

FIG. 6. (a) The sound-speed profiles corresponding to $\vartheta_1=-50$, $-25,0,25,50$. (b) The predicted peak arrival times as functions of ϑ_1.

The set of background states is defined in the following as EOF-1 variations of the basic reference profile over the ϑ_1 interval $[-50,50]$, covering 2.5 standard deviations of the corresponding amplitude, with a step equal to 2. The influence coefficients $\partial g_i/\partial\vartheta_l$ are calculated for the 33 peak arrivals of Fig. 6(b) at each background state using a KRAKEN[28]-based normal-mode code.

A time-variable parameter domain (search interval) is considered for ϑ_1, ± 10 about the historical mean value of ϑ_1 for each day of the year; the anticipated maximum standard deviation from historical data[29] is 1.9. The restriction of the parameter domain for ϑ_1 significantly reduces the computational burden by avoiding calculations for unnatural model states which lie outside the anticipated variability range for each season. For the remaining two EOFs the parameter domains are taken to cover ± 2.5 standard deviations of the corresponding amplitudes, i.e., the interval $[-7.5,7.5]$ for ϑ_2 and $[-2.5,2.5]$ for ϑ_3. The discretization steps are set to $\delta\vartheta_1=2/3$, $\delta\vartheta_2=0.75$, and $\delta\vartheta_3=0.25$.

An observation error of 10 ms is used for all peaks except for the cutoff peak, which is subject to a significant range-dependence effect caused by the large-scale warming trend from north to south. It was shown in a previous study[19] that this causes a cold bias (time delay) to the cutoff peak depending on the background state—the effect is weaker in winter than in summer. In accordance with that study a variable-time correction, linearly varying from 70 ms at $\vartheta_1=-50$ to 150 ms at $\vartheta_1=50$, is applied to the cutoff peak to account for range dependence; after the correction, the observation/model error is set to 50 ms for that peak.

B. Inversion results

Figure 7 shows the distribution of discrete model states identifying the maximum number of peaks in each daily reception. The population density is denoted by the gray scale increasing from white (zero density) to black (maximum density). The gross seasonal trend is seen in the evolution of the first EOF amplitude. The other two EOFs exhibit no major seasonal behavior except for the second one in summer. Also, their probability masses lie away from the boundaries of the search intervals, confirming the proper definition of these intervals. In Fig. 8 the mean values and standard deviations (error intervals) of these distributions are shown. The time-variable search interval for ϑ_1 is also shown in this figure. These estimates for the parameter vector have been obtained from the observed travel-time data without having provided any explicit solution to the identification problem.

The number of peaks matched in each reception is shown in Fig. 9. On the average, 28–30 peaks out of the 33

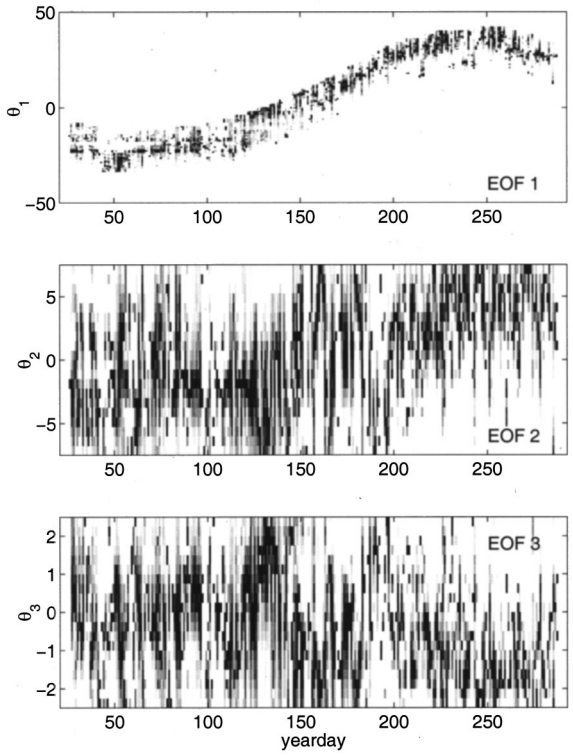

FIG. 7. The distributions of the EOF amplitudes corresponding to the discrete model states identifying the maximum number of peaks in each reception.

model peaks can be identified. In a few receptions the scheme could match as much as 33 peaks, i.e., associate all model peaks with observed ones. During the two periods of low SNR receptions, a lower number of peaks is matched; the drop in the matching index is a warning for possible irrelevance of the selected peaks.

The *a posteriori* distribution of the predicted peak arrival times corresponding to the population of the selected model states for each reception is shown in Fig. 10. The tracks of the 33 model arrivals are recognized in this figure. Nevertheless, these are predicted arrival times corresponding to the more likely model states for each reception and not the identified peaks of each reception. The two periods of low SNR receptions are recognized through systematic discontinuities in the tracks of Fig. 10 pointing to the irrelevance of the selected peaks.

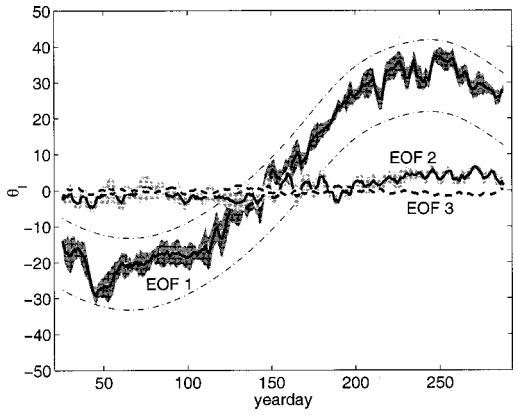

FIG. 8. The mean values and standard deviations (error intervals) of the EOF amplitudes corresponding to the populations of Fig. 7. The dash–dotted lines describe the time-variable parameter domain for ϑ_1.

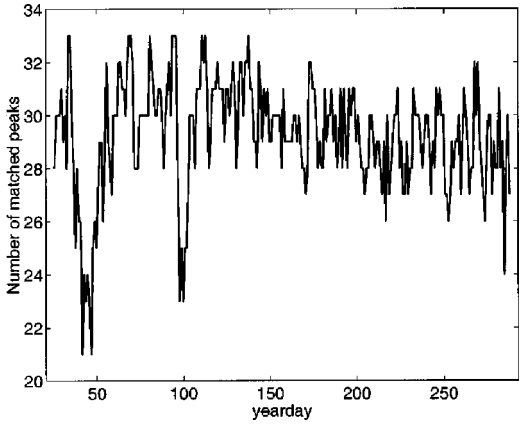

FIG. 9. The number of peaks matched in each reception.

Figure 11 shows the distributions of the depth-averaged temperatures over three layers: a surface layer from the surface down to 150 m, an intermediate layer from 150 to 600 m, and a deep layer from the surface down to 2000 m, representing the total heat content of the water column. A depth-dependent conversion relation, based on historical temperature and salinity data, has been used for obtaining temperature profiles from sound-speed profiles.[19] The gray scale in Fig. 11 represents the population densities of the temperatures corresponding to the more likely model states for each reception. XBT data and also data from conductivity-temperature-density (CTD) measurements during the deployment/recovery cruises are shown in Fig. 11 as crossed circles and squares, respectively. Finally, the dashed lines represent the historical mean temperatures for each day of the year.

From Fig. 11 it is seen that the gross seasonal changes are limited in the surface layer. The observed variability in the intermediate layer, below 150 m, is mainly due to mesoscale activity. The surface layer also determines the evolution of the heat content over the entire water column, represented by the 0–2000-m layer, as shown in the lower panel of Fig. 11. The populations of model states selected using the matching principle give a satisfactory description of the actual evolution described by the XBT data in all three layers.

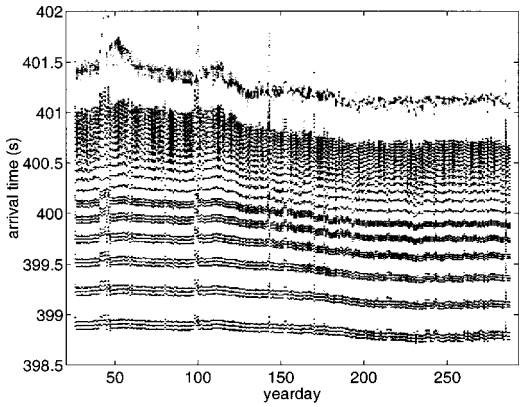

FIG. 10. The distribution of the predicted peak arrival times corresponding to the population of the selected model states for each reception.

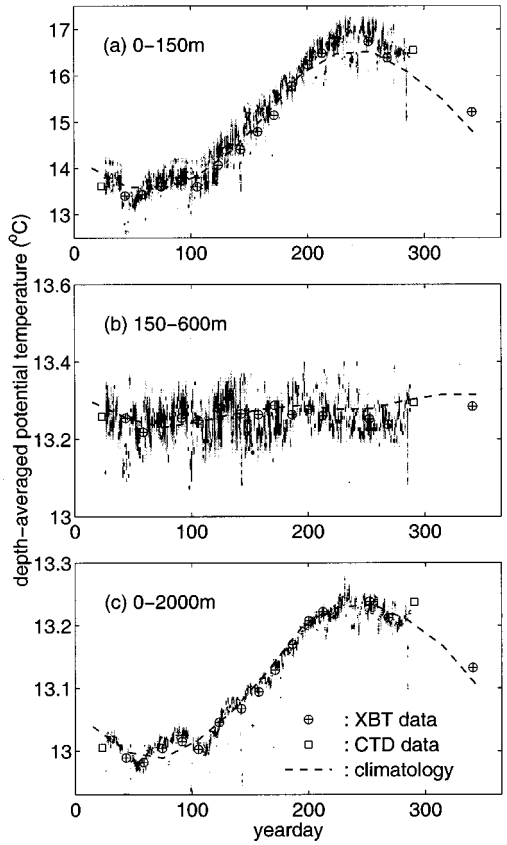

FIG. 11. The distribution of depth-averaged potential temperatures in the 0–150, 150–600, and 0–2000-m layers, corresponding to the discrete model states identifying the maximum number of peaks in each reception, compared with CTD data from the deployment/recovery cruises, with independent XBT data, and also with mean temperatures from the climatology.

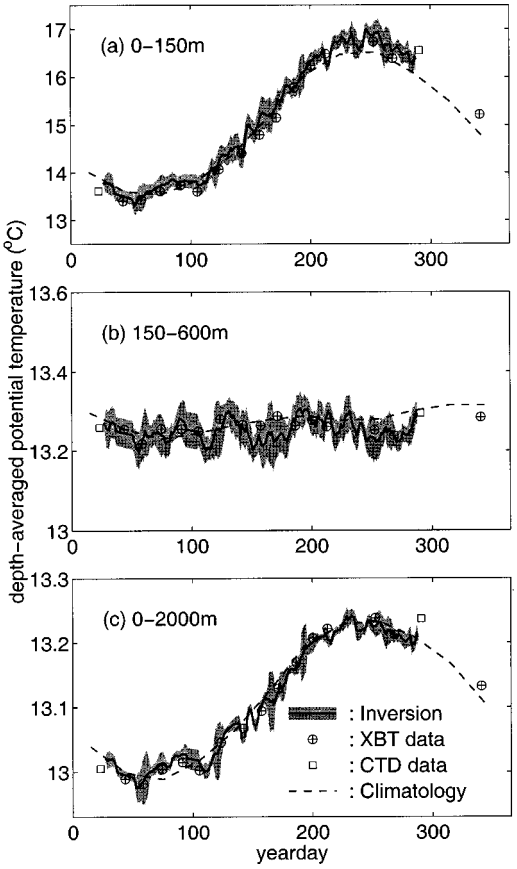

FIG. 12. The mean values and standard deviations (error intervals) of the potential temperatures in the 0–150, 150–600, and 0–2000-m layers, corresponding to the populations of Fig. 11, compared with CTD data from the deployment/recovery cruises, with independent XBT data, and also with mean temperatures from the climatology.

The increased spread of the populations in the intermediate and shallow layers, compared to the deep layer, is due to the larger ambiguity in the identification of the intermediate and late arrivals (cf. Fig. 4), associated with these two layers, compared to the well-separated early arrival groups associated with the deep layer.

A clearer picture of the recovered depth-averaged temperatures over the three layers is shown in Fig. 12 in terms of mean values and standard deviations (error intervals) of the distributions of Fig. 11. The results have been smoothed using a five-reception sliding average, whereas the results corresponding to receptions with SNR lower than 10 dB have been ignored. It is seen that the recovered mean temperatures give a satisfactory description of the actual conditions, the XBT data lying in most cases within the estimated error limits. A comparison of the inversions with the climatological data shows that there are deviations from the climatological mean conditions in all three layers and this is also confirmed by the XBT data. The amplitude of the seasonal signal in the surface layer is 10%–20% larger in the observations than in the historical data.

Figure 13 shows a comparison of the XBT temperature profiles in the upper 300 m with the corresponding inversion results (averaged over the time window of each XBT sample) and associated standard deviations (error bars). A fair agreement between the inversion results and the XBT profiles is seen, the observed deviations lying within the inversion error bars in most cases. The inversion results underlying the left-most profile fall within the first low-SNR period. The seasonal temperature variability spans about 12 °C at the surface and nearly disappears below 150-m depth. It is also seen that deviations between XBT data and inversions are in general larger in the surface layer than in the deeper layers, and this is consistent with the inversion errors shown. The physical reason for the reduced tomography sensitivity near the sea surface lies in the particular temperature and

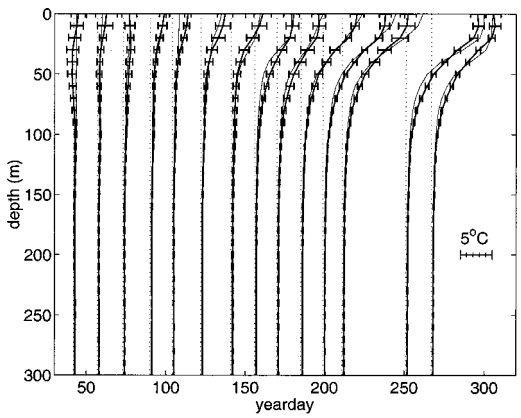

FIG. 13. Comparison of the XBT temperature profiles (deviations from 13.03 °C—light lines) with the corresponding inversion results (heavy lines) and inversion errors.

sound-speed conditions in the Mediterranean, which give rise to either surface-reflected propagation in winter or channeled propagation with a shallow axis in summer. In both cases a very small fraction of the propagation time is spent in the near-surface layer, resulting in a poorer acoustic sampling of smaller depths.

IV. DISCUSSION AND CONCLUSIONS

An inversion approach for travel-time data was proposed which bypasses the explicit solution of the identification problem. This approach uses the linearized model relations between sound-speed and arrival-time perturbations about a set of background states, to calculate arrival times and associated model errors on a fine grid of model states discretizing the sound-speed parameter space. The corresponding model peaks (arrivals) are allowed to associate with observed peaks if their time distance is smaller than a tolerance which depends on the particular peak, the background state, and the discretization step. Accordingly, each discrete model state can explain (identify) a number of peaks in a particular reception. The model states that explain the maximum number of observed peaks are considered the more likely parametric descriptions of the particular reception. Their population forms the matched-peak solution of the inversion problem.

The matched-peak method can be considered an extension of the matched-field approach to the case of travel-time data. The use of the linearized model relations between sound-speed and arrival-time variations accelerates the calculations significantly.

Since the method is based on the number of peaks identified by each model state rather than on inversions for all possible peak identifications in each reception (as is the case in the approaches simultaneously addressing the inversion and identification problem), there is no need to set up the identification space, i.e., the set of all trial identification functions for each reception. The calculation of the number of peaks identified by each model state is a much easier computational task than the setup of the identification space.

A significant advantage of the matched-peak approach is that each reception can be analyzed independently of the previous receptions, i.e., no constraints are posed using identification or inversion results from the previous reception(s). This has an important consequence that there is no need for initialization of the inversion procedure, i.e., no need for additional initialization (commonly hydrographic) data, and also that acoustic data with gaps can be treated. Even though previous-reception results are commonly used in existing methods to assure a smooth evolution of the peak tracks and the inversion results, this strategy may cause errors in a number of cases (e.g., complicated track geometry, peaks fading in and out, discontinuities in the data, or low SNR receptions). In this connection the independent treatment of each reception may result in a nonsmooth evolution of the inversion results, but at the same time it adds to the robustness of the analysis.

The matched-peak inversion approach was initially devised as a simple means to obtain first inversion results from tomography travel-time data, offering an automatic alternative to the usual tracking–identification–inversion approach and also avoiding the difficulties and possible uncertainties associated with the simultaneous solution of the identification and inversion problem (automatic identification/inversion scheme). Despite its simplicity, the application to 9-month-long travel-time data from the Thetis-2 experiment provided very satisfactory results. The inversion results from a particular section ($W3-H$) were presented here for which systematic XBT observations exist, permitting detailed comparisons.

The robustness of the matched-peak approach has proven particularly valuable in cases of problematic evolution of arrival patterns, either due to nonsmooth evolution of arrival times or due to missing receptions. Such cases were encountered in $W3-H$ and the other Thetis-2 sections, and quite a few of them could not be handled at all by the automatic identification/inversion scheme. With the matched-peak approach all sections—13 in total —have been automatically processed; the systematic results will be published elsewhere.

The matched-peak inversion approach provides no explicit solution for the identification problem. If the solution of this problem is of interest, the matched-peak approach can still provide a means to build up the identification space—the set of all possible identification (association) functions—in a model-based fashion, independently of previous-step constraints.

ACKNOWLEDGMENTS

This work was partially supported by the European Union MAST-III program under Contract No. MAS3-CT97-0147. Fruitful discussions with U. Send (IfM, Kiel) F. Gaillard (IFREMER, Brest), and D. Mauuary (LIS, Grenoble) as well as comments by the anonymous reviewers are acknowledged.

[1] W. H. Munk and C. Wunsch, ''Ocean acoustic tomography: A scheme for large scale monitoring,'' Deep-Sea Res. **26A**, 123–161 (1979).
[2] W. H. Munk, P. F. Worcester, and C. Wunsch, *Ocean Acoustic Tomography* (Cambridge University Press, New York, 1995).
[3] W. H. Munk and C. Wunsch, ''Ocean acoustic tomography: Rays and modes,'' Rev. Geophys. Space Phys. **21**, 777–793 (1983).
[4] J. L. Spiesberger and P. F. Worcester, ''Perturbations in travel time and ray geometry due to mesoscale disturbances: A comparison of exact and approximate calculations,'' J. Acoust. Soc. Am. **74**, 219–225 (1983).
[5] E. C. Shang, ''Ocean acoustic tomography based on adiabatic mode theory,'' J. Acoust. Soc. Am. **85**, 1531–1537 (1989).
[6] G. A. Athanassoulis and E. K. Skarsoulis, ''Arrival-time perturbations of broadband tomographic signals due to sound-speed disturbances. A wave-theoretic approach,'' J. Acoust. Soc. Am. **97**, 3575–3588 (1995).
[7] E. K. Skarsoulis, G. A. Athanassoulis, and U. Send, ''Ocean acoustic tomography based on peak arrivals,'' J. Acoust. Soc. Am. **100**, 797–813 (1996).
[8] E. K. Skarsoulis, ''An adaptive scheme for ocean acoustic tomography of large sound-speed variations,'' in *Proceedings of the 3rd European Conference on Underwater Acoust.*, edited by J. S. Papadakis (Crete University Press, Herakion, 1996), pp. 803–808.
[9] B. D. Dushaw, P. F. Worcester, B. D. Cornuelle, and B. M. Howe, ''Variability of heat content in the central north Pacific in summer 1987 determined from long-range acoustic transmissions,'' J. Phys. Oceanogr. **23**, 2650–2666 (1993).
[10] J. L. Spiesberger, R. C. Spindel, and K. Metzger, ''Stability and identification of ocean acoustic multipaths,'' J. Acoust. Soc. Am. **67**, 2011–2017 (1980).
[11] G. R. Legters, N. L. Weinberg, and J. G. Clark, ''Long-range Atlantic

acoustic multi-path identification,'' J. Acoust. Soc. Am. **73**, 1571–1580 (1983).
[12] R. Hippenstiel, E. Chaulk, and J. H. Miller, ''An adaptive tracker for partially resolved acoustic arrivals with application to ocean acoustic tomography,'' J. Acoust. Soc. Am. **92**, 1759–1762 (1992).
[13] J. H. Miller, J. F. Lynch, C. S. Chiu, E. L. Westreich, J. S. Westreich, R. Hippenspiel, and E. Chaulk, ''Acoustic measurements of surface gravity wave spectra in Monterey Bay using mode travel-time fluctuations,'' J. Acoust. Soc. Am. **94**, 954–974 (1993).
[14] F. R. Martin-Lauzer and D. Mauuary, ''Probabilistic ray identification: A new tool for ocean acoustic tomography,'' in Proceedings ICASSP 94 (Adelaide, 1994).
[15] D. Mauuary, ''Detection, estimation et identification pour la tomographie coustique oceanique. Etude theorique et experimentale,'' Ph.D. thesis, Institut National Polytechnique de Grenoble, 1994.
[16] B. M. Howe, P. F. Worcester, and R. C. Spindel, ''Ocean acoustic tomography: Mesoscale velocity,'' J. Geophys. Res. **92**, 3785–3805 (1987).
[17] P. F. Worcester, ''An example of ocean acoustic multipath identification at long range using both travel time and arrival angle,'' J. Acoust. Soc. Am. **70**, 1743–1747 (1981).
[18] U. Send, ''Peak tracking by simultaneous inversion: Toward a one-step acoustic tomography analysis,'' J. Atm. Ocean. Technol. **13**, 1116–1122 (1996).
[19] E. K. Skarsoulis and U. Send, ''One-step analysis of nonlinear traveltime data in ocean acoustic tomography,'' J. Atmos. Ocean. Technol. (in press).
[20] A. Tolstoy, *Matched Field Processing for Underwater Acoustics* (World Scientific, Singapore, 1993).
[21] J.-P. Hermand and W. I. Roderick, ''Acoustic model-based matched-filter processing for fading time-dispersive ocean channels: Theory and experiment,'' IEEE J. Ocean Eng. **OE-18**, 447–465 (1993).
[22] J.-P. Hermand, ''Broad-band geoacoustic inversion in shallow water from waveguide impulse response measurements on a single hydrophone: Theory and experimental results,'' IEEE J. Ocean Eng. **OE-24**, 41–66 (1999).
[23] J. L. Spiesberger, ''Ocean acoustic tomography: Travel time biases,'' J. Acoust. Soc. Am. **77**, 83–100 (1985).
[24] W. H. Munk and C. Wunsch, ''Biases and caustics in long-range acoustic tomography,'' Deep-Sea Res. **32**, 1317–1346 (1985).
[25] J. F. Lynch, J. H. Miller, and C. S. Chiu, ''Phase and travel-time variability of adiabatic acoustic normal modes due to scattering from a rough sea surface, with applications to propagation in shallow-water and high-latitude regions,'' J. Acoust. Soc. Am. **85**, 83–89 (1989).
[26] Thetis-2, A pilot tomography system for monitoring the western Mediterranean basin, Final Report, edited by U. Send, EU MAST-2 project CT91-0006, March 1996.
[27] U. Send, G. Krahmann, D. Mauuary, Y. Desaubies, F. Gaillard, T. Terre, J. Papadakis, M. Taroudakis, E. Skarsoulis, and C. Millot, ''Acoustic observations of heat content across the Mediterranean Sea,'' Nature (London) **385**, 615–617 (1997).
[28] M. B. Porter and E. L. Reiss, ''A numerical method for ocean acoustic normal modes,'' J. Acoust. Soc. Am. **76**, 244–252 (1984).
[29] P. Brasseur, ''The MED2 hydrographic data base (http://modb.oce.ulg.ac.be),'' Oceanogr. Lit. Rev. **42**, 414–415 (1995).

The transmission of Lamb waves across adhesively bonded lap joints

M. J. S. Lowe
Department of Mechanical Engineering, Imperial College, London SW7 2BX, United Kingdom

R. E. Challis
School of Electrical and Electronic Engineering, University of Nottingham, Nottingham NG7 2RD, United Kingdom

C. W. Chan
Department of Mechanical Engineering, Imperial College, London SW7 2BX, United Kingdom

(Received 23 June 1999; accepted for publication 3 December 1999)

The transmission of Lamb waves across adhesively bonded lap joints is investigated using finite element analysis. The studies consider three modes for excitation and reception, s_0, a_0, and a_1, applied to lap joints consisting of parallel aluminum sheets bonded with an epoxy adhesive. Transmission coefficient results for a two-dimensional range of bond thicknesses and bond overlap lengths are presented for all three modes. The transmission coefficients are calculated from the spectra of the received and transmitted signals using an approach which is insensitive to the presence of multimode signals and reverberated signals, and which approximates to a power transmission coefficient. Detailed analysis is then performed for one of the modes in order to investigate the nature of the mode conversion in the overlap region of the joint. It is found that the relative amplitudes of the different modes which propagate in the overlap region can be estimated reliably and simply from the properties of the incident wave mode. As well as demonstrating the physics of the mode conversion behavior, the study provides a basis for the selection of modes for nondestructive evaluation (NDE) of the bond region and for measuring the bond dimensions. [S0001-4966(00)01603-9]

PACS numbers: 43.35.Cg [HEB]

INTRODUCTION

The transmission of Lamb waves across adhesively bonded joints has important industrial relevance. There is a clear need for the development of techniques for the inspection of adhesively bonded metal and composite joints which are in ever increasing use in safety-critical applications such as those found in the aerospace and automotive industries. Lamb waves, which could be transmitted in the plate on one side of a joint and received in the plate on the other side, appear to offer the potential for cheap and convenient *in situ* inspection.

There are two areas of need for inspection. First, in mass production industries in which automated assembly methods may be used, it is important that the dimensions of adhered joints, such as adhesive layer thickness and overlap length, are within tolerance and are measurable. Second, there is a need in all industries which use adhesive joints to detect defects such as voids in the adhesive or local separation of the adhesive from one of the adherends. Conventional techniques to measure the dimensions or detect defects rely mainly on the use of normal incidence scanning which is performed over a two-dimensional area containing the overlap region. This technique is time consuming and access to the joint area is a prerequisite. Lamb wave techniques have the potential for greatly increased speed of inspection of large regions of material because each measurement inspects along a line rather than just at a single point. Furthermore, they have the added advantage that they do not require direct access to the region.

A considerable amount of work has been carried out on techniques for the inspection of adhesively bonded joints using ultrasonic reflection or transmission through the joints, reported for example in Refs. 1–9. Comprehensive studies into the science and technology of adhesive bonds can be found in the texts by Lee and Neville[10] and Kinloch.[11]

The fundamental behavior of Lamb waves in plate structures has been reported widely.[12–14] Studies of waves in more complicated plate systems have included composite plates[15–17] and bonded structures.[18–26] Rokhlin[26] has employed both analytical and experimental methods to look at the interaction of Lamb waves with adhered metal lap joints. He has also reported work on an important related topic, the transmission of Lamb waves across spot-welded lap joints.[27,28] Because of the predominantly analytical nature of Rokhlin's work on the adhered joints, the number of different cases investigated was limited to those with simple boundary conditions (e.g., parallel overlapped sheets coupled acoustically with a water layer). This limitation can be overcome by employing a numerical method such as the finite element technique which has been used successfully to model Lamb wave propagation in plates.[29–33] Recently, Challis *et al.*[34] have demonstrated experimentally that the principal bond dimensions of adhesively bonded T-joints can be determined by careful processing of transmitted Lamb wave signals.

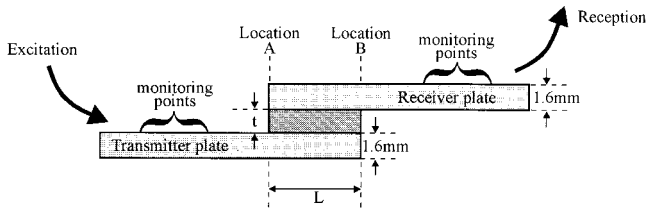

FIG. 1. Schematic of a lap joint showing the concept of transmission of Lamb waves from transmitter plate to receiver plate, principal dimensions, and finite element monitoring locations.

In this paper we apply the finite element modeling technique to study in detail Lamb wave transmission across an adhered metal lap joint. The objective is to investigate the physics of Lamb wave propagation across adhered joints, and to predict the influence of the dimensions of the bond on the transmission coefficients of the modes. The findings have relevance to both the measurement of bond dimensions and the detection of defects. All of the finite element modeling was conducted using the general purpose program FINEL, developed at Imperial College.[35] The program simulates, in the time domain, the propagation of the waves and their interactions at boundaries in the overlap region

We present the results of two studies. In the first study we consider separately three modes: s_0, a_0, and a_1. Each mode is excited in an aluminum plate (the transmitter plate), travels across an adhesive lap joint, and is then received in the second aluminum plate (the receiver plate), as shown in Fig. 1. We predict the amount of energy in the received mode as a function of the two key dimensions of the adhesive layer: the overlap length and the bond thickness. In the second study, we focus on one of these modes, s_0, and one size of joint. We examine in detail the Lamb wave activity within the overlap region, that is to say, the effects of mode conversion. This provides evidence of the main factors which govern the transmissibility of Lamb waves across adhesive lap joints and consequently enables us to make deductions concerning the potential for the exploitation of the modes.

I. DISPERSION CURVE CONSIDERATIONS: CHOICE OF EXCITATION SIGNAL FOR s_0, a_0, AND a_1 MODES

The first task with any technique involving Lamb waves is to decide on appropriate regimes on the dispersion curves for exciting the required Lamb modes. We aim for two ideals.[36] (1) a single mode should be excited, in order to limit the complexity of the received signals; (2) the choice of frequency should be such that the wave is relatively nondispersive, so that signal shapes are retained as the wave packet propagates.

Figure 2(a) and (b) show the phase velocity and group velocity dispersion curves for the first six Lamb modes in an aluminum plate. These, and all the other dispersion curves and mode shapes in this paper, were calculated using a general purpose dispersion curve program, DISPERSE, which was developed at Imperial College.[37,38]

From the group velocity dispersion curves, it can be seen that dispersion of the s_0 and a_0 modes is relatively small at about 1 MHz mm, and that operation above 1.5 MHz-mm could result in the spurious excitation of other modes. Operation at very low frequency-thickness would result in the propagation of signals which are temporally (and spatially) long and this could cause practical problems due to reverberation and interference. A frequency-thickness of 1 MHz-mm would therefore seem to be reasonable for the s_0 and a_0 modes. In this work this corresponds to an excitation center frequency of 625 kHz for aluminum plates of 1.6-mm thickness.

It is convenient to excite the a_1 mode at its maximum group velocity because dispersion is kept to a minimum and also at this point it is the fastest of all possible modes. This means that it would be the first signal of a group of modes to be received when several are mode converted. However, the frequency at which this occurs is relatively close to the cutoff frequency for the s_1 mode, which has a wave number similar to that of the a_1 mode. This can be seen by the close proximity of their phase velocities in the region of this frequency in Fig. 2(a). The implication of this is that it would be difficult to resolve the two modes in the wave number domain and hence it would be virtually impossible to obtain transmission coefficient results for the a_1 mode alone. Decreasing the frequency would reduce the excitation of the s_1 mode, so a frequency of 1.4 MHz was eventually chosen, corresponding to a frequency-thickness of 2.24 MHz-mm; this gives a working compromise between the avoidance of the excitation of the s_1 mode whilst achieving relatively low dispersion.

The signals which were used in the study consisted of five cycles of the chosen center frequency, windowed by a Hanning function. This choice was made in order to give a good compromise between the needs for a narrow bandwidth, for mode selectivity, and a short time duration to give temporal separation of multiple signals.

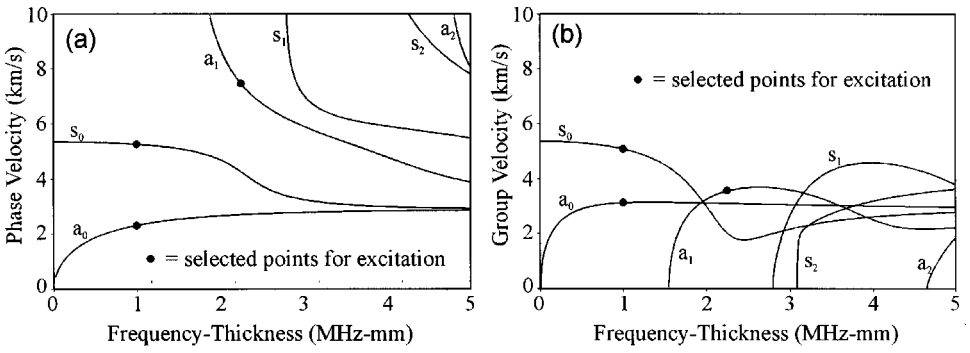

FIG. 2. Dispersion curves for an aluminum plate: (a) phase velocity; (b) group velocity.

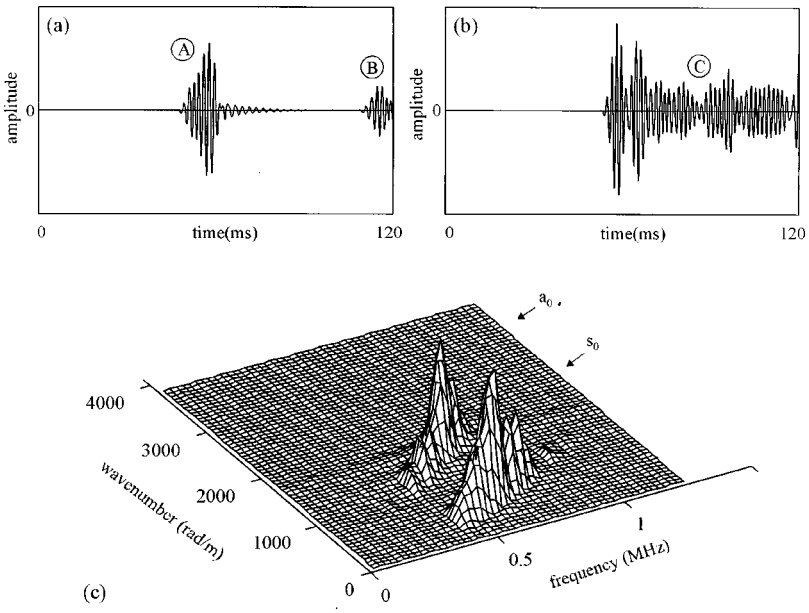

FIG. 3. Predictions of transmitted signals across a lap joint when s_0 mode is incident: (a) time record for bond length 2 mm and bond thickness 0.2 mm; (b) time record for bond length 26 mm and bond thickness 1.4 mm; (c) 2D-FFT of transmitted signal for second case (length 26 mm, thickness 1.4 mm).

II. DETERMINATION OF TRANSMISSION COEFFICIENTS ACROSS AN ADHESIVE LAP JOINT

We started by performing a number of finite element calculations, for each of the three modes in turn, to predict the transmission coefficient of the given mode across a bonded joint. By repeating the analyses for ranges of bond thickness and bond length we could then express the transmission coefficients as functions of these two parameters of the joint. Thus the aim of each finite element analysis was to propagate an s_0, a_0 or a_1 mode in the transmitter plate and to measure the response of the same mode in the receiver plate, expressing the ratio of their strengths as a transmission coefficient.

A. Description of finite element models of joints

Figure 1 shows a schematic of the adhesive joint configuration which was modeled. Four-noded linear elements were used to represent the two-dimensional section in plane strain. The elements representing the 1.6-mm-thick aluminum plates were each 0.2 mm square, so there were 16 elements through the thickness of each plate, and at least 12 elements per wavelength along the plate. This comfortably satisfies the threshold of eight elements per wavelength which the authors have found from experience to be a good limit for accurate modeling. Sufficient lengths of plate were modeled such that reverberations of the signals along the lengths of the plates could be avoided. The mesh for the epoxy layer was chosen to be of similar refinement to the meshes for the plates, the number of elements through its thickness varying according to the thickness being modeled. Perfect bonding was assumed between the aluminum and the epoxy. The following bulk material properties were assumed for the aluminum and the epoxy, respectively: longitudinal velocities 6120 and 2200 m/sec, shear velocities 3100 and 1100 m/sec, densities 2700 and 1000 kg/m^3. All of the finite element analyses assumed perfectly elastic materials, thus neglecting any damping properties. The aluminum has negligible damping properties and is therefore accurately modeled in this way. However, the adhesive material can damp the sound significantly, and the effects of this will be examined later in this paper.

The excitation of each chosen input mode was achieved by prescribing the displacements at the nodes across the thickness of the remote end of the transmitter plate, over the time period of the signal. According to the earlier discussion, the signals that were used consisted of five cycles of the target frequency in a Hanning window. In order to excite the desired mode without exciting any other modes which could exist at the same frequency, the amplitudes of the displacements (in both in-plane and out-of-plane directions) at each node across the thickness of the plate were scaled by the amplitudes of the displacement mode shapes at the appropriate depth in the plate. Furthermore, by performing this scaling in the frequency domain, it was possible to account for changes of the mode shape over the frequency bandwidth of the signal.[31,39] This method ensures reliably that only the desired mode is excited. The input signal was the only boundary condition which was applied to the models.

Explicit time marching was employed, assuming a diagonal mass matrix. The time step was chosen to satisfy the stability limit L/C, where L is the element length and C is the wave speed of the fastest wave present.[40] Preparatory solutions using part of the model representing just one plate were used to confirm that the idealization accurately predicted the expected propagation behavior of the dispersion curves of Fig. 2.

B. Signal processing to extract modal information

Results of one of the simulations, for the s_0 mode and a joint with 2-mm bond length and 0.2-mm bond thickness, are shown in Fig. 3(a). The figure shows a signal received after propagating across the joint. Specifically, the plot is of the time record of the displacement component in the direction normal to the plate, at one of the finite element nodes on the top surface of the receiver plate. This received signal is clearly rather different in shape from the incident windowed

tone burst. We identify three phenomena which can be responsible for this: (1) in general, several possible modes can propagate within the overlap region, interfering with each other and each transmitting energy at a different velocity; (2) the modes within the overlap region can reflect as well as transmit at the ends of the overlap, so that they reverberate over the length of the overlap region, emitting energy into the receiver plate at each reverberation; (3) both s_0 and a_0 modes can be transmitted into the receiver plate by mode conversion from the modes in the overlap region. Thus there are several signals together in region ''A'' in the figure, corresponding to some combination of these effects. For this particular case, in which the overlap length is short, the reverberations die away very rapidly. The signals in region ''B'' correspond to reflections from the remote end of the receiver plate, are not of interest, and should therefore be ignored.

Figure 3(b) shows the received signal for another s_0 case, that of a much longer bond, of length 26 mm, and a thickness of 1.4 mm. Here it can be seen that the reverberations in the overlap length, marked region ''C,'' are of significant amplitude and duration. Also, the first arrival of the five-cycle signal can just be identified before the start of the reverberations.

Since our interest is to predict transmission coefficients for the same type of mode as that which is incident, it is necessary to separate the multimode components in the received signals. In the current example, in which the s_0 mode is incident, the aim therefore is to separate the a_0 and s_0 components in the receiver plate and retain only the s_0. This can be done easily using a two-dimensional Fourier transform (2D-FFT)[41] which decomposes the signal into its frequency and wave number domains. Instead of monitoring the received signal at just 1 node, 64 nodes at intervals of 0.4 mm were monitored on the receiver plate, as shown schematically in Fig. 1. While performing the transform, a Hanning window was applied to the space domain.

Figure 3(c) shows a plot of the 2D-FFT of the results of the second case [Fig. 3(b)], clearly identifying separately the transmission of the two modes. The 2D spectrum also exhibits extrema along the ''ridges'' of both modes; in the transform of the input signal these ridges would be smooth. These extrema are the result of the interference between the directly transmitted mode (e.g., s_0) and those modes which are of the same type (s_0) which have arisen due to reverberations in the overlap region. The plot therefore shows that the transmitted amplitude is extremely sensitive to the value of frequency.

C. Calculation of a transmission coefficient

A conventional approach for determining a transmission coefficient for a mode would be to measure the amplitude of a particular component of displacement in the receiver plate, at a particular frequency, and then to divide this by the amplitude of the corresponding component in the transmitter plate. Such an approach would yield transmission coefficient values for any chosen frequency within the bandwidth of the signal. However, as seen in the 2D-FFT plot, the received amplitude of a mode varies dramatically with frequency because of interference between the directly transmitted signal and the reverberating signal. The frequency values associated with the interference extrema in the spectrum may in fact be useful for the characterization of the joint, and indeed Challis *et al.*[34] have found that these features are particularly important to the successful operation of an artificial neural network (ANN) scheme to estimate bond dimensions from Lamb wave signals that have traversed a joint. However, in the present work we are interested in determining a single scalar measure of the strength of transmission, without sensitivity to a precise chosen value of frequency. We therefore prefer a measure which depends on the whole spectrum of the signal rather than a single frequency.

Alleyne and Cawley have shown[41] that the frequencies and wave numbers of positions on the ridge of a mode in the 2D-FFT plot correspond to locations on the dispersion curve for the mode, and that the amplitude of the plot at any of these positions may be used to determine transmission or reflection coefficients at the given frequency-wave number. Provided that the 2D-FFT is applied in the same manner to both the received and the incident modes, the coefficient is thus given by the ratio of the 2D-FFT amplitudes in the two signals. The conditions of validity require that certain aspects are identical for both the measured and the reference signals, including the thickness and material of the plates, the component which is monitored (typically a surface displacement in a particular direction), the mode, and the processing parameters and windows which are used for the 2D-FFT. For a given mode and frequency, the power flow of the mode is proportional to the square of its amplitude,[14] the constant of proportionality being a function of the mode, the properties of the plate, the frequency, and the choice of the component which is used to define its amplitude. Given the above conditions which are placed on the 2D-FFT calculation, the constant of proportionality is the same for both the incident and the received signal at any chosen frequency. In this case the square of the transmission coefficient at that frequency may therefore be identified as the power transmission coefficient.

A simple procedure for calculating a scalar measure of transmission over the full spectrum of the signal is to sum values over the area (ω and k) of the 2D-FFT plot which represents the received signal, and then divide the total by the value found in the same way for the incident signal. We choose to sum the squares of the amplitudes in this manner, thus yielding a transmission coefficient which is an approximate measure of the proportion of power transmitted. This is not an exact power transmission coefficient, primarily because it neglects the variation with frequency of the constant of proportionality between the square of the wave amplitude and the power flow. However, the coefficients which are thus calculated for our rather narrow band signals are likely to be dominated by the terms around the center frequency. We should also observe that this approach assumes that the shape of the variation of the 2D-FFT plot with wave number, at any particular frequency, is the same for both the incident and the received signals; that is to say that the wave number spectra of the two signals being compared differ only by an amplitude scale factor. In fact this is the case because the wave number spectrum at a particular frequency is deter-

TABLE I. Configurations of bonds analyzed using finite element analysis.

Bond thickness, t (mm)	Bond length, L (mm)							
	2	6	10	14	18	22	26	30
0.2	s_0	s_0	s_0	s_0	s_0	s_0	s_0	s_0
0.4	a_0, a_1	a_0, a_1	a_0, a_1	a_0, a_1	a_0, a_1	a_0, a_1	a_0, a_1	a_0, a_1
0.6	s_0	s_0	s_0	s_0	s_0	s_0	s_0	s_0
0.8	a_0, a_1	a_0, a_1	a_0, a_1	a_0, a_1	a_0, a_1	a_0, a_1	a_0, a_1	a_0, a_1
1.0	s_0	s_0	s_0	s_0	s_0	s_0	s_0	s_0
1.2	a_0, a_1	a_0, a_1	a_0, a_1	a_0, a_1	a_0, a_1	a_0, a_1	a_0, a_1	a_0, a_1
1.4	s_0	s_0	s_0	s_0	s_0	s_0	s_0	s_0
1.6	a_0, a_1	a_0, a_1	a_0, a_1	a_0, a_1	a_0, a_1	a_0, a_1	a_0, a_1	a_0, a_1
1.8	s_0	s_0	s_0	s_0	s_0	s_0	s_0	s_0
2.0	a_0, a_1	a_0, a_1	a_0, a_1	a_0, a_1	a_0, a_1	a_0, a_1	a_0, a_1	a_0, a_1

mined by the spatial sampling of the 2D-FFT which was identical for both incident and received signals. Indeed, this was also confirmed by numerical checks which were performed on several of the results. Thus we take this approach for its simplicity to implement, and recognize that it yields a coefficient which approximates, for a narrow-band signal, to the power transmission coefficient. For reference, and to distinguish this from the displacement transmission coefficient which we will use in the detailed study later, we shall refer to this as the power transmission coefficient. Formally, and expressed in dB, its definition is

$$\text{power transmission coefficient} = T \approx 10 \log \frac{\Sigma_\omega \Sigma_k B_{\omega k}^2}{\Sigma_\omega \Sigma_k A_{\omega k}^2}, \quad (1)$$

where $A_{\omega k}$ is the amplitude of the 2D-FFT plot of the incident signal at frequency ω and wave number k, $B_{\omega k}$ is the same for the received signal, and the summations are carried out over all sampled points in ω and k for the part of the 2D-FFT plot representing the chosen mode.

D. Transmission coefficient results

The simulations were repeated for each of the combinations of bond length (L) and bond thickness (t), and for each of the mode types, shown in Table I. Each analysis yielded a single value of power transmission coefficient. The full sets of transmission coefficients for the matrix of bond lengths and thicknesses were then plotted.

Figure 4(a) shows a plot of the power transmission coefficient plotted against bond length and bond thickness for the s_0 mode. The plot shows that when the bond thickness is small (below 1 mm), the transmission coefficient is relatively low. If the bond thickness is 1 mm or above, then the transmission coefficient starts off low at small bond lengths and rises relatively rapidly with bond length. For bonds whose lengths are larger than 15 mm and thicknesses are larger than 1 mm the transmission coefficient is fairly constant at about -2 dB. Similar behavior in the variation of the transmission coefficient with overlap length was observed by Rokhlin[26] in a numerical and experimental study of the Lamb wave transmission coefficient between two metal sheets coupled together by a water layer. He obtained a maximum transmission coefficient of about -4 dB. This is lower than the

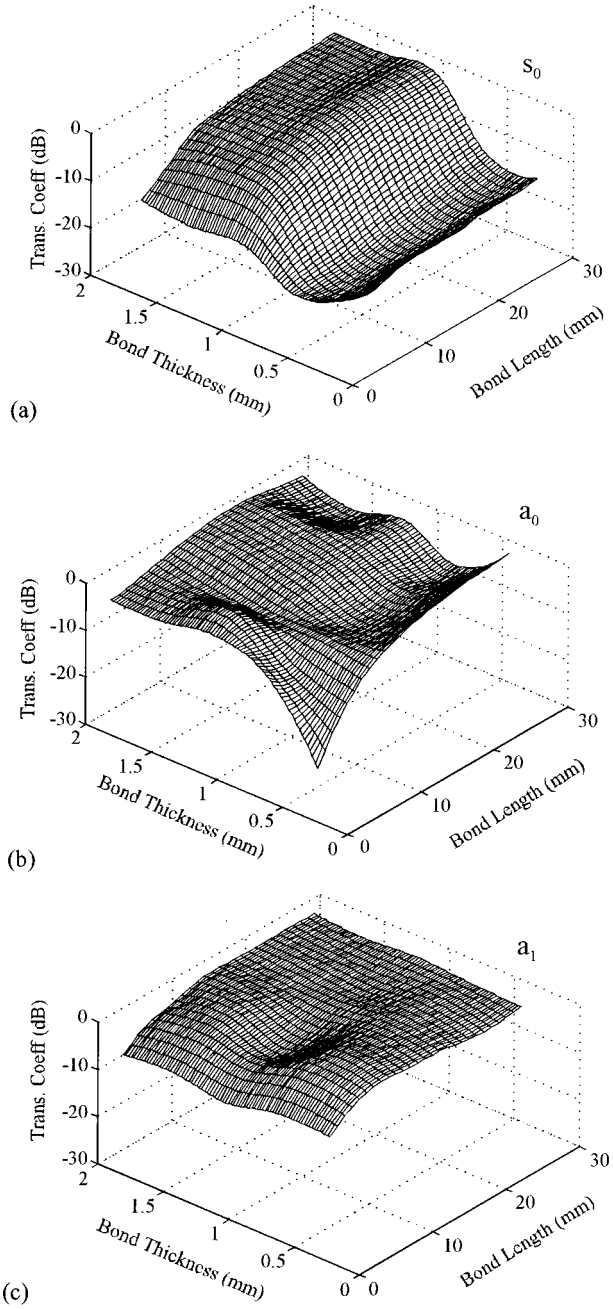

FIG. 4. Transmission coefficient versus bond length and bond thickness for (a) s_0 mode; (b) a_0 mode; (c) a_1 mode.

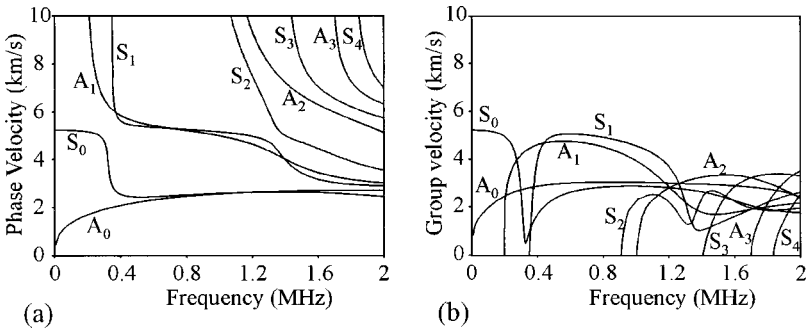

FIG. 5. Dispersion curves for overlap region: (a) phase velocity; (b) group velocity.

values obtained in this present work and could possibly be attributed to the loss in transmission due to the water not supporting transverse stresses.

Figure 4(b) shows a plot of the transmission coefficient versus bond length and bond thickness for the a_0 mode. It can be seen that, apart from the case where the bond length and bond thickness are very small, the transmission coefficient is consistently large, larger than -10 dB. At large bond lengths there appear to be maxima and minima in the bond thickness direction.

Figure 4(c) shows a plot of the transmission coefficient versus bond length and bond thickness for the a_1 mode. The transmission coefficient remains relatively high and constant throughout the calculated range of bond lengths and thickness, with just one shallow minimum.

III. INVESTIGATION OF PHYSICS OF TRANSMISSION PHENOMENA

The power transmission coefficient results show the influence of the bond dimensions on the transmission of the modes, but they give no understanding of the physics of the transmission of the energy across the joint. As well as satisfying scientific curiosity, such an understanding is important if reliable Lamb wave techniques are to be developed to estimate bond dimensions and to detect bond flaws. In support of this aim, we now present results of further finite element simulations to investigate the physics of the transmission. The simulations include both propagating and evanescent modes, but in the interests of clarity we have limited our discussion of the physical phenomena to the propagating modes alone. In any case the evanescent modes are likely to be insignificant in all but the very shortest joints.

Having separated the target transmitted mode from any other modes in the receiver plate, using the 2D-FFT, we are still left with two phenomena which we have identified as contributing to the transmission behavior: the possibility of multiple modes in the overlap region, and reverberation of these modes in the overlap region. We will consider these effects sequentially. First we will examine the mode conversion and the existence of modes in the overlap region, neglecting any reverberation, leading to an understanding of the direct transmission across the joint. Then we will consider the way in which reverberations modify this behavior.

We consider a bond of 0.4-mm thickness, and restrict the study to the s_0 mode.

A. Mode conversion and ''carrier modes'' in the overlap region

The wave in the transmitter plate may convert to one or more modes at the location where it first meets the adhesive layer, shown as location A in Fig. 1. These new waves which then travel in the bonded region are the natural modes of the three-layer system of aluminum-adhesive-aluminum. On arrival at the end of the bonded region, shown as location B in Fig. 1, further mode conversion takes place to the Lamb waves which then travel in the receiver plate. The waves which travel in the bonded region are referred to here as the ''carrier modes,'' signifying their role in carrying the energy across the joint.

Figure 5 shows the phase and group velocity dispersion curves for the three-layer plate consisting of a 0.4-mm-thick layer of adhesive between two aluminum plates of thickness 1.6 mm. It can be seen that at the target frequency of 625 kHz, there are four possible modes, labeled A_0, S_0, A_1, and S_1. The labeling system follows the conventional Lamb wave labels for convenience, although strictly these waves are not Lamb waves because the plate consists of three layers rather than one. The capital letters for labeling are used here to signify modes in the overlap region, to distinguish them from the lower case letters used to denote the modes in the transmitter and receiver plates. In general it must be assumed that the incident s_0 mode can mode convert in some proportion to each of these four modes.

Figure 6(a) shows a schematic of a finite element model which was used to predict the strength of the conversion to each of the carrier modes. In most respects, including all the discretization details, this model was the same as the models of the full joint which were described earlier. However, a sufficiently long bonded region was modeled such that the mode converted waves could be received in the joint, and did not continue to a receiver plate, as indicated. An s_0 mode was generated at the remote end of the transmitter plate. The

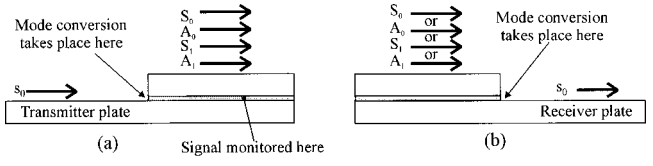

FIG. 6. Schematic of finite element models used for study of mode conversion. Plates are 1.6-mm thick, adhesive is 0.4-mm thick. (a) For mode conversion from s_0 to carrier modes; (b) for mode conversion from carrier modes to s_0.

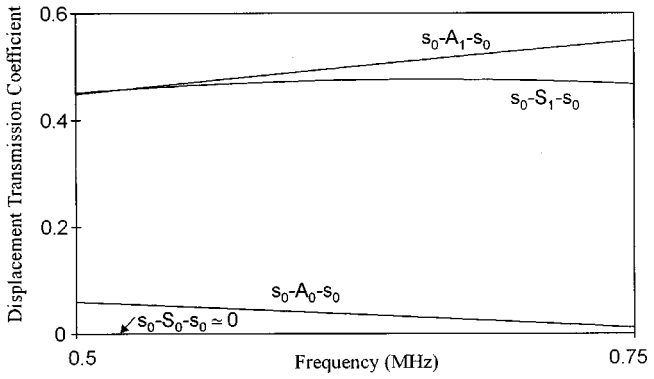

FIG. 7. Separate contributions from the four carrier modes to the transmission of s_0 across the whole joint, calculated without considering reverberations.

four carrier modes were received separately, yielding the strengths of transmission from the s_0 mode in the transmitter plate to each of the carrier modes in the overlap region. Scattered bulk waves and nonpropagating modes at the discontinuity were neglected. The separate reception of each of the carrier modes required particular attention because the zero-order and first-order mode pairs (Fig. 5) each have very similar velocities, so that they are not easily separated, even using a 2D-FFT. An additional property, the modal symmetry, was therefore exploited in addition to the 2D-FFT. A series of 64 nodes was monitored along the center line of the adhesive layer. A 2D-FFT of the in-plane displacements here reveals only the two symmetric carrier modes (S_0 and S_1), which are well separated in velocity and therefore easily resolved by the 2D-FFT; similarly, a 2D-FFT of the out-of-plane displacements reveals and resolves the two antisymmetric modes A_0 and A_1.

Figure 6(b) shows a schematic of a second finite element model which was used to predict the mode conversion, this time for conversion from the carrier modes in the overlap region to the s_0 mode in the receiver plate. Finite element analyses were conducted to study incidence of each of the four carrier modes. In each case, the carrier mode was excited in the overlap region, and a 2D-FFT was performed to determine the strength of transmission to the s_0 mode in the receiver plate. Having predicted functions for transmission from the transmitter plate to the overlap region, and from the overlap region to the receiver plate, it remains just to combine these results to show how much each of the carrier modes contributes to the overall transmission. This was done by multiplying the results of the two finite element models in the frequency domain for each of the four carrier modes in turn. The combination is shown in Fig. 7. The four curves show the displacement transmission coefficients (the power transmission coefficient approach is not needed here) for each of the four carrier modes. Thus, for example, the curve labeled ''s_0-A_1-s_0'' shows the transmission coefficient for s_0 in the transmitter plate, to A_1 in the overlap region, to s_0 in the receiver plate. We emphasize again that the transmission coefficients are meaningful only because we are comparing like quantities in the transmitter plate and the receiver plate: we record the normal displacement at the surface of the plate, both plates are identical, and the incident and transmitted signals are of the same mode.

B. Transmission across a joint if reverberations are neglected

If reverberations are neglected then the overall transmission across the joint is given by some combination of contributions from the four carrier modes which we have just examined, in other words some combination of the separate curves of Fig. 7. We examine here the contributions and how these combinations are effected.

It can be seen in Fig. 7 that most of the energy is transported by the two first-order modes in the overlap region, with transmission amplitudes at least an order of magnitude larger than those for the zero-order modes. An insight into why the first-order modes dominate in this case can be gained by comparing the mode shapes of the input mode to the mode shapes of the carrier modes. Figure 8(a) shows the displacement mode shapes of the s_0 mode in the transmitter plate. Figures 8(b) to 8(e) show the displacement mode shapes of the S_0, A_0, S_1 and A_1 modes, respectively, in the overlap region. All of the mode shapes shown were calculated at a frequency of 625 kHz. Intuitively, we would expect to excite modes in the overlap region if the mode shape in the bottom layer of the overlap region (the part of the overlap region occupied by the transmitter plate) is similar to the mode shape in the transmitter plate. Indeed this is a sound

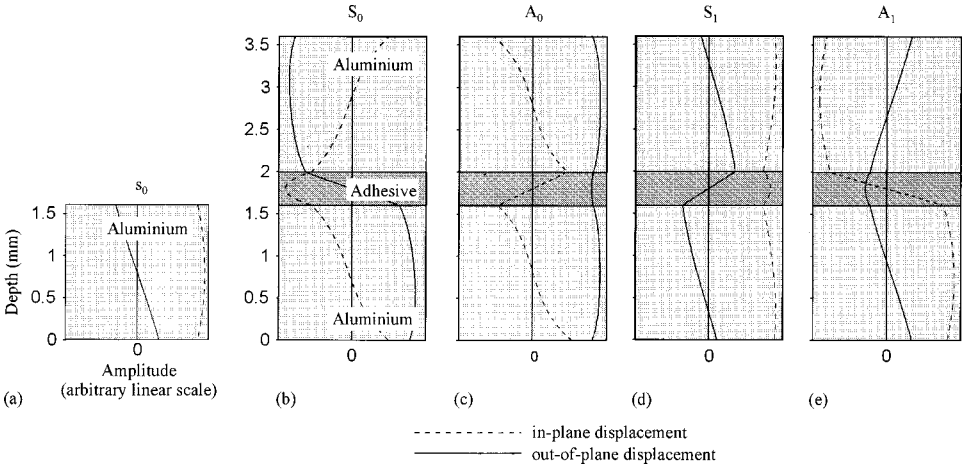

FIG. 8. Displacement mode shapes of (a) s_0 mode in transmitter plate; (b) S_0 mode in overlap region; (c) A_0 mode in overlap region; (d) S_1 mode in overlap region; (e) A_1 mode in overlap region.

TABLE II. Power transmission coefficients, predicted by mode combination, of s_0 across a bond with 0.4-mm adhesive thickness.

Signal composition	Power transmission coefficient (dB) Bond length 10 mm	Bond length 30 mm	Bond length 100 mm	Bond length 500 mm
Direction transmission only (no reverberations, no damping)	−26	−19	−9.2	−2.6
Direct transmission+1 set of reverberations (no damping)	−22	−16	−7.6	−2.1
Direct transmission+2 sets of reverberations (no damping)	−20	−15	−6.4	−1.7
Direct transmission+damping	−27	−20	−11	−9.9
Direct transmission+1 set of reverberations+damping	−23	−17	−9.8	−8.9
Direct transmission+2 sets of reverberations+damping	−21	−16	−9.4	−8.9

intuition, consistent with the logic of normal mode theory published by Auld,[14] and expressed also by Ditri[42] when he stated that a mode will not be excited if its field distribution is orthogonal to the excitation field. Similarly we should expect that the carrier modes arriving at the end of the joint will best convert to the s_0 mode in the receiver plate if their mode shapes in the top layer are well matched to those of s_0. The S_1 and A_1 modes in either layer have very similar mode shapes to the s_0 mode in the single plate, whereas the mode shapes of the S_0 and A_0 modes are totally different. It is therefore not surprising to see that the S_1 and A_1 modes dominate in the overlap region.

From these findings we propose that a simplified, yet insightful, analysis of the transmission behavior may be achieved by assuming that the energy from an incident s_0 mode is transmitted through the overlap region solely by the S_1 and A_1 carrier modes. Furthermore, these modes are coupled to the incident and transmitted s_0 waves according to the parts of their mode shapes which match the s_0 waves at the ends of the overlap region. From similar arguments, and utilizing knowledge of the mode shapes in Fig. 8, it seems probable that we would also be able to predict the dominant carrier modes for the other two incident modes of interest, a_0 and a_1. In both cases the displacements are antisymmetric so the S_0 and A_0 modes should dominate. However, the detailed study of these other incident modes is not pursued here.

The combination of the S_1 and A_1 contributions to the total transmitted signal must take into account the different speeds of these carrier modes in the overlap region and the length of the overlap. This is because the two contributions interfere, constructively or destructively, when they mode convert to the s_0 mode in the receiver plate. The nature of the interference depends on the relative phases of the contributions of the two carrier modes to the s_0 mode at mode conversion. The summation, incorporating the phases, can be performed in the frequency domain using the expression

$$A = \left| A_{s_1} e^{i(\omega t - k_1 x)} + A_{A_1} e^{i(\omega t - k_2 x)} \right|, \tag{2}$$

where A is the resultant amplitude of the combined mode in the receiver plate, A_{S_1} and A_{A_1} are the amplitudes of the s_0 mode due to the S_1 and A_1 carrier modes, respectively (shown in Fig. 7), k_1 and k_2 are the wave numbers of the S_1 and A_1 modes, respectively, and x is the length of the overlap. All of the amplitudes and the wave numbers are frequency dependent. Each of the two contributions incorporates, with the harmonic exponent, a phase which varies in both distance and time, and so the summation must be carried out with complex quantities. The sum is then itself an harmonic function and the resultant amplitude A, which is real valued, is expressed as its magnitude. It is assumed that the mode conversion from the s_0 mode to each carrier mode takes place without phase delay of the components in the lower layer, and similarly when considering the mode conversion from the carrier modes to the s_0 mode in the upper layer; this is reasonable given the simplified description of the mode conversion which has been adopted, as described earlier. However, it is necessary to recognize that there can be a phase difference between the components in the lower and upper layers of the overlap region. For example, Fig. 8 shows that the in-plane displacement has the same sign in both upper and lower plates for S_1, but has opposite sign for A_1. Therefore, if both modes are generated equally such that their displacements are in phase in the lower plate, their displacements will be in opposite phase (at the same location on the joint) in the upper plate. To account correctly for this, a phase delay of 180 deg must be applied to the A_1 mode when performing the combinations calculations.

The first row of Table II shows power transmission coefficients for the 0.4-mm thick joint, for four different bond lengths, predicted by combining the contributions of the S_1 and A_1 carrier modes according to Eq. (2). It can be seen that the strength of transmission increases markedly with the bond length, just as was found in the full model results in Fig. 4(a). This variation can be explained using the results of the combination of the carrier mode contributions. It was shown in Fig. 7 that the amplitudes of the contribution from the S_1 and A_1 carrier modes are approximately equal. It was also argued that a 180-deg phase shift must be applied to A_1 in addition to any phase difference associated with their different propagation speeds. It follows that for a zero length overlap the S_1 and A_1 contributions should cancel (approximately), but as the length of the overlap is increased the interference should change gradually from destructive to

TABLE III. Transmission coefficients of s_0 at 625 kHz for four bond thicknesses. Overall figure is predicted value without reverberations or damping for a joint with a bond length of 20 mm.

Bond thickness (mm)	Transmission coefficient (dB)		
	s_0-S_1-s_0	s_0-A_1-s_0	Overall
0.2	−6.7	−5.5	−24.2
0.4	−6.4	−5.7	−22.6
0.6	−6.5	−5.6	−19.3
0.8	−7.0	−5.3	−12.0

constructive. Thus the transmission should vary from weak to strong as the bond length is increased. The maximum transmission coefficient should occur when the interference is entirely constructive, when the overlap length is such that one of the waves has traveled half a wavelength more than the other. At 625 kHz, the wave numbers of S_1 and A_1 are 0.1157 and 0.1170/mm, respectively, so the overlap length would need to be about 400 mm for the maximum transmission (neglecting damping). The remaining information in Table II will be introduced later.

We can consider also the variation of the transmission coefficient with the bond thickness. The finite element models which were used to predict the transmission coefficients from the transmitter plate to the overlap region and from the overlap region to the receiver plate were modified and rerun for three more different thicknesses of the adhesive layer. The transmission coefficients for each of the two carrier modes, s_0-S_1-s_0 and s_0-A_1-s_0, were then calculated and their values at 625 kHz are shown, together with the earlier values for the 0.4-mm joint, in Table III. The table also shows their combination, using Eq. (2), for a bond length of 20 mm.

It is clear from these results that the transmission by the individual carrier modes is rather insensitive to the bond thickness. Yet the overall transmission coefficient increases with bond thickness, consistent with the plotted function in Fig. 4(a). The reason for this is again the difference between the wave numbers of the S_1 and A_1 modes and the resulting interference between their contributions when mode converting to s_0 in the receiver plate. The wave numbers of these modes at 625 kHz are shown for the four bond thicknesses in Table IV. It can be seen that the difference between the wave numbers increases as the bond thickness increases. Consequently, the change of phase between the modes after traveling the 20-mm length of the bond also increases, as shown. The change of phase reduces the destructive interference, thereby increasing the transmission coefficient.

Thus the simple analysis using Eq. (2) demonstrates that the strength of transmission is determined by the interference of the contributions from the two carrier modes, and that the two parameters which most strongly affect this interference are the overlap length and the wave number relationship between the two carrier modes.

TABLE IV. Wave numbers of carrier modes at 625 kHz and changes of phase between them after traveling 20 mm.

Bond thickness (mm)	S_1 wave number (/mm)	A_1 wave number (/mm)	Change of phase after 20 mm (deg)
0.2	0.1121	0.1112	6.5
0.4	0.1170	0.1157	9.4
0.6	0.1185	0.1169	12
0.8	0.1238	0.1196	30

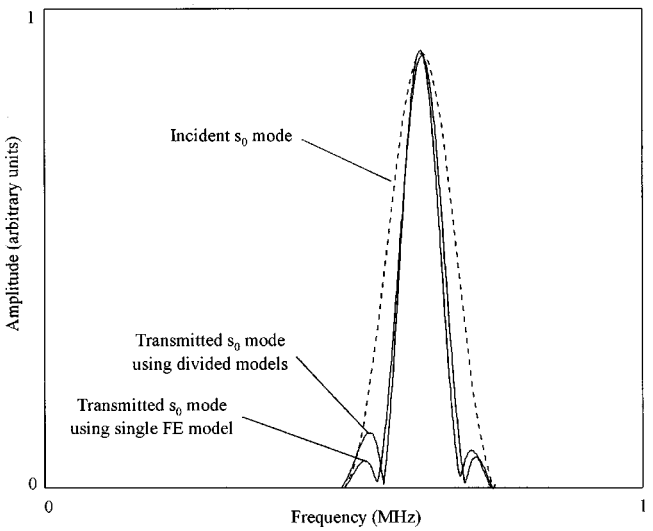

FIG. 9. Amplitude spectra of transmitted s_0 mode across a joint with bond length 500 mm, thickness 0.4 mm. Results shown for a finite element model of the whole joint and prediction using mode combination. The reference spectrum of incident mode is shown for comparison. Reverberations are neglected.

An additional finite element simulation of transmission across a whole joint was conducted specifically for comparison with these combined mode predictions. This model differed from the previous models only in its use of a large overlap length of 500 mm so that reverberation signals would separate in time and could therefore be gated out when monitoring the signal in the receiver plate.

The results of the combined mode analysis and of the full finite element analysis are compared in Fig. 9. The figure shows the amplitude frequency spectra of the transmitted s_0 mode using the two methods, and also the spectrum of the incident mode for reference, all plotted to the same scale. It can be seen that the correlation between the two methods is very good, implying that the combining model, although simplified, is representative of the true behavior. The spectra also show that at the center frequency (coincidentally) there is almost perfect transmission of the s_0 mode across the joint, and that there are two frequencies within the bandwidth at which the contributions due to S_1 and A_1 cancel, resulting in null transmission.

Finally, a simplified prediction, using Eq. (2), of the power transmission coefficient for ranges of bond length and bond thickness is presented in Fig. 10. In order to calculate these coefficients, the transmission contributions of A_1 and S_1 were assumed to be equal and independent of frequency. Their wave numbers were also assumed to be independent of frequency and were fixed to the values at the center frequency of 625 kHz. The prediction was therefore very much simplified but had the attraction of not being reliant on any of the numerical results of the finite element studies. The figure illustrates again the increase in the strength of the

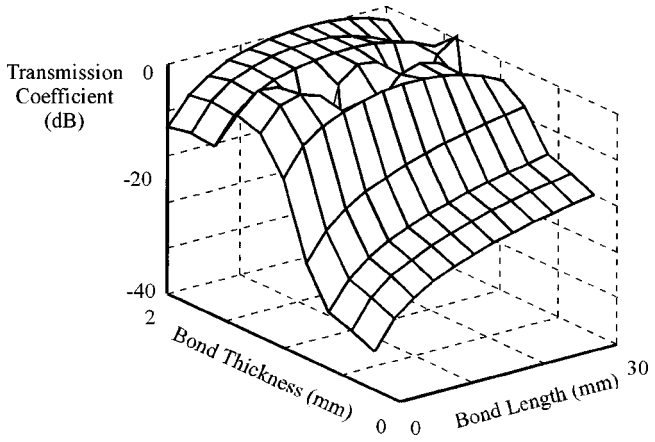

FIG. 10. Predicted power transmission coefficient using simple mode combination model.

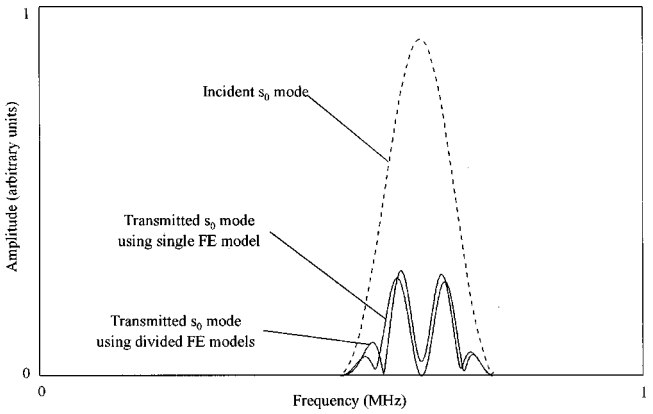

FIG. 11. Amplitude spectra of transmitted s_0 mode across the joint of Fig. 9, showing contribution solely from first reverberation. Results shown for a finite element model of the whole joint and prediction using mode combination. Reference spectrum of incident mode is shown for comparison.

transmission as either the bond length or the bond thickness is increased. Furthermore, comparison with Fig. 4(a) shows that the trends of this simplified prediction agree fairly well with the full finite element modeling which represents wave transmission across the whole structure with no decomposition into individual modes. The quantitative differences between the plots are due to the absence of reverberations in the simplified analysis as well as the above assumptions.

C. Effects of reverberations and damping

So far the analysis of the phenomena has addressed only the transmission in mode conversion at the ends of the overlap. However, reflection as well as transmission can take place at both of these discontinuities, so that there can be reverberation of the carrier modes along the length of the joint between A and B (Fig. 1). Thus the transmitted wave which leaves the joint and propagates in the receiver plate is followed by a succession of smaller signals from the reverberations, as seen earlier in the results of Fig. 3.

The consideration of reverberations is complicated by the need to account for large numbers of combinations of modes. In principle each mode can convert in various proportions to all of the others on each occasion of incidence at either end of the joint. For a single reverberation, which we define as one extra round trip within the overlap region, there are $64(=4^3)$ possible combinations of modes contributing to the final transmitted signal. For example, using the terminology which we introduced earlier, one such single reverberation signal is s_0-A_1-S_1-A_1-s_0, in which the A_1 carrier mode is excited in the overlap region, mode converts to S_1 on reflection at the receiver end of the overlap, mode converts back to A_1 on reflection at the transmitter end, and finally excites s_0 in transmission on arrival back at the receiver end. If double reverberations are considered, consisting of two extra round trips in the overlap region, then there are 1024 $(=4^5)$ possible combinations.

The building block for the study of the reverberation behavior is the reflection coefficient of a carrier mode at an end of the overlap region. Finite element analyses, using the models of Fig. 6, were used to predict the 16 coefficients given by the four possible incident carrier modes and four possible reflected carrier modes. Each reverberation combination could then be calculated by multiplying the relevant coefficients. Considering the 64 single reverberations, it was found that only 8 make a significant contribution. Not surprisingly, bearing in mind the earlier findings of the direct transmission, these are the eight combinations of the A_1 and S_1 carrier modes. All eight of these have very similar transmission coefficients, ranging from -17 to -18 dB. After these eight, the next largest has a transmission coefficient of -50 dB. Thus the single reverberations could be studied sensibly using only eight combinations. Similarly, the double reverberations could be studied using only 32 combinations. Analyses of further reverberations involving more than two round trips were not considered.

The overall transmission was again given by contributions of the combinations and their interference according to Eq. (2). In calculating these it was necessary to take care of phase reversals at the mode conversion and between the symmetric and antisymmetric modes.

Comparisons between the results of the finite element model of the whole joint, with 500-mm overlap length, and of the mode combining model for single reverberations, are shown in Figs. 11 and 12. Figure 11 shows the transmission spectra for the reverberation signal on its own. The results are very encouraging, showing good agreement and confirming the validity of the mode combination approach. Figure 12 shows the spectra when the directly transmitted signal is

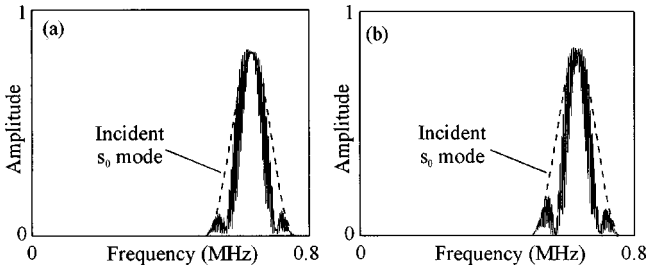

FIG. 12. Amplitude spectra of transmitted s_0 mode across joint of Fig. 9, taking both direct and single reverberation signals into account. Results shown for (a) finite element model of the whole joint, (b) prediction using mode combination. Reference spectrum of incident mode is shown for comparison.

also included. Here we can see the numerous local minima which result from the spectral interference between the direct signal and the reverberation signal. Good agreement between the two methods is also demonstrated by the similarity between parts (a) and (b) of the figure. Although not shown, equally good agreement was found when the double reverberations were taken into account.

The second and third rows of Table II show the predictions, using mode combination, for the single and double reverberations. It can be seen that there is an increase in the contribution to the transmission as each set of reverberations is added. Both the first and second sets are therefore seen to be significant. The results also show that the transmission coefficient consistently increases as the bond length is increased, as was found in the finite element predictions in Fig. 4(a).

All of the modeling work so far has ignored any damping losses of the waves. This is a reasonable assumption for the aluminum material but may not be for the adhesive layer. If damping by the adhesive is significant, it will be particularly influential on the reverberating modes because of their additional distances of travel in the overlap region. It was therefore considered to be useful to extend the analysis work to incorporate some estimates of damping losses.

The attenuation of a carrier mode is in fact one of its modal properties and it can be calculated if the bulk damping properties of the materials are known. The bulk longitudinal and shear attenuations in the adhesive material were taken to be 1.3 dB wavelength and 2.4 dB/wavelength, respectively; these are typical values for a hard epoxy such as Araldite AV119, according to Challis and Cocker.[8] When these were included in the calculation of the modal solutions for the A_1 and S_1 modes it was found that moderate losses were predicted: at 625 kHz the amplitudes of A_1 and S_1 are reduced by about 10% and 15%, respectively, in 100 mm of travel. The introduction of these attenuation properties in the adhesive has a negligible effect on the wave numbers and velocities of the modes.

These attenuation values were introduced into the calculation of the transmission coefficients simply by reducing the amplitudes of the carrier modes according to their distances traveled. Overall transmission coefficients for the s_0 mode, calculated from the mode combination results, are given in the last three rows of Table II. By comparing with the other results in the table, it can be seen that the coefficients for all cases are reduced by the damping in the adhesive layer, and that, as should be expected, the damping has the greatest influence when the joints have long bond lengths. It is also evident that the damping reduces the relative contribution of the reverberations to the overall transmission, in particular of the second set. Indeed it seems that, with the exception of very short bonds, the second set of reverberations makes very little contribution. It is therefore improbable that third or higher sets of reverberations would contribute significantly in any realistic bonds.

IV. DISCUSSION AND CONCLUSIONS

One of the stated objectives of the work was to investigate the sensitivity of the transmission of Lamb waves across a lap joint to the dimensions of the joint. The motivation for this is the possible development of a rapid technique for performing quality checks on sheet metal bonding in-process. Previous work published by Todd and Challis[34] has shown clearly that the dimensions of an adhesively bonded T-joint have a significant influence on the transmission across that type of joint. Their approach was to train a neural network to categorize the joints from the very complicated transmitted signals and they showed that the system could be configured to make very reliable and rapid estimates of dimensions. The approach taken in this study of lap joints was rather different, addressing the nature of the transmission behavior in order to understand the factors which will affect sensitivity and identify the most suitable testing conditions. Having said this, however, the neural network may still remain the most appropriate technology for rapid in-process inspection. The results of the finite element simulations, shown in Fig. 4, demonstrate that the transmission is indeed influenced by the two dimensions of the joint, bond length and bond thickness. None of the modes shows an ideal monotonic variation over the full ranges of the two parameters, but there are areas of sensitivity in all three graphs. The appropriate selection for maximum sensitivity would depend on the target dimensions of the joint being tested and their expected variabilities. In general it is most likely that the s_0 mode will be the most sensitive, particularly for bond lengths up to about 15 mm. The lowest sensitivity is predicted when the bond is both very long and very thick.

Turning to the practical exploitation of these results, it is clear that it is not possible to extract both dimensions from the measurement of a single transmission coefficient, but a measurement of one dimension may be feasible in many cases if the other is known. This could arise if the construction procedure results in a much more precise control of one dimension than the other. Failing this, two other alternatives are suggested. First, a separate thickness measurement could be made, for example using a normal incidence ultrasonic measurement, at a single point in the overlap region. The thickness is a lot easier to measure than the length and could be monitored in this way without reducing the speed of the inspection process. Thus the joint would still be monitored without recourse to area scanning. The second possibility is the exploitation of two different Lamb modes to give both of the dimensions. Indeed this is implicitly achieved when a neural network is used with a multimode signal. A two-mode approach may be possible for certain ranges of the parameters where two of the modes are sensitive to the dimensions, but the sensitivity of a_0 and a_1 is in general rather weak, implying that the estimation may be poorly conditioned. In a practical implementation it would also be necessary to consider the influence of other parameters which have not been considered in the work to date. These would include variability of the material properties, the possibility of variations in thickness over the overlap region, and the influence of irregular details (cusps in the adhesive for example) at the ends of the overlap region.

The study of the nature of the transmission of the s_0 mode across the joint has revealed phenomena which are both interesting and descriptive. The excitation of the ''car-

rier''modes in the three-layer overlap region is governed by the degree to which their mode shapes match the mode shapes of the incident wave. In the case of the s_0 mode incident, this results in significant energy being propagated only in the S_1 and A_1 carrier modes, each with approximately the same amplitude. The transmission in the receiver plate is then initiated by the combination of these two modes when they arrive at the end of the overlap region and mode convert in transmission to the s_0 mode. The strength of this transmitted s_0 mode is determined by the summation of these two components, which can be destructive or constructive, according to their relative phases when the mode conversion takes place. The bond length affects this summation because the modes travel at different speeds and the distance of travel therefore determines the phase difference between them. The bond thickness affects the summation because it affects the difference between the speeds of the carrier modes. Finally, it has been shown that the complete transmitted signal is composed of a series of transmitted signals, due to reverberations of the carrier modes in the overlap region, in addition to the directly transmitted component. The contributions due to reverberations are in general significant, particularly if the adhesive material has low damping properties.

The analysis of the carrier modes also suggests that it may be feasible to use the transmission measurements to detect defects in the adhesive bond. The mode shapes of the carrier modes, plotted in Fig. 8, show that all four carrier modes generate significant strain in the adhesive layer. Although not studied in detail here, the implication is that perturbations of the properties of the adhesive layer and its adhesion to the aluminum layers are likely to affect the modal properties of the carrier modes. Therefore if the bond dimensions are well known then it may be possible to detect anomalies in the bond line from measurements of the transmission coefficient. The antisymmetric modes A_0 and A_1 induce shear strain in the bond line and may therefore be sensitive to disbonded regions or reduced shear stiffness of the adhesive. The symmetric modes S_0 and S_1 induce compression of the adhesive and could therefore be sensitive to changes in the bulk modulus of the adhesive.

Finally, as products of this work, we propose the utility of the techniques presented here for the study of transmission across bonded joints. The mode combination procedure provides insight to the physics of the transmission, indicating the carrier modes which dominate in the transmission of the energy. It also allows for the estimation of the transmission coefficient for ranges of bond dimensions without the need to perform multiple simulations of the whole joint. The approach for calculating the transmission coefficient using the 2D-FFT may be useful in general for measuring the strength of a chosen mode in a multimode signal without the adverse effects of interference which are encountered in the usual measurements of peaks in time or frequency.

[1] R. D. Adams and J. Coppendale, ''Measurement of the elastic moduli of structural adhesives by a resonant bar technique,'' J. Mech. Eng. Sci. **18**, 149–158 (1976).

[2] G. A. Alers, P. L. Flynn, and M. J. Buckley, ''Ultrasonic techniques for measuring the strength of adhesive bonds,'' Mater. Eval. **35**, 77–84 (1977).

[3] C. W. Yew and X. W. Wang, ''Using ultrasonic waves to estimate the quality of adhesive bonds in plate structures,'' J. Acoust. Soc. Am. **77**, 1813–1823 (1985).

[4] R. B. Thompson and D. O. Thompson, ''Past experiences in the development of tests for adhesive bond strength,'' J. Adhes. Sci. Technol. **5**, 583–599 (1991).

[5] C. C. H. Guyott and P. Cawley, ''Evaluation of the cohesive properties of adhesive joints using ultrasonic spectroscopy,'' NDT Int. **21**, 233–240 (1988).

[6] C. C. H. Guyott, P. Cawley, and R. D. Adams, ''The non-destructive testing of adhesively bonded structure: A review,'' J. Adhes. **20**, 129–159 (1986).

[7] R. E. Challis, T. Alper, A. K. Holmes, and R. P. Cocker, ''Near-plane acoustic propagation measurements in thin layers of adhesive polymer,'' Meas. Sci. Technol. **2**, 59–68 (1991).

[8] R. E. Challis and R. P. Cocker, ''Ultrasonic compression wave propagation in adhesive polymers described as a signal filtering process,'' Ultrasonics **33**, 311–319 (1995).

[9] W. Wang and S. I. Rokhlin, ''Evaluation of interfacial properties in adhesive joints of aluminum alloys using angle-beam ultrasonic spectroscopy,'' J. Adhes. Sci. Technol. **5**, 647–666 (1991).

[10] H. Lee and K. Neville, *Handbook of Epoxy Resins* (McGraw-Hill, New York, 1967).

[11] A. J. Kinloch, *Durability of Structural Adhesives* (Applied Science, London, 1983).

[12] H. Lamb, ''On waves in an elastic plate,'' Proc. R. Soc. London, Ser. A **93**, 114–128 (1917).

[13] I. A. Viktorov, *Rayleigh and Lamb Waves* (Plenum, New York, 1970).

[14] B. A. Auld, *Acoustic Fields and Waves in Solids*, 2nd ed. (Krieger, Malabar, FL, 1990).

[15] N. Guo and P. Cawley, ''The interaction of Lamb waves with delaminations in composite laminates,'' J. Acoust. Soc. Am. **94**, 2240–2246 (1993).

[16] N. Guo and P. Cawley, ''Lamb wave reflection for the quick NDE of large composite laminates,'' Mater. Eval. **52**, 404–411 (1994).

[17] A. H. Nayfeh and D. E. Chimenti, ''Ultrasonic plate waves in three-dimensional braided composites,'' J. Acoust. Soc. Am. **97**, 2056–2062 (1995).

[18] G. A. Alers and R. B. Thompson, ''Application of trapped modes in layered media to the testing of adhesive bonds,'' Proceedings of the 1975 IEEE Ultrasonics Symposium, 138–142 1976.

[19] S. I. Rokhlin, ''Interface properties characterization by interface and Lamb waves,'' in *Review of Progress in Quantitative NDE*, edited by D. O. Thompson and D. E. Chimenti (Plenum, New York, 1986), Vol. 5, pp. 1301–1308.

[20] A. Mal, P. C. Xu, and Y. Bar-Cohen, ''Analysis of leaky Lamb waves in bonded plates,'' Int. J. Eng. Sci. **27**, 779–791 (1989).

[21] Y. Bar-Cohen, A. K. Mal, and C.-C. Yin, ''Ultrasonic evaluation of adhesive bonding,'' J. Adhes. **29**, 257–274 (1989).

[22] P. B. Nagy and L. Adler, ''Adhesive joint characterization by leaky guided interface waves,'' in *Review of Progress in Quantitative NDE*, edited by D. O. Thompson and D. E. Chimenti (Plenum, New York, 1989), Vol. 8, pp. 1417–1424.

[23] P. B. Nagy, D. V. Rypien, and L. Adler, ''Dispersive properties of leaky interface waves in adhesive layers,'' in *Review of Progress in Quantitative NDE*, edited by D. O. Thompson and D. E. Chimenti (Plenum, New York, 1990), Vol. 9, pp. 1247–1254.

[24] C. Teller, K. Diercks, Y. Bar-Cohen, and A. Mal, ''Recent advances in the application of leaky Lamb waves to the nondestructive evaluation of adhesive bonds,'' J. Adhes. **30**, 243–261 (1989).

[25] M. J. S. Lowe and P. Cawley, ''The applicability of plate wave techniques for the inspection of adhesive and diffusion bonded joints,'' J. Nondestruct. Eval. **13**, 185–199 (1994).

[26] S. I. Rokhlin, ''Lamb wave interaction with lap-shear adhesive joints: Theory and experiment,'' J. Acoust. Soc. Am. **89**, 2758–2765 (1991).

[27] S. I. Rokhlin, S. Meng, and L. Adler, ''In-process ultrasonic evaluation of spot welds,'' Mater. Eval. **47**, 935–943 (1989).

[28] S. I. Rokhlin and F. Bendec, ''Coupling of Lamb waves with the aperture between two elastic sheets,'' J. Acoust. Soc. Am. **73**, 55–60 (1983).

[29] H. A. Sabbagh and T. F. Krile, ''Finite element analysis of elastic wave scattering from discontinuities,'' Proceedings of the 1972 IEEE Ultrasonics Symposium, 216–219 1973.

[30] M. Koshiba, S. Karakida, and M. Suzuki, ''Finite-element analysis of Lamb waves scattering in an elastic plate waveguide,'' IEEE Trans. Sonics Ultrason. **SU31**, 18–25 (1984).
[31] D. N. Alleyne, ''The nondestructive testing of plates using ultrasonic Lamb waves,'' Ph.D. thesis, University of London, 1991.
[32] A. Mal, Z. Chang, D. Guo, and M. Gorman, ''Lap joint inspection using plate waves,'' *Nondestructive Evaluation of Bridges and Highways*, edited by S. B. Chase (SPIE, Washington, 1996), pp. 128–137.
[33] C. W. Chan, ''The ultrasonic nondestructive evaluation of welds in plastic pipes,'' Ph.D. thesis, University of London, 1996.
[34] C. P. D. Todd and R. E. Challis, ''Quantitative classification of adhesive bondline dimensions using Lamb waves and artificial neural networks,'' IEEE Trans. Ultrason. Ferroelectr. Freq. Control **46**, 167–181 (1999).
[35] D. Hitchings, *FE77 User Manual* (Version 2.40, Imperial College internal report, 1995).
[36] D. N. Alleyne and P. Cawley, ''The practical excitation and measurement of Lamb waves using piezoelectric transducers,'' in *Review of Progress in Quantitative NDE*, edited by D. O. Thompson and D. E. Chimenti (Plenum, New York, 1994), Vol. 13, pp. 181–188.
[37] M. J. S. Lowe, ''Matrix techniques for modeling ultrasonic waves in multilayered media,'' IEEE Trans. Ultrason. Ferroelectr. Freq. Control **42**, 525–542 (1995).
[38] B. N. Pavlakovic, M. J. S. Lowe, D. N. Alleyne, and P. Cawley, ''Disperse: A general purpose program for creating dispersion curves,'' in *Review of Progress in Quantitative NDE*, edited by D. O. Thompson and D. E. Chimenti (Plenum, New York, 1997), Vol. 16, pp. 185–192.
[39] B. N. Pavlakovic, D. N. Alleyne, M. J. S. Lowe, and P. Cawley, ''Simulation of Lamb wave propagation using pure mode excitation,'' in *Review of Progress in Quantitative NDE*, edited by D. O. Thompson and D. E. Chimenti (Plenum, New York, 1998), Vol. 17, pp. 1003–1010.
[40] K.-J. Bathe, *Finite Element Procedures in Engineering Analysis* (Prentice-Hall, New Jersey, 1982).
[41] D. N. Alleyne and P. Cawley, ''A two-dimensional Fourier transform method for the quantitative measurement of Lamb modes,'' in *Review of Progress in Quantitative NDE*, edited by D. O. Thompson and D. E. Chimenti (Plenum, New York, 1991), Vol. 10, pp. 210–208.
[42] J. J. Ditri, ''Some results on the scattering of guided elastic *SH* waves from material and geometric waveguide discontinuities,'' J. Acoust. Soc. Am. **100**, 3078–3087 (1996).

A two-frequency acoustic technique for bubble resonant oscillation studies

K. Ohsaka and E. H. Trinh[a)]
Jet Propulsion Laboratory, California Institute of Technology, Pasadena, California 91109

(Received 15 February 1999; revised 10 November 1999; accepted 8 December 1999)

A two-frequency acoustic apparatus has been developed to study the dynamics of a single gas or vapor bubble in water. An advantage of the apparatus is its capability of trapping a bubble by an ultrasonic standing wave while independently driving it into oscillations by a second lower frequency acoustic wave. For a preliminary application, the apparatus is used to study resonant oscillations. First, near-resonant coupling between the volume and the $n=3$ shape oscillation modes of air bubbles at room temperature is studied, where n is the mode number. The stability boundary, amplitude versus frequency, of the volume oscillation forms a wedge centered at the resonant frequency, which qualitatively agrees with a theoretical prediction based on a phase-space analysis. Next, the resonant volume oscillations of vapor bubbles are studied. The resonant radius of vapor bubbles at 80 °C driven at 1682 Hz is determined to be 0.7 mm, in agreement with a prediction obtained by numerical simulation.
[S0001-4966(00)03703-6]

PACS numbers: 43.35.Ei, 43.35.Yb [HEB]

INTRODUCTION

Single bubble dynamics has been experimentally studied using acoustic techniques for several decades. The techniques involve trapping a bubble in a fluid host and driving it into either a volume (radial) or shape oscillation mode. Trapping of a bubble is accomplished by ultrasonic standing waves generated in the fluid. The bubble is trapped at a pressure antinode if its equilibrium radius, R_0, is smaller than the resonant radius, R_{res}, or at a node if R_0 is larger than R_{res}. For the bubble trapped at a pressure antinode, the time-varying ultrasonic pressure field is used to directly drive the bubble into oscillations.[1,2] This technique does not allow for the variation in the driving frequency, and is only practical for small bubbles (typically $R_0<100\,\mu$m) because of the weakening trapping capability at longer wavelengths. For the bubble trapped at a pressure node, modulation of the ultrasonic standing wave can be used to drive the bubble into oscillations.[3,4] This technique allows the variation of the driving frequency, but it uses the modulated acoustic radiation pressure to deform the trapped bubble; therefore, only the shape oscillations can be induced directly. However, in principle, the volume oscillation can be induced through nonlinear coupling between the shape and volume oscillations. In light of these limitations associated with existing techniques, we have developed an apparatus which employs two separate acoustic waves to independently trap a bubble at a node and drive it into volume and shape oscillations. In this paper, we describe the apparatus and evaluate its basic performances.

Volume and/or shape oscillations of gas or vapor bubbles play a major role in phenomena occurring in nature and in industrial processes. For example, part of ocean ambient noise originates from oscillating bubbles created by natural processes. It is known that the efficiency of mass and heat transports in industrial processes is enhanced by oscillating bubbles in fluids. An improved understanding of the fundamentals of bubble oscillations should contribute to better predictions of natural phenomena and more precise control of industrial processes. An additional objective of this study is to preliminary apply the present apparatus to verify some theoretically predicted features of oscillating bubbles. First, we consider the coupling between the volume and shape modes, which occurs because the bubble dynamics are intrinsically nonlinear. So far, this subject has mainly been studied theoretically.[5–8] Some of the predictions can be verified experimentally such as the existence of the two–one resonant coupling and the threshold amplitude boundary for near-resonant coupling. Next, the vapor bubble resonance, which has unique features due to the interaction between dynamic and thermal processes.[9–12] It has been predicted that a vapor bubble has two resonant radii at the same frequency, and that these radii are significantly smaller than the resonant radius of gas bubbles at the same frequency.

I. EXPERIMENT

A. Apparatus

Figure 1 schematically depicts the apparatus. The cell is a hollow cylindrical quartz tube whose outer diameter, wall thickness, and length are 15, 1, and 73 mm, respectively. The cell is approximately half-filled with water in which a bubble is trapped. The bottom of the cell is directly cemented to the hollow cylindrical transducer. This transducer is driven at around 104 kHz to create an ultrasonic standing wave for trapping a bubble at a node. The broadband audio speaker placed above the cell is operable up to 10 kHz and is used for driving the bubble into oscillations. The top section of the cell is inserted into the loosely closed sound guide (cavity) of the speaker without physically contacting it. The trapped

[a)]Currently at the NASA Headquarters, Washington, D.C.

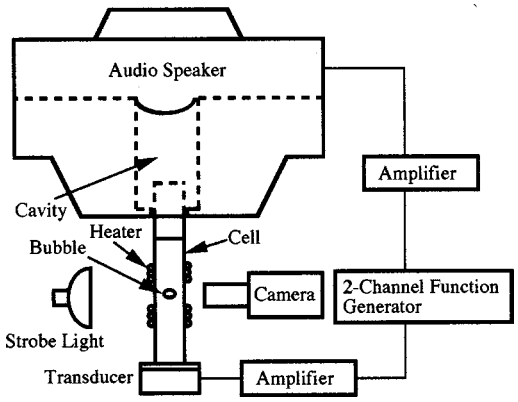

FIG. 1. Schematic diagram of experimental apparatus showing the key parts.

bubble responds to the ambient gas pressure variation in the cavity, and oscillates in either the volume or shape oscillation mode. For the vapor bubble trapping, the nichrome heaters wound around the cell are used to raise the water temperature which is measured by a thermocouple. A single air bubble is introduced in the water with a hypodermic syringe, and is trapped at a location between the two heaters, where the vertical temperature gradient is minimal at elevated temperatures. The content of the bubble is initially air but it quickly become a mixture of air and saturated water vapor. The trapped bubble is back illuminated by the strobe light and its motion is monitored by the camera with a telescopic lens. The images of the bubble are recorded at 30 frames per second on videotape for later analysis.

B. Acoustic pressure estimation

We could not measure the ultrasound pressure because of technical difficulties. The ultrasound pressure was much higher than the driving acoustic pressure; however, the bubble was trapped near a node of the ultrasonic standing wave; therefore, the pressure variation at the bubble position was expected to be small. The ultrasonic pressure could not directly induce noticeable volume or low mode shape oscillations because its frequency was too high. However, the ultrasound pressure could sometimes produce the capillary waves on the bubble surface.

The driving acoustic pressure generated by the audio speaker was estimated at room temperature using a dummy cell whose dimensions were exactly same as those of the actual cell. The dummy cell was placed under the audio speaker at exactly the same position as the actual cell and a calibrated hydrophone was inserted into the water from the bottom of the cell. There were two reasons to take this indirect method to estimate the pressure. First, the hydrophone could not be inserted into the water when a bubble was trapped because its presence disturbed the stability of the trapped bubble. Second, the magnitude of the driving audio frequency pressure was significantly lower than that of the ultrasonic pressure ($\sim 10^4$ Pa) for bubble trapping, thus making the measurement of the audio frequency pressure variations difficult, if not impossible. The driving pressure generated by the audio speaker was correlated to the preamplified signal (input voltage) which was fed to the speaker through an amplifier.

C. Oscillation amplitude determination at the threshold

The input voltage was directly correlated with the amplitude of the volume oscillation in the following manner: We first measured the amplitude of the volume oscillation at a predetermined input voltage, typically, 0.1 V. In some cases, the shape oscillation was induced below 0.1 V, then a reduced voltage was selected. Second, we gradually increased the input voltage until the volume mode turned into the a shape mode. Finally, the threshold amplitude was determined by linearly extrapolating the value at 0.1 V to the input voltage at the threshold.

D. Operation procedure

1. Mode coupling

Outgassed distilled water was first introduced into the cell to a level about halfway to the top, then the ultrasonic transducer was turned on. The frequency was selected at around 104 kHz and then the water height was adjusted to generate a standing wave in the water. An air bubble was introduced in the water using a hypodermic syringe with a thin-gauge needle. The mode of the standing wave was not precisely known but bubbles could easily be trapped at several locations. We chose one near the axial center of the cell halfway to the surface. Once the bubble was stabilized, the audio speaker was turned on to drive the bubble. When the input voltage was low, the bubble was always driven in the volume mode. The speaker was tuned to the frequency, f_0, which approximately satisfies $f_0 = 2 f_n$, where f_n was the resonant frequency of the shape oscillation with the mode n. Then, the input voltage was gradually increased until the volume mode turned into a shape mode to determine the upper threshold value. Next, the input voltage was gradually reduced until the shape mode turned back to the volume mode to determine the lower threshold. The apparatus could generate a variety of the shape oscillation modes by varying the driving frequency. Some of them were simple and could be assigned to low order resonant modes. However, the majority displayed complicated and periodically changing shapes. We decided to study coupling between the volume and the axisymmetric $n = 3$ shape oscillations.

2. Vapor bubble resonance

Outgassed distilled water was first introduced into the cell to a level about halfway to the top. The heater was turned on and the temperature rise was monitored by an immersed thermocouple. Once the temperature reached a predetermined value, the ultrasonic transducer was turned on and the water height was adjusted to generate a standing wave in the water. Then, the thermocouple was withdrawn from the water because its presence disturbed the stability of the trapped bubble. A bubble was introduced in the water with a hypodermic syringe. The content of the bubble was a

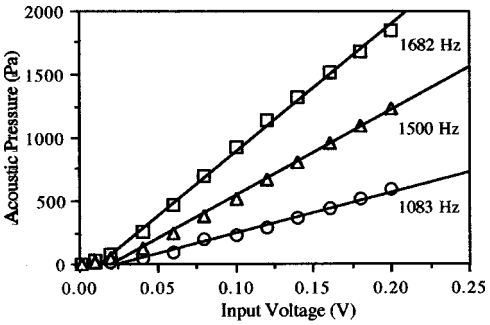

FIG. 2. The driving low frequency pressure as a function of the input voltage at three driving frequencies, determined with the dummy cell.

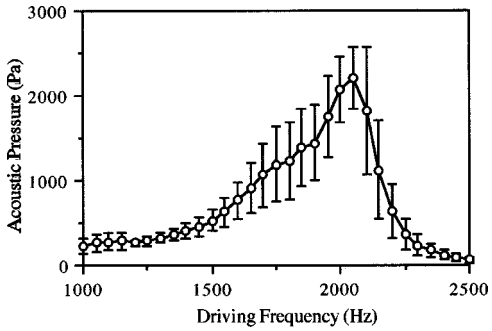

FIG. 3. The driving low frequency pressure as a function of the driving frequency when the input voltage is maintained at 0.1 V.

mixture of air and saturated water vapor (roughly, 50/50 at 80 °C). The audio speaker was then turned on to drive the bubble in the volume oscillation.

Two methods were employed to find evidence of the vapor bubble resonance in acoustic pressure fields. First, we measured the growth rate of vapor bubbles under the assumption that the growth rate increased as the bubble resonated because the growth rate was proportional to the oscillation amplitude. In order to determine the growth rate as a function of the bubble radius, we drove vapor bubbles at constant input voltage but various frequencies between 2.6 and 2.8 kHz depending on the bubble size. The images of the oscillating bubble are recorded on videotape. Second, we directly measured the oscillation amplitude of bubbles as a function of radius at constant input voltage and driving frequency. For this measurement, the driving frequency was fixed at 1682 Hz. The input voltage was initially set at low value and gradually increased to a predetermined value, 0.1 V or just below the threshold value when the volume mode turned into the shape mode at the input voltage below 0.1 V. The images of the bubbles in the volume mode at the threshold were recorded on videotape to determine the amplitude in later analysis.

For comparison with the observed resonant frequency, the theoretical resonant frequency, f_n of the shape oscillation with the mode, n, is calculated by

$$(2\pi f_n)^2=(n-1)(n+1)(n+2)\frac{\sigma}{\rho R_0^3}, \tag{1}$$

where σ is the surface tension, R_0 is the equilibrium radius, and ρ is the fluid density.

E. Image analysis procedure

The images of the oscillating bubbles taken under continuous back illumination were used to determine the growth rate of the vapor bubbles. On the other hand, the images taken under strobe illumination revealed the volume variation in a slow motion. These images were used to determine the oscillation amplitude. For the measurements, the video tapes were reviewed and the images of bubbles were captured at a certain time interval and transferred into a computer using a commercially available software program. The 2-D image of the bubble was distorted into an oblate shape by the curvature of the cell wall in addition to the actual deformation due to the acoustic pressure. Because the actual deformation was minimal and the vertical length was not optically distorted, we determined the actual radius of the bubble from the vertical bubble length and the known magnification of the image. The sequential images allowed us to determine either the growth rate or the maximum and minimum radii from which we calculated the amplitude of the volume oscillation. The possible errors due to the finite number of pixels of the camera were considered when the radius was measured.

II. RESULTS

Figure 2 shows an example of the driving pressure as a function of the input voltage at three driving frequencies. This example shows that the pressure is a function of both the input voltage and the driving frequency. It was noticed that the magnitude of the pressure was sensitive to the position of the water surface; therefore, the measurement was repeated at different surface positions near the surface position in the actual cell. It is found that the pressure always linearly increased as the voltage increased independent from the surface position. The offset from the origin seen in the figure is due to a minimum input voltage which is required to drive the audio speaker.

Figure 3 shows the driving pressure as a function of the driving frequency when the input voltage is maintained at 0.1 V. The peak at around 2 kHz is due to the cavity resonance which intensifies the driving pressure. The open circles are the average of the five measurements. The error bars represent the standard deviation, σ. To estimate the pressure in the actual cell at different input voltages, the

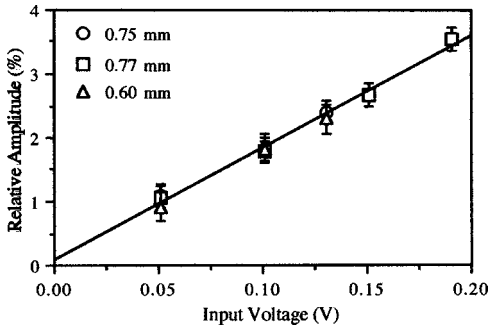

FIG. 4. The correlation between the input voltage and the relative amplitude for three different bubbles, driven at 1682 Hz.

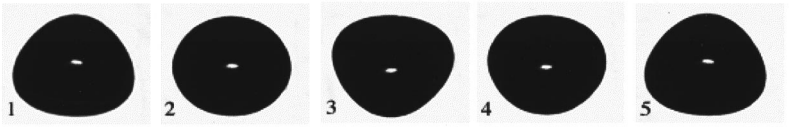

FIG. 5. Images of oscillating bubble in the $n=3$ axisymmetric shape mode. The images are optically distorted due to the curvature of the cell. The spot near the center of the images is the highlight created by the illuminating light.

average value at 0.1 V at a corresponding frequency in Fig. 3 was selected and linearly interpolated (extrapolated) to the different input voltages. We did not use the driving frequencies near the resonant frequency in order to avoid large uncertainties involved in the pressure estimation.

To establish the correlation between the input voltage and the relative amplitude, the amplitude was measured at several input voltages. Figure 4 shows the correlation for three different bubbles driven at 1682 Hz at room temperature. As it is seen in the figure, the relative amplitude linearly increases as the input voltage increases. The offset from the origin is negligible. Although, for these three bubbles, the linear coefficient happens to be roughly the same, it should be different depending on the bubble radius, but the linear correlation is expected to be valid at small amplitudes for any size of bubbles.

Figure 5 shows the images of the oscillating gas bubble, $R_0=0.6\,\mathrm{nm}$, in the axisymmetic $n=3$ mode driven at 1083 Hz. The observed resonant frequency is 542 ($=1083/2$) Hz. The theoretical resonant frequency is calculated to be 580 Hz using Eq. (1) with the surface tension taken to be 72 mN/m. The bright spot near the center of the images is the highlight created by the back illuminating light. The images represent one cycle of the shape oscillation. Note that the images are optically distorted in the horizontal direction due to the curvature of the cell wall.

Figure 6 shows the amplitude variations of the bubble in Fig. 5, oscillating in the volume mode at slightly below the threshold and in the shape mode at slightly above the threshold. The time is a reduced scale whose unit is approximately 1.2×10^{-4} s. The relative amplitude of the volume mode is defined as the actual amplitude divided by R_0. For the shape mode, the relative amplitude is given by the vertical length between the top edge and the center of the image divided by R_0. The figure reveals a significant magnitude difference between the two modes at a similar driving pressure, and the resonant coupling condition, $f_0\cong 2f_3$, being satisfied. A hysteresis effect is observed in the transition between the volume and $n=3$ shape oscillations. As a result, the upper and lower thresholds are slightly different and they are determined to be 0.078 V and 0.070 V, respectively, in terms of the input voltage for this particular bubble. The experimental threshold pressure is estimated to be roughly 3×10^2 Pa using the value in Fig. 3.

Figure 7 shows the stability boundary, amplitude versus frequency, of gas bubble, $R_0=0.44\,\mathrm{mm}$, which is driven into the $n=3$ shape oscillation with the two–one resonant coupling condition. The observed resonant frequency is 900 Hz. The theoretical resonant frequency is calculated to be 925 Hz using Eq. (1) with the surface tension taken to be 72 mN/m. The open circles represent the measured threshold values. The straight lines are drawn to construct the boundary. The threshold amplitude at the resonant frequency is approximately 1.2%.

Figure 8 is a collection of typical results of the measured radius as a function of time for bubbles oscillating in different modes. Bubbles *a*, *b*, and *e* are in the volume mode. Bubble *c* is in the shape mode. Bubble *d* is in the stationary condition. As it is seen in the figure, the growth rate of bubbles in the stationary condition or undergoing shape oscillations is practically zero. On the other hand, the growth rate of the bubbles in the volume mode is positive and depends on the bubble radius. The growth rate appears to be linear and is determined by a linear regression method.

Figure 9 shows the measured growth rate as a faction of the bubble radius. For this presentation, the growth rates of the bubbles driven at the frequencies between 2.7 and 2.8 kHz are selected. The 95% confidence interval of each measured growth rate is shown by the bars. As seen, the growth rate seems showing two peaks at approximately 0.4 and 0.8 mm. The peaks may be attributed to increasing in the oscillation amplitude around these radii.

Figure 10 summarizes the results of the amplitude measurement for both vapor and air bubbles driven at 1682 Hz. The figure shows the relative amplitude as a function of the bubble radius when the input voltage is maintained at 0.1 V.

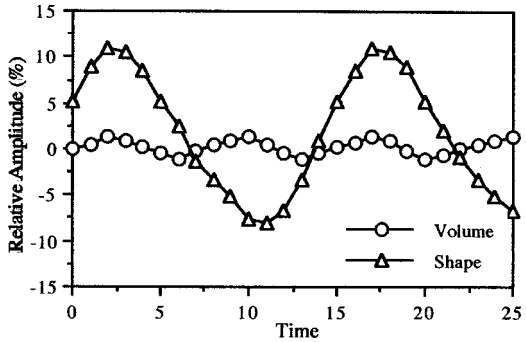

FIG. 6. The amplitude variation of bubble ($R_0=0.6\,\mathrm{mm}$) oscillating in the volume and $n=3$ shape modes, driven at 1083 Hz. The calculated resonant frequency is 580 Hz.

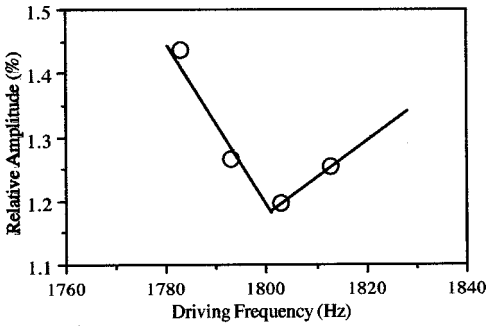

FIG. 7. The stability boundary, amplitude versus frequency, of the volume mode for the bubble ($R_0=0.44\,\mathrm{mm}$) driven into the $n=3$ shape mode. The calculated resonant frequency is 925 Hz.

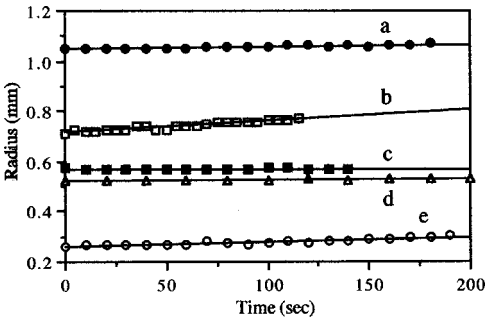

FIG. 8. The measured radius as a function of time for bubbles oscillating in different modes. The growth rate, driving frequency, and the oscillation mode of individual bubble are (a) 8.3×10^{-5} mm/s, 2.63 kHz, volume, (b) 4.6×10^{-4}, 2.74, volume, (c) 0, 2.71, shape, (d) no driving pressure, and (e) 1.8×10^{-4}, 2.69, volume.

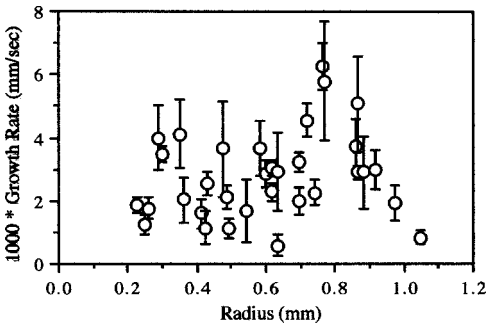

FIG. 9. The measured growth rate as a function of the bubble radius for the bubbles driven at the frequencies between 2.7 and 2.8 kHz are selected. The 95% confidence interval of each measured growth rate is shown by the bars.

The open circles represent the vapor bubbles at 80 °C. The solid circles represent the air bubbles at room temperature. It should be noted that for some vapor bubbles, the volume mode could not be maintained at 0.1 V because it turned into the shape mode. In that case, the amplitude was determined at a reduced input voltage. Then the amplitude was extrapolated to that of 0.1 V assuming the linear correlation. This correction is reflected in the large error bars of some data. Relatively large scattering of the vapor bubble data is partially due to the spatial instability caused by fluid convection around the bubble. As seen in the figure, the amplitude of the air bubbles is relatively constant throughout the measured size range. On the other hand, the amplitude of the vapor bubble shows the peak centered at 0.7 mm, which can be attributed to resonance.

III. DISCUSSION AND SUMMARY

We have developed a two-frequency acoustic apparatus which traps a bubble in a liquid host with a fixed frequency ultrasonic standing wave, and drives the bubble into oscillations with a variable low frequency sound wave. In order to demonstrate its capability, the apparatus is used to verify some theoretically predicted features associated with the resonant oscillations of gas and vapor bubbles. The apparatus, or more precisely the diagnostic technique, will undergo improvements to reduce experimental uncertainties. The dummy cell technique produced a wide range scattering of the acoustic pressures (see Fig. 3). This wide range scattering is partially due to the resonance of the cavity of the speaker, which is not always reproducible. We discarded the data which showed no resonance. For this reason, we presented the acoustic pressure values simply as an estimate of order of magnitude in this paper. An improvement of this technique is necessary for a more reliable estimation. The current imaging technique employs a standard video camera which has limited spatial and temporal (30 frame/s) resolutions. The implementation of a high speed camera or a laser scattering method for sizing the bubbles will allow us to perform better quantitative analysis.

We studied the so-called two–one near resonant coupling between the volume and the $n=3$ shape oscillations of the air bubbles. Feng and Leal[7,8] theoretically studied the two–one resonant coupling using a phase-space analysis technique. They showed that the stability boundary of the volume oscillation formed a wedge centered at the frequency twice of the resonant frequency of the $n=3$ shape oscillation. The present result shows that the stability boundary forms a similar wedge, in agreement with their prediction. At this moment, it is not possible to verify other theoretical predictions such as the threshold and wedge angle which are functions of the bubble size and the mode of the shape oscillation. A more detailed study will be presented elsewhere.[13] The difference between the observed and calculated resonant frequencies is partially due to the frequency shift caused by the drop deformation. One may doubt the present comparison because the ultrasound pressure for trapping the bubble is much higher than the driving pressure and may affect the threshold value. In fact, on some occasions, high frequency capillary waves were visible on the bubble surface even when the low frequency driving pressure was not present. Although these surface disturbances generally tend to induce shape oscillations, it is not obvious how the capillary waves interact with the volume oscillation in the present experiment. Ultimately, this question can be answered if the experiment is performed under negligible ultrasonic pressure, which can be realized in a microgravity environment.

We drove vapor bubbles into volume oscillation to study resonance. First, we measured the growth rate of the oscillating vapor bubbles and found two peaks on the plot of the growth rate versus radius (Fig. 9). These peaks are interpreted as the result of the harmonic (peak at ~0.4 mm) and subharmonic (~0.8 mm) radial responses. However, this re-

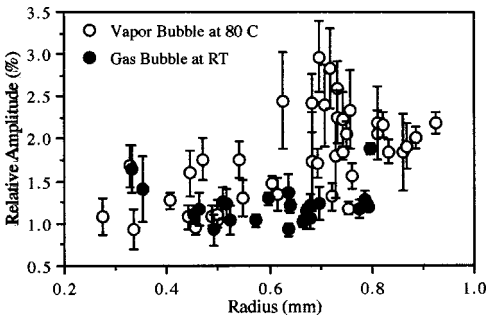

FIG. 10. The relative amplitudes as a function of the bubble radius for air and vapor bubbles, driven at 1682 Hz when the input voltage is maintained at 0.1 V.

sult is based on the assumption of the growth rate being proportional to the oscillation amplitude. In order to avoid ambiguity related to the assumption, we employed the second approach which directly measured the amplitude of the volume oscillation. The result clearly shows a peak in the amplitude, which suggests a resonant response (Fig. 10). In order to exclude the possibility that the peak was caused by the apparatus characteristics, we also measured the oscillation amplitude of air bubbles under the same conditions except that the water was at room temperature. As it is seen in the figure, the air bubbles do not show the peak. Hao and Prosperetti[12] carried out a numerical study of vapor bubble resonance to examine the predictions of earlier analytical studies, such as the existence of two resonant radii. A relevant result of their study for comparison with the present result is the larger resonant radius of vapor bubble at 80 °C. They predict that the resonant radius of vapor bubble at 80 °C is 0.7 mm when the bubble is driven at around 1680 Hz. This prediction agrees with the present result which shows that the amplitude of the volume oscillation has the peak centered at 0.7 mm when the vapor bubbles are driven at 1682 Hz. The resonance is relatively weak (small peak height), which is probably due to the significant presence of the noncondensable gas (air) in the vapor bubbles. The reason why some of the vapor bubbles whose radii are close to 0.7 mm do not resonate is not known, but we suspect the presence of the ultrasonic pressure field which is much stronger than the driving pressure field. The dynamic response of the vapor bubble near the smaller resonant radius (<0.1 mm) could not be tested because the minimum radius of bubbles which could be studied with the present apparatus was approximately 0.2 mm.

ACKNOWLEDGMENTS

We would like to thank Dan Barber for his help to construct the apparatus and Professor Prosperetti for providing his results prior to publication and his comments on an early version of this manuscript. The research described in the paper was carried out at the Jet Propulsion Laboratory, California Institute of Technology, under contract with the National Aeronautics and Space Administration.

[1] R. G. Holt and L. A. Crum, ''Acoustically forced oscillations of air bubbles in water: Experimental results,'' J. Acoust. Soc. Am. **91**, 1924–1932 (1992).
[2] D. F. Gaitan, L. A. Crum, C. C. Church, and R. A. Roy, ''Sonoluminescene and bubble dynamics for a single, stable, cavitation bubble,'' J. Acoust. Soc. Am. **91**, 3166–3183 (1992).
[3] T. J. Asaki, P. L. Marston, and E. H. Trinh, ''Shape oscillations of bubbles in water driven by modulated ultrasonic radiation pressure: Observations and detection with scattered laser light,'' J. Acoust. Soc. Am. **93**, 706–713 (1993).
[4] E. H. Trinh, D. B. Thiessen, and R. G. Holt, ''Driven and freely decaying nonlinear shape oscillations of drops and bubbles immersed in a liquid: experimental results,'' J. Fluid Mech. **364**, 253–272 (1998).
[5] J. E. Ffowcs-Williams and Y. P. Cuo, ''On resonant nonlinear bubble oscillations,'' J. Fluid Mech. **224**, 507–529 (1991).
[6] M. S. Longuet-Higgins, ''Resonance in nonlinear bubble oscillations,'' J. Fluid Mech. **224**, 531–549 (1991).
[7] Z. C. Feng and L. G. Leal, ''On energy transfer in resonant bubble oscillations,'' Phys. Fluids A **5**, 826–836 (1993).
[8] Z. C. Feng and L. G. Leal, ''Bifurcation and chaos in shape and volume oscillations of a periodically driven bubble with two-to-one internal resonance,'' J. Fluid Mech. **266**, 209–242 (1994).
[9] R. D. Finch and E. A. Neppiras, ''Vapor bubble dynamics,'' J. Acoust. Soc. Am. **53**, 1402–1410 (1973).
[10] T. Wang, ''Effects on evaporation and diffusion on an oscillating bubble,'' Phys. Fluids **17**, 1121–1121 (1974).
[11] P. L. Marston, ''Evaporation-condensation resonance frequency of oscillating vapor bubbles,'' J. Acoust. Soc. Am. **66**, 1516–1521 (1979).
[12] Y. Hao and A. Prosperetti, ''The dynamics of vapor bubble in acoustic fields,'' Phys. Fluids **11**, 2008 (1999).
[13] K. Ohsaka and E. H. Trinh, ''Resonant coupling of oscillating gas and vapor bubbles in water: An experimental study,'' Phys. Fluids **12**, 283 (2000).

Line source representation for laser-generated ultrasound in aluminum

Johanna R. Bernstein and James B. Spicer
Department of Materials Science and Engineering, The Johns Hopkins University, Baltimore, Maryland 21218

(Received 12 July 1999; revised 2 November 1999; accepted 3 December 1999)

Modeling the ultrasound generated by a laser source is critical for using noncontact laser-generated ultrasonic systems for the characterization of material properties. In this work, a laser line source was modeled and verified experimentally by measuring the ultrasonic shear wave signal generated in aluminum with a broadband laser generation/electromagnetic acoustic transducer (EMAT)-detection system. Results of calculations and experiments show that the amplitude directivity of a laser line source is identical to that of a point source in the plane perpendicular to the line axis while the temporal dependence differs. © *2000 Acoustical Society of America.* [S0001-4966(00)02403-6]

PACS numbers: 43.35.Zc [HEB]

INTRODUCTION

The generation of ultrasound in metals by pulsed laser irradiation has allowed noncontact methods to be developed for the investigation of material properties.[1,2] An understanding of the generation mechanisms and resulting wave field propagation is critical in interpretation of results, particularly for nondestructive characterization of materials. Ultrasound generated by a pulsed laser source can occur by various mechanisms including the photothermoelastic effect, which does not damage the surface.[3] Generally, a point source has been used for most practical applications.[4,5] In certain cases, it is advantageous to use a laser line source rather than a point; for example, to enhance the wave directivity. In addition, the description of a laser line source is simplified since the system model is two dimensional, thus eliminating some associated mathematical complexity. Examples of applications which fall into this category are the study of ultrasonic diffraction at a crack[6,7] and modeling of seismic wave fields.[8]

Two models for thermoelastically induced stress have been used previously to represent a laser line source. The first model, consisting of a single-sided stress, was used by Hutchins *et al.*[9] to produce longitudinal and shear directivity patterns at the wave front. This model derives from examining the action of a single-sided mechanical radiator on a free surface.[10] Mourad *et al.*[11] modeled a laser line source as a cylindrical shear stress dipole. While directivity patterns were not calculated, waveforms were predicted for two angles, 0° (on epicenter) and 50°, which matched reasonably well with experimentally obtained signals.

In this work, the displacements generated by a laser line source are calculated using the shear-stress dipole model. The in-plane results are assessed by measuring the shear wave amplitude directivity pattern in an aluminum half-cylinder as detected by an electromagnetic acoustic transducer (EMAT). An EMAT detector, which is sensitive to velocity, was chosen over a contact transducer or an optical detector for practical reasons. An EMAT does not require extensive surface preparation for efficient detection as does an interferometer. In addition, an EMAT can be used at relatively high temperatures, without sacrificing sensitivity. Other advantages include flexibility in coil design to allow either narrow-band or broadband detection. In this work, a broadband coil design was used in anticipation of signal frequency analysis. The signal bandwidth was measured to be about 10 MHz.

This work concentrates on in-plane shear waves for two reasons. First, in the thermoelastic regime, a laser source allots more energy to the shear wave than the longitudinal wave.[4] This means that thermoelastically generated shear waves have greater amplitude than longitudinal waves. Second, as will be shown, the shear directivity pattern has a sharp peak in amplitude at a well-defined angle. In contrast, the longitudinal directivity peak is very broad. Thus the sharp peak in shear amplitude and its localization make it more desirable for use in flaw detection systems.

I. THEORY: ULTRASONIC GENERATION WITH A LASER LINE IN METALS

Generation of ultrasound in a bulk metal using a laser line source can be modeled using techniques developed for Lamb's problem for a transient line load on a half-space.[12] Under certain conditions, absorption of a laser pulse at the surface of an opaque sample creates a thermoelastic stress in the material. Representation of the thermoelastic stresses on the surface comes from the geometric considerations of the direction of thermally induced stresses on the surface and the shape of the laser pulse. For this work, a simplified model is used that assumes no thermal conduction or optical penetration below the surface of the sample. For practical applications, these effects are small and apply primarily to the generation of the longitudinal ultrasonic wave.[5,13] Since this work is concerned with the generation of shear waves, these effects can be neglected.

It has been shown that a spherical source includes a volume expansion that is equivalent to three mutually perpendicular dipoles.[14] The volume expansion results from thermal expansion of the material due to the localized heat-

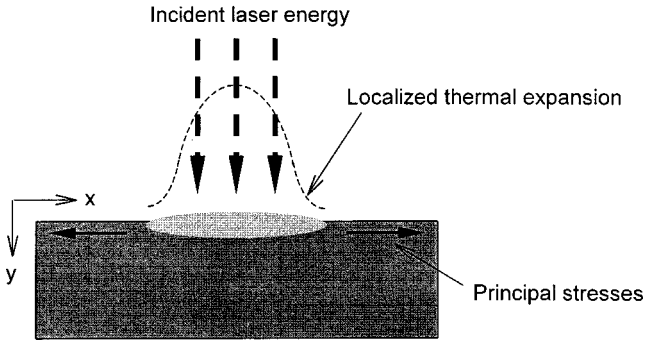

FIG. 1. Absorption of the laser energy from the line source creates a shear stress dipole at the surface.

ing. The effect of the surface is to reduce the volume expansion to two mutually perpendicular dipoles in the plane of the surface. This representation forms the basis for the surface center of expansion model for a laser point source.[4] A line source may be represented as a series of point sources, thus in a similar way, we can define a surface line of expansion represented by two equal and opposite stresses perpendicular to the line direction, as shown in Fig. 1. Summing the dipoles parallel to the line axis gives a net stress equal to zero in that direction. The remaining stresses are mathematically equivalent to the derivative of a delta function in the spatial variable x, $\delta'(x)$, the shear stress dipole perpendicular to the line axis on the surface.

The time dependence of the laser pulse, or pulse shape, can be represented by a range of functions characterized by a rise time and a pulse duration.[15] Typical pulse durations for a Q-switched laser pulse are usually in the range of 10 to 50 ns. Considering the arrival time of an ultrasonic pulse in a large specimen, for example 25-mm thick, the pulse duration is relatively small. On this scale, the pulse shape can be represented instead by a delta function in time, $\delta(t)$. In fact, assuming no heat conduction or dissipation of any kind inside the absorbing material, the resulting ultrasonic source has a temporal dependence that can be modeled as a Heaviside step function in time, $H(t)$.

Since a line source is infinite in a given direction, the overall coordinate system can be reduced to two dimensions. Assuming that the surface of the half-space on which laser excitation occurs is specified by the plane $y=0$, and the surface normal is specified as the y-direction, the long dimension of the line source can be made parallel to the z-direction, as is shown in Fig. 2. The stress boundary conditions on the surface are

$$\tau_y = 0, \tag{1a}$$

$$\tau_{xy} = -A\delta'(x)H(t), \tag{1b}$$

where A is a constant amplitude factor related to the pulse energy and the thermal and elastic properties of the material. The initial conditions are homogeneous.

To calculate displacements associated with the given boundary conditions, it is convenient to use a Helmholtz representation for the displacements,

$$u = \frac{\partial \phi}{\partial x} + \frac{\partial \psi}{\partial y}, \tag{2a}$$

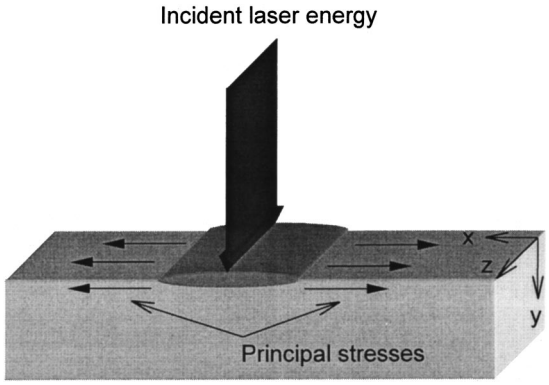

FIG. 2. The long dimension of the laser line is aligned with the z-direction, reducing the mathematical problem to a two-dimensional problem in x and y.

$$v = \frac{\partial \phi}{\partial y} - \frac{\partial \psi}{\partial x}, \tag{2b}$$

where u and v are the displacements in the x and y directions. In (2), ϕ and ψ represent the scalar and vector Helmholtz potentials, respectively. As such, both ϕ and ψ satisfy the two-dimensional wave equations

$$\frac{\partial^2 \phi}{\partial x^2} + \frac{\partial^2 \phi}{\partial y^2} = s_L^2 \ddot{\phi}, \tag{3a}$$

$$\frac{\partial^2 \psi}{\partial x^2} + \frac{\partial^2 \psi}{\partial y^2} = s_T^2 \ddot{\psi}, \tag{3b}$$

where s_L and s_T are the slownesses defined by the reciprocal of the wave speeds, c_L and c_T.

The relevant stresses in terms of the potentials are given by

$$\tau_y = \lambda\left(\frac{\partial^2 \phi}{\partial x^2} + \frac{\partial^2 \phi}{\partial y^2}\right) + 2\mu\left(\frac{\partial^2 \phi}{\partial y^2} - \frac{\partial^2 \psi}{\partial x \partial y}\right), \tag{4a}$$

$$\tau_{xy} = \mu\left(2\frac{\partial^2 \phi}{\partial x \partial y} - \frac{\partial^2 \psi}{\partial x^2} + \frac{\partial^2 \psi}{\partial y^2}\right). \tag{4b}$$

Solutions to Eqs. (3a) and (3b), subject to the conditions given in (1), can be found using Laplace methods. Equations for the initial and boundary conditions are transformed using a single-sided Laplace transformation in t followed by a double-sided Laplace transform in x. This development largely follows that of Achenbach.[12] Only the pertinent equations will be described here.

Using the transforms of Eqs. (1), (3), and (4), solutions for the transformed potentials become

$$\hat{\hat{\phi}} = \frac{A}{\mu p^2}\frac{2\eta^2 \gamma_T}{R(\eta)} e^{-p\gamma_L y}, \tag{5a}$$

$$\hat{\hat{\psi}} = -\frac{A}{\mu p^2}\frac{\eta(s_T^2 - 2\eta^2)}{R(\eta)} e^{-p\gamma_T y}, \tag{5b}$$

where

$$R(\eta) = 4\gamma_L \gamma_T \eta^2 + (s_T^2 - 2\eta^2)^2, \tag{6}$$

which is the Rayleigh function, and

$$\gamma_L=(s_L^2-\eta^2)^{1/2}, \tag{7a}$$

$$\gamma_T=(s_T^2-\eta^2)^{1/2}. \tag{7b}$$

Equation (6) has two roots at $\pm s_R$ at the Rayleigh slowness, or the reciprocal of the Rayleigh wave speed, c_R. The parameters p and η are the transform variables in t and x, respectively.

The wave potentials are now substituted into the transforms of Eqs. (2a) and (b) so that

$$\hat{\bar{u}}=\frac{A}{\mu p}\left[\frac{2\eta^3\gamma_T}{R(\eta)}e^{-p\gamma_L y}+\frac{\eta\gamma_T(s_T^2-2\eta^2)}{R(\eta)}e^{-p\gamma_T y}\right], \tag{8a}$$

$$\hat{\bar{v}}=\frac{A}{\mu p}\left[-\frac{2\eta^2\gamma_L\gamma_T}{R(\eta)}e^{-p\gamma_L y}+\frac{\eta^2(s_T^2-2\eta^2)}{R(\eta)}e^{-p\gamma_T y}\right]. \tag{8b}$$

These equations represent the transforms of the displacements in the x and y directions. To express these solutions in direct space and time, the Cagniard–de Hoop method is used. The inverse double-sided Laplace transform in η is written as follows:

$$\bar{u}=\frac{A}{\mu}\frac{1}{2\pi i}\left[\int_{\eta_L-i\infty}^{\eta_L+i\infty}\left(\frac{2\eta^3\gamma_T}{R(\eta)}\right)e^{-p(\gamma_L y-\eta x)}d\eta+\int_{\eta_T-i\infty}^{\eta_T+i\infty}\left(\frac{\eta\gamma_T(s_T^2-2\eta^2)}{R(\eta)}\right)e^{-p(\eta_T y-\eta x)}d\eta\right], \tag{9a}$$

$$\bar{v}=\frac{A}{\mu}\frac{1}{2\pi i}\left[\int_{\eta_L-i\infty}^{\eta_L+i\infty}\left(\frac{2\eta\gamma_L\gamma_T}{R(\eta)}\right)e^{-p(\gamma_L y-\eta x)}d\eta+\int_{\eta_T-i\infty}^{\eta_T+i\infty}\left(\frac{\eta^2(s_T^2-2\eta^2)}{R(\eta)}\right)e^{-p(\eta_T y-\eta x)}d\eta\right]. \tag{9b}$$

The first term in each integral in Eqs. (9a) and (b) represents the displacements in the x and y directions due to the longitudinal wave. The second term represents the displacements due to the shear wave.

In order to facilitate the second integration in p, the integration path is deformed so that for the first integral in (9a) and (b),

$$\eta_L=-\frac{t}{r}\cos\theta\pm i\sin\theta\left(\frac{t^2}{r^2}-s_L^2\right)^{1/2} \tag{10a}$$

and for the second term,

$$\eta_T=-\frac{t}{r}\cos\theta\pm i\sin\theta\left(\frac{t^2}{r^2}-s_T^2\right)^{1/2}, \tag{10b}$$

where the following substitutions were made for x and y:

$$x=r\cos\theta \quad \text{and} \quad y=r\sin\theta,$$

where θ is the observation angle, and r is the distance from the source to the observation point.

For the integration in the complex η-plane, shown in Fig. 3, the branch points between $\pm s_L$ and $\pm s_T$ must be considered. These singularities lie on the real axis. The integration path for the longitudinal branch remains between $\pm s_L$ on the real axis so that no poles or branch cuts need be considered in the integration as shown in Fig. 3(a). The final inversion for the first integral in Eqs. (9a) and (9b) gives

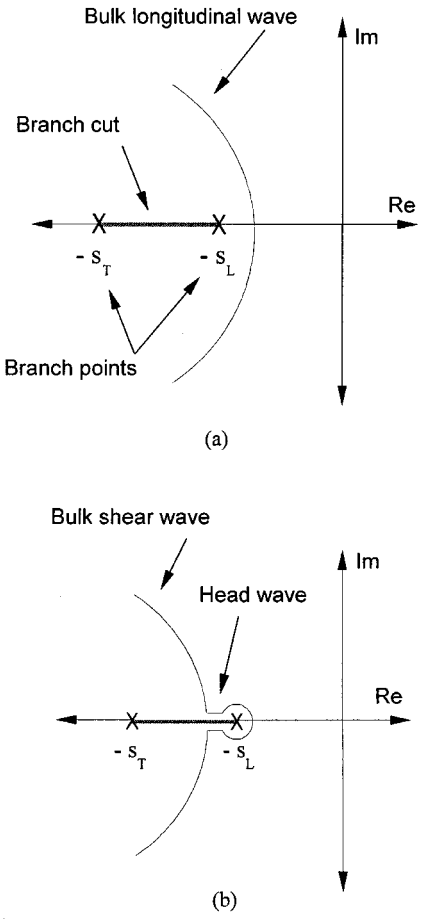

FIG. 3. Cagniard integration paths for (a) the longitudinal branch and (b) the shear branch, including the contribution from the head.

$$u_L=\frac{A}{\mu\pi}\mathrm{Im}\left\{\left[\frac{2\eta^3\gamma_T}{R(\eta)}\right]_{\eta=\eta_{L+}}\frac{\partial\eta_{L+}}{\partial t}\right\}H(t-s_L r), \tag{11a}$$

$$v_L=-\frac{A}{\mu\pi}\mathrm{Im}\left\{\left[\frac{2\eta^2\gamma_L\gamma_T}{R(\eta)}\right]_{\eta=\eta_{T+}}\frac{\partial\eta_{T+}}{\partial t}\right\}H(t-s_T r), \tag{11b}$$

where u_L and v_L represent the displacements in the x and y directions due to the arrival of the longitudinal wave.

For the second integral in Eqs. (9a) and (9b), the point at which the integration path, η_T, crosses the real axis must be examined more closely. If $\cos\theta<s_L/s_T$, then the integration path for the shear branch will not cross the branch cut between $-s_T$ and $-s_L$, thus

$$u_T=-\frac{A}{\mu\pi}\mathrm{Im}\left\{\left[\frac{\eta\gamma_T(s_T^2-2\eta^2)}{R(\eta)}\right]_{\eta=\eta_{T+}}\frac{\partial\eta_{T+}}{\partial t}\right\}\times H(t-s_t r), \tag{12a}$$

$$v_T=-\frac{A}{\mu\pi}\mathrm{Im}\left\{\left[\frac{\eta^2(s_T^2-2\eta^2)}{R(\eta)}\right]_{\eta=\eta_{T+}}\frac{\partial\eta_{T+}}{\partial t}\right\}\times H(t-s_t r). \tag{12b}$$

If, however, $\cos\theta > s_L/s_T$, then the path must be integrated around the branch cut between $-s_T\cos\theta$ and $-s_L$ which will add another term to the shear branch. This path, shown in Fig. 3(b), which represents the head wave, is integrated for $t_{TL} < t < s_T r$, where t_{TL} is defined by

$$t_{TL} = s_L\cos\theta + r\sin\theta(s_T^2 - s_L^2)^{1/2}. \tag{13}$$

Using the same methods, the displacement equations for the head wave are given by

$$u_{TL} = \frac{A}{\mu\pi}\,\mathrm{Im}\left\{\left[\frac{\eta\gamma_T(s_T^2 - 2\eta^2)}{R(\eta)}\right]_{\eta=\eta_{TL}}\frac{\partial\eta_{TL}}{\partial t}\right\} \times[H(t-t_{TL}) - H(t-s_T r)], \tag{14a}$$

$$v_{TL} = \frac{A}{\mu\pi}\,\mathrm{Im}\left\{\left[\frac{\eta^2(s_T^2 - 2\eta^2)}{R(\eta)}\right]_{\eta=\eta_{TL}}\frac{\partial\eta_{TL}}{\partial t}\right\} \times[H(t-t_{TL}) - H(t-s_T r)]. \tag{14b}$$

Note that the integration path in the complex plane will never cross the real axis at $\eta < -s_T$ so that the pole at $-s_R$ need not be considered since $s_R < s_T$. This means that the contribution from the Rayleigh wave will not be included in the solution and must be calculated separately. Thus the complete solutions for the displacements, not including the contributions from the Rayleigh wave, can be expressed as

$$u = u_L + u_{TL} + u_T, \tag{15a}$$

$$v = v_L + v_{TL} + v_T, \tag{15b}$$

where u_L, v_L, u_T, and v_T are given by Eqs. (11) and (12).

Using the method of wave front expansions,[4] directivity patterns for the shear and longitudinal waves can be shown which vary in magnitude according to the observation angle. These expressions are found by allowing $t \to s_L r+$ for u_L and v_L, and $t \to s_T r+$ for u_T and v_T. At $t = s_L r$ and $t = s_T r$, the wave front amplitude appears as a singularity. However, allowing t to approach $s_L r$ and $s_T r$ gives a measure of the wave front amplitudes. Substitution for t in these expressions gives the following coefficients for the directivity patterns. For the longitudinal wave,

$$A_L \propto \frac{s_T^3\cos\theta\sin 2\theta(s_T^2 - s_L^2\cos^2\theta)^{1/2}}{4s_L^3\cos^2\theta\sin\theta(s_T^2 - s_L^2\cos^2\theta)^{1/2} + (s_T^2 - 2s_L^2\cos^2\theta)^2}, \tag{16}$$

and for the shear wave,

$$A_T \propto \frac{-s_T^4\cos 2\theta\sin 2\theta}{s_T^4(1-2\cos^2\theta)^2 + 4s_T^3\cos^2\theta\sin\theta(s_L^2 - s_T^2\cos^2\theta)^{1/2}}, \tag{17}$$

using

$$A_L = u_L\cos\theta + v_L\sin\theta,$$

$$A_T = -u_T\sin\theta + v_T\cos\theta,$$

which come from the relationship between the particle motion and the propagation direction of the wave mode. The amplitude directivity patterns are shown in Fig. 4. Note that if the line source is described as a series of point sources, there will be a small epicentral displacement resulting from the angular directivity of each summed point. However, these displacements will arrive at a later time and are accounted for in the temporal dependence of the wave front. Thus they are not a factor in the amplitude directivities at the wave front.

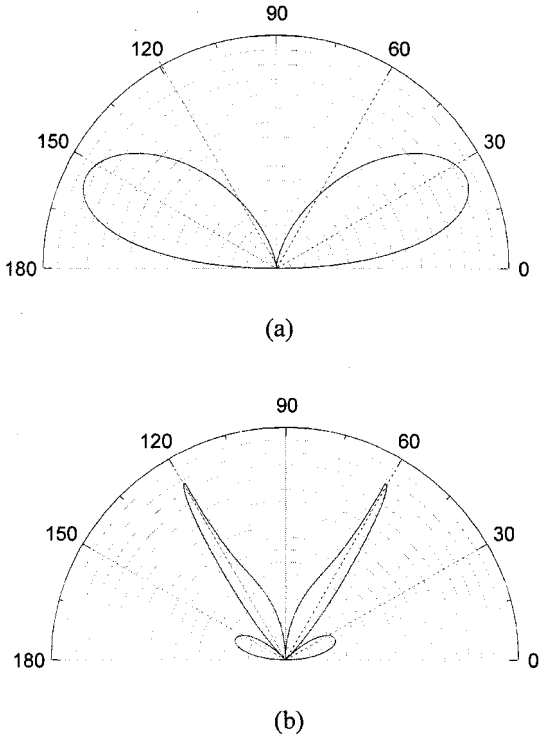

FIG. 4. (a) Longitudinal and (b) shear directivity patterns for a laser line source.

Comparison of Eqs. (16) and (17) with those presented by Rose[4] show that both the longitudinal and the shear directivities for a line source are exactly the same as those for a point source. The only difference between Eqs. (16) and (17) and the results given by Rose is in the definition of the propagation angle. Rose defines the angle from the surface normal, rather than from the surface. Comparing (16) and (17) to other line source models, Scruby and Drain[2] state that a single-frequency aperture function can be used to multiply the point source models to produce a line source directivity. They acknowledge that the longitudinal line source directivity should resemble that for a point source as shown by Hutchins *et al.*[9] However, unlike a point source, the shear directivity given for a line source by Hutchins *et al.* contains a significant amplitude in the epicentral direction, a result of using a single-sided shear stress model at the surface.

II. EXPERIMENTS

A pulsed laser line source was used to generate an ultrasonic wave field in an aluminum half-cylinder ($r = 40$ mm) in order to validate the results of the modeling. The ultrasonic energy was detected around the circumference of the half-cylinder using a broadband EMAT sensitive to shear waves. The experimental setup is illustrated in Fig. 5. The laser used to generate the ultrasound was a *Q*-switched, pulsed Nd:YAG (1.064 μm). The laser beam was expanded with a planoconcave spherical lens followed by a double

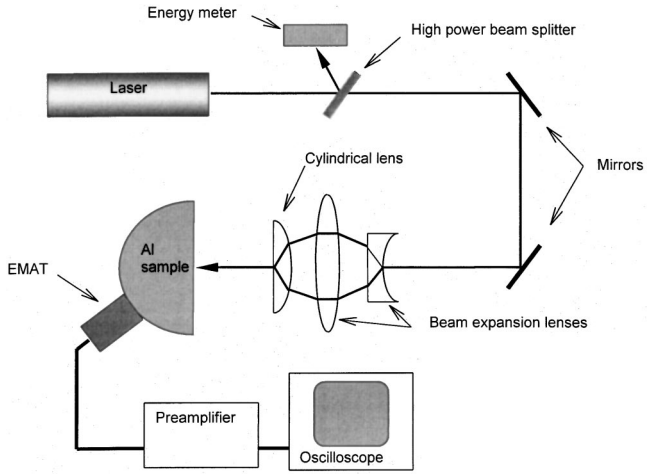

FIG. 5. Experimental setup for measuring line source directivity with an EMAT receiver.

convex lens, and focused to a line with a cylindrical lens onto the center of the flat face of the aluminum half-cylinder. The laser line was approximately 80 mm long, and 250 μm wide. Pulse duration was approximately 20 ns. The energy incident on the surface of the aluminum was approximately 1 mJ or less. The EMAT footprint measured 25.4 by 3 mm with the long dimension of the EMAT oriented along the long dimension of the laser line. The differential signal received from the EMAT was sent through a series of preamplifiers before being recorded by a digital oscilloscope. The signals were transferred using LabView software to a computer for storage and analysis. Time trace signals were recorded from 0 to 90° along the circumference of the cylinder at 0.5° intervals.

III. RESULTS AND DISCUSSION

Several important features appear in both the calculated and measured shear directivity patterns, shown in Fig. 6. The first feature is the peak in amplitude at 30°. The second is the minimal energy detected at 0°. In the calculated pattern, Fig. 6(a), no energy is predicted to propagate on the epicenter and very little is measured as shown in Fig. 6(b). This is convincing evidence that a laser line can be modeled as a shear stress dipole. The model used by Hutchins *et al.*,[9] shown in Fig. 6(c), predicts that a significant amount of laser energy propagates in the epicentral direction. However, as shown by the measured results, a single-sided shear stress model does not correctly predict the directivity. In fact, Jilek and Ceverny[8] calculated the directivity patterns for both radiating and single-sided horizontal point forces. The directivity patterns for the single-sided horizontal point force are identical to those for the line source directivities presented by Hutchins *et al.*[9]

Note, however, that in the measured pattern, Fig. 6(b), a significant amount of laser energy is measured at angles greater than 30°. It would appear that the amplitude directivity at 30° is not as sharp when compared to the calculated pattern. This apparent widening may be explained by two related factors, the footprint size of the coil in the EMAT detector and the subsequent detection of the head wave. At

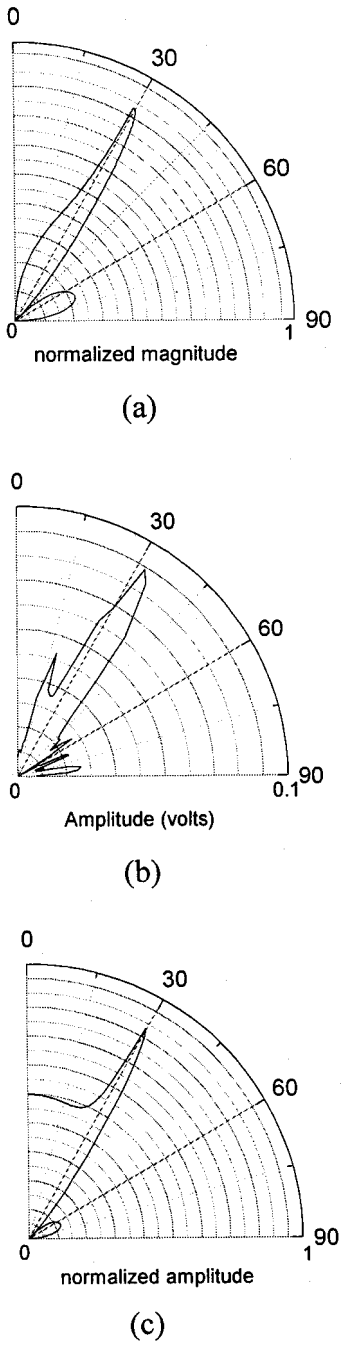

FIG. 6. (a) Calculated shear directivity pattern. (b) Measured shear directivity pattern. (c) Shear directivity as calculated by Hutchins *et al.* (Ref. 9).

the wave front, the contribution of the head wave should not be significant. In reality, at the critical angle, $\theta_c = \cos^{-1}(c_L/c_T)$, and at angles near the critical angle, the head wave is difficult to separate from the shear wave in time. Several features of the EMAT allow the head wave to be detected. The first is the finite width of the sensing coil. The coil itself spans approximately 2°. The error is further compounded by the ability of an EMAT to tolerate a small liftoff from the surface, i.e., the face of the EMAT does not actually need to be in contact with the surface to sense the ultrasonic signal. Because the surface of the EMAT is flat relative to the curve of the half-cylinder, the EMAT can detect energy on either side of the detector contact point. Near the critical

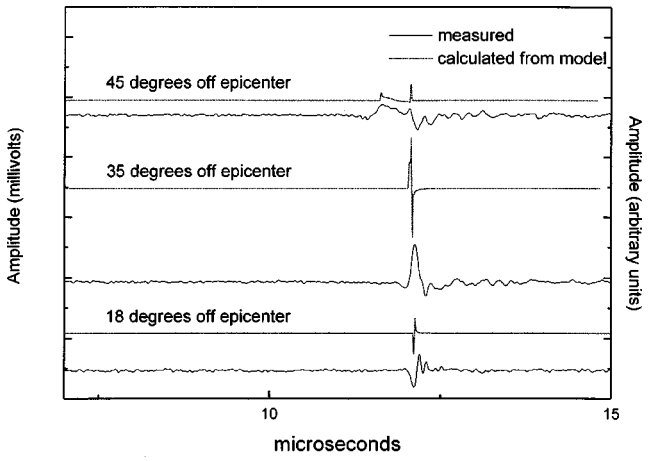

FIG. 7. Calculated shear waveforms, including the head wave arrival. Note that angles are given in degrees from the epicentral direction.

angle, the head wave follows just behind the shear wave. Thus at certain angles, the EMAT is unable to separate the shear wave arrival from the head wave. Figure 7 shows a comparison of calculated and measured waveforms that illustrate the effect of the head wave at angles close to θ_c for aluminum ($\theta_c = 30°$). The calculated signal at 35° clearly shows the head wave arrival just ahead of the bulk shear wave arrival. The signal content of the measured waveforms is lower than the calculated waveforms because of the limit in bandwidth sensitivity of the EMAT detector. The difficulty in separating the head wave arrival from the bulk shear wave arrival, combined with the limited bandwidth sensitivity of the EMAT, means that in practicality, the head wave may be confused for the bulk shear wave as seen in the measured waveform at 35°.

Consideration of the size of the detector and the role it plays in the shape of the received signal may explain the experimental results reported by Hutchins *et al.* If the footprint of the receiver spans a degree or more, the measured amplitude can only be considered an average over the footprint area. It is likely that the earlier reported results coincidentally matched the calculated directivity since the detector behaved as an area receiver rather than as a point receiver. Thus it is critical to determine the necessary resolution of the measurement in relation to the size of the detector. Footprint size must be considered carefully.

IV. CONCLUSIONS

As shown by the calculations in Sec. I and confirmed by the experimental results, the shear directivity of a line source can be modeled by a shear stress dipole. In addition, in two dimensions, the amplitude directivity pattern produced by a laser line source is identical to that produced by a point source. These results were validated by shear wave experiments in an aluminum half-cylinder. However, the temporal dependence of the wave front arrival of the line source differs from that of the point source. For a point source, as shown by Rose,[4] the shape of the wave front can be described by a delta function in time. Using the same wave front expansion method, the shape of the wave front for a line source is represented by a reciprocal square root singularity. Thus the amplitude directivities for a point source and a line source are the same; however, the shapes of the respective waveforms in time will be different.

ACKNOWLEDGMENTS

Funding for this research was provided by McDermott International, Inc. through the Center for Nondestructive Evaluation, The Johns Hopkins University.

[1] A. M. Aindow, R. J. Dewhurst, D. A. Hutchins, and S. B. Palmer, ''Laser-generated ultrasonic pulses at free metal surfaces,'' J. Acoust. Soc. Am. **69**(2), 449 (1981).
[2] C. B. Scruby and L. E. Drain, *Laser Ultrasonics: Techniques and Applications* (Adam Hilger, Bristol, 1990).
[3] R. M. White, ''Generation of elastic waves by transient surface heating,'' J. Appl. Phys. **34**(12), 3559 (1963).
[4] L. R. F. Rose, ''Point-source representation for laser-generated ultrasound,'' J. Acoust. Soc. Am. **75**(3), 723 (1984).
[5] P. A. Doyle, ''On epicentral waveforms for laser-generated ultrasound,'' J. Phys. D **19**, 1613 (1986).
[6] J. R. Bernstein, ''Ultrasonic crack diffraction in metals: Investigations using laser generated ultrasonic shear waves and broadband EMAT detection,'' Ph.D. dissertation, The Johns Hopkins University, 1999.
[7] J. D. Achenbach, A. K. Gautesen, and H. McMaken, *Ray Methods for Waves in Elastic Solids* (Pitman, London, 1982).
[8] P. Jilek and V. Cerveny, ''Radiation patterns of point sources situated close to structural interfaces and to the earth's surface,'' PAGEOPH **148**(1/2), 175 (1996).
[9] D. A. Hutchins, R. J. Dewhurst, and S. B. Palmer, ''Directivity patterns of laser-generated ultrasound in aluminum,'' J. Acoust. Soc. Am. **70**(5), 1362 (1981).
[10] G. F. Miller and H. Pursey, ''The field and radiation impedance of mechanical radiators on the free surface of a semi-infinite isotropic solid,'' Proc. R. Soc. London, Ser. A **223**, 521 (1954).
[11] A. Mourad, B. Castagnede, and E. Mottay, ''Green functions for cylindrical elastic waves in aluminum: Comparison between theory and experiments,'' J. Appl. Mech. **61**, 219 (1994).
[12] J. D. Achenbach, *Wave Propagation in Elastic Solids* (North-Holland, New York, 1973).
[13] K. Telschow and R. Conant, ''Optical and thermal parameter effects on laser generated ultrasound,'' J. Acoust. Soc. Am. **88**, 1494 (1990).
[14] K. Aki and P. G. Richards, *Quantitative Seismology* (W. H. Freeman, San Francisco, 1980).
[15] J. F. Ready, *Effects of High-Power Laser Radiation* (Academic, New York, 1971).

A study on ultrasonic solid horns for flexural mode

Guangping Zhou[a] and Mingxuan Li
Institute of Acoustics, Chinese Academy of Sciences, Beijing 100080, People's Republic of China

(Received 24 September 1998; accepted for publication 1 July 1999)

The transfer matrix method is introduced into the analysis of ultrasonic flexural solid horns. The frequency and magnification equations of a horn are derived by using the transfer matrix method. Analyzed are the characteristics of three types of circular cross-section horns: exponent, cone, and catenary. The results are partly verified experimentally. © *2000 Acoustical Society of America.* [S0001-4966(99)04210-1]

PACS numbers: 43.38.Ja, 43.38.Ar [SLE]

INTRODUCTION

High power ultrasonic techniques, such as ultrasonic cleaning, ultrasonic welding, ultrasonic cutting, and ultrasonic motors, are all based on the ultrasonic vibration system—the key part of any ultrasonic equipment. Ultrasonic solid horns, also called ultrasonic concentrators, are very important in the vibration system of high intensity ultrasonic equipment. The horns act either as amplifiers, which magnify vibration displacement or vibration velocity, or as concentrators, which concentrate the ultrasonic energy onto a small area. The ultrasonic longitudinal vibration horns have been studied intensively and extensively. The results also apply to ultrasonic torsional horns as the modeling equation of torsional vibration of horns is of the same form as that of the longitudinal vibration of horns. However, there are very few studies on ultrasonic flexural vibration of horns.

In the range of ultrasonic frequency, the effects of rotary inertia and shear deformation become very evident; the errors are unacceptably large according to Bernoulli–Euler theory. Therefore Timoshenko theory must be used.[1] Based on Timoshenko theory, Yuji Watanabe and Eiji Mori[2] analyzed the step-type ultrasonic flexural horn. But no study was made on other types of ultrasonic flexural horns. The main reason is that the analytical solution is difficult to find for a flexural vibration rod with arbitrary vari-cross-section. Thus numerical and approximate methods, such as the finite element method and Rayleigh–Ritz method, are used for analyzing nonuniform beams in engineering mechanics.

By dividing a nonuniform beam into a number of uniform element beams, Williams and Banerjee[3] analyzed nonuniform beams for natural frequency. In light of this idea, the transfer matrix method is introduced into the vibration analysis of ultrasonic flexural solid horn. Further, the characteristics of several types such as exponential, conic, and catenary of circular-cross-section horns, are analyzed. This study presents the theoretical fundamental for the application of ultrasonic flexural solid horns.

I. METHOD

Consider a beam of length l, having a uniform cross-section. Let the X coordinate measure positions along the beam, and the Y coordinate the transverse displacements of the beam from its normal configuration. According to the Timoshenko theory, the transverse displacement V_b due to bending and the transverse displacement V_s due to shear of a uniform beam can be expressed as[4,1]

$$V_b = C_1 chn_1 X + D_1 shn_1 X + C_2 \cos n_2 X + D_2 \sin n_2 X, \quad (1)$$

$$V_s = \Phi_1 [C_1 chn_1 X + D_1 shn_1 X] + \Phi_2 [C_2 \cos n_2 X + D_2 \sin n_2 X], \quad (2)$$

where

$$\Phi_1 = \frac{\frac{\omega^2}{Co^2} + n_1^2}{C_s^2 C}, \quad \Phi_2 = \frac{-\frac{\omega^2}{Co^2} + n_2^2}{C_s^2 C}.$$

$$n_1 = \omega M \sqrt{-1 + N\sqrt{1 + a^2/\omega^2}},$$

$$n_2 = \omega M \sqrt{1 + N\sqrt{1 + a^2/\omega^2}},$$

$$C = \frac{A_0 \rho}{EI}, \quad a = 2\sqrt{C} \Big/ \left(\frac{1}{C_S^2} - \frac{1}{C_0^2}\right),$$

$$M = \frac{1}{\sqrt{2}} \sqrt{\frac{1}{C_s^2} + \frac{1}{Co^2}},$$

$$N = \frac{C_0^2 - C_s^2}{C_0^2 + C_s^2}, \quad Co = \sqrt{\frac{E}{\rho}}, \quad C_S = \sqrt{\frac{K'G}{\rho}},$$

and E is the Young's modulus, G the shear modulus, ρ the mass density, I the moment of inertia of the cross-section, A_0 the cross-sectional area, and K' the shear coefficients.

The effect of distorting the beam is to produce bending moments and shear forces in the beam. Let Y, Ψ, M, and F denote the total transverse displacement, the rotational angle, the bending moment, and the shear force, respectively (Fig. 1). Because $Y = V_b + V_s$, $\Psi = \partial V_b / \partial X$, $M = EI(\partial^2 V_b / \partial X^2)$, and $F = -K' A_0 G(\partial V_s / \partial X)$, from Eqs. (1) and (2), the vibration parameters of the beam can be written in the following form:

$$Y = (1 + \Phi_1) C_1 chn_1 X + (1 + \Phi_1) D_1 shn_1 X + (1 + \Phi_2) C_2 \cos n_2 X + (1 + \phi_2) D_2 \sin n_2 X, \quad (3)$$

[a]Corresponding address: Dept. of Research and Development, Shenzhen Polytechnic, Shenzen 518055, Guangdong Province, P.R. China, electronic mail: zhougp@szpt.edu.cn

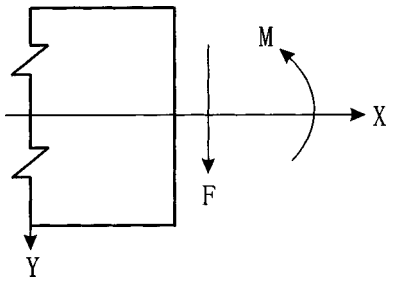

FIG. 1. Bending moment and shear force in a beam.

$$\Psi = C_1 n_1 shn_1 X + D_1 n_1 chn_1 X - C_2 n_2 \sin n_2 X + D_2 n_2 \cos n_2 X, \tag{4}$$

$$M = EI[C_1 n_1^2 chn_1 X + D_1 n_1^2 shn_1 X - C_2 n_2^2 \cos n_2 X - D_2 n_2^2 \sin n_2 X], \tag{5}$$

$$F = -K' A_0 G[\Phi_1 (C_1 n_1 shn_1 X + D_1 n_1 chn_1 X) + \Phi_2 (-C_2 n_2 \sin n_2 X + D_2 n_2 \cos n_2 X)]. \tag{6}$$

Let Y_1, Ψ_1, M_1, F_1 and Y_2, Ψ_2, M_2, F_2 denote, respectively, the vibration parameters at the left end and the right end of the beam, from Eqs. (3) to (6), the following equations hold:

$$\begin{aligned} Y_1 &= a_{11} Y_2 + a_{12} \Psi_2 + a_{13} M_2 + a_{14} F_2, \\ \Psi_1 &= a_{21} Y_2 + a_{22} \Psi_2 + a_{23} M_2 + a_{24} F_2, \\ M_1 &= a_{31} Y_2 + a_{32} \Psi_2 + a_{33} M_2 + a_{34} F_2, \\ F_1 &= a_{41} Y_2 + a_{42} \Psi_2 + a_{43} M_2 + a_{44} F_2, \end{aligned} \tag{7}$$

where

$$a_{11} = \frac{(1+\Phi_1) n_2^2 chn_1 1 + (1+\Phi_2) n_1^2 \cos n_2 l}{n_1^2 (1+\Phi_2) + n_2^2 (1+\Phi_1)},$$

$$a_{12} = \frac{n_1 \Phi_1 (1+\Phi_2) \sin n_2 l - n_2 \Phi_2 (1+\Phi_1) shn_1 l}{n_1 n_2 (\Phi_2 - \Phi_1)},$$

$$a_{13} = \frac{(1+\Phi_1)(1+\Phi_2)(chn_1 l - \cos n_2 l)}{EI[n_1^2 (1+\Phi_2) + n_2^2 (1+\Phi_1)]},$$

$$a_{14} = \frac{(1+\Phi_2) n_1 \sin n_2 l + (1+\Phi_1) n_2 shn_1 l}{K' A_0 G n_1 n_2 (\Phi_2 - \Phi_1)},$$

$$a_{21} = \frac{n_2 n_1^2 \sin n_2 l - n_1 n_2^2 shn_1 l}{n_1^2 (1+\Phi_2) + n_2^2 (1+\Phi_1)},$$

$$a_{22} = \frac{\Phi_2 chn_1 l - \Phi_1 \cos n_2 l}{\Phi_2 - \Phi_1},$$

$$a_{23} = \frac{-n_1 (1+\Phi_2) shn_1 l - n_2 (1+\Phi_1) \sin n_2 l}{EI[n_1^2 (1+\Phi_2) + n_2^2 (1+\Phi_1)]},$$

$$a_{24} = \frac{chn_1 l - \cos n_2 l}{K' A_0 G (\Phi_2 - \Phi_1)},$$

$$a_{31} = \frac{EI n_1^2 n_2^2 (chn_1 l - \cos n_2 l)}{n_1^2 (1+\Phi_2) + n_2^2 (1+\Phi_1)}, \tag{8}$$

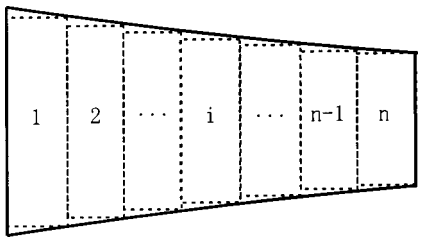

FIG. 2. Ultrasonic solid horn.

$$a_{32} = \frac{-EI(\Phi_2 n_1 shn_1 l + \Phi_1 n_2 \sin n_2 l)}{\Phi_2 - \Phi_1},$$

$$a_{33} = \frac{n_1^2 (1+\Phi_2) chn_1 l + n_2^2 (1+\Phi_1) \cos n_2 l}{n_1^2 (1+\Phi_2) + n_2^2 (1+\Phi_1)},$$

$$a_{34} = \frac{-EI(n_1 shn_1 l + n_2 \sin n_2 l)}{K' A_0 G (\Phi_2 - \Phi_1)},$$

$$a_{41} = \frac{K' A_0 G[n_2^2 n_1 \Phi_1 shn_1 l - n_1^2 n_2 \Phi_2 \sin n_2 l]}{n_1^2 (1+\Phi_2) + n_2^2 (1+\Phi_1)},$$

$$a_{42} = \frac{K' A_0 G(\cos n_2 l - chn_1 l) \Phi_1 \Phi_2}{\Phi_2 - \Phi_1},$$

$$a_{43} = \frac{K' A_0 G[n_1 \Phi_1 (1+\Phi_2) shn_1 l + n_2 \Phi_2 (1+\Phi_1) \sin n_2 l]}{EI[n_1^2 (1+\Phi_2) + n_2^2 (1+\Phi_1)]},$$

$$a_{44} = \frac{\Phi_2 \cos n_2 l + \Phi_1 chn_1 l}{\Phi_2 - \Phi_1}.$$

The matrix form of Eq. (7) is

$$\begin{bmatrix} Y_1 \\ \Psi_1 \\ M_1 \\ F_1 \end{bmatrix} = \begin{bmatrix} a_{11} & a_{12} & a_{13} & a_{14} \\ a_{21} & a_{22} & a_{23} & a_{24} \\ a_{31} & a_{32} & a_{33} & a_{34} \\ a_{41} & a_{42} & a_{43} & a_{44} \end{bmatrix} \begin{bmatrix} Y_2 \\ \Psi_2 \\ M_2 \\ F_2 \end{bmatrix}, \tag{9}$$

where $[a_{ij}]$ is a 4×4 matrix which is dependent on the material, the sizes, and the frequency of the beam.

A ultrasonic solid horn shown in Fig. 2 can be divided into n uniform element beams.[3] Let Y_i, Ψ_i, M_i, F_i and Y_{i+1}, Ψ_{i+1}, M_{i+1}, F_{i+1} denote, respectively, the vibration parameters at the left end and the right end of the ith element beam. Then the vibration parameters satisfy the following equation:

$$\begin{bmatrix} Y_i \\ \Psi_i \\ M_i \\ F_i \end{bmatrix} = \begin{bmatrix} a_{11}^i & a_{12}^i & a_{13}^i & a_{14}^i \\ a_{21}^i & a_{22}^i & a_{23}^i & a_{24}^i \\ a_{31}^i & a_{32}^i & a_{33}^i & a_{34}^i \\ a_{41}^i & a_{42}^i & a_{43}^i & a_{44}^i \end{bmatrix} \begin{bmatrix} Y_{i+1} \\ \Psi_{i+1} \\ M_{i+1} \\ F_{i+1} \end{bmatrix}, \tag{10}$$

where $[a_{ij}^i]$ is the matrix of ith element beam. Because of the continuity of displacement and rotational angle and the equilibrium of moment and shear force at the conjunction position of any two adjacent element beams, it leads to

$$\begin{bmatrix} Y_1 \\ \Psi_1 \\ M_1 \\ F_1 \end{bmatrix} = \begin{bmatrix} A_{11} & A_{12} & A_{13} & A_{14} \\ A_{21} & A_{22} & A_{23} & A_{24} \\ A_{31} & A_{32} & A_{33} & A_{34} \\ A_{41} & A_{42} & A_{43} & A_{44} \end{bmatrix} \begin{bmatrix} Y_{n+1} \\ \Psi_{n+1} \\ M_{n+1} \\ F_{n+1} \end{bmatrix}, \tag{11}$$

where $[A_{ij}]$ is the gross matrix of the horn. It equals the product of the n element matrices, i.e., $[A]=[a^1]\times[a^2]\cdots[a^n]$.

For a free–free ultrasonic solid horn, substituting $M_{n+1}=F_{n+1}=M_1=F_1=0$ into Eq. (11) leads to

$$\begin{vmatrix} A_{31} & A_{32} \\ A_{41} & A_{42} \end{vmatrix} = A_{31}A_{42}-A_{41}A_{32}=0, \tag{12}$$

which is the frequency equation of a ultrasonic flexural solid horn.

The magnification of the horn is defined as

$$M_p=\left|\frac{Y_{n+1}}{Y_1}\right|.$$

From Eqs. (11) and (12), the magnification M_p can be written as

$$M_p=\left|\frac{A_{32}}{A_{11}A_{32}-A_{12}A_{31}}\right|. \tag{13}$$

Based on the above method, the following results on vibration analysis concerning the exponential, conic, and catenary flexural solid horns are gained.

II. VIBRATION ANALYSIS ON FLEXURAL SOLID HORNS

Accompanying the application of the ultrasonic longitudinal vibration system, many types of solid horns have been exploited to meet different engineering demands. Among them, the simplest and most conventional ones are the exponential, conic, catenary, and step types. The step-type solid horn was treated in Ref. 2. The aim of this paper is to analyze the resonance characteristics and magnification of the other three types of flexural solid horns, i.e., exponential, conic, and catenary types.

In this study, it is assumed that the ratio of the maximum diameter to the length of the horn is less than or equal to 1 for the first and the second mode, and that the ratio is less than or equal to 0.5 for the third and the fourth mode. Such a limitation is to assure the validity of Timoshenko theory. Fortunately, most engineering applications conform to this limitation.

The numerical computation method is employed and 45# carbon steel is taken for samples in the study. The materials parameters are as follows: $E=210\,\text{GPa}$, $G=80\,\text{GPa}$, $\rho=7.8\times10^3\,\text{kg/m}^3$.

A. Resonant characteristics of the horns

Based on Eq. (12), the relations between the resonant frequency and the size parameters of the horns are analyzed. The size parameters of a horn are the diameter of the large end D_1, the diameter of the small end D_2, and the length L.

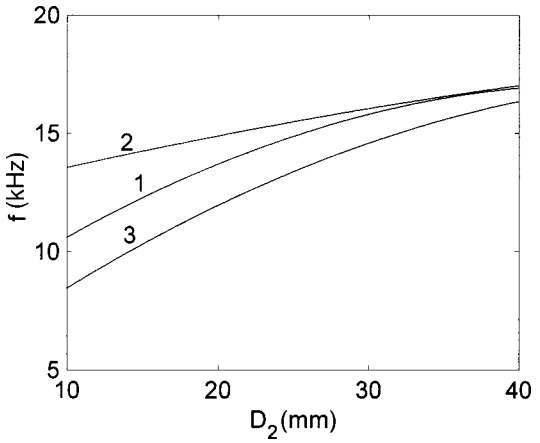

FIG. 3. Frequency vs D_2.

Let the coordinates of the large end and the small end be $X=0$ and $X=L$, respectively. Thus the diameters of the cross-section for the three types of horns can be expressed as

exponential $D=D_1e^{-\beta x}$,

conic $D=D_1(1-\alpha X)$,

catenary $D=D_2chr(L-X)$,

where $\beta=\ln(D_1/D_2)/L$, $\alpha=(D_1-D_2)/(D_1L)$, $r=\text{arcch}(D_1/D_2)/L$. When the horn is divided into n element beams with uniform cross-section as in Fig. 2, accordingly, the diameter of ith element beam is

exponential $D_i=D_1e^{-(\beta L/n)i}$,

conic $D_i=D_1\left(1-\frac{\alpha L}{n}i\right)$,

catenary $D_i=D_2chrL\left(1-\frac{1}{n}i\right)$.

In the computation, the length of each element beam is taken to be 0.5 mm.

For all the three types of horns, the computation shows that the resonance frequency for a given L increases when D_1 or D_2 increases, and the resonance frequency for given D_1 and D_2 decreases when L increases. Figures 3 and 4 are two examples of computation results. Figure 3 shows the

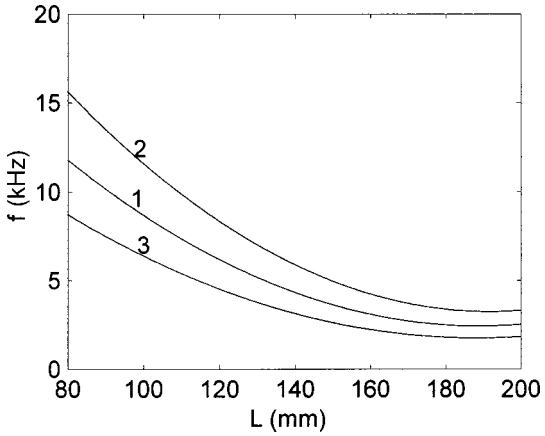

FIG. 4. Frequency vs L.

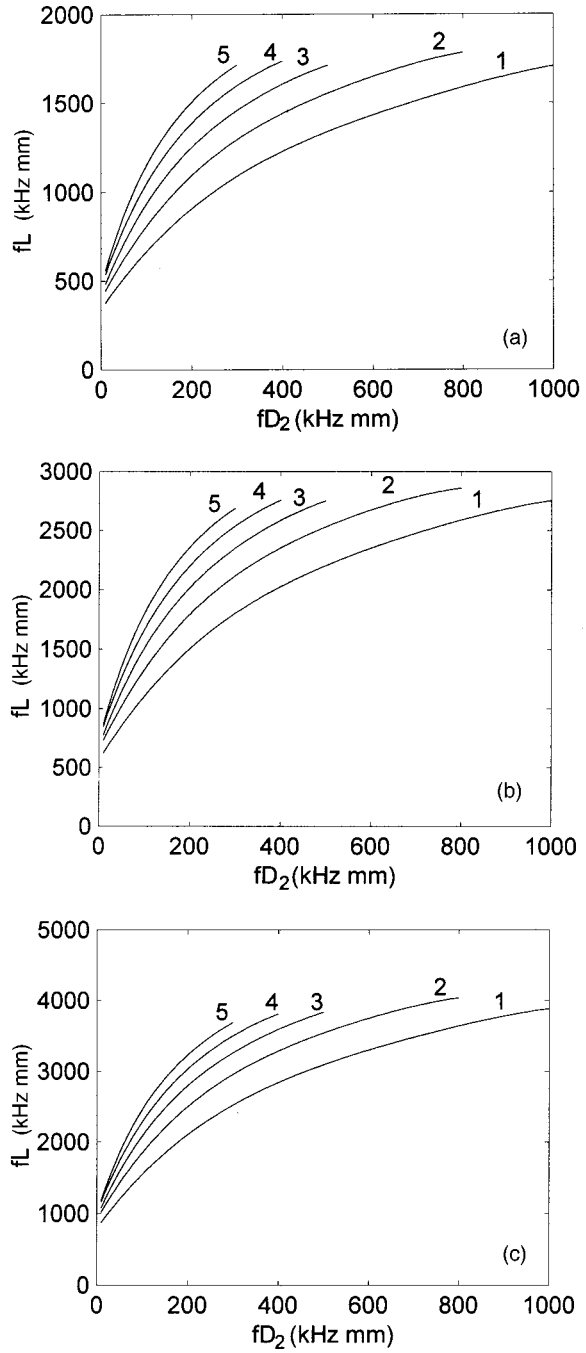

FIG. 5. Resonance curves of conic-type horn. (a) First mode, (b) second mode, and (c) third mode.

relation between the frequency of the second mode and D_2 when $L=150$ mm and $D_1=50$ mm. ''1,'' ''2,'' and ''3'' denote the exponential, the conic, and the catenary type, respectively. Figure 4 shows the relation between the frequency of the first mode and the length of the horn when

TABLE I. The magnification of an exponential horn at different modes.

Mode No.	f (kHz)	M_p
1	7.426	3.38
2	17.21	3.59
3	28.40	4.10

TABLE II. The relation between magnification and end diameters for exponent horns. (The first mode, 15 kHz.)

D_1/D_2	D_1 (mm)	D_2 (mm)	M_p
2	50	25	2.69
2	40	20	2.61
2	30	15	2.54

$D_1=40$ mm and $D_2=20$ mm; ''1,'' ''2,'' and ''3'' have the same meaning as in Fig. 3.

Further study on the relation between the resonance frequency f and the size parameters D_1, D_2 and L of the horn shows that for a certain type of horn if the ratio of D_1 to D_2 is given, the relation between fL (the product of f and L) and fD_2 (the product of f and D_2) is independent of the values of D_1 and D_2. Naturally, for different values of D_1/D_2, there exist different fL vs fD_2 curves. These curves are called resonance curves of the horn. Figure 5 shows the resonance curves of a conic-type solid horn for D_1/D_2 equals 1, 2, 3, 4, and 5, respectively. (a), (b), and (c) represent the first, the second, and the third modes, respectively. There exist similar resonance curves for the exponential- and the catenary-type horns, which are not plotted here for simplicity. These curves can be used in designing of horns.

B. The magnification of horns

The magnification of the three types of flexural solid horns is studied by using Eq. (13).

It is found that the magnification of a horn operating at a higher mode is greater than that at lower mode for certain size parameters. Table I is an example of computation results for an exponent-type horn.

For any type of horn, if the horn is kept operating at a fixed frequency of a given mode and the value of D_1/D_2 is constant, the magnification will vary with the values of D_1 and D_2. Table II shows an example for an exponent-type horn.

In addition, the relation between magnification M_p and N (the ratio of D_1 to D_2) is investigated. In computing, the large end diameter of the horns D_1 is given. Figure 6 is an example for an exponent-type horn with $D_1=50$ mm, N from 1.1 to 5. It can be seen from Fig. 6 that the magnification increases with N.

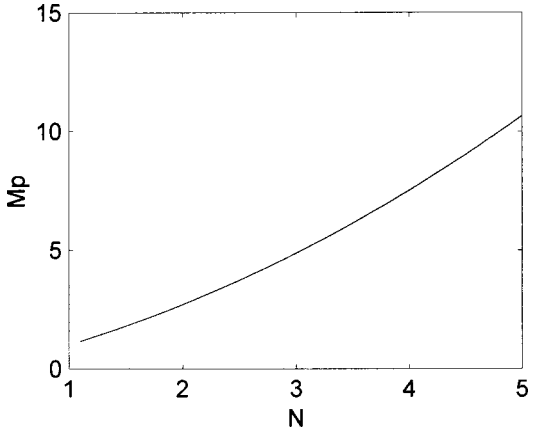

FIG. 6. M_p vs N curve of an exponential horn.

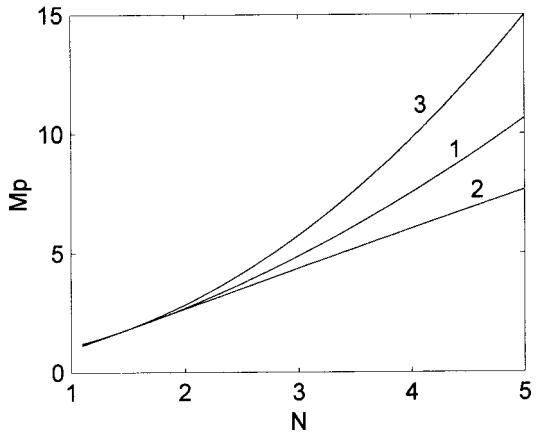

FIG. 7. Comparison of magnification.

It is also found that for a given type of horn the above-mentioned M_p vs N curves for different modes and frequencies are almost the same.

For comparing the magnification between different types of horn, a great deal of computation was conducted for horns with the end diameter ratio from 1.1 to 5 and a fixed value of D_1. The computation results show that the magnification of the catenary horn is the greatest and that of the conic horn is the smallest in the three types of horn when the horns are of the same end diameters. As an example, Fig. 7 shows the magnification of the three types of horn when $D_1=50$ mm and N changes. ''1,'' ''2,'' and ''3'' have the same meaning as in Fig. 2.

III. VERIFICATION

To verify the theoretical results, four solid horns are manufactured. The size parameters of the horns are listed below:

No. 1 conic, $D_1=50$ mm, $D_2=10$ mm, and $L=150$ mm.

TABLE III. Measured results of resonance frequency.

Horn No.	Mode No.	Calculated (kHz)	Measured (kHz)	Error (%)
1	1	6.200	6.397	−3.18
	2	13.549	13.650	0.75
	3	22.376	22.501	0.56
	4	31.807	32.079	0.86
2	1	9.656	9.846	−1.97
	2	20.955	21.253	−1.42
	3	33.237	33.805	1.71
	4	44.080	44.750	1.52
3	1	6.891	7.047	−2.25
	2	16.350	16.520	1.04
	3	27.511	27.824	−1.14
	4	39.064	39.580	1.33
4	1	7.426	7.184	3.26
	2	17.206	17.399	−1.12
	3	28.402	28.605	−0.71
	4	39.441	39.750	−0.78

TABLE IV. Comparison on the magnification computed in two methods.

Horn No.	Mode No	Matrix method	FEM	Error (%)
1	1	6.92	6.88	0.50
	2	7.71	7.73	−0.26
	3	8.45	8.43	0.24
	4	10.16	9.76	3.94
3	1	2.48	2.47	0.40
	2	2.56	2.55	0.39
	3	2.69	2.67	0.74
	4	3.13	3.02	3.51

No. 2 conic, $D_1=50$ mm, $D_2=20$ mm, and $L=120$ mm.

No. 3 exponential, $D_1=40$ mm, $D_2=20$ mm, and $L=130$ mm.

No. 4 exponential, $D_1=50$ mm, $D_2=20$ mm, and $L=130$ mm.

The measured results of the resonance frequency are shown in Table III. It can be seen from the data that the theoretical results agree with the measured ones well.

Limited by the experimental condition, the magnification of horn was not verified experimentally. As a comparison, the results from both metrix method and finite element method (FEM) are shown in Table IV. It is clear that both results are in good agreement.

IV. CONCLUSIONS

Based on the study, the following conclusions can be drawn:

(1) The transfer matrix method might be an efficient one for analysing flexural ultrasonic horns;
(2) For certain length of horn, the resonance frequency of exponential, conic, and catenary horns increases when the large end diameter or the small end diameter increases; For certain end diameters, the frequency decreases when the length increases;
(3) The relation between resonance frequency and size parameters of the three types of horns conform to the resonance curves;
(4) For given end diameters, the magnification of the catenary horn is greater than that of the exponential horn, which is in succession greater than that of the conic horn.

[1] Eiji Mori, ''New bolt clamped flexural mode ultrasonic high power transducer with one dimensional construction,'' Ultrasonics International 89 Conference Proceedings, pp. 256–261 (1989).
[2] Yuji Watanabe and Eiji Mori, ''A Study on transducer-stepped type solid horn for flexural mode ultrasonic high power transducer with one dimensional construction,'' Ultrasonics International 91 Conference Proceedings, pp. 435–438 (1991).
[3] F. W. Williams and J. R. Banerjee, ''Flexural vibration of axially loaded beams with linear or parabolic taper,'' J. Sound Vib. **99**, 121–138 (1985).
[4] Julius Miklowitz, ''Flexural wave solution of coupled equations representing the more exact theory of bending,'' J. Appl. Mech. **20**, 511–514 (1953).

Chirp response of an active-controlled thickness-drive tunable transducer

Hasan A. B. Alwi[a)]
Department of Physics, Universiti Kebangsaan Malaysia, Bangi 43600, Malaysia

John R. Carey and Brian V. Smith
School of Electronic and Electrical Engineering, University of Birmingham, Birmingham B15 2TT, United Kingdom

(Received 31 October 1998; accepted for publication 22 November 1999)

The chirp response of a thickness-drive tunable transducer for wide range time-bandwidth and sweep rates chirp signals is demonstrated experimentally and computationally. The computational evaluation uses recursive digital-filter model based on the *z*-transform method. The model is limited to simple lossless structure with no front and backing layers. The model and experimental results show that there is no limit on the maximum sweep rate of the chirp signal but practically the limit is determined by the limitation of the circuit that generates the control voltage that simulates a variable electric load. © *2000 Acoustical Society of America.* [S0001-4966(00)00703-7]

PACS numbers: 43.38.Yn, 43.30.Yj [SLE]

INTRODUCTION

In long range sonar, a swept frequency signal or ''chirp'' is used to improve range resolution and signal-to-noise ratio but the advances in this technique are limited by the requirement of wide bandwidth transducers. For the efficient transmission of sound, transducers are normally operated at a resonance, and are inherently narrow bandwidth. The design of wide bandwidth transducers presents considerable problems. The conventional methods of bandwidth widening trades off between the sensitivity and the bandwidth of the transducer.

Lately there has been considerable interest in designing a wide-band transducer by controlling or tailoring the frequency response by the application of active piezoelectric adjacent layers.[1–15] A tailored or controlled-response sonar transducer may be defined as a piezoelectric ceramic transducer that employs additional adjacent active ceramic elements or stack of elements of modify the transfer function of either a single ceramic element or stack of elements. The purpose of controlling or tailoring can be to widen the bandwidth of the original single element or stack of elements[6–9] or to obtain a multiple-resonance transducer[7,10,14,15] or to tune it[1–6,11–13] by varying the resonance frequency continuously across a wide range of frequencies. The tunable transducer, as the latter is called, has the advantage of a wider operating frequency range[11,13] than the conventional fixed frequency, wide bandwidth transducer.

Generally a tunable transducer consists of two identical ceramic elements as shown in Fig. 1. The two elements are the ''drive ceramic'' and the ''control ceramic'' which are mechanically coupled. The drive ceramic is driven electrically by a voltage source called the ''drive voltage source'' V_d and therefore provides the acoustic power to the load. The control ceramic varies or tunes the resonance frequency of the drive ceramic. Two methods of ''tuning'' are ''passive control'' [1–8] and ''active control.'' [1,2,3,9,10] In passive control the resonance frequency of the drive ceramic is varied by applying either a capacitive or inductive load across the control ceramic. A change in this electric load changes the acoustical characteristics of the control ceramic and this is subsequently seen by the driving element as a change in the acoustic impedance. It is the variation in the reactive part of this acoustic impedance which causes the variation in the resonance frequency of the driving element; the variation of the resistive part only modifies the amplitude of the driving element conductance. Figure 2(a) shows the driving element conductances measured, with the transducer in water, for a range of different inductances connected across the electrical terminals of the control ceramic. These curves demonstrate that the resonance frequency of the transducer is tunable between the first harmonic frequency $f_{1s}=210\,\mathrm{kHz}$ and the second overtone frequency $f_{3s}=760\,\mathrm{kHz}$ obtained with 0 μH. Figure 2(b) shows the electroacoustic efficiency ξ of the transducer at each resonance frequency approximated by

$$\xi=\left(\frac{G_{\mathrm{air}}-G_{\mathrm{water}}}{G_{\mathrm{air}}}\right)\times 100\%, \tag{1}$$

where G_{air} and G_{water} are the driving element conductances measured with the transducer in air and water respectively. Figure 2(b) shows that the efficiency with passive control is between 15% and 80% over the tunable range of 550 kHz.

In active control as in Fig. 1, a voltage source called the ''control voltage source'' V_c with predetermined values of amplitudes and phases relative to those of the drive voltage source replaces the passive electric load. The control voltage source is driven in synchronism with the drive chirp signal so that the transducer is always at resonance over the tunable frequency range and this leads to the concept of a tunable transducer. The efficiency of active-controlled tunable transducer is similar to the passive control transducer provided that the voltage source V_c accurately simulates the actual inductances. Although active control is attractive, it is difficult to realize the equivalent pure variable inductance accurately. The equivalent variable inductance obtained has large series resistance which dissipates power from the drive ce-

a)Corresponding author.

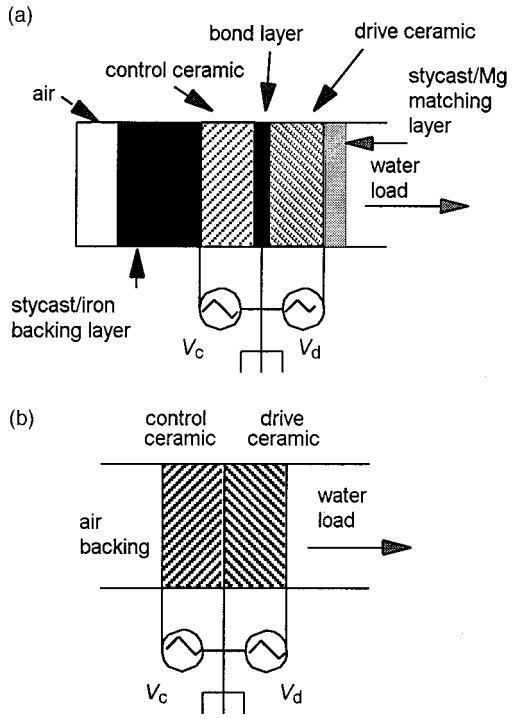

FIG. 1. The (a) real and (b) ideal tunable transducer with active-control tuning.

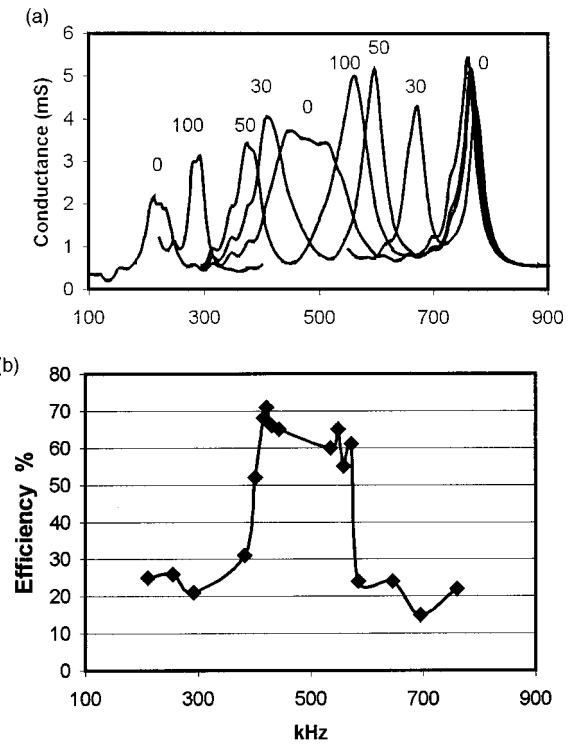

FIG. 2. (a) Measured conductances in water under passive control. (The numbers by the curves indicate the values of inductances L connected across the control ceramic in μH.) (b) The efficiency under passive control over the tunable frequency range.

ramic voltage source and therefore lowers the efficiency.

The tunable transducer has potential application in long range sonar because it is always operated at resonance which is required for a transducer to produce high-amplitude, low-frequency signals. In this paper, it will be shown that it also has the ability to be instantaneously switched between several discrete frequencies to produce the chirp signals that is commonly used in active sonars.

The results analyzed by Alwi[11,13] give the steady-state response of the transducer while in a practical application the transducer may be driven and controlled by a swept-frequency signal so as to generate a large time-bandwidth product signal. This requires that the transient response be investigated similar to the air-backed single-plate transducer.[11,16] As has been shown by Alwi,[11,16] a chirp signal with a fast sweep rate can modify the response of a fixed frequency transducer. The intention of this paper is to investigate the chirp response of the active-controlled tunable transducer. This requires the procedure adopted by Challis[17] and Alwi,[11,16] that is the modeling of the ideal tunable transducer shown in Fig. 1(b) as a recursive digital-filter based on z-transform method. Both the experimental and the modeling results in this paper show that the active control tunable transducer is a versatile transmitter for chirp signals with wide bandwidth between 210 kHz and 760 kHz and sweep durations between 1.15 s and 57 μs. This corresponds to sweep rates ranging from 0.47 MHz/s to 9600 MHz/s.

The viability of a similar structure as a chirp signal transmitter has also been experimentally verified by Hossack.[9] In his work the front layer is treated as an active matching layer to obtain a wide bandwidth transducer between the first harmonic f_{1s} and the second overtone f_{3s} of the transducer when the front layer electrical terminals are short-circuited. A different form of active control was employed by applying a suitable voltage across the front matching layer. He managed to transmit a chirp signal with sweep rate of 300 000 MHz/s from 1.5 MHz to 3 MHz over a 5-μs interval or a time-bandwidth product TB=7.5. The differences between the two transducers are that the tunable transducer is narrow bandwidth but tunable between f_{1s} and f_{3s} while Hossack's is a wide bandwidth transducer between these two frequencies. Another difference is that Hossack's transducer is driven from the rear ceramic layer because the front layer is considered a matching layer but for the tunable transducer it is driven from the front layer.

I. THE DIGITAL-FILTER MODEL OF AN ACTIVE-CONTROLLED THICKNESS-DRIVE TUNABLE TRANSDUCER

The tunable transducer used in the experiment is shown in Fig. 1(a); it comprises two identical PZT4 plates coupled

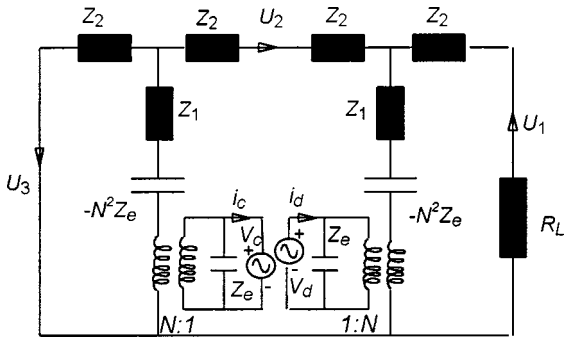

FIG. 3. Mason equivalent-circuit model of the ideal tunable transducer.

together by a thin layer of glue. The plates' diameters of 50.0 mm and thicknesses of $l=4.25$ mm were carefully chosen to avoid the coupling of other planar modes of vibration so that the one-dimensional Mason equivalent-circuit model[18] can be safely used to predict the transducer characteristics. As already indicated, the two plates are designated the drive ceramic and the control ceramic. The drive ceramic is driven electrically by a constant voltage source V_d and radiates into the water load through a λ/4 matching layer of Stycast-magnesium composite. The control ceramic is positioned at the rear of the drive ceramic and is in contact with it through a thin bonding layer. At the rear of the control ceramic is a passive layer of Stycast-fillite composite, which acts as a low-impedance backing.

The mathematics in the modeling of the complex structures in Fig. 1(a) as a recursive digital-filter model is intractable, hence, the transducer is treated as ideal, as shown in Fig. 1(b), with the following assumptions:[11]

(1) zero thickness for the bonds between the ceramics;
(2) zero thickness front-matching or coupling layer;
(3) an air-backing;
(4) the two ceramics are considered identical and lossless.

For the real transducer with a larger number of layers included in the modeling, the model become numerically unstable too quickly, which limits the modeling to a very short frequency range. Assumption (1) increases the resonance frequencies[13] while assumptions (2), (3), and (4) increase the Q value at each resonance frequency. A high Q resonance causes resonance ringing visible in the modeling. As explained in Alwi,[13] the losses in the ceramic limit the tunable range between the first harmonic f_{1s} and the second overtone f_{3s}. Hence, another effect of assumption (4) is to make the ideal transducer tunable beyond those frequency limits.

The modeling is based on the Laplace transform of the Mason equivalent-circuit shown in Fig. 3. Here, U_1, U_2, and U_3 are the front-face, middle-face, and back-face velocities of the transducer faces, respectively; N is the electromechanical transformation ratio; Z_e is the reactance of the clamped capacitance C_0; i_d and i_c are the currents at the drive and control ceramics electrical terminals; and R_L is the water load. The impedances Z_1 and Z_2 in the T-network represent the ceramic as a losslss, mechanical transmission line of length l, where

$$Z_1 = jZ_c \tan\left(\frac{\omega l}{2v_c}\right), \tag{2a}$$

$$Z_2 = \frac{-jZ_c}{\sin(\omega l/v_c)}, \tag{2b}$$

$$Z_e = \frac{1}{j\omega C_0}. \tag{2c}$$

Here, Z_c is the mechanical impedance of the ceramic plates, ω is the radial frequency, and v_c is the sound velocity in the ceramic plates.

The discrete-time model of the transducer is realized by taking the Laplace transform[17] of the Mason equivalent-circuit in Fig. 3. The Laplace transform of the Mason equivalent-circuit is identical, but with Z_1, Z_2, and Z_e as functions of the Laplace variables s:

$$Z_1 = \frac{2Z_c}{e^{sT_p} - e^{-sT_p}}, \tag{3a}$$

$$Z_2 = \frac{Z_c(1-e^{-sT_p})}{(1+e^{-sT_p})}, \tag{3b}$$

$$Z_e = \frac{1}{sC_0}, \tag{3c}$$

where $T_p = l/v_c$ is the propagation time for an acoustic wave to travel across the ceramic plate from one electrode to the other.

By using conventional circuit analysis, the relationship between the variables in Fig. 3 can be shown to be expressable in matrix form:[17]

$$\begin{pmatrix} R_L+Z_1+Z_2 & Z_1 & 0 & NZ_e & 0 \\ Z_1 & 2(Z_1+Z_2) & Z_1 & NZ_e & NZ_e \\ 0 & Z_1 & Z_1+Z_2 & 0 & NZ_e \\ NZ_e & NZ_e & 0 & Z_e & 0 \\ 0 & NZ_e & NZ_e & 0 & Z_e \end{pmatrix} \begin{pmatrix} U_1 \\ U_2 \\ U_3 \\ i_d \\ i_c \end{pmatrix} = \begin{pmatrix} 0 \\ 0 \\ 0 \\ V_d \\ -V_c \end{pmatrix}. \tag{4}$$

From this matrix equation the Laplace transform of the front-face velocity U_1 at the output terminals can be obtained when an input voltage V_d is applied with V_c short-circuited as:

$$\frac{U_1(s)}{V_d} = \frac{N\left\{\frac{3N^2Z_2}{sC_0} + Z_1Z_2 - 2Z_c^2\right\}}{\left\{\frac{4Z_2N^4+R_LN^4}{s^2C_0^2} + \frac{(-4N^2Z_2^2-4Z_1N^2Z_2-2R_LN^2Z_1-4R_LN^2Z_2)}{sC_0} + R_LZ_1^2+2Z_1Z_c^2+2Z_2Z_c^2+2R_LZ_c^2\right\}}. \tag{5}$$

Similarly, the Laplace transform of the front-face velocity U_1 at the output terminals when an input voltage V_c is applied with V_d short-circuited is:

$$\frac{U_1(s)}{V_c}=\frac{NZ_2\left\{\dfrac{N^2}{sC_0}-Z_1\right\}}{\left\{\dfrac{4Z_2N^4+R_LN^4}{s^2C_0^2}+\dfrac{(-4N^2Z_2^2-4Z_1N^2Z_2-2R_LN^2Z_1-4R_LN^2Z_2)}{sC_0}+R_LZ_1^2+2Z_1Z_c^2+2Z_2Z_c^2+2R_LZ_c^2\right\}}. \tag{6}$$

Equations (5) and (6) are obtained from matrix Eq. (4) with the help of the Maple V (Release 2.0a) symbolic processor. The Laplace transform Eqs. (5) and (6) are arranged in negative powers of s so that the z transform of s^{-1} is obtained from

$$s^{-1}=\frac{T_m}{2}\frac{(1+z^{-1})}{(1-z^{-1})}, \tag{7a}$$

$$s^{-2}=\frac{T_m^2}{12}\frac{(1+10z^{-1}+z^{-2})}{(1-z^{-1})^2}, \tag{7b}$$

where $T_m=T_p/m$ is the sampling interval and m, an integer, is the number of samples per propagation time T_p.

The z-transform of Z_1 and Z_2 are

$$Z_1=\frac{2Z_c}{z^m-z^{-m}}, \tag{8a}$$

$$Z_2=\frac{Z_c(1-z^{-m})}{(1+z^{-m})}. \tag{8b}$$

The time delay e^{-ST_P}, which is associated with transducer reverberation in Eqs. (3a) and (3b), can be represented in powers of z by substituting

$$e^{sT_p}=e^{smT_m}=z^m. \tag{9}$$

Equations (8a) and (8b) are substituted into Eq. (5) to get the z-transform of the front-face velocity $U_1(z)$ due to the drive voltage V_d alone. Using the symbolic processor, factorization and expansion of $U_1(z)$ were performed. Finally, $U_1(z)$ was arranged such that it is collected on the same power of z, z^m:

$$\frac{U_1(z)}{V_d(z)}=\frac{\left\{\begin{array}{c}a_0z^{2m}+a_1z^{2m-1}+a_2z^{2m-2}+a_3z^m+a_4z^{m-2}+a_5z^{m-1}+a_6z^0\\+a_7z^{-1}+a_8z^{-2}+a_9z^{-m}+a_{10}z^{-m-1}+a_{11}z^{-m-2}+a_{12}z^{-2m}\\+a_{13}z^{-2m-1}+a_{14}z^{-2m-2}+a_{15}z^{-3m}+a_{16}z^{-3m-1}+a_{17}z^{-3m-2}+a_{18}z^{-4m}+a_{19}z^{-4m-1}+a_{20}z^{-4m-2}\end{array}\right\}}{\left\{\begin{array}{c}b_0z^{2m}+b_1z^{2m-1}+b_2z^{2m-2}+b_3z^m+b_4z^{m-1}+b_5z^{m-2}+b_6z^0\\+b_7z^{-1}+b_8z^{-2}+b_9z^{-m}+b_{10}z^{-m-1}+b_{11}z^{-m-2}+b_{12}z^{-2m}\\+b_{13}z^{-2m-1}+b_{14}z^{-2m-2}+b_{15}z^{-3m}+b_{16}z^{-3m-1}+b_{17}z^{-3m-2}+b_{18}z^{-4m}+b_{19}z^{-4m-1}+b_{20}z^{-4m-2}\end{array}\right\}}, \tag{10}$$

where the a and b coefficients are given in the Appendix.

By dividing with the highest power of z, in this case by z^{2m}; the z-transform of $U_1(z)$ is arranged in negative power of z as

$$\frac{U_1(z)}{V_d(z)}=\frac{\left\{\begin{array}{c}a_0+a_1z^{-1}+a_2z^{-2}+a_3z^{-m}+a_4z^{-m-1}+a_5z^{-m-2}+a_6z^{-2m}\\+a_7z^{-2m-1}+a_8z^{-2m-2}+a_9z^{-3m}+a_{10}z^{-3m-1}+a_{11}z^{-3m-2}+a_{12}z^{-4m}\\+a_{13}z^{-4m-1}+a_{14}z^{-4m-2}+a_{15}z^{-5m}+a_{16}z^{-5m-1}+a_{17}z^{-5m-2}\\+a_{18}z^{-6m}+a_{19}z^{-6m-1}+a_{20}z^{-6m-2}\end{array}\right\}}{\left\{\begin{array}{c}b_0+b_1z^{-1}+b_2z^{-2}+b_3z^{-m}+b_4z^{-m-1}+b_5z^{-m-2}+b_6z^{-2m}\\+b_7z^{-2m-1}+b_8z^{-2m-2}+b_9z^{-3m}+b_{10}z^{-3m-1}+b_{11}z^{-3m-2}+b_{12}z^{-4m}\\+b_{13}z^{-4m-1}+b_{14}z^{-4m-2}+b_{15}z^{-5m}+b_{16}z^{-5m-1}+b_{17}z^{-5m-2}\\+b_{18}z^{-6m}+b_{19}z^{-6m-1}+b_{20}z^{-6m-2}\end{array}\right\}}. \tag{11}$$

The significance of multiplication by z^{-n} in the z-transform of Eq. (11) is to delay the time waveform by n sample periods, thus Eq. (11) can be interpreted as a recurrence relationship between the sampled version of input $V_d(n)$ and output $U_1(n)$, as

$$\begin{aligned}U_1(n)=\frac{1}{b_0}\{&a_0V_d(n)+a_1V_d(n-1)+a_2V_d(n-2)+a_3V_d(n-m)+a_4V_d(n-m-1)\\&+a_5V_d(n-m-2)+a_6V_d(n-2m)+a_7V_d(n-2m-1)+a_8V_d(n-2m-2)\\&+a_9V_d(n-3m)+a_{10}V_d(n-3m-1)+a_{11}V_d(n-3m-2)+a_{12}V_d(n-4m)\\&+a_{13}V_d(n-4m-1)+a_{14}V_d(n-4m-2)+a_{15}V_d(n-5m)+a_{16}V_d(n-5m-1)\end{aligned}$$

$$+a_{17}V_d(n-5m-2)+a_{18}V_d(n-6m)+a_{19}V_d(n-6m-1)+a_{20}V_d(n-6m-2)\}$$

$$-\frac{1}{b_0}\{b_1u_1(n-1)+b_2U_1(n-20+b_3U_1(n-m)+b_4U_1(n-m-1)$$

$$+b_5U_1(n-m-2)+b_6U_1(n-2m)+b_7U_1(n-2m-1)+b_8U_1(n-2m-2)$$

$$+b_9U_1(n-3m)+b_{10}U_1(n-3m-1)+b_{11}U_1(n-3m-2)+b_{12}U_1(n-4m)$$

$$+b_{13}U_1(n-4m-1)+b_{14}U_1(n-4m-2)+b_{15}U_1(n-5m)+b_{16}U_1(n-5m-1)$$

$$+b_{17}U_1(n-5m-2)+b_{18}U_1(n-6m)+b_{19}U_1(n-6m-1)+b_{20}U_1(n-6m-2)\}. \quad (12)$$

Equation (12) represents the transducer as a recursive digital-filter which calculates the nth sample of the output waveform $U_1(n)$ in terms of the nth and previous samples of the drive voltage input waveform $V_d(n)$ acting alone and the previously calculated samples of the output waveform. Equation (12), with different a coefficients, shown in the Appendix, also represents the recurrence relationship between $U_1(t)$ and the sampled version of the control voltage source $V_c(t)$ acting alone, which is by replacing $V_d(t)$ with $V_c(t)$. The total response is then obtained by summation of the time sampled responses from each source. The computations were performed using Turbo C++ (version 3.0).

A. Chirp response of multiple-resonance transducer

The validity of the digital-filter model is demonstrated by investigating the chirp response with the simplest excitation, that is, with the control ceramic short-circuited. Under such simple excitation the transducer behaves as a multiple-resonance transducer. Chirp signals with a sweep rate of 100 MHz/s are considered with the number of samples per propagation $m=3$, which represents a sampling frequency of 3.2 MHz. According to the bilinear transformation, a good discrete representation of analog frequencies can be obtained by up to one-quarter of the sampling frequency. Hence the number of samples $m=3$ is sufficient for the frequency range under consideration.

Figure 4(a) shows the envelope of the chirp response obtained by evaluating the recursive digital filter Eq. (12) twice to calculate the outputs due to the real $\Re$ and imaginary $\Im$ parts of the input as

$$U_1(n)=\sqrt{\Re^2+\Im^2}. \quad (13)$$

Figure 4(a) shows the short-circuit resonance frequencies which represent the first harmonic f_{1s}, the first overtone f_{2s}, and the second overtone f_{3s}. The three resonances can be seen in the conductance measurements of Fig. 2(a) with 0 μH. Switch-on transient and resonance ringings are visible in the chirp responses of Fig. 4(a) because the Q values in the modeling are higher than in the measured values due to assumptions (2), (3), and (4) above. In addition, above about 500 kHz a small degree of ringing may be observed which gradually increases in amplitude with increasing frequency. This is due to numerical instabilities as explained in Sec. B.

B. Digital-filter modeling error

The cause of numerical instabilities is investigated by looking at the impulse response with the control-ceramic short-circuited shown in Fig. 4(b). The impulse response diverges and this indicates numerical instability in the computation of the chirp responses in Fig. 4(a). A sweep rate of 100 MHz/s, which corresponds to sweep duration of 7 ms, requires the whole of the impulse response and the effect of the diverging impulse response is seen as the high-frequency oscillations in the chirp response.

From this illustration, it is clear that the level of instability is less with faster sweep rates chirp signals because the chirp signals take a shorter time to cover the frequency range of interest. Figure 5 shows impulse responses with m equal to 20 and 100 superimposed. The impulse response with the larger m value, curve b, diverges at an earlier time, which appears as a higher level of high-frequency oscillation in the chirp responses. The conclusion is that there is a lower limit to the sweep rate of chirp signals for a particular value of m for the digital-filter model to be accurate.

Although useful information on the chirp responses has been obtained from this digital-filter model, it is only suitable for the ideal case only. For the real transducer with a larger number of layers, the impulse response diverges at an even earlier time which limits the modeling to a short frequency range unless fast sweep rates are considered.

C. Chirp responses of active-controlled tunable transducer

In active control the variable inductive load is simulated by V_c. The required amplitude of V_c and its phase relationship with the drive voltage V_d to simulate a variable inductive loads is shown in Fig. 6(a) and (b), which were obtained from steady-state analysis of Mason equivalent-circuit in Fig. 3. This shows that the amplitude of V_c is nearly always larger than that of V_d and its phase is very nearly always at either $+90°$ or $-90°$ with respect to V_d. Although V_c is generally larger than V_d, which is the inherent disadvantage of tunable transducer, no power is contributed by V_c; the radiated acoustic power is contributed by V_d alone.

By applying the variable control voltage V_c simultaneously in synchronism with V_d, a continuous curve in Fig. 6(c) is obtained. This curve represents the peaks of the resonances at each frequency if a variable electric load is applied

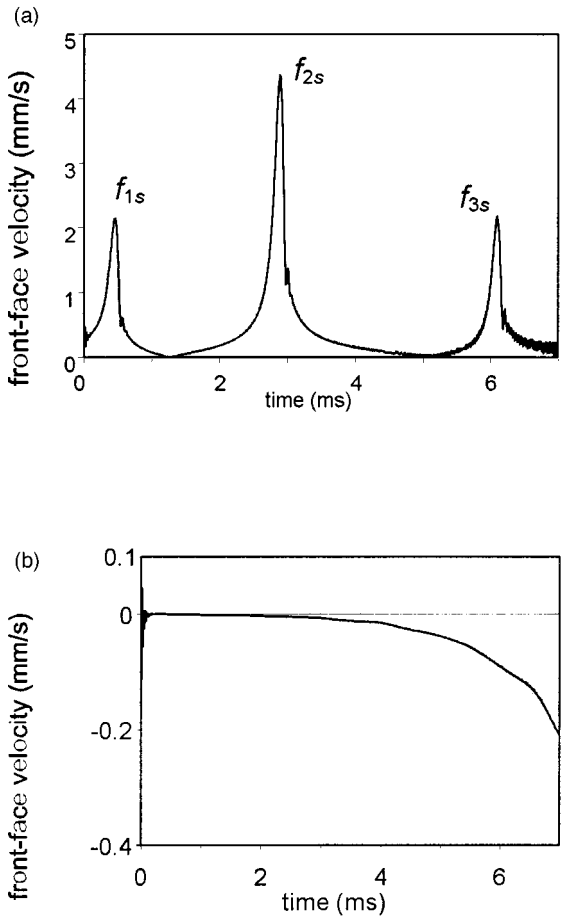

FIG. 4. (a) Chirp response with $V_c = 0$ and (b) impulse response.

to the control ceramic such as to obtain a wide tunable frequency range. The effect of assumption (4) can be seen in Fig. 6(c) because the tunable range of ideal tunable transducer is not limited between the first harmonic f_{1s} and the second overtone f_{3s}.

In this section the digital-filter model developed above is applied to the active-controlled tunable transducer. A very slow sweep rate is desirable to get the steady-state response, but the aim of this paper is to investigate the ability to tune the transducer at higher sweep rates and these are shown in Fig. 7. The sweep rates of 7500 MHz/s and 9600 MHz/s were simulated because they were the two highest sweep rates that could be produced by the signal generator used. Its

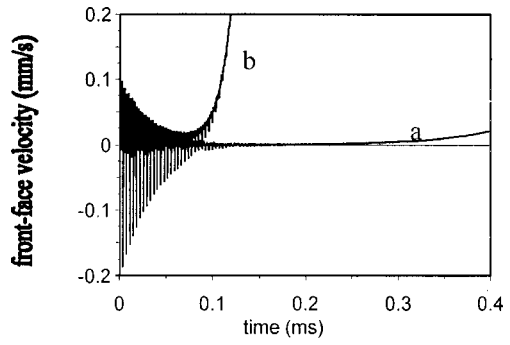

FIG. 5. Impulse responses with $V_c = 0$ for (a) $m = 20$, (b) $m = 100$.

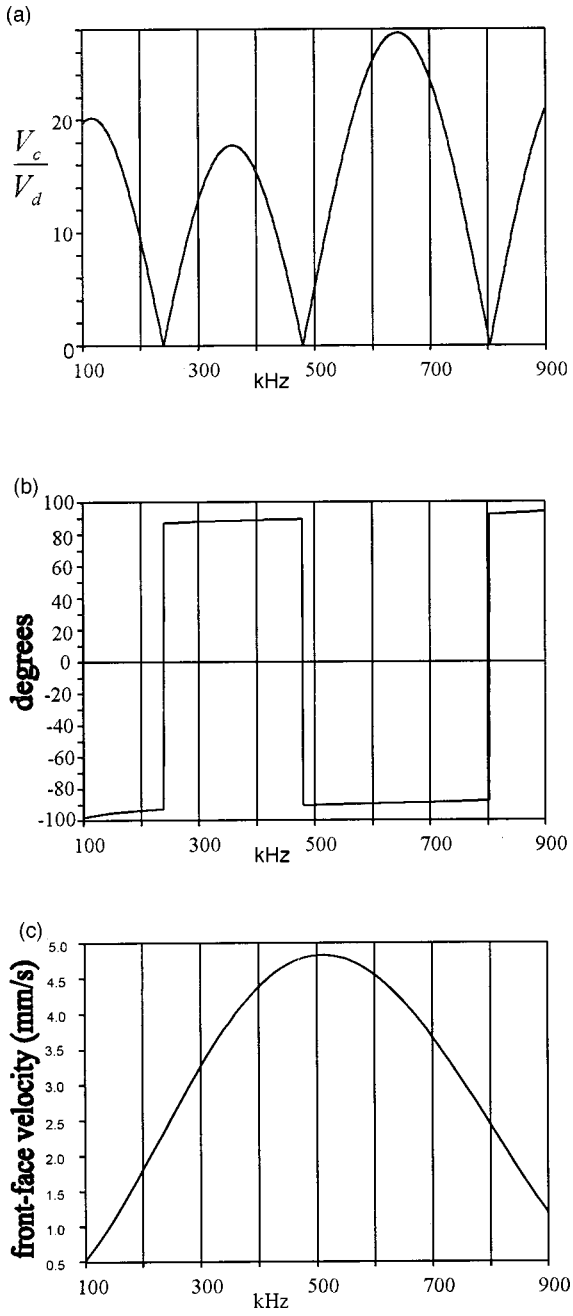

FIG. 6. (a) Magnitudes of V_c and (b) phases of V_c relative to V_d required for resonance at each frequency; (c) the envelope of the front-face velocity.

envelope is similar to the curve in Fig. 6(c). No computational instabilities are observed at high sweep rates because the instabilities occur at higher frequencies than the frequencies displayed. Even though the amplitudes and phases of V_c used above were obtained from the steady-state response, these results suggest that there is no limit on the maximum rate of sweep, other than those set by practical limitations.

II. EXPERIMENTAL RESULTS

The circuit for replacing the variable inductive and capacitive loads by a variable voltage source, V_c, has been realized by Steel.[1–3] In this paper the work is extended to

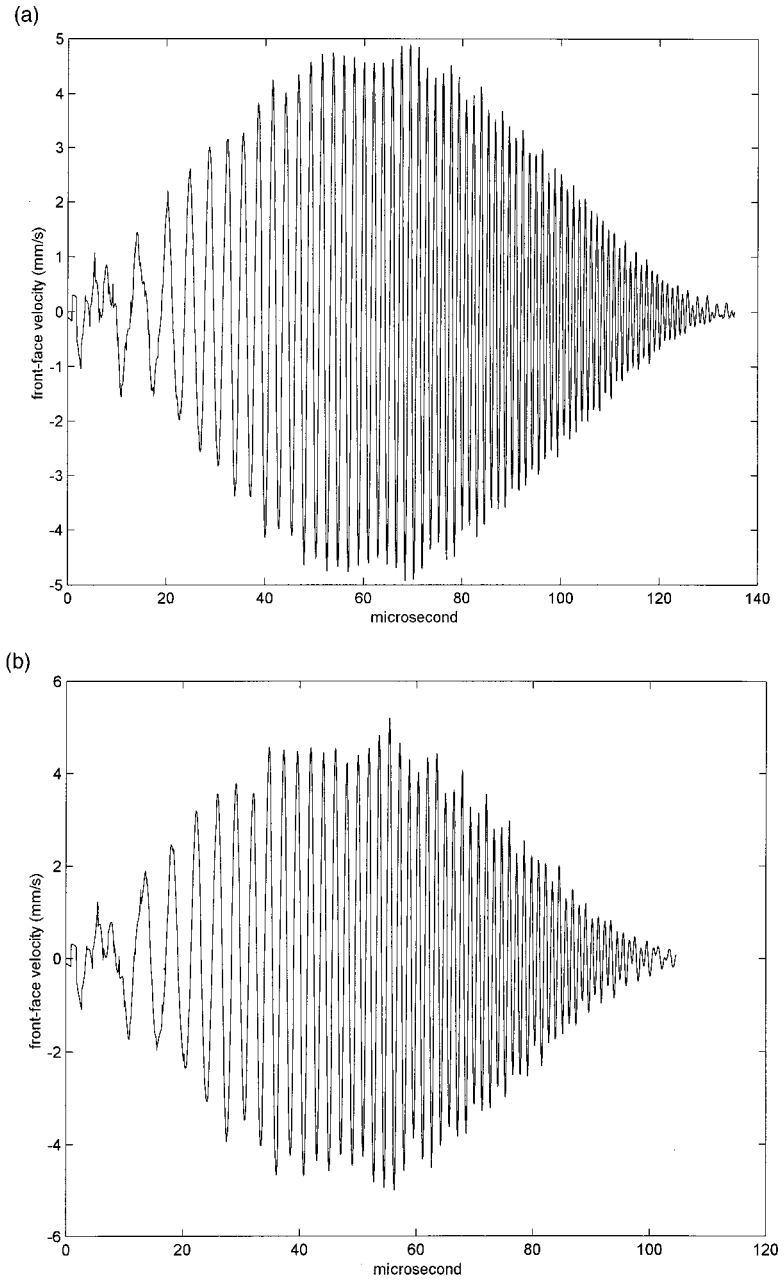

FIG. 7. The computed chirp waveform of the front-face velocity for sweep rate. (a) 7500 MHz/s, (b) 9600 MHz/s.

determine the maximum rate of change of the tuned resonance frequency. This necessitates modifications to the circuit by Steel such that the control voltage V_c can be a swept frequency source with a variable sweep rate.

In this work only the variable inductive loads were simulated by the voltage source V_c with the values of inductances achieved shown as curve a in Fig. 8(a). It is drawn superimposed with the actual inductances to obtain resonances at a particular frequency, and this is shown as curve b. The variable capacitive loads were not required because the tunable capacitive ranges are narrow,[13] which for the real transducer the resonances can be obtained by the short-circuit harmonics f_{1s}, f_{2s}, and f_{3s}. The actual inductances' series resistances are very small and are drawn as curve b in Fig. 8(b). As a comparison, the equivalent series resistances simulated by V_c are large, approximately 100 Ω to 120 Ω, which are contributed by inaccuracy with the V_c circuit in determining its amplitudes and phases. Although active control is attractive, it is difficult to realize the equivalent pure variable inductance even for the ideal tunable transducer.[11] The large series resistance implies that some power from V_d is lost in V_c and therefore lower the efficiency of the active-controlled tunable transducer and lowers the Q value at each resonance frequency.

The experimental setup is shown in block diagram of Fig. 9. Both the PVDF hydrophone and the transducer under test (TUT) were immersed in a water tank. A pair of chirp signals V_d and V_c were applied simultaneously to the transducer and the radiated acoustic signal was detected by the hydrophone. The output voltage of the hydrophone was then amplified and envelope detected. The output voltage of the envelope detector was then recorded by a spectrum analyzer for later analysis.

The chirp signal generator (SG) with variable sweep rate

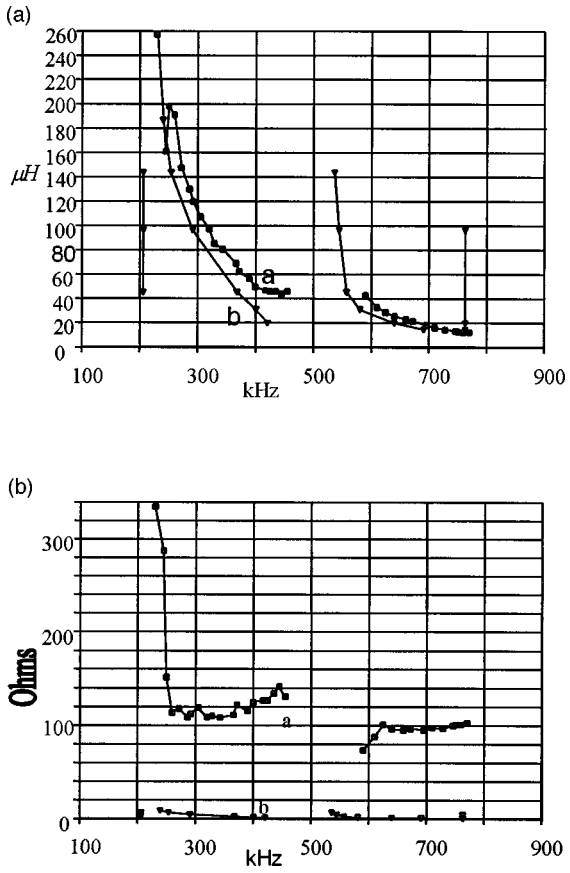

FIG. 8. Values of (a) variable inductance required for resonance at each frequency, (b) the equivalent series resistance. Curve a is the experimental values of V_c and curve b is the actual values of passive inductance L.

drives a power amplifier (PA) for the drive voltage V_d. SG also drives a digital circuit (cct) which sets the phases and amplitudes of V_c equal to the voltage across a passive inductance. Another power amplifier (PA) is required to increase the voltage level of V_c.

Figure 10(a) shows the envelope of the chirp responses measured with sweep rate of 0.47 MHz/s which is slow enough to be considered as a steady-state response. Curve a is obtained with $V_c=0$ which shows the short-circuit resonances at the natural harmonics f_{1s}, f_{2s}, f_{3s}. From Alwi[11,13] the tunable range of the real tunable transducer is defined as between the first harmonic $f_{1s}=210$ kHz and the second overtone $f_{3s}=760$ kHz which is a tunable range of 550 kHz.

Curve b of Fig. 10(a) is the envelope of the chirp response under active control so that the transducer is always at resonances between f_{1s} and f_{3s}. If f_{1s} and f_{3s} are considered as the half-power points of a fixed, wide bandwidth transducer, the tunable transducer has equivalent bandwidth of 550 kHz. If the time at these two harmonics, Fig. 10(a), are 0.280 and 1.456 s, the time-bandwidth product TB of the active control chirp signal is 646 800.

In Fig. 10(b) to Fig. 11(d) are shown the chirp responses for sweep rates of 5.05 to 9600 MHz/s. For the slow sweep rates of lower than 88.89 MHz/s, Figs. 10(a)–(e), the responses are shown as their envelopes. For rates faster than

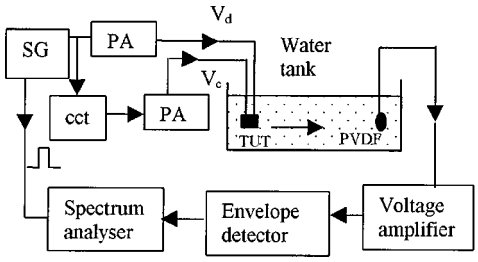

FIG. 9. Block schematic diagram showing the experimental arrangement.

1587 MHz/s, Figs. 11(a)–(e), the actual waveforms are displayed.

From the chirp response measurements, the tunable transducer under active control is capable of transmitting chirp signals with the maximum sweep rates of 1587 MHz/s in Fig. 11(a). This is faster than the 351 MHz/s for the single-plate transducer.[16] For rates faster than 1587 MHz/s, Figs. 11(b)–(e), ringings above the second overtone $f_{3s}=760$ kHz similar to the single-plate transducer are seen. The ringing associated with the f_{3s} overtone becomes more pronounced with faster sweep rates. The computation in Fig. 7 does not show the resonance ringings because the ideal tunable transducer is tunable well beyond the tunable range defined above, but for the real tunable transducer the losses in the ceramic limit the tunable range between $f_{1s}=210$ kHz and $f_{3s}=760$ kHz.[11,13]

The advantage of an active control tunable transducer is that it is a good transmitter of fast sweep rates and large time-bandwidth chirp signals which suggests that it has potential application in long-range sonar. The sweep rates and the corresponding time-bandwidth TB of the chirp signals are tabulated in Table I.

III. CONCLUSION

The transient analysis that has been used in this paper demonstrates that modeling based on a digital-filter is useful although it has only been possible to apply it to the ideal tunable transducer. The effect of numerical instabilities which occur toward the high-frequency end of the response is reduced by using faster sweep rates and smaller values of m. The oscillations with slow sweep rate chirps and the corresponding diverging impulse responses seem to be inherent in the z-transform method. The divergence is stronger with higher m values. It can be concluded that there is a lower limit to the sweep rate for particular value of m for this digital-filter model to be accurate.

The modeling shows that there is no limit to the maximum rate of sweep for the active-control tunable transducer although the values of the control voltage were obtained from the steady-state analysis apart from the limitations of the voltage control circuitry. The experimental maximum rate of sweep attained by active control was 1587 MHz/s which is faster than the maximum sweep rates for the single-plate transducer. The tunable transducer is a versatile transmitter of chirp signals with large time-bandwidth and fast sweep rates.

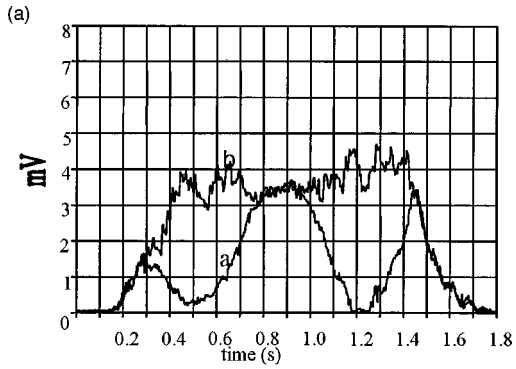

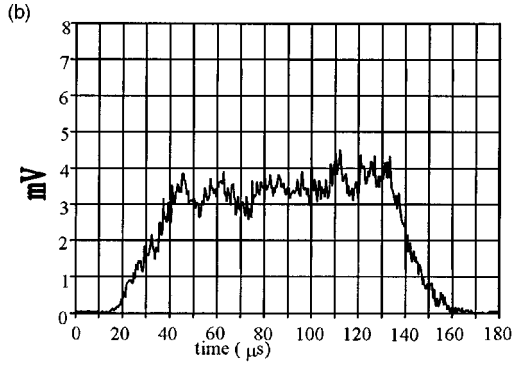

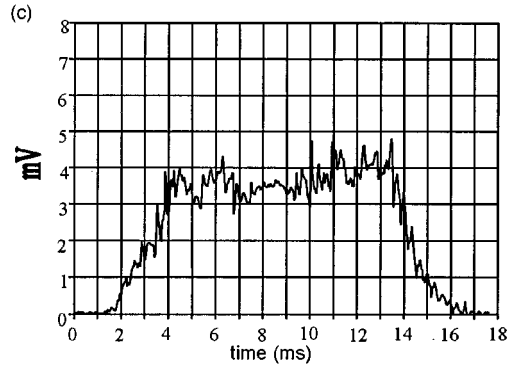

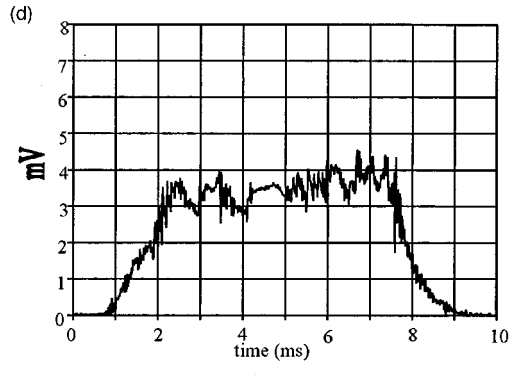

FIG. 10. (a) The envelope of the measured radiation with sweep rate 0.47 MHz/s, a $V_c = 0$, b active control. For faster sweep rates (a) 0.47, (b) 5.05, (c) 49.38, (d) 88.89 MHz/s with active control.

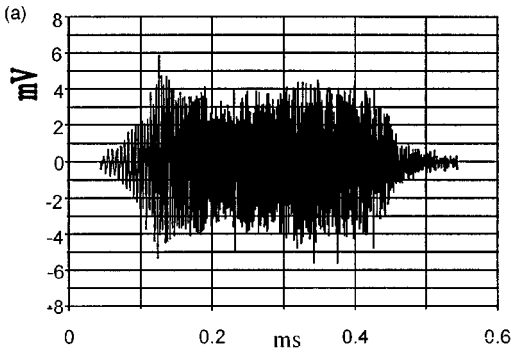

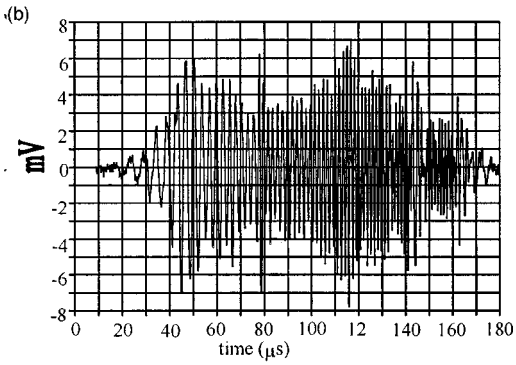

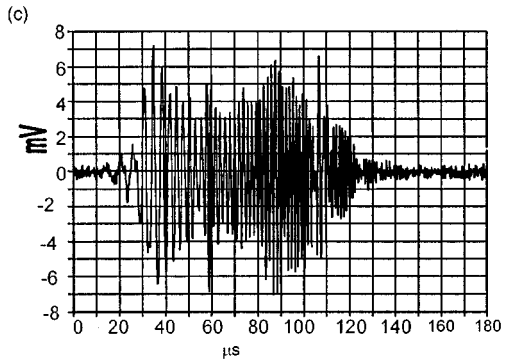

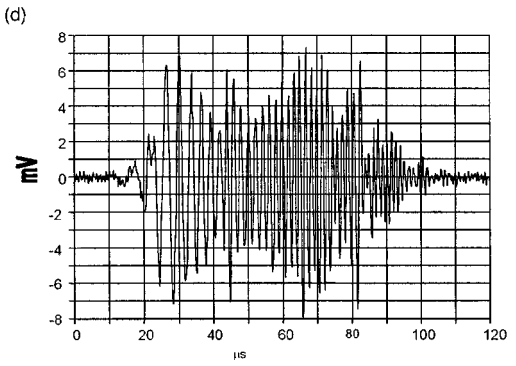

FIG. 11. The actual chirp waveform of the radiation with sweep rate (a) 1587, (b) 4762, (c) 7500, (d) 9600 MHz/s with active control.

TABLE I. Sweep rates and time-bandwidths of chirp signals for tunable transducer.

Sweep rate (MHz/s)	Time-bandwidth (TB)
5.05	57 620
49.38	6182
88.89	3487
1587	187
4762	62
7500	47
9600	35

ACKNOWLEDGMENT

One of the authors, Hasan A. Alwi, wishes to acknowledge the financial support by the Government of Malaysia to the author during his study at University of Birmingham, United Kingdom.

APPENDIX: THE DIGITAL-FILTER MODEL OF A TUNABLE TRANSDUCER

The coefficients a of Eq. (12) with $V_c=0$ are on the left while the coefficients a of Eq. (12) with $V_d=0$ are on the right in Table AI. The coefficients b of Eq. (12) for both cases are:-

$$b_0=\frac{N^4T_m^2}{C_0^2}\left(\frac{R_L}{2}+\frac{Z_c}{3}\right)-\frac{N^2T_m}{C_0}(3Z_c^2+2Z_cR_L)+2Z_c^2R_L+2Z_c^3,$$

$$b_1=\frac{N^4T_m^2}{C_0^2}\left(5R_L+\frac{10Z_c}{3}\right)-4Z_c^2R_L-4Z_c^3,$$

TABLE AI. a coefficients of the digital-filter model.

	$V_c=0$	$V_d=0$
a_0	$\frac{NZ_c}{2C_0}(3N^2T_m-4Z_cC_0)$	$\frac{N^3Z_cT_m}{2C_0}$
a_1	$4NZ_c^2$	0
a_2	$-\frac{NZ_c}{2C_0}(3N^2T_m+4Z_cC_0)$	$-a_0$
a_3	$-2NZ_0^2$	$-2NZ_c^2$
a_4	a_1	$4NZ_c^2$
a_5	a_3	a_3
a_6	$\frac{NZ_c}{2C_0}(4Z_cC_0-9N^2T_m)$	$3a_2$
a_7	$-a_1$	0
a_8	$\frac{NZ_c}{2C_0}(4Z_cC_0+9N^2T_m)$	$-a_6$
a_9	a_1	a_4
a_{10}	$2a_7$	$4a_3$
a_{11}	a_1	a_4
a_{12}	a_8	$-a_6$
a_{13}	$-a_1$	0
a_{14}	a_6	a_6
a_{15}	a_3	a_3
a_{16}	a_1	a_4
a_{17}	a_3	a_3
a_{18}	a_2	a_6
a_{19}	a_1	0
a_{20}	a_0	$-a_6$

$$b_2=\frac{N^4T_m^2}{C_0^2}\left(\frac{R_L}{12}+\frac{Z_c}{3}\right)+\frac{N^2T_m}{C_0}(3Z_c^2+2Z_cR_L)+2Z_c^2R_L+2Z_c^3,$$

$$b_3=\frac{N^4T_m^2}{C_0^2}\left(\frac{R_L}{6}\right)-\frac{N^2T_m}{C_0}(2Z_c^2+2Z_cR_L)+4Z_c^2R_L+4Z_c^3,$$

$$b_4=\frac{N^4T_m^2}{C_0^2}\left(\frac{5R_L}{3}\right)-8Z_c^2R_L-8Z_c^3,$$

$$b_5=\frac{N^4T_m^2}{C_0^2}\left(\frac{R_L}{6}\right)+\frac{N^2T_m}{C_0}(2Z_c^2+2Z_cR_L)+4Z_c^2R_L+4Z_c^3,$$

$$b_6=-\frac{N^4T_m^2}{C_0^2}\left(\frac{R_L}{12}+Z_c\right)+\frac{N^2T_m}{C_0}(2Z_cR_L-3Z_c^2)+2Z_c^2R_L+2Z_c^3,$$

$$b_7=-\frac{N^4T_m^2}{C_0^2}\left(\frac{5R_L}{6}+10Z_c\right)-4Z_c^2R_L-4Z_c^3,$$

$$b_8=-\frac{N^4T_m^2}{C_0^2}\left(\frac{R_L}{12}+Z_c\right)-\frac{N^2T_m}{C_0}(3Z_c^2+2Z_cR_L)+2Z_c^2R_L+2Z_c^3,$$

$$b_9=-\frac{N^4T_m^2}{C_0^2}\left(\frac{R_L}{3}\right)+\frac{N^2T_m}{C_0}(4Z_c^2),$$

$$b_{10}=-\frac{N^4T_m^2}{C_0^2}\left(\frac{10R_L}{3}\right),$$

$$b_{11}=-\frac{N^4T_m^2}{C_0^2}\left(\frac{R_L}{3}\right)-\frac{N^2T_m}{C_0}(4Z_c^2),$$

$$b_{12}=\frac{N^4T_m^2}{C_0^2}\left(Z_c-\frac{R_L}{3}\right)-\frac{N^2T_m}{C_0}(3Z_c^2+2Z_cR_L)+2Z_c^2R_L-2Z_c^3,$$

$$b_{13}=\frac{N^4T_m^2}{C_0^2}\left(\frac{-5R_L}{6}+10Z_c\right)-4Z_c^2R_L-4Z_c^3,$$

$$b_{14}=\frac{N^4T_m^2}{C_0^2}\left(Z_c-\frac{R_L}{12}\right)-\frac{N^2T_m}{C_0}(3Z_c^2+2Z_cR_L)+2Z_c^2R_L-2Z_c^3,$$

$$b_{15}=\frac{N^4T_m^2}{C_0^2}\left(\frac{R_L}{6}\right)+\frac{N^2T_m}{C_0}(2Z_cR_L-2Z_c^2)+4Z_c^2R_L-4Z_c^3,$$

$$b_{16}=\frac{N^4T_m^2}{C_0^2}\left(\frac{5R_L}{3}\right)-8Z_c^2R_L+8Z_c^3,$$

$$b_{17}=\frac{N^4T_m^2}{C_0^2}\left(\frac{R_L}{6}\right)+\frac{N^2T_m}{C_0}(2Z_c^2-2Z_cR_L)+4Z_c^2R_L-4Z_c^3,$$

$$b_{18}=\frac{N^4T_m^2}{C_0^2}\left(\frac{R_L}{12}-\frac{Z_c}{3}\right)-\frac{N^2T_m}{C_0}(3Z_c^2-2Z_cR_L)+2Z_c^2R_L-2Z_c^3,$$

$$b_{19}=\frac{N^4T_m^2}{C_0^2}\left(\frac{5R_L}{6}-\frac{10Z_c}{3}\right)-4Z_c^2R_L+4Z_c^3,$$

$$b_{20}=\frac{N^4T_m^2}{C_0^2}\left(\frac{R_L}{12}-\frac{Z_c}{3}\right)+\frac{N^2T_m}{C_0}(3Z_c^2-2Z_cR_L)+2Z_c^2R_L-2Z_c^3.$$

[1] G. A. Steel, ''Techniques for tailoring sonar transducer responses,'' Ph.D. Thesis, University of Birmingham, United Kingdom (1986).
[2] G. A. Steel, B. V. Smith, and B. K. Gazey, ''Tunable sonar transducer,'' Electron. Lett. **22**, 758–759 (1986).
[3] G. A. Steel, B. V. Smith, and B. K. Gazey, ''Active electronic-control of the response of a sonar transducer,'' Proc. Inst. Acoust. **9**, 79–87 (1987).
[4] S. K. Jain and B. V. Smith, ''Tunable sandwich transducer,'' Electron. Lett. **24**, 311–312 (1988).
[5] W. Chenghao and Z. Zheying, ''Principle of piezoelectric-tunable transducer,'' Chin. J. Acoust. **2**, 16–24 (1983).
[6] B. A. Kasatkin and N. Y. Pavin, ''Piezoelectric transducer with controlled response characteristics,'' Sov. Phys. Acoust. **29**, 418–419 (1983).
[7] B. A. Kasatkin and Y. V. Matvienko, ''Cylindrical piezoelectric transducer with controllable characteristics,'' Sov. Phys. Acoust. **28**, 384–386 (1982).
[8] S. Yamamizu and N. Chubachi, ''Ultrasonic transducer composed of two piezoelectric layers with variable weighting,'' Jpn. J. Appl. Phys. **24**, Suppl. 24(1), 68–70 (1985).
[9] J. A. Hossack and A. Auld, ''Improving the characteristics of a transducer using multiple Piezoelectric layers,'' IEEE Trans. Ultrason. Ferroelectr. Freq. Control **40**, 131–139 (1993).
[10] B. Hamonic and J. N. Decarpigny, ''Multifrequency tonpiltz,'' in *Proceedings Power Sonic and Ultrasonic Transducer Design* (Springer-Verlag, Heidelberg, 1988), pp. 103–105.
[11] H. A. B. Alwi, ''Tunable transducers: The tunable range and the chirp responses,'' Ph.D. Thesis, University of Birmingham, United Kingdom (1995).
[12] H. A. B. Alwi, Brian V. Smith, and John R. Carey, ''Tunable transducers,'' Proc. Inst. Acoust. **17**, 173–182 (1995).
[13] Hasan A. B. Alwi, Brian V. Smith, and John R. Carey, ''Factors which determine the tunable frequency range of tunable transducers,'' J. Acoust. Soc. Am. **100**, 840–847 (1996).
[14] Gregg D. Larson, Peter H. Rogers and Walter Munk, ''State switched transducers: A new approach to high-power, low-frequency, underwater projectors,'' J. Acoust. Soc. Am. **103**, 1428–1441 (1998).
[15] S. Saitoh, M. Izumi, and Y. Mine, ''A dual frequency ultrasonic probe for medical applications,'' IEEE Trans. Ultrason. Ferroelectr. Freq. Control **42**, 294–300 (1995).
[16] Hasan A. B. Alwi, Brian V. Smith, and John R. Carey, ''Chirp response of a single-plate transducer,'' J. Acoust. Soc. Am. **100**, 3655–3664 (1996).
[17] R. E. Challis and J. A. Harrison, ''Rapid solutions to the transient response of piezoelectric elements by *z*-transform technique,'' J. Acoust. Soc. Am. **74**, 1773–1680 (1983).
[18] D. A. Berlincourt, D. R. Curran, and H. Jaffe, ''Piezoelectric and piezomagnetic materials and their function in transducers,'' in *Physical Acoustics*, edited by W. P. Mason (Academic, New York, 1964), Vol. 1, Part A.

The measurement of structural mobilities of a circular cylindrical shell

Ruisen Ming, Jie Pan, and Michael P. Norton
Department of Mechanical and Materials Engineering, The University of Western Australia, Nedlands 6907, Australia

(Received 14 April 1999; revised 17 November 1999; accepted 21 November 1999)

Structural mobility is useful for the estimation of structural power flows in coupled systems. Although the methods of measuring structural mobilities are easily found for one-dimensional beam structures, few are available for cylindrical shells. In this paper, a new method is proposed for the measurement of the structural mobilities of a circular cylindrical shell. A point force excitation is used instead of circumferential modal forces which are difficult to implement in practice. This method utilizes the least squares technique to obtain the transfer function components of different circumferential modes from the measured data. Experiments were carried out on a circular cylindrical shell with different end conditions excited by a point force to verify the feasibility of this proposed method. © *2000 Acoustical Society of America.* [S0001-4966(00)00603-2]

PACS numbers: 43.40.Ey, 43.20.Ye [CBB]

INTRODUCTION

Circular cylindrical shells are important elements of many types of industrial and defense structures. For the control of noise and vibration in coupled cylindrical shell systems, it is necessary to characterize the structural wave field and the vibrational energy transmission across structural joints. This characterization can be made by using structural mobility functions.[1] The theoretical calculation of structural mobilities of a circular cylindrical shell has been studied by several authors.[1–4] However, the experimental measurement of the structural mobilities has received scant attention, perhaps due to the difficulties in practically implementing a desirable circumferential modal force or in experimentally decomposing the wave components of different circumferential modes. To date few methods are available for measuring the structural mobilities of a circular cylindrical shell.

The structural vibration of a circular cylindrical shell exhibits a two-dimensional modal pattern, presented by the superposition of axial and circumferential modes. The vibrational components of different circumferential modes are orthogonal to each other and are required to be decomposed in the analysis. Jong and Verheij have proposed a method[5] to experimentally decompose the acceleration components of $n=0,1,2$ circumferential modes at frequencies below the $n=3$ cutoff frequency in the wave field where the higher order circumferential modal responses become insignificant. This method utilizes the symmetrical nature of a circular cylindrical shell and a group of phase matched accelerometers on the shell surface to obtain the circumferential modal amplitudes and phases. This method cannot be applied to the near wave field or the frequencies above the $n=3$ cutoff frequency because higher order ($n>2$) circumferential modal responses are significant and the simple addition and subtraction of the signals measured on eight symmetrical positions cannot eliminate the effect of the higher order ($n>2$) circumferential modal responses. Recently the authors[6] have successfully applied the method of least squares to decompose the vibration components of different circumferential modes. Theoretically this method has no frequency limit and can be applied to the case where the vibration is the superposition of many circumferential modes. It has been demonstrated that in the far wave field at frequencies below the $n=3$ cutoff frequency, these two methods give comparable results.[6]

In this paper, a new method is proposed and its theoretical basis is outlined for the measurement of structural mobilities in a circular cylindrical shell. A point force excitation is employed instead of a desirable circumferential modal force excitation which is difficult to implement in practice. Therefore, the response of the shell is the superposition of different circumferential modes. This proposed method uses an array of phase matched accelerometers to simultaneously measure dynamical responses at several positions around the cross section of interest in a circular cylindrical shell. Then the method of least squares is used during the data processing to decompose the transfer function components of different circumferential modal accelerations to the input force. A series of experiments was carried out under laboratory conditions to verify the feasibility of this proposed method.

I. STRUCTURAL MOBILITIES

A. Prediction

Consider a circular cylindrical shell of thickness h, radius a and length L. Let the shell be referenced to a cylindrical coordinate system (r,θ,x) where x is taken in the axial direction of the shell, θ measures the angle in the circumferential direction, and the r axis is directed outward along the radial direction, as shown in Fig. 1. If only a radial force per unit area, F, acts on the shell surface and if u, v and w represent the displacement components of the shell middle surface in the axial, tangential and radial directions, respectively, the equation of motion (Reissner–Naghdi–Berry theory) for an element of shell can be written as[7,8]

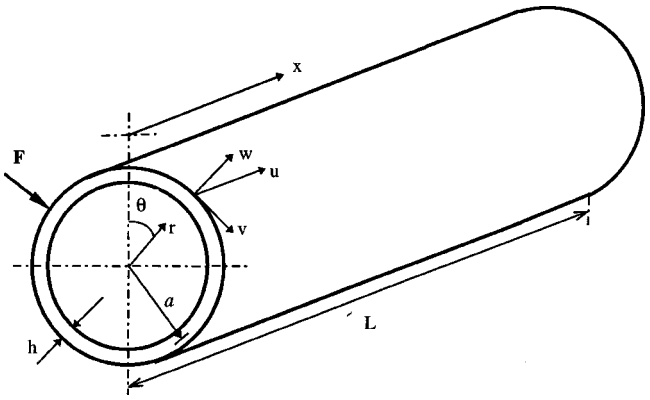

FIG. 1. Coordinates for a circular cylindrical shell.

$$\left[\frac{\partial^2}{\partial x^2}+\frac{1-\mu}{2a^2}\frac{\partial^2}{\partial\theta^2}-\frac{1}{c_p^2}\frac{\partial^2}{\partial t^2}\right]u+\frac{1+\mu}{2a}\frac{\partial^2 v}{\partial x\,\partial\theta}+\frac{\mu}{a}\frac{\partial w}{\partial x}=0; \tag{1a}$$

$$\frac{1+\mu}{2a}\frac{\partial^2 u}{\partial x\,\partial\theta}+(1+\beta^2)\left[\frac{1-\mu}{2}\frac{\partial^2}{\partial x^2}+\frac{1}{a^2}\frac{\partial^2}{\partial\theta^2}-\frac{1}{c_p^2}\frac{\partial^2}{\partial t^2}\right]v+\left[\frac{1}{a^2}\frac{\partial}{\partial\theta}-\beta^2\left(\frac{1}{a^2}\frac{\partial^3}{\partial\theta^3}+\frac{\partial^3}{\partial x^2\,\partial\theta}\right)\right]w=0; \tag{1b}$$

$$\frac{\mu}{a}\frac{\partial u}{\partial x}+\left[\frac{1}{a^2}\frac{\partial}{\partial\theta}-\beta^2\left(\frac{1}{a^2}\frac{\partial^3}{\partial\theta^3}+\frac{\partial^3}{\partial x^2\,\partial\theta}\right)\right]v+\frac{1}{a^2}\left[1+\beta^2\nabla^4+\frac{a^2}{c_p^2}\frac{\partial^2}{\partial t^2}\right]w=-\frac{F}{B}, \tag{1c}$$

where μ is the Poisson's ratio, c_p is the phase speed of an extensional wave propagating in a thin plate, $\beta^2=h^2/12a^2$, $\Delta^2=a^2(\partial^2/\partial x^2)+\partial^2/\partial\theta^2$ is a Laplacian type operator, $B=Eh/(1-\mu^2)$ is the extensional rigidity. At cross section x, the effective transverse force S_x, the bending moment M_x, the extensional stress N_x and the effective shear stress T_x can be expressed as[8]

$$S_x=D\left(\frac{2-\mu}{a^2}\frac{\partial^2 v}{\partial x\,\partial\theta}-\frac{4-3\mu}{a^2}\frac{\partial^3 w}{\partial x\,\partial\theta^2}-\frac{\partial^3 w}{\partial x^3}\right); \tag{2a}$$

$$M_x=D\left(\frac{\mu}{a^2}\left(\frac{\partial v}{\partial\theta}-\frac{\partial^2 w}{\partial\theta^2}\right)-\frac{\partial^2 w}{\partial x^2}\right); \tag{2b}$$

$$N_x=B\left(\frac{\partial u}{\partial x}+\frac{\mu}{a}\left(\frac{\partial v}{\partial\theta}+w\right)\right); \tag{2c}$$

$$T_x=\frac{B(1-\mu)}{2)}\left(\frac{1}{a}\frac{\partial u}{\partial\theta}+(1+2\beta^2)\frac{\partial v}{\partial x}-4\beta^2\frac{\partial^2 w}{\partial x\,\partial\theta}\right), \tag{2d}$$

where $D=Eh^3/(12(1-\mu^2))$ is the bending rigidity of the shell.

The displacement components of the wave propagating in a finite circular cylindrical shell can be expressed in the following forms:[9]

$$u=\sum_{n=0}^{\infty}u_n=\sum_{n=0}^{\infty}\sum_{s=1}^{m}U_{ns}\cos(n\theta+\theta_{n0})\times\exp(-ik_{ns}x+i\omega t+i\pi/2), \tag{3a}$$

$$v=\sum_{n=1}^{\infty}v_n=\sum_{n=1}^{\infty}\sum_{s=1}^{8}V_{ns}\sin(n\theta+\theta_{n0})\times\exp(-ik_{ns}x+i\omega t), \tag{3b}$$

$$w=\sum_{n=0}^{\infty}w_n=\sum_{n=0}^{\infty}\sum_{s=1}^{m}W_{ns}\cos(n\theta+\theta_{n0})\times\exp(-ik_{ns}x+i\omega t), \tag{3c}$$

where θ_{n0} is a constant number representing the polarization angle of nth circumferential mode; ω is the radian frequency; n is the circumferential modal number; k_{ns} is the axial wave number and subscript s corresponds to the axial wave number solutions. In general, $\theta_{n0}=n\theta_{10}$ does not hold. For a single force excitation, however, this relation will hold. For the breathing mode ($n=0$), the tangential component of displacement is zero (actually the pure torsional wave exists but is uncoupled with other wave components in circular cylindrical shells) and the characteristic equation of the system is sixth order. Therefore, three pairs ($m=6$) of axial wave number solutions exist for a finite circular cylindrical shell. Each pair of solutions has the same magnitude but different phases representing the axial waves simultaneously propagated along cylindrical shells in both positive and negative directions. For $n>0$, however, the characteristic equation of the system is eighth order and four pairs ($m=8$) of axial wave number solutions are possible. A pure imaginary or complex wave number corresponds to an evanescent wave which is important at positions near the source but becomes insignificant at positions more than one wavelength away from the source. Only the wave with a pure real wave number can propagate along cylindrical shells. For each n and s pair, the coefficient ratios, $\alpha_{uns}=U_{ns}/W_{ns}$ and $\alpha_{vns}=V_{ns}/W_{ns}$, can be obtained by solving Eqs. (1a) and (1b).

Substituting Eq. (3) into (2) gives the stress and moment resultant vectors at the two ends, $x=0$ and $x=L$, of the cylindrical shell as

$$Q|_{x=0}=[S_x\quad M_x\quad N_x\quad T_x]^T|_{x=0}=\sum_{n=0}^{\infty}J_n[G_n,-G_n]A_n^0X_n; \tag{4a}$$

$$Q|_{x=l}=[S_x\quad M_x\quad N_x\quad T_x]^T|_{x=L}=\sum_{n=0}^{\infty}J_n[G_n,-G_n]A_n^LX_n, \tag{4b}$$

where $G_n(1,s)=-(iD/a^3)((k_{ns}a)^3+(4-3\mu)n^2k_{ns}a+(2-\mu)nk_{ns}a\alpha_{vns})$;

$$G_n(2,s)=\frac{D}{a^2}((k_{ns}a)^2+\mu n^2+n\mu\alpha_{vns});$$

$$G_n(3,s)=\frac{B}{a}(k_{ns}a\alpha_{uns}+\mu n\alpha_{vns}+\mu);$$

$$G_n(4,s)=\frac{1-\mu}{2}\frac{B}{a}(n\alpha_{uns}+(1+2\beta^2)k_{ns}a\alpha_{vns}+4n\beta^2k_{ns}a)\quad(s=1,2,3,4);$$

$J_n = \text{diag}\{\cos(n\theta+\theta_{n0}), \cos(n\theta+\theta_{n0}), \cos(n\theta+\theta_{n0}), \sin(n\theta+\theta_{n0})\}$, $A_n^0 = \text{diag}\{E_m, B_m\}$, $A_n^L = \text{diag}\{B_m, E_m\}$ and $B_m = \text{diag}\{\exp(-ik_{n1}L), \exp(-ik_{n2}L), \ldots, \exp(-ik_{nm}L)\}$ are diagonal matrices; E_m is an $m\times m$ unit matrix ($m=3$ for $n=0$ and $m=4$ for $n>0$); $X_0=[W_{01}, W_{02}, \ldots, W_{06}]^T$ and $X_n=[W_{n1}, W_{n2}, \ldots, W_{n8}]^T$ ($n>0$). X_n can be determined by solving the matrix equations resulting from the end boundary conditions. For the calculation of structural mobilities of a finite cylindrical shell, a free end condition is usually assumed at the end of $x=0$ and a desirable external force vector is assumed to act on it. For example, for the calculation of the radial force mobilities, only one external radial force is assumed to act on the end of $x=0$ and this external force vector may consist of many circumferential modal forces, that is, $F=\Sigma_{n=0}^{\infty}[F_n,0,0,0]^T$. The force equilibrium at the end of $x=0$ gives a matrix equation, $Q|_{x=0}=F$. The boundary condition at the other end ($x=L$) will depend on practical considerations. For a free end condition, $Q|_{x=l}=0$. For a simply supported end condition, $[M_x, N_x, \partial w/\partial x, u]^T|_{x=l}=0$, where M_x and N_x can be obtained from Eq. (4b). For a clamped end condition, $[u, v, w, \partial w/\partial x]|_{x=l}=0$. After X_n is determined, all the components of displacement at any position of the shell can be calculated and then the structural mobilities can be evaluated from the ratios of the corresponding velocity components at the desirable position to the acting external circumferential force.

B. Measurement

It is difficult in practice to generate a force which only excites a single circumferential mode. If a point force is applied to a circular cylindrical shell, the response of the shell will be the superposition of different circumferential modal components ($n=0,1,2,\ldots$). This is because a point force is the sum of different circumferential modal forces (theoretically the circumferential modal number ranges from 0 to infinite). For example, if a point force f_0 acts at the position ($x=0$, $\theta=\theta_0$), the radial force per unit area can be expressed as

$$F = f_0\,\delta(x-0)\,\delta(a\theta-a\theta_0) = \sum_{n=0}^{\infty} F_n \cos(n(\theta-\theta_0)), \tag{5}$$

where $F_n=(1/\Lambda_n)f_0\delta(x-0)$; Λ_n is equal to 2π for $n=0$ and π for $n>0$.

By definition, the structural mobility of the nth circumferential mode is the ratio of the nth circumferential modal velocity to the nth circumferential modal force. For example, the input radial force mobility of the nth circumferential mode can be expressed as

$$Y_n^{wF} = \frac{\dot{w}_n}{F_n} = \frac{\Lambda_n \ddot{w}_n}{i\omega f_0} = \frac{\Lambda_n H_n^{wF}}{i\omega}, \tag{6}$$

where H_n^{wF} is the transfer function of the nth circumferential modal radial acceleration component to the input point force. Similarly, the cross mobility Y_n^{vF}, the ratio of the tangential velocity component to the radial force component of the nth circumferential mode, can be expressed as

$$Y_n^{vF} = \frac{\dot{v}_n}{F_n} = \frac{\Lambda_n \ddot{v}_n}{i\omega f_0} = \frac{\Lambda_n H_n^{vF}}{i\omega}, \tag{7}$$

where H_n^{vF} is the transfer function of the tangential acceleration component of the nth circumferential mode to the input point force. The above equations show that the measurement of the structural mobility for the nth circumferential mode is the measurement of the transfer function of the nth circumferential modal acceleration component to the input point force. In order to determine the structural mobility, it is necessary to extract the corresponding transfer function component of the desirable circumferential mode from the measured transfer function signal.

Since the accelerometer is attached on the shell outer surface during the measurement, its output signal is not equal to the acceleration component of the shell middle surface unless the accelerometer main axis is lying along the radial direction. The relationships between the measured transfer function signals and the transfer function of the acceleration components on the shell middle surface to the input point force are given by[7]

$$\begin{aligned} H_m^{uF} &= H^{uF} - d\frac{\partial H^{wF}}{\partial x};\\ H_m^{vF} &= \left(1+\frac{d}{a}\right)H^{vF} - \frac{d}{a}\frac{\partial H^{wF}}{\partial \theta}; \quad H_m^{wF} = H^{wF}, \end{aligned} \tag{8}$$

where d is the distance between the main axis of the rotational accelerometer and the shell middle surface; H_m^{uF}, H_m^{vF} and H_m^{wF} are the measured transfer function signals when the main axis of the accelerometer is lying along the axial, tangential and radial directions, respectively. To calculate H^{uF} and H^{vF}, it is necessary to know H^{wF} and its first order derivative first. The first order derivative of H^{wF} can be estimated from the data measured at two adjacent cross-sections close to the cross-section of interest.

Substituting Eq. (3) into (8) gives

$$\begin{aligned} H_m^{uF} &= \sum_{n=0}^{\infty}\left(H_n^{uF} - d\frac{\partial H_n^{wF}}{\partial x}\right)\cos[n\theta+\theta_{n0}]\\ &= \sum_{n=0}^{\infty} H_{mn}^{uF}\cos[n\theta+\theta_{n0}]; \end{aligned} \tag{9a}$$

$$\begin{aligned} H_m^{vF} &= \sum_{n=1}^{\infty}\left[\left(1+\frac{d}{a}\right)H_n^{vF} + \frac{nd}{a}H_n^{wF}\right]\sin[n\theta+\theta_{n0}]\\ &= \sum_{n=0}^{\infty} H_{mn}^{vF}\sin[n\theta+\theta_{n0}]; \end{aligned} \tag{9b}$$

$$H_m^{wF} = \sum_{n=0}^{\infty} H_n^{wF}\cos[n\theta+\theta_{n0}]. \tag{9c}$$

Note that the modal transfer function components, H_{mn}^{uF}, H_{mn}^{vF} and H_n^{wF}, are complex numbers and they are characterized by an amplitude and phase (or real and imaginary parts). When the structural wave field is dominated by several circumferential modes, the measured transfer functions will be approximately equal to the sum of those dominating transfer

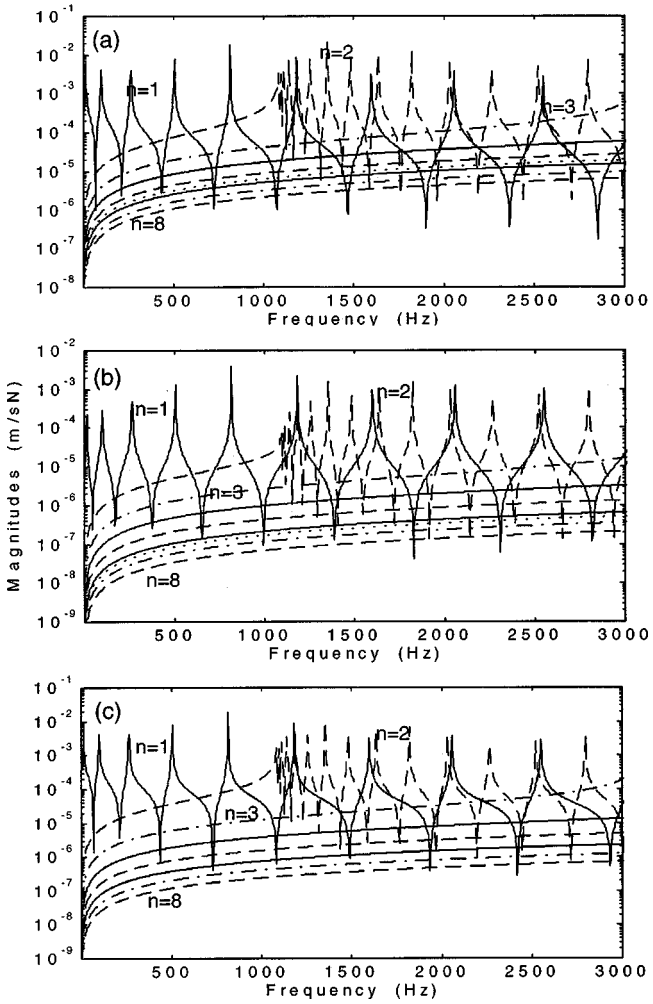

FIG. 2. Predicted magnitudes of the radial force mobilities [(a) Y^{wF}; (b) Y^{uF}; (c) Y^{vF}] of a finite steel circular cylindrical shell under the free–free end conditions for different circumferential modes: $n=0$ (- - - - -); $n=1,4,6$ (------); $n=2,5,8$ (— — —) and $n=3,7$ (———).

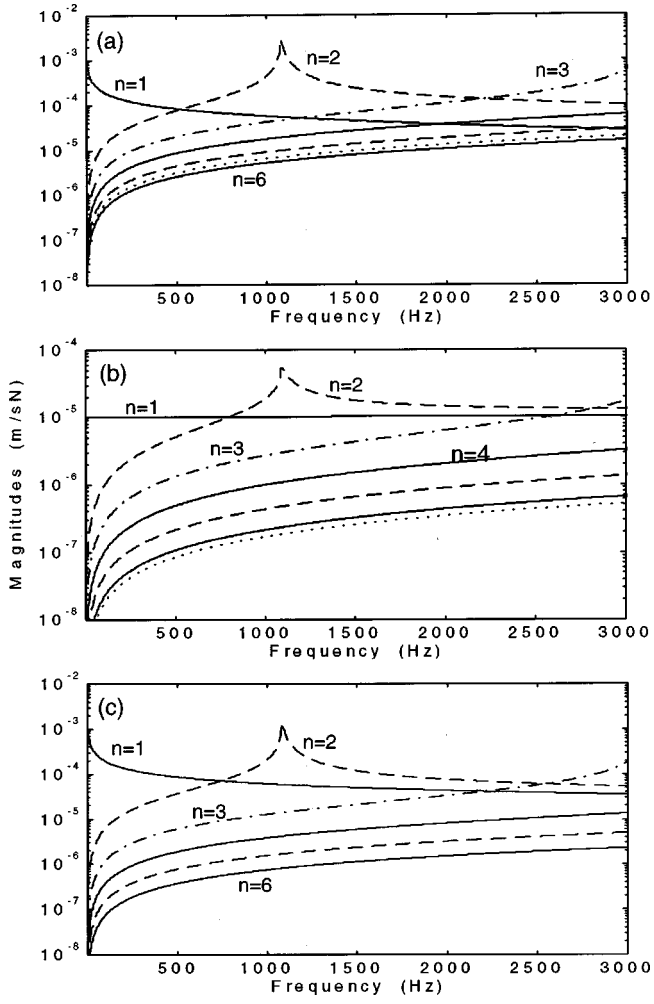

FIG. 3. Predicted magnitudes of the radial force mobilities [(a) Y^{wF}; (b) Y^{uF}; (c) Y^{vF}] of a semi-infinite steel circular cylindrical shell for different circumferential modes: $n=0$ (- - - - -); $n=1,4,6$ (------); $n=2,5$ (— — —) and $n=3$ (———).

function components (that is, the summations in the above equations are taken by only considering these dominating circumferential modes). For a circular cylindrical shell at frequencies below the mth cutoff frequency, the responses of the higher order ($n>m$) circumferential modes at the source position do not display any resonance peak and they decrease with increasing circumferential number n. Therefore, the measured transfer functions in a frequency range can be approximately decomposed into a finite number of dominating circumferential modal components. In order to determinate all three orthogonal modal transfer function components at frequencies where m circumferential modes dominate, it is required to perform the measurements on at least $N=2m$ [or $N=2m-1$ if the breathing ($n=0$) mode is included] positions (for a single force excitation, $\theta_{n0}=n\theta_{10}$ holds, N will reduces to $m+1$) in the three orthogonal directions at the cross-section of interest. The required minimum measurement position number depends on the unknown coefficient number of the circumferential modes of interest. It is also noted that the separation distance between adjacent accelerometers should be less than $\pi a/m$ to satisfy the Nyquist spatial sampling criterion.[10]

Although theoretically a vector containing N unknown quantities can be determined from N experimental data, the solution is usually unreliable because of measurement errors and ill conditioned coefficient matrices due to the selection of inappropriate measurement locations. A reliable solution needs more than N measurement positions.[11] The method of least squares[11] can be used to extract H_{mn}^{uF}, H_{mn}^{vF} and H_n^{wF} from the measured real and imaginary parts of H_m^{uF}, H_m^{vF} and H_m^{wF} at more than N positions around a cross-section. For example, at frequencies where m circumferential modes dominate, these dominating radial transfer function components can be obtained from the minimization of its error function e_w

$$e_w=\sum_{i=1}^{N}\left[H_{m,i}^{wF}-\sum_m H_n^{wF}\cos(n\theta+\theta_{n0})\right]^2, \tag{10}$$

where $N(>(2m-1))$ is the total number of the measurement positions on the cross section of interest and $H_{m,i}^{wF}$ is the measured radial transfer function component at position i. To obtain a minimum value of the error function, both H_n^{wF} and θ_{n0} need to be adjusted. The minimization of e_w is divided into two steps. The first step is to find optimal H_n^{wF} for a

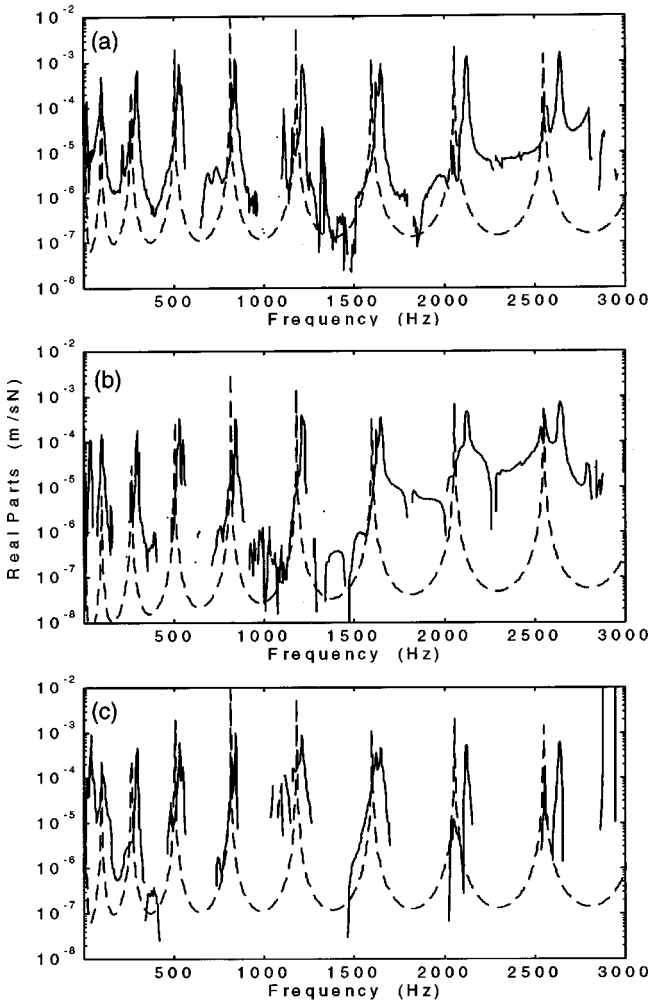

FIG. 4. Measured (-------) and predicted (— — — –) real parts of the radial force mobilities of a finite steel circular cylindrical shell under the free–free end conditions for $n=1$: (a) Re$\{Y_1^{wF}\}$; (b) Re$\{Y_1^{uF}\}$; (c) negative values of Re$\{Y_1^{vF}\}$.

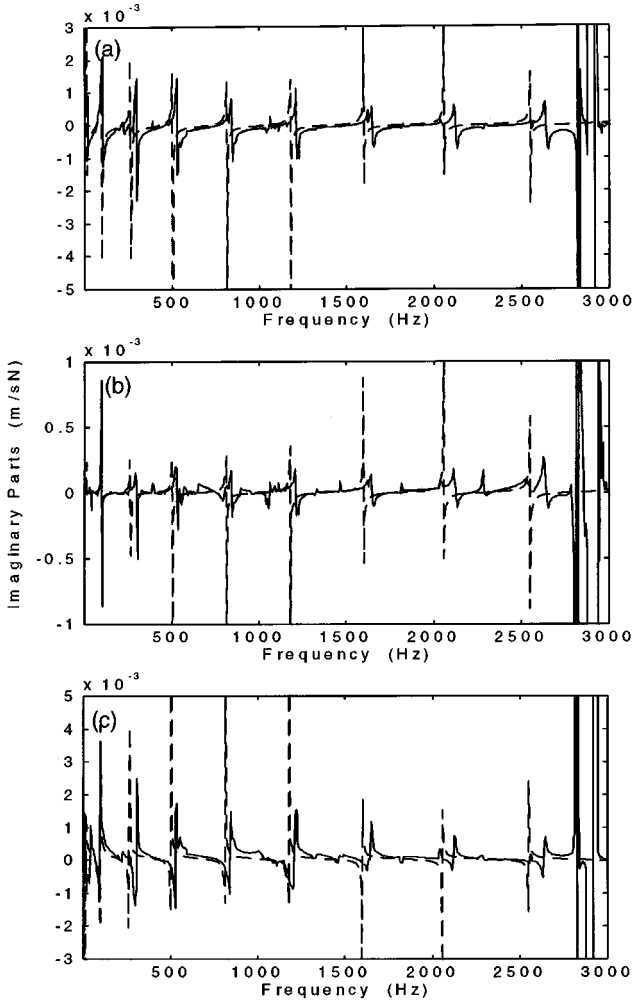

FIG. 5. Measured (--------) and predicted (— — — –) imaginary parts of the radial force mobilities of a finite steel circular cylindrical shell under the free–free end conditions for $n=1$: (a) Im$\{Y_1^{wF}\}$; (b) Im$\{Y_1^{uF}\}$; (c) Im$\{Y_1^{vF}\}$.

given θ_{n0}. The second step is to determine the optimal θ_{n0} by finding the minimum value of the error $e_w(\theta_{n0})$. The final result of the two minimizations gives rise to the modal amplitude of the transfer function and the true value of the polarization angle θ_{n0}.

II. RESULTS AND DISCUSSIONS

A. Experimental setup

A 2.2-m-long steel circular cylindrical shell of $a=32.5$ mm and $h=1.7$ mm was used in the experiment. Two types of end conditions were chosen: (1) free–free end conditions; (2) free-damped end conditions. For the case of free–free end conditions, the cylindrical shell was supported (nearly point contact) at positions 0.5 m away from both ends by two piano wire fixed on a frame via two very soft foam pads. Due to very low damping in the shell structure, light ($1.6\,\mathrm{kg/m^2}$) damping strips (Idikell) were attached to the shell outer surface (covering about 60% of the total surface area) to increase the energy dissipation in the shell. The mass loading of the damping strips is small (surface mass density ratio is less than 8%) and the effect on the structural wave field should be negligible. For the case of free-damped end conditions, the shell was supported at a position 0.5 m away from its free end by a piano wire with a very soft foam pad and its another end was buried (0.5 m) in a dry sand filled box which intended to provide an effectively absorptive termination for all circumferential modes and wave types. For both cases, the (free) end of interest was driven in the radial direction by a mechanical shaker fed with a pseudo-random noise signal.

To measure the driving force, an impedance head was mounted at the driving location. The shaker and the impedance head were connected by a steel rod of 30 mm in length and 1 mm in diameter to avoid possible axial and tangential force excitations. Since the excitation was stable, the responses at different positions around the cross section of interest were measured by one (B&K 4375) accelerometer at different times. Therefore, the measured data should contain no phase matching error. For the measurement of axial and tangential acceleration components, an aluminum cube of 10 mm side dimensions was used to construct a rotational accelerometer. The masses of the accelerometer and the cube are 2.4 g and 2.7 g, respectively. The predicted normalized mass loading errors of measured accelerations are negligible

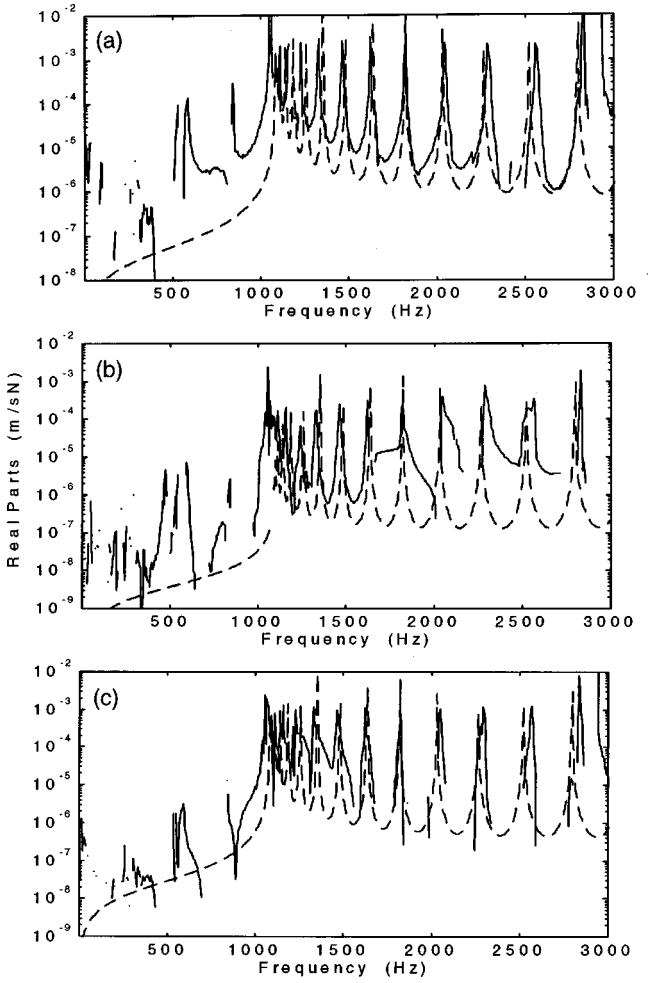

FIG. 6. Measured (--------) and predicted (— — — –) real parts of the radial force mobilities of a finite steel circular cylindrical shell under the free-free end conditions for $n=2$: (a) Re$\{Y_1^{wF}\}$; (b) Re$\{Y_1^{uF}\}$; (c) negative values of Re$\{Y_1^{vF}\}$.

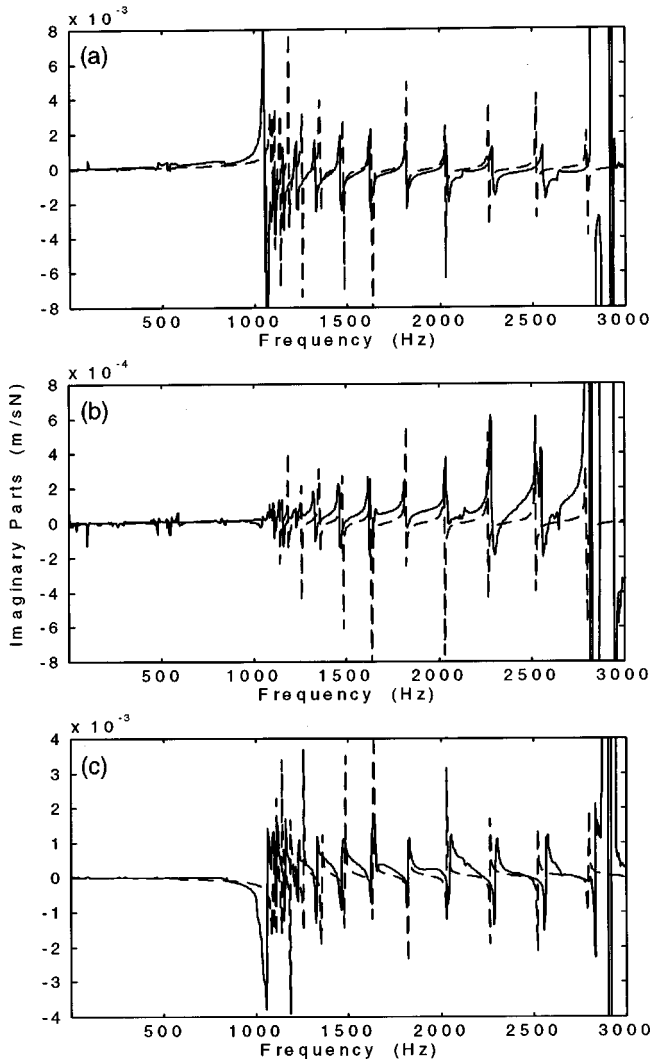

FIG. 7. Measured (-------) and predicted (— — — –) imaginary parts of the radial force mobilities of a finite steel circular cylindrical shell under the free–free end conditions for $n=2$: (a) Im$\{Y_1^{wF}\}$; (b) Im$\{Y_1^{uF}\}$; (c) Im$\{Y_1^{vF}\}$.

in the frequency range of interest. The transverse sensitivity of the accelerometer was measured using a B&K 4294 Calibration Exciter and an aluminum cube. Two points were marked on the accelerometer in the two orthogonal transverse axes, one of them has a minimum transverse sensitivity reading. The transverse sensitivity components in the two orthogonal transverse axes were 0.91% and 2.67%, respectively, at 159 Hz. During the measurements, the two orthogonal transverse axes (or the marked points) were directed along the axial, tangential or radial directions, respectively, depending on which acceleration component is of primary interest. The errors due to the presence of accelerometer transverse sensitivity were eliminated using the following equation during data processing:

$$\begin{bmatrix} u \\ v \\ w \end{bmatrix} = \begin{bmatrix} 1 & \alpha_{x\theta} & \alpha_{xr} \\ \alpha_{\theta x} & 1 & \alpha_{\theta r} \\ \alpha_{rx} & \alpha_{r\theta} & 1 \end{bmatrix}^{-1} \begin{bmatrix} u_m \\ v_m \\ w_m \end{bmatrix}, \tag{11}$$

where $\alpha_{x\theta}$ is the tangential component of the transverse sensitivity of the accelerometer whose main axis is directed along the axial direction; (u_m, v_m, w_m) are the measured acceleration signals.

The frequency range of analysis was set up to 3 kHz (from the Love–Timoshenko theory,[8] the predicted cutoff frequencies of the $n=2,3$ circumferential modes are 1079 Hz and 3053 Hz, respectively). In order to know the dominating circumferential mode number at frequencies of interest and then to determine the measurement position number at the cross-section of interest, the magnitudes of low order circumferential modal mobility components are predicted, as shown in Fig. 2 for a finite steel cylindrical shell with free–free end conditions and in Fig. 3 for a semi-infinite steel cylindrical shell. It can be seen that the mobility components of $n=1,2,3$ circumferential modes dominate at frequencies of interest. The measured transfer functions in Eq. (9) should be approximately equal to the sum of the $n=1,2,3$ circumferential modal components. Due to the point force excitation, $\theta_{n0}=n\theta_{10}$ holds. Therefore, at least four unknown quantities are required to be determined for the estimation of circumferential modal mobility components at frequencies of interest. To assess the effect of the summation number in Eq. (9) on the measurement accuracy, different sets of circumferential modes ($n=1,2,3$; $n=1,2,3,4$, $n=1,2,3,4,5$ and

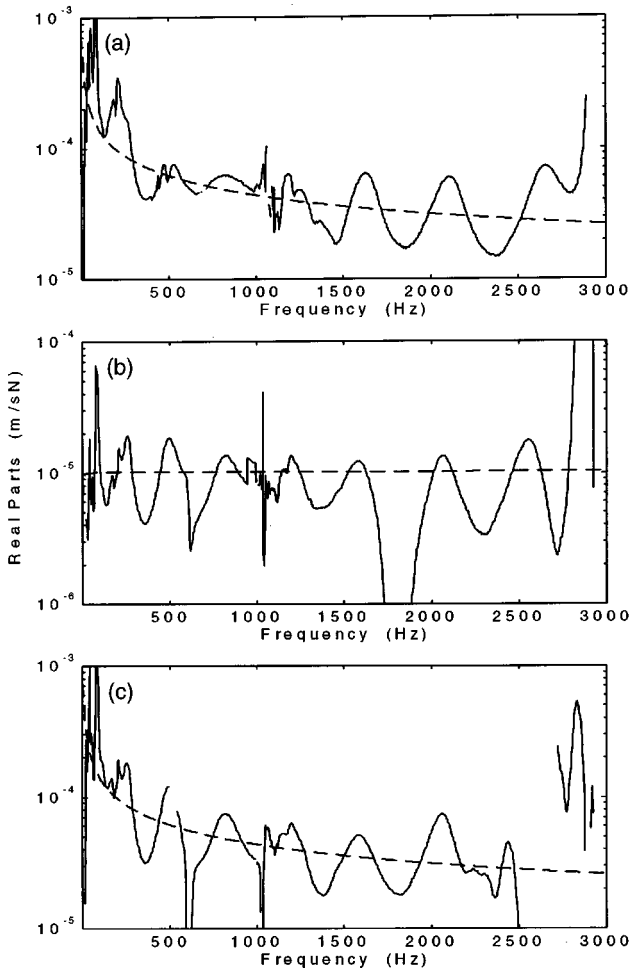

FIG. 8. Measured (-------) and predicted (— — — –) real parts of the radial force mobilities of a finite steel circular cylindrical shell under the free-damped end conditions for $n=1$: (a) Re$\{Y_1^{wF}\}$; (b) Re$\{Y_1^{uF}\}$; (c) negative values of Re$\{Y_1^{vF}\}$.

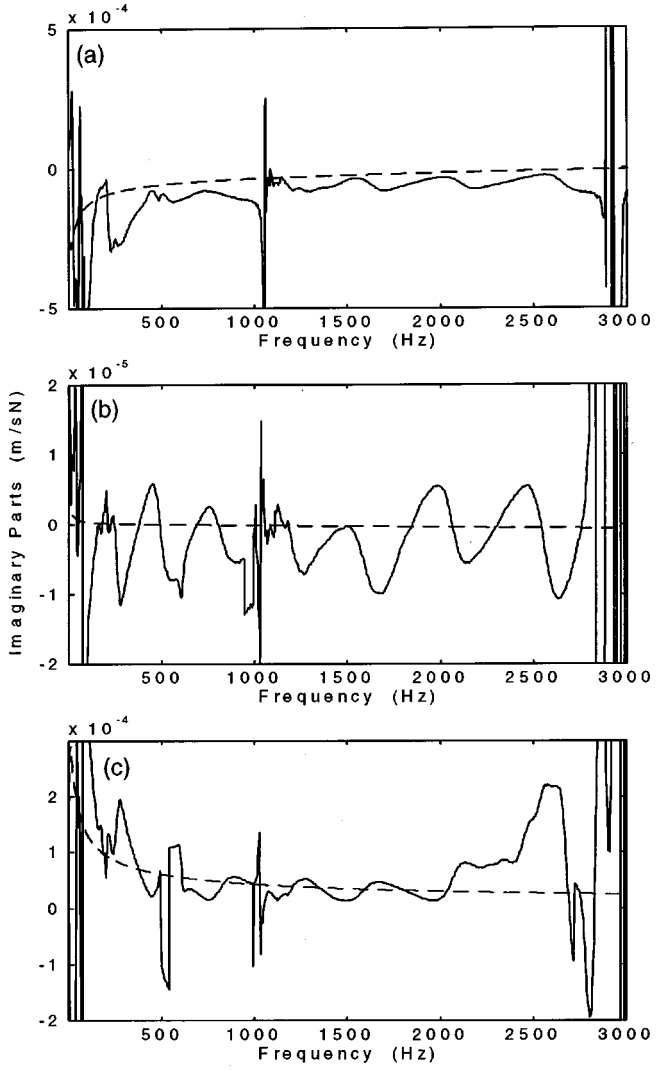

FIG. 9. Measured (-------) and predicted (— — — –) imaginary parts of the radial force mobilities of a finite steel circular cylindrical shell under the free-damped end conditions for $n=1$: (a) Im$\{Y_1^{wF}\}$; (b) Im$\{Y_1^{uF}\}$; (c) Im$\{Y_1^{vF}\}$.

$n=0,1,2,3,4,5$) are considered in the date processing for estimating the $n=1,2$ circumferential modal mobility components from the same measurement data. It is shown that all the results agree well, especially at frequencies close to the resonance frequencies. The results shown in the following figures are obtained by considering 4 ($n=1,2,3,4$) circumferential modes only from data measured on 12 positions. Twelve measurement positions were uniformly distributed (the radial angle between the neighboring positions was 30°) around the free end cross section. For the calculation of the axial transfer function component, the first order derivative of H_n^{wF} was estimated from the data measured around the cross-section of the free end and that of 15 mm away from the free end. Every measured transfer function signal (both real and imaginary parts) was recorded in a dual-channel real-time frequency analyzer.

B. Measurement of structural mobilities

For the cylindrical shell under test, the mobility component of the breathing ($n=0$) mode is quite small compared with those of $n=1,2$ circumferential modes at most frequencies, as shown in Figs. 2 and 3. The measured $n=0$ mobility components were much higher than the predicted ones at most frequencies and they were the residues. Therefore, the measured mobility curves of the breathing ($n=0$) mode will not be shown in the following. Only the mobility components of $n=1,2$ circumferential modes were considered in the analysis.

Figures 4–7 show the comparisons of the measured and predicted real and imaginary parts of the input and cross radial force mobilities of the finite circular cylindrical shell under the free–free end conditions for $n=1$ and 2, respectively. In Figs. 4(c) and 6(c) the negative values of the real parts of the cross mobility Y_n^{vF} are shown. It can be seen that both the predicted and measured mobility curves show peaks at the resonant frequencies. The predicted resonant frequencies are slightly lower at all frequencies for $n=1$ and at frequencies above 1.82 kHz for $n=2$ but little higher than the measured ones at frequencies below 1.82 kHz for $n=2$. The measured $n=2,3$ cutoff frequencies are 1028 Hz and 2884 Hz which are slightly lower than the predicted ones. These could result from the errors in the assumption of the shell material properties in the predictions. At frequencies below the $n=2$ cutoff frequencies, the measured $n=2$ circumferen-

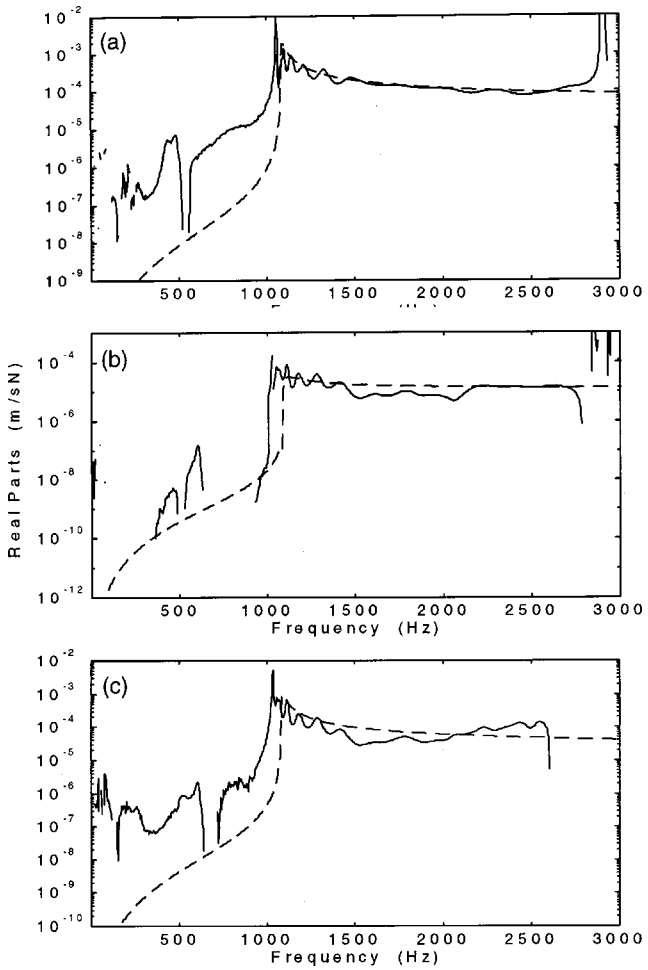

FIG. 10. Measured (-------) and predicted (— — — —) real parts of the radial force mobilities of a finite steel circular cylindrical shell under the free-damped end conditions for $n=2$: (a) Re$\{Y_1^{wF}\}$; (b) Re$\{Y_1^{uF}\}$; (c) negative values of Re$\{Y_1^{vF}\}$.

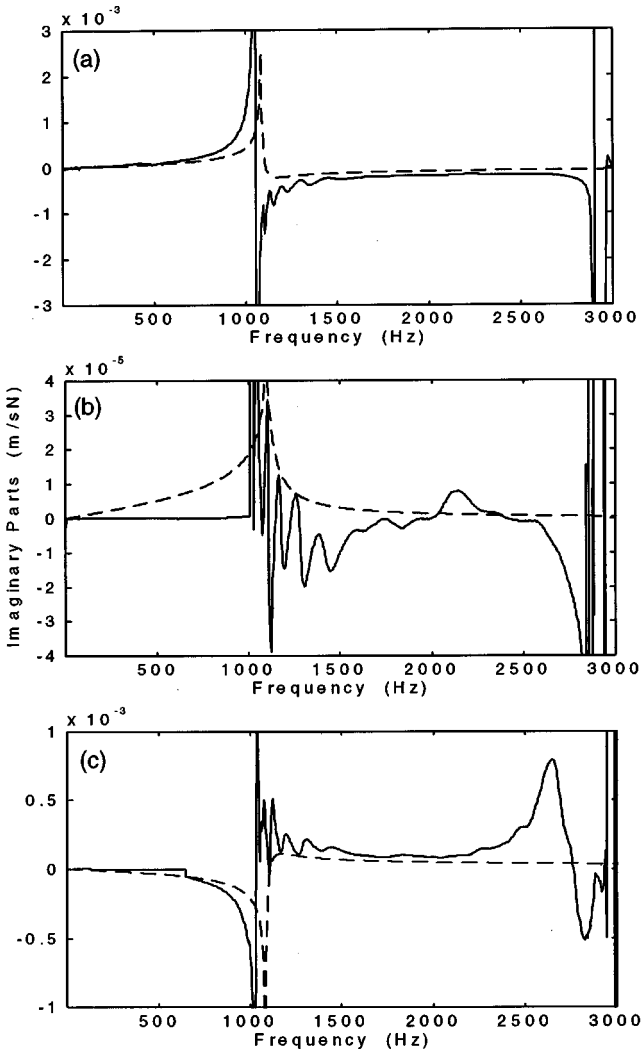

FIG. 11. Measured (-------) and predicted (— — — —) imaginary parts of the radial force mobilities of a finite steel circular cylindrical shell under the free-damped end conditions for $n=2$: (a) Im$\{Y_1^{wF}\}$; (b) Im$\{Y_1^{uF}\}$; (c) Im$\{Y_1^{vF}\}$.

tial modal mobility components do not agree well with the predicted ones. This is because the residual effects of resonances of the $n=1$ circumferential mode. At frequencies above 2884 Hz, the measured curves shown in those figures were not correct because the dominating circumferential modes are different.

From Figs. 4 and 6, it can be seen that a large error could be present in the measured mobilities at nonresonant frequency, especially for cross mobilities. At some nonresonant frequencies especially for Y_n^{vF}, the measured real parts of the mobilities are in opposite signs with or much higher than the predicted values (for clearness, the negative values of Re$\{Y_n^{wF}\}$ and Re$\{Y_n^{uF}\}$ and the positive values of Re$\{Y_n^{vF}\}$ are not shown in the figures). This is because the measurement accuracy of a translational acceleration is usually higher than that of a rotational acceleration, and because the dissipation loss factor of the shell was so small that the wave field was very reactive at nonresonant frequencies. In a very reactive wave field, the measured signals could contain large errors. This indicates that in a reactive wave field, the axial and tangential mobilities at the nonresonant frequencies may not be accurately measured by using this proposed method.

Figures 8–11 show the comparisons of the measured and predicted real and imaginary parts of the input and cross radial force mobilities of the finite circular cylindrical shell under the free-damped end conditions for $n=1$ and 2, respectively. Figures 8(c) and 10(c) show the negative real parts of the cross mobility Y_n^{vF}. It can be seen that the measured mobility curves under the free-damped end conditions is smoother than those under the free–free end conditions shown in Figs. 4–7, even at the troughs, except for the frequencies very close to the cutoff frequencies where a big jump or fluctuation is observed. The reason is that the damped end gave a very effectively absorptive termination. Again, at frequencies above the $n=3$ cutoff frequency, the mobility curves are not correct because of the same reason for Figs. 4–7. The measured mobility curves fluctuate while the predicted ones do not. The frequency averages of the measured real parts of the mobilities are slightly smaller than their predicted ones while those of the measured imaginary parts of the mobilities are a little larger than their predicted ones. This is because the predictions were made based on the semi-infinite circular cylindrical shell model but this assumed model does not accurately represent the actual cylindrical shell system. The damped end absorbed most but not

all of the incident energy. From these figures it may be concluded that for cylindrical shells with free-damped end conditions this proposed method gives accurate results.

III. CONCLUSIONS

A new method is proposed in this paper to measure the structural mobilities of a circular cylindrical shell. This method utilizes a point force excitation instead of circumferential modal forces which are difficult to implement in practice. The method of least squares is employed to obtain the transfer functions of different circumferential modal acceleration components to the input point force. The outlined theory has been experimentally verified on a steel circular cylindrical shell of different end conditions. The measured results show that this proposed method is successful in measuring the structural mobilities of a circular cylindrical shell. The measurement accuracy of this method, however, depends on the acceleration components of interest and the properties of structural wave field. A radial force mobility is usually more accurately measured than the axial or tangential ones because the measurement accuracy of a translational acceleration is higher than that of a rotational one. The absorption in the nonexcitation end will reduce measurement error especially at nonresonant frequencies. Although only a radial force excitation was demonstrated in the experiment, this new method can be applied in principle to the cases of other force excitations such as axial force excitation or acoustical source excitation.

ACKNOWLEDGMENT

Support for this work from Australian Research Council is gratefully acknowledged.

[1] R. S. Ming, J. Pan, and M. P. Norton, ''The mobility functions and their application in calculating power flow in coupled cylindrical shells,'' J. Acoust. Soc. Am. **105**, 1702–1713 (1999).
[2] P. A. Franken, ''Input impedances of simple cylindrical structure,'' J. Acoust. Soc. Am. **32**, 473–477 (1960).
[3] M. Heckl, ''Vibrations of point-driven cylindrical shells,'' J. Acoust. Soc. Am. **34**, 1553–1557 (1962).
[4] C. R. Fuller, ''The input mobility of an infinite circular cylindrical elastic shell filled with fluid,'' J. Sound Vib. **87**, 409–427 (1983).
[5] C. A. F. de Jong and J. W. Verheij, ''Measurement of energy flow along pipes,'' *Second International Congress on Recent Developments in Air and Structure-borne Sound and Vibration*, March 1992, Auburn University, pp. 577–585 (1992).
[6] J. Pan, R. Ming, and M. P. Norton, ''The measurement of structure-borne sound power flows on an elastic cylindrical shell,'' Technical Report, Centre for Vibration and Noise Control, Department of Mechanical and Materials Engineering, The University of Western Australia, Australia (1999) (submitted to J. Sound Vib.).
[7] M. C. Junger and D. Feit, *Sound, Structures and Their Interaction* (The MIT Press, Cambridge, MA, 1972).
[8] A. W. Leissa, *Vibration of Shells* (NASA SP-288, Washington DC, 1973).
[9] C. R. Fuller, ''The effects of wall discontinuities on the propagation of flexural waves in cylindrical shells,'' J. Sound Vib. **75**, 207–228 (1981).
[10] C. R. Fuller, S. J. Elliott, and P. A. Nelson, *Active Control of Vibration* (Academic, New York, 1996).
[11] D. G. Rees, *Foundations of Statistics* (Chapman and Hall, New York, 1987).

Free localized vibrations of a semi-infinite cylindrical shell

Julius D. Kaplunov
Institute for Problems in Mechanics, Russian Academy of Sciences, Pr. Vernadskogo 101-1, Moscow 117526, Russia

Leonid Yu. Kossovich and Maria V. Wilde
Department of Mathematical Theory of Elasticity and Biomechanics, Saratov State University, Astrakhanskaya str. 83, Saratov 410601, Russia

(Received 2 February 1999; revised 25 October 1999; accepted 27 October 1999)

Free vibrations of a semi-infinite cylindrical shell, localized near the edge of the shell are investigated. The dynamic equations in the Kirchhoff–Love theory of shells are subjected to asymptotic analysis. Three types of localized vibrations, associated with bending, extensional, and super-low-frequency semi-membrane motions, are determined. A link between localized vibrations and Rayleigh-type bending and extensional waves, propagating along the edge, is established. Different boundary conditions on the edge are considered. It is shown that for bending and super-low-frequency vibrations the natural frequencies are real while for extensional vibrations they have asymptotically small imaginary parts. The latter corresponds to the radiation to infinity caused by coupling between extensional and bending modes. © *2000 Acoustical Society of America.* [S0001-4966(00)02602-3]

PACS numbers: 43.40.Ey [CBB]

INTRODUCTION

The phenomenon of the edge resonance has been thoroughly investigated for elastic plates and rods (Refs. 1–5 and others). It represents the special case of resonances related to nonpropagating vibration modes localized near edges. The associated frequencies are weakly dependent on body sizes. These features of the edge resonance are of interest for the structural design of prolonged waveguides which can often be simulated as semi-infinite bodies.

In this paper we study free vibrations of a semi-infinite circular cylindrical shell localized near the edge of the shell. In contrast to Ref. 6 we do not use the term ''edge resonance'' when dealing with free vibrations. The shell motion is assumed to be described by the 2D equations of the classical Kirchhoff–Love theory of shells. Our analysis is based on asymptotic techniques traditional in the theory of shells.[7–9]

The problem considered is analogous to those for bending and extension of a semi-strip subjected to certain mixed boundary conditions on its sides. For them, in contrast to the boundary conditions corresponding to traction-free sides, we can easily derive explicit formulas for edge eigenvalues which form an infinite spectrum (see Appendices A and B). In addition, study of the mixed boundary conditions on the sides of a semi-strip clarifies a link between edge-localized vibrations and Rayleigh-type bending and extensional waves propagating along a traction-free edge.

Three types of free localized shell vibrations are revealed. Two of them become similar to bending and extensional vibrations of a semi-strip as the wave number in the circumferential direction increases. The natural frequencies of bending shell vibrations are real ones while the natural frequencies of shell extensional vibrations possess asymptotically small imaginary parts, corresponding to the radiation to infinity because of coupling between bending and extensional modes. In the latter case we start from the concept of complex natural frequency widespread for the problems in acoustics involving radiation (e.g., see Refs. 10 and 11). The third vibration type is associated with super-low-frequency vibrations (their natural frequencies tend to zero) occurring at relatively small wave numbers in the circumferential direction. They follow the semi-membrane asymptotic behavior.[7]

Apart from the case of a traction-free edge, other boundary conditions are considered. It is shown that free localized vibrations exist under the following conditions:

(i) the edge of a shell is not clamped in the transverse direction (for bending vibrations);
(ii) the edge of a shell is not clamped in the longitudinal and circumferential directions (for extensional vibrations); and
(iii) the edge of a shell is not clamped in the transverse and circumferential directions (for super-low-frequency vibrations).

To the best of our knowledge only a few papers deal with a semi-infinite cylindrical shell. Among them we mention Ref. 12 in which the dispersion equation for the extensional surface wave generalizing the classical Rayleigh one is derived from the membrane theory of shells. The imaginary parts of extensional natural frequencies and the bending and super-low natural frequencies cannot be estimated using membrane theory.

I. STATEMENT OF THE PROBLEM AND AN EXACT ANALYSIS

Consider free vibrations of a semi-infinite circular cylindrical shell. Let the midsurface of the shell be referred to the coordinates (s,θ), where s $(0\leqslant s<\infty)$ is the meridian arc

length and θ ($0 \leqslant \theta < 2\pi$) is the angular coordinate. We also introduce the dimensionless variable $\xi = s/R$ ($0 \leqslant \xi < \infty$), where R is the radius of the midsurface.

We start from the equations of the Kirchhoff–Love theory of shells.[7] After separating the angular coordinate by the formulas

$$u(\xi,\theta) = u(\xi)\sin n\theta, \quad v(\xi,\theta) = v(\xi)\cos n\theta,$$
$$w(\xi,\theta) = w(\xi)\sin n\theta,$$

they become

$$\frac{d^2u}{d\xi^2} - \frac{1}{4}\nu_4 n^2 u - \frac{1}{4}\nu_1 n\frac{dv}{d\xi} - \nu\frac{dw}{d\xi} + \nu_2\lambda u = 0,$$
$$\frac{1}{4}\nu_1 n\frac{du}{d\xi} + \frac{1}{4}\nu_4\frac{d^2v}{d\xi^2} - n^2 v + \frac{1}{3}\eta^2\left[\nu_4\frac{d^2v}{d\xi^2} - n^2 v\right] - nw + \frac{1}{3}\eta^2 n\left(\nu_3\frac{d^2w}{d\xi^2} - n^2 w\right) + \nu_2\lambda v = 0, \tag{1}$$
$$-\nu\frac{du}{d\xi} + nv - \frac{1}{3}\eta^2 n\left(\nu_3\frac{d^2v}{d\xi^2} - n^2 v\right) + w + \frac{1}{3}\eta^2\left[\frac{d^4w}{d\xi^4} - 2n^2\frac{d^2w}{d\xi^2} + n^4 w\right] - \nu_2\lambda w = 0,$$

with

$$\lambda = \frac{\rho\omega^2 R^2}{E}, \quad \eta = \frac{h}{R}, \quad \nu_1 = 2(1+\nu),$$
$$\nu_2 = 1-\nu^2, \quad \nu_3 = 2-\nu, \quad \nu_4 = 2(1-\nu),$$

where u and v are the tangential displacements of the midsurface along the axes ξ and θ, respectively, w is the transverse displacement of the midsurface, λ is the dimensionless frequency parameter, ω is the circular frequency, E is Young's modulus, ν is Poisson's ratio, $2h$ is the thickness, ρ is the mass density, η is the small geometrical parameter, and $n = 0,1,2,...$ is the circumferential wave number.

We impose traction-free boundary conditions at $\xi = 0$. They can be written as

$$\frac{du}{d\xi} - \nu n v - \nu w = 0, \tag{2a}$$
$$nu + \frac{dv}{d\xi} + \frac{4}{3}\eta^2\left(\frac{dv}{d\xi} + n\frac{dw}{d\xi}\right) = 0, \tag{2b}$$
$$-\nu n v + \frac{d^2w}{d\xi^2} - \nu n^2 w = 0, \tag{2c}$$
$$-\nu_3 n\frac{dv}{d\xi} + \frac{d^3w}{d\xi^3} - \nu_3 n^2\frac{dw}{d\xi} = 0. \tag{2d}$$

The general solution is presented as

$$u(\xi) = \sum_{i=1}^{4} B_i u_i e^{-r_i\xi}, \quad v(\xi) = \sum_{i=1}^{4} B_i v_i e^{-r_i\xi}, \quad w(\xi) = \sum_{i=1}^{4} B_i w_i e^{-r_i\xi}, \tag{3}$$

where B_i are arbitrary constants and r_i is the ith root of the characteristic equation

$$a_0 r^8 + a_1 r^6 + a_2 r^4 + a_3 r^2 + a_4 = 0, \tag{4}$$

where

$$a_0 = \eta_1^2(1 + \tfrac{4}{3}\eta^2),$$
$$a_1 = -4\eta_1^2 n^2\left(1 + \frac{1}{3}\eta^2\right) + \eta_1^2 b\lambda\left(1 + \frac{4}{3}\eta^2\frac{1-\nu}{3-\nu}\right),$$
$$a_2 = 1 + \frac{4}{3}\eta^2 - \lambda\left(1 + \frac{4}{3}\eta^2\right) + 6\eta_1^2 n^4\left(1 + \frac{\nu_2}{18}\eta^2\right) - 3\eta_1^2 b n^2\lambda\left(1 + \frac{2}{9}\eta^2\frac{\nu_2}{3-\nu}\right) + \eta_1^2\nu_1\nu_2\lambda^2 - 2\eta_1^2(4-\nu^2)n^2,$$
$$a_3 = 2n^2\lambda\left(1 + \frac{1}{3}\eta^2\frac{\nu^2-2}{1-\nu}\right) + (3+2\nu)\lambda \times\left(1 + \frac{4}{3}\eta^2\frac{1}{3+2\nu}\right) - b\lambda^2\left(1 + \frac{4}{3}\eta^2\frac{1-\nu}{3-\nu}\right) - 4\eta_1^2 n^6 + 3\eta_1^2 b n^4\lambda - 2\eta_1^2\nu_1\nu_2 n^2\lambda^2 + 8\eta_1^2 n^4 - 4\eta_1^2 n^2, \tag{5}$$
$$a_4 = -n^4\lambda\left(1 - \frac{1}{3}\eta^2\frac{3+\nu}{1-\nu}\right) - n^2\lambda\left(1 + \frac{2}{3}\eta^2\frac{1}{1-\nu}\right) + \nu_1\lambda^2 + bn^2\lambda^2\left(1 + \frac{2}{3}\eta^2\frac{1}{3-\nu}\right) - \nu_1\nu_2\lambda^3 + \eta_1^2 n^8 - \eta_1^2 b n^6\lambda + \eta_1^2\nu_1\nu_2 n^4\lambda^2 - 2\eta_1^2 n^6 + \eta_1^2 n^4$$

with $\eta_1^2 = \eta^2 3\nu_2$ and $b = (1+\nu)(3-\nu)$. To provide either for the decay of the solution at infinity or to satisfy the radiation condition, we choose roots with $\mathrm{Re}\, r_i > 0$ or $\mathrm{Re}\, r_i = 0$, $\mathrm{Im}\, r_i > 0$.

By substituting Eqs. (3) into boundary conditions (2) we arrive at a linear system in the constants B_i. It can be written as

$$c_{ij}B_j = 0, \quad i,j = \overline{1,4,} \tag{6}$$

where the coefficients c_{ij} are defined as

$$c_{1j} = r_j u_j + \nu n\nu_j + w_j,$$
$$c_{2j} = nu_j - r_j\nu_j - \tfrac{4}{3}\eta^2(r_j\nu_j + r_j n w_j),$$
$$c_{3j} = -\nu n\nu_j + (r_j^2 - \nu n^2)w_j,$$
$$c_{4j} = -r_j[-\nu_3 n\nu_j + (r_j^2 - \nu_3 n^2)w_j], \quad j = \overline{1,4.}$$

By equating the determinant of this system to zero we obtain an equation for determining the natural frequencies λ. It is

$$\det(c_{ij}) = 0. \tag{7}$$

Inspection of numerical data shows that at $n \geqslant 2$, Eq. (7) has two roots corresponding to the sought after natural frequencies of the localized vibrations of the shell. One of them (Λ_1) is real, while the second (Λ_2) is complex valued with a small imaginary part.

To establish the asymptotic behavior of natural frequencies as $\eta \to 0$ we utilize approximate forms of the Kirchhoff–Love theory of shells. To this end we present the parameters n and λ as

$$n \sim \eta^{-q}, \quad \lambda \sim \eta^{-2a}. \tag{8}$$

In doing so we suppose that the quantities q and a satisfy the inequalities

$$0 \leqslant q < 1, \quad a < 1.$$

These inequalities define the range of applicability of the Kirchhoff–Love theory of shells expressed in terms of a wavelength (the first inequality) and a frequency (the second inequality).[8] They state that a wavelength is much greater than the thickness of the shell and the period of vibration considerably exceeds the time that elastic waves propagate the distance between the faces of the shell.

We investigate localization of bending, semi-membrane, and extensional vibrations. Bending and extensional vibrations are similar, in a sense, to those of a plate. Semi-membrane vibrations are specific only for a cylindrical shell. They are super-low-frequency ones, i.e., their natural frequencies tend to zero as the relative shell thickness decreases.

Asymptotic analysis in Ref. 9 (see also Ref. 8) yields the following.

Bending vibrations ($a = 2q - 1$, $\frac{1}{2} \leqslant q < 1$):

Asymptotic behavior 1.1: $\dfrac{\partial}{\partial \xi} \sim \eta^{-q}, \quad u \sim \eta^{q},$

$v \sim \eta^{q}, \quad w \sim \eta^{0},$

Asymptotic behavior 1.2: $\dfrac{\partial}{\partial \xi} \sim \eta^{-q}, \quad u \sim \eta^{2-3q},$

$v \sim \eta^{2-3q}, \quad w \sim \eta^{0}.$

Super-low-frequency semi-membrane vibrations ($a = 2q - 1$, $0 \leqslant q < \frac{1}{2}$):

Asymptotic behavior 2.1: $\dfrac{\partial}{\partial \xi} \sim \eta^{1/2-2q}, \quad u \sim \eta^{1/2},$

$v \sim \eta^{q}, \quad w \sim \eta^{0},$

Asymptotic behavior 2.2: $\dfrac{\partial}{\partial \xi} \sim \eta^{1/2}, \quad u \sim \eta^{1/2},$

$v \sim \eta^{1-q}, \quad w \sim \eta^{0}.$

Extensional vibrations ($a = q$, $q \geqslant 0$):

Asymptotic behavior 3.1: $\dfrac{\partial}{\partial \xi} \sim \eta^{-q}, \quad u \sim \eta^{-q},$

$v \sim \eta^{-q}, \quad w \sim \eta^{0},$

Asymptotic behavior 3.2: $\dfrac{\partial}{\partial \xi} \sim \eta^{1/2-(1/2)q},$

$u \sim \eta^{1/2+(1/2)q}, \quad v \sim \eta, \quad w \sim \eta^{0}.$

The physical meaning of these formulas is clarified in Secs. II–IV. Below we return back to Eqs. (1) and construct approximate equations for determining solutions that possess the assumed asymptotic behaviors.

We write out the solutions of boundary value problem (1) and (2) as

$$u(\xi) = u_b(\xi) + \eta^{\kappa} u_a(\xi), \quad v(\xi) = v_b(\xi) + \eta^{\kappa} v_a(\xi), \quad w(\xi) = w_b(\xi) + \eta^{\kappa} w_a(\xi), \tag{9}$$

where the quantities with the subscript ''b'' denote solutions possessing the asymptotic behaviors 1.1, 2.1, and 3.1 (the basic displacement field) while the quantities with the subscript ''a'' denote solutions possessing the asymptotic behaviors 1.2, 2.2, and 3.2 (the additional displacement field). All these solutions can be defined from the above-mentioned approximate equations. In the theory of shells this approach is known as the separation method.[7] To determine the quantity κ we construct below an iterative process for satisfying boundary conditions (2). In common to all the formal asymptotic methods the existence of such a process justifies the use of the chosen asymptotic behaviors in superposition (9). Estimates for the roots Λ_i ($i = 1,2$) will follow from asymptotic considerations for bending and super-low-frequency vibrations (Λ_1) and for extensional vibrations (Λ_2).

II. BENDING VIBRATIONS

Let the indices q and a be related by the formula $a = 2q - 1$. For the sake of simplicity we suppose that $q > \frac{1}{2}$. First we obtain a system for determining the quantities u_b, v_b, w_b in Eqs. (9). Taking into account the asymptotic behavior 1.1 we set

$$\xi = \eta^{q} \xi_*, \quad n = \eta^{-q} n_*, \quad \lambda = \eta^{2-4q} \lambda_*, \quad u_b = \eta^{q} u_b^*, \quad v_b = \eta^{q} v_b^*, \quad w_b = \eta^{0} w_b^*, \tag{10}$$

and assume that the quantities with the asterisk have the same asymptotic order and differentiation with respect to the variable ξ_* does not change the asymptotic order of unknowns. By substituting Eqs. (10) into Eqs. (1) and retaining only asymptotic leading terms we arrive at the following equations:

$$\frac{d^2 u_b^*}{d\xi_*^2} - \frac{1}{4}\nu_4 n_*^2 u_b^* - \frac{1}{4}\nu_1 n_* \frac{dv_b^*}{d\xi_*} - \nu \frac{dw_b^*}{d\xi_*} + O(\eta^{2-2q}) = 0, \tag{11a}$$

$$\frac{1}{4}\nu_1 n_* \frac{du_b^*}{d\xi_*} + \frac{1}{4}\nu_4 \frac{d^2 v_b^*}{d\xi_*^2} - n_*^2 v_b^* - n_* w_b^* + O(\eta^{2-2q}) = 0, \tag{11b}$$

$$\frac{1}{3}\left(\frac{d^4 w_b^*}{d\xi_*^4} - 2n_*^2 \frac{d^2 w_b^*}{d\xi_*^2} + n_*^4 w_b^*\right) - \nu_2 \lambda_* w_b^* + O(\eta^{4q-2}) = 0. \tag{11c}$$

A system for u_a, v_a, w_a can be obtained in a similar way. Setting

$$\xi=\eta^q\xi_*,\quad n=\eta^{-q}n_*,\quad \lambda=\eta^{2-4q}\lambda_*,$$
$$u_a=\eta^{2-3q}u_a^*,\quad v_a=\eta^{2-3q}v_a^*,\quad w_a=\eta^0 w_a^* \tag{12}$$

in Eqs. (1), we have

$$\frac{d^2u_a^*}{d\xi_*^2}-\frac{1}{4}\nu_4 n_*^2 u_a^*-\frac{1}{4}\nu_1 n_*\frac{dv_a^*}{d\xi_*}+O(\eta^{4q-2})=0, \tag{13a}$$

$$\frac{1}{4}\nu_1 n_*\frac{du_a^*}{d\xi_*}+\frac{1}{4}\nu_4\frac{d^2v_a^*}{d\xi_*^2}-n_*^2 v_a^*+O(\eta^{4q-2})=0, \tag{13b}$$

$$\frac{1}{3}\left(\frac{d^4w_a^*}{d\xi_*^4}-2n_*^2\frac{d^2w_a^*}{d\xi_*^2}+n_*^4 w_a^*\right)-\nu_2\lambda_* w_a^* - \nu\frac{du_a^*}{d\xi_*}+n_* v_a^*+O(\eta^{4q-2})=0. \tag{13c}$$

Boundary conditions (2) become

$$\eta^0\left(\frac{du_b^*}{d\xi_*}-\nu n_* v_b^*-\nu w_b^*\right)+\eta^\kappa\left(\eta^{2-4q}\left(\frac{du_a^*}{d\xi_*}-\nu n_* v_a^*\right)+O(\eta^0)\right)=0, \tag{14a}$$

$$\eta^0\left(n_* u_b^*+\frac{dv_b^*}{d\xi_*}\right)+O(\eta^{2-2q})+\eta^\kappa\left(\eta^{2-4q}\left(n_* u_a^*+\frac{dv_a^*}{d\xi_*}\right)+O(\eta^{2-2q})\right)=0, \tag{14b}$$

$$\eta^{-2q}\left(\frac{d^2w_b^*}{d\xi_*^2}-\nu n_*^2 w_b^*\right)+O(\eta^0)+\eta^\kappa\left(\eta^{-2q}\left(\frac{d^2w_a^*}{d\xi_*^2}-\nu n_*^2 w_a^*\right)+O(\eta^{2-4q})\right)=0, \tag{14c}$$

$$\eta^{-3q}\left(\frac{d^3w_b^*}{d\xi_*^3}-\nu_3 n_*^2\frac{dw_b^*}{d\xi_*}\right)+O(\eta^{-q})+\eta^\kappa\left(\eta^{-3q}\left(\frac{d^3w_a^*}{d\xi_*^3}-\nu_3 n_*^2\frac{dw_a^*}{d\xi_*}\right)+O(\eta^{2-5q})\right)=0. \tag{14d}$$

It follows from (14a) and (14b) that $\kappa=4q-2$. From (14c) and (14d) we conclude that Eqs. (11) have to be subjected to homogeneous boundary conditions. They are

$$\frac{d^2w_b^*}{d\xi_*^2}-\nu n_*^2 w_b^*+O(\eta^{4q-2})=0,\qquad \frac{d^3w_b^*}{d\xi_*^3}-\nu_3 n_*^2\frac{dw_b^*}{d\xi_*}+O(\eta^{4q-2})=0. \tag{15}$$

The nonhomogeneous boundary conditions for Eqs. (13) can be written as

$$\frac{du_a^*}{d\xi_*}-\nu n_* v_a^*+\left(\frac{du_b^*}{d\xi_*}-\nu n_* v_b^*-\nu w_b^*\right)+O(\eta^{4q-2})=0,$$
$$n_* u_a^*+\frac{dv_a^*}{d\xi_*}+\left(n_* u_b^*+\frac{dv_b^*}{d\xi_*}\right)+O(\eta^{2-2q})=0. \tag{16}$$

We begin with solving Eq. (11c) with boundary conditions (15). As a result we determine the natural frequency Λ_1 and the natural form $w_b(\xi)$. Then the functions $u_b(\xi)$, $v_b(\xi)$ can be found from nonhomogeneous Eqs. (11a) and (11b). To determine $u_a(\xi)$, $v_a(\xi)$ we have to consider Eqs. (13a) and (13b) with boundary conditions (16). To within the error $O(\eta^{4q-2})$ we can set $w_a=0$.

Boundary value problem (11c) and (15) coincides with that for plate bending. The latter is considered in Appendix A. By utilizing the results of Appendix A we write out the asymptotic formula

$$\Lambda_1\approx\eta_1^2 n^4(1-\nu)((3\nu-1)+2\sqrt{(1-\nu)^2+\nu^2}). \tag{17}$$

As it could be expected, for the large wave numbers ($n\gg\eta^{-1/2}$) the shell curvature has little effect on localized vibrations. In this case the natural form is associated with a Rayleigh-type bending wave.

It follows from the consideration above that the leading-order asymptotic behavior of the natural frequency λ does not depend on boundary conditions (2a) and (2b) corresponding to a traction-free edge in the longitudinal and circumferential directions. Therefore, we should expect the appearance of localized bending vibrations in other cases as well. Let the edge of the shell be clamped in the longitudinal and circumferential directions. Then Eqs. (14a) and (14b) are replaced by

$$\eta^q u_b^*+\eta^{\kappa+2-3q}u_a^*=0,\qquad \eta^q v_b^*+\eta^{\kappa+2-3q}v_a^*=0. \tag{18}$$

As above we have $\kappa=4q-2$, i.e., boundary conditions (15) should not be changed. Therefore Eq. (17) holds. The same result takes place for an edge clamped only in one of these directions.

Numerical data are given in Table I for different types of boundary conditions. Here $\Lambda_1=\Lambda_1^{\mathrm{ex}}$ are the exact values of natural frequencies calculated from Eq. (7) and $\Lambda_1=\Lambda_1^{\mathrm{as}}$ are their asymptotic values determined by Eq. (17). The relative error is given by $\varepsilon=|\Lambda_1^{\mathrm{as}}-\Lambda_1|/\Lambda_1\times 100\%$. The problem parameters are $h=0.03$, $R=1$, and $\nu=0.3$.

III. SUPER-LOW-FREQUENCY VIBRATIONS

Consider the second type of localized vibrations. Let us determine the quantities u_b, v_b, w_b in solution (9) starting from the asymptotic behavior 2.1. To this end we set

$$\xi=\eta^{-1/2+2q}\xi_*,\quad n=\eta^{-q}n_*,\quad \lambda=\eta^{2-4q}\lambda_*,$$
$$u_b=\eta^{1/2}u_b^*,\quad v_b=\eta^q v_b^*,\quad w_b=\eta^0 w_b^*. \tag{19}$$

Asymptotic simplification of Eqs. (1) leads to an equation in the function v_b^*. It is

$$\frac{d^4v_b^*}{d\xi_*^4}+\left(\frac{1}{3\nu_2}n_*^4(n_*^2-1)^2-\lambda_* n_*^2(n_*^2+1)\right)v_b^*+O(\eta^{1-2q})=0. \tag{20}$$

The latter coincides with the governing equation in the semimembrane theory of shells.[7]

The quantities u_b^*, w_b^* are expressed in terms of v_b^* by

TABLE I. Bending natural frequencies.

	Λ_1^{ex}					
n	(2a)–(2d)	$u=0$, (2b)–(2d)	(2a), $v=0$, (2c), (2d)	$u=0$, $v=0$, (2c), (2d)	Λ_1^{as}	ε
15	16.384 916	16.384 957	16.432 125	16.437 565	16.626 278	1.473
16	21.244 877	21.244 899	21.296 670	21.304 097	21.523 353	1.311
17	27.110 936	27.110 944	27.166 597	27.176 007	27.429 992	1.177
18	34.112 905	34.112 906	34.171 920	34.183 433	34.476 249	1.065
19	42.388 448	42.388 450	42.450 423	42.464 260	42.800 062	0.971
20	52.083 079	52.083 092	52.147 677	52.164 163	52.547 248	0.891
21	63.350 153	63.350 192	63.417 048	63.436 624	63.871 508	0.823
22	76.350 864	76.350 947	76.419 690	76.442 938	76.934 425	0.764
23	91.254 233	91.254 384	91.324 540	91.352 220	91.905 464	0.714
24	108.237 106	108.237 353	108.308 289	108.341 402	108.961 973	0.670
25	127.484 132	127.484 514	127.555 345	127.595 223	128.289 179	0.631

$$n_*^3 u_b^* = -n_*^2 \frac{dv_b^*}{d\xi_*} - \eta^{1-2q} \frac{2\nu_2}{1-\nu} \frac{d^3 v_b^*}{d\xi_*^3} + O(\eta^{2-4q}),$$
$$n_* w_b^* = -n_*^2 v_b^* - \eta^{1-2q} \nu \frac{d^2 v_b^*}{d\xi_*^2} + O(\eta^{2-4q}). \tag{21}$$

Now we consider the asymptotic behavior 2.2. Let us substitute the relations

$$\xi = \eta^{1/2} \xi_*, \quad n = \eta^{-q} n_*, \quad \lambda = \eta^{2-4q} \lambda_*,$$
$$u_a = \eta^{1/2} u_a^*, \quad v_a = \eta^{1-q} v_a^*, \quad w_a = \eta^0 w_a^* \tag{22}$$

into Eqs. (1). By making elementary transformations we obtain

$$\frac{1}{3\nu_2} \frac{d^4 w_a^*}{d\xi_*^4} + w_a^* + O(\eta^{1-2q}) = 0. \tag{23}$$

This equation corresponds to a static boundary layer. The functions u_a^*, v_a^* are related to the function w_a^* by

$$u_a^* = -\frac{\nu}{3\nu_2} \frac{d^3 w_a^*}{d\xi_*^3} + O(\eta^{1-2q}),$$
$$v_a^* = -\frac{2+\nu}{3\nu_2} n_* \frac{d^2 w_a^*}{d\xi_*^2} + O(\eta^{1-2q}). \tag{24}$$

Then we substitute solution (9) into boundary conditions (2) utilizing relations (19) and (22). In addition we express u_b^*, w_b^* in terms of v_b^* by Eqs. (21) and u_a^*, v_a^* in terms of w_a^* by Eqs. (24) to obtain

$$-\eta^{1-2q} \frac{d^2 v_b^*}{d\xi_*^2} + O(\eta^{2-4q}) + \eta^\kappa O(\eta^{1-2q}) = 0,$$
$$\eta^{3/2-3q} \frac{d^3 v_b^*}{d\xi_*^3} + O(\eta^{5/2-5q}) + \eta^\kappa \left(\eta^{1/2-q} \frac{1}{3\nu_2} n_*^3 \frac{d^3 w_a^*}{d\xi_*^3} + O(\eta^{3/2-3q}) \right) = 0,$$
$$\eta^{-2q} \nu n_* (n_*^2 - 1) v_b^* + O(\eta^{1-4q}) + \eta^\kappa \left(\eta^{-1} \frac{d^2 w_a^*}{d\xi_*^2} + O(\eta^{-2q}) \right) = 0,$$
$$\eta^{1/2-4q} \nu_3 n_* (n_*^2 - 1) \frac{dv_b^*}{d\xi_*} + O(\eta^{3/2-6q}) + \eta^\kappa \left(\eta^{3/2} \frac{d^3 w_a^*}{d\xi_*^3} + O(\eta^{-1/2-2q}) \right) = 0. \tag{25}$$

Analysis of these equations yields $\kappa = 1-2q$. It also reveals a possibility for separating them into two groups: the homogeneous boundary conditions for the function v_b^*,

$$\frac{d^2 v_b^*}{d\xi_*^2} + O(\eta^{1-2q}) = 0, \quad \frac{d^3 v_b^*}{d\xi_*^3} + O(\eta^{1-2q}) = 0, \tag{26}$$

and the nonhomogeneous boundary conditions for the function w_a^*,

$$\frac{d^2 w_a^*}{d\xi_*^2} + \nu n_* (n_*^2 - 1) v_b^* + O(\eta^{1-2q}) = 0,$$
$$\frac{d^3 w_a^*}{d\xi_*^3} + O(\eta^{1-2q}) = 0. \tag{27}$$

An asymptotic estimate for a natural frequency follows from basic boundary value problem (20) and (26). It is given by

$$\Lambda_1 \approx \lambda_1 \tag{28}$$

with

$$\lambda_1 = \eta_1^2 \frac{n^2 (n^2-1)^2}{n^2+1}.$$

It is clear that for $\lambda = \lambda_1$ the roots of the characteristic equation corresponding to Eq. (20) are equal to zero (i.e., λ_1 represents the lowest critical frequency). Thus the asymptotic behavior 2.1 does not describe localized vibrations. However, we could expect that the value λ_1 defines the leading-order behavior of the sought after natural frequency. Let us assume

$$\Lambda_1 = \lambda_1 (1-\delta), \tag{29}$$

where $\delta \sim \eta^{4d}$ with unknown $d>0$. In this case we have

Asymptotic behavior 2.1a: $\frac{\partial}{\partial \xi} \sim \eta^{1/2-2q+d}$,

$$u \sim \eta^{1/2+d}, \quad v \sim \eta^{q}, \quad w \sim \eta^{0}.$$

By introducing the relations

$$\xi = \eta^{-1/2+2q-d}\xi_*, \quad n = \eta^{-q} n_*, \quad \lambda = \eta^{2-4q}\lambda_*,$$

$$\lambda_* = \lambda_{1*}(1-\eta^{4d}\delta_*), \quad u_b = \eta^{1/2+d} u_b^*, \tag{30}$$

$$v_b = \eta^{q} v_b^*, \quad w_b = \eta^{0} w_b^*,$$

where

$$\lambda_{1*} = \frac{1}{3\nu_2}\frac{n_*^2(n_*^2-1)^2}{n_*^2+1},$$

we obtain the following equation in the function v_b^*:

$$\frac{d^4 v_b^*}{d\xi_*^4} - \eta^{1-2q-2d}\lambda_{1*}(2n_*^2+(1-2\nu))\frac{d^2 v_b^*}{d\xi_*^2} + \lambda_{1*} n_*^2(n_*^2+1)\delta_* v_b^* + O(\eta^{1-2q+2d}) = 0, \tag{31}$$

and the expressions for the functions u_b^*, w_b^*:

$$n_*^3 u_b^* = -n_*^2\frac{dv_b^*}{d\xi_*} - \nu_1\left[\eta^{1-2q+2d}\frac{d^3 v_b^*}{d\xi_*^3} + \eta^{2-4q}\left(\frac{\nu}{3\nu_2}n_*^4(n_*^2-1) - \lambda_{1*}(\nu n_*^2-1)\right)\times\frac{dv_b^*}{d\xi_*}\right] + O(\eta^{2-4q+4d}), \tag{32}$$

$$n_* w_b^* = -n_*^2 v_b^* - \eta^{1-2q+2d}\nu\frac{d^2 v_b^*}{d\xi_*^2} + O(\eta^{2-4q}).$$

A refined equation for the static boundary layer can be written as

$$\frac{1}{3\nu_2}\frac{d^4 w_a^*}{d\xi_*^4} + w_a^* - \eta^{1-2q}\frac{4}{3\nu_2}n_*^2\frac{d^2 w_a^*}{d\xi_*^2} + O(\eta^{2-4q}) = 0. \tag{33}$$

The expressions for the quantities u_a^*, v_a^* are

$$u_a^* = -\frac{\nu}{3\nu_2}\frac{d^3 w_a^*}{d\xi_*^3} - \eta^{1-2q}\frac{1-2\nu}{3\nu_2}n_*^2\frac{dw_a^*}{d\xi_*} + O(\eta^{2-4q}), \tag{34}$$

$$v_a^* = -\frac{2+\nu}{3\nu_2}n_*\frac{d^2 w_a^*}{d\xi_*^2} + \eta^{1-2q}\frac{1}{3\nu_2}n_* \times((5+2\nu)n_*^2 - \nu_1\nu_3)w_a^* + O(\eta^{2-4q}).$$

By taking into account Eqs. (9), (22), (30), (32), and (34) we rewrite boundary conditions (2) as

$$-\eta^{1-2q+2d}\frac{d^2 v_b^*}{d\xi_*^2} - \eta^{2-4q}\nu\left(\frac{1}{3\nu_2}n_*^4(n_*^2-1) - \lambda_{1*}n_*^2\right)v_b^* + O(\eta^{2-4q+4d}) + \eta^{\kappa}\left(-\eta^{1-2q}\frac{1}{3\nu_2}n_*^3\frac{d^2 w_a^*}{d\xi_*^2} + O(\eta^{2-4q})\right) = 0, \tag{35a}$$

$$\eta^{3/2-3q+3d}\frac{d^3 v_b^*}{d\xi_*^3} + \eta^{5/2-5q+d}\times\left(\frac{1}{3\nu_2}n_*^2(\nu n_*^4 + (2-3\nu)n_*^2 - \nu_4) - \lambda_{1*}(\nu n_*^2-1)\right)\frac{dv_b^*}{d\xi_*} + O(\eta^{5/2-5q+4d}) + \eta^{\kappa}\frac{1}{3\nu_2}n_*^3\left(\eta^{1/2-q}\frac{d^3 w_a^*}{d\xi_*^3} - \eta^{3/2-3q}(2n_*^2-\nu)\frac{dw_a^*}{d\xi_*} + O(\eta^{5/2-5q})\right) = 0, \tag{35b}$$

$$\eta^{-2q}\nu n_*(n_*^2-1)v_b^* + O(\eta^{1-4q+2d}) + \eta^{\kappa}\left(\eta^{-1}\frac{d^2 w_a^*}{d\xi_*^2} + O(\eta^{-2q})\right) = 0, \tag{35c}$$

$$\eta^{1/2-4q+d}\nu_3 n_*(n_*^2-1)\frac{dv_b^*}{d\xi_*} + O(\eta^{3/2-6q+3d}) + \eta^{\kappa}\times\left(\eta^{-3/2}\frac{d^3 w_a^*}{d\xi_*^3} - \eta^{-1/2-2q}\nu_3 n_*^2\frac{dw_a^*}{d\xi_*} + O(\eta^{1/2-2q})\right) = 0 \tag{35d}$$

with $\kappa = 1-2q$.

Let us express the second and third derivatives of w_a^* starting from Eqs. (35c) and (35d) and substitute them into Eqs. (35a) and (35b). The result is

$$-\eta^{1-2q+2d}\frac{d^2 v_b^*}{d\xi_*^2} + \eta^{2-4q}\nu n_*^2\lambda_{1*}v_b^* + O(\eta^{2-4q+4d} + \eta^{3-6q}) = 0,$$
$$\eta^{3/2-3q+3d}\frac{d^3 v_b^*}{d\xi_*^3} - \eta^{5/2-5q+d}(\nu_3 n_*^2 + (1-2\nu))\lambda_{1*}\frac{dv_b^*}{d\xi_*} + O(\eta^{5/2-5q+4d}) - \eta^{5/2-5q}\frac{\nu}{3\nu_2}n_*^3(n_*^2-1)\frac{dw_a^*}{d\xi_*} + O(\eta^{7/2-7q}) = 0. \tag{36}$$

It follows from Eqs. (36) that

$$d = \tfrac{1}{3} - \tfrac{2}{3}q < \tfrac{1}{2} - q.$$

To obtain boundary conditions for the function v_b^* we have to express the first derivative of w_a^* in terms of v_b^*. Since this derivative may be found to within the error $O(\eta^{1-2q})$, we can start from initial boundary value problem (23) and (27). Finally, we have

TABLE II. Deviations from the critical frequency [asymptotic values corresponding to Eqs. (40) and (42)].

	(2a)–(2d)			$u=0$, (2b)–(2d)		
n	$\Delta_{ex}\times 10^6$	$\Delta_{as}\times 10^6$	ε	$\Delta_{ex}\times 10^6$	$\Delta_{as}\times 10^6$	ε
2	0.000 051 72	0.000 071 92	39.07	0.000 021 42	0.000 028 54	33.24
3	0.001 165 76	0.001 899 92	62.98	0.000 485 34	0.000 753 99	55.35
4	0.008 548 25	0.015 586 67	82.34	0.003 557 79	0.006 185 57	73.86
5	0.037 637 43	0.075 090 02	99.51	0.015 646 51	0.029 799 50	90.45
6	0.122 888 77	0.264 998 14	115.64	0.051 079 37	0.105 164 58	105.88
7	0.328 850 29	0.761 071 91	131.43	0.136 966 03	0.302 031 59	120.52
8	0.762 641 41	1.886 775 93	147.40	0.319 248 56	0.748 767 52	134.54
9	1.586 556 94	4.187 872 07	163.96	0.669 961 80	1.661 958 13	148.07
10	3.029 250 32	8.527 035 55	181.49	1.295 722 16	3.383 956 30	161.16

$$\frac{d^2v_b^*}{d\xi_*^2}-\eta^d\nu n_*^2\lambda_{1*}v_b^*+O(\eta^{4d})=0, \tag{37a}$$

$$\frac{d^3v_b^*}{d\xi_*^3}-\eta^d(\nu_3 n_*^2+1-2\nu)\lambda_{1*}\frac{dv_b^*}{d\xi_*}-\frac{\sqrt{2}\nu^2}{(3\nu_2)^{5/4}}n_*^4(n_*^2-1)^2 \times v_b^*+O(\eta^{3d})=0. \tag{37b}$$

By neglecting the term of the order $O(\eta^d)$ in Eqs. (31) and (37) we obtain the following boundary value problem: the equation of motion,

$$\frac{d^4v_b^*}{d\xi_*^4}+\lambda_{1*}n_*^2(n_*^2+1)\delta_*v_b^*+O(\eta^d)=0, \tag{38}$$

and the boundary conditions at $\xi=0$,

$$\frac{d^2v_b^*}{d\xi_*^2}+O(\eta^d)=0, \tag{39a}$$

$$\frac{d^3v_b^*}{d\xi_*^3}-\frac{\sqrt{2}\nu^2}{(3\nu_2)^{5/4}}n_*^4(n_*^2-1)^2v_b^*+O(\eta^d)=0. \tag{39b}$$

By solving this problem we obtain to within the error $O(\eta^d)$

$$\Lambda_1\approx\lambda_1(1-(2\nu^2)^{4/3}(\eta_1^2n^2(n^2-1))^{2/3}). \tag{40}$$

Since $\Lambda_1<\lambda_1$, the associated natural form describes exponentially decaying vibrations.

If the edge is clamped in the longitudinal direction, then Eqs. (37a) and (39a) are replaced by

$$\frac{dv_b^*}{d\xi_*}+O(\eta^{5d})=0. \tag{41}$$

Since we do not change boundary condition (37b), the value of the index d is the same as for a traction-free edge.

In the latter case the sought after asymptotic formula becomes

$$\Lambda_1\approx\lambda_1(1-\nu^{8/3}(\eta_1^2n^2(n^2-1))^{2/3}). \tag{42}$$

Numerical analysis for $n\ll\eta^{-1/2}$ ($q<\frac{1}{2}$) shows that for an edge clamped in the circumferential direction, super-low-frequency free localized vibrations do not occur. In this case, localized vibrations appear beginning with $n\sim\eta^{-1/2}$ ($q=\frac{1}{2}$).

Comparison of numerical and asymptotical results is presented in Table II. Since exact and approximate values are close to the lowest critical frequency λ_1, we calculate the deviations $\Delta_{ex}=\lambda_1^{ex}-\Lambda_1^{ex}$ and $\Delta_{as}=\lambda_1-\Lambda_1^{as}$, and the relative error $\varepsilon=|\Delta_{as}-\Delta_{ex}|/\Delta_{ex}\times 100\%$, where λ_1^{ex} is the exact value of the lowest critical frequency. The value Λ_1^{as} is calculated by Eq. (40) for a traction-free edge and by Eq. (42) for an edge clamped in the longitudinal direction. The problem parameters are $h=0.001$, $R=1$, and $\nu=0.3$.

Asymptotic values for the natural frequencies can be refined by solving boundary value problem (31) and (37). In this case we determine the quantity δ to within the error $O(\eta^{3d})$. For an edge clamped in the longitudinal direction, condition (37a) should be replaced by condition (41). The refined asymptotic values Δ_{as} are compared with the exact values Δ_{ex} in Table III.

TABLE III. Deviations from the critical frequency (refined asymptotic values).

	(2a)–(2d)			$u=0$, (2b)–(2d)		
n	$\Delta_{ex}\times 10^6$	$\Delta_{as}\times 10^6$	ε	$\Delta_{ex}\times 10^6$	$\Delta_{as}\times 10^6$	ε
2	0.000 051 72	0.000 051 85	0.26	0.000 021 42	0.000 021 45	0.14
3	0.001 165 76	0.001 174 23	0.73	0.000 485 34	0.000 486 85	0.31
4	0.008 548 25	0.008 674 42	1.48	0.003 557 79	0.003 577 04	0.54
5	0.037 637 43	0.038 599 73	2.56	0.015 646 51	0.015 773 80	0.81
6	0.122 888 77	0.127 824 04	4.02	0.051 079 37	0.051 648 65	1.11
7	0.328 850 29	0.348 263 30	5.90	0.136 966 03	0.138 922 52	1.43
8	0.762 641 41	0.825 725 05	8.27	0.319 248 56	0.324 806 72	1.74
9	1.586 556 94	1.763 916 37	11.18	0.669 961 80	0.683 630 14	2.04
10	3.029 250 32	3.474 155 48	14.69	1.295 722 16	1.325 755 42	2.32

IV. EXTENSIONAL VIBRATIONS

Consider the third type of localized vibrations assuming that $q>0$. The asymptotic behavior 3.1 yields

$$\xi=\eta^q\xi_*,\quad n=\eta^{-q}n_*,\quad \lambda=\eta^{-2q}\lambda_*,$$
$$u_b=\eta^{-q}u_b^*,\quad v_b=\eta^{-q}v_b^*,\quad w_b=\eta^0 w_b^*. \tag{43}$$

By substituting these equations into Eqs. (1) and neglecting quantities of the order $O(\eta^{2q})$ we obtain the following closed system in the functions u_b^* and v_b^*:

$$\frac{d^2u_b^*}{d\xi_*^2}-\frac{1}{4}\nu_4 n_*^2 u_b^*-\frac{1}{4}\nu_1 n_*\frac{dv_b^*}{d\xi_*}+\nu_2\lambda_* u_b^*+O(\eta^{2q})=0,$$
$$\frac{1}{4}\nu_1 n_*\frac{du_b^*}{d\xi_*}+\frac{1}{4}\nu_4\frac{d^2v_b^*}{d\xi_*^2}-n_*^2 v_b^*+\nu_2\lambda_* v_b^*+O(\eta^{2q})=0. \tag{44}$$

The latter coincides with the 2D equations of plate extension.

The function w_b^* is expressed in terms of u_b^*, v_b^* as

$$w_b^*=-\frac{1}{\nu_2}\lambda_*^{-1}\left(\nu\frac{du_b^*}{d\xi_*}-n_* v_b^*\right)+O(\eta^{2q}). \tag{45}$$

In the case of the asymptotic behavior 3.2 we have

$$\xi=\eta^{1/2+(1/2)q}\xi_*,\quad n=\eta^{-q}n_*,\quad \lambda=\eta^{-2q}\lambda_*,$$
$$u_a=\eta^{1/2+(1/2)q}u_a^*,\quad v_a=\eta^1 v_a^*,\quad w_a=\eta^0 w_a^*. \tag{46}$$

By introducing relations (46) into Eqs. (1) and keeping only leading terms we obtain the following equation in w_a^*:

$$\frac{1}{3\nu_2}\frac{d^4w_a^*}{d\xi_*^4}-\lambda_* w_a^*+O(\eta^{1-q}+\eta^{2q})=0. \tag{47}$$

It represents the equation for beam bending.

The functions u_a^*, v_a^* are

$$u_a^*=\frac{\nu}{3\nu_2}\lambda_*^{-1}\frac{d^3w_a^*}{d\xi_*^3}+O(\eta^{1-q}+\eta^{2q}),$$
$$v_a^*=\frac{2+\nu}{3\nu_2}n_*\lambda_*^{-1}\frac{d^2w_a^*}{d\xi_*^2}+O(\eta^{1-q}+\eta^{2q}). \tag{48}$$

Let us substitute Eqs. (9) into boundary conditions (2) and take into account Eqs. (43), (45), (46), and (48). We obtain

$$\eta^{-2q}\left(\frac{du_b^*}{d\xi_*}-\nu n_* v_b^*\right)+O(\eta^0)+\eta^\kappa O(\eta^{1-q})=0, \tag{49a}$$

$$\eta^{-2q}\left(n_* u_b^*+\frac{dv_b^*}{d\xi_*}\right)+O(\eta^{2-2q})+\eta^\kappa\left(\eta^{1/2-(1/2)q}\frac{2(1+\nu)}{3\nu_2}n_*\lambda_*^{-1}\frac{d^3w_a^*}{d\xi_*^3}+O(\eta^{3/2-(3/2)q}+\eta^{1/2+(3/2)q})\right)=0, \tag{49b}$$

$$\eta^{-2q}B_\nu+O(\eta^0)+\eta^\kappa\left(\eta^{-1-q}\frac{d^2w_a^*}{d\xi_*^2}+O(\eta^{-2q})\right)=0, \tag{49c}$$

$$\eta^{-3q}\frac{d}{d\xi_*}B_{\nu_3}+O(\eta^{-q})+\eta^\kappa\left(\eta^{-3/2-(3/2)q}\frac{d^3w_a^*}{d\xi_*^3}-\eta^{-1/2-(5/2)q}\nu_3 n^{-2}\frac{dw_a^*}{d\xi_*}+O(\eta^{1/2-(3/2)q})\right)=0, \tag{49d}$$

with

$$B_\alpha=-\alpha n_* v_b^*-\frac{1}{\nu_2}\lambda_*^{-1}\left(\frac{d^2}{d\xi_*^2}-\alpha n_*^2\right)\left(\nu\frac{du_b^*}{d\xi_*}-n_* v_b^*\right).$$

Examination of these equations yields $\kappa=1-q$. In analogy to the consideration above, these equations can be separated. The homogeneous boundary conditions for the functions u_b^*, v_b^* are

$$\frac{du_b^*}{d\xi_*}-\nu n_* v_b^*+O(\eta^{2q})=0,\quad n_* u_b^*+\frac{dv_b^*}{d\xi_*}+O(\eta^2)=0, \tag{50}$$

and the nonhomogeneous ones for w_a^* are

$$\frac{d^2w_a^*}{d\xi_*^2}+B_\nu+O(\eta^{1-q}+\eta^{2q})=0,\quad \frac{d^3w_a^*}{d\xi_*^3}+O(\eta^{1/2-(1/2)q})=0. \tag{51}$$

Basic boundary value problem (44) and (50) coincides with that for localized extensional vibrations of a semi-strip considered in Appendix B. Thus, the leading-order asymptotics for the natural frequency Λ_2 are determined from the frequency equation coinciding with Eq. (B6). In this case the natural form is associated with a Rayleigh-type extensional wave.

The procedure above allows for the estimation of only the real part of the natural frequency. However, as we have already mentioned, it also has a small imaginary part caused by the radiation to infinity. The latter corresponds to the effect of small-amplitude bending vibrations on the extensional vibrations considered. As follows from the asymptotic behaviors 3.1 and 3.2 and Eqs. (9), the contribution of the propagating mode for tangential displacements is of the order $O(\eta^{3/2+q/2})$. Let us estimate this imaginary part. For the sake of simplicity we assume that $q>\frac{1}{3}$.

First of all, we take into account terms of the order $O(\eta^{1-q})$ and $O(\eta^{3/2-3q/2})$ in Eqs. (47)–(49). By expressing the second- and third-order derivatives of the function w_a^* in refined Eqs. (49a) and (49b) from Eqs. (49c) and (49d) we arrive at refined boundary conditions for Eqs. (44). They are

$$\eta^{-2q}\left(\frac{du_b^*}{d\xi_*}-\nu n_* v_b^*\right)+O(\eta^0)+\eta^{2-2q}\frac{1}{3}(-n_*^2\lambda_*^{-1}+\nu)B_\nu+O(\eta^{3-3q})=0,$$
$$\eta^{-2q}\left(n_* u_b^*+\frac{dv_b^*}{d\xi_*}\right)+O(\eta^{2-2q})+\frac{\nu_1}{3\nu_2}n_*\lambda_*^{-1}\times\left(-\eta^{2-2q}\frac{d}{d\xi_*}B_{\nu_3}+\eta^{5/2-5/2q}(\nu_3 n_*^2-(\nu_1-\nu^2)\lambda_*)\times\frac{dw_a^*}{d\xi_*}+O(\eta^2)\right)=0. \tag{52}$$

TABLE IV. Extensional natural frequencies (free edge).

n	Re Λ_2^{ex}	Λ_R	ε_1	Im $\Delta_2^{ex}\times 10^4$	Im $\Lambda_2^{as}\times 10^4$	ε_2
5	8.260 577	8.071 621	2.287	0.016 664	0.007 732	53.603
6	11.813 252	11.623 134	1.609	0.023 086	0.012 196	47.169
7	16.011 212	15.820 377	1.192	0.031 655	0.017 931	43.355
8	20.854 663	20.663 350	0.917	0.042 529	0.025 037	41.129
9	26.343 706	26.152 052	0.728	0.055 902	0.033 610	39.877
10	32.478 393	32.286 484	0.591	0.071 983	0.043 738	39.239
11	39.258 757	39.066 645	0.489	0.090 983	0.055 506	38.993
12	46.684 814	46.492 536	0.412	0.113 114	0.068 994	39.005
13	54.756 576	54.564 157	0.351	0.138 588	0.084 278	39.188
14	63.474 052	63.281 508	0.303	0.167 615	0.101 432	39.485
15	72.837 245	72.644 588	0.265	0.200 404	0.120 527	39.858

It is clear that the leading-order imaginary term corresponds to the term of the order $O(\eta^{5/2-5q/2})$ in these equations. It is also evident that the first-order derivative of w_a^* can be determined from boundary value problem (47) and (51), i.e., to within the error $O(\eta^{1/2-q/2})$. By neglecting the real part of this derivative we obtain the boundary conditions

$$\frac{du_b^*}{d\xi_*}-\nu n_* v_b^*+O(\eta^{2q})=0,$$
$$n_* u_b^*+\frac{dv_b^*}{d\xi_*}+i\eta^{5/2-(1/2)q}(3\nu_2\lambda_*)^{-5/4}\nu_1 n_* \times(-\nu_3 n_*^2+(\nu_1-\nu^2)\lambda_*)B_\nu+O(\eta^2)=0. \tag{53}$$

The neglect of the real terms in Eqs. (53) does not effect the asymptotic behavior of the sought after imaginary part. By solving boundary value problem (44) and (53) we have

$$\mathrm{Im}\,\Lambda_2\approx\eta_1^{5/2}(\Lambda_R)^{-5/4}\times\frac{\nu_1 r_1 n^2(\nu_3 n^2-(\nu_1-\nu^2)\Lambda_R)^2}{(n^2/r_1 r_2)[(3-\nu)n^2-4\nu_2\Lambda_R]-2(2n^2-\nu_1\Lambda_R)} \tag{54}$$

with

$$r_1=\sqrt{n^2-\nu_1\Lambda_R},\quad r_2=\sqrt{n^2-\nu_2\Lambda_R},$$

where Λ_R is the real part of the natural frequency corresponding to the root of Eq. (B6).

Equation (54) shows that $\mathrm{Im}\,\Lambda_2$ is less than the error $O(\eta^{2-2q})$ in the Kirchhoff–Love theory of shells.[8] However, as it can be easily seen, refinement of the Kirchhoff–Love theory does not influence the estimate given by Eq. (54).

Localized vibrations occur also in the cases in which the edge is not traction-free in the transverse direction. Let transverse displacement and the angle of rotation be equal to zero on the edge. Then boundary conditions (49c) and (49d) must be replaced by

$$-\eta^0\frac{1}{\nu_2}\lambda_*^{-1}\left(\nu\frac{du_b^*}{d\xi_*}-n_* v_b^*\right)+O(\eta^{2q})+\eta^\kappa w_a^*=0,$$
$$-\eta^{-q}\frac{1}{\nu_2}\lambda_*^{-1}\frac{d}{d\xi_*}\left(\nu\frac{du_b^*}{d\xi_*}-n_* v_b^*\right)+O(\eta^q)+\eta^\kappa\eta^{-1/2-(1/2)q}\frac{dw_a^*}{d\xi_*}=0. \tag{55}$$

In this case we have $\kappa=0$. The nonhomogeneous boundary conditions for the additional boundary value problem become

$$w_a^*-\frac{1}{\nu_2}\lambda_*^{-1}\left(\nu\frac{du_b^*}{d\xi_*}-n_* v_b^*\right)+O(\eta^{2q})=0,$$
$$\frac{dw_a^*}{d\xi_*}+O(\eta^{1/2-(1/2)q})=0. \tag{56}$$

The leading-order asymptotic for the natural frequency is equal to Λ_R as above. Let us estimate the imaginary part by assuming that $q>0$. We determine the third-order derivative of the function w_a^* starting from boundary value problem (47) and (56) and keep only its imaginary part. The boundary conditions for the functions u_b^* and v_b^* become

$$\frac{du_b^*}{d\xi_*}-\nu n_* v_b^*+O(\eta^{2q})=0,$$
$$n_* u_b^*+\frac{dv_b^*}{d\xi_*}+i\eta^{1/2+(3/2)q}3\nu_1(3\nu_2\lambda_*)^{-5/4}n_* \times\left(\nu\frac{du_b^*}{d\xi_*}-n_* v_b^*\right)+O(\eta^{1+q}+\eta^{1/2+(7/2)q})=0. \tag{57}$$

By solving problem (44) and (57) we obtain

$$\mathrm{Im}\,\Lambda_2\approx\eta_1^{1/2}(\Lambda_R)^{-1/4}\times\frac{\nu_1 r_1 n^2}{(n^2/r_1 r_2)[(3-\nu)n^2-4\nu_2\Lambda_R]-2(2n^2-\nu_1\Lambda_R)}. \tag{58}$$

Comparison of asymptotical and numerical results is presented in Tables IV and V for a traction-free edge and an edge clamped in the transverse direction, respectively. The relative errors are $\varepsilon_1=|\Lambda_R-\mathrm{Re}\,\Lambda_2^{ex}|/\mathrm{Re}\,\Lambda_2^{ex}\times 100\%$ and ε_2

TABLE V. Extensional natural frequencies (edge clamped in the transverse direction).

n	Re Λ_2^{ex}	Λ_R	ε_1	Im Λ_2^{ex}	Im Λ_2^{as}	ε_2
5	8.228 298	8.071 621	1.904	0.027 319	0.034 445	26.084
6	11.777 310	11.623 134	1.309	0.029 710	0.037 733	27.003
7	15.972 037	15.820 377	0.950	0.031 736	0.040 756	28.423
8	20.812 562	20.663 350	0.717	0.033 500	0.043 570	30.059
9	26.298 910	26.152 052	0.558	0.035 066	0.046 213	31.788
10	32.431 087	32.286 484	0.446	0.036 474	0.048 713	33.555
11	39.209 090	39.066 645	0.363	0.037 752	0.051 090	35.331
12	46.632 913	46.492 536	0.301	0.038 922	0.053 362	37.102
13	54.702 549	54.564 157	0.253	0.039 998	0.055 541	38.860
14	63.417 992	63.281 508	0.215	0.040 993	0.057 638	40.603
15	72.779 236	72.644 588	0.185	0.041 917	0.059 661	42.330

$=|\mathrm{Im}\,\Lambda_2^{as}-\mathrm{Im}\,\Lambda_2^{ex}|/\mathrm{Im}\,\Lambda_2^{ex}\times 100\%$, and the value $\mathrm{Im}\,\Lambda_2^{as}$ is calculated by Eq. (54) or (58). The problem parameters are the same as in Tables II and III.

V. CONCLUDING REMARKS

Among the localized vibrations considered in this paper, the bending and extensional ones show little dependence on the shell curvature. It is likely that they occur in the case of a shell of arbitrary shape as well. At the same time super-low-frequency semi-membrane vibrations are characteristic only of a cylindrical shell.

The consideration above shows that for a shell localized vibrations take place not only at a traction free edge. The point is that for all the vibrations analyzed in the leading order we satisfy only two boundary conditions corresponding to a traction-free edge in the theories of plate bending and extension and in the semi-membrane theory of shells.

ACKNOWLEDGMENTS

The work was partly supported by INTAS (Grant No. INTAS-96-2113) and in the case of the first author also by the Russian Foundation of Basic Research (Grant Nos. 98-15-96017 and 99-01-01123).

APPENDIX A: Bending vibrations of a semi-strip

Consider the free localized bending vibrations of a semi-strip. Let its middle surface occupy the region $x\geqslant 0$, $-b\leqslant y\leqslant b$ in the plane (x, y) and its thickness be equal to $2h$. Let us introduce the dimensionless coordinates $x_1=\pi x/b$, $y_1=\pi y/b$. The equation of motion in the Kirchhoff theory of plates is

$$\tfrac{1}{3}\,\eta^2\Delta^2 w-(1-\nu^2)\lambda w=0, \tag{A1}$$

where w is the transverse displacement, Δ is the Laplace operator, and $\eta=h\pi/b$ is the relative half-thickness of the semi-strip.

The boundary conditions on the traction-free edge $x_1=0$ can be written as

$$\frac{\partial^2 w}{\partial x_1^2}+\nu\frac{\partial^2 w}{\partial y_1^2}=0,\quad \frac{\partial^3 w}{\partial x_1^3}+(2-\nu)\frac{\partial^3 w}{\partial x_1\partial y_1^2}=0, \tag{A2}$$

while the boundary conditions on the simple-supported edges $y_1=\pm\pi$ are

$$w=\frac{\partial^2 w}{\partial y_1^2}=0. \tag{A3}$$

A particular solution of Eq. (A1) satisfying boundary conditions (A3) can be written as

$$w=e^{-rx_1}\sin ny_1, \tag{A4}$$

where $n=1,2,...$, $\mathrm{Re}\,r>0$. By substituting representation (A4) into Eq. (A1) we obtain a characteristic equation in the parameter r. In the range $0<\lambda<\eta_1^2 n^4$ this equation possesses two real roots,

$$r_{1,2}=\sqrt{n^2\mp\eta_1^{-1}\lambda^{1/2}}, \tag{A5}$$

where

$$\eta_1^2=\frac{\eta^2}{3(1-\nu^2)}.$$

By inserting the general solution of Eq. (A1) into boundary conditions (A2) we arrive at the frequency equation

$$r_1(r_1^2-(2-\nu)n^2)(r_2^2-\nu n^2)-r_2(r_2^2-(2-\nu)n^2)(r_1^2-\nu n^2)=0. \tag{A6}$$

In the range $0<\lambda_0<\eta_1^2 n^4$ at $v\neq 0$ it has the root

$$\lambda=\eta_1^2 n^4(1-\nu)((3\nu-1)+2\sqrt{(1-\nu)^2+\nu^2}). \tag{A7}$$

Equation (A7) defines the sought after natural frequency. The associated natural form can be presented as

$$w=C[-(r_2^2-\nu n^2)e^{-r_1x_1}+(r_1^2-\nu n^2)e^{-r_2x_1}]\sin ny_1. \tag{A8}$$

Natural frequency (A7) and natural form (A8) correspond to the Rayleigh-type bending wave investigated for the first time in Ref. 13.

APPENDIX B: Extensional vibrations of a semi-strip

Consider the free localized vibrations of a semi-strip described in Appendix A and subjected to generalized plane stress. The equations of motion are

$$\begin{aligned}&\frac{\partial^2 u}{\partial x_1^2}+\frac{1-\nu}{2}\frac{\partial^2 u}{\partial y_1^2}+\frac{1+\nu}{2}\frac{\partial^2 v}{\partial x_1\partial y_1}+(1-\nu^2)\lambda u=0,\\ &\frac{1+\nu}{2}\frac{\partial^2 u}{\partial x_1\partial y_1}+\frac{1-\nu}{2}\frac{\partial^2 v}{\partial x_1^2}+\frac{\partial^2 v}{\partial y_1^2}+(1-\nu^2)\lambda v=0.\end{aligned} \tag{B1}$$

Here u and v are the displacements along the coordinates x, y, and $\lambda=\rho\omega^2 b^2/E\pi^2$ is the dimensionless frequency.

Boundary conditions on the edges take the form

$$\frac{\partial u}{\partial x_1}+\nu\frac{\partial v}{\partial y_1}=0, \quad \frac{\partial u}{\partial y_1}+\frac{\partial v}{\partial x_1}=0 \quad \text{at} \quad x_1=0, \tag{B2}$$

$$u=\frac{\partial v}{\partial y_1}=0 \quad \text{at} \quad y_1=\pm\pi. \tag{B3}$$

Solutions of Eqs. (B1) obeying boundary conditions (B3) can be written as

$$u=u_0 e^{-rx_1}\sin ny_1, \quad v=v_0 e^{-rx_1}\cos ny_1, \tag{B4}$$

where r, u_0, and v_0 are constants, $n=1,2,....$ To ensure that the solution decays as x_1 approaches infinity we require $\mathrm{Re}\, r>0$. By substituting Eqs. (B4) into Eqs. (B1) we arrive at a characteristic equation possessing two real positive roots in the range $0<\lambda<n^2/2(1+\nu)$. They are

$$r_1=\sqrt{n^2-2(1+\nu)\lambda}, \quad r_2=\sqrt{n^2-(1-\nu^2)\lambda}. \tag{B5}$$

Then by introducing the general solution of system (B1) into boundary conditions (B2) we obtain the frequency equation

$$(n^2-(1+\nu)\lambda)^2-r_1 r_2 n^2=0. \tag{B6}$$

It can be easily verified that in the range $0<\lambda<n^2/2(1+\nu)$ Eq. (B6) has the unique root corresponding to a natural frequency. In this case the natural form is given by

$$\begin{aligned} u&=C[r_1(n^2+r_2^2)e^{-r_1x_1}-2r_1n^2e^{-r_2x_1}]\sin ny_1,\\ v&=Cn[-(n^2+r_2^2)e^{-r_1x_1}+2r_1r_2e^{-r_2x_1}]\cos ny_1. \end{aligned} \tag{B7}$$

Equations (B7) describe a surface wave. The latter represents an analog of the Rayleigh wave[14] for plate extension. In fact, Eq. (B6) can be rewritten as

$$\left(2-\frac{c_R^2}{c_2^2}\right)^2-4\sqrt{1-\frac{c_R^2}{c_1^2}}\sqrt{1-\frac{c_R^2}{c_2^2}}=0,$$

where $c_1=[E/\rho(1-\nu^2)]^{1/2}$, $c_2=[E/2\rho(1+\nu)]^{1/2}$, and $c_R=\omega b/n\pi$. This equation coincides with that for the phase velocity of the Rayleigh wave.

[1] E. A. G. Shaw, ''On the resonant vibrations of thick barium titanate disks,'' J. Acoust. Soc. Am. **20**, 38–50 (1956).

[2] D. C. Gazis and R. D. Mindlin, ''Extensional vibrations and waves in a circular disk and a semi-infinite plate,'' J. Appl. Mech. **27**, 541–547 (1960).

[3] P. J. Torvik, ''Reflection of wave trains in semi-infinite plates,'' J. Acoust. Soc. Am. **41**, 346–353 (1967).

[4] P. J. Torvik and J. J. McClatchey, ''Response of an elastic plate to a cyclic longitudinal force,'' J. Acoust. Soc. Am. **44**, 59–64 (1968).

[5] V. T. Grinchenko and V. V. Meleshko, ''On the resonance for a semi-infinite strip,'' Prikladnaya Mekhanika **16(2)**, 58–63 (1980) [English translation: Sov. Appl. Mech.].

[6] I. Roitberg, D. Vassiliev, and T. Weidl, ''Edge resonance in an elastic semi-strip,'' Q. J. Mech. Appl. Math. **51**, 1–13 (1998).

[7] A. L. Goldenveizer, *Theory of Elastic Thin Shells* (Pergamon, Oxford, 1961).

[8] J. D. Kaplunov, L. Yu. Kossovich, and E. V. Nolde, *Dynamics of Thin Walled Elastic Bodies* (Academic, San Diego, 1998).

[9] A. L. Goldenveizer, V. B. Lidskii, and P. E. Tovstik, *Free Vibrations of Thin Elastic Shells* (Nauka, Moscow, 1979).

[10] G. C. Gaunard and D. Brill, ''Acoustic spectrogram and complex-frequency poles of a resonantly excited elastic tube,'' J. Acoust. Soc. Am. **75**, 1680–1693 (1984).

[11] J. Sanchez Hubert and E. Sanchez Palencia, *Vibrations and Coupling of Continuous Systems* (Springer-Verlag, Berlin, 1989).

[12] R. A. Bagdasaryan, M. V. Belubekyan, and K. B. Kazaryan, ''Rayleigh-type waves in a semi-infinite closed cylindrical shell,'' in *Wave Problems in Mechanics*, edited by A. I. Vesnitskii and V. I. Erofeev (Nijnii Novgorod Branch of Mechanical Engineering Institute, Nijnii, Novgorod, 1992), pp. 87–93.

[13] Yu. K. Konenkov, ''On a Rayleigh-type bending wave,'' Akust. Zh. **6**, 124–126 (1960) [English translation: Sov. Acoust.].

[14] Lord Rayleigh, ''On waves propagated along the surface of an elastic solid,'' Proc. London Math. Soc. **17**, 4–11 (1885).

Sound propagation in street canyons: Comparison between diffusely and geometrically reflecting boundaries

Jian Kang[a)]
The Martin Centre, University of Cambridge, 6 Chaucer Road, Cambridge CB2 2EB, United Kingdom

(Received 8 December 1998; revised 10 November 1999; accepted 14 November 1999)

This paper systematically compares the sound fields in street canyons with diffusely and geometrically reflecting boundaries. For diffuse boundaries, a radiosity-based theoretical/computer model has been developed. For geometrical boundaries, the image source method has been used. Computations using the models show that there are considerable differences between the sound fields resulting from the two kinds of boundaries. By replacing diffuse boundaries with geometrical boundaries, the sound attenuation along the length becomes significantly less; the RT30 is considerably longer; and the extra attenuation caused by air or vegetation absorption is reduced. There are also some similarities between the sound fields under the two boundary conditions. For example, in both cases the sound attenuation along the length with a given amount of absorption is the highest if the absorbers are arranged on one boundary and the lowest if they are evenly distributed on all boundaries. Overall, the results suggest that, from the viewpoint of urban noise reduction, it is better to design the street boundaries as diffusely reflective rather than acoustically smooth. © *2000 Acoustical Society of America.* [S0001-4966(00)04902-X]

PACS numbers: 43.50.Vt, 43.50.Sr, 43.28.Fp, 43.20.Fn [MRS]

INTRODUCTION

Sound propagation in street canyons has been investigated for a number of years. A common manner of solving the problem is to use the image source method or ray-tracing techniques by assuming that the building facades and street ground are perfectly smooth and thus geometrically reflective. This assumption is appropriate in certain situations and the previous work on this aspect has contributed significantly towards a fundamental understanding of the behavior of sound in street canyons.[1–6] However, since there are always some irregularities on building or ground surfaces, the consideration of pure geometrical reflection appears to be unreasonable in many cases.[2,7] Consequently, a number of models have been proposed for taking diffuse reflections into account. Bullen and Fricke,[8] in order to consider the effects of scattering from objects and protrusions in streets, analyzed the sound field in terms of its propagating modes. In a model suggested by Davies,[9] the sound field was assumed to be the sum of a multiply geometrically reflected field and a diffuse field that was fed from scattering at boundaries at each reflection of the geometrical field. Wu and Kittinger,[10] using Chien and Carroll's method[11] of describing a surface by a mixed reflection law with an absorptivity or reflectivity parameter and a smoothness or roughness parameter, developed a model for predicting traffic noise L_{A10}. Heutschi[12] suggested modeling sound propagation by a continuous energy exchange within a network of predefined points located on individual plane surfaces, and in this way it was possible to define any characteristic directivity pattern for the reflections. In addition to the above models, the boundary element method was also proved to be useful for studying the sound field in street canyons.[13]

Previous work, however, has mainly focused on improving the accuracy of prediction models, and little has been published on the differences and similarities between the sound fields formed by diffusely and geometrically reflecting boundaries. Given the significant differences between the two kinds of sound fields in long enclosures, observed both experimentally and theoretically,[14–19] an investigation of street canyons is important to better understand the behavior of sound and is also useful for the design of new buildings.

The real world is somewhere between the sound fields under the two idealized boundary conditions.[10,15] Consider a general condition, namely, when a sound ray is incident on a boundary, a fraction U_g of the incident power is reflected geometrically, a fraction U_d is reflected diffusely, and the rest is absorbed. A street which consists of a mixture of boundaries, some geometrically reflective and some diffusely reflective, can be represented using $U_g=0$ and $U_d=0$. For a rectangular street canyon with such a general condition, it can be demonstrated that at a given source–receiver distance the average length of reflected sound path and the average order of reflection are between those resulting from diffuse and geometrical boundaries. Consequently, the true sound field should be between the two limits. As a calculation example, Davies has shown that, with $U_g=0.6, U_d=0.3$, the attenuation curve along the length is between those with $U_g=0.3$, $U_d=0.6$ and $U_g=0.9$, $U_d=0$.[9] Experimental evidence shows that in long enclosures the sound attenuation along the length becomes systematically greater with an increasing amount of diffusers on boundaries, or with better diffusers.[16–18]

The objective of this paper is to systematically analyze and compare the sound fields in street canyons resulting from both diffusely and geometrically reflecting boundaries. For diffuse boundaries, a computer model has been developed using the radiosity technique. This model is based on the

[a)]Present address: School of Architecture, The University of Sheffield, Western Bank, Sheffield S10 2TN, United Kingdom.

assumption that the sound energy reflected from a boundary is dispersed over all directions according to the Lambert cosine law. For geometrical boundaries, the conventional image source method is used. The compared indices are mainly the sound pressure level (SPL) and reverberation. The latter has been demonstrated to be a useful index for streets.[7]

For the sake of convenience, the boundary absorption is assumed to be independent of the angle of incidence. Excess attenuation due to ground interference and temperature- or wind-gradient-induced refraction is not taken into account in the calculation. These omissions are not thought to be of great significant for the comparison between the two kinds of boundaries.[7,9] The absorption coefficient is assumed to be uniform in a boundary. With some strong absorption elements, such as open windows or gaps between buildings as sound energy sinks, it has been demonstrated that the trend of the comparison results will not change systematically.

The main interest of this paper is the situation where street boundaries have reasonable effects on the sound energy at a receiver. If the direct sound is dominant, such as the case when a receiver is very close to high-density traffic and there is no barrier in between, it is unimportant to consider the effect of street boundaries, or to compare the two kinds of boundaries.

The paper begins with a description of the models. A series of computed results is then analyzed.

I. MODEL FOR DIFFUSELY REFLECTING BOUNDARIES

The radiosity method was first developed in the 19th century for the study of radiant heat transfer in simple configurations.[20–22] By considering relatively high frequencies, the method has recently been used in the field of room acoustics.[19,23,24] An important feature of this application is that the time factor must be taken into account. With similar principles, the radiosity method can also be used for the study of street canyons.

Basically, the model outlined in this paper divides the building facades and the ground of a street into a number of patches (i.e., elements) and replaces the patches and receivers with nodes in a network. The sound propagation in the street can then be simulated by energy exchange between the nodes. The energy moving between pairs of patches depends on a form factor, which is defined as the fraction of the sound energy diffusely emitted from one patch which arrives at the other by direct energy transport. The main steps of the model are described below.

A. Patch division

The first step of the model is to divide each boundary into a number of patches. Consider an idealized street canyon with a length of X, width of Y, and height of Z, as illustrated in Fig. 1. The boundaries are defined as G, ground; A, building facade at $y=0$; and B, building facade at $y=Y$. Also define the patches along the length, width, and height as l $(l=1,...,N_X)$, m $(m=1,...,N_Y)$, and n $(n=1,...,N_Z)$, respectively.

The model is more accurate with finer patch parametrization, but there is a square-law increase of calculation time

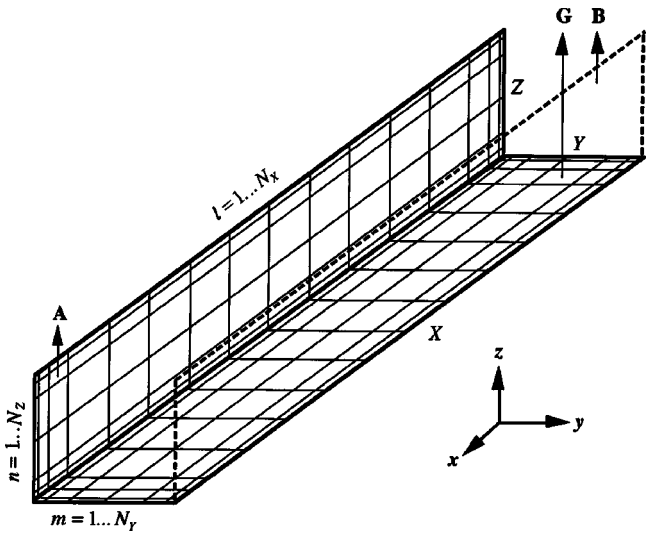

FIG. 1. Three-dimensional projection of an idealized street showing an example of patch division.

with the number of patches. To reduce the patch number, the boundaries are so divided that a patch is smaller when it is closer to an edge. This is because, for a given patch size, form factor calculations become less accurate as the patch moves closer to an edge.[25] For the convenience of computation, the division of boundaries is made using geometrical series (see Fig. 1).

If a dimension is not large, for example, along the width, the patch size dd_m increases from the edges to the center, namely,

$$dd_m = k_m q_y^{m-1} \quad \left(1 \leqslant m \leqslant \frac{N_Y}{2}\right)$$
$$= k_m q_y^{N_Y - m} \quad \left(\frac{N_Y}{2} < m \leqslant N_Y\right), \tag{1}$$

where $q_y (q_y > 1)$ is the ratio between two adjacent patches, N_Y should be an even number, and

$$k_m = \frac{Y}{2} \frac{1-q_y}{1-q_y^{N_Y/2}}. \tag{2}$$

For a relatively large dimension, for example, along the length, the patch size dd_l increases from $l=1$ to $N_X/4$, decreases from $l=3N_X/4+1$ to N_X, and is constant between $l=N_X/4+1$ and $3N_X/4$. In this way extreme differences in patch size can be avoided. The patch sizes can be determined by

$$dd_l = k_l q_x^{l-1} \quad \left(1 \leqslant l \leqslant \frac{N_X}{4}\right)$$
$$= k_l q_x^{N_X/4-1} \quad \left(\frac{N_X}{4} < l \leqslant \frac{3N_X}{4}\right)$$
$$= k_l q_x^{N_X-1} \quad \left(\frac{3N_X}{4} < l \leqslant N_X\right), \tag{3}$$

where q_x $(q_x > 1)$ is the ratio between two adjacent patches, N_X should be divisible by 4, and

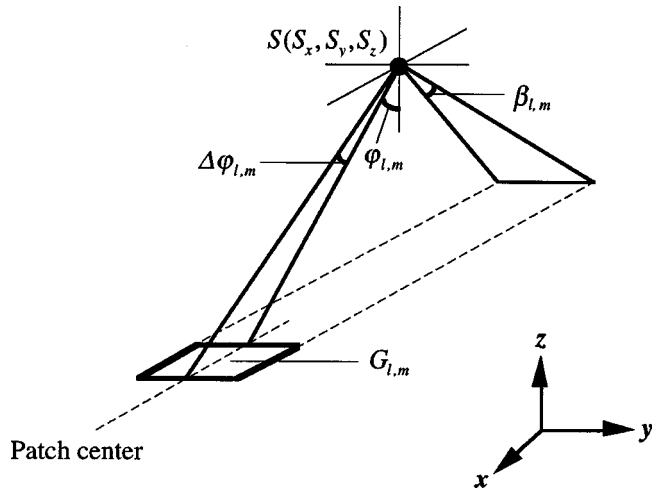

FIG. 2. Distribution of the energy from a point source to a patch on the ground.

$$k_l=\frac{X}{2}\frac{1}{\dfrac{1-q_x^{N_X/4}}{1-q_x}+\dfrac{N_X}{4}q_x^{N_X/4-1}}. \tag{4}$$

Correspondingly, the coordinates of the center of a patch, for example, $G_{l,m}$, can be determined by

$$d_l=-\frac{1}{2}dd_l+\sum_{l=1}^{l} dd_l$$

and (5)

$$d_m=-\frac{1}{2}dd_m+\sum_{m=1}^{m} dd_m.$$

B. First-order patch sources

The next step of the model is to distribute the sound energy of an impulse source to the patches. The patches can then be regarded as sound sources, which are called first-order patch sources below. The basic principle of the source energy distribution is that the energy fraction at each patch is the same as the ratio of the solid angle subtended by the patch at the source to the total solid angle. Consider a point source S at (S_x,S_y,S_z). A first-order patch source, $G_1(t)_{l,m}$, for example (see Fig. 2), can be calculated by

$$\begin{aligned}G_1(t)_{l,m}&=K(1-\alpha_{G_{l,m}})e^{-MS_{l,m}}\frac{1}{4\pi}\\&\quad\times\int_0^{\beta_{l,m}}\int_{\varphi_{l,m}}^{\varphi_{l,m}+\Delta\varphi_{l,m}}\cos\varphi\,d\varphi\,d\beta\\&=K(1-\alpha_{G_{l,m}})e^{-MS_{l,m}}\frac{1}{4\pi}|\sin(\varphi_{l,m}+\Delta\varphi_{l,m})\\&\quad-\sin\varphi_{l,m}|\beta_{l,m}\quad\left(t=\frac{S_{l,m}}{c}\right),\end{aligned} \tag{6}$$

where t $(t=0,...,\infty)$ is the time and $t=0$ represents the moment at which the source generates an impulse. Here c is the speed of sound in air, K is a constant in relation to the sound power of the source, and $\alpha_{G_{l,m}}$ is the angle-independent absorption coefficient of patch $G_{l,m}$. To consider buildings with a lower height than Z, the absorption coefficient can be given as 1. Here M (Np/m) is the intensity-related attenuation constant in air. $S_{l,m}$ is the mean beam length between the source and patch $G_{l,m}$, which can be approximated by the distance from the source to the center of the patch, namely,

$$S_{l,m}=\sqrt{[d_l-S_x]^2+[d_m-S_y]^2+S_z^2}. \tag{7}$$

Here $\varphi_{l,m}$, $\Delta\varphi_{l,m}$, and $\beta_{l,m}$ are the angles determining the location of patch $G_{l,m}$ with reference to the source, which can be calculated by

$$\sin(\varphi_{l,m}+\Delta\varphi_{l,m})=\frac{d_l+\frac{1}{2}dd_l-S_x}{\sqrt{(d_l+\frac{1}{2}dd_l-S_x)^2+(d_m-S_y)^2+S_z^2}}, \tag{8}$$

$$\sin\varphi_{l,m}=k_\varphi\frac{d_l-\frac{1}{2}dd_l-S_x}{\sqrt{(d_l-\frac{1}{2}dd_l-S_x)^2+(d_m-S_y)^2+S_z^2}}, \tag{9}$$

and

$$\begin{aligned}\beta_{l,m}=&\left|\arctan\left|\frac{d_m+\frac{1}{2}dd_m-S_y}{S_z}\right|\right.\\&\left.-k_\beta\arctan\left|\frac{d_m-\frac{1}{2}dd_m-S_y}{S_z}\right|\right|.\end{aligned} \tag{10}$$

In Eq. (9) k_φ is used to consider the source position which is between the two sides of patch $G_{l,m}$. That is, $k_\varphi=-1$ when $d_l-dd_l/2\leqslant S_x\leqslant d_l+dd_l/2$, otherwise $k_\varphi=1$. Similarly, in Eq. (10) $k_\beta=-1$ when $d_m-dd_m/2\leqslant S_y\leqslant d_m+dd_m/2$, and $k_\beta=1$ otherwise.

If a source is directional, a term in Eq. (6) representing the radiation strength of the source in the direction of patch $G_{l,m}$ should be added.

C. Form factors

In an idealized street canyon, as illustrated in Fig. 1, the relative location of any two patches is either orthogonal or parallel. For orthogonal patches, the form factor can be calculated using Nusselt's method.[22] That is, the computing form factor is equivalent to projecting the receiving patch onto a unit hemisphere centered about the radiation patch, projecting this projected area orthographically down onto the hemisphere's unit circle base, and dividing by the area of the circle. As an example, Fig. 3 illustrates the calculation from emitter $A_{l',n'}$ $(l'=1,...,N_X,n'=1,...,N_Z)$ to receiver $G_{l,m}$. By considering the absorption of patch $A_{l',n'}$ and air absorption, the energy emitted from $A_{l',n'}$ to $G_{l,m}$, $AG_{(l',n'),(l,m)}$, can be calculated by

$$\begin{aligned}AG_{(l',n'),(l,m)}=&(1-\alpha_{A_{l',n'}})e^{-Md_{(l',n'),(l,m)}}\frac{1}{2\pi}\\&\times|\cos^2\gamma_{(l',n'),(l,m)}-\cos^2(\gamma_{(l',n'),(l,m)}\\&+\Delta\gamma_{(l',n'),(l,m)})|\vartheta_{(l',n'),(l,m)},\end{aligned} \tag{11}$$

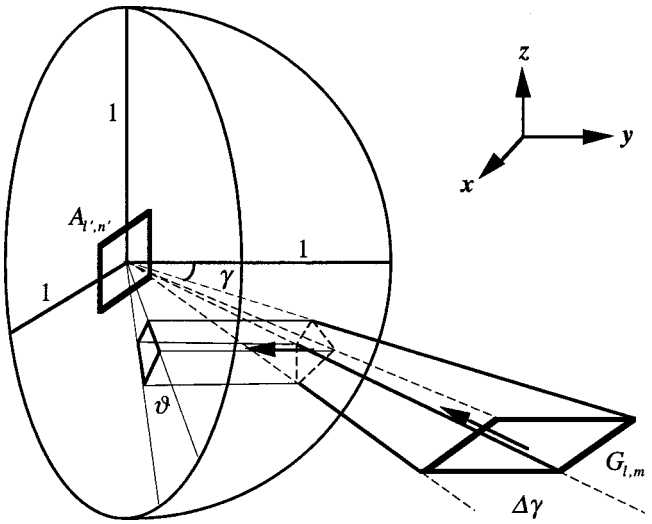

FIG. 3. Determination of the form factor from emitter $A_{l',n'}$ to an orthogonal patch $G_{l,m}$.

where $d_{(l',n'),(l,m)}$ is the mean beam length between patches $A_{l',n'}$ and $G_{l,m}$. It can be approximated using the distance between the centers of the two patches:

$$d_{(l',n'),(l,m)}=\sqrt{(d_l-d_{l'})^2+d_m^2+d_{n'}^2}. \tag{12}$$

Here $\gamma_{(l',n'),(l,m)}$, $\Delta\gamma_{(l',n'),(l,m)}$, and $\vartheta_{(l',n'),(l,m)}$ are the angles for determining the relative location of the two patches:

$$\cos\gamma_{(l',n'),(l,m)}=\frac{d_m-\frac{1}{2}dd_m}{\sqrt{(d_l-d_{l'})^2+(d_m-\frac{1}{2}dd_m)^2+d_{n'}^2}}, \tag{13}$$

$$\cos(\gamma_{(l',n'),(l,m)}+\Delta\gamma_{(l',n'),(l,m)})=\frac{d_m+\frac{1}{2}dd_m}{\sqrt{(d_l-d_{l'})^2+(d_m+\frac{1}{2}dd_m)^2+d_{n'}^2}}, \tag{14}$$

$$\vartheta_{(l',n'),(l,m)}=\left|\arctan\left|\frac{d_l-\frac{1}{2}dd_l-d_{l'}}{d_{n'}}\right|-k_\vartheta\arctan\left|\frac{d_l+\frac{1}{2}dd_l-d_{l'}}{d_{n'}}\right|\right|. \tag{15}$$

In Eq. (15) k_ϑ is used to consider the case where the two patches have the same coordinate in the length direction. That is, $k_\vartheta=-1$ when $l=l'$, otherwise $k_\vartheta=1$.

For parallel patches, the form factor can be calculated by a method developed by Cohen and Greenberg,[22,26] that is, projecting the receiving patch onto the upper half of a cube centered about the radiation patch. Consider patches $A_{l',n'}$ $(l'=1,...,N_X, n'=1,...,N_Z)$ and $B_{l,n}$. For example, the energy emitted from $A_{l',n'}$ to $B_{l,n}$, $AB_{(l',n'),(l,n)}$, can be calculated by

$$AB_{(l',n'),(l,n)}=(1-\alpha_{A_{l',n'}})e^{-Md_{(l',n'),(l,n)}}\times\frac{Y^2dd_ldd_n}{\pi[(d_l-d_{l'})^2+(d_n-d_{n'})^2+Y^2]^2}, \tag{16}$$

where $d_{(l',n'),(l,n)}$ is the mean beam length between the two patches, which can be approximated using the distance between the centers of the two patches:

$$d_{(l',n'),(l,n)}=\sqrt{(d_l-d_{l'})^2+(d_n-d_{n'})^2+Y^2}. \tag{17}$$

D. Energy exchange between patches

Using the form factors obtained above, the sound energy of each first-order patch source can be redistributed to other patches and, consequently, the second-order patch sources can be generated. Continue this process and the kth-order patch sources can be obtained $(k=1,...,\infty)$. This process is ''memory-less,'' that is, the energy exchange between patches depends only on the form factors and the patch sources of preceding order. The calculation of a kth-order patch source can be made by summing the contribution from all the $(k-1)$th-order patch sources, except those which are on the same boundary as the kth-order patch source considered. For example, to calculate a kth-order patch source on the ground, $G_k(t)_{l,m}$, the contribution from the patches on the two facades should be summed:

$$\begin{aligned}G_k(t)_{l,m}=&\sum_{l'=1}^{N_X}\sum_{n'=1}^{N_Z}AG_{(l',n'),(l,m)}\times A_{k-1}\left(t-\frac{d_{(l',n'),(l,m)}}{c}\right)_{l'n'}\\&+\sum_{l'=1}^{N_X}\sum_{n'=1}^{N_Z}BG_{(l',n'),(l,m)}\times B_{k-1}\left(t-\frac{d_{(l',n'),(l,m)}}{c}\right)_{l'n'}\\&\left(t-\frac{d_{(l'n'),(l,m)}}{c}\geqslant 0\right).\end{aligned} \tag{18}$$

E. Energy from patches to receiver

Consider a receiver R at (R_x,R_y,R_z). The energy response at the receiver can be determined by taking all orders of patch sources into account. For the kth-order patch sources, the energy at receiver R at time t can be written as

$$E_k(t)=E_k(t)_G+E_k(t)_A+E_k(t)_B, \tag{19}$$

where, for example, the contribution from the patch sources on boundary G is $E_k(t)_G$, which can be determined by

$$E_k(t)_G=\sum_{l=1}^{N_X}\sum_{m=1}^{N_Y}\left[\frac{G_k\left(t-\frac{R_{l,m}}{c}\right)_{l,m}}{\pi R_{l,m}^2}\cos(\xi_{l,m})\right]e^{-MR_{l,m}}\left(t-\frac{R_{l,m}}{c}\geqslant 0\right), \tag{20}$$

where $\xi_{l,m}$ is the angle between the normal of patch $G_{l,m}$ and the line joining the receiver and the patch:

$$\cos(\xi_{l,m}) = \frac{R_z}{\sqrt{(d_l - R_x)^2 + (d_m - R_y)^2 + R_z^2}}. \tag{21}$$

In Eq. (20) $R_{l,m}$ is the mean beam length between receiver R and patch $G_{l,m}$. Again, it can be approximated using the distance between the receiver and the patch center:

$$R_{l,m} = \sqrt{(d_l - R_x)^2 + (d_m - R_y)^2 + R_z^2}. \tag{22}$$

A more accurate calculation of $R_{l,m}$ can be made by subdividing patch $G_{l,m}$ into N_l by N_m ($N_l, N_m \geqslant 1$) equal elements and then calculating their average distance to the receiver:

$$R_{l,m} = \frac{1}{N_l N_m} \sum_{i=1}^{N_l} \sum_{j=1}^{N_m} \sqrt{\left[d_l - \frac{1}{2}dd_l + \frac{dd_l}{N_l}\left(i - \frac{1}{2}\right) - R_x\right]^2 + \left[d_m - \frac{1}{2}dd_m + \frac{dd_m}{N_m}\left(j - \frac{1}{2}\right) - R_y\right]^2 + R_z^2}. \tag{23}$$

A similar method can also be used for the calculations in Eqs. (10), (12), and (17).

By considering all orders of patch sources as well as the direct energy transport from source to receiver, the energy response at receiver R can be given by

$$L(t) = 10 \lg\left[E_d(t) + \sum_{k=1}^{\infty} E_k(t)\right] - L_{\text{ref}}, \tag{24}$$

where L_{ref} is the reference level. The direct energy can be calculated by

$$E_d(t) = \frac{1}{4\pi r^2} e^{-Mr} \quad \left(t = \frac{r}{c}\right), \tag{25}$$

where r is the source–receiver distance:

$$r = \sqrt{(S_x - R_x)^2 + (S_y - R_y)^2 + (S_z - R_z)^2}. \tag{26}$$

By introducing a term r/c to translate the arrival time of direct sound to zero, the decay curve can be obtained by the reverse-time integration of $L(t)$. Consequently, the early decay time (EDT) and RT30 (reverberation time obtained from -5 to -35 dB on a decay curve using linear regression) can be determined. The steady-state SPL at receiver R can be calculated by

$$L = 10 \lg \sum_{\Delta t} 10^{L(t)/10}. \tag{27}$$

By considering more boundaries, the above theory can also be used for rectangular enclosures. Such an extended model has been shown to correctly calculate the acoustic characteristics of a cube,[19] which can be regarded as a validation of the algorithms.

II. MODEL FOR GEOMETRICALLY REFLECTING BOUNDARIES

With geometrically reflecting boundaries, the sound propagation in a street canyon can be calculated using the image source method. Figure 4 illustrates the distribution of image sources in an idealized street, as shown in Fig. 1. For calculation convenience, the image sources are divided into four groups, namely A1, A2, B1, and B2. Groups A1 and A2 represent the reflections between two facades, and groups B1 and B2 include the reflection from the street ground. With reference to Fig. 4, the energy from an image source to a receiver R at (R_x, R_y, R_z) can be easily determined. First, consider an image source i ($i = 1,...,\infty$) in group A1. For odd values of i the energy to the receiver is

$$E_i(t) = \frac{1}{4\pi d_i^2} (1 - \alpha_A)^{(i+1)/2} (1 - \alpha_B)^{(i-1)/2} e^{-Md_i} \quad \left(t = \frac{d_i}{c}\right), \tag{28}$$

where α_A and α_B are the absorption coefficient of facades A and B, respectively. Here d_i is the distance from the image source i to the receiver:

$$d_i^2 = (S_x - R_x)^2 + [(i-1)W + S_y + R_y]^2 + (S_z - R_z)^2. \tag{29}$$

For even i,

$$E_i(t) = \frac{1}{4\pi d_i^2} (1 - \alpha_A)^{i/2} (1 - \alpha_B)^{i/2} e^{-Md_i} \quad \left(t = \frac{d_i}{c}\right) \tag{30}$$

with

$$d_i^2 = (S_x - R_x)^2 + (iW - S_y + R_y)^2 + (S_z - R_z)^2. \tag{31}$$

For an image source i ($i = 1,...,\infty$) in group A2, with odd values of i the sound energy to the receiver is

$$E_i(t) = \frac{1}{4\pi d_i^2} (1 - \alpha_A)^{(i-1)/2} (1 - \alpha_B)^{(i+1)/2} e^{-Md_i} \quad \left(t = \frac{d_i}{c}\right) \tag{32}$$

with

$$d_i^2 = (S_x - R_x)^2 + [(i+1)W - S_y - R_y]^2 + (S_z - R_z)^2. \tag{33}$$

For even i,

$$E_i(t) = \frac{1}{4\pi d_i^2} (1 - \alpha_A)^{i/2} (1 - \alpha_B)^{i/2} e^{-Md_i} \quad \left(t = \frac{d_i}{c}\right) \tag{34}$$

with

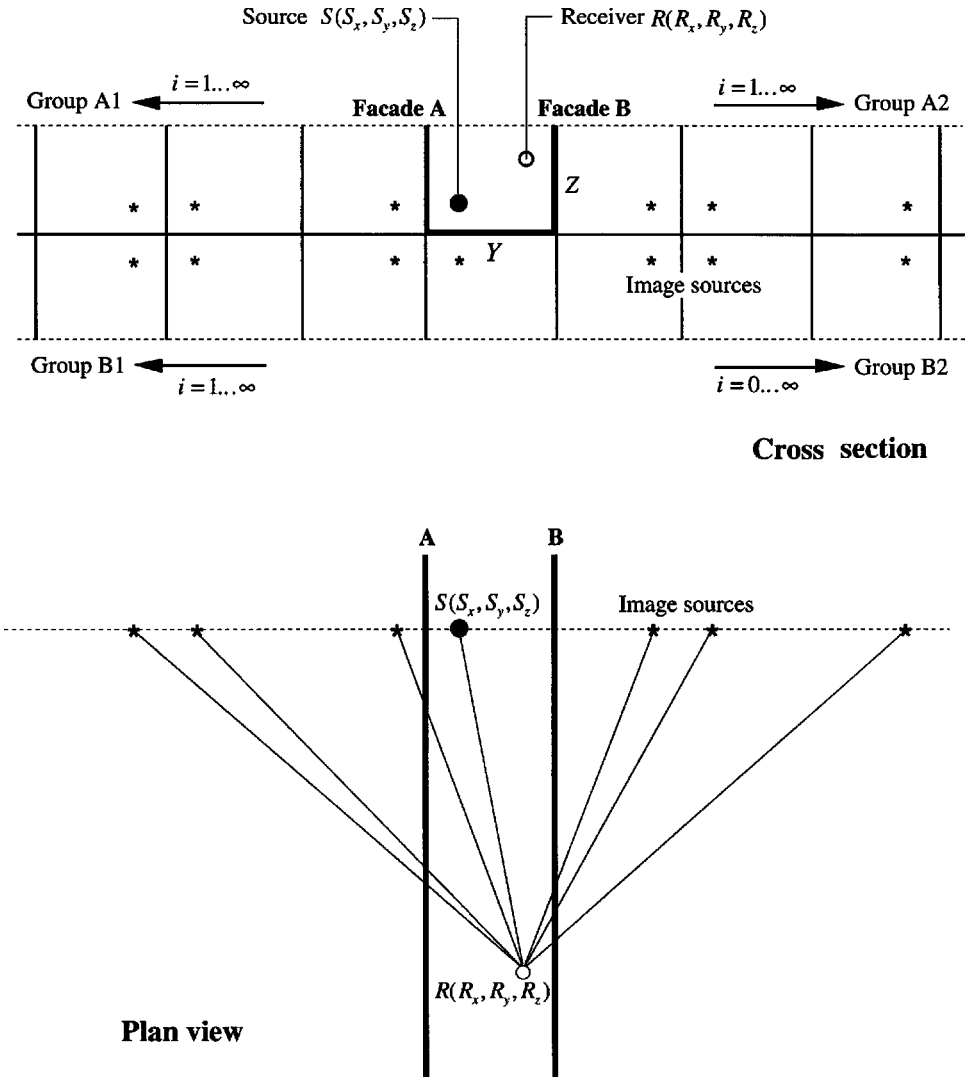

FIG. 4. Distribution of the image sources in an idealized street canyon.

$$d_i^2=(S_x-R_x)^2+(iW+S_y-R_y)^2+(S_z-R_z)^2. \quad (35)$$

For groups B1 and B2, the energy from the image sources to the receiver can be determined using Eqs. (28)–(35) but replacing the term S_z-R_z with S_z+R_z and, also, considering the ground absorption α_G. By summing the energy from all the image sources in groups A1, A2, B1, and B2, and taking direct sound transfer into account, the energy response at the receiver can be obtained. Consequently, the acoustic indices such as EDT, RT30, and steady-state SPL can be determined in a similar manner to Eqs. (24)–(27).

III. COMPUTATION

The sound fields in street canyons resulting from both diffusely and geometrically reflecting boundaries were analyzed using C-program representations of the above models. For convenience, the calculations assumed idealized street layouts. Namely, that the buildings were continuous along a street and of constant height. In most calculations, the street length was 120 m, a point source was positioned at $x=30$ m, the source–receiver distance along the length was 1–60 m ($x=31-90$ m), and the facades and ground were assumed to have a uniform absorption coefficient of 0.1.[2,9,10] With this configuration the calculation results should not be significantly affected by extending the street length.[14,19] In other words, the results can be generalized to represent a longer street. Figure 5 illustrates the geometry of such a typical street. Except where indicated, the calculations below correspond with this configuration. Note that the source–receiver distance refers to the horizontal distance along the canyon length.

Typically, calculations were made with $N_X=60$, $q_x=1.2$, $N_Y=N_Z=8$, and $q_y=q_z=1.5$. Using these parameters the program calculated the form factors and the energy distribution to first-order patch sources accurate to four decimal places.

A. Sound attenuation along the length

Figure 6 shows the extra SPL attenuation along the length caused by replacing geometrically reflecting boundaries with diffusely reflecting boundaries. The calculation is based on two street layouts, namely $Y=20$ m, $Z=6$ m, and $Y=20$ m, $Z=18$ m. The receivers are along two lines in the length direction, namely (31–90 m, 2 m, 1 m) and (31–90 m, 18 m, Z), which represent relatively high and low SPL in a cross section, respectively. The source is at (30 m, 6 m, 1 m). From Fig. 6 it is interesting to note that in comparison with geometrical boundaries, the SPL with diffuse boundaries de-

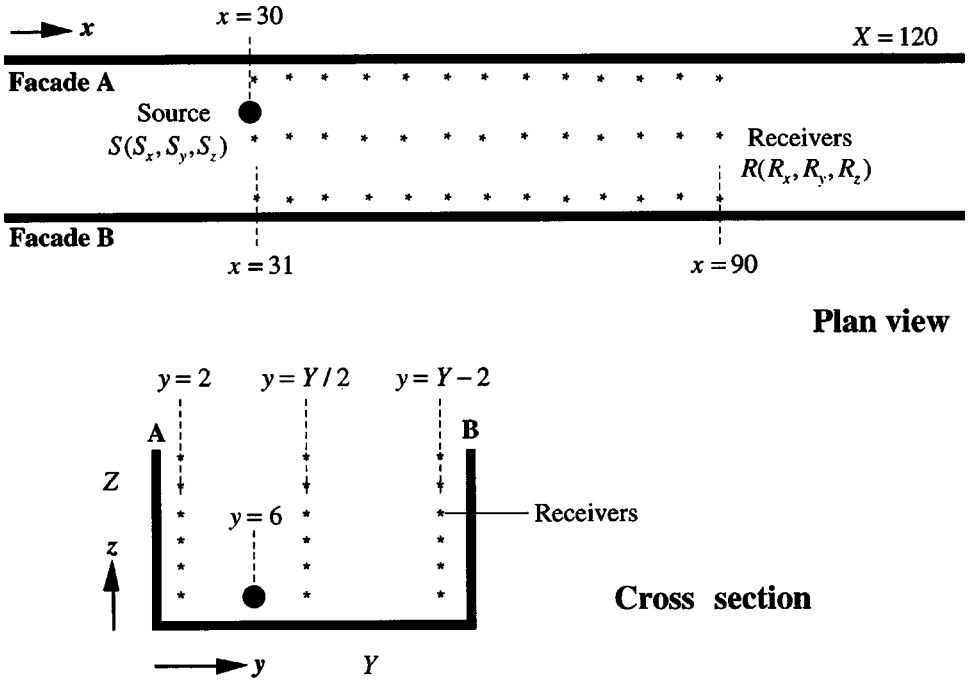

FIG. 5. Plan and cross section of an idealized street showing the source position and receiver lines used in calculation. The units in this figure are meters.

creases significantly with increasing source–receiver distance. The main reason is that, with diffuse boundaries, the total energy loss becomes greater because the average sound path length is longer, especially at the receivers in the far field. For this reason, if air or vegetation absorption is included, the difference between diffuse and geometrical boundaries is even greater. This is supported by calculation results. In the near field, with diffuse boundaries there is a slight increase in SPL, which is possibly due to the energy reflected back from farther boundaries.[16] As expected, this increase becomes less with increasing source–receiver distance in the length and/or width direction.

In long enclosures similar differences between the two kinds of boundaries have been obtained, both theoretically[15,19] and experimentally.[16–18]

From Fig. 6 it can also be seen that, with $Z=18$ m, the extra attenuation is less than that with $Z=6$ m, both along (31–90 m, 2 m, 1 m) and (31–90 m, 18 m, Z). For receivers along (31–90 m, 2 m, 1 m), an important reason for the difference between $Z=6$ and 18 m is that, with diffuse boundaries, the sound energy increases with increasing street height and this energy increase is proportionally greater for a longer source–receiver distance, whereas, with geometrical boundaries, the sound attenuation is not affected by the change in street height because S_z and R_z are less than 6 m. For receivers along (31–90 m, 18 m, Z), a notable reason for the difference between $Z=6$ and 18 m is that in comparison with (31–90 m, 18 m, 6 m), the sound attenuation along (31–90 m, 18 m, 18 m) is considerably less, both with diffuse and geometrical boundaries. Given that along (31–90 m, 18 m, 18 m) the sound attenuation is only 6 dB with geometrical boundaries, the 4-dB extra attenuation caused by replacing geometrical boundaries with diffuse boundaries is significant. If the street width is reduced to 10 m, with geometrical boundaries the sound attenuation along (31–90 m, 8 m, 18 m) increases to 7 dB. Replacing geometrical boundaries with diffuse boundaries, the extra attenuation increases to 5 dB.

B. Street height and width

As mentioned above, with diffusely reflecting boundaries the SPL at a receiver is affected by the street height. Figure 7 shows a comparison between $Z=6$, 18, and 30 m in the sound attenuation with reference to the SPL at 1 m from the source. For this calculation the street width is 20 m, the source is at (30 m, 6 m, 1 m), and the receivers are at (31–90 m, 2 m, 1 m). From Fig. 7 it can be seen that the sound attenuation becomes less with the increase of street height. In the near field, say within 10 m from the source, the SPL

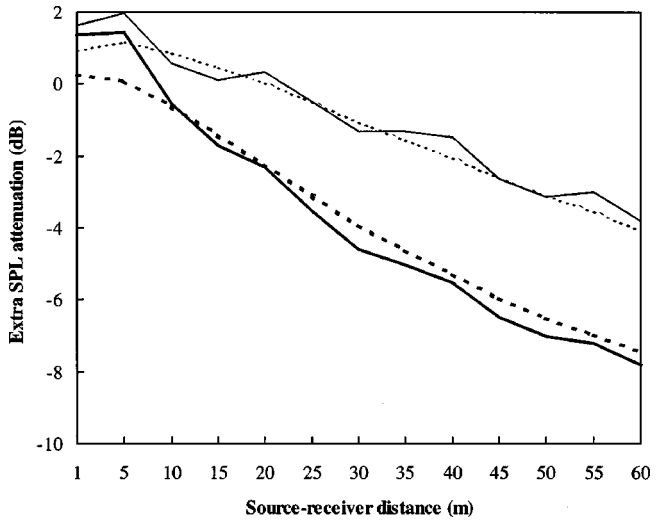

FIG. 6. Extra SPL attenuation along the length caused by replacing geometrically reflecting boundaries with diffusely reflecting boundaries. $Z=6$ m: ———, receivers along $y=2$ m and $z=1$ m: - - -, receivers along $y=18$ m and $z=6$ m. $Z=18$ m:———, receivers along $y=2$ m and $z=1$ m; ⋯, receivers along $y=18$ m and $z=18$ m.

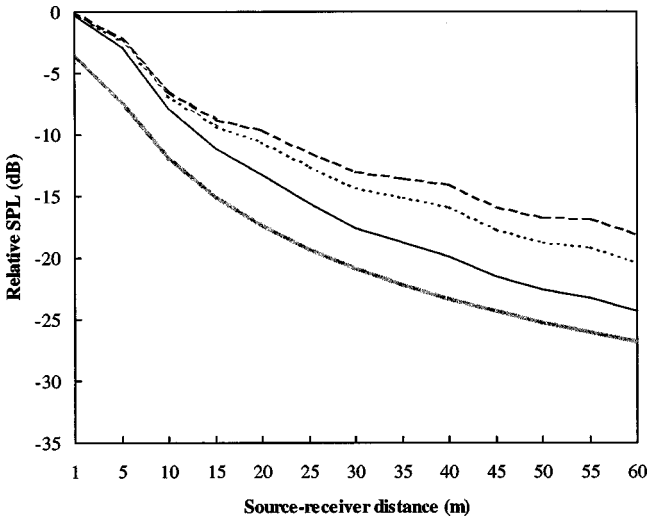

FIG. 7. Sound attenuation along a street canyon with diffusely reflecting boundaries. ———, $Z=6$ m; ⋯, $Z=18$ m; – – –, $Z=30$ m; grey line, free field.

difference between the three street heights is insignificant, which suggests that the SPL at the receivers in this range is dominated by the boundaries under 6 m. From Fig. 7 it is also seen that the attenuation curves are concave. In other words, the attenuation per unit distance becomes less with the increase of source–receiver distance. The attenuation curve in the free field is also shown in Fig. 7. It is interesting to note that the difference between $Z=6$ m and the free field is only about 2–4 dB.

To investigate the effect of street width, the extra SPL attenuation along the length caused by moving facade B from $y=10$ to 40 m was calculated with $Z=18$ m, for both diffuse and geometrical boundaries. This corresponds to a change in height/width ratio of 1.8 to 0.45. Figure 8 shows the average extra attenuation along two lines of receivers near facade A, namely (31–90 m, 2 m, 1 m) and (31–90 m, 2 m, 18 m), again with a point source at (30 m, 6 m, 1 m). The difference in extra attenuation between the two kinds of

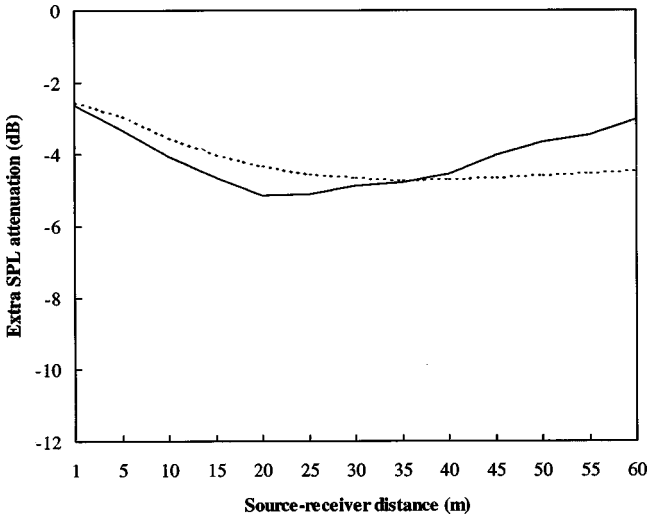

FIG. 8. Extra attenuation along the length caused by moving facade *B* from $y=10$ m to 40 m. ———, diffusely reflecting boundaries; ⋯, geometrically reflecting boundaries.

boundaries is generally insignificant. Interestingly, the maximum extra attenuation occurs at distance from the source of 20 m with diffuse boundaries and 35 m with geometrical boundaries. This is probably because in the near field, the SPL is dominated by the initial reflections from facade A such that facade B is relatively less effective. In the very far field the average sound path length is already long and consequently the effect caused by moving facade B away is proportionally less.

C. Sound distribution in cross sections

To investigate the SPL variation in the width and height direction, calculations were performed at 54 receiver locations in a cross section with a distance of 5 m from the source, for both diffuse and geometrical boundaries. In the calculation, the cross section was $Y=20$ m and $Z=18$ m, the source was at (30 m, 6 m, 1 m), and the receivers were along three lines in the height direction with $y=2$, 10, and 18 m. The results show that for both kinds of boundaries the difference between the maximum and minimum SPL in the cross section is about 7 dB.

The SPL variation in a cross section decreases as the distance between the cross section and the source increases. For both diffuse and geometrical boundaries, the SPL difference was calculated between two lines of receivers along the length, (31–90 m, 2 m, 1 m) and (31–90 m, 18 m, *Z*), which represent relatively high and low SPL in a cross section. Both $Z=6$ and 18 m were considered. The results show that when the source–receiver distance increases from 1 to 15 m, the SPL difference decreases from 10 to about 2 dB. With $Z=18$ m the SPL variation is systematically greater than that with $Z=6$ m, but the difference is only around 1 dB.

The source position may also affect the sound distribution in a cross section. For a street with a cross section of $Y=20$ m and $Z=18$ m, the SPL difference caused by moving a point source from (30 m, 3 m, 1 m) to (30 m, 17 m, 1 m) was calculated for both kinds of boundaries. The results show that for both kinds of boundaries, at receivers (31–90 m, 2 m, 1 m) the SPL difference with the two source positions is significant in the near field but becomes negligible beyond a certain range, say with a source–receiver distance of 15 m. At receivers (31–90 m, 2 m, 18 m), the SPL difference caused by moving the source is less than 1 dB.

D. Reverberation

Reverberation in street canyons is useful for investigating multiple reflections.[27–29] Also, it has been experimentally proven that with a given SPL, noise annoyance is greater with a longer reverberation time.[30]

A comparison of RT30 and EDT between diffusely and geometrically reflecting boundaries is shown in Fig. 9, with a street width of 20 m, three street heights of 6, 18, and 30 m, a point source at (30 m, 6 m, 1 m), and receivers along (31–90 m, 2 m, 1 m). It is interesting to note that, in comparison with diffuse boundaries, the EDT with geometrical boundaries is shorter with a relatively high height/width ratio and is longer when this ratio is relatively low, whereas the RT30 is much longer with any aspect ratio. An important

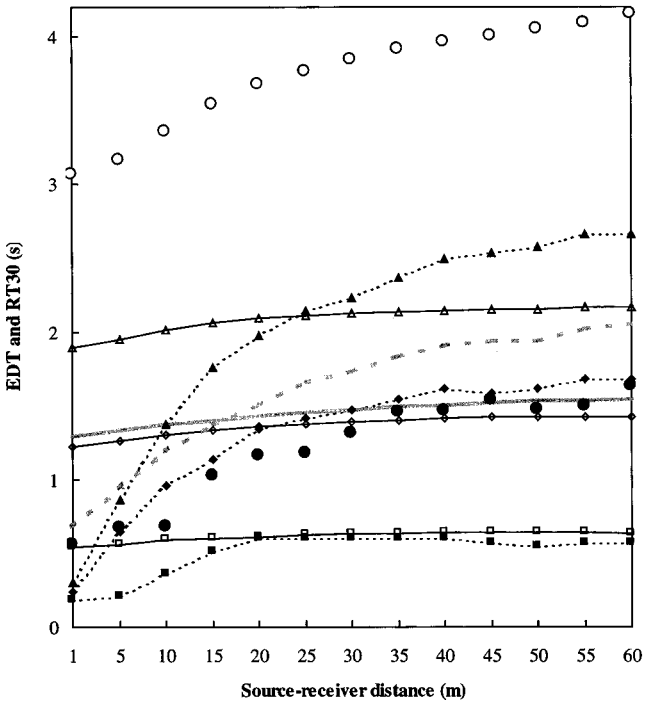

FIG. 9. Comparison of reverberation time between diffusely and geometrically reflecting boundaries. Diffusely reflecting boundaries: □, RT30, $Y=20$ m and $Z=6$ m; ■, EDT, $Y=20$ m and $Z=6$ m; ◇, RT30, $Y=20$ m and $Z=18$ m; ◆, EDT, $Y=20$ m and $Z=18$ m; △, RT30, $Y=20$ m and $Z=30$ m; ▲, EDT, $Y=20$ m and $Z=30$ m; grey line, RT30, $Y=10$ m and $Z=18$ m; dotted grey line, EDT, $Y=10$ m and $Z=18$ m. Geometrically reflecting boundaries: ○, RT30, $Y=20$ m and $Z=6-30$ m; ●, EDT, $Y=20$ m and $Z=6-30$ m.

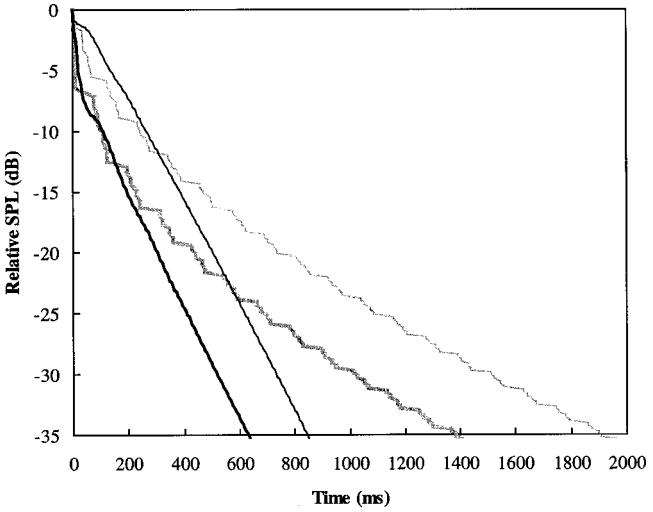

FIG. 10. Comparison of decay curves with diffusely and geometrically reflecting boundaries. Diffusely reflecting boundaries: ———, 5 m from source; ———, 40 m from source. Geometrically reflecting boundaries: thick grey line, 5 m from source; thin grey line, 40 m from source.

reason for the difference in RT30 is that, with geometrical boundaries, the image sources are well separated (see Fig. 4) and, thus, the ratio of initial to later energy at a receiver is less than that with diffuse boundaries. A similar phenomenon occurs in long enclosures with a strongly absorbent ceiling, where the reverberation can be reduced by putting diffusers on smooth boundaries.[17,18] From Fig. 9 it can also be seen that, for both diffuse and geometrical boundaries, the RT30 and EDT increase with the increase of source–receiver distance. This is again similar to the situation in long enclosures.[14,19]

Corresponding to Fig. 9, Fig. 10 shows the decay curves at two typical receivers, 5 and 40 m from the source, where the street height is 18 m. From the decay curves the abovementioned differences between diffuse and geometrical boundaries and the differences between near and far fields can be clearly seen.

The effect of street height on reverberation is similar to that on SPL. In Fig. 9 it is seen that with geometrical boundaries, because S_z and R_z are less than 6 m, the reverberation times are constant with the three street heights, whereas with diffuse boundaries the RT30 and EDT become longer with the increase of street height. Figure 9 also demonstrates the effect of street width on reverberation, as can be seen by comparing cross sections 20 by 18 m^2 and 10 by 18 m^2. As expected, with a given street height the RT30 and EDT are shorter with a greater street width because sky absorption is increased.

Calculation has shown that the reverberation becomes shorter with air absorption, which is expected. It is interesting to note that the change in reverberation caused by air absorption is more significant than that in SPL. This is because the SPL depends mainly on early reflections, whereas reverberation is dependent on multiple reflections, for which the air absorption is more effective due to the longer sound path.

E. Distribution of boundary absorption

To investigate the variation in sound attenuation caused by the location of absorption in the cross section, calculations were made with three distribution schemes of a constant amount of absorption: I, one side wall strongly absorbent; II, two side walls strongly absorbent; and III, all three boundaries evenly absorbent. In these calculations the cross section was $Y=20$ m and $Z=6$ m, the source was at (30 m, 6 m, 1 m), and the SPL in a cross section was represented by the average of two receivers, namely, $y=2$ m, $z=1$ m, and $y=18$ m, $z=6$ m. The absorption coefficients of the boundaries were distribution I, $\alpha_A=0.9$ and $\alpha_B=\alpha_G=0.05$; distribution II, $\alpha_A=\alpha_B=0.475$ and $\alpha_G=0.05$; and distribution III, $\alpha_A=\alpha_B=\alpha_G=0.209$.

Figure 11 shows the extra attenuation caused by replacing distribution III with distributions I and II. The extra attenuation with distribution I is typically 1–4 dB in the case of geometrical boundaries, and 1 dB with diffuse boundaries. With distribution II the extra attenuation is systematically less than that with distribution I, but still noticeable. A simplified model for explaining the differences between the different distribution schemes is that, after hitting each boundary once, the remaining energy of a reflection is the lowest with distribution I, and the highest with distribution III. Assume that the original energy of a reflection is 1. The remaining energy is then $0.1\times0.95^2=0.09$ with distribution I, $0.525^2\times0.95=0.26$ with distribution II, and $0.791^3=0.49$ with distribution III. From Fig. 11 it is also apparent that

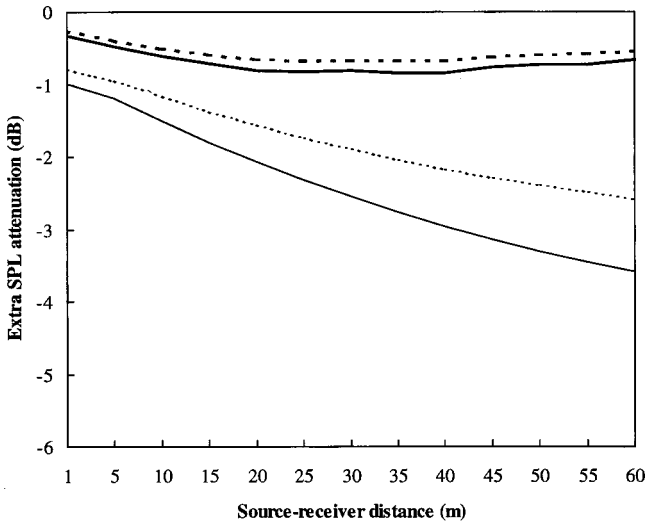

FIG. 11. Extra SPL attenuation along the length caused by replacing distribution III with distributions I and II. Diffusely reflecting boundaries: ———, distribution I; - - -, distribution II. Geometrically reflecting boundaries: ———, distribution I; ⋯, distribution II.

with geometrical boundaries the differences between the three distributions are greater than those with diffuse boundaries. This is probably because geometrical boundaries are more affected by the reflection rule described above.

F. Multiple sources

The above calculations are all based on a single source. This is useful to gain a basic understanding of sound propagation in street canyons. Practically, the results are representative of certain typical types of urban noise, such as low-density traffic. They are also useful for considering noise propagation from a junction to a street. However, in many cases it is necessary to take multiple sources into account.

Consider a typical and simplified configuration as follows. A street canyon is 120 m long and there are evenly distributed point sources along the length. The source spacing is 10 m. With a single source at any location, the SPL attenuation is linear along the length, and this attenuation is 15 dB at 60 m from the source. A treatment, such as replacing geometrical boundaries with diffuse boundaries, or adding absorbers on facades, can bring an extra attenuation that increases linearly along the length, and this extra attenuation is 8 dB at a source–receiver distance of 60 m. With this configuration the extra SPL attenuation caused by the treatment in the case of multiple sources can be readily calculated.[31] To consider the multiple sources as moving vehicles, calculation is made at a range of typical receivers, from $x=60\,\mathrm{m}$, with no horizontal distance from a source, to $x=65\,\mathrm{m}$, halfway between two sources. At these receivers, the extra SPL attenuation with multiple sources is about 2–4 dB. This is less than that with a single source, as expected, but still significant.

IV. CONCLUSIONS

The sound fields in street canyons with diffusely and geometrically reflecting boundaries have been analyzed and compared. For diffuse boundaries a radiosity-based theoretical/computer model has been developed. For geometrical boundaries, the conventional image source method has been used.

Considerable differences between the sound fields resulting from the two kinds of boundaries have been observed. By replacing diffuse boundaries with geometrical boundaries in street canyons, the sound attenuation along the length becomes considerably less, typically by 4–8 dB with a source–receiver distance of 60 m; the RT30 is significantly longer, typically by 100%–200%; and the extra SPL attenuation caused by air or vegetation absorption is reduced. With moving traffic, about 2–4 dB extra attenuation can be obtained by using diffuse boundaries. It is noted that this extra attenuation may be diminished if a receiver is very close to the traffic. Nevertheless, if a barrier is inserted to reduce the direct sound, the use of diffuse boundaries can still be effective.

The above results suggest that, from the viewpoint of urban noise reduction, it is better to design the building facades and the ground of a street canyon as diffusely reflective rather than acoustically smooth. Although it might be unrealistic to design all the boundaries as pure diffusely reflective, some diffuse patches on a boundary, or boundaries with a high diffuse coefficient, are helpful in making the sound field fairly close to that resulting from diffuse boundaries, especially when multiple reflections are considered.[32] Similar to diffuse boundaries, street furniture, such as trees, lampposts, fences, barriers, benches, telephone boxes, bus shelters, and so on, can also be effective in reducing noise. With the same principle as for a single street canyon, diffuse boundaries and street furniture are also useful for reducing ''background'' noise of a city, which is produced by the general distribution of sources throughout the city.[7]

There are also some similarities between the sound fields formed by diffusely and geometrically reflecting boundaries. For both kinds of boundaries the sound distribution in a cross section is generally even unless the cross section is very close to the source. Also, the extra attenuation along the length caused by widening the street is very similar between the two kinds of boundaries. Interestingly, the sound attenuation along the length with a given amount of absorption is the highest if the absorbers are arranged on one boundary and the lowest if they are evenly distributed on all boundaries. This result is especially useful for the design of a street canyon formed by barriers.

The marked differences between the two kinds of sound fields in street canyons suggest that, for practical calculation, it is essential to investigate the characteristics of the boundaries, and then to consider diffuse and geometrical reflection in an integrative way. In this respect, further work is needed.

ACKNOWLEDGMENTS

The author is indebted to Dr. R. J. Orlowski, P. Richens, Dr. G. R. Moore, Dr. D. Robinson, and Professor D. J. Oldham for useful discussions, and to the reviewers and the editor of this paper for many valuable suggestions. Thanks must also go to the Lloyd's Foundation for their financial support.

[1] F. M. Weiner, C. I. Malme, and C. M. Gogos, ''Sound propagation in urban areas,'' J. Acoust. Soc. Am. **37**, 738–747 (1965).
[2] H. Kuttruff, ''Zur Berechnung von Pegelmittelwerten und Schwankungsgrößen bei Straßenlärm,'' Acustica **32**, 57–69 (1975).
[3] M. V. Sergeev, ''Scattered sound and reverberation on city streets and in tunnels,'' Sov. Phys. Acoust. **25**, 248–252 (1979).
[4] R. Y. Vinokur, ''Propagation of sound generated by a point source in certain built-up urban environments,'' Sov. Phys. Acoust. **25**, 377–379 (1980).
[5] M. M. Radwan and D. J. Oldham, ''The prediction of noise from urban traffic under interrupted flow conditions,'' Appl. Acoust. **21**, 163–185 (1987).
[6] D. J. Oldham and M. M. Radwan, ''Sound propagation in city streets,'' Bldg. Acoust. **1**, 65–88 (1994).
[7] R. H. Lyon, ''Role of multiple reflections and reverberation in urban noise propagation,'' J. Acoust. Soc. Am. **55**, 493–503 (1974).
[8] R. Bullen and F. Fricke, ''Sound propagation in a street,'' J. Sound Vib. **46**, 33–42 (1976).
[9] H. G. Davies, ''Multiple-reflection diffuse-scattering model for noise propagation in streets,'' J. Acoust. Soc. Am. **64**, 517–521 (1978).
[10] S. Wu and E. Kittinger, ''On the relevance of sound scattering to the prediction of traffic noise in urban streets,'' Acustica **81**, 36–42 (1995).
[11] C. F. Chien and M. M. Carroll, ''Sound source above a rough absorbent plane,'' J. Acoust. Soc. Am. **67**, 827–829 (1980).
[12] K. Heutschi, ''Computermodell zur Berechnung von Bebauungszuschlägen bei Straßenverkehrslärm,'' Acustica **81**, 26–35 (1995).
[13] D. C. Hothersall, K. V. Horoshenkov, and S. E. Mercy, ''Numerical modelling of the sound field near a tall building with balconies near a road,'' J. Sound Vib. **198**, 507–515 (1996).
[14] J. Kang, ''Reverberation in rectangular long enclosures with geometrically reflecting boundaries,'' Acust. Acta Acust. **82**, 509–516 (1996).
[15] H. Kuttruff, ''Stationäre Schallausbreitung in Langräumen,'' Acustica **69**, 53–62 (1989).
[16] J. Kang, ''Experimental approach to the effect of diffusers on the sound attenuation in long enclosures,'' Bldg. Acoust. **2**, 391–402 (1995).
[17] J. Kang, ''Improvement of the STI of multiple loudspeakers in long enclosures by architectural treatments,'' Appl. Acoust. **51**, 169–180 (1997).
[18] J. Kang, ''Scale modelling for improving the speech intelligibility of multiple loudspeakers in long enclosures by architectural acoustic treatments,'' Acust. Acta Acust. **84**, 689–700 (1998).
[19] J. Kang, ''Reverberation in rectangular long enclosures with diffusely reflecting boundaries,'' Acust. Acta Acust., submitted for publication.
[20] R. Siegel and J. Howell, *Thermal Radiation Heat Transfer* (Hemisphere, Washington, DC, 1981), 2nd ed.
[21] F. X. Sillion and C. Puech, *Radiosity and Global Illumination* (Morgan Kaufmann, 1994).
[22] J. D. Foley, A. van Dam, S. K. Feiner, and J. F. Hughes, *Computer Graphics: Principle and Practice* (Addison–Wesley, Reading, MA, 1990), 2nd ed.
[23] G. R. Moore, ''An approach to the analysis of sound in auditoria,'' Ph.D. dissertation, University of Cambridge, UK, 1984.
[24] T. Lewers, ''A combined beam tracing and radiant exchange computer model of room acoustics,'' Appl. Acoust. **38**, 161–178 (1993).
[25] R. Stibbs, ''The prediction of surface luminances in architectural space,'' Working Paper No. 54, Center for Land Use and Built Form Studies, University of Cambridge, 1971.
[26] M. F. Cohen and D. P. Greenberg, ''The hemi-cube: A radiosity solution for complex environments,'' Comput. Graph. **19**, 31–40 (1985).
[27] E. Schröder, ''Nachhall in geschlossenen bebauten Straßen,'' Lärmbekämpfung **17**, 11–18 (1973).
[28] P. Steenackers, H. Myncke, and A. Cops, ''Reverberation in town streets,'' Acustica **40**, 115–119 (1978).
[29] N. W. M. Ko and C. P. Tang, ''Reverberation time in a high-rise city,'' J. Sound Vib. **56**, 459–461 (1978).
[30] J. Kang, ''Experiments on the subjective assessment of noise reduction by absorption treatments,'' Chinese Noise and Vibration Control **5**, 20–28 (1988).
[31] J. Kang, ''Acoustics in long enclosures with multiple sources,'' J. Acoust. Soc. Am. **99**, 985–989 (1996).
[32] H. Kuttruff, ''A simple iteration scheme for the computation of decay constants in enclosures with diffusely reflecting boundaries,'' J. Acoust. Soc. Am. **98**, 288–293 (1995).

The adaptive beam-tracing algorithm

I. A. Drumm and Y. W. Lam
School of Acoustics and Electronic Engineering, The University of Salford, Salford M5 4WT, United Kingdom

(Received 21 June 1999; revised 6 October 1999; accepted 26 October 1999)

The most popular models to predict sound propagation in architectural spaces involve the tracing of rays, images, or beams. Most current beam-tracing methods use conical or triangular beams that may produce overlaps and holes in the predicted sound field. Hence a new method has been developed whereby the shape of reflected beams is governed by the shape of reflecting surfaces so as to produce a geometrically perfect description of the sound propagation for halls with occluding surfaces. The method also facilitates the calculation of diffuse sound propagation by managing the energy transfer from a specular model to a diffuse model. This adaptive beam-tracing method compares well with other methods in terms of speed and accuracy. © *2000 Acoustical Society of America.* [S0001-4966(00)03602-X]

PACS numbers: 43.55.Ka, 43.55.Gx [JDQ]

INTRODUCTION

There are a number of different modeling techniques currently used to predict the acoustics of auditoria. The most popular include ray tracing, the image method, and various forms of beam tracing. Ray tracing (Kulowski[1]) creates a dense spread of rays, which are subsequently reflected around a room and tested for intersection with a spherical detector. The energy attenuation of the intersecting rays and distances traveled are used to construct an echogram. Although relatively simple to implement, the algorithm has inherent systematic errors (Lehnert[2]) whereby spurious reflections can be created due to using a nonpoint detector whilst other valid reflections are missed as the rays diverge. The image method as demonstrated by Borish,[3] and Lee and Lee,[4] overcomes these problems by instead calculating images of the sound sources in reflecting walls. Hence when considering the specular case, rather than providing a statistical evaluation of a sound's likely incidence at a spherical representation of the detector, the image method provides exact information at a point detector. Higher-order images are in turn calculated and so on until an echogram is produced. Although initially much faster than ray tracing, the image method slows exponentially with increasing orders of reflection as the number of possible, though not necessarily valid, images increases. Invalid images must be eliminated with validity and visibility tests. Some applications, such as Vorlander,[5] use a hybrid of the two methods to improve speed and accuracy; however, this still requires a large number of initial rays and suffers from missing images later on.

By using beams (i.e., rays with volume), a point detector can be used whilst eliminating the need to calculate and validate an exponentially increasing number of images. Popular beam-tracing methods utilize conical beams (Maercke and Martin[6]) or triangular beams (Lewers[7]). Beams are reflected around a room and tested for illumination of the detector. However, since cones and triangles represent approximations of the propagating sound field, overlaps and missing reflections can happen and so have to be compensated for statistically.

Modeling the specular propagating sound field without holes or overlaps requires the cross-sectional shape of reflected child beams to be governed by the shape of reflecting surfaces (Fig. 1). One way of doing this is to determine for each parent beam the polygon–polygon intersections of the beam with reflecting walls (as suggested by Stephenson[8]). For simple rooms without occluding surfaces, each polygon of intersection would define the cross-sectional area of a new reflecting beam. For a room with occluding surfaces, the algorithm would need to be extended, as occlusions, reflecting walls, and beam cross sections would simultaneously define possible sections of illumination and subsequent reflected child beams. The algorithm would have to evaluate all possible combinations of multiple polygon intersections and select only those that correctly represent areas of parent beam illumination. The adaptive beam-tracing algorithm was developed and implemented to efficiently describe the specular propagating sound field without holes or overlaps for relatively complicated halls with occluding planes.

Rather than using polygon–polygon intersection, as suggested by Stephenson, the algorithm starts from a suitable point on a reflecting surface and then proceeds to map out the area illumination of this and all other surfaces illuminated by the parent beam. During the processes of describing one area of illumination, the algorithm tests for other adjacent, occluded, or occluding surfaces encountered. Hence, the description process sets itself up to handle those illuminated surfaces as well. The algorithm has also been designed to take care of awkward surface combinations, such as surfaces, completely within beam areas.

As well as specular sound propagation, the adaptive beam-tracing algorithm facilitates the calculation of diffuse sound propagation by providing, on a reflection-by-reflection basis, information for use in a later radiant exchange. The exact areas of illumination by beams on walls, with respect to time, can represent diffuse energy leaving the specular system for the diffuse system. Diffuse energy imparted on walls can then be reradiated and exchanged between walls, thus creating a diffuse echogram. Specular and diffuse com-

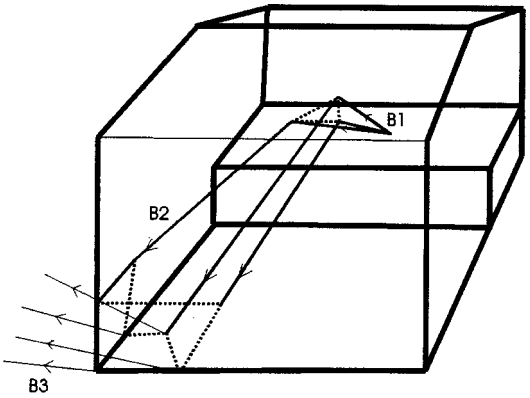

FIG. 1. A beam traced adaptively. The first beam ($B1$) is reflected to create a child beam ($B2$); $B2$ in turn spawns numerous child beams, such as $B3$ formed from the sections of planes illuminated.

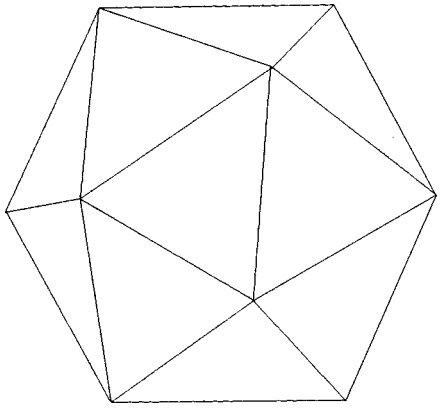

FIG. 2. An icosahedron used for creating an omnidirectional source.

ponents can then be combined, eliminating the need for empirical and statistical adjustments.

I. IMPLEMENTATION

A. Representing three-dimensional (3D) world space

The algorithm was written in C++ to run on a Windows 95, PC operating system. The C++ programming language provides a fast and flexible object-oriented paradigm ideal for governing the creation, manipulation, and interaction of geometric objects such as vectors, rays, beams, and planes.

All theoretical objects in the model were represented in 3D world space (Hill[9]), i.e., in terms of positions and directions within a 3D coordinate system (x,y,z). Fundamental object types within the world space include

(a) Vectors
(b) Polygons, each represented by a series of vectors comprising its verticies.
(c) Planes, each represented by a polygon, associated sound absorption, and diffusion coefficients and the equation of a plane

$$D=\mathbf{p}\cdot\mathbf{n}, \tag{1}$$

where $\mathbf{n}$ is the unit normal to the plane, $\mathbf{p}$ is any point on the plane, and D is the plane coefficient.
(d) Rays, each represented by the equation

$$\mathbf{r}=\mathbf{s}+\mathbf{c}t, \tag{2}$$

where $\mathbf{s}$ is the ray source vector, $\mathbf{c}$ is the unit direction vector and t is time traveled.
(e) Beams, each consisting of a collection of rays that describe its shape diverging from common source vector $\mathbf{s}_{bm}$. The beam will be used for scanning for specular images and recording energy losses from the specular system. As will be shown later, a useful value to associate with each beam is sound source energy minus losses to absorption and diffusion.

B. The omnidirectional source

How the initial spread of beams is constructed to describe the first-order ominidirectional sound field is arbitrary so long as the whole sound field is represented without duplications. However, too few highly diverging beams or too many small beams reduce efficiency. A useful starting point is 20 beams of equal cross section as given by an icoshedron (Fig. 2). An icosahedron with 20 sides is defined by the 12 coordinates

$$(0,\pm F,\pm 1),(\pm 1,0,\pm F),(\pm F,\pm 1,0), \tag{3}$$

where F is the golden ratio $[(\mathrm{sqrt}(5)+1]/2=1.618\,03$.

All initial beams will have equal dimensions and associated sound energy.

C. The main loop

Every beam is in turn passed to the main loop (Fig. 3) that pushes the beam onto a stack, i.e., a temporary collection area where beams await processing. The beam is then popped off this stack and tested for illumination of the detector. To speed things up only the planes that may influence the shape of subsequent sections of illumination are used.

The algorithm then tests for the nearest wall illuminated by the beam, i.e., the nearest intersection of a beam's constituent ray with a wall. This intersection will be the starting point for mapping out the first section of illumination. Subsequent adjacent sections of illumination are tested for during this mapping process. The algorithm maps out all illuminated sections using a progressive description process that automatically takes into account all plane edges, including those of occluding planes.

Each section of illumination is used to make a new reflected child beam. So long as the child beam's order of reflection is not higher than the maximum specified order of reflection, it is pushed on to the beam stack. The beam will later be popped off by the main loop to be used to determine new sections of illumination and new child beams. The main loop continues to pop off beams until none are left.

D. Finding sections of illumination

Central to the adaptive beam-tracing algorithm is its ability to determine the exact sections of planes illuminated by a beam. These sections of illumination are subsequently used to determine the cross sections of reflected beams. Hence unlike triangular and conical beam tracing methods, there are no gaps or overlaps in the predicted sound field.

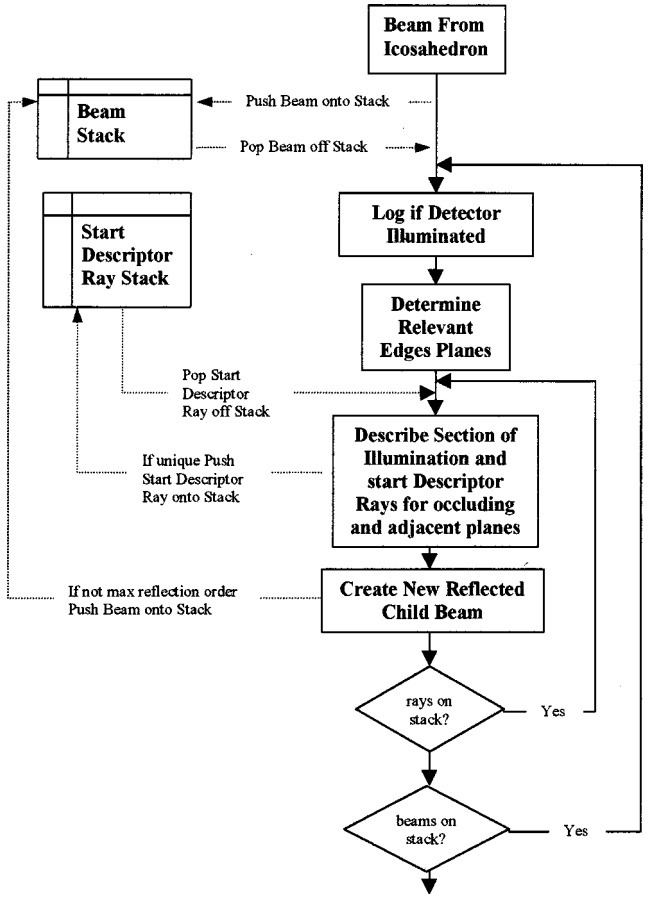

FIG. 3. Schematic diagram for main loop of beam-tracing algorithm.

As shown in Fig. 4, the algorithm has to deal with all manner of illumination scenarios, including single planes, multiple planes, corners, occluding planes, and even planes that could cause holes in the reflected beams. The algorithm uses the fact that the sides or edges of the beam, and edges of every plane illuminated, will determine the boundaries of illuminated sections.

Two important new terms will be used...

1. Edge planes

An edge plane is the triangle that forms the side of a beam or the trapezium formed by extrapolating a plane's side

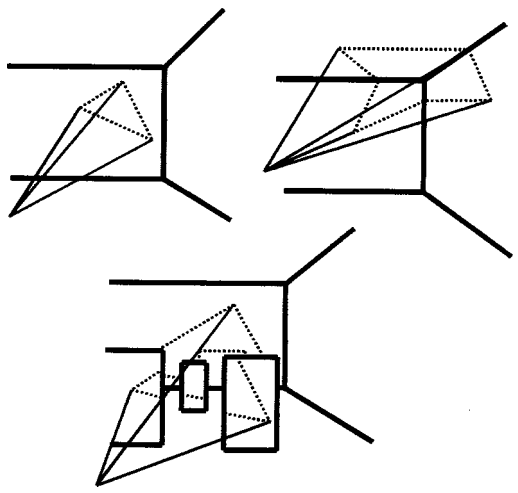

FIG. 4. Different ways in which a beam can illuminate planes.

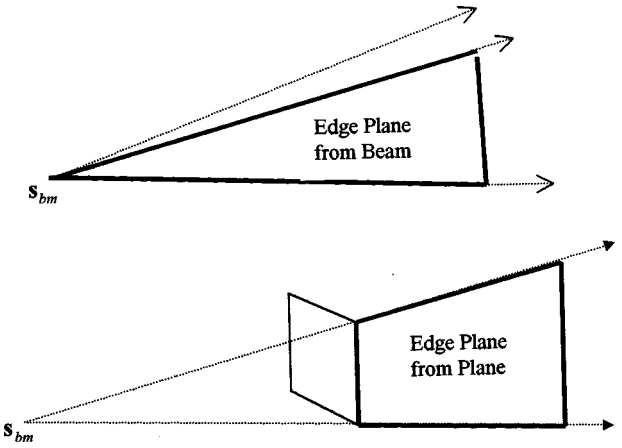

FIG. 5. The formation of edges of planes from a beam side and a plane side, respectively.

to a very large distance relative to the current beam's source (Fig. 5). The edge plane can also be represented by its normal $\mathbf{n}_e$ a point on the edge plane $\mathbf{p}_e$ (such as a vertex), and its plane coefficient D, where

$$D = \mathbf{n}_e \cdot \mathbf{p}_e . \tag{4}$$

2. Descriptor rays

A descriptor ray is the intersection of an edge plane with the current plane being illuminated. The progress of descriptor rays is used to determine the sections of illumination. A descriptor ray $\mathbf{r}_d$ can be represented by

$$\mathbf{r}_d = \mathbf{s}_d + \mathbf{c}_d t, \tag{5}$$

where t is the time or distance a ray travels, $\mathbf{s}_d$ is initially the first intersection of a beam's ray with a given illuminated plane, and subsequently the intersection of the previous descriptor ray with the current edge plane. The vector $\mathbf{c}_d$ is as the cross product of an edge plane normal $\mathbf{n}_e$ with the illuminated plane normal $\mathbf{n}_p$,

$$\mathbf{c}_d = \mathbf{n}_e \times \mathbf{n}_p \quad \text{or} \quad \mathbf{c}_d = \mathbf{n}_p \times \mathbf{n}_e . \tag{6}$$

The algorithm describes sections of illumination by

(a) finding the nearest plane intersecting with a constituent ray of the beam,
(b) creating a descriptor ray along the intersection of the beam edge plane with the plane surface,
(c) finding the nearest valid edge plane that the descriptor ray intersects,
(d) using this edge plane to create a new descriptor ray along the current plane.

Hence, descriptor rays are used to find a closed section of illumination.

As the current section of illumination is mapped out, extra descriptor rays are also created along any adjacent planes and occluding planes (Fig. 6). These extra descriptor rays are set aside as the starting points for the mapping out of other sections' illumination for other adjacent, occluding, or occluded planes. Hence, all sections of illumination of all illuminated planes are eventually found. At the start of de-

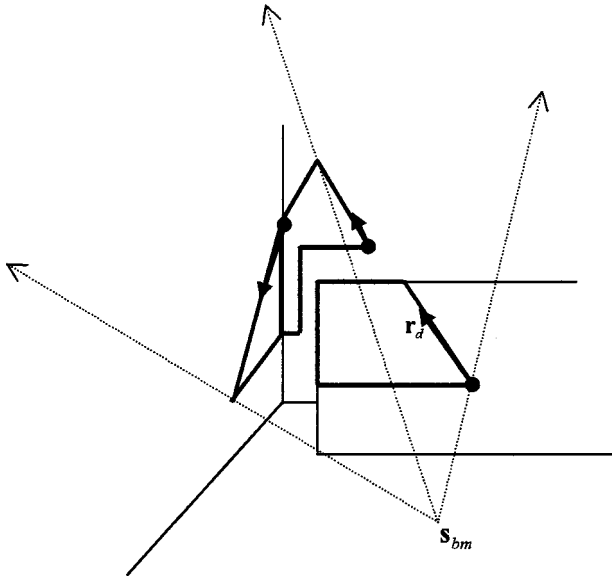

FIG. 6. Descriptor rays mapping out a section of illumination. During this process adjacent sections illuminated by the beam are found with new starting descriptor rays being set aside for subsequent mapping.

scribing any section of illumination the algorithm keeps a record of initial descriptor rays so that no section is described twice.

3. Sense rules

For descriptor rays to map out sections of illumination they must follow the correct sense, i.e., clockwise or anticlockwise relative to the beam source. The sense of the descriptor ray is dependent on the sense of the beam and any planes it may encounter. Sense can be determined using cross product and triple scalar product. Given three concurrent vertices of a plane $\mathbf{v}_1$, $\mathbf{v}_2$, $\mathbf{v}_3$ and the beam source $\mathbf{s}_{bm}$, it can be shown that the triple scalar product T indicates the plane sense

$$T=(\mathbf{v}_2-\mathbf{s}_{bm})((\mathbf{v}_2-\mathbf{v}_1)\times(\mathbf{v}_3-\mathbf{v}_2)), \tag{7}$$

where $T>0$ is a positive clockwise turn and $T<0$ is a negative anticlockwise turn.

To ensure the correct sense of the description process, a large set of sense rules governing the direction of the descriptor ray had to be determined and implemented. These sense rules form the crux of the test to determine the best direction the next descriptor ray should proceed in. For instance, when a descriptor ray encounters an edge plane, the next descriptor ray must turn clockwise or anticlockwise depending on whether the edge plane belongs to a beam, the current plane, or an occluding plane.

4. Best direction

When a descriptor ray encounters a corner, a number of edge planes may be intersected simultaneously. Hence there may be a number of possible directions the new descriptor ray may take. The intersected edge creating the sharpest turn will correspond to the correct mapping, since it will represent an occluding plane, or the beam or current plane boundary if there are no occlusions.

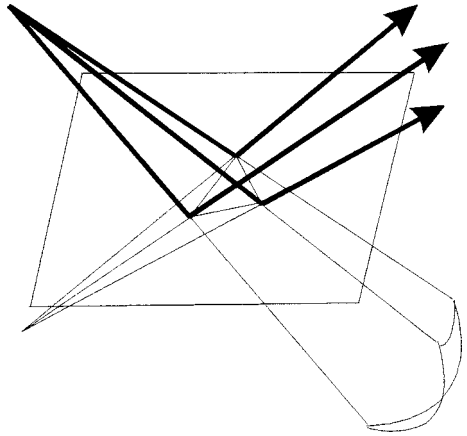

FIG. 7. A reflected child beam constructed from the beam source image of the parent beam and the vertices of the area of illumination.

5. Dealing with concave sections

Since the algorithm relies heavily on point in boundary tests, all of a hall's planes (and newly created child beams) must have convex cross sections. Hence, all concave sections of illumination generated must be subdivided into convex polygons.

6. Dealing with holes

Any plane lying completely within a beam was identified, so as to eliminate the possibility of holes within the reflected beam cross section. When such a plane is encountered, the beam is subdivided with respect to a point on the plane and the resulting child beams are pushed onto the beam stack.

E. Detector illuminated

1. Illumination test

Whether the detector is illuminated by a beam was determined by creating a ray that originates from the current beam source and passes through the detector. If this ray intersects with a visible beam cross section, then the point is within the beam.

2. Building the specular echogram

When the detector is illuminated by a beam, the current beam energy and ray time are stored. Hence, as child beams are created and reflected, an echogram of the room is compiled.

F. Reflecting beams

Creating reflected child beams requires finding the image of the parent beam source in the reflecting plane. Given that the distance or time t of the beam source $\mathbf{s}$ from a plane with nearest point $\mathbf{p}$ is

$$t=\mathbf{p}-\mathbf{s}\cdot\mathbf{n}, \tag{8}$$

then the image of the beam source s_i relative to the plane is

$$\mathbf{s}_i=\mathbf{p}+2t\mathbf{n}. \tag{9}$$

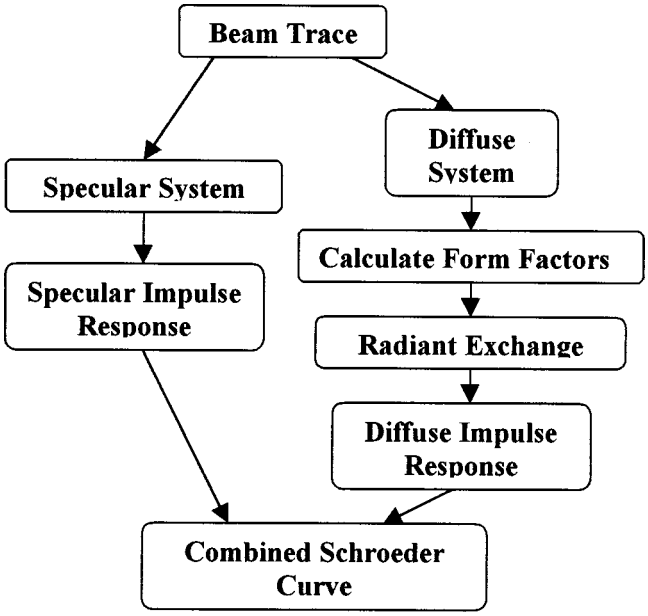

FIG. 8. Schematic diagram representing the relationship between specular and diffuse models.

For each section of illumination, new beam rays are created that intersect with its respective vertices and originate from the new beam source (Fig. 7).

Upon reflection, specular beam energy is lost to wall absorption and the diffuse system. Hence, given the parent beam energy E_b, the wall absorption coefficient α, and diffusion coefficient δ, the reflected beam energy E_r is

$$E_r = E_b(1-\alpha)(1-\delta). \tag{10}$$

Note that the beam energy in the specular model is essentially the original source energy minus energy lost to wall absorption and diffusion after reflections. The beam's specular energy value is independent of the beam's cross-sectional area. On finding the detector, the energy incident on the detector takes account of $1/r^2$ and air attenuation, where r is the distance the beam has traveled.

The diffuse model requires the proportion of diffuse sound energy that the beam has imparted to the wall with respect to time, and so is dependent on the beam's cross-sectional area. This energy is proportional to $\Delta\Omega/\Omega$, where $\Delta\Omega$ is the solid angle subtended by an area of illumination and Ω is the solid angle subtended by a sphere. The solid angle subtended by the beam is calculated by extrapolating all constituent beam rays to an equal arbitrary distance L.

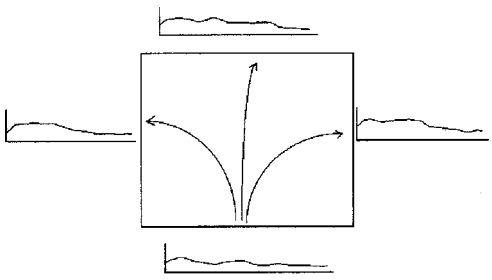

FIG. 9. Diffuse energy from plane reradiated to other planes.

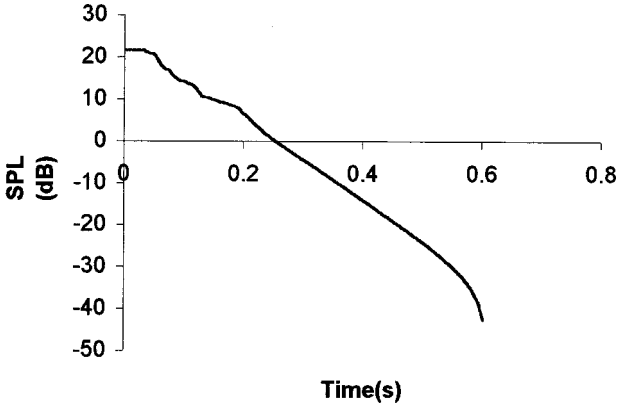

FIG. 10. Sound pressure level decay profile as determined by backward integration.

The resulting extrapolated polygon of area A is used to determine the proportion of energy incident E_d, as shown by Eq. (11),

$$E_d \propto \frac{\Delta\Omega}{\Omega} E_b \delta(1-\alpha) \propto \frac{E_b A \delta(1-\alpha)}{4\pi L^2}. \tag{11}$$

G. The diffuse system

During the specular beam-tracing process, time and plane dependent energy information passes to the diffuse system (Fig. 8). Every wall is assigned a plane impulse response that serves as a record of diffuse energy imparted by beams with respect to time. The plane impulse response consists of energy bins at discrete time intervals Δt. When a beam is incident on a wall, the imparted beam energy E_d is added to the time bin corresponding to the average time the beam has traveled.

1. Radiant exchange

Upon completion of the specular beam-tracing process, a separate diffuse sound profile is calculated using radiant exchange. For every time interval of every plane impulse response, the corresponding diffuse energy is reradiated to all other planes (Fig. 9). Each receiving plane hence has a proportion of this energy added to its plane impulse response at a time interval corresponding to an average distance between the radiating and receiving planes. These energy portions received will in turn be reradiated to other planes later on during the exchange process, and so on. The exchange process cycles through successive time intervals redistributing energy until an arbitrary time that is much greater that the maximum selected order of beam reflection.

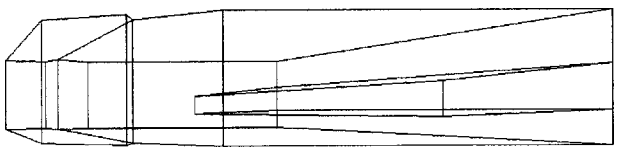

FIG. 11. Concert hall with stage area and balcony ~32×24×13 m.

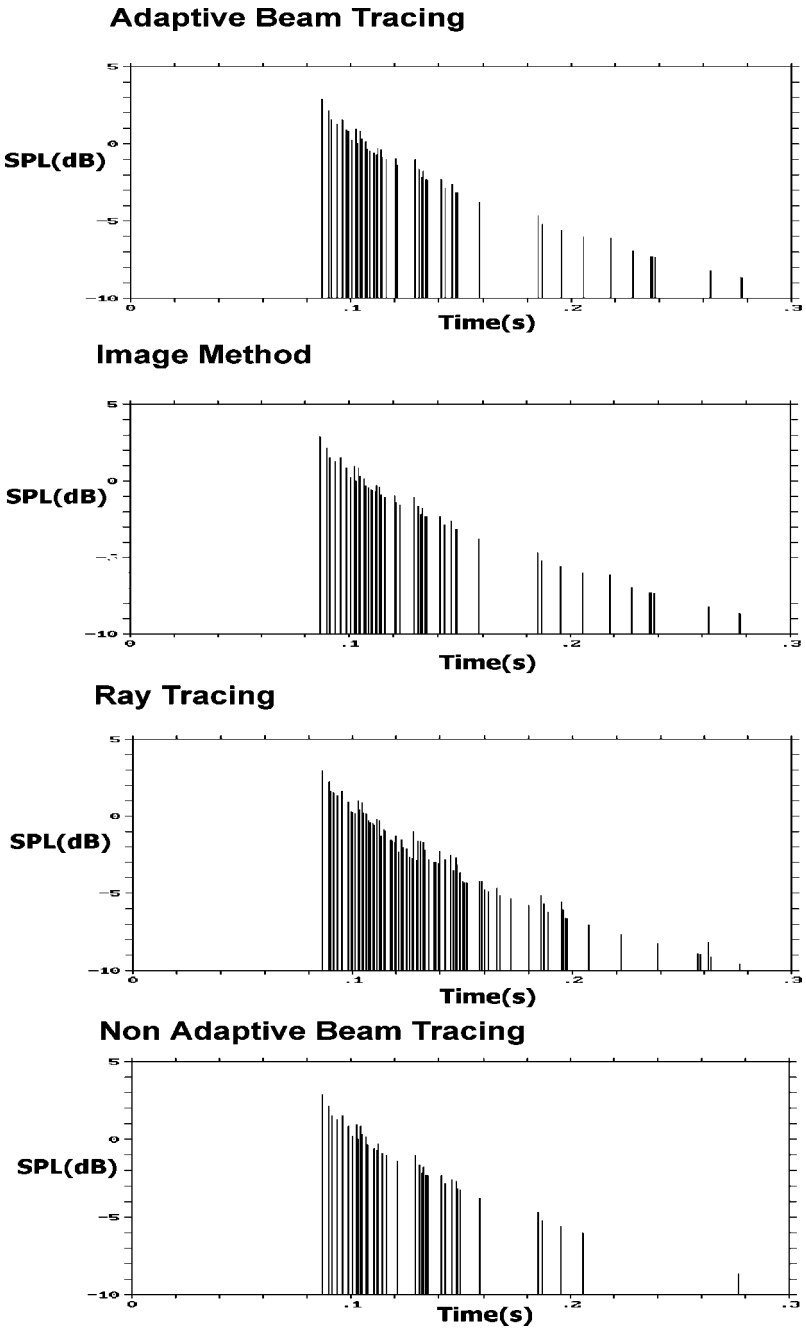

FIG. 12. Predicted impulse responses for hall using adaptive beam tracing, the image method, ray tracing, and nonadaptive beam tracing.

2. Form factors

How much diffuse energy each plane receives is dependent on a form factor between the radiating and receiving planes. The plane form factor F_{ij} between two surfaces i and j is the fraction of energy diffusely emitted from i that reaches j (Lewers[7]).

3. The diffuse echogram

When the radiant exchange process is completed, diffuse energy at the detector can be calculated. For each time interval of each plane impulse response, diffuse energy is reradiated to the detector. Hence, a diffuse impulse response at the detector is built up, allowing for the form factors and distances between the detector and radiating planes.

4. Crossover to totally diffuse

The adaptive beam-tracing algorithm, like all other methods, can only calculate specular reflections to a finite order. Hence remaining energy is assumed to pass to a totally diffuse system to be later used in a radiant exchange. This can be implemented by assuming plane diffusion coefficients have the value 1 for high orders of reflection. However, an abrupt crossover can leave artifacts in the predicted sound decay curve. Thus a more gradual crossover to totally diffuse over a range of high-order reflections was implemented.

H. Recombining specular and diffuse components

Given specular and diffuse impulse responses, the two must be combined to produce an accurate profile of the

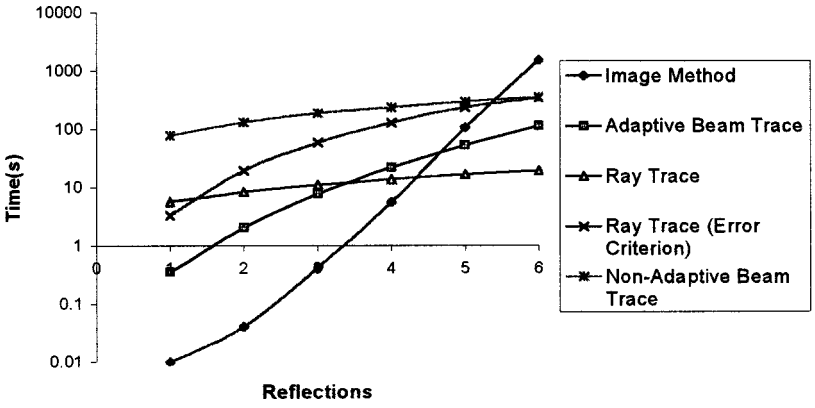

FIG. 13. Time profiles for adaptive beam tracing, the image method, ray tracing, and nonadaptive beam tracing.

room's acoustics. Clarity and Deulikiet can be calculated simply by integrating specular and diffuse energies with respect to time.

$$C_{80}=10\log_{10}\frac{\int_0^{80\ \mathrm{ms}}E(t)dt}{\int_{80\ \mathrm{ms}}^{\infty}E(t)dt}. \tag{12}$$

In order to calculate reverberation time and early decay time, a profile of sound energy decay is needed. This is done by combining specular and diffuse impulse responses. Then using a backwards integration method,[10] a decay profile is built up (Fig. 10). A linear regression on the resultant curve can be used to determine reverberation time (RT) and early decay time EDT.

II. COMPARISONS AND DISCUSSION

A. Comparison with the image method and ray tracing

Comparisons of the adaptive beam-tracing algorithm for accuracy and speed were made with an implementation of ray tracing, the image method, and nonadaptive triangular beam tracing. All methods were tested with the same hall data to produce a specular echogram of sound energy incident on the detector with respect to time.

The ray-tracing algorithm was implemented to use a spherical detector, and a record of rays intersecting was built up. The home-made method was simply used to demonstrate ray tracing's inherent errors when applied to finding image sources and its expensive time profile. Rays with the same plane-to-plane path would sometimes be recorded, while other valid ray paths were missed. These systematic errors for ray tracing were demonstrated by Lehnert,[2] who subsequently suggested a criterion for ray density based on detector size and the mean free path of the hall. The image method used was based on an efficient algorithm (Lee and Lee[4]) which takes account of obstructions and invalid images. The nonadaptive triangular beam-tracing method was based on Lewer's implementation.

Given hall data for a simple concert hall with a stage and balcony (Fig. 11), impulse responses were predicted for the adaptive beam-tracing algorithm, nonadaptive beam-tracing algorithm, the image method, and ray tracing (Fig. 12). The adaptive beam-tracing algorithm correlates well with the image method implemented, without exhibiting the degree of duplicated and missing images predicted with nonadaptive beam tracing and ray tracing. This implementation of adaptive beam tracing may very occasionally miss a reflection due to calculation ambiguities when mapping-out areas of illumination, and the image method may generate spurious images within the balcony volume. However both cases are very rare, and have a negligible bearing on the final results.

Comparisons of calculation time were made for the different methods using a relatively slow 486 personal computer. Figure 13 shows that ray tracing can be fast with an arbitrary number of rays used across a range of orders of reflection; however, systematic errors increase. When applying an error criterion to specify the number of rays used for a given detector size (Lehnert[2]), ray tracing was demonstrated to be much slower than beam tracing. The image method is the fastest for low orders of reflection, but calculation times increase exponentially with orders of reflection or number of planes used. Nonadaptive triangular beam trac-

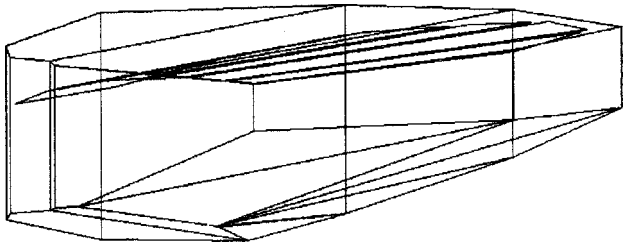

FIG. 14. Sheffield Hallam Concert Hall ~23×19×8 m.

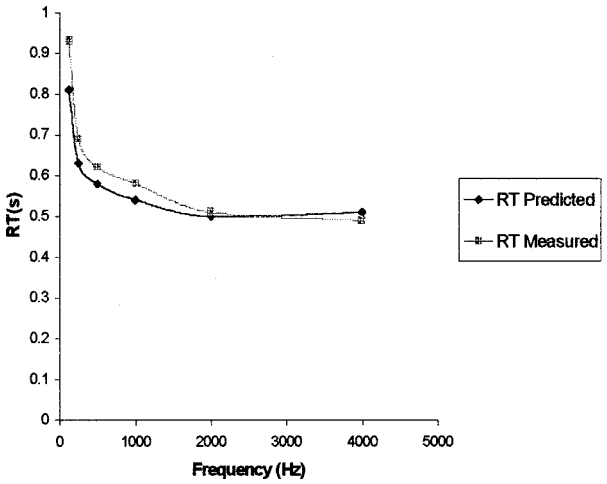

FIG. 15. Comparisons of measured and predicted RTs for Sheffield Hallam Concert Hall.

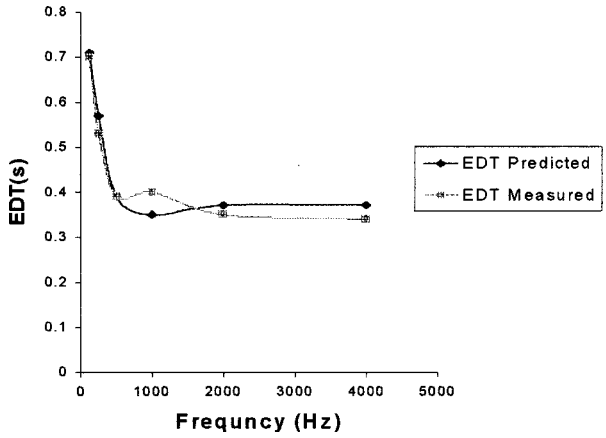

FIG. 16. Comparisons of measured and predicted EDTs for Sheffield Hallam Concert Hall.

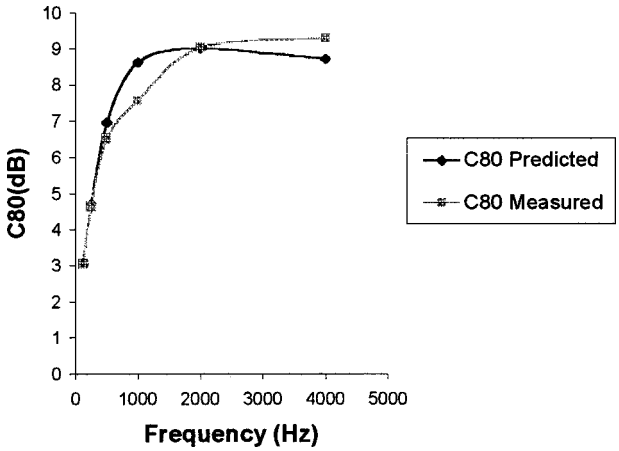

FIG. 17. Comparisons of measured and predicted C80s for Sheffield Hallam Concert Hall.

ing requires a large spread of initial beams for workable accuracy, unlike the adaptive beam-tracing algorithm, which starts with 20. With adaptive beam tracing, the number of child beams generated and their divergence is limited by the number of planes in the hall. For example, a given hall with 17 planes spawned 5200 child beams after six orders of reflection. The number of child beams generated does not become unmanageable at higher orders of reflection. Although calculation of exact areas of beam illumination adds to CPU overhead, the adaptive beam-tracing algorithm compares well with other methods for all but the lowest orders of reflection and simplest of halls.

B. Comparison with measured data

The adaptive beam-tracing algorithm was applied to a number of real halls, for comparisons with measured results. This was to demonstrate the algorithm's ability to cope with relatively complicated scenarios without the need for empirical fixes. For example, measurements of reverberation time, early decay time, and clarity index were made across a range of frequencies for a lecture hall that is also used for music performances (Fig. 14). The adaptive beam-tracing algorithm was implemented on a representation of this hall, based on architectural data and known surface absorption coefficients. The use of this hall data demonstrates the algorithm's ability to handle relatively complex models that include reflectors and obscuring planes.

The walls, ceiling, and reflectors were assumed to have a diffusion coefficient of 0.1. Soft seating was assumed to have a diffusion coefficient of 0.7. These were values estimated in an earlier study (Howarth[11]). For each frequency, the algorithm calculated RT, EDT, and C80.

The results for RT (Fig. 15) show a good correlation with measured, although usually less than predicted, demonstrating a possible loss of predicted energy for higher orders of reflection. However, this may in part be due to an overestimation of absorption coefficient and the algorithm ignoring hall resonance and outside noise like traffic.

The results for EDT (Fig. 16) and C80 (Fig. 17) show some variance with frequency. These can be improved by calculating to higher orders of reflection, although at the expense of fast computation.

III. CONCLUSIONS

The adaptive beam-tracing algorithm shows improvements in speed over other methods. The algorithm seeks to eliminate systematic errors resulting from overlaps and omissions in predicted sound propagation, whilst facilitating an integrated calculation of specular and diffuse systems, thus removing the need for statistical and empirical adjustments.

The algorithm copes well with complicated halls by inherently dealing with occluding planes. However, relative to ray tracing and the image method, the adaptive beam-tracing algorithm is difficult to implement because it relies on sophisticated techniques to map out sections of illumination. Certain complicated plane alignments can confuse the algorithm, creating effects similar to optical illusions. Hence, the algorithm must be able to deal with these by using a degree of artificial intelligence. There is plenty of scope to improve the algorithm's reliability and efficiency.

In conclusion, the adaptive beam-tracing algorithm provides a logical and complete way to model sound propagation. Though difficult to implement, the algorithm has many advantages over existing methods.

[1] A. Kulowski, ''Algorithmic representation of the ray tracing technique,'' Appl. Acoust. **18**, 449–469 (1984).
[2] H. Lehnert, ''Systematic errors of the ray-tracing algorithm,'' Appl. Acoust. **38**, 207–221 (1993).
[3] J. Borish, ''Extension of the image model to arbitrary polyhedra,'' J. Acoust. Soc. Am. **75**, 1827–1836 (1984).
[4] H. Lee and B. Lee, ''An efficient algorithm for image method technology,'' Appl. Acoust. **24**, 87–115 (1988).
[5] M. Vorlander, ''Simulation of transient and steady state sound propagation in rooms using a new combined ray tracing/image source algorithm,'' J. Acoust. Soc. Am. **86**, 172–178 (1989).
[6] D. Van Maercke and J. Martin, ''The prediction of echograms and impulse responses within the Epiduare software,'' Appl. Acoust. **38**, 93–114 (1993).
[7] T. Lewers, ''A combined beam tracing and radiant exchange computer model of room acoustics,'' Appl. Acoust. **38**, 161–178 (1993).
[8] U. M. Stephenson, ''Quantized pyramidal beam tracing—a new algorithm for room acoustics and noise emmission prognosis,'' Acust. Acta Acust. **82**, 517–525 (1996).
[9] F. S. Hill, *Computer Graphics* (Macmillan, New York, 1990), pp. 305–424.
[10] M. R. Schroeder, ''New method for measuring reverberation time,'' J. Acoust. Soc. Am. **37**, 409–412 (1965).
[11] M. J. Howarth, ''The application of advanced computer models to the prediction of sound in enclosed spaces,'' Ph.D. thesis, The University of Salford, United Kingdom, 1998.

Prediction of sound transmission loss through multilayered panels by using Gaussian distribution of directional incident energy

Hyun-Ju Kang[a)]
Acoustics Laboratory, Korea Institute of Machinery and Materials, P.O. Box 101, Yusung, Taejon 305-600, Korea

Jeong-Guon Ih
Department of Mechanical Engineering, Korea Advanced Institute of Science and Technology, Science Town, Taejon 305-701, Korea

Jae-Seung Kim and Hyun-Sil Kim
Acoustics Laboratory, Korea Institute of Machinery and Materials, P.O. Box 101, Yusung, Taejon 305-600, Korea

(Received 29 January 1999; revised 13 October 1999; accepted 2 December 1999)

In this study, a new prediction method is suggested for sound transmission loss (STL) of multilayered panels of infinite extent. Conventional methods such as random or field incidence approach often give significant discrepancies in predicting STL of multilayered panels when compared with the experiments. In this paper, appropriate directional distributions of incident energy to predict the STL of multilayered panels are proposed. In order to find a weighting function to represent the directional distribution of incident energy on the wall in a reverberation chamber, numerical simulations by using a ray-tracing technique are carried out. Simulation results reveal that the directional distribution can be approximately expressed by the Gaussian distribution function in terms of the angle of incidence. The Gaussian function is applied to predict the STL of various multilayered panel configurations as well as single panels. The compared results between the measurement and the prediction show good agreements, which validate the proposed Gaussian function approach. © *2000 Acoustical Society of America.* [S0001-4966(00)01703-3]

PACS numbers: 43.55.Rg, 43.55.Nd, 43.50.Gf [JDQ]

INTRODUCTION

Conventionally, the prediction of sound transmission loss (STL) of various panel systems has been carried out by analytical or semiempirical methods under the assumption that the panels are infinitely extended and the incident sound field on the panel is random.[1] The random incidence approach, which is based on the perfectly diffuse sound field on the wall being tested, is mathematically convenient to calculate the STL of panels. The perfectly diffuse sound field is identical to the uniform directional distribution of incident energy, which means that the incident energy on the wall is uniform over all angles of incidence. However, it is well-known that the prediction using the uniform distribution frequently results in disagreement with measurements.[2] The disagreement is due to the fact that the uniform distribution does not fully reflect the actual sound field incident on the wall. However, this implies that the directional distribution of incident energy plays an important role in the analysis of STL.

A common approach to overcome the observed discrepancy is the field incidence method that truncates the angle of incidence up to a certain limit angle $\phi_{\lim}$. The limit angle $\phi_{\lim}$ has been empirically determined; it is chosen to give a best fit with the experimental data. Beranek[2] concluded that the limit angle of 78° gave an adequate fit for single panels, and named it ''the field incidence method.'' Typical values[3] of $\phi_{\lim}$ vary from 70° up to 85°. The explanation, which is usually given to justify the empirical correction, is that the sound field near the wall of a reverberation chamber is not perfectly diffuse, so that no sound energy is incident on the panels above the near grazing angle, say, 78°.

It should be noted that the field incidence approach[2,3] was initiated by matching the measurement with the prediction for limp panels. The idea of the limp panel is that the panel impedance considering the mass only, i.e., $Z=j\omega m$, is independent of the angle of incidence, where ω and m denote the radian frequency and the mass of panel per unit area, respectively. In principle, the approach is not applicable to the angle-controlled region, where STL is sensitive to the angle of incidence. The mass–spring–mass resonance[4]-controlled region is an example of this. Consequently, the method works fairly well for thin single panels but often fails for multilayered panels with cavities. In previous work,[5] the limit angle was determined by matching the predicted STL with the measured one for the single limp panel. Then, the obtained limit angle was directly applied to double-wall cases.

It should also be noted that variation of the limit angle in using the field incidence method yields an appreciable change in the predicted STL even for a single panel. Using

[a)]Author to whom correspondence should be addressed. Electronic mail: kanghj@mailgw.kimm.re.kr

the expression for sound transmission coefficient $\tau(\omega)$ by Sewell,[6] i.e., $\tau(\omega)=Z^{-2}[\ln(\sec^2\phi_{\lim})]$, one can readily observe the variation of predicted STL with the limit angle. For example, if $\phi_{\lim}$ is changed from 70° to 85°, there is a 4 dB difference in the predicted STL.

Disagreement between the measured and the predicted STL of a double wall with air cavity can also be found in the earlier work by London.[4] Assuming the diffuse sound field, London had derived an explicit expression for the oblique incidence transmission coefficient and showed the existence of the mass–spring–mass resonance. The coefficient was then integrated over all angles of incidence to obtain the average coefficient at a fixed frequency. An additional term defined as the wall resistivity was introduced into the panel impedance to make the predicted STL conform to the measured ones, but no clear explanation or experimental evidence for this term was shown. Mulholland *et al.*[7] managed to replace this additional term by a more physically meaningful one. They also used the limit angle approach and, in addition, the multiple reflection method, which takes into account the absorption of the cavity between panels, was employed as well. The role of the absorption was to reduce the excessive effects caused by mass–spring–mass resonances. However, unrealistic values of the absorption coefficient for the air cavity were required in order to obtain a good fit to the experiment. Cummings and Mulholland[8] made corrections to this work by considering the absorption of the edges in the cavity. However, the modified model was again found to be of limited usefulness, because an absorption value of almost unity was required for a reasonable match between predicted and measured results. By using the mode coupling method for two rooms having a common double wall, Guy[9] showed that the angle of incidence is related not to mass–spring–mass resonance frequency but to the excitation term only. However, his model seems to lack generality, because the adopted size of the panel, which was comparable to the diameter of an impedance tube, was very small.

De Bruijn[10] investigated the influence of diffuseness on the STL of the single-leaf walls with finite size by means of a modified spatial correlation function as the exciting pressure. In order to describe the degree of diffuseness in the vicinity of the wall of a reverberation chamber, he modified the spatial correlation function by introducing the scale coefficients obtained from measurements. By means of this correlation function, an excellent agreement between theory and experiment was achieved in the mass-controlled region. However, no examples were given for the multilayered panels.

In this paper, the incoming sound energy on the wall in a reverberation chamber is numerically investigated. The focus is on directional diffusion, and to derive a weighting function for the directional distribution of incidence energy, which could replace the conventional concept of the full or truncated uniform distribution. The weighting function is applied to the single and multilayered panels and the predicted results are compared with experimental data.

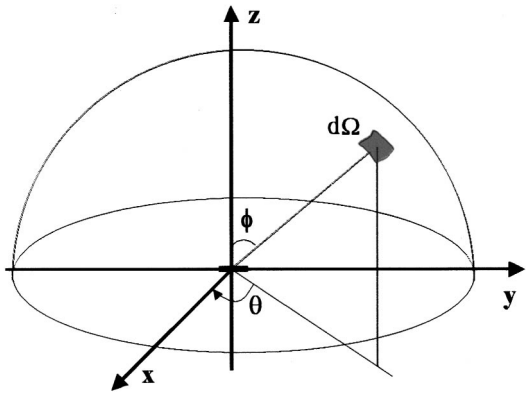

FIG. 1. Description of the solid angle.

I. REVIEW ON THE EFFECTS OF INCIDENCE ANGLE ON STL

A. Average sound transmission coefficient over the angle of incidence

In principle, the average sound transmission coefficient $\tau(\omega)$[11,12] can be obtained from the oblique incidence transmission coefficients of the panels by weighting the directional energy density, $D(\boldsymbol{\xi})$, and integrating over the solid angle as follows:

$$\tau(\omega)=\frac{\int\int\tau(\omega,\boldsymbol{\xi})D(\boldsymbol{\xi})\boldsymbol{\xi}\cdot\mathbf{n}\,d\Omega}{\int\int D(\boldsymbol{\xi})\boldsymbol{\xi}\cdot\mathbf{n}\,d\Omega}. \tag{1}$$

Here, $\boldsymbol{\xi}$ and $\mathbf{n}$ represent the unit directional and normal vectors incident on the wall under consideration, respectively, and Ω denotes the solid angle as shown in Fig. 1. $D(\boldsymbol{\xi})$ means the energy density per unit solid angle in the propagation direction.

Because the information on the directional energy density on a wall has not been available, $D(\boldsymbol{\xi})$ has usually been assumed to be independent of $\boldsymbol{\xi}$. This is equivalent to assuming that plane waves are incident from all directions with equal probability, which means the condition of a perfect diffuse sound field.[13,14] If the sound field on a wall is perfectly diffuse, $D(\boldsymbol{\xi})$ is equal to $E/4\pi$, where E is the energy density. Substituting this condition into Eq. (1), the average transmission coefficient reduces to

$$\tau(\omega)=\frac{\int_0^{2\pi}\int_0^{\pi/2}\tau(\omega,\phi)\cos\phi\sin\phi\,d\phi\,d\theta}{\int_0^{2\pi}\int_0^{\pi/2}\cos\phi\sin\phi\,d\phi\,d\theta}$$

$$=\frac{\int_0^{\phi_{\lim}}\tau(\omega,\phi)\cos\phi\sin\phi\,d\phi}{\int_0^{\phi_{\lim}}\cos\phi\sin\phi\,d\phi}, \tag{2}$$

where θ and ϕ are the azimuth angle and the cone angle, respectively, as can be seen in Fig. 1. Note that the limit angle, $\phi_{\lim}$, is 90° for the random incidence and 70°–85° for the field incidence transmission on the right side of Eq. (2).

A double panel with an air cavity is a typical example for multilayered partitions. The sound transmission coefficient of such layered partition can be approximated by[15]

$$\tau(\omega,\phi)=\left|\frac{-2j(\rho_0c_0\sec\phi)^2/(kd\cos\phi)}{\left[Z+\dfrac{\rho_0c_0}{\cos\phi}-\dfrac{j\rho_0c_0}{kd\cos^2\phi}\right]^2+\left(\dfrac{\rho_0c_0}{kd\cos^2\phi}\right)^2}\right|. \tag{3}$$

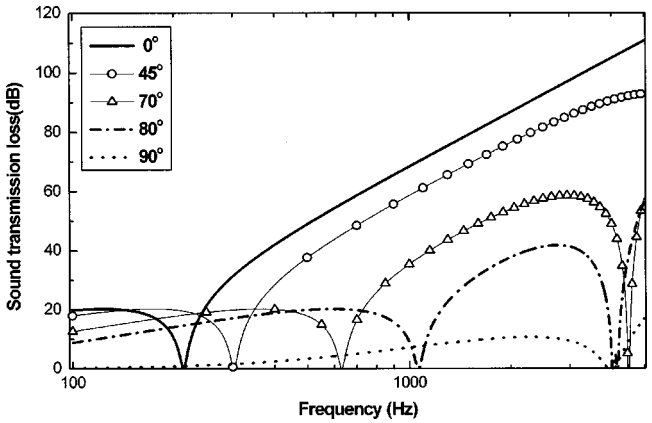

FIG. 2. Variation of predicted transmission losses with the angle of incidence for a double window composed of glass (3 mm), air (19 mm), and glass (3 mm).

where $k=\omega/c_0$ is the wave number in air, c_0 and ρ_0 denote the density of air and the speed of sound, respectively, d is the depth of cavity, and Z denotes the panel impedance. In the low-frequency range, the masses of two skin panels combined with the stiffness of air trapped in the cavity make the mass–spring–mass resonance at f_0. When the absorption in the cavity is negligible, f_0 is given by[4]

$$f_0=\frac{f_{0,1}}{\cos\phi}, \tag{4}$$

where $f_{0,1}=(1/2\pi)((\rho_0 c_0^2/d)((m_1+m_2)/m_1m_2))^{1/2}$ denotes the mass–spring–mass resonance frequency with respect to the normal incidence. It is noted that f_0 is a continuous function of the incident angle and one can observe in Fig. 2 that each STL curve for the particular incident angle has a sharp dip corresponding to the mass–spring–mass resonant frequency, f_0. Because the STL at a fixed frequency is the averaged value over all angles of incidence and the contribution of the dip to the average would be large, the averaged STL above $f_{0,1}$ will be appreciably underestimated. When the concept of limit angle is applied to the calculation of STL, quite different trends can be observed for various choices of $\phi_{\lim}$. Figure 3 displays the effect of various limit angles on the predicted STL for a double-glazed glass window, and also shows the measured values.[16] The random incidence case yields significantly lower STL values above 250 Hz than the measured one due to the aforementioned effect of the mass–spring–mass resonance. One can also find that the field incidence method shows the rapid rise at certain frequencies corresponding to $f=f_{0,1}/\cos\phi_{\lim}$ that can be inferred from Eqs. (3) and (4). Therefore, the choice of limit angle exerts a strong influence on the predicted STL of a double panel with air cavity.

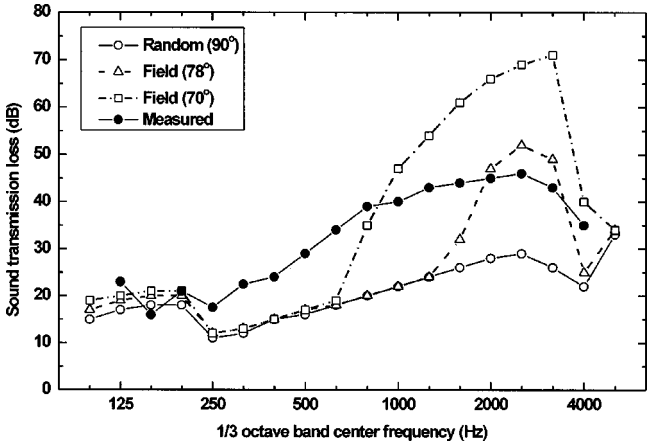

FIG. 3. Comparison of the measured (Ref. 16) with the predicted STL by adopting the different limit angles for a double window composed of glass (3 mm), air (19 mm), and glass (3 mm).

B. Comments on the diffuse sound field in reverberation chambers

One of the widely used assumptions for the infinite panel theory is that the sound field under consideration is perfectly diffuse. As stated by Schultz,[14] there are two criteria for the clear meaning of the diffuse sound field: one is for spatial diffusion and the other for directional diffusion. The criterion for spatial diffusion is that the total energy density is uniform at all points in the room and each volume element radiates equally in all directions. The criterion for directional diffusion is that the energy will flow in all directions with an equal probability and the angle of incidence on the boundaries of the room is randomly given. However, these criteria, especially the directional diffusion, are applicable only to a mathematically ideal room, and actual reverberation chambers cannot satisfy the criteria perfectly. Several factors have already been pointed out to explain why the sound field near the bounding surface of a room is not diffuse. One of them is the Waterhouse effect,[17,18] which mentions the increase of energy density in the reverberation chamber due to the interference between incident and reflected waves at the bounding surfaces. Another nondiffusing mechanism of importance is the so-called tunneling effect[19,20] in the actual test facility. In general, the depth of the specimen is much smaller than that of the test opening so that the remaining part of the opening may form standing wave patterns like a shallow duct. The foregoing effects have been attributed to form a nonuniform sound field on the bounding surfaces. In addition, geometrical shapes of the actual reverberation chamber can also be a reason of the nonuniform directional distribution of the incident energy on the bounding surface. If a large and irregularly shaped room is considered, the sound field can be analyzed by using the ray-tracing technique.[21] If the role of reflecting walls is simply to reduce the intensity of the wave by absorption and all the reflections are specular, it is doubtful that all angles of incidence on the bounding surfaces are equally probable. This geometrical consideration would have been a basis for the field incidence method, but the method assumes a perfect shadow zone above a limit angle. De Bruijn's[10] work on the influence on the STL by using the spatial correlation function also suggests a possible way to solve the problem.

II. NUMERICAL SIMULATIONS FOR THE DISTRIBUTION OF DIRECTIONAL ENERGY DENSITY

When the directional distribution of the incident energy on the wall is not uniform, one must know how much energy

per unit solid angle arrives on the small area element of the wall in order to calculate the average transmission coefficient. In general, measurement of angular distribution of an incident wave imposes several problems, one of which is the difficulty of extracting only the incident wave from the sound field. It is commonly viewed as an unmeasurable quantity, as stated by Schultz.[14] In this work, we investigate the directional energy densities by numerical simulation.

A. Numerical simulations for the directional distribution of incident energy

The directional energy density $D(\xi)$, i.e., the incident sound energy E per unit solid angle, can be calculated by using the ray-tracing technique. Consider an infinitesimal area dS of which cone and azimuth angles are ϕ and θ, respectively, the same as shown in Fig. 1. The incoming energy at an incident angle ϕ within the constant angular interval can be obtained as

$$E(\phi)=\sum_{i=1}^{n} E_i \quad \text{for } \phi_j \leqslant \phi \leqslant \phi_{j+1}. \tag{5}$$

Here, ϕ_j, ϕ_{j+1} represent the upper and the lower angle within the jth and $(j+1)$th angular interval, respectively, n denotes the number of incoming sound rays within the interval, $E_i=E_0(1-\alpha)^{\gamma}$ is the incident energy corresponding to each incoming sound ray within the interval, and E_0, α, and γ denote the radiated energy from the sound source, the absorption coefficient of bounding surface, and the number of reflections, respectively. The directional energy density $D(\xi)$ is given by

$$D(\xi)=E(\phi)/dA. \tag{6}$$

In this expression, the area dA is expressed as

$$dA=\int_0^{2\pi} d\theta \int_{\phi_j}^{\phi_{j+1}} \sin\phi \, d\phi = 2\pi \int_{\phi_j}^{\phi_{j+1}} \sin\phi \, d\phi. \tag{7}$$

If the room is perfectly diffuse, $D(\xi)$ in Eq. (6) should be uniform over all angles of incidence.

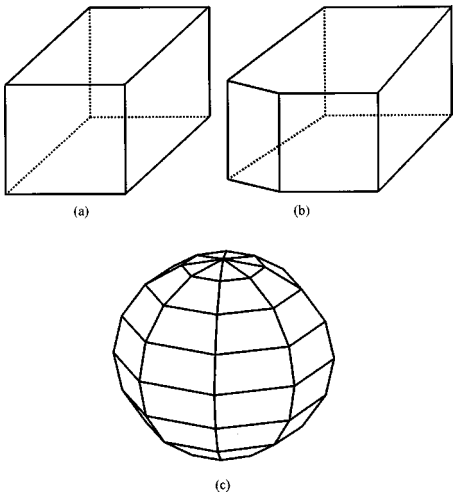

FIG. 4. Test models for numerical simulations. (a) cube, (b) reverberation chamber, (c) sphere.

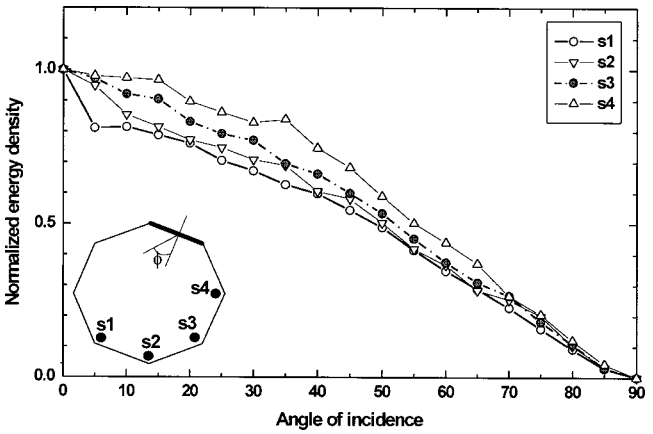

FIG. 5. Calculated directional distribution of incident energy by Eq. (6) for the sphere model. S1–S4 describe the source positions.

Three models were selected for testing the angular dependency of the incident energy on the bounding surface: sphere, reverberant room, and cube, as shown in Fig. 4. The sphere model as a polyhedron, which is composed of 64 patches, was chosen to expect more uniform probabilities for grazing incidence than the others. The dimensions of three models were adjusted such that the reverberation time (7 s) and the volume (225 m^3) were almost the same. The number of rays from the omnidirectional point source was large enough to make the sound field spatially diffuse by checking sound pressures at various locations. The absorption coefficient α of the wall was 0.02.

The energy density was estimated at every 5° interval. The incoming energy density to the receiving surface will vary with each model and with each source position of the same model as well. For comparison purposes, the energy density of each angle of incidence was normalized to that of the normal incidence.

The simulated results for each source position in the sphere model are presented in Fig. 5. It is seen that the incident energy decreases with increasing angle of incidence and varies with four source positions, especially at near-normal incidence. For the cube and reverberation room model, calculations were done repeatedly by changing the source position at every corner on the floor in Fig. 4. Figure 6 shows the

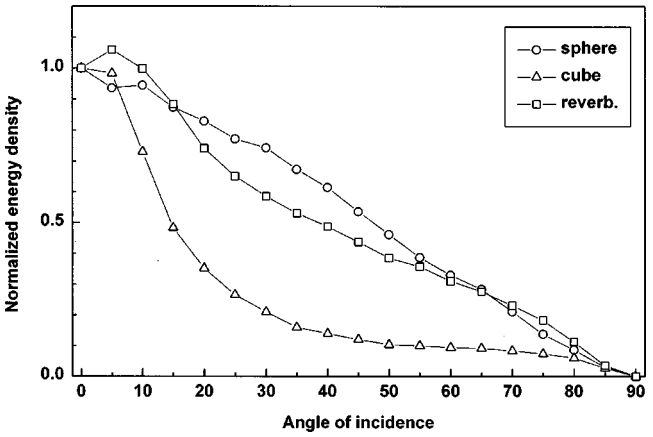

FIG. 6. Comparison of calculated directional energy densities for three geometrical models.

averaged values for all source positions. It is obvious that the incident energy is not uniformly distributed over the angle of incidence, and also that its distribution varies according to the room shapes. As expected, the directional energy distribution of the cubic model is more concentrated on the angles near normal incidence than other models, which agrees with the work of Josse and Lamure.[22] They found that the contribution to the sound transmission through the common wall between two cubic rooms is mainly due to the sound energy of near-normal incident angles.

It was concluded that the directional distribution of the incident energy on a bounding surface in an actual test room is a function in terms of the angle of incidence and with the parameters concerning source position, room shape, and frequency which also affect the directional distribution.

B. Distribution function of the directional energy on a wall

For an appropriate function representing the curves in Fig. 6, the function should enable one to take into account the parameters as mentioned above. In addition, it is desirable for the function to be able to represent the limiting case, the uniform distribution in the diffuse sound field.

There are various candidates for the function to approximate the curves in Fig. 6, such as cosine, polynomial, and Gaussian distribution functions. In order to approximate the curve shapes, the polynomial function might have three or four coefficients. For simplicity, this function is excluded. The following high-order cosine function might also be a good candidate:

$$G(\phi)=\cos^{2\beta}(\phi). \tag{8}$$

Here, β is a constant to reflect the effects of the parameters. However, it can be seen that this function is inappropriate to express all curves in Fig. 6 because of the behavior near the grazing incidence when β is greater than 1.

The Gaussian function can also be a candidate. It is thought that this function matches with the idea that many probability functions for the random variables in nature would be approximately Gaussian. The normalized Gauss distribution, which has zero mean and assumes the vertical symmetry of the incident energy, is represented as

$$G(\phi)=\exp(-\beta\phi^2). \tag{9}$$

Here, β is assumed to reflect all the involved parameters. It is noteworthy that this function properly describes the limiting case, i.e., $\lim_{\beta\to 0}G(\phi)=1$ as the case with the uniform distribution.

Figure 7 compares the ray-tracing simulation result and the Gaussian curve with $\beta=1$. It can be seen that the Gaussian curve with a proper value of β within the range of 1–2 corresponds well to the simulation curves of a reverberation chamber as well as other models. Therefore, using Gaussian function, one can revise Eq. (1) as

$$\tau(\omega)=\frac{\int_0^{\pi/2}G(\phi)\tau(\omega,\phi)\sin\phi\cos\phi\,d\phi}{\int_0^{\pi/2}G(\phi)\sin\phi\cos\phi\,d\phi}. \tag{10}$$

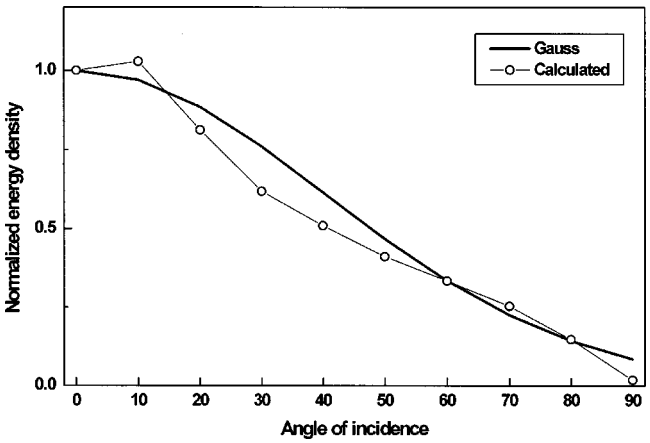

FIG. 7. Comparison of the calculated directional energy densities with Gauss distribution with $\beta=1$.

One can interpret $G(\phi)$ in Eq. (10) as a weighting function for incident sound energy. Also, note that the limit angle is $\pi/2$ here.

III. TESTS FOR VARIOUS PANEL CONFIGURATIONS

The average transmission coefficient $\tau(\omega)$ over the angle of incidence can be obtained by using Eq. (2). Alternatively, one can use Eq. (10) for Gaussian incidence with a proper value of β.

A. Single panels

The impedance Z for a thin single panel consists of the contributions from mass and bending stiffness of the panel, and can be approximated by[1,11]

$$Z=j\omega m-j(\omega^3 D/c_0^4)\sin^4\phi, \tag{11}$$

where $D=D(1-j\eta)$ is the complex bending stiffness and η denotes the loss factor of the panel. The oblique incidence transmission coefficient for a single panel is given by

$$\tau(\phi,\omega)=\left|1+Z\cos\phi/2\rho_0 c_0\right|^{-2}. \tag{12}$$

Figure 8 shows the STL values calculated by using the different methods, and compares them with the predicted

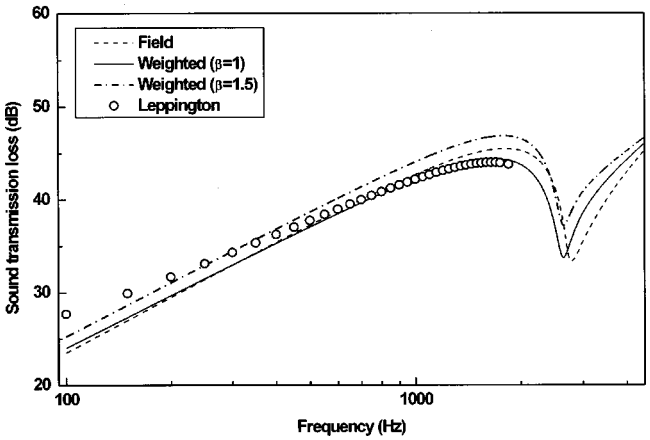

FIG. 8. Comparison of the theoretical STLs by using three different methods for a single steel panel (4.5 mm). Field: from field incidence method in Eq. (2) with $\phi_{\lim}=78°$; Weighted: using Gauss weighting function in Eq. (10) with $\beta=1$ or 1.5; Leppington: from Leppington's theory (Ref. 23).

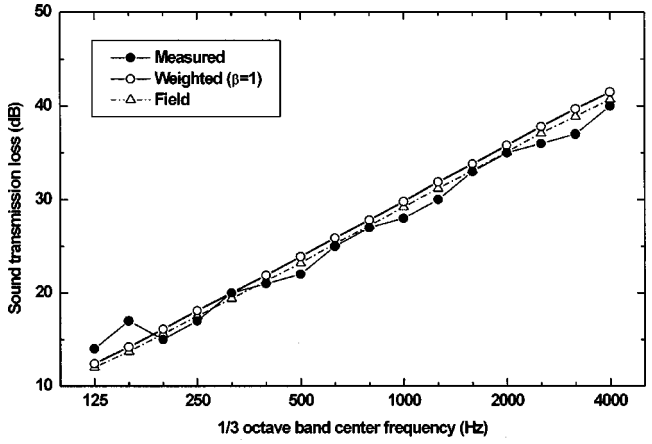

FIG. 9. Comparison of measurement (Ref. 3) with predictions for a limp steel panel ($t=0.9$ mm). Field: from field incidence method in Eq. (2) with $\phi_{\lim}=78°$; Weighted: using Gauss weighting function in Eq. (10) with $\beta=1$.

curves according to Leppington's expression[23] which is an extension of Sewell's work.[6] These predicted STL curves agree reasonably well, except for about 3 dB differences at the coincidence region. This discrepancy may be explained by the finite size effect near the critical frequency, f_{cr}. In the Gauss function approach, the curve of ''weighted ($\beta=1.5$)'' is consistently higher than that of ''weighted ($\beta=1$)'' by about 2 dB. It is noted that Leppington's expression is valid only for $f<f_{cr}$. In Fig. 8, the angular step in the integration was $\Delta\phi=0.01°$.

For the limp panel, Fig. 9 compares the measured data[3] with the STL curves predicted by the field incidence method and the Gaussian weighting method with $\beta=1$. The agreement is very good, i.e., within 2 dB error. For a single steel panel, Fig. 10 shows the comparison of the measurement and the predicted one using the Gaussian weighting method with $\beta=1$ and field incidence method, in which excellent agreements can also be observed.

B. Double panels

The oblique incidence transmission coefficient $\tau(\omega, \phi)$ of double panels with air cavity can be obtained from Eq.

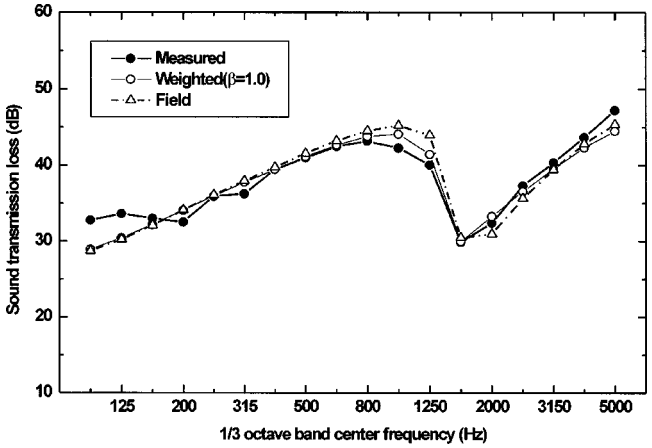

FIG. 10. Comparison of the measured with the predicted STL for a steel panel ($t=7.8$ mm). Field: from field incidence method in Eq. (2) with $\phi_{\lim}=78°$; Weighted: using Gauss weighting function in Eq. (10) with $\beta=1$.

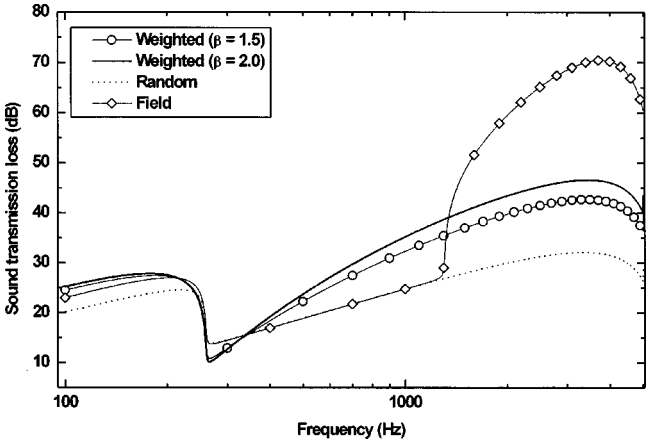

FIG. 11. Variation of the theoretical STLs with each method for a double panel composed of steel (2.2 mm), air (6 mm), and steel (2.2 mm). Weighted: using Gauss weighting function in Eq. (10) with $\beta=1$ or 1.5; Random: from random incidence method in Eq. (2) with $\phi_{\lim}=90°$; Field: from field incidence method in Eq. (2) with $\phi_{\lim}=78°$.

(3). Figure 11 is the detailed narrow-band theoretical results that show how the angle-averaged STL of a double panel with an air cavity varies with frequency according to several different approaches. The angular resolution of the integration was $\Delta\phi=0.0025°$, which assured the convergence of the calculation. Below the lowest mass–spring–mass resonance frequency $f_{0,1}$, all three curves follow mass law quite well, although the random incidence curve based on the fully uniform distribution is lower than the other curves by about 3–5 dB. When $f>f_{0,1}$, the random incidence curve is much lower than the weighted curves. It is observed that the Gauss function approach reduces the excessive effect of the mass–spring–mass resonance. The field incidence curve is similar to the random incidence curve, but it has an abrupt jump above the frequency corresponding to $f=f_{0,1}/\cos\phi_{\lim}$ as stated in Eq. (4). One can also find that for curves of Gauss function approach the mean difference between cases with $\beta=1.5$ and 2.0 is about 2 dB.

In general, it is observed that at $f=f_{0,1}$, the predicted STL of a double panel with an air cavity shows much lower values than the measured one. For example, Fig. 3 displays the significant differences between the measured and the predicted values at $f=f_{0,1}$, e.g., 250 Hz. This implies that a damping mechanism comes into play for mass–spring–mass resonance. In practice, the reason for such a damping may be explained by the friction between panel edges and the frame of test opening when the panels show a mass-like motion and the air cavity acts like a spring. The damping named here as boundary damping may be recognized as a kind of mounting effect.[24] By considering the terms in Eq. (4), assumption of a complex mass of the panel provides an easy way of including such a damping. Hence, the complex surface density[25] of panel, m', is introduced as

$$m=m(1-j\eta_B), \quad \eta_B=\eta_b/\sqrt{f/f_{0,1}} \quad \text{for } f_{0,1}<f<f_c, \quad (13)$$

where η_b is the loss factor for boundary damping and η_B denotes the resultant loss factor. The effect of η_B on the STL of multilayered panels can be found mainly in the vicinity of $f=f_{0,1}$.

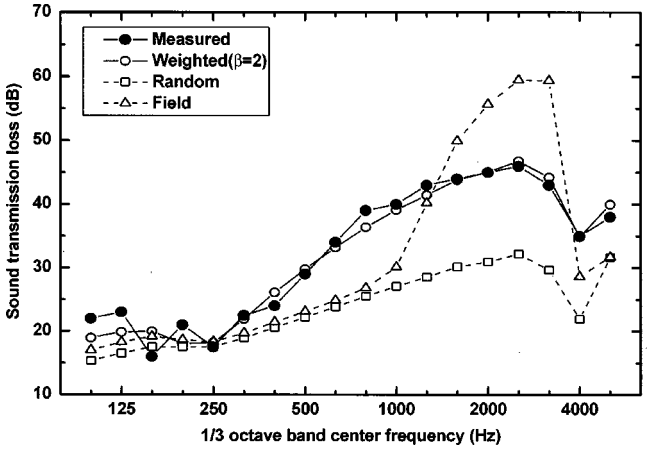

FIG. 12. Comparison of measured (Ref. 16) and predicted STL for a double-glazed window composed of glass (3 mm), air (19 mm), and glass (3 mm).

Using Eqs. (3) and (13), the STL can be predicted for a double panel with an air cavity. As a typical example, a double-glazed window was selected, which is very sensitive to the angle of incidence, as illustrated in Figs. 2 and 3. The values for β and η_b used here were 2.0 and 0.2, respectively. Figure 12 shows a comparison of measured and predicted STL curves. The Gaussian function method agrees very well with the measurement,[16] while the field and random incidence methods yield very poor results.

A double panel lined with porous materials such as glass wool can be analyzed with the poroelastic model,[25–27] which allows three propagating waves within the core material: a fluid-borne longitudinal wave, a solid-borne longitudinal wave, and a solid-borne transverse-shear wave. However, two solid-borne waves are negligible since the glass wool employed in this example does not show significant elastic behaviors. Because of the high absorptive characteristics of the glass wool, the panel system under consideration is less sensitive to the angle of incidence than the case of an air cavity. Figure 13 illustrates such a tendency. Unlike the case of an air cavity, the field incidence curve shows similar pattern to the weighted curve. The difference between measured[28] and predicted results does not in general exceed 2 dB.

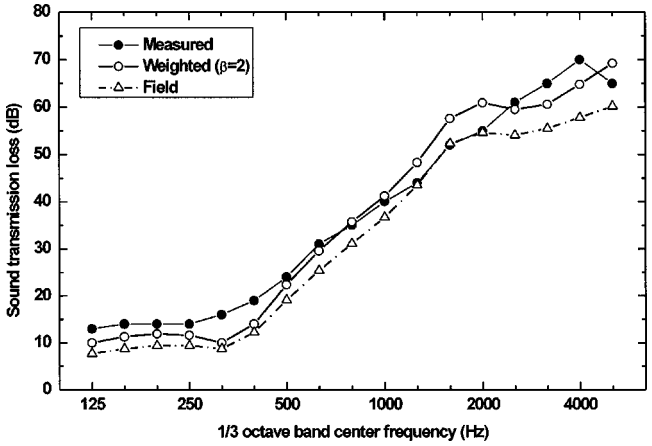

FIG. 13. Comparison of measured (Ref. 28) and predicted STL of a double panel composed of plywood (3 mm), glass wool (45 mm), and plywood (3 mm).

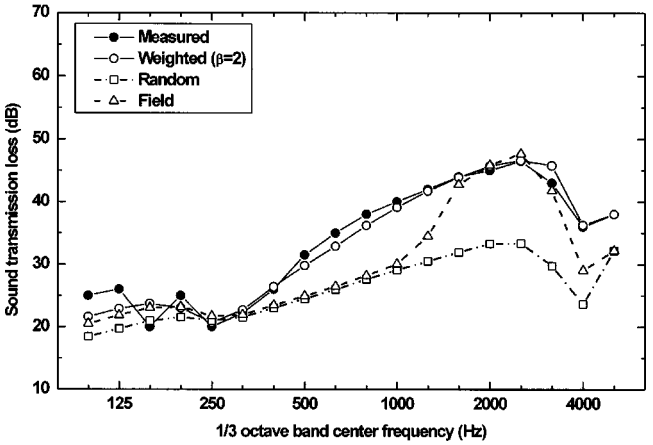

FIG. 14. Comparison of measured (Ref. 16) and predicted STL for a triple-glazed window composed of glass (3 mm), air (3 mm), glass (3 mm), air (10 mm), and glass (3 mm).

C. Triple panels

For the triple panel with air cavities, the oblique incidence transmission coefficient[11] can be derived by using the transfer matrix method

$$\tau(\omega,\phi)=\big|1+(X_1+X_2+X_3)+X_1X_2(1-e^{-j\sigma_1})+X_2X_3(1-e^{-j\sigma_2})+X_1X_3(1-e^{-j(\sigma_1+\sigma_2)})+X_1X_2X_3(1-e^{-j\sigma_1})(1-e^{-j\sigma_2})\big|^{-2}. \quad (14)$$

Here, $X_i=Z_i\cos\phi/2\rho_0c_0$ represents the specific impedance of the ith panel, Z_i denotes the impedance of the ith panel, d_i is the ith cavity depth, and $\sigma_i=2kd_i\cos\phi$.

The STL of triple panels, in principle, will be more complicated than the case of double panels because there are various mass–spring–mass resonances and critical frequencies. Using Eqs. (10), (13), and (14), the STL of triple partitions with air cavities can be predicted. The values for β and η_b are the same as those in the cases of double panels. Figure 14 shows a comparison of predicted and measured[16] STL curves for a triple-glazed glass window with cavities. Similar to the foregoing result with double panels, the prediction using the Gaussian function agrees very well with the measurement. In contrast, the random incidence method produces the greatly underestimated STL above $f=f_{0,1}$ and the field incidence method also yields low STL over the midfrequency range.

It is worth noting that the different values of β were chosen to obtain the best agreement. The use of the different values of β may be explained by the fact that the radiated pressure[29] from the panel, which depends on the panel configurations, will affect the sound field in the vicinity of the wall being tested. Further study on this matter is required.

IV. CONCLUDING REMARKS

Numerical simulation for the directional distribution of incident energy on a wall in the reverberation chamber indi-

cates that the distribution is a function of the angle of incidence, rather than the uniform distribution. This angular distribution in a reverberation chamber can be approximately expressed by the Gauss distribution function. The formula of the average transmission coefficient was then revised by employing this directional weighting function, instead of using the limit angle approach of the field incidence method. The revised formula was applied to typical configurations of single, double, and triple panels, and showed good agreement with the measured data.

In deriving the weighting function, the basic assumption that the sound field at the middle positions in the room is diffuse was not altered, except at the bounding surface. Therefore, the overall previous framework of the infinite panel approach has not been changed. In addition, the complex mass of panels was introduced in order to consider boundary damping as a function of frequency. This enabled one to predict the more accurate values at the lowest mass–spring–mass resonance frequency.

It is believed that the use of a directional weighting function, employing here the Gaussian distribution function, would be generally useful in predicting the sound transmission loss of multilayered partitions with improved accuracy.

ACKNOWLEDGMENTS

The authors would like to thank Professor J. S. Bolton for his valuable comments. This work was partially supported by the Ministry of Science and Technology of Korea.

[1] L. Cremer and M. Heckl, *Structure-Borne Sound* (Springer, New York, 1973), Chap. V.
[2] L. L. Beranek, *Noise Reduction* (McGraw-Hill, New York, 1971), Chap. 13.
[3] R. E. Jones, ''Inter-comparisons of laboratory determinations of airborne sound transmission loss,'' J. Acoust. Soc. Am. **66**, 148–164 (1979).
[4] A. London, ''Transmission of reverberant sound through double walls,'' J. Acoust. Soc. Am. **22**, 270–279 (1950).
[5] J. S. Bolton, N. M. Shiau, and Y. J. Kang, ''Sound transmission through multi-panel structures lined with elastic porous materials,'' J. Sound Vib. **191**, 317–347 (1996).
[6] E. C. Sewell, ''Transmission of reverberant sound through a single-leaf partition surrounded by an infinite rigid baffle,'' J. Sound Vib. **12**, 12–32 (1970).
[7] K. A. Mulholland, H. D. Parbook, and A. Cummings, ''The transmission loss of double panels,'' J. Sound Vib. **6**, 324–334 (1967).
[8] A. Cummings and K. A. Mulholland, ''The transmission loss of finite sized double panel in a random incidence sound field,'' J. Sound Vib. **8**, 126–133 (1968).
[9] R. W. Guy, ''The transmission of airborne sound through a finite panel air gap, panel and cavity configuration—a steady state analysis,'' Acustica **49**, 323–333 (1981).
[10] A. D. Bruijn, ''Influence of diffusivity on the transmission loss of a single-leaf wall,'' J. Acoust. Soc. Am. **47**, 667–675 (1970).
[11] B. H. Sharp, ''A study of techniques to increase the sound insulation of building elements,'' Wyle Laboratory Report No. WR 73-5 (1973).
[12] A. D. Pierce, *Acoustics: An Introduction to Its Physical Principles and Applications* (Acoustical Society of America, New York, 1994), Chap. 6.
[13] H. Kuttruff, *Room Acoustics* (Applied Science, London, 1973), Chap. IV.
[14] T. J. Schultz, ''Diffusion in reverberant rooms,'' J. Sound Vib. **16**, 17–28 (1971).
[15] F. Fahy, *Sound and Structural Vibration* (Academic, London, 1985), Chap. 4.
[16] J. D. Quirt, ''Sound transmission through windows: II. Double and triple glazing,'' J. Acoust. Soc. Am. **74**, 534–542 (1983).
[17] R. V. Waterhouse, ''Patterns in reverberant sound fields,'' J. Acoust. Soc. Am. **27**, 247–258 (1955).
[18] R. V. Waterhouse, ''Output of a sound source in reverberation chamber and other reflecting environments,'' J. Acoust. Soc. Am. **30**, 4–13 (1958).
[19] R. W. Guy and P. Sauer, ''The influence of sills and reveals on sound transmission loss,'' Appl. Acoust. **17**, 453–476 (1984).
[20] R. E. Halliwell and C. C. Warnock, ''Sound transmission loss: Comparison of conventional techniques with sound intensity techniques,'' J. Acoust. Soc. Am. **77**, 2094–2110 (1985).
[21] A. Krokstad, S. Strom, and S. Sorsdal, ''Calculating the acoustical room response by the use of a ray tracing technique,'' J. Sound Vib. **8**, 118–125 (1967).
[22] R. Josse and C. Lamure, ''Transmission du son par une paroi simple,'' Acustica **14**, 267–280 (1964).
[23] F. G. Leppington, K. H. Heron, E. G. Broadbent, F. R. S., and S. M. Mead, ''Resonant and non-resonant acoustic properties of elastic panels. II. The transmission problem,'' Proc. R. Soc. London **412**, 309–337 (1987).
[24] W. A. Utley and B. L. Fletcher, ''The effect of edge conditions on the sound insulation of double windows,'' J. Sound Vib. **26**, 63–72 (1973).
[25] J. F. Allard, *Propagation of Sound in Porous Media* (Elsevier, London, 1993), Chap. 4.
[26] M. A. Biot, ''Theory of propagation of elastic waves in a fluid-saturated porous solid: I. Low frequency range,'' J. Acoust. Soc. Am. **28**, 168–178 (1956).
[27] M. A. Biot, ''Theory of propagation of elastic waves in a fluid-saturated porous solid: II. Higher frequency range,'' J. Acoust. Soc. Am. **28**, 179–191 (1956).
[28] Anonymous, *Handbook of Noise and Vibration Treatment* (Kibodang, Tokyo, 1982), Chap. 6 (in Japanese).
[29] P. H. White and A. Powell, ''Transmission of random sound and vibration through a rectangular double wall,'' J. Acoust. Soc. Am. **40**, 821–832 (1966).

Maximum-likelihood approach to strain imaging using ultrasound

M. F. Insana,[a] L. T. Cook, M. Bilgen, P. Chaturvedi, and Y. Zhu
Department of Radiology, University of Kansas Medical Center, 3901 Rainbow Boulevard, Kansas City, Kansas 66160-7234

(Received 4 January 1999; revised 8 September 1999; accepted 19 November 1999)

A maximum-likelihood (ML) strategy for strain estimation is presented as a framework for designing and evaluating bioelasticity imaging systems. Concepts from continuum mechanics, signal analysis, and acoustic scattering are combined to develop a mathematical model of the ultrasonic waveforms used to form strain images. The model includes three-dimensional (3-D) object motion described by affine transformations, Rayleigh scattering from random media, and 3-D system response functions. The likelihood function for these waveforms is derived to express the Fisher information matrix and variance bounds for displacement and strain estimation. The ML estimator is a generalized cross correlator for pre- and post-compression echo waveforms that is realized by waveform warping and filtering prior to cross correlation and peak detection. Experiments involving soft tissuelike media show the ML estimator approaches the Cramér–Rao error bound for small scaling deformations: at 5 MHz and 1.2% compression, the predicted lower bound for displacement errors is 4.4 μm and the measured standard deviation is 5.7 μm. [S0001-4966(00)00903-6]

PACS numbers: 43.60.Cg, 43.60.Gk, 43.80.Vj [JCB]

INTRODUCTION

Bioelasticity imaging provides important diagnostic information about soft tissue stiffness not available with other imaging modalities. It is based on the principles of manual palpation, a standard diagnostic technique, but promises greater sensitivity and spatial resolution. Numerous approaches to bioelasticity imaging have been proposed.[1–23] A common feature of each technique is a force that is carefully selected to displace the tissue in a way that can be tracked using standard imaging technology, often ultrasonics or magnetic resonance. Analysis of the estimated displacement field yields an image of an elasticity modulus or strain.

We study strain estimation from tissue displacements caused by *static* compression. Static compression minimizes the viscous effects of tissue dynamics. Local displacements are detected from changes in the ultrasonic echo fields recorded before and after compression. Unfortunately, the object motion necessary for strain contrast also can produce noise as coherence is reduced between waveforms recorded before and after compression. The performance of strain imaging for visualizing stiffness variations is often noise limited.

In a typical two-dimensional (2-D) strain imaging experiment, we confine all motion in the body to the image plane. We then scan the tissue with broadband pulse-echo ultrasound to record a radio-frequency echo field at high spatial resolution from the region of interest. This precompression echo field is a reference by which the position of scatterers after compression can be compared. Next we compress, hold, and re-scan the tissue to record the position of displaced scatterers. The displacement field is measured from the pre- and post-compression echo fields using a sequence of signal processing techniques that varies with the presumed nature of the deformation. Gradients of displacement are estimates of strain tensor components.[24] One primary objective of the image formation algorithm is to maximize coherence between the pre- and post-compression waveforms to be cross correlated.

When object deformation is accurately described by scaling spatial coordinates of the echo signal, then waveform *companding* applied before 1-D cross correlation has been found to produce low-noise time delay estimates[25] and strain images.[26] More complex deformations require image filtering[27] or warping[28,29] techniques to improve coherence at the expense of processing time. For very complex motions, compressions must be applied incrementally and accumulated to avoid waveform decorrelation.[11,30] We will show that a maximum-likelihood approach to displacement estimation can be implemented for strain imaging through least-squares techniques.

The amount of compression we apply depends on our ability to balance the requirements for (a) high coherence between pre- and post-compression echo fields, (b) accurate displacement estimation, and (c) high strain contrast between background and targets. Large compressions increase object contrast for strain but decrease waveform coherence particularly if cross correlation is the only displacement estimator. We also know from experience that choosing a compressor geometry and boundary restraints that yield a uniform stress field in the medium being imaged reduces decorrelation errors and simplifies the resulting strain patterns. The challenge for designing bioelasticity imaging systems is to control a large number of coupled variables that influence task

[a]Current address: Biomedical Engineering, University of California, One Shields Avenue, Davis, CA 95616. Electronic mail: mfinsana@ucdavis.edu

performance. Yet most of what is known about strain imaging is empirical.

An excellent introduction to signal analysis for motion estimation in bioelasticity imaging is found in the extensive literature on time delay estimation for sonar and radar[31,32] and for blood velocity estimation.[33,34] These works explore velocity and range estimation for spread target, spread velocity situations using wide-band signals (total bandwidths between 20% and 100%). Our study extends the conditions by analyzing wide-band maximum-likelihood estimation of slowly fluctuating (i.e., strain constant over a pulse volume) spread targets that move in a plane or volume.

Specifically, this paper investigates a maximum-likelihood approach to displacement and strain estimation to provide a rigorous strategy for designing and evaluating strain image formation algorithms and instrumentation. The goals are to find principles that guide experimental design and predict error bounds. Our viewpoint is from the traditional time-delay estimation literature where much is known about motion detection, albeit largely in one dimension and without signal decorrelation. We first describe a comprehensive ultrasonic waveform model that includes deformation of the scattering medium consistent with static compression of biological tissues. Second, the concept of coherence is developed for strain imaging. Coherence is at the core of algorithm design and performance assessment. Third, the maximum-likelihood strategy for displacement estimation is developed. Fourth, error bounds for displacement and strain estimates are found, verified with simulation, and compared with phantom experiments. The results are a rigorous framework for future developments of strain imaging using ultrasound.

I. ULTRASONIC WAVEFORM MODEL

We model an ultrasonic echo waveform $r(\mathbf{x})$ as the sum of a random process $\overline{r}(\mathbf{x})$, which we refer to as the noise-free echo signal, and a signal-independent noise process $n(\mathbf{x})$. Each is a function of position (boldface) $\mathbf{x}=(x_1,x_2,x_3)^t$, a vector of Euclidean 3-space. The transpose of $\mathbf{x}$ is indicated by $\mathbf{x}^t$. For incident plane waves and far-field observation, it is well known that the scattered pressure from a random medium is the sum of spherically diverging waves.[35] However, modeling echo signals recorded during a pulse-echo experiment requires that we also include the point-spread function for the imaging system.

A. Echo signals

An echo signal may be described as a function of the scattering amplitude $\Phi(\mathbf{u})$ and pulse-echo transfer function $\tilde{H}(\mathbf{u})$[36] at spatial frequency $\mathbf{u}$,[37]

$$\overline{r}(\mathbf{x})=\mathcal{F}^{-1}\{\tilde{H}(\mathbf{u})\Phi(\mathbf{u})\}, \tag{1}$$

where $\mathcal{F}\{\tilde{h}(\mathbf{x})\}=\tilde{H}(\mathbf{u})$ is the forward 3-D Fourier transform of the pulse-echo point-spread function $\tilde{h}(\mathbf{x})$ and $\mathcal{F}^{-1}\{\tilde{H}(\mathbf{u})\}=\tilde{h}(\mathbf{x})$ is its inverse.

The amount of acoustic energy scattered depends on the microscopic distribution of three coupled tissue properties: mass density $\rho(\mathbf{x})$, bulk compressibility $\kappa(\mathbf{x})$, and specific acoustic impedance $z(\mathbf{x})$. For local plane waves $z(\mathbf{x})=\pm\sqrt{\rho(\mathbf{x})/\kappa(\mathbf{x})}$. Specifically, the scattering amplitude describes a spatial-frequency distribution of scattered energy from the random *spatial fluctuations* in mass density $\Delta\rho(\mathbf{x})/\rho(\mathbf{x})$, compressibility $\Delta\kappa(\mathbf{x})/\kappa_0$, and impedance $\Delta z(\mathbf{x})/z_0$ according to[35,38]

$$\begin{aligned}\Phi(\mathbf{u})&=\pi u_1^2\mathcal{F}\left\{\frac{\Delta\kappa(\mathbf{x})}{\kappa_0}-\frac{\Delta\rho(\mathbf{x})}{\rho(\mathbf{x})}\right\}\\&=-2\pi u_1^2\mathcal{F}\left\{\frac{\Delta z(\mathbf{x})}{z_0}\right\}=\frac{1}{2\pi z_0}\mathcal{F}\left\{\frac{\partial^2 z(\mathbf{x})}{\partial x_1^2}\right\}.\end{aligned} \tag{2}$$

The spatial-frequency component u_1 corresponds to the spatial coordinate parallel to the axis of the ultrasound beam x_1, and κ_0 and z_0 are the spatial averages of the corresponding quantities. To find the final form of Eq. (2), we used the relation $\Delta\kappa(\mathbf{x})/\kappa_0-\Delta\rho(\mathbf{x})/\rho(\mathbf{x})=-2\Delta z(\mathbf{x})/z_0$ and the derivative theorem for Fourier transforms.[39] The equation shows that sound is scattered wherever the second derivative of the acoustic impedance in the direction of the transmitted beam axis is nonzero. Scattering may be considered as a high-pass filter of the object function z, attenuation as a low-pass filter, and the point-spread function as a band-pass filter. Combining Eqs. (1) and (2), we find

$$\begin{aligned}\overline{r}(\mathbf{x})&=\frac{1}{2\pi z_0}\int_{-\infty}^{\infty}d\mathbf{x}'\tilde{h}(\mathbf{x}-\mathbf{x}')\frac{\partial^2 z(\mathbf{x}')}{\partial x_1'^2}\\&=[h\otimes z](\mathbf{x}),\quad \text{where } h(\mathbf{x})\triangleq\frac{1}{2\pi z_0}\frac{\partial^2\tilde{h}(\mathbf{x})}{\partial x_1^2}.\end{aligned} \tag{3}$$

The symbol $\otimes$ denotes 1-D, 2-D, or 3-D convolution depending on the dimension of $\mathbf{x}$. While h is deterministic, z is an ergodic, zero-mean, Gaussian random process.

The final form of Eq. (3) was introduced to strain imaging by Bertrand and colleagues[27,40] to relate the echo signal directly to the impedance distribution. Therein, signals from a deformed scattering medium can be written in terms of the object function $z(\mathbf{x})$ through a coordinate transformation on $\mathbf{x}$. The quantity h is the sensitivity function. It includes the point-spread function of the ultrasound system, but, more precisely, it is the mapping between the object function z and the echo signal $\overline{r}$. Notice that for an ideal imaging system where $\tilde{h}(\mathbf{x})=\delta(\mathbf{x})$, the Dirac delta function, then

$$\overline{r}(\mathbf{x})=\frac{1}{2\pi z_0}\frac{\partial^2 z(\mathbf{x}')}{\partial x_1'^2}\bigg|_{\mathbf{x}'=\mathbf{x}}.$$

B. Object deformation and coordinate transformation

Strain is estimated through a process that correlates ultrasonic waveform segments recorded before and after a static stress field is applied to the medium being imaged. To be able to evaluate strain estimators, we need a model of the ultrasonic waveform that is both accurate and mathematically tractable. An essential component of such a model is the ability to express coordinates of the impedance distribution before deformation, labeled $\tilde{\mathbf{x}}$, in terms of those after deformation, $\mathbf{x}$, viz., $z(\tilde{\mathbf{x}}(\mathbf{x},t_j))$ where

$$\tilde{\mathbf{x}}(\mathbf{x},t_j)=(\tilde{x}_1(x_1,x_2,x_3,t_j),\tilde{x}_2(x_1,x_2,x_3,t_j),$$
$$\tilde{x}_3(x_1,x_2,x_3,t_j))^t,$$

$j=0,1,2,...$, and $\tilde{\mathbf{x}}(\mathbf{x},t_0)=\mathbf{x}$. The time variable denotes the waveform field recorded during the jth compression at time t_j. In this analysis single-compression strain images are studied: t_0 indicates the time of recording for the precompression waveform field and t_1 is the time of recording following the first compression. However, the analysis is easily extended to multicompression techniques. The corresponding waveforms, expressed in the post-compression coordinates $\mathbf{x}$, at each t_j are given by

$$r(\mathbf{x},t_j)=\overline{r_j}(\mathbf{x})+n_j(\mathbf{x})$$
$$=\left[\int_{\mathcal{S}} d\mathbf{x}'\,h(\mathbf{x}-\mathbf{x}')z(\tilde{\mathbf{x}}(\mathbf{x}',t_j))\right]+n_j(\mathbf{x}), \qquad (4)$$

where $\mathcal{S}$ is the region of support as discussed below and defined as usual.[41] Noise processes $n_j(\mathbf{x})$ are signal independent, zero-mean, bandpass white, and Gaussian with power spectral density G_n, i.e.,

$$E\{n^*(\mathbf{x})z(\mathbf{x})\}=0, \quad E\{n(\mathbf{x})\}=0,$$
$$E\{n^*(\mathbf{x})n(\mathbf{x}')\}=G_n\delta(\mathbf{x}-\mathbf{x}'),$$

where n^* is the complex conjugate of n and $E\{\cdots\}$ denotes expectation.[42]

At time t_0, Eq. (4) reduces to $r(\mathbf{x},t_0)=[h\otimes z](\mathbf{x})+n_0(\mathbf{x})$, the pre-compression echo waveform. At t_1, the post-compression acoustic impedance field is described by $z(\tilde{\mathbf{x}}(\mathbf{x},t_1))$ that explicitly relates the pre-compression position of the impedance field $\tilde{\mathbf{x}}$ to the post-compression position $\mathbf{x}$. We refer to the set of radio-frequency (rf) waveforms in a scan plane acquired at frame time t_j as an *echo field*.

An affine mapping between $\tilde{\mathbf{x}}$ and $\mathbf{x}$ is defined by the linear transformation matrix $\mathbf{A}$, the translation vector $\boldsymbol{\tau}_a$, and the equations

$$\begin{aligned}\mathbf{x}(\tilde{\mathbf{x}},t_j)&=\mathbf{A}\tilde{\mathbf{x}}+\mathbf{A}\boldsymbol{\tau}_a\\ \tilde{\mathbf{x}}(\mathbf{x},t_j)&=\mathbf{A}^{-1}\mathbf{x}-\boldsymbol{\tau}_a\end{aligned} \quad \text{for } j\geqslant 0, \qquad (5)$$

where

$$\mathbf{A}=\left(\begin{array}{ccc}\frac{\partial x_1}{\partial\tilde{x}_1} & \frac{\partial x_1}{\partial\tilde{x}_2} & \frac{\partial x_1}{\partial\tilde{x}_3}\\ \frac{\partial x_2}{\partial\tilde{x}_1} & \frac{\partial x_2}{\partial\tilde{x}_2} & \frac{\partial x_2}{\partial\tilde{x}_3}\\ \frac{\partial x_3}{\partial\tilde{x}_1} & \frac{\partial x_3}{\partial\tilde{x}_2} & \frac{\partial x_3}{\partial\tilde{x}_3}\end{array}\right)_{(\mathbf{0},t_j)}, \quad \boldsymbol{\tau}_a=\left(\begin{array}{c}\tau_{a,1}\\ \tau_{a,2}\\ \tau_{a,3}\end{array}\right)_{t_j}. \qquad (6)$$

$\mathbf{A}$ and $\boldsymbol{\tau}_a$ are implicit functions of t_j since the transformation at any $\tilde{\mathbf{x}}$ varies for each level of compression; e.g., at $j=0$, $\boldsymbol{\tau}_a=\mathbf{0}$, and $\mathbf{A}=\mathbf{I}$, the identity matrix. Another example is the deformation of a homogeneous and incompressible (Poisson's ratio $\simeq 0.5$) medium, where the object is uniformly squeezed by a small amount along the x_1-axis. In this case, the deformation may be described as a scaling of the echo coordinates, and $\mathbf{A}$ is diagonal with nonzero elements $A_{11}=1-s$, $A_{22}=A_{33}=1/\sqrt{1-s}\simeq 1+s/2$. If Eqs. (5) and (6) are to accurately represent the effects of strain s, two conditions must be satisfied: the mapping from $\tilde{\mathbf{x}}$ to $\mathbf{x}$ must be linear over $\mathcal{S}$, and the components of the transformation matrix must be linear functions of strain as in the example above. Both conditions are satisfied if the applied deformations are small.

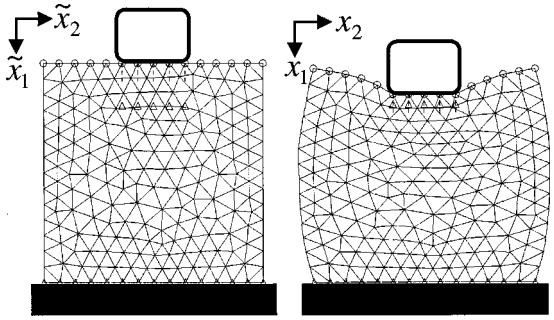

FIG. 1. Deformation of an elastically uniform medium.

Many biological tissues are linear-elastic and incompressible for small deformations.[24] Shear modulus is the material property that describes the deformation of an incremental volume into an equal volume of altered shape. A volume cannot be transformed into a plane, a line, or a point by this operation, so the matrix $\mathbf{A}$ must have rank 3. The mapping from one space to the other is one to one, the inverse $\mathbf{A}^{-1}$ exists, and the Jacobian of the forward transformation, which is the determinant of $\mathbf{A}$, $\det\mathbf{A}$, is nonzero. Furthermore, for incompressible media, $\det\mathbf{A}=1$, which means the volume is conserved. Equation (5) is critical for describing how physical deformation of the object affects coherence between the pre- and post-compression waveforms. In our experience with tissuelike media, deformations are often spatially smooth, particularly over the dimensions of the ultrasonic pulse volume. So the first line of Eq. (5) may be considered a first-order Maclaurin series expansion of $\mathbf{x}(\tilde{\mathbf{x}},t_j)$. It is an accurate approximation of $\mathbf{x}$ in a neighborhood of $\tilde{\mathbf{x}}=\mathbf{0}$. The deformation of a large object region in a strain image may be described by segmenting echo fields into neighborhoods and determining the first-order Maclaurin series for each (Fig. 1).

C. Waveform warping

Our original deformation model was limited to scaling.[43] Large displacement errors were found when using correlation techniques if either of the signals to be cross correlated were scaled relative to the other. To minimize the effects of scaling deformation on displacement estimation, waveforms were compressed and expanded—companded—in one,[30,43] two,[26] or three[44] dimensions prior to correlation. The purpose was to eliminate the scaling component of deformation over the dimensions of the correlation data kernel size and larger. Companding significantly reduces strain noise whenever scaling is the principal deformation.

For more general types of motion, we *warp* the pre-compression echo field prior to cross correlation.[29] Warping may be achieved by applying the transformation $\mathbf{x}(\tilde{\mathbf{x}},t_0)=\mathbf{B}\tilde{\mathbf{x}}+\mathbf{B}\boldsymbol{\tau}_b$ to $r(\tilde{\mathbf{x}},t_0)$ to find $r(\mathbf{B}^{-1}\mathbf{x}-\boldsymbol{\tau}_b,t_0)$. The criterion for selecting $\mathbf{B}$ and $\boldsymbol{\tau}_b$ is that they maximize the magnitude squared coherence function defined in Eq. (12) below. Using the notation of Eq. (5) and the post-compression coordinates

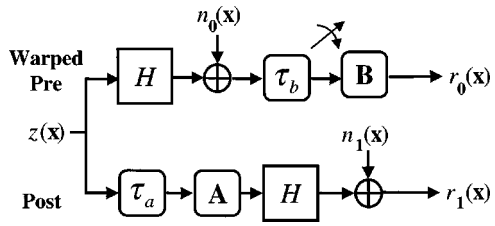

FIG. 2. Ultrasonic waveform model of Eq. (7).

x, the waveforms for single-compression static strain imaging using pulse-echo ultrasound signals, Eq. (4), may be written as

$$
\begin{aligned}
r(\mathbf{x},t_0) &= [h\otimes z](\mathbf{x}) + n_0(\mathbf{x}), && \text{Pre}\\
r_0(\mathbf{x}) &\triangleq r(\mathbf{B}^{-1}\mathbf{x}-\boldsymbol{\tau}_b, t_0),\\
&= \left[\int_{\mathcal{S}} d\mathbf{x}' h(\mathbf{B}^{-1}\mathbf{x}-\boldsymbol{\tau}_b-\mathbf{x}')z(\mathbf{x}')\right]\\
&\quad + n_0(\mathbf{B}^{-1}\mathbf{x}-\boldsymbol{\tau}_b), && \text{Warped Pre}\\
&= \overline{r}_0(\mathbf{x}) + n_0(\mathbf{B}^{-1}\mathbf{x}-\boldsymbol{\tau}_b), && (7)\\
r_1(\mathbf{x}) &\triangleq r(\mathbf{x},t_1)\\
&= \left[\int_{\mathcal{S}} d\mathbf{x}' h(\mathbf{x}-\mathbf{x}')z(\mathbf{A}^{-1}\mathbf{x}'-\boldsymbol{\tau}_a)\right] + n_1(\mathbf{x}), && \text{Post}\\
&= \overline{r}_1(\mathbf{x}) + n_1(\mathbf{x}).
\end{aligned}
$$

Matrix **A** is a linear transformation that describes the physical deformation of the impedance field from a force applied to the object, and **B** is the linear transformation that describes the warp applied to the precompression echo field through signal processing. Eq. (7) is illustrated in Fig. 2.

Warping cannot fully restore lost coherence even for noise-free waveforms. First, the sensitivity function h introduces a null space[45] in which small-scale object deformations cannot be observed using echo waveforms. Consequently, echo formation and object deformation are not commutative operations (Fig. 2). Second, a typical strain image is generated from a plane of echo data. While **A** is given by Eq. (6), **B** has the form

$$
\mathbf{B} = \begin{pmatrix} \dfrac{\partial x_1}{\partial \tilde{x}_1} & \dfrac{\partial x_1}{\partial \tilde{x}_2} & 0\\ \dfrac{\partial x_2}{\partial \tilde{x}_1} & \dfrac{\partial x_2}{\partial \tilde{x}_2} & 0\\ 0 & 0 & 1 \end{pmatrix}, \quad \boldsymbol{\tau}_b = \begin{pmatrix} \tau_{b,1}\\ \tau_{b,2}\\ 0 \end{pmatrix}. \tag{8}
$$

Here too is a null space that reduces coherence in a manner that cannot be recovered by signal processing. The first cause for coherence loss is minimized using highly focused, high bandwidth ultrasound pulses. The second cause is minimized by finely sampling data from a volume instead of a plane or restricting all motion to the scan plane. Nevertheless, we show below that filtering and cross correlating r_0 and r_1 is the maximum-likelihood strategy for estimating displacement. Equation (7) extends our previous 1-D waveform model[46] to three dimensions.

D. Definitions

A few important quantities and relations well known from the literature are stated below without proof and in the notation of this paper.

We assume 2-D echo fields, $r_j(\mathbf{x})$, $j=0,1$, are acquired from the object in a rectangular region defined by the set $\mathcal{S}$ of measure $\mathcal{S}'$.[41] The Fourier series coefficient estimates $\hat{R}_{jk}$ of the 2-D echo field are[47]

$$
\hat{R}_{jk} = \frac{1}{\mathcal{S}'}\int_{\mathcal{S}} d\mathbf{x} r_j(\mathbf{x}) e^{-i2\pi \mathbf{u}_k^t \mathbf{x}}. \tag{9}
$$

Wave vectors $\mathbf{u}_k$ define points on an infinite 2-D grid.[48] For convenience, the two integer indices required to define the grid are lumped into a single index $k=1,\ldots,N$ that enumerates all N frequency points within $\mathcal{S}$.[49] $\hat{R}_{jk}$ is a complex, Gaussian random process because the real waveform $r_j(\mathbf{x})$ is Gaussian.

The Fourier transform of $r_j(\mathbf{x})$ is[47]

$$
R_j(\mathbf{u}) = \lim_{\mathcal{S}'\to\infty} \mathcal{S}'\hat{R}_{jk} = \int_{-\infty}^{\infty} d\mathbf{x} r_j(\mathbf{x}) e^{-i2\pi \mathbf{u}^t \mathbf{x}}, \tag{10}
$$

where **u** is a continuous 2-D spatial frequency variable. It has been shown[50,51] that if the dimensions of the support function are large compared to those of the correlation area in r_j plus the translation $\boldsymbol{\tau}_a$, then the cross power spectral density is

$$
\begin{aligned}
G_{r_0 r_1}(\mathbf{u}_k) &= \mathcal{S}'^2 E\{\hat{R}_{0k}^* \hat{R}_{1k'}\} \xrightarrow[\mathcal{S}',N\to\infty]{} G_{r_0 r_1}(\mathbf{u})\\
&= E\{R_0^*(\mathbf{u}) R_1(\mathbf{u})\}. \qquad (11)
\end{aligned}
$$

If $G_{r_0 r_0}(\mathbf{u})$ and $G_{r_1 r_1}(\mathbf{u})$ are the autospectral densities, then the complex coherence and magnitude squared coherence (MSC) functions are, respectively,

$$
\begin{aligned}
\gamma_{r_0 r_1}(\mathbf{u}) &\triangleq \frac{G_{r_0 r_1}(\mathbf{u})}{\sqrt{G_{r_0 r_0}(\mathbf{u}) G_{r_1 r_1}(\mathbf{u})}},\\
|\gamma_{r_0 r_1}(\mathbf{u})|^2 &= \frac{|G_{r_0 r_1}(\mathbf{u})|^2}{G_{r_0 r_0}(\mathbf{u}) G_{r_1 r_1}(\mathbf{u})},
\end{aligned} \tag{12}
$$

where $0 \leqslant |\gamma_{r_0 r_1}(\mathbf{u})|^2 \leqslant 1$.[52]

Finally, the Fourier transform of a single realization of a scalar random function whose vector coordinates undergo a linear transformation and translation is given by

$$
\mathcal{F}\{z(\mathbf{A}^{-1}\mathbf{x}-\boldsymbol{\tau}_a)\} = \det \mathbf{A} Z(\mathbf{A}^t \mathbf{u}) e^{-i2\pi \mathbf{u}^t \mathbf{A} \boldsymbol{\tau}_a}. \tag{13}
$$

Related results are derived in Appendix A and in Ref. 27.

II. POWER SPECTRAL DENSITY AND COHERENCE

The goal of this section is to express power spectral density functions of the pre- and post-compression waveforms in terms of the signal model of Eq. (7).

A. Cross-spectral density

Assume two-dimensional echo fields are recorded using a linear array transducer. For a rectangular support region $\mathcal{S}$ with dimensions $\mathcal{S}'=T_1T_2$,[41] we find from Eqs. (9) and (11) that

$$E\{\hat{R}_{0k}^{*}\hat{R}_{1k'}\}=\frac{1}{\mathcal{S}'^2}\int_{\mathcal{S}}d\mathbf{x}\int_{\mathcal{S}}d\mathbf{x}'\,\phi_{r_0r_1}(\mathbf{x},\mathbf{x}')\times e^{i2\pi(\mathbf{u}_k^t\mathbf{x}-\mathbf{u}_{k'}^t\mathbf{x}')}. \tag{14}$$

Using Eqs. (45) and (47) from Appendix A and the Wiener–Kinchin theorem,[53] the mean cross correlation function for the echo waveforms is[25]

$$\begin{aligned}\phi_{r_0r_1}(\mathbf{x},\mathbf{x}')&\triangleq E\{r_0^{*}(\mathbf{x})r_1(\mathbf{x}')\}\\&=\det\mathbf{A}\det\mathbf{B}\int_{-\infty}^{\infty}d\boldsymbol{\xi}H(\boldsymbol{\xi})H^{*}(\mathbf{B}^t\boldsymbol{\xi})\\&\quad\times E\{Z(\mathbf{A}^t\boldsymbol{\xi})Z^{*}(\mathbf{B}^t\boldsymbol{\xi})\}\\&\quad\times e^{i2\pi\boldsymbol{\xi}^t(\mathbf{x}'-\mathbf{x}-\mathbf{A}\boldsymbol{\tau}_a+\mathbf{B}\boldsymbol{\tau}_b)}.\end{aligned} \tag{15}$$

Notice that r_0 and r_1 are individually stationary processes but jointly nonstationary. Equations (14) and (15) may be extended to three dimensions to track motion within a scan-volume data set.[44]

Combining Eqs. (14) and (15) and integrating with respect to $\mathbf{x}$ and $\mathbf{x}'$ we find

$$\begin{aligned}E\{\hat{R}_{0k}^{*}\hat{R}_{1k'}\}&=\frac{\det\mathbf{A}\det\mathbf{B}}{\mathcal{S}'}\int_{-\infty}^{\infty}d\boldsymbol{\xi}H(\boldsymbol{\xi})H^{*}(\mathbf{B}^t\boldsymbol{\xi})\\&\quad\times E\{Z(\mathbf{A}^t\boldsymbol{\xi})Z^{*}(\mathbf{B}^t\boldsymbol{\xi})\}e^{-i2\pi\boldsymbol{\xi}^t(\mathbf{A}\boldsymbol{\tau}_a-\mathbf{B}\boldsymbol{\tau}_b)}\\&\quad\times T_1\frac{\sin\pi(\xi_1-u_{1k})T_1}{\pi(\xi_1-u_{1k})T_1}\frac{\sin\pi(\xi_1-u_{1k'})T_1}{\pi(\xi_1-u_{1k'})T_1}\\&\quad\times T_2\frac{\sin\pi(\xi_2-u_{2k})T_2}{\pi(\xi_2-u_{2k})T_2}\frac{\sin\pi(\xi_2-u_{2k'})T_2}{\pi(\xi_2-u_{2k'})T_2}.\end{aligned} \tag{16}$$

Increasing T_1 and T_2 while holding $\mathbf{u}_k$ and $\mathbf{u}_{k'}$ constant yields[54]

$$E\{\hat{R}_{0k}^{*}\hat{R}_{1k'}\}\simeq\begin{cases}\dfrac{\det\mathbf{A}\det\mathbf{B}}{\mathcal{S}'}H(\mathbf{u}_k)H^{*}(\mathbf{B}^t\mathbf{u}_k)E\{Z(\mathbf{A}^t\mathbf{u}_k)Z^{*}(\mathbf{B}^t\mathbf{u}_k)\}e^{-i2\pi\mathbf{u}_k^t(\mathbf{A}\boldsymbol{\tau}_a-\mathbf{B}\boldsymbol{\tau}_b)} & \text{for } k'=k\\ 0 \quad \text{for } k'\neq k\end{cases}. \tag{17}$$

Selection of harmonic frequencies, e.g., $u_{1k}=k/T_1$, is sufficient to ensure that frequency components of the cross-spectral density are orthogonal. The approximation in Eq. (17) approaches an equality as (a) $\mathcal{S}'$ becomes large or the other factors in the integrand do not vary over the frequency interval and (b) the displacement becomes small, specifically, $\tau_{a1}\ll T_1$. Weighting the data with an apodized window function correlates frequency components and can interfere with the orthogonality that must be achieved if data warping followed by cross correlation is to be a maximum-likelihood estimator, as discussed below. The orthogonality condition depends only on properties of the measurement and not the object.

B. Autospectral density

Following the above development, and combining Eqs. (11), (A3), and (A5) yields

$$E\{\hat{R}_{0k}^{*}\hat{R}_{0k'}\}=\begin{cases}\dfrac{(\det\mathbf{B})^2}{\mathcal{S}'}(|H(\mathbf{B}^t\mathbf{u}_k)|^2E\{|Z(\mathbf{B}^t\mathbf{u}_k)|^2\}\\ \quad+E\{|\hat{N}_{0Bk}|^2\}) \quad \text{for } k'=k\\ 0 \quad \text{for } k'\neq k\end{cases},$$

$$E\{\hat{R}_{1k}^{*}\hat{R}_{1k'}\}=\begin{cases}\dfrac{1}{\mathcal{S}'}((\det\mathbf{A})^2|H(\mathbf{u}_k)|^2E\{|Z(\mathbf{A}^t\mathbf{u}_k)|^2\}\\ \quad+E\{|\hat{N}_{1k}|^2\}) \quad \text{for } k'=k\\ 0 \quad \text{for } k'\neq k\end{cases}. \tag{18}$$

For white noise, $E\{|\hat{N}_{0Bk}|^2\}=E\{|\hat{N}_{1k}|^2\}=G_n/\mathcal{S}'^2$. Equations (17) and (18) show that the spectral density functions of the pre- and post-compression echo fields depend on the pulse-echo transfer function of the ultrasonic imaging system via H, the physical deformation via $\mathbf{A}$ and $\boldsymbol{\tau}_a$, and the applied warp via $\mathbf{B}$ and $\boldsymbol{\tau}_b$.

C. Complex coherence

The next section will show the importance of the MSC function for modeling the performance of strain imaging. An expression for MSC is found by substituting Eqs. (17) and (18) into Eq. (12). For a continuous frequency variable, we find

$$|\gamma_{r_0r_1}(\mathbf{u})|^2=\frac{|\gamma_{z_0z_1}(\mathbf{u})|^2\mathrm{SNR}(\mathbf{u})}{1+\mathrm{SNR}(\mathbf{u})}, \tag{19}$$

where

$$|\gamma_{z_0z_1}(\mathbf{u})|^2=\frac{E\{Z(\mathbf{A}^t\mathbf{u})Z^{*}(\mathbf{B}^t\mathbf{u})\}E\{Z^{*}(\mathbf{A}^t\mathbf{u})Z(\mathbf{B}^t\mathbf{u})\}}{E\{|Z(\mathbf{A}^t\mathbf{u})|^2\}E\{|Z(\mathbf{B}^t\mathbf{u})|^2\}} \tag{20}$$

is the MSC for the object function,

$$\mathrm{SNR}(\mathbf{u})\triangleq\frac{S/N_0(\mathbf{u})S/N_1(\mathbf{u})}{1+S/N_0(\mathbf{u})+S/N_1(\mathbf{u})} \tag{21}$$

is the net signal-to-noise ratio,[55] and

$$S/N_0(\mathbf{u}) = \frac{|H(\mathbf{B}^t\mathbf{u})|^2 E\{|Z(\mathbf{B}^t\mathbf{u})|^2\}}{E\{|N_0(\mathbf{B}^t\mathbf{u})|^2\}},$$
$$S/N_1(\mathbf{u}) = \frac{(\det\mathbf{A})^2|H(\mathbf{u})|^2 E\{|Z(\mathbf{A}^t\mathbf{u})|^2\}}{E\{|N_1(\mathbf{u})|^2\}} \tag{22}$$

are channel signal-to-noise ratios corresponding to the warped pre- and post-compression echo waveforms, respectively. The echo waveform MSC is the frequency-space analog to the correlation coefficient. It depends on the object function MSC and SNR($\mathbf{u}$) that includes properties of the imaging system, scattering medium, and noise.

MSC defines the similarity between r_0 and r_1. Intuition tells us that it will be easier to measure displacement if r_0 is similar to r_1, e.g., rigid-body displacement. More intuition about Eq. (19) is found through examples. First, in a simple ideal case, the channel signal-to-noise ratios are large at all frequencies in the bandwidth, $S/N_0 \simeq S/N_1 \gg 1$, and we compress the object a small amount ($<1\%$ of its size) and warp the waveforms accordingly; $\mathbf{A}=\mathbf{B}\simeq\mathbf{I}$. Then SNR($\mathbf{u}$) $\simeq 0.5 S/N_j$ and $|\gamma_{r_0r_1}(\mathbf{u})|^2 \simeq 1$. Low-compression strain images are contrast limited. In a second, more complicated ideal situation, we physically deform the object a substantial amount, say 5% to 10%, to ensure ample strain contrast. Then we apply the perfect warp, i.e., $\mathbf{B}=\mathbf{A}$. In this case, $|\gamma_{z_0z_1}|^2 \simeq 1$ and yet $|\gamma_{r_0r_1}|^2 < 1$ because $S/N_0 \neq S/N_1$ unless all scatterers are resolved by the ultrasonic imaging system such that $|H(\mathbf{B}^t\mathbf{u})|^2 \simeq |H(\mathbf{u})|^2$ over all frequencies for which $|Z(\mathbf{u})|^2$ is nonzero. Unfortunately the bandwidth of the object response is usually much broader than that of the imaging system, and the resulting null space leads to a loss of coherence even for a perfect warp. High-compression strain images are noise limited. Third, if the warp does not match the physical deformation, $\mathbf{B}\neq\mathbf{A}$, then coherence is lost regardless of SNR($\mathbf{u}$) because $|\gamma_{z_0z_1}|^2 < 1$. Ultrasonic attenuation reduces coherence only at frequencies where $S/N_j \not\gg 1$. We show in the next section that accurate displacement estimates require that we design the experiment and image formation algorithm to achieve MSC close to one.

III. MAXIMUM-LIKELIHOOD DISPLACEMENT ESTIMATION

The maximum-likelihood (ML) estimator for displacement selects the estimate $\hat{\boldsymbol{\tau}}$ that maximizes the value of the likelihood function $p(\hat{\mathbf{R}}|\boldsymbol{\theta})$,[56,57] or a monotonic transformation of $p(\hat{\mathbf{R}}|\boldsymbol{\theta})$. $\boldsymbol{\theta}$ is a vector of all unknown real parameters that affect the data, viz., the elements of $\mathbf{A}$, $\mathbf{B}$, $\boldsymbol{\tau}_a$, $\boldsymbol{\tau}_b$, $|H_k|^2$, $E\{|\hat{Z}_{jk}|^2\}$, and $E\{|\hat{N}_{jk}|^2\}$. It is convenient to define the complete data vector $\hat{\mathbf{R}}=(\hat{R}_{01},\hat{R}_{11},\ldots\hat{R}_{0k},\hat{R}_{1k},\ldots\hat{R}_{0N},\hat{R}_{1N})^t$ of length $2N$. It interlaces Fourier-series coefficient pairs from the warped pre- and post-compression echo fields over all N frequencies.[51] Since each value of $\hat{R}_{0k}$ and $\hat{R}_{1k}$ is a complex, Gaussian random variable, the likelihood function is multivariate, complex, and Gaussian in $2N$ dimensions:

$$p(\hat{\mathbf{R}}|\boldsymbol{\theta}) = \frac{\mathcal{S}'^{4N}}{(2\pi)^{2N}\det(\mathbf{Q})}\exp\left(-\frac{\mathcal{S}'^2}{2}\hat{\mathbf{R}}^\dagger\mathbf{Q}^{-1}\hat{\mathbf{R}}\right), \tag{23}$$

where $\hat{\mathbf{R}}^\dagger$ is the complex conjugate transpose (adjoint) of $\hat{\mathbf{R}}$, $E\{\hat{\mathbf{R}}\}=\mathbf{0}$, and

$$\mathbf{Q} \triangleq \mathcal{S}'^2 E\{\hat{\mathbf{R}}\hat{\mathbf{R}}^\dagger\}$$

is a spectral density matrix. The effects on $\hat{\mathbf{R}}$ of object deformation, translation, rotation, and data warping are completely specified by $\mathbf{Q}$.

The $2N\times 2N$ Hermitian matrix $\mathbf{Q}$ may be thought of as an $N\times N$ block-diagonal matrix of 2×2 Hermitian submatrices $\mathbf{Q}_{kk'}$. Since the frequency components are orthogonal, $\mathbf{Q}_{kk'}=\mathbf{Q}_k\delta_{kk'}$, where $\delta_{kk'}$ is the Kroneker delta function, and[50]

$$\mathbf{Q}_k = \begin{pmatrix} G_{r_0r_0}(\mathbf{u}_k) & G^*_{r_0r_1}(\mathbf{u}_k) \\ G_{r_0r_1}(\mathbf{u}_k) & G_{r_1r_1}(\mathbf{u}_k) \end{pmatrix}. \tag{24}$$

Each of the N submatricies $\mathbf{Q}_k=\mathcal{S}'^2E\{\hat{\mathbf{R}}_k\hat{\mathbf{R}}_k^\dagger\}$, where $\hat{\mathbf{R}}_k=(\hat{R}_{0k},\hat{R}_{1k})$, are statistically independent. Also,

$$\det\mathbf{Q}_k = G_{r_0r_0}(\mathbf{u}_k)G_{r_1r_1}(\mathbf{u}_k)(1-|\gamma_{r_0r_1}(\mathbf{u}_k)|^2)$$

and

$$\mathbf{Q}_k^{-1} = \begin{pmatrix} \frac{1}{G_{r_0r_0}(\mathbf{u}_k)} & \frac{-\gamma^*_{r_0r_1}(\mathbf{u}_k)}{\sqrt{G_{r_0r_0}(\mathbf{u}_k)G_{r_1r_1}(\mathbf{u}_k)}} \\ \frac{-\gamma_{r_0r_1}(\mathbf{u}_k)}{\sqrt{G_{r_0r_0}(\mathbf{u}_k)G_{r_1r_1}(\mathbf{u}_k)}} & \frac{1}{G_{r_1r_1}(\mathbf{u}_k)} \end{pmatrix} \times(1-|\gamma_{r_0r_1}(\mathbf{u}_k)|^2)^{-1}. \tag{25}$$

In practice, waveforms always contain noise, so $(1-|\gamma_{r_0r_1}(\mathbf{u}_k)|^2)>0$ and $\mathbf{Q}_k^{-1}$ exists.

The logarithm of the likelihood function is

$$\ln p(\hat{\mathbf{R}}|\boldsymbol{\theta}) = 4N\ln\mathcal{S}' - 2N\ln 2\pi - \ln\det\mathbf{Q} - \frac{\mathcal{S}'^2}{2}\hat{\mathbf{R}}^\dagger\mathbf{Q}^{-1}\hat{\mathbf{R}}. \tag{26}$$

The first three terms of Eq. (26) can be ignored since they are independent of τ_a and weakly dependent on $\mathbf{A}$. Expanding the last term, we find

$$\ln p(\hat{\mathbf{R}}|\boldsymbol{\theta}) \simeq -\frac{\mathcal{S}'^2}{2}\sum_{k=1}^{N}\frac{1}{1-|\gamma_{r_0r_1}(\mathbf{u}_k)|^2}\left[\frac{|\hat{R}_{0k}|^2}{G_{r_0r_0}(\mathbf{u}_k)} + \frac{|\hat{R}_{1k}|^2}{G_{r_1r_1}(\mathbf{u}_k)} - \frac{\hat{R}^*_{0k}\hat{R}_{1k}\gamma^*_{r_0r_1}(\mathbf{u}_k)}{\sqrt{G_{r_0r_0}(\mathbf{u}_k)G_{r_1r_1}(\mathbf{u}_k)}} - \frac{\hat{R}_{0k}\hat{R}^*_{1k}\gamma_{r_0r_1}(\mathbf{u}_k)}{\sqrt{G_{r_0r_0}(\mathbf{u}_k)G_{r_1r_1}(\mathbf{u}_k)}}\right]. \tag{27}$$

Again, the first two terms in the square brackets are weakly dependent on the motion parameters and therefore can be safely ignored for our purposes. The remaining two terms may be written as

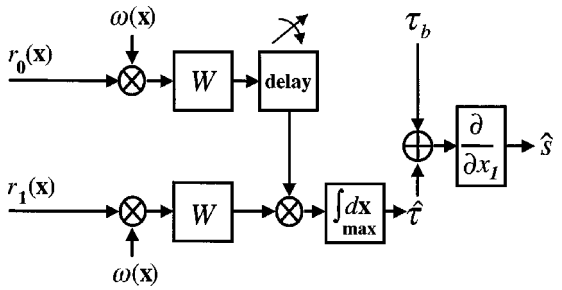

FIG. 3. Generalized cross correlator and strain estimator. The quantity $\omega(\mathbf{x})$ is a window function.

$$\ln p(\hat{\mathbf{R}}|\boldsymbol{\theta}) \simeq \mathcal{S}'^2 \sum_{k=1}^{N} \mathrm{Re}\{\hat{R}_{0k}^* \hat{R}_{1k} W^2(\mathbf{u}_k) \times e^{-i2\pi \mathbf{u}_k^t (\mathbf{A}\boldsymbol{\tau}_a - \mathbf{B}\boldsymbol{\tau}_b)}\}, \tag{28}$$

where $\mathrm{Re}\{\cdots\}$ is the real part of the argument and

$$W^2(\mathbf{u}_k) = \frac{|\gamma_{r_0 r_1}(\mathbf{u}_k)|}{\sqrt{G_{r_0 r_0}(\mathbf{u}_k) G_{r_1 r_1}(\mathbf{u}_k)}(1-|\gamma_{r_0 r_1}(\mathbf{u}_k)|^2)}$$

is a real function of frequency. For large $\mathcal{S}'$, Eq. (11) can be used to express the log-likelihood function of Eq. (28) as an integral over a continuous frequency variable,

$$\ln p(\hat{\mathbf{R}}|\boldsymbol{\theta}) \simeq \mathcal{S}' \int_{-\infty}^{\infty} d\mathbf{u}\, \mathrm{Re}\{R_0^*(\mathbf{u}) R_1(\mathbf{u}) W^2(\mathbf{u}) \times e^{-i2\pi \mathbf{u}^t (\mathbf{A}\boldsymbol{\tau}_a - \mathbf{B}\boldsymbol{\tau}_b)}\}. \tag{29}$$

The first factor in the braces of Eq. (29), $R_0^*(\mathbf{u}) R_1(\mathbf{u})$, is the frequency-space representation of the cross correlation between echo waveforms *for a specific data kernel*. The second factor, $W^2(\mathbf{u})$, is a filter function that weights the Fourier coefficients of the data based on coherence. The third (phase) factor is a function of the physical displacement $\mathbf{A}\boldsymbol{\tau}_a$ and warp displacement $\mathbf{B}\boldsymbol{\tau}_b$. If we write

$$R_0^*(\mathbf{u}) R_1(\mathbf{u}) = \hat{G}_{r_0 r_1}(\mathbf{u}) = |\hat{\gamma}_{r_0 r_1}(\mathbf{u})| e^{i2\pi \mathbf{u}^t \hat{\boldsymbol{\tau}}} \sqrt{G_{r_0 r_0}(\mathbf{u}) G_{r_1 r_1}(\mathbf{u})}, \tag{30}$$

where $G_{r_0 r_1}(\mathbf{u}) = E\{\hat{G}_{r_0 r_1}(\mathbf{u})\}$, then

$$\ln p(\hat{\mathbf{R}}|\boldsymbol{\theta}) \simeq \mathcal{S}' \int_{-\infty}^{\infty} d\mathbf{u} \frac{|\hat{\gamma}_{r_0 r_1}(\mathbf{u})||\gamma_{r_0 r_1}(\mathbf{u})|}{(1-|\gamma_{r_0 r_1}(\mathbf{u})|^2)} \times \mathrm{Re}\{e^{-i2\pi \mathbf{u}^t (\mathbf{A}\boldsymbol{\tau}_a - \mathbf{B}\boldsymbol{\tau}_b - \hat{\boldsymbol{\tau}})}\}. \tag{31}$$

ML estimates of displacement are those that satisfy $\partial \ln p(\hat{\mathbf{R}}|\boldsymbol{\theta})/\partial \hat{\boldsymbol{\tau}} = \mathbf{0}$. Equation (29) is one way to view the ML strategy: (a) Warp the echo fields in a way that maximizes the coherence between r_0 and r_1 (Fig. 2). (b) Increase the relative weighting of frequency components with the highest coherence using W. (c) Cross correlate r_0 and r_1 to find $\hat{\boldsymbol{\tau}}$ at the peak value and add to $\mathbf{B}\boldsymbol{\tau}_b$. Hence, the ML strategy for displacement estimation in acoustic strain imaging (Fig. 3) is consistent with the generalized cross correlator approach described by Knapp and Carter if it is extended to higher spatial dimensions.[25,50] Maximizing waveform coherence also maximizes the peak of the cross correlation function.

The phase factor in Eq. (31) is unity at all frequencies only when the estimate is accurate: $\hat{\boldsymbol{\tau}} + \mathbf{B}\boldsymbol{\tau}_b = \mathbf{A}\boldsymbol{\tau}_a$. Otherwise, motion along all three axes affects displacement estimates along each axis, and the integrand becomes an oscillating function of frequency with decreasing envelope. The oscillations, which are about zero, increase in frequency as $\mathbf{A}\boldsymbol{\tau}_a - \mathbf{B}\boldsymbol{\tau}_b - \hat{\boldsymbol{\tau}}$ deviates further from zero, dramatically reducing the value of the log-likelihood function. The mean log-likelihood function is maximum when $E\{\hat{\boldsymbol{\tau}}\} = \mathbf{A}\boldsymbol{\tau}_a - \mathbf{B}\boldsymbol{\tau}_b = \mathbf{0}$, $\mathbf{A} = \mathbf{B} \simeq \mathbf{I}$, and $\boldsymbol{\tau}_a = \boldsymbol{\tau}_b$, which is also a situation that provides uninteresting strain images. The challenge for medical imaging applications is to achieve maximum-likelihood estimation for displacement in less optimal but more interesting situations.

A. Relationships

The log-likelihood function of Eq. (29) is related to important estimation criteria found in the literature. By beginning the derivation with Fourier coefficients of the data, Eq. (29) becomes the characteristic function of l_r, the classical log-likelihood function defined by Van Trees for zero-mean random signals:[31]

$$\begin{aligned} l_r(\boldsymbol{\theta}) &= \mathcal{F}^{-1}\{\ln p(\hat{\mathbf{R}}|\boldsymbol{\theta})\} \\ &= C \int_{-\infty}^{\infty} d\mathbf{y} \int_{-\infty}^{\infty} d\mathbf{x} \int_{-\infty}^{\infty} d\mathbf{x}'\, \mathrm{Re}\{r_0^*(\mathbf{y}-\mathbf{x}) w(\mathbf{x}) \\ &\quad \times w(-\mathbf{x}') r_1(\mathbf{B}\boldsymbol{\tau}_b - \mathbf{A}\boldsymbol{\tau}_a + \mathbf{y} - \mathbf{x}')\}, \end{aligned} \tag{32}$$

where $w(\mathbf{x}) = \mathcal{F}^{-1}\{W(\mathbf{u})\}$ is a filter function and C is a constant. We can further define

$$r_{0w}(\mathbf{y}) \triangleq \int_{-\infty}^{\infty} d\mathbf{x} r_0(\mathbf{y}-\mathbf{x}) w(\mathbf{x})$$

and

$$r_{1w}(\mathbf{y}) \triangleq \int_{-\infty}^{\infty} d\mathbf{x} r_1(\mathbf{B}\boldsymbol{\tau}_b - \mathbf{A}\boldsymbol{\tau}_a + \mathbf{y} - \mathbf{x}) w(-\mathbf{x})$$

as filtered echo fields, and write Eq. (32) as a wide-band ambiguity function Λ:[58]

$$\Lambda(\mathbf{B}, \boldsymbol{\tau}_b) = \mathrm{Re}\left\{ \int_{-\infty}^{\infty} d\mathbf{y} r_{0w}^*(\mathbf{y}) r_{1w}(\mathbf{y}) \right\}. \tag{33}$$

The view from Eq. (33) is somewhat different from Eq. (29) although the result is the same. Equation (33) suggests we should filter the 2-D echo fields and cross correlate waveforms in the six-dimensional space defined by the motion parameters B_{11}, B_{12}, B_{21}, B_{22}, τ_{b1}, τ_{b2}. The peak value of Λ gives joint ML estimates of the motion parameters such that $\mathbf{B} = \mathbf{A}$ and $\boldsymbol{\tau}_b = \boldsymbol{\tau}_a$.

B. Implementation

Least-squares techniques in elasticity imaging are common,[16,29] but are they consistent with the ML approach? The principal criterion of least-squares algorithms is to mini-

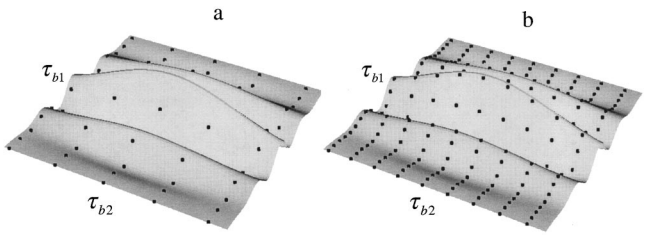

FIG. 4. Sampled ambiguity functions using (a) companding and (b) warping algorithms.

mize a matching energy function E_m. Using the filtered echo waveforms of Eq. (33), we express the matching energy as

$$E_m = \int d\mathbf{x} |r_{0w}^*(\mathbf{x}) - r_{1w}(\mathbf{x})|^2$$
$$= \int d\mathbf{x} |r_{0w}(\mathbf{x})|^2 + \int d\mathbf{x} |r_{1w}(\mathbf{x})|^2$$
$$- 2\,\mathrm{Re}\left\{ \int d\mathbf{x} r_{0w}^*(\mathbf{x}) r_{1w}(\mathbf{x}) \right\}. \quad (34)$$

The first two terms on the right side of Eq. (34) are proportional to the energy in the respective echo fields. In the absence of severe echo decorrelation, for which no algorithm can successfully estimate motion, the energy terms are approximately constant and not of interest. Minimizing the matching energy is equivalent to maximizing the third term—the wide-band ambiguity function of Eq. (33). Consequently, the ML estimator is implemented by the least-squares approach to motion estimation.

The exact ML algorithm for strain imaging would exhaustively search the relevant parameter space of the ambiguity function for the largest peak value, and thus obtain estimates for each motion parameter. Given the model of Eq. (5), there are 2 parameters that define motion in 1-D echo fields,[59] 6 parameters for 2-D echo fields, and 12 parameters for 3-D echo fields. Sampling limitations of echo fields and long computational times are practical considerations that restrict the extent of the search, so we compromise.

For example, the internal motion from a very small compression applied along the transducer beam can be approximated by 1-D translation and scaling. The optimal solution for this motion estimation problem is provided by the wide-band ML estimator for a spread target with constant displacement gradient.[34]

Larger compression produces greater strain contrast, which is desirable, but it also produces larger, more complex motion and hence poses a greater challenge to the algorithm. Normally we impose boundary conditions that confine movement to the scan plane of the linear array transducer. A block matching algorithm is used to measure local displacements in two spatial dimensions, i.e., $\mathbf{B}\boldsymbol{\tau}_b$, for each data segment (Fig. 1). The sampled waveforms are companded and then cross correlated to estimate the residual displacement $\hat{\boldsymbol{\tau}}$.[26] The nature of ultrasonic beamforming using a linear array results in echo fields that are sampled finely along x_1 and coarsely along x_2. The ambiguity function for this situation is illustrated in Fig. 4(a), where τ_{bi} is the displacement estimate along x_i obtained from block matching. Equation (33) for continuous data is represented by the shaded surface. The same values for sampled data are shown as points. In this example, sparse sampling along x_2 leads to an estimation error.

We reduce displacement estimation errors using a warping algorithm that searches for an ambiguity function peak in a sparsely sampled six-parameter space.[29] Our least-squares warping algorithm begins with the same block-matching algorithm used in companding and ends with a perturbation technique that finely tunes the block-matching estimates. Observing the same two parameters of the ambiguity function, we find in Fig. 4(b) that the perturbation component of the algorithm extends the number of sampled points about those determined using block matching. Hence we explain the reduced noise seen with warping versus companding as the consequence of a more thorough sampled ambiguity function in the plane of the displacement vector [Fig. 4(a) versus Fig. 4(b)] and a modest extension of the search to include motion parameters from the coordinate transformation matrix **B** (not shown in Fig. 4).

IV. CRAMÉR–RAO VARIANCE BOUNDS

The log-likelihood function also provides a means for determining a lower bound on estimation variance based on the information available from the data. The link between the two is the Fisher information matrix **J** with components[60]

$$J_{ii'} = -E\left\{ \frac{\partial^2 \ln p(\hat{\mathbf{R}}|\boldsymbol{\theta})}{\partial\theta_i \partial\theta_{i'}} \right\}. \quad (35)$$

The variance of an unbiased estimate $\hat{\theta}_i$ is bounded from below by

$$\mathrm{var}(\hat{\theta}_i) = E\{(\hat{\theta}_i - \theta_i)^2\} \geqslant (\mathbf{J}^{-1})_{ii}. \quad (36)$$

A. Displacement

Applying Eq. (31) to Eqs. (35) and (36) and assuming each displacement is independent of other parameters in $\boldsymbol{\theta}$, the displacement variance about the true value[61] and along x_1 is bounded by

$$\mathrm{var}(\hat{\tau}_1) = E\{(\hat{\tau}_1 - (\mathbf{A}\boldsymbol{\tau}_a - \mathbf{B}\boldsymbol{\tau}_b)_1)^2\}$$
$$\geqslant \frac{A_{12}^2 Y_1 + A_{22}^2 Y_2}{(A_{11}A_{22} - A_{12}A_{21})^2 Y_1 Y_2}. \quad (37)$$

Y_1 and Y_2 are frequency integrals (Appendix B) that summarize the effects of the pulse bandwidth and beam width on displacement variance, respectively.[62] Both are functions of the deformation parameters. Equation (37) is derived in Appendix B for two spatial dimensions where we assume $\boldsymbol{\tau}_a$ and **A** are independent. When the displacement and deformation parameters for 2-D motion are coupled, the size of **J** increases from 2×2 to 6×6, and the variance bound is reduced if information is added. Reduced variance for joint range-velocity estimation has been demonstrated.[31,34]

Equation (37) shows how object deformation and rotation reduce the information content of the echo signals with regard to displacement estimation.

1. Example 1

An incompressible medium is deformed in two dimensions by a scaling transformation, i.e., $A_{11}=A_{22}^{-1}$ and $A_{ij}=A_{ji}=0$. The corresponding variance bound is

$$\mathrm{var}(\hat{\tau}_1)\geqslant\frac{1}{A_{11}^2 Y_1}=\left(2\mathcal{S}'A_{11}^2\int_0^\infty d\mathbf{u}(2\pi u_1)^2\frac{|\gamma_{r_0r_1}(\mathbf{u})|^2}{(1-|\gamma_{r_0r_1}(\mathbf{u})|^2)}\right)^{-1}. \tag{38}$$

The same result was found in one dimension by Knapp and Carter for $A_{11}=1$.[50] Scaling increases the displacement variance directly through the factor A_{11} and indirectly by decreasing the MSC.

2. Example 2

An object is sheared either axially (along x_1) or laterally (along x_2):

$$\mathbf{A}=\begin{pmatrix}1 & A_{12}\\ 0 & 1\end{pmatrix}(\text{axial}) \quad \text{and} \quad \mathbf{A}=\begin{pmatrix}1 & 0\\ A_{21} & 1\end{pmatrix}(\text{lateral}).$$

From Eq. (37) the corresponding variance bounds are

$$\mathrm{var}(\hat{\tau}_1)\geqslant\frac{1}{Y_1}+\frac{A_{12}^2}{Y_2}(\text{axial}) \quad \text{and} \quad \mathrm{var}(\hat{\tau}_1)\geqslant\frac{1}{Y_1}(\text{lateral}). \tag{39}$$

Rotation occurs when $A_{12}=-A_{21}$. Since Y_1 and Y_2 are each functions of $\mathbf{A}$, the relative effects of each motion are not immediately obvious from Eqs. (38) and (39). We did compare variances for axial and lateral shear using simulations,[63] and found that a given amount of axial shear always produces more displacement variance than the same amount of lateral shear.[64] The largest variance for axial shear occurred with the widest ultrasound beam.

For purposes of comparison and illustration, we now examine specific examples of the scaling-only result for 1-D signal and noise sequences that are described by the bandpass white, autospectral density functions

$$G_{\bar{r}_0\bar{r}_0}(u)=G_{\bar{r}_1\bar{r}_1}(u)=G_s\left[\mathrm{rect}\left(\frac{u-u_0}{U_0}\right)+\mathrm{rect}\left(\frac{u+u_0}{U_0}\right)\right]$$

and

$$G_{n_0n_0}(u)=G_{n_1n_1}(u)=G_n\left[\mathrm{rect}\left(\frac{u-u_0}{U_0}\right)+\mathrm{rect}\left(\frac{u+u_0}{U_0}\right)\right]$$

with center frequency u_0, bandwidth U_0, and power spectral densities G_s and G_n. The value of $\mathrm{rect}((u-u_0)/U_0)$ is unity over U_0 that is centered at u_0 and zero elsewhere.

3. Example 3

With no deformation or rotation, $|\gamma_{z_0z_1}(u)|^2=1$ for all u. In addition, assume the channel signal-to-noise ratios are equal and large, $S/N_0(u)=S/N_1(u)=G_s/G_n\gg 1$, so that Eq. (19) gives $\mathrm{SNR}(u)=G_s/2G_n$. Combining Eqs. (19) and (38) we find

$$\mathrm{var}(\hat{\tau}_1)\geqslant\left(4\pi^2\mathcal{S}'\frac{G_s}{2G_n}2\int_{u_0-U_0/2}^{u_0+U_0/2}du u^2\right)^{-1}=\left(4\pi^2\mathcal{S}'\frac{G_s}{G_n}U_0u_0^2\left(1+\frac{U_0^2}{12u_0^2}\right)\right)^{-1},$$

exactly the variance bound found by numerous investigators[65] for passive radar and sonar systems[66] at high SNR and for time-independent time delay. Lacking deformation, this example is a trivial result for strain imaging.

4. Example 4

Given the assumptions above, but allowing the object function to decorrelate because of a scaling deformation, i.e., $|\gamma_{z_0z_1}(u)|^2\leqslant 1$, Eq. (38) reduces to the result of Walker and Trahey [Eq. (20) in Ref. 67]. Converting our notation to theirs, $|\gamma_{z_0z_1}(u)|^2\leftrightarrow\rho^2$, $G_s/G_n\leftrightarrow\mathrm{SNR}^2$, $\mathcal{S}'\leftrightarrow T$, $u_0\leftrightarrow(1/c_0+i\alpha_0/2\pi)2f_0$, and $U_0/u_0\leftrightarrow B$. The two sets of results are compared in Sec. VI below.

The new contribution that Eq. (37) makes to the vast existing literature on time-delay estimation is to reveal how two-dimensional motions in the object couple to increase displacement variance along one direction—that parallel to the ultrasound beam.

B. Strain

If the total displacement vector is $\mathbf{v}=\hat{\boldsymbol{\tau}}+\mathbf{B}\boldsymbol{\tau}_b$, the Eulerian strain tensor is[24]

$$\epsilon_{mn}=\frac{1}{2}\left[\frac{\partial v_n}{\partial x_m}+\frac{\partial v_m}{\partial x_n}\right]$$

and the longitudinal strain along the beam axis is

$$s\triangleq\epsilon_{11}=\frac{\partial v_1}{\partial x_1}. \tag{40}$$

In practice, however, strain is estimated from the difference equation

$$\hat{s}=\frac{v_1^{(2)}-v_1^{(1)}}{\Delta T}, \tag{41}$$

where the superscript numbers in parentheses label the positions of two displacement estimates from waveform segments along the beam that are separated by the axial distance ΔT. By error propagation,

$$\mathrm{var}(\hat{s})=\frac{(\mathrm{var}(\hat{\tau}_1^{(1)})+\mathrm{var}(\hat{\tau}_1^{(2)})-2\,\mathrm{cov}(\hat{\tau}_1^{(1)},\hat{\tau}_1^{(2)}))}{\Delta T^2}\simeq\frac{2\,\mathrm{var}(\hat{\tau}_1)}{T_1\Delta T}. \tag{42}$$

The last form makes use of a conservative approximation for the covariance[68] that was shown to be reasonably accurate.[69] The lower bound on strain error is found by combining Eqs. (37) and (42).

V. METHODS

A. Simulations

We explored the consequences of Eqs. (37) and (42) for strain imaging through the use of 2-D echo waveform simulations. Echo fields from a linear array were generated from their Fourier-domain representations, Eqs. (A3) and (A5). We set $\mathbf{B}=\mathbf{I}$ and $\boldsymbol{\tau}_a=\boldsymbol{\tau}_b=\mathbf{0}$ to isolate the effects of object deformation on displacement variance and to be consistent with the assumptions leading to Eq. (37). Quantities $z(\mathbf{x})$ and $n_j(\mathbf{x})$ were assigned samples of a Gaussian, white random process as given by $\mathcal{N}(0,S/N(\mathbf{u}_0))$ and $\mathcal{N}(0,1)$, respectively. $S/N(\mathbf{u}_0)=100$ (20 dB) for all the data. This object function simulates scattering from a medium with randomly positioned particles, each smaller than the smallest wavelength in the pulse, and with sufficient number density to produce fully developed speckle. The noise function represents electronic fluctuations and quantization errors. The 2-D point-spread function was a Gaussian-modulated sine wave

$$\tilde{h}(\mathbf{x})=(2\pi L_1 L_2)^{-1}\exp\left(-\frac{1}{2}\left(\frac{x_1^2}{L_1^2}+\frac{x_2^2}{L_2^2}\right)\right)\sin(2\pi u_0 x_1).$$

L_1 and L_2 are spatial parameters that determine the pulse length and beam width, respectively. The temporal carrier frequency of the pulse was $u_0 c_0/2=f_0=5$ MHz. The effective temporal bandwidth was computed assuming the expression[70]

$$\frac{\int_0^\infty du_1|\tilde{H}(u_1)|^2}{|\tilde{H}(u_0)|^2}=\frac{c_0}{4\sqrt{\pi}L_1}.$$

Setting $2L_1/c_0=0.1\,\mu$s gave an effective bandwidth of 2.8 MHz (56%). Including the above details into Eq. (A3) yields for two-dimensional data structures

$$R_0(u_1,u_2)=H(u_1,u_2)Z(u_1,u_2)+N_0(u_1,u_2), \tag{43}$$

where

$$H(u_1,u_2)=C' u_1^2 e^{-\alpha}\,\mathrm{sgn}(u_1)e^{-2\pi^2(|u_1|-u_0)^2L_1^2}e^{-2\pi^2u_2^2L_2^2},$$

where u_1 and u_2 are spatial-frequency variables corresponding to x_1 and x_2, respectively, and C' is a complex constant. The attenuation parameter $\alpha=2d\alpha_0|f|/20\log e$ increases linearly with temporal frequency f. The attenuation constant $\alpha_0=0.05\,\mathrm{dB\,mm^{-1}\,MHz^{-1}}$ is valid over a $d=40$ mm depth. The high-pass filtering effects of Rayleigh scattering and low-pass filtering effects of attenuation in Eq. (43) nearly cancel for Gaussian pulses, as shown in Appendix C. Although scattering and attenuation were included in these simulations, they could have been ignored without a significant loss of accuracy.

Pre-compression echo waveforms were computed using $r_0(\mathbf{x})=\mathcal{F}^{-1}\{R_0(\mathbf{u})\}$. The function $\mathrm{sgn}(u_1)=|u_1|/u_1$, $\mathrm{sgn}(0)=0$, ensures that r_0 is analytic. Post-compression echo waveforms were found in a similar manner using Eq. (A5) and the appropriate linear transformation matrix $\mathbf{A}$. Waveforms were oversampled at 400 Msamples/s along the ultrasonic beam axis to minimize errors introduced by sampling. Each waveform in the echo field was simulated assuming a lateral aperture shift of 0.18 mm. Adjacent waveforms were correlated through the Gaussian lateral beam parameter L_2 in Eq. (43) to simulate the experimental measurement conditions described below.

Displacements were measured from 5-μs segments of simulated echo data using cross correlation but *without warping* ($\mathbf{B}=\mathbf{I}$). In each case the displacement was zero ($\boldsymbol{\tau}_a=\mathbf{0}$) and the object deformation, i.e., elements of $\mathbf{A}$, were known.

B. Measurements

We also examined the efficiency of the cross correlator for displacement estimation using phantom measurements.

A 5-MHz linear array (Q2000, 5L45, 60% bandwidth, Siemens Ultrasound, Inc.) was used to scan a graphite-gelatin phantom. In the scan plane, the array was dynamically focused on receive with a constant relative aperture of $f/2$. Perpendicular to the scan plane, the focal properties were fixed at $f/4.5$ and the aperture was 10 mm. The line density of the scan plane was 4.9 A-lines/mm, so the lateral sampling interval was 0.20 mm. Echoes were recorded at 45 Msamples/s for an axial sampling interval of 0.017 mm. Each scan plane spanned approximately 40×40 mm (200 A-lines×2340 samples/A-line) and was centered at a depth of 45 mm. At the 45-mm depth, the measured lateral and elevational beam widths (−6 dB) were 0.7 mm and 1.5 mm, respectively. The correlation coefficient was 0.88 ± 0.03 between adjacent A-lines and 0.63 ± 0.05 between every third A-line.

The phantom was a graphite-gelatin block of dimensions 100 mm×100 mm×74 mm (height).[71] The block was elastically homogeneous on any scale larger than the pulse volume. It was placed on an immovable surface and compressed from above with a rigid plate in which the array transducer was flush mounted. The two side surfaces of the phantom parallel to the scan plane were restrained to prevent motion out of the plane. The remaining two phantom surfaces were free to move. All phantom surfaces were lubricated to encourage free-slip boundary conditions.

The phantom block was warmed to 21 °C, pre-loaded 4% of its 74 mm height under computer control, and electronically scanned to obtain the pre-compression echo field. It was then further compressed, held, and re-scanned at 1.2%, 2.4%, and 3.6% of its pre-loaded height (71 mm). In each case, we selected a sub-region of 50 A-lines×5.7 μs (256 pts) near the center of the echo field where there was minimal lateral motion. The pre- and post-compression waveforms were shifted to remove any time delay ($\boldsymbol{\tau}_b=\boldsymbol{\tau}_a$) but not warped ($\mathbf{B}=\mathbf{I}$). Consequently, $E\{\hat{\tau}_1\}\simeq 0$ and the deformation was predominantly axial scaling with minimal lateral scaling, shearing, or rotation. Displacement was measured for every fourth waveform in the sub-region using cross correlation. The variance $\mathrm{var}(\hat{\tau}_1)$ was computed from 16 uncorrelated echo segments 5.7 μs in duration.

The following displacement variances for simulated and experimental data represent those for unbiased, zero-mean estimates that could result from residual deformation after warping.

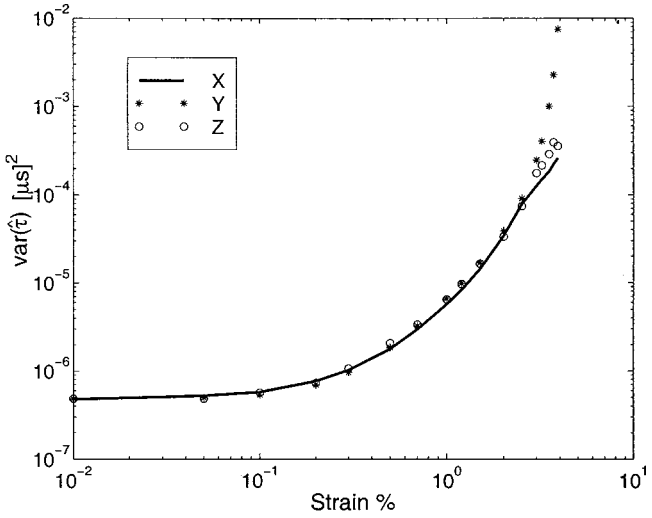

FIG. 5. Predicted displacement variances.

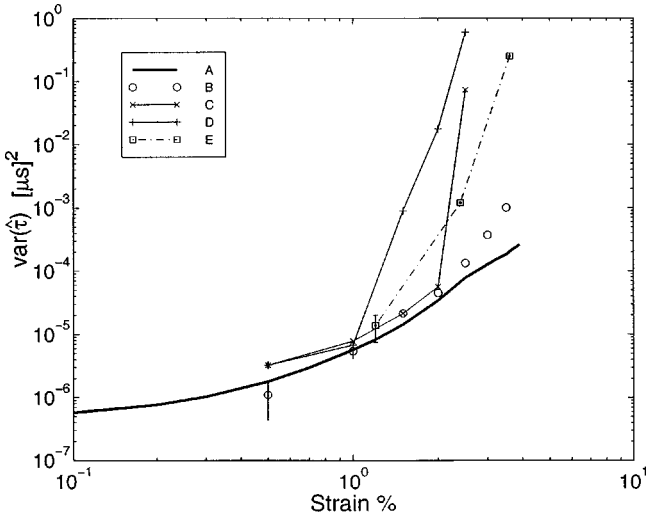

FIG. 6. Predicted versus measured displacement variances (see Sec. VI).

VI. RESULTS AND DISCUSSION

Simulated echo data provide us the means to compute the analytic predictions of Eq. (37) for arbitrary spectra and verify the results for elementary motions. Experimental echo data show us the *efficiency* of the cross correlator for displacement estimation under controlled conditions using tissuelike media and clinical ultrasonic instrumentation.

Figure 5 shows the analytic results for displacement variance as a function of the applied strain up to 4%. Simulated data were used to estimate $|\gamma_{r_0 r_1}(\mathbf{u})|^2$ for each value of applied strain. Results from 200 independent waveforms were averaged to find each point plotted. Because the deformation is limited to scaling, Eq. (38) applies. However, to facilitate comparisons with predictions from the literature, the Y_1 integral was reduced to one dimension, along u_1. Extending the frequency integral in Eq. (38) to two dimensions yields similar curves with slightly greater variances.

The open circles labeled *Z* in Fig. 5 are the results for a flat, band-pass signal spectrum and noise spectrum using Eq. (38). The asterisks labeled *Y* show the results from Walker and Trahey[67] also for flat, band-pass spectra. Values indicated by the solid line marked *X* are the results for a Gaussian echo spectrum and flat, band-pass noise spectrum using Eq. (38). Gaussian signal spectra and flat band-pass noise spectra are representative of those for strain imaging in biological media. As explained in the previous section, the channel signal-to-noise ratios at the center frequency u_0 and the effective bandwidths U_0 for the flat and Gaussian signal spectra were set equal. In general, however, the shape of the signal and noise spectra can influence the curves in Fig. 5 because SNR is a function of frequency. It is a coincidence that the variances for flat and Gaussian signal spectra coincide for realistic system and tissue parameters. The similarity of the results suggests that spectral shape is not a dominant factor determining variance for strain imaging.

The displacement variance at 0.1% strain is an important result. We routinely match scaling components of an applied strain using companding and warping methods to an average of 0.1%. Figure 5 shows that efforts to match **B** to **A** closer than 0.1% will not improve strain image noise since the precision of the cross correlator does not change below 0.1% applied strain. The precision of the cross correlator is highest in this low strain range. Assuming that ± 2 standard deviations of the displacement error is the tolerance for reliable measurements, the smallest measurable displacement at 0.1% applied strain under these typical measurement conditions is $2\sqrt{5.74\times 10^{-7}}\,\mu s^2 = 1.5$ ns or 1.2 μm. With respect to the wavelength at 5 MHz, this is less than 3° of phase!

In Fig. 6, the analytic results for the Gaussian signal spectrum shown as the solid line in Fig. 5 are reproduced as the solid line labeled A. Figure 6 results represented by the open circles labeled B are the displacement variances measured using simulated echo data for axial scaling only, $A_{11} = 1-s$. Agreement with the analytic results is nothing more than verification of programming. Results represented by $\times$labeled C and by+labeled D are variances measured using simulated echo data for axial and lateral scaling, where in C, $A_{11}=1-s$ and $A_{22}=1/2(1-s)$, and in D, $A_{11}=1-s$ and $A_{22}=1/(1-s)$. The former case represents unconstrained motion in a central plane of a homogeneous, incompressible cube. The latter case is similar but includes boundary conditions that prohibit any motion out of the plane. Decoherence from in-plane motion lateral to the beam axis increases the displacement variance by orders of magnitude. Doubling the lateral motion by adding boundary constraints halves the strain at which the sudden increase begins. Because the Cramér–Rao approach describes errors based on the information content of the waveforms, the analytic results are technique independent. Displacement variance increases with aliasing caused by undersampling the data, particularly in nonaxial directions. Aliasing errors are not reflected by Eq. (37), where we assume the data are continuous with large time-bandwidth product. The Cramér–Rao approach establishes the best-possible estimation performance and consequently the standard by which the efficiency of real estimators is measured. Our simulated echo fields were sampled at a rate of 400 Msamples/s to minimize sampling errors. Typical experimental data are sampled at much lower rates, in this case 45 Msamples/s, and interpolated.

Finally, phantom measurements are plotted in Fig. 6 at

the three values of applied strain indicated by the squares and marked E. The most remarkable feature of the experimental results is the relatively high efficiency of cross correlation for displacement estimation with 1.2% strain: The variance measured in a tissuelike phantom is only 30% larger than the lower bound. Using the two-standard deviation criteria discussed above, the data point at 1.2% applied strain shows the precision for displacement to be 7.4 ns or 5.7 μm. The predicted variance was 4.4 μm. This is the first experimental evidence to suggest that cross correlation can be an efficient estimator of ultrasonic displacement in the Cramér–Rao sense when deformation is minimized through warping. Agreement between prediction and measurement was found despite subtle differences in the parameters used to generate analytical results and phantom measurements. For the analysis, the peak frequency was 5 MHz, the bandwidth was 56%, the channel signal-to-noise ratio at the peak frequency was 20 dB, the window length was 5 μs, and the attenuation coefficient slope was 0.5 $\mathrm{dB\,cm^{-1}\,MHz^{-1}}$. For the phantom measurements the peak frequency was 4.2 MHz, the bandwidth was 60%, the channel signal-to-noise ratio at the peak frequency was 17 dB, the window length was 5.7 μs, and the attenuation slope was 0.4 $\mathrm{dB\,cm^{-1}\,MHz^{-1}}$.

VII. SUMMARY

A mathematical model is proposed to describe the ultrasonic waveforms recorded during strain imaging. From this model, the ML strategy for displacement and strain estimation is derived. In addition, a lower bound on displacement variance was found, verified using simulated echo data, and compared with experimental data obtained using a tissuelike phantom.

The ML strategy for image formation is to find the global peak of the ambiguity function. We implement an approximation to the ML strategy by filtering waveforms to favor frequency components with the highest coherence and then warping the pre-compression echo field to match the physical deformation recorded by the post-compression echo field. Finally, warped pre-compression and post-compression waveforms are cross correlated and the net displacement field is differentiated along the direction of the ultrasound beam axis to estimate strain. The ML approach to displacement and strain estimation is consistent with the generalized cross correlator, ambiguity function, and least-squares approaches described in the time-delay literature. It is possible to implement exactly only when the spectral properties of the signal and noise are known and the data are oversampled.

In most practical situations, errors predicted by the Cramér–Rao approach cannot be achieved because the assumptions of continuous echo waveforms and large time-bandwidth products are unrealistic for imaging. This variance bound ignores essential design issues relating noise, spatial resolution and aliasing. Nevertheless, the ML strategy is a rigorous, broad framework for designing systems and algorithms for strain imaging.

ACKNOWLEDGMENTS

The authors gratefully acknowledge helpful discussions with Michel Bertrand, Roch Maurice, Ed Titlebaum, Bill Walker, and Harry Barrett. This work was supported in part by the Whitaker and National Science Foundations BES 9708221.

APPENDIX A

The Fourier transforms of the echo signals $r_1(\mathbf{x})$ and $r_2(\mathbf{x})$ are derived below.

From Eq. (7),

$$r_0(\mathbf{x}) = \overline{r}_0(\mathbf{x}) + n_0(\mathbf{B}^{-1}\mathbf{x} - \boldsymbol{\tau}_b),$$

$$r_1(\mathbf{x}) = \overline{r}_1(\mathbf{x}) + n_1(\mathbf{x}).$$

Therefore,

$$\begin{aligned}
\overline{r}_0(\mathbf{x}) &= \int_{-\infty}^{\infty} d\mathbf{x}'\, h(\mathbf{B}^{-1}\mathbf{x} - \boldsymbol{\tau}_b - \mathbf{x}')\, z(\mathbf{x}') \\
&= \int_{-\infty}^{\infty} d\mathbf{x}' \left[\int_{-\infty}^{\infty} d\boldsymbol{\xi} H(\boldsymbol{\xi}) e^{i2\pi \boldsymbol{\xi}^t (\mathbf{B}^{-1}\mathbf{x} - \boldsymbol{\tau}_b - \mathbf{x}')} \right] \\
&\quad \times \left[\int_{-\infty}^{\infty} d\boldsymbol{\zeta} Z(\boldsymbol{\zeta}) e^{i2\pi \boldsymbol{\zeta}^t \mathbf{x}'} \right], \\
&= \int_{-\infty}^{\infty} d\boldsymbol{\xi} \int_{-\infty}^{\infty} d\boldsymbol{\zeta} H(\boldsymbol{\xi}) Z(\boldsymbol{\zeta}) e^{i2\pi \boldsymbol{\xi}^t (\mathbf{B}^{-1}\mathbf{x} - \boldsymbol{\tau}_b)} \\
&\quad \times \int_{-\infty}^{\infty} d\mathbf{x}' e^{i2\pi (\boldsymbol{\zeta} - \boldsymbol{\xi})^t \mathbf{x}'}.
\end{aligned} \tag{A1}$$

The integral over $\mathbf{x}'$ is $\delta(\boldsymbol{\xi} - \boldsymbol{\zeta})$. Substituting $\mathbf{u}'^t = \boldsymbol{\xi}^t \mathbf{B}^{-1}$ into Eq. (A1) and noting that $d\boldsymbol{\xi} = \det \mathbf{B}\, d\mathbf{u}'$ we find

$$\overline{r}_0(\mathbf{x}) = \det \mathbf{B} \int_{-\infty}^{\infty} d\mathbf{u}' H(\mathbf{B}^t \mathbf{u}') Z(\mathbf{B}^t \mathbf{u}') e^{i2\pi \mathbf{u}'^t (\mathbf{x} - \mathbf{B}\boldsymbol{\tau}_b)}. \tag{A2}$$

The Fourier transform of $\overline{r}_0(\mathbf{x})$ is

$$\begin{aligned}
\overline{R}_0(\mathbf{u}) &= \int_{-\infty}^{\infty} d\mathbf{x} \overline{r}_0(\mathbf{x}) e^{-i2\pi \mathbf{u}^t \mathbf{x}} \\
&= \det \mathbf{B} \int_{-\infty}^{\infty} d\mathbf{u}' H(\mathbf{B}^t \mathbf{u}') Z(\mathbf{B}^t \mathbf{u}') e^{-i2\pi \mathbf{u}'^t \mathbf{B}\boldsymbol{\tau}_b} \\
&\quad \times \int_{-\infty}^{\infty} d\mathbf{x} e^{i2\pi (\mathbf{u}' - \mathbf{u})^t \mathbf{x}} \\
&= \det \mathbf{B} H(\mathbf{B}^t \mathbf{u}) Z(\mathbf{B}^t \mathbf{u}) e^{-i2\pi \mathbf{u}^t \mathbf{B}\boldsymbol{\tau}_b},
\end{aligned}$$

and consequently

$$R_0(\mathbf{u}) = \det \mathbf{B} (H(\mathbf{B}^t \mathbf{u}) Z(\mathbf{B}^t \mathbf{u}) + N_0(\mathbf{B}^t \mathbf{u})) e^{-i2\pi \mathbf{u}^t \mathbf{B}\boldsymbol{\tau}_b}. \tag{A3}$$

Similarly, for $\overline{r}_1(\mathbf{x})$,

$$\overline{r_1}(\mathbf{x}) = \int_{-\infty}^{\infty} d\mathbf{x}' h(\mathbf{x}-\mathbf{x}') z(\mathbf{A}^{-1}\mathbf{x}' - \boldsymbol{\tau}_a)$$
$$= \int_{-\infty}^{\infty} d\mathbf{x}' \left[\int_{-\infty}^{\infty} d\boldsymbol{\xi} H(\boldsymbol{\xi}) e^{i2\pi \boldsymbol{\xi}^t(\mathbf{x}-\mathbf{x}')} \right] \times \left[\int_{-\infty}^{\infty} d\boldsymbol{\zeta} Z(\boldsymbol{\zeta}) e^{i2\pi \boldsymbol{\xi}^t(\mathbf{A}^{-1}\mathbf{x}' - \boldsymbol{\tau}_a)} \right],$$
$$= \int_{-\infty}^{\infty} d\boldsymbol{\xi} \int_{-\infty}^{\infty} d\boldsymbol{\zeta} H(\boldsymbol{\xi}) Z(\boldsymbol{\zeta}) e^{i2\pi(\boldsymbol{\xi}^t\mathbf{x} - \boldsymbol{\zeta}^t\boldsymbol{\tau}_a)} \delta(\boldsymbol{\xi} - \mathbf{A}^{-1t}\boldsymbol{\zeta}),$$
$$= \det \mathbf{A} \int_{-\infty}^{\infty} d\boldsymbol{\xi} H(\boldsymbol{\xi}) Z(\mathbf{A}^t\boldsymbol{\xi}) e^{i2\pi \boldsymbol{\xi}^t(\mathbf{x} - \mathbf{A}\boldsymbol{\tau}_a)}. \quad \text{(A4)}$$

The last form was found by noticing that the delta function is nonzero only at $\boldsymbol{\zeta} = \mathbf{A}^t\boldsymbol{\xi}$ and that $d\boldsymbol{\zeta} = \det \mathbf{A}\, d\boldsymbol{\xi}$. Finally,

$$R_1(\mathbf{u}) = \det \mathbf{A} H(\mathbf{u}) Z(\mathbf{A}^t\mathbf{u}) e^{-i2\pi \mathbf{u}^t \mathbf{A}\boldsymbol{\tau}_a} + N_1(\mathbf{u}). \quad \text{(A5)}$$

Warping the data affects all components of $R_0(\mathbf{u})$ whereas the physical deformation affects only the object function in $R_1(\mathbf{u})$.

APPENDIX B

The Fisher information component that defines the lower bound on displacement variance measured along the ultrasound beam, Eq. (37), is derived below.

We assume the displacements are independent of other parameters in $\boldsymbol{\theta}$, 2-D object motion (plane-strain state), and 2-D data structure (scan plane from a linear array). Then, from Eqs. (31) and (35),

$$-E\left\{ \frac{\partial^2 \ln p(\hat{\mathbf{R}}|\boldsymbol{\tau}_a)}{\partial \tau_{a1}^2} \right\}_{\hat{\boldsymbol{\tau}} = \mathbf{A}\boldsymbol{\tau}_a - \mathbf{B}\boldsymbol{\tau}_b}$$
$$= 4\pi^2 \mathcal{S}' \int_{-\infty}^{\infty} d\mathbf{u} \frac{|\gamma_{r_0 r_1}(\mathbf{u})|^2}{(1-|\gamma_{r_0 r_1}(\mathbf{u})|^2)} (A_{11}u_1 + A_{21}u_2)^2,$$
$$-E\left\{ \frac{\partial^2 \ln p(\hat{\mathbf{R}}|\boldsymbol{\tau}_a)}{\partial \tau_{a2}^2} \right\}_{\hat{\boldsymbol{\tau}} = \mathbf{A}\boldsymbol{\tau}_a - \mathbf{B}\boldsymbol{\tau}_b}$$
$$= 4\pi^2 \mathcal{S}' \int_{-\infty}^{\infty} d\mathbf{u} \frac{|\gamma_{r_0 r_1}(\mathbf{u})|^2}{(1-|\gamma_{r_0 r_1}(\mathbf{u})|^2)} (A_{12}u_1 + A_{22}u_2)^2,$$
$$-E\left\{ \frac{\partial^2 \ln p(\hat{\mathbf{R}}|\boldsymbol{\tau}_a)}{\partial \tau_{a1} \partial \tau_{a2}} \right\}_{\hat{\boldsymbol{\tau}} = \mathbf{A}\boldsymbol{\tau}_a - \mathbf{B}\boldsymbol{\tau}_b}$$
$$= 4\pi^2 \mathcal{S}' \int_{-\infty}^{\infty} d\mathbf{u} \frac{|\gamma_{r_0 r_1}(\mathbf{u})|^2}{(1-|\gamma_{r_0 r_1}(\mathbf{u})|^2)} (A_{11}u_1 + A_{21}u_2) \times (A_{12}u_1 + A_{22}u_2).$$

Completing the squares and integrating, we find that terms linear in frequencies u_1 and u_2 integrate to zero. Factoring the components of $\mathbf{A}$ out of the remaining integrals allows the following simplifications:

$$J_{11} = A_{11}^2 Y_1 + A_{21}^2 Y_2,$$
$$J_{22} = A_{12}^2 Y_1 + A_{22}^2 Y_2,$$
$$J_{12} = J_{21} = A_{11}A_{12}Y_1 + A_{21}A_{22}Y_2,$$

where

$$Y_1 \triangleq 2\mathcal{S}' \int_0^{\infty} d\mathbf{u} (2\pi u_1)^2 \frac{|\gamma_{r_0 r_1}(\mathbf{u})|^2}{(1-|\gamma_{r_0 r_1}(\mathbf{u})|^2)},$$
$$Y_2 \triangleq 2\mathcal{S}' \int_0^{\infty} d\mathbf{u} (2\pi u_2)^2 \frac{|\gamma_{r_0 r_1}(\mathbf{u})|^2}{(1-|\gamma_{r_0 r_1}(\mathbf{u})|^2)}. \quad \text{(B1)}$$

The determinant of the Fisher information matrix is

$$\det \mathbf{J} = (A_{11}A_{22} - A_{12}A_{21})^2 Y_1 Y_2.$$

Finally, we arrive at Eq. (37):

$$\text{var}(\hat{\tau}_1) \geqslant (\mathbf{J}^{-1})_{11} = \frac{A_{12}^2 Y_1 + A_{22}^2 Y_2}{(A_{11}A_{22} - A_{12}A_{21})^2 Y_1 Y_2}.$$

APPENDIX C

We show that the sensitivity function for a Gaussian point-spread function is approximately Gaussian. The function

$$H(f, f_0, \sigma) = C' |f|^m e^{-\alpha} \text{sgn}(f) e^{-2\pi^2 (|f| - f_0)^2 \sigma^2},$$
$$f_0, \sigma, \alpha > 0, \quad \text{(C1)}$$

is a 1-D temporal-frequency representation of the sensitivity function described by Eq. (43). The high-pass factor $|f|^m$ defines the scattering function, where $0 \leqslant m \leqslant 2$, $m = 0$ is for specular reflection, and $m = 2$ is for Rayleigh scattering; the low-pass factor $\exp(-\alpha)$ defines attenuation losses; the remainder represents the point-spread function of a Gaussian-modulated sine wave with center frequency f_0 and pulse duration σ.

We find that

$$H(f, f_1, \sigma_1) = C_1 \text{sgn}(f) e^{-2\pi^2 (|f| - f_1)^2 \sigma_1^2}$$
$$= \lim_{\sigma \to \infty} H(f, f_1, \sigma), \quad \text{(C2)}$$

where the constants

$$C_1 = C' f_1^m e^{-\alpha} e^{-2\pi^2 (f_1 - f_0)^2 \sigma^2},$$
$$f_1 = \frac{-\alpha + 4\pi^2\sigma^2 f_0 + \sqrt{16\pi^2\sigma^2 m + (\alpha - 4\pi^2\sigma^2 f_0)^2}}{8\pi^2\sigma^2},$$

and

$$\sigma_1 = \sigma \frac{f_1^2 e^{-\alpha(f_1 - f_0)} e^{-\alpha^2/8\pi^2\sigma^2} e^{-2\pi^2 (f_1 - f_0)^2 \sigma^2}}{\frac{1}{4\pi^2\sigma^2}\left(1 + \frac{\alpha^2}{4\pi^2\sigma^2}\right) - f_0 \frac{\alpha}{2\pi^2\sigma^2} + f_0^2}.$$

That is, for narrow-band transmission, the sensitivity function is Gaussian with $\sigma_1 \simeq \sigma$ and f_1 given above. It is also a very good approximation for broadband transmission. For example, let $f_0 = 5$ MHz, $\sigma = 0.1$ μs (effective bandwidth $= 2.8$ MHz), $m = 2$, and $\alpha = 2.3$ [$= 0.05$ dB/mm/MHz $\times (2 \times 40$ mm$) \times 5$ MHz$/(20 \log e)$]. We find that $f_1/f_0 = 0.97$, $\sigma_1/\sigma = 1.11$, and $|H(f, f_0, \sigma) - H(f, f_1, \sigma_1|/C_1 < 0.026$. Consequently, we may use a 1-D Gaussian sensitivity function when the 1-D point-spread function is Gaussian without significant error. The situation can be more complicated when modeling the point spread function at higher spatial dimensions.

[1] L. S. Wilson and D. E. Robinson, Ultrason. Imaging **4**, 71 (1982).
[2] R. J. Dickinson and C. R. Hill, Ultrasound Med. Biol. **8**, 263 (1982).
[3] M. Tristam *et al.*, Ultrasound Med. Biol. **12**, 927 (1986).
[4] T. A. Krouskop, D. Dougherty, and S. F. Levinson, J. Rehabil. Res. Dev. **24**, 1 (1987).
[5] K. A. Wear and R. L. Popp, IEEE Trans. Ultrason. Ferroelectr. Freq. Control **34**, 368 (1987).
[6] R. Adler, J. Rubin, P. Bland, and P. Carson, Ultrasound Med. Biol. **16**, 561 (1990).
[7] P. DeJong, T. Arts, A. Hoeks, and R. Reneman, Ultrason. Imaging **12**, 84 (1990).
[8] Y. Yamakoshi, J. Sato, and T. Sato, IEEE Trans. Ultrason. Ferroelectr. Freq. Control **37**, 45 (1990).
[9] R. Lerner, S. Huang, and K. Parker, Ultrasound Med. Biol. **16**, 231 (1990).
[10] I. Céspedes, J. Ophir, H. Ponnekanti, Y. Yazdi, and X. Li, Ultrason. Imaging **15**, 73 (1993).
[11] M. O'Donnell, A. Skovoroda, B. Shapo, and S. Emelianov, IEEE Trans. Ultrason. Ferroelectr. Freq. Control **41**, 314 (1994).
[12] K. Raghavan and A. Yagle, IEEE Trans. Nucl. Sci. **41**, 1639 (1994).
[13] S. Emelianov, A. Skovoroda, M. Lubinski, and M. O'Donnell, Acoust. Imaging **21**, 241 (1995).
[14] C. Sumi, A. Suzuki, and K. Nakayama, IEEE Trans. Biomed. Eng. **42**, 193 (1995).
[15] E. Chen, R. Adler, P. Carson, W. Jenkins, and W. O'Brien, Ultrasound Med. Biol. **21**, 1153 (1995).
[16] F. Kallel and M. Bertrand, IEEE Trans. Med. Imaging **15**, 299 (1996).
[17] M. Fatemi and J. F. Greenleaf, Science **280**, 82 (1998).
[18] K. Nightingale, R. Nightingale, T. J. Hall, and G. E. Trahey, Ultrason. Imaging **20**, 62 (1998) (abstract only).
[19] L. Axel and L. Dougherty, Radiology **171**, 841 (1989).
[20] E. R. McVeigh and E. A. Zerhouni, Radiology **180**, 677 (1991).
[21] R. Muthupillai *et al.*, Science **269**, 1854 (1995).
[22] D. Plewes, I. Betty, S. Urchuk, and I. Soutar, J. Magn. Reson Imaging **5**, 733 (1995).
[23] T. Chenevert, A. Skovoroda, M. O'Donnell, and S. Emelianov, Magn. Reson. Med. **39**, 482 (1998).
[24] Y. Fung, *Biomechanics: Mechanical Properties of Living Tissues*, 2nd ed. (Springer-Verlag, New York, 1993).
[25] C. H. Knapp and G. C. Carter, J. Acoust. Soc. Am. **61**, 1545 (1977).
[26] P. Chaturvedi, M. F. Insana, and T. J. Hall, IEEE Trans. Ultrason. Ferroelectr. Freq. Control **45**, 179 (1998).
[27] R. L. Maurice and M. Bertrand, IEEE Trans. Med. Imaging **18**, 593 (1999).
[28] F. Yeung, S. F. Levinson, D. Fu, and K. J. Parker, IEEE Trans. Med. Imaging **17**, 945 (1998).
[29] Y. Zhu, P. Chaturvedi, and M. F. Insana, Ultrason. Imaging **21**, 127 (1999).
[30] T. Varghese, J. Ophir, and I. Céspedes, Ultrasound Med. Biol. **22**, 1043 (1996).
[31] H. L. VanTrees, *Detection, Estimation and Modulation Theory, Part III* (Wiley, New York, 1971), pp. 9–22, 170–175.
[32] G. C. Carter, *Coherence and Time Delay Estimation* (IEEE Press, Piscataway, NJ, 1993).
[33] M. Azimi and A. C. Kak, Ultrason. Imaging **7**, 1 (1985).
[34] K. W. Ferrara and V. R. Algazi, IEEE Trans. Ultrason. Ferroelectr. Freq. Control **38**, 1 (1991).
[35] P. M. Morse and K. U. Ingard, *Theoretical Acoustics* (McGraw-Hill, New York, 1968), p. 427.
[36] A. Macovski, Proc. IEEE **67**, 484 (1979).
[37] Ordinarily, the magnitude of the spatial frequency variable $u=|\mathbf{u}|$ is $2f/c_0$ in mm^{-1}, where f is the temporal frequency variable in MHz and c_0 is the mean longitudinal sound speed in mm/μs. Only when it is necessary to include acoustic attenuation explicitly in the analysis will we define u as a complex variable: $u=((1/c_0)+i(\alpha_0/2\pi))2f$, where α_0 is an attenuation constant measured in $\mathrm{mm}^{-1}\,\mathrm{MHz}^{-1}$.
[38] M. F. Insana and D. G. Brown, ''Acoustic scattering theory applied to soft biological tissues,'' in *Ultrasonic Scattering in Biological Tissues*, edited by K. K. Shung and G. A. Thieme (CRC Press, Boca Raton, 1993), pp. 75–124.
[39] R. N. Bracewell, *The Fourier Transform and Its Applications*, 2nd ed. (McGraw-Hill, New York, 1978), p. 117.
[40] F. Kallel, M. Bertrand, and J. Meunier, IEEE Trans. Ultrason. Ferroelectr. Freq. Control **41**, 105 (1994).
[41] The set $\mathcal{S}$ is taken to be a Cartesian product of intervals, i.e., $\mathcal{S}=\mathcal{S}_1\times\mathcal{S}_2\times\mathcal{S}_3$, where $\mathcal{S}_i=\{y:-T_i/2\leqslant y\leqslant T_i/2, y\in\Re\}$. With this definition $\mathcal{S}'\triangleq\int_{\mathcal{S}}d\mathbf{x}=T_1T_2T_3$.
[42] Throughout the paper, $E\{\psi\}$ represents $E\{\psi\}_{z,n}=\int dz\, dnp(z,n)\psi$. However, where explicitly noted, expectations are taken over one random variable while holding the others fixed. For example, $\overline{r}(\mathbf{x})=E\{r(\mathbf{x})\}_{n|z}=\int dnp(n|z)r(\mathbf{x})$.
[43] M. Bilgen and M. F. Insana, J. Acoust. Soc. Am. **99**, 3212 (1996).
[44] M. F. Insana, P. Chaturvedi, T. J. Hall, and M. Bilgen, Proc IEEE Ultrason Symp **97CH36118**, 1435 (1997).
[45] H. H. Barrett, J. N. Aarsvold, and T. J. Roney, ''Null functions and eigenfunctions: Tools for the analysis of imaging systems,'' in *Progress in Clinical and Biological Research*, edited by D. Ortendahl and J. Llacer, Vol. 363 (1989 Information Processing in Medical Imaging Conference Proceedings, New York, 1991), pp. 211–226.
[46] M. Bilgen and M. F. Insana, IEEE Trans. Signal Process. **46**, 2589 (1998).
[47] A. Papoulis, *The Fourier Integral and Its Applications* (McGraw-Hill, New York, 1962).
[48] H. H. Barrett, J. L. Denny, R. F. Wagner, and K. J. Myers, J. Opt. Soc. Am. **12**, 834 (1995).
[49] The index k is a function of (k_1,k_2,k_3) such that $k>k'$ implies $|\mathbf{u}_k|\geqslant|\mathbf{u}_{k'}|$. Also, $u_{1k}=k_1/T_1$, $u_{2k}=k_2/T_2$, and $u_{3k}=k_3/T_3$. Since $r_j(\mathbf{x})$ is real, then $\hat{R}_{jk}=\hat{R}^*_{jk'}$ if $\mathbf{u}_k=-\mathbf{u}_{k'}$.
[50] C. H. Knapp and G. C. Carter, IEEE Trans. Acoust. Speech, Signal Process. **24**, 320 (1976).
[51] V. H. MacDonald and P. M. Schultheiss, J. Acoust. Soc. Am. **46**, 37 (1969).
[52] G. C. Carter, C. H. Knapp, and A. H. Nuttall, IEEE Trans. Audio Electroacoust. **21**, 337 (1973).
[53] H. Urkowitz, *Signal Theory and Random Processes* (Artech House, Norwood, MA, 1983).
[54] At $k=k'$, $\int_{-\infty}^{\infty}dx(\sin\pi xT/\pi xT)(\sin\pi xT/\pi xT)=(1/\pi^2T^2)\pi\min\{\pi T,\pi T\}=1/T$. See I. S. Gradshteyn, I. M. Ryzhik, and A. Jeffrey, *Table of Integrals, Series, and Products, 5/e* (Academic, San Diego, 1994), Eq. 3.741.3.
[55] E. Weinstein and A. J. Weiss, IEEE Trans. Acoust. Speech, Signal Process. **32**, 1064 (1984).
[56] S. M. Kay, *Fundamentals of Statistical Signal Processing: Estimation Theory* (PTR Prentice Hall, Englewood Cliffs, NJ, 1993), Chaps. 7 and 15.
[57] J. L. Melsa and D. L. Cohn, *Decision and Estimation Theory* (McGraw-Hill, New York, 1978), pp. 180–182.
[58] Q. Jin, K. M. Wong, and Z.-Q. Luo, IEEE Trans. Signal Process. **43**, 904 (1995).
[59] M. Bilgen, M. F. Insana, and L. T. Cook, Proceedings of the IEEE Symposium Time Frequency and Time Scale Analy (1998), pp. 65–68.
[60] H. L. VanTrees, *Detection, Estimation and Modulation Theory, Part I* (Wiley, New York, 1968).
[61] Displacement estimates are generally biased (Ref. 46). However, by examining the variance of estimates about the true value, which is the case when $\mathbf{A}\simeq\mathbf{B}$ and $\boldsymbol{\tau}_a\simeq\boldsymbol{\tau}_b$, bias may be ignored.
[62] R. N. McDonough and A. D. Whalen, *Detection of Signals in Noise*, 2nd ed. (Academic, San Diego, 1995), pp. 409–422.
[63] M. Bilgen, M. F. Insana, T. J. Hall, and M. Bertrand, Ultrason. Imaging **20**, 60 (1998) (abstract only).
[64] R. L. Maurice and M. Bertrand, IEEE Trans. Ultrason. Ferroelectr. Freq. Control **46**, 584 (1999).
[65] A. H. Quazi, IEEE Trans. Acoust. Speech, Signal Process. **29**, 527 (1981).
[66] Quazi (Ref. 65) defines a *passive* system for localization as one that compares two echo-signal measurements. An *active* system locates targets by matched filtering one echo-signal with the transmitted pulse.
[67] W. F. Walker and G. E. Trahey, IEEE Trans. Ultrason. Ferroelectr. Freq. Control **42**, 301 (1995).
[68] I. Céspedes, M. F. Insana, and J. Ophir, IEEE Trans. Ultrason. Ferroelectr. Freq. Control **42**, 969 (1995).
[69] M. Bilgen, M. F. Insana, T. J. Hall, and P. Chaturvedi, Ultrason. Imaging **19**, 209 (1997).
[70] K. S. Shanmugan and A. M. Breipohl, *Random Signals: Detection, Estimation, and Data Analysis* (Wiley, New York, 1988), pp. 146–148.
[71] T. J. Hall, M. Bilgen, M. F. Insana, and T. A. Krouskop, IEEE Trans. Ultrason. Ferroelectr. Freq. Control **44**, 1355 (1997).

On the mechanoelectrical coupling in the cochlear outer hair cell

Alexander A. Spector[a)]
Department of Biomedical Engineering and Center for Computational Medicine and Biology, Johns Hopkins University, Baltimore, Maryland 21205

(Received 15 February 1999; revised 4 October 1999; accepted 29 November 1999)

Outer hair cell electromotility, a manifestation of the interconnection between the mechanical and electrical processes occurring in outer hair cells, is believed to be an important contribution to the active cochlea. Two modes of mechanoelectrical coupling in the outer hair cell wall are studied: the potential shift caused by mechanical loading under the wall charge preservation conditions and the current (transferred charge) caused by mechanical loading under the voltage-clamp conditions. By using the previously reported elastic moduli of the wall and components of the active force, the potential shift under the charge preservation conditions is derived. This shift is expressed in terms of the wall strains and the active force derivatives with respect to the wall potential. The magnitudes of the potential shift corresponding to the conditions of cell inflation, axial stretch (compression), and the micropipet aspiration are estimated. In the last case, the distribution of the potential shift along the cell wall is also demonstrated. The potential shift can reach -20–-40 mV under the conditions of the micropipet aspiration or cell inflation. Such shift is much smaller under the condition of cell stretch (compression). The current and the charge transfer caused by the cell stretch under the voltage-clamp conditions is analyzed, and shows good agreement of predictions with experimental data. © *2000 Acoustical Society of America.* [S0001-4966(00)02203-7]

PACS numbers: 43.64.Bt, 43.64.Ld, 43.64.Nf [RDF]

INTRODUCTION

Outer hair cells are currently considered the major candidate for the active element in the cochlea providing the ear with the amplification and fine frequency selectivity. The cell activity is related to a specific coupling between the cell's mechanical and electrical characteristics. There are several modes of such coupling. The wall potential changes result in the length changes (electromotility), active force generation, and the transwall charge transport. Mechanical loading of the cell results in the transwall current and the wall capacitance changes. In studying effects of coupling in the outer hair cell wall, we distinguish between the electromechanical effects related to the mechanical responses to changes of the electrical parameters and the mechanoelectrical effects related to reciprocal phenomena.

Iwasa (1994) theoretically predicted effects of the membrane tension on the molecular motor behavior and on the corresponding transwall current and the nonlinear capacitance. Kakehata and Santos-Sacchi (1995) developed experiments demonstrating the effects of the membrane tension under the condition of cell inflation on the transwall current and the nonlinear capacitance peak shift. The same experiment was done by Gale and Ashmore (1994) using the patch-clamp technique. Gale and Ashmore (1994) also developed an experiment under the condition of cell stretch and reported the corresponding current, transferred charge, and nonlinear capacitance. In this case, they observed much smaller changes of the electrical characteristics than under the condition of cell inflation. Tolomeo and Steele (1995) (also, Tolomeo, 1996) analyzed Gale and Ashmore's (1994) experiment from the standpoint of a linear piezoelectric model.

We study an effect that can be considered reciprocal to the charge movement caused by mechanical loading under the voltage-clamp conditions. We analyze here the wall potential shift caused by mechanical loading under the wall charge preservation conditions. Such conditions can be experimentally provided by the current clamp of the cell wall. To estimate the corresponding potential shift, we apply an electroelastic model (Spector, 1999) that includes an equation relating the transferred charge, wall potential, and local strains. Because of relatively small values of the potential shift, we use a linearized version of the model along with the previously reported values of the elastic moduli and the active forces per unit of the potential change (Spector *et al.*, 1998b; Spector, 1999).

We characterize the conditions of the wall under mechanical loading of different modes by using an average strain, and we derive analytical expressions for the potential shift in terms of this parameter. Three modes of mechanical loading are considered, corresponding to cell inflation, cell stretch (compression), and the micropipet aspiration. The coefficients in the expression for the potential shift differ depending on a particular mode of mechanical loading. In the cases of cell inflation and the micropipet aspiration, the potential shift can reach -20–-40 mV for the 10% strain level. The shifts corresponding to stretch, or compression, are much smaller.

In the case of the micropipet aspiration, we also consider the potential shift distribution depending on the location on the cell wall. Here, the potential shift variation is caused by

a)Electronic mail: aspector@bme.jhu.edu

 0001-4966/2000/107(3)/1435/7/$17.00

the nonuniformity of the strains. We present the potential shift distribution along the central cross section of the wall made perpendicular to the cell axis. We show that both the value and sign of the potential shift varies along this cross-section.

The potential shift caused by mechanical loading can be considered a prepulsing before the application of the voltage-clamp technique. Prepulsing is known to shift the nonlinear capacitance distribution in the opposite direction. The obtained direction (sign) of the potential shift, as well as the relative values of these shifts under conditions of cell inflation and stretch, is consistent with the experimental observations of Santos-Sacchi *et al.* (1998) and Gale and Ashmore (1994).

We can hypothesize that the potential shift caused by mechanical loading makes its contribution to the tension effect on the capacitance shift through prepulsing of the cell wall. Therefore, the obtained potential shift can have a dual effect on the nonlinear capacitance. First, it changes the value of the capacitance following a Boltzmann-type dependence for the wall potential. Second, it may contribute to a shift of the whole Boltzmann-type function in the direction opposite to the potential shift.

In addition to the potential shift effect, we consider the process of the charge transport caused by mechanical loading under the voltage-clamp conditions. By using our previous estimates of the parameters of the cell's passive and active behavior, we obtain a range of the transwall current (transferred charge) that corresponds to the condition of cell stretch. We show good agreement of our predictions with the data of Gale and Ashmore (1994) in terms of both the current and the transferred charge. Our predictions also agree with the results of Tolomeo and Steele (1995, 1998) obtained with a different theoretical approach.

I. BASIC RELATIONSHIPS

The full system of constitutive equations for the outer hair cell wall that corresponds to the model of a mechanically linear and electrically nonlinear shell can be presented in the following form:

$$N=[\mathbf{C}]\epsilon+[\mathbf{B}]k+f(E), \tag{1}$$

$$M=[\mathbf{B}]\epsilon+[\mathbf{D}]k, \tag{2}$$

$$d=-f'(E)\epsilon-f_0'(E). \tag{3}$$

Here, N is 3D vector of the resultant forces, M is 3D vector of the bending and twisting moments, ϵ is 3D vector of the strain, k is 3D vector of the curvature change, $[\mathbf{C}]$ is the matrix of the generalized in-plane stiffnesses, $[\mathbf{D}]$ is the matrix of the bending and twisting stiffnesses, and $[\mathbf{B}]$ is the matrix representing mechanical coupling between the bending and in-plane characteristics. Also, in Eqs. (1)–(3), d is the electrical displacement, f is 3D vector of the isometric active force, E is the electric field inside the cell wall, and function f_0' is determined by the cell-wall electrical permittivity. Equations (1)–(3) are valid for arbitrary stress–strain state of the wall.

The presented equations correspond to an advanced version of the shell theory (e.g., Flügge, 1960). A simplified version of the system (1)–(3) where the cross-terms with the matrix $[\mathbf{B}]$ are neglected can be derived on the basis of a thermodynamic potential [electric enthalpy $W(\epsilon,E)$] (Spector, 1999). In that system, the vectors $N(N_x,N_\theta,S)$ and $M(M_x,M_\theta,H)$ have the first two components that are, respectively, the longitudinal and circumferential components of the in-plane resultant force and the longitudinal and circumferential components of the bending moment. The last components of these vectors are given by the equations

$$S=N_{\theta x}=N_{x\theta}-M_{\theta x}/a, \tag{4}$$

$$H=0.5(M_{x\theta}+M_{\theta x}), \tag{5}$$

where $N_{x\theta}$ and $N_{\theta x}$ are the shear components of the resultant force in the x- and θ-cross sections of the wall, and $M_{x\theta}$ and $M_{\theta x}$ are the twisting moments in the same cross sections of the wall.

The cell wall has effective anisotropy determined by the cell cytoskeleton. The cytoskeleton is made of two protein networks inclined at a small angle with respect to the natural $x\theta$ axes. Neglecting the effect of this angle, we assume orthotropy in these axes of the mechanical and electrical properties of the cell. Because of this, we have

$$f_{x\theta}=0,\ \ f_{x\theta}'=0, \tag{6}$$

where $f_{x\theta}$ is the third component of the vector f in Eq. (1).

Below, we consider variations of the wall electric field (wall potential) small enough to linearize the system of constitutive equations at the point of the resting potential. Since the electric field does not create bending effects, electromechanical coupling in constitutive Eqs. (1)–(3) is described by the first (vector) and the last (scalar) equations. Also, the shear component of the resultant force is not affected by the electric field because of the orthotropic properties of the wall [Eq. (6)]. The linearized equations describing electromechanical coupling in the outer hair cell wall take the form

$$N_x=\frac{\partial W}{\partial \epsilon_x}=C_{11}\epsilon_x+C_{12}\epsilon_\theta+f_x'(E_0)(E-E_0), \tag{7}$$

$$N_\theta=\frac{\partial W}{\partial \epsilon_\theta}=C_{12}\epsilon_x+C_{22}\epsilon_\theta+f_\theta'(E_0)(E-E_0), \tag{8}$$

$$-d=\frac{\partial W}{\partial E}=f_x'(E_0)\epsilon_x+f_\theta'(E_0)\epsilon_\theta+f_0''(E_0)(E-E_0). \tag{9}$$

This form of the constitutive relations is equivalent to the common form of equations for linear piezoelectric plates where the C-, f_x'-, and f_θ'-, and f_0''-coefficients represent, respectively, the elastic, piezoelectric, and dielectric properties of the cell wall (e.g., Tiersten, 1969).

The last coefficient on the right-hand side of Eq. (9) can be interpreted as

$$f_0''(E_0)=-eh, \tag{10}$$

where e is the wall capacitance determined under zero-strain conditions, and h is the wall thickness. The outer hair cell-wall capacitance is the sum of a linear capacitance independent of the wall potential and a nonlinear capacitance that

depends on the wall potential and has a typical bell shape (Gale and Ashmore, 1994; Kakehata and Santos-Sacchi, 1995). The linearization of the original equations is done at the point of the resting potential. This means that the total (nonlinear) capacitance in Eq. (10) corresponds to the point of the resting potential. Below, we discuss an example where we compare the results obtained after linearization with those computed on the basis of the variable capacitance.

The full matrix of the system (7)–(9)

$$[\mathbf{T}]=\begin{bmatrix} C_{11} & C_{12} & f'_x(E_0) \\ C_{12} & C_{22} & f'_\theta(E_0) \\ f'_x(E_0) & f'_\theta(E_0) & f''_0(E_0) \end{bmatrix}, \tag{11}$$

is symmetric. The system (7)–(9) is conservative with the potential equal to the quadratic part of W. The original nonlinear system is also conservative with the potential W. These properties provide the effectiveness of the application of numerical methods to both the linearized and original systems.

Now, we concentrate on Eq. (9). We consider two cases: the voltage-clamp conditions ($\Delta\Psi=0$) and the wall charge preservation conditions ($d=0$). Taking into account the relationship between the electric field E and the wall potential variation $\Delta\Psi$

$$E=-\frac{\Delta\Psi}{h}, \tag{12}$$

and using the coefficients

$$e_x=\frac{df_x}{d\Delta\Psi}, \quad e_\theta=\frac{df_\theta}{d\Delta\Psi}, \tag{13}$$

the voltage-clamp conditions are described by the following equation for the surface density of the transferred charge expressed in terms of the mechanical strains:

$$\frac{d}{h}=\frac{dQ}{dS}=e_x\epsilon_x+e_\theta\epsilon_\theta. \tag{14}$$

The surface density of the corresponding current that is determined by the strain rates can be written in the following form:

$$\frac{di}{dS}=\frac{d^2Q}{dS\,dt}=e_x\frac{d\epsilon_x}{dt}+e_\theta\frac{d\epsilon_\theta}{dt}. \tag{15}$$

If we assume the wall charge preservation, then the potential shift caused by mechanical loading of the cell is determined by the equation

$$\Delta\Psi=-(e_x\epsilon_x+e_\theta\epsilon_\theta)/e. \tag{16}$$

To compare the potential shift due to different modes of mechanical loading, we use a universal strain parameter

$$\epsilon^*=(\epsilon_x^2+\epsilon_\theta^2)^{1/2}. \tag{17}$$

Note that the $\epsilon_{x\theta}$ component does not enter the ϵ^* parameter because this component does not affect the potential shift.

II. POTENTIAL SHIFT CAUSED BY MECHANICAL LOADING

A. Cell inflation

We consider the wall potential shift under the condition of cell inflation. Experimentally, additional fluid delivered via the micropipet is used to inflate the cell (Iwasa and Chadwick, 1992). The physical reason for the potential shift is additional turgor pressure created in the cell wall. The additional pressure causes the longitudinal and circumferential strains determined by the cell length and radius changes. A similar effect can be achieved by changing the concentration of the solution outside the cell (Chertoff and Brownell, 1994; Ratnanather *et al.*, 1996) or by other types of mechanical or electrical stimulation of the cell. In the case under consideration, Eq. (16) can be rewritten in the form

$$\Delta\Psi=-[e_x\epsilon_x(p)+e_\theta\epsilon_\theta(p)]/e, \tag{18}$$

where p is inflation (additional) pressure.

The strain components entering the right-hand side of Eq. (18) can be expressed in terms of the universal strain by using the equations of equilibrium

$$C_{11}\epsilon_x+C_{12}\epsilon_\theta=0.5pa, \tag{19}$$

$$C_{12}\epsilon_x+C_{22}\epsilon_\theta=pa, \tag{20}$$

where a is the cell radius. From Eqs. (19) and (20), we derive

$$\epsilon_x=-(1+\alpha^2)^{-0.5}\epsilon^*, \quad \epsilon_\theta=\alpha(1+\alpha^2)^{-0.5}\epsilon^*, \tag{21}$$

where

$$\alpha=\frac{2C_{11}-C_{12}}{2C_{12}-C_{22}}. \tag{22}$$

We substitute the passive in-plane moduli and the coefficients of the active force e_x and e_θ (Spector *et al.*, 1998b; Spector, 1999). We treat the fraction (22) by using the asymptotic representations of the ratios C_{11}/C_{22} and C_{12}/C_{22} (Spector *et al.*, 1999). As a result, we obtain the following expression for the potential shift under the condition of cell inflation:

$$\Delta\Psi=-0.23\epsilon^*. \tag{23}$$

B. Axial loading

The conditions of cell axial loading are provided by applying to the cell a force along the cell axis. In experiments in isolated cells, these conditions are achieved by application to one end of the cell of either an elastic fiber compressing the cell (Holley and Ashmore, 1988; Hallworth, 1997) or a micropipet stretching the cell (Iwasa and Adachi, 1997). In both cases the second end of the cell is held by another micropipet. Under *in vivo* conditions, the outer hair cell is located between the reticular lamina and basilar membrane, and the major component of mechanical loading is axial loading. The direct result of axial loading of the cylindrical outer hair cell is the cell-length change. Because of incompressibility of the liquid core inside the cell, the length changes are accompanied by corresponding radius changes. Under the condition of cell axial loading, the expression for the wall potential shift takes the form

$$\Delta\Psi = -(e_x\epsilon_x + e_\theta\epsilon_\theta) = -(e_x - 0.5e_\theta)\frac{\epsilon_x}{e}. \tag{24}$$

In Eq. (24), the volume preservation condition is taken into account. In the case of cell stretch, we obtain

$$\epsilon^* = (\epsilon_x^2 + \epsilon_\theta^2)^{1/2} = 1.12\epsilon_x. \tag{25}$$

In the case of cell compression, the right-hand side in (25) has the opposite sign. By substituting this relationship along with our previous estimates of the coefficients e_x and e_θ, we obtain

$$\Delta\Psi = -0.034\epsilon^* \tag{26}$$

for cell stretch, and

$$\Delta\Psi = 0.034\epsilon^* \tag{27}$$

for cell compression.

C. Micropipet aspiration

In the micropipet aspiration experiment (Sit *et al.*, 1997), aspiration pressure is applied to the cell wall via the micropipet attached normally to the cell-wall side surface. As a result, a portion of the cell wall is aspirated inside the micropipet, and its height, measured in the experiment, characterizes the level of the strains corresponding to the applied pressure. Under the condition of the micropipet aspiration, the strain field is not uniform and varies from point to point. The same is true for the potential shift. The nonuniformity of the strain along the cell wall also accompanies *in vivo* conditions. This is because of the specialized geometry of the organ of Corti where outer hair cells are inclined both longitudinally and radially with respect to the basilar membrane (Ulfendahl, 1997). Such inclination results in moments that bend the cell and create nonuniform strains in its wall. Thus, it might generate nonuniformity of the cell-wall potential under physiological conditions. Halter *et al.* (1997) also discussed the nonuniformity of the outer hair cell-wall potential, a nonuniformity caused by purely electrical properties of the cell wall.

For wall potential shift under the condition of the micropipet aspiration experiment, we have the following expression:

$$\Delta\Psi = -\left[\frac{e_x}{e}\epsilon_x(x,\theta,\Delta p) + \frac{e_\theta}{e}\epsilon_\theta(x,\theta,\Delta p)\right], \tag{28}$$

where Δp is aspiration pressure. We first consider a characteristic value of the potential shift having in mind a comparison of the shifts corresponding to different modes of the mechanical load. Then, we consider the potential shift distribution along the cell wall.

As a reference value, we choose $\Delta\Psi(0,0,\Delta p)$. This value corresponds to the potential shift at the cross section of the cell surface and the micropipet axis. Under the condition of the micropipet aspiration, the circumferential component of the strain is the major one (see the Appendix)

$$\epsilon_\theta \gg \epsilon_x. \tag{29}$$

Therefore, the expression for the potential shift takes the form

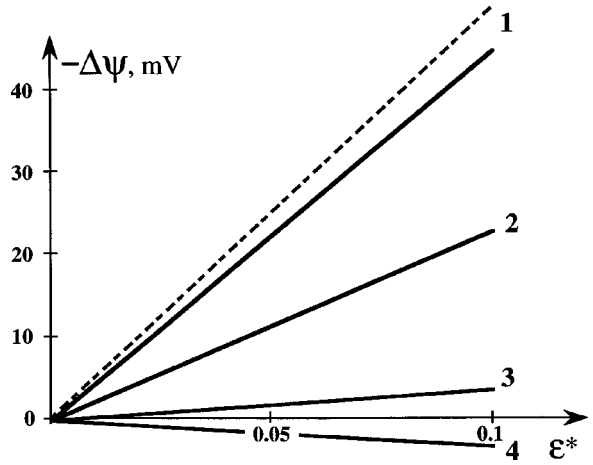

FIG. 1. Outer hair cell-wall potential shift vs characteristic strain under conditions of mechanical loading of different modes. 1—micropipet aspiration (solid line—capacitance estimated at the resting potential, dashed line—variable capacitance), 2—cell inflation, 3—cell stretch, and 4—cell compression.

$$\Delta\Psi = -\frac{e_\theta}{e}\epsilon^*. \tag{30}$$

Substituting our estimate of the e_θ coefficient, we obtain

$$\Delta\Psi = -0.45\epsilon^*. \tag{31}$$

For comparison purposes, we plot Eqs. (23), (26), (27), and (31) in Fig. 1 where cases 1–4 correspond, respectively, to the micropipet aspiration, inflation, stretch, and compression modes of the cell mechanical loading. For each of these four conditions, the local potential shift is determined by the local two-component strain field. The relative values of the two components of the strain and their signs can result in different values of the potential shift that correspond to the same overall level of the strains in the wall. For example, in the case of axial loading of the cell, two strain components cancel out their effects on the potential shift, and it results in relatively low values of the potential shift. For cell compression and cell stretch (Fig. 1), the absolute values of the shift are the same, but their signs are opposite because of the corresponding strains.

We also consider the micropipet aspiration experiment, where the potential shift is the most significant among the four considered conditions, from the standpoint of the accuracy of the linearization of the function f_0'. Such linearization results in the use of the nonlinear and total capacitances calculated at the point of the resting potential. In Fig. 1, we give the additional graph (dashed line) that was developed on the basis of the nonlinear function f_0'. The corresponding equation for the potential shift under the condition of the micropipet aspiration was solved numerically. The small difference between the two functions confirms the accuracy of the linearization approach.

We discuss now the distribution of the potential shifts along the cell. To show the variation of the potential shift, we choose the central cross section of the cell perpendicular to its axis. In this case, we have

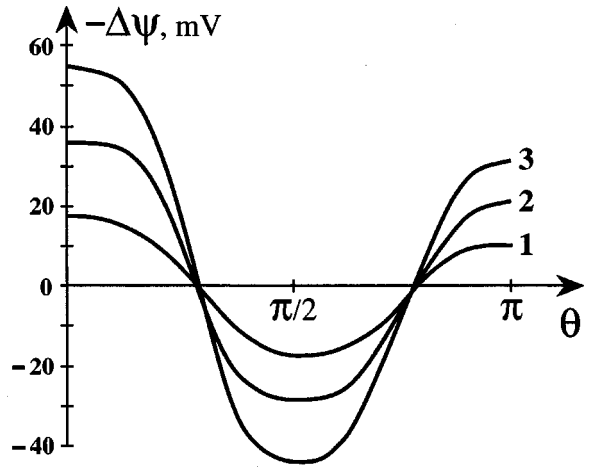

FIG. 2. Distributions of the potential shifts along the central cross section of outer hair cell (because of the symmetry, one half of the cross section is considered) under the condition of the micropipet aspiration (1—$\epsilon^*=4\%$, 2—$\epsilon^*=8\%$, and 3—$\epsilon^*=12\%$).

$$\Delta\Psi(\theta)=-\frac{e_\theta}{e}\epsilon_\theta(\theta,\Delta p). \tag{32}$$

It can be shown (see the Appendix) that under the micropipet aspiration condition the circumferential component ϵ_θ of the strain is proportional to the normal component w of the displacement. Spector *et al.* (1998a) obtained the following expression for the w-component:

$$w(\theta)=A(a_2\cos 2\theta+a_3\cos 3\theta+a_4\cos 4\theta), \tag{33}$$

where

$$a_2\approx 0.118, \quad a_3\approx 0.031, \quad a_4\approx 0.0014, \tag{34}$$

and A is a constant depending on the wall properties and dimensions of the micropipet. Because of the proportionality between ϵ_θ and w, and taking into account our definition of ϵ^* for this case, we obtain

$$\epsilon_\theta(\theta)=\frac{\epsilon^*}{a_2+a_3+a_4}(a_2\cos 2\theta+a_3\cos 3\theta + a_4\cos 4\theta). \tag{35}$$

From this equation, we find the following expression for the potential shift along the central cross section of the cell:

$$\Delta\Psi=-\frac{e_\theta\epsilon^*}{e(a_2+a_3+a_4)}(a_2\cos 2\theta+a_3\cos 3\theta + a_4\cos 4\theta). \tag{36}$$

This function is plotted in Fig. 2 for three values of the strain parameter ϵ^*.

In the micropipet aspiration experiment, the strains are localized around the miropipet, whereas with the other considered conditions, the strains are uniform and accompanied by the corresponding length and radius changes.

III. ANALYSIS OF THE CURRENT CAUSED BY MECHANICAL LOADING UNDER THE VOLTAGE-CLAMP CONDITIONS

We consider a phenomenon reciprocal to the potential shift under conditions of the wall charge preservation. We analyze now the current caused by mechanical loading under the voltage-clamp conditions. Data on this effect are provided by the experiment with cell stretch (Gale and Ashmore, 1994). This experiment was done under conditions of the cell's axial displacement applied stepwise. The corresponding high (but finite) strain rate and the transient current were reported as functions of time. We make our predictions in terms of both the current and the charge transferred during the transient period and compare them with experimental data.

We use Eq. (15), take into account the volume preservation condition, and assume that the current is uniform along the cell surface. Equation (15) can be rewritten in the following form:

$$i\Big/\left(S\frac{d\epsilon_x}{dt}\right)=e_x-0.5e_\theta, \tag{37}$$

where i is the total current through the cell wall. Similarly, Eq. (14) can be interpreted as

$$Q/(S\epsilon)=e_x-0.5e_\theta, \tag{38}$$

where Q is the total charge transferred during the transient period.

The right-hand side in (37) and (38) is small with respect to e_x and e_θ. For an accurate estimate, we use the following representation (Spector *et al.*, 1999):

$$e_x-0.5e_\theta=-\frac{\xi_a L}{\pi a C_{22}}\frac{d\epsilon_x^a}{d\Delta\Psi}. \tag{39}$$

Here, ξ_a is the axial stiffness of the cell, L is the cell length, and ϵ_a is the longitudinal component of the electromotile strain. From Santos-Sacchi's (1992) data on electromotility, the derivative on the right-hand side of Eq. (34) can be estimated as

$$\frac{d\epsilon_x^a}{d\Delta\Psi}=-0.3V^{-1}. \tag{40}$$

We use the following range (Holley and Ashmore, 1988; Russell and Schauz, 1995; Ulfendahl *et al.*, 1998) for the cell axial stiffness:

$$\gamma_a=\frac{\xi_a L}{\pi a C_{22}}=(1-3)\times 10^{-3}. \tag{41}$$

Taking this range into account, we obtain the estimate

$$e_x-0.5e_\theta=(0.3-0.9)\times 10^{-3}\ \text{N/Vm}. \tag{42}$$

We substitute this estimate along with the value of the surface area for a 45-μ-long cell and obtain a range for the left-hand side in Eq. (39) [and for the right-hand side in Eqs. (37) and (38)]. This range is presented in Table I (column 1). In columns 2 and 3 are estimates of the left-hand-side expression in Eq. (39) based on the coefficients obtained in Tolomeo and Steele (1995) and (1998), respectively. Gale

TABLE I. Characteristics (N/Vm) of mechanoelectrical coupling under conditions of cell inflation voltage clamp. Theoretical results are expressed in terms of $e_x - 0.5e_\theta$ [Eqs. (37) and (38), right-hand side]. Experimental data are given in terms of peak current [Eq. (37), left-hand side] and transferred charge [Eq. (38), left-hand side].

Theoretical prediction (present paper)	Theoretical prediction[a]	Theoretical prediction[b]	Experiment[c] (based on peak current)	Experiment[c] (based on transferred charge)
$(0.3-0.9)\times10^{-3}$	0.35×10^{-3}	0.8×10^{-3}	0.9×10^{-3}	0.41×10^{-3}

[a]Tolomeo and Steele (1995).
[b]Tolomeo and Steele (1998).
[c]Gale and Ashmore (1994).

and Ashmore (1994) presented experimental values of the peak current vs the strain rate. We give in column 4 the left-hand side of Eq. (37) expressed in terms of the experimental peak current. We use the time course of the Gale and Ashmore (1994) experiment to estimate the total transferred charge. With this estimate, we calculate the left-hand side in Eq. (38) and present it in column 5 of the table.

IV. DISCUSSION

The effect of the outer hair cell-wall potential shift might be important for cell functioning. Equations (27) and (31) show that this shift can reach $-(20--40)$ mV for the 10% strain level, a significant level for the cell-wall nonlinear capacitance that depends on the wall potential. By using the voltage-dependent nonlinear capacitance (Gale and Ashmore, 1994; Kakehata and Santos-Sacchi, 1995), it can be shown that the corresponding change reaches 25%. The potential shift discussed earlier corresponds to the conditions of the wall charge preservation. This condition means that there is no charge flux out of or in the cell wall, but the movement of the charges inside the wall is not restricted. To provide such conditions perfectly, the currents out of and in the cell have to be clamped. However, under the action of a purely mechanical load, these conditions can be reasonably assumed. There are a number of experiments (e.g., Holley and Ashmore, 1988; Hallworth, 1997; Sit *et al.*, 1997) in which the cell is under mechanical load of different modes, and no restrictions are imposed on the wall potential. The total wall charge preservation can be assumed for these experiments.

The capacitance that enters Eq. (14) corresponds to zero-strain conditions. Such capacitance can be either determined directly on the basis of an experiment under isometric conditions or derived from zero-stress capacitance. Given the complicated relationship between the wall capacitance and the wall stresses (Iwasa, 1994; Kakehata and Santos-Sacchi, 1995), neither zero-strain nor zero-stress conditions are provided in the available experiments (Housley and Ahsmore, 1992; Gale and Ashmore, 1994; Kakehata and Santos-Sacchi, 1995). Because of this, we use the values of Gale and Ashmore (1994) that are reasonably close to other data (Housley and Ashmore, 1992; Kakehata and Santos-Sacchi, 1995).

The magnitude of the cell-wall potential shift can be directly measured under the conditions of the current clamp. We discuss below some indirect experimental confirmations of the potential shift effect. If a purely mechanical load is applied to the outer hair cell, and after this the voltage clamp is used, then the initial potential shift can be interpreted as a prepulsing of the cell wall. Santos-Sacchi *et al.* (1998) showed that prepulsing causes a shift of the whole nonlinear capacitance curve in the direction opposite to prepulsing. Therefore, based on our predictions, we can expect that the capacitance curve shifts in the depolarization direction under the condition of cell inflation or stretch. In addition, we can expect the shift corresponding to the cell-stretch condition to be much smaller than that for the cell-inflation condition. This expectation is consistent with the experimental data of Kakehata and Santos-Sacchi (1995) and Gale and Ashmore (1994) with cell inflation and cell stretch. Note that prepulsing even considered within a broad range can cause a smaller shift of the capacitance curve than that caused by cell inflation (Santos-Sacchi *et al.*, 1998; Kakehata and Santos-Sacchi, 1995). Therefore, the effect of the wall potential shift can be a component of the total effect of the mechanical stress on the electrical characteristics (nonlinear capacitance) of the cell wall.

Our analysis of the current (transferred charge) under the voltage-clamp conditions agrees with experimental data (Table I). The experimental result of Gale and Ashmore (1994) expressed in terms of the peak current (column 4) coincides with the upper bound of our range (column 1). The experimental result of Gale and Ashmore (1994) expressed in terms of the total transferred charge (column 5) is close to the middle point of our range. Our data are also consistent with the predictions of Tolomeo and Steele (1995, 1998) (columns 2 and 3) that were based on a different theoretical approach. Tolomeo (1996) gave a prediction that was about 50% higher than our upper bound (Table I, column 1) for the ratio given on the left-hand side of Eq. (39). Tolomeo (1996) represented this ratio in terms of the wall compliance (but not stiffness) coefficients. The discrepancy can be explained by the high sensitivity of the stiffness and compliance coefficients obtained as a result of treatment of several independent experiments.

The phenomenon of the outer hair cell-wall potential shift, discussed in the present paper, is important to the cell's performance *in vivo*. Here, such shifts are determined under different modes of strains and for the extreme case of zero current in or out of the cell. Similar analysis can be developed when the current [left-hand side in Eq. (9)] is prescribed, and a strain field is generated in the cell wall. Such a case mimics the *in vivo* conditions when the cell-wall potential is established as a result of the receptor current and strains caused by mechanical forces in the organ of Corti. Another conclusion important to the understanding of *in vivo* conditions is that the resulting potential can be nonuniform along the cell, reflecting the nonuniformity of the strain field in the cell wall.

ACKNOWLEDGMENTS

The work was supported by Research Grant Nos. KO1 AG00732, from the National Institute on Aging, and RO1 DCO2775, from National Institute on Deafness and other

Communication Disorders. The author thanks Dr. Popel, Dr. Brownell, and Dr. Raphael for stimulating discussions and comments.

APPENDIX

We derive here some estimates used in our analysis of the potential shift under the conditions of the micropipet experiment. These estimates are based on the asymptotic analysis in terms of the small parameter $\epsilon = h^2/12a^2$ used by Spector *et al.* (1998a). The strain components ϵ_x and ϵ_θ are related to the displacement components u, v, and w by the following equations:

$$\epsilon_x = \frac{\partial u}{\partial x}, \quad \epsilon_\theta = \frac{w}{a} + \frac{\partial v}{a\partial\theta}. \tag{A1}$$

In the Spector *et al.* (1998a) analysis, the strain and displacement components were expressed in terms of a potential function Φ and expanded in Fourier series in terms of the θ coordinate. For Fourier coefficients (denoted by n superscript) of the w and v components of the displacement, we have the following estimates (Spector *et al.*, 1998a):

$$\frac{w^n}{a} = \left[A_{22}\frac{\partial^4}{\partial x^4} + \frac{2A_{12}+A_{66}}{a^2}\frac{\partial^4}{\partial x^2\partial\theta^2} + A_{11}\frac{\partial^4}{\partial\theta^4}\right]\Phi^n \sim A_{11}\frac{\partial^4}{\partial\theta^4}\Phi^n \sim C_3, \tag{A2}$$

$$\frac{\partial v^n}{a\partial\theta} = \left[\frac{A_{11}}{a^5} - \frac{A_{66}+A_{12}}{a^2}\frac{\partial^3}{\partial\theta\partial x^2}\right]\Phi^n \sim A_{11}\frac{\partial^4}{\partial^4\theta}\Phi^n \sim C_3. \tag{A3}$$

Here, the A coefficients are the components of the compliance matrix. The Fourier coefficient of the Ψ function is expressed by the formula

$$\Phi^n = -C_1 g_1(x) + C_2 g_2(x) - C_3 g_3(x) + C_4 g_4(x). \tag{A4}$$

The eigenfunctions g_1, g_2, g_3, and g_4 are given in Spector *et al.* (1998a).

From the estimates (A2) and (A3), it follows that two terms in the representation of ϵ_θ are asymptotically equal to each other. Therefore, the strain component ϵ_θ is proportional to the displacement component w.

The longitudinal component of the strain can be estimated as

$$\epsilon_x^n = \frac{\partial u^n}{\partial x} = \left[\frac{A_{12}}{a}\frac{\partial^4}{\partial x^4} - \frac{n^2 A_{11}}{a^3}\frac{\partial^2}{\partial x^2}\right]\Phi^n \sim \epsilon^{0.5} C_3. \tag{A5}$$

From Eq. (A5), we obtain

$$\epsilon_x \ll \epsilon_\theta. \tag{A6}$$

Chertoff, M. E., and Brownell, W. E. (**1993**). ''Characterization of outer hair cell turgor,'' Am. J. Physiol. **266**, 467–479.

Flügge, W. (**1960**). *Stresses in Shells* (Springer, Berlin).

Gale, J. E., and Ashmore, J. F. (**1994**). ''Charge displacement induced by rapid stretch in the basolateral membrane of the guinea-pig outer hair cell,'' Proc. R. Soc. London, Ser. B **255**, 243–249.

Hallworth, R. (**1997**). ''Modulation of OHC force generation and stiffness by agents known to affect hearing,'' in *Diversity in Auditory Mechanics*, edited by E. R. Lewis, G. R. Long, R. F. Lyon, P. M. Narins, C. R. Steele, and E. Hecht-Poinar (World Scientific, Singapore), pp. 524–530.

Halter, J. A., Kruger, R. P., Yium, M. J., and Brownell, W. E. (**1997**). ''The influence of the subsurface cisterna on the electrical properties of the outer hair cell,'' NeuroReport **8**, 2517–2521.

Holley, M. C., and Ashmore, J. F. (**1988**). ''A cytoskeletal spring in cochlear outer hair cell,'' Nature (London) **335**, 635–637.

Housley, G. D., and Ashmore, J. F. (**1992**). ''Ionic currents of outer hair cells isolated from the guinea-pig cochlea,'' J. Physiol. (London) **448**, 73–98.

Iwasa, K. H. (**1994**). ''A membrane motor model for the fast motility of the outer hair cell,'' J. Acoust. Soc. Am. **94**, 2216–2224.

Iwasa, K. H., and Adachi, M. (**1997**). ''Force generation in the outer hair cell of the cochlea,'' Biophys. J. **73**, 546–555.

Iwasa, K. H., and Chadwick, R. S. (**1992**). ''Elasticity and active force generation of cochlear outer hair cells,'' J. Acoust. Soc. Am. **92**, 3169–3173.

Kakehata, S., and Santos-Sacchi, J. (**1995**). ''Membrane tension directly shifts voltage dependence of outer hair cell motility and associated gating charge,'' Biophys. J. **68**, 2190–2197.

Ratnanather, J. T., Zhi, M., Brownell, W. E., and Popel, A. S. (**1996**). ''The ratio of elastic moduli of cochlear outer hair cell derived from osmotic experiment,'' J. Acoust. Soc. Am. **99**, 1025–1028.

Russell, I. J., and Schauz, C. (**1995**). ''Salicylate ototoxicity: Effects on the stiffness and electromotility of outer hair cells isolated from the guinea pig cochlea,'' Aud. Neurosci. **1**, 309–320.

Santos-Sacchi, J. (**1992**). ''On the frequency limit and phase of outer hair cell motility: effects of the membrane filter,'' J. Neurosci. **12**, 1906–1916.

Santos-Sacchi, J., Kakehata, S., and Takahashi, S. (**1998**). ''Membrane potential affects the voltage dependence of motility related gating charge in the outer hair cell,'' J. Physiol. (London) **510.1**, 225–235.

Sit, S. P., Spector, A. A., Lue, A. J.-C., Popel, A. S., and Brownell, W. E. (**1997**). ''Micropipet aspiration of the outer hair cell lateral wall,'' Biophys. J. **72**, 2812–2819.

Spector, A. A. (**1999**). ''A nonlinear electroelastic model of the cochlear outer hair cell,'' in *Applied Mechanics in the Americas*, edited by P. B. Gonçalves, I. Jasiuk, D. Pamplona, C. Steele, H. I. Weber, and L. Bevilacqua (American Academy of Mechanics, Rio de Janeiro, Brazil), Vol. 6, pp. 19–22.

Spector, A. A., Brownell, W. E., and Popel, A. S. (**1999**). ''Nonlinear active force generation by cochlear outer hair cell,'' J. Acoust. Soc. Am. **105**, 2414–2420.

Spector, A. A., Brownell, W. E., and Popel, A. S. (**1998a**). ''Analysis of the micropipet experiment with the anisotropic outer hair cell wall,'' J. Acoust. Soc. Am. **103**, 1001–1006.

Spector, A. A., Brownell, W. E., and Popel, A. S. (**1998b**). ''Estimation of elastic moduli and bending stiffness of the anisotropic outer hair cell wall,'' J. Acoust. Soc. Am. **103**, 1007–1011.

Tiersten H. F. (**1969**). *Linear Piezoelectric Plate Vibrations* (Plenum, New York).

Tolomeo, J. A. (**1996**). ''Models of the Structure and Motility of the Auditory Outer Hair Cell,'' Ph.D. thesis, Stanford University.

Tolomeo, J. A., and Steele, C. R. (**1995**). ''Orthotropic properties of cochlear outer hair cell wall,'' J. Acoust. Soc. Am. **97**, 3006–3011.

Tolomeo, J. A., and Steele, C. R. (**1998**). ''A dynamic model of outer hair cell motility including intracellular and extracellular fluid viscosity,'' J. Acoust. Soc. Am. **103**, 524–534.

Ulfendahl, M. (**1997**). ''Mechanical responses of the mammalian cochlea,'' Prog. Neurobiol. (Oxford) **53**, 331–380.

Ulfendahl, M., Chan, E., McConnaughey, W. B., Prost-Domansky, S., and Elson, E. L. (**1998**). ''Axial and transverse stiffness measures of cochlear outer hair cells suggests a common mechanical basis,'' Pflügers Arch-Eur. J. Physiol. **436**, 9–15.

Frequency characteristics of sound transmission in middle ears from Norwegian cattle, and the effect of static pressure differences across the tympanic membrane and the footplate

Magne Kringlebotn
Norwegian University of Science and Technology, Department of Physics, N-7491 Trondheim, Norway

(Received 2 July 1999; revised 16 November 1999; accepted 19 November 1999)

For 23 cadaver ears from Norwegian cattle, frequency characteristics for the round-window volume displacement relative to the sound pressure at the eardrum have been measured, and are compared to earlier results for human ears [M. Kringlebotn and T. Gundersen, J. Acoust. Soc. Am. **77**(1), 159–164 (1985)]. For human as well as for cattle ears, mean amplitude curves have peaks at about 0.7 kHz. At lower frequencies, the mean amplitude for cattle ears is about 5 dB smaller than for human ears. The amplitude curves cross at about 2 kHz, and toward higher frequencies the amplitude for cattle ears becomes increasingly larger. If amplitude curves are roughly approximated by straight lines above 1 kHz, the slope for cattle ears is about -5 dB/octave as compared to about -15 dB/octave for human ears. The phase of the round-window volume displacement lags behind the phase of the sound pressure at the tympanic membrane. The phase lag is close to zero below 0.2 kHz, but increases to about 3.5π at 20 kHz for cattle ears, as compared to less than 2π for human ears. Further investigations are needed in order to explain the observed differences. Sound transmission in the ear decreases with an increasing static pressure difference across the tympanic membrane, especially at frequencies below 1 kHz, where pressure differences of 10 and 60 cm water cause mean transmission losses of about 10 and 26 dB, respectively, the losses being somewhat larger for overpressures than for underpressures in the ear canal. At higher frequencies, the transmission losses are smaller. For small overpressures, and in a limited frequency range near 3 kHz, even some transmission enhancement may occur. Static pressure variations in the inner ear have only a minor influence on sound transmission. Static pressures relative to the middle ear in the range 0–60 cm water cause mean sound transmission losses less than 5 dB below 1 kHz, and negligible losses at higher frequencies.
[S0001-4966(00)05602-2]

PACS numbers: 43.64.Bt, 43.64.Ha [BLM]

INTRODUCTION

The middle-ear frequency characteristics of human cadaver ears have been measured by various investigators (Gundersen, 1971; Kringlebotn and Gundersen, 1985; Vlaming and Feenstra, 1986; Gyo *et al.*, 1987; Brenkman *et al.*, 1987; overview in Goode *et al.*, 1989), and for cat ears by Guinan and Peake (1967).

The purpose of the present investigation is to expand our knowledge about the frequency characteristics of sound transmission in different mammalian ears. The frequency characteristics will be measured for various static pressures across the tympanic membrane and the footplate. Cadaver ears from Norwegian cattle have been used, because of their size, robustness, and availability. Size and robustness are about as for human ears.

The observed differences in frequency characteristics for human and cattle ears may be a key to a better understanding of the acoustomechanical functioning of the ear, and will be of special interest in connection with middle-ear models. A model for the middle ear should be able to mimic the frequency characteristics of different mammalian ears just by adjusting the model parameters. If a successful model is obtained, e.g., for the cattle ear, it should therefore be applicable also to the human ear.

It is well known that the tympanic membrane works most efficiently, i.e., with an optimum sound transmission, when there is no static pressure across it. A common experience is a feeling of pressure in the middle ear when the atmospheric pressure is changed, accompanied by a degraded hearing sensitivity. The same effects may be caused by the slow absorption of air in the middle-ear cavity. Normally, the Eustachian tube opens and permits a pressure equalization. But if the Eustachian tube for some reason is blocked, large and even painful pressure differences may build up.

Is sound transmission in the ear also affected by a static pressure in the inner ear? Lempert *et al.* (1949) found that pressures up to 68 cm of water applied to the perilymph, in no instance gave any effect upon the cochlear potentials for pure tones in the monkey. For human ears, Békésy (1960a) observed no change in sound transmission as the internal pressure in the cochlea was continuously increased until just before the inner ear started to drip.

On the other hand, in experiments performed on cat ears, and for a constant 100-Hz sound pressure at the stapes, Lynch *et al.* (1982) found about 20 dB loss in cochlear potential when a static pressure difference of only 20 cm water was applied across the stapes footplate. But it should be emphasized that this result was obtained for sound input to the

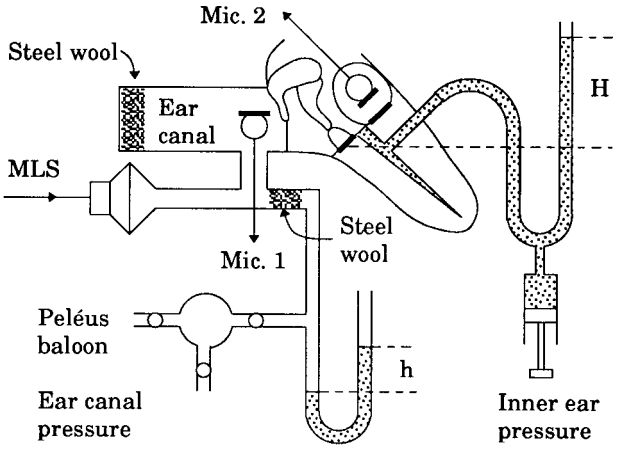

FIG. 1. Experimental setup for measuring the frequency characteristics of the volume displacement in the round window relative to the sound pressure at the tympanic membrane, for varying static pressure differences across the tympanic membrane and the stapes footplate.

oval window and with a disarticulated incudo-stapedial joint, and not for sound input to the tympanic membrane.

METHOD

Applying cement to the ear bone

To cement tubes to the ear bone, coating tissue is first sufficiently removed from the contact area which is carefully dried with absorbing paper towel. To improve attachment, some Loctite 401 (Manufacturer: Loctite Corporation, Dublin, Ireland) is applied, and the tube is then cemented to the bone by means of plastic padding elastic (Manufacturer: AB Hisingeplast, Gøteborg, Sweden). Plastic padding elastic hardens in about 10 min, or even faster if a larger than normal amount of hardener is used. In order to block the openings of the perilymphatic duct and the inner ear meatus, only a careful drying of the surrounding tissue and some Loctite is needed before the openings are coated with cement.

Measuring the middle-ear frequency characteristics

The experimental setup is shown schematically in Fig. 1, and permits measurement of sound transmission in the ear for varying static pressure differences across the tympanic membrane and the stapes footplate. The opening of the ear canal is closed with steel wool and covered with cement. The steel wool reduces the sound-pressure variations in the ear canal due to standing waves. A hole to the ear canal is drilled in front of the eardrum. A glass tube is cemented to the hole, and connected to a loudspeaker. Microphone 1 is directed toward the eardrum through an arm of the glass tube, and measures the input sound pressure about 2 mm in front of the eardrum. The microphone cable is made airtight by means of silicon and fits airtightly into an access tube arm not shown in Fig. 1. Microphone 2 measures the output sound pressure in a small enclosure cemented to the round window. The enclosure includes a small microphone adapter made of aluminum and with a 1-mm diameter hole. The microphone input tube fits exactly into this hole, so that the sound pressure in the air-filled enclosure is exposed to the microphone. The microphones are small electret microphones with built-in amplifiers (Knowles Type 3046).

The volume of the enclosure around the round-window membrane is of the order of 30 mm^3. When approximated by a sphere, its diameter will be of the order 4 mm and small compared to the wavelength in the audible range (the wavelength at 20 kHz is 17 mm). In air at 0 °C, the density is $\rho_o = 1.293\,kg/m^3$ and the velocity of sound $c_o = 331.3\,m/s$. The acoustic compliance for the enclosed air volume V at standard atmospheric pressure and arbitrary temperature is

$$C = \frac{V}{\rho_0 c_0^2}, \tag{1}$$

corresponding to an acoustic impedance, as seen by the round-window membrane,

$$Z_e = \frac{1}{j\omega C}, \tag{2}$$

where ω is the angular frequency. The measured frequency characteristics of the middle ear are not influenced by this impedance, because it is very small, about $4.7T\Omega/\omega$ (SI-units), as compared to the input impedance at the human oval window including the stapes, which at low frequencies is about $326T\Omega/\omega$, and larger at higher frequencies (Merchant *et al.*, 1996). Preliminary measurements of the acoustic input impedance at the oval window in Norwegian cattle indicate that it is of the same order of magnitude as in human ears.

If p is the sound pressure in the enclosed air volume V, the volume displacement S of the round-window membrane will be given by

$$S = \frac{p/Z_e}{j\omega} = pC = p\frac{V}{\rho_0 c_0^2}. \tag{3}$$

Relative to the sound pressure p_d at the eardrum,

$$\left|\frac{S}{p_d}\right|(\mathrm{dB}\ \ re\ \ 10^{-6}\mathrm{mm^3/Pa}) = 20\log\left(\frac{V}{0.142}\right) + \left|\frac{p}{p_d}\right|(\mathrm{dB}). \tag{4}$$

Correspondingly, the relative phase is given by

$$\arg\left(\frac{S}{p_d}\right) = \arg\left(\frac{p}{p_d}\right). \tag{5}$$

The static pressure in the air tight ear canal, relative to the atmospheric pressure in the open middle ear, is regulated to negative and positive values by means of a Peléus balloon (a small rubber balloon having three inlet/outlet sphere valves), and is measured by a water-filled manometer. The pressure is given by the level difference h. The opening of the tube arm to the manometer is filled with steel wool, in order to reduce the effect of standing waves.

The static pressure in the inner ear is regulated through the endolymphatic duct by means of a water-filled syringe, and is measured by another manometer. The resulting pressure difference across the stapes footplate is given by the water level H, relative to the height level of the oval window. The connection to the endolymphatic duct is made in the following way. The endolymphatic sac is cut close to the

opening of the duct. A small steel tube is guided into the sac and cemented to the bone. It is important to avoid blocking of the tube by air bubbles, or by tissue pressed against its inner opening. Water from a syringe is therefore sprayed into the tube so that air bubbles are driven out and replaced by water. A male syringe cone terminates the steel tube opening, and is connected to a female syringe cone at the opening of a silicon tube to the manometer. The applied static pressure is communicated to the scala media, but due to the yielding Reissner's membrane, the static pressure will be constant in the whole inner ear. Only overpressures were used here.

The perilymphatic duct in cattle ears is narrow and long as in humans. In cases where the inner-ear static pressure is varied, leaks through the perilymphatic duct are avoided by covering the opening with cement.

A computer that simultaneously generates and analyzes MLS (maximum length sequence) signals is used to derive the middle-ear transfer function from microphone 1 to microphone 2. The computer is equipped with a suitable soundcard (Fiji from Turtle Beach Systems, Inc.), and software (WinMLS, Morset Sound Development, Trondheim, Norway). The microphone signals are fed via measuring amplifiers (B&K Type 2606 and 2610) to the two line inputs of the sound card.

The MLS signal from the computer is fed to the loudspeaker via an equalizer and an amplifier, and from the loudspeaker via the glass tube to the ear canal. In order to improve the signal-to-noise ratio, the equalizer is adjusted until a fairly flat spectrum is obtained for the eardrum microphone MLS signal. The overall sound-pressure level for the MLS spectrum at the eardrum is estimated to be less than 90 dB, i.e., well below the (acoustomechanical) linearity limit of the ear. For the human ear, Gundersen (1971) reported a linearity limit of about 115 dB SPL and for the cat ear, Nedzelnitsky (1980) found only small departures from linearity up to 140 dB SPL.

The MLS method facilitates the measuring of acoustical transfer functions. It takes about 30 sec or less to measure and store the input and output MLS impulse responses. The transfer function amplitude and phase are then computed by performing fast Fourier transforms on the impulse responses.

RESULTS

For cadaver ears from Norwegian cattle, mean frequency characteristics for the volume displacement in the round window relative to the sound pressure at the eardrum are shown in Figs. 2 and 3, together with earlier published results for human ears (Kringlebotn and Gundersen, 1985). Data points±standard deviations have been connected by spline curve fitting.

In Fig. 4, similar frequency characteristics are shown for varying static pressure differences across the tympanic membrane. The corresponding changes in sound transmission relative to the sound transmission for zero static pressure difference across the tympanic membrane are shown in Figs. 5 and 6, and low-frequency amplitude changes in Fig. 7. Sound transmission changes due to static overpressures in the inner ear are shown in Fig. 8.

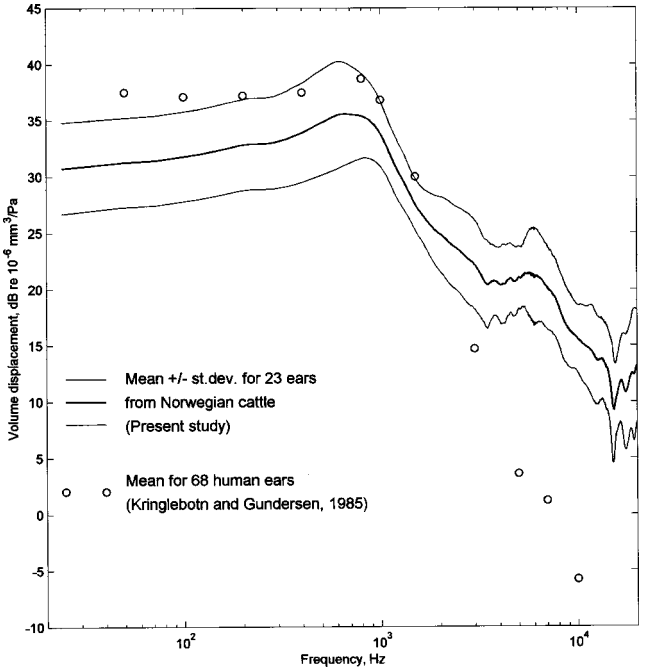

FIG. 2. Round-window volume displacement relative to sound pressure at the eardrum.

DISCUSSION

The sound volume displacements in the cochlear windows are equal (Kringlebotn, 1995; Voss *et al.*, 1996). For a known footplate area, the displacement of the stapes will then be determined by the volume displacement in the oval window.

The sound transmission from the tympanic membrane to the inner ear is measured with an open middle ear. How will sound transmission be affected by opening the middle ear?

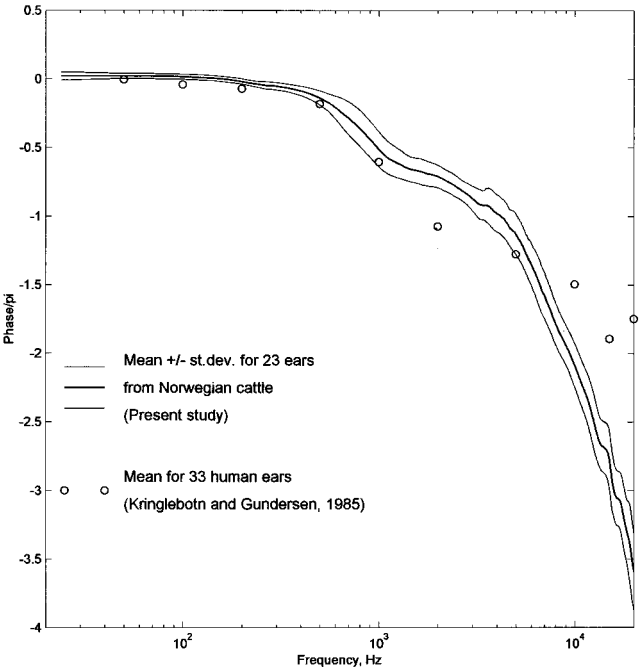

FIG. 3. Round-window volume displacement phase relative to sound pressure at the eardrum.

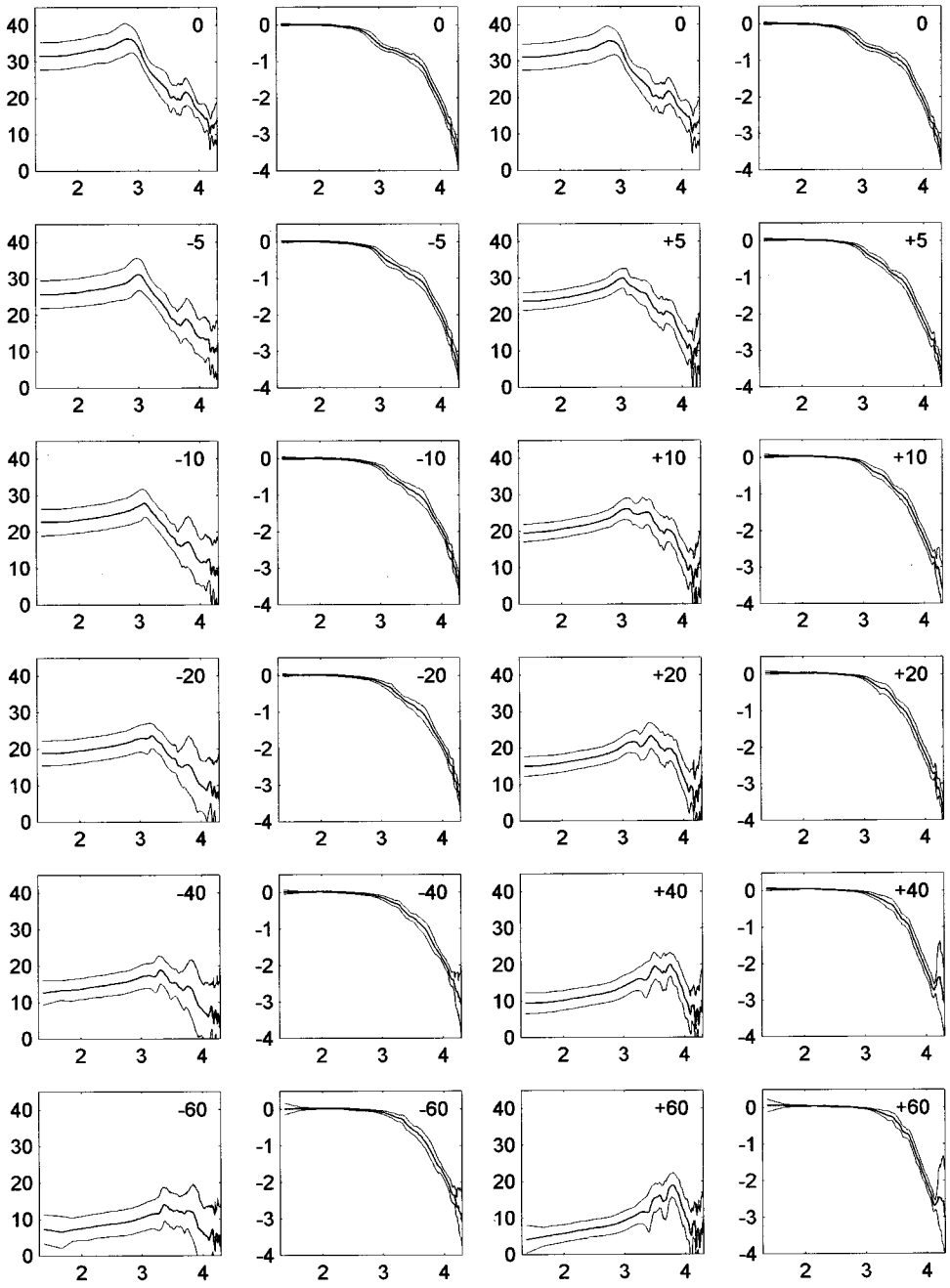

FIG. 4. Mean frequency characteristics ± standard deviations for round-window volume displacement relative to sound pressure at the eardrum, for varying static pressures in the ear canal relative to the middle ear (18 ears for underpressures, 21 for overpressures). As functions of log(frequency/Hz), columns 1 and 3 show amplitudes in dB re 10^{-6} mm^3/Pa and 2 and 4 phases in units of π. The static pressures in cm water are indicated in the upper right corners.

This question has been discussed by Rosowski *et al.* (1990), and by Zwislocki (1962). For the human ear, Zwislocki concludes: ''Since the impedance of the middle-ear cavities is low by comparison to other parts of the middle ear, its effect on the impedance at the eardrum and on the sound transmission to the inner ear is not critical.'' It may be argued that the same conclusion is valid also for the cattle ear.[1] By opening the middle ear, possible influence of large interindividual variations in the middle-ear cavities is excluded.

The air-conducted sound pressures acting on the cochlear windows are not exactly equal, and will contribute to sound transmission. Maximum contribution is obtained by shielding the round window, as in the present experimental setup. But even then the ossicular coupled sound to the inner ear is predominant in human ears (Peake *et al.*, 1992), and in particular for an open middle ear. This will also be the case for cattle ears: the equivalent sound pressure at the stapes footplate for ossicular coupled sound to the inner ear is 15–30 dB higher than at the eardrum (own measurements), and still higher relative to the air-conducted sound pressure at the oval window.

The cadaver ears were stored in a plastic bag that was moistened inside, and at a temperature just above the melting point of water. There was apparently no change in their acoustomechanical behavior during the first 10 days after death. Freezing and thawing is a more suspicious process, and will in any case result in rupture of Reissner's membrane (Kringlebotn, 1999). However, Rosowski *et al.* (1990) have reported that human ''cadaver ears can be maintained in the frozen state for several months with little change'' and that ''unfixed cadaver ears have middle ear input immittances that are indistinguishable from those of living subjects in the

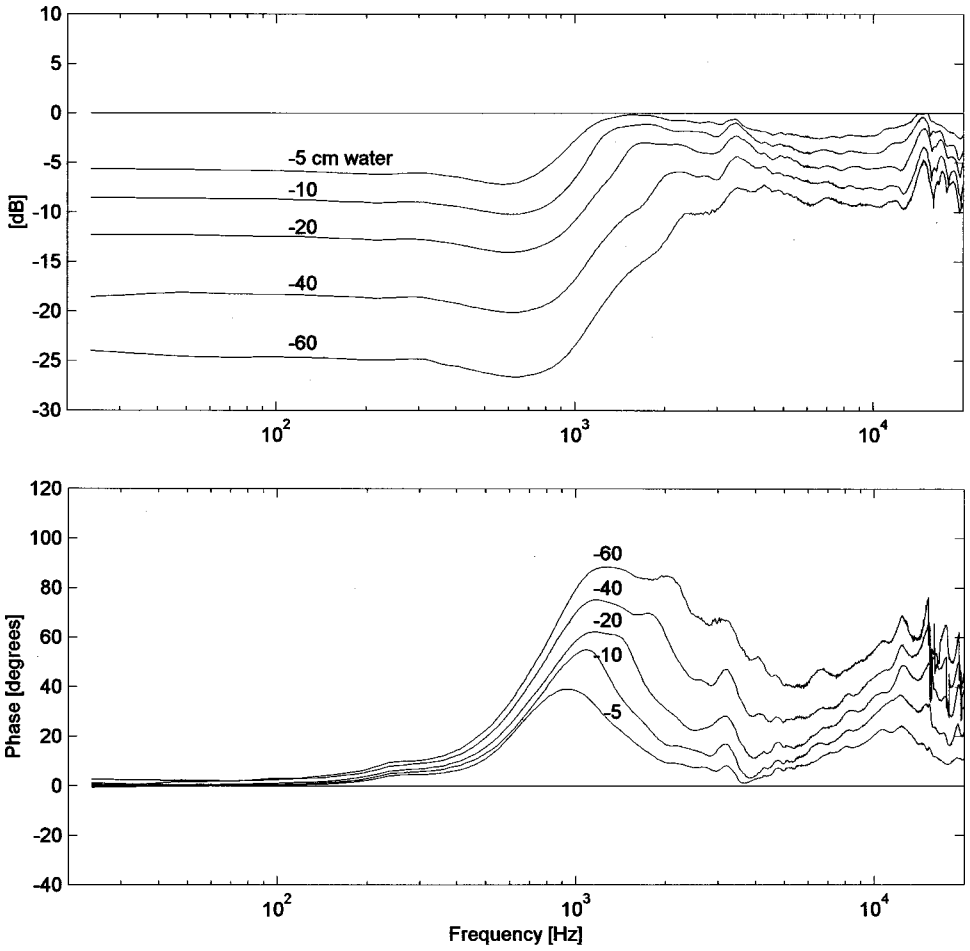

FIG. 5. Mean changes in round-window volume displacement amplitude and phase relative to sound pressure at the eardrum, for varying static underpressures in the ear canal relative to the middle ear (18 ears).

0.1- to 2-kHz range.'' It is to be expected that these statements are valid also for cattle ears.

Normally, the middle ears had a pale appearance, and with the eardrum in an excellent shape. But in some cases, the middle ears had a blood-colored appearance. The tensor tympani may then be swollen and the eardrum ruptured, probably due to impulsive strain when the animal is slaughtered. Holes in the eardrum are always located to the *pars flaccida* region, and appear as small tears. For zero static pressure difference across the tympanic membrane, the holes are closed by restoring forces, and do not seem to have any significance for the sound transmission in the ear.

For 23 cadaver ears from Norwegian cattle, frequency characteristics for the volume displacement in the round window relative to the sound pressure at the eardrum have been measured. In Figs. 2 and 3 they are compared to earlier results for human ears (Kringlebotn and Gundersen, 1985). The mean amplitude curves for cattle ears as well as for human ears have peaks at about 0.7 kHz. At lower frequencies the mean amplitude for cattle ears is about 5 dB smaller than for human ears. The amplitude curves cross at about 2 kHz, and toward higher frequencies the sound transmission in cattle ears becomes increasingly larger. If amplitude curves are roughly approximated by straight lines above 1 kHz, the slope for cattle ears is about -5 dB/octave as compared to about -15 dB/octave for human ears.

For Norwegian cattle, the mean area of the oval window is about 2.3 mm^3 (Kringlebotn, 1999), and for the human footplate about 3.2 mm^2 (Békésy, 1960b). The volume displacement in the cochlear windows is the product of this area and the stapes displacement. The amplitude ratio for cattle ears relative to human ears is therefore about $20 \cdot \log(3.2/2.3) = 2.9$ dB larger for stapes displacements than for volume displacements.

The phase of the windows volume displacement lags behind the phase of the sound pressure at the tympanic membrane. The phase lag is close to zero below 0.2 kHz, but increases to about 3.5π at 20 kHz for cattle ears, as compared to less than 2π for human ears.

In order to explain the observed differences, further investigations are needed. The differences are especially interesting in connection with middle-ear models, as a middle-ear model should be able to mimic the frequency characteristics for cattle ears as well as for human ears, just by adjusting the model parameters.

If the sensitivity of the ear is determined by the volume displacement in the cochlear windows, the cattle ear as compared to the human ear has somewhat less sensitivity at low frequencies, but increasingly higher sensitivity toward higher frequencies above about 2 kHz. This is somewhat paradoxical on the background of the cattle low-frequency ''communication sounds.'' But other more high-frequency sounds are probably equally important in the animal life, e.g., warning sounds.

An overview of the middle-ear frequency characteristics for various static pressure differences across the tympanic

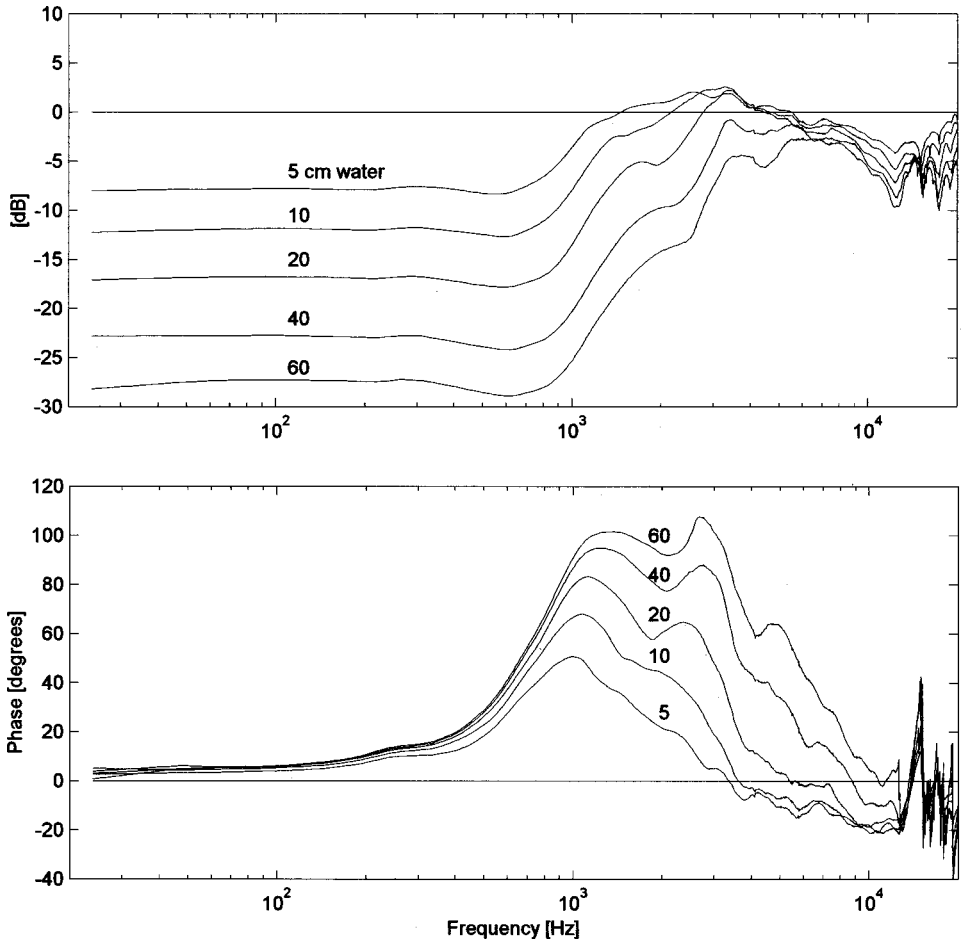

FIG. 6. Mean changes in round-window volume displacement amplitude and phase relative to sound pressure at the eardrum, for varying static overpressures in the ear canal relative to the middle ear (21 ears).

membrane is given in Fig. 4. The most striking effects of increasing the pressure difference are that the low-frequency part of the amplitude curve is displaced toward lower levels, and that the relatively flat low-frequency parts of the amplitude and phase curves are extended in the high-frequency direction. The response peak related to resonance for the middle-ear system is also displaced toward higher frequencies. The changes in amplitude and phase are seen more clearly in Figs. 5 and 6. Below about 1 kHz the sound transmission loss is approximately constant for a given static pressure difference across the tympanic membrane. The loss is a maximum at about 6–700 Hz, and gradually decreases up to about 3 kHz. At higher frequencies the loss is less than 10 dB. For small overpressures in the ear canal and in a limited frequency range near 3 kHz even some transmission enhancement may occur. It is apparent from Fig. 4 that standard deviations for amplitude values are generally larger for underpressures than for overpressures in the ear canal.

The results for cattle ears in Figs. 5–7 may be compared to those obtained for human ears. For four human subjects and pressure difference ± 40 cm water, Rabinowitz (1981) found a mean low-frequency transmission loss of 16.4 dB, as compared to 20.7 dB for cattle ears, see Fig. 7. In a recent work by Murakami *et al.* (1997), the magnitudes of the displacement amplitudes of the umbo and stapes were measured in the frequency range 0.2–3.5 kHz at a constant eardrum input of 134 dB SPL, and for static pressures in the middle ear relative to the ear canal: ± 5, ± 10, and ± 20 cm water. The amplitude curves for transmission changes in human and cattle ears are rather similar, but the effect of static pressures is larger in cattle ears. The results for human ears may have been influenced by nonlinearity effects due to the high eardrum input of 134 dB SPL. At 200 Hz, the mean transmission loss for human ears at 20 cm water under- and overpressure in the ear canal is about 7.5 and 8.5 dB, as compared to 12.7 and 16.7 dB in cattle ears. For human ears and pressures up to 20 cm water, sound transmission is enhanced near 2.5 kHz, not only for overpressures in the ear canal, but also for underpressures. The enhancement effect is somewhat less pronounced for cattle ears. Johansen (1948) offers a qualitative explanation for this effect. He represents the middle-ear system by mass, stiffness, and resistance. When the stiffness is increased by a static pressure across the tympanic membrane, the resonance is shifted toward higher frequencies where enhancement occurs, while the enhancement at the original resonance frequency is removed. That is just what is observed for cattle ears as well as for human ears. In addition, the largest enhancement is to be expected for the largest changes in stiffness, i.e., for overpressures in the ear canal. This expectation is also confirmed by the observed results.

Generally, the largest sound transmission changes are for *positive* pressures in the ear canal (negative middle-ear pressures), see Figs. 5–7. This is in agreement with data for umbo and stapes displacements in the human ear (Murakami *et al.*, 1997), and also with normal tympanograms (Feldman and Wilber, 1976). A normal tympanogram has a rather simi-

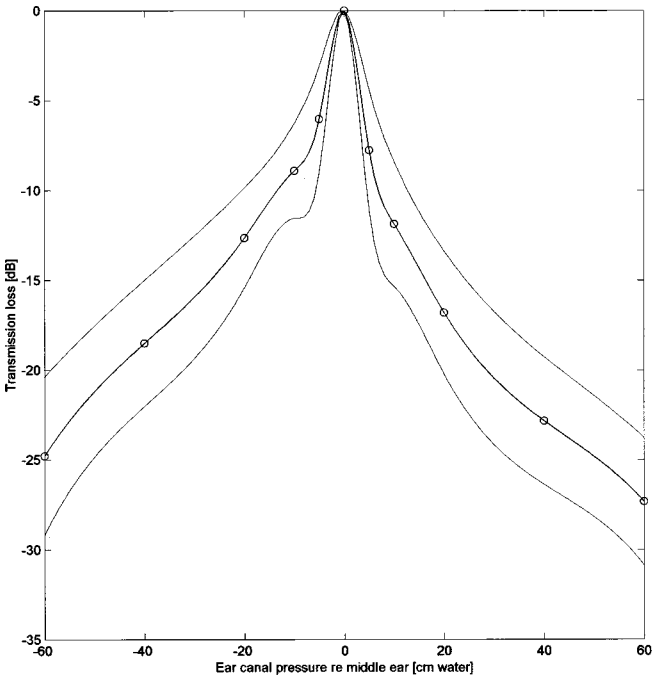

FIG. 7. Mean middle-ear sound transmission losses ± standard deviations in the low-frequency range 72–360 Hz, for varying static pressures in the ear canal relative to the middle ear (18 ears for underpressures, 21 for overpressures). Data points ± standard deviations have been connected by spline curve fitting.

lar shape as the curve in Fig. 7, which shows the sound transmission dependence on ear canal pressure at low frequencies.

It is interesting to note that at low frequencies, the change in stapes displacement is smaller than the change in umbo displacement (Murakami *et al.*, 1997). A possible explanation is that the decrease in umbo displacement for increasing static pressures is partly compensated for by an improved ossicular sound transmission due to a stiffness increase in the incudo-mallear and incudo-stapedial joints. For completely stiff joints (and ossicles), the displacement change expressed in dB should be the same for umbo and stapes.

The tympanic membrane and the annular ligament are nonlinear system elements. Their stiffnesses increase when a static pressure is applied at the eardrum or the footplate. The result will be a reduction in sound transmission at low frequencies, and an increase in the frequency range in which the system is stiffness controlled, see Figs. 5, 6, and 8. To the author's knowledge, a decisive test of the relative importance of these stiffnesses has not been made. Experiments with immobilized stapes (Békésy, 1960c) indicate that sound transmission is affected by stiffness changes for the tympanic membrane. The author's own middle-ear model (Kringlebotn, 1988) indicates that the stiffness of the annular ligament is the most critical for sound transmission.

Stiffening the tympanic membrane and increasing its mass by coating it partly or totally with Loctite 401 had surprisingly little effect on sound transmission. The transmission loss at low frequencies was less than 3 dB. The experimental finding that the total stiffness increase is larger for inward than for outward static displacement of the tympanic membrane (Fig. 7) probably reflects a similar asymmetry for the stiffness of the annular ligament (Lynch *et al.*, 1982; Fig. 10, in agreement with the author's own measurements in cattle ears). Changes in sound transmission therefore seem to be determined mainly by stiffness changes for the annular ligament.

Sound transmission is almost independent of the inner ear pressure. Békésy (1960a) and Lempert *et al.* (1949) found no dependence at all. Figure 8 shows that pressures in the range 0–60 cm water cause mean sound transmission losses less than 5 dB below 1 kHz, and negligible losses at higher frequencies. It should be noted that mean transmission losses are even smaller, as ears with undetectable changes were excluded. The reason for missing changes is probably that the pressure at the opening of the endolymphatic duct was not communicated to the inner ear fluid, due to blocking of the duct by squeezed tissue or air bubbles. Another possibility is simply that the changes were too small to be detected.

Why is sound transmission so insensitive to changes in the inner ear pressure? If the pressure force at the footplate mainly was counteracted by the stiffness of the annular ligament, this stiffness would be strongly dependent on the inner ear pressure, as it is for an ear with an interrupted ossicular chain when a static pressure is applied at the outer side of the footplate (Lynch *et al.*, 1982; Fig. 10, in agreement with the author's own measurements in cattle ears). But this is not the case. The reason must be that the static displacement of the footplate and thus the stiffness change are effectively reduced by a predominating counteracting force from the ossicular chain.

A static pressure at the eardrum corresponds to a considerably larger pressure at the footplate, the author's own measurements in cattle ears indicate about 15 dB larger. In agreement with the results in Figs. 5, 6, and 8, the effect of a static pressure at the eardrum will thus be considerably larger than when the same pressure is applied at the footplate. It may be noted that the frequency characteristics for 60 cm water overpressure in the inner ear resemble those for 5 cm underpressure in the ear canal.

The total stiffness is a minimum and the middle-ear system works most efficiently when the static pressure across the tympanic membrane is close to zero. In all ears, sound transmission is definitely larger for a zero applied pressure at the eardrum than for ± 5 cm water. Initially, the stapes need not be in its optimum position. It may have been displaced by the anvil or by a static pressure in the inner ear. But for an intact ossicular chain, the effect of a possible asymmetry is very small. One of the six ears underlying Fig. 8 had a maximum sound transmission at a nonzero inner ear pressure, the maximum at about 10 cm water being only 0.8 dB larger than at zero pressure.

CONCLUSIONS

Cattle ears may be used with advantage to gain experience in acoustomechanical experiments. They are robust and of convenient size, i.e., about the same size as human ears. And at least for the author, they are easily available.

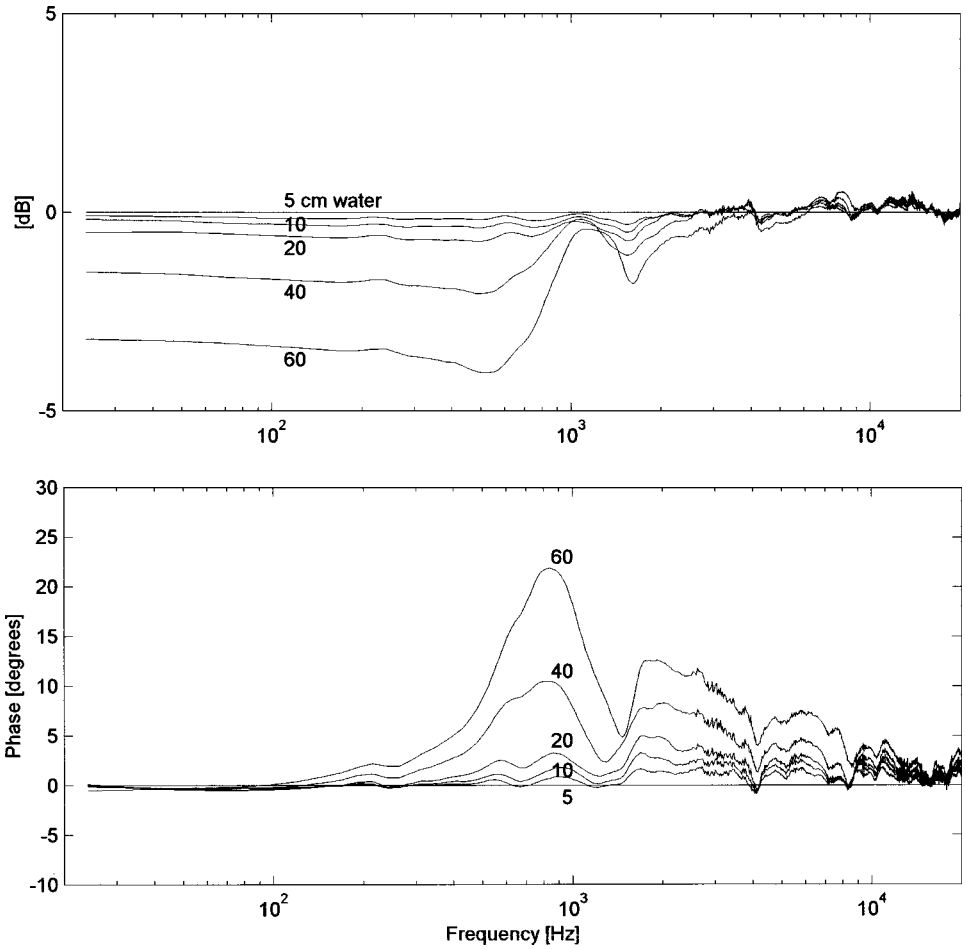

FIG. 8. Mean changes in round-window volume displacement amplitude and phase relative to sound pressure at the eardrum, for varying static overpressures in the inner ear relative to the middle ear (6 ears).

Frequency characteristics for the volume displacement in the round window relative to the sound pressure at the tympanic membrane differ markedly for human and cattle ears, especially at high frequencies. It is a challenging task to find the reasons for these discrepancies. It would have been very satisfying if a middle-ear model could be developed that is able to mimic the middle-ear frequency characteristics for the human as well as for the cattle ear, just by choosing the appropriate parameter values.

Sound transmission in the ear decreases with an increasing static pressure difference across the tympanic membrane, especially at low frequencies, where changes in sound transmission are determined by the stiffness changes of the tympanic membrane and the annular ligament. The stiffness change for the annular ligament seems to predominate. At higher frequencies, the transmission losses are smaller, and in a limited frequency range near 3 kHz even an enhancement may occur. Static pressure variations in the inner ear have only a minor influence on sound transmission.

ACKNOWLEDGMENTS

The author is indebted to Trondheim Slaktehus for easy access to temporal bones from Norwegian cattle. Preliminary reports on this work were presented at the Joint ASA/EAA/DEGA Meeting in Berlin, March 14–19, 1999.

[1]Mean eardrum areas for cat, human, and cattle are about 40, 60, and 95 mm^2, respectively (the first two values are taken from Wever and Lawrence, 1954, and Kringlebotn, 1988), while the corresponding equivalent volumes V_d for the eardrum input compliance at low frequencies are 0.34, and 0.7 cm^3, and unknown for cattle. The value 0.34 is calculated from the mean eardrum reactance 0.33 GΩ at 200 Hz (Lynch *et al.*, 1994), 0.7 is from Rabinowitz, 1981. The equivalent volume for the human tympanic membrane when calculated from the mean eardrum reactance 0.277 GΩ at 200 Hz for 15 cadaver ears (Rosowski *et al.*, 1990) is only 0.4 cm^3, indicating stiffer tympanic membranes than in live ears. The volume of the middle ear cavities V_c in cat is about 1 cm^3 (Peake *et al.*, 1992). By visual inspection, the volume of the middle-ear cavities in cattle is estimated to be about 6 cm^3, which is the same as the mean value in humans (Molvær *et al.*, 1978). By opening the middle ear, the compliance at the eardrum and the sound transmission in the middle ear at low frequencies is increased by a factor $1+V_d/V_c$, i.e., about 1 dB in humans (0.6 dB for $V_d = 0.4\,cm^3$), 2.5 dB in cat — and less than 3 dB in cattle, provided that $V_c \approx 6\,cm^3$ and $V_d < 2.5\,cm^3$, which seems quite probable.

Békésy, G. von (**1960a**). *Experiments in Hearing* (McGraw-Hill, New York), p. 434.

Békésy, G. von (**1960b**). *Experiments in Hearing* (McGraw-Hill, New York), p. 102.

Békésy, G. von (**1960c**). *Experiments in Hearing* (McGraw-Hill, New York), p. 98.

Brenkman, C. J., Grote, J. J., and Rutten, W. L. C. (**1987**). ''Acoustic transfer characteristics in human middle ears studied by a SQUID magnetometer method,'' J. Acoust. Soc. Am. **82**(5), 1646–1654.

Feldman, A. S., and Wilber, L. A. (**1976**). *Acoustic Impedance and Admittance—The Measurement of Middle Ear Function* (Williams and Wilkins, Baltimore, MD), Fig. 14.4.

Goode, R. L., Nakamura, K., Gyo, K., and Aritomo, H. (**1989**). ''Comments on 'Acoustic transfer characteristics in human middle ears studied by a SQUID magnetometer method' [J. Acoust. Soc. Am. **82**, 1646–1654 (1987)],'' J. Acoust. Soc. Am. **86**(6), 2446–2449.

Guinan, J. J., and Peake, W. T. (**1967**). ''Middle-ear characteristics of anesthetized cats,'' J. Acoust. Soc. Am. **41**(5), 1237–1261.
Gundersen, T. (**1971**). *Prostheses in the Ossicular Chain* (University Park Press, Baltimore, MD), p. 43.
Gyo, K., Aritomo, H., and Goode, R. L. (**1987**). ''Measurement of the ossicular vibration ratio in human temporal bones by the use of a video measuring system,'' Acta Otolaryngol. **103**, 87–95.
Johansen, H. (**1948**). ''Relation of audiograms to the impedance formula,'' Acta Otolaryngol. Suppl. **74**, 65–75.
Kringlebotn, M., and Gundersen, T. (**1985**). ''Frequency characteristics of the middle ear,'' J. Acoust. Soc. Am. **77**(1), 159–164.
Kringlebotn, M. (**1988**). ''Network model for the human middle ear,'' Scand. Audiol. **17**, 75–85.
Kringlebotn, M. (**1995**). ''The equality of volume displacements in the inner ear windows,'' J. Acoust. Soc. Am. **98**(1), 192–196.
Kringlebotn, M. (**1999**). ''Rupture pressures of membranes in the ear,'' presented at the Joint ASA/EAA/DEGA Meeting in Berlin, March 14–19, 1999.
Lempert, J., Wever, E. G., Lawrence, M., and Meltzer, P. E. (**1949**). ''Perilymph: Its relation to the improvement of hearing which follows fenestration of the vestibular labyrinth in clinical otosclerosis,'' Arch. Otolaryngol. **50**, 377–387.
Lynch III, T. J., Nedzelnidsky, V., and Peake, W. T. (**1982**). ''Input impedance of the cochlea in cat,'' J. Acoust. Soc. Am. **72**(1), 108–130.
Lynch III, T. J., Peake, W. T., and Rosowski, J. J. (**1994**). ''Measurements of the acoustic input impedance of cat ears: 10 Hz to 20 kHz,'' J. Acoust. Soc. Am. **96**(4), 2184–2209.
Merchant, S. N., Ravicz, M. E., and Rosowski, J. J. (**1996**). ''Acoustic input impedance of the stapes and cochlea in human temporal bones,'' Hear. Res. **97**, 30–45.
Molvær, O. I., Vallersnes, F. M., and Kringlebotn, M. (**1978**). ''The size of the middle ear and the mastoid air cell,'' Acta Otolaryngol. **85**, 24–32.
Murakami, S., Gyo, K., and Goode, R. L. (**1997**). ''Effect of middle ear pressure change on middle ear mechanics,'' Acta Otolaryngol. **117**, 390–395.
Nedzelnitsky, V. (**1980**). ''Sound pressures in the basal turn of the cat cochlea.'' J. Acoust. Soc. Am. **68**(6), 1676–1689.
Peake, W. T., Rosowski, J. J., and Lynch III, T. J. (**1992**). ''Middle-ear transmission: Acoustic versus ossicular coupling in cat and human,'' Hear. Res. **57**, 245–268, Fig. 12.
Rabinowitz, W. M. (**1981**). ''Measurement of the acoustic input immittance of the human ear,'' J. Acoust. Soc. Am. **70**(4), 1025–1035.
Rosowski, J. J., Davis, P. J., Donahue, K. M., Merchant, S. M., and Coltrera, M. D. (**1990**). ''Cadaver middle ears as models for living ears: Comparisons of middle ear input immitance,'' Ann. Otol. Rhinol. Laryngol. **99**, 403–412.
Vlaming, M. S. M. G., and Feenstra, L. (**1986**). ''Studies on the mechanics of the normal human middle ear,'' Clin. Otolaryngol. **11**, 353–363.
Voss, S. E., Rosowski, J. J., and Peake, W. T. (**1996**). ''Is the pressure difference between the oval and round windows the effective acoustic stimulus for the cochlea?,'' J. Acoust. Soc. Am. **100**(3), 1602–1616.
Wever, E. G., and Lawrence, M. (**1954**). *Physiological Acoustics* (Princeton University Press, Princeton, NJ).
Zwislocki, J. (**1962**). ''Analysis of the middle-ear function. Part I: Input impedance,'' J. Acoust. Soc. Am. **34**(8), 1514–1523.

Individual differences in external-ear transfer functions of cats

Li Xu[a] and John C. Middlebrooks[b]
Kresge Hearing Research Institute, University of Michigan, 1301 East Ann Street, Ann Arbor, Michigan 48109-0506

(Received 6 July 1999; accepted for publication 7 December 1999)

Knowledge of the direction-dependent filter characteristics of the external ears is useful for the study of spatial hearing in experimental animals. The present study examined individual differences in the directional components of external-ear transfer functions (directional transfer functions, DTFs) among 24 anesthetized cats. Ears were fixed in a frontal position. Inter-cat differences in DTFs were quantified across a mid-frequency range from 8 to 16 kHz and across 30 locations in the horizontal plane and vertical midline. Across cats, DTFs showed similar direction dependence, but tended to differ in regard to the center frequencies of spectral features, such as spectral peaks and notches. Certain mid-frequency notches, for instance, varied in frequency across cats by nearly a factor of 2. Scaling of DTFs in frequency could reduce the overall differences between pairs of cats. Scale factors that minimized inter-cat differences ranged as high as 1.57 and correlated moderately with cats' body weights. Nevertheless, appreciable individual differences remained after frequency scaling. Inter-cat differences in DTFs were substantially larger than differences that resulted from variability in positioning the ears. The results suggest some guidelines regarding the conditions under which it is acceptable to apply DTF measurements from one cat to another. © *2000 Acoustical Society of America.* [S0001-4966(00)02903-9]

PACS numbers: 43.64.Ha, 43.66.Pn, 43.66.Qp [BLM]

INTRODUCTION

As a sound passes from a free-field source to the ear canal, its spectrum is transformed by interaction with the head and external ear. The transfer function is commonly known as the head-related transfer function (HRTF) (Butler, 1987; Morimoto and Ando, 1980; Wightman and Kistler, 1989a). The HRTF varies with the angle of incidence of sound, so the spectrum of the sound in the ear canal carries directional information.

Domestic cats are widely used as experimental animals for studies of spatial hearing, both for cortical physiology (Brugge *et al.*, 1994, 1996, 1998; Imig *et al.*, 1990; Middlebrooks and Pettigrew, 1981; Middlebrooks *et al.*, 1998; Rajan *et al.*, 1990; Xu *et al.*, 1998, 1999) and for psychophysics (Casseday and Neff, 1973; Jenkins and Masterton, 1982; Huang and May, 1996; May and Huang, 1996; Populin and Yin, 1998). Knowledge of cats' HRTFs can guide physiological study of specific spatial cues (e.g., Rose *et al.*, 1966) and can inspire models of spatial sensitivity (e.g., Middlebrooks, 1987; Rice *et al.*, 1992). In several recent studies, cat HRTFs have been used for synthesis of a virtual auditory space (Brugge *et al.*, 1994, 1996, 1998; Chan *et al.*, 1993; Delgutte *et al.*, 1999; Nelken *et al.*, 1997; Reale *et al.*, 1996).

Human HRTFs show prominent differences among listeners (Mehrgardt and Mellert, 1977; Middlebrooks, 1999a; Shaw, 1966; Wightman and Kistler, 1989a). The functional significance of such individual differences is demonstrated by studies of virtual sound localization. When human subjects listen through HRTFs recorded from other subjects, they show substantial errors in localization (Middlebrooks, 1999b; Wenzel *et al.*, 1993). This raises concern about the validity of generalizing HRTFs measured from any particular cat to a variety of other cats.

The present study characterized the individual differences in cat HRTFs across a sample of 24 cats. Particular attention was paid to the directional components of HRTFs, which are known as directional transfer functions (DTFs; Middlebrooks and Green, 1990). The results showed that the amount of individual differences in cat DTFs is comparable to, if not larger than, that of inter-subject differences in human DTFs. The individual differences could be reduced by frequency scaling, and the scale factors were related to the body weights of the animals. That indicates that there existed a relationship between the physical sizes of the animals and the frequencies of the prominent spectral features in the external-ear transfer functions.

I. METHOD

A. Animal preparation

Twenty-four purpose-bred adult cats (11 females and 13 males) were used in this study. Three of them were supplied by Sinclair Research Center, MO, and the rest were supplied by Harlan Industrials, Inc., IN. Weights ranged from 2.4 to 6.1 kg. For the 21 cats obtained from Harlan Industrials, Inc., three shared a father, six pairs shared fathers, and the remaining six cats were not related directly. Measurements of the head-related transfer function were preceded by single-unit recording in the right auditory cortex (Furukawa *et al.*, 2000; Middlebrooks *et al.*, 1998; Xu *et al.*, 1998, 1999). Each cat was anesthetized for surgery with isoflurane, then was transferred to α-chloralose for single-unit recording followed by acoustic measurement. A stainless-steel fixture was attached

[a]Electronic mail: leehsu@umich.edu
[b]Electronic mail: jmidd@umich.edu

to the frontal bones with screws and dental cement. A midline scalp incision was made, the temporalis muscle was retracted on the right side, and a recording chamber was positioned over the right auditory cortex. Portions of scalp and temporalis muscle were removed to accommodate the recording chamber, and the scalp incision was closed to minimize distortion of the ears. The presence of the skull opening and recording chamber almost certainly influenced details of external-ear transfer functions. Nevertheless, essentially the same opening and chamber were present in all animals, so there should have been minimal influence on the inter-cat differences. Also, inter-cat differences that varied with body weight and gender (Sec. II C) would not have been affected by the recording chamber.

The animal was transferred to the center of a sound-attenuating chamber with the cat's interaural axis centered in the sound chamber. The body of the cat was supported in a canvas sling, and its head was supported from behind by a bar attached to the skull fixture. Under anesthesia, the relaxed pinna position tended to be lateral and downward in comparison to the pinna position of an alert cat. Care was taken to restore the normal-appearing position of the pinnae. Both ears were supported by a pair of curved wire supports so that the pinnae resumed a symmetrical forward position that resembled the pinna position adopted by a cat attending to a frontal sound.

B. Experiment setup and acoustic system

Experiments were conducted in a sound-attenuating chamber that was lined with acoustical foam (Illbruck) to suppress reflections of sounds at frequencies >500 Hz. Sound stimuli were presented from loudspeakers (Pioneer model TS-879 two-way coaxials) mounted on two circular hoops, 1.2 m in radius, one in the horizontal plane and one in the vertical midline plane. On the horizontal hoop, 18 loudspeakers spaced by 20 degrees covered 360 degrees. On the vertical hoop, 14 loudspeakers spaced by 20 degrees ranged from 60 degrees below the frontal horizon, up and over the top, to 20 degrees below the rear horizon. Vertical locations were labeled continuously in 20-degree steps from -60 to $+200$ degrees. Since the vertical and horizontal hoops shared speakers at 0 and 180 degrees, the total number of locations was 30. Experiments were controlled with an Intel-based personal computer. Acoustic stimuli were synthesized digitally, using equipment from Tucker-Davis Technologies. The sampling rate for audio output was 100 kHz, with 16-bit resolution.

C. Measurements of transfer functions

A $\frac{1}{2}$-in. probe microphone (Larson-Davis model 2540) was used for the acoustic measurements. The stainless-steel probe tube that connected to the $\frac{1}{2}$-in. microphone had an inner diameter of 3.2 mm and an outer diameter of 4.0 mm. The probe tube was inserted approximately 2 mm into the ear canal through a vertical incision at the posterior base of the pinna. The probe stimuli delivered from each of the 30 loudspeakers were pairs of Golay codes (Foster, 1986; Golay, 1961; Zhou *et al.*, 1992) that were 81.92 ms in duration. Recordings from the microphone were amplified, then were digitized at a rate of 100 kHz, yielding a spectral resolution of 12.2 Hz from 0 to 50 kHz.

Before each experiment, the frequency responses of the loudspeakers were measured using the Golay stimuli and the $\frac{1}{2}$-in. microphone positioned in the center of the sound chamber in the absence of the animal. The influence of the frequency responses of the loudspeakers was eliminated by dividing them from the ear-canal spectra. The resulting transfer functions were head-related transfer functions (HRTFs). A similar procedure has been used in previous studies of cats' external-ear transfer functions (Musicant *et al.*, 1990; Rice *et al.*, 1992). In the present study, our analysis was based on the direction-specific components of the HRTFs, referred to as directional transfer functions (DTFs). The DTF for each sound source location was obtained by dividing the HRTF for each location by the root-mean-squared HRTF averaged across all 30 locations (Middlebrooks and Green, 1990; Middlebrooks, 1999a). In control experiments performed in three cats, recordings from the probe microphone in the ear canal were made simultaneously with recordings from a Knowles miniature microphone (model 1934) that was placed at a deeper position in the ear canal. Consistent with such dual-microphone recordings in humans (Middlebrooks *et al.*, 1989; Middlebrooks and Green, 1990), HRTFs measured at the two sites were quite different, whereas DTFs computed for the two recording sites were nearly identical.

D. Data analysis

We convolved each DTF in the linear frequency scale with a bank of bandpass filters to obtain samples spaced equally on a logarithmic scale (Middlebrooks, 1999a). The purposes of this procedure were (1) to roughly equalize the number of samples per perceptual critical band and (2) to facilitate scaling of DTFs in frequency. The filter bank consisted of 118 triangular filters. The 3-dB bandwidth of the filters was 0.0571 oct, filter slopes were 105 dB per oct, and the center frequencies were spaced in equal intervals of 0.0286 oct from 3 to 30 kHz. The interval of 0.0286 oct was chosen to give intervals of 2% in frequency. As a consequence of bandpass filtering, the very sharp peaks or notches in the DTFs were blunted, which resembled the perceptual consequence of filtering by the cochlea (Glasberg and Moore, 1990).

Individual differences between DTFs were quantified by a metric that will be referred to as the inter-subject spectral difference. That metric was computed across the 36 filter-bank components from 8 to 16 kHz. That mid-frequency band was chosen because it contains prominent direction-dependent spectral features (Musicant *et al.*, 1990; Neti *et al.*, 1992; Rice *et al.*, 1992) and because our preliminary tests indicated that it captured the most systematic differences in the DTFs among cats. Behavioral studies have demonstrated that cats can accurately localize noise that is limited to mid-frequencies (Huang and May, 1996), and we have shown that mid frequency sounds have the strongest influence on cat neuronal signaling of sound locations (Xu *et al.*, 1999). The spectral difference was computed as follows. For each pair of cats, the dB amplitudes of the 36

components of DTFs were subtracted, component by component, to form a difference spectrum for each source direction. Then, the variance across the 36 components of the difference spectrum was computed. Finally, the variance was averaged across the 30 tested directions for each pair of cats.

We quantified systematic frequency differences between the DTFs of pairs of cats by using a frequency-scaling procedure (Middlebrooks, 1999a). That procedure served as a tool to quantify frequency disparities between DTFs and to evaluate the relationship between the physical sizes of the animals and the spectral features of their DTFs. For each pair of cats, the set of 30 DTFs from one cat was scaled upward by 2%, alternating with downward 2% scaling of the other cat's set of DTFs. Amplitudes of the DTFs were not adjusted. After each scaling, the spectral difference was computed between 8 and 16 kHz. This procedure was repeated until the scale factor was found that produced the minimum spectral difference between any given pair of cats. That was termed the optimal scale factor. The percent reduction in the inter-subject spectral differences as a result of optimal frequency scaling was also computed.

II. RESULTS

A. General properties of cat DTFs

For the 24 cats used in the present study, DTFs were measured from all 24 left ears and 22 of the right ears. For the 22 cats in which both ears were measured, the spectral differences in DTFs between left and right ears averaged 11.3 dB^2. The right ear was somewhat more distorted than the left by the right-sided skull opening and recording chamber (see Sec. I). That asymmetry presumably contributed to the left/right spectral differences. Our subsequent data analysis was based on recordings from the 24 left ears. Figure 1(a) shows 14 DTFs of one cat (cat 19) before they were processed with the bandpass filter bank. Filtering with the bandpass filter bank resulted in significant smoothing of the spectra and yet preserved the major spectral features [thick line in Fig. 1(b)]. One of the prominent features in the cat DTFs was the mid-frequency notches, as has been emphasized in previous studies of cat HRTFs (Musicant *et al.*, 1990; Rice *et al.*, 1992). Generally, the notch center frequencies tended to increase systematically as source elevation increased. The trend often was violated, however, for DTFs at lowest elevations. Also, the DTFs at the highest locations (+80 and +100 degrees) in about half of the cats failed to show any obvious spectral features such as notches or peaks.

Changes in the position of a cat's ears can produce systematic changes in HRTFs (Middlebrooks and Knudsen, 1987; Young *et al.*, 1996). When we compared DTFs among different cats, we attempted to position the ears in a ''normal-appearing'' forward position that was consistent across all subjects. In six cats, we tested the reliability with which a consistent ear position could be attained. In each of the six cats, the ears and the probe microphone were positioned twice, once by each of two investigators, and two sets of DTF measurements were made. Figure 1(b) (thin and thick lines) shows examples of DTFs measured by two different experimenters. The two measurements matched each other fairly well at all locations and across frequencies. The spectral difference between the two measurements computed across all 30 locations was 3.25 dB^2. The spectral differences of the two replicated measurements in the other five cats were 0.56, 2.83, 3.04, 5.80, and 7.10 dB^2. These spectral differences are considerably smaller than the spectral differences between pairs of cats (detailed later in Fig. 4). In another subset of three cats, we deliberately changed the pinna to extreme forward and backward positions beyond those that could normally be obtained in a behaving cat. This was done by pulling a thin string attached to the tip of the pinna and by pushing or retracting the wire support of the pinna. We found that the spectral differences between those extreme pinna positions averaged 14.19 dB^2 ($n=9$, i.e., three cats times three possible combinations of pinna positions), which was smaller than the mean spectral differences between pairs of cats (detailed later in Fig. 4). Young *et al.* (1996) tested the influence of more moderate change of ear position on spectral notches of cat HRTFs. Data illustrated in their figure 6 showed that inter-cat differences were substantially larger than differences resulting from changes in ear position. Therefore, we were confident that the individual differences in cat DTFs were not solely due to the differences in ear position.

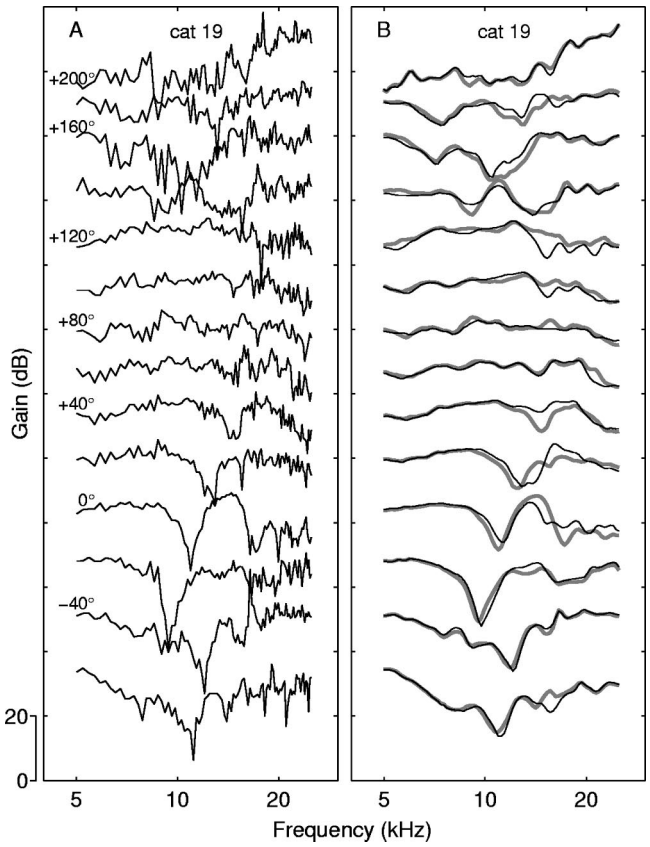

FIG. 1. Directional transfer functions (DTFs) from the left ear of one cat (cat 19) for the 14 elevation locations in the vertical midline plane. (a) Unfiltered DTFs. (b) Two sets of measurements processed by a bank of bandpass filters (see Sec. I for details). Thick lines are from the same set of measurements as shown in (a). Thin lines are after a second experimenter repositioned the probe tube microphone and the pinnae.

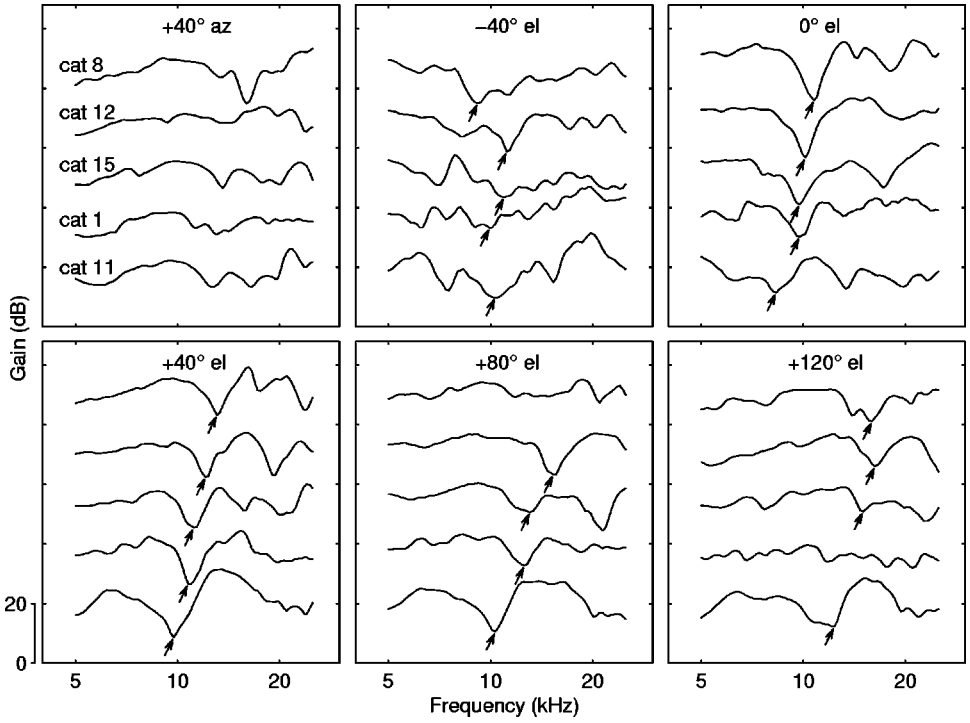

FIG. 2. The DTFs from five cats for selected locations. The upper left panel represents DTFs for a location in the horizontal plane 40 degrees ipsilateral to the ear that contained the microphone, and the other five panels represent DTFs for −40- to 120-degree elevations in 40-degree steps in the vertical midline plane as labeled above the DTFs. Arrows indicate the spectral notches defined in the text. In all panels, DTFs from the five cats are ordered based on the spectral notch frequencies in the DTFs for +40-degree elevation. The same order is given by a rank of body weights of the cats; that is, DTFs for the lightest cat are placed on the top and those for the heaviest cat at the bottom. Cats 8, 12, 15, 1, and 11 had body weights of 2.5, 2.9, 3.6, 4.0, and 6.1 kg, respectively.

B. Individual differences

Despite some similarity in the general features of the DTFs from different cats, we observed substantial individual differences in the DTFs. Figure 2 plots DTFs from five cats at six locations. The upper left panel represents DTFs at ipsilateral 40 degrees on the horizontal plane. The rest of the panels represent DTFs from five midline elevation locations at −40 to +120 degrees in 40-degree steps. Arrows in those panels indicate mid-frequency notches in the DTFs. A spectral notch was defined here as a spectral minimum in the frequency range between 5 and 20 kHz, bounded on either side by slopes that were ⩾5 dB high. The DTFs plotted in each panel are ordered based on the spectral notch frequencies defined at +40 degrees elevation, and the order of cats is the same across all panels. The inter-subject differences in the DTFs included differences in the detailed shape of each DTF and in the frequencies of the prominent spectral features such as spectral notches and peaks.

The prominent mid-frequency spectral notches highlight the individual differences among cat DTFs. Figure 3 summarizes the inter-subject differences in the spectral notch center frequencies in the DTFs of the 14 elevation locations. Figure 3(a) plots the center frequencies of notches for the five cats whose DTFs are shown in Fig. 2. Each line represents data from one of the cats. The lines are broken at locations at which no spectral notches could be identified. In frontal lo-

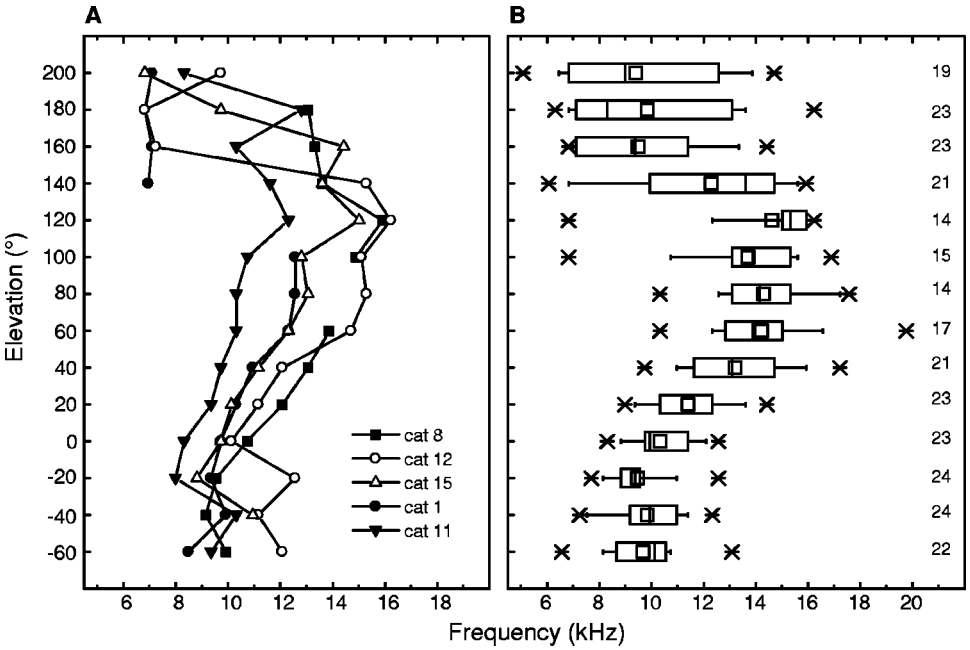

FIG. 3. Individual differences in the spectral notch center frequencies of the DTFs. (a) Each line plots for one of the five cats shown in Fig. 2 the spectral notch frequencies in the DTFs for the 14 elevation locations. (b) The box plot summarizes the distribution of spectral notch frequencies in the 14 elevation DTFs of all 24 cats. At each elevation, the mean is represented by the small square and the minimum and maximum are represented by the asterisks. The three vertical bars represent the 25, 50 and 75 percentiles and the ends of the two horizontal bars represent the 5 and 95 percentiles of the distribution. The number to the right indicates the number of cats at each elevation at which mid-frequency notches could be identified.

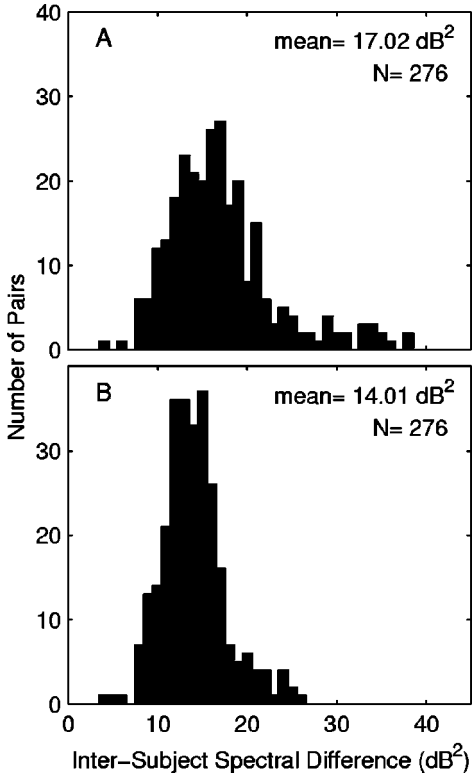

FIG. 4. Distributions of inter-subject spectral differences in DTFs before (a) and after (b) frequency scaling. Values were computed for all 276 possible pairwise combination of 24 cats.

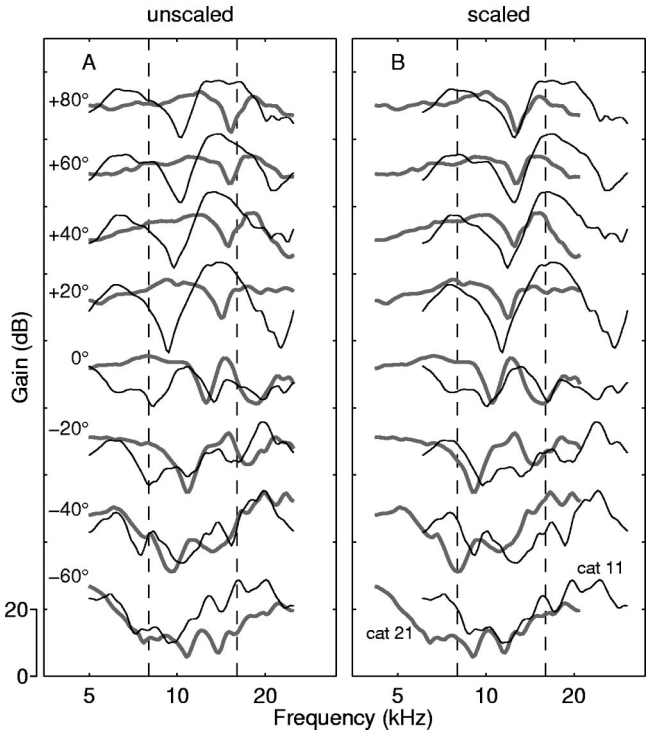

FIG. 5. Examples of frequency scaling between a pair of cats (cat 11 and cat 21). (a) The DTFs from cat 11 (thin lines) and cat 21 (thick lines) for the eight frontal elevation locations before frequency scaling. (b) At optimal frequency scaling, DTFs from cat 11 (thin lines) were scaled upward by 1.219 and those from cat 21 (thick lines) were scaled downward by 1.195, a combined relative scaling of 1.457. The vertical grid lines indicate the frequency band (8–16 kHz) over which quantitative comparisons were made.

cations, notch frequencies increased systematically as source elevation increased from −20 to +80 degrees. In rear locations, notch frequencies also increased as sources moved up from the rear horizon. Individual differences in the notch frequencies of cat DTFs were apparent. The lines were roughly parallel to each other, at least for frontal locations, suggesting that the set of all DTFs from one cat could be aligned with that of another cat by scaling in frequency.

The distributions of the individual differences in spectral notch frequency among the sample of 24 cats are illustrated in Fig. 3(b) in a box-plot format. In this format, the mean notch frequency at each location is represented by the small square and the minimum and maximum values are represented by the asterisks. The three vertical lines represent 25, 50, and 75 percentiles and the ends of the two horizontal bars represent 5 and 95 percentiles of the distribution, respectively. The number of cats in which mid-frequency notches could be identified varied from elevation to elevation. Those numbers are given in a column on the right side of Fig. 3(b). There was a clear trend that the spectral notch center frequencies varied systematically with the frontal midline elevation. Nevertheless, the inter-subject differences in the spectral notch frequencies could be as large as 1 oct for most locations in elevation. The variation was especially large in the rear locations. The smallest range of notch frequencies was found at 0 degrees elevation at which they varied over only 0.60 oct in our sample of 24 cats. The extent of the individual differences in the spectral notch frequencies can also be appreciated from another perspective. If one makes a vertical line in Fig. 3(b) anywhere between 10 and 12 kHz, it passes within the distribution of notch frequencies at all elevations. That means that a notch at, say, 11 kHz could signal nearly any location among one or more of the cats in our sample.

We computed the spectral differences in the DTFs averaged across all 30 locations for each pair of cats. These spectral differences were computed across 36 frequency components from 8 to 16 kHz (see Sec. I for details). The distribution of the spectral differences across all of the 276 pairwise combination of cats is shown in Fig. 4(a). The mean of the distribution was 17.02 dB^2 and the spectral differences of 9.5% of pairs were $\geqslant$25 dB^2.

C. Frequency scaling

The notch data in Fig. 3(a) showed that inter-cat differences in notch frequencies tended to be fairly constant across most locations. That suggests that inter-cat alignment of spectral features could be improved, and spectral differences decreased, by scaling the sets of DTFs for each pair of cats by a single scale factor. That procedure was followed as described in Sec. I. An example is shown for one pair of cats in Fig. 5. Panels (a) and (b) show the eight frontal-midline DTFs of the two cats (cat 11 and cat 21) before and after frequency scaling. At optimal scaling, the DTFs from cat 11 were scaled upward by 2% ten times and the DTFs from cat 21 were scaled downward nine times, resulting in a total relative scale factor of 1.457 ($1.02^{10}/1.02^{-9}=1.457$). Note that the prominent spectral features (e.g., notches) in the two sets of DTFs matched well after frequency scaling. The spectral difference of this pair of cats was reduced by 51.3% from

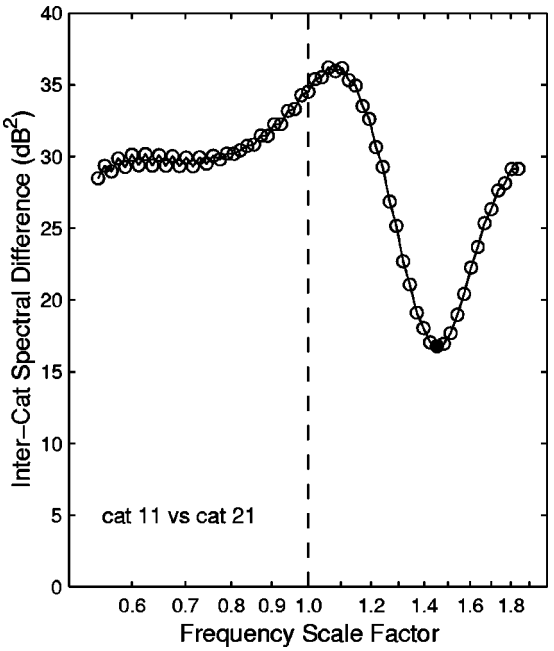

FIG. 6. Spectral difference as a function of frequency scale factor for the pair of cats represented in Fig. 5 (cat 11 versus cat 21). The optimal scale factor is indicated by the filled symbol.

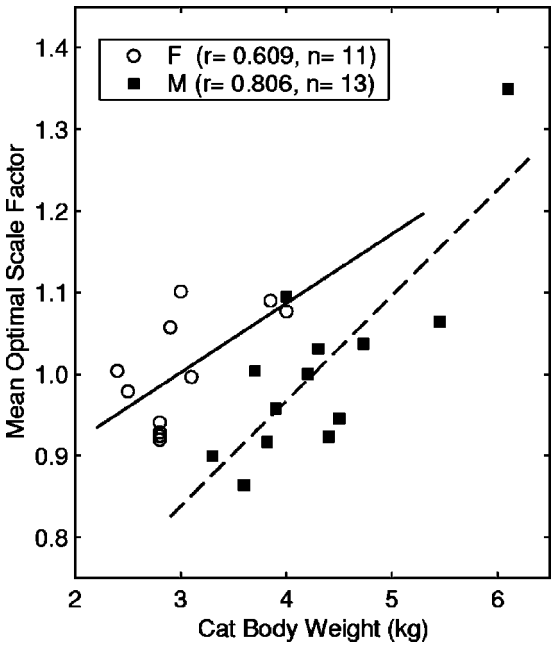

FIG. 8. Relationship between cat body weight and mean frequency scale factor. Eleven female and 13 male cats are represented by the circles and squares, respectively. Solid and dashed lines are linear fits to the data from female and male cats, respectively.

34.5 dB^2 before scaling to 16.5 dB^2 after. Figure 6 shows the spectral differences for this pair of cats as a function of relative scale factor.

The distribution of spectral differences for the 276 pairs of cats after scaling is shown in Fig. 4(b). The mean was 14.01 dB^2. Only one pair showed a spectral difference $\geqslant$25 dB after scaling. Figure 7(a) and (b) shows the distributions of the optimal frequency scale factor and the percent reduction of spectral differences by frequency scaling. For this illustration, all pairs were ordered such that the optimal scale factor was $\geqslant$1. The optimal scale factors ranged from 1 to 1.57 with a median of 1.10. The percent reduction in the inter-subject spectral differences accomplished by frequency scaling had a median of 11.5%, ranging from 0% to 60.7%. A substantial amount of spectral difference remained even after frequency scaling due to nonsystematic differences in the DTFs among cats that could not be removed by frequency scaling.

The spectral details of a DTF result from the physical

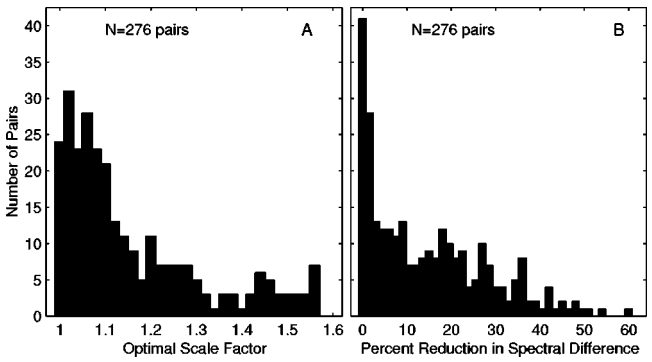

FIG. 7. Distributions of optimal scale factor (a) and percent reduction of spectral difference by frequency scaling (b). Values were computed for all 276 possible pairwise combination of 24 cats.

interaction of an incident sound wave with the head and pinnae. For that reason, one would expect that the frequencies of spectral features depend on the sizes of the head and pinnae as well as the shapes of the pinnae. We used the body weight of each cat as a single number to represent its overall size. The body weights correlated somewhat with the frequencies of spectral features in the DTFs. For example, for the DTFs of the five cats shown in Fig. 2, which were sorted by the notch frequency in the DTF for +40 degrees elevation, the body weights fell in order such that the lightest cat was represented by the top line and the heaviest cat by the bottom line. In general, spectral features in the DTFs of a smaller cat tended to fall in a higher frequency region than those of a bigger cat (Fig. 2). We summarized the frequencies of spectral features in each cat's DTFs as the geometric mean of the optimal scale factor between that cat and every other cat. Figure 8 plots the mean optimal scale factor for each cat as a function of its body weight. The circles represent female cats and squares represent male cats. The solid and dashed lines are linear (least-square) fits for each set of data. Within each gender, mean scale factor correlated with body weight. Correlation coefficients (r) were 0.609 for females and 0.806 for males. The correlation was reduced to 0.547 when females and males were combined. The gender differences were interesting. We measured the pinna sizes in a few cats and found that female cats tended to have bigger pinnae compared to male cats of similar body weights. Conversely, given males and females having heads and ears of similar sizes, the males tended to be more muscular and, thus, heavier. We speculate that the gender differences would disappear if we could use the pinna or head size to correlate with the scale factors. Unfortunately, we did not have ear and head measurements from every cat. In a recent study of individual differences in human DTFs, we found no indication

of a gender effect that could not be accounted for by the tendency of females to be smaller than males (Middlebrooks, 1999a). The correlation between the body weights and the optimal scale factor is further evidence that the inter-cat differences that we observed were not entirely due to different ear positions among cats.

III. DISCUSSION

The general properties of the directional components of HRTFs (i.e., DTFs) that we studied were similar to previous studies of cat HRTFs, but we noted considerable individual differences in the HRTFs among cats. In the following, we compare our results to previous studies of cat HRTFs and discuss the implications of individual differences in HRTFs for studies of spatial hearing.

A. Comparison with previous studies

Previous descriptions of cat external-ear transfer functions have emphasized characteristics of the direction dependence of the transfer functions that are consistent among cats. Musicant and colleagues (1990) measured the HRTFs from six cats for sounds at numerous horizontal and vertical locations. They observed prominent spectral notches in the 8–18 kHz frequency region. Individual differences were considered small. Rice and colleagues (1992) confirmed and extended the observations of the spectral notches in the HRTFs. They focused on a slightly larger frequency range (5–18 kHz) and proposed a sound-localization scheme based on the mid-frequency notch frequencies in the two ears. Again, they emphasized the similarities rather than differences in the HRTFs among the five cats used in that study.

Our measurements of individual DTFs were largely consistent with previous studies in regard to the general location dependence of spectral features. In general, we found that spectral features in the mid-frequency region shifted to higher frequency as sound source moved from lower elevation to higher elevation in the front midline (Fig. 1). The same was true for rear midline locations, but variability there was much greater. We sampled lower elevations than in previous studies, i.e., -60 degrees rather than -30 degrees (Musicant *et al.*, 1990; Rice *et al.*, 1992). At -40- and -60-degree elevations, mid-frequency notches tended to be wide and blunt (Figs. 1 and 2). The center frequencies of those notches tended to shift to higher frequency with decreasing elevation, which was counter to the trend at elevations $\geqslant -20$ degrees. In a behavioral study, May and Huang (1996) tested cat's head orientation to sounds presented as low as -45 degrees elevation and found that response errors increased dramatically compared to those at more centric locations. They attributed these increased errors to the poorer quality of spectral cues at lower elevations. We note that most single neurons in the cat superior colliculus show spatial tuning centered above -30 degrees (Middlebrooks and Knudsen, 1984). Also, coding of low elevations by neurons in the cat's auditory cortex tends to be relatively inaccurate (Xu *et al.*, 1998).

In the present study, optimal scale factors served as global measures of inter-cat differences in the frequencies of spectral features. In the sample of 24 cats, optimal scale factors ranged as high as 1.57 with a median value of 1.10. Individual spectral notches varied across a larger range, up to a factor of 2 in some cases (Fig. 3). Although previous studies have measured smaller samples of cats, one can see instances of variation in the frequencies of spectral features. In the study by Wiener and colleagues (1966), the center frequencies of mid-frequency notches in five cats ranged from approximately 10 to 13 kHz for sound sources at 0 degrees azimuth and 0 degrees elevation (a factor of 1.3; measured from fig. 6 in Wiener *et al.*, 1966). However, in that study, the authors focused on the low-frequency features of the external-ear transfer functions and largely ignored the individual differences in frequencies higher than 10 kHz. In the data illustrated by Musicant and colleagues (1990), three cats showed similar directional dependence of HRTFs, and it is difficult to see any differences in frequencies of spectral features. Rice and colleagues (1992; Fig. 11) showed HRTFs from four cats that appeared very similar. A fifth animal showed a mid-frequency notch that was displaced upward by a factor of $\sim$1.15, but the authors discussed several experimental factors that might have produced that difference. An additional cat measured in the same laboratory (Young *et al.*, 1996, Fig. 3) showed a HRTF for location at 0 degrees azimuth, 0 degrees elevation that was quite similar in shape to the HRTFs shown in the 1992 report but was displaced upward in frequency by a factor of $\sim$1.3. Considering the smaller sample sizes of previous studies, the magnitude of inter-cat variation in published data is roughly in line with the present observations. We consider in the next section whether that magnitude of variation is likely to be significant for studies of spatial hearing.

The magnitudes of individual differences in cats are roughly comparable to those observed in a similar study in humans (Middlebrooks, 1999a). Optimal scale factors for DTFs from pairs of humans were somewhat smaller than our results in cats: humans exhibited a median of 1.06 and maximum of 1.38 compared to median of 1.10 and maximum of 1.57 in cats. The reduction of spectral differences by frequency scaling was more efficient in humans than in cats: median and maximum percent reductions were 15.5% and $\sim$80%, respectively, in humans compared to 11.5% and 60.7% in cats. The lower percentage reduction in cats indicates that efforts to tailor DTFs from one subject for use with another might be less satisfactory in cats than in humans (Middlebrooks, 1999b). We speculate that inter-cat differences in ear position might contribute spectral differences that remain after optimal frequency scaling.

B. Implications of individual differences for physiological studies of spatial hearing

When human subjects listen through headphones to sounds that have been filtered by HRTFs measured from their own ears, they report a well localized ''virtual target'' that appears to originate from the location of the original free-field source (Wightman and Kistler, 1989b). Virtual localization technology has been applied recently to physiological studies in cats (Brugge *et al.*, 1994, 1996, 1998; Chan *et al.*, 1993; Delgutte *et al.*, 1999; Nelken *et al.*, 1997; Reale *et al.*, 1996) and other species (Hartung and Sterbing,

1997; Keller *et al.*, 1998). This approach offers several advantages, including the potential for independent manipulation of various acoustic parameters and the ability to deliver spatial cues under conditions in which it would be impossible to achieve high-quality free-field conditions (i.e., due to interference from experimental apparatus or due to necessary surgical distortion of the external ear).

When human subjects attempt to localize virtual sources that have been synthesized using HRTFs measured from other listeners' ears (''nonindividualized'' HRTFs) they show an increase in localization error, particularly in the vertical and front/back dimensions (Wenzel *et al.*, 1993). Systematic trends in errors can be related to the optimal frequency scale factors between subjects' own DTFs and the DTFs from which virtual targets are synthesized (Middlebrooks, 1999b). When small subjects localize targets that are synthesized from larger subjects' ears, the most common errors are front/back confusions. When large subjects localize targets that are synthesized from smaller subjects' ears, the most common error is an upward bias in responses. This increase in localization error resulting from use of nonindividualized DTFs raises concern about the use of nonindividualized DTFs in physiological experiments in cats, since systematic frequency differences as small as the median value in our sample of cats (i.e., 1.10) produce conspicuous localization errors in humans.

Based on the observations in the present study, we can speculate on some of the likely consequences of using nonindividualized DTFs in cat physiological experiments. We observed that the general shapes of DTFs and the general spatial dependence of DTFs are quite similar across cats. This indicates that basic studies of sensitivity to particular spectral features and, perhaps, studies of the general characteristics of spatial receptive fields would not suffer from use of nonindividualized DTFs. Indeed, Reale and colleagues (1996) examined the receptive fields of cortical neurons in a cat using stimuli synthesized with HRTFs from three other cats. Receptive fields measured in the three conditions differed at near-threshold stimulus levels but were quite similar at higher levels. We note, however, that the HRTFs used in that study were themselves quite similar. In a study in the guinea-pig inferior colliculus, Hartung and Sterbing (1997) found that receptive fields of units changed substantially when stimuli synthesized from another guinea pig's HRTFs were exchanged for those synthesized from an animal's own HRTFs.

Spectral features (i.e., peaks and notches) at particular frequencies corresponded to different locations in different cats. Thus, one might expect to encounter errors in experiments in which spatial sensitivity of neurons would be compared to an independent spatial reference, such as when auditory and visual modalities are compared in the superior colliculus (e.g., Middlebrooks and Knudsen, 1984; Wallace *et al.*, 1998). Similarly, one might expect to find distortions in any systematic progression of spatial tuning in such a midbrain structure, particularly since (at least in humans) use of nonindividualized DTFs in psychophysical procedures can result in a high rate of front/back confusions that are greater than 90 degrees in magnitude.

We recently have presented results of a study that examined the locations that are signaled by cortical neurons when presented with narrow bandpass stimuli (Xu *et al.*, 1999). By using narrow-band sounds, that study emphasized fine details of DTFs. Stimuli were presented in a free field, so cats were exposed to stimuli filtered by their own DTFs. Physiological results showed a close correspondence with the output of a model of spectral recognition that was based on DTFs measured from each cat's own ears. That correspondence would have been largely obscured had we used nonindividualized DTFs. Indeed, two sets of DTFs that were used as examples in the report showed optimal scale factors, one cat to the other, of only 1.025, yet inter-cat differences in details of the DTFs produced markedly different results in the acoustical model and in the physiology.

We regard our measurements of inter-cat differences in DTFs as conservative. All the measurements in the present study were from domestic short hair cats supplied from one of two breeding colonies. Similarly, previous studies appear to have used purpose-bred domestic short hair cats. We have by no means explored the great variability that can be found among other breeds of cats. A visit to any cat show reveals a wide variety of shapes and sizes of heads and ears. The potential for error derived from a mismatch between cats and DTFs is large. Nevertheless, the present results indicate that under certain conditions DTFs are generally similar among cats. We urge caution in interpreting results obtained with nonindividualized DTFs, but affirm that such procedures are acceptable for studies of spatial hearing when suitable care is taken to match animals by breed, size, and gender.

ACKNOWLEDGMENTS

We acknowledge the expert technical assistance by Zekiye Onsan. Shigeto Furukawa helped in DTF measurements. Shigeto Furukawa, Ewan Macpherson, Brian Mickey, and David Moody made valuable comments on an early draft of the manuscript. This research was supported by NIH Grant Nos. RO1 DC00420 and T32 DC00011.

Brugge, J. F., Reale, R. A., and Hind, J. E. (**1996**). ''The structure of spatial receptive fields of neurons in primary auditory cortex of the cat,'' J. Neurosci. **16**, 4420–4437.

Brugge, J. F., Reale, R. A., and Hind, J. E. (**1998**). ''Spatial receptive fields of primary auditory cortical neurons in quiet and in the presence of continuous background noise,'' J. Neurophysiol. **80**, 2417–2432.

Brugge, J. F., Reale, R. A., Hind, J. E., Chan, J. C. K., Musicant, A. D., and Poon, P. W. F. (**1994**). ''Simulation of free-field sound sources and its application to studies of cortical mechanisms of sound localization in the cat,'' Hear. Res. **73**, 67–84.

Butler, R. A. (**1987**). ''An analysis of the monaural displacement of sound in space,'' Percept. Psychophys. **41**, 1–7.

Casseday, J. H., and Neff, W. D. (**1973**). ''Localization of pure tones,'' J. Acoust. Soc. Am. **54**, 365–372.

Chan, J. C. K., Musicant, A. D., and Hind, J. E. (**1993**). ''An insert earphone system for delivery of spectrally shaped signals for physiological studies,'' J. Acoust. Soc. Am. **93**, 1496–1501.

Delgutte, B., Joris, P. X., Litovsky, R. Y., and Yin, T. C. T. (**1999**). ''Receptive fields and binaural interactions for virtual-space stimuli in the cat inferior-colliculus neurons,'' J. Neurophysiol. **81**, 2833–2851.

Foster, S. (**1986**). ''Impulse response measurement using Golay codes,'' in *I.E.E.E. 1986 Conference on Acoustics, Speech, and Signal Processing, Vol. 2* (I.E.E.E., New York), pp. 929–932.

Furukawa, S., Xu, L., and Middlebrooks, J. C. (**2000**). ''Coding of sound-source location by ensembles of cortical neurons,'' J. Neurosci. **20**, 1216–1228.

Glasberg, B. R., and Moore, B. C. J. (**1990**). ''Derivation of auditory filter shapes from notched noise data,'' Hear. Res. **47**, 103–138.

Golay, M. J. E. (**1961**). ''Complementary series,'' IRE Trans. Inf. Theory **7**, 82–87.

Hartung, K., and Sterbing, S. J. (**1997**). ''Generation of virtual sound sources for electrophysiological characterization of auditory spatial tuning in the guinea pig,'' in *Acoustical Signal Processing in the Central Auditory System*, edited by J. Syka (Plenum, New York), pp. 407–412.

Huang, A. Y., and May, B. J. (**1996**). ''Sound Orientation behavior in cats. II. Mid-frequency spectral cues for sound localization,'' J. Acoust. Soc. Am. **100**, 1070–1080.

Imig, T. J., Irons, W. A., and Samson, F. R. (**1990**). ''Single-unit selectivity to azimuthal direction and sound pressure level of noise bursts in cat high-frequency primary auditory cortex,'' J. Neurophysiol. **63**, 1448–1466.

Jenkins, W. M., and Masterton, R. B. (**1982**). ''Sound localization: Effects of unilateral lesions in central auditory system,'' J. Neurophysiol. **47**, 987–1016.

Keller, C. H., Hartung, K., and Takahashi, T. T. (**1998**). ''Head-related transfer functions of the barn owl: Measurement and neural responses,'' Hear. Res. **118**, 35–46.

May, B. J., and Huang, A. Y. (**1996**). ''Sound orientation behavior in cats. I. Localization of broadband noise,'' J. Acoust. Soc. Am. **100**, 1059–1069.

Mehrgardt, S., and Mellert, V. (**1977**). ''Transformation characteristics of the external human ear,'' J. Acoust. Soc. Am. **61**, 1567–1576.

Middlebrooks, J. C. (**1987**). ''Binaural mechanisms of spatial tuning in the cat's superior colliculus,'' J. Neurophysiol. **57**, 688–701.

Middlebrooks, J. C. (**1999a**). ''Individual differences in external-ear transfer functions reduced by scaling in frequency,'' J. Acoust. Soc. Am. **106**, 1480–1492.

Middlebrooks, J. C. (**1999b**). ''Virtual localization improved by scaling nonindividualized external-ear transfer functions in frequency,'' J. Acoust. Soc. Am. **106**, 1493–1510.

Middlebrooks, J. C., and Green, D. M. (**1990**). ''Directional dependence of interaural envelope delays,'' J. Acoust. Soc. Am. **87**, 2149–2162.

Middlebrooks, J. C., and Knudsen, E. I. (**1987**). ''Changes in external ear position modify the spatial tuning of auditory units in the cat's superior colliculus,'' J. Neurophysiol. **57**, 672–687.

Middlebrooks, J. C., and Knudsen, E. I. (**1984**). ''A neural code for auditory space in the cat's superior colliculus,'' J. Neurosci. **4**, 2621–2634.

Middlebrooks, J. C., Makous, J. C., and Green, D. M. (**1989**). ''Directional sensitivity of sound-pressure levels in the human ear canal,'' J. Acoust. Soc. Am. **86**, 89–108.

Middlebrooks, J. C., and Pettigrew, J. D. (**1981**). ''Functional classes of neurons in primary auditory cortex of the cat distinguished by sensitivity to sound location,'' J. Neurosci. **1**, 107–120.

Middlebrooks, J. C., Xu, L., Eddins, A. C., and Green, D. M. (**1998**). ''Codes for sound-source location in non-tonotopic auditory cortex,'' J. Neurophysiol. **80**, 863–881.

Morimoto, M., and Ando, Y. (**1980**). ''On the simulation of sound localization,'' J. Acoust. Soc. Jpn. (E) **1**, 167–174.

Musicant, A. D., Chan, J. C. K., and Hind, J. E. (**1990**). ''Direction-dependent spectral properties of cat external ear: New data and cross-species comparisons,'' J. Acoust. Soc. Am. **87**, 757–781.

Nelken, I., Bar Yosef, O., and Young, E. D. (**1997**). ''Response of Field AES neurons to virtual-space stimuli,'' in *Psychophysical and Physiological Advances in Hearing*, edited by A. R. Palmer, A. Rees, A. Q. Summerfield, and R. Meddis (Whurr, London), pp. 504–512.

Neti, C., Young, E. D., and Schneider, M. H. (**1992**). ''Neural network models of sound localization based on directional filtering by the pinna,'' J. Acoust. Soc. Am. **92**, 3140–3156.

Populin, L. C., and Yin, T. C. (**1998**). ''Behavioral studies of sound localization in cat,'' J. Neurosci. **18**, 2147–2160.

Rajan, R., Aitkin, L. M., Irvine, D. R. F., and McKay, J. (**1990**). ''Azimuthal sensitivity of neurons in primary auditory cortex of cats. I. Types of sensitivity and the effects of variations in stimulus parameters,'' J. Neurophysiol. **64**, 872–887.

Reale, R. A., Chen, J., Hind, J. E., and Brugge, J. F. (**1996**). ''An implementation of virtual acoustic space for neurophysiological studies of directional hearing,'' in *Virtual Auditory Space*, edited by S. Carlile (Springer-Verlag, Heidelberg), pp. 153–183.

Rice, J. J., May, B. J., Spirou, G. A., and Young, E. D. (**1992**). ''Pinna-based spectral cues for sound localization in cat,'' Hear. Res. **58**, 132–152.

Rose, J. E., Gross, N. B., Geisler, C. D., and Hind, J. E. (**1966**). ''Some neural mechanism in the inferior colliculus of the cat which may be relevant to localization of a sound source,'' J. Neurophysiol. **29**, 288–314.

Shaw, E. A. G. (**1966**). ''Earcanal pressure generated by a free sound field,'' J. Acoust. Soc. Am. **39**, 465–470.

Wallace, M. T., Meredith, M. A., and Stein, B. E. (**1998**). ''Multisensory integration in the superior colliculus of the alert cat,'' J. Neurophysiol. **80**, 1006–1010.

Wenzel, E. M., Arruda, M., Kistler, D. J., and Wightman, F. L. (**1993**). ''Localization using nonindividualized head-related transfer functions,'' J. Acoust. Soc. Am. **94**, 111–123.

Wiener, F. M., Pfeifer, R. R., and Backus, A. S. N. (**1966**). ''On the sound pressure transformation by the head and auditory meatus of the cat,'' Acta Oto-Laryngol. **61**, 255–269.

Wightman, F. L., and Kistler, D. J. (**1989a**). ''Headphone simulation of free field listening. I. Stimulus synthesis,'' J. Acoust. Soc. Am. **85**, 858–867.

Wightman, F. L., and Kistler, D. J. (**1989b**). ''Headphone simulation of free-field listening. II: Psychophysical validation,'' J. Acoust. Soc. Am. **85**, 868–878.

Xu, L., Furukawa, S., and Middlebrooks, J. C. (**1998**). ''Sensitivity to sound-source elevation in non-tonotopic auditory cortex,'' J. Neurophysiol. **80**, 882–894.

Xu, L., Furukawa, S., and Middlebrooks, J. C. (**1999**). ''Auditory cortical responses in the cat to sounds that produce spatial illusions,'' Nature (London) **399**, 688–691.

Young, E. D., Rice, J. J., and Tong, S. C. (**1996**). ''Effects of pinna position on head-related transfer functions in the cat,'' J. Acoust. Soc. Am. **99**, 3064–3076.

Zhou, B., Green, D. M., and Middlebrooks, J. C. (**1992**). ''Characterization of external ear impulse responses using Golay codes,'' J. Acoust. Soc. Am. **92**, 1169–1171.

Influence of primary frequencies ratio on distortion product otoacoustic emissions amplitude. I. Intersubject variability and consequences on the DPOAE-gram

A. Moulin[a)]

UPRESA CNRS 5020 Neurosciences et systèmes sensoriels. Perception et mécanismes auditifs. 8, avenue Rockefeller 69530 LYON Cedex 08, France and Laboratoire de physiologie sensorielle, Centre Hospitalier Lyon-Sud, 69495 Pierre-Bénite Cedex, France

(Received 16 April 1999; accepted for publication 1 November 1999)

Distortion product otoacoustic emissions (DPOAEs) are used widely in humans to assess cochlear function. The standard procedure consists of recording the $2f1\text{-}f2$ DPOAE amplitude as a function of the $f2$ frequency, using a fixed $f2/f1$ ratio (DPOAE-gram), close to 1.20. DPOAE amplitude, as recorded in the DPOAE-gram, shows a wide range of values in normal-hearing subjects, which can impair the predictive value of the DPOAE-gram for hearing thresholds. This study is aimed at comparing intersubject variability in $2f1\text{-}f2$ DPOAE amplitude according to three paradigms: a fixed $f2/f1$ ratio, such as the DPOAE-gram, a variable ratio DPOAE-gram ($f2/f1$ adapted to frequency) and an ''optimum'' DPOAE-gram, where the $f2/f1$ is adapted both to subject and frequency. The $2f1\text{-}f2$ DPOAE amplitude has been investigated on 18 normally hearing subjects at ten different $f2$ frequencies (from 0.75 to 6 kHz), using an $f2$ fixed, $f1$ sweep paradigm, and allowed to define, for each frequency, the $f2/f1$ ratio giving the greatest $2f1\text{-}f2$ DPOAE amplitude (or optimum ratio). Results showed a large intersubject variability of the optimum ratio, especially at frequencies below 1.5 kHz, and a significant decrease of the optimum ratio with frequency. The optimum DPOAE-gram was underestimated by up to 5.8 dB on average (up to 14.9 dB for an individual subject) by the fixed ratio DPOAE-gram, and by up to 3 dB on average (up to 10.6 dB for an individual subject) by the variable ratio DPOAE-gram. Intersubject variability was slightly but significantly reduced in the optimum DPOAE-gram versus the fixed-ratio DPOAE-gram. Lastly, correlations between tone-burst evoked otoacoustic emission (TBOAE) amplitudes and maximum DPOAE amplitudes were significantly greater than correlations between TBOAE amplitudes and fixed-ratio DPOAE amplitudes. [S0001-4966(00)03102-7]

PACS numbers: 43.64.Jb [BLM]

INTRODUCTION

It is now widely accepted that cochlear status can be assessed objectively in humans by otoacoustic emissions (OAEs), recorded for the first time in 1978 (Kemp, 1978). Otoacoustic emissions are sounds originating from the outer hair cells of the internal ear and can be recorded in the external auditory meatus. Depending on the stimulus parameters used to record OAEs, different types of otoacoustic emissions have been defined. The most widely used in assessing cochlear status in humans are transiently evoked otoacoustic emissions (TEOAEs), generated by click stimuli, and distortion product otoacoustic emissions (DPOAEs), generated by two pure tones of different frequencies $f1$ and $f2$ (with $f1<f2$) (Kemp, 1979). When stimulated by two pure tones of different frequencies $f1$ and $f2$ (primary frequencies), cochlear nonlinearities give rise to OAEs at frequencies corresponding to algebraic combination of $f1$ and $f2$, or distortion products. Most studies have dealt with $2f1\text{-}f2$, which is of greatest amplitude over a wide range of stimuli. It is now well accepted that the $2f1\text{-}f2$ DPOAE is generated primarily at a cochlear place corresponding to the region of the primary frequencies, as shown by pure tone exposure experiments (Martin *et al.*, 1987) and isosuppression experiments (Brown and Kemp, 1984; Harris *et al.*, 1992; Kummer *et al.*, 1995; Gaskill and Brown, 1996; Abdala *et al.*, 1996). Furthermore, distortion products have been shown in basilar membrane responses to originate in the basilar membrane region corresponding to the primary frequencies, and then propagate to the region corresponding to their distortion frequency (Robles *et al.*, 1991, 1997).

Like other types of OAEs, DPOAE presence and amplitude are decreased in cochlear hearing loss. The first and now most usual method of studying DPOAEs in clinical applications (Martin *et al.*, 1990) consists of recording $2f1\text{-}f2$ DPOAE amplitude as a function of primary frequencies, for fixed primary levels, and for a fixed $f2/f1$ ratio, which defines the separation of the two primary frequencies (DPOAE-gram). A good correlation between the DPOAE-gram pattern and the audiogram could be found in patients, using DPOAE-grams recorded at 65, 75 and 85 dB SPL (Martin *et al.*, 1990; Harris and Probst, 1991; Lonsbury-Martin *et al.*, 1993). However, the intersubject variability of DPOAE amplitude is such that it precludes precise prediction of the pure tone audiogram of a given subject using a DPOAE-gram (see, for instance, Probst and Hauser, 1990; Lasky *et al.*, 1992; Suckfüll *et al.*, 1996). Lower primary levels (at or lower than 62 dB SPL) allow a better sensitivity of the DPOAE-gram with a better correlation between DPOAE amplitude and auditory threshold at the corresponding primary

[a)]Electronic mail: amoulin@olfac.univ-lyon1.fr

frequency (Avan and Bonfils, 1993). Because it is generated at the $f2$ place, at the basal end of the $f1$ traveling wave, the $2f1$-$f2$ DPOAE amplitude is more dependent on the level of L1 than on the level of L2, as shown in human data by Gaskill and Brown (1990) and Whitehead *et al.* (1995a, c). Furthermore, Whitehead *et al.* (1995a, c) showed that lowering the level of $f2$ relative to the level of $f1$, at moderate L1 levels, increased $2f1$-$f2$ amplitude by less than 3.5 dB in normal-hearing subjects, but increased the reduction of DPOAE amplitude in subjects with sensorineural hearing loss when compared to normals. This suggests that using L1>L2 might help to separate normal hearing from abnormal hearing using DPOAE amplitude. Several studies have shown that DPOAE amplitude can be used to separate normal-hearing subjects from subjects having a hearing threshold above 20 dB HL (Gorga *et al.*, 1993). Using statistical analysis by receiver operating characteristic curves, Stover *et al.* (1996b) have shown that primary levels of 65/55 dB SPL allowed a better differentiation between normal-hearing and hearing impaired subjects. In this study, a level of L1=65 dB SPL has been chosen as it is now one of the most commonly used in clinical applications. A difference of only 5 dB between L1 and L2 has been chosen (L2=60 dB SPL), because increasing the level of L1 well above L2 decreases the amplitude of upper sideband DPOAEs such as $2f2$-$f1$ or $3f2$-$2f1$. A compromise of only 5 dB allowed us to be close to the usual parameters used in clinical applications, without impairing the recording of upper sideband DPOAEs which are described in the companion paper.

Most studies using the DPOAE-gram use a fixed $f2/f1$ around 1.20 for all the frequency and level ranges. It is well known that $2f1$-$f2$ DPOAE amplitude increases as the $f2/f1$ frequency ratio increases from 1.01, up to an optimal ratio beyond which DPOAE amplitude decreases. The optimal $f2/f1$ ratio is then defined as the $f2/f1$ ratio giving the DPOAE of greatest amplitude. Several studies have defined, in humans subjects, the optimal ratio for different stimuli conditions: Harris *et al.* (1989) reported on five adult human subjects, optimum ratios at three different primary levels (65, 75, and 85 dB SPL), and three different $2f1$-$f2$ frequencies (1, 2.5, and 4 kHz), changing $f2/f1$ by changing both $f1$ and $f2$ frequencies. They showed a decrease of the optimum $f2/f1$ ratio as a function of frequency and level, and obtained an average ratio of 1.22 across the three frequencies and three stimulus levels tested. This ratio of 1.22 has subsequently been widely used as the standard set parameter for clinical $2f1$-$f2$ DPOAE-gram. However, the parameters used for the DPOAE-gram have changed: the primary levels used now tend to be lower than 70 dB SPL, and different for $f1$ and $f2$ (L1>L2). Furthermore, Harris *et al.* (1989) kept the $2f1$-$f2$ frequency fixed, and changed both $f1$ and $f2$, so that, for instance, for a DPOAE at 1 kHz, the $f2$ frequency was modified from 1220 to 1860 Hz for an $f2/f1$ ranging from 1.10 to 1.30, which represents a substantial frequency range. The modification of DPOAE amplitude could then be attributed not only to the $f2/f1$ ratio, but to the changing place of DPOAE generation as well ($f2$ frequency). Applying their results to a standard DPOAE-gram is therefore not straightforward, but, from Harris *et al.*'s data, we would expect a change in the optimum ratio with frequency and level. In addition, Harris *et al.*'s reported some degree of intersubject variability, showing asymmetrical amplitude versus $f2/f1$ ratio functions between ears of a subject. Using a fixed $f1$ and varying $f2$ to change $f2/f1$, Gaskill and Brown (1990) obtained an average ratio of 1.225, using stimulus levels below 65 dB SPL, but reported only slight variations with frequency and subjects. More recently, Abdala (1996) studied in great detail the $2f1$-$f2$ DPOAE amplitude versus $f2/f1$ ratio function (ARF) (i.e., DPOAE amplitude as a function of $f2/f1$) in humans and neonates at 1500 and 6000 Hz, using a fixed $f2$ and a varying $f1$, and showed a significantly lower ratio at 6 kHz than at 1.5 kHz, and a decrease in the $f2/f1$ ratio with decreasing level separation of the primary frequencies from 15 to 0 dB (L1>L2). A similar decrease in the optimum ratio with frequency was obtained in adults by Lasky (1998), using a fixed $f2$ and varying $f1$, at 60 dB equilevel primaries, for six different $f2$ frequencies between 1 and 8 kHz. It is therefore likely that using a fixed $f2/f1$ ratio for the DPOAE-gram does not give the greatest amplitude DPOAE response one would expect when using an $f2/f1$ adapted to frequency and primary levels. Moreover, none of these studies have specifically addressed the intersubject variability of the amplitude versus $f2/f1$ ratio functions and its consequences on intersubject variability of DPOAE amplitude. To address this issue, amplitude ratio functions have been systematically studied as a function of ten different $f2$ frequencies, in a group of normally hearing subjects, to determine mean values and variability of ARFs (and optimum $f2/f1$ ratio) as a function of frequency. The DPOAE-gram has been reconstructed at each $f2/f1$ ratio to see the consequence of ARF variability on the DPOAE-gram pattern. Lastly, interrelations between DPOAE amplitude and tone-burst-evoked OAE (TBOAE) amplitude recorded in the same subjects were analyzed to determine to what extent modifying the $f2/f1$ ratio could modify the relationship between DPOAEs and other types of OAEs.

I. MATERIAL AND METHODS

A. Subjects

Eighteen normally hearing adult human subjects (ten women, eight men), aged between 24 and 46 years [mean =31.4 years, standard deviation (s.d.)=6 years], were tested. None of the subjects had any history of significant otologic disease and all exhibited pure tone audiometric thresholds in both ears equal to or better than 15 dB HL at standard audiometric frequencies and a normal middle ear function assessed by impedance measurements. No significant differences according to gender were found in auditory thresholds, nor in age.

B. OAE recordings

1. Material

All recordings were made in a soundproof room.

Tone-burst-evoked OAEs (TBOAEs) and distortion product OAEs (DPOAEs) were recorded using respectively Otodynamics ILO88 version 5.50c software (TBOAEs) and

ILO92 Analyzer, version 1.35 software (DPOAEs). A standard adult ILO92 DPOAE probe with three ports was used. The two tone stimuli were generated by two separate loudspeakers and the recording of the response was measured by a microphone incorporated into the probe. The probe was sealed in the external auditory meatus with a foam ear tip. Search for spontaneous otoacoustic emissions (SOAEs) was done for all subjects, using the SOAE search facility of the ILO88 software.

Subjects were comfortably seated in an armchair, and instructed to remain as quiet as possible. Only one ear per subject was tested, chosen at random. TBOAE and DPOAE recordings were performed in two recording sessions, whose order was randomized across subjects.

2. DPOAE recordings

Amplitudes of the $2f1\text{-}f2$ DPOAEs were recorded as a function of $f2/f1$ ratio to obtain DPOAE amplitude versus $f2/f1$ ratio functions. The $f2/f1$ ratio was modified from 1.02 to 1.50 by fixing the $f2$ primary frequency, and changing $f1$ primary frequency in steps varying from 12 Hz at low frequencies to 72 Hz at high frequencies, corresponding to a step change of $f2/f1$ between 0.012 and 0.02. Each sweep was preceded by a ''probe check fit'' procedure that allowed an assessment of the probe fitting using a real-time fast Fourier transform (FFT) analysis of the ear canal response to wideband clicks. The levels of the primaries were monitored during the sweep, so that if the difference between the actual levels of the primaries and their expected values was greater than 1.5 dB, the stimulus levels were set again.

Primary levels were fixed at 65 dB SPL for $f1$ (L1) and 60 dB SPL for $f2$ (L2). Ten different $f2$ frequencies were tested in a random order for each subject: 757, 879, 1000, 1257, 1500, 2002, 3003, 4004, 5005, and 6006 Hz. Each sweep contained a minimum of ten frequency steps or measurement points and, for each point, 128 signal samples were averaged. The DPOAEs were considered as present when their amplitude was greater than the mean noise floor plus 2 standard deviations. The mean noise floor was obtained from the average amplitude of the five spectral components on either sideband of the $2f1\text{-}f2$ frequency.

3. TBOAE recordings

Tone-burst stimuli were nonlinear, five-cycle-long tone-bursts, two-cycle rising time, one-cycle plateau and two-cycle fall time, generated at ten different frequencies, corresponding to the frequencies chosen as $f2$ frequencies for DPOAE recordings, i.e., 750, 880, 1000, 1250, 1500, 2000, 3000, 4000, 5000, and 6000 Hz. Stimulus intensities were adjusted prior to recording for each subject and for each frequency in order to obtain an intrameatal intensity between 65 and 68 dB SPLpe (peak equivalent sound pressure level). The recording time window was 25 ms for the 750- and 880-Hz stimuli, and 15 ms for greater frequencies, with corresponding repetition rates of 40 and 60 Hz, respectively. Noisy responses exceeding 3.1 mPa were rejected and an average of 300 responses were performed for each subject at each frequency. The different frequencies were presented randomly to each subject.

4. Intrasubject variability assessment

In order to study the intrasubject variability of DPOAE amplitude as a function of $f2/f1$ ratio, the DPOAE recordings were repeated several months apart in three subjects, at 1, 1.5, 2, 3, 4, and 6 kHz, using the same equipment and recording rooms. However, due to the length of time between the different recording sessions (2 years in one case), the same probe could not be used for each of the sessions. For subject 1, DPOAE recordings were repeated twice, at 10 weeks apart, and 2 years apart. For subjects 17 and 18, the recordings were repeated once, at 45 weeks apart, and at 36 weeks apart, respectively.

C. Data analysis

1. DPOAE

For each $f2$ frequency, the $f2/f1$ ratio giving the greatest DPOAE amplitude (termed as ''optimum $f2/f1$ ratio'') and the greatest DPOAE amplitude obtained over the $f2/f1$ ratio range (termed as ''maximum DPOAE amplitude'') was obtained from each subject. The DPOAE amplitude as a function of $f2/f1$ was then smoothed according to a three-point running average method, and the optimum $f2/f1$ and the maximum DPOAE amplitude obtained with the smoothed functions were obtained for each subject.

In order to obtain parameters describing the overall pattern of each amplitude ratio function, a nonlinear regression analysis, using a third-degree polynomial function, was performed between the DPOAE amplitude as a function of the $2f1\text{-}f2$ DPOAE frequency, for each of the ten $f2$ frequencies tested, and for each subject [following the technique described by Abdala (1996)]. Correlation coefficients (R) obtained from this nonlinear regression analysis ranged between 0.62 and 0.9996. Five individual functions (out of 180) did not reach statistical significance ($p>0.05$) and were therefore excluded. To study the pattern of the amplitude versus DPOAE frequency functions, the two DPOAE frequencies for which DPOAE amplitude was equal to the optimum amplitude minus 3 dB were obtained for each function. The bandwidth defined by the difference between these two DPOAE frequencies was used to calculate a Q value (cf. Abdala, 1996), as the ratio of the DPOAE frequency giving the greatest DPOAE amplitude, divided by the bandwidth. The Q value was used as an indicator of the width of the ARF. This technique allowed us to obtain the Q value, the optimum DPOAE amplitude, and $f2/f1$ ratio by taking into account the whole ARF function, and not only a few points.

The DPOAE-grams were calculated for each subject using ten points (corresponding to the ten $f2$ frequencies tested), and for fixed $f2/f1$ ratios, ranging from 1.04 to 1.40, by 0.02 steps. An ''optimum'' DPOAE-gram was calculated for each subject, and consisted of the greatest DPOAE amplitude obtained over an $f2/f1$ sweep for each $f2$ frequency.

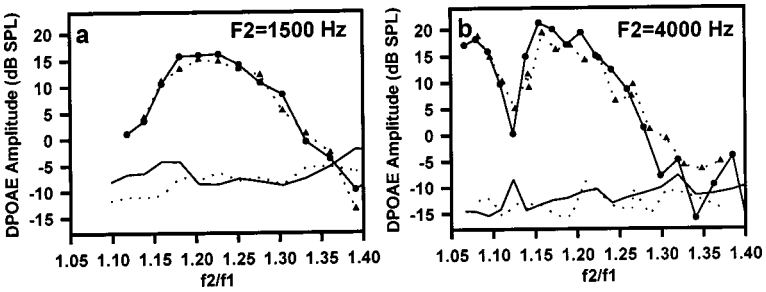

FIG. 1. Reproducibility of $2f1$-$f2$ DPOAE amplitude as a function of $f2/f1$, recorded twice at a 45-week interval, with an $f2$ fixed, $f1$ sweep method, for a single subject at 1.5 kHz (a) and 4 kHz (b). The DPOAE amplitude is represented by symbols, and noise floor by lines.

2. TBOAEs and SOAEs

The amplitudes of TBOAEs were obtained for each stimulus frequency for each subject. Only data at least 3 dB above the noise and showing a reproducibility greater than 70% were selected. At 5 and 6 kHz, only 12 subjects out of 18 met these criterions. Intrameatal stimulus intensities ranged from 65.6 to 67.6 dB SPLpe, with an average of 66.12 dB SPLpe.

The SOAEs were defined as present when synchronized transiently evoked otoacoustic emissions were present more than 60 ms after the click stimulus, and were at least 3 dB above the noise floor. Eight subjects (seven women, one man) out of 18 presented SOAEs.

3. Statistical analyses

Analyses of the optimum $f2/f1$ ratios, Q values and DPOAE amplitude as a function of frequency were performed by analysis of variance for repeated measurements (Anova-R). The intersubject variability in DPOAE-grams was compared with the variability obtained in the optimum DPOAE-gram using Snedecor and Cochran's test.

Student t-test was used to analyze the differences in DPOAE amplitude functions and TBOAE amplitudes according to SOAE presence.

Correlation analysis was used to analyze relationships between $f2/f1$ optimum ratios, DPOAE amplitudes, primary frequencies, and TBOAE amplitudes. Pearson's correlation coefficients are specified as ''r.'' Steiger's test (Steiger, 1980) was used to compare the correlations obtained between DPOAE amplitudes and TBOAE amplitudes and the correlations obtained between DPOAE amplitudes and TBOAE amplitudes.

The level of statistical significance chosen was 5% and is specified for each test as p.

II. RESULTS

A. DPOAE presence

Across all frequencies, $2f1$-$f2$ DPOAE presence was above 92% across $f2/f1$ ratios below 1.30 and decreased rapidly for greater $f2/f1$ ratios. At frequencies below 2000 Hz, presence above 92% was obtained for $f2/f1$ ratios up to 1.34. More detailed results concerning DPOAE presence is presented in the companion paper (Moulin, 2000).

B. Intrasubject variability of ARFs (Fig. 1)

To assess the intrasubject variability of ARFs, the maximum DPOAE amplitude for each ARF was calculated. When averaged across the three subjects, the differences in maximum DPOAE amplitude ranged between 1.4 dB at 1.5 kHz and 2.8 dB at 3 kHz (for raw data). When considered as a function of $f2/f1$, the average, across the three subjects, of the maximum difference in amplitude obtained at two different recordings, across all frequencies, was between 3 and 7 dB for low ratios (<1.28), and between 4.6 and 11.5 dB for $f2/f1$ above 1.28. Figure 1 shows an example of ARF reproducibility, at 1.5 kHz [Fig. 1(a)] and 4 kHz [Fig. 1(b)], for a subject. The mean noise floor plus 2 standard deviations is shown as lines without symbols on the figure.

C. Intersubject variability of amplitude ratio functions (Fig. 2)

Figure 2 shows smoothed ARFs with $f2$ at 1 and 5 kHz for different normal-hearing adults, with the noise floor as dotted lines. Both the shape of the ARF and the optimum $f2/f1$ ratio vary from subject to subject. At 1 kHz, at the ratio of 1.22, subjects 9, 11 and 17 show very similar DPOAE amplitude, whereas at a greater ratio, subjects 14 and 17 show substantially greater DPOAE amplitude than subjects 4 and 11. At smaller ratios than 1.22, subject 9 show larger DPOAE amplitude than subjects 11, 14 and 17. At 5 kHz,

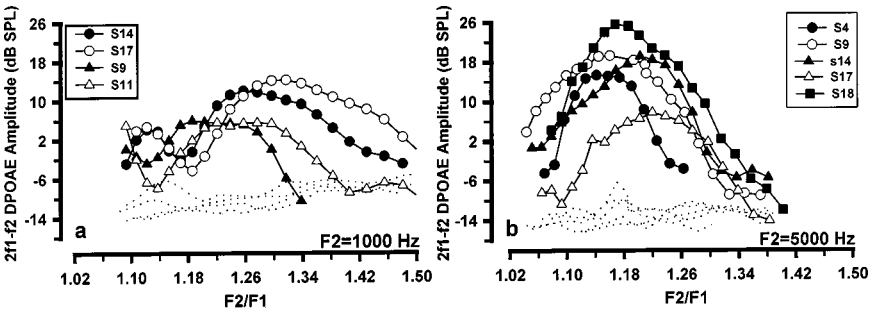

FIG. 2. The $2f1$-$f2$ DPOAE amplitude as a function of $f2/f1$ for different normal-hearing subjects, recorded with an $f2$ fixed, $f1$ sweep method, with $f2$ fixed at 1 kHz (a) and at 5 kHz (b). Primary levels are set at 65 dB SPL for $f1$ and 60 dB SPL for $f2$. Data have been smoothed according to a three-point running average. Noise floor is shown for each subject as dotted lines (mean noise +2 standard deviations).

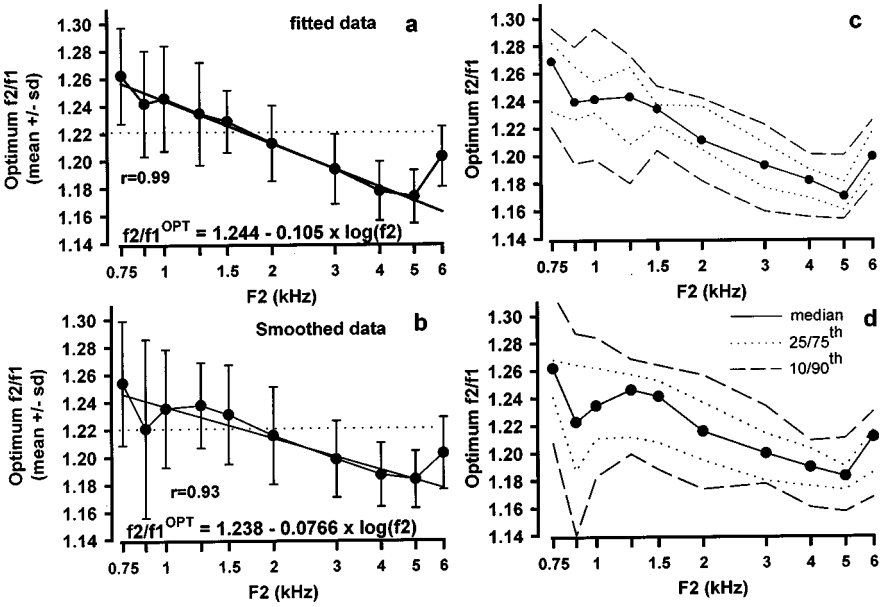

FIG. 3. Optimum $f2/f1$ for $2f1$-$f2$ DPOAE amplitude recorded at 65 and 60 dB SPL, obtained in 18 normal-hearing subjects (mean ± standard deviation: left panels; median and percentiles: right panels). Optimum ratios have been obtained for each ARF after smoothing using a three-point running average (smoothed data: lower panels) and using a third-degree polynomial fit (fitted data: upper panels).

according to the ratio chosen, subject 4 shows greater or smaller amplitude than subject 17. According to the $f2/f1$ ratio chosen, the relative amplitudes of DPOAEs from one subject to another change.

D. Optimum $f2/f1$ as a function of frequency

The optimum $f2/f1$ decreased significantly with increasing $f2$ frequencies from 750 Hz to 5 kHz [Anova-R, $F(17,9)=4.47$, $p<0.0001$] (Fig. 3). Similar results were obtained for the three methods used to obtain the optimum ratio (raw data, smoothed data, or third-degree polynomial fit). Across all subjects, the decrease of the optimum $f2/f1$ was linear as a function of $f2$ frequency in kHz (Fig. 3), following the functions obtained for each of the methods used:

Optimum $f2/f1=1.244-0.105\,05\log(f2)$, with $r=0.99$, $p<0.001$ (polynomial fit).

Optimum $f2/f1=1.238-0.0766\log(f2)$, with $r=0.93$, $p<0.001$ (smoothed data)

Optimum $f2/f1=1.228-0.0684\log(f2)$, with $r=0.89$, $p<0.001$ (raw data).

A significant correlation between the optimum $f2/f1$ obtained by a polynomial fit and $f2$ frequency between 750 and 5000 Hz was observed for 17 subjects out of 18.

However, at 6 kHz, the optimum ratio was significantly greater than the ratios obtained at 4 and 5 kHz, whatever method was used to calculate the $f2/f1$ ratios (paired t-tests on fitted data, $t=4.46$, $p<0.0005$ between 6 and 5 kHz, $t=3.79$, $p<0.005$ between 6 and 4 kHz) (Fig. 3).

No statistically significant correlation was obtained between the optimum $f2/f1$ ratio and the maximum DPOAE amplitude.

Intersubject variability of the optimum ratio decreased with increasing frequency (Fig. 3) and was significantly larger at lower frequencies than at higher frequencies: the standard deviations obtained at 1 and 1.5 kHz were significantly greater than the standard deviations obtained at 4, 5, and 6 kHz (t-test, $p<0.05$). Furthermore, the interpercentile range and the range of the optimum ratio decreased significantly linearly with the logarithm of the $f2$ frequency [$r=0.77$ $p<0.01$ (interpercentile range), and $r=0.87$, $p<0.005$ (range) for fitted data, $r=0.80$, $p<0.01$ and $r=0.87$, $p<0.005$ for smoothed data, and $r=0.66$, $p<0.05$ and $r=0.71$, $p<0.05$ for raw data].

The pattern of the amplitude versus ratio function varied with frequency: the Q values increased significantly as frequency increased [$F(9,149)=3.3$, $p<0.005$ (Anova-R)] (Fig. 4). A significant correlation between the Q values and the logarithm of the $f2$ frequency (in kHz) was obtained on mean data (Fig. 4): $Q_{F2}=3.65+1.92*\log[f2(\mathrm{Hz})]$ ($r=0.95$, $p<0.0001$). No correlations were found between Q values and maximum DPOAE amplitude.

E. DPOAE amplitude as a function of $f2/f1$ and frequency

The DPOAE amplitude as a function of frequency and $f2/f1$ ratio showed a non-monotonic behavior, as a function of frequency, with lowest amplitudes in the 3-kHz region, and greater amplitudes around 1.5 kHz and above 5 kHz, whatever the $f2/f1$ ratio (Fig. 5). However, the DPOAE-gram pattern was quite different according to the ratio chosen: higher ratios favor lower frequencies, whereas lower $f2/f1$ ratios favor higher frequencies. The maximum DPOAE

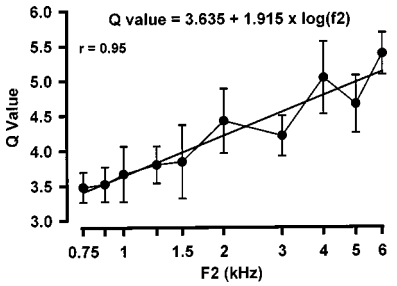

FIG. 4. The $2f1$-$f2$ DPOAE ARF tuning (Q value) calculated from a third-degree polynomial fit on individual ARFs (mean ± standard error of the mean), obtained in 18 normal-hearing subjects, using an $f2$ fixed, $f1$ sweep method, with primary levels at 65 and 60 dB SPL.

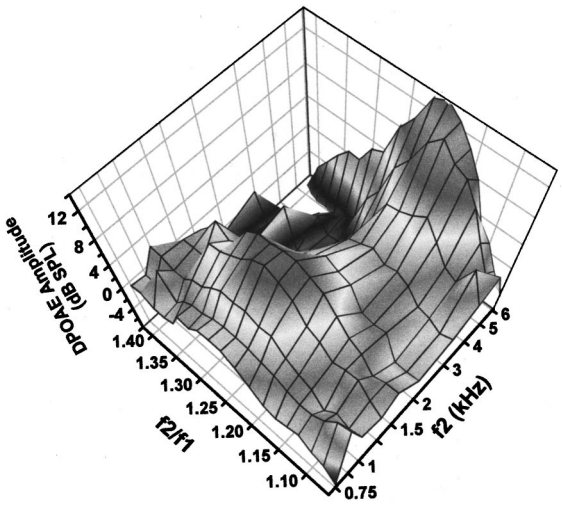

FIG. 5. The $2f1$-$f2$ DPOAE amplitude (dB SPL) as a function of $f2$ (DPOAE-gram), for $f2/f1$ ratios ranging from 1.06 to 1.40, in a group of 18 normal-hearing subjects, at 65 (L1) and 60 dB SPL (L2).

amplitudes were statistically significantly greater in subjects presenting SOAEs, at frequencies ranging from 3 to 6 kHz. When individual $f2/f1$ ratios were considered, subjects presenting SOAEs showed significantly greater DPOAE amplitude at 2, 3, 4, 5, and 6 kHz, mainly at low $f2/f1$ ratios. SOAE presence did not show any statistically significant influence on Q values [$F(1,13)=3.27$, $p=0.09$]. Detailed data about SOAEs for each subjects and further analysis are included in the companion paper (Moulin, 2000).

The optimum DPOAE-gram showed significantly larger DPOAE amplitude across all the ten frequencies than any of the fixed ratio DPOAE-grams, whether raw data or smoothed data were considered [Fig. 6(a) and (b)] ($p<0.01$). For individual subjects, the differences in amplitude between the optimum DPOAE-gram and a DPOAE-gram constructed by taking the optimum ratio at each frequency (DPOAE-gram^{Fvar}) could reach 10.6 dB (for raw data) and 8.3 dB (for smoothed data). When differences were taken between the optimum DPOAE-gram and the 1.22 fixed ratio DPOAE-gram (DPOAE-gram$^{1.22}$), the differences could reach, for an individual subject, 13.3 dB (for smoothed data) and 14.9 dB (for raw data). The mean differences between the optimum DPOAE-gram and the fixed ratio DPOAE-grams increased greatly when the fixed ratio used was far from the optimum ratio at the frequency considered, especially at high frequencies (Fig. 7).

Intersubject variability of DPOAE amplitude tended to be lower in the optimum DPOAE-gram than at fixed ratio DPOAE-grams: Standard deviations of the DPOAE-gram$^{1.22}$ were significantly greater than standard deviations of the optimum DPOAE-gram at 0.75, 1 and 1.5 kHz ($p<0.05$) [Fig. 6(a)]. At several different $f2/f1$ and frequencies, standard deviation of DPOAE amplitude was significantly lower in the optimum DPOAE-gram than in the fixed ratio DPOAE-gram, as shown in Fig. 8. The interpercentile range obtained for the optimum DPOAE-gram was 14.8% smaller using raw data (8.8% smaller using smoothed data) than the interpercentile range obtained for fixed ratio DPOAE-grams, across the ten frequencies and across ratios from 1.14 to 1.32.

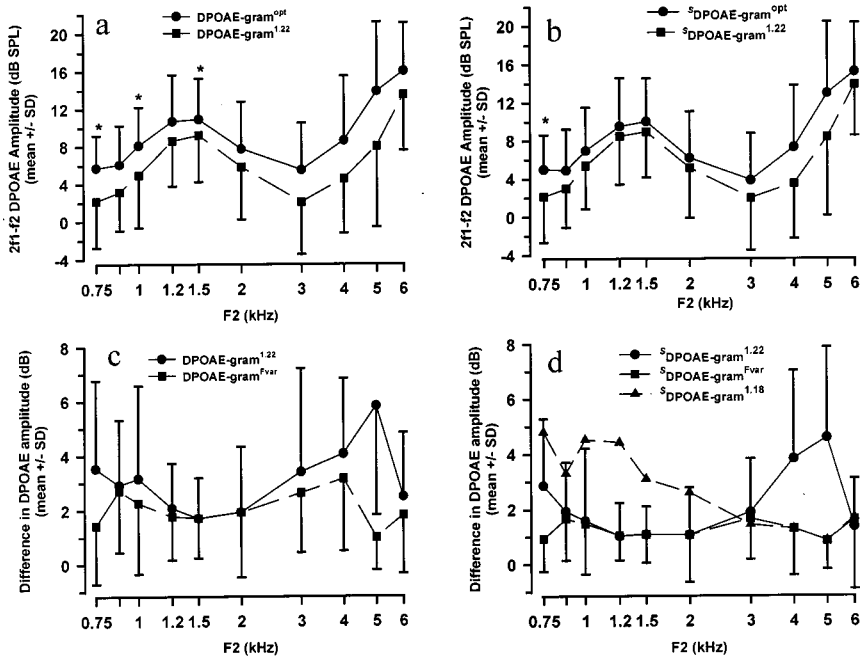

FIG. 6. The DPOAE-gram obtained by taking the greatest DPOAE amplitude for each subject and $f2$ frequency, over a 1.02 to 1.50 $f2/f1$ range (''Optimum'' DPOAE-gram or DPOAE-gram^{opt}, circles), and standard DPOAE-gram obtained with a fixed $f2/f1$ of 1.22 (DPOAE-gram$^{1.22}$, squares), with raw data (a) and smoothed data (b). (c) and (d) show the mean differences in dB obtained between the ''optimum'' DPOAE-gram, and the standard DPOAE-gram for an $f2/f1$ at 1.22 (circles), and the mean differences in dB obtained between the ''optimum'' DPOAE-gram and the DPOAE-gram obtained by taking a variable $f2/f1$ ratio across the $f2$ frequencies (squares, DPOAE-gram^{Fvar}). (c) Has been obtained from raw data and (d) from smoothed data. In addition, (d) shows the mean differences in dB obtained between the ''optimum'' DPOAE-gram, and the standard DPOAE-gram for an $f2/f1$ at 1.18 (triangles, DPOAE-gram$^{1.18}$). In (a), standard deviations of the optimum DPOAE-gram and fixed ratio DPOAE-gram have been compared, with * for $p<0.05$. The difference in DPOAE amplitude between the two DPOAE-grams is statistically significant whatever the $f2$ frequency.

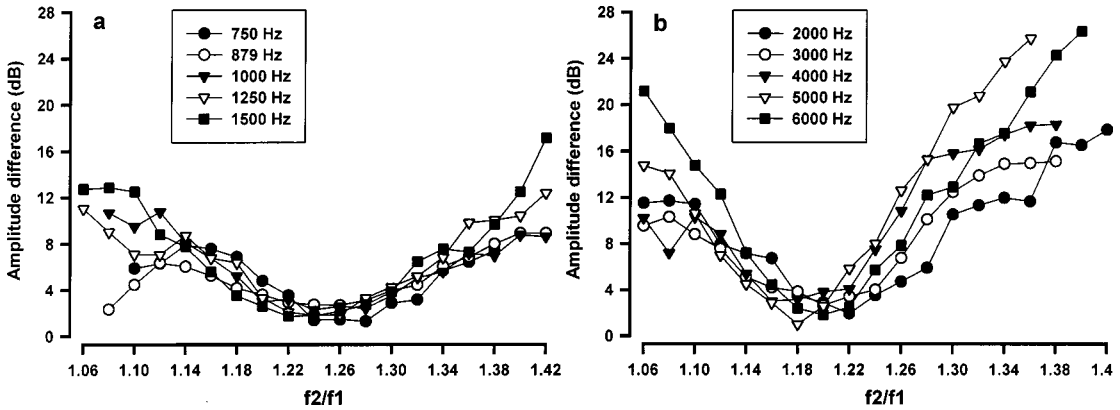

FIG. 7. Mean differences in dB (raw data) observed in 18 normal-hearing subjects between the optimum DPOAE-gram and the fixed ratio DPOAE-gram as a function of frequency ($f2$, kHz) and $f2/f1$.

F. Correlations between DPOAE amplitude and tone-burst evoked otoacoustic emissions amplitude (Fig. 9)

The mean echo amplitude was 6.34 dB SPLpe (s.d. $=5.8$), and ranged from 0.63 dB SPLpe at 6 kHz (s.d.$=6.5$) to 9.41 SPLpe at 1 kHz (s.d.$=4.12$). Subjects presenting SOAEs showed significantly greater TBOAE amplitude from 1250 Hz to 6 kHz.

Significant positive correlations were found between DPOAE amplitude (raw data and smoothed data) and TBOAE amplitude for 1.5 kHz ($r=0.54$, $n=16$, $p<0.05$), 2 kHz ($r=0.58$, $n=17$, $p<0.05$), 3 kHz ($r=0.82$, $n=17$, $p<0.001$) and 4 kHz ($r=0.90$, $n=17$, $p<0.0001$).

Correlations between TBOAE amplitude and the maximum DPOAE amplitude (Fig. 9, black dots) were significantly greater than correlations obtained between TBOAE amplitude and DPOAE amplitude recorded at a fixed ratio (Fig. 9, white dots), especially at 3 and 4 kHz. Correlations between DPOAE amplitude taken at the optimum ratio (black dots) and TBOAE amplitude, and correlations between DPOAE amplitude recorded at a $f2/f1$ fixed at 1.28 and TBOAE amplitude (white dots) are shown at 1.5 kHz [Fig. 9(a)] and 3 kHz [Fig. 9(b)]. Correlations between TBOAE and maximum DPOAE amplitude were significantly greater than correlations between TBOAE and DPOAE amplitude recorded at ratios 1.24 at 1.25 kHz; 1.24 to 1.34 at 1.5 kHz; 1.22, 1.24 and 1.30 at 2 kHz [Fig. 9(c)]; 1.20 to 1.34 at 3 kHz; 1.12 to 1.32 at 4 kHz [Fig. 9(d)], 1.22 to 1.30 at 5 kHz, and 1.24 at 6 kHz. The correlations obtained between TBOAE amplitude and smoothed data DPOAE amplitude did not differ significantly from the correlations obtained between TBOAEs and raw data DPOAE amplitude.

III. DISCUSSION

Repetitive measurement of DPOAE amplitude for several $f2/f1$ ratios showed a greater intrasubject variability for high $f2/f1$ (up to 13.6 dB) than at $f2/f1$ close to the optimum ratio (up to 4.4 dB), which can be explained by the smaller DPOAE amplitude at the ratios far from the optimum ratio, and by the greater noise floor of the recordings at lower DPOAE frequencies (recorded at high $f2/f1$ ratios) (Fig. 1). The slightly greater mean intrasubject variability obtained

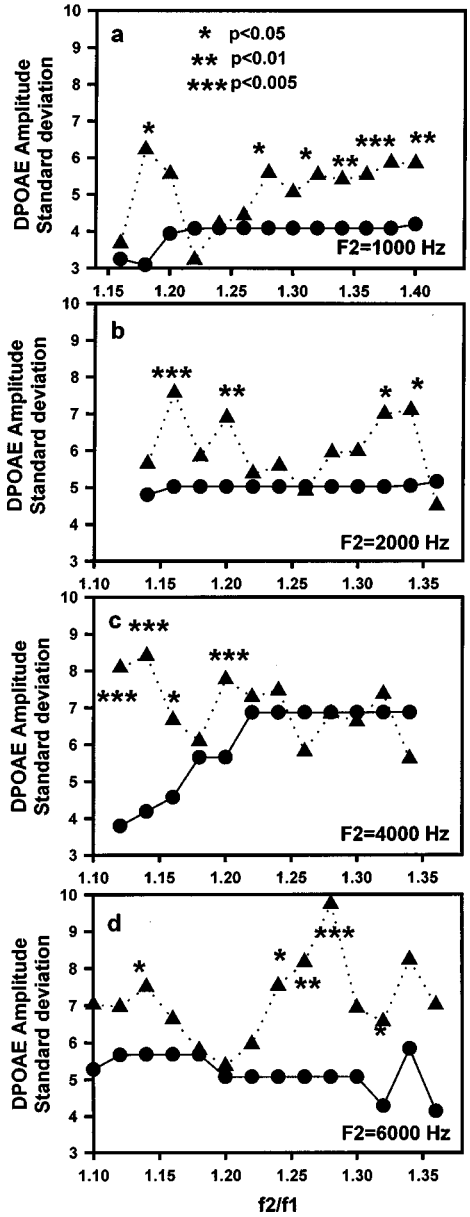

FIG. 8. Intersubject variability in DPOAE amplitude as a function of the $f2/f1$ ratio (triangles), compared to the intersubject variability of the optimum DPOAE amplitude (circles). Comparisons have been done using the same subjects for each $f2/f1$, hence the variation of the optimum DPOAE amplitude variance with $f2/f1$ due to variation in the number of subjects.

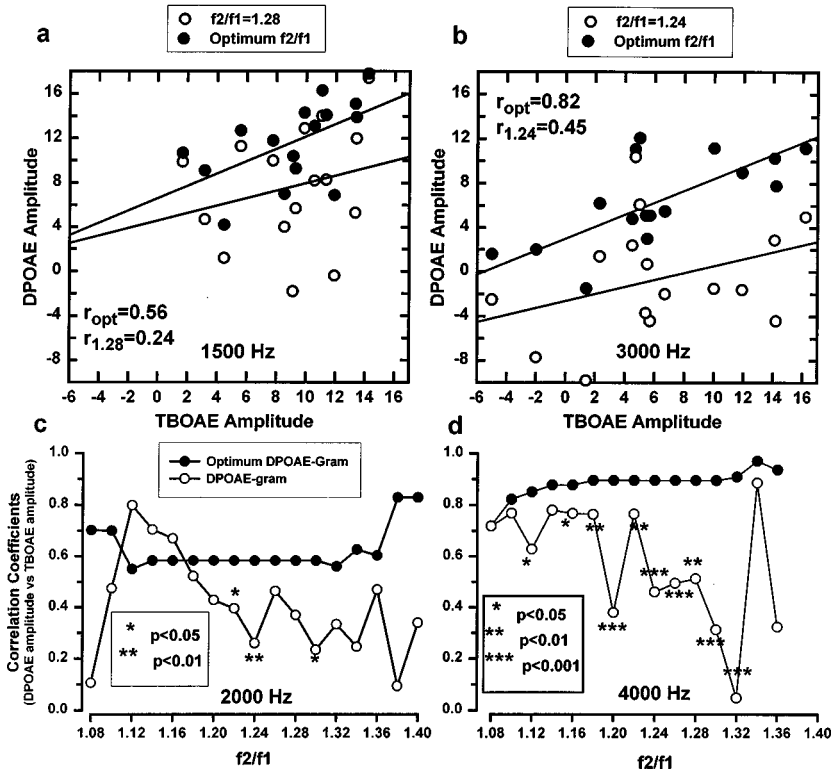

FIG. 9. Correlations between TBOAE amplitude at 1500 Hz (a) and at 3000 Hz (b) and $2f1$-$f2$ DPOAE amplitude taken at a fixed $f2/f1$ (white dots) (correlation coefficients $r_{1.24}$ and $r_{1.28}$), and at the optimum ratio (black dots) (correlation coefficient r_{opt}). The bottom panels show the correlations coefficients obtained between DPOAE amplitude (obtained at a fixed ratio: white dots, and taken as the maximum amplitude over the ratio range: black dots) and TBOAE amplitude for each $f2/f1$, for $f2$ at 2000 Hz (c) and $f2$ at 4000 Hz (d). Correlation coefficients have been compared by Steiger's test, and statistical significance is specified for each $f2/f1$ with * for $p<0.05$;** for $p<0.01$, and *** for $p<0.0001$. The number of subjects varies slightly for each ratio as not all subjects presented a DPOAE for a given $f2/f1$ ratio and correlation coefficients have been compared in exactly the same subjects.

here than in Roede *et al.* (1993) and Franklin *et al.* (1992) studies can be explained by our small sample size, and a substantially longer period of time between the different measurements taken. The pattern of the ARFs showed very good reproducibility over long periods of time for each of the three subjects tested repeatedly in this study, which is in agreement with Brown *et al.* (1992) and Gaskill and Brown (1990). The intersubject variability of ARFs shown in Fig. 2 therefore cannot be attributed simply to intrasubject variability.

In order to assess the influence of the variability of the ARF on the fixed ratio DPOAE-gram, the optimum $f2/f1$ for each frequency tested needed to be obtained. Harris *et al.* (1989) showed decreasing optimum ratios at 1, 2 and 4 kHz, and Abdala (1996) reported a significantly lower optimum $f2/f1$ at 6 kHz than at 1 kHz. Our results agree with a systematic variation of the optimum ratio according to frequency, and show significant decrease of optimum $f2/f1$ ratio, as a function of $f2$ frequency, for a frequency range of 750 Hz to 6 kHz in humans (Fig. 3). Allen and Fahey (1993) reported the equation of the variation of the frequency of the maximum distortion peak with $f2$, in a single human ear, at 65 dB SPL equilevel primaries, and for $f2$ above 1 kHz: Frequency of distortion $=0.5\times f2^{1.04}$, which becomes, translated in terms of optimum $f2/f1$, optimum $f2/f1=1.2058-0.0444\log(f2)$ (with $f2$ in kHz), which gives a ratio of 1.21 at 750 Hz and 1.17 at 6 kHz. Compared to our results, Allen and Fahey's results show similar $f2/f1$ ratios at high frequencies, but a smaller $f2/f1$ at low frequencies. However, the fact that their equation has been obtained in a single human ear, and at frequencies greater than 1 kHz, could account for this difference, the frequencies below 1.5 kHz, in our data set, giving the largest $f2/f1$ ratios.

The greater optimum $f2/f1$ ratio obtained at 6 kHz (Fig. 3) can be explained by underestimation of the primary levels, due to standing waves within the outer ear canal of the subjects. These standing waves can be responsible for great variation in the primary intensities at the eardrum, so that the sound pressure level of primaries at the probe tip can underestimate the levels of the primaries at the ear drum by up to 20 dB SPL (Siegel and Hirohata, 1994; Whitehead *et al.*, 1995b). It is highly likely that at 6 kHz, the sound pressure level at the ear drum was underestimated. Optimum $f2/f1$, for a given frequency, increases as primary levels increase (Harris *et al.*, 1989; Moulin *et al.*, 1999). The greater optimum ratio obtained at 6 kHz can therefore be explained by a higher level of primaries at 6 kHz than at lower frequencies, which yielded greater optimum ratios. According to Siegel (1994), the influence of standing waves on the primary levels at the eardrum can occur at frequencies as low as 3 kHz. Therefore, it is not impossible that the optimum ratios obtained at frequencies above 3 kHz, have been overestimated. If that is the case, the dependency of the optimum ratio on the $f2$ frequency would even be greater than the results described here, and therefore could have more influence on the DPOAE levels obtained with an iso-ratio paradigm. The other possible consequence of the standing wave problem would be an added intersubject variability in the primary levels at the eardrum and, therefore, on the optimum $f2/f1$ ratios. However, our results show a significantly larger intersubject variability in the optimum $f2/f1$ at low frequencies, where there should be much less effect of the standing waves on primary levels. This greater intersubject variability at low frequencies is more probably due to the lesser tuning of the amplitude versus ratios functions at low frequencies, as shown in the Q value data (Fig. 4). Admittedly, noise floor at

low frequencies is always greater than at high frequencies. However, as only DPOAE above the noise floor plus 2 standard deviations have been taken into account, and indeed, DPOAE amplitude around the optimum ratio was well above the noise floor (see for instance, Figs. 1 and 2), it is not likely that the noise floor had a significant influence on Q values and on the optimum ratio variability. This greater intersubject variability in the optimum $f2/f1$ at low frequencies leads to greater variability in DPOAE amplitude, as the standard deviation obtained in the optimum DPOAE-gram tends to be smaller than standard deviation obtained in the fixed ratio DPOAE-grams for $f2$ at 0.75 to 1.5 kHz (Fig. 6).

Whatever the $f2/f1$ used, the DPOAE-grams showed a dip around the 3-kHz region, with high level DPOAEs at the 1.5- and 6-kHz regions (Fig. 5). The levels obtained in this study for $f2/f1$ ratios of 1.20 and 1.22 are within less than 3 dB of the levels obtained by Lonsbury-Martin *et al.* (1990) in a sample of 44 ears (22 subjects), using an $f2/f1$ ratio of 1.21 and equilevel primary levels at 65 dB SPL, and within 4 dB of the levels obtained by Smurzynski *et al.* (1992) using equilevel primaries at 65 dB SPL and an $f2/f1$ ratio ranging from 1.18 to 1.23. The slightly higher levels obtained here can be attributed to the 5-dB difference between the primaries levels used here, as lowering L2 increases $2f1$-$f2$ level by a few dB when L1=65 dB SPL (Whitehead *et al.*, 1995a). Moreover, Hauser and Probst (1991) showed that the maximum $2f1$-$f2$ level was reached by 10-dB difference between L1 and L2 at 1 and 2 kHz and 5 dB at 4 kHz with L1 fixed at 65 dB SPL (and L1>L2). Our results demonstrate that this dip in the DPOAE-gram cannot be attributed to the $f2/f1$ chosen as it is constant over the ratios tested, and is only slightly reduced in the optimum DPOAE-gram.

Results presented here show a substantial difference in DPOAE amplitude between the optimum DPOAE-gram and the standard 1.22 fixed ratio DPOAE-gram, as differences up to 14 dB for an individual subject could be obtained and up to 5.8 dB on average data (Fig. 7). The greatest differences were found at high frequencies, which reflects the greater tuning of the ARFs at these high frequencies: A slight departure from the optimum ratio, at frequencies above 3 kHz, leads to a greater loss of DPOAE amplitude than at frequencies below 2 kHz. The use of a fixed ratio close to the optimum ratio (as, for instance, 1.22) would probably not result, in normal hearing subjects, in an absent DPOAE that would be present if an optimum ratio adapted to both frequency and subject was used, at 65 dB SPL, as DPOAE amplitudes recorded at 65 dB SPL in normal-hearing subjects are quite large. However, if the DPOAE amplitude, and not only DPOAE presence, is to be taken into account, the choice of the $f2/f1$ used might have a substantial influence. The use of primary levels of 65 dB was motivated by the fact that it is similar to primary levels used in DPOAE-grams. Furthermore, by yielding an average ratio across frequencies close to 1.20, 65-dB primary levels represent the level at which the least difference between optimum DPOAE-gram and fixed-ratio DPOAE-gram would be obtained. Indeed, optimum $f2/f1$ depends strongly on primary levels (Moulin *et al.*, 1999), and comparison between fixed 1.22 $f2/f1$ DPOAE-gram with optimum DPOAE-gram at low primary intensities are likely to show much greater differences between both methods. Admittedly, the optimum DPOAE-gram seems unrealistic: obtaining the optimum DPOAE-gram for each of the ten frequencies tested would require recording sessions too long to be useful in day-to-day clinical applications. However, based on the results presented here, if the search for the optimum DPOAE-gram is based on the normative data of the optimum $f2/f1$ as a function of frequency, the number of recording points necessary to obtain the maximum DPOAE amplitude decreases greatly. Using the same $f2$ frequencies as presented here, and an $f2$ fixed, $f1$ sweep method, with a step change of $f2/f1$ of 0.01 and a ratio range equal to the 10th and 90th percentiles of the data set, the maximum DPOAE amplitude could be obtained with only four points at high frequencies (Table I). Furthermore, intersubject variability of the optimum ratio, at frequencies above 3 kHz, is low compared to the variability observed at lower frequencies. High-frequency DPOAE amplitudes can therefore be well approximated taking an $f2/f1$ adapted to the frequency tested, without requiring individual adaptation for each subject.

TABLE I. Frequency parameters adapted to find the optimum $f2/f1$ for each subject and $f2$ frequency, by modifying $f2/f1$ over the interpercentile range, and the full range of optimum $f2/f1$ ratios obtained in normal-hearing subjects, using smoothed ARFs (the number of steps is adapted to a change of $f2/f1$ of 0.01).

	10th–90th percentile		Full range	
$f2$ (Hz)	Starting $f1$ (Hz)	No. of steps	Starting $f1$ (Hz)	No. of steps
757	575	7	573	11
879	683	10	662	15
1001	779	7	760	10
1257	991	5	974	8
1501	1188	5	1159	10
2002	1593	6	1561	10
3003	2434	4	2423	8
4004	3313	3	3259	7
5005	4135	4	4103	6
6006	4884	4	4820	6

There is a significant but small decrease of intersubject variability in DPOAE amplitude from the fixed ratio DPOAE-gram to the optimum DPOAE-gram (Fig. 8), which shows that most of the DPOAE amplitude variability observed in the DPOAE-gram is not due to the ARF variability. Other factors, such as age (Lonsbury-Martin *et al.*, 1991; Dorn *et al.*, 1998) and small variations in hearing thresholds (Dorn *et al.*, 1998), have been suggested to have an influence on DPOAE amplitude (in the absence of middle ear pathology). Whether a 14% decrease in the interpercentile range of DPOAE amplitude obtained in the present study is sufficient to increase the sensitivity of the DPOAE amplitude in discriminating normal-hearing versus hearing impaired subjects needs to be assessed. Nevertheless, the decrease in intersubject variability is greater for low frequencies (below 1.5 kHz), i.e., for frequencies where the sensitivity and specificity of the DPOAE test is known to be the lowest (Kim *et al.*, 1995; Gorga *et al.*, 1993).

Results presented here show correlations between fixed

ratio DPOAE amplitudes and TBOAE amplitudes (Fig. 9) that are similar to correlations obtained between DPOAE amplitude and click evoked OAE frequency-band amplitudes in Smurzynski and Kim (1992) and in Moulin *et al.* (1993). This agrees with the similarities between TEOAEs and TBOAEs described by Prieve *et al.* (1996). Correlations increased greatly (above 0.80), especially at high frequencies, when the maximum DPOAE amplitude was taken into account, which argues for a common mechanism responsible for TBOAE and DPOAE generation. The intersubject variability observed in OAE amplitude in normal-hearing subjects would then be more linked to intersubject variability in cochlear status than to an added variability due to the technique used. The relatively low correlations obtained previously between transiently evoked OAE amplitude and fixed ratio DPOAE amplitudes could be attributed to the added variability of DPOAE amplitude obtained at a fixed $f2/f1$ ratio. Results show that correlations between DPOAE amplitude and TBOAE amplitude are greater at small $f2/f1$ ratios, which agrees with the greater correlations obtained by Knight and Kemp (1999) between transiently evoked OAEs and DPOAE amplitudes, when using a 1.05 $f2/f1$ ratio. The correlations between TBOAEs and DPOAE amplitude have been performed with the TBOAE frequency band centered at the $f2$ frequency place. Once generated at the $f2$ place, the $2f1\text{-}f2$ DPOAE propagates towards the apex, to its frequency specific place, and backwards towards the base of the cochlea. The DPOAE recorded in the outer ear canal can be composed of a direct component, coming from the $f2$ place, and of an indirect DPOAE component, coming from the DPOAE place. Recent studies suggest that the indirect component can have a substantial influence on DPOAEs recorded in the ear canal, especially at low to moderate primary levels (Stover *et al.*, 1996a; Brown *et al.*, 1996) and Kemp and Knight (1999) suggested that low $f2/f1$ $2f1\text{-}f2$ DPOAEs come from reflection from their distortion product frequency place. If the DPOAE component coming from the DPOAE place has some influence on DPOAE amplitude as recorded in the outer ear canal, then DPOAEs recorded at different frequencies, with an $f2$ fixed, might have different origin. This could explain the greater correlations with TBOAE amplitude we obtain at low $f2/f1$, where DPOAE frequency is high and close to $f2$ frequency, than at greater ratios, where DPOAE frequency is much lower than the TBOAE center frequency. This issue will be further developed in the companion paper (Moulin, 2000), where influence of spontaneous OAEs and correlations between the different lower-sideband DPOAE and TBOAE amplitude will be described.

IV. CONCLUSION

Our results show a substantial modification of the optimum $f2/f1$ with frequency, which can lead to substantial amplitude differences and greater intersubject variability in DPOAE amplitude when an iso-ratio paradigm such as the DPOAE-gram is used. Furthermore, correlations between TBOAE amplitude and maximum DPOAE amplitude are significantly greater than correlations obtained with fixed ratio DPOAE amplitudes. Therefore, using a fixed ratio paradigm contributes to the intersubject variability observed in DPOAE amplitude in normal-hearing subjects, but is not the main factor at the origin of this variability.

ACKNOWLEDGMENTS

The author wishes to thank Nouzhra Merzoug for her excellent technical assistance, Paul Smith for his corrections of the manuscript, and the three anonymous reviewers for their comments and help.

Abdala, C. (**1996**). ''Distortion product otoacoustic emission ($2f1\text{-}f2$) amplitude as a function of $f2/f1$ frequency ratio and primary tone level separation in human adults and neonates,'' J. Acoust. Soc. Am. **100**, 3726–3740.

Abdala, C., Sininger, Y. S., Ekelid, M., and Zeng, F. G. (**1996**). ''Distortion product otoacoustic emission suppression tuning curves in human adults and neonates,'' Hearing Res. **98**, 38–53.

Allen, J. B., and Fahey, P. F. (**1993**). ''A second cochlear-frequency map that correlates distortion product and neural tuning measurements,'' J. Acoust. Soc. Am. **94**, 809–816.

Avan, P., and Bonfils, P. (**1993**). ''Frequency specificity of human distortion product otoacoustic emissions,'' Audiology **1**, 12–26.

Brown, A. M., and Kemp, D. T. (**1984**). ''Suppressibility of the $2f1\text{-}f2$ stimulated acoustic emissions in gerbil and man,'' Hearing Res. **1**, 29–37.

Brown, A. M., Gaskill, S. A., and Williams, D. M. (**1992**). ''Mechanical filtering of sound in the inner ear,'' Proc. R. Soc. London, Ser. B **1327**, 29–34.

Brown, A. M., Harris, F. P., and Beveridge, H. A. (**1996**). ''Two sources of acoustic distortion products from the human cochlea,'' J. Acoust. Soc. Am. **100**, 3260–3267.

Dorn, P. A., Piskorski, P., Keefe, D. H., Neely, S. T., and Gorga, M. P. (**1998**). ''On the existence of an age/threshold/frequency interaction in distortion product otoacoustic emissions,'' J. Acoust. Soc. Am. **104**, 964–971.

Franklin, D. J., McCoy, M. J., Martin, G. K., and Lonsbury-Martin, B. L. (**1992**). ''Test/retest reliability of distortion-product and transiently evoked otoacoustic emissions,'' Ear Hearing **6**, 417–429.

Gaskill, S. A., and Brown, A. M. (**1990**). ''The behavior of the acoustic distortion product, $2f1\text{-}f2$, from the human ear and its relation to auditory sensitivity,'' J. Acoust. Soc. Am. **88**, 821–839.

Gaskill, S. A., and Brown, A. M. (**1996**). ''Suppression of human acoustic distortion product: Dual origin of $2f1\text{-}f2$,'' J. Acoust. Soc. Am. **100**, 3268–3274.

Gorga, M. P., Neely, S. T., Bergman, B. M., Beauchaine, K. L., Kaminski, J. R., Peters, J., and Jesteadt, W. (**1993**). ''Otoacoustic emissions from normal-hearing and hearing-impaired subjects: Distortion product responses,'' J. Acoust. Soc. Am. **93**, 2050–2060.

Harris, F. P., and Probst, R. (**1991**). ''Reporting click-evoked and distortion-product otoacoustic emission results with respect to the pure-tone audiogram,'' Ear Hearing **6**, 399–405.

Harris, F. P., Probst, R., and Xu, L. (**1992**). ''Suppression of the $2f1\text{-}f2$ otoacoustic emissions in humans,'' Hearing Res. **64**, 133–141.

Harris, F. P., Lonsbury-Martin, B. L., Stagner, B. B., Coats, A. C., and Martin, G. K. (**1989**). ''Acoustic distortion products in humans: Systematic changes in amplitude as a function of $f2/f1$ ratio,'' J. Acoust. Soc. Am. **85**, 220–229.

Hauser, R., and Probst, R. (**1991**). ''The influence of systematic primary-tone level variation L2-L1 on the acoustic distortion product emission $2f1\text{-}f2$ in normal human ears,'' J. Acoust. Soc. Am. **89**, 280–286.

Kemp, D. T. (**1978**). ''Stimulated acoustic emissions from within the human auditory system,'' J. Acoust. Soc. Am. **64**, 1386–1391.

Kemp, D. T. (**1979**). ''The evoked cochlear mechanical response and the auditory microstructure—evidence for a new element in cochlear mechanics,'' Scand. Audiol. Suppl. **979**, 35–47.

Kemp, D. T., and Knight, R. (**1999**). ''Virtual DP reflector explains DPOAE wave' and place' fixed dichotomy,'' Assoc. Res. Otolaryngol Abstr. **22**, 396.

Kim, D. O., Paparello, J., Jung, M. D., Smurzynski, J., and Sun, X. (**1995**). ''Distortion product otoacoustic emission test of Sensorineural Hearing Loss: Performance Regarding Sensitivity, Specificity and Receiver Operating Characteristics,'' Acta Otolaryngol. (Stockh) **116**, 2–11.

Knight, R. D., and Kemp, D. T. (**1999**). ''Relationships between DPOAE and TEOAE amplitude and phase characteristics,'' J. Acoust. Soc. Am. **106**, 1420–1435.

Kummer, P., Janssen, T., and Arnold, W. (**1995**). ''Suppression tuning characteristics of the $2f1\text{-}f2$ distortion-product otoacoustic emission in humans,'' J. Acoust. Soc. Am. **98**, 197–210.

Lasky, R., Perlman, J., and Hecox, K. (**1992**). ''Distortion-product otoacoustic emissions in human newborns and adults,'' Ear Hearing **6**, 430–441.

Lasky, R. E. (**1998**). ''Distortion-product otoacoustic emissions in human newborns and adults. I. Frequency effects,'' J. Acoust. Soc. Am. **103**, 981–991.

Lonsbury-Martin, B. L., Cutler, W. M., and Martin, G. K. (**1991**). ''Evidence for the influence of aging on distortion-product otoacoustic emissions in humans,'' J. Acoust. Soc. Am. **89**, 1749–1759.

Lonsbury-Martin, B. L., McCoy, M. J., Whitehead, M. L., and Martin, G. K. (**1993**). ''Clinical testing of distortion-product otoacoustic emissions,'' Ear Hearing **1**, 11–22.

Lonsbury-Martin, B. L., Harris, F. P., Stagner, B., Hawkins, M. D., and Martin, G. K. (**1990**). ''Distortion product emissions in humans: II. Relations to acoustic immitance and stimulus frequency and spontaneous otoacoustic emissions in normally hearing subjects,'' Ann. Otol. Rhinol. Laryngol. 99 Suppl. **147**, 15–29.

Martin, G. K., Lonsbury-Martin, B. L., Probst, R., Scheinin, S. A., and Coats, A. C. (**1987**). ''Acoustic distortion products in rabbit ear canal. II. Sites of origin revealed by suppression contours and pure tone exposures,'' Hearing Res. **28**, 191–208.

Martin, G. K., Ohlms, L. A., Harris, F. P., Franklin, D. J., and Lonsbury-Martin, B. L. (**1990**). ''Distortion product emissions in humans. III. Influence of sensorineural hearing loss,'' Ann. of Otol. Rhinol. Laryngol. 99 Suppl. **147**, 30–42.

Moulin, A. (**2000**). ''Influence of primary frequencies ratio on distortion product otoacoustic emissions amplitude. II. Interrelations between multicomponent DPOAEs, tone-burst-evoked OAEs, and sontaneous OAEs,'' J. Acoust. Soc Am. **107**, 1471–1486.

Moulin, A., Jourdain, F., and Collet, L. (**1999**). ''Using acoustic distortion products in clinical applications: influence of $f2/f1$ on DPOAE-grams,'' British Society of Audiology Short Papers Meeting on Experimental Studies of Hearing and Deafness, September 1998, University College London, Br. J. Audiol. **33**, 89.

Moulin, A., Collet, L., Veuillet, E., and Morgon, A. (**1993**). ''Interrelations between acoustic distortion products, transiently evoked otoacoustic emissions and spontaneous otoacoustic emissions,'' Hearing Res. **65**, 216–233.

Prieve, B. A., Gorga, M. P., and Neely, S. T. (**1996**). ''Click and tone-burst evoked otoacoustic emissions in normal hearing and hearing-impaired ears,'' J. Acoust. Soc. Am. **99**, 3077–3086.

Probst, R., and Hauser, R. (**1990**). ''Distortion product otoacoustic emissions in normal and hearing-impaired ears,'' Am. J. Otolaryngol. **4**, 236–243.

Robles, L., Ruggero, M. A., and Rich, N. C. (**1991**). ''Two-tone distortion in the basilar membrane of the cochlea,'' Nature (London) **349**, 413–414.

Robles, L., Ruggero, M. A., and Rich, N. C. (**1997**). ''Two-tone distortion in the basilar membrane of the chinchilla cochlea,'' J. Neurophysiol. **77**, 2385–2399.

Roede, J., Harris, F. P., Probst, R., and Xu, L. (**1993**). ''Repeatability of distortion product otoacoustic emissions in normally hearing humans,'' Audiology **5**, 273–281.

Siegel, J. H. (**1994**). ''Ear canal standing waves and high frequency sound calibration using otoacoustic emission probes,'' J. Acoust. Soc. Am. **95**, 2589–2597.

Siegel, J. H., and Hirohata, E. T. (**1994**). ''Sound calibration and distortion product otoacoustic emissions at high frequencies,'' Hearing Res. **2**, 146–152.

Smurzynski, J., and Kim, D. O. (**1992**). ''Distortion-product and click-evoked otoacoustic emissions of normally-hearing adults,'' Hearing Res. **2**, 227–240.

Steiger, J. H. (**1980**). ''Tests for comparing elements of a correlation matrix,'' Psychol. Bull. **87**, 245–251.

Stover, L. J., Neely, S. T., and Gorga, M. P. (**1996a**). ''Latency and multiple sources of distortion product otoacoustic emissions,'' J. Acoust. Soc. Am. **99**, 1016–1024.

Stover, L., Gorga, M. P., Neely, S. T., and Montoya, D. (**1996b**). ''Towards optimizing the clinical utility of distortion product otoacoustic emission measurements,'' J. Acoust. Soc. Am. **100**, 956–967.

Suckfull, M., Schneeweiss, S., Dreher, A., and Schorn, L. (**1996**). ''Evaluation of TEOAE and DPOAE measurements for the assessment of auditory thresholds in sensorineural hearing loss,'' Acta Otolaryngol. (Stockh) **116**, 528–533.

Whitehead, M. L., McCoy, M. J., Lonsbury-Martin, B. L., and Martin, G. K. (**1995a**). ''Dependence of distortion-product otoacoustic emissions on primary levels in normal and impaired ears. I. Effects of decreasing L2 below L1,'' J. Acoust. Soc. Am. **97**, 2346–2358.

Whitehead, M. L., Stagner, B. B., Lonsbury-Martin, B. L., and Martin, G. K. (**1995b**). ''Effects of ear-canal standing waves on measurements of distortion-product otoacoustic emissions,'' J. Acoust. Soc. Am. **98**, 3200–3214.

Whitehead, M. L., Stagner, B. B., McCoy, M. J., Lonsbury-Martin, B. L., and Martin, G. K. (**1995c**). ''Dependence of distortion-product otoacoustic emissions on primary levels in normal and impaired ears. II. Asymmetry in L1, L2 space,'' J. Acoust. Soc. Am. **97**, 2359–2377.

Influence of primary frequencies ratio on distortion product otoacoustic emissions amplitude. II. Interrelations between multicomponent DPOAEs, tone-burst-evoked OAEs, and spontaneous OAEs

A. Moulin[a)]

UPRESA CNRS 5020 Neurosciences et systèmes sensoriels. Perception et mécanismes auditifs. 8, avenue Rockefeller 69530 LYON Cedex 08, France and Laboratoire de physiologie sensorielle, Centre Hospitalier Lyon-Sud, 69495 Pierre-Bénite Cedex, France

(Received 16 April 1999; accepted for publication 1 November 1999)

Distortion product otoacoustic emissions (DPOAEs) are used widely in humans to assess cochlear function. It is well known that $2f1\text{-}f2$ DPOAE amplitude increases as the $f2/f1$ ratio increases from 1.0 to about 1.20, and then decreases as the $f2/f1$ ratio increases above 1.20, showing an amplitude ratio function, which is thought to be related to cochlear filtering properties. Different lower sideband DPOAEs are believed to show the same amplitude ratio functions as the $2f1\text{-}f2$ DPOAE, with a magnitude peak situated at a constant DPOAE frequency relative to $f2$. More recently, several studies have suggested the involvement of a DPOAE component coming from its own distortion product place as well as the DPOAE component coming from the $f2$ place. To investigate DPOAE generation sites and the importance of the DPOAE frequency place, amplitude ratio functions of $2f1\text{-}f2$, $3f1\text{-}2f2$, $4f1\text{-}3f2$ and $2f2\text{-}f1$, $3f2\text{-}2f1$, $4f2\text{-}3f1$ DPOAE components have been systematically studied in 18 normally hearing subjects, using an $f2$ fixed, $f1$ sweep method, and an $f1$ fixed, $f2$ sweep method, at ten different $f2$ frequencies. Results show a dependency of the distortion magnitude peak on $f2$ frequency for each lower sideband DPOAE, and a small frequency shift of the distortion peak for the high order lower sideband DPOAE components. Strong correlation between the different lower sideband DPOAE amplitude were obtained, whether they were recorded with the same $f1$ (and a different $f2$) or with the same $f2$ (and a different $f1$), suggesting that lower side-band DPOAE amplitude does not depend on small variations in the $f2$ frequency. Moreover, correlations between DPOAE amplitude and tone-burst evoked otoacoustic emissions (TBOAEs) are highly significant for TBOAEs centered at the $f2$ frequency and at $\frac{1}{2}$ octave below the $f2$ frequency, suggesting some degree of importance of the cochlear status at frequencies below $f2$ in DPOAE amplitude. Subjects presenting spontaneous otoacoustic emissions showed a greater lower sideband DPOAE amplitude recorded for low $f2/f1$ ratios, and a distortion magnitude peak shifted towards higher frequencies. The best correlation between upper sideband DPOAE amplitude and lower sideband DPOAE amplitude occurred for lower sideband DPOAEs generated by an $f2$ frequency $\frac{1}{2}$ octave to 1 octave below the primaries used to generate upper sideband DPOAEs, suggesting a site of generation basal to $f2$ for the upper sideband DPOAEs. Correlations between TBOAE amplitude and upper sideband DPOAE amplitude agreed with a site of upper sideband DPOAE generation basal to $f2$, and which would move with the DPOAE frequency itself. [S0001-4966(00)03202-1]

PACS numbers: 43.64.Jb, 43.64.Kc [BLM]

INTRODUCTION

It is well known that cochlear status can be assessed objectively by otoacoustic emissions, or sounds emitted by the ear, originating in the outer hair cells' system of the organ of Corti. Distortion product otoacoustic emissions (DPOAEs) are otoacoustic emissions evoked by two pure tones of different frequencies (primary frequencies $f1$ and $f2$, with $f1<f2$) at frequencies corresponding to algebraic combinations of $f1$ and $f2$. Although multiple combination DPOAEs can be obtained, numerous studies have focused on $2f1\text{-}f2$ DPOAEs, especially in humans, since it is the component of greatest amplitude over a wide range of stimulus parameters. Numerous suppression studies have shown in animals and humans that the $2f1\text{-}f2$ is suppressed by a third tone in the primary frequency region (Brown and Kemp, 1984; Harris *et al.*, 1992; Kummer *et al.*, 1995; Abdala *et al.*, 1996). It is now generally accepted that the $2f1\text{-}f2$ DPOAE site of generation is in the cochlear region corresponding to the primary frequencies, more precisely for some studies at the $f2$ place. Once generated, the $2f1\text{-}f2$ DPOAE propagates in two directions: backwards from the $f2$ place to the base of the cochlea (and can be recorded in the outer ear canal as an otoacoustic emission) and towards its own apical frequency place (Robles *et al.*, 1991, 1997; Brown *et al.*, 1992). The DPOAE amplitudes vary according to the ratio of the primary frequencies: when the separation

a)Electronic mail: amoulin@olfac.univ-lyon1.fr

between the two primary frequencies increases ($f2/f1$ increases), $2f1$-$f2$ DPOAE amplitude increases up to an optimum $f2/f1$ of about 1.20 and then decreases as $f2/f1$ increases further. The decrease of DPOAE amplitude as the two primaries grow apart is easy to explain by the separation of the two traveling waves along the cochlear partition, until the overlapping region between $f2$ and $f1$ traveling waves is not sufficient to elicit a DPOAE. However, the decrease of DPOAE amplitude as the two primaries get closer to one another is still under discussion. When lower sideband DPOAE components ($2f1$-$f2$, $3f1$-$2f2$, $4f1$-$3f2$) are recorded as a function of their DPOAE frequency, using an $f2$ fixed, $f1$ sweep method, their amplitude peaks at the same distortion frequency (Brown *et al.*, 1992; Allen and Fahey, 1993a, b). Several authors (Brown *et al.*, 1992; Allen and Fahey, 1993a) have suggested the presence of a second filter, tuned to about half an octave relative to the $f2$ frequency, that would be responsible for this tuning of the lower sideband DPOAE responses. However, the same tuning of the DPOAE response has been observed without filtering in a nonlinear cochlea model (Matthews and Molnar, 1986), and without the need for a second filter in a computational model of the cochlea (Kanis and deBoer, 1997). Kanis and deBoer (1997) attributed this filtering to suppression between several DPOAE components coming from the DPOAE frequency places and the primaries.

Results concerning cochlear traveling time delays recorded in humans have shown the same interdependency of the different lower sideband DPOAEs: $3f1$-$2f2$ and $2f1$-$f2$ DPOAEs show similar latency provided they have the same distortion frequency and same $f2$ frequency (Moulin and Kemp, 1996). This would suggest that the DPOAEs recorded in the outer ear canal are composed mainly of the component coming from the $f2$ place. However, other evidence suggests that the DPOAE component coming from the DPOAE place itself might have a significant influence on the DPOAEs recorded in the outer ear canal (Gaskill and Brown, 1996), especially at low to moderate primary levels (Brown *et al.*, 1996; Stover *et al.*, 1996). Kemp and Knight (1999) have suggested that $2f1$-$f2$ DPOAE recorded at very low $f2/f1$ ratios are a reflection from the DPOAE frequency place itself, rather than from the $f2$ place. If there is a significant participation of the DPOAE place in DPOAE amplitude, then correlation between the amplitude of the different lower sideband DPOAE components and tone-burst-evoked OAE (TBOAE) amplitudes might differ according to the $f2/f1$ ratio, and to the order of the DPOAE components: high-order lower sideband DPOAEs ($3f1$-$2f2$, $4f1$-$3f2$) might show correlations with OAE amplitude recorded at lower frequencies. To this aim, correlations between TBOAE amplitude and multi-component DPOAE amplitudes recorded at different $f2/f1$ ratios have been performed in 18 normal-hearing subjects, for frequencies ranging from 0.75 to 6 kHz. In addition, as subjects with spontaneous OAEs (SOAEs) present greater DPOAE amplitude (see, for instance, Lonsbury-Martin *et al.*, 1990; Ozturan and Oysu, 1999), the influence of SOAE presence on DPOAE amplitude recorded as a function of $f2/f1$ will be investigated. The different $f2/f1$ ratios have been obtained by, first, keeping $f2$ fixed and varying $f1$ and, second, by keeping $f1$ fixed and varying $f2$. With $f2$ fixed, a high degree of correlation is expected between the maximum amplitude of the different lower sideband DPOAEs, as they have the same $f2$ frequency (and therefore the same generation site) when their DPOAE frequencies are made equal. However, when recording the maximum DPOAE amplitude as a function of $f2/f1$ for different lower sideband DPOAEs using an $f2$ sweep, $f1$ fixed method, the correlations between the different lower sideband DPOAE maximum amplitudes are made when the DPOAEs have the same frequency but different $f2$ frequencies, and therefore a different generation site. To see the importance of the $f2$ place in the DPOAE amplitude recorded in the outer ear canal, results concerning correlations between multicomponent DPOAE amplitude obtained at different $f2/f1$ will be compared using an $f2$ fixed, $f1$ sweep method and using an $f2$ sweep, $f1$ fixed method. Correlations with TBOAE amplitude and the influence of SOAE presence on DPOAE amplitude versus $f2/f1$ ratio will be analyzed.

Upper sidebands have been thought to carry very little useful information for clinical application, until recently (Erminy *et al.*, 1998; Nelson *et al.*, 1999). Several studies have brought arguments for a different generation site for $2f2$-$f1$ than for lower sideband DPOAEs (Brown and Kemp, 1985; Martin *et al.*, 1987; Whitehead *et al.*, 1996). Moulin and Kemp (1996) observed a significantly longer latency for lower sideband DPOAEs when latency was calculated using DPOAE phase gradient, with an $f2$ sweep method versus an $f2$ fixed, $f1$ sweep method. Such difference was not observed for $2f2$-$f1$ DPOAEs. The longer latency observed when $f2$ is modified was attributed to an additional delay due to the peak of the $f2$ traveling wave (Moulin and Kemp, 1996) or to a greater proportion of the cochlear filter response time near the $2f1$-$f2$ DPOAE site of generation (Bowman *et al.*, 1997, 1998). The absence of such a difference in $2f2$-$f1$ latency data argues in favor of a DPOAE generation site further from the primary frequencies region. Using ipsilateral suppression techniques, DPOAEs onset latencies and amplitude correlations, Martin *et al.* (1998) suggested a $2f2$-$f1$ DPOAE generation site more basal to the primary frequencies and closer to the $2f2$-$f1$ DPOAE frequency itself. If the place of $2f2$-$f1$ DPOAE generation is close to the DPOAE frequency itself, then the place of generation should be different when the primary frequencies $f2/f1$ ratio is modified, and for higher-order upper sideband DPOAEs ($3f2$-$2f1$ and $4f2$-$2f1$). This study systematically investigates presence and amplitude characteristics of upper sideband DPOAE amplitude in humans subjects, as a function of $f2/f1$ ratios, and its relationship with TBOAE amplitude.

I. MATERIAL AND METHODS

A. Subjects and OAE recordings

The same population as described in the companion paper (Moulin, 2000) has been tested according to the same stimulus and recording parameters. The DPOAEs have been recorded as a function of $f2/f1$ using Otodynamics's ILO92

software and hardware in one ear of each subject, with $f2$ fixed at ten different frequencies, and presented in a random order for each subject: 757, 879, 1000, 1257, 1500, 2002, 3003, 4004, 5005 and 6006 Hz. Primary levels were fixed at 65 dB SPL for $f1$ (L1) and 60 dB SPL for $f2$ (L2). For each $f2$ frequency, $f1$ was varied from a ratio of 1.04 to 1.50, by steps ranging from 0.012 (at low frequencies) to 0.02 (at high frequencies). In addition, DPOAE amplitude was recorded as a function of $f2/f1$ using a fixed $f1$ frequency and a varying $f2$. The $f2$ was varied from a ratio of 1.04 to 1.50, by steps ranging from 0.012 to 0.02 depending on frequencies. For the $f1$ fixed, $f2$ sweep method, the $f1$ fixed frequencies have been chosen so that the ratio of $f2$ fixed/$f1$ fixed frequencies was around 1.20.

For each measurement point, 128 signal samples were averaged. The $2f1$-$f2$, $3f1$-$2f2$, $4f1$-$3f2$, $2f2$-$f1$, $3f2$-$2f1$, and $4f2$-$3f1$ DPOAE components have been recorded. The DPOAEs were considered as present when their amplitude was greater than the mean noise floor plus 2 standard deviations (calculated for each DPOAE component as the mean of the five spectral components on either sideband of the DPOAE frequency).

Tone-burst-evoked OAEs (TBOAEs) were recorded using Otodynamics ILO88 version 5.50c software at the ten different frequencies corresponding to the frequencies chosen for DPOAE recordings, with an intrameatal stimulus intensity ranging between 65 and 68 dB SPLpe (peak equivalent sound pressure level). Subjects were also tested for presence of spontaneous otoacoustic emissions, using the SOAE search facility of the ILO88 software, which records synchronized SOAEs. Details of the SOAEs obtained are presented in Table I.

TABLE I. Details of spontaneous otoacoustic emissions (frequency and amplitude) in a group of 18 normal-hearing subjects.

Subject	Frequency (Hz)	Amplitude (dB SPL)
S3	916	6.5
	1147	10.6
S4	1660	5.8
	1721	2.6
	2185	1
	2502	−3.5
	3455	0.3
	3833	4.5
S5	1440	−7.2
	2332	−2.3
	2856	0.6
S6	1135	11.9
	1636	10.6
	2283	1
	4565	−7.7
S7	1992	−4.2
	2578	0.1
S9	1175	1.3
	4895	−3.5
S11	1184	−8.9
	1514	−7.9
	1831	−1.7
	2161	−2.9
	2747	1
	4700	−7.7
S18	1000	10.3
	1221	2.9
	1599	3.9
	2832	−1.3
	3564	−1.3

B Data analysis

1. DPOAEs

For each subject and $f2$ frequency, the $f2/f1$ ratio giving the greatest DPOAE amplitude (termed as ''optimum $f2/f1$ ratio'') and the greatest DPOAE amplitude (termed as ''maximum DPOAE amplitude'') recorded over the $f2/f1$ ratio range was obtained. The DPOAE amplitude as a function of $f2/f1$ was then smoothed according to a three-point running average method, and the optimum $f2/f1$ and the maximum DPOAE amplitude obtained with the smoothed functions were obtained for each subject. Similar analysis was performed using the $f1$ fixed, varying $f2$ amplitude ratio functions.

2. Statistical analyses

Analyses of the optimum $f2/f1$ ratio DPOAE amplitude as a function of frequency were performed by analysis of variance for repeated measurements (Anova-R).

Student *t*-test was used to analyze the differences in DPOAE amplitude functions and TBOAE amplitude according to SOAE presence.

Correlation analysis was used to analyze relationships between $f2/f1$ optimum ratios, DPOAE amplitude, primary frequencies, and TBOAE amplitude. Pearson's correlation coefficients are specified as ''*r*.''

The level of statistical significance chosen was 5%, and is specified for each test as *p*.

II. RESULTS

A. DPOAE presence

The DPOAE presence decreased as the $f2/f1$ ratio increased (Fig. 1). Lower sideband DPOAEs decreased more

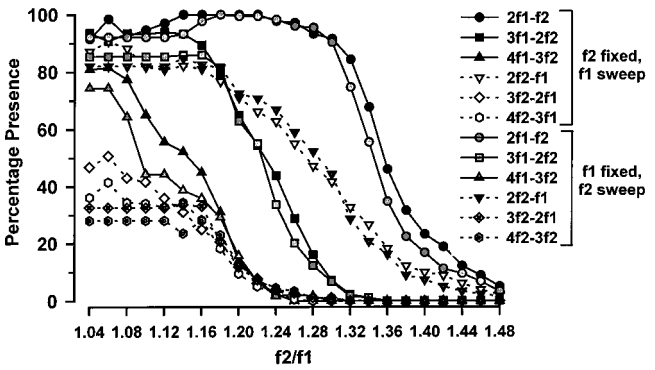

FIG. 1. The DPOAE percentage presence as a function of $f2/f1$ ratio, for each DPOAE component recorded with an $f1$ sweep, $f2$ fixed method (black symbols for lower sideband DPOAEs and open symbols for upper sideband DPOAEs) and with an $f1$ fixed, $f2$ sweep method (grey symbols for lower sideband DPOAEs and dotted symbols for upper sideband DPOAEs) for 18 normal-hearing subjects tested at ten frequencies (0.75 to 6 kHz).

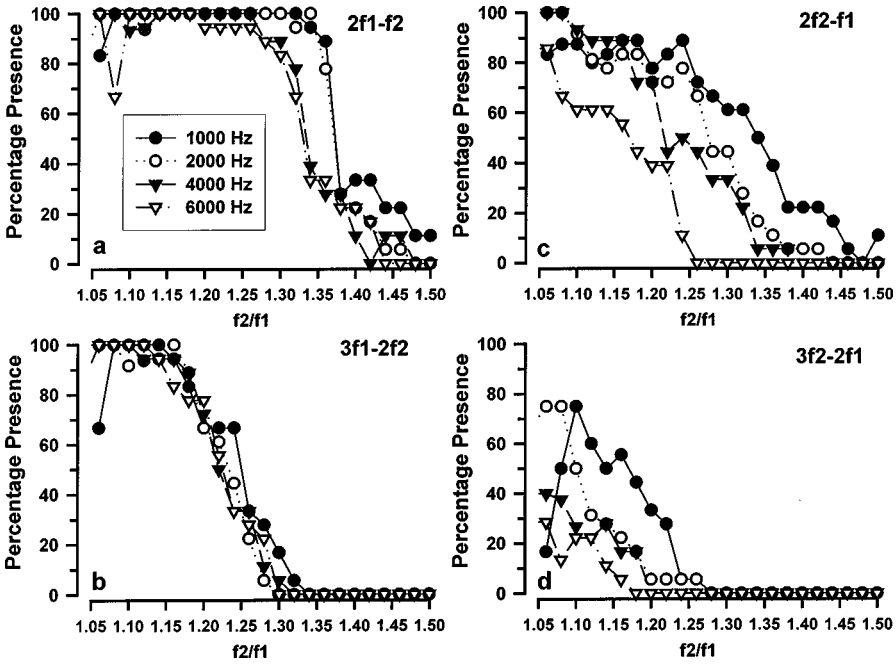

FIG. 2. The DPOAE percentage presence as a function of $f2/f1$ ratio for different $f2$ frequencies (1, 2, 4 and 6 kHz) and for lower sideband DPOAEs [(a) $2f1$-$f2$, (b) $3f1$-$2f2$] and upper sideband DPOAEs [(c) $2f2$-$f1$ and (d) $3f2$-$2f1$] for 18 normal-hearing subjects. DPOAEs have been recorded using an $f1$ sweep, $f2$ fixed method.

abruptly with increasing $f2/f1$ ratios than upper sideband DPOAEs, and were more present across the ratio range. Similar findings were obtained whether an $f2$ fixed, $f1$ sweep method or an $f1$ fixed, $f2$ sweep method was used.

The $2f1$-$f2$ DPOAEs tended to show a greater presence at high $f2/f1$ ($f2/f1>1.30$) at low frequencies than at high frequencies [Fig. 2(a)], but the decrease of $3f1$-$2f2$ presence with increasing $f2/f1$ showed a very similar pattern across frequency [Fig. 2(b)].

Upper sideband DPOAEs presence varied greatly not only according to $f2/f1$ ratio, but also according to frequency, as shown for $2f2$-$f1$ [Fig. 2(c)] and $3f2$-$2f1$ [Fig. 2(d)]: DPOAE presence decreased with increasing frequencies, with only 28% at 6 kHz versus 75% at 1 kHz for $3f2$-$2f1$.

B. DPOAE amplitude

Results presented here have been obtained on DPOAEs recorded using an $f2$ fixed, $f1$ sweep method. Results concerning DPOAEs recorded using an $f1$ fixed, $f2$ sweep method are presented only when different to the $f2$ fixed, $f1$ sweep method.

1. Amplitude ratio functions

a. Lower sideband DPOAEs. As expected from previous work (see, for instance, Brown *et al.*, 1992), lower sideband DPOAE amplitude increased with $f2/f1$ (modified with $f2$ fixed, $f1$ sweep) up to an optimum ratio beyond which it decreased [Fig. 3(a)]. The optimum ratio of $4f1$-$3f2$ was significantly lower than the optimum ratio of $3f1$-$2f2$, which was significantly lower than $2f1$-$f2$ optimum ratio. Each lower sideband DPOAE optimum $f2/f1$ showed a significant decrease as a function of frequency [Fig. 4(a)]. Here $F(9,178)=4.21$, $p<0.0001$ for $2f1$-$f2$, $F(9,170)=9.25$, $p<0.0001$ for $3f1$-$2f2$, $F(9,114)=3.93$, $p<0.0005$ for $4f1$-$3f2$. The corresponding $f2/f1$ ratio versus frequency functions were (with $f2$ in kHz)

$$f2/f1_{\mathrm{opt}(2f1\text{-}f2)}=1.238-0.08\times\log(f2),$$
$$r=0.93(p<0.005),$$
$$f2/f1_{\mathrm{opt}(3f1\text{-}2f2)}=1.143-0.05\times\log(f2),$$
$$r=0.92(p<0.004),$$
$$f2/f1_{\mathrm{opt}(4f1\text{-}3f2)}=1.119-0.04\times\log(f2),$$
$$r=0.68(p<0.05).$$

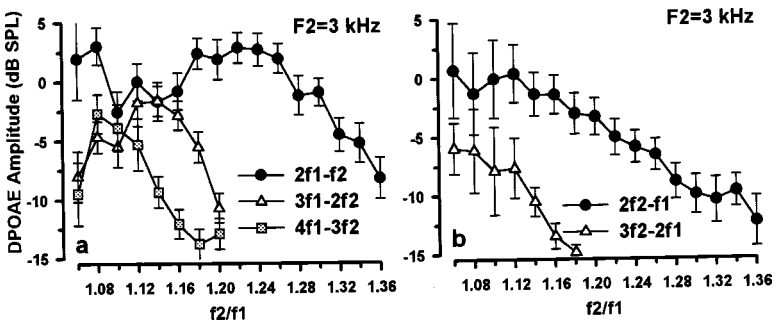

FIG. 3. Mean DPOAE amplitude (± sem) as a function of $f2/f1$ calculated on 18 normal-hearing subjects, with $f2$ fixed at 3 kHz. Lower sideband DPOAE components are shown in (a), and upper sideband components are shown in (b).

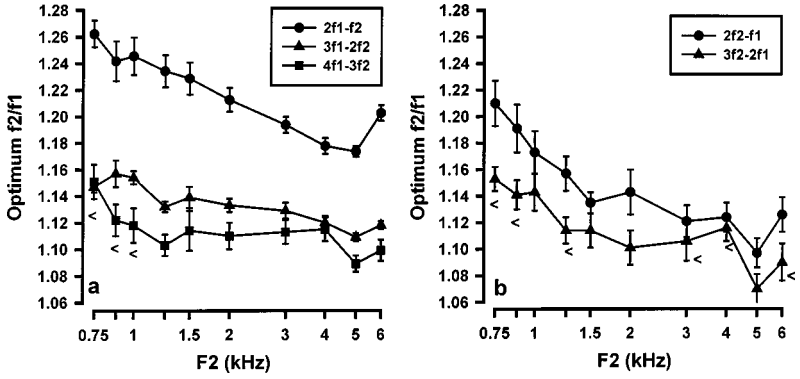

FIG. 4. Optimum $f2/f1$ (mean ± sem) as a function of frequency for lower sideband DPOAEs (a) and upper sideband DPOAEs (b). ''<'' indicates when the number of subjects is lower than 10.

b. Upper sideband DPOAEs. Upper sideband DPOAEs showed a quite different pattern from lower sideband DPOAEs, as a function of $f2/f1$: average data showed a decrease of amplitude as a function of $f2/f1$ for each frequency [see, for instance, data at 3 kHz in Fig. 3(b)]. However, intersubject variability of the pattern of the amplitude ratio functions for upper sideband DPOAEs (Fig. 5) was greater than the intersubject variability of the lower sideband DPOAEs. Figure 5 shows a similar tuning of the $2f2\text{-}f1$ as for lower sideband DPOAEs for two subjects (S9 and S18) who presented high-frequency SOAEs.

The optimum $f2/f1$ was obtained for each subject and frequency (using the $f2$ fixed, $f1$ sweep method), and decreased significantly as a function of frequency [Fig. 4(b)]: $F(9,163)=6.6$, $p<0.0001$ for $2f2\text{-}f1$, $F(9,85)=7.5$, $p<0.0001$ for $3f2\text{-}2f1$, and $F(9,82)=2.77$, $p<0.01$ for $4f2\text{-}3f2$.

$$f2/f1_{\mathrm{opt}(2f2\text{-}f1)}=1.176-0.115\times\log(f2),$$
$$r=0.94(p<0.0005),$$
$$f2/f1_{\mathrm{opt}(3f2\text{-}2f1)}=1.135-0.073\times\log(f2),$$
$$r=0.85(p<0.004) \quad \text{with } f2 \text{ in kHz.}$$

The optimum ratios of $3f2\text{-}2f1$ and $4f2\text{-}3f1$ could not be obtained for each subject and frequency due to the low presence of these components.

2. DPOAE amplitude and optimum f2/f1

There was no correlation between DPOAE amplitude and $f2/f1$ optimum ratios for upper sideband DPOAEs.

There was no correlation between $2f1\text{-}f2$ DPOAE amplitude and $f2/f1$ optimum ratios when all frequencies were pooled together. Per frequency analysis showed an increase of the optimum $f2/f1$ as DPOAE amplitude increased at 750 Hz ($r=0.56$, $p<0.02$, $n=17$) and at 1 kHz ($r=0.54$, $p<0.03$).

However, the $3f1\text{-}2f2$ optimum ratio decreased significantly as $3f1\text{-}2f2$ DPOAE amplitude increased ($r=0.31$, $n=162$, $p<0.0001$ for smoothed data). Per frequency analysis showed a significant decrease of 4 kHz DPOAE optimum ratio as DPOAE amplitude increased ($r=0.64$, $n=17$, $p<0.01$).

The $4f1\text{-}3f2$ optimum ratio decreased significantly as $4f1\text{-}3f2$ DPOAE amplitude increased ($r=0.49$, $p<0.0001$, $n=89$ for smoothed data). Per frequency analysis showed a significant decrease of 3 kHz DPOAE optimum ratio as DPOAE amplitude increased ($r=0.77$, $n=13$, $p<0.01$) at 4 kHz ($r=0.66$, $n=11$, $p<0.03$), and a tendency at 5 and 6 kHz.

3. DPOAE-grams

The optimum DPOAE-grams reconstructed from the multi-component data showed a nonmonotonic pattern for each lower sideband DPOAE component, with a dip around 3 kHz and two peaks around 1.5 and 6 kHz [Fig. 6(a)]. Anova-R shows significant differences across frequencies for each component [$F(9,170)=6.6$, $p<0.0001$ for $3f1\text{-}2f2$ and $F(9,114)=4.7$, $p<0.0001$ for $4f1\text{-}3f2$].

The $3f1\text{-}2f2$ DPOAE component amplitude was significantly lower than the $2f1\text{-}f2$ DPOAE amplitude (paired t-tests, $p<0.001$ at each of the ten frequencies), significantly greater than the $4f1\text{-}3f2$ DPOAE amplitude for frequencies greater than 879 Hz (paired t-tests, $p<0.0005$), and significantly greater than the $2f2\text{-}f1$ DPOAE component at all frequencies except 879 Hz and 3 kHz.

For upper sideband DPOAEs, the optimum DPOAE-gram is nonmonotonic, showing two regions of high levels DPOAEs, around 0.8 and 3 kHz, respectively, and a region of lower level around 1.5 kHz. [Fig. 6(b)], with DPOAE amplitude significantly different across frequencies [Anova-R, $F(9,163)=3.1$, $p<0.005$ for $2f2\text{-}f1$, $F(9,85)=2.2$, $p<0.05$ for $3f2\text{-}2f1$]. The $4f2\text{-}3f1$ DPOAE component showed very low levels across the frequency range, with a dip around 1.5 kHz and around 4 kHz, but still showed sta-

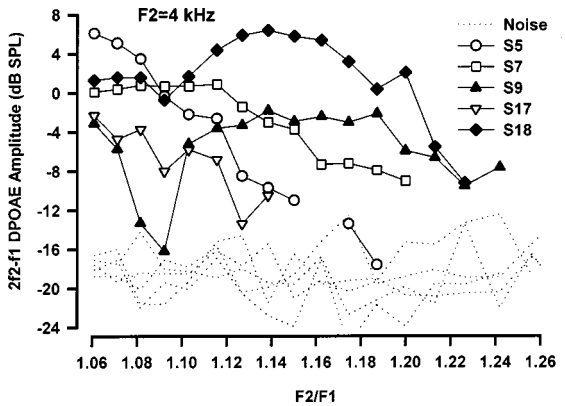

FIG. 5. Upper sideband $2f2\text{-}f1$ DPOAE amplitude as a function of $f2/f1$, for individual subjects, at 4 kHz. The noise floor (calculated as the average of the spectral components on either sideband of the DPOAE frequency, plus 2 standard deviations) is specified as dotted lines.

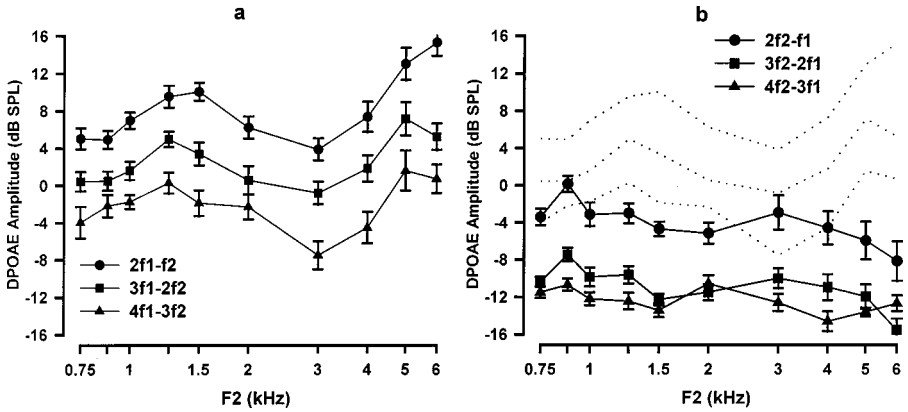

FIG. 6. The DPOAE amplitude (dB SPL, mean ± sem of 18 normal-hearing subjects' data) as a function of $f2$ frequency, for lower sideband DPOAE components (a) and upper sideband DPOAE components (b). The maximum DPOAE amplitude over the ratio range has been taken for each subject and $f2$ frequency, in order to obtain optimum DPOAE-grams. In (b), the dotted lines represent the optimum DPOAE-gram pattern of lower sideband DPOAEs.

tistically significant differences across frequencies [Anova-R $F(9,82)=3.7$, $p<0.005$ for $4f2\text{-}3f1$]. The $2f2\text{-}f1$ DPOAE amplitude was significantly greater than the $3f2\text{-}2f1$ DPOAE amplitude at all frequencies except 4 and 6 kHz (paired t-tests, $p<0.01$). There was no statistically significant differences between $4f2\text{-}3f1$ DPOAE amplitude and $3f2\text{-}2f1$ DPOAE amplitude at any of the ten frequencies tested, but the number of subjects presenting both a $3f2\text{-}2f1$ and a $4f2\text{-}3f1$ DPOAE component was small (from four to eight subjects depending on frequency).

The optimum DPOAE-gram pattern differed between the lower sideband DPOAE component groups [Fig. 6(a)] and the upper sideband DPOAE component groups [Fig. 6(b)], but they were quite similar within one DPOAE component group, except for the $4f2\text{-}3f1$ DPOAE component.

4. Influence of SOAEs

Lower sideband DPOAEs showed significantly greater DPOAE amplitude in SOAE positive subjects from 3 to 6 kHz for the $2f1\text{-}f2$ DPOAE, and only at 5 kHz for both $3f1\text{-}2f2$ and $4f1\text{-}3f2$ DPOAEs. For upper sideband DPOAEs, a significant difference was observed at 2, 4 and 5 kHz for $2f2\text{-}f1$ and at 1.2, 2 and 5 kHz for $3f2\text{-}2f1$ DPOAEs.

The influence of SOAEs on lower sideband DPOAE amplitude was greater for $f2/f1$ at or lower than the optimum ratio, whether an $f2$ fixed or an $f2$ sweep method was used [Fig. 7(a)–(d)]. The SOAE+ subjects showed a tendency towards a lower optimum ratio than SOAE− subjects at 4 and 5 kHz ($p<0.07$) (Fig. 7), with a significant difference at 1000 Hz ($p<0.01$). When the optimum ratio was obtained by the fitting procedure, SOAE+ subjects showed a significantly lower optimum ratio [$F(1,16)=6.9$, $p<0.05$], with a statistical significance at 1 kHz ($p<0.01$), 757 Hz and 3 kHz ($p<0.05$).

For upper sideband DPOAEs, the influence of SOAE presence on DPOAE amplitude did not show a consistent pattern as a function of $f2/f1$: it was obtained at low ratios for $f2$ at 5 kHz (i.e., for a $2f2\text{-}f1$ DPOAE frequency at 5370 Hz) [Fig. 7(e)] and at greater ratio for $f2$ at 4 kHz (corresponding to DPOAE frequencies ranging from 4430 to 4610) [Fig. 7(f)].

C. Relations between multi-component DPOAE amplitudes

1. Maximum DPOAE amplitude

a. Lower sideband DPOAEs. There were highly significant correlations between the maximum DPOAE amplitude of the different lower sideband DPOAE components (Table II), whether DPOAEs were recorded using an $f2$ fixed or an $f2$ sweep method, leading to the following equations:

$$A_{3f1\text{-}2f2}=0.9114\times A_{2f1\text{-}f2}-6.2141, \quad r=0.90,$$

$$A_{4f1\text{-}3f2}=0.7146\times A_{2f1\text{-}f2}-9.7201, \quad r=0.73,$$

$$A_{4f1\text{-}3f2}=0.8525\times A_{3f1\text{-}2f2}-5.3347, \quad r=0.81.$$

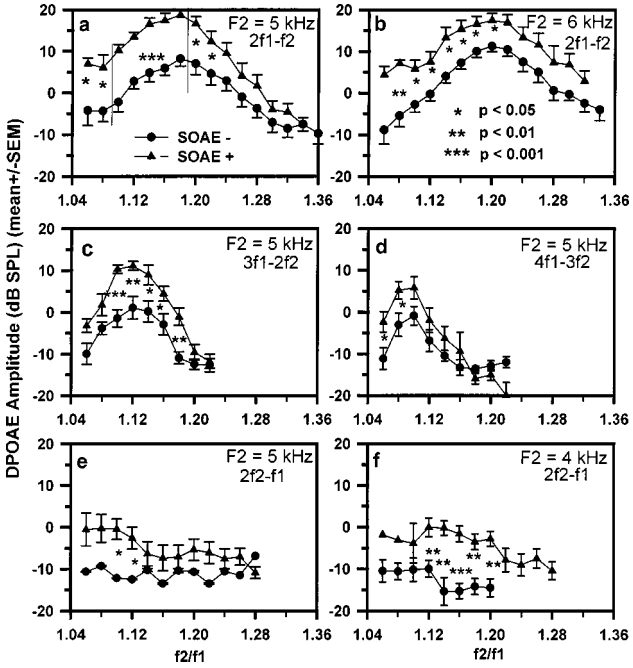

FIG. 7. The DPOAE amplitude (mean ± sem) as a function of $f2/f1$ ratio for subjects presenting SOAEs (SOAE+ subjects, triangles) and for subjects presenting no SOAEs (SOAE− subjects). The top four panels represent lower sideband DPOAEs: $2f1\text{-}f2$ with $f2$ at 5 kHz (a) and $f2$ at 6 kHz (b); $3f1\text{-}2f2$ (c) and $4f1\text{-}3f2$ (d), recorded with $f2$ fixed at 5 kHz. The bottom panels represent upper sideband DPOAEs ($2f2\text{-}f1$) recorded with $f2$ fixed at 5 kHz (e) and 4 kHz (f). Statistical significant differences between SOAE+ subjects and SOAE− subjects are specified (unpaired t-tests), with *** for $p<0.001$, ** for $p<0.01$ and * for $p<0.05$. In (a), the two vertical lines represent the ratios for which $p<0.001$.

TABLE II. Correlations between maximum DPOAE amplitude of different DPOAE components (r=correlation coefficient, n=number of point, p=level of significance with NS for nonsignificant).

		$3f1$-$2f2$	$4f1$-$3f2$	$2f2$-$f1$	$3f2$-$2f1$	$4f2$-$3f1$
$2f1$-$f2$	r	0.90	0.73	0.19	0.14	0.14
	p	$p<0.0001$	$p<0.0001$	$p<0.02$	NS	NS
	n	169	115	164	96	91
$3f1$-$2f2$	r		0.82	0.22	0.28	0.01
	p		$p<0.0001$	$p<0.01$	$p<0.03$	NS
	n		111	155	64	60
$2f2$-$f1$	r				0.62	0.26
	p				$p<0.0001$	$p<0.05$
	n				80	75
$3f2$-$2f1$	r					0.29
	p					$p<0.08$
	n					40

Analysis per frequency showed similar results, with significant correlations between $2f1$-$f2$ and $3f1$-$2f2$ obtained at all frequencies above 750 Hz ($r>0.85$, $p<0.0001$) (at 750 Hz, $r=0.49$, $p<0.10$, $n=13$), and significant correlations between $2f1$-$f2$ and $4f1$-$3f2$ at all frequencies above 879 Hz ($r>0.51$, $p<0.05$) (at 750 and 879 Hz, the number of subjects showing both $2f1$-$f2$ and $4f1$-$3f2$ was 4 and 6, respectively). The $3f1$-$2f2$ DPOAE amplitude increased significantly with $4f1$-$3f2$ DPOAE amplitude for all frequencies above 879 Hz ($r>0.65$, $p<0.01$).

There was no significant difference between the correlations obtained using an $f2$ sweep, $f1$ fixed method (maximum DPOAE amplitude recorded at different $f2$) and correlations obtained using an $f1$ sweep, $f2$ fixed method (maximum DPOAE amplitude recorded for the same $f2$). The correlations obtained using an $f2$ sweep method were slightly greater than correlations obtained using an $f1$ sweep method.

b. Upper sideband DPOAEs. Correlations between lower sideband and upper sideband DPOAE amplitudes are summarized in Table II. There was a weak but significant correlation between the $2f2$-$f1$ DPOAE amplitude and the $2f1$-$f2$ DPOAE amplitude, all subjects and frequencies taken into account. Analysis per frequency found significant correlations between the $2f1$-$f2$ DPOAE amplitude and the $2f2$-$f1$ DPOAE amplitude for $f2$ at 1.5, 2 and 4 kHz ($p<0.05$), and a tendency at 3 kHz ($r=0.44$, $n=16$, $p<0.10$). A significant correlation was obtained between $2f2$-$f1$ DPOAE amplitude and $3f1$-$2f2$ DPOAE amplitude at 4 kHz ($r=0.63$, $n=16$, $p<0.01$), 5 kHz ($r=0.61$, $p<0.02$, $n=15$) and 6 kHz ($r=0.67$, $n=17$, $p<0.03$), and a tendency at 3 and 1.5 kHz ($p<0.10$).

Significant correlations between the different upper sideband DPOAE amplitudes were obtained (Table II).

2. Correlations between multicomponent DPOAE amplitudes with different primary frequencies: Comparison between upper sideband DPOAEs and lower sideband DPOAEs

a. Maximum DPOAE amplitude. Amplitude correlations were performed when the primary frequencies used to generate $2f2$-$f1$ were shifted below primary frequencies used to generate $2f1$-$f2$ frequencies (Table III). Analysis per frequency showed no correlations between $2f1$-$f2$ DPOAE amplitude and $2f2$-$f1$ DPOAE amplitude at frequencies lower than 1.2 kHz. A trend towards better correlations between $2f1$-$f2$ DPOAE amplitude and $2f2$-$f1$ DPOAE amplitude, when the primary frequencies used to generate

TABLE III. Correlations (r=correlation coefficient, n=number of point, p=level of significance with NS for nonsignificant) between maximum $2f1$-$f2$ DPOAE amplitude and the maximum upper sideband DPOAE amplitudes, for each frequency, when the primary frequencies were identical (difference of 0 octave), and when primary frequencies used to generate upper sideband DPOAEs were shifted below primary frequencies used to generate $2f1$-$f2$, by $\frac{1}{4}$-octave steps. Empty cells in the table account for the combination of frequencies which were not recorded: for instance, a difference of 1 octave lower than $f2$ at 5 kHz would require an $f2$ frequency at 2500 Hz, which was not part in the ten frequencies tested in this study.

Frequency shift (octave)	$f2$ (Hz)	750	879	1000	1250	1500	2000	3000	4000	5000	6000
	r	0.06	0.09	0.00	0.16	0.52	0.49	0.44	0.80	0.39	0.41
0	n	15	18	16	17	18	17	16	17	15	15
	p	NS	NS	NS	NS	$p<0.05$	$p<0.05$	NS	$p<0.0001$	NS	NS
	r		0.27	0.13	0.25	0.47				0.8	0.61
$-\frac{1}{4}$	n		16	18	16	17				17	16
	p		NS	NS	NS	NS				$p<0.0001$	$p<0.05$
	r			0.32	0.51	0.50	0.61	0.68	0.78		0.58
$-\frac{1}{2}$	n			16	18	16	18	17	16		18
	p			NS	$p<0.05$	$p<0.05$	$p<0.01$	$p<0.005$	$p<0.001$		$p<0.05$
	r				0.53	0.45	0.75			0.6	
$-\frac{3}{4}$	n				16	18	17			16	
	p				$p<0.05$	NS	$p<0.001$			$p<0.05$	
	r					0.34	0.60	0.64	0.62		0.47
-1	n					16	16	18	17		17
	p					NS	$p<0.05$	$p<0.005$	$p<0.01$		NS
	r							0.54		0.75	
$-\frac{5}{4}$	n							17		17	
	p							$p<0.05$		$p<0.001$	
	r						0.38	0.23	0.48		0.55
-1.5	n						16	18	18		18
	p						NS	NS	$p<0.05$		$p<0.05$

TABLE IV. Correlations (r=correlation coefficient, n=number of point, p=level of significance with NS for nonsignificant) between maximum $2f1$-$f2$ DPOAE amplitude and the maximum upper sideband DPOAE amplitudes when the primary frequencies were identical (difference of 0 octave) and when primary frequencies used to generate upper sideband DPOAEs were shifted below primary frequencies used to generate $2f1$-$f2$ (primary frequencies ranging from 2 to 6 kHz) by $\frac{1}{2}$ octave steps.

$f2_{(2f1\text{-}f2)}/f2_{(\text{upper-side DPOAEs})}$		$2f1$-$f2$ vs $2f2$-$f1$	$2f1$-$f2$ vs $3f2$-$2f1$	$2f1$-$f2$ vs $4f2$-$3f1$
	r	0.34	0.02	0.05
0 octave	n	64	32	12
	p	<0.006	NS	NS
	r	0.56	0.52	0.16
$-\frac{1}{2}$ octave	n	68	38	19
	p	<0.0001	<0.001	NS
	r	0.60	0.55	0.46
-1 octave	n	67	40	24
	p	<0.0001	<0.0005	<0.03
	r	0.31	0.21	0.48
-1.5 octave	n	67	38	29
	p	<0.02	NS	<0.01

$2f2$-$f1$ are $\frac{1}{4}$ to $\frac{3}{4}$ octave below the primary frequencies used to generate $2f1$-$f2$, is shown in Table III. Empty cells in the table account for the combination of frequencies which were not recorded: for instance, a difference of 1 octave lower than $f2$ at 5 kHz would require an $f2$ frequency at 2500 Hz, which was not part of the ten frequencies tested in this study.

Correlations between $2f1$-$f2$ DPOAE and upper sideband DPOAEs have been performed with increasing differences between the primary frequencies used to record $2f1$-$f2$ and primary frequencies used to record upper sideband DPOAEs. The differences between the two sets of primaries are multiples of $\frac{1}{2}$ octave, so that the intermediary frequencies of 879, 1257, and 5000 Hz have been deleted from the calculations. The best correlations between $2f1$-$f2$ and $2f2$-$f1$ are obtained when the $2f2$-$f1$ primaries are $\frac{1}{2}$ and 1 octave below the $2f1$-$f2$ primaries, and the best correlations between $2f1$-$f2$ and $3f2$-$2f1$ are obtained when the $3f2$-$2f1$ primaries are $\frac{1}{2}$ and 1 octave below the $2f1$-$f2$ primaries (Table IV). The best correlations between $2f1$-$f2$ and $4f2$-$3f1$ are obtained when $4f2$-$3f1$ primaries are 1.5 octave below the $2f1$-$f2$ primaries.

Correlations between $2f2$-$f1$ and $3f2$-$2f1$ DPOAE amplitudes have been performed when shifting the primary frequencies by $\frac{1}{2}$ octave. The only significant correlations found were when the primaries used to record $2f2$-$f1$ and the other sideband DPOAEs ($3f2$-$2f1$ and $4f2$-$3f1$) were identical.

b. DPOAE amplitude recorded per f2/f1 ratios. Correlations have been performed with $2f1$-$f2$ maximum DPOAE amplitude and $2f2$-$f1$ DPOAE amplitude recorded per $f2/f1$ ratio, by shifting primary frequencies eliciting the $2f2$-$f1$ DPOAE 0, $\frac{1}{2}$ or 1 octave below primary frequencies eliciting the $2f1$-$f2$ DPOAE. Correlations coefficients are shown in Fig. 8(a) (using an $f1$ sweep method) and in Fig. 8(b) (using an $f2$ sweep method). The most significant correlations are obtained when the difference between the two sets of primary frequencies was $\frac{1}{2}$ octave whatever sweep method was used. For the $f2$ sweep method, the correlations obtained with a difference of 1 octave in primary frequencies increased for $f2/f1$ above 1.20 [Fig. 8(b)].

D. DPOAE optimum ratios

1. Lower sideband DPOAEs

The $3f1$-$2f2$ optimum ratio increased significantly with the $2f1$-$f2$ ratio ($r=0.523$, $n=165$, $p<0.0001$) [Fig. 9(a)]. Per frequency analysis showed a significant correlation at 1250 Hz ($r=0.64$, $p<0.01$), 1.5 kHz ($r=0.49$, $p<0.04$), 3 kHz ($r=0.54$, $p<0.05$), and a tendency at 2 kHz and 5 kHz ($p<0.1$). A significant correlation was also found between the $4f1$-$3f2$ optimum ratio and the $3f1$-$2f2$ ($r=0.63$, $n=91$, $p<0.0001$), with significant correlation at 1.2 kHz ($r=0.77$, $p<0.01$) and 4 kHz ($r=0.73$, $p<0.005$). However, no significant correlations were obtained between $2f1$-$f2$ optimum ratio and $4f1$-$3f2$ $f2/f1$.

If the DPOAEs are of maximum amplitude when they have the same DPOAE frequency and the same $f2$, then the optimum ratio of $3f1$-$2f2$ can be deducted from the optimum ratio of $2f1$-$f2$ using

$$3f'1\text{-}2f2 = 2f1\text{-}f2 \tag{1}$$

with $f2/f1$ the optimum ratio of $2f1$-$f2$ and $f2/f1'$ the optimum ratio of $3f'1$-$2f2$.

By rearranging Eq. (1), we obtain (with R for optimum ratio)

$$R_{3f1\text{-}2f2} = 3 \times R_{2f1\text{-}f2}/(2 + R_{2f1\text{-}f2}). \tag{2}$$

This function is displayed in Fig. 9(b) along with its linear approximation (obtained for a ratio range from 1.05 to 1.50) and the regression line obtained from real data. The linear approximation was considered close enough to the real function as the correlation coefficient was greater than 0.997.

2. Upper sideband DPOAEs

There was a significant correlation between $2f1$-$f2$ optimum ratio and $2f2$-$f1$ optimum ratio ($r=0.28$, $n=163$,

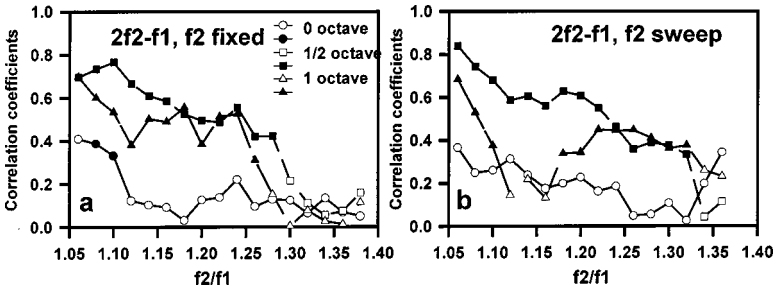

FIG. 8. Correlation coefficients obtained between $2f2$-$f1$ DPOAE amplitude recorded per $f2/f1$ ratio, and $2f1$-$f2$ DPOAE maximum amplitude, with $f2$ frequency generating the $2f1$-$f2$ DPOAE 0, $\frac{1}{2}$ and 1 octave above the $f2$ frequency generating the $2f2$-$f1$ DPOAE. The DPOAEs have been recorded using an $f1$ sweep, $f2$ fixed method (a), and an $f2$ sweep, $f1$ fixed method (b). Black symbols represent statistically significant correlations.

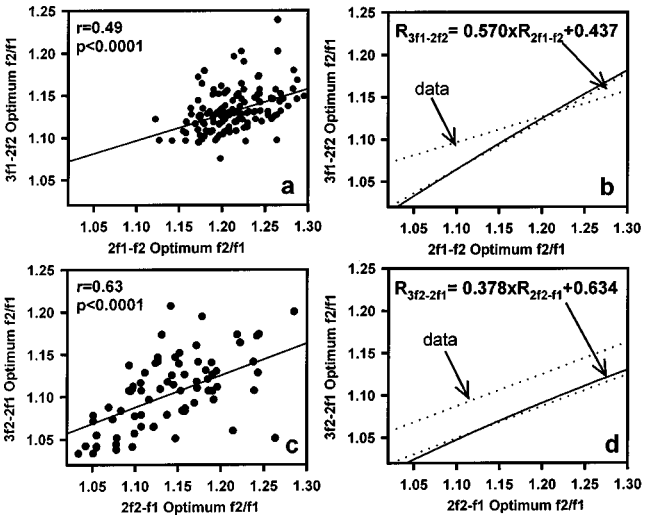

FIG. 9. Correlations obtained between the optimum ratios of different DPOAE components (obtained using an $f1$ sweep, $f2$ fixed method): lower sideband DPOAEs [top panels, (a) and (b)], and upper sideband DPOAEs [bottom panels, (c) and (d)]. Correlation coefficients are specified as ''*r*,'' with the corresponding level of statistical significance (p). In the right panels (b and d), the linear regressions obtained from data are repeated (dotted line specified as ''data'') and the function for which the DPOAE components are of equal frequency (with equal $f2$, and therefore different $f1$ and $f2/f1$) and their linear approximation are specified as solid lines (equations specified with ''*R*'' as $f2/f1$ ratio). (a) and (b) show correlation between $3f1$-$2f2$ and $2f1$-$f2$ optimum $f2/f1$ ratios and (c) and (d) show correlation between $3f2$-$2f1$ and $2f2$-$f1$ optimum $f2/f1$ ratios.

$p=0.0003$). Per frequency analysis showed a significant correlation at 879 Hz ($r=0.56$, $n=18$, $p<0.02$). No significant correlations were obtained at other frequencies.

There was a highly significant correlation between the $2f2$-$f1$ and the $3f2$-$2f1$ optimum ratios [Fig. 9(c)]. Per frequency analysis showed a significant correlation obtained at 1257 Hz ($r=0.79$, $n=7$, $p<0.05$), at 2000 Hz ($r=0.75$, $n=10$, $p<0.02$), at 3000 Hz ($r=0.88$, $n=9$, $p<0.005$), and at 5 kHz ($r=0.92$, $n=7$, $p<0.005$).

In the same way as for lower sideband DPOAEs, the $f2/f1$ ratios for which the $2f2$-$f1$ and $3f2$-$2f1$ DPOAE frequencies are equal, with the same $f2$, can be calculated, giving Eq. (3):

$$R_{3f2\text{-}2f1}=2\times R_{2f2\text{-}f1}/(1+R_{2f2\text{-}f1}). \tag{3}$$

The data obtained and the function given by the equation are shown in Fig. 9(b).

There was no significant correlations between lower sideband and upper sideband optimum ratios when the $f2$ frequencies of the upper sideband DPOAEs were shifted below the $f2$ frequencies of the lower sideband DPOAEs.

E. Correlations between different DPOAE component amplitudes as a function of $f2/f1$

Correlations between $2f1$-$f2$ and $3f1$-$2f2$ DPOAE amplitudes, and correlations between $2f2$-$f1$ and $3f2$-$2f1$ DPOAE amplitudes, were performed for each $f2/f1$ ratio combination, by 0.02 ratio steps, for the $f2$ fixed, $f1$ sweep method, and for the $f1$ fixed, $f2$ sweep method. The ratio pairs giving the greatest correlations were the ratio pairs corresponding to the two components having the same DPOAE frequency, i.e., the ratios of $2f1$-$f2$ corresponding to the ratio of $3f1$-$2f2$ according to the function defined by Eq. (2). The greatest correlations between $2f1$-$f2$ and $3f1$-$2f2$ DPOAE amplitude are shown in Fig. 10(a) and (b) as black dots, and significant correlations as triangles. The regression line from these data is very close to the theoretical line defined by Eq. (2). When an $f1$ fixed, $f2$ sweep method is chosen, the $f2/f1$ ratios of $2f1$-$f2$ and $3f1$-$2f2$ giving the same DPOAE frequency, with the same $f1$ (and a different $f2$), are linked by the equation:

$$R_{3f1\text{-}2f2}=0.5+0.5R_{2f1\text{-}f2}. \tag{4}$$

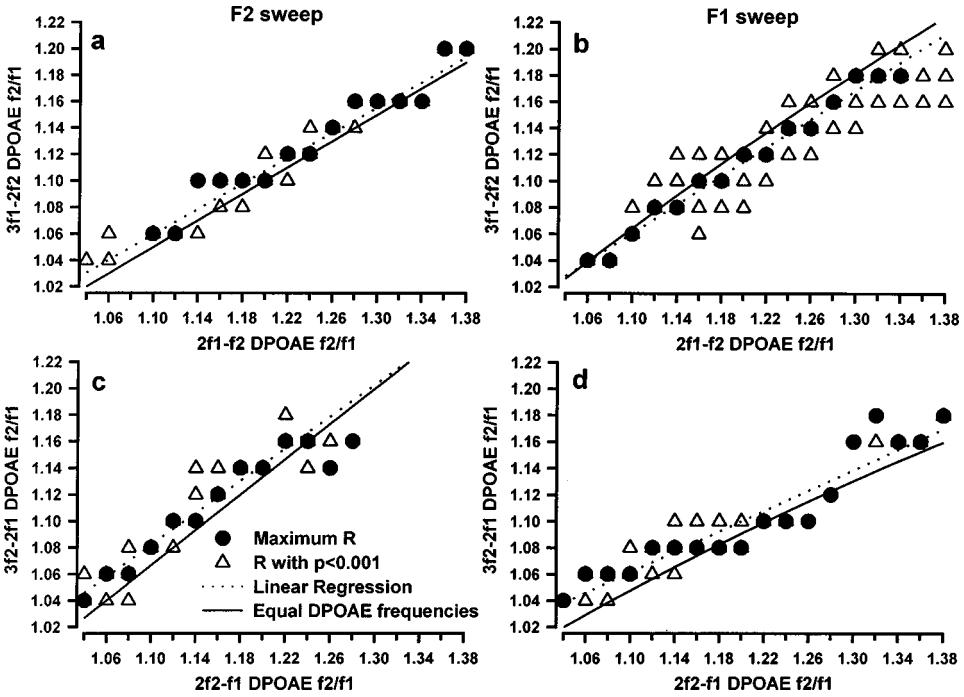

FIG. 10. The $3f1$-$2f2$ $f2/f1$ ratio for which $3f1$-$f2$ DPOAE amplitude correlates significantly with $2f1$-$f2$ DPOAE amplitude, as a function of $2f1$-$f2$ $f2/f1$ ratio [(a) and (b)]. The $3f2$-$2f1$ $f2/f1$ ratio for which $3f2$-$2f1$ DPOAE amplitude correlates significantly with $2f2$-$f1$ DPOAE amplitude, as a function of $2f2$-$f1$ $f2/f1$ ratio [(c) and (d)]. Black dots represent the greatest (and significant) correlations obtained, whereas white triangles represent the significant correlation obtained. The solid line represents the $f2/f1$ ratios for which the two DPOAE frequencies are equal (with one primary frequency fixed), and the regression line obtained from the pairs of $f2/f1$ showing the best correlations is specified as a dotted line. Data were obtained using an $f2$ sweep, $f1$ fixed method [(a) and (c)] and using an $f2$ fixed, $f1$ sweep method [(b) and (d)].

Similarly, for upper sideband DPOAEs,

$$R_{3f2\text{-}2f1}=(2R_{2f2\text{-}f1}+1)/3. \quad (5)$$

For upper sideband DPOAEs, the $f2/f1$ ratio pairs giving the greatest correlations tended to be the ratio pairs corresponding to the two components having the same DPOAE frequency [Eqs. (3) and (5)], whether an $f1$ sweep [Fig. 10(d)] or an $f2$ sweep method [Fig. 10(c)] was chosen. There was no significant difference in the correlation coefficients obtained by an $f1$ sweep versus an $f2$ sweep method, but correlation coefficients obtained using an $f2$ sweep method tended to be greater.

F. Correlations between DPOAE amplitude and TBOAE amplitude

1. Maximum DPOAE amplitude

Significant positive correlations were found between maximum $2f1\text{-}f2$ DPOAE amplitude and TBOAE amplitude for 1.5 kHz ($r=0.54$, $n=16$, $p<0.05$), 2 kHz ($r=0.58$, $n=17$, $p<0.05$), 3 kHz ($r=0.82$, $n=17$, $p<0.001$) and 4 kHz ($r=0.90$, $n=17$, $p<0.0001$). In the same way, $3f1\text{-}2f2$ DPOAE amplitude increased significantly with TBOAE amplitude ($r=0.408$, $n=141$, $p<0.0001$), as did $4f1\text{-}3f2$ DPOAE amplitude ($r=0.356$, $n=97$, $p<0.005$). Analysis per frequency showed correlations between $3f1\text{-}2f2$ DPOAE amplitude from frequencies ranging from 1.5 to 6 kHz ($p<0.05$), and between $4f1\text{-}3f2$ DPOAE amplitudes for frequencies at 2 kHz and above 3 kHz ($p<0.05$).

Statistically significant correlations were obtained between upper sideband DPOAE amplitude and TBOAE amplitude with $r=0.49$, $n=132$, $p<0.0001$ for $2f2\text{-}f1$ and $r=0.48$, $n=78$, $p<0.0001$ for $3f2\text{-}2f1$. No significant correlation was obtained between $4f2\text{-}3f1$ DPOAE amplitude and TBOAE amplitude.

Amplitude correlations were performed when the primary frequencies used to generate DPOAEs were shifted below ($-\frac{1}{2}$ and -1 octave) and above ($+\frac{1}{2}$ and $+1$ octave) frequencies used to generate TBOAEs (Table V). In order to perform correlations between DPOAEs and the same set of TBOAE frequencies, whatever the frequency shift between TBOAE frequencies and primary frequencies, 1.5-, 2- and 3-kHz TBOAE frequencies were selected. Lower sideband DPOAE amplitude increased highly significantly with TBOAE amplitude for $f2$ frequencies at the same frequency as TBOAEs, and $\frac{1}{2}$ octave above, with better correlations with $f2$ $\frac{1}{2}$ octave above. The correlations between $2f2\text{-}f1$ DPOAE amplitude and TBOAE amplitude were highly statistically significant ($p<0.005$) for primary frequencies from $\frac{1}{2}$ octave above to 1 octave below TBOAE frequencies. For $2f2\text{-}f1$ and $3f2\text{-}2f1$, the greatest correlations were obtained when DPOAE primary frequencies were at or $\frac{1}{2}$ octave below TBOAE frequencies.

2. DPOAE amplitude per f2/f1 ratio and TBOAE amplitude

For TBOAE frequencies ranging from 750 to 2000 Hz, correlations were made between TBOAE amplitude and DPOAE amplitude recorded at different ratios, with $f2$ at or above TBOAE frequencies. The respective frequencies of TBOAEs and multi-component DPOAEs for $f2$ at 2 kHz, for the $f1$ sweep method and the $f2$ sweep method, are shown in Fig. 11.

For both $2f1\text{-}f2$ and $3f1\text{-}2f2$, the greatest correlations were obtained for a difference of $\frac{1}{2}$ octave between $f2$ and TBOAE frequency, with DPOAE amplitude increasing significantly with TBOAE amplitude for $f2/f1$ ranging from 1.10 to 1.32 (for ratios ranging from 1.06 to 1.18 for $3f1\text{-}2f2$). Significant correlations were obtained for a difference of 1 octave, for ratios ranging from 1.10 to 1.26 (1.08 to 1.16 for $3f1\text{-}2f2$), and for $f2$ corresponding to TBOAE frequencies for ratios ranging from 1.06 to 1.34 (for 1.06 to 1.20 for $3f1\text{-}2f2$). When TBOAE frequencies were 1.5 octave below $f2$ frequencies, significant correlations were obtained be-

TABLE V. Correlations between maximum DPOAE amplitude of different DPOAE components and TBOAE amplitude, with different frequency shifts between TBOAE center frequency and $f2$ frequency. TBOAEs at 1.5, 2 and 3 kHz have been selected, in order to correlate DPOAE amplitude to the same set of data (r=correlation coefficient, n=number of point, p=level of significance with NS for nonsignificant).

$f2_{(\text{DPOAEs})}$-f(TBOAEs)		Lower sideband DPOAEs			Upper sideband DPOAEs	
		$2f1\text{-}f2$	$3f1\text{-}2f2$	$4f1\text{-}3f2$	$2f2\text{-}f1$	$3f2\text{-}2f1$
	r	0.30	0.39	0.22	0.34	0.21
1 octave	n	53	52	45	47	22
	p	<0.05	<0.01	NS	<0.05	NS
	r	0.71	0.65	0.47	0.61	0.26
1/2 octave	n	53	52	42	49	27
	p	$p<0.0001$	$p<0.0001$	<0.005	<0.0001	NS
	r	0.62	0.55	0.44	0.65	0.44
0 octave	n	53	53	37	51	30
	p	$p<0.0001$	$p<0.0001$	$p<0.01$	<0.0001	<0.05
	r	0.29	0.28	0.36	0.66	0.43
$-\frac{1}{2}$ octave	n	53	53	32	41	31
	p	<0.05	<0.05	<0.05	<0.0001	<0.05
	r	0.10	0.01	0.24	0.48	0.35
-1 octave	n	52	53	23	49	28
	p	NS	NS	NS	<0.005	<0.07

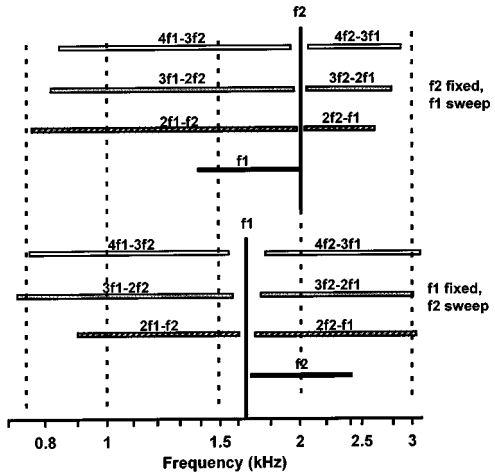

FIG. 11. Frequencies of multicomponent DPOAEs recorded with an $f2$ fixed at 2 kHz, and with a corresponding $f1$ fixed, $f2$ sweep method ($f1$ fixed at 1.6 kHz). Dotted lines represent center frequencies of TBOAEs with which correlations between DPOAE amplitude and TBOAE amplitude have been performed.

tween $3f1\text{-}2f2$ and TBOAE amplitude for ratios of 1.06, 1.08, 1.12, 1.20 and 1.22, but no significant correlations were obtained between $2f1\text{-}f2$ and TBOAE amplitude [Fig. 12(a)].

For $2f2\text{-}f1$, the greatest correlations were obtained for $f2$ corresponding to TBOAE frequencies for ratios ranging from 1.04 to 1.28 [Fig. 12(c)]. There were significant correlations for $\frac{1}{2}$ octave difference between TBOAE and $f2$ frequencies at a ratio of 1.08, for 1 octave difference at ratios ranging from 1.12 to 1.25, and for 1.5 octave difference at a single ratio of 1.10. No significant correlations were obtained between TBOAE amplitude and $3f2\text{-}2f1$ DPOAE amplitude.

For TBOAE frequencies ranging from 2000 to 6000 Hz, correlations were made between TBOAE amplitude and DPOAE amplitude recorded at different ratios, with $f2$ at or below TBOAE frequencies.

For both $2f1\text{-}f2$ and $3f1\text{-}2f2$, the greatest correlations were obtained when there was no difference between $f2$ and TBOAE frequencies, for $f2/f1$ ratios ranging from 1.04 to 1.16 (and 1.10 to 1.14 for $3f1\text{-}2f2$). Significant correlations were obtained between $2f1\text{-}f2$ DPOAE amplitude and TBOAE frequencies $\frac{1}{2}$ octave above $f2$ frequencies, for ratios ranging from 1.10 to 1.32 (at ratios 1.12 and 1.16 for $3f1\text{-}2f2$), and correlations were obtained with 1 octave difference for ratios between 1.10 to 1.18 (ratio of 1.06 and 1.08 for $3f1\text{-}2f2$) [Fig. 12(b)]. No correlations were obtained for 1.5 octave difference.

For $2f2\text{-}f1$ [Fig. 12(d)], the greatest correlations were obtained for $f2$ corresponding to TBOAE frequencies for ratios ranging from 1.04 to 1.26 (for 1.10 ratio for $3f2\text{-}2f1$), and for $f2$ $\frac{1}{2}$ octave below TBOAE frequency for ratios ranging from 1.06 to 1.28 (1.10 and 1.14 for $3f2\text{-}2f1$). Significant correlations were also found with 1-octave difference, for ratios from 1.14 to 1.28 and 1.5-octave difference for ratios ranging from 1.12 to 1.28. The correlation coefficients obtained between $2f2\text{-}f1$ DPOAE amplitude and TBOAE amplitude tended to increase when $f2/f1$ ratios increased from 1.04 to 1.22.

The same analysis was performed using an $f1$ fixed, $f2$ sweep method, and showed similar findings as the $f2$ fixed, $f1$ sweep method.

III. DISCUSSION

A. Lower sideband DPOAEs and DPOAE tuning

When lower sideband DPOAEs are recorded as a function of the primary frequencies separation, with $f2$ fixed (and therefore varying $f1$), their amplitude reaches a maximum value at a common DPOAE frequency value (Gaskill and Brown, 1990; Brown *et al.*, 1992; Brown and Williams,

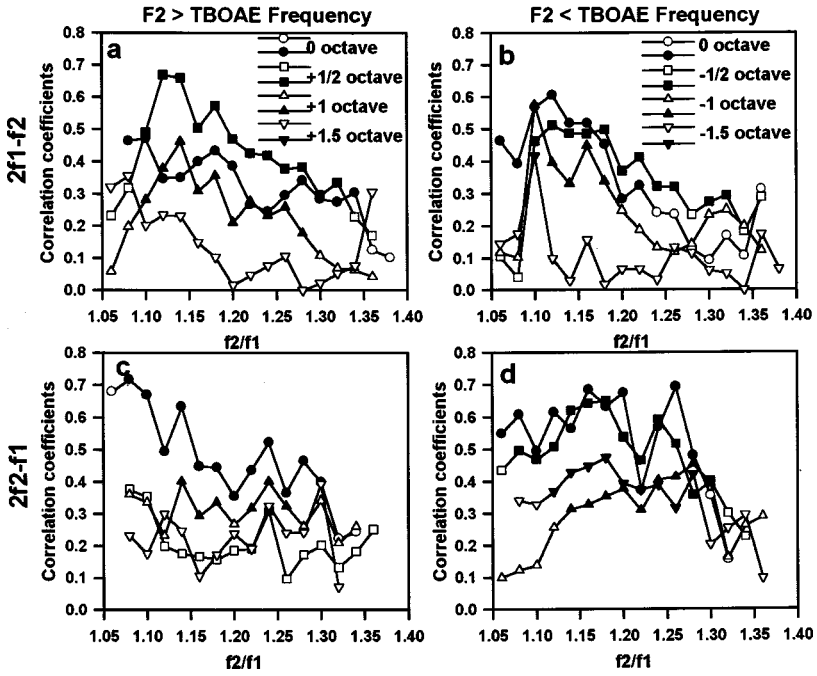

FIG. 12. Correlation coefficients obtained between DPOAE amplitude recorded per $f2/f1$ ratio, and TBOAE amplitude, with $f2$ frequency generating the DPOAEs 0, $\frac{1}{2}$ and 1 octave above the TBOAE center frequency (TBOAE frequencies ranging from 750 to 2000 Hz) [(a) and (c)] and 0, $\frac{1}{2}$ and 1 octave below the TBOAE center frequency (TBOAE frequencies ranging from 2000 to 6000 Hz) [(b) and (d)]. Black symbols represent statistically significant correlations. The DPOAEs have been recorded using an $f1$ sweep, $f2$ fixed method. Upper panels show correlations obtained between TBOAE and $2f1\text{-}f2$ DPOAE amplitude, and lower panels show correlations between TBOAEs and $2f2\text{-}f1$ DPOAE amplitude.

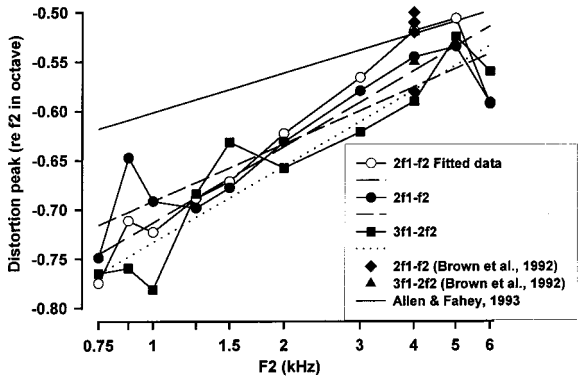

FIG. 13. Maximum DPOAE amplitude peak frequency, relative to $f2$ (in octaves), as a function of $f2$ frequency, obtained from $2f1$-$f2$ amplitude ratio functions (black circles) fitted with a third degree polynomial ($2f1$-$f2$ fitted data, white circles) and from $3f1$-$2f2$ DPOAE amplitude ratio functions (black squares). Data obtained by Brown *et al.* (1992) are specified as diamonds and triangles, and the function obtained by Allen and Fahey (1993a) on a human ear is specified as a solid line.

1993; Allen and Fahey, 1993a, b). Brown *et al.* (1992) and Allen and Fahey (1993a, b) hypothesized the presence of a second filter, whose place is linked to the $f2$ place, but tuned to much lower frequency. This ''second filter'' would be responsible for this tuning of the lower sideband DPOAE responses. Brown *et al.* (1992) have shown, in humans, that the $3f1$-$2f2$ and $2f1$-$f2$ DPOAEs amplitude reached their maximum for a common DPOAE frequency, which was situated around $\frac{1}{2}$ octave below $f2$, for $f2$ at 4 kHz. The results presented here show that this second filter is tuned to different frequencies relative to $f2$ along the cochlear partition. The frequency place of the magnitude peak for each of the lower sideband DPOAEs, relative to $f2$ (in octave) for each $f2$ frequency tested, is shown Fig. 13, along with Brown *et al.*'s results obtained at 4 kHz for four subjects (using $2f1$-$f2$ and $3f1$-$2f2$ data), and Allen and Fahey's results obtained in a single human ear at six different $f2$ frequencies. Results at 6 kHz show a distortion peak further from the $f2$ peak than at 5 kHz: this is due to the greater optimum ratio obtained at 6 kHz for all lower sideband DPOAEs than at 5 kHz, explained by an underestimation of the primary levels at the eardrum (cf. the companion paper, Moulin, 2000). Our results, at 4 kHz, show a distortion peak further from the $f2$ place than Brown *et al.*'s results. This can be attributed to the lower levels of primaries used by Brown *et al.* (1992) (55 dB/40 dB vs 65 dB/60 dB in this study). As optimum ratios for $2f1$-$f2$ tend to decrease as primary levels decrease (Harris *et al.*, 1989; Moulin *et al.*, 1999), the distortion peak would be expected to be closer to the $f2$ place in Brown *et al.*'s data, which is the case. The recording method ($f1$ sweep versus $f2$ sweep) should have an influence on the optimum DPOAE $f2/f1$ ratio: If the second filter is linked to the $f2$ frequency, then the filter moves as $f2$ is swept. When $2f1$-$f2$ and $3f1$-$2f2$ have the same DPOAE frequency, with a fixed $f1$, then for a given $f2/f1$ ratio, $f2$ of $3f1$-$2f2$ is lower than $f2$ of $2f1$-$f2$. The filter would be at greater frequency for $2f1$-$f2$ DPOAE than for $3f1$-$2f2$, hence the maximum DPOAE amplitude for $2f1$-$f2$ would be at greater DPOAE frequency than for $3f1$-$2f2$. Hence, the corresponding $f2/f1$ ratio for $2f1$-$f2$ would be lower than predicted by the formula equating the $2f1$-$f2$ and the $3f1$-$2f2$ DPOAE frequencies. The theoretical difference in $f2/f1$ ratios due to the difference in $f2$ frequencies can be calculated using $f2/f1_{\mathrm{opt}(2f1\text{-}f2)} = 1.238 - 0.08 \times \log(f2)$, but ranges from 0.001 62 for a ratio of 1.10 to 0.006 334 for a ratio of 1.50, which is too small (lower than the smallest step of $f2/f1$ change in our protocols) to be observed in the relations between optimum ratios of $2f1$-$f2$ and $3f1$-$2f2$ for the $f2$ fixed versus the $f1$ fixed methods.

Interrelations between the amplitudes of different lower sideband DPOAEs seem to be more robust than the relation between optimum ratios of the same lower sideband DPOAEs. On average data across 18 subjects, the optimum DPOAE-grams obtained for the three lower sideband DPOAEs showed a very similar pattern across frequencies, whereas the functions describing optimum $f2/f1$ ratios as a function of frequency showed more differences between the $2f1$-$f2$ DPOAE and the $3f1$-$2f2$ DPOAE. Furthermore, when DPOAE amplitude correlations between different lower sideband DPOAEs are considered per $f2/f1$ ratio (by 0.02 $f2/f1$ steps), the pairs of $2f1$-$f2$ and $3f1$-$2f2$ ratios where the strongest correlations are obtained vary according to a function very close to the theoretical function obtained when equating $2f1$-$f2$ DPOAE and $3f1$-$2f2$ DPOAE frequencies, for a fixed $f2$ [Eq. (2)] ($f1$ sweep method) and for a fixed $f1$ [Eq. (4)] ($f2$ sweep method). According to the second filter hypothesis, DPOAE amplitude tuning would be due to a second filter tuned at a frequency half an octave below the $f2$ frequency. Therefore, each lower sideband DPOAE would peak at the same distortion frequency, provided they have the same $f2$ frequency, and, therefore, the relation between $3f1$-$2f2$ and $2f1$-$f2$ optimum ratios should follow Eq. (2) (Fig. 9). This is not the case. According to our results, the different lower sideband DPOAE amplitude ratio functions peak at slightly different frequencies, for a fixed $f2$: $3f1$-$2f2$ peaks at a greater ratio, and therefore at a lower DPOAE frequency than $2f1$-$f2$ DPOAE, when $2f1$-$f2$ DPOAE $f2/f1$ is below 1.22. Similar results are obtained between $4f1$-$3f2$ DPOAE and $2f1$-$f2$ DPOAE optimum ratios: the $4f1$-$3f2$ distortion magnitude peak is at greater $f2/f1$ than expected, i.e., at a lower frequency than $2f1$-$f2$. When compared to the $3f1$-$2f2$ DPOAE, $4f1$-$3f2$ DPOAE peaks at a lower frequency. The DPOAE amplitude peak is shifted towards low frequencies as the order of the lower sideband DPOAE increases. Such low-frequency shift of the place of the distortion peak with different lower sideband DPOAEs can be seen in one subject in Brown *et al.* (1992) [Fig. 3(d)], where the $3f1$-$2f2$ DPOAE amplitude shows a downwards frequency shift *re* $2f1$-$f2$ DPOAE amplitude peak, for a fixed $f2$ of 4 kHz. A similar downwards frequency shift of $3f1$-$2f2$ relative to $2f1$-$f2$ DPOAE frequency is shown, for another human subject, at 4 kHz, by Brown and Williams (1993) [Fig. 1(b)]. Although, admittedly, this difference in the distortion peak frequency (for a fixed $f2$, and for different lower sideband DPOAEs) is small, it is not in favor of the hypothesis of a

second filter tuned at a fixed frequency relative to $f2$. Once generated, according to the second filter hypothesis, the DPOAE amplitude response is filtered, but such a filter would have to be tuned to slightly different frequencies for each lower sideband DPOAE, for a fixed $f2$. This cannot be conceived without involving the $f1$ frequency, as it is the only different parameter between the $2f1$-$f2$ and $3f1$-$2f2$ recorded at the same DPOAE frequency and the same $f2$ frequency. Recently, Martin (1999) suggested the possible involvement of the second harmonic of $f1$, interacting with $f2$ to produce a $2f1$-$f2$ that then would influence the original DPOAE amplitude. Suppression of the DPOAE components by the primary frequencies is one of the contributing factor of the DPOAE amplitude tuning (Kanis and de Boer, 1997). It is likely that the amount of such a suppression varies according to the separation of $f2$ and $f1$, and therefore would be different for $2f1$-$f2$ and $3f1$-$2f2$ recorded at the same DPOAE frequency (with $f2$ fixed). Kanis and de-Boer (1997) showed that DPOAE amplitude tuning can be achieved without the need for a second filter, and explained this tuning by saturation of the active process within the cochlea. Furthermore, their model showed a downwards frequency shift of the distortion peak with increasing order of the lower sideband DPOAE components. The results presented here do not agree with the second filter hypothesis tuned to a fixed frequency relative to $f2$ frequency, and are more in agreement with the Kanis and de Boer hypothesis, as suggested, as well by the influence of SOAEs on DPOAE amplitude. The significantly greater TBOAE and DPOAE amplitudes observed in subjects presenting SOAEs, at frequencies above 3 kHz, can be explained by the fact that seven out of eight subjects presenting SOAEs had SOAE frequencies above 3.5 kHz. It is well known that evoked OAE amplitudes are greater in subjects presenting SOAEs (Lonsbury-Martin *et al.*, 1990; Moulin *et al.*, 1993; Abdala, 1996; Ozturan and Oysu, 1999). However, data about the influence of SOAEs on DPOAE amplitude ratio function are meager. Results presented here show that the difference between DPOAE amplitude recorded in subjects presenting SOAEs and subjects presenting no SOAEs is greater for low $f2/f1$ ratios for $2f1$-$f2$, for ratios close to the optimum ratio for $3f1$-$2f2$, and for ratios lower than the optimum $f2/f1$ for $4f1$-$3f2$. Moreover, the $2f1$-$f2$ DPOAE optimum ratio tends to shift towards low ratios in subjects showing SOAEs. If SOAE+ subjects had a greater traveling wave amplitude, for the same stimulus level, than SOAE− subject, then a greater optimum $f2/f1$ in SOAE+ subjects would be expected, with greater DPOAE amplitude at $f2/f1$ greater than the optimum ratio. This is not the case, suggesting that the greater DPOAE amplitude in SOAE+ subjects is of different origin than the increase of DPOAE amplitude due to an increase of stimulus intensity, i.e., an increase of traveling wave amplitude. SOAE presence is associated with high-amplitude DPOAE components, which is likely to favor multiple interactions between several waves originating from the locations of the primaries of the multiple DPOAE components, and of the SOAE frequencies, modifying the suppression of the DPOAE components by the primaries as $f2/f1$ decreases from the optimum ratio to lower ratio.

B. Lower sideband DPOAEs and generation sites

Most of the available literature about DPOAEs suggests that lower sideband DPOAEs are generated at the $f2$ place. However, new evidence suggests that, in some cases [i.e., at low $f2/f1$ ratios according to Kemp and Knight (1999); in some ears according to Gaskill and Brown (1996); and at low to moderate primaries levels according to Brown *et al.* (1996)], the DPOAE recorded in the outer ear canal can be the product of a DPOAE coming from the $f2$ place and a more delayed DPOAE coming from its own frequency place. Although our use of optimum ratios and primaries levels of 65 dB would not favor this hypothesis, correlations between TBOAE amplitude and lower sideband DPOAE amplitude is greater for TBOAE frequencies $\frac{1}{2}$ octave below the $f2$ frequency. Figure 11 explains the relative frequencies of TBOAEs and DPOAEs tested on a logarithmic scale: The TBOAE frequencies $\frac{1}{2}$ octave, even 1 octave, below $f2$ still correspond to DPOAE frequencies and $f1$ frequency. The greatest correlations between fixed ratio DPOAE amplitude and TBOAE amplitude are obtained for low ratios, i.e., for high DPOAE frequencies, whether the TBOAE frequency is centered on the $f2$ frequency or $\frac{1}{2}$ octave below. The greater correlation between TBOAE and DPOAE amplitude for $\frac{1}{2}$-octave difference persists for all $f2/f1$, suggesting that there is no significant frequency shift in DPOAE generation with $f1$ sweep. Indeed, if the DPOAE site of generation was moving as DPOAE frequency decreases, then correlations between DPOAE amplitude and TBOAE amplitude recorded $\frac{1}{2}$ and 1 octave below $f2$ would increase, and high-order sideband DPOAEs would show correlations for lower TBOAEs frequencies. As this is not the case, the DPOAE site of generation does not seem to move with decreasing $f1$, but DPOAEs recorded at a given $f2$ seem to reflect cochlear status at the frequencies at and below the $f2$ frequency. When an $f2$ sweep method is used, similar correlations between DPOAE and TBOAE amplitudes are obtained, suggesting that DPOAE amplitude does not depend strongly on the precise $f2$ place. This agrees with the strong correlations between the maximum amplitude of each lower sideband DPOAE, obtained by varying $f2/f1$ with $f2$ sweep, which are not different from the correlations obtained with an $f1$ sweep method. With the $f2$ sweep method, when the different lower sideband DPOAEs have the same DPOAE frequency, with a fixed $f1$, $f2$ is different (for instance, for $f2/f1$ at 1.20, $f2$ is equal to 4531 for $4f1$-$3f2$, 4673 Hz for $3f1$-$2f2$ and 5098 Hz for $2f1$-$f2$). If the $f2$ frequency place had an important role in the DPOAE amplitude recorded in the outer ear canal, weaker correlations between maximum multi-component DPOAE amplitudes would be expected when using an $f2$ sweep method. If anything, the correlations obtained with an $f2$ sweep method tend to be greater than correlations obtained using an $f1$ sweep method. Similarly, amplitude correlations between different lower sideband DPOAEs for each $f2/f1$ tended to be greater for the $f2$ sweep method. This argues for a less important role of the precise $f2$ place in lower sideband DPOAE amplitude than previously thought. The small variations of DPOAE amplitude seem to be more linked to the $f2/f1$ ratio (and to the multiple interactions between different DPOAE compo-

nents) than to the precise $f2$ frequency place. This agrees with Heitmann *et al.*'s findings (1998), who found that the $2f1$-$f2$ DPOAE amplitude microstructure can be suppressed by adding a tone close to the $2f1$-$f2$ DPOAE frequency, suggesting that the amplitude microstructure is not linked to cochlear status at the $f2$ place, but to interferences between two components coming from two different generation sites. Lower sideband DPOAEs are tuned slightly differently from one another, with a low-frequency shift for $3f1$-$2f2$ and $4f1$-$3f2$ magnitude peaks relative to the $2f1$-$f2$ peak. Furthermore, the DPOAE tuning varies with $f2$ frequency, and its center frequency is at a lower frequency place relative to $f2$ at low frequencies than at high frequencies. Subjects presenting SOAEs have greater lower sideband DPOAE amplitude at low $f2/f1$ ratio and a smaller optimum $f2/f1$. Similarities between an $f1$ sweep, $f2$ fixed method and an $f2$ sweep, $f1$ fixed method in correlations obtained between amplitudes of the different lower sideband DPOAEs suggest that DPOAE amplitude is not strongly dependent on the precise place of the $f2$ frequency. Correlations between TBOAEs and DPOAEs suggest that lower sideband DPOAEs reflect cochlear status at frequencies around $f2$ and at lower frequencies.

C. Upper sideband DPOAEs

Upper sideband DPOAEs have been neglected in humans comparatively to lower sideband DPOAEs. Indeed, they are of smaller amplitude than the $2f1$-$f2$ DPOAE, especially when the primary levels are set to favor the recording of $2f1$-$f2$ by lowering the level of L2 relative to L1. Furthermore, most studies use an $f2/f1$ ratio around 1.20, which is optimum for $2f1$-$f2$ recording for most stimulus parameters, but is too high for good $2f2$-$f1$ recordings. The results presented here show a decrease of the presence of upper sideband DPOAEs as a function of $f2/f1$, which agrees with Erminy *et al.*'s results (1998), which showed a lower $2f2$-$f1$ DPOAE presence for an $f2/f1$ at 1.20 than at 1.12. Two major differences with lower sideband DPOAEs can be seen: First, the decrease of the upper sideband with increasing $f2/f1$ ratio is shallower than that of lower sideband DPOAEs, but it occurs from a smaller ratio than lower sideband DPOAEs. The shallower decrease with increasing $f2/f1$ is the same whether the $f2/f1$ ratio has been modified using an $f2$ fixed, $f1$ sweep method, or an $f1$ fixed, $f2$ sweep method. Hence, it is linked to the $f2/f1$ ratio rather to the DPOAE frequency itself, as the step change in $2f2$-$f1$ DPOAE frequency with $f2/f1$ ratio is doubled in the $f2$ sweep method versus the $f1$ sweep method. Second, upper sideband DPOAE presence is frequency dependent. Even for small $f2/f1$, presence of higher-order upper sideband DPOAEs ($3f2$-$2f1$ and $4f2$-$3f1$) is very low ($<50\%$), and is down to 0% for a $f2/f1$ of 1.20, which could explain why data available in humans are so meager. The second major difference with lower sideband DPOAEs is the strong frequency dependence of upper sideband DPOAE presence. Results presented here show a decrease of DPOAE presence as $f2$ frequency increases for $2f2$-$f1$ and $3f2$-$2f1$, whereas the decrease of the corresponding lower sideband DPOAE, $3f1$-$2f2$, with increasing ratio has the same pattern whatever the $f2$ frequency.

The influence of primary frequency separation on upper sideband DPOAE amplitude is different from the tuning of lower sideband DPOAEs. The average data presented for $f2$ at 3000 Hz (Fig. 3) suggests that there is a steady decrease of upper sideband DPOAE amplitude with increasing $f2/f1$ ratios. However, this is not universally true, especially at low frequencies, where $2f2$-$f1$ DPOAE amplitude increases as $f2/f1$ increases up to a ratio of 1.20, and then decreases. Individual data at 4 kHz (Fig. 5) show the same kind of tuning of $2f2$-$f1$ DPOAE amplitude versus ratio functions, as for lower sideband DPOAEs, for two subjects presenting high-frequency SOAEs. The optimum ratios eliciting the greatest $2f2$-$f1$ and $3f2$-$2f1$ DPOAE amplitudes for a fixed $f2$ frequency decrease as frequency increases, and this decrease is sharper for upper sideband DPOAEs than lower sideband DPOAEs. This could explain the much lower $2f2$-$f1$ DPOAE amplitude than $2f1$-$f2$ DPOAE amplitude obtained at high frequencies by Martin *et al.* (1998), using a fixed ratio of 1.21 and 75 dB SPL equilevel primaries. From our data set, a ratio of 1.21 is optimum only for $f2$ frequencies below 1 kHz. The optimum ratio is below 1.16 for frequencies above 1.2 kHz. Admittedly, if the optimum ratio of $2f2$-$f1$ DPOAE behaves the same way as optimum ratio of $2f1$-$f2$, it increases with primary levels (Harris *et al.*, 1989; Moulin *et al.*, 1999), so that the optimum ratios for Martin *et al.*'s data are very probably greater than the optimum ratios described here for 65 dB/60 dB primary levels, especially since we used a lower $f2$ level which does not help $2f2$-$f1$ recordings. However, even with this taken into account, the strong dependency of the $2f2$-$f1$ optimum ratio on primary frequencies makes an $f2/f1$ ratio of 1.21 far too high for $2f2$-$f1$ recordings at high frequencies, and can explain the amplitude difference between the $2f1$-$f2$ and $2f2$-$f1$ DPOAE-grams observed by Martin *et al.* (1998), and the decrease of $2f2$-$f1$ amplitude with frequency observed by Moulin *et al.* (1993) with equilevel primaries and a fixed ratio of 1.17. Nelson *et al.* (1999) observed a better signal-to-noise ratio for $2f2$-$f1$ than for $2f1$-$f2$ at low frequencies, and attributed this to the lower noise floor observed for $2f2$-$f1$ compared to $2f1$-$f2$. This is true, however, at low frequencies; $2f2$-$f1$ optimum ratios are similar to $2f1$-$f2$ DPOAE optimum ratios, therefore $2f2$-$f1$ and $2f1$-$f2$ are likely to be of similar amplitude at low frequencies at a 1.20 $f2/f1$ ratio, whereas at higher frequencies, the optimum ratio of $2f2$-$f1$ being very small compared to $2f1$-$f2$ optimum ratio, $2f2$-$f1$ DPOAE amplitude decreases greatly with frequency in a classic fixed ratio recorded method such as the DPOAE-gram. Lastly, the upper sideband DPOAE ''optimum'' DPOAE-grams do not show a steady decrease in amplitude with increasing $f2$ frequencies.

As seen above, lower sideband DPOAE-grams show a similar pattern whatever order the DPOAE components are. Similar findings are obtained for upper sideband DPOAEs:

the $2f2\text{-}f1$ and $3f2\text{-}2f1$ DPOAE-grams show the same pattern with frequency. However, this pattern is quite different from the lower sideband DPOAEs when the same primary frequencies are considered, but similarities can be seen if the primary frequencies of upper sideband DPOAEs are shifted to the right, i.e., towards high frequencies, by about $\frac{1}{2}$ octave. Moreover, differences in DPOAE amplitude due to SOAE presence are obtained for lower $f2$ frequencies (from 2 kHz for $2f2\text{-}f1$ and $3f2\text{-}2f1$ DPOAEs) than lower sideband DPOAEs (significant differences obtained from 3 kHz with $2f1\text{-}f2$ and 5 kHz for $3f1\text{-}2f2$ DPOAE). This bring arguments in favor of a different site of DPOAE generation for upper sideband DPOAEs, situated at greater frequencies than $f2$. Furthermore, $2f2\text{-}f1$ DPOAE amplitude is better correlated with $2f1\text{-}f2$ DPOAE amplitude when the $2f2\text{-}f1$ primary frequencies are $\frac{1}{2}$ to $\frac{3}{4}$ octave below the $f2$ frequency generating the $2f1\text{-}f2$ DPOAE, which gives a ratio of frequencies between 1.5 and 1.7 between the two sets of primaries, which agrees with the ratio of 1.6 obtained by Martin *et al.* (1998). Admittedly, these correlations show a spread of results, with significant correlations obtained with primaries shifted from $\frac{1}{4}$ to $-\frac{5}{4}$ octaves for $f2$ at 5 kHz. This could be attributed to the fact that the maximum DPOAE amplitude has been recorded over a large ratio range at 65 dB SPL primary levels, and would thus reflect cochlear properties over a substantial frequency range. Similarly, when the maximum DPOAE amplitude was correlated to TBOAE amplitude, the greatest correlation between upper sideband DPOAE and TBOAE amplitude were obtained when TBOAE center frequency was 0 to $\frac{1}{2}$ octave above the $f2$ frequency used to generate upper sideband DPOAEs, whereas correlations between lower sideband DPOAEs and TBOAEs were greater for TBOAE frequencies at or lower than the $f2$ frequencies used to generate lower sideband DPOAEs (Fig. 12). This strongly suggests a difference in generation site, with upper sideband DPOAEs generated more basally than lower sideband DPOAEs. However, several questions arise: it is accepted that the different lower sideband DPOAEs are generated at a common place, namely the $f2$ place. Do the upper sideband DPOAE show the same pattern? The similarities between the optimum DPOAE-grams obtained between the $2f2\text{-}f1$ and the $3f2\text{-}2f1$ DPOAEs argue in favor of a common generation site for upper sideband DPOAEs. However, correlations between the optimum amplitude for each upper sideband DPOAEs, with a common $f2$, are much weaker than the same correlation obtained for lower sideband DPOAEs (Table II). If the $2f2\text{-}f1$ DPOAE is generated close to its frequency, its generation site is likely to be modified with the $f2/f1$ ratio, as its frequency moves. In addition, the generation site of higher-order upper sideband DPOAE would be basal to the $2f2\text{-}f1$ DPOAE generation site. The correlation of maximum DPOAE amplitude between lower sideband DPOAEs and upper sideband DPOAEs showed stronger correlation when the primaries generating $2f2\text{-}f1$ and $3f2\text{-}2f1$ DPOAEs were $\frac{1}{2}$ to 1 octave below primaries generating $2f1\text{-}f2$ DPOAEs, which gives a ratio between 1.5 and 2 between the two sets of primaries. The correlation between $4f2\text{-}3f1$ and $2f1\text{-}f2$ were greater for a difference of 1 to 1.5 octave between the two sets of primaries, and were not significant for only $\frac{1}{2}$-octave difference, suggesting that the place of generation of the $4f2\text{-}3f1$ is more basal than the other upper sideband DPOAEs' place of generation. However, this could be explained by the fact that for $2f2\text{-}f1$ and $3f2\text{-}2f1$, the maximum DPOAE amplitude over the ratio range was obtained, whereas the optimum $f2/f1$ ratio for the $4f2\text{-}3f1$ is so small that it is likely to have been overestimated by our calculation procedure. The maximum DPOAE amplitude of the $4f2\text{-}3f1$ would be then recorded at a higher frequency than for other upper sideband DPOAEs, which would explain a better correlation with very low primary frequencies, whereas $2f2\text{-}f1$ and $3f1\text{-}2f2$ both show a similar behavior. Correlations between different upper sideband DPOAEs when the primary frequencies generating the $4f2\text{-}3f1$ were shifted towards lower frequencies than the primaries eliciting the $2f2\text{-}f1$ response showed significant correlations between maximum DPOAE amplitude of the different upper sideband DPOAEs only when the primaries were identical. This would argue for a common site of upper sideband generation. However, these correlations have been obtained using the maximum DPOAE amplitude obtained over the same ratio range, which could involve different sites of generation for different orders of DPOAEs. One way to solve this problem is to study correlations between $2f1\text{-}f2$ maximum DPOAE amplitude (and TBOAE amplitude) and upper sideband DPOAE at different ratios. Results showed a better correlation between $2f1\text{-}f2$ maximum amplitude recorded at lower primaries and $2f2\text{-}f1$ DPOAE amplitude recorded per $f2/f1$ ratio, when upper sideband DPOAEs are recorded at greater $f2/f1$ ratio, i.e., at greater DPOAE frequencies. This is more pronounced when an $f2$ sweep method is used, with which the upper sideband DPOAE frequencies increase more rapidly with the $f2/f1$ ratio. Furthermore, correlations between TBOAE amplitude and $2f2\text{-}f1$ DPOAEs increase as the ratio increases, i.e., as the $2f2\text{-}f1$ DPOAE frequency becomes higher, for differences of $\frac{1}{2}$ and 1 octave between TBOAE frequency and $f2$ frequency. This agrees with a site of DPOAE generation dependent upon the DPOAE frequency itself. Correlation between the different upper sideband DPOAEs amplitude should be greater when the different upper sideband frequencies are at the same frequency. Mathematical equations have been derived to see for which $f2/f1$ ratio pairs the $2f2\text{-}f1$ and $3f2\text{-}2f1$ were of equal frequencies (for a fixed primary frequency) [Eqs. (3) and (5)]. The pairs of $f2/f1$ ratios showing the best correlations between $2f2\text{-}f1$ and $3f2\text{-}2f1$ DPOAE amplitudes follow Eqs. (3) and (5). However, as the amplitude per $f2/f1$ has been considered only for $f2/f1$ differing by 0.02 steps, a small variation from the function described by Eqs. (3) and (5) cannot be seen in our data set.

ACKNOWLEDGMENTS

The author wishes to thank Nouzhra Merzoug for her excellent technical assistance and three anonymous reviewers for their helpful comments.

Abdala, C. (**1996**). ''Distortion product otoacoustic emission ($2f1$-$f2$) amplitude as a function of $f2/f1$ frequency ratio and primary tone level separation in human adults and neonates,'' J. Acoust. Soc. Am. **100**, 3726–3740.

Abdala, C., Sininger, Y. S., Ekelid, M., and Zeng, F. G. (**1996**). ''Distortion product otoacoustic emission suppression tuning curves in human adults and neonates,'' Hearing Res. **98**, 38–53.

Allen, J. B., and Fahey, P. F. (**1993a**). ''Evidence for a second cochlear map,'' in *Biophysics of Hair Cell Sensory Systems*, edited by H. Duifhuis, J. W. Horst, P. van. Dijk, and S. M. van Netten (World Scientific, Singapore), pp. 296–303.

Allen, J. B., and Fahey, P. F. (**1993b**). ''A second cochlear-frequency map that correlates distortion product and neural tuning measurements,'' J. Acoust. Soc. Am. **94**, 809–816.

Bowman, D. M., Brown, D. K., and Eggermont, J. J. (**1997**). ''The effect of sound intensity on $f1$-sweep and $f2$-sweep distortion product otoacoustic emissions phase delay estimates in human adults,'' J. Acoust. Soc. Am. **101**, 1550–1679.

Bowman, D. M., Eggermont, J. J., Brown, D. K., and Kimberley, B. P. (**1998**). ''Estimating cochlear filter response properties from distortion product otoacoustic emission (DPOAE) phase delay measurements in normal hearing human adults,'' Hearing Res. **119**, 14–26.

Brown, A. M., and Kemp, D. T. (**1984**). ''Suppressibilitiy of the $2f1$-$f2$ stimulated acoustic emissions in gerbil and man,'' Hearing Res. **13**, 29–37.

Brown, A. M., and Kemp, D. T. (**1985**). ''Intermodulation distortion in the cochlea: Could basal vibration be the major cause of round windows CM distortion?'' Hearing Res. **19**, 191–198.

Brown, A. M., and Williams, D. (**1993**). ''A second filter in the cochlea,'' in *Biophysics of Hair Cell Sensory Systems*, edited by H. Duifhuis, J. W. Horst, P. van Dijk, and S. M. van Netten (World Scientific, Singapore), pp. 72–77.

Brown, A. M., Gaskill, S. A., and Williams, D. M. (**1992**). ''Mechanical filtering of sound in the inner ear,'' Proc. R. Soc. London, Ser. B **1327**, 29–34.

Brown, A. M., Harris, F. P., and Beveridge, H. A. (**1996**). ''Two sources of acoustic distortion products from the human cochlea,'' J. Acoust. Soc. Am. **100**, 3260–3267.

Erminy, M., Avan, P., and Bonfils, P. (**1998**). ''Characteristics of the Acoustic Distortion product $2f2$-$f1$ from the normal human ear,'' Acta Otolaryngol. (Stockh) **118**, 32–36.

Gaskill, S. A., and Brown, A. M. (**1990**). ''The behavior of the acoustic distortion product, $2f1$-$f2$, from the human ear and its relation to auditory sensitivity,'' J. Acoust. Soc. Am. **88**, 821–839.

Gaskill, S. A., and Brown, A. M. (**1996**). ''Suppression of human acoustic distortion product: Dual origin of $2f1$-$f2$,'' J. Acoust. Soc. Am. **100**, 3268–3274.

Harris, F. P., Probst, R., and Xu, L. (**1992**). ''Suppression of the $2f1$-$f2$ otoacoustic emissions in humans,'' Hearing Res. **64**, 133–141.

Harris, F. P., Lonsbury-Martin, B. L., Stagner, B. B., Coats, A. C., and Martin, G. K. (**1989**). ''Acoustic distortion products in humans: Systematic changes in amplitude as a function of $f2/f1$ ratio,'' J. Acoust. Soc. Am. **85**, 220–229.

Heitmann, J., Waldman, B., Schnitzler, H. U., Plinkert, P. K., and Zenner, H. P. (**1998**). ''Suppression of distortion product otoacoustic emissions (DPOAEs) near $2f1$-$f2$ removes DP-gram fine structure–Evidence for a secondary generator,'' J. Acoust. Soc. Am. **103**, 1527–1531.

Kanis, L. J., and de Boer, E. (**1997**). ''Frequency dependence of acoustic distortion products in a locally active model of the cochlea,'' J. Acoust. Soc. Am. **101**, 1527–1531.

Kemp, D. T., and Knight, R. (**1999**). ''Virtual DP reflector explains DPOAE wave' and place' fixed dichotomy,'' Assoc. Res. Otolaryngol. Abstr. **22**, 396.

Kummer, P., Janssen, T., and Arnold, W. (**1995**). ''Suppression tuning characteristics of the $2f1$-$f2$ distortion-product otoacoustic emission in humans,'' J. Acoust. Soc. Am. **98**, 197–210.

Lonsbury-Martin, B. L., Harris, F. P., Stagner, B., Hawkins, M. D., and Martin, G. K. (**1990**). ''Distortion product emissions in humans: II. Relations to acoustic immitance and stimulus frequency and spontaneous otoacoustic emissions in normally hearing subjects,'' Ann. Otol. Rhinol. Laryngol. 99 Suppl. **147**, 15–29.

Martin, G. K. (**1999**). ''Generation of distortion product otoacoustic emissions: Insights from suppression studies,'' Assoc. Res. Otolaryngol. Abstr. **22**, 210.

Martin, G. K., Jassir, D., Stagner, B. B., Whitehead, M. L., and Lonsbury-Martin, B. L. (**1998**). ''Locus of generation for $2f1$-$f2$ vs $2f2$-$f1$ distortion-product otoacoustic emissions in normal-hearing humans revealed by suppression tuning, onset latencies, and amplitude correlations,'' J. Acoust. Soc. Am. **103**, 1957–1971.

Martin, G. K., Lonsbury-Martin, B. L., Probst, R., Scheinin, S. A., and Coats, A. C. (**1987**). ''Acoustic distortion products in rabbit ear canal. II. Sites of origin revealed by suppression contours and pure tone exposures,'' Hearing Res. **28**, 191–208.

Matthews, J. W., and Molnar, C. E. (**1986**). ''Modeling intracochlear and ear canal distortion products ($2f1$-$f2$),'' in *Peripheral Auditory Mechanisms*, edited by J. B. Allen, J. L. Hall, A. Hubbard, S. T. Neely, and A. Tubis (Springer-Verlag, Berlin), pp. 258–265.

Moulin, A. (**2000**). ''Influence of primary frequencies ratio on distortion product otoacoustic emissions amplitude. I. Intersubject variability and consequences on DPOAE-gram,'' J. Acoust. Soc. Am. **107**, 1460–1470.

Moulin, A., and Kemp, D. T. (**1996**). ''Multi-component acoustic distortion product otoacoustic emissions phase in humans. II. Implications for distortion product otoacoustic emissions generation,'' J. Acoust. Soc. Am. **100**, 1640–1662.

Moulin, A., Jourdain, F., and Collet, L. (**1999**). ''Using acoustic distortion products in clinical applications: influence of $f2/f1$ on DPOAE-grams,'' British Society of Audiology Short Papers Meeting on Experimental Studies of Hearing and Deafness, September 1998, University College London, Br. J. Audiol. **33**, 89.

Moulin, A., Collet, L., Veuillet, E., and Morgon, A. (**1993**). ''Interrelations between acoustic distortion products, transiently evoked otoacoustic emissions and spontaneous otoacoustic emissions,'' Hearing Res. **65**, 216–233.

Nelson, K., Gorga, M. P., Neely, S. T., Dorn, P. A., and Cohn, E. (**1999**). ''Can low frequency DPOAEs be detected more reliably at $2f2$-$f1$ than at $2f1$-$f2$?'' Assoc. Res. Otolaryngol. Abstr. **22**, 408.

Ozturan, O., and Oysu, C. (**1999**). ''Influence of spontaneous otoacoustic emissions on distortion product otoacoustic emission amplitudes,'' Hearing Res. **127**(1–2), 129–136.

Robles, L., Ruggero, M. A., and Rich, N. C. (**1991**). ''Two-Tone distortion in the basilar membrane of the cochlea,'' Nature (London) **349**, 413–414.

Robles, L., Ruggero, M. A., and Rich, N. C. (**1997**). ''Two-Tone distortion in the basilar membrane of the chinchilla cochlea,'' J. Neurophysiol. **77**, 2385–2399.

Stover, L. J., Neely, S. T., and Gorga, M. P. (**1996**). ''Latency and multiple sources of distortion product otoacoustic emissions,'' J. Acoust. Soc. Am. **99**, 1016–1024.

Whitehead, M. L., Stagner, B. B., Martin, G. K., and Lonsbury-Martin, B. L. (**1996**). ''Visualization of the onset of distortion-product otoacoustic emissions, and measurement of their latency,'' J. Acoust. Soc. Am. **100**, 1663–1678.

The mechanical waveform of the basilar membrane. II. From data to models—and back

Egbert de Boer[a)]
Room D2-226, Academic Medical Center, University of Amsterdam, Meibergdreef 9, 1105 AZ, Amsterdam, The Netherlands

Alfred L. Nuttall[b)]
Oregon Hearing Research Center, NRC04, Oregon Health Sciences University, 3181 SW Sam Jackson Park Road, Portland, Oregon 97201-3098 and Kresge Hearing Research Institute, University of Michigan, 1301 E. Ann Street, Ann Arbor, Michigan 48109-0506

(Received 10 May 1999; revised 1 October 1999; accepted 29 November 1999)

Mechanical responses in the basal turn of the guinea-pig cochlea are measured with low-level broad-band noise as the acoustical stimulus [for details see de Boer and Nuttall, J. Acoust. Soc. Am. **101**, 3583–3592 (1997)]. Results are interpreted within the framework of a classical three-dimensional model of the cochlea that belongs to a very wide class of nonlinear models. The use of linear-systems analysis for this class of nonlinear models has been justified earlier [de Boer, Audit. Neurosci. **3**, 377–388 (1997)]. The data are subjected to inverse analysis with the aim to recover the ''effective basilar-membrane impedance.'' This is a parameter function that, when inserted into the model, produces a model response, the ''resynthesized'' response, that is similar to the measured response. With present-day solution methods, resynthesis leads back to an almost perfect replica of the original response in the spatial domain. It is demonstrated in this paper that this also applies to the response in the frequency domain and in the time domain. This paper further reports details with regard to geometrical properties of the model employed. Two three-dimensional models are studied; one has its dimensions close to that of the real cochlea, the other is a stylized model which has homogeneous geometry over its length. In spite of the geometric differences the recovered impedance functions are very similar. An impedance function computed for one model can be used in resynthesis of the response in the other one, and this leads to global amplitude deviations between original and resynthesized response functions not exceeding 8 dB. Discrepancies are much larger (particularly in the phase) when a two-dimensional model is compared with a three-dimensional model. It is concluded that a stylized three-dimensional model with homogeneous geometric parameters will give sufficient information in further work on unraveling cochlear function via inverse analysis. In all cases of a sensitive cochlea stimulated by a signal with a stimulus level of 50 dB SPL per octave or less, the resulting basilar-membrane impedance is found to be locally active, that is, the impedance function shows a region where the basilar membrane is able to amplify acoustic power or to reduce dissipation of power by the organ of Corti. Finally, the influence of deliberate errors added to the data is discussed in order to judge the accuracy of the results. [S0001-4966(00)02703-X]

PACS numbers: 43.64.Kc, 43.64.Bt [RDF]

INTRODUCTION

In the first paper of the present series (de Boer and Nuttall, 1997b-GLIDE) we presented experimental data on the response of the basilar membrane (BM) to click and noise stimuli. We now turn to the theoretical side. Quantitative interpretation of experimental data on the response of the cochlea is only possible within a well-defined *frame of reference*. In our case the proper frame of reference is *a model of the mechanics of the cochlea*, i.e., a conceptional construction describing how different mechanical parts of the cochlea interact and cooperate to achieve that organ's remarkable performance. For the work presented in this paper a model of the cochlea is utilized in which acoustic waves propagate through fluid channels in close interaction with the mechanics of the BM and its associated structures. The model is briefly described in the Appendix. It is assumed that on its way the wave may be amplified in power by a specific frequency- and place-dependent mechanism [proposed by Kim *et al.* (1980), theoretically founded by de Boer, 1983, and coined as the ''cochlear amplifier'' by Davis (1983)]. The region where amplification occurs, the region of ''activity,'' is spatially limited and such a model is called ''locally active'' (de Boer, 1993, 1996).

Furthermore, it is assumed that the elements of this mechanism of the model are *nonlinear*, and that they are the *only* nonlinear elements of the model. The Appendix describes not only the model we used but also the class of nonlinear models to which it belongs (which encompasses almost all of the models published to date) and indicates under which conditions *linear-systems theory* can be applied

a)Electronic mail: e.deboer@amc.uva.nl
b)Electronic mail: nuttall@ohsu.edu

to a model of this class. The present paper will treat data obtained at low stimulus levels where nonlinear effects are small enough to be neglected. We will use three-dimensional models which support all types of waves, long, intermediate and short waves. In addition, we will briefly study a two-dimensional model. All models will be linear.

We performed physiological–mechanical experiments on the response of the BM using wide bands of flat-spectrum random noise as stimulus signals. The responses have been converted into input–output cross-correlation functions (ccfs). This technique is a prerequisite for interpretation of the data in terms of linear-systems theory (see the Appendix). A central place in our work is occupied by the inverse-solution method that has been described in three earlier papers, de Boer (1995a,b), de Boer and Nuttall (1999), henceforth to be called INV-1, INV-2, and INV-3, respectively. In the inverse procedure the measured response in the frequency domain for a fixed location x is first converted into a hypothetical response in the x domain for a fixed frequency. The inverse procedure yields the ''effective BM impedance'' $Z_{\mathrm{BM}}(x,\omega)$ of the model, where the independent variable x is the longitudinal coordinate of the model and the parameter ω is the radian frequency. The variables x and ω are assumed to ''scale,'' i.e., one can be traded for the other using the assumed cochlear map. Furthermore, we computed (''resynthesized'') the response of a model which uses the BM impedance function $Z_{\mathrm{BM}}(x,\omega)$, recovered by inverse analysis, as its BM impedance function.

The inverse-solution method will be applied to various types of models, to be described in Sec. I B. The nature of the results remains the same, only details differ. The most severe test of the integrity of the entire chain of procedures, starting with the spectral response, going via inverse analysis to resynthesis of the spatial response and ending with the response in the frequency domain, is performed by computing the impulse response of the model, and comparing it with the impulse response in the data. The deviations are found to remain within reasonable boundaries, in particular, all the dominant features of the impulse response are preserved. In the first paper of the present series of papers (de Boer and Nuttall, 1997b-GLIDE)—which we will refer to as ''Part I''—we reported on a typical frequency modulation in the impulse response of the BM, the ''glide.'' The resynthesized impulse response is found to include a good representation of the glide. That means that a cochlear model with the function $Z_{\mathrm{BM}}(x,\omega)$—as recovered by inverse analysis—is capable of simulating the glide. We reported earlier (Part I) that not all current models of the cochlea are able to do that.

I. METHOD AND RESULTS I—FROM THE DATA TO A MODEL

A. Data

We have collected data on movements of the basilar membrane (BM) in the basal turn of the guinea-pig cochlea with a laser velocimeter (cf. Nuttall *et al.*, 1990; Nuttall and Dolan, 1996). The measurement and data processing techniques used in the present work have been described in Part I. For the experiments described here[1] *bands of flat-spectrum pseudo-random noise* were used as acoustical stimuli. ''Stimulus level'' is defined as the SPL of one octave of the stimulus signal around the best frequency (BF). We measured the velocity of the BM at a location tuned to a frequency between 16 and 18 kHz as a function of time and computed input–output cross-correlation functions (ccf's). The accuracy of the spectrum of a ccf usually is sufficient only over a narrow range of frequencies around the BF. In order to obtain a useful ccf spectrum over a wider frequency range, we constructed *composite ccf spectra* by combining ccf spectra obtained with flat-spectrum stimuli of different bandwidths, center frequencies and intensities in the same animal (see INV-3 for details). The composite ccf spectrum should be interpreted as if it had been possible to measure the ccf spectrum in one experiment with constant stimulus power density over the entire frequency range from below 1 kHz to over 25 kHz. The composite ccf spectrum is measured and processed in such a way that it represents *the ratio of BM-to-stapes velocity*. For the description of the modest amount of smoothing applied to the composite spectrum we refer to INV-3, Appendix B. The corresponding ccf waveform is obtained from the composite ccf spectrum via (inverse) Fourier transformation. When the stimulus level is so low that the cochlea is operating like a linear system, we may consider the ccf waveform as an estimate of the impulse response.

B. Models

The underlying model is a member of the class of models described in the Appendix. In this paper we will assume that a linear model is sufficient. For higher stimulus levels a nonlinear model would be needed. However, for a nonlinear model, the composite ccf spectrum can still be interpreted as the input–output ccf spectrum of a *linear* model, namely, the ''comparison model'' as described in the Appendix. The corresponding ccf waveform then becomes the impulse response of the comparison model.

The model to be used is *three-dimensional* and supports long, intermediate as well as short waves. We will consider two versions of this model. In one, model ''3dm,'' the cross sections of the channels and the width of the BM all vary with x (the longitudinal coordinate), and we will refer to this model as the ''realistic'' model. Figure 1 shows the BM width $b_{\mathrm{BM}}(x)$ and the channel cross-sectional areas as functions of the longitudinal coordinate x. We adopted the data for this figure from the paper by Mammano and Nobili (1993) who used data published by Fernández (1952). For our purpose (all relevant frequencies are above 5 kHz) it will be sufficient to include only the most basal part. Therefore, the model will have a length of 6 mm [$L=6$ (mm)]. In Fig. 1 the corresponding segments of the curves are shown by solid lines. The remaining part of the length (curves drawn by dashed lines) is not included in our model. In the second version of the model, to be denoted by ''3ds,'' the cross sections of the two channels are the same and constant over the length L of the model. Likewise, the width of the BM (which is the movable part of the partition between the two channels) is constant, it is ε times the width b of the model. To conform with earlier work (INV-1 to INV-3) we made b

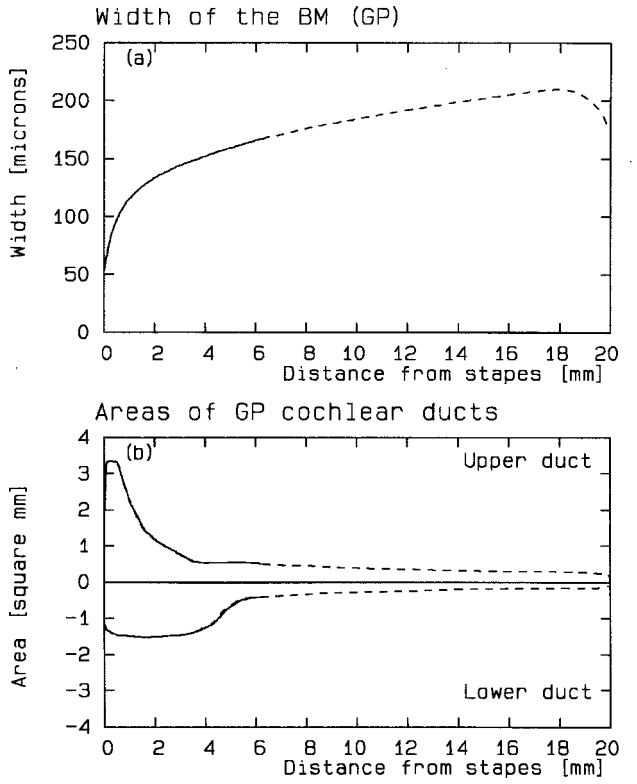

FIG. 1. Width of the basilar membrane (BM) and cross-section area of cochlear ducts for the guinea pig. Modified from Fig. 1 in Mammano and Nobili (1993). Dashed lines: original data. The segment shown by solid curves is used for the model in this paper. In this segment the data have been slightly smoothed to remove discontinuities.

equal to 1 (mm) and ε equal to 0.2. The height h of each channel is also 1 (mm). The dimensions differ considerably between the two models, particularly in the basal region, but we will see further on what the effect of this discrepancy is. We will call this model the ''stylized'' model. In addition to three-dimensional models we will consider a two-dimensional model, to be labeled ''2d.'' This model has the same outer dimensions as the ''stylized'' three-dimensional model but the BM is assumed to move *uniformly* over the entire width b of the model. A few words about units. We will use mm (millimeter) as the unit for length and g (gram) as the unit of mass. As a result the density of water is 10^{-3} (not 1 as in the cgs system).

Before the inverse solution can be applied, it is necessary to transform the response, measured at one location as a function of *frequency* (f), to the response at one frequency (e.g., the best frequency, BF) as a function of *location* (x). We assume that frequency and place ''scale'' in the sense described by (among others) Zweig (1976) and Zweig *et al.* (1976). In particular, the (radian) frequency $\omega(x)$ $(2\pi f)$ corresponding to location x is

$$\omega(x) = \omega_{\max} \exp(-\tfrac{1}{2}\alpha x), \tag{1}$$

where $\omega_{\max}$ is the radian frequency corresponding to the location of the stapes ($x=0$) and α is a constant. Scaling implies that the BM impedance function $Z_{\mathrm{BM}}(x,\omega)$ has the corresponding property in its dependence on x and ω. It is found as the impedance for one frequency, as a function of x, but it can be transformed to a function of ω for a given value of x. We use the following parameters:

$$\alpha = 0.5\,(\mathrm{mm}^{-1}),\ \omega_{\max} = 2\pi 45\,(\mathrm{kHz}),\ L = 6\,(\mathrm{mm}),\ N = 700. \tag{2}$$

The value of α is ''borrowed'' from Greenwood (1961), and that of $\omega_{\max}$ is extrapolated from Cooper and Rhode's (1992) findings (their Fig. 10, corrected for a shift of 1.7 mm).[2] The mapping is assumed to be the same in all models that we will consider. The parameter N is the number of sections in which the length L is divided.

The model equation has been solved with the full-matrix technique described in INV-3, which is based on papers by Allen (1977) and by Mammano and Nobili (1993). This technique was chosen because an alternative, faster and more economical technique (de Boer, 1998) could only be used for model ''3ds.'' In the inverse solution the boundary condition at the stapes side is formulated in terms of the ''virtual stapes velocity'' which is defined as the stapes velocity for which the volume of fluid in one channel of the model is conserved (INV-3). This definition can be used for model ''3ds.'' For model ''3dm'' we have to reinterpret the virtual stapes velocity because the BM width $b_{\mathrm{BM}}(x)$ varies with x. In our formulations the BM velocity $v_{\mathrm{BM}}(x,\omega)$ is defined as the *point velocity* of the center of the BM. For model ''3dm'' the virtual stapes velocity must then be computed as (minus) the fluid *volume* velocity density—which is $b_{\mathrm{BM}}(x)v_{\mathrm{BM}}(x,\omega)$—integrated over x divided by the area of the stapes (which is taken as the area of the upper channel in Fig. 1 at $x=0$).

Executing a forward solution for the chosen model (resynthesis) is a way of ''going from the model back to the data.'' When the *same* model is used for inverse analysis and resynthesis, the resulting response is identical (within plotting accuracy) to the response used as input to the inverse procedure. As a result of smoothing the BM impedance function small deviations occur (cf. INV-3), and we have seen to it that these are less than 2 dB in amplitude. We will explore more subtle relations between experimental data and resynthesized response in Secs. II and III.

C. Results (I)

The *upper* panel (a) of Fig. 2 shows, for one experiment, the measured composite ccf spectrum transformed from the frequency to the place domain. The abscissa is the longitudinal coordinate x (labeled ''location''). We have divided the length L of the model (6 mm) into N (700) sections. The solid line shows the amplitude, and the dashed line the phase. The amplitude is normalized to 0 dB at the peak (see the legend for the maximal BM-to-stapes velocity ratio[3] and the virtual stapes velocity). The response shown is the response of the model under consideration, for stimulation by a tone with its frequency equal to the BF.

In the *lower* panel (b) of Fig. 2 the computed BM impedance $Z_{\mathrm{BM}}(x,\omega)$ resulting from the inverse solution is presented, the solid line showing the real part and the dashed line the imaginary part. The impedance function is computed for model ''3dm'' (the ''realistic'' model). As in earlier papers (INV-1 to INV-3), the ordinate scale for the impedance

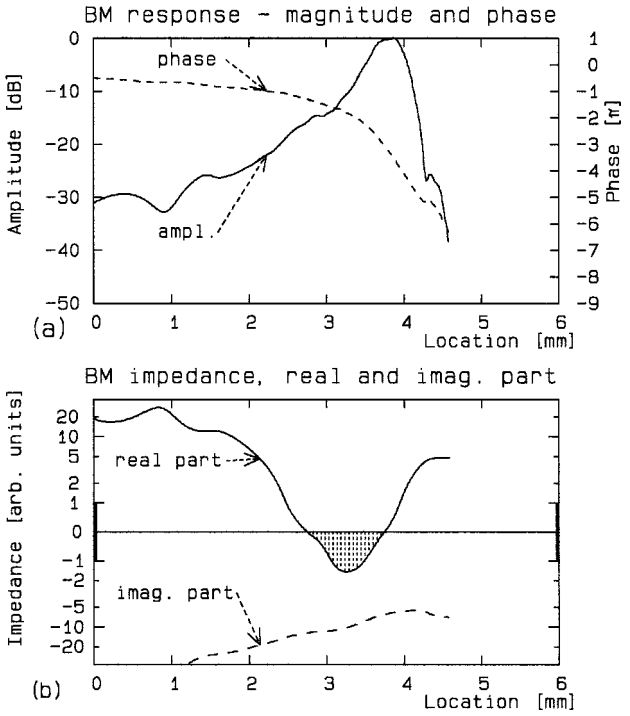

FIG. 2. Upper panel: Measured response (amplitude and phase) transformed to the x domain. Experiment 7619, stimulus level 50 dB. Maximal response amplitude level in this figure is normalized to 0 dB on the ordinate. Lower panel: BM impedance (real and imaginary parts) resulting from inverse solution for model ''3dm'' (the ''realistic'' model). The impedance scale is nonlinear: values from -1 to $+1$ are shown linearly, larger values are logarithmically compressed. The norm ''1'' corresponds to 2 g $mm^{-2} s^{-1}$, or 2000 kg $m^{-2} s^{-1}$. Best frequency (BF): 16.6 kHz. Maximal BM-to-stapes velocity ratio: 112.4. Virtual stapes velocity: $2.26-0.5i$. The filled area shows the region where the BM impedance is ''active'' (i.e., where the real part is negative). The right-hand end point of this region coincides with the response peak (cf. de Boer, 1983). Length (L) of model: 6 mm. Number of sections (N): 700.

is nonlinear: small values are plotted linearly and large values are compressed logarithmically. See the legend to the figure.

In earlier work (e.g., INV-2 and INV-3) it was found that a *locally active model* is needed to simulate data from a good preparation at low stimulus levels. Figure 2 and later figures confirm this: there invariably is a region of x where the real part of the BM impedance is negative. This region lies basalward from—in our figure to the left of—the location of the largest response, and extends from the point where the response amplitude starts its final rise toward the peak to the location of the peak itself. In Fig. 2 the ''active'' region is indicated by shading.

Figure 3 shows response and BM impedance functions for four other experiments. In each of the four panels the upper and lower panels of Fig. 2 are merged. The ordinate scales for amplitude and phase are shown on the sides of the figure. The BM impedance is plotted on the same nonlinear ordinate axis as in Fig. 2; the impedance scale is placed in the middle. Of the abscissa only the region from 1 to 5 mm is shown to present more details in the region of the response peak. Response amplitude is plotted by solid and response phase by dashed lines. The real part of the BM impedance is plotted by solid and the imaginary part by dashed lines whereby the impedance curves are drawn with thickened lines. Curves are labeled in the upper left panel, the general shape and the line thickness serve to identify the curves in the other panels. See the legend for experiment codes, BFs, maximum BM-to-stapes ratios and values of the virtual stapes velocity for the four experiments. Figure 3 has been prepared for the same ''realistic'' model (''3dm'') as Fig. 2.

Figures 2 and 3 serve to illustrate the large variability in the BM response and, especially, in the recovered impedance function. We observe that in all records the real part of the BM impedance is negative (the model is ''locally active'') in the region where the response amplitude rises to its peak. Over this region the BM is enhancing the power of the cochlear wave, and it has been demonstrated earlier that actual amplification does occur in the model, but also that it is less than anticipated (INV-3). In panels (b) and (c) we observe secondary lobes where the real part of the BM impedance $Z_{BM}(x,\omega)$ is negative. Such lobes always correspond to regions where the response amplitude is rising rapidly. We should not expect appreciable amplification in these regions, however, because the imaginary part of the impedance is too large.[4]

In some experiments we found that the ''active'' region extends all the way to the left, and includes the location of the stapes ($x=0$). We have come to the conclusion that this type of finding is most probably due to errors in the data. The arguments for this conclusion come from the study described in Sec. IV. Here we recall that the influence of data errors generally increases from the right (the region just beyond the peak) to the left (the region of the stapes) (an effect amply illustrated in INV-2 and INV-3). That the model has to be ''locally active'' in the response peak region is a much more ''robust'' finding than a similar property in the basal region.

II. RESULTS II—BACK TO THE DATA: ''CROSS-FERTILIZATION''

Our next task is to explore differences between various models. In order to find out what is essential and what is not, we derive the BM impedance function for one model and execute resynthesis with another one. We will call this procedure ''cross-fertilization.'' We found it more rewarding than mere inspection of BM impedance functions, as will become apparent further on. It is recalled that, when the *same* model is used for inverse analysis and resynthesis, the resynthesized response is virtually identical to the response that serves as the input to the inverse procedure (INV-3).

Figure 4 shows response and BM impedance function for one of our experiments, the same as in Fig. 2. The BM impedance is computed for the ''realistic'' model (''3dm''), as before. Next, resynthesis is done, but this time with the ''stylized'' model (''3ds''), in which model the geometry is independent of x. The result is labeled with the code ''3dm-3ds,'' and it is seen to be similar in shape to the input response. It has a somewhat smaller slope of the amplitude curve and also a steeper phase curve. These two features are obviously due to the taper in dimensions that the ''3dm'' model exhibits and that is absent in the ''3ds'' model. Deviations in the amplitude are limited to 8 dB.

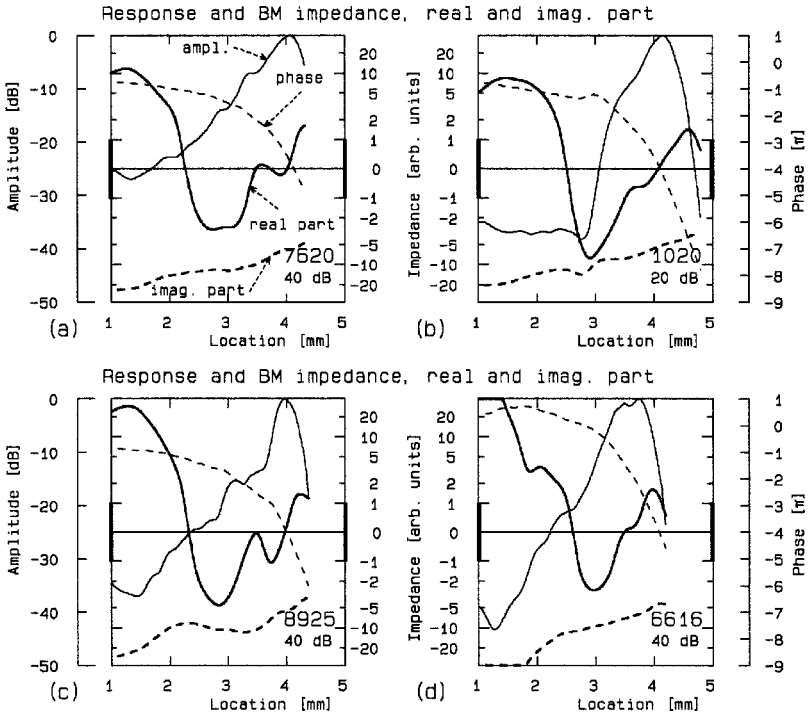

FIG. 3. Response and BM impedance in four experiments. The two panels of Fig. 2 are merged into one. Of the abscissa only the section from 1 to 5 mm is shown. Inverse solution for model ''3dm'' (as in Fig. 2). Panels (a)–(d). Experiment: 7620, 1020, 8925 and 6616. Best frequency (BF): (a) 16.3, (b) 16.0, (c) 16.7, and (d) 17.6 (kHz). Maximal BM-to-stapes velocity ratio: (a) 289, (b) 377, (c) 1003, and (d) 335. Virtual stapes velocity: (a) $1.26-0.474i$, (b) $0.338-0.038i$, (c) $1.059-1.27i$, and (d) $0.77+0.33i$.

The converse procedure is illustrated by Fig. 5. The BM impedance is computed for the ''stylized'' model (''3ds''). The first thing that meets the eye is that the BM impedance function in Fig. 5 is not much different from the one shown in Fig. 4. Resynthesis is done with the ''realistic'' model (''3dm''), and, as before, the differences between the models turn out to be moderate. This time the resynthesized response (labeled ''3ds-3dm'') is about 5 dB larger in amplitude at the response peak, and the phase slope is seen to be slightly smaller than for model ''3ds.'' In both Figs. 4 and 5 the *variations* of the amplitude in the region of the response peak are reasonably well reconstructed, and the same is true for the *variations* of the phase. It should now be clear that ''cross fertilization'' is better suited to illustrate differences between models than mere observation of the BM impedance function. We conclude that the effect of the taper in model dimensions on the response is relatively small. Sizable effects in the stapes region (near $x=0$)—where model ''3dm'' is highly inhomogeneous—can only be expected for much lower frequencies (cf. the ''breaking of symmetry'' treated by Shera and Zweig, 1991).

We now turn to the *two-dimensional model* (see Sec. I B). Figure 6 shows, in the lower panel, the BM impedance function for the three-dimensional ''stylized'' model (''3ds''), the same function as in Fig. 5. Resynthesis is carried out for the two-dimensional model (''2d''), again with the full-matrix method (see Allen, 1977 and Sondhi, 1978). The resynthesized response is labeled ''3ds-2d'' (upper panel). Now we see larger differences, especially in the *initial slope* of the phase curve. In point of fact, this comparison is somewhat unfair. In the basal region of this two-dimensional model, the width of the BM is 1 mm, which is five (or more) times that in the other two models (see Sec. I B). This implies that in the long-wave approximation the phase variations will be more than two times what they are in the three-dimensional model [de Boer (1996), Eq. (4.2.8) with H replaced by the quotient of channel cross-section area and BM width], and this is indeed what we observe.

III. RESULTS III—BACK TO THE DATA: IMPULSE RESPONSE

When inverse solution and resynthesis are done with the same mathematical formalism, the resynthesized response is virtually identical to the response that has served as the input to the inverse solution. This input response was, as recalled, the response imposed on the model in the *place* domain (the x domain). Likewise, the resynthesized response is a model response in the x domain for a fixed frequency. However, we originally started from a response measured in the *frequency (f) domain*, for a fixed location, and we may well inquire into the properties of the resynthesized response in the f domain.

For a sensitive test we turn to the *time (t) domain*. Let the input signal to the analysis be the impulse response corresponding to the composite ccf spectrum and assume that we have obtained the resynthesized response in the x domain. To obtain the resynthesized *impulse* response it is first necessary to retransform the resynthesized response from the x to the f domain. This is done by inverting the frequency-to-place transformation that the original response underwent. That procedure includes undoing the amplitude compensation described in INV-2 and the phase compensation described in INV-3. The resynthesized frequency response is now known from the frequency f_0 corresponding to $x=0$ upward but *it is unknown for lower frequencies*, f_0 being of the order of 5 kHz. Without further ado, the transformed function is linearly extrapolated down to zero frequency with constant phase and amplitude proportional to frequency. A Fourier transformation then produces the resynthesized impulse response. The so-obtained impulse response, (b), is

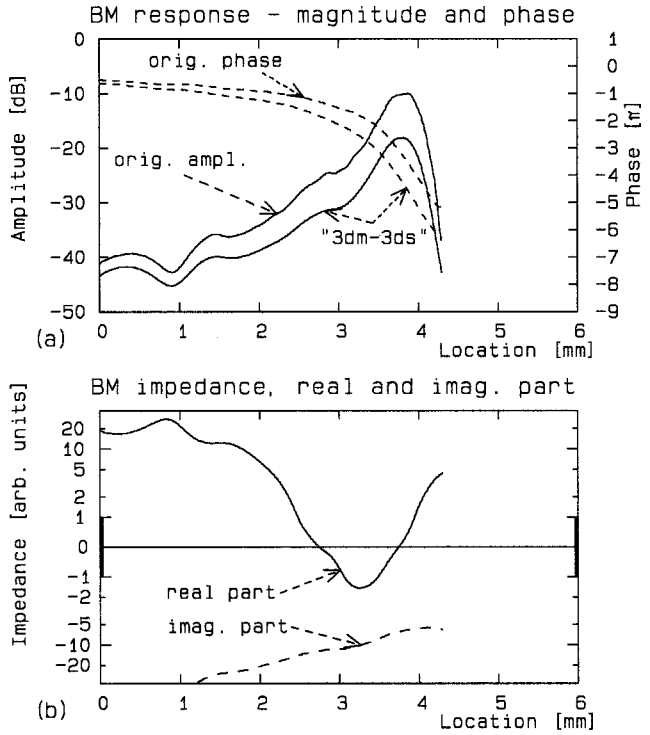

FIG. 4. ''Cross fertilization I.'' Experiment 7619. Upper panel: original response, plotted with respect to stapes velocity but with the amplitude shifted down by 10 dB. Lower panel: BM impedance computed for the ''*realistic*'' model (''3dm''). Resynthesis is done with the ''*stylized*'' model (''3ds''), the amplitude is labeled ''3dm−3ds'' in the upper panel. The resynthesized phase is shown by the lower dashed curve.

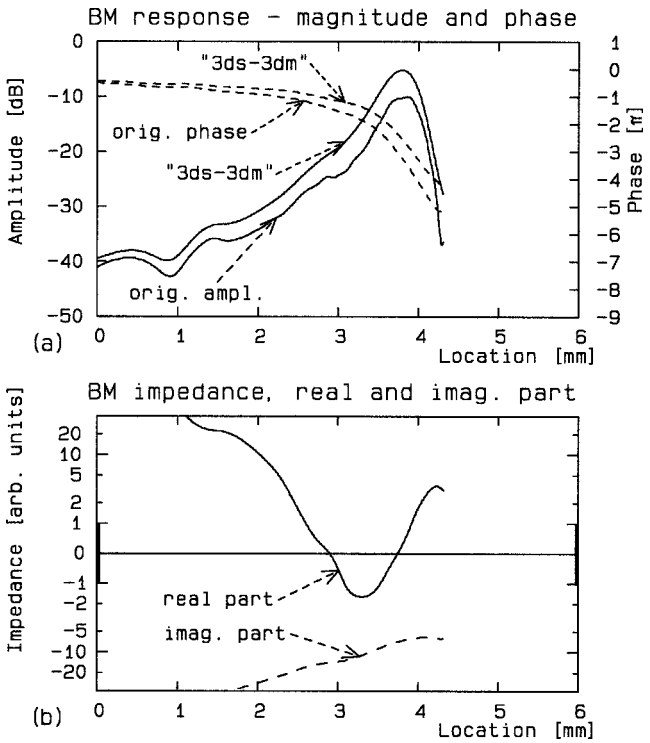

FIG. 5. ''Cross fertilization II.'' Experiment 7619. Upper panel: original response as in Fig. 4. Lower panel: BM impedance computed for the ''*stylized*'' model (''3ds''). Resynthesis is done with the ''realistic'' model (''3dm''), the amplitude is labeled ''3ds−3dm'' in the upper panel. The resynthesized phase is shown by the upper dashed curve.

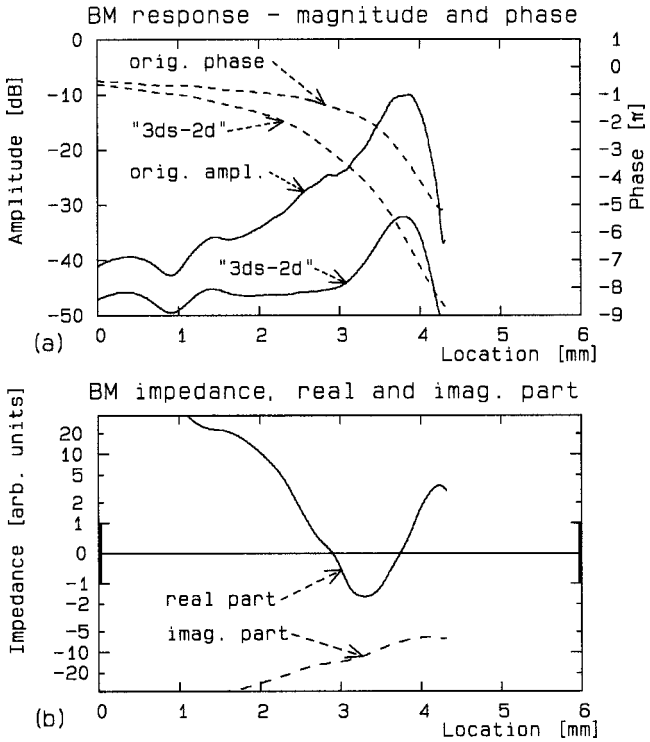

FIG. 6. ''Cross fertilization III.'' Experiment 7619. Upper panel: original response as in Fig. 4. Lower panel: BM impedance computed for the ''*stylized*'' model (''3ds''). Resynthesis is done with the *two-dimensional* model (''2d''), amplitude and phase are labeled ''3ds−2d'' in the upper panel. Note the large deviations in the phase slope (see text).

shown in Fig. 7, together with the original one, (a), on vertically displaced coordinate axes. For this figure the ''stylized'' model is used. Amplitude scaling is the same for the two responses. We observe a very close correspondence be-

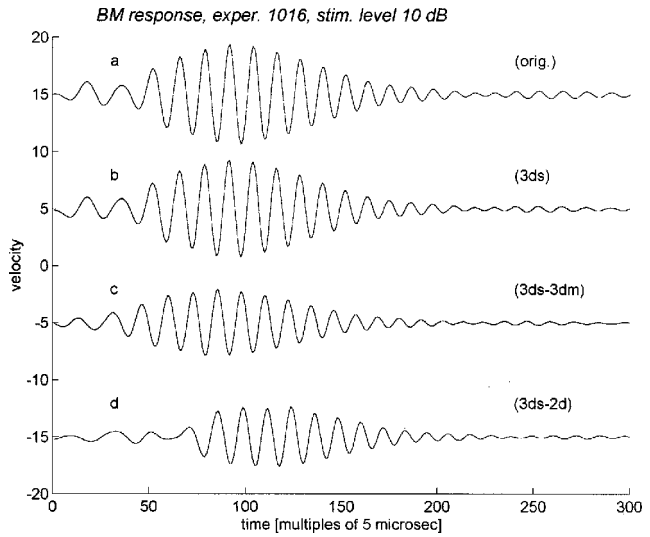

FIG. 7. Resynthesis in the time domain. Experiment ''1016.'' Maximal BM-to-stapes velocity ratio: 291. Best frequency (BF): 16.6 kHz. Virtual stapes velocity: $1.23-0.49i$. Curve (a): original impulse response (i.e., the ccf that corresponds to the composite ccf spectrum). Curve (b): resynthesized impulse response for the ''3ds'' model as described in the text. Curves (a) and (b) have the same normalization factor. Curve (c): ''cross fertilization,'' from model ''3ds'' to model ''3dm.'' Curve (d): ''cross fertilization,'' from model ''3ds'' to model ''2d.'' Normalization factors of curves (c) and (d) are selected for clarity (see text).

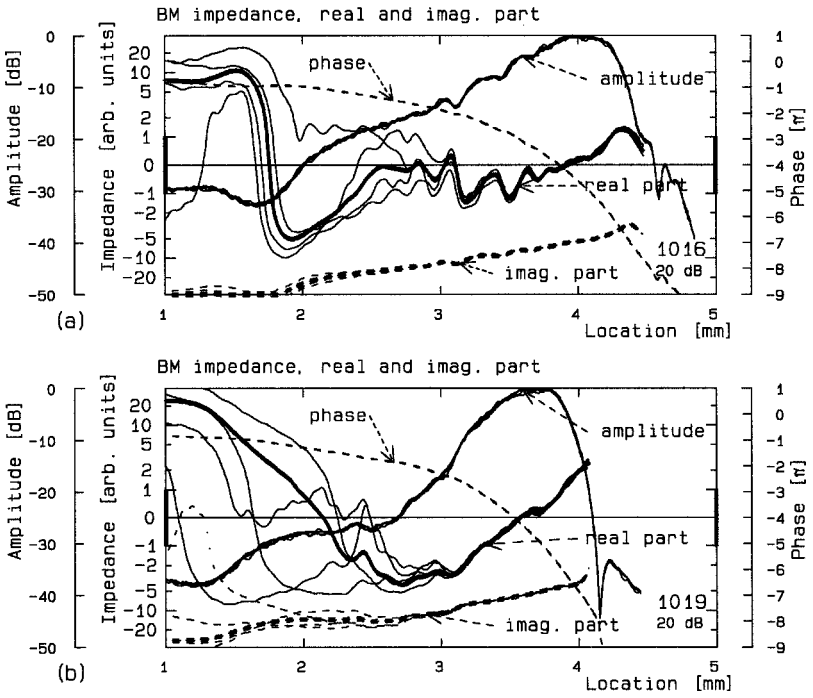

FIG. 8. Effect of deliberate errors added to the ccf data. Response and impedance panels merged as in Fig. 3. Panels (a) and (b): two experiments, 1016 and 1019. In each panel five response and impedance curves have been superimposed, four of them corrupted by noise (see text). Note how the computed BM impedance is the most stable against these errors in the region of the response peak. Deviations become larger when going to the left, a well-known effect from earlier work (see references in text).

tween the curves, in particular with respect to *the timing of the zero crossings*. Clearly, the rather crude way we handled frequencies below 5 kHz has little influence on the ultimate impulse response. We have obtained equivalent results with the ''3dm'' model.

It is interesting to consider effects of ''cross fertilization'' on the impulse response. Curve (c) of Fig. 7 shows the impulse response arising when we start with the ''3ds'' model and do resynthesis with the ''3dm'' model (as we did in Fig. 5). We show this impulse response with a 6 dB smaller amplitude (compare Fig. 5). The result is of the same general type as curves (a) and (b) but shows a few characteristic differences. The small deviation in phase slope that we saw in the peak region in Fig. 5 translates itself into a small shift of the group delay and a change in the shape of the waveform envelope. The timing of the zero-crossings of the original impulse response is not preserved in this response. Curve (d), finally, shows the impulse response corresponding to Fig. 6, resynthesized for the two-dimensional model. To compensate for the large amplitude difference seen in Fig. 6, we show the impulse response with a 12 dB larger amplitude. Apart from the initial oscillations and the shift in group delay, this curve resembles the original one reasonably well. The same applies to curve (c). This correspondence results from good agreement in the peak region which in its turn is due to the fact that two- and three-dimensional models support *short waves* equally well (note that in the peak region short waves dominate, see, e.g., INV-3, Sec. II).

On close inspection it is seen that during the course of the impulse response the frequency of the oscillations increases gradually. This effect is called the ''glide'' and has been extensively reported in Part I. This feature is retained in the resynthesized impulse response [curve (b)] (as well as in the other resynthesized impulse responses). In fact, this means that we have here a model of the cochlea that faithfully simulates all major and many subtle aspects of the cochlear response. The resulting model is characterized by its BM impedance function, and not by being constructed from elements that functionally correspond to mechanical structures of the cochlea. In this sense the model is abstract.

IV. RESULTS IV—BACK TO THE DATA: VARIABILITY

The inverse-solution method is often described as an ''ill-posed problem.'' In INV-3 it has been argued why this epithet does not always automatically apply to cochlear mechanics. Here we will illustrate the same topic from another side. We will take the data in the form of a composite ccf spectrum (obtained, processed and smoothed according to the standard procedure described in this and previous papers) and *deliberately corrupt them by adding a random noise signal*. The ccf spectrum has components spaced by approximately 50 Hz (see, for instance, Part I), and each of these components is multiplied by a complex number $(1+\beta c)$, where β is a small coefficient and c is a random complex number with unity amplitude and random phase. The values of c for the different components are independent of each other. The resulting spectrum is not smoothed in any additional way, and is used as the input signal of the inverse procedure.

Typical results are shown by Fig. 8, panels (a) and (b), for two experiments. In each panel five sets of response and impedance curves have been superimposed; one is the original set of curves, the other four result from corruption by noise. The impedance function corresponding to the original response is shown by two thickened lines (real and imaginary parts). The impedance functions due to corruption of the response are shown by normal lines. For this figure β was chosen as 0.2, implying average amplitude errors of the order of 1.5 dB. In both panels the impedance functions are observed to overlap well in the region of the response peak

and slightly to the left of it. This strengthens the conclusion that ''local activity'' is a robust feature of our procedure. More to the left of the peak the impedance due to the corrupted response starts to deviate markedly from the original function, and this is true over the entire range down to the stapes region. Near the stapes the real part tends to become negative, and the imaginary part to become less negative. A definite trend in accumulation of errors from right to left is evident. This behavior is typical for results of the inverse procedure (see for the explanation INV-1 and INV-3).

In going from the raw data to the composite ccf spectrum, a moderate amount of smoothing has been applied (see INV-3, Appendix B). As a result the errors in the original data (the ccf spectrum) are not independent from frequency to frequency. Therefore, the original response curves are smooth and the average amplitude error appears as less than 1 dB. The artificial errors that we have introduced in this section are much more ''severe'' in that they are *statistically independent*. The findings in Fig. 8 illustrate how critical is the method used in smoothing data.

We now come back to the point described in Secs. I C and II: in some of our data sets the BM impedance appears to be ''active'' all the way to the stapes location. By adding random ''errors'' of the same magnitude to such data it proved almost always possible to reverse this and to achieve a situation where there is no ''activity'' in the basal region. In this way we became convinced that ''activity'' in the stapes region is a variable and unstable property. It is only in the region of the response peak where the property of ''local activity'' is robust.

Possible influences of measurement errors can generally be estimated from repeating the same experiment a few times. In our experiments there also is a systematic error: we used *pseudo-random noise*, which means that one segment of a noise signal (in our case 20 ms long) is repeated over and over, without gaps (see Part I). We performed a few experiments in which four or five *different* noise signals were used as stimulus; these signals were based on different noise period waveforms. The BM velocity records were obtained within minutes of each other, and each record underwent the same inverse analysis. One of the aims of this test was to try to find evidence of corrugations in the BM mechanics. The term corrugation is used here in the sense discussed by Zweig and Shera (1995) as a component of BM impedance that is a function of location x, differs from animal to animal, and *does not scale*. The results were disappointing in that the processed ccf spectra showed random deviations not exceeding 1 dB, and the BM impedance functions showed corresponding deviations. No particular trend that could possibly be ascribed to irregularities of BM mechanics could be discerned.

V. REVIEW, CONCLUSIONS AND OUTLOOK

In combining experimental findings and theory we should keep one thing in mind: All our conclusions will only be valid under the assumption *that the real cochlea operates as the type of model that we are considering*. In the course of the analysis we convert the response, measured as a function of frequency at one location, to a model response distributed over the length of the model for a particular frequency (the BF). Implicit is here that the cochlea ''scales,'' i.e., that it converts frequency to place in a regular manner. We have found that inverse analysis is relatively insensitive to details of the conversion (i.e., the form of the cochlear map), yet scaling is a prerequisite for the entire procedure. Of course, this implies that we must interpret the resulting BM impedance, which is a function of x and ω, in the same ''scaling'' sense. The recovered BM impedance is found as a function of x for fixed ω. Conversely, for a fixed value of x, the BM impedance should show the corresponding behavior as a function of (log) ω. This means that for a higher frequency the region of activity lies more basalward, etc.[5] The same concept of inverse scaling is involved in the computation of the resynthesized impulse response (Sec. III).

In this paper we first went ''from data to models.'' We applied inverse analysis to data on the movement of the basilar membrane (BM) in response to noise stimuli. Two three-dimensional models were studied in this paper; one had its dimensions close to that of the real cochlea, the other one had homogeneous geometry over its length. Additionally, a two-dimensional model was treated. With all three models the BM impedance has to be ''locally active'' in order to match the measured response (at the levels employed in this study). It was found that in three-dimensional models the taper of BM width and cross-sectional area does not create more than a global effect. The two-dimensional model (in the form defined in Sec. I B) does not support the long-wave part of the cochlear wave correctly, but gives a fair representation of the short-wave part. Our conclusion at this point is that, to study global properties of cochlear models, it is sufficient to use the ''stylized'' model, ''3ds.'' This has the additional advantage that a very efficient and universal solution method is available (de Boer, 1998).

Apart from ''cross fertilization'' (Sec. II), we went ''back to the data'' in another way: we considered the resynthesized *impulse response*. We reestablished the consistency of the entire procedure, going from a measured response in the f domain, via the f-to-x transformation and the inverse solution to the BM impedance function in the x domain, via the forward solution for the model and, finally, via the x-to-f transformation back to the f domain. Resynthesis of impulse responses proved to be faithful to the original [Fig. 7, curves (a) and (b)].

All resynthesized impulse responses show the ''glide.'' Compared to the narrow-band ccf spectra analyzed in Part I, the composite ccf spectrum as it is used here has a much more extended low-frequency segment. We have ascertained that this feature has an enhancing effect on the glide (not shown). Thus the glide is not an artifact of the data processing method. On the contrary: when we have data covering a wider frequency range, the glide is slightly more pronounced.

From the results in Fig. 8(a) and (b) we conclude that the ''wiggles'' and random deviations that we normally find in the recovered BM impedance function are mainly due to measurement errors. No recognizable component of these fluctuations can be attributed to spatial irregularities in the

mechanical properties of the BM. The influence of errors is particularly large in the basal region.

In all experiments described here the stimulus level was low enough to neglect the contribution of distortion products to *the response to noise stimuli*. For stimuli of higher levels the cochlea will certainly show more pronounced nonlinearity. In this case linear analysis is justified, too—but only for certain purposes (the EQ-NL theorem, see the Appendix). Activity has been found to decrease with increasing stimulus level (de Boer and Nuttall, 1997a-DAM). A most remarkable nonlinear effect of the cochlea is the property that, as the stimulus level varies, the timing of the individual cycles of the impulse-response waveform is almost invariant [de Boer and Nuttall (1997b-GLIDE) and references cited therein; see also Recio *et al.*, 1998]. In this connection, we stress that zero-crossings of the impulse response are preserved in resynthesis [curves (a) and (b) of Fig. 7]. Results on nonlinear effects associated with changes in stimulus level will be published elsewhere.

As a final note, it should be stressed that our model contains an abstract function, the BM impedance, $Z_{\mathrm{BM}}(x,\omega)$, as its main parameter function. Our model remains abstract since it is not yet composed of elements of which each would replicate a specific mechanical component of the cochlea. The work presented here has laid solid foundations for further explorations in this direction. We are now more confident in relating certain components of the BM impedance to the dynamics of mechanical elements in the cochlea.

ACKNOWLEDGMENTS

The authors are indebted to (in alphabetical order) Gary Dootz, Anders Fridberger, Meng He Guo, Bob Masta, Darren Miller, Irina Omelchenko, Edward Porsov and Jiefu Zheng, for their help in setting up and performing the experiments. Thanks are due to Jont Allen, Renato Nobili, Fabio Mammano and Christopher Shera who shared their experience in MATLAB programming with us. Three JASA reviewers presented us with useful feedback designed to make our work more accessible to readers who are not thoroughly familiar with cochlear modeling. This work was supported by NIH (No. NIDCD-DC-00141), and VA Rehabilitation Research & Development Center (Grant RCTR-597-0160, Portland, VAMC), and is a continuation of project No. SLW 01.011 (NWO, The Netherlands).

APPENDIX: CLASS OF COCHLEAR MODELS, AN OVERVIEW

In the type of model used in this paper the basilar membrane (BM) forms a part of the cochlear partition that is located between two narrow fluid-filled channels stretched out in the x direction. It is assumed that outer hair cells (OHCs) of the organ of Corti are able to cause a local sound pressure $p_{\mathrm{OHC}}(x,t)$ (an oscillating pressure, on a cycle-to-cycle basis) which, in its turn, gives rise to an additional component $p_{\mathrm{add}}(x,t)$ of the sound pressure $p(x,t)$ near the BM in the fluid. By way of this pressure the OHCs are thought to enhance and sharpen the frequency response of the system to a degree compatible with results from recent mechanical measurements of BM motion at low stimulation levels—including our own.

The basic form of the model is linear. In the *nonlinear* version of the model the ''active'' process in the outer hair cells (OHCs) is nonlinear. It is assumed that there exists a *nonlinear instantaneous* relation between the (radial) stereociliary deflection $d_{\mathrm{cilia}}(x,t)$ (considered as a function of time t) and the pressure $p_{\mathrm{OHC}}(x,t)$ that is locally produced by the OHCs. The nonlinear relation should be compressive. All frequency dependence around OHC-bound processes is included in two *linear frequency- and location-dependent* transformations:

(a) between BM displacement $d_{\mathrm{BM}}(x,t)$ and ciliary excitation $d_{\mathrm{cilia}}(x,t)$, and
(b) between OHC output $p_{\mathrm{OHC}}(x,t)$ and the corresponding component $p_{\mathrm{add}}(x,t)$ of the channel pressure $p(x,t)$ near the BM.

It is for nonlinear models of this class that the EQ-NL theorem holds (de Boer, 1997). This theorem is formulated in terms of the input–output cross-correlation function (ccf) for a wideband noise signal with uniform spectral density as input. The theorem states that the ccf of the nonlinear model is equal to the ccf of a *linear* ''comparison model'' and it defines exactly how that comparison model must be constructed. If the actual cochlea functions as the model considered here, we will use the EQ-NL theorem to interpret the data. That interpretation will always be in the language of *linear-systems theory*. Then, it is legitimate to use all concepts of linear-systems theory including ''impedance'' and ''impulse response,'' and, in particular, it is permitted to use the inverse-solution method to find the BM impedance $Z_{\mathrm{BM}}(x,\omega)$. Formally, this impedance is the BM impedance of the ''companion model'' mentioned earlier. On a final note, we will tacitly assume that the model is zero-point stable, which means that it does not go into spontaneous oscillation. On the experimental side, this implies that we assume that spontaneous otoacoustic emissions of the cochlea are either absent or suppressed by the stimulus we used in our experiments.

[1]This study was consistent with NIH guidelines for humane treatment of animals and was reviewed and approved by the University of Michigan Committee on Use and Care of Animals and the Oregon Health Sciences Committee on the Use and Care of Animals.

[2]In earlier work (INV-3) a higher value was selected for $\omega_{\max}$, namely $2\pi 60$ (kHz). This was done to extend the region over which the wave in the model is of the long-wave type.

[3]In INV-3 data from the same animal were used, at the stimulus level of 40 dB and unfiltered. Here the data are taken at 50 dB, and the response is filtered; as a result, the maximal BM-to-stapes ratio is smaller than in INV-3—where it was 177.

[4]Assume the imaginary part to dominate the BM impedance. In the short-wave region the amplification in dB per mm then is inversely proportional to the square of the imaginary part.

[5]Scaling of the impedance involves an extra factor ω, see Eqs. (2.2.a, b and c) in de Boer (1991).

Allen, J. B. (**1977**). ''Two-dimensional cochlear fluid model: New results,'' J. Acoust. Soc. Am. **61**, 110–119.

Cooper, N. P., and Rhode, W. S. (**1992**). ''Basilar membrane mechanics in the hook region of cat and guinea-pig cochleae: Sharp tuning and nonlinearity in the absence of baseline position shifts,'' J. Acoust. Soc. Am. **63**, 163–190.
Davis, H. (**1983**). ''An active process in cochlear mechanics,'' Hear. Res. **9**, 79–90.
de Boer, E. (**1983**). ''No sharpening? A challenge for cochlear mechanics,'' J. Acoust. Soc. Am. **73**, 567–573.
de Boer, E. (**1991**). ''Auditory physics. Physical principles in hearing theory. III,'' Phys. Rep. **203**, 125–231.
de Boer, E. (**1993**). ''Some like it active,'' in *Biophysics of Hair Cell Sensory Systems*, edited by H. Duifhuis, J. W. Horst, P. van Dijk, and S. M. van Netten (World Scientific, Singapore), pp. 3–21.
de Boer, E. (**1995a**). ''The 'inverse' problem solved for a three-dimensional model of the cochlea. I. Analysis,'' J. Acoust. Soc. Am. **98**, 896–903 (INV-1).
de Boer, E. (**1995b**). ''The 'inverse problem' solved for a three-dimensional model of the cochlea. II. Application to experimental data sets,'' J. Acoust. Soc. Am. **98**, 904–910 (INV-2).
de Boer, E. (**1996**). ''Mechanics of the cochlea: modeling efforts,'' in *The Cochlea*, edited by P. Dallos, A. N. Popper, and R. R. Fay (Springer-Verlag, New York), pp. 258–317.
de Boer, E. (**1997**). ''Connecting frequency selectivity and nonlinearity for models of the cochlea,'' Aud. Neurosci. **3**, 377–388.
de Boer, E. (**1998**). ''A method for forward and inverse solutions of a three-dimensional model of the cochlea,'' J. Acoust. Soc. Am. **103**, 3725–3728.
de Boer, E., and Nuttall, A. L. (**1997a-DAM**). ''On cochlear cross-correlation functions: connecting nonlinearity and 'activity','' in *Diversity in Auditory Mechanisms*, edited by E. R. Lewis, G. R. Long, R. F. Lyon, P. M. Narins, C. R. Steele, and E. Hecht-Poinar (World Scientific, Singapore), pp. 291–297.
de Boer, E., and Nuttall, A. L. (**1997b-GLIDE**). ''The mechanical waveform of the basilar membrane. I. Frequency modulations ('glides') in impulse responses and cross-correlation functions,'' J. Acoust. Soc. Am. **101**, 3583–3592.
de Boer, E., and Nuttall, A. L. (**1999-INV-3**). ''The 'inverse problem' solved for a three-dimensional model of the cochlea. III. Brushing up the solution method,'' J. Acoust. Soc. Am. **105**, 3410–3420.
Fernández, C. (**1952**). ''Dimensions of the cochlea (guinea-pig),'' J. Acoust. Soc. Am. **24**, 519–523.
Greenwood, D. D. (**1961**). ''Critical bandwidth and the frequency coordinates of the basilar membrane,'' J. Acoust. Soc. Am. **33**, 1344–1356.
Kim, D. O., Neely, S. T., Molnar, C. E., and Matthews, J. W. (**1980**). ''An active cochlear model with negative damping in the partition: Comparison with Rhode's ante- and post-mortem observations,'' in *Psychophysical, Physiological and Behavioural Studies in Hearing*, edited by G. v. d. Brink and F. A. Bilsen. (Delft U.P., Delft), pp. 7–14.
Mammano, F., and Nobili, R. (**1993**). ''Biophysics of the cochlea: Linear approximation,'' J. Acoust. Soc. Am. **93**, 3320–3332.
Nuttall, A. L., and Dolan, D. F. (**1996**). ''Steady-state sinusoidal velocity responses of the basilar membrane in guinea pig,'' J. Acoust. Soc. Am. **99**, 1556–1565.
Nuttall, A. L., Dolan, D. F., and Avinash, G. (**1990**). ''Measurements of basilar membrane tuning and distortion with laser Doppler velocimetry,'' in *The Mechanics and Biophysics of Hearing*, edited by P. Dallos, C. D. Geisler, J. W. Matthews, M. A. Ruggero, and C. R. Steele (Springer-Verlag, Berlin), pp. 288–295.
Recio, A., Rich, N. C., Narayan, S. S., and Ruggero, M. A. (**1998**). ''Basilar-membrane responses to clicks at the base of the chinchilla cochlea,'' J. Acoust. Soc. Am. **103**, 1872–1989.
Shera, C. A., and Zweig, G. (**1991**). ''A symmetry suppresses the cochlear catastrophe,'' J. Acoust. Soc. Am. **89**, 1276–1289.
Sondhi, M. M. (**1978**). ''Method for computing motion in a two-dimensional model,'' J. Acoust. Soc. Am. **63**, 1468–1477.
Zweig, G. (**1976**). ''Basilar membrane motion,'' Cold Spring Harbor Symp. Quant. Biol. **40**, 619–633.
Zweig, G., and Shera, C. A. (**1995**). ''The origin of periodicity in the spectrum of evoked otoacoustic emissions,'' J. Acoust. Soc. Am. **98**, 2018–2047.
Zweig, G., Lipes, R., and Pierce, J. R. (**1976**). ''The cochlear compromise,'' J. Acoust. Soc. Am. **59**, 975–982.

The mechanical waveform of the basilar membrane. III. Intensity effects[a)]

Egbert de Boer[b)]
Room D2-226, Academic Medical Center, University of Amsterdam, Meibergdreef 9, 1105 AZ, Amsterdam, The Netherlands

Alfred L. Nuttall[c)]
Oregon Hearing Research Center, NRC04, Oregon Health Sciences University, 3181 SW Sam Jackson Park Road, Portland, Oregon 97201-3098 and Kresge Hearing Research Institute, University of Michigan, 1301 E. Ann Street, Ann Arbor, Michigan 48109-0506

(Received 10 May 1999; revised 1 October 1999; accepted 29 November 1999)

Mechanical responses in the basal turn of the guinea-pig cochlea were measured with broad-band noise stimuli and expressed as input–output cross-correlation functions. The experiments were performed over the full range of stimulus intensities in order to try to understand the influence of cochlear nonlinearity on frequency selectivity, tuning, signal compression and the impulse response. The results are interpreted within the framework of a nonlinear, locally active, three-dimensional model of the cochlea. The data have been subjected to inverse analysis in order to recover the basilar-membrane (BM) impedance, a parameter function that, when inserted into the (linearized version of that) model, produces a model response that is similar to the measured response. This paper reports details about intensity effects for noise stimulation, in particular, the way the BM impedance varies with stimulus intensity. In terms of the underlying cochlear model, the decrease of the ''activity component'' in the BM impedance with increasing stimulus level is attributed to saturation of transduction in the outer hair cells. In the present paper this property is brought into a quantitative form. According to the theory [the EQ-NL theorem, de Boer, Audit. Neurosci. **3**, 377–388 (1997)], the BM impedance is composed of two components, both intrinsically independent of stimulus level. One is the passive impedance Z^{pass} and the other one is the ''extra'' impedance Z^{extra}. The latter impedance is to be multiplied by a real factor γ $(0 \leqslant \gamma \leqslant 1)$ that depends on stimulus level. This concept about the composition of the BM impedance is termed the ''two-component theory of the BM impedance.'' In this work both impedances are entirely derived from experimental data. The dependence of the factor γ on stimulus level can be derived by using a unified form of the outer-hair-cell transducer function. From an individual experiment, the two functions Z^{pass} and Z^{extra} are determined, and an approximation $(Z^{\text{pass}}+\gamma Z^{\text{extra}})$ to the BM impedance constructed. Next, the model response (the ''resynthesized'' response) corresponding to this ''artificial'' impedance is computed. The same procedure is executed for several stimulus-level values. For all levels, the results show a close correspondence with the original experimental data; this includes correct prediction of the compression of response amplitudes, the reduction of frequency selectivity, the shift in peak frequency and, most importantly, the preservation of timing in the impulse response. All these findings illustrate the predictive power of the underlying model.
 [S0001-4966(00)02803-4]

PACS numbers: 43.64.Kc, 43.64.Bt [RDF]

INTRODUCTION

It is well known that there exists a close relation between nonlinearity, amplitude compression and frequency selectivity in the cochlea. When stimulus intensity is increased, the degree of nonlinearity in the operation of the cochlea increases, and this affects frequency selectivity, i.e., the way simultaneously presented stimulus components of different frequencies are handled, and it also affects the response amplitude (causing compression). When the stimulus contains one dominant frequency component (or a very narrow band of such components), the distribution of nonlinearity over the length of the cochlea differs from that for a wideband noise stimulus. This entails that the relation between responses to wideband stimuli and pure tones is not straightforward. The same is true for the relation between responses to strong clicks and wideband stimuli. In the former case the degree to which the system is driven into nonlinearity will vary greatly in time—starting small, increasing rapidly and decreasing more slowly—and in the latter case the degree of nonlinearity will be fluctuating less but continually. Would it ever be possible to link responses to clicks, pure tones and noise signals to each other, for all levels of stimulation? It is too early to attempt to understand the behavior of the cochlea for stimuli that are *completely* general, and contain rapid variations in level, time and fre-

[a)]Preliminary results of the subject treated in Sec. V were presented at the ARO 1999 Midwinter meeting (abstract No. 344).
[b)]Electronic mail: e.deboer@amc.uva.nl
[c)]Electronc mail: nuttall@ohsu.edu

quency content. In the present paper the first steps of such a most desirable study are undertaken, with the use of simple stimuli. In all our modeling work we firmly base the parameters of the model on the analysis of experimental data on the mechanical response of the basilar membrane (BM).

Experimental and theoretical details of our work are given in two previous publications in this series of papers (de Boer and Nuttall, 1997b, GLIDE, and 2000, DMD) which will be referred to as Part I and Part II, respectively. Briefly, we measured the velocity of the basilar membrane (BM) in the basal part of the guinea-pig cochlea, in a region where the best frequency (BF) is between 15 and 18 kHz. In Part I we described and commented upon the frequency modulation of the impulse response (the ''glide''). In Part II we critically analyzed the various types of model that can be used in inverse analysis.

The work in Part II relates directly to a linear system because only low-level stimuli were considered. In the present paper we describe and analyze how the cochlea differentially reacts to *noise stimuli of widely varying levels*. The nonlinear model ''$\mathcal{M}$-$\mathcal{NL}$'' underlying the analysis contains response-enhancing elements (outer hair cells, OHCs) that assist in amplifying the cochlear wave and are nonlinear. In fact, these cells are the only nonlinear elements of the model. For this type of model the data can be interpreted via the EQ-NL theorem. The structure of the model and the meaning of the theorem are briefly reviewed in Appendix A. The proof of the theorem is given in de Boer (1997). A prerequisite is that data have to be acquired in the form of input–output cross-correlation functions (ccf's) for wideband noise stimuli with constant power density. By using the EQ-NL theorem, we are considering a *nonlinear* model of the cochlea but our conclusions will always refer to a *linear* model, the ''comparison model'' (defined in the same Appendix), which we will call here model ''$\mathcal{M}$-$\mathcal{L}in$.''

Analysis starts with the inverse solution procedure. The model that will be used is three-dimensional and allows for long, intermediate and short waves to propagate in it. The input to the inverse procedure is the velocity response $v_{\mathrm{BM}}(x,\omega)$ derived from the ccf spectrum data via a frequency-to-place transformation, and the result is the BM impedance $Z_{\mathrm{BM}}(x,\omega)$, both of which are functions of location x and radian frequency ω (see Part II). The computed impedance, then, is the BM impedance of model ''$\mathcal{M}$-$\mathcal{L}in$.'' In the present paper responses are treated to strong stimuli that bring the cochlea into a definite state of nonlinearity. At different levels of stimulation the impedance function will be different, and at each stimulus level model ''$\mathcal{M}$-$\mathcal{L}in$'' has to be equipped with the appropriate impedance in order to simulate the measured response. It is via the variations of $Z_{\mathrm{BM}}(x,\omega)$ with stimulus level that we will interpret nonlinear effects in the real cochlea.

In more detail, the EQ-NL theorem predicts that the BM impedance $Z_{\mathrm{BM}}(x,\omega)$ is a linear combination of two invariant functions, $Z^{\mathrm{pass}}(x,\omega)$ and $Z^{\mathrm{extra}}(x,\omega)$, whereby the second is multiplied by the (real) coefficient γ, which is between 0 and 1. The term $Z^{\mathrm{pass}}(x,\omega)$ is the impedance of the BM when the OHCs do not function. The function $Z^{\mathrm{extra}}(x,\omega)$ represents the maximal contribution that can be given to the BM impedance and refers to the condition with the weakest possible stimulation. The coefficient γ reflects the efficiency with which these OHCs operate when they are processing weak ($\gamma \approx 1$) or strong ($\gamma < 1$) signals. This principle is called the ''two-component theory of the BM impedance'' (more details are given in Sec. III). The two functions $Z^{\mathrm{pass}}(x,\omega)$ and $Z^{\mathrm{extra}}(x,\omega)$ do not depend on stimulus level; γ is the only parameter that depends on stimulus level. It should be noted that the two-component theory results immediately from the EQ-NL theorem. In the development of cochlear mechanics a related principle has been used (see, e.g., Neely and Kim, 1986) but that was simply posed as a hypothesis. In the current work the component impedances are directly derived from experimental data.

The main theme of this paper is to explore the two-component theory. In Sec. III and Appendix B it is shown how the coefficient γ can be calculated when a realistic type of OHC transduction function is assumed. The coefficient γ then becomes a function $\gamma(L)$ of stimulus level L—stimulus level being defined as the sound pressure level (SPL) of one octave of the noise stimulus centered at the best frequency (BF) of the location from where the measurement is made. When the forward solution of the model (resynthesis) is carried out with the two-component impedance using the appropriate value for $\gamma(L)$, the resulting response is found to correspond very closely to the original response used as the input to the inverse procedure, for all values of L. This implies not only that at all levels L the resynthesized response has the same frequency selectivity and tuning as the original response, but also that the amplitude of the resynthesized response shows the same signal compression as the original data (Sec. IV). In the final stage of the work reported in this paper, Sec. V, it is shown that the two-component theory of the BM impedance also accounts for the fact that the timing of the oscillations in the impulse response remains nearly invariant when the stimulus level varies.

I. GENERAL INTENSITY EFFECTS

Data were collected on movements of the basilar membrane (BM) in the basal turn of the guinea-pig cochlea with a laser velocimeter (cf. Nuttall *et al.*, 1990; Nuttall and Dolan, 1996).[1] *Bands of flat-spectrum pseudo-random noise* were used as acoustical stimuli and the velocity of the BM at a location tuned to a frequency between 15 and 18 kHz was measured as a function of time. From stimulus and response signals input–output cross-correlation functions (ccf's) were computed (see Part I), and the ccf spectrum was derived from the ccf waveform. Furthermore, *composite ccf spectra* were obtained by combining sections of ccf spectra measured with flat-spectrum stimuli of different bandwidths, central frequencies and intensities in the same animal (see de Boer and Nuttall, 1999, INV-3). With this technique the composite ccf spectrum accurately represents the input–output relation over a wide frequency range, from below 1 to over 25 kHz, and over a response range of more than 50 dB (a single wideband noise produces either good accuracy in the peak region or in the low-frequency region, but not in both). In this case the ''stimulus level'' is the SPL of one octave of the noise signal that has been used for the frequency band

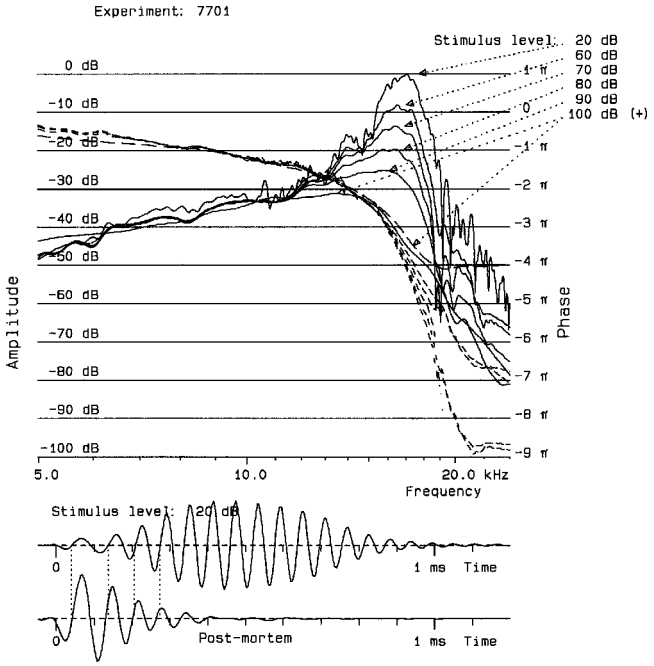

FIG. 1. Upper panel: Composite ccf spectra for various stimulus levels (velocity divided by stapes velocity). Experiment: 7701. *Solid lines*: amplitude; *dashed lines*: phase. Stimulus levels: 20, 60, 70, 80 and 90 dB for live animal, and 100 dB for dead animal (amplitude labeled with ''+,'' phase with coarser dashing). Maximum ratio of BM to stapes velocity at BF for the 20-dB response: 669, shown as 0 dB. Middle panel: impulse response for 20-dB stimulation. Lower panel: impulse response for the dead animal. Notice that the zero-crossings of the two impulse responses are nearly the same (see the dotted vertical lines).

around the BF (the SPL of the lower bands is higher). The composite ccf spectrum is always derived as the (complex) ratio of BM to stapes velocity. Examples of composite ccf spectra for low- and high-level stimuli will be discussed presently.

The waveform corresponding to the composite ccf spectrum is obtained via the (inverse) Fourier transform. At a very low level of stimulation we can assume that the cochlea is linear, and thus we can interpret the so-obtained ccf waveform (remember that it has been measured with a wideband noise input) as the impulse response of the cochlea. For higher stimulus levels the ccf waveform can be similarly interpreted as an impulse response but this time of model ''$\mathcal{M}$-$\mathcal{L}in$.'' Typical variations of such impulse-response waveforms with stimulus level have been reported in Part I but will be analyzed more deeply here.

Figure 1, upper panel, shows the composite ccf spectrum, amplitude (solid lines) and phase (dashed lines), for five values of the stimulus level L, from 20 to 90 dB, measured in a normally sensitive animal. In addition, there is a pair of curves for the same animal post-mortem [labeled (+), stimulus level 100 dB, amplitude and phase curves indicated with two arrows]. The response functions are compensated for the stapes response. All curves are superimposed whereby the amplitude curve at the lowest stimulus level is normalized to 0 dB at its peak. See the legend for the maximum BM-to-stapes velocity of this response. The responses have undergone no extra smoothing as in earlier publications (de Boer and Nuttall, 1999, INV-3, Part II). At the lower frequencies the amplitude curves (solid lines) more or less overlap, implying linear behavior of the cochlea. It is seen that the response peak gradually diminishes in height and moves to lower frequencies with increasing stimulus level. The phase curves (dashed lines) overlap a great deal, but the one corresponding to the post-mortem response (shown with coarser dashes) has the shallowest average slope. The lower two panels of the figure show two impulse responses (inverse Fourier transforms of the ccf spectra), one corresponding to the lowest stimulus level and the other to the post-mortem condition. For these impulse responses the frequency response has been smoothed as detailed in Part II. Note that the low-level impulse response displays six to seven oscillations before it reaches its maximal amplitude and that the frequency of the oscillations increases with time (the ''glide'' as described in Part I). The post-mortem impulse response dies out through most of its course. It should be noted also that the zero-crossings of these two impulse responses are almost the same, especially the first few (see the vertical dotted lines in the figure). This is an intriguing property of the cochlea to which we will return later in this paper.

For the cochlear model to be used for inverse analysis we can choose among several possibilities (see Part II). A three-dimensional model can be given a uniform shape (the ''stylized'' model) or its dimensions can be chosen to approximate the real cochlea (the ''realistic'' model). We have selected the stylized model because our analysis in Part II has shown that there are no major differences in the inverse-analysis results. In the computations we have used the fast and economical approximation method described in de Boer (1998).[2] In the stylized model the BM moves over its own width εb (a constant fraction ε of the model width b) according to a centered half-period of a sine function over the width εb, as if it were hinged at its inner and outer edges (see de Boer, 1981). The remaining parts of the partition between the two channels in the model remain stationary. These parts represent the bony spiral lamina and the outer section of the spiral ligament. Fluid motion in the model is three-dimensional.

As in Part II we will use the following model parameters:

$$\varepsilon = 0.2, \quad b = 1\,(\mathrm{mm}), \quad h = 1\,(\mathrm{mm}),$$
$$\rho = 10^{-3}\,(\mathrm{g\,mm^{-3}}), \quad L = 6\,(\mathrm{mm}), \tag{1}$$

and the following parameters in the frequency-to-place transformation (cf. de Boer and Nuttall, 1999, INV-3):

$$\alpha = 0.5\,(\mathrm{mm^{-1}}), \quad \omega_{\max} = 2\pi 45\,(\mathrm{kHz}). \tag{2}$$

The meanings of the symbols are given in the cited papers. A model length of 6 mm is sufficient to accommodate the high frequencies that we are considering here. We made N, the number of sections in the longitudinal direction, equal to 700 and occasionally used values up to 1400.

Figure 2 shows, for the same experiment as Fig. 1, the response functions $v_{\mathrm{BM}}(x,\omega)$, i.e., the ccf spectra converted from the frequency to the x domain, panel (a) the amplitude and panel (b) the phase (*dashed* curves in both panels). Of the abscissa x only the most interesting part (from 2 to 5

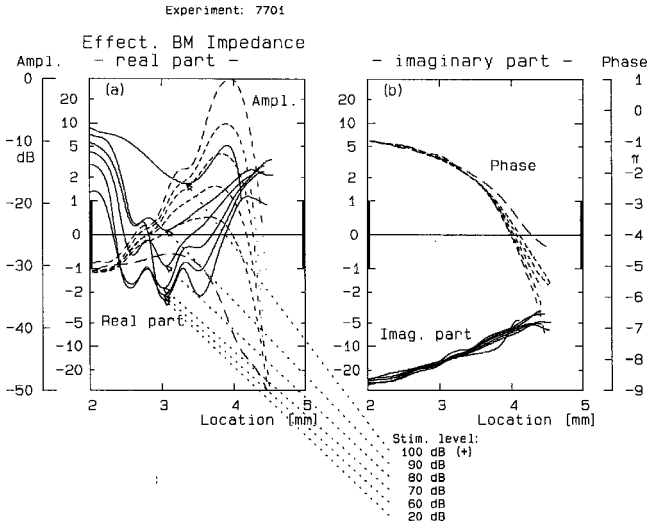

FIG. 2. Response and BM impedance. Experiment: 7701. *Dashed curves*: original responses in the x domain, amplitude and phase (ordinate scales on the sides). See Eq. (2) for the parameters used in the f-to-x transformation. Stimulus levels: 20, 60, 70, 80, and 90 dB for live animal, 100 dB for dead animal (shown with coarser dashes). The constant ω is made equal to 2π times the best frequency, 16.6 kHz, at the 20-dB stimulus level. *Solid curves*: BM impedance $Z_{\mathrm{BM}}(x,\omega)$ recovered by inverse solution, real [panel (a), left] and imaginary parts [panel (b), right]. The ''stylized'' three-dimensional model is used, see text. Number of sections (N): 700. ''Unit'' of impedance (see thick vertical bars along sides of panels): 2 (g mm^{-2} s^{-1})=2000 (kg m^{-2} s^{-1}). Smaller impedance values are plotted linearly, larger ones are logarithmically compressed.

mm) is shown. The constant ω is made equal to 2π times the best frequency (BF) at the lowest stimulus level. The maximum response amplitude at the lowest stimulus level is normalized to 0 dB. Data smoothing is as described in Part II. Dashes are longer for the post-mortem curves.

The *solid* curves in Fig. 2 show the *BM impedance* $Z_{\mathrm{BM}}(x,\omega)$ computed with the inverse method, panel (a) the real and panel (b) the imaginary part. The ordinate scales for the impedance are nonlinear (compressed for large values), as was the case for the impedance figures in Part II. The reference value for the impedance is given in the legend. In both panels the zero point for the impedance is in the center of the ordinate scale. It is stressed that, by their very nature, impedance functions show large variations near the left margin of the figure; these variations are mostly due to data errors (see Part II).

Where the *real part* of $Z_{\mathrm{BM}}(x,\omega)$ is negative, the wave in the model is amplified (its power is increased), and because the region of ''activity'' is limited in length we call the model ''locally active.'' In the region just to the left of the response peak, the real part of the impedance has the largest excursion into the domain of negative values at the lowest stimulus level, and this negative excursion is observed to decrease as stimulus level increases. For the post-mortem case, the real part is positive. The solid curves in panel (b), showing the *imaginary* part of the impedance, overlap very much in the ''active'' region. They are all in the logarithmic region of the ordinate scale; apparently, relative variations of the imaginary part with stimulus level are much smaller than those of the real part. In the absolute sense, the variations are of similar magnitude as those of the real part. It is noted that,

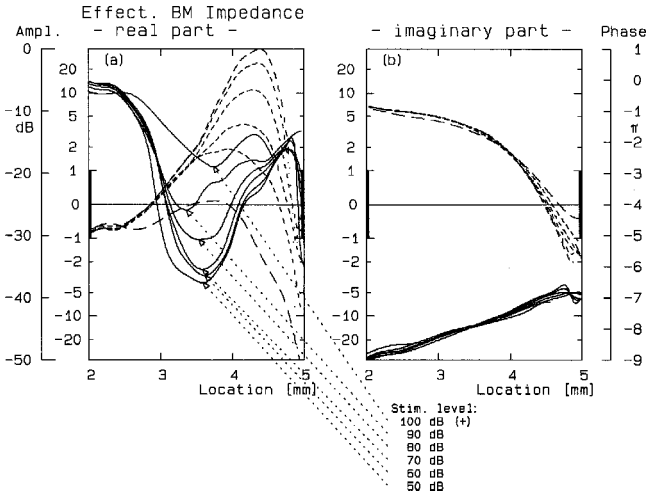

FIG. 3. Response and BM impedance. Experiment: 7611. *Dashed curves*: original responses. *Solid curves*: BM impedance $Z_{\mathrm{BM}}(x,\omega)$ recovered by inverse solution. Layout as Fig. 2. Stimulus levels: 50, 60, 70, 80, and 90 dB for live animal, 100 dB for dead animal.

at the right side of the peak, the *imaginary* part does not show a clear tendency to move toward or to cross the zero line. For low stimulus levels the place of the response peak is not primarily defined by ''resonance'' of mass and stiffness of the BM (a zero-crossing of the imaginary part) but is closely related to the place where the *real* part crosses the zero line, from negative to positive (cf. de Boer, 1983).

Figures 3 and 4 show results from two other experiments. These figures confirm what is concluded from Fig. 2. The three figures together illustrate the large variability in input data and impedance functions. [These figures should be complemented with the findings reported in de Boer and Nuttall (1997a, DAM).] We infer that, with increasing stimulus level, the BM impedance function is more and more ''deprived'' of a special component. We will call this variable component the ''extra'' component. For low stimulation levels this component causes the model to become ''active,''

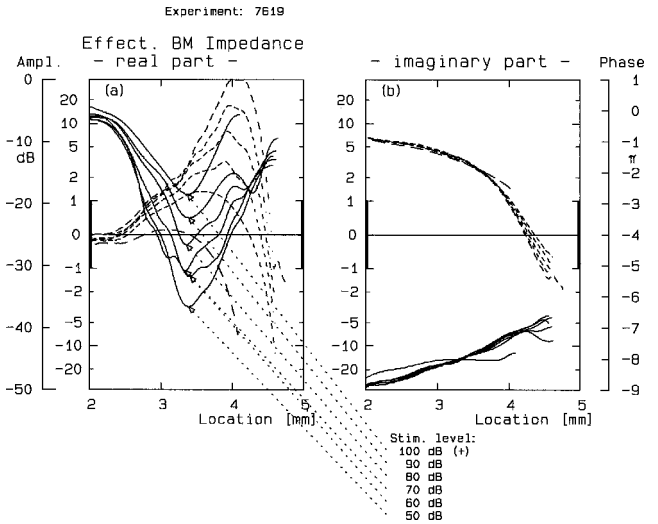

FIG. 4. Response and BM impedance. Experiment: 7619. *Dashed curves*: original responses. *Solid curves*: BM impedance $Z_{\mathrm{BM}}(x,\omega)$ recovered by inverse solution. Layout as Fig. 2. Stimulus levels: 50, 60, 70, 80, and 90 dB for live animal, 100 dB for dead animal.

i.e., to produce wave amplification. For stronger stimuli this component still tends to diminish power dissipation in the model. In our figures the variations are the most conspicuous in the real part. We found the same trends in 17 other experiments. This idea will be worked out in later sections of this paper.

Resynthesized response curves in the x domain overlap the original ones so well that there is no need to illustrate them. One important consequence is that *amplitude compression* is the same in original and resynthesized responses. This entails that model ''$\mathcal{M}$-$\mathcal{L}in$'' is capable of demonstrating the correct input–output amplitude function of the cochlea. The proviso is that at each stimulus level the appropriate BM impedance function is used. The variations of the impedance are obviously of the right type to explain amplitude compression.

In de Boer and Nuttall (1999, INV-3) it has been reported that resynthesis of the *impulse response* is virtually perfect. We found the same feature in this study, for various values of the stimulus level L. Therefore, there is no need for a figure. We want to stress one particular feature of these results: *The timing of individual cycles of the ccf waveform is nearly the same for all stimulus levels*, and this is true for original as well as for resynthesized responses. Therefore, model ''$\mathcal{M}$-$\mathcal{L}in$'' with its level-dependent BM impedance is also capable of reproducing the near-invariance of timing. The earliest report about this near-invariance property in *mechanical* impulse responses of the cochlea appears to be Robles *et al.* (1976), while more specific data are given in Ruggero *et al.* (1992) and, more recently, in Recio *et al.* (1998). For responses of primary auditory-nerve fibers a similar property has been found in PSTH histograms (Kiang *et al.*, 1965) and in revcor functions, see, e.g., Carney and Yin (1988), Carney (1993) and Carney *et al.* (1999). We confirmed this property for mechanical data in Part I (the end of Sec. II C). In particular, we found that the course of the ''instantaneous frequency,'' evaluated for a low stimulus level, neatly lines up with that at higher levels (the relation between instantaneous frequency and timing of zero-crossings should be obvious). One conclusion to be drawn is that near-invariance of timing is not specifically linked with nonlinearity (cf. Sec. II B in Recio *et al.*, 1998). In a way quite the opposite can be stated: near-invariance persists despite nonlinearity (all our resynthesized responses are obtained with a linear model). In Part I it was proposed that the ''glide'' (the general rise in instantaneous frequency with time in the impulse response) should be one of the marks by which the validity of a cochlear model is to be judged. We can now go one step further and propose that the near-invariance of the timing of oscillations in the resynthesized impulse response should also be considered in judging the validity of a cochlear model. Our model ''$\mathcal{M}$-$\mathcal{L}in$,'' at each stimulus level provided with the appropriate BM impedance function, passes the test of acceptance. This is not too impressive a result, however, so we will try to analyze this intriguing near-invariance property more deeply.

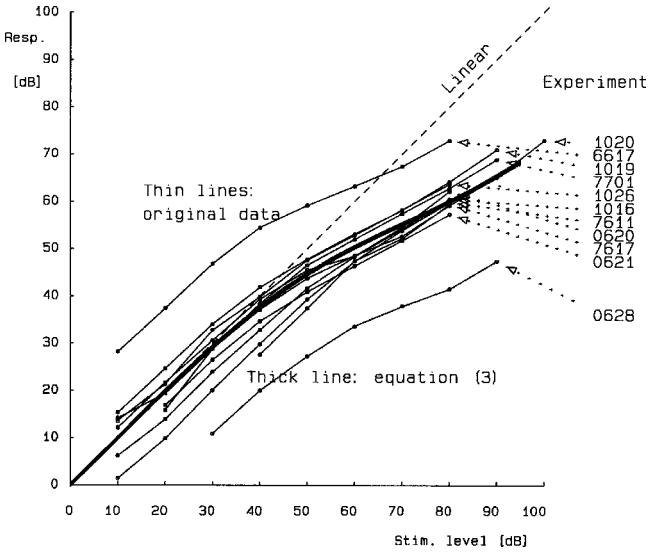

FIG. 5. Amplitude of response as a function of stimulus level L. See text. Dashed line shows linear relation. Thick line follows Eq. (3).

II. SIGNAL COMPRESSION IN THE DATA

For better understanding intensity effects we must embark upon more detailed theoretical considerations. In particular, we need to know *how the average transduction of the OHCs in the model depends on stimulus level*. The result will be applied to the computation of model responses. As the first step, we will formalize how the amplitude of the response to noise stimuli depends on stimulus level. Figure 5 illustrates measured response amplitude versus stimulus level L. The curves connecting small circles show the total power (in arbitrary units) over the ccf spectrum for 11 experiments as functions of stimulus level. The thick continuous curve depicts an average function matched to the data. We used the following expression for this curve:

$$v_{\mathrm{rms}} = \exp[\{2/(1+(L/80)^4) - 2 + (L/20)\} \ln(10)], \quad (3)$$

where v_{rms} is the response amplitude and L is in dB. The particular function in Eq. (3) is not based on any physiological reasoning; it is chosen as a convenient expression involving a maximal compression of 40 dB. For $L=0$ (dB) v_{rms} is normalized to 1. Note that the curves of Fig. 5 refer to stimulation by bands of noise. The amplitude compression shown reflects mainly the compression in the frequency region around the best frequency (BF), but this is of the same order as the compression of single pure tones in that range. Equation (3) will be used in Sec. III to describe the amplitude of the input to OHCs in the model.

III. THEORY: TWO COMPONENTS OF THE BM IMPEDANCE

We have reported on the effect of stimulus intensity on the BM impedance earlier (de Boer and Nuttall, 1997a, DAM). In the stimulus-level range from 10 to 40 dB the *real part* of the BM impedance $Z_{\mathrm{BM}}(x,\omega)$ in the ''active'' region was found to vary little, but from 50 dB on it gradually became less negative to become positive at the highest levels (90–100 dB). The *imaginary* part of the impedance did not vary much (in the relative sense). Our present results show

the same properties but in greater detail. With model ''$\mathcal{M}$-$\mathcal{NL}$'' these results can be explained in a qualitative way. With the stimulus level increasing, the signal at the input to the OHCs makes larger and larger excursions and there will be more and more saturation in the (nonlinear) transfer function of these cells. As a result the average transduction of individual components of the noise signal decreases and ''activity'' decreases likewise.

Let us make this reasoning more precise. In the nonlinear model ''$\mathcal{M}$-$\mathcal{NL}$'' we assume that OHCs give rise to an additional component $p_{\rm add}(x,t)$ of the sound pressure $p(x,t)$ in the fluid near the BM (see Appendix A). In the linear model ''$\mathcal{M}$-$\mathcal{L}in$'' this component is written as $p_{\rm add}(x,\omega)$, which is no longer a real function of location x and time t but a complex function of x and ω. The pressure component $p_{\rm add}(x,\omega)$ will be proportional to the efficiency of OHC transduction $\gamma(L)$ (for wideband noise stimuli γ is a function of L, and not of x or ω, see Appendix A). The additional pressure component $p_{\rm add}(x,\omega)$, when divided by the (complex) BM velocity $v_{\rm BM}(x,\omega)$, will produce an *additive* contribution to the BM impedance $Z_{\rm BM}(x,\omega)$, and this contribution will also be proportional to $\gamma(L)$. Hence, the BM impedance $Z_{\rm BM}(x,\omega)$ can be written as the sum of a ''passive'' term $Z^{\rm pass}(x,\omega)$ that represents the ''dead'' or ''passive'' cochlea (with no functioning of OHCs at all), and an additional term $\gamma(L)Z^{\rm extra}(x,\omega)$ that is solely due to OHC transduction:

$$Z_{\rm BM}(x,\omega)=Z^{\rm pass}(x,\omega)+\gamma(L)Z^{\rm extra}(x,\omega). \tag{4}$$

The parameter $Z^{\rm extra}(x,\omega)$ represents the *maximum* contribution that can be given to the BM impedance. All x-dependent quantities in this relation are complex functions, but the coefficient $\gamma(L)$ is real. Note that the parameters $Z^{\rm pass}(x,\omega)$ and $Z^{\rm extra}(x,\omega)$ do not depend on L, whereas $\gamma(L)$ goes down from 1 to 0 with increasing L. We will call this concept the two-component theory of the BM impedance. It is valid for all models to which the EQ-NL theorem applies. We can rewrite relation (4) in terms of the impedance $Z^{\rm weak}(x,\omega)$ which is the BM impedance for the intact cochlea with a very low level of stimulation [$\gamma(L)=1$], as follows:

$$Z_{\rm BM}(x,\omega)=Z^{\rm pass}(x,\omega)+\gamma(L)[Z^{\rm weak}(x,\omega)-Z^{\rm pass}(x,\omega)]. \tag{5}$$

This expression is ''closer to experiments'' than Eq. (4) since its constituents can directly be derived from data. It is stressed that *only the coefficient* $\gamma(L)$ *depends on the stimulus level* L; the other parameters in the equations are invariant functions of x and do not depend on L.

We can now ask three principal questions:

(A) Does the BM impedance vary with stimulus level L as predicted?

(B) If that is the case, does the two-component theory predict the correct dependence of amplitude and phase of the response upon L, for each individual experiment?

(C) Can the two-component theory simulate the near-invariance of timing of the impulse response?

Note that all three questions are concerned with the *predictive* power of the model; we are no longer in the *descriptive* state. For all values of L, Eq. (4) or (5) should provide a good approximation to the actual BM impedance. It should be remembered, though, that the constituent impedances $Z^{\rm weak}(x,\omega)$ and $Z^{\rm pass}(x,\omega)$ in Eq. (5) have considerable intrinsic errors, especially $Z^{\rm weak}(x,\omega)$.

In the present section question (A) will be treated, and in the next two sections questions (B) and (C). According to the reasoning underlying the EQ-NL theorem, OHC transduction should be proportional to the average slope of the transducer's transfer function, averaged over the OHC input signal's excursions (de Boer, 1997). In Appendix A this is expressed by Eq. (A1). The OHC input signal is proportional to $v_{\rm rms}$ as expressed by Eq. (3) of Sec. II. Thus, given an acceptable OHC transfer function $F(.)$, the average slope, i.e., the transducer efficiency γ, can be calculated for every value of $v_{\rm rms}$. In Appendix B it is shown how the calculation is done, with a transfer function $F(.)$ firmly based on experimental data. The calculation contains the response amplitude $v_{\rm rms}$ normalized by the factor v_1. The function γ gradually decreases from 1 to 0 with increasing $v_{\rm rms}$. For the chosen function $F(.)$, making $v_{\rm rms}$ equal to v_1 makes γ equal to 0.513.

A rough estimate of the normalization factor v_1 can be obtained with the data from Fig. 4 in de Boer and Nuttall (1997a, DAM), which figure shows the BM impedance averaged over a fixed region of x (in fact, the ''active'' region for the lowest stimulus level) as a function of L, for seven experiments. We averaged these results over the seven experiments, and found the real part of the BM impedance to reduce its negative-going excursion to one-half its maximal value around the stimulus level of 73 dB. When we choose v_1 equal to 1100, the function $\gamma(L)$ reduces to 0.5 for L equal to 73. We further verified that *on the average* the negative-going excursion of the real part of the BM impedance indeed varies with L in approximately the same way as our calculated function $\gamma(L)$. In this way question (A) posed above has been answered in the affirmative. We may conclude that the concepts inherent in our nonlinear model are realistic. Therefore, let us go ahead and try to make the prediction more refined. This will be done by including resynthesis, and going from the average over experiments to individual experiments.

IV. APPLICATION TO INDIVIDUAL EXPERIMENTS I: BM RESPONSE

In this section we will address question (B) of Sec. III. We will use $\gamma(L)$ calculated according to Appendix B to predict $Z_{\rm BM}(x,\omega)$ for every value of stimulus level L, and compute model response curves for this choice. Instead of averaged impedance values we will now handle *full functions of x obtained in a single experiment*. The procedure is as follows.

(i) Take, from the collection of responses (ccf's) in one animal, two responses, one for the ''live'' animal, with a weak stimulus, and one post-mortem. Choose a value for v_1.

(ii) Derive from the two responses the two impedance functions $Z^{\rm weak}(x,\omega)$ and $Z^{\rm pass}(x,\omega)$, for all x over the entire range.

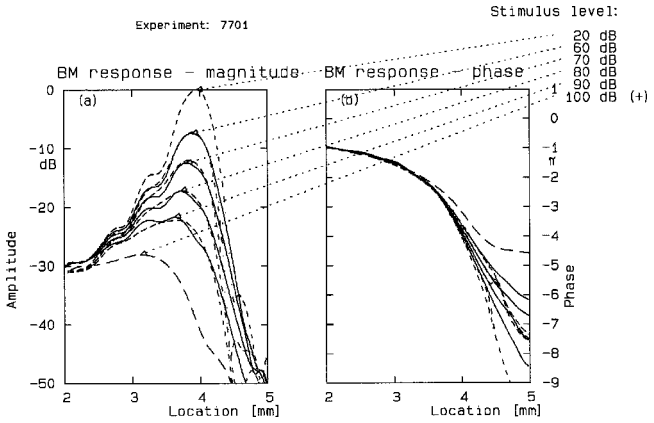

FIG. 6. Resynthesis of response when BM impedance is composed of two components as in Eqs. (4) and (5). Experiment: 7701. *Dashed curves*: original responses (the 20-dB and the post-mortem responses included). *Solid curves*: resynthesized responses with predicted impedance function. Stimulus levels: 60, 70, 80, and 90 dB. Normalization constant v_1: 2440.

(iii) Calculate, for a given stimulus level L, the value of $\gamma(L)$ according to Appendix B.
(iv) Find the ''predicted'' BM impedance function from Eq. (5).
(v) Perform resynthesis in model ''$\mathcal{M}$-$\mathcal{L}in$'' with this impedance.
(vi) Compare the model response $v_{\mathrm{BM}}(x,\omega)$ with the actual response data for the same value of L.
(vii) Do steps (iii) through (vi) for every stimulus level L, keeping the normalizing factor v_1 the same.

It turns out that for every experiment v_1 has to be given its ''own'' value to obtain the best-fitting result over the entire range of L.

We illustrate the outcome with a figure that applies to experiment 7701 (the one used for Figs. 1 and 2). The function $Z^{\mathrm{weak}}(x,\omega)$ refers to the stimulus level of 20 dB, and we choose $Z^{\mathrm{pass}}(x,\omega)$ from the post-mortem case. Then, for stimulus levels from 50 to 90 dB, the ''predicted'' BM impedance is computed from Eq. (5) and the response is resynthesized for that impedance.

Figure 6 shows the resulting responses in the x domain. The original responses are shown by dashed lines [the responses on which $Z^{\mathrm{weak}}(x,\omega)$ and $Z^{\mathrm{pass}}(x,\omega)$ are based are included], and the resynthesized responses by solid lines. Recall that in this resynthesis the BM impedance function is simply a linear combination of two fixed x-dependent components, and it is only one of the coefficients, $\gamma(L)$, that varies with stimulus level L. The value of the normalization factor v_1 giving the best fit for this experiment is 2440. The efficiency $\gamma(L)$ then reduces to 0.5 for L equal to 86 dB. The resynthesized response functions are seen to resemble the original ones and to follow their variations with stimulus level. It is evident that the two-component theory predicts not only the correct frequency selectivity and tuning but also the correct amplitude compression in the input–output function.[3] Moreover, it produces the correct response phase. Thus, question (B) of Sec. III has been answered.

There is one aspect of this result that seems, at first sight, unsatisfactory. To calculate the efficiency coefficient

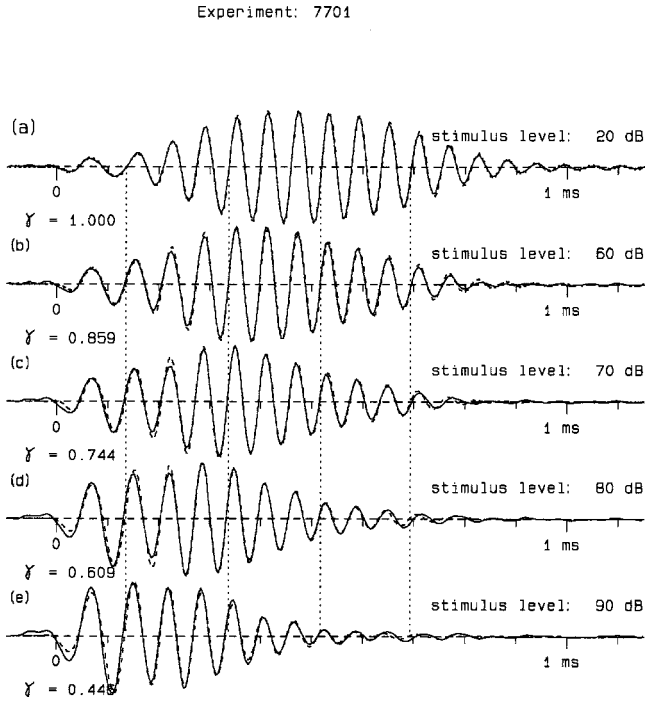

FIG. 7. Resynthesis of impulse response when BM impedance is composed of two components as in Eqs. (4) and (5). Experiment: 7701. Stimulus levels as indicated. *Dashed lines*: original impulse responses. *Solid lines*: resynthesized impulse responses with predicted impedance function. Note how well the timing of the zero-crossings is preserved (see vertical dotted lines).

$\gamma(L)$ we started from Eq. (3) as expressing the signal amplitude value as a function of L. We then used this to calculate $\gamma(L)$, substituted $\gamma(L)$ in the BM impedance expression Eq. (5) and found the resynthesized response to show the ''correct'' amplitude compression. This seems like circular reasoning, we started from and ended with the same ''compression.'' We could have followed a different path, namely, starting with uncompressed BM velocity values, calculating $\gamma(L)$, and using that in resynthesis. We would then find too much compression, and we could use the newly computed BM velocity (which is too small) to recalculate $\gamma(L)$, and to do another resynthesis (producing too large an amplitude). After a number of iterations we would end up by finding that the ''correct'' type of compression in the measured velocity values corresponds with the ''correct'' compression of resynthesized amplitude values. And this is just what we did in a straightforward way.

V. APPLICATION TO INDIVIDUAL EXPERIMENTS II: IMPULSE RESPONSE

A most critical test forms the impulse response [question (C) of Sec. III]. Figure 7 shows the impulse responses corresponding to the curves in Fig. 6; the one corresponding to the 20-dB condition is included. The original impulse responses are the dashed lines. The impulse responses computed with the ''two-component theory'' are shown by solid lines. For different conditions the curves have been normalized to show the same maximum amplitude but *original and resynthesized impulse responses have always been normalized by the same factor*. At many places the solid lines completely cover the dashed lines. At the lowest levels the cor-

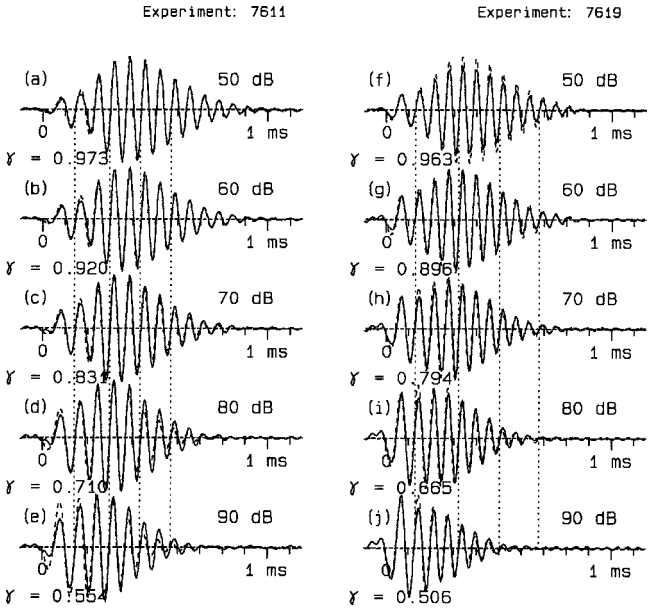

FIG. 8. Resynthesis of impulse responses in two more experiments. Left, experiment 7611. Right, experiment 7619. Normalization constants: 2200 and 1830, respectively. Vertical dotted lines assist in judging near-invariance of timing.

respondence is seen to be almost perfect, as expected because $\gamma(L)$ is close to 1. At higher levels the resynthesized waveforms are very similar to the original ones, but there appear small deviations, in the course of the envelope waveform as well as in the phase of the oscillations. Four vertical dotted lines are added to the figure to illustrate that the zero-crossings are nearly invariant with stimulus level.

Figure 8 shows results for the experiments used for Fig. 3 [panels (a)–(e)] and Fig. 4 [panels (f)–(j)]. For all three experiments illustrated by Figs. 7 and 8 the correspondence between original and resynthesized impulse responses is outstanding, the more so when we take into account how the BM impedance is represented by Eq. (5) as the sum of two terms both having considerable inherent errors. We found corresponding results in 11 other experiments, envelope variations were similar to those shown in Figs. 7 and 8, and the zero-crossings were never more than 0.1 period different between original and resynthesized responses. As implied earlier, v_1 had to be adjusted to each individual experiment but one value then served for all stimulus levels. The largest variations of v_1 with respect to the earlier mentioned value of 1100 amounted to a factor of 3, mostly upward. What is important here is that *the model's impulse response displays almost the same near-invariance of timing as the original impulse response*. In this way, question (C) posed in Sec. III has also been answered in the affirmative. For different values of L the BM impedance functions in the model differ only in the second term of Eq. (5). Apparently, this is one condition to leave the phase of the impulse-response oscillations nearly the same. We have not been able to prove that this condition is necessary (in the mathematical sense).

The condition is not sufficient either. From Part I we recall that one locally active model of the cochlea, Geisler and Sang (1995), qualitatively shows the correct ''glide'' property while another one, Neely and Kim (1986), does not. If we vary the feedback factor in these models—to mimic variations of stimulus level—we find that the Geisler–Sang model approximately shows the near-invariance property while the Neely–Kim model does not. It is important to note that *both* models obey the conditions for the EQ-NL theorem, and their BM impedances thus should obey Eqs. (4) and (5). Therefore, the model property that corresponds to near-invariance of timing in the impulse response is a subtle one. Further study is needed to work out the exact connection.

VI. SUMMARY AND CONCLUSIONS

For stimulation by weak signals it is generally agreed that the cochlea operates as a linear system. In Part II of this series it has been shown that in that case the stimulus–response relation of the cochlea can be simulated by that of a well-chosen model. Characteristically, that model is locally active. In the present paper the procedure is extrapolated to the case where the cochlea is nonlinear. By invoking the EQ-NL theorem the result can be interpreted in terms of a linear model (''$\mathcal{M}$-$\mathcal{L}in$''). When stimulus level increases, the degree of activity in model ''$\mathcal{M}$-$\mathcal{L}in$'' is found to decrease (Figs. 2–4).

In this paper one further step is taken: from *analysis* to *prediction*. First, the EQ-NL theorem predicts that the BM impedance is a linear combination of two components, the ''two-component theory of the BM impedance.'' This is expressed by Eq. (4). Second, the same theorem provides the way to *calculate* the reduction of activity as a function of stimulus level. Given the functional form of OHC transduction, only one parameter, the scaling factor v_1, is involved. The result is the (real) transduction efficiency coefficient $\gamma(L)$ which goes from 1 to 0 with increasing L. With this theory the variations in the BM impedance function with stimulus level can be explained quite well. For the best fit to the average of an earlier data set, $\gamma(L)$ should reduce to 0.5 when the stimulus level is 73 dB. However, for each of the experiments illustrated by Figs. 6–8 the stimulus level L at which $\gamma(L)$ reduces to 0.5 is larger than 80 dB. That level is indeed found to be higher than 73 dB in the majority of the 14 experiments in which we tested the ''two-component theory of the BM impedance.''

These findings can be compared to published data for the guinea pig. In Yates *et al.* (1989) the local cochlear microphonic (CM) potential is reduced to 50% of its maximum value by a tone of 83 dB SPL (see Fig. 4 of that paper); see also Geisler *et al.* (1990). Patuzzi *et al.* (1989) report [see their Fig. 1(c)] that the CM reduces to 50% at slightly over 80 dB SPL. Measuring the CM potential can be seen as estimating the efficiency of the OHCs. Given the enormous differences in experimental technique, the agreement with our estimates is satisfactory.

The same two-component theory of the BM impedance has been applied to *individual experiments*. For each experiment the appropriate value of the scaling factor v_1 has to be selected. With the two-component impedance the model is capable of reproducing all aspects of the processing that noise signals undergo in the cochlea, for all stimulus levels. In the frequency domain this property includes correct reproduction of

(i) variation of frequency selectivity,
(ii) the downward shift of the peak frequency, and
(iii) compression of the response amplitude with varying stimulus level (see Fig. 6).

In the time domain typical characteristics of the impulse response are simulated:

(i) the shape of the envelope of the impulse response, and
(ii) the glide.

In the measured time-domain responses a long-known property is confirmed:

(iii) With increasing stimulus level the timing of the individual oscillations remains approximately constant; this near-invariance is also accurately simulated by the model's impulse response (see Figs. 7 and 8).

Characteristic is the fundamental property that the BM impedance is a linear combination of two fixed impedance functions [Eq. (4)] and that only the coefficient $\gamma(L)$ of one of these varies with stimulus level L. It follows that *one* model now explains *all* manifestations of nonlinearity due to variations in the noise stimulus level L. Only one parameter, v_1, needs to be adapted to an individual experiment but one value serves for all levels L. This illustrates the far-reaching potential of the two-component theory. In Sec. V we explained that the two-component theory for the BM impedance is not a necessary-and-sufficient condition for near-invariance.

In Sec. I we proposed that the near-invariance of the timing of oscillations in the (resynthesized) impulse response should be taken into account in judging the validity of a cochlear model. We have found in Sec. V that a model that is provided with a BM impedance that consists of two components of which only the coefficient of one of the components varies with stimulus level [as in Eq. (4)] is indeed capable of explaining near-invariance of timing in the impulse response. Therefore, with the two-component theory of the BM impedance, we can quantitatively understand the way in which cochlear nonlinearity, frequency selectivity, peak frequency, signal amplitude and impulse-response (waveform *and* timing) vary with stimulus level. All this applies only to the case of stimulation by wideband noise, and under the assumption that the real cochlea operates as the model we have been using, of course.

ACKNOWLEDGMENTS

The work for this paper was carried out in two countries. The authors are indebted to (in alphabetical order) Gary Dootz, Anders Fridberger, Meng He Guo, Bob Masta, Darren Miller, Irina Omelchenko, Edward Porsov and Jiefu Zheng, for their help in setting up and performing the experiments. Fruitful discussions with Laurel Carney on the relation between neural timing and stimulus intensity are gratefully acknowledged. Two anonymous JASA reviewers provided useful suggestions for improving the text. The USA part of this work has been supported by NIH, under Grant No. NIDCD-DC-00141, and VA Rehabilitation Research & Development Center (Grant No. RCTR-597-0160, Portland, VAMC); the part carried out in The Netherlands is the continuation of project No. SLW 01.011 of the Netherlands Foundation for Scientific Research (NWO).

APPENDIX A: THE EQ-NL THEOREM—BASIS AND MEANING

For the purpose of this paper it is necessary to review the basic premises of the cochlear model in somewhat greater detail than has been done in previous papers. This has specifically to do with the elements of the model that are assumed responsible for amplifying the cochlear fluid wave and are also assumed to be the sources of nonlinearity. Consider a model ''$\mathcal{M}$-$\mathcal{NL}$'' of the cochlea consisting of two elongated fluid-filled channels separated by the ''cochlear partition'' containing the organ of Corti. Along the entire length of the model, a part of the width of the partition is occupied by a flexible membrane, the basilar membrane (BM). It is assumed that outer hair cells (OHCs) of the organ of Corti are able to cause a local sound pressure $p_{\mathrm{OHC}}(x,t)$ (an oscillating pressure, on a cycle-to-cycle basis) which gives rise to an additional component $p_{\mathrm{add}}(x,t)$ of the sound pressure $p(x,t)$ near the BM in the fluid. By way of this extra pressure the OHCs may enhance and sharpen the frequency response of the system via amplification of the cochlear wave. Transduction in the OHCs is assumed to be nonlinear (saturating) and instantaneous which makes the model *nonlinear*. All other signal transformations in the model are linear (but are place and frequency dependent).

We also consider a ''comparison model,'' called ''$\mathcal{M}$-$\mathcal{L}in$'' in this paper, which is *linear* and identical in structure and functioning to the nonlinear model when that works with extremely weak signals. Responses and variables in this model are expressed in the frequency or ω domain. In model ''$\mathcal{M}$-$\mathcal{L}in$,'' $p_{\mathrm{OHC}}(x,\omega)$ and $p_{\mathrm{add}}(x,t)$ both have to be multiplied by the (real) factor γ that is called the *transduction efficiency coefficient*. Let γ be 1 for optimal operation of the model, corresponding to stimulation with very weak signals. The coefficient γ will be smaller in a model that represents a strongly stimulated or deteriorated cochlea and zero in a ''dead'' cochlea. Saturation of the OHCs in the nonlinear model ''$\mathcal{M}$-$\mathcal{NL}$'' thus corresponds to a decrease of γ in the linear model ''$\mathcal{M}$-$\mathcal{L}in$.'' The EQ-NL theorem states the following correspondence between the two models, the nonlinear model under study and the linear model:

> *The input–output cross-correlation function (ccf) for the nonlinear model ''$\mathcal{M}$-$\mathcal{NL}$'', determined with a wideband random-noise input signal with a given stimulus level, is equal to the ccf for model ''$\mathcal{M}$-$\mathcal{L}in$'' that has exactly the same structure and the same parameters, but in which all OHCs are linear and operate with a reduced efficiency coefficient γ.*

Further properties are described by the following:

> *With wideband flat-spectrum random-noise stimuli the efficiency coefficient γ is the same for all OHCs and for all frequencies. With stronger stimuli γ will be reduced more and more.*

The acronym EQ-NL has been chosen to emphasize the aspects of ''equivalence'' and ''nonlinearity.'' For the proof of the theorem, see de Boer (1997). The main argument in this proof is that at the input to each nonlinear OHC transducer a composite noise signal is present (with a near-Gaussian distribution and a large number of components) which causes each component of that signal to be *compressed* (in the average) to exactly the same degree (the factor γ). Note that for one OHC this compression is *the same for all frequencies* because the nonlinearity involved is memoryless and the component amplitudes are small. The latter condition requires that all signals have a large number of degrees of freedom.[4] In its concentration upon the handling of small-amplitude components, the EQ-NL theorem forms an extension to the pseudo-linear solution method advocated by Kanis and de Boer (1993), which has proven useful in the study of two-tone suppression and distortion-product generation (Kanis and de Boer, 1994, 1997).

For a no-memory transducer with transducer characteristic $F(.)$ and input signal u the average transduction coefficient γ is given by

$$\gamma = \int_{-\infty}^{\infty} F'(u)P(u)du, \tag{A1}$$

where $P(u)$ is the probability density of the signal u, $F'(.)$ is the derivative of $F(.)$ which should be a monotonically decreasing function of the magnitude of its argument, and $F'(0)$ is assumed to be equal to 1. Then, for very small signals the coefficient γ is equal to 1. For stronger signals γ expresses, by its reduction from 1, the *average state of saturation* in the system. How γ can actually be calculated is detailed in Appendix B.

If we assume that the functioning of the actual cochlea can be described by the nonlinear model under consideration, the signals involved in the theory can be replaced by the ones used and obtained in the experiment, and conclusions about the cochlea can be formulated in terms of properties of the linear ''comparison model,'' model ''$\mathcal{M}$-$\mathcal{L}in$.'' In order to carry out the entire procedure on recorded data, stimulation has to occur with wideband flat-spectrum noise signals and ''responses'' are to be acquired in the form of input–output cross-correlation functions (ccfs).

APPENDIX B: THE EFFICIENCY OF TRANSDUCTION

Let the input to one outer hair cell (OHC) be the deflection $d_{\mathrm{cil}}(x,t)$ of the OHC stereocilia. The output is the local pressure $p_{\mathrm{OHC}}(x,t)$ mentioned in Appendix A. Express the nonlinear instantaneous transduction function of the OHC by

$$p_{\mathrm{OHC}}(x,t) = S_0 d_1 F[d_{\mathrm{cil}}(x,t)/d_1], \tag{B1}$$

where $F(.)$ is a saturating no-memory nonlinear real function that is equal to its argument for very small values of the argument and remains finite for extreme values of the argument, d_1 is a scaling factor for $d_{\mathrm{cil}}(x,t)$, and S_0 is a constant. Assume the signal $d_{\mathrm{cil}}(x,t)$ to be narrow-band noise with a large number of degrees of freedom. Transduction of each of the many (small) components of $d_{\mathrm{cil}}(x,t)$ will be determined by the average slope $F'(.)$ of the function $F(.)$, averaged over all values of the signal $d_{\mathrm{cil}}(x,t)$ [see Eq. (A1)]. Because $d_{\mathrm{cil}}(x,t)$ is a linear transform of BM displacement $d_{\mathrm{BM}}(x,t)$, the function $F'(.)$ can also be averaged over the distribution of $d_{\mathrm{BM}}(x,t)$ provided a different normalization constant is introduced instead of d_1. Similarly, we can work with the normalized BM *velocity* $v_{\mathrm{BM}}(x,t)$ instead of the normalized BM *displacement*. This leads to the alternative formulation

$$p_{\mathrm{OHC}}(x,t) = Z_0 v_1 F[v_{\mathrm{BM}}(x,t)/v_1], \tag{B2}$$

where we have introduced another constant Z_0 instead of S_0 and a new scaling factor, v_1. We will take care of the filtering between BM velocity and ciliary deflection, and the associated phase difference, later. Because this filtering is assumed to be linear, the ratio of the coefficients v_1 and d_1 does not depend on stimulus level.

In model ''$\mathcal{M}$-$\mathcal{L}in$'' (see Appendix A), OHC transduction is written as

$$p_{\mathrm{OHC}}(x,\omega) = \gamma Z_1(x,\omega) v_{\mathrm{BM}}(x,\omega). \tag{B3}$$

This pressure can be represented by a complex number, and its amplitude will be proportional to the real coefficient γ. There will also be a phase shift that is part of the transformation between BM velocity and ciliary displacement. This phase shift does not vary with stimulus level and the transformation can thus adequately be represented by the complex coefficient $Z_1(x,\omega)$. Another phase shift is relevant: that between the local OHC-generated $p_{\mathrm{OHC}}(x,\omega)$ and the corresponding component $p_{\mathrm{add}}(x,t)$ of the pressure $p(x,\omega)$ near the BM. This phase shift does not vary with stimulus level either. Equation (B3) has the following counterpart for the pressure component $p_{\mathrm{add}}(x,t)$:

$$p_{\mathrm{add}}(x,\omega) = \gamma Z_2(x,\omega) v_{\mathrm{BM}}(x,\omega). \tag{B4}$$

The entire space- and frequency-dependent filtering in the feedback path—from the BM via $p_{\mathrm{OHC}}(x,\omega)$ and $p_{\mathrm{add}}(x,t)$ back to the BM—and both phase shifts involved are included in the (complex) coefficient $Z_2(x,\omega)$. By using complex functions we thus have incorporated the phase shifts and filtering that we formerly omitted. A more detailed formulation is found in Kanis and de Boer (1993).

In good approximation the probability distribution of $d_{\mathrm{cil}}(x,t)$ as well as $v_{\mathrm{BM}}(x,t)$ will be Gaussian. We then find the efficiency coefficient γ of OHC transduction as the average slope $F'(u)$ of $F(u)$ over the values of $[v_{\mathrm{BM}}(x,t)/v_1]$ for a Gaussian distribution [see Eq. (A1)]:

$$\gamma = \int_{-\infty}^{\infty} F'(a v_{\mathrm{rms}}/v_1) P_{\mathrm{G}}(a)\, da, \tag{B5}$$

where v_{rms} is the rms value of $v_{\mathrm{BM}}(x,t)$ and $P_{\mathrm{G}}(.)$ stands for the Gaussian probability density function with unity variance. When we know the form of $F(u)$ and the value of v_1, we can calculate γ as a function $\gamma(L)$ of stimulus level L because v_{rms} is assumed to depend on L in the way expressed by Eq. (3) of the main text.

The exact form of the nonlinear transfer function $F(u)$ is not critical. As the basis for $F(u)$ the hyperbolic tangent function as used in the work of Kanis and de Boer (1993) is taken. A weighted sum of two such functions has a two-stage

variation of the slope which corresponds better to the nonlinear odd-order character of hair-cell transfer functions (cf. Geisler, 1998, Figs. 8.3 and 8.5):

$$F(u)=[\tanh w+c\tanh(w/c)]/(1+c), \tag{B6}$$

where

$$w=(1+c)u/2. \tag{B7}$$

The parameter c is a constant which must be nonzero. For every value of c the function $F(u)$ has unity slope at $u=0$ and it reaches $+1$ for $u\rightarrow\infty$ and -1 for $u\rightarrow-\infty$. For $c=1$, $F(u)$ reduces to a single tanh function. The parameter c is taken equal to 0.2. For $u=1$, $F(u)$ is equal to 0.613. Substitution of Eq. (B6) into Eq. (B5) yields the efficiency coefficient γ as a function of $v_{\rm rms}/v_1$. For $v_{\rm rms}$ equal to v_1, γ becomes equal to 0.513. Application of Eq. (3) of the main text gives γ as a function $\gamma(L)$ of stimulus level L.

[1]This study was consistent with NIH guidelines for humane treatment of animals and was reviewed and approved by the University of Michigan Committee on Use and Care of Animals and the Oregon Health Sciences Committee on the Use and Care of Animals.

[2]MATLAB® programs for inverse and forward model solutions using sparse matrices can be requested from the first author (preferably via e-mail).

[3]The slight flattening of the curves to the right is due to smoothing of the BM impedance function.

[4]The number of degrees of freedom is $2WT$, where W is the bandwidth and T is the period of the pseudo-random noise. In our experiments $2WT$ is minimally of the order of 40. For the strongest stimuli it is of the order of 180. These values are large enough for the formalism described to be applicable.

Carney, L. H. (**1993**). ''A model for the responses of low-frequency auditory-nerve fibers in cat,'' J. Acoust. Soc. Am. **93**, 401–417.

Carney, L. H., and Yin, T. C. T. (**1988**). ''Temporal coding of resonances by low-frequency auditory nerve fibers: Single fiber responses and a population model,'' J. Neurophysiol. **60**, 1653–1677.

Carney, L. H., McDuffy, M. J., and Shekhter, I. (**1999**). ''Frequency glides in the impulse response of low-frequency auditory-nerve fibers,'' J. Acoust. Soc. Am. **105**, 2384–2391.

de Boer, E. (**1981**). ''Short waves in three-dimensional cochlea models: Solution for a 'block' model,'' Hear. Res. **4**, 53–77.

de Boer, E. (**1983**). ''No sharpening? A challenge for cochlear mechanics,'' J. Acoust. Soc. Am. **73**, 567–573.

de Boer, E. (**1997**). ''Connecting frequency selectivity and nonlinearity for models of the cochlea,'' Aud. Neurosci. **3**, 377–388.

de Boer, E. (**1998**). ''A method for forward and inverse solutions of a three-dimensional model of the cochlea.'' J. Acoust. Soc. Am. **103**, 3725–3728.

de Boer, E., and Nuttall, A. L. (**1997a-DAM**). ''On cochlear cross-correlation functions: connecting nonlinearity and 'activity','' in *Diversity in Auditory Mechanisms*, edited by E. R. Lewis, G. R. Long, R. F. Lyon, P. M. Narins, C. R. Steele, and E. Hecht-Poinar (World Scientific, Singapore), pp. 291–297.

de Boer, E., and Nuttall, A. L. (**1997b-GLIDE**). ''The mechanical waveform of the basilar membrane. I. Frequency modulations (''glides'') in impulse responses and cross-correlation functions,'' J. Acoust. Soc. Am. **101**, 3583–3592.

de Boer, E., and Nuttall, A. L. (**1999-INV-3**). ''The 'inverse problem' solved for a three-dimensional model of the cochlea. III. Brushing-up the solution method,'' J. Acoust. Soc. Am. **105**, 3410–3420.

de Boer, E., and Nuttall, A. L. (**2000-DMD**). ''The mechanical waveform of the basilar membrane. II. From data to models—and back,'' J. Acoust. Soc. Am. **107**, 1487–1496.

Geisler, C. D. (**1998**). *From Sound to Synapse* (Oxford U.P., Oxford).

Geisler, C. D., and Sang, C. (**1995**). ''A cochlear model using feed-forward outer-hair-cell forces,'' Hear. Res. **86**, 132–146.

Geisler, C. D., Yates, G. K., Patuzzi, R. B., and Johnstone, B. M. (**1990**). ''Saturation of outer hair cell receptor currents causes two-tone suppression,'' Hear. Res. **44**, 241–256.

Kanis, L. J., and de Boer, E. (**1993**). ''Self-suppression in a locally active nonlinear model of the cochlea: A quasi-linear approach,'' J. Acoust. Soc. Am. **94**, 3199–3206.

Kanis, L. J., and de Boer, E. (**1994**). ''Two-tone suppression in a locally active nonlinear model of the cochlea,'' J. Acoust. Soc. Am. **96**, 2156–2165.

Kanis, L. J., and de Boer, E. (**1997**). ''Frequency dependence of acoustic distortion products in a locally active model of the cochlea,'' J. Acoust. Soc. Am. **101**, 1527–1531.

Kiang, N. Y.-S., Watanabe, T., Thomas, E. C., and Clark, L. F. (**1965**). *Discharge Patterns of Single Fibers in the Cat's Auditory Nerve* (MIT, Cambridge, MA).

Neely, S. T., and Kim, D. O. (**1986**). ''A model for active elements in cochlear biomechanics,'' J. Acoust. Soc. Am. **79**, 1472–1480.

Nuttall, A. L., and Dolan, D. F. (**1996**). ''Steady-state sinusoidal velocity responses of the basilar membrane in guinea pig,'' J. Acoust. Soc. Am. **99**, 1556–1565.

Nuttall, A. L., Dolan, D. F., and Avinash, G. (**1990**). ''Measurements of basilar membrane tuning and distortion with laser Doppler velocimetry,'' in *The Mechanics and Biophysics of Hearing*, edited by P. Dallos, C. D. Geisler, J. W. Matthews, M. A. Ruggero, and C. R. Steele (Springer-Verlag, Berlin), pp. 288–295.

Patuzzi, R. B., Yates, G. K., and Johnstone, B. M. (**1989**). ''Outer hair cell receptor current and its effect on cochlear mechanics,'' in *Cochlear Mechanisms: Structure, Function and Models*, edited by J. P. Wilson and D. T. Kemp (Plenum, New York), pp. 169–176.

Recio, A., Rich, N. C., Narayan, S. S., and Ruggero, M. A. (**1998**). ''Basilar-membrane responses to clicks at the base of the chinchilla cochlea,'' J. Acoust. Soc. Am. **103**, 1872–1989.

Robles, L., Rhode, W. S., and Geisler, C. D. (**1976**). ''Transient response of the basilar membrane measured in squirrel monkeys using the Mössbauer effect,'' J. Acoust. Soc. Am. **59**, 926–939.

Ruggero, M. A., Rich, N. C., and Recio, A. (**1992**). ''Basilar membrane responses to clicks,'' in *Auditory Physiology and Perception*, edited by Y. Cazals, L. Demany, and K. Horner (Pergamon, London), pp. 85–91.

Yates, G. K., Geisler, C. D., Patuzzi, R. B., and Johnstone, B. M. (**1989**). ''Saturation of receptor currents accounts for two-tone suppression,'' in *Cochlear Mechanisms: Structure, Function and Models*, edited by J. P. Wilson and D. T. Kemp (Plenum, New York), pp. 177–187.

The dynamic range of inner hair cell and organ of Corti responses

M. A. Cheatham[a] and P. Dallos
Audiology and Hearing Sciences, Communication Sciences and Disorders, The Hugh Knowles Center, Frances Searle Building, 2299 North Campus Drive, Northwestern University, Evanston, Illinois 60208-3550

(Received 22 March 1999; revised 8 November 1999; accepted 29 November 1999)

Inner hair cell (IHC) and organ of Corti (OC) responses are measured from the apical three turns of the guinea pig cochlea, allowing access to regions with best, or most sensitive, frequencies at approximately 250, 1000, and 4000 Hz. In addition to measuring both ac and dc receptor potentials, the average value of the half-wave rectified response (AVE_{HR}) is computed to better reflect the signal that induces transmitter release. This measure facilitates comparisons with single-unit responses in the auditory nerve. Although IHC ac responses exhibit compressive growth, response magnitudes at high levels depend on stimulus frequency. For example, IHCs with moderate and high best frequencies (BF) exhibit more linear responses *below* the BF of the cell, where higher sound-pressure levels are required to approach saturation. Because a similar frequency dependence is observed in extracellular OC responses, this phenomenon may originate in cochlear mechanics. At the most apical recording location, however, the pattern documented at the base of the cochlea is not seen in IHCs with low BFs around 250 Hz. In fact, more linear behavior is measured *above* the BF of the cell. These frequency-dependent features require modification of cochlear models that do not provide for longitudinal variations and generally depend on a single stage of saturation located at the synapse. Finally, behavior of dc and AVE_{HR} responses suggests that a single IHC is capable of coding intensity over a large dynamic range [Patuzzi and Sellick, J. Acoust. Soc. Am. **74**, 1734–1741 (1983); Smith *et al.*, in *Hearing—Physiological Bases and Psychophysics* (Springer, Berlin, 1983); Smith, in *Auditory Function* (Wiley, New York, 1988)] and that information compiled over wide areas along the cochlear partition is not essential for loudness perception, consistent with psychophysical results [Viemeister, Hearing Res. **34**, 267–274 (1988)]. © *2000 Acoustical Society of America.* [S0001-4966(00)02303-1]

PACS numbers: 43.64.Ld, 43.64.Nf, 43.64.Tk [RDF]

INTRODUCTION

Recordings from the auditory nerve provide a relatively complete description of longitudinal variations in cochlear function (Kiang, 1984; Ruggero, 1992), i.e., variations that depend on best frequency (BF). The addition of basilar-membrane measurements to this database makes it possible to compare mechanical and neural responses to the same stimulus in the same species (Narayan *et al.*, 1998). This allows the transformation from basilar-membrane motion to neural activity to be investigated. Because mechanical measures are presently restricted to basal and apical ends of the cochlea, a strategy was developed (Yates *et al.*, 1990; Cooper and Yates, 1994) to use the neural data to estimate mechanical preprocessing at all cochlear locations. This approach is based on the premise that basilar-membrane mechanics are nonlinear, but only in the region around BF, and that hair cell nonlinearities are frequency independent (Patuzzi and Sellick, 1983). Based on these relationships, rate-intensity functions obtained well below BF can be used as a reference because mechanical input to the IHC is linear in this frequency region. Nonlinear mechanical contributions can then be estimated from rate-intensity functions recorded at the BF of the nerve fiber. Unfortunately, this derived input–output technique is appropriate only in the basal, high-frequency region of the cochlea where linear mechanical responses are recorded below BF on the tails of the response curves (Rhode, 1971; Sellick *et al.*, 1982; Nuttall and Dolan, 1996; Ruggero *et al.*, 1997). In the apical, low-frequency region of the cochlea, however, response curves do not exhibit a tail segment, with the result that mechanical responses are generally nonlinear, although to a lesser degree than in the base (Rhode and Cooper, 1996, 1997). Because of this restriction, recordings from individual hair cells at several locations along the cochlear spiral are useful when evaluating how mechanical inputs are transduced and modified prior to spike initiation. By documenting how sound pressure and frequency are coded in the peripheral auditory system (Crawford and Fettiplace, 1981), the processes that underlie intensity coding may be revealed.

In this report, receptor potentials produced by mammalian inner hair cells (IHC), as well as voltages recorded extracellularly in the organ of Corti (OC) fluid space, are obtained and compared. The latter is thought to reflect outer hair cell (OHC) receptor currents (Dallos and Cheatham, 1976; Russell and Sellick, 1983; Dallos and Evans, 1995). Because OHCs respond to basilar-membrane displacement (Dallos, 1973; Nedzelnitsky, 1974; Dancer and Franke,

[a]Author to whom correspondence should be addressed. Electronic mail: m-cheatham@nwu.edu

1980), these extracellular measurements can be used as an indicator of mechanical events. By inspecting input–output functions obtained for inputs below, at, and above BF, it is possible to learn if the compression exhibited by these responses is frequency dependent. Additional comparisons between OC, IHC, and neural results allow the sources of these variations to be estimated. Although a frequency dependence has been observed for high-level responses measured in IHCs with moderate and high BFs (Russell and Sellick, 1978; Sellick and Russell, 1979; Zwislocki and Chatterjee, 1995; Chatterjee and Zwislocki, 1997, 1998), companion data for IHCs in the apex of the cochlea are required.

Previous reports focused on the level dependence of either ac (Russell and Sellick, 1978; Dallos, 1985a; Russell *et al.*, 1986; Dallos and Cheatham, 1990; Chatterjee and Zwislocki, 1998) or dc (Russell and Sellick, 1978; Patuzzi and Sellick, 1983; Dallos, 1985a; Russell *et al.*, 1986; Goodman *et al.*, 1982) receptor potentials. Depending on the BF of the location under study, however, this may not be sufficient. For example, in turn 4, at the apex of the cochlea, the ac receptor potential is large and probably controls transmitter release at low stimulus levels (Schmiedt and Zwislocki, 1978; Cheatham and Dallos, 1993). Conversely, at the base of the cochlea the dc receptor potential controls transmitter release because the ac component is reduced by filtering at the IHC's basolateral membrane (Russell and Sellick, 1978). Between these two extremes, however, some combination of both ac and dc components may provide a better indication of the level-dependent properties of the IHC, which ultimately provide the substrate upon which neural processing is based. This proposal assumes that ac and dc components of the receptor potential are integrated at the synapse and that this combined potential induces the release of neurotransmitter. This latter response is approximated by computing the average value of the half-wave rectified response. By evaluating the dynamic range of ac, dc, and average voltages, it may be possible to learn whether intensity coding is determined at a relatively narrow location along the cochlear partition (Patuzzi and Sellick, 1983; Delgutte, 1987; Smith, 1988; Viemeister, 1988) or whether integration over wide spatial areas is required (Chatterjee and Zwislocki, 1998).

I. METHODS

Inner hair cell responses are recorded in anesthetized guinea pigs using the lateral approach (Dallos *et al.*, 1982). Windows made in the cochlear bone overlying scala media in turns 2, 3, and 4 allow access to regions along the cochlear partition where BFs are approximately 4000, 1000, and 250 Hz, respectively. The latter values refer to that frequency where the greatest sensitivity is demonstrated at low input levels. A recording electrode is advanced through the spiral ligament and *stria vascularis* into the scala media fluid space. After contacting a Hensen cell at the periphery of the OC, small advances are made to acquire the IHC measurements. An ideal electrode track is roughly parallel to, but slightly below, the reticular lamina, to avoid disruption of the tectorial membrane. The condition of the cochlea is determined by monitoring the endocochlear potential (EP), as well as the cochlear potentials recorded in the organ of Corti fluid space. In spite of the fact that the data included here are the best in our collection, variations in response magnitude (Dallos, 1985b) make it difficult to obtain quantitative comparisons between experiments and between recordings made in a single preparation. The fact that these recordings are highly labile probably reflects a decrease in OHC feedback which results in more linear responses. These procedures (Dallos, 1985a; Cheatham and Dallos, 1992) were approved by the National Institutes of Health and by Northwestern University's Institutional Review Committee.

In these experiments, signals are generated using a programmable frequency synthesizer (model 5100, Rockland Systems), gated by a custom-made device and attenuated prior to delivery at the driver (Beyer DT-48). Signal durations vary with frequency such that longer durations are used for lower frequency inputs. All signals, however, are at least 10 ms long. Because cochlear potentials do not adapt (Davis, 1957; Kiang and Peake, 1960), these variations in signal length do not influence the measurements. Signal levels were not changed randomly but varied sequentially, beginning with the lowest level where the largest number of samples were averaged. As stimulus level increased, the number of samples decreased to avoid fatiguing the ear.

The sound pressure at the tympanic membrane is monitored with a probe tube inserted into the sound tube and connected to a miniature microphone (Knowles BT-1751). This concentric assembly is cemented to the external *osseous meatus* forming a closed system. Because the Knowles microphone is nonlinear for high-level inputs, the linearity of the sound system is determined in a coupler using a Brüel & Kjær 1/2-in. condenser microphone (type 4134). These measurements indicate that distortion in the sound is at least 60 dB down from the fundamental, except for low-frequency inputs below ~250 Hz where the distortion is only 40 dB down.

Input–output functions for ac and dc receptor potentials are measured for tone bursts below, at, and above the BF of the IHC. Companion measures are also collected for the cochlear microphonic (CM) measured extracellularly in the OC fluid space. Recorded responses are preamplified and capacitance compensated by optimizing square-wave responses (Cell Explorer model 8700, Dagan Corp.). Signals are then low-pass filtered to prevent aliasing and gain-controlled to avoid saturating the analog-to-digital converter. Fast Fourier transforms of averaged response waveforms are determined off-line to provide the magnitudes of both ac and dc components. Waveform segments, obtained during the steady-state portion of the response, are windowed prior to transformation using a Hanning function. Although data are acquired using a PDP 11/73 (Digital Equipment Corp.), data analysis is performed on a Power Macintosh G3 (Apple Computer, Inc.) using IGOR PRO (WaveMetrics, Lake Oswego, OR).

In some cases, inner hair cell ac and dc receptor potentials are used to obtain a combined voltage that better reflects the signal that induces transmitter release. This approach uses a half-wave rectified version of the averaged response waveform because single units respond to unidirectional movements of the basilar membrane (Brugge *et al.*, 1969) and because rectification is thought to occur at the synapse

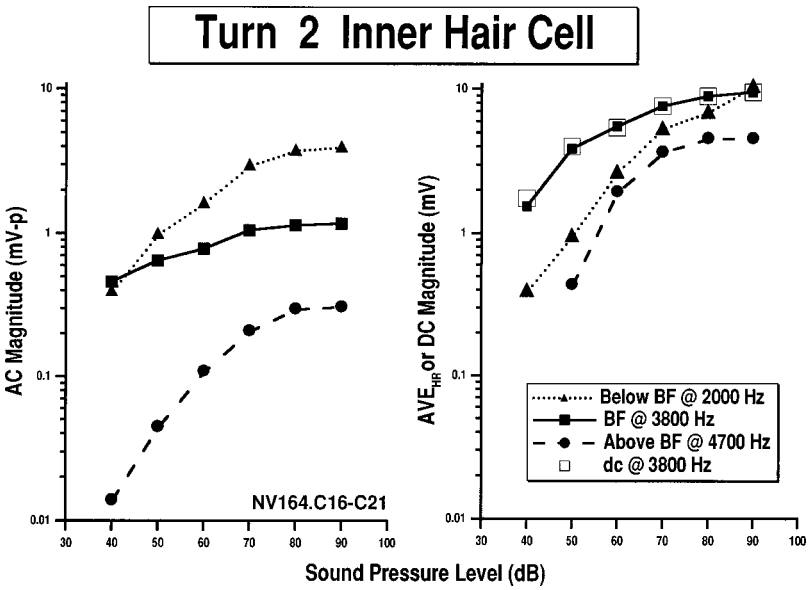

FIG. 1. Input–output functions from a second-turn IHC are plotted for inputs below BF at 2000 Hz (dotted lines and triangles), at BF at 3800 Hz (solid lines and squares), and above BF at 4700 Hz (dashed lines and circles). The ac receptor potential in mV-peak is plotted on the left ordinate versus sound-pressure level; the AVE_{HR} potential, on the right. The right panel also includes data points for the dc receptor potential measured at 3800 Hz (open squares). The endocochlear potential (EP) in this preparation was +79 mV, the resting potential of the cell, −20 mV. In this and all figures, sound-pressure level is measured in dB *re*: 20 μPa.

(Schroeder and Hall, 1974; Smith and Brachman, 1982; Allen, 1983). In this process, all data points within an integer multiple of response cycles are added together. The result is then divided by the total number of points to provide the average value of the half-wave rectified waveform, referred to as AVE_{HR}. It should be remembered that the average voltage for a half-wave rectified sinusoid corresponds to $1/\pi$ (peak). The recorded IHC waveforms, however, are not sinusoidal because hair cell responses are distorted. Consequently, the computed values for the half-wave rectified IHC responses are not simply $1/\pi$ (peak) because of the harmonic and dc components present in the intracellular response.

II. RESULTS

A. Turn 2

Input–output functions are plotted for a second-turn IHC in Fig. 1. In the left panel, magnitude of the ac receptor potential is plotted along the ordinate; sound-pressure level is along the abscissa. Functions are provided for inputs below BF at 2000 Hz (dotted lines and triangles), at BF at 3800 Hz (solid lines and squares), and above BF at 4700 Hz (dashed lines and circles). Although all three functions exhibit compression, the magnitude of high-level responses depends on stimulus frequency. For example, the magnitude near saturation for the input below BF exceeds that at 3800 Hz, while responses at 4700 Hz approach saturation at the lowest magnitude. In other words, as frequency increases, the magnitude of high-level responses decreases. Although it is understood that the recording electrode attenuates high-frequency responses at 12 dB/oct above ~3500 Hz (Baden-Kristensen and Weiss, 1983; Cody and Russell, 1987), corrections for this filtering were not applied to the ac values reported here. It should be stated, however, that the principal features of the frequency dependence exhibited here in second turn do not change when the data at and above BF are corrected using a generic compensation (Cheatham and Dallos, 1993).

In order to better approximate the voltage that drives transmitter release, the AVE_{HR} potential recorded in the IHC is determined and plotted on the right-hand-side of Fig. 1. The dc input–output function is also included for comparison and plotted with open squares. Because the ac receptor potential is filtered by the cell's basolateral membrane (Russell and Sellick, 1978), the AVE_{HR} potential approximates the dc receptor potential when recordings are made near BF in the basal half of the cochlea. Although this AVE_{HR} voltage exhibits compressive growth, the approach to saturation occurs at higher levels than those observed for the fundamental ac component, plotted on the left. This behavior may relate to the greater dynamic range observed for the dc receptor potential (Goodman *et al.*, 1982; Patuzzi and Sellick, 1983; Nuttall, 1984; Cody and Russell, 1987). Responses for the CM measured outside the IHC in the organ of Corti fluid space are shown in Fig. 2. Again, frequency-dependent compression is expressed in the extracellular responses. Because these measurements reflect OHC receptor currents, they imply that basilar-membrane displacements may also approach saturation at lower magnitudes as stimulus frequency increases.

B. Turn 3

Although data from second turn are similar to results recorded in first-turn IHCs (Russell and Sellick, 1978; Patuzzi and Sellick, 1983; Russell *et al.*, 1986) and in gerbil IHCs with BFs around 2500 Hz (Zwislocki and Chatterjee, 1995; Chatterjee and Zwislocki, 1997, 1998), it is important to determine if this frequency dependence can be generalized to other recording locations. Consequently, results are provided for third turn where BFs are between 800 and 1000 Hz. Data in Fig. 3 are obtained for an IHC and for the CM recorded in the OC. In the left panel, the near-BF response (solid lines and squares) reaches the highest magnitude, while inputs both above and below BF generate responses with lower magnitudes. In other words, these data do not show greater linearity for low-frequency inputs. The AVE_{HR} inner hair cell voltage is plotted in the center panel. Again,

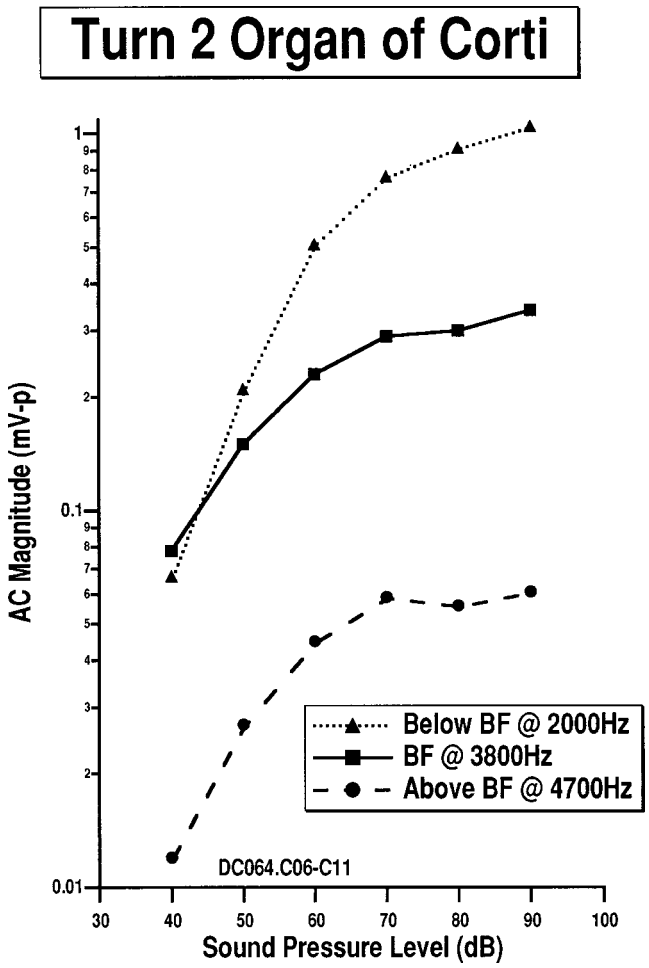

FIG. 2. Input–output functions for the potential recorded in the organ of Corti fluid space are plotted here. Line styles and stimulus frequencies are the same as in Fig. 1. The EP was +79 mV.

the highest magnitudes are achieved near best frequency where a sloping saturation is observed above ~40 dB. The function for the dc receptor potential is also appended for comparison. In contrast to second-turn results, the dc voltage is less than the AVE_{HR} potential, consistent with the idea that filtering of the ac receptor potential by the cell's basolateral membrane is less severe at this more apical recording location which has a lower BF. This suggests that both ac and dc components combine to drive transmitter release at this location. The CM recorded outside the IHC, and plotted on the right, also demonstrates that inputs both below and probably above BF achieve lower magnitudes than do inputs at BF.

Additional results from turn 3 are included in Fig. 4. In this example, IHC data are shown for the individual ac and dc receptor potentials recorded at BF, as well as for the AVE_{HR} intracellular potential. The ac responses at the fundamental ($f_0 = 900$ Hz), and at the second harmonic ($2f_0 = 1800$ Hz), are appended. Data indicate that even when the fundamental component of the ac response (solid lines and squares) approaches saturation, the dc receptor potential (dotted line and circles) and the second harmonic (solid lines and open squares) continue to increase. In fact, even-order distortion products continue to grow, even though the ac response at the fundamental appears relatively constant when plotted on this logarithmic scale. These increases are reflected in the AVE_{HR} response (dashed lines and triangles).

C. Turn 4

Results from turn 4 are provided in Fig. 5. Again, the ac magnitude, as well as the AVE_{HR} potential, is plotted for this IHC with BF at 230 Hz. Although the ac response at BF (solid lines and squares) is recorded at the lowest sound-pressure level, it exhibits asymptotic growth above 60 dB. At 70 Hz (dotted lines and triangles), the cell is less sensitive

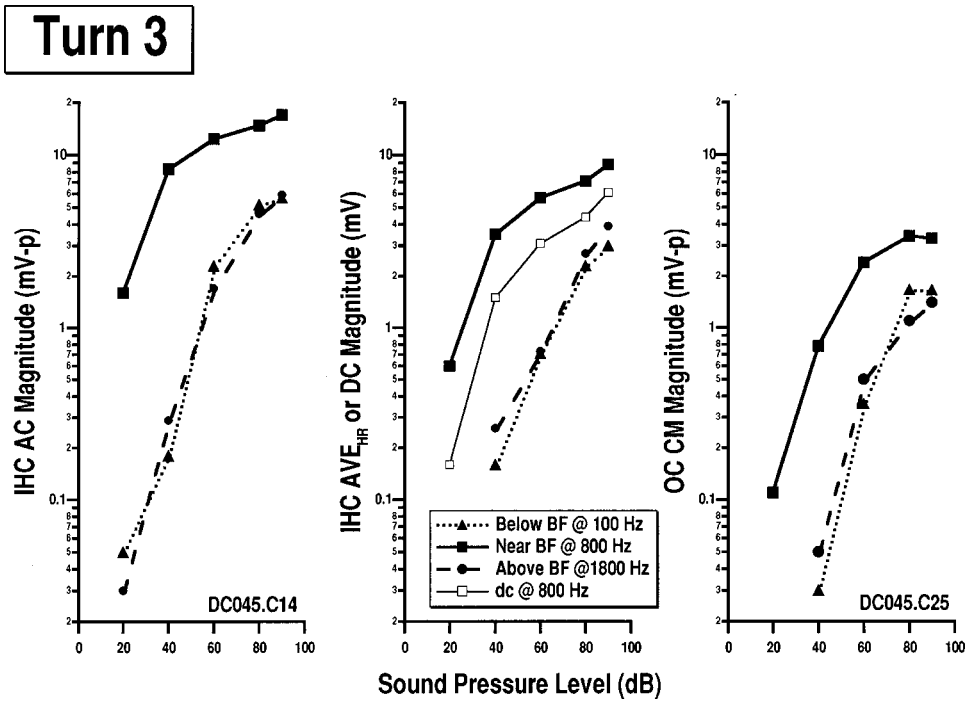

FIG. 3. Data are recorded in third turn of the guinea pig cochlea below BF at 100 Hz, near BF at 800 Hz, and above BF at 1800 Hz. Functions on the left are for the ac receptor potential; those in the center, for the IHC's AVE_{HR} potential. This panel also includes the dc receptor potential measured at 800 Hz. The EP recorded in scala media was +69 mV; the resting potential of the cell, −25 mV. Companion organ of Corti measures are plotted on the right.

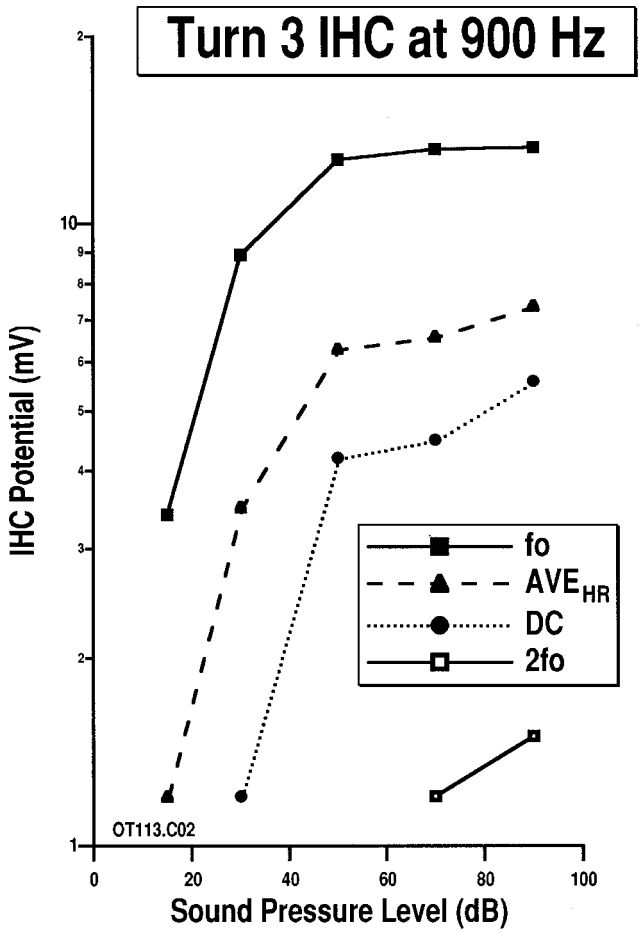

FIG. 4. Data from turn 3 are collected from another IHC with BF at 900 Hz. Potentials for the ac response at the fundamental and second harmonic are plotted, along with results for the dc receptor potential and for the AVE_{HR} potential. The second harmonic at 1800 Hz is small because this potential suffers from filtering at the cell's basolateral membrane to a greater degree than the fundamental. The EP was +70 mV; the resting potential, −24 mV.

but the response also approaches saturation around 60 dB, albeit at a lower magnitude than at 230 Hz. These responses below BF are similar to those in third turn, where response magnitude at high levels is also lower for inputs below BF. For data at 700 Hz (dashed lines and circles), obtained above the BF of the cell, the responses are more linear and saturation is not observed even at 90 dB, the highest level used in this experiment. This contrasts with results from second turn (Fig. 1), where the most linear behavior is recorded *below* the BF of the IHC. In other words, these response patterns, observed at the apex of the cochlea, are opposite those in turn 2. Results for the AVE_{HR} potential, plotted on the right, are similar to those for the fundamental component of the ac receptor potential, except that the asymptotic growth at BF is more gradual. This may reflect inclusion of distortion products generated at high levels in fourth turn. At 90 dB, the dc receptor potential is 0.7 mV, the second harmonic 1.7 mV-peak, and the third harmonic 3.5 mV-peak. Recordings from the OC fluid space are shown in Fig. 6. In turn 4, the frequency dependence evident in the magnitude of high-level responses is similar to that in third turn (Fig. 3), i.e., inputs both above and below BF approach saturation at lower magnitudes than at BF. Consequently, the OC data obtained above BF differ from the responses recorded in nearby IHCs at 700 Hz.

III. DISCUSSION

A. Comparisons with previous results

Data collected from the basal turn of the guinea pig cochlea (Russell and Sellick, 1978; Patuzzi and Sellick, 1983; Russell *et al.*, 1986; Cody and Russell, 1987) and from the middle turn of the gerbil cochlea (Zwislocki and Chatterjee, 1995; Chatterjee and Zwislocki, 1997, 1998) indicate that more linear ac responses are measured for inputs below the BF of the IHC. In addition, at high stimulus levels, response magnitudes decrease as stimulus frequency increases, such that inputs above (below) BF achieve lower (greater) magnitudes than those at BF. This same frequency dependence is documented here in second turn for IHCs with BFs around 4000 Hz (Fig. 1, left) and for the CM response measured extracellularly in the OC fluid space (Fig. 2). An explanation for these results is offered in Fig. 7. A similar approach was used by Sellick and Russell (1979).

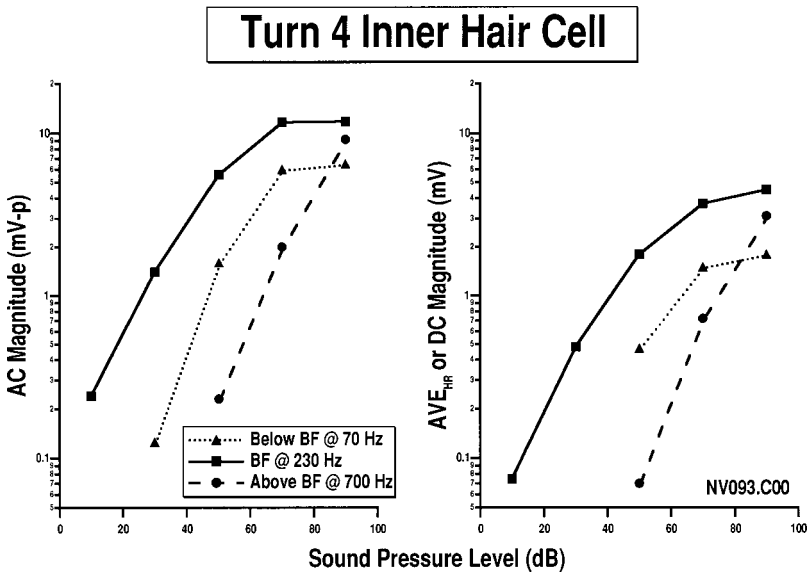

FIG. 5. Input–output functions from an IHC in turn 4 are provided for inputs below BF at 70 Hz, at BF at 230 Hz, and above BF at 700 Hz. The AVE_{HR} potential is plotted on the right-band side. The EP was +55 mV; the resting potential of the IHC, −24 mV.

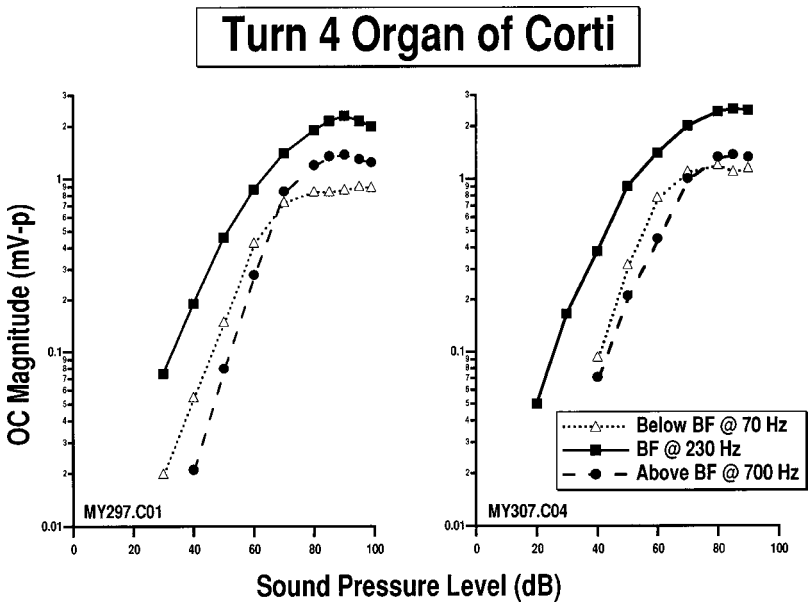

FIG. 6. Two examples of organ of Corti measurements in fourth turn are provided here. The functions are collected at the same stimulus frequencies as in Fig. 5. The EPs in these experiments were +72 mV. This value is higher than in Fig. 5 because the OC results were collected on the first penetration of the organ. In turn 4, the EP is especially vulnerable to the multiple tracks usually required to obtain hair cell recordings.

Cochlear mechanics are represented on the left-hand side of this schematic by the basilar membrane–outer hair cell–tectorial membrane (BM–OHC–TM) complex. It is assumed that nonlinear OHCs sharpen mechanical responses at low levels, via active feedback (Mountain *et al.*, 1983; Neely and Kim, 1983; de Boer, 1983). Because of this mechanical coupling, a greater gain is expressed at low levels which serves to sharpen the basilar membrane's frequency response. In order to demonstrate these level-dependent changes, high- and low-level gain functions are plotted with dotted and solid lines, respectively. The high-level measurement is plotted relative to that obtained at low levels to emphasize the changes in gain. This is achieved by using the low-level function as a reference and assigning a value of 0 dB to its peak response. The high-level function is then shifted vertically to compensate for changes in level. If this were a linear system, the two plots would superimpose. Notice, however, that large changes in gain occur around BF and that the function associated with passive, high-level responses peaks at a lower frequency. The similarity of the two functions at low and very high frequencies indicates more linear behavior observed well below and well above BF.

Measures from the OC, obtained at the output of this mechanical stage of processing, are depicted below. It is emphasized that the frequency dependence observed in the OC response cannot be explained by filtering at the OHC's basolateral membrane. This is because the CM primarily reflects OHC receptor currents and not OHC receptor potentials (Dallos and Cheatham, 1976; Russell and Sellick, 1983; Dallos and Evans, 1995). In other words, the latter, but not the former, are low-pass filtered by resistances and capacitances associated with the OHC's basolateral membrane. Consequently, the more linear responses below BF probably relate to the more linear mechanical responses seen in this frequency region (Patuzzi and Sellick, 1983). In fact, mechanical responses measured at the base of the cochlea are highly compressive (Rhode, 1971; Sellick *et al.*, 1982; Nuttall and Dolan, 1996; Ruggero *et al.*, 1997) but only around the BF of the recording location. This frequency dependence results in migration of the peak basilar-membrane response to lower frequencies as stimulus level increases.

The IHC representation on the right includes a nonlinear transducer. In this case, the set point, indicated by the sym-

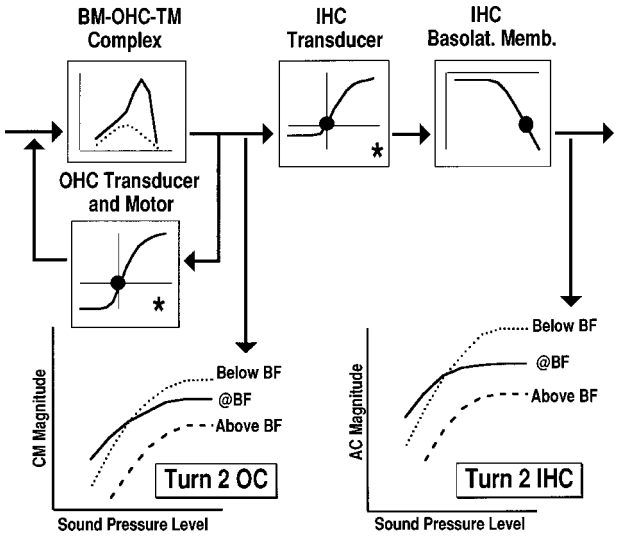

FIG. 7. This schematic illustrates input–output relationships observed in second turn and plotted in Figs. 1 and 2. It is intended to represent responses recorded from high-frequency regions of the cochlea. Mechanical input to the IHC is indicated on the left by the basilar membrane–OHC–tectorial membrane complex. The use of two bandpass filters and a nonlinear element is similar to earlier renditions (Engebretson and Eldredge, 1968; Pfeiffer, 1970). The presentation, however, has been modernized to include active OHC feedback (Mountain *et al.*, 1983; Neely and Kim, 1983; de Boer, 1983). This is indicated by the sharper mechanical response and the increase in peak frequency. In order to demonstrate the changes in gain observed with increasing level, high-level responses (dotted lines) are plotted relative to low-level responses (solid lines). The latter are shifted vertically to adjust for the change in level. The IHC is described on the right by its transducer function and by the low-pass filter associated with the cell's basolateral membrane. The symbol on the high-frequency slope of this function indicates that the BFs of cells in second turn are well above the cutoff frequency of this filter. The transfer function sketches, plotted as functions of input amplitude rather than stimulus frequency, are labeled with asterisks to lessen confusion. Generalized input–output functions at the output of the mechanical system and at the output of the IHC are shown at the bottom for frequencies below, at, and above BF. Portions of this depiction appear elsewhere (Dallos and Cheatham, 1990; Cheatham and Dallos, 1992).

bol placed at the origin, is located at a position along the transducer operating curve that produces a dc receptor potential at lower levels than for nearby OHCs. This is because IHCs in the base appear to be more asymmetrical than neighboring OHCs (Russell and Sellick, 1983; Cody and Russell, 1987). A low-pass filter associated with resistances and capacitances in the hair cell's basolateral membrane is also included. The BF of second-turn IHCs is shown by the symbol placed along the high-frequency slope of the filter function that serves to attenuate ac receptor potentials. Input–output relationships for IHCs with moderate and high BFs are summarized at the bottom. These functions for the ac receptor potential are similar to those for the CM measured extracellularly in the OC fluid space.

Although the IHC data show that the magnitude of high-level responses decreases with increasing frequency, it is not always possible to demonstrate an exaggerated frequency dependence in the IHC's ac receptor potential over and above that already exhibited in the CM which represents the mechanics. Theoretically, when the OC frequency dependence is subtracted, the reductions in magnitude associated with filtering by the IHC's basolateral membrane should remain. In other words, a decrease of 6 dB per octave should occur above the cutoff frequency at ~470 Hz (Dallos, 1983). The fact that this is difficult to demonstrate in IHC ac responses may relate to several possibilities. First, the gross CM response suffers from phase cancellation that tends to lower response magnitude as stimulus frequency increases. The CM responses at and above BF may, therefore, overestimate the decrease in magnitude observed for high-level responses. Second, the leak conductance associated with all intracellular recording serves to increase the cutoff frequency of the membrane filter (Kros and Crawford, 1990; Kros, 1996), thereby reducing differences between OC and hair cell responses at and above BF. Consequently, in our limited sample, we have only one second-turn IHC that shows a greater frequency dependence for inputs above BF than measured in the OC fluid space.

It is also acknowledged that an exaggerated frequency dependence at the IHC level would not be expected to affect single-unit activity at the base of the cochlea where the AVE_{HR} potential is dominated by the dc receptor potential. In fact, rate-intensity functions obtained for single units with high BFs are well described by models (Sachs and Abbas, 1974; Sachs *et al.*, 1989) that incorporate nonlinear cochlear mechanics and a transducer nonlinearity (Zwislocki, 1973; Schroeder and Hall, 1974). This is because filtering of the ac response at the basolateral membrane does not influence magnitude of the high-level dc responses that control transmitter release and, presumably, discharge rate. Although a few examples in the literature show that rate-intensity functions above BF saturate at lower rates than inputs at and below BF (Sachs and Abbas, 1974; Geisler *et al.*, 1974; Ruggero, 1992), Jackson and Relkin (1998) obtained additional support for these observations. Their results suggest that this behavior is probably determined by cochlear mechanics, as indicated by the schematic in Fig. 7. In fact, basilar-membrane measurements suggest that inputs above BF approach saturation at lower magnitudes than inputs at BF (Robles *et al.*, 1986; Ruggero and Rich, 1991).

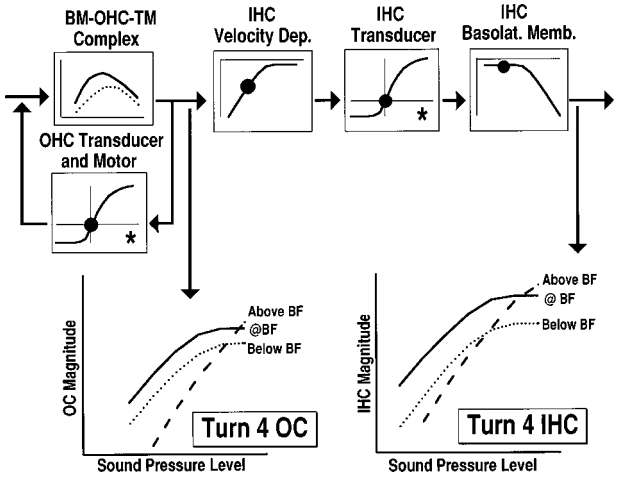

FIG. 8. This schematic is similar to that in Fig. 7 except that it is meant to describe response patterns at the extreme apex of the cochlea. The BM–OHC–TM complex is based on recordings from Reissner's membrane near the 200-Hz place in the guinea pig cochlea (Cooper and Rhode, 1995). The high-level function (dotted line) is plotted relative to the low-level function (solid line), as in Fig. 7. In other words, the graph shows relative gain as a function of frequency. In contrast to the second-turn response pattern in Fig. 7, the IHC representation includes the high-pass filter associated with the velocity dependence of the cell. Because this process is effective only below ~500 Hz, it was not included in the previous schematic. The symbol placed along the low-frequency slope indicates that the BFs of IHCs in turn 4 are below the cutoff frequency of this filter. Conversely, the symbol on the basolateral membrane function indicates that the BFs of cells in fourth turn are within the passband of this low-pass filter. As before, input–output relationships are summarized at the output of the mechanical stage and at the output of the IHC.

B. Results from the apex of the cochlea

The schematic in Fig. 7 does not explain IHC results obtained in turn 4 where more linear behavior is observed above, and not below, BF (Fig. 5). These apical responses are, therefore, modeled in Fig. 8. Mechanical measurements from the apex of the cochlea (Cooper and Rhode, 1995; Rhode and Cooper, 1996, 1997) indicate a shallow tip region and responses that are nonlinear throughout much of the response area, although to a lesser extent than in the base. This more linear mechanical behavior is indicated here by the high- and low-level gain functions, plotted with dotted and solid lines, respectively. In this schematic, the relative gain is smaller than in Fig. 7 and the high-level function peaks at a slightly higher, not a lower, frequency than does the low-level function. This behavior is representative of that observed in mechanical responses measured from Reissner's membrane at the very apex of the guinea pig cochlea where BF lies between 200 and 350 Hz. Although these measurements are from Reissner's and not the basilar membrane, Cooper and Rhode (1995) confirm von Békésy's (1960) original observation that movements of Reissner's membrane are coupled to local movements of the cochlear partition, at least at low frequencies. These mechanical measurements from Reissner's membrane, taken at the most apical recording location tested [Cooper and Rhode, 1995, Figs. 12 and 13(B)], as well as those from the reticular lamina

[Khanna and Hao, 1999, Fig. 5(B)], both exhibit steeper slopes below rather than above BF. Consequently, the data are consistent with those from single units with very low BFs (Rose *et al.*, 1971; Kiang *et al.*, 1977; Liberman and Kiang, 1978; Kiang *et al.*, 1986; Cooper and Rhode, 1995), where the tails of frequency-response functions are observed above, not below, BF. It has also been observed that the tip of the tuning curve shifts upwards in the presence of furosemide for single units with low BFs (Sewell *et al.*, 1984).

The IHC representation on the right in Fig. 8 is modified to include the velocity dependence of the IHC transducer. Due to the free-standing nature of their stereocilia (Lim, 1972), IHCs respond to basilar-membrane velocity, not basilar-membrane displacement, at low frequencies below ~500 Hz (Sellick and Russell, 1980; Nuttall *et al.*, 1981; Russell and Sellick, 1983; Dallos and Santos-Sacchi, 1983; Patuzzi and Yates, 1987). This property is depicted here by the high-pass filter at the input to the cell. Because the BFs of turn 4 IHCs, indicated by the symbol, are located along the low-frequency slope of the filter function, mechanical inputs at and below BF are reduced relative to those above BF. In contrast to responses obtained at more basal locations, the BFs of turn 4 IHCs lie within the passband of the basolateral-membrane filter, again shown by the symbol that designates BF. Consequently, attenuations due to low-pass filtering are negligible. Input–output functions predicted for turn 4 IHCs are appended below.

The schematic in Fig. 8 suggests that response magnitudes for inputs well above BF exceed those at lower frequencies because mechanical inputs are more linear in this region. This is supported by mechanical data obtained from Reissner's membrane in the guinea pig cochlea (Cooper and Rhode, 1995) and from the basilar membrane in the chinchilla cochlea (Rhode and Cooper, 1996). In the region at and below BF, a compressive nonlinearity is described. Somewhat less compressive behavior is documented in the region above BF, and well above BF, the responses are linear. If this description characterizes the mechanical input to IHCs with very low BFs, then input–output functions obtained above BF should continue to grow, even at levels where inputs at and below BF are approaching saturation. The more linear inputs above BF would be effectively coupled to the IHC because they are not attenuated by the high-pass filter associated with ciliary mechanics, i.e., by the low-frequency velocity dependence of the IHC.

If this explanation is correct, then OC responses measured at the output of the BM–OHC–TM complex should exhibit input–output relationships that are qualitatively similar to those shown for IHCs. These OC responses are indicated on the left. The frequency dependence of this turn 4 OC prediction is similar to that for the IHC except that the responses are not attenuated by high-pass filtering. This characterization differs from that measured extracellularly in turn 4 (Fig. 6), where the magnitude of high-level responses is greatest at the BF of the recording location, with responses both below and above BF approaching saturation at lower magnitudes. Although these OC responses are similar to those recorded in turn 3 (Fig. 3), they are inconsistent with the mechanical curves drawn here in Fig. 8 to represent basilar-membrane displacements at the extreme apical end of the cochlea.

This discrepancy may relate to the possibility that OC measurements at high levels do not represent mechanical responses from localized regions at the very apex of the cochlea. In fact, gross recordings pick up potentials originating from more basal locations because of the poor electrical insulation between apical turns (Békésy, 1960; Misrahy *et al.*, 1958). Mechanical responses, obtained in the chinchilla cochlea at a place with BF between 500–800 Hz, indicate that frequency-response functions are either symmetrical or asymmetrical with steeper slopes above BF. This description is compatible with measurements from turn 3 (Fig. 3). These results suggest that OC measurements in turn 4 reflect a more symmetrical mechanical filter because the gross recording electrode integrates potentials from more basal cochlear locations. In fact, turn 4 OC frequency response functions obtained at moderate and high levels display cancellation notches above BF between 400 and 500 Hz (Cheatham and Dallos, 1997). This evidence of interaction between local and remote contributions to the gross response complicates input–output relationships measured extracellularly from the OC at the apex of the cochlea. Consequently, when comparing OC (Fig. 6) and IHC (Fig. 5) input–output functions, it must be remembered that the OC function measured above BF does not necessarily reflect mechanical input to the IHC in turn 4. This is because the extracellular potential at 700 Hz is probably dominated by responses originating in turn 3.

It should be emphasized that IHC recordings from turn 4 (Dallos, 1986; Cheatham and Dallos, 1998a), as well as single-unit recordings from auditory-nerve fibers with very low BFs (Rose *et al.*, 1971; Kiang *et al.*, 1977; Liberman and Kiang, 1978; Kiang *et al.*, 1986; Cooper and Rhode, 1995), imply that cochlear mechanics at the extreme apex of the cochlea are asymmetrical but in a direction opposite to that observed at more basal cochlear locations. Although recent mechanical measurements at the apex of the guinea pig cochlea (Cooper and Rhode, 1995; Khanna and Hao, 1999) show a reverse asymmetry, their existence is foreshadowed by the long-standing neural data. The observation of steeper slopes below BF probably reflects filtering at the input to the cochlea by the middle ear. Because basilar-membrane displacement at low frequencies is proportional to stapes velocity (Dallos *et al.*, 1974), the middle-ear functions as a high-pass filter with a cutoff frequency at ~600 Hz in the guinea pig (Johnstone and Taylor, 1971; Décory *et al.*, 1990; Cooper and Rhode, 1995). This discussion suggests that basilar-membrane mechanics are probably always asymmetrical with steeper slopes above best frequency. However, filtering by the middle ear tends to eliminate the asymmetry in turn 3 and to reverse the asymmetry in turn 4 of the guinea pig cochlea.

C. Implications for cochlear models

Inner hair cell and organ of Corti data imply that frequency-dependent compression originates in cochlear mechanics and that further modifications are associated with the various stages of filtering at the IHC. The degree to which these features interact varies longitudinally along the co-

chlear partition, making it difficult to extrapolate from results recorded at only one cochlear location (Geisler and Cai, 1996). In addition, rate-intensity functions at the single-unit level depend on both spontaneous rate and duty cycle (Ohlemiller *et al.*, 1991; Relkin and Doucet, 1991), implying that the synapse between IHC and auditory-nerve dendrite can influence saturation. However, when the IHC's dc receptor potential controls transmitter release, this synaptic influence is frequency independent. Consequently, the synapse cannot account for the frequency dependence documented here at the hair cell level, especially in turn 2 where the AVE_{HR} potential is dominated by the IHC's dc receptor potential. These results suggest that cochlear models, where saturation is solely a synaptic feature (Sachs and Abbas, 1974; Sachs *et al.*, 1989; Yates, 1990), must be modified to account for the frequency dependence observed prior to the synapse, as suggested by Jackson and Relkin (1998). This is required by both the hair cell (Russell and Sellick, 1978; Russell *et al.*, 1986; Zwislocki and Chatterjee, 1995) and mechanical (Robles *et al.*, 1986; Ruggero and Rich, 1991) data.

D. Implications for intensity coding

When IHC input–output functions for the ac component, measured at the fundamental, are compared with those for the AVE_{HR} potential, the ac response can exhibit greater compression (Figs. 1 and 4). This feature may relate to the shapes of input–output functions for the dc receptor potential measured in IHCs. At low levels, these functions grow with a slope which is roughly twice the slope of the ac component. In addition, dc input–output functions show a sloping saturation when measured from IHCs with high BFs in the basal turn (Goodman *et al.*, 1982; Patuzzi and Sellick, 1983; Nuttall, 1984; Cody and Russell, 1987). This behavior is confirmed here for IHCs recorded in turn 2 (Fig. 1) and turn 3 (Figs. 3 and 4) of the guinea pig cochlea. The sloping saturation exhibited by both dc and AVE_{HR} potentials allows the input to the synapse, and presumably input to the auditory-nerve fiber, to grow with increasing level, albeit slowly (Patuzzi and Sellick, 1983; Smith *et al.*, 1983; Smith, 1988). Consequently, auditory-nerve fibers with high thresholds should be able to increase discharge rate, even at high levels. If only the ac receptor potential induces transmitter release, then nerve fibers with low spontaneous rates and high thresholds (Sachs and Abbas, 1974; Liberman, 1978; Kim and Molnar, 1979; Palmer and Evans, 1979) would not be able to process high-level BF inputs very well.

This latter possibility prompted resurrection of the early suggestion (Stevens and Davis, 1936; Steinberg and Gardner, 1937) that information must be integrated across a relatively wide extent of the cochlea in order to account for intensity coding over the entire dynamic range of hearing. In its most recent version, Chatterjee and Zwislocki (1998) suggest that this proposed integration occurs over a distance equivalent to at least 1/2 octave, basal to the BF place. This distance corresponds to ~0.75 mm in the gerbil cochlea, which is about 11 mm in length (Plassman *et al.*, 1987; Müller, 1996). This integration region represents the spatial difference between the peaks of high-(80 dB) and low-(30 dB) level iso-input functions measured for the intracellular ac response. Chatterjee and Zwislocki suggest that single units with low thresholds, and with BFs equal to the stimulus frequency, should convey information at low stimulus levels. Conversely, single units with high thresholds, and with BFs greater than the stimulus frequency, should convey information at high stimulus levels. However, if one evaluates the dc and/or AVE_{HR} potentials, this integration may not be essential for intensity coding. This suggestion is based on the following argument.

It is usually assumed that the dc receptor potential is primarily produced by asymmetries associated with the hair cell transducer and that the transducer itself exhibits soft rectifying characteristics. This behavior, originally demonstrated in bullfrog saccular hair cells (Hudspeth and Corey, 1977), has also been observed *in vivo* at the base (Russell and Sellick, 1983; Cody and Russell, 1987; Russell and Kössl, 1991) and apex (Dallos and Cheatham, 1989) of the guinea pig cochlea, as well as *in vitro* in the cultured mouse organ of Corti (Kros *et al.*, 1995) and in chick vestibular hair cells (Ohmori, 1987). In order to demonstrate similarities among hair cell transducer functions, a selection is provided in Fig. 9 to facilitate comparisons. In this figure, the data are normalized by plotting all values relative to the peak depolarizing response, which is given a value of 1.0. The abscissa has also been normalized because some data are obtained from *in vitro* preparations (Hudspeth and Corey, 1977; Ohmori, 1987; Kros *et al.*, 1995), where the input is displacement of the hair bundle, while others are taken from *in vivo* preparations (Crawford and Fettiplace, 1981; Russell and Sellick, 1983; Cheatham and Dallos, 1999) where the input is sound pressure in pascals. It is emphasized that functions obtained from *in vivo* guinea pig preparations were measured at frequencies well below BF to avoid being influenced by preceding mechanical nonlinearities (Rhode, 1971; Sellick *et al.*, 1982; Nuttall and Dolan, 1996; Ruggero *et al.*, 1997). Although all functions are asymmetrical, only the negative, hyperpolarizing potentials exhibit hard saturation. The positive, depolarizing responses approach saturation but much more gradually.

It is acknowledged that only the curves obtained from neonatal mouse OHCs and from chick vestibular hair cells are true transducer functions. For these, receptor currents were measured in response to displacement of the hair bundle. In all other examples, receptor potentials were recorded. Because of the overall similarity of the functions (Hudspeth, 1983), contributions by voltage- and time-dependent ion channels in the hair cell's basolateral membrane appear to be minimal. This possibility probably reflects the leak associated with all microelectrode recordings (Kros and Crawford, 1990; Kros, 1996). Consequently, additional distortions associated with ion-channel kinetics will also influence postsynaptic activity. Taken together, the soft rectification apparent in the hair cell transducer and the nonlinearities associated with channel activity should allow AVE_{HR} and/or dc receptor potentials to grow slowly with increasing level. This is demonstrated in Fig. 10, where AVE_{HR} potentials obtained near BF are plotted for IHCs in turns 2, 3, and 4. Because the logarithmic scale makes it difficult to see

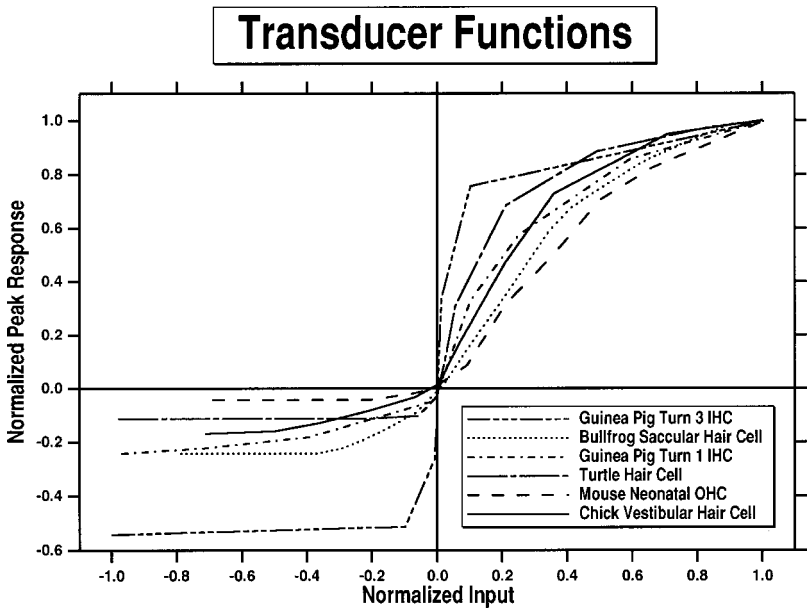

FIG. 9. Transducer functions are plotted on normalized axes to facilitate comparisons of sensory transducers in a variety of preparations. The *in vivo* results are from guinea pig turn 3 (Cheatham and Dallos, 1999) and turn 1 (Russell and Sellick, 1983), and from the turtle cochlea (Crawford and Fettiplace, 1981). The *in vitro* data represent vestibular hair cells from bullfrog (Hudspeth and Corey, 1977) and chick (Ohmori, 1987), as well as cochlear outer hair cells from a neonatal organ culture in the mouse (Kros *et al.*, 1995). Only the chick and mouse results, however, provide true transducer functions. In all other preparations the receptor potential, rather than the receptor current, was measured. Consequently, these data are better described as pseudotransducer functions to acknowledge contributions from the cell's basolateral membrane and, for results recorded in turn 3, from nonlinearities present at the input to the cell (Dallos and Cheatham, 1989). Some of the data for Fig. 9 were obtained on a PC equipped with WINDOWS 95 and using IPHOTOPLUS (version 1.2, Ulead Systems, Inc.) to scan the original graphs on a Mustek scanner (model 600 11 CD). A cursor was then moved along the scanned functions to obtain a sufficient number of data points so that the curves could be reconstructed. This was accomplished using DIGIMATIC software (version 2.0, FEB, Inc.).

small changes in magnitude, these functions are plotted on a linear ordinate to visualize growth at high levels. This idea was suggested by Goodman *et al.* (1982) because discharge rates recorded in auditory-nerve fibers are plotted on a linear scale. Notice that all input–output functions increase with increasing level and saturation is not observed, even at 90 dB.

Another feature should also be considered when evaluating dynamic range at the IHC level. Patuzzi and Sellick (1983) suggested that mechanical input to the IHC may not saturate the transducer because of compression in the basilar-membrane response around BF (Rhode, 1971; Sellick *et al.*, 1982; Nuttall and Dolan, 1996; Ruggero *et al.*, 1997). In this region, basilar-membrane displacement grows ~0.2 dB/dB (Ruggero *et al.*, 1997), implying that the mechanical nonlinearity determines cochlear dynamic range (Yates *et al.*, 1990). This idea is reminiscent of the gain-control mechanism originally offered by Rose *et al.* (1971) and given a mechanical basis in the nonlinear basilar-membrane model of Kim *et al.* (1973). Taken together, the soft rectification inherent in the transducer and the compressed mechanical input to the IHC could allow dc and/or AVE_{HR} potentials to grow slowly with increasing level (Goodman *et al.*, 1982; Smith *et al.*, 1983; Nuttall, 1984; Cody and Russell, 1987). In fact, the sloping saturation observed at high levels in auditory-nerve fibers with high thresholds (Sachs and Abbas, 1974; Palmer and Evans, 1979; Winter *et al.*, 1990; Winter and Palmer, 1991; Zagaeski *et al.*, 1994) may relate to the sloping saturation documented in the IHC's dc receptor potential (Goodman *et al.*, 1982; Patuzzi and Sellick, 1983; Nuttall, 1984; Cody and Russell, 1987). It is acknowledged that magnitude notches have been observed in dc input–output functions at high levels, usually above 90 dB (Dallos and Cheatham, 1989; Cheatham and Dallos, 1998b). Although these nonmonotonicities are not a consistent feature of rate-intensity functions recorded from hair cells or from single units in the auditory nerve (McGee *et al.*, 1982; Liberman and Kiang, 1984; Kiang *et al.*, 1986; Ruggero and Rich, 1989; Cai and Geisler, 1996), the implications for intensity coding suggested here should not be generalized to higher level inputs above ~90 dB.

The intracellular data reported here and elsewhere suggest that IHC input–output relationships can accommodate single units that differ in threshold and dynamic range (Liberman, 1978; Palmer and Evans, 1979; Winslow and Sachs, 1988; Winter and Palmer, 1991), as suggested by Patuzzi and Sellick (1983) and by Smith *et al.* (1983). In other words, rate information from a small pool of auditory-nerve fibers may provide the primary code for intensity discrimination (Delgutte, 1987; Viemeister, 1988). This explanation is consistent with psychophysical data on the perception of loudness, where spread of excitation is not critical for maintaining performance at high sound levels (Viemeister, 1974, 1983; Moore and Raab, 1974; Hellman, 1978). One should not assume, however, that the spread of excitation, which increases the number of responding nerve fibers, is unimportant. In fact, this secondary mechanism may be useful at high levels (Carlyon and Moore, 1984; Viemeister and Bacon, 1988; Relkin and Doucet, 1997), especially in the basal half of the cochlea where temporal processing of signals near BF is not possible. The nonlinear spread of excitation, as well as the ability of subjects to

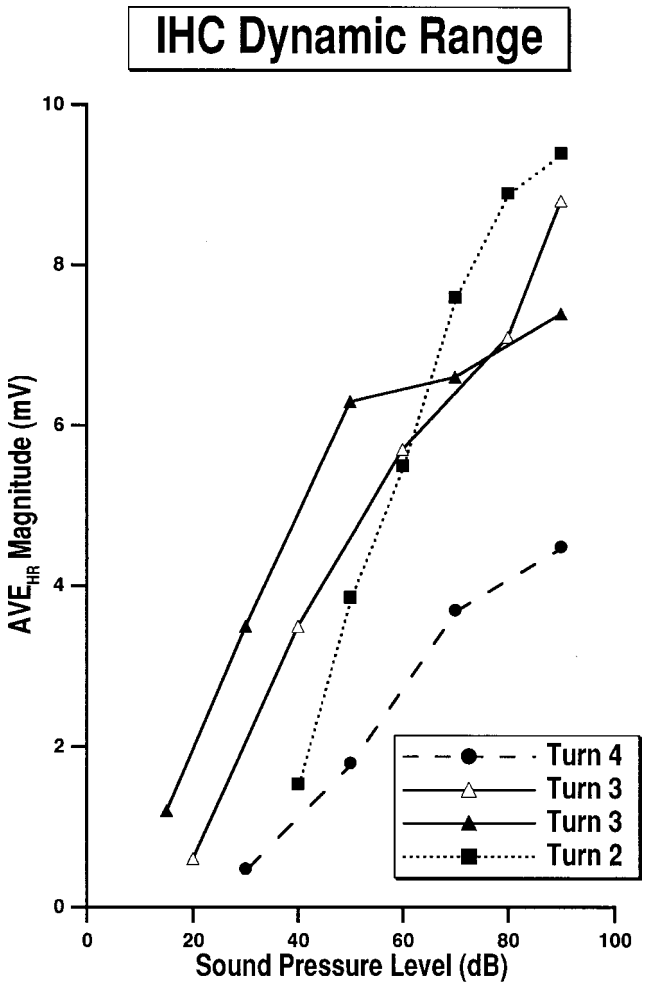

FIG. 10. Input–output functions are plotted for the AVE_{HR} potential computed near BF for four IHCs. The results from turn 2 are replotted from Fig. 1 (3800 Hz), those from turn 3, from Figs. 3 (800 Hz) and 4 (900 Hz), and those from turn 4, from Fig. 5 (230 Hz). In this graph, however, the data are presented on a linear ordinate to emphasize response changes at high levels.

utilize information from different regions within the excitation pattern (Florentine and Buus, 1981), may well explain the near miss to Weber's law, i.e., the relative improvement in intensity discrimination observed at high levels (see Moore, 1989).

ACKNOWLEDGMENTS

This work was supported (in part) by Research Grant No. 5 R01 DC00089 from the National Institute on Deafness and Other Communicative Disorders, the National Institutes of Health. Gulam Emadi is gratefully acknowledged for writing the computer software that allows the AVE_{HR} potential to be computed. We also appreciate comments on the manuscript by Neal Viemeister, Monita Chatterjee, and an anonymous reviewer.

Allen, J. B. (**1983**). ''A hair cell model of neural response,'' in *Mechanics of Hearing*, edited by E. de Boer and M. A. Viergever (Delft University Press, Delft, The Netherlands), pp. 193–202.

Baden-Kristensen, K., and Weiss, T. F. (**1983**). ''Receptor potentials of lizard hair cells with free-standing stereocilia: Responses to acoustic clicks,'' J. Physiol. (London) **335**, 699–721.

Brugge, J. F., Anderson, D. J., Hind, J. E., and Rose, J. E. (**1969**). ''Time structure of discharges in single auditory nerve fibers of the squirrel monkey in response to complex periodic sounds,'' J. Neurophysiol. **32**, 386–401.

Cai, Y., and Geisler, C. D. (**1996**). ''Temporal patterns of the responses of auditory-nerve fibers to low-frequency tones,'' Hear. Res. **96**, 83–93.

Carlyon, R. P., and Moore, B. C. J. (**1984**). ''Intensity discrimination: A severe departure from Weber's law,'' J. Acoust. Soc. Am. **76**, 1369–1376.

Chatterjee, M., and Zwislocki, J. J. (**1997**). ''Cochlear mechanisms of intensity and frequency coding. I. The place code for pitch,'' Hear. Res. **111**, 65–75.

Chatterjee, M., and Zwislocki, J. J. (**1998**). ''Cochlear mechanisms of frequency and intensity coding. II. Dynamic range and the code for loudness,'' Hear. Res. **124**, 170–181.

Cheatham, M. A., and Dallos, P. (**1992**). ''Physiological correlates of off-frequency listening,'' Hear. Res. **59**, 39–45.

Cheatham, M. A., and Dallos, P. (**1993**). ''Longitudinal comparisons of IHC ac and dc receptor potentials recorded from the guinea pig cochlea,'' Hear. Res. **68**, 107–114.

Cheatham, M. A., and Dallos, P. (**1997**). Unpublished results.

Cheatham, M. A., and Dallos, P. (**1998a**). ''Auditory filter shape: implications from IHC recordings,'' in *Psychophysical and Physiological Advances in Hearing*, edited by A. R. Palmer, A. Rees, A. Q. Summerfield, and R. Meddis (Whurr, London), pp. 73–80.

Cheatham, M. A., and Dallos, P. (**1998b**). ''The level dependence of response phase: Observations from cochlear hair cells,'' J. Acoust. Soc. Am. **104**, 356–369.

Cheatham, M. A., and Dallos, P. (**1999**). ''Contributions by inner and outer hair cells to the summating potential,'' Abs. Assoc. Res. Otolaryngol, pp. 182–183.

Cody, A. R., and Russell, I. J. (**1987**). ''The responses of hair cells in the basal turn of the guinea-pig cochlea to tones,'' J. Physiol. (London) **383**, 551–569.

Cooper, N. P., and Yates, G. K. (**1994**). ''Nonlinear input–output functions derived from the responses of guinea-pig cochlear nerve fibers: Variations with characteristic frequency,'' Hear. Res. **78**, 221–234.

Cooper, N. P., and Rhode, W. S. (**1995**). ''Nonlinear mechanics at the apex of the guinea-pig cochlea,'' Hear. Res. **82**, 225–243.

Crawford, A. C., and Fettiplace, R. (**1981**). ''Non-linearities in the responses of turtle hair cells,'' J. Physiol. (London) **315**, 317–338.

Dallos, P. (**1973**). *The Auditory Periphery* (Academic, New York).

Dallos, P. (**1983**). ''Some electrical circuit properties of the organ of Corti: I. Analysis without reactive elements,'' Hear. Res. **12**, 89–119.

Dallos, P. (**1985a**). ''Response characteristics of mammalian cochlear hair cells,'' J. Neurosci. **5**, 1591–1608.

Dallos, P. (**1985b**). ''Membrane potentials and response changes in mammalian cochlear hair cells during intracellular recording,'' J. Neurosci. **5**, 1609–1615.

Dallos, P. (**1986**). ''Neurobiology of cochlear inner and outer hair cells: Intracellular recordings,'' Hear. Res. **22**, 185–198.

Dallos, P., and Cheatham, M. A. (**1976**). ''Production of cochlear potentials by inner and outer hair cells,'' J. Acoust. Soc. Am. **60**, 510–512.

Dallos, P., and Cheatham, M. A. (**1989**). ''Nonlinearities in cochlear receptor potentials and their origins,'' J. Acoust. Soc. Am. **86**, 1790–1796.

Dallos, P., and Cheatham, M. A. (**1990**). ''Effects of electrical polarization on inner hair cell receptor potentials,'' J. Acoust. Soc. Am. **87**, 1636–1647.

Dallos, P., and Evans, B. N. (**1995**). ''High-frequency motility of outer hair cells and the cochlear amplifier,'' Science **267**, 2006–2009.

Dallos, P., and Santos-Sacchi, J. (**1983**). ''AC receptor potentials from hair cells in the low-frequency region of the guinea pig cochlea,'' in *Mechanisms of Hearing*, edited by W. R. Webster and L. M. Aitkin (Monash University Press, Clayton, Australia), pp. 11–16.

Dallos, P., Cheatham, M. A., and Ferraro, J. (**1974**). ''Cochlear mechanics, nonlinearities, and cochlear potentials,'' J. Acoust. Soc. Am. **55**, 597–605.

Dallos, P., Santos-Sacchi, J., and Flock, Å (**1982**). ''Intracellular recordings from cochlear outer hair cells,'' Science **218**, 582–584.

Dancer, A., and Franke, R. (**1980**). ''Intracochlear sound pressure measurements in guinea pig,'' Hear. Res. **2**, 191–205.

Davis, H. (**1957**). ''Biophysics and physiology of the inner ear,'' Physiol. Rev. **37**, 1–49.

de Boer, E. (**1983**). ''No sharpening? A challenge to cochlear mechanic,'' J. Acoust. Soc. Am. **7**, 567–573.

Décory, L., Franke, R. B., and Dancer, A. L. (**1990**). ''Measurement of

eardrum acoustic impedance,'' in *The Mechanics and Biophysics of Hearing*, edited by P. Dallos, C. Geisler, J. Matthews, M. Ruggero, and C. Steele (Springer, New York), pp. 270–277.
Delgutte, B. (**1987**). ''Peripheral auditory processing of speech information: Implications from a physiological study of intensity discrimination,'' in *The Psychophysics of Speech Perception*, edited by M. E. H. Schouten and M. Nijhof (Dordrecht, The Netherlands), pp. 333–353.
Engebretson, A. M., and Eldredge, D. H. (**1968**). ''Model for the nonlinear characteristics of cochlear potentials,'' J. Acoust. Soc. Am. **44**, 548–554.
Florentine, M., and Buus, S. (**1981**). ''An excitation-pattern model for intensity discrimination,'' J. Acoust. Soc. Am. **70**, 1646–1654.
Geisler, C. D., and Cai, Y. (**1996**). ''Relationships between frequency-tuning and spatial-tuning curves in the mammalian cochlea,'' J. Acoust. Soc. Am. **99**, 1550–1555.
Geisler, C. D., Rhode, W. S., and Kennedy, D. T. (**1974**). ''Responses to tonal stimuli of single auditory nerve fibers and their relationship to basilar membrane motion in the squirrel monkey,'' J. Neurophysiol. **37**, 1156–1172.
Goodman, D. A., Smith, R. L., and Chamberlain, S. C. (**1982**). ''Intracellular and extracellular responses in the organ of Corti of the gerbil,'' Hear. Res. **7**, 161–169.
Hellman, R. P. (**1978**). ''Dependence of loudness growth on skirts of excitation patterns,'' J. Acoust. Soc. Am. **63**, 1114–1119.
Hudspeth, A. J. (**1983**). ''Mechanoelectrical transduction by hair cells in the acousticolateralis sensory system,'' Annu. Rev. Neurosci. **6**, 187–215.
Hudspeth, A. J., and Corey, D. P. (**1977**). ''Sensitivity, polarity and conductance changes in the responses of vertebrate hair cells to controlled mechanical stimuli,'' Proc. Natl. Acad. Sci. USA **74**, 2407–2411.
Jackson, B. S., and Relkin, E. M. (**1998**). ''A frequency-dependent saturation evident in rate-intensity functions of the chinchilla auditory nerve,'' Hear. Res. **126**, 75–83.
Johnstone, B. M., and Taylor, K. J. (**1971**). ''Physiology of the middle ear transmission system,'' J. Otolaryngol. Soc. Aust. **3**, 226–228.
Khanna, S. M., and Hao, L. F. (**1999**). ''Reticular lamina vibrations in the apical turn of a living guinea pig cochlea,'' Hear. Res. **132**, 15–33.
Kiang, N. Y.-s. (**1984**). ''Peripheral neural processing of auditory information,'' in *Handbook of Physiology, The Nervous System*, edited by I. Darian-Smith (American Physiological Society, Bethesda, MD), Vol. 3, pp. 639–674.
Kiang, N. Y.-s., and Peake, W. T. (**1960**). ''Components of electrical responses recorded from the cochlea,'' Ann. Otol. Rhinol. Laryngol. **69**, 448–459.
Kiang, N. Y.-s., Liberman, M. C., and Baer, T. (**1977**). ''Tuning curves of auditory nerve fibers,'' J. Acoust. Soc. Am. **61**, S27.
Kiang, N. Y.-s., Liberman, M. C., Sewell, W. F., and Guinan, J. J. (**1986**). ''Single unit clues to cochlear mechanisms,'' Hear. Res. **22**, 171–182.
Kim, D. O., and Molnar, C. E. (**1979**). ''A population study of cochlear nerve fibers: Comparisons of spatial distributions of average rate and phase-locking measures of responses to single tones,'' J. Neurophysiol. **42**, 16–30.
Kim, D. O., Molnar, C. E., and Pfeiffer, R. R. (**1973**). ''A system of nonlinear differential equations modeling basilar-membrane motion,'' J. Acoust. Soc. Am. **54**, 1517–1529.
Kros, C. J. (**1996**). ''Physiology of mammalian cochlear hair cells,'' in *The Cochlea*, edited by P. Dallos, A. N. Popper, and R. R. Fay (Springer, New York), pp. 318–385.
Kros, C. J., and Crawford, A. C. (**1990**). ''Potassium currents in inner hair cells isolated from the guinea-pig cochlea,'' J. Physiol. (London) **421**, 263–291.
Kros, C. J., Lennon, G. W. T., and Richardson, G. P. (**1995**). ''Transducer currents and bundle movements in outer hair cells of neonatal mice,'' in *Active Hearing*, edited by Å. Flock, D. Ottoson, and M. Ulfendahl (Elsevier Science, Oxford), pp. 113–125.
Liberman, M. C. (**1978**). ''Auditory nerve responses from cats raised in a low-noise chamber,'' J. Acoust. Soc. Am. **63**, 442–455.
Liberman, M. C., and Kiang, N. Y.-s. (**1978**). ''Acoustic trauma in cats: Cochlear pathology and auditory nerve activity,'' Acta Oto-Laryngol. Suppl. **358**, 1–63.
Liberman, M. C., and Kiang, N. Y.-s. (**1984**). ''Single neuron labelling and chronic cochlear pathology. IV. Stereocilia damage and alterations in rate- and level-functions,'' Hear. Res. **16**, 75–90.
Lim, D. (**1972**). ''Fine morphology of the tectorial membrane: Its relationship to the organ of Corti,'' Acta Oto-Laryngol. **96**, 199–215.
McGee, J., Walsh, E. J., Gorga, M. P., Farley, G. R., and Javel, E. (**1982**). ''Population study of nonmonotonic response-intensity curves in auditory nerve fibers,'' J. Acoust. Soc. Am. **71**, S18.
Misrahy, G. A., Hildreth, K. M., Shinabarger, E. W., and Gannon, W. J. (**1958**). ''Electrical properties of wall of endolymphatic space of the cochlea (guinea pig),'' Am. J. Physiol. **194**, 396–402.
Moore, B. C. J. (**1989**). *An Introduction to the Psychology of Hearing* (Academic, London).
Moore, B. C. J., and Raab, D. H. (**1974**). ''Pure-tone intensity discrimination: Some experiments relating to the 'near miss' of Weber's law,'' J. Acoust. Soc. Am. **55**, 1049–1054.
Mountain, M. C., Hubbard, A. E., and McMullen, T. A. (**1983**). ''Electromechanical processes in the cochlea,'' in *Mechanics of Hearing*, edited by E. de Boer and M. A. Viergever (Delft University Press, Delft, The Netherlands), pp. 119–126.
Müller, M. (**1996**). ''The cochlear place-frequency map of the adult and developing mongolian gerbil,'' Hear. Res. **94**, 148–156.
Narayan, S. S., Temchin, A. N., Reccio, A., and Ruggero, M. A. (**1998**). ''Frequency tuning of basilar membrane and auditory nerve fibers in the same cochlea,'' Science **282**, 1882–1884.
Nedzelnitsky, V. (**1974**). ''Measurement of sound pressure in the cochlea of anesthetized cat,'' in *Facts and Models in Hearing*, edited by E. Zwicker and E. Terhardt (Springer, Berlin), pp. 45–53.
Neely, S. T., and Kim, D. O. (**1983**). ''An active cochlear model showing sharp tuning and high sensitivity,'' Hear. Res. **9**, 123–130.
Nuttall, A. L. (**1984**). ''Dynamic aspects of guinea pig inner hair cell receptor potentials with transient asphyxia,'' Hear. Res. **16**, 1–16.
Nuttall, A. L., and Dolan, D. F. (**1996**). ''Steady-state sinusoidal velocity responses of the basilar membrane in guinea pig,'' J. Acoust. Soc. Am. **99**, 1556–1565.
Nuttall, A. L., Brown, M. C., Masta, R. I., and Lawrence, M. (**1981**). ''Inner hair cell responses to velocity of basilar membrane motion in the guinea pig,'' Brain Res. **211**, 171–174.
Ohlemiller, K. K., Echteler, S. M., and Siegel, J. H. (**1991**). ''Factors that influence rate-versus intensity relations in single cochlear nerve fibers of the gerbil,'' J. Acoust. Soc. Am. **90**, 274–287.
Ohmori, H. (**1987**). ''Gating properties of the mechano-electrical transducer channel in the dissociated vestibular hair cell of the chick,'' J. Physiol. (London) **387**, 589–609.
Palmer, A. R., and Evans, E. F. (**1979**). ''On the peripheral coding of the level of individual frequency components of complex sounds at high sound levels,'' Exp. Brain Res. **2**, 19–26.
Patuzzi, R., and Sellick, P. M. (**1983**). ''A comparison between basilar membrane and inner hair cell receptor potential input–output functions in the guinea pig cochlea,'' J. Acoust. Soc. Am. **74**, 1734–1741.
Patuzzi, R. B., and Yates, G. K. (**1987**). ''The low-frequency response of inner hair cells in the guinea pig cochlea: Implications for fluid coupling and resonance of the stereocilia,'' Hear. Res. **30**, 83–98.
Pfeiffer, R. R. (**1970**). ''A model for two-tone inhibition of single cochlear nerve fibers,'' J. Acoust. Soc. Am. **48**, 1373–1378.
Plassman, W., Peetz, W., and Schmidt, M. (**1987**). ''The cochlea in gerbilline rodents,'' Brain Behav. Ecol. **30**, 82–101.
Relkin, E. M., and Doucet, J. R. (**1991**). ''Recovery from prior stimulation. I. Relationship to spontaneous firing rates of primary auditory neurons,'' Hear. Res. **51**, 215–230.
Rhode, W. S. (**1971**). ''Observations of the vibration of the basilar membrane in squirrel monkeys using Mössbauer technique,'' J. Acoust. Soc. Am. **49**, 1218–1231.
Rhode, W. S., and Cooper, N. P. (**1996**). ''Nonlinear mechanics in the apical turn of the chinchilla cochlea *in vivo*,'' Aud. Neurosci. **3**, 101–121.
Rhode, W. S., and Cooper, N. P. (**1997**). ''Nonlinear mechanisms in the apical turn of the chinchilla cochlea,'' in *Diversity in Auditory Mechanics*, edited by E. R. Lewis, G. R. Long, R. F. Lyon, P. M. Narins, C. R. Steele, and E. Hecht-Poinar (World Scientific, Singapore), pp. 318–324.
Robles, L., Ruggero, M. A., and Rich, N. C. (**1986**). ''Basilar membrane mechanics at the base of the chinchilla cochlea. I. Input–output functions, tuning curves, and response phases,'' J. Acoust. Soc. Am. **80**, 1364–1374.
Rose, J. E., Hind, J. E., Anderson, D. J., and Brugge, J. F. (**1971**). ''Some effects of stimulus intensity on response of auditory nerve fibers in the squirrel monkey,'' J. Neurophysiol. **34**, 685–699.
Ruggero, M. A. (**1992**). ''Physiology and coding of sound in the auditory nerve,'' in *The Physiology of the Mammalian Auditory CNS*, edited by R. Fay and A. N. Popper (Springer, New York), pp. 34–92.
Ruggero, M. A., and Rich, N. C. (**1989**). ''Peak-splitting: Intensity effects in cochlear afferent responses to low frequency tones,'' in *Cochlear*

Mechanisms—Structure, Function and Models, edited by J. P. Wilson and D. T. Kemp (Plenum, London), pp. 259–266.
Ruggero, M. A., and Rich, N. C. (**1991**). ''Application of a commercially-manufactured Doppler-shift laser velocimeter to the measurement of basilar-membrane vibration,'' Hear. Res. **51**, 215–230.
Ruggero, M. A., Rich, N. C., Recio, A., and Narayan, S. S. (**1997**). ''Basilar membrane responses to tones at the base of the chinchilla cochlea,'' J. Acoust. Soc. Am. **101**, 2151–2163.
Russell, I. J., and Sellick, P. M. (**1978**). ''Intracellular studies of hair cells in the guinea pig cochlea,'' J. Physiol. (London) **284**, 261–290.
Russell, I. J., and Sellick, P. M. (**1983**). ''Low-frequency characteristics of intracellularly recorded receptor-potentials in guinea-pig cochlear hair cells,'' J. Physiol. (London) **338**, 179–206.
Russell, I. J., and Kössl, M. (**1991**). ''The voltage responses of hair cells in the basal turn of the guinea-pig cochlea,'' J. Physiol. (London) **435**, 493–511.
Russell, I. J., Cody, A. R., and Richardson, G. P. (**1986**). ''The responses of inner and outer hair cells in the basal turn of the guinea-pig cochlea and in the mouse cochlea grown *in vitro*,'' Hear. Res. **22**, 199–216.
Sachs, M. B., and Abbas, P. J. (**1974**). ''Rate versus level functions for auditory-nerve fibers in cats: Tone burst stimuli,'' J. Acoust. Soc. Am. **56**, 1835–1847.
Sachs, M. B., Winslow, R. L., and Sokolowski, B. H. A. (**1989**). ''A computational model for rate-level functions from cat auditory-nerve fibers,'' Hear. Res. **41**, 61–69.
Schmiedt, R. A., and Zwislocki, J. J. (**1978**). ''Low frequency neural and cochlear-microphonic tuning curves in the gerbil,'' J. Acoust. Soc. Am. **64**, 502–507.
Schroeder, M. R., and Hall, J. L. (**1974**). ''Model for mechanical to neural transduction in the auditory receptor,'' J. Acoust. Soc. Am. **55**, 1055–1060.
Sellick, P. M., and Russell, I. J. (**1979**). ''Two-tone suppression in cochlear hair cell,'' Hear. Res. **1**, 227–236.
Sellick, P. M., and Russell, I. J. (**1980**). ''Responses of inner hair cells to basilar membrane velocity during low frequency auditory stimulation in the guinea pig cochlea,'' Hear. Res. **2**, 439–446.
Sellick, P. M., Patuzzi, R., and Johnstone, B. M. (**1982**). ''Measurement of basilar membrane motion in the guinea pig using the Mössbauer technique,'' J. Acoust. Soc. Am. **72**, 131–141.
Sewell, W. F. (**1984**). ''The effects of furosemide on the endocochlear potential and auditory-nerve fiber tuning curves in cats,'' Hear. Res. **14**, 305–314.
Smith, R. L. (**1988**). ''Encoding of sound intensity by auditory neurons,'' in: *Auditory Function*, edited by G. M. Edelman, W. E. Gall, and W. M. Cowan (John Wiley and Sons, Inc., New York), pp. 243–274.
Smith, R. L., and Brachman, M. L. (**1982**). ''Adaptation in auditory nerve fibers: A revised model,'' Biol. Cybern. **44**, 107–129.
Smith, R. L., Frisina, R. D., and Goodman, D. A. (**1983**). ''Intensity functions and dynamic responses from the cochlea to the cochlear nucleus,'' in *Hearing—Physiological Bases and Psychophysics*, edited by R. Klinke and R. Hartmann (Springer, Berlin), pp. 112–118.
Steinberg, J. C., and Gardner, M. B. (**1937**). ''The dependence of hearing impairment on sound intensity,'' J. Acoust. Soc. Am. **9**, 11–23.
Stevens, S. S., and Davis, H. (**1936**). ''Psychophysical acoustics: Pitch and loudness,'' J. Acoust. Soc. Am. **8**, 1–13.
Viemeister, N. F. (**1974**). ''Intensity discrimination of noise in the presence of band-reject noise,'' J. Acoust. Soc. Am. **56**, 1594–1600.
Viemeister, N. F. (**1983**). ''Auditory intensity discrimination at high frequencies in the presence of noise,'' Science **221**, 1206–1208.
Viemeister, N. F. (**1988**). ''Intensity coding and the dynamic range problem,'' Hear. Res. **34**, 267–274.
Viemeister, N. F., and Bacon, S. P. (**1988**). ''Intensity discrimination, increment detection, and magnitude estimation for 1-kHz tones,'' J. Acoust. Soc. Am. **84**, 172–178.
Von Békésy, G. (**1960**). *Experiments in Hearing* (McGraw-Hill, New York).
Winslow, R. L., and Sachs, M. B. (**1988**). ''Single-tone intensity discrimination based on auditory nerve rate responses in backgrounds of quiet, noise and stimulation of the crossed olivocochlear bundle,'' Hear. Res. **35**, 165–190.
Winter, I. M., and Palmer, A. R. (**1991**). ''Intensity coding in low-frequency auditory-nerve fibers of the guinea pig,'' J. Acoust. Soc. Am. **90**, 1958–1967.
Winter, I. M., Robertson, D., and Yates, G. K. (**1990**). ''Diversity of characteristic frequency rate-intensity functions in guinea pig auditory nerve fibers,'' Hear. Res. **45**, 191–202.
Yates, G. K. (**1990**). ''Basilar membrane nonlinearity and its influence on auditory nerve rate-intensity functions,'' Hear. Res. **45**, 203–219.
Yates, G. K., Winter, I. M., and Robertson, D. (**1990**). ''Basilar membrane nonlinearity determines auditory nerve rate-intensity functions and cochlea dynamic range,'' Hear. Res. **45**, 203–219.
Zagaeski, M., Cody, A. R., Russell, I. J., and Mountain, D. C. (**1994**). ''Transfer characteristics of the inner hair cell synapse: Steady-state analysis,'' J. Acoust. Soc. Am. **95**, 3430–3434.
Zwislocki, J. J. (**1973**). ''On intensity characteristics of sensory receptors: A generalized function,'' Kybernetik **12**, 169–183.
Zwislocki, J. J., and Chatterjee, M. (**1995**). ''On the neural code for loudness and its cochlear correlates,'' in *Advances in Hearing Research*, edited by G. A. Manley, G. M. Klump, C. Köppl, H. Fastl, and H. Oeckinghaus (World Scientific, London), pp. 241–249.

Mathematical modeling of vowel perception by users of analog multichannel cochlear implants: Temporal and channel-amplitude cues

Mario A. Svirsky
Department of Otolaryngology-HNS, Indiana University School of Medicine, 702 Barnhill Drive RR-044, Indianapolis, Indiana 46202-5200

(Received 22 March 1999; revised 6 July 1999; accepted 18 October 1999)

A ''multidimensional phoneme identification'' (MPI) model is proposed to account for vowel perception by cochlear implant users. A multidimensional extension of the Durlach–Braida model of intensity perception, this model incorporates an internal noise model and a decision model to account separately for errors due to poor sensitivity and response bias. The MPI model provides a complete quantitative description of how listeners encode and combine acoustic cues, and how they use this information to determine which sound they heard. Thus, it allows for testing specific hypotheses about phoneme identification in a very stringent fashion. As an example of the model's application, vowel identification matrices obtained with synthetic speech stimuli (including ''conflicting cue'' conditions [Dorman *et al.*, J. Acoust. Soc. Am. **92**, 3428–3432 (1992)] were examined. The listeners were users of the ''compressed-analog'' stimulation strategy, which filters the speech spectrum into four partly overlapping frequency bands and delivers each signal to one of four electrodes in the cochlea. It was found that a simple model incorporating one temporal cue (i.e., an acoustic cue based only on the time waveforms delivered to the most basal channel) and spectral cues (based on the distribution of amplitudes among channels) can be quite successful in explaining listener responses. The new approach represented by the MPI model may be used to obtain useful insights about speech perception by cochlear implant users in particular, and by all kinds of listeners in general. [S0001-4966(00)00302-7]

PACS numbers: 43.64.Me, 43.66.Ba, 43.71.Es, 43.71.Cq [RVS]

INTRODUCTION

Cochlear implants (CIs) are extremely helpful to postlingually deafened listeners. These devices are excellent sensory aids to lipreading, and many patients obtain enough phonetic information from their devices to achieve significant levels of auditory-only, open-set word recognition. However, the range of speech perception performance shown by cochlear implant users remains wide, and even users who perform relatively well may benefit from alternative speech processing strategies (Wilson *et al.*, 1991). Unfortunately, our basic understanding of the sensory, perceptual, and cognitive mechanisms CI users employ to perceive speech still lags behind the substantial clinical benefit that postlingually deafened adults with CIs obtain with their devices. In particular, we do not know the exact combination of acoustic dimensions that are employed by CI users to understand speech, how sensory information about the different acoustic dimensions is represented and combined, and how that information is used to perform speech identification. These questions are important for two reasons. From a clinical standpoint, increased basic knowledge of the perceptual mechanisms employed by CI users will likely result in better ways to help them understand speech, and to guide the search for better speech processing strategies. In addition, knowledge about how listeners with an impoverished input signal (such as that provided by a CI) understand speech may shed light on the perceptual mechanisms used by listeners with normal hearing.

Stimulation strategies for cochlear implants are frequently classified according to the type of waveform delivered by the device. Although most CI users today use pulsatile stimulation strategies, the use of analog strategies (in particular the simultaneous analog stimulation or SAS strategy, as implemented in the Clarion device, manufactured by Advanced Bionics Corp. in Sylmar, CA) is on the rise. Subjects in this study were users of the compressed analog (CA) stimulation strategy, which is very similar to SAS and has been used successfully to provide substantial speech perception to postlingually deaf subjects with multichannel cochlear implants. Figure 1 illustrates how the CA stimulation strategy is implemented in the Ineraid multichannel CI. The incoming speech signal is filtered into four overlapping frequency bands, with crossover frequencies at approximately 700 Hz, 1.4 kHz, and 2.3 kHz. The filters are broad, with slopes of 12 dB per octave. An analog representation of each filter output is delivered to an intracochlear electrode. Stimulation amplitudes for each electrode are referenced to the individual listener's thresholds in each electrode. The listener can perform minor volume and sensitivity adjustments using the speech processor's control knobs, but there are no frequency-dependent adjustments available (i.e., no ''tone'' control). In the Ineraid CI used by subjects in this study, intracochlear electrodes are placed at 4-mm intervals, with the most basal electrode placed about 8–10 mm from the base of the cochlea and the most apical 20–22 mm from the base. Electrodes closer to the base of the cochlea are associated with filters that have higher cutoff frequencies. Using

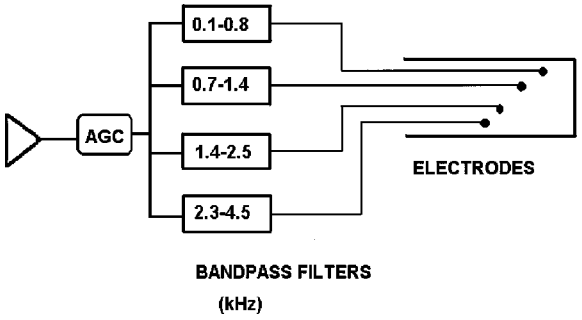

FIG. 1. Simplified block diagram of the ''compressed analog'' stimulation strategy for cochlear implants.

this strategy, a typical patient can have a fluent one-on-one conversation (with the help of lipreading) and can also achieve significant speech reception scores without lipreading (cf. Tye-Murray and Tyler, 1989; Dorman *et al.*, 1989; Rabinowitz *et al.*, 1992).

There are different kinds of acoustic cues that may be used by listeners with the CA strategy. One possibility is that at least the first formant ($F1$) is encoded by a *temporal* code, that is, by neurons discharging synchronously with the period of $F1$. This is certainly plausible: examination of the waveforms output by the lowest frequency channel of the Ineraid device in response to different vowels (see Fig. 2) reveals that the $F1$ period is well represented and could conceivably be employed by Ineraid cochlear implant users to discriminate some vowels. For example, the waveforms delivered to channel 1 in response to /u/, /ɛ/, and /æ/ are quite distinct, reflecting the periodicity of different $F1$ values: 350 Hz for /u/, 500 Hz for /ɛ/, and 700 Hz for /æ/ (see Fig. 2). Psychophysical studies of the rate pitch (i.e., the pitch associated with the repetition rate of a periodic stimulation waveform) of electrical stimuli lend further support to the idea that CA users may obtain frequency information from the waveform sent to channel 1: CI users detect increases in pitch when the frequency of a pulse train or a sinusoid is increased up to 300–500 Hz, and some subjects still detect pitch differences when rate is increased up to 1000 Hz (Shannon, 1993). Therefore, the studies of sinusoid waveform discrimination cited above suggest that cochlear implant users may have the temporal processing capabilities to extract some $F1$ information from a low-pass-filtered version of the speech signal, delivered to a single electrode. Further support for temporal encoding of $F1$ frequency is found in experiments where single channel cochlear implant users identify vowels at above-chance levels (Rosen and Ball, 1986; Tyler *et al.*, 1989; Rabinowitz and Eddington, 1995) because, in these experiments, $F1$ information obtained from the stimulation waveform is essentially the only reliable cue for vowel identification.

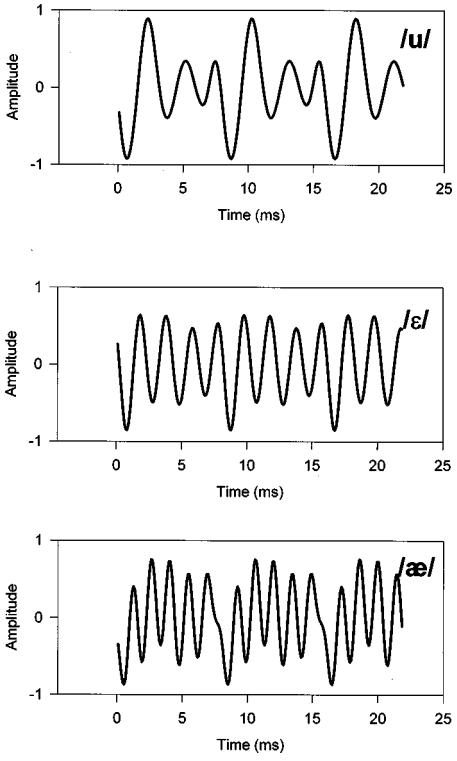

FIG. 2. Channel 1 output waveform in response to vowels /u/, /ɛ/, and /æ/.

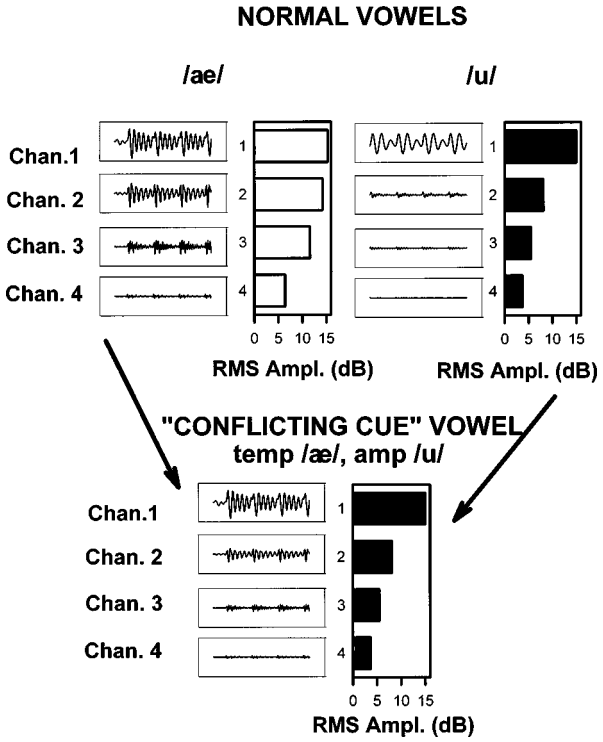

FIG. 3. The top panel shows stimulation waveforms delivered by the Ineraid implant to each channel in response to the vowels /æ/ and /u/. The bar charts indicate the rms amplitude in each channel. The bottom panel shows a ''conflicting-cue'' vowel, where the waveforms corresponding to /æ/ are amplified or attenuated so that the rms amplitude in each channel is the same as for /u/.

Another mechanism that users of the CA strategy may employ to identify vowels is by comparing the amplitude of stimulation delivered to different electrodes. Since the spectra of different vowels have peaks in unique locations of the $F1-F2$ plane (Peterson and Barney, 1952; Hillenbrand *et al.*, 1995), the stimulation amplitudes delivered to each electrode are vowel dependent. For example, the top panels of Fig. 3 show stimulation amplitudes in each channel of the Ineraid device, in response to different vowels. The /u/ sound (right panel) has very low $F1$ and $F2$ frequencies, with prac-

TABLE I. Vowel identification by six Ineraid users (from Dorman *et al.*, 1992). ''Conflicting-cue'' vowels with stimulation waveforms corresponding to vowel *x* and channel amplitudes corresponding to vowel *y* are denoted ''temp *x*, amp *y*.'' The last column lists the predominant response given by subjects in response to a conflicting-cue vowel. Amp indicates that subjects heard the vowel specified by channel amplitudes at least 66% of the time. Amp-temp indicates that subjects heard the vowel specified by channel amplitudes about half of the time, and they heard the vowel specified by the waveforms delivered to each channel the other half of the time. Neither indicates that, most of the time, subjects heard a vowel different from that specified by channel amplitudes and from that specified by channel waveforms.

Stimulus	Response			Type of response
	u	ɛ	æ	
u	99	0	1	
ɛ	0	96	4	
æ	0	8	92	
temp u, amp ɛ	0	84	16	Amp
temp u, amp æ	0	63	37	Neither
temp ɛ, amp u	93	3	3	Amp
temp ɛ, amp æ	10	23	67	Amp
temp æ, amp u	90	7	3	Amp
temp æ, amp ɛ	0	47	53	Amp-temp

tically all the $F1$ energy and a substantial amount of the $F2$ energy falling in the low-frequency filter associated with channel 1. Consequently, stimulation amplitude for channel 1 in response to /u/ is much higher than other channel amplitudes. The vowel /æ/ has higher formants than /u/ and $F1$, for example, is 700 Hz. This means that $F1$ energy for /æ/ goes partly to channel 1 and partly to channel 2. Consequently, the amplitudes in channels 1 and 2 are quite similar for /æ/, and channels 3 and 4 receive more energy than with /u/ as the input. In summary, stimulation amplitudes for each channel depend on vowel identity and also on the loudness of the input. A loudness change has the same effect on all channel amplitudes when they are measured in dB. Therefore, ratios of channel amplitude remain largely unaffected by variations in input loudness, and may be better cues for vowel identity than loudness levels in individual channels.

While both types of cues (temporal and channel-amplitude) are potentially useful, the specific cue or combination of cues that are actually employed by users of the CA strategy remains to be determined. In an interesting study designed to address this question, Dorman *et al.* (1992) presented synthetic ''conflicting-cue'' vowels to a group of subjects. The synthesized waveforms presented to each channel specified one vowel, but the amplitudes were manipulated to specify a different vowel (see Fig. 3). In general, subjects perceived the vowel that was specified by channel amplitudes rather than the one specified by the electrical stimulation waveforms (see Table I), leading Dorman *et al.* to conclude that users of the CA strategy mostly rely on information contained in channel amplitudes to identify vowels. However, responses to two of the six vowels presented in that study suggest that cues other than channel amplitude were also employed by these subjects. The vowel with /æ/ waveforms and /ɛ/ amplitudes elicited a roughly equal number of /æ/ and /ɛ/ responses and, surprisingly, the vowel with /u/ waveforms and /æ/ amplitudes elicited a majority of /ɛ/ responses.

TABLE II. Physical characteristics of the stimuli used by Dorman *et al.* (1992).

	rms levels (dB)				$F1$	$F2$	$F3$
	Ch 1	Ch 2	Ch 3	Ch 4	(Hz)	(Hz)	(Hz)
u	15	7	6	1	350	1250	2200
ɛ	10	6	12	9	500	1700	2500
æ	11	10	9	6	700	1500	2400
temp u, amp ɛ	10	6	12	9	350	1250	2200
temp u, amp æ	11	10	9	6	350	1250	2200
temp ɛ, amp u	15	7	6	1	500	1700	2500
temp ɛ, amp æ	11	10	9	6	500	1700	2500
temp æ, amp u	15	7	6	1	700	1500	2400
temp æ, amp ɛ	10	6	12	9	700	1500	2400

The aim of the current study was to determine the cues employed by users of the Ineraid cochlear implant to identify vowels, as well as the specific way in which these cues are combined. These questions were addressed with a novel modeling approach. A mathematical model is proposed that explains vowel identification based on estimates of psychophysical performance along the acoustic dimensions hypothesized to be relevant. The mathematical framework of the proposed model is a multidimensional extension of Durlach and Braida's single-dimensional model of loudness perception (Durlach and Braida, 1969; Braida and Durlach, 1972), which is in turn based on signal detection theory and on earlier work by Thurstone (1927a,b), among others. The multidimensional model is conceptually similar to that proposed by Braida (1991) to explain integration of visual and auditory information in consonant identification. The confusion matrices generated by the model were compared to the Dorman *et al.* data.

I. METHODS

A. The data

The data to be fit by the model came from the identification experiment conducted by Dorman *et al.* (1992). The stimuli were /u/, /æ/, /ɛ/, and six ''conflicting-cue'' vowels where the temporal waveforms delivered to each channel specified one vowel but channel gains were manipulated so that the rms amplitude of each channel specified another vowel. The vowels were steady state, 200 ms long, and they were generated with the KLATT synthesizer (Klatt and Klatt, 1990). Six subjects took part in an identification test where the possible responses were /u/, /æ/, and /ɛ/. These subjects were selected for their superior vowel identification performance. Figure 3 illustrates an example of a conflicting-cue vowel created with channel waveforms corresponding to /æ/ and rms amplitudes corresponding to /u/ (denoted as [temp /æ/, amp /u/]). Table II lists the principal acoustic characteristics of all the vowels in this study.

Table I shows Dorman *et al.*'s data, averaged across the six subjects. The top three lines simply show that subjects were able to identify the normal, nonconflicting-cue vowels quite successfully. The bottom six lines show subject responses to the conflicting-cue vowels. Four of these lines show that the preponderant response was based on the channel-amplitude cues. For example, when subjects were presented with vowel [temp /ɛ/, amp /u/], they responded /u/ 93% of the time. Similar responses (based on channel-amplitude cues) were obtained for vowels [temp /æ/, amp /u/] and [temp /u/, amp /ɛ/]. The three other conflicting-cue vowels present a more mixed picture; [temp /ɛ/, amp /æ/] received 67% /æ/ responses (corresponding to its channel amplitudes) but also a substantial number of other responses; [temp /æ/, amp /ɛ/] received roughly equal numbers of responses according to temporal and channel-amplitude cues, and, finally (and most interestingly), when subjects were presented with a vowel that combined the temporal waveforms of /u/ and the channel amplitudes of /æ/ the preponderant response was /ɛ/, a vowel that had neither the temporal characteristics nor the channel amplitudes of the stimulus.

B. The multidimensional phoneme identification (MPI) model

Svirsky (1991; Svirsky and Svirsky, 1992) has proposed a mathematical model that predicts phoneme identification based on a listener's discrimination along specified perceptual dimensions. The model incorporates an *internal noise model* to account for basic sensitivity, a *decision model* that allows for response bias, and a *multidimensional perceptual space*. The MPI model is a multidimensional extension of the Braida and Durlach (1972) model of intensity resolution in one-interval paradigms, which is in turn based on earlier work by Thurstone (1927a,b), among others. In the MPI model, the percept associated with each stimulus presentation is represented as a point in a multidimensional space where all dimensions are statistically independent. Due to perceptual noise, the same stimulus elicits somewhat different percepts every time it is presented to a subject. The model postulates that all percepts elicited by different presentations of the same token are normally distributed along each perceptual dimension. The mean of each multidimensional Gaussian distribution is determined by the physical characteristics of the stimulus, and the standard deviations along each dimension are equal to the listener's just-noticeable difference (jnd) along the relevant perceptual dimension. In other words, large jnd's along the relevant perceptual dimensions result in greater uncertainty as to the location of a given stimulus in perceptual space. This is modeled with a broader Gaussian distribution for this stimulus, as exemplified in Fig. 4 for a specific two-dimensional perceptual space. The two perceptual dimensions in Fig. 4 are first formant frequency (which the subject estimates based on the waveform presented to channel 1) and the ratio of amplitudes presented to channels 4 and 1. Three Gaussian distributions are depicted in each panel, corresponding to the vowels /u/, /æ/ and /ɛ/. The top panel shows distributions that may be found with an average subject whose jnd's along each dimension are large enough that some overlap exists. The

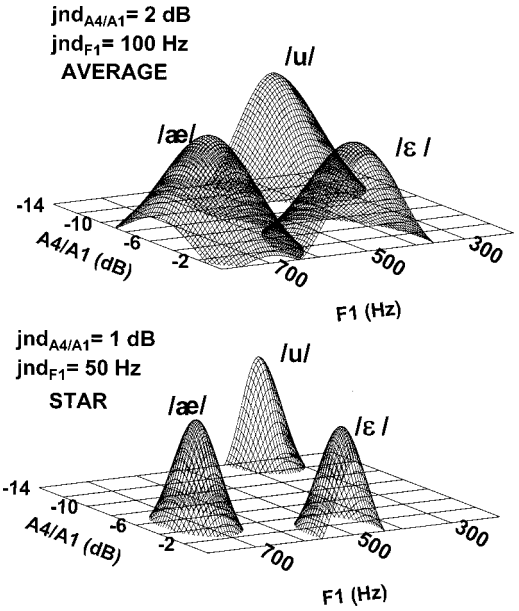

FIG. 4. Example of a specific two-dimensional perceptual space. The two perceptual dimensions are first formant frequency and the ratio of amplitudes presented to channels 4 and 1. Three Gaussian distributions are depicted in each panel, corresponding to the vowels /u/, /æ/, and /ɛ/. The vertical dimension represents the probability that a given vowel will cause a percept in that location of the perceptual space. The bottom panel shows distributions with smaller standard deviations, as would be found in a ''star'' subject with relatively small jnd's along both perceptual dimensions. The top panel shows distributions that may be found with an average subject whose jnd's along each dimension are double those of the star subject. Overlap between these distribution means that the ''average'' subject would make some vowel identification errors.

overlap between different distributions indicates that this subject will make some identification errors due to his insufficient sensitivity along the relevant perceptual dimensions. The bottom panel shows distributions with smaller standard deviations, as would be found in a ''star'' subject with excellent discrimination capabilities (i.e., jnd's that are half the size of the normal subject's) along both perceptual dimensions. Given the smaller jnd's, there is no overlap between the three distributions in this example.

The model postulates that subjects establish their responses by partitioning the perceptual space into nonoverlapping response regions, one region for each possible response. Consequently, each point in the perceptual space belongs to one, and only one, of the response regions. Subject responses are determined by the response region where a given percept falls. In principle, the perceptual space could be partitioned in an infinite number of ways. However, in this study it was assumed that subjects partition the perceptual space in an optimal way (i.e., it was hypothesized that subjects show no response bias). Consequently, perceptual performance is limited only by the overlap between distributions corresponding to different vowels (as illustrated in the bottom panel of Fig. 4). To summarize, the model can be described in a mathematically precise fashion as follows. According to the *internal noise model*, in a perceptual space with m dimensions, the Gaussian probability function S associated with stimulus E_i is

$$S(E_i) = S_i(x_1, x_2, \ldots, x_m)$$

$$= \frac{1}{JND_1 JND_2 \ldots JND_m (\sqrt{2\pi})^m} \times e^{-(x_1 - T_{i1})^2/2JND_1^2} e^{-(x_2 - T_{i2})^2/2JND_2^2} \ldots e^{-(x_k - T_{im})^2/2JND_m^2},$$

where x_j is the value of stimulus E_i along dimension j, T_{ij} is the average value of stimulus i over dimension j, and jnd is the subject's just-noticeable difference (jnd) along dimension j. Each nth presentation of stimulus E_i results in a sensation which is modeled as a point which varies stochastically in a multidimensional space, following the Gaussian distribution $S(E_i)$. We shall denote this point as $S(E_i, n)$. The stochastic variation of $S(E_i, n)$ arises from a combination of ''sensation noise,'' which is a measure of the observer's sensitivity to stimulus differences along the relevant dimension, and ''memory noise,'' which is related to uncertainty in the observer's internal representation of the experimental context. Note that these two kinds of noise (or uncertainty) are different from the variability resulting from separate utterances of the same speech sound, which can be more conveniently modeled by employing one Gaussian distribution for each utterance. Once the value of $S(E_i, n)$ has been determined, a *decision model* is applied to determine the subject's response to the stimulus. The decision model associates a ''response center'' R_k with each possible response, thus creating a partition of the multidimensional space into response regions (one region for each response center). Response region r_k consists of the points that are closer to R_k than to any other response center. When calculating distances we assume that the multidimensional space is Euclidean and that the dimensions are orthogonal. Response regions determine a subject's responses: when a stimulus falls in response region r_k (or, equivalently, when a stimulus is closer to response center R_k than to any other response center), the subject's response is k. One interpretation of the response center concept is that it reflects a subject's expected sensation in response to a stimulus (e.g., a prototype of the subject's phoneme category). If the percept associated with a stimulus is close to the expected sensation, the stimulus is identified correctly. If the percept corresponding to stimulus ''1'' is closer to the expected sensation for stimulus ''2'' than to the expected sensations for any other stimulus, the subject responds ''2'' instead of ''1,'' thus making an identification error.

To generalize this concept and make it precise, cell ik in the response matrix (i.e., the percentage of ''k'' responses to the ''i'' stimulus) is determined by the multiple integral of distribution S_i over the region r_k. In other words, the predicted response matrix for a set of stimuli E_i is obtained by integrating all the $S(E_i)$ distributions over each multidimensional response region.

$$\text{Cell}_{ik} = \int_{r_k} S_i(x_1, x_2, \ldots, x_m) dx_1 dx_2 \ldots dx_m .$$

To use the MPI model the following steps must be taken. *First*, hypothesize what are the relevant perceptual dimensions. *Second*, measure the mean location of each phoneme along each postulated perceptual dimension (this is uniquely determined by the physical characteristics of the stimuli and the selected perceptual dimensions). *Third*, estimate (or better yet, measure) the subjects' just-noticeable difference (jnd) along each perceptual dimension, using appropriate psychophysical tests. The *fourth* step is to estimate (or measure) the response bias along each postulated perceptual dimension. This step may be considered optional if we assume (as in the present study) that the subject is an ideal observer. Note that these steps differ in nature. Specifying the perceptual dimensions is a basically arbitrary (although, one would hope, well informed) decision that may be validated or contradicted by the fit between model output (i.e., a predicted confusion matrix) and the real data. The jnd's and response bias, on the other hand, are measurable psychophysical parameters. Finally, stimulus values along each dimension are measurable physical quantities that are uniquely determined once the dimensions are chosen.

In this study, the four steps described above were handled as follows. Two kinds of perceptual dimensions were considered: a ''temporal'' dimension that is related to information presented to an individual channel (specifically, this dimension is $F1$, the first formant frequency, evaluated from the waveform presented to channel 1) and a number of ''channel-amplitude'' dimensions that are encoded by information presented to different channels (i.e., the ratios of amplitudes presented to channels 2, 3, and 4 with respect to channel 1 amplitude). The temporal dimension is named $F1$ and the channel-amplitude dimensions are named A2/A1, A3/A1, and A4/A1. These kinds of dimensions (or others conceptually very similar) had already been proposed in the Dorman *et al.* (1992) study. The second step to implement the MPI model is to determine the location of each stimulus along each dimension (i.e., the value of $F1$, A2/A1, and the other dimensions for each one of the vowels in this study). All this information can be determined from the data in Table II, which describes the physical characteristics of the stimuli. The third step involves determining or estimating the listener's jnd's along each specified acoustic dimension. In the present study, jnd's were free parameters used to optimize the model's fit to the data. It was assumed that all channel-amplitude jnd's were the same, so the number of free parameters was two: a jnd for $F1$ and a channel-amplitude jnd. The $F1$ jnd was allowed to vary between 50 and 300 Hz, in 10-Hz steps, and the channel-amplitude jnd was allowed to vary between 0.1 and 5 dB, in 0.1 dB steps. Finally, it was assumed that listeners were ideal observers, and thus response bias was zero. The model was implemented by numerically integrating the Gaussian distributions corresponding to a given stimulus and jnd [see Eq. (2)] over the three response regions corresponding to the three possible responses in the experiment: /u/, /æ/, and /ɛ/. In total, nine Gaussian distributions (corresponding to the nine stimuli used in the experiment) were integrated over three regions each (corresponding to the three possible responses), to obtain a 9×3 response matrix that attempted to fit the data shown in Table I. Because each row in the matrix adds up to 100%, the data to be fit by the model has 18 degrees of

TABLE III. Best fit obtained with a four-dimensional model that includes one temporal dimension ($F1$) and three channel-amplitude dimensions (A2/A1, A3/A1, and A4/A1). This fit was obtained for jnd values of 120 Hz for $F1$ and 2.6 dB for the channel-amplitude ratios. The fitted matrix is quite close to the data: it does not have any errors greater than 20 percentage points, and it has only four cells with errors between 10 and 20 percentage points (indicated in underlined numbers). The predominant type of response predicted by the model is indicated in the right column. The second most frequent type of response is also indicated between parentheses, when it exceeds 30% of the total responses. The type of response for the predicted data is quite close to that observed in the listeners (see Table I).

Stimulus	Response			Type of response
	u	ɛ	æ	
u	99	0	1	
ɛ	0	95	5	
æ	0	5	95	
temp u, amp ɛ	0	98	2	Amp
temp u, amp æ	9	58	33	Neither
temp ɛ, amp u	98	0	2	Amp
temp ɛ, amp æ	2	31	67	Amp (temp)
temp æ, amp u	88	0	12	Amp
temp æ, amp ɛ	0	64	36	Amp (temp)

freedom and the number of free parameters (as discussed above) is 2.

Finally, the whole process was repeated for several other choices of dimensions. The first two choices were models with only one type of dimension: temporal-only (i.e., $F1$) and channel-amplitude-only (i.e., A2/A1, A3/A1, A4/A1). Although simple examination of the original data set reveals that these dimension choices are insufficient to explain all the experimental data, it is interesting to show how the MPI model fails when an inappropriate set of dimensions is chosen. Then, the MPI model was run using all possible subsets of the channel-amplitude dimensions combined with the temporal dimension, to determine whether a subset of the four-dimensional model may be just as effective in fitting the data.

II. RESULTS

Table III shows the best fitting matrix generated by the four-dimensional model, i.e., the matrix with minimum rms difference with respect to the actual data (shown in Table I). This best fit was obtained for jnd values of 120 Hz for $F1$ and 2.6 dB for channel amplitude ratios. The jnd for $F1$ is broadly consistent with the literature on rate pitch perception by cochlear implant users (Townshend *et al.*, 1987) and the jnd for channel amplitude ratios is comparable to (but higher than) data on jnd's for intensity discrimination, which range from a fraction of a dB to 1–2 dB, depending on presentation level, task performed by the subject, etc. (Hochmair-Desoyer, 1981; Douek *et al.*, 1977; Fourcin *et al.*, 1979). This is reasonable because even though discrimination of amplitude ratios in different electrodes may be mediated by estimating the separate loudness of each electrode, it is still a more complex task than intensity discrimination in a single electrode.

The predicted matrix is quite close to the observed data: it does not have any errors greater than 20 percentage points, and it has very few cells with errors between 10 and 20 percentage points. The mean square error is less than 8%. Furthermore, the model explains the subjects' excellent performance with the natural vowels; it explains the three conflicting-cue vowels where subjects give a preponderance of responses (80% or more) according to channel amplitudes; it also explains why [temp /ɛ/, amp /æ/] should receive about two thirds of /æ/ responses (based on its channel amplitudes), and some /ɛ/ responses (based on the temporal waveform of channel 1); it explains why [temp /æ/, amp /ɛ/] should receive a substantial number of /ɛ/ responses based on channel amplitudes, and many /æ/ responses based on the temporal waveforms; and, most importantly, the model explains why the vowel with the temporal waveforms of /u/ and the channel amplitudes of /æ/ ([temp /u/, amp /æ/]) should receive a majority of /ɛ/ responses and some /æ/ responses.

Table IV shows the results obtained with different dimension choices. As expected, the temporal-only and the channel-amplitude-only models resulted in a much poorer fit than the four-dimensional model. However, two other choices of dimensions resulted in fits that were just as good as that obtained with the four-dimensional model. One of these choices included the $F1$, A2/A1 and A4/A1 dimensions

TABLE IV. Characteristics of the best-fit matrices obtained with different choices of perceptual dimensions. The first four columns indicate which dimensions were used; the next two columns indicate the jnd values that yielded the best fit; and the last three columns list different measures of fit between predicted matrices and observed data: rms difference, number of cells with errors between 10 and 20 percentage points, and number of cells with errors greater than 20 percentage points.

Dimensions				Amplitude jnd	Frequency jnd	rms	Cells with errors from 10 to 20%	Cells with errors >20%
A2/A1	A3/A1	A4/A1	$F1$					
X	X	X	X	2.6	120	7.3	4	0
			X	N/A	260	38.8	6	19
X	X	X		4.9	N/A	14.7	3	6
X			X	1.2	110	9.0	4	2
	X		X	1.7	130	8.9	5	2
		X	X	1.9	130	7.3	5	0
X	X		X	2.3	130	7.6	5	0
X		X	X	2.7	140	7.1	5	0
	X	X	X	2.5	120	7.7	5	0

and the other one included only $F1$ and A4/A1. The differences between predictions obtained with the four-dimensional model and these two alternative choices of dimensions were quite minor. On one hand, the rms differences between predicted and observed matrices for the alternative choices of dimensions were as small as or even slightly smaller than those for the four-dimensional model, but on the other hand, the four-dimensional model resulted in fewer cells with errors greater than 10%.

III. DISCUSSION

It was already clear from the original study by Dorman *et al*. that listeners must have used some combination of temporal and channel-amplitude cues to identify vowels, but many questions remained unanswered. Why were there so many /ε/ responses to the stimulus [temp /u/, amp /æ/], given that /ε/ had neither the temporal nor the channel-amplitude characteristics of the stimulus? Why didn't this happen with any of the other five conflicting-cue vowels? Why did the stimulus [temp /æ/, amp /ε/] receive a substantial number of responses following the temporal characteristics, as well as many responses following the channel-amplitude characteristics of the stimulus, and why didn't this happen with the other conflicting-cue vowels? Why did three of the conflicting-cue vowels receive 84% or more responses according to channel-amplitude cues, and why didn't this happen with the other conflicting-cue vowels? Why were listeners able to identify the nonmodified vowels so well? The main finding of this study is that an extremely simple model incorporating one temporal cue and three channel-amplitude cues was successful in explaining all these questions in a strictly quantitative fashion. Moreover, the best fit was achieved with jnd parameter values that seem quite plausible.

It should be noted that the data set under analysis is consistent with several different choices of dimensions, as indicated in Table IV. All these choices include the $F1$ dimension and different subsets of channel-amplitude dimensions. However, not just any subset of channel-amplitude dimensions combined with the $F1$ dimension results in equally good fits: some subsets result in greater rms difference between observed and predicted data, and in some cells having errors greater than 20 percentage points. Future studies of individual listeners should explore whether the dimensions employed in a listening task may be subject dependent or even task dependent.

It may be particularly interesting to explore why the model correctly fit the seemingly strange responses to [temp /u/, amp /æ/]. It is rather difficult to visualize this in a space with four dimensions, but it can be illustrated with a two-dimensional space (see Fig. 5 where the dimensions are $F1$ and A4/A1, the ratio of amplitudes in channels 4 and 1). Filled circles show the location of the three normal vowels used in the Dorman *et al.* experiment. The empty circle shows the location of the conflicting-cue vowel [temp /u/, amp /æ/]. As the figure shows, this conflicting-cue vowel is closer to /ε/ than to either of the other two vowels. This result is also true in the tetradimensional perceptual space used by the model, explaining why the observed responses

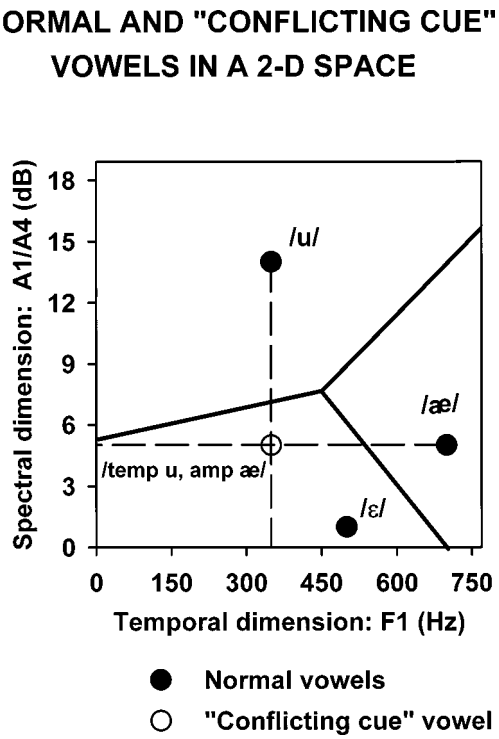

FIG. 5. Filled circles show the location of the three normal vowels used in the Dorman *et al.* experiment, in a two-dimensional perceptual space that incorporates the temporal dimension and one of the channel-amplitude dimensions used in this study. The heavy black lines indicate the boundaries between the three response regions, which correspond to the three possible responses: /u/, /ε/, and /æ/. The empty circle shows the location of the conflicting-cue vowel [temp /u/, amp /æ/]. As the figure shows, this conflicting-cue vowel is closer to /ε/ than to any of the other two vowels. Assuming jnd's of 120 dB for $F1$ and 2.6 dB for A4/A1, equal geometric distances in this figure represent equal perceptual distances.

are a necessary consequence of the postulated perceptual space.

If the specific dimensions proposed in this study were indeed the ones employed by listeners who use the CA stimulation strategy, these listeners would have difficulty identifying vowels uttered with extreme values of spectral tilt, due to its different effect on the amplitude of the different stimulation channels. This unfortunate inability to perform talker normalization in the face of spectral tilt differences would be a direct consequence of the CI listeners' limited ability to identify the frequency of a spectral peak, which forces them to rely on more indirect ways of determining vowel identity. Normal listeners, using their ability to discriminate fine differences in formant frequency, are known to identify vowels accurately even in the face of variability in spectral tilt, breathiness, loudness, and many other acoustic parameters. Conceivably, CI users could adapt to the spectral tilt of a single talker by determining the talker's long-term spectral tilt and adjusting the response centers of different vowels accordingly. However, this strategy would not be as useful when trying to identify vowels in a multitalker test.

More refined versions of mathematical models such as these may be useful both to answer basic research questions and for clinical use. One example of possible clinical use may be the fitting of newer speech processors like that of the

Clarion device, which can implement the state-of-the-art continuous Interleaved sampling strategy as well as a version of the compressed-analog strategy (named SAS) in a variety of electrode configurations. The best method that clinicians have at their disposal among the different strategies and electrode configurations that may be available with a specific implant is to let the patient use each strategy or electrode configuration for at least a few weeks (for training purposes) and measure perceptual performance at the end of the training period. In order to rule out possible learning effects, a reversal design (A-B-A) is necessary, further complicating the testing. Models like the ones proposed here may be used to predict a subject's maximum achievable perceptual performance with a given strategy or electrode configuration by measuring the subject's psychophysical performance along the relevant perceptual dimensions and using it as input to the model. There is some evidence that psychophysical performance does not change dramatically after cochlear implantation (Brown *et al.*, 1995; Svirsky *et al.*, 1999). This is in contrast to speech perception, which requires weeks or even months to reach asymptote after implantation. The psychophysical tests would not require weeks or months of training, so the whole process of determining which strategy to use would be considerably shortened. The MPI model has already been used in several preliminary studies to explain vowel perception by users of formant-extracting pulsatile cochlear implants (Svirsky, 1991; Svirsky and Svirsky, 1992; Blamey and Svirsky, 1993) and to explain vowel and consonant perception by users of the SPEAK strategy, a vocoder-like scheme used with cochlear implants (Svirsky and Meyer, 1997, 1998). In the case of vowel perception, the model was able to predict the large majority of vowel pairs that were or were not confused by subjects. This was achieved both for individual and for group data, and it was done using one free parameter when jnd data were not available or no free parameters when it was possible to obtain jnd data from the subjects. Group consonant data were also fit by the model quite well: most of the consonant pairs that were or were not confused in an 18-consonant confusion matrix were predicted by the model, using three free parameters.

The traditional approach to investigate the relation between psychophysical variables and speech perception by CI users has been to perform correlational analyses between those variables and speech perception scores, usually with modest results (Tyler *et al.*, 1982; Hochmair-Desoyer *et al.*, 1985; Shannon, 1989). More complex psychophysical parameters have resulted in higher correlations with speech perception scores from CI users, and may hold more promise (Collins *et al.*, 1994; Nelson *et al.*, 1995; Dorman *et al.*, 1996). Although these studies have provided important information, any correlations between psychophysics and speech perception, by their very nature, cannot explain the *mechanisms* CI users employ to identify speech sounds. A correlation does not imply causality, it may be a byproduct of both the psychophysical parameter and the speech perception scores being correlated with a third variable. Simply stating that speech perception is related to one specific psychophysical variable does not explain how listeners may actually use acoustic information to arrive at a higher-level decision involving categorization and labeling of speech sounds. In addition, finding correlations between speech perception and psychophysics does not explain how listeners may *combine* various acoustic cues to label the speech sounds they heard. Finally, performing a linear correlation involves the underlying hypothesis of a linear relation between the psychophysical parameter and the speech perception score. Consequently, it may not be reasonable to hypothesize or expect a high correlation between psychophysical and speech perception measures, even when there is an underlying relation between the two variables, because it is unlikely that this relation will be truly linear.

In contrast to the simple calculation of linear correlations, the MPI model provides new ways to test competing hypotheses about the psychophysical dimensions that underlie speech perception by CI users. The MPI mathematical description states in precise terms what the relevant information is that CI users extract from the acoustic signal, how they combine information from different perceptual dimensions, and how they use this information to identify speech sounds. It is important to point out that the prediction provided by the MPI model is not simply a speech perception score on a given test, but an entire confusion matrix. In other words, the MPI model makes specific predictions as to which pairs of vowels or consonants should be more easily confused by a given CI user. Because the MPI model makes such specific predictions about patterns of perceptual behavior, its hypotheses are more easily falsifiable than those used in the simple correlational approach. Consequently, the approach represented by the MPI model may be helpful in advancing our understanding of the role of sensory discrimination abilities and their relation to speech perception by CI users.

Although the present study has shown the feasibility of using the MPI model to fit group data, one of the most interesting potential uses of the model is the examination of individual data. This can be done either using free parameters (as was done in this study) or by measuring the listeners' jnd's along each dimension and then generating predictions without free parameters. A preliminary study (Meyer *et al.*, 1999) has shown that the model's predictions based on the listeners' own jnd's may represent an overestimate of actual performance. This suggests that a listener's ability to extract and integrate acoustic information from different sources in real time may be limited not only by psychophysical factors, but also by more central, cognitive factors. Studies are underway that will employ the MPI model to assess its validity in fitting individual data and the role of higher-order cognitive factors in phoneme identification.

ACKNOWLEDGMENTS

This research was funded by NIDCD Grant No. R01-DC03937, Contract No. N01-DC-2-2402 and a grant from CONICYT (Uruguay). Ashesh Shah provided valuable help modifying figures and running various versions of the model. Important suggestions were made by many colleagues, in particular Don Eddington, Bill Rabinowitz, Mike Dorman, Joe Tierney, Melanie Matthies, Ted Meyer, Karen I. Kirk,

David Pisoni, Peter Blamey, an anonymous reviewer, Rosalie Uchanski and (last but not least) Lou Braida.

Blamey, P. J., and Svirsky, M. A. (**1993**). ''Identification of vowels and stimulation channels by cochlear implant users,'' Speech Communication Group Working Papers, Vol. IX, pp. 35–62.

Braida, L. D. (**1991**). ''Crossmodal Integration in the Identification of Consonant Segments,'' Q. J. Exp. Physiol. (**1981**) **43A**(3), 647–677.

Braida, L. D., and Durlach, N. I. (**1972**). ''Intensity Perception II. Resolution in one interval paradigms,'' J. Acoust. Soc. Am. **51**, 483–502.

Brown, C. J., Abbas, P. J., Bertschy, M., Tyler, R. S., Lowder, M., Takahashi, G., Purdy, S., and Gantz, B. J. (**1995**). ''Longitudinal assessment of physiological and psychophysical measures in cochlear implant users,'' Ear Hear. **16**(5), 439–449.

Collins, L. M., Wakefield, G. H., and Feinman, G. R. (**1994**). ''Temporal pattern discrimination and speech recognition under electrical stimulation,'' J. Acoust. Soc. Am. **96**, 2731–2737.

Dorman, M. F., Smith, L., Smith, M., and Parkin, J. (**1992**). ''The coding of vowel identity by patients who use the Ineraid cochlear implant,'' J. Acoust. Soc. Am. **92**, 3428–3432.

Dorman, M. F., Smith, L. M., Smith, M., and Parkin, J. L. (**1996**). ''Frequency discrimination and speech recognition by patients who use the Ineraid and continuous interleaved sampling cochlear-implant signal processors,'' J. Acoust. Soc. Am. **99**, 1174–1184.

Dorman, M. F., Hannley, M. T., Dankowski, K., Smith, L., and McCandless, G. (**1989**). ''Word recognition by 50 patients fitted with the Symbion multichannel cochlear implant,'' Ear Hear. **10**(1), 44–49.

Douek, E., Fourcin, A. J., Moore, B. C. J., and Clarke, G. P. (**1977**). ''A new approach to the cochlear implant,'' Proc. R. Soc. Med. **70**, 379–383.

Durlach, N. I., and Braida, L. D. (**1969**). ''Intensity perception. I. Preliminary theory of intensity resolution,'' J. Acoust. Soc. Am. **46**, 372–383.

Fourcin, A. J., Rosen, S. M., Moore, B. C., Douek, E. E., Clarke, G. P., Dodson, H., and Bannister, L. H. (**1979**). ''External electrical stimulation of the cochlea: clinical, psychophysical, speech-perceptual and histological findings,'' Br. J. Audiol. **13**, 85–107.

Hillenbrand, J., Getty, L. A., Clark, M. J., and Wheeler, K. (**1995**). ''Acoustic characteristics of American English vowels,'' J. Acoust. Soc. Am. **97**, 3099–3111.

Hochmair-Desoyer, I. J., Hochmair, E. S., and Stiglbrunner, H. K (**1985**). ''Psychoacoustic Temporal Processing and Speech Understanding in Cochlear Implant Patients,'' in *Cochlear Implants*, edited by R. A. Schindler and M. M. Merzenich, pp. 291–303.

Hochmair-Desoyer, I. J., Hochmair, E. S., Burian, K., and Fischer, R. E. (**1981**). ''Four years of experience with cochlear prostheses,'' Med. Prog. Technol. **8**, 107–119.

Klatt, D. H., and Klatt, L. C. (**1990**). ''Analysis, synthesis, and perception of voice quality variations among female and male talkers,'' J. Acoust. Soc. Am. **87**, 820–857.

Meyer, T. A., Svirsky, M. A., Kaiser, A. R., Simmons, P. M., and Lai, T. T. (**1999**). ''Predicting consonant perception with the Multidimensional Phoneme Identification (MPI) model for individual cochlear implant users,'' ARO **22**, 719.

Nelson, D. A., Van Tassell, D. J., Schroder, A. C., Soli, S., and Levine, S. (**1995**). ''Electrode ranking of 'place pitch' and speech recognition in electrical hearing,'' J. Acoust. Soc. Am. **98**, 1987–1999.

Peterson, G. E., and Barney, H. L. (**1952**). ''Control methods used in a study of the vowels,'' J. Acoust. Soc. Am. **24**, 175–184.

Rabinowitz, W. M., Eddington, D. K., Delhorne, L. A., and Cuneo, P. A. (**1992**). ''Relations among different measures of speech reception in subjects using a cochlear implant,'' J. Acoust. Soc. Am. **92**, 1869–1881.

Rabinowitz, W. M., and Eddington, D. K. (**1995**). ''Effects of channel-to-electrode mappings on speech reception with the Ineraid cochlear implant,'' Ear Hear. **16(5)**, 450–458.

Rosen, S., and Ball, V. (**1986**). ''Speech perception with the Vienna extracochlear single-channel implant: a comparison of two approaches to speech coding,'' Br. J. Audiol. **20**(1), 61–83.

Shannon, R. V. (**1989**). ''Detection of gaps in sinusoids and pulse trains by patients with cochlear implants,'' J. Acoust. Soc. Am. **85**, 2587–2592.

Shannon, R. V. (**1993**). ''Psychophysics,'' in *Cochlear implants: Audiological Foundations*, edited by R. S. Tyler (Singular, San Diego).

Svirsky, M. A. (**1991**). ''A mathematical model of vowel perception by users of pulsatile cochlear implants,'' Presented at the 22nd Annual Neural Prosthesis Workshop, Bethesda, MD, 22–24 October.

Svirsky, M. A., and Meyer, T. A., (**1997**). ''A mathematical model of vowel perception by cochlear implantees who use the SPEAK stimulation strategy,'' presented at the Twentieth ARO Midwinter Meeting, St. Petersburg, FL.

Svirsky, M. A., and Meyer, T. A. (**1998**). ''A mathematical model of consonant perception by cochlear implant users with the SPEAK strategy,'' J. Acoust Soc. Am. **103**, 2977(A).

Svirsky, M. A., Meyer, T. A., Kaiser, A. R., Basalo, S., Silveira, A., Suarez, H., Lai, T. T., and Simmons, P. M. (**1999**). ''Learning how to perceive vowels with a cochlear implant: The role of discrimination and labeling,'' Assoc. Res. Otolaryngol. Abs., p. 720.

Svirsky, M. A., and Svirsky, S. H. (**1992**). ''A multidimensional mathematical model of vowel perception by users of pulsatile cochlear implants,'' J. Acoust. Soc. Am. **92**, 2416A–2417A.

Thurstone, L. L. (**1927a**). ''A law of comparative judgement,'' Psychol. Rev. **34**, 273–286.

Thurstone, L. L. (**1927b**). ''Psychophysical analysis,'' Am. J. Psychol. **38**, 368–389.

Townshend, B., Cotter, N., Van Compernolle, D., and White, R. L. (**1987**). ''Pitch perception by cochlear implant subjects,'' J. Acoust. Soc. Am. **82**, 106–115.

Tye-Murray, N., and Tyler, R. S. (**1989**). ''Auditory consonant and word recognition skills of cochlear implant users,'' Ear Hear. **10**, 292–298.

Tyler, R. S., Tye-Murray, N., Moore, B. C. J., and McCabe, B. (**1989**). ''Synthetic two-formant vowel perception by some of the better cochlear implant patients,'' Audiology **28**, 301–315.

Tyler, R. S., Summerfield, Q., Wood, E. J., and Fernandes, M. A. (**1982**). ''Psychoacoustic and phonetic temporal processing in normal and hearing-impaired listeners,'' J. Acoust. Soc. Am. **72**, 740–752.

Wilson, B. S., Finley, C. C., Lawson, D. T., Wolford, R. D., Eddington, D. K., and Rabinowitz, W. M. (**1991**). ''Better speech recognition with cochlear implants,'' Nature (London) **352**, 236–238.

Auditory brainstem responses with optimized chirp signals compensating basilar-membrane dispersion[a)]

Torsten Dau,[b)] Oliver Wegner, Volker Mellert, and Birger Kollmeier
Carl von Ossietzky Universität Oldenburg, AG Medizinische Physik, Graduiertenkolleg Psychoakustik, D-26111 Oldenburg, Germany

(Received 15 July 1998; revised 25 October 1999; accepted 29 November 1999)

This study examines auditory brainstem responses (ABR) elicited by rising frequency chirps. The time course of frequency change for the chirp theoretically produces simultaneous displacement maxima by compensating for travel-time differences along the cochlear partition. This broadband chirp was derived on the basis of a linear cochlea model [de Boer, ''Auditory physics. Physical principles in hearing theory I,'' Phys. Rep. **62**, 87–174 (1980)]. Responses elicited by the broadband chirp show a larger wave-V amplitude than do click-evoked responses for most stimulation levels tested. This result is in contrast to the general hypothesis that the ABR is an electrophysiological event most effectively evoked by the onset or offset of an acoustic stimulus, and unaffected by further stimulation. The use of this rising frequency chirp enables the inclusion of activity from lower frequency regions, whereas with a click, synchrony is decreased in accordance with decreasing traveling velocity in the apical region. The use of a temporally reversed (falling) chirp leads to a further decrease in synchrony as reflected in ABR responses that are smaller than those from a click. These results are compatible with earlier experimental results from recordings of compound action potentials (CAP) [Shore and Nuttall, ''High synchrony compound action potentials evoked by rising frequency-swept tonebursts,'' J. Acoust. Soc. Am. **78**, 1286–1295 (1985)] reflecting activity at the level of the auditory nerve. Since the ABR components considered here presumably reflect neural response from the brainstem, the effect of an optimized synchronization at the peripheral level can also be observed at the brainstem level. The rising chirp may therefore be of clinical use in assessing the integrity of the entire peripheral organ and not just its basal end. © *2000 Acoustical Society of America.* [S0001-4966(00)02603-5]

PACS numbers: 43.64.Qh, 43.64.Ri [RDF]

INTRODUCTION

It is generally assumed that the conventional auditory brainstem response (ABR) is an electrophysiological event evoked by *onset* of an acoustic stimulus. Whether the stimulus is an acoustic click, tone pip, tone burst, or noise burst, the ABR is assumed to be effectively evoked by the first few milliseconds of the stimulus, and is generally unaffected by further stimulation (e.g., Hecox *et al.*, 1976; Kodera *et al.*, 1977; Debruyne and Forrez, 1982; Gorga and Thornton, 1989; Van Campen *et al.*, 1997). Because of its abrupt onset, the acoustic click is often thought to be an ideal stimulus for eliciting a detectable ABR. Clicks or impulsive stimuli are also used under the assumption that their wide spectral spread, inherent in transient signals, elicits synchronous discharges from a large proportion of cochlear fibers (e.g., Kodera *et al.*, 1977; Gorga and Thornton, 1989; van der Drift *et al.*, 1988a,1988b).

Additionally, it is generally observed that if a long-duration tone burst (>8 ms) is employed, a second response can be evoked at stimulus *offset*. This offset response resembles onset ABR morphology and occurs within 8 ms after stimulus offset. It has been termed ''offset ABR'' or ''off potential of the brainstem'' (Kodera *et al.*, 1977; Brinkman and Scherg, 1979).

When a transient stimulus progresses apically along the basilar membrane (BM), single-unit activity is less synchronous with the preceding activity from basal units (Tsuchitani, 1983) because of temporal delays imposed by the traveling wave. This results in an asynchronous pattern of auditory-nerve-fiber firing along the length of the cochlear partition. In addition, it is likely that activity generated from the single units in more synchronous basal regions would be out of phase with activity from some apical units. As a consequence, the combination of phase cancellation and loss of synchronization *bias* the evoked potential to reflect activity from more basal, high-frequency regions of the cochlea (e.g., Neely *et al.*, 1988).

More evidence about the interaction between basilar-membrane dispersion and the synchrony of neural responses can be derived from studies on the compound action potential (CAP) which represents auditory-nerve activity. When stimulated with a click, only auditory-nerve units tuned above 2–3 kHz contribute to synchronous activity in the N_1P_1 complex (Dolan *et al.*, 1983; Evans and Elberling, 1982). In order to determine if cochlear units tuned below 2–3 kHz could be recruited into the CAP response, Shore and Nuttall (1985) used tone bursts of exponentially rising frequency to hypothetically activate synchronous discharges of VIIIth-nerve fibers along the length of the cochlear parti-

[a)]Part of this research was presented at the 21st Midwinter meeting of the Association for Research in Otolaryngology [Dau *et al.*, ''Auditory brainstem responses (ABR) with optimized chirp signals compensating basilar-membrane dispersion,'' ARO, S33 (1998)].

[b)]Electronic mail: torsten.dau@medi.physik.uni-oldenberg.de

tion. Their equations defining the frequency chirps were calculated to be the inverse of the delay-line characteristic of the guinea pig partition. Shore and Nuttall (1985) recorded CAPs in response to the rising chirp and compared them to CAP waveforms evoked by corresponding falling chirps as well as clicks. Their analysis of the CAP waveforms showed narrower N_1 widths and larger N_1 and P_1 amplitudes for rising sweeps when compared to falling sweeps. Their results supported the hypothesis underlying the derivation of the rising sweep: spectral energy with the appropriate temporal organization, determined by basilar-membrane traveling wave properties, increases CAP synchrony. In a later study, Shore *et al.* (1987) provided evidence that the timing of discharges in the ventral cochlear nuclei (VCN) reflects cochlear partition motion as demonstrated for VIIIth-nerve fibers and inner hair cells (Brugge *et al.*, 1969; Geisler *et al.*, 1984; Rose *et al.*, 1971; Russell and Sellick, 1978; Sellick *et al.*, 1982). However, unlike VIIIth-nerve fibers, responses of VCN neurons to rapid frequency sweeps were more complex, showing directional preferences.

The present paper followed the same strategy of generating an ''optimized'' stimulus causing maximal synchronous activation at the level of the VIIIth nerve, but deals with brainstem recordings in human subjects. The latencies of the brainstem potentials can be separated into mechanical and neural components. The mechanical component is due to mechanical BM travel time, and varies with intensity and frequency in an orderly manner, while the remaining neural component is assumed to be independent of both intensity and frequency (e.g., Neely *et al.*, 1988). We attempted to compensate for the frequency-dependent mechanical component in order to increase synchrony at a peripheral level, which may also lead to increased synchrony at higher stations in the brainstem. Our question was whether such a stimulus would be appropriate and effective for ABR recordings. Of course, there is a large difference between events in single-unit electrical fields, and the signals which are recorded by electrodes which are remote from the neural sources. Single-unit electrical fields are rapidly attenuated in the extracellular space and are unmeasurable at more than a few millimeters distance. Also, the effectiveness of neural centers as dipole generators producing a detectable far-field response depends on the number of involved neural sources and on morphological features such as dendritic orientation. However, the mechanical component of BM travel time should affect single-unit electrical-field responses and whole ensemble far-field responses in a similar way. Hence, the time-frequency distribution of a stimulus can be expected to have a distinct effect on ABR.

ABRs elicited by broadband, frequency-sweeping stimuli are compared with click-evoked responses. The underlying chirp stimulus was generated on the basis of the (linear) basilar-membrane model by de Boer (1980).

I. THE CHIRP STIMULUS

The equations describing the stimulus were derived based on the following considerations: (i) Since the mechanical properties of the cochlear partition result in a spatial separation of frequency components of an acoustic signal, the desired stimulus must have a wideband frequency spectrum to excite a maximal number of nerve fibers (see also Shore and Nuttall, 1985). (ii) Since there is also a *temporal* dispersion of displacement maxima along the cochlea partition, the temporal spacing of frequency components of the wideband signal must be adjusted to provide maximum synchrony of discharge across frequency. A low-frequency tone requires more time to reach its place of maximum displacement, near the apex of the cochlea, than does a higher-frequency tone that elicits a maximum closer to the base. The idea is to generate a stimulus in which the high-frequency components are delayed relative to the low-frequency components by an appropriate amount. This should produce *synchronous* displacement maxima and neural discharges resulting from *all* frequency components. The acoustic signal must therefore be a rising frequency chirp. The time course of the chirp developed in the present study is determined by the traveling-wave velocity along the partition as derived by de Boer (1980), and the functional relationship between stimulus frequency and place of maximum displacement (Greenwood, 1990).

De Boer (1980) developed a cochlear model in which—as physical simplifications—he assumed that the fluids of the canals around the basilar membrane would be incompressible and that all viscosity effects were negligible. All movements were assumed to be so small that the fluid as well as the BM operate linearly. All time-dependent variables were considered to vary as $e^{i\omega t}$, with ω representing radian frequency. Since the dynamics of the BM is certainly nonlinear, in some conditions this linear approach must be considered as a first-order approximation. It was further assumed by de Boer (1980) that various parts of the BM are not mechanically coupled to each other and that all coupling occurs via the surrounding fluid. De Boer described the mechanics of the cochlear partition by a single function of the coordinate x, the impedance $\xi(x)$, which is dominated by a stiffness term $c(x)/i\omega$. The fluid movements in the other two directions were assumed not to contribute to the mechanical pattern of movement of the cochlear partition.

The wave equation for the hydromechanical problem was then given by

$$\frac{d^2}{dx^2}\psi(x) - \frac{2i\omega\rho}{h(x)\xi(x)}\psi(x) = 0, \tag{1}$$

with $\psi(x)$ as the wave function, $h(x)$ as the ''effective'' height of the scala, and the density ρ. The impedance ξ is the critical factor and is composed of three parts, a mass part, a resistance part, and a stiffness part,

$$\xi(x) = i\omega m(x) + r(x) + \frac{c(x)}{i\omega}. \tag{2}$$

The mass term $m(x)$ does not depend much on x in the cochlea, but the stiffness $c(x)$ varies over a large range as a function of x (e.g., Békésy, 1960). It is assumed in the following that *only* stiffness contributes to $\xi(x)$, while mass and resistance $r(x)$ are neglected. Due to the variations of the stiffness, the velocity of propagation depends strongly on x. The stiffness was shown to be mainly responsible for the

occurrence of traveling waves propagating along the cochlear partition. De Boer developed the *exponential model* assuming that $c(x)$ varies approximately as an exponential function of x: $c(x)=C_0e^{-\alpha x}$. This results in the wave equation

$$\frac{d^2}{dx^2}\psi(x)+D_0^2e^{\alpha x}\psi(x)=0, \tag{3}$$

where $D_0=\omega\sqrt{2\rho/hC_0}$. The solution of this equation was given as $\psi(x)=\arctan Y_0(z)/J_0(z)$, where $z=(2D_0/\alpha)e^{\alpha x/2}$, and J_0 and Y_0 represent Bessel and Weber function of zero order, respectively. This leads to the local propagation constant

$$k(x)=\frac{d}{dx}\psi(x)=\frac{\alpha/\pi}{J_0^2(z)+Y_0^2(z)}. \tag{4}$$

The speed of propagation is generally given by $\gamma(x)=\omega/k(x)$. The exact expression for the exponential model therefore is

$$\gamma(x)=\frac{\pi\omega}{\alpha}(J_0^2(z)+Y_0^2(z)). \tag{5}$$

This expression shows dispersion with respect to frequency since γ is dependent on ω.

The above equations are used in the present paper to generate the chirp stimulus that compensates dispersion on the BM. The propagation time $t_\omega(x)$ needed to arrive at the place of resonance x is given by

$$\begin{aligned}t_\omega(x)&=\int_0^x\frac{1}{\gamma}dx'=\frac{1}{\omega}\int_0^x k(x')dx'\\&=\frac{1}{\omega}\int_0^x\frac{d}{dx'}\psi(x')dx'=\frac{1}{\omega}(\psi(x)-\psi(0)),\end{aligned} \tag{6}$$

leading to

$$t_\omega(x)=\frac{1}{\omega}\left(\arctan\frac{Y_0(z(x))}{J_0(z(x))}-\arctan\frac{Y_0(z(0))}{J_0(z(0))}\right). \tag{7}$$

For the frequency-place transformation, the mapping proposed by Greenwood (1990) was used,

$$x=x(f)=L-\tilde{c}\log(af+1)=L-c\ln(af+1), \tag{8}$$

with $a=0.006\,046\,\mathrm{Hz}^{-1}$, $\tilde{c}=16.7\,\mathrm{mm}$, $c=\tilde{c}/\ln 10$, and $L=34.85\,\mathrm{mm}$ representing BM length. It follows that

$$\begin{aligned}z(x)=z(x(f))&=\frac{2D_0}{\alpha}e^{\alpha/2[L-c\ln(af+1)]}\\&=\frac{2D_0}{\alpha}(af+1)^{-(\alpha/2)c}e^{(\alpha/2)L}.\end{aligned} \tag{9}$$

Thus $t_\omega(x)$ is given by

$$\begin{aligned}t_\omega(x)&=t_\omega(x(f))\\&=\frac{1}{\omega}\left(\arctan\frac{Y_0\left[\frac{2D_0}{\alpha}(af+1)^{-(\alpha/2)c}e^{(\alpha/2)L}\right]}{J_0\left[\frac{2D_0}{\alpha}(af+1)^{-(\alpha/2)c}e^{(\alpha/2)L}\right]}-\arctan\frac{Y_0\left(\frac{2D_0}{\alpha}\right)}{J_0\left(\frac{2D_0}{\alpha}\right)}\right).\end{aligned} \tag{10}$$

Using the variable transformation $t\to t_0-t$, and with $\kappa:=(4\pi/\alpha)\sqrt{2\rho/hC_0}e^{(\alpha/2)L}$, the function $t=t(f)$ for the ''optimal'' input frequency $\omega=2\pi f$ is given by

$$t_0-t(f)=\frac{1}{2\pi f}\left(\arctan\frac{Y_0[f\kappa(af+1)^{-(\alpha/2)c}]}{J_0[f\kappa(af+1)^{-(\alpha/2)c}]}-\arctan\frac{Y_0\left(\frac{2D_0}{\alpha}\right)}{J_0\left(\frac{2D_0}{\alpha}\right)}\right). \tag{11}$$

From this relation, the inverse function $f(t)=t^{-1}(f)$ was derived numerically. This function for the change of the instantaneous frequency was then temporally reversed and integrated over time to derive the instantaneous phase $\varphi=2\pi\int_0^t f(t')dt'$ of the resulting chirp, which has the general form $s(t)=A(t)\sin(\varphi(t)-\varphi(t_0))$. This is referred to as the ''exact chirp'' throughout this paper (cf. Fig. 1, upper panel, solid curve).

If one uses only an *asymptotic* expression for the propagation constant, namely $k(x)\approx D_0e^{\alpha x/2}$, the speed of propagation results in $\gamma(x)\approx\sqrt{(hC_0/2\rho)}e^{-\alpha x/2}$, which is independent of ω so that there is no dispersion with respect to frequency. The asymptotic expression agrees well with the exact one for frequencies higher than about 5 kHz [for details, see de Boer (1980), p. 147]. For lower frequencies, some small deviations occur for low x-values, i.e., near the cochlear windows. In this region, the asymptotic expression does not hold true any more; however, the extent of this effect is not very large. For the asymptotic case, the instantaneous frequency $f(t)=t^{-1}(f)$ can be easily derived analytically. With

$$\psi(x)=\int_0^x k(x')dx'+\psi(0)=D_0\frac{2}{\alpha}(e^{\alpha x/2}-1)+\psi(0), \tag{12}$$

and Eq. (6), the travel time $t(f)$ to the resonance place $x(f)$ is directly given by

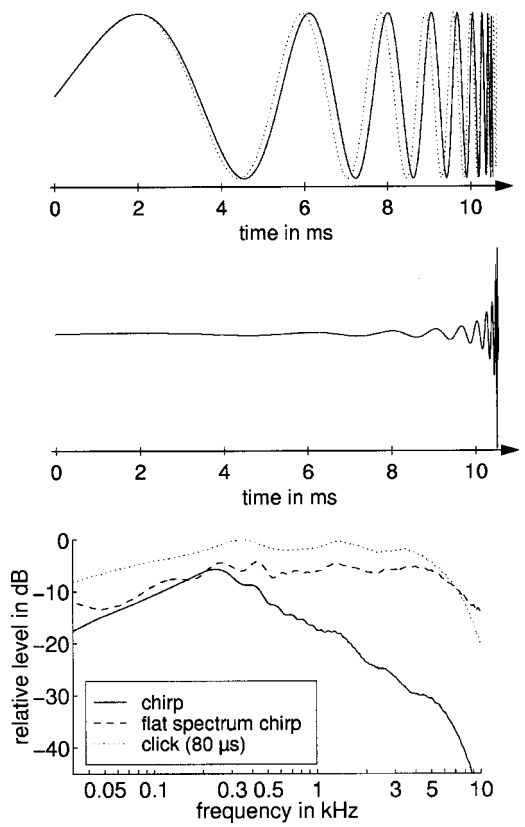

FIG. 1. Top panel: Waveform of the broadband rising (0.1–10.4-kHz) chirp stimulus. The equations defining the chirp were calculated to be the inverse of the delay-line characteristic of the cochlear partition on the basis of the linear cochlea model by de Boer (1980). The solid curve represents the exact chirp, the dotted curve shows the approximated chirp (for details, see text). Middle panel: Waveform of a modified chirp referred to as ''flat-spectrum chirp'' whose phase characteristic is the same as that of the original (exact) chirp. Bottom panel: Acoustic spectra of chirp (solid curve), click stimulus (dotted curve), and flat-spectrum chirp (dashed curve), as used in the present study (for details, see text).

$$t=\frac{1}{\omega}D_0\frac{2}{\alpha}(e^{\alpha x/2}-1)$$

$$=\frac{1}{\omega}D_0\frac{2}{\alpha}(e^{\alpha x/2(L-c\,\ln(af+1))}-1)$$

$$=\frac{2}{\alpha}\sqrt{\frac{2\rho}{hC_0}}((af+1)^{-\alpha c/2}e^{(\alpha/2)L}-1). \tag{13}$$

With $t\rightarrow t_0-t$, and $\beta:=2/\alpha\sqrt{2\rho/hC_0}$, the function $f(t)$ is given by

$$f=\frac{1}{a}\left(\left[e^{(\alpha/2)L}\left(1+\frac{t_0-t}{\beta}\right)\right]^{-2/\alpha c-1}\right). \tag{14}$$

From this, the instantaneous phase φ and the resulting chirp $s(t)$ can easily be derived as above. This is referred to as the ''approximated chirp'' in the rest of this paper (cf. Fig. 1, upper panel, dotted curve).

II. METHOD

A. Subjects

Ten normal-hearing subjects (audiometric thresholds 15 dB HL or better) with no history of hearing problems were chosen: two females and eight males. The subjects were between 21 and 35 years of age, and were either paid or volunteered for the experiment.

B. Apparatus

The experiments were carried out with a PC-based computer system which controlled stimulus presentation and recording of evoked potentials. A DSP card (Ariel DSP32C) converted the digitally generated stimulus (25 kHz, 16 bit) to an analog waveform. The output of the DSP card was connected to a digitally controlled audiometric amplifier, which presented the stimulus through an insert earphone (Etymotic Research ER-2) to the subject.

Electroencephalic activity was recorded from the scalp via silver/silver chloride electrodes, attached to the vertex (positive) and the ipsilateral mastoid (negative). The forehead served as the site for the ground electrode. Interelectrode impedance was maintained below 5 kΩ. Responses were amplified (80 dB) and bandpass filtered (95–1640 Hz, 6 dB/oct) with a commercially available ABR preamplifier (Hortmann Neurootometrie).[1] Extra amplification (Kemo VBF/40) was used to reach the optimum range for the A/D converter. This amplification was in the range from 10 to 16 dB, resulting in a total amplification of 90–96 dB. The amplified signal was digitized by the DSP card (25 kHz, 16 bit), which also performed artifact rejection and signal averaging. Responses were recorded for 26 ms following the stimulus onset.

C. Stimuli and procedure

Broadband chirps as described in Sec. I were used as stimuli. The chirps started and ended with zero amplitude. If not explicitly stated otherwise, no windowing was applied to the stimuli. Chirp-evoked potentials were compared with click-evoked responses. The click had a duration of 80 μs.

The upper panel of Fig. 1 shows the waveforms of the exact (solid curve) and the approximated chirp (dotted curve), both derived in Sec. I. The stimuli have a flat temporal envelope. Since the value for the speed of propagation γ for lower frequencies is lower for the exact chirp (at places near the cochlear windows), it has a slightly longer duration (10.52 ms instead of 10.48 ms for the approximated chirp). Since for both chirps the instantaneous frequency changes slowly at low frequencies relative to the changes in the high-frequency region, their spectra are dominated by the low frequencies. This is shown in the lower panel of Fig. 1 (solid curve). The (acoustic) magnitude spectrum decreases continuously with increasing frequency. The dashed curve in the lower panel indicates the spectrum of a modified chirp which is used later in the study. This modified chirp has a flat amplitude spectrum corresponding to that of the click (dotted curve), while the phase characteristic is the same as that of the original (exact) chirp. The spectra were obtained (at the same sensation level of the stimuli) by coupling the ER-2 insert earphone to a Brüel and Kjær ear simulator (type 4157) with a 1/2-in. condenser microphone (type 4134), a 2669 preamplifier, and a 2610 measuring amplifier. The spectra were obtained from fast Fourier transforms (FFTs) of

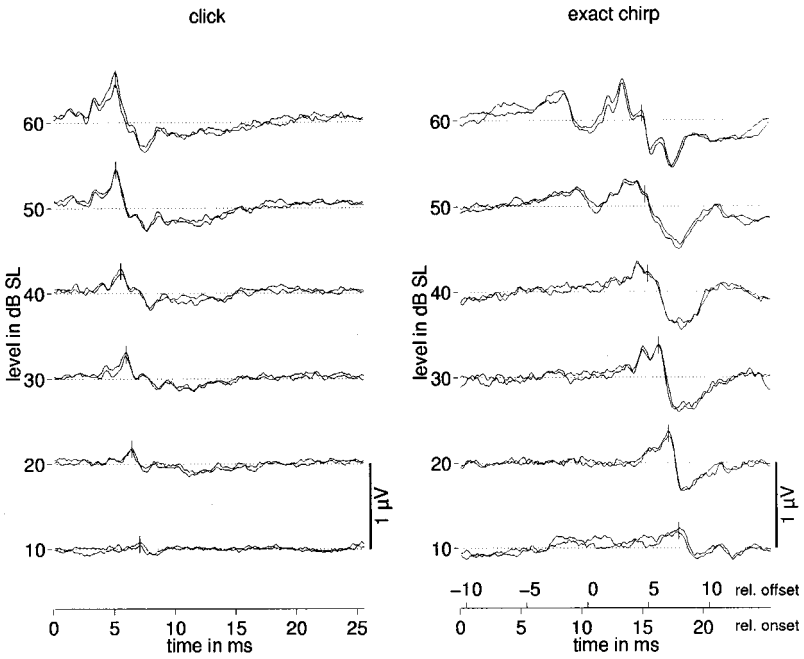

FIG. 2. ABR from subject CR, evoked by a click (left panel) and a broadband chirp (right panel). The stimulation level varied from 10 to 60 dB SL, as indicated. Waveforms are the average of 2000 responses. At each level, two waveforms are superimposed to show response replicability. The small vertical line indicates wave-V peak. Stimulus presentation rate was 20/s.

100-trial time-domain averages of the stimulus over an analysis time of 64 ms using a sampling rate of 25 kHz (Stanford Research Systems SR780). The waveforms were not windowed prior to FFT. The middle panel of Fig. 1 shows the corresponding temporal waveform of the modified chirp, referred to as the ''flat-spectrum chirp'' throughout this paper. This stimulus starts with very small amplitudes at low frequencies and increases nonlinearly in amplitude with time.

The subject lay on a couch in an electrically shielded, soundproof room, and electrodes were attached. The subject was instructed to keep movement at a minimum, and to sleep if possible. The lights were turned out at the beginning of the session. Each session lasted between one and two hours, depending on the subject's ability to remain still. The ear of stimulation was chosen randomly, i.e., for each subject one ear was chosen and then maintained. The acoustic signals were delivered at a mean repetition rate of 20 Hz for all stimulus conditions. A temporal jitter of ± 2 ms was introduced to minimize response superimposition from preceding stimuli. Thus the resulting interstimulus interval (ISI) was equally distributed between 48 and 52 ms. Each trial consisted of 1000 to 4000 averages, depending on the quality of the response. For each stimulus condition, two independent trials were stored in separate buffers. These are illustrated as superimposed waveforms in the figures to show response replicability.

First, to determine the sensation level (SL) of both the click and the chirp stimulus, the absolute hearing thresholds were measured individually with an adaptive 2AFC procedure. At the beginning of each ABR recording session, the first trial was a 60-dB SL presentation of a stimulus. Then intensity was decreased in steps of 10 dB down to 10 dB SL. At the same sensation level, chirp and click represent nearly the same root-mean-square (rms) value (if calculated across the same temporal interval of 10.5 ms).

Wave-V (peak-to-peak) amplitude was analyzed in the different stimulus and level conditions. The amplitude was measured from the peak to the largest negativity following it. For each stimulus and level condition, wave-V amplitude was averaged across subjects. A Wilcoxon matched-pairs signed-rank test ($\alpha=0.05$) was used to verify whether the response amplitude differed significantly for the two stimuli. Throughout the present paper, responses are plotted for one exemplary subject (CR). Average data for the wave-V amplitude are given in a summary figure (Fig. 3).

III. RESULTS

A. Click- versus chirp-evoked potentials

Figure 2 shows the ABR for subject CR obtained with a click (left panel) and a rising broadband chirp (right panel), respectively. Responses for different stimulus levels are shown on separate axes displaced along the ordinate and labeled with the sensation level (dB SL). For the click stimulus, the abscissa represents recording time relative to click onset. In the case of the chirp stimulus, a dual abscissa is used representing recording time relative to stimulus onset and offset. Wave-V peak is marked by small vertical bars for both stimuli. It can be seen in the figure that the wave-V latencies for the two stimuli, relative to stimulus onset, are shifted by the duration of the chirp stimulus which equals 10.5 ms. Thus the latency values relative to stimulus offset are the same in both conditions. The key observation is that the wave-V amplitude is typically larger for chirp stimulation than for click stimulation. For subject CR, the difference is large at stimulation levels of 10–40 dB SL, but is less pronounced at 50 dB SL. At 60 dB SL, for this subject, the click response is slightly larger than the chirp response. At the two highest stimulation levels, earlier activity in response to the chirp becomes visible with a first response peak at about 8–9 ms after chirp onset. These observations at high levels are probably due to cochlear upward spread of excitation, a well-known phenomenon from many other studies in

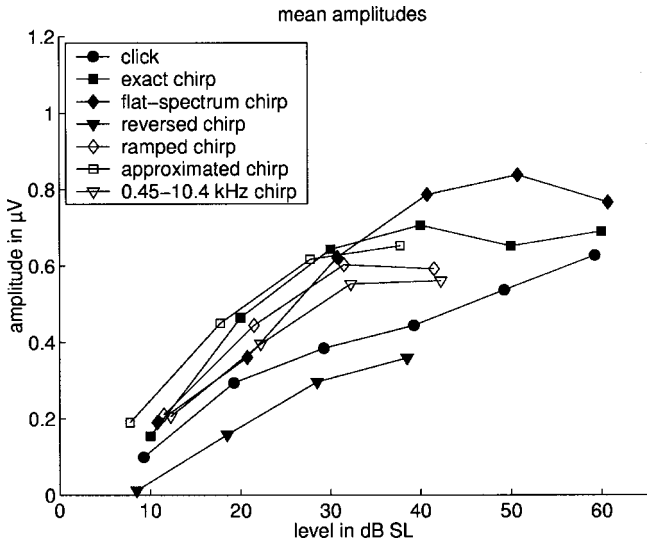

FIG. 3. Average ABR data for wave-V amplitude, as a function of the stimulation level. Different symbols indicate different stimulus conditions. ●: click; ■: exact chirp; ◆: flat-spectrum chirp; ▼: reversed chirp; ◇: ramped chirp; □: approximated chirp; ▽: 0.45–10.4-kHz chirp.

this field. At high levels, the early low-frequency energy in the chirp stimulates basal regions and produces a response.

Figure 3 shows the wave-V amplitude obtained with different stimuli, including the chirp (filled boxes) and the click (filled circles), averaged across subjects. Amplitude values are plotted as a function of stimulation level. Wave-V amplitude was significantly larger ($p<0.05$; $N=10$) for the chirp than for the click, for the levels of 20–40 dB SL. For 50 and 60 dB SL, the average wave-V amplitude was still larger for the chirp than for the click, but the difference was not significant ($p>0.05$). For the lowest stimulation level, 10 dB SL, four of the subjects showed no clear wave-V peak in either the chirp or in the click condition. The number of the remaining subjects was too small to reveal a significant difference in the ABR.

B. Exact versus approximated chirp

On the basis of the exponential model (de Boer, 1980) reviewed in Sec. I, the exact solution and a relatively simple approximation for the generation of a stimulus compensating BM dispersion were derived (see Fig. 1). The question is whether the difference in the time course of the two stimuli is of relevance for the corresponding evoked brainstem potentials.

Figure 4 shows ABR for subject CR elicited by the exact chirp (left panel) and by the approximated chirp (right panel). The stimulation level ranged from 10 to 40 dB SL in each case. The potentials are almost identical in both conditions. The average data across subjects for the approximated chirp are indicated as open boxes in Fig. 3. Wave-V amplitude does not differ significantly between the two stimuli for all levels ($p>0.05$; $N=6$).

C. Stimulation with ramped chirps

It could be argued that the relatively abrupt *offset* of the chirp is responsible for the generation of wave-V amplitude. Although such an argument would *not* explain the observation of an increased amplitude compared to the click response, a chirp stimulus was generated with sufficiently long ramps to preclude the possibility that purely onset- and offset effects are responsible for wave-V amplitude generation. A rise time of 3 ms and a fall time of 0.5 ms were applied.[2] Figure 5 shows the corresponding ABR recordings for subject CR (solid lines). In addition, the corresponding data with the exact chirp without ramps are replotted in the figure and indicated as dotted lines. In comparison with the original chirp without ramps, there is only a slight decrease in amplitude for this subject. This is most likely due to the attenuation of frequencies higher than about 6 kHz that normally also contribute to the generation of wave-V amplitude. Note, however, that the overall level of the ramped chirp had to be increased by 2 dB to yield the same sensation level.

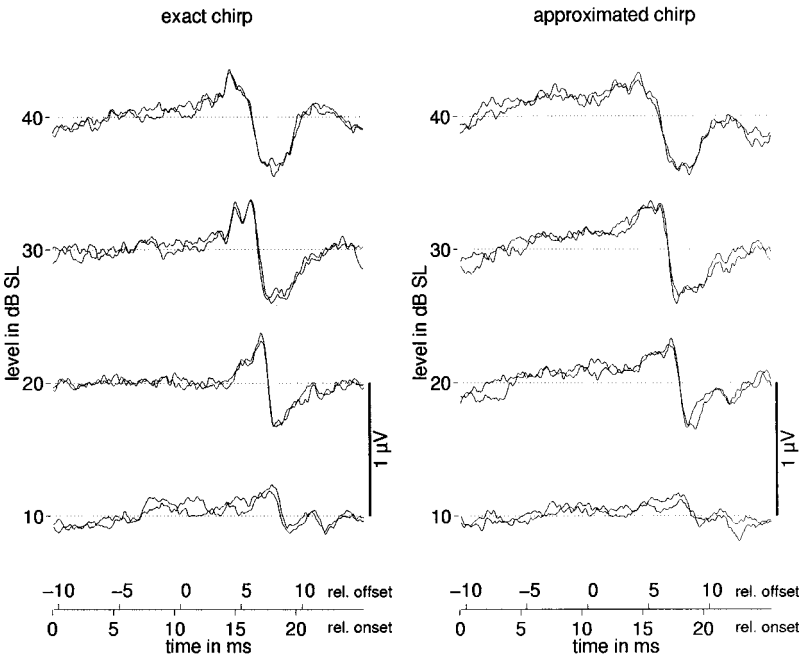

FIG. 4. ABR from subject CR, elicited by the exact broadband chirp (left panel) and the approximated chirp (right panel). Parameters as in Fig. 2, but only for stimulation levels of 10–40 dB SL.

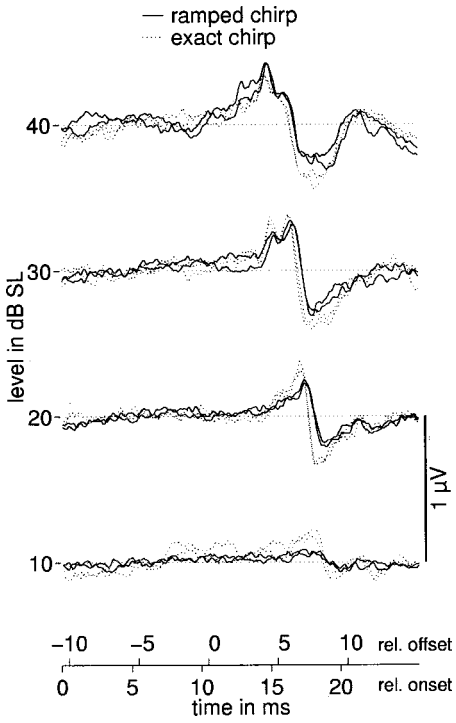

FIG. 5. ABR from subject CR, evoked by the ramped broadband chirp. In addition, the potentials evoked by the original chirp without ramps are replotted from Fig. 2 and indicated as dotted curves.

Average data across subjects obtained with the ramped chirp are indicated in Fig. 3 (open diamonds). Like the original chirp without ramps, the ramped chirp elicits a significantly larger amplitude ($p<0.05$; $N=10$) than the click for the stimulation levels 20–40 dB SL. The difference is not significant for 10 dB SL.

All results taken together show that wave-V amplitude is increased when a rising broadband chirp is used instead of a click. This is the case although the duration of the chirp is about 10 ms, which is a factor of 125 longer than the click duration. This result is in contrast to the generally accepted view in the literature that the conventional ABR is an electrophysiological event only evoked by onset or offset of an acoustic stimulus.

D. Effects of direction of frequency sweeping

If the argument holds that the ''optimized'' temporal course of the frequency sweeping is responsible for maximal synchronization, then a temporally *reversed* broadband chirp should yield a smaller response amplitude. The reversed chirp starts with high frequencies and sweeps nonlinearly in time toward low frequencies. The onset is therefore much steeper than that of the original chirp, so that one should expect a larger response if ABR is determined by the steepness of the stimulus onset. The magnitude spectra of the reversed chirp and the original chirp, of course, are identical.

Figure 6 (left panel) shows the ABR for the reversed chirp (subject CR). For comparison, the right panel of Fig. 6 shows the ABR elicited by the rising chirp, for the same range of stimulation levels (10–40 dB SL), replotted from Fig. 2. It is apparent from the figure that in the case of the falling chirp, wave-V amplitudes are generally much smaller than those obtained with the rising chirp. The responses are also considerably smaller than those elicited by the click (see Fig. 2).

The average data for the reversed chirp are indicated as filled downward triangles in Fig. 3. Wave-V amplitude is significantly smaller ($p<0.05$; $N=10$) for the reversed chirp than for the rising chirp (filled boxes) for all stimulation levels 10–40 dB SL. The reversed-chirp amplitude was also significantly smaller than the click response (filled circles) for the levels 20–40 dB SL ($p<0.05$; $N=10$), while the difference was not significant for 10 dB SL.

However, because of the long duration of the chirp (10.52 ms), the response to the early (high-frequency) part may interfere with responses to the later (low-frequency) part

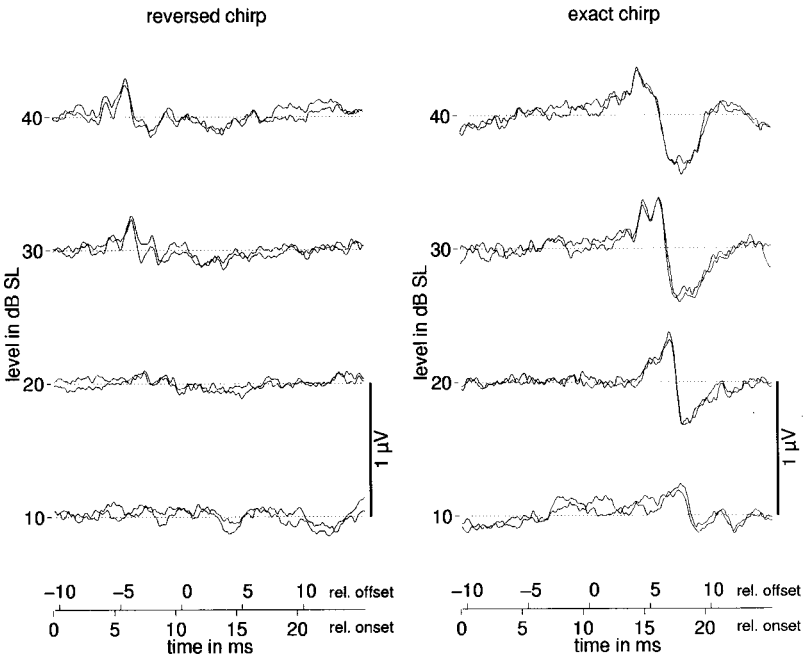

FIG. 6. Left: ABR from subject CR, elicited by the temporally reversed broadband chirp (10.4–0.1 kHz). Parameters as in the previous figures. Right: ABR's from the same subject, elicited by the rising broadband chirp (replot from Fig. 2, but only for the levels 10–40 dB SL).

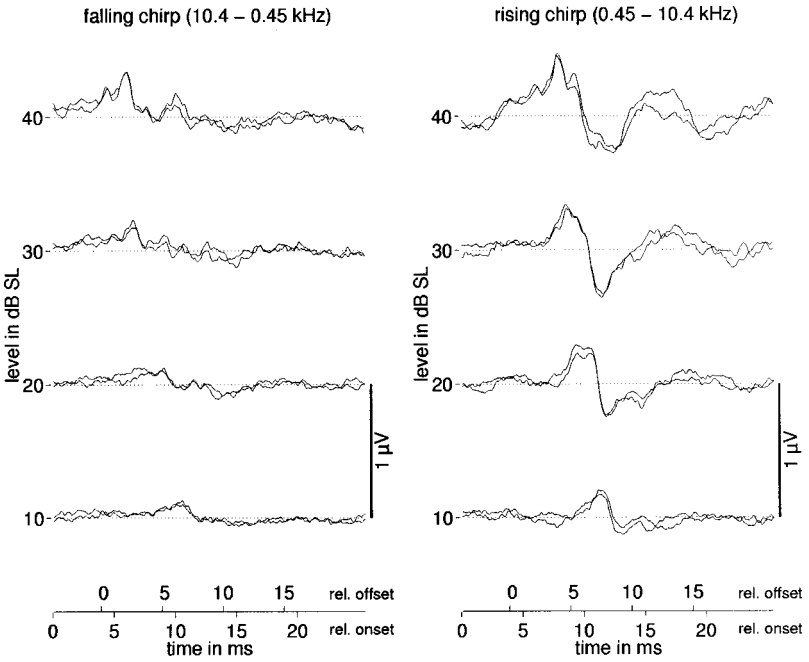

FIG. 7. ABR from subject CR, elicited by the 3.92-ms chirp with a spectrum in the frequency range between 0.45 and 10.4 kHz. Left: Temporally reversed (falling) chirp (10.4–0.45 kHz); right: rising chirp (0.45–10.4 kHz).

of the stimulus. For this reason, a further experiment was run with a shorter chirp (3.92 ms), whose spectrum stretches from about 0.45 to 10.4 kHz (in contrast to 0.1 to 10.4 kHz as before). Figure 7 shows, for subject CR, the brainstem potentials evoked by the falling chirp (left panel) in comparison with the corresponding rising chirp (right panel). As in Fig. 6, the amplitude of wave V is much smaller in the case of stimulation with the falling chirp than with the rising chirp. Note that the responses evoked by the two reversed chirps (from Figs. 6 and 7) are almost identical, whereas the responses evoked by the two rising chirps differ to some extent. The average data for the 0.45–10.4 kHz chirp are indicated as open downward triangles in Fig. 3. There is no significant difference in wave-V amplitude between the two chirps for 10 dB SL. However, for the levels 20–40 dB SL, the amplitude is significantly larger ($p<0.05$; $N=6$) for the 0.1–10.4 kHz chirp than for the 0.45–10.4 kHz chirp. This difference in wave-V amplitude directly reflects the contribution of the low-frequency components (100–450 Hz) to the ABR in the case of the rising chirp.

These results are compatible with the hypothesis that compensation of travel time differences across frequency causes an optimal synchronization, whereas the reversed stimulation leads to a less effective activation (although the onset of the reversed chirp is much steeper than that of the rising chirp). Falling sweeps probably produce sequential activation of high-frequency fibers followed by low-frequency fibers. This may lead to a desynchronized neural activation at the brainstem level, as implied by the results of Shore and Nuttall (1985) at the level of VIIIth nerve and CN. In ''far-field'' recordings as considered in the present study, the observed effects may also be reflected by phase cancellation of the potentials due to superimposition of wave V from one frequency and wave V from another frequency (e.g., Scherg and von Cramon, 1985, see discussion).

E. Effects of spectral composition

It is not clear which spectral shape is optimal for broadband stimulation. It is also not clear how and at which level integration *across* frequency is realized in the auditory system. Hence, it may be argued that the observed differences between responses evoked by a click and a chirp stimulus are produced by their different spectral shape. To rule out this argument, ABR elicited by the flat-spectrum chirp from Fig. 1 (middle panel), with a flat amplitude spectrum corresponding to that of the click, are compared to click-evoked responses.

Figure 8 shows the corresponding ABR for this chirp for subject CR (solid curves). For direct comparison, the corresponding click-evoked responses for the same subject (replotted from Fig. 2, left panel) are indicated as dotted curves. Wave-V amplitudes are much larger for the chirp than for the click. The amplitudes are even larger than for the ''normal'' rising chirp without specific spectral weighting (Fig. 2, right panel), particularly at the highest stimulation levels. The average data for wave-V amplitude, obtained with the flat-spectrum chirp, are plotted as filled diamonds in Fig. 3. Wave-V amplitude is significantly larger ($p<0.05$; $N=10$) for this chirp than for click stimulation for *all* levels (10–60 dB SL). However, the difference in amplitude obtained with the flat-spectrum chirp and the original rising chirp (cross symbols) was not statistically significant.

A similar approach has been earlier described in a study by Lütkenhöner *et al.* (1990). They also generated a rising chirp stimulus with a flat amplitude spectrum where—in contrast to the present study—the course of the instantaneous frequency was estimated from the relationship between the stimulus frequency and the experimentally obtained latency of the corresponding frequency-specific ABR. The authors also found a larger wave-V amplitude with chirp than with click stimulation. However, the differences were smaller

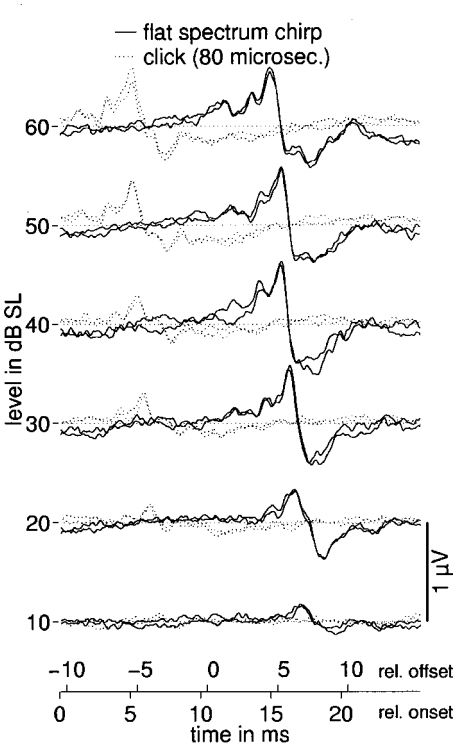

FIG. 8. ABR from subject CR elicited by the rising chirp with flat amplitude spectrum (from Fig. 1, bottom panel). For direct comparison, click-evoked responses (dotted curves) for the same subject are replotted from Fig. 2.

than those presented here, particularly at higher stimulation levels.

In summary, the presented data demonstrate that both dispersed timing as well as spectral composition of the stimulus strongly influence the potential pattern. The dispersed timing appears to be the dominant factor.

IV. GENERAL DISCUSSION

A. Stimulus presentation: SL versus peSPL

In the present study, chirps and clicks were presented at the same sensation level. However, the corresponding peak-equivalent sound pressure level (peSPL) at the same sensation level, averaged across subjects, was about 12 dB *lower* for the chirp than for the click. For example, at threshold (0 dB SL), the mean (and standard deviation) of the peSPL was 45.9 ± 3.7 dB for the click while it was 33.5 ± 3.6 dB for the chirp. It is unclear which measure is appropriate for ABR. Temporal integration of signal energy involved in behavioral threshold measures probably occurs at more central stages of auditory processing, and is most likely not reflected in ABR. Nevertheless, in many studies the stimuli are presented at the same hearing level (HL) to investigate potential amplitude in relation to the (normalized) average hearing threshold (0 dB HL). The strategy in the present study is thus very similar to the HL measure, but hearing thresholds are determined individually. Whatever the proper calibration for ABR may be, if the responses obtained in the present study were plotted at the same peSPL instead of the same dB SL, the differences in the potential amplitude between chirp and click stimulation would be even larger.

B. Role of wave V behavior—Spectral integration

By applying the derived response technique, Don and Eggermont (1978) revealed narrow-band contributions to the ABR from specific portions of the BM. They found that nearly the *whole* cochlear partition can contribute to the brainstem response. In their recordings, the amplitude behavior of wave V, as a function of the central frequency (CF) assigned to each narrow band, was different from waves I and III, depending upon the frequency range. Don and Eggermont found that for CFs below 2 kHz, the amplitudes for waves I and III drop rapidly as CF is decreased, whereas there is an increase in the amplitude of wave V. Therefore, at low CFs the only clear contribution to the ABR is to wave V. This indicates that the representation of cochlear activity in the various peaks probably is quite different for wave I and III on one hand, and wave V on the other hand (Don and Eggermont, 1978). Above 2 kHz, the wave-V behavior is the same as for the earlier waves. Thus wave-V amplitude shows a flatter ''frequency response'' than the earlier waves and has an amplitude distribution which is nearly constant over the entire CF range.

By using a synchronizing chirp instead of a click as the stimulus, activity from *all* cochlear locations can contribute to the amplitude of wave V, which therefore is generally larger than that evoked by a click. This was demonstrated in the present study. Don and Eggermont (1978) stated that the discrepancy in the behavior of wave V with respect to the earlier waves suggests some sort of neural reorganization at the level where wave V is generated.[3] The sharp initial positive potential is most likely generated by the lateral lemniscus as it enters in the inferior colliculus (IC), while the slow negative potential following this is likely a dendritic potential of the inferior colliculus (Hashimoto, 1982; Møller and Jannetta, 1982, 1986; Moore, 1987a,1987b). The central nucleus of the IC (ICC) is a purely auditory processing center; it is the main center for spatial auditory integration receiving most of the ascending information from auditory brainstem nuclei, and it has a curved laminar arrangement of cells, axons, and dendrites (e.g., Gummer and Zenner, 1996) which leads to an effective response. The convergence of pathways activates a large number of neurons in the IC, the wave-V potential therefore is of rather large amplitude, that obviously results from integration of activity from the whole range of auditory frequencies, and hence includes responses elicited by low-frequency stimulus components.

Interestingly, clear peaks corresponding to the earlier waves I–III could *not* be observed in the case of the original rising chirp (without specific spectral weighting) for any of the stimulation levels tested in the present study. This observation was true for all subjects, even if not investigated quantitatively. At the highest levels (50 and 60 dB SL), the early low-frequency energy of the chirp probably stimulates basal regions of the BM due to upward spread of excitation, producing a response at about 8–9 ms after stimulus onset (as earlier mentioned in Sec. III A). However, it is not clear how these high-level responses are related to waves I–III. In contrast, we observed that, for the highest stimulation level of 60 dB SL, most of the subjects clearly showed the typical early peaks in their responses to the click as well as to the

flat-spectrum chirp. In particular, the potential patterns at this level were very similar for these two stimuli for each subject. Thus it appears that the spectral composition of the stimulus mainly determines the response pattern at high levels.[4]

C. Assumption of linearity of BM characteristic

The chirp stimuli used in the present study were derived on the basis of a linear cochlea model (de Boer, 1980). It was assumed that the movements are so small that the fluid as well as the basilar membrane operate linearly. Over the normal range of hearing, the assumption of linearity may be well justified for the fluid (de Boer, 1980). With regard to the BM, however, its dynamics are certainly more complicated (e.g., Rhode, 1971; Ruggero, 1992). At low levels, BM dynamics may indeed be considered as nearly linear. However, at higher levels, nonlinear cochlear mechanics complicate the responses to a frequency-changing signal. Ruggero and Rich (1983), for example, demonstrated that VIIIth-nerve fibers' phase response changes at high intensities, resulting in two peaks which are 90° out of phase, instead of one peak commonly seen in period histograms. Since our interest in the present study was mainly focused on effects at levels between absolute threshold and about 40 dB SL, the assumption of linearity in the model calculations may be well justified. Also, the predictions of the linear model were primarily used for the correction of the dispersive behavior of the BM, which can be assumed to vary less with level than, e.g., the amplitude tuning characteristic for a certain frequency. Of course, a more general description for an extended level range would need to take nonlinear effects into account. The equations used so far should therefore be considered as a first-order approximation.

V. SUMMARY AND CONCLUSIONS

A chirp stimulus was developed which theoretically produces synchronous discharges of VIIIth-nerve fibers along the length of the human cochlear partition. The equations defining the chirp were calculated to be the inverse of the delay-line characteristic of the cochlear partition on the basis of the linear cochlea model by de Boer (1980). The stimulus was tested for eliciting ABR. The underlying idea was to determine if units tuned to low CFs (below 2 kHz) could be recruited synchronously into the brainstem response. It was shown in the present study that, in most level conditions, the chirp evokes a significantly larger wave-V amplitude than the click when presented at the same sensation level. This is the case, although the duration of the chirp is about 10 ms, which is a factor of 125 longer than the click-duration used here. Since at the same sensation level, the peak-equivalent sound pressure level (peSPL) is about 12 dB *smaller* for the chirp than for the click, the difference in wave-V amplitude of the ABR recordings would be even larger if the stimuli would be presented at the same peSPL, or at the same peak-to-peak equivalent sound pressure level (ppeSPL). Thus the conventional ABR should not be considered as an electrophysiological event purely evoked by the onset or offset of an acoustic stimulus. Instead, an appropriate temporal organization, determined by BM traveling wave properties, may increase neural synchrony at the level where wave V is generated. The temporally reversed chirp stimulus led to a smaller wave-V amplitude compared to the rising chirp and to the click. This may be due to desynchronized neural activation at the level where wave V is generated, as a result of sequential activation of high- followed by low-frequency fibers. Alternatively, the reduced potential amplitude may also result from cancellation in the ''far-field'' by superposition of wave V from one frequency on wave V from another frequency.

It was observed that not only temporal organization of the stimulus, but also its spectral shape, influences the ABR pattern. The phase characteristic of the chirp, combined with a flat spectral distribution (as in case of the click), led to a large wave-V amplitude, but also to a more pronounced pattern of the earlier waves (at high stimulation levels), which is comparable to that evoked by the click. In contrast, responses evoked by the rising chirp without specific spectral weighting did not show clear earlier peaks I–III. This may be due to cancellation of overlapping responses at high stimulation levels where the early low-frequency energy in the chirp stimulates basal regions of the BM due to upward spread of excitation. Alternatively, or in addition, this may also be due to biased frequency representations at the level of the neural generators for waves I–III, while the generator for wave V probably has a flatter frequency response.

The use of the rising frequency chirp enables the inclusion of activity from lower-frequency regions, whereas with a click or a falling chirp synchrony is decreased in accordance with decreasing traveling velocity in the apical region. The rising frequency chirp may therefore be of clinical use in assessing the integrity of the entire peripheral organ, and not just its basal end.

ACKNOWLEDGMENTS

We would like to thank our colleagues of the research group ''AG Medizinische Physik,'' the graduate school ''Psychoakustik,'' and the Sonderforschungsbereich 517 ''Neuronale Grundlagen kognitiver Leistungen'' at the Universities Oldenburg and Bremen for fruitful discussions on the content of this paper, and Steve Colburn, Michael Heinz, Stefan Uppenkamp, and Sebastian Hoth for critical reading of an earlier version of this paper. Two anonymous reviewers provided very helpful and fruitful criticism. This study was supported by the Deutsche Forschungsgesellschaft (DFG).

[1]In the official data sheet of the preamplifier, a ''hard-wired'' high-pass cutoff frequency of 30 Hz is given. Unfortunately, we could not replicate this value and found a 3-dB cutoff of 95 Hz. The problem is that this setting will cut out a substantial portion of the wave-V amplitude, which results in smaller responses overall, particularly for responses from lower-frequency stimulus energy. Since the chirp has much of its energy in the low-frequency region, one can expect that an even larger chirp-evoked wave-V amplitude than observed in the present study will be obtained with a more appropriate filter setting.

[2]A larger fall time than 0.5 ms would also attenuate energy at medium frequencies. For example, if a fall time of 1 ms were used, frequencies around 2.5 kHz would be attenuated by about 3 dB. Higher frequencies would be attenuated up to 12 dB more than in the case of the shorter ramp. We think that a 0.5-ms fall time and a 3-ms rise time for the chirp is more than a fair choice for the comparison of chirp and click efficiency in evoking ABR. In addition, in a preliminary study, we performed an experiment

where the stimulus consisted of a *continuous* alternating sequence of chirps: each rising chirp was followed by the temporally reversed (falling) chirp. Results showed ''peaked'' response patterns whereby amplitude and (relative) latency of the peaks directly corresponded to those obtained with ''single'' rising chirps. The results further clearly demonstrate the importance of considering the effects of basilar-membrane traveling wave on the formation of the ABR, at least for wave V.

[3]In a recent study, Don *et al.* (1997) presented a new derived-response measure where the wave-V amplitude of a stacked ABR was constructed by temporally aligning wave V of each derived-band ABR, and then summing the time-shifted responses. They found that the stacked response amplitude can detect small acoustic intracanalicular tumors in patients missed by standard ABR measures. It might be very interesting to compare the stacked wave-V amplitude obtained with the click with the chirp-evoked response amplitude obtained with the ''standard'' derived responses measure. Such experiments are currently in progress to specify the usefulness of the chirp for retrieving frequency-specific information.

[4]The orientation of the electrode configuration certainly plays a role in the shape of the potential pattern observed in the far-field. It has been shown that there are differences in click-evoked responses in horizontal and vertical dipole orientations (e.g., Galbraith, 1994). Wave V is best seen in the vertical channel, while earlier components are well defined in the horizontal channel. Using a spatio-temporal dipole model, Scherg and Von Cramon (1985) demonstrated a predominantly horizontal orientation underlying waves I–III. These horizontal dipoles appeared to reflect transverse propagation along the auditory nerve to the ipsilateral cochlear nucleus (CN), and then via second-order neurons crossing the midline to the contralateral superior olivary complex (SOC). Thus it might be of interest to also investigate chirp-evoked ABR recordings in horizontal dipole orientations.

Békésy (**1960**). *Experiments in Hearing* (McGraw-Hill, New York).

de Boer, E. (**1980**). ''Auditory physics. Physical principles in hearing theory I,'' Phys. Rep. **62**, 87–174.

Brinkmann, R., and Scherg, M. (**1979**). ''Human on- and off-potentials of the brainstem. Influence of stimulus envelope characteristics,'' Scand. Audiol. **8**, 27–32.

Brugge, J. F., Anderson, D. J., Hind, J. E., and Rose, J. E. (**1969**). ''Time structure of discharges in single auditory nerve fibers of the squirrel monkey in response to complex periodic sounds,'' J. Neurophysiol. **32**, 386–401.

Debruyne, F., and Forrez, G. (**1982**). ''On-effect in brainstem electric response audiometry,'' Otolaryngology **44**, 36–42.

Dolan, D. F., Teas, D. C., and Walton, J. P. (**1983**). ''Relation between discharges in auditory nerve fibers and the whole nerve response shown by forward masking: An empirical model for the AP,'' J. Acoust. Soc. Am. **73**, 580–591.

Don, M., and Eggermont, J. J. (**1978**). ''Analysis of the click-evoked brain stem potentials in man using high-pass noise masking,'' J. Acoust. Soc. Am. **63**, 1084–1092.

Don, M., Masuda, A., Nelson, R., and Brackmann, D. (**1997**). ''Successful detection of small acoustic tumors using the stacked derived-band auditory brain stem response amplitude,'' Am. J. Otolaryngol. **18**(5), 608–621.

Evans, E. F., and Elberling, C. (**1982**). ''Location-specific components of the gross cochlear action potential: An assessment of the validity of the high-pass masking technique by cochlear nerve fibre recording in the cat,'' Audiology **21**(3), 204–227.

Galbraith, G. L. (**1994**). ''Two-channel brain-stem frequency-following responses to pure tone and missing fundamental stimuli,'' Electroencephalogr. Clin. Neurophysiol. **92**, 321–330.

Geisler, C. D., Rhode, W. S., and Kennedy, D. T. (**1984**). ''Responses to tonal stimuli of single auditory nerve fibers and their relation to basilar membrane motion in the squirrel monkey,'' J. Neurophysiol. **37**, 1156–1172.

Gorga, M. P., and Thornton, A. R. (**1989**). ''The choice of stimuli for ABR measurements,'' Ear Hear. **10**, 217–230.

Greenwood, D. D. (**1990**). ''A cochlear frequency position function for several species—29 years later,'' J. Acoust. Soc. Am. **87**, 2592–2605.

Gummer, A. W., and Zenner, H.-P. (**1996**). ''Central processing of auditory information,'' in *Comprehensive Human Physiology*, edited by R. Greger and U. Windhorst (Springer, Berlin), Vol. 1.

Hashimoto, I. (**1982**). ''Auditory evoked potentials from the human midbrain: Slow brainstem responses,'' Electroencephalogr. Clin. Neurophysiol. **53**, 652–657.

Hecox, K., Squires, N., and Galambos, R. (**1976**). ''Brainstem auditory evoked responses in man. I. Effect of stimulus rise-fall time and duration,'' J. Acoust. Soc. Am. **60**, 1178–1192.

Kodera, K., Yamane, H., and Suzuki, J. (**1977**). ''The effect of onset, offset and rise-decay times of tone bursts on brainstem response,'' Scand. Audiol. **6**, 205–210.

Lütkenhöner, B., Kauffmann, G., Pantev, C., and Ross, B. (**1990**). ''Verbesserung der Synchronisation auditorisch evozierter Hirnstammpotentiale durch Verwendung eines die kochleären Laufzeitunterschiede kompensierenden Stimulus,'' Arch. Otolaryngol. Suppl. II, 157–159.

Møller, A. R., and Jannetta, P. J. (**1982**). ''Evoked potentials from the inferior colliculus in man,'' Electroencephalogr. Clin. Neurophysiol. **53**, 612–620.

Møller, A. R., and Jannetta, P. J. (**1986**). ''Simultaneous surface and direct brainstem recordings of brainstem auditory evoked potentials (BAEP) in man,'' in *Evoked Potentials*, edited by R. Q. Cracco and I. Bodis-Wollner (Alan R. Liss, New York), pp. 227–234.

Moore, J. K. (**1987a**). ''The human auditory brain stem: A comparative view,'' Hear. Res. **29**, 1–32.

Moore, J. K. (**1987b**). ''The human auditory brain stem as a generator of auditory evoked potentials,'' Hear. Res. **29**, 33–43.

Neely, S. T., Norton, S. J., Gorga, M. P., and Jesteadt, W. (**1988**). ''Latency of auditory brain-stem responses and otoacoustic emissions using tone-burst stimuli,'' J. Acoust. Soc. Am. **83**, 652–656.

Rhode, W. S. (**1971**). ''Observations of the vibration of the basilar membrane in squirrel monkeys using the Mössbauer technique,'' J. Acoust. Soc. Am. **49**, 1218–1231.

Rose, J. E., Hind, J. E., Anderson, D. J., and Brugge, J. F. (**1971**). ''Some effects of stimulus intensity on response of auditory nerve fibers in the squirrel monkey,'' J. Neurophysiol. **34**, 685–699.

Ruggero, M. A. (**1992**). ''Responses to sound of the basilar membrane of the mammalian cochlea,'' Curr. Opin. Neurobiol. **2**(4), 449–456.

Ruggero, M. A., and Rich, N. C. (**1983**). ''Chinchilla auditory nerve responses to low-frequency tones,'' J. Acoust. Soc. Am. **73**, 2096–2108.

Russell, I. J., and Sellick, P. M. (**1978**). ''Intracellular studies of hair cells in the mammalian cochlea,'' J. Physiol. (London) **284**, 261–290.

Scherg, M., and Von Cramon, D. (**1985**). ''A new interpretation of the generators of BAEP waves I–V: Results of a spatio-temporal dipole model,'' Electroencephalogr. Clin. Neurophysiol. **62**, 290–299.

Sellick, P. M., Patuzzi, R., and Johnstone, B. M. (**1982**). ''Measurement of basilar membrane motion in the guinea pig using the Mössbauer technique,'' J. Acoust. Soc. Am. **72**, 131–141.

Shore, S. E., and Nuttall, A. L. (**1985**). ''High synchrony compound action potentials evoked by rising frequency-swept tonebursts,'' J. Acoust. Soc. Am. **78**, 1286–1295.

Shore, S. E., Clopton, B. M., and Au, Y. N. (**1987**). ''Unit response in ventral cochlear nucleus reflect cochlear coding of rapid frequency sweeps,'' J. Acoust. Soc. Am. **82**, 471–478.

Tsuchitani, C. (**1983**). ''Physiology of the auditory system,'' in *Bases of Auditory Brain-Stem Evoked Responses*, edited by E. J. Moore (Grune and Stratton, New York).

Van Campen, L. E., Hall, J. W., and Grantham, D. W. (**1997**). ''Human offset auditory brainstem response: Effects of stimulus acoustic ringing and rise-fall time,'' Hear. Res. **103**, 35–46.

van der Drift, J. F. C., Brocaar, M. P., and van Zanten, G. A. (**1988a**). ''Brainstem response audiometry. I. Its use in distinguishing between conductive and cochlear hearing loss,'' Audiology **27**, 260–270.

van der Drift, J. F. C., Brocaar, M. P., and van Zanten, G. A. (**1988b**). ''Brainstem response audiometry. II. Classification of hearing loss by discriminant analysis,'' Audiology **27**, 271–278.

Studies of interaural attenuation to investigate the validity of a dichotic difference tone response recorded from the inferior colliculus in the chinchilla

Sally Arnold
Department of Speech Language Pathology, Buffalo State College, Buffalo, New York 14222-1095 and Center for Hearing and Deafness, State University of New York at Buffalo, Buffalo, New York 14214-3007

Robert Burkard
Center for Hearing and Deafness, Department of Communicative Disorders and Sciences, and Department of Otolaryngology, State University of New York at Buffalo, Buffalo, New York 14214-3007

(Received 20 September 1999; accepted for publication 30 November 1999)

In a previous paper (Arnold and Burkard, 1998) a dichotic $f2$-$f1$ difference tone (DT) auditory evoked potential from the chinchilla inferior colliculus (IC) was measured while presenting $f1$ (2000 Hz) to one ear and $f2$ (2100 Hz) to the other ear. This measurement paradigm could be used as a means to study binaural processing in an unanesthetized animal model. However, it is possible that this response is actually generated peripherally, as a result of acoustic crossover. The purpose of the present set of experiments was to investigate whether the dichotic DT is a true binaural phenomenon. Recordings were made from chronically implanted IC electrodes in unanesthetized, monaural chinchillas (left cochlea destroyed). In experiment 1, interaural attenuation (IA) was measured in two ways. First, IA was measured by comparing IC evoked potential thresholds obtained when stimulating the normal right ear and the dead left ear, using tone bursts (0.5–8 kHz). Mean values of interaural attenuation ranged from 50–65 dB across frequency (55 dB at 2000 Hz). Next, the DT was measured monaurally using $f1=2000$ and $f2=2100$ ($L1=L2$). By comparing the mean DT input/output functions for monaural stimulation of the right and left ears, a mean value of IA for the tonal pair was estimated ($\approx$69 dB). In experiment 2, the DT was measured with right monaural stimulation, while varying the relative levels of the primaries. A small DT could be seen with primary levels up to 30 dB apart, but not for greater level differences. Differences substantially greater than 30 dB would be expected in the crossover situation based upon IA. In experiment 3, the stimuli were presented dichotically ($f1$ to right ear, $f2$ to left ear and vice versa, $L1=L2$) to determine whether acoustic crosstalk to the normal right ear would generate a DT. No DT was reliably observed in this condition. Taken together, these results suggest that the dichotic DT is a true binaural phenomenon, and not simply attributable to acoustic crossover. [S0001-4966(00)02003-8]

PACS numbers: 43.64.Qh, 43.64.Ri [LHC]

INTRODUCTION

When the ear is stimulated by two frequencies, $f1$ and $f2$ (termed *primaries*), nonlinearity in the auditory system produces additional frequencies or *distortion products* which are not present in the stimulus pair. One such nonlinearity is the simple difference tone (DT), which is a distortion product whose frequency corresponds to $f2$-$f1$. The DT has been measured using scalp-recorded auditory evoked potentials (AEPs), both in animal models (Chertoff and Hecox, 1990; Chertoff *et al.*, 1992; Dolphin *et al.*, 1994) and in humans (Chertoff and Hecox, 1990; Rickman *et al.*, 1991).

In a previous study (Arnold and Burkard, 1998), we made extensive measurements of the AEP DT in near-field recordings from the inferior colliculus (IC) of awake chinchillas. At that time, we also observed what appeared to be a *dichotic* DT by presenting $f1$ (2000 Hz) to one ear and $f2$ (2100 Hz) to the other ear. Specifically, a component in the AEP corresponding to the $f2$-$f1$ difference frequency (100 Hz) was obtained for moderate to high levels (40–80 dB SPL) of the primary tones ($L1=L2$). The amplitude of the dichotic DT was symmetrical for the stimulus conditions: $f1$ to right ear—$f2$ to left ear, and vice versa. Similarly, the amplitude of the response was similar whether recording from the right or left IC (see Arnold and Burkard, 1998, Fig. 6).

This measurement paradigm could be used as a means to study binaural processing in an unanesthetized animal model. However, the question arises as to whether the response observed to dichotic stimulation is caused by stimulus crossover between ears, and hence is really a response to monaural stimulation with an amplitude difference between primary tones. In the present study, a series of experiments was conducted in unilaterally deafened chinchillas to determine if the dichotic DT is a true binaural phenomenon.

In order for crossover to generate the DT, the monaural DT must be elicited with unequal primary levels, since interaural attenuation (IA) would reduce the intensity of the crossover tone. Our strategy then, was first to measure the

amount of IA in the chinchilla, in order to determine the relative levels of the two primary tones that would be mixing at the periphery in the crossover situation. While only the IA value in the region of 2000 Hz is of relevance to the present study, it was considered useful to have measurements of IA across a range of frequencies, for future studies in our laboratory. To this end, we measured IA for tone bursts of several frequencies, by comparing the threshold of the IC evoked potential (ICP) to stimulation of the normal and destroyed ears. In addition, since stimulus type may affect IA, we also measured IA for the specific two-tone stimulus pair that was used in our previous paper (Arnold and Burkard, 1998).

In addition to measurements of IA, we evaluated the DT magnitude when the primary tones were presented monaurally at unequal levels. If a reliable DT could be obtained when the two primary tones differed in level by a value approximating the IA, then it is possible that the binaural DT observed by Arnold and Burkard (1998) was generated monaurally. As an additional test of the validity of the dichotic DT, we determined whether a response to dichotic stimulation could be observed in the monauralized animals.

METHODS

Subjects

Six young adult chinchillas (weight 379–594 grams, 5 males, 1 female) were used as subjects. The animals were anesthetized with ketamine (45–71 mg/kg) and acepromazine (0.54–0.84 mg/kg) and a left cochleotomy was performed by opening the bulla posteriorly and mechanically destroying the cochlea. For evoked response recording, a tungsten electrode was implanted in the left IC using stereotaxic coordinates. The electrode was advanced while acoustically stimulating the right ear with a tone burst. The presence of a large amplitude diphasic or triphasic response was taken as evidence of appropriate electrode placement. A common electrode was implanted 1–2 cm anteriorly on the dura. Electrode impedances ranged from 14.6 to 50.5 kΩ across animals. The animals were allowed to recover for at least two weeks prior to data collection.

Stimuli and electrophysiological recording

Stimuli were generated using the D/A converter(s) (16 bits, 62 kHz) on one (ICP studies) or two (DT studies) TMS320C25-based digital signal processing boards (Spectrum Signal Processing), located in a personal computer. The output of each D/A converter was low-pass filtered and routed through a custom-built, computer-controlled attenuator to an Etymotic ER2 insert earphone, which was held in the ear canal(s) with a foam insert.

To record the ICP, which is the onset evoked response from the IC to transient stimuli, brief tone bursts at octave intervals between 0.5–8.0 kHz were used. The tone bursts (2-ms rise/fall, 1-ms plateau, cosine-shaped onset/offset, alternating polarity) were presented at a rate of approximately 20 per second. The DT was measured using two tones ($f1 = 2000$ and $f2 = 2100$ Hz) presented simultaneously. Each tone was generated on a separate signal processing board and routed to a separate ER2 earphone. The two tones were then either routed to the same ear (for monaural stimulation) or to separate ears (for dichotic stimulation). The two-tone stimulus was presented for a duration of 232 ms, with approximately 30 ms between repetitions. For all monaural stimulus conditions, the nonstimulated ear canal was occluded with a foam plug to minimize crossover by air conduction.

For monitoring stimulus level, the flexible probe tube of an Etymotic ER-7c probe microphone was threaded through the foam insert housing of the earphone in one or both ear canals. This allowed for real-ear calibration of all stimuli, using the sensitivity specification of the microphone for voltage to sound pressure level (SPL) conversion. For the two-tone stimulus pair, the microphone output was routed to the A/D converter of a signal processing board, and the magnitude of the primary tones was determined by computing the Fourier coefficients at $f1$ and $f2$. For dichotic presentation of $f1$ and $f2$, the outputs of two ER-7c microphones, one in each ear canal, were mixed electrically prior to the Fourier computations.

For electrophysiological measurements, the animals were placed in a restraint device (Snyder and Salvi, 1994) in a sound-attenuating chamber. Animals were tested without anesthesia for all recordings. Electrical activity was recorded between the active IC electrode and the common electrode.

The electrical activity was amplified (10 000X) and filtered (30–3000 Hz) with a Stanford Research System model SR560 bioamplifier. After amplification and filtering, the electrical activity was fed to the A/D converter on a third Spectrum Signal Processing board.

For recording the ICP with tone bursts, response collection began at stimulus onset and continued for 15.36 ms, with a sampling period of 60 μs. Responses to 100 stimulus presentations were averaged in the time domain to obtain the ICP waveform.

For recording the DT, response collection began at stimulus onset and continued for 232 ms, using a sampling rate of 31 kHz. Responses to 25 stimuli were averaged in the time domain. The amplitude of the DT was obtained by computing the Fourier coefficient at the $f2$-$f1$ frequency (100 Hz) over the final 132 ms of stimulus presentation, following Blackman windowing of the waveform. The initial 100 ms were not included, to eliminate the contribution of onset responses.

Procedures

For each animal, the data in the three experiments described below were collected during two recording sessions on two consecutive days. The data for experiments 1a, 1b, and 3 were collected during the first session, while the data for experiment 2 were collected during the second session.

Experiment 1a. Interaural attenuation for tone bursts

Using the tone burst stimuli (0.5–8.0 kHz), the ICP was recorded for monaural stimulation of the normal right ear. An intensity series was obtained using stimulus levels ascending from -20 to 80 dB SPL in 5-dB steps. An intensity series was also recorded for stimulation of the destroyed left

ear (10 to 110 dB SPL in 5-dB steps). For each intensity series, ICP threshold was defined as the lowest stimulus level at which a response could be discerned visually. Interaural attenuation was computed by comparing the threshold for the right and left ear at each tone burst frequency.

Experiment 1b. Interaural attenuation for the two-tone stimulus pair

The DT was recorded using the 2000–2100 Hz two-tone stimulus, with equal level primaries ($L1=L2$). Input–output functions were measured for the DT, with primary tone levels increasing from −20 to 80 dB SPL in 10-dB steps. Input–output functions were measured with both primaries presented to the normal right ear and to the dead left ear.

Experiment 2. Effect of primary tone level difference upon the monaural DT

DT input/output functions were measured for monaural stimulation of the right ear, using primary level differences from 10 to 60 dB ($L1>L2$, and $L2>L1$). Input–output functions were measured in 10-dB steps over a range of intensities; the minimum intensity was always −20 dB SPL for the less intense primary tone, while the maximum intensity was always 80 dB SPL for the more intense primary tone. An input–output function with equal level primaries was also measured at this time as a baseline for comparison. The order of presentation of stimulus pairs was randomized across animals.

Experiment 3. Dichotic DT

In this experiment, the DT was measured dichotically, with $f1$ (2000 Hz) presented to the right ear and $f2$ (2100 Hz) presented to the left ear and vice versa. Input–output functions were again measured over a range from −20 to 80 dB SPL ($L1=L2$). These data were collected in conjunction with the monaural DT data in experiment 1b. The order of the four conditions (monaural right, monaural left, dichotic-$f1$ to right ear, dichotic-$f2$ to right ear) was randomized across animals.

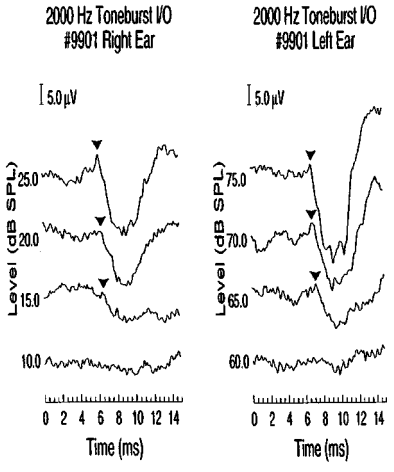

FIG. 1. Example of raw data from animal #9901, showing IC potentials near threshold for right and left ears. Stimulus was a 2000-Hz tone burst. For each waveform in which a response was judged to be present, the arrow shows the location of the positive peak of the ICP.

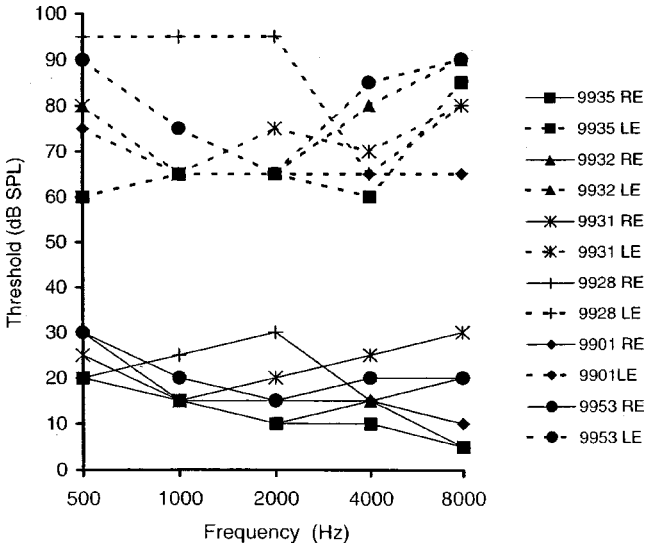

FIG. 2. Individual IC potential thresholds across tone burst frequency, for right and left ear stimulation.

RESULTS

Experiment 1a. Interaural attenuation for tone bursts

An example of an ICP intensity series from one animal is shown in Fig. 1. Data are shown for a 2000-Hz tone burst stimulus, at intensity levels just above and below threshold. It can be seen that the threshold of the ICP for the right ear is 15 dB SPL, while the threshold for the dead left ear is 65 dB SPL.

Figure 2 shows the ICP thresholds across frequency for the right and left ears of all six animals. Considering all frequencies together, ICP thresholds for the right ear ranged from 5–30 dB SPL, while for the left ear, the thresholds ranged from 60–95 dB SPL.

The amount of IA has been estimated by subtracting the right ear thresholds from the left ear thresholds. These values are shown in Table I, for each animal across frequency. Mean values of IA for the tone burst stimuli were between 54.2–55.8 dB from 500–4000 Hz, and rose to 66.7 dB at 8000 Hz. A one-way repeated measures ANOVA indicated that the IA did not vary significantly with frequency

TABLE I. Individual and mean values of interaural attenuation (in dB) across tone burst frequency, obtained by subtracting right ear thresholds from left ear thresholds.

Animal	500 Hz	1000 Hz	2000 Hz	4000 Hz	8000 Hz
9935	40	50	55	50	80
9932	60	50	55	65	85
9931	55	50	55	45	50
9928	75	70	65	50	60
9901	45	50	50	50	55
9953	60	55	50	65	70
Mean	55.8	54.2	55.0	54.2	66.7
s.d.	12.4	8.0	5.5	8.6	14.0
Range	40–75	50–70	50–65	45–65	50–85

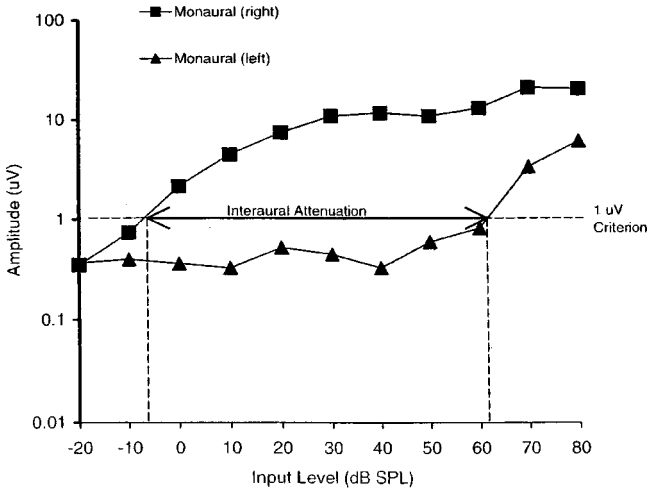

FIG. 3. Mean DT input–output functions, for monaural right and monaural left conditions. ($f1=2000$, $f2=2100$ Hz). Interaural attenuation is estimated by comparing the stimulus levels at which the curves cross an arbitrary 1 μV amplitude criterion.

($p>0.05$). It is possible, however, that the lack of a significant frequency effect is due to the small sample size ($N=6$), which limited the power of the ANOVA. At 2000 Hz, the frequency of $f1$ for the DT measures (below), mean IA was 55 dB.

Experiment 1b. Interaural attenuation for the two-tone stimulus pair

The DT input–output functions, averaged across the six animals, are shown for stimulation of the right and left ears in Fig. 3. For the right ear, the amplitude of the DT rises from 0.35 μV at −20 dB SPL to 20.3 μV at 80 dB SPL. For left ear stimulation, reflecting crossover to the right ear, the curve is flat until the stimulus level is greater than 40–50 dB SPL, then begins to rise. The on-line data processing resulted in no raw time or frequency domain waveforms to judge DT threshold for each animal. Instead, we used the magnitude of the horizontal shift for the left ear curve as a measure of IA. Specifically, the magnitude of IA was obtained by comparing the intensity levels at which the average curves cross an arbitrary amplitude criterion of 1 μV, as shown in Fig. 3. This value, computed using linear interpolation, was 68.8 dB, which is somewhat higher than the 55 dB of IA that was seen for the 2000-Hz tone burst stimulation.

Experiment 2. Effect of primary level difference upon the monaural DT

The DT input–output functions for right monaural stimulation, using unequal primary tone levels, is shown in Figs. 4(a) ($L1<L2$) and 4(b) ($L1>L2$). The input–output function for equal level primaries is also plotted in both graphs as a baseline for comparison. By comparing Fig. 4(a) and (b), it can be seen that the effect of primary tone level difference upon the DT amplitude is highly similar, regardless of which primary tone is larger. DT amplitude decreases systematically with increasing primary tone level difference. A DT response (i.e., an increase in DT amplitude with increasing primary tone level) can be seen with level differences as large as 30 dB, but not when primaries differ by 40–60 dB. At 80 dB SPL, the amplitude of the DT for equal level primaries is greater than 18 μV. The amplitude at 80 dB SPL decreases to approximately 7–9 μV for a 10-dB difference in primary levels, 3 μV for a 20-dB difference, and 1 μV for 30-dB difference. For primary differences of 40–60 dB, the DT response appears to be absent—the curves are flat across intensity level, the maximum amplitude at 80 dB SPL remaining between 0.3–0.6 μV.

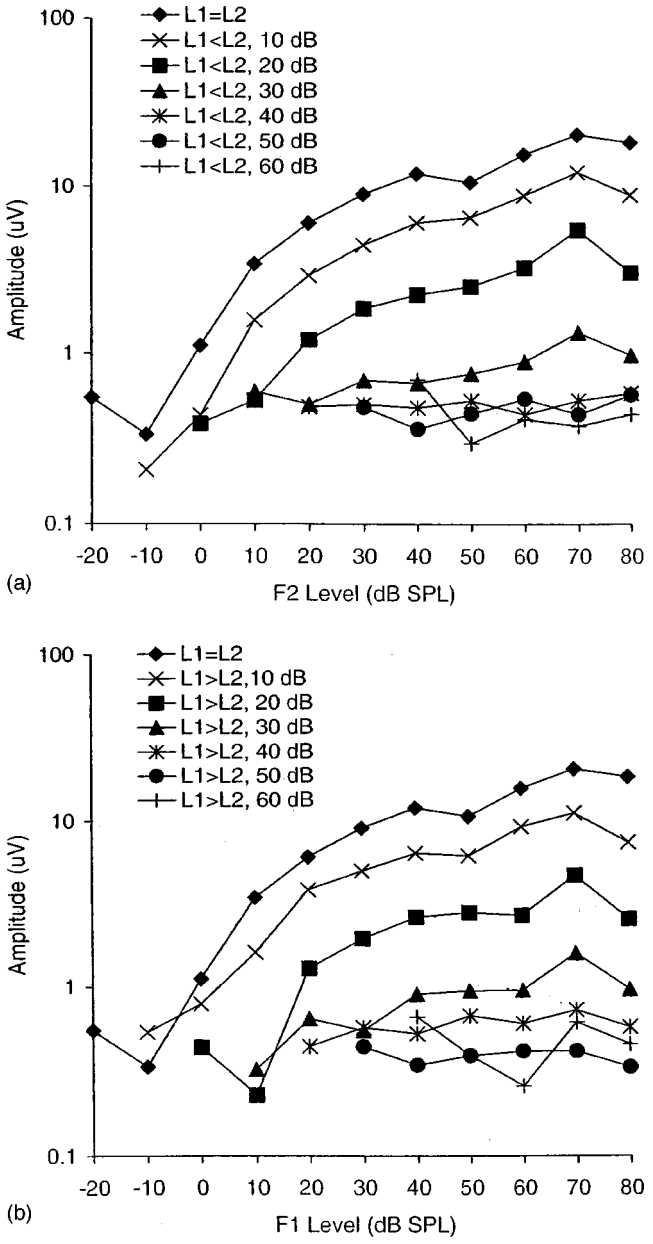

FIG. 4. Mean DT input–output functions ($f1=2000$, $f2=2100$ Hz), for equal level primaries, and for level differences from 10–60 dB. (a) $L1<L2$, (b) $L1>L2$. The abscissa shows the intensity of the higher level tone. Because the intensity of the lower primary was never below −20 dB SPL, the number of data points per curve is not equal.

Experiment 3. Dichotic DT with dead ear

Figure 5 shows the DT input–output functions for dichotic stimulation. The curves for monaural stimulation of the right and left ears, from Fig. 3, are replotted for compari-

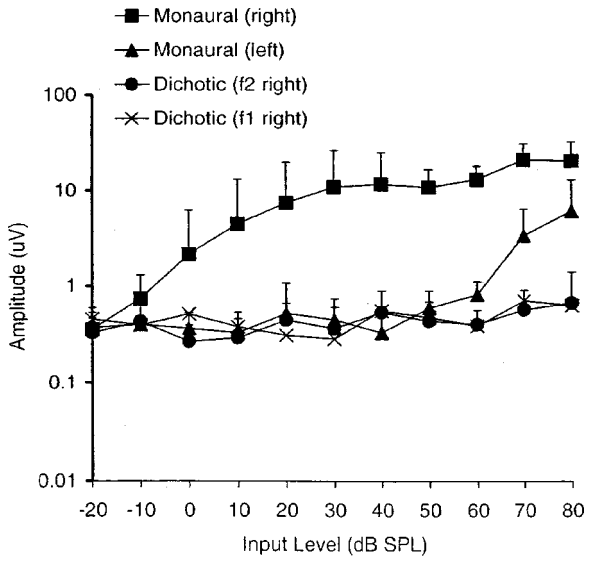

FIG. 5. Mean DT input–output functions, for the two dichotic conditions ($f2$ to right ear, $f1$ to left ear, and vice versa). ($f1=2000$, $f2=2100$ Hz). The monaural right and left conditions from Fig. 3 are replotted here for comparison. Error bars indicate +1 s.d.).

son. The curves for the two dichotic conditions ($f2$ to right ear, and $f1$ to right ear) are virtually overlapping. There does not appear to be a reliable DT response for the dichotic conditions. The curves remain relatively flat across stimulus intensity; specifically, mean response magnitude of the DT does not vary significantly with primary tone level for either curve (one-way repeated measured ANOVA, $p>0.05$).

DISCUSSION

The dichotic DT

The purpose of this study was to determine whether the dichotic DT is a true binaural phenomenon or is actually generated peripherally with primary tones of unequal level, due to acoustic crossover. To this end, we measured the IA in a group of chinchillas, in order to estimate the primary level difference that would exist at the periphery during binaural stimulation if crossover were occurring. We then determined, for monaural stimulation, what degree of level difference between the two primaries, if any, would generate a DT. Finally, as an additional test, we replicated the binaural stimulus condition in cochleotomized animals.

The results of this study showed that, when using monaural stimulation with unequal primary levels, the DT could not be elicited with level differences greater than 30 dB. Substantially larger primary level differences would be expected in a crossover situation, based upon the IA values for 2000 Hz measured here (55 dB for tone bursts, ≈69 dB for the $f1$-$f2$ tonal pair). Therefore, it is unlikely that the dichotic DT observed in the previous study (Arnold and Burkard, 1998) could have been an artifact due to crossover, but rather appears to be a real phenomenon. This conclusion is further supported by the observation that, in the present study, dichotic stimuli did not elicit a DT in monauralized animals.

The dichotic stimulus paradigm is similar to that used in human psychophysical studies to measure the phenomenon of binaural beats. That is, when two tones of slightly different frequency are presented, one to each ear, listeners report a sensation of amplitude fluctuation, roughness, or ''beating'' (Licklider *et al.*, 1950; Perrott and Musicant, 1977; Perrott and Nelson, 1969). While binaural beats appear to be most easily heard for low frequency primary tones, beat detection has been measured up to an $f1$ frequency of 1400–1500 Hz (Licklider *et al.*, 1950; Perrott and Nelson, 1969), for difference frequencies as high as 80–160 Hz (Perrott and Nelson, 1969). The dichotic DT measured from the IC is perhaps a physiological correlate of this psychophysical phenomenon.

Several previous physiological studies have attempted to find a neural basis for the perception of binaural beats. The binaural response properties of single auditory neurons in the cat IC have been studied using a dichotic, two-tone stimulus pair (Kuwada *et al.*, 1984; Kuwada *et al.*, 1979; Yin and Kuwada, 1983). It has been noted that some cells exhibit a pattern of discharges that is phase locked to the difference or beat frequency. While most cells respond only up to a 10-Hz difference frequency, phase-locking up to a difference frequency of 80 Hz has been observed.

A binaural-beat stimulus has been used to record the near-field evoked potential from the superior olivary complex of the cat (Wernick and Starr, 1968). Periodicity in the binaural response corresponding to the difference frequency was noted when the two tones were close in frequency (<100 Hz). In another evoked potential study, the scalp-recorded frequency following response (FFR) in humans was measured with a dichotic paradigm in which a 500-Hz tone burst was presented to one ear and a 540-Hz tone burst was presented to the opposite ear (Hink *et al.*, 1980). The authors noted amplitude fluctuations in the FFR waveform corresponding to the frequency difference between the two tone bursts (i.e., 40 Hz).

In our previous study (Arnold and Burkard, 1998) we were able to measure a small dichotic DT to a difference frequency of 100 Hz. As we did not systematically explore the effect of primary tone frequency or difference frequency upon the amplitude of the dichotic DT, the ideal stimulus paradigm to elicit this response is unknown at this time, and awaits further parametric studies. Based upon single unit studies (Kuwada *et al.*, 1979; Yin and Kuwada, 1983) we would expect to see a larger dichotic response for lower difference frequencies. Nevertheless, because the dichotic DT can be easily measured from the IC in awake chinchillas, it appears to hold promise as a means to study binaural processing.

Interaural attenuation

In the present study, the mean values of IA, measured for the tone burst stimuli, ranged from 54 to 67 dB across frequency (overall mean: 57 dB). These values are in fairly good agreement with previous measures of IA in the chinchilla (Clark and Bohne, 1987; Mast, 1970; Teas and Nielsen, 1975), despite differences in experimental procedures. Mast (1970) measured IA in a group of seven chinchillas by recording the cochlear microphonic (CM) from the round window, and comparing the level of ipsilateral and

contralateral stimulation required to produce a constant CM response of 50 μV. He found that IA was >60 dB for all frequencies tested, across a range from 0.2–10 kHz (specific values of IA were not reported). Teas and Nielsen (1975), recording the CM using basal turn differential electrodes, also compared isopotential CM curves (0.3 μV criterion) for ipsilateral and contralateral stimulation in a group of chinchillas. The value of IA thus obtained (bulla sealed condition) ranged from 40–72 dB across frequencies from 0.3 to 14.3 kHz (overall mean: 55 dB). Clark and Bohne (1987), in one chinchilla with left cochleotomy, measured behavioral threshold shift following ossicular removal on the right side. While this procedure does not technically measure *interaural* attenuation, it does measure crossover from air conduction stimulation to bone conduction on the same side. They found attenuation values from 41–81 dB in the frequency range from 0.125–16.0 kHz (overall mean: 60 dB). Upon comparing the present data with the Teas and Nielsen (1975) and the Clark and Bohne (1987) studies, it is apparent that the overall mean value of IA averaged across frequency is quite similar, ranging from 55–60 dB.

Interaural attenuation has been measured in other species, using a variety of methods. In the guinea pig, IA has been measured using the isopotential CM technique (Teas and Nielsen, 1975), and by comparing ipsilateral and contralateral thresholds of the compound action potential following destruction of one inner ear with the drug sisomicin (Popelar *et al.*, 1994). In cats, IA has been measured by comparing the response of single auditory nerve fibers to ipsilateral and contralateral stimulation (Caird *et al.*, 1980; Gibson, 1982), and by comparing right and left ear thresholds of the brainstem auditory evoked potential in cats with unilateral genetic deafness (Mair *et al.*, 1979). In rats, IA has been estimated by comparing the threshold of the brainstem auditory evoked response for the two ears following surgical destruction of one cochlea (Megerian *et al.*, 1996), and following ossicular disruption (Burkard *et al.*, 1990) in the manner of Clark and Bohne (1987).

While measures of IA have been made in several species, it is not feasible to directly compare data across studies, since the amount of crossover measured will depend upon several factors, including the particular species studied, the experimental method employed (Caird *et al.*, 1980; Gibson, 1982), the manner of coupling of the sound source to the ear (Gibson, 1982), whether the bulla is open or closed (Gibson, 1982; Teas and Nielsen, 1975), as well as the specific frequencies tested.

Effect of unequal primary levels upon the monaural DT

In the present study, we found that the amplitude of the DT measured from the IC with monaural stimulation was maximal for equal level primary tones ($L1=L2$), and decreased in a systematic manner as either $L1$ or $L2$ was decreased re: the other primary. This general pattern of findings has been shown previously, in both physiological (Smoorenburg *et al.*, 1976) and psychophysical (Goldstein, 1967; Humes, 1979; Zwicker, 1979) studies of the $f2$-$f1$ difference tone.

Recording from single neurons in the anteroventral cochlear nucleus of the cat, Smoorenburg *et al.* (1976) used a two-tone stimulus, and measured the response of neurons that were phase locked to the $f2$-$f1$ difference frequency. They found that the amplitude of the response was maximal for $L1=L2$, and became progressively smaller as $L2$ was decreased below a fixed $L1$, up to the maximum difference tested (40 dB).

In human psychophysical studies, detection of the $f2$-$f1$ difference tone has been measured extensively when stimulating monaurally with two tones, $f1$ and $f2$. Several studies have examined the strength of the perceived DT for unequal levels of the primary tones. Zwicker (1979) found that the amplitude of the perceived DT was maximal for equal level primaries, and decreased systematically as the level of one primary tone was decreased below the other. For a given primary level difference, the amplitude was fairly symmetrical for $L1>L2$ and $L2>L1$, consistent with our data. Other psychophysical studies of the DT with unequal primary levels have shown a qualitatively similar pattern of results (Goldstein, 1967; Humes, 1979). Thus the literature is in agreement with our findings concerning the effects of unequal primary levels upon the DT.

ACKNOWLEDGMENT

This work was supported in part by Grant No. R01DC03600 from the National Institute on Deafness and Other Communicative Disorders, National Institutes of Health.

Arnold, S., and Burkard, R. (**1998**). ''The auditory evoked potential difference tone and cubic difference tone measured from the inferior colliculus of the chinchilla,'' J. Acoust. Soc. Am. **104**, 1565–1573.

Burkard, R., Feldman, M., and Voigt, H. F. (**1990**). ''Brainstem auditory-evoked response in the rat. Normative studies, with observations concerning the effects of ossicular disruption,'' Audiology **29**, 146–162.

Caird, D., Gottl, K., and Klinke, R. (**1980**). ''Interaural attenuation in the cat, measured with single fibre data,'' Hear. Res. **3**, 257–263.

Chertoff, M. E., and Hecox, K. E. (**1990**). ''Auditory nonlinearities measured with auditory-evoked potentials,'' J. Acoust. Soc. Am. **87**, 1248–1254.

Chertoff, M. E., Hecox, K. E., and Goldstein, R. (**1992**). ''Auditory distortion products measured with averaged auditory evoked potentials,'' J. Speech Hear. Res. **35**, 157–166.

Clark, W. W., and Bohne, B. A. (**1987**). ''Attenuation and protection provided by ossicular removal,'' J. Acoust. Soc. Am. **81**, 1093–1099.

Dolphin, W. F., Chertoff, M. E., and Burkard, R. (**1994**). ''Comparison of the envelope following response in the Mongolian gerbil using two-tone and sinusoidally amplitude-modulated tones,'' J. Acoust. Soc. Am. **96**, 2225–2234.

Gibson, D. J. (**1982**). ''Interaural crosstalk in the cat,'' Hear. Res. **7**, 325–333.

Goldstein, J. L. (**1967**). ''Auditory nonlinearity,'' J. Acoust. Soc. Am. **41**, 676–689.

Hink, R. F., Kodera, K., Yamada, O., Kaga, K., and Suzuki, J. (**1980**). ''Binaural interaction of a beating frequency-following response,'' Audiology **19**, 36–43.

Humes, L. E. (**1979**). ''Perception of the simple difference tone ($f2$-$f1$),'' J. Acoust. Soc. Am. **66**, 1064–1074.

Kuwada, S. Yin, T. C., Syka, J., Buunen, T. J., and Wickesberg, R. E. (**1984**). ''Binaural interaction in low-frequency neurons in inferior colliculus of the cat. IV. Comparison of monaural and binaural response properties,'' J. Neurophysiol. **51**, 1306–1325.

Kuwada, S., Yin, T. C., and Wickesberg, R. E. (**1979**). ''Response of cat inferior colliculus neurons to binaural beat stimuli: Possible mechanisms for sound localization,'' Science **206**, 586–588.

Licklider, J. C. R., Webster, J. C., and Hedlum, J. M. (**1950**). ''On the frequency limits of binaural beats,'' J. Acoust. Soc. Am. **22**, 468–473.
Mair, I. W. S., Elverland, H. H., and Laukli, E. (**1979**). ''Brain-stem responses of the cat and interaural attenuation,'' Arch. Oto-Rhino-Laryngol. **222**, 113–118.
Mast, T. E. (**1970**). ''Binaural interaction and contralateral inhibition in dorsal cochlear nucleus of the chinchilla,'' J. Neurophysiol. **33**, 108–115.
Megerian, C. A., Burkard, R. F., and Ravicz, M. E. (**1996**). ''A method for determining interaural attenuation in animal models of asymmetric hearing loss,'' Audiol. Neuro-Otol. **1**, 214–219.
Perrott, D. R., and Musicant, A. D. (**1977**). ''Rotating tones and binaural beats,'' J. Acoust. Soc. Am. **61**, 1293–1297.
Perrott, D. R., and Nelson, M. A. (**1969**). ''Limits for the detection of binaural beats,'' J. Acoust. Soc. Am. **46**, 1477–1481.
Popelar, J., Erre, J.-P., Aran, J.-M., and Cazals, Y. (**1994**). ''Plastic changes in ipsi-contralateral differences of auditory cortex and inferior colliculus evoked potentials after injury to one ear in the adult guinea pig,'' Hear. Res. **72**, 125–134.
Rickman, M. D., Chertoff, M. E., and Hecox, K. E. (**1991**). ''Electrophysiological evidence of nonlinear distortion products to two-tone stimuli,'' J. Acoust. Soc. Am. **89**, 2818–2826.
Smoorenburg, G. F., Gibson, M. M., Kitzes, L. M., Rose, J. E., and Hind, J. E. (**1976**). ''Correlates of combination tones observed in the response of neurons in the anteroventral cochlear nucleus of the cat,'' J. Acoust. Soc. Am. **59**, 945–962.
Snyder, D. L., and Salvi, R. J. (**1994**). ''A novel chinchilla restraint device,'' Lab Anim. **23**, 42–44.
Teas, D. C., and Nielsen, D. W. (**1975**). ''Interaural attenuation versus frequency for guinea pig and chinchilla CM response,'' J. Acoust. Soc. Am. **58**, 1066–1072.
Wernick, J. S., and Starr, A. (**1968**). ''Binaural interaction in the superior olivary complex of the cat: An analysis of field potentials evoked by binaural-beat stimuli,'' J. Neurophysiol. **31**, 428–441.
Yin, T. C., and Kuwada, S. (**1983**). ''Binaural interaction in low-frequency neurons in inferior colliculus of the cat. II. Effects of changing rate and direction of interaural phase,'' J. Neurophysiol. **50**, 1000–1019.
Zwicker, E. (**1979**). ''Different behaviour of quadratic and cubic difference tones,'' Hear. Res. **1**, 283–292.

Acoustic mechanisms that determine the ear-canal sound pressures generated by earphones

Susan E. Voss
Eaton-Peabody Laboratory, Massachusetts Eye and Ear Infirmary, 243 Charles Street, Boston, Massachusetts 02114, Speech and Hearing Sciences Program, Harvard–M.I.T. Division of Health Sciences and Technology, Cambridge, Massachusetts 02139, Research Laboratory of Electronics, Massachusetts Institute of Technology, Cambridge, Massachusetts 02139, and Department of Otolaryngology, Massachusetts Eye and Ear Infirmary, 243 Charles Street, Boston, Massachusetts 02114

John J. Rosowski
Eaton-Peabody Laboratory, Massachusetts Eye and Ear Infirmary, 243 Charles Street, Boston, Massachusetts 02114, Department of Otolaryngology, Massachusetts Eye and Ear Infirmary, 243 Charles Street, Boston, Massachusetts 02114, and Department of Otology and Laryngology, Harvard Medical School, Speech and Hearing Sciences Program, Harvard–M.I.T. Division of Health Sciences and Technology, Cambridge, Massachusetts 02139

Christopher A. Shera
Eaton-Peabody Laboratory, Massachusetts Eye and Ear Infirmary, 243 Charles Street, Boston, Massachusetts 02114, Department of Otolaryngology, Massachusetts Eye and Ear Infirmary, 243 Charles Street, Boston, Massachusetts 02114, and Department of Otology and Laryngology, Harvard Medical School

William T. Peake
Eaton-Peabody Laboratory, Massachusetts Eye and Ear Infirmary, 243 Charles Street, Boston, Massachusetts 02114, Department of Electrical Engineering and Computer Science, Massachusetts Institute of Technology, 77 Massachusetts Avenue, Cambridge, Massachusetts 02139, Research Laboratory of Electronics, Massachusetts Institute of Technology, Cambridge, Massachusetts 02139, and Speech and Hearing Sciences Program, Harvard–M.I.T. Division of Health Sciences and Technology, Cambridge, Massachusetts 02139

(Received 4 August 1999, accepted for publication 3 December 1999)

In clinical measurements of hearing sensitivity, a given earphone is assumed to produce essentially the same sound-pressure level in all ears. However, recent measurements [Voss *et al.*, Ear and Hearing (in press)] show that with some middle-ear pathologies, ear-canal sound pressures can deviate by as much as 35 dB from the normal-ear value; the deviations depend on the earphone, the middle-ear pathology, and frequency. These pressure variations cause errors in the results of hearing tests. Models developed here identify acoustic mechanisms that cause pressure variations in certain pathological conditions. The models combine measurement-based Thévenin equivalents for insert and supra-aural earphones with lumped-element models for both the normal ear and ears with pathologies that alter the ear's impedance (mastoid bowl, tympanostomy tube, tympanic-membrane perforation, and a ''high-impedance'' ear). Comparison of the earphones' Thévenin impedances to the ear's input impedance with these middle-ear conditions shows that neither class of earphone acts as an ideal pressure source; with some middle-ear pathologies, the ear's input impedance deviates substantially from normal and thereby causes abnormal ear-canal pressure levels. In general, for the three conditions that make the ear's impedance magnitude lower than normal, the model predicts a reduced ear-canal pressure (as much as 35 dB), with a greater pressure reduction with an insert earphone than with a supra-aural earphone. In contrast, the model predicts that ear-canal pressure levels increase only a few dB when the ear has an increased impedance magnitude; the compliance of the air–space between the tympanic membrane and the earphone determines an upper limit on the effect of the middle-ear's impedance increase. Acoustic leaks at the earphone-to-ear connection can also cause uncontrolled pressure variations during hearing tests. From measurements at the supra-aural earphone-to-ear connection, we conclude that it is unusual for the connection between the earphone cushion and the pinna to seal effectively for frequencies below 250 Hz. The models developed here explain the measured pressure variations with several pathologic ears. Understanding these mechanisms should inform the design of more accurate audiometric systems which might include a microphone that monitors the ear-canal pressure and corrects deviations from normal. [S0001-4966(00)03403-2]

PACS numbers: 43.64.Yp, 43.64.Bt [BLM]

INTRODUCTION

A. A basic problem in audiometric testing

A common clinical test of hearing sensitivity is the pure-tone ''audiogram'' in which the lowest sound-pressure level at which the subject can hear a tone is determined at several frequencies. For the testing, a loudspeaker may generate a sound field around the subject, but more typically an earphone is coupled to the subject's ear; in either case, the subject indicates whether or not the sound is perceived so as to determine the hearing ''threshold'' versus frequency, i.e., the ''audiogram.'' In this study we focus on the acoustic response in the ear canal with two earphone configurations, namely an insert and a supra-aural earphone.

Ear-canal sound-pressure levels during audiometric tests are not generally measured. Instead, the level of the sound stimulus is determined by the setting of an attenuator that controls the electric input to the sound source, and it is assumed that the earphone's calibration (sound-pressure output per volt input) is independent of variation in the acoustic properties of individual ears (e.g., Burkhard and Corliss, 1954; Shaw, 1974; Kruger and Tonndorf, 1977, 1978; Borton *et al.*, 1989; Wilber, 1994). In other words, it is assumed that an earphone's sound-pressure output is not greatly affected by the impedance of the ear to which it is coupled. However, measurements with two earphone configurations (insert and supra aural) of the pressures generated in ear canals of pathologic middle ears show pressure levels that differ from normal by as much as 35 dB (Voss *et al.*, in press). These variations introduce errors of the same size in the measurement of audiograms.

The pressure generated by an earphone can also be affected by acoustic leaks between the earphone and the ear. As Zwislocki *et al.* (1988) write, ''Supra-aural earphones have low reliability at low frequencies because of variable and unstable coupling between the earphone and the ear. Air leaks occurring between the earphone cushion and the pinna produce variable amounts of sound-pressure loss at low frequencies (typically below 500 Hz), accompanied by small, variable amounts of sound-pressure enhancement at somewhat higher frequencies (between 500 and 1000 Hz).''

The theory presented here investigates the acoustic mechanisms that affect the ear-canal pressure level generated by two types of audiologic earphones, an insert earphone and a supra-aural earphone. We combine measurements of the Thévenin equivalents for the earphones with models for (a) the ear canal, (b) the normal middle ear, (c) the middle ear with specific pathologies, and (d) leaks in the earphone-ear connection, and we use these models to predict how these different conditions affect the ear-canal pressures generated by the earphones. We compare these predictions to our recent measurements (Voss *et al.*, in press).

B. Ear impedance and middle-ear pathology

Some middle-ear pathologies have been shown to alter the ear's input impedance (e.g., Zwislocki, 1962; Zwislocki and Feldman, 1970); other pathologies can also be expected to cause large changes in the ear's impedance. For example, tympanic-membrane perforations[1] provide a direct connection between the ear canal and the middle-ear air space [Fig. 1(B)], which reduces the impedance at the tympanic membrane for low frequencies (Voss, 1998). Similarly, tympanostomy tubes,[2] which are inserted through the tympanic membrane to manage middle-ear disease [Fig. 1(C)], also reduce the low-frequency impedance of the middle ear via the same mechanism. Our third pathological configuration, ''mastoid bowl,'' results from ''canal-wall down'' mastoid surgery (see, e.g., Nadol, 1993, pp. 104–106). This procedure, which is performed to remove middle-ear disease, opens the mastoid portion of the middle-ear air spaces and externalizes this space by connecting it to the ear canal by removal of a portion of the posterior and superior bony-canal

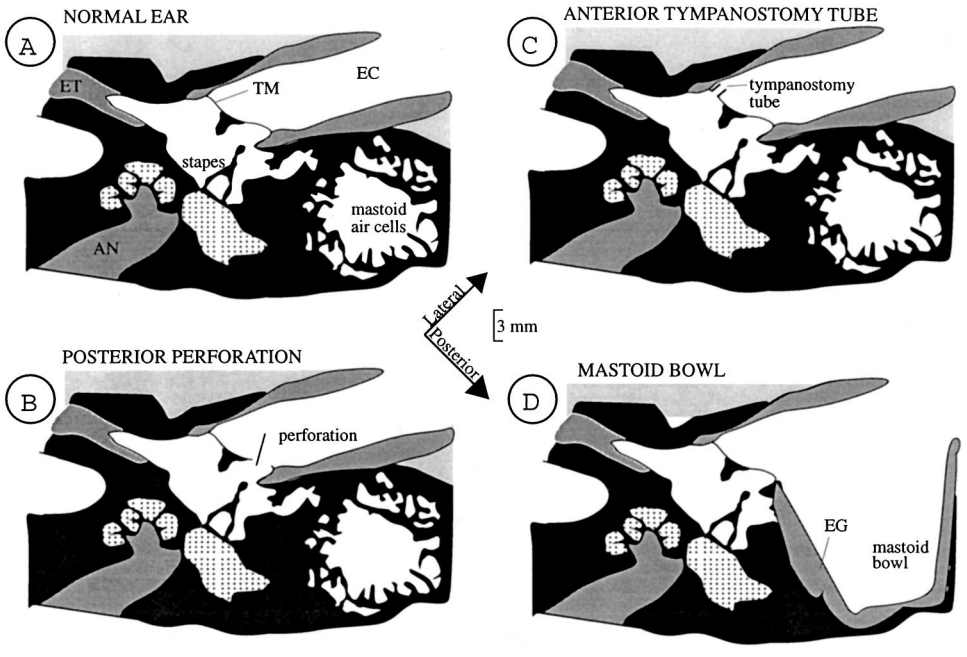

FIG. 1. Structural modifications in three middle-ear pathologies. All four figures portray a horizontal section through the middle ear at the level of the stapes. Bone is black, fluid is dotted, air is white, and soft tissue is gray. (ET=Eustachian tube; AN=auditory nerve; EC=ear canal; TM=tympanic membrane.) (A) Normal ear. (B) Perforation of the tympanic membrane. (C) Tympanostomy tube in the tympanic membrane. (D) Mastoid-bowl cavity connecting to the ear canal. (EG =Epithelial graft.)

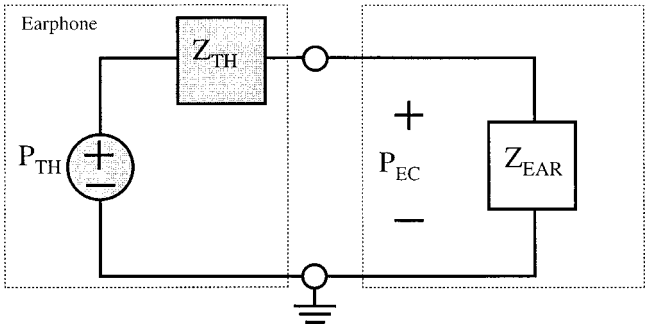

FIG. 2. Electric-circuit analog that represents acoustic variables for an earphone coupled to an ear. The earphone is represented by its Thévenin equivalent (shaded gray): a pressure source P_{TH} and an impedance Z_{TH}. Z_{EAR}, the acoustic load on the earphone, is represented by the white block. P_{EC} is the pressure generated by the earphone in the ear canal. The labeled quantities are acoustic quantities with sound pressure analogous to voltage relative to ''ground'' and volume velocity analogous to current (i.e., the ''impedance analogy'').

wall. The resulting ''mastoid bowl'' introduces a 1 to 6 cm^3 air volume to the external ear (Merchant, 1997) [Fig. 1(D)].

Other middle-ear pathologies have been shown to increase the ear's impedance magnitude relative to normal. Abnormal growth in the petrous bone can reduce movement of the stapes in otosclerosis (Zwislocki and Feldman, 1970), and fluid in the middle-ear cavity can impede tympanic membrane and ossicular motion in otitis media (Berry *et al.*, 1975).

The goal of this paper is to understand the mechanisms through which such pathologies alter sound pressures generated in the ear canal by insert and supra-aural earphones.

C. Theory

Audiometric practice assumes that the ear-canal pressure P_{EC} is nearly independent of the ear to which the earphone is coupled. In this section we examine the constraints that make this assumption accurate.

In the analog-circuit model of Fig. 2, P_{EC} can be expressed in terms of the earphone's Thévenin parameters, P_{TH} and Z_{TH}, and the ear's impedance, Z_{EAR}:

$$\frac{P_{EC}}{P_{TH}} = \frac{1}{1+Z_{TH}/Z_{\mathrm{EAR}}}, \tag{1}$$

where P_{TH} is proportional to the input voltage applied to the earphone. The ratio between the ear-canal pressure generated in a test ear and the pressure generated in an average normal ear can be expressed in terms of $\Delta Z \equiv Z_{\mathrm{EAR}} - Z_{\mathrm{EAR}}^{\mathrm{NORMAL}}$ as

$$\frac{P_{EC}}{P_{EC}^{\mathrm{NORMAL}}} = 1 + \frac{\Delta Z_{\mathrm{EAR}}/Z_{\mathrm{EAR}}^{\mathrm{NORMAL}}}{1+Z_{\mathrm{EAR}}/Z_{TH}}, \tag{2}$$

where $Z_{\mathrm{EAR}}^{\mathrm{NORMAL}}$ is the impedance of an average normal ear and Z_{EAR} is the impedance of the test ear. Thus, for $|P_{EC}/P_{EC}^{\mathrm{NORMAL}}|$ to be approximately one, the term $(\Delta Z_{\mathrm{EAR}}/Z_{\mathrm{EAR}}^{\mathrm{NORMAL}})/(1+Z_{\mathrm{EAR}}/Z_{TH})$ in Eq. (2) must have a magnitude that is much less than one. If $|Z_{\mathrm{EAR}}/Z_{TH}| \to \infty$, so that the earphone acts as an ideal pressure source, the approximation would hold for any finite $|\Delta Z_{\mathrm{EAR}}|$. However, our measurements show that typical earphones do not approximate pressure sources, but rather $0.9 < |1+Z_{\mathrm{EAR}}/Z_{TH}| < 3$.

Consequently, to satisfy the assumption that P_{EC} is nearly independent of Z_{EAR}, impedance variations among ears, ΔZ_{EAR}, must be small relative to $Z_{\mathrm{EAR}}^{\mathrm{NORMAL}}$. We show here that this constraint is also violated for some middle-ear pathologies. For example, using the ER-3A insert earphone in an ear with a 4-cm^3 mastoid bowl at 1000 Hz, $\Delta Z_{\mathrm{EAR}}/Z_{\mathrm{EAR}}^{\mathrm{NORMAL}} \approx -0.8$, so that (with $1+Z_{\mathrm{EAR}}/Z_{TH} \approx 1$) $|P_{EC}/P_{EC}^{\mathrm{NORMAL}}| \approx 0.2$, and the sound pressure in the ear is about -14 dB relative to the assumed calibration value, which leads to an overestimate of hearing loss by about 14 dB.

I. THÉVENIN EQUIVALENTS FOR EARPHONES

A. Measurement methods

An insert earphone (Etymōtic ER-3A) and a supra-aural earphone (TDH-49 with an MX-41/AR cushion) were each modified to include a microphone (Voss *et al.*, in press and Fig. 3). The insert earphone was coupled to the standard yellow-foam ear plug (Earlink™; uncompressed diameter 14 mm, length 12 mm), and a flexible probe tube (Etymōtic Research ER7-14C) was threaded through the foam plug. One end of the probe tube extended 3 mm beyond the medial end of the plug, and the other end was coupled to the microphone. With the supra-aural earphone, a steel tube was inserted through the earphone's cushion so that one end was at the earphone's output port and the other end exited along the cushion's outer circumference. A flexible probe tube (Etymōtic Research ER7-14C) was placed through the steel tube; the inner end of the probe tube was less than 1-mm lateral to the earphone port and the other end coupled to the microphone. The flexible probe fit snugly in the steel tube.

The Thévenin equivalents were determined for each earphone from pressure measurements in two ''reference loads'' of theoretically known impedance (see, e.g., Rabinowitz, 1981; Allen, 1986; Lynch *et al.*, 1994). The reference loads were a short closed cavity and a long open tube, which are described further in Fig. 3.

The pressure measurements were made using an Ariel DSP-16+ board with SYSid™ software (e.g., Voss and Allen, 1994). The software reports the Fourier transform of the sampled and averaged time-domain response. The responses to chirp stimuli were sampled at 50 kHz and averaged over 200 repetitions. The DFT length was 2048 points for all measurements except those made in the long open tube that attached to the supra-aural earphone [Fig. 3(D)], which had a DFT length of 8192 points.

The impulse response computed from the pressure measurement made in the long open tube attached to the supra-aural earphone showed energy that was delayed by more than 10 ms in time relative to the electric stimulus. This energy appeared to result from reflections in the tube at locations remote to the earphone. Because such reflections are not included in the uniform tube model that is used for the theoretical impedance of the long tube, to remove their effects we set the impulse response to zero for all times greater

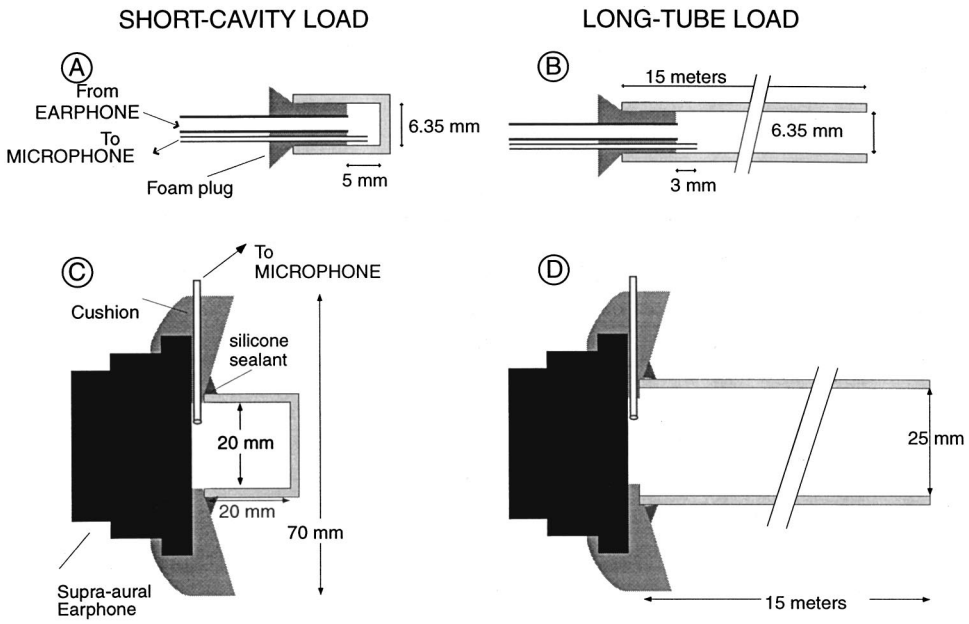

FIG. 3. Schematic showing how the insert [(A) and (B)] and the supra-aural [(C) and (D)] earphones were coupled to the microphone-probe tube and to the calibration loads. (A) The insert earphone coupled to the short closed tube with a rigid termination, inner diameter i.d.=6.35 mm and length $l=2$ mm from the microphone's probe tube. (B) The insert earphone coupled to the long tube with an open termination with i.d.=6.35 mm and length $l=15$ m. (C) The supra-aural earphone coupled to the short closed tube with a rigid termination, i.d.=20 mm and length $l=20$ mm. (D) The supra-aural earphone coupled to the tube with an open termination, i.d.=25 mm and length $l=15$ m.

than 10 ms and used the DFT of this signal as the pressure frequency response.

The theoretical impedances of all reference loads were calculated from the equations of Egolf (1977). For each earphone, the pressure measurements made in the two loads were combined with the loads' theoretical impedances to calculate the Thévenin pressure source and impedance: P_{TH}^{I} and Z_{TH}^{L} for the insert earphone and P_{TH}^{SA} and Z_{TH}^{SA} for the supra-aural earphone.

B. Results: Thévenin equivalents

Our measurements of the Thévenin pressures and impedances for both insert and supra-aural earphones are shown in Fig. 4. The Thévenin acoustic output impedances are nearly identical for the two (ER-3A) insert earphones, where ''Earphone A'' has an electric input impedance of 50 Ω and ''Earphone B'' has an electric input impedance of 10 Ω, and the two Thévenin pressures differ by about 5 dB at most frequencies. The Thévenin impedance magnitude of the supra-aural earphone is about one tenth that of the insert earphones.

These descriptions of the earphones are used in Sec. III to predict the pressure that the earphones generate in ear canals.

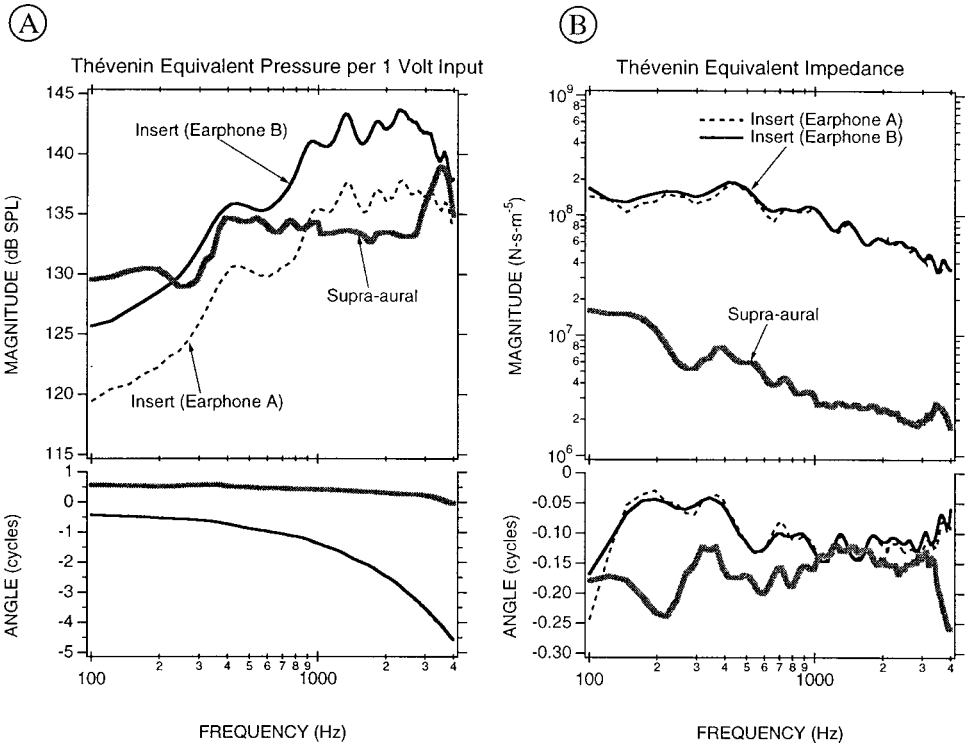

FIG. 4. Thévenin equivalents for the insert earphone and the supra-aural earphone. (A) Thévenin pressures. (B) Thévenin impedances. UPPER: Magnitudes. LOWER: Angles. The Thévenin pressure angles for the insert earphones correspond to a constant delay of about 1.1 ms—the time it takes sound to travel about 35 cm—which is the length of plastic tubing through which sound generated by the insert earphone must travel. Earphone A is an ER-3A insert earphone with a nominal input impedance of 50 Ω and earphone B is an ER-3A with an input impedance of 10 Ω. The angles of the equivalent pressure of the two insert earphones are essentially identical.

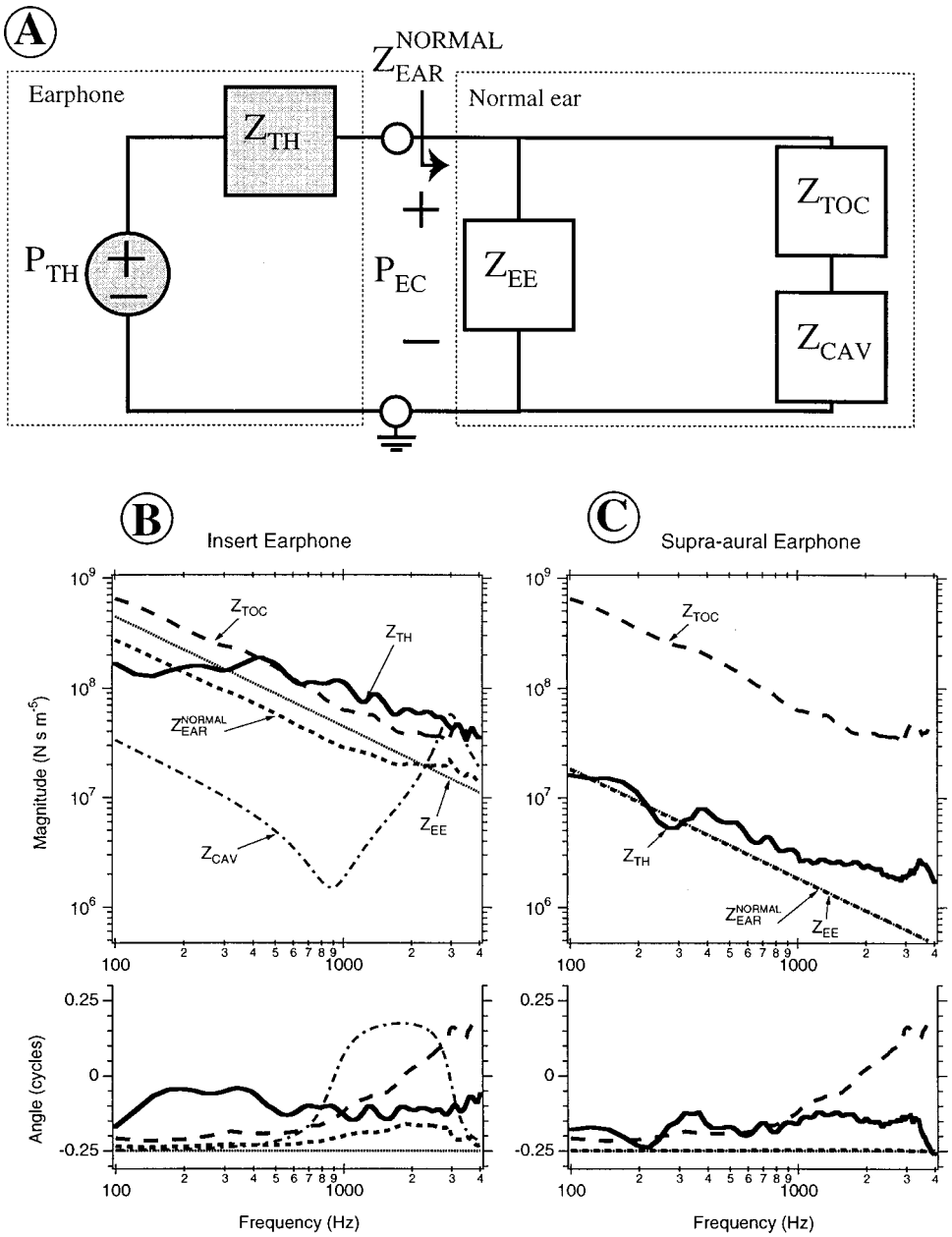

FIG. 5. (A) Lumped-element model for the normal middle ear connected to an earphone represented by its Thévenin equivalent circuit P_{TH} and Z_{TH} (shaded gray). $Z_{\mathrm{EAR}}^{\mathrm{NORMAL}}$, the driving-point impedance of the ear, is the load driven by the earphone. Z_{EE} represents the external-ear air space between the tympanic membrane and the earphone as a compliance corresponding to $V_{EE}^{I}=0.5\ \mathrm{cm}^3$ and $V_{EE}^{SA}=12.0\ \mathrm{cm}^3$ for the insert and the supra-aural earphones, respectively. Z_{TOC} represents the tympanic membrane (T), ossicular chain (O), and cochlea (C), and the values used for Z_{TOC} are means from measurements in normal temporal bones ($N=9$) (Voss, 1998), which are comparable to the measurements of Rosowski *et al.* (1990). The standard deviation for $|Z_{\mathrm{TOC}}|$ is less than 6 dB at all frequencies, and the standard deviation for $\angle Z_{\mathrm{TOC}}$ is less than 0.05 cycles below 1000 Hz and less than 0.10 cycles above 1000 Hz. Z_{CAV} represents an average middle-ear cavity and is defined in Fig. 6. (B) Impedance magnitudes and angles with the insert earphone. (C) Impedance magnitudes and angles with the supra-aural earphone.

II. MODELS FOR EARS COUPLED TO EARPHONES

A. Goals and approach

We propose simple circuit models to represent two earphone configurations (i.e., insert and supra-aural) coupled to a normal ear, coupled to four types of pathologic ears, and incorporating acoustic leaks between the supra-aural earphone and the ear. Our goal is to use these models to test our understanding of the acoustic mechanisms that are important in determining the ear-canal sound pressure generated under these different conditions. In the next section (Sec. III) we use these models to make predictions for the ear-canal sound pressure in each of the configurations.

We plot our model predictions for a frequency range of 100–4000 Hz, which contains the important audiologic frequencies. The lumped-element analog model is accurate only when the dimensions of the ear canal and ear are small relative to the wavelength of sound. With the insert earphone and a normal ear, the largest dimension is the ear-canal length of about 13 mm, which is 15% of the 88-mm wavelength of sound at 4000 Hz; thus, the lumped model should accurately represent the acoustic variations for frequencies up to 4000 Hz. With the supra-aural earphone and a normal ear, the largest dimension of the ear is much larger than with the insert earphone: the ear-canal length plus the distance from the ear canal to the earphone is about 50 mm. Here, the frequency at which the largest dimension is 15% of a wavelength is only 1050 Hz. Thus, with the supra-aural earphone the lumped model becomes inaccurate at lower frequencies than with the insert earphone.

B. The normal ear

The lumped-element model for the normal middle ear [Fig. 5(A)] consists of three impedances. Z_{EE} represents the external-ear (EE) air space between the tympanic membrane

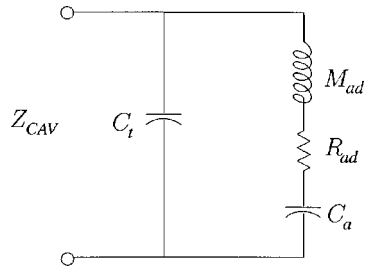

FIG. 6. Lumped-element model that represents the middle-ear cavity impedance Z_{CAV} (Voss, 1998). Element values determined by Voss (1998) from measurements of Z_{CAV} made on temporal bones are: $C_t = 4.2\times10^{-12}$ F, where C_t has an equivalent volume V_t of 0.6 cm^3; $M_{ad} = 722$ H; $R_{ad} = 0.05\times10^6\sqrt{f}\,\Omega$, where f is frequency (in Hz); and $C_a = V_a/(\rho c^2)$, where V_a is the volume of the antrum and other mastoid air cells. Here, unless noted otherwise, $V_a = 5.9$ cm^3 ($C_a = 42\times10^{-12}$ F), which when added to the tympanic-cavity volume of 0.6 cm^3, results in the total middle-ear cavity volume of 6.5 cm^3 as measured (average) by Molvaer *et al.* (1978). In cases where the middle-ear cavity volume is varied, the tympanic-cavity volume remains constant at 0.6 cm^3, and the volume of the antrum and other mastoid air cells, V_a, is varied.

and the earphone and is modeled as a compliance [i.e., $Z_{EE} = 1/(j\omega C_{EE})$] with a value appropriate for the external-ear air space (i.e., $C_{EE} = V_{EE}/(\rho c^2)$, where ρ is the density of air, c is the speed of sound in air, and V_{EE} is the external-ear air volume). External-ear air volumes for the insert earphone and the supra-aural earphone are selected as $V_{EE}^{I} = 0.5$ cm^3 and $V_{EE}^{SA} = 12.0$ cm^3 respectively.[3] [Z_{EE} is plotted in Fig. 5(B) and (C) for both cases.] The impedance that represents the external-ear air volume is assumed constant for all middle-ear conditions and is placed in parallel with the impedances that represent the middle ear to represent the portion of the volume velocity generated by the earphone that compresses the air in the external-ear; the rest of the volume velocity represents movement of the tympanic membrane. We will see that the external-ear volume plays an important role in the ear's impedance; the difference between the insert earphone's smaller external-ear volume and the supra-aural earphone's larger external-ear volume is partially responsible for earphone-linked differences in the effects of altered middle-ear impedances on ear-canal pressures.

Our lumped-element model represents the middle ear by two impedances in series: Z_{TOC} and Z_{CAV}. Z_{TOC} represents the tympanic membrane (T), ossicular chain (O), and cochlea (C), and the Z_{TOC} we use [see Fig. 5(B) and (C)] is the mean from temporal-bone measurements (Voss, 1998; Fig. 4-2). Z_{CAV} represents the middle-ear cavity. The model we use for Z_{CAV} (Fig. 6) is the same topology used in Kringlebotn's (1988) middle-ear model, but some of the element values were determined from measurements of Z_{CAV} on human temporal bones (Voss, 1998, pp. 168–173). In this model, C_t represents the compliance of the tympanic cavity, with $C_t = V_t/(\rho c^2)$, M_{ad} and R_{ad} represent the ''tubelike'' aditus ad antrum that connects the tympanic cavity and the mastoid cavity (Voss, 1998, pp. 168–169); and C_a represents the compliance of the antrum and other air cells, with $C_a = V_a/(\rho c^2)$, where V_a is the total volume of the antrum and other mastoid air cells. The impedance Z_{CAV} is plotted in Fig. 5(B).

In a normal ear, $|Z_{\mathrm{TOC}}| \gg |Z_{\mathrm{CAV}}|$ so that the ear's input impedance, $Z_{\mathrm{EAR}}^{\mathrm{NORMAL}}$, is well approximated by the parallel combination of Z_{EE} and Z_{TOC}. Since $|Z_{EE}| < |Z_{\mathrm{TOC}}|$ for both earphone configurations, Z_{EE} plays an important role in determining Z_{EAR}. The impedance values for $Z_{\mathrm{EAR}}^{\mathrm{NORMAL}}$ are plotted in Fig. 5(B) and (C). Because the external-ear volume is much larger with the supra-aural earphone than with the insert earphone, the driving-point impedance magnitude of the normal ear, $|Z_{\mathrm{EAR}}^{\mathrm{NORMAL}}|$, is much smaller with the supra-aural earphone than with the insert earphone.

Figure 5(B) and (C) allows comparison of the Thévenin-impedance magnitudes for each source to that of the normal ear. Neither Thévenin impedance meets the condition required for a nearly ideal pressure source, namely that $|Z_{TH}| \ll |Z_{\mathrm{EAR}}^{\mathrm{NORMAL}}|$ (Sec. C of the Introduction). In fact, for both earphone configurations $|Z_{TH}| > |Z_{\mathrm{EAR}}^{\mathrm{NORMAL}}|$ for frequencies above 700 Hz. Thus, for ear-canal pressures to be nearly independent of the attached ear, pathologic changes in Z_{EAR} must be small relative to the normal value for Z_{EAR}. Subsequent sections of this paper determine whether this condition is met for either earphone configuration with ears having middle-ear pathologies and earphone-ear connections with acoustic leaks.

C. Pathologic ears

1. Scope

To create models for three pathologic conditions (mastoid-bowl ear, tympanostomy-tube ear, and tympanic-membrane-perforation ear) and one condition that approximates pathological ears with ''high-impedances,'' we modify the lumped-element model for the normal ear [Fig. 5(A)] by adding elements.

2. Mastoid-bowl ear

The effect of the mastoid bowl [Fig. 1(D)] is represented by an added impedance Z_{BOWL} in parallel with the ear-canal air space and the normal middle-ear components [Fig. 7(A)]. Z_{BOWL} is a compliance, with an equivalent volume equal to the physical volume of a mastoid bowl, which can range from about 1 to 6 cm^3 (Merchant, 1997). The additional air volume acts to decrease the magnitude of the ear's driving-point impedance; the greater the bowl's volume, the more the impedance magnitude decreases relative to normal. The impedance magnitudes for the driving-point impedance of an ear with a mastoid bowl, $Z_{\mathrm{EAR}}^{\mathrm{MB}}$, with bowl volumes of 1 cm^3 and 6 cm^3 are compared to the Thévenin impedances of the two sources in Fig. 7(B) and (C).

For the insert earphone, $|Z_{\mathrm{EAR}}^{\mathrm{MB}}| < |Z_{\mathrm{EAR}}^{\mathrm{NORMAL}}|$ for both bowl volumes, and the impedance of the mastoid bowl is approximately the driving-point impedance of the ear $Z_{\mathrm{EAR}}^{\mathrm{MB}}$. Moreover, the condition that variations in Z_{EAR} must be small relative to $Z_{\mathrm{EAR}}^{\mathrm{NORMAL}}$ (Sec. C of the Introduction) is grossly violated for the insert earphone; with the larger mastoid bowl the ear's impedance magnitude $|Z_{\mathrm{EAR}}^{\mathrm{MB}}|$ decreases to about 1/7 the value for a normal ear.

The relative impedance magnitudes are somewhat different with the supra-aural earphone. In this case, the additional volume introduced by the mastoid bowl is less than the 12-cm^3 air volume between the source and the tympanic

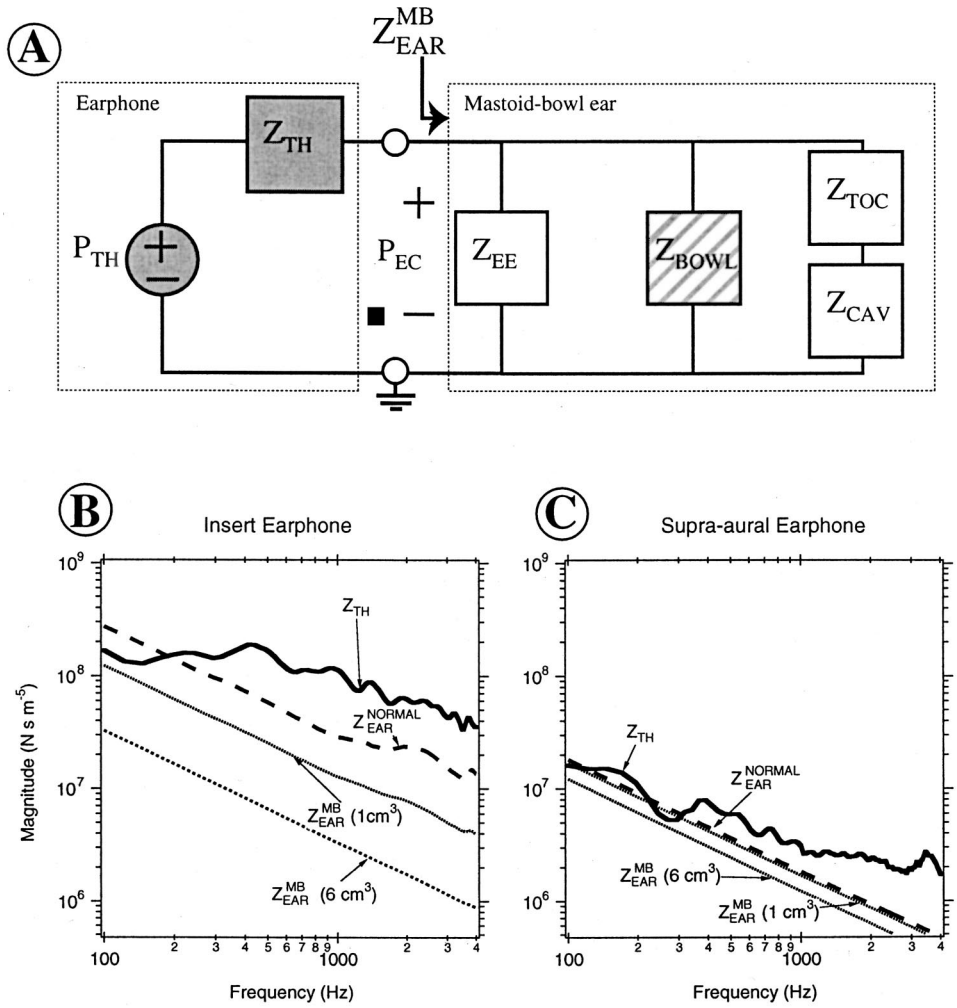

FIG. 7. (A) Lumped-element model for an earphone with Thévenin source characteristics (shaded gray) P_{TH} and Z_{TH} that is connected to an ear with a mastoid bowl (MB). The white blocks are identical to the normal middle ear of Fig. 5(A). The striped box labeled Z_{BOWL} is a compliance with an equivalent volume equal to the volume of the mastoid bowl. (B) Impedance values for the model of *A* with the insert earphone. Z_{EAR}^{MB} the driving-point impedance of the ear with a mastoid bowl (*MB*), is shown for two mastoid bowl volumes, 1 and 6 cm^3, that span the usual range. (C) Impedance values for the model of *A* with the supra-aural earphone.

membrane in the normal ear. Therefore, the effect of a mastoid bowl, though it still reduces the driving-point impedance magnitude, is much smaller with the supra-aural earphone. With a mastoid volume of 6.0 cm^3, the impedance magnitude decreases by less than a factor of 2 relative to the normal ear. Thus, the condition required for constant ear-canal pressures—that variations in Z_{EAR} must be small relative to $Z_{\mathrm{EAR}}^{\mathrm{NORMAL}}$—is more closely approximated with the supra-aural earphone.

The frequency range for which the lumped-element model is valid depends on the largest dimensions of the ear. A mastoid bowl modifies the ear canal and increases the external-ear and ear-canal dimensions relative to normal. With the insert earphone and a normal ear the largest dimension was identified as the effective ear-canal length of about 13 mm; a mastoid bowl may increase this dimension and thus reduce the upper valid frequency limit of 4000 Hz. With the supra-aural earphone, the largest dimension of about 50 mm probably does not increase much with the addition of a mastoid bowl, and the upper limit for our model probably remains at about 1000 Hz. As we will see (Sec. III C), the ''simple'' lumped-element model of Fig. 7(A) fails to capture pressure extrema that occur in the experimental data at frequencies above 1000 Hz with the supra-aural earphone. In order to increase the valid frequency range for the model of a supra-aural earphone coupled to a mastoid-bowl ear, we will represent the external ear (i.e., Z_{EE}) by several lumped elements (Sec. III E).

3. Tympanostomy-tube ear

The tympanostomy tube is modeled as a lossy tube, with impedance Z_{TUBE}, connecting the ear-canal air space to the middle-ear cavity space [Fig. 8(A)]; the volume velocity through Z_{TUBE} contributes to the volume velocity into Z_{CAV}.

The impedance Z_{TUBE} is calculated from the lossy equations of Egolf (1977), with the length of the tube $l = 2.1$ mm and the diameter $d = 1.27$ mm corresponding to the dimensions of a Baxter™ tympanostomy tube. To compute Z_{TUBE}, we reduce Egolf's two-port network model of a tube to a one-port element by computing the input impedance of the two-port network terminated with an impedance of zero. Z_{TUBE} is approximately a mass in series with a small resistance [$|Z_{\mathrm{TUBE}}|$ as plotted in Fig. 8(B)].

The impedance magnitudes for an ear with a tympanostomy tube $Z_{\mathrm{EAR}}^{\mathrm{TUBE}}$ are plotted for both earphone configurations [Fig. 8(B) and (C)]. Here, because of the tube's connection to it, the middle-ear cavity impedance Z_{CAV} becomes an important element in the model. At the lowest frequency plotted (100 Hz), $|Z_{\mathrm{TUBE}}| \ll |Z_{\mathrm{TOC}}|$ and $|Z_{\mathrm{TUBE}}| \ll |Z_{\mathrm{CAV}}|$, independent of earphone configuration; thus, the driving-point impedance Z_{EAR} is essentially the parallel combination of

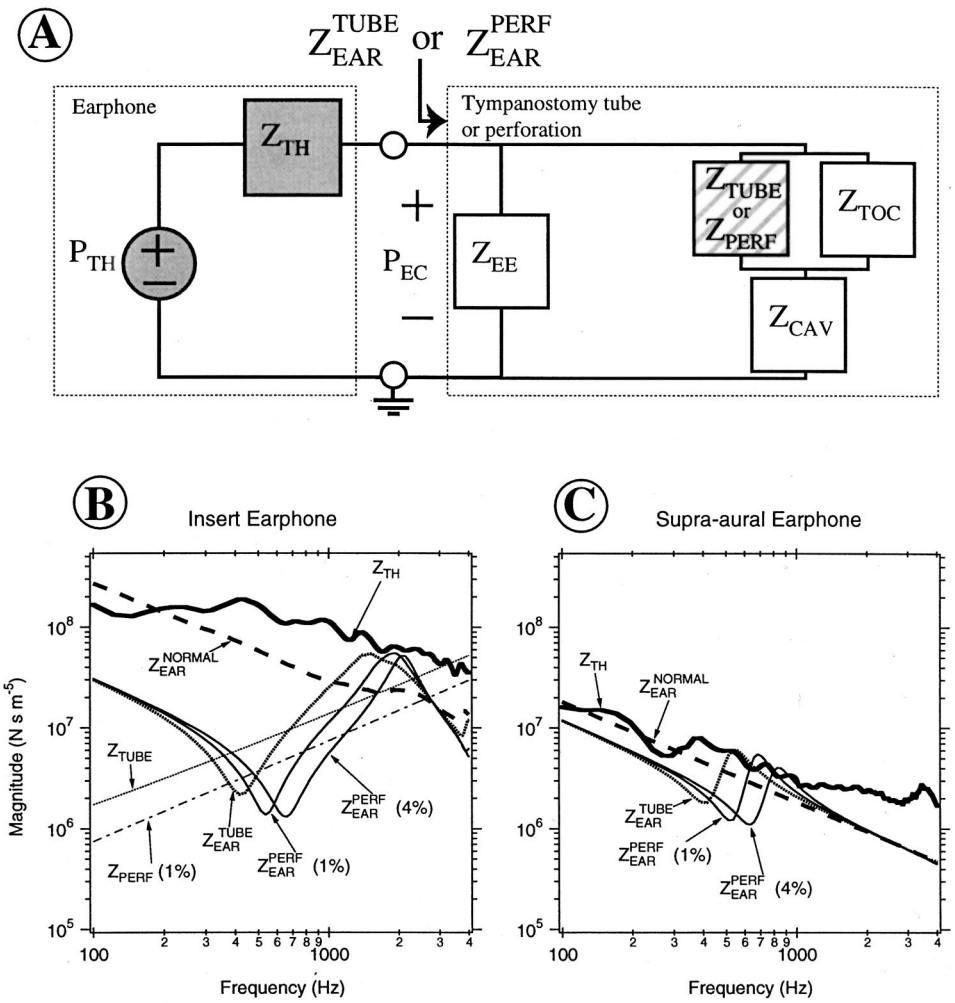

FIG. 8. (A) Model for ears with either a tympanostomy tube (TUBE) or tympanic-membrane perforation (PERF). Z_{EAR}^{TUBE} is the driving-point impedance of the ear with a tympanostomy tube, and Z_{EAR}^{PERF} is the driving point impedance of the ear with a perforation, where the percent of tympanic-membrane area covered by the perforation is indicated. The white blocks are identical to the normal middle ear of Fig. 5(A). The box with stripes is an approximation for a lossy tube that represents a tympanostomy tube (Z_{TUBE}) or a circular orifice with negligible thickness that represents a tympanic-membrane perforation (Z_{PERF}) (see text for details). (B) Impedance values for the model with the insert earphone. (C) Impedance values with the supra-aural earphone.

two compliance-dominated impedances, Z_{EE} and Z_{CAV}. As frequency increases, Z_{TOC} remains relatively unimportant; Z_{TUBE}, which can be approximated by an acoustic mass, M_{TUBE}, increases in magnitude; and a series resonance between the acoustic mass of the tube and the ''effective'' compliance of the middle-ear cavity[4] occurs between 300 and 400 Hz. This resonance results in an impedance-magnitude minimum at frequency f_{min}, which depends on the dimensions of the tympanostomy tube and the middle-ear cavity volume and is independent of the type of earphone (i.e., insert or supra-aural). The depth of the impedance minimum does depend on the earphone type because the driving-point impedance Z_{EAR} depends on Z_{EE}, which changes with earphone type. As frequency increases further, a peak at frequency f_{max} occurs as a result of a parallel resonance between the compliance of the external-ear volume and the effective middle-ear cavity compliance and the mass of the tube. The frequency f_{max} depends on the external-ear volume and is thus different for the two earphones.

Large variations of Z_{EAR}^{TUBE} relative to Z_{EAR}^{NORMAL} occur in ears with tubes [Fig. 8(B) and (C)]. The magnitude variations are larger for the insert earphone than for the supra-aural earphone, but the supra-aural earphone variations can be substantial near the resonant frequencies. Thus, the condition (Sec. C of the Introduction) required for constant ear-canal pressures—that variations in Z_{EAR} must be small relative to Z_{EAR}^{NORMAL}—is not met at some lower frequencies for ears with tympanostomy tubes.

4. Tympanic-membrane perforations

The model for a tympanic-membrane perforation is identical in topology to the tympanostomy tube; the perforation's impedance Z_{PERF} is placed between the external-ear volume and the middle-ear cavity, and the impedance Z_{PERF} is calculated using equations from Morse and Ingard (1968, pp. 480–483) for a circular orifice with negligible thickness, where $Z_{PERF}=j\omega M_{PERF}+R_{PERF}$ is the series combination of $M_{PERF}=\rho/d$ with ρ the density of air and d the perforation's diameter, and $R_{PERF}=1/[4\pi(d/2)^2]\sqrt{2\rho\omega\mu}\ln(d/h)$ with h the larger of two quantities: (1) half the thickness of the tympanic membrane, where the thickness of the tympanic membrane equals 0.1 mm (Lim, 1970), or (2) the thickness of the viscous boundary layer $d_v=\sqrt{2\mu/(\rho\omega)}$, where μ is the absolute viscosity of air. The calculated $|Z_{PERF}|$ with a 1-mm-diameter perforation is included in Fig. 8(B).

Impedance magnitudes for the ear with two different sized tympanic-membrane perforations Z_{EAR}^{PERF} (covering 1% and 4% of the tympanic-membrane area[5]) are plotted for both earphones [Fig. 8(B) and (C)]. The impedance's behav-

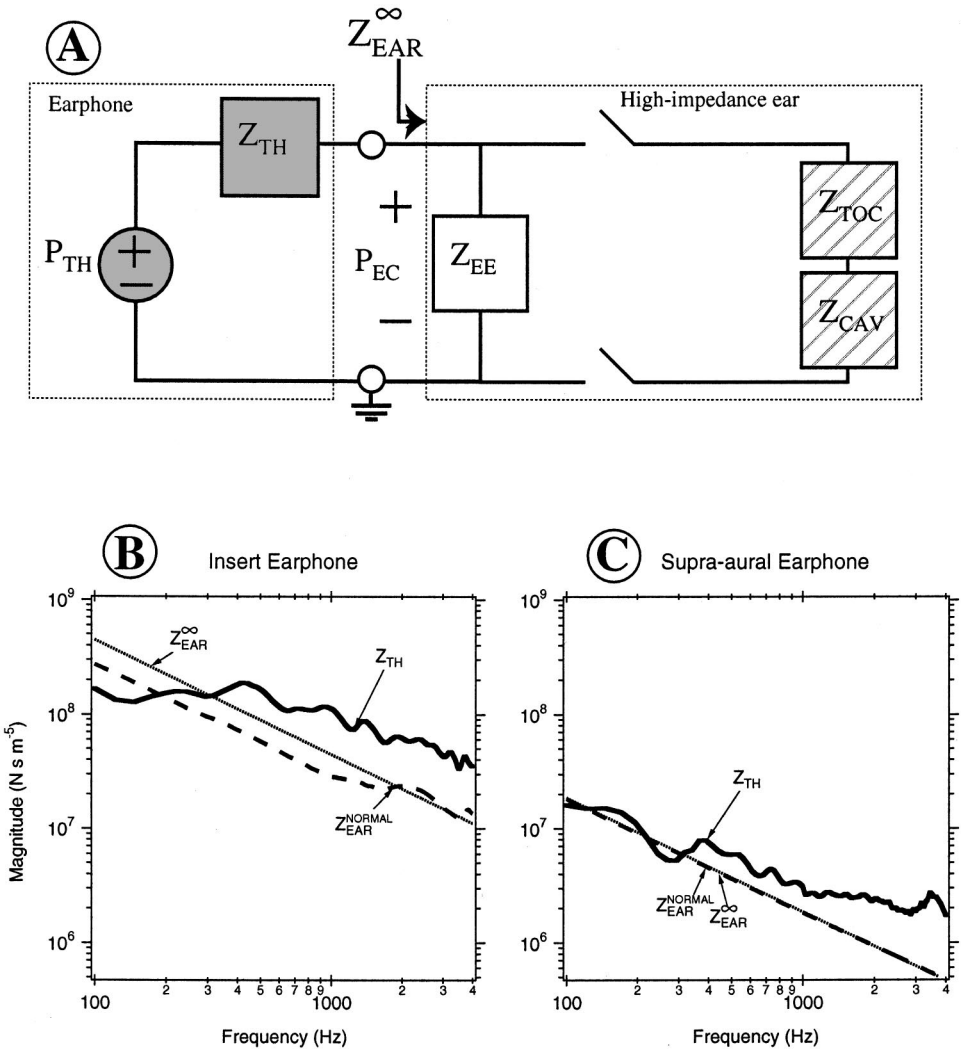

FIG. 9. (A) Model for an ear with a pathology that results in an infinite impedance magnitude at the tympanic membrane. Here, the impedances that represent the middle-ear are disconnected by an open switch. The impedance Z_{EE} that represents the ear-canal air–space is identical to the normal middle ear of Fig. 5(A). Z_{EAR} is the driving-point impedance of the ear and suprascripts refer to the ''normal-'' and the ''infinite-'' impedance conditions. (B) and (C) Impedance values for the model above with the insert earphone (B) and the supra-aural earphone (C).

ior is similar to the condition with the tube. At the lowest frequencies, the driving-point impedance magnitude $|Z_{\mathrm{EAR}}^{\mathrm{PERF}}|$ is essentially the parallel combination of the compliance-dominated impedances Z_{EE} and Z_{CAV}. As frequency increases, a minimum and maximum occur in $|Z_{\mathrm{EAR}}^{\mathrm{PERF}}|$, as with the tymanostomy tube. A series resonance between the perforation's mass and the effective middle-ear cavity compliance results in an impedance minimum, and a parallel resonance between the external-ear volume and the effective middle-ear cavity compliance and the perforation's mass results in an impedance maximum. Thus, as in the case with the tube, the frequency of the impedance minimum is independent of the earphone, and the frequency of the impedance maximum depends on the earphone. The condition (Sec. C) of the Introduction) required for constant ear-canal pressures—that variations in Z_{EAR} must be small relative to $Z_{\mathrm{EAR}}^{\mathrm{NORMAL}}$—is not met at some lower frequencies.

5. ''High-impedance'' ear

Pathologies that can increase the impedance of the ear include otosclerosis and a fluid-filled middle-ear cavity. An ''infinite-impedance'' middle ear represents an upper limit for the effect of pathologies that increase the ear's impedance: with the impedance magnitude at the tympanic membrane infinite,[6] the earphone's load impedance is that of the ear-canal air space Z_{EE} [Fig. 9(A)].

In Fig. 9(B) and (C), the effect of the ''infinite-impedance'' middle ear is shown for each earphone. The impedance magnitude that the earphone must drive, $|Z_{\mathrm{EAR}}^{\infty}|$, increases relative to $|Z_{\mathrm{EAR}}^{\mathrm{NORMAL}}|$ with both earphones, but not by a large factor. For the insert earphone, the impedance increases by less than a factor of 2 at all but the lowest frequencies, and for the supra-aural earphone, the impedance increases by an indistinguishable amount. The reason for these small impedance changes is that the external-ear volume limits the driving-point impedance. With this external-ear ''buffer,'' the impedance that the earphone must drive can never exceed the impedance of the external-ear volume. For example, with the insert earphone, at 1000 Hz, the second term of Eq. (2) is $(\Delta Z_{\mathrm{EAR}}/Z_{\mathrm{EAR}}^{\mathrm{NORMAL}})/(1+Z_{\mathrm{EAR}}/Z_{TH}) \approx 0.45$, so that $|P_{\mathrm{EC}}/P_{\mathrm{EC}}^{\mathrm{NORMAL}}| \approx 1.45$, and the sound pressure in the ear is only about 3 dB greater than the assumed calibration value. Thus, for ears with pathologies that increase the impedance magnitude, variations in $|Z_{\mathrm{EAR}}^{\infty}|$ relative to $|Z_{\mathrm{EAR}}^{\mathrm{NORMAL}}|$ are small and the condition that variations in Z_{EAR} must be small relative to $Z_{\mathrm{EAR}}^{\mathrm{NORMAL}}$ is met.

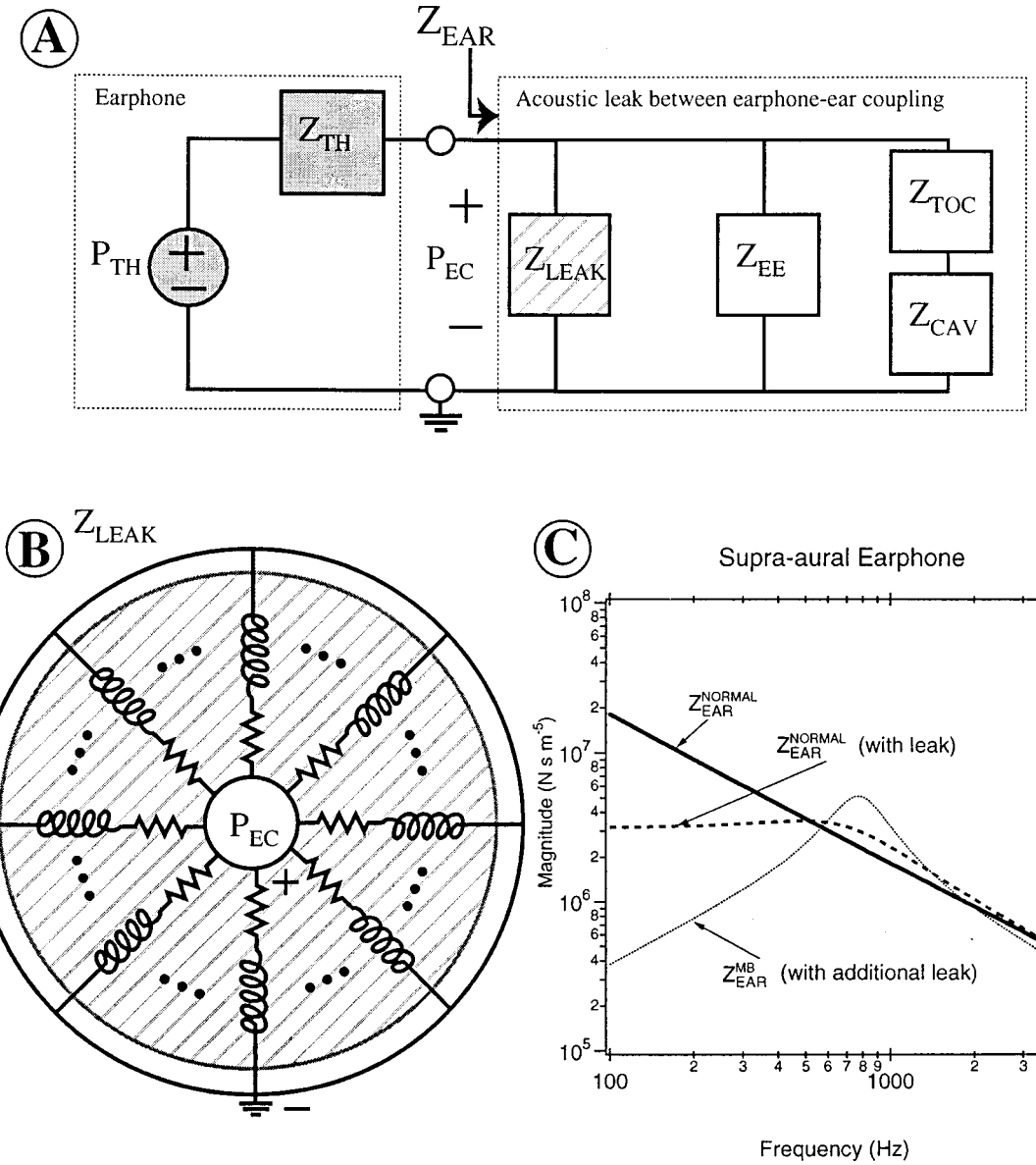

FIG. 10. (A) Model for a normal ear with a leak between the earphone and the ear. The impedances Z_{EE}, Z_{TOC}, and Z_{CAV} are identical to the normal middle ear of Fig. 5(A). The impedance labeled Z_{LEAK} (striped) represents the leak. (B) Model for the acoustic leak. The striped annular region represents the cushion of a supra-aural earphone, across which there are several small pathways that connect the air in the center of the cushion to the surrounding air. Here, eight independent air pathways are represented, each by a frequency-dependent acoustic mass in series with a frequency-dependent acoustic resistance. The three dots between each air pathway indicate the possibility of more elements in the array. The calculations shown here use 150 total pathways so that $Z_{\mathrm{LEAK}}=(1/150)[R_{\mathrm{LEAK}}(f)+j\omega M_{\mathrm{LEAK}}(f)]$. (C) Model predictions for the driving-point impedance magnitude for the normal ear with and without the leak shown here $|Z_{\mathrm{EAR}}^{\mathrm{NORMAL}}|$ [array of 150 ''tubelike'' leaks as in (B)] and the driving-point impedance magnitude for a mastoid-bowl ear $|Z_{\mathrm{EAR}}^{MB}|$ with an additional larger leak described in the text.

D. Acoustic leaks between the earphone and the ear

As demonstrated later [Fig. 11(B) and Fig. 13], our measurements with the supra-aural earphone (Voss *et al.*, in press) are consistent with acoustic leaks occurring at the earphone-ear connection. Here, we propose circuit models for the supra-aural earphone configuration with an acoustic leak in the earphone-ear connection with a normal ear and with an ear with a mastoid bowl. We do not know the spatial configuration of the leaks, which probably differ among ears; our models for the normal and the mastoid-bowl ears represent possible leak configurations.

To motivate the configuration of our model [Fig. 10(A)], consider the connection between a supra-aural earphone and a normal ear. For no leaks to occur, around its entire periphery the earphone cushion must abut the pinna. Here, we propose a model in which gaps occur between the pinna and the cushion in the normal ear. We represent these connections to the space around the earphone as an array of small tubes ($N=150$), indicated schematically in Fig. 10(B), each with a length $l_{\mathrm{leak}}=2.5\,\mathrm{cm}$, which corresponds to the distance from the central hole of the earphone cushion to its outer edge, and a radius $r_{\mathrm{leak}}=0.0125\,\mathrm{cm}$ (for a total leak area of $150\pi r_{\mathrm{leak}}^2=0.08\,\mathrm{cm}^2$). The impedance for each tube in the array is calculated from the lossy equations of Egolf (1977) with a terminating impedance of zero.[7] Each tube in the array is indicated schematically in Fig. 10(B) by a frequency-

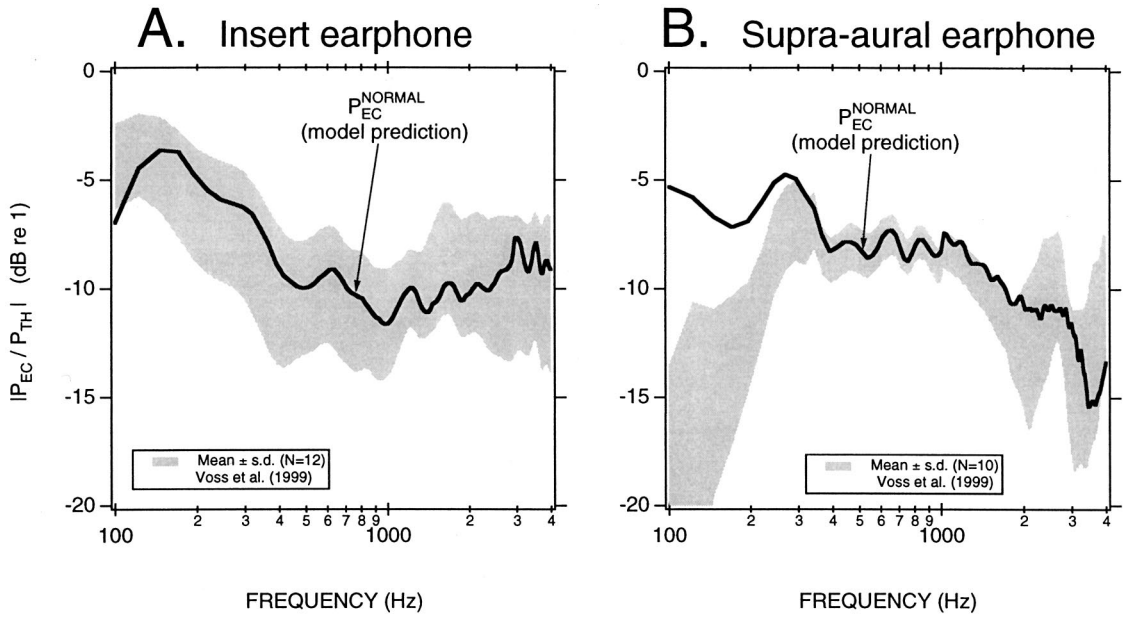

FIG. 11. Normal ears: Ear-canal pressure relative to the Thévenin equivalent P_{TH} for the insert earphone (A) and the supra-aural earphone (B). Solid lines are model predictions for the normal ear using the model of Fig. 5(A). Gray-shaded regions are the means plus and minus one standard deviation from measurements on populations of subjects with normal ears. The vertical scale is $20\log_{10}(|P_{EC}/P_{TH}|)$.

dependent mass in series with a frequency-dependent resistance. These leak-model parameters were chosen because they produce an ear-canal pressure that matches average measurements made on normal ears with the supra-aural earphone. Other leak configurations that match the measurements can also be found, as there are several free parameters in this model (i.e., r_{leak}, l_{leak}, N). With the leak configuration proposed here, Fig. 10(C) shows that the ear's driving-point impedance magnitude (with a leak) is reduced for frequencies below 500 Hz, slightly increased for frequencies between 500 and 1000 Hz due to a parallel resonance between the mass of the leak and the compliance of the normal ear, and roughly normal for frequencies above 1000 Hz where the leak's impedance magnitude becomes much greater than the ear's normal impedance magnitude and as a result the leak is effectively plugged.

Our measurements of ear-canal pressures generated by the supra-aural earphone show the largest low-frequency reductions in ear-canal pressure in ears with mastoid bowls, suggesting that larger leaks occur with mastoid-bowl ears than with other types of ears. (Reasons for these larger leaks are discussed below in Sec. III D.) We model the additional leak as a single pathway between the air space under the earphone cushion and the atmosphere. This pathway, which is larger than any of the single pathways for a leak with a normal ear, is represented by an acoustic mass $M_{\text{leak}}^{MB}=\rho_{\text{leak}}^{MB}/A_{\text{leak}}^{MB}$ whose impedance is calculated as $Z_{\text{leak}}^{MB}=j\omega M_{\text{leak}}^{MB}$. Figure 10(C) shows the predicted driving-point impedance for an ear with a 3-cm^3 mastoid bowl, an array of small leaks identical to those shown for the normal ear, and an additional leak with $l_{\text{leak}}^{MB}=1$ cm and $A_{\text{leak}}^{MB}=0.2\,\text{cm}^2$ that is placed in parallel with the leak for the normal ear. Figure 10(C) shows that with the given configuration, the mastoid-bowl ear's driving-point impedance magnitude is reduced for frequencies below 500 Hz (by nearly a factor of 100 at 100 Hz), increased relative to normal for frequencies between 500 and 1500 Hz, and nearly unchanged for frequencies above 1500 Hz.

III. MODEL PREDICTIONS

A. Plan

In this section, we use the models to predict the ear-canal pressure generated in each of the two earphone configurations in normal and pathologic ears. We are particularly interested in showing how the ear-canal pressures change from normal when the ear's impedance changes due to pathology or when an acoustic leak exists between the ear and the supra-aural earphone; thus, we plot ear-canal pressures relative to those in normal ears [i.e., Eq. (2)]. We include measurements (Voss *et al.*, in press) with the model predictions where possible.

B. The normal ear

In Fig. 11 measurements are compared to the model predictions (with no representation of a leak at the earphone-ear connection) for normal ears. For an earphone that acts as an ideal pressure source, the ratio $|P_{EC}/P_{TH}|$ would correspond to 0 dB (i.e., $P_{EC}=P_{TH}$). In Fig. 11, the measurements show that with either earphone $|P_{EC}/P_{TH}|<-5$ dB for most frequencies, and thus neither earphone approximates an ideal pressure source. The model predictions for the insert earphone approximate the mean of the measurements and are within one standard deviation of the mean at most frequencies; thus, the model predictions are consistent with the measurements. In contrast, the model predictions for the ear-canal pressures generated by the supra-aural earphone are consistent with the measurements above 250 Hz, but below 250 Hz the measurements and model differ by about 10 dB.

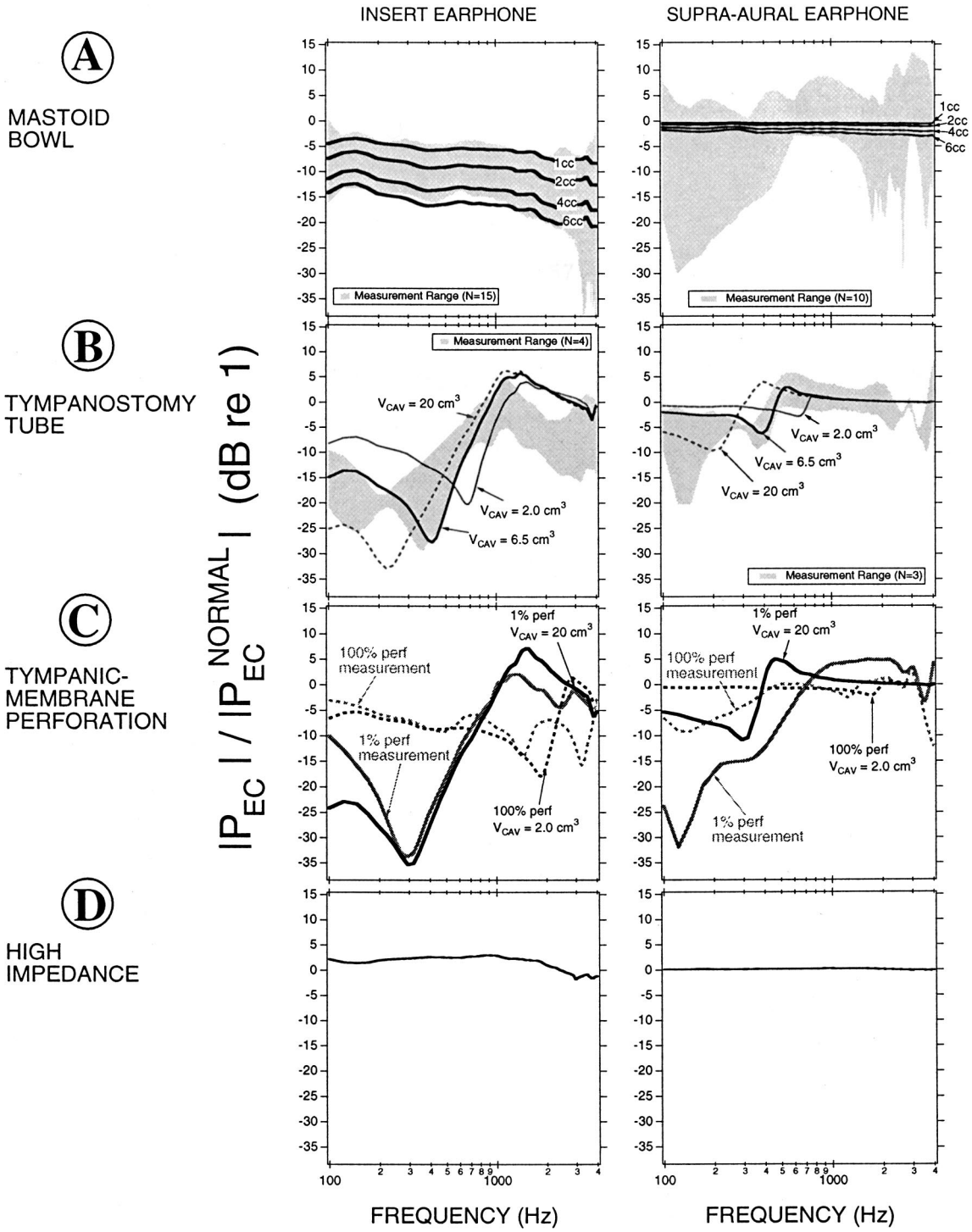

FIG. 12. Model predictions for the ear-canal pressures generated in ears with middle-ear pathologies with the insert earphone (LEFT) and the supra-aural earphone (RIGHT). Pressures are in dB relative to the pressure generated in a normal ear (Fig. 11). All model predictions are in black lines. Gray shaded regions (lines) indicate the range (value) of measurements made on subjects (Voss *et al.*, 1999). (A) Mastoid-bowl ears. (B) Tympanostomy-tube ears. The measurement ranges summarize measurements on ears with Baxter™ tympanostomy tubes. Model predictions are shown for three choices of middle-ear cavity volume V_{CAV}. (C) Perforations of the tympanic membrane. The perforation diameter was estimated visually, using an otoscope, for the human subjects, and the model's middle-ear cavity volume V_{CAV} was selected to fit the measurements. The 100% perforation refers to a case with no tympanic membrane. (D) ''High-impedance'' ear. No measurements were made for this condition. In the model (Fig. 9) $|Z_{TOC}+Z_{CAV}|$ was made infinite.

An explanation of this difference in terms of a leak between the earphone's cushion and the ear will be discussed further in Sec. III D below. As measurements made by Shaw (1966, Fig. 2) with the TDH supra-aural earphone show a similar low-frequency difference between pressures generated in a coupler and pressures generated in normal ears, this result seems to be representative of other measurements.

C. Pathologic ears

1. Mastoid bowl

a. Model predictions. The model predicts [Fig. 12(A)] that a mastoid bowl reduces the ear-canal pressure generated by both the insert and the supra-aural configurations and that the pressure reduction increases as mastoid-bowl volume in-

creases; the reduction is much greater with the insert earphone than with the supra-aural earphone. With the insert earphone and a mastoid bowl of 6 cm^3, the reduction is between 15 and 20 dB, whereas with the supra-aural earphone it is only 2–3 dB. This difference is a consequence of the impedances shown in Fig. 7: The volume of the mastoid bowl has dramatic effects on the driving-point impedance Z_{EAR} with an insert earphone because the insert earphone faces an external-ear volume of only 0.5 cm^3; addition of the 6-cm^3 bowl increases the total volume by a factor of 12. Conversely, with the supra-aural earphone the external-ear volume of 12.0 cm^3 is increased by only a factor of 1.5 by the 6-cm^3 bowl, which changes the impedance magnitude $|Z_{EAR}|$ by a factor of about 0.7 (or -1 dB) at all frequencies.

b. Comparison to measurements. Measurements of ear-canal pressures made on human subjects are generally consistent with the model predictions [Fig. 12(A)]. For the insert earphone, the measurement range is very close to the model's range for volumes of 1 cm^3 to 6 cm^3. With the supra-aural earphone, the range of the measurements is much larger than the model predictions, with both a systematic reduction in pressure below about 500 Hz and increases in pressure between 500 and 1000 Hz; these features could result from acoustic leaks between the earphone cushion and the ear; this possibility is discussed in Sec. III D.

Differences between the measurements and the supra-aural earphone model predictions also occur at frequencies above 1000 Hz. Here, the ear-canal pressure measurements (individual measurements are shown in Fig. 14) show sharp pressure extrema that differ by at least 15 dB from the range of pressures measured in the normal ears; these extrema are not predicted by our simple lumped model, whose validity at these frequencies was questioned earlier (Sec. II A). These extrema are further discussed in Sec. III E below in terms of a more complex model.

2. Tympanostomy tube

a. Model predictions. The model predicts that a tympanostomy tube introduces a low-frequency minimum in ear-canal pressure (relative to a normal ear) which depends on the volume of the middle-ear cavity as well as the tube's dimensions [Fig. 12(B)]. For frequencies above 1000 Hz, the changes from normal are less than 5 dB in both earphone configurations. Model predictions are plotted for an average size middle-ear cavity of 6.5 cm^3 and two extreme volumes that correspond to the range of anatomical measurements in a population of normal temporal bones: 2.0 cm^3 and 20 cm^3 (Molvaer *et al.,* 1978). The changes in ear-canal pressure are again larger for the insert earphone than for the supra-aural earphone, but the general behavior is similar for the two earphones. As the middle-ear cavity volume increases, both the frequency and the level of the pressure minimum decrease. For the same middle-ear cavity volume, the two earphone configurations have pressure minima at the same frequency.

b. Comparison to measurements. Measurements of the ear-canal pressures made on human subjects with Baxter™ tympanostomy tubes are consistent with the model predictions shown here. The gray shaded regions of Fig. 12(B) indicate the range of measurements on a small population of subjects (insert earphone $N=4$; supra-aural earphone $N=3$). Because the model predictions are highly dependent on the middle-ear cavity volumes, which are unknown in the patient population, it is impossible to compare an individual measurement to the model. With anatomically reasonable volume variations, the supra-aural earphone model predicts the measured range, and the insert-earphone model predicts the measured range for frequencies below about 1000 Hz and pressures that are 5–10 dB greater than the measurements for frequencies above 1000 Hz. One explanation for this 5–10 dB difference between the model predictions and the measurements involves the choice of the model parameters. In the model, the component Z_{TOC} is determined from temporal-bone measurements on normal ears (Fig. 5). However, the measurements in Fig. 12(B) are from ears with histories of middle-ear disease, which can reduce the stiffness of the tympanic membrane (Unge *et al.,* 1995). In fact, reducing the model $|Z_{TOC}|$ does result in a reduced ear-canal pressure that more closely approximates the measurements in the 1000–4000 Hz range. Variations of Z_{TOC} from normal are also likely in ears with tympanic-membrane perforations, but the issue is less important in ear's with mastoid bowls because with a mastoid bowl, the additional ear-canal volume dominates the ear's input impedance to frequencies greater than 4000 Hz.

Measurements with both an insert earphone and a supra-aural earphone were made on three subjects with Baxter™ tympanostomy tubes. As the model predicts, low-frequency pressure minima occurred at the same frequencies with both earphones (Fig. 4 of Voss *et al.*, in press).

3. Tympanic-membrane perforations

a. Model predictions. According to the model, the changes in the ear-canal pressure generated with a perforated tympanic membrane depend on both the middle-ear cavity volume and the diameter of the perforation. Model predictions are plotted [Fig. 12(C)] for perforations of two extreme sizes for which we also have measurements: 1% and 100% of the tympanic-membrane area. As we do not have measurements of the middle-ear cavity volumes in individual subjects, volumes were chosen to make the model prediction and the measurement similar.[8] In general, the smaller perforation behaves similarly to the tympanostomy tube: A low-frequency pressure minimum occurs at the same f_{min} for both earphones, and the pressure minimum is smaller with the insert earphone than with the supra-aural earphone. The larger perforations behave more like mastoid bowls with a relatively constant loss as a function of frequency.

b. Comparison to measurements. Figure 12(C) compares model predictions for two perforations with measurements of ear-canal pressure in ear canals with the same size perforations (1% and 100% perforations). Here, we plot individual measurements instead of measurement ranges, because the perforation diameter, which is a parameter in our data, has a large effect on the ear-canal pressure. Just as with the tympanostomy-tube case, model predictions using

middle-ear cavity volumes consistent with the normal range of anatomical measurements are similar to the measured values. An exception occurs with the supra-aural earphone at the lowest frequencies where the measured pressure with a 1% perforation is substantially below the (no leak) model.

4. High-impedance ear

Figure 12(D) shows model predictions for a ''high-impedance'' ear. The predicted ear-canal pressure generated by either earphone is no more than 3 dB greater than in the normal ear. As described above (Sec. II C 5), the maximum driving-point impedance magnitude $|Z_{\mathrm{EAR}}|$ is limited by the volume of the external ear. Thus, with either earphone, the terminating impedance magnitude $|Z_{\mathrm{EAR}}|$ can only increase a small amount when $|Z_{\mathrm{TOC}}+Z_{\mathrm{CAV}}|$ goes to infinity and the ear-canal pressure remains nearly unchanged. [For the highest frequencies shown, 2000–4000 Hz, there is a slight reduction in pressure with the insert-earphone configuration attached to the ''high-impedance'' ear because at these frequencies the magnitude of the impedance of the external-ear space is less than the magnitude of the normal ear impedance (Fig. 9).]

Our conclusion that a high-impedance ear has only small effects on ear-canal pressures depends on the volume of the external ear, i.e., the conclusion assumes that the external-ear volume is that of a normal adult-sized ear with $V_{EE}^{I}=0.5\,\mathrm{cm}^3$ for the insert earphone or $V_{EE}^{SA}=12\,\mathrm{cm}^3$ for the supra-aural earphone. Here we consider the effects of extreme changes in these volumes on ear-canal pressures. For example, consider the case of a smaller volume, as may be appropriate for a young child with a shorter and narrower ear canal than an adult (Keefe *et al.*, 1993). As V_{EE} approaches zero, the ear-canal pressure will be determined by the impedance of the middle ear. In the limiting case, with a high-impedance middle ear, the earphone's terminating impedance will be high and the ear-canal pressure will approach the Thévenin pressure P_{TH}. As shown in Fig. 11, the pressures generated in normal ears are only 5–10 dB below P_{TH}; thus, a small V_{EE} coupled with a high-impedance middle ear can never increase the ear-canal pressure by more than about 10 dB.

D. Acoustic leaks between the earphone and ear

At frequencies below 250 Hz, the ear-canal pressures generated by a supra-aural earphone in normal ears were smaller than those predicted by our (leak free) model [Fig. 11(B)]. Figure 13 compares these results of Fig. 11(B) to the model prediction with the array of small ''tubelike'' leaks (Sec. II D) between the pinna and the supra-aural earphone cushion. The model predictions with this array of small leaks is consistent with the measurements and with the hypothesis that the supra-aural earphone is difficult (if not impossible) to seal acoustically around the pinna and as a result there are low-frequency pressure reductions in ear-canal pressure. We conclude that there are always small acoustic leaks between a supra-aural earphone and a pinna that result in reduced ear-canal sound pressures at frequencies below about 250 Hz. In support of this conclusion, we note that our measurements on ten subjects all showed smaller ear-canal pressures

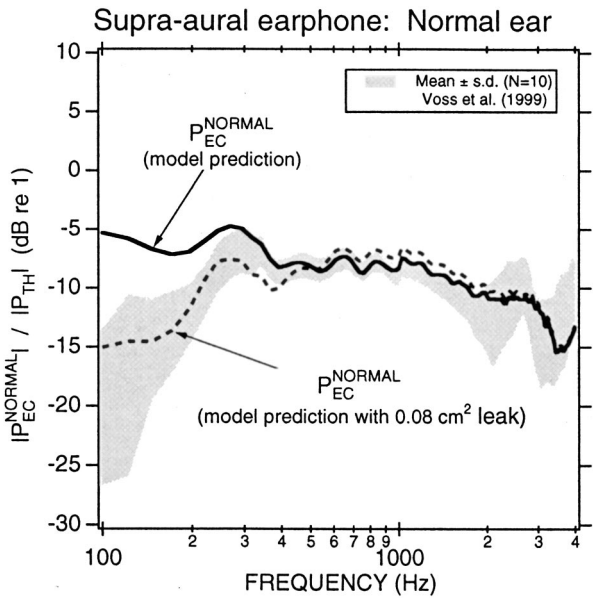

FIG. 13. Model predictions for ear-canal pressures (relative to the earphone's Thévenin pressure P_{TH}) generated in a normal ear when there is a leak between the cushion of the supra-aural earphone and the pinna. Model for the leak has an array ($N=150$) of ''tubelike'' leaks, each with $r_{\mathrm{leak}}=0.0125$ cm and $l_{\mathrm{leak}}=2.5$ cm. Also shown is the model prediction for the normal ear with no leak. The gray shaded region is the mean plus and minus one standard deviation from the measurements on 10 normal ears (Voss *et al.*, in press).

than predicted by our model, and measurements of ear-canal pressure in ten ears made by Shaw (1966, Fig. 2) were all reduced relative to the pressure measured in a coupler.

Our measurements of ear-canal pressures in ears with mastoid bowls show large reductions at low frequencies that are also not accounted for by our model of a mastoid-bowl cavity [Fig. 12(A)]. These pressure reductions are consistent with larger acoustic leaks in the earphone-to-ear connection than the leaks proposed for a normal ear. Effects of the surgery might lead to larger leaks with mastoid-bowl ears. The surgery includes an incision in the skin behind the pinna. As the incision heals, the scar can pull the posterior portion of the pinna flange closer to the skull. This ''bent'' configuration may introduce a larger leak between the supra-aural earphone cushion and pinna flange (Merchant, 1999).

Figure 14 compares the ear-canal pressures generated by the supra-aural earphone in three ears with mastoid bowls to our model prediction for a leak in the earphone-to-ear connection of a mastoid-bowl ear. The model includes two types of leaks: the array of small ''tubelike'' leaks that accounts for the normal ear's earphone-to-ear connection [Fig. 10(B)] and one larger leak that might occur in a region where the earphone cushion does not parallel the pinna. The model has features that are generally consistent with most of the measurements: the pressure reductions are greatest at the lower frequencies and increases with frequency until a maximum is reached around 500 Hz. It is possible to predict ear-canal pressures with features consistent with each measurement by associating an appropriate ''leak area'' and ''leak length'' with the measurement; measurements with the larger low-frequency pressure reductions have larger leak areas and measurements with the smaller low-frequency pressure re-

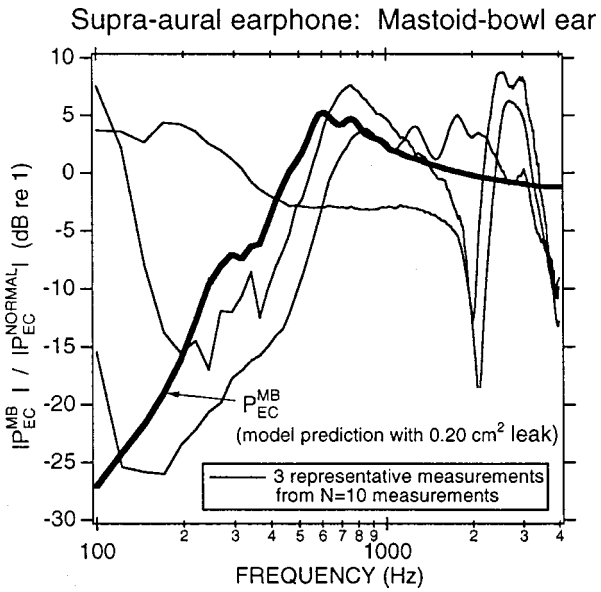

FIG. 14. Model predictions for ear-canal pressures generated in ears when there is a leak between the cushion of the supra-aural earphone and the pinna of a mastoid-bowl ear (bowl volume 3 cm^3) with both the same array of ''tubelike'' leaks shown in Fig. 13 and one additional larger leak (one tube-shaped leak with area 0.12 cm^2 and length 1 cm^2). Also shown are three measurements selected from a total of ten measurements made on mastoid-bowl ears (thin black lines); these three measurements are representative of the total range and general shape of all measurements (Voss *et al.*, in press).

ductions have smaller leak areas associated with them. We conclude that most of our measurements made on mastoid-bowl ears are consistent with larger-than-normal leaks in the earphone-to-ear connection of the supra-aural earphone.

E. Sharp pressure extrema with a supra-aural earphone and a mastoid-bowl ear

Our measurements of ear-canal pressures generated by the supra-aural earphone coupled to ears with mastoid bowls exhibit sharp pressure extrema that typically include a pressure minimum near 2000 Hz of about -20 dB (relative to normal) and a pressure maximum near 2500 Hz of about 10 dB (relative to normal) [Fig. 14 and Fig. 3 from Voss *et al.* (in press)]. Such sharp pressure extrema are not seen in either (1) the measurements on normal ears [Fig. 11(B) and Fig. 2 from Voss *et al.* (in press)] or (2) the model predictions shown with our ''simple'' lumped-element model of Fig. 7(A). Here, we propose an amendment to the model that predicts these pressure extrema at the higher frequencies without affecting the low-frequency behavior with the supra-aural earphone and mastoid-bowl cavity configuration.

As discussed in Sec. II C 2, the ''simple'' lumped-element model with the supra-aural earphone and mastoid-bowl cavity configuration becomes inaccurate at frequencies above 1000 Hz, where the dimensions of the external-ear air volume approach the wavelength of sound. Here, we increase the model's frequency range by adding elements to allow a pressure change along the ear canal between the air space under the earphone and the concha to the mastoid-cavity volume [Fig. 15(A)]. Instead of representing the external-ear air space as a lumped compliance with volume $V_{EE}=12$ cm^3 [i.e., as in Fig. 7(A)], we separate this total air volume into three regions: 1. The air volume within the concha and under the supra-aural earphone cushion ($V'_{EE}=11$ cm^3) is represented by C'_{EE}; 2. The ear canal itself is represented as a ''Π'' network where two compliances—each equal to $0.5C_{EC}$ and representing one-half of the ear-canal volume—are connected by an acoustic mass M_{EC} that is determined by the ear-canal dimensions, $M_{EC}=\rho l_{EC}/(\pi r_{EC}^2)$, where l_{EC} is the ear-canal length and r_{EC} is the ear-canal radius; and 3. The air volume of the mastoid-bowl cavity is represented by the compliance C_{BOWL}.

Here, we choose model-element values for the distributed model [Fig. 15(A)] of the external ear with a mastoid bowl. Values for C'_{EE} and C_{BOWL} are obtained from equivalent volumes defined in the preceding paragraph. The ear-canal dimensions determine the values for the M_{EC} and the $0.5C_{EC}$ of the ''Π'' network. After mastoid surgery, the ear canal is often wider-than-normal, and the canal is shorter-than-normal because the ''tubelike'' part of the canal is terminated by the mastoid-bowl cavity. To define M_{EC} for a mastoid-bowl ear, we use an ear-canal length $l_{EC}^{MB}=1.0$ cm and an ear-canal radius $r_{EC}^{MB}=0.56$ cm. These dimensions also define $0.5C_{EC}=0.5V_{EC}/(\rho c^2)$, where $V_{EC}=1.0$ cm^3 is the ear-canal volume, which is equal to the ear-canal volume computed for a normal ear with average dimensions (i.e., an ear-canal length $l_{EC}^{\mathrm{NORMAL}}=2.5$ cm and an ear-canal radius $r_{EC}^{\mathrm{NORMAL}}=0.36$ cm).

For frequencies below 1000 Hz, the ''distributed model'' [Fig. 15(A)] and the ''simple'' model [Fig. 7(A)] make the same predictions for the ear-canal pressure with a mastoid-cavity bowl [Fig. 15(B)]. Only as frequency increases above 1000 Hz do spatial variations become significant and the ''distributed'' representation of the ear canal has large effects on the model predictions compared to the ''simple'' model [Fig. 15(B)]. In particular, the distributed ear-canal model leads to sharp pressure extrema, with a pressure minimum that results from a series resonance between the mass of the ear canal and the compliance of the mastoid-bowl cavity and a pressure maximum that results from a parallel resonance between the mass of the ear canal and the compliances of the external ear and the mastoid-bowl cavity. As indicated in Fig. 15(B), the volume of the mastoid bowl influences the frequencies of the model's pressure extrema, with the larger mastoid-bowl volume producing extrema at lower frequencies. Since these pressure extrema are similar in magnitude and frequency to those measured on subjects with mastoid bowls [Fig. 14 and Fig. 3 of Voss *et al.* (in press)], we conclude that the pressure extrema result from resonances between the ear-canal and the air spaces of the external ear and the mastoid bowl.

Next, we test whether our ''simple'' model for the normal ear is adequate for the frequency range 100–4000 Hz that we have considered. A distributed model for the external ear of a normal ear is similar to the model for the mastoid-bowl ear [Fig. 15(A)] except the compliance that represents the mastoid bowl, C_{BOWL}, is removed, and the dimensions of the ear canal that define M_{EC} and $0.5C_{EC}$ correspond to a normal ear canal (i.e., an ear-canal length $l_{EC}^{\mathrm{NORMAL}}=2.5$ cm and an ear-canal radius $r_{EC}^{\mathrm{NORMAL}}=0.36$ cm). With a normal

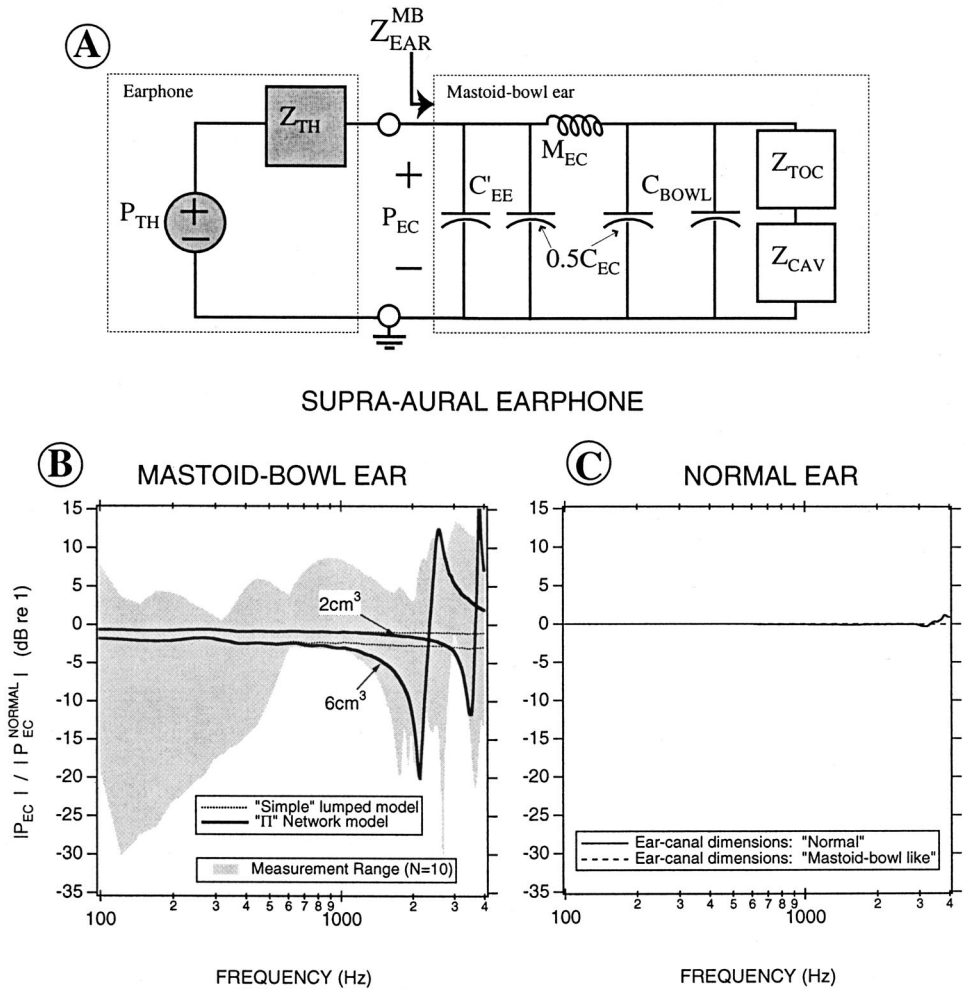

FIG. 15. (A) Modified representation of the external-ear air volume in the model of the supra-aural earphone coupled to a mastoid-bowl ear. The ear canal is modeled as a ''Π'' network with two compliances ($0.5C_{EC}$) connected by mass M_{EC}. The external-ear air volume lateral to the ear canal and the mastoid-bowl cavity remain represented by compliances: C'_{EE} and C_{BOWL}, respectively. (B) Model predictions for the mastoid-bowl ear with the ear-canal represented by both the simple model of Fig. 7(A) (dotted lines) and the ''Π'' network defined above (solid lines) with ear-canal dimensions for a mastoid-bowl ear (i.e., $l_{EC}=1.0$ cm; $r_{EC}=0.56$ cm). Model predictions are shown for two bowl volumes (2 cm^3 and 6 cm^3). The model predictions for each bowl volume (indicated on plot) overlap at the lowest frequencies. (C) Model predictions for the normal ear with the ear-canal represented by the ''Π'' network defined above relative to the model predictions with the simple model of Fig. 5(A). The solid line are calculations made with ear-canal dimensions of a normal ear (i.e., $l_{EC}=2.5$ cm; $r_{EC}=0.36$ cm), and the dashed lines are calculations made with ear-canal dimensions of a mastoid-bowl ear (i.e., $l_{EC}=1.0$ cm; $r_{EC}=0.56$ cm), where both sets of ear-canal dimensions result in an ear-canal volume of 1.0 cm^3.

ear, the two model topologies (i.e., the ''simple'' lumped model and the distributed model) predict nearly identical ear-canal pressures [Fig. 15(C)]. Additionally, as shown in Fig. 15(C), the dimensions of the ear canal have little effect on the model prediction as long as the total volume is constant (i.e., l_{EC}^{NORMAL} and r_{EC}^{NORMAL} lead to model predictions that are nearly identical to model predictions made with l_{EC}^{MB} and r_{EC}^{MB}). Thus, for a supra-aural earphone coupled to a normal ear, the ''simple'' lumped external-ear compliance is adequate and the distributed representation of the ear canal is unnecessary for frequencies up to 4000 Hz.

IV. DISCUSSION

A. Summary of results

Our lumped-element model explains how the sound pressure generated in abnormal ears differs from normal. These differences can lead to significant errors in hearing tests, when it is assumed that the earphone produces the same sound-pressure level in all tested ears.

Middle-ear pathology can both increase and decrease the ear's impedance relative to normal. Both an insert-earphone model and a supra-aural-earphone model predict that ear-canal pressures will be altered when the impedance of the middle ear is reduced. In general, changes from normal are larger with the insert earphone because the insert-earphone's small external-ear volume (relative to the supra-aural earphone) results in a higher load impedance which can be greatly reduced as a result of pathology (mastoid bowl, tympanostomy tube, tympanic-membrane perforation). On the other hand, when the ear's impedance magnitude increases relative to normal, the ear-canal pressure generally increases by less than 3 dB relative to normal, because the impedance of the air–space volume between the tympanic membrane and the earphone generally places an upper limit on the load impedance on the earphone.

The earphone's output can also be affected by acoustic leaks between the ear and the earphone. Here, our supra-aural earphone model predicts that such leaks lead to reduced ear-canal sound pressures at low frequencies and slightly increased ear-canal pressures near the resonant frequency between the mass of the leak and the compliance of the ear's load.

B. Pressure in the ear canal versus pressure at the tympanic membrane

We have focused on variations in the ear-canal pressure P_{EC} generated at the output of the earphone. Inter-ear variations in the pressure generated by the earphone—at the earphone's location—are important to quantify because they are currently assumed negligible when testing hearing.

Another fundamental issue that remains to be addressed deals with determining whether generating a constant sound pressure in the external ear leads to an accurate test of hearing acuity for all ears. For example, at higher frequencies, standing waves can be generated in the ear canal, and the pressure generated at the earphone may not be representative of the pressure at the tympanic membrane. Neely and Gorga (1998) have recently suggested that sound intensity level might provide a more useful measure than sound-pressure level in these circumstances.

Another possibility for improved hearing testing would be to test hearing with free-field sound. In this way, effects of ear-canal standing waves and external-ear filtering would be included in the hearing test in a manner similar to real-world hearing situations.

C. Insert versus supra-aural earphones

Differences between insert earphones and supra-aural earphones have been discussed extensively in the literature. In general, supra-aural earphones are purported to have a larger high-frequency dynamic range than many insert earphones (Zwislocki *et al.*, 1988), while insert earphones provide several advantages over supra-aural earphones, including the reduction of leaks in the earphone-to-ear connection and increased interaural attenuation (Killion and Villchur, 1989). Our measurements and models show advantages and disadvantages for both the insert and the supra-aural earphones. The ear's impedance has a larger effect on the sound pressure generated by the insert earphone than by the supra-aural earphone. Variations in low-frequency pressures that result from leaks are a bigger problem with supra-aural earphones than with insert earphones. We also expect variations in pressure along the ear canal to be larger with supra-aural earphones than with insert earphones as a result of the larger distance between the earphone and the tympanic membrane with the supra-aural earphone.

D. Conclusions

Our model represents mechanisms that can cause systematic ear-canal pressure variations of up to 35 dB in abnormal ears relative to normal; in many cases, pressure variations are as much as 15 dB at several frequencies. To reduce the problem of unknown variations in ear-canal sound-pressure levels, a microphone to monitor ear-canal pressures could be built into commercial audiometers, as suggested many years ago (Harris, 1978). The addition of such a microphone to an insert earphone would result in a system that maintains all of the advantages of an insert earphone and also controls ear-canal pressures close to the tympanic membrane; such a microphone is also a necessary feature of an audiologic system designed to measure the sound intensity level in the ear canal. The models presented here can be used to help define the range of ear-canal pressures such a system would need to correct.

ACKNOWLEDGMENTS

This work was supported by training and research grants from the NIDCD. We thank two anonymous reviewers for helpful comments.

[1]According to Sadé (1982), tympanic-membrane perforations affect 0.5%–30% of any community.

[2]It is estimated that 1.3% of American children (aged 8 months to 16 years) have tympanostomy tubes at a given time (Bright *et al.*, 1993).

[3]The ear canal has a length of about 28 mm and a diameter of about 7 mm (Wever and Lawrence, 1954, pp. 416). The insert earphone assembly extends about 15 mm into the ear canal: the 12 mm length of the foam plug plus 3 mm for the probe-tube extension. Thus, the ear-canal volume between the probe tube and the tympanic membrane accounts for the external-ear air volume of $V_{EE}^{I}=0.5\ \mathrm{cm}^3$. The supra-aural earphone couples to the ear via a cushion that rests along the edge of the pinna. Here, we use a total external-ear air volume of $V_{EE}^{SA}=12\ \mathrm{cm}^3$, where 1.0 cm^3 accounts for the ear-canal volume (Shaw, 1974), 4.0 cm^3 accounts for the concha volume (Shaw, 1974), and 7.0 cm^3 accounts for the air volume under the cushion that is lateral to the concha, which we measured by filling the earphone cushion with water from a calibrated syringe.

[4]An ''effective'' middle-ear cavity compliance can be defined for conditions in which Z_{CAV} has an angle of approximately -0.25 cycles. Because of the effect of M_{ad}, the ''effective'' middle-ear compliance depends on frequency. At the lower frequencies where the effect of M_{ad} is negligible, the ''effective'' compliance is the total compliance C_t+C_a. For frequencies much greater than the parallel resonant frequency between the mass M_{ad} and the compliances C_a and C_t, the ''effective'' compliance is C_t [see the plot of Z_{CAV} in Fig. 5(B)]. In general, when $\angle Z_{\mathrm{CAV}}\approx -0.25$ (cycles), the ''effective'' compliance $C_{\mathrm{eff}}\approx 1/(\omega|Z_{\mathrm{CAV}}|)$ where $\omega=2\pi f$.

[5]Perforations that cover 1% and 4% of the tympanic-membrane area correspond to circular perforations with diameters of 1 mm and 2 mm, respectively, assuming a tympanic-membrane area of 70 mm^2, which is the median of the 55 mm^2 to 85 mm^2 range given by Wever and Lawrence (1954, p. 416).

[6]A possible complication might occur in the process of altering the impedance at the tympanic membrane Z_{TM} from its normal value to an infinite magnitude. We assume a process in which the impedance Z_{TM} varies such that $|Z_{TM}^{\mathrm{NORMAL}}|\leqslant|Z_{TM}|\leqslant\infty$ with the angle of Z_{TM} equal to the angle of Z_{TM}^{NORMAL}. To simplify our discussion here, we consider admittances, where for example, $Y_{TM}=1/Z_{TM}$, $Y_{EE}=1/Z_{EE}$, and $Y_{TH}=1/Z_{TH}$. For all cases represented by Fig. 9, $|Y_{NET}|=|Y_{TH}+Y_{EE}+Y_{TM}|$ decreases when $|Y_{TM}|$ decreases from $|Y_{TM}^{\mathrm{NORMAL}}|$ to zero, and therefore $|P_{EC}|$ increases. It is, however, conceivable that some values of Y_{TM} could occur which would produce an increase in $|Y_{NET}|$, when $|Y_{TM}|$ decreases. For instance, if $Y_{EE}=j\omega B_{EE}$ and $Y_{TM}^{\mathrm{NORMAL}}=-j\omega B_{EE}=-j\omega B_{TM}$, the sum $Y_{EE}+Y_{TM}$ would be zero and as $B_{TM}\rightarrow 0$, the sum would increase in magnitude. Because the imaginary part of Y_{TM} is generally positive (as is $B_{EE}=C_{EE}$), this effect will not occur for most conditions. For conditions (e.g., frequencies above 2000 Hz) where the imaginary part of Y_{TM} can be negative (see, e.g., Rosowski *et al.*, 1990, Fig. 10), the angles are rarely more positive than 1/8 of a period, so the resonance will not produce a sharp increase in $|Y_{NET}|$ and any deviation from a uniform decrease in $|Y_{NET}|$ will not be dramatic.

[7]A terminating impedance that represents a radiation impedance results in essentially the same tube impedance as the terminating impedance of zero.

[8]The model prediction was compared visually to the data with different model volumes until the model and data had similar magnitudes below 1000 Hz.

Allen, J. B. (**1986**). ''Measurement of eardrum acoustic impedance,'' in *Peripheral Auditory Mechanisms*, edited by J. B. Allen, J. L. Hall, A. Hubbard, S. T. Neely, and A. Tubis (Springer-Verlag, New York), pp. 44–51.

Berry, Q. C., Andrus, W. S., Bluestone, C. D., and Cantekin, E. I. (**1975**). ''Tympanometric pattern classification in relation to middle ear effusions,'' Ann Otol. **84**, 56–64.

Borton, T. E., Nolen, B. L., Luks, S. B., and Meline, N. C. (**1989**). ''Clinical applicability of insert earphones for audiometry,'' Audiology **28**, 61–70.

Bright, R. A., Moore, R. M., Jeng, L. L., Sharkness, C. M., Hamburger, S. E., and Hamilton, P. M. (**1993**). ''The prevalence of tympanostomy tubes in children in the United States, 1988,'' American Journal of Public Health **83**, 1026–1028.
Burkhard, M. D., and Corliss, E. L. R. (**1954**). ''The response of earphones in ears and couplers,'' J. Acoust. Soc. Am. **26**, 679–685.
Egolf, D. (**1977**). ''Mathematical modeling of a probe-tube microphone,'' J. Acoust. Soc. Am. **61**, 200–205.
Harris, J. D. (**1978**). ''Proem to a quantum leap in audiometric data collection and management,'' Heart Vessels Suppl. **18**, 1–29.
Keefe, D. H., Bulen, J. C., Arehart, K. H., and Burns, E. M. (**1993**). ''Ear-canal impedance and reflection coefficient in human infants and adults,'' J. Acoust. Soc. Am. **94**, 2617–2638.
Killion, M. C., and Villchur, E. (**1989**). ''Comments on ''Earphones in audiometry'' [Zwislocki *et al.*, J. Acoust. Soc. Am. **83**, 1688–1689 (1988)],'' J. Acoust. Soc. Am. **85**, 1775–1778.
Kringlebotn, M. (**1988**). ''Network model for the human middle ear,'' Scand. Audiol. **17**, 75–85.
Kruger, B., and Tonndorf, J. (**1977**). ''Middle ear transmission in cats with experimentally induced tympanic membrane perforations,'' J. Acoust. Soc. Am. **61**, 126–132.
Kruger, B., and Tonndorf, J. (**1978**). ''Tympanic membrane perforations in cats: Configurations of losses with and without ear canal extensions,'' J. Acoust. Soc. Am. **63**, 436–441.
Lim, D. (**1970**). ''Human tympanic membrane an ultrastructural observation,'' Acta Oto-Laryngol. **70**, 176–186.
Lynch, T. J., Peake, W. T., and Rosowski, J. J. (**1994**). ''Measurements of the acoustic input impedance of cat ears: 10 Hz to 20 kHz,'' J. Acoust. Soc. Am. **96**, 2184–2209.
Merchant, S. N. (**1997**). Personal communication.
Merchant, S. N. (**1999**). Personal communication.
Molvaer, O., Vallersnes, F., and Kringlebotn, M. (**1978**). ''The size of the middle ear and the mastoid air cell,'' Acta Oto-Laryngol. **85**, 24–32.
Morse, P. M., and Ingard, K. U. (**1968**). *Theoretical Acoustics* (McGraw-Hill, New York).
Nadol, Jr., J. B. (**1993**). ''Osseous Approaches to the Temporal Bone,'' *Surgery of the Ear and Temporal Bone*, edited by J. B. Nadol, Jr. and Harold F. Schuknecht (Raven Press, New York), Chap. 9, pp. 99–110.
Neely, S. T., and Gorga, M. P. (**1998**). ''Comparison between intensity and pressure as measures of sound level in the ear canal,'' J. Acoust. Soc. Am. **104**, 2925–2934.
Rabinowitz, W. M. (**1981**). ''Measurement of the acoustic input immittance of the human ear,'' J. Acoust. Soc. Am. **70**, 1025–1035.
Rosowski, J. J., Davis, P. J., Merchant, S. N., Donahue, K. M., and Coltrera, M. D. (**1990**). ''Cadaver middle ears as models for living ears: comparisons of middle ear input impedance,'' Ann. Otol. Rhinol. Laryngol. **99**, 403–412.
Sadé, J. (**1982**). ''Prologue,'' in *Proceedings of the Second International Conference of Cholesteatoma and Mastoid Surgery*, edited by J. Sadé (Kugler Publications, Amsterdam), p. 1.
Shaw, E. A. G. (**1966**). ''Earcanal pressure generated by circumaural and supraaural earphones,'' J. Acoust. Soc. Am. **39**, 471–479.
Shaw, E. A. G. (**1974**). ''The external ear,'' in *Handbook of Sensory Physiology*, edited by W. D. Keidel and W. D. Neff (Springer-Verlag, Berlin), Chap. 14, pp. 455–490.
Unge, M. von W. D., Dirckx, J., and Bagger-Sjöbäck, D. (**1995**). ''Shape and displacement patterns of the gerbil tympanic membrane in experimental otitis media with effusion,'' Hear. Res. **82**, 184–196.
Voss, S. E. (**1998**). ''Effects of tympanic-membrane perforations on middle-ear sound transmission: measurements, mechanisms, and models,'' Ph. D. thesis, MIT.
Voss, S. E., and Allen, J. B. (**1994**). ''Measurement of acoustic impedance and reflectance in the human ear canal,'' J. Acoust. Soc. Am. **95**, 372–384.
Voss, S. E., Rosowski, J. J., Merchant, S. N., Thornton, A. R., Shera, C. A., and Peake, W. T. (**in press**). ''Middle-ear pathology can affect the ear-canal sound pressure generated by audiologic earphones,'' Ear Hear. (in press).
Wever, E. G., and Lawrence, M. (**1954**). *Physiological Acoustics* (Princeton University Press, Princeton, NJ).
Wilber, L. A. (**1994**). ''Calibration, puretone, speech and noise signals,'' in *Handbook of Clinical Audiology*, edited by J. Katz (Williams & Wilkins, Baltimore, MD), Chap. 6, pp. 73–94.
Zwislocki, J. (**1962**). ''Analysis of the middle-ear function. Part 1: Input impedance,'' J. Acoust. Soc. Am. **34**, 1514–1523.
Zwislocki, J., and Feldman, A. (**1970**). ''Acoustic impedance in normal and pathological ears,'' American Speech and Hearing Association Monograph **15**, 1–42.
Zwislocki, J., Kruger, B., Miller, J. D., Niemoeller, A. F., Shaw, E. A., and Studebaker, G. (**1988**). ''Earphones in audiometry,'' J. Acoust. Soc. Am. **83**, 1688–1689.

Separate mechanisms govern the selection of spectral components for perceptual fusion and for the computation of global pitch[a)]

Jeffrey M. Brunstrom[b)] and Brian Roberts
School of Psychology, University of Birmingham, Edgbaston, Birmingham B15 2TT, England

(Received 24 February 1999; revised 20 September 1999; accepted 30 November 1999)

The perceptual fusion of harmonics is often assumed to result from the operation of a template mechanism that is also responsible for computing global pitch. This dual-role hypothesis was tested using frequency-shifted complexes. These sounds are inharmonic, but preserve a regular pattern of equal component spacing. The stimuli had a nominal fundamental ($F0$) frequency of 200 Hz ($\pm$20%), and were frequency shifted either by 25.0% or 37.5% of $F0$. Three consecutive components (6–8) were removed and replaced with a sinusoidal probe, located at one of a set of positions spanning the gap. On any trial, subjects heard a complex tone followed by an adjustable pure tone in a continuous loop. Subjects were well able to match the pitch of the probe unless it corresponded with a position predicted by the spectral pattern of the complex. Peripheral factors could not account for this finding. In contrast, hit rates were not depressed for probes positioned at integer multiples of the $F0$(s) corresponding to the global pitch(es) of the complex, predicted from previous data [Patterson, J. Acoust. Soc. Am. **53**, 1565–1572 (1973)]. These findings suggest that separate central mechanisms are responsible for computing global pitch and for the perceptual grouping of partials. © *2000 Acoustical Society of America.* [S0001-4966(00)01503-4]

PACS numbers: 43.66.Ba, 43.66.Hg, 43.66.Fe [DWG]

INTRODUCTION

A periodic complex tone is typically perceived as a single, coherent, entity with a well-defined global pitch. Pattern recognition models usually assume that the global pitch of a periodic complex tone corresponds to the fundamental ($F0$) frequency of the harmonic ''template'' that best fits the distribution of neural signals corresponding to its resolved partials (e.g., Gerson and Goldstein, 1978; Duifhuis *et al.*, 1982; Scheffers, 1983a, 1983b). Recent findings suggest that the perceptual fusion of harmonically related partials may also be performed by a template-based mechanism. Brunstrom and Roberts (1998) asked subjects to listen to a repeating loop comprising a periodic complex tone followed by an adjustable pure tone. On any trial, 2–4 consecutive components (components 6 and above) were removed from the complex (originally comprising harmonics 1–14) and were replaced with a sinusoidal ''probe'' located at one of a set of regularly spaced positions spanning the gap in the complex. Subjects were instructed to match the pitch of the adjustable tone to the pitch of the probe. They were generally less able to match the pitch of the probe when it corresponded to a harmonic position in the complex than when it did not. This was the case even when the partials at both harmonic positions directly adjacent to the probe were missing. This finding is consistent with a template-based account of complex-tone perception, because it demonstrates that spectral cohesion is primarily determined by a central process that is sensitive to overall harmonic pattern rather than one based solely on local interactions between neighboring partials.

Lin and Hartmann (1998) also proposed the operation of a mechanism of this kind, following their investigation of the pitch-shift phenomenon. Matches to a mistuned harmonic are typically somewhat displaced from the true frequency in the same direction as the mistuning (e.g., Hartmann *et al.*, 1990). Hence, the difference between the pitch shifts resulting from mistuning a target component by +8% or −8%, known as the *pitch-shift gradient*, should be positive if that component behaves harmonically. Lin and Hartmann exploited this measure to assess the ''harmonic status'' of a given target frequency in different spectral contexts. They confirmed that a target frequency corresponding to a harmonic position was typically associated with a positive pitch-shift gradient, and further demonstrated that the gradient usually remained positive even when harmonics adjacent to the target frequency were removed. This led Lin and Hartmann to interpret a positive pitch-shift gradient as evidence for the presence of an active template slot at the target frequency.

A common template mechanism may be used both to determine the global pitch of a periodic complex tone and to fuse its partials perceptually. According to this ''dual-role hypothesis,'' the auditory system first selects the best-fitting harmonic template for the distribution of components in the complex and then partial pitches at integer multiples of this template's $F0$ frequency are inhibited (Bregman, 1990, pp. 243–244). Indeed, Bregman (1990) has argued that this hypothesis may explain why frequency-shifted complexes (e.g., Patterson, 1973) not only have a weaker global pitch than harmonic complexes, but also sound less well fused. Specifically, he suggests that the frequency tolerance of each slot will restrict the set of partials in these stimuli that are passed

[a)]Part of this research was presented at the Joint 137th Meeting of the Acoustical Society of America and 2nd Convention of the European Acoustics Association, Berlin, Germany, March 1999 [J. Acoust. Soc. Am. **105**, 1188 (A) (1999)].

[b)]Current address: Department of Human Sciences, Loughborough University, Loughborough, Leicestershire LE11 3TU, England; electronic mail: J.M.Brunstrom@Lboro.ac.uk

by a harmonic template, leading to a less salient (and perhaps ambiguous) global pitch. Furthermore, he also reasoned that if the auditory system inhibits the pitches of partials that fall close to integer multiples of the $F0$ of the best quasiharmonic template fit, then a mismatch will exist between the frequencies at which partial-pitch suppression is applied and the distribution of partials in the complex. Partials whose pitches are not suppressed are presumed not to fuse with their neighbors, thus reducing the overall perceptual cohesion of the complex.

Although the dual-role hypothesis provides a parsimonious account of template operation in the processes of pitch perception and spectral grouping, some evidence is difficult to reconcile with this account. Moore (1987) noted a substantial mismatch between the degree of mistuning that is sufficient for a harmonic to be heard out clearly as a separate tone (1.3%–2.1%; Moore *et al.*, 1986) and the degree of mistuning after which a harmonic no longer contributes to the global pitch of a complex tone (>8%; Moore *et al.*, 1985). Moreover, Roberts and Brunstrom (1998) have provided evidence that the grouping of concurrent partials cannot always be explained in terms of harmonic relations. They asked subjects to match the pitch of a partial mistuned from its original frequency in a regular inharmonic complex, created by applying either a frequency shift or a small degree of spectral stretch to the partials of a harmonic complex. Shifting was achieved by adding a fixed increment to the frequency of each partial, and stretching was achieved by adding a cumulative increment to the frequency spacing between partials with increasing component number. Subjects were able to match a mistuned partial in these shifted or stretched complexes almost as well as they could match one in an unmodified harmonic complex. This unexpected sensitivity to the spectral structure of these inharmonic complexes suggests that their partials must be perceptually fused, because good matching performance implies that the other (nontarget) partials were consistently less salient than the mistuned target. Roberts and Brunstrom (1998) argued that their stimuli could not be fitted well enough by a single harmonic template for the observed sensitivity to small degrees of mistuning imposed on a single partial to be accounted for in this way. Furthermore, in both shifted and stretched conditions, the direction and magnitude of the pitch shifts associated with the mistuned partials were broadly similar to those found in the harmonic condition. These findings were taken to suggest that spectral patterns other than harmonic relations can be used to group components in a complex tone. This contrasts with what is known about the computation of global pitch for complex tones. Since Schouten's (1938, 1940a) discovery of the ''residue,'' many of the classic studies of pitch perception have employed frequency-shifted complexes (e.g., de Boer, 1976; Patterson, 1973; Schouten, 1940b; Schouten *et al.*, 1962). The results of these studies have indicated consistently that the global pitch (or pitches) of these sounds can best be understood in terms of their quasiharmonic structure.

I. EXPERIMENT 1

The first experiment was designed to explore this apparent pitch/grouping dissociation further. Roberts and Brunstrom's (1998) study was restricted to exploring the effects of mistuning a single component (2–11) in a set of consecutive components (1–12), and so the immediate neighbors of the target partial were always present. To establish that their findings for regular inharmonic complexes reflected the operation of a pattern recognition mechanism, it is necessary to demonstrate that the auditory system is also sensitive to the mistuning of partials whose immediate neighbors are absent. Therefore, an adapted version of the profiling method previously used by Brunstrom and Roberts (1998) was employed. The experiment sought to determine the pattern of partial-pitch suppression that is induced within a spectral gap in a frequency-shifted complex tone. Evidence of perceptual suppression positioned at integer multiples of the global pitch evoked by the complex would be consistent with Bregman's (1990) dual-role hypothesis of spectral fusion. Alternatively, evidence for suppression at positions predicted by the spectral pattern of these complexes would demonstrate a dissociation between the mechanisms responsible for pitch computation and those responsible for perceptual fusion.

A. Method

1. Overview and conditions

On any trial, subjects listened to a repeating cycle of a complex ''test tone'' followed by an adjustable, pure, ''comparison tone.'' Test tones were created by applying a frequency shift to periodic complex tones (harmonics 1–14) and then removing components 6, 7, and 8. In each case, partials were shifted by adding a frequency increment of either 25.0% (condition 1) or 37.5% (condition 2) of the $F0$ frequency of the test tone. A single ''probe'' was then inserted at one of 25 possible positions across the frequency range spanning the gap created in the spectrum of the test tones. The probe positions that were used ranged from halfway (arithmetic mean) between component numbers 5 and 6 to halfway between component numbers 8 and 9, and were equally spaced in units of $0.125\times$component spacing. The component spacing is equal to the nominal $F0$ frequency in both conditions. Figure 1 shows a schematic of the test tones used in conditions 1 and 2, for a nominal $F0$ of 200 Hz. Probe positions shown in bold represent occasions when the frequency of the probe coincides with a position that is consistent with the spectral pattern established by the other components in the test tone (the ''spectral frame''). These probes are described henceforth as *spectrally in-tune*.

Subjects were instructed to match the pitch of the comparison tone to the pitch of a pure-tone-like sound embedded in the test tone. If the salience of the probe changes as its frequency is varied in relation to the spectral frame, then the number of times that it is successfully matched should also vary. A difficulty in detecting the probe (that cannot be accounted for simply in terms of partial masking) is taken to indicate that it has been perceptually suppressed.

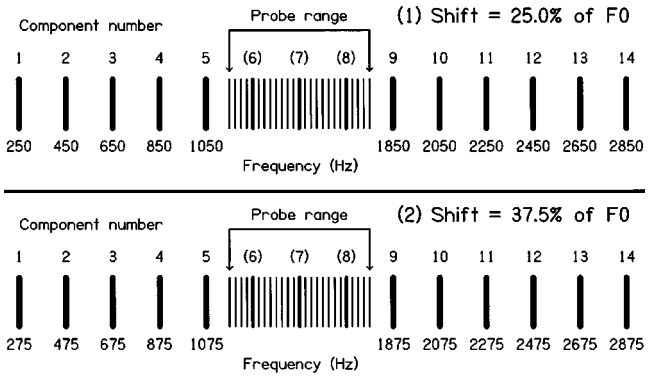

FIG. 1. Schematic of the test tones and probe ranges used for conditions 1 and 2 of experiment 1. Components comprising the test tones are shown heavy and in bold. For each condition, spectrally in-tune probe positions are shown in bold and the corresponding component numbers are given in brackets. A nominal $F0$ frequency of 200 Hz is assumed.

2. Estimating the global pitch(es) of the test tones

The dual-role hypothesis predicts that evidence for perceptual suppression will be found at integer multiples of the global pitch(es) of the test tones. The global pitch(es) of the test tones used in conditions 1 and 2 can be estimated accurately from the data of Patterson (1973). In his study, subjects adjusted the $F0$ frequency of a periodic complex tone (pulse train) to match as closely as possible the perceived global pitch(es) of a set of frequency-shifted complex tones. For a periodic complex with an $F0$ of 200 Hz, comprising partials 1–12 at equal amplitude, a frequency shift of 50 Hz (25.0% of $F0$) gave global pitch estimates of about 211 and 94 Hz. A frequency shift of 75 Hz (37.5% of $F0$) gave global pitch estimates of about 216 and 97 Hz. In both cases, the lower value can be attributed to the listener making an octave error, such that the frequency-shifted stimuli are processed as approximating a set of odd-numbered harmonics (see Patterson, 1973, for a full discussion).

The main difference between our frequency-shifted complexes and the stimuli used by Patterson (1973) is that our stimuli contained a spectral gap. The choice of components 6–8 for removal to create this gap was in response to two constraints. First, Patterson (1973) found that pitch matches were almost unchanged when the set of components in his shifted complexes was reduced from 1–12 to 1–6. However, the global pitch(es) heard were found to be sensitive to the presence or absence of the lower-numbered partials, particularly 3–5. This finding is consistent with Ritsma's (1967) conception of the ''dominant region.'' Hence, higher-numbered components must be selected to minimize the effect of the spectral gap on global pitch. Second, for an $F0$ of 200 Hz, only harmonics below about the eighth are generally considered to be resolved by the auditory system (see Plomp, 1976). Therefore, the set 6–8 was chosen to minimize the effects of component removal on global pitch while preserving some degree of frequency resolution across the probe range. Informal listening tasks in our laboratory have confirmed that listeners typically hear global pitches consistent with Patterson's (1973) values, as quoted above.

3. Subjects

The same six subjects were tested in both conditions. All of them reported having normal hearing, all had some prior experience with similar listening tasks, and three were musically trained.

4. Stimuli

Following the procedure developed by Brunstrom and Roberts (1998), the $F0$ frequency of the test tones was roved to reduce the likelihood of ceiling effects on performance, which can arise from across-trial learning. Specifically, the $F0$ frequency was chosen randomly on each trial from a rectangular distribution with a width of $\pm 20\%$ around 200 Hz. The durations of the test tones and the adjustable tones were 420 and 310 ms, respectively, both including linear onset and offset ramps of 20 ms each. Test tones were followed by a 200-ms silent interval and adjustable tones were followed by a 500-ms silent interval. The durations of the silent intervals were chosen to create a rhythm that clearly defined the within-cycle order of the tones. The probe and all components in the spectral frame began in sine phase. Also as before, each partial in the spectral frame was set to 60 dB SPL, and the probe and adjustable tone were both set to 54 dB SPL. Setting the probe level at 6 dB below that of the test-tone partials made it more difficult to match, which further reduced the chance of ceiling effects on performance.

All stimuli were generated using MITSYN software (see Henke, 1990). Stimuli were synthesized at a sampling rate of 16 kHz and played back via a 16-bit digital-to-analog converter (Data Translation DT2823). They were low-pass filtered (corner frequency=5.2 kHz, roll-off=100 dB/oct.) and presented binaurally over Sennheiser HD 480-13II earphones. The levels of the stimuli were set using a programmable attenuator (0.25-dB steps), and were calibrated with a sound-level meter (Brüel and Kjaer, type 2209, linear weighting) connected to the earphones by an artificial ear (type 4153). Stimuli were played to the listeners in a double-walled sound-attenuating chamber (Industrial Acoustics 1201A).

5. Procedure

The adjustable tone was controlled using a trackball mouse with two different sensitivity settings, which could be selected freely via a mouse button. The default setting was a coarse control. The fine control was ten times more sensitive. The initial frequency of the adjustable pure tone was chosen randomly from the range 1.5–13.5×component spacing. The range was restricted to this region to prevent matches either to the global pitch of the test tone, or to the prominent edge pitch (Kohlrausch and Houtsma, 1992) associated with the highest component present. At the end of each trial, subjects were given feedback on their performance via a computer screen. If the match was within $\pm 1.0\times$component spacing of the test tone from the probe frequency, then the message ''within range'' was displayed. Above and below this range, the message ''much too high'' or ''much too low'' was displayed, as appropriate. Subjects were given unlimited time to complete each trial and were free to rest between trials.

Subjects were tested in each session with six consecutive sets of all probe positions, each in a new randomized order, giving a total of 150 trials (6×25). Each subject was run three times in condition 1 and then three times in condition 2. The first session of each condition was for practice, and these data were discarded. Therefore, for each subject, the main experiment yielded a total of 12 responses per probe position in each condition.

6. Data analysis

Matching ability may be quantified by classifying each response as either a hit or a miss. This classification is not straightforward, because the pitch of the probe may not be the same when it is heard within the test tone as when it is heard in isolation. As noted earlier, the pitch of a mistuned partial in a periodic or a frequency-shifted complex tone is typically shifted in the same direction as the mistuning (Hartmann *et al.*, 1990; Hartmann and Doty, 1996; Lin and Hartmann, 1998; Roberts and Brunstrom, 1998). Therefore, any algorithm for classifying responses should be able to accommodate systematic pitch shifts of moderate size. Here, we have used a two-stage procedure similar to that adapted from Hartmann *et al.*'s (1990) original version by Roberts and Brunstrom (1998). First, all responses in the general vicinity of the probe were flagged as possible hits. To pass this stage, responses had to fall within ±0.5×component spacing from the frequency of the probe. This was a stricter criterion than that used in the previous studies (see below for discussion). Second, those responses that survived the first stage were entered into a recursive clustering algorithm that rejected individual responses until the standard deviation of those that remained fell below 2.5% of the probe frequency. On each cycle of the recursion, the response most distant from the mean was removed. This approach was based on the assumption that genuine matches would be clustered together and that outliers were likely to be chance matches. Following Roberts and Brunstrom (1998) and Brunstrom and Roberts (1998) in cases where only two responses remained, the data point farther away from the probe frequency was rejected. In cases where only one response passed the first stage, it was accepted as a hit.

Brunstrom and Roberts (1998) noted in their study that incorrect matches tended to cluster around the components that defined the edges of the spectral gap in the test tones (*gap-edge components*; see Brunstrom and Roberts, 1998, for discussion). This is a potential problem for the classification of matches to probes near the ends of the probe range, because the clustering criterion may not differentiate between true matches to the probe and matches to a gap-edge component. Nevertheless, it is possible to estimate the reliability of the hit rates calculated for matches to probes around the ends of the probe range. Following Brunstrom and Roberts (1998), reliability was quantified by determining the number of responses classified as hits that also fell within ±0.5×component spacing around the proximal gap-edge component. This value was then used to calculate the proportion of hits that were considered ambiguous. A low proportion indicates that the vast majority of responses classified as hits to a particular probe were indeed genuine attempts to match its pitch, rather than attempts to match the pitch of a nearby gap-edge component.

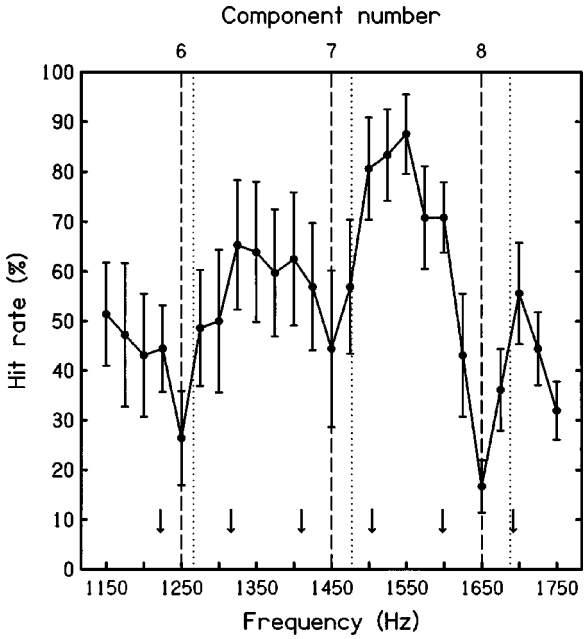

FIG. 2. Mean hit rates for six subjects, with intersubject standard errors, for all probe positions used in condition 1 of experiment 1. A nominal $F0$ frequency of 200 Hz is assumed. Each spectrally in-tune probe position is marked with a vertical dashed line. Integer multiples of 211 and 94 Hz are indicated with dotted lines and arrows, respectively. These global pitch estimates are based on data from Patterson (1973).

The initial criterion used by Brunstrom and Roberts (1998) was that responses should fall within ±1.0 ×component spacing from the position of the probe. However, the tendency to match the gap-edge components was greater in the current study (see Sec. IV B for discussion). A preliminary analysis revealed that a high proportion of hits to probes positioned near to the gap-edge components could be considered ambiguous when the original criterion was used, making the associated hit-rate measures difficult to interpret. Therefore, to limit this problem, we have used a narrower range for our initial criterion (±0.5×component spacing from the frequency of the probe). This modification was found to reduce greatly the proportion of hits to probes near the gap-edge components that were classified as ambiguous, while still leaving scope for pitch-shift effects of moderate size. Furthermore, the change in criterion had only a negligible effect on the number of matches classified as hits to probes in the middle of the range, defined here as those probes falling between the positions corresponding to (missing) components 6 and 8. In both conditions, the change in criterion reduced the hit rate to one of these probes by just over 1%. Hit rates to all other probes were unaffected.

B. Results

Figures 2 and 3 show the mean hit rates and intersubject standard errors for all probe positions in condition 1 (shift =25.0% of $F0$) and condition 2 (shift=37.5% of $F0$), respectively. Vertical dashed lines represent spectrally in-tune probe positions. In both conditions, hit rates form a profile

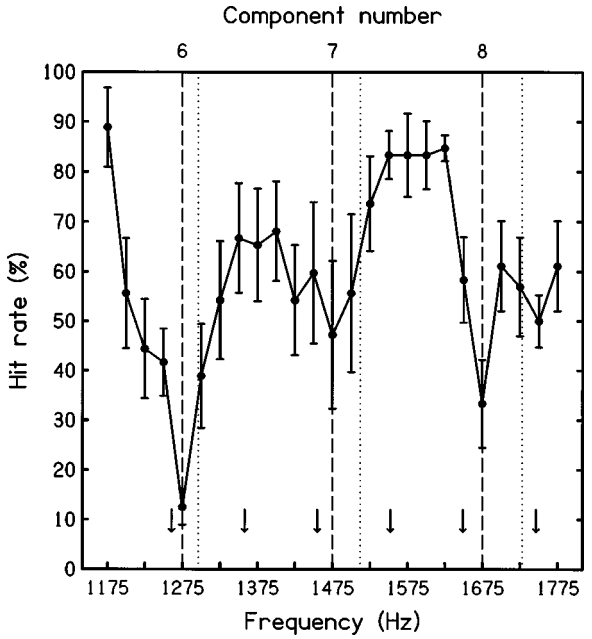

FIG. 3. Mean hit rates for six subjects, with intersubject standard errors, for all probe positions used in condition 2 of experiment 1. A nominal $F0$ frequency of 200 Hz is assumed. Each spectrally in-tune probe position is marked with a vertical dashed line. Integer multiples of 216 and 97 Hz are indicated with dotted lines and arrows, respectively. These global pitch estimates are based on data from Patterson (1973).

that is characterized by three distinct and regularly spaced troughs in performance, each centered around a spectrally in-tune probe position. These troughs are too narrow and too specific in location to be explained in terms of partial masking.[1] From left to right in each profile, these troughs are referred to as the *lower*, *middle*, and *upper* minima in performance. In condition 1, the lower, middle, and upper minima represent reductions in performance of approximately 25%, 20%, and 40%, respectively. In condition 2, these values were about 50%, 20%, and 30%, respectively. The occurrence of a minimum at the middle spectrally in-tune position, as well as at the lower and upper ones, is consistent with the operation of a template mechanism (see Sec. III for discussion). In addition, two less pronounced minima were found at probe positions 11 and 24 for condition 2 (see Fig. 3). The first one is minor enough to be ignored. The second is discussed further below.

Integer multiples of the $F0$ frequencies corresponding to the higher and lower (suboctave) global pitches, estimated from Patterson's (1973) data, are depicted in Figs. 2 and 3 with dotted lines and with arrows, respectively. There is no evidence for a consistent pattern of minima in performance at, or near, these values.

As noted in Sec. I A 6, the proximity of probes near the ends of the probe range to the gap-edge components made it necessary to assess the degree to which the computed hit rates for these probe positions might have been inflated by the spurious inclusion of matches to those components. Table I shows the degree of ambiguity associated with hits to probes near the ends of the ranges used in the two conditions. For a given probe position, ambiguity is expressed as the percentage of hits that also fell within $\pm 0.5\times$component spacing of the proximal gap-edge component. For both conditions, the set of probes analyzed in this way extended inwards from each end of the range to include the probe positions corresponding to the lower and upper minima in performance. These positions are shown in bold in Table I. At the edges of the probe range, about 65%–95% of hits were ambiguous, making it difficult to gauge the accuracy of performance at these positions. However, the degree of potential overlap between matches to the probe and matches to the nearby gap-edge component decreased markedly toward the spectrally in-tune probe positions. Consequently, for the probes corresponding to the lower and upper minima in performance and for probes in directly adjacent positions, only 0%–3% of the responses classified as hits can be considered to be ambiguous. Indeed, the ambiguity was often small even for probes two steps away from the minima. This indicates that the sloping sides of the troughs in the hit-rate profiles represent a genuine decrement in ability to match the pitch of the probe correctly.

Our measure of ambiguity is also relevant for interpreting the additional minimum in performance observed at probe position 24 in condition 2. This minimum can probably be regarded as spurious, because its occurrence relies on the high hit rate to probe position 25, for which the degree of ambiguity was 64% (see Table I).

Average hit rates, collapsed across probe positions, were 54% and 58% for conditions 1 and 2, respectively. These rates are somewhat lower than the 80% reported by Brunstrom and Roberts (1998, expt. 1, condition 2) for probes tested in a similar manner in a comparable harmonic context (nominal $F0 = 200$ Hz; harmonics 6, 7, and 8 removed). This discrepancy is considered further in Sec. IV B.

C. Discussion

Before accepting that the results of this experiment require an explanation in terms of central mechanisms, it is important to evaluate whether or not they can be accounted

TABLE I. Ambiguity associated with hits to probes near the ends of the probe range in conditions 1 and 2 of experiment 1. Results are rounded to the nearest percentage point. Results for probe positions corresponding to spectrally in-tune probe positions are shown in bold.

Condition 1 (frequency shift=25.0% of $F0$)											
Probe position	1	2	3	4	**5**	⋯	**21**	22	23	24	25
% ambiguous hits	86	35	0	0	**0**	⋯	**0**	0	10	44	66
Condition 2 (frequency shift=37.5% of $F0$)											
Probe position	1	2	3	4	**5**	⋯	**21**	22	23	24	25
% ambiguous hits	94	70	22	3	**0**	⋯	**0**	0	5	6	64

for in terms of peripheral ones. Two aspects of peripheral processing require consideration here: (i) the role of intermodulations between the probe and neighboring components in the spectral frame, and (ii) the role of nonlinear distortion products generated by the components of the spectral frame. These issues are considered in turn.

1. Frequency selectivity and modulation depth

One possibility is that limitations in frequency resolution result in intermodulations between the probe and neighboring partials in the spectral frame of sufficient magnitude to influence subjects' ability to locate the probe. Consider, for example, a frequency-shifted test tone with a nominal $F0$ frequency of 200 Hz. A probe located at the spectrally in-tune position corresponding to component 6 might interact with component 5 in the spectral frame to generate an intermodulation of 200 Hz. This is the same rate as the intermodulations generated by pairs of neighboring partials in the spectral frame. However, a probe mistuned from this in-tune position would generate a different local rate of intermodulation, which might act as a salient cue for the listener and lead to a higher hit rate for that probe. The same argument would apply to probes in the region of the missing eighth component. For probes in the region of the missing seventh component, the argument can be extended to intermodulations in the region of the octave (400 Hz).

An initial assessment of the likelihood of explaining our data in this way can be obtained by applying Glasberg and Moore's (1990) formulas for calculating equivalent rectangular bandwidths (ERB's) to our frequency-shifted stimuli. The separation of the probe corresponding to component 7 from its closest neighbors was found to range from 1.96 ERB's (component 9 in condition 2) to 2.53 ERB's (component 5 in condition 1). This degree of spectral isolation suggests that local interactions between the probe and the spectral frame are small. However, auditory filters are not rectangular, and so interactions will not be entirely absent even for separations of 2 ERB's or more. Therefore, we used Glasberg and Moore's (1990) program to compute excitation patterns for the spectral frame alone and for the spectral frame plus the probe corresponding to component 7. These excitation patterns, which include an equal loudness correction, are shown in Fig. 4.

The excitation that spreads from the two gap-edge components of the spectral frame to the probe frequency can be regarded, to a first approximation, as equivalent to the sidebands generated by sinusoidal amplitude modulation of a pure-tone carrier. The amount of excitation that spreads from these components to the probe frequency is -18 dB, relative to the excitation level generated by the probe itself. The sensitivity of the ear to the resulting modulation of the probe can be estimated by comparison with measures of the temporal modulation transfer function (TMTF; Viemeister, 1979).[2] Recent measures of the broadband TMTF indicate a detection threshold for 400-Hz modulation of about -13 dB when a continuous carrier is used (Strickland and Viemeister, 1996) and about -10 dB when a gated carrier is used (Strickland and Viemeister, 1997). The depth of modulation occurring at the probe frequency in our stimulus is

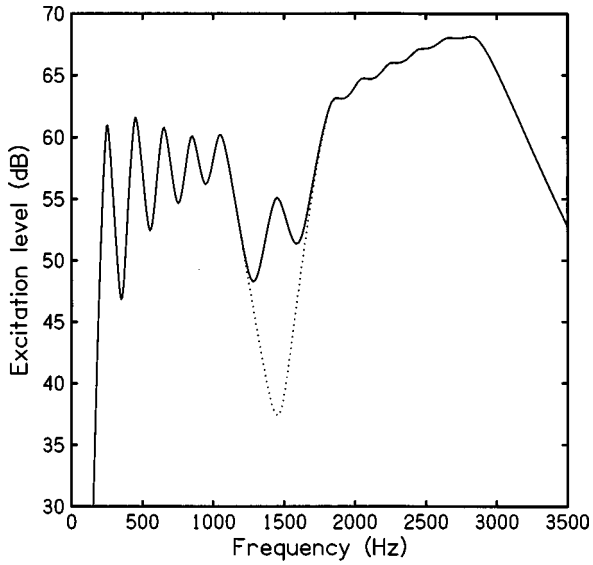

FIG. 4. The solid line represents the excitation pattern for a test tone comprising the spectral frame and a probe at the spectrally in-tune position corresponding to the missing 7th component. The dotted line represents the excitation pattern for the spectral frame alone. A frequency shift of 25.0% on a nominal $F0$ frequency of 200 Hz is assumed, giving a probe frequency of 1450 Hz. The difference in excitation level between the two plots at the probe frequency is 18 dB.

below both of these values. From this, we can conclude that local interactions cannot account for the minimum in the hit-rate profile associated with the missing seventh component. This demonstrates that the overall pattern of results cannot be explained by local interactions, even if these interactions have made some contribution to the other minima in the profile.

2. Combination tones

A number of studies have measured the distortion products resulting from nonlinearities in the auditory periphery, using either cancellation or threshold methods (e.g., Plomp, 1965; Goldstein, 1967; Greenwood, 1972; Smoorenburg, 1972; Zwicker and Fastl, 1973). Goldstein (1967) found that the most prominent combination tone generated from a pair of primaries (f_1 and f_2) was the cubic difference tone ($2f_1$-f_2). This result is relevant to our experiment, because it suggests that pairs of partials in the spectral region above the gap may have generated significant combination tones at the frequencies corresponding to the missing components. A probe located at one of the spectrally in-tune positions might then have been reduced in level (and hence in salience) through phase cancellation, leading to a local hit-rate minimum. Clearly, this possibility must be explored before the role of a hypothetical central template can be evaluated.

Consider a complex tone with a nominal $F0$ frequency of 200 Hz that has been frequency shifted by 25.0% of $F0$, as used in condition 1. Cubic difference tones corresponding to the missing components 6 (1250 Hz), 7 (1450 Hz), and 8 (1650 Hz) can arise from the component pairs 9 and 12 (1850 and 2450 Hz), 9 and 11 (1850 and 2250 Hz), and 9 and 10 (1850 and 2050 Hz), respectively. The frequency ratios for these pairs of primaries are 1.32, 1.22, and 1.11, respectively. Goldstein (1967) observed that the level of the

cubic difference tone is highly dependent on the frequency ratio of the primaries, declining by over 40 dB as the ratio is increased from 1.10 to 1.25. It follows from this that the hit-rate minimum associated with the missing eighth component is by far the most likely to have been affected by auditory nonlinearity. Therefore, it was decided to perform a supplementary experiment in order to evaluate the effect of combination tones on pitch-matching performance in this spectral region.

II. EXPERIMENT 2

A. Method

1. Overview

The extent to which a cubic difference tone at the frequency of the missing eighth component influenced the local hit-rate profile in experiment 1 was assessed by changing the starting phase of the probe, relative to that of the components in the spectral frame. If these hit-rate minima resulted from phase cancellation between a spectrally in-tune probe and a cubic difference tone at the same frequency, then it must be possible to abolish such a minimum by changing the relative phase of the probe. Indeed, a phase shift of 180° might be expected to produce a local *maximum* in hit rate, owing to phase *addition* between the in-tune probe and the combination tone. In contrast, the preservation of the hit-rate minimum across changes in relative probe phase would demonstrate that the apparent perceptual suppression of a spectrally in-tune probe is not an artifact resulting from auditory nonlinearity. Except where indicated below, all aspects of the stimuli, procedure, and data analysis were identical to those used in experiment 1.

2. Stimuli and conditions

Only the spectral frame employed in condition 1 of experiment 1 was used (nominal $F0$ frequency=200 Hz, frequency shift=25.0% of $F0$), because there was no reason to expect that the magnitude of any combination tones generated should depend on the degree of shift. There were four conditions, which differed only in the starting phase of the probe relative to that of the other components (which all began in sine phase). For conditions 1–4, the relative starting phase of the probe was 0, 90, 180, and 270°, respectively. Hence, the phase relations between the probe and the spectral frame in condition 1 were identical to those used in condition 1 of experiment 1. Five probe positions were tested in each condition, centered on the missing eighth component. These positions were the spectrally in-tune position and the two consecutive probe positions above and below it (equivalent to probe positions 19–23 in condition 1 of experiment 1).

3. Subjects and procedure

Four subjects took part in this experiment, two of whom had previously participated in experiment 1. The two new subjects were trained prior to the main experiment using stimuli identical to those of condition 1 in experiment 1 (i.e., using the full set of probe positions across the spectral gap). A third trainee was rejected before the main experiment, because his overall hit rate (collapsed across probe positions) did not exceed 30%. The data presented below represent 200 trials for each subject (5 probe positions×4 conditions×10 sets). The stimuli within each consecutive set were presented in a new random order.

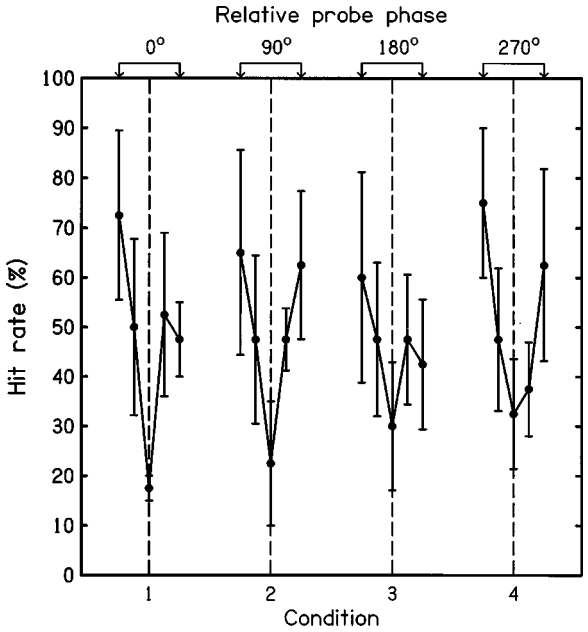

FIG. 5. Mean hit rates for four subjects, with intersubject standard errors, for all probe positions tested in experiment 2. The four conditions differ only in the starting phase of the probe relative to the components of the spectral frame. In each case, the vertical dashed line represents the spectrally in-tune probe position corresponding to the missing 8th component.

B. Results and discussion

Figure 5 shows the mean hit rates and intersubject standard errors for the probe positions tested in the four conditions. The vertical dashed lines represent the spectrally in-tune probe position for each condition. There is a clear hit-rate minimum associated with this position in all four conditions. The hit-rate profiles show some variation across condition, but the differences are not marked given that fewer subjects were tested and fewer judgments were made per probe position compared with experiment 1. To the extent that the variations might reflect the presence of a cubic difference tone at the spectrally in-tune position, it is still clear that phase cancellation cannot explain the common feature of a hit-rate minimum at this position in all four conditions. Given that the magnitude of the cubic difference tone will have been markedly lower at the frequencies corresponding to the missing sixth and seventh components (Goldstein, 1967), we can also conclude that the hit-rate minima associated with these positions in experiment 1 cannot be accounted for by phase cancellation. Therefore, it is now appropriate to consider what kind of central mechanisms might account for our findings.

III. ASSESSMENT OF A QUASIHARMONIC MODEL

The characteristic minima in the hit-rate profiles for conditions 1 and 2 in experiment 1 were not found at integer multiples of the $F0$'s corresponding to the global pitches estimated from Patterson's (1973) data. Instead, in both con-

ditions, the locations of these minima were consistent with the pattern established by the spectral frame of the test tones. This implies the operation of a grouping mechanism that is responsive to common spectral spacing rather than one that is sensitive only to harmonic structure. However, before accepting this conclusion, it is instructive to consider whether or not, for each condition, a harmonic template with an $F0$ other than one predicted from Patterson's data might account for the positions of the minima found in our hit-rate profiles.

To determine potential candidate $F0$'s, it is necessary first to establish the error associated with estimates of the center frequency of each region of partial-pitch suppression, as represented by troughs in the hit-rate profiles. Given that the probe range was tested only at discrete intervals, the true center frequency of a trough may lie between probe positions, rather than corresponding exactly with the observed minimum in a profile. The resolution of our profiling technique is proportionately greater at the higher end of the probe range, because of the equal-linear spacing between consecutive probe positions. Therefore, estimates of these center frequencies will be most accurate around the upper minima in performance. For these troughs in the profiles obtained in experiment 1, the hit rates were markedly higher at probe positions immediately adjacent to the spectrally in-tune position. Therefore, it is reasonable to conclude that the upper minima in performance, evident in Figs. 2 and 3, show the center frequencies of these regions of perceptual suppression (for a nominal $F0$ of 200 Hz) to within ± 1 probe position. This indicates that our profiling technique is capable of resolving the center frequency of a region of partial-pitch suppression to within about 1.5% of its true value. Therefore, we determined which harmonic templates have $F0$'s such that the center frequencies of three consecutive slots would fall within a bandwidth of $\pm 1.5\%$ around the spectrally in-tune probe positions in each condition (assuming a nominal $F0$ of 200 Hz). Candidate templates ($F0$ frequency quantized in 1-Hz steps) that passed this criterion were then explored to establish whether or not they could offer a plausible quasiharmonic account of the hit-rate profiles observed.

For experiment 1, this criterion was met by five $F0$'s in condition 1 (181, 206, 207, 208, and 209 Hz), and by four $F0$'s in condition 2 (184, 210, 211, and 212 Hz). Thus the observed pattern of hit-rate minima in both conditions is broadly consistent with the slot positions of a number of harmonic templates. Nevertheless, for the reasons discussed below, we reject the notion that any of these hypothetical templates produced the observed pattern of results. For use in a simple model, we took $\pm 2\%$ as a liberal estimate of the bandwidth of the slots in a hypothetical harmonic template. This estimate was based on Hartmann *et al.*'s (1990) finding that a low-numbered harmonic (1–7) can be matched with near-ceiling accuracy if it is mistuned by $\pm 2\%$. However, it should be noted that both Hartmann *et al.* (1990) and Roberts and Brunstrom (1998) have shown that partials can often be heard as segregated tones when mistuned by considerably less than this, sometimes even below $\pm 1\%$. For the test tones used in each condition, we examined which of the lower, more resolved, components in the spectral frame (1–5) would pass through slots of $\pm 2\%$ bandwidth in our candidate harmonic templates. Given that our template model was defined in the frequency domain, like that of Duifhuis *et al.* (1982) and of Scheffers (1983a, 1983b), we did not apply it to the less-well-resolved upper components (9–14) in the spectral frame.

For condition 1 (shift=25.0% of $F0$), four of the five candidate harmonic templates have slots that would pass component 5 ($F0$'s=206, 207, 208, and 209 Hz) and, of these, one has a slot that would also pass component 4 ($F0 = 209$ Hz). None of them would pass components 1–3. Therefore, the best-fitting candidate template passes only two of the five resolved components in the lower part of the spectral frame (4 and 5). For condition 2 (shift=37.5% of $F0$), three of the candidate templates have slots that would pass component 5 ($F0$'s=210, 211, and 212 Hz), but none of these would pass any of the other low-numbered components. Therefore, it is clear that although our candidate harmonic templates have slots that are near-coincident with the minima in our hit-rate profiles, none have slots that will readily accept the majority of resolved components in the lower part of the spectral frame. Hence, it is difficult to envisage how any of the candidate templates could underlie the perceptual fusion of our test-tone components. Were it the case that these partials did not fuse at least moderately well, then they would provide competing, salient, alternatives for listeners to match instead of the probe. This possibility is difficult to reconcile with the accurate performance observed for many of the probes at positions other than those predicted by the pattern of the spectral frame. Furthermore, it is doubtful that sufficient test-tone components would pass through slots in our candidate templates to activate any of them to an appreciable extent.

Finally, it is worth noting that the hit-rate profiles for both conditions of experiment 1 provide evidence to indicate that both the lower and upper sets of partials in the spectral frame contributed to the pattern of partial-pitch suppression found within the probe range. Specifically, the minima associated with the spectrally in-tune probes directly adjacent to components in the spectral frame (missing components 6 and 8) are lower than the minimum associated with the nonadjacent in-tune probe (missing component 7). Brunstrom and Roberts (1998, expt. 1) observed this effect for harmonic stimuli directly comparable with the frequency-shifted stimuli used here, and attributed it to an attenuation of perceptual suppression with distance from the set of partials evoking template activity. Their second experiment, which used a different $F0$ for the lower and for the upper set of harmonics, ruled out the possibility that this effect was merely caused by greater masking of probes closer to components of the harmonic frame. This is because the hit-rate minima associated with each set became progressively less pronounced for positions farther away from the *specific* set of harmonics responsible for generating them, rather than becoming less pronounced with distance from *either* set.

Given the above discussion, it seems reasonable to assume an equivalence in the way these profiles have originated for frequency-shifted and harmonic stimuli. The implications of this interpretation are considered below.

IV. DISCUSSION

A. Spectral pattern as a cue for grouping

The hit-rate profiles reported here for frequency-shifted complex tones are similar in general form to those reported for harmonic stimuli by Brunstrom and Roberts (1998, expt. 1). In both cases, we have evidence for the perceptual suppression of partial pitch in the middle of a three-component spectral gap, centered on the missing 7th component, despite the absence of its immediate neighbors in the complex tone (components 6 and 8). Furthermore, our evaluation of the role of peripheral factors in determining the salience of the probe has indicated that these factors cannot provide a satisfactory account of our data. Instead, like Brunstrom and Roberts (1998), we regard the evidence of partial-pitch suppression in more spectrally isolated positions as easiest to reconcile with the operation of a central pattern-recognition mechanism.

As noted earlier, it was observed in informal listening tasks that the global pitches of the test tones used in conditions 1 and 2 of experiment 1 were close to the values estimated from Patterson's (1973) data. Harmonic templates having $F0$'s corresponding to these global pitches do not have slots that are centered in the regions of the probe range where performance is suppressed. Moreover, as we have seen, it is difficult to account for the positions of the hit-rate minima for either condition in terms of the activation of any one harmonic template. Instead, we propose that the positions of the observed minima result from the activation of a mechanism that is sensitive to predictable spectral spacing between concurrent components. The existence of such a mechanism has been proposed previously by Roberts and his colleagues (Roberts and Bregman, 1991; Roberts and Bailey, 1993a, 1993b, 1996a, 1996b; Roberts, 1998). These authors have systematically explored the perceptual salience of an added even harmonic relative to the salience of its neighbors in an otherwise odd-harmonic series. Typically, for $F0$'s of 100 and 200 Hz, the single even harmonic is heard out more easily than its odd-harmonic neighbors. Roberts and Bregman's (1991) original proposal that this effect occurs because the even harmonic is inconsistent with the regular spectral pattern formed by the odd harmonics has been supported by subsequent research. In particular, Roberts and Bailey (1996b) and Roberts (1998) have demonstrated a similar even–odd difference in component salience in regular but inharmonic complex tones, created by applying either a frequency shift or a spectral stretch transformation to ''odds-plus-even'' harmonic stimuli.

One might speculate that the perceptual fusion of partials in both harmonic and regular inharmonic sounds (like shifted and stretched complex tones) is performed by a common mechanism that responds to a general form of spectral regularity based on an equal or near-equal spacing between consecutive components (see Roberts and Brunstrom, 1998, p. 2336). This interpretation would require abandoning the notion that harmonic relations *per se* have a special status in auditory grouping. While it may be premature to accept this conclusion, the proposal offers a parsimonious account of our findings that merits further consideration.

B. Similarities and differences in hit-rate profiles for shifted and harmonic stimuli

The idea that a common mechanism underlies the perceptual grouping of both harmonic and regularly structured inharmonic sounds rests on similarities in the ways these sounds appear to be processed by the auditory system. The hit-rate profiles reported here for frequency-shifted complexes are comparable in general form to those reported by Brunstrom and Roberts (1998) for harmonic complexes. In particular, local minima in performance were observed in both cases for probes at positions consistent with the pattern of component spacing defined by the spectral frame, irrespective of whether or not these positions were directly adjacent to partials present in the spectral frame. Also, the minima observed at nonadjacent positions were less pronounced than those observed at adjacent ones. Brunstrom and Roberts (1998) attributed this effect to an attenuation of partial-pitch suppression with distance from the set of partials that evoked it.

Despite the considerable similarities, there is one difference between the hit-rate profiles reported here for experiment 1 and those reported by Brunstrom and Roberts (1998) that merits discussion. It is a difference in the overall hit rate, when collapsed across probe positions and subjects, for comparable shifted and harmonic stimuli. This is best illustrated with reference to condition 2 of experiment 1 by Brunstrom and Roberts (1998), for which the nominal $F0$ frequency, roving range, duration, component levels, component phases, component range (1–14), and spectral gap (6–8) were identical to those employed here for conditions 1 and 2 in experiment 1. The overall hit rates were 80% (six subjects; data from Brunstrom and Roberts, 1998), 54%, and 58% (six subjects; data from the current study) for stimuli that were harmonic, shifted by 25.0% of $F0$, and shifted by 37.5% of $F0$, respectively.

Only part of this discrepancy can be explained in terms of differences in the subjects used and differences in the way the responses were classified. First, three of the six subjects who took part in experiment 1 had previously taken part in the study of Brunstrom and Roberts (1998, expt. 1). All of these subjects obtained lower hit rates for our shifted stimuli than for the harmonic stimuli, though the differences were smaller (mean=82% for harmonic stimuli, means=70% and 69% for stimuli shifted by 25.0% and 37.5% of $F0$, respectively). Second, the change in the initial acceptance criterion for classifying responses as hits [from those within $\pm 1.0 \times$component spacing of the target frequency (Brunstrom and Roberts, 1998) to those within $\pm 0.5 \times$component spacing in the current study] had a negligible effect on the number of responses classified as hits to probes away from the extremes of the probe range. Despite this, hit rates were found to be generally depressed across the whole probe range.

It would appear that there is a genuine, overall, reduction in matching performance of at least 10% for the shifted stimuli compared with the harmonic stimuli. This suggests a need for caution before assuming a complete perceptual equivalence between harmonic and shifted stimuli in terms of auditory grouping. In particular, the reduction in overall hit rate implies that frequency-shifted complex tones are less

perceptually coherent, leading to an increased tendency for partials in the spectral frame to act as salient false targets for subjects to match. To explore this idea further, we determined which components were matched for all responses classified as misses both in our experiment 1 and in condition 2 of Brunstrom and Roberts (1998, expt. 1). This was achieved by dividing the frequency range into equal units of $\pm 0.5\times$component spacing around each of the partials in the spectral frame, and counting the misses falling within each unit as matches to the corresponding component number. The analysis did not reveal great differences between the harmonic and shifted stimuli in the way misses were distributed across the spectrum. In all cases, roughly half of the misses were matches to one of the gap-edge components, particularly the lower one. These partials are known to have salient pitches (Kohlrausch and Houtsma, 1992). The rest of the misses were scattered across the spectrum. Therefore, whatever the cause of the difference in hit rates between harmonic and shifted stimuli, it cannot easily be attributed to a change in the patterns of errors made by subjects. Further investigation is required to assess whether or not this difference is of real importance. Overall, it is the similarities between the hit-rate profiles for harmonic and for shifted stimuli that are most striking.

C. Separate templates for computing global pitch and for spectral grouping?

We noted earlier the disparity between the degree of mistuning required to cause a harmonic to stand out as a separate pure tone ($\pm 1.3\%$–2.1%; Moore *et al.*, 1986) and the degree required to exclude it from the calculation of global pitch (greater than $\pm 8\%$; Moore *et al.*, 1985). Indeed, Moore *et al.* (1985) showed that the contribution of a low harmonic (1–6) to the global pitch of a complex tone did not even begin to decline until it was mistuned by more than $\pm 3\%$. Furthermore, both Hartmann *et al.* (1990) and Roberts and Brunstrom (1998) have shown that mistuned harmonics in the range 4–8 tend to be the ones that are most easily segregated from a periodic complex tone. This set of components differs somewhat from the range defining the dominant region in pitch perception (components 2–5; Ritsma, 1967). These findings imply that the hypothetical template mechanism governing grouping is different from that governing pitch, even for the processing of harmonic stimuli. The experiments reported here have been able to demonstrate formally their separate actions by using regular inharmonic sounds, leading to different predictions concerning the pattern of partial-pitch suppression within a spectral gap.

On the basis of these findings, we propose the existence of two template mechanisms[3] with distinct roles and properties. The pitch template is envisaged as responsive only to harmonic patterns, but to allow individual partials to deviate considerably from true harmonicity before they are excluded (i.e., it has wide slots). This allows the computation of global pitch for a wide range of quasiharmonic stimuli, the strength and ambiguity of which will be determined by the number of partials passed by the template for a given $F0$. The grouping template is envisaged as responsive to spectral structure in a broader sense than harmonic relations alone, but to be relatively intolerant of the deviation of components from predicted frequencies (say about $\pm 1.5\%$; cf. Moore *et al.*, 1986). This allows both harmonic and frequency-shifted sounds to be heard as coherent, even in the absence of a clear and unambiguous global pitch, but prevents the accidental fusion of partials that are not patterned in a way consistent with the spectral distribution of the others. The question of why the auditory system might have evolved a grouping mechanism that can respond to spectral patterns other than harmonicity remains unclear. However, Roberts and Brunstrom (1998) noted that sounds emitted by many natural sources exhibit marked nonlinearities that are manifest as significant departures from harmonicity (see, e.g., Gaver, 1993; McIntyre *et al.*, 1983). Musical examples include the sounds produced by bells, chimes, gongs, and drums (Pierce, 1992). Perhaps we require a mechanism that is capable of grouping the components of these kinds of sound.

V. CONCLUDING REMARKS

The profiling method previously introduced by Brunstrom and Roberts (1998) has been used to provide further evidence for a grouping mechanism that is sensitive to broader aspects of spectral regularity than harmonic relations alone. Neither intermodulations generated by local interactions between neighboring partials nor combination tones generated by the components of the spectral frame offer a satisfactory explanation of our data at a peripheral level. Our findings are consistent with Roberts and Bregman's (1991) original interpretation of the even–odd difference in component salience for ''odds-plus-even'' harmonic stimuli, and also with Roberts and Brunstrom's (1998) finding that listeners can detect small mistunings imposed on partials in both frequency-shifted and spectrally stretched complex tones (at least for small degrees of stretch). Therefore, as a working proposal, we suggest that the perceptual grouping of components in all of these sounds, and, indeed, in sounds comprising consecutive harmonics, can best be understood in terms of a single mechanism that constructs templates of optimum fit to regions of common spectral spacing (i.e., equal or near-equal spacing between successive components). This suggestion leads to a specific prediction concerning the sensitivity of the ear to different degrees of shift or stretch; namely that any degree of shift can be tolerated but large degrees of stretch cannot. Notwithstanding the outcome of an empirical evaluation of our proposal, it is reasonable to conclude at this point that Bregman's dual-role hypothesis can be rejected. Furthermore, the evident dissociation between the selection of components for perceptual fusion and for the computation of global pitch is incompatible with the idea that pitch has primacy in spectral grouping (e.g., Hartmann, 1988, 1996).

Harmonicity has long been considered a key factor in grouping, and has been incorporated into models ranging from early attempts to separate two concurrent voices (e.g., Parsons, 1976) to recent, more comprehensive, attempts to simulate auditory scene analysis (e.g., Brown and Cooke, 1994a, 1994b). Contemporary models of pitch perception based on autocorrelation (e.g., Meddis and O'Mard, 1997) also typically assume a common periodicity-based mechanism for pitch computation and for spectral grouping. Our

findings suggest that models of this kind are too limited to provide a truly general account of the grouping of concurrent spectral components.

ACKNOWLEDGMENTS

This research was supported by Research Grant No. 6/S04782 from the Biotechnology and Biological Sciences Research Council (U.K.). Our thanks go to Brian Moore, Roy Patterson, Nick Hill, and Chris Plack for helpful discussions, comments, and suggestions. We are grateful to the reviewers for their comments on an earlier version of this manuscript.

[1]The hit rate for a particular probe does not provide a pure measure of its perceptual segregation. In particular, the salience of a given probe will also be influenced by its proximity to the gap-edge components of the spectral frame. All other factors being equal, a probe in the middle of the probe range will attract more hits than one toward either end, because its relative spectral isolation reduces the extent of its partial masking. However, the difference in partial-masking effects between adjacent probe positions will be small. Therefore, while comparisons of hit rate for widely separated probes may require careful interpretation, local comparisons provide a fairly unambiguous measure of relative perceptual segregation.

[2]Thresholds for the TMTF are expressed on a decibel scale in units of $20\log(m)$, where m is the modulation index. This index is a measure of the depth of modulation applied to the carrier (ranging from 0 to 1). Our estimate of the difference between the two computed excitation patterns in the level of excitation at the probe frequency can be compared directly with TMTF thresholds for the same rate of modulation (400 Hz). This is because the level of the sidebands generated when sinusoidal amplitude modulation is applied to a carrier is similarly dependent on the modulation index. Specifically, Hartmann (1995, p. 29) gives the level of each of the two sidebands, relative to the carrier, as $L=20\log(m/2)$.

[3]The term ''template mechanism'' implies the use of centrally stored information, but a central response that is stimulus-driven cannot be ruled out at present.

Bregman, A. S. (**1990**). *Auditory Scene Analysis: The Perceptual Organization of Sound* (MIT Press, Cambridge, MA).

Brown, G. J., and Cooke, M. (**1994a**). ''Computational auditory scene analysis,'' Comput. Speech Lang. **8**, 297–336.

Brown, G. J., and Cooke, M. (**1994b**). ''Perceptual grouping of musical sounds: A computational model,'' J. New Music Res. **23**, 107–132.

Brunstrom, J. M., and Roberts, B. (**1998**). ''Profiling the perceptual suppression of partials in periodic complex tones: Further evidence for a harmonic template,'' J. Acoust. Soc. Am. **104**, 3511–3519.

de Boer, E. (**1976**). ''On the 'residue' and auditory pitch perception,'' in *Handbook of Sensory Physiology*, edited by W. D. Keidel and W. D. Neff (Springer-Verlag, Berlin), Vol. 5, pp. 479–583.

Duifhuis, H., Willems, L. F., and Sluyter, R. J. (**1982**). ''Measurement of pitch in speech: An implementation of Goldstein's theory of pitch perception,'' J. Acoust. Soc. Am. **71**, 1568–1580.

Gaver, W. W. (**1993**). ''What in the world do we hear?: An ecological approach to auditory event perception,'' Ecological Psychol. **5**, 1–29.

Gerson, A., and Goldstein, J. L. (**1978**). ''Evidence for a general template in central optimal processing for pitch of complex tones,'' J. Acoust. Soc. Am. **63**, 498–510.

Glasberg, B. R., and Moore, B. C. J. (**1990**). ''Derivation of auditory filter shapes from notched-noise data,'' Hear. Res. **47**, 103–138.

Goldstein, J. L. (**1967**). ''Auditory nonlinearity,'' J. Acoust. Soc. Am. **41**, 676–689.

Greenwood, D. D. (**1972**). ''Masking by combination bands: Estimation of the levels of the combination bands $(n+1)f_1-nf_h$,'' J. Acoust. Soc. Am. **52**, 1144–1154.

Hartmann, W. M. (**1988**). ''Pitch perception and the segregation and integration of auditory entities,'' in *Auditory Function*, edited by G. M. Edelman, W. E. Gall, and W. M. Cowan (Wiley, New York), pp. 623–645.

Hartmann, W. M. (**1995**). ''The physical description of signals,'' in *Hearing: Handbook of Perception and Cognition*, 2nd ed., edited by B. C. J. Moore (Academic Press, London), pp. 1–40.

Hartmann, W. M. (**1996**). ''Pitch, periodicity, and auditory organization,'' J. Acoust. Soc. Am. **100**, 3491–3502.

Hartmann, W. M., and Doty, S. L. (**1996**). ''On the pitches of the components of a complex tone,'' J. Acoust. Soc. Am. **99**, 567–578.

Hartmann, W. M., McAdams, S., and Smith, B. K. (**1990**). ''Hearing a mistuned harmonic in an otherwise periodic complex tone,'' J. Acoust. Soc. Am. **88**, 1712–1724.

Henke, W. L. (**1990**). MITSYN: A coherent family of high-level languages for time signal processing, software package (Belmont, MA).

Kohlrausch, A., and Houtsma, A. J. M. (**1992**). ''Pitch related to spectral edges of broadband signals,'' in *Processing of Complex Sounds by the Auditory System*, edited by R. P. Carlyon, C. J. Darwin, and I. J. Russell (Oxford University Press, Oxford), pp. 81–88.

Lin, J.-Y., and Hartmann, W. M. (**1998**). ''The pitch of a mistuned harmonic: Evidence for a template model,'' J. Acoust. Soc. Am. **103**, 2608–2617.

McIntyre, M. E., Schumacher, R. T., and Woodhouse, J. (**1983**). ''On the oscillations of musical instruments,'' J. Acoust. Soc. Am. **74**, 1325–1345.

Meddis, R., and O'Mard, L. (**1997**). ''A unitary model of pitch perception,'' J. Acoust. Soc. Am. **102**, 1811–1820.

Moore, B. C. J. (**1987**). ''The perception of inharmonic complex tones,'' in *Auditory Processing of Complex Sounds*, edited by W. A. Yost and C. S. Watson (Erlabum, Hillsdale, NJ), pp. 180–189.

Moore, B. C. J., Glasberg, B. R., and Peters, R. W. (**1985**). ''Relative dominance of individual partials in determining the pitch of complex tones,'' J. Acoust. Soc. Am. **77**, 1853–1860.

Moore, B. C. J., Glasberg, B. R., and Peters, R. W. (**1986**). ''Thresholds for hearing mistuned partials as separate tones in harmonic complexes,'' J. Acoust. Soc. Am. **80**, 479–483.

Parsons, T. W. (**1976**). ''Separation of speech from interfering speech by means of harmonic selection,'' J. Acoust. Soc. Am. **60**, 911–918.

Patterson, R. D. (**1973**). ''The effects of relative phase and the number of components on residue pitch,'' J. Acoust. Soc. Am. **53**, 1565–1572.

Pierce, J. R. (**1992**). *The Science of Musical Sound* (Freeman, New York).

Plomp, R. (**1965**). ''Detectability threshold for combination tones,'' J. Acoust. Soc. Am. **37**, 1110–1123.

Plomp, R. (**1976**). *Aspects of Tone Sensation* (Academic Press, London).

Ritsma, R. J. (**1967**). ''Frequencies dominant in the perception of the pitch of complex sounds,'' J. Acoust. Soc. Am. **42**, 191–198.

Roberts, B. (**1998**). ''Effects of spectral pattern on the perceptual salience of partials in harmonic and frequency-shifted complex tones: A performance measure,'' J. Acoust. Soc. Am. **103**, 3588–3596.

Roberts, B., and Bailey, P. J. (**1993a**). ''Spectral pattern and the perceptual fusion of harmonics. I. The role of temporal factors,'' J. Acoust. Soc. Am. **94**, 3153–3164.

Roberts, B., and Bailey, P. J. (**1993b**). ''Spectral pattern and the perceptual fusion of harmonics. II. A special status for added components?'' J. Acoust. Soc. Am. **94**, 3165–3177.

Roberts, B., and Bailey, P. J. (**1996a**). ''Regularity of spectral pattern and its effects on the perceptual fusion of harmonics,'' Percept. Psychophys. **58**, 289–299.

Roberts, B., and Bailey, P. J. (**1996b**). ''Spectral regularity as a factor distinct from harmonic relations in auditory grouping,'' J. Exp. Psychol. **22**, 604–614.

Roberts, B., and Bregman, A. S. (**1991**). ''Effects of the pattern of spectral spacing on the perceptual fusion of harmonics,'' J. Acoust. Soc. Am. **90**, 3050–3060.

Roberts, B., and Brunstrom, J. M. (**1998**). ''Perceptual segregation and pitch shifts of mistuned components in harmonic complexes and in regular inharmonic complexes,'' J. Acoust. Soc. Am. **104**, 2326–2338.

Scheffers, M. T. M. (**1983a**). ''Sifting vowels: Auditory pitch analysis and sound segregation,'' Doctoral thesis, University of Groningen, The Netherlands.

Scheffers, M. T. M. (**1983b**). ''Simulation of auditory analysis of pitch: An elaboration on the DWS pitch meter,'' J. Acoust. Soc. Am. **74**, 1716–1725.

Schouten, J. F. (**1938**). ''The perception of subjective tones,'' Proc. K. Ned. Akad. Wet. **41**, 1086–1093.

Schouten, J. F. (**1940a**). ''The residue, a new component in subjective sound

analysis,'' Proc. K. Ned. Akad. Wet. **43**, 356–365. Reprinted in *Forty Germinal Papers in Human Hearing* (1969), edited by J. D. Harris (Journal of Auditory Research, Groton, CT).
Schouten, J. F. (**1940b**). ''The perception of pitch,'' Philips Tech. Rev. **5**, 286–294.
Schouten, J. F., Ritsma, R. J., and Cardozo, B. L. (**1962**). ''Pitch of the residue,'' J. Acoust. Soc. Am. **34**, 1418–1424.
Smoorenburg, G. F. (**1972**). ''Audibility region of combination tones,'' J. Acoust. Soc. Am. **52**, 603–614.
Strickland, E. A., and Viemeister, N. F. (**1996**). ''Cues for discrimination of envelopes,'' J. Acoust. Soc. Am. **99**, 3638–3646.
Strickland, E. A., and Viemeister, N. F. (**1997**). ''The effects of frequency region and bandwidth on the temporal modulation transfer function,'' J. Acoust. Soc. Am. **102**, 1799–1810.
Viemeister, N. F. (**1979**). ''Temporal modulation transfer functions based on modulation thresholds,'' J. Acoust. Soc. Am. **66**, 1364–1380.
Zwicker, E., and Fastl, H. (**1973**). ''Cubic difference sounds measured by threshold- and compensation-method,'' Acustica **29**, 336–343.

The perceptual tone/noise ratio of merged iterated rippled noises

Roy D. Patterson
Centre for the Neural Basis of Hearing, Physiology Department, Cambridge University, Cambridge CB2 3EG, United Kingdom

William A. Yost
Parmly Hearing Institute, Loyola University, 6525 North Sheridan Road, Chicago, Illinois 60626

Stephen Handel
Department of Psychology, University of Tennessee, 307 Austin Peay Building, Knoxville, Tennessee 37996

A. Jaysurya Datta
MRC Applied Psychology Unit, 15 Chaucer Road, Cambridge CB2 2EF, United Kingdom

(Received 23 June 1997; revised 15 October 1998; accepted 22 October 1999)

Iterated rippled noise (IRN) is constructed by delaying a random noise by d ms, adding it back to the same noise, and repeating the process iteratively. When two IRNs with the same power but slightly different delays are added together, the perceptual tone/noise ratio of the ''merged'' IRN is markedly reduced with respect to that of either of the component IRNs. In this paper, the reduction in the perceptual tone/noise ratio is measured for IRNs in which one of the delays is always 16 ms and the other is either 16 ± 0.1 ms or 16 ± 1.1 ms. The component IRNs have the same number of iterations, and the number varies across conditions from 4 to 256. The perceptual tone/noise ratio is measured using a discrimination matching procedure developed for single IRNs; each merged IRN is compared with a range of ''standard'' stimuli having varying proportions of a complex tone and a broadband noise [Patterson *et al.*, J. Acoust. Soc. Am. **100**, 3286–3294 (1996)]. For single IRNs, the function relating the signal-to-noise ratio of the matching standard to the number of iterations in the IRN was found to be essentially straight. This relationship was explained in terms of the height of the first peak in the autocorrelation of the stimulus wave, or by the first peak in the summary autocorrelogram produced by a time-domain auditory model. For the merged IRNs in the current experiment, the matching-point functions are found to have pronounced downward curvature, in addition to being well below the function for single IRNs. To account for the reduction in the perceptual tone/noise ratio of merged IRNs, the *autocorrelation* model was extended to include a simple rule for combining adjacent peaks in the autocorrelation function of the wave, and the *autocorrelogram* model was revised to improve the simulation of the ''loss of phase locking'' at higher frequencies in the autocorrelogram. © *2000 Acoustical Society of America.*
[S0001-4966(00)03302-6]

PACS numbers: 43.66.Ba, 43.66.Hg, 43.66.Jh, 43.66.Mk [JWH]

INTRODUCTION

Rippled noise (RN) is constructed by delaying a random noise by d ms and adding it back to the same noise. Iterated rippled noise (IRN) is constructed by repeating the delay-and-add process n times and it is designated IRN(d,n). IRN sounds produce a two-component perception with (1) a tonal foreground with a complex, raspy timbre and a pitch corresponding to a frequency of $1/d$ Hz, and (2) a noisy background hiss, typical of the original noise. As the number of iterations increases, the tonal component becomes more prominent and the noise component becomes less prominent. With two iterations or less, the dominant perception is noise, with eight iterations or more, the dominant perception is that of a buzzy tone. Patterson *et al.* (1996) measured the perceptual tone/noise ratio in IRN sounds with from 1 to 16 iterations using a discrimination matching experiment. On each trial, an IRN was presented in one interval and a ''standard'' stimulus was presented in the other; the standard was composed of the sum of a broadband noise and a complex tone, and the ratio of the energy in the tone to that in the noise was varied over trials to find the value where the perceptual tone/noise ratio of the standard matched that of the IRN. The experiment showed that the standard with a tone/noise ratio of 0 dB has the same perceptual tone/noise ratio as an IRN with between 1 and 2 iterations, and the tone/noise ratio of the matching standard has to be increased 3.8 dB per doubling of the number of iterations in the IRN stimulus to maintain the match in perceived tone/noise ratio.

Yost *et al.* (1996) and Patterson *et al.* (1996) explained the discrimination of IRN sounds in terms of time-interval processing based on autocorrelation (AC): in one case, AC was applied directly to the stimulus wave (the ''simple AC model''); in the other case, a computational version of Licklider's (1951) auditory autocorrelation model was used to produce autocorrelograms (ACGs) and this ''ACG model'' was used to produce summary autocorrelograms (SCs) (Meddis and Hewitt, 1991). For single IRNs, the perceptual

tone/noise ratio of an IRN is an exponential function of the height of the first peak in the AC of the wave (Yost, 1996), or the first peak in the SC (Yost *et al.*, 1996). Following Patterson *et al.* (1996), the first peaks in the AC and SC functions are referred to as AC1 and SC1, respectively. The heights of the peaks are designated $h1$ and $h1'$, respectively, and they are normalized with respect to the height at zero lag. Yost *et al.* (1996) have shown that differences in $h1$ can explain the discrimination of IRN sounds differing in *n*, and Patterson *et al.* (1996) have shown that $h1'$ provides a quantitative description of the discrimination-matching data for single IRNs. The simple AC model and the ACG model are reviewed in Secs. II and III, respectively.

The current paper presents the results of a new discrimination-matching experiment with concurrent IRNs. The study was motivated by the perception produced when two IRNs with slightly different delays are merged by simple addition. Provided the difference in delay is less than about 8% of the delay, the sound is perceived to have a single pitch, and the primary change in the perception is a progressive reduction in the perceived tone/noise ratio as the difference in delay increases. This is a problem for the simple AC model because the temporal resolution of the autocorrelation function is the same as that of the stimulus wave. The stimuli in these experiments have a relatively wide bandwidth (3700 Hz) and so the peaks in the AC are very narrow, and as soon as the difference in delay exceeds *0.2 ms*, the first peak in the autocorrelation function splits into a pair of narrow peaks. The heights of the two peaks drop immediately to half the original value and remain at this level as the delay difference increases further. The ACG models presented in Patterson *et al.* (1996) exhibit the same behavior. However, that is not what is heard. Listeners hear a single pitch and the perceived tone/noise ratio decreases gradually as the delay difference increases out to about 1.6 ms. In this paper, we present a discrimination-matching experiment designed to measure the decrease in the perceived tone/noise ratio of merged IRNs, and, subsequently, we show how both the simple AC model and the ACG model can be modified to explain the perceived tone/noise ratio of merged IRNs. A brief study of pitch matching to merged IRNs is presented in the Appendix.

I. MEASURING THE PERCEPTUAL TONE/NOISE RATIO OF MERGED IRNs

Following Patterson *et al.* (1996), a complex tone and a random noise were combined in varying proportions to produce a set of ''standard'' stimuli in which the perceived tone/noise ratio could be expressed in decibels. These stimuli were then matched to merged IRN stimuli with from 4 to 256 iterations in a discrimination matching experiment to provide a quantitative measure of the perceptual tone/noise ratio of merged IRN sounds. The test and standard stimuli all had the same energy and they were all bandpass filtered between 800 and 4500 Hz. The difference in delay between the two-component IRNs in the merged IRN was either 0.1 or 1.1 ms. The values were chosen on the basis of informal listening: 0.1 ms is a small time difference that, nevertheless, produces a clear reduction in perceptual tone/noise ratio; 1.1 ms is a large difference that produces a further reduction in pitch strength without producing the perception of two simultaneous pitches.

A. Method

1. Stimuli

a. Standard. The tonal component of the standard stimuli (SS) was IRN(16,256) as in Patterson *et al.* (1996) to make the physical and perceptual characteristics of the standard stimuli similar to those of the test stimuli. Five samples of Gaussian noise, 1.25 s in duration, were generated digitally, stored, and used to produce five samples of IRN(16,256). We used the add-same procedure described in Yost *et al.* (1996). Standard stimuli with 11 different tone/noise ratios were produced by adding IRN(16,256) with a fixed level to random noise that varied in level from 3 dB above to 12 dB below the level of the IRN(16,256) in 1.5-dB steps. There were 20 samples of each standard tone/noise ratio, produced by combining the five IRN(16,256)'s with each of four random noises after they had been attenuated to the appropriate level. They were equated for energy and they are referred to by their tone/noise ratio. Thus, the range of standards is from SS(−3), the least tonal, to SS(12), the most tonal. Perceptually, the hiss masks the tone in SS(−3) and the tone masks the hiss in SS(12). In between, the standard stimuli produce two-component perceptions that sound very much like those produced by the merged IRN stimuli.

b. Test. The two IRNs in each merged pair always had the same number of iterations, *n*, and differed only in their delay. In every case one of the IRNs had a delay of 16 ms. In one set of conditions, the delay of the second IRN was either 15.9 or 16.1 ms, a difference of 0.1 ms. In this set, the timbre and pitch of the merged IRN were very similar to those of a simple IRN with a delay of 16 ms. In the second set of conditions, the delay of the second IRN was 14.9 or 17.1 ms, a difference of 1.1 ms. The timbre of the tonal component of these merged IRNs is richer than that of a single IRN, but they are still clearly IRNs, and the listeners found no problem in comparing them to the standard stimuli.

For merged IRNs, the perceptual tone/noise ratio of stimuli with 1 or 2 iterations is so low that it is difficult to measure. As a result, the minimum number of iterations in the present experiment was 4. Moreover, merged IRNs with 16 iterations produce a perception with a substantial noise component. Accordingly, this end of the range was extended to include merged IRNs with 256 iterations. Five samples of each form of merged IRN were generated using the addsame procedure as in Patterson *et al.* (1996). For comparison purposes, single IRNs with a 16-ms delay and 4 iterations were generated to provide a replication of the IRN(16,4) condition in Patterson *et al.* (1996).

c. Standard and test. All of the standard and test stimuli were normalized to produce a longterm spectrum level of 47 dB SPL. The stimuli were generated digitally and output by a high-quality, 12-bit D/A converter at a sampling rate of 10 kHz into an anti-aliasing filter with a cutoff of 4500 Hz. The stimuli were high-pass filtered to exclude the region of re-

solved harmonics (as defined by Houtsma and Smurzynski, 1990). The cutoff of the filter was 800 Hz and the rate of attenuation was 48 dB/oct in the region below the cutoff frequency. After filtering, the stimuli were presented binaurally over Sennheiser HD-414 headphones to listeners seated in double-walled sound-attenuating booths. The energy in these stimuli is above the dominance region (Ritsma, 1967; Bilsen and Ritsma, 1970), which for these low-pitched stimuli is around the seventh harmonic of $1/d$ (Patterson and Wightman, 1976). As a result, the pitch strength of the stimuli was weaker than that of equivalent broadband stimuli. However, in the previous experiment (Patterson *et al.*, 1996), the matching of bandpass IRNs to bandpass standard stimuli produced virtually identical values to those obtained when matching broadband IRNs to broadband standard stimuli. Thus we feel confident that the data from the current experiments would generalize to broadband merged IRNs.

2. Procedure

The experimental details are very similar to those in Patterson *et al.* (1996): On each trial, the listeners were presented with a test stimulus and a standard stimulus in random order, and asked to select the sound with the higher tone/noise ratio. Over trials the noise level in the standard was varied to determine the ratio of IRN(16,256) energy to random-noise energy required to produce an equal probability of choosing the test and standard stimuli. Each trial consisted of a warning interval, silent gap, stimulus interval, silent gap, stimulus interval, and response interval terminated by the listener's response. The durations of the intervals were 250, 500, 1250, 500, and 1250 ms, respectively. There was a 2-s silent interval between trials and there was no feedback.

For each of the merged IRNs in the test set, standard stimuli with a range of tone/noise ratios were selected to generate a psychometric function; that is, the SS with the largest tone/noise ratio was clearly more tonal than the test stimulus, and the SS with the smallest tone/noise ratio was clearly less tonal than the test stimulus. Conditions from the central portion of the psychometric function, where the perceived tone/noise ratios of the test and standard stimuli were similar, were presented 12 times within a block; conditions towards the ends of the psychometric functions were presented 8 or 4 times, as they simply mark where the functions asymptote. The trials for all nine psychometric functions [4 iteration values (4, 8, 16, 256) by 2 delay differences, plus the single IRN(16,4)] were randomly ordered within one large block (560 trials) and presented in four runs of 140 trials each. This procedure was used so that the context for each trial was the full range of tone/noise ratios. Each block was presented to each listener on successive days and the order of runs was counterbalanced across listeners.

A roving level paradigm was used to discourage the use of loudness cues for discrimination and encourage the use of the perceived tone/noise ratio. For each interval of every trial, the stimuli were independently attenuated by between 0 and 10 dB—the specific value being drawn randomly from a uniform distribution. The longterm spectrum level of 47 dB SPL refers to stimuli with 0 dB of roving attenuation. There were four listeners: one was author SH, two were visiting scientists, and the fourth was a graduate student experienced in auditory experiments who was paid at an hourly rate. All four listeners had normal hearing.

B. Results

Preliminary analyses found no evidence of practice effects across blocks for any listener, so individual psychometric functions were plotted for each combination of merged IRN and listener. In each case, the psychometric functions for the four listeners were similar in shape and position, so they were averaged across listeners. These psychometric functions showed that there were no differences between the matches produced by the two merged IRNs with the smaller delay difference; that is, no difference between the match to a merged IRN composed of IRN(16,n) and IRN(15.9,n), and the match to a merged IRN composed of IRN(16,n) and IRN(16.1,n). Similarly, there were no differences between the matches produced for the two merged IRNs with the larger delay differences; that is, no difference between the match to IRN(16,n) with IRN(14.9,n), and the match to IRN(16,n) with IRN(17.1,n). So the data were combined within each delay difference. Merged IRNs composed of an IRN(16,n) with IRN(15.9,n) or IRN(16.1,n) will be designated IRNM(16,0.1,n), and merged IRNs composed of an IRN(16,n) with IRN(14.9,n) or IRN(17.1,n) will be designated IRNM(16,1.1,n). The fact that they are merged IRNs is marked in the name itself (IRNM) and by the addition of the third parameter indicating the absolute value of the delay difference.

The average psychometric functions are plotted in Figs. 1 and 2 using open symbols. The abscissa is the tone/noise ratio of the standard stimulus and the ordinate is the proportion of trials on which the listeners chose the standard stimulus. The parameter is the number of iterations. All of these psychometric functions are very steep with slopes around 20%/dB in the region from 25%–75% correct. The bold line with open double triangles, or ''hour glasses,'' shows the average psychometric function for IRN(16,4). The data gathered in the current experiment were virtually indistinguishable from those in Patterson *et al.* (1996) and so the bold lines in Figs. 1 and 2 present the average psychometric function for the two experiments combined.

The data for IRNM(16,0.1,4) in Fig. 1 (open squares) show that the psychometric function for the merged stimulus with four iterations is shifted a little over 3 dB to the left of that for the single IRN(16,4) (open hour glasses), indicating that the perceptual tone/noise ratio is reliably reduced by the addition of IRN(16.1,4) to IRN(16,4). As the number of iterations increases from 4 to 256, the psychometric functions for the merged stimuli shift to the right by about 5 dB, indicating that the perceptual tone/noise ratio increases with n, as in the earlier experiment. However the size of the effect is substantially less for the merged IRNs; for single IRNs the tone/noise ratio rises 15 dB as the number of iterations increases from 1 to 16 (Patterson *et al.*, 1996). The data for IRNM(16,1.1,n) in Fig. 2 show a similar pattern but with a somewhat greater reduction in perceptual tone/noise ratio, that is, a greater leftwards shift in the psychometric func-

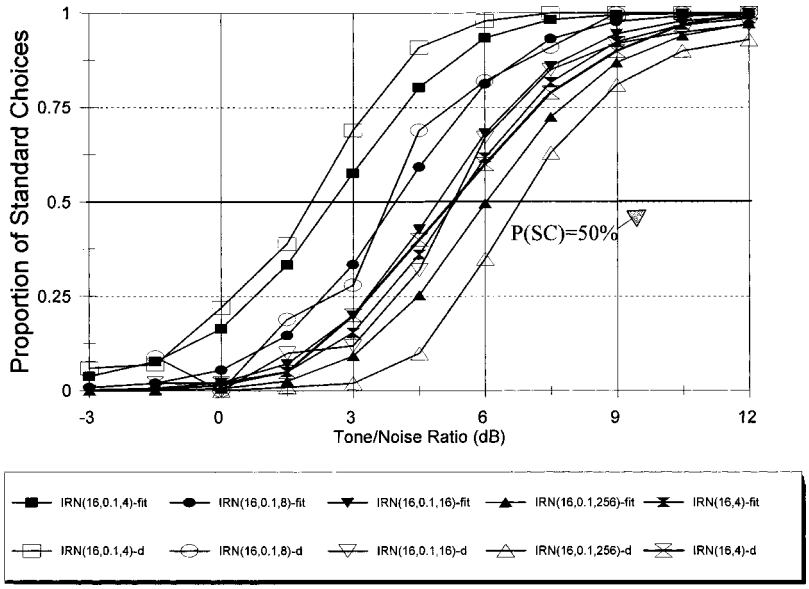

FIG. 1. Average psychometric functions for merged IRNs with a delay difference of 0.1 ms, IRNM(16,0.1,*n*); that is, the proportion of standard choices plotted as a function of the signal-to-noise ratio of the standard stimulus. The open symbols show the **data**; the filled symbols show the **fit** from the simple AC model. The bold line with open symbols shows the average data for the single IRN(16,4). A merged IRN with dd of 0.1 has to have 256 iterations to be more tonal than a single IRN with four iterations.

tions. The tone/noise ratio for the most tonal IRNM with 256 iterations is still less than that for IRN(16,4).

The central portions of the psychometric functions are essentially linear, so lines were fitted to the points between 10% and 90% on each function to estimate the ''matching point:'' that is, the tone/noise ratio of the standard stimulus that led to an equal probability of listeners choosing the test or standard stimulus as the one with the stronger tone/noise ratio. The matching points for IRNM(16,0.1,*n*) and IRNM(16,1.1,*n*) are presented in Fig. 3 by inverted and upright open triangles, respectively. The matching-point data for the single IRNs from the earlier experiment are presented by open squares. The data show that the perceived tone/noise ratio in merged IRNs is much lower than that of single IRNs and the slopes of the functions relating signal/noise ratio to *n* are shallower for merged IRNs.

II. THE SIMPLE AUTOCORRELATION MODEL AND MERGED IRNs

The remainder of the paper is concerned with quantitative descriptions of the discrimination matching data with single and merged IRNs. In this section, we show that the ''simple'' autocorrelation (AC) model of Yost *et al.* (1996), in which autocorrelation is applied directly to the stimulus wave, can be extended in a straightforward manner to describe the merged IRN data including the shape of the psychometric functions. The model is interesting inasmuch as it shows that the perceptual tone/noise ratio of merged IRNs is closely related to the statistics of the stimuli, and it leads to a simple rule for predicting the perceptual tone/noise ratio of merged IRNs. The form of the extended AC model does not, however, shed much light on the functioning of the auditory system. In Sec IV we show that the multi-channel, autocorrelogram (ACG) model of Patterson *et al.* (1996) can also explain the merged IRN data provided the model is extended to simulate auditory loss of phase locking. The time-domain model is considerably more complicated than the simple AC model, but it has the advantage of explaining the relationship between delay difference and perceived tone/noise ratio in auditory terms.

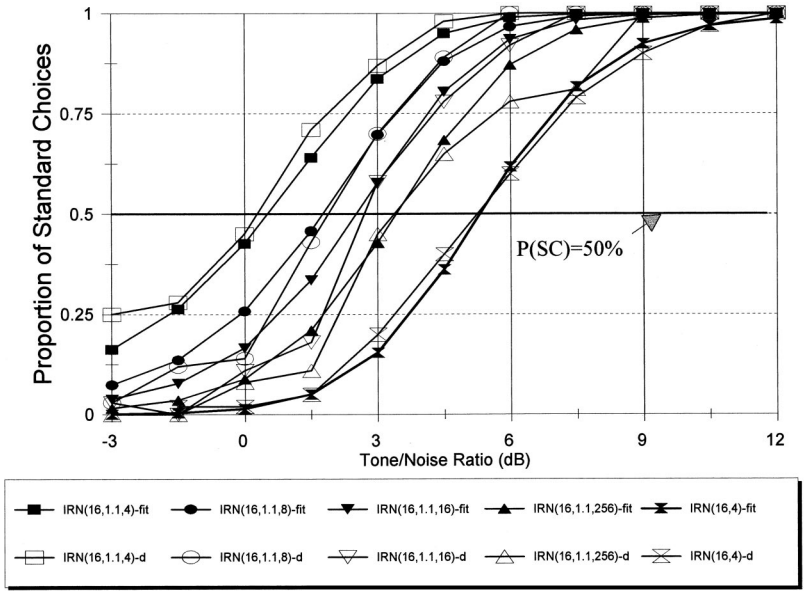

FIG. 2. Average psychometric functions for merged IRNs with a delay difference of 1.1 ms, IRNM(16,1.1,*n*); that is, the proportion of standard choices plotted as a function of the signal-to-noise ratio of the standard stimulus. The open symbols show the **data**; the filled symbols show the **fit** from the simple AC model with the limiting constant, *c*, set to 0.2. The bold line shows the average data for the single IRN(16,4). None of these merged IRNs is more tonal than a single IRN with four iterations.

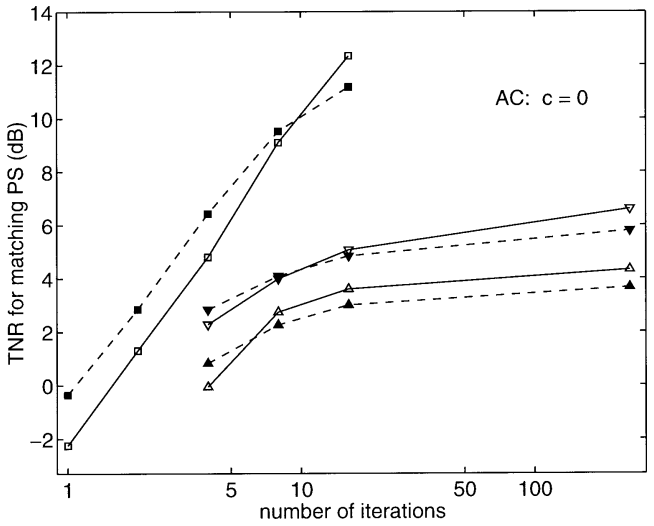

FIG. 3. Matching-points for single IRNs (squares) and merged IRNs with delay differences of 0.1 ms (inverted triangles) and 1.1 ms (upright triangles). The base delay is 16 ms. The matching point is the signal-to-noise ratio of the standard stimulus that leads to an equal probability of the listener choosing the test or standard stimulus as the one with the stronger tone-to-noise ratio. The solid lines show observed values. The dashed lines show values from the simple AC model in which pitch strength is an exponential function of the number of iterations.

A. The AC model and the PS measure for merged IRNs

Yost *et al.* (1996) refer to the perceptual tone/noise ratio of IRN as its pitch strength (PS), and they have shown empirically that the PS of a single IRN is an exponential function of $h1$, the height of the first peak in the normalized autocorrelation function of the IRN wave. Thus, PS $=k10^{h1}$. The proportionality constant, k, has a value of 0.8. In Patterson *et al.* (1996), $h1$ was measured empirically for both the test and standard stimuli by calculating the average value for all of the tokens of each type of stimulus in the experiment. Then, these values were used to fit psychometric functions to the data set as a whole. The matching points produced by this autocorrelation model are shown by filled squares in Fig. 3; they show the signal-to-noise ratio of the standard stimulus required to produce the same $h1$ as the corresponding IRN(16,n). The model provides reasonable estimates of the matching points overall, so the simple AC model was extended to the case of merged IRNs.

Using the longterm autocorrelation function, Yost *et al.* (1996) showed that the height of AC1 for single IRNs is

$$h1_{\mathrm{IRN}}=n/(n+1). \tag{1}$$

Recently, Bilsen (personal communication) and Hartmann (personal communication) have both shown how the same relationship can be derived using the longterm power spectrum of the stimulus. To explain the matching-point data for merged IRNs, the expression has to be extended both to merged IRNs and the standard stimuli. The latter are composed of an IRN(16, 256) and a random noise limited to the same spectral band. Without the noise, $h1$ is simply 256/(256+1). The noise reduces $h1$ as it increases in level relative to the IRN. For convenience, since the IRN(16,256) is perceived as a *f*igure against the noise back*g*round, we will refer to the their energies as f and g, respectively, and to the *r*atio of the noise power to the IRN power as $r_{g/f}$ (in linear terms). In this case,

$$h1_{\mathrm{SS}}=n/[(n+1)(1+r_{g/f})]=256/[257(1+r_{g/f})]. \tag{2}$$

When g and f are measured in decibels, $r_{g/f}$ is $10^{(g-f)/10}$. When the background level is low, $h1$ converges on $n/(n+1)$; when their levels are equal, $h1$ is $0.5\times n/(n+1)$.

The longterm autocorrelation function of a broadband, merged IRN wave has narrow peaks at both of the component delays. In the current studies, the two IRNs have the same number of iterations and so the heights of these peaks are the same, and they are both half the height of the first peak in a single IRN. If the first peak is designated $h1_{\mathrm{IRNM}}$ then

$$h1_{\mathrm{IRNM}}=0.5\cdot n/(n+1). \tag{3}$$

B. The merging of AC1 and AC2 in the AC model

The data show that PS does not immediately drop to half its previous value when the delay of one IRN departs a fraction of a millisecond from that of the other; rather, PS decreases progressively as the difference between the delays increases. If we make the simple assumption that PS decreases linearly as the delay difference, dd, increases over some limited range, then the relationship between $h1_{\mathrm{IRNM}}$ and dd is

$$h1_{\mathrm{IRNM}}=p_{\mathrm{dd}}n/(n+1). \tag{4}$$

The proportionality constant p_{dd} decreases from 1 to 0.5 as dd increases from 0 to about 2 ms. This modified AC model was used to calculate psychometric functions from the matching experiment with merged IRNs. As in Patterson *et al.* (1996), we assume that the psychometric function is a cumulative normal function of the difference in pitch strength between $\mathrm{PS}_{\mathrm{IRNM}}$ and $\mathrm{PS}_{\mathrm{SS}}$, that is, a cumulative normal function of

$$\mathrm{PS}_{\mathrm{IRNM}}-\mathrm{PS}_{\mathrm{SS}}=k10^{p_{\mathrm{dd}}n/(n+1)}-k10^{256/[257(1+r_{g/f})]}. \tag{5}$$

The k value was 0.8 as in the earlier paper. The data sets for IRNM(16,0.1,n) and IRNM(16,1.1,n) were fitted separately, varying p_{dd} in steps of 0.0125 to determine the values that produced the best fit in terms of the minimum squared residual. The values of p_{dd} for IRNM(16,0.1,n) and IRNM(16,1.1,n) were 0.80 and 0.69, respectively. The psychometric functions produced by this model for the 0.1-ms condition are presented in Fig. 1 by filled symbols. The model underestimates the tone/noise ratio of IRNM(16,0.1,4) a little (compare the open and filled squares), and it overestimates the tone/noise ratio of IRNM(16,0.1,256) a little (open and filled upright triangles), but it is a reasonable fit given that there are 45 data points and only on free parameter, p_{dd}. The fit to the data for the larger delay difference (1.1) is similar in form but slightly more accurate; the fit is omitted for brevity. The model underestimates the tone/noise ratio of IRNM(16,1.1,4) as it does for IRNM(16,0.1,4) in Fig. 1, but it does not overestimate the tone/noise ratio of IRNM(16,1.1,256). The fit presented with the 1.1-ms data in Fig. 2 is described in the next subsection.

For each psychometric function, a line was fitted to points between 20% and 80%, and the abscissa value where the line crossed the 50% line was taken to be the tone/noise ratio of the standard that matched that merged IRN. The matching-point functions produced by this modified AC model for both sets of merged IRN data, and for the single IRN data, are presented in Fig. 3 by filled symbols and dashed lines. The fits are surprisingly good for a model with only one free parameter, p_{dd}; the matching-point functions for the merged IRNs have downwards curvature similar to that of the data and the vertical position is approximately correct.

C. Limitation of the linear merging of peaks

A detailed examination of the fit in Fig. 3 reveals that the curvature of the matching-point functions from the model is a little greater than that of the data, and the matching points from the model fall consistently above the observed values for smaller values of n. The discrepancy indicates that there is a lower limit to the linear relationship between dd and $h1$ [Eq. (4)]. To test this hypothesis, we inserted a small limiting constant, c, into the denominators of the equations for $h1$ as follows,

$$h1_{\mathrm{IRN}} = n/(n+1+c), \tag{6}$$

$$h1_{\mathrm{IRNM}} = p_{\mathrm{dd}} n/(n+1+c), \tag{7}$$

and

$$h1_{\mathrm{SS}} = 256/[(257+c)(1+r_{g/f})], \tag{8}$$

respectively. The psychometric functions for both merged and single IRNs were refitted using Eqs. (6)–(8) and varying c in small steps to find the minimum rms residual. The optimum value of c was found to be 0.2 and matching points were extracted from the psychometric functions associated with this fit. The psychometric functions for the merged IRNs with a dd of 1.1 are presented by filled symbols in Fig. 2. This version of the model still underestimates the tone/noise ratio of IRNM(16,1.1,4) a little (open and filled squares), but otherwise it is highly accurate. The fit to the data for the smaller delay difference (0.1) is similarly improved chiefly for IRNM(16,0.1,4); the overestimate of the tone/noise ratio for IRNM(16,0.1,256) remains like that in Fig. 1. The fit is omitted for brevity. With regard to the matching-point data, the inclusion of c reduces the rms deviation for the fit to the single IRN from 2.02 to 0.76 dB; for the merged IRN data, the average rms deviation is reduced from 0.30 to 0.14 dB. This indicates that there is a significant departure from the linear relationship between $h1$ and dd for small values of n, and that Eqs. (6)–(8) should be used whenever conditions with small n are involved. The values of p_{dd} for delay differences of 0.1 and 1.1 were found to be 0.81 and 0.695, respectively, which is virtually the same as without c. It is not, however, obvious why the lower limit to the relationship between $h1$ and dd should be 0.2.

III. AUTOCORRELOGRAM MODELS AND MERGED IRN'S

In the final section of their paper, Patterson *et al.* (1996) present two multi-channel, time-domain, versions of Licklider's (1951) autocorrelation model of pitch perception, and demonstrate that autocorrelograms (ACGs) produced by these models produce matching points similar to those observed with single IRNs. In this section, we briefly review these ACG models, and note that when applied to merged IRNs, they have the same problem as the simple AC model; as the delay difference of the merged IRN increases from zero, the height of the first peak drops too quickly to explain the PS of merged IRNs. The failure is attributed to insufficient loss of phase locking at high frequencies in these auditory models. One of the models is modified to produce greater loss of phase locking, after which it is shown to provide a good explanation of the matching-point data from both single and merged IRNs.

A. Existing ACG models and phase locking

The ACG model of Patterson *et al.* (1996) has three stages like most other models of this type: In the first stage, a gammatone auditory filterbank is used to simulate the spectral analysis performed by the cochlea, and, in the second, a bank of two-dimensional, adaptive-thresholding units is used to simulate neural transduction. These two stages are taken directly from the auditory image model (AIM) described in Patterson *et al.* (1992) and Patterson (1994). Together they produce a simulation of the neural activity pattern (NAP) produced by the cochlea in response to a sound. The final stage consists of a bank of autocorrelators, one for each channel of the cochlea simulation. These autocorrelators convert the NAP into an array of autocorrelation functions referred to as an ''autocorrelogram'' (Meddis and Hewitt, 1991). The IRN stimuli produce autocorrelograms (ACGs) with concentrations of activity in the columns around the IRN delay and integer multiples of the delay. An example is presented in Fig. 8 of Patterson *et al.* (1996); the software package for producing these autocorrelograms is described in Patterson *et al.* (1995). The relative strength of the IRN pitch is assumed to be determined by the amount of activity at the IRN delay, which is estimated by averaging across channels to produce a summary autocorrelogram (SC) and measuring the height, $h1'$, of the first peak, SC1. The model of Meddis and Hewitt (1991) is very similar except that the neural transduction stage is simulated by a bank of Meddis (1986) haircells. In Patterson *et al.* (1996), $h1'$ values were calculated for the single IRNs and test stimuli with the ACG models of both Patterson *et al.* (1996) and Meddis and Hewitt (1991). The two models produced virtually identical matching-point values, *and the values were the same as those of the simple AC model* (Yost *et al.*, 1996) where autocorrelation is applied directly to the stimulus wave.

The neural transduction stages of these ACG models have a known deficiency; they do not accurately represent the loss of phase locking observed in the auditory nerve at frequencies above about 1000 Hz. There is essentially no loss of phase locking in the model of Patterson *et al.* (1996)

and the loss of phase locking in Meddis and Hewitt (1991) is considerably less than that observed physiologically. As a result, these original ACG models have the same problem as the simple AC model; the peaks produced by IRNs are narrow and $h1'$ drops too rapidly with delay difference to explain the PS of the merged IRNs.

In the cochlea, the inner haircell receptor potential oscillates at the stimulus frequency up to very high frequencies, but the haircell membrane *low-pass filters* the receptor potential, which results in a progressive reduction with increasing frequency in the synchrony index as measured in primary auditory nerve fibers (e.g., Johnson, 1980). The receptor potential is strongly asymmetric and so the oscillation is essentially a half-wave rectified version of basilar membrane motion. As a result, the effect of the low-pass filter is like that of a leaky integrator, or temporal window; high frequency components are reduced in level, low-frequency components are augmented in level, and there is a small increase in overall level that increases with the time constant of the low-pass filter. Thus, the low-pass filtering does not cause the overall firing rate to decrease with increasing center frequency; rather the degree of phase locking decreases because the oscillating component on which it depends becomes an ever smaller portion of the total potential as frequency increases. Excellent illustrations of the physiological processes are presented in Weiss and Rose (1988a, Fig. 1) and Russell and Palmer (1992, Fig. 1). To simulate the perceptual effects of the loss of phase locking, a bank of low-pass filters with variable order was added to the transduction stage of AIM[1] (Release 8.2, 1997), one for each channel of the auditory filterbank. The default cutoff frequency was 1200 Hz and the default order was two, so the rate of attenuation beyond the cutoff frequency was 12 dB per octave. Autocorrelograms of single IRN stimuli produced with AIM are illustrated in Yost *et al.* (1998, Figs. 4 and 5) and Griffiths *et al.* (1998, Fig. 2). The temporal detail becomes more and more blurred as filter center frequency increases in these autocorrelograms, but the overall level of activity remains roughly constant.

With regard to the fitting of the merged IRN data, the important relationship is that between the filtering action of the haircell and the synchrony index used to summarize temporal precision in primary fibers. Weiss and Rose (1988a) have studied this relationship and concluded that, to explain the rapid loss of synchrony above the cutoff frequency, it is necessary to assume that there are at least four consecutive stages of simple low-pass filtering applying no less than 24 dB/oct of attenuation above the cutoff frequency. They argue that there are three extra stages of low-pass filtering in the haircell beyond that observable at the cell membrane, and they speculate as to their origin. Subsequently, Weiss and Rose (1988b) make a detailed comparison of the cutoff frequencies and attenuation rates of the synchrony indices measured in alligator lizards, guinea pigs, and cats. They report that the cutoff frequency varies considerably from about 400 Hz in lizards to about 1200 Hz in cats, but that the rate of loss of synchrony beyond the cutoff frequency is remarkably uniform across species. Accordingly, we set the order of the low-pass filters in AIM to four (24 dB/oct slope) and fitted

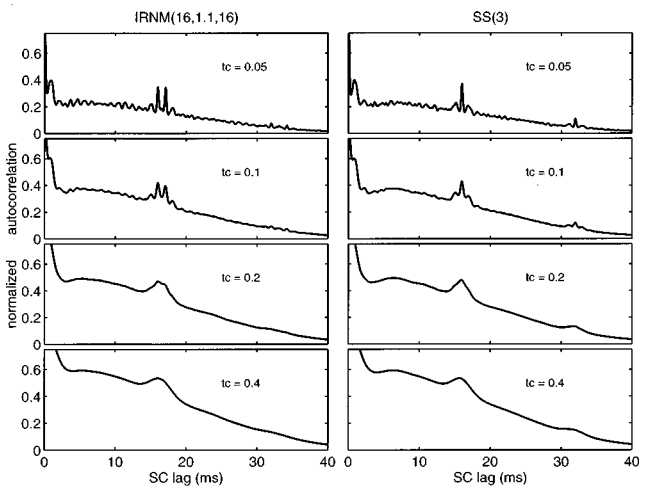

FIG. 4. Summary autocorrelograms for IRNM(16,1.1,16), where the component IRNs have delays of 16 and 17.1 ms (left column), and the standard stimulus that produces a matching pitch strength [SS(3)] (right column). The rows show the effect when loss of phase locking is simulated by low-pass filtering each channel of the NAP with cutoff frequencies of 3200, 1600, 800, or 400 Hz. The peaks of the component IRNs merge as the cutoff frequency is lowered to 800 Hz (left column).

the merged IRN data repeatedly, varying the time constant, tc, between fits. The best temporal resolution is in channels near the low-frequency edge of the stimulus (0.8 kHz), whereas the effect of the number of stages is most pronounced at frequencies well above the cutoff. As a result, the fitting process is more sensitive to the cutoff frequency of the low-pass filter rather than the order within the range being considered (two to four stages).

B. PS and the phase-locking time constant

Four versions of the ACG model with tc values of 0.05, 0.1, 0.2, and 0.4 ms were created to produce models with cutoff frequencies of approximately 3200, 1600, 800, and 400 Hz, respectively. The SCs produced by these models in response to a merged IRN with 16 iterations and a 1.1-ms delay difference [IRNM(16,1.1,16)] are presented in the left-hand column of Fig. 4; the right-hand column shows the SCs produced by the same ACG models in response to the standard stimulus [SS(3)] with matching pitch strength. The upper left-hand panel shows that when dd is 1.1 and tc is 0.05, the peaks at the merged IRN delays are narrow and do not interact. In this case, the relationship between $h1'$ and dd decreases too rapidly to explain the PS of merged IRNs. As tc increases from 0.1 to 0.2, the peaks merge progressively, and, when tc is 0.4, the peaks are completely merged. This is the important aspect of the simulation of loss of phase locking for present purposes, and it indicates that the time constants of interest are in the range from 0.1 to 0.4 ms. As a result, these three versions of the ACG model were fitted to the merged IRN data.

For each value of tc, we generated a sequence of 10 ACGs at 40-ms intervals, for 20 samples of each type of test and standard stimulus in both the single- and merged-IRN experiments—a total of 5600 ACGs for each time constant [10*20*(5+4+4)+10*20*(15)]. We used 20 samples of

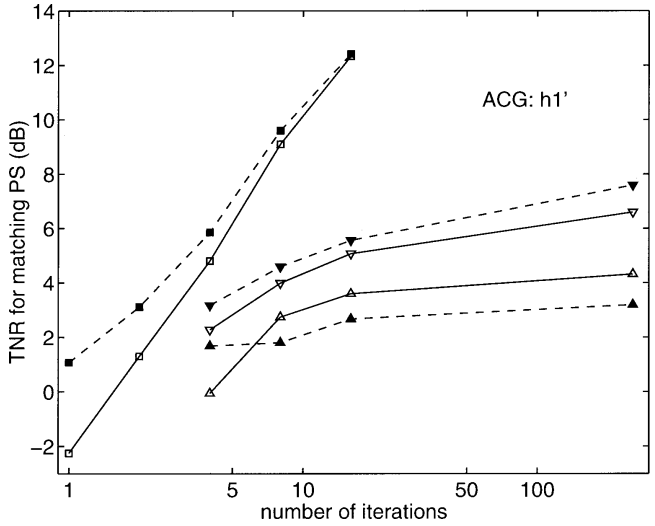

FIG. 5. Matching-points for single IRNs (squares) and merged IRNs with delay differences of 0.1 ms (inverted triangles) and 1.1 ms (upright triangles), as in Fig. 3. The dashed lines show values from an ACG model in which pitch strength is associated with the height of the first peak in the summary autocorrelogram.

each stimulus type because the merged IRN stimuli exhibited considerable variability. The SCs were produced for each ACG, and the 10 SCs for a given sample were then averaged to produce the basic summary of pitch-strength information for that sample of that stimulus type with that time constant. Thus, the analysis is based on three sets of 560 average SCs, one set for each time constant. For each test and standard stimulus, we averaged the SCs for the 20 samples and determined $h1'$ for that stimulus type. For each of the single and merged IRNs, we determined the standard stimulus whose $h1'$ was just greater than that of the given test stimulus, and the standard stimulus whose $h1'$ was just less than that of the test stimulus. Then, by interpolation, we determined the signal-to-noise ratio of the standard stimulus whose pitch strength would match that of the given IRN (single or merged).

The ACG models with time constants of 0.1, 0.2, and 0.4 ms all produced good fits with rms errors of 1.4, 1.3, and 1.5 dB, respectively. The average rms deviation for the 0.2-ms model is comparable to that for the simple autocorrelation model (1.3), and, in that case, the matching points of the single and merged IRNs were fitted separately. The observed matching points are compared with those from the ACG model with the 0.2-ms time constant in Fig. 5; the fit is quite similar to that of the simple AC model when c is zero (Fig. 3). Thus, when the ACG model is modified to include loss of phase locking, it immediately produces a good fit to the matching-point data of both single and merged IRNs taken together; the only free parameter is the time constant.

The summary ACGs exhibit two additional effects that are not observed in the AC of the stimulus wave: (1) The summary ACGs slope downwards to the right. This is because the duration of the segment used to calculate the autocorrelation in the auditory model is limited to 70 ms (Patterson *et al.*, 1996), and this limits the amount of activity that can occur at long lags. (2) Low-pass filtering causes the correlation values at shorter lags to increase with tc in these normalized ACGs; for example, the value at 5 ms increases from just over 0.2 to just under 0.6 as tc increases from 0.05 to 0.4 ms. As the low-pass filter smoothes the neural activity pattern, it reduces the differences between points that are close in time. This increases the correlation at shorter delays, and the effect increases with tc. Neither of these properties of the auditory model is important, however, when modeling the perceptual tone/noise ratio of the current IRNs.

The implications of the ACG model for the pitch values produced by merged IRNs are considered in the Appendix. Briefly, the study indicates that listeners match to the average delay when dd is 0.1 and to the shorter of the two delays when dd is 1.1.

C. Pitch strength and the SC peak at 32 ms

The primary discrepancy between the observed matching points and those of the ACG model in Fig. 5 is for merged IRNs with a 0.1-ms delay difference (down-pointing triangles). All four model values are greater than the observed values. Moreover, the same discrepancy exists when the time-constant is 0.1 or 0.4 ms; this set of four matching points move vertically as a group as the time constant is varied. There are no free parameters in the ACG model to adjust the grand mean of the matching points from the model to the grand mean of the observed matching points; there is only the one fitting parameter, tc. In this sense, the fit of the ACG model with loss of phase locking is surprisingly good. On the other hand, there remains a consistent deviation which suggests that there may be something more to be learned from the data. Accordingly, we briefly considered modifications to the pitch strength measure to determine whether the rms error could be reduced and what it might mean in terms of the ACG model.

The SCs of the standard stimulus, SS(3), in the right-hand column of Fig. 4 contain a secondary peak at 32 ms associated with higher-order iterations. The peak is small or absent in the SCs for IRNM(16,1.1,16) in the left-hand column. If pitch strength is determined by the sum of the periodicity information in the 16- and 32-ms regions, then we may have been underestimating the PS of the standard stimulus relative to that of the test stimulus by a small amount. Yost (1997) has argued that the height of the largest peak in the AC function can explain the data on PS and PS discrimination in virtually all cases, and that secondary peaks do not appear to contribute to PS. Nevertheless, we thought it worth investigating whether the inclusion of the peak at 32 ms in the PS measure would affect the matching points produced by the ACG model.

The analysis was limited to the 0.2-ms time constant. The PS values were recalculated adding the height of the SC function at 32 ms to $h1'$, and recalculating the matching points for the single and merged IRNs as before. The modification reduced the rms deviation of the fit from 1.3 to 1.0 dB, but at the same time, it led to an underestimation of the observed matching points for IRNs with eight or more iterations. The main effect was simply to lower all of the matching points produced by the model rather than improving the pattern of the fit, which suggests that the peak at 32 ms does not play an important role in determining PS.

IV. SUMMARY AND CONCLUSIONS

Combining two IRNs with the same number of iterations and slightly different delays reduces the perceived tone-to-noise ratio substantially, and the reduction increases with the difference between the delays up to 1.1 ms, at least. When measured with a ''standard stimulus'' composed of an IRN(d,256) and a random noise, the average effect is equivalent to a reduction of 4 dB in the signal-to-noise ratio of the standard when the delay difference is as little as 0.1 ms. In this case, the delay difference is only 0.62% of the base delay, 16 ms. When the delay difference is 1.1 ms, or 6.8% of the base delay, the average effect is equivalent to a reduction of 7 dB.

The simple AC model of Yost *et al.* (1996) was modified to make provision for interaction between peaks that occur in close proximity in the AC function, and, with this provision, the model produced excellent fits to the matching-point data and to the psychometric functions from experiments with single and merged IRNs.

The ACG model described by Patterson *et al.* (1996) was also shown to produce a good fit to the matching-point data when the degree of low-pass filtering in the neural transduction module was increased to improve the simulation of the loss of phase locking observed in the auditory nerve. The order of the filter was increased to four and the cutoff frequency was reduced to about 800 Hz. The advantage of the ACG model is that the merging of the component IRNs arises naturally from the loss of phase locking, and the same model can explain other perceptual phenomena such as auditory masking.

ACKNOWLEDGMENTS

These studies were conceived while R. Patterson was a visiting scientist at Parmly Hearing Institute of Loyola University, Chicago. S. Handel was supported while at the Applied Psychology Unit by a professional development award from the Graduate School, University of Tennessee, Knoxville. A. J. Datta was supported by DERA Grant No. ASF/3208 to the MRC Applied Psychology Unit. The authors would like to thank Stefan Uppenkamp for assistance with the pitch matching experiments in the Appendix and Christian Sumner for his assistance with the ACG modeling which was performed with support from ATR-HIP in Kyoto, Japan. The authors would also like to thank Frans Bilsen and Bill Hartmann for their helpful comments on previous versions of the paper.

APPENDIX: PITCH VALUES IN HIGH-PASS-FILTERED MERGED IRNs

The summary autocorrelograms produced by the ACG model (left-hand column of Fig. 4) suggest that it might be possible to produce another estimate of the time constant of phase locking by measuring the pitches produced by merged IRNs as a function of delay difference, dd, and noting the smallest dd for which the merged IRN produces two distinct pitches. This critical stimulus could then be presented to the revised ACG model and the time constant, tc, could be varied to determine the smallest value that produced a double-peaked summary autocorrelogram, SC. A pilot study was performed to measure the pitches produced by merged IRNs and to evaluate the potential for estimating the phase-locking time constant.

1. Method

Listeners were presented trials containing two 500-ms observation intervals, both of which contained merged IRNs whose component IRNs all had 16 iterations. The first interval contained the test stimulus, IRNM(16,dd,16), a merged IRN with an average delay that was always 16 ms and a dd that varied with condition. For example, IRNM (16,08,16) was made up of one IRN with a delay of 15.6 ms and one with a delay of 16.4 ms. The second interval contained the comparison stimulus, IRNM(dc,0.4,16), a merged IRN with dd fixed at 0.4 and an average delay, dc, that was varied over trials in the region of the delays of the test stimulus. For example, IRNM(14.8,0.4,16) was made up of one IRN with a delay of 14.6 ms and one with a delay of 15.0 ms. We used a merged IRN as the comparison stimulus to minimize timbre differences between the test and comparison stimuli. On each trial, listeners were required to indicate whether the pitch of the second interval was higher, the same, or lower than that of the first interval. There was no trial-by-trial feedback. There were six test IRNMs with dd values of 0.4, 0.8, 1.2, 1.6, 2.4, or 3.2 ms.

Trials were grouped into sets of nine during which the test stimulus was fixed to simplify the task, and at the start of each set of nine trials, the test stimulus was played three times on its own. Within the set of nine trials, the average delay of the comparison stimulus, dc, was varied over a range of 1.8 ms in 0.2-ms steps. In one set of nine trials the dc range was centered on the shorter of the two delays in the test stimulus; in a counterbalancing set, it was centered on the longer of the two delays in the test stimulus. The 12 sets of trials generated in this way were presented as a group in a random order in one run. In a separate run the comparison stimuli were all shifted up 0.1 ms, so that the data from the combined set of 24 runs would have a delay resolution of 0.1 ms.

In one condition, the order of the trails within a set was randomized so that the pitch of the comparison stimulus was not predictable. However, the PS of these high-pass-filtered IRNMs is weak and sometimes the pitch is ambiguous, so this condition is relatively difficult. Accordingly, in another condition, the comparison stimuli were presented in order of their delay, with the initial delay being either longer than the longer delay of the test stimulus, or shorter than the shorter delay of the test stimulus. In these conditions, the listener could hear the pitch of the comparison stimulus approaching that of the test stimulus on successive trials which made it, arguably, easier to identify the matching point.

Three experienced listeners participated in the experiment. They were given several initial training runs with the cutoff of the highpass filter at 0.4 kHz to produce stimuli with stronger pitches. The entire experiment was then performed first with the high-pass cutoff at 0.4 kHz and then with it at 0.8 kHz, the value in the main experiment.

Psychometric functions were produced by assigning val-

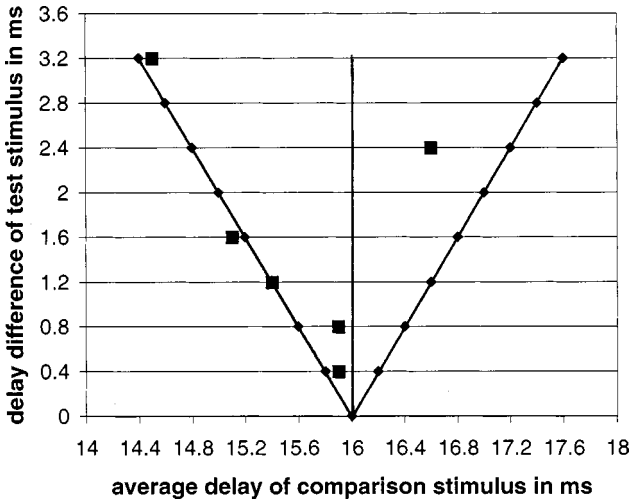

FIG. A1. Average pitch matches for three listeners to merged IRNs with delay differences in the range 0.4 to 3.2 ms. The base delay was 16 ms and the stimuli had 16 iterations. The left and right diagonal lines show the positions of matches to the shorter and longer delays of the merged IRN, respectively. The stimuli were highpass filtered at 0.8 kHz as in the main experiment.

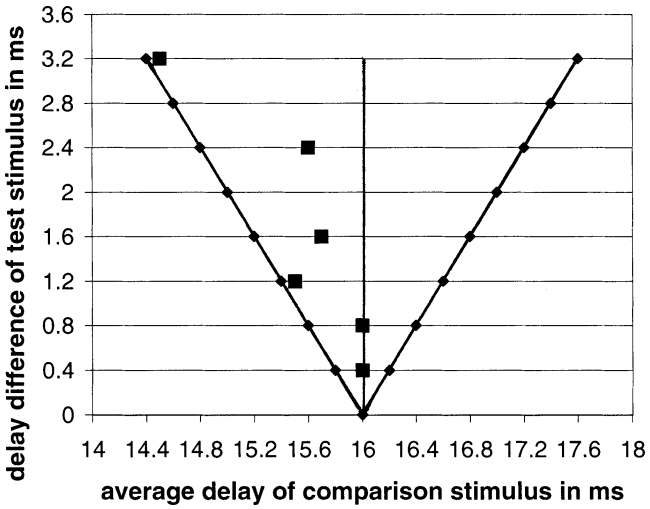

FIG. A2. Average pitch matches for three listeners to merged IRNs with delay differences in the range 0.4 to 3.2 ms. The base delay was 16 ms and the stimuli had 16 iterations. The left and right diagonal lines show the positions of matches to the shorter and longer delays of the merged IRN, respectively. The stimuli were high-pass filtered at 0.4 kHz.

ues of 1, 0.5, and 0 to responses indicating that the second interval contained the ''higher,'' ''same,'' or ''lower'' pitch, respectively, and plotting response value as a function of dc, the average delay of the comparison stimulus. Examination of the individual psychometric functions indicated that there was good agreement over conditions and across listeners for values of dd up to 1.2 ms. Consequently, the data were averaged across listeners and over procedures (blocked versus random) and psychometric functions were fitted to the average data by eye to determine the average pitch match for each delay difference. The pitch match was taken to be the value of dc where the value of the psychometric function was 0.5.

2. Results for small dd and the higher filter cutoff

The pitch matches for the condition with the high-pass cutoff of the filter at 0.8 kHz are presented by squares in Fig. A1. The ordinate is the delay difference of the test stimulus, IRNM(16,dd,16) and the abscissa is the average delay of the comparison stimulus, dc, that produced a pitch match. The vertical line at 16 ms is where pitch matches occur if listeners match to the average of the two delays in the test stimulus. The negative diagonal to the left of the vertical line is where they occur if listeners match to the shorter of the delays in the test stimulus (higher pitch), and the positive diagonal is where they occur if listeners match to the longer of the two delays (lower pitch).

The data show that, when the delay difference is small (0.4 or 0.8 ms), listeners matched to a value just below the average delay of the test stimulus (squares at 15.9 ms). When the delay difference is 1.2 or 1.6, listeners matched to the shorter of the delays in the test stimulus. In these four conditions, the average psychometric functions were steep, indicating (a) that there is no ambiguity in the match and (b) that all three listeners produced the same match. This was true even in those runs where the pitch of the comparison stimulus started well below the pitch of the longer delay and progressed regularly upwards through the region of the longer delay; listeners continued to indicate that the comparison pitch was lower than the test pitch up until it reached the region of the shorter delay (higher pitch). With regard to the perceived pitch in the main experiment of the paper, this indicates that there was one dominant pitch in all conditions of that experiment. When the delay difference was 0.1, listeners were most probably hearing the pitch associated with the average of the two delays (1/16 ms). When the delay difference was 1.1, they were most probably hearing the pitch associated with the shorter of the two delays (1/14.9 ms).

These pitch data are consistent with the modified ACG model in which the time constant of the low-pass filters is 0.2 ms. Consider the summary ACG for the IRNM(16,1.1,16) when tc is 0.2 in the left-hand column of Fig. 4. The peaks of the two component delays are largely merged into one broad-topped peak. A close examination, however, reveals that there are two, minor, local maxima on top of the broad peak, and the one associated with the shorter delay (on the left) is higher than the one associated with the longer delay, due to the gradual decline in the ACG function with increasing lag. Thus, strictly speaking, when tc is on the order of 0.2, the ''first peak in the SC'' does actually occur at the shorter delay, and this could be used to explain listeners matching to the shorter delay. The difference between the heights of the local maxima is small, and to explain the dominance of the higher pitch, one would probably need to postulate that the difference is enhanced in a subsequent stage of processing. For present purposes, however, it is sufficient to note that the model is not inconsistent with the data of the pilot study.

3. Results for small dd and the lower filter cutoff

When the cutoff of the low-pass filter is reduced to 0.4 kHz, the pitch strength increases; the matching pitch values,

however, are similar to those with the higher cutoff as shown in Fig. A2. When dd is small (0.4 or 0.8 ms), the matches are at the average delay of the comparison stimulus, 16 ms, and when dd is 1.2 ms, the match is 15.5 ms, close to the shorter delay of this merged IRN, 15.4 ms. Again the psychometric functions are steep for these conditions, indicating that the listeners heard one dominant pitch and it was the same for all of them. When dd was 1.6 ms, two of the listeners produced inconsistent matching to comparison stimuli with delays between the two delays of the merged IRN, indicating that the pitch was ambiguous. The third listener matched consistently to the shorter delay. The results suggest that the dominance of the pitch associated with the first peak is less than complete with delays of 1.6 ms or more, for some listeners.

4. Results for larger dd

All of the listeners matched to the shorter delay in both filter conditions when dd was 3.2 ms, and the psychometric functions are steep, indicating that the pitch of the shorter delay dominated the perception. However, when dd was 2.4 ms and dc was between the delays of the test stimulus, the matching varied with listener, filter condition, and procedure. The one consistent aspect of the data occurred with the high-pass-filter cutoff at 0.4 kHz: in this case, when dc progressed regularly from shorter to longer delays, all three listeners matched to the shorter delay, and when it progressed regularly from longer to shorter delays, all three listeners matched to the longer delay. It is this pattern of matching that the procedure was intended to reveal, but this is the only condition in which it occurred consistently. When the order of the comparison stimuli was random and dc was between the delays of the test stimulus, the data were inconsistent and the psychometric functions were relatively shallow. For large dd, then, it appears that the stimulus is capable of eliciting two different matches, but, on any one presentation, the perception seems to settle on one of the two pitches and it is difficult, if not impossible, to switch attention voluntarily to the other pitch.

[1]Release 8.2 is the current default version of the AIM software package which is available on the internet at http://www.mrc-cbu.cam.ac.uk/personal/roy.patterson/aim or by anonymous ftp from ftp.mrc-cbu.cam.ac.uk.

Bilsen, F. A., and Ritsma, R. J. (**1970**). ''Some parameters influencing the perceptibility of pitch,'' J. Acoust. Soc. Am. **47**, 469–476.

Griffiths, T. D., Beuchel, C., Frackowiak, R. S. J., and Patterson, R. D. (**1998**). ''Analysis of temporal structure in sound by the brain,'' Nat. Neurosci. **1**, 422–427.

Houtsma, A. J. M., and Smurzynski, J. (**1990**). ''Pitch identification and discrimination for complex tones with many harmonics,'' J. Acoust. Soc. Am. **87**, 304–310.

Johnson, D. H. (**1980**). ''The relationship between spike rate and synchrony in responses of auditory-nerve fibers to single tones,'' J. Acoust. Soc. Am. **68**, 1115–1122.

Licklider, J. C. R. (**1951**). ''A duplex theory of pitch perception,'' Experientia **7**, 128–133.

Meddis, R. (**1986**). ''Simulation of mechanical to neural transduction in the auditory receptor,'' J. Acoust. Soc. Am. **79**, 702–711.

Meddis, R., and Hewitt, M. J. (**1991**). ''Virtual pitch and phase sensitivity of a computer model of the auditory periphery: I. Pitch identification,'' J. Acoust. Soc. Am. **89**, 2866–2882.

Patterson, R. D. (**1994**). ''The sound of a sinusoid: Spectral models,'' J. Acoust. Soc. Am. **96**, 1409–1418.

Patterson, R. D., and Wightman, F. L. (**1976**). ''Residue pitch as a function of component spacing,'' J. Acoust. Soc. Am. **59**, 1450–1459.

Patterson, R. D., Allerhand, M., and Giguere, C. (**1995**). ''Time-domain modelling of peripheral auditory processing: A modular architecture and a software platform,'' J. Acoust. Soc. Am. **98**, 1890–1894.

Patterson, R. D., Handel, S., Yost, W. A., and Datta, A. J. (**1996**). ''The relative strength of the tone and noise components in iterated rippled noise,'' J. Acoust. Soc. Am. **100**, 3286–3294.

Patterson, R. D., Robinson, K., Holdsworth, J., McKeown, D., Zhang, C., and Allerhand, M. (**1992**). ''Complex sounds and auditory images,'' in *Auditory Physiology and Perception, Proceedings of the 9th International Symposium on Hearing*, edited by Y. Cazals, L. Demany, and K. Horner (Pergamon, Oxford), pp. 429–446.

Ritsma, R. J. (**1967**). ''Frequencies dominant in the perception of the pitch of complex sounds,'' J. Acoust. Soc. Am. **42**, 191–198.

Russell, I., and Palmer, A. (**1992**). ''Filtering due to the inner hair-cell membrane properties and its relation to the phase-locking limit in cochlear nerve fibers,'' in *Auditory Physiology and Perception, Proceedings of the 9th International Symposium on Hearing*, edited by Y. Cazals, L. Demany, and K. Horner (Pergamon, Oxford), pp. 199–207.

Weiss, T. F., and Rose, C. (**1988a**). ''Stages of degradation of timing information in the cochlea: A comparison of hair-cell and nerve-fiber responses in the alligator lizard,'' Hear. Res. **33**, 167–174.

Weiss, T. F., and Rose, C. (**1988b**). ''A comparison of synchronization filters in different auditory receptor organs,'' Hear. Res. **33**, 175–180.

Yost, W. A. (**1996**). ''The pitch strength of iterated rippled noise,'' J. Acoust. Soc. Am. **100**, 3329–3335.

Yost, W. A. (**1997**). ''Pitch strength of iterated rippled noise when the pitch is ambiguous,'' J. Acoust. Soc. Am. **101**, 1644–1648.

Yost, W. A., Patterson, R. D., and Sheft, S. (**1996**). ''A time domain description for the pitch strength of iterated rippled noise,'' J. Acoust. Soc. Am. **99**, 1066–1078.

Yost, W. A., Patterson, R. D., and Sheft, S. (**1998**). ''The role of the envelope in processing iterated rippled noise,'' J. Acoust. Soc. Am. **104**, 2349–2361.

Effects of ipsilateral and contralateral precursors on the temporal effect in simultaneous masking with pure tones

Sid P. Bacon[a] and Eric W. Healy
Psychoacoustics Laboratory, Department of Speech and Hearing Science, Arizona State University, Tempe, Arizona 85287-1908

(Received 1 September 1999; revised 5 November 1999; accepted 26 November 1999)

In tone-on-tone masking, thresholds often decrease as the onset of the signal is delayed relative to the onset of the masker, especially when the frequency of the masker is higher than the frequency of the signal. This temporal effect was studied here by using a tonal ''precursor,'' whose offset preceded the onset of the tonal masker (and signal). Under the right conditions, the precursor can reduce or eliminate the temporal effect by decreasing the threshold for a signal at masker onset, presumably for the same reason that the threshold decreases as a signal is delayed relative to the onset of a masker. In the present study, the frequency of the signal was 4000 Hz, and the frequency of the masker and precursor was typically 5000 Hz. In experiment 1, the precursor was presented to the ear receiving the masker and signal (ipsilateral precursor); in experiment 2, it was presented to the opposite ear (contralateral precursor). The results from experiment 1 can be summarized as follows: the ipsilateral precursor (a) reaches its maximum effectiveness (in reducing the temporal effect) for precursor durations of 200–400 ms; (b) is ineffective once the delay between its offset and the onset of the masker reaches about 50–100 ms; (c) is generally ineffective when its level is 10 or more dB lower than the level of the masker, but is effective when its level is equal to or greater than the level of the masker; and (d) becomes progressively less effective as its frequency is either increased or decreased relative to the frequency of the masker. The results from experiment 2 can be summarized simply by stating that the contralateral precursor is ineffective in reducing the temporal effect. These results suggest that the effect of the precursor may be mediated peripherally.
 [S0001-4966(00)01003-1]

PACS numbers: 43.66.Dc, 43.66.Mk, 43.66.Ba [DWG]

INTRODUCTION

Numerous investigators have shown that the threshold for a brief signal can be higher if that signal is presented near the beginning of a longer duration masker than if it is presented well after masker onset (e.g., Samoilova, 1959; Scholl, 1962; Zwicker, 1965a, b; Elliott, 1965, 1967, 1969; Green, 1969; Fastl, 1976, 1977, 1979; Bacon and Viemeister, 1985b; McFadden and Wright, 1990, 1992; Schmidt and Zwicker, 1991; Wright, 1997). The masker that is typically used to observe this temporal effect is either a broadband noise or a tone; the broadband noise maskers usually overlap the signal spectrally, whereas the tonal maskers usually do not. The effect with broadband noise maskers is usually termed ''overshoot,'' whereas that with tonal maskers is known by a variety of names, including overshoot. In the present paper, we refer to the phenomenon—regardless of masker type—simply as a temporal effect. As yet, a satisfactory understanding of the mechanisms underlying the temporal effect does not exist, nor is it even clear whether the underlying processes are the same for broadband and tonal maskers.

There are some similarities between the results obtained with the two types of masker that could be taken as evidence that the mechanisms underlying the temporal effect with the two are the same. For example, the time course of the effect—determined by measuring the threshold for a brief signal as a function of its temporal position within the masker—is similar for noise and tonal maskers (for noise: Zwicker, 1965a, b; Elliott, 1965, 1969; Fastl, 1976; for tones: Green, 1969; Bacon and Viemeister, 1985b; Bacon and Moore, 1986a). Moreover, for both types of masker, the existence of masker energy at frequencies above the signal frequency appears to be most important (for noise: McFadden, 1989; Schmidt and Zwicker, 1991; Bacon and Smith, 1991; Carlyon and White, 1992; Overson *et al.*, 1996; for tones: Bacon and Viemeister, 1985a, b; Bacon and Moore, 1986b). Finally, the temporal effect with both types of masker is reduced by cochlear hearing loss (for noise: Carlyon and Sloan, 1987; Champlin and McFadden, 1989; McFadden and Champlin, 1990; Bacon and Takahashi, 1992; for tones: Bacon *et al.*, 1989; Kimberly *et al.*, 1989).

However, there are also some differences in the results with broadband and tonal maskers that could be taken as evidence that the mechanisms underlying the temporal effect with the two types of masker are different. For example, the effect with broadband maskers is considerably larger at high than at low signal frequencies (Zwicker, 1965a; Fastl, 1976; Bacon and Takahashi, 1992), whereas the effect with tonal maskers is essentially independent of signal frequency (Bacon and Moore, 1986a). In addition, the effect with broadband maskers requires fairly short signals (Fastl, 1976), whereas the temporal effect with tonal (or off-frequency narrow-band noise) maskers has been observed with both

[a]Electronic mail: spb@asu.edu

short (e.g., Bacon and Viemeister, 1985a, b) and long (Viemeister, 1980; McFadden and Wright, 1992) signals. Finally, the effect with broadband maskers declines at high masker levels (Bacon, 1990), whereas the effect with tonal maskers continues to increase or reaches an asymptote at high masker levels (Green, 1969; Bacon and Viemeister, 1985a).

One of the most popular explanations for the temporal effect in simultaneous masking is peripheral adaptation (Green, 1969; Viemeister, 1980; Bacon and Viemeister, 1985a, b; Bacon and Smith, 1991). This is based on the fact that, at the level of the auditory nerve, the response to an increment in level (the signal) is independent of where in time that increment occurs, whereas the initially large response to a pedestal (the masker) declines or adapts over time (Smith and Zwislocki, 1975; Smith, 1977, 1979). Thus, the neural signal-to-masker ratio increases with time. Although appealing, this explanation cannot account for various aspects of the results, such as: the temporal effect with tonal maskers is largest for maskers higher in frequency than the signal (Bacon and Viemeister, 1985a, b); the effect with noise maskers depends upon frequency regions outside the critical band centered at the signal frequency (Zwicker, 1965b; McFadden, 1989; Bacon and Smith, 1991; Schmidt and Zwicker, 1991; Carlyon and White, 1992); and the size of the temporal effect is typically much larger than the 3–5 dB that is predicted on the basis of neural adaptation (e.g., Zwicker, 1965a, b; Viemeister, 1980; Bacon and Viemeister, 1985a; McFadden, 1989; Bacon, 1990).

Others have argued that the ''cochlear amplifier'' is somehow involved in the temporal effect (Champlin and McFadden, 1989; Kimberley *et al.*, 1989; McFadden and Champlin, 1990; von Klitzing and Kohlrausch, 1994). This is based primarily on the fact that temporary hearing loss due to aspirin ingestion (McFadden and Champlin, 1990) or acoustic overstimulation (Champlin and McFadden, 1989) as well as permanent sensorineural hearing loss (Kimberley *et al.*, 1989; Bacon *et al.*, 1989; Bacon and Takahashi, 1992) significantly reduces the temporal effect. However, given that the action of the cochlear amplifier itself is essentially instantaneous, and apparently does not diminish during the course of (nondamaging) stimulation, the amplifier itself—or even in combination with peripheral adaptation—cannot completely account for the temporal effect.

Recently, it has been suggested that the efferent system may be involved in the temporal effect with broadband noise maskers (Schmidt and Zwicker, 1991; Turner and Doherty, 1997), presumably through the influence of neurons from the medial olivocochlear system on the outer hair cells (cochlear amplifier). The majority of these neurons responds best to ipsilateral stimulation, with a minority responding best to contralateral stimulation (Liberman, 1988). The efferent system requires about 200 ms to reach its maximum effectiveness (e.g., Warren and Liberman, 1989), and thus its time course is consistent with the time course of the temporal effect. Furthermore, physiological experiments conducted at the level of the auditory nerve (Kawase and Liberman, 1993; Kawase *et al.*, 1993) have demonstrated that activation of the efferent system can enhance the neural response to a tonal signal embedded in noise. Thus, it is possible that the decrease in threshold with increasing signal delay reflects the relatively slow activation of the efferent system. Turner and Doherty (1997) conducted a psychophysical experiment to evaluate this possibility. They measured the temporal effect both with and without a contralateral ''precursor,'' a 200-ms broadband noise (presented to the ear opposite that receiving the signal and masker) whose offset preceded the onset of their broadband masker by 10 ms. Their precursor reduced or eliminated the temporal effect by reducing the threshold for a signal near masker onset (it had no effect when the signal was presented in the temporal center of their 400-ms masker). Although many others had previously shown that a precursor can reduce or eliminate the temporal effect with broadband maskers (e.g., Zwicker, 1965a; McFadden, 1989; Bacon and Smith, 1991; Overson *et al.*, 1996), the precursor in those studies was always presented to the ipsilateral ear, and thus the effect of the precursor could have been mediated at least partly by, for example, peripheral adaptation. In Turner and Doherty's study, however, because the precursor was presented to the contralateral ear, its effect could not be mediated via peripheral adaptation.

To date, no one has used precursors—ipsilateral or contralateral—with tonal maskers.[1] Thus, the purpose of the present study was to examine in detail the effects of both ipsilateral and contralateral precursors on temporal effects with tonal maskers, with the hope of providing additional insight into the processing underlying this temporal effect. In a companion paper (Bacon and Liu, submitted), we describe our work on the influence of ipsilateral and contralateral precursors on the temporal effect with broadband noise maskers.

I. GENERAL METHOD

A. Apparatus and stimuli

All stimuli were digitally generated and produced at a 50-kHz sampling rate using a digital array processing card (TDT AP2) and digital-to-analog converter, or DAC (TDT DD1). In conditions without a precursor, the signal (quiet thresholds) or signal and masker (masked thresholds) were presented through a single channel of the DAC. When the precursor was presented to the ipsilateral ear, the precursor, masker, and signal were presented through that same single channel. When the precursor was presented to the contralateral ear, the precursor was presented through a second channel. The output of each channel was low-pass filtered at 8 kHz (TDT FT6), attenuated (TDT PA4), and routed via a headphone buffer (TDT HB6) to a TDH-49P headphone mounted in an MX/51 cushion.

The signal was a 4000-Hz tone; its duration was 20 ms. Unless stated otherwise, the masker was a 5000-Hz tone with a duration of 400 ms. This masker-signal frequency ratio (1.25) is one where the temporal effect is usually maximal (Bacon and Viemeister, 1985a; Bacon and Moore, 1986a). The signal was presented either at the beginning (0-ms delay) or in the temporal center (190-ms delay) of the masker; the difference between those two thresholds defines the magnitude of the temporal effect. The precursor was typically a 5000-Hz tone; its duration was either varied systematically

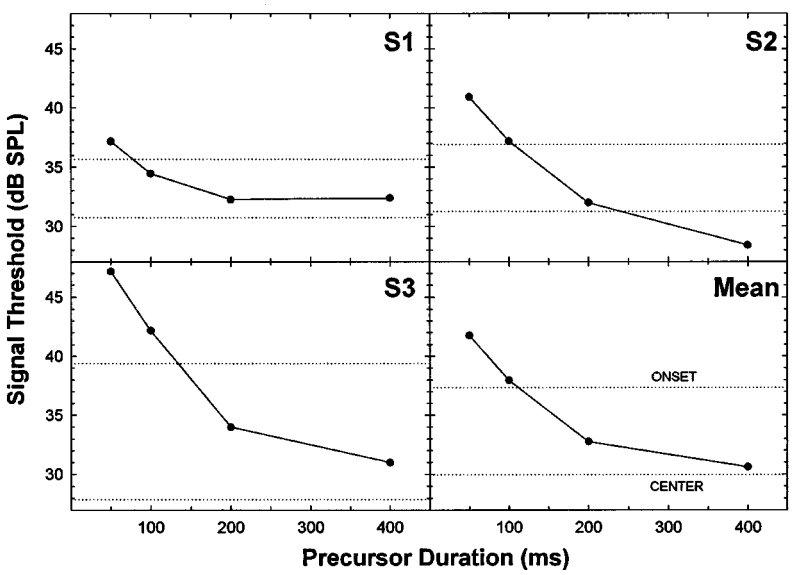

FIG. 1. The threshold for a 20-ms signal presented at the beginning of a 400-ms masker is shown as a function of the duration of a preceding precursor; there was no delay between precursor offset and masker onset. The signal frequency was 4000 Hz, and the masker and precursor frequency was 5000 Hz. The horizontal dotted lines indicate the threshold without a precursor, in which case the signal was presented at the onset (top line) or in the temporal center (bottom line) of the masker. The quiet threshold for the signal was 18.3, 24.4, and 17.1 dB SPL for subjects S1, S2, and S3, respectively.

(experiment 1a) or was fixed at 400 ms. The delay between the offset of the precursor and onset of the masker was either varied systematically (experiment 1b) or was fixed at 0 ms. Throughout, all stimulus durations include 10-ms $\cos^2$ rise/fall times, and all durations and delays are determined from 0-voltage points. The level of the signal was varied adaptively via the array processor. Unless otherwise stated (see experiment 1c), the levels of the masker and precursor were fixed at 80 dB SPL. A similar set of conditions in which the signal was at 1000 Hz and the masker and precursor were at 1250 Hz is described in the Appendix.

B. Procedure

The conditions within a given experiment were tested in random order. Testing was completed in a single-walled, sound-attenuating chamber located within an acoustically treated room. An adaptive, two-interval forced-choice paradigm was used with a three-down, one-up decision rule that tracked 79.4% correct (Levitt, 1971). The signal was presented in one of the two intervals (chosen at random), and the subjects' task was to choose the interval that contained the signal by pressing one of two buttons on a response panel. Lights were used to indicate when the signal might occur and to provide correct-answer feedback. The time between the two observation intervals always included 500 ms of silence. A run consisted of 12 reversals; the threshold estimate for a given run was the mean level at the last 10 reversals. The initial step size of 5 dB was reduced to 2 dB after the second reversal. Runs were discarded on the rare occasions when the standard deviation of the threshold estimate was greater than 5 dB. Three threshold estimates, obtained on separate days, were averaged to produce a threshold for a given condition. If the standard deviation of this average was greater than 3 dB, an additional estimate was obtained and included in the average. This continued until the standard deviation was less than 3 dB, or a total of six estimates was obtained and averaged. Most (96%) of the thresholds obtained here had a standard deviation less than 3 dB.

C. Subjects

Three individuals participated. Of these, two were female (S2 and S3) and one was male (S1). They ranged in age from 21–33 years, and had thresholds of 15 dB HL or lower (ANSI, 1989) for octave test frequencies from 500 to 8000 Hz. The subjects had at least 3 h of practice prior to data collection. Except for S1 (the second author), the subjects were paid for their participation.

II. EXPERIMENT 1: IPSILATERAL PRECURSORS

The first experiment explored various aspects of the effects of ipsilateral precursors. In particular, we examined the effects of precursor duration (experiment 1a), precursor-masker delay (experiment 1b), relative precursor level (experiment 1c), and relative precursor frequency (experiment 1d). The purpose of this experiment was to determine whether ipsilateral precursors reduce the temporal effect with tonal maskers, and to explore the conditions under which this occurs. This experiment will thus provide data for comparison with contralateral tonal precursors (experiment 2), and for comparison with comparably obtained data in the literature with noise maskers and ipsilateral noise precursors.

A. Experiment 1a: Precursor duration

1. Rationale and conditions

The purpose of this experiment was to assess the effect of precursor duration, and to determine the duration that provides maximum effectiveness. Thresholds were measured for the signal positioned at the beginning or the temporal center of the masker, both with and without a precursor. When present, the duration of the precursor was 50, 100, 200, or 400 ms. There was no delay between the offset of the precursor and the onset of the masker.

2. Results

The individual and mean results are shown separately in Fig. 1. Within each panel, the dotted horizontal lines represent the thresholds obtained without a precursor, where the

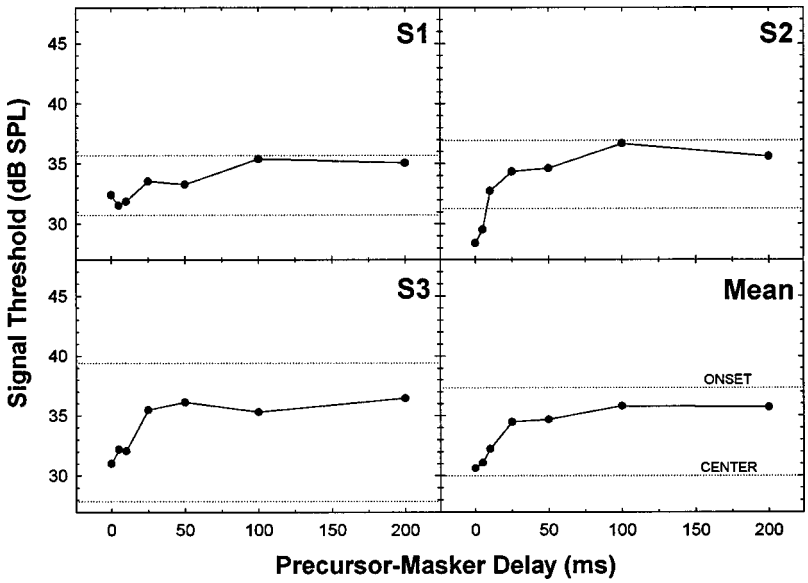

FIG. 2. As Fig. 1, except the threshold is shown as a function of the precursor–masker delay. The precursor duration was 400 ms.

signal delay was either 0 ms (top line) or 190 ms (bottom line). The magnitude of the temporal effect (difference between these two thresholds) varies across subjects from about 5 to 12 dB, and is about 7 dB on average. The magnitude of the effect and the size of the variability across subjects is comparable to that seen by others (e.g., Bacon and Viemeister, 1985b; Bacon and Moore, 1986a). The circles in Fig. 1 indicate how the threshold for a signal at the beginning of the masker (0-ms delay) is affected by the precursor. Thresholds decrease markedly as the duration of the precursor increases from 50 to 200 ms, and then either remain constant (S1) or decrease a bit more (S2 and S3) as the duration increases from 200 to 400 ms. The time course of this effect is similar to that observed when measuring the threshold for a brief signal as a function of the temporal position of that signal within a longer duration masker (Bacon and Viemeister, 1985b; Bacon and Moore, 1986a), as would be expected. These results are also broadly similar to the results obtained with both noise (Carlyon, 1987; Bacon and Smith, 1991) and harmonic complex (Viemeister, 1980) precursors and maskers.

For all subjects, the 50-ms precursor elevated thresholds relative to the no-precursor condition by about 2 to 8 dB (compare the left-most circle with the top dotted line), perhaps as a result of increasing the difficulty of the listening task [i.e., the transient nature of the brief precursor may have made it more difficult to detect the brief signal (see Bacon and Moore, 1987)]. The 400-ms precursor, on the other hand, reduced the threshold to a value similar to that obtained in the no-precursor condition when the signal was presented in the temporal center of the masker (compare the right-most circle with the bottom line).[2] Further, because the 400-ms precursor had no appreciable effect on threshold when the signal was presented in the temporal center of the masker (data not shown, but average thresholds changed by less than 0.3 dB), these results indicate that a 400-ms precursor effectively eliminates the temporal effect with tonal maskers. For this reason, a 400-ms precursor was used in the remaining experiments.

B. Experiment 1b: Precursor–masker delay

1. Rationale and conditions

The purpose of this experiment was to determine how long it would take to ''recover'' from the effect of the precursor. The precursor had a duration of 400 ms, and the onset of the masker followed the offset of the precursor by 0, 5, 10, 25, 50, 100, or 200 ms. The signal was positioned at the beginning of the masker.

2. Results

The results are shown in Fig. 2. The dotted lines are replotted from Fig. 1, as is the point at the 0-ms delay. In general, the threshold increases as the precursor–masker delay increases from 0 to 100 ms, but then changes very little thereafter (for S3, threshold changes very little for delays beyond 25 ms). At the longest delays, the threshold is essentially equal to the threshold obtained without a precursor (S1 and S2) or 2–3 dB below it (S3), indicating that at this delay the precursor has little effect. The time course of this recovery is similar to that observed previously with noise precursors and maskers (Zwicker, 1965a; Elliott, 1969; Carlyon, 1987; Bacon and Smith, 1991; Overson *et al.*, 1996; but see McFadden, 1989), although it is considerably shorter than the recovery observed by Viemeister (1980) using an (incomplete) harmonic complex for a precursor and masker.

C. Experiment 1c: Relative precursor level

1. Rationale and conditions

The purpose of this experiment was to determine whether the effectiveness of the precursor is influenced by its relative level. The duration of the precursor was 400 ms, and the precursor–masker delay was 0 ms; the signal was presented at the beginning of the masker (0-ms delay). The level of the masker was 70 or 80 dB SPL, and the level of the precursor was less than, equal to, or greater than the level of the masker. The lower masker level was included to allow for a larger range of precursor levels greater than the masker

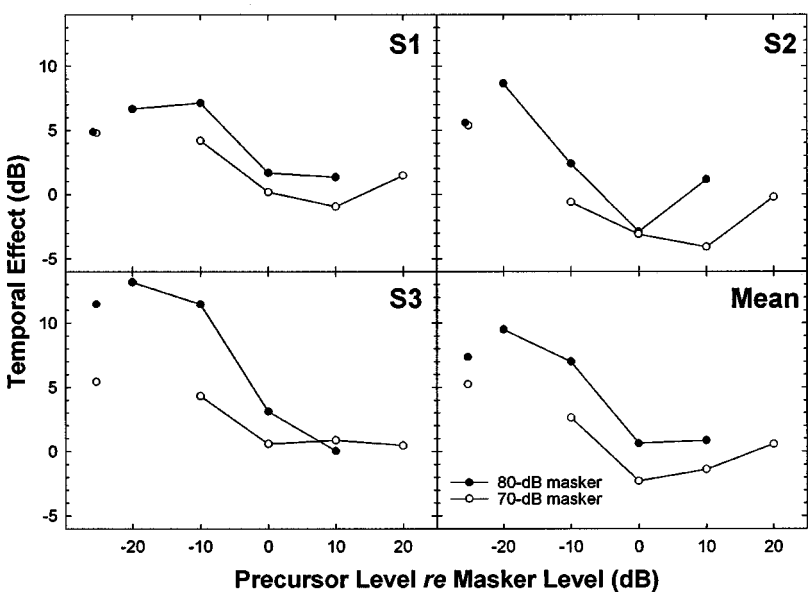

FIG. 3. The size of the temporal effect is shown as a function of the level of the precursor relative to the level of the masker. The temporal effect is defined as the difference in the threshold for a 20-ms signal presented at the beginning of the 400-ms masker (and preceded by a precursor) and the threshold for the signal presented in the temporal center of the masker (but without a preceding precursor). The signal frequency was 4000 Hz, and the masker and precursor frequency was 5000 Hz. The precursor duration was 400 ms, and the precursor–masker delay was 0 ms. The masker level was 80 dB SPL (filled circles) or 70 dB SPL (unfilled circles). The unconnected symbols to the left indicate the temporal effect obtained without a precursor.

level. In particular, we did not wish to use a precursor level greater than 90 dB SPL, and thus the lower masker level allowed a maximum relative level of 20 dB.

2. Results

The results for both masker levels are plotted in Fig. 3 in terms of the size of the temporal effect at the various precursor levels. The temporal effect is defined as the difference between the threshold at the onset of the masker (with a precursor) and the threshold in the temporal center of the masker (but without a precursor). The unconnected points at the far left of each panel represent the size of the temporal effect without a precursor; it is either independent of masker level (S1 and S2) or larger at the higher level (S3). For the most part, the precursor is effective in largely reducing or eliminating the temporal effect only if its level is equal to or greater than the level of the masker. There is a tendency for the precursor to be somewhat less effective in reducing the temporal effect at a relative level of 20 dB as compared to 10 dB; this may reflect forward masking of the signal by the more intense precursor. Nevertheless, even at this higher relative level, the precursor reduces the temporal effect. The similar shape of the two curves within a panel suggests that it is the relative level, and not the absolute level, of the precursor that is important. These results are broadly similar to the results obtained in previous investigations using noise precursors and maskers (Zwicker, 1965a; Carlyon, 1987; Bacon and Smith, 1991; Hicks and Bacon, 1992; but see Carlyon, 1989).

D. Experiment 1d: Relative precursor frequency

1. Rationale and conditions

In experiments 1a–c, the precursor and masker had the same frequency as one another (5000 Hz), and hence the precursor could be viewed as an extension (backward in time) of the masker. The purpose of this experiment was to determine whether the precursor must have the same frequency as the masker to be effective. In this experiment, the frequency of the masker was fixed at 5400 Hz, and the frequency of the precursor was varied from three semitones below to four semitones above 5400 Hz. For each semitone separation, the corresponding frequency (in Hz) was as follows: −3.0, 4541; −2.0, 4811; −1.0, 5097; −0.5, 5246; 0.0, 5400; 0.5, 5558; 1.0, 5721; 2.0, 6061; 3.0, 6422; and 4.0, 6804. The masker frequency was chosen to be as high as possible while still producing at least 5 dB of masking for a signal in its temporal center. By having the highest possible masker frequency, a greater range of precursor frequencies below the masker frequency could be used without the precursor being too close in frequency to (and hence possibly masking) the signal. Precursor duration was 400 ms, and precursor–masker delay was 0 ms. The signal was presented at the beginning of the masker (0-ms delay).

2. Results

The results are shown in Fig. 4, where threshold is plotted as a function of the relative precursor frequency (in semitones). The dotted horizontal lines have the same meaning as in the previous figures, except these are now for the 5400-Hz masker. The temporal effect is smaller here than with the 5000-Hz masker (Figs. 1–3), ranging from about 4–6 dB. Although there are some slight individual differences, all subjects show a degree of tuning with regard to relative precursor frequency: the precursor is most effective (thresholds are lowest) when its frequency is either equal to the masker frequency or one to two semitones below it. These results indicate that the precursor need not be equal in frequency to the masker to be effective. The patterns in Fig. 4 are asymmetric, in that thresholds increase more rapidly as the precursor moves above the masker frequency than as the precursor moves below the masker frequency. The asymmetry is similar to that which is generally observed in peripheral auditory filtering at moderately high levels (i.e., the high-frequency side is sharper than the low-frequency side). By the time the precursor is either three semitones below the masker frequency or one to two semitones above it, the threshold in the presence of the precursor is similar to that

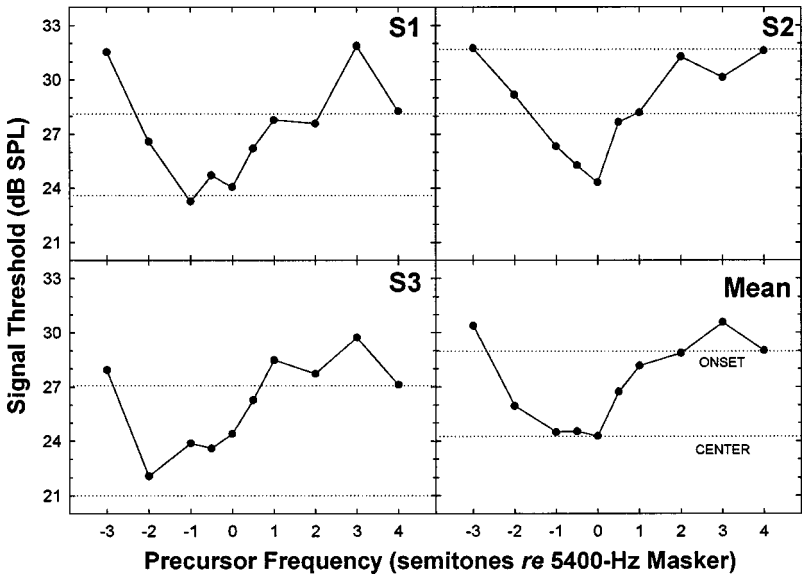

FIG. 4. The threshold for a 20-ms signal presented at the beginning of a 400-ms masker is shown as a function of the frequency of the precursor relative to the frequency of the masker, in semitones. The masker frequency was 5400 Hz, and the signal frequency was 4000 Hz. The actual precursor frequency, from left to right along the abscissa, was: 4541, 4811, 5097, 5246, 5400, 5558, 5721, 6061, 6422, and 6804 Hz. The precursor duration was 400 ms, and the precursor-masker delay was 0 ms. The horizontal dotted lines indicate the threshold without a precursor, in which case the signal was presented at the onset (top line) or in the temporal center (bottom line) of the masker.

obtained without the precursor (top dotted line), indicating that, in those conditions, the precursor is ineffective. On the low-frequency side, the precursor may be ineffective, in part, because it now forward masks the 4000-Hz signal.

III. EXPERIMENT 2: CONTRALATERAL PRECURSORS

A. Rationale and conditions

Turner and Doherty (1997) recently showed that a broadband noise precursor can reduce or eliminate the temporal effect with broadband noise maskers when the precursor is presented to the ear opposite that receiving the masker and signal. The purpose of this experiment was to determine whether a similar effect could be observed with a tonal precursor and masker. The precursor and masker had a frequency of 5000 Hz, and the signal had a frequency of 4000 Hz. The duration of the precursor was 400 ms, and there was no delay between the offset of the precursor and the onset of the masker. The signal was presented at the beginning (0-ms delay) or in the temporal center (190-ms delay) of the masker.

Subjects received at least 1 h of practice with the contralateral precursor prior to data collection, and one additional practice run prior to each threshold estimate. These estimates were obtained over 3 separate days.

B. Results

The results are shown in Table I (precursor present), along with the results obtained in experiment 1 without a precursor (precursor absent). As can be seen, the contralateral precursor has little effect on threshold, whether the signal is presented at the beginning or in the temporal center of the masker. The threshold in the presence of the precursor tends to be within about 1.5 dB of that obtained without a precursor; the most notable exception is for S3 in the 0-ms condition, where the contralateral precursor increased threshold by 4.1 dB. The lack of a clear decrease in threshold for a signal at the beginning of the masker differs from the results in experiment 1 with an ipsilateral precursor. The results also differ from those of Turner and Doherty (1997) obtained with a broadband noise masker and contralateral broadband noise precursor.

IV. DISCUSSION

Although a considerable amount of research has focused on temporal effects with tonal maskers, no one has previously used tonal precursors to study these effects (but see footnote 1). Numerous investigators have, however, used noise precursors to examine temporal effects with broadband noise maskers (e.g., Zwicker, 1965a; McFadden, 1989; Bacon and Smith, 1991; Overson *et al.*, 1996), although, as mentioned in the Introduction, it is unclear whether the mechanisms underlying the temporal effects with the two types of masker are the same. The use of precursors provides certain advantages, in that they allow the examination of various properties of the temporal effect that would otherwise not be testable; indeed, only the information from experiment 1a could be obtained without precursors. The remainder of this section focuses on a discussion of possible mechanisms that might underlie the temporal effect with tonal maskers.

As discussed in the Introduction, it is unclear what mechanisms underlie the temporal effect with tonal maskers, although several possibilities have been proposed. The most popular explanation is adaptation of auditory-nerve fibers,

TABLE I. Results from experiment 2. The contralateral precursor was either absent (data from experiment 1) or present. Thresholds (in dB SPL) are given for the conditions where the signal was at the beginning (0-ms delay) or in the temporal center (190-ms delay) of the masker. The size of the temporal effect (in dB) is also given.

	Precursor absent			Precursor present		
	0	190	TE	0	190	TE
S1	35.7	30.7	5.0	36.9	29.5	7.4
S2	36.9	31.3	5.6	35.3	28.8	6.5
S3	39.4	27.9	11.5	43.5	27.7	15.8
Mean	**37.3**	**30.0**	**7.3**	**38.6**	**28.7**	**9.9**

but it has also been suggested that the temporal effect may be influenced by the cochlear amplifier and by the efferent system. These possibilities are not necessarily mutually exclusive.

The peripheral adaptation explanation depends on the fact that the neural signal-to-masker ratio at the level of an auditory-nerve fiber improves as a signal is delayed relative to the onset of a masker (Smith and Zwislocki, 1975; Smith, 1977, 1979). Although peripheral adaptation probably cannot, by itself, completely account for the temporal effect, certain aspects of the present results are consistent with an adaptation-based explanation. In particular, the temporal characteristics in terms of the growth and recovery are broadly similar to those seen at the level of the auditory nerve. For example, Harris and Dallos (1979) measured the response to a short-duration, fixed-level signal presented after a longer duration ''adaptor.'' The onset response to the signal was reduced by the adaptor. If we assume that, in the psychophysical experiments, the onset response to the masker is at least partly responsible for the higher threshold for a signal near masker onset, and that the precursor can reduce that onset response, then the physiological results of Harris and Dallos may be relevant to understanding how the precursor may influence the threshold for a signal near masker onset. Harris and Dallos measured the growth of their adaptation effect by varying the duration of their adaptor. The effectiveness of the adaptor increased with increasing adaptor duration up to about 100 ms. In the present study, the effectiveness of the precursor was complete or nearly complete for a precursor duration of about 200 ms. Harris and Dallos measured the recovery function by varying the delay between their adaptor and signal. The onset response to the signal was near its unadapted level for delays longer than 50 ms, consistent with the present results showing a nearly complete recovery of the temporal effect for precursor–masker delays of about 50–100 ms.

The effect of relative precursor level is also consistent with an adaptation-based explanation. If the precursor influences masked threshold by producing a certain amount of adaptation, then one would expect the amount of that adaptation to decrease with decreasing level. In the present study, the precursor was essentially ineffective when its level was 10 or more dB lower than the masker level. The precursor was maximally effective when its level was equal to or higher than the level of the masker. In some isolated cases (Fig. 3, S1 and S2 at a 70-dB masker level), the most effective precursor was 10 dB higher in level than the masker, possibly because the precursor was producing even more adaptation than when it was equal in level to the masker. At an even higher relative level (20 dB), however, the precursor often became less effective, possibly because it was now (forward) masking the signal.

The effect of relative precursor frequency is also consistent with an explanation based on adaptation. In particular, if one assumes that the precursor will be effective if it produces sufficient excitation at the masker frequency place, then the pattern of results seen in Fig. 4 can be understood in terms of spread of excitation. At a general level, the broader tuning towards the low-frequency side probably reflects the greater upward than downward spread of excitation from the precursor to the masker frequency. More specifically, the tendency for the precursor to be effective only when its frequency is from -2 to 0.5 semitones *re* the masker frequency may reflect the fact that only those precursor frequencies produce excitation at the masker frequency that is within 3 dB of the excitation produced by the 5400-Hz masker [as determined by an excitation pattern analysis based on Glasberg and Moore (1990)].

Although the present results are consistent with an explanation based on peripheral adaptation, certain aspects of the results in the literature are inconsistent with the possibility that the temporal effect is based solely on adaptation of auditory-nerve fibers. In particular, the effect is largest for maskers higher in frequency than the signal (Bacon and Viemeister, 1985a, b), despite the fact that the amount of neural adaptation is independent of stimulating frequency (Rhode and Smith, 1985). Also, the size of the effect is usually much larger than the 3–5 dB that is predicted on the basis of peripheral adaptation (e.g., Bacon and Viemeister, 1985a, b; Bacon and Moore, 1986a). Thus, it seems clear that some other processing must be involved.

The present study was motivated largely by the recent results of Turner and Doherty (1997), which suggested that the temporal effect with broadband noise maskers was influenced by the efferent system. They showed that a broadband precursor presented to the ear contralateral to that receiving the broadband masker and tonal signal could reduce or eliminate the temporal effect. The influence of the efferent system is presumably through the outer hair cells, as they are suspected of being important for the temporal effect (Champlin and McFadden, 1989; Kimberly *et al.*, 1989; McFadden and Champlin, 1990; Bacon and Takahashi, 1992; von Klitzing and Kohlrausch, 1994). The present study, however, did not find an effect of a contralateral precursor. The difference between the two studies is almost certainly not due to individual differences, as we have duplicated the difference in results between the two types of masker within a single subject (data not shown here). In particular, one subject in a companion paper with noise precursors and maskers (Bacon and Liu, submitted) was evaluated with the stimuli used here in experiment 2; that subject showed an effect of a contralateral precursor with noise but not with tones.

The lack of an effect with a contralateral tonal precursor could indicate one of two things. One possibility is that the efferent system is not involved, and that the temporal effect with tonal maskers is mediated peripherally, or at least at a level in the nervous system prior to where inputs from the two ears interact. Inasmuch as the efferent system may be involved in the temporal effect with broadband noise maskers, this would suggest that the mechanisms underlying the temporal effect with the two types of masker are at least somewhat different. As discussed in the Introduction, this possibility is suggested by several differences in the results with the two types of masker.

The other possibility is that the efferent system is involved with the temporal effect, but that the contralateral tonal precursor is ineffective in generating a sufficiently

strong response in those efferent neurons that synapse in the cochlea being stimulated by the masker and signal. The difference in effectiveness between ipsilateral and contralateral tonal precursors may reflect the fact that the majority of efferent neurons from the medial olivocochlear system respond best to ipsilateral stimulation (Liberman, 1988). More research is obviously needed in order to further clarify the precise mechanisms which underlie the temporal effect with both types of masker, and whether those mechanisms are the same.

ACKNOWLEDGMENTS

This research was supported by NIDCD Grant No. DC01376. We thank the two anonymous reviewers for their helpful comments on a previous version of this manuscript.

APPENDIX: OBSERVATIONS AT A SIGNAL FREQUENCY OF 1000 Hz

The original plan was to use a signal frequency of 1000 Hz. Data were collected from S1 at this frequency before we recruited and began testing the other subjects. His results are shown in Fig. A1. The levels and durations were similar to those in experiment 1, with the exception that the rise/fall times were doubled to 20 ms (and thus the signal duration was doubled to 40 ms, see below). The masker and precursor frequency was 1250 Hz (except when the effect of relative precursor frequency was evaluated). Panel (a) shows the effect of precursor duration, panel (b) the effect of precursor–masker delay, panel (c) the effect of relative precursor level (masker level of 80 dB SPL), and panel (d) the effect of relative precursor frequency (masker frequency of 1450 Hz; note the change in *y*-axis range). The results from this subject at 1000 Hz are similar to his results at 4000 Hz. Surprisingly, however, for the other two subjects the (ipsilateral) precursor was ineffective at this lower frequency. We tested three other subjects (including the first author) at a 1000-Hz signal frequency, using a 400-ms precursor and a 0-ms precursor–masker delay. None of the additional subjects (and thus only one of the six subjects tested) showed an effect of the precursor, other than that the precursor sometimes *elevated* threshold for a signal at masker onset. In contrast, when we recruited additional subjects (including the first author) to evaluate the generality of the effect for a 4000-Hz signal, the precursor lowered the threshold for a signal at masker onset in eight of the nine subjects (it had no effect in the ninth subject). Thus, the effect is clearly more common at the higher frequency.

The verbal reports of the subjects, as well as our own impressions, shed some light on these differences across frequency. In particular, the onsets and offsets at the higher test frequency sounded smoother than they did at the lower test frequency, and consequently the listening task with the precursor was much easier at the higher frequency. In fact, the precursor was only partially effective in eliminating the temporal effect for S1 at the lower frequency with the 10-ms rise/fall time; with a 20-ms rise/fall time, however, we obtained the data shown in Fig. A1. The perceptual differences at the two frequencies are probably related to the fact that the *relative* spectral spread of the stimulus is narrower at the higher frequency (where the relative spread is the width of the acoustic spectrum divided by the width of the critical band). Although this is obviously related to spectral splatter, we do not believe that the temporal effect *per se* is due to such splatter (see also Bacon and Viemeister, 1985a). The splatter due to gating the masker is the same whether a precursor is present or not; the fact that a precursor can eliminate the temporal effect indicates that splatter is not responsible for the temporal effect. The similarity in the results at 1000 and 4000 Hz for S1 strongly suggests that the mechanisms underlying the effect at the two frequencies are the same.

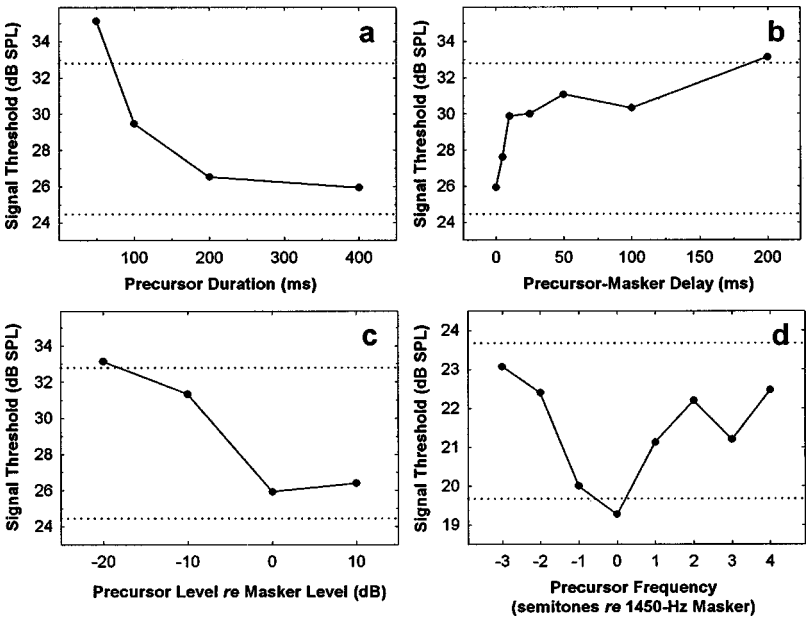

FIG. A1. The results for S1 with a signal frequency of 1000 Hz. The thresholds are for a 40-ms signal presented at the beginning of an 80-dB, 1250-Hz, 400-ms masker. The precursor was identical to the masker unless otherwise indicated. The precursor–masker delay was 0 ms unless otherwise indicated. The dotted lines in each panel have the same meaning as in Figs. 1, 2, and 4. Panel (a): Signal threshold as a function of precursor duration. Panel (b): Signal threshold as a function of precursor–masker delay. Panel (c): Signal threshold as a function of the level of the precursor relative to the level of the masker. Panel (d): Signal threshold as a function of the frequency of the precursor relative to the frequency of a 1450-Hz masker (note the change in *y*-axis range). The actual precursor frequency, from left to right along the abscissa, was: 1219, 1292, 1369, 1450, 1536, 1628, 1724, and 1827 Hz.

[1]In the context of a series of conditions, Viemeister (1980) examined the effect of a precursor on the temporal effect with a tonal masker (his condition E). However, in the condition he employed (800-Hz masker and precursor, 1000-Hz signal), there was no temporal effect. This is consistent with other studies (e.g., Bacon and Viemeister, 1985a) showing that the temporal effect with tonal maskers exists primarily when the masker is higher in frequency than the signal.

[2]For S2, the threshold in the presence of the 400-ms precursor was slightly, but consistently lower than the threshold obtained when the signal was in the temporal center of a masker not preceded by a precursor. This can be seen not only in Fig. 1, but also in Figs. 2–4. This suggests that a 190-ms masker-signal delay (20-ms signal temporally centered in a 400-ms masker) is not sufficiently long for this subject to achieve a ''steady-state'' masked threshold. This has been observed in some of the other subjects tested previously (e.g., Bacon and Viemiester, 1985b; Bacon and Moore, 1986a).

ANSI (**1989**). ANSI S3.6-1989, *Specifications for Audiometers* (American National Standards Institute, New York).

Bacon, S. P. (**1990**). ''Effect of masker level on overshoot,'' J. Acoust. Soc. Am. **88**, 698–702.

Bacon, S. P., Hedrick, M. S., and Grantham, D. W. (**1989**). ''Temporal effects in simultaneous pure-tone masking in subjects with high-frequency sensorineural hearing loss,'' Audiology **27**, 313–323.

Bacon, S. P., and Liu, L. (**1999**). ''Effects of ipsilateral and contralateral precursors on overshoot,'' J. Acoust. Soc. Am. (submitted).

Bacon, S. P., and Moore, B. C. J. (**1986a**). ''Temporal effects in simultaneous pure-tone masking: Effects of signal frequency, masker/signal frequency ratio, and masker level,'' Hear. Res. **23**, 257–266.

Bacon, S. P., and Moore, B. C. J. (**1986b**). ''Temporal effects in masking and their influence on psychophysical tuning curves,'' J. Acoust. Soc. Am. **80**, 1638–1645.

Bacon, S. P., and Moore, B. C. J. (**1987**). ''Transient masking and the temporal course of simultaneous tone-on-tone masking,'' J. Acoust. Soc. Am. **81**, 1073–1077.

Bacon, S. P., and Smith, M. A. (**1991**). ''Spectral, intensive, and temporal factors influencing overshoot,'' Q. J. Exp. Psychol. **43A**, 373–399.

Bacon, S. P., and Takahashi, G. A. (**1992**). ''Overshoot in normal-hearing and hearing-impaired subjects,'' J. Acoust. Soc. Am. **91**, 2865–2871.

Bacon, S. P., and Viemeister, N. F. (**1985a**). ''Simultaneous masking by gated and continuous sinusoidal maskers,'' J. Acoust. Soc. Am. **78**, 1220–1230.

Bacon, S. P., and Viemeister, N. F. (**1985b**). ''The temporal course of simultaneous tone-on-tone masking,'' J. Acoust. Soc. Am. **78**, 1231–1235.

Carlyon, R. P. (**1987**). ''A release from masking by continuous, random, notched noise,'' J. Acoust. Soc. Am. **81**, 418–426.

Carlyon, R. P. (**1989**). ''Changes in the masked thresholds for brief tones produced by prior bursts of noise,'' Hear. Res. **41**, 223–236.

Carlyon, R. P., and Sloan, E. P. (**1987**). ''The 'overshoot' effect and sensory hearing impairment,'' J. Acoust. Soc. Am. **82**, 1078–1081; See also J. Acoust. Soc. Am. **83**, 1193 (1988).

Carlyon, R. P., and White, L. J. (**1992**), ''Effect of signal frequency and masker level on the frequency regions responsible for the overshoot effect,'' J. Acoust. Soc. Am. **91**, 1034–1041.

Champlin, C. A., and McFadden, D. (**1989**), ''Reductions in overshoot following intense sound exposures,'' J. Acoust. Soc. Am. **85**, 2005–2011.

Elliott, L. L. (**1965**). ''Changes in the simultaneous masked threshold of brief tones,'' J. Acoust. Soc. Am. **38**, 738–746.

Elliott, L. L. (**1967**). ''Development of auditory narrow-band frequency contours,'' J. Acoust. Soc. Am. **42**, 143–153.

Elliott, L. L. (**1969**). ''Masking of tones before, during, and after brief silent periods in noise,'' J. Acoust. Soc. Am. **45**, 1277–1279.

Fastl, H. (**1976**). ''Temporal masking effects: I. Broad band noise masker,'' Acustica **35**, 287–302.

Fastl, H. (**1977**). ''Temporal masking effects: II. Critical band noise masker,'' Acustica **36**, 317–331.

Fastl, H. (**1979**). ''Temporal masking effects. III. Pure tone masker,'' Acustica **43**, 282–294.

Glasberg, B. R., and Moore, B. C. J. (**1990**). ''Derivation of auditory filter shapes from notched-noise data,'' Hear. Res. **47**, 103–138.

Green, D. M. (**1969**). ''Masking with continuous and pulsed sinusoids,'' J. Acoust. Soc. Am. **46**, 939–946.

Harris, D. M., and Dallos, P. (**1979**). ''Forward masking of auditory nerve fiber responses,'' J. Neurophysiol. **42**, 1083–1107.

Hicks, M. L., and Bacon, S. P. (**1992**). ''Factors influencing temporal effects with notched-noise maskers,'' Hear. Res. **64**, 123–132.

Kawase, T. K., Delgutte, B., and Liberman, M. C. (**1993**). ''Antimasking effects of the olivocochlear reflex. II. Enhancement of auditory-nerve responses to masked tones,'' J. Neurophysiol. **70**, 2533–2549.

Kawase, T. K., and Liberman, M. C. (**1993**). ''Antimasking effects of the olivocochlear reflex. I. Enhancement of compound action potentials to masked tones,'' J. Neurophysiol. **70**, 2519–2532.

Kimberley, B. P., Nelson, D. A., and Bacon, S. P. (**1989**). ''Temporal overshoot in simultaneous-masked psychophysical tuning curves from normal and hearing-impaired listeners,'' J. Acoust. Soc. Am. **85**, 1660–1665.

Levitt, H. (**1971**). ''Transformed up–down methods in psychoacoustics,'' J. Acoust. Soc. Am. **49**, 467–477.

Liberman, M. C. (**1988**). ''Response properties of cochlear efferent neurons: Monaural vs binaural stimulation and the effects of noise,'' J. Neurophysiol. **60**, 1779–1798.

McFadden, D. (**1989**). ''Spectral differences in the ability of temporal gaps to reset the mechanisms underlying overshoot,'' J. Acoust. Soc. Am. **85**, 254–261.

McFadden, D., and Champlin, C. A. (**1990**). ''Reductions in overshoot during aspirin use,'' J. Acoust. Soc. Am. **87**, 2634–2642.

McFadden, D., and Wright, B. A. (**1990**). ''Temporal decline of masking and comodulation detection differences,'' J. Acoust. Soc. Am. **88**, 711–724.

McFadden, D., and Wright, B. A. (**1992**). ''Temporal decline of masking and comodulation masking release,'' J. Acoust. Soc. Am. **92**, 144–156.

Overson, G. J., Bacon, S. P., and Webb, T. M. (**1996**). ''The effect of level and relative frequency region on the recovery of overshoot,'' J. Acoust. Soc. Am. **99**, 1059–1065.

Rhode, W. S., and Smith, P. H. (**1985**). ''Characteristics of tone-pip response patterns in relationship to spontaneous rate in cat auditory nerve fibers,'' Hear. Res. **18**, 159–168.

Samoilova, I. K. (**1959**). ''Masking of short tone signals as a function of the time interval between masked and masking sounds,'' Biofizika **4**, 550–558.

Schmidt, S., and Zwicker, E. (**1991**). ''The effect of masker spectral asymmetry on overshoot in simultaneous masking,'' J. Acoust. Soc. Am. **89**, 1324–1330.

Smith, R. L. (**1977**). ''Short-term adaptation in single auditory nerve fibers: Some poststimulatory effects,'' J. Neurophysiol. **40**, 1098–1112.

Smith, R. L. (**1979**). ''Adaptation, saturation, and physiological masking in single auditory-nerve fibers,'' J. Acoust. Soc. Am. **65**, 166–178.

Smith, R. L., and Zwislocki, J. J. (**1975**). ''Short-term adaptation and incremental responses in single auditory-nerve fibers,'' Biol. Cybern. **17**, 169–182.

Turner, C. W., and Doherty, K. A. (**1997**). ''Temporal masking and the 'active process' in normal and hearing-impaired listeners,'' in *Modeling Sensorineural Hearing Loss*, edited by W. Jesteadt (Erlbaum, Hillsdale, NJ), pp. 387–396.

Viemeister, N. F. (**1980**). ''Adaptation of masking,'' in *Psychophysical, Physiological, and Behavioural Studies in Hearing*, edited by G. Van den Brink and F. A. Bilsen (Delft University Press, Delft, The Netherlands), pp. 190–199.

von Klitzing, R., and Kohlrausch, A. (**1994**). ''Effect of masker level on overshoot in running- and frozen-noise maskers,'' J. Acoust. Soc. Am. **95**, 2192–2201.

von Scholl, H. (**1962**). ''Das dynamische Verhalten des Gehörs bei der Unterteilung des Schallspektrums in Frequenzgruppen,'' Acustica **12**, 101–107.

Warren III, E. H., and Liberman, M. C. (**1989**). ''Effects of contralateral sound on auditory-nerve responses. I. Contributions of cochlear efferents,'' Hear. Res. **37**, 89–104.

Wright, B. A. (**1997**). ''Detectibility of simultaneously masked signals as a function of masker bandwidth and configuration for different signal delays,'' J. Acoust. Soc. Am. **101**, 420–429.

Zwicker, E. (**1965a**). ''Temporal effects in simultaneous masking by white-noise bursts,'' J. Acoust. Soc. Am. **37**, 653–663.

Zwicker, E. (**1965b**). ''Temporal effects in simultaneous masking and loudness,'' J. Acoust. Soc. Am. **38**, 132–141.

Detection of quasitrapezoidal frequency and amplitude modulation

Aleksander Sek
Institute of Acoustics, Adam Mickiewicz University, 85 Umultowska, 61-614 Poznan, Poland

Brian C. J. Moore[a)]
Department of Experimental Psychology, University of Cambridge, Downing Street, Cambridge CB2 3EB, England

(Received 3 August 1999; accepted for publication 8 December 1999)

It has been proposed that the detection of frequency modulation (FM) of sinusoidal carriers can be mediated by two mechanisms; a place mechanism based on FM-induced amplitude modulation (AM) in the excitation pattern, and a temporal mechanism based on phase locking in the auditory nerve. The temporal mechanism appears to be ''sluggish'' and does not play a role for FM rates above about 10 Hz. It also does not play a role for high carrier frequencies (above about 5 kHz). This experiment provided a further test of the hypothesis that the effectiveness of the temporal mechanism depends upon the time spent close to frequency extremes during the modulation cycle. Psychometric functions for the detection of AM and FM were measured for two carrier frequencies, 1 and 6 kHz. The modulation waveform was quasitrapezoidal. Within each modulation period, P, a time T_{SS} was spent at each extreme of frequency or amplitude. The transitions between the extremes, with duration T_{trans} had the form of a half-cycle of a cosine function. The modulation rate was 2, 5, 10, or 20 Hz, giving values of P of 500, 200, 100, and 50 ms. T_{SS} varied from 0 ms (sinusoidal modulation) up to 160, 80, 40, or 20 ms, for rates of 2, 5, 10, and 20 Hz, respectively. The detectability of AM was not greatly affected by modulation rate or by the value of T_{SS}, except for a slight improvement with increasing T_{SS} for the lowest modulation rates; this was true for both carrier frequencies. For FM of the 6-kHz carrier, the pattern of results was similar to that found for AM, which is consistent with an excitation-pattern model of FM detection. For FM of the 1-kHz carrier, performance improved markedly with increasing T_{SS}, especially for the lower FM rates; there was no change in performance with T_{SS} for the 20-Hz modulation rate. The results are consistent with the idea that detection of FM of a 1-kHz carrier is partly mediated by a sluggish temporal mechanism. That mechanism benefits from greater time spent at frequency extremes of the modulation cycle for rates up to 10 Hz.
[S0001-4966(00)04003-0]

PACS numbers: 43.66.Fe, 43.66.Hg, 43.66.Ba [RVS]

INTRODUCTION

It has been proposed that the frequency discrimination of steady pulsed tones is largely based on temporal information (cues derived from phase locking) for frequencies up to 4–5 kHz (Moore, 1973a, b, 1974; Goldstein and Srulovicz, 1977; Sek and Moore, 1995; Moore, 1997; Micheyl *et al.*, 1998). Above 4–5 kHz, frequency discrimination is thought to depend on place mechanisms (Moore, 1973b; Sek and Moore, 1995). The mechanisms underlying the detection of frequency modulation (FM) of sinusoidal carriers are thought to depend on the modulation rate. For sinusoidal modulation with rates above about 10 Hz, detection is probably largely based on excitation-pattern cues (Zwicker, 1956; Zwicker and Fastl, 1990; Moore and Sek, 1994a, 1995; Sek and Moore, 1995; Saberi and Hafter, 1995). FM results in modulation of the excitation level at each place on the pattern, so the FM is effectively transformed into amplitude modulation (AM). Thus, the FM can be detected as AM, either by using information from the single point on the excitation pattern where the AM is greatest (Zwicker, 1956; Zwicker and Fastl, 1990) or by combining information from different parts of the excitation pattern (Moore and Sek, 1994a). For very low FM rates (around 2 Hz), temporal information may also play a role (Moore and Sek, 1995, 1996; Plack and Carlyon, 1995; Sek and Moore, 1995); the short-term pattern of phase locking can be used to estimate the momentary frequency, and changes in phase locking over time indicate that FM is present. A similar temporal mechanism probably plays a role in the detection of FM of the fundamental frequency ($F0$) of harmonic complex tones, when those tones are bandpass filtered so as to contain only unresolved harmonics (Plack and Carlyon, 1994, 1995; Shackleton and Carlyon, 1994; Carlyon *et al.* (submitted)). Indeed, for such tones, place information is not available at all, so subjects are forced to rely on temporal information.

The temporal mechanism may become less effective for modulation rates above about 5 Hz because it is ''sluggish,'' and cannot follow rapid changes in frequency. Consistent with this idea, thresholds for detecting FM of the $F0$ of harmonic complex tones containing only unresolved harmonics increase with increasing modulation rate over the

a)Electronic mail: bcjm@cus.cam.ac.uk

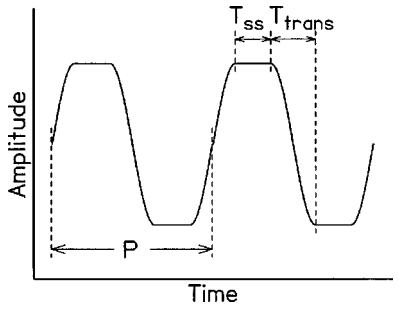

FIG. 1. Example of the waveform of a quasitrapezoidal modulator. The period is denoted by P, the duration of each steady state part by T_{SS}, and the duration of each transition by T_{trans}.

range 1 to 20 Hz, reaching 20% (defined as the peak deviation in $F0$ divided by the mean $F0$) for a modulation rate of 20 Hz (Carlyon *et al.* (submitted)). In the case of sinusoidal carriers, performance does not worsen so much with increasing modulation rate (Zwicker and Fastl, 1990; Moore and Sek, 1995, 1996; Sek and Moore, 1995), presumably because the place mechanism ''takes over'' from the temporal mechanism for modulation rates above about 5 Hz.

The temporal mechanism may become less effective for modulation rates of 5 Hz and above because the time spent at frequency extremes is too short for useful temporal information to be extracted. A long time at frequency extremes may be required because the temporal mechanism normally integrates information over a relatively long time window (Micheyl and Carlyon, 1998; White and Plack, 1998). To test this idea, we (Moore and Sek, 1995) measured psychometric functions for the detection of FM and AM using quasitrapezoidal modulation with a rate of 5 periods per second and carriers of 250, 1000, and 6000 Hz. The waveform of such a modulator is illustrated in Fig. 1. With quasitrapezoidal modulation, the stimuli spend more time at extremes of frequency or amplitude than is the case with sinusoidal modulation. We found that performance was better for 5-Hz trapezoidal modulation than for 5-Hz sinusoidal modulation. More importantly, for the two lower carrier frequencies only, the improvements were markedly greater for FM than for AM detection. This is consistent with the idea that the use of phase-locking information depends on the time that the stimuli spend at frequency extremes.

The experiment reported here is similar to that described above (Moore and Sek, 1995), but it extends that work in several ways. In our earlier work, we used only a single modulation rate (5 Hz) and compared sinusoidal modulation with quasitrapezoidal modulation in which, within each modulation period of 200 ms, 60 ms was spent at each extreme of frequency or amplitude. The transitions between the extremes had the form of a half-cycle of a cosine function, each transition lasting 40 ms. In the present experiment, we used modulation rates of 2, 5, 10, and 20 Hz. For each rate, the duration spent at each extreme of frequency or amplitude was varied over a wide range. We wished to see whether we could find any evidence for the use of temporal information at modulation rates above 5 Hz when the stimuli had relatively long segments at their frequency extremes. We also wished to explore how effectively the quasi-steady-state segments could be used to improve FM detection for very low modulation rates.

I. METHOD

A. Procedure

Psychometric functions were measured for the detection of AM alone and FM alone, using a two-interval, two-alternative, forced-choice (2AFC) task. On each trial, two successive stimuli were presented, one modulated and the other unmodulated. The order of the two stimuli in each pair was random. Subjects were required to identify the interval with the modulated sound by pressing the appropriate button on the response box. Subjects were tested in a double-walled sound-attenuating chamber. Correct-answer feedback was provided by lights on the response box. The method for determining psychometric functions was the same as described by Moore and Sek (1992, 1994a, b); the reader is referred to those papers for details. Briefly, each run of 55 trials started with five trials where the signal contained a highly detectable amount of modulation, so that subjects ''knew what to listen for.'' Scores for these five trials were discarded. In subsequent trials, five different modulation depths were used, in a repeating sequence going from larger values to smaller ones. Thus, subjects received a ''reminder'' (easy) stimulus once every five trials. Each point on each psychometric function was based on 200 judgments.

B. Stimuli

The carrier frequency was 1 or 6 kHz. The pattern of frequency or amplitude change over time had the form illustrated in Fig. 1; within each modulation period P, a time T_{SS} was spent at each extreme of frequency or amplitude. The transitions between the extremes, with duration T_{trans}, had the form of a half-cycle of a cosine function. The modulation rate was 2, 5, 10, or 20 Hz, giving values of P of 500, 200, 100, and 50 ms. The following values of T_{SS} were used: for $P=500$ ms, $T_{SS}=0$, 5, 10, 20, 40, 80, and 160 ms; for $P=200$ ms, $T_{SS}=0$, 5, 10, 20, 40, and 80 ms; for $P=100$ ms, $T_{SS}=0$, 5, 10, 20, and 40 ms, for $P=50$ ms, $T_{SS}=0$, 5, 10, and 20 ms. The value of T_{trans} was equal to $(P-2T_{SS})/2$. The smallest value of T_{trans} was 5 ms, which occurred for the highest modulation rate for $T_{SS}=20$ ms. We did not use values of T_{trans} less than 5 ms, as we wanted to avoid audible spectral splatter. When T_{SS} was equal to 0, the modulation was sinusoidal. Modulation depths for the FM stimuli are specified in terms of the peak deviations from the mean values. Modulation depths for the AM stimuli are specified in terms of the modulation index, m. The mean level of the stimuli was 70 dB SPL. The silent interval between the two stimuli in each trial was 500 ms. All stimuli had 20-ms raised-cosine rise/fall ramps and 1-s overall durations. The modulation was applied throughout the whole stimulus. The modulation started with its ac component at a positive-going zero-crossing.

To generate FM stimuli with the appropriate pattern of frequency changes, we made use of the fact that the instantaneous frequency is the time derivative of the instantaneous phase, so the instantaneous phase as a function of time can

be derived from the integral of the instantaneous frequency over time. Assume that the instantaneous frequency is

$$f_i(t) = f_c + \Delta F(t), \tag{1}$$

where $\Delta F(t)$ is the desired change in instantaneous frequency over time and f_c is the carrier frequency. The instantaneous phase is then

$$\theta(t) = \int_0^t (f_c + \Delta F(\lambda))d\lambda = f_c t + \int_0^t \Delta F(\lambda)d\lambda, \tag{2}$$

where λ is a dummy variable. The time waveform is given by

$$x(t) = \sin 2\pi\left(f_c t + \int_0^t \Delta F(\lambda)d\lambda \right). \tag{3}$$

The equations specifying ΔF over one complete modulation period are given in terms of $Z(t)$

$$Z(t) = \sin(2\pi t/2T_{\text{trans}}) \quad \text{for} \quad 0 < t < 0.5T_{\text{trans}}, \tag{4}$$

$$Z(t) = 1 \quad \text{for} \quad 0.5T_{\text{trans}} < t < 0.5(P - T_{\text{trans}}), \tag{5}$$

$$Z(t) = \sin(2\pi t/2T_{\text{trans}}) \quad \text{for} \quad 0.5(P - T_{\text{trans}}) < t < 0.5(P + T_{\text{trans}}), \tag{6}$$

$$Z(t) = -1 \quad \text{for} \quad 0.5(P + T_{\text{trans}}) < t < P - 0.5T_{\text{trans}}, \tag{7}$$

$$Z(t) = \sin(2\pi t/2T_{\text{trans}}) \quad \text{for} \quad P - 0.5T_{\text{trans}} < t < P, \tag{8}$$

where $\Delta F = \Delta f Z(t)$, and Δf represents the peak deviation of the instantaneous frequency from the carrier frequency.

Stimuli were generated using a Tucker-Davis array processor (TDT-AP2) in a host PC, and a 16-bit digital-to-analog converter (TDT-DD1) operating at a 50-kHz sampling rate. They were attenuated (TDT-PA4) and sent through an output amplifier (TDT-HB6) to a Sennheiser HD414 earphone. The headphone was chosen for its relatively smooth frequency response. This was important, since if the frequency response is irregular, FM can be transformed into a combination of FM and AM. Measurements using a probe microphone close to the eardrum showed that the response was very flat from 100 up to 1100 Hz. Around 6000 Hz, the response varied smoothly by ±2 dB over the range 5–7 kHz. For the range of frequency deviations used in this experiment (typically less than ±1% around 6000 Hz), the amount of spurious AM induced by the FM would have been less than 0.12 dB.

C. Subjects

Three subjects were tested. One was author A.S. The other two subjects were paid for their services. All subjects had absolute thresholds less than 20 dB HL at all audiometric frequencies and had no history of hearing disorders. All had extensive previous experience in similar psychoacoustic tasks.

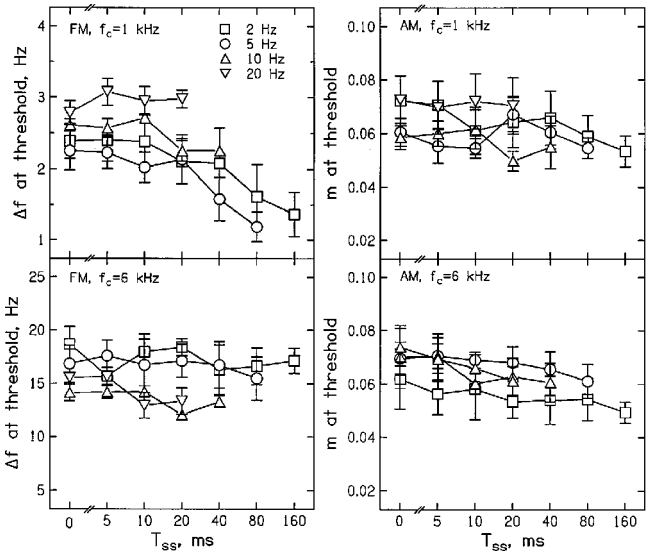

FIG. 2. Thresholds ($d' = 1$) for the detection of FM (left) or AM (right) plotted as a function of T_{SS}. The parameter is the modulation rate, as shown in the key. Results are shown for carrier frequencies of 1 kHz (top) and 6 kHz (bottom). Results shown are the mean for three subjects. Error bars indicate ±1 standard error across subjects.

II. RESULTS

A. Form of the psychometric functions

Following Egan *et al.* (1969), psychometric functions for the detection of FM and AM were fitted with equations of the form $d' = km^\alpha$ of $d' = k\Delta f^\alpha$, where m is the modulation index for AM and Δf is the mean-to-peak frequency deviation for FM; k and α are constants. Previously, we have found that $\alpha \approx 2$ for both AM and FM detection (Moore and Sek, 1992, 1994a) although α was sometimes a little less than 2 for low modulation rates (Moore and Sek, 1995). For the present results, the same general pattern was observed. For FM, the value of α, averaged across carrier frequencies and values of T_{SS}, was 1.5, 1.8, 1.8, and 2.0 for modulation rates of 2, 5, 10, and 20 Hz, respectively. For AM, the corresponding values were 1.7, 1.7, 1.8, and 2.0. Since the values of α did not vary systematically with T_{SS} or with carrier frequency, and the values were all reasonably close to 2, we decided to analyze all of the data with the value of α fixed at 2; thus, only the single parameter k was varied to fit the psychometric function to the data for a specific subject and condition. The value of k is referred to here as the *slope* of the psychometric function (note that some researchers have described α as the slope), and it can be regarded as one way of quantifying performance; high slopes are associated with good performance.

B. Thresholds for AM and FM detection

The fitted psychometric functions were used to derive the values of m and Δf giving a d' value of 1. These values of m and Δf are taken as the thresholds for detecting AM and FM. The pattern of results was similar across subjects (although subject OM had somewhat higher overall thresholds than the other subjects), and mean thresholds are plotted in Fig. 2. Consider first the thresholds for AM detection

(right panels). Thresholds are similar for the carrier frequencies of 1 and 6 kHz, which is consistent with earlier work on the detection of AM at low rates for different carrier frequencies (Riesz, 1928; Zwicker, 1956; Moore and Sek, 1995). Thresholds do not vary markedly with modulation rate or with T_{SS}, although there is a trend for thresholds to decrease slightly with increasing T_{SS}. This is consistent with the results of Moore and Sek (1995) and it indicates that the mechanism underlying AM detection does not benefit greatly from the presence of longer segments at amplitude extremes. Possibly, the detection of AM depends more on the *changes* in the stimuli than on the time spent at extremes. Equivalently, one might argue that AM is detected using the modulation *per se*, as opposed to taking samples of the amplitude at different points during the modulation cycle, as assumed by ''snapshot'' theories (Dooley and Moore, 1988). Indeed, there may be specific mechanisms for detecting and analyzing AM (Kay, 1982; Dau *et al.*, 1997a, b).

Consider now the results for FM detection. For the 6-kHz carrier, the pattern of results was similar to that found for AM; the thresholds were not affected markedly by modulation rate or by the value of T_{SS}. However, there was a trend for thresholds to increase with decreasing modulation rate. A similar trend was found by Moore and Sek (1995) and Sek and Moore (1995). For the 1-kHz carrier, there were reasonably clear effects of modulation rate and of T_{SS}. Thresholds were lower for the 2- and 5-Hz rates than for the 10- and 20-Hz rates. For the 20-Hz rate, there was no effect of T_{SS}. Except for the 20-Hz rate, thresholds decreased with increasing T_{SS}, the decrease being greatest for the modulation rates of 2 and 5 Hz. These results indicate that, for the 1-kHz carrier only, performance is better for stimuli that spend more time close to frequency extremes. This is consistent with the hypothesis that FM detection for a 1-kHz carrier can be mediated by a temporal mechanism that is sluggish.

To confirm the statistical significance of the trends described above, within-subjects analyses of variance (ANOVAs) were conducted on the thresholds, separately for each modulation rate (as there were different values of T_{SS} for each rate) and modulation type (FM or AM). The factors were T_{SS} and carrier frequency. For the FM data, thresholds were expressed as $\Delta f/f_c$, where f_c is the carrier frequency. When expressed in this way, the overall threshold values were similar for the two carrier frequencies. The outcomes of the ANOVAs are summarized in Table I.

Consider first the ANOVAs conducted on the data for FM detection. The main effect of T_{SS} is highly significant for all modulation rates except 20 Hz. The main effect of f_c is not significant for any modulation rate. The interaction of T_{SS} and f_c is highly significant for modulation rates of 2 and 5 Hz, confirming the trend for thresholds to decrease markedly with increasing T_{SS} at 1 kHz, but to change only slightly with T_{SS} at 6 kHz. The interaction of T_{SS} and f_c is not significant for the 10-Hz modulation rate and reaches a moderate significance level for the 20-Hz rate. In the latter case, thresholds decreased more with increasing T_{SS} at 6 kHz than at 1 kHz, the opposite trend to that found for the modulation rates of 2 and 5 Hz. Overall, the ANOVAs confirm that the pattern of results is different for the two lowest modulation rates and for the highest modulation rate, and they confirm that large effects of T_{SS} are only observed for the lower modulation rates and for the 1-kHz carrier.

TABLE I. Results of the ANOVAs conducted on the thresholds for FM and AM detection.

Modulation type	Modulation rate, Hz	Factor	F value	Significance level
FM	2	T_{ss}	6.11(6,12)	0.004
		f_c	5.74(1,2)	ns
		$T_{ss}\times f_c$	5.71(6,12)	0.005
	5	T_{ss}	9.30(5,12)	0.002
		f_c	3.22(5,10)	ns
		$T_{ss}\times f_c$	7.12(5,10)	0.004
	10	T_{ss}	8.22(4,8)	0.006
		f_c	5.56(1,2)	ns
		$T_{ss}\times f_c$	0.94(4,8)	ns
	20	T_{ss}	3.69(3,6)	ns
		f_c	6.68(1,2)	ns
		$T_{ss}\times f_c$	6.34(3,6)	0.027
AM	2	T_{ss}	3.67(6,12)	0.026
		f_c	6.54(1,2)	ns
		$T_{ss}\times f_c$	1.49(6,12)	ns
	5	T_{ss}	4.36(5,10)	0.023
		f_c	2.15(1,2)	ns
		$T_{ss}\times f_c$	4.0(5,10)	0.03
	10	T_{ss}	3.05(4,8)	ns
		f_c	1.05(1,2)	ns
		$T_{ss}\times f_c$	1.03(4,8)	ns
	20	T_{ss}	2.06(3,6)	ns
		f_c	0.94(1,2)	ns
		$T_{ss}\times f_c$	1.83(3,6)	ns

Consider now the ANOVAs conducted on the data for AM detection. The main effect of T_{SS} is significant for the modulation rates of 2 and 5 Hz, confirming the slight trend for thresholds to decrease with increasing T_{SS}, but there is no significant effect for the modulation rates of 10 and 20 Hz. The main effect of f_c is not significant for any modulation rate. The interaction of T_{SS} and f_c is marginally significant for the modulation rate of 5 Hz, but is not significant for any other modulation rate. Overall, the ANOVAs confirm that the pattern of results was similar for the two carrier frequencies.

C. Effects of T_{SS} on the slopes of the psychometric functions

To show the effects of varying T_{SS} more clearly, the slopes of the psychometric functions, quantified by the parameter k, were plotted relative to the slope obtained for $T_{SS}=0$, i.e., relative to the slope obtained for sinusoidal modulation. The mean results across subjects are shown in Fig. 3. For AM, the slope ratios hardly change with T_{SS}, except for a slight trend for the ratios to increase for the longest values of T_{SS} at the lowest modulation rates.

For FM at 6 kHz, the pattern of results was very similar to that found for AM. This is consistent with the idea that FM for high carrier frequencies is detected via the modulation in excitation level that it produces. For FM at 1 kHz, the pattern of results was very different. The slope ratio hardly changed with T_{SS} for the 20-Hz modulation rate. However,

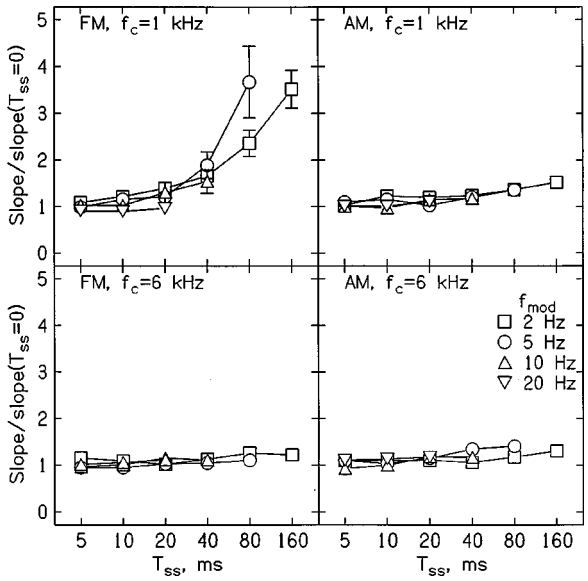

FIG. 3. Slopes of the psychometric functions, relative to the slope obtained for $T_{SS}=0$, plotted as a function of T_{SS}. Data are shown for FM (left) and AM (right). The parameter is the modulation rate, as shown in the key. Results are shown for carrier frequencies of 1 kHz (top) and 6 kHz (bottom). Results shown are the mean for three subjects. Error bars indicate ±1 standard error across subjects.

for the lower rates the slope ratios increased markedly once the value of T_{SS} exceeded 20 ms. This confirms the benefit obtained from the longer time spent at frequency extremes. It appears that the largest value of T_{SS} used with the 20-Hz rate, i.e., 20 ms, was not sufficient to confer any benefit.

To confirm the statistical significance of the trends described above, within-subjects ANOVAs were conducted on the slope ratios, separately for each modulation rate (as there were different values of T_{SS} for each rate). The factors were: T_{SS}, modulation type (AM or FM) and carrier frequency. For the 2-Hz modulation rate all of the main effects were significant: for T_{SS}, $F(6,12)=43.1$, $p<0.001$; for modulation type, $F(1,2)=55.2$, $p=0.018$; for carrier frequency, $F(1,2)=24.8$, $p=0.038$. The two-way interaction of T_{SS} and carrier frequency was significant, $F(6,12)=22.1$, $p<0.001$, as was the two-way interaction of T_{SS} and modulation type, $F(6,12)=18.3$, $p<0.001$. Finally, the three-way interaction was highly significant; $F(6,12)=15.4$, $p<0.001$. The three-way interaction confirms the effect that is obvious in the data; T_{SS} had a large effect only for FM and for the 1-kHz carrier. For the 5-Hz modulation rate, the main effect of T_{SS} was significant, $F(5,10)=15.2$, $p<0.001$, but the main effects of modulation type and carrier frequency were not significant. The two-way interaction of T_{SS} and carrier frequency was significant, $F(5,10)=10.7$, $p<0.001$, as was the two-way interaction of T_{SS} and modulation type, $F(5,10)=10.1$, $p<0.001$. Again, the three-way interaction was highly significant; $F(5,10)=8.55$, $p=0.002$. For the 10-Hz modulation rate, the main effect of T_{SS} was significant; $F(4,8)=17.4$, $p<0.001$. However, none of the other main effects or interactions was significant. A similar pattern was observed for the 20-Hz rate. Only the main effect of T_{SS} was significant; $F(3,6)=6.4$, $p=0.027$.

The results of the ANOVAs confirm the main trends visible in the data. For FM of the 1-kHz carrier, increasing T_{SS} produced a large improvement in performance for the two lower modulation rates, but not for the higher rates. For FM of the 6-kHz carrier, and for AM of both carriers, increasing T_{SS} led to only very small improvements in performance.

III. DISCUSSION

Our results are consistent with the hypothesis that FM detection is mediated by two mechanisms—a place mechanism which is effective for all carrier frequencies and all modulation rates (at least up to the 20-Hz rate used here), and a temporal mechanism which is effective only for carrier frequencies below 4–5 kHz and for low modulation rates. For a given modulation rate, the effectiveness of the temporal mechanism can be increased by the use of quasitrapezoidal modulation, so that the stimuli spend more time at frequency extremes. However, there is little benefit from values of T_{SS}, less than 20 ms.

To quantify the time spent close to frequency extremes, we calculated the durations, T_E, over which our stimuli were within 10% of their frequency extremes. When T_{SS} is 0, these durations are about 72, 29, 14, and 7 ms per half-cycle for modulation rates of 2, 5, 10, and 20 Hz, respectively. It appears from our earlier research (Sek and Moore, 1995; Moore and Sek, 1995, 1996) that the 72- and 29-ms durations are sufficiently long to allow the temporal mechanism to function effectively, while the durations of 14 and 7 ms are not. Thus, a minimum value of T_E above 14 ms, and probably close to 29 ms, seems to be needed for operation of the temporal mechanism. The effects of varying T_{SS} found in the present experiment are broadly consistent with this estimate. For the modulation rate of 10 Hz, performance improved when T_{SS} was increased from 10 to 20 ms, corresponding to an increase in T_E from about 24 to 34 ms. For the modulation rate of 20 Hz, the largest value of T_E used was about 27 ms (for $T_{SS}=20$ ms), which was not enough to give a clear improvement in performance relative to that obtained for smaller values of T_E.

It is instructive to compare the present results with our earlier measurements of thresholds for detecting steps in frequency linked by glides of various durations (Sek and Moore, 1999). One goal of our earlier experiment was to determine whether there is a mechanism for detecting frequency changes *per se*, as opposed to comparing the initial and final frequencies of the stimuli. Subjects discriminated a 500-ms sinusoid of constant frequency from a sinusoid with three parts: an initial part with constant frequency, a downward frequency glide, and a final part with constant frequency. The overall duration was 500 ms, and the glide duration was varied from 5 to 500 ms. In one special case, the portion of the stimuli when a glide might occur was replaced by a brief silent interval. Performance was better when a brief glide was present than when no glide was present, but worsened with increasing glide duration. The overall pattern of results could be explained reasonably well by a model in which it was assumed that information from sampling the endpoint frequencies (which depended on the duration of the frequency plateaus on either side of the glide) was combined

with information from the glide (which was assumed to be independent of glide duration). For center frequencies from 0.5 to 4 kHz, the best fit to the data was obtained using a model in which the two sources of information were partially independent, perhaps being derived by different mechanisms—a temporal mechanism for endpoint sampling and a place mechanism for glide detection. For a frequency of 6 kHz, the best fit was obtained using a model in which the two sources of information were based on a common mechanism, presumably a place mechanism.

The results of the present experiment for a center frequency of 1 kHz are broadly consistent with the model described above. The improvement in performance with increasing T_{SS} found for the lower modulation rates can be interpreted as reflecting an increasing contribution from the endpoint sampling mechanism, based on phase-locking information. However, the present results for a center frequency of 6 kHz did not show any large effect of T_{SS}, whereas our earlier experiment showed that thresholds were about a factor of 1.8 lower for detecting a 200-ms frequency transition bounded by 150-ms plateaus in frequency than they were for detecting a pure transition lasting 500 ms. The discrepancy is presumably related to the difference in the stimuli between the two experiments; the previous experiment used stimuli containing a single downward frequency transition with a frequency plateau on each side, whereas the present experiment used stimuli with alternating upward and downward frequency transitions connected by frequency plateaus. A possible interpretation of the discrepancy is that at high frequencies (when phase locking is no longer available) the endpoint sampling mechanism becomes ineffective when the stimuli have repeating modulations in frequency. Performance may then be based exclusively on the changes in the stimuli.

IV. SUMMARY AND CONCLUSIONS

We have measured psychometric functions for the detection of AM and FM for two carrier frequencies, 1 and 6 kHz, using quasitrapezoidal modulation. Within each modulation period, P, a time T_{SS} was spent at each extreme of frequency or amplitude. The transitions between the extremes had the form of a half-cycle of a cosine function. The following conclusions can be drawn from our results:

(1) For both AM and FM detection, the value of d' was approximately proportional to the square of the modulation depth. However, for modulation rates of 2 and 5 Hz, the values of d' were proportional to the modulation depth raised to a power slightly less than 2; this was true for both AM and FM detection.
(2) The detectability of AM was not greatly affected by modulation rate or by the value of T_{SS}, except for a slight improvement with increasing T_{SS} for the lowest modulation rates; this was true for both carrier frequencies.
(3) For FM of the 6-kHz carrier, the pattern of results was similar to that found for AM, which is consistent with an excitation-pattern model of FM detection.
(4) For FM of the 1-kHz carrier, performance improved markedly with increasing T_{SS}, especially for the lower FM rates; there was no significant change in performance with T_{SS} for the 20-Hz modulation rate. The results are consistent with the idea that detection of FM of a 1-kHz carrier is partly mediated by a sluggish temporal mechanism. That mechanism benefits from greater time spent at frequency extremes of the modulation cycle for rates up to 10 Hz.
(5) The time spent close to frequency extremes was quantified as the duration, T_E, over which the stimuli were within 10% of their frequency extremes during each half-cycle of the stimuli. The data are consistent with the idea that T_E has to be about 29 ms or more for the temporal mechanism to be effective in FM detection.

ACKNOWLEDGMENTS

This work was supported by the Wellcome Trust (Grant Number 056767/Z/99/Z) and by the Medical Research Council (UK). We thank Hedwig Gockel for helpful tips.

Carlyon, R. P., Moore, B. C. J., and Micheyl, C. (**2000**). ''The effect of modulation rate on the detection of frequency modulation and mistuning of complex tones,'' J. Acoust. Soc. Am. (submitted).

Dau, T., Kollmeier, B., and Kohlrausch, A. (**1997a**). ''Modeling auditory processing of amplitude modulation: I. Detection and masking with narrowband carriers,'' J. Acoust. Soc. Am. **102**, 2892–2905.

Dau, T., Kollmeier, B., and Kohlrausch, A. (**1997b**). ''Modeling auditory processing of amplitude modulation: II. Spectral and temporal integration,'' J. Acoust. Soc. Am. **102**, 2906–2919.

Dooley, G. J., and Moore, B. C. J. (**1988**). ''Duration discrimination of steady and gliding tones: A new method for estimating sensitivity to rate of change,'' J. Acoust. Soc. Am. **84**, 1332–1337.

Egan, J. P., Lindner, W. A., and McFadden, D. (**1969**). ''Masking-level differences and the form of the psychometric function,'' Percept. Psychophys. **6**, 209–215.

Goldstein, J. L., and Srulovicz, P. (**1977**). ''Auditory-nerve spike intervals as an adequate basis for aural frequency measurement,'' in *Psychophysics and Physiology of Hearing*, edited by E. F. Evans and J. P. Wilson (Academic, London).

Kay, R. H. (**1982**). ''Hearing of modulation in sounds,'' Physiol. Rev. **62**, 894–975.

Micheyl, C., and Carlyon, R. P. (**1998**). ''Effects of temporal fringes on fundamental-frequency discrimination,'' J. Acoust. Soc. Am. **104**, 3006–3018.

Micheyl, C., Moore, B. C. J., and Carlyon, R. P. (**1998**). ''The role of excitation-pattern cues and temporal cues in the frequency and modulation-rate discrimination of amplitude-modulated tones,'' J. Acoust. Soc. Am. **104**, 1039–1050.

Moore, B. C. J. (**1973a**). ''Frequency difference limens for narrow bands of noise,'' J. Acoust. Soc. Am. **54**, 888–896.

Moore, B. C. J. (**1973b**). ''Frequency difference limens for short-duration tones,'' J. Acoust. Soc. Am. **54**, 610–619.

Moore, B. C. J. (**1974**). ''Relation between the critical bandwidth and the frequency-difference limen,'' J. Acoust. Soc. Am. **55**, 359.

Moore, B. C. J. (**1997**). *An Introduction to the Psychology of Hearing*, 4th ed. (Academic, San Diego).

Moore, B. C. J., and Sek, A. (**1992**). ''Detection of combined frequency and amplitude modulation,'' J. Acoust. Soc. Am. **92**, 3119–3131.

Moore, B. C. J., and Sek, A. (**1994a**). ''Effects of carrier frequency and background noise on the detection of mixed modulation,'' J. Acoust. Soc. Am. **96**, 741–751.

Moore, B. C. J., and Sek, A. (**1994b**). ''Discrimination of modulation type (AM or FM) with and without background noise,'' J. Acoust. Soc. Am. **96**, 726–732.

Moore, B. C. J., and Sek, A. (**1995**). ''Effects of carrier frequency, modulation rate and modulation waveform on the detection of modulation and the discrimination of modulation type (AM vs FM),'' J. Acoust. Soc. Am. **97**, 2468–2478.
Moore, B. C. J., and Sek, A. (**1996**). ''Detection of frequency modulation at low modulation rates: Evidence for a mechanism based on phase locking,'' J. Acoust. Soc. Am. **100**, 2320–2331.
Plack, C. J., and Carlyon, R. P. (**1994**). ''The detection of differences in the depth of frequency modulation,'' J. Acoust. Soc. Am. **96**, 115–125.
Plack, C. J., and Carlyon, R. P. (**1995**). ''Differences in frequency modulation detection and fundamental frequency discrimination between complex tones consisting of resolved and unresolved harmonics,'' J. Acoust. Soc. Am. **98**, 1355–1364.
Riesz, R. R. (**1928**). ''Differential intensity sensitivity of the ear for pure tones,'' Phys. Rev. **31**, 867–875.
Saberi, K., and Hafter, E. R. (**1995**). ''A common neural code for frequency- and amplitude modulated sounds,'' Nature (London) **374**, 537–539.
Sek, A., and Moore, B. C. J. (**1995**). ''Frequency discrimination as a function of frequency, measured in several ways,'' J. Acoust. Soc. Am. **97**, 2479–2486.
Sek, A., and Moore, B. C. J. (**1999**). ''Discrimination of frequency steps linked by glides of various durations,'' J. Acoust. Soc. Am. **106**, 351–360.
Shackleton, T. M., and Carlyon, R. P. (**1994**). ''The role of resolved and unresolved harmonics in pitch perception and frequency modulation discrimination,'' J. Acoust. Soc. Am. **95**, 3529–3540.
White, L. J., and Plack, C. J. (**1998**). ''Temporal processing of the pitch of complex tones,'' J. Acoust. Soc. Am. **103**, 2051–2063.
Zwicker, E. (**1956**). ''Die elementaren Grundlagen zur Bestimmung der Informationskapazität des Gehörs,'' Acustica **6**, 356–381.
Zwicker, E., and Fastl, H. (**1990**). *Psychoacoustics—Facts and Models* (Springer, Berlin).

Level discrimination of sinusoids as a function of duration and level for fixed-level, roving-level, and across-frequency conditions

Andrew J. Oxenham[a)]
Institute for Hearing, Speech, and Language, and Department of Speech-Language Pathology and Audiology (133FR), Northeastern University, Boston, Massachusetts 02115

Søren Buus
Institute for Hearing, Speech, and Language, and Communication and Digital Signal Processing Center, Department of Electrical and Computer Engineering (442DA), Northeastern University, Boston, Massachusetts 02115

(Received 7 May 1999; revised 17 August 1999; accepted 28 October 1999)

The ability of listeners to detect level differences between two sinusoidal stimuli in a two-interval forced-choice procedure was measured as a function of duration and level in three conditions: (1) the pedestal was fixed in level and the stimuli in the two intervals had the same frequency of either 1 or 2 kHz (fixed-level condition); (2) the pedestal was roved in level over a 20-dB range from trial to trial, but the stimuli still had the same frequency of either 1 or 2 kHz (roving-level condition); and (3) the pedestal was roved in level over a 20-dB range and the two stimuli differed in frequency, such that one was around 1 kHz while the other was around 2 kHz (across-frequency condition). In the fixed-level conditions, difference limens decreased (improved) with both increasing duration and level, as found in previous studies. In the roving-level conditions, difference limens increased and the dependence on duration and level decreased. Difference limens in the across-frequency conditions were generally highest and showed very little dependence on either stimulus duration or level. The results may be understood in terms of different internal noise components with additive variances: In the fixed-level conditions, sensation noise, which is dependent on stimulus attributes such as duration and level, is dominant. In more difficult conditions, where trace-memory and/or across-channel comparisons are required, a more central, stimulus-independent noise dominates. [S0001-4966(00)02502-9]

PACS numbers: 43.66.Fe, 43.66.Ba [RVS]

INTRODUCTION

In a recent study, Buus *et al.* (1997) made a distinction between ''loudness discrimination'' and ''level discrimination.'' Level discrimination (also termed intensity discrimination) was used to describe measurements of difference limens for stimuli that differ only in level, while loudness discrimination was used to describe measurements where the listener is required to judge the loudness of stimuli differing in more than one dimension (e.g., in level and duration, or in level and frequency). It was suggested that the difference between the two measures may reflect different underlying processes. For two otherwise identical sounds, level discrimination may be based on an optimal combination of independent information from different frequency channels (Florentine and Buus, 1981). For two unlike sounds, loudness discrimination may be based on the overall sensation of loudness, rather than a combination of information from independent frequency channels.

Buus *et al.* proposed that this distinction is not merely semantic, and that the difference may be reflected in the dependence of the difference limen (DL) on stimulus duration and stimulus level. Level discrimination is dependent on stimulus duration: generally, the just-noticeable change in level, ΔL_{DL} [defined as $20\log(1+\Delta p/p)$, where p is the sound pressure of the standard and Δp is the just-noticeable change in pressure], decreases by about a factor of 2 for every tenfold increase in duration (Henning, 1970; Florentine, 1986). In contrast, Buus *et al.* (1997) reported that loudness difference limens, when comparing tones of different durations, seemed to be independent of duration. Also, DLs for level discrimination generally decrease monotonically with increasing stimulus level, at least for band-limited stimuli, giving rise to the well-known ''near-miss'' to Weber's law (McGill and Goldberg, 1968). For loudness discrimination at 5 kHz, however, DLs seemed to be maximal at medium sound levels and decrease somewhat at both low and high sound levels, as predicted by the slope of the derived loudness function (Buus *et al.*, 1997).

Most previous studies have assumed that level discrimination is based on an internal variable related to loudness (e.g., Durlach and Braida, 1969), and much effort has gone into relating the form of the loudness function to level DLs (e.g., Hellman and Hellman, 1990; Allen and Neely, 1997). The suggestion by Buus *et al.* that the form of the loudness function may underlie loudness discrimination, but not level discrimination, is contrary to the basic tenet of these studies

[a)]Present address: Research Laboratory of Electronics, Rm. 36-763, Massachusetts Institute of Technology, Cambridge, MA 02139. Electronic mail: oxenham@mit.edu

and, if true, has important theoretical consequences.

While the distinction between loudness and level discrimination is a possible interpretation of the data of Buus *et al.* (1997), other interpretations exist. For instance, Durlach, Braida, and colleagues (e.g., Durlach and Braida, 1969; Lim *et al.*, 1977; Braida *et al.*, 1984) have proposed that intensity discrimination is limited by a number of different internal noise sources, including sensation noise and various other noise sources related to memory processes or comparisons of unlike stimuli. Sensation noise is assumed to reflect the fundamental coding inaccuracy at an early stage in the auditory system, and should not be affected by changes in experimental paradigm. In fact, in the models of Durlach and colleagues, sensation noise is assumed to be constant in all conditions. It may be, however, that sensation noise could be more accurately modeled by allowing it to be dependent on certain stimulus parameters, such as stimulus duration (representing the increasingly accurate neural representation of level with increasing duration) and level (by assuming that the near-miss to Weber's law represents a fundamental improvement in neural coding at high levels through, for example, the recruitment of off-frequency auditory-nerve fibers). Memory and other more ''central'' noise, on the other hand, should not depend on the stimulus itself, but would be expected to depend on experimental parameters, such as the interstimulus interval or whether the stimuli are roved in level across trials. Which of these two noise categories dominates will depend on the exact conditions tested. Thus, it is at least conceivable that different paradigms will reveal different dependencies on parameters such as stimulus duration, without it being necessary to postulate different underlying mechanisms.

The purpose of this study was to investigate further the differences between level discrimination and loudness discrimination by measuring DLs as a function of duration and level for both paradigms. Three conditions were tested. The first condition was a simple level-or intensity-discrimination task (Jesteadt *et al.*, 1977; Florentine, 1986) in which the listener was instructed to select the more intense of two otherwise identical tones, and the pedestal level was kept constant within a run.

The second condition was again level discrimination, but with the overall level of the stimuli roved over a range of 20 dB from trial to trial. While the effects of stimulus duration and level have been previously investigated for fixed-level discrimination, very few studies have employed a roving-level paradigm to examine these parameters. Berliner *et al.* (1977) measured performance in fixed-level and roving-level conditions for durations between 200 and 1250 ms and found no noticeable difference in the dependence of sensitivity on duration. However, it seems that the dependence of sensitivity on duration may be greater at durations below about 200 ms (Henning, 1970; Florentine, 1986), and no data comparing fixed-level with roving-level discrimination seem to exist for these durations. A number of studies have found improved performance at the ends of a given level range (both high and low) in roving-level conditions (Berliner and Durlach, 1973; Berliner *et al.*, 1977), and this has been ascribed to a ''perceptual anchor'' effect (Braida *et al.*, 1984): performance at the extreme intensities of a given range seems to be governed primarily by context coding (i.e., a long-term memory representation of the maximum and minimum levels of a stimulus range), while mid-range performance may be governed primarily by a trace mode, which is related to a rapidly degraded short-term memory representation of a stimulus. So far, however, no studies have examined the effect of level, independently of stimulus range, for roving-level conditions.

The third condition was designed to require loudness, rather than level, discrimination, as defined by Buus *et al.* (1997). In each trial two tones, one at 1 kHz and the other at 2 kHz, were presented in random order and listeners were asked to select the louder one. Our use of two frequencies separated by an octave should preclude the use of within-channel level cues and should force listeners to use a cue related to overall loudness. In this condition, the overall level across trials was also roved to rule out the possibility that listeners based their judgments solely on the within-trial level of one of the two frequencies, while ignoring the other (Lim *et al.*, 1977). Based on the findings of Buus *et al.* for tones of different durations, one might expect DLs for tones of different frequencies also to be independent of stimulus duration. Also, according to the theory of Buus *et al.*, the DL for loudness discrimination is inversely proportional to the slope of the loudness function. Thus, according to the data of Florentine *et al.* (1996), the DL for loudness discrimination should be maximal at medium sound levels and should decrease at low and high levels, in contrast to what is generally found for level discrimination.

In summary, this study is designed to test the hypothesis that loudness discrimination and level discrimination reflect different underlying mechanisms. If the hypothesis is correct, DLs for across-frequency comparisons should be independent of duration and should depend on level in a way that is different from the level dependence observed in level discrimination experiments. If, on the other hand, both tasks reflect the same underlying mechanism, it may be possible to account for all the results within a framework of two noise classes, as described above. Specifically, changes in performance in roving-level and across-frequency conditions may be accountable in terms of additional, stimulus-independent noise, representing the additional load of trace memory and/or across frequency comparisons.

I. EXPERIMENT 1: LEVEL AND LOUDNESS DISCRIMINATION AS A FUNCTION OF STIMULUS DURATION

A. Stimuli and apparatus

The stimuli were tone bursts at either 1 or 2 kHz, gated on and off with 5-ms raised-cosine ramps. Difference limens were measured for stimulus durations of 5, 15, 50, 150, and 500 ms, measured at the half-amplitude points of the envelope. The stimuli were generated digitally at a sampling rate of 50 kHz and played out via a TDT digital-to-analog converter (DD1). The stimuli were low-pass filtered at 20 kHz (TDT FT5) and passed through a programmable attenuator

(TDT PA4) before being presented via a headphone amplifier (TDT HB6) to one earpiece of a Sony MDR-V6 headset.

B. Procedure

Three different conditions were tested. These are referred to as the fixed-level, roving-level, and across-frequency conditions, and are described in detail below.

1. Fixed-level and roving-level conditions

In the fixed-level condition, ΔL_{DL} was measured using a fixed pedestal level of 65 dB SPL. In the roving-level condition, ΔL_{DL} was measured with the pedestal level roved across trials over a range from 55 to 75 dB SPL, uniformly distributed in steps of 1 dB. For these two conditions, ΔL_{DL} was measured at frequencies of 1 and 2 kHz using a 2IFC method with a three-down one-up adaptive interleaved tracking procedure. Within each run, a given trial was selected at random from four independent tracks. Each trial consisted of two intervals, marked by lights on the response box, separated by a silent interstimulus interval (ISI) of 700 ms. Both intervals contained the pedestal; in one interval, chosen at random, a second sinusoid (the signal) with the same duration, frequency, and phase as the pedestal was added to the pedestal to produce a level increment. The listener's task was to choose the interval with the increment, and correct-answer feedback was provided after each trial. Initially, the signal level in each track was 5 dB above that of the pedestal, resulting in an initial ΔL of 8.9 dB. For the first two reversals in each track, the signal level was varied in steps of 5 dB. Thereafter, the step size was reduced to 2 dB for the final four reversals. The threshold for each track was defined as the mean of the last four reversals, and the overall threshold for the run was defined as the mean threshold level across the four tracks. Once the threshold for the run had been determined, it was transformed into units of ΔL, using the equation $\Delta L = 20 \log[(p_1 + p_0)/p_0]$, where p_1 and p_0 are the sound pressures of the signal and the pedestal, respectively. Three such estimates of the threshold value of $\Delta L(\Delta L_{\mathrm{DL}})$ were obtained on different days for each duration and frequency combination. The final threshold estimate was the geometric mean of the three estimates of ΔL_{DL}.

2. Across-frequency condition

The across-frequency condition, was designed to prevent listeners from using within-channel cues in performing loudness discrimination. In each trial, one interval contained a tone with a nominal frequency of 1 kHz, while the other interval contained a tone with a nominal frequency of 2 kHz. Although the excitation patterns of these two tones would not be expected to overlap greatly, it is at least conceivable that one auditory filter, centered at the point where the excitation patterns cross, would carry reliable information as to the relative levels of the two tones. To reduce the reliability of such a cue, the frequencies of the tones were roved from trial to trial by $\pm 5\%$. Except for the frequency rove and the different frequencies across intervals, the stimuli were generated and presented in the same way as in the second condition. Which of the two nominal frequencies was presented first was randomized from trial to trial. As in the second condition, a 20-dB level rove was imposed on the stimuli, with the 1-kHz pedestal level ranging from 55 to 75 dB SPL. The pedestal level of the 2-kHz tone was set so as to approximate the loudness of the 1-kHz pedestal for each listener individually, as described below. In two of the four tracks, the standard interval was the 1-kHz tone; in the other two tracks, the standard interval was the 2-kHz tone. The interleaving ensured that listeners could not tell which was the standard based solely on the frequency. Again, the averages of the third to the sixth reversals in each track were used to estimate the DL. In contrast to the other conditions, a track did not terminate after six reversals, but its probability of presentation was reduced. If a track with six or more reversals was selected, the random selection procedure was repeated. If the same occurred on the second selection, a third random selection was made. The third selection was then used without regard to the number of reversals already made on the selected track. Thus, only after three selections would a track with six or more reversals be presented. The reason for this procedure was to avoid the possibility that all but one track would terminate, leaving a single track for which it would be possible (using the feedback provided) to distinguish between the standard and the signal intervals based simply on frequency.

The signal levels at threshold for the two tracks with the 1-kHz tone as pedestal were averaged and converted to units of ΔL, and the same was done for the two tracks with the 2-kHz tone as pedestal. Then, the two estimates of ΔL_{DL} were averaged to provide an unbiased estimate of ΔL_{DL}, as described in the Appendix. The preliminary experiment, described below, provided an estimate of equal loudness levels for the 1- and 2-kHz tones for each listener. However, the accuracy of the estimated DL does not depend critically on the accuracy of the equal-loudness balances. As shown in the Appendix, by measuring DLs for both the 1 and 2-kHz tones as pedestals, any bias towards selecting one or other frequency can be eliminated from the estimate of the overall sensitivity.

Prior to collecting data for the across-frequency condition, a preliminary experiment was run to determine for each listener separately the level difference necessary to make the 1- and 2-kHz tones sound equally loud within the level range of 55 to 75 dB SPL. Signal durations of 5, 50, and 500 ms were tested. In this experiment, six independent tracks were interleaved within each run. In three of the tracks, the level of the 1-kHz tone was fixed and the level of the 2-kHz tone was varied; in the other three tracks, the level of the 2-kHz tone was fixed and the 1-kHz tone was varied. The fixed level of the three tracks at each frequency was set to 55, 65, and 75 dB SPL. For each trial, one of the tracks was chosen at random, as was the order of presentation (fixed or varied tone first). Thus, listeners had no way of distinguishing the fixed from the varied tones. Listeners were asked to select which of the two intervals contained the louder tone. No feedback was provided, as the correct answer depended on the listener's perception of loudness. The starting level of the varied tone in each track was set randomly over a range of ± 10 dB relative to the fixed tone. An adaptive 2IFC procedure with a one-down one-up rule was used in each track to

determine the point of subjective equality. The level of the varied tone was initially altered in steps of 4 dB. After the first five reversals, the step size was reduced to 2 dB for the final four reversals. Threshold was defined as the mean of the last four reversals in each track. Each condition was repeated three times, and the mean of all conditions, pooled across durations and levels for each subject, was taken as the level difference required to produce equal loudness for 1- and 2-kHz tones.

The results from this preliminary experiment were used in the across-frequency condition to adjust the relative levels of the 1- and 2-kHz tones for each listener individually. The 1-kHz pedestal was set to the nominal level in each trial, as determined by the roving procedure, and the 2-kHz tone was adjusted by the difference found in the preliminary experiment. The level difference between 1- and 2-kHz tones judged to be equally loud ($L_{2k}-L_{1k}$) ranged from -4.7 dB for S7 to $+5$ dB for S2. The average across listeners was 0.1 dB. A repeated-measures analysis of covariance with pedestal level and log(pedestal duration) as continuous variables showed a main effect of subject ($F_{6,350}=265$; $p<0.05$) and a significant interaction between subject and pedestal duration ($F_{6,350}=2.61$; $p<0.05$) and subject and pedestal level ($F_{6,350}=2.39$; $p<0.05$), but no main effects of duration or level. This shows that duration and level could have significant effects on loudness balancing, but that the effects were not consistent across listeners. These relatively small effects were ignored and only the mean difference for each subject was used.

C. Subjects

Seven female listeners participated as subjects. All had absolute thresholds of 15 dB HL or less at octave frequencies between 250 and 8000 Hz, and none reported any history of hearing disorders or difficulties. The ages of the listeners ranged from 19 to 44 years (mean age 25.4 years). All were college students who were paid for their participation. Listeners received 1–2 h training in each condition before data were collected.

Data were collected individually in 2-h sessions. For subjects 1 and 2, the conditions were tested in an interleaved manner, such that all conditions were completed at approximately the same time. For the remaining five listeners, the fixed-level condition was completed first, followed by the roving-level condition, and finally the across-frequency condition. The reasoning behind this ordering was that listeners, having been exposed to roving-level and across-frequency conditions, may use the same, nonoptimal, strategy in discriminating stimuli in the fixed-level condition. Richards (1992) found that prior exposure to roving-level conditions impaired listeners' performance in a tone-in-noise detection task, and we hypothesized that the same might apply to our conditions.

D. Results

The results from the individual listeners are plotted in Fig. 1. Filled symbols represent the fixed-level conditions and open symbols represent the roving-level conditions.

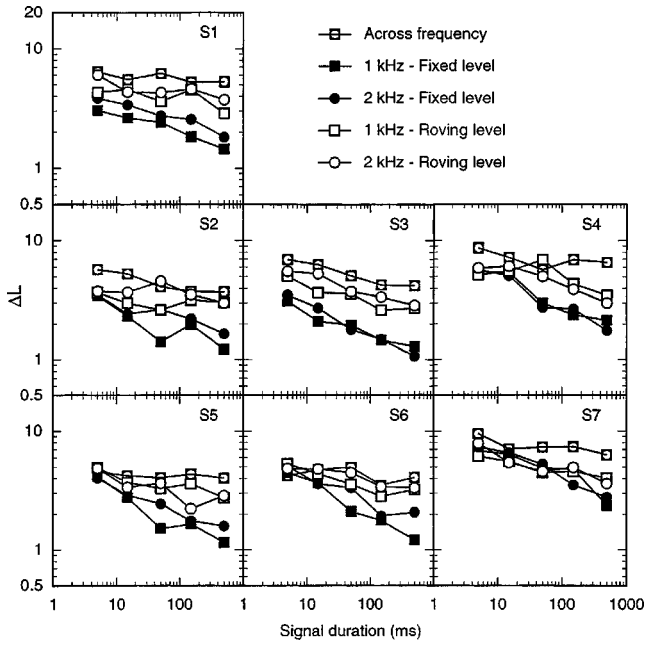

FIG. 1. Individual data from experiment 1. Difference limens in ΔL are shown as a function of pedestal duration for the fixed-level (filled symbols), roving-level (open symbols), and across-frequency (circles in squares) conditions. Squares and circles represent pedestal frequencies of 1 and 2 kHz, respectively.

Squares and circles represent measurements using a 1- and 2-kHz tone, respectively. The circles-in-squares represent the across-frequency conditions. The results are reported in units of ΔL, plotted on a logarithmic axis. This is consistent with the method used by Florentine (1986) and also has some theoretical justification. In studies of a wide range of level discrimination conditions in both normal-hearing and hearing-impaired listeners, Buus and Florentine (1991) and Buus *et al.* (1995) found that d' can be reasonably approximated as being proportional to ΔL, and that this relationship holds over a wider range for ΔL than for either ΔI or Δp. As changes in performance should be stated as ratios, and not differences, of ΔL or d', it is appropriate to plot ΔL on a logarithmic axis. For a more detailed discussion, see Buus and Florentine (1991) and Buus *et al.* (1995).

Generally, the results are rather similar across the seven subjects. In particular, the results from subjects 1 and 2 do not seem very different from those of the other five subjects, suggesting that the order of presentation of the conditions did not have a strong effect on the results. The trends in the individual data are also reflected in the geometric mean data, shown in Fig. 2. Error bars represent $\pm$ one standard error across listeners. Regression slopes [log(ΔL) against log(duration)] for the mean data are shown in Table I.

Consider first the data from the fixed-level conditions (filled symbols). Thresholds decrease with increasing duration over the range of durations tested. Listeners seem slightly, but consistently, more sensitive at 1 kHz than at 2 kHz. The regression slopes for the two frequencies of -0.22 and -0.21, respectively, are shallower than the slope of -0.38 found by Florentine (1986) at 1 kHz for a 65-dB SPL pedestal. However, the slope estimates in that study varied in a relatively nonsystematic way with pedestal frequency and

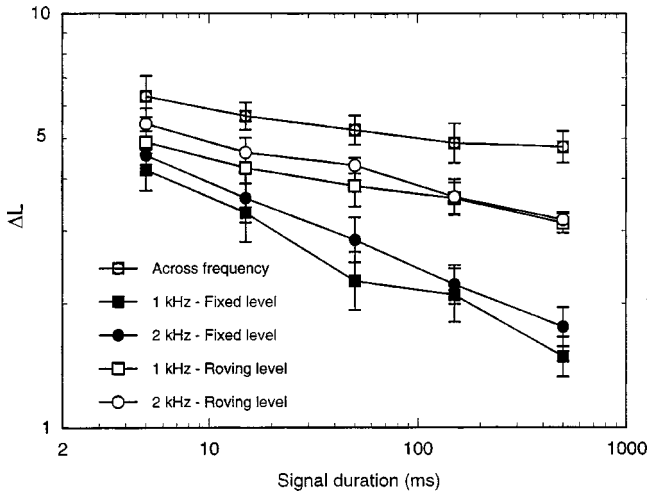

FIG. 2. Mean data from experiment 1. The axes and symbols are the same as in Fig. 1. Error bars represent ±1 standard error of the mean across the seven listeners.

level, with estimates ranging from −0.2 to −0.38. Thus, the slope estimates for the fixed-level conditions found in this study are at least within the range of those found previously.

In comparing overall thresholds across different studies, care must be taken to equate levels of performance. In most previous studies, an adaptive procedure tracking the 70.7% correct point on the psychometric function has been used, whereas the present experiment tracked the 79.4% correct point. Assuming unbiased responses, these two scores correspond to d''s of 0.78 and 1.16, respectively. As ΔL is approximately proportional to d' (Buus *et al.*, 1995), equal performance would be reflected by a ΔL_{DL} 1.5 times greater for the 79.4% conditions than for the 70.7% conditions. At a pedestal duration of 500 ms, the mean value of ΔL_{DL} at 1 kHz found here is 1.49 dB. This is very comparable with the ΔL's of 1.42 and 1.06 dB found at 1 kHz for levels of 60 and 70 dB SPL, respectively, by Florentine *et al.* (1987). If the different levels of performance are taken into account, by dividing our ΔL_{DL} by 1.5, our listeners performed somewhat better on average. In contrast, using the same pedestal level of 65 dB SPL, Florentine (1986) found a mean ΔL_{DL} at 1 kHz of 0.4 dB (equivalent to about 0.6 dB at 79.4% correct). Jesteadt *et al.* (1977) found a ΔL_{DL} of about 1 dB for a 1-kHz pedestal at a sensation level of 40 dB, which was presumably lower than 65 dB SPL. The reasons for such discrepancies have been discussed in detail by Florentine *et al.* (1987), and seem to be primarily due to amount of practice and motivation. Despite the reduced overall sensitivity relative to some earlier studies, the dependence of ΔL_{DL} on duration for the fixed-level conditions is consistent with previous studies (Henning, 1970; Florentine, 1986).

TABLE I. Slopes of $\log(\Delta L_{\mathrm{DL}})$ as a function of log(duration) for the mean data in experiment 1. All slopes are significantly greater than zero ($p<0.01$).

Frequency (kHz)	Fixed level	Roving level	Across frequency
1	−0.22	−0.092	−0.062
2	−0.21	−0.11	

Consider next the roving-level conditions (open symbols). As expected (Berliner and Durlach, 1973; Berliner *et al.*, 1977), DLs are higher than in the fixed-level conditions. Interestingly, however, the deterioration in performance is much less marked at short durations than at long durations. This pattern of results is observed in all listeners and is reflected in shallower slopes for the function relating $\log(\Delta L)$ to log(duration), as can be seen in Table I.

Finally, performance in the across-frequency condition (circles in squares) shows even less dependence on duration than in the roving-level condition. Nevertheless, some improvement with increasing duration is evident in nearly all listeners, and the mean ΔL_{DL} decreases from 6.3 to 4.8 dB as duration is increased from 5 to 500 ms. As indicated in Table I, the slope for the mean data of −0.062 is still significantly different from zero ($p<0.01$).

Mean discrimination thresholds in the across-frequency condition never exceed 7 dB, even for the shortest durations. The value of 7 dB is the best an optimal detector could achieve if the judgment was based simply on a single-frequency, across-trial analysis, without comparing the two frequencies within one trial (Green, 1988, p. 19). Thus, it appears that listeners were in fact comparing levels across frequency, as desired.

E. Discussion

The finding that the across-frequency condition results in a greatly reduced dependence on duration relative to the fixed-level conditions is consistent with Buus *et al.*'s (1997) distinction between loudness discrimination and level discrimination, as described in the introduction. However, this distinction does not predict the observed reduction in duration dependence due to level roving. Despite the level roving, it should still be possible to compare excitation patterns across the two intervals, and so duration dependence should not be affected. A possible explanation for the results from all three conditions was outlined in the Introduction, and assumes the presence of at least two independent internal noise sources (Durlach and Braida, 1969). The first noise source is associated with the sensory coding of the stimulus, and has been referred to as ''sensation noise.'' In the various versions of this model to date, this noise has been assumed to be constant. However, it seems reasonable to assume that it would depend on stimulus duration—a parameter not yet accounted for in this framework. The second noise source is independent of stimulus characteristics and instead depends on experimental conditions, such as whether level roving is used (Berliner and Durlach, 1973; Berliner *et al.*, 1977) or across-frequency comparisons are made (Lim *et al.*, 1977). This noise may consist of several components, including various short- and long-term memory processes, and inaccuracies in comparing level across frequency. For our purposes, it is sufficient to group all these sources together in one stimulus-independent component, termed ''central noise.''

Thus, we may restrict ourselves to defining two internal noise sources, with zero means and variances of $\sigma_s^2(T)$ and σ_c^2, where $\sigma_s^2(T)$ is the variance associated with sensation noise, σ_c^2 is the variance associated with central noise, and T

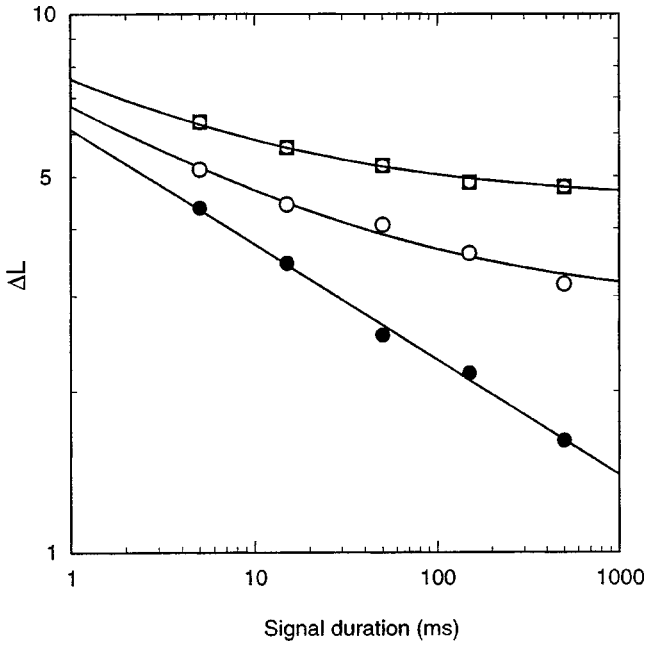

FIG. 3. Mean data from experiment 1, averaged across the two pedestal frequencies. The filled and open circles represent the fixed-level and roving-level conditions, respectively. The circles in squares represent the across-frequency condition. The curves are fits using the model described in the text.

is the stimulus duration in ms. If ΔL is proportional to d' (Buus *et al.*, 1995), it follows that, for a given d', ΔL at threshold (ΔL_{DL}) is proportional to σ, the total internal noise standard deviation. This is because $d' = k\Delta L/\sigma$, where k is a constant. The total internal noise variance for the fixed-level condition can be derived by letting $k = 1/d'$. Thus $\sigma^2 = \Delta L_{\mathrm{DL}}^2$. This overall σ^2 can be thought of as the sum of $\sigma_s^2(T)$ and σ_c^2. In the roving-level and across-frequency conditions, we assume that the value of $\sigma_s^2(T)$ remains the same as in the fixed-level condition, while the value of σ_c^2 increases, reflecting the increased difficulty of the task.

The question of whether simply increasing the value of σ_c^2 can account both for the increase in thresholds and the decreasing dependence on duration can be answered by finding a value of σ_c^2 that best fits the data, while keeping the value of $\sigma_s^2(T)$ fixed for a given duration across conditions. This was done by first fitting the data from the fixed-level conditions. The value for σ^2 as a function of pedestal duration was estimated by fitting a curve to the mean values of ΔL_{DL}^2. The data from the roving-level and across-frequency conditions were then predicted by increasing the value of σ_c^2 (which is independent of T) to best match the data.

The predictions using this model are shown as curves in Fig. 3. The data are taken from Fig. 2, averaged across the two frequencies in the fixed-level and roving-level conditions. The predicted curve for the fixed-level condition is a simple power function that described the data well, namely, $\Delta L_{\mathrm{DL}}^2 = e^{3.62}T^{0.427}$. As the parameters for the curve were fitted to the data, it is not surprising that the fit is good. The other two curves are more interesting. They represent the effect of increasing the duration-independent component of the noise variance. It can be seen that by increasing the duration-independent central noise variance, it is possible to account well for both the increase in thresholds and the decrease in duration dependence for both the roving-level and across-frequency conditions. The constants added to the values of ΔL_{DL}^2 in order to fit the data from the roving-level and across-frequency conditions were 8.2 and 20.1, respectively.

The data and the results from the modeling suggest that it may not be necessary to invoke two different mechanisms to account for level discrimination and loudness discrimination. Instead, these two tasks may form part of a continuum: in some conditions, with low uncertainty and high similarity of stimuli, sensation noise may dominate, producing a strong dependence on stimulus duration. In other conditions, central noise may dominate, in which case the duration dependence is much reduced.

In this experiment, both roving-level and across-frequency conditions resulted in a reduction in the dependence of ΔL_{DL} on duration. The pattern of results was well described by assuming that performance is limited by two internal noise sources, termed sensation noise and coding noise (Durlach and Braida, 1969). If sensation noise depends on the stimulus characteristics, such as duration, then it may also be responsible for changes in level discrimination with pedestal level. As suggested by McGill and Goldberg (1968), the ''near-miss'' to Weber's law, whereby performance improves with increasing level, may be explained in terms of improved coding accuracy, or a relative decrease in sensation noise, with increasing level. Thus, measuring level discrimination as a function of overall level provides another opportunity to attempt to separate the effects of sensation noise and coding noise. Also, as described below, different predictions follow from the different theories under consideration.

II. EXPERIMENT 2: LEVEL AND LOUDNESS DISCRIMINATION AS A FUNCTION OF STIMULUS LEVEL

In the second experiment we examined the dependence of ΔL_{DL} on stimulus level in the same three conditions tested in experiment 1. Using tones with the same frequency (5 kHz) but different durations, Buus *et al.* (1997) found that difference limens were generally highest at medium levels and lower at low and high levels. They related this finding to the shallower loudness function they found at medium sound levels and proposed that, unlike level discrimination (where performance generally improves monotonically with level), loudness discrimination was dependent on the slope of the loudness function. This predicts that ΔL_{DL} should follow the near-miss to Weber's law in the fixed-level and roving-level conditions, but be a nonmonotonic function in the across-frequency condition with ΔL_{DL} being roughly inversely proportional to the slope of the loudness function as found, for instance, by Florentine *et al.* (1996).

In the framework of Durlach, Braida, and colleagues, the near-miss to Weber's law is accounted for by a steepening of the function relating level to internal representation (Braida *et al.*, 1984), while the sensation noise remains constant. This would predict that, while overall performance may depend on various experimental manipulations, the dependence of ΔL on pedestal level should remain unchanged. Thus,

according to this model, the three conditions should produce parallel functions when $\log(\Delta L_{DL})$ is plotted as a function of pedestal level.

A third hypothesis can be formulated as follows: The near-miss to Weber's law may be due to a relative decrease in sensation noise with increasing level (McGill and Goldberg, 1968), consistent with the idea that the near-miss is due to additional information being provided by off-frequency channels (Viemeister, 1972; Moore and Raab, 1974; Viemeister, 1974; Florentine and Buus, 1981). In this case, roving the level, or forcing listeners to compare stimuli with different frequency would be equivalent to adding stimulus-independent noise. As in experiment 1, this would predict that the slope of the function relating $\log(\Delta L_{DL})$ to stimulus level should become increasingly shallow, as the stimulus-independent noise begins to dominate.

These three different predictions were tested here using the three conditions from experiment 1, with the pedestal duration fixed at 500 ms and the mean pedestal level varied parametrically.

A. Stimuli and procedure

The method of generating the stimuli was the same as that in experiment 1. As in experiment 1, three conditions were tested: fixed-level and roving-level level discrimination, and across-frequency loudness discrimination. For the first two conditions, only 1-kHz pedestals were used, as experiment 1 showed no great differences between pedestals of 1 and 2 kHz. For the third condition, 1- and 2-kHz tones were compared. The stimuli had a half-amplitude duration of 500 ms and were gated using 5-ms raised-cosine ramps. The fixed-level condition was tested at pedestal levels of 25, 50, and 80 dB SPL (except for S4 who was tested at 30, 50, and 80 dB SPL). The roving-level condition was tested with pedestal levels in the ranges of 15–35 dB (20–40 dB for S4), 40–60 dB, and 70–90 dB SPL. The rove range was thus always 20 dB, but the median level varied from low to high. This is different from most other roving-level experiments, in which the rove range and the overall level range generally covary. The across-frequency condition was tested with the same 1-kHz pedestal levels as in the roving-level condition. The level of the 2-kHz pedestal was adjusted for each listener and level range to provide roughly equal loudness across the two frequencies, as described below. In an attempt to improve the overall performance of listeners, and to further reduce the influence of coding noise in the fixed-level condition, the ISI was reduced to 250 ms for all three conditions.

The same procedures were used as in experiment 1. Again, interleaved tracks, as described in experiment 1, were used to estimate thresholds, and the mean of three runs was defined as the final threshold.

B. Subjects

Three subjects from experiment 1, S3, S4, and S5, participated in this experiment. Their ages were 23, 44, and 21 years, respectively. This experiment was carried out after experiment 1, and so listeners already had considerable experience in level-discrimination tasks. Listeners were given a further 2 h of practice on the new conditions before data were collected.

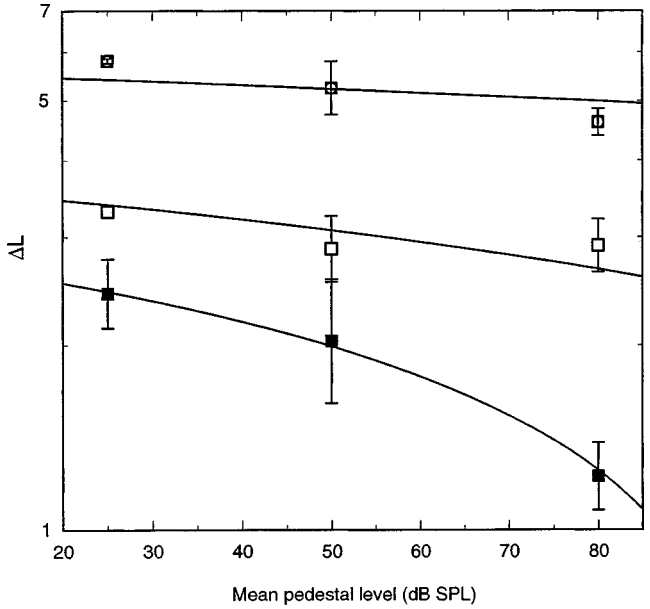

FIG. 4. Mean data from experiment 2. Difference limens in ΔL are plotted as a function of mean pedestal level. The filled and open squares represent the fixed-level and roving-level conditions, respectively. The circles in squares represent the across-frequency condition. Error bars represent ± 1 standard error of the mean across the three listeners. The curves are fits using the model described in the text.

C. Preliminary experiments

Before any data were collected, absolute thresholds at 1 and 2 kHz were measured for the three listeners using a two-interval two-alternative forced choice adaptive procedure with a three-down one-up tracking rule that tracks the 79.4% correct point on the psychometric function. In the actual experiment, the lowest level range was selected such that the lowest level presented was at least 5 dB above absolute threshold at both 1 and 2 kHz. For S3 and S5, this was 15–35 dB. For S4, the levels had to be increased by 5 dB to meet this criterion.

As in experiment 1, a preliminary experiment was conducted to determine points of subjective equality for the loudness of the 1- and 2-kHz tones for the three different level ranges and the three listeners individually. This was done as in experiment 1, except that only the 500-ms durations were tested. The three level ranges were tested separately, using fixed levels of 15, 25, and 35 (20, 30, and 40 for S4), 40, 50, and 60 dB, and 70, 80, and 90 dB SPL. The mean differences for each of the level ranges and each of the listeners were used in the across-frequency condition to set the level of the 2-kHz pedestal.

D. Results and discussion

The data from the three listeners were rather similar and therefore only the mean results are shown in Fig. 4. Error bars represent ± 1 s.e. of the mean. The data at the lowest level are shown as having a mean pedestal level of 25 dB

SPL, although the levels for S4 were in fact 5 dB higher. The fixed-level condition (solid squares) shows a typical decrease in ΔL with increasing pedestal level, often referred to as the ''near-miss'' to Weber's law. Previous studies of the ''near-miss'' have generally quoted slopes in terms of $10\log(\Delta I)$, or intensity increment level, as a function of $10\log(I)$, or pedestal level (McGill and Goldberg, 1968; Viemeister, 1972). In these units, the slope of the mean data from the fixed-level condition is 0.93, which is consistent with results from previous studies (Rabinowitz *et al.*, 1976).

In contrast, both the roving-level (open squares) and the across-frequency (circles in squares) conditions show much less dependence on overall level, with slopes [$10\log(\Delta I)$ as a function of $10\log(I)$] closer to unity, of 0.99 and 0.97, respectively. The curves in the figure are model fits, described below. As in experiment 1, there seems to be no qualitative difference between the results from level discrimination (fixed and roving level) and loudness discrimination across frequency. Instead, the deterioration in performance due to both level roving and across-frequency comparisons leads to a reduced dependence on overall level.

As with the data in experiment 1, it is possible to derive predictions based on the effects of stimulus-dependent sensation noise and stimulus-independent central noise. Again, the results from the fixed-level condition were used to derive an initial estimate of internal variance. Performance in the other two conditions was predicted by assuming the addition of level-independent central noise. This was achieved as described for experiment 1. The predictions are shown as solid curves in Fig. 4. The equation used to derive the noise variance for the fixed-level condition was $\Delta L^2 = -0.0802L + 7.98$, where L is the nominal pedestal level in dB SPL. The constants added to the values of ΔL_{DL}^2 in order to fit the data from the roving-level and across-frequency conditions were 5.5 and 23.3, respectively. These values are reasonably similar to the ones found in experiment 1 of 8.2 and 20.1, considering that only a subset of the original listener group was used in experiment 2. The similarity of these values lends some support to the idea that roving-level and across-frequency conditions may deteriorate performance in a way that is stimulus independent.

The predictions capture the trend of reduced level dependence in the roving-level and across-frequency conditions. However, the actual data show a smaller-than-predicted effect of level in the roving-level condition, and a greater-than-predicted effect of level in the across-frequency condition. While the fit is not quite as convincing as in experiment 1, the trend is captured sufficiently to suggest that the data can be explained in terms of an increase in stimulus-independent central noise relative to stimulus-dependent sensation noise.

No deterioration in performance at medium levels was found in the across-frequency condition. Based on the assumption that the loudness DL is inversely proportional to the slope of the loudness function (Buus *et al.*, 1997), and the fact that the loudness function seems to be shallower at medium levels than at high or low levels at 1 kHz, at least when measured using loudness integration (Florentine *et al.*, 1996), a deterioration at medium levels would have been expected. Such a mid-level deterioration in DLs was found by Buus *et al.* (1997) at 5 kHz in a comparison of long- and short-duration tones, which was quantitatively consistent with the change in the slope of the derived loudness function. A number of parameter differences could account for the different pattern of results observed here, including the use of equal-duration but different-frequency tones, the use of feedback, and the lower frequencies tested here. It should be noted, however, that a mid-level deterioration in DLs has been observed before in traditional level discrimination tasks at frequencies above about 2 kHz, but not below (Penner *et al.*, 1974; Carlyon and Moore, 1984; Long and Cullen, 1985; Florentine *et al.*, 1987; Oxenham and Moore, 1995). Thus, the mid-level deterioration observed by Buus *et al.* at 5 kHz may in part be a reflection of an effect also observed in traditional level-discrimination tasks.

The results are also inconsistent with the predictions of the models explored by Durlach, Braida, and colleagues. Generally in these models, sensation noise is assumed to be constant, and when the near-miss to Weber's law has been accounted for, this has been achieved by a steepening of the function relating sound level to an internal sensation variable (e.g., Braida *et al.*, 1984). Thus it seems that their model would predict parallel functions in Fig. 4.

The present results may also have some implications for models that attempt to relate the slope of the loudness function to ΔL_{DL} (Hellman *et al.*, 1987; Hellman and Hellman, 1990; Allen and Neely, 1997). If ΔL_{DL} as a function of level is determined by the slope of the loudness function, changing the experimental parameters should result in a parallel shift in thresholds, as predicted by the models of Durlach and colleagues. The fact that the relation between ΔL_{DL} and level depends on experimental manipulations seems to indicate that there exists a dissociation between the loudness function and level discrimination, which is not accounted for by models that postulate a direct relation between the slope of the loudness function and level discrimination.

III. SUMMARY

In experiment 1, level discrimination was measured for 1- and 2-kHz tones as a function of stimulus duration for three conditions: (1) within-frequency comparisons with a fixed pedestal level of 65 dB SPL; (2) within-frequency comparisons with the pedestal level roved uniformly between 55 and 75 dB SPL; and (3) across-frequency comparisons with the pedestal level roved uniformly between 55 and 75 dB SPL. As found previously (Florentine, 1986), discrimination in the fixed-level condition improved with pedestal duration. Roving the pedestal level produced a greater deterioration in performance for long than for short tones, leading to less dependence of discrimination thresholds on duration. Across-frequency comparisons produced a further deterioration in performance and even less duration dependence. However, there was no qualitative difference between the results of the within-frequency and the across-frequency roved conditions.

In experiment 2, ΔL_{DL}'s for the same three conditions were measured as a function of pedestal level using 500-ms tones. In the fixed-level condition, the expected improvement

with increasing pedestal level was observed. Roving the pedestal level over a 20-dB range increased ΔL_{DL}'s and reduced the dependence on overall level, producing a relationship much closer to Weber's law than that observed in the fixed-level condition. Across-frequency comparisons produced a further reduction in performance. Again, there was no qualitative difference between the results of the within-frequency and across-frequency roved conditions.

The results do not provide support for a distinction between level discrimination and loudness discrimination, whereby level discrimination is performed using independent information from multiple frequency channels and loudness discrimination is based on an overall sensation of loudness (Buus *et al.*, 1997). Instead, the results may be understood within a framework similar to that suggested by Durlach, Braida, and colleagues (Durlach and Braida, 1969; Berliner and Durlach, 1973; Berliner *et al.*, 1977; Lim *et al.*, 1977). In this approach, as adapted here, two separate internal noise sources are required. The first, termed sensation noise, represents the variance associated with the initial coding of the stimulus. This noise is assumed to be independent of experimental manipulations, such as roving level or changing the interstimulus interval, but (unlike in the formulation of Durlach and colleagues) is assumed to be dependent on stimulus parameters, such as duration and level. The second noise, termed central noise, is assumed to be the variance added by higher, perhaps more cognitive, processes, such as memory and across-frequency processing (Lim *et al.*, 1977). This noise is not dependent on stimulus parameters, but is dependent on experimental manipulations. The increase in ΔL_{DL}'s and the reduction in their dependence on duration and level in the roving-level and across-frequency conditions can be explained in terms of an increase in the stimulus-independent central noise, which represents the increased difficulty of the tasks, while leaving the initial coding of the stimuli (sensation noise) unaffected.

ACKNOWLEDGMENTS

This work was supported by NIH Grant Nos. R01 DC 00187 and R01 DC 03909. Two reviewers provided helpful comments on an earlier version of this paper.

APPENDIX: DERIVING ΔL

In the across-frequency conditions, ΔL_{DL} was derived from four interleaved tracks, in which two used a 1-kHz standard and a 2-kHz comparison tone, and two used the opposite. If the two tones are not calibrated exactly for equal loudness, the two pairs of interleaved tracks will not converge on the same ΔL. Even in this case, the ''true'' ΔL_{DL} can be calculated quite simply, as follows:

Assume two tones at different frequencies where tone 1 is fixed at level L_{1F} and tone 2 is adjusted to be 1 DL above the fixed tone 1, such that

$$L_{2V} = L_{1F} + K + \Delta L_{DL}, \tag{A1}$$

where L_{2V} is the (varied) level of tone 2, L_1 is the (fixed) level of tone 1, K is the level difference necessary for equal loudness, and ΔL_{DL} is the ''true'' DL. The quantity $L_{2V} - L_{1F}$ is then the measured DL. Similarly, when tone 2 is fixed, and tone 1 is set to be 1 DL above tone 2,

$$L_{1V} = L_{2F} - K + \Delta L_{DL}, \tag{A2}$$

where ΔL_{1V} is the varied level of tone 1, L_{2F} is the fixed level of tone 2, and $L_{1V} - L_{2F}$ is the measured DL. Adding A1 and A2 and rearranging the terms gives

$$2\Delta L_{DL} = (L_{2V} - L_{1F}) + (L_{1V} - L_{2F}). \tag{A3}$$

The terms $(L_{2V} - L_{1F})$ and $(L_{1V} - L_{2F})$ are the two measured DLs, ΔL_1 and ΔL_2, respectively, so,

$$\Delta L_{DL} = (\Delta L_1 + \Delta L_2)/2. \tag{A4}$$

Equation A4 shows that the ''true'' ΔL_{DL} can be found as the average of the DLs measured when L_1 is varied and when L_2 is varied, even if the fixed levels did not yield equal loudness. Strictly speaking, then, it would not have been necessary in the experiments to adjust the levels of the tones to approximate equal loudness, as any difference could be dealt with *post hoc*. However, as feedback was provided, it was desirable to have the two pedestals as close to equal loudness as possible.

Allen, J. B., and Neely, S. T. (**1997**). ''Modeling the relation between the intensity just-noticeable difference and loudness for pure tones and wide-band noise,'' J. Acoust. Soc. Am. **102**, 3628–3646.

Berliner, J. E., and Durlach, N. I. (**1973**). ''Intensity perception. IV. Resolution in roving-level discrimination,'' J. Acoust. Soc. Am. **53**, 1270–1287.

Berliner, J. E., Durlach, N. I., and Braida, L. D. (**1977**). ''Intensity perception. VII. Further data on roving-level discrimination and the resolution and bias edge effects,'' J. Acoust. Soc. Am. **61**, 1577–1585.

Braida, L. D., Lim, J. S., Berliner, J. E., Durlach, N. I., Rabinowitz, W. M., and Purks, S. R. (**1984**). ''Intensity perception XIII. Perceptual anchor model of context-coding,'' J. Acoust. Soc. Am. **76**, 722–731.

Buus, S., and Florentine, M. (**1991**). ''Psychometric functions for level discrimination,'' J. Acoust. Soc. Am. **90**, 1371–1380.

Buus, S., Florentine, M., and Poulsen, T. (**1997**). ''Temporal integration of loudness, loudness discrimination, and the form of the loudness function,'' J. Acoust. Soc. Am. **101**, 669–680.

Buus, S., Florentine, M., and Zwicker, T. (**1995**). ''Psychometric functions for level discrimination in cochlearly impaired and normal listeners with equivalent-threshold masking,'' J. Acoust. Soc. Am. **98**, 853–861.

Carlyon, R. P., and Moore, B. C. J. (**1984**). ''Intensity discrimination: A severe departure from Weber's Law,'' J. Acoust. Soc. Am. **76**, 1369–1376.

Durlach, N. I., and Braida, L. D. (**1969**). ''Intensity perception. I. Preliminary theory of intensity resolution,'' J. Acoust. Soc. Am. **46**, 372–383.

Florentine, M. (**1986**). ''Level discrimination of tones as a function of duration,'' J. Acoust. Soc. Am. **79**, 792–798.

Florentine, M., and Buus, S. (**1981**). ''An excitation-pattern model for intensity discrimination,'' J. Acoust. Soc. Am. **70**, 1646–1654.

Florentine, M., Buus, S., and Mason, C. R. (**1987**). ''Level discrimination as a function of level for tones from 0.25 to 16 kHz,'' J. Acoust. Soc. Am. **81**, 1528–1541.

Florentine, M., Buus, S., and Poulsen, T. (**1996**). ''Temporal integration of loudness as a function of level,'' J. Acoust. Soc. Am. **99**, 1633–1644.

Green, D. M. (**1988**). *Profile Analysis* (Oxford U. P., Oxford).

Hellman, R. P., Scharf, B., Teghtsoonian, M., and Teghtsoonian, R. (**1987**). ''On the relation between the growth of loudness and the discrimination of intensity for pure tones,'' J. Acoust. Soc. Am. **82**, 448–453.

Hellman, W. S., and Hellman, R. P. (**1990**). ''Intensity discrimination as the driving force for loudness. Application to pure tones in quiet,'' J. Acoust. Soc. Am. **87**, 1255–1265.

Henning, G. B. (**1970**). ''A comparison of the effects of signal duration on frequency and amplitude discrimination,'' *in Frequency Analysis and Periodicity Detection in Hearing*, edited by R. Plomp and G. F. Smoorenburg (Sijthoff, Leiden).

Jesteadt, W., Wier, C. C., and Green, D. M. (**1977**). ''Intensity discrimination as a function of frequency and sensation level,'' J. Acoust. Soc. Am. **61**, 169–177.
Lim, J. S., Rabinowitz, W. M., Braida, L. D., and Durlach, N. I. (**1977**). ''Intensity perception. VIII. Loudness comparisons between different types of stimuli,'' J. Acoust. Soc. Am. **62**, 1256–1267.
Long, G. R., and Cullen, J. K. (**1985**). ''Intensity difference limens at high frequencies,'' J. Acoust. Soc. Am. **78**, 507–513.
McGill, W. J., and Goldberg, J. P. (**1968**). ''Pure-tone intensity discrimination and energy detection,'' J. Acoust. Soc. Am. **44**, 576–581.
Moore, B. C. J., and Raab, D. H. (**1974**). ''Pure-tone intensity discrimination: some experiments relating to the 'near-miss' to Weber's Law,'' J. Acoust. Soc. Am. **55**, 1049–1054.
Oxenham, A. J., and Moore, B. C. J. (**1995**). ''Overshoot and the 'severe departure' from Weber's law,'' J. Acoust. Soc. Am. **97**, 2442–2453.
Penner, M. J., Leshowitz, B., Cudahy, E., and Richard, G. (**1974**). ''Intensity discrimination for pulsed sinusoids of various frequencies,'' Percept. Psychophys. **15**, 568–570.
Rabinowitz, W. M., Lim, J. S., Braida, L. D., and Durlach, N. I. (**1976**). ''Intensity perception. VI. Summary of recent data on deviations from Weber's law for 1000-Hz tone pulses,'' J. Acoust. Soc. Am. **59**, 1506–1509.
Richards, V. M. (**1992**). ''The detectability of a tone added to narrow bands of equal-energy noise,'' J. Acoust. Soc. Am. **91**, 3424–3435.
Viemeister, N. F. (**1972**). ''Intensity discrimination of pulsed sinusoids: the effects of filtered noise,'' J. Acoust. Soc. Am. **51**, 1265–1269.
Viemeister, N. F. (**1974**). ''Intensity discrimination of noise in the presence of band-reject noise,'' J. Acoust. Soc. Am. **56**, 1594–1600.

Relationships among age-related differences in gap detection and word recognition

Karen B. Snell
Audiology Department, Rochester Institute of Technology, 52 Lomb Memorial Drive, Rochester, New York 14623-0887

D. Robert Frisina
International Center for Hearing and Speech Research, Rochester Institute of Technology, 52 Lomb Memorial Drive, Rochester, New York 14623-0887 and Otolaryngology Division, University of Rochester School of Medicine and Dentistry, Rochester, New York 14642-8629

(Received 20 August 1997; revised 5 February 1999; accepted 19 November 1999)

The relationships among age-related differences in gap detection and word recognition in subjects with normal hearing or mild sensorineural hearing loss were explored in two studies. In the first study, gap thresholds were obtained for 40 younger and 40 older subjects. The gaps were carried by 150-ms, modulated, low-pass noise bursts with cutoff frequencies of 1 or 6 kHz. The noise bursts were presented at an overall level of 80 dB SPL in three background conditions. Mean gap thresholds ranged between 2.6 and 7.8 ms for the younger age group and between 3.4 and 10.0 ms for the older group. Mean gap thresholds were significantly larger for the older group in all six conditions. Gap thresholds were not significantly correlated with audiometric thresholds in either age group but the 1-kHz gap thresholds increased with age in the younger group. In the second study, the relationships among gap thresholds, spondee-in-babble thresholds, and audiometric thresholds of 66 subjects were examined. Compared with the older subjects, the younger group recognized the spondees at significantly lower (more difficult) spondee-to-babble ratios. In the younger group, spondee-in-babble thresholds were significantly correlated with gap thresholds in conditions of high-frequency masking. In the older group, spondee-in-babble thresholds, gap thresholds, and audiometric thresholds were not significantly correlated, but the spondee-in-babble thresholds and two audiometric thresholds increased significantly with age. These results demonstrate that significant age-related changes in auditory processing occur throughout adulthood. Specifically, age-related changes in temporal acuity may begin decades earlier than age-related changes in word recognition. © *2000 Acoustical Society of America.* [S0001-4966(00)01303-5]

PACS numbers: 43.66.Mk, 43.71.Lz, 43.66.Sr [JWH]

INTRODUCTION

Studies of age-related changes in speech perception have shown that older adults experience more problems understanding speech in everyday communication and require more favorable speech-to-noise ratios when compared with younger adults (e.g., CHABA, 1988). Some studies suggest that many of the presumed age-related differences in speech understanding can be predicted by a loss in absolute sensitivity (e.g., Humes *et al.*, 1994). However, there remains considerable interest in studying other age-related factors that may contribute to poorer speech understanding in older adults (e.g., Stuart and Phillips, 1996; Divenyi and Haupt, 1997a, 1997b, 1997c). Central changes induced by age-related peripheral pathology such as tonotopic reorganization or decreases in inhibition (Willott, 1996) are one type of factor that may add to or interact with the effects of hearing loss. Age-related differences in the central auditory system itself, e.g., changes in spontaneous neural activity and the development of inhibition (Ison *et al.*, 1998), are a second. Furthermore, changes in audition may underlie age-related differences in working memory (Pichora-Fuller *et al.*, 1995), and selective attention (Barr and Giambra, 1990).

Several studies have demonstrated age-related differences in temporal processing (see Fitzgibbons and Gordon-Salant, 1996 for a review) and parallel changes in the auditory brainstern (Boettcher *et al.*, 1996; Walton *et al.*, 1997) that do not appear to be induced by peripheral hearing loss. Schneider *et al.* (1994) in a study of subjects with normal hearing or mild high-frequency loss reported age-related differences in gap detection thresholds that were not significantly correlated with audiometric thresholds. However, a limitation in other studies of age-related changes in auditory processing has been the challenge, regardless of species, in matching younger and older age groups for absolute sensitivity. When age is confounded with hearing loss, it is difficult to differentiate differences in auditory processing that are age-related only from those reflecting the interaction of age with hearing loss.

The effects of deficits in temporal resolution, if any, on speech perception remain unclear. Several investigators have reported significant correlations between measures of temporal resolution in quiet and word recognition in noise. For example, Tyler *et al.* (1982) studied 16 normal-hearing [mean age=23 years; standard deviation (s.d.)=6] and 16 hearing-impaired adults (mean age=53 years; s.d.=14). They reported significant correlations between gap thresholds obtained with noise bursts in quiet and word recognition scores obtained in noise after combining the data for the two groups and partialing out the effects of absolute thresholds. In contrast are the results of a study by Divenyi and Haupt

(1997c). They studied the performance of 45 older (mean age=64.4 years; s.d.=4.4) and 16 younger adults (mean age =22.1 years; s.d.=3.5) on 34 auditory measures. Divenyi and Haupt reported little correlation between gap detection thresholds obtained in quite and various measures of word recognition obtained in a background of speech babble or reverberation. They suggested that in order to detect a correspondence between gap detection thresholds and speech perception tasks, both should be measured in the presence of competing stimuli. Similarly, Fitzgibbons and Gordon-Salant (1996) suggested that limitations in temporal processing in older listeners become more evident as the level of stimulus complexity and the demands of the listening task increase. While the inability to discriminate gaps carried by acoustically simple stimuli in quiet backgrounds may explain little of the variation in speech perception in quiet among older adults, greater sensitivity to the temporal characteristics of complex stimuli may contribute to speech understanding in complex listening conditions (Drullman, 1995).

Recently, Strouse *et al.* (1998) studied the relationship between temporal resolution and speech perception in 12 younger and 12 older subjects with clinically normal hearing. Although the older listeners were found to perform more poorly than younger listeners on both temporal resolution and speech perception measures, temporal resolution measures were uncorrelated with speech perception measures in both age groups. Strouse *et al.* suggested that the correlations might have been more robust if temporal resolution and speech perception had been measured in more similar conditions. Strouse *et al.* also noted that the analysis was limited by the small number of subjects in each group.

In separate reports from this lab, age-related differences in speech perception in noise (Frisina and Frisina, 1997) and temporal processing (Snell, 1997) in adults with normal hearing have been discussed. Frisina and Frisina (1997) compared spondee recognition scores obtained in babble and high-frequency noise by 10 younger adults with those of 10 older adults and reported better performance by the younger group. Snell (1997) found that in both quiet and noisy backgrounds, the gap thresholds of 20 younger adults were significantly smaller than were those of 20 older adults. Because of the relatively small group sizes in those studies, we were unable to examine the relationships among the measures of temporal resolution and word recognition. The primary goal of this study was to extend our previous work by examining the relationships among age-related differences in gap detection and word recognition in larger groups of younger and older subjects. In addition, the contributions of age and absolute sensitivity within each age group were explored.

I. STUDY 1

In our first study, the effects of age and absolute thresholds on the gap thresholds of 80 subjects were examined. An analysis of the gap thresholds for 40 of these subjects, consisting of 20 matched pairs of younger and older listeners, has been previously reported (Snell, 1997). The 6 experimental conditions in the current study represent a subset of the original 24 conditions. Doubling the sample size while decreasing the number of conditions permitted a more rigorous analysis.

TABLE I. Mean absolute thresholds (dB HL) and standard deviations (dB) for the younger and older subjects in the first study.

	Mean absolute threshold (dB HL) Frequency (kHz)					
	0.25	0.50	1	2	4	8
	Younger subjects ($N=40$)					
Mean	7.8	8.5	7.7	8.5	11.7	8.9
s.d.	(5.6)	(6.1)	(6.4)	(7.9)	(11.0)	(11.5)
	Older subjects ($N=40$)					
Mean	9.0	9.4	8.2	9.4	14.6	21.8
s.d.	(5.9)	(8.3)	(7.5)	(9.1)	(10.2)	(12.3)

A. Method

Forty younger (20 men, 20 women) and 40 older (13 men, 27 women) adults served as subjects. Fewer older men participated in this study because older men with normal clinical audiometric results were difficult to locate despite extensive audiometric screening of potential subjects. Younger subjects ranged in age from 17 to 40 years (mean age of 26.4 years); older subjects were between 61 and 82 years of age (mean age of 68.3 years). Shown in Table I are the mean audiometric thresholds (ANSI S3.6-1989) and standard deviations. Note that the mean thresholds of the two age groups differ by less than 3 dB at octaves between .25 and 4 kHz, while the difference increases to 12.9 dB at 8 kHz. An initial analysis of variance (ANOVA) was carried out on the thresholds using a repeated measures design (SYSTAT, 1997) with one between (two age groups) and one within factor (five audiometric frequencies: 0.25, 0.5, 1, 2, and 4 kHz). The main effect of frequency was significant $[F(4,312)=13.078;\ p<0.0005]$. The main effect of age $[F(1,78)=0.768;\ p=0.384]$ and the interaction (frequency by age) were not $[F(4,312)=0.663;\ p=0.618]$. While the effect of age was not significant at frequencies between 0.25 and 4 kHz, a subsequent one-way ANOVA of the 8-kHz audiometric thresholds indicated a significant effect of age $[F(1,78)=23.178;\ p<0.0005]$.

Gaps were shaped with 1-ms cosine-squared rise–fall envelopes and placed in the 150-ms signal noise bursts 100 ms after noise burst onset. The stimuli were low-pass noise bursts, digitized with cutoff frequencies of 1 or 6 kHz, and randomly generated for each presentation [Tucker Davis Technologies (TDT) AP2]. These signals will be referred to as the 1- and 6-kHz noise burst carriers throughout the remainder of the paper. The random noise bursts were digitally modulated in amplitude with 20-Hz sinusoids to achieve a modulation depth of 13% to achieve a somewhat more speechlike waveform envelope. The noise bursts were transduced by a 16-bit D/A converter (TDT DD1), attenuated (TDT PA4) to an overall level of 80-dB sound-pressure level (SPL), routed through a signal mixer (TDT SM 3) and headphone buffer (TDT HB5), and then led to an earphone (Beyer DT48). Noise bursts were presented in three background conditions. In the first condition no background noise

was present. In the second condition, continuous white noise was digitally generated (TDT WG1), attenuated (TDT PA4) to an overall level of 45 dB SPL [spectrum level (N_0) $=4$ dB], and mixed with the gated noise bursts. This level was sufficient to shift absolute thresholds of the signal noise bursts by at least 10 dB as well as mask spectral splatter (Moore *et al.*, 1992). In the third condition, a high-frequency masker was present in addition to the noise floor. The spectrum level of the high-frequency masker was fixed at 20 dB below the spectrum level of the noise burst and its cutoff frequencies were 6 and 12 kHz. The high-frequency masker was gated on and off with the signal noise burst but did not contain a gap at 100 ms after onset. The purpose of this high-frequency masker was to minimize the potential contribution of auditory fibers tuned to high frequencies where our subject groups were not well matched. Thus in the noise floor and high-frequency masker condition, the gap was partially filled by the high-frequency masker as well as by the continuous white noise floor. These three conditions are referred to in the remainder of this paper as quiet (Q), noise floor (NF), and noise floor and high-frequency masker (NF+HF masker) conditions. In summary, gap thresholds were obtained for two noise burst carriers that differed in cutoff frequency (1 and 6 kHz) and three background conditions for a total of six conditions.

Gap thresholds were obtained in an adaptive, two-interval, forced-choice (2 IFC) procedure to estimate the 79% point on the psychometric function. Within each condition, two threshold estimates were obtained and averaged to obtain a single threshold estimate. The order of conditions was randomized across sessions and subjects. Each subject practiced for about one and one-half hours prior to data collection. Subjects listened during six to eight sessions each lasting one to one and one-half hours.

B. Results and discussion

The mean gap detection thresholds for the 80 subjects in the six experimental conditions are shown in Fig. 1. Age is shown on the abscissa; the gap threshold in ms is plotted on the ordinate. The three panels on the left represent gap thresholds obtained with the 6-kHz noise burst carrier in backgrounds of quiet, continuous noise floor, and noise floor and high-frequency masker. The three panels on the right represent thresholds obtained with the 1-kHz noise burst carrier in backgrounds of quiet, continuous noise floor, and continuous noise floor with a high-frequency masker. The ordinate scale used for the right panels is expanded to encompass the wider range of gap thresholds obtained with the 1-kHz noise bursts. Note that in each plot, there is overlap between the gap thresholds of the younger and older groups. Generally, however, the distributions for the younger and older subjects are different, and whereas gap thresholds for many younger and older subjects were the same, some older subjects had higher gap thresholds.

These gap thresholds were analyzed in a repeated measure ANOVA (SYSTAT, 1997) with one between factor (age group) and two within factors (cutoff frequency of the noise burst, background condition). The ANOVA results indicated significant main effects of age [$F(1,78)=19.618$, $p<0.0005$], cutoff frequency [$F(1,78)=893.740$, $p<0.0005$], and background condition [$F(2,156)=6.672$, $p<0.002$]. The interaction between age and cutoff frequency [$F(1,78)=0.003$, $p<0.003$] was also significant. The interactions between age and background [$F(2,156)=2.318$, $p<0.103$] and cutoff-frequency and background [$F(2,156)=1.156$, $p<0.317$] were not. The three-way interaction, cutoff frequency, background, and age, was also significant [$F(2,156)=3.985$, $p<0.021$].

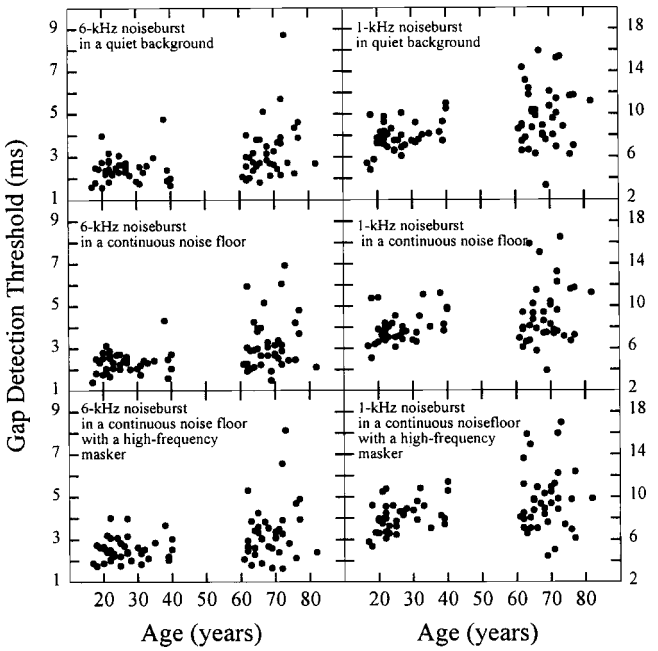

FIG. 1. Six scatter plots with age (years) on the abscissa and gap detection threshold (ms) on the ordinate. The three panels on the left show data obtained with a gated, modulated noise burst low passed at 6 kHz at an overall level of 80 dB SPL. The three panels on the right represent data obtained with a gated, modulated noise burst low passed at 1 kHz at an overall level of 80 dB SPL. The top panels represent the two conditions with a quiet background. The middle panels contain thresholds obtained with a continuous white noise floor in the background. The bottom panels represent conditions with a continuous white noise floor and a gated high-frequency masker. The high-frequency masker was gated, had cutoff frequencies of 6 and 12 kHz, and was presented at a spectrum level 20 dB below that of the noise burst carrier. Each data point represents the mean gap thresholds (ms) of one subject.

The significant interaction between age and cutoff frequency reflects the larger between-group differences in gap thresholds found with the 1-kHz compared with the 6-kHz noise burst carriers. That is, the mean gap thresholds of the younger group were 0.6 to 0.8 ms smaller than those of the older group when obtained with the 6-kHz noise bursts, while they were 1.3 to 2.2 ms smaller when obtained with the 1-kHz noise bursts. The significant three-way interaction reflects an interaction between frequency and background that differs with age group. In the younger group, the mean gap threshold in the noise floor and high-frequency masking condition was significantly poorer than in the quiet and noise floor conditions but only with the 6-kHz noise burst carrier. In the older group, the mean gap thresholds in the noise floor condition and the noise floor and high-frequency-masking condition were significantly poorer than in the quiet condition but only with the 1-kHz noise burst carrier. *Post-hoc* comparisons using Bonferroni-adjusted probabilities re-

TABLE II. Correlation matrices for gap thresholds and audiometric thresholds for younger and older groups. Gap thresholds were obtained with modulated noise bursts at an overall level of 80 dB SPL. The noise bursts had low-pass cutoff frequencies of 1 or 6 kHz. Three background conditions were used: quite (Q), continuous white noise floor (NF), and continuous white noise floor and gated high-frequency masker (NF+HF masker). Before the matrices were estimated, one younger subject was identified as an outlier and eliminated. (With the probabilities adjusted by the Bonferroni method, none of the coefficients was significant at the relaxed level of $p<0.10$.)

Audiometric threshold (dB HL)	Gap thresholds (ms)					
	6-kHz low-pass noise burst			1-kHz low-pass noise burst		
Frequency (kHz)	Q	NF	NF+HF masker	Q	NF	NF+HF masker
	Younger subjects ($N=39$)					
0.25	0.10	0.00	−0.06	−0.12	0.12	−0.02
0.50	0.12	0.15	−0.02	−0.24	−0.05	−0.21
1.00	0.09	0.10	−0.03	−0.21	−0.01	−0.21
2.00	−0.05	−0.03	−0.14	−0.03	0.11	−0.13
4.00	0.20	0.11	0.08	0.17	0.20	0.02
8.00	−0.08	−0.10	−0.09	0.28	0.22	0.29
	Older subjects ($N=40$)					
0.25	0.13	0.09	0.12	0.07	0.21	0.12
0.50	0.11	0.00	0.06	−0.01	0.17	0.02
1.00	0.17	0.13	0.10	0.05	0.23	0.25
2.00	0.19	0.15	0.22	0.03	0.16	0.11
4.00	−0.02	−0.08	0.05	−0.01	0.03	0.03
8.00	0.12	0.04	−0.07	0.23	0.40	0.13

vealed the mean gap thresholds of the younger group were smaller than those of the older group in all six conditions.

1. Absolute thresholds and gap thresholds

A Pearson correlation matrix for the six gap thresholds and six audiometric thresholds was estimated for each age group. Outlying cases were detected and eliminated using a robust procedure outlined by Hadi (1994). The Hadi outlier identification and estimation option (SYSTAT, p. 319) identifies specific subjects as outliers (if there are any) and then uses the acceptable cases to estimate the requested matrix in the usual way. In brief, a robust covariance matrix is used to iteratively compute Mahalanobis distances, adding cases, and updating the covariance matrix until an internal limit based on a chi-square statistic is exceeded. The cases not entered are identified as outliers. The remaining cases are then used to compute the Pearson correlation coefficients in the usual way.

The Hadi procedure identified one subject in the younger group as an outlier prior to matrix estimation. As shown in Table II, the resulting 36 correlation coefficients between gap thresholds and absolute thresholds ranged from −0.09 to 0.279 for the younger group and from −0.08 to 0.397 for the older group. All coefficients failed to achieve significance at $p<0.10$ using Bonferroni-adjusted probabilities to provide protection for multiple tests. We conclude that for these subjects with relatively normal hearing or mild hearing loss, gap thresholds are not significantly correlated with absolute thresholds.

2. Age and gap thresholds

Pearson correlations between gap thresholds and age were also examined. Two younger and five older subjects were identified as outliers by the Hadi procedure and the remaining acceptable cases (38 younger and 35 older) were used to compute the 12 correlation coefficients shown in Table III. The results shown at the bottom of the table indicate that none of the gap thresholds of the older subjects increased with age. This finding contrasts with the results for the younger group where three coefficients (0.512, 0.503, and 0.481) were significant at a Bonferroni-adjusted $p<0.01$. These represent correlations within the younger group between the gap thresholds obtained with the 1-kHz noise burst and age. This suggests that within the younger group and regardless of background condition, gap thresholds increase with age when the gap carrier is a modulated noise burst low passed at 1 kHz.

Could age-related increases in audiometric thresholds (if any) within the younger group have contributed to these age-related increases in gap thresholds? To answer this question, recall that the analysis summarized in Table II indicated that

TABLE III. Correlation coefficients between six gap thresholds and age for the younger and older subjects in the first study. The six gap threshold conditions are the same as those described in Table II. Outliers (two younger, five older subjects) were eliminated before the matrices were estimated.

	Gap threshold (ms)					
	6 kHz low-pass noise burst			1-kHz low-pass noise burst		
	Q	NF	NF+HF masker	Q	NF	NF+HF masker
	Younger subjects ($N=38$)					
Age (years)	0.11	0.00	0.04	0.51[a]	0.50[a]	0.48[a]
	Older subjects ($N=35$)					
Age (years)	0.13	0.15	0.23	0.04	0.03	−0.02

[a]Bonferroni-adjusted probability, $p<0.01$.

TABLE IV. Correlations among gap thresholds obtained with noise bursts at overall level of 80 dB SPL for younger and older groups in the first study. The low-pass cutoff frequencies of the noise bursts (1 and 6 kHz) and the background conditions (Q, NF, and NF+HF masker) are the same as those described in Table II. Before the matrices were estimated, two younger and seven older subjects were eliminated as outliers using the Hadi procedure. Only coefficients with Bonferroni-adjusted probabilities $p<0.10$ were retained in the matrices.

	Gap thresholds (ms)					
	6-kHz noise burst			1-kHz noise burst		
	Q	NF	NF+HF masker	Q	NF	NF+HF masker
	Younger subjects ($N=38$)					
6-kHz noise burst						
Q	1.000					
NF	0.676[a]	1.000				
NF+HF masker	0.842[a]	0.805[a]	1.000			
1-kHz noise burst						
Q				1.000		
NF				0.776[a]	1.000	
NF+HF masker				0.801[a]	0.784[a]	1.000
	Older subjects ($N=33$)					
6-kHz noise burst						
Q	1.000					
NF	0.719[a]	1.000				
NF+HF masker	0.847[a]	0.696[a]	1.000			
1-kHz noise burst						
Q	0.673[a]	0.797[a]	0.498[b]	1.000		
NF	0.489[b]	0.468[b]		0.747[a]	1.000	
NF+HF masker	0.509[b]	0.645[a]		0.785[a]	0.846[a]	1.000

[a]Significant at a Bonferroni-adjusted $p<0.01$.
[b]Significant at Bonferroni-adjusted $p<0.05$.

there were no significant relationships (at an Bonferroni-adjusted $p=0.10$) between the six gap thresholds and the six audiometric thresholds in either age group. Were there age-related increases in audiometric thresholds for the younger group? The correlation coefficients between age and the audiometric thresholds at 0.25, 5, 1, 2, 4, and 8 kHz were 0.04, −0.06, −0.04, 0.04, 0.38, and 0.24, respectively, for non-outlying cases (38 younger subjects). None of these coefficients was significant at a Bonferroni-adjusted $p=0.05$, though the coefficient between age and the audiometric threshold at 4 kHz (0.38) had a Bonferroni-adjusted $p=0.09$. We conclude that the age-related changes in gap thresholds in younger subjects cannot be attributed to age-related changes in their audiometric thresholds.

3. Patterns among gap thresholds

To further explore age-related differences in gap thresholds, correlations among the six gap thresholds were computed. The Hadi procedure identified two younger and seven older subjects as outlying cases. Shown in the top panel of Table IV is the matrix that represents the remaining 38 younger subjects; the lower matrix represents the remaining 33 older subjects. For purposes of clarity, correlation coefficients with Bonferroni-adjusted probabilities exceeding 0.10 were deleted. As in Tables II and III, conditions are ordered by the low-pass cutoff frequency of the noise burst and background condition (quiet, continuous noise floor, or continuous noise floor with gated high-frequency masker). Note that fewer correlation coefficients are significant in the matrix of the younger subjects. To illustrate that the correlations follow a pattern, a set of correlations within each matrix has been outlined by a rectangle. Coefficients falling outside the rectangles are correlation coefficients between gap thresholds obtained with two 6-kHz noise bursts or with two 1-kHz noise bursts. Coefficients within a box are between a gap threshold obtained with a 1-kHz noise burst and a gap threshold obtained with a 6-kHz noise burst. In the matrix for the younger group shown at the top, all nine correlation coefficients (enclosed by the top rectangle) failed to achieve significance. This suggests that the mechanisms underlying gap detection in the younger subjects may vary significantly depending on whether the carrier is a 1 or 6-kHz noise burst. This pattern is consistent with age-related increases in the gap thresholds with one carrier (the 1-kHz noise burst), but not the other (the 6-kHz noise burst) shown in Table III.

The pattern in the lower correlation matrix in Table IV representing the older age group contrasts with that of the younger subjects. Note that seven of the nine correlation coefficients enclosed by the bottom rectangle are significant. That is, the strength of correlation between gap thresholds obtained with carriers differing in their spectral characteristics is similar to that between gap thresholds obtained with carriers with the same spectra. That is, older subjects with relatively better acuity for gaps carried by 6-kHz noise bursts will generally have relatively better acuity for gaps carried by 1-kHz noise bursts.

To explore the generality of this finding, gap thresholds that had been obtained with noise bursts at an overall level of 70-dB SPL were also correlated. Aside from the lower presentation level, the method used to obtain these gap thresholds was identical to that previously described. Similarly, comparisons between age groups using Bonferroni-adjusted

TABLE V. Correlations among gap thresholds obtained with noise bursts at overall level of 70 dB SPL for younger and older groups in the first study. The low-pass cutoff frequencies of the noise bursts (1 and 6 kHz) and the background conditions (Q, NF, and NF+HF masker) are the same as those described in Table II. Before the matrices were estimated, the Hadi procedure identified and eliminated four older subjects as outliers. Only coefficients with Bonferroni-adjusted probabilities $p<0.10$ were retained in the matrices.

	Gap thresholds (ms)					
	6-kHz noise burst			1-kHz noise burst		
	Q	NF	NF+HF masker	Q	NF	NF+HF masker
	Younger subjects ($N=40$)					
6-kHz noise burst						
Q	1.000					
NF	0.778[a]	1.000				
NF+HF masker	0.542[a]	0.718[a]	1.000			
1-kHz noise burst						
Q				1.000		
NF	0.548[a]	0.482[b]		0.599[a]	1.000	
NF+HF masker			0.505[b]	0.772[a]	0.559[a]	1.000
	Older subjects ($N=36$)					
6-kHz noise burst						
Q	1.000					
NF	0.875[a]	1.000				
NF+HF masker	0.890[a]	0.902[a]	1.000			
1-kHz noise burst						
Q	0.560[a]	0.664[a]	0.632[a]	1.000		
NF	0.550[a]	0.677[a]	0.548[a]	0.789[a]	1.000	
NF+HF masker	0.550[a]	0.66[a]	0.591[a]	0.737[a]	0.849[a]	1.000

[a]Significant at a Bonferroni-adjusted $p<0.01$.
[b]Significant at Bonferroni-adjusted $p<0.05$.

probabilities revealed the mean gap thresholds of the younger group were smaller than those of the older group in all six conditions at the lower presentation level. The matrices for the six gap thresholds computed after elimination of outliers (no younger subjects, four older subjects) are shown in Table V. Note that the general patterns are similar to those seen in Table IV. In the matrix for the younger subjects shown in the upper panel, more than half of the correlations between noise bursts that differed in cutoff frequency failed to reach significance. In contrast, the gap thresholds of the older group are correlated regardless of the cutoff frequency of the noise burst. We conclude that in younger adults, the mechanisms underlying gap detection vary significantly depending on whether the carrier is a 1 or 6-kHz noise burst, but that gap detection in older adults may be less dependent on the spectral characteristics of the gap carrier.

4. Summary

To summarize, gap thresholds were obtained with gated, modulated noise bursts at an overall level of 80 dB SPL. Gap thresholds of the younger subjects were significantly smaller than those of the older subjects. The gap thresholds were not significantly related to audiometric thresholds in either age group. Within the younger age group, the 1-kHz gap thresholds increased with age in all three background conditions whereas the 6-kHz gap thresholds did not. Within the older group, gap thresholds were not significantly correlated with age.

Correlations among gap thresholds for noise bursts at overall levels of 70 and 80 dB SPL were also examined. At both levels (and across levels as well), gap thresholds of younger adults tended to be uncorrelated when the carriers differed in the cutoff frequency. That is, the strength of correlation among the gap detection thresholds was influenced by the carrier spectra. Gap thresholds obtained with carriers that were dissimilar in spectra were less correlated. This pattern was consistent with our finding that an age-related increase in gap thresholds occurred only with noise bursts low passed at 1 kHz. Thus within this younger group of subjects, there was a significant relationship between gap thresholds and age and there were significant relationships among gap thresholds but primarily among carriers similar in spectra. In contrast, gap thresholds of the older subjects tended to be correlated regardless of whether the carriers differed in cutoff frequency. However, gap thresholds did not increase significantly with age nor were gap thresholds significantly related to audiometric thresholds within the older group of subjects.

II. STUDY 2

The second study examined relationships among gap thresholds, two measures of word recognition in noise, age, and absolute sensitivity. Many of the subjects in the first study had also completed several speech perception studies. But given the limitations of a correlational approach, only a few speech measures could be included in the analysis, and we therefore focused on the relationship between word recognition and temporal acuity. Our purpose was to determine whether word recognition was significantly correlated with

TABLE VI. Mean absolute thresholds (dB HL) and standard deviations (dB) for the subjects in the second study.

	Mean absolute threshold (dB HL) Frequency (kHz)					
	0.25	0.50	1	2	4	8
	Younger subjects ($N=27$)					
Mean	7.4	7.6	6.8	8.1	12.4	10.0
s.d.	(6.1)	(7.0)	(7.4)	(8.4)	(12.4)	(13.2)
	Older subjects ($N=39$)					
Mean	9.0	8.8	7.8	9.4	14.2	21.8
s.d.	(6.0)	(7.7)	(7.0)	(9.3)	(10.0)	(12.4)

gap detection when both were measured in relatively complex background conditions.

A. Method

Of the 80 subjects in Study I, spondee-in-babble thresholds were available for 66 subjects (17 younger women, 10 younger men, 27 older women, and 12 older men). Shown in Table VI are their mean audiometric thresholds (ANSI S3.6-1989) and standard deviations. A repeated measures design with one between (two age groups) and one within factor (five audiometric frequencies: 0.25, 0.5, 1, 2, and 4 kHz) was used to analyze these thresholds in an ANOVA. The results indicated the effect of frequency was significant [$F(4,256)=13.196$; $p<0.0005$], but the effect of age group [$F(1,64)=0.628$; $p=0.431$] and their interaction (frequency and age group) were not [$F(4,256)=0.066$; $p=0.992$]. While the groups did not differ significantly in audiometric thresholds between 0.25 and 4 kHz, the results of a one-way ANOVA at 8 kHz indicated that the effect of age group was significant [$F(1,64)=13.693$; $p<0.0005$]. Note that these results are substantially the same as those reported for the subjects in the first study.

Spondee-in-babble (spondee/B) thresholds were obtained with 11 spondees (drawbridge, eardrum, grandson, northwest, padlock, playground, railroad, sidewalk, toothbrush, woodwork, and workshop) from a commercially available CD recording of the CID W-1 word lists (Q-Mass Speech Audiometry Materials, Vol. 1). Two of the 11 spondees were among the six spondees identified by Cheesman (1992) as homogeneous with respect to difficulty in various levels of multitalker babble. The spondees were stored on a hard drive of a computer. During playback (TDT AP 2), the spondees were transduced by a 16-bit D/A converter (TDT DAC1), attenuated (TDT PA4 and Grason-Stadler GS1-16), and led to a single earphone (Beyer DT48) in a circumaural cushion. The presentation level was 30 dB SL with reference to each subject's speech recognition threshold (SRT) for the same set of spondees in quiet. This level (30 dB SL) was held constant during a run and corresponded to mean overall sound-pressure levels of 56.0 and 60.5 dB SPL for the younger and older groups, respectively. Subjects listened with the same ear used for the gap detection study.

The spondee presented on each trial was randomly selected from the set of 11 spondees. Twelve-talker speech babble from the recorded Revised Spin Test (Cosmos Corporation), also stored on the same computer hard drive, was used in both spondee /B tasks. During playback (TDT AP2), the babble level was attenuated (TDT PA4) from trial to trial following a one-down, one-up rule. The initial step size of 5 dB was decreased to 2 dB after the first six trials and each run terminated after 12 reversals. In one condition, a broadband noise (TDT WG1) was high-pass filtered at 4 kHz (TDT PF1) and presented at an overall level of 60 dB SPL. In the other condition, no high-frequency masker was present. Spondee/B thresholds for both conditions, i.e., the condition with the high-frequency masker and the condition without it, were obtained during two separate sessions. Within each condition, two threshold estimates were obtained and averaged, given that they generally varied by less than 3 dB.

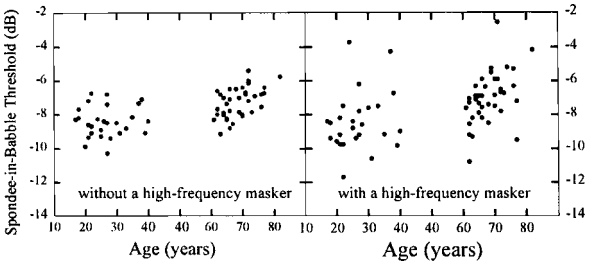

FIG. 2. Two scatter plots showing age (years) on the abscissa and spondee-in-babble thresholds on the ordinate. The spondees were presented at 30 dB SL with respect to the subject's speech reception threshold in quiet (SRT) and the babble level was adaptively varied. The right and left panels represent background conditions with and without high-frequency masking noise, respectively. The high-frequency masker was a high-pass noise with a lower cutoff frequency of 4 kHz presented at an overall level of 60 dB SPL. Each panel contains the raw data points for all 66 subjects (27 younger, 39 older) in the second study.

Eight gap conditions from Study 1 were selected based on their similarity to the spondee/B conditions. In these conditions, the 1- and 6-kHz noise burst carriers were presented at overall levels of 70 and 80 dB SPL in two backgrounds, the continuous white noise floor, with and without the high-frequency masker. As in Study 1, the contributions of absolute thresholds and age to the spondee/B thresholds were also examined.

B. Results and discussion

The spondee-in-babble (spondee/B) thresholds with and without the high-frequency masker for the two groups can be seen in Fig. 2. Age is shown on the abscissa and the spondee-in-babble thresholds on the ordinate. The right and left panels contain the individual data for background conditions with and without the high-frequency masker, respectively. Note that in both panels the distributions representing the younger subjects appear to be slightly lower and that thresholds in the condition with the high-frequency masker appear to have larger variance. The results of a repeated-measures ANOVA with one between (age group) and one within (background condition) factor indicated that the main effect of age group was significant [$F(1,59)=26.659$, $p<0.001$]. However, the main effect of background [$F(1,59)=0.708$, $p=0.404$] and its interaction with age [$F(1,59)=0.220$, $p=0.641$] were not. That is, the younger

subjects were able to recognize spondees at significantly lower spondee-to-babble ratios regardless of whether the high-frequency masker was present, but the spondee-in-babble thresholds were not significantly different with and without the high-frequency masker.

1. Absolute thresholds and spondee/B thresholds

Correlations between the two spondee/B thresholds and the audiometric thresholds were examined for each of the subject groups after exclusion of cases identified as outliers (no younger subjects, one older subject). Within the younger group, the 12 correlation coefficients between the two spondee/B thresholds and the six audiometric thresholds (0.25, 0.5, 1, 2, 4, and 8 kHz) ranged from -0.12 to 0.35. Within the older group, the corresponding correlations ranged from -0.08 to 0.28. None of the Bonferroni-adjusted probabilities was significant at $p<0.10$, indicating that the influence of audiometric thresholds on the spondee/B thresholds was not significant in either age group. We conclude that spondee-in-babble thresholds are not significantly related to audiometric thresholds in subjects with normal hearing or mild hearing loss.

2. Age and spondee/B thresholds

The relationships between age and the two spondee/B thresholds within each of the age groups were examined after the Hadi procedure indicated that neither group contained outliers. In the younger group, spondee/B thresholds were not significantly related to age, i.e., neither correlation coefficient (0.21 and 0.08 for the conditions with and without high-frequency masking, respectively) was significant. In the older group, both spondee/B thresholds increased significantly with age, i.e., both correlation coefficients (0.48 and 0.53 for the conditions with and without high-frequency masking, respectively) were significant (Bonferroni-adjusted $p<0.01$).

Could these age-related increases in spondee/B thresholds within the older group reflect age-related increases in audiometric thresholds? Recall that in the previous section, we reported that all 12 correlations between spondee/B and audiometric thresholds for the older age group were not significant, indicating that there was no relationship between audiometric thresholds and spondee/B thresholds within the older group. Were there age-related increases in audiometric thresholds similar to those age-related changes found in spondee/B threshold? The correlation coefficients for the acceptable cases (38 older subjects, one case eliminated as an outlier) between age and the audiometric thresholds at 0.25, 5, 1, 2, 4, and 8 kHz were 0.42, 0.34, 0.21, 0.42, 0.29, and 0.02, respectively. The coefficients between age and the audiometric thresholds at 0.25 and 2 kHz and Bonferroni-adjusted p-values of 0.043 and 0.042, respectively. This indicates that within the older subject group, two of the six audiometric thresholds increased significantly with age. Thus although spondee/B thresholds were not significantly related to any of the audiometric thresholds, it is interesting to note that age-related increases in audiometric thresholds (at 0.25 and 2 kHz) and spondee/B thresholds were present in the older subjects.

To summarize, spondee/B thresholds did not vary with age within the younger group of subjects. Within the older group of subjects, spondee/B thresholds were not significantly related to any of the audiometric thresholds. However, both spondee/B thresholds and two audiometric thresholds (at 0.25 and 2 kHz) significantly increased with age. Since spondee/B thresholds were not significantly correlated with these two audiometric thresholds, independent, underlying age-related changes apparently resulted in increased thresholds for both measures.

3. Gap thresholds and spondee-in-babble thresholds

Pearson correlations were used to examine the relationships between the spondee-in-babble thresholds and the four gap thresholds obtained at an overall level of 70 dB SPL. The correlation coefficients resulting after elimination of outlying cases (none in the younger group, three in the older group) are shown in the top half of Table VII. Note that the relationships between the spondee-in-babble and gap thresholds appear stronger in the younger group. The eight coefficients for the older group range between -0.18 and 0.11, strongly suggesting that the gap and speech measures are unrelated in the older age group. In contrast, four coefficients for the younger group range from 0.19 to 0.31; the other four range from 0.36 to 0.49. Three correlations were significant at $p<0.10$ after the probabilities were corrected for multiple comparisons.

Similarly, the relationships between the spondee-in-babble thresholds and the four gap thresholds obtained at an overall level of 80 dB SPL were examined. The correlation coefficients resulting after elimination of outlying cases (none in the younger group, one in the older group) are shown in the bottom half of Table VII. Note that in the younger group, the relationships between the spondee-in-babble thresholds and two gap thresholds are significant at a Bonferroni-adjusted $p<0.05$. Note also it is generally the gap thresholds obtained with the noise burst carrier low passed at 6 kHz that are significantly correlated. It may be that the similarity in bandwidth of the 6-kHz carrier to that of the spondees produced a stronger relationship between these measures. Two of the relationships between 6-kHz gap thresholds and the spondee-in-babble thresholds for the 27 younger subjects are illustrated in Fig. 3. In both panels, the spondee-in-babble thresholds were obtained in the presence of high-frequency masking. The top panel shows the relationship between gap and spondee-in-babble thresholds when the gap carrier was presented at an overall level of 70 dB SPL in a continuous noise floor with a high-frequency masker. The bottom panel shows data for gaps obtained with an 80-dB SPL carrier without a high-frequency masker. In both panels, poorer spondee-in-babble thresholds are associated with poorer gap thresholds. We conclude that some measures of temporal acuity are related to word recognition in noise in younger adults.

TABLE VII. Correlations between the spondee-in-babble and gap-thresholds. The correlations at the top and bottom represent gap thresholds obtained with 70 and 80 db SPL noise bursts, respectively. The background conditions (NF,NF +HF masker) for the gap thresholds are as described in Table II. Three older subjects were eliminated as outliers before computing the upper matrix; one older subject was eliminated before computing the lower matrix.

Gap thresholds (ms)	Spondee-in-babble threshold (dB)	
	Without high-frequency masker	With high-frequency masker
Noise burst carrier level=70 dB SPL		
	Younger subjects ($N=27$)	
1-kHz noise burst/NF	0.31	0.36
1-kHz noise burst/NF +HF masker	0.19	0.50[a]
6-kHz noise burst/NF	0.30	0.50[a]
6-kHz noise burst/NF +HF masker	0.31	0.49[a]
	Older subjects ($N=36$)	
1-kHz noise burst/NF	0.11	−0.05
1-kHz noise burst/NF +HF masker	0.00	−0.18
6-kHz noise burst/NF	−0.05	−0.08
6-kHz noise burst/NF +HF masker	−0.06	−0.08
Noise burst carrier level=80 dB SPL		
	Younger subjects ($N=27$)	
1-kHz noise burst/NF	0.13	0.21
1-kHz noise burst/NF +HF masker	0.18	0.14
6-kHz noise burst/NF	0.15	0.57[b]
6-kHz noise burst/NF +HF masker	0.26	0.53[b]
	Older subjects ($N=38$)	
1-kHz noise burst/NF	0.14	0.04
1-kHz noise burst/NF +HF masker	−0.14	−0.07
6-kHz noise burst/NF	−0.15	−0.06
6-kHz noise burst/NF +HF masker	−0.11	−0.08

[a]Bonferroni-adjusted probability $p<0.10$.
[b]Bonferroni-adjusted probability $p<0.05$.

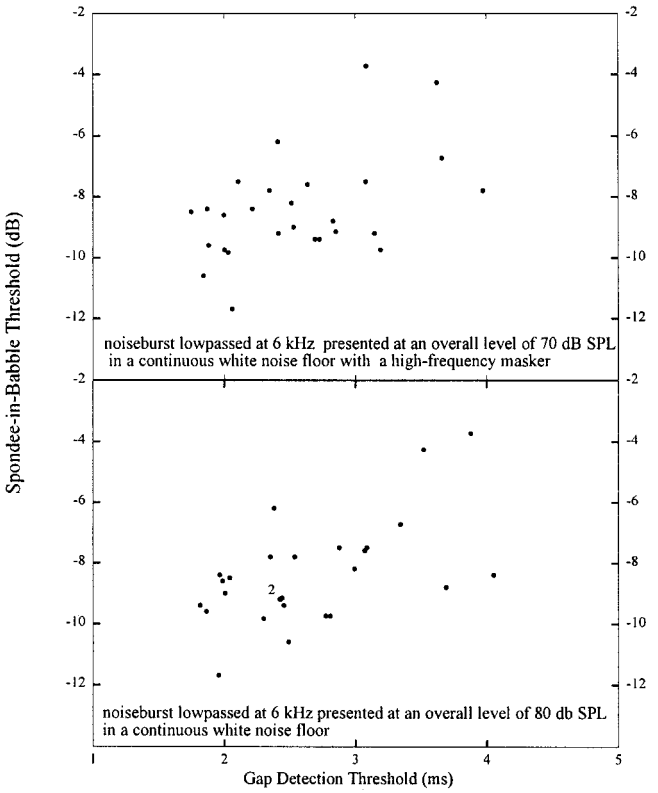

FIG. 3. Two scatter plots for the younger subjects in the second study showing gap detection thresholds (ms) on the abscissa and spondee-in-babble thresholds on the ordinate. The gaps were obtained with gated, modulated, noise burst carriers low passed at 6 kHz. The top panel represents gap detection with a noise burst at an overall level of 70 dB SPL in a background of continuous white noise and high-frequency masker. The bottom panel represents gap detection with an 80-dB SPL noise burst in a background of continuous white noise. The spondee-in-babble thresholds were measured in a background of high-frequency masking noise. Each data point represents the mean thresholds of one of the 27 younger subjects. Two data points that overlie one another are below and to the right of the ''2'' in the lower panel.

III. GENERAL DISCUSSION AND CONCLUSION

The goal of this study was to explore the relationships among gap detection and word recognition in noise, age, and absolute sensitivity in younger and older subjects with clinically normal hearing or mild hearing loss. In the first experiment, significant differences between mean thresholds of the younger ($N=40$) and older ($N=40$) groups of subjects were found on six measures of gap detection. The mean gap thresholds of the younger group were smaller in all conditions. Within each age group we examined the relationships among gap thresholds, audiometric thresholds, and age. Gap thresholds were not significantly related to audiometric thresholds in either group. In the younger age group, the gap thresholds obtained with a noise burst carrier low passed at 1 kHz increased significantly with age. This increase in the 1-kHz gap thresholds can not be attributed to age-related increases in audiometric thresholds. In the older age group, gap thresholds did not significantly increase with age.

The pattern of correlations among the gap thresholds differed between the age groups. Significant correlations were found among the gap thresholds of younger subjects primarily when the gap thresholds were obtained with noise burst carriers having similar spectra. Gap thresholds obtained with carriers of disparate spectra were generally not correlated. In contrast, most of the gap thresholds of the older subjects were significant correlated regardless of carrier spectra.

To summarize, gap detection thresholds are not related to audiometric thresholds in subjects with clinically normal hearing and age-related increases in gap detection thresholds are not dependent on changes in absolute sensitivity. Significant age-related changes in temporal acuity begin relatively early in adulthood, and gap detection in younger adults appears to be more sensitive to the spectral characteristics of the gap carrier than it is later in life.

In the second experiment, we explored the relationship between gap thresholds and spondee-in-babble thresholds in 66 of the 80 subjects who participated in the first study. Spondee-in-babble thresholds were not significantly correlated with audiometric thresholds in either age group. Although spondee-in-babble thresholds did not increase with

age in the younger group, spondee-in-babble thresholds did increase with age in the older group, and the correlation coefficients were of moderate strength (0.55 and 0.45 for the spondee-in-babble conditions with and without high-frequency masking, respectively). Within the older group, two audiometric thresholds (0.25 and 2 kHz) also increased with age.

Correlations between gap and spondee-in-babble thresholds were examined. Specifically, correlations were examined between eight gap thresholds obtained at two overall levels (70 and 80 dB SPL) in two background conditions (a continuous noise floor with and without a gated high-frequency masker) and two spondee-in-babble thresholds obtained in similar conditions (with and without a high-frequency masker). In the younger group, the correlations between the gap and the spondee-in-babble thresholds ranged from 0.13 to 0.53. The correlations were stronger for the gap thresholds obtained with the noise burst carrier low passed at 6 kHz and the spondee-in-babble condition with the high-frequency masker. This suggests that some of the variation in word recognition in noise by younger listeners is related to temporal acuity as measured in a gap detection task using a wide band (6-kHz), modulated noise burst. In the older group, correlations between gap thresholds and spondee-in-babble thresholds ranged from -0.18 to 0.14. This suggests that differences in spondee-in-babble thresholds within the older group cannot be explained by variations in gap thresholds as measured in this study.

Finally, note that within the younger age group, the relationships among age, temporal acuity, and spondee-in-babble thresholds depend very much on the spectral characteristics of the noise burst carrier. The mean gap thresholds of the younger adults increased with age, but only with noise bursts low passed at 1 kHz. That is, the earliest age-related differences in temporal processing occurred with stimuli whose spectral characteristics have been associated with poorer gap detectability (e.g., Snell *et al.*, 1994). These 1-kHz gap thresholds were not significantly correlated with spondee-in-babble thresholds. In contrast, when the upper cutoff frequency of the noise burst was increased to 6 kHz (resulting in a carrier more speechlike in bandwidth and upper-cutoff frequency), age-related differences in gap thresholds were first detected in the comparisons between age groups. Yet it was the 6-kHz gap thresholds that were significantly correlated to the spondee-in-babble thresholds of the younger subjects. Thus although age-related changes in gap detection may begin as early as the third and fourth decades with a relatively narrow-band gap carrier, these declines may be of little consequence for word recognition in noise. Of greater importance may be that performance with more speechlike gap carriers is significantly related to word recognition in noise by younger adults. Age-related declines in performance on both of these tasks appear slightly later in life, e.g., when comparing the performance of younger and older groups of subjects.

A. Relation to previous studies

Our conclusions complement those of a study by Humes *et al.* (1994) of 50 older subjects whose audiometric thresholds were on average 20 to 40 dB less sensitive than those of our older adults. Humes *et al.* concluded that hearing loss was the primary factor associated with differences in speech perception in quiet among the elderly hearing impaired. We found that absolute sensitivity contributes little to the recognition of spondees-in-babble and noise by younger and older subjects with good hearing. Humes *et al.* reported that age does not explain much of the variation in speech perception in the elderly once hearing loss has been considered. In our group of older listeners, age was significantly correlated with both spondee-in-babble thresholds and with two audiometric thresholds, those at 0.25 and 2 kHz. However, spondee-in-babble thresholds were not significantly correlated with audiometric thresholds. Humes *et al.* did not measure temporal resolution but suggested that this auditory capability might underlie observed systematic individual differences in speech perception in noise at high intensities. We measured temporal resolution and spondee recognition at moderate intensity levels and found that temporal resolution could explain some of the variation in spondee-in-babble thresholds but only in younger subjects.

Van Rooij *et al.* (1990) studied 72 elderly hearing-impaired and 24 younger normal-hearing subjects. They concluded that much of the variation in speech perception could be attributed to high-frequency hearing loss that increased with age and the remainder to a ''general performance decrement indicated by a general slowing of performance and a reduced memory capacity.'' Since the average audiometric thresholds of their older subjects were 10 to 60 dB less sensitive than the subjects in our study, it is not surprising they found high-frequency hearing loss to be of greater importance for speech perception. Similarly, van Rooij and Plomp (1992) concluded hearing loss is the most important predictor of speech perception in older adults when hearing loss is present. In addition, they reported an increase in the number of significant correlations among related measures of temporal resolution and among related measures of speech perception in older adults. Just such an increase can be seen in the matrices of Tables IV and V, where gap thresholds of our older subjects are more highly and significantly interrelated than are the gap thresholds of the younger group.

Strouse *et al.* (1998) examined the correlations among three measures of speech perception and eight measures of temporal resolution obtained from 12 younger and 12 elderly adults with normal audiometric thresholds between 0.25 and 4 kHz. They concluded that there was no evidence that individual differences in speech perception were related to temporal resolution and suggested that this may be because speech is processed in different ways than nonspeech stimuli. We suggest that there is evidence that spondee recognition in a background of babble and high-frequency noise may be related to temporal resolution in younger adults. In part, our different conclusions reflect different methods. For example, Strouse *et al.* obtained gap thresholds with gated 1-kHz sinusoids presented at low-intensity levels (4, 8, and 16 dB SL) and measured speech perception in a voice onset time (VOT) task with consonant–vowel syllables presented at preferred listening levels in a quiet background. In our study, gap detection was measured using stimuli designed to be

more speechlike in waveform. A continuous background noise floor or babble and similar high-frequency maskers were used in both the gap detection and spondee-recognition tasks to further increase the similarity as well as the complexity of the acoustic backgrounds. Interestingly, the strongest correlation in the Strouse *et al.* study between temporal resolution and speech perception was obtained with the highest intensity level gap carrier and a word recognition task in a masking level difference (MLD) paradigm. The correlation between these two measures for the younger group was -0.448, indicating a correlation of moderate strength, though nonsignificant in their study.

That the correlation was of moderate strength but nonsignificant followed from the number of subjects per age group in the Strouse *et al.* (1998) study. Each age group had only 12 subjects. Let us assume that there is a real correlation between speech perception and temporal resolution in the two populations represented by the two age groups. Assume that the correlation is moderate ($r=.50$) in the younger group and small ($r=.30$) in the older group. Holding the likelihood of a Type I error to .05 and the likelihood of a Type II error to .20, the necessary group sizes to detect those two real correlations are 28 and 85 (Cohen, 1992). Thus the likelihood of detecting any real correlation between speech perception and temporal resolution was small in Strouse *et al.*'s study simply because of the small samples.

Lutman (1991) studied temporal resolution in older adults with and without hearing loss. Though there were many differences in methodology, the results are consistent in that we find no association between age and gap detection thresholds in subjects over 60 years of age.

B. Summary

Relationships among measures of temporal acuity, speech perception, and absolute sensitivity were studied in two groups of subjects with normal hearing or mild hearing loss. Significant differences in gap detection thresholds and spondee-in-babble thresholds were found between groups of younger (17 to 40 years) and older (61 to 82 years) subjects.

Within the younger group of subjects, gap detection thresholds increased with age in conditions where the noise burst carrier was low passed at 1 kHz. These increases in gap thresholds could not be attributed to age-related changes in absolute sensitivity since the gap thresholds were not correlated with the audiometric thresholds nor did the audiometric thresholds increase with age within the younger age group. Spondee-in-babble thresholds were significantly correlated with gap thresholds within the younger group of subjects but only when the gap thresholds were obtained with noise bursts low passed at 6 kHz.

In the older subject group, the spondee-in-babble thresholds, gap thresholds, and audiometric thresholds were not significantly correlated. Gap thresholds of older subjects did not increase with age. Spondee-in-babble thresholds and audiometric thresholds at 0.25 and 2 kHz increased with age. However, these increases probably reflect independent underlying factors since spondee-in-babble were not significantly correlated with audiometric thresholds in the older subjects.

Together, these findings suggest that age-related changes in auditory processing occur over many decades and that the declines in word recognition in noise seen in older adults may reflect changes that begin decades earlier. That age-related changes in auditory processing occur throughout the adult life span supports the suggestion by Stuart and Phillips (1996) that the dichotomization of young versus old listener is likely oversimplified and misleading. The possibility of different aging patterns for temporal acuity and word recognition in noise warrants further study.

ACKNOWLEDGMENTS

This research was supported by the Rochester International Center for Hearing and Speech Research and a grant from NIA (No. AG09524). Chris Turner helped with the experimental design and calibration. Cindy Hogan, Donald Sims, Frances Mapes, Ajit Janardan, and Neil Rekhi assisted with data collection, Christopher Cox reviewed the analyses, and Beth Hickman provided programming support. We are grateful to Joe Hall and two anonymous reviewers for their insightful comments.

ANSI (**1989**). ANSI S3.6-1989, ''Specifications for Audiometers'' (American National Standards Institute, New York).

Barr, R. A., and Giambra, L. M. (**1990**). ''Age-related decrement in auditory selective attention,'' Psychol. Aging **5**, 597–599.

Boettcher, F. A., Mills, J. H., Swerdloff, J. L., and Holley, B. L. (**1996**). ''Auditory evoked potentials in aged gerbils: Responses elicited by noises separated by a silent gap,'' Hear. Res. **102**, 167–178.

Cheesman, M. F. (**1992**). ''An automated technique for estimating speech reception thresholds in multi-talker babble,'' JSLPA **16**, 223–227.

Cohen, J. (**1992**). ''A power primer,'' Psychol. Bull. **112**, 155–159.

Committee on Hearing, Bioacoustics, and Biomechanics (CHABA): Working Group on Speech Understanding (**1988**). ''Speech understanding and aging,'' J. Acoust. Soc. Am. **83**, 859–895.

Divenyi, P. L., and Haupt, K. M. (**1997a**). ''Audiological correlates of speech understanding deficits in elderly listeners with mild-to-moderate hearing loss. I. Age and lateral asymmetry effects,'' Ear Hear. **18**, 42–61.

Divenyi, P. L., and Haupt, K. M. (**1997b**). ''Audiological correlates of speech understanding deficits in elderly listeners with mild-to-moderate hearing loss. II. Correlation analysis,'' Ear Hear. **18**, 100–113.

Divenyi, P. L., and Haupt, K. M. (**1997c**). ''Audiological correlates of speech understanding deficits in elderly listeners with mild-to-moderate hearing loss. III. Factor representation,'' Ear Hear. **18**, 189–201.

Drullman, R. (**1995**). ''Speech intelligibility in noise: Relative contribution of speech elements above and below the noise level,'' J. Acoust. Soc. Am. **98**, 1796–1798.

Fitzgibbons, P. J., and Gordon-Salant, S. (**1996**). ''Auditory temporal processing in elderly listeners,'' J. Am. Acad. Audiol **7**, 183–189.

Frisina, D. R., and Frisina, R. D. (**1997**). ''Speech recognition in noise and presbycusis: Relations to possible neural mechanisms,'' Hear. Res. **106**, 95–104.

Hadi, A. S. (**1994**). ''A modification of a method for the detection of outliers in multivariate samples,'' J. R. Stat. Soc. Series. B. **56**, No. 2.

Humes, L. E., Watson, B. U., Christensen, L. A., Cokely, C. G., Halling, D. C., and Lee, L. (**1994**). ''Factors associated with individual differences in clinical measures of speech recognition among the elderly,'' J. Speech Hear. Res. **37**, 465–474.

Ison, J. R., Agrawal, P., Pak, J., and Vaughn, W. J. (**1998**). ''Changes in temporal acuity with age and with hearing impairment in the mouse: A study of the acoustic startle reflex and its inhibition by brief decrements in noise level,'' J. Acoust. Soc. Am. **104**, 1696–1704.

Lutman, M. E. (**1991**). ''Degradations in frequency and temporal resolution with age and their impact on speech identification,'' Acta Oto-Laryngol. Suppl. **476**, 120–126.

Moore, B. C. J., Peters, R. W., and Glasberg, B. R. (**1992**). ''Detection of temporal gaps in sinusoids by elderly subjects with and without hearing loss,'' J. Acoust. Soc. Am. **92**, 1923–1932.

Pichora-Fuller, M. K., Schneider, B. A., and Daneman, M. (**1995**). ''How young and old adults listen to and remember speech in noise,'' J. Acoust. Soc. Am. **97**, 593–608.

Q-Mass Speech Audiometry (**1992**), Vol. 3, Qualitone, 4931 W. 35th Street, Minneapolis, MN 55416.

Revised Speech-in-Noise (SPIN) Test (**1987**), Cosmos Distributing, Inc., Winnepeg, Manitoba, Canada.

Schneider, B. A., Pichora-Fuller, M. K., Kowalchuk, D., and Lamb, M. (**1994**). ''Gap detection and the precedence effect in young and old adults,'' J. Acoust. Soc. Am. **95**, 980–991.

Snell, K. B. (**1997**). ''Age-related changes in temporal gap detection,'' J. Acoust. Soc. Am. **101**, 2214–2220.

Snell, K. B., Ison, J. R., and Frisina, D. R. (**1994**). ''The effects of signal frequency and absolute bandwidth on gap detection in noise,'' J. Acoust. Soc. Am. **96**, 1458–1464.

Strouse, A., Ashmead, D. H., Ohde, R. N., and Grantham, D. W. (**1998**). ''Temporal processing in the aging auditory system,'' J. Acoust. Soc. Am. **104**, 2385–2399.

Stuart, A., and Phillips, D. P. (**1996**). ''Word recognition in continuous and interrupted broadband noise by young normal-hearing, older normal-hearing, and presbyacusic listeners,'' Ear Hear. **17**, 478–489.

SYSTAT for Windows: Statistics, Version 7.0, SPSS, Inc., Chicago, IL, 1997.

Tyler, R. S., Summerfield, Q., Wood, E. J., and Fernandes, M. A. (**1982**). ''Psychoacoustic and phonetic temporal processing in normal and hearing-impaired listeners,'' J. Acoust. Soc. Am. **72**, 740–752.

van Rooij, J. C. G. M., and Plomp, R. (**1990**). ''Auditive and cognitive factors in speech perception by elderly listeners. II: Multivariate analyses,'' J. Acoust. Soc. Am. **88**, 2611–2624.

van Rooij, J. C. G. M., and Plomp, R. (**1992**). ''Auditive and cognitive factors in speech perception by elderly listeners. III. Additional data and final discussion,'' J. Acoust. Soc. Am. **91**, 1028–1033.

Walton, J. P., Frisina, R. D., Ison, J. E., and O'Neill, W. E. (**1997**). ''Neural correlates of behavioral gap detection in the inferior colliculus of the young CBA mouse,'' J. Comp. Physiol. A **181**, 161–176.

Willott, James, F. (**1996**). ''Anatomic and physiologic aging: A behavioral neuroscience perspective,'' J. Am. Acad. Audiol. **7**, 141–151.

Tori of confusion: Binaural localization cues for sources within reach of a listener

Barbara G. Shinn-Cunningham[a)]
Departments of Cognitive and Neural Systems and Biomedical Engineering, Hearing Research Center, Boston University, Boston, Massachusetts 02215

Scott Santarelli and Norbert Kopco
Department of Cognitive and Neural Systems, Hearing Research Center, Boston University, Boston, Massachusetts 02215

(Received 19 August 1999; revised 5 November 1999; accepted 7 December 1999)

To a first-order approximation, binaural localization cues are ambiguous: many source locations give rise to nearly the same interaural differences. For sources more than a meter away, binaural localization cues are approximately equal for any source on a cone centered on the interaural axis (i.e., the well-known ''cone of confusion''). The current paper analyzes simple geometric approximations of a head to gain insight into localization performance for nearby sources. If the head is treated as a rigid, perfect sphere, interaural intensity differences (IIDs) can be broken down into two main components. One component depends on the head shadow and is constant along the cone of confusion (and covaries with the interaural time difference, or ITD). The other component depends only on the relative path lengths from the source to the two ears and is roughly constant for a sphere centered on the interaural axis. This second factor is large enough to be perceptible only when sources are within one or two meters of the listener. Results are not dramatically different if one assumes that the ears are separated by 160 deg along the surface of the sphere (rather than diametrically opposite one another). Thus for nearby sources, binaural information should allow listeners to locate sources within a volume around a circle centered on the interaural axis on a ''torus of confusion.'' The volume of the torus of confusion increases as the source approaches the median plane, degenerating to a volume around the median plane in the limit. [S0001-4966(00)04803-7]

PACS numbers: 43.66.Qp, 43.66.Pn [DWG]

INTRODUCTION

The most robust, static cues for determining sound source direction in anechoic space are differences between the signals reaching the left and right ears (i.e., the interaural intensity differences, or IIDs; and interaural time differences, or ITDs). Other cues, such as spectral content and overall sound intensity, depend on the ability of the listener to tease apart acoustic attributes that are due to source content from attributes that are due to source position.

A. Cones of confusion: Binaural cues for relatively distant sources

Interaural time differences result mainly from differences in the path length from the source location to the two ears. In the simplest approximation, iso-ITD locations form a hyperbolic surface of rotation symmetrical about the interaural axis (e.g., see von Hornbostel and Wertheimer, 1920; cited in Blauert, 1997, p. 179). For distances more than a meter from the head, these hyperbolic surfaces approximate cones centered on the interaural axis (i.e., the well-known ''cones of confusion''). A better approximation takes into account the effects of a spherical head on the path lengths to the ears (e.g., see Mills, 1972; Molino, 1973); however, even these iso-ITD contours depend only on the angle from source to interaural axis for distant sources. Empirical measurements of ITD as a function of source direction show that these approximations are quite accurate (e.g., see Mills, 1972).

For relatively distant sources, IIDs arise primarily because of acoustic interference of the head (e.g., see Mills, 1972). In particular, for frequencies whose wavelengths are small relative to the dimensions of the head, the ear farther from the source generally receives less energy than the nearer ear. For sources more than a meter away and assuming a simple spherical head model, the IID at a given frequency is roughly constant for all sources at the same angle from the interaural axis. Thus for distant sources, a spherical head model predicts that iso-IID contours fall on the same cones of confusion as iso-ITD contours (although the magnitude of the IID at a particular direction generally varies with frequency).

When human subjects localize sounds, they often make errors in which the perceived location falls near the same cone of confusion as the actual source, but is at the wrong location on the cone of confusion. Such errors can be explained by the fact that to a first-order approximation, binaural cues can only resolve source position to within a cone of confusion and other less robust cues must be used to disambiguate location on a particular cone of confusion. It is noteworthy that in a large percentage of cone-of-confusion er-

a)Author to whom correspondence should be addressed; electronic mail: shinn@cns.bu.edn

rors, the perceived source location is near the true location mirrored about a vertical plane passing through the interaural axis, resulting in ''front/back'' confusions (e.g. see Makous and Middlebrooks, 1990; Wenzel *et al.*, 1993; Wightman and Kistler, 1999).

One cue for resolving this confusion is the spectrum of the signal reaching the eardrum, which varies with source position due to the acoustic effects of the head, pinnae, and torso (e.g., see Shaw, 1997). However, despite the fact that the spectrum of the signal at the eardrum also depends on the spectrum of the source signal itself, a number of experiments support the idea that a major cue for resolving cone-of-confusion ambiguities is the spectral content of the signals reaching the eardrums (e.g., see Roffler and Butler, 1968; Butler and Planert, 1976; Butler and Humanski, 1992; Wenzel *et al.*, 1993; Gilkey and Anderson, 1995; Wightman and Kistler, 1997b; Hofman *et al.*, 1998; Kulkarni and Colburn, 1998).

ITD and IID cues are not perfectly constant for sources on the same cone of confusion because the ears are not diametrically opposed to one another, the head is not a perfect sphere, and the head and ears are not perfectly symmetric about the interaural axis (e.g., see Molino, 1973; Searle *et al.*, 1976; Searle *et al.*, 1976a; Middlebrooks *et al.*, 1989; Duda and Martens, 1998). Such asymmetries probably aid in localizing sound sources (e.g., see Searle *et al.*, 1976b). For instance, the pattern of IID across frequencies may help to resolve source location on a cone of confusion for distant sources (e.g., see Middlebrooks *et al.*, 1989; Duda, 1997; Wightman and Kistler, 1997b). However, such cues are not as robust or systematic as other binaural cues; they tend to be extremely complex functions of both frequency and source location (see discussions in Middlebrooks *et al.*, 1989; Wightman and Kistler, 1997a). Recent analysis suggests that torso reflections cause a peak in the IID between 2–5 kHz, with the frequency of the peak varying with angle around the interaural axis (Avendano *et al.*, 1999). This low-frequency IID peak is grossly front–back symmetric, a trait which may explain why front/back reversals are the most common cone-of-confusion errors.

It is clear that binaural cues (particularly IIDs) arising from distant sources actually differ to some degree for different locations on the same cone of confusion. However, the variations in binaural cues on any given cone of confusion tend to be smaller and/or less consistent than the variations across different cones of confusion. Thus analyzing binaural cues for a simplified, symmetrical head model can provide insight into sound localization behavior by describing how gross binaural cues vary with source location.

B. Interaural intensity differences as a cue for source distance

A number of researchers have previously pointed out that for a nearby point source, IIDs vary with source position differently than do ITDs. If one assumes that ITDs convey in which cone of confusion a source is contained (an angle that will be called the ''angle between the source cone and the interaural axis'' throughout this paper), then IIDs can be used to determine source distance (e.g., see Hartley and Fry, 1921; Firestone, 1930; Wightman and Firestone, 1930; Coleman, 1963; Hirsch, 1968; Molino, 1973; Brungart and Rabinowitz, 1996; Duda and Martens, 1998; Brungart and Durlach, 1999; Brungart and Rabinowitz, 1999). Due to limitations in available computational power, most early studies of the binaural differences arising from a point source near the listener were limited to a very restricted set of positions and frequencies (e.g., Hartley and Fry, 1921; Firestone, 1930; Wightman and Firestone, 1930; Hirsch, 1968; Molino, 1973). While these papers point out that IID cues can disambiguate source location once the ITD is known, they do not explicitly show how reliable IID spatial cues are or how these cues change with source location.

Recently, Duda and Martens (1998) and Brungart and Rabinowitz (1999) computed how the signals reaching a rigid spherical head vary with distance and direction of a point source. Both groups discuss the fact that IIDs provide distance information for nearby sources. Brungart and Rabinowitz (1999) further point out that the IID grows as the source moves lateral to the head, as well as increasing with frequency and decreasing with distance. In analyzing behavioral localization data for nearby sources, Brungart and Durlach (1999) show that the ability to judge source distance increases as source azimuth increases, consistent with the idea that the IID magnitude generally increases with source laterality. In a preliminary model of localization for nearby sources, Brungart (1998) assumes that IID decreases exponentially with source distance and that the exponent power increases with source azimuth. By taking into account the perceptual sensitivity to ITD and IID information, this model was able to predict an observed improvement in distance perception with increasing source azimuth for sources restricted to within 30 deg of the horizontal plane.

These studies demonstrate that IIDs provide unique information about source location for nearby sources, but that the amount of spatial information gained from the IID depends on the spatial position of the source. The current analysis shows quantitatively how IID depends on the angle between source cone and interaural axis and the distance of the source from the head. By calculating surfaces for which binaural cues are constant (and thereby specifying which source positions cannot be disambiguated on the basis of binaural cues), insight can be gained into sound source localization for nearby sources.

The analyses below examine how binaural cues vary with source location; however, they exclude any consideration of the acoustic effects of the shoulders, torso, or pinnae. Thus, while the current analyses may help to explain some aspects of sound localization for nearby sources, they cannot explain perceptual results that depend on these acoustic effects.

I. INTERAURAL DIFFERENCES FOR AN ACOUSTICALLY TRANSPARENT HEAD

For a spherical head, interaural differences will vary with frequency. However, if one treats the head as acoustically transparent, interaural differences depend only on source position relative to the two ears and are independent

of frequency. This section considers this simplified case in order to gain insight into more realistic approximations (treated in later sections).

A. Interaural time differences

Ignoring the acoustic effects of the head itself, the ITD τ depends only on Δ, the difference in the path lengths to the two ears. Specifically,

$$\tau = \frac{\Delta}{c}, \tag{1}$$

where c is the speed of sound (343 m/s). By definition, an iso-ITD surface for point receivers in free space is the locus of positions at which Δ is constant. Assuming that two ears are located in a rectilinear coordinate system at $(r,0,0)$ and $(-r,0,0)$ (which puts the center of a head of radius r at the origin), this surface is given by

$$\frac{4}{\Delta^2}x^2 - \frac{4}{4r^2-\Delta^2}(y^2+z^2) = 1. \tag{2}$$

These iso-ITD surfaces form the ''traditional'' cones of confusion (e.g., see Blauert, 1997).

The just-noticeable difference (JND) for ITD is roughly 10–20 μs for a reference with 0 ITD and increases by roughly a factor of 2–3 for larger reference ITDs (e.g., see Durlach and Colburn, 1978). Of course, these JNDs measure the best performance that can be achieved in a simple discrimination experiment when there is no stimulus uncertainty (e.g., see Braida and Durlach, 1988). In fact, the ability to extract ITD information will generally be worse if the subject must attend to a large range of stimuli (e.g., see Koehnke and Durlach, 1989; Shinn-Cunningham *et al.*, 1998). In order to gain insight into the spatial information conveyed by the ITD, one can compute the iso-ITD surfaces that should lead to detectable changes in ITD as a function of spatial location. The left side of Fig. 1 shows ITD contours spaced at 50-μs increments for an arbitrary plane containing the interaural axis.

One can see from the symmetry of Eq. (2) that the iso-ITD contours are three-dimensional surfaces formed by rotating the depicted one-dimensional contours around the interaural axis. ITD information should allow listeners to determine a sound source location to within the volume delineated by an adjacent pair of iso-ITD surfaces. The gray area on the left of the graph shows the cross section of such a volume taken through an arbitrary plane containing the interaural axis for a source at the position labeled ''○.'' Of course, if the head were not acoustically transparent, the path from source to ear would not always be direct (i.e., sound would have to travel around the head) and the sound wave would be reflected and diffracted by the head. As a result, the acoustically transparent head analysis generally underestimates ITDs.

B. Interaural intensity differences

The IIDs that occur for sound sources very close to the listener help to disambiguate source positions that result in nearly identical ITD values. Like ITDs, IIDs restrict source location to a two-dimensional surface. For sources near the head, iso-IID surfaces differ from iso-ITD surfaces and thus provide unique information about source position.

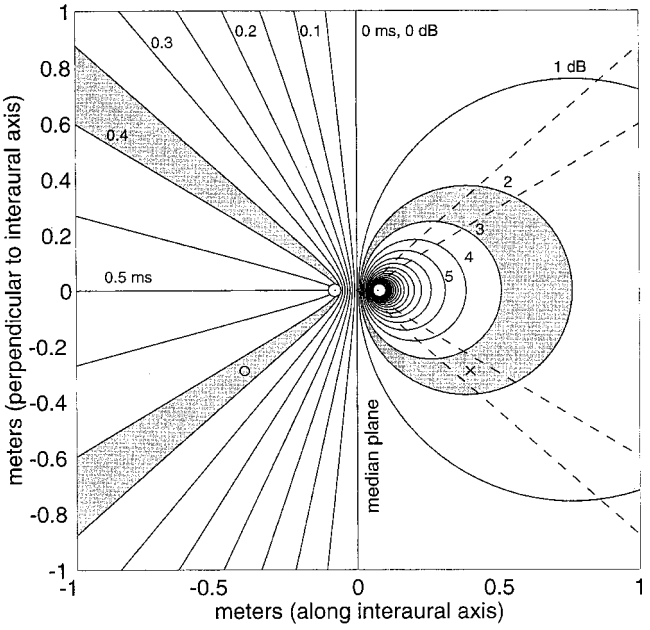

FIG. 1. Iso-ITD and iso-IID contours as a function of spatial location for an acoustically transparent head. The left side of the figure shows iso-ITD contours spaced every 50 μs. The right side of the figure shows iso-IID contours spaced every 1 dB. By symmetry, these contours are identical for any arbitrary plane containing the two ears (small circles). All spatial units are in meters. The abscissa is parallel to the interaural axis and the ordinate perpendicular to the interaural axis. The gray filled areas show the regions of space that are consistent with the ITD for a source at the position marked by ''○'' and the IID for a source at the position marked by ''×.'' The dashed line repeats the iso-ITD contours that delineate the ''cone of confusion'' for the source at ''×.'' The intersection of the area enclosed by these dashed lines and the filled area on the right are the only locations consistent with both ITD and IID cues for a source at ''×.''

One major component of the IID for nearby sources arises due to differences between the path lengths to the two ears. The energy transmitted to a point in space from a uniformly radiating point source is inversely proportional to the square of the distance from the source. Assume that the ''left'' and ''right'' point receivers are located at distances of d_L and d_R, respectively, from a uniformly radiating point source. Then the square of the ratio d_L/d_R equals the ratio of the intensity reaching the right receiver over the intensity reaching the left receiver. The resulting IID will be constant for all positions at which the ratio $k = d_L/d_R$ is constant. The IID α (in dB) is given by

$$\alpha = 20\log_{10} k. \tag{3}$$

Again assuming that two ears are located at $(r,0,0)$ and $(-r,0,0)$, the iso-IID surfaces are given by

$$(x-x_\alpha)^2 + y^2 + z^2 = d_\alpha^2,$$

$$x_\alpha = -r\frac{(1+k^2)}{(1-k^2)}, \tag{4}$$

$$d_\alpha = \left| \frac{2rk}{1-k^2} \right|.$$

These iso-IID surfaces constitute perfect spheres of radius d_α, whose centers fall on the interaural axis at $(x_\alpha,0,0)$. Both the distance from the center of the sphere to the nearer ear and the radius of the sphere increase with decreasing IID magnitude (as k approaches one). As the IID approaches zero, the magnitudes of both d_α and x_α grow to infinity and the iso-IID sphere degenerates to the entire median plane. The iso-IID sphere degenerates to a point at the position of the nearer ear as the IID magnitude increases (k approaches zero or infinity).

The just-noticeable difference (JND) in IID is approximately 0.8 dB, independent of frequency and reference IID (e.g., see Mills, 1960; Hershkowitz and Durlach, 1969; Mills, 1972). The right side of Fig. 1 shows iso-IID contours at 1-dB separations for source positions on an arbitrary plane containing the interaural axis. As with iso-ITD curves, rotating these iso-IID curves around the interaural axis generates iso-IID surfaces in 3-space. In other words, gross IID information alone should allow subjects to determine source location to a volume of space whose bounding surfaces are iso-IID spheres separated by one JND. The shaded gray area on the right side of Fig. 1 shows the cross section of such a volume (through a plane containing the interaural axis) for a source at location ''×.''

C. Tori of confusion

The goal of this analysis is to estimate how well subjects can judge source position based only on robust, binaural cues. It is generally accepted that ITD and IID are separately computed in individual frequency channels. Both types of binaural information have a limited resolution; however, both are available to help determine source location. A listener should be able to determine source location to within the intersection of the volumes separately determined by IID and ITD information. In other words, based on binaural cues, a subject should be able to determine source location to within a volume whose four bounding surfaces are the two iso-IID spheres and two iso-ITD cones described above.

For the source at location ''×'' in Fig. 1, the listener should be able to judge the location of the source as somewhere within the gray area on the right half of the figure based on IID information alone. ITD information constrains the source to be between the dashed lines on the right side of the figure. In the horizontal plane, the intersection of these constraints forms two roughly square regions positioned symmetrically about the interaural axis. Rotating these areas around the interaural axis defines the locus of positions for which the binaural cues are consistent with those from a source at position ''×.''

The extent of the resulting volume of space varies dramatically with source position. For source positions that are near the head and on the interaural axis, IID cues alone will restrict the source position to a relatively small region of space. In contrast, both iso-IID and iso-ITD surfaces degenerate to the same surface for a source on the median plane so that gross binaural cues only determine source position to a broad swatch of space within about 5 deg of the median plane. For intermediate locations, iso-IID and iso-ITD surfaces are nearly perpendicular to one another and the combination of cues provides much more information than either cue taken alone. In these cases, the intersection of the IID and ITD volumes is a torus-shaped volume.[1] We call these volumes ''tori of confusion[2]'' (after the ''cones of confusion'') to reflect the additional constraints on source location derived from the IID for a nearby source. If the source is more than 2 meters away, the change in IID with source position is too gradual to provide spatial information (at least for an acoustically transparent head), and the source can only be localized to a volume around the correct cone of confusion.

This analysis demonstrates why one should not think of IID as providing distance information about nearby sources, *per se*. Instead, IID cues provide information about the location of the source in both distance and direction. In addition, distance perception (based on binaural information) does not depend on source azimuth, but rather on the angle between the source cone and the interaural axis. In the next section, these transparent-head iso-IID and iso-ITD surfaces are compared to those derived for a simple rigid, spherical head model.

II. INTERAURAL DIFFERENCES FOR A RIGID, SPHERICAL HEAD

Treating the head as rigid sphere, Rabinowitz and his colleagues (Rabinowitz *et al.*, 1993) derived how the pressure on the surface of a rigid sphere varies for a point source at an arbitrary location. This analysis has previously been applied to the problem of determining how sound pressure varies with source position for nearby sources (e.g., see Duda and Martens, 1998; Brungart and Rabinowitz, 1999). The current analysis focuses on how much spatial information binaural cues convey as a function of source position and how these results differ (and are similar to) the simple analysis given in the previous section.

The current computations also use the spherical head model presented by Rabinowitz *et al.* (1993). The point receivers (ears) are assumed to be at opposite ends of one diameter of a rigid sphere of radius 8 cm. From these assumptions, interaural differences depend only on source distance and cone-of-confusion angle (solutions will be symmetrical about the interaural axis). The complex pressure on the surface of the sphere was calculated for a uniformly radiating point source at all directions, distances between 12 cm and 10 m, and frequencies ranging from 20 to 20 000 Hz. The ratio of the RMS pressures on opposite sides of the sphere were then computed in order to determine interaural differences in intensity and time as a function of sound frequency and source position. These results were then smoothed in frequency using a 1/3-octave-wide kernel.

A. Interaural time differences

ITD was estimated from the phase of the ratio of the complex transfer functions for the right and left ears. The interaural phase difference was nearly linear (after unwrap-

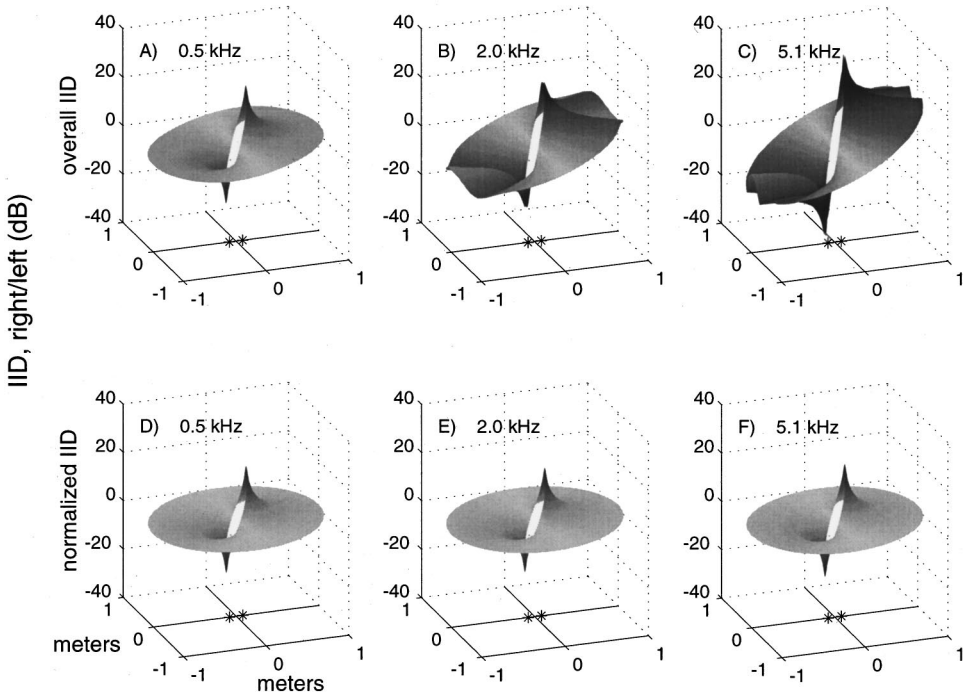

FIG. 2. IID as a function of spatial location in an arbitrary plane through the interaural axis using a spherical head model with diametrically opposed ears. The interaural intensity difference (right ear relative to left ear, in decibels) is plotted in the vertical dimension. The (x,y) position corresponds to the location of the source relative to a head centered at (0,0) of radius 8 cm. The locations of the ears are shown by asterisks in the x-y plane at the bottom of the figure. The median plane is located at $x=0$. The top row (panels A, B, and C) shows the overall IID for three different frequencies (500, 2000, and 5100 Hz). The bottom row (panels D, E, and F) shows the normalized IID (total IID less the IID that arises for a source infinitely far, i.e., 10 m, from the sphere) for the same three frequencies.

ping the phase) up to 6 kHz for all distances and angles. Since ITDs are generally assumed to be relatively unimportant above 2 kHz, a single ITD value was estimated for each source location by averaging the slope of the interaural phase versus frequency function for frequencies below 2 kHz.

At any particular location, the expected ITD using a spherical head model is larger than that predicted in the earlier analysis, as expected (i.e., the iso-ITD surfaces are more closely spaced). This difference in ITD magnitude arises primarily because the path length to the far car is longer for a rigid sphere compared to an ''invisible'' head, increasing the ITD for a given source location. Although the ITD increases slightly as the source approaches the ear along a particular cone of confusion, the resulting distance information is negligible for most source positions. As a result, the spatial information conveyed by the ITD for a rigid head follows roughly the same geometry as predicted by the analysis in the previous section; namely, the ITD determines source location to near a particular cone of confusion. In general, the volumes of the cones of confusion are smaller than for the case of an acoustically transparent head.

B. Interaural intensity differences

The top half (panels A, B, and C) of Fig. 2 plots the IID as a function of source position for an arbitrary plane through the interaural axis. In general, the magnitude of the IID increases as the source approaches either ear (consistent with the analysis for an acoustically transparent head). In addition, the IID becomes more complex and grows in magnitude as frequency increases. At low frequencies (500 Hz and below, see panel A), the IID function is shaped nearly identically to the IID function for an acoustically transparent head. However, even for low frequencies, the IID magnitude at a particular location is larger when the head is treated as a rigid sphere rather than acoustically transparent. As frequency increases, the IID begins to show a directional dependence, with the IID increasing as the source position moves away from the median plane (e.g., see panels B and C). The IID actually decreases for mid and high frequencies as the source position approaches the interaural axis. This results from the fact that the sound waves traveling around the head add in phase at the far ear as the source approaches the interaural axis, thereby increasing the intensity of the sound at the far ear and decreasing the IID (the so-called ''acoustic bright spot''). In the limit, for sources relatively far from the head, the iso-IID surfaces must approach the cones of confusion. For these distances, the IID at a given frequency depends only on the angle from the source to the interaural axis.

In order to gain further insight into the dependence of the IID on source position, the IID for a source very far from the head (i.e., for a source at 10 m) was calculated for all possible cone-of-confusion angles. For each source position, the IID that occurs for a source at 10 meters in that direction was subtracted from the overall IID to form ''normalized IIDs'' (i.e., the IID was normalized by subtracting the IID for a source from the same direction, but at an effectively infinite distance). The normalized IIDs are plotted in the bottom half of Fig. 2 (panels D, E, and F) for the same frequencies shown in the top half of the figure.

At low frequencies, IID is approximately zero for sources far from the head and the normalization has little effect (panels A and D). For higher frequencies, the IID for a distant source accounts for a large percentage of the overall IID. Once this distant-source IID is removed, the only positional dependence in the IID is nearly identical to the form predicted by the analysis for an acoustically transparent head, independent of frequency (compare panels B and C with E and F). In other words, while the magnitude of the normalized IID is slightly larger than the IID predicted for an acoustically transparent head, the shape is virtually identical.

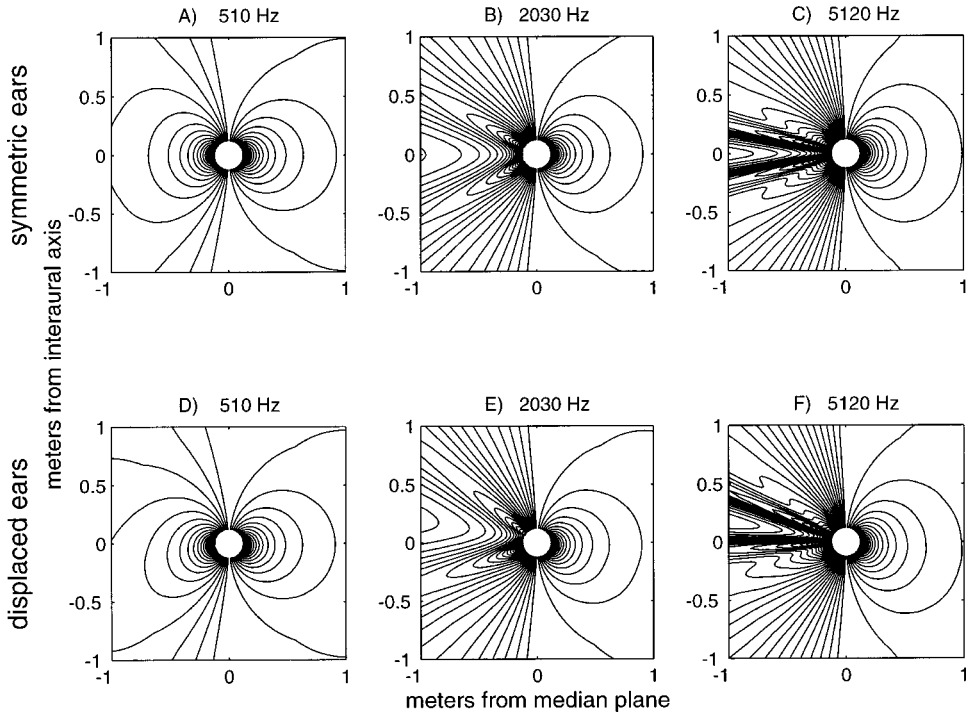

FIG. 3. Iso-IID contours as a function of spatial location in a plane through the interaural axis using a spherical head model. The spherical head is centered at (0,0) and the ears are located at (±0.08,0) m. The left half of each panel shows the overall iso-IID contours. The right half of each panel shows the iso-IID contours that remain after the IID that arises for a source infinitely far (i.e., 10 m) from the head is subtracted. Contours are shown for 1-dB increments, starting at 1 dB (contour nearest to the median plane). The top row shows the IID for three different frequencies (500, 2000, and 5100 Hz) assuming that the ears are diametrically opposed. In these panels (A, B, and C), the results are valid for an arbitrary plane containing the interaural axis. The bottom row shows the IID for the same three frequencies when the ears are displaced 10 deg behind the center of the head in the horizontal plane. In these panels (D, E, and F), the results are valid for the horizontal plane.

Iso-IID contours derived from the plots in Fig. 2 are shown in the top row (panels A, B, and C) of Fig. 3 (the bottom row is discussed in the next section). The left side of each panel shows the full iso-IID contours and the right side of each panel shows the corresponding normalized iso-IID contours. For low frequencies (e.g., see panel A), iso-IID contours are grossly similar to the iso-IID contours for an acoustically transparent head. At intermediate frequencies (e.g., panels B and C), the iso-IID contours become complex, varying both with the angle from the interaural axis and the relative distance from the source to the two ears. Once the head-shadow IID component (i.e., the component present for sources infinitely far from the head) is removed from the IID surfaces (right half of each panel), the remaining iso-IID contours depend mainly on the relative distance from the source to the two ears, like iso-IID contours for an acoustically transparent head. The main distinction between the two cases is that the IIDs for an acoustically transparent head are slightly smaller in magnitude than those that arise for a spherical head. As a result, the volumes of spatial uncertainty delineated by the iso-IID contours for the normalized IIDs are slightly smaller than from those predicted by an acoustically transparent head.

This analysis shows that the IIDs that arise for a rigid, spherical head model can be broken down into two components. The first component is frequency-dependent but distance-independent. As expected, the magnitude of this distant-source component increases dramatically with frequency. For frequencies below about 500 Hz, this factor is negligible; at high frequencies, this ''head shadow'' dominates the overall IID. The second component, the ''normalized IID,'' varies with the relative distance from the source to the two ears and conveys roughly the same spatial information predicted for an acoustically transparent head. While this relative-distance component increases with frequency, the frequency dependence is not pronounced.

C. Tori of confusion

ITD information for a rigid spherical head conveys information about the angle between the source cone and the interaural axis. Although the ITD increases slightly as the source approaches the head, these deviations from the perfect ''cones of confusion'' are small in perceptual terms (as pointed out previously; e.g., see Brungart, 1998; Brungart and Rabinowitz, 1999).

Spatial information conveyed by the IIDs varies dramatically with frequency. At low frequencies (below 500 Hz), the IID information is essentially the same as predicted for an acoustically transparent head. At high frequencies, the IID primarily conveys information about source direction, but also conveys some information about the relative distances from the source to the two ears. At intermediate frequencies, the IID varies with angle from the interaural axis and with relative distance to the two ears.

In other words, at both intermediate and high frequencies, part of the information conveyed in the IID covaries with the information conveyed in the ITD. Combining ITD and IID information will restrict the possible source position to a torus of confusion. However, if the source is broadband, combining spatial information in the IIDs in different frequency bands will restrict the source location to the same torus of confusion, since mid- and high-frequency IIDs contain spatial information similar to the information conveyed by ITD.

It must be pointed out that the spherical-head approximation becomes increasingly less accurate as frequency increases. In particular, above about 6 kHz, spectral notches and peaks that depend on the angle around the interaural axis

(the angle around the torus of confusion) will begin to arise in the signals at the ears due to the acoustic effects of the pinnae. These notches and peaks will cause changes not only in the energy pattern at the individual ear drums, but will result in IIDs since the effects are different at the left and right ears. Also, for frequencies between 2 and 5 kHz, torso reflections may affect the IID (Algazi *et al.*, 1999). Thus the IID analysis for a rigid spherical head model is most useful for relatively low frequencies.

Overall, this analysis shows that when sources are within a meter of the listener, low- and mid-frequency IID information should allow listeners to localize a source to within a torus of confusion. This IID information is further refined by the ITD cues, which partially covary with IIDs at mid and high frequencies. Many of the observations made for the acoustically transparent head analysis continue to hold. For instance, the volume of a torus of confusion increases as the angle between the source cone and the interaural axis increases until it degenerates to the entire median plane. The toroidal volume decreases as the angle between the source cone and the interaural axis decreases and as the source moves closer to the nearer ear. For sources beyond 2 meters from the listener, IID changes so gradually with distance that it conveys no useful spatial information beyond that contained in the ITD and the torus of confusion degenerates into a cone of confusion.

III. INTERAURAL DIFFERENCES FOR DISPLACED EARS

Human ears are not diametrically opposed on the head. For instance, in their analysis of the range dependence of the HRTF, Duda and Martens (1998) assumed that the ears were located 10 deg behind the diameter parallel to the interaural axis. This asymmetry is relatively small, but complicates the geometry of iso-binaural surfaces. In particular, the rotational symmetry that is assumed in the above discussion no longer holds; instead of symmetrical tori of confusion, binaural cues will allow the listener to locate the source to within some skewed volume. In this section, we examine the effect of displacing the ears backward on the head.

The same rigid spherical head model was used to calculate the transfer function from a point source in space to point receivers on the surface of a rigid sphere (Rabinowitz *et al.*, 1993). However, the point receivers were assumed to be angularly displaced backward by 10 deg in the horizontal plane. Of course, for a head in which the ears are angularly displaced, different planes containing the x-axis yield slightly different iso-IID and iso-ITD contours (i.e., binaural differences are no longer constant on a cone of confusion). While full rotational symmetry no longer holds, binaural cues are mirror symmetric about the horizontal plane [i.e., the binaural differences that occur for a source at (x,y,z) are equal to those for a source at $(x,y,-z)$]. Such symmetry is consistent with up/down and down/up reversals that are occasionally reported in the literature (e.g., see Wenzel *et al.*, 1993). The only plane containing the x-axis and the two ears is the horizontal plane $(z=0)$; results in this plane show the greatest (front–back) asymmetry. As a result, the distortion of the iso-binaural contours from those seen in the analysis for the symmetrically placed ears will be greatest through the horizontal plane.

A. Interaural time differences

Iso-ITD contours that arise for a spherical head with the ears displaced are nearly indistinguishable from the iso-ITD contours for a head with diametrically opposed ears. The biggest difference is that the ITD is slightly smaller at positions near an azimuth of 90 deg when the ears are displaced. This is explained by the observation that if a source moves from 78 to 79 deg in the horizontal plane, it moves away from the left (far) ear and toward the right (near) ear, causing an increase in the ITD. However, a source at 80 deg azimuth is directly opposite the left ear, so as a source moves from azimuth 80 to 81 deg, it actually moves closer to the far ear (around the back of the head) as well as moving closer to the near ear. As a result, for sources located at azimuths between 80 and 100 deg, the difference in the path lengths to the two ears does not change significantly with azimuth and the magnitude of the ITD is reduced for locations to the side of the head. Thus the main effect of positioning the ears behind the center of the head is to decrease ITD magnitude.

B. Interaural intensity differences

The bottom row (panels D, E, and F) of Fig. 3 plots overall- and normalized-iso-IID contours for locations in the horizontal plane when the ears are displaced. It should be emphasized that nonhorizontal planes containing the x-axis would yield different iso-IID contours. In particular, since only the horizontal plane bisecting the head passes through the ears, the iso-IID contours for this plane show the greatest asymmetry (and reach the largest values).

Looking first at the iso-IID contours for the overall IID (left half of each panel), the IID function is no longer front–back symmetric (compare top and bottom rows in Fig. 3). There are two factors influencing the IID as a function of location in the horizontal plane. The first can be ascribed to differences in the ratio of the path lengths to the two ears. This factor is maximal for sources located 100 deg to the side of the median plane for sources in the horizontal plane containing the ears and increases as the source approaches the head. The second factor depends on the head shadow and varies with the direction between source and head as well as with frequency. The relative importance of this second factor increases with frequency.

The maxima of the normalized iso-IID functions (right half of each panel) are skewed toward an azimuthal angle of 100 deg (in line with the near ear). Nonetheless, this spatial dependence is similar to the spatial dependence exhibited for the symmetrical case. The IID information consists of a component that varies with azimuthal angle and a component that varies with the relative path length from source to the two ears.

C. Distorted tori of confusion

Because of the asymmetry for angularly displaced ears, the combination of IID/ITD information taken across fre-

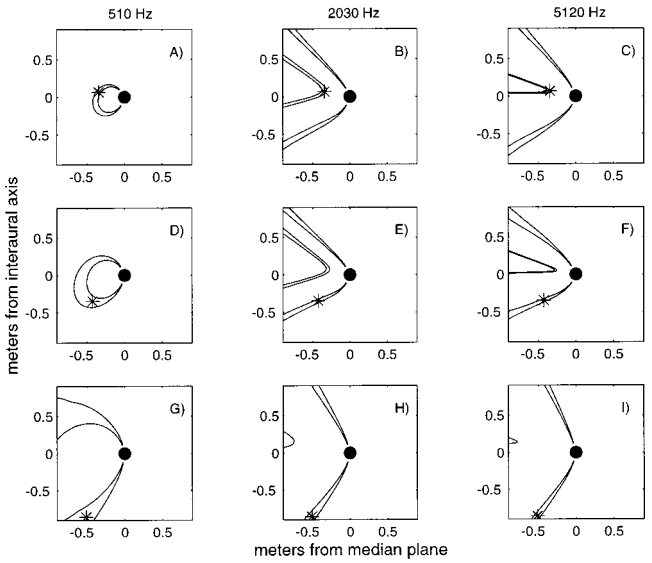

FIG. 4. Constraints on spatial location due to the IID for a spherical head model in which the ears are angularly displaced. Each row corresponds to one source location (plotted as an asterisk in each panel). The solid circle in the middle of the panel shows the head. Each column corresponds to a different frequency. In each plot, the source is constrained to fall within the area delineated by the drawn contours by the IID in the corresponding frequency range.

quency no longer forms a symmetrical torus of confusion. ITD information constrains the source to be on a distorted cone of confusion. In order to gain insight into how the IID would constrain locations for sources at various locations in the horizontal plane, Fig. 4 shows the locations in the horizontal plane that are consistent with the IID in different frequencies (columns) for a source in various locations (rows).

Figure 4 shows that the tori of confusion are skewed by the angular displacement of the ears, but many of the observations made for the symmetrical model still hold. In particular, IID information will constrain the source location to within some volume of space. The size of the volume decreases as the source nears an ear and increases as sources approach the median plane. In general, there are locations both in front of and behind the listener that could give rise to the observed IID cues at each frequency, consistent with front/back and back/front reversals. At lower frequencies, the source position is constrained in both distance and direction, similar to predictions from an acoustically transparent head analysis. As frequency increases, iso-IID contours vary more dramatically with source direction than source distance and provide information that is similar to the information in the ITD. For some source positions, the IID in moderate and high frequencies constrains the source to fall within one of two spatial bands (e.g., see panels C and D), roughly corresponding to two different cones of confusion (one of which contains the actual source location). This occurs because the IID is not monotonic with source azimuth (see Fig. 2) so that there can be two or more connected regions of space consistent with the IID in mid and high frequencies. Looking across these spatial constraints, broadband IID information (with or without ITD information) restricts the source location to within a volume of space that forms a distorted torus of confusion.

IV. SUMMARY AND DISCUSSION

These results show that when sources are close to one ear, IIDs vary dramatically with source position and frequency so that using only binaural cues, a broadband sound source can be located to somewhere on a ''torus of confusion.'' ITD cues determine source position to within a cone of confusion. IIDs vary with both distance and direction for sources, but are only significant for sources within one or two meters of the head and close to the interaural axis.

There are two main components of the IID: one that depends primarily on the ratio of the path lengths from the source to the two ears and one that depends on the direction from the source to the center of the head. The relative importance of these two factors depends on frequency, primarily because the magnitude of the second factor increases with frequency.

Of course, the acoustic signals at the ears of a real listener include many effects not considered here. In particular, the effects of the shoulders, torso, and pinnae are known to be acoustically significant and to affect localization judgments. However, the current results demonstrate how gross binaural cues vary with direction and distance. In addition, the current analysis is most accurate at low frequencies, precisely the frequencies at which IIDs do not occur for distant sources.

When one considers the problem of how to estimate source position from the acoustic cues available at the eardrums, the importance of the ''extra-large'' IIDs that can occur for sources very near the listener becomes clear. It has been reported that ITD cues dominate judgments of source direction for broadband sounds (Wightman and Kistler, 1992). In these experiments, IID and spectral shape cues derived from individually measured head-related transfer functions (HRTFs) were pitted against interaural phase information (derived from a different spatial location using the individualized HRTFs). In the study, the measured HRTFs were taken for relatively distant sources, where only the head shadow contributed to the IID. The results show that as long as the source signal contained low frequencies, judgments of source direction were dominated by the ITD cue. In contrast, many headphone experiments in which ITD and IID cues are pitted against one another (e.g., see the review in Durlach and Colburn, 1978, as well as Buell *et al.*, 1994; Buell and Trahiotis, 1997) show that a large, broadband IID favoring one ear biases judgments of source direction toward that ear, even when ITD cues indicate a different direction. From the current analysis, we see that a large, low-frequency IID only occurs for sources near the ear *and* close to the interaural axis. Thus in many dichotic headphone studies, the low-frequency IID in the imposed broadband IID restricts the possible source location to be a very small volume of space close to the ear. A parsimonious explanation for all of these results is that both ITD and IID information are used to determine source position, but that low-frequency ITD information is generally more reliable than head-shadow cues. Only very large, low-frequency IIDs (which can only occur when sources are very near one ear) are sufficiently reliable to overcome the dominance of low-frequency ITD information. In fact, if the auditory system treats ITD and IID infor-

mation as separate, independent channels of spatial information, a maximum-likelihood estimation approach (e.g., see Duda, 1997), will predict dual source images (as are often reported in the literature) for ITD/IID pairings that are inconsistent.

It should also be pointed out that energy differences in the signals reaching the two ears are important for spatial unmasking in many real-world listening situations. Thus the pattern of spatial unmasking for sources close to the listener may be different than when sources are more than a meter away. If a source is near the interaural axis and close to the head, the ''better ear'' advantage will be more pronounced than when a source is at the same direction but distant from the head. However, the extra-large IIDs that arise in such a situation may actually decrease the binaural component of spatial unmasking (e.g., see Colburn and Durlach, 1965). The question of how these two factors play out under free-field listening conditions is relevant for understanding spatial unmasking in true ''cocktail party'' situations, where talkers may be fairly close to the listener.

Finally, it must be emphasized that above 6 kHz, large IIDs will arise due to the interaction of the pinnae with the sound waves. At intermediate frequencies, torso effects will alter the IID. However, the analysis presented here is most useful for predicting the IID for the very frequencies which are normally assumed to have zero IID for ''naturally occurring,'' free-field sources. This analysis demonstrates how the unique low-frequency IIDs for sources near the listener depend upon spatial position, and how these IIDs may allow listeners to determine where on the cone of confusion a source is located.

ACKNOWLEDGMENTS

This work was supported in part by AFOSR Grant No. F49620-98-1-0108. The authors gratefully acknowledge assistance from Jay Desloge and Douglas Brungart with code for the analysis of the spherical head model. Nat Durlach, Wesley Grantham, Fred Wightman, and an anonymous reviewer provided valuable feedback and criticisms of earlier drafts of this work. A more extensive description of this work is available as Technical Report CAS/CNS-TR-99-026 from the Boston University Department of Cognitive and Neural Systems.

[1]It should be pointed out that the cross-sectional area of the ''torus of confusion'' is not circular, although the word ''torus'' often conjures an image of a solid of rotation with a perfectly circular cross section. The more general definition of torus includes any solid created by rotation of a fixed cross-sectional area about an (in this case interaural) axis. Indeed, the cross-sectional shape of the torus of confusion varies with spatial location of the source. For sources very close to one ear, the cross-sectional area is roughly trapezoidal; for sources near the median plane, the cross section is much more asymmetrical and significantly larger.

[2]We have previously used the more colloquial term ''doughnuts of confusion'' to describe the volume of spatial uncertainty.

Algazi, V. R., Avendano, C., and Duda, R. O. (**1999**). ''Low-frequency ILD elevation cues,'' J. Acoust. Soc. Am. **106**(4), 2237.

Avendano, C., Algazi, V. R., and Duda, R. O. (**1999**). ''A head-and-torso model for low-frequency binaural elevation effects,'' in *Proceedings of the 1999 IEEE Workshop on Applications of Signal Processing to Audio and Acoustics*, New Paltz, NY.

Blauert, J. (**1997**). *Spatial Hearing*, 2nd ed. (MIT Press, Cambridge, MA).

Braida, L. D., and Durlach, N. I. (**1988**). ''Peripheral and central factors in intensity perception,'' in *Auditory Function: Neurobiological Bases of Hearing*, edited by G. M. Edelman, W. E. Gall, and W. M. Cowan (Wiley, New York), pp. 559–583.

Brungart, D. S. (**1998**). ''Preliminary model of auditory distance perception for nearby sources,'' in *Proceedings of the NATO AS1 on Auditory Computational Hearing*, Il Ciocco, Italy.

Brungart, D. S., and Durlach, N. I. (**1999**). ''Auditory localization of nearby sources II: Localization of a broadband source in the near field,'' J. Acoust. Soc. Am. **106**(4), 1956–1968.

Brungart, D. S., and Rabinowitz, W. M. (**1999**). ''Auditory localization of nearby sources I: Head-related transfer functions,'' J. Acoust. Soc. Am. **106**(3), 1465–1479.

Brungart, D. S., and Rabinowitz, W. R. (**1996**). ''Auditory localization in the near field,'' in *Proceedings of the Third International Conference on Auditory Display*, Palo Alto, CA.

Buell, T. N., and Trahiotis, C. (**1997**). ''Recent experiments concerning the relative potency and interaction of interaural cues,'' in *Binaural and Spatial Hearing in Real and Virtual Environments*, edited by R. Gilkey and T. Anderson (Erlbaum, New York), pp. 139–150.

Buell, T. N., Trahiotis, C., and Bernstein, L. R. (**1994**). ''Lateralization of bands of noise as a function of combinations of interaural intensitive differences, interaural temporal differences, and bandwidth,'' J. Acoust. Soc. Am. **95**(3), 1482–1489.

Butler, R. A., and Humanski, R. A. (**1992**). ''Localization of sound in the vertical plane with and without high-frequency spectral cues,'' Percept. Psychophys. **51**, 182–186.

Butler, R. A., and Planert, N. (**1976**). ''The influence of stimulus bandwidth on localization of sound in space,'' Percept. Psychophys. **19**, 103–108.

Colburn, H. S., and Durlach, N. I. (**1965**). ''Time-intensity relations in binaural unmasking,'' J. Acoust. Soc. Am. **38**(1), 93–103.

Coleman, P. D. (**1963**). ''An analysis of cues to auditory depth perception,'' Psychol. Bull. **60**, 302–315.

Duda, R. O. (**1997**). ''Elevation dependence of the interaural transfer function,'' in *Binaural and Spatial Hearing in Real and Virtual Environments*, edited by R. Gilkey and T. Anderson (Erlbaum, New York), pp. 49–76.

Duda, R. O., and Martens, W. L. (**1998**). ''Range dependence of the response of a spherical head model,'' J. Acoust. Soc. Am. **104**(5), 3048–3058.

Durlach, N. I., and Colburn, H. S. (**1978**). ''Binaural phenomena,'' in *Handbook of Perception*, edited by E. C. Carterette and M. P. Friedman (Academic, New York), pp. 365–466.

Firestone, F. A. (**1930**). ''The phase difference and amplitude ratio at the ears due to a source of pure tone,'' J. Acoust. Soc. Am. **2**, 260–270.

Gilkey, R. H., and Anderson, T. R. (**1995**). ''The accuracy of absolute localization judgments for speech stimuli,'' J. Vestib. Res. **5**(6), 487–497.

Hartley, R., and Fry, T. (**1921**). ''The binaural location of pure tones,'' Phys. Rev. **18**, 431–442.

Hershkowitz, R. M., and Durlach, N. I. (**1969**). ''Interaural time and amplitude JND's for a 500 Hz tone,'' J. Acoust. Soc. Am. **46**, 1464–1467.

Hirsch, H. R. (**1968**). ''Perception of the range of a sound source of unknown strength,'' J. Acoust. Soc. Am. **43**(2), 373–374.

Hofman, P. M., Van Riswick, J. G. A., and Van Opstal, A. J. (**1998**). ''Relearning sound localization with new ears,'' Nat. Neurosci. **1**(5), 417–421.

Koehnke, J., and Durlach, N. J. (**1989**). ''Range effects in the identification of lateral position,'' J. Acoust. Soc. Am. **86**, 1176–1178.

Kulkarni, A., and Colburn, H. S. (**1998**). ''Role of spectral detail in sound-source localization,'' Nature (London) **396**, 747–749.

Makous, J. C., and Middlebrooks, J. C. (**1990**). ''Two-dimensional sound localization by human listeners,'' J. Acoust. Soc. Am. **87**(5), 2188–2200.

Middlebrooks, J. C., Makous, J. C., and Green, D. M. (**1989**). ''Directional sensitivity of sound-pressure levels in the human ear canal,'' J. Acoust. Soc. Am. **86**, 89–108.

Mills, A. W. (**1960**). ''Lateralization of high-frequency tones,'' J. Acoust. Soc. Am. **32**, 132–134.

Mills, A. W. (**1972**). ''Auditory localization,'' in *Foundations of Modern Auditory Theory*, edited by J. V. Tobias (Academic, New York), pp. 303–348.

Molino, J. (**1973**). ''Perceiving the range of a sound source when the direction is known,'' J. Acoust. Soc. Am. **53**, 1301–1304.

Rabinowitz, W. R., Maxwell, J., Shao, Y., and Wei, M. (**1993**). ''Sound localization cues for a magnified head: Implications from sound diffraction about a rigid sphere,'' Presence **2**(2), 125–129.

Roffler, S. K., and Butler, R. A. (**1968**). ''Factors that influence the localization of sound in the vertical plane,'' J. Acoust. Soc. Am. **43**, 1255–1259.

Searle, C. L., Braida, L. D., Cuddy, D. R., and Davis, M. F. (**1976a**). ''Binaural pinna disparity: Another auditory localization cue,'' J. Acoust. Soc. Am. **57**, 448–455.

Searle, C. L., Braida, L. D., Davis, M. F., and Colburn, H. S. (**1976b**). ''Model for auditory localization,'' J. Acoust. Soc. Am. **60**, 1164–1175.

Shaw, E. A. G. (**1997**). ''Acoustical features of the human external ear,'' in *Binaural and Spatial Hearing in Real and Virtual Environments*, edited by R. Gilkey and T. Anderson (Erlbaum, New York), pp. 25–48.

Shinn-Cunningham, B. G., Durlach, N. J., and Held, R. M. (**1998**). ''Adapting to supernormal auditory localization cues I. Bias and resolution,'' J. Acoust. Soc. Am. **103** (6), 3656–3666.

von Hornbostel, E. M., and Wertheimer, M. (**1920**). ''Uber die Wahrnehmung der Schallrichtung [On the perception of the direction of sound],'' Sitzungsber. K. Preuss. Akad. Wiss. 388–396.

Wenzel, E. M., Arruda, M., Kistler, D. J., and Wightman, F. L. (**1993**). ''Localization using nonindividualized head-related transfer functions,'' J. Acoust. Soc. Am. **94**, 111–123.

Wightman, E. R., and Firestone, F. A. (**1930**). ''Binaural localization of pure tones,'' J. Acoust. Soc. Am. **2**, 271–280.

Wightman, F. L., and Kistler, D. J. (**1992**). ''The dominant role of low-frequency interaural time differences in sound localization,'' J. Acoust. Soc. Am. **91**, 1648–1661.

Wightman, F. L., and Kistler, D. J. (**1997a**). ''Factors affecting the relative salience of sound localization cues,'' in *Binaural and Spatial Hearing in Real and Virtual Environments*, edited by R. Gilkey and T. Anderson (Erlbaum, New York), pp. 1–24.

Wightman, F. L., and Kistler, D. J. (**1997b**). ''Monaural sound localization revisited,'' J. Acoust. Soc. Am. **101**(2), 1050–1063.

Wightman, F. L., and Kistler, D. J. (**1999**). ''Resolution of front-back ambiguity in spatial hearing by listener and source movement,'' J. Acoust. Soc. Am. **105**(5), 2841–2853.

Effects of phase duration and electrode separation on loudness growth in cochlear implant listeners

Monita Chatterjee,[a] Qian-Jie Fu, and Robert V. Shannon
Department of Auditory Implants and Perception, House Ear Institute, 2100 W. Third Street, Los Angeles, California 90057

(Received 29 March 1999; revised 13 September 1999; accepted 26 November 1999)

Loudness estimates were obtained in a group of four adult subjects implanted with the Nucleus-22 multielectrode cochlear implant device, for a range of pulse amplitudes and different fixed phase durations and electrode separations. The stimulus was a 200-ms long train of biphasic pulses presented at 500 pulses/s. Subjects estimated loudness as a number from 0 (''don't hear it'') to 100 (''uncomfortably loud''). Loudness was found to grow exponentially with pulse amplitude, at a rate that was dependent upon the phase duration as well as the electrode separation. An equation of the form $L = e^{(\lambda + \gamma M)(D^{\theta})I}$, where L is the estimated loudness, M is the separation between electrodes of a stimulating pair, D is the phase duration, I is current amplitude, and λ, γ, and θ are constants, appears to describe the observed data adequately. The findings are remarkably consistent across subjects. © *2000 Acoustical Society of America.* [S0001-4966(00)01103-6]

PACS numbers: 43.66.Ts, 43.66.Cb, 43.66.Ba [DWG]

INTRODUCTION

Electrical stimulation of the auditory nerve in cochlear implant listeners is often conducted using bipolar stimulation with trains of biphasic current pulses. Experimental studies in the past have shown that both phases of a biphasic pulse will evoke neural excitation. Measured in units of current, psychophysical threshold is known to decrease with increasing per-phase duration (hereafter referred to as ''phase duration'') of the pulses (Pfingst *et al.*, 1995; Smith and Finley, 1997). In bipolar stimulation, threshold also decreases with increasing separation between the two electrodes of a stimulating pair (Abbas and Brown, 1991; Pfingst *et al.*, 1995). Together, these results indicate that, at least at threshold, the electrically stimulated auditory system integrates information over time as well as over cochlear distance. If linearity holds, the rate of integration of such information should be constant as either phase duration or current amplitude is increased. Shannon (1985), studying changes in threshold and loudness for constant charge pulsatile stimuli as a function of phase duration, found that, in fact, the system was not linear—i.e., equal charge did not necessarily produce equal loudness or equal threshold. More recently, Zeng *et al.* (1998) have shown that under conditions of equal loudness, pulse amplitude and phase duration are not related by a simple reciprocal relationship, but rather, by a compressive power function.

In a previous study of loudness growth in individuals implanted with the Nucleus-22 implant system, Chatterjee (1999) found that the loudness L (estimated as a number on a scale from 0 to 100) of a 200-ms, 500-pulses/s train of biphasic, 200-μs/phase current pulses can be approximated by a simple exponential function of the form $L = e^{(c + kM)I}$, where I is the amplitude of each pulse in microamperes, M is the separation between the two electrodes of the stimulating pair ($M = 1$ for adjacent electrodes), and c and k are constants. It was observed that these relations held regardless of electrode location, and were consistent across subjects.

Zeng *et al.* (1998) measured the interaction of phase duration and pulse amplitude using a loudness-balancing technique for various combinations of electrode separations and pulse rates. Along equal loudness contours, the product ID^{θ} is constant, where I and D represent current amplitude and phase duration, respectively, and the exponent θ changes linearly from approximately 0.7 near threshold to approximately 0.5 near uncomfortable loudness. If linearity held, the product $I*D$ would be constant at equal loudness. Instead, Zeng *et al.*'s work shows that the product $I*D^{\theta}$ is constant at equal loudness. Within the range of conditions tested in their study, the authors found this relationship between phase duration and pulse amplitude to be relatively independent of electrode separation and electrode location. We may therefore assume that the effects of electrode separation M and phase duration D are orthogonal, and propose a general equation of the form

$$L = e^{g(M)f(D)I}, \tag{1}$$

where $g(M)$ represents the change in the exponent of the loudness function with electrode separation M, and $f(D)$ represents the change in the exponent of the loudness function with phase duration D. Based upon Zeng *et al.*'s results, we would expect $f(D)$ to be a compressive power function of D, with an exponent lying within the range 0.5–0.7. Based on our previous study, $g(M)$ appears to be a roughly linear function of M.

In Chatterjee (1999), loudness functions were measured for a fixed phase duration of 200 μs/phase, and a diverse set of electrode locations and separations. The present experiments were designed to study and quantify the effect of phase duration on the shape of the loudness function. To this end, we obtained loudness functions for a limited set of elec-

[a]Corresponding address: M. Chatterjee, Dept. of Auditory Implants and Perception, House Ear Institute, 2100 W. Third St., Los Angeles, CA 90057. Electronic mail: monita@hei.org

TABLE I. Potentially relevant information about subjects.

Subject	Gender	Age (years)	Etiology of deafness	Age at onset of profound hearing loss in both ears (years)	Date of implantation	Insertion depth (No. of rings out)	Baseline scores (CUNY sentence recognition test)	Baseline scores (NU6 word list)	Value of the exponent θ	Values of λ and γ
N3	M	58	Unknown	45	5/90	3	79.4%	24.0%	0.534	$\lambda = 3.164e\text{-}04$ $\gamma = 4.237e\text{-}05$
N4	M	42	Trauma	35	7/92	4	99.0%	70.0%	0.530	$\lambda = 1.735e\text{-}04$ $\gamma = 6.816e\text{-}05$
N7	M	57	Unknown	47	1st - LE, 10/91 2nd - LE, 2/95 3rd - RE, 11/95 (current implant)	0	99.0%	48.0%	0.561	$\lambda = 1.864e\text{-}04$ $\gamma = 4.988e\text{-}05$
N14	M	65	Unknown	61	11/96	0	47.0%	18.0%	0.641	$\lambda = 3.808e\text{-}04$ $\gamma = 3.267e\text{-}05$

trode separations and a number of phase durations. The results allow us to directly measure $f(D)$ and to test the validity of Eq. (1).

I. METHODS

Subjects were four postlingually deafened adult male users of the Nucleus-22 cochlear implant system with varying levels of speech recognition in quiet (see Table I for detailed information). All subjects are highly trained, having participated in a number of psychophysical experiments in the laboratory. These subjects had also participated in the experiments described in the previous publication (Chatterjee, 1999).

Stimuli were delivered through a custom research interface (Shannon *et al.*, 1990). All stimuli were 200-ms-long trains of biphasic pulses, presented at 500 pulses/s. Two variables of stimulation were explored in this study. Phase duration D was one variable. Another variable was the electrode separation M, defined as the difference between the electrodes of a stimulating pair. In our terminology, $M=1$ for adjacent electrodes, and $M=21$ for the furthest separation between electrodes possible in the 22-electrode Nucleus implant (stimulation between electrodes 1 and 22). Note that M is related to the term ''stimulation mode'' in popular clinical use; thus, stimulation between adjacent electrodes ($M=1$) is described as the bipolar mode (BP), and the widest separation between electrodes is described as BP+20. Electrodes are numbered from 1 (most basal) to 22 (most apical). Accurate estimates of current delivered were obtained from the manufacturer's amplitude calibration tables for each subject's device. Loudness functions were measured using the following procedures.

A. Dynamic range estimation

First, thresholds in quiet were measured using a standard 3-down, 1-up, 2-interval forced-choice procedure. Next, the subject was presented with a soft stimulus (one presentation of the 200-ms, 500-pulses/s-pulse train) close to threshold. By pressing the left and right mouse buttons, the subject could increase or decrease the level of the stimulus in small incremental steps (0.2 dB). The subject received a single presentation of the stimulus each time he pressed a mouse button.

The subject was asked to increase the level until the loudness reached a maximum acceptable level. The subject indicated to the experimenter the loudness at each step (using a number from 0 to 100, as described below). This gave us an idea of the approximate dynamic range for each mode of stimulation. Subjects tended to be conservative in estimating the maximum acceptable level during the first session. In pilot runs, a subject would sometimes estimate a stimulus to be only moderately loud, even though its amplitude had been set to the maximum level previously obtained. We would then increase the amplitude in very small steps, until the subject estimated it to be at the maximum acceptable loudness. The true range was estimated more accurately after several runs of this nature.

B. Loudness estimates

Based upon pilot runs, a number of amplitudes (minimum eight) were selected to cover the dynamic range appropriately. As the set of amplitudes was selected according to the loudness estimates obtained in the pilot runs, they were not the same for each subject or for each condition for a given subject. At each amplitude selected, the subject was presented with a sequence of six presentations of the same stimulus (stimulus set). The first presentation was intended as a cue to alert the subject. Next, the remaining five repetitions were presented to the subject (interstimulus interval was 300 ms). An LED flashing in synchrony with each presentation served as a visual cue. The subject was asked to select a number from a scale of 0 (don't hear it) to 100 (too loud) to match the subjective magnitude of the perceived overall loudness of the stimulus set. This procedure was used because, during pilot runs, some subjects occasionally reported changes in the loudness of the stimulus between the first and third presentations of the stimulus.

Before beginning the data collection procedure, the subject was presented with an ascending sequence (0.2-dB steps) of the 200-ms pulse train from threshold to the maxi-

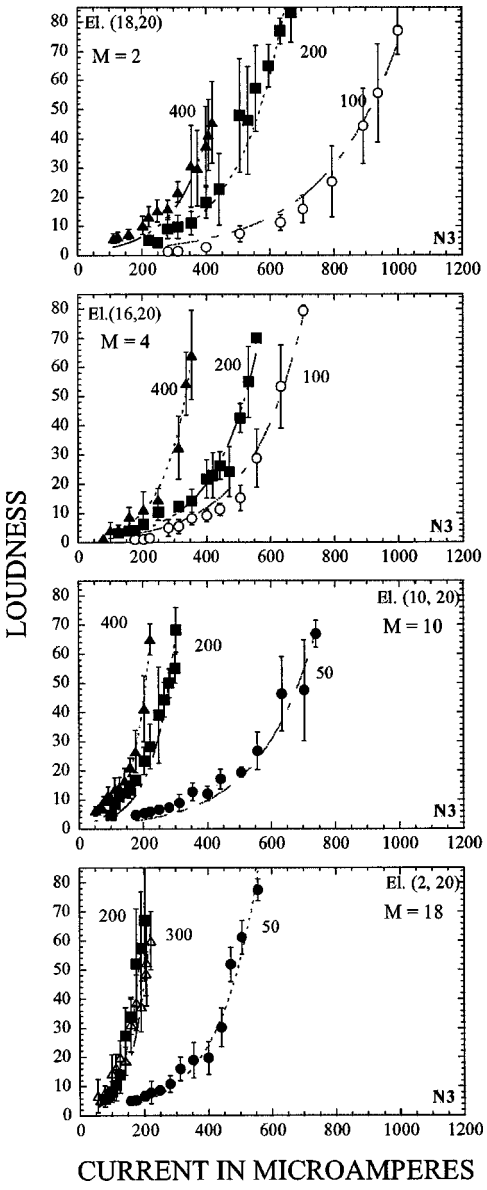

FIG. 1. Loudness growth as a function of pulse amplitude. Parameter: Phase duration. Each panel corresponds to results obtained with a different stimulating electrode pair. Results for subject N3. The dotted lines represent the best fitting exponential approximation to the data [Eq. (2)].

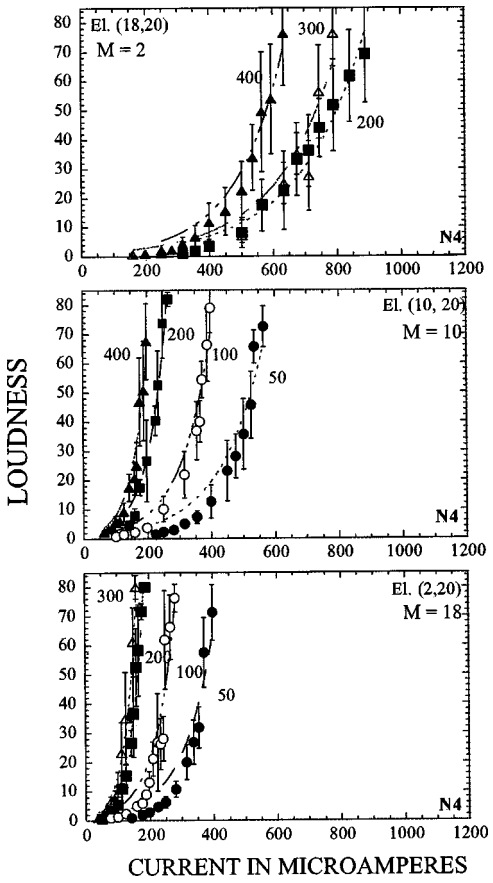

FIG. 2. As in Fig. 1: loudness growth as a function of pulse amplitude for subject N4.

mum acceptable level, in order to give them some orientation as to the range of stimuli that might be used, as well as to ensure that the loudest stimuli were not too loud. Each loudness function is based upon a minimum of four to a maximum of eight independent loudness estimates at each amplitude level. The mean and standard deviation of all loudness estimates made for a particular electrode pair were computed at each amplitude.

At current levels close to threshold, subjects did not always hear all six presentations, but were asked to judge the overall loudness of the ones that were audible. As the softest sound was always presented at a higher level than threshold, subjects never used ''0'' to judge the loudness, but fractions were allowed and often used.

Loudness functions were obtained using a number of phase durations D at each of a number of electrode separations M. One repetition consisted of loudness estimates obtained for each of the set of selected current amplitudes for a particular condition (combination of M and D). One run consisted of a number of such repetitions (usually three to four). The experimenter ensured a rough randomization of the presentation sequence of the stimuli in each repetition. This was done by presenting each set of amplitudes in each repetition in a different order, decided previously by the experimenter. Subjects most easily recognized the softest and loudest sounds, while sounds in between the two ends of the range were more difficult to judge.

II. RESULTS AND ANALYSIS

All loudness functions obtained with the four subjects are shown in Figs. 1–4. The different panels correspond to loudness functions obtained with different (fixed) electrode pairs (separations). In each panel, each function corresponds to loudness estimates obtained with a different phase duration. The loudness functions obtained with a phase duration of 200 μs/phase were published previously (Chatterjee, 1999). It is apparent from the results that, for a fixed electrode pair (or separation), longer phase durations result in a steeper loudness function.

In each case, the data were fit with an equation of the form used by Chatterjee (1999)

$$L = a^{\alpha I}, \tag{2}$$

where the value of the parameter α controls the steepness of the function. The dashed lines in Figs. 1–4 represent the

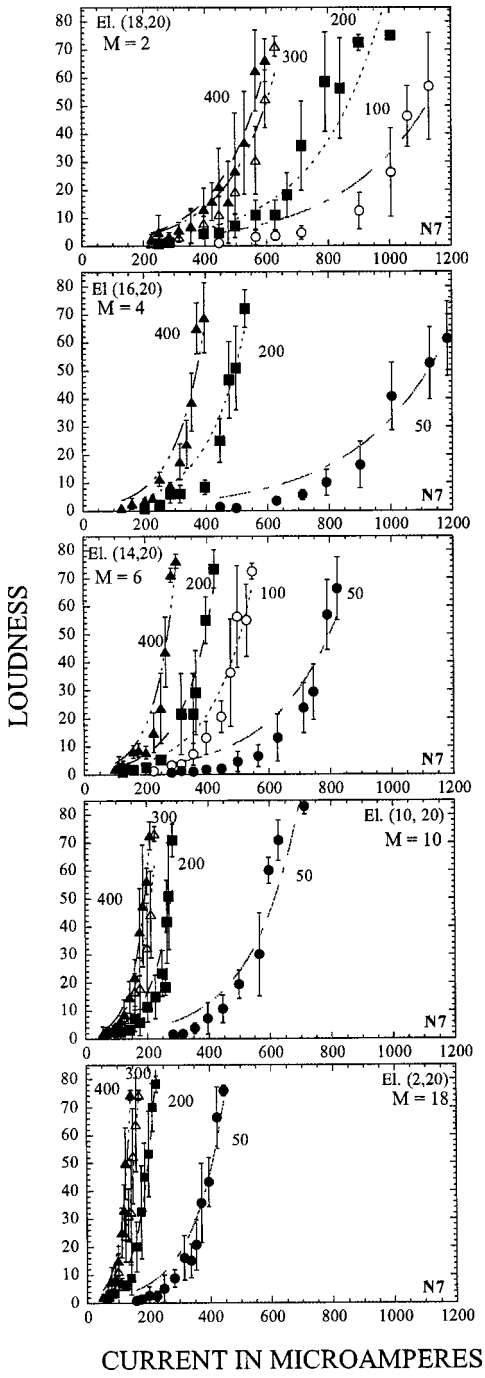

FIG. 3. As in Fig. 1: loudness growth as a function of pulse amplitude for subject N7.

curve fits corresponding to each electrode separation and phase duration.

According to the hypothesis stated in the Introduction, the exponent α should correspond to $g(M)*f(D)$. The symbols in Fig. 5 show the exponents corresponding to each loudness function, plotted against the phase duration. Each panel shows results from a different subject. Note that the different symbols correspond to the exponents obtained with different electrode pairs (electrode separations M). It is apparent from the functions in Fig. 5 that, for a fixed M, $f(D)$ is a monotonically increasing function of D.

To directly compare the shapes of the exponent-phase duration functions across electrode separations, we normal-

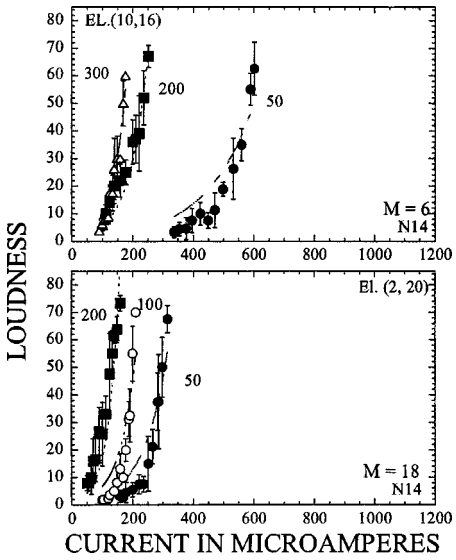

FIG. 4. As in Fig. 1: loudness growth as a function of pulse amplitude for subject N14.

ized the exponents by dividing each set of exponents in Fig. 5 by the exponent obtained at a phase duration of 200 μs. If $f(D)$ and $g(M)$ are independent, this normalization should yield the same function regardless of electrode separation, as shown below.

Using the term $\alpha_{n(M)}$ to describe the normalized exponents for a particular M, and the term $|f(D)|_{D=200}$ to signify the value of $f(D)$ for $D=200$ μs/phase, and assuming $g(M)$ and $f(D)$ are independent, we can write

$$\alpha_{n(M)}=g(M)*\frac{f(D)}{g(M)*|f(D)|_{D=200}},$$

or

$$\alpha_{n(M)}=\frac{f(D)}{|f(D)|_{D=200}}. \tag{3}$$

Thus, $\alpha_{n(M)}$ should be a function of D only, independent of electrode separation M. For a particular subject and electrode pair, $|f(D)|_{D=200}$ is a constant. Figure 6 shows the normalized exponents plotted against the phase duration D. It is apparent that for each subject, the normalized values of the exponent for the different electrode separations fall along a single function of phase duration, indicating that $g(M)$ and $f(D)$ are indeed independent. We fit the pooled, normalized data with the equation

$$\alpha_{n(M)}=\mu D^{\theta}, \tag{4}$$

where $\alpha_{n(M)}$ is the normalized value of the exponent α, μ is a constant (presumably equal to $1/(|f(D)|_{D=200})$, D represents the phase duration, and θ is the exponent of the power function. The dotted lines and the equations in Fig. 6 show the results of the fit. The best-fitting power functions have exponents θ ranging from 0.530 to 0.641 across subjects. [We note here that attempts to fit the pooled, normalized exponents with linear functions also yielded good approximations. The power function was selected for two reasons: (1) we wished to be consistent with the Zeng *et al.* study

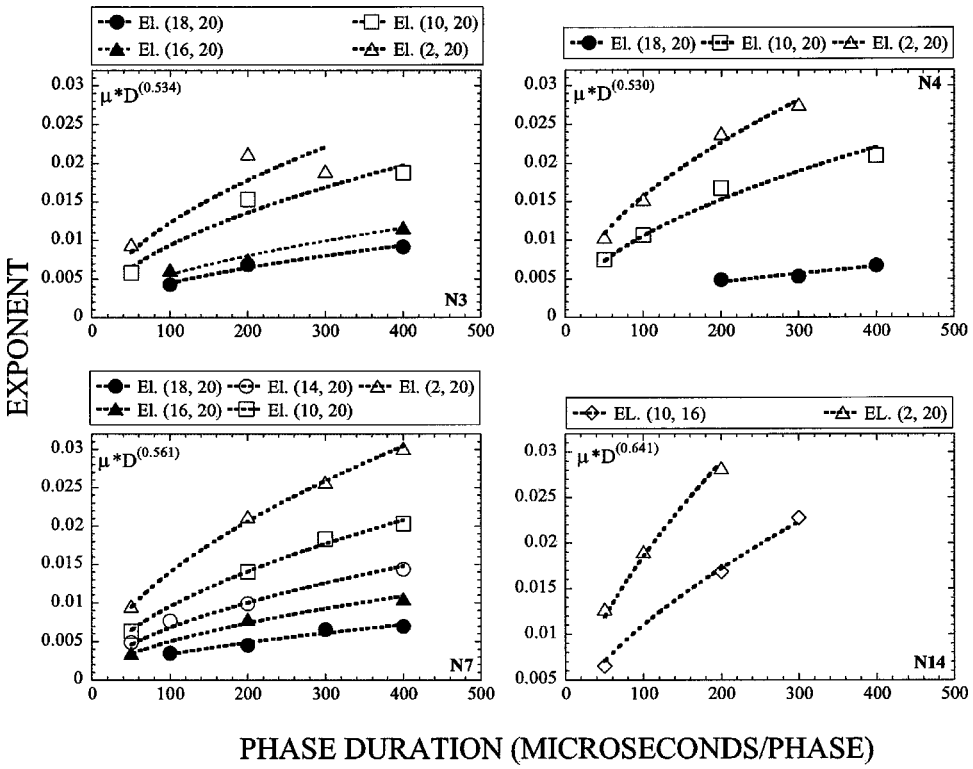

FIG. 5. The best-fitting exponents plotted against the phase duration. Each panel represents data from a different subject. Within each panel, the different symbols correspond to exponents obtained with a different electrode separation. Dashed lines show curve fits following Eq. (5).

cited previously, and (2) in each subject, the fits obtained with the power function accounted for more of the variance than those obtained with the linear function.]

Using the value of θ for each subject obtained from the curve fits in Fig. 6, we fit the original data in Fig. 5 with the equation

$$\alpha = \mu_M D^{\theta}, \tag{5}$$

where μ_M, a multiplicative constant, is the only parameter to be fit, and is dependent upon M. Recalling Eq. (1), it becomes clear that the function relating μ_M and M is identical to $g(M)$, presumably a monotonically increasing function of the electrode separation. Equation (5) (dotted lines in Fig. 5) provides a satisfactory fit to the data, accounting for 86.5% (subject N3) to 99.4% (subject N14) of the variance. Figure 7 plots the best-fitting values of μ_M against M for each subject. The resulting function, $g(M)$, is a monotonically increasing function of M. The dashed lines in Fig. 7 show the results of linear curve fits to the data. It is apparent that a function of the form

$$g(M) = \lambda + \gamma M \tag{6}$$

describes the data reasonably well. From Fig. 7, we see that λ ranges from 1.735e-04 in subject N4 to 3.808e-04 in subject N14, while γ ranges from 3.267e-05 in subject N14 to 6.816e-05 in subject N4. These values are listed in Table I.

We can now write, at least for pulsatile stimuli presented at moderate rates, a more general equation describing the

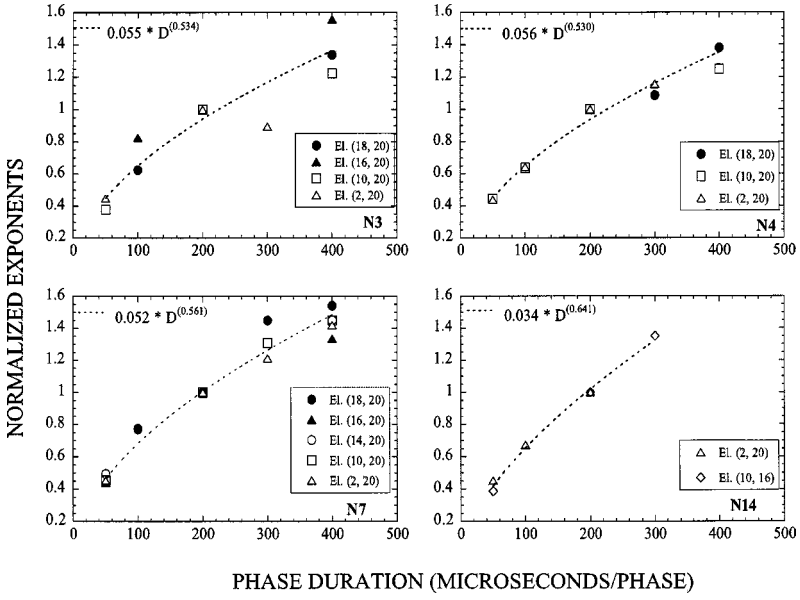

FIG. 6. The exponents from Fig. 5 have been normalized and replotted against the phase duration. Normalization involved dividing each exponent by the value of the exponent at a phase duration of 200 μs/phase for that electrode pair. The dashed lines and equations show the best-fitting power function to the normalized exponents. Each panel shows exponents for a different subject; each symbol within a panel shows exponents obtained with a different electrode pair/separation.

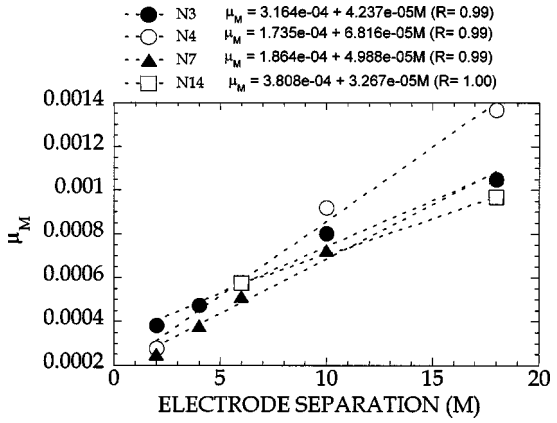

FIG. 7. Values of the multiplicative constant μ obtained from the curve fits shown in Fig. 5, plotted against electrode separation M.

growth of loudness as a function of phase duration and electrode separation

$$L = e^{(\lambda + \gamma M) D^{\theta} I}, \tag{7}$$

where λ, γ, and θ are subject-dependent constants, M is the electrode separation, and I is current amplitude.

The previously cited study (Chatterjee, 1999) was conducted at a fixed phase duration (D) of 200 μs/phase. Substituting 200 for D, and the expression for $g(M)$ given in Eq. (6), we obtain

$$L = e^{(\lambda + \gamma M)(200^{\theta}) I}. \tag{8}$$

In Fig. 8, we have plotted estimated exponents for each subject from the present study, alongside the values of the exponents obtained in the previous study using 200-μs/phase pulses and a larger number of electrode separations and locations. Given the considerable variability encountered in subjective measures of magnitude, the close correspondence between these variables is reassuring.

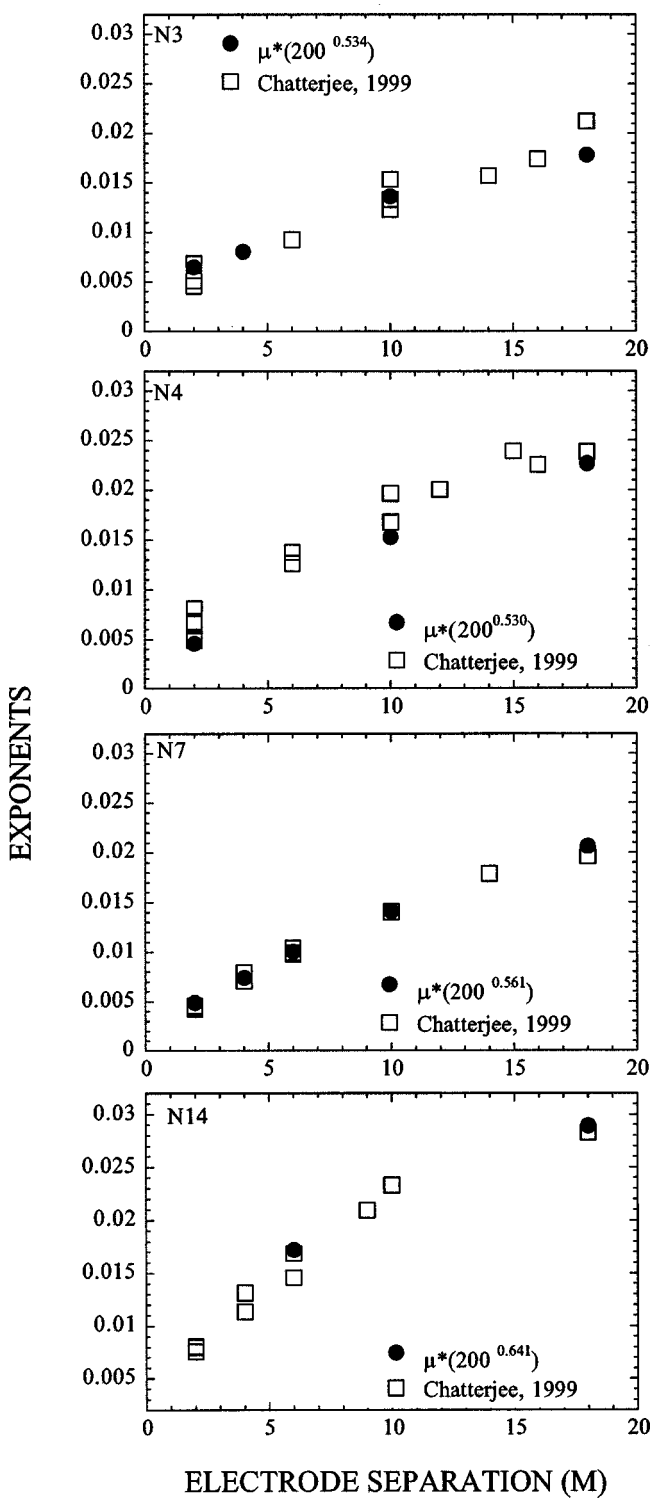

FIG. 8. Pooled exponents obtained in a previous study (Chatterjee, 1999) using a fixed phase duration of 200 μs/phase (open symbols), plotted alongside the function predicted by Eq. (8), using values obtained in the current study (closed symbols). The exponents (open symbols) in the previous study were obtained using a more diverse set of electrode locations and separations than the present study.

III. DISCUSSION

Although the small size of the subject pool and the limited set of experimental conditions does not allow us to make broad generalizations, our directly measured loudness functions add to the findings in our previous study as well as confirm the hypothesized independence of the functions $f(D)$ and $g(M)$. To some extent, the present findings are strengthened by the consistency across subjects, particularly considering the large variation in their performance in speech tests. Based upon our set of data, we now have a more general equation [Eq. (7)] to describe the perceived loudness of steady-state pulsatile stimuli in electrical stimulation as a function of both the separation M between electrodes of a stimulating pair and the phase duration D. Whether these relations will hold for other stimulus conditions remains to be seen.

At a fixed loudness L_0, we can write

$$L_0 = e^{(\lambda + \gamma M)(D^{\theta}) I},$$

or

$$I D^{\theta} = \frac{\ln(L_0)}{(\lambda + \gamma M)}. \tag{9}$$

Thus, at equal loudness, the product ID^{θ} is constant for a fixed electrode pair (i.e., fixed M). This result is in agreement

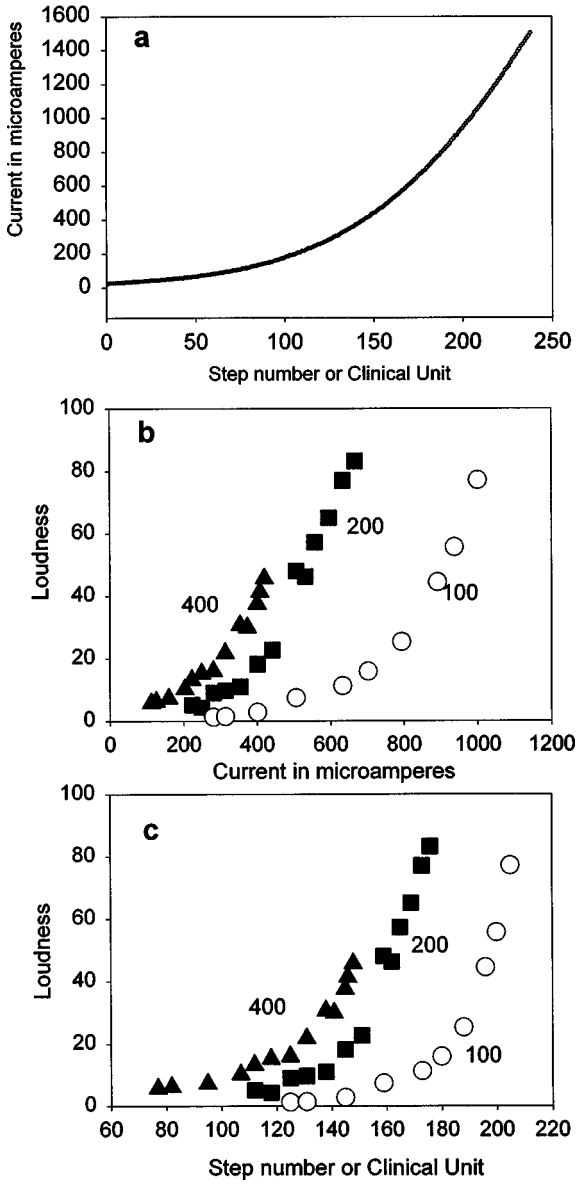

FIG. 9. (a) Clinical units (amplitude step) vs current in microamperes for subject N3's device. (b) Loudness estimates made by subject N3 for stimulation on electrode pair (18, 20), as a function of current in microamperes. Loudness functions were obtained using three different phase durations (shown next to each plot): 100, 200, and 400 μs/phase. Data are replotted from Fig. 1 (top panel). (c) Data of (b), plotted as a function of step numbers or clinical units.

with the fundamental finding of the Zeng *et al.* (1998) study, which was conducted under conditions of equal loudness. In addition, our present findings show that the constant relating I and D^{θ} is inversely related to the electrode separation M. According to Zeng *et al.*, the exponent θ is loudness dependent, decreasing from 0.7 at threshold to 0.5 at high levels. Although our data are adequately described using a single value of θ, methodological differences between the two studies may underlie some of the discrepancy: Zeng *et al.* used a loudness-balancing technique, whereas we used magnitude estimation to measure loudness. It is at least encouraging that our observed value of θ lies well within the range of values from the Zeng *et al.* study.

The subjects' sensitivity to changes in stimulation parameters is controlled by the exponential nature of the loudness function. Thus, when the electrodes of the pair are close together (i.e., M is small), changes in phase duration D result in small changes in perceived loudness, while stimuli with large electrode separations evoke larger changes in loudness for similar changes in phase duration. Similarly, for stimuli with short phase durations, loudness will change slowly with increasing electrode separation, while for stimuli with long phase durations, loudness will change rapidly with increasing electrode separation. In addition, for fixed electrode separations, the rate of change of loudness with phase duration will depend directly upon the current amplitude I. These effects can be seen in the loudness functions plotted in Figs. 1–4.

It is evident from the above observations that the greatest changes in perceived loudness occur at current levels that are near the upper limit of the dynamic range for a particular stimulus. However, the discrete steps in the Nucleus-22 device follow an approximately logarithmic function of current amplitude, so that one step near threshold results in a small change in current, but one step at higher levels results in a large change in current. This is illustrated in Fig. 9(a), which plots current amplitude in microamperes against step number (or clinical unit) for subject N3's device. In Fig. 9(b), we have plotted examples of loudness estimates obtained in this subject as a function of current in microamperes (the same data are plotted in Fig. 1, top panel). The three loudness estimates were obtained when stimulating electrode pair (18,20) with three phase durations. Figure 9(c) shows the same loudness estimates as a function of clinical units. It becomes clear from a study of Fig. 9 that the compressive transformation from current amplitude to clinical units shown in Fig. 9(a) has the potentially deleterious effect of steepening an already steep loudness function and providing larger amplitude increments in the region of the function that is most sensitive to such changes.

Mechanisms underlying the relationships quantified here are unclear, as sources of nonlinearity in the electrically stimulated auditory system are largely unknown. At threshold, physiological experiments indicate that electrically stimulated primary auditory neurons function as leaky integrators (Moxon, 1971; Parkins and Columbo, 1987; van den Honert and Stypulkowski, 1984). However, the parameter dependence of such integration has not been examined in depth at the auditory-nerve level. As electrode separation increases, the geometry of the stimulating electrical field may change considerably. It is known that neural excitability depends strongly on the geometry as well as the dynamics of the stimulating electrical field, both of which may be expected to change with changes in electrode separation or changes in temporal aspects of the stimulus, such as phase duration. It has also been suggested (van den Honert and Stypulkowski, 1984) that the site of neural excitability changes with current amplitude, jumping from dendritic excitation at low current amplitudes to axonal excitation at high current amplitudes. If so, the temporal aspect of neural response (which is dictated by the membrane properties) may be expected to change from low to high current amplitudes also, resulting in an amplitude-dependent time-domain re-

sponse. These issues will become even more critical when considering dynamic stimuli with overlapping excitation patterns and time-varying amplitudes.

Although it is not strictly necessary to describe the growth of loudness in electrical stimulation with an exponential function, some sort of expansive nonlinearity appears to be present. Zeng and Shannon (1992, 1994) have proposed that such an expansion of the compressed cochlear output may be occurring in the central auditory pathways of normally hearing listeners. According to their theory, the cochlear compression is absent in cochlear implant patients; the expansion works directly on the auditory-nerve output to the brain (assumed to be linearly related to input current amplitude). Whether the expansive nonlinearity is peripherally or centrally located, our present study has further defined the parameter space upon which it operates. It is now apparent that the expansion works not only on the input current amplitude, but on a function of current amplitude, phase duration, and electrode separation.

It is important to keep in mind that these findings are valid only for stimulation of one electrode pair at a time. Given recent advances in the field of cochlear implant technology, it is only to be expected that the growth of loudness of complex stimuli, involving simultaneous stimulation of multiple electrode pairs, will be an important area of research in the near future.

ACKNOWLEDGMENTS

This work was supported by NIDCD Grant Nos. RO1 DC01526-05 and RO3 DC03519-01. We thank Cochlear Corporation for the amplitude calibration tables for each subject's device. Dr. D. Wesley Grantham and two anonymous reviewers provided helpful criticism of the manuscript. Above all, we are grateful to the subjects for their patient and enthusiastic participation in these experiments.

Abbas, P. J., and Brown, C. J. (**1991**). ''Electrically evoked auditory brainstem response: Growth of response with current level,'' Hear. Res. **51**(1), 123–137.

Chatterjee, M. (**1999**). ''Effects of stimulation mode on threshold and loudness growth in multielectrode cochlear implants,'' J. Acoust. Soc. Am. **105**, 850–860.

Moxon, E. C. (**1971**). ''Neural and mechanical responses to electrical stimulation of the cat's inner ear,'' Ph.D. thesis, Massachusetts Institute of Technology, Cambridge, MA.

Parkins, C. W., and Columbo, J. (**1987**). ''Auditory-nerve single-neuron thresholds to electrical stimulation from scala tympani electrodes,'' Hear. Res. **31**, 267–286.

Pfingst, B. E., Miller, A. L., Morris, D. J., Zwolan, T. A., Spelman, F. A., and Clopton, B. M. (**1995**). ''Effects of electrical current configuration on stimulus detection,'' Ann. Otol. Rhinol. Laryngol. Suppl. **166**, 127–131.

Shannon, R. V. (**1985**). ''Threshold and loudness functions for pulsatile stimulation of cochlear implants,'' Hear. Res. **18**, 135–143.

Smith, D. W., and Finley, C. C. (**1997**). ''Effects of electrode configuration on psychophysical strength-duration functions for single biphasic electrical stimuli in cats,'' J. Acoust. Soc. Am. **102**, 2228–2237.

van den Honert, C., and Stypulkowski, P. H. (**1984**). ''Physiological properties of the electrically stimulated auditory nerve II. Single fiber recordings,'' Hear. Res. **14**, 225–243.

Zeng, F. G., and Shannon, R. V. (**1992**). ''Loudness balance between electric and acoustic stimulation,'' Hear. Res. **60**(2), 231–235.

Zeng, F.-G., and Shannon, R. V. (**1994**). ''Loudness-coding mechanisms inferred from electric stimulation of the human auditory systems,'' Science **254**, 564–566.

Zeng, F.-G., Galvin, J. J., and Zhang, C. (**1998**). ''Encoding loudness by electric stimulation of the auditory nerve,'' NeuroReport **9**(8), 1845–1848.

Place-pitch sensitivity and its relation to consonant recognition by cochlear implant listeners using the MPEAK and SPEAK speech processing strategies

Gail S. Donaldson and David A. Nelson
Department of Otolaryngology, University of Minnesota, Minneapolis, Minnesota 55455

(Received 13 November 1998; revised 28 July 1999; accepted 19 November 1999)

Two related studies investigated the relationship between place-pitch sensitivity and consonant recognition in cochlear implant listeners using the Nucleus MPEAK and SPEAK speech processing strategies. Average place-pitch sensitivity across the electrode array was evaluated as a function of electrode separation, using a psychophysical electrode pitch-ranking task. Consonant recognition was assessed by analyzing error matrices obtained with a standard consonant confusion procedure to obtain relative transmitted information (RTI) measures for three features: stimulus (RTI stim), envelope ($\mathrm{RTI\,env}_{[\mathrm{plc}]}$), and place-of-articulation ($\mathrm{RTI\,plc}_{[\mathrm{env}]}$). The first experiment evaluated consonant recognition performance with MPEAK and SPEAK in the same subjects. Subjects were experienced users of the MPEAK strategy who used the SPEAK strategy on a daily basis for one month and were tested with both processors. It was hypothesized that subjects with good place-pitch sensitivity would demonstrate better consonant place-cue perception with SPEAK than with MPEAK, by virtue of their ability to make use of SPEAK's enhanced representation of spectral speech cues. Surprisingly, all but one subject demonstrated poor consonant place-cue performance with both MPEAK and SPEAK even though most subjects demonstrated good or excellent place-pitch sensitivity. Consistent with this, no systematic relationship between place-pitch sensitivity and consonant place-cue performance was observed. Subjects' poor place-cue perception with SPEAK was subsequently attributed to the relatively short period of experience that they were given with the SPEAK strategy. The second study reexamined the relationship between place-pitch sensitivity and consonant recognition in a group of experienced SPEAK users. For these subjects, a positive relationship was observed between place-pitch sensitivity and consonant place-cue performance, supporting the hypothesis that good place-pitch sensitivity facilitates subjects' use of spectral cues to consonant identity. A strong, linear relationship was also observed between measures of envelope- and place-cue extraction, with place-cue performance increasing as a constant proportion ($\sim$0.8) of envelope-cue performance. To the extent that the envelope-cue measure reflects subjects' abilities to resolve amplitude fluctuations in the speech envelope, this finding suggests that both envelope- and place-cue perception depend strongly on subjects' envelope-processing abilities. Related to this, the data suggest that good place-cue perception depends both on envelope-processing abilities and place-pitch sensitivity, and that either factor may limit place-cue perception in a given cochlear implant listener. Data from both experiments indicate that subjects with small electric dynamic ranges ($<$8 dB for 125-Hz, 205-μs/ph pulse trains) are more likely to demonstrate poor electrode pitch-ranking skills and poor consonant recognition performance than subjects with larger electric dynamic ranges. [S0001-4966(00)01403-X]

PACS numbers: 43.66.Ts, 43.66.Hg, 43.66.Jh, 43.71.Ky [JWH]

INTRODUCTION

Recent developments in cochlear implant speech processing strategies have resulted in significant improvements in implant listeners' speech recognition performance. As a result, users of the newest generation of speech-processing strategies commonly achieve high levels of speech recognition under favorable listening conditions (e.g., Dorman, 1993; Skinner *et al.*, 1994; Tyler *et al.*, 1996). At present, we have only a limited understanding of how such high levels of speech recognition are achieved by the better implant performers or, conversely, why some implant listeners still perform poorly with the same prostheses and speech-processing strategies. Related to this, there exists relatively little information concerning the psychophysical abilities underlying speech recognition in electric hearing, or how such abilities may vary as a function of stimulation parameters that differ among speech-processing strategies.

One psychophysical ability thought to be important for speech recognition in electric hearing is place-pitch sensitivity, i.e., the ability to distinguish among electrodes on the basis of tonotopically mediated pitch, or timbre. Theoretically, cochlear implant listeners with good place-pitch sensitivity can make use of the spectral information in speech if it is well-represented in the electrical stimulus. Such spectral information contributes primarily to discrimination of the vowel height and frontness features (related to $f1$ and $f2$ frequency, respectively) and the consonant place-of articula-

tion feature, since these phonemic features are coded predominantly by spectral cues. Townshend *et al.* (1987) were the first investigators to examine place-pitch sensitivity in cochlear implant listeners, using psychophysical electrode pitch-ranking and electrode discrimination tasks. They showed that some implantees exhibit relatively strong place-pitch sensitivity consistent with the normal tonotopic organization of the cochlea, whereas others perceive little change in pitch as a function of electrode location. This finding, confirmed in several later studies (see below), suggests that place-pitch sensitivity may be an important factor limiting speech recognition ability in some cochlear implant users.

Only a few studies have examined the relationship between place-pitch sensitivity and speech recognition, and these studies are limited to subjects using the Nucleus $f0/f1/f2$ or MPEAK speech processing strategies. Busby *et al.* (1993) showed that discrimination of electrode trajectories by four late-deafened cochlear implant subjects predicted the degree to which speech recognition performance improved with a multichannel device ($f0/f1/f2$ strategy) relative to a single-channel device. Nelson *et al.* (1995) evaluated the relationship between place-pitch sensitivity and consonant recognition in eight postlingually deafened subjects using the Nucleus MPEAK or $f0/f1/f2$ strategy. Several subjects exhibited good or excellent place-pitch sensitivity; however, none of the subjects demonstrated particularly good place-of-articulation performance. This led the authors to conclude that spectral cues to consonant identity are not coded very effectively by the MPEAK and $f0/f1/f2$ strategies. Even so, a weak correlation between place-pitch sensitivity and consonant place-cue performance was reported. Nelson *et al.*'s impression that the $f0/f1/f2$ and MPEAK strategies provide only minimal place-cue information was subsequently supported by place-cue data reported by Parkinson *et al.* (1996) in a comparison study of the $f0/f1/f2$ and MPEAK strategies. Zwolan *et al.* (1997) examined the relationship between electrode discrimination and speech recognition in 11 users of the Nucleus MPEAK strategy. A considerable range of electrode discrimination performance was observed across subjects, with several subjects demonstrating excellent performance; however, no significant relationship between electrode discrimination and speech recognition was observed. In general, the above studies suggest that many cochlear implant patients possess good place-pitch sensitivity, but that place-pitch sensitivity is not strongly related to speech recognition performance with the $f0/f1/f2$ or MPEAK speech-processing strategies.

The present experiments were motivated by the MPEAK-SPEAK comparison study of Skinner *et al.* (1994), which showed that some but not all users of the MPEAK speech-processing strategy can achieve improved speech recognition performance with SPEAK. We were especially interested in the individual differences apparent in Skinner *et al.*'s data, in particular, the demonstration that subjects who achieved equivalent levels of performance with MPEAK sometimes exhibited considerably different levels of performance with SPEAK. Because SPEAK provides a more detailed spectral characterization of the speech waveform than MPEAK, we hypothesized that subjects showing the greatest gains with SPEAK were those subjects who were best able to use this spectral information, i.e., those with good place-pitch sensitivity. Skinner *et al.* did not analyze speech recognition data in terms of spectral versus temporal speech cues; thus it is not possible to determine whether the improvements demonstrated by their subjects were primarily related to spectral cues as our hypothesis would predict.

The studies described here specifically evaluated the relationship between place-pitch sensitivity and consonant recognition in cochlear implant subjects using the MPEAK and SPEAK strategies. The first experiment compared consonant recognition performance with MPEAK and with SPEAK in a single group of subjects. Subjects were experienced users of the MPEAK strategy, and their performance with SPEAK was evaluated after they used the SPEAK strategy on a daily basis for one month. The findings from this first experiment were somewhat surprising: Although subjects demonstrated a wide range of place-pitch sensitivity as measured by our electrode pitch-ranking task, their place-cue performance was equally poor with the SPEAK strategy as with the MPEAK strategy, and there was no systematic relationship between place-pitch sensitivity and consonant place-cue performance with either strategy.

Subsequent examination of several cochlear implant listeners' performance over time with the SPEAK strategy showed that performance on the consonant place-cue measure sometimes continued to improve well beyond the first month of use. This suggested that the relatively short SPEAK trial used in our first experiment may have provided an inaccurate picture of the relationship between place-pitch sensitivity and consonant recognition. As a result, we reevaluated this relationship in a second study using subjects with substantially more SPEAK experience. Data from the second study showed the expected positive relationship between place-pitch sensitivity and consonant place-cue performance, consistent with our hypothesis. In addition, this study indicated that consonant place-cue performance depends not only on place-pitch sensitivity but also on subjects' ability to resolve amplitude fluctuations in the speech signal.

EXPT 1: PLACE-PITCH SENSITIVITY AND CONSONANT RECOGNITION WITH MPEAK VERSUS SPEAK

Methods

Subjects

Fourteen postlingually deafened adult subjects participated in the first experiment. All were experienced users of the Nucleus 22-electrode implant, having used their implants continuously for at least one year. Twelve were clinical users of the MPEAK speech-processing strategy implemented on the Mini Speech Processor and two were clinical users of the $f0/f1/f2$ strategy implemented on the Wearable Speech Processor. All subjects were native speakers of American English. Subjects provided informed consent to participate in the study and were paid on an hourly basis for their participation. Demographic data and other information describing the subjects are provided in Table I.

TABLE I. Description of 14 cochlear implant subjects who participated in expt. 1: Subject identifying code, gender, age, etiology of deafness (implanted ear), duration of bilateral severe-to-profound hearing loss prior to implantation, depth of electrode array insertion (mm from the round window, with 25 mm representing complete insertion), duration of implant use prior to the study, and duration of MPEAK use prior to the study. To provide readers with an indication of subjects' clinical performance levels with MPEAK (or $f0/f1/f2$), subjects' scores for the NU-6 monosyllabic word test (% correct words and % correct phonemes) are also shown.

Subj	m/f	Age (yrs)	Etiology of deafness	Duration (yrs)	Depth (mm)	CI use (yrs)	MPEAK use (yrs)	Nu-6 % words	Nu-6 % phons
AJA	*m*	48	skull fracture	10	20	6.4	4.7	22	43
AMB	*m*	51	progressive SNHL	1	25	1.6	1.6	40	63
BRL	*f*	49	progressive SNHL	25	20	3.2	3.2	8	27
EJQ	*f*	52	mumps, progressive SNHL	9	22	8.0	8.0	0	12
FXC	*m*	68	progressive SNHL	4	25	4.1	4.1	16	44
JMS	*f*	48	progressive SNHL	36	25	4.9	4.9	8	34
JWB	*m*	60	cochlear otosclerosis	4	20	8.5	⋯	6	22
KRK	*m*	66	familial SNHL noise exp.	5	24	5.1	5.1	6	27
LMF	*f*	24	meningitis	12	21	6.8	6.8	0	4
MAS	*f*	65	genetic/progressive SNHL	10	25	2.4	2.4	28	52
PLF	*f*	67	otosclerosis	<1	25	1.4	1.4	14	40
REC	*m*	71	traumatic noise exposure	15	25	5.5	5.5	6	27
RFM	*m*	62	Meniere's disease	1	22	6.4	⋯	8	28
TVB	*m*	46	progressive SNHL	8	22	4.7	4.7	12	37

Study design

Each subject completed a one-month trial with the SPEAK strategy implemented on a loaner Spectra processor, and underwent consonant confusion testing four times. Ten subjects who were clinical users of the MPEAK strategy completed the following standard (ABBA) protocol: (1) testing with MPEAK 2–4 weeks prior to the beginning of the SPEAK trial (**MPK-1** condition); (2) testing with SPEAK on the first day of the one-month trial (**SPK-1** condition); (3) repeat testing with SPEAK at the conclusion of the one-month trial (**SPK-2** condition); and (4) repeat testing with MPEAK approximately 4 weeks later (**MPK-2** condition). Comparisons of consonant recognition with the MPEAK and SPEAK strategies, described below, are based on data from these ten subjects. Four additional subjects (two MPEAK users and two $f0/f1/f2$ users) provided data for the SPK-1 and SPK-2 conditions but were unable to complete the standard test protocol for the MPK-1 and/or MPK-2 conditions. Data for these subjects are included in analyses that compare electrode pitch-ranking performance and consonant recognition with the SPEAK strategy. A psychophysical electrode pitch-ranking task was used to measure place-pitch sensitivity across the electrode array in each subject. In most cases, this testing was performed within the three-month time period spanned by consonant recognition testing.[1]

Speech processor maps

Subjects used their usual, clinical maps for testing with MPEAK. The SPEAK map created for each subject initially used the same thresholds (*T*-levels) and most comfortable loudness levels (*C*-levels) as the MPEAK map. In a few cases, *C*-levels were subsequently reduced by a constant small percentage across electrodes to compensate for increased overall loudness with the SPEAK strategy. Other SPEAK parameters were set to their default values, including the frequency allocation table which varied according to the number of electrodes activated in a subject's map. All subjects used the Cochlear Corp. ''Stimulus Level'' intensity coding scheme for both the MPEAK and SPEAK strategies. Over the range of levels used here, this coding scheme holds current amplitude constant at approximately 1 mA, and varies pulse duration in logarithmic steps between 19 and 400 μs/ph (Cochlear Corp., 1996).

The MPEAK and SPEAK speech-processing strategies typically employ bipolar stimulation in which the active and return members of a given electrode pair are closely spaced electrodes along the cochlear array. In this report, electrodes are numbered in increasing order from the most apical (1) to the most basal (22) electrode along the array, and a given bipolar electrode pair is referred to by its more basal member. Two expt. 1 subjects were programmed with a bipolar separation of 0.75 mm (BP mode); all others were programmed with a bipolar separation of 1.5 mm (BP+1).

Consonant recognition procedures

Stimuli. Stimuli used in the consonant confusion procedure were 19 /aCa/ disyllables spoken by each of three female talkers and three male talkers, where $C = /p,t,k,b,d,g,f,\theta,s,ʃ,v,ð,z,ʒ,m,n,r,l,j/$. These were identical to the stimuli used by Van Tasell *et al.* (1992) in their ''unprocessed'' condition. The 114 tokens (19 stimuli×6 talkers) were digitized by Van Tasell *et al.* at a sampling rate of 10 kHz with 12-bit resolution.

Test procedure. The subject was seated approximately 1 meter in front of a pair of high-quality loudspeakers and a video screen in a sound-isolated room. Speech tokens were played from computer memory at 10 kHz, amplified, and presented through the speakers. The presentation level of individual tokens varied over a 5-dB range between 60–65 dB SPL (slow response, A-weighting scale) in the sound field at the location of the subject's head. This level is consistent with a conversational or slightly raised vocal effort by a speaker 1 m from the listener (Pearsons *et al.*, 1976; Skinner *et al.*, 1997). The speech processor was set to the ''normal''

TABLE II. Envelope and place categories of Van Tasell *et al.* (1992) that were used for information transmission analyses in the present study.

Category #	Envelope feature	Place feature
1	/b,d,g,v,ð,ʒ,z/ (voiced fricatives and plosives)	/b,p,f,v,m/ (front)
2	/p,t,k/ (voiceless plosives)	/d,s,j,t,n,z,ð,1,θ/ (mid)
3	/f,s,θ,ʃ/ (voiceless fricatives and affricates)	/k,ʃ,ʒ,r,g/ (back)
4	/m,n,r,l,j/ (nasals and glides)	

(rather than the noise-reduction) setting, and subjects were instructed to adjust the processor's sensitivity control such that stimuli were comfortably loud. A standard test block consisted of one presentation each of all 114 tokens, in randomized order. The stimulus was presented once on each trial, and the subject used a computer mouse to select his or her response from a list of 19 alternatives displayed on the video screen. Correct-answer feedback was provided immediately after each stimulus presentation, as recommended by Van Tasell *et al.* (1992). A practice block of 38 randomly selected tokens was presented initially, followed by 5 standard blocks. Testing was usually completed in a single 2–3 hour session; however, it was occasionally necessary to carry over testing to a second session. In the latter case, a practice block was obtained at the beginning of each test session. A pooled confusion matrix was created from the five standard blocks of data for a particular subject and test condition. Each pooled matrix represented 30 observations (5 blocks×6 tokens) per stimulus.

Analysis. Information transmission analysis was performed on the pooled consonant confusion matrices to obtain measures of *relative transmitted information for stimulus* (RTI stim), *relative transmitted information for envelope conditional on place* ($\mathrm{RTI\,env}_{[\mathrm{plc}]}$), and *relative transmitted information for place conditional on envelope* ($\mathrm{RTI\,plc}_{[\mathrm{env}]}$). RTI stim represents the proportion of all available stimulus information that is successfully transmitted to the listener, with possible values ranging from 0 to 1. It was computed in the manner described by Miller and Nicely (1955). $\mathrm{RTI\,env}_{[\mathrm{plc}]}$ represents the subject's ability to extract and use low-frequency temporal information in the speech waveform (envelope and periodicity), whereas $\mathrm{RTI\,plc}_{[\mathrm{env}]}$ represents the subject's ability to utilize available spectral cues to consonant place-of-articulation. $\mathrm{RTI\,env}_{[\mathrm{plc}]}$ and $\mathrm{RTI\,plc}_{[\mathrm{env}]}$ were computed via sequential information analysis (SINFA), using the modified envelope categories described by Van Tasell *et al.* (1992) and the place categories *front, middle*, and *back*. Category membership for the envelope and place features used in SINFA analyses are shown in Table II. The conditional values $\mathrm{RTI\,env}_{[\mathrm{plc}]}$ and $\mathrm{RTI\,plc}_{[\mathrm{env}]}$ were computed because the envelope and place feature sets shown in Table II are not completely orthogonal. These conditional measures can be viewed as independent indicators of subjects' abilities to use temporal (envelope) and spectral cues in the acoustic speech waveform (Van Tasell *et al.*, 1992).

Electrode pitch-ranking procedures

The stimuli and procedures used for the electrode pitch-ranking task were similar to those described by Nelson *et al.* (1995). Stimuli were 500-ms trains of 125 Hz, 205 μs/ph biphasic pulses presented at current amplitudes yielding constant, comfortable loudness across electrodes as determined by the loudness balancing procedure described below. Stimulation was bipolar, with bipolar mode matched to that used in the subject's speech processor (BP or BP+1). Electrodes were stimulated directly (bypassing the speech processor) using a specialized interface (Shannon *et al.*, 1990) controlled through the parallel port of an 80–486 computer running custom software.

Current amplitudes used in the electrode pitch-ranking task were determined by balancing loudness to a common level of ''medium loud'' across electrodes. To accomplish this, estimates of threshold and maximum acceptable loudness were first obtained for each usable electrode in the subject's array, using an ascending method of limits procedure. In this procedure, the current amplitude of the pulse train stimulus (500-ms pulse trains separated by 500-ms silent intervals) was raised slowly from below threshold to a level where the subject first reliably heard the tone (i.e., could tap his or her finger in synchrony with the tone). After this level was recorded, the current amplitude of the stimulus was gradually increased further. The subject indicated loudness changes by sliding his or her finger along a printed loudness scale, and stimulation was terminated when maximum acceptable loudness was reached. After a short pause, a second ascent was completed, and average threshold and maximum acceptable loudness values were computed from the two values of each. The range of current amplitudes yielding a loudness percept of ''medium loud'' was then determined for one electrode near the middle of the array by slowly raising and lowering current levels over the range of amplitudes yielding medium to loud percepts. The current amplitude on this reference electrode was then set to the approximate midpoint (in logarithmic amplitude units) of the medium loud range. Following this, current amplitudes on each of the remaining electrodes were adjusted to produce similar loudness by presenting the reference stimulus alternately with an adjustable stimulus on each new electrode. The current amplitude on the nonreference electrode was adjusted by the experimenter until the stimulus on that electrode was judged to be equally loud as the stimulus on the reference electrode. Once loudness matches were obtained on all usable electrodes in the subject's array, the loudness-balanced stimuli were played back to the subject in random order to ensure that no stimulus was noticeably louder or softer than the others. If any irregularities in loudness were noted by the subject, the loudness balance procedure was repeated on the electrodes in question and the stimuli were again checked for equal loudness using the playback procedure.

Loudness balancing was intended to ensure that loudness differences between stimuli would not distract subjects from judging pitch differences between stimuli presented on two different electrodes. However, it could not guarantee that all discriminable loudness differences between electrode pairs had been eliminated. For this reason, additional steps

were taken to ensure that subjects could not use loudness cues to improve their pitch-ranking performance. First, subjects were not given feedback on the electrode pitch-ranking task. Thus even if small loudness differences could be discriminated on a given stimulus pair, the subject could not use the loudness cue to improve performance. Second, stimuli were presented in randomized blocks consisting of 10 trials each of 6 to 10 electrode pairs, and the ordering of individual pairs was also randomized.

Pitch-ranking data were obtained using a 2IFC procedure in which two electrodes were stimulated in sequence, separated by a 500-ms silent interval. On each two-interval trial, the subject's task was to select the stimulus that was ''higher in pitch'' or ''sharper.'' The term ''sharpness'' was included in our instructions because subjects in our previous study (Nelson *et al.*, 1995) reported that some stimulus pairs differed in sharpness rather than pitch. A correct response was scored when the subject chose the stimulus presented to the more basal electrode. Feedback was withheld in order to eliminate the possibility that subjects could correctly order stimuli in the case of pitch reversals, i.e., when stimuli were perfectly discriminable but the more apical electrode produced a higher pitch. As indicated above, this also removed the possibility that any remaining loudness differences between stimuli could be used to improve performance. All possible pairs of electrodes separated by distances of 0.75, 1.5, 3.0, and 4.5 mm (1st, 2nd, and 4th diagonals of the comparison matrix) were tested in each subject. Additional electrode separations of 6.0 and 7.5 mm (8th and 10th diagonals) were tested in most subjects whose data did not approach perfect performance at 4.5 mm separation. Note that the term ''electrode separation,'' as used here, refers to the distance between the basal (or apical) members of each of the two electrode pairs stimulated on a given trial, and not to the distance between electrodes in a single electrode pair, which we refer to as ''bipolar separation.''

Subjects were initially trained to perform the pitch-ranking task using widely spaced pairs of electrodes. Following training, data were obtained for 5 to 8 electrode pairs at a time, with 10 trials per comparison pair presented in random order within the block of 50 to 80 trials. Comparisons within a given block of 50 to 80 trials involved a limited region of the electrode array (basal, middle, or apical) and a fixed electrode separation. Blocks of trials with larger and smaller electrode separations were alternated, so that subjects were not required to endure long stretches of trials that involved very difficult comparisons. After one complete data set (10 trials/comparison) was obtained for all electrode separations, two additional data sets were obtained. This resulted in a total of 30 trials per comparison. Three or four two-hour sessions were typically required to complete the entire electrode pitch-ranking procedure.

A merged comparison matrix was constructed for each subject's pitch-ranking data, with comparison scores expressed as percent correct responses. The average percent correct scores obtained in the 1st, 2nd, 4th, and 6th diagonals of the matrix were computed to arrive at mean percent correct pitch-ranking scores for electrode separations of 0.75, 1.5, 3.0 and 4.5 mm. These mean percent correct scores were then translated to units of perceptual sensitivity (d') using the conversion tables of Hacker and Ratcliffe (1979). A d' value of 3.29 was assigned to perfect performance.

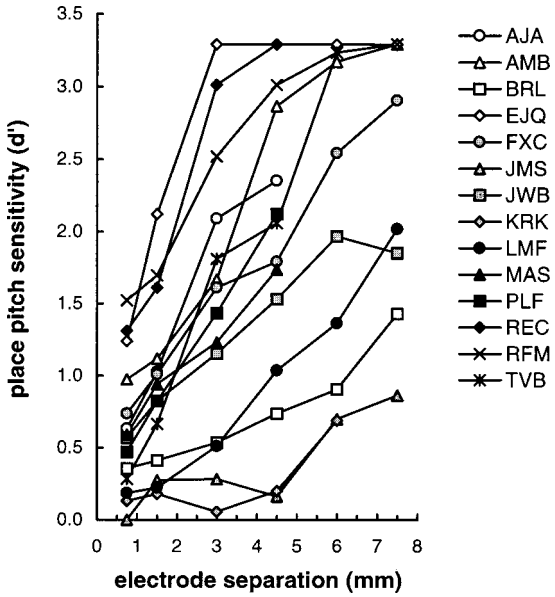

FIG. 1. Average place-pitch sensitivity (d') across the electrode array as a function of electrode separation, for 14 subjects in expt. 1. Perfect discrimination corresponds to $d' = 3.29$.

Results and discussion

Electrode pitch ranking

Figure 1 shows average place-pitch sensitivity as a function of electrode separation for each of the 14 subjects who participated in expt. 1. There was considerable variability in subjects' performance at all electrode separations. At the narrowest separation (0.75 mm, corresponding to the distance between adjacent electrodes in the Nucleus array), place-pitch sensitivity (d') ranged from 0.13 to 1.52; however, only 3 of 14 subjects achieved performance better than $d' = 1$. Performance improved systematically as electrode separation increased from 0.75 to 4.5 mm for most subjects, with the result that 11 of 14 subjects demonstrated place-pitch sensitivity of $d' = 1$ or better at an electrode separation of 4.5 mm. Two subjects (JMS and KRK) demonstrated unusually poor pitch-ranking performance. For these subjects, performance was near chance for electrode separations of 0.75 to 4.5 mm and improved only slightly for wider electrode separations.

It should be noted that pitch reversals were common at narrow electrode separations, but occurred less often at wider electrode separations. Specifically, 13 of 14 subjects demonstrated one or more pitch reversals at an electrode separation of 0.75 mm, whereas only 2 of 14 subjects demonstrated any pitch reversals at the 4.5-mm separation. It is also noteworthy that place-pitch sensitivity did not vary systematically with distance along the electrode array in most cases. Only two subjects demonstrated clear differences in place-pitch sensitivity in the apical versus basal halves of the implanted array and, even for these subjects, differences were not dramatic.

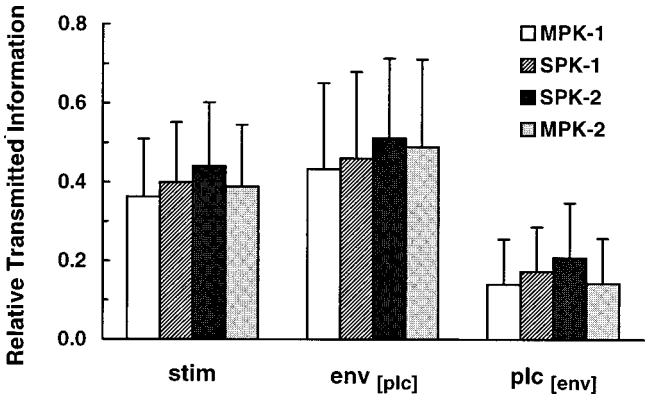

FIG. 2. Mean consonant recognition data for ten subjects who followed the standard expt. 1 protocol. Relative transmitted information (RTI) measures for the stimulus, envelope, and place features are shown for the four consonant recognition tests obtained with MPEAK and SPEAK, in the order obtained (see text). Error bars represent 1 standard deviation (s.d.).

Consonant recognition

Group data. Figure 2 shows mean consonant recognition data as a function of test condition for the ten subjects who followed the standard testing protocol. Mean scores for RTI stim ranged from 36.3% to 44.1%, depending on test condition (MPK-1, SPK-1, SPK-2 or MPK-2). Mean scores for RTI $\text{env}_{[\text{plc}]}$ (50.1%–60.6%) were considerably higher than those for RTI $\text{plc}_{[\text{env}]}$ (12.9%–20.7%) for all test conditions, reflecting subjects' strong reliance on envelope cues to consonant identification.

Comparison of mean scores for the first and second tests with MPEAK showed a small but significant improvement in envelope-cue recognition, with RTI $\text{env}_{[\text{plc}]}$ increasing from 43.4% for MPK-1 to 49.0% for MPK-2 (paired *t*-test, $p < 0.05$). This improvement may be attributable to the experience that subjects accrued with the test materials between the MPK-1 and MPK-2 time points or, possibly, to a more general improvement in envelope-cue perception that occurred as the result of the subjects' intervening experience with SPEAK (Skinner *et al.*, 1994, p. 24). Mean scores for RTI stim and RTI $\text{plc}_{[\text{env}]}$ were comparable for the MPK-1 and MPK-2 conditions. As expected, mean performance with SPEAK improved between the first and last days of the one-month trial period (SPK-1 versus SPK-2 conditions). Improvements were statistically significant ($p < .01$) for all three features (RTI stim, RTI $\text{env}_{[\text{plc}]}$ and RTI $\text{plc}_{[\text{env}]}$) both for the subset of ten subjects shown in Fig. 1 and for the entire group of 14 subjects who were tested with SPEAK.

Comparisons between MPEAK and SPEAK performance were made using data from the second test with each processor (MPK-2 and SPK-2 conditions, respectively). Overall transmission of stimulus information (RTI stim) and transmission of spectral information (RTI $\text{plc}_{[\text{env}]}$) were slightly higher with SPEAK than with MPEAK and these differences were statistically significant (paired *t* tests, $p < .05$). Transmission of envelope information (RTI $\text{env}_{[\text{plc}]}$) was similar for the two strategies. In general, these findings indicate that consonant place-of-articulation cues were transmitted slightly better with the SPEAK strategy than with the MPEAK strategy, and that improvements in place-cue transmission with SPEAK resulted in slightly better overall consonant recognition with that strategy.

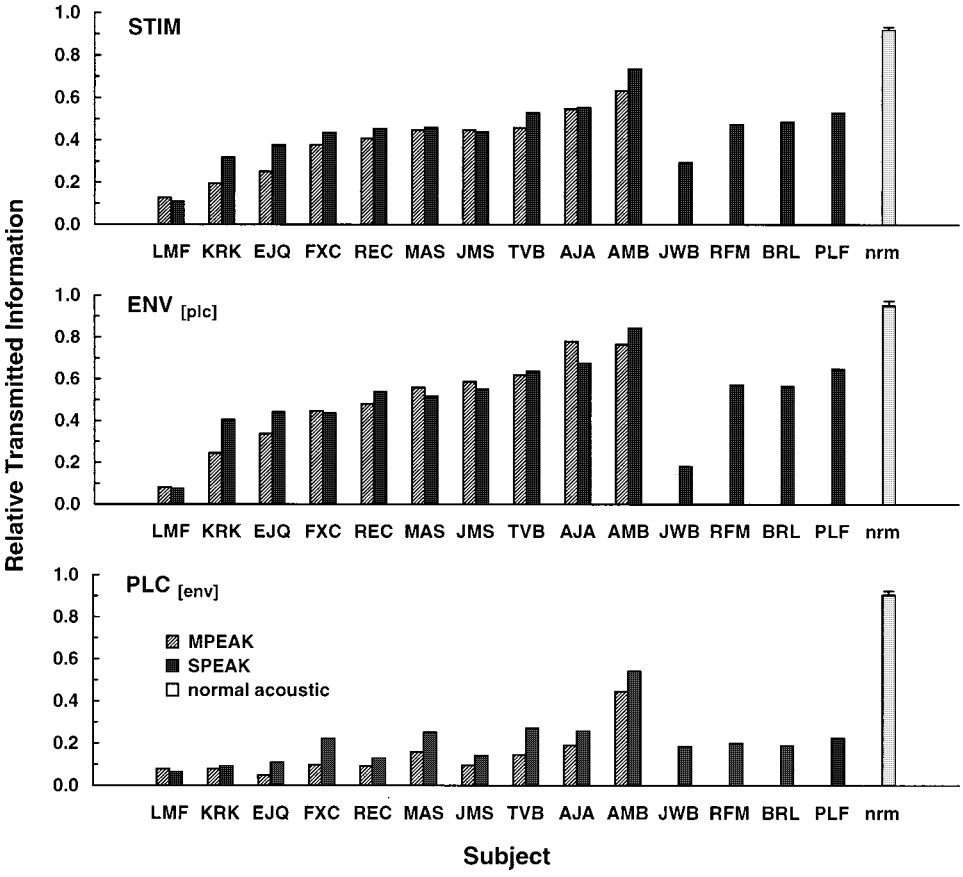

FIG. 3. Consonant recognition data for ten subjects who followed the standard expt. 1 protocol (MPEAK and SPEAK data), and for four subjects who provided SPEAK data only. Relative transmitted information (RTI) values for stimulus, envelope (conditional on place), and place (conditional on envelope) are shown in the top, middle, and bottom panels, respectively, as a function of speech-processing strategy. Mean values for four normal-hearing acoustic listeners (nrm) are also shown. Error bars indicate 1 s.d.

Individual data. Figure 3 shows individual subjects' consonant recognition data for the MPEAK and SPEAK processors. Data for the stimulus, envelope, and place features are shown in the top, middle, and bottom panels, respectively. Within each panel, data are shown for the ten subjects who followed the standard testing protocol (in order of increasing performance for the stimulus feature) and for the four subjects tested with SPEAK only (in similar order). Mean data for four normal-hearing, acoustic subjects are shown to the far right of each panel for reference purposes.

Performance on the stimulus feature (RTI stim), which represents overall transmitted information for the consonant stimuli, varied considerably across subjects with scores ranging from 11.8% (subject LMF with MPEAK) to 73.4% (subject AMB with SPEAK). A similar pattern of scores across subjects was obtained for the envelope feature. In contrast, scores for the place feature were almost uniformly low, with only one subject (AMB) scoring above 30% with either the MPEAK or the SPEAK processing strategy. Differences in individual subjects' performance with the MPEAK versus SPEAK strategies were small, with only three subjects (KRK, EJQ, and AMB) demonstrating more than 5% improvement in overall performance (RTI stim) with SPEAK. Two of these subjects, KRK and EJQ, were relatively poor performers. For these subjects, the overall improvement with SPEAK stemmed primarily from improved transmission of envelope cues (RTI $\text{env}_{[\text{plc}]}$). The third subject, AMB, was a considerably better performer. In his case, improved performance with SPEAK appeared to stem from small improvements in both envelope- and place-cue transmission (RTI $\text{env}_{[\text{plc}]}$ and RTI $\text{plc}_{[\text{env}]}$).

Place-pitch sensitivity and consonant place-cue performance

Although six of the ten subjects who were tested with MPEAK demonstrated good or excellent place-pitch sensitivity as estimated by the electrode pitch-ranking task, only one of these six (AMB) extracted more than 20% of the available place-of-articulation information from the consonant stimuli with the MPEAK strategy. Consistent with this, correlations between place-pitch sensitivity (d') and place-cue perception (RTI $\text{plc}_{[\text{env}]}$ scores) with MPEAK all failed to reach significance. It is noteworthy that the correlations between place-pitch sensitivity and RTI $\text{plc}_{[\text{env}]}$ became systematically stronger as electrode separation was increased from 0.75 to 4.5 mm for the pitch-ranking measure, since this suggests that place-pitch sensitivity within relatively narrow frequency regions may be less important to consonant recognition than place-pitch sensitivity across wider frequency distances. The left panel of Fig. 4 demonstrates the relationship between RTI $\text{plc}_{[\text{env}]}$ and place-pitch sensitivity at the 4.5-mm electrode separation where the strongest relationship was observed.

Correlations between place-pitch sensitivity and consonant place-of-articulation (RTI $\text{plc}_{[\text{env}]}$) were somewhat stronger for SPEAK than for MPEAK; however, they still did not approach statistical significance. Once again, correlations between place-pitch sensitivity and RTI $\text{plc}_{[\text{env}]}$ increased as electrode separation increased from 0.75 to 4.5 mm for the place-pitch measure, suggesting that consonant place-of-articulation cues predominantly involve spectral contrasts across relatively broad frequency regions. The strongest relationship between RTI $\text{plc}_{[\text{env}]}$ and place-pitch sensitivity was again observed for an electrode separation of 4.5 mm ($r = 0.350$, $p = 0.220$). This relationship is illustrated in the right panel of Fig. 4.

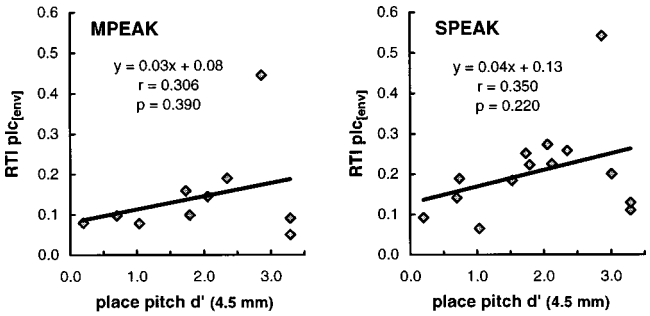

FIG. 4. Scatterplots showing average place-pitch sensitivity for electrode pairs separated by 4.5 mm versus performance on the consonant place-of-articulation feature (RTI $\text{plc}_{[\text{env}]}$). Data for the MPEAK and SPEAK speech-processing strategies are shown in the left and right panels, respectively.

There was no systematic relationship between place-pitch sensitivity at any electrode separation and improvement on the place-of-articulation feature (RTI $\text{plc}_{[\text{env}]}$) with SPEAK relative to MPEAK. Thus our hypothesis that subjects with the best place-pitch sensitivity would achieve the greatest improvements in consonant place-of-articulation performance with SPEAK was not supported by the expt. 1 data.

Summary and explanation of findings

The 14 subjects who participated in expt. 1 demonstrated a wide range of performance on the electrode pitch-ranking task, with several subjects exhibiting excellent place-pitch sensitivity even at small electrode separations. However, only one subject (AMB) demonstrated any substantial ability to extract consonant place-of-articulation cues with either the MPEAK or SPEAK speech-processing strategy. With respect to MPEAK, these results echo the findings of Nelson *et al.* (1995) and support their conclusion that consonant place-cue information is not well represented in the MPEAK-encoded stimuli. The finding that good place-pitch sensitivity did not translate into good place-cue perception with SPEAK was more surprising, since the SPEAK strategy provides considerably more detail concerning the spectral characteristics of speech than MPEAK.

A possible explanation for subjects' poorer-than-expected place-cue performance with SPEAK was that a relatively short duration (one month) of SPEAK use was provided in our protocol. It is possible that subjects require a longer period of daily experience with SPEAK to make full use of the additional spectral information that it provides. To examine this possibility, we evaluated the effect of additional experience on consonant recognition performance in three subjects (AMB, FXC, and TVB) who upgraded permanently to SPEAK following their participation in expt. 1. Consonant recognition had been obtained several times from each of these subjects over a 12–18-month time period following

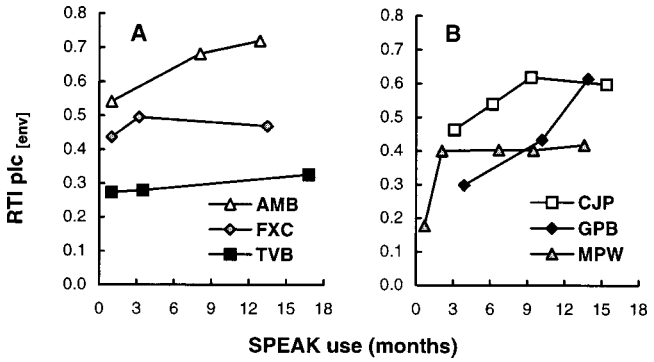

FIG. 5. Relative transmitted information for consonant place-of-articulation ($RTI\,plc_{[env]}$) as a function of duration of SPEAK use. (a) Data for three subjects who participated in expt. 1 and subsequently upgraded to SPEAK. Data points at 1 month are the SPK-2 data from expt. 1; subsequent data points represent the number of months of continuous use following upgrade to SPEAK. (b) Data for three subjects who received SPEAK at initial hookup. Additional information concerning these subjects is provided in Table III.

their processor upgrade, in conjunction with another experiment. Scores for the consonant place-of-articulation feature ($RTI\,plc_{[env]}$) derived from these data are shown in Fig. 5(a). It is apparent that subject AMB improved substantially in his ability to extract place-of-articulation cues as he gained additional experience with SPEAK over a time course of 12 months. In contrast, subjects FXC and TVB demonstrated relatively stable performance for $RTI\,plc_{[env]}$ as experience with SPEAK increased from 1 month to 14 months and 17 months, respectively. It should be noted that $RTI\,plc_{[env]}$ scores for each of these subjects were nearly identical for the MPK-1 and MPK-2 test conditions in expt. 1. This suggests that subjects had achieved stable performance with the test materials prior to time that the data in Fig. 5 were obtained, and argues against the possibility that the improvements shown for subject AMB in Fig. 5 were related to increased familiarity with the test materials rather than improved speech perception *per se*.

Corresponding data for three other subjects who received SPEAK as their first speech processor are shown in Fig. 5(b). One subject (MPW) achieved stable performance on the $RTI\,plc_{[env]}$ feature within three months of initial hookup; however, the remaining two subjects (CJP and GPB) showed clear improvements in the place measure over the first 9 months and 14 months of use, respectively. In general, then, the data in Fig. 5 suggest that a subject's ability to extract spectral information from SPEAK-encoded speech stimuli may continue to improve with experience over the course of several months to a year, or even longer. This suggests that the relatively short period of SPEAK experience provided in expt. 1 may have been a factor in our failure to identify a relationship between place-pitch sensitivity and consonant place-cue performance. To determine whether this was the case, we reevaluated the relationship between place-pitch sensitivity and consonant recognition in expt. 2, using subjects with greater SPEAK experience.

EXPT 2. PLACE-PITCH SENSITIVITY AND CONSONANT RECOGNITION IN EXPERIENCED SPEAK USERS

Subjects

Expt. 2 participants were 12 adult users of the Nucleus 22-electrode implant who had used the SPEAK processing strategy on a daily basis for at least one year. As in expt. 1, all subjects were postlingually deafened and were native speakers of American English. Seven subjects in this group had upgraded to SPEAK after using the $f0/f1/f2$ or MPEAK processing strategy; the remaining five subjects had used the SPEAK strategy continuously since implant hookup. Again, all subjects provided informed consent to participate in the study and were paid on an hourly basis for their participation. Additional information concerning expt. 2 subjects is provided in Table III.

Design and procedures

Each subject underwent consonant recognition testing and electrode pitch-ranking testing, using procedures identical to those described in expt. 1. Subjects used their usual

TABLE III. Description of 12 cochlear implant subjects who participated in expt. 2: Subject identifying code, gender, etiology of deafness (implanted ear), duration of bilateral severe-to-profound hearing loss prior to implantation, age at implantation, depth of electrode array insertion (mm from the round window, with 25 mm representing complete insertion), duration of implant use prior to the study, and duration of SPEAK use prior to consonant testing. To provide readers with an indication of subjects' clinical performance levels with SPEAK, scores for the NU-6 monosyllabic word test (% correct words and % correct phonemes) are also shown.

Subj	m/f	Age (yrs)	Etiology of deafness	Duration (yrs)	Depth (mm)	CI use (yrs)	SPEAK use (yrs)	Nu-6 % words	Nu-6 % phons
AGF	*m*	70	noise exposure	25	20	8.2	1.9	0	23
AMB	*m*	49	progressive SNHL	1	25	4.9	1.1	68	81
CJP	*m*	29	maternal rubella	<1	23	1.3	1.3	70	87
DAW	*f*	57	otosclerosis	10	25	1.0	1.0	36	57
EES	*f*	54	Cogan's syndrome	4	17	8.7	1.8	12	40
FXC	*m*	64	progressive SNHL	4	25	5.7	1.1	8	30
GPB	*m*	57	meningitis	<1	25	1.2	1.2	56	75
JPB	*m*	52	progressive SNHL	4	24	6.4	1.8	52	76
MPW	*m*	31	genetic/progressive SNHL	<1	20	1.1	1.1	66	83
RFM	*m*	56	Meniere's disease	1	22	8.9	1.2	4	25
TVB	*m*	41	progressive SNHL	8	22	6.3	1.4	24	58
WPS	*m*	66	noise exposure	<1	25	2.9	2.9	32	52

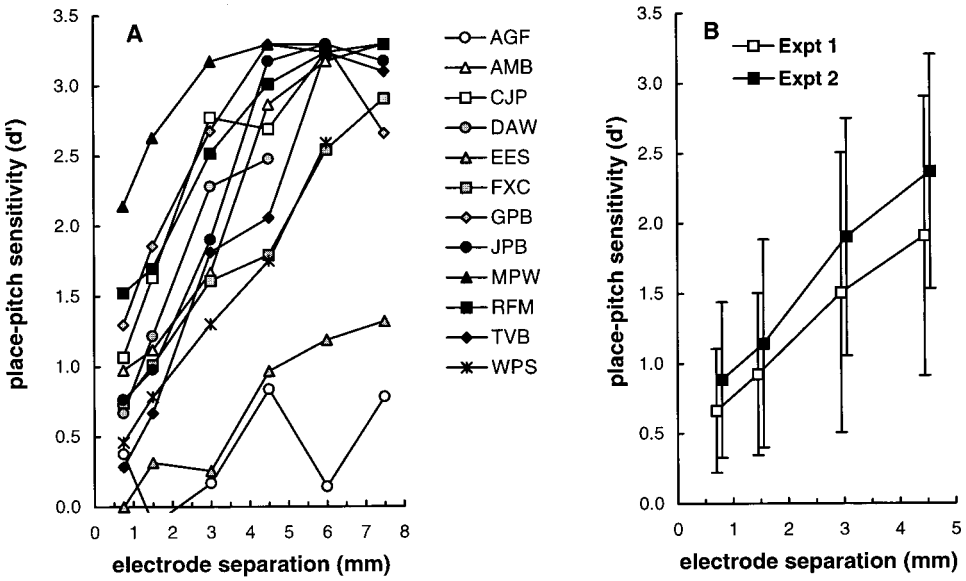

FIG. 6. (a) Average place-pitch sensitivity (d') across the electrode array as a function of electrode separation, for 12 subjects in expt. 2. Perfect discrimination corresponds to $d'=3.29$. (b) Comparison of mean place-pitch sensitivity obtained by 14 expt. 1 subjects and 12 expt. 2 subjects. Error bars represent 1 s.d.

(clinical) SPEAK maps implemented on their own Spectra 22 speech processors for consonant recognition testing. Speech processor parameters were set to their default values, as in expt. 1. One subject was programmed with a bipolar separation of 0.75 mm (BP mode); all others were programmed with a bipolar separation of 1.5 mm (BP+1). As in expt. 1, bipolar separations used in the electrode pitch-ranking task matched those used in subjects' SPEAK maps.

Results and discussion

Electrode pitch ranking

Figure 6(a) shows average place-pitch sensitivity as a function of electrode separation for each of the 12 subjects who participated in expt. 2. Data for subjects AMB, FXC, RFM, and TVB, who participated in expt. 1, are replotted from Fig. 1. Subjects demonstrated a wide range of place-pitch sensitivity, similar to that observed in expt. 1. One subject (MPW) demonstrated exceptionally good pitch-ranking performance, particularly for narrow electrode separations; two others (EES and AGF) exhibited unusually poor pitch-ranking performance at all electrode separations. As noted later, both of these subjects also demonstrated small electrical dynamic ranges. Figure 6(b) compares mean electrode pitch-ranking performance for subjects in expts. 1 and 2. Average place-pitch sensitivity was somewhat higher for the expt. 2 participants at all electrode separations; however, intersubject variability was similar for the two groups.

Consonant recognition

Figure 7 summarizes consonant recognition performance for individual subjects in expt. 2. Subjects are ordered along the *x*-axis according to their performance on the stimulus feature. As in expt. 1, subjects demonstrated a wide range of overall performance and achieved considerably higher transmitted information scores for the envelope feature ($\mathrm{RTI\,env}_{[\mathrm{plc}]}$) than for the place feature ($\mathrm{RTI\,plc}_{[\mathrm{env}]}$). Average performance for the stimulus feature increased 27% relative to the SPK-2 performance obtained in expt. 1 (44.6% for expt. 1 versus 56.8% for expt. 2). Corresponding increases for the envelope and place features were 20.2% and 76.4%, respectively, suggesting that additional experience with SPEAK had a considerably greater impact on place-cue performance than on envelope-cue performance. Related to this, 8 of 12 subjects in this experiment exhibited $\mathrm{RTI\,plc}_{[\mathrm{env}]}$ scores greater than 30%, as compared to a single subject (AMB) in expt. 1.

Place-pitch sensitivity and place-cue perception

In contrast to the findings of expt. 1, a positive relationship was observed between place-pitch sensitivity and consonant place-cue perception ($\mathrm{RTI\,plc}_{[\mathrm{env}]}$). As in the first experiment, correlations between place-pitch sensitivity and $\mathrm{RTI\,plc}_{[\mathrm{env}]}$ became stronger as electrode separation increased from 0.75 to 4.5 mm. They approached statistical significance at electrode separations of 1.5 and 3.0 mm ($r=0.535$, $p=0.07$ and $r=0.563$, $p=0.06$, respectively) and reached statistical significance at an electrode separation of 4.5 mm ($r=0.711$, $p<0.05$). A scatterplot of $\mathrm{RTI\,plc}_{[\mathrm{env}]}$ versus average place-pitch sensitivity at 4.5-mm electrode separation is shown in Fig. 8. Note that there was no systematic relationship between place-pitch sensitivity for adjacent electrodes (0.75-mm electrode separation) and place-cue perception, even though subjects demonstrated a wide range of place-pitch sensitivity for this condition. This suggests that fine spectral resolution is not necessary for consonant place-cue discrimination with the SPEAK strategy.

Envelope- versus place-cue performance

Another result that emerged from the expt. 2 data was a strong positive relationship between the envelope- and place-cue measures. This relationship is implied in Fig. 3, where it can be seen that subjects who achieved the highest scores on the envelope feature ($\mathrm{RTI\,env}_{[\mathrm{plc}]}$) also tended to achieve the highest scores on the place feature ($\mathrm{RTI\,plc}_{[\mathrm{env}]}$.) Figure 9 demonstrates the relationship between $\mathrm{RTI\,env}_{[\mathrm{plc}]}$ and $\mathrm{RTI\,plc}_{[\mathrm{env}]}$ more directly. Here $\mathrm{RTI\,plc}_{[\mathrm{env}]}$ is plotted as a function of $\mathrm{RTI\,env}_{[\mathrm{plc}]}$ and a linear function fitted to the plotted data indicates that $\mathrm{RTI\,plc}_{[\mathrm{env}]}$ increases as a constant

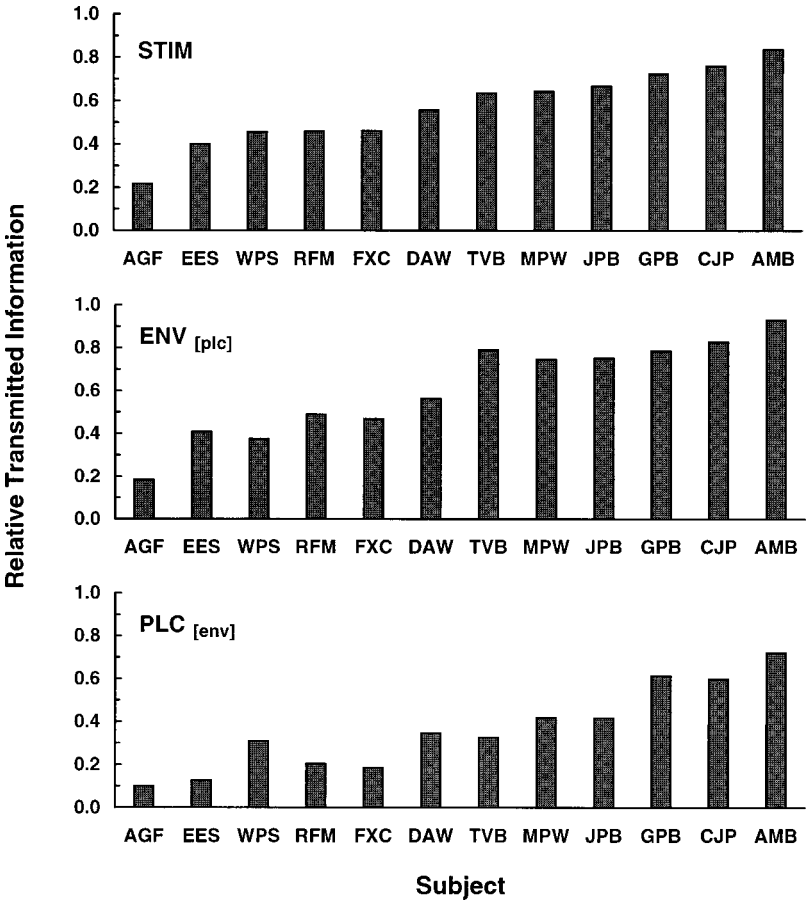

FIG. 7. Consonant recognition data for 12 experienced users of the SPEAK strategy. Relative transmitted information (RTI) values for stimulus, envelope (conditional on place), and place (conditional on envelope) are shown in the top, middle, and bottom panels, respectively.

proportion (~0.8) of RTI $env_{[plc]}$. This finding suggests that both envelope and place-cue measures may depend on a common underlying ability, possibly the ability to detect amplitude fluctuations in the envelope of the speech waveform. A mutual dependence of envelope-cue and place-cue perception on envelope following seems reasonable given that envelope-cue perception involves the detection of amplitude fluctuations in a single-channel representation of the stimulus and place-cue perception involves the detection of patterns of amplitude fluctuations across several frequency channels or electrodes. In this sense, RTI $env_{[plc]}$ can be viewed as a measure of overall envelope-processing ability, independent of place-pitch sensitivity (channel separation), and RTI $plc_{[env]}$ can be viewed as a measure of subjects' combined ability to resolve envelope fluctuations and to utilize place-pitch cues.

To get a better feel for the relationship between place-pitch sensitivity, envelope following, and place-cue perception, it is helpful to consider the data for individual subjects shown in Figs. 6(a) and 7. In general, these individual data support the contention that subjects' place-cue perception reflects both their envelope-processing abilities (as indicated by scores on the consonant envelope-cue measure) and their place-pitch sensitivity. First, consider the five subjects who achieved the highest scores on the consonant place-cue measure RTI $plc_{[env]}$: MPW, JPB, GPB, CJP, and AMB (Fig. 7, bottom panel). Each of these subjects demonstrated high envelope-cue scores (Fig. 7, middle panel), suggesting that they possess good envelope-processing abilities. In addition, each exhibited good or excellent place-pitch sensitivity at all electrode separations. For these subjects, then, it appears that the combination of good envelope-processing skills and good place-pitch sensitivity permitted relatively high performance on the consonant place-cue feature. There is no obvious explanation for differences in place-cue performance within this group, in particular to explain the fact that GPB, CJP, and AMB achieved higher place-cue scores (60%–72%) than MPW and JPB (42%). However, it is noteworthy that subject AMB, who achieved the highest score on the place-cue measure (72%), was distinguished from the others in this group by his very high score on the envelope-cue measure (93%) but not by his place-pitch sensitivity, which was second poorest among the subjects in this group at narrow electrode separations (0.75–3.0 mm). This supports our impression that envelope-processing is at least as important as place-pitch sensitivity in determining consonant place-cue perception.

The next group of five subjects in the bottom panel of Fig. 7 (WPS, RFM, FXC, DAW, and TVB) exhibited a reduced ability to extract consonant place cues (RTI $plc_{[env]}$ scores between 19% and 35%). One of these subjects, TVB, demonstrated excellent envelope-cue performance but only moderate place-pitch sensitivity, suggesting that place-cue extraction may have been limited by place-pitch sensitivity rather than envelope-processing ability. Two others in this group, RFM and DAW, demonstrated excellent place-pitch sensitivity but only moderate envelope-cue performance. For these subjects, envelope-processing skills rather than place-

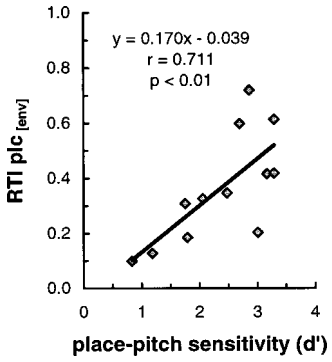

FIG. 8. Relative transmitted information for consonant place-of-articulation (RTI $plc_{[env]}$) as a function of average place-pitch sensitivity (d') for electrode pairs separated by 4.5 mm. Data are for 12 experienced users of the SPEAK strategy.

pitch sensitivity may have been the factor limiting place-cue extraction. The remaining subjects in this group, WPS and FXC, demonstrated low-to-moderate envelope cue scores and only moderate place-pitch sensitivity, suggesting that both envelope-processing skills and place-pitch sensitivity may have limited place-cue performance.

The final two subjects shown in Fig. 7, AGF and EES, were unable to extract meaningful amounts of place-cue information from the consonant stimuli (RTI $plc_{[env]}$ scores $<13\%$). These subjects demonstrated unusually poor place-pitch sensitivity, in addition to poor (AGF) or moderately poor (EES) performance on the envelope-cue measure. In effect, it appears that these subjects had little chance of extracting spectral information from the consonant stimuli, given the dual limitations of poor envelope processing and poor place-pitch sensitivity.

In general, then, the individual data support the notion that both envelope-processing abilities and place-pitch sensitivity are prerequisites for place-cue extraction with the SPEAK strategy. It appears that both factors are necessary and that neither alone is sufficient for achieving good consonant place-cue perception. An important implication of these findings is that spectral information cannot provide an alternative source of information about consonant identity in those cochlear implant subjects who obtain limited temporal information. This suggests that improved strategies for encoding spectral speech features will be most effective among

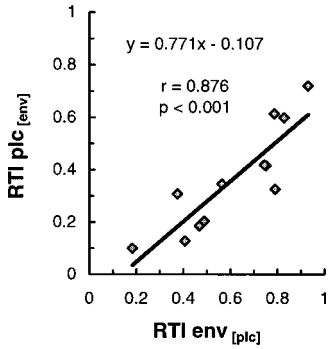

FIG. 9. Spectral versus envelope measures of consonant recognition (RTI $plc_{[env]}$) versus (RTI $env_{[plc]}$) for 12 experienced users of the SPEAK strategy. A strong linear relationship between the two measures is observed, as indicated by the regression fit (heavy line).

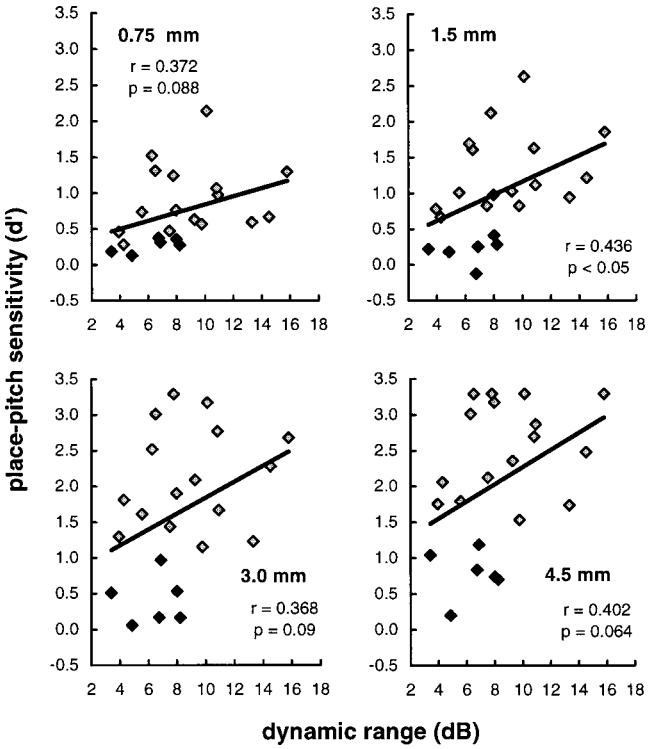

FIG. 10. Place-pitch sensitivity (d') at four electrode separations (0.75, 1.5, 3.0, and 4.5 mm) as a function of dynamic range (dB μA). Dynamic range data were taken from measurements obtained for the electrode pitch-ranking procedure, and represent average values across electrodes for 205-μs/ph, 125-Hz, 500-ms pulse trains. Data are shown for all 22 subjects who participated in expts. 1 and 2. Filled symbols indicate data for six subjects who demonstrated the poorest place-pitch sensitivity (AGF, BRL, EES, JMS, KRK, and LMF).

listeners who demonstrate good temporal-cue recognition. It further suggests that efforts to improve consonant perception among poorer-performing subjects (who have limited recognition for both temporal and spectral cues) should focus on improving subjects' perception of temporal cues.

Dynamic range versus place-pitch sensitivity and consonant recognition

Figure 10 shows place-pitch sensitivity at each of four electrode separations as a function of dynamic range for 22 subjects who participated in expts. 1 and 2. There is a clear trend for place-pitch sensitivity to increase with dynamic range at each electrode separation, although the correlation between place-pitch sensitivity and dynamic range is statistically significant only at an electrode separation of 1.5 mm (upper right panel). Note that the six subjects with the poorest place-pitch sensitivity across electrode separations (filled symbols) all possess average dynamic ranges less than 8 dB. This indicates that subjects with small dynamic ranges may be most ''at risk'' for poor place-pitch sensitivity and, therefore, poor consonant place-cue perception.

Relationships between dynamic range and the consonant recognition measures RTI $env_{[plc]}$ and RTI $plc_{[env]}$ are illustrated in Fig. 11 for expt. 2 participants. Subjects' scores for the envelope feature (RTI $env_{[plc]}$) tended to increase with dynamic range (panel A). However, linear regression failed

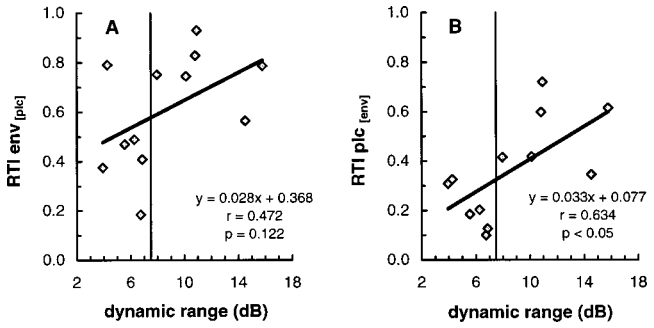

FIG. 11. (a) RTI $\text{env}_{[\text{plc}]}$ as a function of dynamic range (dB μA) for 12 experienced users of the SPEAK strategy. Dynamic range data represent the average values across electrodes for 125-Hz, 205-μs/ph, 500-ms pulse trains. The vertical line indicates a dynamic range of 7.5 dB (see text). (b) As in a, but showing RTI $\text{plc}_{[\text{env}]}$ versus dynamic range.

to yield a statistically significant regression coefficient, primarily due to the performance of one subject (TVB) who exhibited a small average dynamic range (3.9 dB μA) but good envelope-cue performance (79.0%). Note that five of six subjects with average dynamic ranges less than 7 dB exhibited envelope scores less than 50% (data points to the left of the vertical line), whereas all six subjects with dynamic ranges greater than 7 dB achieved scores greater than 50% (points to the right of the vertical line). Place-cue performance also increased with dynamic range for these 12 subjects (panel B) and linear regression of RTI $\text{plc}_{[\text{env}]}$ on dynamic range yielded a significant correlation coefficient ($r=0.634$, $p<0.05$). Again, there was a clear performance difference between subjects whose dynamic ranges were 7 dB and smaller versus those whose dynamic ranges were 8 dB or greater. This finding, that subjects with small dynamic ranges perform poorly on place-cue recognition, is not altogether surprising, since these subjects (with one exception) demonstrated low scores for the envelope-cue measure [Fig. 11(a)] and since a tight coupling was previously demonstrated between envelope- and place-cue performance (Fig. 9).

Summary

The 12 subjects who participated in expt. 2 had considerably greater experience with the SPEAK speech-processing strategy (1.0–2.9 years) than the subjects in expt. 1 (1 month), and also demonstrated considerably better consonant place-cue performance. Mean place-pitch sensitivity for the expt. 2 subjects was slightly higher than that observed for expt. 1 subjects, but the range of performance was similar. In contrast to the expt. 1 results, a significant relationship was observed between place-pitch sensitivity and place-cue performance. This supports our hypothesis that the detailed spectral information provided by the SPEAK encoding strategy is best utilized by subjects with good place-pitch sensitivity. A strong linear relationship was observed between individual subjects' scores on the consonant envelope- and place-cue measures, RTI $\text{env}_{[\text{plc}]}$ and RTI $\text{plc}_{[\text{env}]}$. This suggests that place-cue perception depends both on envelope-processing abilities and place-pitch sensitivity. Finally, the combined electrode pitch-ranking data from expts. 1 and 2 show that poor place-pitch sensitivity is most likely to occur in subjects with small average dynamic ranges ($<$ 8 dB for the test stimulus used here), indicating that subjects with small dynamic ranges are most ''at risk'' for poor consonant recognition.

GENERAL DISCUSSION

The present results indicate that the SPEAK processing strategy can provide meaningful levels of consonant spectral-cue transmission in cochlear implant listeners who possess adequate place-pitch sensitivity and envelope-processing skills. They also confirm earlier findings of Nelson *et al.* (1995) and Parkinson *et al.* (1996) which showed that the MPEAK strategy provides very limited consonant spectral-cue information. Prior to summarizing our conclusions from the present research, we would like to comment briefly on several issues related to the effects of experience on speech recognition performance and place-pitch sensitivity, and concerning the generalizability of the present findings to other speech stimuli and listening conditions.

Effects of experience

Results from our first experiment highlight the importance of experience with a new speech-processing strategy as a factor in speech recognition performance. Several studies have shown that performance increases over time following a change in speech-processor configuration (Tyler *et al.*, 1986; Parkinson *et al.*, 1996; Rosen *et al.*, 1998) and suggest that improvements may depend on the nature of the processing change as well as the speech materials being evaluated. However, many important issues concerning the effects of experience on implant speech recognition have not been addressed. For example, it is not known whether the time course of improvement to asymptotic performance for consonant temporal cues is more rapid than that for spectral cues, as suggested by the present data, or whether rates of improvement vary as a function of speech materials or speech-processing strategy. Such issues have considerable importance for the evaluation and design of speech-processing strategies and also for the evaluation of post-implant speech recognition performance in individual patients. Thus it will be important to address them in future studies. It should be noted that, although experience was a limiting factor in the present experiments, it may or may not have similar importance in other experiments involving cochlear implant speech recognition.

A possible weakness of the present study is that it did not evaluate the influence of SPEAK experience on place-pitch sensitivity as measured with our electrode pitch-ranking task. Since the SPEAK strategy provides an enhanced representation of spectral speech cues, it is possible that use of this strategy could sharpen the spatial resolution of neural responses in the electrically stimulated auditory system. Such improvements could parallel or underlie the improvements in consonant place-cue perception observed in Fig. 5 as a function of increasing experience with the SPEAK strategy. In the present experiments, electrode pitch-ranking testing was most often performed prior to consonant identification testing with SPEAK; thus if SPEAK experi-

ence served to improve place-pitch sensitivity, electrode pitch-ranking measures would have underestimated place-pitch sensitivity at the time of consonant testing. We suspect that this would have been a small effect, since longitudinal measures of place-pitch sensitivity that we have obtained in several SPEAK subjects indicate minimal or no improvement over time. Nonetheless, such effects could exist in some subjects. It is important to note that underestimation of place-pitch sensitivity would not have altered the study's major finding related to place-pitch sensitivity, i.e., that most subjects have moderate or good place-pitch sensitivity but that only a subset of these achieve meaningful amounts of consonant place-cue perception.

Generalizability of the present findings

The present research evaluated subjects' use of spectral cues under optimal listening conditions (moderately loud stimuli in quiet) and for a particular subset of speech stimuli (consonants). Thus we can only speculate as to whether findings would generalize to other speech stimuli or would hold true under less optimal listening conditions. The dependence of spectral cue transmission on envelope processing in addition to place-pitch sensitivity may apply uniquely to consonant stimuli, owing to their brief durations and their low intensities relative to the vowel segments of speech. Vowel stimuli may depend more strongly on place-pitch sensitivity alone, such that subjects with poor performance on consonant envelope cues (indicating poor envelope-processing abilities) may be able to achieve high levels of vowel recognition on the basis of spectral information only. A recent study by Fishman *et al.* (1997) suggests that fine spectral resolution may be more important for vowel recognition than for consonant recognition. This is generally consistent with the present finding that consonant place-cue performance is more strongly related to place-pitch sensitivity at wider electrode separations than at narrower ones. It also suggests that relationships between place-pitch sensitivity and spectral-cue performance might exhibit a different pattern for vowel stimuli than for consonant stimuli. With respect to the issue of listening conditions, recent research has suggested that fine spectral resolution is more important to speech recognition in noise than in quiet (Delhorne *et al.*, 1997; Dorman *et al.*, 1997). Consistent with this, subjects in the Skinner *et al.* (1994) study showed the largest speech recognition improvements with SPEAK relative to MPEAK for sentence materials presented in a background of speech babble. In general, we would expect place-pitch sensitivity at narrow electrode separations to be important for perception of spectral cues to vowel identity and for the perception of consonant spectral cues under unfavorable signal-to-noise conditions. Additional research is needed to evaluate these predictions.

Clinical implications

The present findings indicate that moderate- and poor-performing SPEAK users rely almost exclusively on temporal cues to consonant identity, most often because they have limited envelope-processing abilities but occasionally because they possess inadequate place-pitch sensitivity. Consonant discrimination does not appear to rely strongly on fine spectral resolution, thus place-pitch sensitivity is probably not the factor limiting consonant place-cue perception in most of these listeners. This suggests that attempts to improve spatial resolution, for example by excluding indiscriminable electrodes from subjects' maps (Zwolan *et al.*, 1997), are unlikely to result in improved consonant recognition among poorer performers. Instead, it may be more beneficial to focus on enhancing temporally based cues. There are currently no well-defined strategies for improving consonant temporal-cue recognition in cochlear implant listeners. However, it is possible that the use of specific stimulus parameters and speech-processing strategies could enhance the transmission of such cues for some individuals. Future research should evaluate this possibility.

CONCLUSIONS

(1) Spectral cues to consonant identity are poorly represented by the MPEAK speech-encoding strategy. Even experienced cochlear implant subjects with excellent place-pitch sensitivity and good envelope-cue performance exhibit very limited consonant place-cue perception with MPEAK.
(2) Experience is an important factor influencing consonant recognition performance with SPEAK. A subjects' ability to make use of the spectral information provided by the SPEAK strategy may improve substantially over the first few months of daily use.
(3) Cochlear implant listeners' ability to extract spectral cues from consonant stimuli with the SPEAK strategy depends on both place-pitch sensitivity and envelope-processing ability. Place-cue performance may be limited by either one of these factors, or both, in a given individual.
(4) Cochlear implant subjects with small electrical dynamic ranges are considerably more likely than other subjects to exhibit poor place-pitch sensitivity and poor consonant recognition with the SPEAK strategy.
(5) Attempts to increase consonant recognition among poorer-performing cochlear implant listeners should focus primarily on improved transmission of temporally based (envelope) cues. Better-performing subjects are more likely to benefit from improved transmission of spectral (place-of-articulation) cues.

ACKNOWLEDGMENTS

This research was supported by NIDCD Grant No. DC00110 and the Lions 5M International Hearing Foundation. Preliminary findings were presented at the 19th Midwinter Research Meeting of the Association for Research in Otolaryngology (February 1996). The authors wish to thank Dianne Van Tasell for providing the digitized stimuli used in consonant recognition experiments; Cochlear Corporation for providing two loaner Spectra processors for use in expt. 1; John Van Essen for writing the computer programs used for the electrode pitch-ranking and consonant recognition procedures; Sharon Smith for creating SPEAK maps for the

expt. 1 subjects; and Tanya Grann and Tara Khetrapal for assisting in data collection and data analysis. We also thank Dr. Rich Tyler and an anonymous reviewer for their helpful comments on an earlier version of this manuscript. Finally, we would like to express our sincere appreciation to the 22 cochlear implant subjects who participated in this research project.

[1]Ten of 14 subjects completed electrode pitch-ranking (EPR) testing within the three months spanned by their consonant recognition test sessions. One additional subject underwent EPR testing six months following his completion of consonant testing, due to scheduling constraints. The remaining three subjects had completed electrode pitch-ranking testing as part of an earlier study (Nelson *et al.*, 1995). These subjects were not retested on the pitch-ranking task as part of this experiment, but were tested on the electrode pitch-ranking task again about a year following the conclusion of this study. In each case, pitch-ranking performance was similar for the earlier and later test points, and the earlier data were used in the present analyses.

Busby, P. A., Tong, Y. C., and Clark, G. M. (**1993**). ''Electrode position, repetition rate, and speech perception by early- and late-deafened cochlear implant patients,'' J. Acoust. Soc. Am. **93**, 1058–1067.

Cochlear Corporation (**1996**). Technical reference manual: Nucleus 22 channel cochlear implant system.

Delhorne, L. A., Eddington, D. K., Noel, V. A., Rabinowitz, W. M., Tierney, J., and Whearty, M. E. (**1997**). ''Speech reception with CIS processing: Longitudinal evaluations and implications from acoustic simulations,'' presented at the 1997 Conference on Implantable Auditory Prostheses, Pacific Grove, California (unpublished).

Dorman, M. F. (**1993**). ''Speech recognition by adult users of cochlear implants,'' in *Cochlear Implants: Audiological Foundations*, edited by R. Tyler (Singular, San Diego), pp. 145–190.

Dorman, J. F., Loizou, P. C., Shannon, R. V., and Brill, S. M. (**1997**). ''Converging evidence from simulations and patients on the number of channels necessary for high levels of speech understanding,'' presented at the 1997 Conference on Auditory Prostheses, Pacific Grove, California (unpublished).

Fishman, K. E., Shannon, R. V., and Slattery, W. H. (**1997**). ''Speech recognition as a function of the number of electrodes used in the SPEAK cochlear implant speech processor,'' J. Speech Hear. Res. **40**, 1201–1215.

Hacker, M. J., and Ratcliffe, R. (**1979**). ''A revised table of d' for M-alternative forced choice.'' Percept. Psychophys. **26**, 168–170.

Miller, G. A., and Nicely, P. E. (**1955**). ''An analysis of perceptual confusions among some English consonants,'' J. Acoust. Soc. Am. **27**, 338–352.

Nelson, D. A., Van Tasell, D. J., Schroder, A. C., Soli, S., and Levine, S. (**1995**). ''Electrode ranking of 'place-pitch' and speech recognition in electrical hearing,'' J. Acoust. Soc. Am. **98**, 1987–1999.

Parkinson, A. J., Tyler, R. S., Woodworth, G. G., Lowder, M. W., and Gantz, B. J. (**1996**). ''A within-subject comparison of adult patients using the Nucleus F0F1F2 and F0F1F2B3B4B5 speech processing strategies,'' J. Speech Hear. Res. **39**, 261–277.

Pearsons, K. S., Bennett, R. L., and Fidell, S. (**1976**). ''Speech levels in various environments,'' Bolt Beranek and Newman Report 321, Canoga Park, CA.

Rosen, S., Faulkner, A., and Wilkinson, L. (**1998**). ''Perceptual adaptation by normal listeners to upward shifts of spectral information in speech and its relevance for users of cochlear implants,'' Abstracts of the 21st Midwinter Research Meeting, Association for Research in Otolaryngology, p. 69.

Shannon, R. V., Adams, D. D., Ferrel, R. L., Polumbo, R. L., and Grandgenett, M. (**1990**). ''A computer interface for psychopysical and speech research with the Nucleus cochlear implant,'' J. Acoust. Soc. Am. **87**, 905–907.

Skinner, M. W., Clark, G. M., Whitford, L. A., Seligman, P. M., Staller, S. J., Shipp, D. B., Shallop, J. K., Everingham, C., Menapace, C. M., Adrndt, P. L., Antogenelli, T., Brimacombe, J. A., Pijl, S., Daniels, P., George, C. R., McDermott, H. J., and Beiter, A. L. (**1994**). ''Evaluation of a new spectral peak coding strategy for the Nucleus 22 channel cochlear implant system,'' Am. J. Otol. **15**, 15–27.

Skinner, M. W., Holden, L. K., Holden, T. A., Demorest, M. E., and Fourakis, M. S. (**1997**). ''Speech recognition at simulated soft, conversational and raised-to-loud vocal efforts by adults with cochlear implants,'' J. Acoust. Soc. Am. **101**, 3766–3782.

Townshend, B., Cotter, N., Van Compernolle, D., and White, R. L. (**1987**). ''Pitch perception by cochlear implant subjects,'' J. Acoust. Soc. Am. **82**, 106–115.

Tyler, R. S., Gantz, B. J., Woodworth, G. G., Parkinson, A. J., Lowder, M. W., and Schum, L. K. (**1996**). ''Initial independent results with the Clarion cochlear implant,'' Ear Hear. **17**, 528–536.

Tyler, R. S., Preece, J. P., Lansing, C. R., Otto, S. R., and Gantz, B. J. (**1986**). ''Previous experience as a confounding factor in comparing cochlear-implant processing schemes,'' J. Speech Hear. Res. **29**, 282–287.

Van Tasell, D. J., Greenfield, D. G., Logemann, J. L., and Nelson, D. A. (**1992**). ''Temporal cues for consonant recognition: Training, talker, generalization and the use in evaluation of cochlear implants,'' J. Acoust. Soc. Am. **92**, 1247–1257.

Zwolan, T. A., Collins, L. M., and Wakefield, G. H. (**1997**). ''Electrode discrimination and speech recognition in postingually deafened cochlear implant subjects,'' J. Acoust. Soc. Am. **102**, 3673–3685.

A self-learning predictive model of articulator movements during speech production

C. Simon Blackburn and Steve Young
Department of Engineering, University of Cambridge, Cambridge CB2 1PZ, England

(Received 19 May 1997; revised 12 April 1999; accepted 19 October 1999)

A model is presented which predicts the movements of flesh points on the tongue, lips, and jaw during speech production, from time-aligned phonetic strings. Starting from a database of x-ray articulator trajectories, means and variances of articulator positions and curvatures at the midpoints of phonemes are extracted from the data set. During prediction, the amount of articulatory effort required in a particular phonetic context is estimated from the relative local curvature of the articulator trajectory concerned. Correlations between position and curvature are used to directly predict variations from mean articulator positions due to coarticulatory effects. Use of the explicit coarticulation model yields a significant increase in articulatory modeling accuracy with respect to x-ray traces, as compared with the use of mean articulator positions alone. © *2000 Acoustical Society of America.* [S0001-4966(00)01502-2]

PACS numbers: 43.70.Aj, 43.70.Bk [AL]

INTRODUCTION

Articulatory models of speech production synthesize acoustic signals from discrete symbolic inputs via intermediate representations in articulatory space. The potential advantages of such an approach over nonarticulatory techniques include: (1) an ability to represent explicitly the effects of phonetic context on sound production; (2) a natural integration of temporal and spatial physiological constraints; (3) an understanding of the acoustic correlates of articulatory gestures and hence their perceptual relevance; (4) a framework for studying higher-level motor control mechanisms; and (5) a tool for the analysis of human speech defects.

The prediction of articulator movements corresponding to a particular textual transcription requires the definition of a spatial representation of the articulatory mechanism, the conversion of text into a temporal phonetic and/or phonological symbolic representation, and the control of the articulatory system to produce articulator trajectories corresponding to these symbols.

Previous attempts to implement models of the articulatory mechanism have focused on the use of parametrized descriptions of articulator positions and movements, often incorporating a principal components analysis of articulatory data (Lindblom and Sundberg, 1971; Maeda, 1979, 1988). Articulatory representations such as these are usually restricted to parametrizations of the lips, tongue, jaw, and velum, coupled to simplified damped mass-spring models of the glottis or explicit models of the glottal waveform (Flanagan *et al.*, 1975; Meyer *et al.*, 1989; Rubin *et al.*, 1981; Sondhi and Schroeter, 1987).

Due to the relative paucity of physical articulatory data previously available from x-ray, MRI, or ultrasound images, the parameters of these models were typically adjusted manually to fit fixed vocal-tract configurations or articulator movements corresponding to particular phonetic contexts. The resulting models were primarily descriptive, and not designed to automatically generate articulator movements from arbitrary phonetic transcriptions.

While early attempts at x-ray filming for articulatory data acquisition were limited by the need to minimize the exposure of the subject's head to radiation (Houde, 1967; Perkell, 1969), recent x-ray microbeam (XRMB) acquisition techniques have enabled the collection of much larger articulatory databases (Abbs *et al.*, 1988; Kiritani *et al.*, 1975; Westbury, 1991). This in turn has enabled the use of *statistical* models of articulatory behavior, in which the parameters are automatically learned from a training set, so that the resulting models can be viewed as ''self-organizing,'' as opposed to systems requiring manual adjustment.

The advantages provided by such an approach are that: (1) the systems are automatically adaptable to new speakers, provided appropriate training data are available (Blackburn and Young, 1996a); (2) many of the difficulties of modeling the dynamics of the articulatory mechanism can be avoided, while still producing good approximations to physical articulator movements (Blackburn, 1996); (3) the necessity for mimicking human physiology can be relaxed if desired (Blackburn and Young, 1995); and (4) it is possible to provide a probabilistic description of speech production which is suitable for use in the context of speech recognition systems (Blackburn and Young, 1996b).

The speech recognition system of Ramsay and Deng is an example of an approach which uses a statistical description of the production system (Ramsay and Deng, 1995a). The system described in this paper similarly uses a statistical model of articulator movement, the parameters of which are automatically extracted from a training data set. In this case, however, x-ray articulator trajectories are used during training, and coarticulatory effects are modeled explicitly. The model can be used to predict articulator movements in any phonetic context.

I. ARTICULATORY VARIABILITY

The spatial trajectories followed by articulators during the production of speech presumably represent a tradeoff between inertial and perceptual constraints. The former dictate

that these movements be as efficient as possible to minimize biomechanical effort (Nelson, 1983), while the latter require that articulator movements be sufficiently precise to produce an acoustic signal intelligible to the listener.

For a given speaker, sources of variability in the acoustic realization of a sound within an utterance include (Perkell and Klatt, 1986): (1) random variations due to the limited precision of muscular control of the articulators and/or limited precision in the neural control signals sent by the brain, (2) systematic variations due to the phonetic and/or prosodic context in which the sound occurs, and (3) variations due to stationary or time-varying noise on the signal, or channel distortion during transmission of this signal. Only the systematic variability arising as a result of the phonetic context during the articulatory production of speech is of interest in this study.

A. Position sampling

A relatively straightforward technique for characterizing articulatory variation is to sample articulator positions over many examples of the production of each phoneme in a speech corpus. The samples obtained would ideally be insensitive to changes in phonetic duration, but would incorporate the effects of coarticulation due to both the right and left phonetic contexts of the phoneme. In addition, since the goal is to develop a self-organizing model, this sampling process should be fully automated.

One of two different strategies is typically used at the symbolic level for specifying the temporal relationships within an utterance: concatenated sequences of (usually phonetic) units, or overlapping sequences of (usually phonological) labels. While the latter approach yields a description of the production mechanism in terms of actual articulatory events (Browman and Goldstein, 1992; Deng and Sun, 1994; Local, 1994; Tatham, 1996), phonological labeling is difficult to automate by comparison with phonetic segmentations. A concatenative system has therefore been used in this work. This temporal representation can then be used to determine appropriate times to sample the articulator positions.

When modeling articulator movements, we assume that: (1) each phonetic segment comprises two basic sections. In the first of these, the articulators are moving away from the positions dictated by the previous phoneme and toward those required for the phoneme in question. In the second section, the articulators start to move to locations corresponding to the following phoneme; (2) there is a subsection of the phonetic segment in which a knowledge of articulator positions is sufficient to define the approximate shapes of the articulator trajectories into and out of the phoneme concerned. This subsection may or may not include a region in which the positions of one or more articulators are held constant; and (3) this subsection roughly corresponds to—or else encompasses—the midpoint of the phoneme.

The requirement that the articulators satisfy positional constraints at the midpoints of phonemes is conceptually different from requiring that the articulators attain and maintain static spectral ''targets,'' although such positional constraints could be interpreted as ''probabilistic targets'' for a speech production controller, or simply as the distributions of articulator positions seen in actual production data, as will be proposed in the following section.

The positional variability of each articulator during the production of each phoneme is therefore characterized by sampling its midpoint position. This technique is duration independent, and represents both an explicit and an implicit model of perceptually relevant articulatory behavior: specific positional constraints are explicitly incorporated, while the shapes of articulator trajectories into and out of phonemes are implicitly modeled.

B. Parametric models

The result of the above sampling process is a set of positions for each phoneme and each articulator. The probability distribution functions of these samples are then approximated by single Gaussian distributions, whose variances represent both random and systematic positional variations. In making this approximation, it is assumed that: (1) the distribution of articulator positions at phonetic midpoints is unimodal; (2) in the limit of a very large number of sample points, this distribution approaches a ''normal'' distribution; (3) a first approximation to articulator positions can be obtained by modeling the positional variation of each articulator independently.

The first of these assumptions implies that a single articulation strategy is used for each phoneme regardless of its context, with variations about the mean position being caused by contextual effects. If a speaker maintains more than one strategy for the production of a given sound (Atal *et al.*, 1978; Levinson and Schmidt, 1983) and chooses amongst these according to the phonetic context, then either a multimodal distribution would need to be used, or else a set of unimodal distributions maintained, and rules used for selecting between them according to the context.

The second assumption predicts the shape of the probability distribution obtained from the sample points. When dealing with real articulatory data, a limited number of different contexts and sample points will be available, and hence the use of a ''normal'' distribution will by definition be approximate. In addition, the nature of the articulatory system is such that many positional distributions will not be symmetrical. For example, when positioning the tongue tip during the production of /s/, there is far greater scope for random or systematic variations due to downward rather than upward movement, due to the presence of the hard palate. This physical constraint will be manifested in the statistical data as a skew on the distribution.

Nevertheless, the single Gaussian distribution model described above serves as a useful approximation which is not only mathematically tractable, but very efficient in its use of parameters. In practice, it proves to be a successful model of systematic articulatory variations.

Finally, each articulator's movements are modeled independently. This is a simplifying assumption which is not valid in the case of the human articulators, but which permits an initial approximation to articulator movements to be relatively easily derived using the positional sampling technique.[1]

II. COARTICULATION MODEL

The degree to which the phonetic context will influence the positions of the articulators during the production of a given sound varies greatly from articulator to articulator and from sound to sound. Factors which determine this variation include: (1) the duration of the current sound and of its neighbors, both relative to each other and in terms of the overall speaking rate; (2) the spatial separation between the desirable articulator positions for adjacent sounds; (3) the degree to which any constraints on articulator positions are perceptually relevant; (4) the physiologically determined speed and precision with which a particular articulator's position can easily be controlled; (5) the amount of articulatory effort used by the speaker.

The first two items determine the underlying geometrical framework for articulatory production. Once a desired articulator position has been specified, the physiological nature of the articulator concerned strongly influences the speed and accuracy with which this position is approached. In normal conversational speech however, the movements of the articulators usually do not directly reflect the physical limits of muscular control, but rather an economy of effort while communicating a message (Lindblom, 1983; Nelson, 1983), since speakers are capable of clearly articulating speech at much higher rates than are typically used in conversation. Within this framework of geometrical constraints and economies of movement, the amount of coarticulation permitted perceptually is largely determined by the degree of specification of an articulator's position in a particular context (Keating, 1988).

Due to the presence of both anticipatory and carryover coarticulatory effects, the articulation of a sound will in general be dependent upon both the preceding and following contexts. Although specific contexts have been identified in which anticipatory effects can be demonstrated over multiple phonemes (Benguerel and Cowan, 1974; Lubker, 1981), a relatively simple, single-neighboring-phoneme bidirectional model of coarticulation is used here as a first approximation to the coarticulation process.

A. Existing target models

Many researchers have proposed models for converting a discrete symbolic representation of an utterance into a smooth articulatory realization, while satisfying both perceptual and physiological constraints. A popular technique is to specify a sequence of underlying goals, and to regard articulator movements as attempts to reach these goals while satisfying biomechanical constraints. The goals may be fixed target points, or else target regions or trajectories.

Several authors have proposed the use of frequency-domain targets (Akagi, 1990; Akagi and Tohkura, 1990; Deng and Braam, 1994; Kuwabara, 1985), possibly supplemented by articulatory goals (Perkell *et al.*, 1995; Stevens *et al.*, 1994). These systems attempt to model a time-domain effect (coarticulation) in the frequency domain, however, and a separate mapping to articulator positions would be required for articulatory synthesis. Alternatively, purely articulatory targets can be used, and linear or nonlinear system dynamics used to generate continuous trajectories (Coker, 1976; Houde, 1967; Kröger *et al.*, 1995; Macneilage, 1970; Mermelstein, 1973; Meyer *et al.*, 1989; Rubin *et al.*, 1981; Saltzman *et al.*, 1988; Shirai and Kobayashi, 1986; Wilhelms *et al.*, 1986; Wilhelms-Tricarico, 1995).

The difficulty here is that context-independent spatial targets which are invariably achieved do not exist for all articulators or all phonemes. Even if exact spatial targets such as these did exist, if fixed dynamics is used to model movements independently of the context, targets would only sometimes be reached. A common solution is to hypothesize *virtual* targets, with constraints to stop articulators moving once they collide, or secondary modifications to trajectories to ensure consonantal requirements are met (Coker, 1976; Mermelstein, 1973; Meyer *et al.*, 1989; Wilhelms *et al.*, 1986).

A more realistic model would require context-sensitive targets and/or dynamics (Kröger *et al.*, 1995; Meyer *et al.*, 1989). Determining and specifying the context-sensitive control parameters is a difficult task, however, which obviates either the advantage of postulating contextually invariant targets, or the use of simple automatic control.

Promising preliminary work has also been described for systems which use control signals to define trajectories or movements (Hirayama *et al.*, 1992; Vatikiotis-Bateson *et al.*, 1994), or attractor regions or equilibrium points in articulatory space (Bailly, 1996; Perrier *et al.*, 1996).

B. Existing window models

An alternative to using specific articulator target points or trajectories is to propose *regions* of articulatory space through which an articulator must pass in order to guarantee intelligibility. This is an inherently attractive approach, since it is both simple and flexible. It can either be used to specify ''corridors'' through which articulator trajectories must pass, or else to set a range of positions which an articulator can satisfy at any point in time. The relative degree of specification of an articulator is explicitly encoded by the size of the perceptually acceptable region, and coarticulatory effects are modeled as variations within these prescribed limits.

An early model proposed along these lines is Keating's ''window'' model of coarticulation (Keating, 1990). This model specifies both the ranges of possible articulator positions and the time intervals over which these restrictions apply, as shown in Fig. 1.

This figure shows a simulated articulator trajectory (solid line), which is constrained to pass through the regions delineated by dashed horizontal lines. Both the duration and the degree of specification of the restriction regions are variable, and there may be intervening intervals of complete underspecification. Keating proposed that the articulator trajectory is free to pass anywhere within these allowable ranges, with the path being chosen to fit as smoothly as possible within the constraints imposed by the context.

This is a descriptive model of articulator movement, which differs from the point target models in that it directly specifies ranges of *achieved* articulator motion, as opposed to indirectly controlling articulator movements through virtual targets which are undershot by the system dynamics. Not only does this model explicitly represent relative degrees of

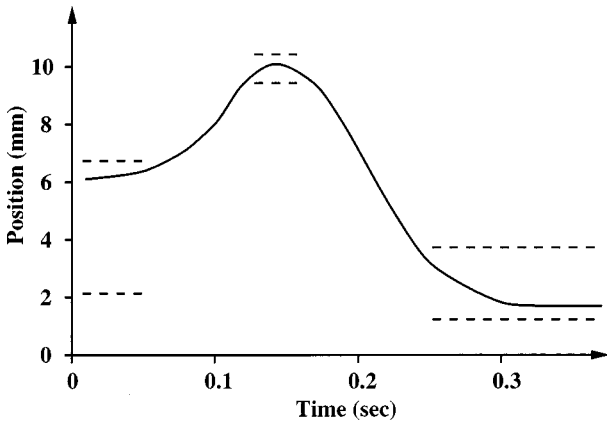

FIG. 1. Simulated articulator trajectory (solid line) using the window model of coarticulation. The trajectory is constrained to pass through the ''windows'' indicated by dashed horizontal lines.

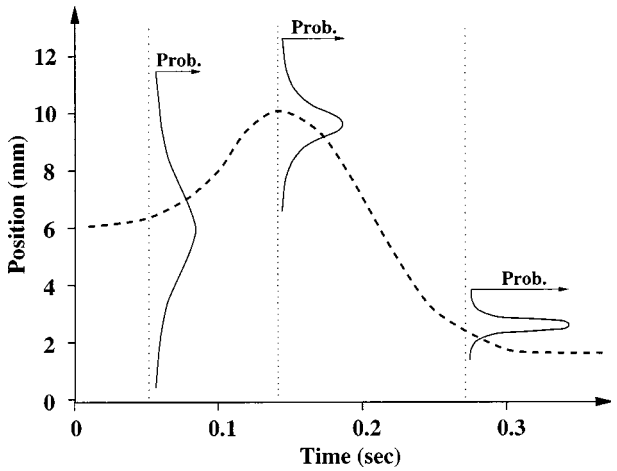

FIG. 2. Simulated articulator trajectory (dashed line) using a probabilistic coarticulation model. The midpoints of successive phonemes are indicated by dotted vertical lines, and associated with each midpoint is a probability distribution. These distributions define the probability that the articulator trajectory will take particular positions at the midpoint concerned.

specification, but it also emphasizes the need for the rate of rise or fall of an articulator at the onset of a particular phoneme to be context dependent.

Guenther has proposed an alternative model based on target regions, which attempts to address the problem of choosing between multiple vocal-tract shapes which result in similar acoustic patterns. Target regions are initially planned in formant space, and are then mapped onto equivalent articulator target regions by selecting articulator movements which best correspond to the desired formant dynamics (Guenther, 1995; Guenther *et al.*, 1998).

C. Proposed probabilistic model

An alternative approach to modeling coarticulatory variation is to use a probabilistic description of articulator movement. Bakis has described a system based on hidden Markov models (HMMs) which uses explicit articulator position targets, which are related to the realized articulator positions by a set of probability distributions at the outputs of the HMMs (Bakis, 1991). Ramsay and Deng have developed a model which uses overlapping phonological gestures as the symbolic inputs to an HMM, whose output distributions represent both formant and articulator position distributions (Ramsay and Deng, 1995a, 1995b). In both cases a probabilistic distribution of possible articulations is produced, rather than a definitive sequence of articulator movements.

A new model is now proposed which is similar to the window model in that regions of articulatory space are specified, but in which a very different description of articulator motion is provided. A self-organizing approach to modeling context-sensitive articulator positions is used, which does not require context-dependent system parameters or rules to be inferred. The key components of this system are: (1) a descriptive probabilistic model of instantaneous articulator positions at the midpoints of phonemes: (2) a predictive probabilistic model of variations in articulator positions at these midpoints due to coarticulatory effects; (3) a simple linear interpolation between coarticulated articulator midpoint positions.

By contrast with Keating's model, this descriptive model does not specify time intervals during which articulators must satisfy a given spatial constraint, but instead specifies articulator positions only at the midpoints of phonemes. Furthermore, instead of postulating a hard-limited region of equally acceptable positions, a smoothly varying probabilistic model is used to specify articulator positions, as demonstrated in Fig. 2.

In this figure, the midpoints of the phonemes being articulated are indicated by dotted vertical lines, and the articulator trajectory is shown as a dashed curve. Against each midpoint line is shown a probability density function (pdf) which represents the probability of observing various articulator positions *at that point in time*. The axes for these pdf's are the articulator position vertically, and increasing probability in the directions shown. Thus, the pdf associated with the midpoint of the left-most phoneme indicates that the most probable (mean) articulator position at this point in time is $\approx$6 mm, with decreasing likelihood above and below this value, and a standard deviation of $\approx$2 mm. In Keating's model, these pdf's would be ''square'' windows rather than smooth functions, with a zero probability that an articulator will be positioned outside the window, and a flat distribution of equal probabilities within the window.

This framework for describing coarticulatory variation is neatly implemented by the technique for characterizing articulatory variability. By automatically sampling a large number of articulator trajectories at times corresponding to the midpoints of phonemes—and modeling the observed variations with unimodal Gaussian distributions—smooth probabilistic ''window'' functions can be obtained automatically. Multiple distributions would be required if it were necessary to allow for the possibility of selecting between alternative articulatory strategies according to the context in which a phoneme appears. Techniques for predicting coarticulatory variation within the ranges described by these distributions, and methods for generating complete articulator

trajectories from them, are described in the following section.

III. PREDICTING VARIABILITY

The goal of the approach to modeling coarticulatory variation taken in this paper is the development of an automated system for predicting variations in articulator positions using a knowledge of the context and the relative durations of the phonetic segments. The positional variation for each articulator is directly modeled at the midpoint of each phoneme using a single Gaussian distribution. This task therefore reduces to the prediction of deviations from an articulator's mean position at these midpoints, and the generation of complete articulator trajectories from the resulting positions.

Articulator movements exhibit both random and systematic positional variation. While random variations are an inherent characteristic of human speech production, their perceptual effects must be negligible or else words would be randomly misperceived by listeners. Of greater interest is that part of the variation which is systematically reproducible, and which *may* therefore be perceptually relevant. Consistent variations in articulator movements due to the phonetic context are motivated by efficiency constraints, whereby articulators move early (or late) toward (or from) perceptually relevant regions, from (or toward) relatively less relevant or ''unspecified'' regions. To predict such movements, information which is correlated with these variations must be extracted in either explicit or rule-based form, from the time-aligned phonetic transcription.

A. Articulator accelerations

If it is assumed that coarticulatory effects are governed by economy of effort considerations and perceptual constraints, the greatest deviations from ''ideal'' articulatory behavior are expected to be observed in regions where the muscular effort required is greatest *and* the position of the articulator concerned is relatively underspecified. While compromises in articulator movements would be desirable wherever relatively large articulatory effort is dictated, such variations are only likely to be observed where the corresponding acoustic effects are perceptually acceptable.

Since the articulators have finite inertial masses, a simple measure related to the muscular effort required at a given point in time is the acceleration of the articulator concerned. In terms of articulator trajectories, the acceleration is the second derivative, or ''curvature'' of the plot, so that regions of relatively high positive or negative articulator acceleration tend to correspond to local minima or maxima in a trajectory, respectively. During the production of phonemes for which an articulator's position is relatively underspecified, the required acceleration of the articulator concerned is expected to be highly correlated with deviations from the mean articulator position, as shown in Fig. 3.

This figure shows both a desired (solid) and an achieved (dashed) simulated articulator trajectory around the midpoint of a phoneme, indicated by a dotted vertical line. To the right of the line marking this midpoint position is a hypothetical pdf describing the observed variation in the simulated articulator's achieved position at the midpoint, computed from many examples in a training data set.

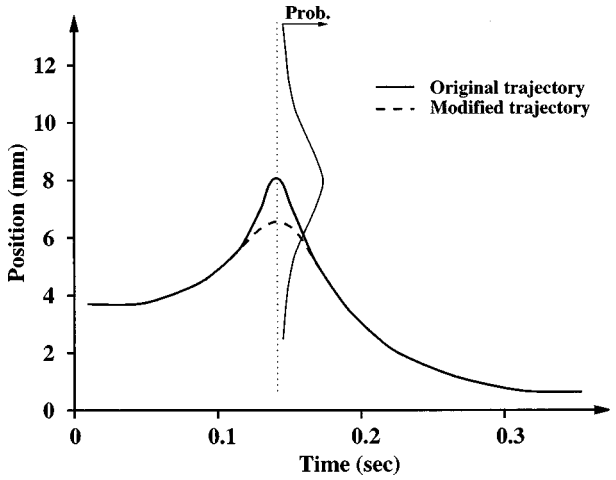

FIG. 3. Variation in the position of a simulated articulator trajectory at the midpoint of a phoneme (dotted vertical line). The pdf associated with the midpoint defines the probability of observing different articulator positions. The large negative acceleration required at the midpoint of the phoneme results in an undershoot of the mean position, which reduces the curvature of the resulting trajectory.

In regions of high acceleration, such as the large negative acceleration near the midpoint of the phoneme in this example, an economy of effort can be obtained by following a less curved trajectory, leading to an undershoot of the mean articulator position as shown. Relatively large positive acceleration demands in turn lead to an overshoot of this mean, which therefore should not be regarded as a ''target'' position, but merely as descriptive of observed articulator traces.

The width of each distribution describing the achieved articulator positions will be determined by physical constraints in the vocal tract, the range of geometrical contexts in which the phoneme occurs—wider ranges leading to wider distributions—and the relative degree of specification of the articulator. Less positional variation will be observed where articulators are physically constrained, or where an articulator's position is perceptually important and increased muscular effort is used to achieve the required acceleration.

1. Estimating curvatures

If articulator curvatures are to be used to predict positional variations, a technique for estimating these from time-aligned trajectories is required. Given a time-aligned phonetic transcription of an utterance, a first approximation to the shape of a corresponding articulator trajectory can be obtained by a simple linear interpolation between that articulator's mean positions at the midpoints of each of the phonemes.

The curvature of the trajectory is then defined as the rate of change in its gradient, which will be infinite at the midpoint of the phoneme, due to the discontinuity at the boundary between the segments. If only the *relative* curvatures of trajectories around the midpoints of phonemes in different contexts are of interest—rather than the absolute values of

these curvatures—then a simple approximate measure can be obtained by taking the difference of the gradients leading out of and into the midpoint of the phoneme.

This simple gradient-differencing technique is therefore used to estimate relative trajectory curvatures (and hence accelerations) from a linear interpolation between successive articulator mean positions. Mean positions are used here instead of actual positions, as these will be the only data available for estimating curvatures when synthesizing initial trajectory estimates for unseen utterances. The resulting estimates of articulator curvatures represent simple approximations to the amount of muscular effort dictated by the phonetic context.

Since the computation of this curvature measure requires a knowledge of articulator mean positions, statistics describing the distribution of curvature estimates are not derived until after the articulator position statistics have been determined. First approximations to articulator trajectory shapes are computed by linear interpolation between successive articulator mean values, where these points are placed at the midpoints of phonemes using a phonetic time alignment. The curvature measure described above is then computed for each articulator over all examples of each phoneme, and the resulting values are modeled using a single Gaussian distribution in each case, in an analogous manner to the positional distributions.

B. Systematic variation prediction

The curvature measure described in the preceding section can be used to predict systematic variations in articulator positions at the midpoints of the phonemes in any time-aligned phonetic string. Articulator positions and curvatures at these midpoints are modeled by the random variables P and C, respectively, each of which in turn has a pdf given by a single Gaussian distribution, with means μ_P, μ_C and variances σ_P^2 and σ_C^2, respectively. The joint pdf of C and P, $f_{C,P}(c,p)$ is then a binormal distribution, so that the conditional pdf $f_{P|C}(p|c)$ is itself a Gaussian, with mean μ and variance σ^2 given by

$$\mu = \mu_P + \rho_{CP}\frac{\sigma_P}{\sigma_C}(c-\mu_C), \tag{1}$$

$$\sigma^2 = \sigma_P^2(1-\rho_{CP}^2), \tag{2}$$

where $\rho_{C,P}$ is the correlation coefficient for the random variables C and P. Using the time-aligned transcription and the techniques described in the preceding section for obtaining a rough prediction of articulator positions, the value c of the curvature of an articulator trajectory at the midpoint of each phoneme is estimated.

The expected articulator position $E[P|C=c]$ will then be given by the mean value μ in Eq. (1) above, known as the ''regression curve'' (Mood *et al.*, 1974). This allows the most likely articulator position at the midpoint of a phoneme to be determined from the estimate of the curvature, the means and standard deviations of the position and curvature distributions, and the correlation coefficient between these two distributions.

The principal characteristics of the resulting model of coarticulatory variation are that: (1) it is entirely statistically based and requires no rule-based input; (2) variability in articulator positions at the midpoints of phonemes is modeled using a single Gaussian distribution for each articulator during the production of each phoneme; (3) the required articulatory effort is estimated by computing the gradient changes (curvatures) of linearly interpolated trajectories at the midpoints of phonemes, which are also modeled using single Gaussian distributions; and (4) correlations between curvature and position statistics are used to predict systematic positional variations from the estimated curvatures in particular contexts.

The model is symmetrical with respect to the right and left contexts of phonemes (anticipatory and carry-over effects, respectively), and considers only the immediate neighbors of a phoneme when computing contextual effects. The effects of context on articulatory transitions into and out of phonemes are modeled implicitly, during the construction of complete articulator trajectories from the coarticulated values at the midpoints of the phonemes.

C. Generation of trajectories

Finally, a technique is required for generating continuous articulator trajectories starting from the coarticulated midpoint positions, which are computed in Eq. (1) from the mean prior positions and curvature information. Since these prespecified values are not precise ''target'' positions or ''attractors'' for the articulators, but represent the most likely positions for the articulators at these points in time, any dynamic system model would therefore have to be such that the dynamics was varied according to the context to ensure the achievement of these positions. Alternatively, the midpoint positions could be connected using explicit linear, piece-wise linear or nonlinear functions.

When choosing amongst these options, it is important to consider the nature of the trajectories being approximated. On the one hand it is clear that actual articulator movements describe smooth curves rather than linear segments, which might lead to the postulation of a dynamic system or curved function model. The caveat to using relatively complex models such as these, however, is that current predictive models of articulator position, including that described in the preceding sections, are relatively crude approximations to human physiology. As a result, it is anticipated that any errors in articulator movements due to the choice of connecting segments will be insignificant by comparison with those due to gross errors in the articulator positions predicted by the model. For example, Meyer *et al.* found in their German-language synthesizer that articulator trajectories which were fitted to second order critically damped transitions using Kalman filtering could be replaced with linearly interpolated trajectories, with ''only small differences'' being observed in the acoustic waveform (Meyer *et al.*, 1989).

Standard linear interpolation was also used as the model for trajectory generation in this system. To enhance the system's robustness to unusual contexts given the small size of the training data set, however, a low-order low-pass filter

was applied to the resulting trajectories to remove very sharp articulator movements which were otherwise observed in approximately 0.3% of data points.

The use of this linear interpolation scheme implies that coarticulatory effects will be introduced even in the absence of the explicit coarticulation model. If mean articulator positions are used at the midpoints of phonemes, rather than modified positions, the phonetic context will still strongly influence the shape of the resulting interpolated trajectory.

IV. DATA SET

The University of Wisconsin (UW) x-ray microbeam database contains articulator traces along with synchronously recorded speech waveforms for 57 speakers of American English, comprising 32 females and 25 males. Articulatory and acoustic data taken from three female (jw16, jw27, and jw29) and three male (jw18, jw24, and jw45) speakers were used in this study.

The articulatory component of the database was recorded by using a narrow x-ray beam to track the movements of gold pellets glued to the tongue, jaw, and lips of subjects who read from a set corpus. Three reference pellets were attached to the subject's head, and eight articulator pellets were tracked relative to these, with the subject's head viewed in profile by the apparatus: UL (upper lip), LL (lower lip), *T*1 to *T*4 (tongue positions 1 to 4 where 1 is closest to the tip), MI (mandibular incisor), and MM (mandibular molar).

Approximately 17 min of data were used per speaker, comprising citation words, sentences, prose passages, counting, and sequences of number names. Three quarters of the data were used for training the system (≈5000 phonemes per speaker), with the remainder reserved for testing. Although nominal word-level transcriptions were provided for each utterance, these were hand-edited to correspond to the actual text spoken, including some utterances which had been truncated during recording.

The raw acoustic signal recorded at 21 739 Hz was notch filtered to remove background noise at 5435 Hz and down-sampled to 16 kHz. The speech was then parametrized into 12-dimensional Mel-frequency cepstral coefficients (MFCCs), along with difference (''delta'') and difference of difference (''delta delta'') parameters. A Hamming window of length 25 ms was applied to the acoustic signal before computing the Fourier transform, and a step size of 10 ms was used between adjacent parametrized speech frames.

The *x* and *y* positions of each articulator pellet were recorded at sample rates which varied according to the accelerations of the articulators, and had been interpolated and resampled at a uniform sampling period of 6.866 ms (≈146 Hz) before inclusion in the database. These waveforms were then reinterpolated, and resampled at intervals of 10 ms to give values corresponding to the centers of the parametrized acoustic frames.

A. Automatic phonetic alignment

A phonetic dictionary was constructed for the 440 words in the x-ray microbeam (XRMB) database using Kai-Fu Lee's Resource Management (RM) 47-phoneme set (Lee, 1989), excluding ''closure'' phonemes as we are using a model in which stop phonemes comprise an occlusion and an optional burst, so that separate closure phonemes are unnecessary. A set of monophone HMMs with two emitting states for each stop and diphthong and three for the other phonemes was then trained using the Hidden Markov Model Toolkit (HTK) (Young *et al.*, 1995) on MFCC parametrized speech from the Defense Advanced Research Projects Agency RM speaker-independent corpus. In the case of stop phonemes, the two HMM states align to the occlusion and burst, respectively, where the burst state is optional; in the case of diphthongs they align to the initial and final voiced sections. In both instances each state is treated as a separate phone, yielding an expanded set of 56 phones.

Separate three-state monophone HMMs corresponding to the tone played at the start of each utterance and the ''good'' and ''rep'' background comments found at the end of many utterances were trained on parametrized speech vectors extracted from 21, 16, and 5 examples of each sound, respectively.

These model sets were combined and used with the hand-edited transcriptions and dictionary to adapt a set of speaker-dependent 5-mixture monophone HMMs using the training data for each speaker. A state-level forced Viterbi alignment of both the training and test data to the transcriptions was then performed, to yield data sets labeled at the subphonemic level suitable for input to the automatic sampling or trajectory synthesis algorithms.

V. RESULTS

The result of the positional sampling algorithm is a set of values describing articulator positions at the midpoints of phonemes for each articulator and each phoneme. Both *x* and *y* values are sampled for each of the eight articulator pellets to yield 16 sampled articulatory variables, except in the case of speaker jw29, for whom only 14 articulator parameters could reliably be estimated, due to frequent tracking errors in the MM pellet during x-ray data collection.

The greatest range of movement is seen in the *x*, or horizontal position of the tongue tip, which has a maximum range of movement of ≈3 cm, as compared with horizontal movements in the incisors of the lower jaw, which exhibit the least displacement at only ≈3 mm. In general terms, the tongue variables and those describing vertical motion in the jaw and lower lip vary more widely than do those describing horizontal lip and jaw movements, as shown in Fig. 4 for the speaker jw18.

A. Discriminatory usefulness

The degree to which an articulator's position is likely to discriminate between two different sounds varies greatly, with the articulators exhibiting the greatest range of movement also proving the most discriminatory. For example, the range of horizontal movement observed at the back of the jaw, MM*x*, is almost identical across all phonemes, with similar mean positions and a standard deviation of ≈1.2 mm being observed in each case (although on average, the jaw extends slightly further during /tʃ/, /f/, and /ʃ/, and retracts slightly for /eɪ/). In fact, a value of 3.15 mm for MM*x* in the data for speaker jw18 falls within one standard deviation of

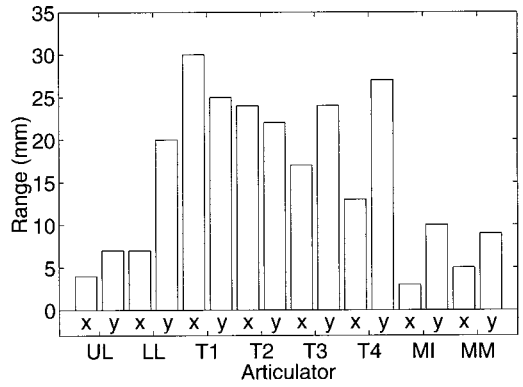

FIG. 4. Bar graph showing approximate maximum ranges of articulator movement for the speaker jw18.

the mean MM*x* position for *every* phoneme sampled, and hence the discriminatory power of this variable is extremely low.

By contrast, both the mean and standard deviation of the vertical positional samples for the tongue tip vary greatly from phoneme to phoneme, so that this articulatory variable is extremely useful for discriminating between phonetic identities. This is as expected, since the position of the tongue tip has a very strong influence on the shape—and hence the acoustic properties—of the vocal tract, as compared with the slight extension and retraction of the jaw.

These differences in discriminatory ability are illustrated in Fig. 5, which plots two standard deviations for each articulatory variable for the speaker jw18. The first of these is the mean standard deviation for the variable concerned, measured at the midpoints of each phoneme *p*.

$$\sigma_{\text{av}} = \sqrt{\frac{1}{N_p}\sum_{p=1}^{N_p}\sigma_p^2}, \tag{3}$$

where N_p is the total number of phonemes, and σ_p is the standard deviation of the articulator's positional samples at the midpoint of the phoneme *p*. The standard deviation of the distribution of the *mean* values of each variable at these midpoints is then computed as

$$\sigma_\mu = \sqrt{\frac{1}{N_p - 1}\sum_{p=1}^{N_p}(\mu_p - \mu)^2}, \tag{4}$$

where μ_p is the mean value of the articulator's positional samples at the midpoint of phoneme *p*, and μ is the mean of the N_p mean positions

$$\mu = \frac{1}{N_p}\sum_{p=1}^{N_p}\mu_p. \tag{5}$$

Relatively large values of σ_μ (unshaded) indicate that the mean position of the articulator varies significantly from phoneme to phoneme. When the value of σ_{av} (shaded) is less than σ_μ, as is the case for the tongue parameters, the articulator's positions are also relatively tightly constrained during the production of each individual phoneme, compared with the variations in mean position observed between different phonemes. This in turn means that, on average, the positions of these articulators are relatively highly specified, and hence discriminatory between phonemes.[2]

Where σ_{av} is relatively large compared with σ_μ however, the position of the articulatory variable concerned is less likely to be strongly correlated with the identity of the phoneme, as is the case for MM*x* as previously described.

B. Parametric position and curvature models

Given a set of statistics for articulator positions, the corresponding trajectory curvatures were estimated at the midpoints of the phonemes from a linear interpolation between successive mean positions. The distributions of both positions and curvatures were then modeled using a single Gaussian distribution for each [articulator, phoneme] pair, thus characterizing the range of variation seen in each case by just two parameters, namely the mean and variance of the Gaussian concerned.

The quality of the matches between the probability density functions of the sampled data and those of the parametric models was assessed using the Kolmogorov–Smirnov (K-S) test (Massey, Jr., 1951). The K-S statistic was computed for each of the position and curvature distributions, and the resulting mean proportions of position and curvature statistics across all six speakers which had greater than 90%, 50%, and 10% probability, respectively, of being drawn from single Gaussian distributions are given in Table I. In general terms, the positional variables have a much better fit to Gaussian distributions than do the curvature measures, and although relatively few distributions have greater than 90% probability of having been drawn from single Gaussians, a minority has extremely poor fits.

By plotting histograms for the articulator distributions which yielded poor matches, it was observed that these were typically either caused by skews on the distributions, or by distribution tails which fell away at non-Gaussian rates, rather than by multimodal distributions. This implies that the speakers in this data set are rarely using more than one articulatory strategy to produce a given phoneme, despite the fact that in some instances very different articulations can be shown to produce similar acoustic results (Atal *et al.*, 1978; Levinson and Schmidt, 1983).

The observed skews arise due to both the limited variety of contexts available in the UW data, and to the physiological limitations imposed on articulator positions in the vocal tract. In addition, for some data sets poor fits to Gaussian distributions result indirectly from errors in the automatic alignment of the training data by HTK and/or mistracked pellet samples which were not identified in the database. Errors such as these typically lead to outliers in the sample distributions for the phoneme concerned, which are poorly modeled by the single Gaussian assumption. In these cases, however, a poor fit to the articulatory data is *desirable* in order to exclude erroneous data points from the statistical models.

C. Correlation coefficients

Correlation coefficients for pairs of curvature and position statistics were computed, and Student's *T*-test (Kreyszig,

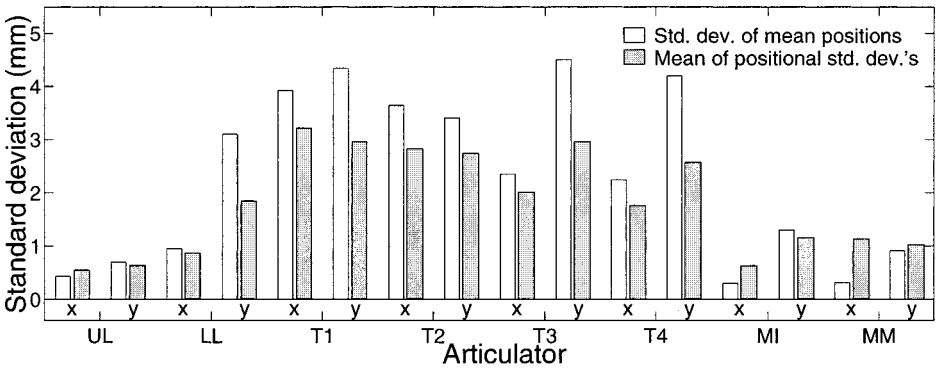

FIG. 5. Bar graph showing comparisons of standard deviations of mean articulator positions σ_μ (unshaded) against average articulator position standard deviations σ_{av} (shaded), as measured at the midpoints of phonemes for the speaker jw18.

1970) was used to compute the significance of each coefficient computed over the data points in the Gaussian position and curvature distributions. Correlation coefficients which were not significant at the 5% level were set to zero, and the remainder retained. Approximately 20% of correlation coefficients were set to zero when this significance test was applied (not counting those whose absolute values had already been less than 0.1).

Strong positive correlations were observed between the position and curvature estimates for most articulators during the production of the different phonemes. A positive curvature value—corresponding to a local minimum in an articulator trajectory, where the articulator's direction of motion is changing rapidly—will therefore tend to result in a position greater than the mean position and vice versa.

The mean significant correlation coefficients obtained for each articulator and averaged over all phonemes are illustrated in Fig. 6 for the speaker jw18; similar results were obtained for the other five speakers.

The *x* and *y* positions of the four tongue pellets show the greatest degree of correlation between curvature and position, with the horizontal positions of the two jaw pellets, MI*x* and MM*x*, showing considerably less correlation than the other articulators.

This is as expected, since the variation in the degree of protrusion of the jaw is not only small in magnitude with respect to the other articulatory variables, but is also rarely discriminatory between phonemes. Much of the variation for these two variables will therefore be random rather than systematic, and hence is not correlated with the curvature measure, which is assumed to be predictive only of systematic positional variations. This lack of correlation for randomly varying parameters allows the removal of a great deal of the random movement seen in actual x-ray articulator traces when synthesizing articulator trajectories.

Figure 7 shows an example of the correlation coefficients between the curvatures and positions of the eight articulator pellets for jw18, sampled at the midpoints of all examples of the phoneme /s/, where the correlation coefficients for *T*3*x*, MI*x*, and MM*x* have been set to zero as their values were insufficiently large to be considered significant.

The relatively low correlation coefficients for lower lip, jaw, and tongue-tip positions in this figure reflect the fact that these articulators are highly constrained in position for the production of /s/. By contrast, the tongue back and upper lip are relatively free to move into positions dictated by neighboring phonemes, as evidenced by the larger correlations for UL and *T*2 to *T*4.

TABLE I. Percentage proportions of articulator position and curvature distributions with greater than 90%, 50%, and 10% probability, respectively, of being drawn from a single Gaussian distribution, averaged over all six speakers

Position			Curvature		
90%	50%	10%	90%	50%	10%
17.7	55.8	87.2	2.7	18.0	53.7

D. Articulator trajectories

Synthetic articulator trajectories corresponding to the time-aligned acoustic test data were generated for each speaker, both with and without using the explicit coarticulation model, where using this model modifies articulator positions at the midpoints of phonemes before linear interpolation, and the model excluding explicit coarticulation simply uses a linear interpolation between successive articulator mean positions. In both cases, a low-order low-pass filter was used to remove the sharp articulator movements observed in 0.3% of data points, due to unusual contexts not observed in the training data.

To assess the effectiveness of the coarticulation model in reducing articulatory error over a large number of utterances the errors between synthetic training and test set trajectories were computed for each speaker with respect to the

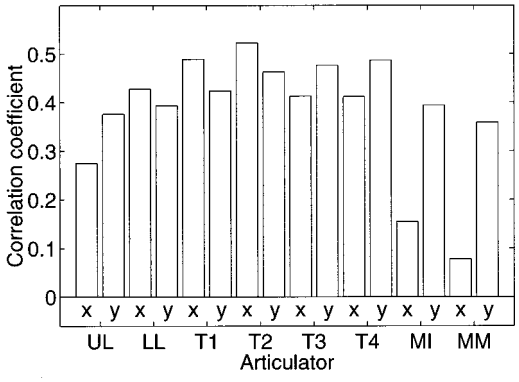

FIG. 6. Bar graph of mean significant correlation coefficients between curvature and position statistics for each articulator over all phonemes, for the speaker jw18.

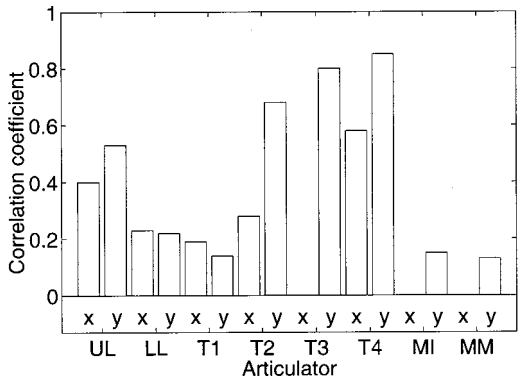

FIG. 7. Correlation coefficients between curvature and position statistics for the phoneme /s/ for jw18.

corresponding x-ray traces. In each case, the coarticulation model gave a reduction in the articulatory error computed over an entire utterance.

Figure 8 shows a bar graph representing a breakdown by articulator of the mean error obtained over the 51 utterances in the test sets averaged over the six UW speakers.

The error for each parameter has been scaled by that articulator's standard deviation over the entire training set to give a more meaningful comparison, since the absolute magnitudes of the positional variations of the articulators vary greatly (Fig. 4). As shown in Fig. 8, each individual articulator's positional error decreases when the coarticulation model is used. The errors in tongue position are generally less than those for lip and jaw position, with the *x* position of the front and back of the jaw (MI*x* and MM*x*) being most poorly modeled.

The poor performance obtained for these latter articulators is not surprising, since horizontal movements of the jaw have relatively little effect on the acoustic signal, as previously described. This implies that much of the variation seen in these variables will be random movement, as evidenced by the correspondingly low mean correlation coefficients in Fig. 6. Since these random variations cannot be modeled, the coarticulation model has relatively little effect on the errors obtained for these articulators, as demonstrated in Fig. 8. This is a desirable result, since it implies that the coarticulation model has the greatest beneficial effect on the positions of the articulators which are most significant acoustically.

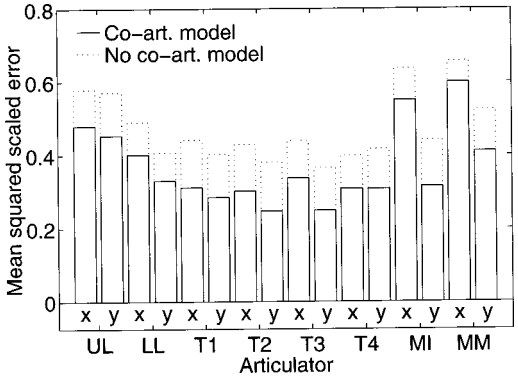

FIG. 8. Normalized test set errors by articulator, with and without coarticulation model, averaged over the six UW speakers.

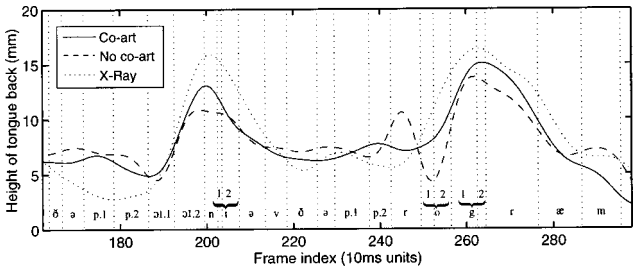

FIG. 9. Movements in the height of the tongue back ($T4y$) for the speaker jw18 during the test set utterance: ''the point of the program.'' Articulator trajectories synthesized both with and without the explicit model of coarticulation are shown, as well as the corresponding x-ray trace. Automatically generated phonetic boundary positions are shown by vertical dotted lines.

A detailed study of the model's performance across the very large number of specific phonetic contexts observed in the data set falls outside the scope of this paper, although it would represent a logical extension of the research. A set of sample trajectories for the test set utterance ''the point of the program'' has been included in Fig. 9, however, to provide an illustrative example of the model's output. This figure shows both synthesized and x-ray articulator traces for the height of the tongue back $T4y$, corresponding to this test utterance for the speaker jw18.

Synthetic trajectories generated both with and without using explicit coarticulation at the midpoints of the phonemes are shown, and a phoneme-level transcription is provided in which phonetic boundaries determined using HTK are shown by vertical dotted lines. The principal effects of using the explicit coarticulation model when synthesizing the articulator trajectory are as follows:

(1) The tongue back is raised to form an occlusion at the rear of the oral tract during the production of /n/ and /g/, as evidenced by the relatively high tongue back around frames 200 and 260, respectively. The use of the explicit coarticulation model to modify articulator positions at the midpoints of these phonemes results in a more accurate approximation to these positional extrema.
(2) An economy of articulatory movement is achieved by the tongue back during the first syllable of ''program.'' The *mean* positions of $T4y$ at the midpoints of the phonemes /r/ and /o/ can be deduced from the synthetic articulator trace produced without coarticulation. The achievement of these mean positions requires relatively rapid changes in the direction of motion of $T4y$—and hence relatively large muscular effort—between frames 240 and 260, as evidenced by the dashed curve. Since the height of the back of the tongue is relatively underspecified during production of these phonemes, however, it is free to follow a trajectory which requires less articulatory effort, as seen in both the x-ray trace and that synthesized using the explicit coarticulation model.

Finally, in the example shown, the model performs relatively poorly in predicting the height of the tongue back around the stop /p/ in ''point.'' The poor performance observed in this instance is not surprising, however, given the substantial variations in tongue-back height observed in the

x-ray trace for the two instances of the same sequence /ð/ /ə/ /p/ in the utterance. This variability may either be due to random variation, or to coarticulatory effects spanning much further than adjacent phonemes, which are not modeled in the current system.

Based on results from many such utterances, as summarized in Fig. 8, use of the explicit coarticulation model yields a significantly closer approximation to the x-ray articulator traces overall, as measured in terms of mean-squared scaled error. Since the relationship between articulator movements and acoustic output is nonlinear, however, the addition of an acoustic mapping would be required to assess the perceptual implications of this modeling improvement. A natural extension of this model, therefore, would be to predict acoustic output suitable for use in either synthesis or recognition of speech (Blackburn and Young, 1996b).

VI. CONCLUSIONS

A trainable statistical model of articulatory movement has been presented. The model is self-organizing, and can be used to predict the movements of articulator flesh points during speech production, from time-aligned phonetic strings.

The system was trained on an x-ray articulatory database, from which suitable values for the model parameters were automatically estimated. Positional variation was characterized by automatically time-aligning the acoustic signal to its transcription, and sampling articulator positions at the midpoints of phonemes.

An explicit time-domain model of coarticulation was then proposed, which used a measure of articulatory effort to predict positional variations at these midpoint positions. This model incorporates both anticipatory and carry-over coarticulatory effects, and the correlations observed between articulatory effort and positional variation were interpretable in terms of expected articulatory behavior.

When complete articulator trajectories were synthesized, the use of the explicit model of coarticulatory variation yielded a significant increase in articulatory modeling accuracy over the use of interpolation between mean articulator positions, when compared with actual x-ray traces from a test data set.

ACKNOWLEDGMENTS

The authors would like to thank John Westbury and his team for making the University of Wisconsin x-ray database available to them. Simon Blackburn gratefully acknowledges the financial support of Trinity College, Cambridge.

[1]While techniques such as principal component analysis could be used to derive a set of independent parameters, an interpretation of the resulting variables in terms of physical constraints on the motion of actual articulators would no longer be meaningful.

[2]The ratio of these two variances is known as Fisher's discriminant.

Abbs, J. H., Nadler, R. D., and Fujimura, O. (**1988**). ''X-ray microbeams track the shape of speech,'' SOMA **2**, 29–34.

Akagi, M. (**1990**). ''Evaluation of a spectrum target prediction model in speech perception,'' J. Acoust. Soc. Am. **87**, 858–865.

Akagi, M., and Tohkura, Y. (**1990**). ''Spectrum target prediction model and its application to speech recognition,'' Comput. Speech Lang. **4**(4), 325–344.

Atal, B. S., Chang, J. J., Mathews, M. V., and Tukey, J. W. (**1978**). ''Inversion of articulatory-to-acoustic transformation in the vocal tract by a computer-sorting technique,'' J. Acoust. Soc. Am. **63**, 1535–1555.

Bailly, G. (**1996**). ''Sensory-motor control of speech movements,'' in *ECSA 4th Tutorial and Workshop on Speech Production Modelling* (ECSA, Autrans, France), pp. 145–154.

Bakis, R. (**1991**). ''Coarticulation modelling with continuous-state HMMs,'' in *IEEE Speech Recognition Workshop* (Arden House, IEEE, New York).

Benguerel, A. P., and Cowan, H. A. (**1974**). ''Coarticulation of upper lip protrusion in French,'' Phonetica **30**, 41–55.

Blackburn, C. S. (**1996**). ''Articulatory methods for speech production and recognition,'' Ph.D. thesis, University of Cambridge.

Blackburn, C. S., and Young, S. J. (**1995**). ''Learning new articulator trajectories for a speech production model using artificial neural networks,'' IEEE International Conference on Neural Networks, 4, pp. 2046–2051.

Blackburn, C. S., and Young, S. J. (**1996a**). ''A self-learning speech synthesis system,'' in *ECSA 4th Tutorial and Workshop on Speech Production Modelling* (ECSA, Autrans, France), pp. 225–228.

Blackburn, C. S., and Young, S. J. (**1996b**). ''Pseudo-articulatory speech synthesis for recognition using automatic feature extraction from X ray data,'' in Proceedings of the International Conference on Speech and Language Processing, Vol. 2, pp. 969–972.

Browman, C., and Goldstein, L. (**1992**). ''Articulatory phonology: an overview,'' Phonetica **49**, 155–180.

Coker, C. H. (**1976**). ''A model of articulatory dynamics and control,'' Proc. IEEE **64**(4), 452–460.

Deng, L., and Braam, D. (**1994**). ''Context-dependent Markov model structured by locus equations: Application to phonetic classification,'' J. Acoust. Soc. Am. **96**, 2008–2025.

Deng, L., and Sun, D. X. (**1994**). ''A statistical approach to automatic speech recognition using the atomic speech units constructed from overlapping articulatory features,'' J. Acoust. Soc. Am. **95**, 2702–2719.

Flanagan, J. L., Ishizaka, K., and Shipley, K. L. (**1975**). ''Synthesis of speech from a dynamic model of the vocal cords and vocal tract,'' Bell Syst. Tech. J. **54**(3), 485–506.

Guenther, F. H. (**1995**). ''A modeling framework for speech motor development and kinematic articulator control,'' Int. Cong. Phonet. Sci. **2**, 92–99.

Guenther, F. H., Hampson, M., and Johnson, D. (**1998**). ''A theoretical investigation of reference frames for the planning of speech movements,'' Psychol. Rev. **105**(4), 611–633.

Hirayama, M., Vatikiotis-Bateson, E., Kawato, M., and Jordan, M. I. (**1992**). ''Forward dynamics modeling of speech motor control using physiological data,'' in *Advances in Neural Information Processing Systems 4*, edited by J. E. Moody, S. J. Hanson, and R. P. Lippmann (Morgan Kaufman, San Mateo, CA), pp. 191–198.

Houde, R. A. (**1967**). ''A study of tongue body motion during selected speech sounds,'' Ph.D. thesis, University of Michigan, Ann Arbor.

Keating, P. A. (**1988**). ''Underspecification in phonetics,'' in *Coarticulation* (UCLA Phonetics Laboratory, Los Angeles), pp. 30–50.

Keating, P. A. (**1990**). ''The window model of coarticulation: articulatory evidence,'' in *Papers in Laboratory Phonology I*, edited by J. Kingston and M. E. Beckman (Cambridge University Press, Cambridge), Chap. 26, pp. 451–470.

Kiritani, S., Itoh, K., and Fujimura, O. (**1975**). ''Tongue-pellet tracking by a computer-controlled x-ray microbeam system,'' J. Acoust. Soc. Am. **57**, 1516–1520.

Kreyszig, E. (**1970**). *Introductory Mathematical Statistics* (Wiley, New York).

Kröger, B. J., Schröder, G., and Opgen-Rhein, C. (**1995**). ''A gesture-based dynamic model describing articulatory movement data,'' J. Acoust. Soc. Am. **98**, 1878–1889.

Kuwabara, H. (**1985**). ''An approach to normalization of coarticulation effects for vowels in connected speech,'' J. Acoust. Soc. Am. **77**, 686–694.

Lee, K.-F. (**1989**). *Automatic Speech Recognition* (Kluwer Academic, Dordrecht).

Levinson, S. E., and Schmidt, C. E. (**1983**). ''Adaptive computation of articulatory parameters from the speech signal,'' J. Acoust. Soc. Am. **74**, 1145–1154.

Lindblom, B. (**1983**). ''Economy of speech gestures,'' in *The Production of*

Speech, edited by P. F. MacNeilage (Springer, New York), Chap. 10, pp. 217–246.
Lindblom, B. E. F., and Sundberg, J. E. F. (**1971**). ''Acoustical consequences of lip, tongue, jaw, and larynx movement,'' J. Acoust. Soc. Am. Suppl. 1 **50**(4, Part 2), S1166–S1179.
Local, J. K. (**1994**). ''Phonological structure, parametric phonetic interpretation and natural-sounding synthesis,'' in *Fundamentals of Speech Synthesis and Speech Recognition*, edited by E. Keller (Wiley, West Sussex, England), Chap. 12, pp. 253–270.
Lubker, J. F. (**1981**). ''Temporal aspects of speech production: Anticipatory labial coarticulation,'' Physica (Utrecht) **38**, 51–65.
MacNeilage, P. F. (**1970**). ''Motor control of serial ordering of speech,'' Psychol. Rev. **77**, 182–196.
Maeda, S. (**1979**). ''An articulatory model based on statistical analysis,'' J. Acoust. Soc. Am. Suppl. 1 **65**, S22.
Maeda, S. (**1988**). ''Improved articulatory model,'' J. Acoust. Soc. Am. Suppl. 1 **84**, S146.
Massey, Jr., F. J. (**1951**). ''The Kolmogorov–Smirnov test for goodness of fit,'' J. Am. Stat. Assoc. **46**, 68–78.
Mermelstein, P. (**1973**). ''Articulatory model for the study of speech production,'' J. Acoust. Soc. Am. **53**, 1070–1082.
Meyer, P., Wilhelms, R., and Strube, H. W. (**1989**). ''A quasiarticulatory speech synthesizer for German language running in real time,'' J. Acoust. Soc. Am. **86**, 523–539.
Mood, A. M., Graybill, F. A., and Boes, D. C. (**1974**). *Introduction to the Theory of Statistics*, 3rd ed. (McGraw-Hill, New York).
Nelson, W. L. (**1983**). ''Physical principles for economies of skilled movements,'' Biol. Cybern. **46**, 135–147.
Perkell, J. S. (**1969**). *Physiology of Speech Production: Results and Implications of a Quantitative Cineradiographic Study* (MIT Press, Cambridge, MA).
Perkell, J. S., and Klatt, D. H., editors (**1986**). *Invariance and Variability in Speech Processes* (Erlbaum, Hillsdale, NJ).
Perkell, J. S., Matthies, M. L., Suirsky, M. A., and Jordan, M. I. (**1995**). ''Goal-based speech motor control: a theoretical framework and some preliminary data,'' J. Phonetics **23**, 23–35.
Perrier, P., Ostry, D. J., and Laboissière, R. (**1996**). ''The equilibrium point hypothesis and its application to speech motor control,'' J. Speech Hear. Res. **39**, 365–378.
Ramsay, G., and Deng, L. (**1995a**). ''Articulatory synthesis using a stochastic target model of speech production,'' Int. Cong. Phone. Sci. **2**, 338–341.
Ramsay, G., and Deng, L. (**1995b**). ''Maximum-likelihood estimation for articulatory speech recognition using a stochastic target model,'' in European Conference on Speech Communication and Technology, Vol. 2, pp. 1401–1404.
Rubin, P., Baer, T., and Mermelstein, P. (**1981**). ''An articulatory synthesizer for perceptual research,'' J. Acoust. Soc. Am. **70**, 321–328.
Saltzman, E. L., Goldstein, L., Browman, C., and Rubin, P. (**1988**). ''Modeling speech production using dynamic gestural structures,'' J. Acoust. Soc. Am. Suppl. 1 **84**, S146.
Shirai, K., and Kobayashi, T. (**1986**). ''Estimating articulatory motion from the speech wave,'' Speech Commun. **5**(2), 159–170.
Sondhi, M. M., and Schroeter, J. (**1987**). ''A hybrid-time-frequency domain articulatory speech synthesizer,'' IEEE Trans. Acoust., Speech, Signal Process. **35**(7), 955–967.
Stevens, K. N., Bickley, C. A., and Williams, D. R. (**1994**). ''Control of a Klatt synthesizer by articulatory parameters,'' in Proceedings of the International Conference on Speech and Language Processing, Vol. 1, pp. 183–186.
Tatham, M. (**1996**). ''Articulatory phonology, task dynamics and computational adequacy,'' in *ECSA 4th Tutorial and Workshop on Speech Production Modelling* (ECSA, Autrans, France), pp. 141–144.
Vatikiotis-Bateson, E., Tiede, M., Wada, Y., Gracco, V., and Kawato, M. (**1994**). ''Phoneme extraction using via point estimation of real speech,'' in Proceedings of the International Conference on Speech and Language Processing, Vol. 2, pp. 631–634.
Westbury, J. (**1991**). ''The significance and measurement of head position during speech production experiments using the X-ray microbeam system,'' J. Acoust. Soc. Am. **89**, 1782–1791.
Wilhelms, R., Meyer, P., and Strube, H. W. (**1986**). ''Estimation of articulatory trajectories by Kalman filtering,'' in *Signal Processing III: Theories and Applications*, edited by J. Biemond, R. P. W. Duin, and J. J. Gerbrands (Elsevier Science, North Holland, Amsterdam), pp. 477–480.
Wilhelms-Tricarico, R. (**1995**). ''Physiological modeling of speech production: methods for modeling soft-tissue articulators,'' J. Acoust. Soc. Am. **97**, 3085–3098.
Young, S. J., Jansen, J., Odell, J. J., Ollason, D., and Woodland, P. C. (**1995**). *The HTK Book* (Entropic Cambridge Research Laboratory and University of Cambridge, Cambridge, England), Version 2.0.

Method for the selection of sentence materials for efficient measurement of the speech reception threshold

Niek J. Versfeld,[a] Laura Daalder, Joost M. Festen, and Tammo Houtgast
Department of Otorhinolaryngology, University Hospital VU, P.O. Box 7057, 1007 MB Amsterdam, The Netherlands

(Received 21 January 1999; revised 2 July 1999; accepted 11 November 1999)

A method is described to select sentence materials for efficient measurement of the speech reception threshold (SRT). The first part of the paper addresses the creation of the sentence materials, the recording procedure, and a listening experiment to evaluate the new speech materials. The result is a set of 1272 sentences, where every sentence has been uttered by two male and two female speakers. In the second part of the paper, a method is described to select subsets with properties that are desired for an efficient measurement of the SRT. For two speakers, this method has been applied to obtain two subsets for measurement of the SRT in stationary noise with the long-term average spectrum of speech. Lastly, a listening experiment has been conducted where the two subsets (each comprising 39 lists of 13 sentences each) are directly compared to the existing sets of Plomp and Mimpen [Audiology **18**, 43–52 (1979)] and Smoorenburg [J. Acoust. Soc. Am. **91**, 421–437 (1992)]. One of the outcomes is that the newly developed sets can be considered as equivalent to these existing sets. [S0001-4966(90)04702-6]

PACS numbers: 43.71.Gv [DOS]

INTRODUCTION

The ability to understand speech depends on both the mode of communication (e.g., live, via the radio, or through a telephone), the listening situation (e.g., in quiet, with interfering speakers, background noise, or reverberation), and the listener's hearing impairment, if any. Redundancy in speech not only makes that its intelligibility is fairly robust against distortions or interfering sounds, but also allows hearing-impaired people to follow a conversation in spite of their hearing loss. Thus, in relatively favorable listening conditions both normal-hearing and hearing-impaired people usually are quite capable of speech understanding. However, where, under increasingly adverse conditions, speech will stay intelligible for the normal hearing, its intelligibility will break down for the hard-of-hearing. The additional effort, or even disability, to understand speech under less favorable conditions is considered by many people as the greatest handicap of their hearing impairment (Kramer *et al.*, 1998). Since the hearing loss based on a tone audiogram appears to be a poor predictor for speech intelligibility in noise, many tests have been developed that assess the communicative abilities by measuring the speech reception threshold, or SRT, in noise for sentences (e.g., Kalikow *et al.*, 1977; Plomp and Mimpen, 1979; Nilsson *et al.*, 1994; Kollmeier and Wesselkamp, 1997).

The present paper deals with a method for development and evaluation of sentence materials to be used in SRT tests. The method has been used to create a new large set of sentence materials for the Dutch language. For that language, two smaller sets already exist (Plomp and Mimpen, 1979; Smoorenburg, 1992). Together, they comprise 260 sentences that can be used to determine 20 thresholds. In a large number of studies, these sets have been utilized to assess the effect of a diversity of parameters on speech reception (e.g., Festen and Plomp, 1990; Duquesnoy, 1983; Middelweerd *et al.*, 1990). However, there are several reasons why the demand for a large set of speech materials has swollen. First, recent developments in hearing aid technology have resulted in an enormous increase of the number of adjustable parameters on a hearing aid. The developments have also enabled the implementation of a variety of signal-processing algorithms, often with the purpose to enhance speech intelligibility in noisy backgrounds. The clear advantage is that the hearing aid can be better adjusted to the individual's needs and can be adapted to the different listening situations. On the other hand, it is evident that evaluation of the algorithms and hearing-aid settings with respect to speech intelligibility requires large amounts of speech materials. Second, there is evidence that the benefit of a hearing aid may improve over time: people have to acclimatize to their hearing aid (Gatehouse, 1992). To be able to investigate these effects, one has to measure the SRT at several instances over time, which also requires a substantial amount of speech materials.

The main goal of the present project was to create a large set of sentence materials that yield equal or better test efficiency as the existing sets, while maintaining the same testing procedure, i.e., the one described by Plomp and Mimpen (1979).

A second goal was to create four sets that are equivalent with respect to intelligibility, but differ with respect to voice quality. To that end, the speech materials have been uttered by two male and two female speakers. With these sets, it then, in principle, becomes possible to test the dependency of the outcomes of a particular signal-processing algorithm upon voice quality. However, it is known that, even with the same word or sentence materials, differences between speak-

[a]Corresponding author. Address: Clinical and Experimental Audiology, Room D2-330, Academic Medical Centre, Meibergdreef 9, 1105 AZ Amsterdam, The Netherlands. Electronic mail: N.J.Versfeld@AMC.UvA.nl

ers can affect intelligibility substantially (e.g., Mullennix *et al.*, 1989; Sommers *et al.*, 1994). To reduce the between-speaker variability as much as possible, a special recording setup has been designed. By instructing a speaker to repeat prerecorded utterances as accurately as possible, it is hoped that variations in amplitude, intonation, speaking rate, etc., is reduced as much as possible.

The first part of the paper describes the creation of the sentence materials, the recording procedure, and an experiment to evaluate the new sentences. The result is a set of about 1300 sentences, where every sentence has been uttered by two male and two female speakers. The second part of the paper describes a method to select subsets with properties that are desired for an efficient measurement of the SRT. It is illustrated by a listening experiment conducted to form two subsets with steep psychometric functions. Lastly, a listening experiment is described where the two subsets (each comprising 39 lists of 13 sentences each) are directly compared to the existing sets of Plomp and Mimpen (1979) and Smoorenburg (1992).

I. CREATION AND EVALUATION OF THE TEST MATERIALS

The creation of the test materials consisted of several steps. First, sentence texts were selected from large databases, whereafter recordings of these materials were made, using two male and two female speakers. Next, a subset of the new materials was sampled and evaluated in a listening experiment, where the speech reception threshold in noise was measured with 12 normal-hearing subjects. Detailed procedures on each of these steps follow.

A. Selection of the sentences

Sentence materials were selected from large databases (mainly back files of major Dutch newspapers) that were available in a digitized (ASCII) format. The initial selection process was automated, and was followed by a manual selection process. To avoid too much homogeneity (e.g., by using only sentences with identical syntax) or too much heterogeneity (e.g., by allowing very short and very long sentences), sentences were selected according to criteria defined by Plomp and Mimpen (1979), as indicated below.

1. Automated selection

A sentence was defined as the sequence of characters between two full stops. The number of syllables in a sentence was estimated by counting the number of isolated vowels. Sentences were selected if (a) the number of syllables was equal to eight or nine, (b) words did not contain more than three syllables, (c) capitals did not occur, except for the initial capital, and (d) punctuation characters were absent. Duplicate sentences were removed. As a result, about 35 000 sentences fulfilled the above conditions.

2. Manual selection

From the set of 35 000 sentences, the sentences were selected that (a) represented conversational speech, (b) did not contain proverbs, exclamations, or questions, (c) did not contain any proper names, (d) were complete (i.e., contained a verb) and were syntactically and grammatically correct, and (e) had semantically neutral contents, i.e., did not deal with topics such as politics, sex, war, or some trendy subject. The manual selection process narrowed down the set to about 1500 sentences. Next, this set was evaluated by members of the audiology group, and a group of seven experts in the field of audiology and speech therapy. Based on their comments, sentences were adapted or discarded. This resulted in a set of 1311 sentences.

B. Recording of the sentence materials

1. Speakers

Via advertisements in a Dutch journal on speech therapy as well as at the Library for the Blind, tape recordings of more than 25 voices of trained speakers were obtained. A speech therapist (the second author) judged these voices on the basis of intonation, loudness, tempo, articulation, breathiness, voice quality, and dialectical influences, resulting in the selection of two male speakers (AM and RB) and two female speakers (HB and MS). They were very experienced book readers from the Library for the Blind.

2. Preliminary recording session

The aim was to create four equivalent sets, in the sense that a sentence was uttered by every speaker in a similar manner with respect to intonation, tempo, etc. To achieve this, all 1311 sentences were uttered by speaker MS in a preliminary session. She was instructed to pronounce the sentences in a natural, clear manner, while maintaining a constant vocal effort. Sentence waveforms were stored directly in separate files on a computer hard disk. In the actual recording session, a sentence waveform was played back via loudspeakers, and the speaker's task simply was to repeat it in a similar manner.

3. Actual recording session

At the actual recording session, the speaker was seated on a chair in the middle of an otherwise empty double-walled sound-proof booth ($4.20\times3.10\times2.20$ m^3). An Altai dynamic microphone was placed about 15 cm in front of the speaker, at chest height, pointed at the speaker's mouth. The microphone signal was routed to a Kawai MX-8SR eight-channel stereo mixer, and the different outputs were routed to Tucker-Davis Technology (TDT) hardware for hard disk recording, a Casio DA-7 DAT recorder for backup purposes, and the hi-fi audio channel of a JVC BR-S605EB S-VHS video recorder. Before storage to hard disk, the signals were routed through a TDT MA2 microphone amplifier, a TDT FT5 anti-aliasing filter (16 kHz), and were digitized with a TDT AD1 16-bit A/D-converter at a sampling frequency of 44.1 kHz.

In addition to the audio recordings, video recordings were made that could be used for audio-visual purposes (such as lip-reading courses). The speaker was facing the window of the sound proof booth, and a Blaupunkt CR-2000S S-VHS video camera was placed outside the booth in front of the window. The speaker was asked to look into the camera when uttering a sentence, so that simultaneously

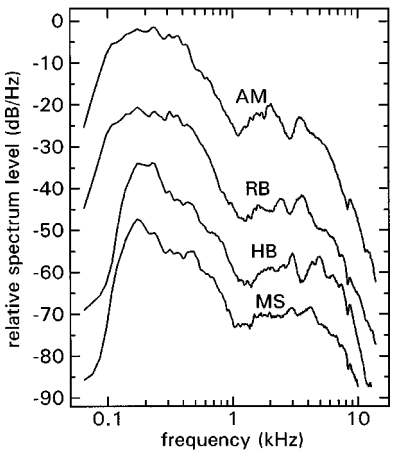

FIG. 1. Long-term average spectrum of speech for male speakers AM and RB and female speakers HB and MS. The curves have been shifted along the ordinate.

video recordings of the face could be made. The video signals were routed to the video channel of the JVC BR-S605EB S-VHS video recorder.

The task of the speaker was to repeat, as accurately as possible, utterances that were presented via loudspeakers. The procedure was self paced, and was controlled by the speaker with a PC mouse. The sequence was as follows: By pushing one out of the three mouse buttons, a sentence was presented via loudspeakers. (All sentences had been equalized with respect to their rms values.) By pushing the same mouse button, this sentence could be repeated. By pushing the second button, the speaker started the hard disk recording, and repeated this sentence. By pushing this button again, the hard disk recording was halted. Automatically afterwards, this newly recorded sentence was played back via loudspeakers, and by pushing one of the mouse buttons the speaker could decide either to listen to this new recording again, to accept the recording and continue with the next sentence, or to make a new recording of the same sentence. Both audio and video signals were monitored throughout the session, and annotations were made of sentences that were not entirely correct. These sentences were repeated at the end of the session. Per speaker, the sessions lasted about 8 h in total, divided over 2 days.

4. Editing the sentences

Silent periods before and after each sentence waveform were eliminated. Sentence waveforms that appeared to be clipped or speech with audible impurities (clicks, noises) were edited or discarded. Lastly, the sentences were equated with respect to their rms value.

5. Long-term average speech spectrum

For each speaker, the long-term average speech spectrum (LTASS) was obtained by concatenation of all sentences in time followed by calculating 4096-point fast Fourier transforms (FFTs), using an overlap-add method with Hanning windowing (50% overlap). The LTASS for each of the four speakers is displayed in Fig. 1. A 2048-tap finite impulse response (FIR) filter was designed to match the LTASS of the individual speaker. Speech noise was generated by filtering white noise with the FIR filter.

6. Evaluation of the sentence materials at comfortable level

To eliminate unclear or ambiguous sentences, a listening experiment was conducted in which four normal-hearing subjects participated. A subject was seated behind a computer terminal and received sentences (uttered by speaker AM) monaurally over headphones at a comfortable level. The subject's task was to type in the sentences on the computer keyboard. Based on these responses, unclear or ambiguous sentences were discarded, which reduced the number of sentences further to 1272.

C. Experiment I. Evaluation of the sentence materials

The purpose of the procedures described above was to create a homogeneous set, i.e., a set of sentences that are equally intelligible in a variety of listening conditions. To evaluate the characteristics of the new set of sentences, and to assess the degree of speaker variability, an experiment was conducted where the speech reception threshold in stationary speech-shaped noise for a subset of sentences was determined. Apart from the fact that such a test is indicative of problems encountered with everyday speech perception, it enables a comparison with the characteristics of existing sets in the literature.

Previous investigators (Plomp and Mimpen, 1979; Smoorenburg, 1992; Nilsson *et al.*, 1994; Kollmeier and Wesselkamp, 1997) developed speech materials solely with the aim to obtain accurate measurements for speech intelligibility in noise. Because intelligibility not only is determined by signal level, but also by contents and level variations within an utterance, these investigators conducted listening experiments on the basis of which the signal level of the individual sentences was adjusted to obtain equal intelligibility in speech noise of a fixed level. As a consequence, the resulting sets have steep psychometric functions for speech intelligibility in noise, enabling efficient measurements. However, this must imply that for other types of noise, or for some type of signal processing, the speech materials are not optimized (although differences in efficiency are expected to be small, when switching between different types of noise). In contrast to previous investigators, it was not our intent (nor would it be feasible) to equate the different sentences with respect to intelligibility by level adjustment. Instead, the aim was to select a subset of sentences that are equally intelligible in a variety of conditions. *In all experiments reported below, sentences have been equalized with respect to their rms values. Thus, in all experiments, the signal-to-noise ratio is defined as the ratio of the rms values of speech and noise, expressed in decibels.*

1. Method

a. Subjects. Twelve subjects (three male and nine female) participated in this experiment. Their age ranged from 20 to 53 years (mean of 26 years). None of them had a hearing loss at the test ear larger than 15 dB at octave fre-

quencies from 250 to 4000 Hz. Subjects were members of the audiology department or university students.

b. Stimuli and apparatus. Sixteen lists and one practice list were created by random sampling of sentences. To be able to study the effect of list length upon the accuracy of the measurement (cf. Nilsson *et al.*, 1994), each list comprised 25 sentences. Within each list, the sentence order was kept fixed. Thus, for each of the four speakers, the 16 lists and the sequential order of the sentences within each list were identical. Stimuli were stored on computer hard disk, and were converted to analog signals with an OROS-AU21 sound card. The sample frequency was 44.1 kHz and the signals were low-pass filtered at 20 kHz. Noise with the long-term average spectrum of speech of the respective speaker (see Fig. 1) served as the masker. The noise level was kept fixed at 70 dBA, and the signal-to-noise ratio was varied by changing the level of the sentences. Noise onset was 500 ms before the sentence onset, and the noise offset was 500 ms after the end of the sentence. The signal-to-noise ratio was defined by the ratio of the rms value of the sentence and the rms value of the speech noise.

c. Design. Apart from the practice list, the experimental design consisted of two parts. In the first part, one list of each speaker was presented. The presentation order was identical for all subjects. Since all subjects received exactly the same stimuli in the same order, the results of this part can be used to study between-subject differences. In the second part 12 lists were presented. The lists were counterbalanced according to a 12×12 digram-balanced Latin square (Wagenaar, 1969). For each subject, the first list was uttered by speaker HB, the second list by speaker AM, etc., such that in the end each subject received three lists of every speaker.

d. Procedure. Prior to the listening experiment, the subject's pure-tone audiogram was determined, and based on these measurements the test ear was chosen. The test ear was either the subject's best ear, or, in the case of no differences, the subject's preferred ear. The subject was informed about his task by a set of written instructions. The subject was seated in a sound-insulated room, received the sentences monaurally to the test ear over Sony MDR-CD999 headphones, and was instructed to repeat it as accurately as possible. In a list, the signal-to-noise ratio was varied according to the adaptive procedure described by Plomp and Mimpen (1979): The first sentence of each list was presented at a signal-to-noise ratio of −8 dB (which is well below the expected speech reception threshold) and was repeatedly presented, each time at a 4-dB higher signal-to-noise ratio, until it was correctly reproduced. A response was considered correct only if the entire sentence was reproduced without mistakes. The subsequent sentences of the list were presented only once, irrespective of the response. Based on the subject's response, the signal-to-noise ratio of the successive sentence was either increased (after an incorrect response) or decreased (after a correct response) by 2 dB. The entire experiment lasted about 1.5 h, breaks included.

2. Calculation of the SRT

Several authors (e.g., Plomp and Mimpen, 1979; Nilsson *et al.*, 1994) advise to estimate the SRT of a list by averaging across the signal-to-noise ratios after sentence #4. This is a very simple method that works well in adaptive procedures. In the present paper, a more sophisticated method will be used, *viz*., the method of fitting a psychometric function to the data using a maximum-likelihood criterion. This method is preferred to the conventional method since not all experiments reported on in this paper use an adaptive procedure. In order to be consistent with respect to data analysis across experiments, this method will be adopted throughout this paper. In fact, the data analysis and selection of sentences in experiment II heavily rely on this technique. An additional advantage of the maximum-likelihood method is that the first sentences of a list can also be taken into account, thereby presumably yielding more reliable estimates.

a. Maximum-likelihood estimation of the SRT. Suppose that data have been collected for one list using the adaptive procedure described in the previous section. Instead of averaging across the signal-to-noise ratios at which the sentences were presented, it is also possible to determine at each signal-to-noise ratio r_i the number of sentences N_i that has been presented together with the number of correct responses k_i. The psychometric function can next be drawn by plotting the proportion of correct responses $p_i = k_i/N_i$ as a function of the signal-to-noise ratio r_i. The function that often is used to describe such data is given by

$$\pi_{\mu,\sigma}(r) = \Phi\left(\frac{r-\mu}{\sigma}\right), \tag{1}$$

where $\Phi(z)$ is the standardized cumulative normal distribution

$$\Phi(z) = \frac{1}{\sqrt{2\pi}} \int_{-\infty}^{z} e^{-t^2/2}\, dt. \tag{2}$$

The function $\pi_{\mu,\sigma}(r)$ links the signal-to-noise ratio to the probability of a correct response, and contains two free parameters, namely μ, the signal-to-noise ratio for which the probability of a correct response will be equal to 0.5, and σ, a measure for the spread of the normal distribution. Smaller values for σ indicate steeper curves. Since the SRT is defined as the signal-to-noise ratio for which 50% of the sentences are correctly repeated, it is, by definition, equal to μ.

Instead of the spread σ, often the steepness S is given. Here S is defined as the increase in intelligibility (in percent per dB) at the 50%-correct point. The two values σ and S are easily convertible by the expression

$$S = \frac{100}{\sigma\sqrt{2\pi}}. \tag{3}$$

At a given signal-to-noise ratio r_i the probability on k_i correct responses out of N_i sentences is given by a binomial distribution:

$$B(\pi_i, N_i, k_i) = \binom{N_i}{k_i} \pi_i^{k_i} [1-\pi_i]^{N_i - k_i}, \tag{4}$$

where π_i is a shorthand notation for $\pi_{\mu,\sigma}(r_i)$. Equation (4) implicitly assumes that all sentences have similar psychometric functions, i.e., μ and σ are not sentence dependent. Given that n different signal-to-noise ratios were addressed

during the data collection, the likelihood on the outcome, assuming the underlying function given by Eq. (1), is given by

$$L = \prod_{i=1}^{n} B(\pi_i, N_i, k_i). \tag{5}$$

The most likely values for the free parameters μ and σ are obtained if L is maximized. In the remainder of this paper, SRTs and slopes of the psychometric functions will be estimated with the maximum-likelihood procedure.

b. Goodness of fit and confidence intervals. Maximization of L is equivalent to minimization of the so-called deviance function D, given by

$$D = -2 \ln\left(\frac{L}{L_0}\right), \tag{6}$$

where L_0 is the likelihood that maximally can be achieved with the given data set, which is for the case that all points p_i are described exactly by Eq. (1), i.e., for $\pi_i = p_i$. Thus, if a perfect fit to the data is obtained, $D=0$, otherwise $D>0$. The value of D for which a maximum-likelihood fit is obtained, i.e., for which D is minimized with respect to μ and σ, will be denoted as D_{ml}.

The standard error of μ can be obtained by variation of μ such that D increases to $D_{\mathrm{ml}}+1$. The same goes for the standard error of σ. The joint standard error for μ and σ can be obtained by simultaneously varying μ and σ, and selecting all pairs for which D is increased to $D_{\mathrm{ml}}+1$. These points usually form an ellipsoid. It can be shown (Cox and Snell, 1989) that D has a χ^2 distribution with $n-f-1$ degrees of freedom, where f is the number of free parameters (here $f=2$). Thus, the (joint) $1-\alpha$ confidence interval of the estimates for μ and σ can be determined by multiplication of the (joint) standard error with χ^2_α.

Finally, it can be shown (see the Appendix) that, by approximation, the standard error of μ depends linearly on the estimate of σ. Thus, an efficient measurement of the SRT can best be achieved by using sentence materials with a steep psychometric function.

3. Results

a. Effect of initial sentence number. In this experiment, the conventional adaptive up–down procedure was used. It converges to the signal-to-noise ratio where on average 50% of the sentences can be reproduced correctly. Since the SRT is not known beforehand, the vicinity of the 50% correct point is reached only after several trials. To avoid bias in the threshold estimate due to initialization effects, both Plomp and Mimpen (1979) and Nilsson *et al.* (1994) do not take into account the first few sentences, and report that the SRT should be estimated by averaging across the signal-to-noise ratio of the fifth and subsequent sentences. Earlier in this paper it was asserted that the present method of calculating the SRT is not affected by initialization effects. To verify this assertion, for each of the 144 lists from the second part of the experiment, the SRT was determined based on ten sentences, namely sentence #P to #$(P+9)$, where P ranged from 1 to 16. The SRT was calculated in two ways, *viz.*, with a curve fit to the data, as described in Sec. I C 2, and with the conventional manner by averaging across the signal-to-noise ratios of these ten sentences. Thus, for $P=5$, the method described by Plomp and Mimpen (1979) and Nilsson *et al.* (1994) was obtained.

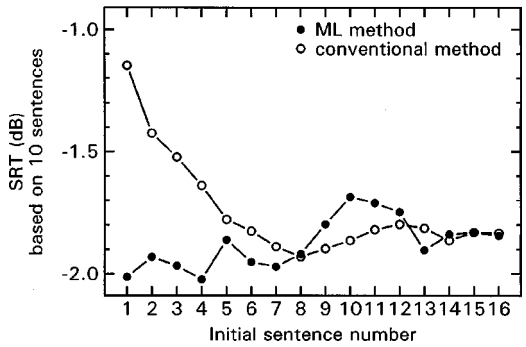

FIG. 2. Speech reception threshold (dB), based on ten sentences, as a function of the initial sentence number. Open symbols indicate the SRTs determined with the conventional method, filled symbols indicate the SRTs as determined with the maximum-likelihood method.

Figure 2 displays the average SRT as a function of the number of the first sentence P taken into account. Open symbols indicate the thresholds estimated with the conventional method of averaging, filled symbols denote the thresholds as obtained with a maximum-likelihood fit. It is clear that the conventional method suffers from bias due to initialization. Indeed, the calculations support, even quantitatively, the decision of Plomp and Mimpen (1979) and Nilsson *et al.* (1994) to omit the first four sentences. It can be seen that the maximum-likelihood method does not display such bias. A two-way (16 [sentence number] by 4 [speaker]) analysis of variance confirms this (conventional method: $F[15,2240]=2.69$, $p<0.0005$; maximum-likelihood method: $F[15,2240]=0.54$, $p>0.5$). No significant interaction was observed, and the (absence of the) initialization effect was evident for all four speakers.

In conclusion, the results show that calculation of the SRT with the maximum-likelihood method using all sentences is justified. In the following, the SRT was calculated using the responses to sentence #2 to #25. Although perhaps not necessary, it was decided to omit the first sentence of a list, because this sentence could have been presented more than once to the same subject, and might contaminate the data in some sense.

b. Consistency between subjects. The first part of the experiment (consisting of four lists per subject) was identical for each subject, and was therefore suitable to quantify between-subject differences. A two-way (12 [subject] by 4 [speaker]) analysis of variance showed a significant effect of speaker ($F[3,33]=7.44$, $p<0.001$), but not of subject ($F[11,33]=1.75$, $p>0.1$). The standard deviation between subjects was on average 1.0 dB and is given in Table I.

c. Interaction between lists and speakers. The results of the second part of the experiment (consisting of 12 lists per subject) were subjected to a two-way (12 [list] by 4 [speaker]) analysis of variance. The outcome again showed a significant effect of both speaker ($F[3,96]=30.0$, $p<0.00001$) and list ($F[11,96]=4.33$, $p<0.00005$).

TABLE I. Results of experiment I. For each speaker the SRT (dB) and the slope S (%/dB) of the psychometric function are given. The last two columns indicate the standard deviation between and within subjects, respectively.

Speaker	SRT (dB)	Slope (%/dB)	Standard deviation between subjects (dB)	Standard deviation within subjects (dB)
HB	−2.6	12.5	0.9	1.0
MS	−1.1	11.1	1.2	0.8
AM	−1.3	12.1	0.9	1.0
RB	−2.4	12.1	1.1	0.8
Average	−1.8	11.9	1.0	0.9

Speaker-specific masking noise was used to decrease the variability across sentences. At the same time, however, this may have resulted in increased between-speaker differences. The finding that the SRTs between speakers differ significantly is unfortunate if the aim is to obtain four equivalent sets. Moreover, the interaction also was found to be significant ($F[33,96]=2.45$ $p<0.0005$). This indicates that lists cannot be considered as equivalent, and that a list resulting in low SRTs for one speaker, will not necessarily do so for another speaker. An unfortunate but important conclusion, therefore, is that the aim to produce lists that are equivalent across speakers has not been met.

d. Interaction between subjects and speakers. The results of a two-way (12 [subjects] by 4 [speakers]) analysis of variance show a significant effect of both subject ($F[11,96]=3.37$, $p<0.001$) and speaker ($F[3,96]=20.6$, $p<0.00001$). Fortunately, the interaction between subjects and speakers was not significant at all ($F[33,96]=0.64$, $p>0.5$), indicating that ordering of speakers with respect to intelligibility is not subject dependent.

e. SRTs and steepness of the psychometric functions. As was noted in Sec. I C 2, the steepness of the psychometric function determines largely the accuracy and efficiency to which the SRT can be measured. For the individual subject, Plomp and Mimpen (1979) and Smoorenburg (1992) found slopes of 20%/dB and 18%/dB, respectively. [The group data of Plomp and Mimpen (1979) displayed a slope of 15%/dB.] To achieve a similar efficiency, the slopes of the functions for the present materials should be at least as steep.

Per subject and speaker, one psychometric function was constructed by pooling the data of three lists, and the SRT and steepness S were determined. For each of the four speakers, Table I displays the SRT (dB) and steepness S (%/dB), averaged across subjects. The average SRT of about −1.8 dB should be compared to the value of −5.6, −5.1, and −2.9 dB, obtained by Plomp and Mimpen (1979), Smoorenburg (1992), and Nilsson *et al.* (1994), respectively. The average slope per subject of about 12%/dB should be compared to the value of 20%/dB and 18%/dB, as obtained by Plomp and Mimpen (1979) and Smoorenburg (1992), respectively. It is clear that these values compare unfavorably with those of the existing materials. It can be shown (cf. the Appendix) that, in order to achieve an accuracy similar to Plomp and Mimpen (1979), 28 sentences are required instead of 10. Recall, however, that the existing materials have been optimized with respect to speech reception in this type of noise. Although this may explain the difference in slope, it cannot account for the differences in SRT.

4. Conclusions from experiment I

In experiment I, the newly recorded sets have been evaluated by measuring the SRT in stationary LTASS noise. The result was that the SRTs for the four speakers ranged from −2.6 to −1.1 dB, and that the average slope of the psychometric functions for an individual subject ranged from 11.1%/dB to 12.5%/dB between speakers. These characteristics do not compare favorably to the sentence materials reported in the literature. Moreover, SRTs of speakers differed significantly, and the aim of producing equivalent lists across speakers was not met.

In the following section, a new method is described to form subsets that do meet some desired characteristics. In this case, one of the most desirable properties of a new set should be a steep psychometric function.

II. THE FORMATION OF A SUBSET FOR EFFICIENT SRT MEASUREMENTS

Efficient measurement of the SRT requires a steep psychometric function of the speech materials. Therefore, it is not only required that the individual sentences in the subset have a steep slope, but also that their individual SRTs are close together (cf. Kollmeier, 1990). In short, a subset can be formed by first determining the slope and SRT of the individual sentences, whereafter a selection criterion is defined to decide whether a sentence is incorporated or discarded. This section describes the method from an experiment conducted to determine a subset for efficient SRT measurement in noise.

A. Experiment II. Intelligibility of the individual sentences

In this experiment the psychometric function of each individual sentence will be evaluated. Thus, for each sentence, the value for μ and σ in Eq. (1) has to be estimated. In order to be able to do so, at least two points of the psychometric function are required. In contrast to the previous experiment, no adaptive procedure will be used, and the signal-to-noise ratio will be kept fixed at either −1 or −4 dB. To keep the experiment within proportions, only sentences uttered by two speakers (*viz.*, HB and RB) are evaluated. Again, the set is evaluated by determination of the intelligibility of the speech in a background of LTASS noise.

1. Method

a. Subjects. In total 48 subjects (11 male, 37 female) participated in this experiment. Their age ranged from 18 to 43 years, and the mean age was 22 years. All subjects had hearing equal to or better than 15 dB HL at octave frequencies from 250 to 8000 Hz. Subjects were mostly university students.

b. Stimuli and apparatus. All 1272 sentences were evaluated. These sentences were uttered both by female speaker HB and male speaker RB. The speech was masked by noise with the LTASS of the speaker (cf. Fig. 1). The signal-to-noise ratio was set at either −1 or −4 dB, and was

chosen to encompass the expected value of the SRT (which was about −2.5 dB, cf. experiment I). The speech noise started 500 ms before the sentence, and continued for 500 ms after the end of the sentence. Sentences and masking noise were stored on computer hard disk and were played out with an OROS-AU21 sound card at 44.1 kHz. The low-pass cut-off frequency was set at 20 kHz. The level of the noise was kept fixed at 70 dBA.

c. Design. The experiment was partitioned into four blocks, each comprising 318 sentences. A block differed from another block with respect to speaker (HB or RB) and signal-to-noise ratio (−1 or −4 dB). The blocks were presented in counterbalanced order according to a 4×4 Latin square. Within each block, presentation order of the sentences was randomized. Thus, each subject received in total 1272 sentences, and each sentence occurred only once.

d. Procedure. For each subject, the experiment started with the determination of the pure-tone audiogram. Next, the subject was asked to be seated in a soundproof booth, and was given a set of written instructions. The subject's task was to listen carefully to the stimuli (that were presented monaurally via Sony MDR-CD999 headphones), and to type in on a computer keyboard as much as they could understand of what was being said. A sentence was presented only once. Subjects could edit the typed text as often as desired, and when they were satisfied with it, they pressed ''Enter.'' If the response was correct, the next sentence was presented automatically after a delay of a few seconds. If the response was incorrect, the correct sentence was displayed, and the next sentence was presented only after the subject pressed the ''Enter'' key again.

Prior to the actual session, a practice list was given, consisting of ten sentences uttered by HB and ten sentences by RB. These sentences did not occur in the actual list. After it was clear that the task was understood by the subject, the actual session was started. The task was completely self-paced, and the subjects were encouraged to take a short break whenever they wanted. The total amount of time required to finish all sentences was estimated at about 6 h. The experiment therefore was split into two or three parts. After about 3 h, the experimenter interrupted the session, and an appointment was made for the next session. If it was clear that the subject could not finish the experiment within a reasonable time limit at the second session, an appointment for a third session was made. The duration of an experiment was on average 6.5 h.

TABLE II. Sentences subdivided by the number of correct responses at a signal-to-noise ratio of −1 dB (abscissa) and −4 dB (ordinate). (a) Speaker HB, (b) speaker RB. The entry in reversed video indicates the expected number of k_{-1} and k_{-4}, given an underlying psychometric function with a SRT of −5.6 dB and a slope of 15%/dB. The thick, medium, and thin solid lines then indicate the boundary where the probability $P(k_{-1},k_{-4})$ exceeds 0.05, 0.01, and 0.001, respectively. The shaded area indicates the 99% confidence interval given by a psychometric function with SRT of −3.9 dB and slope $S=15\%/\mathrm{dB}$. Sentences within this area are taken into account into the final set.

(a) Speaker HB

Number of correct responses at a signal-to-noise ratio of -4 dB \ Number of correct responses at a signal-to-noise ratio of -1 dB	0	1	2	3	4	5	6	7	8	9	10	11	12
12	0	0	0	0	0	0	0	0	0	0	4	11	42
11	0	0	0	0	0	0	0	0	0	3	5	17	51
10	0	0	0	0	0	0	0	0	1	4	10	23	46
9	0	0	0	0	0	0	0	0	2	2	18	22	39
8	0	0	0	0	0	0	0	1	3	11	19	33	41
7	0	0	0	0	0	0	0	3	2	6	15	30	29
6	0	0	0	0	0	0	1	0	10	10	22	26	23
5	0	0	1	0	0	2	8	5	8	12	10	23	21
4	0	1	0	0	1	3	3	9	15	19	20	21	14
3	1	0	1	4	5	5	3	10	12	20	14	13	4
2	0	3	3	2	11	5	12	9	11	18	19	6	5
1	1	2	7	7	9	13	10	18	16	8	21	13	3
0	12	11	20	18	19	16	17	17	15	13	7	2	0

(b) Speaker RB

Number of correct responses at a signal-to-noise ratio of -4 dB \ Number of correct responses at a signal-to-noise ratio of -1 dB	0	1	2	3	4	5	6	7	8	9	10	11	12
12	0	0	0	0	0	0	0	0	0	0	3	7	23
11	0	0	0	0	0	0	0	0	0	2	5	14	50
10	0	0	0	0	0	0	0	0	0	3	8	17	29
9	0	0	0	0	0	0	0	0	2	2	10	20	24
8	0	0	0	0	0	0	0	1	5	4	19	26	34
7	0	0	0	0	0	0	1	1	4	7	20	18	30
6	0	0	0	1	0	1	0	4	5	20	17	19	20
5	0	0	0	0	0	0	2	7	10	13	21	27	12
4	0	0	0	1	2	3	4	11	11	28	21	17	16
3	0	0	0	2	5	3	7	6	10	24	16	13	7
2	0	0	5	5	6	6	15	20	17	18	18	15	6
1	3	5	6	5	16	17	16	23	16	13	14	5	3
0	27	18	24	27	24	21	25	20	21	6	4	6	1

2. Results

a. General. All incorrect answers were checked manually for typing errors and other nonrelevant mistakes. At a signal-to-noise ratio of −1 dB, 76% and 71% of the responses were correct for speakers HB and RB, respectively. At −4 dB, these values were 43% and 37%, respectively. Thus, for speaker HB, the SRT was −3.4 dB with a slope of 11.7%/dB, whereas for RB this was −2.9 dB with a slope of 11.8%/dB. In comparison with the previous experiments, SRTs were more than 0.5 dB better, but slopes were slightly less steep. The differences may be due to the experimental method. The SRTs for the individual subjects ranged from −1.3 to −5.1 dB, with a standard deviation of 0.8 dB.

b. Method of selection. The intelligibility of a sentence is characterized by two numbers, *viz*., the number of correct responses k_{-1} at −1 dB and the number of correct responses k_{-4} at −4 dB. Since for both speakers, for each sentence, and for both signal-to-noise ratios, 12 responses were obtained, k_{-1} and k_{-4} range between 0 and 12 (inclusive). Table II yields the number of sentences as a function of k_{-1} (abscissa) and k_{-4} (ordinate). Table IIa displays the results obtained with speaker HB, Table IIb those with speaker RB.

For example, with speaker HB, the number of sentences for which all 12 responses were correct at −1 dB, and 10 responses were correct at −4 dB equals 46. For speaker RB this number equals 29. The sum across all entries must be equal to 1272.

Suppose one wants to select the sentences that may have originated from a psychometric function characterized by a given SRT of μ and a given slope σ. For a given sentence, the probability of obtaining k_{-4} correct responses at −4 dB and k_{-1} correct responses at −1 dB is derived from Eq. (4), and is written as

$$P(k_{-4},k_{-1}) = B(\pi_{-4},N_{-4},k_{-4}) \cdot B(\pi_{-1},N_{-1},k_{-1}), \tag{7}$$

where $N_{-1}=N_{-4}=12$ and π_i is defined in Eq. (1). Thus, for each cell in Table II, the probability $P(k_{-4},k_{-1})$ can be determined for a given value of μ and σ. Let us, for example, set the value for μ to −5.6 dB, and the steepness S to 15%/dB (i.e., σ=2.66 dB), which are the values reported by Plomp and Mimpen (1979). Then, according to Eq. (1), the probability of a correct response at −4 and −1 dB then is equal to 0.73 and 0.96, respectively. The most likely values for a pair k_{-4} and k_{-1}, given $N=12$, therefore will be 9 and 12, respectively, and, according to Eq. (7), $P(9,12)=0.152$. In Table IIa, this entry is indicated in reversed video. Similarly, the probability $P(k_{-4},k_{-1})$ can be calculated for all other combinations of k_{-4} and k_{-1}. It is clear that pairs (k_{-4},k_{-1}) remote from the most likely pair, yield low probabilities. Selection takes place by taking into account only the sentences in the cells for which $P(k_{-4},k_{-1})$ exceeds some value P_0. For example, if $P_0=0.05$, the sentences of only 8 cells [*viz.*, (7,12), (8,11), (8,12), (9,11), (9,12), (10,11), (10,12), and (11,12)] are selected. This results in 284 sentences for speaker HB and 230 sentences for speaker RB. The SRT of this subset for HB and RB can be recalculated, and indeed appears to be −5.7 and −5.6 dB, respectively. The steepness of these sets even are 17.1%/dB and 17.2%/dB, respectively. Although the specifications for the subsets are satisfactory, the number of sentences selected is far too low. By decreasing the value of P_0 from 0.05 to, for example, 0.01, the number of selected cells, hence the number of selected sentences, increases to 490 for HB and 373 for RB, but the specifications of these subsets are less good (slopes between 14%/dB and 15%/dB). Decreasing P_0 even further to 0.001 increases the number of sentences to 641 and 524 for HB and RB, respectively, but results in SRTs of −5.4 and −5.2 dB, and slopes of 13.7%/dB and 14.1%/dB for HB and RB, respectively. Thus, there is a tradeoff between the number of sentences included and the specifications. Selection of large subsets with low SRTs and steep slopes is not possible due to the heterogeneity of the materials [cf. Kollmeier's (1990) convolution model].

Since the absolute value of the SRT is far less important than the slope, it was decided to maximize the number of included sentences by variation of μ and P_0, with the restriction that the steepness of the subsets should at least be 15%/dB. By taking μ equal to −3.9 dB, and P_0 equal to 0.001, the subset formed for HB consisted of 783 sentences, with a SRT of −4.0 dB and a steepness of 15.1%/dB. For RB, 726 sentences were selected, with a SRT of −3.8 dB and a steepness of 15.2%/dB. The selected cells are shaded in Table IIa and b. The value for P_0 appears to be equivalent to the 99% joint confidence interval of μ and σ. A number of the selected sentences occurs in both subsets. By assigning these sentences to either set, one set of 509 sentences was created for speaker HB, and a second set containing 510 *different* sentences was created for speaker RB. The SRT and slope for these sets were recalculated and were −3.88 dB and 15.4%/dB for speaker HB and −3.86 dB and 15.0%/dB for speaker RB, respectively.

c. Formation of lists. All sentences were transcribed to phonemes with the grapheme-to-phoneme converter of Kerkhoff and Rietveld (1994). Next, the sentences were grouped in lists of 13 sentences. The latter number was adopted from Plomp and Mimpen (1979). In order to match the phonemic content of each list as closely as possible to the mean phonemic distribution, a matching procedure was designed that started by the selection of the sentences containing the rarest phoneme, and dividing them evenly across lists. Next, the sentences containing the one-but-rarest phoneme were selected and again were divided across lists. This process was repeated until all phonemes were selected. A sentence was randomly assigned to a list, but the phonemic distribution across lists was kept as constant as possible. A χ^2 criterion was used as a goodness-of-fit measure between observed and expected frequencies. Thus, in the matching procedure it was attempted to minimize

$$X^2 = \sum_{l=1}^{L} \sum_{p=1}^{P} \frac{(o_{pl}-e_p)^2}{e_p}, \tag{8}$$

where l and p denote the list number and phoneme number, respectively, and L and P denote the maximum number of lists and phonemes, respectively. Here, $L=39$ and $P=39$. The observed frequency of phoneme p in list l is denoted by o_{pl}, and the expected frequency of phoneme p (i.e., the mean frequency) is denoted by e_p. The consequence of this criterion is that the rare phonemes are very evenly distributed across lists, whereas larger (absolute) differences occur for the more common phonemes. The entire matching procedure was repeated until the value of X^2 did not decrease any further. Next, it was verified that for each list the different sentences did not resemble each other too much with respect to words or contents. The resulting values of X^2 ranged from 13.4 to 46.0, indicating that the distribution of the individual lists matched the average distribution very well $\{p[X^2=13.4,\ \text{d.f.}=38]=0.999,\ p(X^2=46.0,\ \text{d.f.}=38)=0.17\}$. Only with one list (list 39 for speaker RB) the distribution deviated significantly from the average distribution ($p[X^2=65.5,\ \text{d.f.}=38]<0.005$). This deviation was caused by the phoneme /c/, occurring three times, whereas the average frequency was only 0.26.

In conclusion, two sets (one with a male speaker, the other with a female speaker) each comprising 39 lists of 13 sentences were created. A sentence occurring in one set did not occur in the other set. Thus, in total 1014 new sentences have been generated that have the property that they are

TABLE III. Results from experiment III. For each set is given the SRT (dB), the slope of the psychometric function (%/dB), and the standard deviation between lists, between subjects and within subjects (in dB).

Speaker	SRT (dB)	Slope (%/dB)	Standard deviation (dB) Between lists	Between subjects	Within subjects
RP (Plomp and Mimpen, 1979)	−4.50	15.9	0.54	0.77	1.07
LP (Smoorenburg, 1992)	−3.66	17.7	0.63	1.11	1.04
HB	−4.11	16.6	0.57	0.82	1.10
RB	−4.00	15.2	0.49	0.77	1.08
Average	−4.07	16.3	0.56	0.80	1.07

equally intelligible when presented in speech-shaped noise at an equal rms level.

B. Experiment III. Evaluation of the final sets

In the previous experiment, intelligibility of the sentences was measured at fixed signal-to-noise ratios. It was already observed that the SRTs of experiments I and II differed by over 0.5 dB, which was ascribed to the different experimental procedure. The present experiment was set up to determine the statistical properties of the newly developed sets, and to compare these to the properties of the existing sets of Plomp and Mimpen (1979) and Smoorenburg (1992). The experimental method was very similar to that of Plomp and Mimpen (1979), as described in experiment I. Therefore, only a short description is given.

1. Method

a. Subjects. Twelve subjects (ten female and two male) participated in this experiment. Their age ranged from 18 to 26 years (with a mean of 22 years). Their pure-tone audiogram did not exceed 15 dB HL at octave frequencies from 250 to 8000 Hz. Subjects were university students.

b. Stimuli. The sentence materials of four sets were evaluated. The first set (set I) comprised the first eight lists of Plomp and Mimpen (1979), which had been uttered by a female speaker RP. The second set (set II) comprised the first eight lists of Smoorenburg (1992), and had been uttered by a male speaker LP. The third and fourth sets (sets III and IV) each comprised the first eight lists from the newly formed sets of speakers HB and RB, respectively. For each speaker, a ninth list was added as a practice list. Within each list, the sentence ordering was kept fixed. All sentences were stored on computer hard disk, at a 16-bits resolution and a sampling frequency of 44.1 kHz. Noise with the LTASS of the respective speaker served as the masker. The noise was presented at a level of 70 dBA.

c. Design. The experiment was partitioned into four blocks, each block comprising a different speaker. The presentation order of the blocks was counterbalanced according to a 4×4 Latin square. Within each block, eight lists were presented, preceded by one practice list. The eight lists also were presented in counterbalanced order according to an 8×8 Latin square. Thus, in total, each subject received 32 lists of 13 sentences plus four practice lists.

d. Procedure. The procedure was identical to the one described in experiment I. The entire experiment lasted about 1.5 h, breaks included.

2. Results

For each list, the SRT was determined with the maximum-likelihood method, using all sentences except for the first one. This resulted in 384 SRTs.

a. Differences between speakers. A two-way (12 [subject] by 4 [speaker]) analysis of variance, with eight replications per cell, shows a significant effect of both subject ($F[11,336]=15.9$, $p<0.000\,01$) and speaker ($F[3,33]=7.96$, $p<0.0005$). The interaction between speaker and subject was not significant. The SRT per speaker is given in Table III, and is on average −4.07 dB. The standard deviation between speakers is 0.35 dB. The SRT of speaker RP [of Plomp and Mimpen (1979)] is lowest, followed by HB and RB. The SRT of speaker LP [of Smoorenburg (1992)] is highest. A *post hoc* Tukey test showed no significant differences between the SRTs of speakers RP and HB, and also no significant differences between the SRTs of speakers HB, RB, and LP. Thus, the average SRT of the two new sets is in between the two existing sets.

For the determination of the slope, the data were pooled across lists for each speaker and subject. For the individual speaker, the slope is given in Table III, and was on average 16.3%/dB. The average slope per set always was larger than 15%/dB.

b. Differences between subjects. For each speaker, the standard deviation between subjects was determined. The values are given in Table III, and were on average 0.80 dB. This value is very similar to the value of 0.78 dB, obtained

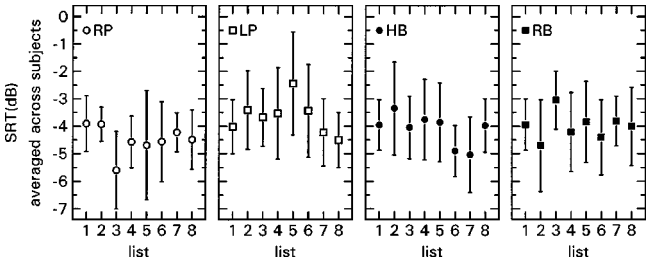

FIG. 3. Results of experiment III. Speech reception thresholds (dB) as a function of list number. Error bars indicate the standard deviation between subjects. Each panel displays the result of a different speaker.

by Nilsson *et al.* (1994). The analysis of variance shows that the effect of subject is much larger than the effect of speaker (cf. Sec. II B 2 a).

c. Differences between lists. Figure 3 displays, for each speaker separately, the average SRT (dB) as a function of list number, as well as the standard deviation between subjects. For each speaker, a one-way analysis of variance was performed. For none of the speakers, large significant effects of list were found ($F[7,88]<2.45$, $p>0.02$). Therefore, lists were considered as equivalent. The standard deviation between lists for each speaker is given in Table III, and was on average 0.56 dB.

d. Test–retest reliability. The reliability of an SRT measurement can be estimated by looking at the within-subject differences. For each speaker, the standard deviation between lists for each individual subject was determined {i.e., the within-cell variance with the two-way (12 [subject] by 4 [speaker]) analysis of variance}. The standard deviations per speaker are given in Table III, and were on average 1.07 dB. This result is in good agreement with previous results of Plomp and Mimpen (1979) and Nilsson *et al.* (1994), who found values of 0.9 and 1.13 dB, respectively.

3. Conclusions from experiment III

Despite the fact that in the selection procedure in Sec. II A higher SRT values were accepted, the results show surprisingly that the two newly developed sets still have similar SRTs and slopes as the existing sets of Plomp and Mimpen (1979) and Smoorenburg (1992).

III. GENERAL DISCUSSION

In the present paper, the selection, recording, and evaluation of new sentence materials for the measurement of the speech reception threshold, as well as a selection procedure to create subsets for efficient measurement of the SRT in LTASS noise has been described. Two sets have been formed that can be viewed as equivalent to the existing sets of Plomp and Mimpen (1979) and Smoorenburg (1992). Each set contains 39 lists of 13 sentences. In one set, sentences were uttered by a female speaker, in the other by a male speaker. The sentences that occur in one set do not occur in the other set.

A. Differences between speakers

Initially, the aim was to create four sets, each with identical sentence materials, but uttered by different speakers. The results of experiment I showed a large effect of speaker, indicating that the overall intelligibility differed between speakers. Moreover, a significant interaction between lists and speakers was found, indicating that the rank-order between speakers with respect to intelligibility differed from list to list (hence also from sentence to sentence). Despite the special recording procedure, where as many variables as possible have been kept fixed, the between-speaker differences apparently still were not small enough.

One possibility is that differences in articulation have played a role. It is known that these differences become more apparent under increasingly adverse listening situations (Mullennix *et al.* (1989). Since, in the present experiments, all speech has been presented near the speech reception threshold, it is conceivable that articulatory differences may have played a significant role. The issue of speaker variability in the sense that listeners have to adjust to the characteristics of a particular speaker (Mullennix *et al.*, 1989) probably has not played a role in the present experiments, since alteration from one speaker to another did not occur earlier than after one list.

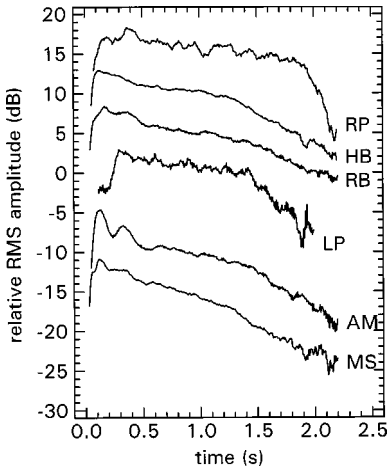

FIG. 4. Mean rms amplitude (dB) as a function of time (s) for male speakers LP, AM, and RB and female speakers RP, HB, and MS. Curves have been shifted along the ordinate.

Alternatively, with speaker MS it was observed that the end of each sentence on average was less intelligible when listening to it in stationary noise. Usually, when uttering a sentence, the level decreases as the sentence proceeds. However, in stationary noise this implies that, at a given overall signal-to-noise ratio, the signal-to-noise ratio at the beginning of a sentence will be higher than at the end. Since the intelligibility of the complete sentence depends crucially on the intelligibility of the individual parts, it is expected that the SRT worsens if the intensity over time increases. For example, sentences with a large decline will, at the SRT, be perfectly intelligible at the beginning, but not at the end. Thus, intelligibility of the complete sentence depends only on the intelligibility of the last (few) words. Therefore, not only the SRT increases, but also the slope of the psychometric function will flatten (and become comparable to, for example, the slope for isolated words).

To investigate to what degree the sets varied with respect to within-sentence intensity course, for each set the rms amplitude as a function of time was calculated. The result is displayed in Fig. 4. Indeed, the decline in speakers AM and MS is larger than those of the other speakers, whereas those for the other four speakers are comparable. As can be seen, the decline is substantial: Although it is difficult to fit a straight line to the curves, it is clear that the intensity declines at least by about 2 dB per second. This indicates that, next to articulatory variation, within-sentence intensity decline has caused differences in intelligibility between sentences or speakers. If one would be able to correct the tem-

poral slope in some way, it seems feasible to decrease variability and create more equivalent sets.

B. Measurement efficiency

In evaluating the sentence materials, the experimental procedure of Plomp and Mimpen (1979) was adopted. Also, a number of methods and strategies described in this paper closely follow those described by Plomp and Mimpen (1979). It is clear that these choices have been made to come to comparable sentence materials that can be used in an identical experimental setup. This also means that these choices are not necessarily the best ones. For example, one could argue that word scoring would result in more accurate results than sentence scoring. Also, a different manner of estimating the SRT of a run could produce more reliable results. In the next paragraphs some of these issues are discussed in light of measurement efficiency.

1. How much variation in the response is allowed?

In the experiments reported in this paper, as well as many other papers on this topic, a response was considered correct only if the entire sentence was reproduced completely correct, i.e., no mistakes whatsoever (articles, tense, plural/singular, etc.) were allowed. To investigate to what extent the SRT changes if small mistakes are allowed (i.e., to investigate the variability in SRT due to the variation in judgment criteria between different investigators), the results from experiment II were reexamined for the first ten subjects. A sentence now was considered correct if the content was more or less understood. If small mistakes are allowed, it is expected that not only the SRT becomes better, but also that the slope becomes steeper. For, at favorable signal-to-noise ratios, the message usually is clear, but small mistakes are still made, whereas at less favorable signal-to-noise ratios the message itself is unclear, independent of small mistakes. The results show that indeed the SRT becomes better, about 0.7 dB, but that the slope hardly changes. Averaged across subjects, the slope slightly increases by 1%/dB, but for the individual subjects slopes either increase or decrease. Thus, the extent to which response variations are allowed changes the SRT, but not the slope. This indicates that judgment criteria hardly affect measurement efficiency.

2. Sentence scoring versus word scoring

Instead of sentence scoring, the number of correctly repeated words could be scored (Kollmeier and Wesselkamp, 1997). To assess the difference between sentence scoring and word scoring, the results of experiment II were reanalyzed, and for every response the number of correctly repeated words (i.e., the number of correctly typed words) was counted. The results of experiment II already showed that, averaged across all sentences, sentence scoring resulted in an SRT of -3.4 and -2.9 dB for speakers HB and RB, respectively. The corresponding slopes were 11.6%/dB and 11.8%/dB, respectively. With word scoring, the SRT drastically improves to -6.1 and -5.6 dB for speakers HB and RB, respectively. However, the slope *decreases* to 10.3%/dB and 10.5%/dB, respectively.

Similar statistics were performed on a subset of the data, *viz*., the sentences for which the individual psychometric function could be determined. This resulted in a subset of 653 sentences for speaker HB and 678 sentences for speaker RB. Again, SRT and slope were determined under sentence scoring or word scoring. With sentence scoring, the SRT of the individual sentences was on average -3.1 dB with a standard deviation of 2.9 dB for speaker HB, and -2.8 dB with a standard deviation of 3.3 dB for speaker RB. Thus, the SRT of the subsets did not differ much from those obtained for the entire set. However, the average slope greatly improved to 15.5%/dB and 15.7%/dB for HB and RB, respectively. Thus, with sentence scoring, measurement efficiency can already greatly be improved by imposing a level correction to each individual sentence, such to produce equal SRTs. With word scoring, SRTs and slopes of the subset were comparable to those of the whole set (SRTs of -6.4 and -5.9 dB for speaker HB and RB, respectively, with standard deviations of 3.4 and 3.1 dB; slopes of 12.8%/dB and 13.0%/dB, respectively). Again, the slopes obtained under word scoring are less steep than those obtained under sentence scoring.

It is known (e.g., Bosman and Smoorenburg, 1995) that the psychometric function for single words is rather shallow (e.g., 6%/dB for CVC words). It is expected that, with word scoring, the psychometric function for a string of N nonrelated words is similar to that for single words (presuming that other factors such as memory span, etc. are ignored), since only averaging takes place. (In other words: It makes no differences whether one scores a list of ten separate words, or one ''sentence'' consisting of ten words.) With sentence scoring, on the other hand, every word in the string needs to be perceived correctly, in order to yield a correct response. Thus, the psychometric function for sentence scoring, Φ_S, is expected to be related to that of single words, Φ_W, via $\Phi_S \approx (\Phi_W)^N$. (Note that this must be an approximation, since Φ_S and Φ_W cannot be Gaussian simultaneously, except for $N=1$.) For values of N greater than unity, Φ_S has a steeper slope, but a worse SRT in comparison with Φ_W. This is precisely what has been observed above. By insertion of the values for the SRT and slope for both Φ_S and Φ_W it is in principle possible to obtain an estimate for N, which can be interpreted as the ''effective'' or ''independent'' number of words of a sentence [cf. the so-called j-factor of Boothroyd and Nittrouer (1988)]. Here, the value for N is between 1.5 and 2.5. The fact that N is smaller than the average number of words in a sentence (about six) originates from the fact that the words in a meaningful sentence are interrelated and redundant.

Word scoring thus produces psychometric functions with relatively shallow slopes. However, this does not imply that the measurement efficiency is smaller, since every word is scored, instead of every sentence. Hence, per sentence, effectively 1.5 to 2.5 (binary) responses are obtained (i.e., the value for N). It can be shown that, in order to obtain an equally reliable estimate of the SRT, word scoring requires about 0.5 to 0.8 times the amount of sentences required with sentence scoring. Therefore, despite the shallower slope, word scoring eventually is more efficient than sentence scor-

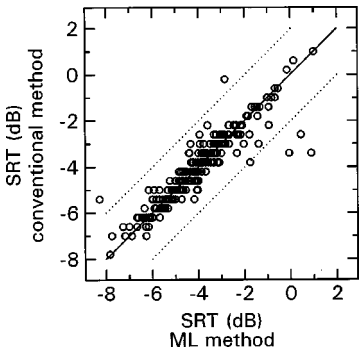

FIG. 5. Comparison between SRTs obtained with the conventional method and those obtained with the maximum-likelihood method. The major diagonal is indicated by a solid line, dotted lines indicate a deviation of 1 dB from the diagonal.

ing. In any case, word scoring requires less sentence materials per SRT estimate, and it therefore is worthwhile to consider this method if one expects to run out of sentence materials. One should keep in mind, however, that word scoring probably is more laborious for the experimenter. It presumably depends on the experimental setting whether word scoring will also be more time efficient.

3. Maximum-likelihood method versus conventional method

The SRTs from the present experiments all have been calculated by fitting a cumulative Gaussian curve to the data with a maximum-likelihood method, using all data but the first sentence. Plomp and Mimpen (1979) and others calculated the SRT by averaging across the signal-to-noise ratios after sentence #4. To investigate the difference between both methods, all 384 SRTs from experiment III were recalculated with the conventional method. Figure 5 displays, for each list, the SRT obtained with the conventional method as a function of the SRT calculated with the maximum-likelihood method. Except for six lists, the deviation between the SRTs of the two calculation methods is less than 1 dB. These six lists are characterized by a large standard deviation, i.e., a bad staircase. Overall, no systematic differences occur; the two methods give very similar results. Given the fact that more trials are taken into account with the maximum-likelihood method, one would expect the spread of the data along the abscissa to be smaller than that along the ordinate. With the present results, this appears not to be true (the standard deviations are 1.93 and 1.75 for the maximum-likelihood method and the conventional method, respectively). This counterintuitive result led us to perform some Monte Carlo simulations. For a range of slopes (from 5%/dB to 25%/dB) and a variety of list lengths (from 13 to 832 trials per list), adaptive runs were simulated. Both calculation methods were performed after each run. Again, in all cases the standard deviation of the SRT estimate was larger for the maximum-likelihood method than for the conventional method, although differences often were small. An explanation for these differences is that the maximum-likelihood method makes no assumptions about the underlying value of the SRT or the steepness of the slope, whereas the conventional method does. Nevertheless, for the present procedure, the method of simple averaging seems to be at least as effective as the more complex maximum-likelihood estimate.

C. Linguistic entropy

Nilsson *et al.* (1994) were surprised about the difference in SRT between their sentence materials (SRT=−2.92 dB) and Plomp and Mimpen's (1979) materials (SRT=−5.6 dB). They examined the range of level variations within the materials, but no systematic differences were found between the sets. They also checked the LTASS of both sets, but these were found to be correct. Lastly, Nilsson *et al.* (1994) hypothesized that differences in linguistic entropy (cf. van Rooij *et al.*, 1991) might be a factor. Informal comparison of the Dutch and English materials did not directly lead to the conclusion that the contents or structure of the English sentences were more difficult than that of the Dutch materials. Nevertheless, it is possible that lexical issues such as the neighborhood density and frequency (e.g., Luce and Pisoni, 1998; Sommers *et al.*, 1997) have a considerable effect on the overall SRT value, for instance, since the English language contains many more words than the Dutch language. Although it is very worthwhile to find out to what degree these issues play a role, it is beyond the scope of the present paper.

IV. SUMMARY

This paper describes a method for the development of speech materials for efficient measurement of the speech reception threshold. A set of 1272 sentences was created and was uttered by two male and two female speakers. For one male and one female speaker, a subset was formed that enables efficient measurement of the speech reception threshold in stationary speech noise. The subset consists of two times 39 lists, each list containing 13 sentences. The subset can be considered as being equivalent to the existing sets of Plomp and Mimpen (1979) and Smoorenburg (1992).

ACKNOWLEDGMENTS

This work was financially supported by the ''Heinsius Houbolt'' foundation and by Philips Hearing Instruments BV. The newspaper database was put at our disposal by David van Leeuwen of TNO Human Factors Research, Soesterberg, The Netherlands. Automated grapheme-to-phoneme conversion and syllable counting was carried out by Joop Kerkhoff of Nijmegen University, Nijmegen, The Netherlands. The authors acknowledge Arjan Bosman, Margreet Langereis, Louis Pols, and many people from the ENT/audiology department of the VU hospital for their critical evaluation of the sentence materials and their participation in the listening experiments. The reviewers are greatly acknowledged for their critical reading of the manuscript. Birger Kollmeier is acknowledged for his detailed comments. Special thanks go to Hilde de Boer, Rob Binnerts, A. Mojet, and Maeve van der Steen, all speakers of the Library for the Blind, for their enthusiasm and willingness to spend hours and hours in a sound-proof booth uttering all sentences.

APPENDIX: CALCULATION OF THE CONFIDENCE INTERVALS OF THE SRT USING A MAXIMUM-LIKELIHOOD METHOD

This Appendix contains the derivation of the confidence interval of the SRT, as determined with a maximum-likelihood method. The result will show that the confidence interval is directly related to the steepness of the psychometric function, and decreases with the increase in the number of sentences in a list.

In this Appendix, the psychometric functions will be based on the logistic function, rather than the cumulative normal distribution that was used in the main text. The shapes of both functions are very similar, and the use of the logistic function is solely for mathematical convenience. The logistic function $\Lambda(r)$ is given by

$$\Lambda(r)=\frac{e^r}{1+e^r}. \tag{A1}$$

Analogous to Eq. (1) in the main text, the psychometric function is defined as

$$\pi_{\mu,\tau}(r)=\Lambda\left(\frac{r-\mu}{\tau}\right), \tag{A2}$$

where μ denotes the signal-to-noise ratio for which the probability of a correct response equals 0.5, hence is equal to the SRT, and where τ is a measure for the steepness of the psychometric function. Near the 50% correct point, the values for σ (in the main text) and τ are related via $\tau=\sigma\sqrt{(\pi/8)}$, and the steepness of the slope, expressed in percent per dB, is given by $S=25/\tau$.

The deviance function, given by Eq. (6) in the main text, can be written out explicitly by insertion of the binomial distribution from Eq. (4). After some simplifications the expression becomes

$$D=2\sum_{i=1}^{n} N_i p_i \ln\left(\frac{p_i}{\pi_i}\right)+2\sum_{i=1}^{n} N_i(1-p_i)\ln\left(\frac{1-p_i}{1-\pi_i}\right). \tag{A3}$$

Here, $p_i=k_i/N_i$, where k_i is the observed number of correct responses out of N_i sentences. Equation (A3) goes for any arbitrary function π. Minimization of the deviance function requires that the first derivatives of D with respect to μ and τ are equal to zero. Thus μ and τ should be varied such that

$$\frac{\partial D}{\partial \mu}=\frac{2}{\tau}\sum_{i=1}^{n} N_i(p_i-\pi_i)=0 \tag{A4}$$

and

$$\frac{\partial D}{\partial \tau}=\frac{2}{\tau^2}\sum_{i=1}^{n} N_i(p_i-\pi_i)(r_i-\mu)=0. \tag{A5}$$

Near the minimum, the second derivative of the deviance function with respect to μ or τ is a measure for the curvature, hence indicative for the standard error. The matrix that contains the second derivatives of D is called Fisher's information matrix and is given by

$$F=\begin{bmatrix} \dfrac{\partial^2 D}{\partial \mu^2} & \dfrac{\partial^2 D}{\partial \mu \partial \tau} \\ \dfrac{\partial^2 D}{\partial \tau \partial \mu} & \dfrac{\partial^2 D}{\partial \tau^2} \end{bmatrix}, \tag{A6}$$

where, with the aid of Eqs. (A4) and (A5),

$$D_{\mu\mu}=\frac{\partial^2 D}{\partial \mu^2}=\frac{2}{\tau^2}\sum_{i=1}^{n} N_i\pi_i(1-\pi_i), \tag{A7}$$

$$D_{\mu\tau}=\frac{\partial^2 D}{\partial \mu \partial \tau}=\frac{\partial^2 D}{\partial \tau \partial \mu}$$
$$=\frac{2}{\tau^2}\sum_{i=1}^{n} N_i\left\{\pi_i(1-\pi_i)\frac{(r_i-\mu)}{\tau}-(p-\pi_i)\right\}, \tag{A8}$$

and

$$D_{\tau\tau}=\frac{\partial^2 D}{\partial \tau^2}$$
$$=\frac{2}{\tau^2}\sum_{i=1}^{n} N_i\frac{r_i-\mu}{\tau}\left\{\pi_i(1-\pi_i)\frac{r_i-\mu}{\tau}-2(p-\pi_i)\right\}. \tag{A9}$$

Near the minimum, the second part of Eqs. (A8) and (A9) are equal to zero. The diagonal elements of the inverse matrix of F yield the variance in the estimate of μ and τ. The variance in the estimate of μ therefore is given by

$$\text{var}\,(\mu)=\frac{D_{\tau\tau}}{D_{\mu\mu}\cdot D_{\tau\tau}-D_{\mu\tau}^2}. \tag{A10}$$

Insertion of Eqs. (A7)–(A9) into Eq. (A10) shows that, near the minimum, var (μ) is proportional to τ^2, hence the standard error is proportional to τ, and thus depends linearly on the steepness of the psychometric function. Also, it can be seen that the standard error of μ is roughly inversely proportional to the square root of the total number of sentences.

Boothroyd, A., and Nittrouer, S. (**1988**). ''Mathematical treatment of context effects in phoneme and word recognition,'' J. Acoust. Soc. Am. **84**, 101–114.

Bosman, A. J., and Smoorenburg, G. F. (**1995**). ''Intelligibility of Dutch CVC syllables and sentences for listeners with normal hearing and with three types of hearing impairment,'' Audiology **34**, 260–284.

Cox, D. R., and Snell, E. J. (**1989**). *Analysis of Binary Data* (Chapman & Hall, London).

Duquesnoy, A. J. (**1983**). ''The intelligibility of sentences in quiet and in noise in aged listeners,'' J. Acoust. Soc. Am. **74**, 1136–1144.

Festen, J. M., and Plomp, R. (**1990**). ''Effects of fluctuating noise and interfering speech on the speech-reception threshold for impaired and normal hearing,'' J. Acoust. Soc. Am. **88**, 1725–1736.

Gatehouse, S. (**1992**). ''The time course and magnitude of perceptual acclimatization to frequency responses: Evidence from monaural fitting of hearing aids,'' J. Acoust. Soc. Am. **92**, 1258–1268.

Kalikow, D. N., Stevens, K. N., and Elliott, L. L. (**1977**). ''Development of a test of speech intelligibility in noise using sentence materials with controlled word predictability,'' J. Acoust. Soc. Am. **61**, 1337–1351.

Kerkhoff, J., and Rietveld, T. (**1994**). ''Prosody in NIROS with FONPARS

and ALFEIOS,'' *Proceedings Department of Language and Speech*, University of Nijmegen, Vol. 18, pp. 106–119.
Kollmeier, B. (**1990**). ''Meßmethodik, Modellierung und Verbesserung der Verständlichkeit von Sprache,'' Habilitationsschrift, Universität Göttingen.
Kollmeier, B., and Wesselkamp, M. (**1997**). ''Development and evaluation of a German sentence test for objective and subjective speech intelligibility assessment,'' J. Acoust. Soc. Am. **102**, 2412–2421.
Kramer, S. E., Kapteyn, T. S., and Festen, J. M. (**1998**). ''The self-reported handicapping effect of hearing disabilities,'' Audiology **37**, 302–312.
Luce, P. A., and Pisoni, D. B. (**1998**). ''Recognizing spoken words: The neighborhood activation model,'' Ear Hear. **19**, 1–36.
Middelweerd, M. J., Festen, J. M., and Plomp, R. (**1990**). ''Difficulties with speech intelligibility in noise in spite of a normal pure-tone audiogram,'' Audiology **29**, 1–7.
Mullennix, J. W., Pisoni, D. B., and Martin, C. S. (**1989**). ''Some effects of talker variability on spoken word recognition,'' J. Acoust. Soc. Am. **85**, 365–378.
Nilsson, M., Soli, S. D., and Sullivan, J. A. (**1994**). ''Development of the Hearing In Noise Test for the measurement of speech reception thresholds in quite and in noise,'' J. Acoust. Soc. Am. **95**, 1085–1099.
Plomp, R., and Mimpen, A. M. (**1979**). ''Improving the reliability of testing the speech reception threshold for sentences,'' Audiology **18**, 43–52.
Smoorenburg, G. F. (**1992**). ''Speech reception in quiet and in noisy conditions by individuals with noise-induced hearing loss in relation to their tone audiogram,'' J. Acoust. Soc. Am. **91**, 421–437.
Sommers, M. S., Nygaard, L. C., and Pisoni, D. B. (**1994**). ''Stimulus variability and spoken word recognition. I. Effects of variability in speaking rate and overall amplitude,'' J. Acoust. Soc. Am. **96**, 1314–1324.
Sommers, M. S., Kirk, K. I., and Pisoni, D. B. (**1997**). ''Some considerations in evaluating spoken word recognition by normal-hearing, noise-masked normal-hearing, and cochlear implant listeners. I. The effect of response format,'' Ear Hear. **18**, 89–99.
van Rooij, J. C. G. M., and Plomp, R. (**1991**). ''The effects of linguistic entropy on speech perception in noise in young and elderly listeners,'' J. Acoust. Soc. Am. **90**, 2985–2991.
Wagenaar, W. A. (**1969**). ''Note on the construction of Digram-Balanced Latin Squares,'' Psychol. Bull. **72**, 384–386.

Measuring the threshold for speech reception by adaptive variation of the signal bandwidth. II. Hearing-impaired listeners[a)]

Ingrid M. Noordhoek,[b)] Tammo Houtgast, and Joost M. Festen
Department of Otolaryngology, University Hospital VU, P.O. Box 7057, 1007 MB Amsterdam, The Netherlands

(Received 18 January 1999; revised 5 July 1999; accepted 8 December 1999)

In a previous study [Noordhoek *et al.*, J. Acoust. Soc. Am. **105**, 2895–2902 (1999)], an adaptive test was developed to determine the speech-reception *bandwidth* threshold (SR*B*T), i.e., the width of a speech band around 1 kHz required for a 50% intelligibility score. In this test, the band-filtered speech is presented in complementary bandstop-filtered noise. In the present study, the performance of 34 hearing-impaired listeners was measured on this SR*B*T test and on more common SRT (speech-reception threshold) tests, namely the SRT in quiet, the standard SRT in noise (standard speech spectrum), and the spectrally adapted SRT in noise (fitted to the individual's dynamic range). The aim was to investigate to what extent the performance on these tests could be explained simply from audibility, as estimated with the SII (speech intelligibility index) model, or require the assumption of suprathreshold deficits. For most listeners, an elevated SRT in quiet or an elevated standard SRT in noise could be explained on the basis of audibility. For the spectrally adapted SRT in noise, and especially for the SR*B*T, the data of most listeners could not be explained from audibility, suggesting that the effects of suprathreshold deficits may be present. Possibly, such a deficit is an increased downward spread of masking. [S0001-4966(00)03203-3]

PACS numbers: 43.71.Ky, 43.71.Gv [DOS]

INTRODUCTION

A common complaint of listeners suffering from sensorineural hearing impairment is that they experience great difficulty in understanding speech in ambient noise. According to some studies, this difficulty is only caused by the fact that part of the speech spectrum is below the absolute threshold (Zurck and Delhorne, 1987; Lee and Humes, 1993). Other studies suggest that suprathreshold deficits (i.e., deficits that show up in a suprathreshold stimulus condition) are also involved (Glasberg and Moore, 1989; Dreschler and Plomp, 1985). In a review, Moore (1996) concluded that, for hearing losses up to about 45 dB, inaudibility of part of the speech spectrum is the dominant source of the difficulty in understanding speech, whereas for greater losses suprathreshold deficits start to play a role.

Aspects of sound perception that may be affected are spectral resolution, temporal resolution, frequency discrimination, and loudness perception. It has proved difficult to relate the reduced ability to understand speech in noise to specific suprathreshold deficits (Moore, 1996). A reason for this may be that correlations between the ability to understand *broadband* speech and auditory functions at a specific frequency were studied. The investigation of the factors underlying a speech-processing deficit may be simplified by restricting the research to a limited frequency region. To find clear correlations with auditory functions at a specific frequency, considering intelligibility for *narrow-band* speech seems more relevant.

For that purpose, the SR*B*T test has been developed (Noordhoek *et al.*, 1999). In this test, the bandwidth of speech around 1 kHz required for a 50% intelligibility score is determined (speech-reception *bandwidth* threshold or SR*B*T). The narrow-band speech is presented in complementary bandstop-filtered noise to ensure that the speech is only audible within the desired frequency band. A procedure comparable to the SRT test in noise (Plomp and Mimpen, 1979) is followed with the difference that the bandwidth of the speech signal, not the signal-to-noise ratio, is changed adaptively.

The SR*B*T of normal-hearing listeners is 1.4 octave under optimal conditions, i.e., when the entire speech dynamic range is above the hearing threshold, but not so loud that audibility is affected by excessive upward spread of masking. Provided that the full dynamic range of speech is above threshold, it is plausible to assume that a broader-than-normal SR*B*T points to a deterioration in sound processing in the 1-kHz frequency region. The SR*B*T test is meant as a research tool to select hearing-impaired listeners suffering from a deficit in speech processing in the 1-kHz frequency region, and may be incorporated in correlation studies of auditory functions at 1 kHz and speech perception.

Although the stimulus in the SR*B*T experiment is an artificial signal, it is not remote from everyday listening situ-

[a)]Part of the SR*B*T data was presented at the 16th International Congress on Acoustics and the 135th Meeting of the Acoustical Society of America [Proceedings of ICA/ASA '98, Seattle, WA, 2613–1614 (1998)] and at the Summerschool and Symposium '98, Bad Zwischenahn, Germany [*Psychophysics, Physiology and Models of Hearing* (1999), World Scientific Publishing, Singapore].

[b)]Current address: TNO Institute of Applied Physics, P.O. Box 155, 2600 AD Delft, The Netherlands. Electronic mail: ingridn@dds.nl

ations. In practice, it often occurs that part of the speech spectrum is masked by ambient noise with a different spectral content, like the sound from traffic, domestic equipment, or music. However, it should be clear that the SR*B*T is *not* designed as a measure for the speech communication ability of hearing-impaired listeners in real life. The human voice is probably the most common source of ambient noise. Therefore, the SRT test for broadband speech in noise, in which the noise spectrum is shaped according to the long-term average speech spectrum, is a more appropriate measure for everyday speech perception.

An alternative measure for a listener's ability to understand *narrow-band* speech is the SRT for bandpass-filtered speech in noise. However, when noise is added to the speech passband, the bandwidth of the speech must be much broader than the SR*B*T in order to allow the listeners to reach a 50% intelligibility score. For a broader speech band around 1 kHz, the correlation between intelligibility and auditory functions at 1 kHz is less obvious. Therefore, the SR*B*T test is preferred to the SRT test for bandpass-filtered speech in noise, when the experimental goal is to find correlations between a listener's ability to understand narrow-band speech and performance on psychoacoustic tests at 1 kHz.

In the present study, 34 hearing-impaired listeners and 10 normal-hearing listeners performed the new SR*B*T test and more common SRT tests. First, the SRT in quiet was measured. Next, the SRT in steady-state speech-shaped noise was measured with the noise fixed at 20 dB above each listener's SRT in quiet. Since even at these levels, it is possible that part of the speech spectrum falls below the hearing threshold, the SRT in noise was also measured with the speech and noise spectra shaped to fit the midline of the dynamic range of each individual listener. Last, the SR*B*T was determined using the same spectral shaping.

The first aim of this paper is to examine to what extent the SR*B*T of the hearing-impaired listeners differs from the SR*B*T of normal-hearing listeners. This is important, because the SR*B*T test is intended to discriminate between listeners with normal and reduced speech processing in the 1-kHz frequency region. The second aim is to investigate whether an elevated SRT or broader-than-normal SR*B*T can be explained simply within the audibility concept (losing part of the full dynamic range of the speech), or require the assumption of suprathreshold deficits. This is of significance for the audiology practice, because when the speech-understanding problem of a hearing-impaired listener is caused by a suprathreshold deficit, intelligibility cannot be restored completely by amplification of the speech signal with a hearing aid.

In this study, audibility is defined as the effective proportion of the speech dynamic range contributing to intelligibility as calculated with the speech intelligibility index, or SII (ANSI, 1997). The SII replaces the older articulation index (ANSI, 1969), and is calculated from the speech and noise spectra, and the hearing threshold. The SII model includes procedures for computing the effect on audibility of self-masking of speech, upward spread of masking, and level distortion (i.e., the decrease of speech intelligibility at high presentation levels), *for normal-hearing listeners*.

A speech-processing deficit is defined as a suprathreshold effect, not included in the SII model, that reduces intelligibility. For example, speech intelligibility can be reduced by spectral spread of masking. If the spread of masking experienced by a hearing-impaired listener in a speech intelligibility test is the same as that experienced by a normal-hearing listener at the same absolute level, this is considered an audibility effect. If the hearing-impaired listener experiences excessive spread of masking, the extent to which the spread of masking exceeds the normal spread of masking is regarded to be a speech-processing deficit.

Thus, if the performance of a hearing-impaired listener on speech intelligibility tests is consistent with the SII model, it is assumed that this listener does not suffer from a suprathreshold speech-processing deficit, and that a possible abnormal SRT or SR*B*T is due only to inaudibility of a part of the speech spectrum. If, on the other hand, performance is worse than predicted by the SII model, it is assumed that this is caused by a speech-processing deficit.

I. METHOD

A. Materials and design

The speech material consisted of eight lists of 13 meaningful everyday Dutch sentences (eight or nine syllables), uttered by a male speaker (Smoorenburg, 1992). For masking, a Gaussian noise was used, shaped according to the long-term average spectrum of the sentences. Both the speech and the noise were digitized at a sampling frequency of 15 625 Hz with 16-bit resolution.

Signals were generated by a personal computer using TDT (Tucker-Davis Technologies) System II hardware. Speech and noise were upsampled by a factor of 2, and were each delivered through a 16-bit D/A converter (TDT DD1) at a 31 250-Hz sampling frequency and low-pass filtered at 16 kHz (TDT FT5). Next, speech and noise were attenuated separately (TDT PA4), and subsequently summed (TDT SM3). The total signal was sent through a programmable filter (TDT PF1), used for frequency shaping. If necessary, the signal was passed through an amplifier.

In this study, our main interest is to compare the results of individual hearing-impaired listeners to the results of the normal-hearing listeners. Therefore, differences among listeners due to order and lists effects were avoided by presenting the lists of sentences and the intelligibility tests in a fixed order. With the eight lists of sentences, two similar blocks (test–retest) of four intelligibility tests were performed. A block consisted of three SRT tests, followed by one SR*B*T test.

The first SRT test was performed in quiet (SRTq), with the original spectrum (i.e., with the programmable filter in bypass mode). The second SRT test was performed in noise (SRTn), with the unmodified spectra for speech and noise. The level of the masking noise was 20 dB above the measured SRTq of each listener. The third SRT test was also performed in noise, with the difference that the speech and noise signals were adapted to the dynamic range of individual listeners (SRTa). The noise spectrum was shaped to fit halfway between hearing threshold and broadband uncom-

TABLE I. Mean pure-tone air-conduction thresholds at octave frequencies in the ear under test of the 34 hearing-impaired listeners. Also given are the standard deviation and the range of thresholds at each frequency.

Threshold (dB HL)	Frequency (Hz)					
	250	500	1000	2000	4000	8000
Mean	29	35	43	49	65	82
s.d.	19	20	17	16	17	22
Minimum	0	−5	0	5	15	15
Maximum	75	75	70	75	100	120

fortable loudness level (see Sec. I C) for frequencies between 250 and 4000 Hz. The shape of the speech spectrum was equal to the shape of the noise spectrum. The signal-to-noise ratio in the adaptive procedure was varied by adjusting the level of the speech. To obtain the desired spectra, the speech and noise signals were filtered, using a finite impulse response (FIR) filter with 160 coefficients, implemented on the TDT PF1-hardware. Below 250 Hz and above 4000 Hz, the frequency response of the filter was flat.

In the SR*B*T procedure, the bandwidth of the speech signal was varied. The speech was bandpass filtered on line with a fixed-center frequency of 1 kHz, using software filters with 256 coefficients. Complementary bandstop noise was added to the speech signal. The noise was filtered off-line, using software filters with 1024 coefficients. Both the (bandpass-filtered) speech and (bandstop-filtered) noise spectra were shaped to fit halfway the dynamic range of the individual listener, using the same FIR filter, implemented on the TDT PF1-hardware as in the preceding SRTa test.

B. Listeners

Thirty-four hearing-impaired persons were selected from the files of the University Hospital VU and served as subjects. Their age ranged from 35 to 88 years, with a mean of 64 years. Their native language was Dutch. Only listeners who could reach an intelligibility score for monosyllabic words in quiet of at least 75% were selected. Four listeners had a mixed hearing loss and 30 listeners suffered from sensorineural hearing loss in both ears. Mean, standard deviation, and range of pure-tone air-conduction thresholds at the ear under test are given in Table I. For each listener, the threshold was at least 40 dB HL at one or more frequencies. Ten normal-hearing listeners, ranging in age from 18 to 33 years, participated in the experiment as a reference group.

C. Procedure

Listeners were seated in a soundproof room. The stimuli were presented monaurally through headphones (Sony MDR-CD999). Generally, the ear with the lowest word intelligibility score in quiet was tested. Only if the risk of overhearing existed or if the listener could not reach a 75% intelligibility score in quiet with this ear, the other ear was tested.

The experiment consisted of two parts. In the first part of the experiment, the dynamic range was determined for each listener by measuring hearing threshold and uncomfortable loudness level (UCL). In the second part of the experiment, the ability of the listener to understand speech was measured with SRT tests in quiet and in noise, and with the SR*B*T test.

1. Dynamic range

Hearing threshold and UCL were measured with 1/3-octave bands of noise at five center frequencies: 250, 500, 1000, 2000, and 4000 Hz. Levels for intermediate 1/3-octave bands were calculated by interpolation. The maximum presentation level was 80 dB SPL in the determination of the hearing threshold and 134 dB SPL in the UCL measurement. If the hearing threshold was higher than 80 dB SPL or the UCL was higher than 134 dB SPL, the levels of 80 or 134 dB SPL were used in the calculation of the midline of the dynamic range.

For the determination of the hearing threshold, a Békésy tracking procedure was used with a step size of 1 dB. The listener was asked to push a button as long as he or she could hear a pulsating noise burst (duration: 300 ms; repetition frequency: 2.4 Hz). As long as the button was pushed, the level of the noise bursts decreased. When the button was released, the level started to increase. The threshold measurement was finished after 11 reversals. The threshold was defined as the average of all but the first reversal levels.

Uncomfortable loudness levels were determined in two steps. First, the UCL of the five 1/3-octave bands of noise was measured individually. Next, the UCL was measured with a broadband noise burst. For determination of the 1/3-octave band UCL, the listener had to push a button as soon as a pulsating noise burst with increasing level (length: 300 ms; repetition frequency: 1.7 Hz) was experienced as uncomfortably loud. The level of the noise burst increased in steps of 3 dB. When the listener pushed the button, the level of the noise burst decreased by a random amount between 21 and 31 dB. The measurement was finished after six responses. The UCL of each band was computed by averaging across the levels at which the button was pushed.

The broadband noise burst had a duration of 4 s and was spectrally shaped according to the narrow-band UCLs. To determine the UCL of the broadband noise burst, the noise burst was generated at gradually increasing levels. After each presentation the listener was asked whether the signal was experienced as uncomfortably loud. If so, this level was considered as the broadband UCL and the corresponding level in each of the five 1/3-octave bands was taken as the new UCL of that band. The broadband UCL was measured, because in the second part of the experiment a broadband masking noise was used, and since the relationship between narrow-band and broadband UCLs varies across listeners (Walker *et al.*, 1984).

2. Speech intelligibility

In the SRT tests, the level of the sentences was changed according to an adaptive procedure (Plomp and Mimpen, 1979). The first sentence of a list was repeated, each time at a 4-dB higher level, until the listener could correctly reproduce the sentence. The subsequent 12 sentences were presented only once, using an up–down procedure with a step size of 2 dB.

The SRTq was defined as the average A-weighted sound-pressure level of sentences 5 to 14. Sentence 14 was not actually presented, but its ''would-be'' level was included in the calculation of the SRT, to use the information provided by the response to sentence 13. The SRTn and SRTa were defined as the average signal-to-noise ratio (in dB) for sentences 5 to 14.

In the SR*B*T test, the first sentence in a list was presented at a 600-Hz bandwidth, much narrower than the bandwidth required for a 50% intelligibility score. This sentence was repeated each time with the bandwidth multiplied by $(1.37)^2$ (a double step), until the listener correctly reproduced the sentence. The other sentences in the list were presented only once. When a sentence was repeated correctly, the bandwidth (in Hz) for the next sentence was divided by 1.37. When the repeated sentence was incorrect, the bandwidth (in Hz) for the next sentence was multiplied by 1.37. This implies that the step size in the SR*B*T procedure was constant on a logarithmic frequency axis. The SR*B*T was defined as the geometric mean of the bandwidth of sentences 5 to 14.

Prior to the speech intelligibility experiment, two lists of 13 sentences were presented, to familiarize the listeners with the procedure. With these lists, an SRTq test and an SRTn test were performed.

II. SII CALCULATIONS

As a consequence of our effort to keep the full dynamic range of the speech audible, presentation levels were different for each listener. This, in turn, may cause differences in audibility, for example because at a higher level the bandstop noise in the SR*B*T experiment produces more spectral spread of masking. The effect of level on audibility is evaluated with the speech intelligibility index (SII).

The SII for a given condition is calculated from the speech and noise spectra, and the hearing threshold (ANSI, 1997). The SII is defined by

$$\mathrm{SII}=\sum_{i=1}^{n} I_i A_i, \tag{1}$$

where n is the number of frequency bands used in the calculations. The band-importance function I_i reflects the importance of frequency band i for speech intelligibility. The band-audibility function A_i is the effective proportion of the dynamic range of speech within band i that contributes to intelligibility. In quiet, a speech sample in band i contributes to intelligibility, when its level is higher than the level of an imaginary internal noise in the ear of the listener. This internal noise is calculated so that, if it were an external noise, it would lead to the pure-tone threshold of the listener. In noise, a speech sample in band i contributes to intelligibility when its level is higher than the level of the masking noise and the imaginary noise. Furthermore, the band-audibility function A_i includes the effects on audibility of self-masking in speech, upward spread of masking, and level distortion (i.e., the decrease of speech intelligibility at high presentation levels).

In the present study, the SII was calculated following the 1/3-octave band procedure of ANSI (1997), using the band-importance function for speech material of average redundancy (Pavlovic, 1987). One modification to the standard SII model was introduced. In the standard SII model, the slope for the upward spread of masking in dB/octave (C_i) due to frequency band i is given by

$$C_i=-80+0.6\cdot BL_i, \tag{2}$$

where BL_i is the level of the masker (in dB SPL) in frequency band i. In our modified SII model, shallower slopes of the masking curves were used for frequencies below 500 Hz, because previous calculations have shown that the standard SII model underestimates the upward spread of masking produced by the low-frequency noise in the SR*B*T experiment (Noordhoek *et al.*, 1999). For 1/3-octave bands with masker frequencies below 500 Hz (i.e., $i<6$), the slope of the masking curve was calculated according to[1]

$$C_i=[1-0.08\cdot(6-i)]\cdot[-80+0.6\cdot BL_i]. \tag{3}$$

The level of speech and noise was measured in 1/3-octave bands with the headphone on a Brüel & Kjær type 4152 artificial ear with a flat-plate coupler. For the SII procedure, these levels were transformed to equivalent free-field levels, using the ''artificial-ear-to-free-field transfer function'' as derived in Noordhoek *et al.* (1999). Next, the free-field levels of speech and noise were converted to spectrum levels, as is required by the SII procedure.

The spectrum level of the imaginary internal noise is

$$X=Q-R, \tag{4}$$

where Q is the observed pure-tone threshold, measured with a psychoacoustical procedure compatible with those used for obtaining the ISO (1961) threshold, and R is the critical ratio in dB (Pavlovic, 1987). The 1/3-octave band-noise threshold is virtually identical to the pure-tone threshold (Berger, 1981; Cox and McDaniel, 1986). Therefore, the spectrum level of the internal noise was calculated as the observed 1/3-octave band-noise threshold (transformed to free-field level) minus the critical ratio in dB.

All measured SRT and SR*B*T values were subjected to SII calculations. The SII for listeners with a sensorineural hearing loss was calculated in the same way as that for normal-hearing listeners. For listeners with a mixed hearing loss, the conductive part of the hearing loss was subtracted from the level of speech, external noise, and internal noise. This means that the conductive part of the hearing loss is considered an attenuation in the transmission system, as suggested by Fletcher (1952).

III. RESULTS

A. Dynamic range

For the normal-hearing listeners, the difference between hearing threshold and narrow-band UCL was on average 98 dB [standard deviation (s.d.) 11 dB]. The individual narrow-band UCLs of the normal-hearing listeners had to be attenuated by 15 dB (s.d. 9 dB) on average to obtain the broadband UCL.

The narrow-band dynamic range of the hearing-impaired listeners ranged from about 30 to 100 dB at each frequency. On average, their narrow-band dynamic range decreased from 70 dB at 250 Hz, to 50 dB at 4 kHz. The attenuation of the narrow-band UCLs needed to obtain the broadband UCL ranged from 10 to 40 dB, with a mean of 25 dB.

B. Speech intelligibility

For the normal-hearing listeners, the average SRTq was 24.0 dBA (s.d. 1.3 dBA). For the hearing-impaired listeners, the SRTq ranged from 23.5 to 84.5 dBA, with a mean of 58.8 dBA. The mean standard error (test–retest) of an individual SRTq was 2.2 dBA.

The level of the masking noise in the subsequent SRTn test was 20 dB above the individually measured SRTq. For one hearing-impaired listener, the resulting level of the masking noise was above the uncomfortable loudness level. For this listener, the level of the masking noise was set at 5 dB above the SRTq.

For the normal-hearing listeners, the average SRTn was −3.6 dB (s.d. 1.1 dB). For the hearing-impaired listeners, the SRTn ranged from −3.4 to +5.8 dB, with a mean of +0.8 dB. The average SRTa was −4.5 dB (s.d. 1.0 dB) for the normal-hearing listeners. For the hearing-impaired listeners, the SRTa ranged from −5.0 to +5.8 dB, with a mean of −1.0 dB. The mean standard error (test–retest) of an individual SRTn and SRTa was 0.96 and 0.85 dB, respectively.

The average SR*B*T of the normal-hearing listeners was 1.44 octave (s.d. 0.13 octave). The SR*B*T of the hearing-impaired listeners ranged from 1.29 to 4.02 octave, with a mean of 2.14 octave. The standard error (test–retest) of an individual SR*B*T was 0.18 octave.

IV. DISCUSSION

A. Relationship between narrow-band and broadband UCLs

In our study, the average narrow-band UCLs (transformed to free-field levels) of the normal-hearing listeners approximately follow the equal loudness contour pattern (see also Walker *et al.*, 1984). The loudness summation formula of Stevens (1956) predicts that the narrow-band UCLs must be attenuated by 14 dB to obtain the broadband UCL. This agrees well with the average attenuation of 15 dB found for the normal-hearing listeners in our study.

Loudness summation is often reduced in hearing-impaired listeners (Moore, 1995). Therefore, an attenuation less than 14 dB would be expected for the broadband UCL of hearing-impaired listeners. However, the average attenuation for the hearing-impaired listeners was significantly higher than for the normal-hearing listeners ($p<0.05$). Therefore, it seems that the broadband UCL can be predicted from the narrow-band UCL on the basis of loudness summation for the average normal-hearing listener, but not for the average hearing-impaired listener. For both groups of listeners, the relationship between narrow-band and broadband UCLs was highly variable, consistent with the findings of Walker *et al.* (1984).

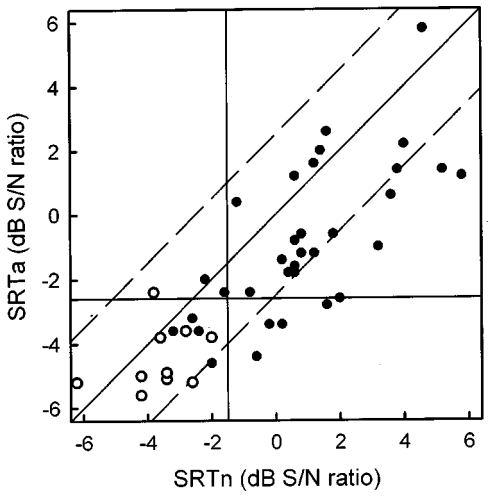

FIG. 1. Speech-reception threshold in noise for speech with an adapted spectrum (SRTa) versus the standard speech-reception threshold in noise (SRTn) for normal-hearing listeners (open circles) and hearing-impaired listeners (filled circles). Solid horizontal and vertical lines represent the one-tailed 95% confidence limit for the data of the normal-hearing listeners. For data points between the dashed lines, SRTa and SRTn are not significantly different ($p<0.05$).

B. SRTa versus SRTn

Figure 1 shows the SRT in noise for speech with an adapted spectrum (SRTa) (i.e., a spectrum halfway the dynamic range) as a function of the SRT in noise for speech with the original spectrum (SRTn) for 10 normal-hearing listeners and 34 hearing-impaired listeners. The upper limit of the one-tailed 95% confidence interval of the SRT of normal-hearing listeners is chosen as the boundary between normal and elevated SRT. The separation between normal and elevated SRTn is indicated with a vertical line at −1.5 dB [i.e., $-3.6\,\mathrm{dB}+t_{0.05}(9)\times 1.1\,\mathrm{dB}$]. Using this criterion, 7 hearing-impaired listeners had a normal SRTn, whereas 27 hearing-impaired listeners had an elevated SRTn. The boundary between a normal and an elevated SRTa lies at −2.6 dB. The SRTa was elevated for 24 of the 34 hearing-impaired listeners.

The solid diagonal line in Fig. 1 shows where SRTn is equal to SRTa. A two-tailed *t* test, using the mean standard error (test–retest) of individual SRT values, showed that for an individual listener the difference between SRTa and SRTn is significant if it exceeds 2.5 dB ($p<0.05$). Thus, for the data points that lie between the dashed lines, the SRTa does not differ significantly from the SRTn. For ten hearing-impaired listeners the SRTa was significantly lower than the SRTn. In other words, for these listeners, speech intelligibility in noise improved when the stimuli were shaped to fit in their dynamic range.

Five listeners with an elevated SRTn had a normal SRTa (see Fig. 1). These listeners probably performed worse than normal-hearing listeners on the SRTn test only because part of the relevant dynamic range of the speech was presented below the hearing threshold. However, for 22 of the hearing-impaired listeners, adapting the spectrum did not bring the SRT in noise back to normal. A possible explanation is that these listeners suffered from excessive spread of masking due to higher presentation levels. Another possibility is that,

TABLE II. Average speech intelligibility index with standard deviation in parentheses for the normal-hearing listeners (NH) and the hearing-impaired listeners (HI), for four intelligibility tests. The SII was calculated according to different procedures. Modifications with respect to the standard SII procedure (ANSI, 1997) are given in the second column. ''Slopes.'' Shallower slopes of the masking curves are used below 500 Hz (see Sec. II). ''Noise.'' The internal noise level is lowered by 3.6 dB (see Sec. IV C). ''Desensitization.'' The speech desensitization factor (Pavlovic *et al.*, 1986) is included in the model (see Sec. IV D). Results for the hearing-impaired listeners that differ significantly ($p<0.05$) from the corresponding result for the normal-hearing listeners are indicated with an asterisk.

Modifications SII		SRTq	SRTn	SRTa	SR*B*T
NH	slopes	0.22(0.07)	0.31(0.04)	0.31(0.03)	0.31(0.03)
HI	slopes	0.26(0.11)	0.31(0.05)	0.36*(0.05)	0.40*(0.10)
NH	slopes, noise	0.31(0.08)	0.32(0.04)	0.31(0.03)	0.31(0.03)
HI	slopes, noise	0.30(0.12)	0.32(0.05)	0.37*(0.05)	0.41*(0.09)
HI	slopes, noise, desensitization	0.24*(0.08)	0.24*(0.05)	0.26*(0.05)	0.30(0.06)

although many efforts were made, parts of the speech spectrum were still below absolute threshold. These possibilities were investigated with the SII model.

C. Results in relation to the SII

The speech intelligibility index is a physical measure designed to be a good predictor for speech intelligibility. It may be interpreted as the proportion of the total speech information available to the listener. For normal-hearing listeners, all conditions of equal intelligibility should result in the same SII. Thus, when the measured SRT and SR*B*T are expressed in SII values, and the SII model is consistent with the results of the normal-hearing listeners in this study, the model will yield identical SII values for the various tests. Then, an elevated SII at 50% intelligibility for a hearing-impaired listener can be considered an indication of deteriorated suprathreshold speech processing, because a listener with a higher-than-normal SII needs more speech information than normal-hearing listeners to reach the 50% intelligibility score.

1. Average SII

The upper two rows of Table II show the average SII values (and standard deviation) for the normal-hearing listeners (NH) and the hearing-impaired listeners (HI). For the normal-hearing listeners, the average SII for the SRTq is 0.22, and the average SII values for the SRTn, SRTa, and SR*B*T are equal: 0.31. Paired *t* tests show that the SII for the SRTq is significantly lower than the SII for the other conditions (Bonferroni test, $p<0.05$; Keren and Lewis, 1993).

Theoretically, a possible cause for the lower SII for the SRTq is an order or list effect, because the sentence lists and conditions were presented in a fixed order. However, for each speech-intelligibility test, the first measurement did not differ significantly from the second measurement (*t* tests for matched samples, $p<0.05$). This suggests that no significant order effect is present. Versfeld *et al.* (submitted) did not find large list effects in the speech material of Smoorenburg (1992) used in this study: the standard deviation between lists was 0.6 dB. Therefore, it seems unlikely that the observed difference in SII in our study is a result of an order or list effect.

In quiet, the SII is very sensitive to the level of the imaginary internal noise, calculated from the hearing threshold [Eq. (4)]. Most likely the SII for the SRTq is too low, because the procedure for the determination of the hearing threshold in the present study using Békésy tracking resulted in thresholds that were systematically a few dB higher than would have been measured using the method of constant stimuli or the method of limits, on which the ISO (1961) threshold is based. The SII for the SRTq becomes equal to the SII in the other conditions when the SII is recalculated with the internal noise level lowered by 3.6 dB.

Rows 3 and 4 of Table II present the SII values calculated with the adapted internal noise level. Note that the adaptation of the internal noise level hardly influences the SII values for conditions other than the SRTq. For the hearing-impaired listeners, the average SII for the SRTq and SRTn is similar to the SII for normal-hearing listeners, but for the SRTa and SR*B*T, the average SII is significantly higher (*t* test for unequal variances, $p<0.05$). Thus, for the average hearing-impaired listener, the SII corresponding to the SRTq and to the SRTn appears to be ''normal'' (i.e., equal to the SII of the normal-hearing listeners), suggesting the absence of the effect of suprathreshold deficits. This is consistent with the idea, mentioned in the Introduction, that the difficulty with understanding speech in background noise is only caused by part of the speech spectrum being below absolute threshold (Zurek and Delhorne, 1987; Lee and Humes, 1993). However, the mean SII for the SRTa and SR*B*T is higher. Therefore, in these conditions the effects of suprathreshold deficits *do* seem to influence speech intelligibility. This agrees with the notion that suprathreshold deficits may affect intelligibility (Glasberg and Moore, 1989; Dreschler and Plomp, 1985).

For the hearing-impaired listeners, the mean SII for the SRTa is *higher* than for the SRTn, although their mean SRTa (-1.0 dB) was 1.8 dB *lower* than their mean SRTn ($+0.8$ dB). This means that by adapting the spectrum, the SRT in noise did not decrease as much as predicted from audibility. The SII model would predict an equal SII for SRTn and SRTa. Thus, the SRTa can be predicted for each listener from the SII for the measured SRTn. On average, the predicted SRTa for the hearing-impaired listeners is -2.9 dB. Hence, when adapting the spectra the SII model predicts a

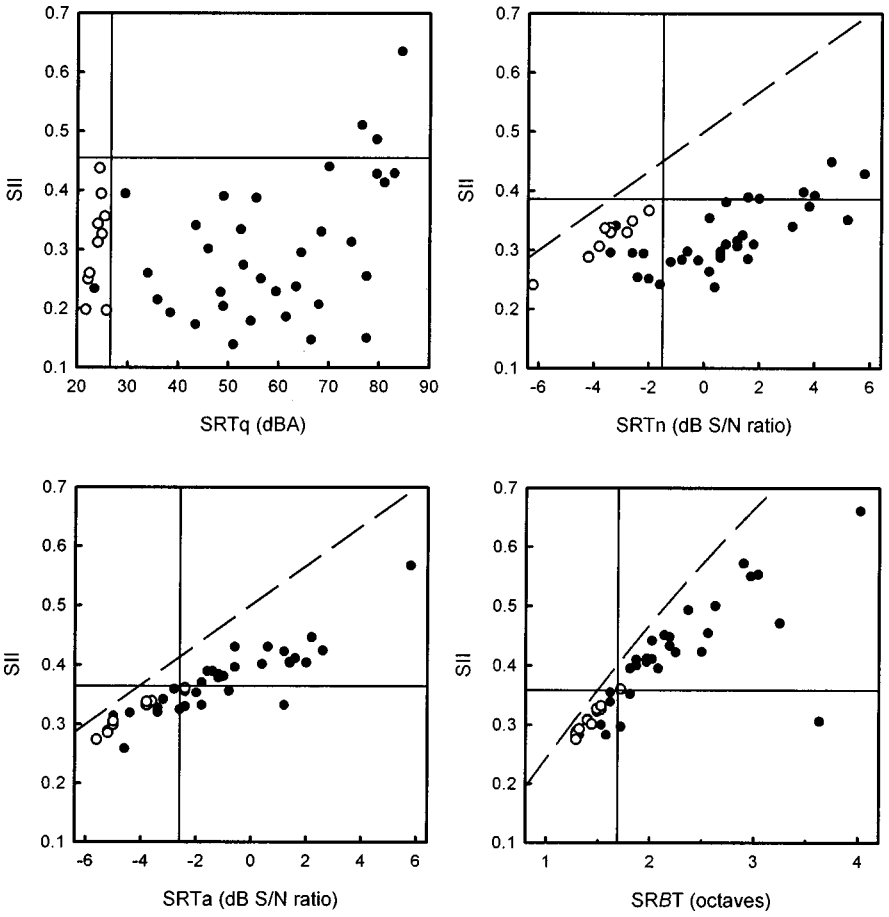

FIG. 2. Speech intelligibility index versus the thresholds on the four intelligibility tests (SRTq, SRTn, SRTa, SR*B*T) for normal-hearing listeners (open circles) and hearing-impaired listeners (filled circles). Solid lines represent the one-tailed 95% confidence limit for the data of the normal-hearing listeners. Dashed lines represent the maximum possible SII as a function of SRT or SR*B*T, i.e., the SII that would have been calculated if the audibility of the speech had not been influenced by the hearing threshold, upward spread of masking, and level distortion.

decrease in the mean SRT in noise of 3.7 dB, instead of the observed 1.8 dB.

The mean SII for the SR*B*T is significantly higher than for the SRTa ($p<0.05$) for the hearing-impaired listeners. Thus, for the average hearing-impaired listener in the present study, the effect of suprathreshold deficits is most obvious for the SR*B*T condition (narrow-band speech in bandstop noise), and to a lesser extent also for SRTa (spectrally adapted broadband speech in broadband noise), but entirely absent for the standard conditions SRTn and SRTq.

One possibility that may explain why the SII varies across condition is that the suprathreshold deficit is frequency dependent. For example, in the frequency regions where the hearing loss is greater, the suprathreshold deficit may be larger [Pavlovic *et al.* (1986)]. Different frequency regions are involved in the different conditions. In the standard conditions, the listeners must use the frequency region where the original speech spectrum is above their hearing threshold. In the SRTa condition, the entire frequency range from 250 to 4000 Hz should contribute. The suprathreshold deficit may be present in the frequency region that is below threshold in the standard conditions, but above threshold in the SRTa condition. This may explain the elevated SII for the SRTa. However, it seems improbable that a frequency-dependent deficit can explain the elevated SII for the SR*B*T, because the frequency range around 1 kHz that is important in the SR*B*T test is also important in the other tests.

Another possible cause for the dependence of the effect of suprathreshold deficits on condition can be found in the different spectra of speech and noise among conditions. For instance, when a hearing-impaired listener experiences excessive upward or downward spread of masking, the degree to which this influences speech intelligibility in a specific condition will depend on the specific spectra of speech and noise.

2. Individual SII

Table II shows that the interindividual spread in SII for the hearing-impaired listeners is substantially larger than the spread in SII for normal-hearing listeners. Therefore, the SII of individual listeners (after the correction of −3.6 dB of the internal noise levels) is considered. In Fig. 2, the SII is plotted as a function of SRT or SR*B*T obtained for the individual normal-hearing listeners (open circles) and hearing-impaired listeners (filled circles). The upper limit of the one-tailed 95% confidence interval of the SII of normal-hearing listeners is chosen as the separation between normal and higher-than-normal SII (horizontal lines). The separation between normal and abnormal SRT or SR*B*T is indicated with a vertical line. The dashed lines in Fig. 2 represent the hypothetically maximum SII given the SRTn, SRTa, and SR*B*T, i.e., the SII that would have been calculated if the audibility of the speech had not been influenced by the known effects of hearing threshold, upward spread of masking, and level distortion. To calculate this hypothetically maximum SII, the full 30-dB dynamic range of the speech was assumed to be audible for all frequency bands in which the speech was not

masked by noise in the same frequency band. Thus, the vertical distance from each data point to the dashed line represents the combined influence of hearing threshold, upward spread of masking, and level distortion.

The horizontal and vertical lines divide the graphs of Fig. 2 in four quadrants. No data points fall in the upper-left quadrant. Data points in the lower-left quadrant correspond to a normal threshold. Data points in the lower-right quadrant correspond to an elevated SRT or a broader-than-normal SR*B*T, but this abnormal threshold can be explained on basis of audibility by the SII model. Finally, data points in the upper-right quadrant correspond to an abnormal threshold that cannot be explained by the SII model. The higher a data point lies above the horizontal line, the larger the speech processing deficit.

a. SRTq. Figure 2 shows that for all but three hearing-impaired listeners the SII for the SRTq is not higher than normal. The most important factor affecting the audibility of the speech in quiet is the hearing threshold. The effect of level distortion is negligible. Indeed, stepwise multiple regression shows that the SRTq (in dBA) can be predicted quite accurately ($R^2=0.92$) from the hearing threshold

$$\mathrm{SRTq}=22.2+0.60\cdot \mathrm{HL}_{0.5}+0.32\cdot \mathrm{HL}_2, \tag{5}$$

where $\mathrm{HL}_{0.5}$ and HL_2 are the hearing threshold in dB HL at 0.5 and 2 kHz, respectively.

b. SRTn. The results on the SRTn test also yield a rather constant SII. Only six of the listeners performed (slightly) worse than predicted on the basis of audibility. The hearing threshold is the most important factor that causes the difference between the individual SII and the dashed line. The SII calculations show that a part of the speech signal (the high frequencies) is still below the hearing threshold, even for the normal-hearing listeners. Audibility of the speech is also affected by upward spread of masking.

c. SRTa. In contrast to most of the elevated thresholds in noise for the *original* spectrum (SRTn), most of the elevated thresholds for an *adapted* spectrum (SRTa) cannot be explained by the SII model. For the normal-hearing listeners, the difference between the obtained SII and maximal possible SII (dashed line) for the SRTa is only caused by upward spread of masking. Upward spread of masking, some level distortion, and the hearing threshold reduce audibility for the hearing-impaired listeners. Thus, the hearing threshold still affects audibility, although speech and noise spectra were spectrally shaped to fit in the dynamic range of individual listeners from 250 to 4000 Hz. The reason is that below 250 Hz and above 4000 Hz, the frequency response of the filter was flat. For most hearing-impaired listeners, the hearing threshold at 8000 Hz was much higher than at 4000 Hz. Therefore, part of the relevant dynamic range of the speech was below the hearing threshold in the frequency region between 4000 and 8000 Hz.

d. SRBT. The SR*B*T was broader than normal for 24 of the 34 hearing-impaired listeners. For 21 hearing-impaired listeners, the broader SR*B*T cannot be accounted for by the SII model. Therefore, also in this condition, additional suprathreshold factors must have affected intelligibility. The difference between the obtained SII and the maximal possible SII (dashed line) is caused by the hearing threshold, upward spread of masking, and some level distortion. Figure 2 shows that for the listener with an SR*B*T of 3.6 octaves, the difference between the actual SII and the dashed line is very large. The reason is that a large part of the relevant dynamic range of the speech was presented below the hearing threshold, due to the extremely narrow dynamic range of this listener.

3. SII across tests

For a convenient discussion of the SII of the hearing-impaired listeners across tests, the listeners are categorized into groups, based on their normal or elevated SII. A measurement error is associated with each result, and this error may cause an SII to fall just on one side of a separation between normal and elevated SII. Therefore, the categorization into groups should not be viewed too absolutely, but only as a means to simplify the discussion of the individual SII across tests. The SII for the SRTq is not used for this categorization, because the SII of only three hearing-impaired listeners is distinct from the SII of normal-hearing listeners.

Considering the SII for the SRTn, SRTa, and SR*B*T, the SII patterns of all but three hearing-impaired listeners can be subdivided into only four groups. Figure 3 shows the average proportion of the speech dynamic range (hatched area) needed for a 50% intelligibility score in the three conditions, for normal-hearing listeners (NH) and the four hearing-impaired groups. The group-averaged SII is shown in the upper-right corner. Double frames contain an elevated SII. Figure 3 displays no large differences in hearing threshold (dashed curves) or in the midline of the dynamic range (thick curves in the middle panels) across the four hearing-impaired groups. Thus, the differences across the groups do not seem related to major differences in hearing threshold or in the presented spectra. Each group of hearing-impaired listeners is discussed below.

a. Group I. Eleven hearing-impaired listeners have a normal SII for thresholds on all three tests. These listeners seem to process suprathreshold speech equally well as normal-hearing listeners. The four listeners with a mixed hearing loss all belong to this group.

b. Group II. Four listeners have an elevated SII for the SR*B*T, but a normal SII for both SRT tests in noise. The speech-understanding problems of these listeners seem to be caused primarily by the specific spectral configuration of the stimulus in the SR*B*T experiment. A possible cause is an increased susceptibility to spread of masking.

c. Group III. Twelve listeners have an elevated SII for both the SR*B*T and the SRTa, but a normal SII for the SRTn. Like the listeners of group II, the elevated SII for the SR*B*T could be related to increased spread of masking. The elevated SII for the SRTa may be caused by a frequency-dependent deficit. Figure 3 shows that the high-frequency part of the spectra of speech and noise is lifted above the hearing threshold in the SRTa condition. It appears that, although the high-frequency part of the speech spectrum is presented to the hearing-impaired listeners of this group, they cannot use it as effectively as normal-hearing listeners.

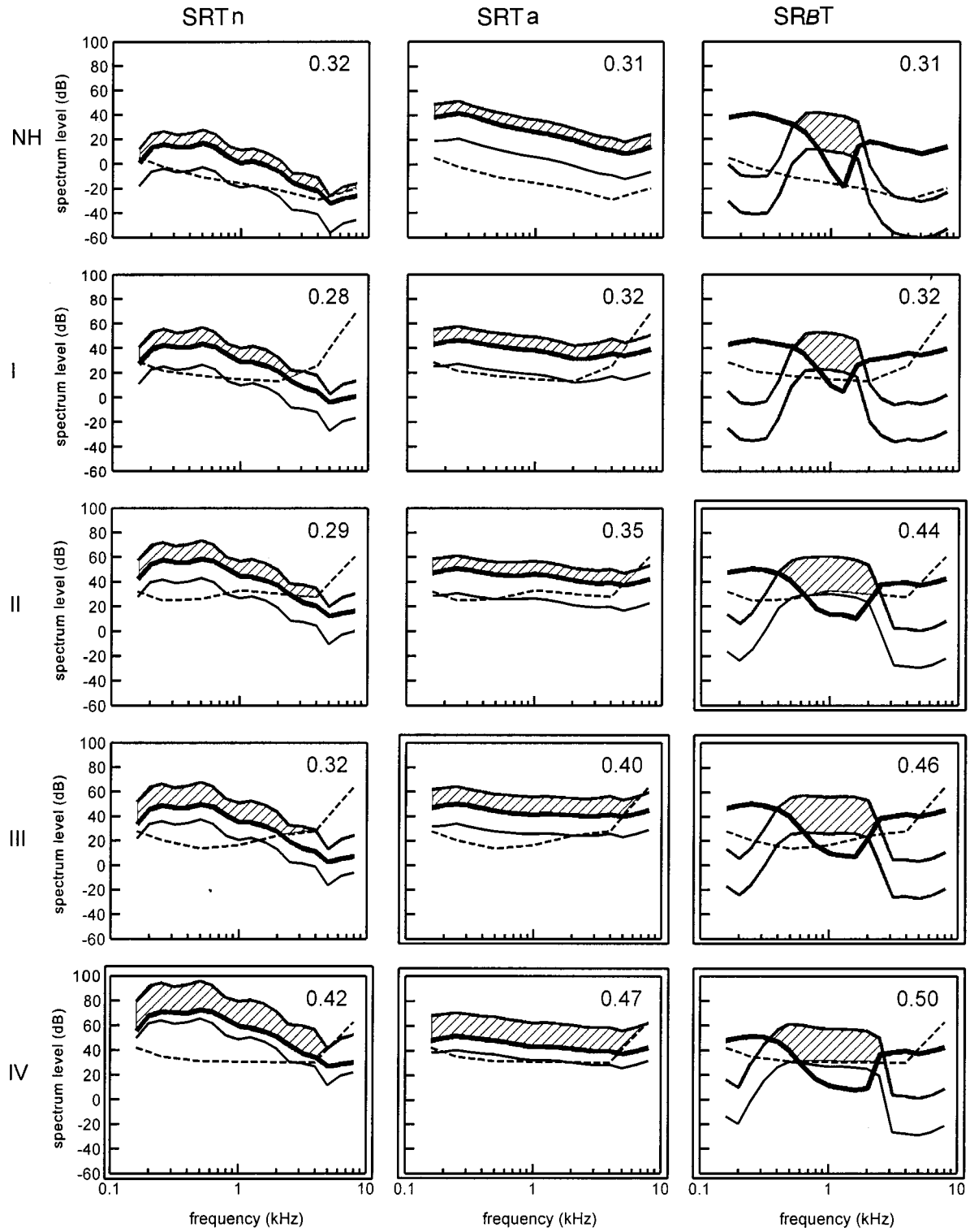

FIG. 3. Average proportion of the speech dynamic range (hatched regions) required for a 50% intelligibility score in three conditions (SRTn, SRTa, and SR*B*T) for normal-hearing listeners (panel set NH) and four groups of hearing-impaired listeners (panel sets I through IV). The 30-dB speech dynamic range is enclosed by the two thin lines. Thick lines are the masker spectra (including upward spread of masking) for the noise. Dashed lines indicate the spectrum level of the imaginary internal noise leading to the average absolute threshold. The group-averaged SII is shown in the upper-right corner. Double frames contain an elevated SII.

The performance of these listeners is consistent with the finding of Ching *et al.* (1998) and Hogan and Turner (1998) that the contribution of audibility to intelligibility is much reduced at high frequencies, where the hearing loss is severe.

d. Group IV. Four listeners have an elevated SII for the SRTn, the SRTa, and the SR*B*T. Two of these listeners also have an elevated SII for the SRTq. The SII for the SRTq of the other two listeners is also high: 0.41 and 0.43. Therefore, the suprathreshold deficit of these listeners does not seem to depend strongly on condition.

Overall, it seems that a normal SII for the SRTn does not imply a normal SII for the SRTa and the SR*B*T (groups

II and III). However, a normal SII for the SR*B*T appears to imply a normal SII for both SRT tests in noise (group I).

D. Modifying the SII model to include suprathreshold deficits

1. Proficiency factor

In the literature, various attempts have been made to modify the articulation index or SII to account for the deterioration in processing of suprathreshold speech, due to the sensorineural hearing loss. Fletcher (1952) proposed using the listener-dependent proficiency factor P for this purpose. Equation (1) then changes to

$$\mathrm{SII} = P \sum_{i=1}^{n} I_i A_i . \tag{6}$$

The proficiency factor depends only on the listener, and not on the listening condition. However, the SII for the listeners of groups II, III, and IV clearly depends on the listening condition (Fig. 3). Therefore, the proficiency factor cannot account for the performance of the listeners from these groups.

2. Speech desensitization factor

Pavlovic *et al.* (1986) proposed using a ''speech desensitization factor'' to account for the deterioration in speech processing of listeners with a sensorineural hearing impairment

$$\mathrm{SII} = \sum_{i=1}^{n} D_i I_i A_i . \tag{7}$$

The desensitization factor D is specified as a function of the hearing loss in each frequency band. It decreases linearly from 1, for hearing losses less than 15 dB HL, to 0, for hearing losses exceeding 95 dB HL. With Eq. (7) the SII values are recalculated. Rows 4 and 5 of Table II show the average SII of the hearing-impaired listeners with and without the desensitization factor. An SII indicated with an asterisk differs significantly from the corresponding SII of the normal-hearing listeners (row 3). At the SR*B*T, the SII of the hearing-impaired listeners becomes equal to the SII of normal-hearing listeners, when the desensitization factor is used. However, at the SRTq, SRTn, and SRTa, the SII of the hearing-impaired listeners becomes lower than the SII of normal-hearing listeners. In these three conditions, the speech desensitization factor seems to overestimate the deterioration in speech processing. It was verified that it is not possible to make the SII values of the hearing-impaired listeners equal to those of the normal-hearing listeners by choosing another linear relation between the desensitization factor D and the hearing loss. Thus, the hearing-loss-dependent speech desensitization factor cannot explain our results.

3. Upward spread of masking

Ludvigsen (1987) modified the articulation index by including a model of auditory masking in cochlearly hearing-impaired listeners. In his model, upward spread of masking increases proportionately with the hearing loss at the frequency being masked. Increased upward spread of masking decreases the SII for the SRTn, the SRTa, and the SR*B*T. It was found to have a larger effect on the SII for the SRTn than on the SII for the SR*B*T. Therefore, increased upward spread of masking also cannot explain why the average SII for the SR*B*T is higher than the average SII for the SRTn.

4. Downward spread of masking

The spectral configuration of the stimulus in the SR*B*T experiment is not only sensitive to the effect of upward spread of masking, but also for the effect of *downward* spread of masking. Increased downward spread of masking may explain the results. The noise spectrum level in the SRTn condition decreases with frequency (Fig. 3). Therefore, the level of downward spread of masking will be negligible compared with the level of the noise that is already physically present in the SRTn condition. Downward spread of masking will have a larger influence on the SII for the SR*B*T, because downward spread of masking from the high-frequency part of the bandstop noise will mask the (physically unmasked) bandpass-filtered speech.

For normal-hearing listeners, the slope of downward spread of masking is very steep, about 100 dB/octave (Zwicker, 1963), and independent of sound-pressure level. Abnormal downward spread of masking for hearing-impaired listeners has been observed by some authors. Glasberg and Moore (1986) measured auditory-filter shapes at three center frequencies (0.5, 1.0, and 2.0 kHz) for five listeners, and at one center frequency (1.0 kHz) for seven listeners with cochlear impairments. The slope of the high-frequency skirt of the filter, which reflects the amount of downward spread of masking, ranged from about 4 to 100 dB/octave. For four listeners, the filter shape could not even be determined at one or two center frequencies, because the filter had too little frequency selectivity. Hearing loss and high-frequency slope were not significantly correlated. Nelson (1991) obtained forward-masked psychophysical tuning curves for 21 listeners with cochlear hearing losses. Ten listeners showed abnormal downward spread of masking when equivalent masker levels were compared. Conversely, none of these listeners showed abnormal upward spread of masking. The high-frequency slopes of their tuning curves ranged from 10 to 87 dB/octave. Abnormal downward spread of masking was only observed in listeners with hearing losses exceeding 40 dB HL. However, not all listeners with a hearing loss greater than 40 dB HL showed abnormal downward spread of masking.

The two above-mentioned studies show that hearing-impaired listeners may experience increased downward spread of masking. The slope of the downward spread of masking varies considerably across the listeners, and cannot be predicted from the hearing loss. Further experiments are required to investigate if, for the individual listener, increased downward spread of masking is indeed related to an elevated SII for the threshold on these intelligibility tests.

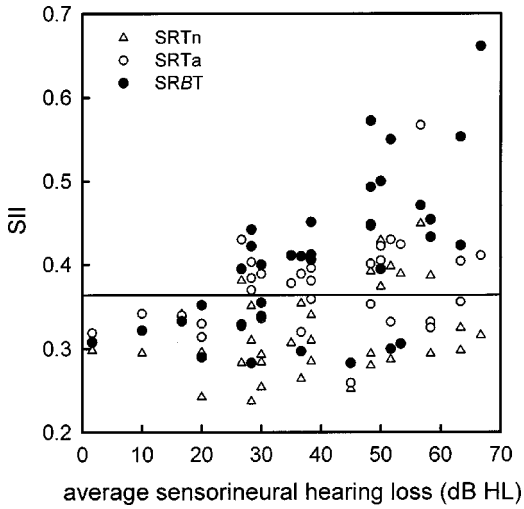

FIG. 4. Speech intelligibility index corresponding to the data of the hearing-impaired listeners on three intelligibility tests (SRTn, SRTa, and SR*B*T) versus their sensorineural hearing loss averaged over the frequencies 0.5, 1, and 2 kHz. The horizontal line represents the one-tailed 95% confidence limit for the SII of the normal-hearing listeners.

E. SII and hearing loss

As mentioned in the Introduction, Moore (1996) argued that factors other than audibility contribute to the difficulties in speech perception for listeners with a cochlear hearing loss greater than about 45 dB. To investigate the relation between SII and hearing loss for the present results, the SII for the SRTn, SRTa, and SR*B*T is plotted as a function of sensorineural hearing loss averaged over the frequencies 0.5, 1 and 2 kHz (Fig. 4). The horizontal line is the 95% confidence limit of the SII of the normal-hearing listeners. Figure 4 shows that only for average hearing losses less than 25 dB, all results can be explained on the basis of audibility by the SII model. For losses greater than 25 dB, suprathreshold factors already seem to influence speech perception for some listeners and intelligibility tests. However, high losses may still be associated with ''normal'' SII values.

V. SUMMARY AND CONCLUSIONS

The speech-understanding ability of 34 hearing-impaired listeners and a reference group of 10 normal-hearing listeners was measured with the SRT test in quiet, the standard SRT test in noise, and an SRT test in noise in which the speech and noise spectra were shaped to fit in the dynamic range of each listener. Furthermore, the threshold for speech reception was measured with the new SR*B*T test (Noordhoek *et al.*, 1999). The SR*B*T is defined as the bandwidth of speech around 1 kHz required for a 50% intelligibility score.

All individual data were converted to SII values, with the assumption that the SII reflects the effect of audibility, and that a higher-than-normal SII value required for a 50% intelligibility score indicates a deterioration in speech processing by factors not included in the SII model. For the normal-hearing listeners, the SII model accounts for the results obtained for all four tests (SII of typically 0.31 for all SRT and SR*B*T values).

For the normal-hearing listeners, the mean SRT in quiet was 24.0 dBA. For the hearing-impaired listeners, the mean SRT in quiet was 58.8 dBA. The mean standard SRT in noise was −3.6 dB for the normal-hearing listeners and +1.0 dB for the hearing-impaired listeners. An elevated SRT in quiet or an elevated standard SRT in noise could be explained on the basis of audibility by the SII model for the great majority of hearing-impaired listeners.

When the speech and noise spectra were adapted to fit in each listener's dynamic range, the SRT in noise improved on average by 0.9 dB for the normal-hearing listeners and 1.8 dB for the hearing-impaired listeners. Yet, the improvement for the hearing-impaired listeners is less than predicted on the basis of audibility by the SII model. For about half of the hearing-impaired listeners, the SRTa corresponds to significantly higher SII values.

On average, the SR*B*T of the normal-hearing listeners was 1.4 octave. The SR*B*T of the hearing-impaired listeners ranged from 1.3 to 4.0 octave. Compared with the normal-hearing reference group, 10 hearing-impaired listeners had a normal SR*B*T, whereas 24 hearing-impaired listeners had a broader-than-normal SR*B*T. Only for three hearing-impaired listeners could the broader-than-normal SR*B*T be explained on the basis of audibility by the SII model.

Eleven of the hearing-impaired listeners performed on all four tests as predicted by the SII model. The data of 23 hearing-impaired listeners on one or more of the intelligibility tests could not be explained by this model. This points to a deterioration in speech processing. The effect of such a speech-processing deficit appeared to depend strongly on the test condition for hearing-impaired listeners. However, a normal SII for the SR*B*T appears to imply a normal SII for both SRTn and SRTa. Thus, it seems that the SR*B*T test is most sensitive for speech-processing deficits. Increased downward spread of masking may be the reason for the elevated SII for the threshold on these three intelligibility tests.

Predicting the elevation of the SII from the hearing loss does not seem possible: for hearing losses greater than 25 dB, elevated SII values were found for some listeners, but for other listeners SII values were still considered normal.

ACKNOWLEDGMENT

This research was supported by the Foundation ''Heinsius-Houbolt Fonds,'' The Netherlands.

[1]It should be mentioned that the shallower slopes of the masking curves for frequencies below 500 Hz hardly influence the calculated SII in the present study (the largest SII decrement was 0.02). Equation (3) decreases the SII most for spectra with a negative spectral tilt and a high sound-pressure level (Noordhoek *et al.*, 1999). In the present study, no spectral tilt was imposed in the SRTn test, and the imposed spectral tilt was positive for spectra presented halfway through the dynamic range. Although the shallower slopes of the masking curves hardly influence the SII in this study, Eq. (3) is still used to be consistent with our previous study.

ANSI (**1969**). ANSI S3.5-1969, ''American national standard methods for the calculation of the articulation index'' (American National Standards Institute, New York).

ANSI (**1997**). ANSI S3.5-1997, ''American national standard methods for calculation of the speech intelligibility index'' (American National Standards Institute, New York).

Berger, E. H. (**1981**). ''Re-examination of the low-frequency (50–1000 Hz) normal threshold of hearing in free and diffuse sound fields,'' J. Acoust. Soc. Am. **70**, 1635–1645.
Ching, T. Y. C., Dillon, H., and Byrne, D. (**1998**). ''Speech recognition of hearing-impaired listeners: Predictions from audibility and the limited role of high-frequency amplification,'' J. Acoust. Soc. Am. **103**, 1128–1140.
Cox, R. M., and McDaniel, D. M. (**1986**). ''Reference equivalent threshold levels for pure tones and 1/3-oct noise bands: Insert earphone and TDH-49 earphone,'' J. Acoust. Soc. Am. **79**, 443–446.
Dreschler, W. A., and Plomp, R. (**1985**). ''Relations between psychophysical data and speech perception for hearing-impaired subjects. II,'' J. Acoust. Soc. Am. **78**, 1261–1270.
Fletcher, H. (**1952**). ''The perception of speech sounds by deafened persons,'' J. Acoust. Soc. Am. **24**, 490–497.
Glasberg, B. R., and Moore, B. C. (**1986**). ''Auditory filter shapes in subjects with unilateral and bilateral cochlear impairments,'' J. Acoust. Soc. Am. **79**, 1020–1033.
Glasberg, B. R., and Moore, B. C. (**1989**). ''Psychoacoustic abilities of subjects with unilateral and bilateral cochlear hearing impairments and their relationship to the ability to understand speech,'' Scand. Audiol. Suppl. **32**, 1–25.
Hogan, C. A., and Turner, C. W. (**1998**). ''High-frequency audibility: Benefits for hearing-impaired listeners,'' J. Acoust. Soc. Am. **104**, 432–441.
International Organization for Standardization (**1961**). ISO R226-1961, ''Normal equal-loudness contours for pure tones and normal threshold of hearing under free field listening conditions'' (available from American National Standards Institute, New York).
Keren, G., and Lewis, C. (**1993**). *A Handbook for Data Analysis in the Behavioral Sciences* (Erlbaum, Hillsdale, NJ).
Lee, L. W., and Humes, L. E. (**1993**). ''Evaluating a speech-reception threshold model for hearing-impaired listeners,'' J. Acoust. Soc. Am. **93**, 2879–2885.
Ludvigsen, C. (**1987**). ''Prediction of speech intelligibility for normal-hearing and cochlearly hearing-impaired listeners,'' J. Acoust. Soc. Am. **82**, 1162–1171.
Moore, B. C. J. (**1995**). *Perceptual Consequences of Cochlear Damage* (Oxford University Press, Oxford).
Moore, B. C. J. (**1996**). ''Perceptual consequences of cochlear hearing loss and their implications for the design of hearing aids,'' Ear Hear. **17**, 133–161.
Nelson, D. A. (**1991**). ''High-level psychophysical tuning curves: Forward masking in normal-hearing and hearing-impaired listeners,'' J. Speech Hear. Res. **34**, 1233–1249.
Noordhoek, I. M., Houtgast, T., and Festen, J. M. (**1999**). ''Measuring the threshold for speech reception by adaptive variation of the signal bandwidth. I. Normal-hearing listeners,'' J. Acoust. Soc. Am. **105**, 2895–2902.
Pavlovic, C. V. (**1987**). ''Derivation of primary parameters and procedures for use in speech intelligibility predictions,'' J. Acoust. Soc. Am. **82**, 413–422.
Pavlovic, C. V., Studebaker, G. A., and Sherbecoe, R. L. (**1986**). ''An articulation index based procedure for predicting the speech recognition performance of hearing-impaired individuals,'' J. Acoust. Soc. Am. **80**, 50–57.
Plomp, R., and Mimpen, A. M. (**1979**). ''Improving the reliability of testing the speech reception threshold for sentences,'' Audiology **18**, 43–52.
Smoorenburg, G. F. (**1992**). ''Speech reception in quiet and in noisy conditions by individuals with noise-induced hearing loss in relation to their tone audiogram,'' J. Acoust. Soc. Am. **91**, 421–437.
Stevens, S. S. (**1956**). ''Calculation of the loudness of complex noise,'' J. Acoust. Soc. Am. **28**, 807–832.
Versfeld, N. J., Daalder, L., Festen, J. M., and Houtgast, T. (**2000**). ''Method for the selection of speech materials for efficient measurement of the speech reception threshold,'' J. Acoust. Soc. Am. **107**, 1671–1684.
Walker, G., Dillon, H., Byrne, D., and Christen, R. (**1984**). ''The use of loudness discomfort levels for selecting the maximum output of hearing aids,'' Aust. J. Audiol. **6**, 23–32.
Zurek, P. M., and Delhorne, L. A. (**1987**). ''Consonant reception in noise by listeners with mild and moderate sensorineural hearing impairment,'' J. Acoust. Soc. Am. **82**, 1548–1559.
Zwicker, E. (**1963**). ''Über die Lautheit von ungedrosselten und gedrosselten Schallen,'' Acustica **13**, 194–211.

Analysis and synthesis of intonation using the Tilt model

Paul Taylor
Centre for Speech Technology Research, University of Edinburgh, Edinburgh EH1 1HN, United Kingdom

(Received 30 December 1998; revised 24 June 1999; accepted 18 October 1999)

This paper introduces the *Tilt* intonational model and describes how this model can be used to automatically analyze and synthesize intonation. In the model, intonation is represented as a linear sequence of events, which can be pitch accents or boundary tones. Each event is characterized by continuous parameters representing amplitude, duration, and tilt (a measure of the shape of the event). The paper describes an event detector, in effect an intonational recognition system, which produces a transcription of an utterance's intonation. The features and parameters of the event detector are discussed and performance figures are shown on a variety of read and spontaneous speaker independent conversational speech databases. Given the event locations, algorithms are described which produce an automatic analysis of each event in terms of the Tilt parameters. Synthesis algorithms are also presented which generate $F0$ contours from Tilt representations. The accuracy of these is shown by comparing synthetic $F0$ contours to real $F0$ contours. The paper concludes with an extensive discussion on linguistic representations of intonation and gives evidence that the Tilt model goes a long way to satisfying the desired goals of such a representation in that it has the right number of degrees of freedom to be able to describe and synthesize intonation accurately. [S0001-4966(00)01802-6]

PACS numbers: 43.72.Ar, 43.72.Ja, 43.72.Ne [JLH]

INTRODUCTION

A. Robust intonational models for speech technology applications

This paper presents a phonetic model of intonation designed specifically to facilitate robust computational analysis and synthesis. While intonational models of various types have been used in text-to-speech (TTS) synthesis for some time, intonation is still typically ignored completely in automatic speech recognition (ASR) systems. Some studies have shown uses for intonation and prosody in ASR systems (Lea, 1980; Waibel, 1986), but these components rarely make up part of state of the art large vocabulary ASR systems. The two most commonly cited reasons (Granstrom, 1997) for the absence of intonation in ASR systems are:

(1) Intonation is not a mature field and much more basic research is needed studying the phonetics and linguistics of intonation before we can apply this knowledge. Specifically, we need to discover a sophisticated and universal intonation model before applications that use such a model can be built.
(2) Intonation has many functions in language, such as helping syntactic disambiguation, distinguishing new/given information, signifying word emphasis, identifying speech acts, etc. None of these alone is significant enough to merit the redesign of an ASR system. In other words, it would take a lot of effort to include a specific intonational component in a recognizer and not much benefit would ensue from its inclusion.

While more basic research will certainly help the development of intonation applications, we do not think this is the main reason for the absence of intonation components in speech recognizers. In a typical contemporary ASR system (e.g., Woodland *et al.*, 1995), the phonetics are modeled by hidden Markov models (HMMs) and the grammar is modeled by a *n*-gram language model. Neither HMMs nor *n*-grams are a particularly ''good'' model of phonetics or grammar and it is known that there are many phenomena in the respective domains that neither can model. Furthermore, the use of HMMs and *n*-grams has not arisen through phonetic/linguistic studies which have advocated their suitability: HMMs and *n*-grams are used because they provide simple and robust techniques for modeling their domains. Crucially they are amenable to automatic training and because of their statistical nature allow principled ways of smoothing, interpolation, merging, analysis, etc. It is our belief that the main reason preventing intonation being used in ASR systems is the lack of an equivalent model for the intonational domain. In other words we disagree with statement (1) above, and argue that instead of fundamental research holding back the application of intonation, it is the lack of a suitable model which is robust, easily trainable, and amenable to statistical interpretation.

The response to the second point stems from the response to the first. For the sake of argument, let us suppose that a 5% relative decrease in word error rate could be achieved if ways were found to use the above cited functions of intonation in an ASR system. If an ASR system builder had to adopt a separate approach for each of these, the addition in complexity to the overall system would probably be deemed to be too great a cost for the potential increase in performance. If, on the other hand, a single robust intonation model could provide the basic information needed to harness all these functions, it would reduce the cost and might swing the balance in favor of using the intonational information.

While other speech technology applications such as TTS have long made use of more traditional intonational models,

we believe that these applications can also benefit from the provision of a robust intonational model. In the past, TTS systems typically had just a single ''voice.'' Recently much attention has been given to the notion of having large numbers of voices in synthesis systems (Hunt and Black, 1996). A logistic requirement of this is that the speech on which these voices are modeled should be acquired quickly which implies automatic transcription techniques for all components including intonation. Hence we need some way to automatically analyze and parameterize data so that the intonational characteristics of a speaker can be captured.

B. Requirements of an intonational model

The basic aim of intonation models is to provide a system of intonational description that is linguistically meaningful in such a way that representations in this system can be automatically derived from the relevant parts of an utterance's acoustics, and that the acoustics can be automatically synthesized from the representation.

By ''linguistically meaningful'' we mean a representation which contains information which is significant to the linguistic interpretation of an utterance's intonation. This excludes effects which are purely redundant, or phenomena which affect the $F0$ contour but which are not important in this sense (e.g., segmental perturbations). We do include phenomena that affect intonation on the syntactic, semantic, pragmatic levels, and also what has traditionally been described as ''paralinguistic,'' but an explanation of how these levels relate to the phonetic Tilt model is outside the scope of this paper.

Existing linguistic representations range from relatively low-level phonetic descriptions such as the Fujisaki model (Fujisaki and Ohno, 1997), the Hirst model (Hirst, 1992), and the RFC model (Taylor, 1995), to higher-level systems such as the IPO model (t'Hart and Collier, 1975), to phonological systems such as Pierrehumbert's (Pierrehumbert, 1980), Ladd's (Ladd, 1996), and ToBI (Silverman *et al.*, 1992). A full discussion of the issue of linguistic representation is given in Sec. IV, but we will now give the main desired properties of such a representation:

(1) Constrained. The representation should be as compact as possible having few degrees of freedom. Specifically, redundancy should be absent so that one part of the representation cannot be derived from another.
(2) Wide coverage. The representation should cover as many intonational phenomena as possible and should be capable of expressing distinctions in utterances which are perceptually different.
(3) Linguistically meaningful. The form of the representation should be such that its parameters can be interpreted and generated by higher-level components.

It is clear that these properties have a tradeoff: an unconstrained system with many degrees of freedom will have wider coverage than a system with few. The notion of providing constrained, compact models is common throughout linguistics and it is a general rule of thumb that a compact representation system with low redundancy and an orthogonal description space is a better linguistic representation than one without these properties. Furthermore the properties of the linguistic representation interact with the two further goals:

Automatic synthesis. The model should have an automatic mechanism for generating $F0$ contours from the linguistic representation.

Automatic analysis. It should be possible to derive the linguistic representation automatically from an utterance's acoustics.

It is fairly easy to design a representation which is a amenable to automatic analysis and synthesis if one is not worried about the linguistic relevance of the representation.

Given the interaction between these desires, we have developed a model of intonation that tackles these problems together in an attempt to provide a reasonable balance between them. The *Tilt model* provides a linguistic representation which is compact, has wide coverage, and is linguistically meaningful. Importantly, the model has been specifically designed to facilitate automatic analysis and synthesis. The following sections now describe the representation system and the analysis and synthesis systems which allow mappings between the representation and the $F0$ contour.

I. OVERVIEW OF THE MODEL

The basic unit in the Tilt model is the *intonational event*. Events occur as instants with nothing between them, as opposed to segmental based phenomena where units occur in a contiguous sequence. The basic types of intonational event are *pitch accents* and (following the popular terminology) *boundary tones*. Pitch accents (denoted by the letter **a**) are $F0$ excursions associated with syllables which are used by the speaker to give some degree of emphasis to a particular word or syllable. In the Tilt model, boundary tones (**b**) are rising $F0$ excursions which occur at the edges of intonational phrases and as well as giving the hearer a cue as to the end of the phrase, can also signal effects such as continuation and questioning. A combination event **ab** occurs when a pitch accent and boundary tone occur so close to one another that only a single pitch movement is observed. There are different kinds of pitch accents and boundary tones: the choice of pitch accent and boundary tone allows the speaker to produce different global intonational tunes which can indicate questions, statements, moods, etc., to the hearer.

The Tilt model can be regarded as a *phonetic* model of intonation in that it describes the intonational phenomena observable in an $F0$ contour. This contrasts with a *phonological* model which is concerned with the underlying structure of the intonation. It is only in a few practical cases that this distinction actually matters much, for example, with the treatment of ''level accents.'' These are pitch accents which have no observable $F0$ behavior and hence should be present in a phonological transcription but not a phonetic one.

The sequence of events in an utterance is called an *intonational stream*. A full intonational description is obtained by joining the intonational stream to the *segmental stream* (the sequence of phones) for the utterance. Bidirectional links can exist between units in one stream and units in the

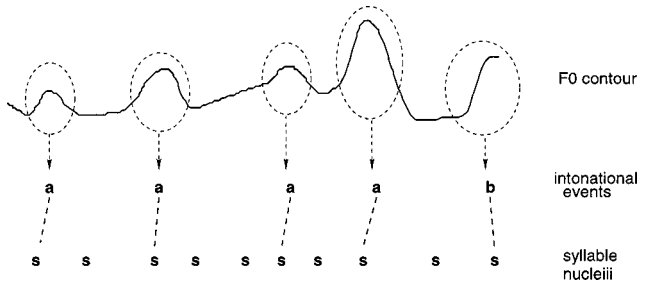

FIG. 1. Schematic representation of $F0$, intonational event stream and segment stream in the Tilt model. The linguistically relevant parts of the $F0$ contour, which correspond to intonational events, are circled. The events, labeled **a** for pitch accent and **b** for boundary are linked to the syllable nuclei of the syllable stream. Note that every event is linked to a syllable, but some syllables do not have events.

other stream, with the restriction that links cannot cross. Events are linked to syllabic nuclei (usually vowels), as shown in Fig. 1. In this way the intonation stream and the segment stream can be analyzed separately and one can still find out whether a particular intonational unit is linked to a particular segment or syllable. In generative phonology such descriptions are called *autosegmental* diagrams consisting of tiers (streams) and association lines (Goldsmith, 1989). Viewing intonation in this way is useful in that one can decouple the intonation part from the segmental part and thus compare intonation descriptions independently of the actual text they are associated with. There is no loss of descriptive power in this; one can still ask whether a syllable or segment is ''accented'' or not.

Unlike traditional intonational phonology schemes (Pierrehumbert, 1980; Silverman *et al.*, 1992) which impose a categorical classification on events, we use a set of continuous parameters. These parameters, collectively known as *Tilt parameters*, are determined from examination of the local shape of the event's $F0$ contour. A previous paper (Taylor, 1995) presented the rise/fall/connection (RFC) model. In this model, each event is fully described by a rise shape, a fall shape, or a rise shape followed by a fall shape. Each event is parameterized by measuring the amplitudes and durations of the rises and falls which can be done by hand or by the curve fitting algorithm described in Sec. IV A. For a rise–fall shape, three points are defined which correspond to the start of the event, the peak (the highest point), and the end of the event. The rise duration is the distance in time from the start of the event to the peak, and the fall duration is the distance from the peak to the end; likewise, the rise amplitude is the difference in $F0$ between the $F0$ value at the peak and at the start, and the fall amplitude is the $F0$ distance from the end to the peak. (Hence rise amplitudes are always positive and fall amplitudes are always negative.) In this way each event is characterized by four parameters: rise amplitude, rise duration, fall amplitude, and fall duration. If an event has only a rise component, its fall amplitude and duration are set to 0. Likewise when an accent only has a fall. These four parameters are ''local'' to the event—a fifth parameter *position* is used to specify the alignment of the event to the syllable and is usually measured as the distance from the start of the vowel. The sections of contour between events are called *connections* (denoted **c**) and are also described by an amplitude and duration. (The connection is described further in Sec. IV C).

While the RFC model can accurately describe $F0$ contours, the mechanism is not ideal in that the RFC parameters for each contour are not as easy to interpret and manipulate as one might like. For instance there are two amplitude parameters for each event, when it would make sense to have only one. The *Tilt* representation helps solve these problems by transforming the four RFC parameters into three Tilt parameters, namely *duration*, *amplitude*, and *tilt* itself. Duration is simply the sum of the rise and fall durations. Amplitude is the sum of the magnitudes of the rise and fall amplitudes. The tilt parameter is a dimensionless number which expresses the overall *shape* of the event, independent of its amplitude or duration. It is calculated by taking the ratio of the differences and sums of the rise and fall amplitudes and durations, as explained in Sec. IV B. The RFC position parameter is kept unchanged in the Tilt representation. The Tilt representation is superior to the RFC representation in that it has fewer parameters without significant loss of accuracy. Importantly, it can be argued (see Sec. VI) that the Tilt parameters are more linguistically meaningful.

Sections III and IV explain how the boundaries of events can be located from an utterance's acoustics and how automatic RFC and Tilt analysis is performed. Section V describes how $F0$ contours can be synthesized from Tilt representations, and the paper concludes with a discussion on the concept of linguistic meaningfulness in intonation and its implications for the Tilt and other models.

II. DATA

The three databases used in the experiments are briefly described below. Further technical details about the corpora and their availability can be found in Appendix B.

A. DCIEM maptask

This is a corpus of 216 dialogues collected by Canada's Defense and Civil Institute of Environmental Medicine (DCIEM) (Bard *et al.*, 1995). Each dialogue consists of recordings of two participants playing a game called the maptask, where one participant describes a route on a map to the other participant. The maps are designed to be confusing, with the aim of eliciting interesting dialogue structures from the participants. The speech is fully spontaneous and contains many disfluencies. The database has a particularly rich variety of types of utterance, e.g., it contains many questions, instructions, statements, confirmations, back-channels, etc. A subset of 25 dialogues (about 2 h of speech) was used here. Two partitions of the corpus were used. The first is a speaker independent set and comprised 20 dialogues for training and 5 for testing with none of the speakers in the training set being in the test set. All the results reported in Secs. IV E and V are on the test set from this partition. One of the speakers in the corpus set appeared in several dialogues and a speaker dependent partition containing just his speech was also used.

B. Boston radio news corpus

This is a corpus of news stories read by professional news reader, collected at Boston University (Ostendorf *et al.*, 1995). A subset of 34 stories of about 48 min from one speaker was used for experiments here.

C. Switchboard

Switchboard is a corpus of about 2000 spontaneous speech dialogues collected live over the US telephone network (Godfrey *et al.*, 1992). Experiments reported here are based on a 1-h subset, chosen (by researchers at ICSI, Berkeley) to achieve maximum acoustic and phonetic variability across the corpus. Within this hour there are about 100 different speakers from all parts of the United States. Fifty minutes were used for training and 10 for testing.

D. Hand labeling

The databases were hand labeled to produce intonational transcriptions. The transcriptions were produced by using an interactive speech analysis tool which displayed the waveform and $F0$ contour, and allowed the labelers to listen to the speech. The labelers were instructed to locate pitch accents and boundaries within each utterance, in accordance with the intonational event model described above. A few extra features were added to make the labeling easier from a human point of view and to help in the error analysis of the automatic system:

- Level accents give the perception of accentuation but have no discernible $F0$ movement associated with them. Although we previously said that these should not be part of a phonetic description of intonation, these were marked in the database as normal pitch accents with an **l** diacritic. The diacritic making allows these to be ignored at a later stage if desired.
- One of the biggest problems in hand labeling intonation is that there are a large number of cases, especially in prenuclear position, where there is a ''hint'' of a pitch accent, but it is difficult to tell with certainty whether it is actually there or not. Often this is because a syllable is clearly perceived as being stressed, but there is only a little $F0$ movement observable in the $F0$ contour. Labelers marked these as being accented and gave them a separate diacritic indicating they were ''minor'' accents.
- In the Tilt model, only rising boundaries are classed as events. Falling boundaries are the default case and are not classified as true events. However, when labeling the corpus it was decided to give the labels **rb** to rising boundaries and **fb** to falling boundaries, again with the idea that the **fb** labels could be ignored later if desired. Normal well-formed utterances always end in one of these two labels. In spontaneous speech, however, many utterances are abandoned and hence it is possible for utterances to end with no boundary event.
- Silence was labeled **sil**.

E. Labeling consistency

In assessing any labeling scheme it is important to give consistency figures. As well as demonstrating the inherent reliability of the task they also serve to set an upper measurable limit of performance for an automatic system (it is conceivable that the system could beat a human labeler, but we would not be able to tell). As the automatic event detector described below is tested against human transcriptions, it is important to know how many errors in the human transcriptions we can expect.

Five labelers were used, all of whom were Edinburgh University Ph. D. students studying various intonation topics. For comparison purposes, each of the labelers transcribed the same DCIEM dialogue. Their transcriptions were compared using a modified form of the dynamic programming scoring algorithm that is standard in the speech recognition field (see Young *et al.*, 1996 for an explanation). This scoring algorithm produces two figures, % correct which gives the total number of events correctly identified and % accuracy which is % correct minus the percentage of false insertions. The standard algorithm is modified to penalize situations where the correct label sequence is present but the timings are wrong. In intonation transcriptions, because of the small number of labels, there is a quite high probability that two label sequences will match by chance. To ensure that this is not taken as correct, a further constraint is enforced whereby labels have to have a temporal overlap of 50% to be considered the same.

The pairwise scores for all the labelers were 81.6% correct with 60.4% accuracy. When ignoring the accents marked with the minor diacritic, the agreement is 88.6% correct with 74.8% accuracy, showing that a large number of errors were caused by minor accents. Looking at the types of events separately, the agreement for pitch accents is 81.6% correct, 58.1% accuracy and the agreement for boundaries is 83.3% correct and 64.1% accuracy. There are very few other studies published on inter-labeling accuracy, but Pitrelli *et al.* (1994) cite an accuracy figure of 80.6%. We feel their higher figure is mostly due to their comparison data having more read speech, as the accent location task is virtually identical to ours.

III. AUTOMATIC DETECTION OF EVENTS

This section describes the first stage of the automatic analysis process, namely determining the approximate event start and end positions as mentioned in Sec. IV A. The second stage, whereby events are assigned Tilt parameters, is discussed in Sec. IV.

A. Detection versus classification

This section describes an *intonational event detector* which locates intonational events from the acoustic information alone. It is important to note the distinction between this type of system and an *intonational classifier* which uses a linguistic segmentation of the utterance to perform intonational analysis. An intonational event detector is analogous to a speech recogniser in that it determines a sequence of linguistic units (words or phones in the case of a speech

recognizer, pitch accents, and boundaries for intonational events) from the acoustic input alone. An intonational classifier, on the other hand, starts with a linguistic segmentation (for purposes of discussion we will assume these are syllables, but words and phones are also possible) and performs a *classification* to determine which one of *N* intonational categories (including unaccented) a linguistic unit has. Each approach has strengths and weaknesses which we will now briefly discuss.

Intonational classifiers have an easier task in some sense because once given a linguistic segmentation, much of the work has already been done. However, in a fully automatic system the linguistic segmentation must be done automatically also, and in certain situations (e.g., when recognizing Switchboard data) the linguistic segmentations can be very error prone. This may weaken classification performance considerably. The systems also differ with respect to alignment and association. The temporal relationship between a pitch accent and its associated syllable is not simple. Experiments with the Tilt model have shown that only about 50% of accents have their peak within the boundaries of the associated syllable: the remainder have either late or early peaks which are actually closer to adjacent syllables. Event detectors show the precise location of events in time but do not (in the first instance) show which syllable or word is accented. Conversely, classifiers show that a certain syllable is accented or unaccented, but do not say where in relation to the syllable the accent is to be found.

The choice of which approach to take is based on what the intonational analysis system is to be used for. Specifically, it depends on whether it is reasonable to assume that a linguistic segmentation is actually available, and which is more important for the particular application: knowing the precise location of the accent or knowing which syllables are accented. Here we report an automatic intonational event detector; work by others has already been performed on intonational classifiers (e.g., Ross and Ostendorf, 1995). The Tilt model itself can work with either approach; all it needs is the approximate location of the events, which both approaches can provide.

A final point concerns accuracy measurements of the systems. It is important to note that it is not possible to meaningfully compare accuracy figures for the two types of system. The accuracy figures for classification systems can always be expected to be considerably higher for two reasons. First, for reasons of system development, the linguistic segmentation is normally assumed to be perfect and so some degradation is to be expected when used with a fully automatic system. Second, and more importantly, classification results normally report how well the system identified unaccented syllables. As these may typically account for 70%–80% of the syllables in the test set, it is important to see the baseline accuracy for such systems as being this figure. In event detection, there is no such baseline and because of insertion errors, figures may even be worse than 0%.

B. Event detector overview

The automatic event detector uses continuous density hidden Markov models to perform a segmentation of the input utterance. A number of units are defined and an HMM is trained on examples of that kind from a pre-labeled training corpus using the Baum–Welch algorithm (Baum, 1972). Each utterance in the corpus is acoustically processed so that it can be represented by a sequence of evenly spaced frames. Each frame is a multi-component vector representing the acoustic information for the time interval centered around the frame.

Recognition is performed by forming a network comprising the HMMs for each unit in conjunction with an *n*-gram language model which gives the prior probability of a sequence of *n* units occurring. To perform recognition on an utterance, the network is searched using the standard Viterbi algorithm to find the most likely path through the network given the input sequence of acoustic vectors.

Using the HTK toolkit (Young *et al.*, 1996), a series of experiments was performed, each following the same experimental procedure. First an HMM set is defined, with each HMM representing one intonational unit (such as **a** or **c**). Each HMM has three states, each of which initially has a single Gaussian which gives the probability density function for the acoustic data. The HMM parameters are initialized using the Viterbi algorithm to provide starting estimates for the model parameters. Training proper is performed using the Baum–Welch algorithm. A number of training iterations are performed until convergence is reached. The single Gaussian is then split into two Gaussian components to form a Gaussian mixture for that state and the Baum–Welch algorithm is run again. This process is repeated for models of 2, 3, 4, 5, 6, 7, 8, 10, 12, 14, 16, 20, 24, and 28 components. All the experiments used the nonembedded form of the Baum–Welch algorithm. In this style of training each HMM is trained on frames of speech lying within the boundaries of its own units only, as opposed to embedded style training where only the sequence of units is given and it is up to the training algorithm to assign frames appropriately. Experiments showed that this style of training consistently produced better results than embedded training.

Testing is performed by running the trained system over test data and comparing the transcriptions to those produced by a hand labeler using the procedure outlined in Sec. III E. This technique simply decides if an event in the automatic transcription corresponds to an event in the reference transcription. In most of the results reported below, all events are treated as the same category, so a pitch accent in the test transcription can be successfully matched to either a pitch accent or boundary tone in the reference transcription. Section III D gives individual scores for pitch accents and boundary tones. The comparison procedure gives %correct and %accuracy for the standard case and for the case where minor accents are ignored. In all cases, the %accuracy for the standard case is taken to be the most important measure, and is the one used for determining the highest scoring system.

Sections III C and III D report experiments on different feature and label configuration for the DCIEM test data. Section III E compares these with results for the Boston Radio News Corpus and Switchboard. It should be noted that none of this data was used in the development of the RFC and Tilt models. The HMM event detector was developed on a train-

TABLE I. Performance in terms of % correct and % accuracy for different feature sets.

Features	% corr	% acc	% major corr	% major acc
$F1$ $F0$ and energy	57.7	26.6	69.6	46.3
$F2$ Normalized $F0$ and energy	61.7	33.6	73.0	51.7
$F3$ Normalized $F0$ and energy+deltas	65.6	43.8	76.7	56.1
$F4$ Normalized $F0$ and energy+deltas+acc	72.7	47.7	81.9	60.7

ing and development test set which are now included in the DCIEM training set, and the test sets for the corpora can properly be considered unseen evaluation data.

C. Features

The super-resolution pitch detection algorithm (Medan *et al.*, 1991) was used to extract $F0$ contours from waveforms for the DCIEM database. This algorithm has been shown to be one of the most accurate $F0$ detection algorithms currently available (Bagshaw *et al.*, 1993), but contours extracted from any state-of-the-art algorithm should be adequate for use in the model. The integrated pitch tracking algorithm (Secrest and Doddington, 1983) was used for Switchboard because it gave better results on telephone speech (which is often missing the fundamental). Rms energy was calculated in the standard way. The $F0$ and rms values were combined to give a feature representation at 10-ms frame intervals.

Table I gives the results for four experiments on different acoustic feature sets. Experiment $F1$ used plain $F0$ and rms energy. Experiment $F2$ used a simple form of speaker and channel normalization, whereby the mean and standard deviation of each speaker's $F0$ and energy was calculated and used to normalize all the data for that speaker.

It has been shown before (e.g., Taylor, 1995) that the *change* in $F0$ is a particularly salient cue to the presence of a pitch accent, and so the normalized $F0$ and energy measures were supplemented by their delta coefficients. Deltas were calculated in the standard way by taking an estimate of the first derivative of a value over a period of four frames. It is also possible to calculate a second order delta which gives the rate of change of the normal delta coefficients. Experiment $F3$ gives the results for the normalized and delta coefficients and experiment $F4$ gives the results for the normalized, delta and delta–delta coefficients. As feature set $F4$ gave the best results, its feature combination was used for all the subsequent experiments.

TABLE II. Description of different label sets.

Name	Labels	Description
$L1$	**sil, c**, and **e**	Major pitch accents and rising boundaries are **e**. Fallingboundaries, minor and level pitch accents are **c**
$L2$	**sil, c, a, ab, b**	Major, minor and level pitch accents are **a**; all rising boundaries are **b**, falling boundaries are **c**
$L3$	**sil, c, a, ab, b**	Normal pitch accents are **a**; rising boundaries are **b**; minorand level pitch accents and falling boundaries are **c**
$L4$	**sil, c, a, fb, rb, afb, arb, m, mfb, mrb, l, lrb, lfb**	full label set

D. Labels

As far as the Tilt model is concerned, there are only five intonation labels, namely **a**, **b**, **ab**, **c**, and **sil**. However, for the reasons described in Sec. II D, a richer label set was used for hand labeling which differentiated rising and falling boundaries, and had diacritics for level and minor accents. A series of experiments were performed to see which label set was the optimal for the HMM event detector. These experiments investigated whether level accents, minor accents, and falling boundaries should be included in the label set.

Four label sets, shown in Table II, were defined to investigate the various issues just outlined. Label set $L1$ is the simplest possible set, where pitch accent and boundary labels are mapped to a single label **e**, representing all events. In sets $L2$ and $L3$, rising boundaries are labeled **b**, falling boundaries are ignored (i.e., they are labeled **c**), and pitch accents are labeled **a**. In set $L2$, level, minor, and normal pitch accents are grouped into a single accent category **a**, while in set $L3$, only normal accents are labeled **a**, level and minor accents are ignored (labeled **c**). In set $L4$, all variations are given their own label, so that level accents are labeled **l**, minor accents **m**, and the combined accent and boundary labels for each (**ab** for normal accents) are also marked separately.

A separate recognition experiment was performed for each set of labels. In testing, as before, the identities of the event labels were treated as equivalent, allowing direct comparison across label sets. It is clear from the results given in Table III that the sets with finer event distinctions out perform the sets where different types of events are grouped together. The best performing set is $L4$, where each possible type of event has its own HMM. Hence this label set was adopted as the standard set in the event detector and used for all the other experiments, including those previously reported on feature usage.

In all the results reported here, events of one label matching events of another are considered correct. To show

TABLE III. Performance in terms of % correct and % accuracy for different label sets.

Labels	% corr	% acc	% major corr	% major acc
$L1$	60.2	43.8	73.4	56.9
$L2$	70.5	46.9	80.4	56.9
$L3$	67.6	44.1	77.9	54.4
$L4$	72.7	47.7	81.9	60.7

TABLE IV. Individual performance in terms of % correct and % accuracy for different labels.

Reference label	Test label	% correct	% accuracy
a	a	71.9	25.9
m	m	3.4	−24.2
l	l	9.8	−52.4
alm	alm	70.9	44.2
fb rb	fb rb	58.0	19.2
rb	rb	55.0	34.8
fb	fb	49.1	−25.9

individual labeling accuracy, however, a set of comparisons were performed where labels had to match their own type to be considered correct. Table IV shows that labels often do not match themselves very well, for instance when **a** accents are compared to **a** accents in the reference transcription the accuracy is only 25.9%. As expected, minor and level accents are extremely difficult to detect and have very low accuracy (−24.2% and −52.4%). However, when **a**, **l**, and **m** accents are allowed to match with each other, the performance is substantially higher. The accuracy for boundary event detection is relatively low at 19.2%. The further results for boundary detection show that the source of errors is almost entirely due to falling boundaries **fb** being missed (−25.9%), the score for rising boundary detection is substantially higher at 34.8% accuracy. These figures tell us two things. First, events which are not distinct acoustically are detected with much lower accuracy than those which have prominent acoustic features. In acoustic terms **fb** is often just a section of flat $F0$ contour, whereas **rb** often has a prominent rising $F0$. Second, although discrimination between the three accent types is poor, collectively they actually produce better accent recognition than when a single model is trained for **a**, **l**, and **m** (label set $L2$ gives 73.1% correct 40.5% accuracy for accents).

E. Datasets

The above results give event detection performance on the speaker independent DCIEM test set (SI-DCIEM). Further experiments were performed on a single speaker subset of this (SD-DCIEM), the Boston University Radio News Corpus (RN) and Switchboard (SWB), all using the $F4$ feature set. Results are shown in Table V. The results for the SI-DCIEM corpus are the same as those in Tables I and III. The SD-DCIEM corpus contains about 30 min from a single speaker, and this was used to examine the differences between a speaker independent and speaker dependent event detector. There is a clear improvement in performance from the speaker independent to the speaker dependent test.

TABLE V. Performance in terms of % correct and % accuracy for different data sets.

Dataset	% corr	% acc	% major corr	% major acc
SI-DCIEM	72.7	47.7	81.9	60.7
SD-DCIEM	82.1	63.1	88.1	70.2
Radio News 3	69.4	49.7	79.4	59.3
Radio News 1	68.9	49.2	n/a	n/a
Radio News 2	67.1	45.7	n/a	n/a
Switchboard	60.7	35.1	71.5	47.4

The three different results of the Radio News corpus correspond to different labeling situations, RN1 corresponds to the $L4$ label set as used in the other experiments, while RN2 and RN3 correspond to transcriptions which have automatically been converted from ToBI transcriptions. The RN corpus had been previously labeled at Boston University using the ToBI scheme and we investigated whether a database already labeled with the ToBI scheme could be converted into the Tilt model scheme. The mapping, which is quite complex, is described in Appendix A. There are two variants. In RN2 all ToBI boundary tones are labeled as **b**, and in RN3 **H**% tones are labeled as **rb**, and **L**% tones are labeled as **fb**. The RN corpus is from a single speaker only and so it is somewhat surprising that the results, although better than SI-DCIEM, are not as good as SD-DCIEM. This result led us to further analysis of the SI-DCIEM where we examined the errors attributed to each of the ten speakers in the test set separately. We found there was quite a large variation in performance, with the best speaker having 76.3% correct and 58.9% accuracy, and the worst 64.3% correct and 33.9% accuracy. The difference in performance between SD-DCIEM and RN lies within this range and hence the differences may be attributed to some speakers being naturally more suited to the approach than others.

It is interesting to note that the best results for the ToBI mapped labels (RN2 and RN3) are nearly the same as the results for the Tilt labels (RN1). This is an important result because it means that the event detection technique described here can be used on databases already labeled with the ToBI scheme. However, although the performance of the RN1 and RN3 is similar, the actual transcriptions they produce are significantly different. The results in the table were obtained by testing the RN1 trained event detector against the test set labeled using RN1. Likewise the RN3 event detector was tested against an RN3 labeled test set. When the RN1 event detector is tested on the RN3 labeled test set, the performance drops to 49.1% correct with 40.2% accuracy. The biggest discernible difference in the two sets is that the Tilt set (RN1) has many more accent labels than the ToBI (RN3) set. Whether this is due to a fundamental difference in the labeling schemes, or just a discrepancy between labelers is difficult to say. In summary then, it is possible to map ToBI labeled data into event labels and train an accurate event detector, but one should not assume that the resulting labeling from this is the same as from a Tilt event detector.

The results for Switchboard are worse than for the other datasets. Accurate word transcription of Switchboard has proved a notoriously difficult task for speech recognition systems, which often perform much worse on this task than others. Many reasons are given for Switchboard's difficulty including disfluencies, ''poor'' pronunciations (i.e., substantially different from citation forms) and low acoustic quality. As regards the performance of the event detector we can probably rule out the spontaneous nature of the speech as being the source of the poorer performance. Although the task is different, the DCIEM corpus is fully spontaneous also and contains highly diffluent speech. The DCIEM corpus is

recorded from speakers of a fairly homogeneous regional accent group, while Switchboard is from speakers from across the entire United States and this may account for some of the worse performance. However, in our opinion it is the differences in acoustic quality which are probably the most important factor. While DCIEM was recorded with high quality close talking microphones in a quiet room, Switchboard was recorded live over the US telephone network. The acoustic quality of Switchboard is very bad in places, with background noise, and telephone network artifacts. The poor acoustic quality affects feature extraction with many more errors in $F0$ being present than with other databases. However, given that Switchboard is such a difficult database, the figures of 60.7% correct and 35.1% accurate may not be too bad.

IV. DERIVING TILT PARAMETERS FROM EVENT BOUNDARIES AND *F*0 CONTOURS

The event detector produces a segmentation of the utterance from which it is possible to derive the start and end positions of the events. This information is used to delimit a region of contour that is first turned into RFC parameters and then Tilt parameters. Each of these processes is now described in turn.

A. Automatic RFC analysis

Automatic RFC analysis involves determining the precise locations of the start, peak, and end positions and using the values to calculate the rise amplitude, rise duration, fall amplitude, and fall duration of the event. This process is explained in more detail in Taylor (1995); here we present a summary.

RFC analysis operates only on sections of $F0$ contour which have been delimited by the event detection procedure. Each of these sections is smoothed using a median smoothing algorithm, and unvoiced regions are interpolated through. This ensures that the RFC analysis sees only smooth fully voiced contours. Smoothing serves a number of purposes. First, median smoothing is useful for removing isolated spurious $F0$ values produced by the errors in the extraction process. Second, it helps remove the natural minor perturbations in $F0$ periods which result from natural variations in the speaker's production. While these perturbations affect speech quality, they are not important in intonation analysis and synthesis and can be removed without distorting the intonational content of the contour. A median filter with a window of about 7–11 points is sufficient to smooth the contour.

After smoothing, a peak-picking algorithm is used to determine whether the event is a rise, fall, or combined rise–fall. If a peak is found, then the event is classified as a combined rise–fall. The peak position (if present) and the start and end position as given by the event detector, are used to define *search regions*. In the case of a single rise or fall event (as shown in Fig. 2) the search regions are defined to be 20% before and after the approximate event detector boundaries. Typically this will correspond to ten 10-ms frames for the start and ten frames at the end. Each start frame position in combination with each end frame position is taken as a potential start and end point, and a $F0$ curve is synthesized

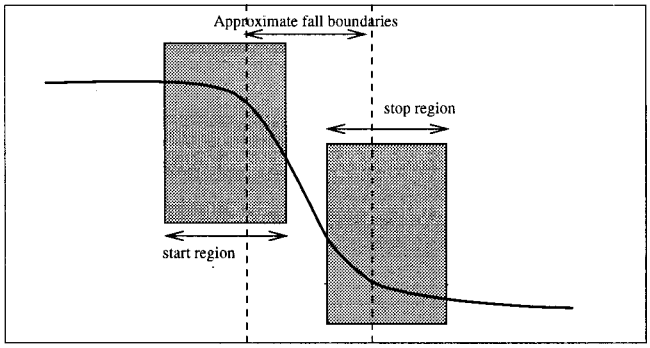

FIG. 2. Search regions for fall accents.

(using the technique described in Sec. V) for each of these start and end combinations (in our example this is $10^2 = 100$ curves). Each of these curves is compared with the values of the actual $F0$ contour at that point and the curve with the lowest Euclidean distance is taken to be the best fit. Compound rise–fall events are treated similarly, but in this case two searches are performed. The first search (to find the rise) defines its start search region as before, but the end position is fixed as the peak. The second search (to find the fall) has a fixed start position at the peak and has a variable end search region as above. This procedure is continued until all the precise start, peak, and end times have been located for every event in the utterance.

B. Automatic tilt analysis

The Tilt representation is easily derived from the RFC representation by application of the equations described below. The *tilt* parameter itself is an abstract description of the $F0$ shape of an event. Tilt is calculated by comparing the relative sizes of the amplitudes and durations of the rises and falls for an event. Amplitude tilt is given by

$$\text{tilt}_{\text{amp}} = \frac{|A_{\text{rise}}| - |A_{\text{fall}}|}{|A_{\text{rise}}| + |A_{\text{fall}}|} \tag{1}$$

and duration tilt is given by

$$\text{tilt}_{\text{dur}} = \frac{D_{\text{rise}} - D_{\text{fall}}}{D_{\text{rise}} + D_{\text{fall}}}. \tag{2}$$

Empirical evidence has shown that these parameters are highly correlated (see Sec. IV E) to the extent that a single parameter can be used for both amplitude and durational tilt. This single value is calculated from the averages of both:

$$\text{tilt} = \frac{|A_{\text{rise}}| - |A_{\text{fall}}|}{2(|A_{\text{rise}}| + |A_{\text{fall}}|)} + \frac{D_{\text{rise}} - D_{\text{fall}}}{2(D_{\text{rise}} + D_{\text{fall}})}. \tag{3}$$

The other two tilt parameters, amplitude and duration, are calculated in terms of the sum of the magnitudes of the rises and falls:

$$A_{\text{event}} = |A_{\text{rise}}| + |A_{\text{fall}}|, \tag{4}$$

$$D_{\text{event}} = D_{\text{rise}} + D_{\text{fall}}. \tag{5}$$

C. Segmental and event based views

So far events have been described using what amounts to local information about their amplitude, duration, and shape. There are a number of ways to describe further information, specifically how events are located in time with respect to the rest of the utterance.

There are two possible formally equivalent ways to do this. The first makes use of the filler unit *connection*, implying a segmentally based view in which all the information is presented as a contiguous sequence of units, one ending where the next starts. In this view, connections take durations such that the total duration of an intonational description can be calculated by summing the durations of the connections and events. Connections also have amplitudes so that the starting $F0$ value of an event following a connection is given by the end $F0$ value of the previous event plus the amplitude of the connection.

An alternative view, which does away with the need for connections, is closer to the philosophy of the event based formulation described in the overview. Connections can be eliminated by explicitly attaching time and distance from baseline parameters to the events. For the $F0$ value we designate a parameter *start-F0* which specifies the height in Hz to the start of the event. The simplest way to specify the position parameter is with respect to the start of the utterance, for example, saying that the start of the event is 2.5 s from the start of the utterance. An alternative is to measure position with respect to the syllable with which the event is associated. In practice we have to use a measure which gives the distance from the start of the nucleus of the syllable (usually the vowel) to the peak (the join between the rise and fall) of the event. If the event is rise only the end of the rise is used, if the event is fall only the start of the fall is used. The start of the nucleus is used because it is easy to locate in a segmented utterance and because the start of the syllable itself (that is, the boundary between the current syllable and the previous one), is often difficult to determine.

Measurement with respect to the start of the utterance (absolute position) and with respect to the associated syllable (syllabic position) each have their own advantages. Absolute position is useful when the intonation stream is produced in isolation and where the syllable stream is not present. Syllabic position is useful in that it behaves similarly to the three proper Tilt parameters, and can be considered to be a local parameter which carries intonational significance.

The information in all the formulations is exactly equivalent and one can be mapped to another without loss of information. The decision to use one rather than another is often made on the basis of the practical application in which the model is being used.

D. Interpretation of tilt parameters

Here we briefly describe the significance of each of the Tilt parameters. Amplitude corresponds to the phonetic prominence of an event. While the correspondence is often complex and dependent on context as Gussenhoven and Rietveld (1988) have shown, in general, it is the case that the bigger the amplitude of an event in a given location the more prominence it will receive. Amplitude is measured using the linear Hertz scale. This has the advantage of being easy to interpret, but some additional processing is often required to obtain a more linguistically representative prominence value. For instance, pitch range often narrows toward the end of an utterance and hence an accent excursion of size x Hz at the start of an utterance will be perceived as less prominent than an accent of x Hz at the end (Liberman and Pierrehumbert, 1984).

Duration is measured in seconds. Compared with the other Tilt parameters, duration does not contain much genuine high-level intonational information. While it would in principle be possible to collapse amplitude and duration into a single quantity of intonational *size*, the correlation studies (described in Sec. IV E) have shown that duration and amplitude are not highly correlated and their amalgamation would result in a substantial loss of synthesis accuracy. The variance in the duration parameter mainly arises because of the interaction between the intonation and segmental streams. Differences in duration are often a function of the size of the voiced interval that an event can be realized within: some syllables are longer than others and crucially some have substantially more voicing. It is common to see events associated with short syllables (e.g., ''pot'') to have short durations, while events associated with longer syllables (e.g., ''strength'') to have longer duration.

Tilt is a measure of event shape and represents the relative sizes of the rise and fall components of an event. A value of $+1.0$ indicates a rise, a value of -1.0 indicates a fall, a value of -0.5 indicates an accent with a rise but which has a larger fall, and a value of 0.0 indicates an event with equal sized rise and fall components. Values of 1.0 are often found in boundary events (pure rises), negative values <-0.3 are often found in down-stepped accents, while values around 0.0 often typify simple hat or H^* style accents. Figure 3 shows five different event shapes with their tilt values. Tilt is dimensionless and is not dependent on amplitude or duration.

In addition to the three core Tilt parameters it is also worth mentioning the significance of the *syllabic position* parameter. As Ladd (1996) points out, when discussing temporal relations, it is important to distinguish *association* from *alignment*. Association describes the structural relationship between the intonation stream and the segment stream by saying which units in one are linked to units in the other. Alignment on the other hand describes the temporal relationship between units, and can be important in distinguishing pitch accent type. The syllabic position parameter is used to represent alignment in the Tilt model. In rise–fall events, syllabic position is the distance between the peak of the event (i.e., the boundary between the rise and fall) and the start of the nucleus of the syllable that the event is associated with (the accented syllable). In simple rise or fall events it is the distance between the start of the event and the start of the vowel of the accented syllable. An event which has the same amplitude, duration, and tilt parameters can signal different effects depending on its position. For instance, what are known as H^* and $H+L^*$ accents in the Pierrehumbert notation can often be realized by a simple falling contour: the

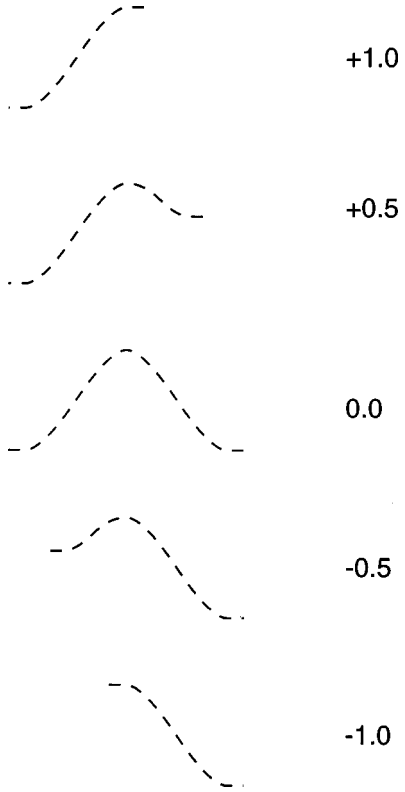

FIG. 3. Examples of five events with varying values of tilt.

difference is that the H^* occurs much later with respect to the vowel than the $H+L^*$. Further discussion of the position parameter is given in Sec. VI D.

E. Modeling accuracy of the tilt and RFC models

The motivation behind mapping RFC parameters into Tilt parameters is to produce a new representation which has less redundancy and is more linguistically meaningful. An assessment of the linguistic relevance of the Tilt model is left to Sec. VI, but here we can give some evidence about the redundancy in the RFC and Tilt representations.

A useful way to examine redundancy in a set of data is to calculate its correlation matrix, which shows the correlation of every parameter against every other parameter. Table VI shows the correlation matrix for the RFC parameters as measured on the DCIEM test set. We can see clearly from the table that a number of parameters are correlated to some extent, for instance, rise amplitude against fall amplitude and rise duration against fall duration.

TABLE VI. Correlation matrix for RFC parameters. Values near 1.0 indicate positive correlation, values near −1.0 indicate negative correlation and values near 0.0 indicate little correlation. Note that the matrix is symmetric and hence only the bottom left corner is shown for clarity.

	Rise amplitude	Rise duration	Fall amplitude	Fall duration
Rise amplitude	1.0			
Rise duration	0.33	1.0		
Fall amplitude	−0.48	−0.04	1.0	
Fall duration	−0.18	−0.46	0.025	1.0

TABLE VII. Correlation matrix for Tilt parameters.

	Amplitude	Duration	Tilt
Amplitude	1.0		
Duration	0.17	1.0	
Tilt	0.06	−0.09	1.0

As explained above, the tilt parameter is calculated by averaging amplitude tilt and duration tilt into a single parameter and it is this which allows the four RFC parameters to be reduced to three Tilt parameters. Is this justified? By combining the two tilt parameters in Eq. (3) we are effectively saying that they are equal: taking the average of the two is simply more robust than using either one alone. We can rearrange the equivalence Eq. (6) to give Eq. (7)

$$\frac{|A_{\text{rise}}|-|A_{\text{fall}}|}{(|A_{\text{rise}}|+|A_{\text{fall}}|)}=\frac{D_{\text{rise}}-D_{\text{fall}}}{(D_{\text{rise}}+D_{\text{fall}})}, \tag{6}$$

$$\frac{|A_{\text{rise}}|}{D_{\text{rise}}}=\frac{|A_{\text{fall}}|}{D_{\text{fall}}}, \tag{7}$$

which states that the magnitude of the gradient of the rise part is equal to the magnitude to the gradient of the fall part. When we actually measure the correlation of the rise and fall gradients for our data we get a high correlation of 0.64, which is higher that any shown in Table VI. The correlation between the amplitude and duration tilt parameters themselves is 0.73. Hence collapsing the amplitude and duration tilt parameters based on correlation is justifiable. Table VII shows the correlation matrix of the tilt parameters for the same data. There is a slight correlation between amplitude and duration (0.17), but virtually no correlation between tilt and amplitude and tilt and duration.

In theory, it is easy to map a set of n-dimensional parameters to a set of $n-1$ dimensional parameters using standard techniques such as principal component analysis. What is more difficult is to achieve parameter reduction without significant loss of information. While the correlation figures just quoted prove that the Tilt system provides a compact set of intonational control parameters which are independent of one another, it is important to prove that little information has been lost in the process. The next section explains how RFC and Tilt representations can be converted back into $F0$ contours and examines the accuracy of this process. Crucially, we show that the reduction of the four RFC parameters to the three Tilt parameters is achieved without significant information loss.

V. TILT SYNTHESIS

The synthesis process of converting Tilt representations into $F0$ contours involves two steps: converting Tilt representations into RFC representations and then converting these into $F0$ contours. Given the Tilt parameters for an event, the RFC parameters can be calculated by equations formed by rearranging Eqs. (3), (4), and (5):

$$A_{\text{rise}}=\frac{A_{\text{event}}(1+\text{tilt})}{2}, \tag{8}$$

$$A_{\text{fall}} = \frac{A_{\text{event}}(1-\text{tilt})}{2}, \tag{9}$$

$$D_{\text{rise}} = \frac{D_{\text{event}}(1+\text{tilt})}{2}, \tag{10}$$

$$D_{\text{fall}} = \frac{D_{\text{event}}(1-\text{tilt})}{2}. \tag{11}$$

The conversion process first involves converting event style descriptions into segmental style descriptions (that is *start* $F0$ and *position* parameters are converted into connection information). Next, Eqs. (8)–(11) are used to produce the RFC parameters for the events. Each event is decomposed into its separate rise and fall components, each of which is synthesized using the following equation:

$$\begin{aligned} f_0(t) &= A_{\text{abs}} + A - 2.A.(t/D)^2, \quad 0 < t < D/2, \\ f_0(t) &= A_{\text{abs}} + 2.A.(1-t/D)^2, \quad D/2 < t < D, \end{aligned} \tag{12}$$

where A is rise or fall amplitude, D is rise or fall duration, and A_{abs} is the absolute $F0$ value at the start of the rise or fall, which is given by the end value of the previous event or connection. Connections are synthesized using straight lines:

$$f_0(t) = A_{\text{abs}} + A.(t/D), \quad 0 < t < D, \tag{13}$$

where A is connection amplitude, D is connection duration, and A_{abs} is as before.

A. Synthesis accuracy

We now address the question of synthesis accuracy. This is measured by taking a Tilt representation for an utterance in the data, synthesizing an $F0$ contour from this and measuring the difference between the synthesized and real contours.

It is well known that listeners are more sensitive to some parts of $F0$ contours then others, for instance, listeners can perceive differences in peak height more readily than valleys. Unfortunately there is no known comparison technique that can mimic this behavior and so we are forced to use a cruder approach whereby all parts of the contour are treated equally. To measure $F0$ contour similarity we use root-mean-squared error and correlation, which are somewhat standard in the literature (e.g., Dusterhoff and Black, 1997; Fujisaki and Ohno, 1997; Ross and Ostendorf, 1994). With root mean squared error, it is not possible to say that one system is better than another if it only has a slightly lower error, but in general the measure is accurate enough to allow confident conclusions to be made about systems with large differences in error. (For example, we cannot really conclude that an error of 14.6 is definitely better than an error of 15.11, but we can state more confidently that a system with an error of 6.94 is better than a system with an error of 15.11.)

Accuracy experiments were conducted on the 1061 utterances in the DCIEM test set. To obtain the Tilt and RFC representations for testing, we used the automatic analysis procedure described in Sec. IV A. This analysis was performed on the events derived from the hand transcriptions and on the events found by the automatic event detection process. For each utterance, the original raw and smoothed $F0$ contours were compared with the contours generated from the RFC and Tilt representations. Table VIII shows the rms error and correlation (ρ) for the comparisons.

TABLE VIII. Accuracy figures for RFC and Tilt synthesis.

Representation	Raw $F0$ rmse	Raw $F0$ ρ	Smooth $F0$ rmse	ρ Smooth $F0$
Complete RFC	14.60	0.651	6.94	0.837
Complete Tilt	14.58	0.647	7.14	0.829
Event only RFC	12.86	0.630	6.82	0.798
Event only Tilt	13.13	0.620	7.15	0.786
Automatic RFC	15.11	0.651	7.16	0.841
Automatic Tilt	15.25	0.644	7.51	0.833

Two clear patterns emerge from the table. First, looking at the first two rows of the table, we see that the artificial contours match the smoothed contours much better than the raw contours. The smoothing technique eliminates $F0$ tracking errors and segmental perturbations, so it can be argued that the smoothed contours are a more meaningful representation to measure against than the raw contours. In a simple attempt to focus on the relevant parts of the contour, the $F0$ regions within the event boundaries were subjected to the same analysis. Rows 3 and 4 show the results. There are slight improvements in rms error and slight reductions in correlation, but the overall pattern is the same as the errors for the complete contour. Rows 5 and 6 show the results for the contours synthesized from automatically detected events. The correlations are about the same and the rms errors are slightly worse than for the hand detected events.

The second pattern we find is that although RFC contours are closer to originals than Tilt contours are to originals, the difference is very small and often insignificant. In other words, the advantage in being able to convert RFC representations into Tilt representations is not at the expense of much synthesis accuracy. To demonstrate this point further, a comparison was conducted between the synthetic RFC contours and the synthetic Tilt contours. The rms error on hand detected events was 0.975 and the correlation was 0.992, on automatically detected events the rms error was 1.26 and the correlation 0.98. To all intents the contours are identical. From the comparison of synthesis accuracy of the Tilt and RFC we can conclude that there is very little information lost in the RFC to Tilt mapping process. While Sec. IV E showed that the three parameters in the Tilt representation are quite independent, the synthesis result shows that the dimension reduction in RFC to Tilt does not throw away much information.

In the Introduction we described one of the goals of an intonation model as being ''wide coverage.'' In fact the test as to whether or not a model has wide coverage can be formulated in terms of a synthesis test. Taken independently from the other two goals, all ''wide coverage'' actually means is that the representation being used, in conjunction with its analysis and synthesis processes, is powerful enough to describe the data under examination. By ''describe'' we mean having the ability to code the original data without information loss. So to check the coverage capability of a

representation, all we have to do is analyze it in terms of the representation, synthesize the data from this, and compare to the original. Representations giving low errors have wide coverage. Of course, it is relatively easy to produce an arbitrary coding scheme which can do this if one does not pay attention to the other goals. But so far we *have* shown that the Tilt model *has* satisfied goals 1, 4, and 5, namely that it uses a constrained representation, and is capable of automatic synthesis and analysis. We now turn to a discussion of the model's fulfilment of the final goal, namely linguistic meaningfulness.

VI. LINGUISTIC MEANING

The most frequent criticism that has been made about the RFC and Tilt models is they are ''only a coding of the $F0$ contour, and are not linguistically meaningful.'' A strict definition of the term linguistically meaningful has been avoided until now, because it is a complex issue and requires discussion in the light of the results reported above. It is difficult to come up with firm (i.e., experimental) evidence for the model's linguistic meaningfulness as there are no simple measures of this, in contrast to the fairly straightforward methods used to demonstrate the Tilt model's success at the other stated goals. However, when we look at this issue more thoroughly, it is clear that it is very difficult to justify the linguistic relevance of *any* existing model of intonation. The following sections discuss various aspects of this issue.

A. Applications

We have stated that the Tilt model has been designed to facilitate intonational processing for speech technology applications, and hence in the first instance we should address the concept of ''linguistically meaningful'' in this sense. For applications, the main requirement is that the Tilt representation is ''usable.'' In a speech analysis environment (e.g., a speech recognition system), this means that Tilt representations should be interpretable by other system components which need to use intonational information. In a synthesis environment (e.g., a text-to-speech system) the requirement is that high-level modules in the system can generate Tilt parameters from other linguistic representations.

The model has been used as the last component in several TTS intonation models. In Taylor and Black (1994) normalized (speaker independent) Tilt parameters were generated from rule based feature descriptions. Speaker specific parameters were then used to produce normal Tilt representations from which $F0$ contours were generated. Black (1997) describes a method for learning Tilt parameters automatically from data and then generating them at synthesis run time. In an extension of this work, Dusterhoff and Black (1997) describe a method for using CART to generate $F0$ contours from high-level information in a text-to-speech system. They do this by training the decision trees to produce Tilt parameters. This study is particularly interesting in that they perform a direct comparison between the Tilt representation and a ToBI labeling of the same data. The Tilt representation gave slightly better performance, showing that at least in this setup it is a useful representation.

The Tilt model has also been successfully applied to speech recognition. Wright and Taylor (1997) describe a system for automatically recognizing the dialogue act of an utterance from an analysis of its intonation. Each utterance is automatically analyzed using the Tilt model and an HMM classifier is used to assign it to one of 12 dialogue act types (such as acknowledgement, yes–no question). This classifier has been used as a component in a speech recognition system and has been shown to help reduce word error rate (Taylor *et al.*, 1998).

While the automatic analysis component has been shown to produce Tilt representations that are useful in systems such as speech recognizers, it is clear that the use of the model in other potential applications is still some way off. For instance, it would be helpful if the analysis system could automatically transcribe data for use for experimental database analysis. Such a use is not recommended, however, as the considerable number of errors produced may have an adverse affect on further analysis.

B. The bias against continuous representations

The Tilt representation uses continuous variables to describe pitch accents, unlike more traditional representations which use discrete categories. Here we take some time to argue that continuous variables can legitimately form part of a linguistic intonational description.

It is traditional in linguistics to deal with categorical (i.e., discrete) representations alone, to such an extent that continuous representations are often deemed unlinguistic in some sense. This has led to properties of intonation that are clearly continuous, such as pitch range and prominence, being largely ignored, and study concentrating on categorical issues only, such as pitch accent type. Despite virtually overwhelming evidence that prominence and pitch range follow regular patterns and have an important linguistic function (Gussenhoven and Rietveld, 1988; Terken, 1991; Ladd, 1996, 1994), these parts of intonation are often called ''paralinguistic'' and omitted from intonational representations simply because of their continuous nature. The bias toward purely discrete representations in linguistics is a hang-over from traditional linguistics and has often been justified because such representations are seen as being properly ''cognitive'' (Pierrehumbert, 1990). Massaro (1998) questions the whole basis of categorical perception in linguistics, explaining that the dominance of this idea arises from equating discrimination with identification, an equivalence which does not really hold. In recent years there has been a growing acceptance of continuous representations in linguistics, partly through the acceptance of connectionist models as legitimate cognitive science. As such, the corollary that only discrete phenomena can be considered cognitive does not hold.

The proponents of what Ladd (1996) terms the Autosegmental-Metrical (AM) school of intonation (Pierrehumbert, 1980; Liberman, 1975; Bruce, 1977) have argued strongly that intonation has a phonological level of representation, in the same way as segmental phonology/phonetics does, and that the sound patterns of intonation are best described with such representations. Much of the evidence for

the phonological level has stemmed from showing that this solved many problems with previous approaches because with a phonology, sound patterns can be described in abstract ways, without having to deal with pitch values directly. This allows meaningful comparison of intonation across speakers who have different pitch ranges, for instance. While we believe that this is one of the major contributions to modern intonation research, we believe the success of this approach is due to the adoption of an *abstract* level of representation in the broad sense, rather than a necessarily *phonological* one in the traditional discrete sense. Just because abstract representations have proved useful, and because they share many similarities with the structures of segmental phonology, it does not follow that abstract intonational representations are necessarily phonological *in the same way*.

A crucial property of segmental phonology is that the connection between the semantic and phonological properties of a lexical item is arbitrary. This is proved by showing that two words (for example, ''pill'' and ''bill'') which sound similar do not necessarily mean similar things. Crucially, we can prove that the segmental phonological space is discrete by showing that is impossible to *perceive* a sound which is half way between a /b/ or a /p/. It has been shown in synthesis experiments that if listeners are played a pattern of words such as ''pill,'' each time with more voicing in the initial stop, at some stage they will start to perceive the word ''bill.'' At no point, however, although the sound pattern is half-way between a normal /p/ and /b/, will the listeners conjure up a half-way semantic image of an entity which is a bit ''bill''-like and a bit ''pill''-like. Thus although there might be an acoustic continuum, there is a sharp perceptual boundary which prohibits interim semantic representations.

There is no evidence that intonation behaves in such a way. It is clear that different acoustic intonation patterns can give rise to different semantic interpretations, but the crucial point is that the connection between intonational sound and meaning is not arbitrary in the same way, and that if intonational sound S_A gives rise to meaning M_A and sound S_B gives rise to meaning M_B, then a sound half-way between S_A and S_B can certainly give rise to a meaning somewhere between M_A and M_B. In other words, there has been no evidence to show that there are strict boundaries between intonational units which signal abrupt changes in meaning. Some studies have shown (Kohler, 1991b, 1991a; Pierrehumbert and Steele, 1989) that subjects do assign distinct semantic categories to certain pitch accent patterns. These studies lend support, however, to the idea that the mapping from the acoustic to semantic space is complex and nonlinear, but do not prove the key point with regard to categories, i.e., that there is a sharp semantic boundary occurring within a continuous acoustic range.

Ladd (1996) in fact uses just this argument as support for there being proper, discrete phonological categories in intonation. In linguistics (including the phonological part of intonation) he claims that ''close similarity of phonetic form is generally of no relevance for meaning'' and states that in contrast ''semantic continua are matched by phonetic ones'' in paralinguistics. Crucially, he does not state the *actual* defining properties of a categorical system, namely that there should be strict and identifiable boundaries between the categories.

Further evidence for problems with categorical intonational classification come from consideration of how one would actually go about producing a phonological inventory for a new accent or language. In segmental linguistics, the classical way to determine the phonological units of a language is via the use of minimal pairs. This is how one can find out whether, for instance, [r] and [l] are distinct phonological units (as in English) or whether they are allophonic (as in Japanese). By knowing that the words ''crown'' and ''clown'' have clearly different meanings, we know that in English [r] and [l] are phonologically distinct units. No one has yet produced an equivalent test for intonational units.

Traditionally the argument about categorization in intonation has revolved about a false dichotomy, namely that the relationship between sound and meaning can either be as in segmental phonology, where the relationship is completely arbitrary, or as in paralanguage, where the relationship is a simple linear one. In fact this is an inappropriate application of the law of the excluded middle and one does not have to choose either of these positions: a third position is that intonation is continuous with regard to both sound and meaning, but that the relationship between the two is highly complex and nonlinear. Adopting such a position can explain why simple attempts to prove direct correspondence between sound and meaning in intonation have failed, but also why it is so hard to produce evidence for categorical boundaries. In this view pitch accents occupy positions in a multidimensional sound space, and in effect what H^* and L^*, etc., represent are points of particular importance in this space. One can think of this as somewhat analogous to how people describe the temperature of an object when they are touching it. Physically, temperature is a continuum with no distinct categories, but it is helpful to have terms such as hot and cold which describe certain temperature situations. This is not troublesome as long as we accept this as just a convention, and we do not insist that underlying temperature is categorical. It is pointless to go further and try to define strict boundaries on what is underlyingly a continuous phenomenon. While there will be a lot of agreement as to what hot and cold represent under these conditions, there will always be temperatures between the two which are impossible to categorize either way. Going back to intonation, it is clear that a typical H^* accent is different from a typical L^* accent, the point is that there are accents in between which could be described as either. We again re-iterate the point that proof of the existence of categories depends on the proof of the existence of category boundaries.

C. Phonetics and phonology in the Tilt model

The Tilt representation as described here can be termed *phonetic* because its purpose is to describe observable linguistic sound phenomena. Although the focus of our paper is on this representation and its relationship with the acoustics, it is useful to informally discuss the relationship between the phonetic Tilt representation and higher-level, phonological representations. The parameters used to describe events in

the Tilt representation are quite literal with respect to measurable acoustic quantities, and hence we have duration and position measure in seconds, and amplitude in Hertz. We advocate that a phonological representation in the Tilt model should have the same parameters as the phonetic representation (with the possible exception of duration, see below), but that their *scales* should be modified so as to represent higher level phenomena more appropriately.

For instance, the amplitude parameter should reflect genuine perceptual prominence, rather than simple acoustic magnitude. Different speakers have different pitch ranges and these differences should be accounted for in a phonological representation. It has been widely shown (Cohen *et al.*, 1982; Pierrehumbert, 1980; Liberman and Pierrehumbert, 1984; Ladd, 1984) that pitch range narrows toward the end of an utterance. This means that a pitch accent at the start of an utterance needs a bigger $F0$ amplitude than an accent at the end to produce an effect of equal prominence in a listener. Hence it would be desirable for phonological Tilt amplitude to be normalized with respect to pitch range and that amplitude should be a measure of perceived prominence.

As stated in Sec. IV D, the duration and position parameters are dependent on the local segmental content of the utterance which is undesirable from a phonological point of view. In fact it is possible that the duration parameter is wholly dependent on segmental content and carries no phonological information at all. If this were the case, then the number of parameters in the phonological Tilt representation could be reduced. The position parameter, which certainly does contain high-level information, should be normalized with respect to the segmental content.

The tilt parameter itself is dimensionless and so is independent of amplitude and time scales. Hence it is possible that this is already as abstract as it needs to be and does not require modification.

It light of our previous discussion we think it is entirely appropriate for the phonological representation to have continuous parameters. The key point about the scales of phonological representation is that events which are perceived as being the same should have the same values in the Tilt representation.

The difference between phonetic and phonological representations in the Tilt model can also be versed in terms of speaker dependence. All speakers of the same accent and language should produce the same phonological representation for say a common neutral fall type of accent. However, the phonetic Tilt parameters of these speakers would be expected to differ, due to speaking style and physiology. Hence a phonetics-phonology component of the model would be responsible for modeling speaker differences.

D. Comparison with the AM/ToBI models

We now discuss the similarities between the Tilt model and the AM/ToBI models. In many respects the models are very similar. Both adopt the same approach to intonational primitives, namely that the intonational representation of an utterance should be a linear sequence of event based intonational entities, associated with syllables/segments in an autosegmental structure. Following from this, both agree that

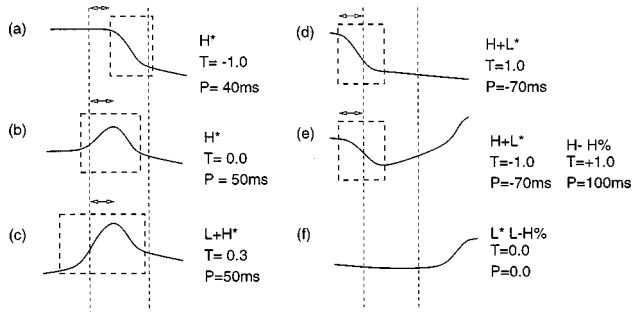

FIG. 4. Examples of Tilt and AM representations for various common types of utterance. The dashed boxes delimit the events, while the dotted vertical lines show the boundaries of the accented vowel.

downdrift in intonation can be accounted for by a combination of pitch accent downstepping and gradual falls in pitch range, and hence that downdrift should not be modeled by global phrase patterns. While the phonetic aspects of the AM are often ignored, both models agree that intonation can be described using a high level abstract sound representation, i.e., a phonology.

Some differences arise from the phonetics/phonology mismatch of the models. Phrase tones (*H-* and *L-*) are used in the AM model as a mechanism to differentiate four types of post-nuclear intonation. Phrase tones are purely phonological units, having no direct $F0$ realization and hence there is no equivalent for these in the Tilt model. In a similar way, there is no equivalent for the low boundary tone (*L*%). Falling post nuclear intonation is usually modeled by a single connection, and only rising boundaries have an event. The observed variation in post nuclear intonation is modeled by using different parameters for the connections and rising events. Level accents may legitimately be part of a phonological representation but are absent from the phonetic one because they have no observable $F0$ behavior. If deemed desirable, such accents could be accommodated in the Tilt model as entities with zero amplitude, duration, and tilt, and hence the issue as to whether or not level accents should be represented may not be of great consequence.

Accepting that Tilt duration is probably a purely phonetic phenomena, we now discuss the relationship of the more phonological Tilt parameters (amplitude, tilt, and position) with respect to the AM model. To simplify the discussion, we assume that these three parameters have been normalized and are represented on phonological scales in the way described in Sec. VI C. Some varieties of the AM model, for example the original Pierrehumbert system (Pierrehumbert, 1980; Ladd, 1987), actually have an amplitude parameter very similar to the type we propose for the phonological Tilt model. Because of the paralinguistic argument, this is often treated separately from the system used to describe accent type. Having accounted for duration and amplitude, we now turn to showing how the the position and tilt parameters relate to the tonal accent classification system of the AM model. Figure 4 shows typical tilt and position parameters for some accent and boundary tone combinations. Figure 5 is an impressionistic plot, with one axis representing tilt and the other position. This plot maps the space of possible pitch accents and shows how tilt and position reflect

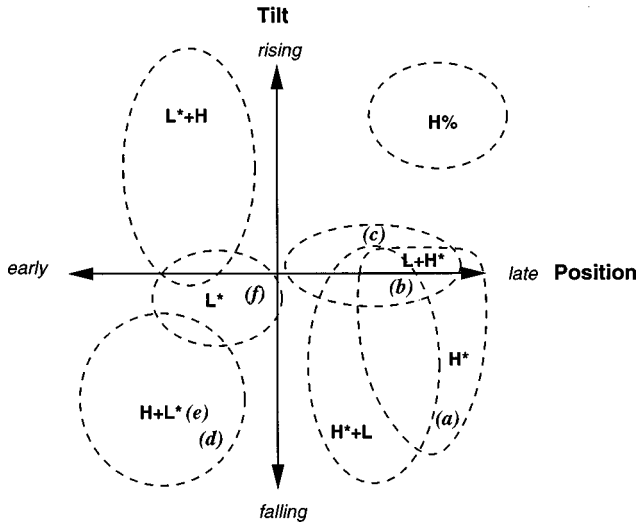

FIG. 5. Two dimensional schematic representation of intonational space. The letters in brackets refer to the example contours in Fig. 4. It is clear from this digram that many AM accents have large overlapping distributions, while there are also substantial areas of this space that are not covered by any AM accent type.

the natural variation in pitch accent types. The relevant AM accents and boundary tones have been marked to show how each relates to the tilt parameters.

As should be clear by now, the main area in where the models disagree is that the Tilt representation uses continuous parameters to model events whereas the AM model uses discrete classes. Although we think that it is an important point in its own right to demonstrate the tenuous nature of categorical descriptions in intonation, we further argue that the adoption of such description mechanisms is actually harmful in that it does not provide a satisfactory means to describe intonational events. The first problem is that because of the difficulty in defining class boundaries, it is very difficult for machines and humans to label naturally occurring speech using the AM system. While it is simple enough for experts to produce canonical examples of different pitch accents and get agreement when labeling these, the situation is very different in natural speech. Leaving the distribution problem aside (see below), it has been our experience that even linguists trained in intonation find it difficult to decide which class a particular accent belongs to. As human labelers must provide the data on which automatic systems are to be trained and tested, badly labeled data cannot be expected to facilitate accurate automatic systems. The second problem is that in naturally occurring speech, the distribution of AM pitch accent types is extremely uneven. In the RN corpus about 79% of all accents in the corpus fall into the H^* category, and 15% into the $L+H^*$ category. From an information theoretic point of view, any classification system which lumps the vast majority of tokens into a single type is not very useful because it does not actually provide tell us much about the tokens. Importantly, within the vast H^* class, there actually is a substantial amount of variation which is linguistically meaningful and this information is lost.

These problems of labeling difficulty and unevenness of distribution are not present in the Tilt model as the continuous parameters express the differences in pitch accents naturally without having to resort to a forced classification.

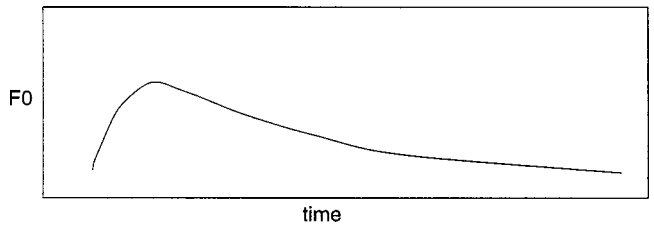

FIG. 6. Fujisaki phrase component.

E. Comparison with the Fujisaki and other models

The Fujisaki model (Fujisaki and Ohno, 1997) has many similarities to the Tilt model. It is a fully formal and quantitative phonetic model and hence has a defined synthesis algorithm. It too models accents as events, with no categorical accent types built in to the model and it uses an amplitude and a duration parameter for event parameterization.

However, the models differ in significant ways. First, the Tilt model allows the gradients of the rise and fall parts of events to vary. While some gradient variation in the rises and falls of the Fujisaki models accents is possible, this is minor and indirect and due to the gradient of the underlying phrase component. From our study of rise and fall pitch accent gradients in our database, it is clear that substantial variation is possible, and that any model which advocates fixed gradients will have substantially worse synthesis accuracy that the Tilt model. Second, the Fujisaki model makes use of a phrase component, which dictates the global shape of the $F0$ contour over the length of a phrase. The shape of this is shown in Fig. 6. Again, we think this is too constrained and cannot account for the wide range of observed long term contour shapes in English. For example, in the contour shown in Fig. 7, the intonation is slowly and steadily rising after the first event. Fujisaki (personal communication) has suggested that this can be modeled by stacking several phrase components on top of each other in short intervals. While such a solution could recreate the shape shown in the contour, it is has a severe price, in that all reference between the position of the phrase component and its linguistic meaningfulness has been lost.

In summary, it seems the Fujisaki model does not have enough degrees of freedom to synthesize English intonation and still keep some sense of linguistic relevance.

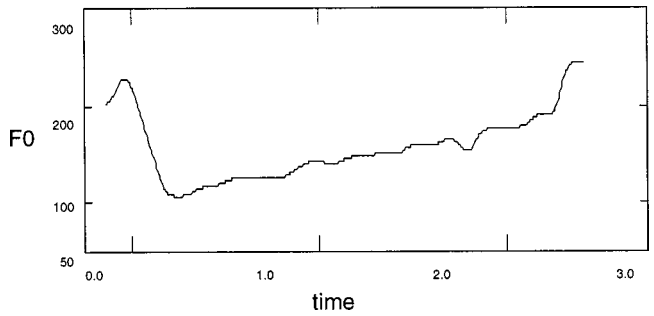

FIG. 7. Contour with slowly rising intonation.

A number of other intonation models have been proposed in more recent years including (Strom, 1995; Portele and Heuft, 1998; Sproat, 1998; Möhler and Conkle, 1998). All of these models have been designed for mainly speech technology purposes and it is striking that they model $F0$ contours with continuous parameters. Some (Portele and Heuft, 1998; Möhler and Conkie, 1998) in particular bear a strong resemblance to the RFC model providing support for the idea that the parameters of the RFC model (and the Tilt model derived from it) are not purely arbitrary.

VII. CONCLUSION

We conclude with an examination of how well the Tilt model has fulfilled the five goals described in the Introduction. The issues of *constraint* and *wide coverage* go hand in hand as they are essentially concerned with the *degrees of freedom* of a model. Put simply, a model with too many degrees of freedom will be able to model the data well but will have a large amount of redundancy in its representation. A model with too few degrees of freedom will have a compact representation but will not be able to synthesize the data accurately nor differentiate certain phenomena. The results in Table VII show that the Tilt representation is compact and has low redundancy, while still producing wide coverage, as shown by the synthesis accuracy results in Table VIII. We therefore conclude that an appropriate balance has been found between constraint and wide coverage. We have stated that the duration parameter may be purely phonetic in nature, and that only amplitude, position, and tilt should be considered as parameters with a phonological correspondence.

The proof of any representation's linguistic meaningfulness is difficult, but we hope that the discussion of this issue in Sec. VI has at least shown that continuous parameters can form the basis of a high-level intonational representation and that, furthermore, the tilt and position parameters map the intonational space elegantly. In the end we take a pragmatic approach to the issue of deciding whether one representation system is better than another. If the bias against continuous representations is removed, we think that the Tilt model compares well against the AM model in that it provides a simple representation which solves many of the problems that categorical representations impose.

A long raging argument in the field has been whether intonation should be regarded as a tonal or contour (shape) phenomenon (see Ladd, 1996). While this may be an interesting theoretical question, for the computational goals presented here, it is somewhat beside the point. For practical purposes, a more important goal than discovering the nature of intonational primitives is to assess a model in terms of the criteria explained in the Introduction. A model with good coverage, accuracy, and linguistic meaningfulness is better than a model without these, regardless of which one is tonal or contour.

It is in the area of automatic analysis that perhaps most future improvement could be made. Spontaneous speaker independent conversational speech is one of the most challenging types of speech for any system, and hence it is a solid achievement that the event detector can achieve the level of success that it does on this task. However, with performance figures on the DCIEM data of 72.7% correct, 47.7% accuracy for all accents and 81.9% and 60.7% for nonminor accents there is obviously room for improvement. It should be pointed out that it is not necessary to use this particular event detection algorithm with the Tilt model: any system that can locate events and give their boundaries can be used. As explained in Sec. III A our system is an event *detector* but there is nothing to stop an event *classifier* (e.g., Ross and Ostendorf, 1995) being used in conjunction with the model. The choice of a classifier or detector essentially depends on whether a phonetic segmentation is available in the application.

Table VIII shows that the Tilt model can synthesize $F0$ contours with a high degree of accuracy. Given that the just noticeable difference for $F0$ in natural speech has been estimated at about 4 Hz (Hess, 1983), the figures for the comparison between the synthesized and smoothed contours show that the synthetic contours are nearly identical to the smoothed ones. Raw contours differ from smoothed ones mainly due to the presence of segmental glitches and perturbations. The Tilt synthesis procedure has not attempted to model these in any way, and hence the errors for the synthetic versus raw comparison are worse.

In summary, we have shown that the Tilt model has been fairly successful at fulfilling our original goals. We have tested the model rigorously on read speech and spontaneous dialogue speech from a number of different speakers in different situations. We think the success of the model has been to find a suitable balance between the conflicting goals, so that the model facilitates automatic analysis and synthesis and provides a useful and elegant linguistic representation of intonation.

ACKNOWLEDGMENTS

The author wishes to acknowledge the support of the U.K. Engineering and Physical Science Research Council, who funded much of the work on automatic analysis and recognition (Grant No. GR J55106). Steve Isard and Bob Ladd both offered detailed comments on all the work reported. The many discussions with them lead to useful insights into how best to explain this work. Thanks also to the two reviewers who offered a considerable amount of advice on how to improve this article. Some of the Tilt theory was developed during my stay at ATR Interpreting Telecommunications labs, and I am grateful to everyone there for their support during that period.

APPENDIX A: MAPPING FROM ToBI TO TILT LABELS

Despite the statement in Sec. VI A that the Tilt and AM models are both based on intonational events, there are important technical differences in the way that AM (i.e., ToBI) and Tilt label files are actually constructed. In Sec. III E we described experiments where a Tilt transcription of the Boston University Radio News (RN) corpus was derived by from the original ToBI transcriptions. We briefly explain how this was done.

The RN corpus was labeled using the guidelines in Beckman and Ayers (1993) and the transcriptions are format-

ted in xwaves xlabel files. Xwaves files contain a list of elements, one per line, where each line contains a label name and a time, normally representing the end of the label. In the ToBI files, the time in each line represents the notional *center* of the pitch accent, e.g., the time of an *H** is marked at its peak. As the Tilt event detector is trained on events whose start and end times are marked, the ToBI transcriptions need to be realigned so as accent start and end times rather than accent middles are marked. There is no single ''right'' way, but we estimate the start and stop times by assuming that the time given is the literal middle of the event, and then marking the start and end times as being $d/2$ before and after this where d is the average duration of an event in another database ($d = 210$ ms in the DCIEM corpus). Connections are inserted between non-contiguous events and phrase tones and low boundary tones are deleted.

APPENDIX B: SOFTWARE AND CORPORA AVAILABILITY

The HTK toolkit was used in the event detection experiments. It is available under licence from Cambridge Entropic Labs, U.K. (Young *et al.*, 1996).

All the other software, including the super resolution pitch detection algorithm, Tilt analysis, Tilt synthesis and transcription comparison code is included in the Edinburgh Speech Tools, a publicly available speech software toolkit available from http://www.cstr.ed.ac.uk/projects/speech_tools.html.

The CART based $F0$ generation algorithm (Dusterhoff and Black, 1997) which uses the Tilt model is implemented in the Festival speech synthesis system, available from the above address.

The original DCIEM, Boston University Radio News and Switchboard databases can be licenced from the Linguistic Data Consortium, http://www.ldc.upenn.edu. These databases contain the original waveforms and transcriptions.

Derived $F0$ and energy contours, and the Tilt model labelings for all the experiments reported here are available from http://www.cstr.ed.ac.uk/projects/intonation.

Bagshaw, P. C., Hiller, S. M., and Jack, M. A. (**1993**). ''Enhanced pitch tracking and the processing of $f0$ contours for computer aided intonation teaching,'' in Proc. Eurospeech '93, Berlin, pp. 1003–1006.

Bard, E. G., Sotillo, C., Anderson, A. H., and Taylor, M. M. (**1995**). ''The DCIEM map task corpus: Spontaneous dialogues under sleep deprivation and drug treatment,'' in Proc. of the ESCA-NATO Tutorial and Workshop on Speech under Stress, Lisbon, pp. 25–28.

Baum, L. E. (**1972**). ''An inequality and associated maximization technique in statistical estimation for probabilistic functions of a Markov process,'' Inequalities **3**, 1–8.

Beckman, M. E., and Ayers, G. M. (**1993**). *Guidlines for ToBI labelling*, Technical Report Version 1.5, Ohio State University.

Black, A. W. (**1997**). ''Predicting the intonation of discourse segments from examples in dialogue speech,'' in *Computing Prosody*, edited by Y. Sagisaka, N. Campbell, and N. Higuchi (Springer, New York), pp. 117–128.

Bruce, G. (**1977**). ''Swedish Word Accents in Sentence Perspective,'' Ph. D. thesis, University of Lund.

Cohen, A., Collier, R., and t'Hart, J. (**1982**). ''Declination: Construct or intrinsic feature of speech pitch,'' Phonetica **39**, 254–73.

Dusterhoff, K., and Black, A. (**1997**). ''Generating intonation contours for speech synthesis using the tilt intonation theory,'' in Proc. ESCA workshop on Intonation: Theory Models and Applications, Athens, pp. 107–110.

Fujisaki, H., and Ohno, S. (**1997**). ''Comparison and assessment of models in the study of fundamental frequency contours of speech,'' in Proc. ESCA workshop on Intonation: Theory Models and Applications, Athens, pp. 131–134.

Godfrey, J., Holliman, E., and McDaniel, J. (**1992**). ''SWITCHBOARD: Telephone speech corpus for research and development,'' in Proc. ICASSP '92, San Fransisco, pp. 517–520.

Goldsmith, J. (**1989**). *Autosegmental and Metrical Phonology* (Blackwell Scientific, New York).

Granstrom, B. (**1997**). ''Applications of intonation—An overview,'' in Proc. ESCA workshop on Intonation: Theory Models and Applications, Athens, pp. 21–24.

Gussenhoven, C., and Rietveld, T. (**1988**). ''Fundamental frequency declination in Dutch: Testing three hypotheses,'' J. Phonetics **16**, 355–369.

Hess, W. (**1983**). *Pitch Determination of Speech Signals* (Springer-Verlag, New York).

Hirst, D. (**1992**). ''Prediction of prosody: An overview,'' in *Talking Machines*, edited by G. Bailley and C. Benoit (North Holland, New York), pp. 199–204.

Hunt, A. J., and Black, A. W. (**1996**). ''Unit selection in a concatenative speech synthesis system using a large speech database,'' in *Proc. ICASSP '96, Atlanta* (IEEE, Bellingham), pp. 373–376.

Kohler, K. J. (**1991a**). ''The perception of accents: Peak height versus peak position,'' in *Studies in German Intonation*, edited by K. J. Kohler (Universität Kiel, Kiel), pp. 72–96.

Kohler, K. J. (**1991b**). ''Terminal intonation patterns in single-accent utterances of German: Phonetics, phonology and semantics,'' in *Studies in German Intonation*, edited by K. J. Kohler (Universität Kiel, Kiel), pp. 53–71.

Ladd, D. R. (**1984**). ''Declination: A review and some hypotheses,'' Phonlogy Yearbook **1**, 53–74.

Ladd, D. R. (**1987**). ''A model of intonational phonology for use with speech synthesis by rule,'' in Proc. European Conference on Speech Technology, Edinburgh, pp. 21–24.

Ladd, D. R. (**1994**). ''Constraints on the gradient variability of pitch range,'' Papers in Laboratory Phonology **3**, 43–63.

Ladd, D. R. (**1996**). *Intonational Phonology*, Cambridge Studies in Linguistics (Cambridge University Press, Cambridge).

Lea, W. A. (**1980**). *Prosodic Aids to Speech Recognition* (Prentice Hall, Englewood Cliffs, NJ).

Liberman, M. (**1975**). ''The Intonational System of English,'' Ph.D. thesis, MIT. Published by Indiana University Linguistics Club.

Liberman, M., and Pierrehumbert, J. (**1984**). ''Intonational invariance under changes in pitch range and length,'' in *Language Sound Structure*, edited by M. Aronoff and R. T. Oehrle (MIT Press, Boston), pp. 157–233.

Massaro, D. W. (**1998**). ''Categorical perception: Important phenomena or lasting myth,'' in Proc. ICSLP '98, Sydney, pp. 2275–2278.

Medan, Y., Yair, E., and Chazan, D. (**1991**). ''Super resolution pitch determination of speech signals,'' IEEE Trans. Signal Process. **39**, 40–48.

Möhler, G., and Conkie, A. (**1998**). ''Parametric modeling of intonation using vector quantization,'' in Proc. Third ESCA/IEEE workshop on speech synthesis, Jenolan Caves, Sydney, pp. 311–314.

Ostendorf, M., Price, P. J., and Shattuck-Hufnagel, S. (**1995**). ''The Boston University radio news corpus,'' Technical Report ECS-95-001, Boston University.

Pierrehumbert, J. B. (**1980**). ''The Phonology and Phonetics of English Intonation,'' Ph.D. thesis, MIT. Published by Indiana University Linguistics Club.

Pierrehumbert, J. B. (**1990**). ''Phonological and phonetic representations,'' J. Phonetics **18**, 375–394.

Pierrehumbert, J. B., and Steele, S. A. (**1989**). ''Categories of tonal alignment in english,'' Phonetica **46**, 181–196.

Pitrelli, J. F., Beckman, M. E., and Hirschberg, J. (**1994**). ''Evaluation of prosodic transcription labeling reliability in the ToBI framework,'' in Proc. ICSLP '94, Yokohama, Vol. 1, pp. 123–126.

Portele, T., and Heuft, B. (**1998**). ''The maximum-based description of $f0$ contours and its application to english,'' in Proc. ICSLP '98, Sydney, pp. 663–666.

Ross, K., and Ostendorf, M. (**1994**). ''A dynamical system model for generating $F0$ for synthesis,'' in Proc. Second ESCA/IEEE Workshop on Speech Synthesis, New York, pp. 131–134.

Ross, K., and Ostendorf, M. (**1995**). ''A dynamical system model for recognising intonation patterns,'' in Proc. Eurospeech '95, Madrid, pp. 993–996.

Secrest, B. G., and Doddington, G. R. (**1983**). ''An integrated pitch tracking algorithm for speech systems,'' in Proc. ICASSP '83, Boston, pp. 1352–1355.

Silverman, K., Beckman, M., Pitrelli, J., Ostendorf, M., Wightman, C., Price, P., Pierrehumbert, J., and Hirschberg, J. (**1992**). ''ToBI: a standard for labelling English prosody,'' in Proc. ICSLP '92, Banff, Vol. 2, pp. 867–870.

Sproat, R. (**1998**). *Multilingual Text-to-Speech Synthesis: The Bell Labs Approach* (Kluwer Academic, New York).

Strom, V. (**1995**). ''Detection of accents, phrase boundaries and sentence modality in German with prosodic features,'' in Proc. Eurospeech 95, Madrid, pp. 2039–2041.

Taylor, P. A. (**1995**). ''The rise/fall/connection model of intonation,'' Speech Commun. **15**, 169–186.

Taylor, P. A., and Black, A. W. (**1994**). ''Synthesizing conversational intonation from a linguistically rich input,'' in Proc. Second ESCA/IEEE Workshop on Speech Synthesis, New York, pp. 175–178.

Taylor, P. A., King, S., Isard, S. D., and Wright, H. (**1998**). ''Intonation and dialogue context as constraints for speech recognition,'' Language and Speech **41**, 491–512.

Terken, J. (**1991**). ''Fundamental frequency and perceived prominence of accented syllables,'' J. Acoust. Soc. Am. **89**, 1768–1776.

t'Hart, J., and Collier, R. (**1975**). ''Integrating different levels of intonation analysis,'' J. Phonetics **3**, 235–255.

Waibel, A. (**1986**). ''Prosody in speech recognition,'' Ph.D. thesis, Carnegie Mellon University, Pittsburgh, Pennsylvania.

Woodland, P., Leggetter, C. J., Odell, J. J., Valtcher, V., and Young, S. J. (**1995**). ''The 1994 HTK large vocabulary speech recognition system,'' in *Proc. ICASSP '95, Detroit* (IEEE, Bellingham), pp. 1–6.

Wright, H., and Taylor, P. A. (**1997**). ''Modelling intonational structure using hidden markov models,'' in Proc. ESCA workshop on Intonation: Theory Models and Applications, Athens, pp. 333–336.

Young, S., Jansen, J., Odell, J., Ollason, D., and Woodland, P. (**1996**). *HTK manual*, Entropic.

Rheo-acoustical study of the shear disruption of reversible aggregates. Ultrasound scattering from concentrated suspensions of red cell aggregates

L. Haider[a)]
Groupe de Recherche en Physique et Biophysique (GRPB), UFR Biomédicale, 45 rue des Sts-Peres, 75270 Paris Cedex 06, France

P. Snabre[b)]
Institut de Science et de génie des matériaux et procédés, UPR 8521, B.P.5 66125 Font-Romeu, France

M. Boynard[c)]
Groupe de Recherche en Physique et Biophysique (GRPB), UFR Biomédicale, 45 rue des Sts-Peres, 75270 Paris Cedex 06, France

(Received 26 May 1999; revised 28 August 1999; accepted 23 November 1999)

Shear-induced disruption of reversible aggregates or clusters in a concentrated suspension is investigated by ultrasound backscattering in the low shear regime. Fractal aggregates are considered as non-Brownian scatterers much smaller than the wavelength with acoustic properties close to those of the surrounding liquid, so that the attenuation of the coherent field is weak and multiple scattering can be neglected. The concept of variance in local particle volume fraction is used to deduce a first-order expression of the ultrasound scattering cross section per unit volume for Rayleigh scatterers in a dense suspension. On the basis of a scaling law for the shear-induced disruption of aggregates, the shear stress dependence of the ultrasonic scattered intensity from a dense suspension of clusters is derived. In a second part, the shear breakup of hardened red blood cell aggregates is investigated in plane–plane flow geometry by ultrasound scattering. Rheo-acoustical experiments are analyzed within the framework of the self-consistent field approximation and the scaling laws currently used in microrheological models. Finally, the ability of ultrasonic, light reflectometry and viscometry methods to provide quantitative information about red blood cell aggregation and membrane adhesiveness is discussed. © *2000 Acoustical Society of America.* [S0001-4966(00)01203-0]

PACS numbers: 43.80.Gx, 43.80.Ev, 43.35.Bf [FD]

INTRODUCTION

Characterization of biological tissues with ultrasound has been a subject of wide interest for at least two decades in the medical field. In general, specific acoustic characteristics such as tissue attenuation or wave phase velocity were believed to be capable of delineating tissues and perhaps disease states from one another.[1] However, the scattering behavior of tissues like liver, heart, kidney or blood is complex and depends on several factors such as the acoustic impedance or compressibility of the scatterers and the surrounding medium, as well as the space distribution and the length scale of scattering inhomogeneities.[2] The interest of using ultrasonic scattering to detect red blood cell aggregation *in vitro*[3–6] as well as *in vivo*[7–9] has been demonstrated for more than 20 years. For example, the fact that blood can be imaged ultrasonically could have significant clinical relevance. Experimental investigations were aimed at elucidating factors affecting the backscattered power of red blood cell aggregates at rest[10,11] and under flowing conditions.[12–16] It is now well established that the echogenicity of blood depends on the shear stress, the hematocrit, the ultrasound frequency and the concentration of macromolecules responsible for red cell aggregation. Among these factors, the shear stress is the most important parameter affecting the blood scattering power under flowing conditions.

The ultrasound scattering technique is well suited for investigating rheological properties of suspensions and particularly the aggregation processes of red blood cells since the aggregates are usually much smaller than the ultrasound wavelength and thus the scattered power from a single aggregate varies as the square of the cluster volume (Rayleigh scattering regime).[17] However, both the internal structure of porous aggregates and coherence effects may influence scattering from suspensions.[18–21] Most of the recent contributions about ultrasound scattering from suspensions concern the Doppler instrumentation[22] and were focused on understanding the relationship between the ultrasonic scattered power and particle volume fraction under different flow conditions.[15,23,24] Little attention has been paid to the ultrasound scattering from a dense distribution of aggregates and most experimental works remain empirical[12,15,22] since multiple hydrodynamic interactions in a concentrated suspension influence the dynamical size of aggregates.[25]

[a)]Present address: 5665 Sherbrooke Ouest, Montreal, Quebec QCH4A 1W6, Canada.
[b)]Electronic mail: snabre@imp-odeillo.fr. Author to whom correspondence should be addressed.
[c)]Electronic mail: boynard@citi2.fr

Non-Newtonian behavior of weakly flocculated suspensions such as blood results from the rupture of aggregates when increasing the shear stress. Several authors have recently proposed microrheological models to describe the rheology of concentrated suspensions of fractal clusters and viscoelastic particles.[26–32] Severe difficulties arising from many body interactions have been roughly resolved by making hydrodynamic assumptions. The microrheological models developed by one of the authors[30–32] is based on a self-consistent field approximation assuming that the viscosity of the effective medium surrounding an aggregate is the viscosity of the suspension. Computer simulations further suggest a power law for the shear stress dependence of the equilibrium radius of aggregates in a shear field.[33] However, little is known about the exact form of the scaling law which depends both on flow type and the reversibility of cluster deformation under the action of external stresses.

In the present paper, shear breakup of aggregates is investigated by ultrasound backscattering in the low shear regime. We consider non-Brownian particles or aggregates smaller than the wavelength and scatterers with acoustic properties close to those of the surrounding liquid so that the attenuation of the coherent incident wave remains negligible and multiple scattering can be ignored. From these assumptions, hydrodynamic effects dominate over Brownian motion and the Rayleigh scattering theory can be used to estimate the single scattered incoherent intensity from a dilute random suspension. In the concentrated regime, particles or aggregates can no longer be considered as independent and correlation effects influence the ultrasonic scattered power because of wavelet interference in a dense distribution of scatterers.[19] The scattered power can be considered as the result of imperfect wave destruction either associated with a packing factor[20,34] or with the variance in local scatterer concentration.[35,36]

The first section concerns ultrasound scattering from a dense suspension of fractal aggregates small compared to the wavelength. A first-order expression of the ultrasound scattering cross section per unit volume for a dense suspension of Rayleigh aggregates is derived from the concept of variance in local particle concentration. The fractal scattering regime for aggregates larger than the ultrasound wavelength is further discussed.

In the second section, a scaling law for the dynamical equilibrium size of aggregates in a shear flow is used to describe the shear stress dependence of the ultrasonic backscattered power from a dense suspension of reversible aggregates.

In the third section, ultrasound scattering from a suspension of hardened red blood cell aggregates is investigated experimentally as a function of particle volume fraction and shear rate in plane–plane flow geometry. The experimental results are discussed on the basis of the Rayleigh scattering theory and scaling laws proposed in the second section.

Light scattering is in many aspects analogous to ultrasound scattering and also provides a way to investigate the shear breakup of red cell aggregates in concentrated suspensions.[25] The viscosity behavior of aggregated suspensions is further strongly influenced by the shear-induced disruption of aggregates.[30,31] The ability of ultrasonic, light reflectometry and viscometry methods to give quantitative information about red blood cell aggregation and membrane adhesiveness is finally discussed.

I. ULTRASONIC SCATTERING FROM A SUSPENSION

Under consideration is a homogeneous distribution of particles of characteristic size a and volume fraction ϕ dispersed in a liquid and probed by an ultrasound wave normally incident upon the half-space of scatterers. Weakly scattering particles small compared to the ultrasound wavelength λ (Rayleigh scattering regime, i.e., low-frequency scattering regime) with acoustic properties (density and compressibility) close to those of the surrounding liquid are considered. The last condition ensures a negligible attenuation of the incident plane wave propagating through the slab. The shear wave propagation and wave mode conversion effects can be ignored since the shear and bulk viscosities of the suspension are relatively small. Therefore, the attenuation of the incident ultrasound wave due to viscous losses is negligible and ultrasound scattering mainly results from the mismatches in the mechanical properties of continuous and particle phases. Theoretical models of ultrasound scattering are based either on the particle approach[20,21,34] or the continuum approach.[35,36] The continuum approach recognizes that particles separated by less than $\lambda/2$ cannot be resolved by the transducer and therefore the suspension can be modeled as a continuum medium in which local fluctuations in density and compressibility give rise to the scattered waves.[35,36] In contrast, the particle approach tracks the position of every particle in the insonified volume and sums the wavelets scattered from individual particles.[20,21] Recently, Mo and Cobbold[36] introduced a new hybrid approach which sums the wavelets from elemental volumes or voxels of size $1/k \approx \lambda/2\pi$ small enough so that the incident wave arrives with the same phase at every particle located within it. In the Rayleigh scattering regime $(ka \ll 1)$, the hybrid model predicts a somewhat isotropic scattered power scaling as the variance of the particle number in a voxel. The ultrasound power scattered from a suspension of Rayleigh aggregates is then sensitive to cluster size and fluctuations of the local particle number in a voxel. In the fractal scattering regime $(ka > 1)$, the aggregates are larger than a voxel and the scattered power becomes strongly anisotropic and influenced by particle correlation within the clusters.

A. Uncorrelated particles

For a random distribution of particles in space, each particle scatters the incident wave unaffected by the presence of the other particles. The addition of intensity scattered by each particle then gives the incoherent scattered intensity from a weakly scattering suspension.[18,20] The directional scattering coefficient $\chi(\mathbf{k},\mathbf{s})$ defined as the power scattered per unit solid angle from a unit volume for an incident plane wave of unit amplitude then scales as the average number n of scatterers per unit volume:[10]

$$\chi(\mathbf{k},\mathbf{s}) = n\sigma(\mathbf{k},\mathbf{s}), \tag{1}$$

where $\mathbf{k}$ and $\mathbf{s}$ are the incident and scattered wave number vectors and $\sigma(\mathbf{k},\mathbf{s})$ the differential scattering cross-sectional area of a single particle. Ultrasound scattering from particles arises from the different modes of vibrations (radial pulsations or back and forth oscillations) in relation with either compressibility or density mismatches. Viscous dissipation effects weakly influence the low-frequency scattering of acoustic waves. The Green's function approach gives the differential scattering cross section $\sigma(\mathbf{k},\mathbf{s})$ of a weak Rayleigh scatterer of volume V and arbitrary shape:[37]

$$\sigma(\mathbf{k},\mathbf{s}) = \pi^2 \nu^4 V^2 (\kappa_o \rho_o)^2 \left[\left(\frac{\kappa_p - \kappa_o}{\kappa_o} \right) + \left(\frac{\rho_p - \rho_o}{\rho_p} \right) \frac{\mathbf{k}\cdot\mathbf{s}}{ks} \right]^2, \tag{2}$$

where κ_p, κ_o and ρ_p, ρ_o are the compressibilities and densities of scatterer and suspending medium, respectively, ν is the ultrasonic frequency and $c_o = 2\pi\nu/k = (\kappa_o \rho_o)^{-1/2}$ is the phase velocity of the incident ultrasound wave in the suspending medium. In the Rayleigh regime, the scattering is nearly isotropic and depends on the fourth power of the ultrasound frequency.

B. Correlated particles

Departure from independent scattering occurs in densely packed systems where the increase in correlation among particles induces interference of the far-field scattered waves.[18,24] The scattering cross section $\chi(\mathbf{k},\mathbf{s})$ can be evaluated by defining the packing factor $W(\mathbf{k},\mathbf{s})$ of the pair-correlated particles that accounts for the coherent addition of the scattered waves:[19,20]

$$\chi(\mathbf{k},\mathbf{s}) = n\sigma(\mathbf{k},\mathbf{s}) W(\mathbf{k},\mathbf{s}). \tag{3}$$

The packing factor $W(\mathbf{k},\mathbf{s})$ describes the orderliness in the spatial arrangement of particles and can be expressed in terms of the statistical pair-correlation function $g(\mathbf{R})$:[19]

$$W(\mathbf{k},\mathbf{s}) = 1 + n \int [g(\mathbf{R}) - 1] e^{i(\mathbf{k}-\mathbf{s})\cdot\mathbf{R}} d\mathbf{R}, \tag{4}$$

where $\mathbf{R}$ is the separation distance between the particles. If the average separation of the scatterers is much smaller than the wavelength, the above relation reduces to

$$W = 1 + n \int [g(\mathbf{R}) - 1] d\mathbf{R}. \tag{5}$$

The application of this model is contingent on the selection of an appropriate pair-correlation function $g(\mathbf{R})$ which mainly depends on particle volume fraction and flow conditions.[38,39] Assuming Rayleigh scatterers and no shear dependence of the pair function in the low shear regime, then the packing factor $W(\phi)$ derived from the Percus–Yevick approximation only depends on the particle volume fraction:[38,40]

$$W(\phi) = \frac{(1-\phi)^4}{(1+2\phi)^2}. \tag{6}$$

The packing factor viewpoint involves complex statistical mechanics and provides unclear physical insight. In the Rayleigh scattering regime, an alternative view-point based on a continuum approach was first proposed by Angelsen[35] to estimate the packing factor from the variance in local particle volume fraction. Mo and Cobbold[36] recently developed a hybrid model which combines both the particle and continuum approaches. In this model, the scattered power is split into a part arising from a crystalline phase, which gives no net contribution because of destructive wave interference, and the other, representing contributions from independent fluctuations in the particle number ω within elemental voxels of volume Ω and size $\approx 1/k$. The scattering cross section per unit volume for a suspension of Rayleigh clusters then scales as the variance $\mathrm{var}(\omega) = \overline{\omega^2} - \overline{\omega}^2$ of the particle number ω averaged over the insonified region:[36]

$$\chi(\mathbf{k},\mathbf{s}) = n\sigma(\mathbf{k},\mathbf{s}) \frac{\overline{\mathrm{var}(\omega)}}{\overline{\omega}} \tag{7}$$

with $n = \overline{\omega}/\Omega$. Alternatively, one can define the space average variance $\overline{\mathrm{var}(\omega)} = \overline{\omega W \phi} = \Omega \phi W(\phi)/V$ of particles in a voxel as a function of the packing factor $W(\phi)$ which unifies Eqs. (3) and (7).

C. Correlated fractal aggregates

Several models of random cluster growth developed in the last decade and supported by experiments lead to tenuous self-similar aggregates with radius of gyration $R(N)$ obeying the scaling relationship:[41]

$$R \approx a N^{1/D}, \tag{8}$$

where N is the number of particles in the cluster, a is the characteristic size of elementary particles and D is called the fractal dimension or Hausdorf–Besicovitch dimension. A fractal dimension less than the Euclidean dimension d corresponds to tenuous structures with porosity increasing with size. The reaction limited aggregation model (RLA) developed by Kolb and Jullien[42] and Weitz and Huang[43] covers reversible flocculation and introduces a sticking probability when two clusters collide. The RLA model produces self-similar clusters with a fractal dimension $D \approx 2$ for $d = 3$.

Ultrasound scattering by a Rayleigh cluster ($Rk \ll 1$) is completely coherent and the differential scattering cross-sectional area $\sigma_a(\mathbf{k},\mathbf{s})$ of an aggregate of arbitrary shape scales as the square of the particle number N:[44]

$$\sigma_a(\mathbf{k},\mathbf{s}) = N^2 \sigma(\mathbf{k},\mathbf{s}) \quad \text{for } kaN^{1/D} \ll 1. \tag{9}$$

From Eq. (7) relevant to the hybrid approach, the directional scattering cross section $\chi_a(\mathbf{k},\mathbf{s})$ from a distribution of Rayleigh aggregates is given by

$$\chi_a(\mathbf{k},\mathbf{s}) = n_a \overline{\sigma_a(\mathbf{k},\mathbf{s})} \frac{\overline{\mathrm{var}_a(\omega)}}{\omega}, \tag{10}$$

where $\overline{\mathrm{var}_a(\omega)}$ is the space average variance of the particle number in a voxel, $n_a = n/\overline{N}$ is the average number of aggregates per unit volume and $\overline{N}$ is the mean particle number in a cluster. Cluster growth increases the variance in particle number because each voxel can gain or lose a larger number of elementary particles. As a first approximation, the variance $\overline{\mathrm{var}_a(\omega)}$ increases linearly with the volume fraction ϕ_a

of aggregates. Therefore, the variance can be roughly approximated by the first-order scaling relation:

$$\overline{\mathrm{var}_a(\omega)} = \frac{\phi_a}{\phi}\,\overline{\mathrm{var}(\omega)} \quad \text{for } N \ll (ka)^{-D}. \tag{11}$$

Substituting for the average variance in Eqs. (9) and (10) gives

$$\chi_a(\mathbf{k},\mathbf{s}) = n_a\,\overline{N^2}\,\frac{\phi_a}{\phi}\,\sigma(\mathbf{k},\mathbf{s})\,\frac{\overline{var(\omega)}}{\omega}. \tag{12}$$

We further define the dimensionless normalized scattering coefficient $\chi_r = \chi_a(\mathbf{k},\mathbf{s})/\chi(\mathbf{k},\mathbf{s})$. Using Eqs. (7) and (12), the dimensionless scattering coefficient χ_r in the Rayleigh scattering regime becomes

$$\chi_r = \frac{\chi_a(\mathbf{k},\mathbf{s})}{\chi(\mathbf{k},\mathbf{s})} = \frac{n_a}{n}\,\frac{\phi_a}{\phi}\,\overline{N^2} = \frac{\overline{N^2}}{\overline{N}}\,\frac{\phi_a}{\phi}, \tag{13}$$

where $\phi_a/\phi = (n_a\overline{V_a})/(nV) = \overline{V_a}/(\overline{NV})$ and $\overline{V_a}$ is the average volume of aggregates. In a dense suspension, multiple hydrodynamic interactions strongly reduce the spread of the aggregate size distribution. For a weak standard deviation of the aggregate size distribution ($\overline{N^2} \approx \overline{N}^2$), then the scattering cross section per unit volume scales as the average volume V_a of clusters without dependence on particle volume fraction and fractal dimension of aggregates because the transducer cannot resolve the internal structure of clusters smaller than voxels:

$$\chi_r \approx \overline{\frac{V_a}{V}} \approx \left(\frac{R}{a}\right)^3 \quad \text{for } N \ll (ka)^{-D}. \tag{14}$$

Far field coherence effects are responsible for the aggregate volume dependence of the scattering coefficient χ_r which would scale as $(n_a/n)\,(\sigma_a/\sigma) \approx N \approx R^D$ when neglecting the variance terms in Eqs. (7) and (10). One can indeed expect no influence of the fractal dimension of aggregates upon the scattering coefficient χ_r because the transducer cannot resolve the internal structure of clusters smaller than voxels. As a consequence, the dimensionless scattering coefficient χ_r scales as the volume of aggregates and can be interpreted as an aggregation index in the Rayleigh scattering regime ($kR \ll 1$).

D. Fractal scattering regime

For aggregates of dimension larger than a voxel ($kR \gg 1$), the hybrid theory is no longer valid and ultrasound scattering becomes strongly anisotropic because of angle-dependent destructive interferences. Considering the scattering wave number $\mathbf{q} = \mathbf{s} - \mathbf{k}$, the choice of a scattering angle θ sets a length scale $1/q = [2k \sin(\theta/2)]^{-1}$ under which scattering remains coherent.[44] Therefore, one may decompose an aggregate into smaller subunits of size $1/q$ with an average number $N_b \approx (qa)^{-D}$ of elementary particles. One subunit scatters coherently a power scaling as N_b^2. In contrast, the scattered waves from different subunits add incoherently and the differential scattering cross-sectional area $\sigma_a(\mathbf{k},\mathbf{s})$ of an arbitrary shape aggregate scales as the average number N/N_b of subunits in the cluster:

$$\sigma_a(\mathbf{k},\mathbf{s}) \approx \frac{N}{N_b} N_b^2 \sigma(\mathbf{k},\mathbf{s}) \approx N^2 S(qR)\,\sigma(\mathbf{k},\mathbf{s}), \tag{15}$$

where $S(qR) \approx N_b/N \approx (qR)^{-D}$ is commonly referred to as the structure factor in coherent optics[44] and describes spatial correlations between particles in fractal structures. The fourth-order frequency law characterizing the Rayleigh scattering regime no longer applies for an aggregate larger than a voxel ($\sigma_a \approx a^6 R^{-D} \lambda^{D-4}$). The crossover from the small $-q$ scattering behavior to the fractal regime is much broader and a more accurate expression of the structure factor $S(qR)$ was proposed by Fisher and Burford.[45] In the case of large aggregates ($qR \gg 1$), the directional scattering cross section $\chi_a(\mathbf{k},\mathbf{s}) = n_a \sigma_a(\mathbf{k},\mathbf{s})$ per unit volume then mainly depends on the scattering angle and the fractal dimension:

$$\chi_a(\mathbf{k},\mathbf{s}) \approx \frac{\phi}{V}(qa)^{-D}\sigma(\mathbf{k},\mathbf{s}). \tag{16}$$

In the fractal scattering regime ($kR \gg 1$), the dimensionless scattering coefficient $\chi_r = \chi_a/\chi \approx (qa)^{-D}/W(\phi)$ can no longer characterize the aggregation state of a suspension since the scattered power mainly involves the fractal dimension of aggregates and becomes insensitive to cluster size. Indeed, light scattering from a suspension of large aggregates is weakly dependent upon the cluster size because the formation of contact points between aggregated rigid particles induces no significant changes in the scattering area per unit volume.[30,31] However, the formation of a large contact area during the aggregation process of deformable particles may significantly lower the scattering area and thus light scattering phenomena become more sensitive to the growth of large clusters.[25,31]

II. RHEO-ACOUSTICAL MODEL

Our purpose in this section is to present a rheo-acoustical model and estimate both the average dynamical size of aggregates in a shear flow and the ultrasound scattered power from a weakly aggregated suspension. The proposed scaling laws only involves physical parameters (fractal dimension, particle adhesive energy, cluster deformability) in contrast to numerous approaches which introduce phenomenological parameters.

Above a critical yield stress, the shear thinning behavior of weakly flocculated suspensions results from the rupture of the spanning network and finite-sized aggregates when increasing the shear stress.[26–32,46] The concept of fractal aggregation was recently introduced in microrheological models to estimate the average size of reversible aggregates in concentrated suspensions.[26–32]

A. Average size of aggregates in a dense suspension at rest

In the diluted regime, the suspension only consists of isolated particles and finite-sized aggregates (Fig. 1). By increasing the particle volume fraction, clusters cannot grow indefinitely without interpenetration. Above the percolation concentration ϕ_g, fractal structures then reach a maximum average size $\hat{R}$ (Fig. 1). In a concentrated suspension, the

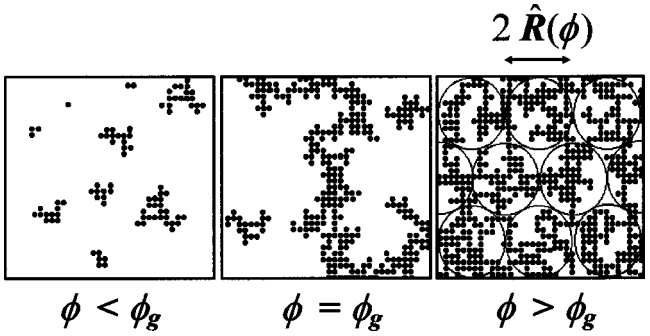

FIG. 1. Structure of an aggregated suspension at rest [$\phi < \phi_g$: finite sized aggregates, $\phi = \phi_g$: an infinite spanning cluster and some isolated aggregates, $\phi > \phi_g$: packing of fractal aggregates of maximum size $\hat{R}(\phi)$].

infinite network can be considered as a collection of fractal aggregates of mean density $\hat{\phi}$ and characteristic dimension $\hat{R}$ packed with a volume fraction ϕ^*.[26,28,30] The condition $\phi = \hat{\phi}\phi^*$ then gives the maximum average size $\hat{R}$ of fractal aggregates at rest:[30]

$$\frac{\hat{R}(\phi)}{a} = \left(\frac{\phi}{\phi^*}\right)^{1/D-3} \quad \text{with} \quad \hat{\phi} \approx \frac{\hat{R}^3}{\hat{N}a^3} \quad \text{and} \quad \hat{N} \approx (\hat{R}/a)^D, \tag{17}$$

where $\hat{N}$ is the mean particle number in a fractal cluster of size $\hat{R}$.

B. Shear breakup of aggregates

Above the yield stress τ_o, the filling space aggregates of average size $\hat{R}(\phi)$ are broken into smaller subunits of size $R < \hat{R}$ corresponding to a dynamical equilibrium between formation and shear breakup of the aggregates. As shown by experimental investigations[47] and computer simulations,[33,48] the shear stress dependence of the equilibrium radius $R(\tau)$ of an isolated fractal aggregate obeys the general power law:

$$\frac{R(\tau)}{a} \approx \left(\frac{\tau^*}{\tau}\right)^m, \tag{18}$$

where the critical shear stress $\tau^* \approx \Gamma/a$ for breaking a bond is related to the surface adhesive energy Γ (adhesive energy per unit contact area) and the characteristic radius a of elementary particles. The exponent m mainly depends on the reversibility of cluster deformation under the action of external stresses.[33,46] Rigid aggregates are broken into secondary clusters of approximately equal parts (large-scale fragmentation process) since elastic deformations are transmitted over the whole structure. On the other hand, soft aggregates are irreversibly deformed by external stresses and split into individual particles and small clusters one by one (surface erosion process).[30,33]

We may introduce a correlation length ξ under which elastic stresses are transmitted and consider the aggregate as a soft assembly of rigid subunits of size ξ.[30] A three-dimensional aggregate of fractal dimension $D \geqslant 2$ strongly interacts with the surrounding fluid and roughly behaves hydrodynamically like an unpermeable compact sphere with a hydrodynamic radius close to the radius of gyration.[46]

In the low shear regime, an unpermeable aggregate of radius R experiences a viscous force $F \approx \tau R^2$ where τ is the viscous stress. The shear force F exerts a bending moment $M \approx F\xi$ on the rigid branches of size ξ located on the outer surface of the aggregate. A bending moment higher than the critical moment $M^* \approx \tau^* a^3 \approx \Gamma a^2$ for breaking a bond leads to the rupture of rigid subunits. The breaking criterion $F\xi \approx \Gamma a^2$ then yields the equilibrium size $R(\tau)$ of unpermeable aggregates in a shear flow:[30]

$$R(\tau) \approx \left(\frac{\Gamma a^2}{\tau \xi}\right)^{1/2}. \tag{19}$$

For soft aggregates, outer chains of size $\zeta \approx a$ are stretched and broken one by one until the cluster reaches a stable size $R(\tau)$:

$$\frac{R(\tau)}{a} \approx \left(\frac{\tau^*}{\tau}\right)^{1/2} \quad \text{with} \quad \tau^* \approx \Gamma/a. \tag{20}$$

In the case of rigid aggregates, the correlation length is the whole size of the aggregate ($\xi \approx R$), and the equilibrium size derived from Eq. (19) then takes the form

$$\frac{R(\tau)}{a} \approx \left(\frac{\tau^*}{\tau}\right)^{1/3} \quad \text{with} \quad \tau^* \approx \Gamma/a. \tag{21}$$

Equations (20) and (21) for soft and rigid aggregates give the upper and lower bounds of the exponent m in the general scaling law (18). Recent computer simulations of the shear-induced disruption of three-dimensional soft aggregates give $m = \frac{1}{2}$.[33] On the other hand, the lower value $m = \frac{1}{3}$ agrees with experimental data from Torres *et al.*[48] for rigid aggregates.

In the general case of Rayleigh aggregates ($kR \ll 1$), the dimensionless scattering coefficient $\chi_r(\tau)$ is derived from Eqs. (14) and (18):

$$\chi_r(\tau) = \left(\frac{R(\tau)}{a}\right)^3 \approx 1 + \left(\frac{\tau^*}{\tau}\right)^{3m} \quad \text{with} \quad \frac{1}{3} \leqslant m \leqslant \frac{1}{2}, \tag{22}$$

where particle adhesiveness and cluster deformability respectively determine the critical shear stress τ^* and the exponent m. The fractal dimension and the average particle volume fraction within the aggregates apparently have no influence on the average size of clusters and the scattering behavior. However, the internal structure of aggregates and the amount of fluid trapped within the aggregates determine both the suspension viscosity and the average shear stress experienced by interacting clusters.[30]

III. ULTRASONIC SCATTERING FROM HARDENED RED BLOOD CELL AGGREGATES

In this section, rheo-acoustical experiments are reported for hardened red blood cells suspended in dextran saline solutions. An 8-MHz piezoelectric ceramic element emits acoustic bursts and detects the backscattered waves from red blood cell aggregates in a shear flow. Human red cells of volume-averaged radius $\approx 2.8\mu$m (average volume $V = 87\ \mu\text{m}^3$) can be considered as Rayleigh scatterers when probed with an 8-MHz ultrasound wave (wavelength $\lambda \approx c_s/\nu$

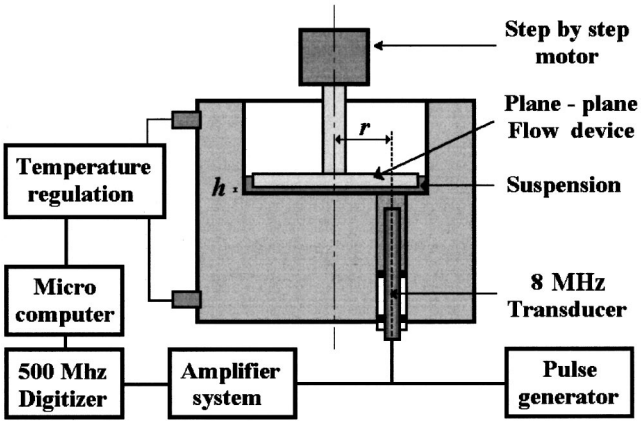

FIG. 2. Schematic representation of the ultrasonic technique to investigate the ultrasound backscattering from a flocculated suspension in a plane–plane flow device.

≈ 200 μm where $c_s \approx 1570$ m/s is the sound velocity in diluted red cell suspensions). For human red cells, the fourth-order frequency law was indeed confirmed by Shung *et al.*[49] in the ultrasound frequency range from 5 to 15 MHz. Furthermore, ultrasound scattering from red cell suspensions is weak since the acoustic properties of erythrocytes such as density $\rho_p \approx 1092\ \mathrm{kg/m^3}$ and compressibility $\kappa_p \approx 34.1 \times 10^{-11}\ \mathrm{m^2/N}$ (Ref. 34) are close to those of physiological saline solution ($\rho_o \approx 1005\ \mathrm{kg/m^3}$, $\kappa_o \approx 44.3 \times 10^{-11}\ \mathrm{m^2/N}$). Based on the above acoustic properties, the Rayleigh formula (2) predicts a backscattering cross-sectional area $\sigma(\mathbf{k}, -\mathbf{k}) \approx 6 \times 10^{-14}\ \mathrm{cm^2}$ for a single red blood cell in saline solution.

In the following, the effect of shear rate and particle volume fraction on the ultrasound scattered power from a suspension of hardened red cell aggregates is investigated and examined within the framework of the rheo-acoustical model.

A. Rheo-acoustical method

The measurement cell consists of a polymethacrylate cylinder (diameter 94 mm) divided into two compartments by a polymethacrylate plate perpendicular to the vertical axis of a plane–plane flow device (Fig. 2). The flow field is generated in the upper compartment between the stationary plate and an upper rotating polymethacrylate plane disk driven by a stepper motor. In the lower compartment, filled with water to ensure good ultrasonic coupling, a transmitter receiver circular transducer (Vermon, France) (incident beam diameter $d \approx 5$ mm) is driven by a pulse function generator which sends 8-MHz frequency electrical pulses (resonant frequency of the transducer) with a repetition rate of 200 Hz. The piezoelectric nonfocused transducer connected to the polymethacrylate plate by an acoustic window filled with water emits short ultrasonic bursts in the direction perpendicular to the plane–plane flow device. The distance $z \approx 41$mm from the piezoelectric ceramic to the insonified volume between the plates was chosen to be in the far field of the transducer (the transition point from near-field zone to far-field zone is located at the distance $z_o \approx d^2/4\lambda \approx 32$ mm). The pulsewidth $\delta t = 0.4$ μs of the ultrasonic bursts was determined from the

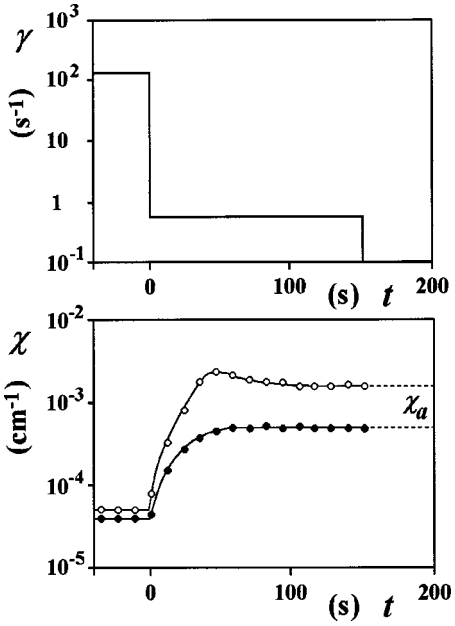

FIG. 3. Ultrasonic backscattering coefficient χ versus time t for normal (○) and hardened (●) red blood cells in 3g% dextran 70-PBS from the flow setting ($\gamma = 0.6\ \mathrm{s^{-1}}$ for $t > 0$) and the establishment of a dynamical equilibrium to flow stoppage ($\phi = 0.15$, $T = 25\ ^\circ\mathrm{C}$ and $I = 150$ mM). The suspension is previously dispersed in an intense flow ($\gamma = 128\ \mathrm{s^{-1}}$ for $t < 0$) before imposing the relevant shear rate $\gamma = 0.6\ \mathrm{s^{-1}}$.

time analysis of the ultrasound wave reflected from the polymethacrylate plate. As a consequence, the axial resolution $\delta z = \delta t c_s/2 \approx 0.3$ mm ($c_s \approx 1570$ m/s is the sound velocity in the suspension) is much less than the gap width 2 mm$< h <$3 mm between the plates. The thickness $e = 3$ mm of the polymethacrylate plate is enough that pulse ringing can be further neglected and the scattered signal can be separated from multiple reflections between the plates. The far-field pattern of the transducer has a 5-degree-wide central lobe so that the lateral resolution δx is of the order of 5 mm.

The water temperature in the lower compartment was maintained to 25 °C and controlled with $\pm 0.5\ ^\circ\mathrm{C}$ accuracy. The average distance $r = 30$ mm from the axis of the transducer to the axis of the plane–plane flow device and the angular velocity of the rotating disk ($8 \times 10^{-5}\ \mathrm{rd\ s^{-1}} < d\theta/dt < 80\ \mathrm{rd\ s^{-1}}$) determine the average local shear rate $\gamma \approx r(d\theta/dt)/h$ experienced by the insonified region across the gap width h between the plates ($10^{-3}\ \mathrm{s^{-1}} < \gamma < 10^3\ \mathrm{s^{-1}}$ for $h = 2.5$ mm).

The ultrasound wave either reflected by the wall surfaces or scattered from the suspension is detected by the same transducer. The radio frequency signal delivered by the transducer was sampled and amplified using a Tektronix 520 digitizer. The digitized signals were downloaded to a microcomputer (Macintosh Centris 650) where gating and power calculations were performed. Time gating of the digitized signal provides a way to measure the rms power P_r and P_s of the echo corresponding either to specular reflections at wall/suspension interfaces (considered as a reference acoustic reflector) or scattering from a specified volume between the plates. The backscattering coefficient $\chi(\mathbf{k}, -\mathbf{k})$ is derived from the relation:[6]

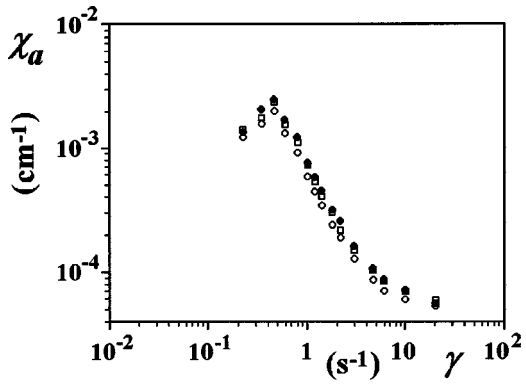

FIG. 4. Ultrasonic backscattering coefficient χ_a versus the shear rate γ for normal red cells in 3g% dextran 70-PBS as a function of the gap width h between the plates [$h=2$mm (●), $h=2.5$ mm (○), $h=3$ mm (□)]. Particle volume fraction $\phi=0.25$, temperature $T=25\,^{\circ}$C, ionic strength $I=150$ mM and liquid viscosity $\mu_o=1.82$ mPa.s.

$$\chi(\mathbf{k},-\mathbf{k})=\left(\frac{\rho_w c_w-\rho_s c_s}{\rho_w c_w+\rho_s c_s}\right)^2 \frac{z^2}{A\,\delta z}\frac{P_s}{P_r}, \tag{23}$$

where ρ_w and ρ_s are the densities of the polymethacrylate wall and the suspension, c_w and c_s are the sound velocities in the two media, z is the distance between the front face of the transducer and the insonified region, A is the cross-sectional area of the ultrasound beam and δz the axial resolution of the transducer. Equation (23) neglects the attenuation compensation of the incident wave. For red cell aggregates in dextran saline solution and particle volume fraction $\phi<0.3$, viscous losses are indeed weak and the extinction of the incident ultrasound wave remains negligible since the scattering mean free path $1/\chi_a$ ranges from 10 up to 100 m depending on cell aggregation extent (Fig. 5).

The shear viscosity of suspensions was determined at 25 °C in a Couette viscometer (RCHAIX-MCCA, France) and calculated with ±3% accuracy from the steady-state torque reading. The sample was previously sheared at high shear rate before imposing the relevant shear rate. The preshearing period eliminates any memory effects due to induced restructuration processes of aggregates in the low shear regime[31] and viscosity measurements no longer depend upon the rheological history of the suspension.

B. Red cell suspensions

Normal human red blood cells are biconcave disks of 8 μm mean diameter and 2 μm thickness when suspended in an isotonic phosphate buffered saline solution (PBS) (osmolarity 300 mOsmol, ionic strength 150 mM and pH=7.4). Blood was obtained from healthy human donors and used on the day of withdrawal. After centrifugation and removal of the plasma and the white-cell–platelet layer, red blood cells were washed twice in PBS (10 mn at 3000 rpm).

Cross-linking of the skeleton proteins in a glutaraldehyde solution produces hardened red cells. The glutaraldehyde treatment has no significant influence on red cell electrophoretic mobility and thus hardly alters the outer surface of the cell.[50] Glutararaldehyde fixed red cells were prepared by suspending one volume of washed cells in 10 volumes of 2% glutaraldehyde saline solution for 60 min at room temperature. Hardened red cells were then washed twice in PBS and finally suspended in dextran 70-PBS solutions (molecular weight 7×10^4).

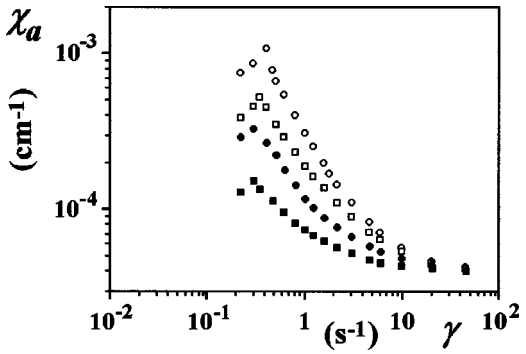

FIG. 5. Ultrasonic backscattering coefficient χ_a versus the shear rate γ for normal red cells in 3g% dextran 70-PBS. Particle volume fraction $\phi=0.1$ (○), $\phi=0.15$ (□), $\phi=0.25$ (●) and $\phi=0.3$ (■).

Above a molecular weight of about 4×10^4, dextran polymer induces aggregation of human red cells.[51,52] The extent of red blood cell aggregation increases with dextran molecular weight and polymer concentration. However, high dextran concentrations ($\varphi>3-5$g%) enhance the repulsive interaction forces and induce suspension restabilization. Reversible red cell aggregation is usually attributed to macromolecular bridging between cell surfaces.[53] However, the nature of red cell interaction in polymer solution remains controversial up to the present time. Indeed, there is good evidence that red cell aggregation in dextran solutions results from polymer depletion, the disaggregation stage at high polymer concentrations arising from the penetration of chains within the cell surface coat.[53]

The fractal dimension of two-dimensional normal or hardened red cell aggregates was determined by one of the authors[30] from optical imaging of clusters between two glass plates after previous dispersion of the suspension. The particle number dependence of the cluster size yields a fractal dimension $D=1.59\pm0.03$ and $D=1.56\pm0.04$, respectively, for normal of hardened red cells in 3g% dextran 80-PBS[30] in good agreement with the predictions of the RLA model ($D\approx1.55$ for $d=2$) representative of reversible flocculation.[42,43]

C. Experimental protocol

The ultrasonic backscattered power from red blood cells suspended in dextran 70-PBS solution was measured in the plane–plane flow device for shear rates in the range $0.1\ \mathrm{s}^{-1}<\gamma<50\,\mathrm{s}^{-1}$. The suspension was first dispersed in an intense flow ($\gamma=128\,\mathrm{s}^{-1}$) before imposing the relevant shear rate at time $t=0$ (Fig. 3). Particle flocculation results in an increase of the ultrasound backscattered power which reaches a stationary level after a delay time of about 2 min. Since the shear flow can induce a stable orientation of deformable particles[31] and an anisotropy of the suspension microstructure, the flow is quickly stopped to suppress any cell orientation. The extrapolated ultrasonic backscattering coefficient χ_a just after flow stoppage is representative of the dynamical aggregation equilibrium for random particle ori-

entation (Fig. 3). For each red cell volume fraction and shear rate, the average coefficient χ_a was determined with an accuracy of about 5% from ten measurements of the rms power backscattered from the suspension.

The steady-state backscattering coefficient χ_a decreases when increasing the shear rate because of the shear breakup of red cell clusters into smaller ones (Fig. 4). Under defined shear rate conditions, the backscattering coefficient $\chi_a(\gamma)$ is weakly dependent upon the gap width 2 mm$\leqslant h \leqslant$3 mm between the plates (Fig. 4), which indicates both a linear velocity profile (constant shear rate across the gap) and a weak influence of the marginal layers clear of particles near the walls.

Figure 4 further shows an increased backscattering coefficient and a shear-induced restructuration of the infinite network for deformable red cell aggregates subjected to low shear rates ranging from 0.2 s^{-1} up to 0.5 s^{-1}. Such a restructuration process preferentially occurs for strongly aggregated deformable particles and results in hysteresis phenomena in the rheology of flocculated suspensions.[31] The previous dispersion of the suspension in an intense flow cancels out any memory effects in the low shear regime. On the other hand, no time-dependent restructuration effect is observed for hardened red cell aggregates (Fig. 3). Rigid particles only establish contact points during adhesion and the low internal variation energy of the suspension associated with particle aggregation then prevents shear-induced restructuration processes at short time scale.[31]

D. Shear break-up of hardened red cell aggregates

Figure 5 shows the shear rate dependence of the ultrasonic backscattering coefficient $\chi_a(\gamma)$ upon the particle volume fraction ϕ for hardened red cells suspended in 3g% dextran 70-PBS ($0.1 \leqslant \phi \leqslant 0.3$). At high shear rates $\gamma > 20\,s^{-1}$, aggregates are broken into individual particles and the backscattering coefficient takes the value $\chi \approx 4\times10^{-5}\,cm^{-1}$ in good agreement with the predictions from Eqs. (3) and (6) based on the Percus–Yevick approximation [$\chi(\mathbf{k},-\mathbf{k}) = \phi\sigma(\mathbf{k},-\mathbf{k})W(\phi)/V \approx 3\times10^{-5}\,cm^{-1}$ with $V \approx 87\,\mu m^3$, $\phi = 0.2$ and $\sigma(\mathbf{k},-\mathbf{k}) \approx 6\times10^{-14}\,cm^2$ as shown in Sec. III]. Particle volume fraction in the range from 0.1 up to 0.3 weakly influences the backscattering coefficient $\chi \approx 4\times10^{-5}\,cm^{-1}$ of nonaggregated particles (Fig. 5) since the scattered power from pair-correlated red cells peaks at $\phi \approx 0.2$.[49] The variance of particle number in a voxel scales as $\phi W(\phi)$ and indeed displays limited changes over the concentration range $0.1 < \phi < 0.3$. Flow disturbances and turbulence effects may further increase local fluctuations in particle concentration and enhance the ultrasound backscattered power. However, no shear rate dependence was observed below 200 s^{-1} for the scattered power from nonaggregated red cells suspensions in agreement with recent experiments from Van Der Heiden *et al.*[54]

We consider now the dimensionless backscattering coefficient $\chi_r = \chi_a/\chi$ and we define the critical disaggregation shear rate γ_c in terms of extrapolated intercept. For hardened red cells in 3g% dextran 70-PBS, Fig. 6 shows a dependence of the ultrasonic experimental data and the extrapolated shear rate γ_c upon the red cell volume fraction. Under defined shear rate conditions, particle crowding increases the viscosity of the suspension and the shear stress experienced by aggregates resulting in a more efficient dispersion of clusters and a lower backscattering coefficient. Raising the particle volume fraction then shifts the critical shear rate $\gamma_c(\phi)$ for cell disaggregation towards lower values (Table I). The critical shear stress τ_c defined as the product of the critical shear rate γ_c and the shear viscosity $\mu(\gamma_c)$ no longer depends on particle volume fraction (Table I). The critical disaggregation shear stress $\tau_c \approx 0.45\,N/m^2$ is representative of the mechanical force required to disrupt a bond for red cells in 3g% dextran 70-PBS. From the Derjaguin theory, the force $F \approx \tau_c a^2$ required to break a bond between two aggregated particles scales as Γa (Γ is the surface adhesive energy). For cells in 3g% dextran 70-PBS ($\tau_c \approx 0.45\,N/m^2$ and $a \approx 4\,\mu m$), we then derive a surface adhesive energy $\Gamma \approx \tau_e a \approx 1.8\times10^{-6}\,N/m$ in good agreement with earlier estimations based either on rheo-optical experiments ($\Gamma \approx 2\times10^{-6}\,N/m$ for red blood cells in 2g% dextran 80)[30,31] or the equilibrium shape of deformable red cell doublets.[55]

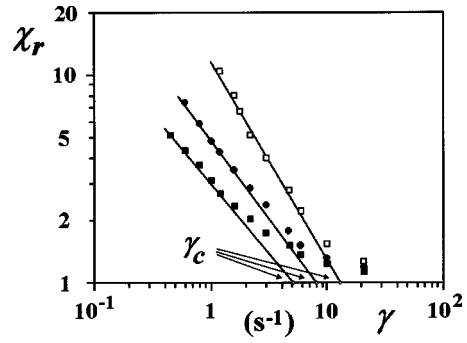

FIG. 6. Dimensionless ultrasonic backscattering coefficient $\chi_r = \chi_a/\chi$ versus the shear rate γ for hardened red cells in 3g% dextran 70-PBS. Particle volume fraction $\phi = 0.15$ (□), $\phi = 0.25$ (●) and $\phi = 0.3$ (■).

The effective medium approximation used in microrheological models states that interacting aggregates behave like isolated clusters in a fluid of viscosity equal to the shear viscosity $\mu(\gamma)$ of the suspension and thus experience an effective shear stress $\tau = \mu(\gamma)\gamma$. Therefore, we have determined the shear viscosity $\mu(\gamma)$ of aggregated red cell suspensions (Fig. 7) and plotted the backscattering coefficient χ_r against the shear stress $\tau = \mu(\gamma)\gamma$ to account correctly for the microrheological conditions around the clusters whatever the particle concentration (Fig. 8). The viscosity $\mu(\gamma)$ of hardened red cell suspensions was determined using a low shear viscometer (LS40 Contraves) and the same experimental procedure. The experimental data $\chi_r(\tau)$ then lie on a single curve since the local shear stress determines the dy-

TABLE I. Experimental values of the critical disaggregation shear rate γ_c, relative shear viscosity $\mu_r(\gamma_c)$ and critical shear stress $\tau_c = \mu_r(\gamma_c)\mu_o\,\gamma_c$ for hardened red cells suspended in 3g% dextran 70-PBS (liquid viscosity $\mu_o = 1.82$ mPa.s).

ϕ	γ_c (s^{-1})	$\mu_r(\gamma_c)$	τ_c (N/m^2)
0.15	12.9	1.92	0.45
0.25	7.3	3.4	0.452
0.30	5	4.93	0.449

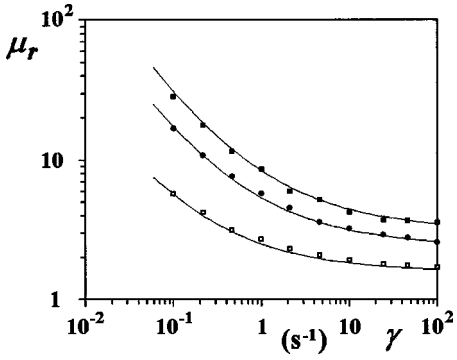

FIG. 7. Relative shear viscosity $\mu_r(\gamma)=\mu(\gamma)/\mu_o$ versus the shear rate γ for hardened red cells suspended in 3g% dextran 70-PBS. Particle volume fraction $\phi=0.15$ (□), $\phi=0.25$ (●) and $\phi=0.3$ (■). Liquid viscosity $\mu_o=1.82$ mPa.s.

namical equilibrium size of interacting aggregates in a dense suspension (effective medium approximation). The master curve $\chi_r(\tau)$ further indicates that correlation effects among individual particles or aggregates only involve the average particle volume fraction since the transducer cannot resolve clusters smaller than a voxel.

Red cell aggregates can be considered as soft clusters undergoing irreversible deformation under shear because of the weak bonding energy and the biconcave shape of erythrocytes which allow particles to roll at their contact points. We may thus estimate the dimensionless scattering coefficient $\chi_r(\tau)$ from Eq. (22) with $m=\frac{1}{2}$ for soft clusters:

$$\chi_r(\tau)=\left(\frac{R(\tau)}{a}\right)^3\approx 1+\left(\frac{\tau^*}{\tau}\right)^{3/2}. \tag{24}$$

For a critical shear stress $\tau^*=0.25$ N/m^2 , the above relation well describes the shear stress dependence of the experimental acoustic curve $\chi_r(\tau)$ (Fig. 9).

The present analysis based on the Rayleigh scattering theory is valid as long as the aggregates remain smaller than voxels. The maximum value $\chi_r\approx 30$ of the backscattering coefficient in the low shear regime corresponds to a mean aggregate diameter $2a\chi_r^{1/3}\approx 25\,\mu$m close to the characteristic size $\lambda/2\pi\approx 30\,\mu$m of voxels when the suspension is probed with 8-MHz ultrasound waves. As a consequence, Rayleigh scattering from blood is no longer valid at low shear rates $\gamma<1\ \mathrm{s}^{-1}$, especially when red cell aggregation is strong and

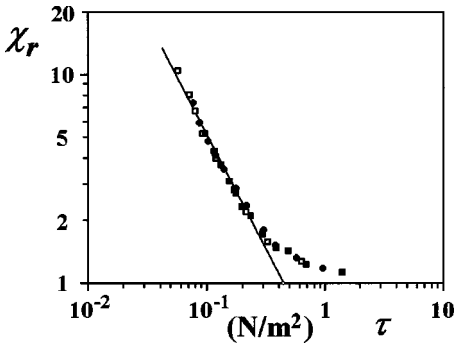

FIG. 8. Dimensionless ultrasonic backscattering coefficient $\chi_r=\chi_a/\chi$ versus the shear stress $\tau=\mu(\gamma)\gamma$ for hardened red cells in 3g% dextran 70-PBS. Particle volume fraction $\phi=0.15$ (□), $\phi=0.25$ (●) and $\phi=0.3$ (■).

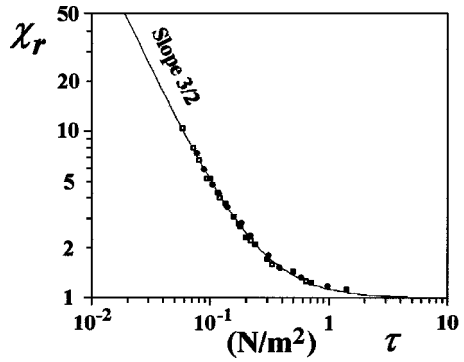

FIG. 9. Dimensionless ultrasonic backscattering coefficient $\chi_r=\chi_a/\chi$ versus the shear stress $\tau=\mu(\gamma)\gamma$ for hardened red cells suspended in 3g% dextran 70-PBS. Particle volume fraction $\phi=0.15$ (□), $\phi=0.25$ (●) and $\phi=0.3$ (■). The solid curve is calculated from Eq. (22) with $m=\frac{1}{2}$ and $\tau^*=0.25$ N/m^2. The rheo-acoustical model predicts a power law scaling as $(\tau^*/\tau)^{3m}$ with an exponent $m=1/2$ for soft clusters.

ultrasound frequency is high ($kR=2\pi\nu R/c_o>1$). A fourth-order frequency dependence of the backscattered power representative of the Rayleigh scattering regime was indeed observed by Yuan and Shung[13] for aggregated whole blood over an extended range from 3.5 to 12.5 MHz. In the fractal scattering regime, the scattered power from a collection of large structures ($kR\gg 1$) becomes sensitive to the fractal dimension of aggregates and Eq. (16) predicts a frequency dependence scaling as ν^{4-D}. For most biological media with a long-ranged structure such as liver, the frequency dependence of the ultrasound scattered power indeed obeys the power law $\chi_a\approx\nu^f$ with $f\approx 2$ (Refs. 56 and 57) which indicates a fractal dimension $D=4-f\approx 2$.

In the case of moderate ultrasound frequencies such that the wavelength is much larger than clusters ($kR\ll 1$), rheo-ultrasonic experiments provide a way to estimate the characteristic size of aggregates and the critical disaggregation shear stress. For red cells in dextran 70-PBS, particle aggregation occurs above the critical dextran concentration $\varphi\approx 1.5$ g% (Fig. 10). As dextran is added, the critical disaggregation shear rate rises and then decreases for polymer concentration higher than 4g% (Fig. 10). The disaggregation behavior at high dextran polymer concentration $\varphi>6$ g% is extremely sensitive to the structure of the outer polymeric coat (or glycocalyx) of biological membranes.[58]

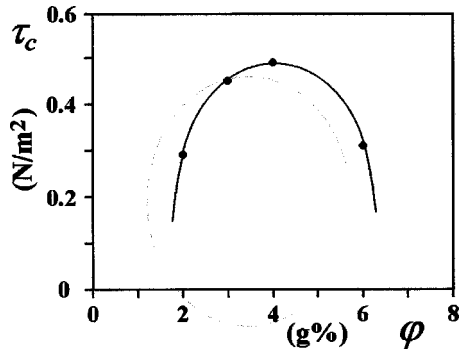

FIG. 10. Critical disaggregation shear stress τ_c versus polymer concentration φ for red blood cells suspended in dextran 70-PBS (particle volume fraction $\phi=0.25$). The critical shear stress τ_c is determined from ultrasound scattering experiments.

E. Ultrasonic, light scattering and viscometry methods

Light scattering is also well suited to study the aggregation of deformable red blood cells and determine the critical disaggregation shear stress.[30,31] The aggregation process of deformable biological membranes leads to large contact areas between adjacent cell surfaces with a uniform gap across which visible radiations are not scattered since the intercellular distance of about 200 Å (Ref. 52) is lower than the light wavelength. As a consequence, light scattering is sensitive to the growth of deformable red cell aggregates much larger than the light wavelength since the scattering cross section per unit volume decreases with cluster size. In contrast to ultrasound scattering in the Rayleigh regime, the diffuse reflectivity of the blood involves the fractal dimension of clusters. When comparing results from rheo-ultrasonic and rheo-optics experiments obtained with close molecular weight dextran solutions (respectively 3g% dextran 70 and 3g% dextran 80), disaggregation shear stresses τ^* differ by a factor 2 [$\tau^* = 0.65$ N/m^2 with the light reflectometry method[30] and $\tau^* = 0.25$ N/m^2 with the ultrasonic method (Fig. 8)]. One may indeed expect a somewhat higher disaggregation shear stress from the rheo-optical method since the light reflectometric technique is sensitive to the contact area between aggregated particles while ultrasound Rayleigh scattering involves the cluster volume.

Viscosity measurements also provide a way to estimate the disaggregation shear stress of weakly flocculated suspensions. A microrheological model proposed by Mills and Snabre[30] leads to a rheological Casson-like equation[59] and confirms that hardened red cell clusters can be considered as soft aggregates of fractal dimension $D = 2$.[30] However, the critical disaggregation shear stresses τ^* determined from rheo-ultrasonic and viscometry experiments are different by a factor of 10 since particle aggregation dominates the rheological behavior in the low shear regime and the shear viscosity is not very sensitive to the presence of small aggregates.[30] Viscosity measurements indeed become less predictive in the high shear regime where the disaggregation is almost complete. The restructuration of clusters in shear flow may further influence the rheological behavior of a weakly aggregated suspension.[31] Particle deformability and adhesiveness indeed favor a shear-induced restructuration of aggregates and a contraction of the spanning network in the low shear regime.[31]

IV. CONCLUSION

In the present paper, an approach for modeling ultrasound scattering from a dense suspension of Rayleigh clusters has been proposed and applied to red blood cell aggregates. In the Rayleigh scattering regime, it was shown that the scattered power scales as the average volume of the aggregates without dependence on the cluster volume fraction or the fractal dimension of aggregates since the ultrasound wave cannot resolve small structures. Conversely, the internal structure of aggregates larger than a voxel ($kR > 1$) influences the scattering behavior.

Studies about ultrasound scattering from a flowing suspension are usually performed in a tube.[12,13,22,54] In nonuniform flows, the space variation of the tangential shear stress induces particle or cluster migration toward the center of the channel.[60] Recent experimental results by Koh *et al.*[61] concerning the flow of concentrated suspensions in a rectangular channel indeed show particle concentrations close to the random packing volume fraction $\phi^* = \frac{4}{7}$ near the central region of the channel and a strong blunting of the velocity profile. As a result of cluster migration favored by particle flocculation, strong correlations among scatterers would lower the ultrasound backscattered power from the central region of a parabolic flow. Such a mechanism likely explains the striking ''black hole'' phenomenon observed in cross-sectional B-mode images of aggregating red cells in a channel flow near the center region of the tube.[62,63]

In the present study, rheo-ultrasonic experiments were performed in a plane–plane flow to investigate the shear breakup of hardened red cell aggregates under well-defined hydrodynamic conditions. The Rayleigh scattering model together with a fractal approach of cluster breakup describes well the ultrasonic experiments. The shear stress dependence of the backscattering coefficient indicates that hardened red cell aggregates can be considered as soft clusters with a fractal dimension $D \approx 2$. The flow-dependent changes of the ultrasound scattered power from red cell clusters further establish the validity of the effective medium approximation used in microrheological models.

Light reflectometry and viscometry methods, as well as ultrasound scattering, can give an estimate of the disaggregation shear stress representative of the mechanical force required to disrupt the bonds between particles.[30] However, particle flocculation dominates the rheological behavior in the low shear regime and, thus, the viscometry method likely underestimates the critical disaggregation shear stress. Viscosity measurements are further strongly dependent on both shear-induced restructuration processes and the formation of a marginal layer free of particles near the viscometer walls. Therefore, scattering techniques sensitive to either cluster volume (ultrasound scattering) or contact area between particles (light scattering) are better suited for determining the critical disaggregation shear stress of red cell suspensions. However, light scattering by red cell aggregates is dependent both on the fractal dimension of clusters and the deformability of particles. For Rayleigh scatterers, the ultrasound scattering technique presents the main advantage to be only sensitive to the characteristic volume of aggregates in concentrated suspensions whatever the deformability of particles and the internal structure of clusters.

Therefore, ultrasound backscattering is a very promising technique to estimate the particle adhesiveness in dense suspensions and assess *in vivo* red blood cell aggregation. Considerable research in ultrasonic scattering was indeed motivated by the potential applications in hematology.[22] The present theoretical and experimental study clearly demonstrates that quantitative information about *in vivo* red blood cell aggregation can be obtained from the analysis of the ultrasound backscattered power.

[1] J. F. Greenleaf, *Tissue Characterization with Ultrasound, Vol. II: Results and Applications* (CRC, Boca Raton, FL, 1996).
[2] J. F. Greenleaf and M. S. Chandra, *Biological System Evaluation with Ultrasound* (Springer-Verlag, New York, 1992).
[3] K. K. Shung and J. M. Reid, Ultrasonic detection of erythrocyte aggregation, in Proceedings of the 29th Annual Conference of the Engineering Medicine and Biology Alliance of Engineers in Medicine and Biolology, Bethesda, MD (1976), pp. 136–145.
[4] K. K. Shung and J. M. Reid, ''Ultrasonic instrumentation for hematology,'' Ultrason. Imaging **1**, 280–289 (1979).
[5] M. Boynard and M. Hanss, ''Ultrasonic blood characterization,'' Acoust. Imaging **10**, 315–324 (1982).
[6] M. Boynard, J. C. Lelievre, and R. Guillet, ''Aggregation of red blood cells studied by ultrasound backscattering,'' Biorheology **24**, 451–461 (1987).
[7] M. K. Wolverson, S. Nouri, J. H. Joist, M. Sundaram, and E. Heiberg, ''The direct visualization of blood flow by real-time ultrasound: Clinical observations and underlying mechanisms,'' Radiology **140**, 443–448 (1981).
[8] B. Sigel, J. Machi, J. C. Beitler, J. R. Justin, and J. C. U. Coelho, ''Variable ultrasound echogenicity in flowing blood,'' Science **218**, 1321–1323 (1982).
[9] B. Sigel, J. Machi, J. C. Beitler, and J. R. Justin, ''Red cell aggregation as a cause of blood-flow echogenicity,'' Radiology **148**, 799–802 (1983).
[10] M. Boynard and J. C. Lelievre, ''An approach of red blood cell aggregation by ultrasonic echography,'' Clin. Hemorheol. **9**, 771–779 (1998).
[11] M. Boynard and J. C. Lelievre, ''Size determination of red blood cell aggregates induced by dextran using ultrasound backscattering phenomenon,'' Biorheology **27**, 39–46 (1990).
[12] Y. W. Yuan and K. K. Shung, ''Ultrasonic backscatter from flowing whole blood: I. Dependence on shear rate and hematocrit,'' J. Acoust. Soc. Am. **84**, 52–58 (1988).
[13] Y. W. Yuan and K. K. Shung, ''Ultrasonic backscatter from flowing whole blood: II. Dependence on frequency and fibrinogen concentration,'' J. Acoust. Soc. Am. **84**, 1195–1200 (1988).
[14] S. Y. Kim, I. F. Miller, B. Sigel, P. M. Consigny, and J. Justin, ''Ultrasonic evaluation of erythrocyte aggregation dynamics,'' Biorheology **26**, 723–736 (1989).
[15] K. K. Shung, G. Cloutier, and C. C. Lim, ''The effects of hematocrit, shear rate and turbulence on ultrasonic doppler spectrum from blood,'' IEEE Trans. Biomed. Eng. **39**, 462–469 (1992).
[16] R. E. N. Shehada, R. S. C. Cobbold, and L. Y. L. Mo, ''Aggregation effects in whole blood: influence of time and shear rate measured using ultrasound,'' Biorheology **31**, 115–135 (1994).
[17] J. W. S. Lord Rayleigh, ''Vibrations of solid bodies,'' in *Theory of Sound* (Dover, New York, 1945), pp. 414–431.
[18] V. Twersky, ''On scattering of waves by random distributions: I. Free space scatterer formalism,'' J. Math. Phys. **3**, 700–715 (1962); ''II. Two space formalism,'' *ibid.* **3**, 724–734 (1962).
[19] V. Twersky, ''Acoustic bulk parameters in distribution of pair-correlated scatterers,'' J. Acoust. Soc. Am. **36**, 1710–1719 (1978).
[20] V. Twersky, ''Low-frequency scattering by correlated distributions of randomly oriented particles,'' J. Acoust. Soc. Am. **81**, 1609–1614 (1987).
[21] L. Y. L. Mo and R. S. C. Cobbold, ''Theoretical models of ultrasonic scattering in blood,'' in *Ultrasonic Scattering in Biological Tissues*, edited by K. K. Shung and G. A. Thieme (CRC, Boca Raton, FL, 1993), Chap. 5, pp. 125–170.
[22] G. Cloutier and Z. Qin, ''Ultrasound backscattering from non-aggregating and aggregating erythrocytes. A review,'' Biorheology **54**, 443–470 (1997).
[23] R. J. Lucas and V. Twersky, ''Inversion of ultrasound scattering data from red blood cell suspensions under different flow conditions,'' J. Acoust. Soc. Am. **82**, 794–799 (1987).
[24] M. Hanss and M. Boynard, ''Ultrasound backscattering from blood: Hematocrit and erythrocyte aggregation dependence,'' in *Ultrasonic Tissue Characterization II*, Special Publication 525, edited by M. Linzer (National Bureau of Standards, Washington, DC, 1979), pp. 165–169.
[25] P. Snabre, M. Bitbol, and P. Mills, ''Cell disaggregation behavior in shear flow,'' Biophys. J. **51**, 795–807 (1987).
[26] P. Mills and P. Snabre, ''The fractal concept in the rheology of concentrated suspensions,'' Rheol. Acta **26**, 105–108 (1988).
[27] P. D. Patel and W. B. Russel, ''A mean field theory for the rheology of phase separated or flocculated dispersions,'' Colloid Surf. **31**, 355–383 (1988).
[28] A. Potanin and N. B. Uriev, ''Microrheological models of aggregated suspension in shear flow,'' J. Colloid Interface Sci. **142**, 385–395 (1991).
[29] R. Wessel and R. C. Ball, ''Fractal aggregates and gels in shear flow,'' Phys. Rev. A **46**, R3008–R3011 (1992).
[30] P. Snabre and P. Mills, ''Rheology of weakly flocculated suspensions of rigid particles,'' J. Phys. III **6**, 1811–1834 (1996).
[31] P. Snabre and P. Mills, ''Rheology of weakly flocculated suspensions of viscoelastic particles,'' J. Phys. III **6**, 1835–1853 (1996).
[32] P. Snabre and P. Mills, ''Rheology of concentrated suspensions of viscoelastic particles,'' Colloids Surf., A **152**, 111–123 (1999).
[33] A. A. Potanin, ''On the computer simulation of the deformation and breakup of colloidal aggregates in shear flow,'' J. Colloid Interface Sci. **157**, 399–410 (1993).
[34] B. A. J. Bascom and R. S. C. Cobbold, ''On a fractal packing approach for understanding ultrasonic backscattering from blood,'' J. Acoust. Soc. Am. **98**, 3040–3049 (1995).
[35] B. A. J. Angelsen, ''A theoretical study of the scattering of ultrasound by blood,'' IEEE Trans. Biomed. Eng. **27**, 61–67 (1980).
[36] L. Y. L. Mo and R. S. C. Cobbold, ''A unified approach to modeling the backscattered Doppler ultrasound from blood,'' IEEE Trans. Biomed. Eng. **39**, 450–461 (1992).
[37] P. M. Morse and K. U. Ingard, *Theoretical Acoustics* (McGraw–Hill, New York, 1968).
[38] L. Tsang, J. A. Kong, and T. Habashy, ''Multiple scattering of acoustic waves by random distribution of discrete spherical scatterers with quasicrystalline and Percus–Yevick approximation,'' J. Acoust. Soc. Am. **71**, 552–558 (1982).
[39] N. J. Wagner and W. B. Russel, ''Light scattering measurements of a hard sphere suspension under shear,'' Phys. Fluids A **2**, 491–502 (1990).
[40] A. Ishimaru and Y. Kuga, ''Attenuation constant of a coherent field in a dense distribution of particles,'' J. Opt. Soc. Am. **72**, 1317–1320 (1982).
[41] B.B. Mandelbrot, *The Fractal Geometry of Nature* (Freeman, New York, 1982).
[42] M Kolb and R. Jullien, ''Chemically limited versus diffusion limited aggregation,'' J. Phys. Lett. **45**, L977–L981 (1984).
[43] D. A. Weitz and J. S. Huang, *Aggregation Gelation*, edited by F. Family and D. P. Landau (North Holland, Amsterdam, 1984), p. 19.
[44] M. Y. Lin, R. Klein, H. M. Lindsay, D. A. Weitz, R. C. Ball, and P. J. Meakin, ''The structure of fractal colloidal aggregates of finite extent,'' J. Colloid Interface Sci. **137**, 263–280 (1990).
[45] M. E. Fisher and R. J. Burford, ''Theory of critical point scattering and correlations. The Ising model,'' Phys. Rev. **156**, 583–622 (1967).
[46] G. Bossis, A. Meunier, and J. F. Brady, ''Hydrodynamic stress on fractal aggregates of spheres,'' J. Chem. Phys. **94**, 5064–5070 (1991).
[47] R. C. Sonntag and W. B. Russel, ''Structure and breakup of flocs subjected to fluid stresses,'' J. Colloid Interface Sci. **115**, 378–389 (1987).
[48] F. R. Torres, W. B. Russel, and W. R. Schowalter, ''Simulations of coagulation in viscous flows,'' J. Colloid Interface Sci. **145**, 51–73 (1991).
[49] K. K. Shung, R. A. Sigelmann, and J. M. Reid, ''Scattering of ultrasound by blood,'' IEEE Trans. Biomed. Eng. **23**, 460–467 (1976).
[50] P. Snabre, H. Baumler, and P. Mills, ''Aggregation of human R.B.C. after heat treatment,'' Biorheology **22**, 185–195 (1985).
[51] P. Snabre, G. Grossman, and P. Mills, ''Effects of dextran polydispersity on red blood cell aggregation,'' Colloid Polym. Sci. **263**, 478–483 (1985).
[52] S. Chien and K. M. Jan, ''Red cell aggregation by macromolecules. Roles of surface adsorption and electrostatic repulsion,'' J. Sup. Structure **1**, 385–409 (1975).
[53] P. Snabre, ''Rhéologie des suspensions concentrées et agrégées de particules déformables. Application à la suspension sanguine,'' State doctorate dissertation. University Paris VII, 1988.
[54] M. S. van der Heiden, M. G. M. de Kroon, N. Bom, and C. Borst, ''Ultrasound backscatter at 30 MHz from human blood: influence of rouleau size affected by blood modification and shear rate,'' Ultrasound Med. Biol. **21**, 817–826 (1995).
[55] R. Skalak, P. R. Zarda, K. M. Jan, and S. Chien, ''Mechanics of rouleau formation,'' Biophys. J. **35**, 771–781 (1981).
[56] F. Dunn, P. D. Edmonds, and W. J. Fry, ''Absorption and dispersion of ultrasound in biological media,'' in *Biological Engineering*, edited by H. P. Schwan (McGraw-Hill, New York, 1969), Chap. 3, p. 205.
[57] C. Javanaud, ''The application of a fractal model to the scattering of ultrasound in biological media,'' J. Acoust. Soc. Am. **86**, 493–496 (1989).
[58] A. Othmane, M. Bitbol, P. Snabre, and P. Mills, ''Influence of altered phospholipid composition of the membrane outer layer on red blood cell

aggregation: relation to shape changes and glycocalyx structure,'' Eur. Biophys. J. **18**, 93–99 (1990).
[59] N. Casson, ''A flow equation for pigment-oil suspensions of printing ink type,'' in *Rheology of Disperse Systems*, edited by C. C. Mills (Pergamon, New York, 1959), pp. 84–102.
[60] P. Mills and P. Snabre, ''Rheology and structure of concentrated suspensions of hard spheres shear induced particle migration,'' J. Phys. II **5**, 1597–1608 (1995).
[61] J. C. Koh, P. Hookam, and L. G. Leal, ''An experimental investigation of concentrated suspension flows,'' J. Fluid Mech. **266**, 1–32 (1994).
[62] Y. W. Yuan and K. K. Shung, ''Echoicity of whole blood,'' J. Ultrasound Med. **10**, 425–434 (1989).
[63] Z. Qin, L. G. Durand, and G. Cloutier, ''Kinetics of the 'black hole' phenomenon in ultrasound backscattering measurements with red blood cell aggregation,'' Ultrasound Med. Biol. **24**, 245–256 (1998).

Ultrasound sensitivity in the cricket, *Eunemobius carolinus* (Gryllidae, Nemobiinae)

Hamilton E. Farris and Ronald R. Hoy
Section of Neurobiology and Behavior, Mudd Hall, Cornell University, Ithaca, New York 14850

(Received 26 July 1999; accepted for publication 15 November 1999)

Extracellular recordings from the cervical connectives in both long- and short-winged *E. carolinus* reveal auditory units that are sensitive to frequencies >15 kHz with best sensitivity at 35 kHz (79 dB SPL threshold). Stimuli in this frequency range also elicit a startle response in long-winged individuals flying on a tether. For single-pulse stimuli, startle and neck connective thresholds decrease with increasing ultrasound duration, consistent with the operation of an exponential integrator with a ~32.5-ms time constant. There is evidence for adaptation to long duration pulses (>20 ms) in the neck connectives, however, as it is more difficult to elicit responses to the later stimuli of a series. For paired-pulse stimuli consisting of 1-ms pulses of 40 kHz, temporal integration was demonstrated for pulse separations <5 ms. For longer pulse separations, startle thresholds were elevated by 3 dB and appear to be optimally combined. Startle thresholds to 5 ms frequency modulated (FM) sweeps (60–30 kHz) and pure tone pulses (40 kHz) did not differ. The characteristics and sensitivity of this ultrasound-induced startle response did not differ between males and females. As in some other tympanate insects, ultrasound sensitivity in *E. carolinus* presumably functions in the context of predation from echolocating bats. © *2000 Acoustical Society of America.* [S0001-4966(90)05502-3]

PACS numbers: 43.80.Lb [WA]

INTRODUCTION

Numerous species in five different insect orders have independently evolved sensitivity to ultrasound, presumably as a consequence of the selective pressure from echolocating, insectivorous bats (see Hoy, 1992 for review). Although much of the behavior and neurophysiological evidence for sensitivity to ultrasound comes from experiments with tympanate moths (Roeder, 1967; Fullard, 1979), sensitivity to ultrasound in Orthopterans has been described in several families (e.g., Tettigoniidae, Libersat and Hoy, 1991; Acrididae, Robert, 1989) including Gryllidae, the family which represents the true crickets. Although this family is composed of at least nine subfamilies (Walker and Mazaki, 1989), most evidence of ultrasound sensitivity comes from members of the subfamily, Gryllinae, commonly referred to as field crickets. For example, Australian field crickets (*Teleogryllus oceanicus*) are sensitive to two spectral ranges: a low-frequency band between 3 and 9 kHz (i.e., male calling song spectrum) and a broad high-frequency band >15 kHz (i.e., the frequency range of echolocating bats; Moiseff *et al.*, 1978). When presented with ultrasound, *T. oceanicus* flying on a tether perform short-latency (~35–55 ms; Nolen and Hoy, 1986) negative phonotactic behaviors that consist in part of the lateral extension of one of the metathoracic legs. This response presumably functions to evade echolocating, insectivorous bats. Using playback experiments in the field, the repulsive effect of ultrasound was demonstrated for a North American field cricket, *Gryllus rubens*. Farris *et al.* (1998) showed that the simultaneous broadcast of batlike ultrasound with a calling song decreases that calling song's attractiveness relative to a song broadcast without ultrasound.

Few studies, however, have examined auditory sensitivity in members of another subfamily, the Nemobiinae, commonly referred to as ground crickets. Like field crickets, members of this subfamily produce species-specific calling songs that function as sexual advertisement signals and attract male and female conspecifics (Farris *et al.*, 1997). Several species of nemobiines are polymorphic for hind wing length such that individuals develop either long hind wings that are capable of flight or short hind wings that are insufficient for flying (see Harrison, 1980 for review). Presumably, nightly phonotactic flights by long-winged individuals should put them at risk from echolocating bats. To determine whether nemobiine crickets are also sensitive to ultrasound, we used both electrophysiological and behavioral assays to examine the auditory sensitivity of *Eunemobius carolinus* (Gryllidae, Nemobiinae), a species in which long-winged individuals perform nocturnal flight-phonotaxis to male calling songs (Farris *et al.*, 1997). In particular, we examined the effects of acoustic stimuli that vary in temporal and spectral structure on the response of auditory units in the cervical connectives. Furthermore, we used the hitherto undescribed ultrasound-induced startle response in flying *E. carolinus* as a behavioral assay of cricket auditory sensitivity. We show that like gryllines, the nemobiine *E. carolinus* is sensitive to ultrasound and that the ultrasound-induced startle response in flying *E. carolinus* is elicited by sounds similar to those emitted by echolocating bats. Some of these results have been previously reported in abstract form (Farris and Hoy, 1997, 1998).

I. GENERAL METHODS

A. Subject animals

The colony, started from individuals sound-trapped in Lafayette County, Mississippi (see Farris *et al.*, 1997), was

reared under a 14 L/10 D hrs light schedule and fed ''cricket chow'' *ad libitem*. Crickets were characterized as having one of three different wing morphologies: (1) Long-winged, possessing fully developed hind wings and thus capable of flying; (2) de-alates, long-winged crickets that have detached their hind wings at the axillary sclerites of the dorsal metathorax and are no longer flight capable; (3) short-winged, possessing undeveloped hind wings and thus never capable of flying.

B. Acoustic stimuli

Stimuli were generated using Tucker Davis Technologies (TDT) 16-bit, digital-to-analog converters and custom-written software (8- or 5-μs sample period for pure tone and frequency modulated stimuli, respectively). Stimuli were amplified using a Harman/Kardon HK6150 integrated amplifier and broadcast from either a Radio Shack Super tweeter (Cat. No. 40-1310b) or an ESS AMT-1 tweeter located 30 cm from the cricket preparation (note that the maximum output frequency for each speaker was different). For experiments in which the carrier frequency was held constant at 40 kHz, the stimuli were broadcast through Panasonic 40-kHz transducers. Stimulus amplitude was adjusted using TDT PA4 programmable attenuators. The stimuli were calibrated at the preparation using a Bruel and Kjaer (B&K) 2608 measuring amplifier (linear weighting, fast: 125-ms integration time) with a (B&K) model 4138 1/8-inch microphone (90° angle of incidence, experiment 1 only) or with a B&K 4135 1/4-inch microphone (0° angle of incidence), B&K 2639 preamp, a B&K 5935 microphone power supply. The calibration system was checked using a B&K 4220 pistonphone calibrator. All sound-pressure levels (dB SPL) are referenced to 20 μPa. Depending on the speaker used, the maximum output level of the system was either 108 or 113 dB SPL. All pulse onset and offset ramps are raised cosine. Pure tone stimuli were calibrated using continuous tones, whereas the calibration signal for FM stimuli was a continuous series of 5-ms FM pulses at 100 pulses/s (50% duty cycle). The amplitude of a single FM pulse was thus corrected by 4.13 dB (the effect of the 50% duty cycle and the 1-ms ramp) to match that of the pure tone stimuli for a given SPL. This calibration signal was used to maintain the temporal relationship of the spectral components within the 5-ms FM sweep. Spectral properties of the FM sweep were analyzed at the position of the cricket preparation using a B&K 4135 1/4-inch microphone (0° angle of incidence), B&K 2639 preamp, a B&K 5935 microphone power supply, and a Hewlett-Packard 3562A signal analyzer.

C. Neurophysiological recordings

The experimental procedure used in this study is the same as that used by Farris *et al.* (1998). Briefly, cold-anesthetized, colony-reared crickets were mounted ventral side up on a platform in a foam-lined Faraday cage that reduced acoustic reflections and electrical noise. The prothoracic legs of the crickets were extended laterally and the tarsi were fixed to small bars using low melting point wax. The acoustic stimuli were presented from loudspeakers 30 cm from the preparation, positioned 0° normal to the longitudinal axis of the cricket. Extracellular recordings were made using a sharpened tungsten electrode inserted ventrally through an opening in the cervical membrane and hooked under the left or right cervical connection between the prothoracic and subesophogeal ganglia. When recording ascending information only, the neck connectives were cut anterior to the placement of the hook electrode. The electrode was insulated using a mixture of mineral oil and Vaseline jelly applied around the connective. The indifferent electrode was inserted into the abdomen. Recordings from the cervical connectives were amplified using a model 1700 AM Systems differential amplifier and bandpass filtered between 10 and 10 000 Hz. The stimuli and neural responses were recorded simultaneously onto tape using a 400-PCM recorder or digitally captured using a TDT AD1 analog-to-digital converter (sampling period: 40 μs) for later analysis. We also monitored the recordings visually using a Tektronix R5030 oscilloscope and aurally using an Archer amplified speaker.

The threshold for eliciting a response in the neck connectives was determined as the minimum sound-pressure level necessary to elicit at least three responses to a series of five pulses. Stimuli were presented at 0.5 pulses/s. In addition to this 3/5 threshold criteria, for experiments that tested the effects of stimulus duration on threshold, we used a 1-out-of-2-down, 0-out-of-2-up adaptive procedure. For this adaptive rule, the amplitude of a single pulse was decreased in 6-dB steps if a response was detected in one out of two presentations. Stimulus step sizes were then changed to 3 and 1 dB for each reversal until a threshold was determined. The minimum interstimulus interval in this procedure was 5 s.

D. Startle response

Long-winged *E. carolinus* were tethered dorsally at the pronotum to a 14-cm-long piece of piano wire using low melting point wax. Flight can easily be initiated by waving the tethered cricket in the air or by giving it small puffs of wind. Once flying, a tethered cricket was positioned in the foam-lined Faraday cage 7 cm from the cage floor and 30 cm from the speakers placed at 90° normal to the cricket. The behavioral components of the startle response consist of an abrupt cessation of flapping, folding of the hind wings, closure of the fore wings, anterior extension of the prothoracic and mesothoracic legs, posterior extension of the metathoracic legs, and dorsal flexion of the head and antennae. Flight usually resumed with the termination of the stimulus. Restarting flight became more difficult with increasing numbers of startle responses in some subjects, however. Thus to help ensure that most subjects would complete the test, we measured the startle threshold using the 1/2-down, 0/2-up adaptive procedure described above. Note that thresholds are statistical constructs and that this adaptive procedure converges on the stimulus level that elicits a response in 30% of the presentations (Levitt, 1971). Without measurement of a second point on each individual's psychometric function (i.e., using a 2-down, 1-up method), it is impossible to know the function's slope and thus extrapolate what change in stimulus level will induce a certain change in the probability of

response. Individuals were required to fly for at least 5 s prior to stimulus presentation (i.e., minimum interstimulus interval was 5 s). This interval was chosen to reduce the probability of any habituation or sensitization.

The hind wings of long-winged crickets were removed for morphometric measurement following an experiment by simply squeezing the wings with a pair of forceps and allowing the cricket to reflexively detach the wings (de-alation). With each detached wing in its folded position, their proximo-distal lengths (along the length of the costal vein) were measured using vernier calipers (0.05-mm resolution). Wing size for an individual was then determined as the average wing length measured for both hind wings.

II. EXPERIMENTS

A. Frequency sensitivity

To determine the effect of stimulus carrier frequency on responses in the neck connectives of long-winged individuals ($N=7$), we measured the threshold for eliciting a detectable neural response to pure tone pulses of 18 frequencies ranging from 2–55 kHz. Pulses were 5 ms in duration with 1-ms ramps and presented at 0.5 pulses/s. The threshold for eliciting a startle response was determined by presenting individual flying crickets ($N=8$) a single 5-ms pulse with 1-ms ramps for 20 frequencies ranging from 2–65 kHz and visually noting whether a startle response occurred. Stimulus frequencies were presented in a pseudorandom order.

B. Wing morph and frequency sensitivity

The frequency responses (2–60 kHz) in the neck connectives of flightless crickets (6 short-winged and 9 long-winged de-alated individuals) were examined using the same protocol as in experiment 1. Wing-morph was determined after the prep was completed by examining the axillary sclerites of the dorsal metathorax for the presence of undeveloped hind wings in short-winged individuals or ''stumps'' from the de-alated wings.

C. Frequency sensitivity of ascending units

Following the measurement of the frequency sensitivity in the neck connectives of six individuals (all de-alates), we examined the tuning of just the ascending units by cutting both connectives anterior to the hook electrode and repeating the measurements for frequencies ranging from 2–60 kHz.

D. Temporal integration: Single pulse

Startle response and neck connective thresholds were measured for stimuli that varied in duration (i.e., duration versus intensity paradigm). A stimulus consisted of a single pulse of 40 kHz with 1-ms ramps that varied in duration from 2–80 ms. The threshold for eliciting a response in the neck connectives was measured using both the 1/2-down, 0/2-up adaptive procedure ($N=10$) and the 3/5-down criteria ($N=10$). Ten different individuals were used in each test. The effect of duration on the startle response was measured for 14 individuals using the 1/2-down, 0/2-up procedure only.

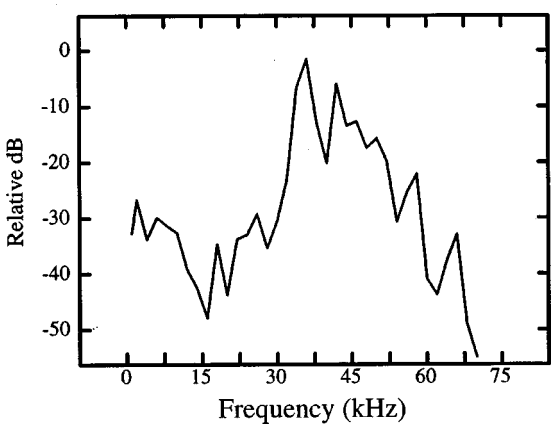

FIG. 1. Amplitude spectrum of a single pulse of the FM sweep used in Sec. II E. Each pulse was 5 ms in duration with 1-ms ramps and consisted of a 60- to 30-kHz linear sweep.

E. Temporal integration: Multipulse

Two different experimental methods were used to assess the temporal integration of multiple pulse stimuli. First, 5-ms pulses consisting of a linear FM sweep from 60 to 30 kHz (Fig. 1) were presented at varying pulse rates to flying crickets to determine the effect of repetition rate (and pulse separation) on startle threshold. The duration and spectral characteristics of the pulses in these stimuli were chosen to model the characteristic search phase pulses of some bats (Simmons, 1987). In trial 1 ($N=10$), the total stimulus duration was 1 s (pulse number varied), whereas in trial 2 ($N=12$) only a pair of pulses was presented. Thresholds were determined for pulse repetition rates ranging from 1 to 181 pulses/s. Each pulse had 1-ms ramps. To assess whether the FM structure of the stimulus had an effect on startle threshold relative to that for a pure tone stimulus, startle threshold to a single 5-ms pulse of 40 kHz (1 ms raised cosine ramps) was also measured for each individual in trial 1 and compared to that for a single FM pulse using a paired *t*-test (Zar, 1989).

Second, the threshold for eliciting a startle response to a pair of 1-ms pulses (0.1-ms ramps) of 40 kHz was measured as a function of pulse separation ($N=20$). For both the duration versus intensity (i.e., single-pulse stimuli in Sec. II D) and paired-pulse paradigms, the response functions were described analytically using a least-squares fit to the means.

F. Effects of sex and wing length on startle threshold

A sample population across several experiments was used to assess the effects of wing size and sex on startle threshold. The threshold for eliciting a startle response to a single 5-ms pulse of 40 kHz with 1-ms ramps was compared between males and females using a Mann–Whitney test of ranks (Zar, 1989). This test was also used to compare male wing length to female wing length (i.e., long-winged). The relationship between wing length and startle threshold was analyzed using linear regression in which wing length and startle threshold were the independent and dependent variables, respectively.

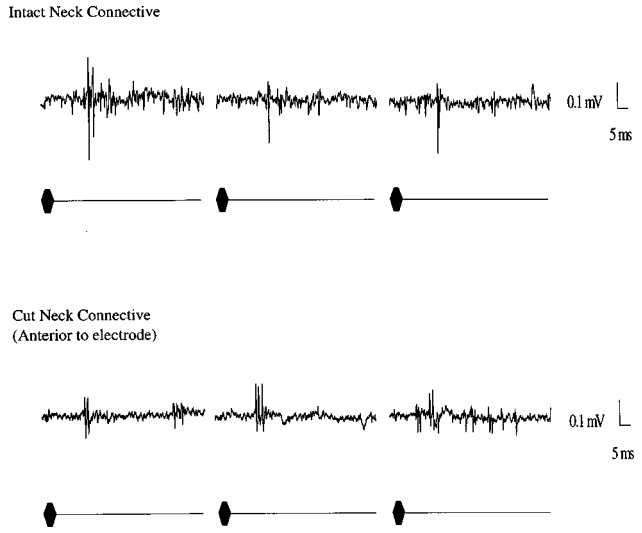

FIG. 2. Responses recorded in the neck connective of a female *E. carolinus* presented with three 5-ms pulses of 40 kHz at 82.3 dB SPL at 0.5 pulses/s. Upper and lower panels are the responses of the same connective in the intact and cut conditions, respectively. Relative to recordings in the intact preps, spike amplitudes were commonly reduced in the cut-connective recordings.

III. RESULTS

A. Frequency sensitivity

Extracellular recordings from the cervical connectives in long-winged *E. carolinus* show recognizable auditory units that are sensitive to frequencies higher than 15 kHz with best sensitivity at 35 kHz (79 dB SPL threshold) (Figs. 2 and 3). This range of frequencies also elicits a startle response in individuals flying on a tether (Fig. 3). The components of the startle response in *E. carolinus* (see Sec. I) do not appear to be directional, which is different from the ultrasound-induced directional steering response in field crickets (Gryllinae) (May and Hoy, 1990).

B. Wing morph and frequency sensitivity

The frequency response curves of neural activity in the neck connectives of both de-alate and short-winged individuals (i.e., both flightless morphs) were similar to those of long-winged individuals. Comparison of the audiograms of the two short-winged groups to that for long-winged crickets shows that best sensitivity occurs at frequencies >20 kHz (Fig. 3). Ultrasound sensitivity was not uniform across the three wing-morphs, however, as long-winged individuals were 5–7 dB more sensitive from 20–30 kHz and 5–7 dB less sensitive above 45 kHz than the two short-winged morphs.

C. Frequency sensitivity of ascending units

The exclusion of any descending information by cutting the neck connective did not change the frequency response in the neck connectives. Figure 4 shows the average tuning in the same preparations prior to and after cutting the connective in six de-alates. Like those for experiments 1 and 2, frequency sensitivity increased for frequencies above 15 kHz. One notable difference between the cut and intact voltage records was that the evoked potentials in the intact connective showed a tri-phasic change in potential, whereas those in the cut connective appeared to bi-phasic (Fig. 2).

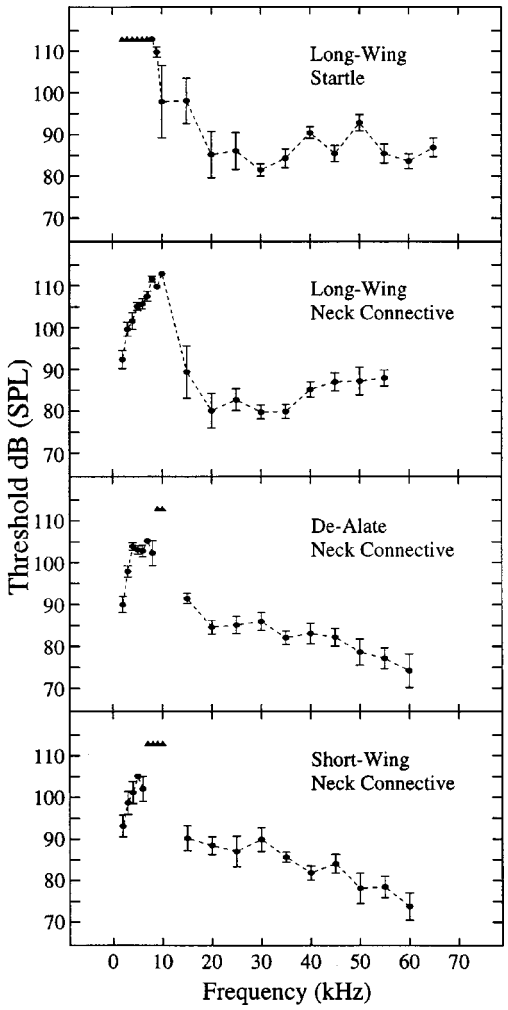

FIG. 3. Frequency tuning curves for the startle response of long-winged individuals flying on a tether and the neural activity recorded in the neck connectives for the three-wing morphs. Circles are the mean thresholds ($\pm$SE) necessary to elicit a response in 1/2 stimulus presentations for the startle response ($N=8$) and 3/5 stimulus presentations for the neck connectives. Sample sizes for the three-wing morphs were: $N=7$, 9, and 6 for the long-winged, de-alates, and short-winged crickets, respectively. Triangles mark frequencies to which <2 individuals responded to stimuli below 113 dB SPL.

D. Temporal integration: Single pulse

Startle response thresholds to single 40-kHz pulses decrease exponentially with increasing pulse duration (Fig. 5). The individual data were normalized to their minima prior to the analysis of the effect stimulus duration on threshold. The dashed curve in each panel of Fig. 5 represents a least-squares fit of the following equation proposed by Plomp and Bouman (1959) for the change in threshold as a function of stimulus duration,

$$\text{Threshold Shift } (T) = -10^{*}\log\left(1-\exp\left(\frac{-T}{\tau}\right)\right),$$

where τ represents the temporal integration (i.e., summation) time constant that describes the rate at which the threshold

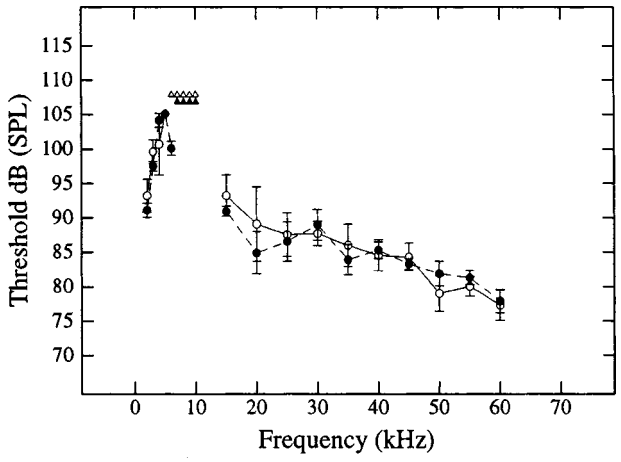

FIG. 4. Frequency tuning curves for intact (●) and cut (○) neck connectives. Values are the mean thresholds (±SE) necessary to elicit a response in 3/5 stimulus presentations ($N=6$, all de-alates). After measuring the frequency response in intact preparations, both connectives were cut anterior to the electrode and measurement of the frequency response was repeated. Triangles mark frequencies in which <2 individuals responded to stimuli below 108 dB SPL. Examples of the responses recorded in the two conditions are shown in Fig. 2.

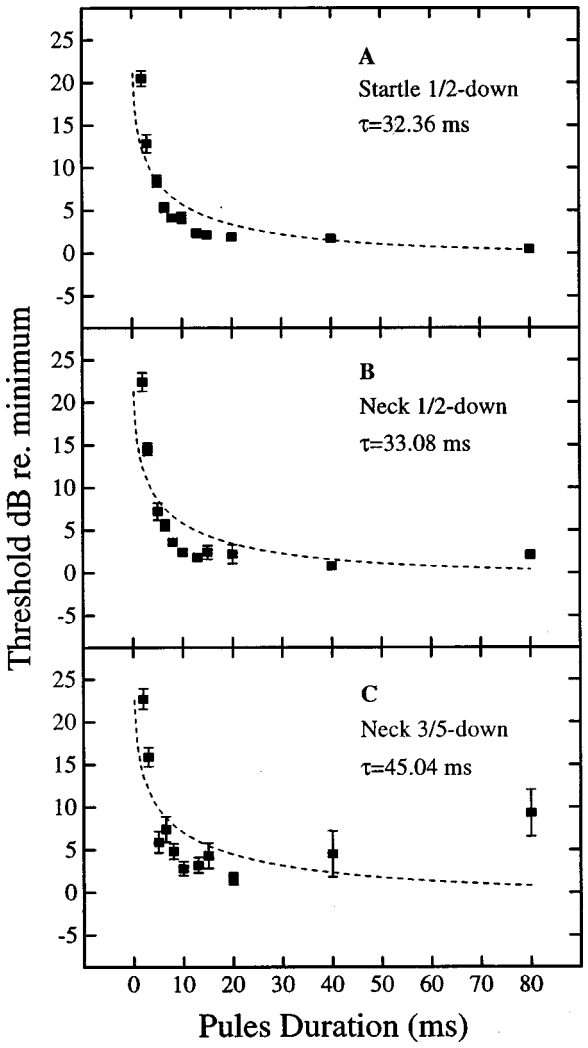

FIG. 5. Relationship between stimulus duration and threshold for eliciting: (A) a startle response ($N=14$), (B) a response in the neck connectives using a 1/2-down adaptive procedure ($N=10$), and (C) a response in the neck connectives using a 3/5-down adaptive procedure ($N=10$). Data were normalized to their minima prior to averaging. Filled squares are the mean thresholds (±SE; in some cases SE is smaller than the symbol) for eliciting a response to 40-kHz pulses with 1-ms ramps at varying durations. The dashed curves represent the least-squares fit to the data using the equation proposed by Plomp and Bouman (1959) for the change in threshold as a function of duration (T) (see text). The time constants (τ) for each fit are noted in each panel.

reaches an asymptote as a function of T, the duration of the stimulus. For the two experiments that used a 1/2-down, 0/2-up procedure, the time constants were virtually the same: 32.36 ms ($r^2=0.726$) and 33.08 ms ($r^2=0.624$) for the startle response and neck connectives, respectively. For the response in the neck connectives measured using a 3/5 threshold criteria, however, there appears to be some evidence for adaptation to pulses longer than 20 ms. During these presentations it was common for a response to be elicited to the first pulse in the five-pulse train, with little response after that (Fig. 6). Thus the thresholds measured at these longer durations are higher (to meet the 3/5 criteria) and there is an apparent increase in τ to 45.04 ms ($r^2=0.421$). Linear regression analysis of the mean threshold versus the logarithm of stimulus duration showed that the slopes for the time-intensity tradeoff for the three data sets in Fig. 5: A, B, and C are: −10.9 dB ($r^2=0.72$), −11.3 dB ($r^2=0.62$), and −7.8 dB ($r^2=0.33$) per decade duration, respectively.

E. Temporal integration: Multipulse

For stimuli consisting of 5-ms FM pulses, there was no salient effect of pulse rate on the startle threshold (Fig. 7). Although the data show a slight increase in sensitivity to pulse rates near 20 pulses/s, this peak is only ~4 dB lower than that for a single pulse in the 1-s pulse train tests [Fig. 7(a)] and at the most 1.5 dB better in the paired-pulse test [Fig. 7(b)]. These thresholds are thus indistinguishable from the rest of the response function, and there does not appear to be any clear multiple pulse integration revealed by this paradigm. These stimuli were chosen to more closely simulate bat biosonar (Simmons, 1987; see discussion). Using a pairwise comparison for each individual in trial 1, we found no significant difference between the startle threshold for a single FM pulse and that for a pure tone 40-kHz pulse ($t=0.34$, $N=10$, $P=0.741$; absolute mean difference $=0.469\pm4.21$ dB).

Startle threshold did depend on pulse separation for the shorter duration, pure tone pulses (1-ms duration, 40 kHz), however (Fig. 8). Thresholds relative to that for a single 1-ms pulse decreased for pulse pairs separated by <10 ms (i.e., 0- to 5-ms interpulse intervals). As in the duration versus intensity tradeoff above, the change in startle threshold as a function of pulse separation can be modeled as a leaky integrator (Zwislocki, 1960) using the following equation:

$$\text{Threshold Shift } (T) = -10^{*}\log\left(1+\exp\left(\frac{-\Delta T}{\tau}\right)\right)+C,$$

where C is a constant that describes the asymptote of the

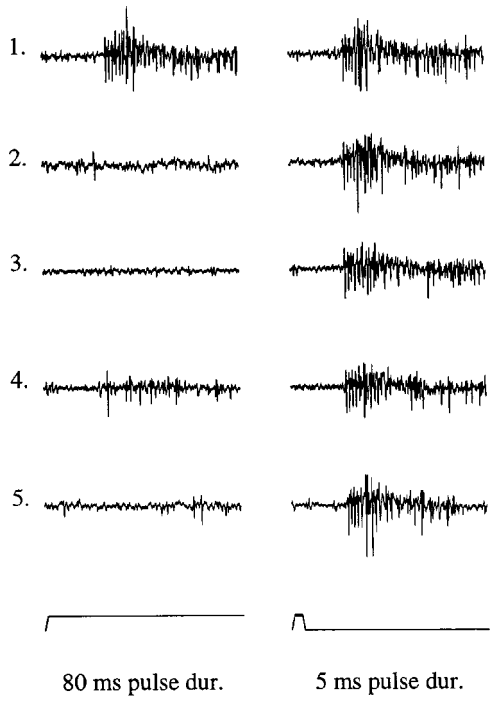

FIG. 6. Demonstration of reduced response to five presentations of pulses with long durations. Traces are the responses recorded in the neck connectives for two different pulse durations (40 kHz, 1 ms-ramps, 90 dB SPL, 2-s pulse period). For the 80-ms stimulus (left column), a response was noted for sweep 1 only (note that trace 4 may contain a response of the same unit that responds in sweep 1). Whereas for the 5-ms stimulus, a response was noted in all five presentations.

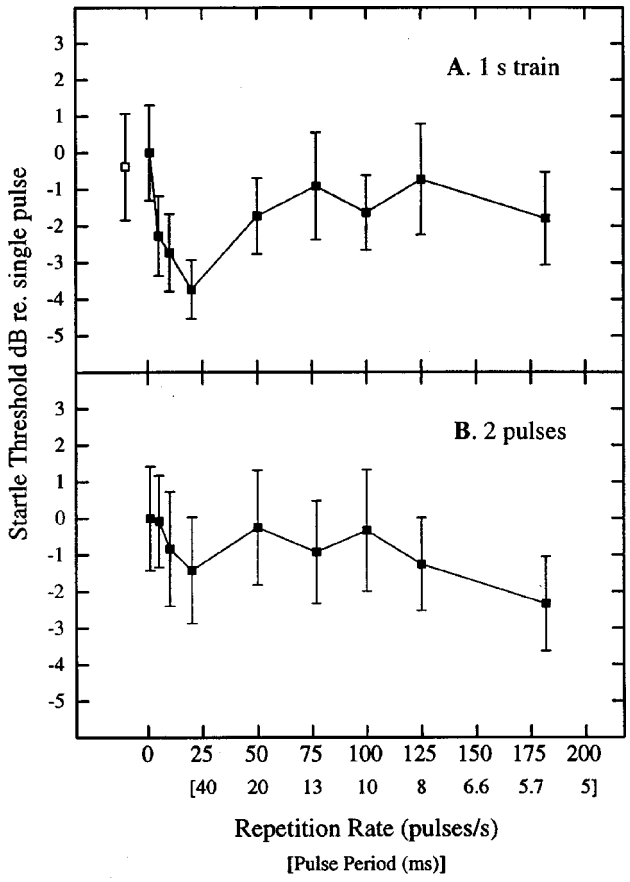

FIG. 7. Relationship between FM pulse repetition rate and startle threshold. Filled squares are the mean thresholds (±SE, *re* 1 FM pulse) necessary to elicit a startle response. (a) Stimuli consisted of a 1-s train of 5-ms pulses (1-ms ramps) of a linear 60–30 kHz FM sweep presented at variable pulse rates ($N=10$). The open square is the mean threshold for eliciting a startle response to a single 5-ms pulse (1-ms ramps) of 40 kHz for the same 11 crickets. There was no difference in pairwise comparison of startle threshold to single pulses of FM and pure tone (40 kHz) ($t=0.34$, $N=10$, $P=0.741$; absolute mean difference $=0.469\pm4.21$ dB). (b) Stimuli consisted of a pair of 5-ms pulses (1-ms ramps) of a linear 60–30 kHz FM sweep presented at variable pulse rates. Corresponding pulse periods (time between the beginning of two successive pulses) are noted on the *x*-axis in brackets.

function and ΔT is the time interval between pulses. A least-squares solution for τ and C showed that the startle threshold changed like that of a leaky integrator with a time constant (τ) of 5.30 ms that reaches an asymptote (C) at -1.30 dB ($r^2=0.803$).

F. Effects of sex and wing length on startle threshold

There was no significant difference between male and female startle thresholds ($U=50$; $N=11$ female, 13 male; $P>0.2$). Startle threshold (i.e., long-winged individuals) did not vary significantly with wing length ($r^2=0.006$, $N=24$; male and female wing sizes were not significantly different, $U=58$, $P>0.2$). Because wing lengths in our study population only ranged from 10.95–12.78 mm, we would expect only a 1.34-dB range in startle thresholds (Forrest *et al.*, 1995; see discussion). It is thus not surprising that regression analysis showed no correlation between *E. carolinus* size and startle threshold.

IV. DISCUSSION

A. Frequency tuning

Without doubt, *E. carolinus* is sensitive to frequencies below 15 kHz, especially those contained in the calling song (see Farris *et al.*, 1997). It was the focus of this study, however, to examine the more salient auditory capabilities in the ultrasound band. Extracellular recordings of neural activity in the neck connectives of *E. carolinus* demonstrate recognizable auditory units that are excited by ultrasound. This physiological tuning is similar to that found in other insects known to use acoustic cues to avoid echolocating bats (Hoy, 1992). For example, general physiological sensitivity to ultrasound in tympanate moths is tuned to frequencies between 20 and 120 kHz and best sensitivity is found near 30 kHz at ~50 dB SPL (e.g., Faure *et al.*, 1993; Waters and Jones, 1996). Sensitivity to this spectrum is noctuid moths reflects the parallel tuning of a pair of peripheral auditory neurons with staggered thresholds called A1 and A2 (Coro and Perez, 1984). In addition to moths, mantids (Dictyoptera), lacewings (Neuroptera), and beetles (Coleoptera) all possess similar ultrasound sensitivity. Although independently evolved (Fullard and Yack, 1993), these convergent auditory systems all mediate ultrasound-induced startle responses that presumably function in the avoidance of echolocating bats.

More closely related to the ground cricket, *E. carolinus* (Gryllidae: Nemobiinae) are the field crickets (Gryllidae: Gryllinae). Sensitivity to ultrasound in the central nervous system (CNS) of gryllines is carried out by a bilateral pair of ascending interneurons called INT-1 (Moiseff and Hoy, 1983; cf. AN2 Wohlers and Huber, 1982), and its tuning

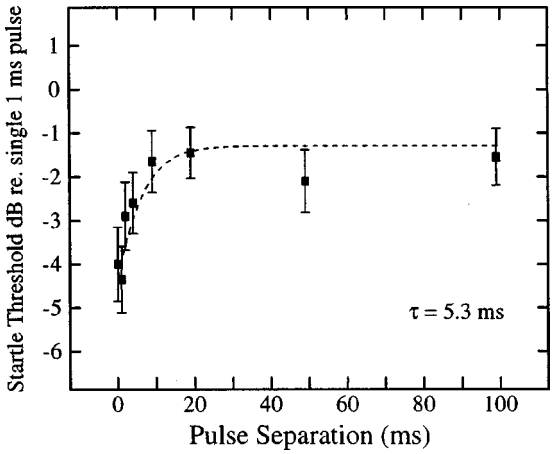

FIG. 8. Relationship between pulse separation and startle threshold. A stimulus consisted of a pair of 1-ms pulses of 40 kHz (0.1-ms ramps) that varied in separation from 0–99 ms. Squares (■) are the mean (±SE) threshold necessary to elicit a startle response relative to the threshold for a single pulse ($N=20$). Dashed curve represents the expected threshold for an integrator with a 5.3-ms time constant (τ) (Zwislocki, 1960).

closely matches the tuning of evasive startle behavior in flying field crickets (Nolen and Hoy, 1986). Similarly, the frequency tuning and temporal integration properties of recognizable auditory units in the neck connective recordings of *E. carolinus* closely match those for the startle response (Figs. 3 and 5). Although we have not yet identified these auditory units by intracellular recording and dye injection, potentials recorded in the neck connectives of *E. carolinus* appeared to be associated with ascending units (Figs. 2 and 4) and may represent the activity of an INT-1 homologue.

Comparison of startle tuning in *E. carolinus* with that of the steering response in field crickets (Gryllidae: Gryllinae) is shown in Fig. 9 (to normalize the energy of stimuli with different durations, thresholds are dB energy *re* a 125-ms, 124-dB SPL tone). Although the broad tuning is similar for all four species, the startle response in *E. carolinus* is elicited by more energy than is field cricket steering. From a proximate point of view, because larger insects can be echolocated with lower levels of sonar (and therefore at greater distances; see Dusenbery, 1992, pp. 284–291 for discussion), Forrest *et al.* (1995) proposed a negative relationship between insect size and startle threshold. Although flying field crickets have ~nine times the cross-sectional area of *E. carolinus* which predicts ~9.5 dB more sensitivity (i.e., the wing lengths of *G. bimaculatus* and *T. oceanicus* are ~three times longer than *E. carolinus*, translating into nine times the cross-sectional area when modeled as sphere), Fig. 9 shows that in the 25–40 kHz range, the thresholds for the field cricket steering response are ~15 dB more sensitive than that for the startle response in *E. carolinus*. The steering response in gryllines and the startle response in *E. carolinus* may not be analogous behaviors, however. Whereas the steering response only changes a cricket's flight direction, the startle response of *E. carolinus* consists of an abrupt stop in flight and a dive to the ground (50-ms latency, Farris, unpublished data). Like the steering response in moths presented with low intensity ultrasound (Roeder, 1967), the steering response in field crickets may thus be more adaptive in avoiding echolocating bats at earlier stages in the attack and is therefore tuned to lower levels of ultrasound.

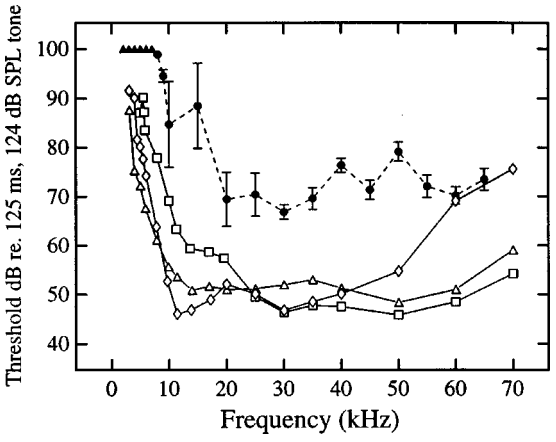

FIG. 9. Frequency tuning of the startle response in *E. carolinus* and the negative steering response in three species of field crickets (Gryllidae: Gryllinae). Circles (●) represent the mean thresholds (±SE) necessary to elicit a startle response in *E. carolinus* ($N=8$ cf. Fig. 3). Squares (□), triangles (△), and diamonds (◇) represent the mean thresholds for eliciting negative phonotaxis in flying *Teleogryllus oceanicus*, *T. commodus*, and *Gryllus bimaculatus*, respectively (Nolen and Hoy, 1986). To accommodate the different duration stimuli, all thresholds are normalized for stimulus energy relative to a 125-ms, 124-dB (*re* 20 μPa) tone, the calibration tone in both studies. Closed triangles mark frequencies in which <2 individuals (*E. carolinus*) responded to stimuli below 99 dB.

Different response criteria used in different studies could account for differences in thresholds. To determine the steering threshold in field crickets, Nolen and Hoy (1986) used a 10/15 response criteria. This method converges on the stimulus level that elicits a 63% response rate (Levitt, 1971). If the three species of field crickets mentioned above had the same psychometric function as *E. carolinus*, then we would expect the stimulus level required to elicit the 63% response rate to be higher than that for the 30% response rate (i.e., 63% steering threshold in the field crickets is higher than the 30% startle threshold in *E. carolinus*). The opposite is true (Fig. 9), however, eliminating this methodological explanation for these comparative differences in behavioral thresholds.

There is evidence that the auditory systems of some insects differ for short- and long-winged individuals. For example, Yager (1990) found that both auditory sensitivity and ear anatomy were associated with wing morphology in mantids; long-winged males were sensitive to ultrasound whereas short-winged (flightless) females were not. Such a correlation between flight capability and ultrasound sensitivity is consistent with the hypothesis that ultrasound sensitivity in mantids functions in the context of avoiding echolocating, aerial-hawking bats.

A similar correlation between macroptery and auditory development has been found in crickets (Ingrisch, 1977). In *Trigonidium cicindeloides* (Gryllidae: Trigoniinae), for example, the development of a tympanic membrane in long-winged individuals only, suggests that like mantids, the acoustic ecology of the two-wing morphs differs and that the development of an ear is more costly for short-winged individuals. Evidence for such tradeoffs associated with the maintenance of flight have also been measured in nemobiine crickets. In *Allonemobius fasciatus*, for example, mainte-

nance of the flight muscles is correlated with the presence of fully developed hind-wings (Tanaka, 1986). Whereas individuals with intact hind-wings maintain the dorsolongitudinal flight muscles (DLFM), individuals with at least one wing de-alated histolyze the DLFM. For females in particular, flight muscle maintenance is negatively correlated with oocyte production. Because ultrasound sensitivity appears to function at least in the context of flight (i.e., detecting aerial hawking bats) and also may be costly to maintain in flightless individuals, we tested whether short-winged and de-alated crickets possessed the same sensitivity as long-winged crickets (hind-wings still attached). Tuning of the responses in the neck connectives of de-alated and short-winged individuals is similar to that in long-winged crickets (Fig. 3). From a functional point of view, these results are interesting and may mean that ultrasound sensitivity still plays a role in the behavioral ecology of flightless crickets. Conversely, the economics of flight muscle maintenance and the maintenance of ultrasound sensitivity may not be analogous. Resources devoted to auditory maintenance presumably are small relative to that for flight muscles and its cost in terms of oocyte (and hypothetically spermatophore) production may not be so significant that selection has produced a noticeable reduction in the sensitivity of flightless morphs. Such traits are of course under the influence of a number of factors such as nutrition, and more study is required to argue this conclusively.

B. Temporal sensitivity

Commonly described as a ''time-intensity tradeoff,'' the decrease in threshold for detecting a signal as its duration increases is usually modeled as an integration process that effectively integrates (or sums) signal energy over a short period of time called the temporal integration time constant (τ). The limits of temporal processing (including integration) in auditory systems are known to vary relative to the specific processing tasks; however, as different experimental procedures testing various aspects of temporal resolution and integration reveal different time constants (Tougaard, 1996; but see Eddins and Green, 1995 for review). In humans, for example, although duration versus intensity experiments suggest integration occurs over ~200 ms, paired-pulse tests reveal a much shorter time constant on the order of 5 ms (Viemeister and Wakefield, 1991). Furthermore, no simple long-term integration seems to occur and the behavior of the human subjects is consistent with a multiple-short-term-look model. In other mammalian taxa, differences between the time constants measured in duration versus intensity and paired-pulse paradigms are comparable to those in humans. In bottle-noise dolphins for example (*Tursiops truncatus*) duration versus intensity integration times range from ~10–200 ms (Johnson, 1968), whereas paired-pulse time constants are as short as 264 μs (Au *et al.*, 1988).

Physiological assays of temporal integration in insects also reveal disparities in τ, reflecting differences in the experimental tasks. For example, in a duration versus intensity paradigm using pure tone ultrasound stimuli, Surlykke *et al.* (1988) found that the A1 receptor in noctuid moths integrates over ~25 ms. A slightly larger time constant (69 ms) was estimated for the peripheral receptors of noctuids; however, when the rise and fall times of the stimuli were also varied with duration (Waters and Jones, 1996). As in humans, paired-pulse paradigms with moths reveal a much shorter temporal integration time constant. Tougaard (1996) showed that the threshold for a response in the A1 cell of noctuids decreases for pairs of clicks separated by <5 ms. This interval is comparable to the 2–3-ms temporal resolution time constant (acuity) also measured for the A1 cell using gap detection and amplitude modulation tests (Surlykke *et al.*, 1988).

Experiments testing the temporal sensitivity of tympanate moths are not limited to the physiological assays of the auditory periphery, however. In addition to evasive flight, the behavioral repertoire of some moths (Arctiidae) presented with ultrasound includes the production of a series of high-frequency clicks. Fullard (1984; Fullard *et al.*, 1994) used this phonoresponse as a behavioral assay of the effects of stimulus temporal structure (i.e., amplitude modulation rate) on the auditory sensitivity of *Cycnia tenera* (Arctiidae). For pulses of pure tone stimuli presented at varying repetition rates, *C. tenera* are most sensitive to rates from 30–50 pulses/s. The response to the playback of actual echolocation attack sequences, however, shows that the *C. tenera* phonoresponse is best tuned to the faster rates of the terminal phase of the echolocation sequence. Thus this defensive behavior appears to function as a jamming signal that decreases the ability of the bat to locate the target moth (Fullard *et al.*, 1994). These experiments do not explore the limits of temporal power integration, however, and it is unclear how to best compare these results to the physiological experiments above.

From a comparative point of view, ultrasound sensitivity presumably functions in similar contexts for *E. carolinus* and many tympanate moths, the detection of insectivorous, echolocating bats. In this study, we examined the temporal integration characteristics of the startle response and responses in the CNS of *E. carolinus* using both the duration versus intensity and multipulse experimental paradigms. For the duration versus intensity paradigm, the time constants estimated for the startle and neck connective responses are nearly the same when using the same adaptive experimental procedure [$\tau \cong 32.5$ ms; Fig. 5(a) and (b)]. Although this integration time is comparatively longer than that for the negative steering response in *T. oceanicus* ($\tau \cong 15.6$ ms; calculated from data in Nolen and Hoy, 1986), the time-intensity slopes for the two responses are similar. The time-intensity slope measured for the startle response in *E. carolinus* and the steering response of *T. oceanicus* are 10.9 and 9.5 dB/decade, respectively, slightly steeper than that for humans (7.5 dB/decade; Florentine *et al.*, 1988). Using the 3/5 adaptive procedure, the multiple presentation of longer pulse durations appears to cause adaptation (Fig. 6) and thus, raise the threshold for longer pulse duration stimuli. As described above, while testing durations >40 ms at levels above the threshold previously determined in the 1/2-down procedure, it was common to observe a larger response to the first pulse in the series of five pulses and then little or no response thereafter. Thus greater levels were required to

meet the threshold criteria at the longer durations which resulted in a greater tau ($\tau = 45.04$ ms).

Two sets of experiments examined temporal integration of multipulse stimuli. One set of experiments measured startle threshold as a function of FM repetition rate (i.e., pulse separation). These tests were designed to test temporal sensitivity while more closely simulating the detection task presented by echolating bats. The results from the FM experiments are similar for the two types of stimuli (1-s trains of FM pulses or a pair of FM pulses). In both cases, startle threshold did not decrease like that of an energy detector with a time constant similar to those measured in the duration versus intensity tests (Fig. 7). For example, for an integrator with a time constant (τ) of 32 ms, thresholds are expected to change by ~ -8 dB as the 1-s pulse train changes rates from 1 to 181 pulses/s (Zwislocki, 1960). In the paired-pulse FM tests, the expected change in threshold is only -3 dB as the energy within the integration interval (τ) is doubled when the separation between the two pulses decreases to less than τ (Zwislocki, 1960). Because these reductions in threshold were not observed in the two stimulus paradigms, the data suggest that: multiple-pulse stimuli are not integrated over the same time as single-pulse stimuli and the 5-ms duration of the FM pulses is longer than the multipulse integration time constant.

Temporal integration of multipulse stimuli was thus examined by measuring the change in startle threshold as a function of the separation of a pair of 1-ms duration pulses of 40 kHz. This stimulus design facilitated the measurement of a shorter multipulse τ, while at the same time controlling for any effect due to FM bandwidth. For pulse separations <5 ms, startle threshold decreases by 3 dB (Fig. 8), suggesting a combination of the two pulses. Because the repetition rate of typical bat sonar does not exceed 200 pulses/s (5–6 ms interpulse interval; see Fullard *et al.*, 1994) such temporal resolution ($\tau = 5.3$ ms) appears adequate for processing even the fastest sonar rates of the attack sequence.

It is interesting to note that the startle threshold for two pulses separated by >5 ms remains ~ 1.7 dB below that for a single pulse. These results are quite similar to those in humans (Viemeister and Wakefield, 1991) and may be explained in part by the optimal combination of two independent samples, the two pulses. Thus the normalized difference between the signal-and-noise and the noise distributions (d') for the two-pulse stimulus increases by a factor of $\sqrt{2}$ relative to that for a single pulse and reduces the threshold. For the human subjects tested by Viemeister and Wakefield (1991), this change translated into an expected decrease in threshold of 1.3 dB, slightly worse than the 1.6 dB they observed. Modeling the expected decrease in threshold for two pulses in *E. carolinus* would require the measurement of more than one point on the startle threshold psychometric function (i.e., probability of a startle response as a function of stimulus intensity), which we did not do.

C. FM versus pure-tone threshold

Although the temporal structure (i.e., amplitude modulation) and intensity of bat biosonar appear to be the most reliable cues of the proximity of aerial-hawking bats, the capacity for frequency analysis in tympanate insects could also contribute to the assessment of predation risk from echolocating bats. For example, the bandwidth of the sonar pulses of the big brown bat, *Eptesicus fuscus*, changes with the stages of the echolocation attack sequence. During the search phase, longer duration (15–20 ms) sonar pulses may have bandwidths <10 kHz, whereas during the approach phase, the bandwidth of the first harmonic may be as large as 40 kHz (60 to 20 kHz FM, 5–10 ms) (Simmons, 1987).

There is no conclusive evidence in tympanate insects for frequency analysis in the ultrasound band, however. In some moths (e.g., noctuids), the auditory receptors show parallel frequency tuning (Surlykke and Miller, 1982; Waters and Jones, 1996), presumably preventing any spectral processing of the signal. In crickets, although behavioral assays and recordings in the CNS have shown sensitivity to frequencies up to 100 kHz (Moiseff *et al.*, 1978; Moiseff and Hoy, 1983), there is unfortunately little information regarding ultrasound sensitivity in the primary auditory units (i.e., the most distal cells of the crista acoustica). In the most extensive such study in crickets, Imaizumi and Pollack (1999) found that across individuals, frequency selectivity in primary units sensitive to ultrasound ($\leqslant 40$ kHz) varied from broad-banded (>20 kHz) to more narrow-banded selectivity (<5 kHz). Unlike moths, the latter type of unit in crickets could provide the neural substrate necessary for frequency analysis in the ultrasound band. As in the physiological assay, the results of behavioral tests of frequency sensitivity to ultrasound also vary, as critical bandwidths centered at 40 kHz range from $\sim$28–50 kHz wide (in direct measurement and critical-ratio calculation) to only 3.55 kHz (using the ratio of the absolute thresholds of broadband noise and single tones) (see Ehret *et al.*, 1982). Consistent with the wider critical bandwidth measure (e.g., 28–50 kHz), Wyttenbach *et al.* (1996) found that habituation of the ultrasound- (20 kHz) induced steering response in flying *T. oceanicus* could only be dishabituated by frequencies <16 kHz. Thus in their experimental paradigm, because frequencies >16 kHz were not distinguished from the 20-kHz habituating stimulus, it appears that the critical band around 20 kHz covers at least the range of ultrasound frequencies tested (16–40 kHz).

We found no difference in startle thresholds for a single 5-ms pulse of 40 kHz (1-ms ramps) and a 5-ms FM sweep (60–30 kHz, 1-ms ramps). Like moths and field crickets, it appears that for *E. carolinus*, frequency tuning in the ultrasound range is broad and that the FM sweep did not probe multiple frequency channels (i.e., critical bands) or spectral regions of a single channel that differed in sensitivity from that of 40 kHz (i.e., an effect of intensity rather than frequency). Unlike humans, for example, where the psychophysical tuning from 0.05–20 kHz is effectively modeled as a bank of overlapping frequency filters (i.e., critical bands) (see Moore, 1995 for review), our results suggest that the broad tuning of the startle response and the response in the neck connectives is representative of a single ultrasound filter with little variation in threshold from 60 to 30 kHz.

In conclusion, this study adds a new taxon to the growing list of insects that are sensitive to ultrasound. Relative to

that in gryllines (field crickets), however, the nemobiine startle response appears comparable in spectral sensitivity only. In addition to the differences in the motor components between the nemobiine and grylline startle responses, salient differences in absolute threshold as well as temporal sensitivity also appear evident. From a comparative point of view, the auditory behavior of *E. carolinus* is not unlike that across a variety of disparate taxa (e.g., mammals).

ACKNOWLEDGMENTS

Helpful input for this project was generously provided by the members of the ''Hoy Lab'' and two anonymous reviewers. A. C. Mason, T. G. Forrest, and M. Oshinsky provided valuable technical help with regard to physiological recordings and computer programming. C. Gilbert and C. Clark offered many useful comments to the manuscript. H. E. Bass kindly provided resources at the University of Mississippi in support of animal collection. This study was presented in partial fulfillment of a doctorate degree at Cornell University. H. E. Farris was supported by NIMH training Grant No. 2 T32 MH15793 and NIH Grant No. R01 DC00103 to R. R. Hoy.

Au, W. W. L., Moore, P. W. B., and Pawloski, D. A. (**1988**). ''Detection of complex echoes in noise by an echolating dolphin,'' J. Acoust. Soc. Am. **83**, 662–668.

Coro, F., and Perez, M. (**1984**). ''Intensity coding by auditory receptors in *Empyreuma pugione* (Lepidoptera, Ctenuchidae),'' J. Comp. Physiol. **154**, 287–295.

Dusenbery, D. B. (**1992**). *Sensory Ecology: How Organisms Acquire and Respond to Information* (W. H. Freeman, New York).

Eddins, D. A., and Green, D. M. (**1995**). ''Temporal integration and temporal resolution,'' in *Hearing*, edited by B. C. J. Moore (Academic, London), pp. 207–242.

Ehret, G., Moffat, A. J. M., and Tautz, J. (**1982**). ''Behavioral determination of frequency resolution in the ear of the cricket, *Teleogryllus oceanicus*,'' J. Comp. Physiol. **148**, 237–244.

Farris, H. E., Forrest, T. G., and Hoy, R. R. (**1997**). ''The effects of calling song spacing and intensity on the attraction of flying crickets (Orthoptera: Gryllidae: Nemobiinae),'' J. Insect Behav. **10**, 639–653.

Farris, H. E., Forrest, T. G., and Hoy, R. R. (**1998**). ''The effect of ultrasound on the attractiveness of acoustic mating signals,'' Physiol. Entomol. **23**, 322–328.

Farris, H. E., and Hoy, R. R. (**1997**). ''Acoustic startle and two-tone suppression in a Nemobiine cricket, *Eunemobius carolinus*,'' 27th Annual Meeting of the Society for Neuroscience, New Orleans, Louisiana, October 25–30, 1997; Soc. Neurosci. Abstracts **23**, 1070.

Farris, H. E., and Hoy, R. R. (**1998**). ''Two-tone suppression of the ultrasound induced startle response in a cricket,'' J. Acoust. Soc. Am. **103**, 2826(A).

Faure, P. A., Fullard, J. H., and Dawson, J. W. (**1993**). ''The gleaning attacks of the northern long-eared bat, *Myotis septentrionalis*, are relatively inaudible to moths,'' J. Exp. Biol. **178**, 173–189.

Florentine, M., Fastl, H., and Buus, S. (**1988**). ''Temporal integration in normal hearing, cochlear impairment, and impairment simulated by masking,'' J. Acoust. Soc. Am. **84**, 195–203.

Forrest, T. G., Farris, H. E., and Hoy, R. R. (**1995**). ''Ultrasound acoustic startle response in scarab beetles,'' J. Exp. Biol. **198**, 2593–2598.

Fullard, J. H. (**1979**). ''Behavioral analyses of auditory sensitivity in *Cycnia tenera* Hubner (Lepidoptera: Arctiidae),'' J. Comp. Physiol. **129**, 79–83.

Fullard, J. H. (**1984**). ''Listening for bats: pulse repetition rate as a cue for a defensive behavior in *Cycnia tenera* (Lepidoptera: Arctiidae),'' J. Comp. Physiol. A **154**, 249–252.

Fullard, J. H., Simmons, J. A., and Saillant, P. A. (**1994**). ''Jamming bat echolation: The dogbane tiger moth *Cycnia tenera* times its clicks to the terminal attack calls of the big brown bat *Eptesicus fuscus*,'' J. Exp. Biol. **194**, 285–298.

Fullard, J. H., and Yack, J. E. (**1993**). ''The evolutionary biology of insect hearing,'' TREE **8**, 248–252.

Harrison, R. G. (**1980**). ''Dispersal polymorphisms in insects,'' Ann. Rev. Ecol. Syst. **11**, 95–118.

Hoy, R. R. (**1992**). ''The evolution of hearing in insects as an adaptation to predation from bats,'' in *The Evolutionary Biology of Hearing*, edited by D. B. Webster, R. R. Fay, and A. N. Popper (Springer-Verlag, New York), pp. 115–130.

Imaizumi, K., and Pollack, G. S. (**1999**). ''Neural coding of sound frequency by cricket auditory receptors,'' J. Neurosci. **19**, 1508–1516.

Ingrisch, S. (**1977**). ''Das Stridulationsorgan der Käfergrille *Trigonidium cicindeloides* (Orthoptera: Gryllidae: Trigoniinae) und Beobachtungen zur Eidonomie und Ethologie,'' Ent. Germ. **3**, 324–332.

Johnson, C. S. (**1968**). ''Relation between absolute threshold and duration-of-tone pulses in the bottlenosed porpoise,'' J. Acoust. Soc. Am. **43**, 757–763.

Levitt, H. (**1971**). ''Transformed up-down methods in psychoacoustics,'' J. Acoust. Soc. Am. **49**, 467–477.

Libersat, F., and Hoy, R. R. (**1991**). ''Ultrasonic startle behavior in bush crickets (Orthoptera; Tettigoniidae),'' J. Comp. Physiol. A **169**, 507–514.

May, M. L., and Hoy, R. R. (**1990**). ''Leg induced steering in flying crickets,'' J. Exp. Biol. **151**, 485–488.

Moiseff, A., and Hoy, R. R. (**1983**). ''Sensitivity to ultrasound in an identified auditory interneuron in the cricket: A possible neural link to phonotactic behavior,'' J. Comp. Physiol. **152**, 155–167.

Moiseff, A., Pollack, G. S., and Hoy, R. R. (**1978**). ''Steering responses of flying crickets to sound and ultrasound: Mate attraction and predator avoidance,'' Proc. Natl. Acad. Sci. USA **75**, 4052–4056.

Moore, B. C. J. (**1995**). ''Frequency analysis and masking,'' in *Hearing*, edited by B. C. J. Moore (Academic, London), pp. 161–205.

Nolen, T. G., and Hoy, R. R. (**1986**). ''Phonotaxis in flying crickets. I. Attraction to the calling song and avoidance of bat-like ultrasound are discrete behaviors,'' J. Comp. Physiol. A **159**, 423–439.

Plomp, R., and Bouman, M. A. (**1959**). ''Relation between hearing threshold and duration for tone pulses,'' J. Acoust. Soc. Am. **31**, 749–758.

Robert, D. (**1989**). ''The auditory behavior of flying locusts,'' J. Exp. Biol. **147**, 279–301.

Roeder, K. D. (**1967**). *Nerve Cells and Insect Behavior* (Harvard University Press, Cambridge, MA).

Simmons, J. A. (**1987**). ''Acoustic images of target range in the sonar of bats,'' Nav. Res. Rev. **39**, 11–26.

Surlykke, A., Larsen, O. N., and Michelsen, A. (**1988**). ''Temporal coding in the auditory receptor of the moth ear,'' J. Comp. Physiol. A **162**, 367–374.

Surlykke, A., and Miller, L. A. (**1982**). ''Central branchings of the three sensory axons from a moth ear (*Agrotis segetum*, Noctuidae),'' J. Insect Physiol. **28**, 357–364.

Tanaka, S. (**1986**). ''De-alation, flight muscle histolysis, and oocyte development in the striped ground cricket, *Allonemobius fasciatus*,'' Physiol. Entomol. **11**, 453–458.

Tougaard, J. (**1996**). ''Energy detection and temporal integration in the noctuid A1 auditory receptor,'' J. Comp. Physiol. **178**, 669–677.

Viemeister, N. F., and Wakefield, G. H. (**1991**). ''Temporal integration and multiple looks,'' J. Acoust. Soc. Am. **90**, 858–865.

Walker, T. J., and Masaki, S. (**1989**). ''Natural history,'' in *Cricket Behavior and Neurobiology*, edited by F. Huber, T. E. Moore, and W. Loher (Cornell University Press, Ithaca, NY), pp. 1–42.

Waters, D. A., and Jones, G. (**1996**). ''The peripheral auditory characteristics of noctuid moths: Responses to the search-phase echolation calls of bats,'' J. Exp. Biol. **199**, 847–856.

Wyttenbach, R. A., May, M. L., and Hoy, R. R. (**1996**). ''Categorical perception of sound frequency by crickets,'' Science **273**, 1542–1544.

Wohlers, D. W., and Huber, F. (**1982**). ''Processing of sound signals by six types of neurons in the prothoracic ganglion of the cricket *Gryllus bimaculatus* L.,'' J. Comp. Physiol. **146**, 161–173.

Yager, D. D. (**1990**). ''Sexual dimorphism of auditory function and structure in praying mantises (Mandtodea; Dicytoptera),'' J. Zool., Lond. **221**, 517–537.

Zar, J. H. (**1989**). *Biostatistical Analysis* (Prentice-Hall, Englewood Cliffs, NJ).

Zwislocki, J. (**1960**). ''Theory of temporal auditory summation,'' J. Acoust. Soc. Am. **32**, 1046–1060.

Masking by harmonic complexes in budgerigars (*Melopsittacus undulatus*)

Marjorie R. Leek
Army Audiology and Speech Center, Walter Reed Army Medical Center, Washington, D.C. 20307

Micheal L. Dent and Robert J. Dooling
Department of Psychology, University of Maryland, College Park, Maryland 20742

(Received 28 July 1999; accepted for publication 11 December 1999)

In humans, masking by harmonic complexes is dependent not only on the frequency content of the masker, but also its phase spectrum. Complexes that have highly modulated temporal waveforms due to the selection of their component phases usually provide less masking than those with flatter temporal envelopes. Moreover, harmonic complexes that are created with negative Schroeder phases (component phases monotonically decreasing with increasing harmonic frequency) may provide more masking than those created with positive Schroeder phases (monotonically increasing phase), even though both temporal envelopes are equally flat. To date, there has been little comparative work on the masking effectiveness of harmonic complexes. Using operant conditioning and the method of constant stimuli, masking of pure tones by harmonic complexes was examined in budgerigars at several different masker levels for complexes constructed with two different fundamental frequencies. In contrast to humans, thresholds in budgerigars differed very little for the two Schroeder-phase waveforms. Moreover, when there was a difference in masking by these two waveforms, the positive Schroeder was the more effective masker—the reverse of that described for humans. Control experiments showed that phase selection was relevant to the masking ability of harmonic complexes in budgerigars. Release from masking occurred when the components were in coherent phase, compared with a complex with random phases selected for each component. It is suggested that these psychoacoustic differences may emerge from structural and functional differences between the avian and mammalian peripheral auditory systems involving traveling wave mechanics and spectral tuning characteristics. [S0001-4966(00)06203-8]

PACS numbers: 43.80.Lb, 43.66.Gf [WA]

INTRODUCTION

Over the years, masking studies involving the detection of pure tones against a background of broadband noise have been conducted in a number of species of birds (Dooling, 1982, 1991; Fay, 1988). Although there are some exceptions (Dooling, 1982; Dooling and Saunders, 1975; Dyson *et al.*, 1998; Langemann *et al.*, 1998), masking patterns in birds are generally similar to those reported for mammals, with critical ratios increasing about 2–3 dB/octave (Fay, 1988; Klump, 1996; Okanoya and Dooling, 1987). In contrast, there is much less comparative data on the masking of pure tones by complex sounds. Recent studies show that in humans and other mammals, masking by complex sounds is influenced by both the frequency content and the temporal characteristics of the maskers. Harmonic complexes used as maskers offer an intriguing array of results that incorporate aspects of both simultaneous and temporal masking. They lend themselves to manipulation of temporal aspects of stimuli while permitting the long-term spectral information to remain constant. Masking by these complex sounds is strongly affected by the temporal waveform shapes, and interpretations of these effects have focused on specific cochlear functions such as traveling wave mechanics and nonlinear active gain (Kohlrausch and Sander, 1995; Carlyon and Datta, 1997a, 1997b; Summers and Leek, 1998).

Explanations for various masking effects traditionally invoke features of the mammalian auditory system. These features are likely to be important in the avian auditory system as well, supported by mechanisms that may or may not be similar to those found in mammals. In general, the best absolute thresholds for birds fall between about 1 and 5 kHz and approach the levels of sensitivity typically reported for humans and other mammals (Dooling, 1982, 1991). Avian audibility curves are typically more narrowly tuned than those of mammals, with sensitivity falling off at about 15 dB/octave below 1 kHz and about 50 dB/octave above 5 kHz (Dooling, 1980, 1982; Okanoya and Dooling, 1987). While many characteristics of hearing in this frequency region are known to be similar in birds and mammals, the special effects of masking by harmonic complexes have not been studied in birds.

In human listeners, Smith *et al.* (1986) reported large differences in masking by harmonic complexes that were identical in long-term spectra, but varied in their phase spectra. By selecting phases according to an algorithm developed by Schroeder (1970), the waveform envelope becomes very flat, and the instantaneous frequency within each period sweeps upward or downward, depending on the sign of the phase equation. Two such ''Schroeder-phase'' complexes are shown in Fig. 1(a) and (b). These two harmonic complexes, one the time-reverse of the other, can produce large

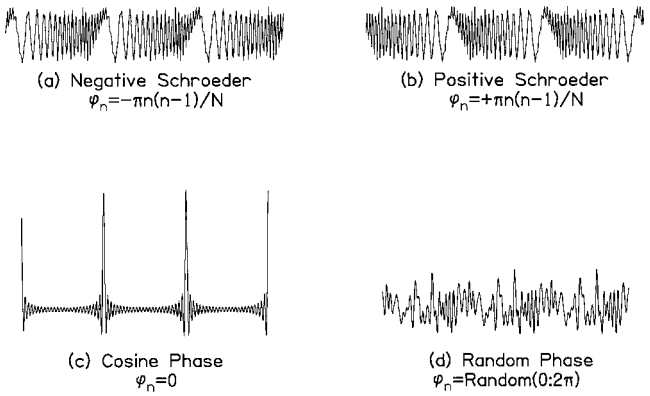

FIG. 1. Temporal waveforms of four harmonic complexes. Three periods (30 ms) are shown for each waveform. Each waveform is constructed of harmonics 2–50 of a fundamental frequency of 100 Hz. All components have equal amplitude. The phase of each component is selected according to the equations shown (φ_n = phase for each component, n; N = total number of components).

differences in masking. The amount of masking for each Schroeder-phase masker is affected by the fundamental frequency of the complex and the frequency location of the signal within the masker bandwidth (Kohlrausch and Sander, 1995). Masking by the positive Schroeder-phase wave may also change dramatically as a function of stimulus level (Carlyon and Datta, 1997b; Summers and Leek, 1998). Summers and Leek (1998) showed that differences in masking by the two Schroeder waveforms were not specific to pure tone signals, in that they also produce a differential amount of interference with speech intelligibility.

While specific cochlear processing mechanisms are thought to underlie the masking of pure tones by harmonic complexes in mammals, possible explanations are much less clear in birds. The masking effects of harmonic complexes in birds are unknown. Moreover, while the inner ears of birds show some general similarities to mammalian inner ears, there are also a host of important differences, including differences in size, morphology, spatial arrangement, and function of cochlear structures (for a review, see Manley, 1990). For these reasons, a comparison of masking by harmonic complexes in mammals and birds might prove useful in trying to understand the relative contributions to masking of various cochlear features and processes. In addition, the manner in which the maskers interact with bird inner ear mechanisms, as revealed by masking differences between Schroeder-phase waveforms, may add to our understanding of important problems in avian hearing such as how the avian auditory system processes complex sounds like species-specific vocalizations.

In this study, we report masking effects of harmonic complexes with phase spectra constructed according to the positive and negative Schroeder algorithms, and some control conditions using cosine-phase [Fig. 1(c)] and random-phase [Fig. 1(d)] maskers. We show for both birds and humans that there is an effect of stimulus phase on masking, as shown by responses to cosine- and random-phase maskers. In contrast to human listeners, however, in whom negative Schroeder complexes are more effective maskers than positive Schroeder complexes, the masking effectiveness of the two Schroeder-phase waveforms in birds is much more similar.

I. METHODS

A. Subjects

Three adult budgerigars (all females) were used as subjects. The birds were kept on a normal day/night cycle correlated with the season and maintained at approximately 90% of their free-feeding weights. For comparison, two humans (laboratory staff members) were also tested in this experiment. All bird and human subjects had hearing within normal limits for their species, as shown by their audiograms.

B. Stimuli

Stimuli consisted of masker harmonic complexes alone and masker-plus-signal, with the pure-tone signal added in-phase to the maskers at appropriate signal-to-masker levels. Stimuli were created digitally, at a sampling rate of 40 kHz, using software from Tucker-Davis Technologies to combine frequencies in the correct phases and amplitudes, followed by an inverse fast Fourier transform (FFT) to create the waveforms. They were created off-line and stored as files for playback during the experiment.

The masking stimuli were positive and negative Schroeder-phase harmonic complexes as shown in Fig. 1(a) and (b), with equal-amplitude components at frequencies that were integral multiples of a fundamental frequency, and starting phases selected according to the Schroeder algorithms as shown in the figure. Maskers included all harmonics of the fundamental frequency from 200 to 5000 Hz. Two fundamental frequencies were used, 50 and 100 Hz. The number of components in the maskers was determined by the fundamental frequency, and was 97 and 49 for the 50- and 100-Hz fundamentals, respectively.

The maskers were 260 ms in duration including 20-ms cosine^2 onset and offset ramps. The tones were 180 ms in duration, including the 20-ms ramps. The signal was temporally centered in the masker, and was always added in-phase with the masker component having the same frequency. Except where noted, the signal frequency was either 2.8 or 2.85 kHz for fundamental frequencies of 100 or 50 Hz, respectively. Signal-to-masker levels were created for testing in 5-dB steps.

C. Testing apparatus—Birds

The budgerigars were tested in a wire cage ($23\times25\times16$ cm) mounted in a sound-isolation chamber (Industrial Acoustics Company, IAC-3). A response panel consisting of two microswitches with light-emitting diodes (LEDs) was mounted on the wall of the test cage just above the food hopper. The microswitch was tripped when the bird pecked the LED. The left microswitch and LED served as the observation key while the right microswitch and LED served as the report key. The behavior of the animals during test sessions was monitored by a video camera system (Sony HVM-322).

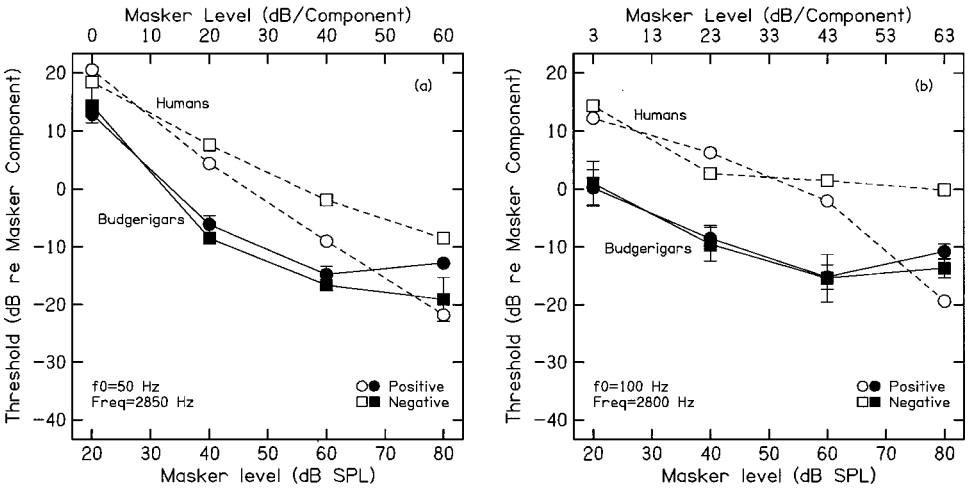

FIG. 2. Mean thresholds are plotted as signal level in dB relative to each component of the masker as a function of overall masker level at the bottom of the figures, and for the level per component of the masker along the top. Average data are shown for budgerigars in solid symbols, and for two human listeners by open symbols. Error bars indicate standard deviations for the three birds. Larger numbers on the ordinate (toward the top of the graphs) indicate more masking and smaller numbers denote less masking. Left panel (a) shows data for a fundamental frequency of 50 Hz, and a signal frequency of 2.85 kHz; right panel (b) shows data for a fundamental frequency of 100 Hz, signal frequency of 2.8 kHz.

Test sessions were controlled by an IBM 486 computer. The digital stimuli were output to a KEF loudspeaker (model 80C) via Tucker-Davis modules at a sampling rate of 40 kHz and presented at masker levels of 20, 40, 60, or 80 dB SPL. Stimulus calibration was performed using a General Radio sound level meter (model 1982). Stimulus intensities were measured with a 1/2-in microphone attached to the sound level meter via a 3-m extension cable. The microphone was placed in front of the response keys in the approximate position occupied by the bird's head during testing. Masker intensities were measured several times during these experiments to ensure that stimulus levels remained constant and the entire system was calibrated.

D. Training and testing procedures—Birds

Birds were trained by standard operant auto-shaping procedures (Dooling and Okanoya, 1995) to peck at the left microswitch key (observation key) during a repeating background until a new stimulus was presented alternately with the background sound. The time between pecking the observation key and the initiation of alternating sounds was random, with a range of 2–7 s. If the bird pecked the right microswitch and LED (report key) within 2 s of this alternating pattern, the food hopper was activated for 2 s. The dependent variable was percent correct on trials involving an alternating sound pattern. A failure to peck the report key within 2 s of sound alternation was recorded as a miss, and a new trial sequence was initiated. Thirty percent of all trials were sham trials in which the target sound was the same as the repeating background sound. A peck to the report key during the 2 s sham trial was recorded as a false alarm, and the lights in the test chamber were extinguished while the repeating background continued. The length of this time-out period was normally 5 s, but varied according to an individual bird's behavior, with longer time-out periods imposed if birds began developing higher false alarm rates. Sessions with a total false alarm rate of 16% or higher were discarded. In all, 14% of the test sessions were discarded, which is typical for these procedures (Dooling and Okanoya, 1995)

For each experimental condition, signal levels in 5-dB steps were presented using the method of constant stimuli (Dooling and Okanoya, 1995). Signal levels within a condition were selected to bracket the presumed threshold, and psychometric functions were developed. At the conclusion of testing, thresholds were defined as the level of the tone detected 50% of the time, adjusted by the false-alarm rate, which corresponded to d' of about 1.5–1.8.

E. Testing apparatus and procedures—Humans

The human subjects were seated in a sound-treated booth, facing a touch-screen terminal. The same stimulus files used for the birds were played through Tucker-Davis modules to one TDH-49 earphone. Stimulus levels were calibrated with the earphone in a 6-cc coupler using a sound level meter.

A standard/two alternative forced choice procedure (S/2AFC) was used to generate abbreviated psychometric functions for each threshold (Macmillan and Creelman, 1991). Correct answer feedback was provided after each trial. Stimuli were tested in 40-trial blocks. For each experimental condition (phase selection and masker level), three to five signal levels were tested. Linear interpolation was used to estimate a threshold level that would produce about 85% correct performance ($d'=1.5$).

II. RESULTS

A. Effects of masker level

Masking by the positive and negative Schroeder-phase maskers as a function of masker level for two fundamental frequencies is shown in Fig. 2. The human data are consistent with previous studies of Schroeder-phase masking in humans (Summers and Leek, 1998; Kohlrausch and Sander, 1995). Human listeners showed larger masking differences as the masker level increased, and the positive Schroeder-phase stimuli were the less effective maskers. At the highest masker levels, the difference in masking for the two phase selections was 15–20 dB. At both fundamental frequencies, however, the birds showed only small masking differences between the two Schroeder-phase maskers. The amount of masking difference increased slightly with increasing level at both fundamental frequencies, as seen with the humans, with masking differences of 5 to 8 dB at the highest masker level for a fundamental of 50 Hz (left panel), and 3–4 dB for

complexes with 100-Hz fundamental frequency. A major difference between the birds and the humans, however, is that the negative Schroeder-phase masker was the less effective masker for the birds.

A two-way analysis of variance (ANOVA) with repeated measures was carried out for the budgerigar data, separately for the two fundamental frequencies. For the 50-Hz fundamental, there was a significant effect of stimulus level ($F_{3,6}=201.90$, $p<0.001$), but no effect of phase selection ($p>0.05$). The interaction between level and phase was also not significant ($p>0.05$). However, a Bonferroni *t*-test indicated that the phase difference at a masker level of 80 dB was significant ($t=3.49$, $p=0.01$). Differences due to phase selection were not significant at any other masker levels. Similar results emerge from the ANOVA for a fundamental frequency of 100 Hz. There was a significant effect of masker level ($F_{3,6}=43.95$, $p<0.001$), with no other significant main effects or interactions. Here again, however, the negative Schroeder masker provided significantly less masking than the positive masker at a stimulus level of 80 dB ($t=2.36$, $p<0.05$).

Within species, in both birds and humans, the overall differences in thresholds between the two fundamental frequencies shown in the two panels of Fig. 2 were minor. However, the masking patterns for the two fundamental frequencies within a species differed somewhat. In budgerigars, larger masking differences between positive and negative Schroeder waves occurred with the lower fundamental frequency [Fig. 2(a)] than the higher one [Fig. 2(b)]. This suggests that some characteristics of the 50-Hz fundamental frequency stimuli might have affected the amount of masking by the positive and negative Schroeder maskers. The maskers generated with the lower fundamental frequency contained more components and a longer period than maskers with a fundamental of 100 Hz, and there was also a different spectral spacing of the components. Either of these aspects of the maskers might have contributed to the Schroeder masking differences observed. This masking difference is especially obvious at the highest masking level, where the greater masking for the positive Schroeder is clearly seen for the 50-Hz fundamental.

Humans also showed some differences in the patterns of masking at the two fundamental frequencies. For a fundamental frequency of 100 Hz, masking by the negative Schroeder phase waveforms did not change as the masker level increased over a 40-dB range (from 40 to 80 dB SPL). This masker became less effective at higher masker levels when the fundamental was 50 Hz. For both fundamental frequencies, however, the positive Schroeder masker became systematically less effective over the range of masker levels from 40 to 80 dB. In all, a drop in relative masking of nearly 25 dB occurred over that masker range for both fundamental frequencies. In contrast, over the same range of masker levels, the amount of masking for budgerigars for both maskers changed by only about 10 dB.

Overall, the budgerigars were more resistant to masking than humans, with most of their thresholds falling below (i.e., less masking) those of the human listeners. Such differences in masking may be related to critical ratios in the frequency region of the signal used here. Critical ratios of budgerigars near 2.8 kHz are smaller than those reported for humans (Dooling and Saunders, 1975; Dooling, 1980, 1982; Farabaugh *et al.*, 1998; Saunders *et al.*, 1979).

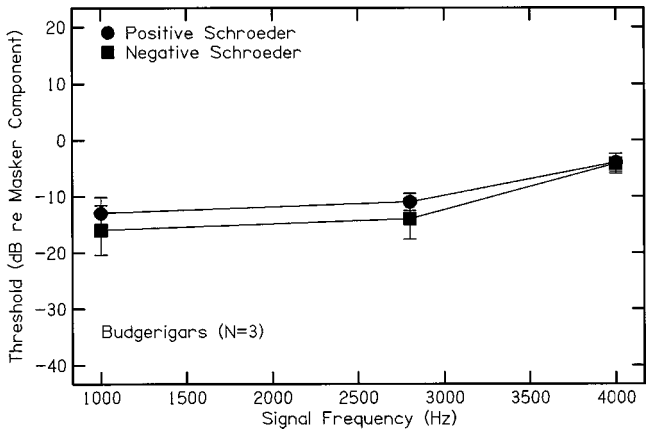

FIG. 3. Mean thresholds as a function of signal level in dB relative to each component of the masker as a function of signal frequency. Maskers had a fundamental frequency of 100 Hz, and were tested at an overall level of 80 dB SPL.

B. Effects of signal frequencies

Because budgerigars are known to have their smallest critical ratios around 2.8 kHz and larger critical ratios at 1.0 and 4.0 kHz, one test of whether the reduced effectiveness of Schroeder maskers for budgerigars compared with humans is related to the unusual shape of the critical ratio function is to test the birds on different signal frequencies. Figure 3 shows the masking for three signal frequencies provided by positive- and negative-phase maskers with a fundamental frequency of 100 Hz, tested at an overall masker level of 80 dB SPL. For signal frequencies of 1.0 and 2.8 kHz, two of the notable masking effects observed earlier are also shown here: small differences between masked thresholds, and those differences are in the reverse order of those shown in humans, with the negative Schroeder masker being less effective for birds. At 4.0 kHz, however, there was an increase in masking and no differences between the positive and negative Schroeder masked thresholds. Recall that critical ratios for these birds around 2.8 kHz are about 2 dB less than they are at 1.0 or 4.0 kHz. Thus the increase in masking by harmonic complexes from 2.8 to 4.0 kHz is consistent with earlier critical ratio results, but the similarity in masked threshold at 1.0 and 2.8 kHz is not. The critical ratios were measured with a continuous broadband noise as the masker, whereas the energy in the maskers used here is discretely distributed, occurring only at whole number multiples of the fundamental. Perhaps the failure to conform completely with critical ratio results is due to the difference in energy spacing within continuous random noise and harmonic complexes used as maskers.

C. Cosine maskers versus random maskers

It might be supposed that, given the results for the two Schroeder maskers, budgerigars are simply less sensitive than humans to phase changes in harmonic maskers. Figure 4

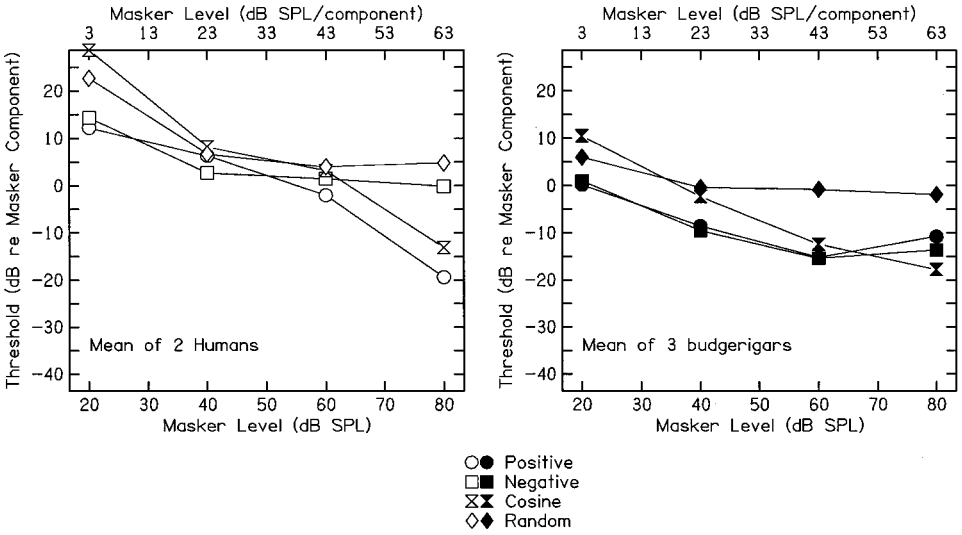

FIG. 4. Thresholds for two Schroeder-phase maskers, the cosine-phase masker, and means of two random-phase maskers as a function of overall masker level. Human data are shown in the left panel; budgerigars are shown in the right panel. The Schroeder-phase data are replotted from Fig. 2.

shows that this is not the case. This figure shows masked thresholds for harmonic maskers constructed with all components in cosine phase or with component phases selected randomly. Results from the Schroeder maskers are replotted from Fig. 2. Masking data for humans are shown in the left panel and for the budgerigars in the right panel. In this experiment, the masker fundamental frequency was 100 Hz, and the signal frequency was 2.8 kHz. For the random phase selections, two different maskers with separate phase draws were used, and the results were averaged.

For both humans and budgerigars, masking by random-phase harmonic complexes changes very little as masker level increases from 40 to 80 dB SPL. However, for both species, there is a release from masking by the cosine-phase stimuli over this range, with masking dropping by 15–20 dB for both birds and humans. Cosine- and random-phase complexes, therefore, produce distinctive patterns of masking that are similar in budgerigars and in humans. The species differences emerge with the Schroeder-phase maskers. In birds, both Schroeder-phase maskers produce a release from masking relative to the random-phase maskers across the entire range of masker levels. In humans, however, it is only the positive Schroeder phase that shows the same release from masking evidenced by the cosine-phase masker. The negative Schroeder phase masker has nearly the same effectiveness as the random-phase masker over the range of masker levels. In aggregate, these results suggest that processing mechanisms involved in masking by harmonic complexes are fundamentally different between humans and birds.

III. DISCUSSION

Masking by harmonic complexes in humans is thought to be influenced by a number of processes in the peripheral auditory system. Schroeder-phase harmonic maskers are particularly intriguing in that they have identical long-term spectra and waveform envelopes, while having temporal fine structure that is reversed. Explanations of the masking differences between the two Schroeder waves observed in human listeners have primarily addressed traveling wave mechanics and within-processing-channel differences in internal crest factors. It is likely, therefore, that the species differences in masking by harmonic complexes observed here might also be related to species differences in the same anatomical and/or physiological factors. The major findings that must be explained here are: (1) birds generally show less overall masking from harmonic complexes than do humans; (2) although clear differences in masking effectiveness of harmonic complexes occur with different phase selections (e.g., cosine-phase maskers relative to random-phase maskers), large differences between the positive and negative Schroeder-phase maskers were not observed in the budgerigars in any of the conditions tested here, in contrast to results from human listeners; and (3) when differences between masking by Schroeder-phase complexes in birds occur, the positive Schroeder waveform is the more effective masker—the reverse of the asymmetry observed in humans.

Turning first to the finding of less masking in the birds than in the human listeners, recall that the frequency analyzing channels at the signal frequency (2.8 kHz) in budgerigars are narrower than those found in humans (Dooling and Saunders, 1975; Dooling and Searcy, 1979, 1985; Saunders *et al.*, 1978a, 1978b, 1979). Less masker power within the relevant critical bands near the signal frequency would result in lower thresholds for the birds than for humans. The bandwidth of the analyzing channel surrounding the signal frequency also determines how many harmonic components will interact to produce a within-channel output waveform. To the extent that the individual components are more nearly resolved by the relatively narrow analyzing channels, the influence of the temporal waveform shape on masking will be reduced.

Within-channel waveform shapes also may be altered by cochlear processes other than the bandwidths of analyzing channels, and these other processes may contribute to the equal effectiveness of positive and negative Schroeder-phase harmonic complexes for the birds. Smith *et al.* (1986), and later, Kohlrausch and Sander (1995), argued that, in humans, because of an interaction between the phase spectrum of the Schroeder-phase maskers and the phase characteristic of the basilar membrane, the positive-phase masker becomes trans-

formed internally (i.e., on the basilar membrane) into a highly modulated waveform, with relatively long intervals of low-amplitude activity—much as is seen externally in a cosine-phase wave. The interaction between the basilar membrane and the negative Schroeder masker, however, does not create such peaks in the internal waveform. Instead, it produces an envelope that is more like its external waveform shape, or like a random-phase wave. Thus the (internally) modulated positive-phase masker would be a poorer masker than the (internally) flat-envelope negative Schroeder masker, as the signal could be detected within the low-amplitude portions of the positive Schroeder waveform. Additional reductions in masking by the positive Schroeder masker might also be due to active gain mechanisms in the mammalian cochlea, which differentially amplify low- and high-amplitude portions of a sound. Carlyon and Datta (1997a) and Summers and Leek (1998) have reported changes in the effectiveness of the positive-phase masker with increasing level that are consistent with the activity of the nonlinear gain mechanism in the cochlea. The contribution of the active gain mechanism was further demonstrated by Summers and Leek by showing a loss of the differential masking effect in human listeners with sensorineural hearing impairment—a condition usually involving damage to active cochlear processing (Patuzzi *et al.*, 1989).

An explanation of the Schroeder masking results in birds that relies on the dynamics of cochlear processing and active nonlinear mechanisms is somewhat problematic. This is because of the small size of the avian basilar papilla, our lack of knowledge regarding the phase characteristics of the avian inner ear, and uncertainty about the existence and characteristics of nonlinear processing in birds. The length of the budgerigar basilar papilla is only about 3 mm—an order of magnitude smaller than the human basilar membrane (Manley *et al.*, 1993). Moreover, the stiffness gradient of the chicken basilar papilla is much steeper than its counterpart in the human cochlea (von Bekesy, 1960). Though there is undoubtedly a traveling wave on the bird basilar papilla, its time course is likely to be much shorter from base to apex than that observed in humans. These, and possibly other structural and functional differences, suggest that the phase characteristics of the inner ears of the two species differ considerably. There is no evidence for the kind of hair cell motility in birds that is responsible for the active gain processes, and therefore nonlinearity, in mammals (Manley, 1995). Other nonlinear gain mechanisms may exist in the avian inner ear, possibly related to the function of the tectorial membrane (Manley, 1995).

Perhaps the most intriguing finding from this study is the reversal in birds of the Schroeder masking effect observed in humans. In the budgerigars, the positive Schroeder-phase maskers were more effective, while in humans, the negative-phase complexes produced the greater amounts of masking. We would expect that species differences in inner ear tuning or neural firing patterns may contribute to these masking differences. Gleich (1994) reported that tuning curves and excitation patterns in birds are generally more symmetrical and change less with increasing stimulus levels than those of mammals. At very high levels, the tuning curves broaden slightly and the excitation patterns begin to show a slightly shallower lower-frequency side than high-frequency side (Gleich, 1994). In contrast, mammalian tuning curves at frequencies above 1 kHz broaden significantly with level, with the low-frequency tail becoming more shallow. Excitation patterns on the mammalian basilar membrane become increasingly asymmetrical with level, as the high-frequency side of the excitation becomes ever more shallow and the low-frequency side remains fairly steep, in contrast to patterns exhibited in birds.

On the basis of tone-on-tone masking studies, budgerigars appear to share with other birds a tuning curve shape that is more symmetrical than that typically found in mammals (Saunders *et al.*, 1979; Dooling and Searcy, 1985). In fact, if budgerigars follow the typical avian patterns of tuning, only at the highest levels might the slightly increased asymmetry contribute to a difference in masking between the negative and positive Schroeder maskers. Thus to the extent that tuning asymmetries observed in mammals are involved in masking differences found there, we might expect less masking differences between Schroeder-phase complexes in birds. Moreover, because the tuning curve asymmetry is opposite to the asymmetry observed in mammals, the direction of any masking difference would be the reverse of that seen in humans. This, of course, is exactly the pattern observed in the budgerigars as masker level increases (see Fig. 2).

While considering the possible contributions of tuning curve shapes to these masking differences, however, it must be remembered that the long-term spectra of the Schroeder complexes are identical, with differences only in the direction of the within-period glides in their instantaneous spectra. Upward-sweeping instantaneous frequencies found in the negative-Schroeder harmonic complex would change the dynamic aspects of neural firing relative to that produced by instantaneous frequencies sweeping downward, as in the positive Schroeder-phase waveform. Differences in Schroeder-phase masking may in part result from the glide-like aspects of the maskers interacting with temporal characteristics of neural firing. For example, Carney *et al.* (1999) reported that, in cats, impulse responses of auditory nerve fibers show an initial upward or downward frequency glide, depending on the best frequency of the neuron in question. Frequency-modulated impulse responses in basilar membrane motion at high frequencies have also been reported (de Boer and Nuttal, 1997; Recio *et al.*, 1998), and several recent auditory models of tuning characteristics in mammals incorporate an upward- or downward-sweeping impulse response (e.g., Irino and Patterson, 1997). These glides in the impulse responses may reflect the phase characteristic of the basilar membrane, and may relate to the Schroeder masking differences observed in humans. It is not clear whether such frequency glides might be found in neural impulse responses in birds, or whether such glides might be reversed relative to those found in mammals, perhaps in conformity with the symmetry characteristics of avian tuning curves.

There are two other minor factors that deserve mention in considering the contrasting findings here from humans and from budgerigars. First, there is a possible contribution from different transducers in the experimental setups. Birds per-

formed this listening task in a sound field, and were free to move around (although in practice, because they were busy pecking the observing key, their heads moved very little in this sound field). Humans listened to these complex sounds over earphones. Informal testing of humans in the same free field as the birds confirmed the human pattern of Schroeder masking effects (i.e., negative producing more masking than positive), but the masking differences were slightly smaller than under earphones. Depending on the size of the room and the amount of reverberation, some phase alterations might occur in some sound fields between the loudspeaker and the ear. However, the masking differences for humans listening in the bird's testing box were still much larger than observed in the birds. The results of this sound field testing make it unlikely that these transducer differences were responsible in any major way for the differences in performance observed between species. Further confirmation that these masking differences are not due to random movements of the birds within the listening boxes may be found in the reliability of response patterns in replications of experimental conditions by the birds, suggesting that the stimuli were controlling responses in a systematic manner.

Finally, the effect of the bird middle ear system on these data is not clear. The middle ears of birds are connected through an interaural pathway in their highly trabeculated skull. It is now known that this interaural pathway can influence the nature of the acoustic stimulus perceived by the binaural auditory system (Coles *et al.*, 1980; Larsen *et al.*, 1997; Lewis, 1983; Rosowski and Saunders, 1980) and probably affects certain binaural phenomena such as sound localization (Park and Dooling, 1991) and binaural masking release (Dent *et al.*, 1997). It is not known whether the interaural pathway differentially distorts the positive and negative Schroeder maskers in ways that affect their masking effectiveness.

IV. CONCLUSIONS

The shape of the temporal waveform has a significant impact on the ability of harmonic complexes to mask pure tones in both humans and budgerigars. In both species, highly peaked waveforms with all components in cosine phase generally produce less masking than random-phase maskers, and the masking differences between the two maskers increase monotonically with stimulus level, again in both species. Significant species differences emerge, however, with other selections of harmonic component phases.

As previously reported in humans, masking by positive and negative Schroeder-phase complexes produce differences in signal threshold that increase as masker level increases from low to moderate levels. The negative Schroeder waveform is usually the more effective masker. These results hold for fundamental frequencies of 50 and 100 Hz.

In budgerigars, however, the two Schroeder phase maskers produced nearly identical thresholds until the highest masker level was reached. When small differences in masking were observed, the direction of masking effectiveness was reversed relative to that found in humans, with the positive Schroeder masker showing the greater masking effects. In addition, in most cases the budgerigars showed less masking than did humans. These differences in masking performance between species are likely due to differences in structure and function of the two auditory peripheries. They may relate to differences in traveling wave characteristics and to different manifestations of active cochlear processing in avian and mammalian ears. A known difference between species relating to shapes and widths of neural tuning curves may emerge as a significant contributor to these observed masking differences.

The differences in masking between budgerigars and humans observed here encourage the use of these types of harmonic complex stimuli in studies relating auditory perception to species-specific structures and processing mechanisms. Stimulus manipulations of both long-term and instantaneous frequencies, as well as control of dynamic aspects of sounds such as temporal envelopes and fine structure, open a broad vista of challenges to comparative explorations of auditory function.

ACKNOWLEDGMENTS

This work was supported by NIH Grants DC-00198 to R.J.D. and DC-00626 to M.R.L. M.L.D. was supported by an Institutional NRSA from NIH (DC-00046). We are grateful to Van Summers for interesting discussions regarding these data. Otto Gleich also provided stimulating and enlightening discussions on the topics addressed in this paper. Special thanks to M. Mavilia, K. Inouye, B. Lohr, and J. Lentz for assistance. The opinions or assertions contained herein are the private views of the authors and are not to be construed as official or as reflecting the views of the Department of the Army or the Department of Defense.

Carlyon, R. P., and Datta, A. J. (**1997a**). ''Excitation produced by Schroeder-phase complexes: Evidence for fast-acting compression in the auditory system,'' J. Acoust. Soc. Am. **101**, 3636–3647.

Carlyon, R. P., and Datta, A. J. (**1997b**). ''Masking period patterns of Schroeder-phase complexes: Effects of level, number of components, and phase of flanking components,'' J. Acoust. Soc. Am. **101**, 3648–3657.

Carney, L. H., McDuffy, M. J., and Shekhter, I. (**1999**). ''Frequency glides in the impulse responses of auditory-nerve fibers,'' J. Acoust. Soc. Am. **105**, 2384–2391.

Coles, R. B., Lewis, D. B., Hill, K. G., Hutchings, M. E., and Gower, D. M. (**1980**). ''Directional hearing in the Japanese quail (*Coturnix coturnix japonica*) II. Cochlear physiology,'' Exp. Biol. **86**, 153–170.

de Boer, E., and Nuttall, A. L. (**1997**). ''The mechanical waveform of the basilar membrane. I. Frequency modulations ('glides') in impulse responses and cross-correlation functions,'' J. Acoust. Soc. Am. **101**, 3583–3592.

Dent, M. L., Larsen, O. N., and Dooling, R. J. (**1997**). ''Free-field binaural unmasking in budgerigars (*Melopsittacus undulatus*),'' Behav. Neurosci. **111**, 590–598.

Dooling, R. J. (**1980**). ''Behavior and psychophysics of hearing in birds,'' in *Comparative Studies of Hearing in Vertebrates*, edited by A. N. Popper and R. R. Fay (Springer-Verlag, New York), pp. 261–288.

Dooling, R. J. (**1982**). ''Auditory perception in birds,'' in *Acoustic Communication in Birds*, edited by D. E. Kroodsma and E. H. Miller (Academic, New York), pp. 95–130.

Dooling, R. J. (**1991**). ''Hearing in birds,'' in *The Evolutionary Biology of Hearing*, edited by D. Webster, R. R. Fay, and A. N. Popper (Springer-Verlag, New York), pp. 545–560.

Dooling, R. J., and Okanoya, K. (**1995**). ''The method of constant stimuli in testing auditory sensitivity in small birds,'' in *Methods in Comparative Psychoacoustics*, edited by G. M. Klump, R. J. Dooling, R. R. Fay, and W. C. Stebbins (Birkhaeuser Verlag, Basel), pp. 161–169.

Dooling, R. J., and Saunders, J. C. (**1975**). ''Hearing in the parakeet (*Melopsittacus undulatus*): Absolute thresholds, critical ratios, frequency difference limens, and vocalizations,'' J. Comp. Physiol. Psychol. **88**, 1–20.
Dooling, R. J., and Searcy, M. H. (**1979**). ''The relation among critical ratios, critical bands, and intensity difference limens in the parakeet (*Melopsittacus undulatus*),'' Bull. Psychon. Soc. **13**, 300–302.
Dooling, R. J., and Searcy, M. H. (**1985**). ''Non-simultaneous auditory masking in the budgerigar (*Melopsittacus undulatus*),'' J. Comp. Psych. **99**, 226–230.
Dyson, M. L., Klump, G. M., and Gauger, B. (**1998**). ''Absolute hearing thresholds and critical masking ratios in the European barn owl: A comparison with other owls,'' J. Comp. Physiol. **182**, 695–702.
Farabaugh, S. M., Dent, M. L., and Dooling, R. J. (**1998**). ''Hearing and vocalizations in native Australian budgerigars (*Melopsittacus undulatus*),'' J. Comp. Psych. **112**, 74–81.
Fay, R. R. (**1988**). *Hearing in Vertebrates: A Psychophysics Databook* (Hill-Fay, Winnetka, Illinois).
Gleich, O. (**1994**). ''Excitation patterns in the starling cochlea: A population study of primary auditory afferents,'' J. Acoust. Soc. Am. **95**, 401–409.
Irino, T., and Patterson, R. D. (**1997**). ''A time-domain, level-dependent auditory filter: The gammachirp,'' J. Acoust. Soc. Am. **101**, 412–419.
Klump, G. M. (**1996**). ''Bird communication in the noisy world,'' in *Ecology and Evolution of Acoustic Communication in Birds*, edited by D. E. Kroodsma and E. H. Miller (Cornell University Press, New York), pp. 321–338.
Kohlrausch, A., and Sander, A. (**1995**). ''Phase effects in masking related to dispersion in the inner ear II. Masking period patterns of short targets,'' J. Acoust. Soc. Am. **97**, 1817–1829.
Langemann, U., Gauger, B., and Klump, G. M. (**1998**). ''Auditory sensitivity in the great tit: Perception of signals in the presence and absence of noise,'' Anim. Behav. **56**, 763–769.
Larsen, O. N., Dooling, R. J., and Ryals, B. M. (**1997**). ''Roles of intracranial air pressure on hearing in birds,'' in *Diversity in Auditory Mechanics*, edited by E. R. Lewis, G. R. Long, P. M. Narins, C. R. Steele, and E. Hecht-Poinar (World Scientific, New Jersey), pp. 253–259.
Lewis, D. B. (**1983**). ''Directional cues for auditory localization,'' in *Bioacoustics, a Comparative Approach*, edited by D. B. Lewis (Academic, London), pp. 233–257.
Macmillan, N. A., and Creelman, C. D. (**1991**). *Detection Theory: A User's Guide* (Cambridge University Press, Cambridge).
Manley, G. A. (**1990**). *Peripheral Hearing Mechanisms in Reptiles and Birds* (Springer-Verlag, Berlin).
Manley, G. A. (**1995**). ''The avian hearing organ: A status report,'' in *Advances in Hearing Research*, edited by G. A. Manley, G. M. Klump, C. Koppl, H. Fastl, and H. Oeckinghause (World Scientific, New Jersey), pp. 219–232.
Manley, G. A., Schwabedissen, G., and Gleich, O. (**1993**). ''Morphology of the basilar papilla of the budgerigar, *Melopsittacus undulatus*,'' J. Morphol. **218**, 153–165.
Okanoya, K., and Dooling, R. J. (**1987**). ''Hearing in passerine and psittacine birds: A comparative study of absolute and masked auditory thresholds,'' J. Comp. Psych. **101**, 7–15.
Park, T. J., and Dooling, R. J. (**1991**). ''Sound localization in small birds: Absolute localization in azimuth,'' J. Comp. Psych. **105**, 125–133.
Patuzzi, R. B., Yates, G. K., and Johnstone, B. M. (**1989**). ''Outer hair cell receptor current and sensorineural hearing loss,'' Hear. Res. **42**, 47–72.
Recio, A., Rich, N. C., Narayan, S. S., and Ruggero, M. A. (**1998**). ''Basilar-membrane responses to clicks at the base of the chinchilla cochlea,'' J. Acoust. Soc. Am. **103**, 1972–1989.
Rosowski, J. J., and Saunders, J. C. (**1980**). ''Sound transmission through the avian interaural pathways,'' J. Comp. Physiol. **136**, 183–190.
Saunders, J. C., Denny, R. M., and Bock, G. R. (**1978a**). ''Critical bands in the parakeet (*Melopsittacus undulatus*),'' J. Comp. Physiol. **125**, 359–365.
Saunders, J. C., Else, D. V., and Bock, G. R. (**1978b**). ''Frequency selectivity in the parakeet (*Melopsittacus undulatus*) studied with psychophysical tuning curves,'' J. Comp. Physiol. Psychol. **92**, 406–415.
Saunders, J. C., Rintelmann, W. F., and Bock, G. R. (**1979**). ''Frequency selectivity in bird and man: A comparison among critical ratios, critical bands, and psychophysical tuning curves,'' Hear. Res. **1**, 303–323.
Schroeder, M. R. (**1970**). ''Synthesis of low-peak-factor signals and binary sequences with low autocorrelation,'' IEEE Trans. Inf. Theory **IT-16**, 85–89.
Smith, B. K., Sieben, U. K., Kohlrausch, A., and Schroeder, M. R. (**1986**). ''Phase effects in masking related to dispersion in the inner ear,'' J. Acoust. Soc. Am. **80**, 1631–1637.
Summers, V., and Leek, M. R. (**1998**). ''Masking of tones and speech by Schroeder-phase harmonic complexes in normally hearing and hearing-impaired listeners,'' Hear. Res. **118**, 139–150.
von Bekesy, G. (**1960**). *Experiments in Hearing* (McGraw-Hill, New York).

A dual passive cavitation detector for localized detection of lithotripsy-induced cavitation *in vitro*

Robin O. Cleveland
Department of Aerospace and Mechanical Engineering, Boston University, Boston, Massachusetts 02215

Oleg A. Sapozhnikov
Department of Acoustics, Physics Faculty, M. V. Lomonosov Moscow State University, Moscow 119899, Russia

Michael R. Bailey and Lawrence A. Crum
Applied Physics Laboratory, University of Washington, Seattle, Washington 98105

(Received 18 June 1999; revised 10 August 1999; accepted 29 November 1999)

A passive cavitation detector (PCD) identifies cavitation events by sensing acoustic emissions generated by the collapse of bubbles. In this work, a dual passive cavitation detector (dual PCD), consisting of a pair of orthogonal confocal receivers, is described for use in shock wave lithotripsy. Cavitation events are detected by both receivers and can be localized to within 5 mm by the nature of the small intersecting volume of the focal areas of the two receivers in association with a coincidence detection algorithm. A calibration technique, based on the impulse response of the transducer, was employed to estimate radiated pressures at collapse near the bubble. Results are presented for the *in vitro* cavitation fields of both a clinical and a research electrohydraulic lithotripter. The measured lifetime of the primary growth-and-collapse of the cavitation bubbles increased from 180 to 420 μs as the power setting was increased from 12 to 24 kV. The measured lifetime compared well with calculations based on the Gilmore–Akulichev formulation for bubble dynamics. The radiated acoustic pressure 10 mm from the collapsing cavitation bubble was measured to vary from 4 to 16 MPa with increasing power setting; although the trends agreed with calculations, the predicted values were four times larger than measured values. The axial length of the cavitation field correlated well with the 6-dB region of the acoustic field. However, the width of the cavitation field (10 mm) was significantly narrower than the acoustic field (25 mm) as bubbles appeared to be drawn to the acoustic axis during the collapse. The dual PCD also detected signals from ''rebounds,'' secondary and tertiary growth-and-collapse cycles. The measured rebound time did not agree with calculations from the single-bubble model. The rebounds could be fitted to a Rayleigh collapse model by considering the entire bubble cloud as an effective single bubble. The results from the dual PCD agreed well with images from high-speed photography. The results indicate that single-bubble theory is sufficient to model lithotripsy cavitation dynamics up to time of the main collapse, but that upon collapse bubble cloud dynamics becomes important. [S0001-4966(00)02503-0]

PACS numbers: 43.80.Sh, 43.25.Yw, 43.35.Ei [FD]

INTRODUCTION

Shock wave lithotripsy (SWL) (Chaussy *et al.*, 1980) is the most common modality for treating kidney stones (Holmes and Whitfield, 1991). Despite the widespread use of SWL, there is no agreement in the literature as to the mechanism by which the shock wave destroys kidney stones. In addition, although early reports indicated that SWL treatment did not lead to appreciable damage to the kidney (Chaussy, 1982; Evan and McAteer, 1996), it is now recognized that a clinical dose of shock waves will induce renal injury in a majority, if not all, treated kidneys (Kaude *et al.*, 1985; Evan and McAteer, 1996). Both the significance of tissue damage, and the mechanisms that are responsible for the damage, are under dispute. There is an incentive therefore to develop techniques that can quantify the action of possible mechanisms in SWL.

One mechanism that appears to play a significant role during SWL, both for stone comminution and tissue damage, is acoustic cavitation. Acoustic cavitation refers to the growth and violent collapse of vapor or gas cavities in response to an acoustic pressure field. Cavitation has been proposed as a mechanism of stone comminution in SWL (Coleman *et al.*, 1987; Crum, 1988; Vogel and Lauterborn, 1988). Studies have shown that the presence of cavitation is critical to stone fragmentation *in vitro* (Sass *et al.*, 1991; Delacretaz *et al.*, 1995). Studies with biological systems demonstrate that significant bioeffects occur when cavitation is present (Delius *et al.*, 1990; Dalecki *et al.*, 1996). Evidence of cavitation events occurring in and around the kidneys of human patients during SWL has been detected (Coleman *et al.*, 1996). These results provide circumstantial evidence that in clinical lithotripsy cavitation could play both a beneficial role in stone destruction and a deleterious role in bioeffects. In this report a refinement of previous cavitation detection systems is presented which can both improve the spatial

specificity and better quantify the strength of cavitation events produced by a lithotripter.

At the focus of an electrohydraulic lithotripter, the pressure waveform consists of a shocked positive pulse, with peak pressure of order 40 MPa and duration 1 μs, followed by a negative tail, of about -10 MPa peak pressure and 4-μs duration (Coleman and Saunders, 1989). The behavior of cavitation bubble dynamics in response to a lithotripsy pressure pulse was predicted by Church (1989) based on the Gilmore–Akulichev model. The model predicts that bubbles will respond with a characteristic ''double-burst'' acoustic signature (discussed in more detail below). Coleman *et al.* (1992) measured the double-burst acoustic signature from cavitation in a lithotripter using passive cavitation detection (PCD). The PCD system consisted of a single focused hydrophone listening for acoustic emissions from the focal region of the lithotripter. The results showed that the measured response was qualitatively in accordance with the Gilmore–Akulichev model. Delacretaz *et al.* (1995) measured a double-burst signature from the cavitation field of an electromagnetic lithotripter using a polyvinylidene fluoride PVDF needle hydrophone. The double burst has also been recorded in patients undergoing clinical SWL (Coleman *et al.*, 1996). Measurements *in vivo* with a pig model indicated that tissue has a constraining effect on bubble dynamics (Zhong *et al.*, 1997, 1998, 1999).

A number of other techniques have been used to monitor lithotripsy-induced cavitation. When foil targets are placed in the focus of a lithotripter they suffer surface pitting due to cavitation. The pitting has been used to measure both the spatial extent and relative intensity of the cavitation (Coleman *et al.*, 1987; Lifshitz *et al.*, 1997; Bailey *et al.*, 1999) but does not give information on the time history of the bubble cloud. Pye and Dineley (1999) have recently published a technique where translation of a small sphere is used to detect cavitation. Sonoluminescence, light emissions from cavitation collapses, has been measured in the focal region of an electrohydraulic lithotripter (Coleman *et al.*, 1992). Laser scattering (Jochle *et al.*, 1996; Huber *et al.*, 1999) and fiber optic transmittance (Delacretaz *et al.*, 1995) provide time history of the bubble dynamics.

Perhaps the best measurements of the *in vitro* cavitation field are provided by high-speed photography (Sass *et al.*, 1991; Huber *et al.*, 1994; Jochle *et al.*, 1996; Zhong *et al.*, 1997, 1999). Video images demonstrate that cavitation in the free field consists of a large cloud of bubbles. This is significant for PCD systems because even with focused hydrophones it appears that detected emissions could come from a number of cavitation events. Difficulty in specifying the location of cavitation events using PCD is compounded in electrohydraulic lithotripters where spark jitter leads to variation in the location of the acoustic and hence the cavitation fields.

An advantage of the PCD over other methods is the ability to observe cavitation *in vivo*. This work describes an acoustic cavitation detection system, the dual PCD, which provides improved spatial information on the location of cavitation events in comparison to a single transducer PCD. The article first addresses the drawbacks associated with using a single focused transducer as a PCD. It proceeds to describe how signals from two focused PCD transducers, in association with a coincidence detection algorithm, can provide improved spatial localization of cavitation events. The dual PCD system is completed by establishing a calibration technique to estimate the pressure radiated by collapsing cavitation bubbles. The dual PCD was used to map the cavitation field of two electrohydraulic lithotripters and results were compared to numerical predictions of single-bubble dynamics. The presence of bubble rebounds detected by the dual PCD was confirmed with high-speed photography. The dual PCD system described here has the potential to detect events *in vivo* and may be a useful tool in elucidating the role of cavitation in clinical lithotripsy by providing a means to correlate cavitation with either stone fragmentation or tissue injury.

I. MATERIALS AND METHODS

A. Lithotripters

The majority of the measurements were conducted in the research electrohydraulic lithotripter at the Applied Physics Laboratory, University of Washington at Seattle (APL-UW), which was designed to mimic the performance of a clinical lithotripter, the Dornier HM3 (Howard and Sturtevant, 1997; Cleveland *et al.*, 2000). Measurements were also taken on a clinical, unmodified, Dornier HM3 lithotripter at Methodist Hospital (Indianapolis, Indiana). Our experiments are focused on the Dornier HM3 because it is the lithotripter in the widest use in the United States (Lingeman, 1996). The acoustic field of the lithotripters was characterized by a broadband polyvinylidene fluoride (PVDF) membrane hydrophone with a 0.5-mm active spot (Model 702, Sonic Industries, Hatboro, Pennsylvania). The calibration value provided with the shock wave hydrophone was confirmed by substitution calibration, up to 20 MHz, with a PVDF membrane hydrophone (type Y-33-7611, GEC-Marconi, Chelmsford, UK) that had been calibrated at National Physical Laboratories (Teddington, UK). The waveforms and acoustic fields measured in the two lithotripters have been determined to be similar (Cleveland *et al.*, 2000). In each lithotripter, peak positive pressure was variable from 25 MPa (12 kV) to 40 MPa (24 kV).

An electrohydraulic lithotripter uses an underwater spark to generate a shock wave. The spark is located at the internal focus ($F1$) of a hemi-ellipsoidal reflector; the reflector focuses the spherical shock wave generated by the spark to the external focus ($F2$) of the ellipsoid. The geometry of the ellipses in the two lithotripters was identical (major half-axis $a=139$ mm, minor half-axis $b=78$ mm; the reflector is truncated to be 14 mm short of complete hemi-ellipsoid). Both lithotripters used an 80-nF capacitor to store the high voltage before discharging it through a refurbished Dornier electrode (Service Trends, Kennesaw, Georgia). Electrodes with between 100 and 2000 sparks were used to limit variability in spark amplitude with electrode age. The water in both lithotripters was degassed to between 2 to 4 ppm of O_2 (approximately half the gas content of tap water) and NaCl added to achieve a conductivity of 650 μS/cm. Gas content

was measured to increase during experiments at a rate of 0.1 ppm/hour. The temperature of the water bath in the APL-UW machine was 20 °C; the HM3 water was maintained at body temperature 37 °C. In the HM3, positioning was achieved using the three-axis hydraulic positioner provided with the HM3, or by the mounting hand-controlled stages on the side of the tank. Positioning in the APL-UW lithotripter was accomplished using a computer-controlled three-axis system (Velmex-Unislide, Bloomfield, NY).

All data were recorded on a digital oscilloscope (Tektronix TDS 744, Beaverton, OR) which has an 8-bit digitizer and sampling rate up to 2 gigasamples/s. The scope was triggered by a photodiode which detected the light flash from the underwater spark discharge. Data were transferred to computer and processed by LabVIEW (National Instruments, Austin, TX). Further processing was done in MatLab (Mathworks, Natick, MA).

B. Bubble dynamics model

Measurements of cavitation activity were compared with results of numerical calculations. The model used for bubble dynamics was the Gilmore–Akulichev formulation (Gilmore, 1952; Akulichev, 1971), with gas diffusion included. The model was proposed and solved numerically for lithotripsy by Church (1989). We have reproduced Church's numerical solution and briefly review the model here; further details can be found elsewhere (Church, 1989; Chol *et al.*, 1993). The Gilmore equation describes the oscillations of a single spherical bubble driven by an acoustic excitation and can be written in the following form:

$$\left(1-\frac{\dot{R}}{c}\right)R\ddot{R}+\frac{3}{2}\left(1-\frac{\dot{R}}{3c}\right)\dot{R}^2=\left(1+\frac{\dot{R}}{c}\right)H+\frac{R}{c}\left(1-\frac{\dot{R}}{c}\right)\frac{dH}{dt}, \tag{1}$$

where R is the bubble radius, a dot indicates a time derivative, t is time, c is the speed of sound in the liquid at the bubble wall, and H is the difference in the liquid enthalpy between the bubble wall and infinity. The expressions for $c=\sqrt{dp/d\rho}$ and $H=\int_{p_\infty}^{p(R)}dp/\rho$ were obtained from the Tait equation of state for the liquid $p=p_0+(c_0^2\rho_0/n)\cdot[(\rho/\rho_0)^n-1]$, where n is the Tait parameter, p_0 is ambient pressure, ρ_0 ambient density, and c_0 small-signal sound speed. The upper limit of the enthalpy integral is the pressure at the water–gas interface, i.e., the bubble wall $p(R)=p_g-2\sigma/R-(4\mu/R)\dot{R}$, where p_g is the pressure in the gas, given below, σ is the coefficient of surface tension, and μ the coefficient of viscosity. The lower limit is $p_\infty=p_0+P(t)$, the pressure at infinity where $P(t)$ is acoustic pressure associated with the lithotripter shock wave.

Gas diffusion was accounted for by Church with a zero-order model for gas diffusion based on a theory by Eller and Flynn (1965). The number of moles of gas $n(t)$ in the bubble is given by the following equation: $n=n_0-4\sqrt{\pi D}\int_0^\tau F(\tau')\times(\tau-\tau')^{-1/2}d\tau'$, where n_0 is the initial number of moles in the bubble, D is the diffusion constant, $\tau=\int_0^t R^4(t')dt'$, $F(\tau)=C_0(p_g/p_0)-C_i$, C_0 the saturation concentration of the gas in the liquid, C_i the initial concentration of gas in the liquid far from the bubble, $p_g=(p_0+2\sigma/R_0)(n/n_0)\times(R_0/R)^{3\eta}(R_{0n}/R_0)^{3(\eta-1)}$ is the pressure in the gas, R_0 the initial radius, R_{0n} the time varying equilibrium radius, and η is the polytropic exponent of the gas.

The radiated pressure was calculated using the Akulichev formulation

$$p_{\mathrm{RAD}}(t)=p_0+\frac{\rho_0 c_0^2}{n}\left[\left(\frac{2}{n+1}+\frac{n-1}{n+1}\times\sqrt{1+\frac{n+1}{rc_0^2}G}\right)^{2n/(n-1)}-1\right], \tag{2}$$

where $G=R(H+U^2/2)$ is an invariant of the bubble motion evaluated at the bubble wall and r is the distance from the center of the bubble. Equation (2) does not account for nonlinear distortion of the radiated pressure as it propagates from the bubble.

The equations were solved using a code written in FORTRAN. The Gilmore equation was integrated using the fourth-order Runge–Kutta solver from Numerical Recipes (Press *et al.*, 1992, pp. 710–722). The diffusion equation was solved using a trapezoidal rule as discussed by Church (1989). The various numerical values used for the parameters were $p_0=10^5$ Pa, $c_0=1485$ m/s, $\rho_0=1000$ kg/m^3, $n=7$, $\sigma=0.0725$ N/m, $\mu=0.001$ Pa.s, $n_0=6.93\times10^{-15}$ moles, $D=2.42\times10^{-9}$ m^2/s, $C_0=0.872$ moles/m^3, $C_1=0.436$ moles/m^3 (i.e., 50% gas saturation), $\eta=1.4$, and $R_0=3$ μm. The acoustic pressure $P(t)$ used as an input to the code was taken from waveforms measured by the shock wave hydrophone system (Sec. I A). The waveforms were sampled at 250 MHz (4 ns) and linear interpolation was used to produce a continuous waveform.

Figure 1 shows a sample calculation of a bubble in response to an acoustic waveform measured in the APL-UW lithotripter. Figure 1(a) shows the measured pressure waveform and a corrected waveform. The corrected waveform has an elongated negative pressure tail (Bailey *et al.*, 1999) to compensate for an underestimation of the negative pressure phase attributed to measurements with PVDF membranes (Wurster *et al.*, 1994). In all the bubble dynamics calculations presented here, corrected pressure waveforms were used for the acoustic input. Figure 1(b) and (c) show the radius of the bubble and the radiated pressure 10 mm away from the bubble as functions of time. The response of a bubble consists of an initial collapse due to the positive-pressure phase of the shock and the corresponding first burst acoustic emission p_S^* (the asterisk indicates a computed value). This is followed by a rapid growth phase driven by the negative-pressure tail of the shock wave. The inertia imparted to the bubble wall by the negative tail is large enough that the bubble continues to grow after the shock wave has passed. From this point inertial cavitation dominates, as there is no external time-varying driving pressure, and the bubble continues to grow for a relatively long period (in excess of 100 μs). Eventually the ambient pressure in the fluid stops the growth and initiates an inward flow of fluid which leads to a second collapse of the bubble and the corresponding second burst of the acoustic emission, p_C^*. These two emissions are the double-burst signature and the time between them is the characteristic time t_C^*. After the second collapse

the bubble undergoes a number of growth and collapse cycles, rebounds, at the collapse of each rebound a pressure wave is radiated $p_R^*, p_{R2}^*, \ldots$ and the time between rebounds is $t_R^*, t_{R2}^*, \ldots$ When the bubble becomes quiescent we note that its radius has increased to approximately 60 μm because of gas diffusion into the bubble.

For the simulation shown in Fig. 1 the characteristic time was about 520 μs, the maximum radius 3 mm, and the rebound time 33 μs. At distance 1 cm from the bubble center the calculated radiated pressures were: $p_S^* = 0.8$, $p_C^* = 68$, and $p_R^* = 0.24$ MPa. These values are similar to those calculated by Church. We note that the radiated pressure expression does not account for nonlinear distortion of the radiated pressure wave. For the pressures predicted, particularly at the second collapse, the radiated pressure wave will form a shock within 10 mm and suffer corresponding nonlinear attenuation which will reduce the collapse pressures p_C^*. Neglect of nonlinear distortion may contribute to calculated radiated pressures being larger than measured values.

C. Cavitation detection receivers

The system for measuring cavitation signals is now presented. Although the dual PCD system consists of two focused receivers, we first discuss the behavior of a single PCD receiver. The individual transducers used in this research were spherical caps of C-5400 lead zirconate titanium (PZT) (Channel Industries, Santa Barbara, CA) with a resonance frequency of 1.08 MHz, aperture diameter of 100 mm, and radius of curvature (focal length) of either 100 or 200 mm. The PZT elements were mounted in a stainless steel housing and were air-backed. When used as receivers of acoustic emissions from shock waves it was necessary to use a high-pass filter (model 3202, Krohn-hite, Avon, MA), with a 300-kHz cutoff frequency, to remove the low-frequency signal of the radial mode of the transducer (approximately 20 kHz). The configuration used here is very similar to that described by Coleman *et al.* (1992).

The use of focused transducers in PCD is based on the desire to detect cavitation events from a confined volume. Although focused transducers have a narrow focal region, the focal region can be relatively long, leading to uncertainty in the axial location of a detected event. The size of the sensitive region of a focused hydrophone can be determined from the radiation pattern of the transducer. Because of reciprocity of the wave equation, the focal region of the transducer as a hydrophone is identical to the focal region of the transducer as a source. The acoustic field of a focused piston source was described theoretically by O'Neil (1949), and it has been shown that a focused piezoelectric transducer behaves very much like an ideal focused piston source (Cathignol *et al.*, 1997). The O'Neil solution for pressure amplitude distribution along the transducer axis for sinusoidal excitation can be written as

$$p = V_0 \rho c \left| \frac{e^{i2\pi z/\lambda} - e^{i2\pi R/\lambda}}{1 - z/F} \right|, \tag{3}$$

where V_0 is the amplitude of the normal velocity of the piston surface, ρ the ambient density of the medium, c the small signal sound speed, z the distance along the axis, λ the wavelength, F the radius of curvature, and R the distance from the observation point to the transducer edge. The axial pressure field described by Eq. (3) achieves a localized region of high amplitude around the geometrical focus $z = F$. The axial length of the ''focal spot'' $\Delta_\parallel$ (full width half-maximum) is given by

$$\Delta_\parallel = \frac{0.6\lambda}{\sin^2(\alpha/2)}, \tag{4}$$

where $\alpha = \arcsin(a/F)$ is the half-aperture angle of the radiator, and a the radius of the transducer. The lateral distribution of the pressure amplitude at the focal plane ($z = F$) may be expressed as follows:

$$p = p_{\max} \left| \frac{2J_1(2\pi r \sin\alpha/\lambda)}{2\pi r \sin\alpha/\lambda} \right|. \tag{5}$$

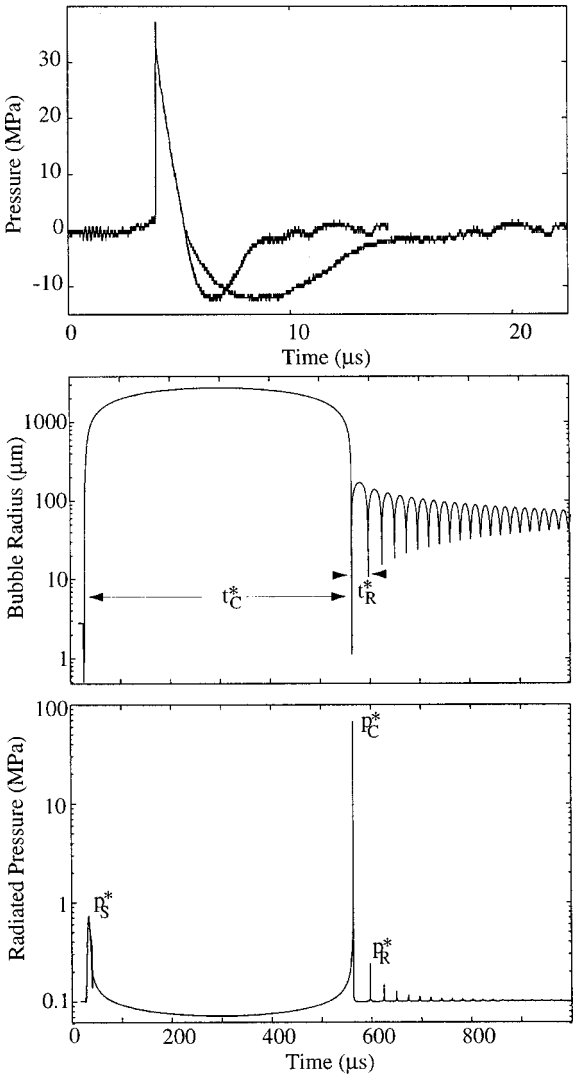

FIG. 1. Predicted bubble dynamics in the APL-UW lithotripter at 24 kV (a) measured acoustic shock wave and corrected shock wave used for bubble dynamics, (b) calculated radius time curve of a 3-μm bubble, (c) calculated radiated pressure 10 mm from the bubble. The scattered pressure p_S*, characteristic time t_C*, radiated collapse pressure p_C*, rebound time t_R*, and radiated rebound pressure p_R* are all indicated. The asterisk * denotes the values are calculated.

TABLE I. Axial and lateral dimensions of sensitive volume for different PCD transducers: 1, 2, Channel Industries, 3 Coleman *et al.* (1992, 1996), 4 Zhong *et al.* (1997).

Hydrophone #	1	2	3	4
f_{res}, MHz	1.08	1.08	1.0	1.0
$2a$ (mm)	100	100	100	38
F (mm)	100	200	120	102
$\Delta_{\parallel}$, mm	13	53	20	105
$\Delta_{\perp}$, mm	2.0	3.9	2.5	5.7

Here p_{max} is the pressure amplitude at the focal point, J_1 the cylindrical Bessel function of the first order, and r the lateral distance. The full width half-maximum diameter of the focal region is

$$\Delta_{\perp} = \frac{0.7\lambda}{\sin\alpha}. \tag{6}$$

Equations (4) and (6) define the axial and lateral dimensions of the sensitive area of a single PCD transducer. When sensing cavitation events from the bubble cloud, a single PCD transducer receives signals coming from all collapsing bubbles sitting in a cigar-shaped volume of dimensions $\Delta_{\parallel}$ by $\Delta_{\perp}$.

Table I presents corresponding values for the PCD transducers we employed (Nos. 1 and 2), the PCD transducer used by Coleman *et al.* (1992, 1996) (No. 3), and the PCD transducer used by Zhong *et al.* (1997) (No. 4). Table I illustrates that all PCD transducers have good spatial resolution, of the order of a few millimeters, in the lateral direction ($\Delta_{\perp}$), but have a poor resolution, of the order of tens of millimeters, in the axial direction ($\Delta_{\parallel}$). The resolution is especially poor for small aperture (i.e., small α) PCD transducers, which can be deduced from the $\sin\alpha$ term in the denominator of both Eqs. (4) and (6).

D. Coincidence detection: dual PCD

Dual PCD, illustrated in Fig. 2, uses two perpendicular confocal transducers to produce a detector with an effective focal dimension proportional to the width, not the length, of the focal region of each transducer. Although each receiver in the dual PCD suffers from the same long focal region as a single PCD, it is possible to take advantage of the fact that signals coming from the union of the two focal regions will have the same arrival time. A coincidence detection algorithm was constructed so that only events that originated from the effective focal region were identified as cavitation events. The transducers were mounted on a rigid frame but each transducer could be independently rotated and moved vertically. Fine alignment was achieved by placing a needle hydrophone at the desired focus; each of the PCD transducers was used as a source and independently positioned so that a maximum signal was recorded at the needle.

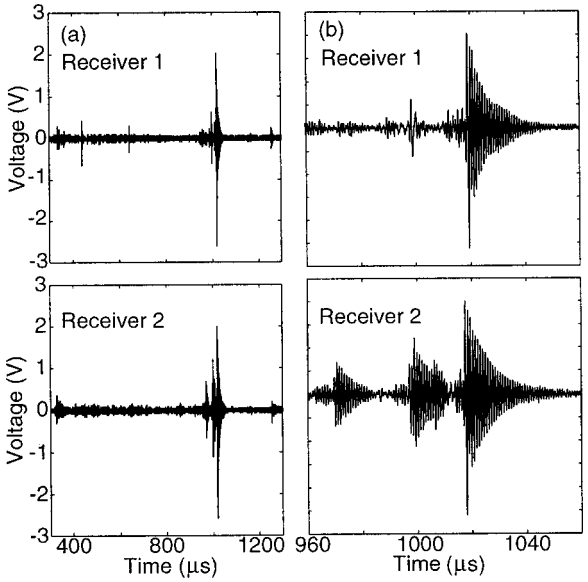

FIG. 3. Dual PCD signals for a single shock wave at 24 kV (a) long time scale, (b) closeup of main burst.

The concept behind the use of coincident detection using the dual PCD is illustrated by an example. Figure 3 presents signals registered by the two confocal PCD transducers (200-mm focal length) aligned with the focal region of the APL-UW lithotripter for a single spark discharge at a voltage of 24 kV. Figure 3(a) shows the signals received by both transducers, where zero time corresponds to the firing of the spark. The travel distance of the shock wave from the electrode to the reflector, and then to $F2$ is 276 mm; the distance from $F2$ to either PCD hydrophone is 200 mm. The time delay for the total distance is 317 μs, assuming a speed of sound 1500 m/s, which corresponds to the first peak seen in Fig. 3(a). This first signal p_S results from nonlinear acoustic scattering, which can be interpreted as being comprised of two inseparable effects: (i) scattering of the lithotripter shock wave from small bubbles or particles that are typically present in water; (ii) acoustic radiation from the bubbles during their first collapse. As described in Sec. I B, the cavitation field then proceeds through a growth and collapse cycle and radiates a second acoustic emission p_C. In Fig. 3 a sec-

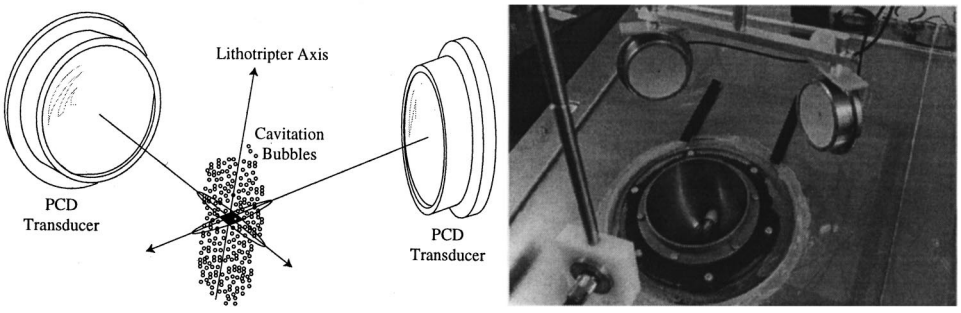

FIG. 2. Diagram of the concept of intersecting focal volumes is shown on the left. The cigar-shaped volumes are the focal regions of the individual transducers; the shaded region is the effective focal volume of the dual PCD. On the right is a photograph of the dual PCD in APL lithotripter. The brass ellipsoidal reflector and spark plug are at the bottom of the tank; the two confocal bowls are also confocal with $F2$ of the ellipsoid.

ond, large amplitude, emission is detected by both PCD transducers at around 1000 μs; however, additional emissions are registered by both transducers before and after this event. Figure 3(b) shows a closeup view of the signal around 1000 μs which consists of a number of ''events.'' Each event consists of a decaying sinusoid, the impulse response of the transducer. The signal from one PCD transducer does not allow one to deduce whether the detected events originated in the focal region or not. The structure of the detected signals becomes clear when comparing signals from the two PCD transducers. Only the signals arriving at similar times and having similar amplitude are of interest, all other signals do not originate near the effective focal region of the dual PCD. It is apparent from the traces that only the burst arriving at 1017 μs is similar on both transducers, therefore only this burst corresponds to a bubble collapsing in the effective focal region. The characteristic time in this case is $t_C = 700\,\mu$s.

Note that, in addition to the main collapse, a further simultaneous collapse, at approximately 1260 μs, is also apparent from the dual PCD traces. This second collapse appears to be from a ''rebound,'' a second growth-and-collapse cycle, and occurs about 240 μs after the main collapse. The rebound will be discussed in more detail in Sec. II.

The signals displayed in Fig. 3 were unwieldy to perform analysis on. Significant data reduction was achieved by demodulating the signals to remove the sinusoidal oscillations yet maintain the structure of the envelope. The demodulation process was carried out in LABVIEW immediately after the waveforms had been transferred from the digital oscilloscope to the computer. A full-wave rectification demodulation process was used; it consisted of taking the absolute value of the signal, followed by a low-pass filter (Butterworth, 300 kHz, second order) and finally decimation by a factor of five. The demodulation process also reduced the peak amplitude of the signal by a factor of 2.5.

Detection of simultaneous events was carried out in post-processing using MatLab by the following procedure. The demodulated signals from each channel were converted from volts to pressure by a calibration factor (described in the following section). The first burst (corresponding to the arrival of the shock) was located by windowing each waveform to within 20 μs of the calculated arrival time of the first burst. The windowed waveforms were oversampled by a factor of five to smooth the signals and then the peak in the cross correlation between the two channels was used to determine the location of the first burst. The second burst, associated with the primary inertial collapse, was determined by finding the location of the maximum signal (for time greater than 20 μs after the first burst) on each channel. The 20-μs delay was used to skip over spurious signals associated with the coda of the first burst. For each of the maxima, the two channels were windowed from -10 to 30 μs around the time of the peak (large enough to capture the impulse response of the PCD), locally resampled and a cross correlation performed. If a maximum occurred in the cross correlation for time shifts less than 3.4 μs (which corresponded to the 5-mm cross-sectional region of the PCD transducers), a coincident event was deemed to have occurred. Rebounds were found by looking for maxima in the recorded signals beyond the primary collapse by performing the same windowing and cross-correlation algorithm.

Once coincident events were identified, the signal (or pulse) amplitudes on each channel were compared to determine if the event had occurred at the focus. Coincident events do not necessarily occur at the focus; because only two transducers were used coincident events could in fact occur anywhere in the equal travel-time plane that bisects the two transducers. However, the focused nature of the transducers meant that events outside of the focal region, but which still lie on the plane of equal travel time, were detected with very low amplitude. These events were identified and excluded on two grounds: (1) if the amplitude of the signals received on the two channels differed by more than a factor of three it was assumed that the bubble was outside of the focal region of one of the transducers and (2) if the amplitude of the signal from the second burst was less than twice the amplitude of the signal received from the first burst, i.e., $p_C < 2p_S$, it was assumed that the bubble was not in the focal region. The signal from the first burst was very consistent and it appeared that there was always some sort of bubble or scatterer present to generate this signal in the focal region of the dual PCD. For a cavitation event to occur in the first side lobe of a PCD and appear to have come from the focal zone (that is, exceed the detection threshold given here) would require a collapse pressure in excess of 30 MPa which was larger than anything we measured. In summary, a ''focal event'' was deemed to have occurred when

(1) The arrival times of the pulses on both channels were close enough for the event to have been somewhere on the plane of constant travel time for the transducers.
(2) The amplitudes of both pulses were consistent with a signal emanating from the focal region of both transducers.

The action of the algorithm is demonstrated in Fig. 4, which shows demodulated signals received by a pair of transducers (PCD#2, $F = 200$ mm) from five consecutive shots. The lithotripter was at a setting of 18 kV and fired approximately every 3 sec (limited by the time necessary to transfer data from the scope to the computer). For the signals in Fig. 4 the focus of the dual PCD was aligned 10 mm in front of $F2$ of the lithotripter. The signal from the second PCD transducer was inverted to assist in visual comparison of the signals. The vertical scale has been calibrated to represent the peak radiated pressure 10 mm from the bubble center as discussed below in Sec. I E.

Locations where a maximum in the cross correlation was detected (not necessarily a focal event) are marked by an ''$\times$.'' The uppermost traces (shot 1 of the five) show no significant emissions on either channel. Shot 2 shows cavitation activity on channel 1 only but no activity on channel 2. The third shot yielded a coincident event (simultaneous signals on both channels) but of such low amplitude that it was assumed the signals did not originate from the focal region of the dual PCD. Shot 4 shows an event and apparent rebound detected on channel 2 but no events on channel 1, which indicates the cavitation collapse was in the focal re-

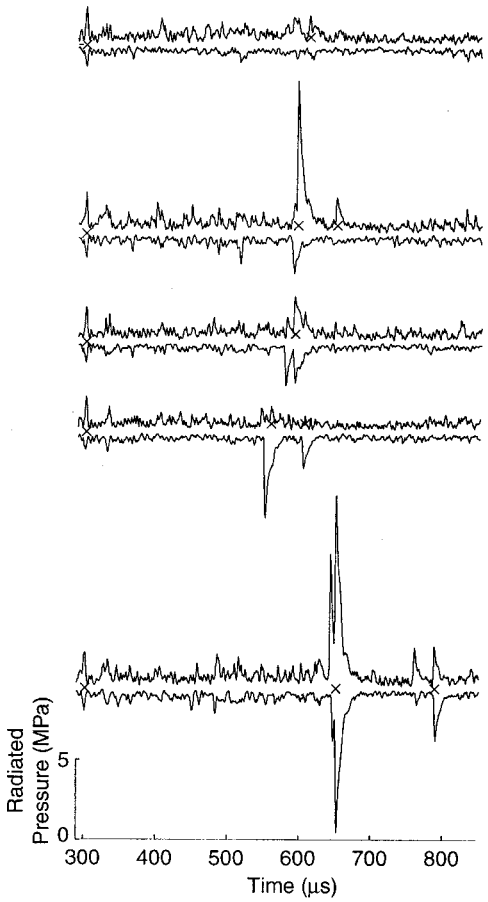

FIG. 4. Five consecutive dual PCD recordings at 18 kV. The radiated pressure is calibrated in terms of the peak pressure at a distance 10 mm from a collapsing bubble. The shape of the waveform is related to the impulse response of the PCD transducer and is not representative of the pressure waveform of the acoustic emission.

gion of transducer 2 but outside the focal region of transducer 1. The last shot shows a large cavitation event at 650 μs and a rebound signal at 800 μs evident on both channels—the algorithm described above identified this as a focal event. The collapse time, or characteristic time, $t_C = 340\,\mu$s, is the time between the first collapse $p_S = 2.2$ MPa and the main collapse $p_C = 12$ MPa. The rebound time t_R was 150 μs and the radiated pressure $p_R = 3.3$ MPa. Note that upon examination of the traces associated with the last shot there appeared to be a second bubble nearby that collapsed a little sooner than the bubble that was detected. This second bubble also appeared to generate a rebound. The coincident detection algorithm rejected this signal as being outside the volume of interest because the signal was disproportionately strong on channel 1.

Measurements taken at the focus of the lithotripters studied here provided simultaneous cavitation events for approximately 2/3 of the shots at 18 kV. Observation with a single PCD transducer would lead one to observe cavitation events in at least 90% of the shots because it does not exclude events outside of the focal region.

E. PCD pressure calibration

In addition to being able to localize cavitation events it was also considered useful to obtain an estimate of the amplitude of the acoustic emission generated by the cavitation collapse. Calculations by Church (1989) predict that the second collapse produces an outgoing shock wave with peak pressure of order 30 MPa at a distance of 1 cm from the bubble. Pressures nearer the bubble would be higher. Vogel and Lauterborn (1988) performed an experiment with a single laser-produced vapor bubble. They measured the amplitude of the pressure wave radiated by a collapsing bubble at a distance of 1 cm from its center. For the same maximum bubble radius as in the calculations of Church, their measurements give a value of about 10 MPa, which is three times less than corresponding computed value. Our goal was to estimate, from the PCD signals, the pressure generated by a bubble excited by a lithotripter pulse.

Calibration of a single PCD system has been reported by Zhong *et al.* (1997). The calibration value was the sensitivity of their transducer at resonance. Based on this technique they report that the pressure 10 mm from a cavitation bubble consisted of a pulse with 1.8 MPa compressive pressure and a 3.3-MPa tensile pressure for a spark discharge of 18 kV. These values are an order of magnitude less than predicted by Church, and in addition, it seems unlikely that a collapsing bubble will produce a stronger tensile pulse than compressive pulse. We discuss below that a resonance calibration is not appropriate for extracting the peak amplitude of pulse-type excitations.

The acoustic waveform detected by the PCD transducer cannot be easily reconstructed from the voltage it produces. The transducer is a high-Q resonator and its response to cavitation emission is a tone burst with exponentially decaying envelope, as seen in Fig. 3(b). Therefore the sensitivity of the transducer at its resonant frequency G_0 cannot be used for determining the pressure amplitude of a wide bandwidth signal such as the radiation from a bubble collapse. The measured voltage $u(t)$ from the PCD transducer can be described as a convolution of the incident acoustic pressure $p(t)$ and $h(t)$ the impulse response of the transducer,

$$u(t) = \int_{-\infty}^{\infty} h(t')p(t-t')dt'. \tag{7}$$

If $h(t)$ is known it is technically possible to recover the pressure waveform by deconvolving the impulse response from the measured signal. Unfortunately, if the pressure pulse is wideband and the receiver narrow band, as is the case here, then the presence of noise leads to significant errors in the inversion process (see, e.g., Press *et al.*, 1992, pp. 547–549).

We propose a new calibration scheme to estimate the amplitude of a pressure wave radiated during lithotripsy bubble collapse. For excitation by a very short pulse, as occurs in emissions from a bubble collapse, a simple approximation for the transducer response can be made which allows a calibration value to be determined from the impulse response of the transducer. If the incident wave is shorter than the resonant period of the transducer (about 1 μs for the PCD transducers used here), the excitation is effectively an impulse function to the PCD transducer and Eq. (7) reduces to

$$u(t) = h(t) \cdot \int_{-\infty}^{\infty} p(r,t')dt', \tag{8}$$

i.e., the PCD transducer responds with its impulse response scaled by a factor that depends on the integral of the acoustic pulse over time.

We determine whether the acoustic pulse from a cavitation bubble is short enough from measurements of Vogel and Lauterborn (1988). They reported that a shock wave emitted by a collapsing bubble has an exponential waveform,

$$p(t) = p_0 \cdot H(t) e^{-t/\tau_0}, \tag{9}$$

where $H(t)$ is the Heaviside step function.[1] Their measurements gave $\tau_0 = 35$ ns and $p_0 = 10$ MPa at 10 mm from the bubble center. We require that the duration of the pulse at the face of the PCD transducer (a distance of 100 mm from the bubble) be short compared to 1 μs. The pulse is intense enough that nonlinear distortion will occur as it propagates from the bubble to the PCD transducer; the distortion will lead to an increase of the duration of the pulse and decrease in amplitude (more rapidly than given by spherical spreading) (see, e.g., Rudenko and Soluyan, 1977, p. 36; Blackstock *et al.*, 1998, pp. 102–110). In the case of spherically spreading shock waves it is possible to use weak shock theory to model the nonlinear effects. For the waveform measured by Vogel and Lauterborn: $p_0 = 10$ MPa, $\tau_0 = 35$ ns, at $r_0 = 10$ mm, spherical spreading, without nonlinear effects, would predict that at $r = 100$ mm, $p = 1$ MPa, and $\tau = 35$ ns. When nonlinear effects are taken into account one calculates $p = 0.41$ MPa and $\tau = 130$ ns. Therefore, nonlinearity distorts the waveform, reducing the peak pressure more than two times and increasing the pulse duration almost four times. The duration is still much shorter than the period of oscillation of the hydrophone (926 ns at 1.08 MHz) and the approximation given in Eq. (8) is valid. A useful property of the nonlinear distortion that we shall also exploit is that the area under pressure curve is independent of nonlinear distortion, i.e., $S(r) = \int_{-\infty}^{\infty} p(r,t')dt'$ will vary according to linear theory (spherical spreading in this case) therefore $S(r) = S(r_0) r_0 / r$. For the Vogel and Lauterborn pulse the time integral at the source is $S(r_0) = p_0 \tau_0$.[2]

We now need to determine $h(t)$, the impulse response of the transducer for Eq. (8). This was done by placing a PZT needle hydrophone of 0.635-mm active element diameter (Dapco Industries, Ridgefield, CT) at the focus of the PCD transducer. The PZT needle had a 6-dB bandwidth that covered the frequency range 1 to 10 MHz. The needle was excited by a short, 0.5-μs duration, electrical pulse; the bandwidth of the needle was broad enough that it generated an acoustic pulse that was as short as the electrical signal. The short duration was confirmed by measuring the acoustic signal with the Marconi PVDF membrane mentioned above. The response of the PCD transducer to the acoustic impulse was similar to those in Fig. 3(b), and it appeared to be an exponentially damped sinusoid, which is typical for a simple damped resonance system. The measured waveform was assumed to be a good representation of the impulse response and was fitted to the following function:

$$h(t) = h_0 e^{-t/\tau^*} \sin 2\pi f_{\text{res}} t, \tag{10}$$

where the parameters h_0, τ^*, and f_{res} were to be determined. The resonant frequency f_{res} was determined from the period of oscillation of the impulse response. The decay constant τ^* was determined from the envelope of the impulse response.

Accurate determination of the parameter h_0 directly from the damped sinusoid was found to be difficult as it involved extrapolation of the exponential envelope. Instead h_0 was determined from the response at resonance G_0; for a sinusoidal excitation $p = p_{\max} \sin 2\pi f_{\text{res}} t$, the peak measured voltage $u_{\max} = G_0 p_{\max}$. Equations (7) and (10) predict that the peak measured voltage is also given by $u_{\max} \approx p_{\max} h_0 \tau^*/2$ and therefore $h_0 = 2G_0/\tau^*$. The sensitivity at resonance G_0 was determined by exciting the PZT needle with a 20-Vpp, 40-cycle tone burst at f_{res}. The 40-cycle pulse was long enough that the transducer attained steady state while avoiding reverberation problems in the tank. First, the field of the needle was measured with the Marconi hydrophone to confirm that it behaved as a spherical wave along the axis and to determine the acoustic pressure at the face of the transducer p_{face}. Then the PZT needle was placed at the focus of one of the PCD transducers and the peak voltage V_R from the transducer was recorded. If the PZT needle were an ideal spherical source the sensitivity of the bowl at resonance would be $G_0 = V_R / p_{\text{face}}$. However, a correction was necessary because the needle source was not perfectly omnidirectional. The PZT needle can be considered a piston source with a directivity function given by $D(\theta) = 2J_1(2\pi a \sin\theta/\lambda)/2\pi a \sin\theta/\lambda$, where a is the source radius, and θ the observation angle from the axis. We measured the transverse amplitude distribution of the PZT needle and it compared well with the Bessel directivity function. As the transducer response is a result of averaging of pressure over its surface, it is necessary to correct for the change in amplitude across the face of the transducer. This procedure gives a 3% correction to the sensitivity of the 100-mm focal length bowl and a 1% correction for the 200-mm focal length bowl, i.e., the effect of the directivity pattern of the PZT needle was very small. The resonant sensitivity for the 100-mm bowl was $G_0 = 111$ V/MPa. For the case of the pair of 200-mm bowls the resonant frequency sensitivities were $G_0 = 118$ and $G_0 = 164$ V/MPa.

Once the response of the transducers had been characterized it was possible to determine the calibration. The short duration of the excitation indicates that the response is given by Eq. (8); it follows from the form of the impulse response that the peak voltage from the transducer will be $u_{\max} = h_0 S(r)$. We noted above that for nonlinear distortion of the exponential pulse the pulse integral $S(r) = p_0 \tau_0 r_0 / r$, where p_0 is the peak pressure and τ_0 the shock wave duration at a distance r_0 from the bubble. It is now possible to determine the peak pressure of the radiated acoustic emission at a distance r_0 from the center of the collapsing bubble,

$$p_0 = u_{\max} \cdot \frac{r\tau^*}{2G_0 r_0 \tau_0}. \tag{11}$$

Here r is distance from the center of the bubble to the surface

of the PCD transducer, that is, the focal distance of the transducer.

For the case of the 100-mm bowl the appropriate values are $r=100\,\text{mm}$, $\tau^*=7.4\ \mu\text{s}$, and $G_0=111\,\text{V/MPa}$. The only value we did not measure was τ_0, which we took to be 35 ns from the measurements of Vogel and Lauterborn (1988). The calibration value relating the maximum voltage at the focusing hydrophone to the peak pressure of the shock waves at the distance 10 mm from the bubble center is

$$\frac{p_0(10\text{mm})}{u_{\max}} \approx 9.5 \frac{\text{MPa}}{\text{V}}. \tag{12}$$

This is the sensitivity for the focusing hydrophone of 100-mm aperture and 100-mm focal length. The sensitivity of the two 200-mm focal length transducers were determined to be 26 and 17 MPa/V. The larger calibration values for the 200-mm transducers are consistent with their reduced solid angle. These calibration values relate the peak in the measured PCD signals to the peak radiated acoustic pressure 10 mm from the bubble. The shape of the measured PCD signals is related to the impulse response of the PCD transducer and is not an accurate representation of the pressure waveform emitted by the bubbles. Recall, that the demodulation process reduced the signal amplitude by a factor of 2.5 and so the calibration values have to be multiplied by 2.5 when applied to demodulated signals.

F. High-speed camera

High-speed camera images of the focal region were taken with a Kodak EktaPro 4540 (San Diego, CA). The APL-UW lithotripter has a water tank made of optically clear acrylic. The focal region was backlit with either a 400- or a 1000-W light bulb which meant that bubbles appeared as dark regions (shadows) on the image. The camera had a maximum frame rate of 40 500 frames per second and stored up to 5120 full frames in memory. The size of each frame at the maximum framing rate was 64×64 pixels. In these experiments, the focal depth was 3 cm and the image area was 9 by 9 mm. The camera was triggered with the photodiode and operated simultaneously with the dual PCD system, see Fig. 5. The digital images obtained by the camera were stored on videotape and analyzed with NIHImage (National Institutes of Health, Bethesda, MD).

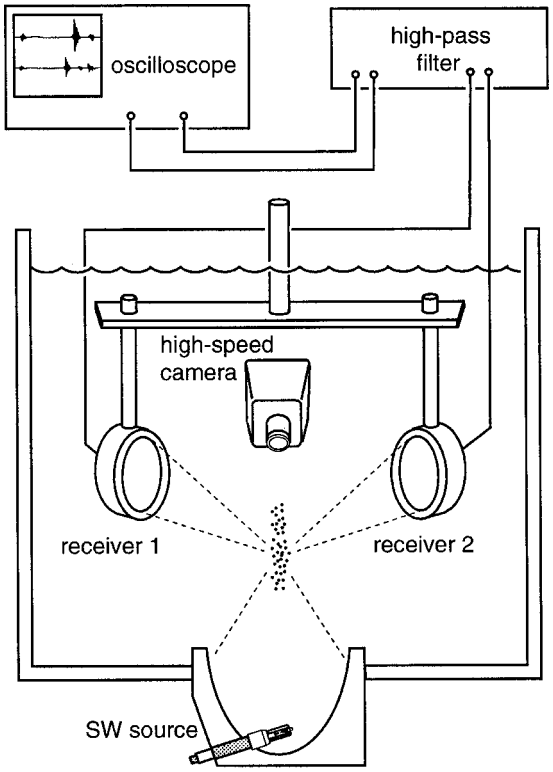

FIG. 5. Setup for high-speed photography and dual PCD.

II. RESULTS

A. Cavitation field of an electrohydraulic lithotripter

We first report on *in vitro* measurements of the cavitation field performed in both the APL-UW lithotripter and the clinical Dornier HM3 lithotripter. Figure 6 shows the characteristic time t_C and collapse pressure p_C of the cavitation at $F2$ for charging voltages between 12 and 24 kV. Twenty shock waves were fired at each voltage and each detected focal event is marked with a ''+.'' The solid line connects the mean values from the focal events. The results from the two lithotripters were similar with an almost monotonic increase in both the radiated pressure at collapse p_C and the characteristic time t_C with applied voltage. The results are in agreement with measurement by others (Coleman *et al.*, 1992; Zhong *et al.*, 1997). We note that the scatter in the measurement of the characteristic time was 20%, whereas the scatter in the peak pressure value was 100%. One reason for the large variation in p_C is that measurements of p_C are highly sensitive to the location of the bubble in the focal region of the dual PCD system, whereas t_C is not. In comparing the two lithotripters we observed that the characteristic times were comparable; however, p_C in the APL-UW lithotripter was about twice that measured in the HM3. One

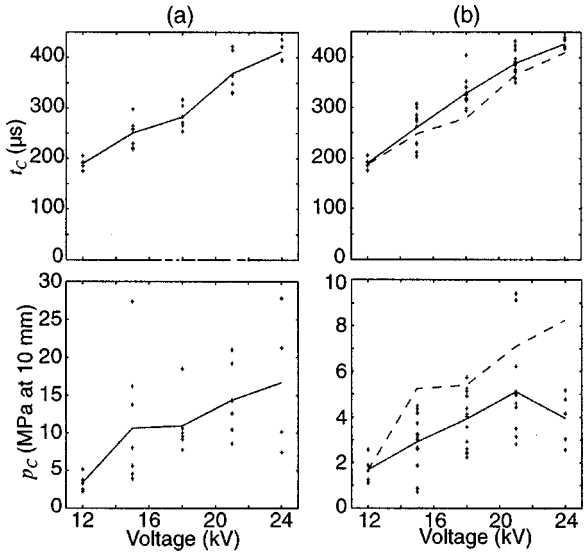

FIG. 6. Measured characteristic time t_C and the radiated collapse pressure p_C as a function of voltage for (a) the APL-UW lithotripter and (b) HM3 lithotripter. The crosses (+) represent individual measurements and the solid line is the mean value. The dashed lines in (b) are mean values for APL-UW lithotripter.

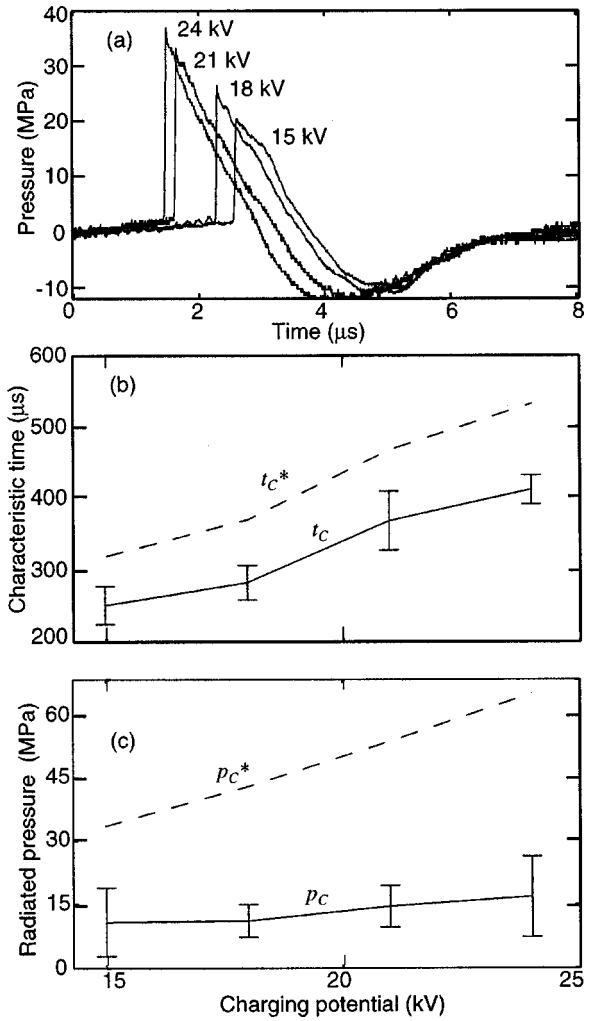

FIG. 7. Comparison between measured and calculated cavitation dynamics (a) measured waveforms used as inputs to the Gilmore–Akulichev model, (b) calculated characteristic time t_C^* (dashed line) and measured t_C (solid line), (c) calculated radiated pressure p_C^* (dashed line) and measured radiated pressure p_C (solid line).

notable difference between the two lithotripters was that the water in the APL-UW lithotripter was at 20 °C and that in the HM3 was at 37 °C. We speculate that the warmer water in the HM3 may have increased diffusion of gas into the bubble and led to a softening of the collapse and reduced radiated pressure.

Figure 7(a) shows pressure waveforms measured at 15, 18, 21, and 24 kV in the APL-UW lithotripter. Plots of the calculated characteristic time t_C^* and calculated collapse pressure p_C^* based on these waveforms are compared to measured values. There is reasonable agreement between the measured and calculated characteristic times. Recall that the negative tail of the pressure waveform was elongated to correct a measurement problem with the hydrophone. The elongation factor was based on the measurements by Wurster *et al.* (1994) and was not used as a free variable to ensure a fit between t_C and t_C^*. Reducing the elongation factor would have brought the calculated values closer to the measured values. Without the correction the calculated characteristic time t_C^* was about one-half of the measured characteristic time t_C. The 20% variation in the measured t_C was reproduced in the calculations by varying the amplitude of the acoustic waveform by 10% (which is the typical variation in the measurements of the peak negative pressure of the shock waves). The comparison between p_C and p_C^* shows that measured and calculated values have the same trends but the calculated values were about four times larger than the measurements. The qualitative correlation between characteristic time, collapse pressure, and discharge voltage has been observed before in both calculations (Church, 1989) and measurements (Coleman *et al.*, 1992). Although correcting the negative phase of the pressure waveforms made it possible to obtain quantitative agreement for the characteristic time; it was not possible to obtain quantitative agreement with the collapse pressure. We have already commented that our model for the radiated pressure neglects nonlinear distortion and that we expect the calculated values to overestimate the pressure. In addition, the model assumes a spherical collapse; in the case of an aspherical collapse one would also anticipate the model to overestimate the radiated pressure. Other losses, such as thermal damping, are also neglected (Church, 1989).

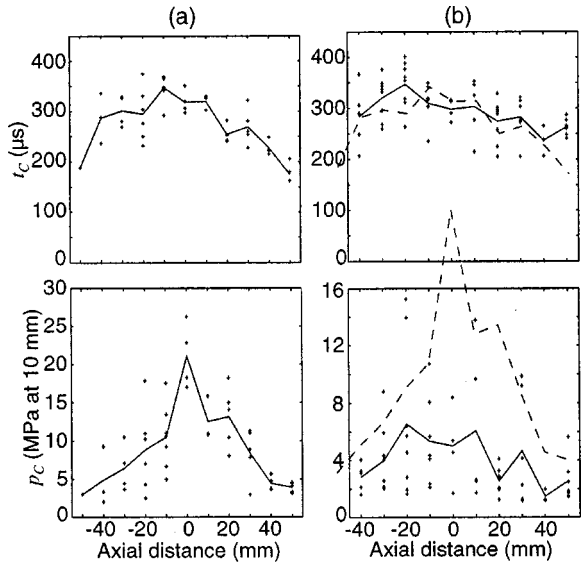

FIG. 8. Axial cavitation field (a) APL-UW lithotripter, (b) HM3 lithotripter (dashed lines are mean values for APL-UW lithotripter). The geometrical focus ($F2$) is at zero and negative distances are toward the source; the spark was fired at 18 kV.

Figure 8 shows the variation of the characteristic time and radiated pressure along the axis of each lithotripter for a fixed charging voltage of 18 kV. The two lithotripters have similar characteristic times but again the radiated pressure in the HM3 is approximately one-half of the APL-UW machine. Data were compared using Student's *t*-test. For the HM3, the maximum t_C occurred at $z=-20$ mm ($p<0.1$); there was no statistically significant peak in p_C. In the APL-UW lithotripter the peak in the characteristic time could not be distinguished between $z=-10$ and $z=0$ mm ($p<0.1$). There was a peak in p_C at $z=0$ mm ($p<0.001$). These results are in agreement with single PCD measurements that showed that the characteristic time peaked about 10 to 20 mm in front of $F2$ (Coleman *et al.*, 1992). It is also consistent with the location of the peak negative pressure in

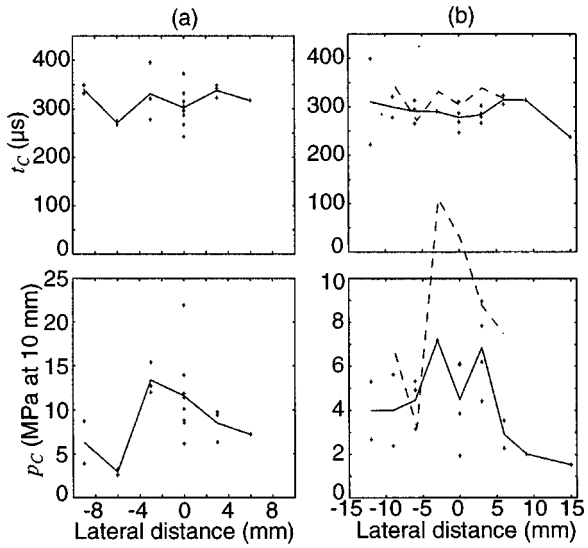

FIG. 9. Lateral scan (at $F2$ and 18 kV) of the cavitation field (a) APL-UW lithotripter, (b) HM3 lithotripter (dashed lines are mean values for APL-UW lithotripter).

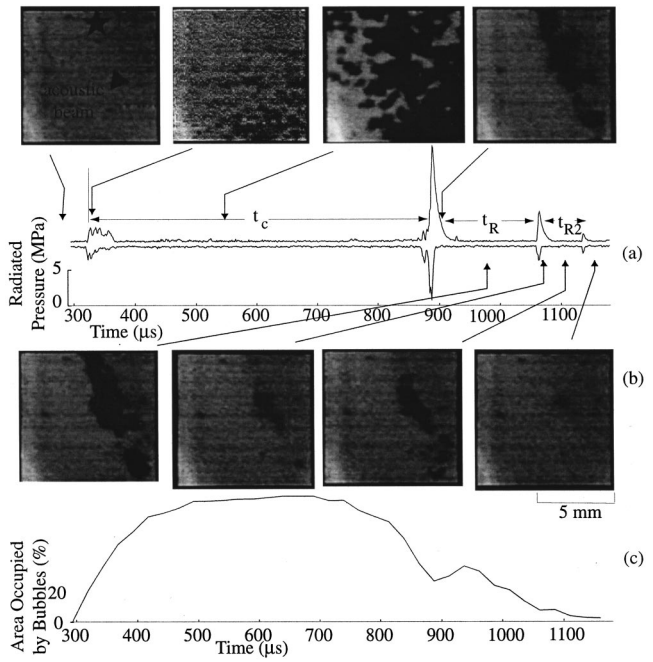

FIG. 10. Bubble rebound as captured by (a) dual PCD, (b) sequence of high-speed camera images and, (c) area occupied by the bubble cloud. The dual PCD traces show spikes representing inertial collapses at 880, 1060, and 1140 μs. These times correspond to a minimum in the size of the bubble cloud.

an electrohydraulic lithotripter as determined by both measurements (Coleman *et al.*, 1989; Cleveland *et al.*, 2000) and numerical simulations (Coleman *et al.*, 1991; Christopher, 1994; Averklou and Cleveland, 1999). The 6-dB length of p_C is approximately 50 mm and it corresponds to (1) the region where the negative pressure in the lithotripter is in excess of -5 MPa (Cleveland *et al.*, 2000), (2) the length of the lithotripsy-induced bubble cloud as determined by high-speed video images (Huber *et al.*, 1994), and (3) the axial size of pitting created in aluminum foil (Bailey *et al.*, 1999).

Figure 9 shows measurements for a transverse scan (at the geometrical focus) of t_C and p_C for a discharge voltage of 18 kV for both lithotripters. Two notable features of the data are (1) that the characteristic time t_C is almost uniform across the beam of the lithotripter and (2) that very few cavitation events were detected more than 5 mm off-axis—despite the fact that the peak negative pressure in the lithotripter exceeds -5 MPa in excess of 10 mm off-axis. Recall that the spatial resolution of the dual PCD is 5 mm and the region of collapse may be even narrower than indicated by Fig. 9. Indeed, high-speed photography presented below shows that the collapse of bubbles occurs almost as a line along the acoustic axis. It appears that during their collapse bubbles are drawn toward the acoustic axis of the lithotripter.

B. High-speed photography and bubble rebound

The apparent rebound signal, seen in Figs. 3 and 4, was investigated using dual PCD and high-speed photography simultaneously. Figure 10 shows (a) dual PCD traces and (b) high-speed video images of the cavitation from a single shot at 18 kV in the APL-UW lithotripter. At 310 μs the shock wave impinged upon bubbles at $F2$ and the first acoustic burst was emitted. The bubbles then grew to form a broad cloud and then collapsed in a line at 900 μs ($t_C = 600\,\mu$s), emitting a second burst measured by the dual PCD. The cloud then rebounded and generated a rebound signal at 1060 μs recorded by the dual PCD. A second rebound was detected at 1140 μs. The correlation between the dual PCD system and the high-speed video images is excellent. It can be seen from the images that although bubbles are generated over a region approximately 8 mm in diameter, the bubbles appear to collapse collectively, as a cylindrical cluster, to a line along the acoustic axis rather than spherically to their center of radius. This is in accordance with other high-speed video images (Zhong *et al.*, 1999) and explains why very few cavitation events were recorded by the dual PCD off-axis (see Fig. 9).

In Fig. 10(c) the size of the bubble cloud is plotted as a function of time. The size of the bubble cloud at each instant was based on the light intensity of each camera frame. The average light intensity $I(t)$ was calculated by averaging over all the pixels [0 (white) to 255 (black)]. A background intensity I_b was obtained from a frame recorded halfway between spark discharge and the arrival of the acoustic wave in the focal area. The corrected intensity $I_c(t) = I(t) - I_b$ was calculated in order to compensate for naturally occurring shadows that varied between tests but were unrelated to the cavitation bubbles. The plot of intensity (bubble cloud size) with time confirms that the bubbles undergo a main growth and collapse followed by rebounds. There is excellent agreement between the minima in the bubble cloud size and the presence of acoustic emissions from the dual PCD.

In Fig. 11 the rebound time t_R and rebound collapse pressure p_R are shown as a function of discharge voltage. These values were obtained from the same data that was used to generate Fig. 6. Rebound events are marked by a ''○'' and the solid line is the average rebound time. The characteristic times t_C associated with the bubbles that had rebounds are marked by ''+'' and the dashed line is the aver-

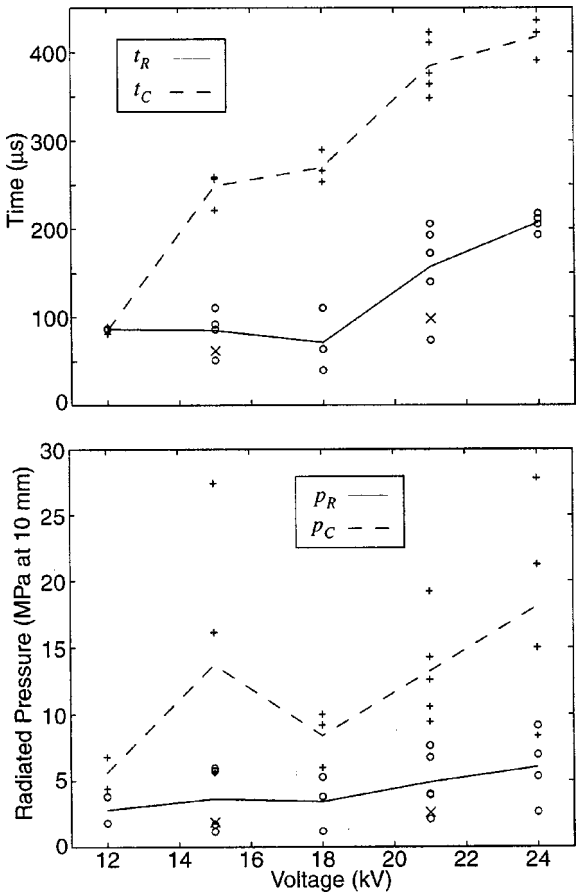

FIG. 11. Bubble duration and collapse pressure for the rebound signal and the main collapse as a function of voltage in the APL-UW lithotripter. Individual rebound events are marked with an ''○'' and the solid line is the mean. Corresponding main collapse events are denoted with a ''+'' and dashed line is the mean. Second rebounds were detected at 15 and 21 kV and are marked by an ''×.''

age value. Only two shots, one at 15 kV and one at 21 kV, produced cavitation that was determined to have two rebounds; these events are marked by ''×.''

In general, the measured rebound times were shorter then the characteristic time $t_R < t_C$ and radiated pressure at rebound was less $p_R < p_C$. Calculations [see, for example, Fig. 1(c)] are in agreement with these trends. The monotonic increase in t_R and p_R with discharge voltage was also in agreement with calculations and is consistent with the fact that at higher voltages the bubbles are driven harder. However, the agreement is qualitative; the measured time t_R was about five times longer than t_R^* and the measured radiated pressure p_R about ten times larger than p_R^*. We note that for the main collapse the measured p_C was smaller than p_C^*. The two second rebound events that were detected had a shorter rebound time and smaller collapse pressure than either the main burst or the rebound, also in qualitative agreement with the model.

Because the main collapse was that of a bubble cloud or cluster it is not surprising that the rebound no longer behaves in accordance with a theory that assumes a single spherical bubble for the entire dynamics. We can model the rebound with the Rayleigh model for a spherical void collapsing in a fluid (see, e.g., Church, 1989). We approximate the collapse time of the void as $t_R/2$. The corresponding maximum bubble radius using Rayleigh's expression is $R_{\max} = (t_R/2)\sqrt{P_0/\rho}/0.915$, where P_0 and ρ are the ambient pressure and density of the liquid. For water, $R_{\max} \approx 5.5 \cdot 10^{-3} t_R$, where $R_{\max}$ is measured in millimeters and t_R in microseconds. The rebound time in Fig. 11 was $t_R = 175\,\mu$s, from which we obtain a maximum bubble size $R_{\max} = 0.5$ mm. This corresponds well to the size of the bubble observed with high-speed photography. It appears that after the main collapse the cavitation field acts as an effective single bubble system; but because of agglomeration of bubbles during the main growth and collapse phase the single rebound bubble is larger than what would be predicted using single-bubble theory for the entire cavitation life cycle.

III. DISCUSSION

The dual passive cavitation detection (dual PCD) system has been developed for the localized detection of cavitation events in the field of a shock wave lithotripter. Two confocal receivers (PCD transducers) were used to detect acoustic emissions from cavitation bubbles. Signal processing techniques were used to resolve coincident signals that originated from a volume approximately 5 mm in diameter. The spatial localization is a significant improvement over a single transducer PCD which is sensitive to signals from a relatively long volume. It was necessary to use both the arrival time and the amplitude of received signals to localize an event to the volume of interest.

A calibration technique was described that was appropriate for estimating the peak pressure of spherically spreading shock waves emitted by collapsing cavitation bubbles. The calibration technique relied on the fact that the pulse duration of the acoustic wave from the cavitation event was much shorter than the resonant period of the PCD transducer. It was also necessary to estimate the pulse duration near the bubble, which was done from previously reported measurements of cavitation bubbles generated by a laser pulse. The calibration is not valid for bubbles collapsing asymmetrically; also for *in vivo* measurements the effects of tissue attenuation would need to be taken into account.

The dual PCD system was used to measure the cavitation fields of two electrohydraulic lithotripters: a Dornier HM3 and the APL-UW research machine. Measurements were compared to predictions of the Gilmore–Akulichev model for a single spherical bubble (Church, 1989). We corroborated previous observations that the cavitation signature can be characterized by two acoustic emissions, ''bursts''; the first associated with the arrival of the lithotripter shock wave and the second, hundreds of microseconds later, resulting from an inertial growth and collapse cycle. The cavitation was quantified in terms of the characteristic time t_C and the radiated pressure at collapse p_C. The two machines were observed to have similar cavitation fields. The measured characteristic times were in agreement with results from single-bubble theory after a correction to the tensile portion of the pressure waveform was applied (Bailey *et al.*, 1999). The peak pressure radiated at the primary collapse of the bubble p_C was measured to be on order of 10 MPa at 10 mm

from the bubble center. The collapse pressure of the APL-UW machine was between 30% to 100% higher than that of the HM3, an effect which may be attributable to the higher water temperature in the HM3. Shot-to-shot variation in p_C was much larger than the variation in t_C and may be because p_C was more sensitive to either variations in the water conditions or shock wave variability associated with the electrohydraulic spark source. The calculated p_C^* values were three to four times larger than the measurements. We suspect that this is because the model is idealized and that effects such as thermal damping of the bubble, asymmetry in bubble shape, and finite-amplitude distortion of the radiated pressure wave have been neglected in the model. The measured values of p_C and t_C increased monotonically with increasing discharge voltage as observed by others (Coleman *et al.*, 1992) and in accordance with calculations.

The dual PCD was used to obtain a spatial map of the cavitation field in both lithotripters. An axial scan of the cavitation field showed that inertial cavitation was detected in the range where the peak negative pressure exceeded -5 MPa. The longest characteristic time and largest radiated pressure occurred approximately 10 to 20 mm in front of the focus which correlated with the location of the maximum peak negative pressure in the lithotripter. These results are consistent with reports that the inertial behavior of lithotripsy-induced cavitation is controlled primarily by the negative pressure of the lithotripsy pulse (Church, 1989; Ding and Gracewski, 1994).

In contrast, a transverse scan at the focus indicated that although t_C was nearly uniform out to 20 mm, p_C dramatically dropped for distances more than 5 mm off-axis. In addition, very few events occurred more than 5 mm off-axis; which was also the size of the sensitive region of the dual PCD. The peak negative pressure in the lithotripters exceeds -5 MPa to a distance of at least 12 mm and so one would expect that cavitation field to be at least 25 mm in diameter. High-speed photography indicated that the lithotripter pulse created a cloud of bubbles that collapsed collectively along the axis rather than individually to their own center. Therefore the response of cavitation bubbles off-axis was not simply related to the negative pressure of the shock wave. It appeared that cloud dynamics strongly affected the off-axis bubble dynamics and high-speed video images indicated that the bubbles were attracted to the axis.

The dual PCD system also provided the ability to detect bubble rebounds that occurred after the main collapse. A single PCD would not provide enough specificity to distinguish between a rebound and a second bubble collapsing with a long t_C. High-speed photography confirmed that the coincident events detected by the dual PCD after the primary collapse did indeed coincide with rebounds of the bubble cloud. Comparison with calculations provided only qualitative agreement. However, the rebound times and maximum bubble radius of the rebound observed on the high-speed photography were in agreement with Rayleigh collapse theory.

In conclusion, we have demonstrated an effective new technique for localized passive cavitation detection in the case of shock wave lithotripsy. An algorithm was developed to ensure that detected events originated from a volume about 5 mm in diameter. A novel calibration technique allowed the peak pressure radiated by the bubble to be estimated. It was seen that the measured characteristic time of the bubbles t_C was close to that predicted by single-bubble theory, whereas the pressure radiated at collapse p_C and subsequent bubble dynamics were not. It appeared that once the bubbles started to collapse, cloud dynamics affected the system and single-bubble theory was no longer appropriate. It is planned to use the dual PCD system *in vivo*. Preliminary results indicate that the coincidence algorithm can be used to localize cavitation *in vivo*, as the variations in speed of sound through tissue are small enough that arrival times across different paths should vary by less than 1.5 μs (a localization error of less than 1 mm). What has not yet been accounted for is the effect of tissue absorption on the calibration technique.

ACKNOWLEDGMENTS

The authors would like to thank Dr. Vera Khokhlova and Dr. Michalakis Averkiou for assistance with coding the solution to the Gilmore equation and Dr. James McAteer for valuable discussions. This work was supported by a grant from NIH, No. P01 DK43881 including a supplementary Fogarty International Research Collaboration Award (FIRCA), Grant No. NIH R03 TW00492, and by a Civilian Research and Development Fund (CRDF) Young Investigator Award No. RB2-131.

[1]Although the area under the waveform curve must be zero for a spherical wave (Landau and Lifshitz, 1987) it is likely that the pressure waveform measured by Vogel and Lauterborn had a long weak negative tail which can be neglected as has been done in Eq. (7). For the purpose of the calibration it is only the energy contained in a time scale much less than 1 μs that is important and so Eq. (7) is appropriate.

[2]For the case of a waveform with a negative tail the integral could be modified to the area of the leading positive portion only. Weak shock theory predicts that the area of the positive section alone will also remain constant.

Akulichev, V. A. (**1971**). in *High-Intensity Ultrasonic Fields*, edited by L. D. Rozenberg (Plenum, New York), pp. 239–259.

Averkiou, M. A., and Cleveland, R. O. (**1999**). ''Modeling of an electrohydraulic lithotripter with the *KZK* equation,'' J. Acoust. Soc. Am. **106**, 102–112.

Bailey, M. R., Blackstock, D. T., Cleveland, R. O., and Crum, L. A. (**1999**). ''Comparison of electrohydraulic lithotripters with rigid and pressure-release ellipsoidal reflectors: II. Cavitation fields,'' J. Acoust. Soc. Am. **106**, 1149–1160.

Blackstock, D. T., Hamilton, M. F., and Pierce, A. D. (**1998**). ''Progressive waves in lossless and lossy fluids,'' in *Nonlinear Acoustics*, edited by M. F. Hamilton and D. T. Blackstock (Academic, New York).

Cathignol, D., Sapozhnikov, O. A., and Zhang, J. (**1997**). ''Lamb waves in piezoelectric focused radiator as a reason for discrepancy between O'Neil's formula and experiment,'' J. Acoust. Soc. Am. **101**, 1286–1297.

Chaussy, C., Brendel, W., and Schmiedt, E. (**1980**). ''Extracorporeally induced destruction of kidney stones by shock waves,'' Lancet **2**, 1265–1268.

Chaussy, C., ed. (**1982**). *Extracorporeal Shock Wave Lithotripsy: New Aspects in the Treatment of Kidney Stone Disease* (Karger, Basel).

Choi, M. J., Coleman, A. J., and Saunders, J. E. (**1993**). ''The influence of fluid properties and pulse amplitude on bubble dynamics in the field of a shock wave lithotripter,'' Phys. Med. Biol. **38**, 1561–1573.

Christopher, P. T. (**1994**). ''Modeling the Dornier HM3 lithotripter,'' J. Acoust. Soc. Am. **96**, 3088–3095.

Church, C. C. (**1989**). ''A theoretical study of cavitation generated by an extracorporeal shock wave lithotripter,'' J. Acoust. Soc. Am. **86**, 215–227.
Cleveland, R. O., Bailey, M. R., Hartenbaum, B., Fineberg, N., Lokhandwalla, M., McAteer J. A., and Sturtevant, B. (**2000**). ''Design and characterisation of a research electrohydraulic lithotripter patterned after the Dornier HM3,'' Rev. Sci. Instrum. (accepted).
Coleman, A. J., Saunders, J. E., Crum, L. A., and Dyson, M. (**1987**). ''Acoustic cavitation generated by an extracorporeal shockwave lithotripter,'' Ultrasound Med. Biol. **13**, 69–76.
Coleman, A. J., and Saunders, J. E. (**1989**). ''A survey of the acoustic output of commercial extracorporeal shock wave lithotripters,'' Ultrasound Med. Biol. **15**, 213–227.
Coleman, A. J., Choi, M. J., and Saunders, J. E. (**1991**). ''Theoretical predictions of the acoustic pressure generated by a shock wave lithotripter,'' Ultrasound Med. Biol. **17**, 245–255.
Coleman, A. J., Choi, M. J., Saunders, J. E., and Leighton, T. G. (**1992**). ''Acoustic emission and sonoluminescence due to cavitation at the beam focus of an electrohydraulic shock wave lithotripter,'' Ultrasound Med. Biol. **18**, 267–281.
Coleman, A. J., Choi, M. J., and Saunders, J. E. (**1996**). ''Detection of acoustic emission from cavitation in tissue during clinical extracorporeal lithotripsy,'' Ultrasound Med. Biol. **22**, 1079–1087.
Crum, L. A. (**1988**). ''Cavitation microjets as a contributory mechanism for renal calculi disintegration in ESWL,'' J. Urol. (Baltimore) **40**, 1587–1590.
Dalecki, D., Raeman, C. H., Child, S. Z., and Carstensen, E. L. (**1996**). ''A test for cavitation as a mechanism for intestinal hemorrhage in mice exposed to a piezoelectric lithotripter,'' Ultrasound Med. Biol. **22**, 493–496.
Delacretaz, G., Rink, K., Pittomvils, G., Lafaut, J. P., Vandeursen, H., and Boving, R. (**1995**). ''Importance of the implosion of ESWL-induced cavitation bubbles,'' Ultrasound Med. Biol. **21**, 97–103.
Delius, M., Denk, R., Berding, C., Liebich, H., Jordan, M., and Brendel, W. (**1990**). ''Biological effect of shock waves: Cavitation by shock waves in piglet liver,'' Ultrasound Med. Biol. **16**, 467–472.
Ding, Z., and Gracewski, S. M. (**1994**). ''Response of constrained and unconstrained bubbles to lithotripter shock wave pulses,'' J. Acoust. Soc. Am. **96**, 3636–3644.
Eller, A., and Flynn, H. G., (**1965**). ''Rectified diffusion during nonlinear pulsations of cavitation bubbles,'' J. Acoust. Soc. Am. **37**, 493–501.
Evan, A. P., and McAteer, J. A. (**1996**). ''*Q*-Effects of shock wave lithotripsy, in *Kidney Stones: Medical and Surgical Management*, edited F. Coe, C. Pak, and G. M. Preminger (Raven, New York), pp. 549–570.
Gilmore, F. R. (**1952**). *The Growth or Collapse of a Spherical Bubble in a Viscous Compressible Liquid* (California Institute of Technology, Pasadena, CA), Rep. No. 26-4, pp. 1–40.
Holmes, S. A. V., and Whitfield, H. N. (**1991**). ''The current status of lithotripsy,'' Br. J. Urol. **68**, 337–344.
Howard, D. D., and Sturtevant, B. (**1997**). ''*In vitro* study of the mechanical effects of shockwave lithotripsy,'' Ultrasound Med. Biol. **23**, 1107–1122.
Huber, P., Debus, J., Peschke, P., Hahn, E. W., and Lorenz, W. J. (**1994**). ''*In vivo* detection of ultrasonically induced cavitation by a fibre-optic technique,'' Ultrasound Med. Biol. **20**, 811–825.
Huber, P., Debus, J., Jöchle, K., Simiantonakis, I., Jenne, J., Rastert, R., Spoo, J., Lorenz, W. J., and Wannenmacher, M. (**1999**). ''Control of cavitation activity by different shockwave pulsing regimes,'' Phys. Med. Biol. **44**, 1427–1437.
Jochle, K., Debus, J., Lorenz, W. J., and Huber, P. (**1996**). ''A new method of quantitative cavitation assessment in the field of a lithotripter,'' Ultrasound Med. Biol. **22**, 329–338.
Kaude, J. V., Williams, C. M., Millner, M. R., Scott, K. N., and Finlayson, B. (**1985**). ''Renal morphology and function immediately after extracorporeal shock-wave lithotripsy,'' Am. J. Roentgenol. **145**, 305–313.
Landau, I. D., and Lifshitz, E. M. (**1987**). *Fluid Mechanics*, 2nd ed. (Pergamon, New York).
Lifshitz, D. A., Williams, Jr., J. C., Sturtevant, B., Conners, B. A., Evan, A. P., and McAteer, J. A. (**1997**). ''Quantization of shock wave cavitation damage *in vitro*,'' Ultrasound Med. Biol. **23**, 461–471.
Lingeman, J. E. (**1996**). ''Extracorporeal shock wave lithotripsy devices: Are we making progress,'' in *New Developments in the Management of Urolithiasis*, edited by J. E. Lingeman and G. M. Preminger (Igaku-Shoin, New York).
O'Neil, H. T. (**1949**). ''Theory of focusing radiators,'' J. Acoust. Soc. Am. **21**, 516–526.
Press, W. H., Teukolsky, S. A., Vetterling, W. T., and Flannery, B. P. (**1992**). *Numerical Recipes in Fortran*, 2nd ed. (Cambridge University Press, Cambridge).
Pye, S. D., and Dineley, J. A. (**1999**). ''Characterization of cavitational activity in lithotripsy fields using a robust electromagnetic probe,'' Ultrasound Med. Biol. **3**, 451–471.
Rudenko, O. V., and Soluyan, S. I. (**1977**). *Theoretical Foundations of Nonlinear Acoustics* (Plenum, New York).
Sass, W., Braunlich, M., Dreyer, H.-P., Matura, E., Folberth, W., Priesmeyer, H.-G., and Seifert, J. (**1991**). ''The mechanisms of stone disintegration by shock waves,'' Ultrasound Med. Biol. **17**, 239–243.
Vogel, A., and Lauterborn, W. (**1988**). ''Acoustic transient generation by laser-produced cavitation bubbles near solid boundaries,'' J. Acoust. Soc. Am. **84**, 719–731.
Wurster, C., Staudenraus, J., and Eisenmenger, W. (**1994**). ''The fibre optic probe hydrophone,'' Nature (London) **2**, 941–944.
Zhong, P., Cioanta, I., Cocks, F. H., and Preminger, G. M. (**1997**). ''Inertial cavitation and associated acoustic emission produced during electrohydraulic shock wave lithotripsy.'' J. Acoust. Soc. Am. **101**, 2940–2950.
Zhong, P., Cioanta, I., Zhu, S., Cocks, F. H., and Preminger, G. M. (**1998**). ''Effects of tissue constraint on shock-wave induced bubble expansion *in vivo*,'' J. Acoust. Soc. Am. **104**, 3126–3129.
Zhong, P., Lin, H., Xi, X., Zhu, S., and Bhogte, E. S. (**1999**). ''Shock wave-inertial microbubble interaction: Methodology, physical characterization and bioeffect study,'' J. Acoust. Soc. Am. **105**, 1997–2009.

LETTERS TO THE EDITOR

This Letters section is for publishing (a) brief acoustical research or applied acoustical reports, (b) comments on articles or letters previously published in this Journal, and (c) a reply by the article author to criticism by the Letter author in (b). Extensive reports should be submitted as articles, not in a letter series. Letters are peer-reviewed on the same basis as articles, but usually require less review time before acceptance. Letters cannot exceed four printed pages (approximately 3000–4000 words) including figures, tables, references, and a required abstract of about 100 words.

Ultrasonic diffraction by a square periodic array of spheres

Benjamin K. Henderson, Vikram K. Kinra,[a] and Albert W. Gonzales
Center for Mechanics of Composites and Department of Aerospace Engineering, Texas A&M University, College Station, Texas 77843-3141

(Received 8 June 1999; accepted for publication 10 December 1999)

Shear waves propagated as a result of the diffraction of a broadband normally incident plane ultrasonic longitudinal pulse by a square periodic array of spherical elastic inclusions are measured at specific angles from the normal. As expected, peaks in the spectra were observed at frequencies given by the condition of constructive interference. © *2000 Acoustical Society of America.* [S0001-4966(00)05503-X]

PACS numbers: 43.20.Gp, 43.35.Cg [DEC]

INTRODUCTION

Diffraction of light by a periodic grating is a well-known phenomenon in optics.[1] When a grating is illuminated by a monochromatic light source, coherent light propagates in the far field only at specific angles from the normal. In this Letter a parallel phenomena in the diffraction of elastic waves is explored. Unlike light, mode conversion exists in solid media, such that a longitudinal (or shear) ultrasonic wave is diffracted as both longitudinal and shear waves. Measured transmission and reflection spectra of a periodic layer of spheres exhibit extrema at cutoff frequencies corresponding to the onset of shear wave diffraction orders.[2,3] In the interest of examining such diffraction phenomena, the measurement of shear waves diffracted by a square periodic array of solid spherical inclusions (scatterers) in a solid matrix in response to a plane longitudinal ultrasonic pulse normal to the array is reported.

I. EXPERIMENTAL METHODS

A cylindrical polyester (viscoelastic) specimen (50-mm diam., 70-mm long) was manufactured containing a layer of glass (elastic) spheres (1.12-mm diam.) at its midplane. The spheres are arranged in a square lattice with an interparticle spacing of 2.63-mm. A schematic of the specimen is shown in Fig. 1. Three inclined planar cuts were machined in the specimen, their normal vectors lying within the plane formed by the cylinder axis and one of the principal directions of the square lattice. For the measurement of transmitted waves, two planes were machined on one side of the specimen, their normals inclined from the axis by nominal (actual measured) angles of 30° (30.0°) and 60° (58.5°). For reflection measurements, one plane was machined on the opposite side, its normal inclined from the axis by a nominal angle of 60° (62.5°).

A schematic of the experimental apparatus used to perform the experiment is shown in Fig. 2. An ultrasonic longitudinal wave transducer (2.25 MHz center frequency, 25.4-mm diam.) is coupled to the excitation surface with a thin layer of high acoustic impedance couplant and connected to a pulser/receiver as a transmitter. A shear wave transducer (2.25 MHz center frequency, 12.7-mm diam.) is affixed to one of the inclined planes with a thin layer of shear couplant to serve as the receiver; the polarization vector of the transducer lies in the plane formed by a principal direction of the lattice and the cylindrical axis. The transmitter is used to send a short-duration broadband pulse and the response of the shear transducer is recorded. A Fourier transform of the received signal yields the spectrum of the shear waves diffracted by the layer at this angle.

II. RESULTS AND DISCUSSION

Consider one line of particles in the principal direction of the square array, as depicted in Fig. 3. As a consequence of the translational symmetry of the lattice and the fact that the excitation is a normally incident longitudinal wave, the

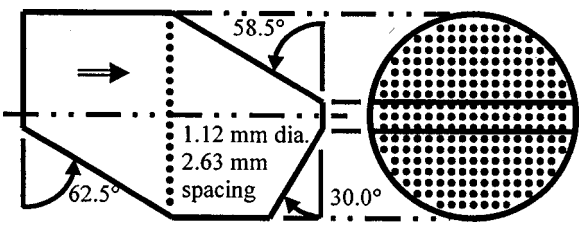

FIG. 1. Drawing of the cylindrical specimen.

[a]Author for correspondence.

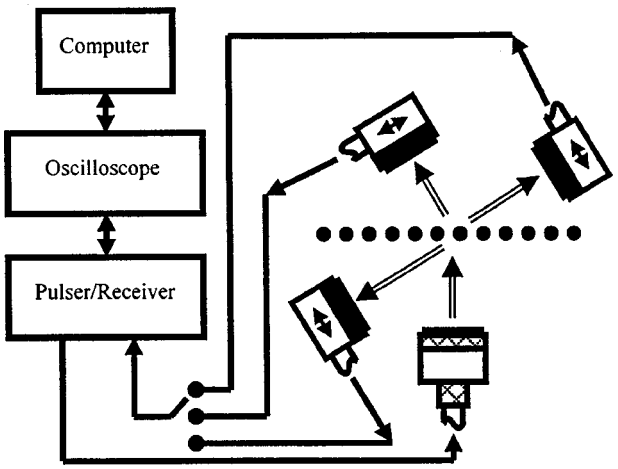

FIG. 2. Schematic of the experimental setup.

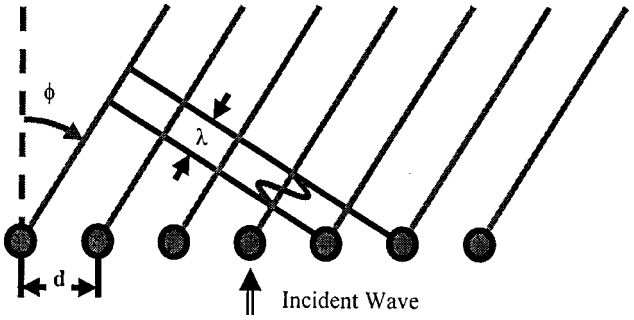

FIG. 3. Kinematic conditions for constructive interference: $d\sin(\phi)=n\lambda$.

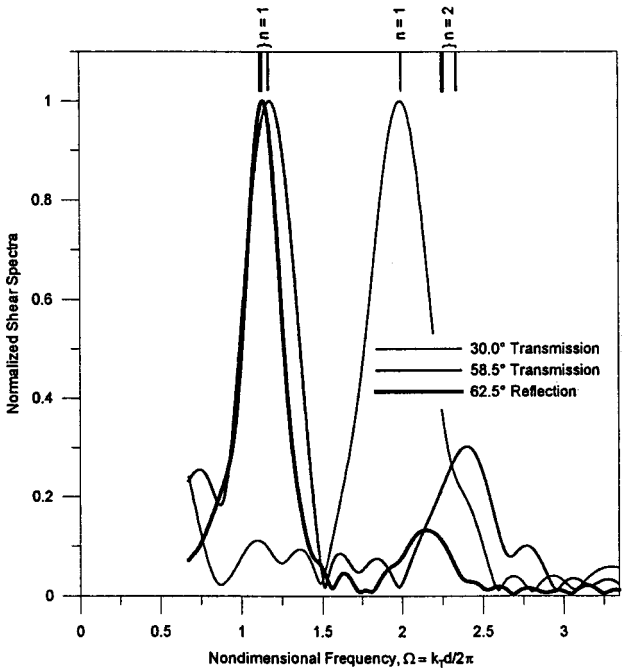

FIG. 4. Shear wave spectra at three angles: 30° transmission, 58.5° transmission, and 62.5° reflection.

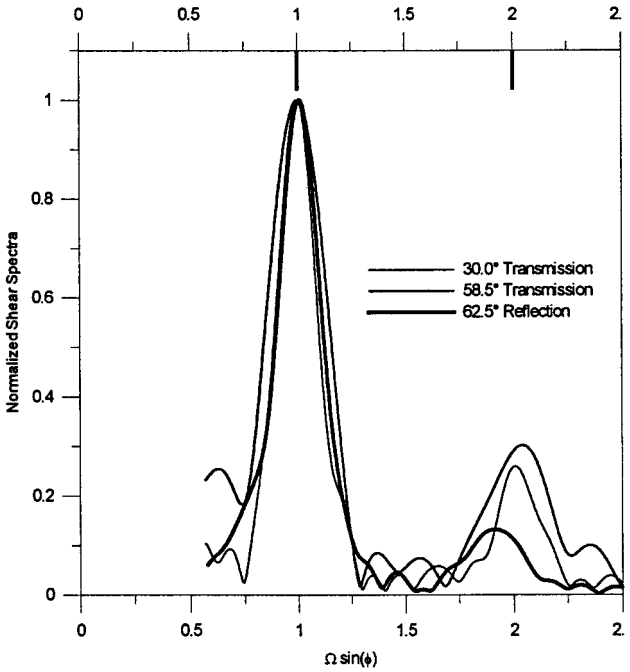

FIG. 5. Shear wave spectra adjusted by angle.

fields scattered by all particles are identical. Following the well-established argument in optics, the kinematic condition for constructive interference is[4]

$$d\sin(\phi)=n\lambda \quad \text{or} \quad \Omega\sin(\phi)=n, \quad n=0,+1,+2,\ldots, \qquad (1)$$

where d is the interparticle distance, ϕ is the angle of inclination from the normal, λ is the wavelength of the shear wave in the matrix, and Ω is a normalized frequency, $\Omega \equiv k_T d/2\pi$, where k_T is the shear wave number in the matrix (see Fig. 3). This constructive interference argument goes through for every line of particles in the two-dimensional array, and therefore for the array as a whole.

Figure 4 is a plot of the scattered shear wave spectra for all three angles. Vertical lines at the top of the graph denote frequencies that satisfy Eq. (1). Note that each spectrum has been normalized by its own maximum value to facilitate comparison. As expected, all three spectra exhibit sharp peaks near their predicted frequencies, indicating that higher-order diffraction does exist for the array of scatterers under consideration. Also note from the figure that the secondary ($n=2$) peaks of the 58.5° and 62.5° spectra are not as sharp as the primary ($n=1$) peaks.

As suggested by Eq. (1), if the received signals are plot ted against $\Omega\sin(\phi)$ instead of Ω, the frequency at which the first maximum occurs in all three curves should be at $\Omega\sin(\phi)=1$. Accordingly, Fig. 5 is a plot of the three shear spectra against $\Omega\sin(\phi)$. As is evident, the primary peaks of all curves are collocated at the expected value. This gives us some additional confidence in our measurements. To ensure reproducibility, a second specimen was manufactured, identical to the specimen of Fig. 1 in all respects except for the absence of the inclined plane for backscattered measurements. The spectra from the two forward scattered planes exhibit peaks at frequencies corresponding to $n=1$, further corroborating the results of Figs. 4 and 5. To avoid clutter, these results are not included in the figures.

III. CONCLUSIONS

The diffraction of a broadband normally incident ultrasonic longitudinal wave by a square periodic array of spherical elastic inclusions in a solid matrix at specific angles from the normal has been measured. The frequencies at which peaks are observed in the shear spectra satisfy the well-known condition of constructive interference.

[1] M. Born and E. Wolf, *Principles of Optics* (Pergamon, New York, 1959), pp. 400–413.

[2] K. Maslov, V. K. Kinra, and B. K. Henderson, ''Elastodynamic Response of Layers of Spherical Particles in Hexagonal and Square Periodic Arrangements,'' J. Mech. Phys. Solids **47**, 2147–2170 (1999).

[3] K. Maslov, V. K. Kinra, and B. K. Henderson, ''Lattice Resonances of a Planar Array of Spherical Inclusions: An Experimental Study,'' Mech. Mater. **31**, 175–186 (1999).

[4] D. Halliday and R. Resnick, *Physics*, 3rd ed. (Wiley, New York, 1986), p. 1048.

Comments on "Ultrasonic flow metering based on transit time differentials which are insensitive to flow profile" [J. Acoust. Soc. Am. 74, 955–959 (1983)]

M. Willatzen[a)]
IN-EV, Danfoss A/S, DK-6430, Nordborg, Denmark

(Received 24 June 1999; revised 9 November 1999; accepted 15 November 1999)

In a 1983 paper by H. Lechner, published in this journal, it was claimed that sound propagation in a flowing media confined by a cylindrical waveguide is characterized by mode phase speeds which, for small flows, do not depend linearly on flow. In particular, Lechner concludes that the phase speed of the fundamental mode changes with minus two times the average upstream flow as compared to the phase speed at zero flow. Downstream, the phase speed of the same mode is left unchanged with flow. In this comment, it is shown that changes in mode phase speeds with respect to flow will change sign when the flow direction is reversed disproving Lechner's claim. Numerical calculations based on Sodha *et al.*'s paper published in *Acustica* [**41**, 232–237 (1979)], being the basis of Lechner's work as well as this work, support the present analytical results for all modes. © *2000 Acoustical Society of America.* [S0001-4966(00)05002-5]

PACS numbers: 43.28.Py, 43.20.My [ANN]

INTRODUCTION

Previous works on ultrasound propagation in flow tubes by H. Lechner[1–3] address the influence of a fluid flow for the phase velocities of the different wavemodes that are allowed to propagate. A main conclusion of Refs. 1–3 is that the fundamental mode does not experience a difference in phase speed in the case of downstream fluid transport subject to laminar flow conditions as compared to the case of a quiet medium, i.e., $c_{p0+}=c$. On the contrary, the phase speed of the same fundamental mode becomes $c_{p0-}=c-2\overline{w}$ in the case of upstream fluid transport under laminar flow conditions, where c is the velocity of freely propagating sound in the motionless fluid and $\overline{w}$ is the mean flow velocity. References 1–3 conclude that the phase speed changes are independent of the profile parameter τ only in the case of fundamental mode propagation and that the various modes experience different phase speed changes for the same mean flow conditions.

In this comment, it is shown that changes in mode phase speeds with respect to flow will change sign when the flow direction is reversed. In particular, for the fundamental mode it is found that $c_{p0+}=c+\overline{w}$ and $c_{p0-}=c-\overline{w}$, in conflict with Lechner's result (Refs. 1–3). Furthermore, as the phase speed changes with respect to flow in Refs. 1–3 do not change sign with reversing flow for any of the possible wavemodes in the case of laminar or mixed flow ($\tau<1$), the present results disagree with those of Lechner for *all* modes. However, the conclusion that phase speed changes become profile independent only for the fundamental mode still holds true. Therefore, flow measurements based on changes in phase speed between downstream and upstream sound propagation situations inevitably lead to measurement errors if the acoustic pulse generated by the transmitting transducer contains several mode components. Numerical results as well as perturbation theory calculations support the conclusions made in the present work. The consequences for the deviation of measurement E utilizing the mth mode from one utilizing the fundamental mode are also discussed. Although the phase speed changes under flow given in Refs. 1–3 are wrong, the deviation of measurement E turns out to be correct. The notation follows Ref. 1 so as to avoid confusion when comparing results to those obtained by Lechner.

I. THEORY

In the case of slowly moving media, i.e., $w_0<<c$, it is possible to determine analytically a solution to the scalar wave equation under flow for sound propagation in cylindrical waveguides:[4]

$$\vec{\nabla}^2\Phi(r,\theta,z)+\frac{\omega^2}{c(r)^2}\Phi(r,\theta,z)=0, \tag{1}$$

where

$$c(r)=c\pm w_0\left(1-(\tau-1)\frac{r^2}{R^2}\right). \tag{2}$$

As the general solution to Eq. (1) depends on the direction of flow, the two cases, (a) sound wave propagation against the flow and (b) sound wave propagation along the flow, shall be treated separately in the following.

II. SOUND WAVE PROPAGATION AGAINST THE FLOW

According to Ref. 4, the general solution to Eq. (1) for azimuthally symmetric modes can be written as

$$\Phi(r,z)=A\exp(-x/2)\,{}_1F_1(\alpha,1,x)\exp(i\beta z), \tag{3}$$

where

a)Electronic mail: mwillatzen@danfoss.dk

$$x=\frac{k_0\sqrt{\delta}}{R}r^2,\quad k_0=\frac{\omega}{c-w_0},$$

$$\delta=2(1-\tau)\frac{w_0}{c},\quad \alpha=\frac{1}{2}-\frac{b}{4},\quad b=\frac{k_0R\chi}{\sqrt{\delta}},$$

$$\chi=1-\frac{\beta^2}{k_0^2},\quad \Delta=\frac{k_0\sqrt{\delta}}{R},\tag{4}$$

$${}_1F_1(a,b,x)=\sum_{n=0}^{\infty}\frac{(a)_n}{(b)_n}\frac{x^n}{n!},\quad (a)_n=\frac{(a+n-1)!}{(a-1)!},$$

and A is an arbitrary constant. The parameter α takes on a set of discrete values describing the different modes allowed for propagation as determined by the boundary conditions at the cylinder wall. Considering the cylinder wall as rigid, such that the radial velocity vanishes at $r=R$, the possible α values are found by the condition

$$\left.\frac{\partial\Phi(r,z)}{\partial r}\right|_{r=R}=0,\tag{5}$$

equivalent to

$$B_1=B_2,\quad B_1=2\alpha_1F_1(\alpha+1,2,\Delta R^2),$$
$$B_2={}_1F_1(\alpha,1,\Delta R^2).\tag{6}$$

A few manipulations based on Eqs. (4) lead to the following relation,

$$(\beta_n^-)^2=k_0^2-\Delta(2-4\alpha_n^-),\tag{7}$$

where α_n^- (β_n^-) denotes the nth solution for α (β) to Eq. (6) ($n=0,1,2,\ \ldots$, where the fundamental mode corresponds to $n=0$). It is well known that, in the limit of vanishing flow, $(\beta_n^-)^2$ must approach $\omega^2/c^2-j_{1n}^2/R^2$, the latter expression being $(\beta_n^-)^2$'s value at zero flow conditions and j_{1n} denotes the nth zero point of the Bessel function J_1. However, since Δ is proportional to $\sqrt{w_0}$ [refer to Eqs. (4)], Δ approaches zero with vanishing flow, and α_n^- takes on the form

$$\alpha_n^-=-\frac{(j_{1n}/2)^2}{\Delta R^2}+\gamma^-+\epsilon^-\Delta R^2\tag{8}$$

to first order in the small quantity ΔR^2 so as to obtain the required result:

$$(\beta_n^-)^2=k_0^2-\Delta(2-4\alpha_n^-)\to\frac{\omega^2}{c^2}-\frac{j_{1n}^2}{R^2}\quad\text{as}\quad w_0\to0.\tag{9}$$

The expression given in Eq. (8) for α_n^- is appropriate whenever $(\Delta R^2)^2\approx(\omega R/c)^2\,w_0/c\ll1$. The parameters γ^- and ϵ^-, introduced in the same equation, must be specified by the boundary conditions given in Eq. (6). In actual fact, Eq. (6) yields two expressions by equating terms proportional to $(\Delta R^2)^0$ on the left- and right-hand sides, and similarly for the terms proportional to $(\Delta R^2)^1$. Collecting terms proportional to $(\Delta R^2)^{-1}$ and equating simply asserts that j_{1n} must be the zero points of the Bessel function J_1.

To zeroth order in ΔR^2, the coefficients B_1 and B_2 reduce to

$$B_1(O[(\Delta R^2)^0])=2\gamma^-J_0(j_{1n}),$$
$$B_2(O[(\Delta R^2)^0])=J_0(j_{1n}),\tag{10}$$

and

$$\gamma^-=\tfrac{1}{2},\tag{11}$$

so as to fulfill $B_1=B_2$.

To first order in ΔR^2, the coefficients B_1 and B_2 reduce to

$$B_1(O[(\Delta R^2)^1])=(2\epsilon^-+2/3)J_0(j_{1n})\Delta R^2+1/12\,\delta_{n0}\Delta R^2,$$
$$B_2(O[(\Delta R^2)^1])=1/2J_0(j_{1n})\Delta R^2,\tag{12}$$

where δ_{n0} is a Kronecker delta, and Eq. (6) yields the following simple result for ϵ^-:

$$\epsilon^-=-\tfrac{1}{8},\quad n=0,$$
$$\epsilon^-=-\tfrac{1}{12},\quad n\neq0.\tag{13}$$

Having determined the parameters γ^- and ϵ^-, we are in a position to write down final expressions for the propagation constant β_n^- and the phase speed c_{pn}^-:

$$\beta_n^-=\sqrt{k_0^2-\Delta(2-4\alpha_n^-)}$$
$$=\sqrt{\frac{\omega^2}{c^2}-\frac{j_{1n}^2}{R^2}}\left[1+\frac{\omega^2/c^2\,(1+4\epsilon^-(1-\tau))\,w_0/c}{\omega^2/c^2-j_{1n}^2/R^2}\right],$$
$$\frac{1}{c_{pn}^-}=\frac{1}{c}\sqrt{1-\left(\frac{cj_{1n}}{\omega R}\right)^2}\left[1+\frac{(1+4\epsilon^-(1-\tau))\,w_0/c}{1-(cj_{1n}/\omega R)^2}\right].\tag{14}$$

III. SOUND WAVE PROPAGATION ALONG THE FLOW

In Ref. 4, the solution to the case where sound propagates along the flow becomes

$$\Phi(r,z)=A\exp(-x/2)\sum_{\nu=0}^{\infty}a_\nu x^\nu\exp(i\beta z),\tag{15}$$

where a_ν satisfies the recurrence relations,

$$a_0=1,\quad a_1=\alpha,$$
$$a_\nu=\frac{\nu+\alpha-1}{\nu^2}a_{\nu-1}-\frac{1}{2\nu^2}a_{\nu-2},\quad \nu\geqslant2,\tag{16}$$

and all the relations given in Eqs. (4) still apply except that k_0 now becomes $\omega/(c+w_0)$. Note that the sign of the term $(1/2\nu^2)a_{\nu-2}$ in the expression for a_ν, $\nu\geqslant2$, is negative as opposed to the wrong (positive) sign of the same term in Eq. (25) of Ref. 4. The negative sign is a point on which Lechner (Ref. 2) and the present author agree.

The possible set of discrete α values are determined by[4]

$$\sum_{\nu=1}^{\infty}\left(\frac{2\nu}{\Delta R^2}-1\right)a_\nu(\Delta R^2)^\nu=1.\tag{17}$$

As in the case of fluid flow against sound wave propagation, α can be written as

$$\alpha_n^+ = -\frac{(j_{1n}/2)^2}{\Delta R^2} + \gamma^+ + \epsilon^+ \Delta R^2, \tag{18}$$

whenever $(\omega R/c)^2 w_0/c \ll 1$. Inserting the previous Eq. (18) for α in Eqs. (16) and (17) allows determination of the parameters γ^+ and ϵ^+. Since Eq. (17) differs from Eq. (6) by the presence of the last term $-(1/2\nu^2)\, a_{\nu-2}$ in Eq. (16) only, and using the fact that this term contributes to first order (and, of course, higher orders) in ΔR^2, γ^+ must be equal to γ^-, i.e.,

$$\gamma^+ = \tfrac{1}{2}, \tag{19}$$

as γ^+ is determined by equating coefficients proportional to $(\Delta R^2)^0$ in Eq. (17).

An extra contribution to ϵ^+ appears, however, due to the term $-(1/2\nu^2)\, a_{\nu-2}$ in Eq. (16), since ϵ^+ is determined by equating terms proportional to $(\Delta R^2)^1$. In actual fact, it is found that

$$\begin{aligned} &B_1 = B_2, \\ &B_1(O[(\Delta R^2)^1]) \\ &\quad = (2\epsilon^+ + 1/3) J_0(j_{1n}) \Delta R^2 - 1/12 \delta_{n0} \Delta R^2, \\ &B_2(O[(\Delta R^2)^1]) = 1/2 J_0(j_{1n}) \Delta R^2, \end{aligned} \tag{20}$$

such that

$$\begin{aligned} &\epsilon^+ = \tfrac{1}{8}, \quad n = 0, \\ &\epsilon^+ = \tfrac{1}{12}, \quad n \neq 0. \end{aligned} \tag{21}$$

As a result, $\epsilon^+ = -\epsilon^-$ and β_n^+, c_{pn}^+ become

$$\begin{aligned} \beta_n^+ &= \sqrt{k_0^2 - \Delta(2 - 4\alpha_n^+)} \\ &= \sqrt{\frac{\omega^2}{c^2} - \frac{j_{1n}^2}{R^2}} \left[1 - \frac{\omega^2/c^2 (1 - 4\epsilon^+ (1-\tau))\, (w_0/c)}{\omega^2/c^2 - j_{1n}^2/R^2} \right], \\ \frac{1}{c_{pn}^+} &= \frac{1}{c} \sqrt{1 - \left(\frac{c j_{1n}}{\omega R} \right)^2} \left[1 - \frac{(1 - 4\epsilon^+ (1-\tau))\, w_0/c}{1 - (c j_{1n}/\omega R)^2} \right], \end{aligned} \tag{22}$$

reflecting the fact that phase speed changes with flow change sign for *all* modes when the flow direction is reversed.

IV. FLOW MEASUREMENT BASED ON PHASE SPEED CHANGES WITH FLOW

In flow meter applications, the quantity of interest is the mean flow $\overline{w}$. If $\overline{w}$ is measured in terms of phase changes with flow, it is necessary to obtain flow-profile-independent phase changes. In other words, the various mode phase speeds should be a function of the mean velocity only. We shall discuss this point next. First, notice that Eqs. (14) and (22) can be rewritten in terms of $\overline{w}$ by use of the identity:

$$\overline{w} = w_0 (1 - \tfrac{1}{2}(1 - \tau)). \tag{23}$$

The phase speeds written as a function of the mean flow velocity now become

$$\begin{aligned} &c_{pn}^{\pm} = c \pm \overline{w}, \quad n = 0, \\ &c_{pn}^{\pm} = c_{pn} \left(1 \pm \frac{2}{3} \frac{[2+\tau]\overline{w}/c}{[1+\tau] c^2/c_{pn}^2} \right), \quad n \neq 0, \end{aligned} \tag{24}$$

where c_{pn} is the phase speed of the nth mode at zero flow. As expected, the fundamental mode changes its phase speed as the mean flow changes only, i.e., the phase speed of the fundamental mode is independent of the flow profile. This conclusion is also reached by Lechner in Refs. 1–3 although he obtains different expressions in $c_{p0}^{\pm}$ with mean flow as compared to the present work. Numerical results based on the general expressions derived by Sodha *et al.*,[4] i.e., direct solution of Eqs. (6) and (17), agree with the analytical expressions found in the present work and therefore disagree with the results given in Refs. 1–3. Notice that the expressions given by Eqs. (6) and (17) serve as the starting point in Lechner's work as well. Perturbation theory allows a broader class of flow profiles to be analyzed in the small flow regime compared to the analysis carried out by Sodha *et al.* and Lechner. Again, perturbation theory[5] agrees with numerical results and the present results in the specific case where flow profiles are described by the relation $w(r) = w_0(1 - (\tau - 1)\, r^2/R^2)$.

A pair of nth order modes transmitted simultaneously downstream and upstream are received with the phase difference $\Delta\phi = \omega b_a (1/c_{pn}^- - 1/c_{pn}^+)$,

$$\begin{aligned} &\Delta\phi = \frac{2\omega b_a \overline{w}}{c^2}, \quad n = 0, \\ &\Delta\phi = \frac{2\omega b_a \overline{w}}{c_{pn} c} \frac{2}{3} \frac{2+\tau}{[1+\tau](c^2/c_{pn}^2)}, \quad n \neq 0, \end{aligned} \tag{25}$$

or the transit time difference $\Delta t = \Delta\phi/\omega$,

$$\begin{aligned} &\Delta t = 2 b_a \overline{w}/c^2, \quad n = 0, \\ &\Delta t = \frac{2 b_a \overline{w}}{c^2} \frac{c_{pn}}{c} \frac{2}{3} \frac{2+\tau}{1+\tau}, \quad n \neq 0. \end{aligned} \tag{26}$$

As the phase speed changes depend on the mode number, errors inevitably arise if the transmitter excites higher-order modes besides the fundamental mode. Defining the measurement error (or the deviation of measurement) E as the relative phase speed difference between a higher-order mode and the fundamental mode provides a measure of the flow meter error due to excitation of higher-order wave modes as a function of different flow profiles:

$$E = \frac{\Delta t - 2 b_a \overline{w}/c^2}{2 b_a \overline{w}/c^2} \tag{27}$$

yields

$$\begin{aligned} &E = 0, \quad n = 0, \\ &E = \frac{c_{pn}}{c} \frac{2}{3} \frac{2+\tau}{1+\tau} - 1, \quad n \neq 0. \end{aligned} \tag{28}$$

This result for E agrees with the expression given in Eq. (5) of Ref. 1. This is so although the phase speeds given by Lechner are wrong. In Fig. 1, calculated measurement errors

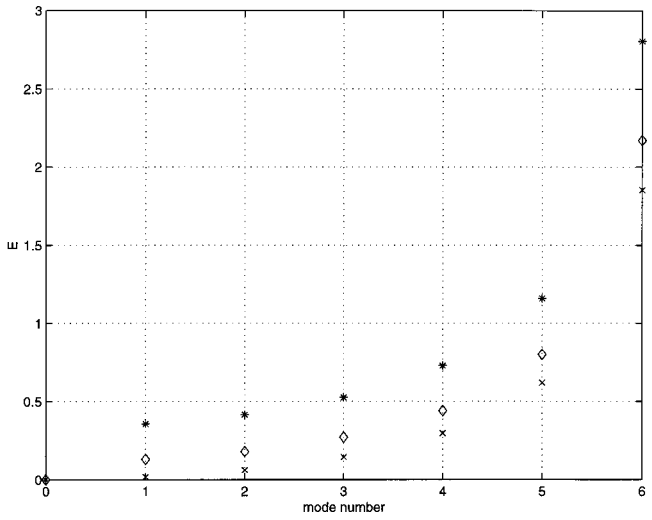

FIG. 1. The deviation of measurement E as a function of mode number. Three curves are shown corresponding to different degrees of turbulence: ''×'' is for $\tau=1$, ''diamond'' is for $\tau=0.5$, and ''asterisk'' is for $\tau=0$. The parameter values used in the calculation are $\omega=2\pi\cdot 10^6$ rad/s, $R=0.006$ m, and $c=1500$ m/s.

E for various wave modes and degrees of turbulence are shown corresponding to the parameter values: $\omega=2\pi\cdot 10^6$ rad/s, $R=0.006$ m, and $c=1500$ m/s being typical values for 0.6 m^3/h energy flow meters used in hot-water supply systems. It is evident that the measurement error increases strongly with increasing mode number as compared to a phase measurement with just the fundamental mode excited in the acoustic pulse. It is not a surprise that the measurement error increases as the turbulence degree approaches zero, due to the stronger flow profile variations over the cylinder cross-sectional area with decreasing τ values. The figure also reveals that the error in the laminar regime is some 36% using the second mode instead of just using the fundamental mode. It is therefore essential that the effects of higher-order modes on the received signal are eliminated to obtain better flow meter accuracy.

V. CONCLUSIONS

It has been shown that previous works by H. Lechner[1–3] on sound propagation in a flowing media confined by a cylindrical waveguide give incorrect expressions for the mode phase speeds. In particular, Lechner concludes that the phase speed of the fundamental mode changes with 2 times the average upstream flow as compared to the phase speed at zero flow. Downstream, the phase speed of the same mode is left unchanged with flow. In this comment, it has been shown that changes in mode phase speeds with respect to flow will change sign when the flow direction is reversed. Numerical calculations based on Sodha *et al.*'s paper,[4] being the basis for this work as well as Lechner's work, support the present analytical results.

ACKNOWLEDGMENTS

The author acknowledges Dr. N. B. O. L Pettit for a careful reading of the manuscript.

[1] H. Lechner, ''Ultrasonic flow metering based on transit time differentials which are insensititve to flow profile,'' J. Acoust. Soc. Am. **74**, 955–959 (1983).
[2] H. Lechner, ''Ultrasonic measurement of volume flow independent of velocity distribution,'' ACTA IMEKO **9**, 279–288 (1982).
[3] H. Lechner, ''Stroemungsprofilunabhaengige Durchflussmessung mit Ultraschall,'' Landis & Gyr Mitteilungen **28**, 16–18 (1981).
[4] M. S. Sodha, A. Kumar, I. C. Goyal, and A. K. Ghatak, ''Sound wave propagation in cylindrical inhomogeneus waveguides,'' Acustica **41**, 232–237 (1979).
[5] M. Willatzen, ''Perturbation theory applied to sound propagation in a flowing media confined by a cylindrical wall,'' submitted to J. Acoust. Soc. Am.

Range estimation and depth discrimination of multiple sources in noisy shallow waters without knowing sound speed profiles

I-Tai Lu[a] and Hsuan-Ling Wu
Polytechnic University, Route 110, Farmingdale, New York 11735

(Received 11 February 1998; revised 15 November 1999; accepted 17 November 1999)

A bottom-mounted horizontal array is proposed for range estimation and depth discrimination of multiple sources where the SSP information of the environment is not required. The two key elements are, first, to use the horizontal array for deriving modal wave numbers and composite modal amplitudes excited by multiple sources in multiple frequencies and, second, to utilize the frequency samples for obtaining unknown source ranges and discriminating source depths. © *2000 Acoustical Society of America.* [S0001-4966(00)05102-X]

PACS numbers: 43.30.Dr. 43.30.Wi [SAC-B]

INTRODUCTION

Source localization technologies are of vital importance for many civil and military applications. There have been many efforts to develop inverse source algorithms such as matched-field (e.g., see Refs. 1 and 2), matched-traveltime (e.g., see Refs. 3 and 4), matched-ray or matched-beam (e.g., see Refs. 5–7), and matched-mode (e.g., see Refs. 8–10) approaches. However, none of the existing methods can work under simultaneous excitations of several sources. Furthermore, all of these algorithms operate properly only when accurate descriptions of the environments are available. Since the environment is time varying and full of noises created by surface ships and other sources, it is impractical to implement any real time monitoring system using these methods.

In this paper, we present a feasibility study of a novel inverse source approach which may lead to the realization of a real time monitoring system consisting of bottom-mounted horizontal arrays. The new algorithm is developed for range estimation and depth discrimination of multiple sources where the sound speed profile (SSP) information of the environment is not required. Numerical simulation shows very promising results. The approach can also be extended to estimate source spectra, which will be discussed in future presentations. Since the information of SSP is not required, the proposed monitoring system based on the new approach is anticipated to function properly disregarding the variation of SSP due to time change (day or night) and seasonal alternation (summer or winter) without performing frequent SSP measurements.

I. FORMULATION

The key ideas of our new approach can be illustrated by a 2-D example using a horizontal array. Consider multisource excitations in a multi-mode shallow water environment. Let the acoustic pressure P_h received by the hth hydrophone at range r_h be represented in terms of mode sums:

$$P_h = \sum_m A_m \exp(-ik_m r_h) + N \tag{1}$$

with

$$A_m = \sum_s a_{ms} \exp(ik_m r_s), \tag{2}$$

where r_s is the range of the sth source, N is an additive noise, k_m is the horizontal wave number of the mth mode, and a_{ms} is the mth mode amplitude due to the sth excitation. Here, A_m is the composite amplitude of the mth mode from all sources. Note that the information about the frequency spectrum and the depth of the sth source (z_s) is contained in the mode amplitudes a_{ms} for every m, and the information of the source ranges r_s is contained in the phase.

II. NOVEL INVERSION APPROACH

For the proposed application, z_s, r_s, k_m, a_{ms}, and A_m are unknowns. In our novel approach, the first step is to estimate A_m and k_m from the measured data P_h for every m at some desired frequencies [using Eq. (1)]. The second step is to obtain the unknown source range r_s and modal amplitudes a_{ms} for every s and m [using Eq. (2)]. Both steps are related to spectral estimation where a large enough array aperture and an sufficient number of sampling frequencies are required in the first and the second steps, respectively. The source spectrum of the sources can be estimated because the mth mode amplitudes a_{ms} of the sth source are obtained for various frequencies. Depth discrimination can be achieved by examining the fundamental mode amplitude a_{1s} excited by every source s, especially when the environment has a downward-refracting SSP. Strong fundamental mode is usually excited by submerged sources. If the SSP or the modal eigenfunctions are approximately known, more accurate source depths can be derived from a_{ms} by a matched-mode procedure.

In a practical implementation, many tough propagation and signal processing issues need to be addressed. Primary concerns are as follows

(a) The receiver array is of finite length.

[a]Electronic mail: itailu@rama.poly.edu

(b) The modal wave numbers $\{k_m\}$ are usually complex due to internal wave scattering, rough surface scattering, SH coupling, bottom absorption, etc.
(c) Noises include both white and colored constituents.
(d) Receivers may be on different depths and, therefore, the mth composite modal amplitude A_m in Eqs. (1) and (2) becomes r_h dependent.
(e) The mth modal amplitude a_{ms} excited by the sth source in Eq. (2) is frequency (or k_m) dependent.
(f) The fact that the estimated values of $\{k_m\}$ obtained from the first inversion step are not equally spaced makes the second spectral estimation step very difficult.
(g) The environment may be range dependent.
(h) The number of surface sources is large.
(i) Some of the sources are moving.

Regarding problems (a)–(c), we have recently developed the SVD-matrix pencil method[11] which can suppress white noise well, estimate complex spectra accurately, and offer high resolution. This approach will not be redundantly described here. Problems (d) and (e) have the same mathematical implication and cause the same difficulty in inversion procedure. They can be tackled by the newly developed complex-spectrum model[11] (see Sec. III). Problem (f) can be overcome by compensation and interpolation techniques (see Sec. IV). Problem (g) is more complicated. Fortunately, the error due to weak range dependance can be quantified numerically. Regarding problem (h), a beam-type source may be employed to model many distributed sources.[7] Regarding problem (i), Doppler shifts due to moving effects can be taken into consideration.[9] Problems (g)–(i) will not be discussed in this paper.

III. COMPLEX-SPECTRUM MODEL

Problem (e) implies that a_{ms} is a function of wave number k_m. Thus, the conventional spectrum estimation approaches cannot be employed directly and the inversion becomes very difficult. Fortunately, if the frequency bandwidth is narrow, a_{ms} can be approximated by a linear function of k_m:

$$
\begin{aligned}
&a_{ms} \approx a_{ms}(k_{m0}) + \frac{\partial a_{ms}(k_{m0})}{\partial k_{m0}}(k_m - k_{m0}),\\
&a_{ms} \approx a_{ms}(k_{m0}) e^{\alpha_{ms}(k_m - k_{m0})},\\
&\alpha_{ms} \equiv \frac{\partial a_{ms}(k_{m0})}{\partial k_{m0}} \Big/ a_{ms}(k_{m0}),
\end{aligned}
\tag{3}
$$

where the linear approximation of $\exp(x) \approx 1+x$, if $|x| \ll 1$, is also employed. From Eq. (3), Eq. (2) can be expressed as

$$
\begin{aligned}
&A_m \approx \sum_s b_{ms} \exp[ik_m \gamma_s],\\
&\gamma_s \equiv r_s - i\alpha_{ms},\\
&b_{ms} \equiv a_{ms}(k_{m0}) \exp[-\alpha_{ms} k_{m0}],
\end{aligned}
\tag{4}
$$

where b_{ms} is a constant complex amplitude and γ_s is a complex spectrum. Now, the frequency-dependent problem is resolved by converting the frequency-dependent spectral amplitude a_{ms} into a constant b_{ms} and by converting the real spectrum r_s into complex spectrum γ_s. In this way, the complex spectrum estimation techniques can then be employed.

Problem (d) implies that A_m is a function of receiver location r_h. It has the same mathematical implication as problem (e) and can be solved by the same approach. If the location-dependent variation is slow, A_m can be approximated as a linear function of r_h. Then, the linear variation can be modeled as a loss factor in the complex wave number term k_m and the remaining amplitude becomes a constant.[11]

IV. COMPENSATION, INTERPOLATION, AND SMOOTHING

In the second step of the proposed inversion approach, A_m and k_m are employed to estimate modal amplitude a_{ms} and range r_s in Eq. (2), or equivalently b_{ms} and γ_s in Eq. (4) for the sth source. The difficulty here is that the estimated wave numbers $\{k_m\}$ are not equally spaced. Therefore, interpolation is required to estimate $\{A_m\}$ with respect to equally spaced $\{k_m\}$ if eigenstructure spectra estimation methods are to be employed. However, A_m is usually a fast-varying function of k_m and may not be approximated as a linear function between adjacent samples of $\{k_m\}$. Thus, before performing interpolation, a range compensation factor r_c has to be found to remove the fast-varying factor in (2):

$$
A'_m = \sum_s a_{ms} \exp(ik_m(r_s - r_x)). \tag{5}
$$

Let NR and NI be the number of zero crossing or sign changing of the real part and the imaginary part of A'_m, respectively, over the entire estimated $\{k_m\}$. The best compensation factor $r_{c,\text{best}}$ corresponds to minimum NR or NI over all possible range compensation factor r_c. In principle, if A'_m in Eq. (5) becomes a slowly varying function of k_m, a conventional linear interpolation procedure can then be employed to estimate $\{A'_m\}$ for equally spaced $\{k_m\}$.

In practice, this method breaks down if estimated values of $\{k_m\}$ are not accurate enough, or if the frequency resolution is too low. Thus, in our approach, the observation time has to be long enough (which ensures that the frequency resolution will be good enough). In addition, a data smoothing technique can be employed to prevent small jittering of the estimated k'_m values.

V. NUMERICAL RESULTS

For convenience, a simplified channel model and source spectra are employed. Consider a shallow water channel with a rigid bottom, a pressure-released surface, and a constant sound speed of 1500 m/s. A bottom-mounted horizontal array with 201 receiving elements is employed to determine the ranges and discriminate the depths of remote sources. The distance between two adjacent receivers is 18.75 m. Consider two sources with (x,z) coordinates (20 000 m, 2 m) and (20 200 m, 50 m), respectively. Note that the surface and the bottom of the water channel are denoted by $z=0$ m and $z=100$ m, respectively, and the center of the receiving array is located at (0 m, 100 m). Both sources emit equal and

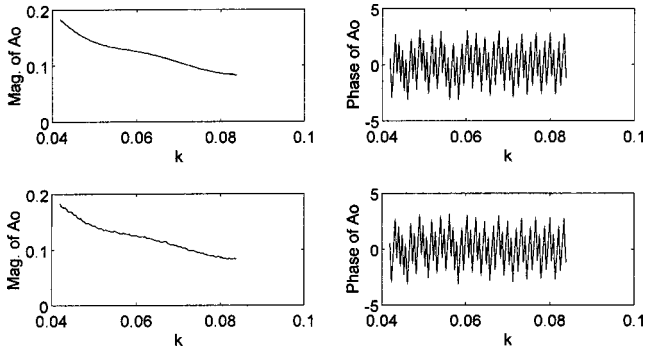

FIG. 1. The magnitude and phase of the composite modal amplitude of the fundamental mode. The SNRs are 30 and 15 dB for the top and bottom plots, respectively.

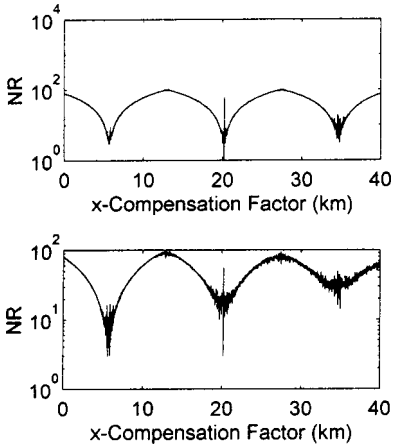

FIG. 2. The zero crossing numbers NR. The SNRs are 30 and 15 dB for the top and bottom plots, respectively.

constant power in the frequency interval between 10 and 20 Hz. The acoustic field is observed in a sufficient long time interval (say, 2 min) to obtain a frequency resolution of about 0.1 Hz. The received field at each sampled frequency by the hth hydrophone is given in (1) where the noise N is generated by a random number generator. Two signal-to-noise ratios SNR=30 and 15 dB are considered.

In the first step of the new inversion approach, the received field P_h is used to estimate composite modal amplitude A_m and the horizontal modal wave number k_m of the fundamental mode $m=0$ [see Eq. (2)] for every frequency. The estimated results are obtained by using the SVD-eigen matrix pencil method outlined in Ref. 11. The magnitude and phase of A_0 are shown in Fig. 1. It can be seen that our approach is very robust and the noise N does not affect these estimates much. Note that this inversion process neither requires nor depends on the channel model or the source parameters. The knowledge about the total number of modes M for each frequency is also not required. In the second step, we need to use A_0 and k_0 to estimate modal amplitude a_{0s} and range r_s for the sth source.

As discussed in Sec. IV, the difficulty here is that the estimated wave numbers $\{k_0\}$ are not equally spaced. Therefore, interpolation is required to estimate $\{A_0\}$ with respect to equally spaced $\{k_0\}$. Before performing interpolation, a range compensation factor $r_{c,\text{best}}$ has to be found to remove the fast-varying factor in Eq. (2). Figure 2 shows NR as functions of r_c with a coarse step ($\Delta r_c=50$ m). The curves of NI is very similar to NR and are omitted. The locations of local minimums are possible solutions of the range compensation factor $r_{c,\text{best}}$. More accurate estimates of $r_{c,\text{best}}$ can be obtained by using a finer step in computing NR and NI. Under low noise conditions, the global minimum in the top figure in Fig. 2 indicates the location of the $r_{c,\text{best}}$ (e.g., $r_{c,\text{best}}\approx 20\,000$ m for SNR=30 dB). However, there may exist range ambiguity under noisy situations because of the existence of multiple local minimums (e.g., SNR=15 dB) and, therefore, one has to take all possible range compensation factors into considerations.

Three compensation factors ($r_c=20\,144$, 5664, and 34 708 m) are considered in this simulation. After interpolation, the SVD-eigen matrix pencil method is employed again in the second step for ten frequency ranges: 10 to 11 Hz, 11 to 12 Hz,..., and 19 to 20 Hz. A set of source ranges $\{r_s,\ s=1,2\}$ and modal amplitudes $\{|b_{ms}|,\ m=0,\ s=1,2\}$ is derived for each frequency range. Note that the modal amplitudes $|b_{ms}|$ can be used to discriminate the source depths and estimate the source spectra. The mean and standard deviation of the estimated source ranges $\{r_s\}$ over the ten frequency ranges are shown in Table I.

Without smoothing, the estimated standard deviations of r_1 and r_2 are of similar order for all compensation factors. Therefore, range ambiguity occurs. Fortunately, the ambiguity can be resolved by a smoothing approach. Figure 3 shows the magnitudes and the phases of the compensated A_0' with the correct $r_c=20\,194$ m. In the middle and bottom parts of Fig. 3, the phase fluctuation is primarily induced by small estimation errors of $\{k_0\}$ for SNR=30 and 15 dB, respectively. These fluctuations can be removed by applying a

TABLE I. Estimation of source locations and mode amplitudes.

	SNR (dB)	Mean (r_1)	Var (r_1)	Mean (r_2)	Var (r_2)	Mean (b_{01})	Mean (b_{02})
$x_c=20\,144$	30	18 829	2325	21 067	1940	0.0271	0.0684
	30(*)	20 033	107	20 199	4	0.0090	0.0856
	15	15 400	2824	20 945	2248	0.0125	0.0835
	15(*)	19 828	376	20 258	134	0.0267	0.0681
$x_c=5664$	30	5096	1417	5798	281	0.0170	0.0397
	15	2703	3145	7541	2826	0.0339	0.0266
$x_c=34\,708$	30	32 269	2995	35 454	1485	0.0377	0.0176
	15	33 559	2131	38 100	2658	0.0403	0.0203

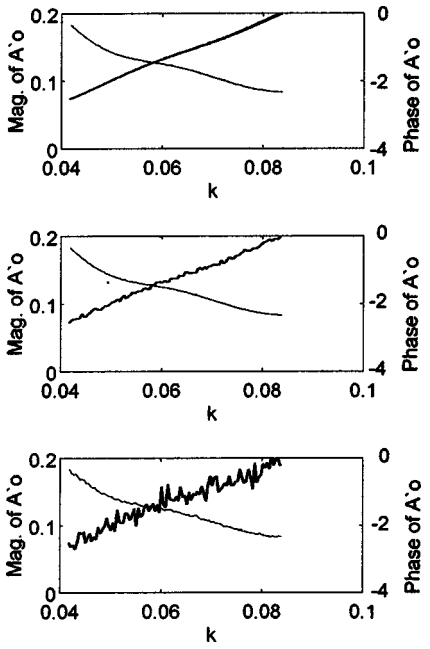

FIG. 3. The magnitude and phase of the compensated composite modal amplitude of the fundamental mode. The SNRs are 30 and 15 dB for the middle and bottom plots, respectively. The smoothed results are shown in the top plots.

smoothing procedure with small perturbations of $\{k_0\}$. The smoothed results are shown in the top of Fig. 3. The results denoted by (*) in Table I are obtained by smoothing both magnitudes and phases in Fig. 3. It is remarkable to note that accurate range estimations with small standard deviations are yielded even with SNR$=15$ dB. Thus, the range ambiguity is resolved and accurate range estimation is obtained.

The averages of the corresponding modal amplitudes $\{|b_{0s}|\}$ are also listed in Table I. For low noise the estimated standard deviations of r_1 and r_2 are small for the correct compensation factor ($r_c=20\,144$ m). One can also see that the second source is more likely than the first source to be an underwater vehicle because of its strong excitation strength of the fundamental mode ($|b_{02}|/|b_{01}|=856/90$).

In practical situations, the smoothing approach may not be employed because the environment is too noisy. The difficulty can be overcome by using a longer receiver array to provide a better estimate of $\{k_0\}$ or by observing the data with a longer period of time to obtain a higher frequency resolution. The ambiguity problem can also be avoided totally by using an inversion technique which does not require equally spaced $\{k_0\}$ in the second step of the proposed inversion procedure. Unfortunately, to the best of our knowledge, no inversion technique can work conveniently with non-equally spaced samples.

VI. CONCLUSIONS

A novel real-time system concept for range estimation and depth detection in shallow waters using bottom-mounted horizontal sonar arrays without knowing the SSP is presented. Novel signal processing algorithms for depth discrimination and range estimation of multiple acoustic sources are developed and examined. The preliminary results show that the proposed approach is very promising. Many practical issues need to be addressed before the proposed real-time monitor system can be realized. If it is proven successful, it will be a fundamental breakthrough in the inverse source applications.

[1] H. P. Bucker, ''Use of calculated sound fields and matched field detection to locate sound in shallow water,'' J. Acoust. Soc. Am. **59**, 368–373 (1976).
[2] M. B. Porter, R. L. Dicus, and R. G. Fizell, ''Simulation of matched-field processing in a deep-water Pacific environment,'' IEEE J. Ocean Eng. **OE-12**, 173–181 (1987).
[3] Y. Luo and G. Schuster, ''Wave equation inversion of skeletized geophysical data,'' Geophys. J. Int. **105**, 289–294 (1991).
[4] Peter Voltz and I. T. Lu, ''A back-propagating ray technique for source localization,'' J. Acoust. Soc. Am. **95**, 805–812 (1994).
[5] I. T. Lu, ''Simultaneous characterization of source and environment using a ray travel-time inversion approach,'' J. Comput. Acoust. **5**, 193–228 (1997).
[6] M. D. Collins and W. A. Kuperman, ''Focalization: Environmental focussing and source localization,'' J. Acoust. Soc. Am. **90**, 1410–1422 (1991).
[7] I. T. Lu, ''Forward modeling and data inversion for beam propagation in a stratified medium: I. Theory,'' J. Acoust. Soc. Am. **91**, 1228–1238 (1992).
[8] T. C. Yang, ''Broadband source localization and signature estimation,'' J. Acoust. Soc. Am. **93**, 1787–1806 (1993).
[9] H-Y. Chen and I.-T. Lu, ''Matched mode processing schemes of a moving point source,'' J. Acoust. Soc. Am. **92**, 2039–2050 (1992).
[10] H. Y. Chen and I. T. Lu, ''Localization of a broadband source using a matched mode procedure in time-frequency domain,'' IEEE J. Ocean Eng. **19**(2), 166–174 (1994).
[11] I. T. Lu, C. M. Qiu, and J. Kwak, ''A novel high-resolution algorithm for complex-spectrum serach,'' J. Acoust. Soc. Am. **104**, 288–299 (1998).

Power law absorption in polymers and other systems

H. J. Wintle[a)]
Department of Physics, Queen's University, Kingston, Ontario, Canada K7L 3N6

(Received 9 March 1999; accepted for publication 17 November 1999)

The theoretical treatment of acoustic absorption which goes as a power of the frequency is quite subtle. In this paper, it is shown that some of the difficulties can be resolved by using a wide distribution of relaxation times which is cut off at a short time limit $\tau_1>0$, and a finite long time limit $\tau_2<\infty$, without altering the general form of the acoustic response. This formalism is used to show that quadratic, linear, and fractional losses can be consistent with the Kramers–Kronig (KK) causal relations. The linear loss in polymers is associated with a weak velocity dispersion, so the group velocity and the phase velocity are quite close. The implications for space charge measurements in insulating polymers are discussed. Using the Helmholtz–Kirchhoff tube absorption as an example, it is also shown that the local approximation for the KK relations is unsatisfactory. © *2000 Acoustical Society of America.* [S0001-4966(00)00403-3]

PACS numbers: 43.35.Cg, 43.35.Mr, 43.20.Hg [HEB]

INTRODUCTION

Pulsed electroacoustic methods have become the preeminent tool for the study of space charge in dielectrics. We are therefore concerned with the acoustic propagation characteristics of insulators at frequencies up to 1 GHz. Our particular interest lies in the insulating polymers, for which the acoustic attenuation α is very nearly a power law of the angular frequency ω

$$\alpha=\alpha_0\omega^y, \tag{1}$$

where α_0 is a constant, and the exponent y is close to one. The theory of this power law regime was studied extensively by Szabo,[1] using Fourier transforms of generalized functions. Two intriguing questions remain, both of technical importance. The first is how a quadratic absorption, $y=2$, can be associated with a dispersionless velocity, of interest for delay lines. The second question applies to the linear case, $y=1$, for which the imaginary part of the propagation constant $\beta=\omega/v$ has a logarithmic behavior. Here, v is the phase velocity. Szabo arbitrarily normalized the frequency ω to 1 rad/s in order to obtain a dimensionless argument to the logarithm, but some clarification is called for in order to understand our polymer materials better. Two related problems are in what way power law responses might hold over the full frequency range $0<\omega<\infty$, and whether the Kramers–Kronig relations can be used for $y>1$.[2] In this paper, we first assemble for convenience the well known equations for the dispersion relations, and we then analyze the particular situations just mentioned.

I. THEORY

A. Velocity formulae

The equations describing the velocity and attenuation of a linear acoustic wave are well known:[3]

$$\frac{1}{v^2}-\left(\frac{\alpha}{\omega}\right)^2=m'/c^2, \tag{2}$$

$$2\alpha=\omega v m''/c^2, \tag{3}$$

where c is a constant reference velocity and m', m'' are the real and imaginary parts of a dimensionless modulus of elasticity. While the choice of c is arbitrary, and the quantities m', m'' must be scaled appropriately,[4] we will choose c to be the high frequency limit, and then the components of the moduli are directly related to susceptibilities χ', χ'' which are entirely analogous to the dielectric case:

$$m'=1+\chi', \tag{4}$$

$$m''=\chi''. \tag{5}$$

We note that Szabo used a different convention for c. The phase velocity can now be obtained from the root of a quadratic equation:

$$\frac{v^2}{c^2}=\frac{-1-\chi'+(1+2\chi'+\chi'^2+\chi''^2)^{(1/2)}}{\chi''^2/2}. \tag{6}$$

When the susceptibilities are small, this equation can be expanded binomially. The expansion must be taken to third order since the constant and first order terms cancel exactly. The result is

$$v\approx c(1-\chi'/2). \tag{7}$$

B. Kramers–Kronig relations

For a complex function which has no poles or essential singularities in the upper half plane, the Cauchy integral formula leads to the Kramers–Kronig (KK) relations, as long as the function vanishes rapidly enough as $z\to\infty$. In the case of an acoustic propagation constant $\gamma=\alpha+i\beta$, care has to be taken since the last condition may not be satisfied. Starting from the complex (Hilbert transform) variant, Jonscher[5] identified the pair of functions:

$$\chi'=A\omega^{y-1}, \tag{8}$$

a)Electronic mail: wintle@ieee.org

$$\chi'' = A\omega^{y-1}\cot(y\pi/2), \quad 0<y<1, \tag{9}$$

which describe a (slightly modified) power law loss with exponent y and amplitude proportional to A. This solution has its problems, since both parts of the susceptibility become infinite as $\omega \to 0$. The real form of the KK relations is

$$\chi' = \frac{2}{\pi}\int_0^\infty \frac{s\chi''(s)}{s^2-\omega^2}ds, \tag{10}$$

$$\chi'' = -\frac{2\omega}{\pi}\int_0^\infty \frac{\chi'(s)}{s^2-\omega^2}ds. \tag{11}$$

These are awkward to handle. Direct substitution shows that Jonscher's formulas would in principle fit for any value of the exponent y, but there is no guarantee that the integrals converge, while unphysical divergences still persist at one or both of the limits $\omega \to 0$ and $\omega \to \infty$.

The safe way to handle the situation is to use a distribution $g(\tau)$ of Debye relaxations with time constant τ. Then it follows that

$$\chi' = A\int_{\tau_1}^{\tau_2} \frac{g(\tau)}{1+\omega^2\tau^2}d\tau, \tag{12}$$

$$\chi'' = A\int_{\tau_1}^{\tau_2} \frac{\omega\tau g(\tau)}{1+\omega^2\tau^2}d\tau, \tag{13}$$

$$\int_{\tau_1}^{\tau_2} g(\tau)d\tau = 1. \tag{14}$$

The KK relations are now automatically satisfied, and the divergences are controlled by limiting the range of the distribution to $\tau_1 < \tau < \tau_2$. Other linear responses such as resonances would also satisfy the KK relations, but we have not used them. We have also ignored the technical difficulty that the simple Debye response lacks a small inertial component.[6]

II. SPECIAL CASES

We now turn to the questions that were raised earlier. The Debye equations are unpleasant to handle in general, but the particular cases of interest can be evaluated analytically. The integrations are easily done by a computer algebra program. We do not claim any originality in this development.

A. Almost quadratic attenuation

If we take the probability density to be

$$g(\tau) = \tau_1\tau_2/[(\tau_2-\tau_1)\tau^2], \tag{15}$$

then we find

$$\chi'/A = 1-\omega\tau_1\tau_2 \times[\arctan(\omega\tau_2)-\arctan(\omega\tau_1)]/(\tau_2-\tau_1), \tag{16}$$

$$\chi''/A = \frac{\omega\tau_1\tau_2}{2(\tau_2-\tau_1)}\ln\left[\frac{\tau_2^2}{\tau_1^2}\left(\frac{1+\omega^2\tau_1^2}{1+\omega^2\tau_2^2}\right)\right]. \tag{17}$$

One can readily check that these satisfy the expected limiting forms $\chi'/A \to 1$ as $\omega \to 0$, $\chi' \propto 1/\omega^2$ as $\omega \to \infty$, $\chi'' \propto \omega$ as $\omega \to 0$, and $\chi'' \propto 1/\omega$ as $\omega \to \infty$. We consider the case of a wide spread of relaxation times, $\tau_2/\tau_1 \gg 1$, and an intermediate frequency such that $\omega\tau_1 \ll 1 \ll \omega\tau_2$. In this frequency range, these equations reduce to the approximate relations

$$\chi'/A \approx 1-\frac{\pi\omega\tau_1\tau_2}{2(\tau_2-\tau_1)}, \tag{18}$$

$$\chi''/A \approx \omega\tau_1\ln(1/\omega\tau_1). \tag{19}$$

The frequency dependent term in the real part of the susceptibility is very small compared with the constant part. On substituting into the acoustic equations, and assuming for simplicity the low susceptibility condition, we find

$$v \approx c(1-A/2), \tag{20}$$

$$\alpha \approx -\omega^2(1-A)A\tau_1\ln(\omega\tau_1)/(2c). \tag{21}$$

Apart from the slowly varying logarithmic term, this represents a quadratic attenuation with an essentially constant phase velocity as originally claimed. The velocity dispersion is not absent, but it largely occurs in the high frequency region $\omega\tau_1 > 1$. This shows it is possible to satisfy the KK relations with $y \approx 2$ over a wide range of frequency, and the doubts raised by Weaver and Pao[2] are not substantiated.

B. Almost linear attenuation

If we now take $g(\tau) \propto 1/\tau$,[7] and proceed in a similar fashion, we obtain

$$\chi'/A = 1-\frac{1}{2}\ln\left(\frac{1+\omega^2\tau_2^2}{1+\omega^2\tau_1^2}\right)\Big/\ln(\tau_2/\tau_1), \tag{22}$$

$$\chi''/A = [\arctan(\omega\tau_2)-\arctan(\omega\tau_1)]/\ln(\tau_2/\tau_1). \tag{23}$$

Again, the low and high frequency limits give the expected Debye type of behavior. In the intermediate zone $\omega\tau_1 \ll 1 \ll \omega\tau_2$ we get

$$\chi'/A \approx 1-\ln(\omega\tau_2)/\ln(\tau_2/\tau_1), \tag{24}$$

$$\chi''/A \approx \pi/[2\ln(\tau_2/\tau_1)]. \tag{25}$$

In the limit of small relaxation strength, it follows from the form of χ' that the phase velocity is almost constant, with a small logarithmic correction, while the attenuation is linear in the frequency:

$$v \approx c\left(1-\frac{A}{2}-\frac{A}{2}\frac{\ln(\omega\tau_2)}{\ln(\tau_2/\tau_1)}\right), \tag{26}$$

$$\alpha \approx \frac{A\pi\omega}{4c\ln(\tau_2/\tau_1)}. \tag{27}$$

In this regime, the angular frequency is scaled to a frequency $1/\tau_2$, and not to some arbitrary value as originally proposed.[1] The group velocity v_g can be readily found:

$$v_g \approx v + v/[2\ln(\tau_2/\tau_1)+\ln(\omega\tau_1)-1]. \tag{28}$$

For a polymer such as polyethylene, the attenuation essentially follows the linear loss form up to at least 1 GHz,[8,9] so $\tau_1 \ll 1/\omega \sim$ 100 ps, and it presumably lies close to the reciprocal of a phonon frequency, 1 to 0.1 ps. At the other extreme, the power law extends down to 1 kHz,[10] so $\tau_2 \gg 1$ ms. Hence the denominator of the correction term is about 45,

and the adjustment to the velocity is about 2 percent. This is negligible, given the present state of acoustic space charge measurements. The actual fit is not good for some polymers[4], so some problems remain.

C. Fractional power law

The two previous cases show that by limiting the range of relaxation times, we can ensure both the convergence of the integrals and acceptable limiting behavior of the physical parameters. Given a span of several decades between τ_1 and τ_2, the material response in the intermediate range of frequency is essentially the same as for the $(0, \infty)$ range in τ. Thus, we can confidently treat other cases using the latter limits for their analytical convenience, always recalling that the finite, nonzero limits must be restored when needed. In this spirit, the fractional absorption regime, $0<y<1$, is easily derived, either from the distribution function method, or by using the Jonscher analysis[5] or Szabo's approach.[1] All three lead to the same results:

$$g(\tau) \propto 1/\tau^y, \tag{29}$$

$$\alpha = A v \omega^y \cot(y\pi/2)/(2c^2), \tag{30}$$

$$v \approx c(1 - A\omega^{y-1}/2) \approx c[1 - \alpha c \tan(y\pi/2)/\omega], \tag{31}$$

where we have again used the small relaxation strength approximation for v. The susceptibilities χ' and χ'' are given by Eqs. (8) and (9).

The case of most interest is $y=1/2$, which corresponds to the propagation of sound in gases in wide tubes. This is the famous Helmholtz–Kirchhoff (HK) absorption (see Rayleigh[11] for an accessible account, and Weston[12] for a detailed study). It is well known that there is quite good agreement between theory and experiment, even in the presence of competing loss mechanisms,[13] and the corrections are important in precision acoustic measurements.[14] We again have a reasonably wide span of relaxation times, since the data extend from a few tens of Hz up to 10 kHz. The kinematic viscosity and thermal diffusivity which underlie the HK loss process do not stem from any specific set of relaxing molecular states, so there is no overt distribution of relaxation times. The use of $g(\tau)$ simply allows us to mimic a linear loss process,[15] and there is no reason for this fictitious density to be normalizable. Even so, there is presumably a high frequency cutoff for which τ_1 is comparable to the mean free time between collisions in the gas.

This solution gives us the opportunity to test how good is the local approximation[1] α_{loc} to the attenuation constant:

$$\alpha_{\mathrm{loc}} \simeq \frac{\pi}{2} \frac{\omega^2}{v^2} \frac{\partial v}{\partial \omega}. \tag{32}$$

By substituting χ' and χ'' from Eqs. (8) and (9) and the moduli from Eqs. (4) and (5) into the velocity equations, eliminating α, and calculating $(\partial v/\partial\omega)$ analytically, we find the theoretical value

$$\alpha_{\mathrm{loc}} = \frac{\alpha(\pi/2)(1-y)\tan(y\pi/2)(v^2/c^2)}{1+\alpha^2 v^2/\omega^2}, \tag{33}$$

$$\approx \alpha(\pi/2)(1-y)\tan(y\pi/2). \tag{34}$$

This is plainly wrong by a factor $\pi/4$ for $y = 1/2$. It yields the correct result only as $y \to 1$. The inverse local transform to find v from α is merely an integration of Eq. (32), with a starting point that can be located at will in the midst of the range of interest,[1] so it does not provide a critical test of the local approximation. However, detailed analysis of some high resolution polymer data[4] showed that this approximation is inadequate even close to $y=1$.

III. DISCUSSION

We have established a number of results connected with acoustic attenuations which follow a power law. The chief conclusion is that the general results obtained by Szabo[1] can be substantiated over a wide frequency range, while at the same time satisfying the KK conditions and avoiding unphysical infinities, by using a representation in terms of an appropriate distribution of relaxation times $g(\tau)$ together with a nonzero lower limit τ_1 and a finite upper limit τ_2. A quadratic absorption goes with an almost dispersionless phase velocity over the region of interest as previously predicted, and the doubt raised by Weaver and Pao[2] over causality has been shown to be groundless. We are not aware of a physical model that accounts for this behavior. The fractional case $(0<y<1)$ has a rather simple structure which has allowed us to show that the relaxation process may be formally represented in terms of a distribution $g(\tau)$, which now need not be normalizable. The physical model is well known for $\alpha = 1/2$ (HK absorption).[11,12]

In addition, we have shown directly from the theory that the nearly local approximation may not be very good. This reinforces an earlier experimental finding[4] that the small absorption test $(\alpha\omega/c)^2 \ll 1$ is inadequate as a criterion for using the local (or smallness) approximation. We have not discussed the situation when the absorption is large for any of the examples studied. Here, the binomial expansion for finding the phase velocity would no longer be valid, but Eq. (6) can always be used.

The losses in polymers approximately follow the linear case $y=1$, and we have confirmed theoretically that the phase velocity is a weak function of frequency. The group velocity does not differ much from the phase velocity, so acoustic methods for space charge detection are not compromised. The physical mechanism leading to this type of loss is not understood. It is unlikely that several polymers having widely different chemical structure would have the same type of distribution of relaxing states, with time constants spread over more than nine decades. Alternatives such as soliton formation[16] are material specific, and also would need an activation energy of 0.6 eV, which seems unacceptably high. We speculate that this type of response may be due to a continuum property, but further investigation is needed. Since the response of the material in the creep regime is not straightforward,[17] it is likely that the viscoelastic

behavior is also not simple. From the distribution $g(\tau) \propto 1/\tau$ given earlier, we can derive the decay function Φ following the removal of a constant stress:

$$\Phi = [E_1(t/\tau_2) - E_1(t/\tau_1)] / \ln(\tau_2/\tau_1), \tag{35}$$

where E_1 is an exponential integral. The function Φ drops sharply at first, and then more slowly, and is reminiscent of the stretched exponential (KWW function). However, the distribution $g(\tau)$ is not very close to the calculated KWW distribution,[18] so the analogy cannot be taken too far.

ACKNOWLEDGMENTS

The author wishes to thank ESTAC (Sarnia, Canada) for their financial support, and Professors G. M. Sessler and R. Gerhard-Multhaupt for their valuable comments.

[1] T. L. Szabo, ''Causal theories and data for acoustic attenuation obeying a frequency power law,'' J. Acoust. Soc. Am. **97**, 14–24 (1995).
[2] R. L. Weaver and Y.-H. Pao, ''Dispersion relations for linear wave propagation in homogeneous and inhomogeneous media,'' J. Math. Phys. **22**, 1909–1918 (1981).
[3] A. B. Bhatia, *Ultrasonic Absorption* (Oxford University Press, London, 1967). (Reprinted by Dover, New York.)
[4] H. J. Wintle, ''Kramers–Kronig analysis of polymer acoustic data,'' J. Appl. Phys. **85**, 44–48 (1999).
[5] A. K. Jonscher, ''A new model of dielectric loss in polymers,'' Colloid Polym. Sci. **253**, 231–250 (1975).
[6] Y. Onodera, ''Breakdown of Debye's model for dielectric relaxation in high frequencies,'' J. Phys. Soc. Jpn. **62**, 4104–4107 (1993).
[7] M. Gevers and F. K. du Pré, ''Power factor and temperature coefficient of solid (amorphous) dielectrics,'' Trans. Faraday Soc. A **42**, 47–55 (1946).
[8] R. Gerhard-Multhaupt and G. M. Sessler, ''Charging and charge-detection methods and their use in the characterization of polymer-electret materials,'' Prog. Colloid Polym. Sci. **78**, 81–87 (1988).
[9] R. Gerhard-Multhaupt, G. M. Sessler, and J. E. West, ''Ultrasonic velocity and absorption in thin polymer films,'' *Conf. Proc. Ultrasonics International* (London, 1985), pp. 317–322.
[10] K. W. Hillier, ''A method of measuring some dynamic elastic constants and its application to the study of high polymers,'' Proc. Phys. Soc. London, Sec. B **62**, 701–713 (1949).
[11] Rayleigh, *The Theory of Sound* (Macmillan, London, 1926), 2nd rev. ed., Vol. 2, pp. 317–328. (Reprinted by Dover, New York.)
[12] D. E. Weston, ''The theory of the propagation of plane sound waves in tubes,'' Proc. Phys. Soc. London, Sec. B **66**, 695–709 (1953).
[13] D. H. Smith and H. J. Wintle, ''The propagation of sound in relaxing gases in tubes at low frequencies,'' J. Fluid Mech. **9**, 29–38 (1960).
[14] A. R. Colclough, T. J. Quinn, and T. R. D. Chandler, ''An acoustic redetermination of the gas constant,'' Proc. R. Soc. London, Ser. A **368**, 125–139 (1979).
[15] G. F. Leal Ferreira and B. Gross, ''Comments on the dielectric theory: Non-Debye models and the superposition principle,'' J. Appl. Phys. **68**, 2526–2528 (1990).
[16] J. L. Skinner and Y. H. Park, ''Soliton model for dielectric relaxation in crystalline polyethylene. Comparison with experiment,'' Macromolecules **17**, 1735–1740 (1984).
[17] P. J. Dixon-Stubbs, ''Creep behaviour of polyethylene and polypropylene,'' J. Mater. Sci. **16**, 389–396 (1981).
[18] M. Dishon, J. T. Bendler, and G. H. Weiss, ''Table of the inverse Laplace transform of the function $e^{-s\beta}$,'' J. Res. Natl. Inst. Stand. Technol. **95**, 433–467 (1980). Note that our $g(\tau)$ is labeled $\rho(u)$ in this paper, but their plots show a different quantity.

The radial motion of a sonoluminescence bubble driven with multiple harmonics

Kirk Hargreaves[a] and Thomas J. Matula
Applied Physics Laboratory, University of Washington, 1013 NE 40th Street, Seattle, Washington 98105

(Received 18 October 1999; accepted for publication 8 December 1999)

Harmonic excitation has been reported to enhance the light emission of a single sonoluminescing bubble by as much as 300% [J. Holzfuss, M. Rüggeberg, and R. Mettin, Phys. Rev. Lett. **81**, 1961–1964 (1998)]. In this paper it is shown that the effect of harmonic excitation on the radial motion of the bubble is consistent with bubble dynamics predictions. Also, it has been suggested that the energetic collapse of a sonoluminescence bubble can be enhanced with the addition of an acoustic ''spike'' drive [W. C. Moss *et al.*, Phys. Lett. A **211**, 69–74 (1996)]. Preliminary attempts to spike the bubble with an acoustic pulse (positive and negative) resulted in a temporary increase in light intensity of $\approx$ 200%; however, a strong acoustic radiation force pushes the bubble away from the antinodal region, suggesting that ''spiking'' the bubble each and every acoustic cycle may not be feasible. © *2000 Acoustical Society of America.* [S0001-4966(00)03603-1]

PACS numbers: 43.35.Ei [HEB]

INTRODUCTION

Single-bubble sonoluminescence (SBSL) refers to the emission of light from an acoustically trapped bubble undergoing large-amplitude, nonlinear, predominantly radial oscillations.[1] Whereas the ''standard'' SBSL technique utilizes a sinusoidal forcing pressure, it has been hypothesized that the addition of a temporally narrow, high-amplitude (spiked) acoustic pulse should dramatically increase the light emission.[2] It has even been shown that the addition of a second harmonic can result in an increase in the light intensity by as much as 300%.[3] These results suggest that enhancing the SBSL light emission may be accomplished with novel excitation mechanisms.

In this paper, we describe measurements of the radial dynamics of a sonoluminescence bubble subject to multifrequency (harmonic) excitation. This effort is designed to supplement the work of Holzfuss *et al.*[3] In addition, these measurements serve as a starting point for measuring the radial motion of a bubble subjected to more unconventional forcing, such as a spike. We will show that the bubble's radial motion is dramatically affected by nonsinusoidal forcing. Furthermore, bubble dynamics equations[4] predict the bubble's radial motion fairly well. With spiked drives, the bubble is observed to move laterally, suggesting that a strong acoustic radiation force affects the bubble, limiting the periodic enhancement of SBSL.

I. HARMONIC ENHANCEMENT

To measure the radial motion of an SBSL bubble under harmonic (multimode) excitation, we utilized a cubical levitation cell (an acrylic box) of (inner) dimensions 5.4 $\times$5.4 cm cross section, by 5.9 cm tall (water filled to the 5.4-cm mark), and 0.16 cm thick. Assuming pressure-release surfaces, one would expect the normal mode frequencies (eigenmodes) to occur at $f=c/(2L)[n^2+m^2+p^2]^{1/2}$, where f, c, and L are the resonance frequency, speed of sound in the fluid, and length of the sides of the cubical cell, respectively, and $m,n,p=1,2,3,....$ For our system, we calculate the fundamental frequency to be near $f=23.74$ kHz (1, 1, 1 mode), with eigenmodes at $1.41f$, $1.73f$, $1.91f$, etc. In addition, harmonics exist at $2f$ (2, 2, 2 mode), $3f$ (3, 3, 3 mode), etc.

In our actual cell, stable sonoluminescence occurred at a fundamental frequency of $f=22.775$ kHz. Furthermore, stable bubble levitation (even sonoluminescence) at $2f$ and $3f$ was obtained. Thus, we were able to levitate bubbles at harmonics of the fundamental, allowing us to synchronize the frequency generators.

The frequency generators (HP 33120A) were synchronized with a 10-MHz clock so that the relative phase difference remained constant. The output from the generators (fundamental and second or third harmonic) was fed into an amplifier (Krohn Hite 7500), whose output drives a piezoelectric transducer (PZT) mounted to the bottom of the cubical levitation cell, filled with degassed ($\approx$100 mmHg), filtered water.

The dynamical motion of the bubble is measured by scattering 30-mW HeNe laser light off the bubble near the critical scattering angle ($\approx$83°), and collecting a large solid angle of the scattered light. This method can be used to measure the overall real-time, presumed spherical motion of the bubble.[1] In the geometrical optics approximation, the collected signal is proportional to the square of the bubble radius; the proportionality constant is determined by imaging the bubble at its maximum size ($R_{\max}$).

Figure 1 shows various measured radius-time, or $R(t)$, curves for a bubble forced at the fundamental and third harmonic. The measured hydrophone voltage (in the absence of the bubble) is also shown. The measured $R(t)$ curves were then fit in a standard way to a bubble dynamics equation,[4] taking into account the measured $R_{\max}$. For the forcing pressure, we used $P_1\sin(\omega_1 t+\Phi_1)+P_3\sin(3\omega_1 t+\Phi_3)$, where P_1, P_3 are the pressure amplitudes of the first and third harmonic, and Φ_1, Φ_3 are the respective phases relative to a

[a]Currently at Synaptics, Inc., 2702 Orchard Parkway, San Jose, CA 95134.

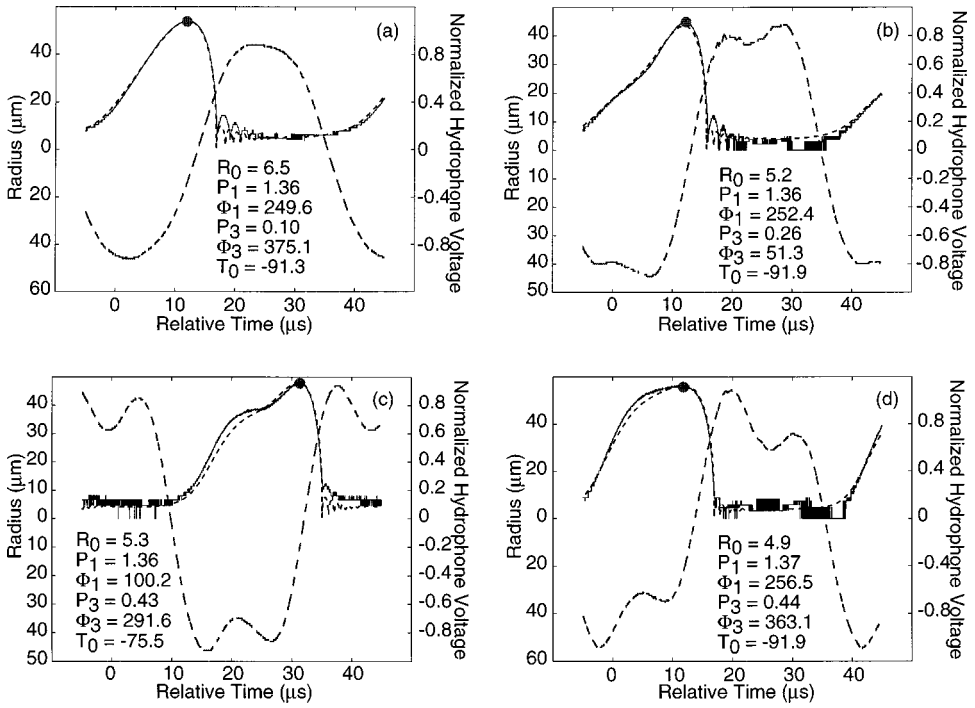

FIG. 1. Measured $R(t)$ curves (solid line) and hydrophone signal (long dashed line) for SBSL bubbles driven with a fundamental (22.775 kHz) and third harmonic. The data represent an average of 100 individual $R(t)$ curves. The fitting parameters are also shown. The fitting parameters include P_1 and P_3, the pressure amplitudes (in atm) of the fundamental and third harmonic, Φ_1 and Φ_3, the respective phases relative to a reference time T_0, in (μs), and the equilibrium radius, R_0, in μm. The $R(t)$ fit is shown as a short dashed line. The measured bubble size (obtained by imaging with a microscope) at its maximum radius is shown as a solid circle.

fixed reference time. The surface tension, liquid viscosity, speed of sound in the liquid, etc. were obtained from accepted values for water.

For each of these curves, the bubble was stable, cycle-to-cycle, and emitting light. Although it was difficult to determine whether or not small changes in the $R(t)$ curve had any effect on the light emission, when large-scale changes to the $R(t)$ curve were made, we found that bubbles that grew to larger maximum sizes emitted more light. The multiparameter fit shows good agreement with the data; thus, we are able to confirm that the addition of higher harmonics affects the bubble in a predictable way.

II. ACOUSTIC PULSE ENHANCEMENT

Our next goal was to affect the bubble's motion much more dramatically, by applying a high-amplitude, acoustic impulse to the bubble during its collapse phase. Moss has predicted that a large spike applied to the bubble during its collapse would impart a higher velocity to the collapse, as well as possibly shock the interior gases.[2] It should also be noted that applying a longer negative pulse during the bubble's growth should force the bubble to grow to a much larger radius, and thus collapse with a greater velocity. We attempted both methods.

For this experiment, a broadband focused immersion transducer[5] (1.88-MHz center frequency, 6.35-cm focal length) was placed near the top of a cylindrical cell such that the bubble was located at the focus of the transducer. The output of a pulse generator was connected to a 400-W power amplifier. The pulse (short positive, or longer negative) was initiated so that it would reach the bubble during various phases of the bubble's collapse (or growth).

In order to observe a change in the light emission or bubble dynamics from the spiked system, we collected data for approximately 100 consecutive acoustic cycles. A subset of some representative data for a negative pulse is shown in Fig. 2. We found that the pulse (positive or negative) produced a large acoustic radiation force on the bubble, causing it to translate out of the laser beam. The light-scattered signal would thus change substantially. The results showed that we would obtain a larger emission intensity only for one or two acoustic cycles, after which the bubble would require a few seconds to come to equilibrium before we could again trigger the pulse. Parenthetically, applying the pulse to the transducer used to levitate the bubble is precluded since the transducer will respond at the system's resonance frequency.

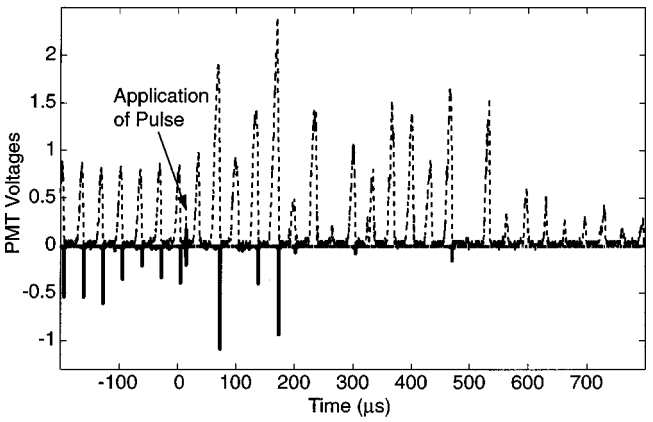

FIG. 2. The dashed curve is the measured voltage from the light-scattering photomultiplier tube (PMT), and represents the radius of the bubble. The solid negative curve is the PMT signal from the bubble emissions. The travel time for the negative pulse to reach the bubble is approximately 40 μs. After an initial doubling of the light emission, the intensity decreases abruptly, probably because of instabilities caused by the bubble's translation. The apparent change in R_{max} toward the right of the figure is probably due to the bubble being forced out of the laser beam, and thus, the scattered intensity decreases. The measured intensity is only approximate, due to the finite digitization rate of the oscilloscope.

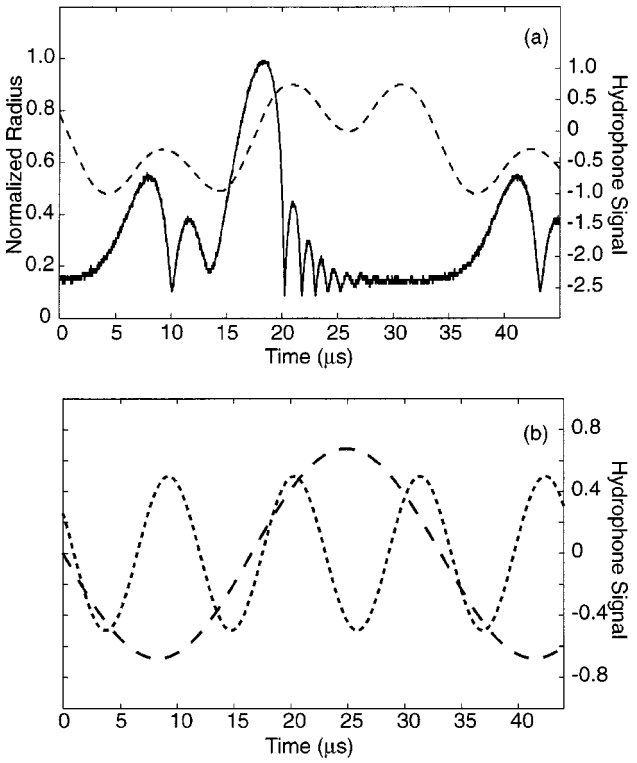

FIG. 3. (a) The driving waveform (dashed line) and bubble's radial response (solid line). (b) Decomposing the driving waveform into its Fourier components (first and second harmonic) shows that the precollapse at 10 μs is apparently due to the increasing harmonic pressure. The bubble then rebounds before going through the main growth phase. The hydrophone voltage amplitudes for P_1 and P_2 were 67.8 and 49.8 mV, respectively, and the relative phase between the components was $\Phi = 148.8°$.

III. DISCUSSION

The multimode frequency experiments show that the bubble oscillations can be dramatically affected. One can understand the shape of the $R(t)$ curve by examining Fig. 3(a), which shows a measured $R(t)$ curve, together with the driving waveform. This particular $R(t)$ curve was obtained with the addition of a second harmonic in a spherical cell ($f_{\text{res}} = 30.170$ kHz).

In Fig. 3(b), the driving waveform is decomposed into its Fourier components (the fundamental and second harmonic). Note that the collapse of the bubble near 10 μs is apparently due to the positive pressure from the second harmonic. The bubble's response between 10 and 14 μs is probably a rebound.

Although the acoustic pulse method for increasing the bubble's collapse velocity was only partially successful, the knowledge gained from such studies can be used in future refinements to the system. For instance, it may be possible to align two confocal acoustic impulse drivers, with the bubble situated in the confocal region. Such a system may prevent the bubble from translating.

As an alternative, a potentially large ''transient'' SBSL bubble may be achieved by using a shock-wave lithotriptor, which can generate very large positive ($\approx$40 MPa) and negative pressure ($\approx$10 MPa) amplitudes at its focus.[6] One might expect the bubble to disintegrate after its collapse, so that real-time monitoring of the bubble would be necessary to observe the ''one-shot'' event.

IV. CONCLUSION

Previous studies have found that harmonic driving of an SBSL bubble can result in changes to the light emission intensity. Our results clearly show that these changes are the results of changes to the bubble's radial motion. Also, we have shown that spiking the bubble can approximately double the light-emission intensity; however, the resulting bubble destabilization suggests that acoustic spiking will work best in a single-shot mode. Such a system may work well with unstable bubbles (such as nitrogen, deuterium, etc.) as well, since the bubble can be driven in a stable fashion at lower pressure amplitudes, and then spiked with a single-shot transient pulse. It may be possible to generate large temperatures and pressures inside the bubble, especially if a lithotriptor pulse can be used as the spiking waveform.

ACKNOWLEDGMENTS

The authors wish to thank V. Bezzerides and C. A. Frensley for help in the laboratory, and L. A. Crum and W. C. Moss for many valuable discussions. This work was supported in part by NSF and DARPA.

[1] B. P. Barber and S. J. Putterman, ''Light scattering measurements of the repetitive supersonic implosion of a sonoluminescing bubble,'' Phys. Rev. Lett. **69**, 3839–3842 (1992).
[2] W. C. Moss, D. B. Clarke, J. W. White, and D. A. Young, ''Sonoluminescence and the prospects for table-top microthermonuclear fusion,'' Phys. Lett. A **211**, 69–74 (1996).
[3] J. Holzfuss, M. Ruggeberg, and R. Mettin, ''Boosting sonoluminescence,'' Phys. Rev. Lett. **81**, 1961–1965 (1998).
[4] R. Löfstedt, B. P. Barber, and S. J. Putterman, ''Toward a hydrodynamic theory of sonoluminescence,'' Phys. Fluids A **5**, 2911–2928 (1993).
[5] Ultan Laboratories, Inc., 1020 E. Boal Ave., Boalsburg, PA.
[6] M. R. Bailey, D. T. Blackstock, R. O. Cleveland, and L. A. Crum, ''Comparison of electrohydraulic lithotripters with rigid and pressure-release ellipsoidal reflectors. I. Acoustic fields,'' J. Acoust. Soc. Am. **104**, 2517–2524 (1998).

Surface wave velocity determination by using reflection coefficient method on the liquid–anisotropic–solid interface

Yang Xu[a] and Tatsuhiko Aizawa
Department of Materials Engineering, The University of Tokyo, 7-3-1 Hongo, Bunkyo-ku, Tokyo 113-8656, Japan

(Received 1 April 1999; accepted for publication 17 September 1999)

Reflection coefficient of a plane wave impinging from liquid onto a liquid–anisotropic–solid interface is useful to theoretically predict the Rayleigh surface wave (RSW) velocity and the pseudo surface wave (PSW) velocity dispersions. In the present letter, several incomplete results proposed by previous investigation are restudied to attempt giving more appropriate physical understanding in theory. It is found that PSW velocity determined by the reflection coefficient analysis is just a nonleaky effect surface wave on the liquid–anisotropic–solid interface but not the leaky one. © *2000 Acoustical Society of America.* [S0001-4966(00)00801-8]

PACS numbers: 43.35.Pt [HEB]

Using incident angle dependence of the reflection coefficient of an infinite plane wave impinging from liquid onto a liquid–cubic–crystal(001) interface, Atalar[1] first analyzed the relation between the Rayleigh surface wave (RSW) and the reflection coefficient. In his theory, a null in the reflection coefficient should define the excitation position for the pseudo surface wave (PSW). Arikan *et al.*[2] extended the above method to deal with any type of anisotropic materials in arbitrary crystallographic orientation. In their more complete theoretical aspects about the reflection coefficient, a more detailed study was done for the null value appearing in the reflection coefficient. Nayfeh[3] derived analytical expression for the reflection coefficient on the liquid–anisotropic–solid interface having the monoclinic symmetry, and calculated RSW and PSW velocity distributions on the interfaces between water and several anisotropic materials.

Peering into both theories by Arikan *et al.* and Nayfeh, several unclear and wrong aspects were found, especially in the latter. The present work is concerned with physical accountability to understand the relation between the reflection coefficient theory and the excitation behavior of RSW and PSW on the liquid–anisotropic–solid interface. According to Arikan *et al.*, a computer program has been developed to analyze the incident angle dependence of reflection coefficient on the liquid–anisotropic–solid interface, and to calculate RSW and PSW velocities on the considered interface. Using Lim and Farnell's method,[4–6] a numerical analysis method was also developed to obtain RSW and PSW velocities on the vacuum–anisotropic–solid interface.

For a longitudinal plane wave impinging from liquid onto a liquid–solid interface, the reflection coefficient R can be expressed by:[7]

$$R=\frac{Z_{\mathrm{tot}}-Z}{Z_{\mathrm{tot}}+Z}, \tag{1}$$

where the Z_{tot} term is a total impedance of the boundary at the presence of longitudinal and transverse waves, and Z term includes the effect of the liquid medium.

Instead of the condition of $Z_{\mathrm{tot}}+Z=0$ for activation of the leaky Rayleigh surface wave (leaky RSW), the condition of $\mathrm{Re}[R]=-1$ and $\mathrm{Im}[R]=0$ were used in Ref. 3 to determine the ''leaky'' RSW velocity. From Eq. (1), obviously $R=-1$ leads to $Z_{\mathrm{tot}}=0$, but $Z\neq 0$. To be noted, $Z_{\mathrm{tot}}=0$ holds for the vacuum boundary condition. Since the Z term has nothing to do with R, the obtained surface wave becomes true RSW on the vacuum–solid interface, but not the ''leaky'' one. Figure 1 illustrated the calculated RSW velocity distribution on the vacuum–InAs(001) interface by Lim and Farnell's method compared with RSW velocity dispersion on the water–InAs(001) interface obtained by using Nayfeh's method. The two curves are just the same with each other. While the leaky RSW velocity analyzed by setting $Z_{\mathrm{tot}}+Z=0$ is larger than RSW velocity. The point to be noted in reality is that the leaky RSW under water loading should be separated into two branches: the original leaky RSW and the induced Rayleigh wave (IRW).[8] The latter appears close to the original PSW branch; it reradiates acoustic energy only into the liquid and does not appear in the vacuum boundary condition.

In Ref. 3 it was stated that the absolute value of the reflection coefficient ($|R|$) cannot identify the existence of RSW and PSW. This proposal is correct and important. Nayfeh insisted that both RSW and PSW can be determined from the two dip positions in $\mathrm{Re}[R]$. Corresponding to these two dip positions, the incident angles θ_R and θ_P are called the Rayleigh critical angle for RSW and PSW, respectively. From the right dip, where $\mathrm{Re}[R]=-1$ and $\mathrm{Im}[R]=0$, RSW velocity can be obtained, and, from the left dip, PSW velocity can be determined. Nayfeh considered that $\mathrm{Im}[R]$ should be also zero in the left dip position. For almost all cases, this consideration is not true: the incident angle θ_{Re} to have minimized $\mathrm{Re}[R]$ is almost not equal to the position θ_{Im} where $\mathrm{Im}[R]=0$. As pointed out by Arikan *et al.*, the null position of the reflection coefficient (corresponding to the minimum location of $|R|$) is different from θ_{Im}. Actually, even along the propagation direction, where the reflection coefficient null exists, $\theta_{\mathrm{Re}}\neq\theta_{\mathrm{Im}}$ is also held.

In our calculation, there exists some propagation direc-

[a]Electronic mail: xuy@dragon.mm.t.u-tokyo.ac.jp

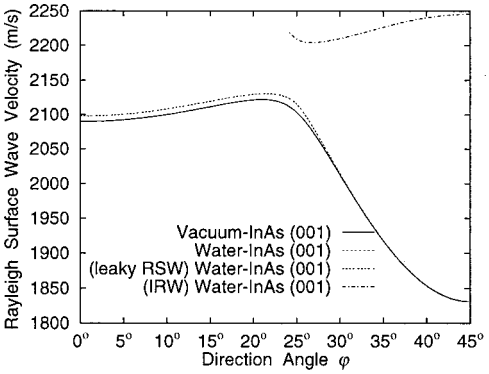

FIG. 1. RSW velocity distributions on InAs(001) plane. The same elastic stiffness and the density as in Ref. 3 are used for computation. To be noted, RSW velocity distribution on the vacuum–InAs(001) interface obtained by Lim and Farnell's method, and that on the water–InAs(001) interface determined by reflection coefficient analysis are overlapped with each other into one curve.

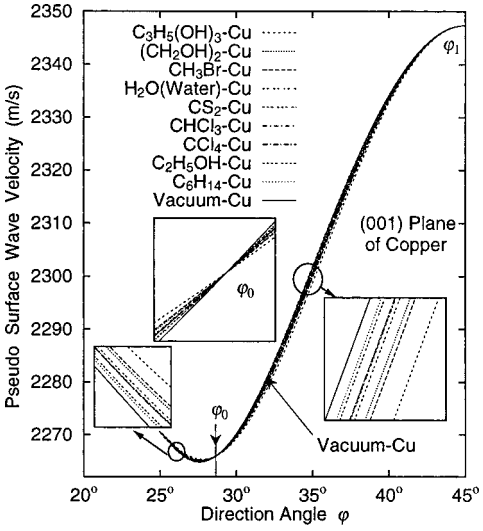

FIG. 2. PSW velocity distributions on several liquid-Cu(001) and vacuum-Cu(001) interfaces. The elastic stiffness is $C_{11}=171.0$ GPa, $C_{12}=124.0$ GPa and $C_{44}=75.6$ GPa, the density is 8.93 g/cm^3.

tions in PSW branch on (001) plane for some cubic crystals, where $\mathrm{Re}[R]=-1$ and $\mathrm{Im}[R]=0$. Nayfeh emphasized that $|R|$ for PSW might become very close to unity but never reaches it: $|R|<1$. Hence he implied that the propagation energy for PSW must be transmitted into the substrate, no matter how small it might be. This speculation might be physically significant, but no proofs were derived in his theory. To be noted, this proof can never be obtained in his theoretical frame.

Figure 2 shows PSW velocity distributions on the interfaces between several practical liquid media and Cu(001) plane calculated by the reflection coefficient method together with PSW velocity dispersion on the vacuum-Cu(001) interface calculated by using Lim and Farnell's method. The viscosity for liquid media was neglected in these calculations. Those velocity dispersion curves intersect at two points—$\varphi_0=28.647\,821°$ and $\varphi_1=45°$: PSW velocities become independent of liquid medium, and just equal to PSW velocities on the vacuum–Cu(001) interface, respectively. Table I listed the values of the real and the imaginary parts of R for several liquid media at $\varphi=\varphi_0$. $\mathrm{Re}[R]=-1$ and $\mathrm{Im}[R]=0$ were satisfied, and the velocities for different boundary conditions are equal to each other up to nine digits. $\mathrm{Re}[R]=-1$ and $\mathrm{Im}[R]=0$ correspond to $Z_{\mathrm{tot}}=0$ and $|R|=1$. From $Z_{\mathrm{tot}}=0$, the properties of liquid have no influence on the PSW velocity; hence every dispersion curve can be coincident at φ_0. From $|R|=1$, the incident energy from the liquid onto the interface is all reflected back to the liquid itself. The above condition is also true to the case when $\varphi=\varphi_1$.

Figure 3 illustrated the cross-section of slowness surface of bulk waves on the water–Cu(001) interface along propagation direction φ_0. When a plane wave with incident angle θ_P impinges from water onto the interface, a PSW is excited. By using Snell's law across the interface, there can exist one possible shear wave together with an evanescent longitudinal wave and an evanescent shear wave.

In order to analyze the structure of this PSW, let us consider that an anisotropic solid occupies a half-space $x_3 \leqslant 0$. The displacement u_j of a surface wave on the half-space of anisotropic solid can be expressed as:[6]

$$u_j=\sum_{n=1}^{3} W_n \alpha_j^{(n)} \exp[ik(l_1x_1+l_2x_2+l_3^{(n)}x_3-vt)], \quad (2)$$

where W_n is a weighting factor for the nth partial wave, $\alpha_j^{(n)}$ the unit polarization component of the partial wave, $i=\sqrt{-1}$, k the wave number, v the surface wave phase velocity, l_1, l_2 and $l_3^{(n)}$ the direction cosines of propagation vector in the coordinate system axes x_1, x_2 and x_3, respectively.

Substituting Eq. (2) into the wave motion equation, the Christoffel equation can be obtained after some mathematic manipulations:

$$|l_i l_l c_{ijkl}-\delta_{jk}\rho v^2|=0, \quad (3)$$

where c_{ijkl} is the elastic stiffness tensor, ρ the density of mass, and δ_{jk} Kronecker's delta. The repeated subscripts denote for summation convention.

TABLE I. Reflection coefficient R for some liquid media along $\varphi_0=28.647\,821°$ direction on Cu(001) plane.

Media	Real part of R	Imaginary part of R	PSW velocity (m/s)
CH_3Br	−1.000 000 000 0	−4.790 438 561 0e−08	2265.909 397 4
$C_3H_5(OH)_3$	−1.000 000 000 0	−1.821 756 264 7e−08	2265.909 397 6
$(CH_2OH)_2$	−1.000 000 000 0	−2.550 945 319 4e−08	2265.909 397 6
H_2O (Water)	−1.000 000 000 0	−5.630 357 027 5e−08	2265.909 397 5
C_6H_{14}	−1.000 000 000 0	−1.221 773 645 7e−07	2265.909 397 5
Vacuum	…	…	2265.909 397 8

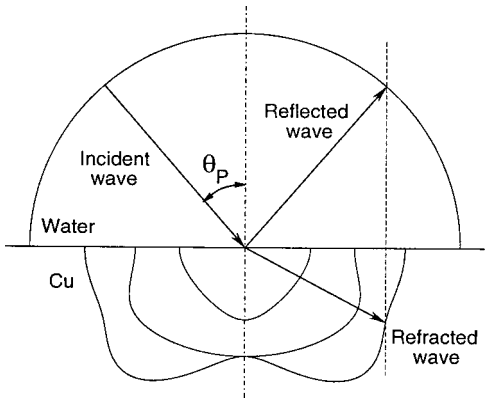

FIG. 3. Cross-section of slowness surface of bulk waves on the water–Cu(001) interface along propagation direction φ_0 with incident angle θ_P.

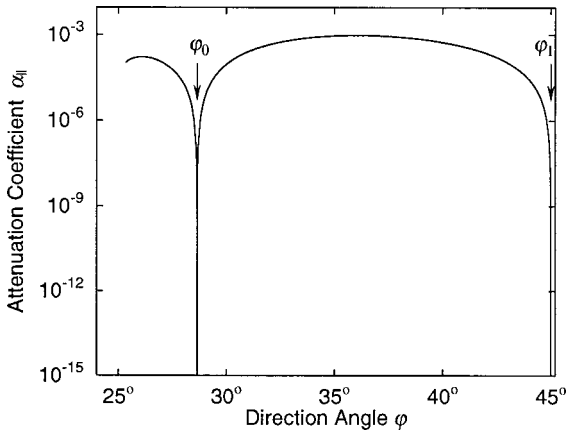

FIG. 4. Attenuation coefficient for PSW as a function of propagation direction on the vacuum–Cu(001) interface.

Some parameters in Eq. (2) for the PSW along φ_0 direction on the water–Cu(001) interface were listed in Table II. In the reflection coefficient analysis method, the direction cosines of l_1 and l_2 are the same values with the incident wave. All of them are real-valued: $\mathrm{Im}[l_1]\equiv 0$ and $\mathrm{Im}[l_2]\equiv 0$. Then the Christoffel equation (3) becomes a sextic equation in l_3 with real coefficients. The six roots of l_3 are real or complex conjugate. The three effective $l_3^{(n)}$'s for the PSW are: $l_3^{(1)}$ and $l_3^{(2)}$, having negative imaginary parts, correspond to two partial surface wave components, and $l_3^{(3)}$, having only a negative real part, represents a general bulk wave along the $-x_3$ direction. Since $W_3=0$, this PSW loses its bulk component which carries energy into the solid, and consists of only two partial surface wave components. In fact, it becomes a two-component surface wave.[9,10] This two-component surface wave is intrinsic to the PSW on the vacuum–anisotropic–solid surface. To be noticed again, among three components of this two-component surface wave, the bulk partial wave component is lost and only two surface partial wave components are working in real.

On the vacuum boundary condition, the structure of a PSW can be expressed as follows. The direction cosines of l_1 and l_2 are usually complex-valued with small positive imaginary part. That is, PSW attenuates along the parallel direction of the surface. Hence, the Christoffel equation (3) becomes a sextic equation in l_3 with complex coefficients. Two components $\{l_3^{(1)}, l_3^{(2)}\}$ among the three effective $l_3^{(n)}$'s for PSW have negative imaginary parts as surface wave components. The other $l_3^{(3)}$ has a negative real part and a small positive imaginary part. This partial wave implies an unusual bulk wave: the amplitude increases along the depth direction of the solid. An attenuation coefficient $\alpha_{||}$ for PSW was theoretically defined by $\alpha_{||}=\mathrm{Im}[k_{||}]/\mathrm{Re}[k_{||}]$ for the wave number $k_{||}$ of PSW. Here, $k_{||}$ is a component of wave number vector $\mathbf{k}$ along the propagation direction on the surface. Figure 4 illustrated variation of this $\alpha_{||}$ for PSW on the vacuum–Cu(001) interface. Obviously seen in this figure, $\alpha_{||}$'s become zero along φ_0 and φ_1 directions. Hence, along these propagation directions, l_1 and l_2 become real. Thus the Christoffel equation (3) for two different methods becomes a same expression. Additionally, the same PSW velocities can be obtained by using these methods: the wave parameters along the φ_0 direction for PSW on the vacuum–Cu(001) interface become equal to that in Table II. It is typical to the two-component surface wave.

From Ref. 9, when a two-component surface wave is excited, the boundary condition determinant becomes really zero valued: $Z_{\mathrm{tot}}=0$. From Eq. (1), $Z_{\mathrm{tot}}=0$ provides $R=-1$; therefore, along φ_0 and φ_1 direction, reflection coefficient R becomes -1. On the other hand, if $R=-1$, then from Eq. (1), $Z_{\mathrm{tot}}=0$ can be obtained. Since the above procedure becomes free from Z term, the properties of liquid have nothing to do with PSW. In other words, use of the condition by $\mathrm{Re}[R]=-1$ and $\mathrm{Im}[R]=0$ for PSW, enables

TABLE II. The values of some parameters along $\varphi_0=28.647\,821°$ direction on the water–Cu(001) interface.

Parameter	Value
$\mathrm{Im}[l_1]$	0
$\mathrm{Im}[l_2]$	0
$l_3^{(1)}$	$0.597\,853\,238\,4-0.265\,852\,725\,9i$
$l_3^{(2)}$	$-0.597\,853\,238\,4-0.265\,852\,725\,9i$
$l_3^{(3)}$	$-0.534\,192\,189\,9$
W_1	1
W_2	$-0.663\,295\,417\,1-0.748\,357\,661\,5i$
W_3	0
v(m/s)	2265.909 397 8

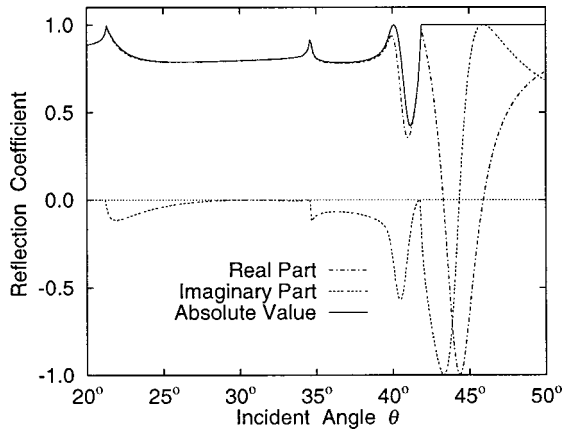

FIG. 5. Incident angle dependence of reflection coefficient along direction angle $\varphi=22°$ on water–InAs (001) interface.

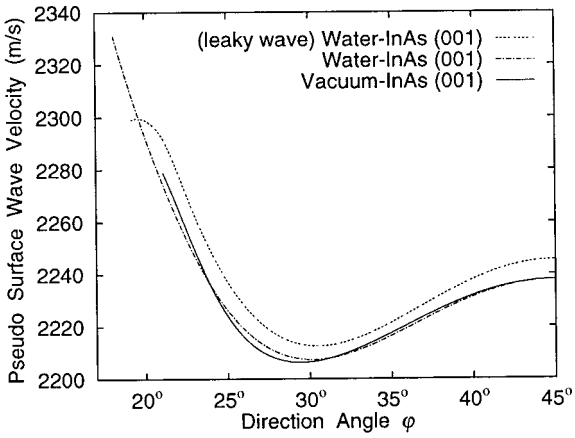

FIG. 6. PSW velocity distributions on InAs(001) plane.

us to make numerical search for the activation position of the two-component surface wave.

Nayfeh indicated that PSW should be excited when $\mathrm{Re}[R]<0$ and $\mathrm{Im}[R]=0$. This definition may underestimate the existence range of PSW. His calculated existence range of PSW on the water–InAs(001) interface was placed from $\varphi=24°$ to 45°. Figure 5 shows $R(\theta)$ for $20°\leqslant\theta\leqslant 50°$ on the water–InAs(001) interface along direction angle $\varphi=22°$. It is obvious from this profile of the reflection coefficient that the dip of $|R|$ at near incident angle $\theta=41.2°$ is not caused by the usual quasi-bulk wave(s), but by the excitation of PSW. Here, $\mathrm{Im}[R]=0$ and $\mathrm{Re}[R]>0$ (but not $\mathrm{Re}[R]<0$). Figure 6 illustrated PSW velocity distribution on the water–InAs(001) interface analyzed by the reflection coefficient method. The existence range is located from 18.1° to 45° which is wider than Nayfeh's estimate. Note that this profile is different from the leaky PSW velocity distribution on the water–InAs(001) interface and the PSW velocity dispersion on the vacuum boundary.

In the reflection coefficient method for a plane wave impinging from liquid onto a liquid–anisotropic–solid interface, the leaky effect was not considered when RSW or PSW are excited. This obtained RSW is not a leaky wave but just equals to the true RSW on the vacuum–solid interface. The PSW is also nonleaky, having no energy leakage from the solid into the liquid.

[1] A. Atalar, ''Reflection of ultrasonic waves at a liquid–cubic–solid interface,'' J. Acoust. Soc. Am. **73**, 435–440 (1981).
[2] O. Arikan, E. Telatar, and A. Atalar, ''Reflection coefficient null of acoustic waves at a liquid–anisotropic–solid interface,'' J. Acoust. Soc. Am. **85**, 1–10 (1989).
[3] A. H. Nayfeh, ''Elastic wave reflection from liquid–anisotropic substrate interfaces,'' Wave Motion **14**, 55–67 (1991).
[4] T. C. Lim and G. W. Farnell, ''Search for forbidden directions of elastic surface-wave propagation in anisotropic crystals,'' J. Appl. Phys. **39**, 4319–4325 (1968).
[5] T. C. Lim and G. W. Farnell, ''Character of pseudo surface waves on anisotropic crystals,'' J. Acoust. Soc. Am. **45**, 845–851 (1969).
[6] G. W. Farnell, ''Properties of elastic surface waves,'' in *Physical Acoustsics, Vol. VI*, edited by W. P. Mason and R. N. Thurston (Academic, New York, 1970), p. 109.
[7] L. M. Brekhovskikh, *Waves in Layered Media*, 2nd ed. (Academic, New York, 1980), p. 45.
[8] S. Tamura, R. E. Vines, and J. P. Wolfe, ''Effects of liquid loading on surface acoustic waves in solids,'' Phys. Rev. B **54**, 5151–5163 (1996).
[9] A. A. Maznev and A. G. Every, ''Secluded supersonic surface waves in germanium,'' Phys. Lett. A **197**, 423–427 (1995).
[10] A. N. Darinskii, V. I. Alshits, J. Lothe, V. N. Lyubimov, and A. L. Shuvalov, ''An existence criterion for the branch of two-component surface waves in anisotropic elastic media,'' Wave Motion **28**, 241–257 (1998).

Flexural edge waves and Comments on "A new bending wave solution for the classical plate equation" [J. Acoust. Soc. Am. 104, 2220–2222 (1998)]

A. N. Norris
Department of Mechanical & Aerospace Engineering, Rutgers University, 98 Brett Road, Piscataway, New Jersey 08854-8058

V. V. Krylov
Department of Civil and Structural Engineering, The Nottingham Trent University, Burton Street, Nottingham NG1 4BU, England

I. D. Abrahams
Department of Mathematics, University of Manchester, Manchester M13 9PL, England

(Received 7 December 1998; accepted for publication 25 September 1999)

A brief review is presented of the theory of flexural edge waves, first predicted in 1960 by Yu K. Konenkov using Kirchhoff plate theory. It is demonstrated that the flexural edge wave is also predicted by Mindlin's plate theory, and that the prediction agrees with measured data. It is noted that the edge wave was erroneously presented as a new type of bending wave solution in a recently published paper in this journal. © *2000 Acoustical Society of America.* [S0001-4966(00)01301-1]

PACS numbers: 43.40.Dx [CBB]

The existence of a flexural wave guided by the free edge of a semi-infinite isotropic elastic thin plate was first demonstrated by Konenkov[1] in 1960. The wave has properties analogous to a Rayleigh wave on an elastic half-space, in that it decays exponentially with distance from the edge. This result was apparently not very widely known in Western scientific circles, not an uncommon situation in the 1960's and 1970's, because it was rediscovered concurrently and independently by Sinha[2] and by Thurston and McKenna,[3] both published in 1974 in ''western'' journals. The first author of this Letter was likewise ignorant of Konenkov's original contribution when he proved that the edge wave also exists on anisotropic plates.[4]

In a recent article[5] in this journal, the now-classical result for the flexural edge wave was again presented as new. The author cited a paper of McKenna *et al.*[6] but apparently did not know the Thurston and McKenna paper,[3] published shortly after and in the same journal, and was also unaware of the sizeable literature on the subject.

The propagation of flexural waves guided by the tip of a wedge or the free end of a ridge on a substrate was studied in some depth by various groups in the 1970's. In 1974 Sinha,[2] using the classical plate theory, obtained an explicit expression for the speed of the flexural edge wave. At about the same time, McKenna *et al.*[6] derived the dispersion relation for a flexural plate edge wave by taking the limit of a wedge with zero internal angle. Thurston and McKenna[3] subsequently discussed in detail the existence and behavior of this wave, and obtained the same wave speed as Sinha.[2] The flexural edge wave speed was also derived from the modes of a thin plate of finite width by taking the limit in which the width becomes infinite.[7]

The classical Kirchhoff plate theory predicts a speed for the edge wave which is in constant proportion to the flexural wave speed. The constant of proportionality is independent of the frequency and depends only on the Poisson's ratio, being slightly less than unity and equal to unity when the Poisson's ratio vanishes. As noted by Thurston and McKenna,[3] this equality reflects the fact that a flexural wave traveling parallel to the edge of a thin plate of zero Poisson's ratio gives no bending moment or shear and hence automatically satisfies the free edge conditions of the classical plate theory.

The edge wave solution of the classical plate theory has been studied by many since then, for instance Refs. 8, 9, and is discussed in at least two monographs.[10,11] The speed of the flexural edge wave was measured and agrees well with finite element calculations,[9] and both the measured speed and the FEM calculations are less than the values predicted by the Kirchhoff plate theory. An explicit expression can also be obtained for the edge wave speed on an anisotropic thin plate.[4] The analog of a flexural Stoneley wave propagating along the line of contact of two joined semi-infinite plates and decaying exponentially in the perpendicular direction has been studied by Zilbergleit and Suslova.[12] Kouzov *et al.*[13] have considered the more general configuration of a starlike nodal junction of thin plates.

Two of the present authors have recently established the existence of edge supported flexural waves on fluid loaded thin plates.[14] However, submerged plates support such waves only under very light fluid loading conditions: for instance, thin plates of aluminum, brass or Plexiglas will support edge waves in air, but not in water.[14]

Previous studies of the flexural edge wave on a semi-infinite plate *in vacuo* have used either the Kirchhoff plate theory or some far more sophisticated analysis based on the full equations, e.g., FEM. We now demonstrate that the essential characteristics of the edge wave are captured by the Mindlin plate theory[15] without much additional effort beyond that required for the Kirchhoff theory. To the best of

our knowledge, the edge wave has not been previously analyzed in the context of Mindlin plate theory. The Mindlin theory for flexural waves incorporates shear-deformation and rotary-inertia, two effects that are absent from the classical Kirchhoff theory. According to Mindlin's theory the displacement at (x,y,z) is $\mathbf{u}=z\boldsymbol{\psi}(\mathbf{x},t)+w(\mathbf{x},t)\mathbf{e}_z$, where $\mathbf{x}=(x,y)$ is the 2-D position on the central plane of the plate, z is the transverse coordinate, with $z=0$ the center plane of the plate and $\boldsymbol{\psi}=(\psi_x,\psi_y)$ is the in-plane vector of rotations.

The equations of motion in the absence of external loading are

$$\frac{\partial M_x}{\partial x}+\frac{\partial M_{xy}}{\partial y}-Q_x=\frac{\rho h^3}{12}\frac{\partial^2\psi_x}{\partial t^2}, \tag{1}$$

$$\frac{\partial M_{xy}}{\partial x}+\frac{\partial M_y}{\partial y}-Q_y=\frac{\rho h^3}{12}\frac{\partial^2\psi_y}{\partial t^2}, \tag{2}$$

$$\frac{\partial Q_x}{\partial x}+\frac{\partial Q_y}{\partial y}=\rho h\frac{\partial^2 w}{\partial t^2}, \tag{3}$$

where ρ is the density and h the thickness. The moments M_x, M_y, and M_{xy}, and the shear forces Q_x and Q_y, are

$$M_x=D\left(\frac{\partial\psi_x}{\partial x}+\nu\frac{\partial\psi_y}{\partial y}\right),\quad M_y=D\left(\frac{\partial\psi_y}{\partial y}+\nu\frac{\partial\psi_x}{\partial x}\right),$$

$$M_{xy}=\frac{1}{2}D(1-\nu)\left(\frac{\partial\psi_x}{\partial y}+\frac{\partial\psi_y}{\partial x}\right),\quad Q_x=\alpha^2\mu h\left(\frac{\partial w}{\partial x}+\psi_x\right), \tag{4}$$

$$Q_y=\alpha^2\mu h\left(\frac{\partial w}{\partial y}+\psi_y\right),$$

where $D=Eh^3/12(1-\nu^2)$ is the bending stiffness, ν is Poisson's ratio, μ is the shear modulus, and $E=2(1+\nu)\mu$ is the Young's modulus. The shear modulus is modified by the factor α^2 in order to better approximate the shear forces, and α may be chosen according to different criteria, but normally, $\alpha^2\leqslant 1$.[16]

Now let the plate occupy $-\infty<x<\infty$, $y\geqslant 0$ with a free edge on $y=0$. We consider the time harmonic *ansatz* of frequency ω:

$$w(\mathbf{x},t)=\mathrm{Re}[(V_1+V_2)e^{-i\omega t}],$$
$$\boldsymbol{\psi}(\mathbf{x},t)=\mathrm{Re}[(\beta_1\boldsymbol{\nabla}V_1+\beta_2\boldsymbol{\nabla}V_2-\mathbf{e}_z\times\boldsymbol{\nabla}V_3)e^{-i\omega t}], \tag{5}$$

where V_1, V_2 and V_3 are given by[15]

$$V_j(\mathbf{x})=A_j e^{i\xi x-\sqrt{\xi^2-k_j^2}\,y},\quad j=1,2,3. \tag{6}$$

The three bulk wave numbers k_1, k_2 and k_3 and the numbers β_1 and β_2 follow by direct substitution into Eqs. (1)–(4) and are given by

$$k_1^2+k_2^2=k_S^2+k_P^2,\quad k_1^2k_2^2=k_S^2k_P^2-k_f^4,\quad k_3^2=\alpha^2k_1^2k_2^2/k_P^2,$$
$$\beta_j=-1+k_S^2/k_j^2,\quad j=1,2, \tag{7}$$

where

$$k_S=\frac{\omega}{\alpha}\sqrt{\rho/\mu},\quad k_P=\omega\sqrt{(1-\nu^2)\rho/E},\quad k_f^2=\omega\sqrt{h\rho/D}. \tag{8}$$

By applying the boundary conditions appropriate to a free edge: vanishing shear force, bending moment and twisting moment, that is, $Q_y(x,0)=0$, $M_y(x,0)=0$, and $M_{xy}(x,0)=0$, respectively, three equations are obtained for A_j, $j=1,2,3$. Setting the resulting determinant to zero, yields, after some simplification, the following dispersion relation for the wave number ξ of the edge wave:

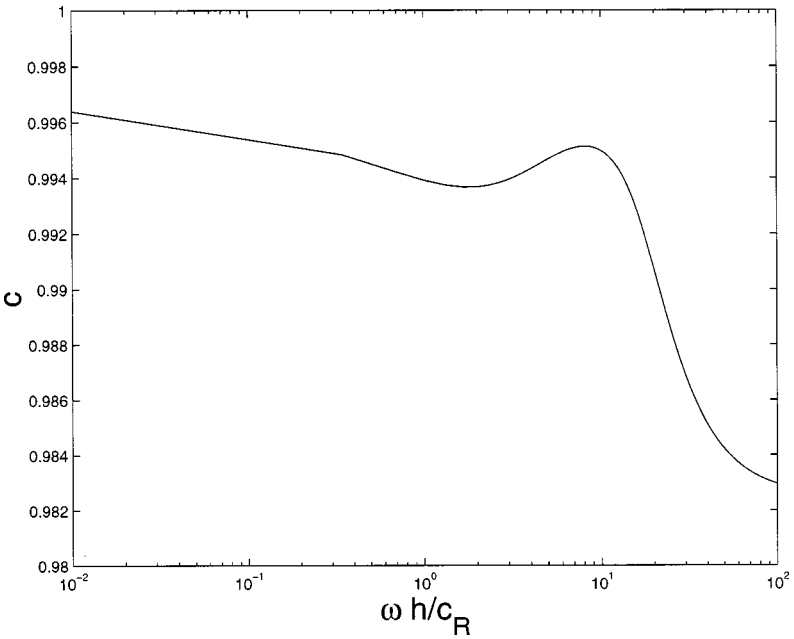

FIG. 1. The dimensionless speed $c=k_1/\xi$ according to Mindlin plate theory plotted against the dimensionless frequency $k_Rh=\omega h/c_R$. The free parameters are $\nu=0.39$, $\alpha=c_R/c_T$. The value at $k_Rh=0$ is given by Eq. (10).

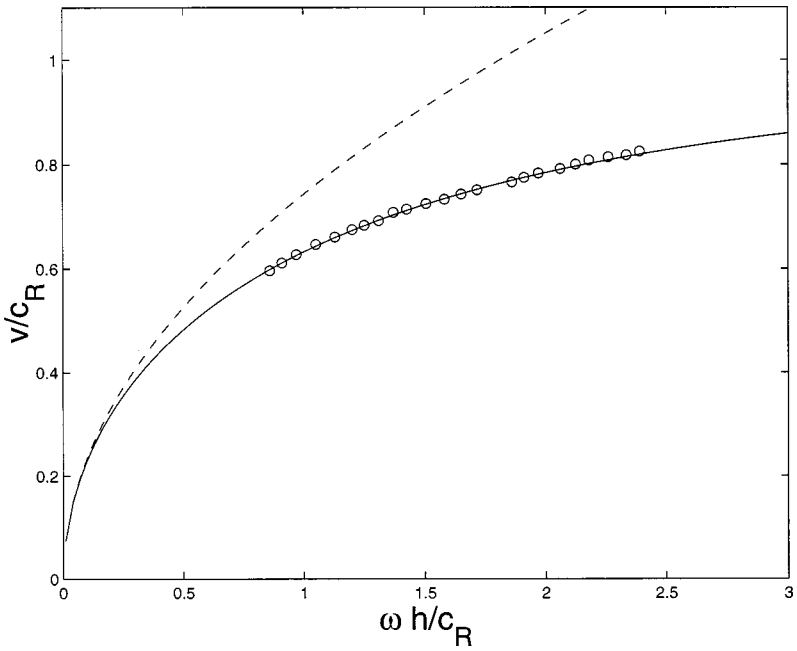

FIG. 2. The edge wave speed v relative to the Rayleigh wave speed c_R according to Mindlin theory (solid curve) and the Kirchhoff theory (dashed curve). The circles represent data from Lagasse and Oliner (Ref. 9).

$$\begin{vmatrix} k_1^2 & k_2^2 & k_3^2 \\ k_S^2 & k_S^2 & 2\xi^2 \\ \dfrac{[(1-\nu)\xi^2-k_1^2](k_S^2-k_1^2)}{\sqrt{\xi^2-k_1^2}} & \dfrac{[(1-\nu)\xi^2-k_2^2](k_S^2-k_2^2)}{\sqrt{\xi^2-k_2^2}} & 2(1-\nu)\xi^2\sqrt{\xi^2-k_3^2} \end{vmatrix} = 0. \tag{9}$$

Let $k_1^2 > k_2^2$, then k_1 is the analog of the classical flexural wave number k_f in the Mindlin theory. The speed of the flexural edge wave relative to the Mindlin flexural wave is $c = k_1/\xi$. Numerical experimentation shows that there is always a root of the dispersion relation for $c \leqslant 1$, with equality again when $\nu = 0$. The fact that $c = 1$ for $\nu = 0$ is a consequence of the fact that the flexural wave automatically satisfies the free edge conditions with no Poisson contraction effect. For nonzero ν the Poisson effect comes into play and the edge wave solution has a small but nonzero component from the other two Mindlin plate waves, and its speed is subsonic relative to the propagating flexural wave. For instance, Fig. 1 shows a plot of c versus frequency. It may be verified by direct calculation that the root of Eq. (9) reduces to the value predicted by Thurston and McKenna[3] in the limit as the dimensionless frequency $k_S h$ approaches zero, that is,

$$c = [-(1-\nu)(1-3\nu) + 2(1-\nu) \times (1-2\nu+2\nu^2)^{1/2}]^{1/4} \quad \text{as } k_S h \to 0. \tag{10}$$

The high frequency limit of the edge wave is of interest. It may be shown by taking the correct limits that at high frequencies ξ is the unique positive solution of

$$(2\xi^2-k_T^2)^2 - 4\xi^2(\xi^2-k_T^2)^{1/2}(\xi^2-k_P^2)^{1/2} = 0 \quad \text{as } k_S h \to \infty, \tag{11}$$

where $k_T = k_S/\alpha$ is the wave number of bulk transverse waves, i.e., $k_T = \omega/c_T$ where $c_T = \sqrt{\mu/\rho}$. The form of Eq. (11) is precisely the same as the equation for the Rayleigh wave on the surface of a half-space, except that the longitudinal wave number k_P in Eq. (11) is the wave number according to membrane theory; see Eq. (8). This has speed $c_P = \sqrt{E/[(1-\nu^2)\rho]}$ as compared with the larger speed of a bulk longitudinal wave, $c_L = c_P(1-\nu)/\sqrt{1-2\nu}$. The membrane Rayleigh wave speed c_R^* is the same as the true Rayleigh wave speed for a material with ν replaced by the value $\nu/(1+\nu)$, leading to a slower speed. Hence, the high frequency limit of the edge wave according to Mindlin's theory is the Rayleigh ''surface'' wave traveling along the narrow surface of a thin plate. The meaning and interpretation of this is unclear since one should be cautious of using the high frequency limit of Mindlin's theory for purposes other than intended. The original goal of Mindlin was to obtain the high frequency asymptote of the fundamental antisymmetric mode of a plate, which is itself the true Rayleigh wave speed c_R if α is chosen as $\alpha = c_R/c_T$. The occurrence of the ''membrane'' Rayleigh wave as the asymptote is therefore all the more interesting since it drops out in the limit independent of the value of α.

Finally, Fig. 2 compares the Mindlin edge wave speed with the Kirchhoff edge wave speed, and also with measured data of Lagasse and Oliner.[9] The speeds are normalized with respect to the Rayleigh wave speed. The Poisson's ratio was

chosen as $\nu=0.39$ so that the Kirchhoff curve agrees with a similar curve in Ref. 9, and $\alpha=c_R/c_T$. We note that a finite element computation by Lagasse and Oliner[9] produced a curve essentially overlying the Mindlin curve of Fig. 2, within the accuracy of the data read from Ref. 9.

Note added in proof. A referee pointed out that Ambartsumyan and Belubekyan[17] came to a conclusion opposite to ours: that the more exact plate theories of Timoshenko–Mindlin type predict that localized edge wave do not exist. After examining their paper, we conclude that the analysis of Ambartsumyan and Belubekyan is in error, and that the edge wave is predicted by Mindlin plate theory.

ACKNOWLEDGMENT

Thanks to Dr. Boris Belinskiy for information on the Soviet era literature.

[1] Yu. K. Konenkov, ''A Rayleigh-type flexural wave,'' Sov. Phys. Acoust. **6**, 122–123 (1960).
[2] B. K. Sinha, ''Some remarks on propagation characteristics of ridge guides for acoustic waves at low frequencies,'' J. Acoust. Soc. Am. **56**, 16–18 (1974).
[3] R. N. Thurston and J. McKenna, ''Flexural acoustic waves along the edge of a plate,'' IEEE Trans. Sonics Ultrason. **21**, 296–297 (1974).
[4] A. N. Norris, ''Flexural edge waves,'' J. Sound Vib. **171**, 571–573 (1994).
[5] C. Kauffmann, ''A new bending wave solution for the classical plate equation,'' J. Acoust. Soc. Am. **104**, 2220–2222 (1998).
[6] J. McKenna, G. D. Boyd, and R. N. Thurston, ''Plate theory solution for guided flexural acoustic waves along the tip of a wedge, '' IEEE Trans. Sonics Ultrason. **21**, 178–186 (1974).
[7] V. A. Veshev, I. I. Klyukin, D. P. Kouzov, and V. D. Lukyanov, ''On oscillating energy propagation in a thin elastic plate of a finite width,'' Sov. Phys. Acoust. **23**, 129–131 (1977).
[8] T. M. Sharon, A. A. Maradudin, and S. L. Cunningham, ''Vibrational modes on a rectangular ridge,'' Lett. Appl. Eng. Sci. **2**, 161 (1974).
[9] P. E. Lagasse and A. A. Oliner, ''Acoustic flexural mode on a ridge of semi-infinite height,'' Electron. Lett. **12**, 11–13 (1976).
[10] A. A. Oliner, Ed., *Acoustic Surface Waves*, Topics Appl., Phys., Vol. 24 (Springer, Berlin, 1978).
[11] S. V. Biryukov, Yu. V. Gulyaev, V. V. Krylov, and V. P. Plessky, *Surface Acoustic Waves in Inhomogeneous Media*, Springer Series on Wave Phenomena, Vol. 20 (Springer, Berlin, 1995).
[12] A. S. Zilbergleit and I. B. Suslova, ''Contact flexural waves in thin plates,'' Sov. Phys. Acoust. **29**, 108–111 (1983).
[13] D. P. Kouzov, T. S. Kravtsova, and V. G. Yakovleva, ''On the scattering of the vibrational waves on a knot contact of plates,'' Sov. Phys. Acoust. **35**, 392–394 (1989).
[14] I. D. Abrahams and A. N. Norris (unpublished).
[15] R. D. Mindlin, ''Influence of rotary inertia and shear on flexural motion of isotropic, elastic plates,'' J. Appl. Mech. **18**, 31–38 (1951).
[16] K. F. Graff, *Wave Motion in Elastic Solids* (Dover, New York, 1991).
[17] S. A. Ambartsumyan and M. V. Belubekyan, ''On bending waves localized along the edge of a plate,'' Int. Appl. Mech. **30**, 135–140 (1994).

Response to "Flexural edge waves and Comments on 'A new bending wave solution for the classical plate equation'" [J. Acoust. Soc. Am. 104, 2220–2222 (1998)]

Christiaan Kauffmann
Delft University of Technology, Faculty of Information Technology and Systems, Department of Technical Mathematics and Computer Science, P.O. Box 5031, 2600 GA Delft, The Netherlands

(Received 15 June 1999; accepted for publication 25 September 1999)

We reply to the preceding letter.

[S0001-4966(00)01401-6]

PACS numbers: 43.40.Dx [CBB]

In a recent publication by the author[1] a flexural wave mode was described that freely propagates down the free edge of a semi-infinite, classical, Kirchhoff plate. In a letter to the editor Norris *et al.*[2] pointed out that Konenkov[3] already described this wave back in 1960. Consequently, this is certainly not a new wave type, although largely unfamiliar. While this was unknown to me before (and supposedly also to the referees) I take the opportunity to thank Norris *et al.* for their letter and to re-confirm that credit should have been given to Konenkov's work. Moreover, I would not have submitted my work for publication if I had been aware of Konenkov's paper.

I take the opportunity to make some remarks of minor importance. This concerns the confusion that might arise from the term *Rayleigh wave*. Konenkov termed his wave *Rayleigh-type flexural wave*. Norris *et al.* emphasize the analogy between the flexural edge-wave and the true Rayleigh wave. My remarks are made to stress the difference between the flexural edge-wave and the Rayleigh wave. First, the amplitude of the Rayleigh wave falls off exponentially with distance from the free surface, while the amplitude of the flexural edge-wave falls off exponentially at *two* different rates. Second, the observation that the amplitude falls off exponentially does not justify such a close correspondence between the flexural edge-wave and the Rayleigh wave: to date, there is a very large number of so-called surface waves, although the Rayleigh wave was the first surface wave identified in the context of elastic waves in solids. Third, the analogy between the Rayleigh wave and the flexural edge-wave breaks down if one considers that the Rayleigh wave and the flexural edge-wave are both transverse waves, i.e., the particle displacements and velocities are perpendicular to the direction of propagation. However, a Rayleigh surface wave has no velocity component that is both perpendicular with respect to the direction of propagation and, simultaneously, parallel to the free surface, whereas the flexural edge-wave has no other velocity component than just that! Note that the analogy requires one to identify the free edge and the free surface as well as the direction of propagation. Consequently, the flexural edge-wave cannot be identified to, nor derived from, the Rayleigh wave.

[1] C. Kauffmann, ''A new bending wave solution for the classical plate equation,'' J. Acoust. Soc. Am. **104**, 2220–2222 (1998).
[2] A. N. Norris, V. V. Krylov, and I. D. Abrahams, ''Flexural edge waves and Comments on 'A new bending wave solution for the classical plate equation,' J. Acoust. Soc. Am. **104**, 2220–2222 (1998),'' J. Acoust. Soc. Am. **107**, 1781–1784 (2000).
[3] Yu. K. Konenkov, ''A Rayleigh-type flexural wave,'' Sov. Phys. Acoust. **6**, 122–123 (1960).

 0001-4966/2000/107(3)/1785/1/$17.00

On the effect of the bending vibration on the acoustic properties of thin poroelastic plates

M. J. Swift, K. V. Horoshenkov, P. Leclaire, and D. C. Hothersall
Department of Civil and Environmental Engineering, University of Bradford, Bradford BD7 1DP, England

K. Fujiwara and H. Torihama
Department of Acoustic Design, Kyushu Institute of Design, Shiobaru 4-9-1, Minami, Fukuoka 815, Japan

(Received 31 August 1999; accepted for publication 18 November 1999)

An experimental study on the effect of bending vibration on the acoustic properties of thin porous plates is presented. Poroelastic plates are tested in a large impedance tube in the lower frequency range. It is shown that bending vibration can be excited by the incident sound and detected by measuring the acoustic impedance of a plate. This effect together with the effect of the flow resistivity on the values of the acoustic impedance of the plate are shown. The data from the large and small impedance tubes illustrate how these effects are reduced with the reduced size of the plate.
 [S0001-4966(00)00803-1]

PACS numbers: 43.50.Gf, 43.20.Tb, 43.40.Dx [MRS]

INTRODUCTION

There are a number of studies which have been carried out on the vibration of plates and structural damping. These have primarily been to investigate behavior of plates which are made from nonporous materials. The results of these studies are widely reported in the literature and a comprehensive summary of them can be found in Ref. 1. On the other hand, some studies have been carried out into the effect of the solid movement on the surface impedance of porous layers.

As an example, particular works by Bardot *et al.*[2] and Allard[3] are concerned with the coupling effect between Biot's slow and fast waves excited in a layer of highly porous fibrous materials with an infinite lateral extend bonded by an impermeable rigid wall. The low rigidity in the thickness of these materials allows compressions and expansions of the porous layer associated with the passage of the airborne acoustic wave. In such a case, the rigid frame approximation where the solid is immobile is no longer valid.

In this article, a coupling between the solid motion and the fluid motion is also studied, but this coupling is of a different nature. Here, the solid movements are eventually taken into account but these correspond to the structural vibration of thin rectangular porous plates.[4] The same assumption is made as in the standard theory of plates (nonporous) that only the in-plane stresses and deformations are considered while the deformations in the thickness are neglected. This assumption is often written in the standard plate theory as $\sigma_{33}=0$ where σ_{33} is the component of the stress tensor normal to the middle surface. As a consequence, the plate is allowed to bend, but its thickness remains constant. Two conditions are required to make this assumption: the plate must be fairly thin and its Young's modulus must be much greater than that of the fluid (air in our case). These requirements are met by our samples.

In this configuration, the triple combination of the bending vibration, the presence of an air gap, and the well-known visco-thermal interaction in the pores are investigated experimentally. Their influence on the surface impedance and the absorption coefficient is studied. It is shown that the absorption coefficient of a thin poroelastic plate can be considerably increased at particular frequencies so that the low frequency acoustic performance can be improved.

I. EXPERIMENTAL PROCEDURE

An investigation has been carried out on three thin porous plates with varying values of flow resistivity, density, and Young's modulus. Two plates have been manufactured from foam granulates which are recovered from automotive waste. The other plate has been manufactured from flint particles consolidated with rubber-epoxy binder (Coustone™). The dimensions of the plates were $0.5\,\mathrm{m}\times0.5\,\mathrm{m}\times10\,\mathrm{mm}$. Other material properties of the plates are listed in Table I.

The measurements have been carried out in the large impedance tube in the Kyushu Institute of Design and in a smaller Bruel and Kjaer 4206 impedance tube available in the University of Bradford. The larger impedance tube allows testing of $0.5\,\mathrm{m}\times0.5\,\mathrm{m}$ samples of acoustic materials in the frequency range of 50–300 Hz (see Fig. 1).

The plates have been tested with 40-mm and 80-mm air gaps, depending on the material properties. They have been clamped in the larger impedance tube along their edges using a strong wooden frame and the edges have been carefully sealed (see Fig. 1). Care was taken to ensure good clamping conditions so that not to distort the panel from its ''natural'' resting position. All gaps between the edges of the frame and the wall of the chamber were blocked using sealing putty. Because of the clamping device, the effective area of the plate exposed to sound was reduced to $0.48\,\mathrm{m}\times0.48\,\mathrm{m}$.

It is assumed that the resonance frequencies for bending vibration in smaller samples tested in the smaller tube are considerably higher. The results from the normal incidence impedance and absorption from the large and small impedance tubes have been compared. From this comparison the effect of structural vibration on the visco-thermal absorption in the material is estimated.

TABLE I. Summary table of material properties.

	YB10	G10	C10
Material	Recycled foam	Recycled foam	Consolidated flint
Plate thickness (m)	0.010	0.010	0.010
Density (kg/m^3)	414	390	1464
Young's modulus (Pa)	2.29×10^7	1.57×10^7	6.20×10^7
Porosity	0.57	0.44	0.40
Flow resistivity, Pa s m^{-2}	190367	743200	31520
Observed resonance frequency, Hz	86.25	76.25	96.25
Frequency of bending wave (mode), Hz	89.02 (3)	82.54 (3)	94.35 (3)

Some nonacoustic properties of the tested materials have been measured. These are the bulk density, Young's modulus, porosity, and flow resistivity. The flow resistivity and porosity have been measured using standard techniques of air flow tube and the method of water saturation under vacuum, respectively. The Young's modulus has been measured using rectangular strips of the material in a standard cantilever setup. The values of these parameters are compiled in Table I.

II. RESULTS AND DISCUSSION

The results for the real and imaginary parts of the surface acoustic impedance from the measurements in the large and small impedance tubes are compared in Figs. 2–4. The absorption coefficient as a function of frequency is shown in Figs. 5–7.

These figures seem to confirm that the vibration of certain modes in a clamped, porous, elastic plate can be generated by airborne sound in the low frequency range. These modes can be detected as resonances in the acoustic surface impedance (see Figs. 2–4). The frequencies corresponding to the bending vibration modes detected from the measurements are listed in Table I. These frequencies are reasonably close to the theoretical values provided by the classical theory of plates.[1] At these frequencies the values of the acoustic surface impedance can differ considerably from those measured in the small impedance tube, in which case the amplitude of vibration is considered to be negligibly small (see Figs. 2–4). In the vicinity of these resonances the absolute value of the imaginary part of the impedance can have a minimum, at which the relaxation processes are particularly pronounced. In this region the absorption in the porous material can be noticeably improved (see Figs. 5–7).

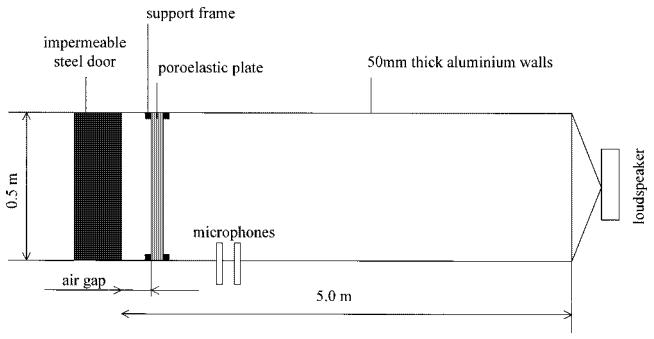

FIG. 1. Experimental setup.

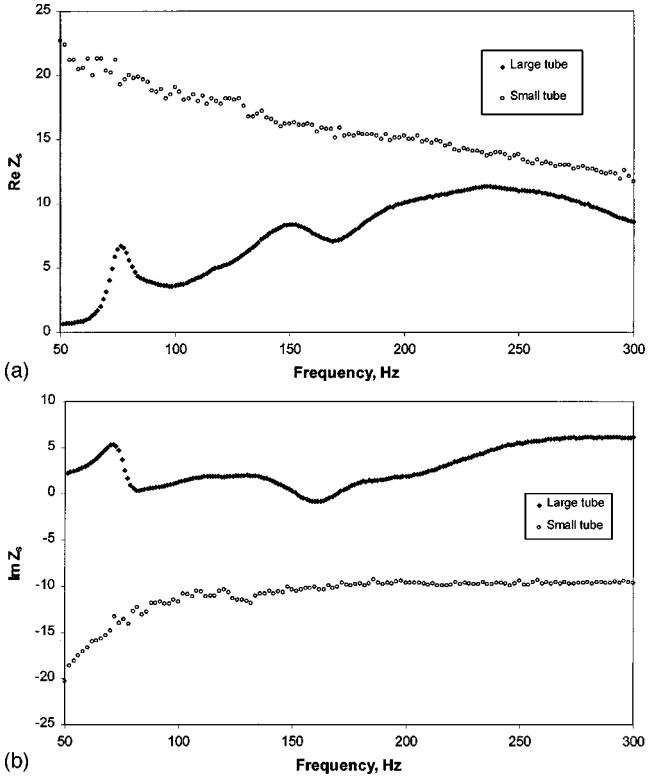

FIG. 2. The real (a) and imaginary (b) parts of the normalized surface impedance of a 10-mm-thick rectangular plate made from consolidated foam G10. 80-mm air gap.

In the case of a porous plate which is manufactured from consolidated foam G10 it is possible to observe two bending modes at frequencies 76.25 Hz and 150 Hz on the curve for the impedance (see Fig. 2). The frequencies of the modes correspond to the minima in the absorption spectrum (see Fig. 5). The minima in the impedance spectrum for this material are observed at 97.5 Hz and 168.75 Hz. At these frequencies the absorption is considerably improved in comparison with the data from the small impedance tube (see Fig. 5).

There is a resonance in the impedance spectrum corresponding to a mode which is clearly observed at 86.25 Hz in the case of a porous plate which is manufactured from consolidated foam YB10 (Fig. 3). There is a local maximum in the absorption spectrum at 76.25 Hz (Fig. 6).

In the case of the Coustone plate (C10) the resonance in the impedance spectrum is observed at 96.25 Hz (see Fig. 4). There is a local minimum in the spectrum immediately above this frequency, which results in some increase in the absorption spectrum at 103.75 Hz.

A precise quantitative analysis of the problem described in this article is still very difficult at the moment because of the lack of theoretical results. Nevertheless, a few remarks can be made from this study and some conclusions can be drawn with a reasonably good degree of confidence:

(1) The acoustical properties of large acoustic panels measured in a large impedance tube clearly exhibit resonances. These are associated with bending structural vibra-

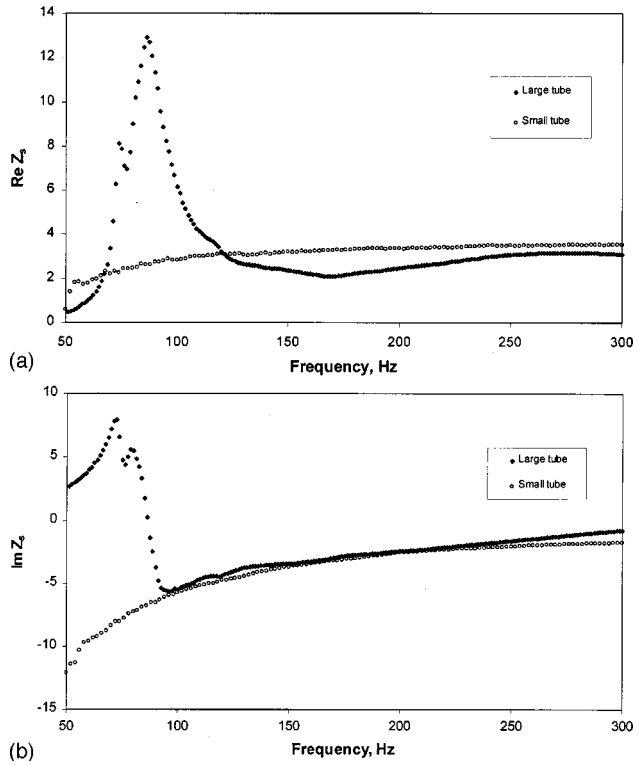

FIG. 3. The real (a) and imaginary (b) parts of the normalized surface impedance of a 10-mm rectangular plate made of consolidated foam YB10. 80-mm air gap.

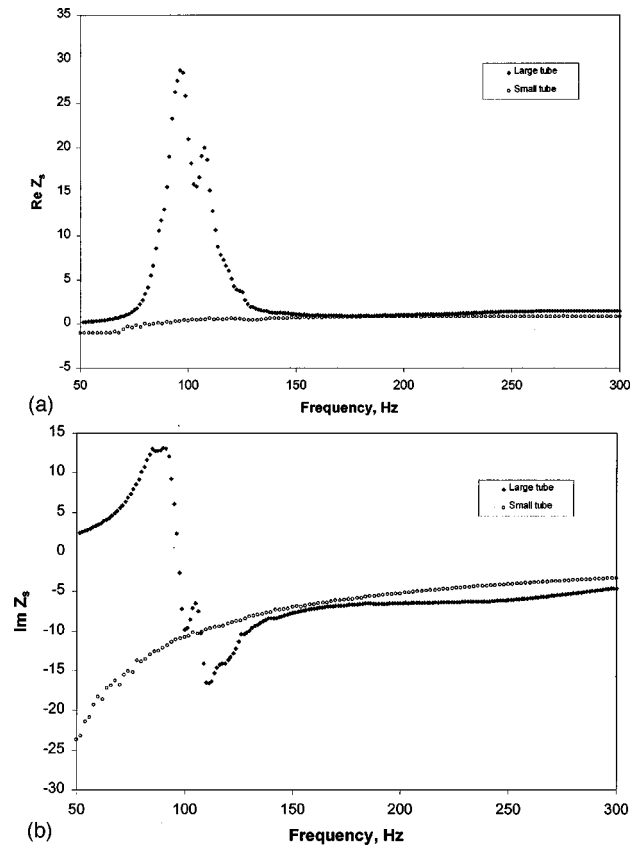

FIG. 4. The real (a) and imaginary (b) parts of the normalized surface impedance of a 10-mm rectangular plate made of the material C10. 40-mm air gap.

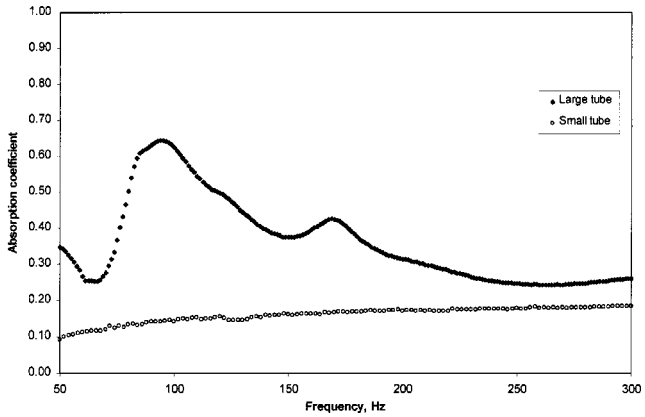

FIG. 5. The normal incidence absorption coefficient of a 10-mm-thick rectangular plate made from consolidated foam G10. 80-mm air gap.

tion of a finite-size, porous plate which has a fairly small thickness and the Young's modulus higher than that of air. The resonance frequencies seem to be close to predictions given by the standard theory of plates. These results show a noticeable enhancement of the absorption coefficient at some frequencies in the low frequency domain where the acoustic absorption is generally low. A physical interpretation of the resonances and of the mechanisms of the enhancement of the absorption coefficient is that a fraction of the acoustic energy carried by the incident sound wave is converted into the vibrational energy used to move the plate. This energy is then partly re-radiated at particular frequencies and partly dissipated in the frame.

(2) It is known that the presence of an air gap with properly chosen dimensions can enhance the low frequency acoustic performances.[3] It is also known that while increasing the absorption coefficient at some frequency areas, an air gap will decrease it at some others.[3] Nevertheless, the combination of an air gap with the structural vibrations could be very useful. Depending on its thickness, the presence of an air gap is thought to favor or hinder the observation of the structural vibration, but not to change the resonance frequencies which are solely dependent upon the plate mechanical properties, the clamping conditions, and the microstructural parameters (porosity, tortuosity and flow resistivity).

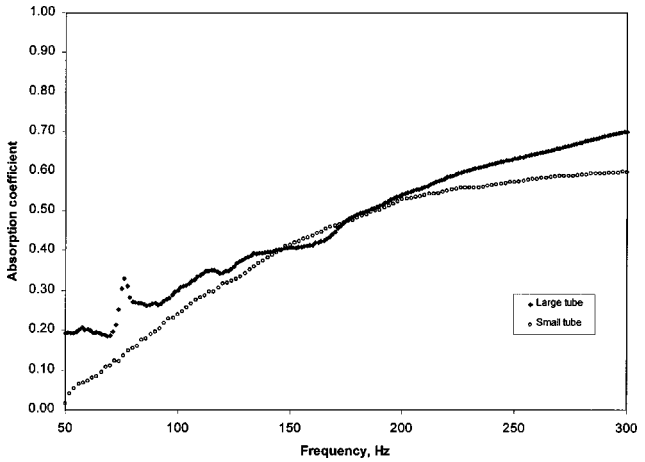

FIG. 6. The normal incidence absorption coefficient of a 10-mm-thick rectangular plate made from consolidated foam YB10. 80-mm air gap.

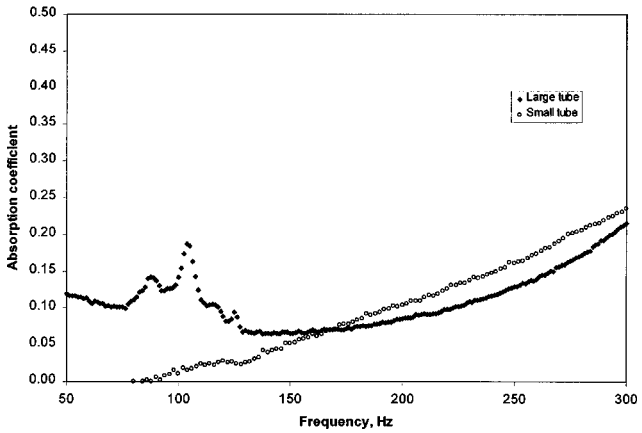

FIG. 7. The normal incidence absorption coefficient of a 10-mm-thick rectangular plate made from Coustone material C10. 40-mm air gap.

(3) The comparison of the damping of the resonances in the three examples investigated in this study shows that peaks in Fig. 5 seem to be smoother than those shown in Figs. 6 and 7. It is thought that particular values of the flow resistivity exist that will result in a maximum loss of energy by viscous frictions at certain frequencies of vibrations of the plate structures. In the optimum case, the phase shift between the solid and fluid motions is maximum and the viscous losses are maximum. This will result in a very smooth resonance peak.

(4) The visco-thermal interactions in porous media have been and are still the subject of active research (see Refs. 3,5). At low frequencies, the compressibility of air in the pores is isothermal and the absorption is dominated by the viscous frictions. At higher frequencies the compressibility is adiabatic and the viscous friction is also predominant. The thermal effects are particularly pronounced in the medium frequency range. Although they have less influence on the absorption than the viscous friction, their effect is not negligible. The combination of the visco-thermal effects and the effects described in (1)–(3) can provide an improved absorption spectrum in the whole frequency range.

III. CONCLUSIONS

An experimental study has been carried out to determine the effect of bending vibration on the acoustic properties of a clamped, porous, elastic plate. It has been shown that bending vibration of certain modes can be excited by incident sound in the plate and affect its acoustic impedance. The corresponding frequencies can be estimated a using a standard theory for clamped porous plates.[1] The measured values of the normal incidence plane wave absorption coefficient suggest that, in the vicinity of these frequencies, the absorption can be significantly improved as a result of relaxation processes which develop in the moving porous frame. In this way, porous plates with improved low frequency absorption can be designed. The experimental data also suggest that the acoustic impedance is more affected in porous plates with higher values of the flow resistivity as a result from a better coupling between airborne sound and bending vibration in the elastic frame.

ACKNOWLEDGMENTS

The authors gratefully acknowledge the support of the Engineering and Physical Sciences Research Council (Grant No. GR/L54905) and the contribution from the British Council in Tokyo toward the travel and expenses connected to the work which was carried out in Kyushu Institute of Design. The authors are also very grateful for the support given by Eric Chadwick and CEP Acoustics Limited, who manufactured and supplied samples of Coustone material.

[1] A. Leissa, *Vibration of Plates* (Acoustical Society of America, New York, 1993).
[2] A. Bardot, B. Brouard, and J. F. Allard, ''Frame decoupling at low frequency in thin porous layers saturated by air,'' J. Appl. Phys. **79**, 8223–8229 (1996).
[3] J.-F. Allard, *Propagation of Sound in Porous Media: Modelling Sound Absorbing Materials* (Elsevier, Amsterdam, 1993).
[4] D. D. Theodorakopoulos and D. E. Beskos, ''Flexural vibrations of poroelastic plates,'' Acta Mech. **103**, 191–203 (1994).
[5] D. Lafarge, P. Lemarinier, J. F. Allard, and V. Tarnow, ''Dynamic compressibility of air in porous structures at audible frequencies,'' J. Acoust. Soc. Am. **102**, 1995–2006 (1997).

Tinnitus and $2f1-f2$ distortion product otoacoustic emissions following salicylate overdose

Thomas Janssen,[a] Paul Boege, Elmar Oestreicher, and Wolfgang Arnold
ENT-Department of the Technical University Munich, Ismaningerstrasse 22, D-81675 München, Germany

(Received 16 July 1999; accepted for publication 3 December 1999)

A 22-year-old woman consumed approximately 10 g of salicylate with suicidal intent. She had a severe hearing loss and a strong tinnitus within 22 h of the overdose, and then 24 h later a subsequent hearing restoration and tinnitus abolishment. Transiently evoked otoacoustic emissions (TEOAEs) and $2f1-f2$ distortion product otoacoustic emissions (DPOAEs) were measured in both states. In the state of intoxication DPOAEs could be recorded well in the frequency range that corresponded to the appearance of the tinnitus despite the 50-dB hearing loss. The corresponding DPOAE I/O-functions were linearized, indicating loss of outer hair cell compression. After recovery, DPOAE level and DPOAE growth were within the normal range and showed normal physiological compression. The TEOAEs were missing in the acute state of intoxication. This case supports the hypothesis that aspirin-induced tinnitus is generated at the outer hair cell level. Whereas TEOAEs only give evidence that something might have changed in the cochlea, DPOAEs are a more useful and robust quantitative indicator of the underlying mechanism of some forms of cochlear tinnitus. [S0001-4966(00)03003-4]

PACS numbers: 43.64.Jb, 43.64.Kc, 43.64.Ri [BLM]

FINDINGS

A young female (22 years) who had just overdosed on salicylates was brought to our attention. She had a severe high-frequency hearing loss associated with a strong tinnitus in both ears. The patient reported that she swallowed all capsules in an aspirin box with suicidal intent. She was unable to give precise information on the dose or how many capsules she swallowed. On the assumption that she swallowed the content of a standard package of aspirin containing, 1000-mg capsules, a dose of 10 g can be estimated. Her approximate height was 165 cm, her weight 60 kg. The patient reported that she did not take additional drugs. Because aspirin-induced tinnitus is known to be reversible (Myers and Bernstein, 1965; McFadden and Pattsmier, 1984; Long and Tubis, 1988; Wier *et al.*, 1988; Stypulkowski, 1990), the patient was not referred for any medical treatment.

The clinical audiogram, measured 22 h after swallowing the aspirin capsules, revealed a sensorineural hearing loss with a 50-dB notch at 6 kHz in both ears, and the patient reported hearing a high-frequency hissing noise in both ears. She estimated the loudness of the tinnitus to be somewhat above the audiometric threshold in the high-frequency region. Forty-six hours after swallowing the aspirin capsules hearing sensitivity had been completely restored and the tinnitus had disappeared (see audiograms for the right ear in Fig. 1).

Distortion product otoacoustic emissions (DPOAEs) and transiently evoked otoacoustic emissions (TEOAEs) were measured in the state of aspirin intoxication and after recovery in both ears immediately after audiogram recording.

The DPOAEs were measured between $f_2=488$ and 8008 Hz (Cubedis/ER10-C instrumentation, Mimosa Acoustics/Ethymotic Research, USA) using a special primary tone level setting ($L_1=0.4L_2+38$ with $20<L_2<65$ dB SPL and $f_2/f_1=1.2$, see Kummer *et al.*, 1998) that accounts for the nonlinear basilar membrane response at the DPOAE generation site at f_2. DP-grams and I/O-functions were constructed. In order to quantify the DPOAE growth, the slope s of the I/O-functions was calculated between $L_2=40$ and 60 dB SPL and plotted against f_2. Calculation between $L_2=40$ and $L_2=60$ dB SPL was chosen because in that range normal and pathological growth differed most (Janssen *et al.*, 1998; Kummer *et al.*, 1998). The TEOAEs were recorded using the nonlinear stimulation mode (ILO-88 instrumentation, Otodymamics, UK).

In the state of intoxication the DP-grams obtained at different primary tone levels from $L_2=50$ dB SPL to $L_2=65$ dB SPL (5-dB steps) followed that of normal-hearing subjects with reduced level. It should be emphasized that the DPOAEs were relatively large, around 6 kHz, where the hearing loss was greatest. In that frequency region, DP-grams were widely spaced in intensity, indicating a linearized (that is, pathological) growth of emission level. After recovery all ten DP-grams from $L_2=20$ dB SPL to $L_2=65$ dB SPL (5-dB steps) were found to have normal levels. The DP-grams were close together at high primary tone levels, demonstrating normal nonlinear compressive growth of emission levels (compare middle panels in Fig. 1). Both ears behaved similarly, therefore only the data of the right ear are presented.

The different DPOAE growth behavior, during aspirin intoxication and after recovery, may be seen more clearly in the slope s of the I/O-functions. In the state of aspirin intoxication, the slope increased with increasing hearing loss (4–6 kHz), and was greatest at the frequencies of maximum hearing loss (6 kHz), indicating increasing loss of compression with increasing hearing loss. After recovery, the slope re-

[a]Electronic mail: T.Janssen@lrz.tu-muenchen.de

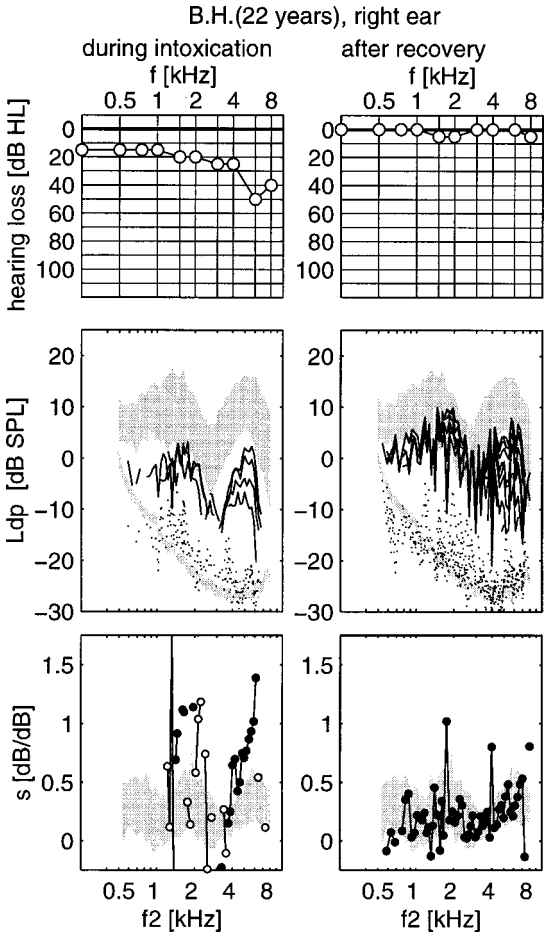

FIG. 1. Audiograms (upper panels), DP-grams showing the level $L_{DP}(f_2)$ at different primary tone levels according to $L_1=0.4L_2+38$ with $20<L_2<65$ dB SPL and $f_2/f_1=1.2$ (middle panels), and slope s (f_2) of the DPOAE I/O functions calculated between $L_2=40$ and $L_2=60$ dB SPL (lower panels) in the right ear during acute aspirin intoxication (left-hand side) and after recovery (right-hand side). Shaded areas indicate ranges of mean ± one standard deviation of the corresponding measures calculated for a normal-hearing subject sample for the DPOAE level (at $L_2=65$ dB SPL only), and the slope s (see Kummer *et al.*, 1998). Dotted lines in the middle panels indicate the noise floor for the different DP-grams. The small lower shaded area represents normal noise condition. In the lower panels open circles show slope values calculated only from two $L_{DP}(L_2)$ values, while filled circles mark slope values calculated from three or more $L_{DP}(L_2)$ values.

turned to its normal range (compare bottom panels in Fig. 1).

In the state of intoxication, in both ears no TEOAEs could be measured. The click level amounted to 74 dB SPL at both ears with a stability of 95% (right ear) or 91% (left ear). The reproducibility of the response was −4% in the right ear and 27% in the left ear. After recovery, TEOAEs were normal in both ears. The level of the TEOAE response was 19.8 dB SPL in the right and 17.2 dB SPL in the left ear. The reproducibility of the response was 86% in the right ear and 87% in the left ear. The click level amounted to 74.4 dB SPL at the left and 75.2 dB SPL at the right ear with a stability of 98% (right ear) or 88% (left ear). The TEOAE data are not shown.

DISCUSSION

Administration of salicylate is known to affect hearing sensitivity and to induce tinnitus (Myers and Bernstein, 1965; Boetcher and Salvi, 1991). Also, otoacoustic emissions have been shown to be affected (McFadden and Plattsmier, 1984; Wier *et al.*, 1988; Long and Tubis, 1988; Brown *et al.*, 1993; McFadden and Pasanen, 1994). To our knowledge there is no report in the literature of DPOAE measurements for a case with salicylate-induced hearing loss with a hearing loss of 50 dB.

In the case reported here, DPOAEs could be measured in the frequency region of the tinnitus despite the 50-dB loss with a nearly normal level. The slope of the I/O-functions, however, increased with increasing hearing loss and, therefore, did correlate with the pathological alteration of the hearing threshold. Normally, no DPOAEs are measurable in ears with a hearing loss of 50 dB or more (Lonsbury-Martin and Martin, 1990). However, in hearing loss ears associated with tinnitus, high emission levels can be recorded in the frequency range that corresponded to the appearance of the tinnitus, despite considerable hearing losses (Janssen *et al.*, 1998). Also, in these ears, the slope of the DPOAE I/O-functions increased with increasing hearing loss, revealing decreased outer hair cell compression.

How can we interpret such DPOAE behavior? A retrocochlear pathology can be excluded because the patient's auditory brainstem responses were normal and comparable between both states. The linearized DPOAE growth indicates a malfunction of cochlear micromechanics near the tinnitus frequency. The steep slope of the DPOAE I/O-function reveals that the low level (more vulnerable) response is affected more than the high level response. The linearized DPOAE growth therefore suggests impairment of active cochlear processes and is strong evidence that a cochlear pathology is the cause for the aspirin-induced hearing loss and tinnitus. This is in accord with the report of Wier *et al.* (1988) who also found steepened DPOAE I/O-functions in volunteers who took 325-mg tablets of aspirin four times per day for four days.

Structural changes in outer hair cells (OHCs) appeared to be the most likely pathological correlate. Outer hair cells perfused with salicylate solution are reported to show a reversible reduction in the turgidity and axial stiffness (Shehata *et al.*, 1991; Russell and Schauz, 1995). Loss of stiffness of OHCs or of their stereocilia and the corresponding alteration in the coupling with the tectorial membrane may play a key role in this process. Assuming that a loss of stiffness is responsible for mechanical disturbances that lead to altered DPOAE growth, we suggest the corresponding tonic changes at the level of the stereocilia of inner hair cells to be one potential correlate of tinnitus of cochlear origin (Janssen *et al.*, 1998).

Such alterations in cochlear micromechanics could also change mechanical tuning. The DPOAEs measured in volunteers during aspirin administration exhibited a downward shift in the frequency of the DPOAE level maximum, which have been interpreted as changes in mechanical tuning (Brown *et al.*, 1993). Correspondingly, models have been proposed in which the basilar membrane/tectorial membrane resonance is determined by its mass and its elastic attachment to the spiral lamina (Allen, 1980) and in which a stereocilia/tectorial membrane resonance allows OHCs to in-

fluence the TM's displacement (Zwislocki, 1980, 1990). Another argument that speaks for changes of the basilar membrane/tectorial membrane resonance is the fact that, during the acute state of intoxication, no TEOAEs were measurable.

Assuming that TEOAEs present unit pulse responses of the nonlinear micromechanical elements (the OHCs), an altered resonance could affect the dynamics of the mechanical ringing after click-stimulation and thereby reduce the TEOAE amplitude drastically. In contrast, when stimulating the resonant circuit with stationary signals (the primaries for eliciting DPOAE), the altered basilar membrane/tectorial membrane resonance could yield a much smaller effect on the output signal (the DPOAE). Obviously, there is an advantage of the DPOAEs over the TEOAEs. The DPOAEs are able to give a qualitative measure of alterations in cochlear micromechanics in salicylate-induced tinnitus of the form described here.

How can one explain the complete restoration from a 50-dB hearing loss and a strong tinnitus within such a short time? Aspirin consumption in doses required to produce tinnitus and hearing loss reversibly eliminates SOAE and reduces DPOAE (McFadden and Plattsmier, 1984; Wier *et al.*, 1988). One explanation for reversible tinnitus and hearing loss therefore is reversible impairment of cochlear micromechanics. It seems reasonable to assume that the effect of salicylate is to remove the OHCs from their role as force feedback elements in that the salicylate molecule partitions into the membrane of the OHC and alters the OHC motor protein (Tunstall *et al.*, 1995).

Our findings carry two implications. First, the effect of salicylate-induced tinnitus on DPOAE might help to better understand the underlying mechanisms of ototoxicity. The fact that DPOAEs in acute acoustic trauma (Janssen *et al.*, 1998) and in salicylate intoxication behave similarly suggests similar pathogenetic mechanisms. This case supports the hypothesis that aspirin-induced tinnitus is generated at the outer hair cell level. Second, whereas TEOAEs only give evidence that something might have changed in the cochlea, DPOAEs are a more useful and robust quantitative indicator of the underlying mechanisms of some forms of cochlear tinnitus.

ACKNOWLEDGMENTS

We thank Dennis McFadden and an anonymous reviewer for their efforts and detailed suggestions to improve this report. Thanks are also extended to Jont Allen and Manfred Kössl for helpful discussions and comments. This study was supported by the Deutsche Forschungsgemeinschaft (Ja597/5-1).

Allen, J. B. (**1980**). ''Cochlear micromechanics—A physical model of transduction,'' J. Acoust. Soc. Am. **68**, 1660–1670.

Boetcher, F. A., and Salvi, R. J. (**1991**). ''Salicylate ototoxicity: Review and synthesis,'' Am. J. Otolaryngol. **12**, 33–47.

Brown, A. M., Williams, D. M., and Gaskill, S. A. (**1993**). ''The effects of aspirin on cochlear mechanical tuning,'' J. Acoust. Soc. Am. **93**, 3298–3307.

McFadden, D., and Pasanen, E. G. (**1994**). ''Otoacoustic emissions and quinine sulfate,'' J. Acoust. Soc. Am. **95**, 3460–3474.

McFadden, D., and Plattsmier, H. S. (**1984**). ''Aspirin abolishes spontaneous otoacoustic emissions,'' J. Acoust. Soc. Am. **76**, 443–448.

Myers, E. N., and Bernstein, J. M. (**1965**). ''Salicylate ototoxicity. A clinical and experimental study,'' Arch. Otolaryngol. **82**, 483–448.

Janssen, T., Kummer, P., and Arnold, W. (**1998**). ''Growth behavior of the $2f1$-$f2$ distortion product otoacoustic emission in tinnitus,'' J. Acoust. Soc. Am. **103**, 3418–3430.

Kummer, P., Janssen, T., and Arnold, W. (**1998**). ''The level and growth behavior of the $2f1-f2$ distortion product otoacoustic emission and its relationship to auditory sensitivity in normal hearing and cochlear hearing loss,'' J. Acoust. Soc. Am. **103**, 3431–3444.

Long, G. R., and Tubis, A. (**1988**). ''Modification of spontaneous and evoked otoacoustic emissions and associated psychoacoustic microstructure by aspirin consumption,'' J. Acoust. Soc. Am. **84**, 1343–1353.

Lonsbury-Martin, B. L., and Martin, G. K. (**1990**). ''The clinical utility of distortion-product otoacoustic emissions,'' Ear Hear. **11**, 144–154.

Russell, I., and Schauz, C. (**1995**). ''Salicylate ototoxicity: Effects on the stiffness and electromotility of outer hair cells isolated from the guinea pig cochlea,'' Aud. Neurosci. **1**, 309–319.

Shehata, W. E., Brownell, W. E., and Dieler, R. (**1991**). ''Effects of salicylate on shape, electromotility and membrane characteristics of isolated outer hair cells from guinea pig cochlea,'' Acta Oto-Laryngol. **111**, 707–718.

Stypulkowski, P. H. (**1990**). ''The mechanism of salicylate ototoxicity,'' Hear. Res. **46**, 113–146.

Tunstall, M. J., Gale, J. E., and Ashmore, J. F. (**1995**). ''Action of salicylate on membrane capacitance of outer hair cells from guinea-pig cochlea,'' J. Physiol. **485**, 739–752.

Wier, C. C., Pasanen, E. G., and McFadden, D. (**1988**). ''Partial dissociation of spontaneous otoacoustic emissions and distortion products during aspirin use in humans,'' J. Acoust. Soc. Am. **84**, 230–237.

Zwislocki, J. J. (**1980**). ''Five decades of research on cochlear mechanics,'' J. Acoust. Soc. Am. **67**, 1679–1685.

Zwislocki, J. J. (**1990**). ''Active cochlear feedback: required structure and response phase,'' in *Mechanics and Biophysics of Hearing*, edited by P. Dallos *et al.* (Springer-Verlag, New York), pp. 114–120.

Limitations in using Golay codes for head-related transfer function measurement

Pavel Zahorik[a)]
Department of Psychology and Waisman Center, University of Wisconsin–Madison, Madison, Wisconsin 53705

(Received 12 July 1999; revised 22 October 1999; accepted 30 November 1999)

Although the use of Golay codes has been recommended for measuring external-ear impulse responses [Zhou *et al.*, J. Acoust. Soc. Am. **92**, 1169–1171 (1992)], this report demonstrates a potential limitation that could arise in applications requiring probe stimulus excitation to last longer than a few hundreds of milliseconds. In such situations, artifacts in the measured impulse responses can result from using Golay codes if the system under evaluation is time variant. These impulse-response artifacts are demonstrated for measurements of human binaural impulse responses (equivalent to head-related transfer functions, or HRTFs) under conditions analogous to small head movements during the measurement procedure. A popular alternative impulse-response measurement technique using maximum-length sequences (MLSs) does not produce artifact-contaminated measurements under the same conditions. © *2000 Acoustical Society of America.* [S0001-4966(00)03303-8]

PACS numbers: 43.66.Yw, 43.64.Ha [DWG]

INTRODUCTION

Modern signal-processing techniques have afforded researchers a variety of methods for measuring the impulse responses of linear time-invariant systems. Popular methods have included periodic pulse testing (Berman and Fincham, 1977), dual-channel fast fourier transform (FFT) analysis (Pope, 1998), time-delay spectrometry (Heyser, 1967), as well as various methods relying on excitation with types of deterministic noise signals. One particular type of deterministic noise signal that has been utilized for impulse-response measurement is the Golay code (Foster, 1986). Given both its superior signal-to-noise ratio when compared to measurements with conventional impulse-signal excitation, as well as its implementational ease, Golay codes have been specifically recommended for measuring human external-ear impulse responses (Zhou, Green, and Middlebrooks, 1992), or equivalently, head-related transfer functions (HRTFs).

External-ear impulse-response measurement using live humans presents a number of challenges to the measurement method employed. In addition to both efficiency and noise immunity requirements, the given measurement method must be able to handle mild violation of system time invariance, since humans are arguably always time-variant systems. Although all methods of impulse-response measurement will produce errors when the system under evaluation is not strictly time invariant, this report shows that the Golay method can produce particularly deleterious artifacts in the measured impulse response under these conditions. As such, users of the Golay method should be aware of these potential limitations.

Following a brief description of the Golay method, these artifacts will be demonstrated by binaural impulse-response measurements made under the time-variant conditions of simulated head movement. Results are compared to measurements made with a popular alternative method of impulse-response measurement using a different deterministic noise signal known as the maximum-length sequence (MLS).

I. THE GOLAY TECHNIQUE

Golay codes, named after their creator, Marcel Golay (1961), are complementary pairs of radix two digital sequences that may be generated by a simple recursive relation (given in Golay, 1961; Foster, 1986; and Zhou, Green, and Middlebrooks, 1992). The codes have the noteworthy property that the sum of the autocorrelation functions for each code is only nonzero at zero lag. Figure 1 demonstrates this complementarity, which holds for circular as well as noncircular autocorrelation. Since complementary pairs of these noise-like codes produce a perfectly flat magnitude spectrum, they appear ideally suited for use as impulse-response measurement excitation signals. Additionally, the system's impulse response can be determined by cross-correlating the responses to each of the codes in the pair with the codes themselves and summing the results. This property avoids the sometimes unstable frequency-domain division operations required for deconvolution by certain other impulse-response measurement techniques (e.g., Wightman and Kistler, 1989). Also, since both codes and responses are radix two, the cross-correlation operations may be efficiently implemented by use of the FFT to multiply complex conjugates in the frequency domain (Zhou, Green, and Middlebrooks, 1992).

Although Zhou, Green, and Middlebrooks (1992) describe implementation of the Golay method with only a single code pair excitation period, additional gains in signal-to-noise ratio can be realized by presenting multiple code periods to the system and averaging the results coherently.

[a)]Current address: Pavel Zahorik, Department of Psychology, University of California-Santa Barbara, Santa Barbara, CA 93106-9660. Electronic mail: zahorik@psych.ucsb.edu

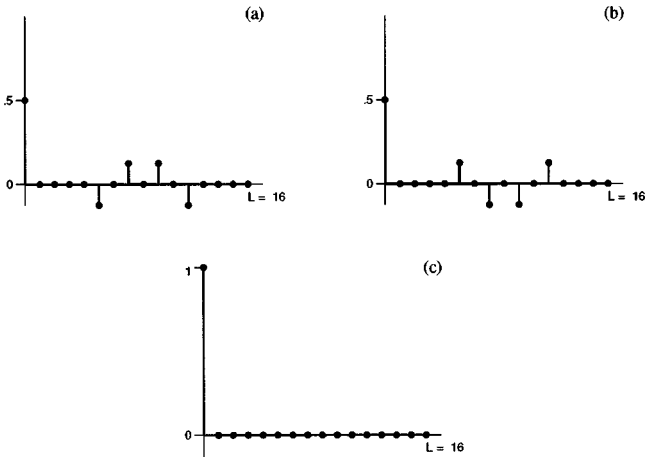

FIG. 1. Length $L=16$ Golay code circular autocorrelation functions for the individual complementary *a* and *b* codes, shown in panels (a) and (b), respectively, along with the sum of the individual autocorrelation functions, shown in panel (c). All functions have been normalized by $2L$.

Measurement of a system's (periodic) impulse response using this style of Golay code implementation proceeds as follows:

(1) Generate a Golay code pair with length, L, sufficient to capture the system's expected impulse response, and avoid potential time-aliasing effects.
(2) Excite the system periodically with k repetitions ($k \geqslant 2$) of the first (*a*) code in the Golay pair. Record and average the k-p most recent results, where $k > p \geqslant 1$.
(3) Wait for one code period.
(4) Excite the system periodically with k repetitions of the second (*b*) code in the Golay pair. Record and average the k-p most recent results.[1]
(5) Cross-correlate the response to the *a* code with the raw *a* code.
(6) Cross-correlate the response to the *b* code with the raw *b* code.
(7) Sum the results of 5 and 6 to arrive at the system's periodic impulse response.

For example, if the system being measured had a true impulse response that was a delta function, and this system were probed with a Golay code pair of length $L=16$, then the results of steps (5) through (7) may be represented by panels (a) through (c) of Fig. 1.

From this example, it may be seen that if the system being measured is time variant, then the Golay code responses are no longer complementary. Returning to this example, consider introducing additional gain into the system between *a* and *b* code probings. Panel (a) of Fig. 1 would look the same, but panel (b) would be scaled by an additional gain factor. The sum would therefore no longer have zeros at all nonzero lags. It would instead have a number of nonzero elements near lag $L/2$, which may all be considered artifacts caused by a time-variant system. Notice as well that if a small time delay were introduced into the system between *a* and *b* probings instead of a gain factor, similar nonzero elements near lag $L/2$ would result.

This complementarity violation may be of particular issue when making impulse-response measurements on live human ears, since it is difficult in this circumstance to guarantee that the system being measured is time invariant. To the extent that live humans are unable to remain perfectly motionless during these measurements, and given that the HRTF is strongly dependent on head position, such systems are always time variant. With the Golay measurement technique, as the length of the codes and/or the number of averages taken become large, a longer period of time elapses between *a* and *b* code presentation. There is therefore a greater chance that the measurement participant is not in exactly the same position for both code presentations, and hence a greater chance of resulting artifacts in the measured impulse response.

Conversely, the possibility of system time variation due to head movement over the course of the measurement is much less likely with short measurement durations. The 20.48-ms total signal duration (no averaging) used by Zhou, Green, and Middlebrooks (1992) in making anechoic HRTF measurements, for example, made it very unlikely that measurements were contaminated by head movement. Noise level and time-aliasing constraints do not always allow for such short measurement durations in all applications, however. For instance, if HRTFs are to be measured in a reverberant room environment, longer codes are required to fully capture the room response and avoid time aliasing. Increased number of averages may also be required to increase signal-to-noise ratio in such applications.

II. A TIME-VARIANT SYSTEM TEST

To demonstrate these impulse-response artifacts, binaural impulse responses were measured from a single human participant under time-varying conditions simulating head movement. Measurements were made both using the Golay technique and a popular alternative technique based on maximum-length sequences (MLSs), a technique that has been described in detail by Rife and Vanderkooy (1989); Borish and Angell (1983); Schroeder (1975, 1979); and Nielsen (1998).

Briefly, MLSs are, like Golay codes, pseudorandom digital sequences with flat-magnitude spectra that are generated via recursion (binary shift registers). They are not, however, made up of two complementary sequences, but instead have only a single 2^n-1 length sequence that must be presented periodically to the system under evaluation. Like the Golay technique, impulse responses are computed in the MLS technique by cross-correlating (circular cross-correlation must be used in this case) the response to the MLS with the raw MLS.

A. Procedure

Binaural impulse responses were measured from a single individual (participant code: SNA) in an anechoic chamber using both Golay and MLS techniques. The sound source was a small loudspeaker (Cambridge SoundWorks Center/Surround IV) with a nominal position of 0° azimuth and 0°

elevation (directly in front of the participant) and 1.4 m in distance. Two conditions of system time variation analogous to that caused by head movements were examined. These conditions were produced by moving the loudspeaker clockwise along a circular arc (via a computer-controlled motor with movement accuracy of approximately 0.1°) either 5° or 10° in azimuth during the measurement process. Movements were initiated at the start of the measurement sequence with a rate chosen such that the desired movement angle would be traversed in the exact time allotted for measurement completion. Preliminary testing confirmed that this form of simulated head movement offered a substantial increase in movement precision and repeatability over actual participant head movement. The effect of noise produced by the are movement apparatus was also found to be minimal, at least −50 dB relative to the signal level. A third, time-invariant condition was also examined in which the loudspeaker remained stationary at 0° azimuth. Additional stationary measurements were made at 5° and 10° azimuth (left-handed coordinates), for purposes of comparison to the time-variant conditions.

Specifically developed software driving PC-controlled Tucker-Davis Technologies D/A and A/D hardware (model PD1) capable of real-time signal averaging was used to implement both Golay and MLS techniques. Binaural microphones (Sennheiser KE4-211-2) were used in a blocked canal (Møller *et al.*, 1995) fashion. For each of the measurement conditions, 100 averages of a 10th-order (1023 point) MLS and 100 averages of a 10th-order (1024 point) Golay code pair (50 contiguous-time averages for the *a* code followed by 50 contiguous-time averages for the *b* code) were obtained sampling at a rate of 50.0 kHz. The periodic stimulus excitation was initiated ten stimulus periods prior to data acquisition in all cases. These parameters yielded a total measurement duration of just over 2 s. The stimulus level at the position of the participant's head was approximately 75 dB SPL.

The participant was instructed to remain as motionless as possible during the duration of the measurements, although no explicit means to prevent movement were employed.

B. Results

Figure 2 displays the measurement results from the participant's left ear, with columns corresponding to measurement technique (Golay or MLS) and rows corresponding to movement angle (0°, 5°, or 10°). Little difference is observed between the two methods when the system is time invariant (0° of movement), other than a slight difference in gain most likely attributable to listener positioning differences in the two conditions. For the time-variant conditions (5° and 10° of movement), however, marked difference may be observed between the two methods, the Golay technique showing substantial artifacts in the time region between 10 and 20 ms. If the impulse-response maximum were shifted back to lag zero, removing the system's pure delay of approximately 4 ms, it can be seen that the Golay code artifacts present for the time-variant conditions do indeed exist about the region of lag $L/2$, which is approximately 10 ms in this case. Additionally, artifact amplitude appears to be positively related to

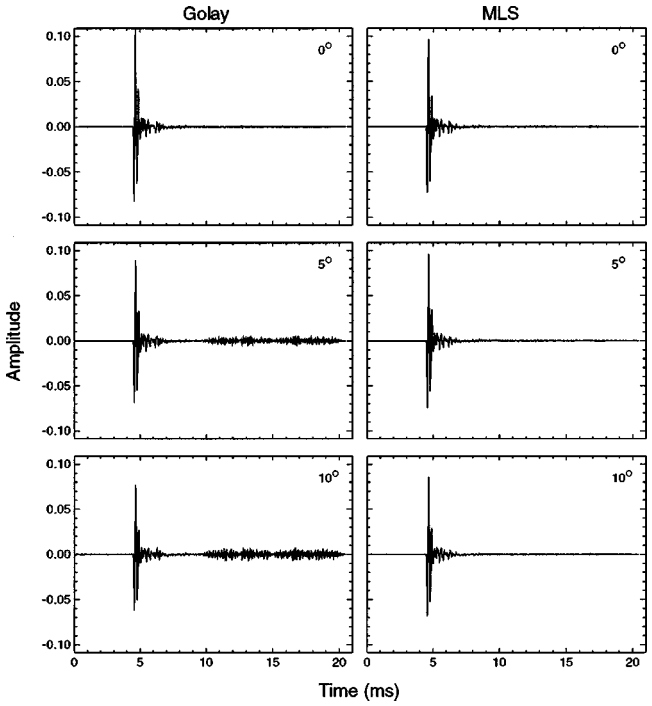

FIG. 2. Binaural impulse responses (left ear displayed) measured using Golay and MLS techniques under conditions of 0°, 5°, or 10° of loudspeaker movement during the measurement procedure.

movement magnitude. Results from the right-ear measurements are very similar to those displayed for the left ear in Fig. 2.

Note that the impulse responses measured in either of the time-variant cases are not expected to be the same as those measured in the time-invariant case. Both measurement techniques return an average response to source positions between either 0° and 5°, or 0° and 10° in these circumstances. This assertion may be verified by examination of Fig. 3, which displays the transfer functions from each of

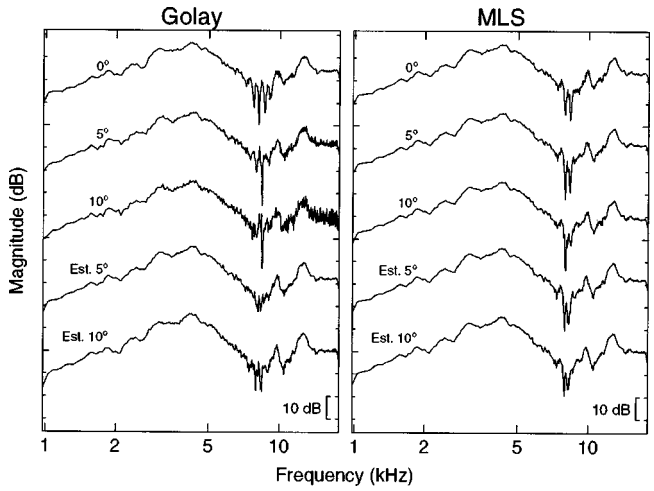

FIG. 3. Measured and estimated transfer functions using Golay and MLS techniques. The measured functions correspond to the impulse responses displayed in Fig. 2 under conditions of 0°, 5°, or 10° of movement. Estimates of the 5° and 10° functions are also displayed, based on the mean of log-magnitude spectra measured at static azimuth angles of 0° and 5° or 0°, 5°, and 10°, respectively. All functions have been displaced by increments of 30 dB for display purposes.

the three measurement conditions, along with estimated transfer functions for each of the movement conditions. These estimated functions are means of the log-magnitude spectra measured at stationary azimuth angles of 0° and 5°, or 0°, 5°, and 10°. For the MLS technique, the estimated functions are quite similar to the measured functions for both 5° and 10° of movement. This suggests that, in the time-variant cases, the MLS technique does not introduce any errors in addition to that of returning an average response to positions over the movement arc. For the Golay technique, however, less similarity exists between the estimated and measured movement condition functions, with the high-frequency noise in the measured functions being a result of the artifacts observed in the impulse responses measured using this technique.

While system time variance has been discussed primarily in terms of variation between successive presentations of the digital sequences, it should also be noted that time variation within the presentation of a single sequence can cause errors. For the MLS technique, Vanderkooy (1994) has shown that these errors are relatively trivial, manifesting themselves simply as uniform noise in the computed impulse response. The precise effect of this form of time variation of Golay codes is unknown, but is likely to be smaller than the between-pair time-variation effects demonstrated.

III. CONCLUSION

The Golay technique for impulse-response measurement has been shown to be susceptible to measurement artifacts caused by time-varying systems. As a result, caution is recommended in interpreting impulse responses measured with this technique if the systems under evaluation are known to be time varying, such as those involving nonstationary humans.

In practice, certain situations are more likely to result in contaminated measurements than others. When both noise level and time-aliasing constraints permit short measurement durations, such as the 20.48-ms duration used by Zhou, Green, and Middlebrooks (1992), these artifacts may be reduced to trivial levels. Likewise, strict control of system movement (e.g., by head immobilization) will undoubtedly reduce or eliminate time-variant artifacts as well. The additional practice of time-windowing measured impulse responses to remove room effects could also potentially remove most, if not all such artifacts. In situations where room effects are of interest, however, such as measuring binaural room impulse responses, the presence of these artifacts is not only much more problematic, but more probable as well. The increase in measurement time required to avoid time aliasing and achieve acceptable signal-to-noise ratios, in such situations, leads to a greater chance of system time variation over the course of the measurement. Not only are measurement artifacts of this type easily misinterpreted as room-response components, but they can also lead to significant errors in reverberant energy calculation.

The MLS technique has been shown to be more robust with respect to violations of system time invariance, and therefore may be considered preferable to the Golay technique for binaural impulse-response measurement applications where assumptions of system time invariance are questionable.

ACKNOWLEDGMENTS

The author gratefully thanks Dr. Ewan Macpherson for his assistance in performing the time-variant test reported in this work, as well as Dr. Fred Wightman, Dr. John Middlebrooks, and Dr. Ewan Macpherson for their helpful comments on earlier drafts of this manuscript. Financial support for this work was provided by NASA (Cooperative Agreement #NCC2-542) and the NIH-NIDCD (No. DC00116).

[1]Although not the averaging method suggested by Foster (1986), it is technically possible to present interleaved series of *a* and *b* code repetitions and average the results. To properly implement this method, a time period with no signal excitation must be inserted between *a* and *b* code presentations, however, in order to avoid capturing part of the response to the *a* code in the *b* code record, or vice versa. This scheme could, for example, take the form: $[a_1, a_2,$ wait, $b_1, b_2,$ wait, $a_3, a_4,$ wait, ..., $b_{k-1}, b_k]$. The extra time periods with no signal excitation make this method less efficient than the suggested method of presenting and averaging all *a* code repetitions followed by all *b* code repetitions, $[a_1, \ldots, a_k,$ wait, $b_1, \ldots, b_k]$.

Berman, J. M., and Fincham, L. R. (**1977**). ''The application of digital techniques to the measurement of loudspeakers,'' J. Audio Eng. Soc. **25**, 370–384.

Borish, J., and Angell, J. B. (**1983**). ''An efficient algorithm for measuring the impulse response using pseudorandom noise,'' J. Audio Eng. Soc. **31**, 478–487.

Foster, S. (**1986**). ''Impulse response measurements using Golay codes,'' in *IEEE, 1986, Conference on Acoustics, Speech, and Signal Processing (ICASSP)* (IEEE, New York), Vol. 2 pp. 929–932.

Golay, M. J. E. (**1961**). ''Complementary series,'' IRE Trans. Inf. Theory **7**, 82–87.

Heyser, R. C. (**1967**). ''Acoustical measurements by time delay spectrometry,'' J. Audio Eng. Soc. **15**, 370.

Møller, H., Sørensen, M. F., Hammershøi, D., and Jensen, C. B. (**1995**). ''Head-related transfer functions of human subjects,'' J. Audio Eng. Soc. **43**, 300–321.

Nielsen, J. L. (**1998**). ''Improvement of signal-to-noise ratio in long-term MLS measurements with high-level nonstationary disturbances,'' J. Audio Eng. Soc. **45**, 1063–1066.

Pope, J. (**1998**). ''Analyzers,'' in *Handbook of Acoustics*, edited by M. J. Crocker (Wiley, New York), pp. 1341–1353.

Rife, D. D., and Vanderkooy, J. (**1989**). ''Transfer-function measurement with maximum-length sequences,'' J. Audio Eng. Soc. **37**, 419–444.

Schroeder, M. R. (**1975**). ''Diffuse sound reflection by maximum-length sequences,'' J. Acoust. Soc. Am. **57**, 149–150.

Schroeder, M. R. (**1979**). ''Integrated-impulse method measuring sound decay without impulses,'' J. Acoust. Soc. Am. **66**, 497–500.

Vanderkooy, J. (**1994**). ''Aspects of MLS measuring systems,'' J. Audio Eng. Soc. **42**, 219–231.

Wightman, F. L., and Kistler, D. J. (**1989**). ''Headphone simulation of free-field listening: I. Stimulus synthesis,'' J. Acoust. Soc. Am. **85**, 858–867.

Zhou, B., Green, D. M., and Middlebrooks, J. C. (**1992**). ''Characterization of external ear impulse responses using Golay codes,'' J. Acoust. Soc. Am. **92**, 1169–1171.